IBN AL-HAITHAM FIRST INTERNATIONAL SCIENTIFIC CONFERENCE

Preface

IHSCICONF2017 is an International Conference on Biology, Chemistry, Computer Science, Mathematics, and Physics, Take place in Baghdad, Iraq, from December 13-14, 2017. IHSCICONF 2017 is assisted by the College of education for pure science – Ibn Al-Haitham \ University of Baghdad and with supporting of the American Chemical Society (ACS) in Iraq.

IHSCICONF 2017 aimed to distills the most current knowledge on a rapidly advancing discipline in one conference. Join key researchers and established professionals in the field of Biology, Chemistry, Computer Science, Mathematics and Physics as they assess the current state-of-the-art and roadmap crucial areas for future research.

We aimed to build an idea-trading platform for the purpose of encouraging researcher participating in this event. The papers to be presented at IHSCICONF 2017 address many grand challenges in sciences. The full papers that presented are peer-reviewed by three expert reviewers.

Editorial Board

Photographs


عمادة كلية التربية للعلوم الصرفة

Keynote Speakers

IHSCICONF-2017

Associate Prof. Dr. Saeed S. Al-Alawi
Kingdom of Bahrain

Ph.D. (Analytical Chemistry) Strathclyde University , Glasgow, UK. Dec. 1981
B.Sc. (Applied Chemistry) Basreh University, Iraq, 1978

Experience and duty occupied

From 1982 to 2015; Associate professor in College of Science.
1991-1995 chairman of Chemistry Department, College of Science, University of Bahrain.
2007 - 2011, Director of Continuous Science Eduction in College of Science.
1991- 2001, Fonder and Chairman of Bahrain Chemical Society
1992-2006; organising a series conferences (Chemistry in Industry) in collaboration with Armco.
1992 - 2002; Organising and performing a series of Cleaner Production workshops in Collaboration with UNEP office in Bahrain.
2002 to 2004: Conducting a series of regional workshop in Bahrain in Chemical safety and Security in collaboration with Sandia laboratory in USA.
Since retirement in 2015, I own consultancy company in Environmental Chemistry.

IHSCICONF-2017

Assist. Prof. Dr. Mohammad Mahdi Ahadian
I. R. Iran

Assistant director of Institute for Nanoscience and Nanotechnoilogy .
Specialization: Surface science, Characterization in nano-scale

Citations	626	446
h-index	15	12
i10-index	20	15

IHSCICONF-2017

Prof. Dr. Ali H. Reshak
Iraq
Resident in the Czech Republic

Full Professor Dr. Senior Scientist
Qualification: B.Sc, M.Sc, Ph.D Physics, Ph.D Eng
h-index 32 + (web of Science) with 4816 citations
The winner of the Abdul Hameed Shoman Award.
Durham University senior fellow (UK).
Recently have been awarded a Honorary Doctorate of Engineering from the University of Malaysia Perlis for my achievements in Sciences and Technology

Present Occupation:

1. Full Professor at West Bohemia University , in Plzen-Czech Republic
2. Full Professor for Special assignments at University of Malaysia Perlis- Malaysia ,
3. Professor at Czech Technical University, Faculty of mechanical Engineering – Prague - Czech Republic ,
4. Visiting Professor at Department of Physics and Astronomy, King Saud University, Saudi Arabia.
5. Editor-In-Chief :Journal of Laser and Optics Advances Specialized Research- JLOASR

IHSCICONF-2017

Prof. Dr. Fuad El Hahj Hassan
France
Lebanese University, Faculty of Sciences, Department of Physics , Beirut-Lebanon

- Maîtrise in Physics (Lebanese University).
- D. E. A “master” Metz University, France.
- PhD thesis in materials sciences at LPLI Institute of Metz University (France).
- Diplôma «TUXEDO Administration and development» BEA System – Tour Manhattan; Paris la défense-France.
- Diplôma « Utilisateur Rational Clearcase (NT) » Rational University – The development company-Franced.
- School on: Electronic-structure calculations and their applications in materials science ICTP – INFM/Democritos – ISMO – IUT (Isphahan) 25 April – 6 May 2005.

IHSCICONF-2017

Prof. Dr. Ram K. Agarwal
India

received his Ph.D (1980)and D.Sc.(2000) PG Diploma in Macromolecular Chemistry from Charles University, Czech Republic in 1981 . He served at Meerut College as a lecturer in Chemistry from 1969 to 1970 and then were invited into Lajpat Rai College (Ch. Charan Singh University, India) as a Senior lecturer to Associate Professor yet retired in June 2011. He was also an Associate Professor at University of South Pacific, Suva, Fiji from 2003 to 2005. In 2008, he became a Professor of Eritrea Inst. of Technology, Asmara, Eritrea. Up till now, He has published a total number of 250 works and supervised 35 Ph.D. students. He has took part in many international activities held in USA, Czech Republic, Egypt, Jordan, Qatar, Poland, Thailand, China, Hong Kong, Korea, Fiji, Bali-Indonesia and Dubai etc. At present, he is the Editor in Chief of Asian Journal of Chemistry with his main research interests covering coordination chemistry and bio-inorganic chemistry fields.

IHSCICONF-2017

Prof. Dr. Suvardhan Kanchi
India
Chemistry

Durban University of Technology · Department of Chemistry , Durban, South Africa.

Dr. Kanchi is the Research Scientist in fabricating the bio-sensors for the identification and quantification of high intensity artificial sweeteners in food stuff's and biological samples. He completed his post doctoral research in Separation and Determination of High Intensity Artificial Sweeteners (Sucralose, Neotame & Stevia glycosides with Capillary Electrophoresis and electrochemical methods (biosensors) in different Food Stuff's from Durban University of Technology, Durban, South Africa. He is associated with the Indian Society of Analytical Scientists (ISAS), India. He is also serving as the Executive Editor for American Journal of Phytomedicine and Clinical Therapeutics; EB member for International Journal of Research in Chemistry and Environment and many more. He is also having several reviewer experiences for many articles

Research Interest

Applied Chemistry, Pharmaceutical Research, Phytomedicine and Clinical Therapeutics, Environmental Technology and Management.

IHSCICONF-2017

أ.د. نبيل محي عبد الحميد علي
جمهورية مصر العربية
عميد كلية الصيدلة / جامعة كفر الشيخ / جمهورية مصر العربية.

الدرجة العلمية : أستاذ الكيمياء الحيوية (تخصص دقيق : بيولوجيا الأورام , مع التركيز على أورام الكبد - التشخيص المبكر لأورام الكبد و إستحداث أدوية من ضمنها الأعشاب لعلاج أورام الكبد ، إضافة إلى دراسة سمية بعض الكيماويات على الكبد فى نماذج تجريبية.

1. بكالوريوس الصيدلة مايو 1985 م . من كلية الصيدلة / جامعة الزقازيق .
2. ماجستيرفى الكيمياء الحيوية مايو 1989 م من كلية الصيدلة / جامعة الزقازيق.
3. دكتوراه فى الكيمياء الحيوية اكتوبر 1999 م من كلية الصيدلة / / جامعة الزقازيق.

Conference Sessions

Al- Mansour Melia Hotel				
Day 1	**Wednesday**	**morning Session**	**Date**	**Dec. 13 , 2017**
Session	**Main**		**venue**	**Cordoba Hall**
9:00 – 10:00	**Ceremony of the Conference Opening Session**			

Al- Mansour Melia Hotel				
Day 1	**Wednesday**	**Keynote Speakers**	**Date**	**Dec. 13 , 2017**
Session Duration	**10:00-11:00**		**venue**	**Cordoba Hall**

Title	Speaker	
The contribution of scientific research toward development and solving the troubles of the country by concentrating on applied aspects of research	**Dr. Walid A. GH. Al- Hilli** (Chemistry) Iraq Advisor to the Prime Minister	
Nanotechnology - the New Horizon	**Prof. Dr. Ali H. Reshak** (Physics , Engineering) Iraq West Bohemia Univ./Czech Rep. Univ. of Malaysia Perlis/ Malaysia.	
Biosensors in Food Applications	**Prof. Dr. S. kanchi** (Environmental Chemistry) India Durban Univ. of Technology/S. Africa	

Al- Mansour Melia Hotel				
Day 1	**Wednesday**	**Keynote Speakers**	**Date**	**Dec. 13 , 2017**
Session Duration	**11:30-12:00**		**venue**	**Cordoba Hall**

Title	**Speaker**	
Difference Between Normal & Cancer Cell	**Prof. Dr. Nabil M. Abdelhamid** (Biochemistry) Egypt Dean of Pharmacy College/Kafrelsheikh Univ./Egypt	
Antioxidant Activity of Methanolic Plant Extract & their effect on Fish spoilage prevention	**Prof. Dr. Saeed S. Al-Alawi** (Analytical Chemistry) Kingdom of Bahrain Advisor in environmental Chemistry	

Al- Mansour Melia Hotel				
Day 1	**Wednesday**	**Keynote Speakers**	**Date**	**Dec. 13 , 2017**
Session Duration	**11:30-12:00**		**venue**	**Al-Hamraa Hall**

Title	**Speaker**	
The full potential-linearized augmented plane wave method within Density functional theory	**Prof. Dr. Fuad Elhaj Hassan** (Physics) France Lebanese Univ., Fac. of Sciences I, Dept. of Physics	
Recent application of nanotechnology in oil and petroleum industry: two examples	**Assist. Prof. Dr. Mohammad M. Ahadian** (Surface Science) I.R. Iran Inst. of Nanosci. & Nanotech./ Sharif University of Technology	

Al- Mansour Melia Hotel				
Day 2	**Thursday**	**Keynote Speakers**	**Date**	**Dec. 14 , 2017**
Session Duration	**9:00-10:00**		**venue**	**Dept. of Physics Seminar Hall 2**

Title	**Speaker**	
Designing of Multifunctional Thiosemicarbazones Derived from Heterocyclic Compounds and Their Metal Coordination Compounds in Biological and Medicinal Inorganic Chemistry	**Prof. Dr. Ram K. Agarwal** (Macromolecular Chemistry) India Editor in Chief of Asian Journal of Chemistry	

Al- Mansour Melia Hotel				
Day 1	**Wednesday**	**Afternoon Session**	**Date**	**Dec. 13 , 2017**
Session	**1bio1a**		**venue**	**Cordoba 2 Hall**

Session Theme	**Biology**
Session Duration	**(1:00 –2:30) pm.**
Session Chair	**Prof. Dr. Abdulhusaain M. Al-Faisal**
Rapporteur	**Assist. Prof. Dr. Ihsan I. Hussain**

Time	**Code**	**Title**	**Author**
1:00-1:12	5	Comparative Analysis Of Various Techniques For Giardia Lamblia Detection And Association With E Coil And Shigella Among Children Attending Al-Imamin Al- Kadhimin Medical City	Rawaa A. Hussein, **Areej A. Hussein**
1:12-1:24	170	The Role Of Staphylococcus Haemolyticus In Men Infertility	**Ghaeda J. Al-Ghizawi**, Zahraa K. Jomaa
1:24-1:36	252	Antifungal Activity Of Solanum Niger Extract Against Microsporum Canis, The Causative Agent Of Ring Worm Disease	**Yasser M. Al-Qertani**
1:36-1:48	260	The Congenital Malformations In White Pregnant Mice Fetus Induced By Metformin Drug	**Faeza N. Toama**, Aziz Kh. Hamid, Asmat J. Jameel
1:48-2:00	317	Checklists Of Parasites Of Stray Cats Felis Catus L. Of Iraq	**Abdulrahman A. Altae**, Abdulrrazzak L. Alrubaie
2:00-2:12	25	Study The Seroprevalence Of Viral Hepatitis And Hiv Among Hemodialysis Patients	**Batool M. Mahdi** Inass M. Kamal

College Of Education For Pure Science (Ibn Al-Haitham)				
Day 2	**Thursday**	**Morning Session**	**Date**	**Dec. 14 , 2017**
Session	**2bio1m**		**venue**	**Biology Dept. Seminar Hall**

Session Theme	**Biology**
Session Duration	**(10:00 – 11:30) am.**
Session Chair	**Prof. Dr. Hussain A. Dawod**
Rapporteur	**Assist. Prof. Dr. Hanadi S.Abdulsahib**

Time	Code	Title	Autho
10:00-10:12	226	Lag Phase And Biomass Determination Of Rhodococcus Pyridinivorans Gm3 For Phenol Degradation	**Mahammed E. Aldefiery**, Gopal Reddy
10:12-10:24	110	Teratogenic Effect Of Levetiracetam Drug On The Development Of The Kidney In Rat Embryo	**Lamyaa H. Alibrahimi**, Nahla A. Al-Bakri
10:24-10:36	47	Effect Of Tamoxifen Citrate Supplement To Smart Medium On Human Sperm Morphology During In Vitro Sperm Activation	**Noor K. Kadhim,** Mohammed B. Fakhrildin, Jabir Hameed
10:36-10:48	73	Seasonal Abundance Of Eggplant Leaf Miner Liriomyza Sativae (Diptera: Agromyzidae) In Plastichous	**Soolaf A.Kathiar**, Sawsan K. Flaih, Hind I. Al Khazraji, Safa K. Ismael
10:48-11:00	51	Assessment Of The Soluble Form Of Fas Ligand In Patients With Asthenozoospermia And Teratozoospermia.	**Ahmed H. Zwamel**, Anam R. Al-Salihi, Sabah N. Alwachi
11:00-11:12	154	Comparison Between Procalcitonin And Traditional Blood Biomarkers In Diagnosis Of Sepsis In Iraqi Wounded Soldiers	**Meroj A. Jasem,** Ali E. Mahmood, Ayser I.Mahmood, Mahmood M. Mustafa, Khalid M. Farhood

College Of Education For Pure Science (Ibn Al-Haitham)				
Day 2	**Wednesday**	**Afternoon Session**	**Date**	**Dec. 14 , 2017**
Session	**2bio1a**		**venue**	**Biology Dept. Seminar Hall**

Session Theme	**Biology**
Session Duration	**12:00 – 1:30 pm.**
Session Chair	**Prof. Dr. kadhim M. Al-Somaida'ee**
Rapporteur	**Lect. Dr. Areej A. Farmann**

Time	Code	Title	Author
12:00-12:12	1	Effects Sprayed Solution Of Salicylic Asid To Prevent Of Wilt Diseases	**Dina Y. Mohammed**
12:12-12:24	188	Influence Of Foliar Application Of Abscisic Acid (Aba) And Vitamin C Of Some Plant Hormones Of Pea Pisum Sativum L.	**Wifak A. Al-Kaisy**, Sahar F. Mahadi
12:24-12:36	216	Determination Of Progesterone, Prolactin, Estradiol, Zinc And Vitamin C In Female Iraqi Patients With Breast Cancer	Hazima M. Al-Abassi, Asmaa M. Almohaidi, **Amenah A. Almsawi**
12:36-12:48	27	Extraction And Preparation Of Pigments From Strelitzia Reginae Flowers As Sensitizer For Dye-Sensitized Solar Cell Application	**Mahmoud A. Alalwani**
12:48-1:00	109	The Study Of Bacterocin Of Pseudomonas Fluorescens And Citrus Limon Effects On Propionibacterium Acnes And Staphylococcus Epidermidis In Acne Patients	**Mais E. Ahmed**
1:00-1:12	224	Antimicrobial Activity Of Some Plants Extracts On Bacteria Isolated From Acne Vulgaris Patients	**Khetam H. Rasool**

Al- Mansour Melia Hotel				
Day 1	**Wednesday**	**Afternoon Session**	**Date**	**Dec. 13 , 2017**
Session	**1chem1a**		**venue**	**Meeting Hall**

Session Theme	**Chemistry**
Session Duration	**(1:00 – 2:30) pm.**
Session Chair	**Prof. Dr. Sarmad B. Dekran**
Rapporteur	**Assist. Prof. Dr. Dhafir T. Ajeel**

Time	**Code**	**Title**	**Autho**
1:00-1:12	15	Three locally clays as a surfaces for adsorption of cephalexin monohydrate from aqueous solution: thermodynamic and desorption equilibrium	**Saja S. Al-Taweel**, Sadoon A. Isa, Ramzi R. Al-Ani
1:12-1:24	184	Preparation and characterization of novel 4,5-dihydro-1H-tetrazol derivatives via azomethine compounds Reaction with sodium azide and evaluation the Biological Activity of them	**Obaid H. Abid**, Hiba M. Tawfeeq
1:24-1:36	293	Synthesis and antifungal activity against of Candida species for Some Heterocyclic Compounds new containing Schiff base or oxazepine or Indolinor imidazo groups and their spectral characterization	**Shaima I. Chyad**, Bari L. Mohammed, Siham Sh. AL-Salihi
1:36-1:48	229	Synthesis, spectroscopic characterization, and antibacterial evaluation of new Schiff bases bearing benzimidazole moiety	**Muayed A. Redayan**, Maha S. Hussein, Ashraf T. Lafta
1:48-2:00	343	Enhance the antioxidant activity For 2,4-di-*tert*-butylephenol by formation hytrocyclic ring at position six	**Raied M. Shakir,** Azhar Ariffin, Mahmood A. Abdulla
2:00-2:12	13	Partial purification of Leucine aminopeptidase (LAP) in Acromegalic Sample of Iraqi Patients	**Taghreed U. Mohammad**

College Of Education For Pure Science (Ibn Al-Haitham)				
Day 2	**Thursday**	**Morning Session**	**Date**	**Dec. 14 , 2017**
Session	**2chem1m**		**venue**	**Prof. Dr. Fahad Ali Hall**

Session Theme	**Chemistry**
Session Duration	**(10:00 – 11:30) am.**
Session Chair	**Prof. Dr. Taqieddeen Abdulhadi**
Rapporteur	**Assist. Prof. Dr. Juman A. Nasir**

Time	Code	Title	Autho
10:00-10:12	291	The FSHR polymorphisms association with polycystic ovary syndrome in women of Erbil, Kurdistan in north of Iraq	**Aesha Sh. Sh. Baban**, Sabah H. Korsheed, Anas Y. Al Hayawi
10:12-10:24	250	Preparation Characterization and Electrical Study of New Polymeric Mixture (Consist of Three Polymers) Nanocomposites	**Entisar E. AL-Abodi**, A. Farouk
10:24-10:36	297	Indirect way for the assay of captopril drug in dosage forms using 1,10-phenanthroline as a selective spectrophotometric agent for Fe(II) via homemade CFIA /Merging zones technique	**Bushra B. Qassim,** Ahmed A. Alwan
10:36-10:48	135	Heavy metals characteristics of settled particles of streets dust from Diwaniyah City- Qadisiyah Governorate - Southern Iraq	**Moutaz A. Al-dabbas,** Khalid H. Mahdi, Raad M. Alkhafaji, Kawther H. Ohays
10:48-11:00	160	Fire retardancy assessment of polypropylene composite filed with nano clay prepared from Iraqi bentonite	**Watheq K. Salih**

College Of Education For Pure Science (Ibn Al-Haitham)				
Day 2	**Thursday**	**Morning Session**	**Date**	**Dec. 14 , 2017**
Session	**2chem2m**		**venue**	**Chemistry Dept. Postgraduate Hall**

Session Theme	**Chemistry**
Session Duration	**(10:00 – 11:30) am.**
Session Chair	**Prof. Dr. Jumbid H. Toma**
Rapporteur	**Assist. Prof. Dr. Taghreed U. Mohammed**

Time	Code	Title	Author
10:00-10:12	129	Synthesis, Characterization and thermal study of Some Transition metal Complexes derived from Quinoxaline-2,3-dione.	**Taghreed M. Musa,** Mahmoud N. Al-jibouri, Bayader F. Abass
10:12-10:24	123	Theoretical Treatment, Microwave Synthesis, Spectroscopic analysis of new Schiff bases derived from 4-Aminoantipyrene	**Ameena N. Seewan,** Zainab Y. Kadhim , Ahmed A Hadi
10:24-10:36	187	Cytotoxic effects of new synthesis heterocyclic derivatives of Amoxicillin on some cancer cell lines	**Muna S. AL-rawi,** Dhuha F. Hussein, Anwar F. Al-Taie, Mohammed M. Al-Halbosiy, Baraa Abdul-Hameed
10:36-10:48	333	Theoretical Investigation for the Effect of Fuel Quality on Gas Turbine Power Plants	**Omar A. khudair,** Khetam A. Abass, Noor S. Abed**,** Khalid H. Ali, Saad Abdulaziz, Ali Chlaib
10:48-11:00	332	Synthesis and spectral studies of heterocyclic azo dye complexes with some transition metals	**Amer J. Jarad,** Ismaeel Y.Majeed , Abaas O. Hussein
11:00-11:12	304	Spectrophotometric and Potentiometric Analysis of Calcichrome and its complex with Calcium ion .	**Ismail K. Al-Hitti**, Omur H. AlOubaydi, Saja S. AlSamarra'ay

Al- Mansour Melia Hotel				
Day 1	**Thursday**	**Afternoon Session**	**Date**	**Dec. 14 , 2017**
Session	**2chem1a**		**venue**	**Prof. Dr. Fahad Ali Hall**

Session Theme	**Chemistry**
Session Duration	**12:00 – 1:30 pm.**
Session Chair	**Prof. Dr. Ahmed Th. Numan**
Rapporteur	**Assist. Prof. Dr. Bushra H. Ali**

Time	**Code**	**Title**	**Autho**
12:00-12:12	296	Synthesis, Characterization and Antimicrobial activity of Mn(II), Co(II), Ni(II),Cu(II), Zn(II) and Cd(II) mixed ligand complexes Schiff base derived from Trimethoprim drug with 8-Hydroxy quinolone	Ahmed Th. Numan, **Eman M. Atiyah**
12:12-12:24	303	Synthesis, Characterization and the Corrosion Inhibition Study of Two Schiff Base Ligands Derived From Urea and Thiourea and Their Complexes with Cu(II) and Hg(II) Ions	**Wasan M. Alwan**
12:24-12:36	161	Synthesis, Spectral And Bacterial Studies Mixed Ligand Complexes of Schiff Base Derived from Methyldopa And Anthranilic Acid With Some Metal Ions	**Lekaa K. Abdul Karim**, Taghreed H. Al-Noor
12:36-12:48	196	Synthesis, Characterization and Antibacterial Activity of 1,4-di[aminomethylene carboxyl] phenylene (H_2L) Complexes Co(II), Cu (II), Zn(II) and Cd (II)	**Jassim S . Sultan,** Salah M. Fezea, Falih H .Mousa
12:48-1:00	227	Modified unzipping technique	**Basma H. Al-Tamimi**, Saad B. Farid, Fadhil A. Ghyad

Al- Mansour Melia Hotel				
Day 1	**Wednesday**	**Afternoon Session**	**Date**	**Dec. 13 , 2017**
Session	**1comp1a**		**venue**	**Cordoba 1 Hall**

Session Theme	**Computer Science**
Session Duration	**(1:00 –2:30) pm.**
Session Chair	**Assist. Prof. Dr. Alyaa K. Abdulhussain**
Rapporteur	**Assist. Prof. Dr. Abdullateef A. Hussain**

Time	Code	Title	Autho
1:00-1:12	263	Achieving Real-Time Tracking Mobile Wireless Sensors Using SE-KFA	Haider K. Hoomod, **Sadeem M. Al-Chalabi**
1:12-1:24	288	A New Heuristic Anonymization Technique for Privacy Preserved Datasets Publication on Cloud Computing	**Yousra A. S.Aldeen**
1:24-1:36	259	Hide for dynamic encryption text based on Corner point	**Firas A. Abdullatif**, Alaa A. Abdullatif, Amna al-saffar
1:36-1:48	269	Network Performance Analysis Based on Network Simulator NS-2	Maan Y. Anad, Naors Y. Anad, **Nawfal A. Zakar**
1:48-2:00	279	Evaluation Methodology between Globalization and Localization Features Approaches for Skin Cancer Lesions Classification	**Hussein M. Ahmed,** Razi J. Al-azawi, Abbas A. Abdulhameed
2:00-2:12	265	Analyzing Study of Path loss Propagation Models in Wireless Communications at 0.8 GHz	Haider K. Hoomod, Intisar Al-Mejibli, **Abbas I. Jabboory**

College Of Education For Pure Science (Ibn Al-Haitham)				
Day 2	**Thursday**	**Morning Session**	**Date**	**Dec. 14 , 2017**
Session	**2comp1m**		**venue**	**Computer Dept. Seminar Hall**

Session Theme	**Computer Science**
Session Duration	**(10:00 – 11:30) am.**
Session Chair	**Assist. Prof. Dr. Jeen J. Estifon**
Rapporteur	**Assist. Prof. Dr. Alaa A. Abdullatif**

Time	**Code**	**Title**	**Author**
10:00-10:12	264	Applying Self-Organizing Map and Modified Radial Based Neural Network for Clustering and Routing Optimal Path in Wireless Network	Haider K. Hoomod, **Tuka K. Jebur**
10:12-10:24	212	Hiding Text in Gray Image Using Mapping Technique	Ahmed A. Abbass, **Hussein L. Hussein**, Sinan A. Naji, Salam Al-augby, Jasim H. Lafta
10:24-10:36	80	secure server login by using third party and chaotic system	Firas A. Abdulatif , **Maan zuhiar**
10:36-10:48	312	Information Hiding In Digital Video Using DCT, DWT and CvT	**Wisam A. Shukur,** Wathiq N. Abdullah, Luheb K. Qurban
10:48-11:00	275	Performance of Case-Based Reasoning Retrieval Using Classification Based on Associations versus Jcolibri and Free CBR: A Further Validation Study	**Ahmed S. Aljuboori**, Frans Coenen, Mohammed Nsaif, David J. Parsons
11:00-11:12	244	Fuzzy-Estimation Control for Improvement Microwave Connection for Iraq Electrical Grid	Haider K. Hoomod, **Mohammed Radi**
11:12-11:24	299	Using Digital Watermarking To Secure Digital Documents	**Awad K. Hammoud**, Hatem N. Mohaisen, Qusay S. Shaker

College Of Education For Pure Science (Ibn Al-Haitham)				
Day 2	**Thursday**	**Afternoon Session**	**Date**	**Dec. 14 , 2017**
Session	**2comp1a**		**venue**	**Computer Dept. Seminar Hall**

Session Theme	**Computer Science**
Session Duration	**12:00 – 1:30 pm.**
Session Chair	**Prof. Dr. Ziyad T. Mustafa**
Rapporteur	**Assist. Prof. Dr. Ahmed N. Rasheed**

Time	Code	Title	Autho
12:00-12:12	245	Transmuted of Rayleigh Distribution with Estimation and Application on Noise Signal	**Suhad Ahmed,** Zainab Qasim
12:12-12:24	243	Fuzzy-Cellular Neural Network for Face Recognition HCI Authentication	Haider K. Hoomod, **Ahmed A. Ali**
12:24-12:36	104	Intelligent cloud computing security using genetic algorithm as a computational tools	**Mazin H. Razuky**
12:36-12:48	56	Comparison of Features Extraction Algorithms Used in the Diagnosis of Plant Diseases	**Mohammed A. Hussein**, Amel H. Abbas
12:48-1:00	330	Medical Image Security Using Modified Chaos-based Cryptography Approach	Methaq T. Gaata, **Shahad Th. Abdullatief**
1:00-1:12	157	New Secure E-mail System Based on Bio-Chaos Key Generation and Modified AES Algorithm	Haider K. Hoomod, **Arkan M. Radi**
1:12-1:24	274	Implementation of 4-way Superscalar Hash MIPS Processor Using FPGA	Safaa S. Omran, **Laith F. Jumma**

Al- Mansour Melia Hotel				
Day 1	**Wednesday**	**Afternoon Session**	**Date**	**Dec. 13 , 2017**
Session	**1math1a**		**Venue**	**Al-Khayam Hall**

Session Theme	**Mathematics**
Session Duration	**(1:00 – 2:30) pm.**
Session Chair	**Assist. Prof. Dr. Ali H. Nasir Alfayadh**
Rapporteur	**Assist. Prof. Dr. Majeed A. Wali**

Time	Code	Title	Author
1:00-1:12	7	On Direct Theorems For Best Polynomial Approximation	**Alaa A. Auad**, Rifaat S. AbdulJabbar
1:12-1:24	306	Generalized Differential Operator On Bistarlike And Biconvex Functions Associated By Quasi- Subordination	Abdul Rahman S. Juma, **Mohammed H. Saloomi**
1:24-1:36	116	Using Approximation Non-Bayesian Computation WITH Fuzzy Data TO Estimation Inverse Weibull Parameters AND Reliability Function	**Nadia H. Al-Noor**, Shurooq A.K. Al-Sultany
1:36-1:48	72	Finite Element Method with Piecewise Linear Function FOR Solving Nanoscale Inas⁄Gaas Quantum Ring Structures	Eman A. Hussain, Jamil A. Al-Hawasy, **Lamyaa H. Ali**
1:48-2:00	67	Classical Artinian Module And Related Topics	Majid M. Abed, **Ghazi F. AL-Sharqi**
2:00-2:12	253	Local Search Heuristic for Multi-CRITERIA Single Machine SCHEDULING Problem	Tariq S. Abdulrazaq, **Abeer O. Akram**

College Of Education For Pure Science (Ibn Al-Haitham)				
Day 2	**Thursday**	**Morning Session**	**Date**	**Dec. 14 , 2017**
Session	**2math1m**		**Venue**	**Prof. Oraibi AlZoba'ee Hall**

Session Theme	**Mathematics**
Session Duration	**(10:00 – 11:30) am.**
Session Chair	**Prof. Dr. Abdurahman H. Majeed**
Rapporteur	**Assist. Prof. Dr. Buthaina N. Shihab**

Time	Code	Title	Author
10:00-10:12	307	Coclosed Rickart Modules	Ghaleb A. Hmood
10:12-10:24	74	Strongly C_11-condition modules and strongly T_11-type modules	Inaam M. Ali Hadi, **Farhan D. Shyaa**
10:24-10:36	320	Application of Weyl Module in the Case of Two Rows	Haitham R. Hassan, **Neeran S. Jasim**
10:36-10:48	90	Weakly coretractable modules	**Shukur N. Alaeashi,** Inaam M. A. Hadi
10:48-11:00	66	Action of Groups on The Projective Plane Over The Field GF(41)	Emad B. AlZangana **Saja A. Joudah**
11:00-11:12	34	Essentially semismall Quasi-Dedekind module relative to a module	**Mukdad Q. Hussain**

College Of Education For Pure Science (Ibn Al-Haitham)				
Day 1	**Thuesday**	**Morning Session**	**Date**	**Dec. 14 , 2017**
Session	**2math2m**		**Venue**	**Central Laboratory Hall**

Session Theme	**Mathematics**
Session Duration	**(10:00 – 11:30) am.**
Session Chair	**Prof. Dr. Ra'ed K. Naji**
Rapporteur	**Prof. Abbas N. Salman**

Time	Code	Title	Author
10:00-10:12	82	Connecting On The Lattice Basis Reductions For Computing The Generators In The ISD Method	**Ruma K. Ajeena**, Sanaa K. Kamal
10:12-10:24	60	Steady State Radial Flow In Anisotropic And Homogenous In Confined Aquifers	**Alaa K. Jabber,** Luma N. M. Tawfiq
10:24-10:36	323	Solved Nth-Order Of Ordinary Differential Equations Using Lie Group	Eman A. Hussain, **Zainab M. Alwan**
10:36-10:48	94	Dynamic Of An SIR Model With Nonlinear Incidence Rate And Regress Of Treatment	**Saba N. Majeed**
10:48-11:00	319	Normalization Bernstein Basis For Solving Fractional Fredholm-Integro Differential Equation	**AbdulKhaleq O. AlJubory**, Shaymaa H. Salih
11:00-11:12	169	The Comparison Between The Bayes Estimator And The Maximum Likelihood Estimator Of The Reliability Function For Negative Exponential Distribution	Hazim M. Gorgees, **Bushra A. Ali,** Raghad I. Kathum

College Of Education For Pure Science (Ibn Al-Haitham)				
Day 1	**Thursday**	**Afternoon Session**	**Date**	**Dec. 14 , 2017**
Session	**2math1a**		**Venue**	**Prof. Oraibi AlZoba'ee Hall**

Session Theme	**Mathematics**
Session Duration	**12:00 – 1:30 pm.**
Session Chair	**Prof. Dr. Saad N. Ali**
Rapporteur	**Assist. Prof. Dr. Salwa S. Abd**

Time	Code	Title	Author
12:00-12:12	177	Fuzzy Fixed Point Theorem For Some Types Of Fuzzy Jungck Contractive Mappings In Hilbert Space	Buthainah A. Ahmed , **Manar F. Dheyab**
12:12-12:24	239	On Some Results Of Topological Groupoid	**Taghreed H. Majeed**
12:24-12:36	325	Common Fixed Points In Modular Spaces	Salwa S. Abed, **Karrar E. Abdulsada**
12:36-12:48	65	When M-Lindelof Sets Are Mx-Semi Closed	Haider J. Ali, **Marwa M. Dahham**
12:48-1:00	101	Analysis On The Cosets Of L-Convex Sets Subgroup	Nada M. Abbas, **Ruma K. Ajeena**
1:00-1:12	46	Quasi - Inner Product Spaces Of Quasi-Sobolev Spaces And Their Completeness	**Jawad K. Kalaf**

Al- Mansour Melia Hotel				
Day 1	**Wednesday**	**Afternoon Session**	**Date**	**Dec. 13 , 2017**
Session	**1phys1a**		**venue**	**Al-Hamraa Hall**

Session Theme	**Physics**
Session Duration	**(1:00 –2:30) pm.**
Session Chair	**Prof. Dr. Sameer A. Mekei**
Rapporteur	**Assist. Prof. Dr. Bushra K. Hassun**

Time	Code	Title	Autho
1:00-1:12	98	Fabrication And Study The Effect Of The Laser On The Properties Of The Compound **Tl2-Xhgxba2-Ysryca2cu3o10+Δ** Superconductor	Abdulkareem D. Ali, **Nihad A. Shafeek**
1:12-1:24	162	Theoretical Estimation Photons Flow Rate Production In Quark_Gluon Interacting At High Energies	**Hadi J. Al-Agealy**, Hayder H. Hussain, Saba M. Hussein
1:24-1:36	166	A New Relation Between Spiral Arm Pitch Angles (P) And The Momentum Parameter Of The Host Spiral Galaxies	**Ismaeel A. AlBaidhany**, Hayfa Gh. Rashid, Nadir F.Habubi, Sami S. Chiad , Nidhal N. Jando, Wasmaa Jabbar,
1:36-1:48	102	Wind Turbine Bearing Diagnostics Based On Vibration Monitoring	**Ali K. Resen**, Faleh H. Mahmood, Hussein T. Kadhim
1:48-2:00	301	The Enhancement Of UV Sensor Response By Zinc Oxide Nanorods / Reduced Graphene Oxide	**Ali A. A. Mohammed**, Suriani A. Bakar, Akram R. Jabur
2:00-2:12	324	Corrosion Protection Of Ductile Cast Iron Under Effect Of Harsh Environments	**Mustafa A. Rajab**, Hussein S. Hassan, Jasem Kh. Hamad

College Of Education For Pure Science (Ibn Al-Haitham)				
Day 2	**Thursday**	**Morning Session**	**Date**	**Dec. 14 , 2017**
Session	**2phys1m**		**venue**	**Prof. Salim Abdulhameed Hall**

Session Theme	**Physics**
Session Duration	**(10:00 – 11:30) am.**
Session Chair	**Prof. Dr. Kareem A. Jasim**
Rapporteur	**Assist. Prof. Dr. Abdulhameed R. Mahdi**

Time	Code	Ti	Autho
10:00-10:12	2	Improved Photoresponse of Porous Silicon Photodetectors By Embedding Titanium Oxide Nanoparticles	Hiba M. Ali, Sameer A. Mekei, **Ahmed N. Abd**
10:12-10:24	21	Fabrication And Characterization Study Of Vacuum Evaporated Znte/N-Si Heterojunction Solar Cell	**Bushra K. Hassun**, Bushra H. Hussein, Auday H. Shaban
10:24-10:36	22	Fabrication And Characterization Of AIAS/P-Si Heterojunction Solar Cell	**Hanan K. Hassun**, Auday H. Shaban, Ebtisam M. Salman
10:36-10:48	23	Effect Of Aluminum On Characterization Of Znte/N-Si Heterojunction Photodetector	Samir A. Maki, **Hanan K. Hassun**
10:48-11:00	331	Utilizing Laser-Induced Breakdown Spectroscopy Method to recognize chemical composition of low-carbon steel in NH3 (NO)4 material	**Nissan S. Oraibi**
11:00-11:12	96	Some Physical Properties Of Polyaniline Blends Films	**Tariq J. Alwan** , Abdulkhaliq S. Jabbar

College Of Education For Pure Science (Ibn Al-Haitham)				
Day 2	**Thursday**	**Morning Session**	**Date**	**Dec. 14 , 2017**
Session	**2phys2m**		**venue**	**Physics Dept. Seminar Hall 2**

Session Theme	**Physics**
Session Duration	**(10:00 – 11:30) am.**
Session Chair	**Prof. Dr. Aleya A. Shihab**
Rapporteur	**Assist. Prof. Dr. Widad H. Jasim**

Time	**Code**	**Title**	**Autho**
10:00-10:12	81	Design And Simulation Of Surface Plasmon Resonance Sensors For Environmental Monitoring	**Aseel I. Mahmood** , Rawa Kh. Ibrahim, Zainab Kh. Ibrahim
10:12-10:24	69	Very High Q-Factor Based On G-Shaped Resonator Type Metamaterial Absorber	**Khalid S. Lateef**
10:24-10:36	93	Numerical Simulation Of Endlessly Single Mode Photonic Crystal Fibers (ESM-12-02)	**Nadia F. Muhammed**, Sudad S. Al-Bassam, Aseel Ibrahim, Shehab A. Kahdum
10:36-10:48	105	The Effect Of Replaced Recycled Glass On Thermal Conductivity Of Brittle Materials	Mustafa A. Mahmoud, Asmaa S. Khalil, **Ali H. Ressen**, Mohammed K. Jawad, Ban M. Mozahim
10:48-11:00	139	The Effect Of Fecl3 Additives On The Optical Parameters Of Pva	**Duha M. A. Latif** , Sami S. Chiad, Khalid H. Abass , Nadir F. Habubi , Muhssen S. Erhayief , Hadi Ahmed Hussin
11:00-11:12	158	Enhance Video Film Using Retnix Method	**Rasha A. Abtan**, Ali A. D. Al-Zuky, Anwar H. Al-Saleh, Haidar J. Mohamad

College Of Education For Pure Science (Ibn Al-Haitham)				
Day 2	**Thursday**	**Morning Session**	**Date**	**Dec. 14 , 2017**
Session	**2phys3m**		**venue**	**Physics Dept. Seminar Hall 1**

Session Theme	**Physics**
Session Duration	**(10:00 – 11:30) am.**
Session Chair	**Prof. Dr. Khalid H. Mahdi**
Rapporteur	**Assist. Prof. Dr. Aisar J. Ibraheem**

Time	Code	Title	Author
10:00-10:12	249	Characterization Of Zno Nanoparticles-PVDF Polymer Visible Photoconductive Detector On Silicon And Porous Silicon	**Asama N. Naje,** Omar Adnan
10:12-10:24	198	Synchronization Of Quantum Cascade Lasers With Negative Optoelectronic Feedback	**Hussein H. Waried**
10:24-10:36	173	Measuring Of Non-Linear Properties Of Spatial Light Modulator With Different Wavelengths	Samar Y. Aldabagh, Sudad S. Ahmed, Aseel I. Mahmood, **Farah G. Khalid**
10:36-10:48	88	Using SAFRAN Software to Assess Radiological Hazards from Dismantling of Tammuz-2 Reactor Core at Al-tuwaitha Nuclear Site	**Mezher A. Gatea**, Anwar A. Ahmed, Saad j. Kadhum, Hasan M. Ali, Abbas H. Muheisn
10:48-11:00	267	Theoretical Calculation Of The Electron Transport Parameters And Energy Distribution Function For CF3I With Noble Gases Mixtures Using Monte Carlo Simulation Program	**Enas A. Jawad**
11:00-11:12	29	Radiological Risk Assessments For Occupational Exposure At Fuel Fabrication Facility Al-Tuwaitha Site Baghdad – Iraq By Using Resrad Computer Code	**Zaidoon H. Ibrahim**, Sameera A. Ibrahim, Marwa K. Mohammed, Auday H. Shaban,

College Of Education For Pure Science (Ibn Al-Haitham)				
Day 2	**Thursday**	**Morning Session**	**Date**	**Dec. 14 , 2017**
Session	**2phys4m**		**venue**	**Chemistry Dept. Hall 4**

Session Theme	**Physics**
Session Duration	**(10:00 – 11:30) am.**
Session Chair	**Prof. Dr. Bashaier M. Saeed**
Rapporteur	**Assist. Prof. Dr. Mustafa K. Jasim**

Time	Code	Title	Author
10:00-10:12	225	Detection Of Increasing Of Tropospheric NO2 Over some Iraqi Cities By Using Satellite Data	**Saadiyah H. Halos**
10:12-10:24	4	OLIFE: Tight Binding Transmission Coefficient Calculation Code	**Zainelabideen Y. Mijbil**
10:24-10:36	68	Design Of Light Trapping Solar Cell System By Using Zemax Program	**Alaa B. Hasan**, Sabah A. Husain
10:36-10:48	70	Practical Study For The Properties Of Hueckel Edge Detection Operator	**Hameed M. Abduljabbar,** Amal J. hatem, Inbethaq M. A. AbdulAmeer
10:48-11:00	100	Chaotic Behavior Of The Rössler Model And Its Analysis By Using Bifurcations Of Limit Cycles And Chaotic Attractors	Kejeen M. Ibrahim, **Raied K. Jamal**, Falah Hasan
11:00-11:12	167	Theoretical Evaluations Of Probability Of Photons Yield Depending On Quantum Chromodynamics Theory	**Hadi J. Al-Agealy**, Mudhafar J. Sahib

College Of Education For Pure Science (Ibn Al-Haitham)				
Day 2	**Thursday**	**Afternoon Session**	**Date**	**Dec. 14 , 2017**
Session	**2phys1a**		**venue**	**Prof. Salim Abdulhameed Hall**

Session Theme	**Physics**
Session Duration	**12:00 –1:30 pm.**
Session Chair	**Prof. Dr. Raad H. Majeed**
Rapporteur	**Assist. Prof. Dr. Farouk I. Hussain**

Time	Code	Title	Author
12:00-12:12	138	Urban Energy And Dispersion Parameters Of Polyvinyl Alcohol Thin Films Doped With Fe	Nadir F. Habubi , **Khalid H. Abass** , Chiad S. Sami , Duha M. A. Latif , Jandow N. Nidhal , Ismaeel Al-Baidhany
12:12-12:24	182	The Role Of Tin Oxide Concentration On The Structural, Morphology And Optical Properties Of In2O3:Sno2 Thin Films	Bushra A. Hasan , **Rusul M. Abdallah**
12:24-12:36	327	Doping And Annealing Effect On Evaporation Of Zno Thin Films	**Auday H. Shaban**, Sameer A. Mekei , Shahd A. Hussain
12:36-12:48	210	Study Of The Effect Of Electromagnetic Fields On Indoor And Outdoor Radon Concentrations	**Lina M. Haider**, Najlaa R. Shareef, Hasssan H. Darwoysh, Hazim L. Mansour
12:48-1:00	215	Effect Of Nanoparticle Size Of Tio2 And Additive Materials To Improve Dye Sensitized Solar Cells Efficiency	**Falah H. Ali**, Dheyaa B. Alwan
1:00-1:12	8	Study Of Vegetation Cover Distribution Using DVI, PVI And WDVI Indices With 2D-Space Plot	**Taghreed A. H. Naji**

College Of Education For Pure Science (Ibn Al-Haitham)				
Day 2	**Thursday**	**Afternoon Session**	**Date**	**Dec. 14 , 2017**
Session	**2phys2a**		**venue**	**Physics Dept. Seminar Hall 2**

Session Theme	**Physics**
Session Duration	**12:00 –1:30 pm.**
Session Chair	**Prof. Dr. Nadir F. Habubi**
Rapporteur	**Assist. Prof. Dr. Alaa B. Hasan**

Time	**Code**	**Title**	**Author**
12:00-12:12	172	Preparing And Study The Effects Of Composite Coatings In Protection Of Oil Pipes From The Risk Of Corrosion That Resulting From The Water Associated With Petroleum Products.	Abdulhameed R. Mahdi, **Mohammed A. Yaseen**
12:12-12:24	189	Recycling The Construction And Demolition Waste To Produce Polymer Concrete	Mohammad T. Hamza, Awham M. Hameed
12:24-12:36	214	Study The Effect Of Flow Rate On Some Physical Properties Of Different Polymeric Solutions	**Akram R. Jabur**, Manar A. Najim, Shereen A. Abdurahman
12:36-12:48	230	The Effect Of MWCNT On Some Physical Properties Of Epoxy Matrix	**Tagreed M. Alsaadi**, Suad H. Aleabi, Entisar E. Al-Obodi, Hadeel A. J. Abbas
12:48-1:00	235	Carbon Nanotubes /Conduct Polymer Nanocomposites For Electronic Devices	**Estabraq T. Abdullaha**, Abdulsattar G. Enadb, Mohammed G. Hamed
1:00-1:12	285	Mathematical Calculations Of Heat Transfer For The CNC Deposition Platform Based On Chemical Thermal Method	**Mohammed Sh. Essa,** Bahaa T. Chiad, Khalil A. Hussein

College Of Education For Pure Science (Ibn Al-Haitham)				
Day 2	**Thursday**	**Afternoon Session**	**Date**	**Dec. 14 , 2017**
Session	**2phys3a**		**venue**	**Physics Dept. Seminar Hall 1**

Session Theme	**Physics**
Session Duration	**12:00 –1:30 pm.**
Session Chair	**Prof. Dr. Harith I. Jaafar**
Rapporteur	**Assist. Prof. Dr. Hameed M. Abduljabbar**

Time	Code	Title	Author
12:00-12:12	31	Computation Of Hazard Indices And Age Group Parameters Of Powder Milk Consumed In Iraq	**Hassan A. Ammer**, Nada F. Kadhim, Mahmood S. Karim
12:12-12:24	121	Arriving A Characteristic Formula To Deducing The Energy Of The Heaviest Particles Producing From The Controlled Thermonuclear Fusion Reactions	Raad H. Majeed, **Osamah N. Oudah**
12:24-12:36	181	Design Of Charged Particle Of Lens Using An Analytical Potential Formula	**Ali H. Hassan**, Mohammed J. Yaseen, Saadi R. Abbas
12:36-12:48	191	Interraction Of(O,Ar)Ions With (Prostat) As Approach Of Cancer Therapy	Bashair M. Saied, **Saad N. Yaacoub**
12:48-1:00	302	Radon Concentration And Dose Assessment In Well Water Samples From Karbala Governorate Of Iraq	**Iman T. Al-Alawy**, Aqeel A. Hasan
1:00-1:12	240	Effect Of Electrical Current Stimulation On Pseudomonas Aeruginosa Growth	Auns Q. Alneami, Eman Gh. Khalil, Rana A. Mohsien **Ali F. Abdulkareem**

College Of Education For Pure Science (Ibn Al-Haitham)				
Day 2	**Thursday**	**Afternoon Session**	**Date**	**Dec. 14 , 2017**
Session	**2phys4a**		**venue**	**Chemistry Dept. Hall 4**

Session Theme	**Physics**
Session Duration	**12:00 –1:30 pm.**
Session Chair	**Prof. Dr. Hazim L. Mansour**
Rapporteur	**Assist. Prof. Dr. Hadi J. Mojebil**

Time	Code	Title	Author
12:00-12:12	124	Structural And Optical Properties Of Colloidal Inzno Nps Prepared By Laser Ablation In Liquid	**Maryam M. Khlewee**, Khawla S. Khashan
12:12-12:24	130	Multispectral And Panchromatic Used Enhancement Resolution And Study Effective Enhancement On Supervised Classification Landcover	**Salama S. Salman** , Wafaa A. Abbas
12:24-12:36	131	Hiding Information Using Different Lighting Color Images	**Ahlam Majead** , Salema Sultan, Rasha Awad
12:36-12:48	136	Enhance The Performance Of Liquid Crystal As An Optical Switch Doped With Cds Quantum Dots	Sudad S. Ahmed, **Rawa Kh. Ibrahim**, Kais Al-Naimee , Asama N. Naje, Omar A. Ibrahim, Khalood A. Majeed
12:48-1:00	137	Spatial And Temporal Analysis Of Mean Air Temperature Seasonally And Annually In Iraq For The Period 1980-2015	Yassen K. AlTimimi, **Aws A. AlKhudhairy**.
1:00-1:12	155	Preparation And Characterization Of Copper Oxide Nanoparticles Decorated Carbon Nanoparticles Using Laser Ablation In Liquid	Farah A. Abdulameer, Khawla S. khashan, Majid S. Jabir

Conference Posters

Al-Mansour Melia Hotel			
Day 1	Wednesday	**Date**	Dec. 13 , 2017
Session	Posters	**Theme**	Biology

Code	Title	Author
190	Irrigation water quality of Al-Gharraf Canal, south of Iraq	Salam H. Ewaid
255	Antimicrobial susceptibility of Enterococcus spp. Isolated from different clinical sources in Kirkuk provency	Hajir A. Shareef, Shara N. Abdullah
294	Antimicrobial Effect of Lactobacillus as a Probiotic Isolated from Yoghurt Products Against Staphylococcus aureus and Escherichia.coli	Israa I. Khalil, Suhail J. Fadihl, Haifaa H. Ali
295	Determain kind and concentration of Heliotropium suaveolens, Plantago major and Silybum marianum plants ingredients and its effect on some plant pathogenic fungi	A. J. Abdlrhmaan, I. A. Abdul Raheem , R. H. Latef

College Of Education For Pure Science (Ibn Al-Haitham)			
Day 2	Thursday	**Date**	Dec. 14 , 2017
Session	Posters	**Theme**	Biology

Code	Title	Author
54	Detection of tox A gene in Pseudomonas aeruginosa that isolates from different clinical cases by using PCR.	Rana M. A. Al-Shwaikh, Abbas F. Alornaaouti
134	Effect of sesame oil on lipid profile and liver enzymes of in male albino rats treated with Carbone tetrachloride (CCl4)	Rashaa F. Abdul-Lattif
186	First Record of Trichodina magna Van As and Basson, 1989 (Ciliophora: Trichodinidae) from Gills of Blue Tilapia Oreochromis aureus (Steindachner, 1864) in Iraq	Kefah N. Abdul-Ameer, Fatima Kh. Atwan
289	Investigate of the ability of Cronobacter sakazakii isolated from clinical samples of children under two years to induce swimming, swarming and biofilm	Luma A. H. Zwein, Tharieyt A. Motlag, Mohamed mousa
316	Pathological and immunological study on infection with Escherichia coli in male BALB/c mice	Intisar H. Ali, Majid S. Jabir, Hanady S.A. Al-Shmgani , Ghassan M. Sulaiman , Ali H. Sadoon
321	The effect of Larinus maculates F. cocoon aqueous extract in some Immunological Aspects of male albino mice	Zainab Thamer Alasady; Hanady Salim Abd Alsaheb; Muna Shukri Mahmod Jwad
326	Seroprevalence of Toxoplasmosis Antibodies among Diabetes Mellitus Type 2 Patients and Assessment some Immunological Markers	Sarah A. Saeed , Israa K. Al-Aubaidi

Al-Mansour Melia Hotel			
Day 1	Wednesday	**Date**	Dec. 13 , 2017
Session	Posters	**Theme**	Chemistry

Code	Title	Author
293	Synthesis and antifungal activity against of Candida species for Some Heterocyclic Compounds new containing Schiff base or oxazepine or Indolinor imidazo groups and their spectral characterization	Shaima I. chyad AL-khazraji, Bari L. Mohammed , Siham Sh. AL-Salihi
223	Cardiovascular Risk Assessement In Osteoporotic Patients Using Osteoprotegerin As A Reliable Predictive Biochemical Marker	Noora W. Rasheed, Ooroba J. Taresh
144	Use of Acidic Hydrolysis and Diazocoupling Reaction for Spectrophotometric Determination of Furosemide in Urine and pharmaceutical Formulation.	Hawraa Ali, Sumayha muhammed
283	New Indirect Spectrophotometric Method for Determination of Hypochlorite using Nile blue	Farha Kh. Omar

College Of Education For Pure Science (Ibn Al-Haitham)			
Day 2	Thursday	**Date**	Dec. 14 , 2017
Session	Posters	**Theme**	Mathematics

Code	**Title**	**Author**
6	Effect of radial magnetic field and heat transfer as well as mass transfer on peristaltic transport of Jeffrey fluid in curved channel.	Tamara Sh. Ahmed, Ahmed M. Abdulhadi
32	Characterizations of p-Hollow-Lifting Modules	Mukdad Q. Hussain, Marrwa A. Salih
43	ON CONTRACTIBLE J-SPACES	Narjis. A. Dawood Suaad G. Gasim &
44	Estimate the Rate of Contamination in Soil for Displaced Persons Camp Using Interpolation Method	Luma N. M. Tawfiq, Israa N. Abood
55	Intuitionistic fuzzy n-fold KU-ideal of KU-algebra	Samy M. Mostafa, Fatema F. Kareem
63	Estimate the Effect of Rainwaters in Contaminated Soil by Using Simulink Technique	Luma N. M. Tawfiq, Mohammed A. Hassan
64	Estimate the Concentration of Heavy Metals in soil for Al- Zafaraniyah City By Using Neural Network	Farah. F. Ghazi
87	Different Estimation Methods for System Reliability in Multi-Components Stress-Strength Model: Exponentiated Weibull Distribution	Abbas N. Salman, Fatima Hadi
114	Comparison between Nonlinear Least Squares Method and Maximum A Posteriori Method	Mustafa M. Kazem
141	On Estimating the Survival Function for the Patients Suffer From the Lung Cancer Disease	Abbas N. Salman, btehal H. Farhan, Maymona M. Ameen, Adel A. Hussein
150	The RSA Algorithm and Diffie-Hellman key exchange with A generated function of primes	Faez Ali AL-Maamori, Mazin S. Rasheed

Code	Title	Author
151	Using simulation technique to overcome the multi-collinearity problem for estimating fuzzy linear regression parameters	Hazim M. Gorgees, Mariam M. Hilal
153	On Reliability Estimation for Exponential Distribution Based on Monte Carlo Simulation	Abbas N. Salman, Taha A. Taha
194	Bayesian Estimation of Reliability Burr Type XII Under Al-Bayyatis Suggest Loss Function with Numerical Solution	Amal A. Mohammed, Sudad K. Abraheem , Nadia J. Fezaa Al-Obedy
203	Strong Convergence of Iteration Processes for Infinite Family of General Extended Mappings	Zena H. Maibed
204	On Solving Modified Regularized Long Wave Equation Using Collocation Method	Hamad S., Luma N. M. Tawfiq, Zainor R. Yahya, Shazalina Mat Zin
217	FIBREWISE IJ-PERFECTBITOPOLOGICAL SPACES	Yousif Y.Yousif , Liwaa. A. Hussain
2018	〖λN〗_αC –Continuous And Contra 〖λN〗_αC –Continuous Mappings In Topological spaces	Nadia M. A. Al- Tabatabai
300	COPRIME MODULES AND OTHER RELATED TOPICS	Inaam.M. Ali, Rasha Ibrahim
308	FIBREWISE SOFT IDEAL TOPOLGICAL SPACES	Yousif Y.Yousif, Mohammed A. Hussain
309	The Approximate Solution of Fractional Damped Burger's Equation and its Statistical Properties	Wurood R. Abd AL- Hussein, Mahmood A, Shamran, Suaad N. Kadhim, Saad N. AL-Azzawi
314	Using the Ridge Regression procedures to Estimate the Multiple Linear Regression Coefficients	Hazim M. Gorgees, Fatimah A. Mahdi
318	Minimax Shrunken Technique for Estimate Burr X Distribution Shape Parameter	Abbas N. Salman, Maymona M. Ameen Ahmed E. Abdul-Nabi

College Of Education For Pure Science (Ibn Al-Haitham)			
Day 1	Wednesday	**Date**	Dec. 13 , 2017
Session	Posters	**Theme**	Physics

Code	Title	Author
234	Influence of Temperature on Nanosecond Pulse Amplification in Thulium Fiber Lasers	Ali Abdulfattah, Stefan Gausmann, Alex Sincore, Joshua Bradford, Nathan Bodnar, Justin Cook, Lawrence Shah, Martin Richardson

College Of Education For Pure Science (Ibn Al-Haitham)			
Day 2	Thursday	**Date**	Dec. 14 , 2017
Session	Posters	**Theme**	Physics

Code	Title	Author
3	The Effects of micro Aluminum fillers In Epoxy resin on the thermal conductivity	Kareem A. Jasim , Rihab Nasser Fadhil
11	The Effect of Oxygen Flow on the Transition Temperature of Hg0.75Pb0.25Sr2-yBayCa2Cu3O8+ δ Superconductors	Kareem A. Jasim, Raghad S. Al- Khafaji
30	Study The Electron Transport Coefficients for $\mathbf{Ar}, \mathbf{O_2}$ and Their Mixtures By Using EEDF Program	Dhuha S. Abdulmajeed, Bushra J. Hussein, Mustafa K. Jassim
40	Experimental study of some shielding parameters for composite shields	Ahmed F. Mkhaiber, Abdulraheem Dheyaa
48	Antibacterial Activity Of ternary semiconductor compounds AgInSe2 Nanoparticles Synthesized by Simple Chemical Method	Alia A. Shehab, Suha. A. Fadaam, Ahmed N. Abd, Mohamed H. Mustafa
49	The partial substitution of copper with nickel oxide on the Structural and electrical properties of Hg$\boldsymbol{Ba_2Ca_2Cu_{3-x}Ni_xO_{8+\delta}}$ superconducting compound	Kareem A. Jasim, Laheeb A. Mohammed
79	Photoluminescence Spectra From The Direct Energy Gap of a-SiQDs	Nidhal M. Abdul-Ameer, Moafak C. Abdulrida, Shatha M. Abdul-Hakeem
91	Measure of Backscatter for small particles of atmosphere by lasers	Mariam M. Abud
112	Synthesis and characterization of porous silicon gas sensors	Roaa Adil abbas, Alwan M. Alwan, Zainab T. Abdulhamied
125	Theoretical discussion of Electron Transport rate constant at TCNQ / Ge and TiO2 System	Hadi J. Al-agealy, Mohsin A. Hassooni , Burhan R. Alshafaay, Ahmed M. Ashwiekh , Abbas K. Sadoon, Raad H. Majeed,

Code	Title	Author
		Rawnaq Q. Ghadhban, Shatha H. Mahdi
156	Repeatability and Reversibility of the Humidity Sensor Based on Photonic Crystal Fiber Interferometer	Suaad S. Hindal, Hanan J. Taher
192	Estimation of geometrical shapes of mass-formed nuclei (A=102-178) from the calculation of deformation parameters for two elements ($\boldsymbol{Sn}$ & $\boldsymbol{Yb}$)	Sameera A. Ebrahiem, Haider A. Zghaier
231	La+3 effectiveness replacement on the ferrite material ($\boldsymbol{Cu_{0.2}Zn_{0.45}La_xFe_{2-x}O_4}$) on the structural and electrical and magnetic features	Farouq I. Hussain, Rusul A. Najem
236	Partial substitution of Zn Effects on the Structural and Electrical Properties of High Temperature Hg0.95Ag0.05Ba2Ca2Cu3O8+δ Superconductors	Noor S. Abed, Sabah J. Fathi, Kareem A. Jassim , Shatha H. Mahdi
254	Investigation of Corrosion Protection in Oil Mineral Reservoirs by Nanocomposites Used as Coating Layers	Abdulhameed R. Al-Sarraf, S A Al-Saaidi
258	Structural properties difference between two types of PE subjected to heat treatment	May A.S. Mohammed
266	Evaluation of the Epoxy/Antimony Trioxide Nanocomposites as Flame Retardant	B. M. Dheyaa1, W H Jassim, N A Hameed2
271	Effect of time variation on coating characteristic of Ti-6Al-4V alloy coated with TiO2 by dip coating method	Shaymaa H. Aneed

Peer review statement

IOP Conf. Series: Journal of Physics: Conf. Series **1003** (2018) 011007 doi:10.1088/1742-6596/1003/1/011007

Peer review statement

All papers published in this volume of *Journal of Physics: Conference Series* have been peer reviewed through processes administered by the proceedings Editors. Reviews were conducted by expert referees to the professional and scientific standards expected of a proceedings journal published by IOP Publishing.

Table of contents

Volume 1003

2018

Previous issue Next issue

IBN AL-HAITHAM FIRST INTERNATIONAL SCIENTIFIC CONFERENCE
13–14 December 2017, Baghdad, Iraq

View all abstracts

Accepted papers received: 4 April 2018
Published online: 25 May 2018

Preface

OPEN ACCESS 011006

Conference Posters

+ View abstract View article PDF

OPEN ACCESS 011007

Peer review statement

+ View abstract View article PDF

Papers

Biology

OPEN ACCESS 012001

Effects Sprayed Solution of Salicylic Acid to Prevent of Wilt Disease Caused by *Fussarium oxysporium*

Dina. Y. M. Yousif

+ View abstract View article PDF

OPEN ACCESS 012002

Seroprevalence occurrence of viral hepatitis and HIV among hemodialysis patients

Inass Mahmood Kamal and Batool Mutar Mahdi

+ View abstract View article PDF

OPEN ACCESS 012003

Seasonal abundance of eggplant leafminer Liriomyza sativae (Blanchard, 1938) (Diptera, Agromyzidae) in plastic-house

S A Kathiar, S K. Flaih, H I Al-Khazraji and S K Ismael

+ View abstract View article PDF

OPEN ACCESS 012004

The study of Bacteriocin of Pseudomonas fluorescens and Citrus limon effects against Propionibacterium acnes and Staphylococcus epidermidis in acne patients

Mais E. Ahmed

+ View abstract View article PDF

OPEN ACCESS 012005

The Role Of Staphylococcus Haemolyticus In Men Infertility

Ghaed'a J. AL-Ghizzawi and Zahraa K. Jomaa

+ View abstract View article PDF

OPEN ACCESS 012006

Chemistry

Modified Unzipping Technique to Prepare Graphene Nano-Sheets

B H Al-Tamimi, S B H Farid and F A Chyad

+ View abstract View article PDF

OPEN ACCESS 012021

Synthesis and spectral studies of heterocyclic azo dye complexes with some transition metals

A J Jarad, I Y Majeed and A O Hussein

+ View abstract View article PDF

OPEN ACCESS 012022

Theoretical Investigation For The Effect of Fuel Quality on Gas Turbine Power Plants

Omar AbdulRazzak khudair, Khetam Alwan Abass, Noor Saadi Abed, Khalid Hussain Ali, Saad AbdulAziz and Ali Chlaib Shaboot

+ View abstract View article PDF

OPEN ACCESS 012023

Heavy metals characteristics of settled particles of streets dust from Diwaniyah City-Qadisiyah Governorate - Southern Iraq

Moutaz A. Al-Dabbas, Khalid H. Mahdi, Raad Al- Khafaji and Kawthar H. Obayes

+ View abstract View article PDF

Computer Science

OPEN ACCESS 012024

Intelligent cloud computing security using genetic algorithm as a computational tools

Mazin H Razuky AL- Shaikhly

+ View abstract View article PDF

OPEN ACCESS 012025

New Secure E-mail System Based on Bio-Chaos Key Generation and Modified AES Algorithm

Haider K Hoomod and A M Radi

+ View abstract View article PDF

OPEN ACCESS 012026

Transmuted of Rayleigh Distribution with Estimation and Application on Noise Signal

Suhad Ahmed and Zainab Qasim

+ View abstract View article PDF

OPEN ACCESS 012027

Hiding Techniques for Dynamic Encryption Text based on Corner Point

Firas A. Abdullatif, Alaa A. Abdullatif and Amna al-Saffar

Mathematics

OPEN ACCESS 012043

COPRIME MODULES AND OTHER RELATED TOPICS

A.M. Inaam and K.I. Rasha

+ View abstract View article PDF

OPEN ACCESS 012044

When *m-lindelof* sets are mx-semi closed

Haider Jebur Ali and Marwa Makki Dahham

+ View abstract View article PDF

OPEN ACCESS 012045

Mathematical analysis on the cosets of subgroup in the group of E-convex sets

Nada Mohammed Abbas and Ruma Kareem K. Ajeena

+ View abstract View article PDF

OPEN ACCESS 012046

Generalized Differential Operator on Bistarlike and Biconvex Functions Associated By Quasi-Subordination

Abdul Rahman S. Juma and Mohammed H. Saloomi

+ View abstract View article PDF

OPEN ACCESS 012047

Essentially semismall Quasi-Dedekind module relative to a module

Mukdad Q Hussain

+ View abstract View article PDF

OPEN ACCESS 012048

The Approximate Solution of Fractional Damped Burger's Equation and its Statistical Properties

Wurood R. Abd AL- Hussein, Mahmood A Shamran, Suaad N. Kadhim and Saad N. AL-Azzawi

+ View abstract View article PDF

OPEN ACCESS 012049

Using the Ridge Regression Procedures to Estimate the Multiple Linear Regression Coefficients

HazimMansoor Gorgees and FatimahAssim Mahdi

+ View abstract View article PDF

OPEN ACCESS 012050

Fibrewise soft ideal topological space

Yousif Y Yousif and Mohammed A H Ghafel

+ View abstract View article PDF

OPEN ACCESS 012051

Application of Weyl Module In The Case Of Two Rows

Haytham R. Hassan and Niran Sabah Jasim

+ View abstract View article PDF

OPEN ACCESS 012052

Solution Of nth-Order Ordinary Differential Equations Using Lie Group

Eman Ali Hussain and Zainab Mohammed Alwan

+ View abstract View article PDF

OPEN ACCESS 012053

Effect of radial magnetic field on peristaltic transport of Jeffrey fluid in curved channel with heat / mass transfer

Ahmed M. Abdulhadi and Tamara S. Ahmed

+ View abstract View article PDF

OPEN ACCESS 012054

On direct theorems for best polynomial approximation

A A Auad and R S AbdulJabbar

+ View abstract View article PDF

OPEN ACCESS 012055

Persons Camp Using Interpolation Method

Luma Naji Mohammed Tawfiq and Israa Najm Abood

+ View abstract View article PDF

OPEN ACCESS 012056

Steady State Radial Flow in Anisotropic and Homogenous in Confined Aquifers

Luma Naji Mohammed Tawfiq and Alaa K Jabber

+ View abstract View article PDF

OPEN ACCESS 012057

Estimate the Effect of Rainwaters in Contaminated Soil by Using Simulink Technique

Luma N M Tawfiq and Mohammed A Hassan

+ View abstract View article PDF

OPEN ACCESS 012058

Estimation of Heavy Metals Contamination in the Soil of Zaafaraniya City Using the Neural Network

Farah F Ghazi

+ View abstract View article PDF

OPEN ACCESS

Taghreed Hur Majeed

+ View abstract View article PDF

OPEN ACCESS 012068

Using Simulation Technique to overcome the multi-collinearity problem for estimating fuzzy linear regression parameters.

Hazim Mansoor Gorgees and Mariam Mohammed Hilal

+ View abstract View article PDF

Physics

OPEN ACCESS 012069

Study the effect of flow rate on some physical properties of different polymeric solutions

A R Jabur, M A Najim and Sh A Abd Al- Rahman

+ View abstract View article PDF

OPEN ACCESS 012070

The Enhancement Of UV Sensor Response By Zinc Oxide Nanorods / Reduced Graphene Oxide Bilayer Nanocomposites Film

Ali A A Mohammed, AB Suriani and Akram R Jabur

+ View abstract View article PDF

OPEN ACCESS 012071

The partial substitution of copper with nickel oxide on the Structural and electrical properties of $HgBa_2$ Ca_2 $Cu_{3x}Ni_x$ $O_{8+\delta}$ superconducting compound

K A Jasim and L A Mohammed

+ View abstract View article PDF

OPEN ACCESS 012072

Repeatability and Reversibility of the Humidity Sensor Based on Photonic Crystal Fiber Interferometer

S S Hindal and H J Taher

+ View abstract View article PDF

OPEN ACCESS 012073

Enhanced photo-response of porous silicon photo-detectors by embeddingTitanium-dioxide nano-particles

Hiba M Ali, Sameer A Makki and Ahmed N Abd

+ View abstract View article PDF

OPEN ACCESS 012074

Design of Light Trapping Solar Cell System by Using Zemax Program

A B Hasan and S A Husain

Partial substitution of Zn Effects on the Structural and Electrical Properties of High Temperature $Hg_{0.95}Ag_{0.05}Ba_2Ca_2Cu_3O_{8+\delta}$ Superconductors

Noor S. Abed, Sabah J. Fathi, Kareem A. Jassim and Shatha H. Mahdi

+ View abstract View article PDF

OPEN ACCESS 012099

Chaotic behaviour of the Rossler model and its analysis by using bifurcations of limit cycles and chaotic attractors

K M Ibrahim, R K Jamal and F H Ali

+ View abstract View article PDF

OPEN ACCESS 012100

Preparation and characterization of copper oxide nanoparticles decorated carbon nanoparticles using laser ablation in liquid

K S Khashan, M S Jabir and F A Abdulameer

+ View abstract View article PDF

OPEN ACCESS 012101

Doping And Annealing Effect On Evaporation Of ZnO Thin Films

Auday H Shaban, Samir A. maki and Shahd A. hussain

+ View abstract View article PDF

OPEN ACCESS 012102

The Effect of Multi Wall Carbon Nanotubes on Some Physical Properties of Epoxy Matrix

Tagreed M. Al-Saadi, Suad hammed Aleabi, Entisar E. Al-Obodi and Hadeel Abdul-Jabbar Abbas

+ View abstract View article PDF

OPEN ACCESS 012103

Preparing and Study the effects of Composite Coatings in Protection of Oil Pipes from the Risk of Corrosion that resulting from Associated water with Petroleum Products

A R Al – Sarraf and M A Yaseen

+ View abstract View article PDF

OPEN ACCESS 012104

Study of the effect of electromagnetic fields on indoor and outdoor radon concentrations

Lina M Haider, N R Shareef, H H Darwoysh and H L Mansour

+ View abstract View article PDF

OPEN ACCESS 012105

Photoluminescence Spectra From The Direct Energy Gap of a-SiQDs

Nidhal M. Abdul-Ameer, Moafak C. Abdulrida and Shatha M. Abdul-Hakeem

+ View abstract View article PDF

OPEN ACCESS 012106

Interaction of (O,Ar)ions with Prostate tissue

Dr. Bashair Mohammed Saied and SaadNafea Yaqoob

+ View abstract View article PDF

OPEN ACCESS 012107

Novel Relationship among Spiral Arm Pitch Angles (p) and momentum parameter of the host spiral galaxies

Ismaeel Al-Baidhany, Hayfa G Rashid, Sami S Chiad, Nadir F Habubi, Nidhal N Jandow, Wasmaa A Jabbar and khalid H Abass

+ View abstract View article PDF

OPEN ACCESS 012108

Effects of FeCl3 additives on optical parameters of PVA

Duha M A Latif, Sami S Chiad, Muhssen S Erhayief, Khalid H Abass, Nadir F Habubi and Hadi A Hussin

+ View abstract View article PDF

OPEN ACCESS 012109

Experimental study of some shielding parameters for composite shields

Ahmed F Mkhaiber and Abdulraheem Dheyaa

+ View abstract View article PDF

OPEN ACCESS 012110

Fabrication & Characterization of AlAS/pSi Heterojunction Solar Cell

Hanan K Hassun, Auday H Shaban and Ebtisam M T Salman

+ View abstract View article PDF

OPEN ACCESS 012111

Design of Magnetic Charged Particle Lens Using Analytical Potential Formula

A H Al-Batat, M J Yaseen, S R Abbas, M S Al-Amshani and H S Hasan

+ View abstract View article PDF

OPEN ACCESS 012112

Effect of Electrical Current Stimulation on Pseudomonas Aeruginosa Growth

Auns Q Alneami, Eman G Khalil, Rana A. Mohsien and Ali F. Albeldawi

+ View abstract View article PDF

OPEN ACCESS 012113

Mathematical Calculations Of Heat Transfer For The CNC Deposition Platform Based On Chemical Thermal Method

Mohammed Sh. Essa, Bahaa T. Chiad and Khalil A. Hussein

+ View abstract View article PDF

OPEN ACCESS 012114

OLIFE: Tight Binding Code for Transmission Coefficient Calculation

Zainelabideen Yousif Mijbil

+ View abstract View article PDF

OPEN ACCESS 012115

Effect of time variation on coating characteristic of Ti-6Al-4V alloy coated with TiO2 by dip coating method

Shaymaa Hashim Aneed

+ View abstract View article PDF

OPEN ACCESS 012116

Study electron transport coefficients for Ar, O_2 and their mixtures by using EEDF program

D S Abdul Majeed, B J Hussein and M K Jassim

+ View abstract View article PDF

OPEN ACCESS 012117

Radon Concentration And Dose Assessment In Well Water Samples From Karbala Governorate Of Iraq

I T Al-Alawy and A A Hasan

+ View abstract View article PDF

OPEN ACCESS 012118

Design and Simulation of Surface Plasmon Resonance Sensors for Environmental Monitoring

Aseel I Mahmood, Rawa Kh Ibrahim, Aml I Mahmood and Zainab Kh Ibrahim

+ View abstract View article PDF

OPEN ACCESS 012119

Theoretical estimation of Photons flow rate Production in quark gluon interaction at high energies

Hadi J. M. Al-Agealy, Hyder Hamza Hussein and Saba Mustafa Hussein

+ View abstract View article PDF

OPEN ACCESS 012120

Influence of Temperature on Nanosecond Pulse Amplification in Thulium Doped Fiber Lasers

Ali Abdulfattah, Stefan Gausmann, Alex Sincore, Joshua Bradford, Nathan Bodnar, Justin Cook, Lawrence Shah and Martin Richardson

+ View abstract View article PDF

OPEN ACCESS 012121

Antibacterial Activity Of ternary semiconductor compounds AgInSe2 Nanoparticles Synthesized by Simple Chemical Method

A A Shehab, S A Fadaam, A N Abd and M H Mustafa

+ View abstract View article PDF

OPEN ACCESS 012122

Theoretical Discussion of Electron Transport Rate Constant at TCNQ / Ge and TiO_2 System

Hadi J M Al-agealy, B Alshafaay, Mohsin A Hassooni, Ahmed M Ashwiekh, Abbas K Sadoon, Raad H Majeed, Rawnaq Q Ghadhban and Shatha H Mahdi

+ View abstract View article PDF

OPEN ACCESS 012123

Hiding Information Using different lighting Color images

Ahlam Majead, Rash Awad and Salema S Salman

+ View abstract View article PDF

OPEN ACCESS 012124

Enhance Video Film using Retnix method

Rasha Awad, Ali A. Al-Zuky, Anwar H. Al-Saleh and Haidar J. Mohamad

+ View abstract View article PDF

OPEN ACCESS 012125

Structural properties different between two types of PE subjected to heat treatment

May Abdul Sattar Mohammed Najeeb, Kareem.A. Jasim and Dr. Nabil.N. Rammo

+ View abstract View article PDF

OPEN ACCESS 012126

Investigation of Corrosion Protection in Oil Mineral Reservoirs by Nanocomposites Used as Coating Layers

Abdulhameed R Al-Sarraf and Samer A Al-Saaidi

+ View abstract View article PDF

OPEN ACCESS 012127

The effect of replaced recycled glass on thermal conductivity and compression properties of cement

A S khalil, M A Mahmoud, A AL-Hathal, M K Jawad and B M Mozahim

+ View abstract View article PDF

OPEN ACCESS 012128

Utilizing Laser-Induced Breakdown Spectroscopy Method to recognize chemical composition of low-carbon steel in $NH_3(NO)_4$ material

Nissan Saud Oraibi

+ View abstract View article PDF

OPEN ACCESS 012129

The role of Tin Oxide Concentration on The X-ray Diffraction, Morphology and Optical Properties of In2O3:SnO2 Thin Films

Bushra A. Hasan and Rusul M. Abdallah

+ View abstract View article PDF

OPEN ACCESS 012130

Performance of Case-Based Reasoning Retrieval Using Classification Based on Associations versus Jcolibri and FreeCBR: A Further Validation Study

Ahmed S. Aljuboori, Frans Coenen, Mohammed Nsaif and David J. Parsons

+ View abstract View article PDF

JOURNAL LINKS

Journal home

Information for organizers

Information for authors

Search for published proceedings

Contact us

Reprint services from Curran Associates

Effects Sprayed Solution of Salicylic Acid to Prevent of Wilt Disease Caused by *Fussarium oxysporium*

Effects Sprayed Solution of Salicylic Acid to Prevent of Wilt Disease Caused by *Fussarium oxysporium*

Dina. Y. M. Yousif*

* Department of Biology., College of Science, Mustansiriyah University. Baghdad-Iraq.

dr.dinayousif33@gmail.com , dr.dinayousif@uomustansiriyah.edu.iq

Abstract.The current search aimed to detective the effect of sprayed solution of salicylic acid on plant and leaves of sweet green pepper (*Capsicum annuum*) for control the pathogen *Fussarium oxysporium* compering with control plant and leaves.Results indicated that, the spray of salicylic acid at concentration 0.5 g/L is effecting the fungal infection through prevent transport fungus *F. oxysporum* to the neighboring green pepper plant. The number of dead green pepper plant after sprayed with solution of salicylic acid and only water they were (4, 6, and 3) (8, 9, and 10) respectively. While the experimental infection of green pepper leaves after inoculated the fungus as local spot by scorching small spots of these leaves with the aid of hot nail. These spots were then exposed to the 0.5 g/L aqueous solution salicylic acid before and after the inoculation of the fungus. The spray of salicylic acid before 24 and 48 hour prevent the development of disease and make a good protection of the mention leaves from infection with this fungus, the diameter of leaves lesion (1,1.5 cm) respectively. while the ability of fungus to grow after 24 and 48 hours from salicylic acid treatment was markedly reduce as compared with control, such treatment show slow growth of pathogen infect.

Key words: Biological control, *Fusarium* wilts, Salicylic acid (SA)

1.Introduction

Fusarium wilt is widespread, which considered one of the most important plant disease**[1]** caused by many forms of the soil-inhabiting pathogenic fungus such as *Fusarium oxysporum* which belongs to class Hyphomycetes **[1,2,3]** consider one of the most important soil-borne plant pathogen (saprophyte). Fusarium wilt, which is also called “yellows”. This self-explanatory name indicates the major symptom of the disease **[2,3,4]**. A deadly vascular wilting syndrome in plants around the world. importance disease, which is particularly severe in countries with warm climate **[5,6]**.

Different managements were used to control this disease **[7,8,9]**. Unfortunately, most these managements have side effect due to the development of resistant strains of pathogens against various chemical fungicides **[10,11,12].**

Salicylic acid is monohydroxybenzoic acid **[13].** It is a natural phenolic compound from White willow (*Salix alba*), that affects a variety of biochemical and molecular events associated with induction of disease resistance **[14,15,16].**That the phenolic compounds present fungitoxic, antibacterial and anti virotical activities **[16,17,18].**

2. Materials & Methods

2.1. Fungi Isolates & Preparation.

F. oxysporum was obtained from my pervious study **[19]**. For preparation fungal inoculum, the isolates of (*F. oxysporum*) Figure (1) were grown on potato dextrose agar (PDA) for 72 hr. at 2 ± 28°C. The inoculum was prepared by flooding the surface of the one agar with10 ml of sterile distilled water and scraping the sporulated aerial mycelium with a loop. The suspensions obtained were used as inoculum in these experiments.

2.2. Plant Preparation.

One and two month old plants of sweet green pepper (*C. annuum*) grown in a row (Cork box), using Peat moss (which sterile by use autoclave at 121 o C for 1 hr. and steam pressure at 15 pound/inch2).

2.3. Preparation Solution of Salicylic acid.

Plants of sweet green pepper (*C. annuum*) were sprayed with solution of salicylic acid at concentration 0.5 gm /L.

2.4 Effect of SA to prevent transport fungus F. oxysporium to plant of sweet green pepper grown in line.

The plant was placed in cork box (90 X 60 cm) contain sterile Peat moss and grown in a row (one after each other), spray the lift line with solution of salicylic acid at concentration 0.5 gm /L, while the right line spray with water only as control treatment. The plant leaved for 24 hr., and then placing inoculum at the converging end of the plant rows. Three replications were made. Kept the treatment in Greenhouse conditions for 2 weeks with irrigation from time to time. In addition to that, record all note about symptom and disease development with count of dead plant 'figure 2'.

2.5 Effect spray SA on Green pepper leaves before and after inoculum with pathogen F. oxysporium

Two month old plants of sweet green pepper (*C.annuum*) scorching a small spots of their leaves with the aid of hot nail. These spots were then spray with 0.5 g/L aqueous solution salicylic acid before and after 24 and 48hr. from inoculated with two drops of inoculum fungus *F. oxysporium* as local spot. Kept the treatments in greenhouse conditions for 10 days with irrigation from time to time.

3. Result & Discussion

When one-month plant of sweet green pepper grown in a row (in a pot) were sprayed with 0.5 g/L solution of salicylic acid the fungal inoculum was placed beside the first plant in the raw. The infection spread in a row slowly to the neighboring plants, whereas in the untreated row the infection spread much faster to the neighboring plant Figure (2A). After one week from inoculum with pathogen (F. oxysporum), were appear on most plants that spray with water only, first noticed on the lower (older) leaves causing the foliage to wilt and turn yellow Figure (2B).

Other disease symptoms which include: vein clearing and leaf epinasty, followed by stunting, the lower leaves, successive, yellowing, progressive wilting, defoliation and, finally, death of the plant **[20,21]**. While, symptoms on root include: weakly, brownish primary and secondary root **[21, 22, 23,24]** as see in 'figure 3'. Disease fungi (*F. oxysporum*) enter through the roots and interfere with the water conducting vessels of the plant. As the infection spreads up into the stems and leaves it restricts water flow causing the foliage to wilt and turn yellow **[20, 22, 23, 24, 25]** as see in 'Figure 3'.

'Figure 4' showed the number of dead green pepper plant after sprayed solution of salicylic acid at 0.5 g/L per each replication. They were: (4, 6, and 3). While showed the number of dead green pepper plant after sprayed with only water, they were: (8, 9, and 10).

Data in 'figure 5' reveal that the leaves of sweet green pepper (*C. annuum*) which treatment with (SA) either before 24 or 48 hr. from inoculum with pathogen (*F. oxysporum*) that reduction of the disease lesion comparing with control .SA prevent growth of the pathogen completely from the first day of treatment and did not show any symptom disease in local spot figure (6). Salicylic acid reduces and prevent growth the pathogen through prevent the metabolism activity of fungus. In addition, the period time before inoculum with pathogen was enough to induced resistance against many necrotic or systemic fungal pathogens in leaves of plants **[33]**. While the diameter of leaves lesion which spray with (SA) either after 24 or 48 hr. from inoculum with *F. oxysporum* were (1,1.5 cm) respectively as seen in 'figure 5'. leaves lesion of sweet green pepper show slow growth of the pathogen and then stopped completely in sixth day as see in 'figure 5'. Growth was observed in the control leaves, the happen development of lesion to success infection after sixth day from start the treatment. There increase in lesion diameter was (2.2 cm). Symptom disease as the following characteristic: brownish soft lesion and start the leaves turn yellow, 'figure 6'.

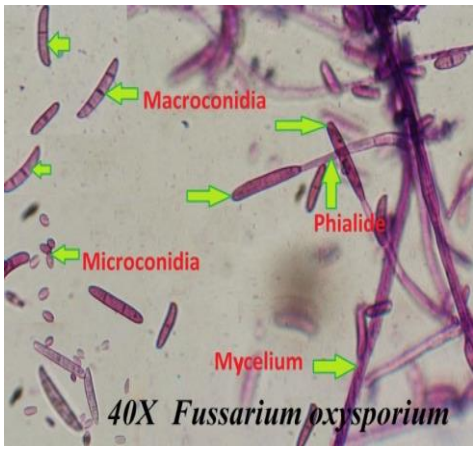

Figure 1. *F. oxysporium* under light microscope 40X show the mycelium and conidia (note macroconidia and microconidia)

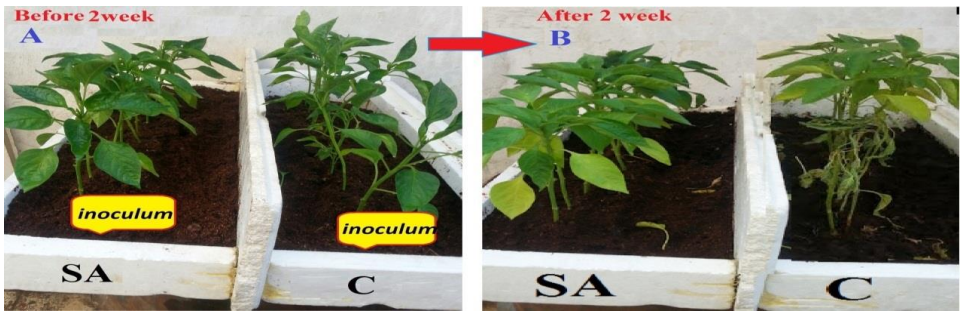

Figure 2. One month old plants of sweet green pepper (*C. annuum*) grown in a row, inoculum with pathogen (*F. oxysporum*),

AS = Spray the lift line with solution of salicylic acid at concentration 0.5 gm /L.
C = Spray the right line with water only.

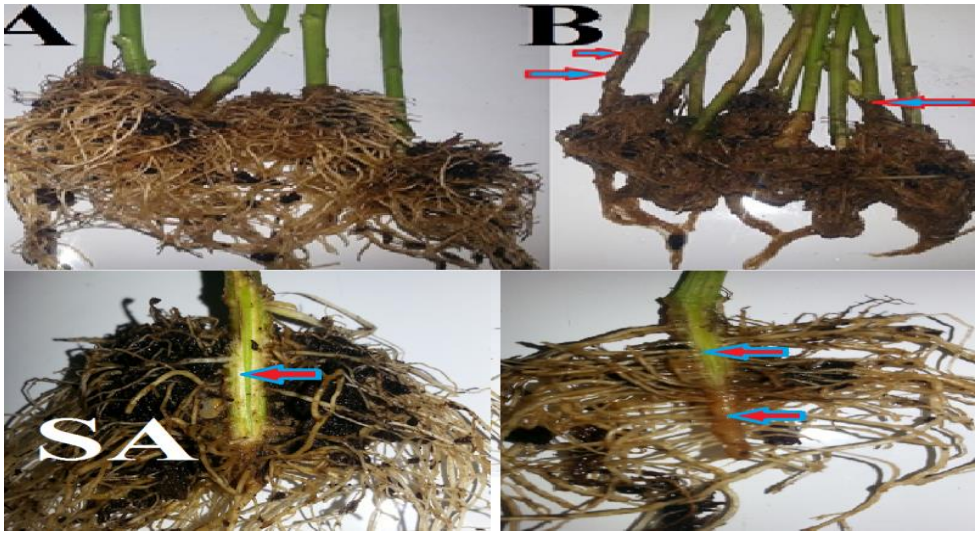

Figure 3. Root plants of sweet green pepper (*C. annuum*), inoculum with pathogen (*F. oxysporum*).

A= Spray with solution of salicylic acid.
B= Spray with water only (note the soft rot root with brownish).

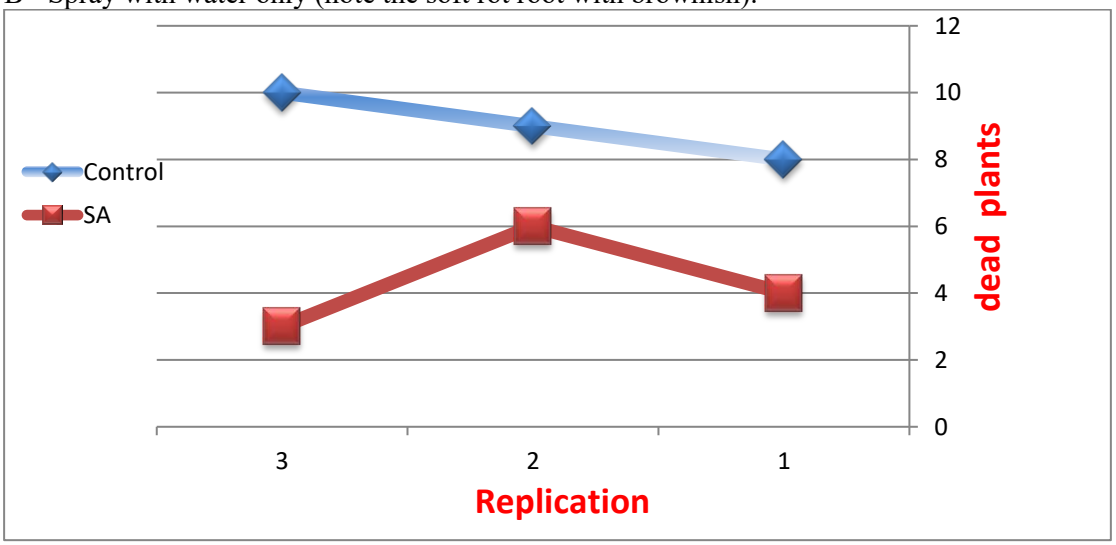

Figure 4. Number of dead green pepper plants.

SA = Spray with solution of salicylic acid and inoculum with pathogen (*F. oxysporum*).
Control = Spray with only water and inoculum with pathogen (*F. oxysporum*).

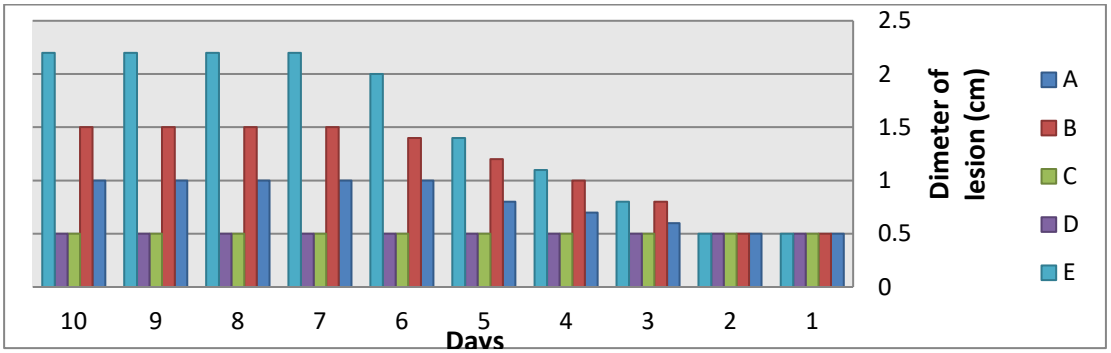

Figure 5. Show the diameter of lesion (cm) by pathogen (*F.oxysporum*) in days.
A = Green pepper leaves inoculum with pathogen after 24hr. spray with (SA).
B = Green pepper leaves inoculum with pathogen after 48 hr. spray with (SA).
C = Green pepper leaves inoculum with pathogen before 24hr. spray with (SA).
D = Green pepper leaves inoculum with pathogen before 48hr. spray with (SA).
E = Inoculum with *F. oxysporium* only (control -).

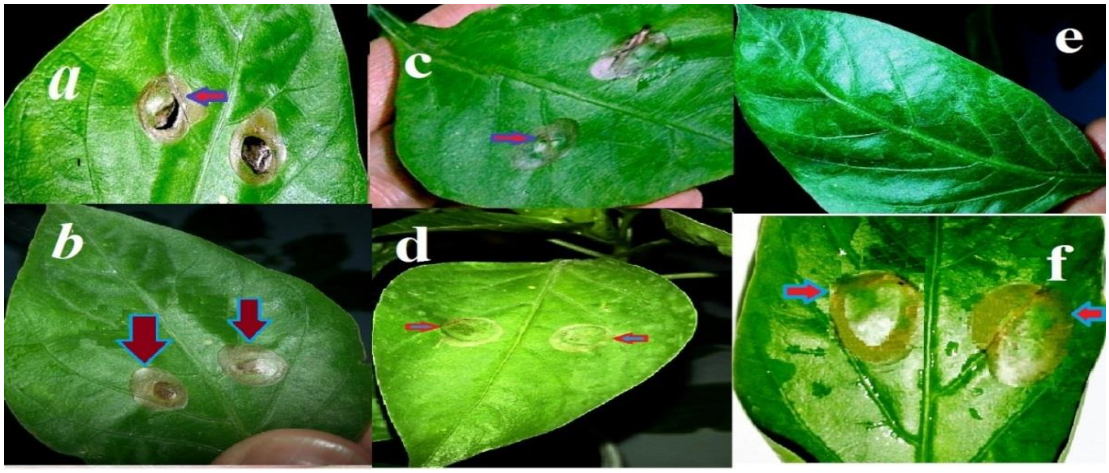

Figure 6. Green pepper leaves with a small spots**.**
a = Spray SA after 24 hr. inoculum with *F. oxysporium.*
b = Spray SA after 48 hr. inoculum with *F. oxysporium.*
c = Spray SA before 24 hr. inoculum with *F. oxysporium.*
d = Spray SA before 48 hr. inoculum with *F. oxysporium.*
e = Spray with water only (control +).
f = Inoculum with *F. oxysporium* only (control -).

Fariduddin *et al*., **[34]** reported that exogenous application of salicylic acid enhanced the net photosynthetic rate, Co2 assimilation and water use efficiency in *Brassica juncea*. Salicylic acid (2-hydroxybenzoic acid) consider as endogenous and exogenous elicitor, plays a crucial role in plant growth and development, and serves as an endogenous signal to activate certain immune responses and to establish disease resistance **[14,16,18]** by induction processes of systemic acquired resistance (SAR) **[26,27].** Various defense-related stimuli have been shown to trigger enhanced SA levels in local and systemic plant tissues. Exogenous application of SA can stimulate particular enzymes catalyzing biosynthetic reactions to produce defense compounds **[28,29]**, and induce reactive oxygen intermediates (ROI) production, pathogenesis-related (PR) gene expression and immunity against various pathogens with bio trophic or hemi bio trophic lifestyles

[29,30,31] .In another words, it's can be affirmed that SA acts in two ways, by inducing resistance in sweet green pepper, and also by the fungitoxic action on the pathogen **[30,31,32]**. SA is known as an antioxidant compound which is involved in prohibition of the activity of reactive oxygen species.

References

[1] Both C. 1977 Fusarium laboratory Guide to the Identification of the Major Species. 1st Ed. Commonwelth. Mycological *Institute*, kew, Surrey England.
[2] Leslie, J. F. and Summerell. B. A. 2006 The *Fusarium* Laboratory Manual. Blackwell, Ames, IA.
[3] Nelson P. E. 1983. Fusarium species. An Ilustrated Manual for Identification. The Penn St. University Press.
[4] Groenewald, S. 1988. Biology, pathogenicity and diversity of *Fusarium oxysporum* f.sp. cubense. University of Pretoria etd. 153: 2-3.
[5] Agrios GN. Plant pathology 5th Ed. Burlington: Elsevier Academic. 2005;922.
[6] Jun ma, L.; Geiser, D.; Proctor, R.; Rooney, A.;Donnell, K.; Trail,F. ;Gardiner, D.; Mnners,J. and Kanzan,K. 2013. *Fusarium* pathogenomics. *Annu.Rev. Microbiol*; 67: 399- 416.
[7] Reid, T. C., Hausbeck, M. K. and Kizilkaya, K. 2002. Use of fungicides and biological control in the suppression of Fusarium crown root rot of asparagus under greenhouse and growth chamber conditions. *Plant Disease*, 86: 493-498.
[8] Abada, K. A. and Ahmed, M. A. 2014. Management Fusarium wilt of sweet pepper by Bacillus strains. *American Journal of Life Sciences* 2 6-2: 19-25
[9] Amini, Jahanshir and Sidovicho, Dzhalilov Fevzi. 2010. The effects of fungicides on *fusarium oxysporum* f. Sp. Lycopersici associated with fusarium wilt of tomato. *Journal of plant protection research* Vol. 50, No. 2: 172-178.
[10] Rajput,abdul qayoom ; arain, m. H; pathan, m. A. ; jiskani, m. M. And lodhi, a. M. 2006. Efficacy of different fungicides against fusarium wilt of cotton caused by *Fusarium oxysporum f. Sp. Vasinfectum*. Pak. *J. Bot*. Vol. 38, Issue 3: 875-880.
[11] Gnanamanickam, S.S. 2002 Biological Control of Crop Diseases. New York. Basel: *Marcel Dekker,* Inc.; 158.
[12] Ahmed. S. Dwaish, Dina. Y. M. Yousif and Siham. N. Lefta (2016). "Use of Spirogyra Sp. Extract Against Multidrug Resistant Bacterial Pathogens." *International Journal of Advanced Research*, Volume 4, Issue 7, 575-579.
[13] Arberg, B. 1981. Plant growth regulators. Monosubstituted benzoic acid. Swedish Agriculture Research, 11, 93–105
[14] Chandra, A., & Bhatt, R. K. 1998. Biochemical and physiological response to salicylic acid in relation to the systemic acquired resistance. *Photosynthetica,* 35, 255–258
[15] Fariduddin Q, Hayat S, Ahmad A. 2003 Salicylic acid influences net photosynthetic rate, carboxylation efficiency, nitrate reductase activity and seed yield in Brassica juncea. *Photosynthetica.* 41: 281–284.
[16] Hayat Q, Hayat S, Irfan M. Ahmad A. 2010 Effect of exogenous salicylic acid under changing environment: A review. *Environmental and Experimental Botany* 6: 14-25.
[17] Hayat S, Fariduddin Q, Ali B, Ahmad A. 2007 Effect of salicylic acid on growth and enzyme activities of wheat seedlings. *Acta Agron*. Hung 53:433–437.
[18] Eraslan F, Inal A, Gunes A, Alpaslan M. Impact of exogenous salicylic acid on growth, antioxidant activity and physiology of carrot plants subjected to combined salinity and boron toxicity. *Sci. Hort.* 113: 120-128.

[19] Yousif, Dina. Y. M.; Dwiash, Ahmed. S. and Shafiq, Shatha Ali. 2015. Antifungal activity of algal spirogyra sp. Against fungal *Fusarium oxysporum. World Journal of Pharmaceutical Research.* Volume 4, Issue 1, 1620-1628.
[20] Fletcher, J. T. 1994. *Fusarium* stem and fruit rot of sweet peppers in the glass house. *Plant Pathology,* 43: 225-227

Seroprevalence occurrence of viral hepatitis and HIV among hemodialysis patients

Seroprevalence occurrence of viral hepatitis and HIV among hemodialysis patients

Inass Mahmood Kamal[1], Batool Mutar Mahdi[2]

[1]AlKindy Teaching Hospital [2]Consultant ImmunologistDirector of HLA research Unit AlKindy College of MedicineUniversity of Baghdad

abas_susan@yahoo.com

Abstract. Patients with chronic renal failure (CRF) were on maintenance invasive haemodialysis (HD) procedure This procedure by itself affects immunity of the patients and became more susceptible to viral infections to investigate the occurrence of HBV HCV and HIV infections in patients with hemodialysis A retrospective study of 430 end stage renal failure patients referred to hemodialysis department at Al-Kindy Teaching Hospital BaghdadIraq from January 2015 to January 2017 Patients were investigated for HBsAg using enzymelabeled antigen test (ForesightEIAUSA) HCV Abs (IgG) specific immunoglobulin using a HCV enzymelabeled antigen test (ForesightEIA USA) and anti HIV Abs (IgG) using enzymelabeled antigen test (ForesightEIA USA). The frequency of HBV infection in the first year was not significant between males (111%) and females (000%) (P= 0295). About HCV also there are no significant differences between males (1263%) and females (931%) (P=0347) After one year of follow up the frequencies of HBV and HCV were not significant between two sexes. Additionally no any one of the patients had HIV infection. This study brings a light on that HBV and HCV were having the same frequencies in both genders and lower occurrence with time Furthermore HIV was not detected in those patients.

Key words virus, haemodialysis, infection.

1 Introduction

One of the treatments of chronic renal failure (CRF) is maintenance invasive hemodialysis (HD) procedure This procedure by itself affects innate immunity like changes in chemotactic factor for leukocytes phagocytic function of neutrophils and monocytes and natural killer cell (1, 2 and 3) Moreover adaptive immunity is affected for example defect in proliferation of T lymphocytes and down regulation of phosphorylation pathways of lymphocytes (4, 5 and 6) Therefore HD patients are more susceptible to blood born viral infection like hepatitis B virus (HBV) hepatitis C virus (HCV) and Human immunodeficiency virus (HIV) due to disturbance in immune system (7).

Infection with these viruses is the main reason of morbidity in HD patients However precautions' must be taken to prevent disseminations of viruses in the unit like available treatments and vaccines (8) In USA after acquiring viruses like HBV in HD patients 60% of them become chronic carriers while in the general population was 5% of them became chronic carrier (9) A study showed that chronic HBV infection had a relation with mortality (10) Additionally there are 170 million hepatitis C virus carriers

worldwide and one of the risk group is HD patients and the risk of death was 157 times more than others in association with liver cirrhosis and hepatocellular carcinoma (1112).

Subsequently infection of liver with viruses was fatal for patients on HD and constitutes 19% of all deaths (13) Additional virus that is important in HD patients is HIV The prognosis of this virus was changed significantly due to administration of Highly Active AntiRetroviral Therapy (HAART) stage of HIV disease at time of dialysis start and T helper (CD4+) lymphocyte count (14, 15 and 16).

The goal of the present study is to investigate the occurrence of viral infection like HBV HCV and HIV in patients with the end stage renal failure on hemodialysis.

2 Patients and methods

A retrospective study of 430 end stage renal failure patients referred to hemodialysis unit of Al-Kindy Teaching Hospital Baghdad Iraq from January 2015 to January 2017 All patients were subject to the process of hemodialysis

Hemodialysis patients were a case for the study if their serum tested positive for HBV HCV and HIV in contrast the patients receiving hemodialysis were considered as a control if their serum tested negative for those three viruses for every case one age and gendermatched control receiving haemodialysis was selected.

The Broad of Medical Ethics has been approved for these patients and accepted their review of Al-Kindy College of Medicine and Al-Kindy Teaching Hospital The knowledgeable permission was obtained from patients Data collected from both groups including demographic information age sex marital status occupation residential status onset of renal failure and hemodialysis history.

Serological testing A 430 patients were investigated for HBsAg using enzymelabeled antigen test (ForesightEIAUSA) HCV Abs (IgG) specific immunoglobulin using a HCV enzymelabeled antigen test (ForesightEIAUSA) and anti HIV Abs (IgG) using enzymelabeled antigen test (ForesightEIA USA) The principle for detection antibodies in the serum are illustrated as follows using leaflet kit.

The microwells are coated with Ags then the serum will be added that contains Abs lead to formation a complex After incubation washing was done and enzyme conjugated with Abs was added After incubation and washing were done substrate A and B were added The color was formed and the reaction was stopped by sulfuric acid The results were interpreted after reading with micro plate reader at 450nm within 30 minutes Samples with optical density below the cutoff were recorded as negative those with optical densities (< 10% > 10%) of the cutoff were equivocal and all others were positive The sample was retested when the absorbance was within 10% of the cutoff level.

Statistical analysis

- Data were analyzed statistically using
- Descriptive statistics frequencies mean and standard deviation
- Inferential statistics Chisquare tests and fisher exact test

All of these were done using Mini Tab statistical software program 1320 A P value $\leq$ 005 was considered to be significant

3 Results

A total of 430 patients with chronic kidney disease (renal failure) were on hemodialysis during the study period The proportion of males 269 (6255%) was more than that of female 161(3744%). Their ages ranged from 16 to 76 years (median=35) (312 ±080). The frequency of HBV infection in the first year was not significant between males (111%) and females (000%) (P= 295) as shown in Table 1. About HCV also there is no a significant difference between males (1263%) and females (931%)(P=0347). After one year of follow up the frequency of HBV and HCV was also not significant between two sexes as was reported in (Table 2) HIV was not affecting any of HD patients There was a

significant reduce in the frequency of infection with HCV while occurrence of HBV was not changed (Table3).

Table1 Frequency of viral infection in patients in the first year of hemodialysis

Viral markers	HD Patients positive for the viruses males		HD Patients negative for the viruses Males		HD Patients positive for the viruses females		HD Patients negative for the viruses Females		P value
	No	%	No	%	No	%	No	%	
HBsAg	3	111	266	9888	0	0	161	100	0295*
Anti HCV Abs	34	1263	235	8736	15	931	146	9068	0347*
Anti HIV Abs	0	0	0	0	0	0	0	0	

Not significant

Table 2 Frequency of viral infection in patients in the second year of haemodialysis

Viral markers	HD Patients positive for the viruses males		HD Patients negative for the viruses Males		HD Patients positive for the viruses females		HD Patients negative for the viruses Females		P value
	No	%	No	%	No	%	No	%	
HBsAg	0	0	269	100	0	0	161	100	100*
Anti HCV Abs	15	557	254	9442	9	559	152	944	100*
Anti HIV Abs	0	0	0	0	0	0	0	0	

Not significant

Table 3 Comparison of viral infection in hemodialysis patients in two years of follow up

Viral markers	HD Patients positive for the viruses 2015		HD Patients positive for the viruses 2016		P value
	No	%	No	%	
HBsAg	3	0697	0	0	0248*
Anti HCV Abs	49	1139	24	558	0002
Anti HIV Abs	0	0	0	0	

Not significant

4 Discussion

Chronic renal failure patients receiving hemodialysis are often acquiring blood borne viral infection over their long treatment period like HBV HCV and HIV. In our study HD patients had HBV and HCV infection and after follow them the percentage of HBV decreased Additionally HCV still in the same percentage. There was no significant difference regarding gender in the frequency of these viruses. There was a significant reduce in the frequency of infection with HCV table3 with time. A study done in Canada demonstrated that two patients (08%) were positive for HBsAg and 9 (38%) had viral HB DNA by PCR (17). This is in agreement with our study (11%) in 2015 and then (00%) in 2016, therefore, the molecular investigation that detects HBVDNA using nested PCR is helpful for patients with antiHB core Ab positive negative for HBsAg and antiHBs Abs (18). It is recommended to analayze HBVDNA annually and biopsy from liver (19) Additional study done in Madhav Nagar city reported that the frequency of HBV and HCV infections in HD patients was 152% and 111% respectively (20, 21). In India the occurrences of HBV were 34% to 42% which is higher than found in our study (22, 23). The lower occurrence of HBV in this study may be caused by sample size method used for detection the virus less blood transfusion and blood products for the patients and screening of blood for bloodborne viral infections before transfusion. The availability of erythropoietin leads to lowering blood transfusion times to the patients. The only three patients with HBsAg positive were treated and recover from the disease Consequently HBV did not detect after one year of follow Management patients with HBV vaccine separation of infected patient on separate machine and habitual surveillance for HBV infected patients in the hospitals leads to lower rates of infection with HBV.

Regarding the frequency of HCV infection was higher than HBV in our study while other studies reported less prevalence of HCV infection in HD patients like Spain (24) and Brazil (25). This may be due to sample size method of detection and screening blood for antibodies against HCV with control measures in hospitals Double infection with two viruses (HBV and HCV) in same patient were not detected in our study while in other studies were 44 %(26, 27). The lower number of the patients who were positive for anti HCV after one year of follow-up was due to their deaths.

About HIV infection there were no cases of this virus in HD patients in our study due to control measures of this disease. The prevalence of this virus varies in different countries depending on district of the countries (28, 29) Within USA about 1% 0f HD patients had HIV due to HIV associated nephropathy (30) HD patients should be investigated by ELISA Western blot and serum HIVRNA for positive cases. The prognosis of HIV infected HD patients has considerably better by using Highly Active AntiRetroviral Therapy (HAART)(31) stage of HIV disease at initiation of dialysis (32) and The CD4+T helper count (33) Infections with these viruses are important cause of death following cardiovascular diseases in HD patients Thus many safety measures must do to limit the dissemination of these viruses (34) There is a need for treatment of HCV endstage renal disease patients and sustained systematic immunization campaigns for HBV infection (35) Investigating hemodialysis patients for antiHBc is important to show latent HBV infection (36) Thus early vaccination and better nutritional conditions improves antiHBV response (37).

5 Conclusions

This study brings a light on that HBV and HCV infections were in the same in both genders though less common with time HIV was not detected in HD patients.

References

[1] Lewis SL, Van Epps DE, Chenoweth DE, 1988, “Alterations in chemotactic factorinduced responses of neutrophils and monocytes from chronic dialysis patients” Clin Nephrol, 30, 63 72

[2] Muniz Junqueira MI, Braga Lopes C, Magalhaes CA, Schleicher CC, Veiga JP, 2005, “Acute and chronic influence of hemodialysis according to the membrane used on phagocytic function

of neutrophils and monocytes and proinflammatory cytokines production in chronic renal failure patients" Life Sci., **77,** 3141 3155

[3] Eleftheriadis T, Kartsios C, Yiannaki E, Kazila P, Antoniadi G, Liakopoulos V, et al, 2008, Chronic inflammation and CD16 natural killer cell zetachain down regulation in hemodialysis patientsBlood Purif, 26**,** 317 321

[4] Eleftheriadis T, Papazisis K, Kortsaris A, Vayonas G, Voyatzi SVargemezis V, 2004, Impaired T cell proliferation and zeta chain phosphorylation after stimulation with staphylococcal enterotoxinB in hemodialysis patients Nephron Clin Pract, 96, 15 20

[5] Eleftheriadis T, Antoniadi G, Liakopoulos V, Kartsios C, Stefanidis I, 2007, Disturbances of acquired immunity in hemodialysis patients, Semin Dial, 20**,** 440 451

[6] Eleftheriadis T, Kartsios C, Yiannaki E, Kazila P, Antoniadi G, Liakopoulos V, et al, 2008, Chronic inflammation and T cell zetachain downregulation in hemodialysis patients, *Am J Nephrol,* **28,** 152 157

[7] Abumwais JQ, Idris OF, 2010, Prevalence of hepatitis C hepatitis B and HIV infection among haemodialysis patients in Jenin District (Palestine), *Iranian Journal of Virology,* **4,** 38 44

[8] Kausz A, Pahari D, 2004, The value of vaccination in chronic kidney disease, Semin Dial, 17 911

[9] Szmuness W, Prince AM, Grady GF, Mann MK, Levine RW, Friedman EA et al 1974 Hepatitis B infection A pointprevalence study in 15 US hemodialysis centers *JAMA,* 227**,** 901-906

[10] Fabrizi F, Martin P, Dixit V, Kanwal F, Dulai G, 2005, HBsAg seropositive status and survival after renal transplantation metaanalysis of observational studies, *Am J Transplant,* **5,** 2913 2921

[11] Yen T, Keeffe EB, Ahmed A, 2003, The epidemiology of hepatitis C virus infection, *J Clin Gastroenterol,* 36**,** 47 53

[12] Fabrizi F, Martin P, Dixit V, Bunnapradist S, Dulai G, 2004, MetaanalysisEffect of hepatitis C virus infection on mortality in dialysis Aliment, Pharmacol Ther, 20**,** 1271 1277

[13] Aghakhani A, Banifazl M, Eslamifar A, Ahmadi F, and Ramezani A, 2012, Viral hepatitis and HIV infection in hemodialysis patients Hepatitis Monthly, 12**,** 463 464

[14] Ahuja TS, Borucki M, Grady J, 2000, Highly active antiretroviral therapy improves survival of HIVinfected hemodialysis patients, *Am J Kidney* Dis, 36**,** 574 580

[15] Ortiz C, Meneses R, Jaffe D, Fernandez JA, Perez G, Bourgoignie JJ, 1988, Outcome of patients with human immunodeficiency virus on maintenance hemodialysis Kidney, *Int,* 34**,** 248253

[16] Perinbasekar S, BrodMiller C, Pal S, Mattana J, 1996, Predictors of survival in HIVinfected patients on hemodialysis, *Am J Nephrol,* **16,** 280 286

[17] Minuk GY, Sun DF, Greenberg R, Zhang M, Hawkins K, Uhanova J, et al, 2004, Occult hepatitis B virus infection in a North American adult hemodialysis patient population Hepatology, **40,** 1072 1077

[18] Hui CK, Sun J, Au WY, Lie AK, Yueng YH, Zhang HY, et al, 2005, Occult hepatitis B virus infection in hematopoietic stem cell donors in a hepatitis B virus endemic, *area J Hepatol,* 42**,** 813 819

[19] Ozdogan M, Ozgur O, Gur G Boyacioglu S, Ozderin Y, Demirhan B, et al, 1997, Histopathological impacts of hepatitis virus infection in hemodialysis patients should liver biopsy be performed before renal transplantation Artif Organs, 21**,** 355 358

[20] Otedo AEO, Mc'Ligeyo SO, Okoth FA, and Kayima JK, 2003, Seroprevalence of hepatitis B and C in maintenance dialysis in a public hospital in a developing country, *South African Medical Journal,* **93,** 380 384

[21] Busek SU, Bab´a EH, Tavares Filho HA, et al, 2002, Hepatitis C and hepatitis B virus infection in different hemodialysis units in Belo Horizonte Minas Gerais Brazil Memorias do Instituto Oswaldo Cruz, 97**,** 775 778

[22] Agarwal SK, Dash SC, and Irshad M, 1999, Hepatitis C virus infection during haemodialysis in, India *Journal of Association of Physicians of India,* 47**,** 1139 1143

[23] Saha D, and Agarwal SK, 2001, Hepatitis and HIV infection during haemodialysis, *Journal of the Indian Medical Association*, **99,** 194 199
[24] Espinosa M, Mart´ınMalo A, Ojeda R, et al, 2004, Marked reduction in the prevalence of hepatitis C virus infection in hemodialysis patients causes and consequences, *American Journal of Kidney Diseases,* 43**,** 685 689
[25] Carneiro MAS, Teles SA, Dias MA, et al, 2005, Decline of hepatitis C infection in hemodialysis patients in Central Brazil a ten years of surveillanceMemorias do Instituto Oswaldo Cruz, **100,** 345 349
[26] Kosaraju K, Faujdar SS, Singh A, and Prabhu R, 2013, Hepatitis Viruses in Heamodialysis Patients an Added Insult to Injury Hepatitis Research and Treatment, **14.**
[27] Reddy GA, Dakshinamurthy KV, Neelaprasad P, Gangadhar T, and Lakshmi V, 2005, Prevalence of HBV and HCV dual infection in patients on haemodialysis, *Indian Journal of Medical Microbiology,* **23,** 41 43
[28] Perez G, OrtizInterian C, Lee H, de Medina M, Cerney M, Allain JP, et al, 1989, Human immunodeficiency virus and human Tcell leukemia virus type I in patients undergoing maintenance hemodialysis in Miami, *Am J Kidney Dis*, 14**,** 39 43
[29] Vigneau C, GuiardSchmid JB, Tourret J, Flahault A, Rozenbaum W, Pialoux G, et al, 2005, The clinical characteristics of HIV infected patients receiving dialysis in France between 1997 and 2002, Kidney *Int,* 67**,** 1509 1514
[30] Eggers PW, Kimmel PL, 2004, Is there an epidemic of HIV Infection in the US ESRD program? *J. Am Soc Nephrol,* 15**,** 2477 2485
[31] Ahuja TS, Borucki M, Grady J, 2000, Highly active antiretroviral therapy improves survival of HIVinfected hemodialysis patients, *Am J. Kidney Dis.*, 36**,** 574 580
[32] Ortiz C, Meneses R, Jaffe D, Fernandez JA, Perez G, Bourgoignie JJ, 1988, Outcome of patients with human immunodeficiency virus on maintenance hemodialysis, Kidney *Int,* **34,** 248 253
[33] Perinbasekar S, BrodMiller C, Pal S, Mattana J, 1996, Predictors of survival in HIVinfected patients on hemodialysis, *Am J Nephrol,* **16,** 280 286
[34] Eleftheriadis T, Liakopoulos V, Leivaditis K, Antoniadi G, Stefanidis I, 2011, Infections in hemodialysis a concise review Part II blood transmitted viral infections Hippokratia, **15,** 120 126
[35] Isnard Bagnis C, Couchoud C, Bowens M, Sarraj A, Deray G, Tourret J, Cacoub P, Tezenas, 2017, du Montcel S Epidemiology update for hepatitis C virus and hepatitis B virus in endstage renal disease in France Liver, *Int* , **37,** 820 826
[36] Ayatollahi J, Jahanabadi S, Sharifyazdi M, Hemayati R, Vakili M, Shahcheraghi SH, 2016, The Prevalence of Occult Hepatitis B Virus in the Hemodialysis Patients in Yazd Iran, Acta Med Iran, **54,** 784 787
[37] Cordova E, Miglia I, Festuccia F, Sarlo MG, Scornavacca G, Punzo G, Menè P, Fofi C, Hepatitis B 2017 vaccination in haemodialysis patients an underestimated problem Factors influencing immune responses in ten years of observation in an Italian haemodialysis centre and literature review, Ann Ig, 292 737

Seasonal abundance of eggplant leafminer Liriomyza sativae (Blanchard, 1938) (Diptera, Agromyzidae) in plastic-house

Seasonal abundance of eggplant leafminer Liriomyza sativae (Blanchard, 1938) (Diptera, Agromyzidae) in plastic-house

S A Kathiar[1], S K. Flaih[2], H I Al-Khazraji[2], S K Ismael[2]

[1]Biology Department, College of Science for Women, University of Baghdad
[2]Plant Protection Department, College of Agriculture, University of Baghdad

Abstract. The eggplant Solanum melongena L. crop is attacked by one of the most common pests which is the leafminer Liriomyza sativae (Blanchard, 1938); therefore, this investigation was conducted to study the seasonal abundance of the eggplant leafminer in eggplant Plastic-house. The results showed that the highest average of infested leaves was 6.67 leaf, the highest average of tunnels by leaf miner was 9.87 tunnels and the highest percent of infestation was recorded 30.5% in 23. April.2017. This study showed the parasitoid Diglyphus isaea (Walker, 1838) (Hymenoptera, Eulophidae) was recorded as a natural enemy to control the pest and the highest incidence of parasitism was 32.2 parasites on average in 16. April. 2017.

1. Introduction

Eggplant S. melongena L. is an important and main agricultural crop that belongs to the Solanaceae family; it contains more than 1400 species that grow on all continents except Antarctica [1]. The family Solanaceae includes tomato, potato, tobacco, and petunia, and contains economically important species, because it is a food source such as potato, tomato or pharmaceutical important or ornamental plants [2]; the eggplant found as a wild crop in India and then distributed to other countries [3] and attacks by many pests, such as: mites, aphids, whiteflies and leafminers [4].

The leafminers are a well-known group of small and similar to flies in morphological features. There are about ten thousand species of leaf miners belong to insect orders, such as, Coleoptera, Diptera, Lepidoptera, and Hymenoptera [5]. The damage by leafminer pests is caused by both larvae and adults; adult females puncture the leaf epidermis with their ovipositor to feed and lay eggs, while larvae mine the palisade mesophyll and consumed the parenchyma tissue 'figure 1' thereby disrupting photosynthesis and cause falling the leaves causing bacteria and fungi attraction [6].

The plant leaves are more attractive to the adult females oviposition and the lower leaf surface is more infested than the upper surface [7]; the control of this pest generally is complicated because of protected habit of leafminers larvae [8]. All Agromyzid species have a very similar lifecycle [9]; in Iran, the study by [10] who reported that the adult of this insect takes eight days, egg stage takes six days, larval stage takes four days with three instars, pupa stage takes from two to seven days till two months depending on the environmental conditions. The duration of each generation is 18-25 days. There are five species belonging to five genera under three families, the parasitoids are: Digylphus isaea (Walker, 1838), Pediobius metallicus (Nees, 1834), Cirrospilus vittatus (Walker, 1838), and Halticoptera circulus (Walker, 1838) of Agromyza [11]; at least 114 species have been recorded as leafminers in Australia [12].

Due to a few studies of leaf miners in Iraq, therefore, the purpose of this study was to evaluate the biological outcomes of leaf miner Agromyza sp. On eggplant leaves in glasshouses.

Figure 1. The damges of eggplant leaves by leafminer

2. Materials and Methods

2.*1 Study area*

The present study was conducted in the plastic house of the College of Agriculture/ University of Baghdad, Iraq during the spring planting season for the period of March to May 2017; in order to study the biological aspects of leafminer on eggplants, the Hagen AL-Mustakabel variety of eggplant was planted in glasshouse (5 m wide x 36 m length x 3 m high) in ten lines and as a five split plots, the space between each plant and other was 70 cm.

2.2 Insect collection

The average of the number of the total leaves per plant, average of infested leaves per plant, average numbers of tunnels per leaf and infestation percentages during months were counted from 19.March.2017 to 28.May.2017. In order to identify the leafminer species, the five eggplant leaf samples were chosen randomly and kept in plastic cases with all information (date and plant length) and took to the laboratory in order to get the parasites that preserved in 70% alcohol to send to the Natural History Research Center and Museum/ University of Baghdad for the purpose of identification.

3. Results and Discussion

The data that presented in (table 1) showed that the highest average of the total number of leaves of eggplant plants 55.33 leaves/plant was counted in 21. May. 2017; while the lowest average of the total number of leaves of eggplant plants 5.20 leaves/plant was counted at the beginning of the growth season in 19. March. 2017 then increase to 7.53 leaves/plant at the beginning of April until the end of April reached to 21 leaves/plant.

The first infestation of leaf miner was recorded at the beginning of growth season and the results were low 0. 3 infested leaves/plant. Later, numbers of infested leaves were increased until it reached its peak 6.67leaves/plant in 23. April. 2017 with significant differences between months. The results also showed that the lowest number of tunnels was 0.67 in 19. March. 2017 then increased to the highest (9.87) in 23. April. 2017. These results are consistent with a study by Flaih [13] who found that the infested leaves by leaf miner and the average number of tunnels per leaf increased gradually then reached the highest when cucumber plant growth reached their the maximum.

The results in 'figure 2' showed that the infestation percentage of eggplant by leafminer *L. sativae*; the highest was 30.5% in 23. April. 2017, while the lowest 2.2% that recorded in 28. May. 2017.

Many important economic crops in the world are often attacked by leafminer that can cause significant yield losses; for example, the *L. sativae* reduce tomato and onion crops production by 80% In Florida [14]; in another investigation the L. sativae reduce tomato production by 70%. Leafminer control with the natural wasp parasitoides, including, *Diglyphus isaea* (Walker), *Diglyphus crassinervis* (Erdös), *Pediobius metallicus* (Nees), *Neohcrysocharis formsa* (Westwood), *Cirrospilus*

vittatus Walker, *Halticoptera circulus* (Walker), *Opius sp*. and *Ratzeburgiola incomplete* Boucek [15, 16].

The highest percentage of parasitism of the parasite Diglyphus isaea on leafminer L. sativae was 32.2% in 16. April. 2017, while the lowest percentage of parasitism was 2.5% in the begning of the study 19. March. 2017 'figure 3'. These results are consistent with a study [17]; in this investigation, the highest percentage of parasitim of Neohcrysocharis formsa on weed leafminer Phytomyza horticola was35%

Table 1. The averages of total number of leaves per plant, average infested leaves per plant and average numbers of tunnels per plant during study period

Date	Average of total number of leaves/plant	Average of infested leaves/plant	Average number of tunnels/leaf
19/03/2017	5.20	0.30	0.67
26/03/2017	6.27	0.67	1.13
02/04/2017	7.53	1.33	3.73
09/04/2017	8.27	1.33	7.00
16/04/2017	10.60	1.47	8.80
23/04/2017	15.87	6.67	9.87
30/04/2017	21.00	5.00	8.00
07/05/2017	32.33	2.00	8.20
14/05/2017	44.93	3.67	5.93
21/05/2017	55.33	1.33	3.40
28/05/2017	54.80	1.27	0.93
L.S.D	4.70	2.55	1.03

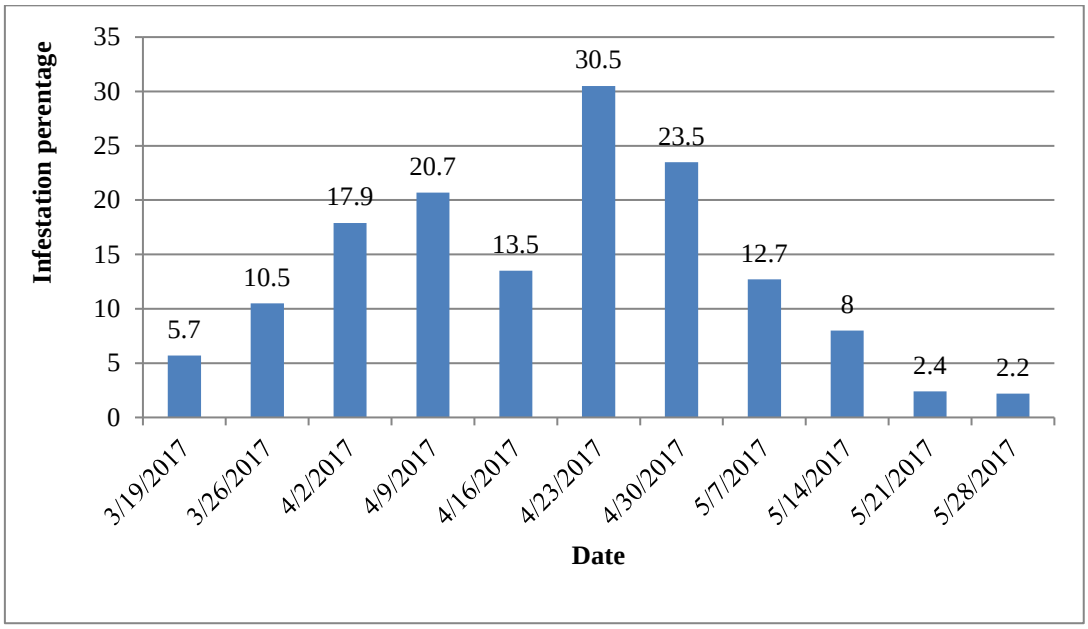

Figure 2. The infestation percentages of eggplant leave by leaf miner L. sativae.

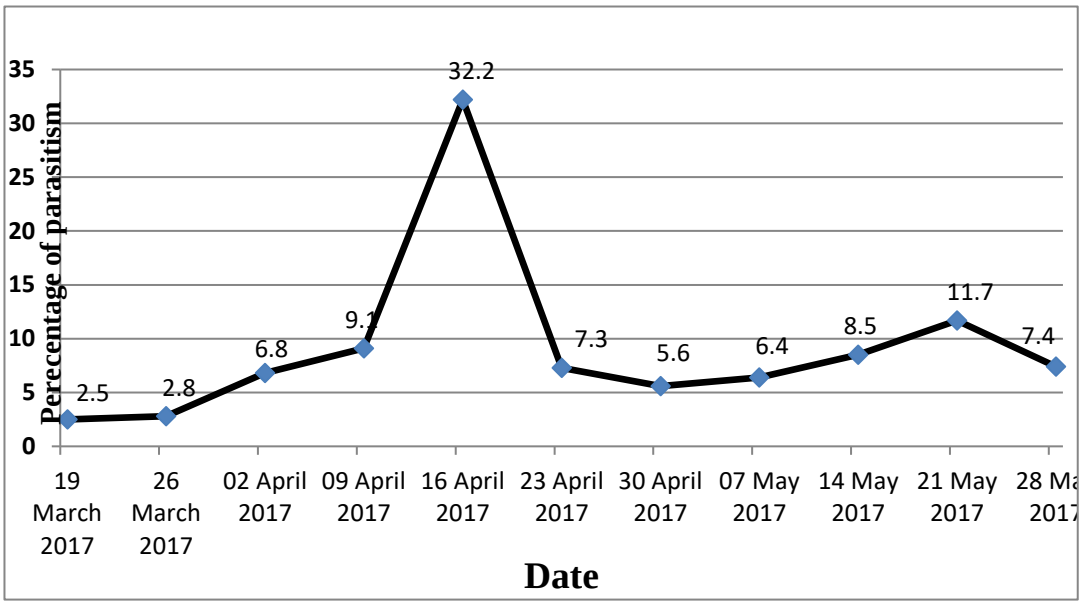

Figure 3. The percentage of parasitism of the parasite Diglyphus isaea on leafminer L. sativae.

References

[1] Frodin D Taxon 2004 **5** pp753-776
[2] Dias G B, Gomes V M and Cunha M D 2013 *Genet. Mol. Res.* **12** pp 6488-6501
[3] Isshiki S, Okuba H and Fujieda K 1994 *Sci. Hort.* **59** pp 171-176
[4] Al-Azzawi A F, Qadu I K and Al-Haidari S 1990 Dar El Hekma for Printing & Publishing 680.
[5] Hespenheide H A 1991 *Annu. Rev. Entomol* **36** pp 535-560
[6] Parella M P, Jones V P, Youngman R R and Lebeck L 1985 Ann. Entomol. Soc. Am.**78** pp 90-93
[7] Salama H S, Ismail I A, Fouda M, Ebadah I and Shehata I 2015 Ecologia Balkanica **7** 2 pp 35-44
[8] Banchio E, Valladares G, Defag M, and Carpinella C. 2003 Ann. appl. Biol. **14** 3 pp 187-193
[9] Ridland P and Malipatil M 2008 Plant Health Australia
[10] Changizi S, Goldasteh Sh, R, Changizi M and Modarres S. 2012 Ent. Zool. **7** 1 pp 474-480
[11] Al Saffar H H 2016 *Int. J. Curr.Microbiol.App.Sci*. **5** 5 pp 742-747
[12] Sinclair R J and Hughes L 2010 Austral Ecol. **35** 3 pp 300-313
[13] Flaih S K 2016 *J. Basic Edu*. **22** 93 pp 29-36.
[14] CABI. Invasive Species Compendium. www.cabi.org. 2017
[15] Mujica N D, Alvites P and Kroschel J 2017 International Potato Center
[16] Abdul R M, Al Saffar H H 2014 *Int. J. Curr. Microbiol. App. Sci*, **3** pp 618-624
[17] Flaih S K 2009 *Iraqi J. Agri. Sci.* pp 76-81

The study of Bacteriocin of Pseudomonas fluorescens and Citrus limon effects against Propionibacterium acnes and Staphylococcus epidermidis in acne patients

The study of Bacteriocin of *Pseudomonas fluorescens* and *Citrus limon* Effects against *Propionibacterium acnes* and *Staphylococcus epidermidis* in acne patients

Mais E. Ahmed
College of Science / University of Baghdad
mais.e.mahmood@gmail.com

Abstract

Research was carried out antibacterial of (Citrus limon) juice on Acnevulgaris. Samples were obtained from individuals having (Pimples) by swabbing their faces. Substances natural from plants are promising to treat disease cause Acnevulgaris, the study in vitro biological activity of the juice, as well as bacterocin cultivated and fruits was investigated on two strain bacteria (*Propionibacterium acnes*, *Staphylococcus epidermidis*). The new antimicrobial (bacteriocin and Citrus juice) is ongoing search. This study used s juice at different concentrations at (20%, 30%, 40%, 60%, 80% and 100%). The Bacteriocin produced from local *P. fluorescens* isolates from wound infection and majority of isolates were found to produce crude Bacteriocin were (P1and P2) in Pseudomonas agar at 37˚C for 24 hrs. Crude Bacteriocin and Citrus limon juice against some pathogenic skin bacteria was find to be effective juice Citrus limon aganist *S.epidermidis* at 100% Concentrations with a range of inhibition zone (18) mm. The isolates of *P. fluorescens* (P2) was positive as producer of Bacteriocin with a wide inhibition growth against gram positive pathogenic bacteria with a range between (10-12) mm.

Key words: Juice extract, Bacteriocin, Pathogenic bacteria

1. Introduction

Pseudomonas fluorescens are gram negative rods aerobic with cells size of from× (2 -3)µm, they are usually occurred in the wild, in the waste water and wound. They occur in contaminated environment with colonization, but no signs of disease [1]. (Pseudomonic acid A) Mupirocin an antibiotic (Bacteriocin) produced by *P. fluorescens*, showed a peaky attributable of activity against Staphylococci and Streptococci and against certain G-ve bacteria, including *Haemophilus influenza* and *Neisseria gonorrhoeae*. There was no cross resistibility between available clinically antibiotics and mupirocin [2]. Proteinaceous toxins are Bacteriocins produced by bacteria to inhibit the growth strain(s) bacterial. Bacteriocins are medicine of interest because they are made by bacteria non-pathogenic in human normally colonize [3].

Citrus limon (L.) is a plant from the northeast and north of Brazil with popular name known “limoeiro” [4]. Oranges and Lemon are an expatriate medicaid plant of the family Rutaceae which are having antitumor activities and the antibacterial possibility in crude of disparate parts as follows (flower, root,

stem and leaves) of Lemon against bacterial strains were shown and reported [5] Flavonoids of Citrus have a big spectrum of biological activities including anti-bacterial, anti-fungal, anti-diabetic, anti-cancer and anti-viral activities [6]. The positive health benefits of part to vitamin C juices have been ascribed in [7].

The formed (emergence) of resistance of microorganisms to antimicrobial drugs is one of the world's current challenges. Second hand, plant- based antimicrobials are Attraction as they are often during many aspect effects associated with synthetic antimicrobials. The finding of new antimicrobial compounds from natural sources is, thus, Acne occurs frequently in individuals with high at acne regions bacteria is observed. *Propionibacterium acnes* are considered to cause inflammation around pores, and aggravate the symptoms [8].

The aim of study: this was to test the production of bacteriocin from commune strain. The main objective of study is anti-bacterial activity of Citrus Lemon against isolates from wound from skin infection. Comparable between Bacteriocin and natural juice extract can be used as an effective antibacterial agent against multidrug resistant bacteria skin infection and moreover it is readily available, safe, cheap and has no side effects.

2. Materials and Methods

Bacterial isolates

Ten isolates of *P. fluorescens* (P 1 to P10) were collected from wound cultures (swabs) from Yarmouk hospitals in Bagdad, Iraq and identified by morphological and Bacteriological tests [9].

Indicator isolates:

Clinical bacterial isolates from wound infections like; methicillin resistant *Staphylococcus epidermidis* (MRSE) were used as indicator isolates. These isolates were identified by morphological and biochemical tests according to [10] and *P. acnes* isolates were obtained from College of Science for Women/ Department of Biology (microbiology lab) /University of Baghdad.

Culture Media using:

MacConkey agar, Kligler Iron agar and Pseudomonas agar that we used, were purchased from Sigma Company, both media. These media were recommended for differentiation of *P. aeruginosa* while mannitol salt and blood agar for *S. epidermidis* for 24 hours in 37°C. Additional chemicals; Indole, Simmen citrate and Urea test were purchased from Merck Millipore company. Every single colony of different (culture) was tested biochemically.

Antibiotic Sensitivity Test:

By using disk diffusion method for sensitivity test of *P. fluorescens* was carried out according to [11] as follows, Bacterial inoculums pure colonies have been prepared by dissolving in normal saline and the turbidity of the bacterial inoculums should be compared with (10^6 cfu/ml) standard McFarland tube(bacterial suspension in Mcfarland =1.5×108 tube. A volume of 0.1 ml spread on Mueller -Hinton agar medium plates and let at room temperature to dry. Five antibiotics Gentamycine CN (01 mg), Ampiciline AM (01 mg), Amoxiline AX (52mg), Erythromycine E (15 mg) and Tetracycline TE (30) were used, by placing the disks of antibiotics on the inoculated period plate and pressed into the agar with a sterile forceps. Then the plates were incubated at 37 ̧C for 24 hours in an inverted position. The results have been read after incubation. The diameters of the complete zone of inhibition were noted and measured by a millimeter (mm).

Antibacterial activity of *Pseudomonas fluorescens*:

Antibacterial activity of *P.fluorescens* isolates against indicator isolates were detected by well diffusion agar method [12]. Each isolate of *P. fluorescens* approximately 10^6 CFU was cultured on nutrient agar, and for 24 hr incubated at 37°C. Agar (blocks diameter, 5mm) including growth were cleared excised from the nutrient agar and upside down placed on the surface of Mueller-Hinton agar seeded made with 0.1ml of ~10^6cells of indicator isolates. Plates incubated for 24 hr at 37°C. then measuring the diameter of the inhibition zones bacteriocin activity

The Extraction of Juice Lemon:

Lemon fruits were obtained from the local markets of Baghdad, with a bactericidal washed and filets into two halvers. Squeeze the juice out from it immediately and the seeds were removed to avoid contamination of the juice lemon during squeezing.

Antibacterial Activity of Lemon Juice by Agar Well Diffusion Method:

The Lemon juice was double or serial dilution which was prepared by using distilled water to obtain concentrations at (20%, 30%, 40%, 60%, 80% and 100%). Equal volume of lemon juice of Nutrient agar was mixed together. Specifically 0.1ml of the organism inoculated (*Staphylococcus. epidermidis* and *Propionibacterium acnes*) was added to each of the tube test containing the different concentrations above. Tubes are incubated at 35^0C for 24 hours anaerobic condition , and then

after 24hours observed of incubation to determine the (MIC), that showed concentration is the lowest and no growths were shown . [13].

3. Results

Ten isolates of *P. fluorescens* (P 1 to P10) were obtained from wound infections and identified with conventional methods Figure (1) and also for further confirmation with API-20 Profile Recognition System.

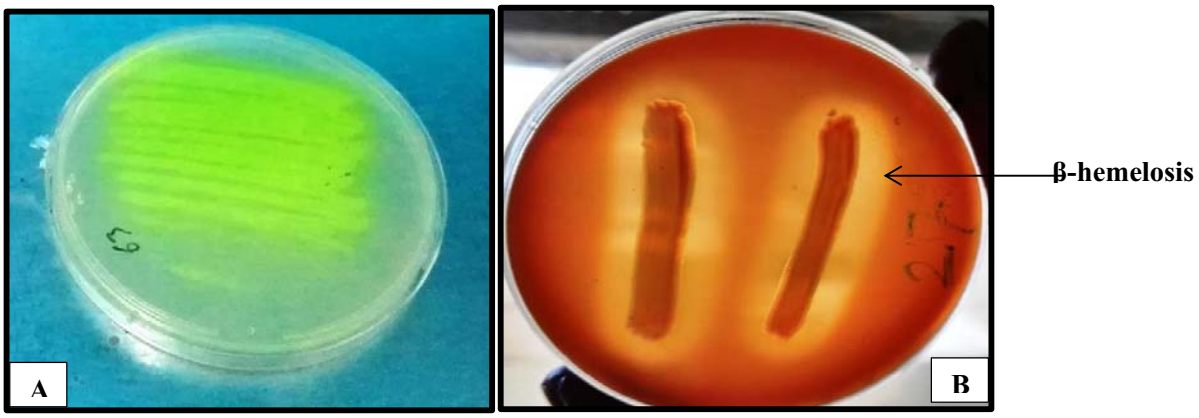

Figure 1. (A) A presumptive *P. fluorescens* on Pseudomonas agar (B) presumptive *P. fluorescens* on blood agar

Antibiotic Sensitivity Tests:

The results of the sensitivity test have shown that (isolates) P2, P1, P4 and P5 more resistant for all antibiotic using (choosing) resistant than P3, P8, P7, P9 and P10 for all type antibiotic using Figure (2), then using resistance *P. fluorescens* (P1 and P2) as bacterocin producers.

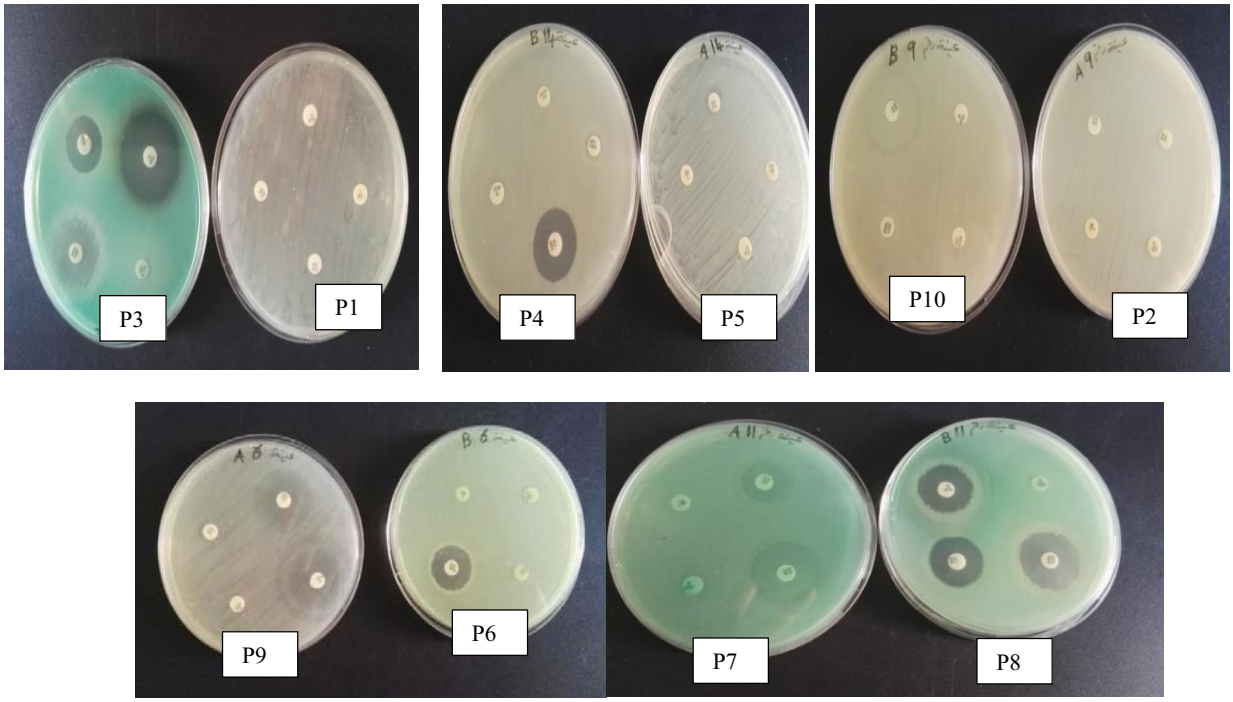

Figure 2. Antibiotic susceptibility test of *P. fluorescens* isolates

The two isolates of *P. fluorescens* the two isolates produced bacteriocin (P1 and P2) with a wide range effect on growth of gram positive *Staphylococcus. epidermidis* as shown in (Figure 3). The P2 (11) strain produced bacterocin more than P1, while the range of inhibition zones aganist *Propionibacterium acnes* by P2 was (12) mm. as in (Figure 4).

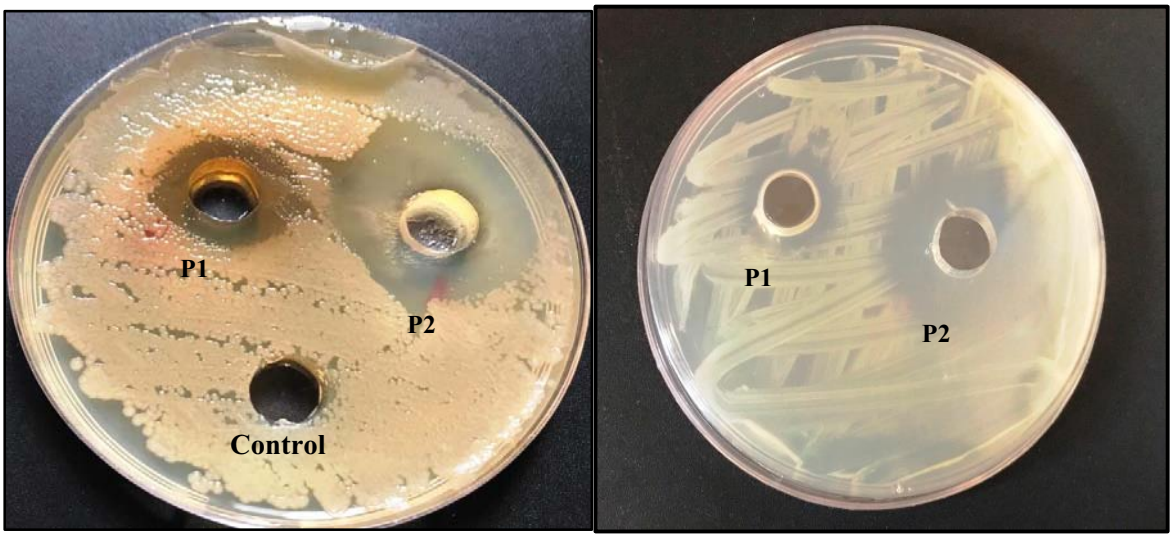

Figure 3. Crude Bacterocin aganist *S. epidermidis* P1 (4mm), P2 (11mm) at 37°C for 24 hr on nutrient agar

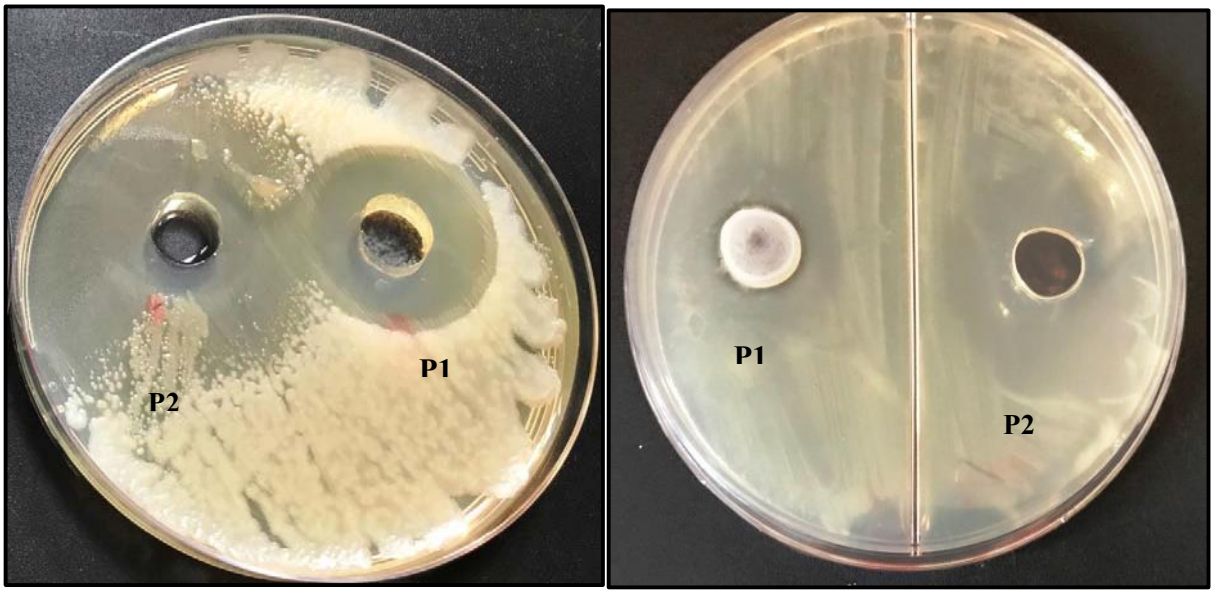

Figure 4. Crude Bacterocin on nutrient agar at 37°C for 24 hr aganist *Propionibacterium acnes* P1 (5mm), P2 (12 mm)

(Table 1) and (figure 5 and 6) showed activity the antibacterial on pimples of Citrus limon. The results of *Citrus limon* as the concentration increases the inhibition zone showed that all concentrations used between (20-100)% were effective on *S. epidermidis* and *Propionibacterium acnes*. The result at concentrations at 20% indicated that there was no clear inhibition of zone. While higher zone was at concentrations of 60%, 80% and 100%.

Table 1: Percentage (%)Citrus limon juice of Antibacterial Activity of (*Propionibacterium acnes* and *Staphylococcus epidermidis*)

Organism	Citrus limon Juice concentrations (%)	Diameter of zone of inhibition (mm)
P. acnes *S. epidermidis*	20	3 2
P.acnes *S. epidermidis*	40	7 7
P. acnes *S. epidermidis*	60	10 11
P. acnes *S. epidermidis*	80	12 14
P.acnes *S. epidermidis*	100	14 18
LSD value	11.894 **	4.275 **
P-value	0.0001	0.0001

Lemon on *Propionibacterium acnes* and *Staphylococcus epidermidis* of the (MIC), the results indicated as Lemon increases observed concentration the broth less turbid becoming an absence of growth was. Also it showed the (MIC) of cleanser on *Propionibacterium acnes.*

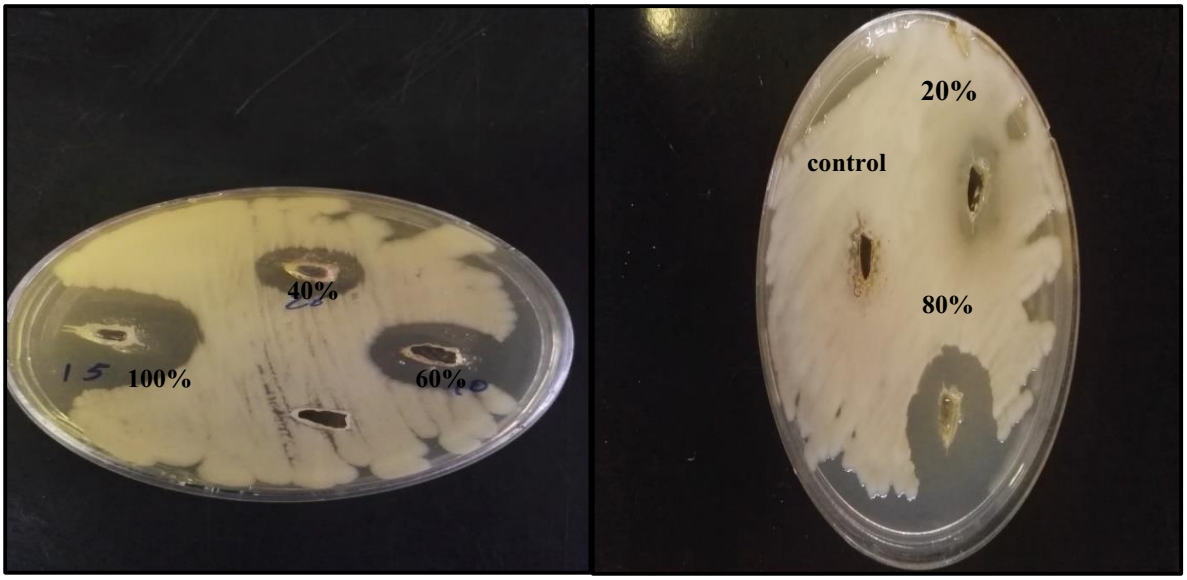

Figure 5. Percentage (%)Citrus limon juice of Antibacterial Activity on ***Propionibacterium acnes***

Figure 6. Antibacterial activity of Citrus limon (%) on *Staphylococcus epidermidis*.

4. Discussion

P. fluorescens isolate (1 and 2) as shown inhibited the growth of pathogenic bacteria and this study agrees with the results of the agar spot method, the substance of *P. fluorescens* isolates from wound inhibit the growth of *S. aureus* isolates at 37ţC for 24hr [14]. Bacteriocin is released action ability of a lysis protein from the cell [15] The research showed the (Lemon juice) is not only an astringent but it is also a very good antimicrobial agent against *P. acnes*, *S. epidermidis* with high inhibition zone camper baterocin. This bacteria is not surprising because they are part of the skin (normal flora) on the skin. The study carried out indicated that (Citrus limon juice) is a very active treatment against the organism that causes Acnevulgaris as seen from the sensitivity test results which showed that Lemon was very effective at all concentrations used in the study (20%,40%,60%,80% and 100%). A similar study conducted by [16] Citrus limon peel and juice extract works as a detoxifying and as an antibacterial agent activity against bacteria also, *P. cnes* inclusive because it contains the citrus acid main that acnes.Acne scars or even marks are also effectively cured with the help of *Citrus limon* juice. Juice can also be very effective in treating Acne when taken orally, apart from treating Acnes when taken orally, it helps to eliminate acid waste from the body, cures constipation, improves digestion process and reduces infections [15]. Cleanser used in the study was also found to be effective, but not as effective as juice. Cleanser was only effective as its concentrations were increased (60%, 80% and 100%).

When limon citrus is applicatively to the skin, it's known to excess oil remove and get rid helps of cells dead [17]. Juice citrus that is very rich in vitamin c also contains acid citric an acid, the citric acid acts to husk the skin a very important treating step in Acne vulgaris [18]. Works as study a detoxifying *Citrus limon* as agent an anti-bacterial. Also effectively cured of juice with the help Acne scars or even marks are juice of citrus limon can also be consumedly in treating Acne effective when orally taken, apart Acnes from treating when taken orally, it helps to acid waste eliminate from the body, treatment constipation, uptrend process digestion and infections reduces [19]. The result agrees with [20] shown juice and extracts from lemon had good antibacterial effect against the two *staphylococci* tested and on *Klebsiella pneumoniae*.

In experiments juice natural had good antibacterial activity against (gram positive) bacteria the natural components against acne-inducing bacteria refer to medicinal plants. The antimicrobial effect of commercial and wild fruits was investigated against these bacteria. Their inhibitory potential on bacterial growth may be utilized in the development of natural drugs or cosmetics to treat acne vulgaris [21].

5. Conclusion

The present study showed that the bacterial specie that causes Acnevulgaris (Pimples), identified as *P.acnes* and *S. epidermidis* was very sensitive to Citrus limon more than crud bacterocin from *P. fluorescens* so as to the very acidic normalizes of *Citrus limon*.

References

[1] Jozef Č, Peter Z , Pavol B and Lucia Z 2012Sanitation process optimalization in relation to the microbial biofilm of *Pseudomonas fluorescens*. *J. Mici. Bio and Food Sci*. (1). 733-741

[2] Josef T, Archana C, Steven R and Alice C 2012 *Pseudomonas fluorescens* HK44: lessons learned from a model whole-cell bioreporter with a broad application history sensors. *J. Agric. Food Chem* (12). 1544-1571.

[3] Farkas-Himsley H, Bacteriocins-are they broad-spectrum antibiotics? *1980 J. Ant. Chem* 6 (4). 424–6.

[4] Elangovan V, Sekar N, and Govindasamy S, 1994, Chemopreventive potential of dietary bioflavonoids against 20methylcholanthrene-induced tumorigenesis, Cancer Letters, (87), 1, 107–113,

[5] Kawaii S, Yasuhiko T, Eriko K, Kazunori O, Masamichi Y, Meisaku K, and Hiroshi F, 2000, Quantitative study of flavonoids in leaves of Citrus plants. *J. Agric. Food Chem*. 48: 3865-3871.

[6] Khanum R, Mahmud S ,Waheed A and Nazir T, 2004, Physico-chemical studies of the essential oil of C. sinensis (var. Mousambi). Chemical Society of Pakistan, p. 209. 4th Intl. and 14th National Chemistry Conference. Organized by Chemical Society of Pakistan, Lahore Chapter.

[7] Rauf A, Uddin G, and Ali J, 2014, Phytochemical analysis and radical scavenging profile of juices of Citrus sinensis, Citrus anrantifolia, and Citrus limonum. *Org. Med. Chem. Lett*. 4:5.

[8] Bardawee S, Tawaha A, and Hudaib M, 2014, Antioxidant, antimicrobial and antiproliferative activities of Anthemis palestina essential oil. BMC Complement. *Altern. Med*. 14:297.

[9] Forbes B, Sahm A and Weissfeld A, 2000, Baily and Scotts diagnostic Microbiology .12th ed. Mosby.

[10] Collee J, Frazer A, Marmion B and Simmon A, 1999, Practical Medical Microbiology 14th ed. Churchul livingstone. Newyork.

[11] BaronE and Finegold S, 1990, Diagnostic Microbiology. 8th Ed., Mosby Company, London.

[12] Line J, Svetoch E, Erslaanov B and Perelygin V, 2008, Isolation and purification of Enteriocin E-760 with broad antimicrobial activity against Gram-positive and Gram– negative bacteria, *Anti. Agents and Chemoth,* 52 (3), 1094- 1100.

[13] Cheesbrough MD, 2000, District Laboratory Practice in Tropical Countries Part 2, Cambridge University Press, UK.

[14] Sinai W, 2009, Characterization of antibacterial substance produced by *Pseudomonas fluorescens*, *Iraq. J. of Sci.,* 50 (2). 267-270.

[15] Margaret A, 1998, Molecular mechanisms of bacteriocin evolution, Annu. *Rev. Genet,* 32. 255–78.

[16] Shinkafi S and Ndanusa H, 2013, Antibacterial Activity of Citrus Limonon Acnevulgaris (Pimples), *Ind J Dermatol,* 2(5),397-409

[17] Sand S, Haug T, Nissen J and Sand O, 2007, The bacterial peptide pheromone plantaricin a permeabilizes cancerous, but not normal, rat pituitary cells and differentiates between the outer and inner membrane leaflet, *J. Membr. Biol*., 216 (2–3). 61–71.

[18] Ferdowsian H and Levin S, 2010, "Does diet really affect acne?''. Skin therapy Lett; 15 (3): 5-12.

[19] Hindi N and Chabuc Z, 2013, Antimicrobial Activity of Different Aqueous Lemon Extracts, *J. Appl. Pharm. Sc.,* 3 (06): 074-078.

[20] Ördögh L, Galgóczy L and Krisch J, 2010, Antioxidant and antimicrobial activities of fruit juices and pomace extracts against acne-inducing bacteria, *Acta Biologica Szegediensis*, 54(1):45-49.

[21] Hassanzadeh P, Bahmani M and Mehrabani D, 2008, Bacterial resistance to antibiotics in acne vulgaris: An in vitro study, *Ind J Dermatol,* 53:122-124.

The Role Of Staphylococcus Haemolyticus In Men Infertility

The Role of Staphylococcus Haemolyticus in Men Infertility

Ghaed'a J. AL-Ghizzawi , Zahraa K. Jomaa

Department of Biology, Education College for Pure Science, Basra University

Corresponding authors email : warkajasem@yahoo.com

Abstract.A total of 80 samples of seminal fluid from infertile men who attending to admitted to clinics and laboratories in Omara city during the period from 2016/6/1 to 2016/12/1 , samples were subjected to semen analysis as recommended by WHO. The age of patients from 20 - 59 year. Another 25 semen sample were collected from fertilized men considered as control group. For this purpose, seminal fluid was cultured on MacConkey agar, Blood agar, Chocolate agar. within the 80 samples recorded *S. haemolyticus* in 14 cases and the rate of infection 18%, all strains was diagnosed by Vitek system 2 Double. The highest percent (64%) record in age group (30 – 39). Primary infertility recorded 94% while 6% recorded for secondary infertility. Also, different species of bacterial isolates were identified in 32 cases by Vitek system 2 douple. The bacterial infection of men genital system affected on fertility.

KEYWORDS**:** Infertility, semen analysis, genital pathogens

1-introduction

Infertility it means the inability to have a child after at least 12 months of unprotected sexual intercourse without using any contraceptive or condon use and affect the cause psychological and social of both spouses (Deka and Sarma , 2010). The incidence of male infertility means of a problem in the genital tract lead to an imbalance and lack of fertility (Askinazy-Elbhar,2005). *Staphylococcus haemolyticus* is a member of the coagulase – negative (Bertin *et al*., 2004). It is a well- known opportunistic bacterial pathogen that is well-known for its highly antibiotic- resistant phenotype (Takeuchi *et al*., 2005). As a gram- positive *Staphylococcus haemolyticus* has a thick peptidoglycan wall outside (Billot- Klein *et al.*, 1996). And it is highly cross- linked and reported cases of infections caused by *S. haemolyticus* dysfunction of organ systems resulting from immune response to a severe infection (Takeuchi, 2005). Primary infertility is infertility which affects the woman or man since the beginning of their lives of marital sexual and caused either hormonal or not integration organisms sexual for caused congenital (La vignera , *et al* .,2012).As for infertility secondary it is the infertility that afflicts woman after having a child or having a pregnancy end abortion child or ectopic pregnancy resulting from bleeding after birth or when the female is in a period of breastfeeding or because of the presence of infections resulting from bacteria . Men infertility occurs due to the inactivity of sperms and their inability to penetrate the membranes of the egg (Kay and Robertson, 1998).

2-Materials and Methods:

This study included the collection of seminal fluid (100) a married men infected infertility aged (20-59 year) 80 infertile men and 20 fertile men is considered control by collecting samples in sterile plastic (cup at the hospital) according to the instructions of where to abstain from ejaculation for at least 48 hours before

a routine examination of a sample of semen and then placed in the incubator for 15 - 30 minutes at least by converting it from a glass to the transparent liquid may be more than one hour if the high viscosity . Included measurements of volume sperm count and movement of sperms and type of sperms been collecting samples from reviewers to clinics and laboratories in Maysan - Iraq. As shown as in fig (1), well culture all samples on media (Blood, Chocolate, MacConky ager) and it was diagnosed by Vitek 2 system. Rapid identification (three hrs), a high level of automation, a simple methodology and taxonomically updated databases (Cheng *et al*,. 2010). All men were instructed to abstain from sexual intercourse or masturbation for 5 days before attending the clinic up arrival at the clinic the men were asked to collect samples by masturbation on site into standard sterile containers know to be free of cystic effects on human spermatozoa (WHO,2010). Before semen collection the men were asked to wash their hands and genitalia with running water and soap. Soon after semen production the samples were promptly liquefied at 37 ºC for about 30 minutes in an incubator before analysis. Finally, statistical analysis was done spss.

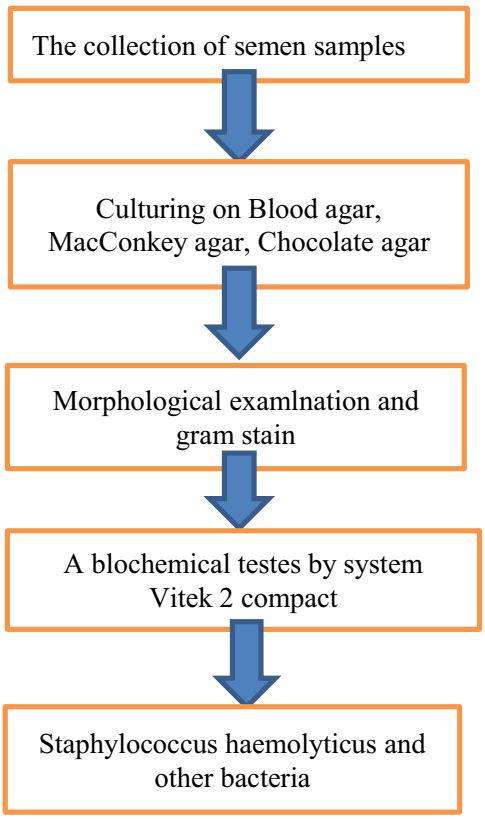

Figure (1) flow chart showing isolation and identification of *Staphylococcus haemolyticus*

3-RESULTS:

The results of the current study showed that can have isolated and diagnosis Staphylococcus haemolyticus of semen by Vitek 2 system, from (80) samples of seminal fluid of infertile men who the reviewers to the clinics and the private laboratories in the province of Maysan. Staphylococcus haemolyticus was diagnosed in 14 patients with rate 17.5%. When analysis semen for patients which infected by this bacterium their effect appeared on the size and nature semen and as well as on the number and efficiency of the tents the appearance of these bacteria also led to the appearance of abnormal sperm. Staphylocuccs

haemolytics infection was affected bacteria in quantity and quality of sperm. Colonies were appeared after (24-48) hours and have cocci shape as shown in the 'figure2', 'figure3', 'figure4'.

Figure 2. colonies Staphylococcus haemolyticus on the blood agar medium.

Figure 3. colonies Staphylococcus haemolyticus on the chocolate agar medium.

Figure 4. colonies *Staphylococcus haemolyticus* on the MacConkey agar medium.

The colonies were stained with gram stain and it appeared Gram positive with purple color as show in 'figure 5'.

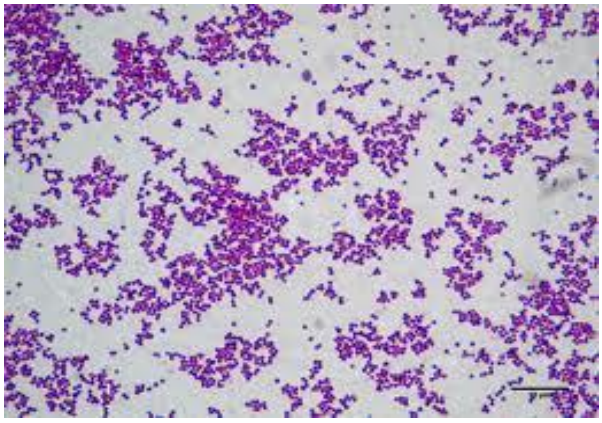

Figure 5. Staphylococcus haemolyticus colonies stained with gram stain (100X).

Many bacteria were isolated from seminal fluid of infertile men (table 1). High percent of isolation from S. *haemolyticus*.

Table 1. bacterial which isolated from patients.

Type of bacteria	Number	Percent
Staphylococcus haemolyticus	14	17.5%
Enterobacter cloacae& *Escherichia coli*	7	8.7%
Klebsiella pneumonia	6	7.5%
Pseudomonas aeruginosa	6	7.5%
Enterococcus faecium	4	5%
Morganella morganii	2	4%

The volume of patient's semen was ranged between 1.5- 3 ml. The infection was affected on appearance of abnormal sperm with high numbers. On the type of sperms, the infection was affected because type A (Active) sperms recorded low in numbers in contract with of types B & C (Butti & Colorless movement) also, type D (Dead) sperms recorded low percent. (table 2).

Table 2. the influence of infection with *Staphylococcus haemolyticus* on seminal fluid analysis of infertile men.

	Count	Volume	Normal	Abnormal	A	B	C	D	RBC.	Pus
1	0	1.5	5	95	5	0	95	0	1	0
2	$10^{6\times}5$	1.5	15	85	15	20	35	30	1	1
3	$10^{6\times}6$	1.5	20	80	15	30	20	20	1	1
4	$10^6\times15$	1.5	20	80	20	40	20	20	2	1
5	$10^6\times65$	1.5	20	80	20	25	35	20	2	1
6	$10^6\times20$	1.5	30	70	25	65	5	5	2	1
7	$10^6\times20$	1.5	35	65	30	30	10	30	2	1
8	$10^6\times30$	1.5	35	65	30	40	15	15	3	2
9	$10^6\times35$	1.5	25	75	40	20	15	25	4	2
10	$10^6\times40$	2.0	40	60	45	40	5	10	4	2

11	10^6×60	2.0	20	80	45	30	15	10	5	2
12	10^6×65	2.0	45	55	30	20	5	45	6	2
13	10^6×80	2.0	40	60	45	35	10	10	6	2
14	10^6×100	3.0	45	55	25	20	30	25	6	2

Type of infertility was determining in current study; Primary infertility percent was 94% while secondary infertility recorded only 6%. Among primary infertility cases a 79% found infected with *Staphylococcus haemolyticus* and 21% in secondary infertility.

Patients were divided in four age groups. The high percent (64%) recorded in patients with age group (30-39). (table -3-).

Table 3. age groups of study patients.

Age	Number	Rate
20-29	2	14%
30-39	9	64%
40-49	2	14%
50-59	1	7%

Table -5- explain the patient's disease which recorded in this study beside infertility. A (4) patients have diabetes and (2) suffered with thyroid gland disease.

Table 4. type of patient's diseases.

Sickness	Number	Rate
Diabetes	4	28%
Thyroid	2	14%

Patients wives of study participants have infection with bacteria a 93.7% percent. Distributed patients among residents the province center Maysan elimination and aspects, as recorded found *Staphylococcus haemolyticus* in elimination and aspects more than the center of the civil, in elimination 9 infections (64.2%) and the center 5 infections (35.7%).

Finally, all medical examination showed statistically significant differences in mean ($P<0.05$).

4-Discussion:

The role of the genital tract microorganisms important factor in male infertility (Keck *et al*, 1998; Ramesh *et al*,.2004). Bacteria is transmitted to the genital tract of the urinary tract or from the digestive system due to the proximity of the opening device of the output of the reproductive system as it becomes opportunistic to pathogenic and caused infections in the epididymis prostate and semen and testicles and thus infertility (Alausa and Osoba ,1978; Hobson *et al*, 2013). More that presences bacteria in semen which cause infertility represented in total bacteria Staphylococcus spp. (Cunningham and Beagley, 2008; Fraczek *et al*. 2012). Identified the current study bacteria *Staphylococcus haemolyticus* in the rate 17.5% the presence of these bacteria it works paralysis in sperm. As it penetrates of sperm and break it excretion enzymes which on the occurrence of deformities (Veznik *et al*, 2004). In addition to the negative impact on the secretion of the gonads and its analysis of blood and appearance of RBC., WBC. and agglutinating of sperm (Qusada *et al*, 1968; Alekwe *et al*, 2013). More bacteria are present in samples she *Staphylococcus haemolyticus* and Escherichia coli in terms of influence on movement and morphology of sperm (Prabha *et al*, 2010). Also the presence of *Enterobacter cloacae* and P*seudomonas aeruginosa* influenced in appearance shapes of abnormal and lack of movement (Merino et al, 1995; Buommino *et al,* 1999). It was appearance of *Klebsiella pneumoniae* and *Enterococcus faecium* and *Morganella morganii* role in infertility by

influencing the movement, quantity and quality of sperm (Claire *et al*., 2013). That presence *Staphylococcus haemolyticus* come through the proper environment for semen because it contains nutrients and this is basic basis in the presence of bacteria (Shalika *et al*, 1996).

Primary and secondary infertility occurs by having bacteria causing adverse and adverse changes in sperms chromosomes thereby causing abnormal and abnormalities of sexual chromosomes represented chromosomes(Y) as the bacteria work to lose semen sperm (Samara *et al*, 2011). Infertility increased in age groups (30-39). It is companion to the presence of bacteria *Staphylococcus haemolyticus* because as a defect in the function sex gland and the descent of abnormal secretions changed the characteristics of semen it is a period of sexual activity (Weng *et al*, 2014). Also recorded the current study accompanying bacteria with diabetes most people with diabetes suffer from cystitis which causes difficulty in dividing the bladder it is difficult to sweep the bacteria outside the body he added that high blood sugar is an appropriate environment for the presence of bacteria diabetes inhibits immunity which is caused by dysfunction in phagocytic cells (Jeanette *et al*, 2005). Thyroid diseases if caused by thyroid diseases lack of secretion of male hormone Testosterone (Paavonen, 1998). The current study was associated with infertility with the presence of bacteria in the districts more than the center of the city to raise health awareness (Lewis *et al*, 1981). 93.7% is the proportion of women infected with infections and because of sexual contract to infection or diseases in one of the spouses will move to the other partner and case to the diseases and thus infertility (Samara *et al*, 2011).

5-Acknowledgments
Authors wishing to acknowledge assistance or encouragement from colleagues, special work by technical staff to the cadre of the national laboratories to collect samples of study and to the Al- Sadr General Hospital for their cooperation with me using the Vitek -2 system in governorate of Mesan.

References:

[1] Alausa, K. and Osoba, A. (1978). The role of sexually transmitted diseases in male infertility in Tropical Africa. Niger. *Med. J.* **8**: 225-229.

[2] Alekw, A. Osamudiamen, I. and Aberare, L. (2013). Association between bacteriospermia and abnormal semen charcteristics, Pak. *J. F. Med. Heal. Sci.* **7**(1):3-6.

[3] Askienazy – Elbhar. (2005). Male genital tract infection: the point of view of the bacteriology. Gynecol. Obstet. Fertil. **33** (9): 691-697.

[4] Bertin, M. Muller, A. Bertrand, X. Cornette, C. Thouverez, M. and Talon, D. (2004). Relationship between glycopeptide use and decresed susceptibility to teicoplanin in isolation of coagulase – negative staphylococci. Eur. *J. Clinmicrobiol infect Dis*. **23** (5): 375-379

[5] Billot – Klein, D. Gutmann, L. Bryant, D. Bell, D. Van Heijenoort, J. and Grewal, J. (1996). Peptidoglycan synthesis and structure in Staphylococcus haemolyticus expressing increasing levels of resistance to glycopeptide. *J. Bacterial* **187** (15): 4696-4703.

[6] Buommino , E. et al,.(1999). Porin from Pseudomonas aeruginosa Induces Apoptosis in an Epithelial Cell Line Dervied from Rat Seminal Vesicles. *Inf. Imm*. **67**: 4794-4800.

[7] Cheng, C. Wong, E. Yan, H. and Mruk, D. (2010). Regulation of spermatogenesis in the microenviroment of the seminiferous epithelium: new insights and advances.Mol Cell. Endocr. 315 (1-2):49-56.

[8] Claire, B. David, G. and Hossein, S. (2013). Sexually Transmitted Infections and Sexual Function in Relation to Male Fertility Empirical College Healthcare NHS 3: 54-149.

[9] Cunningham, K. and Bealgley, W. (2008). Male genital tract chlamydial infection: implications for pathology and infertility. Biol. Repro. **79**(2):180-189.

[10] Deka and S. Sarma. (2010). Psychological aspects of infertility. *Briti. J. Med. Pract.* **3**(3) article a336. 40.

[11] Fraczek M, Piasecka M. and Gaczarzewicz, D. et al. (2012). Membrance stability and mitochondrial activity of human – ejaculated spermatozoa during in vitro experimental infection with Eschericha coli, Staphlylococcus haemolyticus and Bacteroides ureolyticus. Andro. 44:315-329.

[12] Jeanette, S. Wessells, H. Chancellor, M. Howards, S. Stamm, W. VanDenEdenm, S. and Mc Vary, K. (2005) Urologic complications of diabetes. Diabetes Care. **28**:177-185.

[13] Hobson, N. Chousolkar, K. and Chenometh, P. (2013). Ureaplasma spp. In semen in Australia: its detection and potential effects. *Aus. Vet. J*., **91**(11):469-473.

[14] Kay, V. and Robertson, L. (`1998). Hyperactivated motility of human spermatozoa. a review of physiological function and application in assisted reproduction. *Hum. Rep. Upd.* (4).776-786.

[15] Keck, C. Gerber – Schafer, C. Clad, A. Wilhelm, C. and Breckwolf, M. (1998). Seminal tract infections: impact on male fertility and treatment options. Hum. Reprod. 8- Update, **4** (6): 891-903.

[16] La Vignera, S. Condorelli, R- Vicari, E. Agata, R. and Calogero, A. (2012). High frequency of sexual dysfunction in patients with male accessory gland infections. Andro. **44** (Supp1 1): 438-446.

[17] Lewis, R. Harrison, R. and Domingue, G. (1981). Culture of seminal fluid infertility *clinic. Fert. Steri*. **35**,194-198.

[18] Paavonen, J. (1998). Pelvic inflammatory disease- from diagnosis to prevention. Derma. Clin. 16:747-56.

[19] Prabha, R. Sandhu, S. and Kaur, K. (2010). Mechanism of sperm immobilization by Escherichia coli. Advan*. Urol. Arti. ID* 240268, pp.6.

[20] Quesada, E. Dukes, C. Deen, G. and Franklin, R. (1968). Genital infection and sperm agglutinating in infertile men*. J. Urolo*. **99**,106-108.

[21] Ramesh Babu, S. Sadhnani, M. Swarna, M. Padmavathi, P. and Reddy, P. (2004). Evaluation of bacterial levels in different subgroups of infertile males. India*. J. Clin. Biochem.*, 19(1): 45-49.

[22] Samara, Z. Rosenberg, S. and Madar –Shapiro, L. (2011). Direct simultaneous detection of sexually transmitted pathogenes from clinical specimens by autocapillary electrophoresis. Diagn Microbiol INFECT Dis; 70:17-21.

[23] Shalika, S. Dugan, K. Smith, R. and Padilla, S. (1996). The effect of positive semen bacterial cultures on in fertilization success. Hum Reprod. **11**: 2789-2792.

[24] Takeuchi, F. (2005). Whole Staphylococcus haemolyticus evolution of human colonizing Staphylococcus *Species J. Bacteiol* **187**: 7292- 7308.

[25] Veznik, Z. Pospisil, L. Svecova, D. Zajicova, A. and Unzeitig, V. (2004). The bacterial in the ejaculate: their influence on the quality and morphology of sperm. Acta Obstet Gynecol Scand, **83**(7):656-60.

[26] Weng, C. Chiu, F. and Lin, L. (2014). Bacterial communiities in semen from men of infertile couples: metagenomics sequencing reveals relationships of seminal microbiota to semen quality. PLoS ONE, **9**. (10) Article ID e110152.

[27] Wold Health Organization (WHO). (2010). Laboratory Manual for the Examination of Human Semen, World Health Organization, Geneva, Switzerland, 5th edition.

Irrigation water quality of Al-Gharraf Canal, south of Iraq

Irrigation water quality of Al-Gharraf Canal, south of Iraq

Salam Hussein Ewaid

Technical Institute of Shatra, Southern Technical University, Iraq

salamalhelali@yahoo.com

Abstract.To evaluate the water quality of Al-Gharraf Canal south of Iraq for irrigation purpose, analysis of 12 physiochemical parameters of water samples by standard methods was carried out at five stations during the year 2016 (water temperature, pH, electrical conductivity, total dissolved solids, bicarbonate, chloride, calcium, magnesium, sulfate, nitrate, sodium, potassium).

Seven irrigation water quality indices were calculated like; sodium percentage (% Na), soluble sodium percentage (SSP), residual sodium bicarbonate (RSBC), Kelly's ratio (KR), permeability index (PI), magnesium adsorption ratio (MAR), and sodium adsorption ratio (SAR).

The results represented as diagrams (Piper, Stiff, Schoeller, Durov, Gibbs, and Wilcox) using AquaChem and RockWork hydro-chemical software.

Chemical analysis for canal water demonstrates the calcic chlorinated water type, the dominance of alkalis water, the major cations was in the order of: Na+ > Ca2+ > K+ > Mg2+ and major anions was: Cl- > SO42- > HCO3- > NO3-, the mean values of the irrigation water quality indices were (in meq/l) were; SAR (2.37), % Na (43.4), PI (%) (52.3), SSP (% (38.1), MAR (%) (34.5), KR (0.61), RSBC (-1.78).

The results indicate the suitability of canal water for irrigational purposes based on the calculated indices for the majority of crops under special management for salinity and permeability control.

The presentation of chemical analysis by diagrams and numbers makes understanding of complex water system too simpler and quicker. This study is a comprehensive assessment towards providing indicators and classification indices on irrigation water quality of the canal ecosystem, which will be the basis for future planning decisions on agricultural demand management measures and water quality monitoring to protect this principal water resource.

Key words: Al-Gharraf, irrigation water, Durov, Piper, SAR, Wilcox, Gibbs.

1.Introduction

Rivers are the main source of water in Iraq and some countries in the Middle East, the region that is known by its shortage of water resources and acute water scarcity problems [1].

The supply of freshwater is essential to the socio-economic development and agriculture is the largest consumer, therefore the water shortage and quality issues cannot be separated or studied in isolation of agriculture [2,3,4].

It is expected that Iraq and the region will suffer from drought caused by climate change with less rainfall and high temperatures affecting peoples and crop yields [5, 6].

Iraq which was considered rich in its water resources, now it is suffering from a water shortage due to the large number of dams and reservoirs constructed on the Euphrates and Tigris in Turkey, Syria, and Iran during the last decades [7, 8].

Salinization is a growing problem affects agriculture in the central and southern Iraq. It is evaluated that around 60% of the cultivated land has been genuinely influenced by saltiness; and 20-30% has been abandoned [9].

Al-Gharraf Canal is a main source of water for agriculture and public water supply in the south of Iraq. It branches from the Tigris upstream of Al-Kut Barrage and flows through Wasit and Dhi-Qar provinces. Its water is utilized for drinking, irrigation, raising livestock and fishing [11].

The major irrigation water quality problems are sodicity, salinity, and alkalinity caused by the presence of large amounts of ions in water, affecting soil's chemical and physical properties causing reduce soil productivity [12].

The common indices used to assess the suitability of water for irrigation are; percent sodium (% Na), residual sodium bicarbonate (RSBC), soluble sodium percentage (SSP), Kelly's ratio (KR), permeability index (PI), magnesium adsorption ratio (MAR), sodium adsorption ratio (SAR) [13, 14, 15, 16].

The hydrochemical classification diagrams of, Piper, Durov, Stiff, Schoeller, Gibbs, and Wilcox have been widely used in the world (but little used in Iraqi studies) to show the ionic concentration in water samples for best understanding of complex water system which becomes quicker and simpler when it presents in graphical forms. Previous studies on water quality in Al-Gharraf region [17, 10] focused only on the general physicochemical characteristics of the canal water. The objective of the present work is to discuss the hydrochemical characteristics of Al-Gharraf Canal water and assessing its suitability for irrigation by applying several quality parameters, classification indices, and diagrams.

2. Materials and methods

2.1 The study area

Al-Gharraf Canal (Figure 1) is the major branch of Tigris River south of Baghdad; its water features are similar to the hydrological features of the Tigris in Al-Kut area. The canal yearly discharge has substantial yearly variance and experiences common and human issues, for example, pollution, salinity, a collection of mud, the growth of plants, misusing and lessening of water levels [18].

The canal passes through several towns and many villages in Wasit and Thi-Qar provinces until ends in the south Mesopotamian marshes [19]. The length of the primary canal is around 230 km, 50-80 m width and 3-7 m depth, irrigates an area of 700,000 hectares, the maximum capacity was about 622 m^3/s, and the drainage area is 435,052 $x10^6$ m^2. It's basin populated by more than million individuals and going through a farming zone of around 215019 h in the south-west of Iraq inside the sediment plain [20].

The canal lies between the north scope (32 Â 27 º - 31 Â 2 º) and east longitude (45 Â 45 º - 46 Â 4 º), this geographical position gives the region features like; the high rate of solar radiation, high temperature, few rain events, low dampness, and high rate of dissipation [19].

Figure 1. The study area and sampling stations [20].

2.2 Field sampling and water analysis

Water samples were collected monthly in pre-cleaned sterilized polyethylene bottles of two-liter capacity during January to December 2016 from five sampling stations on the canal (Figure 1). Samples were preserved and examined according to the standard methods of the American Public Health Association (APHA) [21].

Some variables were measured *in situ* including; water temperature (T) (ºC), pH, and, electrical conductivity (EC) (µS/cm) by using the WTW multi-meter model Multi 340i. Total dissolved solids (TDS) measured by a temperature controlled oven. The concentrations of Ca^{+2}, Mg^{+2} were measured by EDTA complex metric titration, K^{+} and Na^{+} by flame photometer model M410, UK, and Cl^{-} by silver nitrate titration method. Sulfate (SO_4^{-2}) was analyzed spectrophotometrically by $BaSO_4$ turbidity method. Nitrate (NO_3^{-}) concentration was analyzed by cadmium reduction method and HCO_3^{-} by acid-base titration method. Determination of the study stations positions by the Global Positioning System (GPS). The concentration values expressed in milligram per liter (mg/l) unless otherwise indicated.

2.3 Irrigation water quality indices

The irrigation water quality indices, like (% Na), (SSP), (KR), (RSBC), (PI), (SAR), and (MAR) were calculated using the result values of water samples analysis and the suitable equations (Table 1).

Table 1. Equations used to calculate the water quality indices and criteria used for classifying irrigation water quality of the study area (concentrations in mill equivalents/liter; meq/l).

Water quality indices	Equations	Water quality criteria	Reference
Sodium Percentage (% Na)	$\mathrm{Na} = \frac{(\mathrm{Na^+ + K^+})\ x100}{\mathrm{Ca^{2+} + Mg^{2+} + Na^+ + K^+}}$	< 20 excellent, 20–40 good, 40–60 permissible, 60–80 doubtful, >80 unsuitable.	[14]
Soluble Sodium Percentage (SSP) (%)	$\mathrm{SSP} = \frac{\mathrm{Na^+}\ x\ 100}{(\mathrm{Ca^{2+} + Mg^{2+} + Na^+})}$	<50 good, > 50 bad	[22]
Residual Sodium bicarbonate (RSBC)	$\mathrm{RSBC} = \mathrm{HCO^-3 - Ca^{2+}}$	< 1.25 Safe	[23]
Kelly ratio (KR)	$\mathrm{KR} = \frac{\mathrm{Na^+}}{(\mathrm{Ca^{2+} + Mg^{2+}})}$	< 1 good, >1 bad.	[24]
Sodium Adsorption Ratio (SAR)	$\mathrm{SAR} = \frac{\mathrm{Na}}{\sqrt{\frac{\mathrm{Ca^{2+} + Mg^{2+}}}{2}}}$	< 10, excellent (S1), 10–18 good (S2), 18–26 doubtful (S3), > 26 unsuitable	[13]
Permeability index (PI) (%)	$\mathrm{PI} = \frac{\mathrm{Na^+ + \sqrt{HCO_3}}}{(\mathrm{Ca^{2+} + Mg^{2+} + Na^+})} \mathrm{x100}$	< 20 excellent, 20–40 good, 40–80 injurious, > 80 unsatisfactory	[25]
Magnesium Adsorption Ratio (MAR) (%)	$\mathrm{MAR} = \frac{\mathrm{Mg^{2+}\ x\ 100}}{(\mathrm{Ca^{2+} + Mg^{2+}})}$	< 50 suitable, > 50 unsuitable.	[26]

2.4 Graphical diagrams

The overall hydrochemical components of irrigation water explained with the most widely utilized graphical diagrams; Piper [27], Durov [28], Stiff [29], Wilcox [14], Schoeller [30], and Gibbs [31] to better explain of the classification and water composition using the analysis result values of the dissolved ions by meq/l. The hydrochemical software, RockWork version 16 and AquaChem 2014.2 software were used to plot these diagrams.

In Piper diagram (Figure 2) the percentage concentration values in meq/l of the main anions (Cl^-, SO_4^{2-}, and HCO_3^-) and cations (Ca^{2+}, Na^+ K^+, and Mg^{2+}) are plotted in two triangles, which were then anticipated further into a diamond-like field and inference is drawn for the chemical composition of water [27].

Durov diagram (Figure 3) is consisting of two ternary diagrams and the percentages of the anions are plotted against that of cations; sides shape the central rectangular, two-fold plot of total anion vs. the total concentrations of the cation [28].

Both the diagrams (Piper and Durov) show differences and similarities because the water samples which have the same qualities will plot together as groups, in the first diagram, the information plotted on the diamond-shaped field will decide the water type. Complexity to this, crossing point of lines reached out from the points in ternary outlines and anticipated on the sub-divisions of paired plot of Durov diagram show the hydro chemical forms required alongside water sort [22].

The canal water quality for irrigation purpose was assessed by Gibbs diagram (Figure 7) which is widely used to explain the relationship of water composition and characteristics [31].

Gibbs suggested that a simple plot of TDS versus the weight ratio of Na^+ / (Na^+ + Ca^{2+}) would provide meaningful information on the relative importance of three major natural mechanisms

controlling surface water chemistry: (1) rock weathering dominance, (2) atmospheric precipitation dominance, and (3) evaporation and fractional crystallization dominance [32, 33].

These two equations are used, the ionic concentration is in meq/l:

Gibbs ratio I (for anion) = $[Cl^-]/ [Cl^-+HCO_3^-]$

Gibbs ratio II (for cation) = $[Na^+ + K^+]/ [Na^+ + K^+ + Ca^{2+}]$

2.5 Stiff Diagram

Stiff diagrams 'Figure 5' are a typical method for showing concoction attributes for individual water tests. A stiff diagram utilizes four parallel, horizontal axes reaching out on each side of a vertical zero axis. Anions and cations are plotted on the left and right of the vertical axis in meq/l. These shapes are frequently included specifically on the site map for quick comparison of all the samples on a single page. Major ion concentrations are appeared to the left and right of the plot centerline and present the graph its shape and size [29].

3. Results and discussion

The results of the physicochemical parameters measured, water quality indices calculated, and diagrams plotted for the canal water samples in the study area are summarized in Tables 2, 3, 4, Figures 2, 3, 4, 5, 6, and discussed as follows:

3.1 General water physiochemical parameters

The temperature variation of the canal water in the study area ranged from 17 to 33°C. Hydrogen ion concentration (pH) was ranging from 7.0 to 8.3; EC value ranging from 1.19 to 1.925 ds/m.

The TDS in the canal water ranged between 760 and 1232 mg/l. Cl^-, SO_4^{2-}, HCO_3^-, and NO_3^- were ranging from 187 to 288, 147 to 210, 102 to 327, and 2.2 to 7.2 respectively. The concentration of Na^+ ranged from 84 to 150 mg/l, Ca^{2+} from 80 to 125 mg/l, Mg^{2+} from 23 to 43 mg/l, and K^+ from 34 to 77 mg/l. From this it was clear that hydrochemistry was dominated by sodium, calcium, chloride and sulfate ions. The relative abundance (in mg/l) of major cations was in the order of: $Na^+ > Ca^{2+} > K^+ > Mg^{2+}$ and major anions was: $Cl^- > SO_4^{2-} > HCO_3^- > NO_3^-$, Table 2 and Table 3.

Table 2. Annual range and mean values of chemical and physical parameters of water samples during the study period. The temperature in ºC, EC in (ds/m) and the rest in mg/L.

	1st Station (Kut)			2nd Station (Hai)			3rd St. (Qalaa)			4th St. (Badaa)			5th St. (Shatra)		
	Range		Mean	Range		Mean	Range		Mean	Range		Mean	Range		Mean
Temp.	17	31	23.7	18	32	24.5	18	32	23	18	33	24	19	33	25.3
pH	7.2	7.6	7.3	7.2	7.6	7.4	7	8.3	7.5	7.2	8.2	7.6	7.4	8	7.8
EC	1.19	1.6	1.37	1.29	1.72	1.51	1.35	1.67	1.61	1.42	1.88	1.651	1.33	1.925	1.76
TDS	760	1023	877	828	1101	967	864	1069	1041	911	1206	1057	854	1232	1128
HCO_3^-	102	140	118	192	270	223	186	327	235	198	324	240	186	318	235
Cl^-	205	275	251	187	216	228	204	282	232	192	282	232	210	288	246
Ca^{+2}	82	114	96	80	120	103	90	125	107	92	107	98	99	120	110
Mg^{+2}	29	43	35	26	41	32	25	27	34	23	39	31	29	36	32
SO_4^{-2}	150	193	171	168	190	175	147	198	181	170	210	190	156	204	180
NO_3^-	2.8	7	4.1	2.8	7.2	4.8	3.3	6.6	4.8	2.8	6.2	4.85	2.2	5.9	2.55
Na^+	91	144	108	88	150	107	96	143	120	104	121	106	84	133	110
K^+	37	57	44	34	57	44	42	63	47	39	67	55	38	77	51

Table 3. Annual mean values of major ions concentration in water samples by meq/l unit.

Stations	Ca^{+2}	Mg^{+2}	Na^{+}	K^{+}	Cl^{-}	SO_4^{-2}	HCO_3^{-}
Kut	4.79	2.88	4.7	1.13	7.07	3.56	1.93
Hai	5.14	2.63	4.65	1.13	6.42	3.64	3.66
Qalaa	5.34	2.8	5.22	1.07	6.54	3.76	3.85
Badaa	4.89	2.55	4.61	1.41	6.54	3.95	3.93
Shatra	5.49	2.63	4.78	1.3	6.93	3.74	2.97

3.2 Water quality indices

Table 4 shows the annual means of water quality indices including: (%Na), (RSBC), (SSP), (KI), (PI), (MAR) and (SAR) in the canal water samples during the study.

Table 4. Annual mean values and results of irrigational water quality indices from the five stations during the study.

Station	Irrigation water quality indices (meq/l)						
	SAR	**% Na**	**PI (%)**	**SSP (%)**	**MAR (%)**	**KR**	**RSBC**
Kut	2.4	43.2	49.2	38.9	37.55	0.61	-2.86
Hai	2.36	42.6	52.8	37.4	33.85	0.60	-1.48
Qalaa	2.4	43.6	53.7	39.07	34.4	0.64	-1.49
Badaa	2.5	44.9	54.7	38.3	34.3	0.62	-0.96
Shatra	2.23	42.8	50.4	37.05	32.4	0.59	-2.52
Mean	2.37	43.4	52.3	38.1	34.5	0.61	-1.78
Result	Excellent	Permissible	Injurious	Good	Suitable	Good	Safe
References	[13]	[14]	[25]	[22]	[26]	[35]	[34]

A. Sodium adsorption ratio (SAR)

The classification of the canal water samples with respect to SAR showed that its mean value is 2.37, all of the samples were <10 and fall under excellent category [13, 39]. SAR calculates the degree to which dissolved cations tend to enter into cation exchange sites in the soil. The high Na concentrations relative to the Ca and Mg affects the soil permeability, contributes to total salinity and toxic to sensitive plants [13, 40].

B. Sodium percentage (% Na)

High percentage of sodium in water decreases plant growth and soil penetrability. Results for Na % ranged from 42.6 % to 44.9 % with a mean of 43.4 %, as shown in Table 4, based on % Na, the canal water was not excellent nor good but permissible for irrigation [14].

C. Permeability index (PI)

In the present study, its values ranged from 49.2 meq/l to 54.7 meq/l with a mean of 52.3. This result suggests that all water samples can be categorized as injurious irrigation water [38].

As proposed by Doneen [25], soil permeability is influenced by a long-term utilization of irrigation water, depending on soil sort and the water content of (Na^{+}, Ca^{2+}, $Mg^{2+,}$ and HCO_3^{-}).

D. Soluble sodium percentage (SSP)

It is a vital factor to study sodium hazard and for adjudging the quality of water for irrigation. The high rate of sodium in water may decrease plant growth and soil penetrability [14].

The soluble sodium percentage values range between 37.05 meq/l to 39.07 meq/l with a mean of 38.1. According to SSP, all of the canal water was good for irrigation [22].

E. Magnesium adsorption ratio (MAR) (%)

It was proposed by Szaboles and Barab [36] for classifying irrigation water quality. MAR values of all the samples varied from 32.4 to 37.55 % with a mean of 34.5 % which was less than 50.0 indicating that water is suitable for irrigation uses. Crops are harmfully affected and the soil becomes more saline if MAR exceeds 50% [15, 26, 37].

F. Kelly Ratio (KR)

The Kelly Ratio values of the study area ranged between 0.59 meq/l to 0.64 meq/l with a mean of 0.61. This indicates that all of the water samples fall within the limit of <1.0 and are considered good for irrigation [35]. When the concentration of Na^+ increases, it will replace Ca^{2+} and cause soil dispersion, where Ca^{2+} has a vital role in the nutrition of plants. In like manner, the take-up of K^+ is stimulated, while the absorption of Na^+ is repressed, by $Ca^{2+,}$ notwithstanding when the concentration of Ca^{2+} is low [24].

G. Residual sodium bicarbonate (RSBC)

Water with high RSBC has high sodium hazard and high pH makes land infertile attributable to deposition of sodium carbonate. Carbonate and bicarbonate are combined with Na^+ when Ca^{2+} and Mg^{2+} precipitated by plant uptake and evaporation to represents a loss of fertility [23].

In this study RSBC values (Table 4) ranged from -2.86 meq/l to -0.96 meq/l with a mean of -1.78, it was less than the critical value of 1.25 meq/l and consider safe for irrigation (Gupta,1989). The negative values indicated that dissolved ions content of Ca^{2+} and $Mg^{2+} > HCO_3^-$ [23].

3.3 Graphical Diagrams

3.3.1 Piper Diagram

The concentrations of the main cations and anions found in the canal water of the study area are plotted from the available data in Piper's diagram to reveal the analogies, dissimilarities, and type of water (Figure 2). The Piper diagram of water classification showed that all canal water samples were in the Na^+, Ca^{2+}, K^+, Mg^{2+} and Cl^-, SO_4^{2-}, HCO_3^-, No_3^- facies, the alkali elements ($Na^+ + K^+$) exceeded alkali-earth ($Ca^{2+} + Mg^{2+}$), the strong acidic anions ($Cl^- + SO_4^{2-}$) exceeded the weak acidic anion HCO_3^-, calcium chloride type of water were predominant in all samples.

3.3.2 Durov Diagram

Durov diagram shows that the type of water samples of the canal from the five stations in all seasons is calcium chloride type demonstrates the dominance of alkalis water with increased portions of earth alkaline, the prevailing anions are chloride and sulfate, cations are sodium and calcium. In general, water chemistry of the study area was dominated by alkalis elements and strong acids 'Figure 3'.

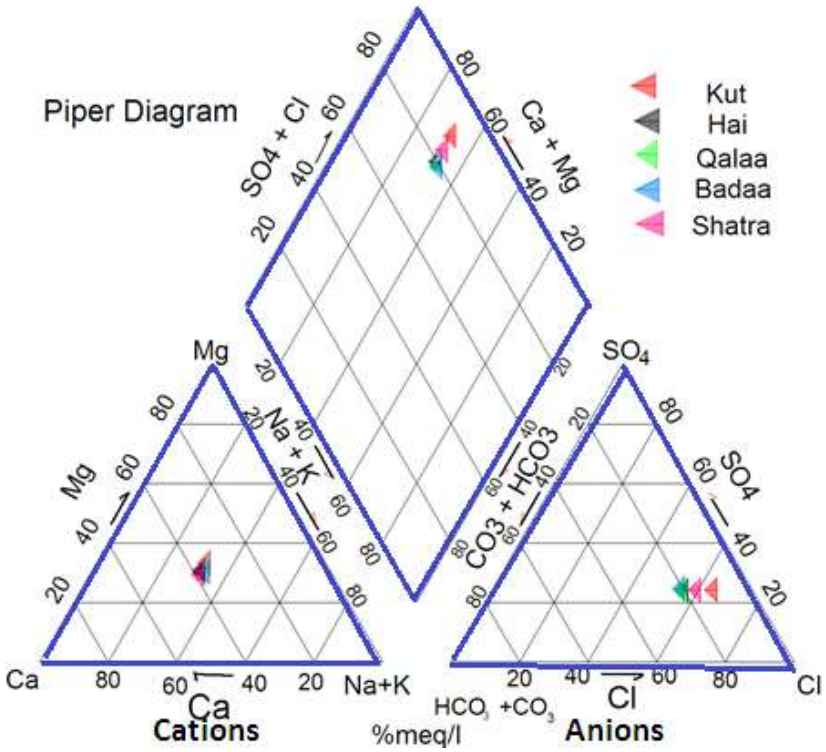

Figure 2. Piper's Diagram showing the major chemical compositions of the canal water samples.

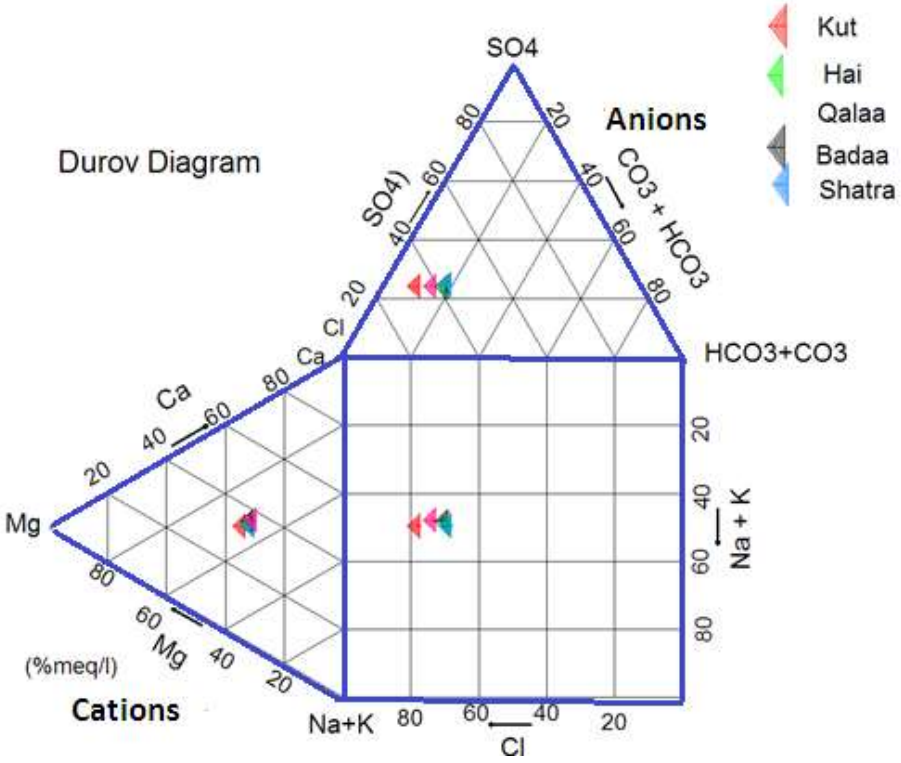

Figure 3. Durov's Diagram showing the chemistry of water samples.

3.3.3 Wilcox Diagram

SAR and EC plotted to get Wilcox diagram which divides waters into C1, C2, C3, and C4 categories on the basis of salinity hazard (EC) and S1, S2, S3 and S4 categories on the basis of sodium hazard (SAR). The results of this study indicate that all samples of the canal were in a C3S1 category with high salinity and low sodium (alkalinity) hazards as shown in 'Figure 4' [14, 41].

The canal water of these samples can be used for irrigation with most crops under special management for salinity control due to high salinity hazards.

When the concentration of chloride ions higher than 4 meq/l, toxicity problems can occur for sensitive crops according to [42]. Waters of Al-Gharraf (Table 3) have more than 4 meq/l and a high risk of salinity, it is fresh brackish water based on Stuyfzand classification [43].

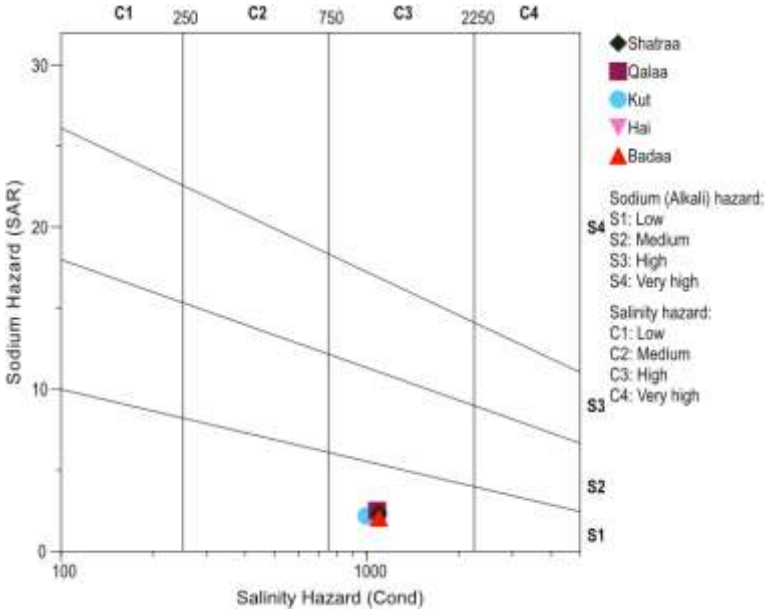

Figure 4. The site of the water samples on the Wilcox Diagram.

3.3.4 Stiff Diagram

The stiff system is a method for showing similarities or differences and changes in water composition explaining the chemical composition in hydrological cross-section. The width of the pattern could be used as an approximate indication of total ionic content [44].

'Figure 5' shows a stiff diagram for one of the study stations, there were little differences in the concentrations of the major dissolved ions (Ca^{2+}, Na^{+}, Mg^{2+}, K^{+}, Cl^{-}, SO_4^{2-}, and HCO_3^{-}) among stations and seasons.

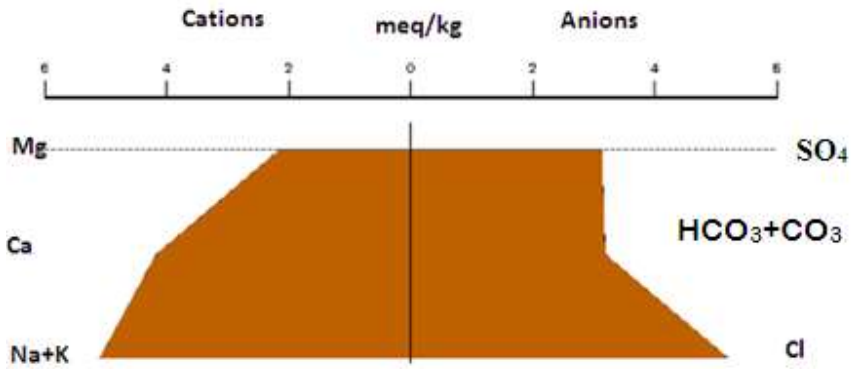

Figure 5. Stiff diagram for one of the study stations shows the water ionic composition.

3.3.5 Schoeller Diagram

The Schoeller diagram is used to study the chemical composition of the canal water, ions concentrations (meq/l) are plotted as shown in 'Figure 6'.

Results specify that lines of similar slope connecting concentrations of different parameters are indicative of water from a similar source. The most water type of high sodium content also has a high concentration of chloride [30].

Schoeller index revealed that base exchange reactions were more predominant than cation-anion exchange reaction. In this area, water samples had higher HCO_3^- values than alkali-earth indicating that water of the study area was of base exchange-softened type [45].

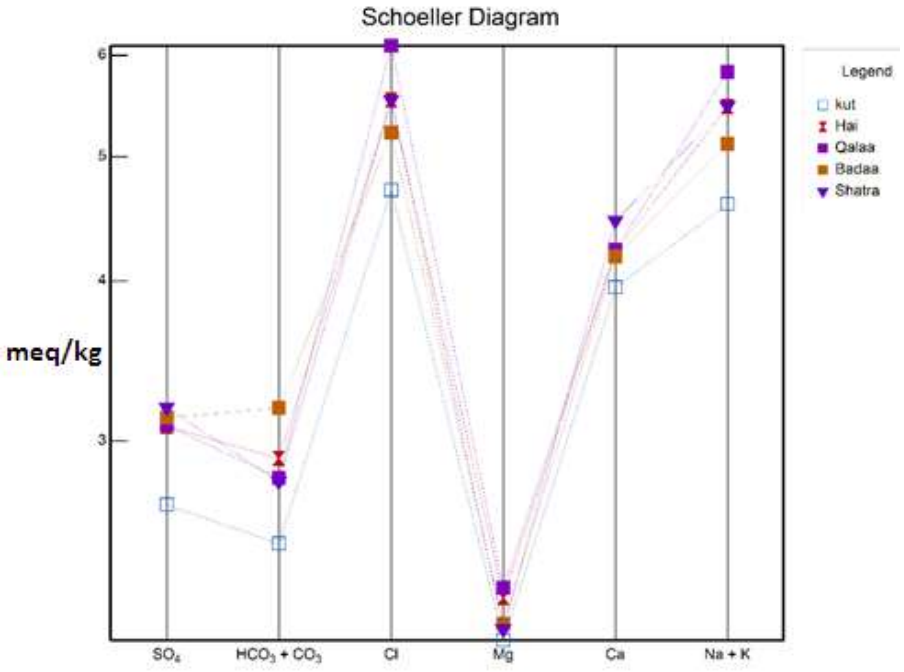

Figure 6. The position of the canal water samples on the Schoeller's diagram.

3.3.6 Gibbs diagram

According to Gibbs diagram, the predominant of all the canal water samples in the study area fall in the evaporation and fractional crystallization dominance field of the diagram and evaporation is the main responsible process for changing the chemistry of the canal water, 'Figure 7' [31].

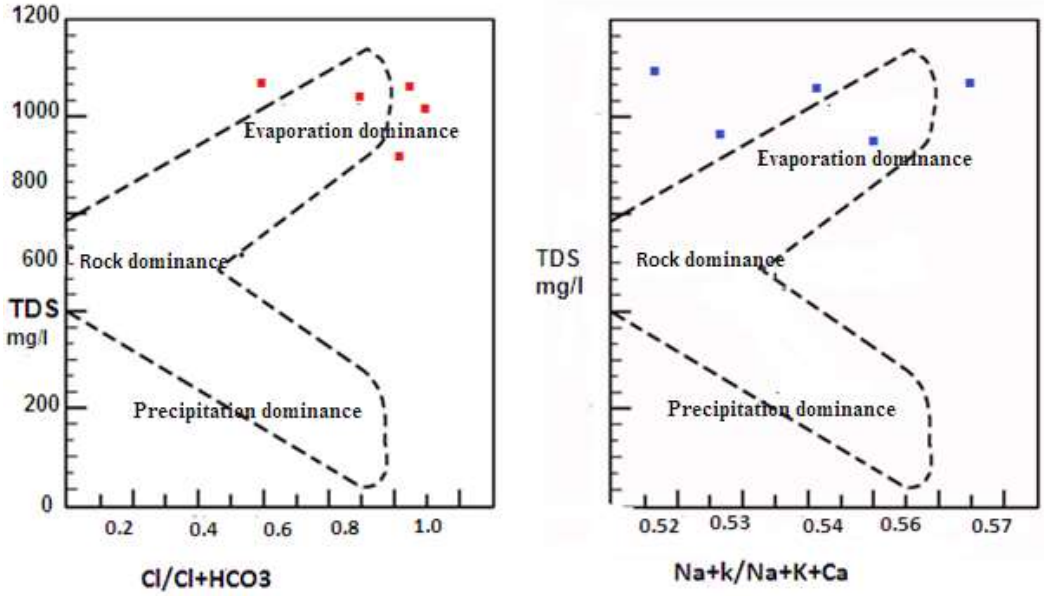

Figure 7. Gibb's diagram plot of the canal water samples.

4. Conclusions

Chemical composition of Al-Gharraf Canal water indicated that the cationic concentrations ranged in the order of $Na^+ > Ca^{2+} > K^+ > Mg^{2+}$, while it is $Cl^- > SO_4^{2-} > HCO_3^- > NO_3^-$ for anions.

The Piper and Durov diagrams showed the predominance of calcic chlorinated (Ca^{2+}- Cl^{-}) type.

The Gibbs plotting suggesting that evaporation and fractional crystallization is the prime process for contributing the ions into the water.

Wilcox diagram reveals that the water quality class is C3–S1 has a high risk of salinization and a low risk of alkalization with low SAR.

RSBC values of the canal water samples belong to good class; the irrigation water does not present any risk of sodicity but has a high risk of salinization, especially for sensitive crops.

References

[1] Al-Ansari, N. (2013). Management of water resources in Iraq: perspectives and prognoses. *Engineering*, *5*(6), 667-684.

[2] Cherfane, C. C., & Kim, S. E. (2012). Arab Region and Western Asia, UNESCWA. *Managing Water under Uncertainty and Risk, UN World Water Development Report*, *4*.

[3] Barr, J., Grego, S., Hassan, E., Niasse, M., Rast, W., & Talafré, J. (2012). Regional challenges, global impacts. *Managing Water under Uncertainty Risk, UN World Water Development Report*, *4*.

[4] Al-Kalbani, M. S., Price, M. F., Ahmed, M., Abahussain, A., & O'Higgins, T. (2016). Water Quality Assessment of Aflaj in the Mountains of Oman. *Environment and Natural Resources Research*, *6*(2), 99.

[5] Al-Ansari, N., & Baban, S. M. (2005). Rainfall trends in the Badia Region of Jordan. *Surveying and Land Information Science*, *65*(4), 233.
[6] Al-Ansari, N. A., Al-Shamali, B., & Shatnawi, A. (2006). Statistical analysis at three major meteorological stations in Jordan. *Al Manara Journal for scientific studies and research*, *12*, 93-120.
[7] UN 2010) Water Resources Management White Paper, United Nations Assistance Mission for Iraq, United Nations Country Team in Iraq, 20 p.
[8] Al-Ansari, N., Knutsson, S., & Ali, A. (2012). Restoring the Garden of Eden, Iraq. *Journal of Earth Sciences and Geotechnical Engineering*, *2*(1), 53-88.
[9] FAO (2011). Country pasture/forage resource profiles: Iraq. FAO, Rome, Italy, p.34.
[10] Ewaid, S. H. (2016a) Water Quality Assessment of Al-Gharraf River, South of Iraq by the Canadian Water Quality Index (CCME WQI). *Iraqi Journal of Science, 2016, Vol. 57, No.2A, pp: 878-885*
[11] Ewaid, S. H. (2016b). Water quality evaluation of Al-Gharraf River by two water quality indices. *Applied Water Science*, 1-7.
[12] Varol, S., & Davraz A. (2015). Evaluation of the groundwater quality with Water Quality Index and multivariate analysis: a case study of the Tefenni plain, Turkey. *Env. Earth Sciences, 73*(4), 1725-1744.
[13] Richard, L. A. (1954). Diagnosis and Improvement of Saline Alkali Soils (pp. 98-99). IBH Publishing Co. Ltd., New Delhi, India.
[14] Wilcox, L.V. (1955). Classification and use of irrigation waters: Washington D.C., United States Department of Agriculture, 19 pp.
[15] Ayers, R. S., & Westcot, D. W. (1989). Water quality for agriculture. Rome: Food and Agriculture Organization of the United Nations. 174 pp.
[16] Nag, S. K. (2014). Evaluation of hydrochemical parameters and quality assessment of the groundwater in Gangajalghati Block, Bankura District, West Bengal, India. *Arabian Journal for Science and Engineering*, *39*(7), 5715-5727.
[17] Al-Abadi, A. M. (2016). Modeling of stage–discharge relationship for Gharraf River, southern Iraq using backpropagation artificial neural networks, M5 decision trees, and Takagi–Sugeno inference system technique: a comparative study. *Applied Water Science*, *6*(4), 407-420.
[18] Ewaid, S. H., Abd, R. S. and Abed, S. A. (2017). Assessment the Performance of Al-Nassriya Water Purification Plant, South of Iraq. May – June 2017 *RJPBCS* 8(3) Page No. 2440.
[19] Ewaid, S. H. and Abed, S. A. (2017a). Water Quality Assessment of Al-Gharraf River, South of Iraq Using Multivariate Statistical Techniques. *Journal of Al-Nahrain Univ., Science.* Vol.20 (2), June, 2017, pp.114-122
[20] Ewaid, S. H., & Abed, S. A. (2017b). Water quality index for Al-Gharraf River, southern Iraq. *The Egyptian Journal of Aquatic Research*, under press.
[21] American Public Health Association (APHA) (2012). Standard methods for the examination of water and wastewater, 27th ed. Washington, DC.
[22] Todd, D.K. and Larry, W.M. (2005). Groundwater hydrology: New Jersey, John Wiley & Son, Inc, 3rd ed., 656 pp.
[23] Eaton, F. M. (1950). Significance of carbonates in irrigation waters. *Soil science*, *69*(2), 123-134.
[24] Kelly, W. P. (1953). Use of Saline Irrigation Water. *Soil Science*, 95: 355-391.
[25] Doneen, L. D. (1964). Notes on water quality in Agriculture Published as a Water Science and Engineering Paper 4001. *Dept. of Water Science and Engineering, Univ. of California*.
[26] Raghunath, H. M., 2007, Groundwater. 3rd edition: New Delhi, India, Wiley Eastern, 364-389.
[27] Piper, A. M. (1944). A graphic procedure in the geochemical interpretation of water-analyses. *Eos, Transactions American Geophysical Union*, *25*(6), 914-928.
[28] Durov, S. A. (1948). Natural waters and graphic representation of their composition. In *Dokl Akad Nauk SSSR* (Vol. 59, No. 3, pp. 87-90).
[29] Stiff Jr, H. A. (1951). The interpretation of chemical water analysis by means of patterns. *Journal of Petroleum Technology*, *3*(10), 15-3.

[30] Schoeller, H. (1965). Qualitative evaluation of groundwater resources. *Methods and techniques of groundwater investigations and development. UNESCO*, *5483*.
[31] Gibbs, R. J. (1970). Mechanisms controlling world water chemistry. *Science*, *170*(3962), 1088-1090.
[32] Feth, J. H., & Gibbs, R. J. (1971). Mechanisms controlling world water chemistry: evaporation-crystallization process. *Science*, *172*(3985), 870-872.
[33] Stallard, R. F., & Edmond, J. M. (1983). Geochemistry of the Amazon: 2. The influence of geology and weathering environment on the dissolved load. *Journal of Geophysical Research: Oceans*, *88* (C14), 9671-9688
[34] Gupta DC (1989). Irrigational suitability of surface water for agricultural development of the area around Mandu, District. *J. App. Hydro.* 2 (2): 63 -71.
[35] Kelly, W. P. (1940). Permissible composition and concentration of irrigation water. In *Proceedings of the American Society of Civil Engineers* (Vol. 66, pp. 607-613).
[36] Szaboles, I., & Darab, C. (1964). The influence of irrigation water of high sodium carbonate content of soils. In Proceedings of 8th international congress of ISSS, Trans, II (pp. 803–812).
[37] Rengasamy, P. (2006). World salinization with emphasis on Australia. *Journal of experimental botany*, *57*(5), 1017-1023.
[38] Reza R, Singh G (2010) Assessment of Heavy Metal Contamination and its Indexing Approach for River Water. International J. of Environmental Science and Technology 7(4): 785-792
[39] Panigrahy, P. I. C., Sahu, S. D., Sahu, B. K., & Sathyanarayana, D. (1996). Studies on the distribution of calcium and magnesium in Visakhapatnam harbour waters, Bay of Bengal. In *Inter. Symposium on Applied Geochemistry, Osmania University, Hyderabad* (pp. 353-340).
[40] Dey, A. K. (2002). Environmental chemistry, 4thed. New Delhi, India: New Age Inter. Publishers, pp 232-252.
[41] Dhok, R. P., Patil, A. S., & Ghole, V. S. (2011). Sodicity and Salinity Hazards in Water Flow Processes in the Soil. *Journal of Chemistry*, *8*(S1), S474-S480.
[42] Bigak, J. W., & Nielsen, D. R. (1972). Irrigation under diverse conditions. In S. A. Taylor & G. L. Ashcroft (Eds.), Physical edaphology: the physics of irrigated and non-irrigated soils. San Francisco: WH Freeman.
[43] Stuyfzand, P. J. (1989). Nonpoint source of trace element in potable groundwater in Netherland. *Proceedings 18th TWSA Water Workings. Testing and Research Institute, KIWA*
[44] Mackenzie, F. T., & Garrels, R. M. (1966). Chemical mass balance between rivers and oceans. *American Journal of Science*, *264*(7), 507-525.
[45] Handa, B. K. (1964). Modified classification procedure for rating irrigation waters. *Soil Science*, *98* (4), 264-269.

Lag phase and biomass determination of Rhodococcus pyridinivorans GM3 for degradation of phenol

IOP Conf. Series: Journal of Physics: Conf. Series **1003** (2018) 012007 doi:10.1088/1742-6596/1003/1/012007

Lag phase and biomass determination of Rhodococcus pyridinivorans GM3 for degradation of phenol

M E J Al-Defiery[1],1and G Reddy[2]

[1] Environmental Research and studies Center, University of Babylon, Iraq.
[2] Department of Microbiology, UCS, University of Osmania, India.
E-mail: al_defiery2004@yahoo.com

Abstract. Among various techniques available for removal of phenol, biodegradation is an eco-friendly and cost effective method. Thus, it is required to understand the process of biodegradation of phenol, such as investigate on lag phase and biomass concentration.

Phenol degrading bacteria were isolated from soil samples of industrial sites in enriched mineral salts medium (MSM) with phenol as a sole source of energy and carbon. One isolate of potential phenol degradation from consortium for phenol degrading studies was identified as Rhodococcus pyridinivorans GM3. Lag phase and biomass determination of R. pyridinivorans GM3 was studied with different phenol concentrations under pH 8.5 at temperature 32 Co and 200 rpm.

Microbial biomass was directly proportional to increasing phenol concentration between 1.0 to 2.0 g/L with a maximum dry biomass of 1.745 g/L was noted after complete degradation of 2.0 g/L phenol in 48 hours.

1. Introduction

Phenol represents a serious ecological problem due to its wide spread use, toxicity and occurrence throughout the environment; hence, it is necessary to develop efficient strategies for its waste management [1]. Whilst Rigo and Alegre [2] reached that among twenty two microorganisms species isolated from wastewaters that containing phenol, Candida parapsilopsis had to be growth capable on a medium with phenol concentration (1.0 g/L). The degradation ability of Streptococcus epidermidis OCS-B was checked up to 200 mg/L concentration within 84 hours and so can be utilized the phenol by bioremediation of contaminated sites [3].

Much attention is paid on microorganisms that can completely degrade phenol, and there are a variety of phenol degrading cultures. Xanthobacter flavus MTCC 9130 can tolerate upto 1100 mg/L phenol concentration, the phase of lag elevated with the raise in concentration of phenol and the temperature of optimum growth was 37°C [4]. Shourian et al. [5] observed that Pseudomonas sp. SA01 degrades phenol at 0.7 g/L after an initial very short lag phase, then rapidly completed within 30 hours. Pseudomonas sp. SA01 was capable to degrade up to 1.0 g/L of phenol concentration and over concentrations of phenol (1.0 g/L) had a potential inhibitory affect growth of bacterial.

When an inoculum of bacteria is first introduced into medium, it will probably require a period to adapt to its new surrounding environment. Irrespective of variation of conditions and microbial strain, the increased phenol concentration leads to the increase in period of the lag phase, thus, extend the time of biodegradation. Moreover, the reduce in the degradation rate by Acinetobacter baumannii; on increase in the initial concentration of phenol from 125 mg/L to 1000 mg/L, an increasing lag phase period from 0 to 48 hours was observed and correspondingly extended the process of degradation from 84 hours to 354 hours [6]. The strain Corynebacterium sp. DJ1 granules had a lag phase of 12 hours at 2000 mg/L phenol concentration and degradation rate was 38.3, 36.4 and 34.7 mg/L per hour at concentration 1.0, 1.5 and 2.0 g/L respectively; however, phenol at 2500 mg/L inhibited microbial growth and degradation [7]. At higher concentration of phenol, the microbial growth inhibition was more and hence the lag phase time get longer for Alcaligenes faecalis to degrade 400, 700 and 1000 mg/L within 6, 12 and 26 hours respectively [8].

The elevated inhibition with the higher levels of phenol was obvious in longed lag period treatment of stream wastewater and can be negatively influenced by the co-pollutants existence [9]. Although the phenol is a poisonous composite which inhibits its possess change even at low concentrations, there are some methods accessible for phenol treatment; the biological treatment is mainly attractive because it has the significant to complete degrade phenol at often with generating minimum production of secondary waste and safe end products [10]. The simple recycle of the biomass by both, chemical and physical methods have been recognized for aromatic wastewaters treatment, but phenols biological degradation is progressively more being documented as a proficient and mild effective cost method [11]. Biomass is important parameter that affect phenol biodegradation rate, whereby it is correlated with differences of microbial growth stage, such as lag phase of microorganism during growth on media containing phenol Therefore, the objective of study is investigate lag phase and determination of biomass concentration of bacterial isolate during phenol biodegradation process.

2. Materials and Methods

2.1. Isolation

Samples were collected from 4 industrial and 4 agriculture sites in Hyderabad. Medium of enrichment for degrading bacteria was conducted to screen sample of soils under aerobic condition. Isolation of phenol degrading bacteria were carried out in enrichment culture containing 1.0 and 1.5 g/L of phenol by sub cultured into fresh MSM for several times. Among 26 isolates, one of the bacterial isolates that were evidenced high degradation of phenol and identified as *Rhodococcus pyridinivorans* GM3 by biochemical characteristics, morphological and microscopic 'Figure (1)'.

2.2. Growth medium

The mineral salts medium includes yeast extract (1.25 g/L), MgCl2.6H2O (0.35 g/L), K2HPO4 (0.35 g/L), Ca(NO3)2 (0.2 g/L), FeCl2 (0.12 g/L) and trace elements (0.2 mg/L of MnSO4. 2H2O, 0.2 mg/L of CuSO4.5H2O, and 0.1 mg/L of Na2MoO4, 0.1 mg/L of ZnSO4.7H2O) with phenol addition as source of sole carbon according to concentration assay[12].

2.3. Phenol estimation

Phenol was determined by method of direct photometric [13]. The supernatant was added 4-amino-antipyrene and using phosphate buffer (pH 6.8) and ammonium hydroxide (0.5N) for adjusted at pH 7.9 ± 0.1. Then, followed by oxidation with $K_3Fe(CN)_6$ and analyzed at 500 nm by spectrophotometer (Shimadzu - Japan) Visible/Ultra Violet recording. The minimum detectable quantity of phenol in this method is 0.1 mg/L.

2.4. Phenol degradation

Phenol degradation was carried out on MSM (50 mL) containing 1.5 g/L of phenol concentrations (at triplicate) with 1% *R. pyridinivorans* GM3 of inoculation and incubated at 32ºC, pH 8.5 and 200

rpm(optimization conditions) [14]. The samples were collected every 8 hours of interval from flasks containing phenol concentration 1.5 g/L respectively and phenol degradation was monitored.

2.5. Lag phase

For studying lag phase of *R. pyridinivorans* GM3 with phenol as sole carbon sources it was carried out in triplicates on MSM with different concentrations of phenol (0.5,1.0,1.5 and 2.0 g/L) at pH 8.5, 32ºC and 200 rpm. Each phenol concentration was estimated at regular intervals of one hour of incubation.

2.6. Growth curve

MSM with 1% glucose was prepared in 250 mL flask and inoculated with 1% actively growing *R. pyridinivorans* GM3 and incubated at 32ºC, pH 8.5 and 200 rpm. Growth was measured at regular intervals as culture optical density (OD) by spectrophotometer (Shimadzu) at 600 nm (in lab of Department of Microbiology- -Science College- Osmania University).

2.7. Determination of biomass concentration

The biomass concentration was determined using the dry weight method. It was carried out on MSM (50 mL) including three phenol concentrations (1.0, 1.5 and 2.0 g/L) at triplicate in flasks (250 mL) and inoculated with 1% *R. pyridinivorans* GM3 and incubated at temperature 32ºC, pH 8.5 and 200 rpm. For every six hours of incubation, biomass was estimated for all phenol concentrations. Fifty mL aliquots in plastic centrifuge tubes (100 mL) were centrifuged for 15 minutes at 5000 rpm [15] on 4ºC. The samples were then rinsed (twice) with de-ionized water and at 105ºC for 24 hours, the pellets were dried, cooled in a dessicator and reweighed. The dry weight of biomass as g/L was estimated by the difference between the first (empty) and the second weight.

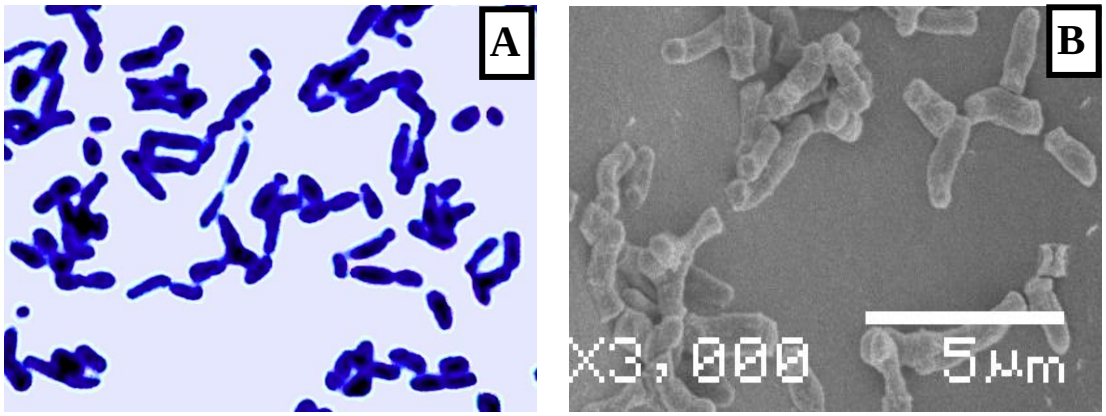

Figure 1. A: Light Microscopic picture of bacterial isolate GM3 with simple staining at magnification 1000X. **B:** Scanning electron micrograph of *R. pyridinivorans* strain GM3

3. Results

The ability of *R. pyridinivorans* GM3 to degrade phenol in batch culture were studied by using MSM containing 1.5 g/L initial phenol concentrations with inoculum size 1%. It is clear from the results that *R. pyridinivorans* GM3 showed 100% degradation within 24 hours at phenol concentration 1.5 g/L which is shown in Figure 2. The results proved that *R. pyridinivorans* GM3 utilized /degraded phenol as sole carbon and energy source.

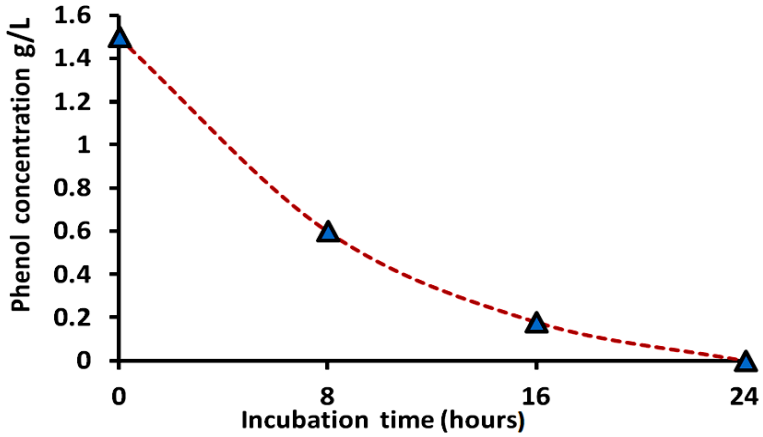

Figure 2. Phenol degradation by *Rhodococcus pyridinivorans* GM3 with initial phenol concentration of 1.5 g/L

3.1. Lag phase of R. pyridinivorans GM3

The isolate bacterial *R. pyridinivorans* GM3 has ability to utilize phenol in MSM was used to study lag phase. Initial concentration of phenol acts a significant role in the process of biodegradation, since some contaminants of hydrocarbon, as well as phenol are recognized to possess inhibitory affect the duration of the lag phase of bacterium (Figure 3). The lag phases to initial 0.5, 1.0, 1.5 and 2.0 g/L phenol concentrations were 2, 3, 4 and 6 hours respectively. The results imply that the lag phase length elevated exponentially with concentration of phenol. The high phenol concentrations may have an inhibitory effect on growth of *R. pyridinivorans* GM3, hence reflected effect of toxic compound in the form of extended lag phase.

When a bacteria population is inoculated into a medium, the growth generally does not start immediately but after some time as known as the lag phase. In the lag phase there is a delay in the growth of bacterial population until the bacteria have become arranged to the surrounding conditions and source of nutrients.

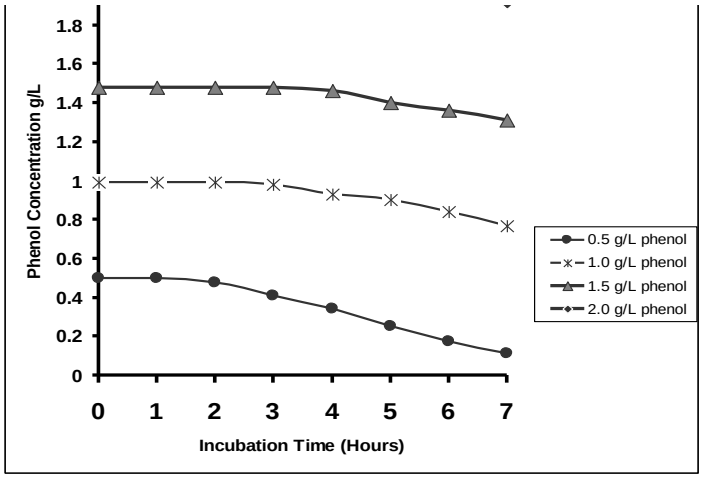

Figure 3. Lag phase of *Rhodococcus pyridinivorans* GM3 with 0.5, 1.0, 1.5 and 2.0 g/L of phenol concentrations

3.2. Growth curve

Growth of GM3 was monitored by measuring turbidity at 600 nm (Figure 4). It is not clear that lag phase from the growth curve but there was less growth in first 4 hours. Growth curve of *R. pyridinivorans* GM3 showed a logarithmic phase extending up to 20 hours and maximum growth occurred at 20 hours (OD 1.324 $\approx 10^9$ CFU/mL), later the culture reached stationary growth.

3.3. Determination of biomass concentration

In order to determine biomass of *R. pyridinivorans* GM3 at varying phenol concentrations, freely suspended cells were inoculated (1%). Figure 5 shows biomass at 1.0, 1.5 and 2.0 g/L phenol concentrations, which were significant with phenol concentration and interdependence among the times needed for phenol degradation. At phenol concentration of 1.0 g/L the dry biomass found was lower than 1.5 and 2.0 g/L phenol concentrations. However, when the phenol concentration was 2.0 g/L it increased to approximately 1.745 g/L (dry biomass) and phenol could be completely degraded only at 48 hours. The biodegradation of phenol can be described by the non-elementary chemical reaction:

Phenol + Nutrients + *R. pyridinivorans* GM3 Cells ⟹ More *R. pyridinivorans* GM3 cells + Products

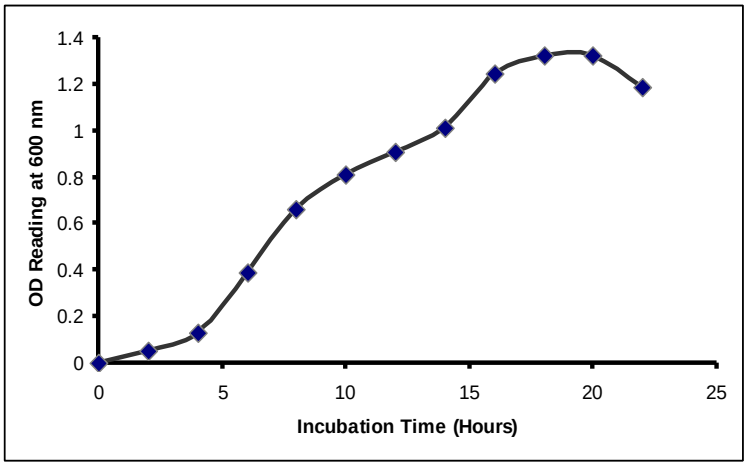

Figure 4. Growth curve of *Rhodococcus pyridinivorans* GM3 in mineral salts medium

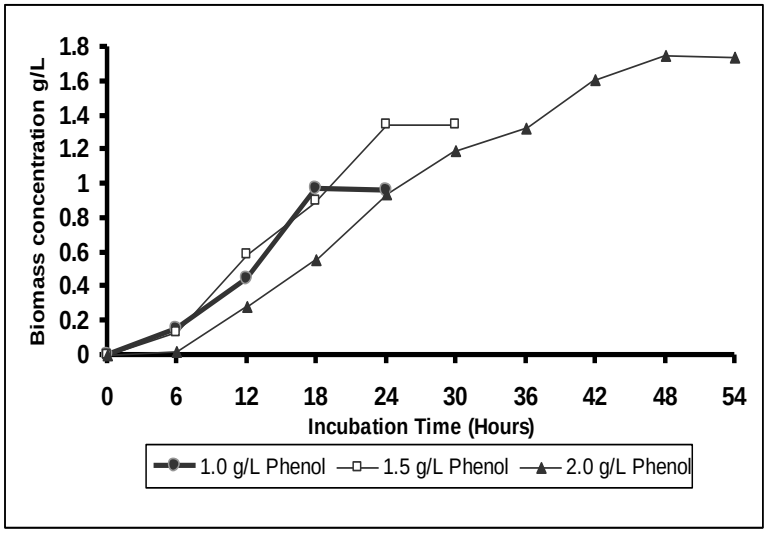

Figure 5. Biomass production of *Rhodococcus pyridinivorans* GM3 with 1.0, 1.5 and 2.0 g/L phenol concentrations

4. Discussion

The isolate *R. pyridinivorans* GM3 could degrade phenol with concentrations of 1.5 g/L in 24 hours. The results implied that GM3 has utilized phenol as sole source of carbon in MSM. Previous reports

suggest that *Rhodococcus* has the ability to degrade a variety of hydrocarbon and fuel additive compounds and could be efficiently used in bioremediation field for elimination of these compounds [16].

It was confirmed that lag phase depends upon the concentration of phenol in the media and when the concentration is increased, the lag phase period also extended concomitantly. The lag phase of *R. pyridinivorans* GM3 was obvious at 2.0 g/L phenol concentration within the first 6 hours of incubation, which might be due to the toxicity of phenol and the use of phenol as sole carbon and energy source. Similarly, Kim *et al*. [9] showed that increased inhibition of degradation with the higher levels of phenol was exhibited the lag phases increased. The correlations between concentration and lag phase imply that regarding inhibition of phenol degradation in kinetic analysis is useful for phenol degradation characterization [17]. Also, these results are in agreement with Oboirien *et al.* [18] whereby increasing initial concentration from 0.1 to 0.25 and 0.5 g/L enlarged the lag phase of *Pseudomonas aeruginosa* growth on pure culture to 8 and 16 hours respectively.

Phenol is not easy to degrade and is toxic to mainly microorganisms at adequately high concentration. The growth rate can inhibit even of those species that have utilizing it by metabolic ability as a substrate used for growth [19]. Since of the nature of phenol inhibitory to *R. pyridinivorans* GM3 populations at high phenol concentrations may completely inhibit bacterial degradation or caused in long lag times following a slightly rate of biodegradation. When increasing the initial concentration of phenol from 100 mg/L to 500 mg/L result to extend lag phase of *Pseudomonas fluorescence* growth from 0 to 66 hours [20].

Microbial bioremediation of a toxic chemical depends mainly on the ability of a microorganism to be viable, survive and tolerance to existing concentration and utilize that the compound as a substrate for growth. Microbial biomass was directly proportional to increasing phenol concentration between 1.0 to 2.0 g/L with a maximum dry biomass of 1.745 g/L was noted after complete degradation of 2.0 g/L phenol in 48 hours. If the toxicant concentration can be dominated or the biomass is big sufficient, numerous very toxic wastes or components can be degrade. Furthermore, by incrementally mounting concentrations of pollutant and waste in environment that can utilize the bacteria for removing this pollution. Growth of *R. pyridinivorans* GM3 varies depending on consumption of phenol and nutrient abundance. In other words, the activity of forming biomass indicated phenol degradation. Therefore, there is significant relation between phenol degradation and growth. Parameters such as concentrations of pollutant, microbial adaptation, tolerance and viable biomass are essential parameters that effect on biodegradation of phenol rate which further depend on the period of culture adapted to phenol [21]. Phenol is difficult to use as a substrate for growth within biodegradable process because the phenol inhibits the activity of innate of most kinds of microorganisms at lower and higher concentrations, also the phenol is toxic to microbial even at skimpy concentration [22]. Moreover, Goudar *et al.* [10] reported that the greater than 1.3 g/L of phenol concentrations were toxic to the culture of microbial. Conversely, phenol showed inhibition to degradation rate of substrate and specific rate of growth over initial concentration of phenol 300 mg/L [23].

In the present study, growth of *R. pyridinivorans* GM3 increased with increasing phenol concentrations. Degradation of organic substrates supplies bacteria with energy source and materials of building for metabolism, new cells growth, maintenance of cell. Attention was focused on phenol toxicity that inhibits growth depending on the concentration of phenolic compound to which microbial cells are exposed. Researchers have described results such as disruption of cell, precipitation of cell protein, inactivation of enzymes and leakage of amino acid from cells [24].

The tolerance of phenol effects on bacteria growth; this implied that they contribute in the processes regulations which are operating through the cell division and/or growth. The solution is to gradually increase the concentrations of contaminant, letting to the microorganism population to acclimatize to the altering conditions and generate the necessary metabolites and enzymes [25]. The step of cell division is mostly sensitive to effect of phenol toxic and its inhibition can be regarded as a response of adaption underneath phenol stress conditions [26]. Therefore, it is required to know the phenol biodegradation process that involved in degradation. Research has been conducted to understand biodegradation of phenol that are among the most prevalent and persistent environmental pollutants.

5. Conclusion

The degradation rates diminished or slowed considerably for length of lag phase when high concentrations of the phenol was used. Adaptation demonstrated that effect of inhibition was take place at high phenol concentration, hence the degradability is rimmed due to the toxicity is a concentration function. However, the rate of biodegradation depends on the state of biomass development. Obviously, the microbial biomass was directly proportional with increasing concentration of phenol.

References

[1] Nair C I, Jayachandran K and Shashidhar S, 2008, Biodegradation of Phenol. *Afr. J. Biotechnol*.**7** pp 4951–4958.

[2] Rigo M and M Alegre R, 2004, *Isolation And Selection of Phenol-Degrading Microorganisms From Industrial Wastewaters And Kinetics Of The Biodegradation*. Folia Microbiol. 49 41–45.

[3] Mohite B V, Jalgaonwala R E, Pawar S and Morankar A, 2010, *Isolation and Characterization of Phenol Degrading Bacteria from Oil Contaminated Soil*. Innov Rom Food Biotechnol. **7** 61–65.

[4] Nagamani A, Soligalla R and Lowry M, 2009, Isolation and characterization of phenol degrading Xanthobacter flavus. Afr. *J. Biotechnol*. **8** 5449–5453.

[5] Shourian M, Noghabi K A, Zahiri H S, Bagheri T, Karballaei G, Mollaei M, Rad I, Ahadi S, Raheb J and Abbasi H 2009 *Efficient Phenol Degradation by A Newly Characterized Pseudomonas sp*. SA01 isolated from pharmaceutical wastewaters. Desalination. **246** 577–594.

[6] Prasad S B C, Babu R S, Chakrapani R and Rao C S V R, 2010, Kinetics of high concentrated phenol biodegradation by Acinetobacter baumannii. Int. *J. Biotechnol. Biochem.* **6** 609–615.

[7] Ho K L, Lin B, Chen Y Y and Lee D J, 2009, Biodegradation of phenol using Corynebacterium sp. DJ1 aerobic granules. Bioresour. Technol. **100** 5051–5055.

[8] Manafi M, Mehrnia M R and Sarrafzadeh M H 2011 Phenol removal from synthetic wastewater by Alcaligenes Faecalis: Online monitoring. *Int. J. Chem*. Environ. Eng. **2** 103–107.

[9] Kim M K, Singleton I, Yin C R, Quan Z X, Lee M and Lee S T 2006 Influence of phenol on the biodegradation of pyridine by freely suspended and immobilized Pseudomonas putida MK1. *Lett. Appl. Microbiol*. **42** 495–500.

[10] Goudar C T, Ganji S H, Pujar B G and Strevett K A 2000 Substrate inhibition kinetics of phenol biodegradation. *Water Environ. Res*. **72** 50–55.

[11] Varma R J and Gaikwad B G, 2010, Continuous phenol biodegradation in a simple packed bed bioreactor of calcium alginate-immobilized Candida tropicalis (NCIM 3556). World *J. Microbiol. Biotechnol*. **26** 805–809.

[12] Al-Defiery M E and Gopal R, 2014, Influence of metal ions concentration on phenol degradation by Rhodococcus pyridinivorans GM3. *Mesop. Environ. J*. **1**(1) 30-38.

[13] Clesceri L S, Greenberg A E and Eaton A D, 1998, *Standard Methods for Examination of Water and Waste Water*. 20th ed. American public health association. Washington. 5530 D, p.5–(43–44).

[14] Al_Defiery M E and Gopal R, 2014, Influence of metal ions concentration on phenol degradation by Rhodococcus pyridinivorans *GM3*. *Mesop. Environ*. *J*. 1(1) pp30-38.

[15] Tuah P B M 2006 *The Performance of Phenol Biodegradation by Candida Tropicalis RETL-Cr1 Using Batch and Fed-batch Fermentation Techniques*. Ph.D. thesis. Faculty of Science, Universiti Teknologi Malaysia, Malaysia. p 58.

[16] Auffret M, Labbe D, Thouand G, Greer C W and Fayolle-Guichard F 2009 Degradation of A Mixture of Hydrocarbons, Gasoline, And Diesel Oil Additives By Rhodococcus Aetherivorans And Rhodococcus Wratislaviensis. Appl. Environ. Microbiol. 75 7774–7782.

[17] Wei Y H, Chen W C, Chang S M and Chen B Y, 2010, Exploring kinetics of phenol biodegradation by Cupriavidus taiwanesis 187. *Int. J. Mol. Sci*. **11** 5065–5076.
[18] Oboirien B O, Amigun B, Ojumu T V, Ogunkunle O A, Adetunji O A, Betiku E and Solomon B O, 2005, Substrate inhibition kinetics of phenol degradation by Pseudomonas aeruginosa and Pseudomonas fluorescence. Biotechnology. **4** 56–61.
[19] Alexievaa Z, Gerginova M, Zlateva P and Peneva N, 2004, Comparison of Growth Kinetics and Phenol Metabolizing Enzymes of Trichosporon Cutaneum R57 and Mutants with Modified Degradation Abilities. Enzyme Microb. Technol. **34** 242–247.
[20] Agarry S E and Solomon B O, 2008, Kinetics of batch microbial degradation of phenols by indigenous Pseudomonas fluorescence. *Int. J. Environ*. *Sci. Technol*. 5 223–232.
[21] Basha K M, Rajendran A and Thangavelu V, 2010, Recent advances in the biodegradation of phenol: *A review. Asian J. Exp. Biol. Sci*. **1** pp 219–234.
[22] Kahru A, Maloverjan A, Sillak H and Pollumaa L 2002 The Toxicity and Fate of Phenolic Pollutants in The Contaminated Soils Associated with The Oil-Shale Industry. Environ. Sci. Pollut. Res. 1 27–33.
[23] Dey S and Mukherjee S, 2010, Performance and kinetic evaluation of phenol biodegradation by mixed microbial culture in a batch reactor. *Int. J. Water Resour. Environ. Eng*. 2 40–49.
[24] Pelczar M J, Chan E C S and Krieg N R, 2006, Microbiology. 5th ed. Tata McGraw-Hill Publishing Company Limited. p.493.
[25] Talley J W and Sleeper P M, 1997, Roadblocks to the implementation of biotreatment strategies. Annuals of New York Academic of Sciences. **829** 16–29.
[26] Putrinš M, Ilves H, Lilje L, Kivisaar M and Horak R 2010 The impact of ColRS two-component system and TtgABC efflux pump on phenol tolerance of Pseudomonas putida becomes evident only in growing bacteria. BMC *Microbiol.* **10/110** 1-12.

Determine kind and concentration of eliotropiumsuaveolens, Plantagomajorand Silybummarianum plants ingredients and its effect on some plant pathogenic fungi

Determain kind and concentration of eliotropiumsuaveolens, Plantagomajorand Silybummarianum plants ingredients and its effect on some plant pathogenic fungi

A J Abdlrahmaan[1], I A Abdul Raheem[2], R H Latef [1]

[1] Department of Biology, College of Women Education, University of Tikrit, Iraq.

[2] Department of Biology, College of Education, Tuzhurmato.

Abstract. A study was conducted on the biology laboratories-Tikrit University to determine the ingredients of three local plants Heliotropiumsuaveolens, Plantagomajor and Silybummarianum and effect its extracts on the growth of fungus Fusariumsolani, Fusariumoxysporum and Alternariaalternate. Results analysis by High performance Liquid Chromotographyte (HPLC) technique showed H. suaveolensplant contain alkaioidic compounds indicine 9.52%, supinine 3.95%, indicine-N-oxide 14.66%, heleurine 33.0%. heliotrine 31.88% and lidelofidine 6.95% and plantago major plant contain salysilic acid34.93%, kampferol 4.55%,gentisic acid 2.72%,vanilic acid 1.67%,chlorogenetic acid 0.70%,coumaric acid 8.59%,ferulic acid 21.42% and aucubin 9.12% While S. marinum contain salichristinA 42.24%,salichristin B 14.89%, salidianin 30.23%, silybins A3.30%,silybins B 2.74%, isosilybins A 4.86% and isosilybins B 1.71% Extract 20 concentration of H.suavelones and P.major showed high inhibition reached100% While S. marinumshoed no effect on fungus growth.

Keywords. Medicinal Plants, Aqueous Extract, Fungi Inhibitory Effect.

1. Introduction

Medicinal plant has big important in agriculture production, it contain active natural ingredients [1] this natural products has effect on other plants and on its environment beside its effect on organisms growth [2] such as using extracts of medicinal and aromatic plants which has one or more materials in its chemical composition able to inhibition fungus and insects growth [3, 4] , There is a wide variety of funga genera causing diseases for human, animals and plants [5, 6, 7] The intensive and indiscriminate use of pesticide in agriculture has caused many problems to the environment such as water, soil, animal and food contamination, poisoning of farmers [8] besides its harmful effect on human health [9, 10] and appearance resistant strain from fungi [11]. The genus Heliotropium is bigger genuses of Boraginaceae family include 220-300 species in Iraq specialize by scorpoid inflorescence shape [12] andplantago majorbelong to the Plantaginaceae family its high reach about 0.5 m give many leaves over the earth directly had about 5-7 lines with small black or yellow or weight, flowers on the head of long stem distrib around roads and in the gardens [13] ,while marianumis one of the important species belong to the silybum genusits annual or biannualplantwith 1-2 m high and simple or branched cavey stem and leaves spiny on the borders has white veins, the flowers is violet or pinky or white [14], distribution in the south of Aljazeera and Sedimentary plain of Iraq and commonly find around the fields and roads [15, 16]. In recent years, antimicrobial properties of plant extracts have been reported with increasing frequency from different parts of the world because plant provide compounds such as alkaloids suponins, volatailoil, coumarins, suponins, flavonoids and glycosides [17], extracts of Zingiberofficinale and Xylopiaethioicaplants inhibited

growth of Fusariumoxysporum [18], a study by [19] find activity extracts of Cmbopogon martini on inhibition growth of Fusariumsolanifungi.Pimpinellaanisum extract with 50 and 75% concentration lead to full growth inhibition of F.solani,R.solani and A.alternata fungus [*20*] and sort rot diseases on potato affected by garlic extract[*21*],extracts of Saliva officinalis.Rosmarinsofficinalis and seed of Cynarscolymns were quite comparable to values obtained with the convential fungicide captain [*22*],turmeric rhizomes inhibited the mycelia growth of A.solani by 38.2% [*23*] and aqueous extracts from Euccalptuscitriodrafresh leaves in 20% concentration were efficient to inhibited in 100% the mycelia growth of Phytophthorasp and Seclerotiumrolfsii and 75% in R. solani and in 45% to A. alternataunder in vitro assays [*24*],while aqueous extract of wild basil at 5% concentration was enough to provide inhibition at 100% mycelia growth of A.alternata [*25*] .Study by [*26*] appeared that crude extract of Lippa alba and R.officinalis has bigger inhibition for A. alternata mycelia growth and the two plants mixture extracts produced better values than isolated extracts with 60% of growth inhibition of A.alternata [*27*].Active inhibition appeared by extract of Neriem oleander leaves against R. solani and F. solani [*28*], also significant effect of N.oleander leaves extract in particular 3% which showed high inhibition activity on fungi colony diameter growth of Pythiumaphandermatum [*29*].

2. Materials and Methods

2.1. determain plants ingrediants

The plants collected from fields and around of the roads(leaves and stems) of three plants were washed by water, The plant dried at the shade and milled then 10gm from the sample put in 50 ml boiled water (90-100C0) for 3 hours then extracted whattman papers no.1 the extraction collected and put in closed glass tube in order measuring the concentration of active ingredients by High Performance Liquid Chromotography (HPLC) apparatus which supplied by Shimadzu company (Japan) type,LC-10A 2000 supplied with spectrum scale (Spectro photo meter – spd – 10A – UV), A sample size 20µl injected on Fast liquid chramotographic column (LC) with diamention(50×4.6mm I.D) by the injector type (Rheodyn-712) at condition show in (table 1)and the data recorded by calculator which drawed the pick area and retention time. Astandard solution of *Heliotropiumlasiocarpium* plant used and speratedpy HPLC apparatus and identification the pick area and retention time of standard solution and comparing it with the pick area and retention time of studed plant sample at the same condition. Concentration of compounds in the sample calculated by the aquation [36]:

$$\text{Conc. Compound in the plant} = \frac{\text{Pick area of compound}}{\text{Pick area of standard pattern}} \times \text{standard pattern conc.} \times \text{delution factor}$$

Table 1. Chromatographics separate condition.

Colum	Mobile Phase	Following rate	Type of detector	Temperature	Fast of recorder paper	Size of injected sample
Reverse Phase Column (50×4.6 mm I.D)	Distill water: Ethanol 70% 2: 80v/v	10 ml/min.	Ultra violate ray 254 nm	$30C^0$10	mml/min	20mg/ml

2.2. Preparing plants extracts

Leaves and stems of three plants were washed by water and soaked in 2% of sodium hypochloride solution for 15 minute and washed with sterilized water and air dried at room temperature, 100gm of each plant milled and used for extraction in 100ml of hot water and the extraction dried by using water path at 60^0Cinorder obtain 8.2gm dried extraction then different concentration 5, 10, 15, 20% prepared from the dried extraction in addition to control 0% [20].

2.3. Isolation and identification of fungi.

Infected parts from potato and Solanum plants were collected, the pathogen was isolated on potato dextrose agar (PDA) medium. Infected piece of plant washed and sterilized by sodium hypochloride

2%then washed and transferred to (PDA) plate were incubated at 25 ±2^{0}C for 10 days. The fungus identification was done with using akey of [30].

2.4. interactionbetween fungi and plant extract

Three petridish (9 cm diameter) prepared for each fungi then disks with 0.5cm transfer from each studied fungi taken from pure culture on age 7 days .Prepared different concentration plant extactionaddad in each treatment(three replication) without control treatment, the dishes incubatedat 25 ±2^{0}C,taken the measurement of fungi culture growth of two opposite diameter of diameter each dish when fungi growth reached in control treatment to edge of the dish then calculation the percentage of inhibition by the equation:

$$\text{Inhibition (\%)} = [(C - T)/C] \times 100 \quad (1)$$

Where, C and T represent the diameter of control and treated colony, respectively. Data on mycelial growth 9 days after incubation (DAI) when mycelial reach edge of petridish were recorded. before addition the mediumantibacterial Amoxicilin added to 1 L of PDA mediumand mix well with the medium then added to the petridish.

3. Results and discussion

The analysis of three studded plants by HPLC apparatus appeared verily H. suaveolensplant containseveral compounds Indicine, Supinine, Indicine-N-oxide, Heleurine, Heliotrine and Linelofidine Figure 1 and table 2, and P.vmajor plant contain the compounds Salysilicacid, Kaempferol, Gentisicacid, Vanilicacid, Chlorogenticacid, Coumaricacid,Ferulic acid and Aucubin Figure 2 and table 3, while S. marinumplant contain, Silychrstin A, Silychrstin B, Silydianin, Silybins A, Silybins B, Isosilybin s A and Isosilybin A Figure 3 and table 4.

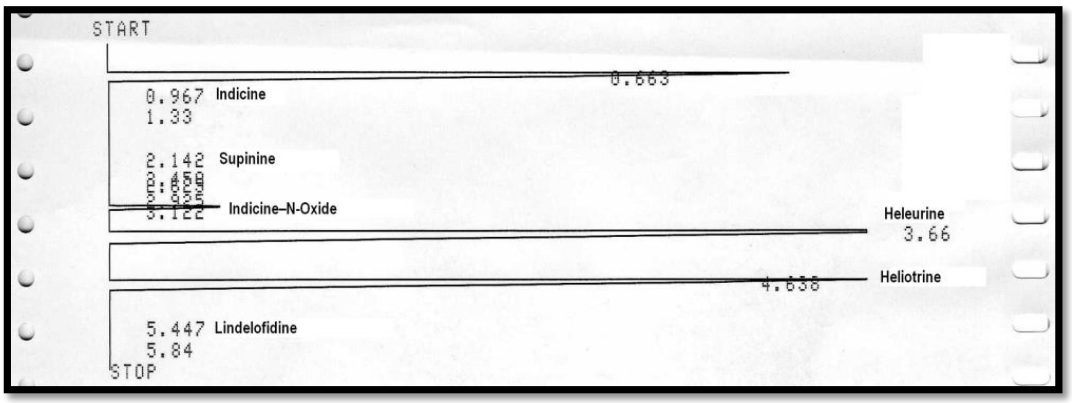

Figure 1. Chromatogram HPLC analysis of studied H. suaveolens plant.

Table 2. Compounds, Pick area and the concentration studied of H. suaveolens plant.

Compounds	Pick area Of plant	Pick area of standard	standard Conc. mg/ml	Compound Conc.	Percentage (%)
Indicine	14222	39148	50	90.82	9.52
Supinine	49530	32824	50	37.72	3.95
Indicine-N-oxide	20682	36977	50	139.83	14.66
Heleurine	46263	36748	50	314.73	33.00
Heliotrine	33423	27478	50	304.08	31.88
Lindelofidine	92870	34983	50	66.36	6.95

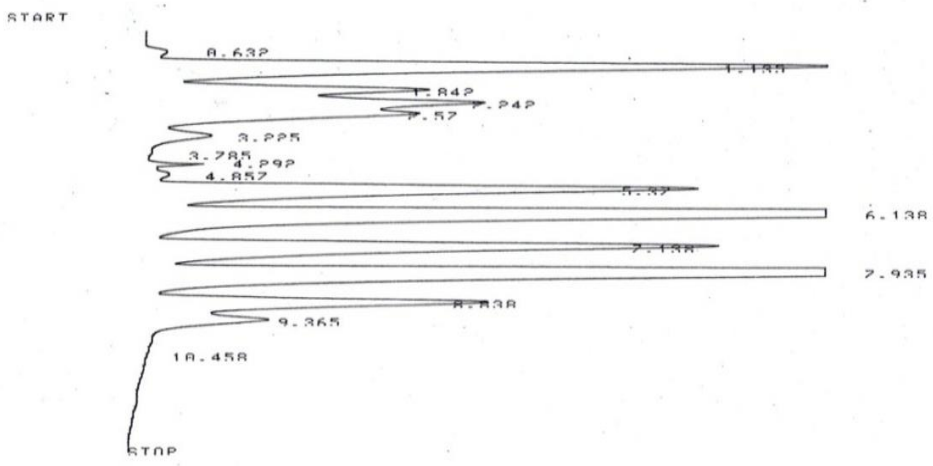

Figure 2. Chromatogram HPLC analysis of studied Plantago major plant.

Table 3. Compounds, Pick area and the concentration of studied P. major plant.

Compounds Of plant	Pick area of standard	Pick area mg/ml	standard Conc. mg/ml	Compound Conc.	Percentage(%)
Salysilic acid	37357	3606	25	90.82	34.93
Kaempferol	133752	3732	25	37.72	4.55
Gentisic acid	13164	3864	25	139.83	2.72
Vanilic acid	3806	18348	25	314.73	1.67
Chlorogentic acid	3510	40005	25	304.08	0.70
Coumaric acid	31321	29463	25	66.36	8.59
Ferulic acid	6315	23819	25	29.13	21.42
Aucubin	31890	28229	25	64.22	9.12

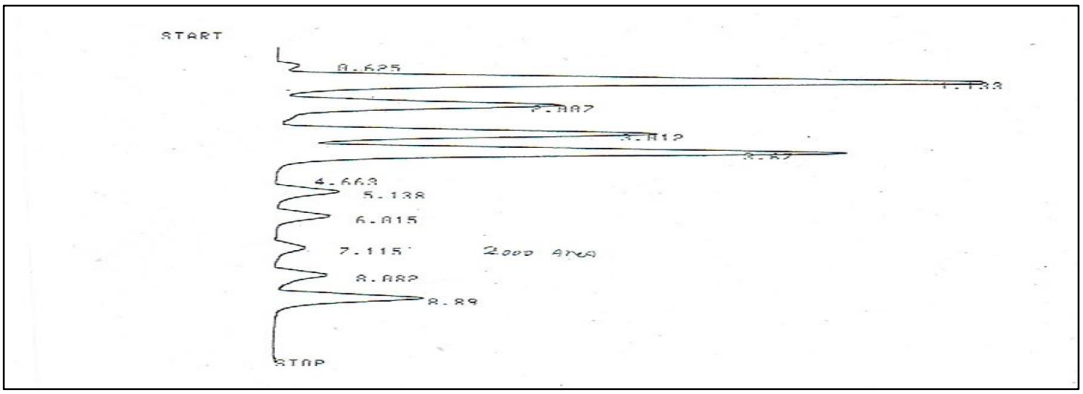

Figure 3. Chromatogram HPLC analysis of Studied *S*. marainum plant.

Table 4. Compounds, Pick area and Concentration of studied S. marinum plant.

Compounds	Pick area Of plant	Pick area of standard	standard Conc. mg/ml	Compound Conc. mg/ml	Percentage (%)
Silychristin A	416853	2583	25	31.98	42.24
Silychristin B	15645	34646	25	11.28	14.89
Silydianin	20637	22533	25	22.89	30.23
Silybins A	3425	34445	25	2.50	3.30
Silybins B	2831	433993	25	2.08	2.74
Isosilybins A	3091	20989	25	3.68	4.86
Isosilybin A	2000	38168	25	1.30	1.71

Plant extracts differ in its effect on fungi growth,the concentration by 15% and 20% ofP.majorplant completely inhibit fungi growth and H.suaveolens plant completely inhibit the fungi growth by 20% concentration,while S.marainumdoesnt show any effect on fungi growth Table 5 and 6.

Table 5. Effect of varians concentration of plant extracts on the radial mycelia growth of Fusarium solani,Fusarium oxysporum and Alternaria alternate (average mm).

	Concentration%				
Extracts	0	5	10	15	20
H.suaveolens	86.61a	71.72b	28.77c	8.95d	0e
P.major	87.19a	36.0b	11.31c	0d	0d
S.marainum	87.30a	86.16a	85.04a	86.62 a	81.33a

***The same letterin the line means no significant differnce between the concentration.**

Table 6. Ihibition concentration of Fusarium solani,Fusarium oxysporum and Alternaria alternate growth at various concentration of plant extracts.

	Concentration%				
Extracts	0	5	10	15	20
*H.*suaveolens	0	17.19	66.78	89.63	100
P.*major*	0	58.71	87.02	100	100
S.*marinum*	0	1.30	2.5	80.77	6.83

Analysis by(HPLC) technique is characterized by in procedure quantitive and qualitative estimation of plant ingrediants by its ability to caculate curves and its high and determine this ingrediants on one operation [31],the author [32] and [33] said verily speration and diagnosis of ingrediants extracted from plants by (HPLC) appratus gave fast results and high accuracy in comparative with other chromotographic methodsand using (HPLC) technique showed high speed and

accuracy on appreciation quantity and quality of volatail oil [34] and [35]. Using this technique appeared existence 15-20 compounds on the volatail oil of Cuminum cyminum[36] and discovery several glycosidic compounds on the Heliotropium sp plant such asQuricting ،Isorahamanine ،Heliotrope ،Isopyrolidine ،Narenginine ،Triterpene [37]. The inhibition on fungi growth due to the alkaloidal compounds in plant extract which prevent fungus growth on severl plant kinds [3] ,this compounds has high treatment efficiency and its toxic [21] exist in the plant and mature seeds contain it more than imature seeds[38] also alkaloidal compound N-oxide is toxic [39] and the inhibition ability of this species due toits high containfrom alkaloid reach (233.71)mg/ml in comparative with low content of another compounds[37],our study agree with [40] whom proved that aqoues and alkholic extract of Heliotropium genus inhibit growth of types of bacteria and fungi and with [41] who showed difference on inhibition activity of Artemisia sp, Achillea spand Saliva officinalis plant extracts against F.oxysporum fungi alsow agree with syudy appeared completely inhibition on F.solani and A.alternata growth when use Pimpinella anism seed extracts [42]. The analysis appeared severel acidic compound in the content of S. marinum and this may lead to inhibition of fungi growth because acidic materials or acid medium affect on enzymes production [43]Organic acids have been used to prevent the growth reproduction of harmful fungi and secreting of aflatoxins. The effect of eight organic acids as antifungal agents on the growth of four fungi were studied. Acetic acid (10%) showed the highest inhibition effect on A. flavus growth being 45.21% while tartaric acid (5%) and citric acid (5%) gave the lowest inhibition effect of 0.42%. Formic, acetic and propionic acids had the highest inhibition effect on A. flavus growth [44].

References

[1] Al-Abed A, Study the activity of antibacterial and antioxidant for crud alkaloid extract of *Tragonumnudatum* L. plant. MSc. Thesis, Coll. of Sci. Univ. of Khasedy Merbah Warkhela, Algeria, 2009.
[2] Al-Eahia S A, Role of natural plant extracts in controlling fungi causing plant diseases. MSc. Thesis, Coll. of Sci. Univ. of the king Suod, Sudia Arabia, 2002.
[3] Afefy F A, Mahmood A A. The plant extracts and Biologicalactive. Al Thakhfaaldenialiberary for publishing (Bor-Sa,ed:Egypt), 2002.
[4] Tadakashimi R, Kukubo, Sakinom M. Antimicrobial activities of Eucalyptus maculate. *Applid Microbiology*, 2004, 39: 60-64.
[5] Agrios S G N. Lossed caused by plant diseases, plant pathogen. [Elsevier: OxfordUK., 2004: 29-45.
[6] Harris C A, Renfree M J, Woolridge. Assessing the risk of pesticide residues to consumer: Food Additive and Contamintation, 2001, 18: 1124-1129.
[7] Kumardas P. Antibacterial activity of leaf extracsof Heliotropiumindicum L. Dep. Bio. life. Sci., 2011, 20: 904-907.
[8] Stangarlin J R, Kuhn O J, assi L, Schwan-Estrada K R F. Control of plant diseases using extracts from medicinal plants and fungi Science against microbial pathogens: communicating current research and technological advances. A. Méndez-Vilas (Ed), 2011.
[9] Chean L. H, Cox J K. Screening of plant exracts for control of powdery mildew in squash. Phytopato, 1995, 88: 545-550.
[10] Minler R T. Prospects for biopesticide for aphid control.Entomophoga, 1997, 42(1-2): 277-24
[11] Hassan M S. Evaluation of some fungi and water extracts of some organic manure efficacy in controlling of Rhizoctoniasolani on tomato Daily *J. Agric. Sci,* 2001, 3(1):61-67.
[12] Al-Musawi A H, Plant classification science, staddition, Dar Al-kutub for printing and distribution, Mosul,Iraq, 1987.
[13] Al-Malkhy Ibn-Al Baitar 1990 Explain Diaskhor Bdoe Book, Bet-Al-Hekma, Khertaj, Tunis.
[14] Rechinger, K. H. Flora of lowland Iraq, Velageven, Gover. Wein, 1964.
[15] Majeed S H. Mahmoud, M. J. Iraqi plantsad herbs between folkloric medicin and scientific research, scientific research council, Biology research center, Drugs toxic and Drugs evaluation, 1988.
[16] Tallas M. Medicinal and plant lexicon, Dar Tallas for distribution and translation studies, Syria, Damascus, 1989.
[17] Cowan M M. Plant products and antimicrobial agents Clinical microbiology, Rev., 1999, 10: 564 - 582.
[18] Okibo R N, Numeka I A. Control of Yam tuber rot with leaf extracts of XylopiaeathipicaL and ZingiberofficinaleL. Africa J. Biotech, 2005, 1(4).
[19] MaolanY S, Kamel A, Al-Husainy S. The natural chemical biological control for welt disease causes and seedling die some vegetable crops in protect house on Riad region King Abdul-Azez city for Application science, 2006.

[20] Al-Janabi H S, Al-Doghchee A H, Al-Jabery W M. Extracts effect of Pimpinellaanisum L plant seeds on growth of Fusariumsolani and comparing its growth with growth of Rhizoctoniasolani and Alternaria alternate on extracts*, Babilon J. Pure Application Sci*., 2015, 1(23): 411-425.

[21] Salman A M, Alaa E H, Effiicincy of some plant extracts Bacillus cerus and antibiotic on controlling soft rot diseases on potato caused by Erwinaiacarotorora Subsp. *carotorora Kufa J. Agric. Sci.,* 2011, 3(2): 151-161.

[22] Paola D D, Andrea C, Diego A, Patricia L, Fernando F, Marco D R Antifungal activity of medicinal plant extrscts against phytophathogenic fungus Alternaria ssp. *Chilean J. Agric. Res*., 2011, 71(2): 231-239.

[23] Balbi-Peña MIB, Becker A, Stangarlin JR, Franzener G, Lopes MC, Schwan-Estrada KRF Control of Alternariasolaniin Control of Alternariasolaniin tomato by Curcuma longa and curcumin - II. In vivo evaluation.FitopatologiaBrasileira., 2006, 31: 401-404.

[24] Bonaldo SM, Schwan-Estrada KRF, Stangarlin JR, Cruz MES, Fiori-Tutida ACG Contribution for the study of antifungal and phytoalexins elicitors in sorghum and soybean activities by eucalyptus (Eucalyptus citriodora). Summa Phytopathologica., 2007, 33:383-387.

[25] Benini PC, Schwan-Estrada KRF, Klais EC, Cruz MES, Itako AT, Mesquini RM, Stangarlin JR, TolentinoJúnior JB, In vitro effect on phytopathogens of essential oil and aqueous crude extract of Ocimumgratissimum harvest in the four seasons. Arquivos do InstitutoBiológico, 2010, 77:677-683.

[26] Gasparin MDG, Moraes LM, Schwan-Estrada KRF, Stangarlin JR, Cruz MES. Effect of crude extract of Lippiaalbaand Rosmarinusofficinalison phytopathogenic fungi. Anuário CCA/UEM. 2000.

[27] Tagami OK, Gasparin MDG, Schwan-Estrada KRF, Cruz MES, Itako AT, Tolentino Júnior JB, Moraes LM, Stangarlin JR Fungitoxicity of Bidenspilosa, Thymus vulgaris, Lippia alba and Rosmarinusofficinalisin the in vitro development of phytopathogens fungi. Semina. Ciências Agrárias., 2009, 30:285-294.

[28] Hadizaadeh I, Pevastegan B, Kolahi M. Antifungal activity of Netle (Uryicadioica L.) Colocynth (CitrullacollcynthL. Schrad) Oleander (Nerium oleander L.) Extracts of plants pathogenic fungi *Pkistan J.Bio.Sci*., 2009,12(1):58-63.

[29] Muhammad N. M. Effect of aqueous extracts of Nerium oleander leaves on the fungi causes Damping off of Cucumber seedling, *Babelon J, Pure and applicated Sci*., 2011, 3(6): 520-542.

[30] Hoking A D, Pitt J I. Mycotixigenic fungi food borne microorganism of public health significance. Food Microbiology Group, 1997:35-55.

[31] Al-Hedwany A KH. Effect fertilization and foliar application on some nutrient elements on quantitative and qualitative of some active compounds in seed of two kind of (Trigonelafoenum L.), Ph.D. Theses Col. Agric.Unvi.Baghdad , Iraq, 2004.

[32] Man KP, HP. Sang, B.H. Young. Determinate on of denseno side by high performance liquid chromatography-evaporative light scatting detector.Chin.J.Pharm. Anal., 1996, 16:412-414.

[33] Yang. S J, LUT. J, Hwang LS. Simoltaneous Determination of Furostanol and Spirostanol Glycoside in Taiwanese Yam (Dioscoreaspp) cultivation by high performance liuid chromatographyJ, of food and Drug Analysis., 2003, 11(4):271-276.

[34] Baswnway R J. Determination and β-Carotene in Some Raw Fruits and Vegtables by high high performance liuid chromatographyJ.Agric. Food, 1986:457.

[35] Chen BH, JR Vhuang JH Line, Cchiu C P. Quantification of provitamin compounds in Chinese vegetables Vegtables by high performance liquid chromatography J .of food protection, 1993, 56(1):51-54.

[36] Al-Bayaty A J A. Effect of humic acid and uxins on growth of (Cimbopogoncitratus L.) plant and its ingrediants. Ph. D Theses, Col. Edu. Univ. Tikrit. Iraq, 2012.

[37] Mohmmad A A. Taxnomic comparative study of species of genus inmedl and north of Iraq. Ph.D. Theses, Col. Edu. Univ. Tikrit. Iraq, 2012.

[38] Mahmodian M, Jalilpour H and Ssalehian P. Toxicity of (Peganum harmala). Review and a case report. Iranian J. of Pharmacology and therapeutic, 2002, 1:14.

[39] Lin, G, Cui, Y Y, Hawes, E M. Characterization of rat liver microsomal metabolites of clivorine, a hepatotoxic otonecine-type pyrrolizidine alkaloid. Drug MetabDispos, 2000, 28:1475–1483.

[40] Mahmoud M J, Redha, F M J, Al-Azawi, M J, Hussein, WA, and Beham, Y T. Alkaloids of Iraqi Heliotropiumramosissimum, Phyto-chemistry and some biochemical Aspects. JBSR. 1987, 18 (1): 127-135.

[41] EsmailF K H. Evaluation of inhibitory activity of some plant extracts on growth of Fusarium. *Iraq J. Sci*., 2010, 41(2):165-172.

[42] Al-JanabiH.J,Al-Doghjee,E H, Al-Jabery, W M. Effect of Pimpinilaanism L.seedextracts on Fusariumsolani fungi andcomparing its growth with growth of fungi Rhizoctoniasolani and Alternaria alternate on oil extract. *Babilon J. Pure Sci*., 2015, 1(23): 441-425.
[43] Emran R, Al-Janabi J K, Al-Janabi H SH. Effect of some environmental condition on growth of Microsporumcanis fungi isolated from Tihecorporis in human and its production from protease enzyme.J. *Babilon,Pure and applied Sci*., 2011, 2(19):1-20.
[44] Abdulnabi A M. Fungi resistance for sever environmental condition.Kenanonline.com/users/abdulnabi/post/472279 2012.

Pathological And Immunological Study On Infection With Escherichia Coli In ale BALB/c mice

Pathological And Immunological Study On Infection With Escherichia Coli In ale BALB/c mice

Intisar H Ali[1], Majid S Jabir[1], Hanady S A Al-Shmgani[2*] , Ghassan M. Sulaiman[1] and Ali H. Sadoon[1]

[1]Biotechnology Division, Applied Science Department, University of Technology, Baghdad, Iraq
[2]Biology Department, college of Education for Pure Sciences/Ibn al-Haitham, University of Baghdad, Iraq

Abstract. Escherichia coli bacteria consider as one of the common responsible for the frequency and severity of infections that it causes hospitalized patients. E. coli simultaneously carries a harmful side in which only a slight genetic recombination can bring about highly pathogenic strain that most frequently causes the scourge of bacterial infections worldwide including sepsis, neonatal meningitis, pneumonia, bacteremia, and traveler's diarrhea. This study was carried out to assessed Escherichia coli infection induced different Pathological and immunological. Following Escherichia coli isolation, identification and counting, the lethal dose (LD-50) was determined before infection. Twenty-two mice were used in this study for 21 days infection, the animals were sacrificed at 3, 6, 9, 12, 15, 18 and 21 days, and tissues of different tissue were collected, examined for bacterial infection. Bacteria and mice Immunization and ELISA were used to detect immunoglobulin G level in serum as well. For histological study, different infected organs were used. The results indicated that the LH50 was 1×109 cell; and all organs were infected after 3 days followed by decreased in infection level shown in brain at day 12, lung, kidney and intestine at day 15 and in liver, spleen and heart at day 21. Moreover, ELISA results revealed that concentration 1:200 of serum in positive and negative state and optimum concentration of Ag 1:40 dilution and compact dilution is 1:1000. In addition, diversity of histopathological alteration occurs in tissue on time-depended manner. This study concluded that the ability of activated E.coli to stimulate the intestinal secretory immune system of germ might result from a retardation of immunological maturity.

Keyword: Escherichia coli infection, histopathological in mice, immunological maturity

Introduction

Escherichia coli are a gram negative bacterium which is responsible for the frequency and severity of infections that it causes hospitalized patients. *E. coli* simultaneously carries a harmful side in which only a slight genetic recombination can bring about highly pathogenic strain that most frequently causes the scourge of bacterial infections worldwide including sepsis, neonatal meningitis, pneumonia, bacteremia, and traveler's diarrhea [1, 2].

There are many physiological changes accrue during infection with EPEC such as transport of iron [3], inflammatory responses initiation, and increase in the cellular permeability [4]. These physiological events are similar to the changes accrue by EPEC of host signaling pathways, such as inositol phosphate fluxes [5], protein kinase C, mitogen-activated protein kinases [6], tyrosine kinase enzyme, myosin light-chain kinase [7], and NF-KB [8].

The motivation of some these lanes have been proven to the biological changes induction of EPEC. Though of achievement over the last 25 year for understand the EPEC illness, there is still needed more studies to comprehend the EPEC activation of biological changes. Earlier studies with different animal models have been reported to investigate host immune reactions such as modulated rabbits and mice [9, 10].

The diseases which are induced by REPEC in animal is comparable to EPEC causes infections [9] but, there are confines to the same model, like genetic and immunological difficulties. However, the present study was done to examine of *Escherichia coli* for BALB/c mice was used for animal immunological and histological studies.

Material and methods

Isolation and identification of Bacteria

In the present study, the samples of bacteria were collected aseptically in sterilized labeled containers from Al-Yarmook Hospital, Baghdad, Iraq, and were brought to the Microbiology Laboratory, Division of Biotechnology, Department of Applied Science, University of Technology. The *E. coli* were isolated by following standard protocol using sterile bacteriological media, including Nutrient agar and MacConky agar. The specimen were aseptically inoculated on the plates and incubated aerobically at 37 °C for 24 hours. The morphological investigation of Bacterial strains have been done using Gram's staining. In the other hand biochemical tests were also included such as , catalase, (MR-VP), gelatin liquefaction test, starch hydrolysis, nitrate reduction test, indole, motility, coagulase, urease, oxidase, TS,I sugar fermentation and Bacterial counting as described by [11].

Laboratory Animals

Male BALB/ mice were the tested animals, which were 8 week old at the beginning of experiments, and their weight was 22 ± 0.5 gram. They had free excess to water and food during experiments. The mice were divided into 2 groups.

Lethal Dose -50 (LD_{50})

The lethal dose-50 was determined in mice before carrying infection efficacy experiments by injecting intraperitoneally (i.p.) different doses of viable *E. coli* suspended in phosphate-buffered saline (PBS). The doses were 1×10^1, 1×10^2, 1×10^3, 1×10^4, 1×10^5, 1×10^6, and 1×10^7 CFU per mouse. Five mice were utilized for each dose group. Another group of five mice were used as control and administered with PBS only. The living and dead mice were detected after 28 days for LD-50 and calculated using the formula as below:

$$\text{Proportional distance} = \frac{50\% - (\text{Mortality at dilution next below})}{(\text{Mortality next above}) - (\text{Mortality next below})}$$

Infection of Mice

Approximately 1×10^7 of *E. coli* cells in 250 µL of PBS were injected interaperitonial into 33 mice. Control animals of 11 mice were received 250 µL of PBS. During the experimental time of treatment, animals were detected every 24 h for observing action and aquatic intake, and mass was measured as well. Following infection, the animals were sacrificed at 3, 6, 9, 12, 15, 18 and 21 days, and tissues of liver, spleen, kidney, lung, brain intestines and intraperiton were collected, examined for bacterial infection and processed for further analysis.

Preparation of E. coli Ag for Immunization

E. coli cells were inoculated into nutrient broth for 24 h at 37°C and then washed with PBS by centrifugation at 3000 rpm for 5 min at 4°C; and then re-suspended to the appropriate density in PBS. Bacterial count were done to verify the number of bacteria at 1×10^7 CFU/ml. Bacterial strain were killed by heating 60°C for 60 min. The sterility of antigens was tested before use according to [12]. Protein concentration has been measured by biuret protein assay according to standard protocol.

Immunization of Mice

The mice were divided equally into two groups, 10 mice of each. The group one was injected subcutaneously 2 times for two weeks with 250 µL containing $1x10^7$ CFU/ml. Second group (control group) was injected subcutaneously with 250 µL of PBS. Serum were collected at 3, 6, 9, 12, 15, 18 and 21 days. Serum samples were stored at -20 ºC until use for analysis by ELISA.

Enzyme-Linked Immunosorbent Assay

ELISA technique are used to measured the level of immunoglobulin G (IgG) in the serum as described techniques by [13]. 200 µl prepared as described above. Diluted 1.5 µg mL^{-1} in carbonate bicarbonate buffer as coating antigen which kept overnight in refrigerator. Plates were washed three times with washing solution (PBS containing 0.1% Tween 20). Blocking solution 200 µl $well^{-1}$ was added (1% BSA in PBS), plates were incubated at 37 °C for 60 min. Then washed three times with washing solution. Diluted 100 µl of each serum samples 1:100 in 1% BSA was distributed into appreciate well, positive and negative control sera were added and then incubated at 37 °C for 60 minutes. Washing the plates three times, 100 µl of anti-IgG peroxidase conjugate diluted 1:1000 in diluents buffer containing 1% Bovine serum albumin were added to each well and plates were incubated at 37 °C for 60 minutes. Washing 3 times again and then add 100 ml of diluted OPD (1 tablet plus 75 ml deionized distilled water and immediately H_2O_2 30% for each diluted OPD) incubated 20 minutes in dark place at room temperature. Absorbance values at 490 nm were measured using ELISA Reader.

Histological study

The histological examination selected organs of treated mice were washed with PBS, fixed in 10% formalin, followed by use of paraffin dispensing module EG 1150H (Leica, Germany), and embedded in paraffin. Sections were prepared by use of a microtome RM2255 (Leica, Germany) and followed by hematoxylin and eosin (H&E) staining. The processing and staining of sections were performed according to a standard procedure used in histopathological laboratories [14].

Results

The biochemical evaluation for *E. coli* showed that colonies growing in MacConkey agar have a ping color due to the presence of fermented lactose sugar and give a positive test in catalase and negative test in urease as shown in Table (1):

Table (1). Biochemical test of *E. coli*

Test	Result
Gram stain	Negative
Oxidase	Negative
Catalase	Positive
Urease	Negative
Coagulase	Positive
Hemolysin	Positive
Fermentation mannitol	Negative

Lethal Dose-50

The results of LD50 for bacteria E. coli in mice after injection subcutaneously with bacteria have proved that the LD50 is (1×10^9 cells) as shown in table 2.

Table (2). LD-50 of infection mice in *E. coli*.

Group	No. of cells	loose	Live	Accumulation of loose effect	Accumulation of living effect	Accumulation percentage	Percentage
1	10^{12}	4	0	12	0	12/12	100
2	10^{11}	3	1	8	1	8/9	88.88

3	10^{10}	2	2	5	3	5/8	62.5
4	10^{9}	8	8	3	3	8/8	50
5	10^{8}	2	2	3	5	3/8	37.5
6	10^{7}	1	3	1	8	1/9	11.11
7	10^{6}	0	4	0	12	0/12	0
8	10^{5}	0	4	0	16	0/16	0
9	PBS	0	4	0	16	0/16	0

Infected organs with E. coli.

After 21 days of infection with *E. coli*. It is noted that all organs of mouse were infected and reached to maximum levels at 3 days of infection. After that the bacterial infection was started to decrease and less infection was recorded in the brain at 12 days of infection as compared to other organs. Low level infection in lung, kidney and intestine were recorded at 15 days while, in liver, spleen and heart was at 21 days as given in Table (3):

Table (3). Spreading of bacteria *E. coli*. in organs of mice.

Day after infection	Liver	spleen	heart	lung	Kidney	intestine	Intraperitoneal space	brain
3	+ + +	+ + +	+ + +	+ + +	+ + +	+ + +	+ + +	+ + +
6	+ + +	+ + +	+ + +	+ + +	+ + +	+ + +	+ + +	+ + +
9	+ + +	+ + +	+ + +	+ + +	+ + +	+ + +	+ + +	+ + +
12	+ + +	+ + +	+ + +	+ + -	+ + +	+ + +	+ + +	- - +
15	+ + -	+ - +	+ + -	+ - -	+ + -	+ + -	+ + -	- - -
18	+ - -	+ - -	+ - -	- - -	- - -	- - -	- - -	- - -
21	+ - -	+ - -	+ - -	- - -	- - -	- - -	- - -	- - -

Histopathological changes

Sections of infected organs were stained with haematoxylin and eosin and then evaluated for histological changes. The tested organs were liver, lung, spleen and kidney.

In the liver, infection with E. coli induces focus suspension and poly focus of neutrophiles, congestion of veins with micro abscess in tissue of liver especially at first days of infection. At second week, a severity infection was characterized by presence of inflammatory cells such as neutrophiles, lymphocyte and macrophage while at third week a signs of prominent central area of necrosis was seen in the infected sections but not in control sections 'Figure (1)'.

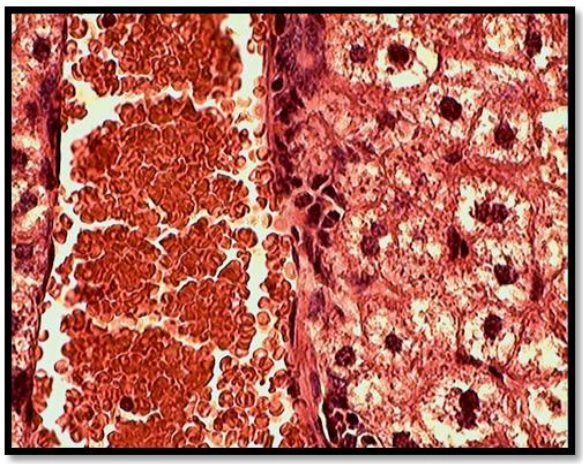

Figure (1): Photograph of liver section showing micro abscess and necrosis in liver cells of infected mice **with** E. coli. (H&E stain; x 400).

In spleen, increase in growth of white core of spleen tissue and contact between with other core and congestion in red core of spleen tissue and eccentric artery, in third week amyloidosis type sago spleen was seen in the infected sections. No abnormal changes were observed in control sections 'Figure (2)'.

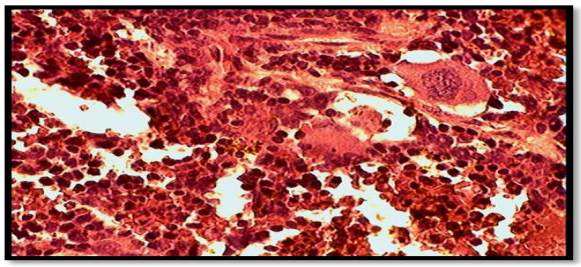

Figure (2): Photograph of spleen section showing amyloid in white core and sago spleen amyloidosis in cells of infected mice with *E. coli*. (H&E stain; x 400).

As shown in 'figure (3)', the pancreas of infected mice with *E. coli* notes suspension around pancreatic cell, pancreatic acini and congestion in vein of pancreatic. After three week later fibroblasts, lymphocyte, macrophages were observed in the pancreatic loop. No abnormal changes were observed in control sections 'Figure (3)'.

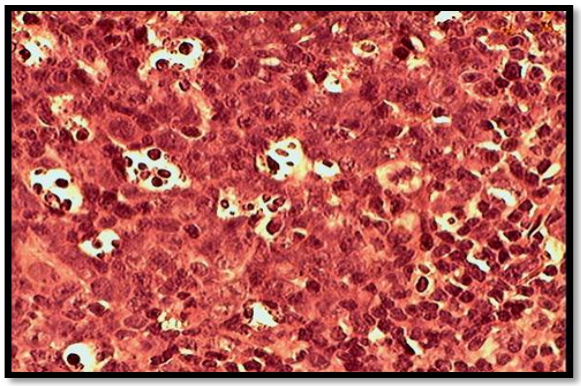

Figure (3): Photograph of pancreatic section showing amyloid in pancreatic ascini and clot in vein of infected mice with *E. coli* . (H&E stain; x 400).

Histopathological examination of lung showed growth in lymphocyte behind tunic and amyloid with congestion in vein and loose size in interstitial pneumonia. No abnormal changes were observed in control sections 'Figure (4)'.

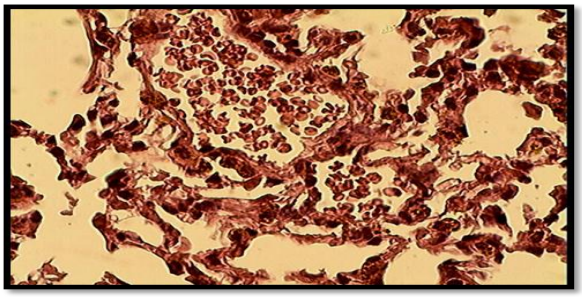

Figure (4): Photograph of lung section notes inflammation and amyloid with lymphocyte of infected mice with *E. coli*. (H&E stain; x 400).

As shown in 'Figure (5)', the infected heart revealed amyliod with neutrophile and macrophage, lymphocyte. Congestion in vein with focal epicarditis and focal mycocarditis was observed at infection in later state. Bacterial contamination was also recorded in lipid tissue surrounding the heart

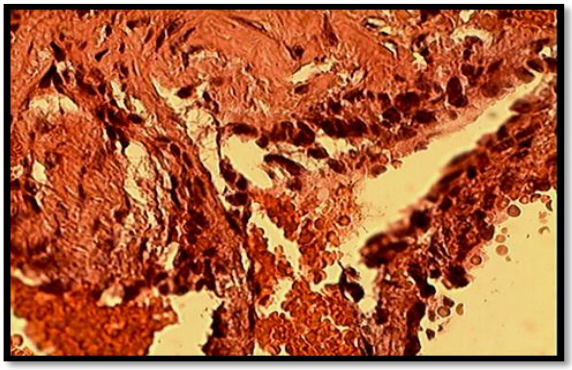

Figure (5): section in heart tissue notes myocarditis and amyloid in epicarditis X 400 (H& E).

The kidney: infection tissue of kidney effect interstitial nephritis and amyloid with macrophage and lymphocyte 'Figure (6)'.

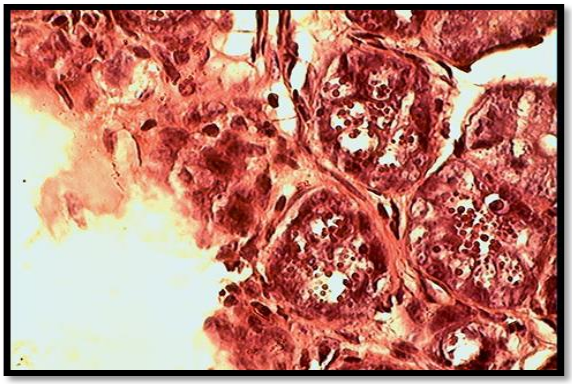

Figure (6): section in kidney tissue notes macrophage, amyloid and lymphocyte X 400 (H& E).

The intestine: infection accuse present of neutrophile in mucus of intestine that lead to congestion of vein in wall of intestine ,advance infection macrophage ,plasma cell and lymphocyte in mucus and secretion mucin 'Figure (7)'.

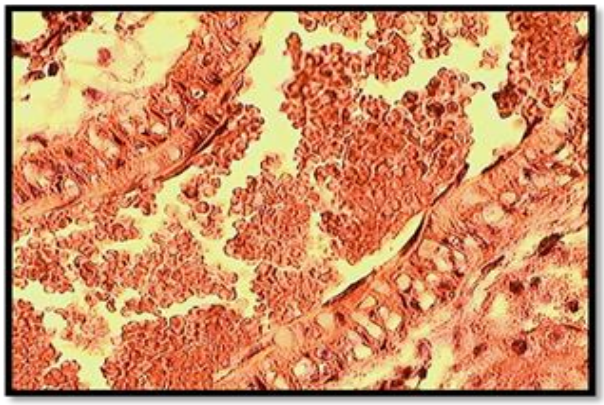

Figure (7): section in kidney notes chronic catarrhal enteritis and mucin in intestine X 400 (H& E).

The brain: congestion in vein and loss white blood cell around perivascular cuffing lymphocyte in all tissue of brain ,with focal gliosis and different change 'Figure (8)'.

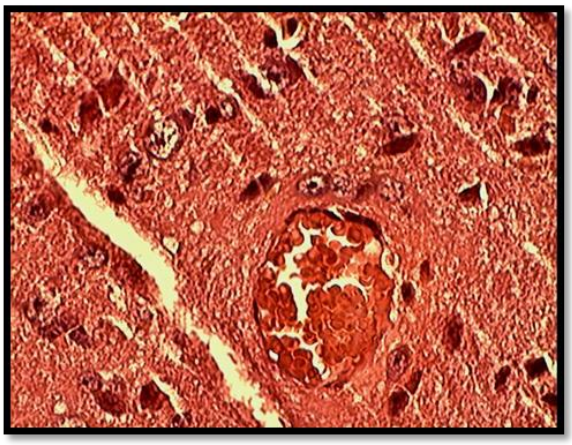

Figure (8): section in brain tissue notes congestion in vein and perivascular cuffing lymphocyte X 400 (H& E).

The peritoneum: notes congestion in vein after infection and present macrophage and lymphocyte 'Figure(9)'.advance infection notes growth in fibroblast and mononuclear cells that lead to chronic peritonitis.

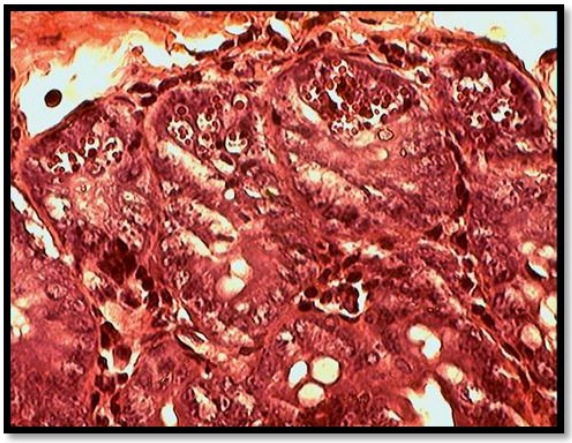

Figure (9): section in peritoneum notes inflammatory in peritoneum and macrophage ,lymphocyte X 400 (H& E).

ELISA result

To detect level of immune response against *E.coli* in detect time table to differential optimum dilution between positive and negative control and detect optimum quantity of Ag we found that concentration 1:200 of serum in positive and negative state and optimum concentration of Ag 1:40 dilution and compact dilution is 1:1000 Table (4).

Table (4) : ELISA results for IgG level.

Groupe	Day	Maximum	Minimum	Average
1	3	0.313	0.201	0.257
2	6	0.379	0.302	0.340
3	9	0.743	0.624	0.683
4	12	1.021	0.942	0.981
5	15	1.034	1.023	1.028
6	18	0.808	0.979	0.893
7	21	0.706	0.892	0.799

Discussion:

The results of present study improved that immunization of male mice by *E. coli* results in activation of immunity in treated group compared with control. These results is in contract with a study of [15] which reported mice immunity stimulation with two doses of the same bacteria vaccines containing O157 or O157:H7; K99 to antibodies in serum. Other study has been reported different immune response parameters such as lymphocyte numbers and spleen weight where the infection with *E. coli* increase the spleen weight and number of lymphocytes after infected with 36× 106 CFU/ml [16]. Other studies have been demonstrated that continuous injection of *E. coli* increases number of immune cells such as intestinal monocytes when we compare the number produced through infection with a live *E. coli* [17].

Several studies have been reported the LD50 dose in mice; for example, Tzong et al. [18] informed that dose of 250μg subcutaneous administrated was sub-toxic to mice, while control PE was toxic at 0.5 and 1μg. Moreover, Armstrong and Merrill [19] have reported the inhibition of protein synthesis by activation of ADP on factor 2 and the lethal dose was at 1μg in *in vivo* and *in vitro* study. Susan et al., [20] documented that toxin had median lethal in mice at i.p injection dose of 0.15μg /22 g. However, Mohawk et al., [21] reported that there is no one reviews all *E. coli* O157:H7 infection features, and many respected mouse prototypes have been established to authorization examination of *E. coli* O157:H7 pathogenesis and disease can be measured.

Histopathological investigation in administrated mice in this study reveal that toxin had a marked effects on different tissues characterize by the presence of inflammatory cells such as neutrophils, lymphocyte and macrophage. Vulcano et al., [22] investigated the histopathological and immunological alteration in mice infected with *E. coli* and suggested that EPEC activates immune action and intestinal histological changes with instruction to use mice as an appropriate model for the proposal and experimental of immuno-biological products for active or passive immunization. Not many *in vivo* researches have studied the differences between *E. coli* improved from patients with renal clinical signs and patients with signs of pyelonephritis. One of the mechanism is that *E. coli* has LPS in its wall, which is consider as a possible elements that generate an inflammatory reaction by motivating cytokine producing inflammatory mediators such as interleukins, TNF-α and CAM.[23]. While LPS stimulation through Toll-Like Receptor-4 (TLR-4) causing cytokines production [24]. Thus in view of the B-cell mitogenicity of bacterial lipopolysaccharide it may well be the Gram-negative component of the intestinal flora which most significantly effects expansion of immunocytes and thereby plays a more fundamental role in the activation, differentiation and maturation of the local immune system [25]. Furthermore, Ogawa *et al*. [26] have reported that STEC infected infant rabbit model shown intragastric epithelial changes including; vacuolation in epithelial cells, detached and necrosis due to increase growth of STEC; cecum and colon epithelial changes were exfoliation of epithelial cells, infiltration of immune cell and mitotic activity. Other studies have been demonstrated that continuous injection of *E. coli* increases number of immune cells such as intestinal monocytes when we compare the number produced through infection with a live *E. coli* [17]. Additionally, higher IgG level in mucosa in cattle has been observed by Martorelli et al., [27] in response to E. coli O157 where the level of IgA was low in serum. Hoffman *et al.* [28] explanation was that production of Stx2 by E. coliO157:H7 throughout infection time might diminish lympho-proliferative responses in intra-gastric epithelial cells and peripheral lymphocytes. It would be interesting if further examination of other protein response in serum and mucosa study.

This finding suggests a relationship between immunization, immune response and histology. Nevertheless, further studies are necessary to investigate the role of antibodies and cellular immunity in the *E. coli* infection. In addition, immune responses improvement can be proposed to control *E. coli* affects.

References:

[1] Savkovic S, Villanueva J, Turner J, Matkowskyj K and Hecht G 2005 Mouse Model of Enteropathogenic *Escherichia coli* Infection *Infect. Immun.* **73** 1161–70.
[2] Peleg A and Hooper D 2010 Hospital-Acquired Infections Due to Gram-Negative Bacteria *The New Eng. J. Medic.* **362** 1804–13.

[3] Greco S, Ravelli P and Fagiuoli S 2011 What can we learn about biofilm/host interactions from the study of inflammatory bowel disease *J. Clin. Period.* **38** 36–43.
[4] Chen H and Frankel G 2005 Enteropathogenic Escherichia coli: unravelling pathogenesis *FEMS Microbiol. Rev.* **29** 83-98.
[5] Scholz R, Imami K, Scott N, Trimble W, Foster L and Finlay B 2015 Novel Host Proteins and Signaling Pathways in Enteropathogenic *E. coli* Pathogenesis Identified by Global Phosphoproteome Analysis *Molec.Cellul. Prot. MCP* **14** 1927–45.
[6] Hommes D, Peppelenbosch M and van Deventer S 2003 Mitogen activated protein (MAP) kinase signal transduction pathways and novel anti-inflammatory targets *Gut* **52** 144–51.
[7] Miao H, Burnett E, Kinch M, Simon E, and Wang B 2000 Activation of EphA2 kinase suppresses integrin function and causes focal-adhesion-kinase dephosphorylation *Nat. Cell. Biol.* **2** 62-69.
[8] Zhuang X, Chen Z, He C, Wang L, Zhou R, Yan D, and Ge B 2017 Modulation of host signaling in the inflammatory response by enteropathogenic Escherichia coli virulence proteins *Cell Mol. Immun.* **14** 237–44.
[9] Tauschek M, Strugnell R and Robins-Browne R 2002 Characterization and evidence of mobilization of the LEE pathogenicity island of rabbit-specific strains of enteropathogenic Escherichia coli *Mol. Microbiol.* **44** 1533-50.

[10] Crepin V, Collins J, Habibzay M and Frankel G 2016 Citrobacter rodentium mouse model of bacterial infection Nature Protocol 11 1851-76.
[11] Ogbulie J, Uwazuoke J and Ogieho S 1998 Introductory Microbiology Practical. *Sprin. Publish. Niger*. 70-120.
[12] Ihssen J, Kowarik M, Dilettoso S, Tanner C, Wacker M and Thöny-Meyer L 2010 Production of glycoprotein vaccines in *Escherichia coli Microb. Cell Factor.* **9** 61.
[13] Snyder D and Marquardt W 1989 Enzyme immunoassay for poultry disease mentoring. In H. G. Purchase; Lawerence, H. Arp. C. H. Domermuth and James E. Pearson (eds). A laboratory Manual for Isolation and Identification of Avian Pathogens. American Association of Avian Pathologist, University of Pennsylvania, New Bolton Center, Kennett Saquare PA. **19348-1692** PP: 201-207.
[14] Luna LG 1968 Manual of histological staining methods of the forces institute of pathology 3rd edition. McGraw. Hillbook, New York. PP: 2258.
[15] Yousif A, Al-Taai N and Mahmood N 2013 Humoral and Cellular Immune Response Induced By E. coli [O157:H7 and O157:H7:K99] Vaccines in Mice *Intern. J. Immun. Res.* **3** 17-20.
[16] Mitasari Z, Gofur A and Listyorini – KnE D 2017 Mus musculus (Linnaeus, 1758) Immune Responses Caused by Escherichia coli (Migula, 1895) Infection. *The 4th International Conference on Biological Science*, 285-293.
[17] Takahashi T, Oka T, Iwata H, Kuwata T and Yamamoto Y 1993 Immune response of mice to orally administered lactic acid bacteria *Biosc. Biotech. Biochem.* **57** 1557-60.
[18] Tzong Y, Chia P, Chien C and Cho, F 1999 A non toxic pseudomonas exotoxin A induce active immunity and passive protective antibody against pseudomonas exotoxin A intoxication. *J. Biom. Scien.* **6** 357-63.
[19] Armstrong S and Merrill A 2001 Application of fluorometric assay for characterization of catalytic competency of domain III fragment of pseudomonas aeruginosa exotoxin A *Biochem.* **292** 26 – 33.
[20] Susan P, Patricia L and Rod M 2005 Structure function analysis of the catalytic domain of exotoxin A from pseudomonas aeruginosa *J. Biochem.* **385** 667 – 75.
[21] Mohawk K and O'Brien A 2011 Mouse Models of *Escherichia coli* O157:H7 Infection and Shiga Toxin Injection *J. Biomed. Biotechn.* **258185**. http://doi.org/10.1155/2011/258185
[22] Vulcano A., Tino-De-Franco M, Amaral J, Ribeiro O, Cabrera W, Bordenalli M, Carbonare C, Álvares E and Carbonare S 2014 Oral infection with enteropathogenic Escherichia coli triggers immune response and intestinal histological alterations in mice selected for their minimal acute inflammatory responses *Microbiol. Immun.* **58** 352-9.

[23] Kafa I, Uysal M, Bakirci S, Ayberk Kurt M 2010 Sepsis induces apoptotic cell death in different regions of the brain in a rat model of sepsis *Acta Neurobiol. Experimen.* **70** 246-60.

[24] McAleer P and Vella A 2008 Understanding how lipopolysaccharide impacts CD4 T-cell immunity *Crit. Rev. Immunol.* **28** 281–99.

[25] Belkaid Y and Hand T 2014 Role of the Microbiota in Immunity and inflammation *Cell* **157** 121–41.

[26] Ogawa M, Shimizu K, Nomoto K, Takahashi M, Watanuki M, Tanaka R, Tanaka T, Hamabata T, Yamasaki S and Takeda Y 2001 Protective effect of Lactobacillus casei strain Shirota on Shiga toxin-producing *Escherichia coli* O157:H7 infection in infant rabbits *Infec. Immun.* **69** 1101-8.

[27] Martorelli L, Hovde C, Vilte D, Albanese A, Zotta E, Ibarra C and Cataldi A 2015 Impact of Infection Dose and Previous Serum Antibodies against the Locus of Enterocyte Effacement Proteins on *Escherichia coli* O157:H7 Shedding in Calves following Experimental Infection *Bio.Med. Res. Internation.* **290679** 8.

[28] Hoffman M, Menge C, Casey T, Laegreid W, Bosworth B and Dean-Nystrom E 2006 Bovine immune response to Shiga-toxigenic Escherichia coli O157:H7 *Clin. Vacc. Immun.* **13** 1322–27.

Seroprevalence occurrence of viral hepatitis and HIV among hemodialysis patients

IOP Conf. Series: Journal of Physics: Conf. Series **1003** (2018) 012010 doi:10.1088/1742-6596/1003/1/012010

Seroprevalence occurrence of viral hepatitis and HIV among hemodialysis patients

Inass Mahmood Kamal[1], Batool Mutar Mahdi[2]

[1]Al-Kindy Teaching Hospital

[2]Al-Kindy College of Medicine University of Baghdad

E-mail:abas_susan@yahoo.com

ABSTRACT.Background: Patients with chronic renal failure (CRF) were on maintenance invasive haemodialysis (HD) procedure. This procedure by itself affects immunity of the patients and became more susceptible to viral infections.

Aim of the study: to investigate the occurrence of HBV, HCV and HIV infections in patients with hemodialysis.

Patients and methods: A retrospective study of 430 end-stage renal failure patients, referred to hemodialysis department at Al-Kindy Teaching Hospital, Baghdad-Iraq from Junuary-2015 to Junuary-2017. Patients were investigated for HBs-Ag using enzyme-labeled antigen test (Foresight-EIA-USA), HCV- Abs (IgG) specific immunoglobulin using a HCV enzyme-labeled antigen test (Foresight-EIA-USA)and anti HIV Abs (IgG) using enzyme-labeled antigen test (Foresight-EIA-USA).

Results: The frequency of HBV infection in the first year was not significant between males (1.11%) and females (0.00%)(P= 0.295). About HCV also there are no significant differences between males (12.63%) and females (9.31%)(P=0.347). After one year of follow up the frequencies of HBV and HCV were not significant between two sexes. Additionally, no any one of the patients had HIV infection.

Conclusions: This study brings a light on that HBV and HCV were having the same frequencies in both genders and lower occurrence with time. Furthermore, HIV was not detected in those patients.

Key words: virus, haemodialysis, infection.

1.Introduction

One of the treatments of chronic renal failure (CRF) is maintenance invasive hemodialysis (HD) procedure. This procedure by itself affects innate immunity like changes in chemotactic factor for leukocytes, phagocytic function of neutrophils and monocytes and natural killer cell (1, 2, and 3). Moreover, adaptive immunity is affected for example defect in proliferation of T lymphocytes and down regulation of phosphorylation pathways of lymphocytes (4, 5 and 6). Therefore, HD patients are more susceptible to blood born viral infection like hepatitis B virus (HBV), hepatitis C virus (HCV) and Human immunodeficiency virus (HIV) due to disturbance in immune system (7).

Infection with these viruses is the main reason of morbidity in HD patients. However, precautions' must be taken to prevent disseminations of viruses in the unit like available treatments and vaccines (8). In USA, after acquiring viruses like HBV in HD patients, 60% of them become chronic carriers, while in the general population was 5% of them became chronic carrier (9). A study showed that chronic HBV infection had a relation with mortality (10). Additionally, there are 170 million hepatitis C virus carriers worldwide and one of the risk group is HD patients and the risk of death was 1.57 times more than others in association with liver cirrhosis and hepatocellular carcinoma (11,12).

Subsequently infection of liver with viruses was fatal for patients on HD and constitutes 1.9% of all deaths (13). Additional virus that is important in HD patients is HIV. The prognosis of this virus was changed significantly due to administration of Highly Active Anti-Retroviral Therapy (HAART), stage of HIV disease at time of dialysis start and T helper (CD4+) lymphocyte count (14, 15 and 16).

The goal of the present study is to investigate the occurrence of viral infection like HBV, HCV and HIV in patients with the end-stage renal failure on hemodialysis.

2. Patients and methods:

A retrospective study of 430 end-stage renal failure patients, referred to hemodialysis unit of Al-Kindy Teaching Hospital, Baghdad-Iraq from January-2015 to Junuary-2017. All patients were subject to the process of hemodialysis.

Hemodialysis patients' were a case for the study if their serum tested positive for HBV, HCV and HIV. In contrast, the patients receiving hemodialysis were considered as a “control” if their serum tested negative for those three viruses. For every case, one age- and gender-matched control receiving haemodialysis was selected.

The Broad of Medical Ethics has been approved for these patients and accepted their review of Al-Kindy College of Medicine and Al-Kindy Teaching Hospital. The knowledgeable permission was obtained from patients. Data collected from both groups including demographic information age, sex, marital status, occupation, residential status, onset of renal failure and hemodialysis history.

2.1 Serological testing

A 430 patients were investigated for HBs-Ag using enzyme-labeled antigen test (Foresight-EIA-USA), HCV- Abs (IgG) specific immunoglobulin using a HCV enzyme-labeled antigen test (Foresight-EIA-USA) and anti HIV Abs (IgG) using enzyme-labeled antigen test (Foresight-EIA-USA).

The principle for detection antibodies in the serum are illustrated as follows using leaflet kit:

The micro-wells are coated with Ags then the serum will be added that contains Abs lead to formation a complex. After incubation, washing was done and enzyme conjugated with Abs was added. After incubation and washing were done; substrate A and B were added. The color was formed and the reaction was stopped by sulfuric acid. The results were interpreted after reading with micro plate reader at 450nm within 30 minutes. Samples with optical density below the cutoff were recorded as negative, those with optical densities (< 10% - > 10%) of the cutoff were equivocal, and all others were positive. The sample was retested when the absorbance was within 10% of the cutoff level.

2.2 Statistical analysis:

Data were analyzed statistically using:

- Descriptive statistics: frequencies, mean and standard deviation.
- Inferential statistics: Chi-square tests and fisher exact test.

All of these were done using MiniTab statistical software program 13.20. A P- value ≤ 0.05 was considered to be significant.

3. Results:

A total of 430 patients with chronic kidney disease (renal failure) were on hemodialysis during the study period. The proportion of males 269 (62.55%) was more than that of female 161(37.44%). Their ages ranged from 16 to 76 years, (median=35), (31.2 ±0.80). The frequency of HBV infection in the first year was not significant between males (1.11%) and females (0.00%)(P= 295) as shown in table -1- About HCV also there is no a significant difference between males (12.63%) and females (9.31%)(P=0.347). After one year of follow up the frequency of HBV and HCV was also not significant between two sexes as was reported in (table-2-). HIV was not affecting any of HD patients. There was a significant reduce in the frequency of infection with HCV while occurrence of HBV was not changed (table-3-).

Table-1- Frequency of viral infection in patients in the first year of hemodialysis.

Viral markers	HD Patients positive for the viruses males No. %	HD Patients negative for the viruses Males No. %	HD Patients positive for the viruses females No. %	HD Patients negative for the viruses Females No. %	P -value
HBs-Ag	3 1.11	266 98.88	0 0	161 100	0.295*
Anti HCV Abs	34 12.63	235 87.36	15 9.31	146 90.68	0.347*
Anti HIV Abs	0 0	0 0	0 0	0 0	-----

* Not significant.

Table-2- Frequency of viral infection in patients in the second year of haemodialysis.

Viral markers	HD Patients positive for the viruses males No. %	HD Patients negative for the viruses Males No. %	HD Patients positive for the viruses females No. %	HD Patients negative for the viruses Females No. %	P -value
HBs-Ag	0 0	269 100	0 0	161 100	1.00*
Anti HCV Abs	15 5.57	254 94.42	9 5.59	152 94.4	1.00*
Anti HIV Abs	0 0	0 0	0 0	0 0	-----

* Not significant.

Table-3- Comparison of viral infection in hemodialysis patients in two years of follow - up.

Viral markers	HD Patients positive for the viruses 2015 No. %	HD Patients positive for the viruses 2016 No. %	P -value
HBs-Ag	3 0.697	0 0	0.248*
Anti HCV Abs	49 11.39	24 5.58	0.002
Anti HIV Abs	0 0	0 0	-----

* Not significant.

4. Discussion:

Chronic renal failure patients receiving hemodialysis are often acquiring blood-borne viral infection over their long treatment period like HBV, HCV and HIV. In our study, HD patients had HBV and HCV infection and after follow them the percentage of HBV decreased. Additionally, HCV still in the same percentage. There was no significant difference regarding gender in the frequency of these viruses. There was a significant reduce in the frequency of infection with HCV table-3- with time. A study done in Canada demonstrated that two patients (0.8%) were positive for HBs-Ag and 9 (3.8%) had viral HB DNA by PCR(17). This is in agreement with our study (1.1%) in 2015 and then (0.0%) in 2016. Therefore the molecular investigation that detects HBV-DNA using nested PCR is helpful for patients with anti-HB core Ab positive, negative for HBs-Ag and anti-HBs Abs (18). It is recommended to analayze HBV-DNA annually and biopsy from liver (19). Additional study done in Madhav Nagar city reported that the frequency of HBV and HCV infections in HD patients was 1.52% and 1.11%, respectively (20, 21). In India, the occurrences of HBV were 3.4% to 42%, which is higher than found in our study (22, 23). The lower occurrence of HBV in this study may be caused by sample size, method used for detection the virus, less blood transfusion and blood products for the patients and screening of

blood for blood-borne viral infections before transfusion. The availability of erythropoietin leads to lowering blood transfusion times to the patients. The only three patients with HBs-Ag positive were treated and recover from the disease. Consequently, HBV did not detect after one year of follow. Management patients with HBV vaccine, separation of infected patient on separate machine, and habitual surveillance for HBV infected patients in the hospitals leads to lower rates of infection with HBV.

Regarding the frequency of HCV infection was higher than HBV in our study while, other studies reported less prevalence of HCV infection in HD patients like Spain (24) and Brazil (25).This may be due to sample size, method of detection and screening blood for antibodies against HCV with control measures in hospitals. Double infection with two viruses (HBV and HCV) in same patient were not detected in our study while in other studies were 4.4 %(26, 27). The lower number of the patients who were positive for anti- HCV after one year of follow-up was due to their deaths.

About HIV infection; there was no cases of this virus in HD patients in our study due to control measures of this disease. The prevalence of this virus varies in different countries depending on district of the countries (28, 29). Within USA about 1% 0f HD patients had HIV due to HIV associated nephropathy (30). HD patients should be investigated by ELISA, Western blot and serum HIV-RNA for positive cases. The prognosis of HIV infected HD patients has considerably better by using Highly Active Anti-Retroviral Therapy (HAART)(31), stage of HIV disease at initiation of dialysis (32) and Th CD4+T helper count (33).

Infections with these viruses are important cause of death following cardiovascular diseases in HD patients. Thus, many safety measures must do to limit the dissemination of these viruses (34). There is a need for treatment of HCV end-stage renal disease patients and sustained systematic immunization campaigns for HBV infection (35). Investigating hemodialysis patients for anti-HBc is important to show latent HBV infection (36). Thus, early vaccination and better nutritional conditions, improves anti-HBV response (37).

4. Conclusions:

This study brings a light on that HBV and HCV infections were in the same in both genders, though less common with time. HIV was not detected in HD patients.

References:

[1] Lewis SL, Van Epps DE, Chenoweth DE. Alterations in chemotactic factor-induced responses of neutrophils and monocytes from chronic dialysis patients. Clin Nephrol. 1988; 30: 63-72.
[2] Muniz-Junqueira MI, Braga Lopes C, Magalhaes CA, Schleicher CC, Veiga JP. Acute and chronic influence of hemodialysis according to the membrane used on phagocytic function of neutrophils and monocytes and pro-inflammatory cytokines production in chronic renal failure patients. Life Sci. 2005; 77: 3141-3155.
[3] Eleftheriadis T, Kartsios C, Yiannaki E, Kazila P, Antoniadi G, Liakopoulos V, et al. Chronic inflammation and CD16+ natural killer cell zeta-chain down regulation in hemodialysis patients.Blood Purif. 2008; 26: 317-321.
[4] Eleftheriadis T, Papazisis K, Kortsaris A, Vayonas G, Voyatzi S,Vargemezis V. Impaired T cell proliferation and zeta chain phosphorylation after stimulation with staphylococcal enterotoxin-B in hemodialysis patients. Nephron Clin Pract. 2004; 96: c15-20.
[5] Eleftheriadis T, Antoniadi G, Liakopoulos V, Kartsios C, Stefanidis I. Disturbances of acquired immunity in hemodialysis patients. Semin Dial. 2007; 20: 440-451.

[6] Eleftheriadis T, Kartsios C, Yiannaki E, Kazila P, Antoniadi G, Liakopoulos V, et al. Chronic inflammation and T cell zeta-chain downregulation in hemodialysis patients. Am J Nephrol. 2008;28: 152-157.
[7] Abumwais JQ and Idris OF, "Prevalence of hepatitis C, hepatitis B, and HIV infection among haemodialysis patients in Jenin District (Palestine)," Iranian Journal of Virology.2010; 4: 38–44.
[8] Kausz A, Pahari D. The value of vaccination in chronic kidney disease. Semin Dial. 2004; 17: 9-11.
[9] Szmuness W, Prince AM, Grady GF, Mann MK, Levine RW, Friedman EA, et al. Hepatitis B infection. A point-prevalence study in 15 US hemodialysis centers. JAMA. 1974; 227: 901-906.
[10] Fabrizi F, Martin P, Dixit V, Kanwal F, Dulai G. HBs-Ag seropositive status and survival after renal transplantation: meta-analysis of observational studies. Am J Transplant. 2005; 5: 2913-2921.
[11] Yen T, Keeffe EB, Ahmed A. The epidemiology of hepatitis C virus infection. J Clin Gastroenterol. 2003; 36: 47-53.
[12] Fabrizi F, Martin P, Dixit V, Bunnapradist S, Dulai G. Metaanalysis:Effect of hepatitis C virus infection on mortality in dialysis. Aliment Pharmacol Ther. 2004; 20: 1271-1277.
[13] Aghakhani A, Banifazl M, Eslamifar A, Ahmadi F, and Ramezani A, "Viral hepatitis and HIV infection in hemodialysis patients," Hepatitis Monthly, 2012; 12: 463–464.
[14] Ahuja TS, Borucki M, Grady J. Highly active antiretroviral therapy improves survival of HIV-infected hemodialysis patients. Am J Kidney Dis. 2000; 36: 574-580.
[15] Ortiz C, Meneses R, Jaffe D, Fernandez JA, Perez G, Bourgoignie JJ. Outcome of patients with human immunodeficiency virus on maintenance hemodialysis. Kidney Int. 1988; 34: 248-253.
[16] Perinbasekar S, Brod-Miller C, Pal S, Mattana J. Predictors of survival in HIV-infected patients on hemodialysis. Am J Nephrol.1996; 16: 280-286.
[17] Minuk GY, Sun DF, Greenberg R, Zhang M, Hawkins K, Uhanova J, et al. Occult hepatitis B virus infection in a North American adult hemodialysis patient population. Hepatology. 2004;40: 1072-1077.
[18] Hui CK, Sun J, Au WY, Lie AK, Yueng YH, Zhang HY, et al. Occult hepatitis B virus infection in hematopoietic stem cell donors in a hepatitis B virus endemic area. J Hepatol. 2005; 42:813-819.
[19] Ozdogan M, Ozgur O, Gur G, Boyacioglu S, Ozderin Y, Demirhan B, et al. Histopathological impacts of hepatitis virus infection in hemodialysis patients: should liver biopsy be performed before renal transplantation? Artif Organs. 1997; 21: 355-358.
[20] Otedo AEO|, Mc'Ligeyo SO, Okoth FA, and Kayima JK,"Seroprevalence of hepatitis B and C in maintenance dialysis in a public hospital in a developing country," South African Medical Journal,2003; 93: 380–384.
[21] Busek SU, Bab´a EH, Tavares Filho HA et al., "Hepatitis C and hepatitis B virus infection in different hemodialysis units in Belo Horizonte, Minas Gerais, Brazil," Memorias do Instituto Oswaldo Cruz. 2002; 97: 775–778.
[22] Agarwal SK, Dash SC, and Irshad M, "Hepatitis C virus infection during haemodialysis in India," Journal of Association of Physicians of India. 1999; 47: 1139–1143.
[23] Saha D and Agarwal SK, "Hepatitis andHIV infection during haemodialysis," Journal of the Indian Medical Association2001;99; 194–199.
[24] Espinosa M, Mart´ın-Malo A, Ojeda R et al., "Marked reduction in the prevalence of hepatitis C virus infection in hemodialysis patients: causes and consequences," American Journal of Kidney Diseases. 2004; 43; 685–689.
[25] Carneiro MAS, Teles SA, Dias MAet al., "Decline of hepatitis C infection in hemodialysis patients in Central Brazil: a ten years of surveillance,"Memorias do InstitutoOswaldoCruz.2005;100; 345–349.

[26] Kosaraju K, Faujdar SS, Singh A, and Prabhu R. Hepatitis Viruses in Heamodialysis Patients: An Added Insult to Injury? Hepatitis Research and Treatment.2013;1-4.
[27] Reddy GA, Dakshinamurthy KV, Neelaprasad P, Gangadhar T, and Lakshmi V, "Prevalence of HBV and HCV dual infection in patients on haemodialysis," Indian Journal of Medical Microbiology.2005; 23: 41–43.
[28] Perez G, Ortiz-Interian C, Lee H, de Medina M, Cerney M, Allain JP, et al. Human immunodeficiency virus and human T-cell leukemia virus type I in patients undergoing maintenance hemodialysis in Miami. Am J Kidney Dis. 1989; 14: 39-43.
[29] Vigneau C, Guiard-Schmid JB, Tourret J, Flahault A, Rozenbaum W, Pialoux G, et al. The clinical characteristics of HIVinfected patients receiving dialysis in France between 1997 and 2002. Kidney Int. 2005; 67: 1509-1514.
[30] Eggers PW, Kimmel PL. Is there an epidemic of HIV Infection in the US ESRD program? J Am Soc Nephrol. 2004; 15: 2477-2485.
[31] Ahuja TS, Borucki M, Grady J. Highly active antiretroviral therapy improves survival of HIV-infected hemodialysis patients. Am J Kidney Dis. 2000; 36: 574-580.
[32] Ortiz C, Meneses R, Jaffe D, Fernandez JA, Perez G, Bourgoignie JJ. Outcome of patients with human immunodeficiency virus on maintenance hemodialysis. Kidney Int. 1988; 34: 248-253.
[33] Perinbasekar S, Brod-Miller C, Pal S, Mattana J. Predictors of survival in HIV-infected patients on hemodialysis. Am J Nephrol. 1996; 16: 280-286.
[34] Eleftheriadis T, Liakopoulos V, Leivaditis K, Antoniadi G, Stefanidis I. Infections in hemodialysis: a concise review. Part II: blood transmitted viral infections. Hippokratia. 2011; 15: 120-126.
[35] Isnard Bagnis C, Couchoud C, Bowens M, Sarraj A, Deray G, Tourret J, Cacoub P, Tezenas du Montcel S. Epidemiology update for hepatitis C virus and hepatitis B virus in end-stage renal disease in France. Liver Int. 2017 37:820-826.
[36] Ayatollahi J, Jahanabadi S, Sharifyazdi M, Hemayati R, Vakili M, Shahcheraghi SH. The Prevalence of Occult Hepatitis B Virus in the Hemodialysis Patients in Yazd, Iran. Acta Med Iran. 2016 ;54:784-787.
[37] Cordova E, Miglia I, Festuccia F, Sarlo MG, Scornavacca G, Punzo G, Menè P, Fofi C. Hepatitis B vaccination in haemodialysis patients: an underestimated problem. Factors influencing immune responses in ten years of observation in an Italian haemodialysis centre and literature review. Ann Ig. 2017;29:27-37.

Theoretical Treatment, Microwave Synthesis and Spectroscopic Analysis of New Schiff Bases Derived from 4-Aminoantipyrene

IOP Conf. Series: Journal of Physics: Conf. Series **1003** (2018) 012011 doi:10.1088/1742-6596/1003/1/012011

Theoretical Treatment, Microwave Synthesis and Spectroscopic Analysis of New Schiff Bases Derived from 4-Aminoantipyrene

A N Seewan [1], Z Y Kadhim [2], A A Hadi [1]

[1]College of Basic Education/Al-Muthanna University, Samawa, Iraq
[2] College of Veterinary Medicine/Al-Muthanna University, Samawa, Iraq

Abstract. The new Schiff base was obtained compounds (I, II, III, IV) derived from 4-aminoantipyrene were synthesized by using microwave technique. And these Schiff bases were verified by some spectral data (IR, UV). HyperChem release 8.0 program was used to calculate the heat of formation ($\Delta H^0 f$) binding energy (ΔEb) and dipole moment (μ) for all compounds, also theoretical vibration frequencies and electronic spectra of compounds were calculated.

Key words: Schiff base**,** 4-Aminoantipyrene, Microwave, 4,4′-Diaminodiphenyl methane

1-Introduction

There are many chemists which are very much focused on the Schiff bases derived from heterocyclic ring with carbonyl compounds. As has been the center of attraction in many areas like biological, clinical, medical, analytical and pharmacological [1,2]. Play as Schiff bases a central role in the field of coordination chemistry and their metal complexes are of great interest for many years [3-5]. Used also for preparation super-conducting [6]. There are many methods for synthesis Schiff bases one of this using a microwave technique. Where the synthesis microwave-assisted is a branch of green chemistry. The application of microwave-assist synthesis in organic chemistry continued to develop at an astonishing pace. Microwave irradiated reactions under solvent free or less solvent conditions are attractive contributory, reduced pollution, low cost and offer high yields together with clarity in processing and handling. The most important advantages of microwave approach are shorter reaction times, simple reaction conditions and enhancements in yields [7-11]. In this study, we report the synthesis a new Schiff base derived from 4-aminoantipyrene by using microwave techniques.

2.Materials and Methods

2.1 Materials

All chemicals and solvents used in the present work were supplied by Merck, BDH, Fluka and Sigma Aldrich and the thermionic device were used to measure the melting point of all prepared compounds and are uncorrected (Table1). Also element C.H.N analyzer was carried out on a EM-017. Mth instrument in laboratory of Chemistry Department, College of Science, Al-Muthanna University. The FTIR spectra in the range (4000-400) cm^{-1}were recorded as KBr disc on FT-IR-8000, single beam path laser, Shimadzu Fourier transform infrared spectrophotometer. The spectra were recorded in the laboratory of Chemistry Department, Al-Muthanna University. UV-Visible spectrophotometer in range (200-600) nm. The microwave irradiation was complete using microwave oven-Panasonic. NN-ST300W in the laboratory of Science Department/College of Basic Education/AL-Muthanna University.

2.2 Methods

2.2.1 Synthesis of new Schiff base compounds

All materials were used further purification.

2.2.2 Synthesis of mono-imines [12,13]

The mono-imines (I,II) prepared by the reaction of the mixture of 0.005 mole of 4-aminoantipyrene with 0.005 mole of aldehyde were dissolved in absolute ethanol (15mL). The mixture was irradiated in microwave oven for 1min. and 300W, then cooled at room temperature, a Schiff base. Finally, a suitable solvent is used to recrystallize the products.

- *4-((4-(Chloro)benzylidene)amino)-1,5-dimethyl-2-phenyl-pyrazol-3-one(I)* : Prepared by reacting 4-aminoantipyrene (1.01gm, 0.005mol) with 4-Clorobenzaldehyde (0.70gm , 0.005mol). Yield = 81%, m.p = 210-212 ^{0}C. IR ($\bar{\upsilon}$,cm^{-1}, KBr disk): 1610 (C=N). Recrystallized with ethanol.
- *4-((4-(Dimethylamino)benzylidene)amino)-1,5-dimethyl-2-phenyl-pyrazol-3-one (II):* Prepared by reacting 4-aminoantipyrene (1.01gm, 0.005mol) and 4-dimethylamino benzaldehyde (0.74gm, 0.005mol). Yield = 81%, m.p = 246-248 0C. IR ($\bar{\upsilon}$, cm-1, KBr disk): 1593 (C=N). Recrystallized with ethanol.

2.2.3 Synthesis of Bis-imines [14,15]

The bis-imines (I,II) prepared by the reaction of the mixture of 0.001 mole of 4,4′-Diaminodiphenylmethane with 0.002 mole of mono-imine were dissolved in absolute chloroform (15mL). The reaction mixture was irradiated in microwave oven for 2min. And 300W, then cooled at room temperature, a good of Schiff base. Finally, a suitable solvent used to recrystallize the products.

- 3,3'-((methylenebis(4,1-phenylene))bis(azanylylidene))bis(N-(4-chlorobenzyli dene)-2,5-dimethyl-1-phenyl-2,3-dihydropyrazol-4-amine)(III):Prepared by reacting 4,4′-Diaminodiphenylmethane (0.198gm, 0.001mol) and compound I (0.65gm , 0.002mol), were dissolved in chloroform (15mL). Yield = 86%, m.p = 190-192 ^{0}C. IR ($\bar{\upsilon}$,cm^{-1}, KBr disk): 1651 (C=N). Recrystallized with ethanol.
- 3,3'-((methylenebis(4,1-phenylene))bis(azanylylidene))bis(N-(4-(dimethyl amino)benzylidene)-2,5-dimethyl-1-phenyl-2,3-dihydropyrazol-4-amine)(IV): Prepared by reacting 4,4′-Diaminodiphenylmethane (0.198gm, 0.001mol) and compound II (0.66gm, 0.002mol). Yield = 86%, m.p = 200-202 ^{0}C. IR ($\bar{\upsilon}$,cm^{-1}, KBr disk): 1649 (C=N). Recrystallized with ethanol.

3.Result and discussion

The compounds(I, II, III, IV) were synthesized by using the microwave technique the reactions involve two steps. The First step involves of the reaction of 4-aminoantipyrene with 4-substituted benzaldehyde to give compounds I and II. The second step involves the reaction of compounds I and II with 4,4′-Diaminodiphenylmethane to give compounds III and IV. The purity of the compounds was checked by TLC. The strategies adopted to obtain the target compounds are:

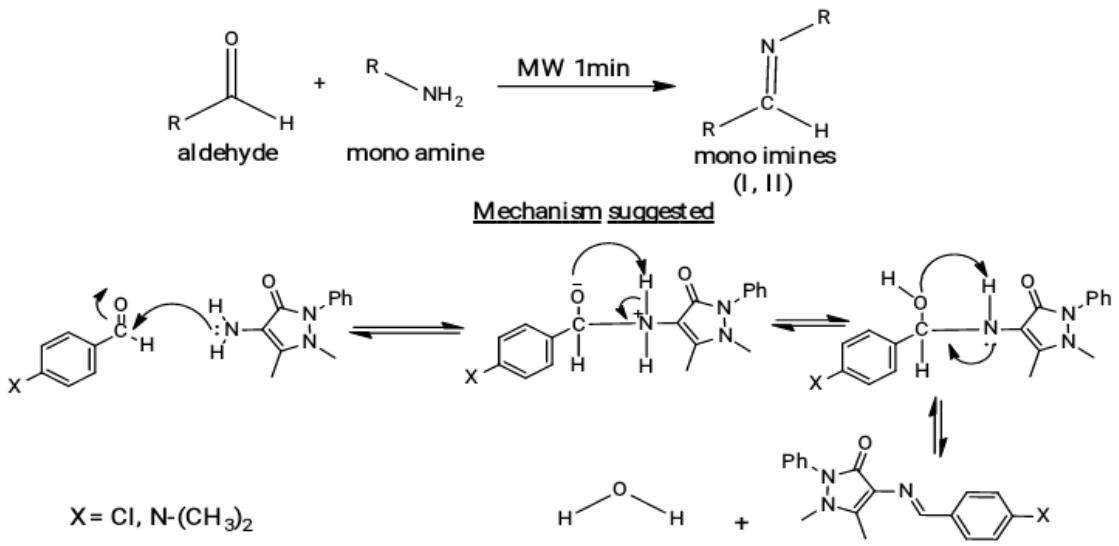

Scheme 1. Mechanism suggested for synthesis of mono-imines

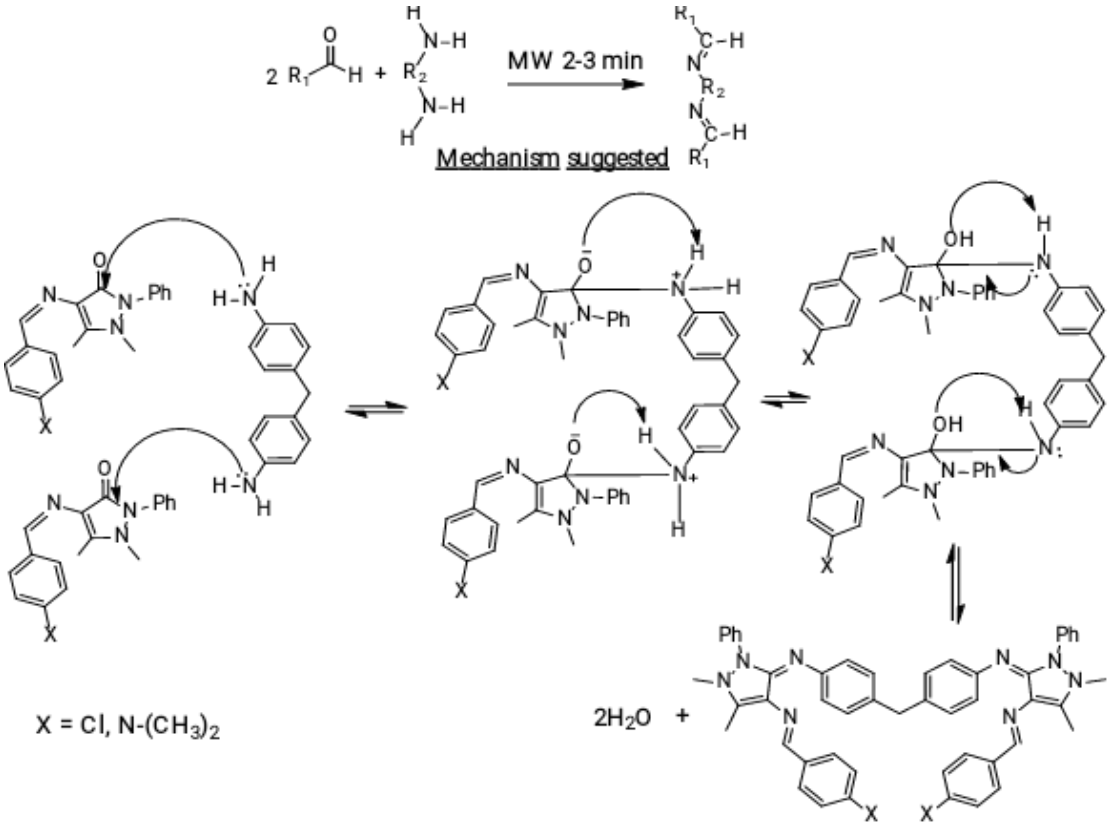

Scheme 2. Mechanism suggested for synthesis of Bis-imines

The analytical data together with some physical properties of the compounds are summarized in Table (1).The calculated values of C.H.N analysis were in a good agreement with the experimental values.

Table 1. Physical data of Schiff base compounds

Comp	Color	Molecular formula	Found (calculated1)			M.wt (g. Mol-1)
			C٪	H٪	N٪	
I	Pale yellow	C18H16N3OCl	65.42 (66.30)	5.10 (4.91)	11.9 (12.89)	325.79
II	Yellow	C20H22N4O	70.50 (71.76)	5.60 (6.57)	15.81 (16.74)	344.13
III	Brown	C49H78N8Cl2	70.65 (69.17)	8.46 (9.17)	13.43 (13.17)	850.10
IV	Dark yellow	C53H90N10	74.51 (73.33)	9.43 (10.30)	17.10 (16.14)	867.34

The important IR spectral data are given in Table (2).The spectrum of Compound (I) indicated the appearance of bands in the region 1593.95, 1570.79, 1649.92 and 3060.75 cm^{-1} which could be attributed to ν(C=N), ν(C=C)aromatic, ν(C=O) and ν(C-H) aromatic respectively [16].The spectrum of the compound (II) exhibits the absorption bands for ν(C=N), ν(C=C) aromatic, ν(C=O) and ν(C-H)aromatic at 1610.61, 1589.40, 1647.26 and 3070.78 cm^{-1} respectively[17]. Figures (1 and 2). The IR spectra of the compounds III and IV arecomplex due to the large number of the groups which have overlapping regions, however few bands have been chosen in order to observe the complement of reaction. The spectra of compounds III and IV characterized by disappearance of stretching frequency of ν(C=O) and appearance of another band due to stretching frequency of ν(C=N) in the region 1651.12 cm^{-1} for compound III and 1649.19 cm^{-1} for compound IV make us a good sign that we are on the correct way in the synthesis. Figures (3 and 4).

The experimental UV-VIS. Spectra of compounds I, II, III, and IV, exhibited λ_{max} in 323, 326, 333,370 nm respectively this absorption band due to (n–π*) transition may be located on the nitrogen atom of the (-C=N-) [18].

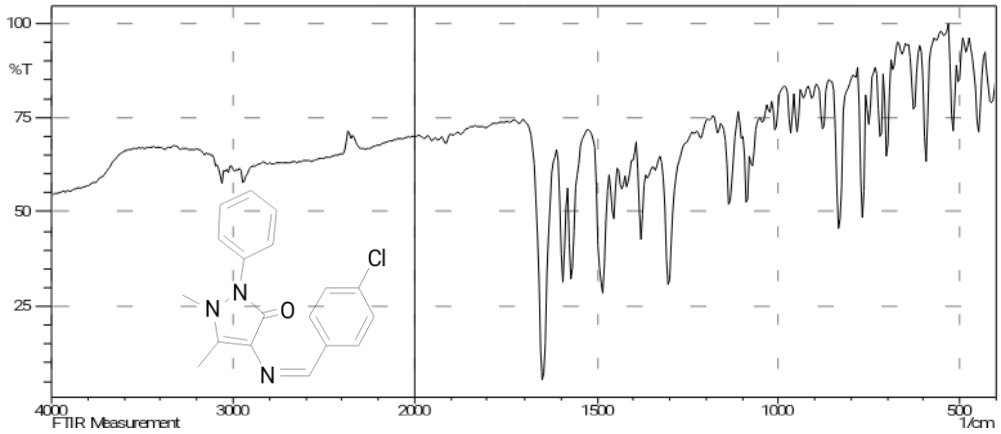

Figure 1. FTIR spectrum of compound I

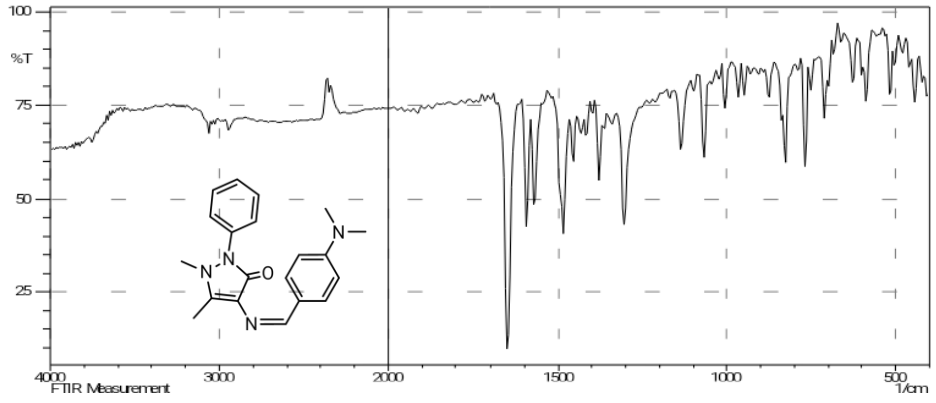

Figure 2. FTIR spectrum of compound II

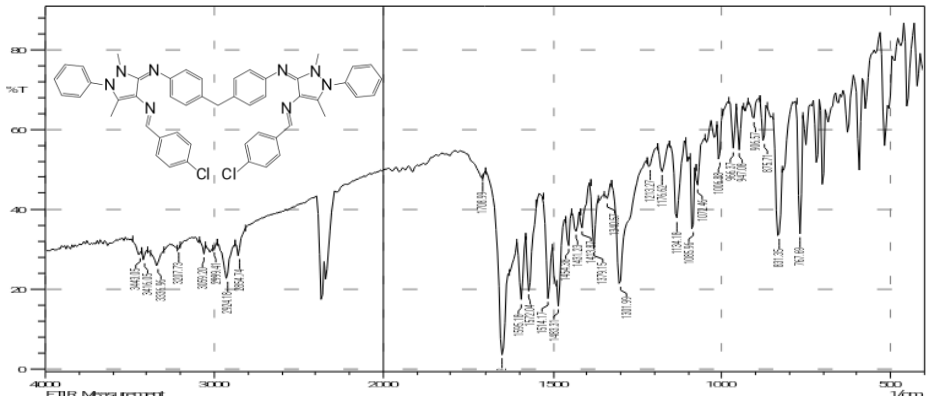

Figure 3. FTIR spectrum of compound III

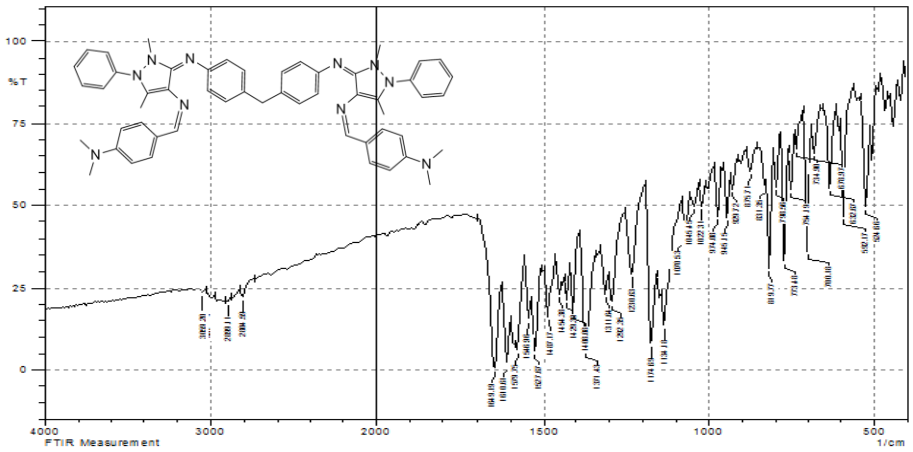

Figure 4. FTIR spectrum of compound IV

4.Theoretical calculation

HyperChem offers ten semi-empirical molecular orbital methods, with options for organic and main group compounds for spectrum simulation [19]. Zerner's INDO (ZINDO/1) level of semi-empirical method was used for evaluating the heat of formation ($\Delta H^{\circ}f.$) and binding energy (ΔE_b) for Schiff base compounds .Parameterization method3 (PM3) level also used to calculate vibration frequencies and ZINDO/S compound used to calculate the electronic spectra table 2.

Table 2. The calculated energies(in $KJmol^{-1}$) and dipole moment (in Debye) for Schiff base compounds.

Comp.	$\Delta H^{\circ}f$	ΔE_b	μ
I	-35670.78	-53817.60	4.1
II	-41370.26	-62606.58	4.5
III	-98231.99	-146447.88	8.6
IV	-110153.99	-164548.83	21.4

All computational chemistry techniques energy such that the system with the lowest energy is more stable. Thus the shape of a molecule corresponds to the shape with the lowest energy [20].As shown in the table the compounds can be arranged according to the increase in thermodynamic stability as follows: IV > III > II > I.

Table 3. Experimental and theoretical vibration frequencies of Schiff base compounds

Symbol	ῡ (C-H) aromatic	ῡ (C=O)	ῡ (C=N)	ῡ (C=C) alkene
I	3060.75* 3086.67** (0.8)	1649.92* 1790.95** (7.9)	1593.95* 1677.67** (4.9)	1570.79* 1600.10* (1.8)
II	3070.78 * 3051.19** (-0.6)	1647.26* 1779.95** (7.5)	1610.61* 1679.84** (4.1)	1589.40* 1631.78** (2.6)
III	3059.20* 3151.31 (2.9)	-------	1651.12* 1595.18* 1650.11**1622.21** (-0.06) (1.6)	1572.04* 1610.35** (2.4)
IV	3059.20* 3010.22** (-0.16)	-------	1649.19* 1610.61* 1700.11**1650.22** (2.9) (2.4)	1574.75* 1666.32** (5.5)

Where *: Experimental frequency, **: Theoretical frequency ( ) :Error%.

The theoretical UV-spectrum of compounds were calculated using ZINDO/S method and appeared some deviations from the experimental values but these deviations in generally acceptable in theoretical calculations [21] .The electronic spectrum of compounds I,II,III, and IV , exhibited λmax at 309.48, 316.12, 320.34, and 368.31 nm respectively. Figures (5-8).

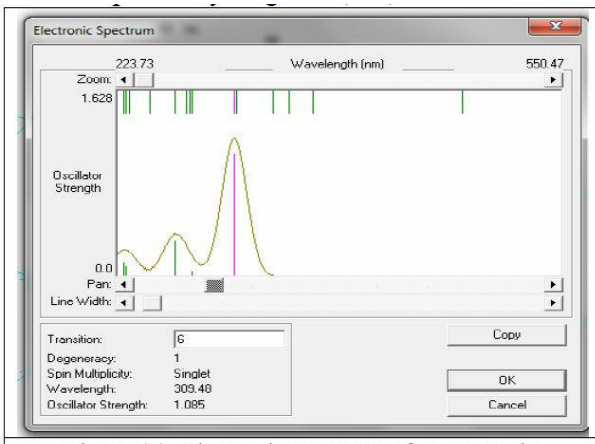

Figure (5): Electronic spectrum of compound I

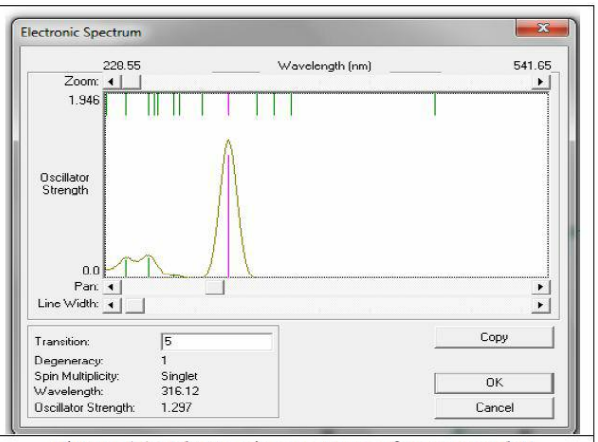

Figure (6): Electronic spectrum of compound II

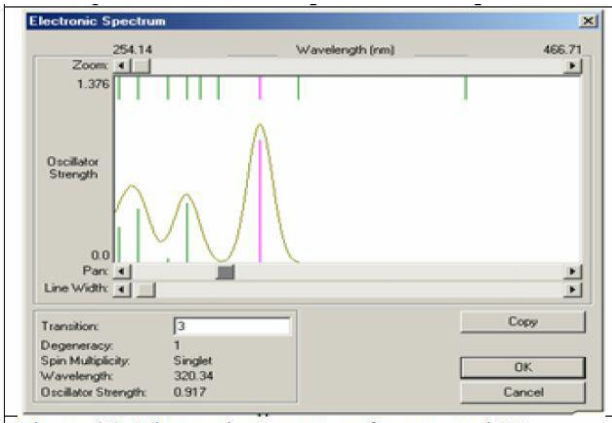

Figure (7): Electronic spectrum of compound III

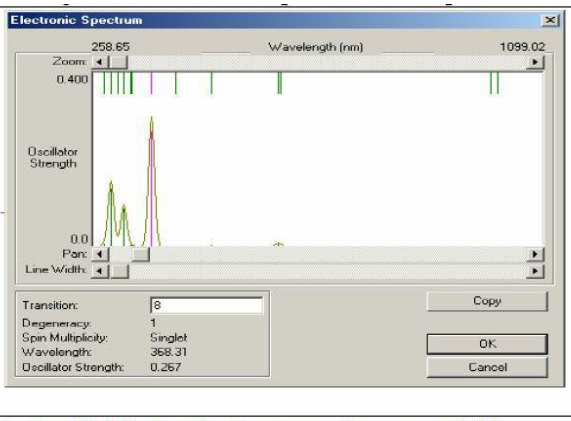

Figure (8): Electronic spectrum of compound IV

5.Conclusions:

The compounds I, II, III, and IV were successfully synthesized by microwave irradiation technique. the physical data as well as FTIR and UV-VIS. Proposed the compounds synthesized. The value calculated energy for the compounds suggested that the compound IV is more stable than the other compounds. The value of theoretical vibrational frequencies and electronic transitions which obtained practically approximately similar to the experimental values.

References

[1] Hohlfeld, T., Zimmermann, N., Webe,r A. A., Jessen, G., Webe,r H., Schroer, K., Hoeltje, H. D and Ebel, R. *J Thromb Haemost,* **6,** 166-173.
[2] Yi, L., Yuanyua,n L., Haowei, W., Xiaohui, X., Ping, W., Fangshi, L., *Molecules* **18**, 877-893.
[3] Cozzi, P. *G., Chem. Soc. Rev.* **33**, 410.
[4] Vicini, P., Geronikaki, A., Incerti, M., Busonera, B., Ooni, G., Kabras, C. A and Colla, L.P., *Bio.org .Med .Chem.* **11**, 4785-4789.
[5] Karia, F. D and Parsinia, P. H *Asian J. Chem.***11** ,991-995.
[6] Ershad, S., Sagathforough, L. A., Nezhad G. K and Kangari, S. *Int. J. Electrochem. Sci.* **4** , 846-854.
[7] Hong, T and Schmilter, A *Zh. Obsheh. Khim.* **83** ,194518g.
[8] Mahajan, K.; Fahmi, N and Singh, R.V. ***Indian J. Chem*.** **46A**, 1221.
[9] Sharma, A. K and Mishra, A. K *Adv. Mat. Lett*., **1(1)**, 59.
[10] Sharma, K., Singh, R., Fahmi, N and Singh, R.V *Spectrochim. Acta*. **75A**, 422.
[11] Garg, R., Saini, M. K., Fahmi, N. and Singh, R.V. *Trans. Met. Chem*. **31**, 362.
[12] Mahajan, K., Swami, M and Singh, R.V *Russ. J. Coord. Chem*. **35**, 179.
[13] Jeena-Pearl, A and Abbs-Fen, T. F. *J. Chem. Pharm. Res.* **5(1)**,115-122.
[14] Mishra, A. P., Tiwarim, Aand Jain, R. K. *"Adv. Mat. Lett."*. **3**, 213-219.
[15] Jain, R and Mishra A. P. *"J.Jordan Chem."*. **7**, 9-21.
[16] AEL, O., Ali, M. S., Saad, E. M and Mostafam S.I., *J. Mol. Struct.* **973**, 69.
[17] Silverstein, R. M., Bassler G. C and Morill, T. C. *"Spectrochemitric identification of organic chemistry"* John wiley and sons.
[18] Kumar, R., Mahiya, K and Mathur, D *Ind. J. Chem*. **50**. 775-780.
[19] Hadi A. A*., International Journal of ChemTech Research*, **9**. 139-142.
[20] Atkins, P. W., Friedman, R. S.,"*Molecular Quantum Molechanics*"Oxford.
Clark, T. A., "*Hand Book of Comput* the last numbered se

Cytotoxic effects of new synthesis heterocyclic derivatives of Amoxicillin on some cancer cell lines

Cytotoxic effects of new synthesis heterocyclic derivatives of Amoxicillin on some cancer cell lines

M S Al-Rawi[1], D F Hussei[1], A F Al-Taie[1], M M Al-Halbosiy[2] and B A Hameed[2]

[1]Department of Chemistry, College of Education Ibn Al- Haitham, University of Baghdad, Iraq.
[2]Biotechnology Research Center –Al-Nahrain University, Iraq.
dr.m1967@yahoo.com

Abstract. A new Schiff base [I] was prepared by refluxing Amoxicillin trihydrate and 4-Hydroxy-3,5-dimethoxybenzaldehyde in aqueous methanol solution using glacial acetic acid as a catalyst. The new 1,3-oxazepine derivative [II] was obtained by Diels- Alder reaction of Schiff base [I] with phthalic anhydride in dry benzene. The reaction of Schiff base [I] with thioglycolic acid in dry benzene led to the formation of thiazolidin-4-one derivative [III]. While the imidazolidin-4-one [IV] derivative was produced by reacting the mentioned Schiff base [I] with glycine and triethylamine in ethanol for 9 hrs. Tetrazole derivative [V] was synthesized by refluxing Schiff base [I] with sodium azide in dimethylformamid DMF. The structure of synthesized compounds[I-V] was characterized by their melting points, elemental analysis CHN-S and by their spectral data; FTIR and ^{1}H NMR spectroscopy. *Two cancer cell lines include: (RD) human pelvic rhabdomyosarcoma and* ($L_{20}B$) the mice intestines carcinoma cell line (which expresses the genes for human cellular receptor for Polio viruses) *were used in this study*. The cytotoxic effect of different concentrations of all the synthesized compounds for 48 hrs was examined. All compounds except [IV] and [V] showed less than 50% inhibition for (L20B), while these compounds exhibit inhibition more than 50% inhibition for (RD).

Key Words: Oxazepine, Thiazolidin-4-one, Imidazolidin-4-one, Tetrazole, β-lactam, Amoxicillin, Anticancer, Cell Line, Cytotoxic effects.

1.Introduction

Amoxicillin is a bacteriolytic containing the β-lactam antibiotic drug of class penicillin [1-2], the first antibiotic developed for the treatment of bacterial infectious diseases have also found new applications as anti-cancer prodrugs. Recently studies have reported on the anticancer properties of the β-lactams: N-methylthio *β*-lactam and N-ethylthio β-lactams, figure (1), a new group of drugs was found to induce apoptotic behavior in a number of cancer cell lines, like human breast, leukemia, prostate, etc. [3-4].

.

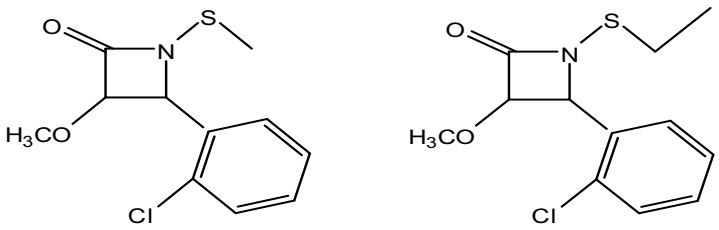

Figure (1). N-methylthio β-lactam and N-ethylthio β-lactams

Heterocyclic compounds containing varies ring are associated with diverse pharmacological activities such as antimicrobial, anti-intiflammatory, analgesic, anticancer against some the cancer cell lines. The rapid development of resistance to existing antimicrobial drugs generates a serious challenge to the scientific community [5].

1,3-oxazepine is unsaturated non homologous seven membered heterocycle, consist of oxygen in position 1and nitrogen in position 3 in addition to the 5 carbon atoms. 1,3-oxazepine derivative as an antitumor agent and colorectal adenocarcinoma [6-7].

Thiazolidin-4-one is used as antioxidant, anticancer, anti-inflammatory, antimicrobial, antifungi may be associated with their affinity to anticancer biotargets, such as non-membrane protein tyrosine phosphatase, JNK-stimulating phosphatase-1, and tumor necrosis factor [8-11].

Imidazoles such as all azoles are five membered ring systems, occurs in the nucleus of purine and in histidine. several imidazolidin derivatives have been examines for antitumor activity against various human tumors. which have shown higher cytotoxic activity and good inhibitory effect at the ovarian cancer cell line [12-13].

Tetrazole cycle is a promising pharmacophore fragment frequently used in the development of anticancer drugs. Over recent 10-15 years, various isomeric forms of tetrazole have been successfully used in the design of promising anticancer drugs [14].

In this study we have used amoxicillin to changes in parent chemical structures and modern classes of antibiotics to evaluate its anti-cancer activity against two cancer cell lines human pelvic rhabdomyosarcoma (RD) and the mouse cell line ($L_{20}B$), an attention for being promise anticancer products.

2. EXPERIMENTAL

2.1. Materials and Instrumentation

All the chemical used in the synthesis were supplied from BDH and Sigma-Aldrich.Standard antibiotic drugs: Amoxicillin trihydrate was supplied by the State Company of Drug Industries and Medical Appliances in Iraq-Samara.

Melting points were registered using electro thermal melting point apparatus and are uncorrected. Infrared spectra was recorded as KBr discs on SHIMADZU 8400s spectrophotometer.^{1}H NMR spectra was recorded on a Bruker - 500 MHz instrument using DMSO as a solvent and TMS as internal reference (ppm), measurement were made at Central lab , Tahran University (Iran). Elemental analysis (C.H.N.S) were carried out using an EuroEA Elemental Analyzer. All reactions was monitored by thin layer chromatography (TLC) and spots were visualized using iodine chamber.

2.2. Synthesis Procedures

All derivatives [I-V] were synthesized according to scheme (1), and all compounds [I-V] gave acceptable elemental analysis, FTIR and ^{1}H NMR spectra that matched data reported in the quote references.

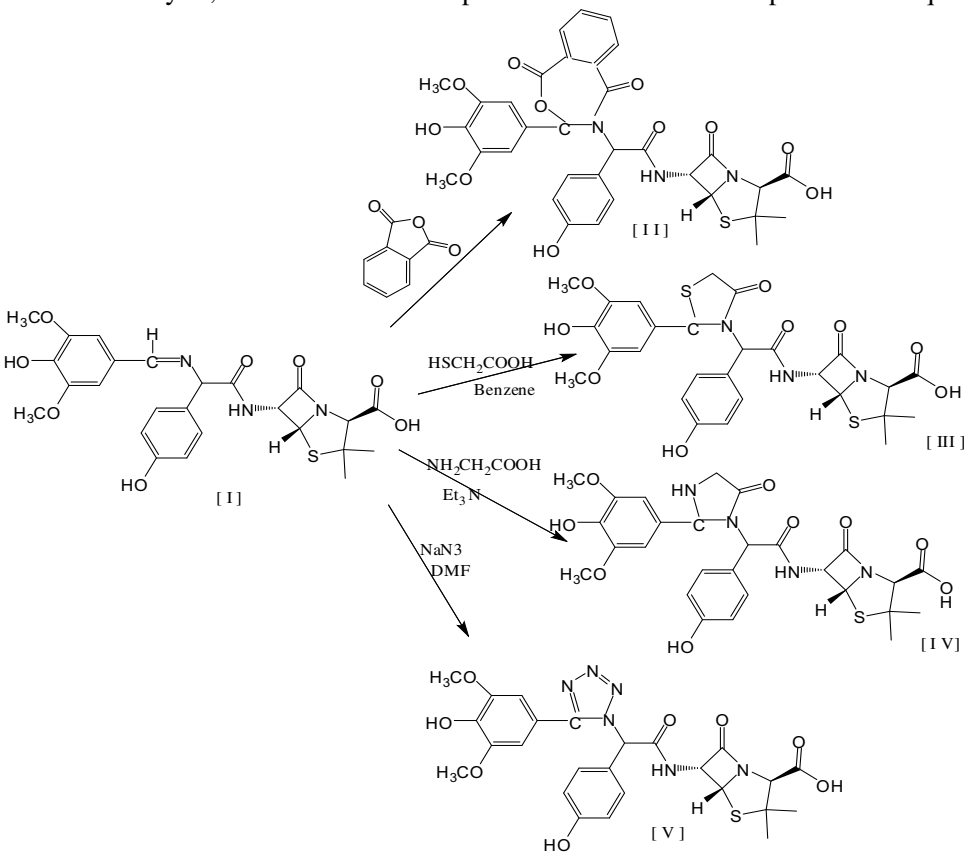

Scheme (1)

2.2.1. Preparation of Schiff Base: 6-{2- [(4-Hydroxy-3,5-dimethoxybenzilidene) amino]-2- (4-hydroxyphenyl) acetyl] amino}-3,3-dimethyl-7-oxo-4-thia- 1-aza-bicyclo[3.2.0] heptane -2- carboxylic acid [I]:

To the stirred solution of amoxicillin trihydrate (0.419gm, 1 mmol) dissolved in 10 ml aqueous methanol (1:1) was added a stirred solution of 4-hydroxy-3,5-dimethoxybenzaldehyde (syringaldehyde) (0.182gm, 1mmol) dissolved in 10 ml methanol and 2 drops of glacial acetic acid . The mixture was stirred and refluxed for 10 hrs at 30 ^{o}C. The solvent was evaporated under vacuum. The pale orange solid obtained was filtered, washed and recrystallized from ethanol. Yield: 71%; m.p. = 205-207 ^{o}C; IR(KBr) ν cm^{-1}: 3275-3420 (s & br, Ph-OH ; & -COOH; O-H); 3010 (s, C-H arom.); 2966 & 2918 (s, C-H aliph.), 1647 (s, C=N), 1665 (s, C=O amide); ^{1}H NMR (TMS) δ ppm: 1.58 (s, 6H, CH_3); 2.49 (1H, CH-S); 3.87 (s, 6H, 2OCH_3); 5.62 (1H,Ph-OH); 6.72-7.12 (4H, Ar-OH); 8.23 (1H,CH= N); 9.76 (1H, H of COOH) . Anal. Calc. for $C_{25}H_{27}N_3O_8S$: C, 56.71; H, 5.10; N,7.93; S,6.04. Found: C, 56.83; H, 4.99; N,7.15; S,5.88.

2.2.2. Preparation of 6-{2- [(4-Hydroxy-3,5-dimethoxyphenyl) -2,3-dihydro benz[1,2e][1,3]- oxazepine-4,7-diones]-2- (4-hydroxyphenyl) acetyl] amino}-3,3-dimethyl-7-oxo-4-thia- 1-aza-bicyclo[3.2.0] heptane -2- carboxylic acid [II]:

A mixture of equimolar amounts (0.53gm, 1 mmol) of Schiff base [I] and phthalic anhydriede (0.148gm, 1 mmol) in dry benzene as a solvent was refluxed for 4 hrs[7], the solvent was removed and the resulting colored crystalline solid recrystallized from petroleum ether to obtained 1,3- oxazipenes [II] . Yield: 78%; m.p. = 220-222 ^{o}C; IR(KBr) ν cm^{-1}: 3290-3400 (s & br, Ph-OH ; & -COOH; O-H); 3030 (s, C-H arom.); 2972 & 2920 (s, C-H aliph.); 1750 (s, C=O lactone ring), 1665 (s, C=O amide) ; 1280 and 1103 cm^{-1} (br, asymetric and symmetric C-O-C) band. ^{1}H NMR (TMS) δ ppm: 1.28 (s, 6H, CH_3); 2.49 (1H, CH-S); 3.88 (s,6H,2OCH_3); 5.40 (s,1H, Ph-OH); 6.67-7.26 (4H, Ar-OH); 8.203-8.64 (m, 6H, Ar-H); 9.40 (1H, H of COOH) . Anal. Calc. for $C_{33}H_{31}N_3O_{11}S$: C, 58.49; H, 4.57; N,6.20; S,4.72. Found: C, 58.98; H, 4.10; N,6.08; S,4.18.

2.2.3. Preparation of 6-{2- [(4-Hydroxy-3,5-dimethoxyphenyl) -1,3-thiazolidin-4-one]-2- (4-hydroxyphenyl) acetyl] amino}-3,3-dimethyl-7-oxo-4-thia- 1-aza-bicyclo[3.2.0] heptane -2- carboxylic acid [III]:

Compound of Schiff base [I] (0.53gm, 1 mmol) and thioglycolic acid (1 mmol) was refluxed in dry benzene (10 mL) for 8hrs [10] . The solvent was evaporated and the reaction mixture was neutralized with sodium bicarbonate solution, filtered off, the product was off white, and recrystallized from petroleum ether (50-60)^{0}C. Yield : 66% m.p = 180-182 ^{0}C**,** IR(KBr) ν cm^{-1}: 3286-3415(s & br, Ph-OH ; & -COOH; O-H); 3026 (s, C-H arom.); 2976 & 2929 (s, C-H aliph.); 1680 (C=O of thiazolidinone ring) ;1662 (s, C=O amide), 1614 (C=C); 896 (C-S); ^{1}H NMR (TMS) δ ppm: 1.17 (s, 6H, CH_3); 2.48 (1H, CH-S); 3.34 (s,2H, CH_2-S); 3.83 (s, 6H, 2OCH_3); 6.69 (s, 1H,Ph-OH); 7.78-7.20 (6H, Ar-H); 9.76 (s,1H, H of COOH); Anal. Calcd. for $C_{27}H_{29}N_3O_9S_2$: C, 53.73; H, 4.80; N, 6.96; S,10.61. Found: C, 52.99; H, 4.64; N, 6.09; S,10.82.

2.2.4. Preparation of 6-{2- [(4-Hydroxy-3,5-dimethoxyphenyl) imidazolidin-4-one]-2- (4-hydroxyphenyl) acetyl] amino}-3,3-dimethyl-7-oxo-4-thia- 1-aza-bicyclo[3.2.0] heptane -2- carboxylic acid [IV]:

A mixture of Schiff base [I] (0.53gm, 1 mmol), glycine (0.075gm, 1mmol) and triethylamine (1mL) in ethanol (20mL) was refluxed for 9hrs[13] . The reaction mixture was neutralized with diluted HCl and then poured into ice-cold water. The precipitate was filtered off, washed with water and recrystallized from ethanol to give [IV].Yield : 71% m.p = 198-200 C; IR(KBr) ν cm^{-1}: 3380(br, NH),3176-3404(s & br, Ph-OH ; & -COOH; O-H); 3006 (s, C-H arom.); 2979 (s, C-H aliph.); 1710 (C=O of imidazolidine ring) ; 1670 (s, C=O amide); ^{1}H NMR (TMS) δ ppm: 9.76 (s,1H, H of COOH); 8.57 (s, 2H, NH-C); 7.02-7.19 (6H, Ar-H); 6.69 (s, 1H,Ph-OH); 3.82 (s, 6H, 2OCH_3); 3.77 (s,2H, CH_2-N); 2.49 (s ,1H, CH-N) ; 1.19 (s, 6H, CH_3); Anal. Calcd. for $C_{27}H_{30}N_4O_9S$: C, 55.29; H,5.11; N, 9.55.; S, 5.46 Found: C, 55.89; H, 4.96; N, 9.50; S, 5.01.

2.2.5. Preparation of 6-{5- [(4-Hydroxy-3,5-dimethoxyphenyl) tetrazole] - 2- (4-hydroxy phenyl) acetyl] amino}-3,3-dimethyl-7-oxo-4-thia- 1-aza-bicyclo[3.2.0] heptane -2- carboxylic acid [V]:

Sodium azide (0.065gm, 1 mmol) was added to a stirring solution of Schiff base [I] (0.53gm, 1 mmol), in dimethylformamid (10 mL), and the mixture was refluxed for 4 hrs with stirring [15], then cooled at room temperature and the precipitate was filtered , washed with cold water. Recrystallized from ethanol to give Yield : 58% m.p = 233-235^{0}C ,IR(KBr) ν cm^{-1}: 3246-3400 (s & br, Ph-OH ; & -COOH; O-H); 3383(br, NH), 3041 (s, C-H arom.); 2964-2806 (s, C-H aliph.); 1658 (s, C=O amide); 1581 (C=C); 1639 (C=N for tetrazole ring); 1496 (N=N) ; ^{1}H NMR (TMS) δ ppm: 1.70 (s, 6H, CH_3); 3.82 (s, 6H, 2OCH_3); 6.67 (1H,Ph-OH); 7.17-7.14 (6H, Ar-OH); 9.34(s,1H, H of COOH) . Anal. Calc. for $C_{25}H_{27}N_6O_8S$: C, 52.53; H, 4.72; N,14.71; S,5. 60. Found: C, 52.93; H, 4.60; N,14.00; S,5.43.

3. Results and Discussion

A major number of pharmacologically active molecules like amoxicillin that have been found for clinical use and synthesized through the derivatization of heterocyclic antibiotics as anticancer drugs clearly form an important part chemotherapeutics with madicinal properties, with its use as antibacterials and also anticancer drugs.

Aim of the present work is describes the synthesis of new heterocyclic compounds [I-V] derived from amoxicillin to produce bio-active compounds. The new Schiff base [I] was synthesized by refluxing equemolare of amoxicillin trihydrate with syringaldehyde in dry benzene with some drops of glacial acetic in good yield. These Schiff base [I] was identified by their melting points, elemental analysis C.H.N-S, FTIR, and 1HNMR spectroscopy. FTIR absorption spectra showed the demise of absorption bands due to NH2 and C=O groups of the starting materials together with presence of new band at 1620 cm-1 which is due to to C=N stretching vibration . The 1,3-oxazepine derivative [II] was obtained by Diels-Alder reaction of Schiff base [I] with phthalic anhydride in dry benzene. Thiazolidin-4-one derivative [III] was synthesized by refluxing Schiff base[I] with one mole of thioglycolic acid was refluxed in dry benzene for 8 hrs. The novel limidazolidin-4-one derivative [IV] was synthesized by refluxing Schiff base [I] with glycin and triethylamine in ethanol for 9hrs. Tetrazole derivative [V] was obtained by addition reaction of Schiff base [I] with sodium azide in dimethylformamid for 7hrs.ecorded in DMSO and show all expected protons. The suggested mechanism to obtain the target products are outlined [III] and [IV], scheme (2).

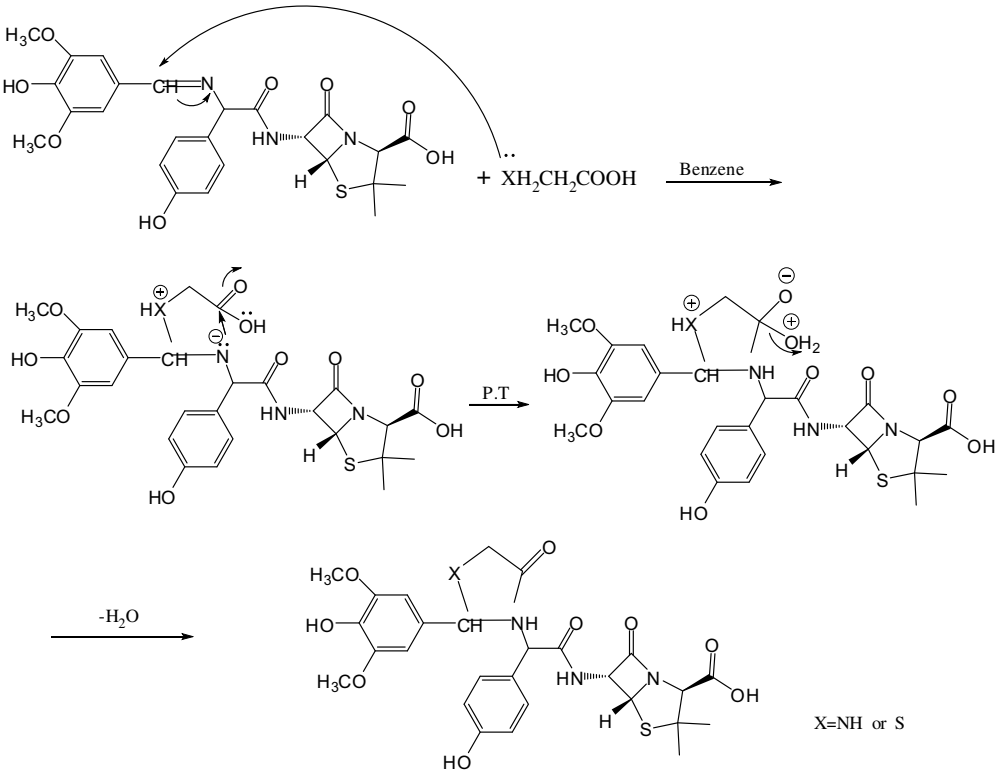

Scheme (2): Mechanism for the derivative compounds [III] and [IV].

3.1 Anticancer screening

All compounds of these study were selected for testing for their anticancer activity, at Bio-technology research center in Al-Nahrain University, Baghdad, Iraq. Two cell lines were used for the evaluation: human pelvic rhabdomyosarcoma (RD) and the mouse cell line ($L_{20}B$) according to the method described by Freshney [17]. Cytotoxicity assay of this demonstrated that synthesized heterocyclic compounds [I –V] caused inhibitory effect on the growth of (RD) and ($L_{20}B$) cell lines except compound [IV] table (1). All compounds except [IV] and [V] showed less than 50% inhibition for mice intestines carcinoma cell line($L_{20}B$), while these compounds exhibit inhibition more than 50% inhibition for human pelvic rhabdomyosarcoma (RD). As the table (1) compound [II] showed there was a potent toxic effect on both cell lines RD&$L_{20}B$ 67.7% and 49.8%, respectively. The heterocyclic derivatives of amoxicillin [I-V] exhibit cytotoxic effects on both cancer cell lines (except [IV] **)** need to further investigation to know mechanism by which the heterocyclic compounds act in comparison to traditional anticancer drug that might get the amoxicillin derivatives an attention for being promise anticancer product.

Table (1): The cytotoxic effect as percent inhibition rate (%IR) of different concentration (µl/well) for all synthesized compounds of after 48 hours exposure on RD and $L_{20}B$ cell lines.

Comp.	Inhibition of cells growth%	Inhibition of cells growth%
[I]	50.8	40.7
[II]	67.7	49.8
[III]	58.0	50.0
[IV]	64.2	-
[V]	51.0	30.4

4. Conclusions

Heterocyclic compounds derived from amoxicillin were synthesized and structurally characterized using spectroscopic techniques. The synthetic way started from reaction between amoxicillin and adequate syringaldehyde in aqueous methanol.

The heterocyclic compounds containing amoxicillin moiety have been estimated for their anticancer activity on both cancer cell lines RD & $L_{20}B$.

Acknowledgment

We thank Dr M M Al-Halbosiy and B A Hameed (Bio-technology research center in Al-Nahrain University, Baghdad, Iraq) for helpful about doing the cytotoxic effects of this compounds on some cancer cell lines.

Also we would like to express our sincere gratitude to: The Central Service Laboratory - College of Education for Pure Sciences ibn Al- Haitham, for their continual support throughout my experimental work.

REFERENCES

[1] Chaudhary N K 2013 *World J. of pharmacy and pharma. Sci.* **2** 6 6016-6025 .
[2] Parashuram M A 2010 *Inter. J.of pharma. sci Rev. and Res*. **3** 2 145.
[3] Banerjee A, Dahiya M, Anand M T and Kumar S 2013 *Asian Pacific J. of Cancer Prevention* **14** 3 2127-2130.
[4] Sreya M and Biplob B 2015 *J. of Cancer Therapy* **6** 849-858.,
[5] Entesar O and Khalida A Th 2016 *Inter. J. of Current Micro. and Appl. Sci*. **5** 2, 2319-7706 511-522.
[6] Dhanya S, Ranjitha C, Rama M and Pai KSR 2014 *Inter. J. of Innov. Res. in Sci Engin. and Technol* **3** 8.
[7] Anila K A, Lincy J. and Mathew G. 2016 *Eur. J. of Pharma and Medi. Res*. **3** 7 330-336.
[8] Alex J, Chaitany S, Shah S and Sharad K 2013 *Acta Pharm*. **63** 397–408.
[9] Sunny J, Anil J, Avneet G and Hemr AJ 2012 *Asian J. Pharm. Clin . Res*. **5** 3. 199-208.
[10] Geronikaki A, Eleftheriou P, Vicini P, Alam A D and Saxena A K 2008 *J. of Med. Chem.*.**51** 5221–5228.
[11] Cutshall N S and Prezhdo M 2005 *Bioorg. Med. Chem. Lett*. **15** 3374–3379.
[12] El-Deeb I M, Bayoumi S M, El-Sherbeny M A Abdel-Aziz A M 2010 *Eur. J. of Medi. Chem* **45** 6 2516-2530.
[13] Singh P, Kaur M, and Verma P 2009 *Bioorg. Med. Chem. Lett*. **19** 3054-3058.
[14] Popova EA, Protas AV, and Trifonov RE 2017 *Anticancer Agents Med Chem.* doi: 10.2174/ 1871520617666170327143148.
[15] Al-Rawi M S, Jumbad H T, Abdul-Jabber A M, Al-Dujaili A H 2013 *American J. of Org.Chem* **3** 1 1-8.
[16] Jumbad H T and Al-Rawi M S 2013 *Al- Mustansiriyah J. Sci* **24** 3.
[17] Freshney I R 2001 Culture of animal cells: A manual for basic technique .Wiley-Liss publication, New York.

Synthesis, Characterization and Antibacterial Activity of 1,4-di[aminomethylene carboxyl] phenylene (H2L) and its Complexes Co(II), Cu (II), Zn(II) and Cd (II)

Synthesis, Characterization and Antibacterial Activity of 1,4-di [aminomethylene carboxyl] phenylene (H_2L) and its Complexes Co(II), Cu (II), Zn(II) and Cd (II)

J S Sultan[1], S M Fezea[1], F H Mousa[2]

[1] Department of chemistry, Collage of Education for pure Sciences, Ibn Al – Haitham, University of Baghdad, Iraq

[2] Ashur University Collage, Iraq

salahmf79@yahoo.com

Abstract. A binucleating tetradentate Schiff base ligand, 1,4- di[amino methylene carboxylic] phenylene (H_2L) and its forth new binuclear complexes [Co(II) , Cu(II) ,Zn(II) and Cd(II)] were prepared via reaction metal (II) chloride with ligand (H_2L) using 2:1 (M:L) in ethanol solvent. The new ligand (H_2L) and its complexes were characterized by elemental microanalysis (C.H.N), atomic absorption, chloride content, molar conductance's magnetic susceptibility, FTIR UV- Vis spectral and, ^1H, ^{13}C- NMR (for H_2L). The antibacterial activity with bacteria activity with bacteria, *Staphylococcus aureus, Bacillus* and *Esccherichia Coli* were studied.

1. Introduction

Schiff base and their metal complexes play an important role in the development of coordination chemistry, resulting in an enormous number of publication, Mohalakshmi and Rajavel have been synthesized $[M_2(L)]X$ type (M(II) = Cu, Ni, VO] X= ClO_4, SO_4^{-2} , L = Schiff base derived from 2-Carboxybenzaldehde and 3,3˜,4,4˜-teraaminobiphenyl . They found to be higher antibacterial activity than the free ligand [1]. Bis (O-vaniline) benzidine and its complexes ($M^{(II)}$= Cu, Co, Mn, Zn) and Sm (III), VO_2(VI) have been synthesized with 3D molecular modeling and analysis for bond lengths and bond angles have also been carried out on Ni- complex [2]. Metal complexes of Schiff bases derived from substituted salicylaldehydes and various amines have been widely investigated because of their applicability. Chelating ligands containg O and N donor atoms show broad biological activity and are special interest because of the variety of ways in which they are bonded metal ions [2, 3-8]. It is well known Schiff bases complexes have numerous applications, such as in the treatment cancer [9], as antibactericide agents and as antifungicide agents [10,11]. Recently one of our group research has studied mixed ligand (1,5- Dimethyl-3-oxo-2- phenyl- 2,3-dihydro- ^1H-pyrazol-4-ylimino) and azide ion forming complexes with Mn(II), Co(II), Ni(II), Zn(II), Cd(II) and Hg(II) ion [12].

Mononuclear complexes $[L.MXH_2O]$, L=[-2-Carboxy methylene amino]phenylimino] acetic acid and, $[LMXH_2O]Cl$ L= pyrimidine-2-ylimino acetic acid with M(II) = Co, Ni, Cu, Cd, Hg and Pb were prepared too [13,14]. This paper described the synthesis spectral and magnetic studies of Schiff base 1,4- di-[amino methylene carboxy] phenylene (H_2L) and its binuclear M(II) = Cu, Co, Zn, and Cd complexes. Indeed, the biological activity of the ligand (H_2L) and its complexes are screened against selected kinds of bacteria *Bacillus cereus, Staphylococcus aureus* and *E.Coli*.

2. Experimental Part

2.1. Chemicals

All chemicals were purchased from BDH, and used without further purifications.

2.2. Instruments

- FTIR spectra were recorded in KBr on Shimadzu- 8300 Spectrophotometer in the range of (4000-400 cm–1).
- The electronic spectra in DMSO were recorded using the UV-Visible spectrophotometer type (spectra 190-900 nm) CECIL, England, with quartz cell of (1 cm) path length.
- The melting point was recorded on "Gallen kamp Melting Point Apparatus".
- The Conductance Measurements were recorded on W. T. W. conductivity Meter.
- Metal analysis. The metal contents of the complexes were determined by atomic absorption (A. A.) technique. Using a shimadzu PR-5. ORAPHIC PRINTER atomic absorption spectrophotometer.
- Balance Magnetic Susceptibility model MSB-MLI Al-Nahrain University
- The characterize of new ligand (H_2L) is achieved by:

A: ^{1}H and ^{13}C-NMR spectra were recorded by using a Bruker 300 MHZ (Switzerland). Chemical Shift of all ^{1}H and ^{13}C-NMR spectra were (ppm) unitδrecorded in downfield from internal reference tetramethylsilane (TMS), using DMSO-d^6 as a solvent, were done at AL-al-Bayt University, AlMafrag, Jordan

B: Elemental analysis for carbon, hydrogen and nitrogen was using a Euro Vector EA 3000 A Elemental Analyses (Italy), analysis (A and B) were done at AL-al-Bayt University, AlMafrag, Jordan.

2.3. Synthesis of ligand (H_2L)

A solution of glyoxylic acid (0.15 g, 2 mmol.) in ethanol (15 ml) was added to a solution of p- phenylene diamine (0.11 g, 1 mmol.) in ethanol (5 ml). The resulting mixture was stirred and refluxed for (4 hrs) Brown powder precipitate was filtered off and recrystallization to the precipitate with hot mixture of methanol: acetone: distilled water (5:5:2) ml to give brown crystals, m.p. (170-172˚C), yield 88 %.

2.4. Synthesis of Co-Complex

A solution of (H_2L) (0.22 g, 1mmol) in ethanol (20 ml) and a solution of $CoCl_2.6H_2O$ (0.48 g, 2.4 mol.) in ethanol (5 ml). The mixture was refluxed and stirred for 30 min. the mixture was filtered and dried. The product was recrystallized from hot methanol, dried over anhydrous calcium chloride the pale brown product obtained, M.p. 110 ˚C, and yield 78%.

A similar method was used to prepare of Cu (II) (0.34 g, 2 mmol, m.p. 115˚C, and yield 76%, Zn (II) (0.24 g, 2 mmol, m.p. 210˚C, and yield 80% and Cd(II) (0.40 g, 2 mmol, m.p. 220˚C, and yield 81% complexes. The physical properties for synthesized ligand (H_2L) and its complexes are shown in table (1).

Table 1. The physical properties for synthesizes ligand (H_2L) and its complexes.

Empirical Formula	Yield %	M.P ˚C	Colour	Found Calc.%					Solubility
				C	H	N	Cl	M	
$H_2L= C_{10}H_8O_4N_2$	82	170-172	Brown	54.54 54.98	3.63 4.14	12.72 13.15			Methanol ,Etanol, Acetone, DMF
$[(Co)_2(L)(H_2O)_7Cl]Cl.9H_2O$	78	110	Pale brown	15.66 15.88	4.96 4.91	3.65 3.84	18.53 19.08	15.40 16.08	DMSO DMF
$[(Cu)_2(L)(H_2O)_7Cl]Cl$	76	115	Pale brown	19.57 20.01	3.26 3.80	4.56 5.11	23.16 22.80	20.71 21.06	=
$[(Zn)_2(L)(H_2O)_2Cl_2]3H_2O$	80	210	Dark brown	20.68 20.23	2.75 3.03	4.82 5.20	24.48 23.98	22.41 23.10	=
$[(Cd)_2(L)(H_2O)_2Cl_2]8H_2O$	81	220	Dark brown	15.70 16.05	3.40 3.39	3.66 4.18	18.58 18.12	29.31 28.80	=

3. Results and Discussion

3.1. Characterization of ligand (H_2L)

In this study, new Schiff base ligand (H_2L) type NO / donor atoms was synthesized according to the used method shown in Scheme (1)

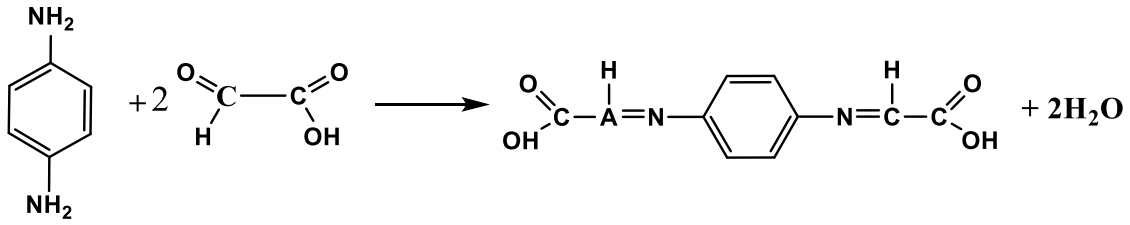

Scheme (1) :Synthesis route of ligand (H_2L)

Spectroscopic methods [FT-IR, UV-Vis, ^{1}H-^{13}C-NMR] along with melting point and element micro-analysis (C.H.N) were used to characterized new ligand (H_2L).

3.1.1. NMR Spectral Data

The ^{1}H.NMR spectrum of ligand H_2L, Figure 1, multiple chemical shifts range δ (6.44-7.40) ppm. May assign to aromatic protons. The proton of carboxylic group appeared as slightly multiple broad δ (9.70, 10.20) ppm. The imine proton (HC=N) is showed as a doublet at δ (8.1, 8.3) ppm. The signal at δ (2.5) ppm, refer to deurated DMSO [15-17].

^{13}C-NMR spectrum of ligand (H_2L). Figure 2, and shows chemical shift for carbonyl group of carboxylic group appeared as expected downfield at (175) ppm. The chemical shifts at (159) ppm was attributed to azomethine group (HC=N). Signals related to aromatic carbon were detected at range (110-130) ppm. Finally, the chemical shift at (40-45) ppm was as due to DMSO-d^6 [18].

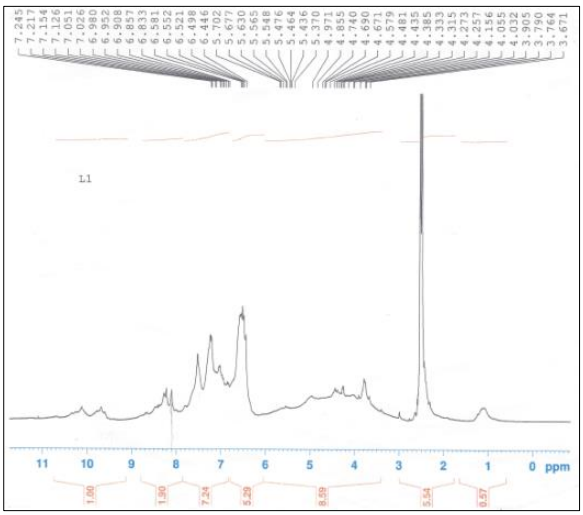

Figure 1. ^{1}H-NMR chart for ligand H_2L

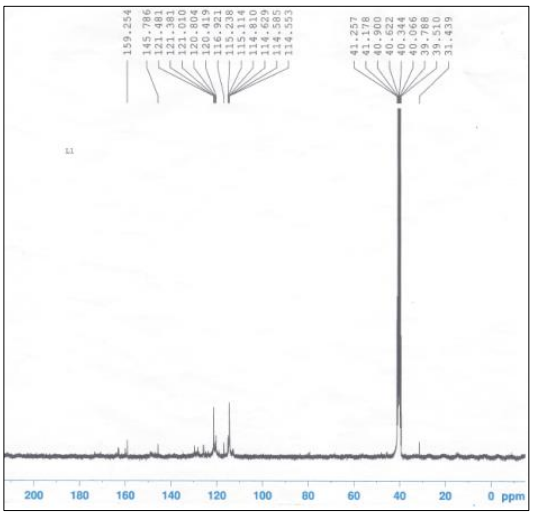

Figure 2. ^{13}C-NMR chart for ligand H_2L

3.2. Characterization of (H_2L complexes)

The complexes of ligand (H_2L) with Co(II), Cu(II), Zn(II), and Cd(II), were prepared via reaction metal (II) chloride salt with ligand (H_2L) using 2:1 (M:L) mole ratio in ethanol solvent respectively. The method of this synthesis shows in scheme 2).

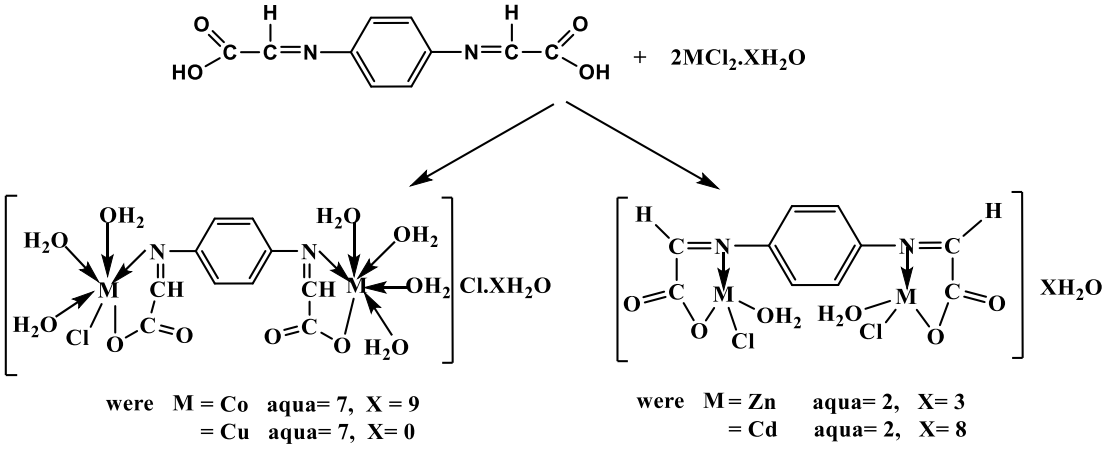

Scheme 2 Synthesis route of (H_2L) Complexes.

Spectroscopic methods [FT-IR, U – Vis, A.A.] along with molar conductivity, elemental microanalysis C, H, N, chloride content, magnetic susceptibility and melting point were used to characterize the prepared ligand complexes. The complexes are stable and soluble in DMSO, DMF

3.2.1. Molar conductance

The molar conductance of the complexes (Co (II), Cu(II)) in DMSO solvent lie in the (52.8, 33.1) S.cm^2 molar $^{-1}$, indicating its electronic nature (1:1) ratio, the molar conductance of the complexes [Zn(II), Cd(II)] in DMSO solvent (12.23, 13.37) S.cm^2 molar $^{-1}$ refer to non-electrolytic nature [19].

3.2.2. Magnetic Susceptibility

The magnetic susceptibility for all complexes were measured at room temperature and the effective magnetic moment (μ_{eff}) values were listed in table (2). The magnetic susceptibility measurement for the dinuclear complexes Co (II) and Cu (II) are (6.79) and (2.54) B.M which suggests the presence of

unpaired electron. Large and permanent magnetizations may be established within the ferromagnetic metals [Co (II) and Cu (II)] [20,21].

Table (2) The molar conductance and magnetic susceptibility of the complexes

Empirical Formula	**Λ M S.cm^2 molar $^{-1}$**	**ratio**	**μ effect BM**
[$(Co_2)(L)(H_2O)_7Cl]Cl.9H_2O$	52.8	1:1	6.79
[$(Cu)_2(L)(H_2O)_7Cl]Cl$	33.1	1:1	2.54
[$(Zn)_2(L)(H_2O)_2Cl_2]3(H_2O)$	12.23	Neutral	-
[$(Cd)_2(L)(H_2O)_2Cl_2]8(H_2O)$	13.37	Neutral	-

3.2.3. FT-IR Spectral data

IR spectral at the ligand (H_2L) figure 3 shows disappearance of ν(C=O) (1795) cm^{-1} and ν(NH_2) (3381, 3373) cm^{-1} in starting material, and appeared new strong bands at (1690 and 1650 cm^{-1}) are due to ν(C=O) of carboxylic group and (HC=N) imines [22, 23]. The stretching band of middle intensity at [3350-3294] cm^{-1} attributed to ν(OH) of carboxylic group compared with precursors which indicates the ligand (H_2L) has been obtained. Bands corresponding to (C—H) aromatic stretching at (3140-3043) cm^{-1}. Band at 829 is due to para disubstuted phenyl [24].

The IR spectra of ligand (H_2L) complexes Cu(II), Zn(II), Cd(II) and Co(II) 'figure 4', table (3) exhibited band at (3396 -3363) cm^{-1} and (987-720) cm^{-1} refer to water coordinate [25]. The bands (835-827) cm^{-1} attributed to p- substituted aromatic [26]. The detected bands of (620) cm^{-1}, (1630) cm^{-1}, (622) cm^{-1} and (1625) cm^{-1} in the IR spectra of all ligand complexes refer to stretching frequency of imine group (HC=N) which were shifted to lower frequency when if compared with that of free ligand (H_2L) (1650) cm^{-1} showing that coordination with the metal ions was occurred via nitrogen atom of imine group (HC=N) [23,24]. The ν(C=O), ν_{asy} (COO) and ν_{sy} (COO) stretching vibrations of the carboxylate group are observed at (1665-1650) cm^{-1} and (1398-1350) cm^{-1}. For all complexes ($\Delta_{asy} - \Delta_{sy}$) equal (313-252) cm^{-1}, supporting, the idea the ligand coordinate through deprotonated oxygen of mono dentate carboxylate [26,27]. New bands are found in the spectra of all complexes in the regions (597-532) cm^{-1}which are attributed to ν (M—N) mode [16]. The bands at (459-412) cm^{-1} refer to ν (M—O) mode [19]. Therefore, from IR spectra, its concluded that the ligand behave an anion tetradentate and bind to the two metals; two imines and two carboxylates, forming octahedral for Co(II), Cu (II) and tetrahydral for Zn(II) and Cd(II) structures.

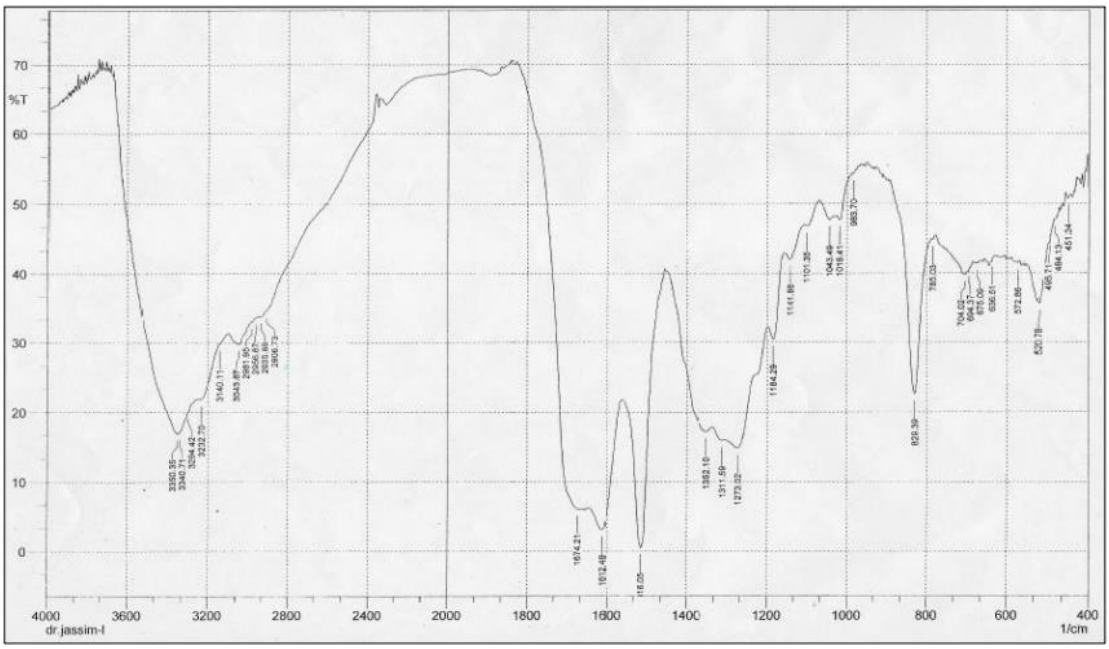

Figure. 3 FT-IR spectrum of ligand H_2L

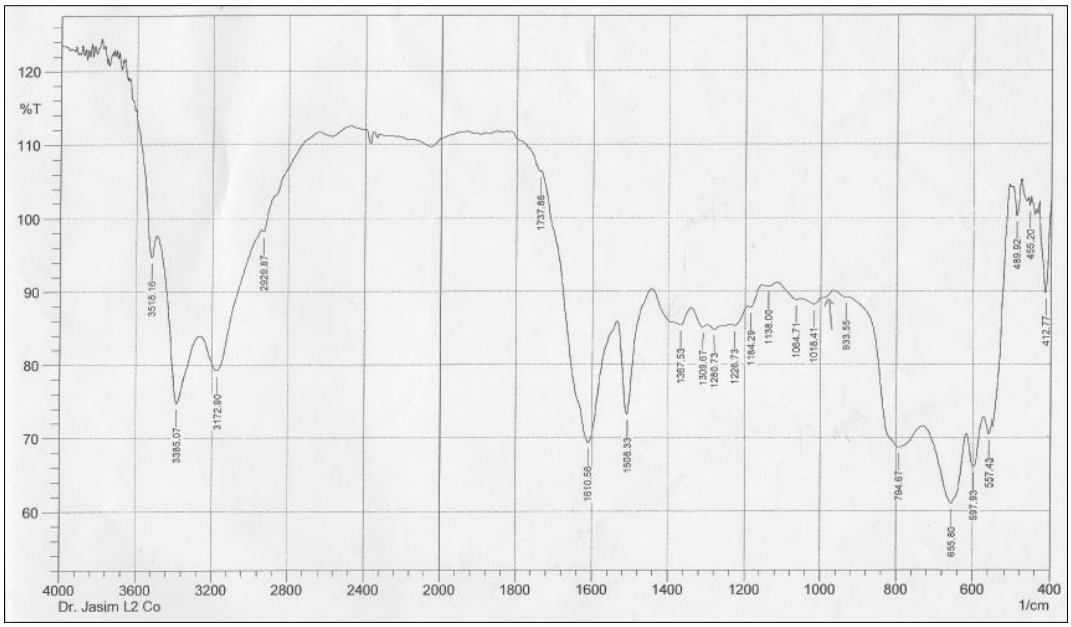

Figure. 4 FT-IR spectrum of Co-complex

Table (3) Infrared spectral data for the precursor, ligand and its complexes

Compound	υOH	υ(NH_2)	υ(C=N)	υ(C-H) Aromatic	υ(C=O)	Y_{asym} COO^-	υ_{sym} COO^-	Δcm^{-1}	P. subs.	aqua	M-N	M-O
Glgoxylic acid	3361				1745							
p-phenylene diamine		3381 3371		3008					825			
L=$C_{10}H_8O_4N_2$			1650	3140 3043	1690	1420	1380		829			
Co-complex	3385		1620	3172	-	1665	1397	268	829	794	557	412
Cu-complex	3363		1630	3120	-	1650	1398	252	827	987	597	441
Zn-complex	3396		1622	3130	-	1662	1350	312	829	735	534	417
Cd-complex	3384		1625	3125	-	1665	1352	313	835	720	532	459

3.2.4. U.V–Vis Spectral Data

The electronic spectral data for ligand (H_2L) and its complexes are summarized in table (4). The electronic spectra for ligand displayed absorption at (266,345) nm (37594-28985) cm^{-1} were attributed to intraligand $\pi \rightarrow \pi^*$, $n \rightarrow \pi^*$, respectively [28]. The UV-Vis spectrum of Co (ΙΙ), complex fig. (5). Displayed broad centered band at (656) nm (15244) $cm^{-1}$was attributed to (d—d) spin allowed electronic transition type $4T_{1g} \rightarrow {}^4A_{2g}$ (ν_3) characteristic octahedral geometry around Co(II) [29]. The UV-Vis spectrum of Cu (II) complex showed broad peak centered at (580) nm (17241) cm^{-1} was assigned to $^2Eg \rightarrow {}^2T_2g$ transition, conforming octahedral geometry around Cu(II) [30]. The electronic spectrum of Zn (II), Cd (II) complexes exhibited charge transfer peaks compared with free ligand in UV.spectrum which are common phenomenon for metal complexes where (d—d) transitions are excluded [31].

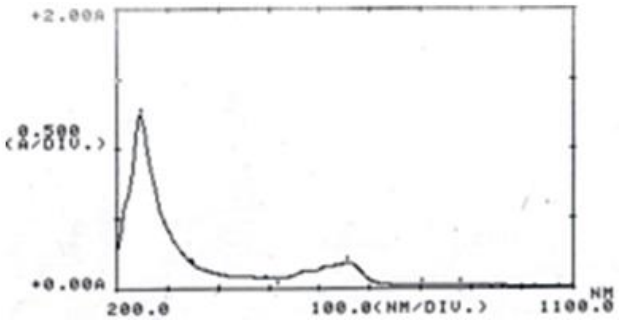

Figure 5. Electronic spectrum of Co-complex

Table (4) Electronic spectral data of the ligand (H_2L) and its complexes

Compound	**λnm**	**ύ wave number cm^{-1}**	**(E_{max} molar^{-1} cm^{-1}**	**Assignment**	**Proposed Structure**
L=$C_{10}H_8O_4N_2$	266	37594	785	$\pi \rightarrow \pi^*$	
	345	28985	1135	$n \rightarrow \pi^*$	
Co-complex	656	15244	185	$^4T_{1g} \rightarrow {}^4A_{2g}$	Distorted octahedral

Cu-complex	580	17241	1023	$^2Eg \rightarrow {}^2T_2g$	Distorted octahedral
Zn-complex	358	27932	1277	C.T	Tetrahedral
Cd-complex	357	28011	1258	C.T	Tetrahedral

Were C.T= Charge transfer

4. Biological activity of the ligand (H_2L) and its Complexes.

Indicating the new ligand (H_2L) and its complexes, exhibited antibacterial activity against four kinds of bacterial *E, Coli*, *Staphylococcus aureus* and *Bacillus cereus* respectively. Table (5) and Table (6) shows the various activities of the ligand and its complexes can be explained on the bases of overtones' concept and Tweeds chelating theory [32-33].

Table (5) the inhibition circle diameter in millimetre for the bacteria after 24 hours in cubation paid and 37˚C

Compounds	Bacillus cereus	StaphylococcusAureus	E.Coli
Ligand H_2L	0	10	13
Co-complex	0	14	15
Cu-complex	0	8	0
Zn-complex	0	10	8
Cd-complex	0	10	0

E.Coli = Escherichia coli

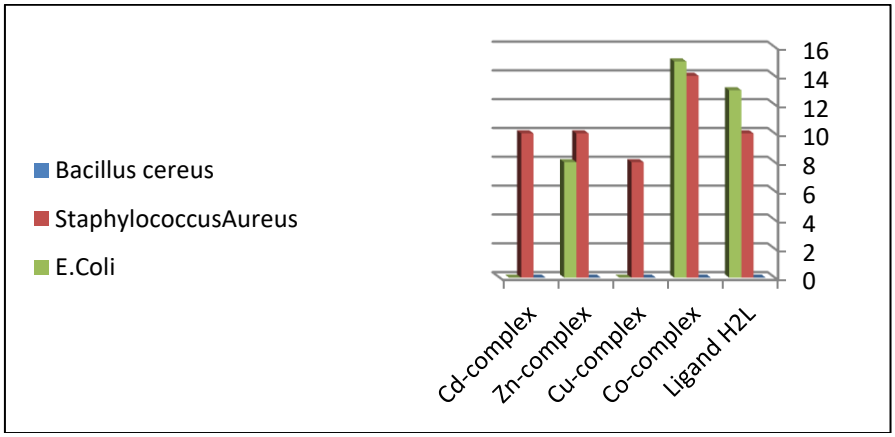

Figure (6) Antibacterial activity of the ligand and its complexes (inhibition zone diameter, mm)

5. Conclusions

The new ligand (H_2L) and its complexes behave tetradentate ligand through its two azomethene nitrogen and two oxygen atom of 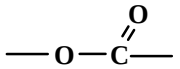 group of two five member ring with central metal ions, Co (II), Cu (II), Cd (II) and Zn(II) forming complexes with molecular formula.

$[M_2L.Cl.7H_2O]Cl.\ XH_2O$ (M = Cu X = 0) (M = Co X = 9)

$[M_2L.Cl_2.2H_2O]Cl.\ XH_2O$ (M = Zn X = 3) (M = Cd X = 8)

The distorted octahedral geometrical structure was suggested for Co(II) and Cu(II) complexes and tetrahedral for Zn(II) and Cd(II) complexes based on the characterization data for all technique.

The antibacterial study showed that the ligand H_2L and its complexes showed various activities to the strain of bacteria taken under study.

References

[1] Mahalakshmi N, and Rajavel R, 2011, Asian J. of Biochemistry and pharmaceutical Research, 1 525
[2] Maurga R. C, Chorurasia J. and Sharma P, 2008, Indian J. of chem. 47 517
[3] Canpolat E and kaya M, 2004, J. Coord. chem. 57 127
[4] Mishra A P, Khare M and Gautam S K, 2002, Synth. React.Inorg. Met-Org. chem. 32 1485
[5] *Fan Y, Bi C, Li J,* 2003, *Synth. React. Inorg. Met. Org. Chem. 33 137*
[6] Canpolat E. and kaya M, 2005, Russ. J. Coord. Chem. 31 790
[7] Maurya R C, Patel P and Rajput S, 2003, Synth. React. Inorg .Met.Org.Chem. 33 817
[8] Vedanayaki S. and Jayaseelan P, 2014, World J. of pharmacy and pharmaceutical Sci. 3 504
[9] Jayasselam P, Akila E, Usharani M, Rajaval R, 2016, J. Saudi. Chem. Soc. 20 625
[10] Rajib l D, Keka S, Kamales M, Egbert k, 2001, Inorg. Chim. Acta. 316 113
[11] Ahmed A S, Saadia A A, Amany H, Doaa H N, 2012, Spectrochim Acta Part A 89 329
[12] Jassim S S, Sajed M L, Dhuha K R, 2015, Open Journal of Inorganic Chemistry 5 102
[13] Jassim S S, Falih H M, 2012, J. Baghdad for Sci. 3 547
[14] Jassim S S, Falih H M, 2012, N.J.C. 48 466
[15] Silverstein M R, Bassler G C, and Morrill T C, 1981, "Spectrometric Identification of Organic Compounds" 4th ed. John Wiley and Sons New York
[16] Tajmir R, 1990, J. Inorg. Biochem. 40 181
[17] Tajmir R, 1991, J. Inorg. Biochem. 42 47
[18] Raman N, Sobha S and Selvaganapayhy M, 2012, Intera. J. of pharma. and Bio. Science 3 251
[19] Kettle S F, 1975, "Coordination Compounds", Thomas Nelson and Sons, London P. 165.
[20] Anupama B, Paadmaja M and Kumari C G, 2012, E. J. Chem.1 389
[21] Trived G S and Desai N C, 1992, J. of Chem. 31 366
[22] Sajjad M Shokoh B and Asad, S 2011, transition met. chem. 36 425
[23] Raj K D and Sharad K M, 2011, J. of Coord. Chem. 13 2292
[24] Fleming and Williams D H, 1966, "Spectroscopic methods in organic chemistry", Ed. McGraw Hill publishing company ltd, London
[25] Dominik C and Branko K, 2011, crystengcomm 13 4351
[26] Geeta B and Ravinder V, 2011, Chem. pharm. Bull. 2 166
[27] Washed M G Refat M S and Megharbel S M, 2009, spectrochimia acta A 4 916
[28] William K, 1987, "Organic spectroscopy" 2nd Edition
[29] Lever, P A B, 1968, "In organic electronic spectroscopy" Elsevier publishing company New York P. 6, 121
[30] Kamellia N and Razie S, 2011, J. of coord. Chem. 11 1859

[31] Choi K Y, Jeon Y M, Lee K C, Ryu, H, Suh M, Park H S, Kim M J and Song Y H, 2004, J. Chem. Cryst. 9 591
[32] Jayablakrishnan C and Natarajan K, 2002, Transition Metal Chemistry 27 75
[33] Tweedy B G, 1964, Phytopatology 55 910

Preparation Characterization and Electrical Study of New Polymeric Mixture (Consist of Three Polymers) Nanocomposites

Preparation Characterization and Electrical Study of New Polymeric Mixture (Consist of Three Polymers) Nanocomposites

Entisar E. AL-Abodi, Azhar Farouk

Department of Chemistry, Collage of Education for Pure Science /Ibn Al-Haitham, University of Baghdad, Baghdad, Iraq.

email: entisaree2000@gmail.com

ABSTRACT. By using hummers' method, graphene oxide (GO) was synthesized and by reducing it gave reduced graphene oxide (RGO). The polymeric blend contains three polymers; Poly Aniline (PANI), Poly Vinyl Acetate (PVAc), and Pecten (Pc) which have been prepared at studied amount. The composites for above polymers with various concentrations of, graphene oxide (GO) and with reduced graphene oxide (RGO)were prepared, and then pour into films (chips). The dielectric constant properties of chips were measured, which its point the electrical conductivity values for the prepared chips increase with increasing of frequency. As well, the electrical conductivity is research in terms of the Arrhenius plot, it is plotted against the reverse temperature for the prepared films at different applied frequencies.

1. Introduction

The interesting of Polymer nanocomposites are increased due they collect the merits of polymers with little amounts of nanoparticle materials [1]. The polymer structure is so important to define , the polarity of polymer and this effectives the on electrical and dielectric properties [2] Conducting polymers offer optical and electrical characteristic of the metal and keep the engaging mechanical properties of polymers leading to extensive range of uses [3]. Using of PANI as matrix materials for more research, because it is much stable in several solvent and air, as well it is shows dramatic changes in its physical properties and electronic structure [4]. In our study, it prepared polymeric mixture consist of three polymers; Poly Aniline(PANI) Poly Vinyl Acetate(PVAc), and Pecten (Pc) and it composite with different concentrations of, graphene oxide (GO) and with reduced graphene oxide (RGO or G). and effect this addition on the electrical properties of the polymeric mixture.

2. Experimental

2.1. Synthesis of Nanoparticles

All materials used in this research from Sigma Aldrich, and it used without any purification. graphene oxide nanosheets (GO) was prepared by Hummer's method [5] by oxidation of graphite with concentrated H_2SO_4, $NaNO_3$, $KMnO_4$. graphene nanosheets (G) were prepared by reduction GO with hydrazine hydride [6].

2.2. Preparation of Composite

Polyvinyl acetate (PVA), (commercial/ German), poly aniline(PANI) and Pecten (Pc), (commercial). Mixture Composite was prepared in the previous paper [7]. Then polymeric mixture nanocomposites were prepared by following: Four 40 ml beakers were prepared with

25 percentages of PANI (5 g in 100 ml disstaled water) Pecten, (12.5g in 100 ml distalled water) PVAc, (0.8070 g) of Ammonium persulphate and (0.367 g) of Aniline chloride) and blended totally under mechanical stirring for 120 minutes at normal temperature. Every composite was blended ultrasonically for 20 minutes with various (GO) composites weights (0.000 ,0.0065,0.015 and 0,029g). By solution casting, the films was prepared, then they let dry at (60ºc) for 130 hour .From measured σ (electrical conductivity) to the above films, it found that the highest value of σ was the film which include 4% Percentage of (GO), that is cause this ratio elected for our research. then repeated this procedure with (G) nanosheets.

2.3. Dielectric Constant Measurement

The dielectric parameter (for prepared films) as a function of frequency is obtained by the complex permittivity.

$$\varepsilon*(\omega) = \varepsilon'(\omega) - \varepsilon''(\omega) \quad (1)$$

where the ε'(the dielectric constant) and ε''(dielectric loss) are the components for the energy storage and energy loss, respectively, in each cycle of the applied electric field. To calculate ε' from measured capacitance C by using following equation:

$$\varepsilon' = \frac{Cd}{\varepsilon_0 A} \quad (2)$$

A is the area of the electrodes, d is the thickness between the two electrodes, ε_0 is the permittivity of the free space, and (ω) is the angular frequency $(\omega = 2\pi f)$., f is applied frequency**.** (ε'' (ω)) is described with equation (3),wereis tangent delta [8] $tan\ \theta\ (\omega)$

$$\varepsilon''(\omega) = \varepsilon'(\omega).tan\theta\ (\omega) \quad (3)$$

Electrical conductivity σ of fabricated chips was determined by expresion (4).

$$\sigma = \varepsilon' \times \varepsilon_0 \quad (4)$$

3. Results and Discussion

3.1. FTIR Characterization

3.1.1FTIR of Nanomaterials

'Figure 1 'shows the FTIR spectrum of GO and G nanosheets, respectively. In (1a), a broad peak at (3431 cm-^{1}) attributed to the stretching vibration of (OH) group, the two peaks at (1618 cm-^{1} and 1720 cm-^{1}) can be referred to the stretching vibration of (C=C) groups and (C=O) groups of carboxylic acid and carbonyl groups present at the edges of GO. The absorption peaks at (1360 cm^{-1} and 1227 cm^{-1}) can be attributed to the stretching vibration of (C-O) group of carboxylic acid and (C-OH) group of alcohol, respectively. In (1b), as we see abscence of stretching vibration for (C=O) group [9].

3.1.2 FTIR of Composites

Proof of polymeric mixture composite, polymeric mixture GO nanocomposite and polymeric mixture G nanocomposite was studded by FT-IR spectroscopy, as appear in the Figure1. From figure (2a), the special absorption peak at (1402 cm^{-1}) for (C-N) group in PANI [10], the peak at (1188 cm-^{1}) due to(C-N+) group [11], which gave electrical conductive of polymeric mixture. The peaks at (3321 cm^{-1} and 3131cm^{-1}) for aromatic(C-H) and (O-H) at acetate group, respectively. The band at (1111cm^{-1}) refer to (C-O-C) group in Pecten [12]. In (2b), there is a clear increase in the peak at (3136 cm^{-1}), which indicates the (OH) group in GO nanosheets Figure (2c) Shows a decrease in the bands at (1111, 1400 cm$^{-1)}$, which indicates of (C-O) group and (C=C) group, another decrease in the peaks at (3410, 32281 cm^{-1}) indicating the weakness of hydroxyl group, which appeared in GO spectrum.

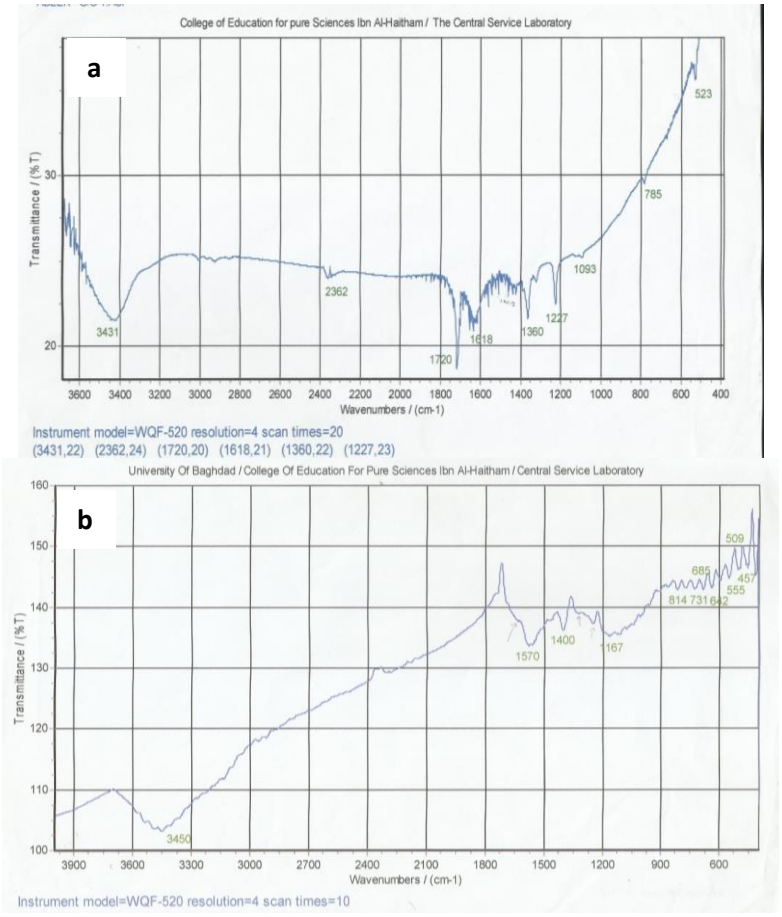

Figure 1. FT-IR spectrum of (a) GO nanosheets and (b) G nanosheets

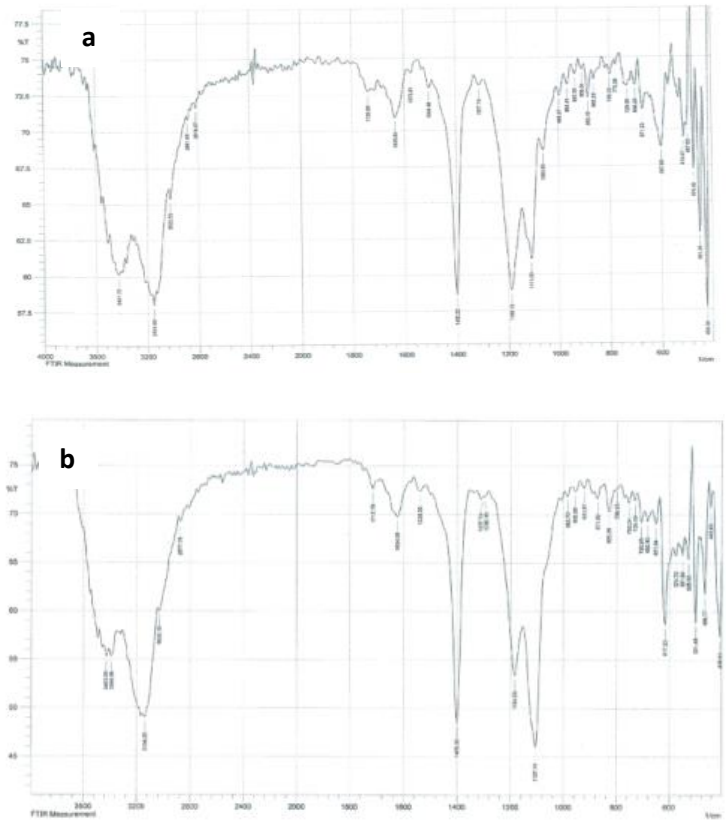

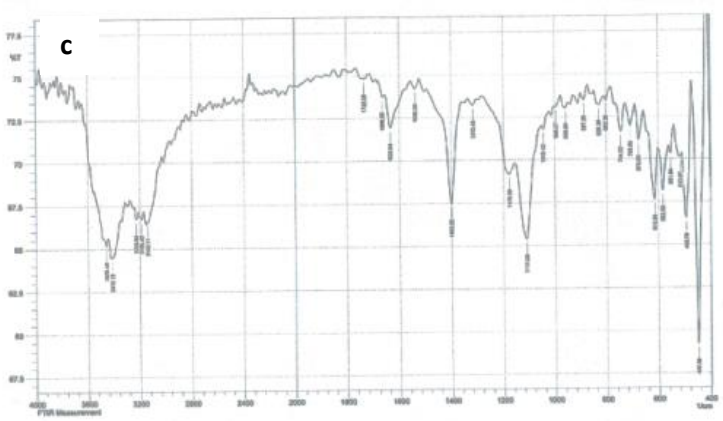

Figure 2. FT-IR spectrum of (a) polymeric mixture composite (b) polymeric mixture GO nanocomposit and (c) polymeric mixture G nanocomposite

3.2. XRD Analysis

'Figure 3' shows the XRD analysis of GO and G nanosheets, the peak at (10.77°) corresponding to GO nanosheets was disappeared in G nanosheets, while the two major peaks are observed at about (25.07,44.47°) [6,13].

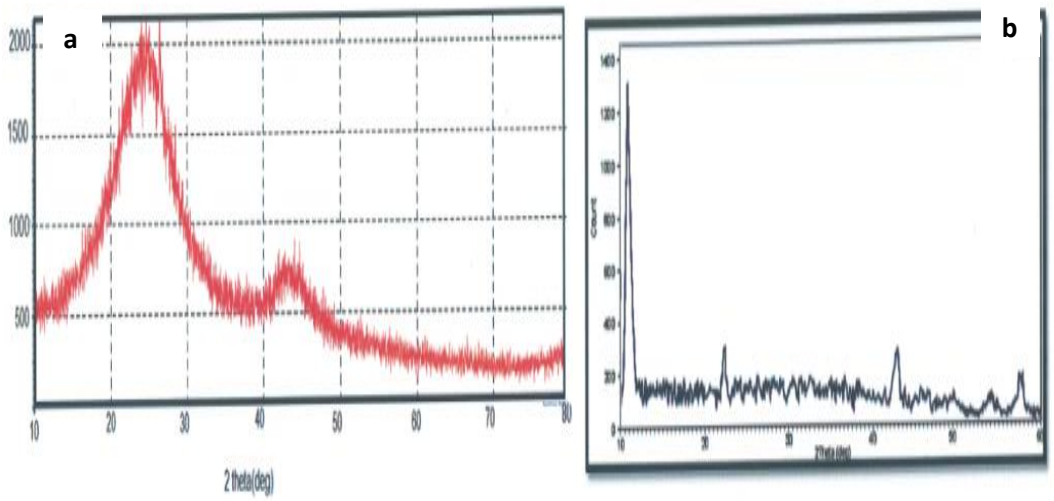

Figure 3. The X-ray diffraction pattern (XRD) of (a) GO nanosheets

and (b) G nanosheets

Figure (4) shows the X-ray diffraction pattern (XRD) of polymeric mixture composite, polymeric mixture GO nanocomposit and polymeric mixture G nanocomposite. In (4a), where the more peaks of diffraction have appeared at (14.01, 19.88 and 25.12), while in (4b), the X-ray diffraction peaks at (12.14, 18.03, 23.22, 26.12, 35.13) [14]. In (4c) a pattern of diffraction showed the spread of G nanosheets within polymeric mixture, the distinctive peaks of G appear at (20.01, 29.47) [15].

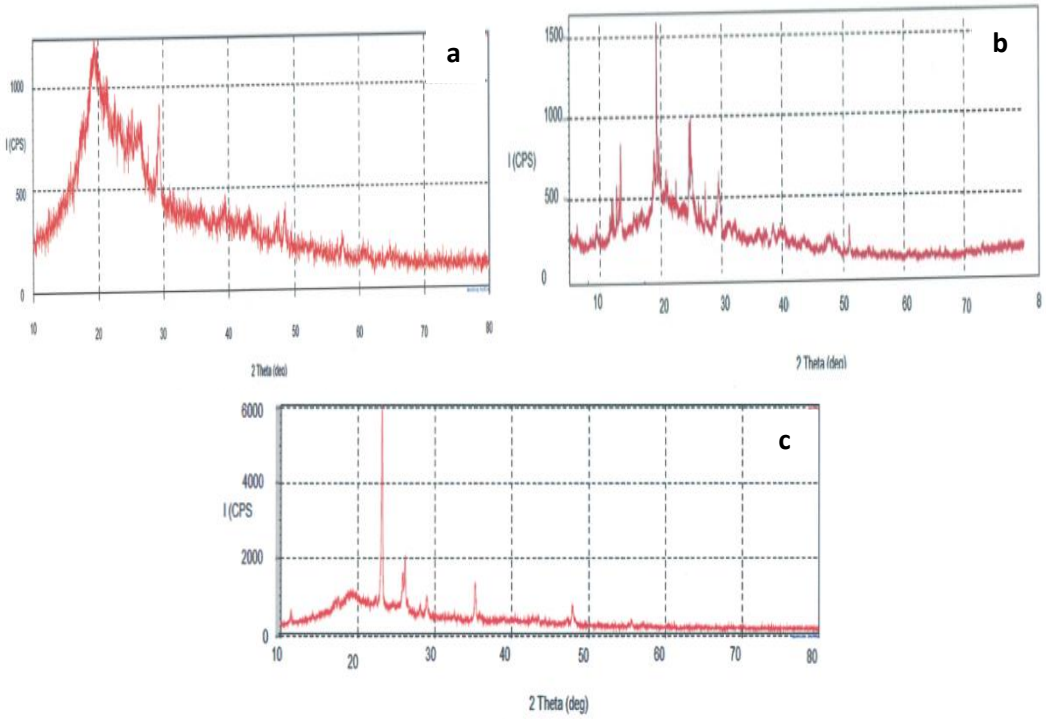

Figure 4. The X-ray diffraction pattern (XRD) of (a) polymeric mixture composite (b) polymeric mixture GO nanocomposit and (c) polymeric mixture G nanocomposite

4. AFM Analysis of Nanomaterials

The synthesized nanomatrials GO and G nanosheets, were investigated by (AFM), the results were almost identical as in 'figures 5' and with nanoparticles size about (25.7 nm). 'Figure 6' shows AFM of polymeric mixture composite. 'Figure 7' shows AFM of polymeric mixture G nanocomposite, which are distributed within the polymeric mixture and are encapsulated in the polymer mixture particles. The size changed from nanoscale to about (371 nm).

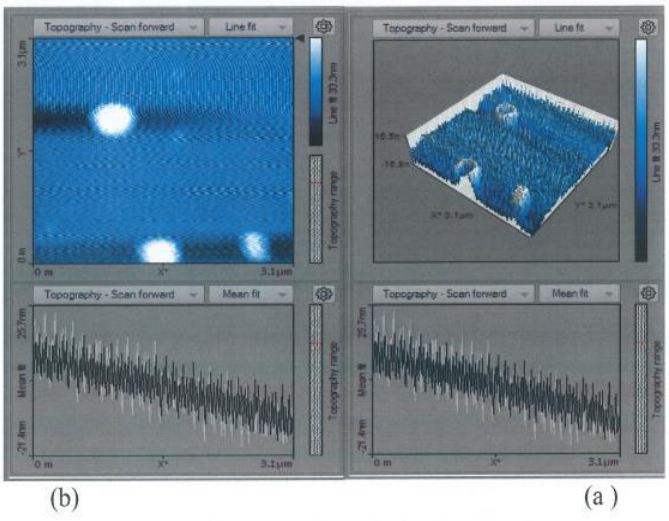

Figure 5. AFM pictures of G nanosheets (a):2-D topographic and (b):3-D topographic

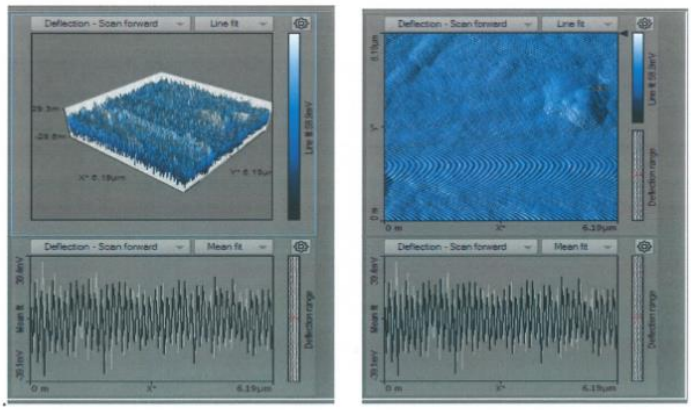

Figure 6. AFM pictures of polymeric mixture composite (a):2-D topographic and (b):3-D topographic

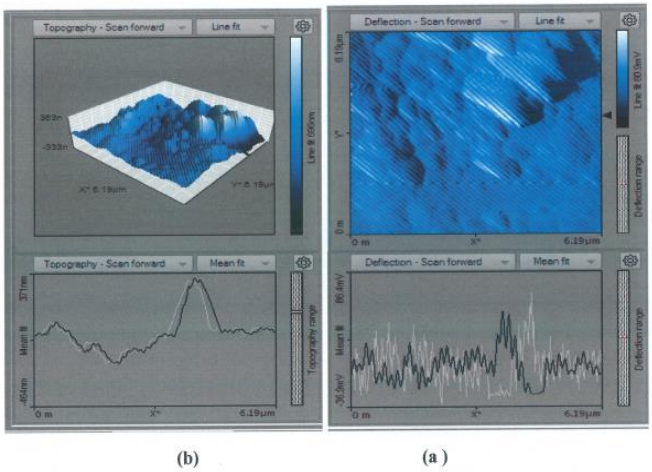

Figure 7. AFM pictures of polymeric mixture G nanocomposite (a):2-D topographic and (b):3-D topographic

5. SEM Analysis

'Figure 8' show the surface morphology of GO and G nanosheets, from this figure it appeared the d-spacing of sheets of G is smaller than GO.

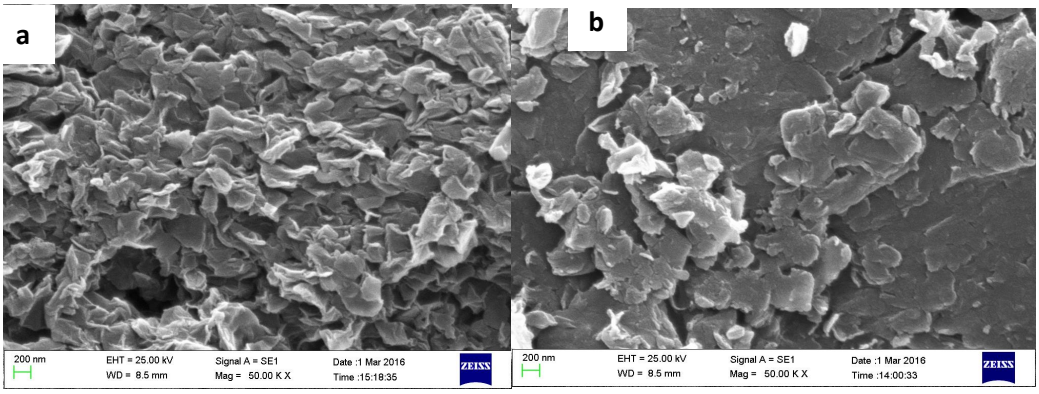

Figure 8. SEM pictures of (a) GO nanosheets and (b) G nanosheets

'Figure 9' shows SEM pictures of polymeric mixture composite, while 'figure 10' of polymeric mixture G nanocomposite which are distributed within the polymeric mixture and encapsulated in the polymer mixture particles.

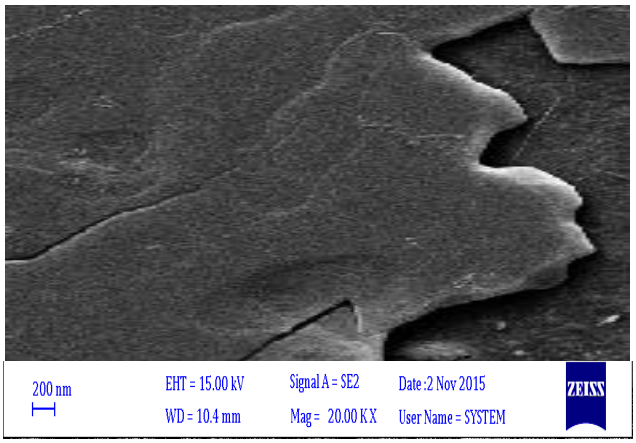

Figure 9. SEM pictures of polymeric mixture composite.

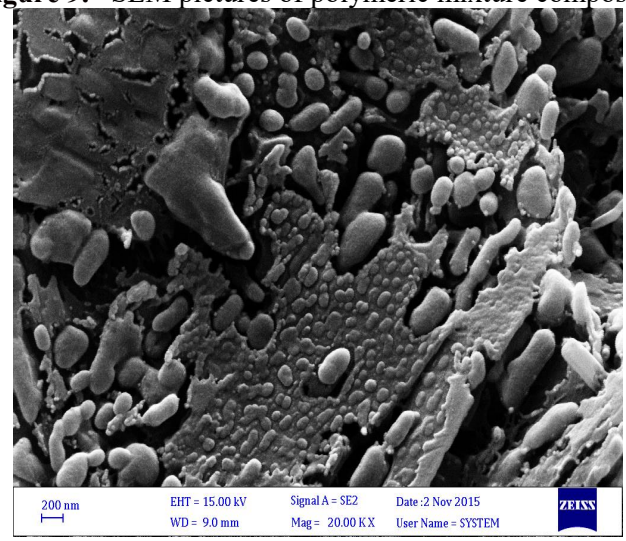

Figure (10). SEM pictures of polymeric mixture G nanocomposite.

6. Electrical properties measurements

The difference in electrical conductivity of the chips prepared from the polymeric mixture composites, polymeric mixture GO nanocomposites, and polymeric mixture G nanocomposites, is shown in Figure (11) and there is a steady increase in the conductivity values by increasing the frequency. The conductivity of the polymeric mixture without the addition of a nanomaterials gave a value of conductivity of (0.514 s/m), which is the conductivity of PANI, which is the only conductive polymer in the polymeric mixture, and the other are non-conductive polymers.

Chips prepared from polymeric compositions with 4% of nanomaterials. The results showed that the electrical conductivity values increased with increasing frequency, with a gradual and stable increase at (100-4000 Hz). The conductivity is clearly and strongly increased at (100000 Hz), as shown in Figure (11) showing the difference in the conductivity values of the composites. The highest conductivity at the frequency (100000 Hz) of the polymeric mixture G nanocomposites is shown. This indicates the effect of the conductivity G nanosheets conductivity on the polymeric mixture as the highest conductivity of GO, which is an electrical insulating material. The conductivity has very little start and oscillates until it becomes zero at the frequency (100000 Hz), This is an indication of the effect of GO sheets scattered within the polymeric mixture on the conductivity on the composites. It is clear that the doping processes effects on the conductivity of the chips prepared from polymeric mixture, that the conductive nanomaterials increase the carriers of the charge (electrons or gaps) and thus increase the conductivity of composites.

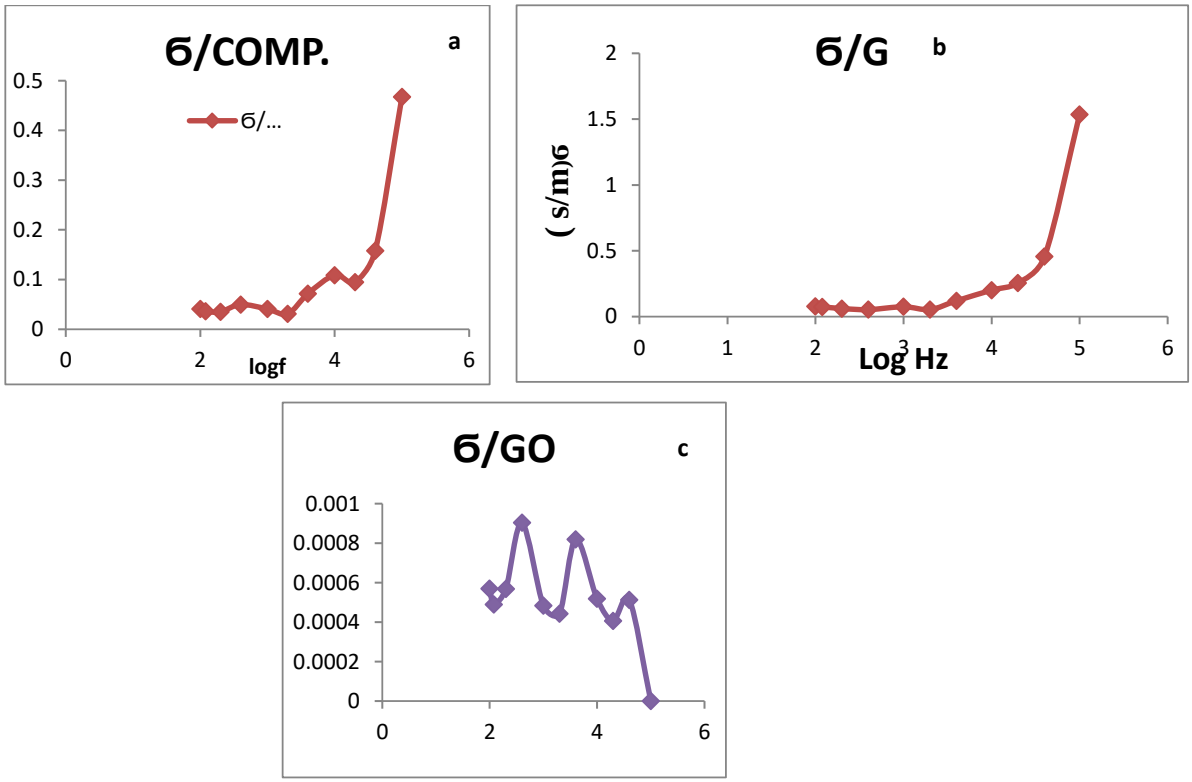

Figure 11. Electrical conductivity measurements of (a) polymeric mixture composite (b) polymeric mixture G nanocomposit and (c) polymeric mixture GO nanocomposite

Figures (12) and (13) were pictorial the variance of real part (ε') and imaginary part (ε'') of dielectric permittivity with frequency for chips prepared from polymeric compositions with 4% of nanomaterials, respectively, at room temperature. In both cases, permittivity arrived higher values at low frequencies, which decreased quickly with increasing of frequency. This is because at low frequency region the alternation of the field is slow, those give more time to induced and permanent dipoles to align themselves to the applied field, leading to enhanced polarization. Enhanced values of (ε') particularly at low frequencies can be referred to interfacial polarization, and/or electrode polarization. Electrode polarization is associated to the buildup of space charges at the specimen-electrode interfaces and is describing by very highly values of real part (dielectric constant) and imaginary part (dielectric loss) of permittivity, these chips have a high ability to store electric energy more than a composite of other chips and is suitable for many applications from capacitors for battery manufacturing but the chips prepared from the triple composite with (GO), which is non-conductive material to the value of the electrical conductivity approach to zero and did not get the electric plug as [16-18].

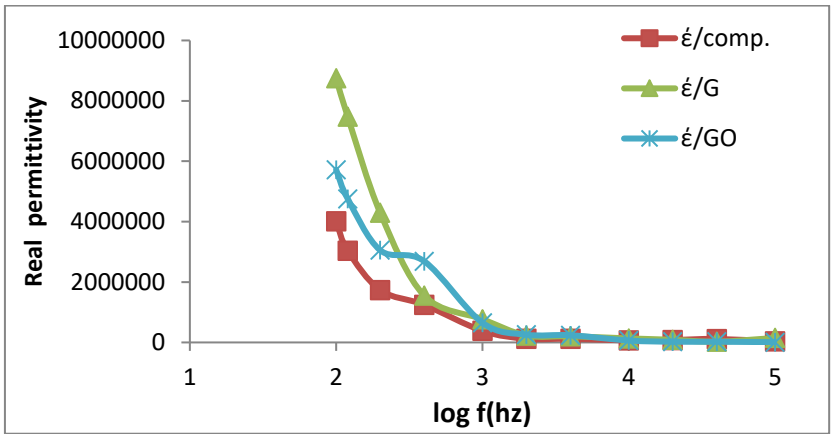

Figure 12. Real permittivity against log frequency for prepared composites.

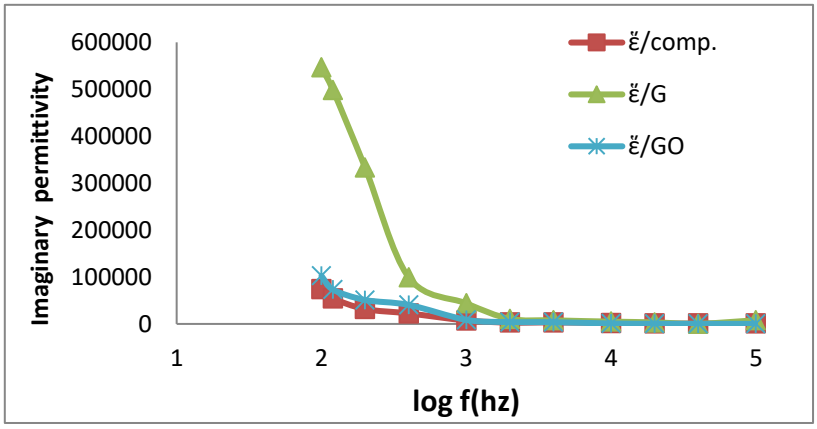

Figure 13. Imaginary permittivity against log frequency for prepared composites.

7. Activation Energy of the Nanoparticles

The study of conductivity, which is the inverse of resistance as a function of temperature, is the best criterion for determining the behavior of conductivity in the chips and membranes by determining the energy values needed for the conductions of the electrical conductions. This energy is an energizing energy which can be determined by drawing the relationship between the logarithm of electrical conductivity and absolute temperature, according to Arrhenius equation [19], which shown in 'figures 14', (15) and (16), respectively and the results of the activation energy for the polymeric mixture composites, polymeric mixture GO nanocomposites, and polymeric mixture G nanocomposites, in tables 1, 2 and 3, Respectively.

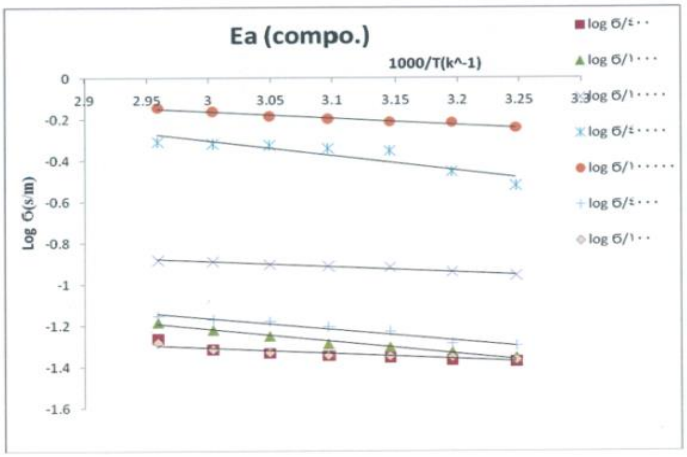

Figure 14. The logarithm of electrical conductivity versus absolute temperatures of polymeric mixture composite.

Table (1): The activation energy values for the polymeric mixture composites.

F	high Ó (65 c°)	Slop	Ea(ev)/molecule
100	0.052334	-0.263	5.219E-05
400	0.054512	-0.336	6.668E-05
1000	0.06557	-0.581	0.0001153
4000	0.070125	-0.536	0.0001064
10000	0.13111	-0.257	5.1E-05
40000	0.492982	-0.714	0.0001417
100000	0.794212	-0.322	6.39E-05

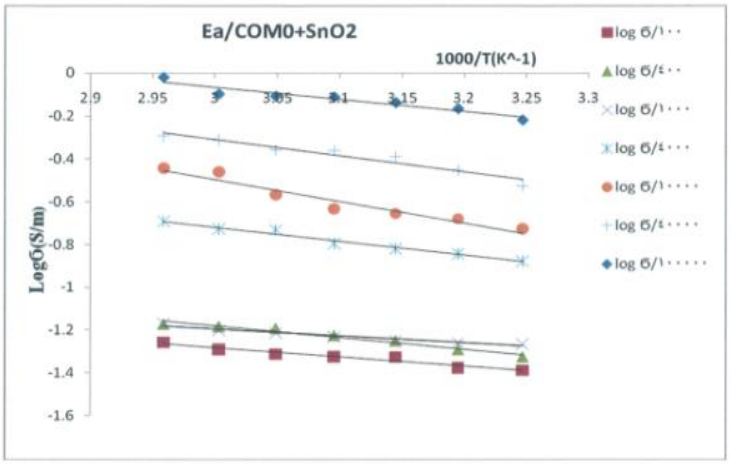

Figure 15. The logarithm of electrical conductivity versus absolute temperature**s** of polymeric mixture GO nanocomposites.

Table (2): The activation energy values for the polymeric mixture GO nanocomposites.

F	high ϭ (65 c°)	Slop	Ea(ev)
100	0.055406	-1.0216	0.0002027
400	0.06756	-0.758	0.0001504
1000	0.068124	-0.653	0.0001296
4000	0.20364	-0.552	0.0001095
10000	0.360655	-0.525	0.0001042
40000	0.51021	-0.436	8.652E-05
100000	0.95849	-0.334	6.628E-05

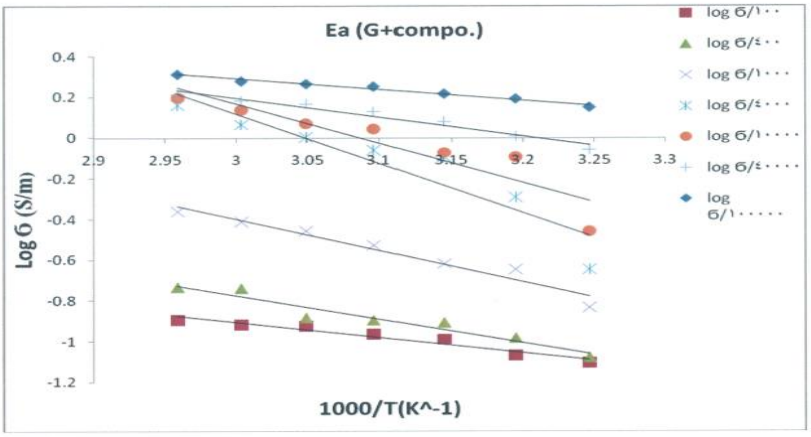

Figure 16. The logarithm of electrical conductivity versus absolute temperature**s** of polymeric mixture G nanocomposite.

Table (3): The activation energy values for the polymeric mixture G nanocomposite.

F	high ϭ (65 c°)	Slop	Ea(ev)
100	0.12787	-0.747	0.0001482
400	0.184641	-1.152	0.0002286
1000	0.436808	-1.537	0.000305
4000	1.456147	-2.426	0.0004814
10000	1.583647	-1.936	0.0003842
40000	1.622633	-0.925	0.0001836
100000	2.057813	-0.53	0.0001052

8. Conclusion

In this work, the dielectric behavior of the polymeric mixture (contain three polymers; Poly Aniline(PANI), Poly Vinyl Acetate(PVAc), and Pecten(Pc) which have been prepared at

studied amount) . with various concentrations of, graphene oxide (GO) and with reduced graphene oxide (RGO) nanocomposite films has been investigated. The results show that the electrical conductivity values for the prepared chips increase with increasing of frequency. As well, the electrical conductivity of above films is research in terms of the Arrhenius plot.

REFERENCES

[1] Peukert W, Schwarzer H-C, Götzinger M, Günther L and Stenger F, 2003, *Adv. Powder Tech* **14** 411.
[2] Jordan J, Jacob K, Tannenbaum R, Sharafb A M.and Jasiukd I **393** 11.
[3] Ghosh P, Sarkar A, Meikap A K, Chattopadhyay S K, Chatterjee S K, Ghosh M, 2006, *Journal of Physics D: Applied Physics* 39 3047.
[4] Zengin H, Zhou W, Jin J, Czerw R, Smith D W, Echegoyen L, Carroll D L, Foulger S H and Ballato J, 2002, *Advanced Materials* **14** 1480.
[5] Hummers W S and Offeman R E, 1958, *J. Am. Chem. Soc.* **80** 1339.
[6] Park S , An J , Potts J R , Velamakanni A , Murali S and Ruoff R S 2011 *Carbon* **49** 3019.
[7] Alobodi E and Farouk A, 2016, International *Journal of Advanced Research in Science, Engineering and Technology* **3** 1484.
[8] Richer R 2002 *Journal of Nano- Crystalline Solids* **305** 35
[9] Chaturvedi A, Tiwari Aand Tiwari A, 2013, *Adv. Mat. Lett* **4** 656.
[10] Kang ET, Neoh KG, Tan KL, 1998, *Progress in Polymer Science* **2** 277.
[11] Trchova M, and Stejskal J, 2011, " The infrared spectroscopy of conducting polymer nanotubes" IUPAC doi:10. 10-02-01, p. 1351.
[12] Bandan G and Proctor R, 2000, *Food Chem.* **68** 327.
[13] Du Q, Zheng M, Zhang L, Wang Y, Chen J, Xue L, Dai W, Ji G and Cao J, 2010, Electrochim. *Acta* **55** 3897.
[14] Nethravathi C, Rajamathi M, Ravishankar N, Basit L and Felser C, 2010, *Carbon* 48 4343.
[15] Tsangaris G M, Psarras G C and Kouloumbi N 1998 *Journal of Materials Science* **33,** 2007.
[16] Gatos K G, Martinez Alcazar J G, Psarras G C, Thomann R, and Karger-Kocsis J, 2007, *Composites Science and Technology* **67** 157.
[17] Psarras G C, Gatos K G, Karahaliou P K, Georga S N, Krontiras C A, and Karger-Kocsis J, 2007, *Express Polymer Letters* **1** 837.
[18] Kalini A, Gatos K G, Karahaliou P K, Georga S N, Krontiras C A, and Psarras G C, 2010, *Journal of Polymer Science Part B: Polymer Physics* **48** 2346.
[19] Saikia D, Chen-Yang Y W, Chen Y T, LiS Y K and Lin I, 2008, *Desalination* **234** 24.

Partial purification of Leucine aminopeptidase (LAP) in Acromegalic Sample of Iraqi Patients

IOP Conf. Series: Journal of Physics: Conf. Series **1003** (2018) 012015 doi:10.1088/1742-6596/1003/1/012015

Partial purification of Leucine aminopeptidase (LAP) in Acromegalic Sample of Iraqi Patients

Taghreed Uloom Mohammad

Department of Chemistry, College of Education for Pure Science

(IbnAL Haitham) University of Baghdad

tagreedaloom@gmailcom

Abstract

Acromagaly is a syndrome caused by increased growth hormone secretion from the frontal lobe of the pituitary gland. A Leucine aminopeptidase (EC 34111) activity has been assayed in (30) patient's sera samples (15 females and 15 males) with acromegaly age range between (30-50) years and (30) sera of healthy as control group (16 females and 14 males) age range between (3050) years. The goal of the research was partial purified of enzyme from sera patients with acromegaly by dialysis gel filtration by using sephdex G50 and ion exchange chromatography by using DEAE cellulose A50. The results showed a single peak by using gel filtration and the activity was reached to 152 U/L. Two isoenzymes were obtained by using ion exchange chromatography and the purity degree of isoenzymse (I, II) were (125) and (128) fold respectively. The current study found that the enzyme showed no significant difference between the healthy and the patients.

Key words Leucine aminopeptidase (LAP)، Acromegaly (Acro) ، Purification**.**

1 Introduction

The rise of growth hormone (GH) secretion reasons Acromegaly (Acro) in addition to high levels of insulin like growth factor1 (IGF1). The occurrence of acromegaly is considered to be 34 cases per million for every year (1). For the reason that GH secretion is pulsatile elevated serum IGF1 heights are a useful showing tool for Acro (2).

The increase of the release of GH has important metabolic effects; the two most significant effect of GH on metabolism in adipose tissue are insulin resistance (IR) and lipolysis (3). Insulin resistance presenting as diabetes or impaired glucose tolerance is found in most Acro patients and contributes to the improved illness Growth hormone makes the expression and secretion of IGF1 thus phenotypes associated with Acro may be as a result of either GH signaling IGF1 signaling or a combnation of both (4). Acro treatment includes surgical treatment often used for transphenoidal route radiotherapy administration of somatostatin analogs for example octreotide or of dopmine agonists (5). Amino peptidases "EC 3411XX" belongs to the group of proteases which are essential enzymes as they play an important role in many life processes They catalyze the hydrolysis of amino acids located at the Nterminus of pepide and are involved in proteins degradation to free amino acids (6).

leucine aminopeptidase "LAP" is well known to be generally spread in organisms from bacteria to humans as well as various cancer cells LAP is normally found in most body fluids and tissues It is mainly abundant in the biliary mucosa and small intestine. Elevated enzyme activity was observed in serum and urine patients with liver pancreatic and biliary diseases Its determination is of significant value in the diagnosis of cancer of the pancreas in addition to metastatic carcinoma of tile liver Malignancies in overall the

nephrotic syndrome and several skin diseases may be related by elevated levels and a physiologic increase happens in the third trimester of pregnancy Animal tests show raises occur with infarction of the small bowel (78).
The aim of this study purification of LAP from serum patients with acromegaly and isolation.

2. Statistical Analysis

The results were analyzed to determine the mean value and standard error of different parameters. The statistical analysis (2012) method was used to study effect of different groups on LAP enzyme test analysis was used to compare a significant between the means values [9].

3. Patients and Methods

3.1. Patients

Thirty people with Acromegaly aged 3050 years were studied "15 female and 15 males" and thirty controls "16 female and 14 male" aged 30-50 years were recruited at the "National Diabetes Center_ Al_Mustansiria university amidst Dec 2015 and the end 0f 2016 In all the patients a previous diagnosis of acromegaly had been promptly decided by their typical clinical features and biochemical findings.

- Determinations of protein concentration this method is based on protein interaction with basal solution and then Folin detector is added to a complex product with a blue colour that depends on the intensity on the amount of proteins (10).
- Determination of LAP activity hydrolysis of the peptide bond of leucinamide is measured according to Mitz and Schlueter (1958) wavelength is measured at 238 nm (11).
- Purification of LAP from sera of patients with acromegaly.

3.2. *. Precipitation by using Ammonium sulfate (40%)*

The method used for precipitation of protein by adding 08 gm of ammonium sulphate was added gradually to 5ml of fresh serum in a beaker with constant stirring at about (4^{o}C) for one hour until the solution became turbid and then it was centrifuge at speed (3500 rpm) for 10 min to spilt the precipitate. The precipitate was dissolved in a less amount of tris buffer solution pH (87) then the activity of enzyme and total protein concentration were measured in it .

3.3. Dialysis

Two mL of protein solution that prepared in the previous step was put into a tightly wrapped cellophane bag from bottom and from top then the pipe was put into a container which contains tris buffer solution (pH=87). This process was done with constant stirring at 4^{o}C.

3.4. Gel Filtration

Two mL of serum was added slowly on the surface of sephadex (G50) column (20x 2 cm) and left for 5min to be absorbed. Twenty Fractions were collected by passing tris buffer solution pH =87 through the column. The process was carried out inside a refrigerator and the flow rate was (2 ml /min).

3.5. on Exchange Chromatography

Two mL of fresh filtered serum was passed through a column of diethyl amino ethyl cellulose A50 column (20x 2 cm). A syringe pump is commonly used to pump various buffer via the column. One salt

commonly used is sodium chloride and forty five fractions were collected by passing different concentration of sodium chloride solution (01 04)M The flow rate was (2ml/4 min).

4. Results and Discussion

Table (1) presents the isolation and partial purification of LAP and isoenzymes from sera patients with acromegaly disease. The LAP activity was reached to (72) U/L by using ammonium sulphate salt in concentration of (40%). The enzyme was partially purified by using dialysis method with tris HCl buffer at (pH=78) the purity degree of LAP was reached to 26 fold which yields (656%) while the purity degree was increase to 451 fold which yields (95%) by using Sephadex G50 column chromatography. This enzyme shows a single peak in Figure (1). The Purification by ion exchange chromatography technique offered several distinct advantage over other conventional methods of separation serum isoenzymes. This enzyme was purified by using DEAE cellulose A50 two isoenzymes were obtained as mentioned in Figure (2). The purity degree of isoenzyme (I) was 125 fold which yields (20%) and isoenzyme (II) was 128 fold which yields (156%).

Table 1 Steps of LAP Enzyme Partial Purification From Acromegaly Patients

Step	*Volum (ml)*	*Activity of enzme U/L*	*Total activity (U)*	*Protein Con (mg/ ml)*	*Total Protein (mg)*	*Specific activity (U/mg)*	*Fold Purification*	*Yield %*
Crude serum	5	653	0032	064	3235	102	1	100
Ammonium sulphate	2	72	0014	053	265	1358	133	45
Dialysis	2	109	0021	040	08	2725	267	656
Sephadex G50	2	152	003	033	6458	4606	451	95
Ion exchange Iso I	2	32	00064	025	05	128	125	20
Ion exchange Iso II	2	25	0005	019	038	1315	128	156

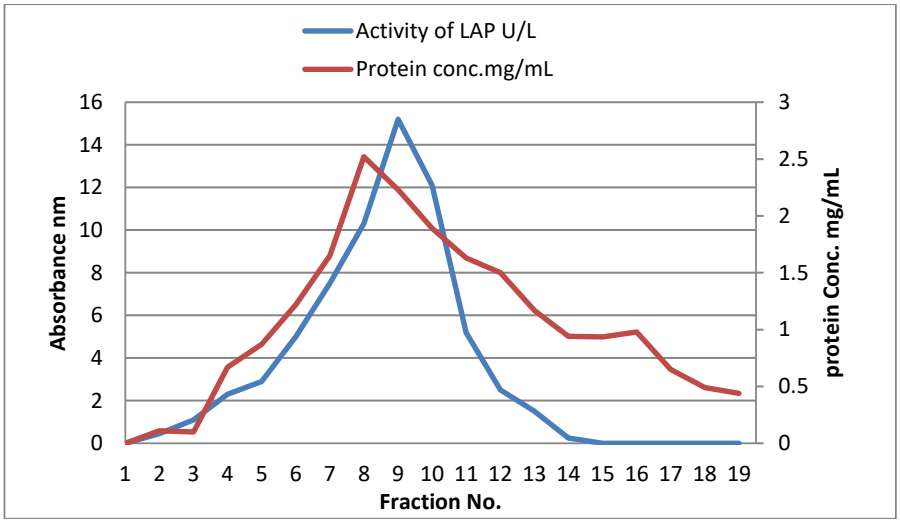

Figure 1. Isolation of LAP from Patient with acromegaly by Gel Filtration.

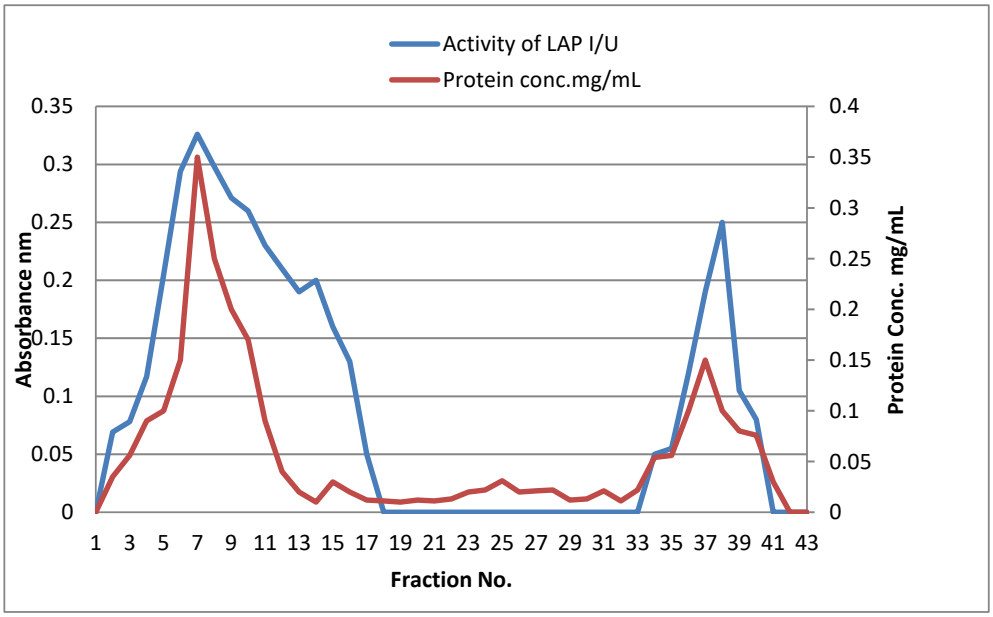

Figure 2. Isolation of LAP Isoenzymes from Patients with Acromegalyic Using by Ion Exchange DEAE–Cellulose A50.

Several previous studies have indicated the use of leucine aminopeptidase in clinical diagnosis for more than 10 years. The high LAP activity of the serum usually indicates a defect in the liver or bile duct. This rise is minimal influenced by injury of the liver parenchyma than by the active involvement of the

biliary tract in the process. There is likewise a prominent raise in LAP activity in sever pancreatitis. High LAP amounts have been found in addition in advanced pregnancy malignancies in some skin diseases and in cases of nephrotic syndrome [12]. In fact, none of the literature has indicated a relationship between the enzyme and Acromegaly except for a previous source found that the activity of the enzyme is normal in some cases such as Paget's disease [13].

5. Conclusion

Two isoenzymes of the purified LAP were obtained from patients with Acromegaly and there was no clear difference in enzyme activity between healthy and patients. Thus the leucine aminopeptidase enzyme is no evidence of the presence of the disease.

Acknowledgments

I would like to thank the University of Baghdad Faculty of Education (Ibn Al-Haitham) Department of Chemistry to help me for complete this article.

References

[1] Narendra, BS. Dharmalingam, M.and Kalra, P. ; 2015. Acromegaloidism Associated with Pitutary Incidentaloma , *Journal of the Association of Physicians of India* **, 63:** 81-79.

[2] Hyae, ML. Sun, HL. InHo, Y. In Kyoung, H. *et al* ; 2015. Acromegaly with Normal InsulinLike Growth Factor1 Levels and Congestive Heart Failure as the First, Clinical Manifestation, **30 (** 3) :395-401.

[3] Satoshi, Y. Kazunori, K. Shingo, M. Ken, T. Shoko, K. et al ; 2016. A case Of Nonalcoholic Steatohepatitis In A Cured Acromegalic Patient With Sever Growth Hormone Deficiency, AACE Clinical Case Rep ,**2** (3) :e194-e195.

[4] Fujio, S. Tokimura, H. et al ;2013. Sever growth hormone deficiency is rare in surgically cured, acromegalics Pituitary ,16:326-332.

[5] Melmed ,S. Ho, K. Klibanski, A. Reichlin, S. Thorner ,M. ;1995. Clinical review 75 Recent advances in pathogenesis diagnosis and management of acromegaly, *J Clin Endocrinol Metab*, 80 : 3395-3402.

[6] Joana, K. and Danuta, G.; 2015. Aminopeptidases isolated from plants of great economic valuerole and characteristics, Chemik, **69** (8): 463-468.

[7] Knight, JA. and Hunter, D T.; 1968. A continuous Spectrophotometric Method for the Determination of Leucine Aminopeptidase, Clinical Chemistry, **14(** 6): 555-564.

[8] Qiuyu, G. Wen, Sh. Lihong, L. and Huimin, M.; 2015. Leucine aminopeptidase may contribute to the intrinsic resistance of cancer cells toward cisplatin as revealed by an ultrasensitive fluorescent probe, Chemical Science, 7:788-792.

[9] Statical Analysis System 2012. User's Guide statistical version 91th Ed, SAS Inst Inc Cary NC USA.

[10] Sadasivam, S. and Manikam, A,; 1992. In Biochemical Methods for Agricultural Science Wily Eastern Limited New Delhi and TNAU, Coimbatore India: p122-123.

[11] Mitz, M. and Schlueter, R.;1958. Direct Spectrophotometric Measurement of the Peptide Bond Application to the Determination of Acylase 1, Biochim Biophys Acta, 27:168.

[12] GABOR, S. A.;1967. Kinetic photometric method for serum leucine aminopeptidase, The Amercan *journal of clinical Pathology*, **47(** 5).

[13] Rutenburg, A .M. Banks, B. M. Pineda,E. P. and Goldbarg, J .A. .A.; comparison of serum aminopeptidase and alkaline phosphatasein the detection of hepatobiliarydisease in anicteric patients, Ann Int Med, **61** :5055-1064.

Composition, Characterization and Antibacterial activity of Mn(II), Co(II),Ni(II), Cu(II) Zn(II) and Cd(II) mixed ligand complexes Schiff base derived from Trimethoprim with 8-Hydroxy quinoline

Composition, Characterization and Antibacterial activity of Mn(II), Co(II),Ni(II), Cu(II) Zn(II) and Cd(II) mixed ligand complexes Schiff base derived from Trimethoprim with8-Hydroxy quinoline

Ahmed T Numan, Eman M Atiyah*, Rehab K. Al-Shemary, Sahira S. Abd_Ulrazzaq**

Department of Chemistry, College of Education for Pure Science, Ibn- Al-Haithem/ University of Baghdad, Baghdad ,Iraq

emanchem12@gmail.com* ,drrehabalshemary@gmail.com**

Abstract. New Schiff base ligand 2-((4-amino-5-(3, 4, 5-trimethoxybenzyl) pyrimidin-2-ylimino) (phenyl)methyl)benzoic acid] = [HL] was synthesized using microwave irradiation trimethoprim and 2-benzoyl benzoic acid. Mixed ligand complexes of Mn((II), Co(II), Ni(II), Cu(II), Zn(II) and Cd(II) are reacted in ethanol with Schiff base ligand [HL] and 8-hydroxyquinoline [HQ] then reacted with metal salts in ethanol as a solvent in (1:1:1) ratio. The ligand [HL] is characterized by FTIR, UV-Vis, melting point, elemental microanalysis (C.H.N), 1H-NMR, 13C-NMR, and mass spectra. The mixed ligand complexes are characterized by infrared spectra, electronic spectra, (C.H.N), melting point, atomic absorption, molar conductance and magnetic moment measurements. These measurements indicate that the ligand [HL] coordinates with metal (II) ion in a tridentate manner through the oxygen and nitrogen atoms of the ligand, octahedral structures are suggested for these complexes. Antibacterial activity of the ligands [HL], [HQ] and their complexes are studied against (gram positive) and (gram negative) bacteria.

1. Introduction

Schiff bases have played a significant role in the development of coordination chemistry and have been implicated as an important point in the development of inorganic biochemistry and optical materials [1].Schiff base metal complexes have been widely studied because they have industrial, antifungal and biological applications [2-4].Schiff bases have played a significant role in the development of coordination chemistry and have been implicated as antreatment and urinary tract infections [5]. Antibiotic 5-(3, 4, 5-trimethoxybenzyl) pyrimidine-2, 4-diamine (Trimethoprim) is used mainly in the treatment of urinary tract infections [6] .Chelating ligands containing O and N donor atoms show broad biological activity and are of special interest because of the variety of ways in which they are bonded to metal ions [7]. Mixed ligands complexes have been studied because of their importance in biological systems [8-9, 10]. Few reports are available on the mixed metal complexes of trimethoprim [11]. Thus, this work is aimed at the synthesis, characterization and biological studies of mixed ligand complexes of trimethoprim and 2- benzoyl benzoic acid Schiff base and mixed ligand complexes with 8-hydroxy quinoline .The metal ion in an octahedral environment. The primary aim of the current study to

determine the structure and geometry of tridentate Schiff base mixed ligand Mn (II), Co (II), Ni (II),Cu (II), Zn (II) and Cd (II) metal complexes.

2. Experimental

2.1. Materials and Methods

All Chemicals employed were of analytical grade and used without further purification. The reagents were used without further purification. FTIR spectra were measured as (KBr disc) utilizing "Shimadzu FTIR-8400S", Fourier Transform Infrared spectrophotometer. ^{1}HNMR and ^{13}CNMR were carried out by using Bruker500 MHz NMR spectrophotometerin central laboratory Isfahan University. Mass spectra were obtained by using Acq Method LOW ENERGY DSD Direct Probe, central lab Isfahan University, Iran. The electronic spectra were recorded in DMSO on a "Shimadzu UV-visible-160 A Ultra Violet-Visible Spectrophotometer" .Elemental microanalyses (C.H.N.) were performed by using a Leco 932 USA Elemental Analyzer. The atomic absorption was measured by using"Varian-AA 775 Atomic Absorption spectrophotometer". Conductivity measurements were made in DMSO for 10^{-3}M of complexes by using (Philips PW9526 Digital Conductivity meter) at room temperature. Magnetic moment (μ_{eff} B.M) for the prepared complexes was measured at room temperature by using Bruker Magnet B.M. Finally, melting points were got by utilizing "Stuart Melting Point Apparatus".

2.2. Synthesis of ligand Schiff Base

(0.1g, 0.34 mmole) trimethoprim is mixed with (0.09g, 0.34 mmole) 2-benzoylbenzoic in (1:1) ratio mole, and the mixture is grinded in ceramic mortar. Then, the contents are subjected to microwave irradiation at (100 Co) for 10 minutes. The reaction product is washed with small portion of benzene as off white of ligand. Weight (0.16g), yield (94%), m.p (96- 98)°C. The ligand [HL] is recognized by FTIR spectral, 1H and 13C NMR, mass spectrum and elemental analysis. The synthesis route of the ligand is shown in figure(1).The microanalysis of results for the ligand [HL] and some of its physical properties are given in Table 1.

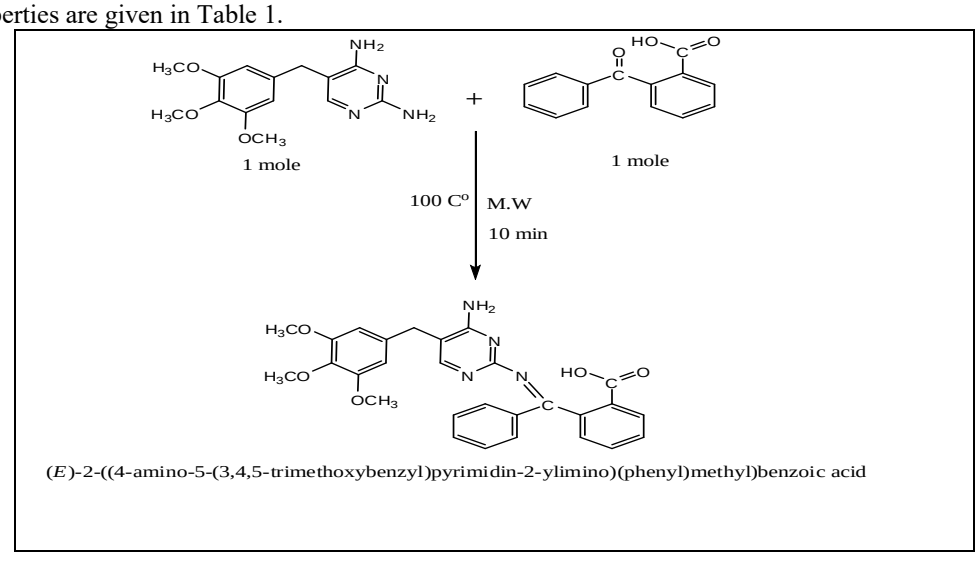

Figure 1. Preparation course of the Schiff base

2.3. General synthesis of mixed ligands complexes

An ethanolic solution (25ml) of metal salts of Mn(II), Co(II), Ni(II), Cu(II), Zn(II) and Cd(II) was added gradually to a stirred ethanolic solution of Schiff base(25ml) and secondary ligand 8-hydroxyquinoline ethanol to get (1:1:1) (metal:HL:HQ) molar ratio. Few drops of KOH solution were added to adjust the pH < 9. The resulting solution was refluxed for about 2 hours. The chelate was precipitated, cooled and then filtered. The result got by washed with small amounts of ethanol and dried. The microanalysis of results for the ligand and some of its physical properties are given in Table 1.

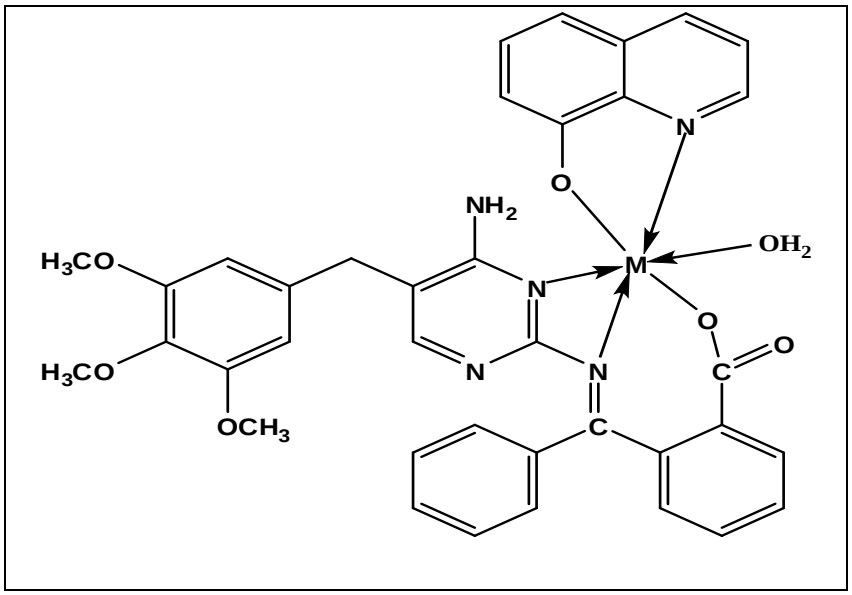

Figure 2. Suggested structure for mixed ligand complexes

Table 1. Some of physical properties and microanalysis of all prepared product

Compound	Empirical Formula (formula wt.)	M.P Dec.	Yield %	Color	Elemental Analyses Found (Calc.) %(calculated)					Molar conductivity (ohm^{-1} cm^2mol^{-1})
					C	H	N	M	Cl	
[HL]	$C_{28}H_{26}N_4O_5$ 498.35	(96-98)	94	Off white	66.34 (66.46)	5.53 (4.26)	10.19 (10.24)	-	-	-
[Mn(L)(Q)(H_2O)]	$C_{37}H_{33}MnN_5O_7$ 714.63	300 <dec.	76	Brown	62.19 (61.25)	4.65 (4.39)	9.80 (8.74)	7.69 (7.48)	Nil	12.3
[Co(L)(Q)(H_2O)]	$C_{37}H_{33}CoN_5O_7$ 718.62	300 <dec.	75	Olive	61.84 (60.65)	4.63 (3.39)	9.75 (9.24)	8.20 (7.88)	Nil	9.9
[Ni(L)(Q)(H_2O)]	$C_{37}H_{33}NiN_5O_7$ 718.38	300 <dec.	71	Pale green	61.86 (61.67)	4.63 (4.39)	9.75 (8.25)	8.17 (7.95)	Nil	8.7
[Cu(L)(Q)(H_2O)]	$C_{37}H_{33}CuN_5O_7$ 723.23	300 <dec.	83	Green	61.45` (60.89)	4.60 (3.36)	9.68 (8.99)	8.79 (8.34)	Nil	10.6
[Zn(L)(Q)(H_2O)]	$C_{37}H_{33}ZnN_5O_7$ 725.10	300 <dec.	80	yellow	61.29 (58.15)	4.59 (4.35)	9.66 (9.16)	9.02 (8.96)	Nil	8.5
[Cd(L)(Q)(H_2O)]	$C_{37}H_{33}CdN_5O_7$ 772.10	300 <dec.	79	Yellow	57.56 (56.78)	4.31 (4.10)	9.07 (8.73)	14.56 (13.88)	Nil	10.2

dec. = Decomposition

3. Results and Discussion

Spectroscopic [FT-IR,^{1}H,^{13}C-NMR,Mass,and UV-Vis].Also molar conductivity, elemental microanalysis, melting point, magnetic sensitiveness, and atomic absorption were applied to portray the synthesized mixed ligand complexes. Some physical properties were listed in Table 1.

3.1. FT-IR Spectra

In the spectra of free [HQ] ligand is found the peak found at 3182 cm^{-1} assigned to the alcohol υ(OH) stretching and this band was absented in the complexes[12].In the spectrum of ligand [HL] the sharp peak found at 3458 cm^{-1} assigned to the υ(OH) stretching of carboxylic acid while the band was disappeared in the complexes, proton of ligand [HL]on complexation and participation of hydroxylic carboxylic anionic (COO^-) oxygen in concent [13].In addition the two peaks at found in range (3468-3455)$cm^{-1}$and (3387-3348)cm^{-1}assigned to stretching of υsym and asy(NH_2), in the ligand and all the mixed complexes [14]. Also the band found at (1664) cm-1is assigned to υ(C=O) group of carboxylic acid of the ligand [HL] [15], this bond disappeared in all the mixed complexes In in the spectra of the mixed complexes,another bands appeared in range(1589-1572) cm^{-1} and (1465-1445) cm^{-1}due to υasym.(COO^-)and υsym.(COO^-)vibration, respectively, (Δυ(COO^-)=υasy.(COO^-)-υasy.(COO^-)) in range (116-127)cm^{-1},indicated the involvement of deprotonated group of (COOH) in bonding and a coordination of metal ions through oxygen atoms of carboxyl groups[16]. In the ligand [HL] spectrum was exhibited the strong band at 1637cm-1due to υ(C=N) stretching vibration, while this bond was shifted towards lower region at (1624-1627) cm^{-1} in the complexes indicating the participating of the azomethine group in the complex formation. Further, the bands observed at (1591) cm^{-1} and (1573) cm^{-1}which were due to υ(C=N) azomethine groups in rings for ligand free [HL] and ligand free [HQ], while these bands were shifted in range(l566- 1553)cm^{-1} and (l523 -l492)cm^{-1}due to the reduction of double bond character carbon nitrogen bond of azomethine group and indicates that (C=N) of the ligand co-ordinate to metal through nitrogen and that was further reflected by the appearance of new band at (586-405)cm^{-1}due to υ(M-N)[17] .The mixed ligand complexes formation was further evidence by the appearance of the ligand band in the complexes (455-405)cm^{-1} assigned as υ(M-O) bonds[18].In the IR spectra of mixed ligand complexes a band was observed around (3356-3197) cm^{-1} to which were assigned to hydrate water molecules [19, 24].

Table 2. The FT-IR spectral data (cm^{-1}) of all the prepared compounds

Compound	$\upsilon(OH)_{HL}$ $\upsilon(OH)_{Q}$	$\upsilon OH-(H_2O)$	$\nu(N-H)_{sym}$ $\nu(N-H)_{asym}$	$\nu(C=N)_{PYR.}$ $\nu(C=N)_{Q}$	$\nu(C=N)_{imine}$	$\nu(C=O)_{carboxi.}$	$\upsilon(COO-)$ asy..	$\upsilon(COO-)$ sy	$\Delta\upsilon$	$\nu(M-OH_2)$	ν (M-N)	ν (M-O)
[HL]	3329	-	3458	1591	1637	1664	-	-	-	-	-	-
			3388	-								
[HQ]	- 3182	-		- 1573	-	-	-	-	-	-	-	-
[Mn(L)(Q)(H_2O)]	-	3356	3468	1553	1625	-	1572	1445	127	702	513	451
			3387	1523							497	408
											482	
[Co(L)(Q)(H_2O)]	-	3197	3468	1562	1624	-	1585	1462	123	771	558	432
			3369	1496							520	408
											497	
[Ni(L)(Q)(H_2O)]	-	3348	3455	1558 1500	1627	-	1581	1465	116	740	547	451
			3352								505	408
											478	
[Cu(L)(Q)(H_2O)]	-	3321	3468	1562	1625	-	1589	1462	128	771	586	443
			3385	1500							559	408
											516	
[Zn(L)(Q)(H_2O)]	-	3217	3460	1558	1627	-	1581	1465	116	732	504	455
			3348	1500							482	405
											470	
[Cd(L)(Q)(H_2O)]	-	3332	3468	1566	1624	-	1577	1458	120	786	493	439
			3353	1492							455	405
											444	

3.2. NMR Spectra

^{1}H-NMR spectrum of the ligand [HL] was recorded in d6-DMSO. The 1H-NMR spectra of [HL] exhibits signal due to proton of (-COOH) group as singlet at δ 12.17 ppm[20].The protons of (NH_2)group as signal at δ 6.62ppm[13] .The proton of (-CH-N) pyrimidine ring as singlet at δ 7.15 ppm. The aromatic protons as multiple at (7.97-7.27) ppm. The (OCH_3) protons as signal at δ3.76ppm.The DMSO signal appeared at 2.5 ppm [21], figure (3).^{13}C NMR spectrum of ligand [HL] displays chemical shifts at (170.2)ppm and (164.1)ppm indicate to (C=N) and C=O groups respectively[22]. At (157.4) ppm and (153.4) ppm were the chemical shifts attributed to C atoms of (C=C) in pyrimidine ring, respectively. Signals attached to aromatic carbon were attached in reign (106.7 - 138.5) ppm. The two chemical shift at (56.6) ppm and (39.6) ppm were referred to C atoms, respectively. Also the chemical shift at (40.2) ppm is due to DMSO d_6 [23],' figure 4'.

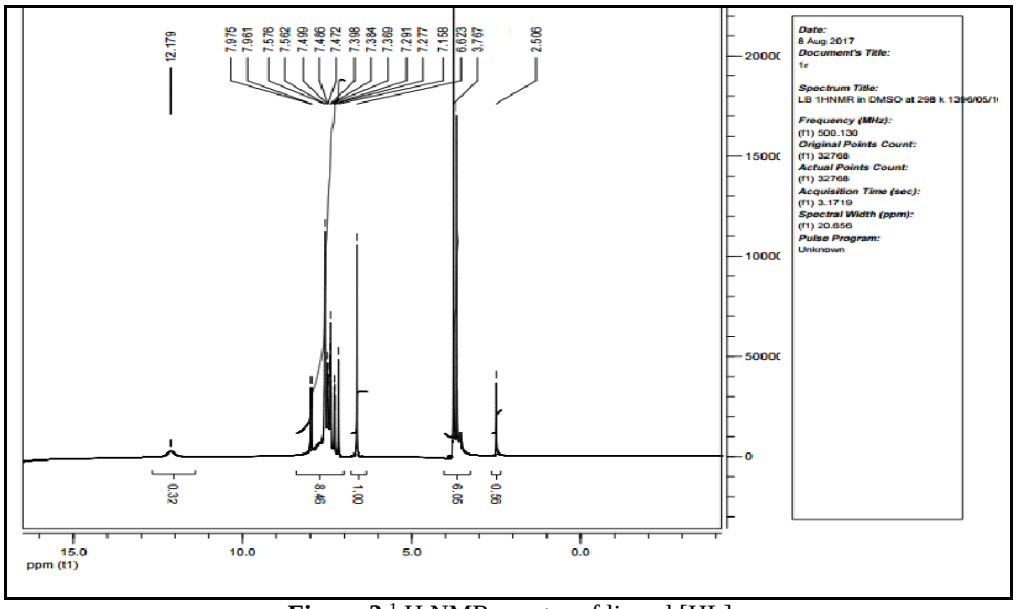

Figure 3.[1] H NMR spectra of ligand [HL]

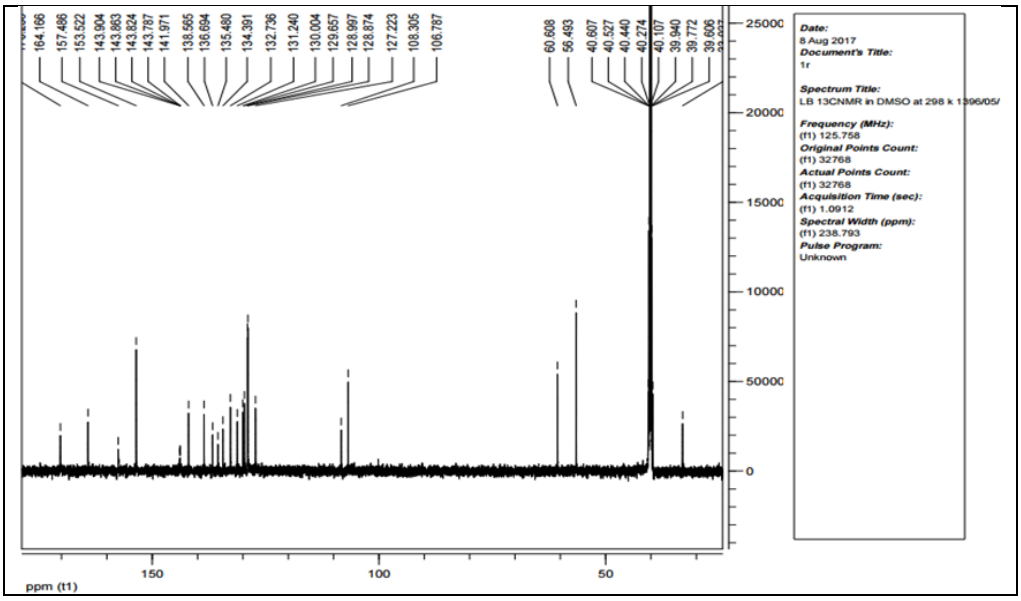

Figure 4. [13]C NMR spectra of ligand [HL]

3.3. Mass Spectra

Mass Spectrum was completed on the ligand [HL] to determine its molecular weight and fragmentation pattern,' Figure 5'.

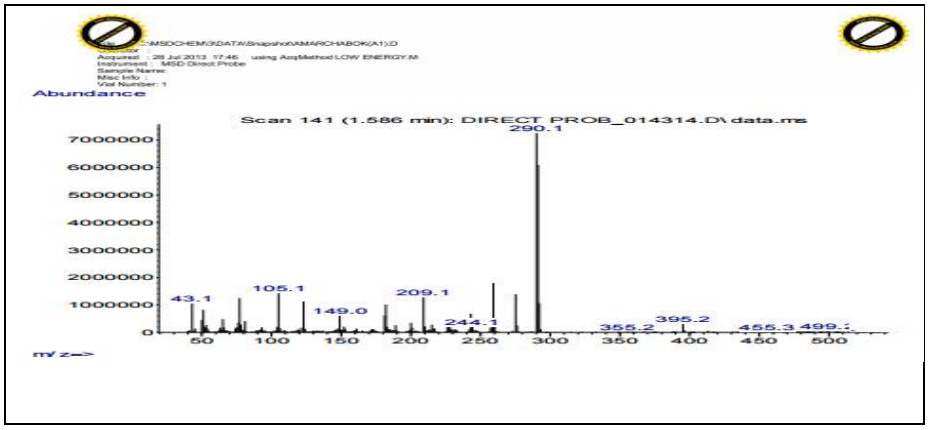

Figure5. Mass spectra of ligand schiff base [HL]

3.4. Electronic spectra, Magnetic moments and conductivity measurements

The electronic spectrum of ligand [HL], exhibit high intense absorption peaks at (279 nm) (35842 cm-1) and (345 nm) (28985 cm^{-1}) which due to ($\pi\rightarrow\pi^*$) and ($n\rightarrow\pi^*$) transitions, respectively [24], the data recorded in Table (3). The electronic spectrum of 8-hydroxy quinolone[HQ], displays high intense absorption bands at (268 nm) (37313 cm^{-1}) and (305 nm) (3278 6cm^{-1}) which designated to ($\pi\rightarrow\pi^*$) and ($n\rightarrow\pi^*$) transition respectively[25], the data recorded in Table (3) .Theses transitions were also found in the spectra of the complexes, but they were shifted towards in range (37037-14265) cm^{-1}.The electronic spectrum of [Mn(L)(Q)(H_2O)] showed two intense peaks in (270nm) (37037 cm^{-1}) and (374nm) (26737cm^{-1}) was assigned to the ligand field respectively. And another intense peak in (392nm) (25510 cm^{-1}) due charge transfer transition.And the peak at visible region at (755 nm) (13245cm^{-1}). This peak is assigned to ($^6A_1g \rightarrow {}^4T_2g(G)$) (d-d) transitions confirming an octahedral structure around (Mn^{+2}) ion complex[26]. The electronic spectrum of [Co(L)(Q)(H_2O)] displayed two intense peaks in (277nm) (36101 cm^{-1}) and (334 nm) (29940 cm^{-1})were assigned to the ligand field. And another intense peak in (401 nm) (24937cm^{-1}) due charge transfer transition. And the peaks at visible region at (687 nm)(14556cm^{-1})and (762nm)(13123cm^{-1}).These peaks are assigned to($^4T_1g \rightarrow {}^4A_2g$)and ($^4T_1g\rightarrow {}^4T_2g$) (d-d)transitions confirming an octahedral structure around (Co^{+2}) ion complex[27]. The electronic spectrum of [Ni(L)(Q)(H_2O)] showed two intense peaks in (275nm) (36363cm^{-1}) and (345nm) (28985cm-1) was assigned to the ligand field respectively. And another intense peak in (408nm) (24509 cm-1) due charge transfer transition. And the peakat visible region at (810 nm)(12345 cm^{-1}). These peak are assigned to($^3A_1g \rightarrow {}^3T_1g$)(d-d)transitions confirming an octahedral structure around (Ni^{+2}) ion complex[28]. The electronic spectrum of [Cu(L)(Q)(H_2O)] showed two intense peaks in (276nm) (36231 cm^{-1}) and (337nm) (29673cm^{-1}) was assigned to the ligand field respectively. And another intense peak in (412nm) (24271cm^{-1}) due charge transfer transition. And the peaks at visible region at (701 nm)(14265cm^{-1})and (859nm)(11641cm^{-1}).These peaks are assigned to ($^2B_1g\rightarrow {}^2B_2g$)and ($^2B_1g \rightarrow {}^2A_1g$)(d-d)transitions confirming an octahedral structure around (Cu^{+2}) ion complex[29]. The electronic spectrum of [Zn(L)(Q)(H_2O)]showed absorption peaks in (277 nm) (36101cm^{-1}) and (340 nm) (29411cm^{-1}) were assigned to the ligand field . And another peak in (419 nm) (23866 cm^{-1}) due charge transfer transition. The absence of absorption peaks at the visible area suggested no(d-d)electronic transitions happened, this is a very well result for an octahedral structure around (Zn^{+2}) ion complex[30,31].The electronic spectrum of [Cd(L)(Q)(H_2O)]showed absorption peaks in (277 nm) (36101cm^{-1}) and (342nm) (29239 cm^{-1}) were assigned to the ligand field .And another intense peak in (412 nm) (24271 cm^{-1}) due charge transfer transition. The disappeared of peaks at the visible area suggested no(d-d)electronic transition same, this is a good result for an octahedral structure around (Cd^{+2}) ion complex [30, 31]. Where a rapprochement between the data recorded of all the prepared compounds are given in Table 3.The molar conductivities indicate that all metal complexes are non-electrolytes [32], Table 3. Magnetic moment together with these values suggest ochtahedral configuration around the Mn(II), Co(II), Ni(II), Cu(II), Zn(II) and Cd(II) metal ions studied, Table 3.

Table 3.UV-Vis spectral and magnetic moments values of the compounds in DMSO

Compounds	λ nm	υ' cm^{-1}	ε_{max} ($molar^{-1}.cm^{-1}$)		Transitions		μeff (BM)
[HL]	279	35842	2111	2260	π→π*		-
	345	28985			n→π*		
[HQ]	268	37313	861		π→π*		-
	305	32786	1966		n→π*		
[Mn(L)(Q)(H_2O)]	270	37037	1675	358	L.F	L.F	5.72
	374	26737	297	10	C.T	^6A_1g	
	392	25510			→^4T_2g(G)		
	755	13245					
[Co(L)(Q)(H_2O)]	277	36101	2400	1956	L.F	L.F	4.72
	334	29940	1508	7	C.T		
	401	24937	6		^4T_1g→^4A_2g	^4T_1g	
	687	14556			→ ^4T_2g		
	762	13123					
[Ni(L)(Q)(H_2O)]	275	36363	2315	1825	L.F	L.F	3.38
	345	28985	1339	20	C.T	^3A_1g →	
	408	24509			^3T_1g		
	810	12345					
[Cu(L)(Q)(H_2O)]	276	37453	2329	763	L.F	L.F	1.81
	337	29673	995	4	C.T		
	412	24271	5		^2B_1g→^2B_2g	^2B_1g	
	701	14265			→^2A_1g		
	859	11641					
[Zn(H_2L)(Q)(H_2O)]	277	36101	2463	1305	L.F	L.F	Dia.
	340	41666	1687		C.T		
	419	23866					
[Cd(L)(Q)(H_2O)]	277	36101	2418	2238	L.F	L.F	Dia.
	342	29239	1368		C.T		
	412	24271					

Dia = Diamagnetic

3.5. Antibacterial Activity Studies:

Finally, the in vitro antibacterial activities of the ligands and their complexes were tested against (*Staphylococcus aureus*), (*Escherichia coli*), (*Enterobacter cloacae*) and (*Bacillus subtilis*) using well diffusion method by nutrient agar as medium at (10^{-3}) mole/liter concentration was prepared by dissolving the compound in DMSO[33] .The zone of inhibition of bacterial evolution around the disc is offered in Ffigure 6,Table 4 displays the obstruction capacity versus the bacteria sample of the synthesized compounds under work.

Table 4 the obstruction capacity versus the bacteria sample of the synthesized compounds under work.

No.	Compound	*Staphylococcus aureus*	*Bacillus subtilis*	*Enterobacter cloacae*	*Esherichia Coli*
1	[HL]	43	34	-	31
2	[HQ]	32	28	25	26
3	[Mn(L)(Q)(H_2O)]	26	24	-	22
4	[Co(L)(Q)(H_2O)]	26	24	-	24
5	[Ni(L)(Q)(H_2O)]	31	28	13	26
6	[Cu(L)(Q)(H_2O)]	34	33	16	30
7	[Zn(L)(Q)(H_2O)]	30	33	25	28
8	[Cd(L)(Q)(H_2O)]	27	30	22	27
C	DMSO	-	-	-	-

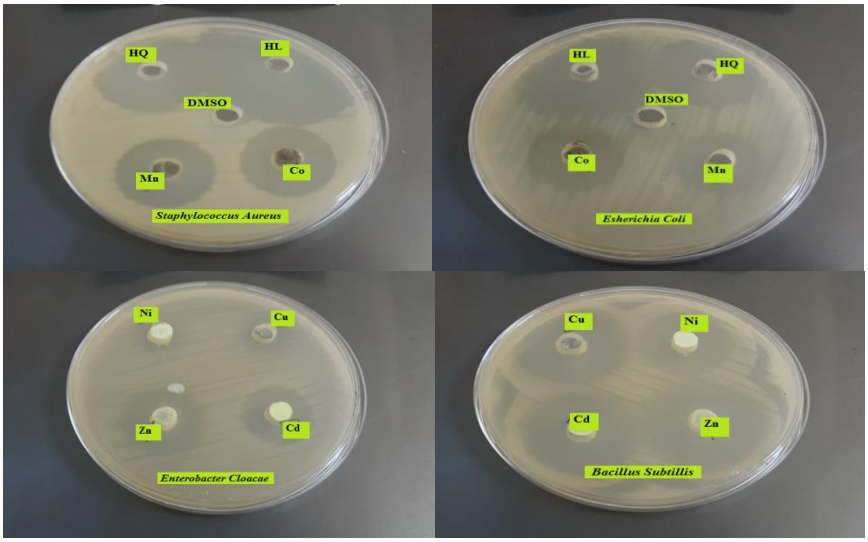

Figure 6. Shows the antimicrobial activity of compounds appear the inhibition zones against pathogenic bacteria (Staphylococcus Aureus, Bacillus Subtilis, Enterobacter Cloacae and Esherichia Coli)

4. Conclusion

Mixed ligand complexes can be a synthetic challenge to tune the properties of the metal complexes and have been shown to exhibit a broad range of the possible geometry of synthesized complexes is octahedral and it is six coordinated metal ligand complexes. The ligand Schiff base [HL], ligand [HQ] and their metal complexes showed broad-spectrum antimicrobial activities against all the microbes used.

Acknowledgement:
The authors express their sincere thanks to the Deanship of Faculty Education for Pure Sciences Ibn-Al-Haithem and Department of Chemistry for their moral back up.

References:

[1] F Tisato, F Refosco, G Bandoli. Structural survey of technetium complexes. *Coord. Chem.* 1994, 135: 325-397.
[2] Kumar, U., S Chandra, *J. Saudi Chem.Soc.* , 2011, 15: 187.
[3] EO Offiong,N Emmanuel, AAAyi, M Sante. Transit. Metal Chem., 2000, 25: 369.
[4] RM Patil and S.R Chaurasiya Asian J. Chem., 2008, 20 (6): 4615.
[5] N Demirezen, D Tarınç, D Polat, M Çeşme, AM Gölcü. *Tümer, SpectrochimicaActaA,* 2012, 94: 243– 255.
[6] Trimethoprim .The American Society of Health-System Pharmacists.Retrieved. (2015).
[7] W Hungand C Lin Inorg. Chem, 2009, 48 (2): 728.
[8]MOAgwara, PTNdifon, NB Ndosiri, AG Paboudam, DM Yufanyi, A Mohamadou Synthesis, characterization andantimicrobial activities of cobalt(II),copper(II) and zinc(II) mixed-ligand complexes containing 1,10-phenanthroline and 2,2-bipyridine. Bull. Chem. Soc. Ethiop., 2010, 24 (3): 383-389.
[9] MO Agwara, JN Foba-Tendo, C Amah, DM Yufanyi, NB Ndosiri. Thermo gravimetric and antimicrobial properties of some divalent metal complexes of hexamethylenetramine. *RJPBCS*, 2012, 3(3): 95-104.
[10] S Matangi, J Pragathi, U Bathini, K Gyana. Synthesis, characterization and antimicrobial activity of transition metal complexes of Schiff base ligand derived from 3-ethoxy salicylaldehyde and 2-(2-aminophenyl) 1-h-benzimidazole. *E-J Chem*, 2012, 9(4): 2516-2523.
[11] ANMAAlaghaz, RS Farag, MA Elnawawy, ADA Ekawy. Synthesis and spectral characterization studies of new trimethoprim-diphenylphosphate metal complexes. *Int. Jour. Sci. Res*., 2013, 5 (1),
[12] K Nakamoto, Y Morimoto, AE Martell. *J. Am. Chem.* Soc. 1961, 83: 4528.
[13] M. R. Silverstein, CGBassler, T TMorrill.Spectrometric Identification of Organic Compounds, 4th Ed., *John-Wiley and Sons Inc*., New York, London, 1981.
[14] D Demartzi-Kovala, JM Tsangaris. Complexes of 2, 4 – Diamine – 5 (3, 4, 5 Ttrimethoxybenzylpyrimidine (Trimethoprim) with palladium (II). *Inorg.Chim.Acta*, 1986, 125: L31-L33.
[15] B Geeta, V Ravinder. Synthesis, characterization and biologicalevaluation of mononuclear Co (II), Ni (II) and Pd(II) complexes, with New N_2O_2schiff base ligand. chem., pharm. Bull., 2011, 95 (2):166-171.
[16] ShK Rakesh, N Munirathnam, SG Ashoka. Asymmetric allylicalkylation by palladium-bisphosphinites, Tetrahedron; Asymmetry, 2008, 19:555–663.
[17] K Nakamoto. Infrared and Raman Spectra of Inorganic and Coordination Compounds.^{5th}Ed *Part B Wiley*; New York, 1997.
[18] Ravich, NS Ran and C Thangaraja. Copper (II), Cobalt (II), Nickel (II) and Zinc (II) Complexes of derived from benzyl -2, 4-dinitrophenyl hydrazones with aniline. *J.Chem.Soc.* 2004, 116(4):215-219.
[19] J A Malcolm, A Gordonk, P R. Nigam. Synthesis and characterization of platinum (II) complexes of L- Ascorbic Acid. *Inorg. Chem*., 1999, 38, 5864-5869.
[20] D Saravanakumar, N Sengottuvelan, G Priyadarshni, M Kandaswamy, H Okawa. Synthesis of unsymmetrical end-off phenoxo and oximinatodibridged Copper (II) and nickel (II) complexes: spectral, electrochemical and magneticproperties. *Polyhedron,* 2004, 23(4): 665-672.
[21] K D Raj and K M Sharad. Synthesis, Spectroscopic and Antimicrobial studies of new Iron (III) complexes, containing Schiff bases and substituted benzoxazole ligands, *J.Coord. Chem.*, 2011, 64 (13):2292-2301.
[22] DH Williams, IFleming.Spectroscopic Methods in Organic Chemistry.^{4th} Ed., *Mcgraw-Hill Book Company (UK) Limited*, 1989:1– 33.
[23] A V Mishchenco,VVLukov, L D Popov. Synthesis and Physicochemical study of complexation of Glyoxylic acid arolhydrazone, with Cu (II) in solution and solid phale, *J. Coord. Chem*., 2011, 64, (11): 1963- 1976.

[24] D Sutton. Electronic Spectra Transition Metal Complexes. 1st Ed., *Mc.Graw-Hill Publishing*, London, 1968.
[25] G Ahn, DC Ware, WA Denny, WR Wilson. Optimization of the auxiliary ligand shell of Cobalt (III) (8- hydroxyquinoline) complexes as model hypoxia-selective radiationactivatedprodrugs. Radiat. res.,in press, 2004.
[26] JE Huheey. Inorganic Chemistry: Principles of Structure and Reactivity. *Harper and Row Publisher*, New York, 1994.
[27] J Awetz, P Melnick, ADelbrgs. Medical Microbiology 4th Edition, *McGraw Hill*, New York, 2007.
[28] NP Priya,SV Arunachalam, N Sathya, V Chinnusamy, C Jayabalakrishnan. Catalytic and Antimicrobial Studies of Binuclear Ruthenium (III) Complexes, Containing Bis-β-Diketones. *Transition Metal Chemistry*, 2009, 34: 437-445
[29] A B P Lever. Inorganic Electronic Spectroscopy. *Elsevier Publishing Company* New York, London, 1968.
[30] K Siddappa, M Mallikarjum, V CReddy. Synthesis, Characterization and Antimicrobial Studies of 3-[(2-Hydroxy-Quinolin-3-Ylmethylene)-Amino]-2-Phenyl- 3H-Quinazolin-4-One and its Metal (II) Complexes. E. J. Chem. 2008, 5(1):155-162.
[31] A. B. P. Lever. Inorganic Electronic Spectroscopy. *Elsevier, Amsterdam*, the Netherlands, 2nd Ed, 1984.
[32] W J Geary. The Use of Conductivity Measurements in Organic Solvents for the Characterization of Coordination Compounds. *J. Coord. Chem. Rev*. 1971, 7: 81-122.
[33] VL Paetznick, JH Rex. Disk Diffusion Method for Determining Susceptibilities of Candida spp. to MK-0991. J. Clin. Microbiol, 1999, 37(5): 1625-1627.

Synthesis, Characterization and the Corrosion Inhibition Study of Two Schiff Base Ligands Derived From Urea and Thiourea and Their Complexes with Cu(II) and Hg(II) Ions

Synthesis, Characterization and the Corrosion Inhibition Study of Two Schiff Base Ligands Derived From Urea and Thiourea and Their Complexes with Cu(II) and Hg(II) Ions

Wasan Mohammed Alwan

Department of Chemistry, College of Education for Pure Science (Ibn Al–Haitham), University of Baghdad, Adhamiyah – Anter square – Baghdad – Iraq

Email : wwoo27@yahoo.com

Abstract. The research includes synthesis of [L1] and [L2] Schiff base ligands by the reaction of vanillin with urea and thiourea respectively in 2:1 mol ratio. The two ligands were reacted with CuII ion in 1:2 mol ratio and HgII ion in 1:1 mol ratio. The prepared compounds have been identified by FTIR, U.V-Vis, 1H-NMR (L1, L2 and HgII complex) spectroscopies, microelemental analysis (C.H.N.S), magnetic susceptibility measurements, atomic absorption, chloride content along with conductivity and melting point measurements. According to applied characterization methods, the proposed general formulas of CuII and HgII complexes were [Cu2LnCl4] and [HgLnCl]Cl, respectively, (where n= 1, 2). The ability of corrosion inhibition with two ligands and their cupper complexes has been studied in diluted hydrochloric acid media.

Keywords: Schiff Base Ligand, Metal Complex, Urea, Thiourea, Corrosion Inhibition. hydrochloric acid media.

1. Introduction

Compounds comprising carbonyl and thion groups have an important position between organic reagents to be used as potential donor ligands with transition metal ions [1, 2]. Thiourea and urea derivatives were considered potentially very versatile ligands, its oxygen, nitrogen and sulfur donor atoms provide a multitude of coordinating possibilities [3]. Schiff bases and their metal complexes owns a wide range of applications as anticarcinogenic, pharmaceutical and antimicrobial reagents, beside the industrial and analytical uses[4-7]. Cu, Hg metals are present as essential elements in tracing amounts in biological systems; also they play an important role in bioinorganic chemistry [8]. Because of the main concerns of corrosion in the durability of materials structure; therefore, many studies were always carried out to develop an effective and economic means of corrosion control. To select an appropriate inhibitor for a certain system may be actually complicated, due to the great variety of corrosion related applications [9]. The corrosion inhibitor adsorbed on the surface of metals as a protective layer, the strength of the adsorption bond depends on the type of the functional group donor atom, the electron density and the polarizability of the functional group. Corrosion inhibitor normally contains oxygen, sulfur and nitrogen atoms. Multiple bonds in the corrosion inhibitor molecules that may facilitate the adsorption on the metal surface [10,11]. Recently Al-Obaidi prepared several mixed ligands complexes of Cu(II) and Zn(II) using benzylidene thiourea obtained by the

condensation of benzaldehyde and thiourea as the primary ligand and acetamide or thioacetamide as an additional ligand[12] .

2. Experimental

Melting points have been measured using an electro thermal apparatus (Stuart). FT-IR spectra were obtained using FT-IR test scan Shimadzu (FT-IR)- 8300 series spectro photometer in the range (400-4000 cm^{-1}); spectra were registered as potassium bromide discs at College of Education for Pure Science Ibn- Al- Haitham / Baghdad University. The electronic spectra of the compounds were achieved using (U.V-Vis) spectrophotometer UV-1800, using quartz cell of (1.0) cm length, in the range (1100-200 nm) with concentration (10^{-3}) M of samples in DMSO solvent at 25°C. Chloride content were determined by potentiometric titration method on (686-titro proceccor-665 dosinat metrome Swiss), while metal contents of the complexes were determined by atomic absorption (A.A) technique using a Shimadzu (AA 680) in Ibn Sina Company, Ministry of Industry, Baghdad-Iraq. Electrical conductivity measurements of prepared complexes carried out at (25˚C) using (10^{-3}–10^{-5}) M solutions of the samples in DMSO solvent using Eutech 150 conductivity meter in central laboratory of College of Education for Pure Science Ibn- Al- Haitham / Bagdad University. ^{1}H-NMR spectra for two ligands and two Hg^{II} complexes were recorded in DMSO-d_6 solution using Brucker, model: ultrashield 400 MHz, origin: Switzerland, at Kashan University, Iran. Microelemental Analysis (C.H.N.S) recorded using, Euro EA 300, at College of Education for Pure Science Ibn- Al- Haitham / Baghdad University. Magnetic moments at 298K were determined with a magnetic susceptibility balance (Sherwood Scientific). Samples were recorded at College of Sciences, Al-Mustansiriyah University.The study of corrosion inhibition has been obtained with a computer-controlled potentiostat (PCI4/750, GAMRY Instruments, Inc., Warminster, PA) and Nikon ME - 600 optical microscope provided with a NIKON camera, DXM-1200F which used to show the images of the surfaces of the electrodes, at Technology / University Baghdad-Iraq.

3. Preparation of the ligands ($L^1$and L^2)

A (2.53g, 16.63mmol) and (1.99g, 13.08mmol) from vanillin dissolved in (15ml) ethanol was mixed with (0.50g, 8.33mmol) and (0.50g, 6.57mmol) from urea or thiourea, respectively, dissolved in (15ml) ethanol and then added few drops of (10% NaOH) to adjust pH of the obtained reaction mixture, then heated with stirring for two hours. The products were filtered off, washed and recrystallized from absolute ethanol[13], Scheme (1) represents synthesis rout of two ligands.

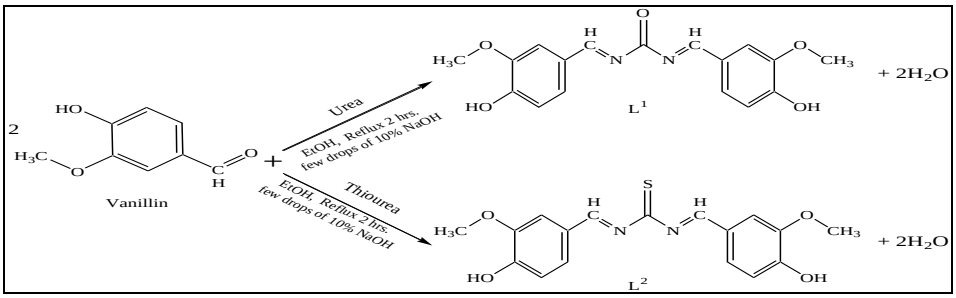

Scheme 1: Synthesis Rout of the L1 and L2

4. Preparation of $[Cu_2L^nCl_4]$

To a (15 ml) ethanolic solution (1.02g, 3.11mmol) of L^1 and (1.10g, 3.19mmol) of L^2, respectively, (10 ml) ethanolic solution (1.06g, 6.22mmol) and (1.09g, 6.39mmol), of cupper(II) chloride have been

added with heating and stirring for 2h. The products were filtered off, washed and recrystallized from absolute ethanol.

5. Preparation of [HgL^{n}Cl]Cl

A similar procedure described to that mentioned in preparation of Cu^{II} complexes was used to prepare the complexes of L^1 and L^2 with [Hg^{II}] ion, but in 1:1 mole ratio.

6. Study of Corrosion inhibition

Electrochemical studies of the Cu^{II} corrosion were obtained with potentiostat polarization. All experiments were carried out with a potentiostat (PCI4/750, GAMRY Instruments, Six different solutions from the prepared compounds were tested for corrosion inhibition study in (0.1M) HCl, two blank solution were used (HCl solution) blank 1 and (HCl + DMSO solution) blank 2. The test solutions include L^1, L^2, [$Cu_2L^1Cl_4$] and [$Cu_2L^2Cl_4$] solutions in one liter of distilled water at room temperature. Platinum electrodes and Ag/AgCl were used as auxiliary and reference electrode, respectively. Working electrodes were immersed into the solution until a steady open circuit potential (OCP) obtained. The exposed area of the tested specimens was (10 mm^2), the data have been adjusted according to the surface area. The sweep was taken from (-200 to + 200) mV relative to (OCP), scan rate (10mV/sec). A linear data fitting of the standard model gives an estimate of the polarization resistance, which is used to calculate (Icorr) and (Ecorr).

7. Metallographic Studies

Preparation of samples included many steps, sampling, grinding, polishing and etching. First, the samples were filed and ground. Grinding was done on a roll grinder using silicon carbide abrasive papers of 220, 320, 400, and 600 grits. Polishing process was done to the samples by using diamond paste of size (1μm) with special polishing cloth and lubricant followed by cleaning with water and alcohol and drying with hot air. Then the samples were scanned using Nikon ME-600 optical microscope provided with a NIKON camera, DXM-1200F.

8. Results and Discussion

shows some physical properties, and microelemental analysis (C.H.N.S) and chloride content and molar conductivity(solvent in DMSO) of the prepared compounds.

Table (1): some physical properties, microelemental analysis (C.H.N.S) ,chloride content and molar conductivity of the prepared compounds.

Empirical formula	M. wt g.mol^{-1}	Yield %	Color	m.p. ^{0}C	C%	H%	N%	S%	(Calc.), Found %		Λm S.cm^2 molar^{-1}
									M%	Cl%	
L^1	328.32	54	Light white	200	(62.19) 62.12	(4.91) 4.82	(8.53) 8.51	-	-	-	-
[$Cu_2L^1Cl_4$]	597.22	51	Light Orange	270	-	-	-	-	(21.28) 21.23	(23.75) 23.70	11.5

[HgL^1Cl]Cl	599.82	53	Light White	250	-	-	-	-	(33.44) 33.43	(11.82) 11.79	35.7
L^2	344.38	64	Light White	230	(59.29) 59.23	(4.68) 4.60	(8.13) 8.10	(9.31) 9.29	-	-	-
$[Cu_2L^2Cl_4]$	613.29	51	Light Orange	290	-	-	-	-	(20.72) 20.70	(23.12) 23.10	14.1
$[HgL^2Cl]Cl$	615.88	53	Light White	280	-	-	-	-	(32.57) 32.50	(11.51) 11.48	38.5

9. FTIR-Spectra of Precursors, Ligands and Complexes

The spectrum of the urea show bands at (3448) cm^{-1} and (3350) cm^{-1} may be attributed to the ν(N-H) asym. and (N-H) sym. of (NH_2) group[14]. The spectrum shows band at (1685) cm^{-1} may attributed to ν(C=O) group[15]. The spectrum of starting material thiourea, shows the bands at (3373) cm^{-1} and (3271) cm^{-1} may be attributed to the ν(N-H) asym. and ν(N-H) sym. bands of ν(NH_2) group[14]. The band at (1248) cm^{-1} attributed to ν(C=S) group[15]. The spectrum of vanillin, shows sharp band at (3180) cm^{-1} belong to ν(OH) may referred to the phenolic group and the band at (2983) cm^{-1} may be referred to the ν(OCH_3) group. The bands at (2947) cm^{-1} and (2848) cm^{-1} may be attributed to stretching vibration of the aldehydic proton. The spectrum shows band at (1678) cm^{-1} attributed to ν(C=O) group and the bands at (1205) cm^{-1} and (1014) cm^{-1} may be belong to the υ(C-O) vibration [15].

FT-IR spectra of L^1 and L^2, Figures (1) and (2), showed broad bands at (3440) cm^{-1} and (3444) cm^{-1}, respectively which assigned to υ(OH) of phenolic groups[16]. The bands at (3013) cm^{-1} and (3063) cm^{-1} may be referred to aromatic ν(C-H)[15] of L^1 and L^2, respectively. The spectra showed two bands at (2833) cm^{-1} and (2841) cm^{-1} referred to stretching vibration of (-OCH_3) group[15,17] for L^1 and L^2 respectively. The spectra have been also showed bands at (2715) cm^{-1} and (2719) cm^{-1} attributed to iminic υ (C-H) vibrations [18] of L^1 and L^2 respectively. The strong bands have been noticed in spectra of L^1 and L^2 at (1591) cm^{-1} and (1658) cm^{-1} may be assigned to υ(C=N) vibrations of imine groups[19,20], the appearance of these bands and disappearance of amine (NH_2) and aldehyde (CHO) bands in the spectra confirms the formation of Schiff base ligands[21]. The bands appeared at (1666) cm^{-1} and (1223) cm^{-1} in the spectrum due to υ(C=O) group for L^1 and υ(C=S) for L^2 [15]. The assignment of characteristic bands are summarized in Table (2).The band at (1591) cm^{-1} in L^1 spectrum may assigned to υ(C=N) stretching, shifted to the lower frequencies in the complexes of Cu^{II} and Hg^{II} and appears at (1587) cm^{-1} and (1579) cm^{-1} respectively, the shift in υ(C=N) suggests weak co-ordination of L^1 to metal ion [19]. While the band at (1658) cm^{-1} for L^2 belong to υ(C=N) shifted to the higher frequencies in the Cu^{II} and Hg^{II} complexes and appears at (1666)cm^{-1} and (1685) cm^{-1} respectively compared with L^2, indicating that azomethine nitrogen is involved in the coordination with the metal ions [20]. The band at (1666) cm^{-1} in the spectrum due to υ(C=O) vibrations in L^1 shifted towards higher values in the complexes Cu^{II} and Hg^{II} respectively and appeared at (1671) cm^{-1} and (1682) cm^{-1} as a result suggests the coordination of ligand to metal ion via the C=O group [22,23].The band at (1223) cm^{-1} in the spectrum due to υ(C=S) stretching vibration in L^2 shifted towards lower values in the complex Cu^{II} and Hg^{II} respectively and appears at (1130) cm^{-1} and (1192) cm^{-1}, this shift indicating the coordination of the sulpher atom of the ligand, referred to the charge transfer from the ligand to the metal [24,25]. The emergence of two new bands in the regions (588) cm^{-1}, (482) cm^{-1} and (503) cm^{-1}, (420) cm^{-1} in the spectra of the L^1 complexes Cu^{II} and Hg^{II} respectively may refer to υ(M-N) and υ(M-O). The appearance of two new bands in the regions (590) cm^{-1}, (480) cm^{-1} and (511) cm^{-1}, (463) cm^{-1} in the spectra of the L^2 complexes Cu^{II} and Hg^{II} respectively may refer to υ(M-N) and υ(M-S). The new bands confirmed the formation of metal

complexes through coordination from the iminic nitrogen, carbonyl and thiocarbonyl groups[12]. The characteristic FT-IR data are presented in Table (2). The spectra of the ligands and complexes were shown in 'Figures (3-6)'.

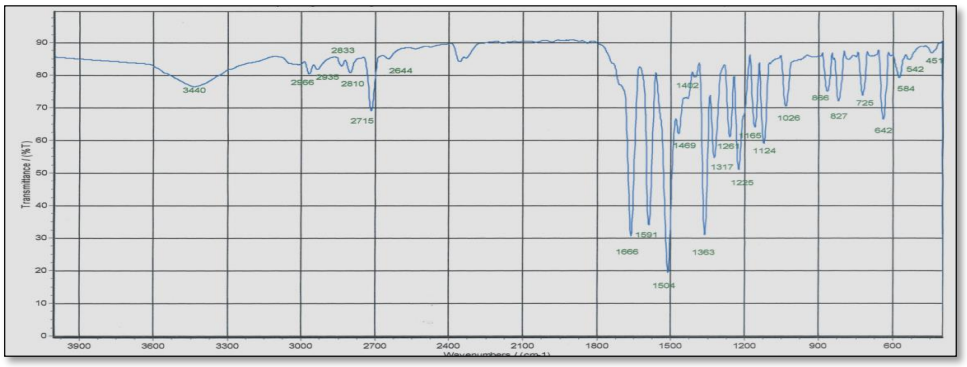

Figure 1: FT-IR spectrum of the L1

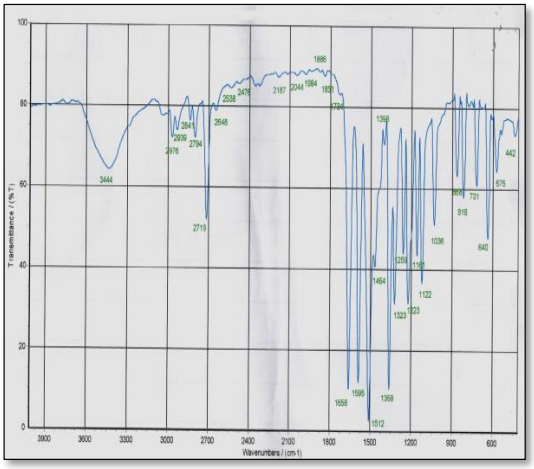

Figure 2: FT-IR spectrum of the L^2

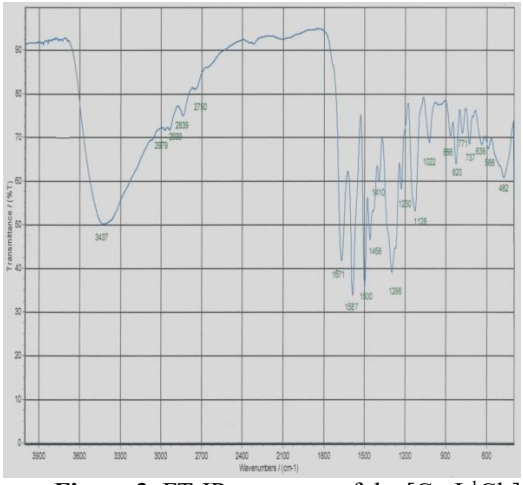

Figure 3: FT-IR spectrum of the $[Cu_2L^1Cl_4]$

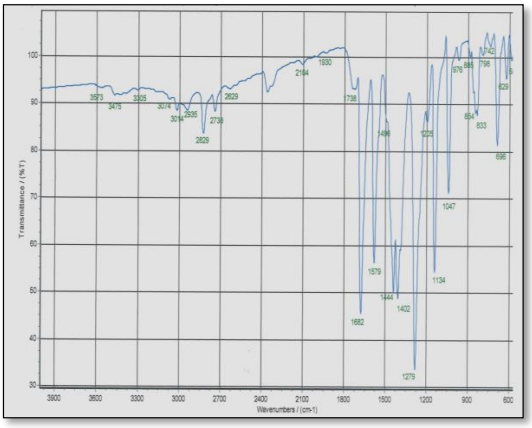

Figure 4: FT-IR spectrum of the [HgL[1]Cl]Cl

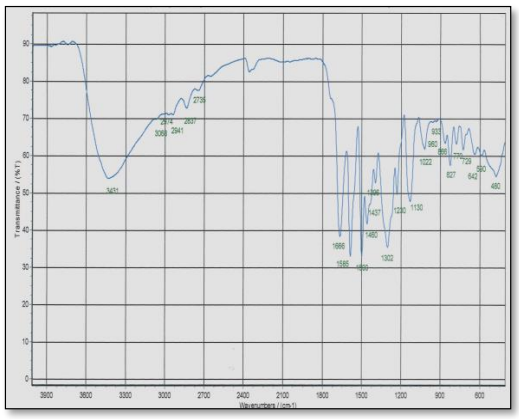

Figure 5: FT-IR spectrum of the $[Cu_2L^2Cl_4]$

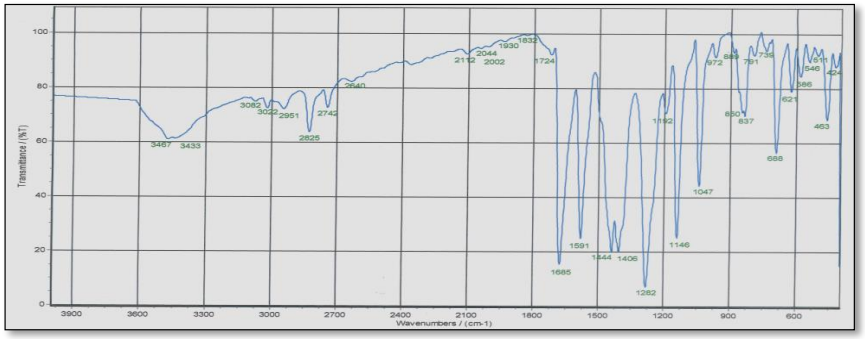

Figure 6: FT-IR spectrum of the [HgL[2]Cl]Cl

Table 2: Infrared data of ligands (cm-1) and starting materials and complexes

Compound	v(OH) $v(NH_2)$	v(C=O) v(C=S)	v(C=N)	v(M-N)	v(M-S) v(M-O)	Additional bands
L^1	3440 -	1666 -	1591	-	-	v(C-H)aro. 3013 $v(OCH_3)$ 2833 v(C=C) 1504
L^2	3444	- 1223	1658	-	-	v(C-H)aro. 3063 $v(OCH_3)$ 2841 v(C=C) 1595 – 1512

$[Cu_2L^1Cl_4]$	3437	1671 -	1587	588	- 482	
$[HgL^1Cl]Cl$	3475	1682 -	1579	503	- 420	
$[Cu_2L^2Cl_4]$	3431	- 1130	1666	590	480 -	
$[HgL^2Cl]Cl$	3433	- 1192	1685	511	463 -	

Electronic Spectra Ligands and magnetic susceptibility for the complexes

Table (3) summarized the electronic data of two ligands and their complexes. The electronic spectra of two ligands (L^1 and L^2) at (10^{-3} M) in ethanol showed one π–π* transition at (267 nm) and (267 nm) and the three peaks at (300 nm), (335 nm) and (383 nm) for L^1 and (305 nm), (345 nm) and (372 nm) for L^2 represented n–π* transition resulted from the presence of the lone pairs of the groups (C-OH, C=O and HC=N groups) of L^1 and (C-OH, C=S and HC=N groups) for L^2[26,19], Figures (7) and (8).

The U.V - Visible spectra of $[Cu_2L^1Cl_4]$, showed in Figure (9) and $[Cu_2L^2Cl_4]$, Figure (10), in (10^{-3}M) ethanol solutions. In each case it was noticed a shift in π–π* and n–π* transitions and intensity change in the complexes compared with those of ligands, indicating the coordination to metal. Two peaks for $[Cu_2L^1Cl_4]$ and $[Cu_2L^2Cl_4]$ complexes at (358 nm) and (358 nm) with high intensities are most probably due to charge transfer transition [27]. The peaks in the visible region can be associated with d-d transitions. The $[Cu_2L^1Cl_4]$ shows peak at (788 nm) assigned to $^2B_1g \rightarrow {}^2A_1g$ while $[Cu_2L^2Cl_4]$ shows two peaks at (716 nm) and (814 nm) assigned to $^2B_1g \rightarrow {}^2B_2g$ and $^2B_1g \rightarrow {}^2A_1g$ suggesting square planar geometry around the Cu^{II} ion[5,27,28]. The magnetic moment values(1.56 and 1.64 BM) for complexes $[Cu_2L^1Cl_4]$ and $[Cu_2L^2Cl_4]$ are indicative of square-planar geometry[28,29].

The U.V / Visible spectra of $[HgL^1Cl]Cl$, Figure (11) and $[HgL^2Cl]Cl$, Figure (12) exhibited peaks at (375 nm) and (375 nm) assigned to charge transfer transitions .Finally Hg^{II} ions belong to d^{10} configuration and they don't have d-d transition. On considering the position of the bands, the tetrahedral structure may be proposed for these complexes [5, 30,31] .

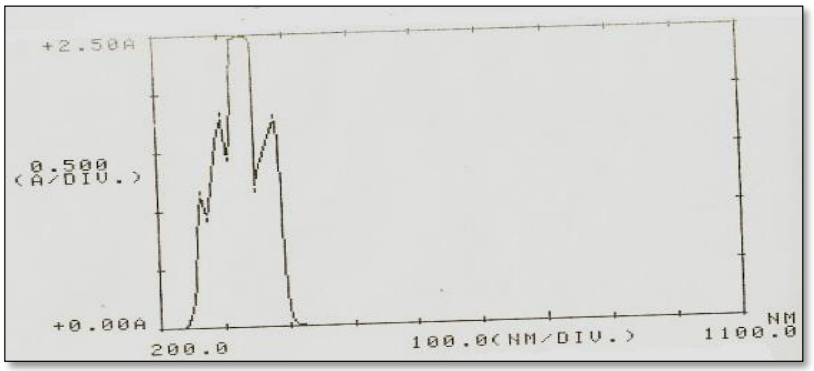

Figure 7: UV spectrum of the L^1

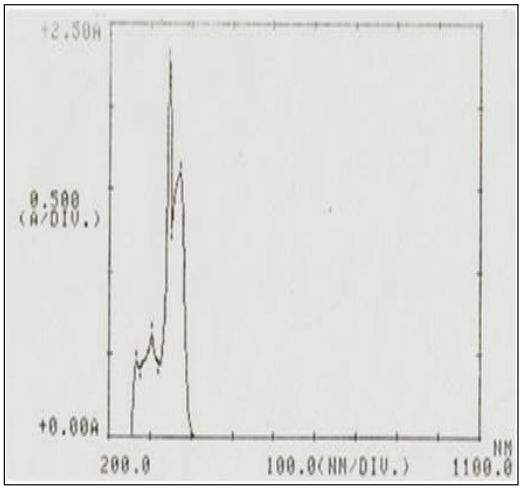

Figure 8: UV spectrum of the L^2

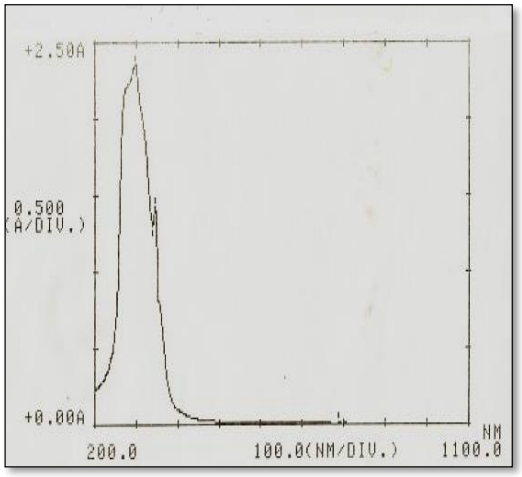

Figure 9: UV spectrum of the $[Cu_2L^1Cl_4]$

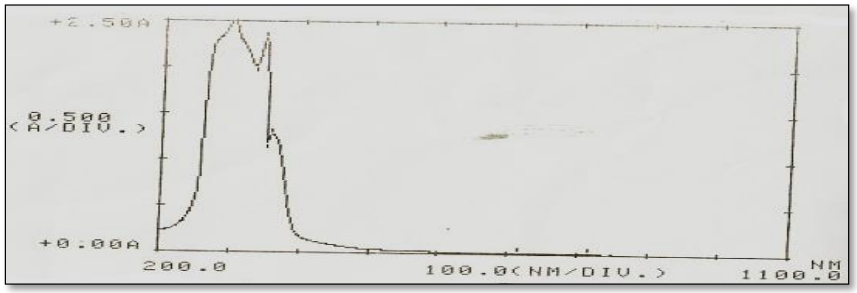

Figure 10: UV spectrum of the $[Cu_2L^2Cl_4]$

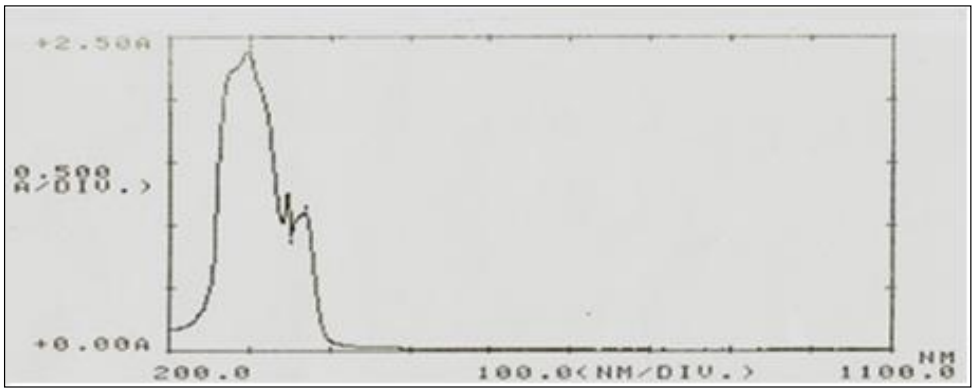

Figure 11: UV spectrum of the $[HgL^1Cl]Cl$

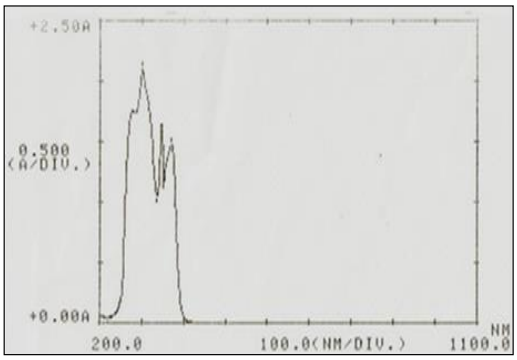

Figure 12: UV spectrum of the $[HgL^2Cl]Cl$

Table 3: Electronic spectral data of ligands and metal complexes

Compound	Transition		ε_{max} molar^{-1} cm^{-1}	Assignment	μeff. (B.M.)	Suggested structure
	λ nm	ν cm^{-1}				
L^1	267	3745	1107	π–π*	-	
	300	3333	1779	n–π*		
	335	2985	2484			
	383	2610	1758			
$[Cu_2L^1Cl_4]$	283	3533	2208	π–π*	1.56	Square planar
	298	3355	2360	n–π*		
	345	2898	1428			
	350	2857	1125			
	358	2793	791	CT		
	788	1269	8	$^2B_1g \rightarrow {}^2A_1g$		
$[HgL^1Cl]Cl$	275	3636	2291	π–π*	Diamagnetic	Tetrahedral
	299	3344	2392	n–π*		
	342	2923	125			
	368	2717	1103			
	375	2666	958	CT		
L^2	267	3745	451	π–π*	-	
	305	3278	634	n–π*		
	345	2898	2283			
	372	2688	1600			
	275	3636	2333	π–π*		
	301	3322	2500			

$[Cu_2L^2Cl_4]$	316	3164	2166	$n–\pi^*$	1.64	Square planar
	345	2898	2314			
	358	2793	1269	CT		
	716	1396	15	$^2B_1g \rightarrow {}^2B_2g$		
	814	1228	10	$^2B_1g \rightarrow {}^2A_1g$		
$[HgL^2Cl]Cl$	258	3875	1750	$\pi–\pi^*$	Diamagnetic	Tetrahedral
	301	3322	2103	$n–\pi^*$		
	350	2857	1708			
	370	2702	1447			
	375	2666	1208	CT		

10. ^{1}HNMR Spectra of Ligands and Their Hg^{II} Complexes

The ^{1}H-NMR spectrum of L^1, Figure (13), exhibits the following signals: (3.75), (6.15), (6.93-7.07) and (9.23) ppm which are assigned to the ($-OCH_3$), (-OH), aromatic and (-CH=N-), protons, respectively. The two signals at (2.49 and 3.5) ppm assigned to protons of solvent (DMSO) and water, respectively.

The ^{1}H-NMR spectrum of $[HgL^1Cl_2]$ complex, Figure (14), exhibits the following signals: (3.7), (7.22-7.49) and 9.63 ppm which are assigned to the ($-OCH_3$), aromatic and (-CH=N) protons, respectively. The signal of (-CH=N-) proton shifted to the downfield region (9.63) ppm due to coordination to Hg^{II} ion. The signal of (-OH) proton disappeared because of exchange with solvent[15,32].

The ^{1}H-NMR spectrum of L^2, Figure (15), exhibits the following signals: (3.66), (6.11), (6.91-7.04) and (9.21) ppm which are assigned to the ($-OCH_3$), (-OH), aromatic and (-HC=N) protons, respectively.

The ^{1}H-NMR spectrum of the $[HgL^2Cl_2]$, Figure (16) exhibits the following signals: (3.78), (6.9), (7.17-7.45) and (9.57) ppm which are assigned to the, ($-OCH_3$), (-OH), (aromatic) and (-HC=N) protons, respectively. The (-CH=N-) shifted to the downnfiled region (9.57) ppm compared to that of free ligand indicating that the azomethine nitrogen involving in coordination with Hg^{II} ion[15,32]. The characteristic ^{1}H-NMR spectral data are presented in Table (4).

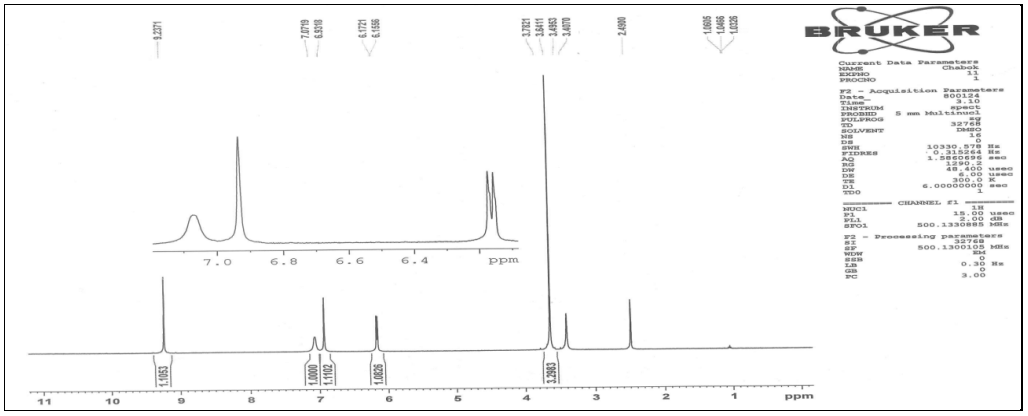

Figure 13: ^{1}H-NMR spectrum for the L^1

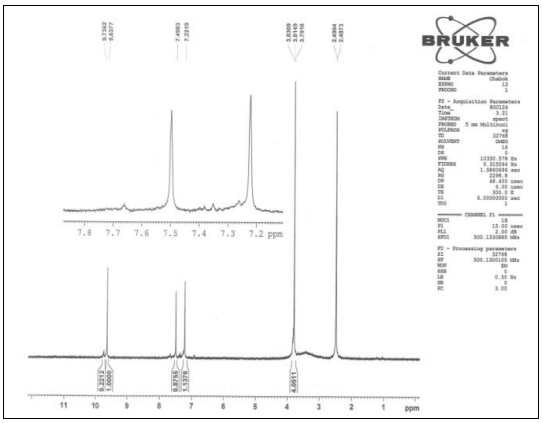

Figure 14: ^{1}H-NMR spectrum of the [HgL^{1}Cl]Cl

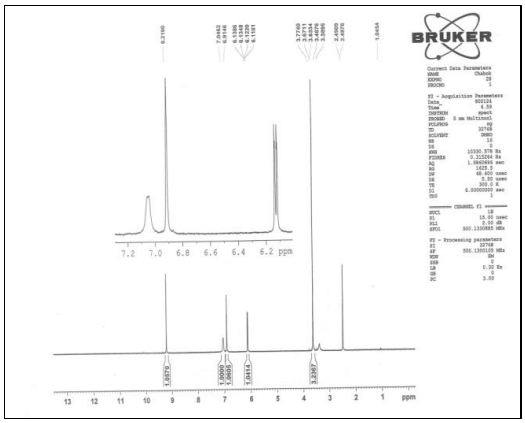

Figure 15: ^{1}H-NMR spectrum for the L^{2}

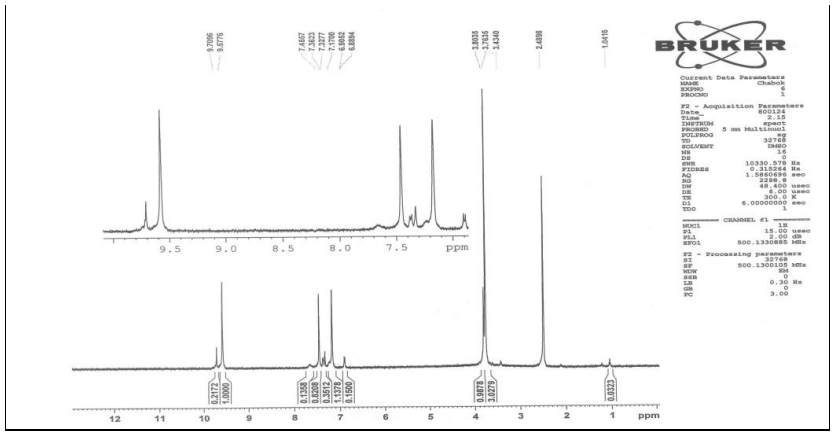

Figure 16: ^{1}H-NMR spectrum of the [HgL^{2}Cl]Cl

Table 4: 1H-NMR Spectral data of two ligands and two HgII Complexes in DMSO-d6

L^1		[HgL^{1}Cl]Cl		L^2		[HgL^{2}Cl]Cl	
(δ) ppm	Assignment	(δ) ppm	Assignment	(δ) ppm	Assignment	(δ) ppm	Assignment
(3.75)	(-OCH_3)	(3.7)	(-OCH_3)	(3.66)	(-OCH_3)	(3.78)	(-OCH_3)
(6.15)	(-OH)	---	(-OH)	(6.11)	(-OH)	(6.9)	(-OH)
(6.93-7.07)	(Ar-H)	(7.22-7.49)	(Ar-H)	(6.91-7.04)	(Ar-H)	(7.17-7.45)	(Ar-H)
(9.23)	(-CH=N)	(9.63)	(-CH=N)	(9.21)	(-CH=N)	(9.57)	(-CH=N)

11. The proposed structure

According to the results obtained from (IR, UV/visible,^{1}H-NMR, microelemental analysis (C.H.N.S), magnetic susceptibility measurements, atomic absorption, chloride content along with conductivity and melting point measurements for the prepared complexes, the proposed molecular structure of the complexes has an square planar Cu^{II} and tetrahedral Hg^{II} structure as shown in Fig.(17) and (18) **.**

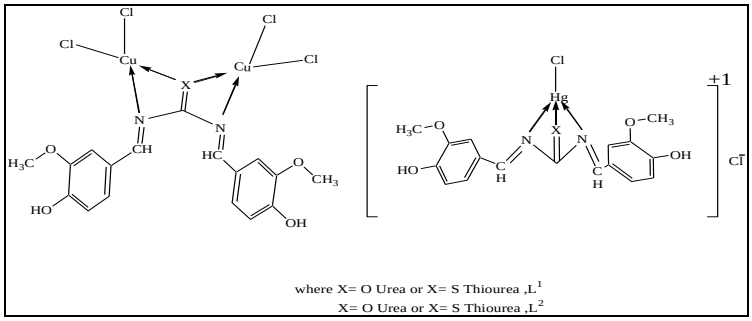

Figure (17): Proposed Structures of Prepared Complexes

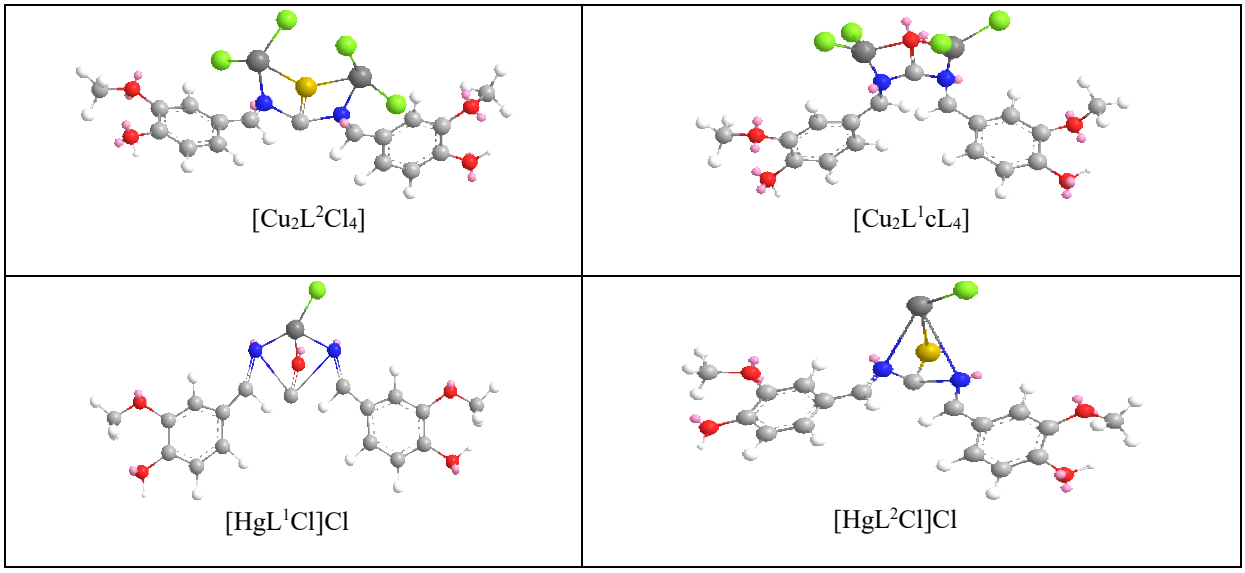

Figure(18): The proposed molecular structure of the complexes

Conclusions

Corrosion inhibition efficiency of two ligands with two copper complexes electrodes in 10% HCl solution have been studied using potentiometric method. All synthesized inhibitors showed inhibition characteristics for copper corrosion in 10% HCl solution. The chelates displaying high surface activity and low solubility in solution. The synthesized inhibitors due to containing one or more functional groups, containing one or more hetero atoms, N, O, S, this may increases the ability of the inhibitor molecule to cover a large surface area of the metal surface[33]. The inhibition efficiency of synthesized inhibitors increased in the following order: L^{2}> blank 1>L^{1}> [$Cu_2L^{2}Cl_4$] > blank 2>[$Cu_2L^{1}Cl_4$], see Figures (19) and (20) and metallographic Figures (21), (22), (23), (24), (25), (26) and (27) show the corrosion inhibition ability of the prepared ligands and two cupper complexes, the results are summarized in Table (5).

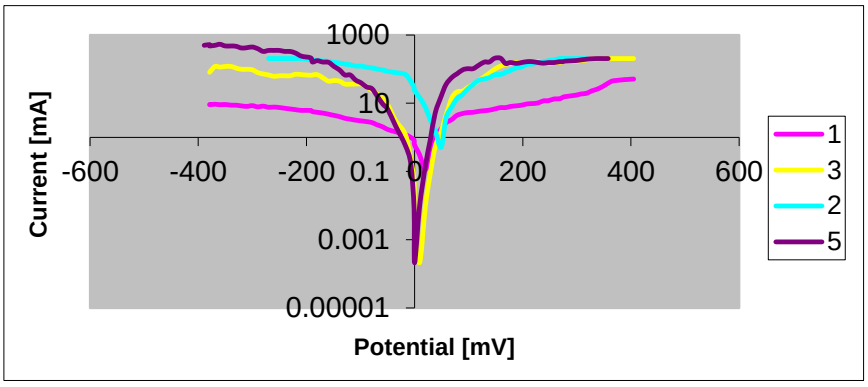

Figure 19: Tafel polarization curves for corrosion in (1 M) HCl in the absence and presence of different concentrations of inhibitors for [1(blank 1), 3(L^1), 2(blank 2), 5($Cu_2L^1Cl_4$)]

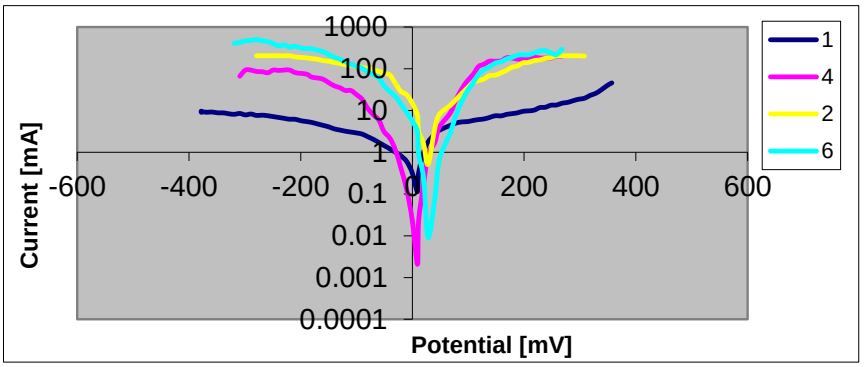

Figure 20: Tafel polarization curves for corrosion in (1 M) HCl in the absence and presence of different concentrations of inhibitors for [1(blank 1), 4(L^2), 2(blank 2), 6($Cu_2L^2Cl_4$)]

Figure 21: Micrograph of the electrode before corrosion

Figure 22: Micrograph of the electrode in blank 1

Figure 23: Micrograph of the electrode in blank 2

Figure 24: Micrograph of the electrode with L^1

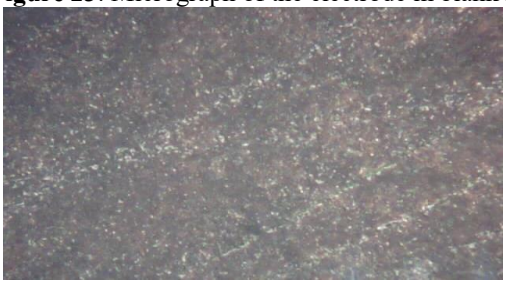

Figure 25: Micrograph of the electrode with L^2

Figure 26: Micrograph of of the electrode with$[Cu_2L^1Cl_4]$

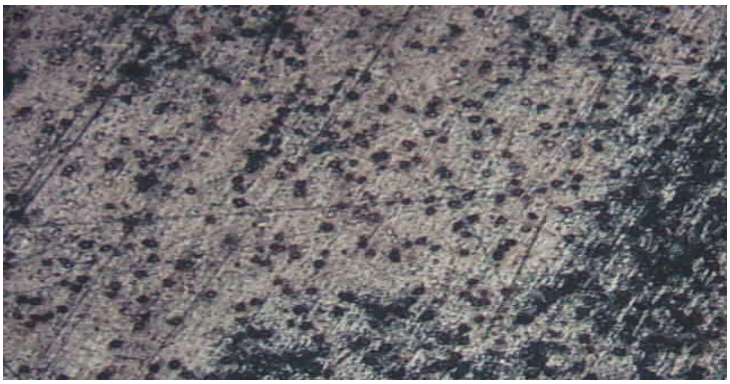

Figure 27: Micrograph of the electrode with $[Cu_2L^2Cl_4]$

Table 5: Results of Corrosion inhibition

Sample No.	Sample Solution	E_{corr}	I_{corr}
1	Blank 1	-68.1 [mv]	768.92 A/cm^2
2	Blank 2	40.5 [mv]	7.71 A/cm^2
3	L^1	-27.0 [mv]	444.97 A/cm^2
4	L^2	25.9 [mv]	992.84 A/cm^2
5	$[Cu_2L^1Cl_4]$	36.0 [mv]	4.34 A/cm^2
6	$[Cu_2L^2Cl_4]$	61.8 [mv]	81.08 A/cm^2

References

[1] H. Arslan, N. Kulcu, and U. Florke, "Synthesis and characterization of copper (II), nickel (II) and cobalt (II) complexes with novel thiourea derivatives", Transit. Metal Chem., 28, 2003,816-819.

[2] D.S. Mansuroglu, H. Arslan, U. Florke, and N., Kulcu, "Synthesis and characterization of nickel and copper complexes with 2,2-diphenyl-N-(alkyl(aryl)carbamothioyl) acetamide: The crystal structures of HL1 and cis-[Ni(L-1)(2)]", J. Coord. Chem., 61, 2008, 3134-3146.

[3] Y.M. Zhang,T.B. Wei, L. Xian, and L.M. Gao, "An efficient synthesis of polymethylene-bis-aroyl thiourea derivatives under the condition of phase-transfer catalysis", Phosphorus, Sulfur Silicon Relat. Elem., 179, 2004, 2007-2013.

[4] A.D. Garnovskii, A.L. Nivorozhkin and V.I. Minkin, "Ligand environment and the structure of schiff base adducts and tetracoordinated metal-chelates", Coord. Chem. Rev. 126(1-2), 1993, 1-69.

[5] A.B.P. Level, "Inorganic Electronic Spectroscopy", New York, 1968, 6,121.

[6] O.E. Offiong, "Synthesis and spectral studies of platinum metal complexes of benzoin thiosemicarbazone", Spectrochim. Acta Part A, 50(13), 1994, 2167-2175.

[7] M.S. El-Shahawi*, M.S. Al-Jahdali, A.S. Bashammakh, A.A. Al-Sibaai, H.M. Nassef, "Spectroscopic and electrochemical characterization of some Schiff base metal complexes containing benzoin moiety", Spectrochimica Acta Part A: Molecular and Biomolecular Spectroscopy 113, 2013 ,459–465

[8] H. Arslan, N. Duran, G. Borekci, C.K. Ozer, and C. Akbay, "Antimicrobial activity of some thiourea derivatives and their nickel and copper complexes", Molecules, 14, 2009, 519-527.

[9] P.R. Roberge, "Handbook of Corrosion Engineering", 2000, McGraw-Hill, http:www.corrosion doctorse.org/ Economics/ introduction.htm-10k.

[10] M.A. Quraishi, M.A.W. Khan, and M. Ajmal, "Influence of some thiazole derivatives on the corrosion of mild steel in hydrochloric acid", Anti-Corros. Methods Mater, 43(2), 1996, 5-8.

[11] R.T. Loto*, C.A. Loto, A.P.I. Popoola, " Corrosion inhibition of thiourea and thiadiazole derivatives : A Review", J. Mater. Environ. Sci. 3 (5) ,2012, 885-894

[12] O.H. Al-Obaidi, "Synthesis, Characterization and Antimicrobial Screening Mixed-Ligand Cu(II) and Zn(II) Complexes: DNA Binding Studies on Cu(II) Complex", open journal of Inorganic Non-metallic Materials , 2, 2012, 59-64.

[13] F.A. Abdlseed, and M.M. El-ajaily, "Complex formation of TiO (IV), Cr (III) and Pb (II) ions using 1,3-bis(2-hydroxybenzylidene)thiourea as ligand", International Journal of Research in Pharmaceutical and Biomedical Sciences, 3(3), 2012, 1031-1037.18

[14] E. Erdem, E.Y. Sari, R. Kilinçarslan and N. Kabay, "Synthesis and characterization of azo-linked Schiff bases and their nickel(II) and zinc(II) complexes", Trans. Met. Chem., 34, 2009, 167-174.

[15] M.Robert, Silverstein, Spectrometric identification of organic compounds 7th edition, John Willey and Son, inc.,2005, p 174.

[16] F. Karipcin and E. Kabalcilar, "Spectroscopic and thermal studies on solid complexes of 4-(2-pyridylazo)resorcinol with some transition metals", Acta. Chim. Slov., 54, 2007, 242-247.

[17] M.J.K. Al-Assadi, "Synthesis and Characterization of Ni2+ and Cu2+ Schiff-base complexes and their study for electrical properties", Journal of Basrah Researches (Sciences), 2011, 37(3A).

[18] G. Socrates, "Infrared Characteristic Group Frequencies", Wiley, New York,1980.

[19] A.N. Al-Shareefi, S.H. Kadhim, and W.A. Jawad, "Synthesis and study of Fe(III), Co(II), Ni(II) and Cu(II) complexes of new Schiff's base ligand derived from 4-amino antipyrine", Journal of Applicable Chemistry, 2(3), 2013, 438–446

[20] D.K. Dey, A. Lycka, S. Mitra, and G.M. Rosair, Simplified synthesis, 1H, 13C, 15N, 119Sn NMR spectra and X-ray structures of diorganotin(IV) complexes con- taining the 4-phenyl-2,4-butanedionebenzoylhydrazone(2-) ligand. Journal Organometallic Chemistry, 689, 2004,

88-95.

[21] J. Sanmartin, M.R. Bermejo, A.M. Garcia-Deibe, I.M. Rivas and A.R. Fernandez, "Zinc and cadmium complexes with versatile hexadentate Schiff base ligands. The supramolecular self-assembly of a 3-D cage-like complex", J. Chem. Soc. Dalton Trans, (22), 2000, 4174-4181.

[22] B.S. Parajon-Costa, E.J. Baran, O.E. Piro, Polyhedron 16 (19) ,1997,3379.

[23] D Gangopadhyay a , S Kumar Singh b , P Sharma a , H Mishra c , V.K. Unnikrishnan d , B. Singh b , R.K. Singh a,*, "Spectroscopic and structural study of the newly synthesized heteroligand complex of copper with creatinine and urea", Spectrochimica Acta Part A: Molecular and Biomolecular Spectroscopy 154 ,2016 ,200–206

[24] I. Dilovic, M. Rubcic, Vrdoljak, V. Novel thiosemicarbazone derivatives as potential antitumor agents: Synthesis, physicochemical and structural properties, DNA interactions and antiproliferative activity. Bioorg. Med. Chem., 16, 2008, 5189–5198. [CrossRef] [PubMed]

[25] L. Lathee, M.R. Prathapachandra Kurup, Spectral and structural studies of copper(II) complexes of thiosemicarbazones derived from salicylaldehyde and containing ring incorporated at N(4)-position. Spectrochim. Acta Part A 2008, 70, 86–93. [CrossRef] [PubMed]

[26] B. Manjula, S.Arul Antony and C. Justin Dhanaraj "Synthesis, spectral characterization, and antimicrobial activities of Schiff base complexes derived from 4-aminoantipyrine", Spectroscopy letters, 47(7), 2014, 518-526.

[27] J. A. McCleverty, T.J. Meyer, Comprehensive Coordination Chemistry: Ligands, Complexes, Synthesis, Purification, and Structure; Pergamon Press: New York, NY, USA, Volume 1, 1987,p. 274.

[28] E. Pahont,u 1,*, D -Carolina Ilies,2,* , S. Shova 3, C. Oprean 4,5,V. Paunescu 5,6, O.T. Olaru 7, F.Stefan Radulescu 8, A. Gulea 9,Tudor Ros,u 10 and D. Draganescu 11 , " Synthesis, Characterization, Antimicrobial and Antiproliferative Activity Evaluation of Cu(II), Co(II), Zn(II), Ni(II) and Pt(II) Complexes with Isoniazid-Derived Compound", Molecules, 2017, 22, 650

[29] R.L. Carlin, Transition Metal Chemistry, 2nd ed.; Marcel Decker: New York, NY, USA, 1965.

[30] S. Karabocek and N. Kaeabocek, Polyhedron, 11, 1997, 1771-1774.

[31] P. Mangaiyarkkarasi1 and S. Arul Antony2*, "Synthesis, Characterization And Biological Significance of Some Novel Schiff Base Transition Metal Complexes Derived from 4-Aminoantipyrine And Dihydropyrimidine of Vanillin", Journal of Applicable Chemistry
, 3 (3), 2014, 997-1006 (International Peer Reviewed Journal)

[32] H. Yin, H. Xu, K. Li, and G. Li, Tin(IV) poly- mers: Part 1. Synthesis of diorganotin esters of thiosali- cylicacid: X-ray crystal structure of polymeric thiosalicy- latodiorganotin. Journal of Inorganic and Organometal- lic Polymers and Materials, 15, 2005 , 319-325 .

[33]F. Mansfeld., "Chemical Industries/28 of Corrosion Mechanisms", Department of Materials Science , University of Southem California , Los Angeles , California,117, 999, 1970.

Synthesis, spectroscopic characterization, and antibacterial evaluation of new Schiff bases bearing benzimidazole moiety

Synthesis, spectroscopic characterization, and antibacterial evaluation of new Schiff bases bearing benzimidazole moiety

Muayed Ahmed Redayan[1], Maha Salih Hussein[2], Ashraf Tark lafta[2]

1 Department of Chemistry, College of Education for pure sciences, Diyala University,
Diyala, Iraq
2 Department of Chemistry, College of Education, Samarra University, Salahaldin, Iraq

mredayan@gmail.com

Abstract. The present work comprise synthesis of new derivatives for Schiff bases bearing benzimidazole ring. Compounds 1(a-d) were prepared by reaction of *o*-pheneylenediamine with a various of amino acids (glycine, alanine, phenyl alanine and tyrosine) in the presence 6N HCl to yielded derivatives of benzimidazole compounds containing free $-NH_2$ group. Then these compounds used to prepare different Schiff bases through reaction with various of aromatic aldehydes. The chemical structure of synthesized compounds were confirmed by FTIR,^{1}H,^{13}C-NMR, and ^{13}C-NMR dept135 spectroscopy. Some selected compounds were evaluated *in vitro* for their antibacterial activity against two types of Gram-positive bacteria namely (*Staphylococcous aureus*, *Bacillus subtilis*) and Gram-negative bacteria namely (*Pseudomonas aeruginosa*, *Escherichia coli*). Most of the results of the antibacterial activity of these compounds were good when compared with the standard antibiotic ampicillin and ciprofloxacin.

1. Introduction

Due to their remarkable biological activity and diverse clinical application, Benzimidazole derivatives occupied a major part in the field of pharmaceutical chemistry and very important field of heterocyclic compounds.The benzimidazole nucleus moiety is existing in many Benzimidazole compounds are consider a promising field of bioactive heterocyclic compounds, Specifically this nucleus is constitution of vitamin-B12 [9]. Because of the immense importance and versatile biological activities displayed by benzimidazole, Attempts have been made from time to time to create libraries of these compounds and evaluation them for biological activities [10]. Schiff base hold a major part in the field of pharmaceutical research due to their high biological activity. Thus, numerous attempts to develop and design of new Schiff base still arouse interest of pharmaceutical and medicinal researchers [11].

Schiff bases which have a various of heterocyclic ring were reported to posses a wide spectrum of biological activities including antiviral [12],anticancer [13],cytotoxic [14]antimicrobial [15],antibacterial [16-17]anticonvulsant [18]. In coordination chemistry of transition metals, metal complexes which derivative from Schiff bases have been usually utilized as chelating ligands in radiopharmaceutical for cancer attack and agrochemicals such as pesticide. Therefore, they constitute a fascinating field of chelating agents effective of coordination with metals ion which use as style for biological systems [19-21].

2. Experimental Section

2.1 General

Melting points were taken in an electrically heated using Stuart SMP[3] instrument and are uncorrected. FT-IR spectra were recorded on (Shimadzu FT-IR- 8400S spectrophotometer at the Chemistry department/ College of education for pure scince/ University of Diyala) by using KBr disc(v,cm^{-1}). The ^{1}H and ^{13}C-NMR spectra were recorded on (Bruker 400MHz at the Jordan University for science and technology /Jordan) by using tetramethylsilane (TMS) as an internal standard and DMSO-d_6 as solvent. The purity of the compounds was checked by TLC on silica gel plates using ultraviolet lamp(365nm and 254nm).

2.2 General procedure for synthesis of compounds 1(a-d) [22].:Asolution of o-phenylenediamine (6.5g, 0.06 mol) and amino acids (glycine, alanine, phenylalanine and tyrosine) (0.12 mol) in 6N hydrochloric acid (20 ml) was heated to reflux with stirring for 6h. The progress of the reaction was monitored by TLC plate. On completion of the reaction, the reaction mixture was cooled to room temperature and the pH was adjusted to 7.2 using 1N sodium hydroxide solution to obtain buff colored product. The product was recrystallized using ethanol as solvent.

(1H-benzo[d]imidazol-2-yl)methanamine(1a): White crystals, yield 66%. m.p: 257 – 259°C, IRν_{max} (KBr/cm^{-1}): NH_2 (3387, 3363), N-H benzimidazole (3288), aromatic C-H (3028), aliphatic C-H (2864, 2754), C=N (1635) , aromatic C=C (1458, 1593). ^{1}H –NMR (400MHz, DMSO – d_6) δ : 3.01 (2H, s, CH_2), 4.38 (1H, s, N-H), 8.58 (2H, s, NH_2), 6.3-6.5 (4H,m,Ar – H). ^{13}C –NMR (400MHz, DMSO) δ : 44.6 (CH_2), 142.3 (C=N of benzimidazole), 114.7 , 117.3 , 134.8 . ^{13}C-Dept 135 NMR (400MHz, DMSO – d_6) δ : 44.4 (CH_2),

1-(1H-benzo[d]imidazol-2-yl)ethanamine(1b): Brown, yield 97%. m.p : 236 – 238°C, IRν_{max} (KBr/cm^{-1}): NH_2 (3387, 3336), N-H benzimidazole(3286), aromatic C-H(3037,3028), aliphatic C-H (2944, 2856), C=N (1633), aromatic C=C (1458-1593).^{1}H –NMR (400MHz, DMSO – d_6) δ : 1.2 (3H, d, CH_3), 3.7 (1H, q, C-H), 5.9 (1H, s, N-H benzimidazole), 8.44 (2H, s, NH_2), 6.54-7.81 *(4H,m,Ar – H).^{13}C–NMR (400MHz, DMSO) δ*: 23.9 (CH_3), 54.3 (CH), 140.9 (C=N of benzimidazole), 140.1, 138.1, 127.1, 119.2,114.9,

(1H-benzo[d]imidazol-2-yl)(phenyl)methanamine (1c) : Off White, yield 98% m.p : 255 – 257°C, IRν_{max} (KBr/cm^{-1}): N-H benzimidazole (3125), aromatic C-H (3064,3034), aliphatic C-H (2960, 2868), C=N (1625), aromatic C=C (1454-1571).

4-(2-amino-2-(1H-benzo[d]imidazol-2-yl)ethyl)phenol (1d) :Dark brown, yield 77% . m.p : 276–278°C, IRν_{max} (KBr/cm^{-1}): NH_2 (3385,3363), N-H benzimidazole (3205) overlap with OH , aromatic C-H (3024), aliphatic C-H (2962, 2885), C=N (1608).aromatic C=C (1456-1591).

2.3 General procedure for the synthesis of compounds 2(a-l) [23]**.:**Compounds 1(a-d) (0.01 mol)were add to asolution of the different substituted benzaldehydes (p-bromobenzaldehyde, p-nitro benzaldehyde, p-hydroxybenzaldehyde) (0.012 mol) in dry ethanol 40 ml in RBF. Two drops of glacial acetic acid were also added to the above mixture. The mixture was refluxed for 8-12h and at the end of the reaction; solvents were partially evaporated then poured in to water. The precipitates

were collected by filtration, washed with ether, dried and compounds 2(a-l) were synthesized and recrystallized from the appropriate solvent like ethanol or ethanol-water.

1-(1*H*-benzo[*d*]imidazol-2-yl)-N-(4-bromobenzylidene)methanamine(2a) :Yellow, yield 87%. m.p : 287-289°C, IRν_{max} (KBr/cm^{-1}): N-H benzimidazole(3321), aromatic C-H (3030,3055), aliphatic C-H (2997, 2875), C=N (1610), aromatic C=C (1448-1531), C-Br (744),

4-((((1*H*-benzo[*d*]imidazol-2-yl)methyl)imino)methyl)phenol (2b) :Brown crystals, yield 93%. m.p : 285-287°C, IRν_{max} (KBr/cm^{-1}): N-H benzimidazole and O-H(3253)over lab, aromatic C-H (3088,3032), aliphatic C-H (2943, 2885), C=N (1610), aromatic C=C (1444-1514),^{1}H –NMR (400MHz, DMSO – d_6) δ : 3.37 (2H, s, CH_2), 5.40 (1H, s, N-H), 9.97 (1H, s, OH),9.41 (1H, s, CH=N), 6.64-7.65 (4H, m, Ar – H). ^{13}C –NMR (400MHz, DMSO) δ : 47.4 (CH_2), 142.7 (C=N of benzimidazole), 156.5 (1H,s,C-OH), 158.7(1H,s,CH=N),115.3 , 118.7 ,122.03, 127.4 130.5 , 136.19)^{13}C-Dept 135 NMR (400MHz, DMSO – d_6) δ : 46.8 (CH_2),

1-(1*H*-benzo[*d*]imidazol-2-yl)-N-(4-nitrobenzylidene)methanamine(2c) :brown crystals, yield 91%. m.p : 293-295 °C, IRν_{max} (KBr/cm^{-1}): N-H benzimidazole(3321), aromatic C-H (3035,3035), aliphatic C-H (2954, 2850), C=N (1604), aromatic C=C (1445,1535), NO_2(1340,1516),

1-(1*H*-benzo[*d*]imidazol-2-yl)-N-(4-bromobenzylidene)ethanamine (2d) :brown crystals, yield 87%. mp : 283-285°C, IRν_{max} (KBr/cm^{-1}): N-H benzimidazole(3321), aromatic C-H (3089,3055), aliphatic C-H (2983, 2879), C=N (1613), C=Br (765), aromatic C=C (1466,1536), ^{1}H –NMR (400MHz, DMSO – d_6) δ : 1.56 (3H, s, CH_3), 5.70 (1H, s, N-H), 3.97 (1H, s, CH),9.11 (1H, s, CH=N), 6.94-7.8 (8H, m, Ar – H). ^{13}C –NMR (400MHz, DMSO) δ : 17.4 (CH_3), 60.6 (CH), 145.7 (C=N of benzimidazole), 160.7(1H,s,CH=N),117.3 , 118.7 ,123.03, 130.4, 138.5 , 140.19

4-((((1*H*-benzo[*d*]imidazol-2-yl)ethyl)imino)methyl)phenol (2e) :Yellow crystals, yield 91%. m.p : 285 – 287°C, IRν_{max} (KBr/cm^{-1}): N-Hbenzimidazole(3265), O-H (3398), aromatic C-H (3095,309), aliphatic C-H (2852 , 2737), C=N (1625), aromatic C=C (1428-1536),

1-(1*H*-benzo[*d*]imidazol-2-yl)-N-(4-nitrobenzylidene)ethanamine(2f) :Red, yield 86%. m.p : 302 – 304°C, IRν_{max} (KBr/cm^{-1}): N-H benzimidazole(3245), aromatic C-H (3117,3029), aliphatic C-H (2962, 2807), C=N (1629), aromatic C=C (1470-1596), NO_2(1557,1338),

1-(1*H*-benzo[*d*]imidazol-2-yl)-N-(4-bromobenzylidene)-2-phenylethanamine (2g) :Yellow crystals, yield 64%. m.p : 274 – 276°C, IRν_{max} (KBr/cm^{-1}): N-H benzimidazole(3317), aromatic C-H (3109,3001),aliphatic C-H (2919, 2828), C=N (1614), aromatic C=C (1466,1547),C-Br (745),

4-((((1-(1*H*-benzo[*d*]imidazol-2-yl)-2-phenylethyl)imino)methyl)phenol (2h) :Yellow crystals, yield 76%. m.p: 285 – 286°C, IRν_{max} (KBr/cm^{-1}): N-H benzimidazole(3285),O-H (3425), aromatic C-H (3137), aliphatic C-H (2971,2876), C=N (1614), aromatic C=C (1459,1537). ^{1}H –NMR (400 MHz, DMSO – d_6) δ : 3.23 (2H, d, CH_2), 4.83 (1H, q, C-H), 5.93 (1H, s, N-H benzimidazole), 9.53 (1H, s, O-H), 8.39 (1H,s,N=C-H), 6.87-8.10 (13H,m,Ar – H). ^{13}C –NMR (400 MHz, DMSO– d_6) δ : 65.8 (C-H), 46.3 (CH_2), 159.8 (=C-H), 163.4 (C-O), 138.3 (C=N of benzimidazole), 113.3 , 117.4 , 120.5, 124.9, 128.7, 130.1 , 133.6 , 139.8 ,^{13}C-Dept 135 NMR (400MHz, DMSO – d_6) δ : 46.1(CH_2),

1-(1*H*-benzo[*d*]imidazol-2-yl)-N-(4-nitrobenzylidene)-2-phenylethanamine (2i) :Yellow crystals, yield 78%. m.p : 294– 296°C, IRν_{max} (KBr/cm^{-1}): N-H benzimidazole(3273), aromatic C-H (3097,2996), aliphatic C-H (2827, 2799), C=N (1605), aromatic C=C (1467-1553), NO_2(1530,1344),

4-(2-(1*H*-benzo[*d*]imidazol-2-yl)-2-((4-bromobenzylidene)amino)ethyl)phenol (2j):
Brown crystals, yield 83%. m.p : 290 – 292 °C, IRν_{max} (KBr/cm^{-1}): O-H(3405), N-H benzimidazole(3205), aromatic C-H (3080,3039), aliphatic C-H (2881,2962), C=N (1608), aromatic C=C (1456-1591), C-Br (740).

4-(2-(1*H*-benzo[*d*]imidazol-2-yl)-2-((4-hydroxybenzylidene)amino)ethyl)phenol (2k) :
Brown crystals, yield 81%. m.p : 304 – 306°C, IRν_{max} (KBr/cm^{-1}): N-H benzimidazole(3205), aromatic C-H (3039,3024), aliphatic C-H (2962, 2885), C=N (1608), aromatic C=C (1456-1591), O-H (3446).

4-(2-(1*H*-benzo[*d*]imidazol-2-yl)-2-((4-nitrobenzylidene)amino)ethyl)phenol (2l) :
Red, yield 64%. mp : 316 – 318°C, IRν_{max} (KBr/cm^{-1}): O-H(3410), N-H benzimidazole(3205), aromatic C-H (3039,3024), aliphatic C-H (2960 , 2897), C=N (1608), aromatic C=C (1456-1591), NO_2 (1456,1591),), ^{1}H –NMR (400 MHZ, DMSO – d_6) δ : 3.56 (2H, s, CH_2), 5.90 (1H, s, N-H), 4.47 (1H, t, CH),9.01 (1H, s, CH=N),9.54(1H,s,OH), 6.97-7.90 (12H, m, Ar – H). ^{13}C –NMR (400 MHZ, DMSO) δ : 47.4 (CH_2), 63.6 (CH), 149.7 (C=N of benzimidazole), 167.7(=CH), 157(C-O) , 153(C-NO_2), 113.3 , 117.7 ,122.03, 131.4, 137.5 , 140.19 , 143.5 ^{13}C-Dept 135 NMR (400 MHZ, DMSO – d_6) δ : 47.2 (CH_2),

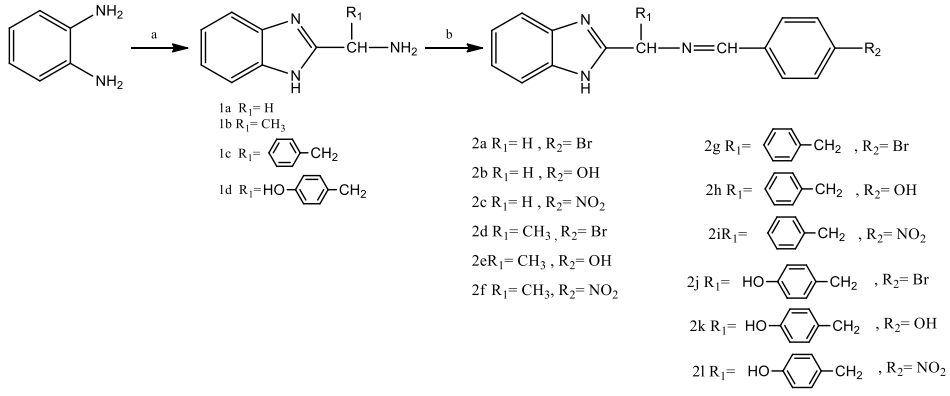

Scheme 1. Synthetic route to the synthesized compounds. Reagents and conditions: (a) Corresponding amino acids, 6N HCl, reflux(8-12)hrs; (b) Corresponding aromatic aldehyde, EtOH/2-3 drops of CH3COOH

Table 1. Physical properties of the compounds.

Comp no .	M.p (°C)	M . wt (g /mole)	M . Formula	Color	Yield %
1a	257-259	147.18	$C_8H_9N_3$	White Crysal	66%
1b	236-238	161.21	$C_9H_{11}N_3$	Brown	97%
1c	255-257	237.31	$C_{15}H_{15}N_3$	Off White	98%
1d	276-278	253.31	$C_{15}H_{15}N_3O$	Dark brown	77%
2a	287-289	314.19	$C_{15}H_{12}BrN_3$	Yellow	87%
2b	285-287	251.31	$C_{15}H_{13}N_3O$	Brown	93%
2c	293-295	280.29	$C_{15}H_{12}N_4O_2$	Brown	91%
2d	283-285	328.21	$C_{16}H_{14}BrN_3$	Brown	87%
2e	285-287	265.32	$C_{16}H_{15}N_3O$	Yellow	91%
2f	302-304	294.31	$C_{16}H_{14}N_4O_2$	Red	86%
2g	274-276	404.31	$C_{22}H_{18}BrN_3$	Yellow	64%
2h	285-286	341.41	$C_{22}H_{19}N_3O$	Yellow	76%
2i	294-296	370.41	$C_{22}H_{18}N_4O_2$	Yellow	78%
2j	290-292	420.31	$C_{22}H_{18}BrN_3O$	Brown	83%
2k	304-306	357.41	$C_{22}H_{19}N_3O_2$	Brown	81%
2l	316-318	386.41	$C_{22}H_{18}N_4O_3$	Red	64%

3. Results and discussion

In the present work, benzimidazole derivatives containing Schiff base moiety were synthesized according to the reaction scheme(1). (1H-benzo[d]imidazol-2-yl)methanamine(1a), 1-(1H-benzo[d]imidazol-2-yl)ethanamine(1b), (1H-benzo[d]imidazol-2-yl)(phenyl)methanamine(1c) and 4-(2-amino-2-(1H-benzo[d]imidazol-2-yl)ethyl)phenol(1d),1(a-d) was prepared by the cyclocondensation reaction of the *o*-pheneylenediamine and amino acids (glycine, alanine, phenyl alanine and tyrosine) in the presence of 6N HCl. The IR spectra of these compounds exhibited broad absorption bands, one of which appearing at(3125-3288) was attributed to the N-H imidazole group. And other, observed at (3336-3421) was assigned to NH_2 stretching frequency. In ^{1}H-NMR spectra of compounds 1(a,d) exhibited two different signals at(δ 8.4-8.5 ppm)which attributed to NH_2 protons and (δ 4.3-5.9 ppm)which assigned to N-H imidazole protons . The ^{13}C-NMR spectra of compounds 1(a,b) exhibited signals at(δ 140.9 – 142.3 ppm) which attributed to the(C=N) group. The Schiff bases compounds 2(a-l) was prepared by the condensation reaction of compounds 1(a-d) with corresponding aromatic aldehyde in the presence of ethanol and few drops of acetic acid .the structure of all compounds 2(a-l) was confirmed by its IR spectra and compounds 2(b,d,h,l) by ^{1}H and ^{13}C-NMR, The IR spectra of these compounds exhibited broad absorption band at (3205-3321)cm^{-1} was attributed to the N-H imidazole group and band at(1604-1629) which assigned to imine group(N=CH).In ^{1}H-NMR spectra of compounds 2(b,d,h,l), the presence of proton of N=CH group was confirmed by one proton singlet at (8.3-9.4)ppm, while signal for imidazole protons of NH group can be observed at (5.4-5.9), ^{1}H-NMR spectra revealed the multiplet at(6.6-8.1)ppm corresponding to the four aromatic protons. The ^{13}C-NMR spectra of compounds 2(b,d,h,l) exhibited signals at(δ 158.7–

167.7 ppm) which attributed to the imine group (-N=CH-),and showed signal at about (δ138.3 – 149.7 ppm) related to benzimidazole (-C=N) group, signals for benzene ring appeared at about δ 113.3 – 143.5 ppm .In ^{13}CNMR, DEPT-135 of compounds(1a,2b,2h and 2l)show negative signals at around (44.4 – 47.2) for CH_2 group.

4. Antibacterial activity

The disk diffusion method was used to screened antibacterial activities of the some compounds synthesized herein against different strains of Gram-positive bacteria namely (*Staphylococcous aureus*, *Bacillus subtilis*) and Gram-negative bacteria (*Pseudomonas aeruginosa*, *Escherichia coli*) The compounds were tested at concentration of (10 mg /ml and 100 mg /ml). The zone of inhibition was measured in millimeters and was compared with reference standard antibiotic namely ampicillin and ciprofloxacin. The test compounds were dissolved in DMSO to obtain solution of different concentration. The results of antibacterial activity of the synthesized compounds are listed in (table 2) which demonstrate that most of compounds displayed significant activities when compared with the standard antibiotic ampicillin and ciprofloxacin .The antibacterial activities of the test compounds are shown briefly below .

1. The compounds (1a, 2a,2f, 2g, 2k) showed high activity against B. subtilis bacteria.
2. The compounds (2a,sf,2g,2k) showed high activity against E. coli bacteria.
3. The compounds (2a,2g,2k) showed high activity against P. aeruginosa bacteria.
4. The compounds (1a,2a,2g,2k) showed good activity against S.aureus bacteria.

Table 2 . Antibacterial activity of synthesized compounds

Comp no.	Concentration (mg / ml)	Zone of inhibition (in mm)			
		Gram-positive		Gram-negative	
		S. aureus	*B. subtilis*	*P. aeruginosa*	*E. coli*
1a	10	11	10	10	13
	100	17	19	12	14
1b	10	12	12	-	-
	100	10	13	11	-
2a	10	14	22	29	25
	100	15	13	12	-
2f	10	14	20	13	23
	100	-	21	-	20
2g	10	15	28	20	22
	100	15	11	-	-
2l	10	14	12	12	13
	100	12	11	15	11
2k	10	16	24	22	27

1c	100	13	12	15	13
	10	11	15	15	16
	100	9	12	11	-
Ampicillin		22	23	-	10
ciprofloxacin		19	23	29	-
DMSO solvent		0	0	0	0

Conclusion

Series of new Schiff base attached to benzimidazole ring have been synthesized successfully by condensation reaction between (1H-benzo[d]imidazol-2-yl)methanamine, 1-(1H-benzo[d]imidazol-2-yl)ethanamine, (1H-benzo[d]imidazol-2-yl)(phenyl)methanamine and 4-(2-amino-2-(1H-benzo[d]imidazol-2-yl)ethyl)phenol with a various of aromatic aldehydes. The compounds (1a, 2a,2f, 2g, 2k) showed high activity against *B. subtilis* bacteria, compounds (2a,sf,2g,2k) showed high activity against *E. coli* bacteria, compounds (2a,2g,2k) showed high activity against *P. aeruginosa* bacteria and compounds (1a,2a,2g,2k) showed good activity against *S.aureus* bacteria.

References

[1] Sawhney S, Vir D, and Kumar P 1989 *Indian. J. Chem.* B **28** 574 - 578
[2] Ibrahim E, Omar A and Khalil M 1980 *European J. Pharm. Sci.* **69** 1348 - 1350
[3] Fatma N, Murthy P and Kumar S 1988 *Indain J. Pharm. Sci.* **50** 265 - 268
[4] Morinaga H, Yanase T and Nomura M 2004 *Endocrinology*. **145** 1860 - 1869
[5] Freeman G, Selleseth D and Rideout J 2000 *Nucleosides, Nucleotides Nucleic Acids* **19** 155 - 174
[6] Ates-Alagoz, Z, Alp M, Kus, C,Yilidiz S, Buyukbing, E andGoker H 2006 *Arch. Pharm. Chem. Life Sci.* 3**39**
[7] Lazer E, Farina P and Oliver J 1987,*Agents Actions*. **21** 2057 - 2059
[8] Jiang S, Meadows S and Anderson S 2002 *Antimicrob. Agents Chemother.* **46** 2569 - 2574
[9] Niel M and Smith M,Heckelman 2001 The Merk Index, 13th ed. Merk Co. Inc. , New Jersey , p.10074
[10] Ansari K and Lal C 2009 *Eur. J Med. Chem.* **44** 4028 - 4033
[11] Vigato P and Tamburini S 2004 *Coord. Chem. Rev*. **248** 1717-2128
[12] Vicini P, Geronikaki A, Incerti M, Busonera B, Poni G, Cabras C and IaColla P 2003 *Bioorg. Med. Chem.* **11** 4785-4789
[13] Sondhi S, Singh N, Kumar A, Lozach O and Meijer L2006 *Bioorg. Med. Chem.* **14** 3758-3765
[14] Tarafder M, Kasbollah A, Saravan N,Crouse K, Ali A and Tin O 2002 *J. Biochem. Mol. Biol. Biophys.* **6**85
[15] Hui-Ming L, Tan S, Li H, Song Y, ZhuH and Tan R 2007 *Eur. J. Med. Chem.* **42** 558-564
[16] Cheng K, Zheng Q, Hou J, Zhou Y, liu C, Zhao J and Zhu H 2010 *Bioorg. Med. Chem.* **18** 2447-2455
[17] Cheng K, Zheng Q, Qian Y, Shi L, ZhaoJ and Zhu H 2009 *Bioorg. Med. Chem.* **17** 7861-7871
[18] Kucukguzel I, Kucukguzel S, Rollas S, Sanis G Ozdemir O, Bayrak I, Altug T and Stables J 2004 *Il Farmaco* **59** 839
[19] Liu G, Liao J, Huang S, Shen G and Yu R 2001 *Anal. Sci.* **17** 1031-1036

[20] BhartiShailendra N, Gonzales Garza M, Cruz-Vega D,Castro-Garza J, Saleem K, Naqui F, Maurya M and Azam A 2002 *Bioorg. Med. Chem. Lett.* **12** 869-871.
[21] Raman N, Selvan A and Manisankar P 2010 *Spectrochim. Acta* A **76** 161-173
[22] Namani V,Goud B, Kumart Y, Kumbham R, Balakrishna K and Bhima B 2015 *Asian J. Chem*. **12** 4575 – 4578
[23] Ajani O, Aderohunmu D, Olorunshola S, Ikpo C and Olanrewaju I 2016 *Orient. J. of Chem*. **32(1)** 109 – 120

Acknowledgment
The authors express their thanks and appreciation to Department of Chemistry, College of Education, Samara University, as well as Department OF Chemistry, College of Education for pure sciences, Diyala University for their support and assistance.

Fire retardancy assessment of polypropylene composite filed with nano clay prepared from Iraqi bentonite

Fire retardancy assessment of polypropylene composite filed with nano clay prepared from Iraqi bentonite

Watheq Kareem Salih

Directorate of Materials Research – Ministry of Science & Technology- Baghdad – Iraq

Corresponding Email: alwathiq316@yahoo.com

Abstract: Fire retardants have an extraordinary importance because of their role in saving the people, property and reducing the damages and minimizing the dangers resulting from fires and burning of polymeric composites which are used in different civil and industrial fields. The work in this paper can be divided into two main stages. In first one nano-clay was manufactured from Iraqi bentonite and it was characterized using AFM, XRD, XRF, SEM, and BET. The AFM test showed the particle size of prepared nano clay was about 99.25 nm. In the second stage, polypropylene/nano clay composites at three low loading percents (0%,2%,4%,6%) were formulated via twin screw extruder. The fire retardancy tests included burning rate according to ASTM:D-635 and maximum flame height of flame according to ASTM:D-3014. Besides, the mechanical tests and thermal behavior of prepared samples were investigated. The results showed that (4%) of nano-clay had the maximum fire retardancy and while at (2%) loading, the maximum value of tensile strength and Yong modulus were obtained. The maximum heat of fusion was recorded for 6% nano clay sample. The final results assessment confirmed on the possibility of using low loadings of prepared nano clay to improve the fire retardancy, mechanical and thermal properties successfully.

Keywords: nano clay, Iraqi Bentonite, polypropylene, fire retardancy, burning rate, polymer composite

1. Introduction

No one could imagine the world without polymeric products. This important sector occupies very outstanding ranking in all industrial, civil and domestic fields. The world demand increases annually. In general, polymers are divided into two main categories thermoplast and thermoset. The polymeric compounds are characterized by a macromolecular structure which is either amorphous or semi-crystalline. Polypropylene (PP) is one of the most important semi-crystalline thermoplast types which is used extensively in many fields for different applications. The annual global need of polypropylene was about 83 million metric tons in 2013 and the expectations of experts

indicate that the expected global demand will increase rapidly to reach 126 million metric tons in 2023[1].

Polypropylene (PP) is a downstream petrochemical product that is derived from the olefin monomer propylene. The polymer is produced through a process of monomer connection called addition polymerization. Polypropylene is a vinyl polymer in which every carbon atom is attached to a methyl group and can be expressed as shown in 'figure 1' [2].

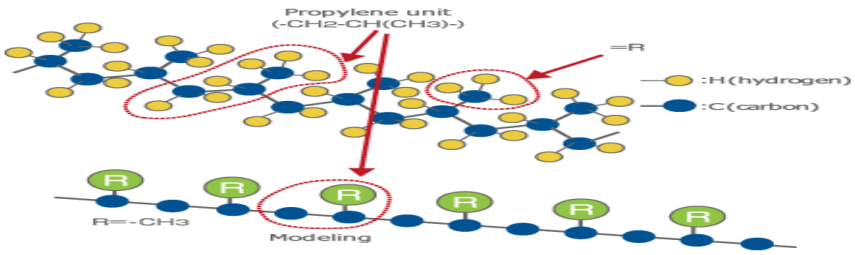

Figure 1 Structure of polypropylene [3]

Polypropylene (PP) is a commodity polymer which offers a combination of outstanding physical, chemical, mechanical, thermal and electrical properties not found in any other thermoplastic [4].Besides, polypropylene is easy to formulate using extruding or molding methods. In spite of these characteristics, PP like other polymers, its resistance against flame and fire is very weak and it is classified as sever flammable one. This drawback of PP limited its role in some products and that provokes the researchers and scientists to improve the flame retardancy of polymer for several decades. In the twentieth century, they used the micro size of different materials, metal oxides, hydroxides, halogens and phosphate-based retardants and the efforts continued in this field. But to achieve a good retardant performance, it must be used high loading of these materials. Typically filler levels required are between 20% - 60% by weight, but lower levels may be acceptable in combination with more effective alternative fire retardants or where the purpose of their inclusion in a formulation is principally to aid smoke suppression [5].The high loadings of micromaterials have negative effects on other properties like mechanical, optical and thermals ones.So, the efforts were focused on finding high-performance fire retardants which their crucial role in saving the people souls and properties using small amounts.

With appearing nanomaterials and the huge developments in synthesis methods and applications, the fire retardants come in a new era. The scientists do their best to develop and to manufacture new polymeric composites filled with nanofillers of different substances which were used previously in micro size. One of the famous nanomaterials using extensively is the nano-clay.

The possibility of manufacturing nano-composites materials with tailored properties at low cost has gained much interest. In fact, there is already more than two decades of research on those materials. Particular interest has been paid to clay nano-platelets and their composites with non-polar thermoplastic polyolefin matrixes, namely polypropylene (PP)[6]

Nano clay is belonged in most cases to Montmorillonite type of clay. Montmorillonite is a 2:1 type consisting of two silicon-oxygen sheets held together by intervening cations with water molecules in the interlayer spaces1. Two outer tetrahedral layers which contain Si and O atoms are fused with an inner octahedral layer containing Al and Mg atoms which are bonded to oxygen or hydroxyl group. Individual clay particle has “platey” structure with a lateral dimension of 200 to *600* nanometers and thickness of only 0.96 nm. These layers organize themselves to form stalks by Vander walls force of attraction between them. The attraction force between layers is relatively weak so polymer molecules can be

intercalated between them so in pristine form, clay is hydrophilic (platelets contain Na^+ or k^+ ions) [7], [8], [9]. The structure of bentonite clarifies in figure 2. Using this type of clay in synthesis nano clay can be attributed to its characteristic properties. The methods of preparation nano-clay are varied

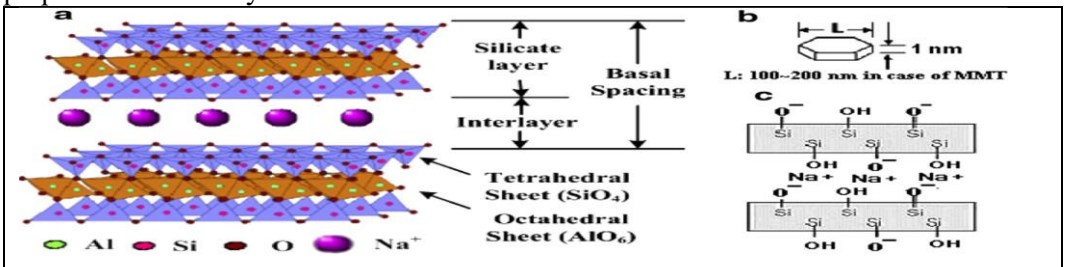

Figure 2 Structure of bentonite clay [10]

1.1 Polymer combustion process mechanism:

Natural and synthetic polymers, when exposed to a source of sufficient heat ,will decompose or 'pyrolysis' evolving flammable volatiles. These mix with the air and, if the temperature is high enough, ignite [11]. The polymer combustion is characterized by a complex combination of condensed and gas phase phenomena. Every phase consists of sets of complex reactions with heat and mass transfer processes [12], [13]. The complex reactions of polymer combustion process in both phases are shown in 'figure3'.

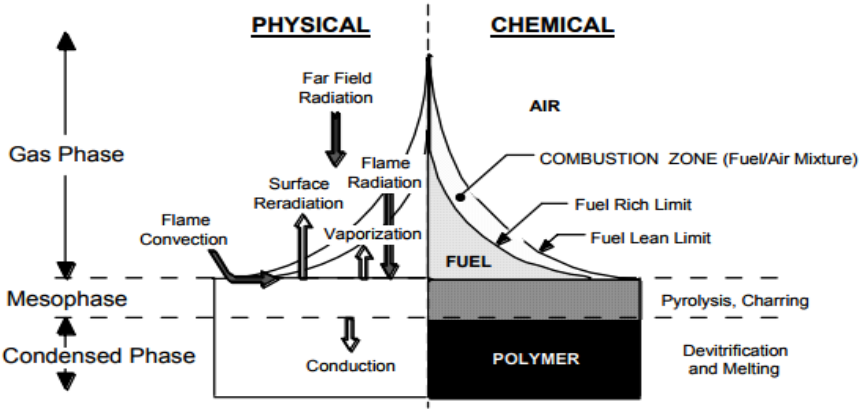

Figure 3 Polymer combustion process mechanism [14]

1.2 Mechanisms of nano-clay fire retardants:

In general, the mechanisms of fire retardants materials either micro conventional retardant or nanomaterials are still unsolved issues in spite there is a huge number of scientific papers dealing with this subject. Thus, what is suitable for specific polymer group it may not effective with other kinds .there are different explanations and opinions but there is no fully understood or complete mechanism valid for all polymers till now.

In previous, the general mechanisms of fire retardants are explained in details [15]. But nanomaterials mechanisms need to interpret depending on their characteristics which particle size of nanomaterials plays a very crucial role besides other properties. But, the proposed mechanisms of nano-clay retardancy performance will be explained

1. Migration mechanism. It is hypothesized that migration of clay particles to the surface of the matrix polymer occurs during burning [16].It is believed that the clay is pushed by the numerous rising bubbles of degradation products and the associated convective flow in the melt from the interior of the sample toward the sample surface, while the matrix polymer because of the pyrolysis with dewetted clay particles are left behind. Further, aggregation of clay layers occurs after the degradation of the organic treatment on the clay interlayers, which makes the clay more hydrophilic and less compatible with the matrix polymer, and thus leads to a clay-rich barrier that slows the rate of mass loss [17]
2. Barrier mechanism: it is a well-accepted mechanism in the condensed phase during burning. It suggested that, under pyrolysis conditions, the clay forms a char-like material that acts as both a barrier to the mass transport of the degradation products to the surface of the degrading polymer and a thermal barrier as in figure 4, preventing additional exposure of the polymer matrix to the heat and oxygen. The barrier function of the clay platelets can provide thermal insulation for the condensed phase and thus increase the thermal stability of the matrix polymer [17],[18]
3. Paramagnetic radical trapping mechanism: It assumes that the structural metals in the clay (especially iron) trap the radicals that form during the polymer degradation, thus slowing down the degradation reaction. This mechanism has an important role with the low loading of nano-clay.[19],[20]

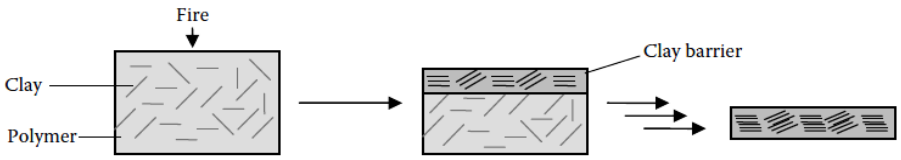

Figure 4 the nano-clay barrier mechanism [17]

Nano cay as fire retardant has been used extensively with different polymers types .table 1 shows the published papers in recent years:

Table 1 Previous published works

	Polymer matrix	Refernces	Notes
Nano clay	Poly (methyl metha- acrylate) PMMA	[21]	
	Boron - Phenolic resins	[22]	
	EVA and LDPE	[23]	
	Epoxy	[24]	
	Polypropylene	[25]	Till 20% loadings
	Polystyrene	[26]	
	polyurethane/polypropylene	[27]	
	vinylester	[28]	
	High-density polyethylene and wood flour composites	[29]	

The aim of present work is to prepare and to characterize a nanoclay from Iraqi bentonite using acid activation method.Besides, nanoclay /polypropylene composite with different loadings are synthesized and the mechanical, thermal and fire retardancy properties are assessed.

2. Experimental Work

2.1 Chemicals & machines :

2.1.1 *Iraqi raw bentonite*: the chemical composition of this clay as in table 2 :

Table 2 chemical composition of Iraqi raw bentonite

Composition	**SiO_2**	**Al_2O_3**	**TiO_2**	**Fe_2O_3**	**CaO**	**MgO**	**K_2O**	**Na_2O**	**Others**
%mass	57..4	17.9	1.6	8.9	5.5	3.5	1.57	1.5	2.13

2.1.2 *Hydrochloric acid* : (36.4) conc. (BHD company), England

2.1.3 Polypropylene: the PP was used in this work was provided by Sabic company (KSA). Its density is 0.902 g/cc and melting flow is 3g/10 min at 2.16 kg load at 230˚C. The process temperture is 235-250 ˚C.

2.14: *Twin screw extruder* (RD11- 100 – 0254) was used to mold the samples. It is Chinese type with 20/25 L/D and motor speed 0-100 RPM. It has three thermal processing 180, 220, 250 C

2.1.5 *Assistant apparatuses*: magnetic stirrer (Chinese), Dry oven (England), tubular furnace (Chinese) thermal press (Chinese)

2.1.6 glassware with different measurements and shapes and filter papers

2.2 Nano clay preparation:

The Iraqi bentonite had been crashed and milled by using mill till fine powder had been obtained.Then clay powder was sieved and 53 microns had been chosen. The 2M hydrochloric solution was prepared and bentonite was added gradually to the solution and mixing for 2 hours using magnetic stirrer.After mixing duration, the solution was filtrated using vacuum filtration. The obtained precipitation was left for 72 hours to dry at room temperature. Then it was calcinated in a tubular furnace for 2 hours at 600 ˚C. The calcinated powder was milled and stored in a sealed desiccator for testing and characterization.

2.3 Nanocomposite synthesis :

Firstly, prepared nanoclay was mixed with polypropylene granules with the different clay loadings(0%,2%,4% and 6% wt.) with sample code (PNC0, PNC2, PNC3, and PNC4) respectively.The nanoclay/PP mixture was extruded using twin screw extruder (180-250 ˚C). The molten has molded in the template with dimensions (20 cm x 10 cm x4 cm) and thermally compressed (10 bar for 10 min). The sheets left for 24 hours at room temperature to dry. Then, the samples were cured in drying oven at 75 ˚C for 2 hours. Then the nanocomposite samples formulated in different shapes and dimensions according to the requirement of every test.

3.Tests and characterization:

3.1 Structural & phase characterization:

The X-ray diffraction (XRD) measurements of the clay samples were recorded with XRD-6000, Shimadzu, Japan equipped with Ni-filtered CuKα radiation (λ = 1.5418 Å) and operated at 40 kV and 30 mA. The diffractograms were recorded in the range of 2θ from 3˚ to 20° at a speed rate of 5 degrees/min. while elemental analysis was conducted using X-ray Fluorescence (XRF) , S2 PUMA Single model , Bruker , USA

3.2 Thermal analysis:
Differential Scanning Calorimetry (DSC) of samples (0%, 2%, 4%, 6%) were performed using DSC TA60,Shimadzu , Japan , with a scanning rate of 10 ˚C/ min. in air atmosphere with temperature range 20 -250 ˚C to assess their thermal behaviour and morphology.

3.3 *Mechanical performance*:
tensile properties of composite samples were investigated using mechanical testing machine (H50KT model, Tinius- Olsen, UK)

Particle size estimation:
Particle size measurements id done using (AA3000 Scanning Probe Microscope Angstrom Advanced Inc, USA) to specify the nano size of prepared nano clay

3.5.Morphology:
the topography of nanoclay and micro bentonite was investigated using scanning electronic microscopy (SEM) (Vega3 model, Tuscan, Czech Republic)

3.6.Specific surface area:
the specific surface area and tests of nanoclay & bentonite were calculated using BET method .the test was conducted using surface area analyzer (SA-9600, Horiba company, USA)

3.7.Hardness:
microhardness (Vicker method) : composite samples were tested using Microhardness tester (MODEL HV-1000A, JINAN Co., China).The applied force was 0.5N for 20 seconds.

3.8. Limited oxygen index (L.O.I):
defined is the minimum Oxygen amount requited to combustion of the polymer or composite.It is expressed as a percentage of O2 concentration.The test is done according to ASTM D2863.

3.9. The rate of Burning (RB):
the burning rate was measued according (ASTM-D 635- *03)*. The test was conducted for three specimens for each sample .the specimen dimension was (100 mm L*13 mm W * 4 mm Thick)

3.10 Maximum flame heigh test(H):
the test is done according to (ASTM D 4804) using metal ruler The test was conducted for two specimens for each sample. Specimen dimension was (100 mm L*10 mm W * 4 mm Thick.)

4.Results & Discussion:

4.1 Nano clay characterization:

4.1.1 Phase & structure characterization:
figure 5 shows the effect of acid treatment on the structure of prepared nanoclay. The comparison between Xray patterns of pristine bentonite without treatment and prepared nanoclay shows that there was a shift in angle occurred between both patterns. Pristine bentonite has a characteristic peak at (2θ=6.7˚ & d001=13.1111˚˚A) whilst nanoclay has characteristic one at (2θ=3.54˚ & d001=24.83˚A). This shift to smaller angle with increasing in d-spacing between interlayers revealed that the distances between clay interlayers

(galleries) of the bentonite were expanded due to the acid and thermal treatments .It is indicated that intercalated structure is formed .This expansion helps the polymer to exfoliate completely or partically with clay. This is in agreement with results obtained by [7], [9],[10],[30]. While the elemental analysis of prepared nano clayshowed some oxides were disappeared as shown in table 3.

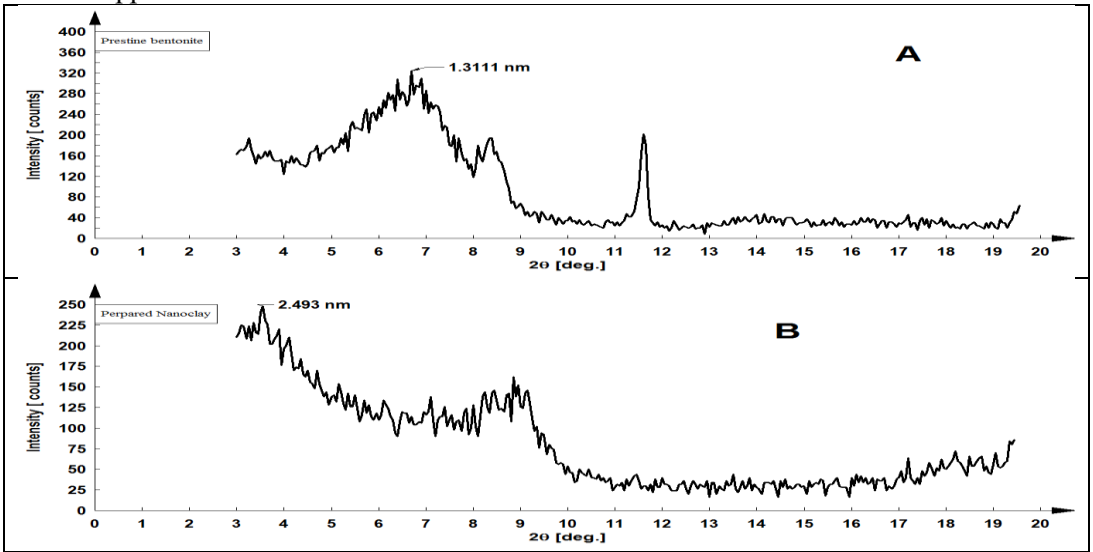

Figure 5 XRD patterns A. Prestine bentonite B. Prepared nano-clay

Table 3 chemical composition of prepared nano clay

Composition	SiO_2	Al_2O_3	TiO_2	Fe_2O_3	CaO	MgO	K_2O	Na_2O	Others
%mass	67.78	16.48	1.336	7.483	2.034	3.485	0.5485	0.227	0.627

4.1.2 Particle size measurement:

The results of particle size (AFM) test showed that the size of prepared clay particle is in the range 70-130 nm and mean diameter is 99.29 nm as shown in figure 6.

Diameter nm	70 nm	80 nm	90 nm	100 nm	110 nm	120 nm	130 nm	Total	Mean Diameter nm
Volume %	7.58	12.12	15.15	15.15	15.91	14.3	19.7	100%	99.29

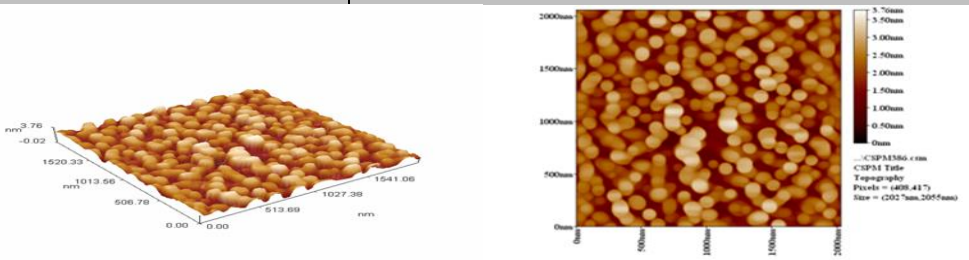

Figure 6 particle size & morphology of prepared nanoclay

4.1.3 Surface area:
surface area results showed the strong effect of synthesis process on surface area values. There is a big difference in surface area between pristine bentonite and prepared nanoclay where the surface area of clay changed from **11 m^2 /g to 60 m^2/g** for pristine bentonite and nanoclay respectively the improvement is about 450%.

4.1.4 .Morphology investigation : The SEM images are listed in figure 7 for both types :

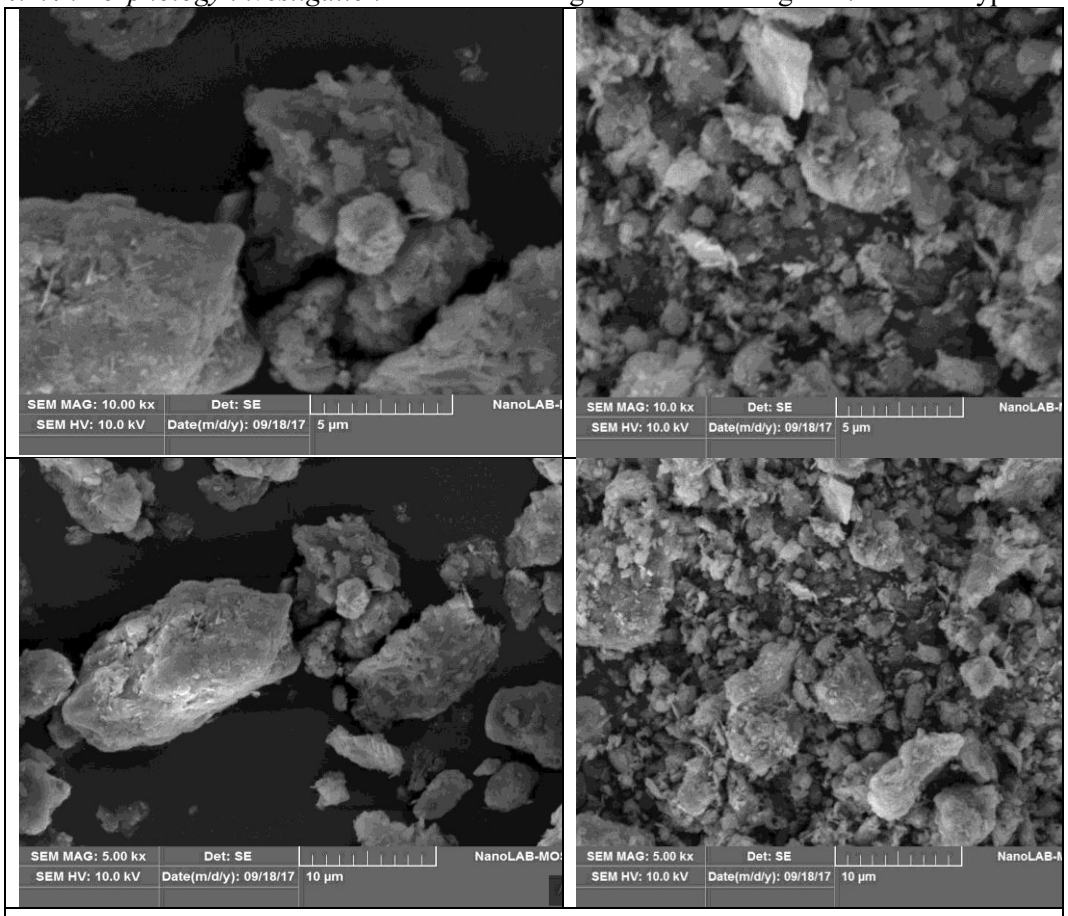

Figure 7 SEM images of pristine Bentonite (left) and nanoclay (right)

The SEM image showed the differences in particle size of pristine (Left) and nano clay (right) at two magnifications (5 kx ,10 kx). The shapes of both types are disorder structural shapes with different sizes which is can be attributed to milling effect in the final step of the preparation process. The disorder of shapes as a result of milling was indicated by Adham et al. [31].

4.2. Polypropylene/ nano clay Composite characterization

4.2.1 Thermal analysis:
the results of thermograms of composite samples showed that change in melting point is not big. The changes were about 5 ˚C from 160 to 165 but the clear changes were detected in heat of fusion for different loading samples. The nanoclay contributed to improving the crystallinity leading to increasing the heat of fusion. The results are shown in 'figure 8'.

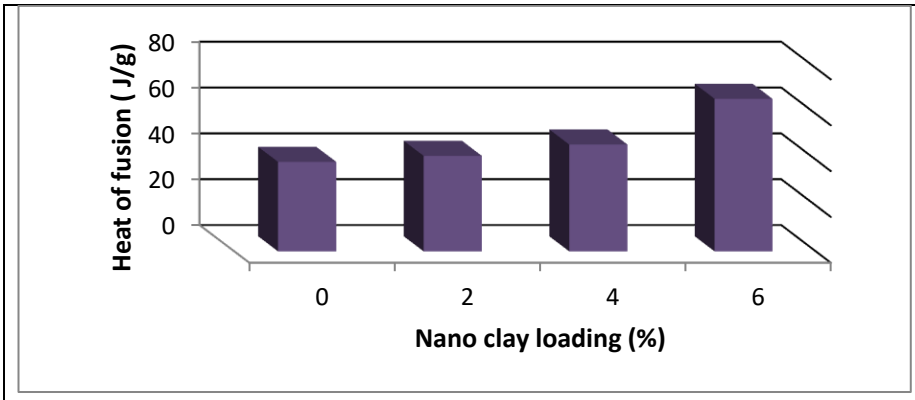

Figure 8 Heat fusion of composite samples

4.2.2. Mechanical behavior:

the results of the tensile test were conducted for composite samples. The results showed that the mechanical properties (Tensile stress& modulus) improved at 2% loading. But with increasing clay loadings, these properties reduced.as shown in 'figure 9'.

Test \ Sample code	PCN0 (0%)	PCN2 (2%)	PCN4 (4%)	PCN (6%)
Tesile stress (MPa)	2196	28.41	24.16	23.71
Tensile modulus (Mpa)	307	398	376	334

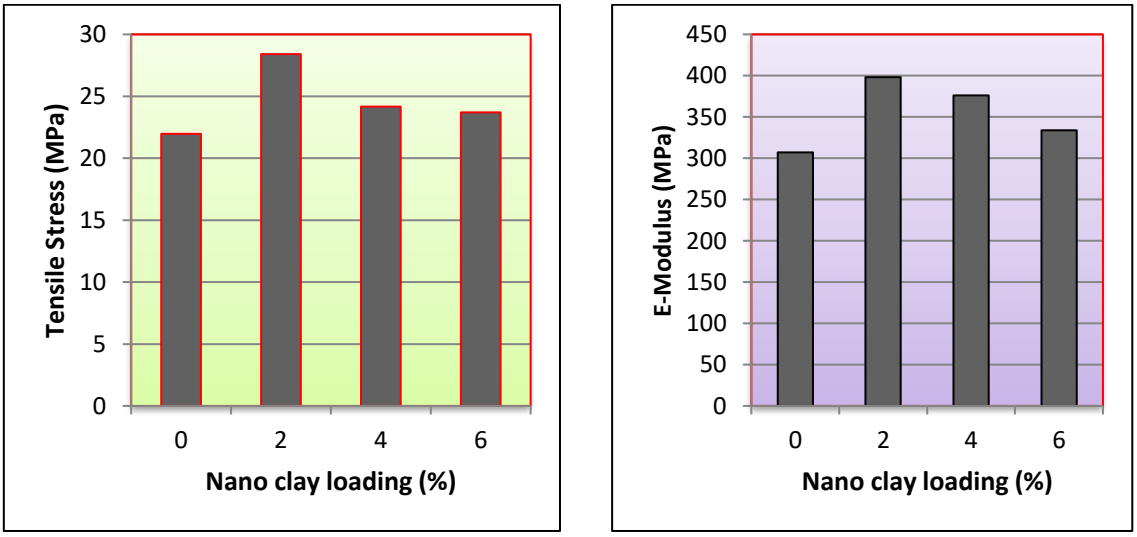

Figure 9 Mechanical tests Left – Tensile test Right- E-modulus

The improvement in mechanical properties (tensile stress & modulus) of nano-clay/PP composite samples compared with virgin PP. can be explained depending on two main factors. Firstly, the extended basal spacing of nano-clay layers (as shown in XRD tests), high aspect ratio and surface area help the intercalation between clay particles and polymer matrix leading to good interfacial connections and to completely or partially exfoliation. Secondly, nano-clay particles have good stuffiness property and when these particles

existed in polymer- particle interface enhance the resistance of composite against external stresses and preventing the sliding and movement of the polymer matrix as a result of a mechanical load applied.

The reducing in tensile stress and modulus with increasing nano-clay concentration can be attributed to two factors. First of all, the agglomeration of nanoparticles which contributes to reducing surface area so the exfoliation and interaction between clay interlayers and polymer chains become weak and poor. Second, the decreasing in the mechanical properties is because of the increasing nano-clay particulate-particulate interfaces instead of polymer- particulate interfaces. This is compatible with the interpretations and results of many researchers who they assured on these facts in their published papers[32],[33],34],[35]

4.2.3 Microhardness (Vickers method):

the results of microhardness tests showed the improvement effect of nanoclay additions on hardness values. The results are listed in table 4.

Table 4 Micro-hardness values

Nanoclay loading	**0%**	**2%**	**4%**	**6%**
Hardness (hv)	33	46	62.3	76.8
% Improvement	-	39.39%	88.78	132.7

The values of hardness increased with nanocaly concentration increasing. The maximum value was recorded for 6% wt. which was 76.8 hv and the improvement percent is about 132.327%.This means polymeric composite resistance to deformation increases with loading increasing because of nanoparticles which working on restraining the movement of polymer chain during the deformation process.

4.3. Fire retardancy tests & assessment :

4.3.1 Limited Oxygen Index (L.O.I) :

this test is a good indication about composite flammability. The results are shown in table 5. It is shown that all samples with different loadings needed Oxygen higher than what virgin PP sample (PCN0) needed. This means that nanoclay additions contributed to sustaining the flammability of polymer.

Table 5 Limited Oxygen Index test results

Sample code / Test	**PNC0**	**PNC2**	**PNC4**	**PNC4**
L.O.I	17.67	18.75	20.85	19.28
% improvement	-	6.1 %	17.99%	9.1%

4.3.2. Rate of Burning (RB): it is measured mm/min.uusing to Eq. according to ASTM: D635

$$RB=60\ X/t \qquad \text{---- (1)}$$

Where: X = burned length of specimen and t =burning time (S)

Depending on the results of the test which are listed in figure 10, the burning rate (RB) of prepared samples were varied with nano clay loadings but it is noticed that all loadings

contributed to reducing the rate of burning compared with the pure sample. But the maximum reducing of RB is recorded for PCN4 (4% wt. loading) where the improvement is about 41% compared with pure PP (PCN0)) .it was noticed that burning was slow on contrary to the burning of the pure sample which was fast and strong. The efficiency is followed the next order

PNC0> PNC2 > PNC6> PNC4

Reducing in RB

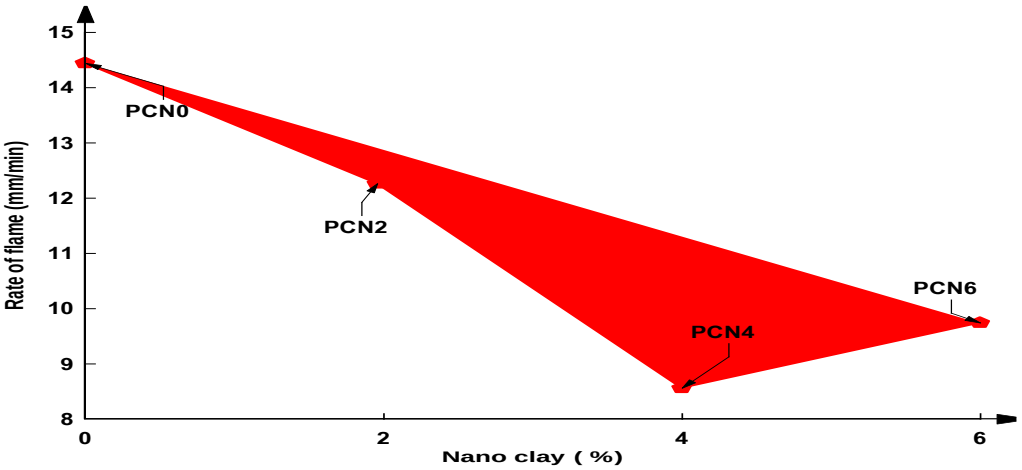

Figure 10 Rate of burning

4.3.3. The ignition time or flame exposure time:
is defined that time required to initiate burning process of the polymer sample.The results are clarified in table 6. The longest time was recorded for PNC4 is about (51s) compared with the time required to initiate burning process of virgin PP (PNC0) was (23 s). The improvement was about 121.7%

Table 6 Ignition time results

Sample code / Ignition time	PNC0			PMC2			PNC4			PNC6		
Exposure time	21	23	25	35	34	36	50	51	52	41	42	41
Mean exposure time	23			35			51			41.3		
% delay improvement	-			52%			121.5			79.6		

4.3.4. Maximum flame height (H):
The results showed the positive role of nanoclay loading on minimizing flame height. Different responses were recorded for different loadings but minimum height was recorded for PCN4 (4%) which was about 8.5 cm compared with the flame height of pure PP which was about 16 cm. Samples efficiency is following the next order and the results are shown in figure 11

PNC0> PNC2 > PNC6> PNC4

Minimizing in flame height

4.3.5. First melt drip time:

it defined as the time required falling down the first drip of the polymeric composite after the glowing process. The results are shown in figure 12 for horizontal and vertical burning tests. The values showed that nano clay loading contributed to increasing the time required for first melt drip. All loadings have a positive effect on delay falling down of drips compared with the pure sample without additions. The PNC4 (4%) recorded the longest time compared to others according to following order:

PNC0< PNC2< PNC6< PNC4

First melt drip time increasing

The polymers with low glass transition temperature melt in time shorter than those polymers with high Tg. The PP has very low Tg (-26 ℃) (josef 2015).When pure PP is subjected to flame , it will decompose and producing short chains with low viscosity because of random cleavage chain of PP structure .The nano clay additions to PP sustain the dripping via changing the viscosity of molten and it becomes more viscous and this leading to increase the time required for falling down first melt drip.

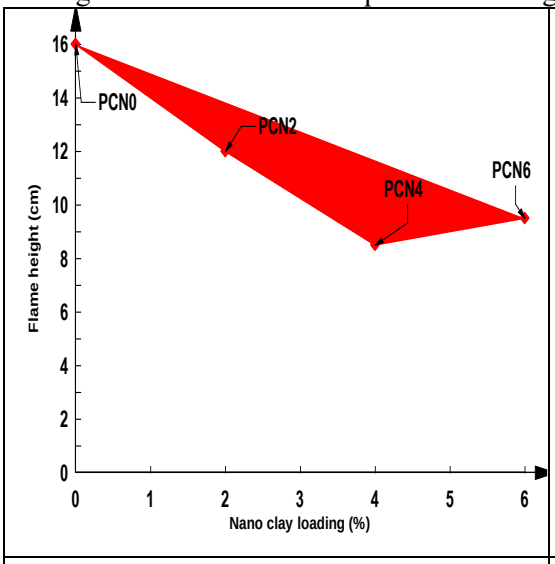

Figure 11 Flame height results

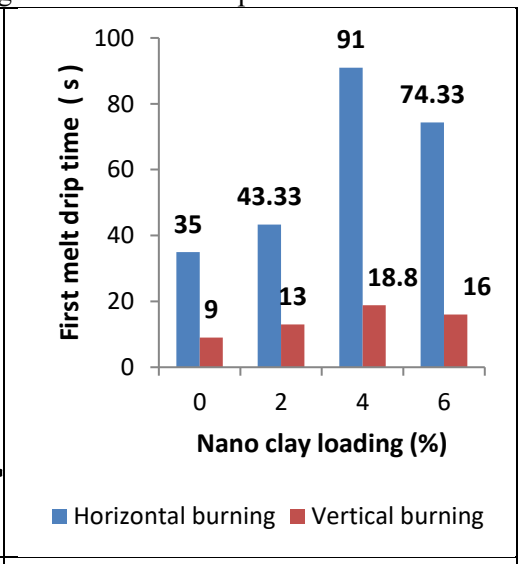

Figure 12 first melt drip time

Depending on the results of thermal and fire retardancy tests in above, it is noticed that nanoclay additions to PP composite have a positive impact on improving the flame retardancy performance compared with virgin PP. The improvements in thermal and fire properties can be attributed to more than a cause. First of all, migration mechanism with barrier played an important role to enhanced retardancy property of the PP/nanoclay composite especially the char formation mechanism do not work well with olefinic polymers which their degradation process depending on scission chains and volatilization processes.

The effect of insulating layer and effect of nanoclay particles is clear from results of L.O.I test and other tests which are mentioned above especially the time of burning increased with increasing clay loadings and the high of flame is shorter than in virgin PP because the clay particles sustained on scission and volatilization processes and making the degradation to be slower.Secondly, the chemical composition of used bentonite contained

on iron metal (7.483%) as shown in table3) . the iron existence led to pragmatic radical reactions which worked to make mass transfer slower.

The deterioration in fire retardancy when the nanoclay loading is more than 6% can be attributed to the agglomeration of particles during manufacturing process

4. Conclusions:

The assessment of results in this work shows that the possibility of synthesis nanoclay from Iraqi bentonite and using it as a fire retardant for polypropylene composites. The results clarified that mechanical properties (tensile stress & modulus) are improved and the maximum value at 2% loading. The thermal & fire test showed the positive role of nanoclay additions on these properties. The results of limited oxygen index, flame rate, height of flame, ignition time and first drip tests indicated to the role of nanoclay in the improvement. The result of 4% loading was the best among all samples relating to fire retardancy. Thermal properties are improved and heat of fusion increased with nanoclay increased

6. Recommendation:

1-Testing nano-clay loadings more than 6% to assess their fire retardancy
2-Testing the effect of using different surfactants on nanoclay particle size and on fire retardant properties

References

[1] Lewandowski S., 2014, Global olefins:cost,demand, prices and trade, HIS association report, London,UK
[2] Maddah H.,2016, Polypropylene as a Promising Plastic: A Review, *American J. Polym .Sci.* , **6** (1): 1-11, doi:10.5923/j.ajps.20160601.01
[3] http://www.primepolymer.co.jp/english/technology/material/pp/03.html
[4] Ahmad S.R.,.Young R. J., and Kinloch J. A.,,2015, Raman Spectra and Mechanical Properties of Graphene/Polypropylene Nanocomposites, *Inter. J. Chem. Eng. Appl*.,**6** (1):1-5
[5] Wilkie C. A. and Morgan A. B.,2010, Fire Retardancy of Polymeric Materials, 2nd CRC publisher,
[6] Azza M. M. (2012). Polypropylene Nanocomposites, Polypropylene, Dr. Fatih Dogan (Ed.), InTech Publisher, Rijeka, Croatia
[7] Bhattacharya S.S. and Aadhar M.,2014, Studies on Preparation and analysis of Organoclay Nano Particles, *Res. J.. Eng. Sci.,* **3** (3): 10-16,
[8] Uddin F.,2008, Clays, Nanoclays, and montmorillonite minerals, *Metal. Mat. Trans. A* ,**30** (12): 2804–14, DOI: 10.1007/s11661-008-9603-5
[9] Manocha S., Patel N. and Manocha L.M.,2008, Development and Characterisation of Nanoclays from Indian Clays, *Def. Sci. J*., **58** (4): 517-24
[10] Motawie A.M., Madany M.M., El-Dakrory A.Z. , Osman H.M., Ismail E.A. , Badr M.M., El-Komy D.A., Abulyazied D.E.,2014, Physico-chemical characteristics of nano-organo bentonite prepared using different organo-modifiers, *Egy. J. Petr*., **23**: 331–38
[11] Horrocks A R and Price D.,2001, Fire retardant materials, Woodhead Publishing, Cambridge,UK
[12] Kashiwagi T., 1994, Polymer combustion and Flammability –role of the condensed phase, 25th Int. symp. Combustion :1423-37, California, USA
[13] Beyler C. and Hirschler M., 2002,Thermal decomposition of polymer , SFPE Handbook of Fire Protection Engineering, 3rd ed.,IEEE, USA

[14] Lyon, R. E., and Janssens, M. L. (2005). Polymer Flammability, U.S. Dep. Transp., Fed. Avi. Admin., Office Avi. Res. , Washington, USA
[15] Hashim A. A., Salih W. K. and Jameel N. J. , 2016, Preparation and Performance Testing of Nano Titanium Dioxide as Fire Retardant of High Density Polyethylene Composite, *Int. J. Cur. Eng. Tech., 6* (4):1104-9
[16] Clerc L., Ferry L., Leroy E., and Cuesta, J.M., 2005, Influence of talc physical properties on the fire retarding behavior of (ethylene-vinyl acetate copolymer / magnesium hydroxide/talc) composites, *Polym. Deg. Stab*., 88, 504-11.
[17] Wilkie C A. and Morgan A. B. ,2010, *Fire Retardancy of Polymeric Materials,* CRC Press, USA
[18] Visakh P.M. and Arao Y., 2015, *Flame Retardants Polymer Blends, Composites and Nanocomposites,* Springer, Switzerland, DOI 10.1007/978-3-319-03467-6
[19] Jimenez P. E. S., Maqueda L. A. P., Perejon A., and. Criado J. ́M,2012, Nanoclay Nucleation Effect in the Thermal Stabilization of a Polymer Nanocomposite: A Kinetic Mechanism Change*, J. Phys. Chem,,* **116** (21):11797-807
[20] Bras M. L., Wilkie C. A. , Bourbigot S. , Duquesne S., Jama C.,2005, *Fire Retardancy of Polymers:New Applications of Mineral Fillers* , RSC, UK
[21] Jash, P. and Wilkie, C.A.:(2005) , Effects of surfactant on the thermal and fire properties Poly (methyl meth-acrylate/nanoclay nanocomposites, *Polym. Degrad. Stab.* **88** (93): 401-406
[22] Wang, D.-C., Chang, G.-W. and Chen, Y,(2008), Preparation and thermal stability of boron-containing phenolic resin/clay nanocomposites*, Polym. Degrad. Stab*. **93** (1), 125-33
[23] Zhang J., Hereida J., Hagena M., Bakirtzisa D., Delichatsiosa M.A ,Finab A., Castrovincib A., Caminob G., Samync F. and Bourbigotc S., (2009,) Effects of nanoclay and fire retardants on fire retardancy of a polymer blend of EVA and LDPE, *Fire Safety J.* , **44** (4), 504–13
[24] Frache, A., Monticelli O., Nocchetti M., Tartaglione G. and Constantino U. 2011, Thermal properties of epoxy resin nanocomposites based on hydrotalcites, *Polym. Degrad. Stab*. **96**: (1) 164-69
[25] Kumar N. and Dahiya J. B.,(2013), Polypropylene-nanoclay composites containing flame retardant additive: Thermal stability and kinetic study in inert atmosphere*, Adv. Mat. Lett.,* **4** (9), 708-713
[26] Kaynak C. and Sipahioglu B. M.,2013, Effects of nanoclays on the flammability of polystyrene with triphenyl phosphate-based flame retardants*, Fire Sci. J*.,**3** (4):339-55
[27] Kannan, M., Thomas, S. and Joseph, K. (2015), Flame-retardant properties of nanoclay filled thermoplastic polyurethane/polypropylene nanocomposites. *J. Vin. Add. Tech*., 21(3), DOI 10.1002/vnl.21523
[28] Raghavendra N, Narasimha Murthy HN, Firdosh Salim, Sridhar R, Angadi Gangadhar Mahesh KR Vishnu , Krishna M,2017, Combined influence of organo modified Indian bentonite nanoclay and fire retardants on thermal and fire behavior of vinylester*, Nanom., Nanoeng. & Nanosy. J.,* **231**(1):34-42
[29] Zhang J., Li G., Wu Q., Li M., Sun X., and Ring D., 2017, Synergistic influence of halogenated flame retardants and nano clay on flame performance of high density polyethylene and wood flour composites*, RCS Adv*, **7** (40): 24895–902, DOI: 10.1039/c7ra03327c
[30] Araujo E. , Leite A., Paz R.,Medeiros V., Melo T. and Lira H.,2011, Polyamide 6 Nanocomposites with Inorganic Particles Modified with Three Quaternary Ammonium Salts, *Mat. J.*, **4 (11)**, 1956-66; doi:10.3390/ma4111956

[31] Adham R.R., Amal M.K.E., Ahmed A.G.2010, Effect of ball milling on the structure of Na -montmorillonite and organo-montmorillonite (Cloisite 30B) ,*Appl. Clay Sci.* **47** (3-4) 196–202
[32] Kohls, D. J. and Beaucage G., (2002), Rational Desing of Reinforced Rubber, *Cur OP. Solid St Mat Sci J.* ,**6** (3):183-94.
[33] Kouini B. and Serier , 2016, studying the effect of nanoclays on mechanical properties of polypropylene/polyamide nanocomposite , *Int. J. chem. Mol. Mat. Metal. Eng*., **10** (3):331- 34
[34] Gupta N. , Lin T. C., and Shapiro .,2007, Clay-Epoxy Nanocomposites: Processing and Properties, *JOM,* **59** (3): 61-65
[35] Yadav S. M. and Yusoh K. B., 2015, Mechanical and physical properties of wood-plastic composites made of polypropylene, wood flour and nanoclay, Kuala Lumpur International Agriculture, Forestry and Plantation conference, Kual lampur, Malaysia

Modified Unzipping Technique to Prepare Graphene Nano-Sheets

Modified Unzipping Technique to Prepare Graphene Nano-Sheets

B H Al-Tamimi1, S B H Farid1 and F A Chyad

Department of Materials Engineering, University of Technology, Baghdad, Iraq

Abstract. Graphene nano-sheets have been prepared via unzipping approach of multiwall carbon nanotubes (MWCNTs). The method includes two chemical-steps, in which a multi-parameter oxidation step is performed to achieve unzipping the carbon nanotubes. Then, a reduction step is carried out to achieve the final graphene nano-sheets. In the oxidation step, the oxidant material was minimized and balanced with longer curing time. This modification is made in order to reduce the oxygen-functional groups at the ends of graphene basal planes, which reduce its electrical conductivity. In addition, a similar adjustment is achieved in the reduction step, i.e. the consumed chemicals is reduced which make the overall process more economic and eco-friendly. The prepared nano-sheets were characterized by atomic force microscopy, scanning electron microscopy, and Raman spectroscopy. The average thickness of the prepared graphene was about 5.23 nm.

1. Introduction

Nanotechnology regarded as a new branch of science which involves study and manipulation the properties of materials at nanoscale. In fact the behavior of a specific material will be changed completely when it becomes at nanoscale. This change in the behavior of materials at nanoscale is rejoiced for the revolutionary changing in the crystal structure and the quantum confinement effects [1,2].

Carbon is an important element in the periodic table which can be exist in many fields, it can found for writing as a graphite and can be use like jewelry as a diamond. In nanoscale, carbon element can be exist in many different forms such as fulluerene, carbon nanotubes (CNTs), nanodiamond (ND), carbon nanoscrolls (CNS), diamond like carbon (DLC) and graphene sheets (GS). All these forms of carbon consisting only carbon element, but they are differ due to the different in the way at which these carbon atoms arrange them self [1,2].

Graphene nano-sheet is a one-atom thick planar sheet of sp2-bonded carbon atoms, which is packed densely in a honeycomb crystal lattice. The graphene lattice posses many fascinating properties including high electron mobility, extraordinary high thermal conductivity, stiffness, and strength. The graphene as a material of high mechanical stress and low density (2.2 gm/cm3), it may be suggested for application in nano-robots, nano-composites and nano-electronics and others [3,4].

Actually it has been understood that the mechanical, thermal, and electronic properties of the graphene are mainly dependent on some factors which are the morphology (shape and size of the planar sheet) and the atomic structure of it as well as the presence or absence of structural defects [5], which in turn depend on the preparation methodology [6,7]. For example the edge of a graphene sheet can be either zigzag-shaped or armchair shaped, or a mixture of both [7]. A zigzag morphology of the graphene is expected to give metallic electrical properties, where a semiconducting or metallic transport is expected with armchair configuration [8].

Essentially, there are two distinctive methodologies that can be employed to produce the graphene. They are bottom-up and the top-down strategies. The first relies on the generation of graphene from suitably designed molecular building blocks undergoing chemical reaction to form covalently linked (2D) networks. The second strategy relies on exfoliation of graphite into graphene [9].Also it is noticed that the graphene can be exist in many forms, it can be exist as a sort of sheet, membranes with some noticed ripples, ribbons and scrolls due to the interactions of Van der Waals between adjacent sheets [5,10].

As a results of that the carbon nanotubes (CNTs) is now produced in large scale, its reasonably to start with the carbon nanotubes to produce the graphene. In fact, carbon nanotubes can be regarded as layers of graphene sheets that rolled up into tubes form. Thus, graphene nanoribbons (GNRs) can be produced by unzipping of these carbon nanotubes. In fact, longitudinal unzipping or cutting and unraveling of multi-wall carbon nanotubes (MWCNTs) can be achieved via exposing it to a strong oxidizing solutions. After that, the oxidized nano-sheets (graphene oxide) can be reduced directly to obtain graphene nano-sheets [11]. The unzipping process of the carbon nanotubes seems to be similar to that occurs to graphite. Where, a linear or spiral cut takes place throughout the oxidation stage that depends upon the initial site of attack and it was noticed that the presence of inherent defects at the surface of nanotubes regarded as a site for cutting or unzipping initiation [12]. On the other side the aggressive effect of the oxidant materials in the oxidation stage had been reported and studied the harmful effect of the oxygen-functional groups which can take place at the edges of the graphene sheets on the properties of the prepared material [13].

In this work, the graphene is prepared from multiwall carbon nanotubes (MWCNTs) through optimized process parameters that reduced the cost via minimizing the amount of the used chemicals and reduce the effect of the oxidants on the final properties of the produced graphene.

2. Materials and Methods

The starting materials were multiwall carbon nanotubes (95%, Nanoshel LLC. USA.), Sulphuric acid (98%, Himedia, India), Potassium Permanganate (99.5%, BDH, UK), Hydrogen Peroxide (30%, Sigma Aldrich, Germany), Ammonium Hydroxide (33%, Sigma Aldrich, Germany), Hydrazine Monohydrate (80%, Schar Lab, Spain), and Hydrochloric acid (35.4%, Gainland Chemical, UK).

An oxidation stage of the carbon nanotubes was first performed to perform the unzipping process and obtain graphene oxide. 150 mg of multiwall carbon nanotubes was suspended in 150 ml of the concentrated sulphuric acid. The solution was stirred via magnetic stirrer for 15 hr. at room temperature. Then, a 450 mg of the potassium permanganate is added and the stirring was continued for additional 3 hr.

After that, the obtained solution was heated at 60°C for 1 hr by means of a water bath. The stirring is continued in order to encourage the reaction. The temperature of water bath was then raised to 75°C and then the solution was let for 1 hr to stabilize. A dark solution is formed, which was allowed to cool to room temperature.

The prepared solution was mixed with 400 ml of iced water and 5 ml of the hydrogen peroxide. Afterward, the solution was filtered via vacuum filtration through cellulous nitrate paper. The final step of the oxidation stage is washing out the obtained graphene oxide. The obtained solid material was dissolved in 150 ml of deionized water and stirred for 1hr. The solution was again filtered and was dissolved once more in 150 ml of ethanol. A final vacuum filtration was performed.

Next to the oxidation stage, the reduction stage is performed to convert the graphene oxide to graphene. The material was suspended in 150 ml of water. A 100 µml of the concentrated ammonium hydroxide and a 100µml of the hydrazine monohydrate were then added. The solution was heated at 90°C for 2hr in a water bath. The resultant solution was vacuum filtered and let to dry in air.

The prepared graphene was characterized by Atomic force microscopy, Scanning electron microscopy, and Raman spectroscopy.

3. Results and Discussions

'Figure (1)' shows 2D and 3D AFM image of the produced graphene nano-sheets. The nano-sheets have ribbons-like appearance due to that they were originated from unzipping of the carbon nanotubes.

Moreover, the morphology reflects the hexagonal character of the graphene lattice. The AFM analysis attached with the figure shows that the minimum thickness was around 1.23 nm, which should correspond to few- graphene sheet. In addition, the maximum thickness of the stacked sheets was 5.23 nm. Figure (1) also reflects regular and uniform microstructure with high surface area at the nanoscale. These characters make this graphene meets the requirement in electronic field and that for the nanocomposites [13].

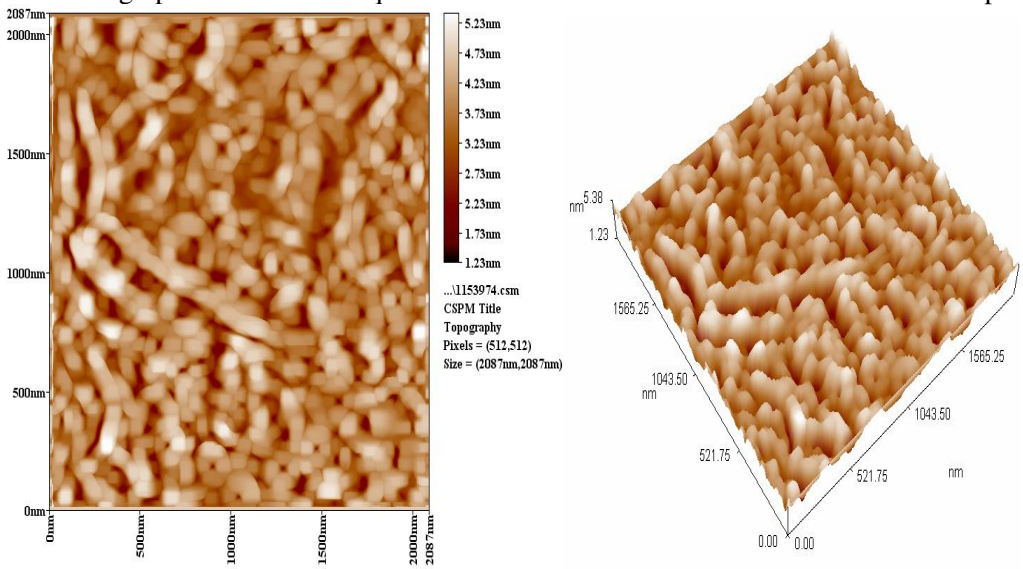

Figure 1. 2D and 3D AFM image of the prepared graphene nano-sheets.

The result of Raman spectroscopy illustrated in 'figure (2)'. The characteristic graphene Raman peaks are obvious. The intensity ratio (ID/IG) of the two main peaks (G at 1605 cm-1 and D 1360 cm-1) is equal to (1.1). This value of the intensity ration indicates that the carbon atoms is nearly all sp2 hybridization and is graphitic with some non-crystalline feature [13], which supports the low thickness observed with the AFM. The figure shows high intensity of the G band, which is another indication of the small thickness of the prepared graphene.

SEM images of the prepared graphene in two different scales are shown in 'figure (3)'. The figure shows that the prepared graphene sheets assemble thin wrinkled paper-like structure. The SEM images are thus conforms the AFM and Raman results. Besides, the SEM images show a dominant character of the microstructure that reflects the stacking of graphene sheets is substantially disordered and the graphene sheets are agglomerated and overlapped.

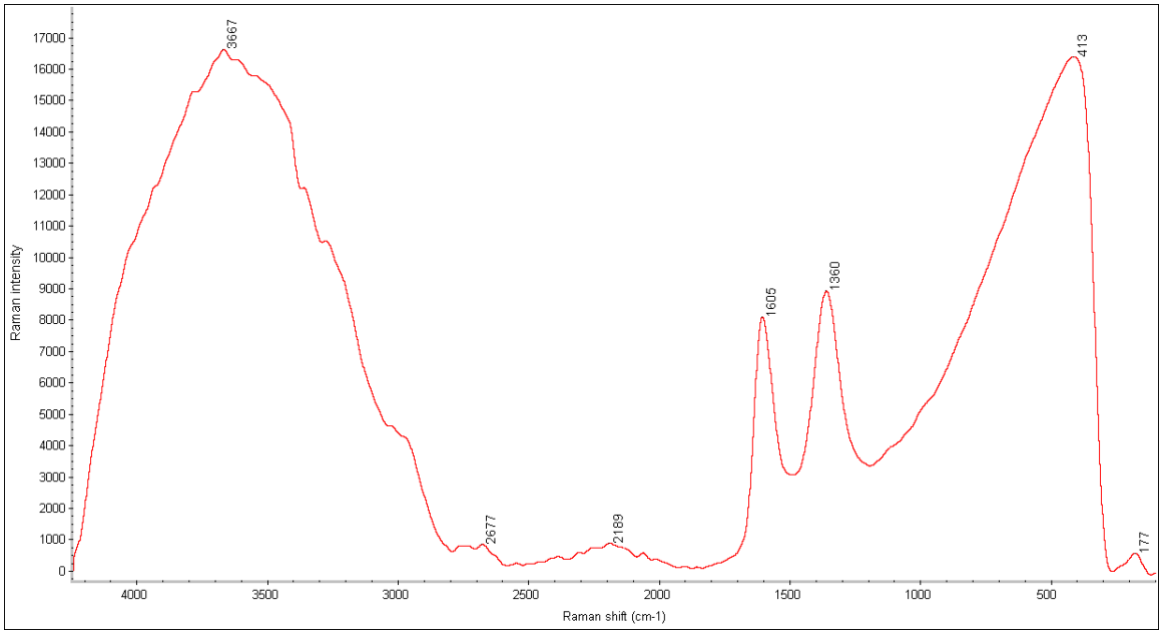

Figure 2. Raman spectrum of the prepared graphene nanoribbons.

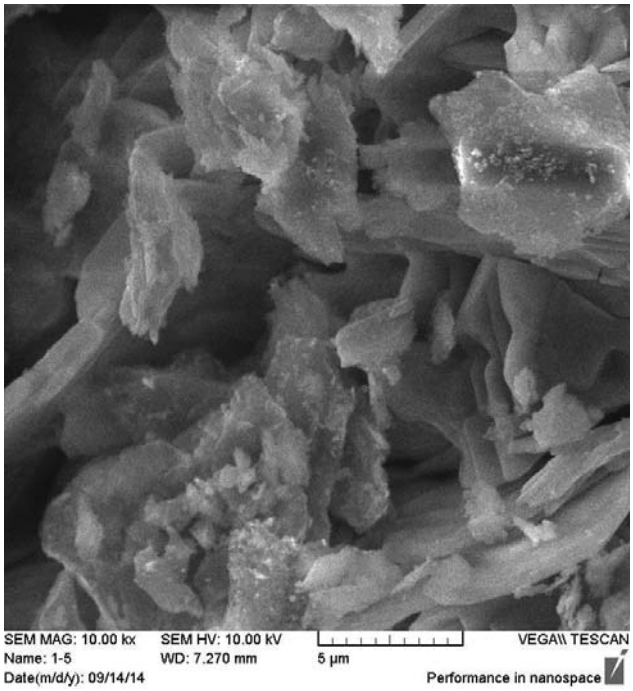

Figure 3. SEM image of the prepared graphene.

4. Conclusions

A modified unzipping technique is used to obtain graphene nano-sheets from MWCNTs. In this work, the used materials for the both the oxidation stage and the reduction stage were reduced. Consequently, the harmful effect of the aggressive chemical is minimized and the overall cost of the process is reduced. The

produced graphene characterized by its high quality and small thickness that make it is suitable for several applications.

6. Acknowledgements
The authors thank the stuff of laboratories in Department of Materials Engineering and the Center of Nanotechnology and Advanced Materials in the University of Technology for the help in the experimental activity.

References

[1] Arshad H W and Imran W K, 2016, Synthesis of Graphene Nano Sheets by the Rapid Reduction of Electrochemically Exfoliated Graphene Oxide Induced by Microwaves*, J.Chem.Soc.Pak*, **38**, No. 01,pp. (11-16).
[2] Balamurugan T, Chellakannu R, Shen-Ming C, Selvakumar P,2017, One-Pot Green Synthesis Of Graphene Nanosheets Encapsulated Gold Nanoparticles for Sensitive and Selective Detection of Dopamine, Scientific Reports, 7.
[3] Stephen W, Ricardo M, John K.G and Claudia C,2010, Production Of Graphene From Graphite Oxide Using Urea As Expansion-Reduction Agent, Elsevier, Carbon, 48, pp. (3463-3470).
[4] M. Gautam, A. H. Jayatissa, and G. U. Sumanasekera,2010, Synthesis And Characterization Of Transferable Graphene by CVD Method, IEEE Nanotechnology Materials and Devices Conference, USA.
[5] Sergey M,2011, Physics And Application Of Graphene – Experiments, Published by Intech, India.
[6] Long Z., Jiajie L, Yi H, Yanfeng M, Yan W and Yongsheng C,2009, Size-Controlled Synthesis Of Graphene Oxide Sheets On a Large Scale Using Chemical Exfoliation, Elsevier, Carbon, 47, pp.(3365-3380).
[7] Van N D and Thanh H P,2010, Graphene and Its One-Dimensional Patterns: From Basic Properties Towards Applications, Advances In Natural Science: Nanoscience And Nanotecgnology, 1, pp. (1-14).
[8] Jessica C D, Jose M R H, Xiaoting J and David A C,2008, Bulk Production Of a New Form Of sp2 Carbon: Crystalline Graphene Nanoribbons, Nano Letters, 8, No. 9, pp. (2773-2778).
[9] Raghu M,2012, Graphene Nanoelectronics- From Materials to Circutes, Published by Springer.
[10] Fang L and Yong Z,2010, Substrate-Free Synthesis of Large Area, Continuous Multi-Layer Graphene Film, Elsevier, Carbon, 48, pp. (2394-2400).
[11] Biwei X, Xifei L, Xia L, Biqiong W, Craig L, Ruying L and Xueliang S,2014, Graphene Nanoribbons Derived From the Unzipping Of Carbon Nanotubes: Controlled Synthesis and Superior Lithium Storage Performance, *The Journal of Physical Chemistry*, **118**, No. 2, pp. (881-890).
[12] Dmitry V K, Amanda L H, Alexander S, Jay R. L, Ayrat D, B. Katherine P and James M T,2009, Longitudinal Unzipping Of Carbon Nanotubes to Form Graphene Nanoribbons, Nature Letters, 458,pp. (872-876).
[13] Dhanraji B. S, Joyashish D, Ajay K, Mohammed A and Vijayaamohanan K P,2011, Electrochemical Unzipping Of Multi-Walled Carbon Nanotubes for Facial Synthesis of High-Quality Graphene Nanoribbons, J. A. C. S. *Journal of American Chemical Society*, **133**, pp. (4168-4171).

Synthesis and spectral studies of heterocyclic azo dye complexes with some transition metals

Synthesis and spectral studies of heterocyclic azo dye complexes with some transition metals

A J Jarad[1], I Y Majeed[1] and A O Hussein[2]

[1]Dept. of Chemistry College of Education for Pure Science -Ibn-Al-Haitham, University of Baghdad, Iraqi

[2]Ministry of education, Babylon Education, Iraqi

Abstruct. 6-(2-benzathiazolyl azo) -3,5-dimethylphenol was formed by grouping the 2-benzothiazole diazonium chloride with 3,5-dimethylphenol. Azo ligand(L) was resolved on the origin by ^{1}H and $^{13}CNMR$, FTIR and UV-V is spectral analysis. Complexation of tridentate ligand (L) with Co^{2+}, Ni^{2+}, Cu^{2+} and Zn^{2+} in aqueous of ethyl alcohol with a 1:2 metal:ligand, and at ideal pH.. The formation of metal chelates are assigned using flame atomic absorption, FTIR and UV-Vis spectral analysis, other than conductivity and magnetic estates. The nature of the metal chelates were carried out by mole ratio and continuous variation mechanism, Beer's law followed the rate (0.0001 - 3×0.0001 M) concentration. High molar absorptivity for the complex solutions were observed. On the origin data an octahedral geometry were described for the metal chelates. Biological activity of the ready compounds were assayed.

Keywords:- heterocyclic azo dyes, complexes, spectral studies, biological activity

1-Introduction

Azo dyes have been widely used in the textile industrial and highest versatile group of produced organic dyes [1]. Heterocyclic azo dyes have been studied highly applications in thermal, optical and medicinal estates, such as antiviral, anti-fungal and antioxidant properties [2-5]. Because of heterocyclic azo dyes colorist, this dyes have been used to evaluate of many elements. Recently, many workers developed a model mechanism for the evaluation of metal ions with heterocyclic azo dyes [6]. Most of metal chelates of azo dyes have been highly studied in the antimicrobial, anti-cancer and analytical application [7-9]. In the last years, the azo dyes and their metal chelates have been extensively used in deying industries [10]. In this work, we produced azo ligand derived from 2-benzothiazole diazoniumchloride with 3,5-dimethylphenol, the metal chelates of azo dye were prepared and identified using different spectral studies.

2-Experimental

2-1-Instrumentation

^{13}C,proton-NMR spectra were recorded on a Brucker-300 MHz Ultra Shield spectrometer at the Al- al- Bayt University using DMSO-d6 as solvent and trimethylsilane as a reference. Electronic spectra were taken on a Schimadzu UV- 160A UV-Vis Spectrophotometer. Fourier transform spectra were registered on a Shimadzu, Fourier transform -IR-8400S in the rate 4000- 400 cm^{-1} with KBr discs. Conductivity was recorded for 0.001 M solutions of complexes, in ethylalcohol at 25°C using Philips PW-Digital Conductimeter. Magnetic properties were completed by using Auto Magnetic Susceptibility Balance Sherwood Scientific instrument at 25C°. Atomic absorption was obtained from using a Shimadzu A.A-160A Atomic Absorption, Flame Emission Spectrophotometer. Other than, m.p were quantities using Stuart Melting Point device.

2-2-Reagents and Materials

Obeying chemicals were used, as collected from provider; CoCl2.6H2O (Fluka); NiCl2.6H2O, CuCl2.2H2O, ZnCl2(Merck); 2-aminobenzothiazole and 3,5-dimethylphenol (Merck).

2-3-synthesis of 2-(benzo[d]thiazol-2-yldiazenyl)-3,5-dimethylphenol(ligand)

(1 mmole, 0.272 gm) of 2-aminobenzothiazol [11] was melted in (10ml) of ethanol formed (2 ml) conc. HCl was diluted in water 10 ml, and diazotized at 5°C and 10% $NaNO_2$ solution, then added gradually and stirring to a cooled of ethyl alcohol (1mmole, 0.345 gm) of 3,5-dimethylphenol. On other hand, (20 ml) of 1M of solution of NaOH was appended to the color dark mixture and precipitation of azo ligand was noticed. This product was filtered and washed number ounce with (1:1) ethylalcohol: water, and dry. The reaction steps were shown in scheme 1.

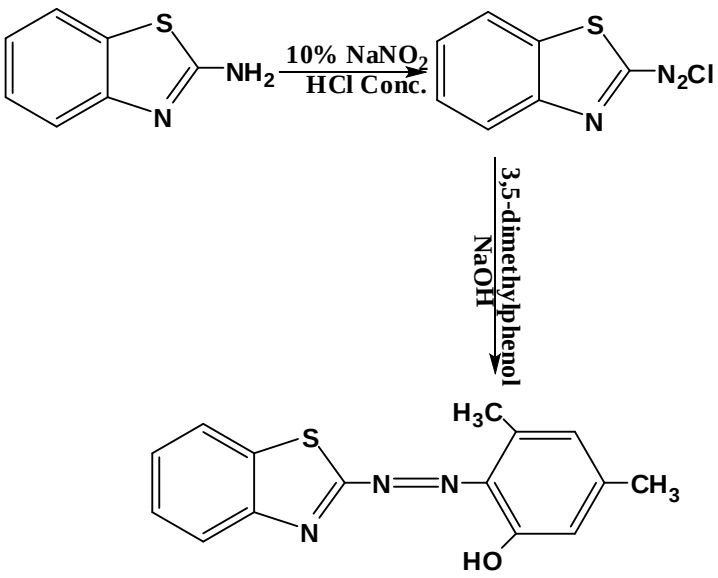

Scheme 1. Preparation of 2-(benzo[d]thiazol-2-yldiazenyl)-3,5-dimethylphenol(ligand).

.

2-4-Buffer Solution series

(0.771gm, 0.01M) of ammonium ethanoate was melted in 1000 milliliter of doubly distilled water for rate pH rate (4-9) was used ethanoic acid or ammonium hydroxide.

2-5-Standard Solution

Series of standard solutions of metal chloride were produced in variant concentration (10^{-5}-10^{-3} M) at pH rate (4-9). On other hand, a series of ethyl alcoholic solutions of ligand within the rate (0.00001-0.001 M) concentrations were also produced.

2-6-synthesis of Metal Complexes

(0.268 g, 2 mmole) of the ligand dissolved in ethanol was appended gradually with stirring to the 0.118, 0.118, 0.085 and 0.068 gm (1 mmole) of $CoCl_2.6H_2O$, $NiCl_2.6H_2O$, $CuCl_2.2H_2O$, $ZnCl_2$, continuously melted in the buffer solution with the required pH. The mixture reaction was cooled and kept dark color precipitate was formed, filtered, then washed number ounces with (1:1) of H_2O: ethylalcohol solution. The preparation technique is shown in scheme-2.

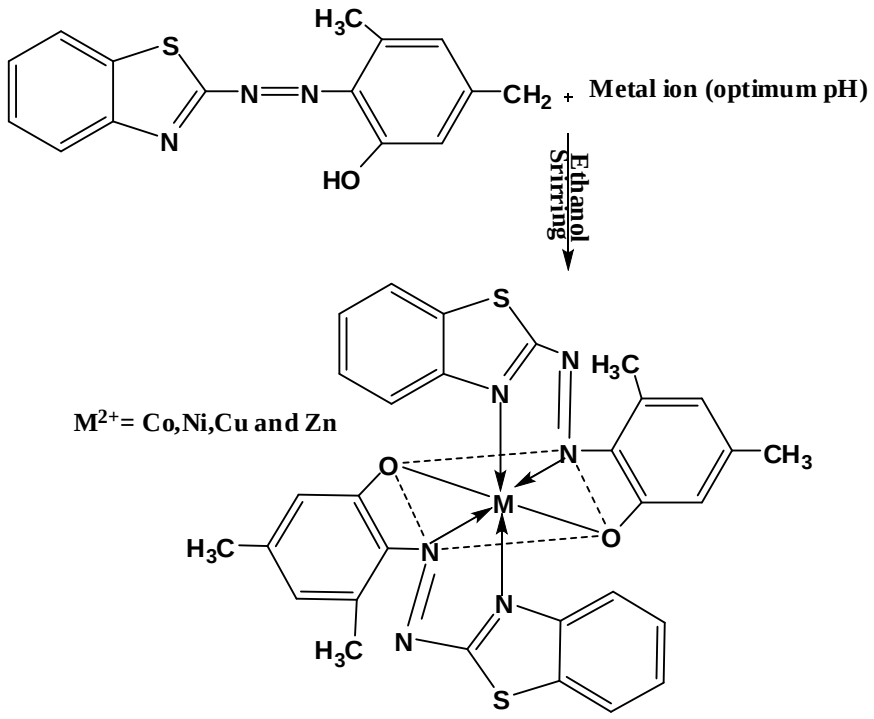

Scheme 2: The expected geometry of the metal chelates.

2-7-Biological Activity Studies

The ligands and Metal chelates were test in vitro for their three types antibacterial activity against bacteria: *Staph. aureus, E-coli* and *Pseudomonas* using the paper disc method. The produced compounds in DMSO solution were applied in vitro by paper disc method. All materials used were sterilized in a hot air oven and colony of each of the tested microorganisms were subculture and

incubated about (8 hours) before introducing into agar plates. The discs (7 mm diameter) were drenched with variant test samples (concentration 1000 ug/ml) drained and then put on the agar plate using sterilized forceps. The plates were kept in incubated under 37°C for (48 hours), finally of the incubation period; the zones of inhibition of the different bacteria were carried out [12]. The values of which are listed in Table (1).

Table 1. Diameters (mm) of deactivation of bacteria for ready compounds.

Compounds	**Staphylococcus aureus**	**E-coli**	**Pseudomonas**
Ligand(L)	10	20	18
$[Co(L)_2]$	14	18	17
$[Ni(L)_2]$	17	21	20
$[Cu(L)_2]$	15	18	18
$[Zn(L)_2]$	15	20	20

3-Results and discussion

The readying of the ligand (HL) a linkup compound 4-nitroaniline with the diazotized derivative in basic medium was carried out. Performed ligand was verified by ^{1}H and ^{13}CNMR, Fourier transform infrared and Ultraviolet-Vis spectral.

3-1-NMR Spectrum

The ^{1}HNMR spectrum of the 2(2-benzothiazolyl azo)-3,5-dimethylphenol (L) in dimethylsulfoxide (Figure 1) show resonance at δ=7.283-8.937 ppm described to phenyl protons [13]. Peak at δ=6.278 ppm assigned to proton of phenol [14]. The resonance at δ=2.598 ppm is assigned to proton of (methyl) groups and the gesture at δ=2.50 assigned to dimethylsulfoxide-d6 [15]. The ^{13}CNMR spectrum of ligand (Figure 2) appeared signals at δ=162.549 and δ=158.537 ppm described to (C-OH) and carbon of thiazole group. The various symbol at (δ=139.829, 133.393, 126.848, 126.586, 123.808, 122.732 and 116.943 ppm lead to carbon atoms of aromatic rings. The signals at δ=34.283 and 21.231 ppm attributed to $\delta(CH_3)$ groups of phenol. The gesture at δ=39.225 ppm due to DMSO-d6 [16].

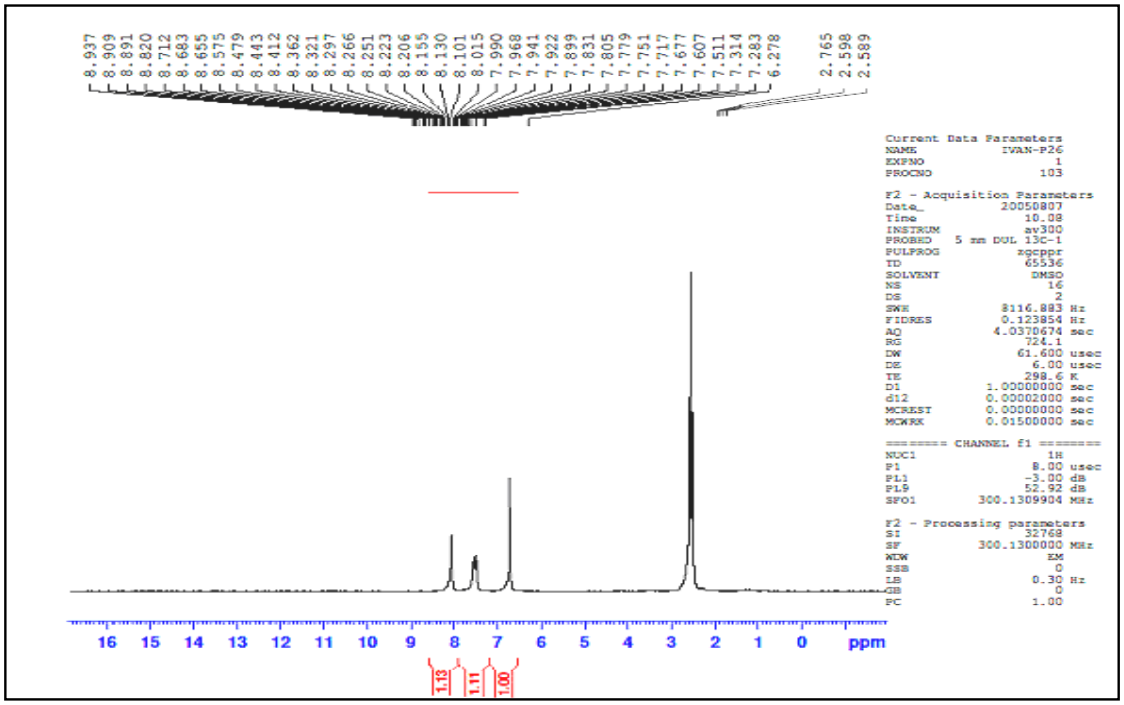

Figure1. [1]HNMR spectrum of the ligand.

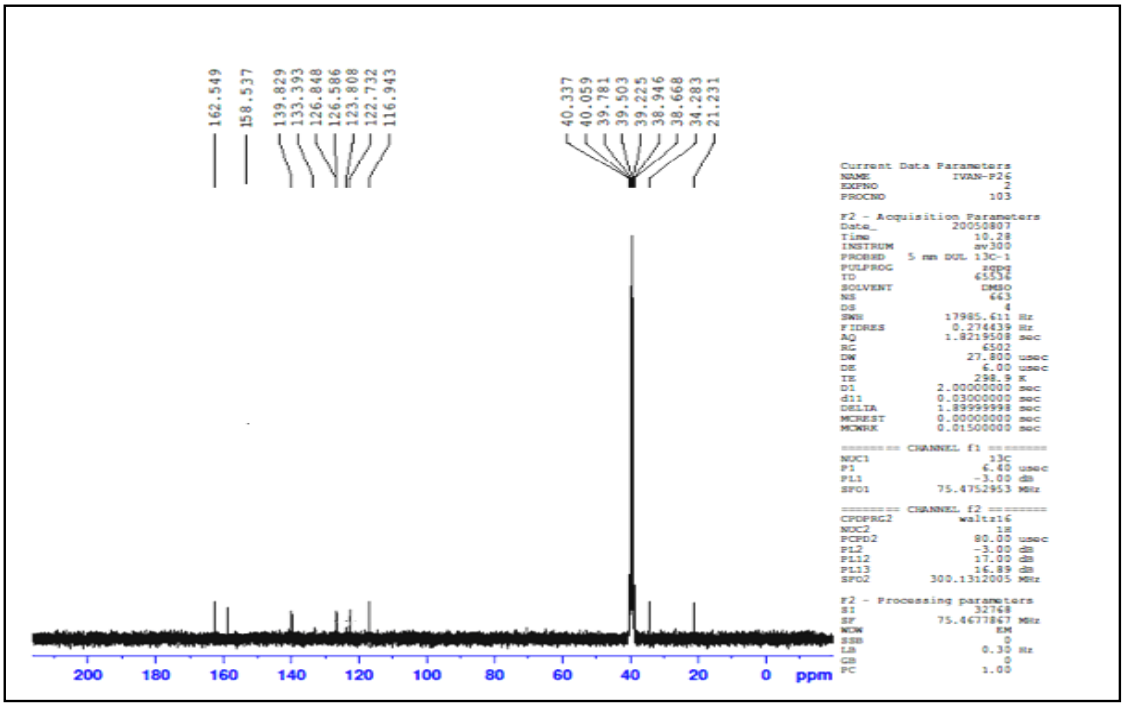

Figure 2. [13]CNMR spectrum of the ligand.

3-2-Physical properties

Metal chelates have been readied by immediate reaction of ethanolic and ligand (L) solution with the aqueous solution of the metal ions at the perfection pH and in a M:L proportion of (1:2). The product of metal content of these complexes were in a good agreements with the calculated values, data recorded in Table 2. The molar conductance of (0.001 M) in ethylalcoholic solutions for these complexes lead to non-electrolytic type [17] data are formed in Table 2. Magnetic estates Table 2 of the produced metal chelates have been happened to a paramagnetic that was accounted for octahedral geometry [18].

Table 2. Physical properties of ligand and metal chelates.

products	**Color**	**Melting points°C**	**Percentage products %**	**M% Calculate (found)**	**Λ_m(S.cm^2.mol^{-1}) in ethanol**	**μ_{eff} (B.M)**
Ligand(L)	Reddish orange	175	75	-	-	-
$[Co(L)_2]$	Brown	194	70	9.91 (8.88)	7.54	4.53
$[Ni(L)_2]$	Reddish brown	220	77	9.76 (9.31)	11.73	3.07
$[Cu(L)_2]$	Deep brown	230	75	10.66 (9.78)	3.42	1.77
$[Zn(L)_2]$	Orange	210	70	10.81 (9.77)	14.32	Di

3-3-Calibration Curve

Variant molar concentration (0.00001–0.001) M of mixed aqueous-ethanol of ligand and metal ions, only the rate (1-3×10^{-4}M) concentration followed Beer's law and produced obvious intense color. Best excellent straight lines were happened together with correlation factor R>0.9980 as showed below (Figure 3).

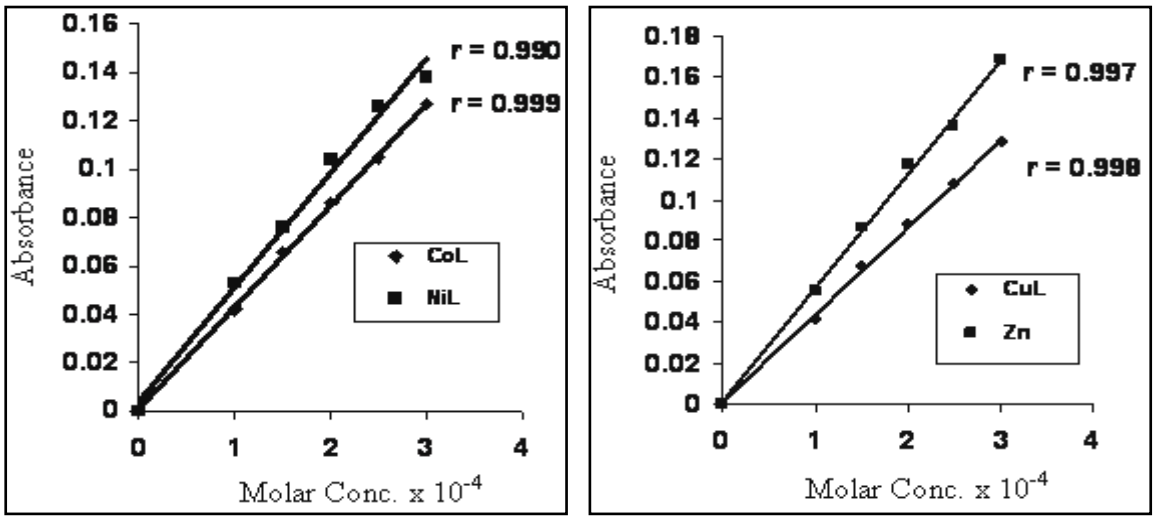

Figure 3. Linear correlation between absorbance and molar concentration.

3-4-Perfect Conditions

To work out coordination between the ready metal ions and ligand under searching for the synthesis of the metal chelates, the spectra of combining solutions for the metal ions and ligand to attain to perfect pH and concentration, as well as firm (λ_{max}) were studies first .Then mole ratio metal to ligand (M:L) was defined to prepare the metal chelates. Perfect concentration was selection for complex solution based on which solution gives the highest absorbance at constant (λ_{max}) at variant pH, and results are assigned in Table-3. The probation results proof that the absorbance of all produced complexes are high and constant in a buffer solution of ammonium ethanoate in the pH extent (4-9). It was found that ready metal chelates had perfect pH as is showed below in Figure (4).

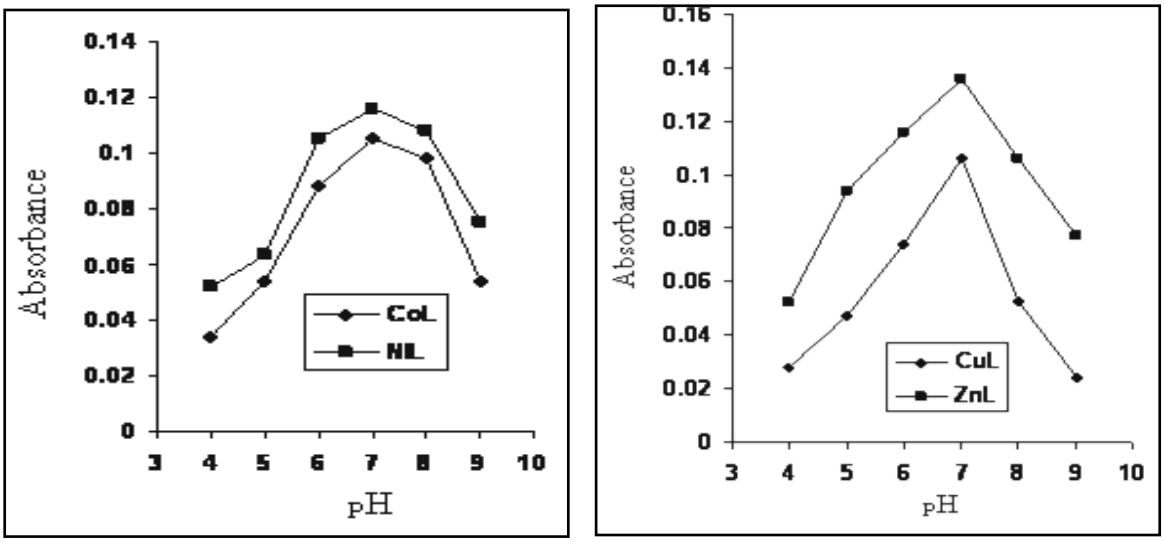

Figure 4. Effect of pH on absorbance (λ_{max}) for metal chelates.

3-5-Ratio of Complexes

Mole ratio and job mechanisms are used to appoint the complexes in solutions. In both procedures the products disclose a (metal:ligand)1:2 ratio. A picked plot is shown in Figure (5). Table 3 outlines the results contained, other than specification for the making complexes.

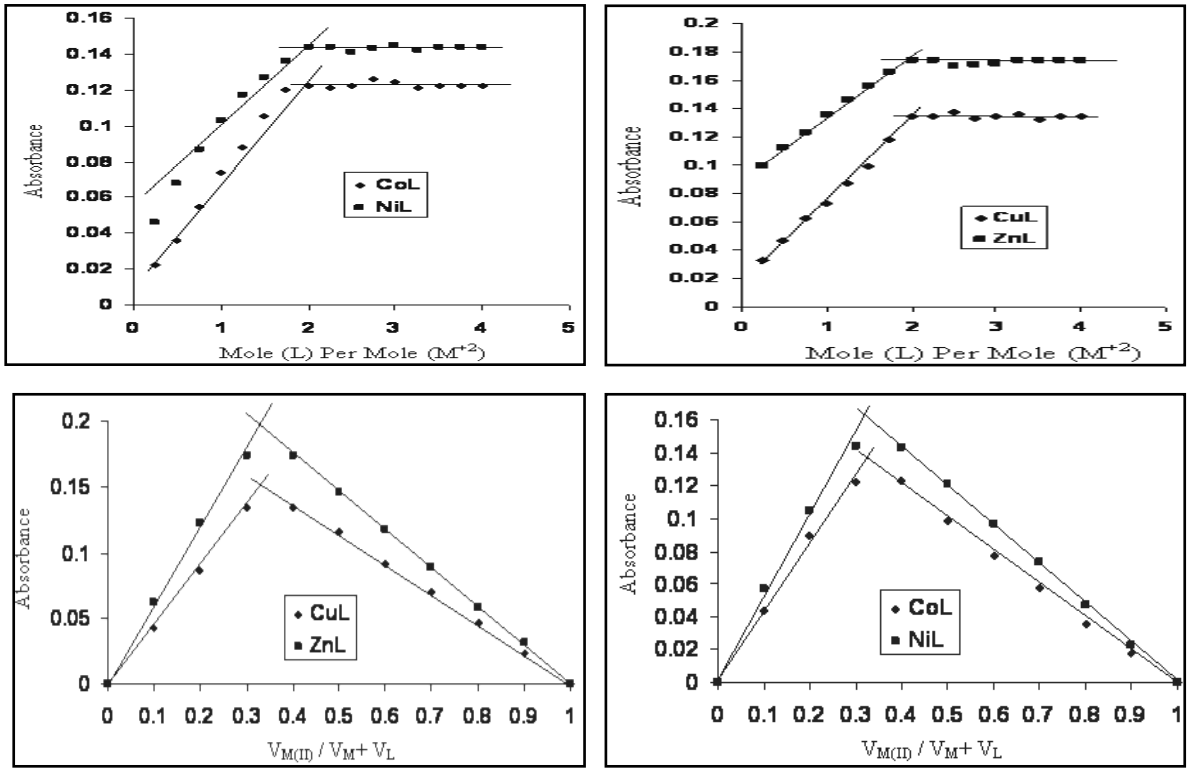

Figure 5. Mole ratio and Job mechanisms for complexes solutions.

3-6-Electronic spectra

Ultraviolet-Vis spectra of the ready azo ligand and their metal chelates mixed in ethanol (0.001 M) were studied and the dataset included in Table 3. The spectrum of the ligand (L) (Figure 6) display peaks at 262 and 408 nm described to (π- π^*) electronic transition [19]. The spectrum of Co^{2+} complex shows peaks at 270 and 416 nm related to ligand felid, other peak at 893 nm lead to electronic transition [20] $^4T_{1g(F)} \rightarrow {}^4T_{2g(F}$ The spectrum of Ni^{2+} complex refers peaks at 268 and 418 nm due to ligand felid, than peaks at 892 and 980 nm were assigned to electronic transition [21] $^3A_{2g(F)} \rightarrow {}^3T_{1g(F)}$ and $^3A_{2g(F)} \rightarrow {}^3T_{2g(F)}$. The Cu^{2+}complex (Figure 7) display peaks at 268 and 420 nm lead to ligand, the peak at 892 nm described to electronic transition [22] $^2E_g \rightarrow {}^2T_{2g}$. The electronic spectrum of Zn^{2+}complex do show the charge transfer, because d-d transition is not possible hence electronic spectrum did not give any fruitful information [23].

Table 3. Conditions for the produced metal chelates and UV-Vis data.

products	**Perfect pH**	**Perfect Molar Concentration. x 0.0001**	**M:L Ratio**	**(λ_{max}) nm**	**ABS**	**ϵ_{max}**
Ligand(L)	-	-	-	262 408	0.510 1.267	510 1267
$[Co(L)_2]$	7	2	1:2	270 416 893	0.433 1.189 0.022	433 1189 22
$[Ni(L)_2]$	7	2	1:2	268 418 892 980	0.358 1.249 0.004 0.023	358 1249 4 23
$[Cu(L)_2]$	7	2	1:2	268 420 892	0.3151 .218 0.023	315 1218 23
$[Zn(L)_2]$	7	2.5	1:2	266 423	0.322 1.124	322 1124

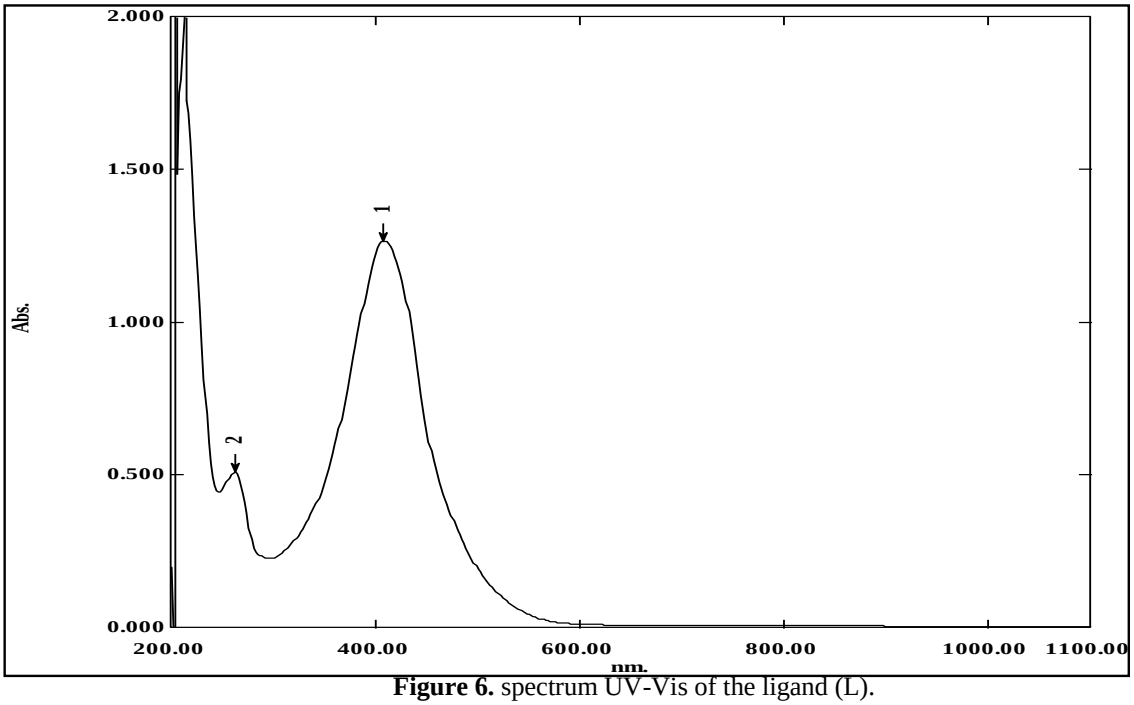

Figure 6. spectrum UV-Vis of the ligand (L).

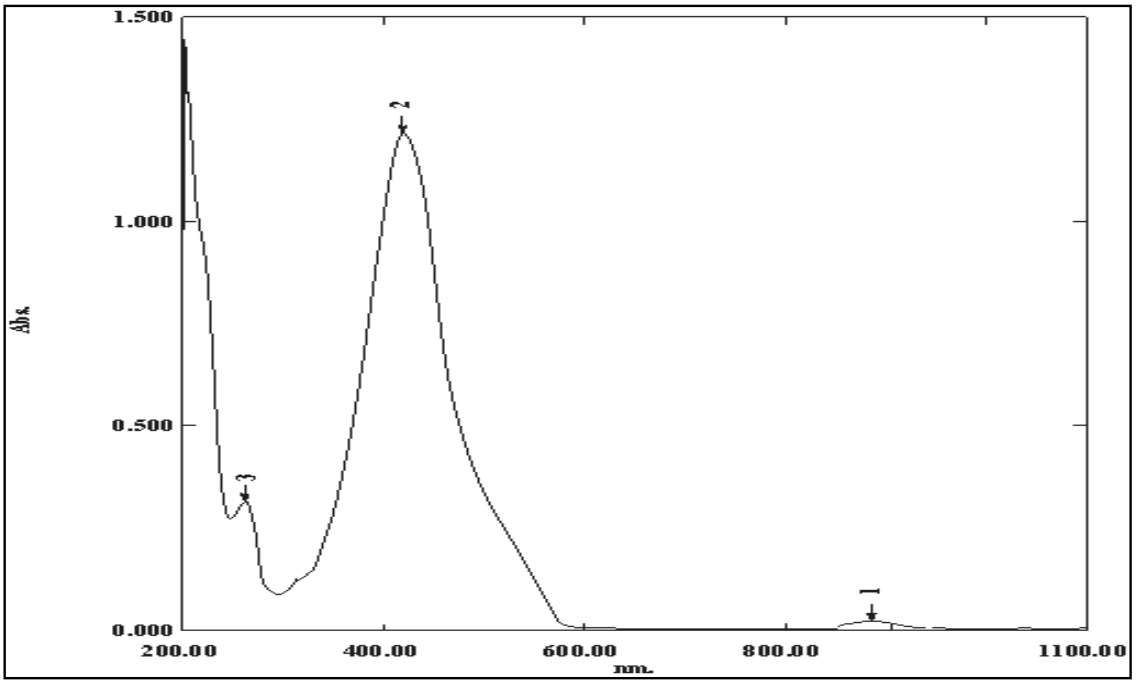

Figure 7. spectrum UV-Vis of the $[Cu(L)_2]$ complex.

3-7-Fourier transforms infrared spectra

FTIR spectra of ready compounds have been formed, data was scheduled in Table (4). Broad band in FTIR spectrum of the ligand (Figure 8) at 3396 cm^{-1} due to υ(OH) phenol, in the metal chelates spectra, disappearance of this band (Figure 9) indicated to coordinate with metal ion [24]. The spectrum show band at 1608 cm^{-1} ascribed to υ(C=N), on chelates a shifted to higher frequency may be lead to coordinate with metal ion [25]. Band at 1461 cm^{-1} due to azo bridge, this band shifted to higher frequency may be result to coordinate with metal ion [26]. The bands at (1454, 1435, 1377, 1311 and 1570 cm^{-1}) due to bending frequency of (δCH_3) and vibration of υ(C=C) [27]. Bands for metal-nitrogen and metal-oxygen [28-29] at the rate (442-572) cm^{-1}. Other than, results protected an octahedral geometry has been offered for the metal chelates.

Table 4. The main frequencies of the ready compounds (cm^{-1}).

Compounds	**)OHυ(**	**υ(C=N) + υ(C=C)**	**υ (N=N)**	**$CH_{3\ as,s}\delta$**	**)M-N(υ + M-O)(υ**
Ligand(L)	3396 br.	1608 sh. 1570 sh.	1461 sh.	1454 sh. 1435 sho. 1377 sh. 1311 sh.	-
$[Co(L)_2]$	-	1630 sh. 1570 sh.	1477 sh.	1453 sh. 1432 sho. 1375 sh. 1310 sh.	530 w. 471 w.
$[Ni(L)_2]$	-	1635 sh. 1571sh.	1477 s.	1450 sho. 1430 sho. 1370 s. 1311 sh.	572 w. 442 w.
$[Cu(L)_2]$	-	1633 sh. 1570 s.	1473 sh.	1455 sh. 1431 sh. 1370 sh. 1310 sh.	570 w. 472 w.
$[Zn(L)_2]$	-	1637 sh. 1570 sh.	1473 s.	1454 sh. 1435 sho. 1377 sh. 1311 sh.	516 w. 493 w.

br = broad, sh = sharp, s = strong, w = weak, sho = shoulder

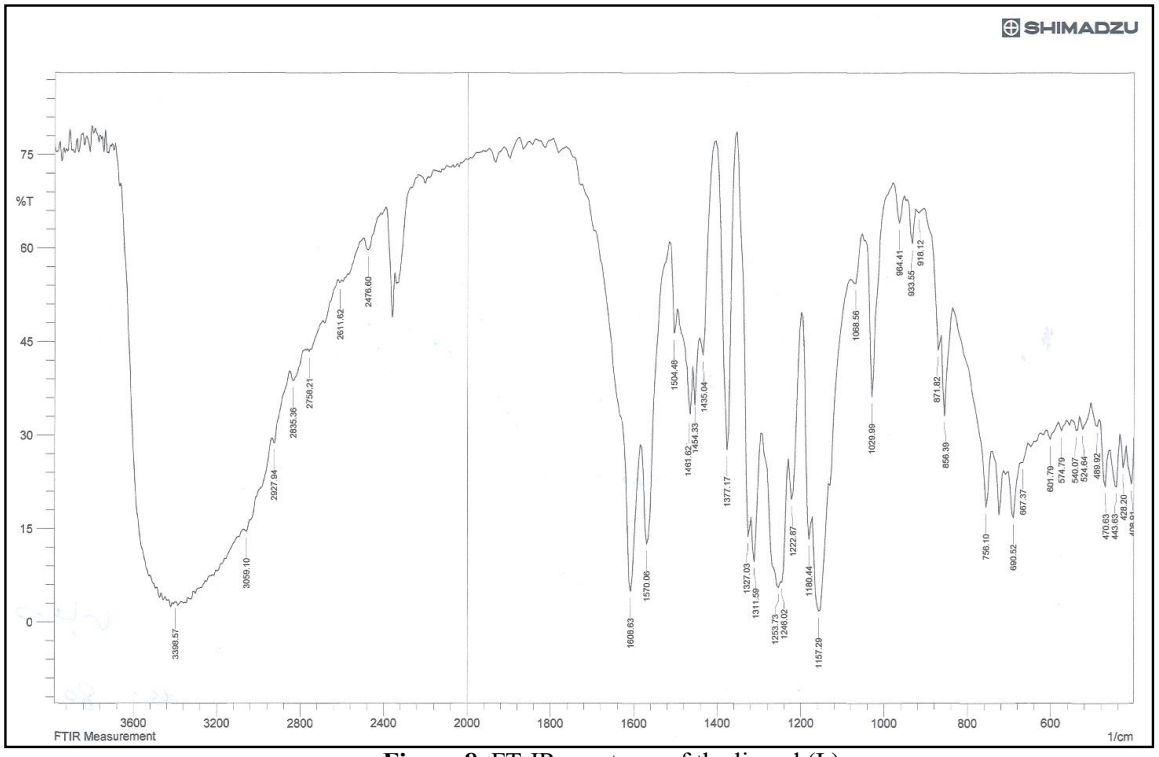

Figure 8. FT-IR spectrum of the ligand (L).

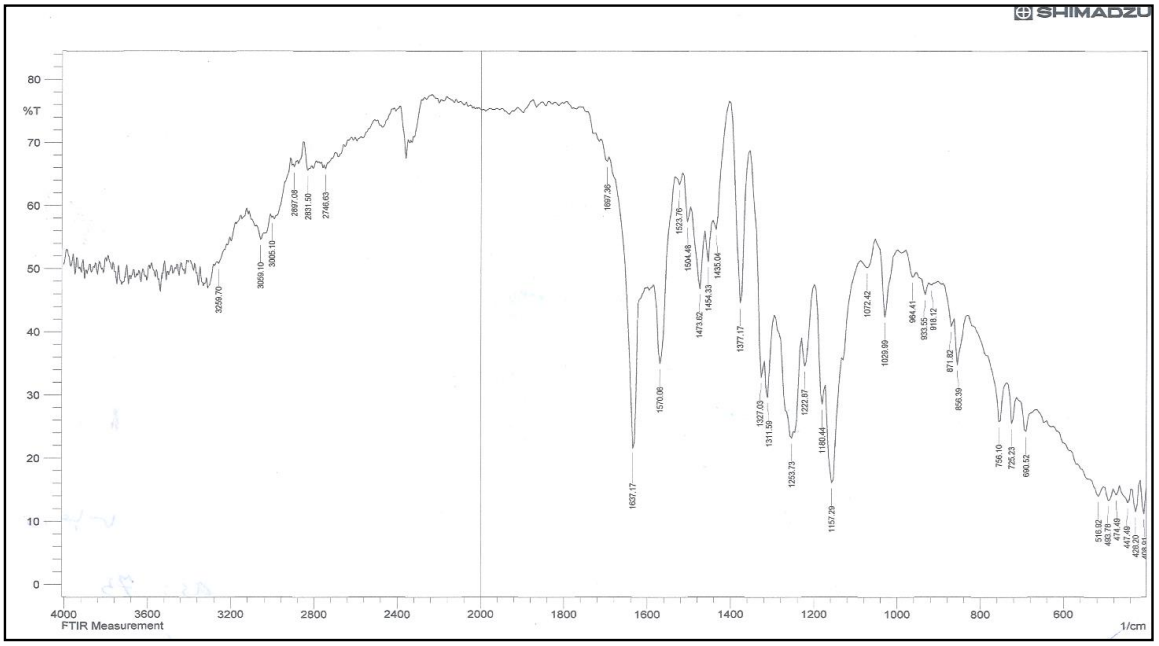

Figure 9. FTIR spectrum of the $[Zn(L)_2]$ complex.

4-Conclusion

In this paper, metal chelates have been produced with the azo ligand (L). The willing compounds are described by melting point, flame atomic absorption, FT-IR and UV-Vis spectral, other than, conductivity and magnetic moment mechanisms. Exploration of antimicrobial activities was lifted out opposite the experimented organism. Other than, analytical data an octahedral structure offered for metal chelates.

References

[1] Khedr A M and Saad FA 2015 *Turk.J.Chem.* **39** 267-280.
[2] Refat M S, El-Sayed M Y and Adam A M A 2013 *J.Mol.Struct*. **1038** 62-72.
[3] Raghavendra K R and Kumar K A 2013 *Int.J.Chem.Tech.Res.* **5** 1756-1760.
[4] Hadham A AH, Al-Amiery A A, Musa A Y and Mohamed A B 2011 *Int.J.Mol.Sci.* **12** 5747-5761.
[5] Sahoo J, Mekap S K and Kumar P S 2015 J.*Taiban University for Science* **9** 187-195.
[6] Karaman Y, Menek N, Bicar F A and Olmez H 2015 *Int.J.Electrochem.Sci.* **10** 3106-3116.
[7] Kirkan B and Gup R 2008 *Turk.J.Chem.* **32** 9-17.
[8] Tureasi C V and Sebe I 2012 *U.P.B.Sci.Bull.* **74** 109-118.
[9] Dhahir S A, Aziz N M and Bakir S 2012 *Tnt.J.Basic.Appl.Sci*. **12** 58-67.
[10] Vadher GB and Zala RV 2011 *Int.J.Chem.Sci.* **9** 87-94.
[11] Nair M LH and Sheela A 2008 *Indian.J.Chem.* **47A** 1787-1792.
[12] Iniama G E, Nfor E N, Okon E D and Iorkpiligh I T 2014 *Int.J.Sci.Techn.Res.* **3** 73-77.
[13] Jarad A J 2013 *Eur.Chem.Bull.* **2** 383-388.
[14] Patel P S and Hathi M V 2010 *J.Chem.Pharm.Res.* **2** 78-85.
[15] Jarad A J and Kadhim Z S 2015 *Int.J.Huma.Art.Med.Sci.* **3** 197-210.
[16] Silverstein R M and Webster F X 1996 *Spectrometric identification of organic compounds*, John Wiley and Sons,6th Ed, New York,180.
[17] Geary W J 1971 *Coord.Chem.Rev.* **7** 81-122.
[18] Pati A J, Donde K J, Raut S S, Patil V R and Lokhande R S 2012 *J.Chem.Pharm.Res*. **4** 1413-1425.
[19] Sharma A, Mehta T and Manish K S 2013 *Der.Chem.Si.* **4** 141-146.
[20] Cotton F A, Williknson G, Murillo C A and Bochman M 2003 *Advanced inorganic chemistry*, 6th edition, John Wiley and Sons, New York.
[21] Raman N, Jeyamurugan R, Sudharsan S, Karuppasamy K and Mitu L 2013 *Arabian.J.Chem*. **6** 235-247.
[22] Srivastava K P, Singh A and Singh S K 2014 *IOSR -J.Appl.Chem.* **7** 16-23.
[23] Al-Noor T H, Ali K F, Jarad A J and Kindeel A S 2013 *Chem.Met.Res.* **3** 26-133.
[24] Al-Naimi S H, Kndeel A S, Jrad A J and Al-Noor T H 2016*Trans.Engin.Sci.* **4** 42-47.
[25] Osowole A A 2008 *E.J.Chem.* **5** 130-135.
[26] Canakei D, Sibiyik O Y and Serin S 2014 *Int.J.Sci.Res.Innov.Tech.* **1** 52-57.
[27] Pallikavil R, Umnathur B and Krishnankuty K 2012 *Arch.Appl.Sci.Res.* **4** 223-2227.
[28] Hakim A A, Ahmed A and Benguzzi S A 2008 J.*Sci.Appl*. **2** 83-90.
[29] 29. Rajavel R, Vadivu M S and Anitha C 2008 *E.J.Chem.* **5** 620-626.

5-Acknoweledgment

The authors are grateful to Dr. Taghreed H. Al-Noor (university of Baghdad-college of Education for Pure Science Ibn-Al-Haitham) for helpful suggestions.

Theoretical Investigation For The Effect of Fuel Quality on Gas Turbine Power Plants

Theoretical Investigation For The Effect of Fuel Quality on Gas Turbine Power Plants

Omar AbdulRazzak khudair[1], Khetam Alwan Abass[1] , Noor Saadi Abed[1], Khalid Hussain Ali[2], Saad AbdulAziz[2], Ali Chlaib Shaboot[2]

[1]Ministry of Science and technology
[2]Ministry of Electricity

omar_franco64@yahoo.com

Abstract. Gas turbine engine power generation is declined dramatically because of the reduction in thermodynamic parameters as a work of turbine, compressor ratio, compressor work, and air mass flow rate and fuel consumption. There are two main objectives of this work, the first is related with the effect of fuel kinds and their quality on the operation of fuel flow divider and its performance specifically gear pump displacement and fuel flow rate to the combustion chambers of gas power plant. AL-DORA gas turbine power plant 35MW was chosen to predict these effects on its performance MATLAB Software program is used to perform thermodynamic calculations.

Fuel distribution stage before the process of combustion and as a result of the kind and its quality, chemical reaction will occur between the fuel and the parts of the gear system of each pump of the flow divider, which causes the erosion of the internal pump wall and the teeth of the gear system, thus hampering the pump operation in terms of fuel discharge.

The discharge of fuel form the eight external gates of flow divider is decreased and varied when going to the combustion chambers, so that, flow divider does not give reliable mass flow rate due to absence of accurate pressure in each of eight exit pipes.

The second objective deals with the stage of fuel combustion process inside the combustion chamber. A comparative study based upon performance parameters, such as specific fuel consumption for gas and gasoil and power generation. Fuel poor quality causes incomplete combustion and increased its consumption, so that combustion products are interacted with the surface of the turbine blades, causing the erosion and create surface roughness of the blade and disruption of gas flow. As a result of this situation, turbulence flow of these gases will increase causing the separation of gas boundary layers over the suction surface of the blade .Therefore the amount of extracted gas will decrease causing retreat work done by turbine, as a result decline of power and gas turbine power plant efficiency causing the drop in the level of electric generation. The fuel quality is found to be a strong function of specific fuel consumption and its effects on the power generation and the efficiency of the gas turbine power plants and hence, the cycle performance shifts towards favorable conditions.

Keywords: power plant, fuel consumption, chemical reaction, flow divider, combustion

1.Introduction

Gas turbine power generating device has been widely used in the developed areas, which are growing shortage of electricity energy, in turbine power plant fuel is used as working fluid. The compressor compresses the air; heat is added to compressed air by burning fuel in the chamber. The hot and high-pressure air then passed to the gas turbine, where it expands and the mechanical work is introduced. The mechanical energy converted to an electrical energy by the gas turbine. The advantages of gas turbine of power plants are fuel flexibility, large power, and small size, lightweight, fast installation time, less investment in engineering, fuel adaptability, less pollution, and simple maintenance.

Gas turbine operates on a natural gas, synthetic gas, landfill gas, and fuel oils, the fuel must be free from chemical impurities and solids. Diesel and gas oil contain sulfur as part of their chemical make-up, this effected seriously on the efficiency of the gas power plant. While the cetane number must be maintained in a specific range where the thermal efficiency of gas turbine is a function of a pressure ratio, ambient air temperature, turbine elements, turbine inlet air temperature, and the efficiency of the compressor enhancements. All these parameters must be improving with time. High sulfur and other contaminations, low cetane number are effecting on fuel quality , is in this work we summarized the parameter affecting on the quality of fuel and how does it affection the work of power plant, which can reduce the power while the ambient temperature has the ability to change the rate of power.

M.S.AL-Rasidi, et al. [1], presented an application of the industrial source complex model for short-term prediction (ISCST3) to determine the impact of SO2 released from four power plants in Kuwait. Four different scenarios were simulated along with their corresponding real case scenarios to analyse the impact of SO2 based on the Sulphur content in the fuel used by the power plants.

The comparison with the real case scenarios show that the predicted maximum hourly average ground level concentration is about 2244.19 μg/m 3, exceeding the allowable KAAQS (hourly standard is 445 μg/m 3), whereas if the fuel used in all power plants is of 0.5% Sulphur content the standard was not exceeded and the maximum hourly predicted concentration was 370.62 μg/m 3.They concluded that there is an urgent need to identify or reduce the effect of sulfur dioxide as a fuel combustion product containing sulfur.

P.Ghosh et al. [2], presented the general composition based predictive for cetane number (CN) that can be universally applied across a wide variety of Diesel fuels, Including process streams and their blend. The cetane number is correlated to a total of 129 different hydrocarbon lumps determined by a combination of supercritical fluid chromatography, gas chromatography, and mass spectroscopic methods. A total of 203 diesel fuels are considered in this study derived from various diesel-range refinery process streams and their commercial blends.

Mehaboob Basha et al. [3], employed a computational study to assess the performance of different gas turbine plants. The work includes the effect of relative humidity, ambient inlet air temperature and types of fuels on gas turbine plants. It has been observed For 70 MW frame, for a decrease of ambient inlet air temperature by 10 °F, plant net output and efficiency have been found to increase by about 5 and 2%, respectively for all fuels. More specifically, plant net output and efficiency for natural gas are higher as compare to other fuels. It has been noticed that turbines operating on natural gas emit less carbon relatively as compared to other fuels.

wong et al.[4] studied the effect of the Ash deposits resulting from the combustion of poor fuel quality and what it causes when depositing it on the moving and stationary blades of turbine of gas stations to generate electricity. It has been observed that chemical and mechanical corrosion occurs on the surfaces of the turbine blades when the fuel is burned, causing the surfaces pitting of these blades to be damaged , which should be replaced due to its effect on the workings of the turbine and the end of its service life. They decide to take into account the economic effects when this type of fuel and caused by the products of this combustion and

suggested to replace these kinds of fuels or add some additives of materials to improve the performance of fuel when burned .

Mike welch et al,[5] Show the presence of sodium, potassium, or vanadium, contaminants commonly found in air in off-shore or in coastal environments or in liquid fuels, further assessment will be required as the reaction of these metals and their salts with sulfur results in the production of sodium and potassium sulfates or vacates, which are highly corrosive to modern materials (for example, nickel alloys) used in the hot gas path components, such as turbine nozzles and rotor blades. Such corrosion can occur after many operating hours.

S.CSinghal[6] studied the characteristics of High temperature solid oxide fuel cells (SOFCs) and its effect on gas turbine power plant performance. They observed that this kind of fuel offer a clean, pollution-free technology to electrochemically generate electricity at high efficiencies. These fuel cells provide many advantages over traditional energy conversion systems including high efficiency, reliability, modularity, fuel adaptability, and very low levels of NOx and SOx emissions. Furthermore, because of their high temperature of operation (~1000°C), pressurized SOFCs can be successfully used as replacements for combustors in gas turbines; such hybrid SOFC–gas turbine power systems are expected to reach efficiencies over 70%. This paper reviews the materials and fabrication methods used for the different cell components, and discusses the performance of cells fabricated using these materials; it also discusses the materials and processing studies that are under investigation to reduce the cell cost.

Penyrat Chinda et al. [7] investigated the effect of Solid Oxide Fuel Cells (SOFCs) as hybrid systems on the gas turbine power plants cycle efficiency. Two models of solid oxide fuel cell and gas turbine power system have been developed based on simple thermodynamic expressions and implemented in MATLAB. They concluded that the performance of this cell is to be the strongest factor of operating temperature (which depends upon the preheating of the input streams) and hence when the heat exchanger properties are varied with the air mass flow rate, the cycle performance shifts towards favorable conditions. Therefore, the factors that control the cycle performance are the SOFC temperature, the turbine inlet temperature, and the exhaust temperature. However, at high SOFC temperatures, the cycle efficiency is high.

2.Theory of calculations:

A flow divider is composed by two or more modular elements (stages) with driving gears mechanically linked by an internal coupling sleeve that causes them to turn at the same speed. Unlike multiple pumps, in which the input power is mechanical (shaft connected to a motor), in a flow divider the input power is hydraulic, i.e. a flow under pressure supplies the modular elements, which are connected to the hydraulic circuits serving the users.

Flow dividers are used on gas turbines to maintain equal flows of liquid fuel to all combustors. They are passive devices that derive their motive power from the energy contained in the fuel delivered by the main fuel pump. Although designs and layouts vary, the fundamental principle of flow-divider operation is the same. Flow dividers are little more than an array of virtually identical, high-precision, spur-gear hydraulic motors (think of them as flow elements) that are mechanically coupled to run at equal rotational speeds, as shown in figure(1),(3)[8]and (2)[9].

Figure (1). Fuel flow divider

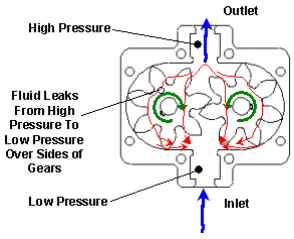

Figure (2). External gear pump

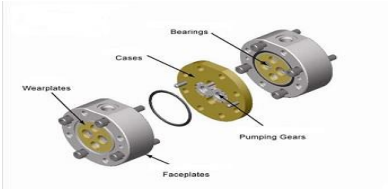

Figure (3).Fuel flow divider components

2.1 Displacement (Z)

Displacement is a volume displaced during one complete gear revolution (cubic inches, cubic gallons or (cubic cm/rev),[9].

Z = 6*W (2D-L)*(L-D)/2 ---------- (1)

Z is the gear pump displacement (cm^3/rev)

L is the length of both gear displacement (cm).

D bore diameter of one of the gear chamber (cm)

W gear width (cm)

2.2 Fuel flow Rate (Q)

Measurement of fluid delivered per unit of time,[9]

*Q = Z*N* ----------*(2)*

Q is the fuel flow rate (l/min)

Z is the gear pump displacement (cm^3)

N is the rotation speed of flow divider per min

2.3 Pump volumetric efficiency (ηv)

Volumetric Efficiency is defined as the ratio of flow rate to the volume displaced per unit of time, so that it can express as,[9]

$\eta_v = Q_{act} / Q_{ide}$ ---------- (3)

η_v is the volumetric efficiency

Q_{act} actual fuel flow rate delivers from flow divider (l/min)

Q_{ide} theoretical fuel flow rate delivers from flow divider (l/min)

2.4 Differential pressure

The differential pressure is the algebraic difference of the discharge pressure and inlet pressure, with terms expressed in like units, [9]

$\Delta p = pd - ps$ ---------- *(4)*

Where

Δp is differential pressure (bar)

P_d discharge Pressure (bar)

p_s Inlet Pressure (bar)

The pump tasks the power from a rotating shaft as shown in eq.(5)

$P_{in} = T \times W$ …….. (5)

Where P_{in} =power input to shaft (watt) or (horsepower).

W= shaft rotational speed (rad/ sec) or (rev/min).

Apportion of this power is dissipated in the pump through coulombs friction and viscous dissipation. This is not easily quantified experimentally. This power will be denoted at (P_{loss})

P_{loss}= (frication), viscous effect (watt or horse power)

The power output that can be derived from the fluid will come out of the pump in equation (6)

$P_{out} = (\Delta p \times Q) = P_{in} - P_{loss} = T \times Q. P_{loss}$… (6)

P_{out}= the power output to fluid system) (watt or horsepower).

Δp = pressure increase between inlet and outlet (PSI) or Pascal.

Q= flow rate through the pump (lit)

Q = fluid density ×pump density × r.p.m(in^3/ sec), equation (6) can expressed using the efficiency in equation (3)

$P_{OUT} = \eta \times P_{in}$ …… (6)

Where: η= mechanical efficiency and $\eta = P_{OUT} / P_{in.}$ This is a function of the fluid viscosity, clearance between internal components, and other variables. Typically, gear pump efficient around (85%).

3. Thermodynamic considerations of gas turbine

Specific fuel consumption (SFC) may be defined as the ratio of fuel used to the amount of power produced by engine, [10]

$$SFC = 3600 * \frac{f}{Wn} - - - - - - - - - - (7)$$

$$\eta_m = \frac{Wn}{f * Qnet} - - - - - - - - - - (8)$$

$$\eta_m = \frac{3600}{s.f.c * Qnet} - - - - - - - - (9)$$

Where

SFC Specific fuel consumption (m^3/MW.hr)

f fuel air ratio

Qnet higher calorific value at constant pressure (kJ//kg)

W_N specific network output (kW)

4. Results and discussion

'Figure (4)' represents the effect of impurities and pollutants for the gasoil fuel used in the operation of the gas station, which is the change in the dimension of the internal wall of the pump between the tips of the teeth, that represents the x- axis while the y axis represents the volume displacement of pump in addition to the amount of change in the flow of fuel. Its noted that the relationship is inverse proportional where the greater the change in this distance create the decreasing of the volume displacement of the pump and causing an increased the process of fuel leakage between the inner wall and the tip of the gear teeth producing low pressure pump and thus decrease the amount of fuel flow to the outside.
This decrease in fuel flow because of the fuel consist of pollutants and impurities, which increase the chemical reaction of fuel and the wall of the internal pump, which causes the wall erosion over time and increase the internal volume. Those particles resulting from the erosion of the wall remain stuck with fuel and may enter between gears teeth cause mechanical wear and the occurrence of surface pitting of the gears teeth .Therefore that fuel flow required will not reach the combustion chamber of the station and the occurrence of incomplete combustion of unequal combustion ratios between fuel and air. The difference in the flow of fuel from one pump to another leads to the lack of balance in the process of combustion within the eight combustion chambers of the station. This phenomenon is working to reduce the efficiency of combustion chambers to produce the temperature required that is satisfied turbine work.

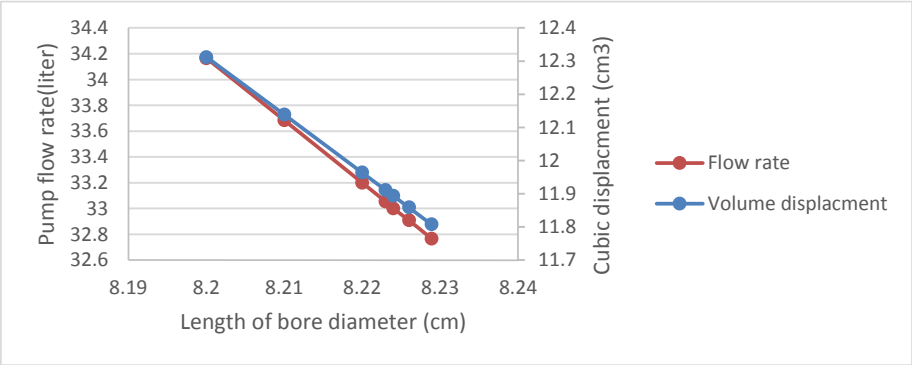

Figure (4). Core length against gear pump displacement and fuel flow rate

'Figure (5) 'shows that the gas turbine cycle efficiency is affected by specific fuel consumption, for diesel fuel .The decreasing of specific fuel consumption leads to a lower cycle efficiency**.** The curves represent the amount of diesel fuel spent for expected and practical situation. It is noticeable from the figure that the relationship between specific fuel consumption and efficiency is inverse proportional so that the gas turbine power plant efficiency begins to decline as the specific fuel expenditure is increased therefore, the gas power station is also decreased The decline for the practical efficiency curve is increased and as different as expected efficiency curve because of the diesel fuel quality used, which in turn reduces the efficiency of the plant.

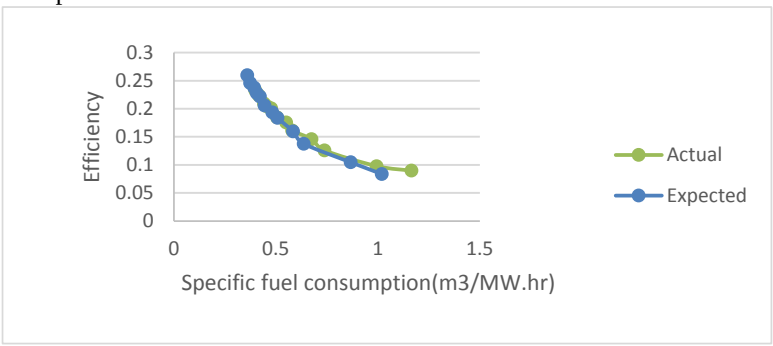

Figure (5). Gasoil fuel efficiency against specific fuel consumption

'Figure (6)' represents the variation of expected and actual specific fuel consumption. The amount of specific fuel start to decrease as the power generation of the plant increases and therefore the station's efficiency will increase due to the nature of the inverse proportion between the specific fuel consumption and the power plant generation. However, actual fuel disbursements for the actual specific fuel consumption are greater than the expected discharge when the power generation.

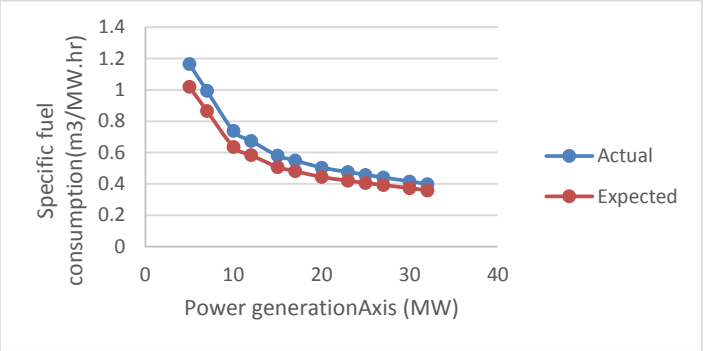

Figure (6). Gasoil fuel efficiency against power generation

'Figure (7)' represents the change of efficiency against the variation of specific fuel consumption for two kinds of fuel, gasoil and gas during plant operation. The efficiency is declined gradually as an increasing of specific fuel consumption and varied inverse proportional linearly. The efficiency of the gas power plant is regular, highly effective and low fuel consumption during gas fuel operation, while the efficiency is lower, higher fuel consumption and less efficient if the use of diesel fuel. The reason is the purity of the gas oil and its impurities, in addition, the

calorific value of gas fuel is higher than gasoil, also there is no harmful residue when the gas fuel is burned, as it is for the diesel fuel used, which seems to leave residues that interact with the surface of the turbine blades.

These waste, which are formed on the turbine blades surface as well as the high temperature inside the turbine, result in a chemical reaction with the blade surface and the formation of blade , which growth the surface roughness, thereby eroding the aerodynamic performance by increasing the region of turbulent gas flow on the blade surface and increasing energy the layers of the walls of those gases.

Thus, the separation of those layers, which leads to increased drag force on blade and reduce the lift and its efficiency. As a result of this phenomenon the stage efficiency will also reduce. The decline in the performance of the whole turbine stages leads to turbine's collapse blade performance and the reduction of the work done, so that the power generation will reduce and is not the same as when using pure gas fuel.

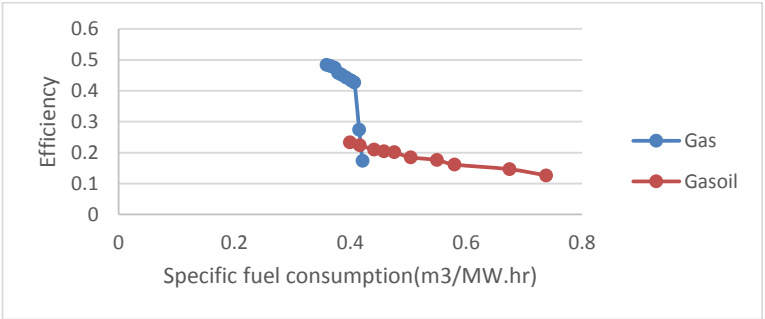

Figure (7). Gas and gasoil efficiency against specific fuel consumption

'Figure (8)' shows the relationship between the change in power generation of plant and the quantity of specific fuel consumption for both diesel and gas fuel where the correlation relationship is inverse between the change in power generation and the amount of specific fuel consumption. The higher the power generation , the less the quality of fuel consumption for both gasoil and gas, while the gasoil fuel consumption values remain lower than gas fuel at any point of power, and this shows that the efficiency of the station will be higher when using gas fuel.

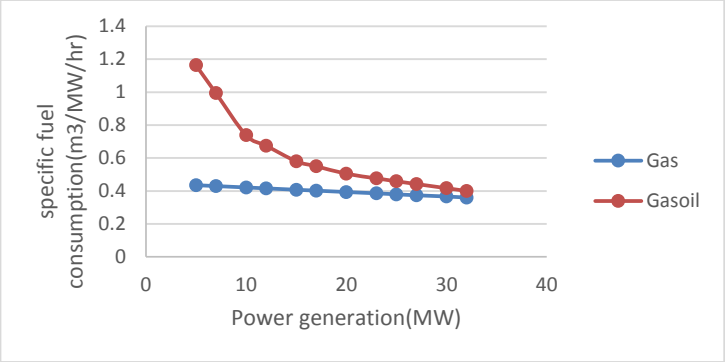

Figure (8). Gas and gasoil specific fuel consumption against power generation

'Figure (9)' represents the relationship between the power generation and the station's efficiency for both diesel and gas. The correlation between the power and efficiency changes is the proportional. As the power generation rise, the efficiency of the station will increases. However, the increase in the efficiency of the plant when using gas fuel is greater than the increase in diesel fuel. Efficiency is increased when the power generation of the station is 15 MW by 0.266 and continue this difference and by 25 percent between the gas and diesel fuel values until the power generation will be 23 MW. Therefore, the use of gas fuel is better to increase power generation and efficiency of the station.

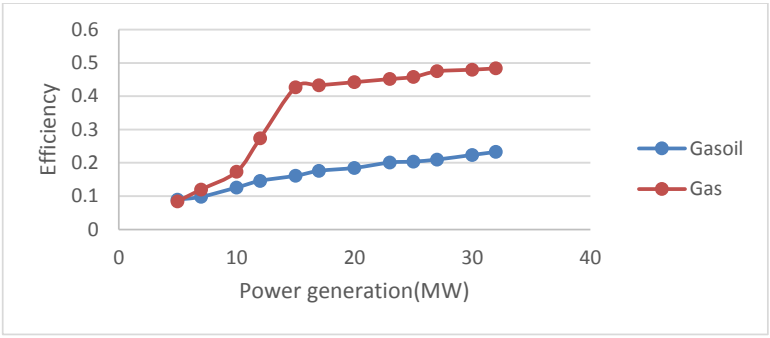

Figure (9). Gas and gasoil efficiency against power generation

References

[1] Al.Rashidi, M S , Nassehi, V, and Wakeman, R, (2005), Air quality modelling of Sulphur dioxide emission from power plant in Kuwait; international conference on modelling, monitoring and management of air Pollution No. 13, Cordoba, Spain. Air Pollution, XIII,79-87.
[2] Ghosh, P and Jaffe , S B,(2006), "Detailed composition based model for predicating the Cetane Number of Diesel fuels" , *Ind. Eng. Chem. Res*., **45**, 346-351 .
[3] Mehaboob Basha, S M Shaahid. Luai Al- Hadhrami.(2012). Impact of fuels on performance

and Efficiency of Gas turbine power plants. Volume **14**, pp558-565.
[4] Wong M A , Frogiel A, Lopez D,(2006). Investigation and analysis of high temperature corrosion and degradation of marine boiler combustion swirler. *Journal of marine, Science and Application* volume **15**, issue1, pp. 86-94.
[5] Mike Welch et. al ,(2014), Combustion , fuels and Emission for industrial gas turbines , turbo machinery laboratory , Texas And M Eng. Experimental station.
[6] S.C Singhal, (2000), Advances in solid oxide fuel cell technology, volume **135**, issues 1-4, pages 305-313.
[7] Penyrat chinda,Pascal Brault,(2012).Thrbhybrid solid oxide fuel cell(SOFC) and gas turbine (GT)system steady state modeling.*International Journal of Hydrogen Energy* .pp.9237-9248.
[8] Roper Pump Company,(2008),Fuel Flow Divider,Po Box 269 ,3757 old Mysville Road Commerce ,GA30529,USA.
[9] Gear Pump Basics,McNally Industries,(2008),340 West Benson Avenue Grantsburg,WI,54840,USA.
[10] H.Cohen, G.F.C. Regens ,(1971**),** Gas Turbine Theory, Second edition, Mc Graw Hill .

Heavy metals characteristics of settled particles of streets dust from Diwaniyah City- Qadisiyah Governorate - Southern Iraq

IOP Conf. Series: Journal of Physics: Conf. Series **1003** (2018) 012023 doi:10.1088/1742-6596/1003/1/012023

Heavy metals characteristics of settled particles of streets dust from Diwaniyah City- Qadisiyah Governorate - Southern Iraq

Moutaz A. Al-Dabbas[1]*, Khalid H. Mahdi[2], Raad Al- Khafaji[2] and Kawthar H. Obayes[3]

[1*] College of Science, University of Baghdad, Baghdad, Iraq,profaldabbas@yahoo.com

[2]College of Education for pure sciences (Ibn Al-Haitham), University of Baghdad,raadalkhafagee@yahoo.com

[3]College of Education, University of Qadisiyah, Qadisiyah Governorate, Iraq.

Abstract. Road-side dust samples were collected from selected areas of Diwaniyah city-Qadisiyah Governorate - Southern Iraq. The heavy metals (Fe, Co, Ni ,Cu, Zn and Pb) in these streets dust samples were studied and used as indicator for pollution by using three of main indices (I- geo, CF, and PLI). Determination of heavy metal in the roadside dust is with XRD and XRF methods. I-geo for Co, Zn, Pb, and Ni in the studied sites shows relative values of class 1, which indicated the slightly polluted, while I-geo for Fe and Cu shows relative values of class 0, which indicated no pollution. The contamination factor for Co, Zn, Pb, and Ni classified as class 2, which indicate moderately contamination, while the contamination factor for Fe and Cu classified as class 1, which indicate low contamination. PLI values in the all of studied sites classified as class 2 (Deterioration on site quality) indicating local pollution, as well as denote perfection with (class 0) of no pollution. The distribution pattern of metals percentages was affected by gases emitted from transportation vehicles as well as the prevailing wind direction.

1. INTRODUCTION

Dust storms are significant phenomena in Iraq and especially in Diwaniyah City which represent a serious natural hazard where the number of day in which dust storms occur is considerable , such phenomenon have a wind speed at least 25 mile/hour , playing an active role in transporting and deposition of material of different sizes led to change in earth surface. These storms are most prevalent in spring and summer when a prevailing north westerly wind known locally as the "Shamal " kicks up the fine desert sand and silt along the Tigris and Euphrates rivers basins towards south part of Iraq (Al-Dabbas et al.,2011, and 2012). Moreover, Al-Dabbas et al.,(2011) estimated that the texture of dust fall out ranged from sandy clayey silt and clayey sandy silt , whereas the quartz, feldspar, and calcite were most of light minerals, and chlorite, illite, montmorillonite, palygoreskite and kaolinite were most of clay minerals in the dust fallout. Soil receives pollutants from different sources including exhaust gases from vehicles, factory chimneys, dust storm etc. Banerjee, 2003, concluded that the composition and quantity of chemical matrix of road dust are indicators of environmental pollution (Khuwaidem, 2007 ;Awadh, 2013). Street dust is typically derived from anthropogenic sources via the interaction of natural solid, liquid or gaseous materials with pollutant (Al-Khashman, 2004 and 2007;Aydin,et al.,2012). The effects of heavy metals in road dust on human health include respiratory system disorders, nervous system interruptions and the risk of cancer in later life (Ferreira- Baptista and Miguel, 2005; Ahmed and Ishiga, 2006). The rapid growth in population and urbanization in Diwaniyah City (of semi-arid to arid climate) exert a pressure on its urban environment. The source of heavy elements can be from the quaternary unconsolidated sediment of the Mesopotamian plain and from river sediments (sand, silt and clay) as natural sources as well as the artificial sources that include industrial sources that supply the heavy metals to the air and causing contamination of the atmosphere (Al-Dabbas et al., 2011). Urbanization and industrial processes development and increase extraction of oil and the subsequent burning of associated gas especially during the past years in Diwaniyah city , these exerts formed a heavy pressure on its urban environment. For these reasons it is necessary to know the main of heavy metals in the dust storm in order to understand their behavior and impact. This work was carried out on roadside dust in twelve selected sites of Diwaniyah City- Qadisiyah Governorate - Southern Iraq 'Figure 1'.

The objective of this study is to elucidate the concentrations and distribution of heavy metals (Fe, Zn, Cu, Co, Pb, and Ni) and assessment of heavy metals pollution in the streets dust particles of Diwaniyah city by using the geo- accumulation (I-geo), contamination factor (CF) ,and Pollution load index (PLI) as first attempt to evaluate the heavy metals pollution in the streets dust samples particles in Diwaniyah city - southern Iraq

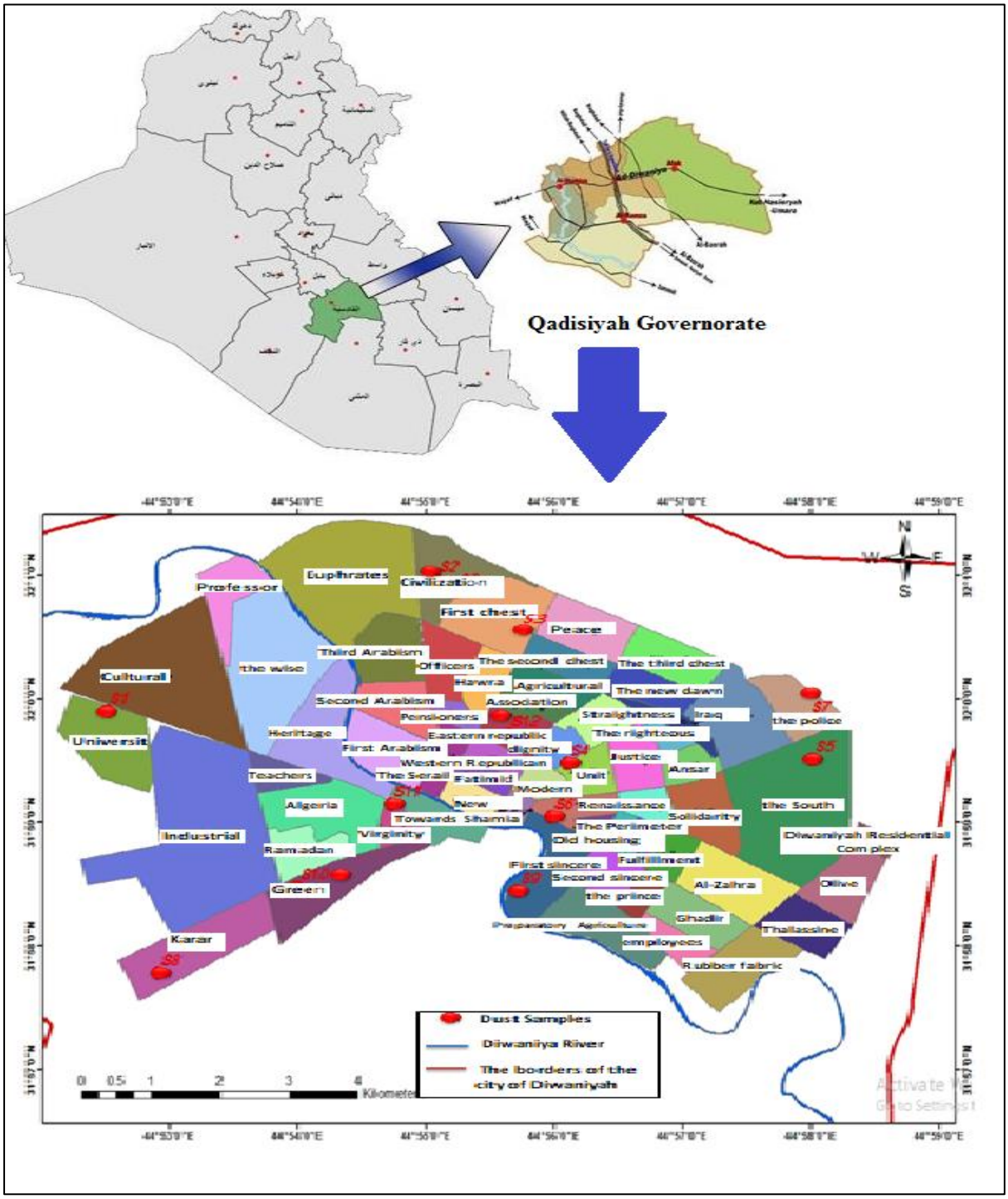

Figure 1: Locations of the collected streets dust samples within Diwaniyah city.

2. METHeDology

The study area is Diwaniyah city that divided by Shatt Al-Diwaniyah (The extension of Shatt Al-Hillah which is an eastern part of Euphrates River). Total of twelve road dust samples were collected (Based on traffic load, major roadways near the fuel stations old military camps) during 2016; five from the western district (the west part of Diwaniyah) and seven from the eastern district (the east part of Diwaniyah) locations were recorded with GPS (Figure 1, Table1). These samples were analyzed in the laboratory of geochemistry in the Geology Department, University of Baghdad by XRD and XRF Methods. Ten grams of samples were powdered to detect the Fe, Co, Zn, Cu, Ni, and Pb elements by XRF and XRD Methods. The results are tabulated in (Table 1).

Table 1: Values of heavy metals for the streets dust samples within Diwaniyah city.

Sample No.	Fe_2O_3 %	Co ppm	Zn ppm	Cu ppm	Ni ppm	Pb ppm
1	2.26	4	130	25	77	45
2	2.86	4	80	25	100	32
3	2.5	4	100	30	100	20
4	2.16	4	80	22	70	22
5	5.26	18	160	45	200	27
6	2.6	4	90	23	86	35
7	4.86	16	88	25	164	17
8	2.73	4	120	37	94	40
9	2.98	4	114	38	100	70
10	3.42	4	190	80	100	110
11	2.82	4	97	30	90	60
12	3.63	4	130	160	130	40
Mean of This study	3.17	6	115	45	109	43
Mean of Al-Jaberi ,2014, results	0.23	29	123	27	119	48

Table 2: CF, I-geo and PLI index for the streets dust samples within Diwaniyah city.

S.No.	Fe2O3 %		Co ppm		Zn ppm		Cu ppm		Ni ppm		Pb ppm		
	CF	I-geo	CF	I-geo	CF	I-geo	CF	I-geo	CF	I-geo	CF	I-geo	PLI
1	0.75	-0.99	0.16	-3.23	1.86	0.31	0.46	-1.72	1.03	-0.55	3.60	1.26	0.85
2	0.95	-0.65	0.16	-3.23	1.14	-0.39	0.46	-1.72	1.33	-0.17	2.56	0.77	0.80
3	0.83	-0.85	0.16	-3.23	1.43	-0.07	0.55	-1.46	1.33	-0.17	1.60	0.09	0.78
4	0.72	-1.06	0.16	-3.23	1.14	-0.39	0.40	-1.91	1.00	-0.69	1.76	0.23	0.67
5	1.75	0.23	0.72	-1.06	2.29	0.61	0.82	-0.88	2.67	0.83	2.16	0.53	1.55
6	0.87	-0.79	0.16	-3.23	1.29	-0.22	0.42	-1.84	1.15	-0.39	2.80	0.90	0.79
7	1.62	0.11	0.64	-1.23	1.26	-0.26	0.46	-1.72	2.19	0.54	1.36	0.14	1.10
8	0.91	-0.72	0.16	-3.23	1.71	0.19	0.67	-1.16	1.25	-0.26	3.20	1.09	0.94
9	0.99	-0.60	0.16	-3.23	1.63	0.12	0.69	-1.12	1.33	-0.17	5.60	1.90	1.05
10	1.14	-0.40	0.16	-3.23	2.71	0.86	1.46	-0.04	1.33	-0.17	5.98	1.99	1.43
11	0.94	-0.67	0.16	-3.23	1.39	-0.11	0.55	-1.46	1.20	-0.32	4.80	1.68	0.93
12	1.21	-0.31	0.16	-3.23	1.86	0.31	2.91	0.96	1.73	0.21	3.20	1.09	1.34
Mean	1.06	-0.56	0.25	-2.88	1.64	0.08	0.82	-1.17	1.46	-0.11	3.45	0.99	1.02

Table 3: Classified grades of I- geo, CF and PLI indices, (after Thomilson et al (1980) and Al-Jaberi and Al-Dabbas, 2014).

I-geo	CF contamination factor	PLI
≤ 0 (class 0), Practically unpolluted		<1 Perfection (class 0
0 < to ≤ 1(class 1), slightly polluted	<1 Low contamination (class 1).	=1 Baseline Level (class 1).
1< to ≤ 2 (class 2), Moderately polluted	1≤CF< 3 Moderate contamination (class 2).	>1 Deterioration on site quality (class 2)
2< to ≤ 3 (class 3), moderately severely polluted	3≤ CF≤6 Considerable Contamination (class 3).	
3< to ≤ 4 (class 4), Severely polluted	>6 Very high Contamination (class 4).	
4< to ≤ 5 (class 5), Severely extremely polluted		
> 5 (class 6), Extremely polluted		

3. RESULT AND DISCUSSION

A-Heavy metals

Metals, a major category of globally-distributed pollutants, are natural elements that have been extracted from the earth and harnessed for human industry and products for millennia. Metals are notable for their wide environmental dispersion from such activity; their tendency to accumulate in select tissues of the human body; and their overall potential to be toxic even at relatively minor levels of exposure. Some metals, such as copper and iron, are essential to life and play irreplaceable roles in, for example, the functioning of critical enzyme systems. Other metals are xenobiotics, i.e., they have no useful role in human physiology (and most other living organisms) and, even worse, as in the case of lead and mercury, may be toxic even at trace levels of exposure. Even those metals that are essential, however, have the potential to turn harmful at very high levels of exposure, a reflection of a very basic tenet of toxicology--"the dose makes the poison. Exposure to metals can occur through a variety of routes. Metals may be inhaled as dust or fume (tiny particulate matter, such as the lead oxide particles produced by the combustion of leaded gasoline).Metals may also be ingested involuntarily through food and drink (Howard Hu, 2002).Six common heavy metals are discussed in this brief: iron, cobalt, zinc, copper, lead, and nickel in the dust particles of the studied area (Table1).Discussion of these heavy metals is as follows:

1-Lead

As a result of human activities, such as fossil fuel burning, mining, and manufacturing, lead and lead compounds can be found in all parts of our environment (includes air, soil, and water). Lead can affect every organ and system in the body. Exposure to lead can damage the brain and kidneys and ultimately cause death (CHSR, 2009). The human body may take the lead through air which ranges between less than (4 Mg /day) and more than (200 Mg/day) according to area where he lives. The averages concentrations of Pb in dust particles of in Diwaniyah city selected sites ranging from 22 ppm in site No. 7 to 110 ppm in site No. 10 with mean value of 43 ppm .

2- Copper

Copper toxicity is contributor to health problems such as anorexia, depression, anxiety, liver and kidney damage, headaches, and allergies (CHSR, 2009). The averages concentrations of Cu in dust particles of in Diwaniyah city selected sites ranging from 17 ppm in site No. 4 to 160 ppm in site No. 12 with mean value of 45 ppm.

3- Iron

The corrosive nature of Iron seems to further increase the absorption. Target organs are the liver, cardiovascular system, and kidneys. Iron exposure in utero, in infancy and childhood may result in low birth rate, anemia, neurological impairment, IQ deficits and growth retardation (CHSR, 2009). The averages concentrations of Fe in dust particles of in Diwaniyah city selected sites ranging from 2.16 % in site No. 4 to 5.26 % in site No. 5 with mean value of 3.17%.

4- Zinc

The excess amount of Zinc can cause system dysfunctions that result in impairment of growth and reproduction ((McCluggage, 1991; Nolan, 2003). The clinical signs of zinc toxicities have been reported as vomiting, diarrhea, bloody urine, liver failure, kidney failure and anemia (Kabata-Pendias and Mukherjee,2007). The averages concentrations of Zn in dust particles of in Diwaniyah city selected sites ranging from 80 ppm in site No. 4 and No.2 to 190 ppm in site No. 10 with mean value of 115 ppm.

5- Nickel

The high Nickel concentrations are carcinogenic to human and animals which result in respiratory system rapid damage and cause health affection , vertigo, bronchitis and Asthma (CHSR,2009). The averages concentrations of Ni in dust particles of in Diwaniyah city selected sites ranging from 70 ppm in site No. 4 to 200 ppm in site No. 5 with mean value of 109 ppm.

6- Cobalt

The cobalt increase rats will cause disturbances in some important organism (CHSR, 2009). The averages concentrations of Cobalt (Co) in dust particles of in Diwaniyah city selected sites ranging from 4 ppm in 10 sites to 18 ppm in site No. 5 with mean value of 6 ppm.

Observed from the concentrations of heavy metals in the dust particles of studied sites (Table 1) that significantly increase of these metals in site No. 5 and No. 10, this increase may be due to urbanization and industrial processes problems, represented by manufacturing, waste flaring associated gas from oil drilling sites, and from vehicle emission.

Comparing the above results with that of Al-Jaberi, 2014, reflect that they are lower for Co, Zn, Ni and Pb except for Fe and Cu values which are higher.

B- Contamination evaluation:

Three indices were selected to evaluate the contamination level of Fe, Co, Zn, Cu, Ni, and Pb in the dust particles. These are contamination factor (CF) ,Geo accumulation index (I- geo), and Pollution Load Index (PLI) (Tables 2 and 3).

1- Geo- accumulation index (I- geo):

The Geo accumulation (I-geo) index means the assessment of contamination by comparing the levels of heavy metal obtained to a background level (Muller, 1969; Gowd et al., 2010). Geo-accumulation index (I- geo) was determined by the following equation according to Muller (1969).

I- geo = log 2 (Cn/1.5 Bn) Where:

Cn = the heavy metals concentration in the sediments and

Bn = the geochemical background concentration of the heavy metals (crustal average) (Muller ,1969;Taylor and McLennan, 1985 ; Lu et al ,2009). This index range from subzero to more than 5 having 7 grades (Table 3). The highest grade (6) reflects a 100-fold enrichment and (0) reflects the background concentration. The Fe_2O_3 was found negative in most of the sites, ranging from -1.06 to -0.31 (Table 2), These results are of (class 0) which indicated that the concentrations of Fe_2O_3 in the dust particles of studied sites are unpolluted and lower than the background (Table 3). While, the samples from sites No. 5 and No.7 show I-Geo of 0.23 and 0.11 respectively, which reflect (class 1) of slightly polluted sites.

The Co was found negative in all the sites, ranging from -1.06 to -3.23 (Table 2), These results are of (class 0) which indicated that the concentrations of Co in the dust particles of studied sites are unpolluted and lower than the background (Table 3).

The Zn was found negative in the sites (No. 2, 3, 4, 6, 7 and 11), ranging from -0.07 to -0.39 (Table 2), These results are of (class 0) which indicated that the concentrations of Zn in the dust particles of studied sites are unpolluted and lower than the background (Table 3). While in the sites (No. 1, 5, 8, 9, 10 and 12), are with positive values I-Geo values ranging from of 0.12 to 0.61 which reflect (class 1) of slightly polluted sites (Table 2).

The Cu was found negative in all the sites, ranging from -0.04 to -1.91 except site No. 12 that has positive value of 0.96 (Table 2). These results are of (class 0) which indicates that the concentrations of Cu in the dust particles of studies sites are unpolluted and lower than the background ,except site No.12 which reflect (class 1) of slightly polluted sites (Table 2).

The Ni was found negative in most of the sites, ranging from -0.17 to -0.69 (Table 2). These results are of (class 0) which indicated that the concentrations of Ni in the dust particles of studied sites are unpolluted and lower than the background (Table 3). While site No. 5, No.7 and No.12 are with positive I-Geo of 0.83, 0.54 and 0.21respectively, which reflect (class 1)of slightly polluted sites (Table 2).

The Pb had positive values in the all of studied sites, some ranging from 0.09 to 0.94 (Table 3); these results are of (class 1) which indicated that the concentrations of Pb in the dust particles of these sites are slightly polluted (Table 2). While, the other sites ranging from 1.09 to 1.99 of (class 2) which indicated moderately polluted.

2- Contamination factor (CF):

Contamination factor (CF) was determined following equation according to Thomilson et al (1980). The level of contamination by metals was established by applying the CF that can be calculated as follows:

CF= Cm Sample/ Cm Background, Tables 2 and 3.

The contamination factor (CF) for Fe, Co, Zn, Cu, Ni, and Pb was calculated in Table 2. Lead (Pb) classified as class 2 representing moderate contamination ranging from 1.36 to 2.80 for some samples. While other samples classified as class 3 representing Considerable contamination in six samples (No. 1, 8, 9, 10, 11, 12) ranging from 3.20 to 5.98. The CF for Ni classified as class 2 which indicate moderately contamination in all the studied sites, ranging from 1.00 to 2.67. It is believed that considerable part of Lead and nickel find their way into the environment as a result of the burning of diesel oil and oil spilling that caused to increase both of nickel in the sediments. The CF for Cu classified as class 1 which indicate Low contamination ranging from 0.40 to 0.82 , except two sites (No.10 and 12) have 1.46 and 2.91 respectively, classified as class 2 representing moderate contamination . It is believed that considerable part of copper finds its way into the environment as a result of the burning of diesel oil and may be due to the disposal of copper-containing wastewater. Zinc (Zn) classified as class 2 representing moderate contamination ranging from 1.14 to 2.71. Zn is come from toxic waste from industrial sources (Thorpe and Harrison, 2008). Cobalt (Co) classified as class 1 representing a low contamination ranging from 0.16 to 0.72. The CF for Fe classified as class 1 which indicate low contamination, ranging from 0.72 to 0.99 except four sites (No. 5, 7, 10, 12) classified as class 2 which indicate Moderate contamination, ranging from 1.14 to 1.75. It is believed that considerable part of iron finds its way into the environment as a result of the burning of diesel oil and may be due to the disposal of iron -containing wastewater.

3- Pollution load index (PLI):

The PLI provides a simple but comparative means for assessing a site quality. Pollution load index (PLI) was determined following equation according to Thomilson et al (1980), where (PLI) is expressed as follows:

PLI = $\sqrt[n]{CF1 \times CF2 \times CF3 \times \ldots..x\ CFn}$, Where:

n= the number of studied metals in each site.

The Pollution Load Index (PLI) for Fe, Co, Zn, Cu, Ni, and Pb was calculated and classified as class 0 with perfection of no pollution ,while five sites were classified as class 2 (Deterioration on site quality) indicating local pollution, ranging from 1.05 to 1.55.

4. CONCLUSION

The heavy metals (Fe, Co, Ni ,Cu, Zn and Pb) in these streets dust samples were studied and used as indicator for pollution by using three of main indices (I- geo, CF, and PLI). In the roadside dust ,the heavy metal contents were determined using XRD and XRF Methods. Comparing the above results

with that of Al-Jaberi, 2014, reflect that they are lower for Co, Zn, Ni and Pb except for Fe and Cu values which are higher. I-geo for Co, Zn, Pb, and Ni in the studied sites shows relative values of class 1, which indicated the slightly polluted, while I-geo for Fe and Cu shows relative values of class 0, which indicated no pollution. The contamination factor for Co, Zn, Pb, and Ni classified as class 2, which indicate moderately contamination, while the contamination factor for Fe and Cu classified as class 1, which indicate low contamination. PLI values in the all of studied sites classified as class 2 (Deterioration on site quality) indicating local pollution, as well as denote perfection with (class 0) of no pollution. The distribution pattern of metals percentages was affected by gases emitted from transportation vehicles as well as the prevailing wind direction.

REFERENCE

[1] Ahmed F, and Ishiga, H., 2006. Trace metal concentrations in street dusts of Dhaka city, Bangladesh, Atmos. Environ., 40: 3835-3844.
[2] Al-Dabbas, M.; Abbas, M.; and Al-Khafaji, R., 2012.Dust storms loads analyses –Iraq, Arab.J.Geosci.5-121-131.
[3] Al-Dabbas, M.; Abbas, M.; and Al-Khafaji, R., 2011.The Mineralogical and Micro-Organisms Effects of Regional Dust Storms over Middle East Region. International Journal of Water Resources and Arid Environments, No. 1 Vol.2, pp- 129-141.
[4] Al-Jaberi , M. H. A. ,2014. Heavy metals characteristics of settled particles during dust storms in Basrah city- Iraq, IJSR ,Volume : 3 , Issue : 10 , ISSN No 2277 – 8179, pp.14-18.
[5] Al-Jaberi , M. H. A. and Al-Dabbas ,M.A. , 2014. Assessment of Heavy Metals Pollution in the Sediments of Iraqi Coastlines, IJSR ,Volume : 3 , Issue : 9 , ISSN No 2277 – 8179, pp.455-459.
[6] Al-Khashman OA, 2004. Heavy metal distribution in dust, street dust and soils from the work place in Karak Industrial Estate, Jordan, Atmospheric Environment, 38, 6803–6812.
[7] Al-Khashman OA ,2007. The investigation of metal concentrations in street dust samples in Aqaba city, Jordan, Environ. Geochem.Health, 29: 197-207.
[8] Awadh, S.M., 2013. Assessment of the potential pollution of cadmium, nickel and lead in the road-side dust in the Karkh district of BaghdadCity and along the highway between Ramadi and Rutba, Western Iraq. Merit Research Journal of Environmental Science and Toxicology, Vol. 1, No.7, pp. 126-135.
[9] Aydin, F.; Aydin, I.; Erdogan, S.; Akba, O; Isik, B; Hamamci, C., 2012.Chemical Characteristics of Settled Particles during a Dust- Storm. Pol. J. Environ.Stud. Vo.21, No.3, pp—33-537.
[10] Banerjee ADK ,2003. Heavy metal levels and solid phase speciation in street dusts of Delhi, India. Environ. Pollut., 123: 95-105.
[11] CHSR. Center for Hazardous Substance Research.2009.Environmental Science and Technology Briefs for Citizens, Kansas State University, as part of the Technical Assistance to Brownfields communities (TAB) program).
[12] Ferreira-Baptista L, ED de Miguel ,2005. Geochemistry and risk assessment of street dust in Luanda, Angola: A tropical urban environment. Atmos. Environ., 9: 4501-45312.
[13] Gowd, S.S.; Reddy, M.R. and Govil, P.K., 2010.Assessment of heavy metal contamination in soils at Jajmau (Kanpur) and Unnao industrial areas of the Ganga Plain, Uttar Pradesh, India. J. Hazardous Mat. Vol. 174, pp-113-121.
[14] Howard Hu, M.D., 2002. Human health and heavy metals exposure. In: Life Support: The Environment and Human Health, Michael McCally (ed), MIT press.
[15] Kabata-Pendias, A. and Mukherjee A.B. 2007. Trace Elements from Soil to Human. Springer-Verlag Berlin Heidelberg. P 561.

[16] Khwedim, K.H.; Al-Anssari, H.R.; and Al- Bassam K., 2009. Study of distribution of some heavy metals in the soil of Basra city- south of Iraq", Iraqi Journal of Science, V.50, No.4,533-542pp.
[17] Lu, X.L.; Wang, K.; Lei, J.H.andZhai, Y., 2009. Contamination assessment of copper, lead, zinc,manganese and nickel in street dust of Baoji, NW China, J. Hazardous Mat. Vol.161, pp-1058-1062.
[18] McCluggage, D., 1991. Heavy Metal Poisoning, NCS Magazine, Published by The Bird Hospital, CO, U.S.A. (www.cockatiels.org/articles/Diseases/metals.html).
[19] Muller, G., 1969. Index of geoaccumulation in sediments of the Rhine River, J. Geol. 2:108-118.
[20] Nolan, K., 2003. Copper Toxicity Syndrome, J. Orthomol. Psychiatry , Vol.12, No.4, pp.270 – 282.
[21] Taylor, S.R., and McLennan, S.M., 1985.The continental crust: its composition and evolution, Blackwell, Oxford.
[22] Thomilson, D.C.; Wilson, D.J.; Harris, C.R. and Jeffrey, D.W., 1980.Problem in heavy metals in Estuaries and the formation of pollution index. Helgol. Wiss. Meeresunlter, No.33, Vol-1–4, pp- 566–575.
[23] Thorpe A, RM Harrison ,2008. Sources and properties of non-exhaust particulate matter from road traffic: A review. Sci. Total Environ., 400(1-3): 270-282. doi:10.1016/j.scitotenv.06.007.

Intelligent cloud computing security using genetic algorithm as a computational tools

IOP Conf. Series: Journal of Physics: Conf. Series **1003** (2018) 012024 doi:10.1088/1742-6596/1003/1/012024

Intelligent cloud computing security using genetic algorithm as a computational tools

Mazin H Razuky AL- Shaikhly

Baghdad College of Economic Sciences University

Abstract. An essential change had occurred in the field of Information Technology which represented with cloud computing, cloud giving virtual assets by means of web yet awesome difficulties in the field of information security and security assurance. Currently main problem with cloud computing is how to improve privacy and security for cloud "cloud is critical security" .This paper attempts to solve cloud security by using intelligent system with genetic algorithm as wall to provide cloud data secure, all services provided by cloud must detect who receive and register it to create list of users (trusted or un-trusted) depend on behavior .The execution of present proposal has shown great outcome.

Keywords. Cloud, cloud service, service seclude, genetic algorithm.

1. Introduction

Currently one of the major topics of many information technology discussions is cloud computing and the key point in them is cloud computing security the main aim is relationship between system stability and security to improve security by using intelligent machine (genetic algorithm) as clear with section 2 cloud computing, section 3 intelligent system, section 4 experimental result and section 5 conclusion.

2. Cloud computing

Cloud computing suppliers convey basic business applications online as administrations which are gotten to from another web administration or programming like a web browser, while the product and information are put away on server [1, 2].

2.1 Cloud service and cloud deployment model type

Cloud administrations conveyance demonstrate is ordinarily alluded to as a SPI and falls into three by and large acknowledged administrations is Saas, Paas and Iaas as show with Figure 1 [3, 17, 19].

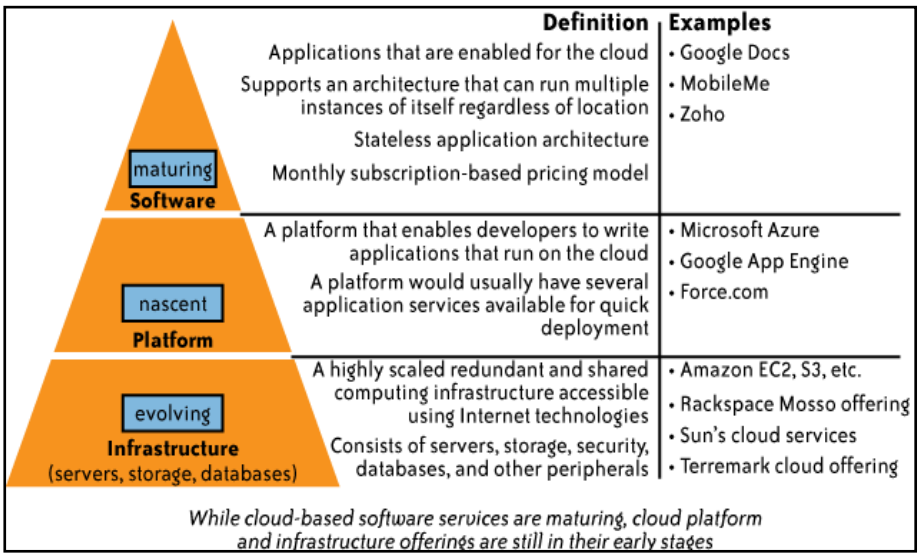

Figure 1. Cloud services delivery model [17]

The cloud services can be implemented in four deployment models:

1. **Public Cloud**: The cloud framework is influenced accessible to the overall population or extensive industry to gathering and is claimed by an association offering cloud administrations.
2. **Private Cloud**: The cloud foundation is worked completely for a solitary association. It might be overseen by the association or an outsider, and may exist on-premises or o-premises.
3. **Community Cloud:** The cloud framework is shared by a few associations and backings a specific group. It might be overseen by the associations or an outsider, and may exist on-premises or o_premises.
4. **Hybrid Cloud**: The cloud infrastructure is a composition of two or more clouds (private, community or public) that are bound together by standardized or proprietary technology that enables portability of data and application [1, 10, 19].

2.2 Scheduler of cloud computing service

Cloud computing administrations have developed in prevalence, the measure of information and assignments to be managed have additionally strongly expanded, requiring a great deal of framework assets and some of the time bringing about extreme asset waste . Aim to schedule these data and tasks more efficiently. In order to analyze the problem at a somewhat detailed level see Figure 2 (module for cloud task scheduling) [4, 5, 6, 18].

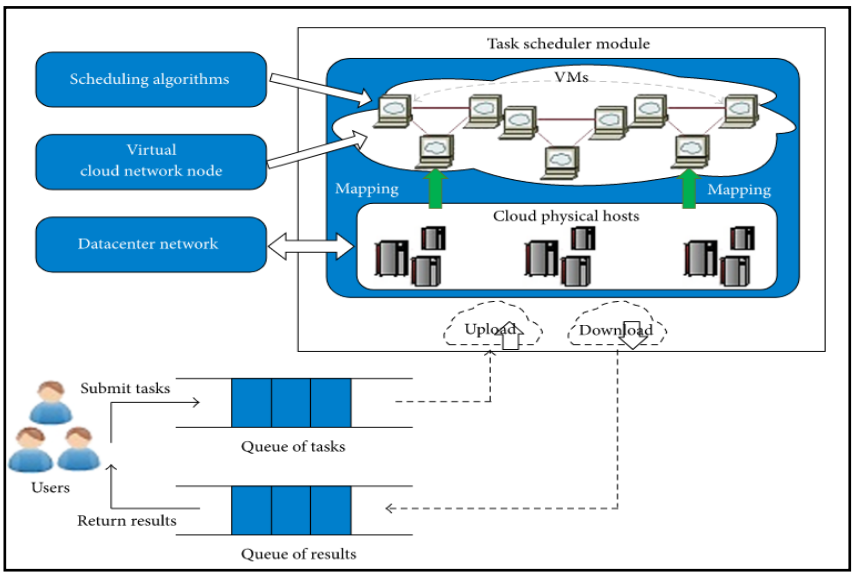

Figure 2. Module for cloud task scheduling [4].

Round-robin (RR) is one of the calculations utilizes by process and system schedulers in registering [7, 8]. As the term is by and large utilized, time cuts (otherwise called time quanta) [9]. Round-robin planning is basic, simple to actualize, and sans starvation. Round-robin planning can likewise be connected to other booking issues, for example, information bundle planning for PC systems. It is a working framework concept [10].

2.3 security and stability relation between us

It is well-known that cloud computing has many potential advantages and many enterprise applications and data are migrating to public or hybrid cloud. But regarding some business-critical applications, the organizations, especially large enterprises, still wouldn't move them to cloud. The market size the cloud computing shared is still far behind the one expected. From the consumers' perspective, cloud computing security concerns, especially data security and privacy protection issues, remain the primary inhibitor for adoption of cloud computing services [9, 10, 19].

Modern computer systems are plagued with stability and security problems: applications lose data, web servers are hacked, and systems crash under heavy load. Many of these problems arise from rare program behaviors. PH (process Homeostasis) is a Linux 2.2 kernel extension which detects unusual program behavior and responds by slowing down that behavior. Inspired by the homeostatic mechanisms organisms use to stabilize their internal environment, pH detects changes in program behavior by observing changes in short sequences of system calls. When pH determines that a process is behaving unusually, it responds by slowing down that process's system calls. If the anomaly corresponds to a security violation, delays often stop attacks before they can do damage. Delays also give users time to decide whether further actions are warranted [11, 12, 13]

2.4 Cloud computing security

Expansion to returning to approaches for particular issues in securing shared registering, history shows us that creating security designs ahead of schedule in the process can pay off extraordinarily as frameworks advance and accumulate more divergent usefulness. Then again, the historical backdrop of business Internet offerings over and over demonstrates that opportunity to-advertise and undermining costs can extraordinarily influence clients even without sound security underpinnings. The circumstance might be fairly extraordinary this time around, in any case, given that quite a bit of distributed computing

targets clients who have broad business reasons (and scars from the past) driving them to regard security as a hoisted need. We close our dialog with what we observe to be a fascinating analogy. Companies, for example, National CSS started by offering moderate calculation for organizations. Time-sharing in the end offered approach to PCs, which conveyed reasonable calculation to the overall population. In a comparative design, distributed computing right now offers reasonable, substantial scale calculation for organizations. In the event that the monetary case wins, at that point we may find that nothing—not even security concerns—will keep distributed computing from turning into a shopper ware. Similarly as the item PC and the Internet achieved the Information Revolution, and made data all around available, moderate, and helpful, so too clouds figuring can possibly realize the Computation Revolution, in which substantial scale calculations turn out to be generally open, reasonable, and valuable. We should trust we can add to this result "and be reasonably safe [14, 15, 16, 19].

3. Intelligent system

This section explains the main item of the proposed algorithm that related with (scheduler of process and stability) as:

3.1 Introduction

Attempted to design intelligent (secure /scheduler) system to improve system stability and security using genetic algorithm as tool. System is described with following sections.

3.2 Record coding

Now explain the coding using in genetic algorithm and as main data for operate system:

1. Ip address 32 bit.
2. Service type (Saas m Iaas and Paas) with two bit as:
   00 don't cure, 01 Saas, 10 Iaas and 11 Paas.
3. Trusted value 4 bit.
4. Block 1 bit.

Table 1 illustrate the representing.

Table 1. Coding representing

186:101:83:167 PAAS	10111010011001010101001110100111 11---wait test 5 bit 4,5
186:142:116:120IAAS	10111010100011100111010001111000 10---wait test 5 bit 4,5

3.3 Intelligent scheduler and security algorithm

While traffic increased attack may be increasing because system inter to critical region (un-stability in system)and attempt to avoid latch process thus using slice time scheduler method for processing (with control on process select).as shown in algorithm 1.

Algorithm 1 main;

Input (query list from different client)
Output (demand service "true or false")

1-Start.
2- Create initial list.

3- While I/O channel on.
    3.1 check stability depend on service.
    3.2 check download depend on service.
    3.3 if download balance error (inter with critical zoon) insert process with special. queue and re-arrange process queue.
    3.4 Start with service after check above depend on service.
    3.5 update service queue.
    3.6 update critical queue.
    Until service queue end,
4-indecte all critical process and random arrange for all without any contiguous same IP request.
5-Save update and flag all request.
6-end,

Algorithm 2 check stability;

Input (system resource (for supplies services), request list, current status, time)
Output (demand service "true or false")

1- Start.
2- If system supply service stabile then
        supply service
 else
        call check_process_status
3- end

Algorithm 3 check download;

Input (current request, download rang, system current statues, time)
Output (demand service "true or false")

1- Start
2- If download in rang then
        demand service
else
        call check_process_status
3- end

Algorithm 4 check_process_status**;**

Input (current request, system current statues,time)
Output (delete process “true or false" // send request in un stable queue)

1- start
2- delay and check
  Start new timer
  If time out then
        delete (save to un balance queue and decrees demand" time , download")
  else
        if luch process then
                delete (save to un balance queue and decrees demand" time ,
        download")

3- end

Algorithm 5 queue operate.

For special process "service time set to low rang"
Input (queue, max. time,system current status)
Output (demand service)

1- Start
2- Demand service using slice time (round robin) scheduler algorithm
// to improve stability and service all request
3- end

4. Experimental results

Running of simulated system with Genetic and slice scheduler feature (in traffic mode) saves the following value from system with fitness, following chart gives sample fragment view, where

X axis = 1.48 sequence of IP as total (divide as request 1-13 SAAS 2-18 request IAAS 3-12 request PAAS)

and Y axis =1..15 fitness value (threat degree)
if fitness value [current IP] = 15-1" (max threat) ***then*** block IP[current],
Where current= current I/O value

Figure 3 and Table 2 give detail on (IP address, 32 bit value for IP , service and trusted value).

1SAAS

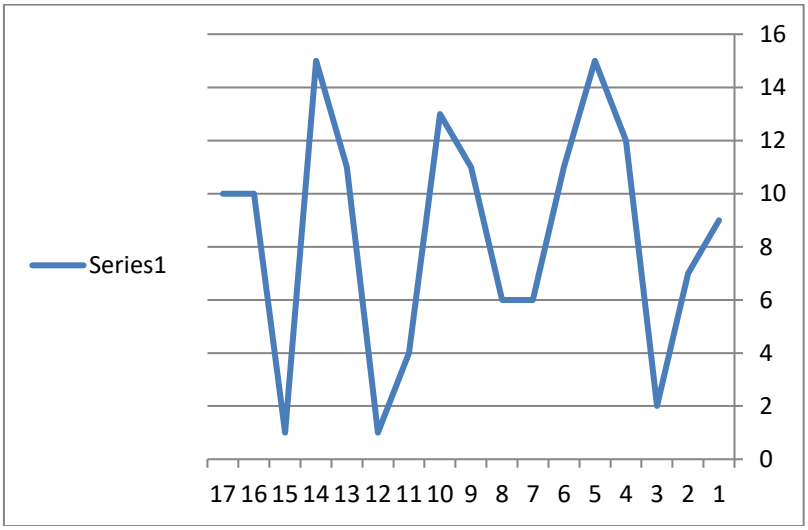

2IAAS

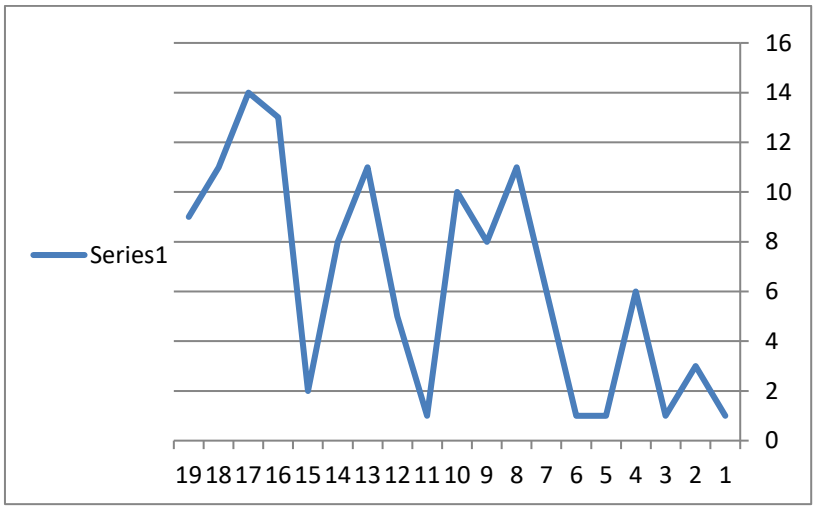

3PAAS

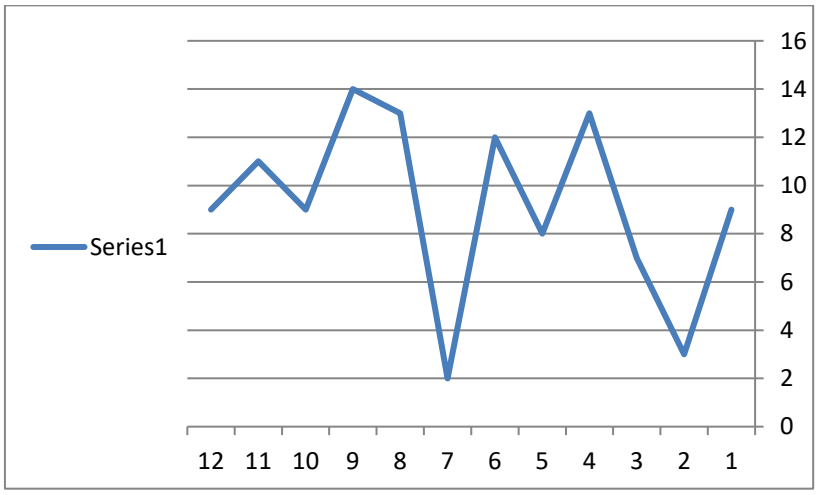

Figure 3(a)

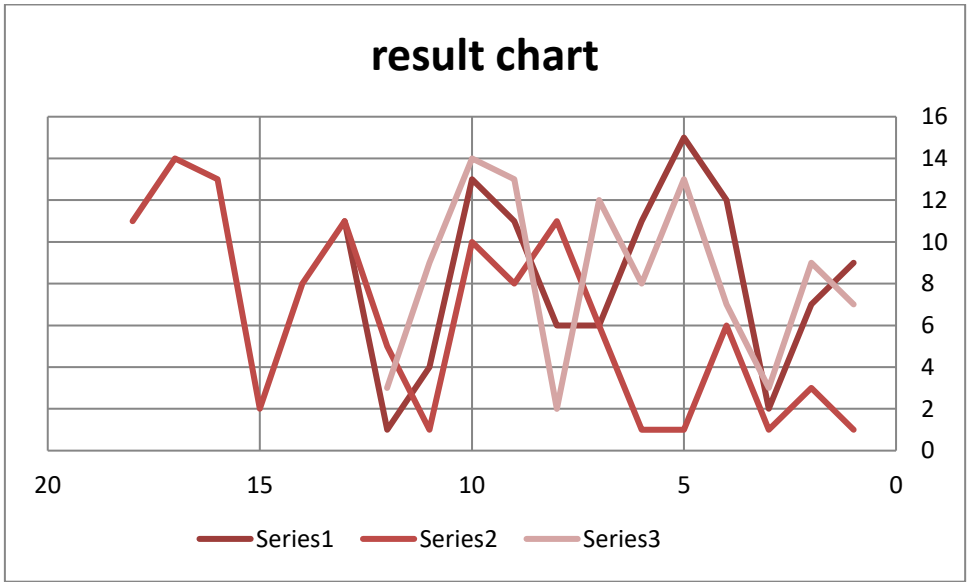

Figure 3. (a, b) results chart

Table 2 Result table

Where S= service T=trusted value

IP Adress	IP address as binary cone	S	T
180:106:90:174	10110100011010100101101010101110	3	3
186:148:123:127	10111010100101000111101101111111	3	7
183:164:59:119	10110111101001000111011011110111	2	1
174:59:171:130	10101110001110111010101110000010	2	3
195:159:92:181	11000011100111110101110010110101	1	9
177:98:135:197	10110001011000101000011111000101	1	7
182:121:134:53	10110110011110011000011000110101	3	9
174:104:110:74	10101110011010000110111001001010	2	1
178:61:93:41	10110010001111010101110100101001	3	3
187:158:200:67	10111011100111101100100001000011	2	6
174:119:210:186	10101110011101111101001010111010	2	1
175:109:48:71	10101111011011010011000001000111	1	2
182:133:120:73	10110110100001010111100001001001	2	1
174:127:90:162	10101110011111110101101010100010	1	12
195:95:163:144	11000011010111111010001110010000	1	15
178:133:65:239	10110010100001010100000111101111	2	6
191:35:122:80	10111111001000110111101001010000	3	7
191:77:102:233	10111111010011010110011011101001	2	11
187:93:38:78	10111011010111010010011001001110	2	8
178:138:203:89	10110010100001010110010110101001	2	10
173:88:124:140	10101101010110000111110010001100	2	1
174:177:167:103	10101110101100011010011101100111	1	11
179:91:167:158	10110011010110111010011110011110	3	13
172:34:142:180	10101100001000101000111010110100	2	5
175:141:73:147	10101111100011010100100110010011	3	8
191:127:233:173	10111111011111111110100110101101	2	11

197:48:42:92	11000101001100000010101001011100	1	6
172:39:80:176	10101100001001110101000010110000	1	6
176:153:221:100	10110000100110011101110101100100	3	12
194:148:192:190	11000010100101001100000010111110	2	8
189:156:64:172	10111101100111000100000010101100	1	11
191:154:166:67	10111111100110101010011001000011	3	2
178:166:198:82	10110010101001101100011001010010	3	13
175:79:232:235	10101111010011111110100011101011	2	2
178:95:168:81	10110010010111111010100001010001	2	13
188:180:80:239	10111100101101000101000011101111	1	13
176:50:147:89	10110000001100101001001101011001	1	4
184:139:44:52	10111000100010110010110000110100	2	14
189:53:190:108	10111101001101011011111001101100	1	1
182:146:218:182	10110110100100101101101010110110	2	11
185:103:149:96	10111001011001111001010101100000	1	11
194:89:56:123	11000010010110010011100001111011	3	14
181:161:118:41	10110101101000010111011000101001	3	9
182:151:157:126	10110110100101111001110101111110	2	9
186:116:98:50	10111010011101000110001000110010	1	15
178:110:68:140	10110010011011100100010010001100	3	11
173:158:193:175	10101101100111101100000110101111	1	1
182:156:95:123	10110110100111000101111101111011	1	10
188:168:99:110	10111100101010000110001101101110	3	9
188:60:133:210	10111100001111001000010111010010	1	10

5. Conclusion

For present study can conclude the following:

1. Results obtained shaved good indication of the present (test with simulated environment of real world).
2. While traffic increase, attaching attack easier.
3. Any change in fitness and time slice gives the new feature to system (the current fitness, time slice may be better).

References

[1] Security and Communication Networks group. Cloud Service Scheduling Algorithm Research and Optimization, SCNG, Article ID 2503153, 2017.

[2} David Wagner, Drew Dean. Intrusion detection via static analysis. In Proceedings of the IEEE Symposium on Security and Privacy, 2001.

[3] Tim Mather, Subra Kumaraswamy, Shahed Latif. Cloud Security and Privacy. O'Reilly Media, Inc., 1005 Gravenstein Highway North, Sebastopol, CA 95472, 2009.

[4] T. Muth, J. Peters, J. Blackburn, E. Rapp, L. Martens. Proteocloud: a full-featured open source proteomics cloud computing pipeline. *Journal of Proteomics*, 2013, 5 I (**12**).

[5] W. Zhao, T. Tao, E. Zio. System reliability prediction by support vector regression with analytic selection and genetic algorithm parameters selection. Applied Soft Computing, 2015, 4 (**I**):15.

[6] Y. M. Wang, H. L. Yin. A two-stage approach based on genetic algorithm for large size flow shop scheduling problem. In Proceedings of the 10th IEEE International Conference on Mechatronics and Automation (IEEE ICMA '13), Takamatsu, Japan, 2013: 376–381.
[7] Arpaci-Dusseau, Remzi H.; Arpaci-Dusseau. Operating Systems Three Easy Pieces. Arpaci-Dusseau Books, Andrea C., 2014.
[8] Jump Zander, Ki Won Sung, Ben Slimane. Fundamentals of Mobile Data Networks. Cambridge University Press, ISBN 1107143217, 2016.
[9] A. Kaleeswaran, V. Ramasam y, P. Vivekanandan. DYNAMIC SCHEDULING OF DATA USING GENETIC ALGORITHM IN CLOUD COMPUTING. India IUP, 2013.
[10] Zai Liji,Uiai Pia. Computer Science and Electronics Engineering. **IEEE** Conference **(**Hangzhou, China) 2012:23-25.
[11] X. Wang, D. Reeves, S.F. Wu, J. Yuill. Sleepy watermark tracing: anactive network-based intrusion response framework. In Proceedings of the IFIPConference on Security, Paris, 2001.
[12] Anil Buntwal Somayaji, Operating System Stability and Security through Process Homeostasis. University of New Mexico, 2002.
[13] Stefan Axelsson. Intrusion detection systems: A taxomomy and survey. Dept. of Computer Engineering, Chalmers University of Technology, conf., 2000.
[14] Vern Paxson, Randy H. Katz. What's New about Cloud Computing Security? University of California, 2010.
[15] A. Stamos, A. Becherer, N. Wilcox. Cloud computing. Security—raining on the trendy new parade. Black Hat USA, 2009.
[16] J. Stokes, T-Mobile, Microsoft. Danger data loss is bad for the cloud, Ars technical, 2009.
[17] Bharat Bhargava, YounSun Cho. Cloud Security and Privacy. Computer Science Purdue University, 2014.
[18] Jump up, Stallings. Operating Systems Internals and Design Principles Pearson. William Press, 2015.
[19] Firas A. Abdulatif, Maan zuhiar. Cloud Security Issues and Challenges: Important Points to Move towards Cloud Storage. IJSR, 2017, 6 (8).

New Secure E-mail System Based on Bio-Chaos Key Generation and Modified AES Algorithm

New Secure E-mail System Based on Bio-Chaos Key Generation and Modified AES Algorithm

Haider K Hoomod, A M Radi

[1] Department of computer Science, college of Education, University Al-Mustansiriya

Drhjnew@gmail.com

Abstract. The E-mail messages exchanged between sender's Mailbox and recipient's Mailbox over the open systems and an insecure Networks. These messages may be vulnerable to eavesdropping and itself poses a real threat to the privacy and data integrity from unauthorized. The E-mail Security includes the following properties (Confidentiality, Authentication, Message integrity). We need a safe encryption algorithm to encrypt Email messages such as algorithm Advanced Encryption Standard (AES) or Data Encryption Standard DES as well as biometric recognition and chaotic system. The proposed E-mail system security is uses modified AES algorithm and use secret key-bio-chaos that consist of biometric (Fingerprint) and chaotic system (Lu and Lorenz). This modification makes the proposed system more sensitivity and randomness. The execution time for both encryption and decryption of proposed system is much less from original AES, in addition to being compatible with all Mail Server.

1. Introduction

The E-mail message transmitted via the internet will be vulnerable to eavesdropping and threats to the privacy of E-mail because it insecure channel [1].there are two protocols, the Simple Mail Transfer Protocol (SMTP) and Post Office Protocol third (POP3). The SMTP, this protocol allows for user send E-mails to another user and not to received E-mail [2], The POP3, This type of protocol enables the user to access the mailbox and download the messages to the computers in addition to providing the possibility to read the message even in the case of the presence of Internet service, Those protocols are unsafe [3,4]. The AES algorithm is one of the most important algorithms that are related to encryption and decryption message contents of e-mail system because has many from characteristics (Secure, accepted Cost, Flexible, Simplest) [5]. However, these algorithms have some shortcomings encryption speed has a poor efficiency at a low level, if the attachments are large, it is, therefore, necessary to develop AES algorithm and make it more efficient in implementing encryption and decryption [6], the algorithm isn't the secret; it's known to the public. The secret is the key. Although encryption is effective in transferring sensitive data across an insecure channel but lacks the handle of long keys because maintenance and sharing of these long and random keys have become a critical problem in encryption systems. These problems are handled well by using a biometrics system that eliminates the need to remember the key or even to exchange it over an open network [7], can be integrated with chaotic mapping that has many important properties corresponding to encryption because Randomization, sensitivity is the initial conditions and control parameters. These features make from chaotic systems a powerful choice in building powerful cryptographic systems and as well as generate a secret key strong has sensitive and random against all types attacks [8]. In this paper will be using

modified AES algorithm, key-bio-chaos that consist of biometric (Fingerprint) and chaotic system (Lu and Lorenz or Lorenz) in the design of a proposed E-mail system security.

2. Advanced Encryption Standard

AES is an encryption algorithm used the symmetric key and used in encrypt/decryption the contents of the message between two parties. The data block length and a key length of AES can be varied according to the requirement. Three key lengths: 128, 192, 256, whose iteration cycle number is 10, 12 and 14 round respectively, AES encryption process is shown in 'figure 1'. Each round consists of the following four steps: SubBytes, ShiftRows, MixColumns, AddRoundKey. There are a number of benefits of AES will be relevant in providing E-mail system security as Secure, accepted Cost, Flexible, Simplest. However, these methods have some shortcomings encryption speed has a poor efficiency at a low level, if the attachments are large, it is, therefore, necessary to develop AES algorithm and make it more efficient in implementing encryption and decryption [9].

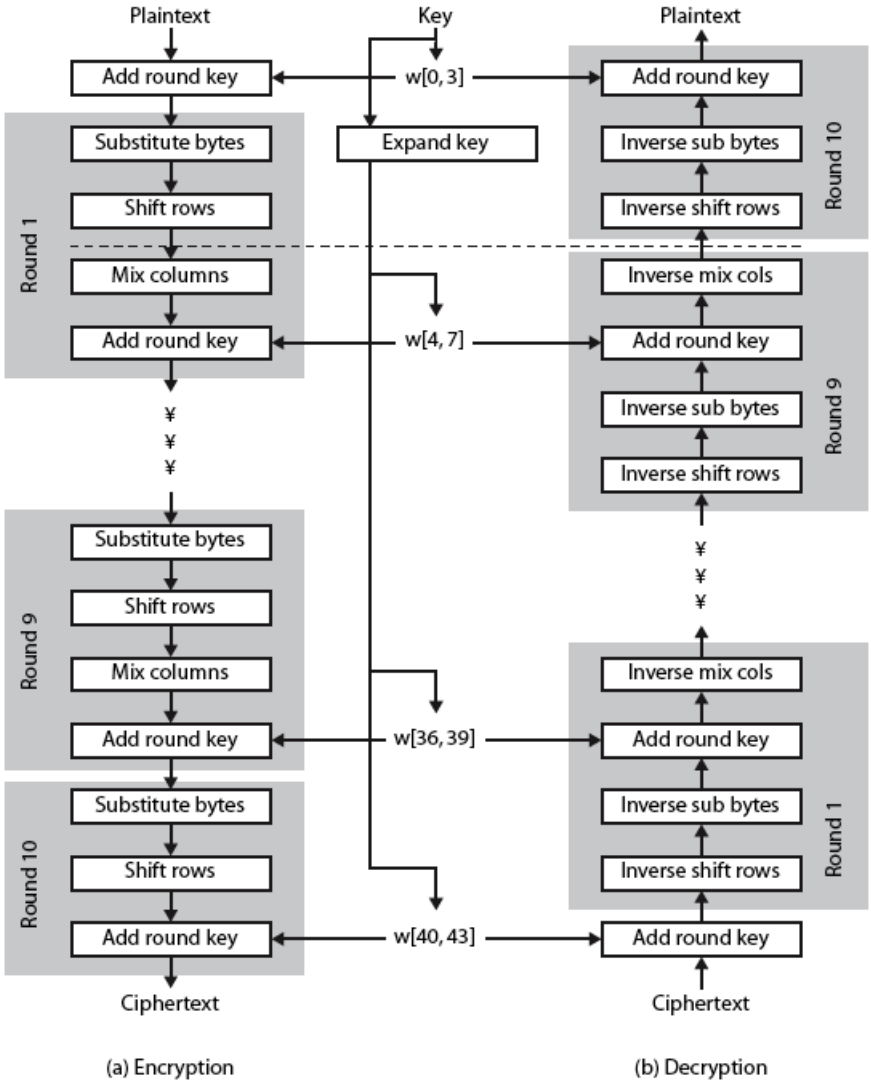

Figure 1. AES Encryption and Decryption process

3. Chaotic Systems

Chaos theory is based on nonlinear behaviours (which are highly sensitive to their initial parameters) , it has enabled structures sensitive equations of this theory from generating unpredictable random

values that correspond with diffusion and confusion principles in order to construct cryptographic systems that have the maximum type of entropy [8] and robust against any type of attacks. We need to use a three-dimension chaotic system such as Lu and Lorenz are suitable to encrypt the three components of the color image and In addition to text.

3.1. Lu Chaotic System

The Lu system is a three dimensions chaotic system and it is described 'as in equation (1), equation (2) and equation (3)' [10]:

$$\bar{X} = a(y - x) \tag{1}$$

$$\bar{Y} = -xz + cy \tag{2}$$

$$\bar{Z} = xy - bz \tag{3}$$

3.2. *Lorenz Chaotic System*

Lorenz system is also three dimensions chaotic system and the Lorenzo system steps and its equations are described 'as in equation (3), equation (4) and equation (5)' [10]

$$\bar{X} = \sigma\,(y - x) \tag{4}$$

$$\bar{Y} = x(\rho - z) - y \tag{5}$$

$$\bar{Z} = xy - \beta z \tag{6}$$

4. Biometric Recognition

Biometric is a technique based on the physiological or behavioral characteristics of humans such as face features, palm, iris, fingerprint, finger or hand geometry, voice, keystroke dynamics, handwritten signature, etc. Usually, common passwords, have many disadvantage factors: Ease of forgotten, stolen, lost, replication, etc. It is worth mentioning that the characteristics of the human body have a uniqueness cannot be repeated. It cannot be copied, stolen or forgotten. It is safe in provides authentication for Email message [11].

This biometric can be used to generate an exclusive and unique key for each individual. These features make biometric a powerful option in building cryptographic systems because it can take advantage of strengths in both fields while encryption provides confidentiality, biometrics provides properties non-repudiation and eliminates the need to remember passwords or to carry codes etc, can integrate it with a number of other technics, such as chaotic systems that make those systems more random and sensitive to the initial information [12].

Amid various Biometric identifications technologies, Fingerprint recognition has been successful due to its two vital characteristics uniqueness and permanence that's ability to stay unchanged over the lifetime and simplicity feature extraction by use image fingerprint [13]. After extracting the fingerprint feature as shown in 'figure 2' it integrates with a chaotic mapping which previously mentioned to produce a key-bio-chaos has characteristic random and sensitivity of initial values use in building strong encryption systems.

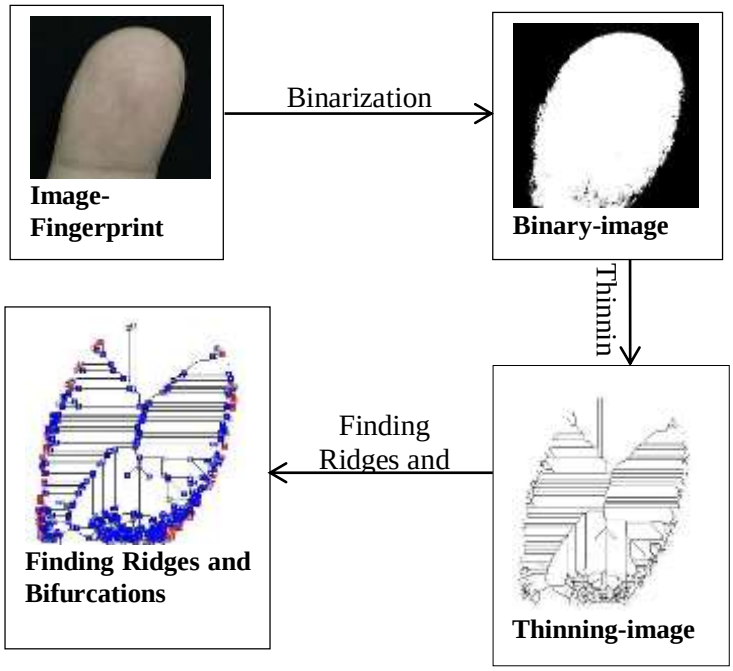

Figure 2. The minutia extraction of Fingerprint

5. The Proposed E-mail system security:

The proposed system consists from two part are modified AES algorithm (MAES) and generate a secret key based on biometric (fingerprint) and chaotic mapping (Lu and Lorenz) and also use protocols (SMTP and POP3) in the sending and receiving In sending and receiving emails.

5.1. Generate secret key

The Lu system taking its initial conditions after extract features fingerprint as shown in figure (2) for generating three random numbers used as inputs to the three equations of Lorenz system to generate random masks, when dealing with Email attachment (image) will produce three random masks, Each mask has size 4096 (4 * 4) equal to the three dimensions of the image (256*256), in the same way implement on the message content (text, file) but use one random mask to be XOR with the encrypted message contents that is produced from modified AES. after that will performing permutation for each block of random masks, The resulting blocks will be used as changing key for modified AES algorithm and the same time multiplication each block of changing key values in number 3 for produce new key to be XOR with the next state coming from shift-rows process in modified AES that will be explained later.

5.2. Modified AES algorithm (MAES)

The MAES, it uses same operations of original AES except for Mix-Columns operation and compensation for it in two XOR and shift-cycle operations as well as has two keys-bio-chaos which mentioned earlier in the process of Generate Key-bio-chaos, each key has size 4*4 byte that changing random values completely in each encryption or decryption process.

After splitting the message contents (file, image, text) to blocks size 4 * 4 byte, each block refers to the state. This state with two keys-bio-chaos are passed to the modified AES algorithm operations for produce encrypted message contents (image, file, text) as shown in ‘figure 3’ that describe the

main encryption steps of modified AES and then to be XOR with mask-bio-chaos which is the output of the Lorenz system mentioned earlier in the process of Generate Key-bio-chaos for produce finial cipher-message contents.This modification adds more sensitivity and randomness to the system and reducing time required in both encryption and decryption for content (Text/Image) message during an exchange of messages between the sender's Mailbox and the recipient's Mailbox via the network using protocols (SMTP,POP3), and In addition to being compatible with all Mailserver.

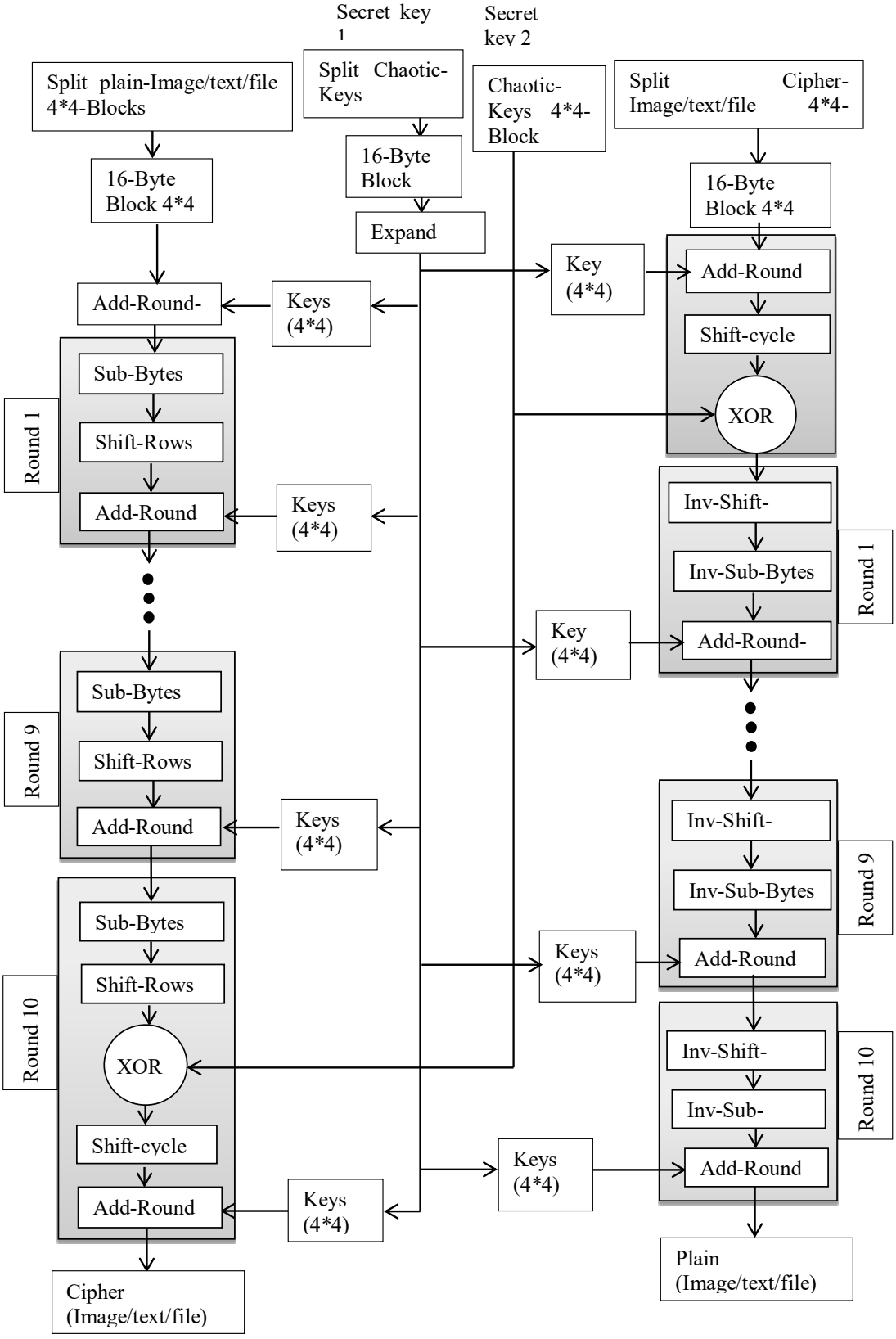

Figure 3 Encryption and Decryption Process of Modified AES

6. The sending and receiving side of the proposed system

The system mainly has two sides. The first side is called “sending side“, the second side is called “receiving side“

6.1. Sending side:

The algorithm (1) describes process encryption of the message contents in this side.

Algorithm (1): Encryption process

Input: Plain-message contents (image, file, text).
Output: Send cipher-message contents (image, file, text).

Step1: Read plain-message contents (image, file, text).
Step2: If attachment (image), resize (256*256).
Step3: Split the message contents (image, file, text) into a set of block size 4*4 byte.
Step4: If size block ≠ 16 byte, add values zeros to length block, block=16 byte.
Step5: Read image fingerprint.
Step6: Extract features fingerprint as shown in section 4.
Step7: apply modified AES algorithm (Encryption process) that take two keys-bio-chaos with pain blocks 16 byte.
Step8: produce message encrypted.
Step9: message encrypted XOR three masks random of image (256*256) / one mask of message contents (file, text).
Step10: output cipher-message (image, file, text).
Step11: The proposed system send cipher-message (image, file, text) via protocol SMTP.
Step12: END

6.2. Receiving Side

This algorithm (2) shows steps of decrypting the message contents in proposed system

Decryption process algorithm (2)

Input: cipher-message contents (image, file, text).
Output: plain-message contents (image, file, text).

Step1: The proposed system received E-mail cipher-message contents (image, file, text) by protocol POP3.
Ste2: Read cipher-message contents (image, file, text)
Step3: Read image fingerprint
Step4: Extract features fingerprint as shown in section 4.
Step5: Message encrypted XOR three masks random of the image (256*256) / one mask of message contents (file, text).
Step6: Split the message contents (image, file, text) into a set of block size 4*4 byte.
Step7: Apply modified AES algorithm (decryption process) that take two keys-bio-chaos 4*4 with blocks 4*4 byte for output decrypt-message.
Step8: If output modified AES algorithm is file or text will go to the condition if output> 0 then plain message = output(The purpose of this process is to remove the excess zeroes that were previously added to the encryption process if the output of modified AES algorithm is file or text).
Step9: Output plain-message (image, file, text).
Step10: END

7. Experimental Results

In this system, A series of tests were execution out on the message contents (body and attachment) which the encrypted in at the originator's point and decryption upon receipt. This tests showing the efficiency of modified AES algorithm compared to the original AES algorithm, The main flaw that is resolved is a waste of time (lost) in the encryption and decryption process in the original AES

algorithm, which need a lot of time when dealing with large data in E-mail attachment (Image, file), also random the key that is based on chaotic (Lu and Lorenz) and biometric (fingerprint) used in this system. This Experiments on a PC with Intel Core i7 CPU @ 2.70GHz, 8G RAM with Windows 8, types experiments are:

7.1. Analysis of the Key Sensitivity:
The proposed system is sensitive to the key change even if it is a slight change, for example, we encrypt the contents of the message with a key (0.4), a small change in the key (0.400000000001) and then execute operation decryption was the result the message was not decrypted.

***7.2.** The Histogram Analysis*
This test shows pixel density levels in message attachments (image) encrypted as graphs. (Table 1) shows the level of density in each level of color before and after encryption in modified AES.

Table 1. Histogram Analysis of the modified AES algorithm

Image		**Histogram**		
		R	G	B
Original	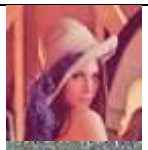	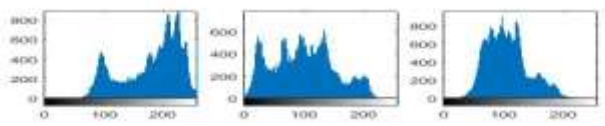		
Encryption		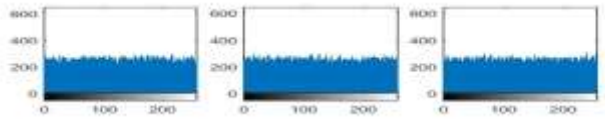		
Original		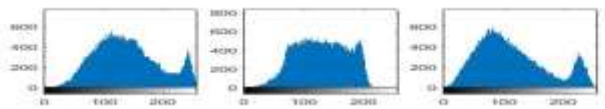		
Encryption		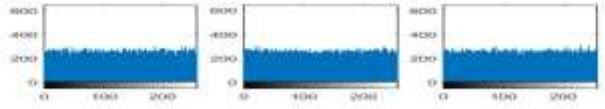		
Original		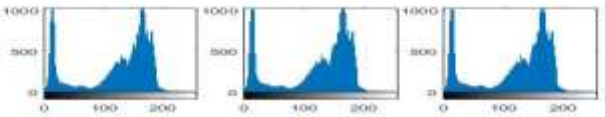		
Encryption		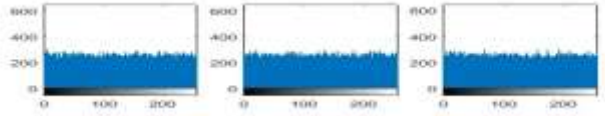		

7.3. Correlation Analysis
In the (table 2) shows correlation analysis between the Email message contents when using the original AES and modified AES based on key-bio-chaos consists from biometric (fingerprint) and chaotic system (Lu and Lorenz).

Table 2. Correlation Analysis between plain and cipher message
(A) attachment (Image), (B) attachment (File), body (Text)

(A)

Attachment (Image)		Correlation Analysis					
		Proposed Modified AES			**Original AES**		
		R	G	B	R	G	B
1	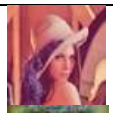	**0.0067**	**-0.0059**	**-0.0037**	**-0.0034**	**0.0050**	**-0.0029**
2	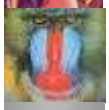	**0.0043**	**-0.0035**	**0.0029**	**0.0028**	**2.3283**	**-6.5870**
3	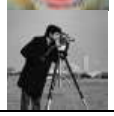	**-0.0049**	**-0.0082**	**-0.0030**	**-0.0041**	**-0.0064**	**0.0033**

(B)

(File.txt)	Correlation Analysis	
	Proposed Modified AES	**Original AES**
16kB	**0.0089**	**0.0015**
12kB	**0.0061**	**-0.0016**

(C)

Characters message	Correlation Analysis	
	Proposed Modified AES	**Original AES**
100	0.0089	-0.0354
250	-0.1511	-0.0136
500	-0.0332	-0.0781

7.4. PSNR Analysis

This PSNR Peak Signal to Noise Ratio reflects the encryption quality. Mean Square Error (MSE) is the cumulative squared error between originally and encryption message contents (Body, Attachment) as shown in (tables 3).

Table 3. PSNR & MSE for Email message contents (A) attachment (Image), (B) attachment (File), body (text)

(A)

Image	**Proposed Modified AES**						**Original AES**					
	MSE			PSNR			MSE			PSNR		
	R	G	B	R	G	B	R	G	B	R	G	B
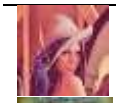	3.5406	3.0059	2.3829	12.6740	13.3851	14.3938	3.5826	2.9842	2.4002	12.6228	13.4165	14.3624
	2.7782	2.4404	2.9982	13.7272	14.2901	13.3962	2.7746	2.4207	3.0123	13.7328	14.3253	13.3758
	3.1433	3.1574	3.1390	13.1909	13.1715	13.1969	2.7649	2.4200	3.0083	13.7481	14.3266	13.3815

(B)

File.txt	Proposed Modified AES	Original AES

	MSE	PSNR	MSE	PSNR
12KB	7.7440	9.2752	7.6475	9.3296
16KB	7.7028	9.2983	7.6711	9.3162

(C)

Characters message	Proposed Modified AES		Original AES	
	MSE	PSNR	MSE	PSNR
100	7.2189	9.5801	8.2035	9.0248
250	7.2711	9.5488	7.4844	9.4232
500	7.5946	9.3598	7.7625	9.2648

7.5. Entropy Analysis

This entropy calculates the uncertainty association of the random values, the good encryption algorithm should give low mutual information of values of the encrypted message contents, and this means that the entropy will be increased, and the entropy equation is as follows in the equation:
In this (table 4), the entropy of the proposed system is better than the original AES algorithm.

Table 4. Entropy Analysis of message attachment
(A) Attachment (image), (B) Attachment (File.txt),
(C) Body (Text)

(A)

Image	**Modified AES**	**Original AES**
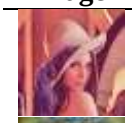	7.9991	7.9992
	7.9992	7.9992
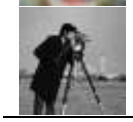	7.9991	7.9972

(B)

File.txt	Modified AES first	Original AES
16KB	7.9882	7.9873
12KB	7.9858	7.9851

(C)

Characters message	Proposed System first	Original AES
100	6.6229	6.4861
250	7.2839	7.2297
500	7.5803	7.5860

7.6. Execution Time

This test calculates the execution time of the encryption process on the message contents (body, attachment) when sending and decrypting the message contents when received. In the (table 5), shows a less execution time in both models of the modified AES (MAES) algorithm function with Generate key-bio-chaos in the proposed system compared to the original AES algorithm.

Table 5. The execution times Encryption (A)Encryption process, (B) Decryption process

(A)

message contents		Execute time encryption	
		Proposed Modified AES first	**Original AES**
Attachment	Image 256*256	9.852044s	101.459606s
	File 12 KB	8.022659s	14.305919s
	File 16 KB	8.517189s	14.954298s
Body	100 characters	7.652578s	8.000599s
	250 characters	7.646128s	8.244076s
	500 characters	7.638534s	8.462815s

(B)

Message contents		Execute time decryption	
		Proposed Modified AES first	**Original AES**
Attachment	Image 256*256	9.119982s	122.015908s
	File 12 KB	7.873978s	14.127101s
	File 16 KB	7.498325s	16.574347s
Body	100 characters	7.604548s	8.474877s
	250 characters	7.692139s	7.974319s
	500 characters	7.651514s	8.118706s

8. Conclusion

E-mail provides an important means of communication between users. In this paper was proposed E-mail system secure capable of providing a high level of security for contents message and speed in encryption and decryption between two parties via an open network, in addition to compatible with all MailServers.

Refrences

[1] Jang J, S Nepal and J Zic 2008 Trusted Email Protocol: Dealing with Privacy Concerns from Malicious Email Intermediaries IEEE
[2] S ANDREW TANENBAUM and J DAVID WETHERALL 2011 COMPUTER NETWORKS FIFTH EDITION.
[3] L Larry Peterson and S Bruce Davie 2003 Computer networks THIRD EDITION
[4] Ms.Priyanka S. Kamthe and Ms.Sonal P. Nalawade 2015 Email Security The Challenges of Network Security *International Journal on Recent and Innovation Trends in Computing and Communication IJRITCC*
[5] K P Singh and S Dod 2016 An Efficient Hardware design and Implementation of Advanced Encryption Standard (AES) Algorithm *International Journal of Recent Advances in Engineering & Technology (IJRAET)*
[6] K R Saraf, V P Jagtap and A K Mishra 2014 Text and Image Encryption Decryption Using Advanced Encryption Standard *International Journal of Emerging Trends & Technology in Computer Science (IJETTCS)*
[7] A G Reddy 2016 An Enhanced Biometric Based Authentication with Key-Agreement Protocol for Multi-Server Architecture Based on Elliptic Curve Cryptography PLOS ONE
[8] M T Mohammed, A E Rohiem, A El-moghazy, and A. Z. Ghalwash 2013 Chaotic Encryption

Based PGP Protocol *International Journal of Computer Science and Telecommunications*
[9] Mathur N, R 2016 AES Based Text Encryption Using 12 Rounds with Dynamic Key Selection Elsevier.
[10] Leonov A. G Leonov and Kuznetsov V. N 2015 Elsevier
[11] Zhu H, Hao X, Zhang Y and Jiang M 2015 A Biometrics-based Multi-server Key Agreement Scheme on Chaotic Maps Cryptosystem *Journal of Information Hiding and Multimedia Signal Processing*
[12] Chandra S, Paul S, Saha B and Mitra S 2013 Generate an Encryption Key by using Biometric Cryptosystems to secure transferring of Data over a Network IOSR *Journal of Computer Engineering (IOSR-JCE)*
[13] Ankit K and Rekha J 2016 Biometrics as a Cryptographic Method for Network Security *Indian Journal of Science and Technology*

Transmuted of Rayleigh Distribution with Estimation and Application on Noise Signal

IOP Conf. Series: Journal of Physics: Conf. Series **1003** (2018) 012026 doi:10.1088/1742-6596/1003/1/012026

Transmuted of Rayleigh Distribution with Estimation and Application on Noise Signal

Suhad Ahmed[1], Zainab Qasim[2]

[1]Ibn – Al – Haitham for Pure Science College, Baghdad University

[2]Ibn – Al – Haitham for Pure Science College, Baghdad University

[1]Suhadahmed12@gmail.com, [2]zainab0qasim1@gmail.com

Abstract. This paper deals with transforming one parameter Rayleigh distribution, into transmuted probability distribution through introducing a new parameter (ʎ), since this studied distribution is necessary in representing signal data distribution and failure data model the value of this transmuted parameter $|\lambda| \leq 1$, is also estimated as well as the original parameter (Θ) by methods of moments and maximum likelihood using different sample size (n=25, 50, 75, 100) and comparing the results of estimation by statistical measure (mean square error, MSE).

Keywords: Rayleigh Distribution, ExponentiatedTransformation,Transmuted Rayleigh, Moment's Method, Maximum Likelihood Method, Application of audio signal.

1. Introduction

Many researcher's work on modifying the given probability distribution, through using either exponentiated to another parameter or using modification to by applying some transformation (like marshull-olkin) which is used in reference Vasile Preda(2011) when the failure rate model af any distribution is not constant, as well as using transmutation to obtain a new family which we apply it in hour research to expand Rayleigh one parameter into two parameters one through transmuted. The one parameter Rayleigh distribution may have high precision in data fitting, but sometimes we want to obtain another family to have better representation for data without any effect of original probability models, this done through exponentiated transformation, or through exponentiated to another parameters, may give best fitting and more flexibility of data, so here we extend one parameter Rayleigh through transmuted of this distribution applying quadratic rank transformation, were this used by Show and Buckely (2009), and Aryal and Tosokos (2009 & 2011)[5], and Aryal (2013), so here we continue the work of extension by applying it to a one parameter Rayleigh to obtain a new $p.d.f$ of two transmuted Rayleigh as well as deriving the new $p.d.f$ and the new CDF, also the formula of rth

moments about origin were derived, then we used moments method for estimation, as well as maximum likelihood method, the application of the studied model is done on datawhich represent audio signal with noise at (*n=100*).

2. Theoretical Aspect

The $p.d.f$ of one scale parameter Rayleigh distribution is;

$$f(x;\theta) = \frac{2\,x}{\theta}\left(e^{-\frac{x^2}{\theta}}\right) \quad x,\theta > 0 \tag{1}$$

Where x is random variable, θ is scale parameter.

0 o/w

The cumulative distribution function is;

$$F_X(x) = \left(1 - e^{-\frac{x^2}{\theta}}\right) \tag{2}$$

Also, The mean and variance are;

$$\boldsymbol{E(x,\theta)} = \sqrt{\frac{\boldsymbol{\pi\,\theta}}{\boldsymbol{4}}}$$

$$\boldsymbol{v(x)} = \boldsymbol{\theta}\left(\boldsymbol{1} - \frac{\boldsymbol{\pi}}{\boldsymbol{4}}\right)$$

The random variable (x) with Rayleigh (one parameter θ), can be transmuted using quadratic rank transmutation, this help in finding more flexible family distribution and is more benefit in representing signal system, also radical distance. The transmutation is done using;

$$\boldsymbol{G(x) = (1+\lambda)F(x) - \lambda[F(x)]^2 |\lambda| \leq 1} \tag{3}$$

Transmuted Rayleigh from by applying equation (3); is obtained and explained in equation (4):

$$\boldsymbol{g(x) = (1+\lambda)f(x) - 2\lambda F(x)f(x)|\lambda| \leq 1}$$

$$\boldsymbol{g(x) = (1+\lambda)\frac{2\,x}{\theta}\left(e^{-\frac{x^2}{\theta}}\right) - 2\lambda\left(1 - e^{-\frac{x^2}{\theta}}\right)\left(\frac{2\,x}{\theta}\right)\left(e^{-\frac{x^2}{\theta}}\right)}$$

$$g(x) = \frac{2\,x}{\theta}\left(e^{-\frac{x^2}{\theta}}\right)\left[(1+\lambda) - 2\lambda\left(1 - e^{-\frac{x^2}{\theta}}\right)\right]$$

$$\boldsymbol{g(x) = \frac{2\,x}{\theta}\left(e^{-\frac{x^2}{\theta}}\right)\left[(1-\lambda) + e^{-\frac{x^2}{\theta}}\right]} \boldsymbol{(4)}$$

This is the new generated $p.d.f$ of transmuted Rayleigh is;

$$\boldsymbol{g(x) = (1+\lambda)f(x) - 2\lambda F(x)f(x)}$$

$$\boldsymbol{= f(x)[(1+\lambda) - 2\lambda F(x)]} \boldsymbol{(5)}$$

$$\boldsymbol{g(x) = \frac{2\,x}{\theta}\left(e^{-\frac{x^2}{\theta}}\right)\left[(1+\lambda) - 2\lambda\left(1 - e^{-\frac{x^2}{\theta}}\right)\right]}$$

$$\boldsymbol{g(x) = \frac{2\,x}{\theta}\left(e^{-\frac{x^2}{\theta}}\right)\left[(1-\lambda) + 2\lambda\left(e^{-\frac{x^2}{\theta}}\right)\right]} \quad (6)$$

The $p.d.f$ is new transmuted Rayleigh with two parameters (θ is scale parameter, and λ is transmution parameter).

Now we derive the formula for rth moments about origin by applying equation (7);

$$\boldsymbol{\mu_r' = E(x^r) = \int_0^\infty x^r\, g(x)dx \;(7)}$$

$$\boldsymbol{= (1-\lambda)\int_0^\infty x^r \frac{2\,x}{\theta}\left(e^{-\frac{x^2}{\theta}}\right)dx + (2\lambda)\int_0^\infty x^r\left(e^{-\frac{x^2}{\theta}}\right)\left(\frac{2\,x}{\theta}\right)\left(e^{-\frac{x^2}{\theta}}\right)dx}$$

$$\boldsymbol{= (1-\lambda)\frac{2}{\theta}\int_0^\infty x^{r+1}\left(e^{-\frac{x^2}{\theta}}\right)dx + \frac{(4\lambda)}{\theta}\int_0^\infty x^{r+1}\left(e^{-2\frac{x^2}{\theta}}\right)dx} \quad (8)$$

$$\boldsymbol{\mu_r' = I_1 + I_2}$$

$$\boldsymbol{I_1 = (1-\lambda)\frac{2}{\theta}\int_0^\infty x^{r+1}\left(e^{-\frac{x^2}{\theta}}\right)dx}$$

Let

$$\boldsymbol{Z = \frac{x^2}{\theta} \quad \rightarrow \theta Z = x^2 \quad \rightarrow \quad x = \sqrt{\theta}Z^{\frac{1}{2}} \quad \rightarrow \quad dx = \sqrt{\theta}\frac{1}{2\sqrt{Z}}dZ}$$

$$I_1 = (1-\lambda)\frac{2}{\theta}\int_0^\infty \left(\sqrt{\theta}Z^{\frac{1}{2}}\right)^{r+1}(e^{-Z})\sqrt{\theta}\frac{1}{2\sqrt{Z}}dZ$$

$$I_1 = \frac{(1-\lambda)}{\theta}\theta^{\frac{r+2}{2}}\int_0^\infty Z^{\frac{r}{2}}(e^{-Z})dZ = (1-\lambda)\left(\theta^{\frac{r}{2}}\right)\Gamma\left(\frac{r}{2}+1\right) \quad (9)$$

$$I_2 = \frac{(4\lambda)}{\theta}\int_0^\infty x^{r+1}\left(e^{-2\frac{x^2}{\theta}}\right)dx$$

Let

$$\boldsymbol{Z = 2\frac{x^2}{\theta} \quad \rightarrow \frac{\theta Z}{2} = x^2 \quad \rightarrow \quad x = \frac{\sqrt{\theta}}{\sqrt{2}}Z^{\frac{1}{2}} \quad \rightarrow \quad dx = \frac{\sqrt{\theta}}{\sqrt{2}}\frac{1}{2\sqrt{Z}}dZ}$$

$$\boldsymbol{I_2 = \frac{(4\lambda)}{\theta}\int_0^\infty \left(\frac{\sqrt{\theta}}{\sqrt{2}}Z^{\frac{1}{2}}\right)^{r+1}\left(e^{-Z}\right)\frac{\sqrt{\theta}}{\sqrt{2}}\frac{1}{2\sqrt{Z}}dZ}$$

$$\boldsymbol{I_2 = \frac{(4\lambda)}{\theta}\frac{(\sqrt{\theta})^{r+2}}{(\sqrt{2})^{r+1}}\frac{1}{2\sqrt{2}}\int_0^\infty Z^{\frac{r}{2}}\left(e^{-Z}\right)dZ}$$

$$I_2 = \lambda\left(\frac{\theta}{2}\right)^{\frac{r}{2}}\Gamma\left(\frac{r}{2}+1\right) \quad (10)$$

Then the formula of r[th] moment about origin is;

$$\boldsymbol{\mu'_r = (1-\lambda)\theta^{\frac{r}{2}}\Gamma\left(\frac{r}{2}+1\right) + \lambda\left(\frac{\theta}{2}\right)^{\frac{r}{2}}\Gamma\left(\frac{r}{2}+1\right)}$$

Applying $[\mu'_r = \frac{\sum_{i=1}^{n} x_i^r}{n}]$ for $(r = 1,2)$, we obtain moment estimator of $(\theta \; and \; \lambda)$

3. Maximum Likelihood Estimator

Let $(x_1, x_2, \dots, x_n)$ be a random variable from $[g(x)]$ then;

$$\boldsymbol{L = \prod_{i=1}^{n} g(x_i) = \frac{2^n}{\theta^n}\prod_{i=1}^{n} x_i\, e^{-\frac{\sum_{i=1}^{n} x_i^2}{\theta}} \prod_{i=1}^{n}\left[(1-\lambda) + 2\lambda e^{-\frac{x_i^2}{\theta}}\right]}$$

$$\boldsymbol{log\, L = n\, log\, 2 - n\, log\, \theta + \sum_{i=1}^{n} log\, x_i - \frac{\sum_{i=1}^{n} x_i^2}{\theta} + \sum_{i=1}^{n} log\left[(1-\lambda) + 2\lambda e^{-\frac{x_i^2}{\theta}}\right]}$$

$$\boldsymbol{\frac{\partial\, log\, L}{\partial \theta} = -\frac{n}{\theta} + \frac{\sum_{i=1}^{n} x_i^2}{\theta^2} + \sum_{i=1}^{n} \frac{2\lambda e^{-\frac{x_i^2}{\theta}}\left(-\frac{x_i^2}{\theta^2}\right)}{\left[(1-\lambda) + 2\lambda e^{-\frac{x_i^2}{\theta}}\right]}}$$

$$\boldsymbol{\widehat{\theta}_{MLE} = \frac{\sum_{i=1}^{n} x_i^2 - 2\lambda \sum_{i=1}^{n} x_i^2 e^{-\frac{x_i^2}{\theta}}\left[(1-\lambda) + 2\lambda e^{-\frac{x_i^2}{\theta}}\right]}{n}} \qquad (11)$$

Since $(|\lambda| \leq 1)$, we can restricted (λ) by this region, we do not estimate it.

4. Simulation

From the CDF of transmuted Rayleigh, we generate random samples of various size $(n = 25,50,75,100)$, using different sets of two parameters (λ, θ), where $(|\lambda| \leq 1)$.

Table (1): Prior values of $(\lambda \; \& \; \theta)$ given for simulation

θ (scale parameter)	λ(transmuted parameter)
1.5	0.9
3	0.7
4.5	0.4

Table(2): MLE and MOM Estimates for $(\lambda \; \& \; \theta)$ when priors values$(\theta = 1.5, \lambda = 0.9)$

	Estimator	MOM	MLE	**Best**

Sample Size (n)	(MSE)	$\hat{\theta}$	$\hat{\lambda}$	$\hat{\theta}$	$\hat{\lambda}$	
25	Estimator	1.2203	0.9785	0.9979	0.8997	**$\hat{\lambda}$ MOM, $\hat{\theta}$MLE**
	(MSE)	(0.0224)	(0.00364)	(0.01304)	(0.01236)	
50	Estimator	1.0114	0.96631	1.0321	0.9946	**$\hat{\lambda}$ MLE, $\hat{\theta}$MLE**
	(MSE)	(0.01302)	(0.0061)	(0.0041)	(0.003)	
75	Estimator	1.0304)	0.90662	1.0314	0.8863	**$\hat{\lambda}$MLE, $\hat{\theta}$MLE**
	(MSE)	(0.00738)	(0.00182)	(0.00715)	(0.00124)	
100	Estimator	1.2205	0.9936	1.0031	0.7793	**$\hat{\lambda}$ MLE, $\hat{\theta}$MLE**
	(MSE)	(0.0094)	(0.00126)	(0.00521)	(0.00124)	

Table(3): MLE and MOM Estimates for (λ & θ) when priors values ($\theta = 3, \lambda = 0.7$)

Sample Size	Estimator (MSE)	MOM		MLE		**Best**
		$\hat{\theta}$	$\hat{\lambda}$	$\hat{\theta}$	$\hat{\lambda}$	
25	Estimator	3.0645	0.9907	3.2461	0.9981	**$\hat{\lambda}$ MLE, $\hat{\theta}$MOM**
	(MSE)	(0.0952)	(0.0891)	(0.0987)	(0.0617)	
50	Estimator	3.9475	1.0062	3.8890	1.0041	**$\hat{\lambda}$ MOM, $\hat{\theta}$MLE**
	(MSE)	(0.3882)	(0.0991)	(0.2061)	(0.1691)	
75	Estimator	3.0062	0.8751	3.0094	0.8082	**$\hat{\lambda}$ MLE, $\hat{\theta}$MOM**
	(MSE)	(0.0632)	(0.0762)	(0.0605)	(0.0415)	
100	Estimator	3.0061	0.7726	3.0021	0.80061	**$\hat{\lambda}$ MLE, $\hat{\theta}$MLE**
	(MSE)	(0.0457)	(0.0329)	(0.0241)	(0.0061)	

Table(4): MLE and MOM Estimates for (λ & θ) when priors values ($\theta = 4.5, \lambda = 0.4$)

Sample Size	Estimator (MSE)	MOM		MLE		**Best**
		$\hat{\theta}$	$\hat{\lambda}$	$\hat{\theta}$	$\hat{\lambda}$	
25	Estimator	5.4706	0.9901	5.3201	0.9802	**$\hat{\lambda}$ MOM, $\hat{\theta}$MLE**
	(MSE)	(0.4921)	(0.0781)	(0.4761)	(0.0851)	
50	Estimator	4.9906	0.8006	4.2031	0.7064	**$\hat{\lambda}$ MLE, $\hat{\theta}$MOM**
	(MSE)	(0.0321)	(0.12542)	(0.1467)	(0.0332)	
75	Estimator	4.6972	0.5006	4.0031	0.4806	**$\hat{\lambda}$ MLE, $\hat{\theta}$MLE**
	(MSE)	(0.08211)	(0.03115)	(0.0445)	(0.0025)	
100	Estimator	4.6652	0.5003	3.9980	0.4772	**$\hat{\lambda}$ MLE, $\hat{\theta}$MLE**
	(MSE)	(0.07013)	(0.0224)	(0.0332)	(0.0013)	

Application

We applied Rayleigh probability distribution on audio signal which have some noise, and noise refers to unwanted audio, so Rayleigh probability distribution work on choosing the best audio signal through replacing the best estimates of parameters through of probability function, and also we apply the data from distribution and the original data and explain these opinion in the following figures

All figures and results are applied in MATAB environment.figure 1 shows the original audio signal and original audio signal with noise.

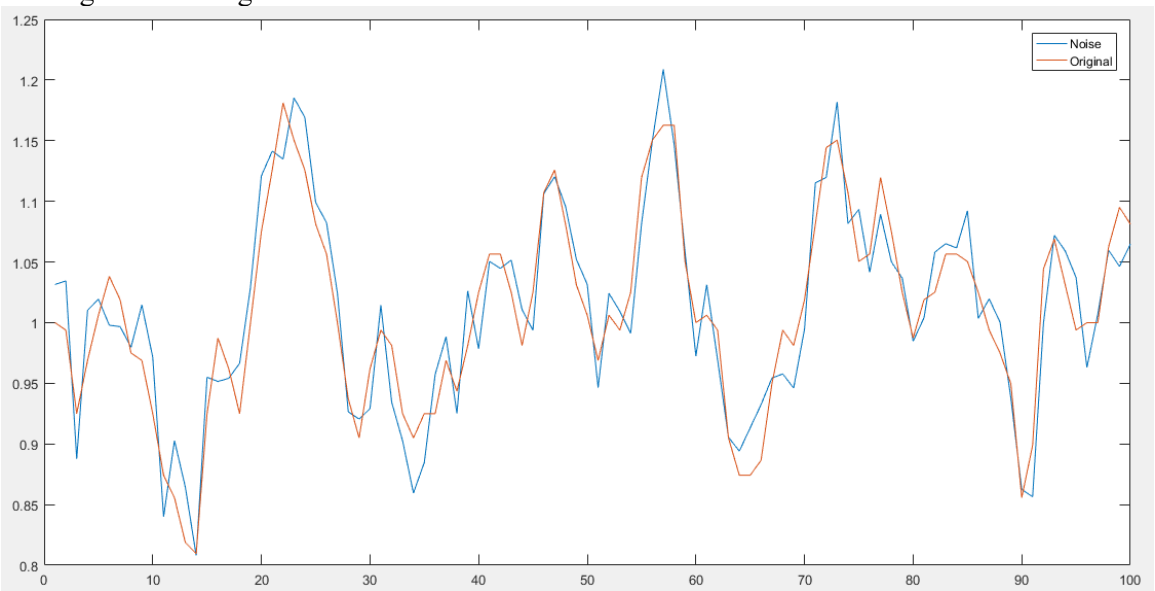

Figure. 1 original and original with noise signal

Now we applied some Rayleigh probability distribution to choose the best set of parameter.

original	X’	S^2	S	C.V
	1.0085	0.0064	0.0798	7.9763

noise	X’	S^2	S	C.V
$\lambda = 0.9\ \ \theta = 1.5$	0.7134	0.0039	0.0622	6.2188
$\lambda = 0.7\ \ \theta = 3$	0.4292	0.0026	0.0512	5.1157
$\lambda = 0.4\ \ \theta = 4.5$	0.2670	0.0013	0.0364	3.6423

Conclusion

The best estimator for (θ) for small size ($n = 25$) and moderate sample size ($n = 50$) and large sample ($n = 75$), are ($\hat{\theta}_{MLE}$&$\hat{\lambda}_{MLE}$), this is related to the important properties of estimation by maximum likelihood method.

$\hat{\lambda}_{MOM}$ is best by MOM with percentage (3/24 *100) while $\hat{\lambda}_{MLE}$ is best with percentage (9/24 *100) and $\hat{\theta}_{MOM}$ is best with percentage (3/24) while $\hat{\theta}_{MLE}$ is best with percentage (9/24 *100%).

In the application of noise audio signal we applied three value of the two parameter (λ & θ) and we see that ($\lambda = 0.4$ & $\theta = 4.5$) are the best estimatorwhen (n =100) since it give the smallest coefficient of variation which is the measure of dispersion .

Summary

For original data, and at computed values of $(\lambda = 0.9, \theta = 1.5), (\lambda = 0.7, \theta = 3), (\lambda = 0.4, \theta = 4.5)$ we find that the best estimator that gives smallest C.V (coefficient of variation).

References

[1]Vasile PREDA, Eugenia PANAITESCU, Roxana CIUMARA,“the modified exponential al poisson distribution”, publishing house of the Romanian academy series A, vol. (12), No. 1, pp.(22-29), 2011

[2] A, Ahmed Z; Nofal, Zohdy M., (2014), “Transmuted Complementary Weibull Geometric Distribution”, Pakistan Journal of Statistics and Operation Research; Lahore10.4.

[2]A. Ahmad, S.P. Ahmadand A. Ahmed, (2014), “Transmuted Inverse Rayleigh distribution: A Generalization of the Inverse Rayleigh Distribution”, Mathematical Theory and Modeling, vol. 4, pp. 90-98.

[3]Afaq Ahmad, S. P Ahmad and A. Ahmed, (2015),”Characterization and Estimation of Transmuted RayleighDistribution”, J. Stat. Appl. Pro. 4, No. 2, 315-321.

[4]Afaq Ahmad, S.P Ahmad and A. Ahmed, (2014), “Transmuted Inverse Rayleigh Distribution: A Generalization ofthe Inverse Rayleigh Distribution”, Mathematical Theory and Modeling, Vol.4, No.7.

[5]Aryal G.R. TsokosCh.p., (2011), Transmuted Weibull Distribution: A Generalization of the Weibull probability distribution”, European Journal of Pure and Mathematics, Vol.4, No.2, 89 – 102.

[6]Ashour, S. and et al. (2013), "Transmuted Exponentiated Lomax distribution", Australian Journal ofBasic and Applied Sciences, vol. 7, pp. 658-667.
[7]F. Merovci. (2013), "Transmuted Rayleigh distribution". Austrian Journal of Statistics, vol. 42, pp. 21-31.
[8]FatonMerovci, (2013), "Transmuted Rayleigh Distribution", AUSTRIAN JOURNAL OF STATISTICSVolume 42, Number 1, 21–31.
[9]FatonMerovci, (2014), "Transmuted Generalized Rayleigh Distribution", J. Stat. Appl. Pro. 3, No. 1, 9-20.
[10]I. Elbatal, (2013), "TRANSMUTED MODIFIED INVERSE WEIBULL DISTRIBUTION: A GENERALIZATION OF THE MODIFIED INVERSE WEIBULL PROBABILITY DISTRIBUTION", International Journal of Mathematical Archive, Vol.4, No.8.
[11]Khan, M. S., and King, R. (2013). Transmuted modified Weibull distribution: A generalizationof the modified Weibull probability distribution. European Journal of Pureand Applied Mathematics, 6, 66-88.
[12]Mahmoud Eltehiwy, Samir Ashour, (2017), "Transmuted Exponentiated Modified Weibull Distribution", International Journal of Basic and Applied Sciences, Vol 6, No 3.
[13]Merovci, F. (2013). Transmuted Lindley distribution. International Journal of OpenProblems in Computer Science and Mathematics, 6.
[14]Muhammad Shuaib Khan, Robert King, (2015), "Transmuted Modified Inverse Rayleigh Distribution", Austrian Journal of Statistics, Volume 44, 17–29.
[15]Muhammad Shuaib Khan, Robert King, Irene Hudson, (2013), "Characterizations of the transmuted inverse Weibull distribution",ANZIAM Journal, Vol.55.
[16]YuzhuTian,MaozieTian , Qianqian Zhu, (2014), "Transmuted Linear Exponential Distribution: A New Generalization of the Linear Exponential Distribution", Communications in Statistics - Simulation and Computation Volume 43, Issue 10.

Hiding Techniques for Dynamic Encryption Text based on Corner Point

IOP Conf. Series: Journal of Physics: Conf. Series **1003** (2018) 012027 doi:10.1088/1742-6596/1003/1/012027

Hiding Techniques for Dynamic Encryption Text based on Corner Point

Firas A. Abdullatif[1], Alaa A. Abdullatif[2], Amna al-Saffar[3]

[123]University of Baghdad\College of Education for pure science-Ibn Al-Haitham\computer science department

Firas.alobaedy@gmail.com, Alaa_3b@yahoo.com, Amnaalsafar1@yahoo.com

Abstract. Hiding technique for dynamic encryption text using encoding table and symmetric encryption method (AES algorithm) is presented in this paper. The encoding table is generated dynamically from MSB of the cover image points that used as the first phase of encryption. The Harris corner point algorithm is applied on cover image to generate the corner points which are used to generate dynamic AES key to second phase of text encryption. The embedded process in the LSB for the image pixels except the Harris corner points for more robust. Experimental results have demonstrated that the proposed scheme have embedding quality, error-free text recovery, and high value in PSNR.

Keywords: steganography, Harris corner point algorithm, dynamic encryption, Dynamic coding table.

1.Introduction

In the past years, due to the proliferation of digital data and its ease of dealing, detection, sharing and reuse, many researchers have invented to work on techniques to increase the security of the transfer of this data and confidentiality, cryptography and Steganography are still the most important techniques[1].

Cryptography is the conversion of plain text to an illegible cipher, Return of the text to its explicit state on the other side depends generally on the algorithm used and the key, where the symmetric algorithm used the same key in both encryption and decryption process, that key must transfer in a secure channel. the different keys named "public and private" are used in asymmetric algorithm that depends on different keys in encryption and decryption process[2].

The algorithms that encrypt data are a blocks cipher algorithms and stream cipher algorithm, Encrypted data can be transmitted in a private channel or public channel, but the key in the symmetrical algorithms must be transmitted by the private channel, unlike the asymmetric methods, one of the keys which is public and does not need to be secret[3] .

In all cases and algorithms the data still present but in an unreadable format, it makes them more vulnerable to the threat[4].

Steganography is an embedding of digital message with the digital data of the cover; the cover may be an image, audio, movie, etc. When hiding in the image as in the proposed method there will be a stego-image. In general, the steganography in the image either in the temporal domain or in the transform domain. There are several techniques for hiding in both domains. Some types of steganography technique use the key and others do not use it, and is mostly used for more robust [5].

During the transfer process, the channel may be monitor intentionally or unintentionally, there are many hackers who wish to reveal the hidden data for different purposes. Therefore, the cover should be preserved with least possible changes. This means that there is a great similarity between the cover and the stego-object, and Difficulty to retrieve the secret message from stego-object at worst case [6].

In this paper, we propose two phases to encrypted text. Firstly the plain text converted to binary depending on dynamic substitution table, then it encrypted by AES algorithm which the dynamic key is generated by corner points. In the end, the data is hidden in the least significant bit exception these corner points.

2. AES Encryption Algorithm

AES is a symmetric cryptography algorithm, It a block cipher algorithm[7]. The length of the cipher keys can be 128, 192, or 256 bits. Both encryption and decryption procedures perform several rounds, due to the size of input/cipher key blocks. Input data in AES is often represented as 4*4 bytes array and it is termed as ‘‘state”[8].Figure 1 shows the AES encrypting steps.

There are four main phases: Add Round Key, Shift Rows, Sub Bytes, and Mix Columns. These four phases are used in every round except first and the last ones. The first round has only Add Round Key, and the last round does not have Mix Columns. The initial key has to be expanded to execute different rounds. The main phases are briefly described below:[[9]

1. Add Round Key: This phase adds a cipher key to a state array by using bitwise Exclusive-OR (XOR).
2. Shift Rows: This phase is a conversion that operates on the rows of a state. Bytes of the state are shifted cyclically to the left and right. The first row remains untouched. The second, third, and fourth rows are shifted by one, two, and three, respectively.
3. Substitute Bytes: This function is nonlinear. It performs a byte-by-byte substitution of the blocks to produce a new byte value. A substitution-box (S-Box) implemented by either a Look-Up Table or Galois Field operation.
4. Mix Columns: is a matrix multiplication with fixed values.

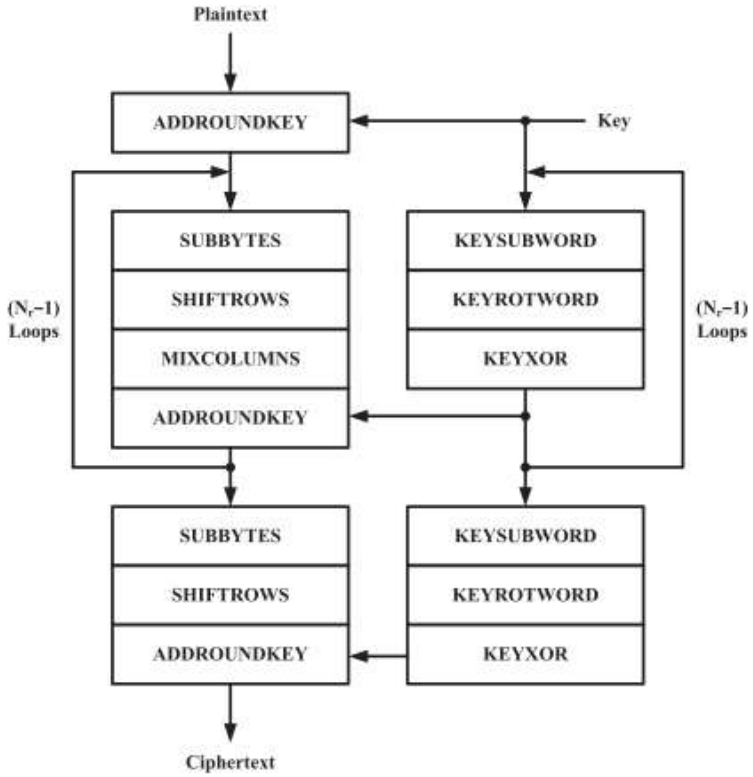

Figure 1. AES Encryption Steps [9]

3. Harris Corner Detection Algorithm

Harris algorithm is a still image algorithm used for the communal edge and edge detector. The amounts of corner functions are extracted that gives a better quantitative measurement that uses a steady operator. A local detection window is designed for it. With a minute shifting the window is shifted in diverse directions, and determined the average difference in intensity. As a corner point, the midpoint of the window is taken. By considering the intensity values in a minute window the point can be predicted. [10]

To identify the corner points, Harris algorithm uses corner detector. In a flat region will not show any difference of intensity in any directions in moving the window. It will show the difference in the edge direction if an edge section is found. But in a corner, there will be a considerable difference in intensity in every direction. The following shows the basic steps of Harris Corner Detection[11][12][13]

1. Compute x and y derivatives of image
   $I_x=G_\delta^x * I$ $I_y=G_\delta^y * I$
2. Compute products of derivatives of every pixel
   $I_{x2}=I_x \cdot I_x$ $I_{y2}=I_y \cdot I_y$
   $I_{xy}=I_x \cdot I_y$
3. Compute the sums of the products of derivatives at each pixel
   $S_{x2}=G_{\delta 1} * I_{x2}$ $S_{y2}=G_{\delta 1} * I_{y2}$
   $S_{xy}=G_{\delta 1} * I_{xy}$
4. Define at each pixel (x,y) the matrix
   $H(x,y)=\begin{vmatrix} S_{x2}(x,y) & S_{xy}(x,y) \\ S_{xy}(x,y) & S_{y2}(x,y) \end{vmatrix}$

5. Compute the response of the detector at each pixel
   $R=Det(H)-K(Trace(H))^2$
6. Threshold on value of R. Compute nonMax suppression

4. Proposed method

In the proposed method two phases are done to encryption the text. First one is convert the plain text to binary code by dynamic substitution table which generated from cover image data. While the second phase is encrypted binary code using the AES algorithm depend on the dynamic key generate by using the Harris corner points .The hiding process for the encrypted code in the image has used the LSB of all image pixels excluding the pixels of corner points. The embedding and extracting processes shown in 'figure 2 'and 'figure 3'.

4.1 Proposed Algorithms

In this section, the algorithms of the proposed method are explained as shown below:

Algorithm 1: Data Embedding Algorithm

Input: plain text, cover image
Output: stego_ image
Step 1: generate dynamic coding table// generate 256 different bytes in coding table for
256 characters that used in computer
i=0, // i the counter of bytes in code table,
j=0 // j the counter of bytes in cover image
while i<= 255 do
temp= 4 bits of MSB of byte[j] catenation with 4 bits of MSB of byte [j+1]
if temp not in code table
code table [char[i]]=temp
i=i+1
end if
j=j+2
end while
step 2: convert the plain text to binary code by substitute character using the code table that generated in step 1
step 3: apply Harris algorithm on cover image to generate corner points.
Step 4:// generate dynamic 128 key for AES algorithm
i=1 ; // i the counter of corner point bytes
key=0
While i<= 32 do
Temp=(bit[0], bit[2], bit[4], bit[5]) from byte[i] of corner point array
Key = key concatenation with Temp
i=i+1
End while
Step 5: apply AES algorithm on binary code that resultant from step2 using key from step 4 .
Step 6: hiding the encrypted data in LSB of the cover image exception the corner points.

Algorithm 2: Data Extracted Algorithm

Input: stego_image
Output: plain text
Step 1: generate the code table from the stego_image as in step 1 in algorithm 1.
Step 2: apply Harris algorithm on stego_image to get corner points.
Step 3: generate dynamic 128 bits key for AES algorithm depending on corner point as in step 4 in algorithm1
Step 4: extract the encrypted text from the LSB of stego_image pixels except corner points.

Step 5: apply AES algorithm on extracted encrypted text using the128 bits key to get the binary code.
Step 6: generate plain text characters by substitute the binary code using the coding table.

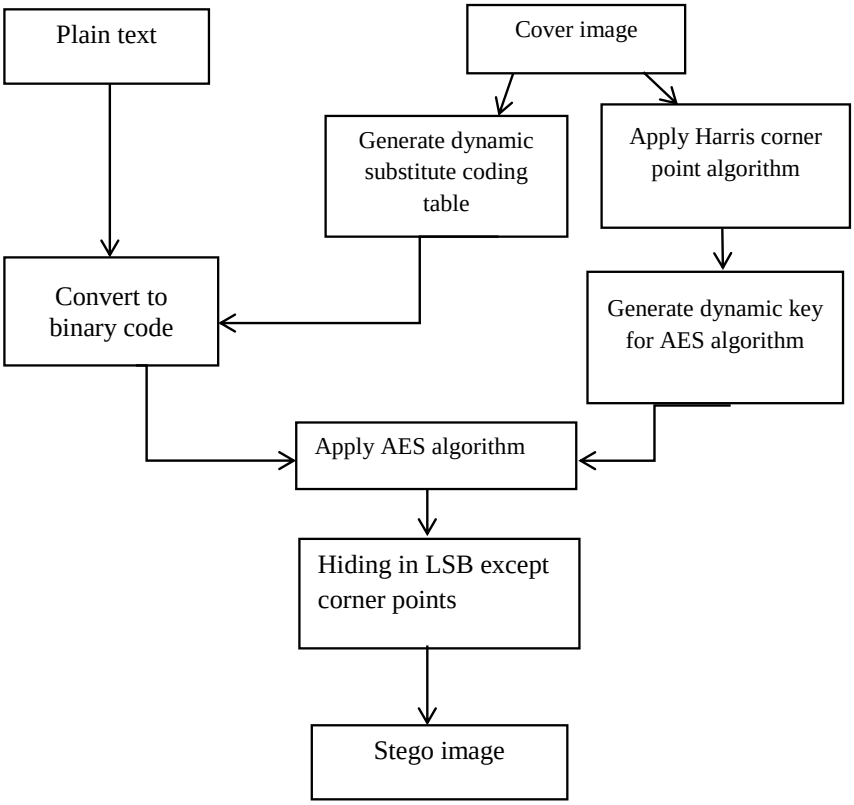

Figure 2. the embedding process

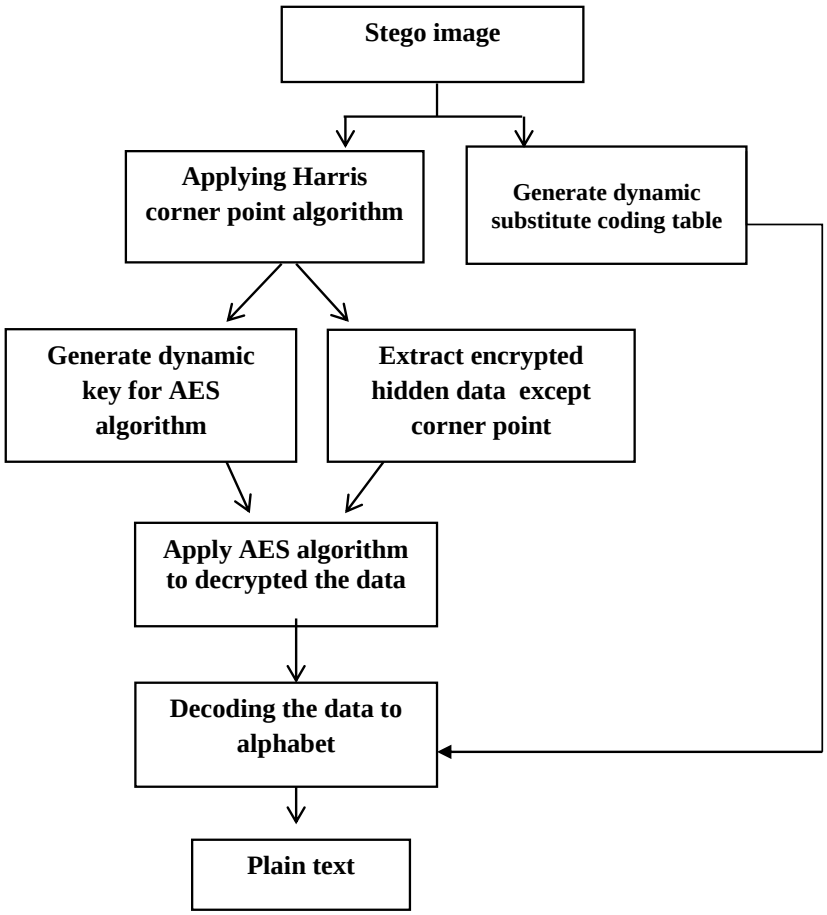

Figure 3. the extracting process

5.Experimental Results and Analysis

The proposed algorithm performed on many images with size 256x256x3, and 70 characters' message. The substitution table size is 256 records generated from the cover image, each record have two fields first to chars and the second to the binary coding. The corner points that generate from Harris algorithm are used to generate a dynamic key for the AES. The first, third, fifth, and sixth bits of each bytes of corner points were used until the end of the 128-bits key. this configuration is to increase the randomness of the key.

table (1) shows the cover image, the image with corner point and the result stego-image of six images as a samples for implement the proposed algorithm to compute the result. we can use image size more than 256*256 that give more load to hide with best result.

Table (1) the cover images, the images with corner points, and the stego-images

Image name	Cover image	image with corner point	stego-image
Baboon image			
Lena image		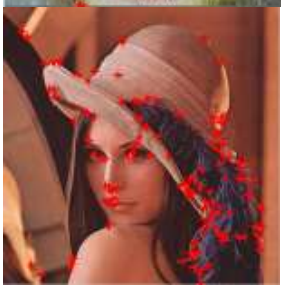	
Barbra image			
Pepper image			
House image			

Light house image

To evaluate the performance of proposed algorithm used parameters such as PSNR and MSE where

$$\mathrm{MSE} = \frac{1}{w \times h} \sum_{i=1}^{w} \sum_{j}^{h} \left(Stego\,(i,j) - Cover\,(i,j) \right)^2 \quad \text{--------- (1)}$$

Where, the Stego(i,j) is the stego_ image and the Cover(I,j) is cover image.

$$\mathrm{PSNR} = 10 \times \log_{10} \frac{255^2}{\mathrm{MSE}}\ (\mathrm{dB}) \quad \text{--------- (2)}$$

The proposed method does not need to exchange any information except cover-image and all information extract from cover-image until the secret message is retrieve , although it does not use the standard coding table and its using a symmetric encryption method that needs to exchange the key before the start of the encryption process.

The cryptographic flaws showed that the encryption text was larger than the original text (as result of standard AES algorithm, although that the proposed algorithm shows good average of PSNR as show in table(2).

Table (2) value of PSNR, and MSE for the proposed algorithm.

Image	PSNR	MSE
Baboon	80.9384	5.2389e-04
Lena	81.0668	5.0863e-04
Barbra	80.8138	5.3914e-04
Pepper	80.385	5.9509e-04
House	80.6163	5.6458e-04
Lighthouse	81.0668	5.0863e-04

6.Conclusion

In this work an efficient method for encryption and hiding is produce. The two phases in encryption process (dynamic substitution table and AES algorithm with dynamic key) are providing more security. To overcome the problem of exchange the key, the two parties generated it dynamically from image. The method of embedding data has used the most common and simplest way is the LSB of image pixels except the corner points extracted from

the Harris algorithm. Although the cryptographic flaws showed that the encryption text was larger than the original text, the proposed method shows high value of PSNR. Also can used two or three LSB in each byte for hiding to increase the capacity of hiding data in cover image with good value of PSNR.

Reference

[1] P. Patil, P. Narayankar, D. G. Narayan, and S. M. Meena, "A Comprehensive Evaluation of Cryptographic Algorithms: DES, 3DES, AES, RSA and Blowfish," *Procedia Comput. Sci.*, vol. **78**, no. December 2015, pp. 617–624, 2016.

[2] S. Sherkhane, A. Waghmare, S. Dalvi, and S. Bamne, "Hybrid Data Encryption using Color code and Armstrong number," vol. **7**, no. 4, pp. 10300–10305, 2017.

[3] S. Wade, A. Gadikar, A. Khan, and V. Deshmukh, "Design Enhance AES Data Encryption and Decryption," vol. **3**, no. 2, pp. 136–138, 2017.

[4] P. Dusane, J. Patil, U. Jain, R. Pandya, C. Engineering, and S. Coet, "Security of Data with RGB Color and AES Encryption Techniques," pp. 3063–3067, 2017.

[5] A. Judice, P. Shamini, D. J. Sree, and H. A. Sree, "An Image High Capacity Steganographic Methods by Modified OPA Algorithm and Haar Wavelet Transform," vol. **14**, no. 3, pp. 125–132, 2014.

[6] A. A. Abdul Latef and F. A. Abdul Latef, "Hiding Encrypted Color Image within MPEG-2 Video," vol. **30**, no. 4, pp. 605–614, 2012.

[7] N. Mathur and R. Bansode, "AES Based Text Encryption Using 12 Rounds with Dynamic Key Selection," *Procedia Comput. Sci.*, vol. **79**, pp. 1036–1043, 2016.

[8] U. Farooq and M. F. Aslam, "Comparative analysis of different AES implementation techniques for efficient resource usage and better performance of an FPGA," *J. King Saud Univ. - Comput. Inf. Sci.*, vol. **29**, no. 3, pp. 295–302, 2017.

[9] K. Shahbazi, M. Eshghi, and R. Faghih Mirzaee, "Design and implementation of an ASIP-based cryptography processor for AES, IDEA, and MD5," *Eng. Sci. Technol. an Int. J.*, 2017.

[10] M. Zhu, W. Wang, B. Liu, and J. Huang, "A Fast Image Stitching Algorithm via Multiple-Constraint Corner Matching," *Math. Probl. Eng.*, vol. 2013, 2013.

[11] P. V. Patil and M. S. C. Chavan, "A Comparative Analysis of Image Stitching Algorithms Using Harris Corner Detection And SIFT Algorithm .," vol. **10**, no. 1, pp. 482–486, 2017.

[12] Mahesh and M. . Subramanyam, "INVARIANT CORNER DETECTION USING STEERABLE FILTERS AND HARRIS ALGORITHM," *Int. J.*, vol. **3**, no. 4, pp. 1638–1645, 2011.

[13] Z. Zhang, H. Lu, X. Li, W. Li, and W. Yuan, "Application of Improved Harris Algorithm in Sub-Pixel Feature Point Extraction," *Int. J. Comput. Electr. Eng.*, vol. **6**, no. 2, pp. 101–104, 2014.

Analyzing Study of Path loss Propagation Models in Wireless Communications at 0.8 GHz

Analyzing Study of Path loss Propagation Models in Wireless Communications at 0.8 GHz

Haider Kadhim Hoomod[1], Intisar Al-Mejibli[2] and Abbas Issa Jabboory[3]

[1] Computer Science Dept., Al-Mustansiriyah University, Baghdad, Iraq
[2] Informatics Systems Management Dept., University of Information Technology and Communication, Baghdad, Iraq
[3]Informatics Institute for Postgraduate Studies, Iraqi Commission for Computer & Informatics, Baghdad, Iraq
Corresponding address: drhjnew@gmail.com, it_abbas@yahoo.com

Abstract. The paths loss propagation model is an important tool in wireless network planning, allowing network planner to optimize the cell towers distribution and meet expected service level requirements. However, each type of path loss propagation model is designed to predict path loss in a particular environment that may be inaccurate in other different environment. In this research different propagation models (Hata Model, ICC-33 Model, Ericson Model and Coast-231 Model) have been analyzed and compared based on the measured data. The measured data represent signal strength of two cell towers placed in two different environments which obtained by a drive test of them. First one in AL-Habebea represents an urban environment (high-density region) and the second in AL-Hindea district represents a rural environment (low-density region) with operating frequency 0.8 GHz. The results of performing the analysis and comparison conclude that Hata model and Ericsson model shows small deviation from real measurements in urban environment and Hata model generally gives better prediction in the rural environment.

Keywords: Hata model, Path loss, Signal strength, Ericsson model, 0.8 GHz.

1. Introduction

In recent years, mobile wireless communications have developed rapidly, leading to make the mobile phones become an integral part of people's lives. Hence the demand on services from mobile wireless communications companies has increased [1][2]. Wireless network planners are looking to improve connectivity between different points. Path loss propagation models is an experimental mathematical formula for characterizing the propagation of radio waves as a distance function between the antennas of transmitter and receiver. These models are designed based on a large dataset collected from specific environments. Propagation model determine is very important parameter in network planning and studies of interference with starting deployment [3].
The remainder of the research is arranged as follows: Section 2 explores the related work .Section 3 describes the path loss propagation models. Radio link budget calculation is explained in section 4. Section 5 details the performance evaluation. In section 6, results and

discussion is presented. The conclusions are discusses in section 7. The last section list the research references.

2. Related Work

Several studies have been completed in the fields of path loss propagation model where good results are obtained. All these studies are very important and play a vital role in wireless network planning. Authors in [4] estimate five path loss propagation models Stanford University Interim (SUI), COST-231, Hata-Okumura Extended Model (called also ECC-33 Model), Ericsson and the Hata-Okumura model. The results of these models compared with actual measured data. The results of comparison show that the ECC-33 model suitable for a suburban environment. In [3] authors gave a brief introduction to loss models, concluding that each model is suitable for a specific environment. While [5] has analyzed and compared the path loss values of the selected models in different environments with frequency 1700 MHz. They concluded that SUI model calculations consistent with measurements data and it is suitable for urban areas, unlike the cost 231 W-I model whose calculations do not correspond to the measure data.
In this research, present four path loss propagation models (Hata Model, ICC-33 Model, Ericson Model and Coast-231 Model) and then calculate the signal strength of theirs. The signal strength of these models are analyzed and comparison with real measured data to see whether these models are accurately used for prediction to the path loss.

3. Path Loss Propagation Models

Generally, some of propagation factors for instance reflection, scattering, diffraction, absorption, and atmospheric particles affect the signal of wireless communication when transmitted through a path [2, 6].
The main benefit for the use of the standard path loss models are time-saving and cost, despite the limited accuracy. Through the results of many measurement efforts, the existing equations are used in empirical models. The following are examples of the path loss propagation models[4, 7]:

a. Free Space Path Loss Model
b. Okumura Model
c. HATA Path Loss Model
d. LHata Model (LHata)
e. COST 231 Extended Hata Model
f. ECC-33 or Hata – Okumura Extended Model
g. Walfisch-Ikegami Model
h. Stanford University Interim (SUI) model
i. Ericson Model

Field data for various environments have been used in the design of all the models mentioned above. In this research, four path loss propagation models were used (HATA, COST 231, ECC-33 and Ericson Models) because they are suitable to be implemented in the study area environment at frequency 0.8 GHz.

3.1 HATA Path Loss Model

This model introduces by Okumura model and it is useful for frequency range 150MHz to 1500MHz. This model is the most widely used in urban area, the path loss equation of this model is [1] [8]:

$$PL(dB) = 69.55+26.16\log_{10}(f)-13.82\log_{10}(hb)-(ahm) + (44.9-6.55\log_{10}(hb))\log_{10}(d) -C \quad (1)$$

$$\text{ahm}=\begin{cases} 3.2(\log(11.75hm))^2-4.97 & in\ urban, f>400MHz \\ (1.1log_{10}(f-0.7)hm-(1.56log_{10}(f-0.8) & in\ open\ area \end{cases} \quad (2)$$

$$C=\begin{cases} 0 & in\ urban \\ 40.49+4.78(log_{10}(f))^2-18.33log_{10}(f) & in\ open\ area \end{cases} \quad (3)$$

Where:
PL = path loss
f(MHz) =Frequency
d (Km) = Distance between transmitter and receiver antennas
hb (m) = Base station antenna height
hm(m)=Mobile station antenna height
C = environment factor

3.2 COST 231 Extended Hata Model

Cost 231model and also called Personal Communication System (PCS) Extension, it is the first model used up to date. This model is an extension of the Okumura-Hata model to cover a wide range of frequencies between (0.5-2 GHz), and is used for medium to small cities [3][4].

$$PL=46.3+33.9\log_{10}(f)-13.82\log_{10}(hb)-\text{ahm}\ (44.9-6.55\log_{10}(hb))\ \log_{10}(d)+C \quad (4)$$

$$\text{ahm}=\begin{cases} 3.2(\log(11.75hm))^2-4.97 & in\ urban, f>400MHz \\ (1.1log_{10}(f-0.7)hm-(1.56log_{10}(f-0.8) & in\ open\ area \end{cases} \quad (5)$$

$$C=\begin{cases} 3 & in\ urban \\ 0 & in\ suburban\ \ or\ rural \end{cases} \quad (6)$$

3.3 ECC-33 or Hata – Okumura Extended Model

It is appropriate model for the Ultra High Frequency (UHF) band, and according to recent recommendations of International Telecommunication Union-Radio communication (ITU-R), it uses up to 3.5GHz. This model proposed based on the Okumura model [4].

$$PL=\ 92.4+20\log(d)+20\log(f)+20.41+9.83\log(d)+7.89\log(f)+9.56(\log(f))^2+\log(hb/200)(13.958+5.8\log(d))^2+Gr \quad (7)$$

$$Gr=\begin{cases} [42.57+13.7\log(f)][\log(hm)-0.585] & in\ median\ city \\ 0.759(hm)-1.862 & in\ larg\ city \end{cases} \quad (8)$$

3.4 Ericson Model

Ericsson model is software provided by Ericsson Company to use for wireless network planner. This model was developed based on the modified Okumura-Hata model for use in differing propagation environments according to the parameters shown in Table (1) [5] [9].

$$PL=k_0+k_1+\log_{10}(d)+k_2\log_{10}(hb)+k_3\log_{10}(hb).\log_{10}(d)-3.2[\log10(11.75hr^2]+44.49\log_{10}(f)-478[\log_{10}(f)]^2 \quad (9)$$

Table 1. Ericson Models parameters

ENVIRONMENT TYPE	K_0	K_1	K_2	K_3
RURAL	45.95	100.6	12	0.1
SUBURBAN	43.20	68.63	12	0.1
URBAN	36.20	30.20	12	0.1

4. Radio Link Budget Calculation

The link budget calculation in the cell is calculates for the farthest point from the cell tower. In order to calculate the maximum coverage, consideration must be given to the minimum signal intensity received by the receiver. The most important parameters of the budget calculation is discussed in the following[6, 10].

Transmitter Power: the maximum transmission power from cell towers antenna typical value from 36-46 dBm.
Antenna Gain: Antenna gain depends mainly on carrier frequency, size of antenna and device type. The cell tower antenna gain is a typical 15-18 dBi.

Losses: Includes cable and body losses on both sides (cell tower antenna and phone). Cable losses depend on the length and type of cable and frequency; it varies from 1-6 dB for cell tower antenna, and phone losses, in practical planning it is considered to be 0 dB[11].

EIRP: Is a stand for Effective Isotropic Radiated Power, the term is used to express how much transmitted power is radiated in the desired direction. It takes into account all type of losses and the gain of the transmitter antenna as:

EIRP (dBm) = Pt (dBm) + Ga (dBi) – Cable losses
(10)
Where:
Pt(dBm): Cell tower transmitting power
Ga(dBi): Antenna gain in reference to isotropic antenna

RX Level: Is a stand for received signal level, which considered the signal strength obtained by the mobile phone from cell tower antenna. It is importing factor who determines that the reception was good or not [12]. The RX level ranges and rating shown in table (2) and mathematical formula to calculate the Rx level is [6][13]:

$$RxLev\ (dBm) = EIRP - Pl - A_{BL} - I_{DM} - L_{SM} - L_{ACC} - G_A \quad (11)$$

Where:
EIRP (dBm)= Effective Isotropic Radiated Power
Pl (dB) = path loss propagation model
ABl (dB) = antenna / body loss.
IDM (dB) = degradation margin of Interference.
LSM (dB) = Log normal shadowing margin.
LACC (dB) = cell tower antenna cable and connector (0 dB).
GA (dB) = Cell tower antenna gain.

Table 2. RX level ranges and rating [14]

VALUE	RATING
-47 TO -10DBM	Very good
-6O TO -47DBM	Good
-75 TO -60DBM	better range of coverage
-90 TO -75DBM	average coverage
-95 TO -90DBM	poor coverage
-110 TO -95DBM	very bad coverage

5. Performance Evaluation

Practically, measured the signal strength by a drive test for two cell towers. First one in AL-Habebea represents an urban environment (high-density region) and the second in AL-Hindea district represents a rural environment (low-density region), Figure (1) and figure (2) show the location maps of the computerized areas of the cell towers (rural and urban) under study in which the drive test was applied.

The path loss propagation of four models (Hata Model, ICC-33 Model, Ericson Model and Coast-231 model) are calculated using the parameters shown in table (3) in MATLAB 2016. Then, the signal strength of these models are computed using equations (11), (12).

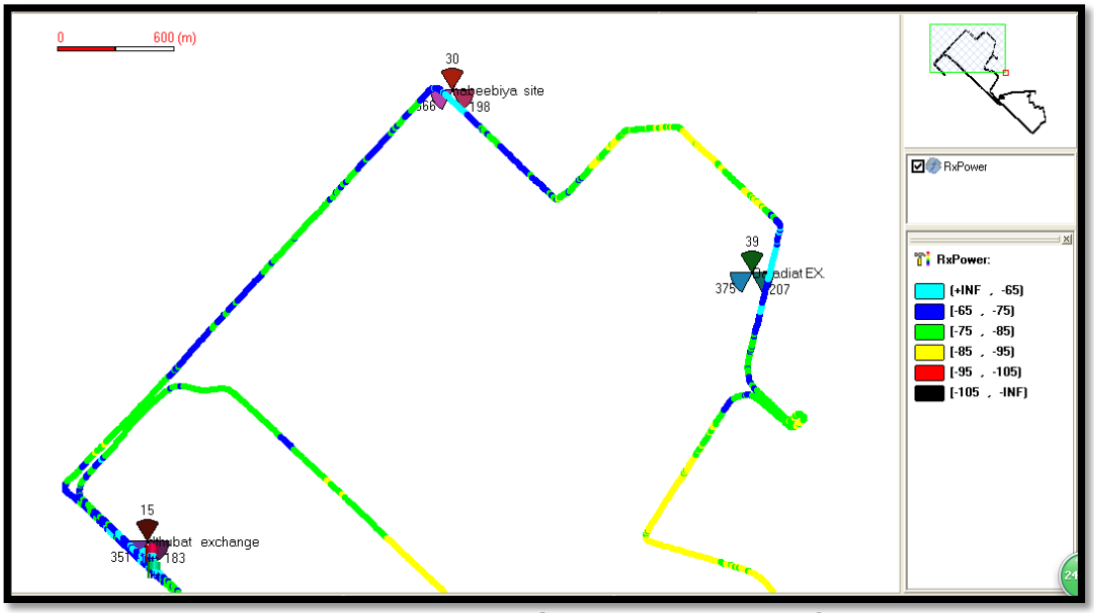

Figure 1. Drive test Simulation Environments in Urban

Figure 2. Drive test Simulation Environments in Rural

Table 3. Path loss parameters

PARAMETERS	VALUE
FREQUENCY	800 MHz
TRANSMITTER POWER	46 dBm
CELL TOWER ANTENNA HEIGHT	20 m urban, 30 m rural
PHONE ANTENNA HEIGHT	1.5 m
ANTENNA GAIN	18 dB
ANTENNA CABLE LOSS	1.5 dB
ANTENNA BOUY LOSS	3 dB
IDM	3 dB
LSM	5 dB for 90% coverage

The root mean square error (RMSE) of signal strength for these four type models has been calculated and compared with measurement data to predicate an appropriate path loss model [4].

$$\text{RMSE}=\sqrt{\frac{\sum_{i=1}^{N}(RX_{mi}-RX_i)^2}{N}} \qquad (12)$$

Where RX_{mi} is the measured signal strength in dBm, RX_i is the calculated signal strength in dBm, and N is the samples number of measured signal strength.

6. Results and Discussion

After calculating the path loss propagation values of the four models as shown in figure (3) and figure (4) and then calculating the RMSE as shown in the table (4)

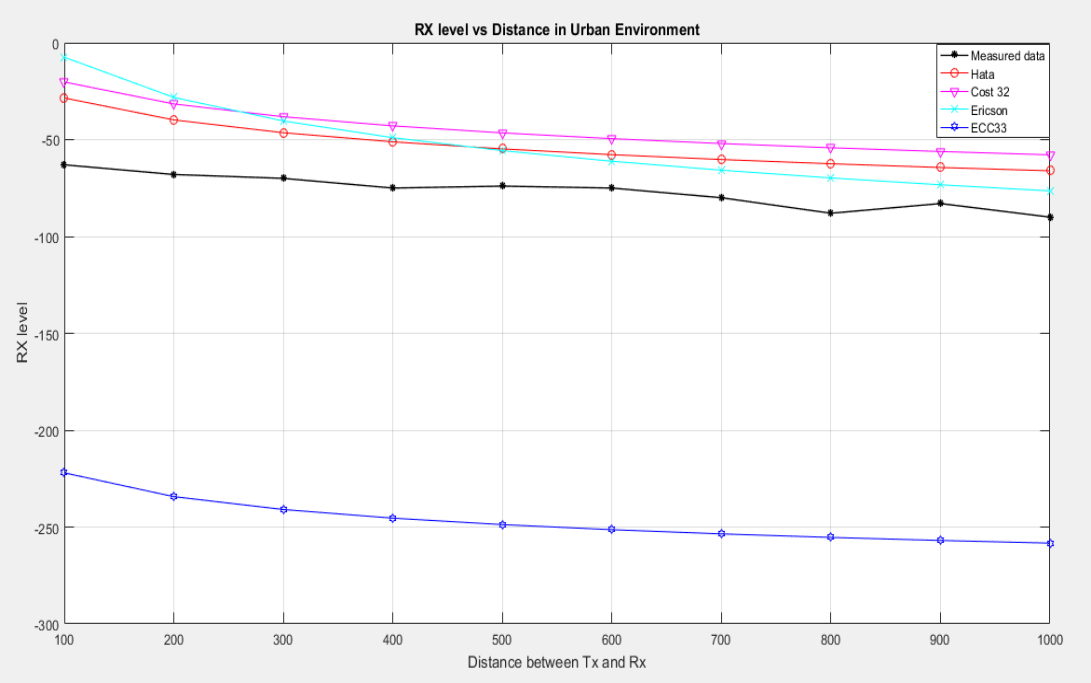

Figure 3. Comparison Signal Strength of Four Models with Measured Data from Urban Area

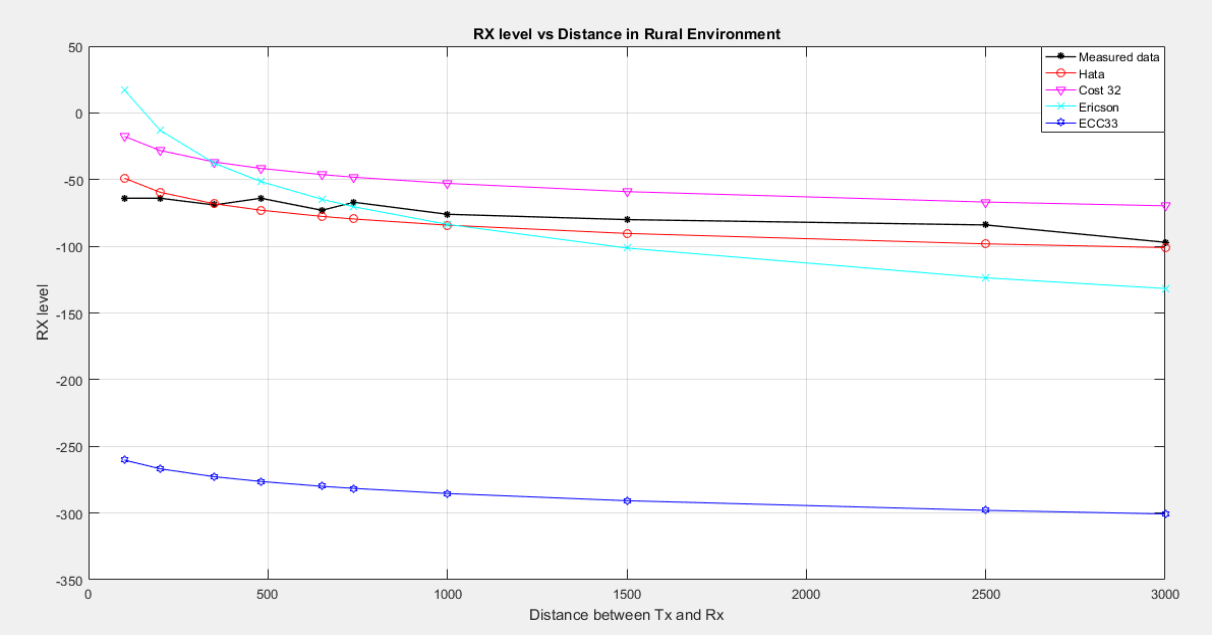

Figure 4. Comparison Signal Strength of Four Models with Measured Data From Rural Area

Table 4. Root Mean Square Error

PATH LOSS MODELS	URBAN	RURAL
HATA MODEL	23.43	4.23
COST 32 MODEL	31.68	27.09
ECC33 MODEL	170.09	207.44
ERICSON MODEL	23.88	7.75

Figure (3) shows the path loss in the urban environments (Al-Habebea) using Hata model and Ericsson model have small deviation compared to other models.
Figure (4) shows the path loss in the rural environments (AL-Hindea) using Hata model has small deviation compared to other models.
The difference in empirical values (the non-straight line graph) to Baghdad's urban environment has many obstacles in the way, such as many nearby high buildings.

7. Conclusions

The mainly objective of this research is to analyze and compare the appropriate path loss propagations model in wireless communication systems in different environment. The measured data and signal strength values of selected empirical path loss models in urban and rural environments are analyzed and compared at frequency 0.8 GHz. Path loss model is the most important parameter for network planners to achieve an acceptable quality of service for the users in wireless systems. This research study the path loss using four models: Hata Model, ICC-33 Model, Ericson Model and Coast-231 Model based on using the same parameters. The results of comparison conclude that the Hatta Model and Ericsson model are better predictive

of the urban environments. In addition to, Hata models generally gives better prediction in the rural environment.

8. References

[1] Z. Nadir, M. Bait-Suwailam, and M. Idrees 2016, "Pathloss Measurements and Prediction using Statistical Models," in *MATEC Web of Conferences*.

[2] H. K. Hoomod, I. Al-Mejibli, and A. IssaJabboory 2017, "Optimizing SOM for cell towers distribution," in *New Trends in Information & Communications Technology Applications (NTICT), 2017 Annual Conference on*, Baghdad, pp. 138-143.

[3] K. J. Parmar and D. V. D. Nimavat 2015, "Comparative Analysis of Path Loss Propagation Models in Radio Communication," *International Journal of Innovative Research in Computer and Communication Engineering*, vol. **3**, pp. 840-844.

[4] M. S. Mollel and M. Kisangiri 2014, "Comparison of Empirical Propagation Path Loss Models for Mobile Communication," *Computer Engineering and Intelligent Systems*, vol. **5**, pp. 1-10.

[5] Y. Zakaria, J. Hosek, and J. Misurec 2015, "Path Loss Measurements for Wireless Communication in Urban and Rural Environments," *American Journal of Engineering and Applied Sciences*, vol. **8**.

[6] D. S. A. Mawjoud 2008, "Evaluation of power budget and Cell coverage Range in Cellular GSM System," *AI-Rafidain Engineering*, vol. **16**, pp. 37-47.

[7] P. K. Sharma and R. K. Singh 2012, "Cell Coverage Area and Link Budget Calculations in GSM System," *International Journal of Modern Engineering Research (IJMER)*, vol. **2**, pp. 170-176.

[8] N. V. K. Ramesh, K. S. Kumar, D. V. Ratnam 2015, A. Hussain, Y. V. S. Jaswanth, and P. S. Chaitanya, "Comparative Analysis Of Path Loss Attenuation At Outdoor For 1.8 Ghz, 2.1 Ghz In Urban Environment," *Journal of Theoretical and Applied Information Technology*, vol. **82**, p. 85.

[9] M. S. Mollel and M. Kisangiri 2014, "An overview of various propagation model for mobile communication," in *Science, Computing and Telecommunications (PACT), 2014 Pan African Conference on*, pp. 148-153.

[10] B. Seifu 2012, "LTE Radio Network Planning: Modeling Approaches for the Case of Addis Ababa," in *Electrical and Computer Engineering Department*. vol. Masters of Science in Electrical Engineering Ethiopia Addis Ababa: Addis Ababa University, p. 108.

[11] A. Obot, O. Simeon, and J. Afolayan 2011, "Comparative analysis of path loss prediction models for urban macrocellular environments," *Nigerian journal of technology*, vol. **30**, pp. 50-59.

[12] O. Shoewu, Adedipe, A. and, and F. O. Edeko 2011, "CDMA network coverage optimization in South-Eastern Nigeria," *American Journal Of Scientific And Industrial Research*.

[13] R. Mardeni and L. Y. Pey 2012, "Path loss model optimization for urban outdoor coverage using Code Division Multiple Access (CDMA) system at 822MHZ," *Modern Applied Science*, vol. **6**, p. 28.

[14] N. T. Makanjuola, O. O. Shoewu, L. A. Akinyemi, and A. A. Ajasa 2015, "Comparative Analysis of GSM Network and IS-95 CDMA Network Using Signal Strength," *The Pacific Journal of Science and Technology* vol. **16**.

Acknowledgment:
The authors wish to acknowledge Watanea Wireless Communication for technical support.

Evaluation Methodology between Globalization and Localization Features Approaches for Skin Cancer Lesions Classification

IOP Conf. Series: Journal of Physics: Conf. Series **1003** (2018) 012029 doi:10.1088/1742-6596/1003/1/012029

Evaluation Methodology between Globalization and Localization Features Approaches for Skin Cancer Lesions Classification

H M Ahmed[1], R J Al-azawi[2], A A Abdulhameed[3]

1Department of Computer Science, Iraqi Commission for Computers and Informatics/ Informatics Institute for postgraduate studies, Baghdad, Iraq.
2Department of Laser and Optoelectronics, University of Technology, Baghdad, Iraq.
3Department of Computer Science, University of Mustansiriyah, Baghdad, Iraq.

Hussein_gqi@yahoo.com

Abstract. Huge efforts have been put in the developing of diagnostic methods to skin cancer disease. In this paper, two different approaches have been addressed for detection the skin cancer in dermoscopy images. The first approach uses a global method that uses global features for classifying skin lesions, whereas the second approach uses a local method that uses local features for classifying skin lesions. The aim of this paper is selecting the best approach for skin lesion classification. The dataset has been used in this paper consist of 200 dermoscopy images from Pedro Hispano Hospital (PH2). The achieved results are; sensitivity about 96%, specificity about 100%, precision about 100%, and accuracy about 97% for globalization approach while, sensitivity about 100%, specificity about 100%, precision about 100%, and accuracy about 100% for Localization Approach, these results showed that the localization approach achieved acceptable accuracy and better than globalization approach for skin cancer lesions classification.

Keywords:Skin cancer, Dermoscopy, Melanoma, image segmentation, Color features, Texture features.

1. Introduction

Cancer is considered one of the largest danger to the humanity, it is predictable to be a major reason for death across the following few years. Depending on the statistics of the (WHO) World Health Organization 13% is the cancer estimation for all the deaths in 2004 in the world, and in 2030 is estimated 12 million people will die of the disease Among all the familiar cancers skin cancer is the main worry in both the developed and the developing countries during the last 40 years with an occurrence that has been increased in recent years [1]. One of the most common cancers in humans is skin cancer, the numeral of the skin tumor treatments growing robustly in the last decade and the cost

of skin tumor was most elevated of all tumors in U.S, around 87,110 new instances of melanoma and roughly 9,730 new melanoma-related deaths in 2017 in U.S [2]. In a modern estimate by the Australian government, the aggregate cost of diagnoses and treatments benign skin cancer was 511 million Australian dollars in 2010 and will be 703 million in 2015 [3]. The continuous rise of skin cancer in the worldwide and the rise medical cost and death average have prioritized to early diagnosis of this tumor [4]. The survival average is very high if cancer diagnosed in its early stages. Therefore, the early diagnosis the skin lesion is important to prevention death [5]. Two main cause that required an early detection of melanoma, firstly reason, localization of melanoma is surface (skin) in the majority of the cases, therefore, the detection manner can be very simple, second reason, the probability of healing of melanoma are large if diagnosed early stage (with the thickness below 1mm) with the 10-years survival rate for the patient as large as 95% [6].

2. Skin Cancer Diagnosis

There are different ways to evaluate and diagnose skin cancers. Most dermatologists depend on biopsy of the lesion for definitive diagnosis. Pathologists then examine histological sections derived from such biopsies to make a definitive diagnosis, this depends on evaluate cell morphology and architectural distribution of the cancer cells.

In some instances, the definite histopathological diagnosis of malignancy is difficult, this is particularly so when there is overlap in morphological features between some malignant and benign lesions [5]. Computer-based automatic diagnosis system appears to be an important tool for such difficult cases. Computer is not more intelligent than the human brain, but it may be able of extracting some information, such as texture features, that may not be easily seen by human eyes [7]. Therefore, it is important to develop efficient schemes for the physicians and pathologists through supporting their decision with computer-aided diagnosis (CAD) systems this is based on digital images. It is hoped that image analysis could help in identifying early skin cancers and aids in early diagnosis to help reduce the death rate caused by these serious diseases [8].

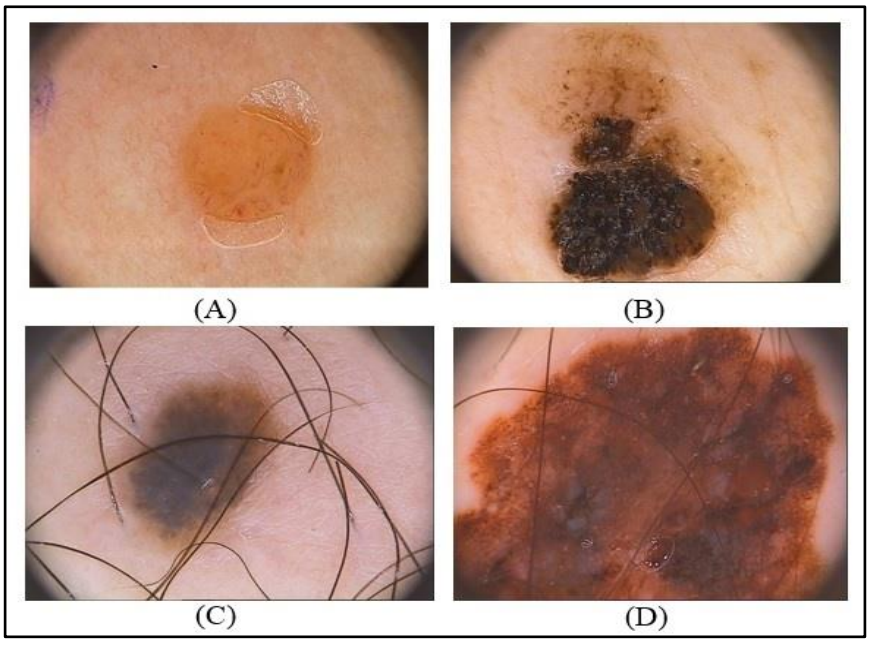

Figure 1. Different types of dermoscopy images for both type benign and melanoma; (A) Benign skin lesion; (B) Melanoma skin lesion; (C) Benign skin lesion with some hair; (D) Melanoma skin lesion with some hair.

3. Related work

There are a number of researches which used images obtained from a dataset of Hospital Pedro Hispano (PH2) as shown in Figure.1. [9]. that is used in this paper, and these researches are as followed below:[10] Suggested algorithm for diagnosis of the melanoma. based on a group of directional filters and explore colors, directional and topology properties of the network.it used 55 images from the dataset (PH2) and achieved result SP = 67% and an SE= 80%. [11] suggested an improved system for automatic diagnosis of melanomas. it uses Adaptive Boosting (AdaBoost) classifier and used 57 images from (PH2) dataset and achieving SE = 78% and SP = 77%. [12] suggested a system to diagnose melanoma. it used a bank of directional filters and a connected component analysis, then used AdaBoost classifier and used 200 images from (PH2) dataset, achieving an SE = 91.1% and an SP = 82.1%. [13] suggested system to diagnoses of melanoma, using texture and color features. The achieved results Sensitivity = 94.1%, Specificity =77.4% are obtained by mixing them both. used 163 images from the (PH2) dataset. [14]. a comparison of performance Big-of-feature classifies by using a manual and automated segmentation. they using KNN classifier and achieve results Sensitivity = 98% and Specificity = 86% for a manual segmentation, and achieved Sensitivity = 88% and Specificity = 82% for an automatic segment, and combining the two segmentation strategies achieve results SE is 98% and SP is 82%. They used 176 images from (PH2) dataset. [15] suggested two different systems for the diagnosis of melanoma. The first system uses the global method and a second system use localization feature. they using AdaBoost, SVM, and KNN classifier. they used 176 images from (PH2) dataset.and achieve results an SE is 96 % , SP is 80% for globalization method and SE is 100% , SP is75 % for localization method.

4. Proposed Method

The proposed method tries to find the skin cancer using image processing by applying specific operation on the image. The hair removing is applied as a pre-processing step. The output of hair removing is used as globalization dataset. Two segmentation method applied using the different method used to find the

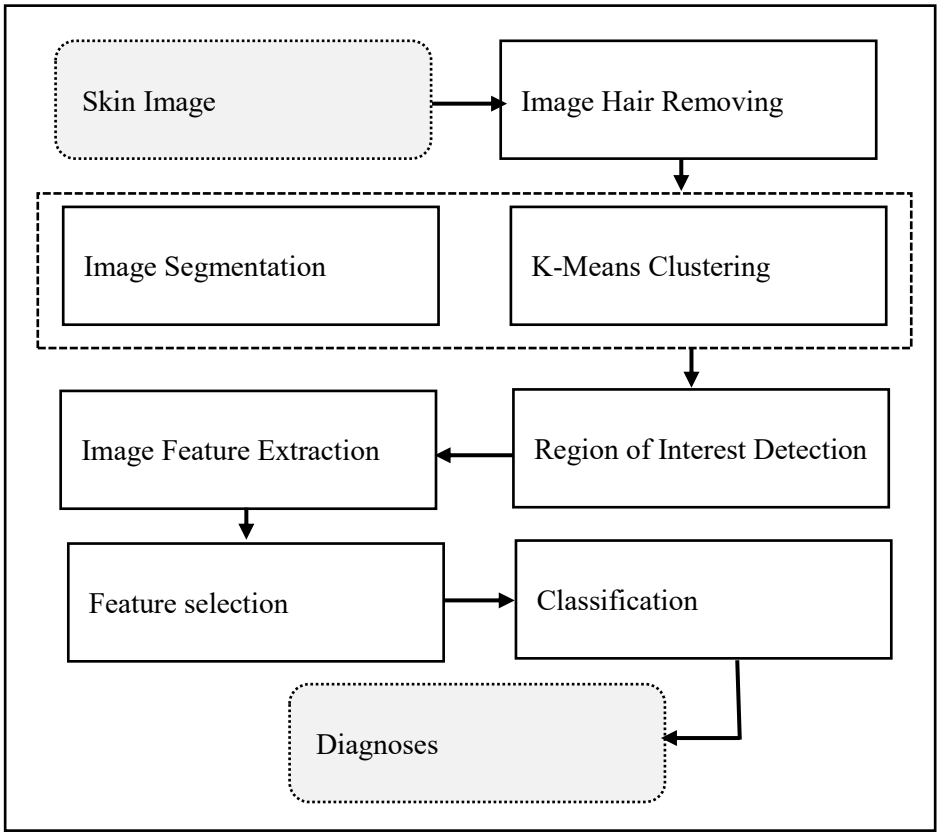

Figure 2. General view of proposed method.

region of interest (ROI) then used as localization dataset. Feature extraction used to find some discriminant characteristics to verify the input image for classification. Extracted features are normalized for standardization features. Features selection used to reduce dimensional features and increase accuracy. The support vector machine used as a classification method. The general view of the proposed method shown in Figure.2. The total steps of the proposed method are five steps as follow:

4.1 Image Hair Removing

The process of hair removal from skin cancer images is a pre-processing of images in the proposed method for diagnosing. The cases through medical images consist of several steps for two kinds of skin image (benign and melanoma). Pre-processing of this kind of image consists of input a color image and extract its three bands RGB. For each band applied the same operation, first applied the median filter with size (3×3), then applied image Closed morphological operation with three masks zero, 45, and 90 degrees. These three results are a union of one output to replace in the input image. These will be used in three ways first as a global feature, second as input to segmentation with thresholding method, and the last as input with segmentation using k-mean clustering. The next step is applied Gaussian smoothing filter for smoothing a removed hair image at last. The size of the filter is 3×3 and the coefficient sigma is equal to 1.1. The total steps of hair removing illustrate in figure 3 in details, and the results are shown in figure 3.

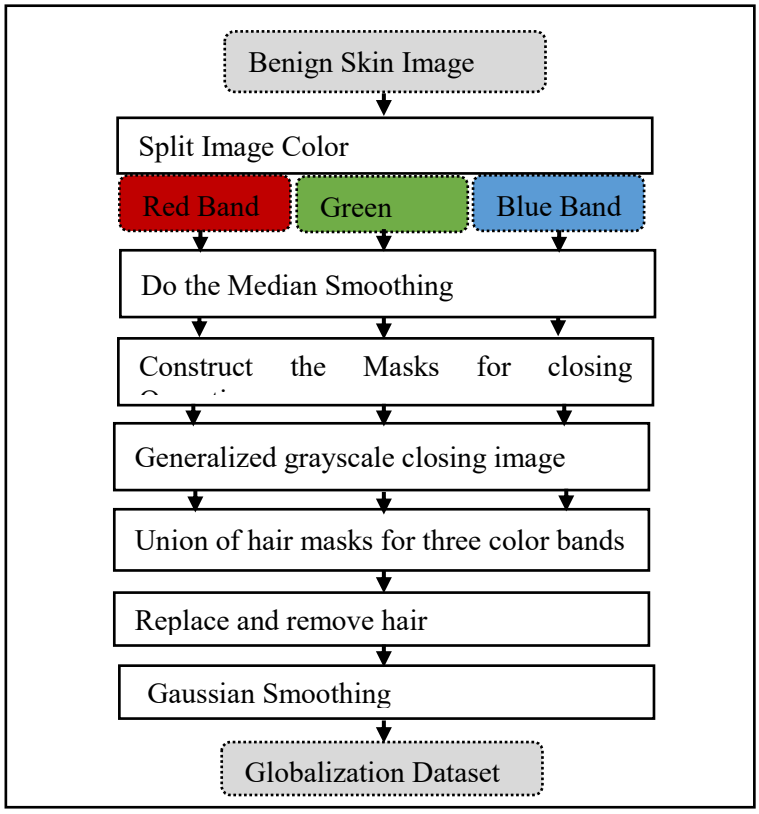

Figure 3. Skin Image Hair Removing (Image Preprocessing)

- *Image Segmentation*

In the proposed method, two segmentation method applied and evaluated to get a better result for The ROI because it is sensitive step and the total feature depend on it, especially structural features depend on the extracted binary image. The first is segmentation using adaptive threshold. The second is

segmentation using K-means clustering. Each one has a specific way and properties to get the ROI. Among the implemented algorithms the Adaptive automatic thresholding technique accomplished the better results and confirm to be useful and firm enough to the automatically skin lesions segmentations in CAD systems. The result is shown in figure 5, And explained more details in [16].

Feature Extraction

Accurate classification depends on a discriminant feature that extracted from ROI. In proposed method several kinds of features are extracted as follow:

Geometric Features

These features depend on the binary mask that deals with the shape of ones in the mask. The binary mask extracted from skin image using two previous segmentation method, from this binary mask geometric feature will extract as follow: Area, Perimeter, distance to Centroid, distance to Centre of Nearest, and standard deviation for each previous features [17].

$$Area = \sum_{i=1}^{m}\sum_{j=1}^{n} I_{white}(i,j) \quad (1)$$

Where m and n is height and width of binary image (object mask) and $Iwhite$ is white pixel in binary image (object).

$$P = Ne + \sqrt{2}No \quad (2)$$

Where Ne is the number of even values and No is the number of odd values in the boundary chain code.

$$D(B,C) = \sqrt{(B_x - C_x)^2 - (B_y - C_y)^2} \quad (3)$$

Where Bx, By are coordinate of boundary points and Cx and Cy are coordinate of centroid point of object.

$$D(B,C) = \sqrt{(B_x - C_{row})^2 - (B_y - C_{col})^2} \quad (4)$$

Where Bx, By are coordinate of boundary points and Crow and Ccol are coordinate of centroid point of geometric center.

$$St = \sqrt{\frac{1}{n}\sum_{i=1}^{n}(x_i - \mu)^2} \quad (5)$$

Where St is standard deviation value, n is size of column data, xi is column data, and μ is mean of column data.

- *Intensity Color Features*

The Intensity color features used in the proposed method, for global and local features, used the intensities of colors band after split them into RGB from this mask color feature will extract as follow: Mean of colors for each band, the variance of Colors, and standard deviation for each previous features [17].

$$\mu = \frac{1}{n}\sum_{i=1}^{n} x_i \quad (6)$$

Where μ is mean value, n is size of column data, and xi is column data.

$$Var = \frac{1}{n-1}\sum_{i=1}^{n}(x_i - \mu)^2 \quad (7)$$

Where Var is variance of column data, n is size of column data, x_i is column data, and is mean of column data.

- *Texture Features*

The Third group features are texture feature, they depend on second order feature (Gray Level Co-occurrence Matrix (GLCM) and Gray-Level Run-Length Matrix (GLRLM)). These features are local feature depend on the relation of two adjacent pixels that give some information about location, the samples of grayscale image matrix. All features obtained from co-occurrence matrix for GLCM while GLRLM depend on run length matrix. These main features are as follow [17]: contrast, correlation, energy, and homogeneity for GLCM, while (Short Run Emphasis, Long Run Emphasis, Gray Level Distribution, Run Length Distribution, Run Percentage, Low Gray-level Run Emphasis, High Gray-level Run Emphasis, Short Run Low Gray-level Emphasis, Short Run High Gray-level Emphasis, Long Run Gray-level Emphasis, Long Run High Gray-level Emphasis) for GLRLM.

- *Features selection*

Features Selection step used to find feature subsets combination that relevant to result. The feature selection restricted chance to find class labels of a given features as filter. Conditional mutual information is modeled to use. This corresponds to the smallest feature subset and starting from this objective function to increased subset using mutual information properties.

- *Classification*

The classification is the last step in this proposed method that used 200 dermoscopy images of lesions for training and testing, where the SVM algorithm is used in this proposed method for diagnoses. Two approaches global and local approach are considered in this proposed method, the global approach depends on the global features while local approach depends on local features from ROI. Two kind of kernel function used for classifying data: linear, and nonlinear (polynomial kernel) function. where the linear kernel function is used for solving the optimization problem and it is much faster than the others. The linear kernel is certainly not more accurate than the others but it is used when a number of features is larger than number of observations (labeled features). While nonlinear function (Polynomial kernel) is used to solving the optimization problem, and it is used usually with high dimension features as kernel trick to make the combinations of features able to split as possible. Kernel function used for solving interference in properties and making features that representing the infected region more separable and increasing accuracy in classification results.

5. Experimental Result

Experimental of the proposed method used Hospital Pedro Hispano (PH^2) dataset. It consists of 200 dermoscopy images of lesions, Hair Removing this step is a pre-processed step. It applied to two kinds of images benign and melanoma. The same procedure applied to them. The operations performed on the images for the purpose of hair removal are done by separating the colors to the RGB band then applied the median filter on each band. Morphological closing operation applied on an image with line structure element. The horizontal line (zero angles), sloped line (45 angles), vertical line (90 angles). from these

three band getting maximum value replaced the hair area that near to dark. The last step is applying Gaussian smoothing filter on the result. The hair removing of skin image is shown in figure 4.

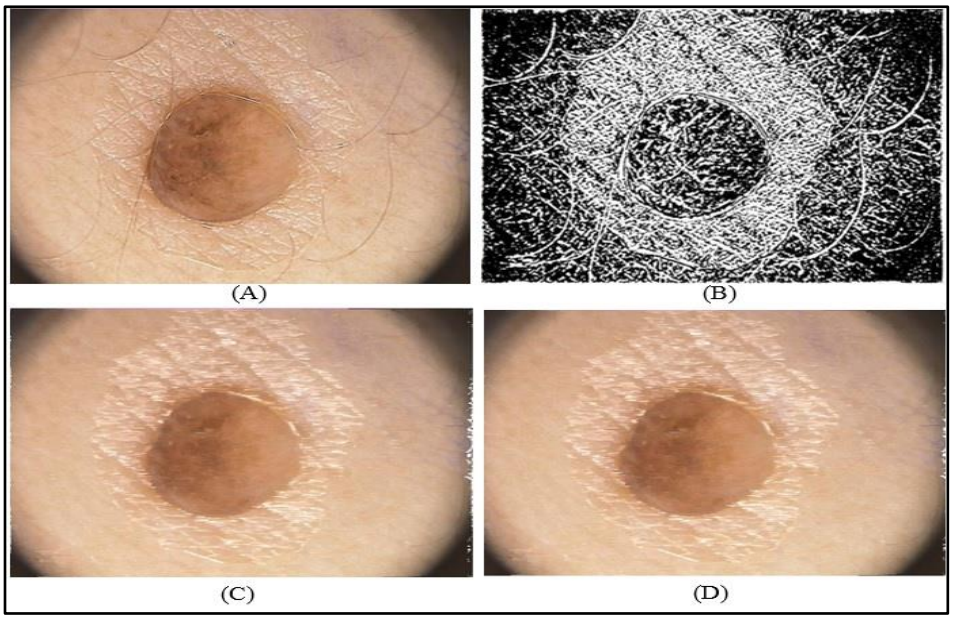

Figure 4. Hair Removal Process: (A) Original Haired Skin Image Cancer(B) Haired Skin Cancer Mask (C) Hair Removing Skin Cancer Image (D) Smoothed Skin Cancer Image

The second step is Segmentation, two algorithms for automatic segmentation of dermoscopy image were executed and assessed for tracking the boundary of skin cancer lesions, including the Adaptive automatic thresholding, K-Means clustering. The result of each algorithm is greatly influenced by the type of images used for analysis. Among the implemented algorithms the Adaptive automatic thresholding

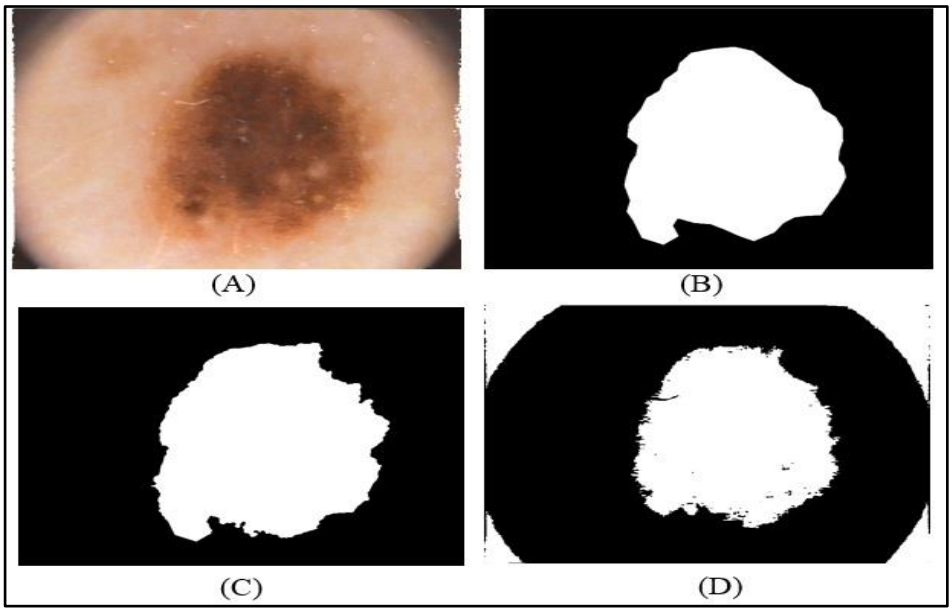

Figure 5. Implemented Segmentation Methods; (A) Original Skin Cancer Images; (B) Ground Truth Lesion Image; (C) Adaptive Automatic Thresholding Cluster Lesions Image; (D) K-Means Cluster Lesion Image.

technique accomplished the better results and confirm to be useful and firm enough to the automatically skin lesions segmentations in CAD systems. The skin image Segmentation step in proposed method and the evaluation of the two methods used to Region of Interest Detection are explained in details in [16]. some of these result is shown in figure 5.
in the evaluation step to Region of Interest Detection, the Adaptive automatic thresholding technique was chosen because it accomplished the better results, after this operation is done the enhanced of segmentation is applied on the result by comparing it with ground truth (GT) lesion mask of the same image get it from a dataset. The comparison applied on each pixel if it is one on proposed segmentation or in GT image the result will be one. Some of these results are shown in Figure 6 and Figure 7.

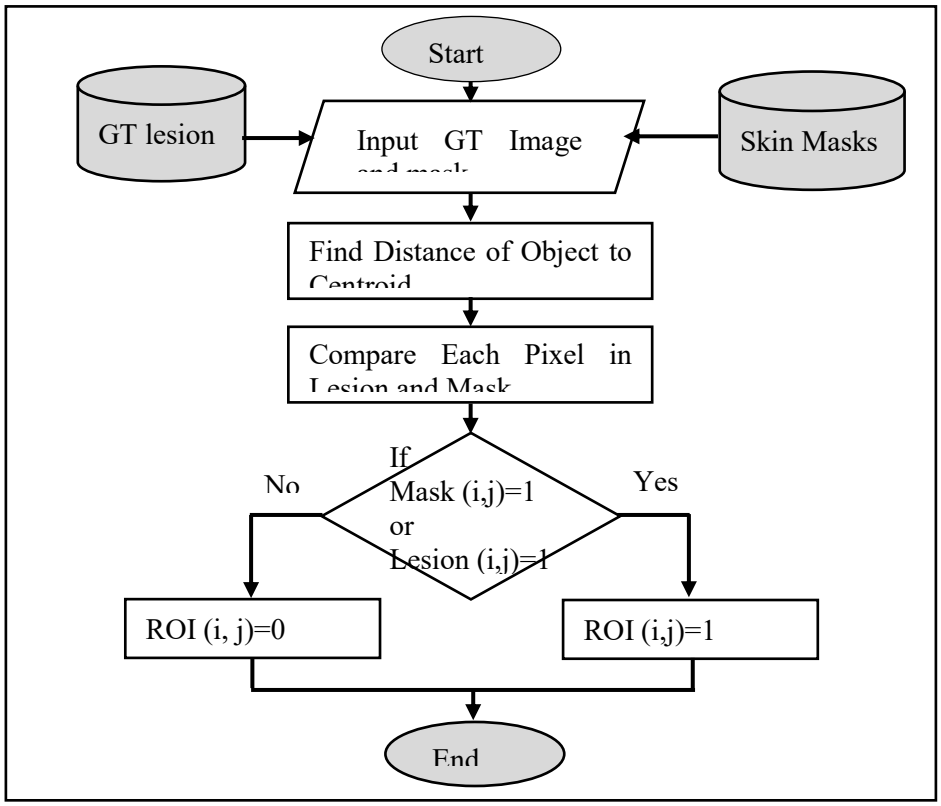

Figure 6. Flowchart Enhanced segmentation methods

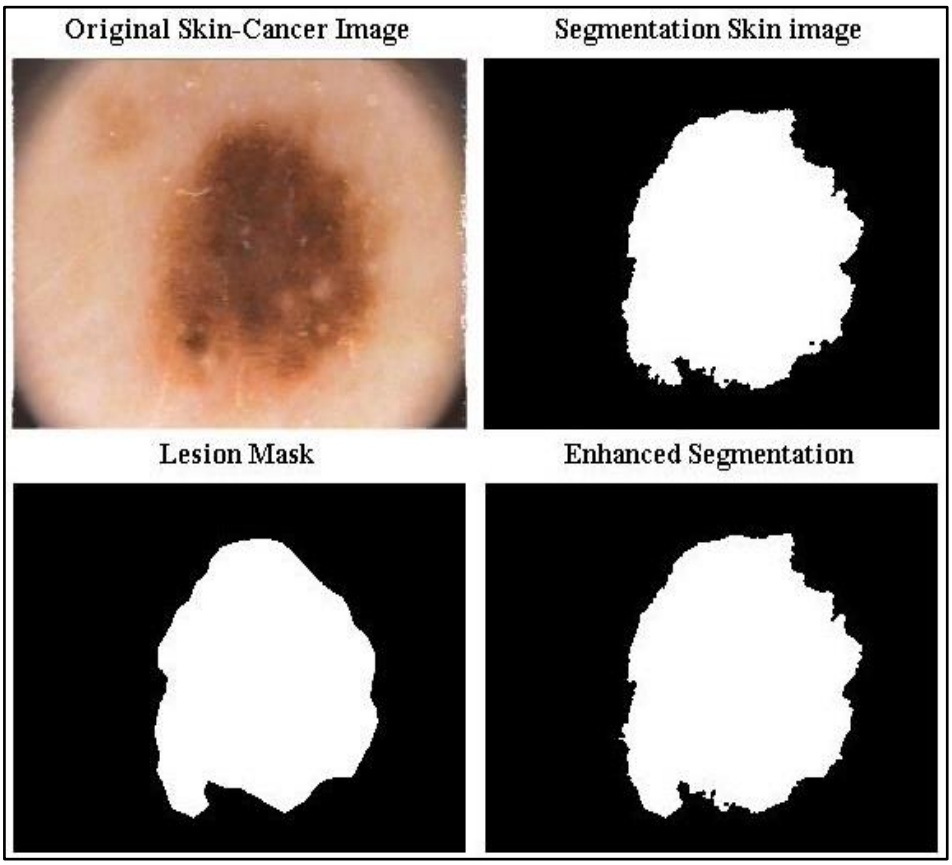

Figure 7. Enhanced segmentation methods for skin cancer image.

The region of interest circularity is calculated after the enhanced operation to determinate cancer. Color ROI important because it used in next step of feature extraction (color features) that detected by select the whole the boundary of the lesion and cover the lesion in a rectangle that shown in figure 8.
Feature extraction applied to find three kinds of features geometric features, color features, and texture feature. Used equation (1 to 7) to calculate geometric and color features and other feature are second

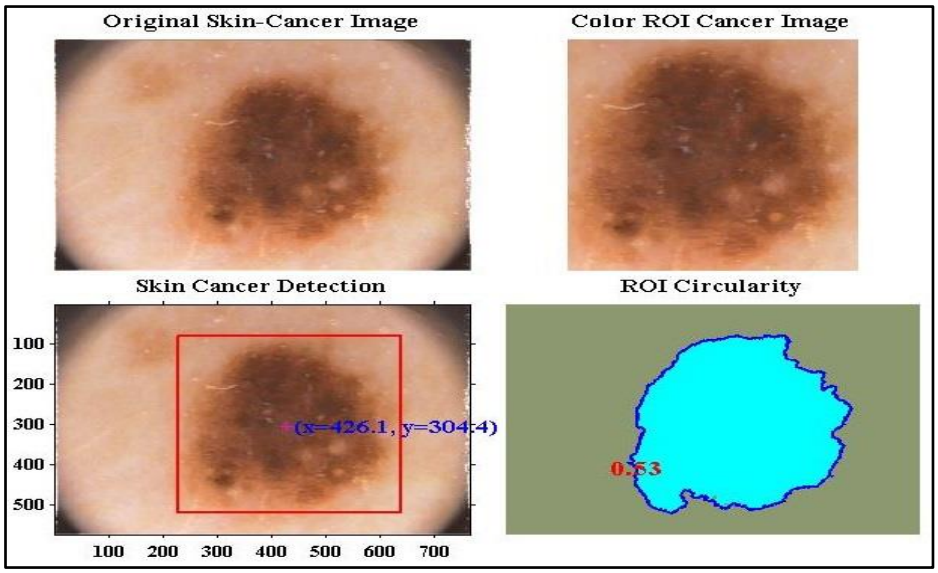

Figure 8. Calculate the color ROI and ROI circularitv.

order (GLCM and GLRLM), There two type of features are produced the global and local features the global features depend on the whole images while local features depend on ROI lesion.
Feature normalization depends on mean and standard deviation for each feature. The normalization of features supports classification step. This necessary for keeping the range of feature close to all in numeric value. The last step before the classification step is feature selection step that used Mutual information method in these step calculate by weighted each feature vector to the class label. These weights will sort from high weight to low weight and then can choose the higher weighted feature that relative to specify the class label. These operations at all reduced complexity of the proposed method.
The classification is the last step in the proposed method, it is used SVM algorithm with two functions (linear and nonlinear (Polynomial kernel)) for diagnoses. The achieved results for each function are shown in table 1, 2.

Table1: Testing Linear and polynomial kernel (Globalization)

t					
Kernels	**Sensitivity**	**Specificity**	**Precision**	**Accuracy**	**Time**
Linear	100%	77%	93%	94%	0.019923 sec
Polynomial	96%	100%	100%	97%	0.021653 sec

Table 2: Testing Linear and polynomial kernel (Localization)

Localization Approach					
kernels	**Sensitivity**	**Specificity**	**Precision**	**Accuracy**	**Time**
Linear	100%	85%	95%	96%	0.019869 sec
Polynomial	100%	100%	100%	100%	0.021965 sec

6. Conclusion

Evaluation and comparison methodology between two approaches are presented for the diagnosis skin cancer image. There two approaches depend on localization and globalization features. Both approaches are tested on PH2 dataset, the experimental result show that localization features approach performance better than globalization features approach, as shown in Table 2 for each kernel linear and polynomial with respect to time. The selected kernel (polynomial kernel) achieved best results: sensitivity is 100%, specificity is 100%, Precision is 100%, and Accuracy is 100%. In other approach (globalization features) the achieve results are shown in Table 1 for each kernel linear and polynomial. The polynomial kernel achieved best results: sensitivity is 96%, specificity is 100%, Precision is 100%, and Accuracy 97%.

References

[1] H. W. Rogers and B. M. Coldiron, “Analysis of skin cancer treatment and costs in the United States Medicare population, 1996-2008.,” Dermatol. Surg., vol. 39, no. 1 Pt 1, pp. 35–42, 2013.
[2] Siegel, R.L., Miller, K.D., Fedewa, S.A., Ahnen, D.J., Meester, R.G., Barzi, A. and Jemal, A., 2017. Colorectal cancer statistics, 2017. CA: a cancer journal for clinicians, 67(3), pp.177-193.
[3] Sinclair, Rodney. "Nonmelanoma skin cancer in Australia." British Journal of Dermatology 168.1 (2013): 1-2.
[4] Bhati, P. and Singhal, M., 2015, November. Early stage detection and classification of melanoma. In Communication, Control and Intelligent Systems (CCIS), 2015 (pp. 181-185). IEEE.

[5] Demir, Cigdem, and Bülent Yener. "Automated cancer diagnosis based on histopathological images: a systematic survey." Rensselaer Polytechnic Institute, Tech. Rep (2005).
[6] Sagar, Chiranjeev, and Lalit Mohan Saini. "Color channel based segmentation of skin lesion from clinical images for the detection of melanoma." In Power Electronics, Intelligent Control and Energy Systems (ICPEICES), IEEE International Conference on, pp. 1-5. IEEE, 2016.
[7] Ruela, Margarida, Catarina Barata, and Jorge S. Marques. "What is the role of color symmetry in the detection of melanomas?." In International symposium on visual computing, pp. 1-10. Springer, Berlin, Heidelberg, 2013.
[8] Sheha, Mariam A., Mai S. Mabrouk, and Amr Sharawy. "Automatic detection of melanoma skin cancer using texture analysis." International Journal of Computer Applications 42, no. 20 (2012): 22-26.
[9] Mendonça, Teresa, Pedro M. Ferreira, Jorge S. Marques, André RS Marcal, and Jorge Rozeira. "PH 2-A dermoscopic image database for research and benchmarking." In Engineering in Medicine and Biology Society (EMBC), 2013 35th Annual International Conference of the IEEE, pp. 5437-5440. IEEE, 2013.
[10] Barata, Catarina, Jorge S. Marques, and Jorge Rozeira. "Detecting the pigment network in dermoscopy images: A directional approach." In Engineering in Medicine and Biology Society, EMBC, 2011 Annual International Conference of the IEEE, pp. 5120-5123. IEEE, 2011.
[11] C. Barata, J. S. Marques, and J. Rozeira, "A system for the automatic detection of pigment network," Proc. - Int. Symp. Biomed. Imaging, pp. 1651–1654, 2012.
[12] Barata C, Marques JS, Rozeira J. A system for the detection of pigment network in dermoscopy images using directional filters. IEEE transactions on biomedical engineering. 2012 Oct;59(10):2744-54.
[13] Marques, Jorge S., Catarina Barata, and Teresa Mendonça. "On the role of texture and color in the classification of dermoscopy images." Engineering in Medicine and Biology Society (EMBC), 2012 Annual International Conference of the IEEE. IEEE, 2012.
[14] Barata, Catarina, Jorge S. Marques, and M. Emre Celebi. "Towards an automatic bag-of-features model for the classification of dermoscopy images: The influence of segmentation." In Image and Signal Processing and Analysis (ISPA), 2013 8th International Symposium on, pp. 274-279. IEEE, 2013.
[15] Barata, Catarina, Margarida Ruela, Mariana Francisco, Teresa Mendonça, and Jorge S. Marques. "Two systems for the detection of melanomas in dermoscopy images using texture and color features." IEEE Systems Journal 8, no. 3 (2014): 965-979.
[16] Al-azawi, Razi J., Abbas Abdulazez Abdulhameed, and Hussein Majeed Ahmed. "A Robustness Segmentation Approach for Skin Cancer Image Detection Based on an Adaptive Automatic Thresholding Technique." American Journal of Intelligent Systems 7, no. 4 (2017): 107-112.
[17] Filipczuk, Paweł, Thomas Fevens, Adam Krzyżak, and Andrzej Obuchowicz. "GLCM and GLRLM based texture features for computer-aided breast cancer diagnosis." Journal of Medical Informatics & Technologies 19 (2012).

A New Heuristic Anonymization Technique for Privacy Preserved Datasets Publication on Cloud Computing

A New Heuristic Anonymization Technique for Privacy Preserved Datasets Publication on Cloud Computing

S. Aldeen Yousra[1,2] ,Salleh Mazleena[2]

1Department of Computer Science, College of Science for Women, University of Baghdad, Baghdad, Iraq

2Faculty of Computing, University Technology Malaysia, UTM, Skudai, Johor, Malaysia

yohrmz_8@yahoo.com[1,2]; mazleena@fc.utm.my[2]

Abstract. Recent advancement in Information and Communication Technologies (ICT) demanded much of cloud services to sharing users' private data. Data from various organizations are the vital information source for analysis and research. Generally, this sensitive or private data information involves medical, census, voter registration, social network, and customer services. Primary concern of cloud service providers in data publishing is to hide the sensitive information of individuals. One of the cloud services that fulfill the confidentiality concerns is Privacy Preserving Data Mining (PPDM). The PPDM service in Cloud Computing (CC) enables data publishing with minimized distortion and absolute privacy. In this method, datasets are anonymized via generalization to accomplish the privacy requirements. However, the well-known privacy preserving data mining technique called K-anonymity suffers from several limitations. To surmount those shortcomings, I propose a new heuristic anonymization framework for preserving the privacy of sensitive datasets when publishing on cloud. The advantages of K-anonymity, L-diversity and (α, k)-anonymity methods for efficient information utilization and privacy protection are emphasized. Experimental results revealed the superiority and outperformance of the developed technique than K-anonymity, L-diversity, and (α, k)-anonymity measure.

1. Introduction

The innovative notion so called cloud computing (CC) with prolific computing resources allows the users to store the data remotely into the cloud for diverse applications [1]. Numerous third-party cloud computing services also offer data support, computing management and internet services including Microsoft Azure, Amazon's EC2, etc. They are not only economic but have great bounciness to rendering progressively the service providers in outsourcing their data to the cloud platform. Organizations recognize opportunities as well as critical values of sharing prosperity of data information through numerous dispersed databases. The sensitive and private data collected from various governmental and non-governmental organizations are rapidly increasing and stored in the electronic repository [2]. In recent times, varieties of data mining techniques on CC are implemented to support the decision-making process. These techniques are used to quotation the hidden information from enormous datasets in form of new models, trends, and diverse

patterns. However, due to privacy reason the personal data of any individual need to be protected during data mining. Privacy in CC implies the individual's personal information (called sensitive data) protection while publishing [2];[3];[4]. Investigates exposed that attackers often detect and goal the information efficiently from third party clouds [5]. Individuals sensitive data information requires supreme privacy protection before being outsourced to the cloud [6]. This issue is widely addressed via anonymization in the form of K-anonymity [7];[8], (a, k)-anonymity [9], L-diversity [10], t-closeness [11], m-invariance [12], etc. The original information that is released to the cloud by data providers necessitates different privacy requirements. Despite many dedicated efforts, an efficient and accurate privacy preserving anonymization technique is far from being achieved [1]. For the first time, I report the design and development of a heuristic anonymization technique for privacy preserving dataset publishing on cloud. The methods for L-diversity, K-anonymity and (a, k)-anonymity are meticulously combined to avoid the adversary from aggressive the dataset privacy. The proposed method overcomes the limitations of heuristic K-anonymity algorithm to efficiently protecting the sensitive datasets privacy from linking attack. This is achieved by integrating the heuristic L–diversity with heuristic (a, k)-anonymity method. A heuristic anonymization technique provides robust privacy to datasets publishing on CC. In achieving so, two major contributions are made:

1. A systematic experimentation on anonymization is introduced. The benefits of K-anonymity, L-diversity and (a, k)-anonymity -anonymity are amalgamated to ensure strong privacy by balancing simultaneously the privacy protection and information utilization.
2. The proposed privacy framework and anonymization technique outperformed the distinct L-diversity measure, and K-anonymity with (a, k)-anonymity measure.

This article is composed of seven sections. Section 2 overviews the literature on related work especially the anonymization method. The discussion about the relationship between cloud computing and preserving of privacy of published data (Section 3). Then, the technique and flowchart of this work are explained in Section 4. Section 5 is explained the experimental results and evaluation Section 6 concludes the paper. 'Figure(1)' illustrates the conceptual framework of this article.

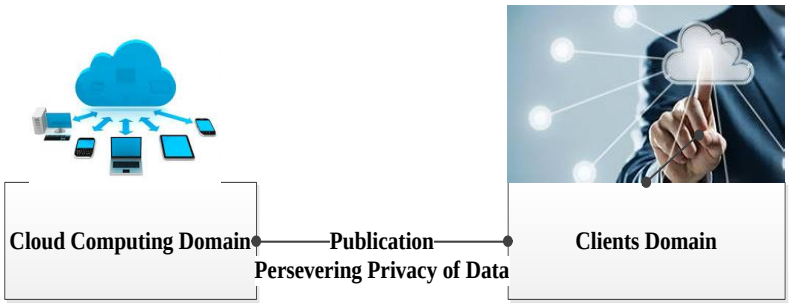

Figure 1. Conceptualization of privacy preserving data publication.

2. Related Work

Currently, the privacy preserved data publishing are conducted broadly in integrated databases [13]. It is important to develop privacy values, such as K-anonymity, (α, k)-anonymity, L-diversity, t-closeness and m-invarance for greatly secured data sharing and mining on cloud. All data supplies undertook this matter by suggesting a third party trusted

approach. They upload the data to confidential third party for anonymization and data integration in which the clients inquire on centralized database [14]. Jiang et al. (2006) suggested a two-party application based model for generating K-anonymous data, which vertically partitioned the sources without revealing the data from site to site [15]. Zhong et al. (2005) presented a solution for K-anonymous generalization for distributed setup by maintaining the end-to-end privacy of original data together with final K-anonymous results [16]. Jurczyk et al. (2009) developed a distributed anonymization algorithm for achieving the anonymity of data providers and subjects [14]. Ciriani et al. (2007) clear the likely threats to K-anonymity that arise from executing the mining on a group of data, where two main methods are considered to syndicate K-anonymity in data mining. Numerous approaches are developed to distinguish K-anonymity violations and to remove them in suggestion rule and cataloguing mining. Despite extensive use of K-anonymous privacy preservation it suffers from various challenges that requires special attention and further improvements [17]. Patil et al., 2013 analyzed the current K-anonymity model and its applications. They addressed some of the multidimensional K-anonymous approach that is accustomed attain the elementary knowledge. Nowadays, majority of the K-anonymity algorithms hang on multidimensional datasets, where nearest neighborhood strategy is incorporated to recover the superiority of anonymity and to decrease the information loss [18]. Generally, the addition of all local anonymized datasets is performed through the secure algorithm. The problem of secured outsourcing of frequent item-set mining on the multi-cloud environments is scrutinized [19]. To provide protection against a knowledgeable attacker with exact support information a K-support anonymity is proposed [20]. [1] suggested a distributed anonymization protocol for privacy-preserving data publishing from numerous data suppliers on cloud. Recently, the scalability issue of sub-tree anonymization over big data on cloud is reported by Zhang et al. (2013) and Zhang et al. (2014). They suggested a hybrid method which combined the Top-Down Specialization (TDS) and Bottom-Up Generalization (BUG). Both TDS and BUG are talented in an extremely scalable manner via a sequence of deliberately designed Map Reduce jobs [21];[22]. Zhang et al. (2014) also proposed a highly scalable two-phase TDS approach using Map Reduce on cloud, where datasets are first divided and anonymized in parallel to create intermediate results [23]. Literature clearly hinted that the existing privacy preserving techniques cannot efficiently protect the privacy from combined attacks including homogeneity, similarity and background knowledge. However, my proposed anonymization technique ensures strong data privacy during publishing in CC. Conversely, it satisfies the privacy need of data providers and individual within the budget. It is significant for anonymous data that already exists in servers as individual databases, where all local anonymized datasets are inserted through the secure algorithm.

3. Privacy Preservation of Published Data

In recent times, numerous data mining techniques are suggested and rummage-sale to assist the decision-making process. These methods mined the concealed information from vast data in the form of new models, trends and different patterns. Privacy in data mining during publication indicates the defense of private information [4]. Repeated studies indicated that attackers often detect and aim the information from third party clouds [5]. Figure 2 demonstrates the three domains of privacy preservation of the stored data, which contain the user domain, cloud domain, and recipient domain. In public practice, any user share the stored data records to the cloud service provider. Service providers further publish these

datasets to any research centre (viz. medical research). For example, hospital assists as the data owner and the medical research centre acts as data recipient. The cloud domain enables the hardware and software infrastructures to the service provider for providing the shared medical records as outsourced storage [24].

Figure 2. Various domains of the stored data privacy preservation.

Before outsourcing the data to cloud for publication, the data privacy (sensitive information of individuals) must be protected or well-preserved. This is determined using data anonymization methods such as K-anonymity, (α, k)-anonymity and L-diversity [25], [26]. The data providers implement various privacy requirements while releasing their original data to the cloud, which often pose a challenge. Numerous privacy preservation methods are accessible for data mining such as K-anonymity, distributed privacy preservation, L-diversity, randomization, taxonomy tree, condensation and cryptographic techniques [27],[28],[29]. To resolution the cloud data mining related privacy preservation problem, this paper proposed a practical solution to the data provider.

4. Heuristic anonymization Technique

The aim heuristic anonymizing techniques for privacy preserving data mining in cloud is to ensure strong confidentiality for data to be published in cloud. The privacy preserving techniques for data publishing are categorized into theoretical and heuristic types. This research proposed a heuristic technique [30]. Although numerous heuristic techniques are introduced to guarantee strong privacy preservation but a unified algorithm is far from being developed. Thus, heuristic K-anonymity, heuristic L-diversity and (α, k) - anonymity techniques are combined to achieve this target. Figure 3 depicts an overview of privacy preserving techniques for published data in cloud environment. It composed of two parts. The first part explains the heuristic K-anonymity technique and its result. The second part explains heuristic L-diversity and (α, k) - anonymity technique to overcome the limitations of the heuristic K-anonymity technique. It is customary to describe datasets and the attack model before introducing the concept of heuristic K-anonymity technique.

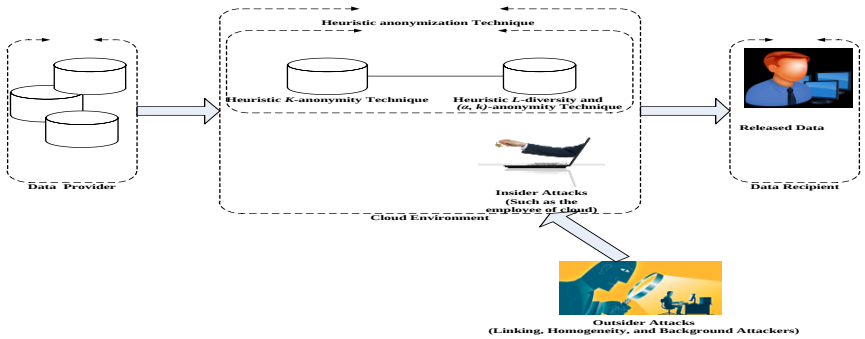

Figure 3. Overview of privacy preserving techniques for published data

I use the bank direct marketing dataset, which is collected from different web sources such as the UCI (University of California at Irvine) Machine Learning Repository. This dataset is implemented and the privacy related performances of proposed heuristic anonymization approach is evaluated. [31],[32], [33], [34] collected and arranged this dataset, which is utilized by [35].

4.1 *Heuristic K-anonymity Technique*

Generally, the procedure starts from promoting an expert in the data to determine the QI, where QI, diversion method, and K values are determined by the user. The user is able to determine QI, K value and diversion method. K value denotes the length of the K group in the resulting K-anonymized data as shown in Figure 4. In this research, K values are changed to examine its effect on other metric. For the first experiment, the value of K is taken as 20. Every group possessed many tuples and the range is increased to 25. This produced a strong privacy at the cost of enhanced information loss. Therefore, it is essential to reduce the K value. In the second experiment, the K value is chosen to be 10. The information loss is still increased. Then, the value of K is changed to 5 and this time the information loss is reduced with lower range. Thus, the trade-off between the privacy and utility of data is achieved. Next, the grouping is performed. The criterion of stopping the technique is based on confirming the condition of reaching a minimum group of set of unique QI with a size equals or more than the K value. Figure 4 demonstrates three diversion methods of performing the K-anonymity including Incremental Range, Incremental Suppression, and Unification.

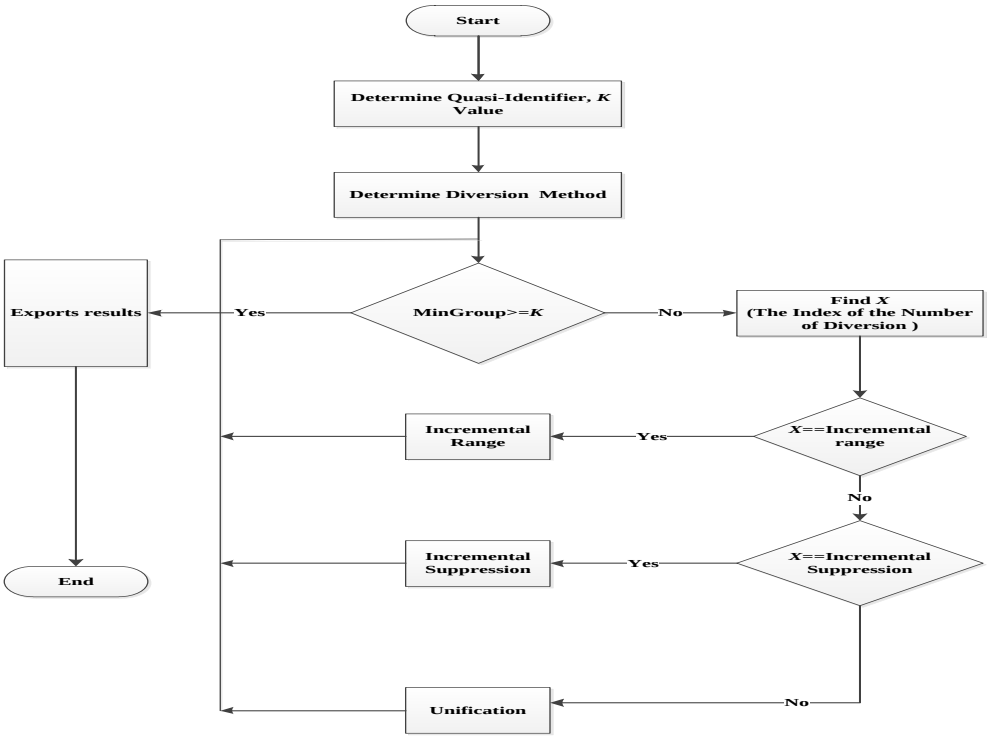

Figure 4. Flowchart of heuristic K-anonymity technique

In the Incremental Range method, the user must select the suitable mode with corresponding attributes. For example, when the attribute is a range of numbers (set of numbers) like Age, Date, Time…etc., the user might select incremental range. Consequently, the user provides the value of increment to combine records together with a sub-range in the Age attribute. For instance, if a user provided 5 as range incremental, then the technique start to generalizing by combining the sub-range 20-24 into one group, then 25-29 into another group and so on. The Incremental Suppression method is performed by incrementally replacing the characters. Thus, different values are included in one group once they are matched each other. This diversion can be used with ZipCode. The third method is the unification, which simply combines more than one of the distinct values of the attributes. This is similar to combine: different cities in the attribute address under the name of the state that includes them. Variable X in the flowchart indicates the index of the number of diversion that is performed on the attribute. In Figure 4, the QI, X (the index of the number of diversion method) and K value are determined. If X is incremental range, then incremental range method is chosen. In this method the attribute is a range of numbers (set of numbers) such as age, date, time, etc. The user might select incremental range, and provide the value of increment to combining the records together with respect to a sub-range in the Age attribute. For X to be incremental suppression, then this method is applied by performing it incrementally to replacing the characters of the attribute to "*". Consequently, once two values or more become matching each other they are included in one group and the diversion is used with ZipCode. Otherwise, the unification method is applied. This operation is iterative until the desired K value is reached. 'Figure(5)' represents the pseudo code of the heuristic K-anonymity steps.

```
1.   INPUT : Quasi_Identifiers, Diversion _Method, K
2.   OUTPUT: K_Anonymized_Table
3.   Main
4.       WHILE(MinGroup<K)
5.           X=Find_Index_of_Min (Diversion _Level[])
6.           IF(Diversion _Method(x)==INCREMENTAL_RANGE)
7.           Incremental_Range(x);
8.     ELSEIF(Diversion _Method(x)==INCREMENTAL_SUPPRESSION)
9.       Incremental_Suppression(x);
10.    ELSEIF(Diversion _Method(x)==UNIFICATION)
11.      Unfication(x);
12.    End While
13.    Diversion _Level[x]++;
14.  END
```

Figure 5. Algorithm representing the pseudo code for Heuristic K-anonymity technique.

4.2. *Heuristic (L-diversity) and (α, k)-anonymity Technique*

K-anonymity is extended using an L-diversity and (α, k)-anonymity methods to maintain a limit of maximum frequency of distance (sensitive) values in the critical attributes. Figure 6 shows a new value of K that is enabled once the K- groups are generated. To overcome the weakness of K-anonymity from homogeneity attack such as the QI group having several tuples with same sensitive attributes value, one needs to achieve L-diversity with (α, k)-anonymity methods. Furthermore, K is increased to enhance the diversity in the data until the achieved maximum frequency is less than 20%. This percentage is selected based on the natural of data as tuneable parameter. In other word, to decrease the frequency of sensitive attributes, this percentage is selected heuristically.

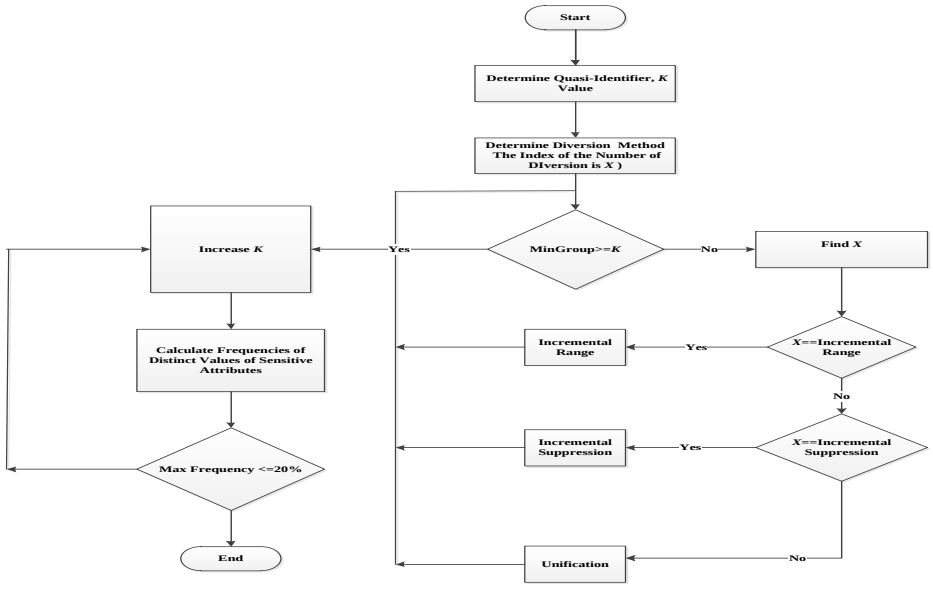

Figure 6. Flowchart of heuristic (L-diversity) and (α, k)-anonymity technique.

'Figure(7)' represents the steps of pseudo code of heuristic (L-diversity) and (α, k)-anonymity. Meanwhile, the frequencies are calculated for distinct values of sensitive attributes. If they meet the condition (less 20%), the loop is ended else it is continued to increase K until the condition is met.

```
1.  INPUT : Quasi_Identifiers, Diversion _Method, K
2.  OUTPUT: K_Anonymized_Table
3.  Main
4.  K_Anonymity(K);
5.  While(Max_Freq()<0.2)
6.     K++;
7.     K_Anonymity(K);
8.     Export_Table
9.  End
```

Figure 7. Pseudo-code for Heuristic (L-diversity) and (α, K)-anonymity.

The frequencies of distinct values of sensitive attributes are measured with respect to L-diversity with (α, k)-anonymity techniques by increasing K to maintain a limit of maximum frequency of distance values in the sensitive attributes. Figure 8 demonstrates the frequency of distinct values with respect to increase K. This demonstrates the spreading of the critical values among the whole equivalent group. It is observed that there is a less possibility of attacking record when the frequencies of critical values are decreased in every equivalent group of tuples. For example, if a record has critical value of high frequency the background or homogeneity attack can affect the individual. There is diversity on critical values to prevent these attacks from breaching the privacy. This histogram illustrates the reduction in frequency value of tuples and increase of diversity in critical values.

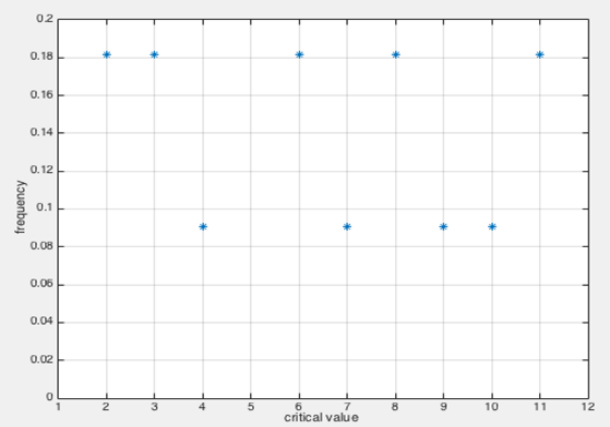

Figure 8. Histogram of distinct values of critical attribute

The experimental results demonstrate that the present heuristic anonymization technique can prevent the privacy breach in distributed datasets on cloud environment. By taking the advantage of K-anonymity, L-diversity and (α, k)-anonymity the unified technique overcomes the weakness of each method. Table 3 enlists the result after applying the heuristic (L-diversity) and (α, k)-anonymity technique. It is clear that the equivalent group contains at least L acceptable values of sensitivity attributes, which has 6053, 643, 1411, 1483, 397, 499, 2235, 0, 1381, 2140, and 5944 balances. This signifies the presence of diversity in sensitive attributes with diminished frequency values. For example, in the first sensitive value (6053) the frequency is reduced with increasing K value, similarly for other critical attributes. Furthermore, the group size is found to increase with the decrease in frequencies values of sensitive attributes. Small group size revealed the higher frequency. These frequencies are reduced by increasing the group size to avoid background and homogeneity attack.

5. Experimental Results and Evaluation

The experimental results demonstrate that the present heuristic anonymization technique can prevent the privacy breach in published datasets on cloud environment. By taking the advantage of K-anonymity, L-diversity and (α, k)-anonymity the unified technique overcomes the weakness of each model. For the first experiment, the value of K is taken as 20. Every group possessed many tuples and the range is increased to 25. Therefore, it is essential to reduce the K value. In the second experiment, the K value is chosen to be 10. Then, the value of K is changed to 5 and this time the information loss is reduced with lower range as shown in Table 1. Table 1 enlists the result after applying the heuristic K-anonymity technique. As shown in Table 1, two groups are resulting from using the proposed technique where K value is 5. The QI attributes that generalized are (age and job). The first group has nine-tuples. Which mean that every tuple in this group has matched with other eight tuples in the same group so; it is hard to distinguish every tuple. The second group has eleven tuples that are indistinguishable. The reason of difference in a number of anonymized tuples in every group, which is based on condition Mingroup ≥ K as shown in 'Figure(4)'.

Table 1. Two groups resulting from applying the method (K=5, QI: age and job)

	Age	**Job**	**Marital**	**Education**	**Balance**
1	90-105	Retired-Services-Admin.-Technician	Divorced	Secondary	1
2	90-105	Retired-Services-Admin.-Technician	Divorced	Primary	712
3	90-105	Retired-Services-Admin.-Technician	Married	Unknown	775
4	90-105	Retired-Services-Admin.-Technician	Married	Unknown	775
5	90-105	Retired-Services-Admin.-Technician	Married	Unknown	775
6	90-105	Retired-Services-Admin.-Technician	Married	Unknown	775
7	90-105	Retired-Services-Admin.-Technician	Divorced	Secondary	1234
8	90-105	Retired-Services-Admin.-Technician	Divorced	Primary	2282
9	90-105	Retired-Services-Admin.-Technician	Married	Secondary	0
1	75-90	Unemployed-Entrepreneur-Self-Employed-Management	Married	Unknown	4984
2	75-90	Unemployed-Entrepreneur-Self-Employed-Management	Married	Unknown	1780
3	75-90	Unemployed-Entrepreneur-Self-Employed-Management	Married	Unknown	4984
4	75-90	Unemployed-Entrepreneur-Self-Employed-Management	Married	Unknown	4984
5	75-90	Unemployed-Entrepreneur-Self-Employed-Management	Married	Unknown	1780
6	75-90	Unemployed-Entrepreneur-Self-Employed-Management	Married	Tertiary	5619
7	75-90	Unemployed-Entrepreneur-Self-Employed-Management	Married	Unknown	1780
8	75-90	Unemployed-Entrepreneur-Self-Employed-Management	Married	Unknown	1780
9	75-90	Unemployed-Entrepreneur-Self-Employed-Management	Married	Primary	6483
10	75-90	Unemployed-Entrepreneur-Self-Employed-Management	Married	Tertiary	0
11	75-90	Unemployed-Entrepreneur-Self-Employed-Management	Married	Secondary	0

Table (2) enlists the result after applying the heuristic (L-diversity) and (α, k)-anonymity technique. It is clear that the equivalent group contains at least L acceptable values of sensitivity attributes, which has 6053, 643, 1411, 1483, 397, 499, 2235, 0, 1381, 2140, and 5944 balances. This signifies the presence of diversity in sensitive attributes with diminished frequency values. For example, in the first sensitive value (6053) the frequency is reduced with increasing K value, similarly for other sensitive attributes. Furthermore, the group size is found to increase with the decrease in frequencies values of sensitive attributes. Small group size revealed the higher frequency. These frequencies are reduced by increasing the group size to avoid threats.

Table 2. Results of heuristic (L-diversity) and (α, k)-anonymity technique

Age	Job	Marital	Education	Balance
75-100	Unknown-Student-Housemaid-Unemployed-Entrepreneur-Blue-Collar	Divorced-Single-Married	Unknown-Primary-Tertiary-Secondary	6053
75-100	Unknown-Student-Housemaid-Unemployed-Entrepreneur-Blue-Collar	Divorced-Single-Married	Unknown-Primary-Tertiary-Secondary	6053
75-100	Unknown-Student-Housemaid-Unemployed-Entrepreneur-Blue-Collar	Divorced-Single-Married	Unknown-Primary-Tertiary-Secondary	643
75-100	Unknown-Student-Housemaid-Unemployed-Entrepreneur-Blue-Collar	Divorced-Single-Married	Unknown-Primary-Tertiary-Secondary	1411
75-100	Unknown-Student-Housemaid-Unemployed-Entrepreneur-Blue-Collar	Divorced-Single-Married	Unknown-Primary-Tertiary-Secondary	1411
75-100	Unknown-Student-Housemaid-Unemployed-Entrepreneur-Blue-Collar	Divorced-Single-Married	Unknown-Primary-Tertiary-Secondary	1483
75-100	Unknown-Student-Housemaid-Unemployed-Entrepreneur-Blue-Collar	Divorced-Single-Married	Unknown-Primary-Tertiary-Secondary	397
75-100	Unknown-Student-Housemaid-Unemployed-Entrepreneur-Blue-Collar	Divorced-Single-Married	Unknown-Primary-Tertiary-Secondary	397
75-100	Unknown-Student-Housemaid-Unemployed-Entrepreneur-Blue-Collar	Divorced-Single-Married	Unknown-Primary-Tertiary-Secondary	499
75-100	Unknown-Student-Housemaid-Unemployed-Entrepreneur-Blue-Collar	Divorced-Single-Married	Unknown-Primary-Tertiary-Secondary	2235
75-100	Unknown-Student-Housemaid-Unemployed-Entrepreneur-Blue-Collar	Divorced-Single-Married	Unknown-Primary-Tertiary-Secondary	0

75-100	Unknown-Student-Housemaid-Unemployed-Entrepreneur-Blue-Collar	Divorced-Single-Married	Unknown-Primary-Tertiary-Secondary	0
75-100	Unknown-Student-Housemaid-Unemployed-Entrepreneur-Blue-Collar	Divorced-Single-Married	Unknown-Primary-Tertiary-Secondary	499
75-100	Unknown-Student-Housemaid-Unemployed-Entrepreneur-Blue-Collar	Divorced-Single-Married	Unknown-Primary-Tertiary-Secondary	1381
75-100	Unknown-Student-Housemaid-Unemployed-Entrepreneur-Blue-Collar	Divorced-Single-Married	Unknown-Primary-Tertiary-Secondary	1381
75-100	Unknown-Student-Housemaid-Unemployed-Entrepreneur-Blue-Collar	Divorced-Single-Married	Unknown-Primary-Tertiary-Secondary	1381
75-100	Unknown-Student-Housemaid-Unemployed-Entrepreneur-Blue-Collar	Divorced-Single-Married	Unknown-Primary-Tertiary-Secondary	2140
75-100	Unknown-Student-Housemaid-Unemployed-Entrepreneur-Blue-Collar	Divorced-Single-Married	Unknown-Primary-Tertiary-Secondary	0
75-100	Unknown-Student-Housemaid-Unemployed-Entrepreneur-Blue-Collar	Divorced-Single-Married	Unknown-Primary-Tertiary-Secondary	5944
75-100	Unknown-Student-Housemaid-Unemployed-Entrepreneur-Blue-Collar	Divorced-Single-Married	Unknown-Primary-Tertiary-Secondary	2140
75-100	Unknown-Student-Housemaid-Unemployed-Entrepreneur-Blue-Collar	Divorced-Single-Married	Unknown-Primary-Tertiary-Secondary	0

The efficiency and effectiveness of the heuristic anonymization technique is compared with the recent art-of-the technique (Zhang et al., 2014). The performance evaluation of the heuristic anonymization technique is carried out using UTD Anonymization ToolBox software, where entropy and execution time are calculated as privacy measure.

Entropy Evaluation: UTD Anonymization Tool Box is used to compare the results of heuristic anonymization technique with K-anonymity and original data as shown in Figure 9. Figure 9 displays that the K-anonymity reduced the entropy level of the data by 13.5% from 0.3823 to 0.3308. However, by implementing the heuristic anonymization technique on the same dataset, the entropy revealed a reduction of 0.75% only, which is much lower compared to K-anonymity technique (13%). This clearly indicates the outperformance of heuristic anonymization technique in preserving the entropy of the data with small percentage difference from the original data. It is important to note that the entropy measure depends on the data. Moreover, the entropy measure of heuristic anonymization technique is observed to be too close to entropy measure of original data. This signifies that the entropy measure for heuristic anonymization technique is superior compared to the entropy measure

of K-anonymity. Besides, the entropy is discerned to be insensitive to the value of K. This can be interpreted with the large amount of data with respect to small ranges of values of K.

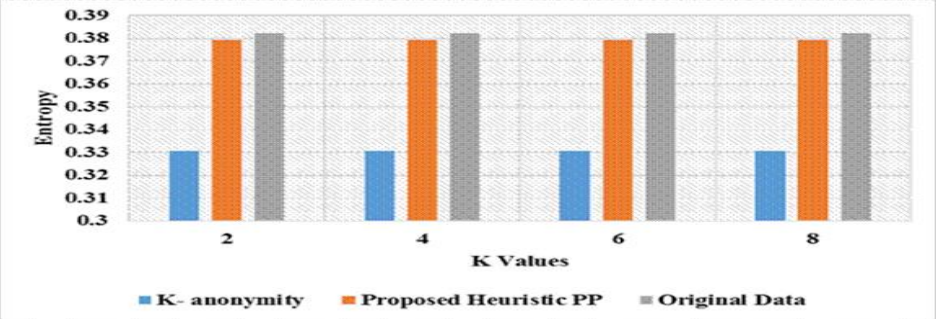

Figure 9. Comparison of entropy measure for K-anonymity and heuristic anonymization technique

Privacy Measure: Privacy being complementary of entropy, the privacy measure of the heuristic anonymization technique is evaluated using UTD Anonymization Tool Box. The privacy is observed to decrease with the increase of information contents. Privacy measure for K-anonymity and heuristic anonymization technique are compared in Figure10. The privacy level is found to enhance in the presence of K-anonymity. Thus, it is established that the heuristic anonymization possesses more utility than the normal K-anonymity. Owing to this attribute the heuristic anonymization technique protects the privacy without increasing information loss, where the preserved privacy level is over 65%. Moreover, the percentage remains the same even with the increase of information and the preserving entropy of the original data does not exceed 10%. Indeed, it is a good performance indicator of the heuristic technique.

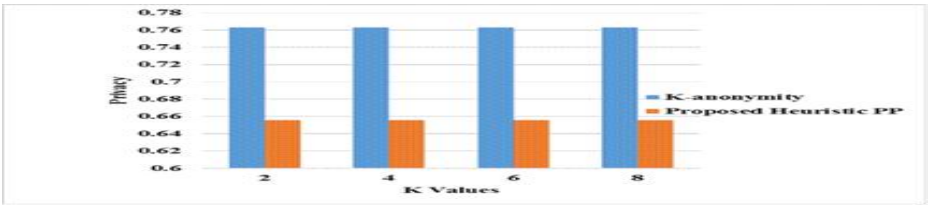

Figure 10. Comparison of privacy for K-anonymity and heuristic anonymization technique

Execution Time: The computational complexity of both K-anonymity and heuristic anonymization technique are evaluated in terms of their execution time as illustrated in Figure 11. It is evident that the heuristic anonymization technique spent less execution time than K-anonymity. The embedment of other models such as L-diversity and (α, k)-anonymity in the heuristic anonymization technique to ensuring the strong privacy without affecting on execution time.

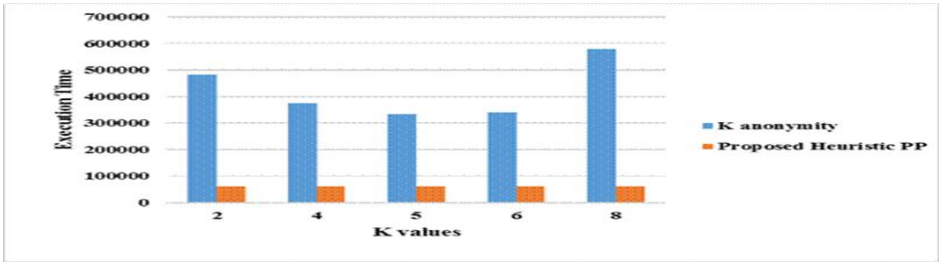

Figure 11. Execution Time for K-anonymity and heuristic anonymization technique

6. Conclusion

This paper provides the basic concept of pilot study on anonymization model and demonstrates that the synergy of different privacy preserving models can provide a strong privacy balance with the information utilization. The detailed correlation between cloud computing and privacy preserving of published data is exemplified. With the materialization of CC technologies, various organizations attempted to leverage the Internet-based paradigm. The main aim is to optimize the utility of computing resources in a flexible and scalable manner. Despite the increased use of cloud-based platforms in diverse business areas, the privacy and security requirements have prevented their adoption in the healthcare and related areas. Actually, the privacy concerns (data utilization requirements) of different data providers (consumers) are quite different. Over the years, numerous techniques are developed to ensure the privacy of sensitive data publication on cloud environment. Yet, no precise and efficient solution for privacy is achieved. To surmount this limitations, present paper proposed a data privacy preserving technique useful for cloud publishing. To achieve high-quality generalization, a novel anonymization technique is developed by unifying the techniques such as heuristic K-anonymity, heuristic L-diversity and (α, k)-anonymity. The need of hybrid solution via the innovative integration of different privacy protection models is justified. The experimental results obtained using the proposed anonymization technique revealed enhanced privacy protection against various attacks and offered the obligatory data for research analysis.

7. References

[1] X. Ding, Q. Yu, J. Li, J. Liu, and H. Jin, “Distributed anonymization for multiple data providers in a cloud system,” in Lecture Notes in Computer Science (including subseries Lecture Notes in Artificial Intelligence and Lecture Notes in Bioinformatics), 2013, vol. 7825 LNCS, no. PART 1, pp. 346–360.

[2] H. Kargupta, S. Datta, Q. Wang, and K. S. K. Sivakumar, “On the privacy preserving properties of random data perturbation techniques,” Third IEEE Int. Conf. Data Min., 2003.

[3] L. Sweeney, “Privacy-Preserving Surveillance using Selective Revelation,” no. October, 2005.

[4] M. Prakash and G. Singaravel, “An approach for prevention of privacy breach and information leakage in sensitive data mining,” Comput. Electr. Eng., pp. 1–7, 2015.

[5] T. Ristenpart and E. Tromer, “Hey, you, get off of my cloud: exploring information leakage in third-party compute clouds,” … Conf. Comput. …, 2009.

[6] S. Kamara, C. Papamanthou, and T. Roeder, “Dynamic searchable symmetric encryption,” … 2012 ACM Conf. …, pp. 965–976, 2012.

[7] R. J. Bayardo and R. Agrawal, “Data privacy through optimal k-anonymization,” in Data Engineering, 2005. ICDE 2005. Proceedings. 21st International Conference on, 2005, 2005, no. Icde, pp. 217–228.

[8] L. Sweeny, "k- Anonymity: A Model For Protecting Privacy," Int. J. Uncertainty, Puzziness Knowledge-Based Syst., vol. 10, no. 5, pp. 557–570, 2002.
[9] R. C. Wong, J. Li, A. W. Fu, and K. Wang, "(α,k)-Anonymity : An Enhanced k -Anonymity Model for Privacy-Preserving Data Publishing," Proc. 12th ACM SIGKDD Int. Conf. Knowl. Discov. Data Min., pp. 754–759, 2006.
[10] A. Machanavajjhala, D. Kifer, J. Gehrke, and M. Venkitasubramaniam, "-Diversity," ACM Trans. Knowl. Discov. Data, vol. 1, no. 1, p. 3–es, 2007.
[11] N. Li, T. Li, and S. Venkatasubramanian, "Closeness: A new privacy measure for data publishing," IEEE Trans. Knowl. Data Eng., vol. 22, no. 7, pp. 943–956, 2010.
[12] X. Xiao and Y. Tao, "M-invariance: towards privacy preserving re-publication of dynamic datasets," SIGMOD Conf., pp. 689–700, 2007.
[13] B. C. M. Fung, K. Wang, R. Chen, and P. S. Yu, "Privacy-preserving data publishing," ACM Comput. Surv., vol. 42, no. 4, pp. 1–53, Jun. 2010.
[14] P. Jurczyk and L. Xiong, "Distributed anonymization: Achieving privacy for both data subjects and data providers," Lect. Notes Comput. Sci. (including Subser. Lect. Notes Artif. Intell. Lect. Notes Bioinformatics), vol. 5645 LNCS, pp. 191–207, 2009.
[15] W. Jiang and C. Clifton, "A secure distributed framework for achieving k-anonymity," VLDB J., vol. 15, no. 4, pp. 316–333, 2006.
[16] S. Zhong, S. Zhong, Z. Yang, Z. Yang, R. N. Wright, and R. N. Wright, "Privacy-enhancing k-anonymization of customer data," Proc. twenty-fourth ACM SIGMOD-SIGACT-SIGART Symp. Princ. database Syst., p. 147, 2005.
[17] V. Ciriani, S. De Capitani di Vimercati, S. Foresti, and P. Samarati, "k-Anonymous data mining: a survey," Adv. Database Syst., pp. 105–136, 2008.
[18] B. B. Patil and A. J. Patankar, "Multidimensional k-anonymity for protecting privacy using nearest neighborhood strategy," in 2013 IEEE International Conference on Computational Intelligence and Computing Research, IEEE ICCIC 2013, 2013, p. IEEE Podhigai; IEEE Signal Processing, Computation.
[19] C. Tai, P. S. Yu, and M. Chen, "Privacy Preserving Frequent Pattern Mining on Multi-cloud Environment," 2013 Int. Symp. Biometrics Secur. Technol., pp. 235–240, Jul. 2013.
[20] C. Tai, P. S. Yu, and M. Chen, "k-Support Anonymity Based on Pseudo Taxonomy for Outsourcing of Frequent Itemset Mining," Proc. 16th ACM SIGKDD Int. Conf. Knowl. Discov. Data Min., pp. 473–482, 2010.
[21] X. Zhang, C. Liu, C. Yang, W. Dou, and J. Chen, "Combining Top-Down and Bottom-Up : Scalable Sub-Tree Anonymization over Big Data using MapReduce on Cloud," 2013.
[22] X. Zhang, C. Liu, S. Nepal, C. Yang, W. Dou, and J. Chen, "A hybrid approach for scalable sub-tree anonymization over big data using MapReduce on cloud," J. Comput. Syst. Sci., vol. 80, no. 5, pp. 1008–1020, Aug. 2014.
[23] X. Zhang, L. T. Yang, C. Liu, and J. Chen, "A scalable two-phase top-down specialization approach for data anonymization using mapreduce on cloud," IEEE Trans. Parallel Distrib. Syst., vol. 25, no. 2, pp. 363–373, 2014.
[24] J. J. Yang, J. Q. Li, and Y. Niu, "A hybrid solution for privacy preserving medical data sharing in the cloud environment," Futur. Gener. Comput. Syst., vol. 43–44, pp. 74–86, 2014.
[25] A. Gkoulalas-Divanis and G. Loukides, "Anonymization of electronic medical records to support clinical analysis," pp. 9–30, 2013.
[26] Y. Xiao, C. Lin, Y. Jiang, X. Chu, and F. Liu, "An Efficient Privacy-Preserving Publish-Subscribe Service Scheme for Cloud Computing," 2010 IEEE Glob. Telecommun. Conf. GLOBECOM 2010, vol. 1, pp. 1–5, Dec. 2010.
[27] A. Sachan, D. Roy, and P. V Arun, An Analysis of Privacy Preservation Techniques in Data Mining. 2013.
[28] Z. Xu and X. Yi, "Classification of Privacy-preserving Distributed Data Mining protocols," in 2011 Sixth International Conference on Digital Information Management, 2011, pp. 337–342.

[29] Hamza, "Attacks on Anonymization-Based Privacy-Preserving : A Survey for Data Mining and Data Publishing," J. Inf. Secur., vol. 2013, no. April, pp. 101–112, 2013.
[30] X. Xiao, "The Hardness and Approximation Algorithms for," arXiv:0912.5426v1, 2010.
[31] S. Moro and R. M. S. Laureano, "Using Data Mining for Bank Direct Marketing: An application of the CRISP-DM methodology," Eur. Simul. Model. Conf., no. Figure 1, pp. 117–121, 2011.
[32] S. Moro, P. Cortez, and P. Rita, "A data-driven approach to predict the success of bank telemarketing," Decis. Support Syst., vol. 62, pp. 22–31, 2014.
[33] K. Bache and M. Lichman, "UCI machine learning repository." 2013.
[34] H. A. Elsalamony, "Bank Direct Marketing Analysis of Data Mining Techniques," Int. J. Comput. Appl., vol. 85, no. 7, pp. 12–22, 2014.
[35] V. Ayala-Rivera, P. McDonagh, T. Cerqueus, and L. Murphy, "A Systematic comparison and evaluation of k-Anonymization algorithms for practitioners," Trans. Data Priv., vol. 7, no. 3, pp. 337–370, 2014.

Acknowledgements
Author is thankful to UCI (University of California at Irvine) Machine Learning Repository for providing the dataset.

Secure Server Login by Using Third Party and Chaotic System

Secure Server Login by Using Third Party and Chaotic System

Firas A Abdulatif[1], Maan zuhiar[2]

[1]Department of Computer Sciences, College of Education for pure science, Baghdad University, Baghdad, Iraq.
[2]Iraqi Commission for Computers & Informatics, Informatics Institute for Postgraduate, Iraq

Abstract. Server is popular among all companies and it used by most of them but due to the security threat on the server make this companies are concerned when using it so that in this paper we will design a secure system based on one time password and third parity authentication (smart phone). The proposed system make security to the login process of server by using one time password to authenticate person how have permission to login and third parity device (smart phone) as other level of security.

Keywords. Server security; one time password; third parity.

1. Introduction

Medium-to-large companies are using the server where computing requirements are high. It is depends on the client server model There are several services provided by the server and the most important one is storage [1].

Many online based application used password to authenticate a particular person from the login system. A password is a string of characters used during authentication process to verify user identity. Passwords can have letters, numbers and special characters and can vary in length. There are two type of password static password and one time password, most companies still use one single static passwords due it is easy to remember. But, when there are more than one systems have different passwords it may be hard to remember. Static passwords have many defects such as easy to decipher and are usually only letters and are often short and are based on topics close to user birthdays and child names. To overcome these defects a new method is discovered known one time password (OTP) [2]. So far OTP is the most effective way to provide secure login to the system. In one time password the password will be generated on the server side and after that will send to the client. This type of password, will be valid for only one login session and even if an attacker succeeds in acquiring an one time password, he may not be able to predict the next one time password [3].

2. Security challenges of server

Server has many disadvantage one of this loss of physical control such that users and tenants cannot access their data.

1- Malicious Insiders: granting powers to the current or former employee or partner to access user data and misuse this access in a way that negatively affects the confidentiality, integrity of data [4].

2- Data Leakage: data leakage is the accidental or unintentional distribution of private or sensitive data to an unauthorized entity. Data leakage poses a serious issue for companies as the number of incidents and the cost to those experiencing them continue to increase

3- SQL injection: this type of attack works on inserting SQL orders that destroy that database [5].

4- Brute force attack: this type of attack try to get user information such as username and password by using automated program to generate a large number of consecutive guesses [6].

5- Denial of service: The denial-of-service attack block legal users from accessing their data. The denial-of-service attack can alter the encryption key or slow the system to block users from using the service by trying to use the wrong password more than once. Therefor cloud service providers should develop a mechanism so that the attackers cannot impact on the services provide by the cloud [6, 7].

6- Account or Service Hijacking: Is a ways of fraud, phishing and vulnerability exploration moreover password credentials used in distributed methods give breadth to this problem. The anxiety with abduction of accounts was the goal of many cloud service providers already consolidated in the market, such as Amazon.

7- Cross-site scripting (XSS) attack: this type of attack commonly found in web applications. It is makes it possible for attackers to inject malicious code into victim's web browser and steal the victim's credentials [8].

8- Insecure Interfaces and Application Programing Interface (API): There are group of APIs or software interfaces provided for users to control and interact with services provided by the server. To protect against accidental and malicious attempts to circumvent, the interfaces must be designed in a safe manner. Organizations and third parties often build upon these interfaces to offer value-added services to their customers [9].

3. Proposed system

The proposed system provide security of data stored on server by using third party authentication and one time password. Using smart phones as a third party because they are used by the owner only and stay with him wherever he are. Using one time password for authentication. This one time password will be usable for one time to prevent unauthorized people from access and manipulate user's data that stored on the server and expiry after half hour until if not used. This one-time passwords will be send to the third party to make sure it only reaches to the authorized person. 'Figure 1' explain the general structure of the propose system.

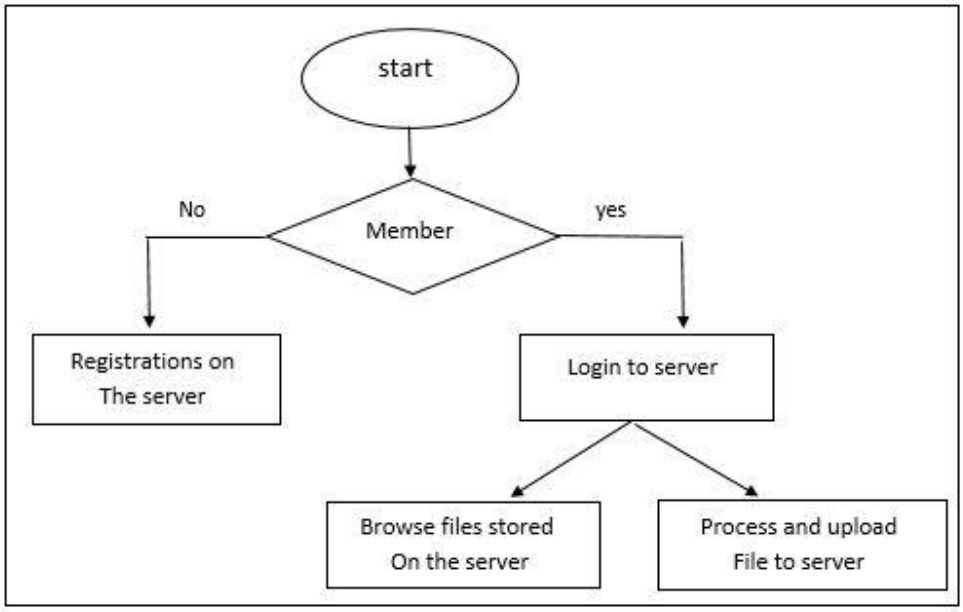

Figure 1. General work flow diagram of the proposed system

The proposed system is implements on remote server and use firebase cloud messaging (FCM) API to send the one time password from server to user. To use the services provided by the server, first user must register on the server by entering the username and static password and then register his smartphone as a third party to complete the registration process; android mobile application design to confirm the account of user on the server and send/ receive notification from server. To complete the smartphone registration process, the user will enter the same user name and static password previously registered in the server. A phone application designed for this purpose will be used to search for the server data base. When the user name and password are found, will send request to the fire base cloud messaging API (application programing interface) asked for registration and then the FCM will response with message of unique string (token) generated for particular user smart phone. This token will be store in the server database according to username and password to using it when send or receive notification on mobile. After token stored in the server database the user complete the process of registration and can login to server at any time and from anywhere by using his information. 'Figure 2' explain the steps of registration process.

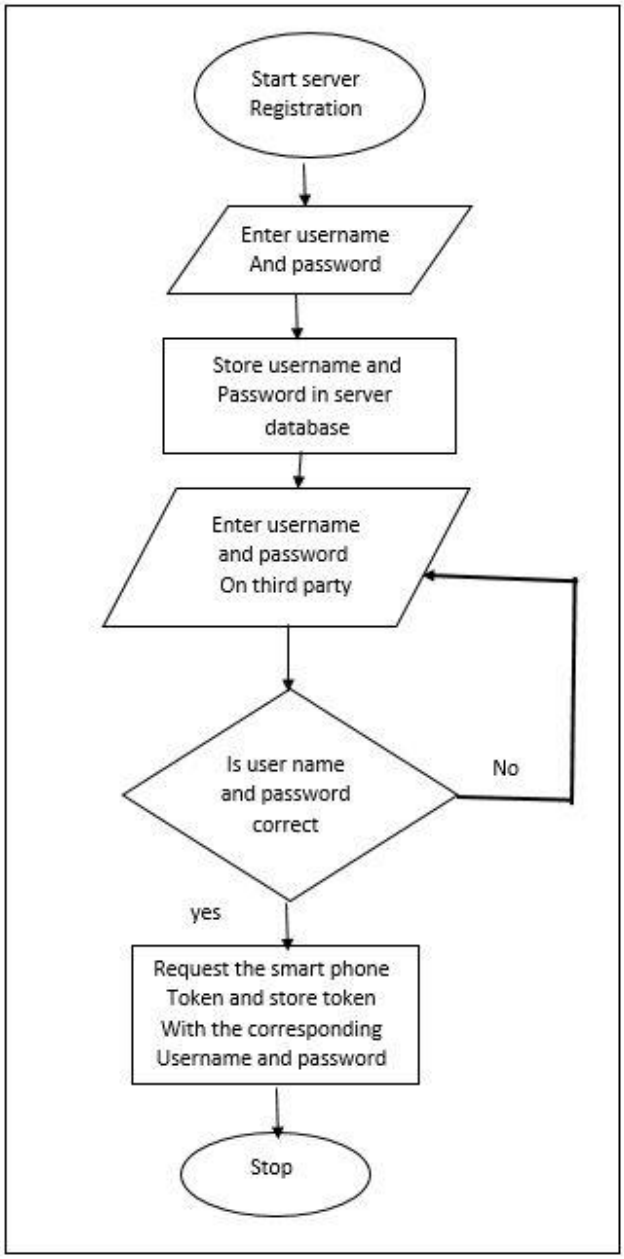

Figure 2. Registration process

After complete the process of registering his account on the server and the corresponding third party device, now can he login to server. He must enter the previously registered user name and if valid system will generate the one time password using chaotic system. This chaotic system is non liner equation called sin map chaotic equation that used to generate random number that cannot be predicted. The one-time password will be expired after half an hour or one use. The sin map is one of the important equations that used in security. It shown 'as in equation (1)'.

$$X_{N+1} = r \sin(\pi X_n) \quad (1)$$

This is sin map chaotic equation. The one time password that generated from the chaotic system will be send to the user on mobile as shown in ‘figure 3’ then the user can used this received password on mobile application with the static password that used in the registration as a password. User input the received password in mobile and after that go to the server and input the static password to login the server and using server storage to store his data, browses his file that stored on the server storage and downloading any file, ‘figure 4’ explain the login operation.

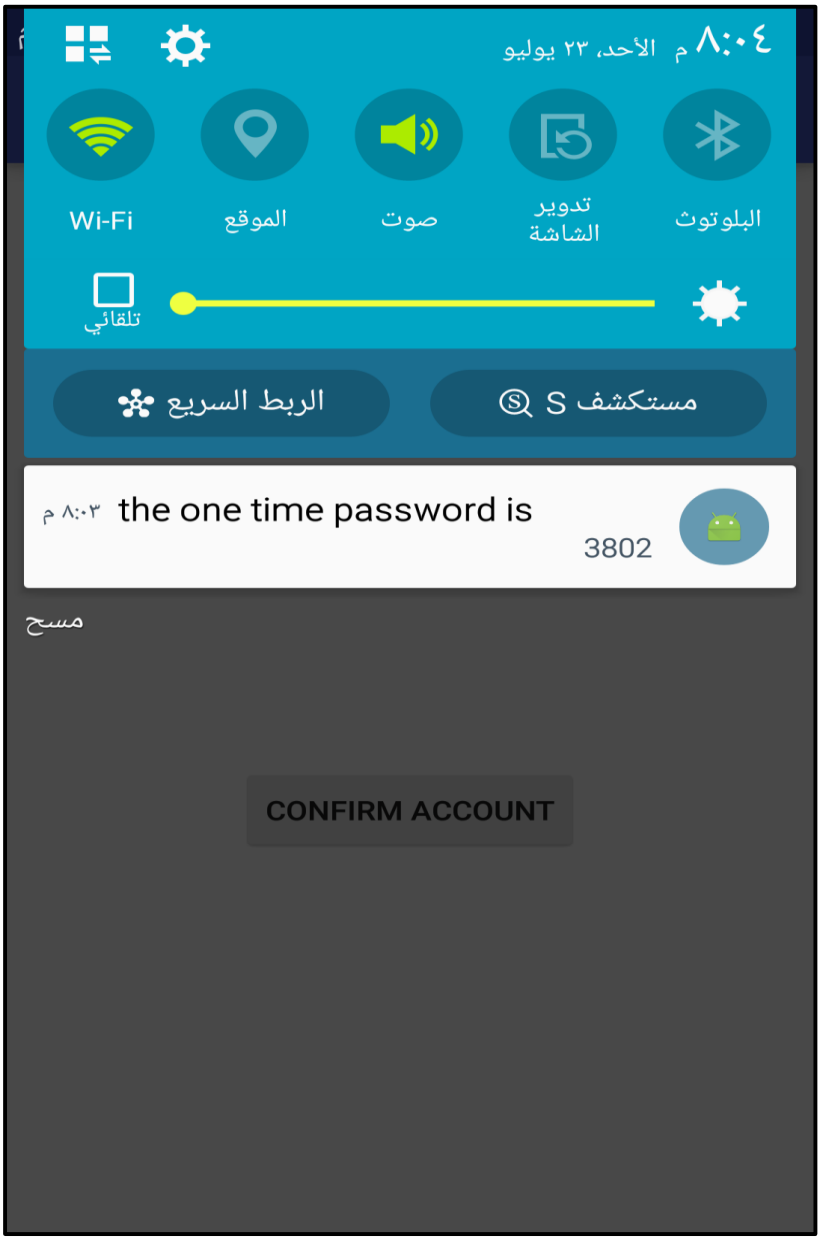

Figure 3. One time password that user received on mobile.

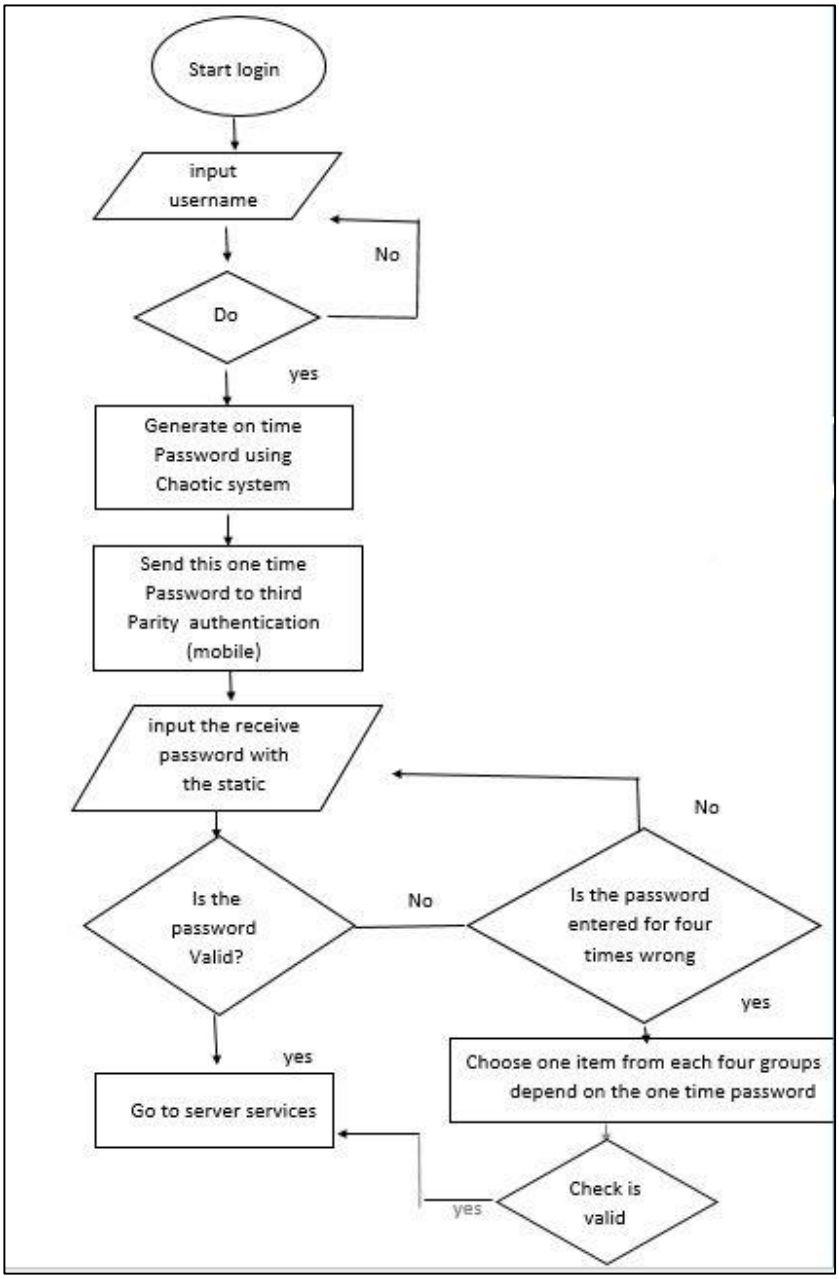

Figure 4. Login process to server storage

When the user login to the server, he can use all the facilities provided by the system such as browses any file that are pre-stored in the server and can download any file and read it and can upload any file to server. The mobile application designed to receive the one-time password that send from server. It is programed by using Java programing languish.

4. Conclusion

Servers offer valuable services but due to security challenges makes both organizations and people are concerned so that a system has been proposed to address these security threat. The proposed system provides a secure way to use the server services by using one-time password, third parity authentication (smart phone). This one time password will be valid only for one time and will be expire after half an hour and the using the third parity device (smart phone) to receive the one time password. The proposed system overcomes the brute force attack and denial of service attack by following the method in case if the user entered the password wrong for more than four times the proposal will offer the user groups of image to select from each group the image have number equal to the password that received on the mobile in the login step. The propose system handle many type of attach such as SQL injection attack and many other type of attack.

Reference

[1] F Abidi and V Singh 2013 Cloud Servers vs. Dedicated Servers – A Survey *Conf. MOOC. IEEE* pp 1–5
[2] M E K, M C A, M Phil, J M Sc, M Phil and D Ph 2013 Secure Login Using Encrypted One Time Password (Otp) and Mobile Based Login Methodology *Int. J. Eng. Sci.* **2** 10 pp 14–17
[3] S Srivastava On The Generation of Alphanumeric One Time Passwords i pp 1–3
[4] Cloud Security Alliance Top Threats to Cloud Computing Security 2010 pp 1–14
[5] C M R Da Silva, J L C Da Silva, R B Rodrigues, G M M Campos, L M Do Nascimento and V C Garcia 2013 Security threats in cloud computing models: Domains and proposals. IEEE Int. Conf. Cloud Comput CLOUD pp 383–389
[6] F A Abdulatif 2017 Cloud Security Issues and Challenges : Important Points to Move towards Cloud Storage International **6** 8 pp 2105–2112
[7] A Hendre and K P Joshi 2015 A Semantic Approach to Cloud Security and Compliance Proc. IEEE 8th Int. Conf. Cloud Comput. CLOUD pp 1081–1084
[8] A Kie, P J Guo and M D Ernst Automatic Creation of SQL Injection and Cross-Site Scripting Attacks
[9] F A A Latef 2012 Web Ranking and Rating Server Usng Web Service pp 411–424

Hiding text in gray image using mapping technique

IOP Conf. Series: Journal of Physics: Conf. Series **1003** (2018) 012032 doi:10.1088/1742-6596/1003/1/012032

Hiding text in gray image using mapping technique

[1] Hussein L. Hussein, [2]Ahmed A. Abbass,, [3]Sinan A. Naji, [4]Salam Al-augby and [5]Jasim H. Lafta

[1] Ibn Al- Haitham College for education, Baghdad University, Baghdad, Iraq.
[2] College education for girls, Kufa University, Najaf, Iraq.
[3] College of Engineering, Univ. of Information Technology and Communications, Baghdad, Iraq.
[4]Faculty of Computer Science and Maths, Kufa University, Najaf, Iraq.
[5]Faculty of Informatics, Debrecen University, Debrecen, Hungary.

Abstract: In order to hide the significant and secret message inside a cover object, Steganography is considered as one of the most used technique because of its strength. This paper presents a new steganography technique that it is difficult to discover or break by a third party. The ASCII Mapping Technique (AMT) is used to create an encoded table by mapping the text message and matching some bits with that of the cover image. The system saves the character parts matching and the location of which part of the pixels. Then change the related flag from zero to one the for matched locations so that they cannot be used again to strength the technique and make it more secure. The proposed t**echnique** was tested and showed low computational cost with effective performance to be used for multi-purpose applications.

1-Introduction.

"Covered writing" is the literal translation of the Steganography term which consists originally from the "steganos" and "graphia" Greek words. Steganography can be considered as a way of concealed communications which is highly related to cryptography [1] [2].

In fact, the protection of messages is the main goal of cryptography and that is the vital difference between cryptography and steganography, by converting it to cipher text, meanwhile the main objective of steganography is to conceal a secret message in a cover object. As a result, the message will be hidden from the unauthorized users [3]. Steganography, Digital watermarking and other information hiding mechanisms is used to solve this problem [4].

Steganography implies embedding process and extracting process. In the embedding process, the new generated image is called stego-image or a cover image and used to carry the secret data. For hiding data, the selected pixels should be chosen secretly by using a special algorithm or secrete key as shown in Figure 1 [5] [6].

The challenges associated with steganography techniques are influenced by the following factors [7] [8]:

1. Invisibility: implies that the stego-image looks very similar to the original image [9] [10].
2. Payload/Capacity: defines the amount of secret data which can be hided in the cover media [11].

3. Robustness against statistical attacks: Peak Signal-to-Noise Ratio (PSNR) and Mean Square Error (MSE) are two most fidelity parameters which are used to measure the robustness against statistical attacks [9] [12] .
4. Computation Complexity: It is a computation of the expensiveness of the embedding and extracting process of a hidden message [2] [13].

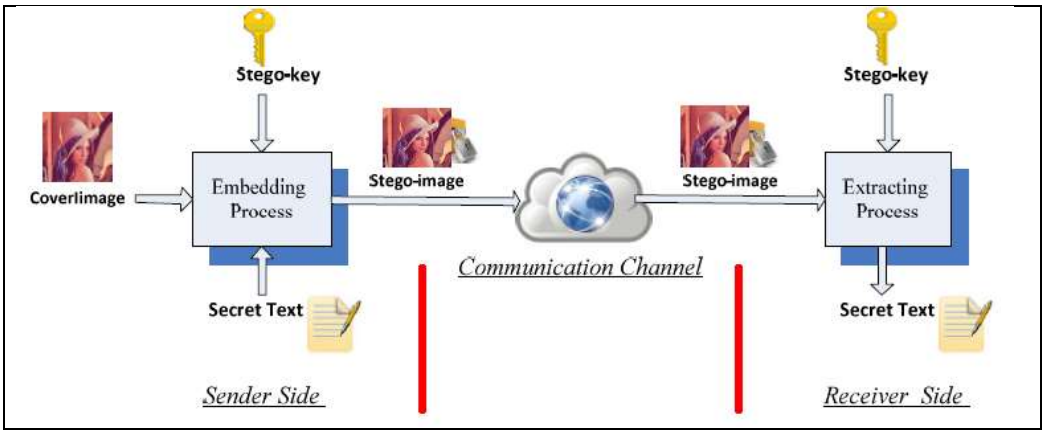

Figure 1: Steganography system

2.Related Works

Many techniques are proposed to improve the steganography techniques. Kukapalli et. al. [8] presented an enhancement method of the Pixel Indicator Method (PIM). The methodology was built on using the last three MSB of each pixel. Blowfish was used as an encrypted algorithm. Taking the advantage of the difference between colors to embed message bit was one of the strength points of this method. Depending on color differences and values of variable N the color will be selected and the authors claimed the detecting of message will be difficult. Moreover, changes in the image will be indistinguishable.

Bhattacharyya et. al. [4] proposed a text steganography method based on ASCII Mapping Technology (AMT). In order to increase the security level, the quantum logic technique was used because of its ability to find a valid embedding position. The Shannon Entropy and Correlation-coefficient values showed that Stego text was generated with minimum or zero degradation using ATM method.

For hiding secret message in an image Satar et. al. [14]designed a simple and efficient model.

In calculation stage of this model, a new binary number of secret messages was conducted by Connective Logical (CL) algorithm while the key was represented by the Most Significant Bit (MSB) of each pixel. Using Operator Negation, OR and XOR helped in the production of a new secret message by calculating the MSB of each pixel that will assist the new secret message by embedding in the LSB of pixels.

Alsarayreh et. al. [7] presented a system to hide secret data inside the image. This work finds the exact matches between the image RGB decimal values and the secret message/data after converting them to ASCII. However, the system generates a key to recover the secret data which is randomly generated based on matched pixels and the secret text. As well as, a Random Key-Dependent Data (RKDD) is generated without performing any changes on the image's pixel values.

One of the concealing information technique that hide information within the spatial domain of any gray scale image is Pixel Mapping Method (PMM) technique. It is firstly proposed by Bhattacharyya et. al. [15]. Some mathematical functions were the basis of choosing embedding pixels where the pixel intensity value of the seed pixel and its 8 neighbors are the cornerstone of this process. The selection was taken in counter clockwise direction. Each two or four bits of the secret message were mapped to data embedding.

This process was conducted in each of the neighboring pixel on the basis of some features of that pixel. In order to retrieve the original information there will be different reverse operation are executed at the receiver side.

Banerjee et. al. [16] presented an improved version of PMM method which is based on special domain. In the first step of this method, the input message is converted into a digital character format in order to deal

with bit stream. For the purpose of embedding in a separate pixel and embedding pixel selection, a 2-bit pair and a mathematical function are adapted. In the next step pixel intensity value and pixel position on image were used as the basis of selection technique. For more embedding in a pixel, a two bit from the secret message were mapped. This embedded pixel is based on the intensity value, previous pixel value and number of one's (in binary) present in that pixel. The concept of previous pixel intensity value is added in this work along with the embedding pixel selection method [16].

3.The Proposed Technique

The main idea of the proposed algorithm is to divide each character (8-Bits) of the secret message into two bits and then search the image pixels for the two similar bits in that image (Each pixel in gray image has 256 gray scale, i.e. in the representation of one pixel in gray image we need one byte). As an expected result of this method, the probability of finding matching pixels that are in relation to characters of the secret messages. The matches are saved and sent to the receiver in separate encrypted channel.

Error! Reference source not found.Error! Reference source not found. shows the structure of the proposed algorithm that can be summarized in the four steps as follows:-

3.1. Embedding algorithm the secret message:

Input : secret text , covered image.
Output : covered image , locations table.
The Technique Consists of the Following Steps
Step-1:

- Select gray scale image.
- Read the secret message.
- The gray scale pixel image and each character of secret message will be represented as binary values.
- Divide each binary value of the pixel image and binary values of each character into four parts of 2-bits long.

Step-2:

- Sequentially, two bits are selected from the data stream after that a search of a two bits similarity in the image pixels will be conducted.
- Save matches location of which part of the pixel.
- Set the flag to one for this location and that part so that cannot be used again.

Step-3: Repeat step 2 until the end of secret message.
Step-4: Output the resulting location table.

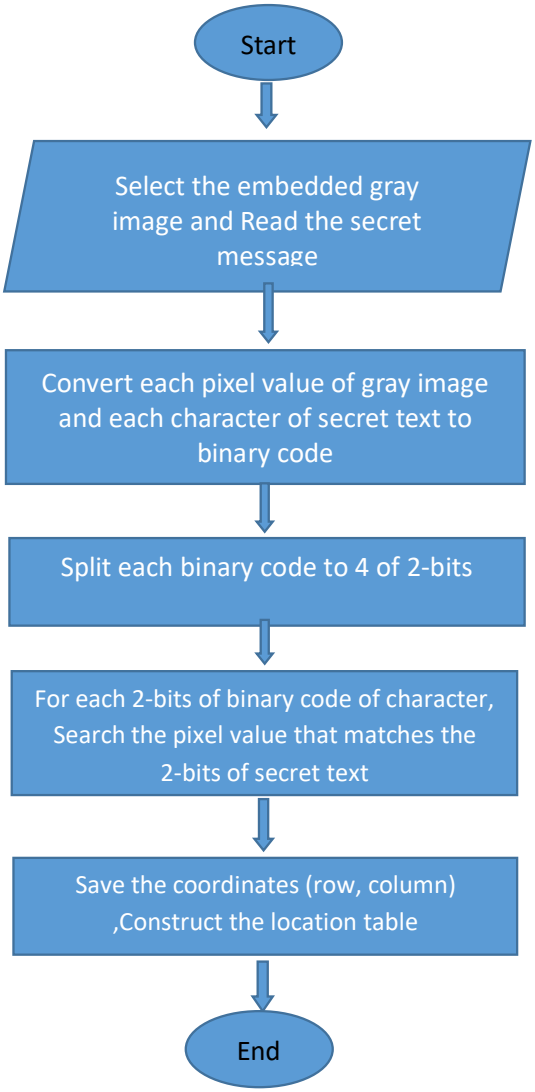

Figure-2. Flowchart of proposed system for mapping technique.

4.Experimental Results

For testing the proposed algorithm, various lengths of secret messages and different sizes of images were taken as depicted in Table-1 where:

INPUT TEXT= 'this free online service allows to … separate files ".

Table 1: The input letters along with their matches locations in the image

Letter	ASCII Code	1st 2-bits location		2nd 2-bits location		3rd 2-bits location		4th 2-bits location	
		Row	Col.	Row	Col.	Row	Col.	Row	Col.
t	01110100	1	14	1	14	1	2	1	3
h	01101000	1	15	1	479	1	3	1	7
i	01101001	1	21	1	490	1	4	1	4
s	01110011	1	22	1	15	1	1	1	1

space	00100000	29	4	1	491	1	10	1	9
f	01100110	1	23	1	492	1	8	1	2
r	01110010	1	24	1	21	1	11	1	8
e	01100101	1	25	1	495	1	9	1	5
e	01100101	1	26	1	496	1	12	1	6
space	00100000	29	9	1	497	1	13	1	12
. . . .	. . .	. . . .	. . . .	. . . .	. . . .	. . . .	. . . .	. . .	. . .
f	01100110	1	315	20	58	1	75	1	56
i	01101001	1	318	20	59	1	27	1	68
l	01101100	1	319	20	60	1	46	1	75
e	01100101	1	331	20	61	1	76	1	69
s	01110011	1	338	1	83	1	87	1	79

5.Conclusion

The system achieved two important goals, which can be summarized as following:

First, we illustrate that the system keeps the cover image unchanged because the image plays the role of the key to encode the secret message.

This is an important issue for the developers and users.

Second, the proposed system uses the mapping technique.

The mapping of each character of the secret message and matching each binary two bits of the stream data to the same two bits in the image was the first step. Secondly, locking the locations in the image will lead to a distribution of every two bits the character of the same bits of the image and will give each character of the secret message a new substitution value. Increasing the probability of finding another matching that has a mapping to characters of the secret message was done by distributing the bits of the characters.

This makes the task of the steganalysis harder to reconstruct the message.

References.

[1] Ingemar J. Cox, Matthew L. Miller, Jeffrey A. Bloom, Jessica ridrich, Ton Kalker, 2007 ," Digital Watermarking and Steganography" ,Second Edition, Morgan Kaufmann Publishers is an imprint of Elsevier, USA.

[2] Mehdi Hussain, 2013,A Survey of Image Steganography Techniques*, International Journal of Advanced Science and Technology*, **54**.

[3] Al-Husainy, M.A.2009, Image Steganography by mapping Pixels to letters. *Journal of Computer science,* **5**(1): p. 33.

[4] Bhattacharyya, S., P. Indu, and G. Sanyal,2013, *Hiding Data in Text using ASCII Mapping Technology (AMT). International Journal of Computer Applications*, **70**(18).

[5] Samagh, R. and S. Rani,2015, Data Hiding using Image Steganography*, International Journal of Emerging Trends in Engineering and Development,*: p. 123-129.

[6] Li;, B., et al.,2011, A Survey on Image Steganography and Steganalysis. *Journal of Information Hiding and Multimedia Signal Processing,.*

[7] Alsarayreh, M.A., M.A. Alia, and K.A. Maria,2017, *A Novel Image Steganographic System Based on Exact Matching Algorithm and Key-Dependent Data Technique. Journal of Theoretical and Applied Information Technology*, **95**(5): p. 1212.

[8] Kukapalli, V.R., B.T. Rao, and M.B.S. Reddy,2014, Image Steganography by Enhanced Pixel Indicator Method Using Most Significant Bit (MSB) Compare,*International Journal of Computer Trends and Technology (IJCTT)*, Volume-**15** Number-3.
[9] Tuama, A.Y., et al.,2017, Randomized Pixel Selection for Enhancing LSB Algorithm Security against Brute-Force Attack. *Journal of Mathematics and Statistics* , **13**((2)): p. 127-138.
[10] Nag, A., et al.,2011, A novel technique for image steganography based on DWT and Huffman encoding. *International Journal of Computer Science and Security,(IJCSS)*, **4**(6): p. 497-610.
[11] Kumar, M. and M. Yadav,2014, Image steganography using frequency domain. *International Journal of Scientific & Technology Research,* **3**(9): p. 226-230.
[12] Goyal, M., Y. Lather, and V. Lather, 2015,Analytical relation & comparison of PSNR and SSIM on babbon image and human eye perception using matlab. *International Journal of Advanced Research in Engineering and Applied Sciences*, **4**(5): p. 108-119.
[13] Chen, P.-Y. and H.-J. Lin, 2006,*A DWT* based approach for image steganography. *International Journal of Applied Science and Engineering,* **4**(3): p. 275-290.
[14] Satar, S.D.M., et al.,2015, A New Model for Hiding Text in an Image Using Logical Connective. *International Journal of Multimedia and Ubiquitous Engineering,* **10**(6): p. 195-202.
[15] Bhattacharyya, S., L. Kumar, and G. Sanyal, 2010,A novel approach of data hiding using pixel mapping method (PMM). *International Journal of Computer Science & Information Security*, p. 1.
[16] Banerjee, I., S. Bhattacharyya, and G. Sanyal, 2013,*Hiding & analyzing data in image using extended PMM.* Procedia Technology, 10: p. 157-166.

Fuzzy-cellular neural network for face recognition HCI Authentication

IOP Conf. Series: Journal of Physics: Conf. Series **1003** (2018) 012033 doi:10.1088/1742-6596/1003/1/012033

Fuzzy-cellular neural network for face recognition HCI Authentication

Haider K. Hoomod, Ahmed abd ali

Al-Mustansyriah University- Education college- computer science Dept.
Drhjnew@gmail.com

Abstract. Because of the rapid development of mobile devices technology, ease of use and interact with humans. May have found a mobile device most uses in our communications. Mobile devices can carry large amounts of personal and sensitive data, but often left not guaranteed (pin) locks are inconvenient to use and thus have seen low adoption while biometrics is more convenient and less susceptible to fraud and manipulation. Were propose in this paper authentication technique for using a mobile face recognition based on cellular neural networks [1] and fuzzy rules control. The good speed and get recognition rate from applied the proposed system in Android system. The images obtained in real time for 60 persons each person has 20 to 60 different shot face images (about 3600 images), were the results for (FAR =0), (FRR =1.66%), (FER =1.66) and accuracy =98.34 Keyword: HCI, HCI authentication, Face recognition, Cellular neural network, Fuzzy.

1.Introduction

Because of the great sophistication of computer technology, Human Computer Interaction (HCI) techniques have become an important component of our lives HCI Interested in the understanding between persons and the Machine [2]. Because of the increased use or spread of mobile devices, interaction between humans and computers has increased Such technologies include PDAs, handheld communicators, pocket music players, two-way pagers, cameras, watches smart, GPS units, medical and work devices, and smartphones.

Mobile devices are rapidly evolving technologies capable of give many services through a wide domain of apps through multiple networks such as the Internet (e.g. e-mail, online banking), amusement (e.g. photos and video games) and the Participation of data (via Bluetooth, laptops/ computers). The increase of functionalities presented by mobile devices enables persons to storage increasing amounts of broad ranging kinds of data from business to personal and sensitive data. and mobile users worry of their devices being missing or stolen. there are a types of security threats that can affect mobile devices. We divide these mobile threats into various types: application threats such as (Malware, Spyware, Privacy Threats and Vulnerable Applications), web threats such as (Phishing Scams, Drive-By Downloads, Browser exploits), network threats such as (Network exploits and Wi-Fi Sniffing) Physical Threats as smartphones are small and carry

with us almost anywhere, it is important to provide security [2], The loss or theft of a device is one of the most prevalent mobile threats. The loss of a valuable mobile device was not as important as personal and sensitive information

Biometrics technologies indicate to recognize individuals depended on their distinguishing biological or behavioral traits. These traits include face, speech, fingerprints, gait, hand-vein, retina, iris, palm-print, ear, and signature. Biometric security systems supply suitability and high stability to persons, it is needless to remember passwords or have physical tokens. Using face recognition for mobile authentication, their acceptable authentication execution and a reliable and user-friendly way are in high requesting for mobile devices. Some of the previous work in face recognition: Fast Face Recognition Based on Wavelet Transform on PCA [4] and using "Prabujeet KaurI" User Authentication in Social Networking Sites using Face Recognition [5] and N.Rajkumar S.Vijayakumar C.Murukesh applied new face recognition method dependent on 2D Level 2 Wavelet decomposition, PCA with singular value decomposition, and Bayesian Classifier is suggested. The results were accurate (PCA, ICA and KPCA ,77, 77 and 87) [6] in 2016 the Naveen S, Shihana Fathima R and Dr. R S Moni are used features employed a form the whole face as well as the eye and nose expected to Local binary pattern (LBP) and Binarized Statistical Image Features (BSIF) are utilized to extract the texture features of the face for recognition and the results (BSIF Accuracy =84.90) and (LBP Accuracy = 47.84) [7]. In this paper we suggest co-authentication system, face recognition and using cellular neural network with fuzzy rules control.

2. Cellular Neural Network (CNN) Background

Standard CNNs, known as Chua-Yang models contains of a rectangular ZxF orders of identical-cells, describing by the states and outputs equations:

$$\frac{dx_i}{dt} = -x_{ij} + \sum_{j\in N_i} A(i,j;k,l)ykl + \sum_{k\in N_i} B(i,j,k,l)ukl \qquad (1)$$

Where (u_{kl}) inputs,(x_{ij}) the states, and (y_{kl}) the cell output in position(i,j), the k and l denoting a generics cell belongs to the neighbor-hood N(i,j) of the cell at position(i,j). The matrices set and threshold {A, B}, that contain the neural (or nonlinear) network weights, and call the cloning-template and defining the network processes execution. There are many advantages and disadvantages to the CNN model. The CNN model additional cells or neurons can be added to the network to extend the network. It can also perform tasks that a linear program cannot. When an element of the neural network fails, it can continue without any problem because of its parallel paradigm. Another advantage of the CNN model is that neural network can learn by adjusting its coupling strengths and does not need to be reprogrammed. It can also be implemented in any application without any problem [8].

3. Face Recognition Background

There are three steps for face recognition: Face Detection, Features Extraction, and Face Recognize 'Figure (1)' shows Face recognize steps. [9]

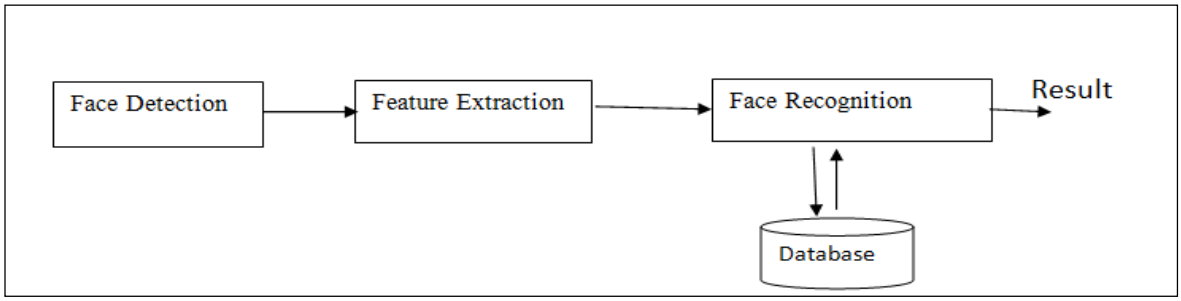

Figure 1. Steps for face recognition: Face Detection, Features Extraction, and Face Recognize

3.1. Face Detection

Face detection as a first stage for face recognitions the major function of this stage is to determine whether human faces show in a given picture. There are many face detection algorithm as Local Binary Pattern (LBP), features whereas Support Vector Machine (SVM), classifier is used with Histogram of Oriented Gradients (HOG).

3.2. Features extraction

The second step of face recognition is Process of extracting important information from a face picture. Features as (eyes, nose and mouth) [10].

3.3Face match

Feature matching is the actual recognition operation. The feature vector features acquired from the features extraction is matched to person face picture register and stored in a database [11].

4.Chaos system

The Henon map is a prototypical two dimentional invertible repeat map with chaotic solutions suggest by the French astronomer Michel Henon [12]

$$Wn + 1 = 1 + aWn2 + bTn \quad (2)$$
$$Tn + 1 = w_n$$

he second equation above can be written as Tn = Wn-1, the Henon map can be written in terms of a single variable with two time delays [13] :

$$Wn{+}1 = 1 + aWn2 + bWn - 1 \quad (3)$$

5. The proposed Modified CNN With Chaos System (HCNN)

In this stage, the Modified Chaotic CNN was used to find optimal face recognition between face features in database and current entered face features. The proposed modifications are in two locations in CNN, the first modification in the outputs of CNN by adding Henon results to (CNN) for improving the making a decision. Second modification was used Henon chaos system in the learning feeding of the CNN in order to increase the learning speed and get acceptable results in stable case by avoiding angle deviation of face image. Also, to optimization the speeding of the learning and detection of case to find the optimal matching for two images face in face recognition system. Figure (2) shows the modification of CNN cells by adding Henon chaos system. The proposed modified CNN equation will be:

$$\frac{dx_i}{dt} = -x_{ij} + \sum_{j\in N_i} A(i,j;k,l) + ch.ykl + ch + \sum_{k\in N_i} B(i,j,k,l)ukl \quad (4)$$

Where the chaos is ch and:

$$ch = Wn + 1 = 1 + aWn2 + bTn \quad (5)$$

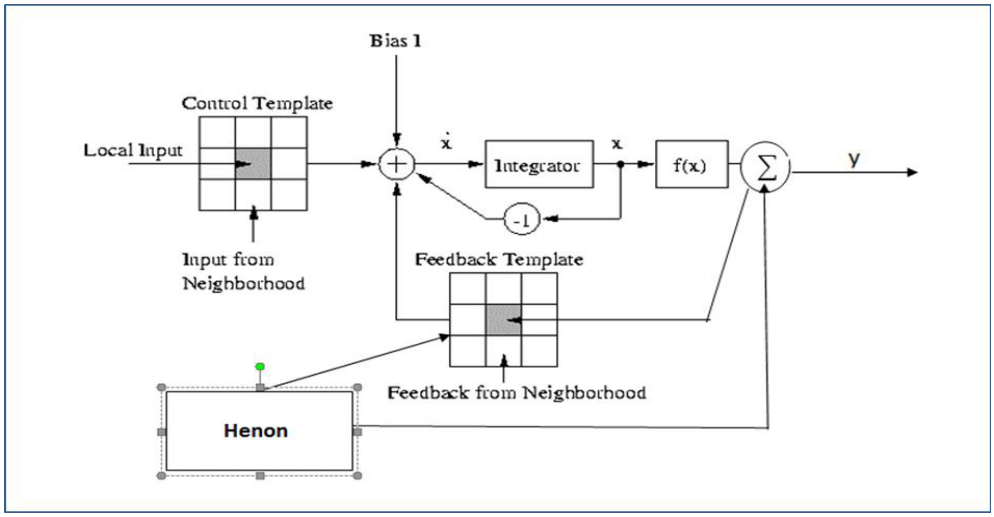

Figure 2. Modification of CNN Cells with Henon

6. The Proposed System

The main aim of the proposed system is to design the authentication system for(HCI), to get high-level identity management processes and a system that is easy and safe to use. The user can be authorize or rejected within a few seconds. The propose system is consists two main stages. First is the face recognition using (PCA) and second face recognition using Henon Cellular Neural Network(HCNN). This stage consists from three steps and named as: face-detection, features extraction, face recognitions and classifications. The flowchart of a face recognition proposed system is presented in Figure (3). The input images obtained from image acquisition devices e.g. Using a camera 2-megapixel and image size (256 * 256) might not be suitable for recognition due to noise or illumination conditions. first step preprocessing to remove noise and fix the illumination, in this stage using Canny edge detection, Canny edge was a multi-stage algorithm that can discover edges with noise at the same time. The two steps preprocessor and the edge detection were merged into one stage when using canny. The next stage-features extraction- includes obtaining important face features from the data. These features are face areas, difference, corner or measurement, (e.g. eyes spacing, Size and shape of nose and mouth) at this stage we were able to extract 70 secondary and primary advantage using the algorithm principal component analysis (PCA). The next is to classify and match features based on the stored face features in database. Second stage in proposed system is the modified cellular neural network by using chaos for face recognition. This modification (as shown in Figure.2) to the CNN is to increase the learning speed and accuracy of the recognition operation.

These two steps of face recognition using (HCNN) work parallel to the image of the face, where the image enters the proposed system in parallel. One enters the system of face recognition and the other enters into the modified (HCNN) and the results goes to the fuzzy rules control and calculated the process where (HCNN) accelerate and corresponding improvement in decision-making. The Algorithm of proposed system is shows in algorithm (1):

Algorithm (1) the proposed system Steps.

Input: face image

Output: ratio of identification

Steps 1: initial camera

Step2: capture image

Step3: face detection (using canny filter)

1: Smoothing removing noise by Gaussian filter with formula

$$g(m,n) = G_\sigma(m,n) * f(m,n) \quad \text{Where} \quad G\sigma = \frac{1}{\sqrt{2\pi\sigma^2}} \exp\left(-\frac{m^2+n^2}{2\sigma^2}\right)$$

2: Compute gradient of g(m , n) using any of the gradient operators with formula

$M(n,n)= \sqrt{g_m^2(m,n) + g_{n(m,n)}^2}$ And $\boldsymbol{\partial(m,n) = tan^{-1}\,[g_n(m.n)/g_m\ (m,n)]}$

3: Threshold M: with formula $M_{T(m,n)} = \begin{cases} M(m,n) & if\ M(m,n) > T \\ 0\ otherwise \end{cases}$

4: Suppress non-maxima pixels in the edges in MT

5 Thresholding

Step4: features extraction using algorithm (PCA).

1: convert face image (i*j) to vector (v)

2: calculate average by using Equation AV= $\frac{1}{M}\sum_{k=1}^{m}$ In

3: fined differential distance by using Equation U=In-AV

4: Find the covariance matrix by using Equation SC= $\frac{1}{M}\sum_{k=1}^{m}$ Un U n

5: selected highest eigenvalue

Step5: Appling (HCNN) modify on result step2

Step6: applied Fuzzy rule control on result step 4 and step 5

Step7: checking stage if ratio accepts then open screen and services
Else Not authentication

Stap8: end

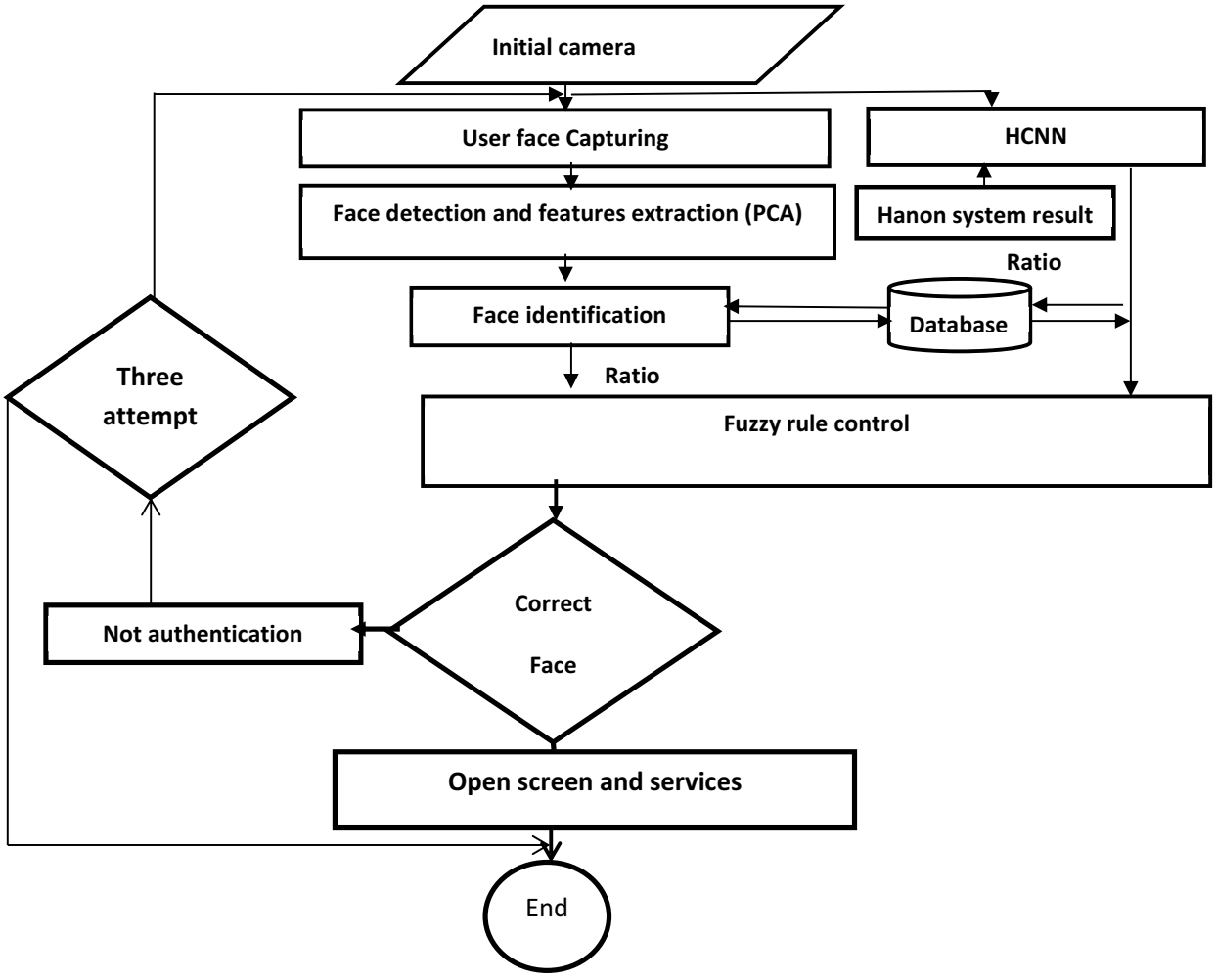

Figure .3 flowchart of a face recognition proposed system

After the matching operation the output will be a ratio for both HCNN and PCA face identification ratios. These values entered into fuzzy control the first step is to convert the matching value (x) into a group of fuzzy variables. This done by giving values to each of a group of membership functions. The values for each membership function f(x) are determined by the original value x and the shape of the membership. Now divide the corresponding ratios into the fuzzifier variables, where the percentages are between (1....45) low and Symbolizes them (LO), (40...70) medium and Symbolizes them (ME) and (60....90) high and Symbolizes them (HI). The proposed fuzzy rules used in this proposed system are:
If HCNN= LO and PCA=LO then flags=0
If HCNN=LO and PCA= ME then flags=0
If HCNN=LO and PCA=HI then flags=0
If HCNN=ME and PCA=LO then flags=0
If HCNN= ME and PCA=ME then flags=1
If HCNN= ME PCA=HI then flags=1
If HCNN=HI and PCA=LO then flags=0
If HCNN=HI and FEPCA= ME then flags=1
If HCNN=HI and FEPCA=HI then flags=1
The Calculation Defuzzification is convert truth values into output from the following equation (6). The algorithm (2) shows steps of fuzzy control and decision making. [14]

$$u = \frac{\sum_{n=1}^{N} Ui\, fi}{\sum_{n=1}^{N} fi} \tag{6}$$

Algorithm (2): fuzzy control and decision making stage

Input: (HCNN) ratio and (PCA) identifier ratio and similarity user face

Output: flag value

Step1: start
Step2: check the similarity of user if no similarity then go to end authentication and display error message
Step3: converting a ratio of (HCNN) and (PCA ratio) into a fuzzy input using:
If ratio <= 45 then LO
Else If 45 <=ratio <= 70 then ME
Else If 70 <=ratio <= 90 then HI
Step4: applied fuzzy rule
Step5: convert truth values into output using Defuzzification operation
Step6: get flags results from step4 and step5
Step7: Compute decision based on the flag:
If flag =1 then
Accept the authentication and open the services and the screen
Else If flag =0 then
Shows message authentication Error
Step7: End.

7.Experimental Results
In this section, experimental results of the proposed methodology are presented. The algorithm has been implemented using android studio 2.2.2. figure (4) shows android studio. The database utilized for face recognition (the images were obtained in real time) comprises and content a 20 to 60 different shot face

images for each person (from 60 persons). The acquisition system for face image is samsung S5 device mobile. The recognition execution is calculate by means of FAR, FRR, F T E, and RR or accuracy. The FAR is the percent mistake of a system that accepts imposter as actual users while FRR is the percent mistake of a system that rejects real person as imposter FER. The Failure to Enroll average is the number of persons who fail in their tried at register and RR or accuracy is the recognition rate, These equations explain below, also calculate time detection and time match. Tables (1), (2) and (3) show results.

$$\text{FRR} = \frac{\text{Number of rejected of an authorized person}}{\text{Total number of attempts}} * 100 \quad (7)$$

$$FAR = \frac{\text{Number of acceptance of an unauthorized person}}{\text{Total number of attempts}} * 100 \quad (8)$$

$$FER = \frac{\text{Number of acceptance of an unauthorized person}}{\text{Total number of attempts}} * 100 \quad (9)$$

$$\text{The recognition rate RR=100-}\frac{FER+FRR}{2} \quad (10)$$

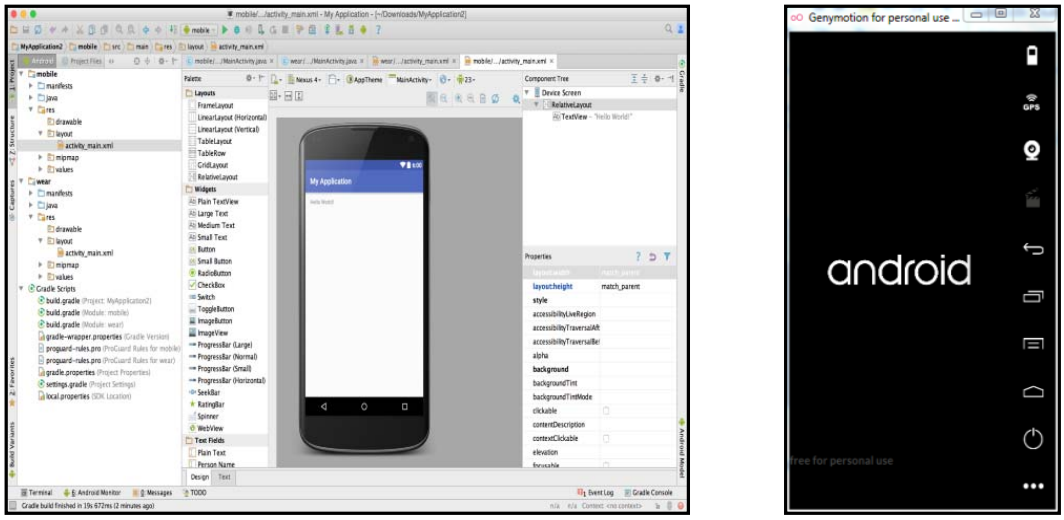

(a) (b)

Figure .4 (a) shows android studio (b) shows genymotion

Table 1. Results for 20 Persons Face Recognition

	PCA	CNN	PCA&CNN
FAR	0/20=0	0/20=0	0/20=0
FRR	3/20= 15%	2/20=10%	1/20=5%
FER	2/20 =10%	2/20=10%	1/20=5%
ACCURACY	87	90	95

Table 2. Results for 60 Persons Face Recognition

	PCA	CNN	PCA&CNN
FAR	1/60=1.6%	0/60=0	0/60=0
FRR	5/60= 8.3%	3/60=5%	1/60=1.66%
FER	4/60 =6.66%	3/60=5%	1/60=1.66%
ACCURACY	92.5	95	98.34

Table 3. The Proposed System Results and Time Computing.

Class	Original image	Gaussian Smoothing	Canny Filter	Feature extraction	Detection time(HCNN)	Matching time
1					690 ms	263 ms
2	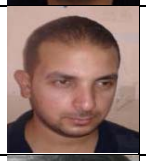		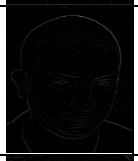	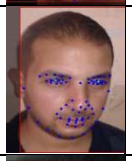	699 ms	180 ms
3			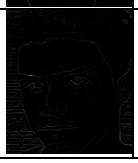	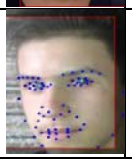	768 ms	290 ms

8. Discussion

The proposed HCI Secure Authentication Technique that was developed to protected the users from threats and concerns related to the safety of their personal information. From the results, we obtained Note that the proposed system is very fast (about 0.0800 sec its less than one second) in the process of detecting and face recognition. Also according to the results obtained through the implementation of the system on 60 people and each person (20 to 60) different situations, we note that the high speed of recognition with good performance. Where 2 images were rejected out of 6000 images due to high deviation of the image of the face. The use of the CNN of recognition led increasing speed of recognition of the system and according to

the results in the tables we notice the matching speed of 140 to 310 millisecond and the speed of detection was 500 to 900 milliseconds (Depending on lighting conditions and angle of face) less than one second. By integrating CNN with Henon and running in parallel with PCA we notice an increased speed learning algorithm and gave it the best results.

Reference

[1] Roman Z´alusk´y, Daniela Duraˇckov´a, 2010 New digital architecture of CNN for pattern recognition *Journal of Electrical engineering*, vol.**61**.no.4,2010,22-228
[2] Renuka R and Suganya V ,Arun Kumar B 2014 Online Hand Written Character Recognition Using Digital Pen for Static Authentication.
[3] Collin Richard Mulliner, 2014 Security of Smart Phones Santa Barbara, July.
[4] Moresh M.Mukhedkar, Samarjeet B. Powalkar, 2015 Fast Face Recognition Based on Wavelet Transform on PCA.
[5] Prabujeet KaurI and Aruni Singh, 2012 User Authentication in Social Networking Sites using Face Recognition.
[6] N.Rajkumar S.Vijayakumar C.Murukesh 2011 Intellectually Combined Face Recognition Using Curvelet Based Principle Component Analysis for Feature Extraction and Bayesian Classifier .
[7] Naveen S, Shihana Fathima R and Dr. R S Moni, 2016 Face Recognition and Authentication Using LBP and BSIF .
[8] Dr. Ing. Kyandoghere Kyamakya 2009 CNN based non-linear image processing for robust.
[9] Ani1 K. Jain, P.W. Duin, and Jianchang Mao 2000 Statistical Pattern Recognition.
[10] Kumud Kundu Sapna Tyagi 2016 Face Recognition Using Pca And Rbf Neural Network .
[11] Erwin Hidayat, Fajrian Nur A, Azah Kamilah Muda, Choo Yun Huoy and Sabrina Ahmad 2011 A Comparative Study of Feature Extraction Using PCA and LDA for Face Recognition.
[12] Henon Map Correlation Dimension Department of Physics, University of Wisconsin, Madison, WI 53706, USA August 29, 1997(,http://sprott.physics.wisc.edu).
[13] Predrag Cvitanovi´c, Roberto Artuso, Per Dahlqvist, Ronnie Mainieri, Gregor Tanner, G´abor Vattay, Nia ll Whelan, and Andreas Wirzba, 2002 Classical and Quantum Chaos version 9.2.3 Feb 26.
[14] Jan Jantzen, 1998 Design of Fuzzy Controllers Technical University of Denmark, Department of Automation, Bldg 326, DK-2800 Lyngby, DENMARK. *Tech*. report no 98-E 864.

Fuzzy-Estimation Control for Improvement Microwave Connection for Iraq Electrical Grid

IOP Conf. Series: Journal of Physics: Conf. Series **1003** (2018) 012034 doi:10.1088/1742-6596/1003/1/012034

Fuzzy-Estimation Control for Improvement Microwave Connection for Iraq Electrical Grid

Haider K. Hoomod And Mohammed Radi

Al-Mustansyriah University- Education college- computer science Dept.
Drhjnew@gmail.com

Abstract. The demand for broadband wireless services is increasing day by day (as internet or radio broadcast and TV etc.) for this reason and optimal exploiting for this bandwidth may be other reasons indeed be there is problem in the communication channels. it's necessary that exploiting the good part form this bandwidth. In this paper, we propose to use estimation technique for estimate channel availability in that moment and next one to know the error in the bandwidth channel for controlling the possibility data transferring through the channel. The proposed estimation based on the combination of the least Minimum square (LMS), Standard Kalman filter, and Modified Kalman filter. The error estimation in channel use as control parameter in fuzzy rules to adjusted the rate and size sending data through the network channel, and rearrangement the priorities of the buffered data (workstation control parameters, Texts, phone call, images, and camera video) for the worst cases of error in channel. The propose system is designed to management data communications through the channels connect among the Iraqi electrical grid stations. The proposed results show that the modified Kalman filter have a best result in time and noise estimation (0.1109 for 5% noise estimation to 0.3211 for 90% noise estimation) and the packets loss rate is reduced with ratio from (35% to 385%).Keyword: error estimate channel, least square, minimum mean square error , fuzzy logic .

1.Introduction

Electricity is one important issues in the word and especially in Iraq it comes second after the security after 2003. The power grid contains: [1]

1- energy production (power station) as a thermal's power station, gas turbine combined cycle power's station and hydro power's station.
2- Transmission: the networks transmission of Iraq be composed of (400kV,132kV) system. Generations was connecting to the132kV or to 400kV systems. The transmission's system of the 400kV especially composed of single's circuit overhead lines' capacity of around 1,000 MVA. This system represents as a power transmitting of highway from the southern regions and northern regions to the centric regions. The networks of 132kV was the sub transmission network that delivered the power to the distribution's networks inside the governorates and also representing the connection between governorates.
3- Distribution' system consists of many substations such as (33/11kV,11/0.4 kV) and overhead lines (33kV, 11kV,0.4 kV) and underground's cables. [1]

The power grid stations contains has(as shown in Fig.1) a national control center linked RTUs, and renewing the PLC and Microwave communication's systems (400kV,132kV) transmission's systems. [1]

As being one of the most important factors to support development, the amount of electrical power demand increased rapidly. During the last six years[3] and There is an increase in

demand for electric energy that mean we need to add an new units in the power station, transmission and Distribution system . [2, 4]

One part of the infrastructure in the power grid in Iraq is a control and communication. Control means work in the same unit as a (micro SCADA) but communication means transfer data or information between units according to the direction of linking these substations in the power grid. In this thesis we will focus in communications of transmission (substation 400k.v, 132k.v).

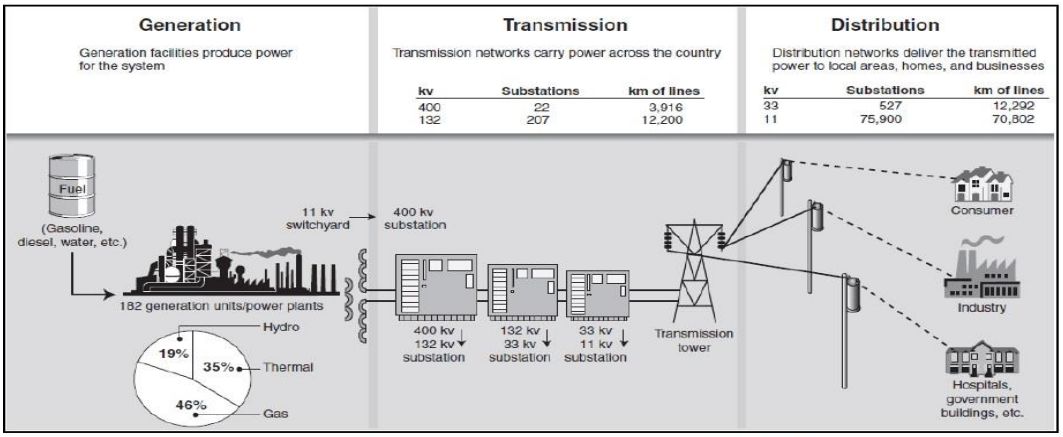

Figure 1. Illustrates the power station, Transmission and Distribution system [2]

More applications of distributing multimedia were became an integrated with computing and communication's environments. For achieving this goal, multimedia applications should be delivering high QoS. This is represented a challenges when distributed multimedia applications were executed on general purposes operating's systems and network that was developing to process best-efforts data and transmission. therefore, they bear high level of troubles in resource allocation when treating continuous media. For solving this challenge, many techniques for QoS adaptations for distributing multimedia system situation are proposed.[10]

The network problem congestions controls stay as critical high priority and issues, principally when increase the demands in using the Internet during delay-time sensitives application with different Qualities of Services (QoSs) requirements'. [7]

Many researches effort a large numbers of difference proposed controls systems. But still no universal acceptable congestions controls solution. Even with techniques of the classical-controls systems proposed in different researches, still don't perform sufficient controlling of the dynamic, and the non-linearities network or in Internet. [7]

For many years, fuzzy logic control is well known Computation Intelligences techniques in the best applications are used in many control researches especially in the networks and communication. [7]

In this section, we explain and discuss some of the control system used the estimation operation in controlling the network QoS, and the researches used in their suggestion the fuzzy control system techniques:

M. Reda and et al (2006) [1], they review the Iraqi-electrical-power systems history and illustrate the methods to enhancement and improved the infrastructures. The electrical-network due to the military operations, substantial damages, and poor maintenances with a very little developments and assessment replacements, that all results in reduction qualities operations and communications. They proposed some solution in the ongoing repairing infrastructure of the gird and stations and connect them with intelligent modern communication system of the Iraqi electricity grid.

Ghulam Abbas and et al (2008) [11], they propose a novel-framework, depend on states-Estimation, for the Networks Management-System approaches to controlling the network

traffics flow, routings, hard-ware malfunction, congestions and resources managing in data transfer network. The aim is to eliminats anomalies events and other dis-crepancies between network models that leads to bad operation in network and reduct the performance and threats the security and integrity of the network. The proposes framework was validate using cases studies that focuse on the congestion-control and have demonstrate favourables result in term of enhancing data deliveries with few packets losses and re-transmissions. The simulation results also suggest that States Estimations basedon congestion-control technique offer system monitoring improving with enhancement control network security.

Yasser Sadri and Sohrab Khanmohammadi(2013) [12], they introduced a QoS-Aware Scheduling technique depend on fuzzy-logic, for traffics managing in WiMAX point to multi point (PMP) network. The proposes technique was attempt to guarantees delays and throughputs QoS requirements. Its consider QoS requirements and radio-quality of users in decision-making processing. A simulation experiment series have achieving to evaluated the proposes scheduling-system performance. Getting the (QoS) for differnt multi-media service are an important issues in IEEE-802.16 (Wi-MAX) network. A scheduling techniques which satisfy the QoS crteria have become important for multi-media network. Also, scheduling-algorithms for wireless network were high complex than that of the wired network due to quality variation of channel and radio-resource limitation. The simulation results illustrate that the proposes technique perform more effective to achieving the QoS requiremts and increase different types traffic performance.

Mehrdad Taki and etal (2016) [13], propose joint's scheduling and link's adaptation techniques was designed by fuzzy-logic. the scheduler was designing for providing difference requirements for throughput and allocating the users shared media in optimal way Depending on their important.coding, transmit power and Adaptive modulation are using an average powers restrictions based on every power supply of the user. Differen bit-error-rate and QoS-delays restrictions were providing to all links. Numerical's evaluation displayed that the proposed schema that based on fuzzy has the execution extremely closing to the analytic approachs, basically minimum complexity.

Abbas Ali Rezaee and Faezeh Pasandideh(2017)[14] , when the patient's body sensors are constantly send the data packets, probably congestions may be happened. This was increasing the loss of packet ratio and hence the efficiency was decreasing and it will be affecting on system overall performance, so the congestion's control is a main challenges. Detecting the Congestions and control it was fundamental for some systems.active queue method's management was proposed here for determining the packet's losing probability. AQM was integrating the early random detections and Fuzzy PID (fuzzy-proportional-integral-derivative) controlling methods jointly. When PID was joined with the fuzzy logic, that was helping to controlling the target buffer's queue. The controller of the fuzzy logic was estimating and adjusting the rates of sending of every node. By using MATLAB and OPNET simulators, the researcher was comparing proposing protocol with Priority-based-Congestion -Control-protocol data-loss-rate.

In this paper we suggest the fuzzy rules control with many channel error (noise) estimations to control the data transferring in the Microwave channels connected the power stations in the Iraqi electrical grid.

2.Channel Estimation Techniques

Many methods for Channel estimation problems based in semi-blind approach are used Least Mean Square(LMS) Algorithms

Estimation algorithm of LMS uses the gradient vector for estimation of the main data. Iterative procedures combined with the LMS method made successful rectifications to the weight vectors in the negative direction of the gradient vectors which results minimum MSE(mean-square-error). In comparing of other algorithms, the LMS algorithm was comparatively easy:

Input: A random process x(n);
Output: e and d.
FIR filter of weights: (w0, w1, …wN-1);
Filter output: $Y(n) = w^T x(n)$;
Error signal: e(n) = d(n) – y(n)
Where d(n) is desired output

From the method of steepest descent, weight vector equation is given by:

$$w(n) = w(n) + {}^{1}/_{2}\ \mu\ [-\nabla(E\{e^2(n)\})] \quad (1)$$

Where μ is the step-size factor that controls the characteristics of convergence of the LMS algorithm

Kalman filters Estimator [24, 25]

The Kalman filters are founded by linearly dynamical system discretized in times domain'. These filters were constituted by a Marko's chains structured by linear factors anxious about the error that include the Gaussian's noises. The system status was represented as a real number vectors. In each increment of discrete time the system was applying linear operators to the state for generating a state was discovered recently that has some data from controls and some noise that mixed with on the system. After that other linearly operator's that mixing with more noises was generating the supervised outputs from the correct state (hidden stat). Kalman's filters may be considered as analogous to Markov's hidden model with different key that the variables of hidden states value in a continuous space (against the Markov hidden model, it's state in discrete space).

For using Kalman's filter for estimating the internal state of an operation, that only sequence of noisy considerations was given a, first should model the operation in conformity of the Kalman's filter framework.

1. Equation of Process

$$X_k = A_{Xk-1} + W_{k-1} \quad (2)$$

Where:

$\boldsymbol{X_k}$ = the state time k to time k-1, A= transition matrix, $\boldsymbol{W_{k-1}}$ = N noise of Gaussian process.

2. Equation of Measurement

$$Z_k = H_{Xk} + v_k \quad (3)$$

Where:

H = measurement matrix, $\boldsymbol{Z_k}$ = observed measured at time k-1 to k, $\boldsymbol{v_k}$ = N noise of Gaussian measurement.

3. Time Update Equation

$$\hat{x}_{\bar{k}} = A\hat{x}_{k-1} + w_k \quad (4)$$

Where:

$\hat{\boldsymbol{x}}_{\bar{\boldsymbol{k}}}$ = A prior estimate of state(s), $\widehat{\boldsymbol{X}}_{\boldsymbol{k}}$ = covariance error estimate for the next step of time k, A= transition matrix, $\boldsymbol{W_k}$ = N noise of Gaussian process.

4. Update Measurement Equations

$$K_k = p_{\bar{k}} H^T (HP_{\bar{k}} H^T + R)^{-1} \quad (5)$$

Where:

Kk = is the Kalman growth (gain), Pk = a posterior error estimate

3. The Proposed System

Many distributed multi-media were become an integral parts of the network environment. Inorder to get this target, the multimedia files should deliver with highest Quality of Services (QoS). The challenges in the multimedia distribution are networks errors and noise in the data

traffic, also data transmission mechainizem between power station of the electrical grid. In the power grid in Iraq, either PLC (power line carrier) used to send data over the lines power phase and the multiplexer (MUX with pilot cable, microwave, fiber optic) also used to send data separately from the transmission power lines with some problems in the network QoS.

The main goal of the proposed system is to improvement the data transfer in the wireless network connected the power stations in Iraqi Electrical Grid. The improvement operation cab done by use the intelligent technique to solve many problems described above by optimization data transfer over the electricity grid. The selection of the Microwave channel due to the limitation of PLC (power line carrier), and because the grid power have many substation uses Microwave network(with 2Mbps bit rate) behind the old (PLC) that has limited capacity channel (64 kbps).

In this research, we proposed the Fuzzy Logic control rules used for adaptive the Microwave network QoS in order to distributed multi-media (lik data parameters, speech phone calls,images, and webcmera videos) and control the transmission in Iraq power grid to improvement the data transmission operation. This goal can be done through calculate the error rate(caused by noises) and estimate the next error rate in the network channel. Depending on the error rates, the best fuzzy rules can apply to take adjust the compression techniques with compression ratio and the number of the multimedia can be send as subchannels transfer(and number of delayed multimedia stored in delayed buffers).

In this s proposed system, the error estimation stage checks the current error rate (like noise ratio) and estimate the error rate in the next period by using four different techniques (Modified Kalman Filter MKF, and LMS) by using the automatic packet generation technique to generated and send testing packets to all active nodes in the network. Estimation vector will be used in the proposed Fuzzy controls commuincation stage.Many compression technques were used like (Lossless and losy)JPEG image compression, Pulse Code Modulation PCM (with different quantization bit levels) for speech compression, and H.264/AVC for web camera videos. There are different compression and quailites degres are used depending on the decision of the proposed Fuzzy control stage.The proposed system was designed to be fasting in the implementation by use the modren algorithms and reduction these algorithms as possible. Figure 2 shows the flowchart of the proposed system.

The proposed system can divide into four stages:

Network stage: in this stage the network paramters, nodes number, sending and receiving test packets are illstrated.

Error Estimator Stage: the error calculated and estimated for the next time periods using the modified kalman filter, Kalman filter, and LMS estimators.

Fuzzy Control Stage: The outputs of the estimators are input to the Fuzzy rule control to adjusted the priorities and compression ratio and types.

Send Media Stage: in this stage, the media sending after applying the fuzzy control rules on the buffered media like speech, web camera video, images, and controlling power station parameters through the subchannels. The sending operation is based on the TCP/IP protocol.

a. 3.1 Proposed Modified Kalman Filter

The first modification is to the Kalman filter in order to make this filter more effective for estimation the error rate, the modification by adding the previous mean noise ratio and the previous covariance of the observation noise at a time.

MKF is not only effective practically but attractive theoretically as well accurately, the optimal states are found with smallest's possible factual errors, recursively. However, there are four phases for describe MKF mathematically as follows:

1. Proposed Modified Equation of process

$$X_k = A_{Xk-1} + (W_{k-1} + MPNR)/2 \quad (1)$$

Where:

$\boldsymbol{X_k}$ = the state time k to time k-1.

A= transition matrix.

$\boldsymbol{W_{k-1}}$ = noise of Gaussian process.

MPNR= The mean of previous noise ratio during the total last time period.

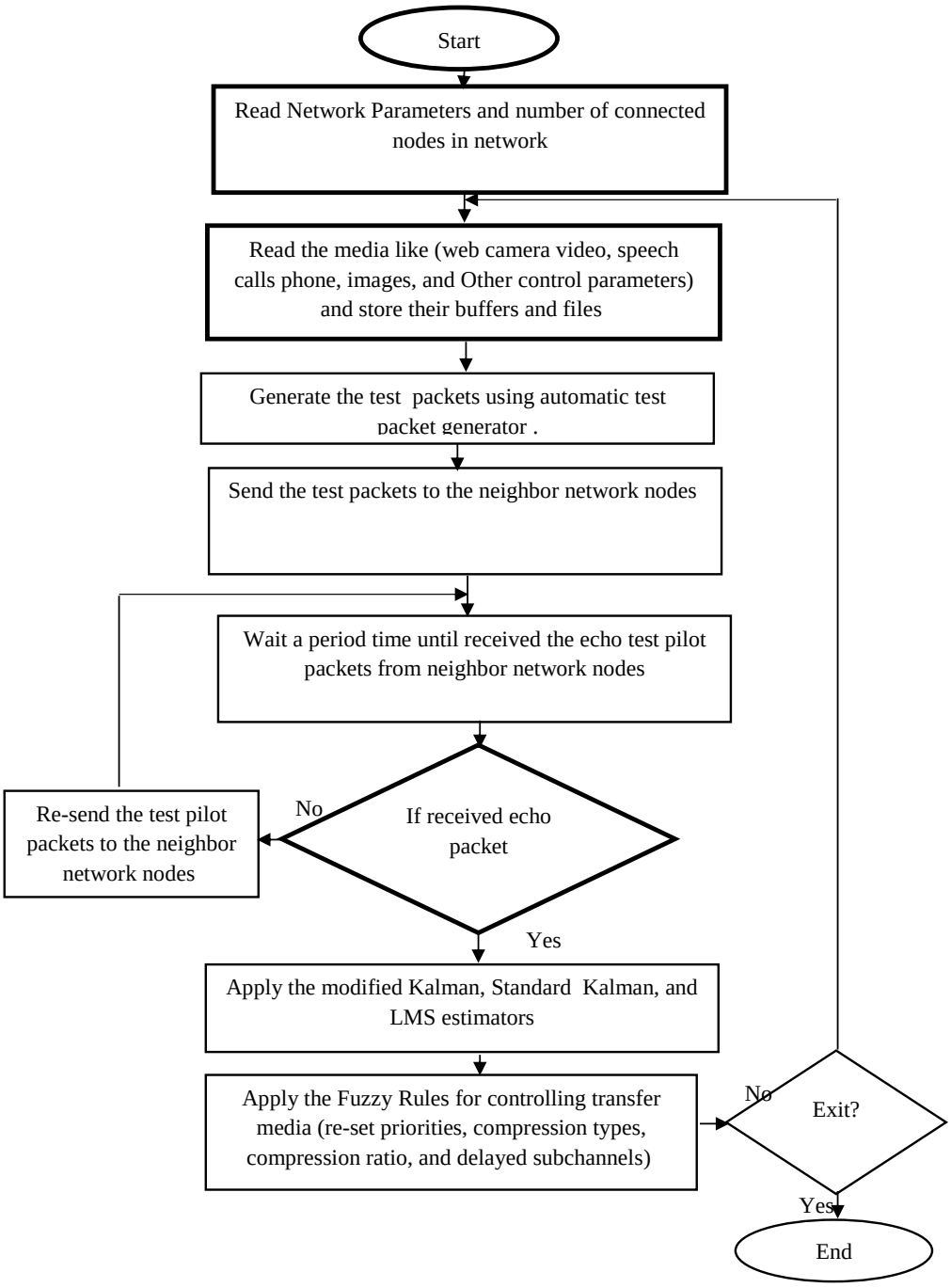

Figure 2. The Flowchart of the proposed system.

2. Proposed Modified Equation of measurement

$$Z_k = H_{Xk} + (v_k + MPNR)/2 \quad (2)$$

Where:
H = measurement matrix.
$\boldsymbol{Z_k}$ = observed measured at time k-1 to k.
$\boldsymbol{v_k}$ = noise of Gaussian measurement.

3. Proposed Modified Time Update Equation

$$\hat{x}_{\bar{k}} = A\hat{x}_{k-1} + (2 * W_k + MPNR)/3 \quad (3)$$

Where:
$\widehat{\boldsymbol{x}}_{\bar{\boldsymbol{k}}}$ = A priori estimate of state.
$\widehat{\boldsymbol{X}}_{\boldsymbol{k}}$ = covariance error estimate for the next time step k.
A= transition matrix.
$\boldsymbol{W_k}$ = noise of Gaussian process.

4. Proposed Modified Equations of measurement update

$$K_k = p_{\bar{k}} H^T (HP_{\bar{k}} H^T + (2R_k + R_{k-1})/3)^{-1} \quad (4)$$

Where:
$\mathbf{K_k}$ = is the Kalman growth (gain).
$\mathbf{P_k}$ = a posterior error estimate.
R= the covariance of the observation noise at a time.

The mechanism of MKF Algorithm clarified as shown in 'figure (3)'. In order to understand the common MKF better. There are three main calculating according to the four main equations that need to be done frequently. **First** one in calculating the Modified Kalman Gain (MKG) to make the estimate zooming into the actual correct value, so we need to calculate each time this MKG. Then its need to calculate the current estimate each time are going to update the estimate. Finally, it is important to re-calculate the new error (the uncertainty) in the estimate. From the figure, it is clear that it is need two things know for calculate the MKG, first one is the error in the estimation (the mean previous error or the original error), and later is the error in the data input, both of these feed into the calculation come up. Secondly, the MKG feeds into the calculation of the current estimate depending upon what the gain is the adjustment to the mean previous estimate that come up with a new estimate of the gain, beside of the gain it is depending upon the mean and previous estimate and with the next iteration the new data comes in. Then it has been used to re-calculate the new estimate, so that it is always feedback in on itself that mean it is need the mean previous estimated that calculated before but if it is the first time it need to take the original estimate. Finally, when the calculation in one and two has been done, then calculation for the error estimation can be achieved for the next time around.

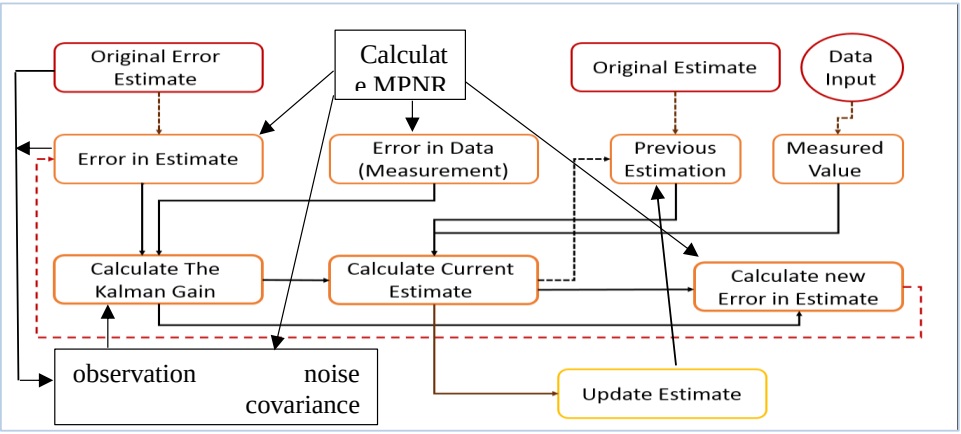

Figure 3. Block diagram of The Proposed Modified Kalman Filter for Estimation

The Fuzzy Control Stage

Fuzzy Control Stage contain the main operation of the controlling the sequence of the transfer media. The outputs of the error estimation stage is a Error Estimation Ratios (EER) Vector passed as input to the Fuzzy rule control stage to adjusted the priorities, compression ratio, compression types, and Sequence of the media.Also the Mean Perivious Noise Ratios (MPNR) will compute from the pervios noise or error estimated for the channel during the work duration.

The average of EER vector(without Mean Perivious Noise Ratios MPNR) will used as the final error estimation value called Mean Final Error ratio (MFER) and compare it with the MPNR, if the MPNR greater than with high difference , then MFER as estimate ratio, if the MPNR close or near the MFER then MFER= (MFER+ MPNR)/2. From this ratio, the proposed system selects the appropriate fuzzy rule to control the sending operation.

The proposed Fuzzy rules are as following(where no. of media in buffers(MB), Initial no. of subchannels (IM), and Compression ratio CR):

Rule 0: if the MPNR greater than with high difference , then MFER as estimate ratio, if the MPNR close or near the MFER then MFER= (MFER+ MPNR)/2.

Rule 1: If (MFER≤5% of the channel capacity) and (MB≤IM) then: No compression, CR=0, no change the priority and sequence of media in transmission buffers, no delay.

Rule 2: If (%5<MFER≤15% from the channel capacity) and (MB≤IM) then: Lossless compression, CR=15%, no change the priority and sequence of media in transmission buffers.

Rule 3: If (%5<MFER≤15% from the channel capacity) and (MB>IM) then: Lossless compression, CR=15%, change the priority and sequence of media in transmission buffers (speech, Parameters, control data, images, and the less priority videos), no delay needed in videos subchannels.

Rule 4: If (%15<MFER≤25% from the channel capacity) and (MB≤IM) then: Lossy compression, CR=15%, change the priority and sequence of media in transmission buffers (speech, Parameters, control data, images, and the less priority videos), and need to delay in last two videos subchannel.

Rule 5: If (%15<MFER≤25% from the channel capacity) and (MB>IM) then: Lossy compression, CR=25%, change the priority and sequence of media in transmission (speech, Parameters, control data, images, and the less priority videos), and need to delay in last three videos subchannel.

Rule 6: If (%25<MFER≤35% from the channel capacity) and (MB≤IM) then: Lossy compression, CR=40%, change the priority and sequence of media in transmission

buffers (speech, Parameters, control data, images, and the less priority videos), and need to delay in last three videos subchannel.

Rule 7: If (%25<MFER≤35% from the channel capacity) and (MB>IM) then: Lossy compression, CR=50%, change the priority and sequence of media in transmission buffers (speech, Parameters, control data, images, and the less priority videos), and need to delay in last five videos subchannel.

Rule 8: If (%35<MFER≤45% from the channel capacity) and (MB≤IM) then: Lossy compression, CR=50%, change the priority and sequence of media in transmission buffers (speech, Parameters, control data, images, and the less priority videos), and need to delay in last four videos subchannel.

Rule 9: If (%35<MFER≤45% from the channel capacity) and (MB>IM) then: Lossy compression, CR=60%, change the priority and sequence of media in transmission buffers (speech, Parameters, control data, images, and the less priority videos), and need to delay in last six videos subchannel.

Rule 10: If (%45<MFER≤60% from the channel capacity) and (MB≤IM) then: Lossy compression, CR=70%, change the priority and sequence of media in transmission buffers (speech, Parameters, control data, images, and the less priority videos), and need to delay in last seven videos subchannel.

Rule 11: If (%45<MFER≤60% from the channel capacity) and (MB>IM) then: Lossy compression, CR=75%, change the priority and sequence of media in transmission buffers (speech, Parameters, control data, images, and the less priority videos), and need to delay in last eight videos subchannel.

Rule 12: If (%60<MFER≤65% from the channel capacity) and (MB≤IM) thenLossy compression, CR=75%, change the priority and sequence of media in transmission buffers (speech, Parameters, control data, images, and the no videos), and need to delay in last three speech and seven images subchannel.

Rule 13: If (%60<MFER≤65% from the channel capacity) and (MB>IM) then: Lossy compression, CR=75%, change the priority and sequence of media in transmission buffers (speech, Parameters, control data, and no images and videos), and need to delay in last four speech subchannel.

Rule 14: - If (%65<MFER≤85% from the channel capacity) and (MB≤IM) then: Lossy compression, CR=75%, change the priority and sequence of media in transmission buffers (speech, Parameters, control data, and the no images videos), and need to delay in last seven speech subchannel.

Rule 15: If (%65<MFER≤85% of the channel capacity) and (MB>IM) then: Lossy compression, CR=75%, change the priority and sequence of media in transmission buffers (speech, Parameters, control data, and no images and videos), and need to delay in last eight speech videos subchannel.

Rule 16: If (MFER>85% of the channel capacity) then the channel very noisy and no valid to transfer data.

Rule 17: The comparison error rate used in the rules (1-16) can be change depend on the other parameters (like the Air temperature, Rain, Light day and night, station location (Urban areas), and frequencies of the main channel). This update rules.

As shown above, the fuzzy rules proposed to use in this stage covered the noise ratio from the 5% to 85%, and choose the rule and their actions depend on these MFER. The priority is very important to make the re-sequence the media in the transfer buffer more effective in sending the important data then others. The compression type and ratio hep in avoid the noises interference by reduced the size of data with keeping the most details as possible. The reduction of data transfer in the channel useful in reduction the noise infection and sending time. The error ratio (noise) can be change during year and locations of the power stations.

4. Results and Discussion

The results from the implementation proposed system in the simulatiom enironments were show the improvement in the increasing number of sending media (subchannels) by at least 3 times, and reduction (with 30-90%) in the losing packet through connection operation for all different

error ratios. Time of the all operations in the proposed system was acceptal and can be consider fasting with average (1-3) second. Also, the modified Kalman Filter estimator has best results of error estimation from the other used estiomators.Also, the modified Kalman filter are more speed from it(with superior from th LMS). Figures (4-7) show the results of the proposed syste. Also, the tables(1-2) show the results of the estimation stage.

Figure 4.The Results of the Sending-Receiving Test Packets

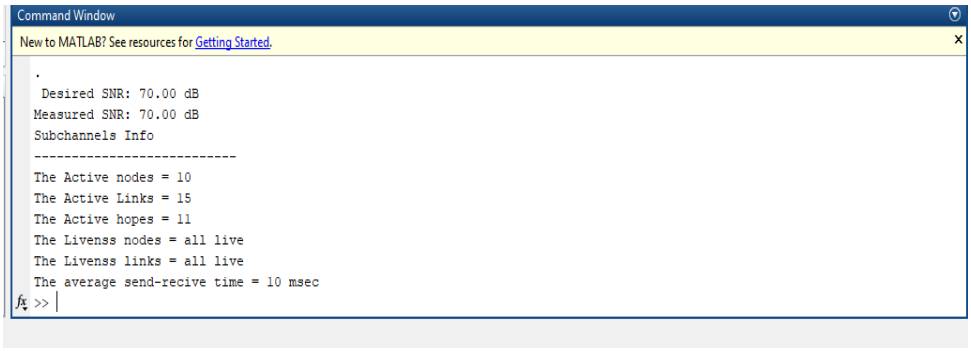

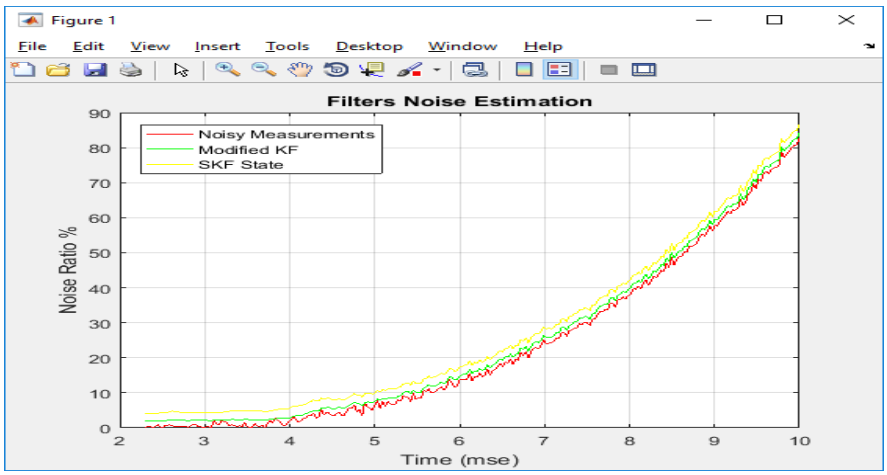

Figure 5 .The Modified Kalman and Standard Kalman Filter Results

This figure shows the results of error estimation by modified Kalman filter (green line) for different types of noise through the time is near to the actual error rate, while the Standard Kalman filter(SKF) (yellow line) has some different from the actual error rate measured.

Table 1. MKF and SKF estimator results

Actual noise ratio	MKF estimation	Time (MKF) sec	SKF estimation	Time (SKF) sec	LMS estimation	Time (LMS) sec
5%	5.011%	0.1109	5.123%	0.1613	6.234%	0.2390
10%	10.041%	0.1278	11.511%	0.1655	12.526%	0.2598
15%	15.102%	0.1341	17.774%	0.1660	17.390%	0.2786
25%	25.109%	0.1398	27.451%	0.1742	28.451%	0.2999
35%	35.197%	0.2109	37.799%	0.2134	38.563%	0.3213
45%	45.412%	0.2231	48.123%	0.2309	48.382%	0.3214
60%	61.345%	0.2786	63.569%	0.2817	64.512%	0.3322
65%	66.209%	0.2823	67.820%	0.2956	67.425%	0.3390
75%	76.561%	0.2851	78.123%	0.3017	79.123%	0.3403
85%	86.341%	0.3109	88.407%	0.3280	88.567%	0.3439
90%	91.890%	0.3211	93.980%	0.3301	94.326%	0.3560

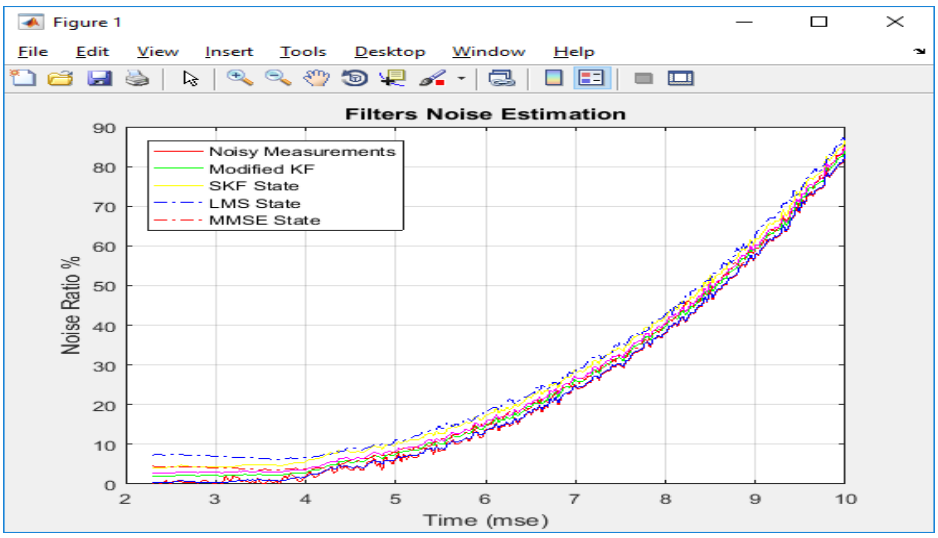

Figure 6. The MMSE, LMS, SKF, and MKF results

As shown in the table (1), the MFK is more accuracy from the SKF and LMS estimator in all ratio of noise. But the time of the SKF is less than operation time in a few msec.

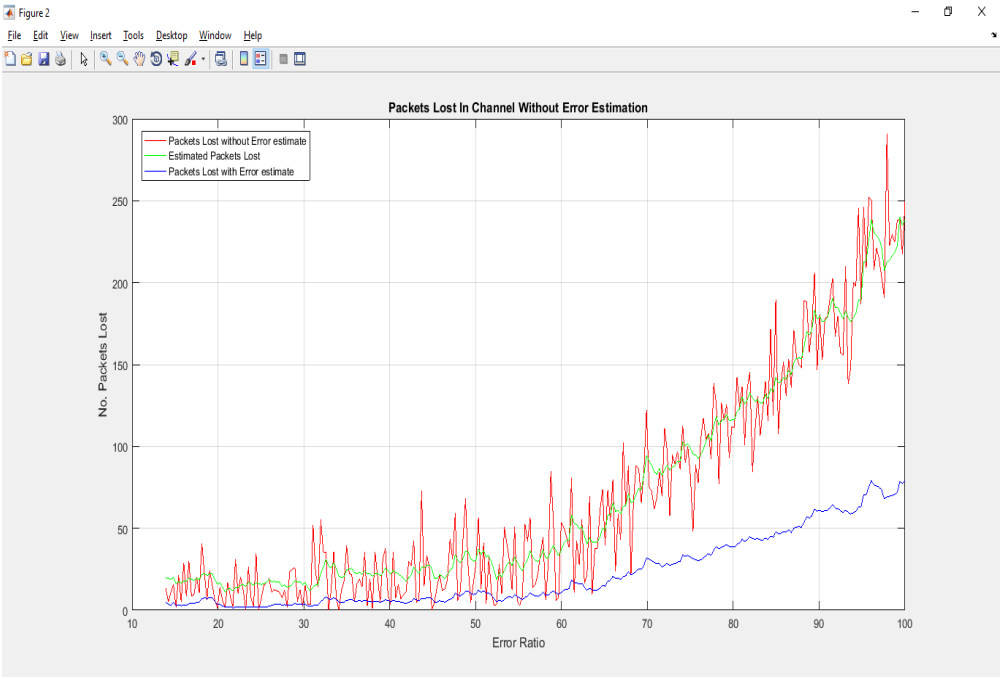

Figure 7. The Comparison Results of testing the network using test packets.
As shown in figure 7, the packets loss rate is reduced with ratio from (35% to 385%)after using the proposed system.

5. Conclusions

In this research, the error estimation filters were used to checks the current error rate in channel communication for the Iraqi Electrical Grids (likes noise ratio) and to estimates the error rate

for the next periods by using the combination of the three different techniques (MKF, SKF, LMS) for the Microwave channel.

Fuzzy rules are used to selects the transformation conditions and parameters for the current environment and estimations noise rates. As shown from the above results, the error(noise) estimation output level will improve and adjusts the data transfer in the noisy channel by help in selection the no. of subchannels, compression ratio, compression type, and the specific delay transfer time for the lowest priority media subchannels passed to the Microwave channel of Iraqi Electrical Grid. The proposed system implements in the simulation environment to test its operation and techniques and get the packet loss rate with (35% to 385%) depends on the noise ratio levels.

Reference

[1] M. Reda, N. Saied, A. Khaldi, M.A.Abdul-Hussain, and A. Ekwue," Iraq Electrical Power Infrastructure – Past, Present and Future Developments and Expectations", Power Systems Conference and Exposition, 2006. PSCE '06. 2006 IEEE PES.

[2] Saif Rashid, Irene Peters, Martin Wickel, and Christoph Magazowski "Electricity Problem in Iraq" , Economics and Planning of Technical Urban Infrastructure Systems, March 18 2012.

[3]Impact of UPFC-based damping controller on dynamic stability of Iraqi power network Lokman H. Hassan1*, M. Moghavvemi1 and Haider A. F. Mohamed2 1Centre for Research in Applied Electronics (CRAE), University of Malaya, 50603 Kuala Lumpur, Malaysia.2Department of Electrical and Electronic Engineering, University of Nottingham Malaysia Campus, 43500 Semenyih, Selangorr, Malaysia. Accepted 25 November, 2010

[4] Mohammed Hammed Yasen ,"Analyse the Problems of the Iraqi Power System", Advances in Energy Engineering, Volume 4, 2016 , doi: 10.14355/aee.2016.04.003.

[5] Pirmez L., Delicato F.C., Pires P.F., Mostardinha A.L., de Rezende N.S., "Applying fuzzy logic for decision-making on Wireless Sensor Networks", IEEE International Symposium on Fuzzy Systems Conference, pp. 1–6 (2007).

[6] Feng Xia, Wenhong Zhao, Youxian Sun, and Yu-Chu Tian1, " Fuzzy Logic Control Based QoS Management in Wireless Sensor/Actuator Networks", Sensors (Basel). 2007 Dec; 7(12): 3179–3191 PMCID: PMC3841889.

[7] Chrysostomos Chrysostomou and Andreas Pitsillides, " Fuzzy Logic Control in Communication Networks ", Hassanien AE., Abraham A., Herrera F. (eds) Foundations of Computational Intelligence Volume 2. Studies in Computational Intelligence, vol 202. Springer, Berlin, Heidelberg.ISBN: 978-3-642-01532-8.

[8] Qiu Gongan , Zhang Shunyi , and Liu Shidong , " Service-aware based fuzzy admission control scheme in multi-service networks", Journal of Electronics (China) July 2007, Volume 24, Issue 4, pp 537–543, Science Press.

[9] Muhammad Mostafa Monowar, Md. Obaidur Rahman, Byung Goo Choi, and Choong Seon Hong, "A Hop by Hop Rate Control Based QoS Management for Real Time Traffic in Wireless Sensor Networks", Ma Y., Choi D., Ata S. (eds) Challenges for Next Generation Network Operations and Service Management. APNOMS 2008. Lecture Notes in Computer Science, vol 5297. Springer, Berlin.

[10] Koliver C., Farines JM., Nahrstedt K., "QoS Adaptation Based on Fuzzy Theory". Soft Computing in Communications. Studies in Fuzziness and Soft Computing, vol. 136(2004). Springer, Berlin, Heidelberg

[11] Ghulam Abbas ; Atulya K. Nagar ; Hissam Tawfik ; J.Y. Goulermas, "A state estimation based framework for control and management of data communication networks", IEEE Distributed Framework and Applications, 2008. DOI: 10.1109/ICDFMA.2008.4784436.

[12] Yasser Sadri and Sohrab Khanmohammadi, "A QoS Aware Dynamic Scheduling Scheme Using Fuzzy Inference System for IEEE 802.16 Networks", Wireless Personal Communications, October 2013, Volume 72, Issue 4, pp 2107–2125, Springer US.

[13] Taki M., Heshmati M., and Omid Y.," Fuzzy-Based Optimized QoS-Constrained Resource Allocation in a Heterogeneous Wireless Network", International Journal of Fuzzy Systems", December 2016, Volume 18, Issue 6, pp 1131–1140, 18: 1131. https://doi.org/10.1007/s40815-016-"0152-6, Springer Berlin Heidelberg.
[14] Abbas Ali Rezaee and Faezeh Pasandideh, " A Fuzzy Congestion Control Protocol Based on Active Queue Management in Wireless Sensor Networks with Medical Applications",Wireless Personal Communications pp 1–28, 21 August 2017. Springer US.
[15] Tirthankar Paul, PriyabratabKarmarkar, SauravDhar,"Comparative study ofchannel estimation algorithms under different channel scenario", International journal of computer application(0975-8887), vol. 34. No. 7, November 2011.
[16] Mohammad NaserFawwazKhasawneh,"Comparison study for Multi- user MIMO channel estimation techniques",August 2009, Jordan University of science and Technology.
[17] Gauri S. Godbole, Shailaja Gaikwad," Comparative Study of Channel Estimation Techniques", 2016 IJEDR | Volume 4, Issue 4 | ISSN: 2321-9939

[18] Ishihara, J.Y.; Terra, M.H.; Campos, J.C.T. (2006). "Robust Kalman Filter for Descriptor Systems". IEEE Transactions on Automatic Control. 51 (8): 1354. doi:10.1109/TAC.2006.878741.
[19] Terra, Marco H.; Cerri, Joao P.; Ishihara, Joao Y. (2014). "Optimal Robust Linear Quadratic Regulator for Systems Subject to Uncertainties". IEEE Transactions on Automatic Control. 59 (9): 2586–2591. doi:10.1109/TAC.2014.2309282.
[20] Simon Fabri, Visakan Kadirkamanathan,"Functional Adaptive Control: An Intelligent Systems Approach", Springer Science & Business Media, Dec 6, 2012.
[21] Brijesh Kumar Patel and Jatin Agarwal," Comparative Study of Bit Error Rate with Channel Estimation in OFDM System for M-ary Different Modulation Techniques", International Journal of Computer Applications (0975 – 8887) Volume 95– No.8, June 2014.

Information Hiding In Digital Video Using DCT, DWT and CvT

Information Hiding In Digital Video Using DCT, DWT and CvT

Wisam Abed Shukur[1], Wathiq Najah Abdullah[2], Luheb Kareem Qurban[3]
[1] University Of Baghdad, College of Education For Pure Sciences/Ibn Al-Haitham Computer Science Dept., Iraq
[2] University Of Baghdad, College of Education For Pure Sciences/Ibn Al-Haitham, Computer Science Dept., Iraq.
[3] University Of Baghdad, College of Education For Pure Sciences/Ibn Al-Haitham, Computer Science Dept., Iraq.
[1]wisam_shukur@yahoo.com, wisam.a.s@ihcoedu.uobaghdad.edu.iq
[2]wathiq79@gmail.com
[3] Laheeb.k.k@ ihcoedu.uobaghdad.edu.iq

ABSTRACT.The type of video that used in this proposed hiding a secret information technique is .AVI; the proposed technique of a data hiding to embed a secret information into video frames by using Discrete Cosine Transform (DCT), Discrete Wavelet Transform (DWT) and Curvelet Transform (CvT). An individual pixel consists of three color components (RGB), the secret information is embedded in Red (R) color channel. On the receiver side, the secret information is extracted from received video. After extracting secret information, robustness of proposed hiding a secret information technique is measured and obtained by computing the degradation of the extracted secret information by comparing it with the original secret information via calculating the Normalized cross Correlation (NC). The experiments shows the error ratio of the proposed technique is (8%) while accuracy ratio is (92%) when the Curvelet Transform (CvT) is used, but compared with Discrete Wavelet Transform (DWT) and Discrete Cosine Transform (DCT), the error rates are 11% and 14% respectively, while the accuracy ratios are (89%) and (86%) respectively. So, the experiments shows the Poisson noise gives better results than other types of noises, while the speckle noise gives worst results compared with other types

of noises. The proposed technique has been established by using MATLAB R2016a programming language.

Keywords: Steganography, DWT, DCT, CvT and Noise.

1. INTODUCTION. The most important concept in any communication process between sender and receiver via the transmission channel is security. Using the advance technology and the world wide web to exchange information leads to increase the challenges and risks. However, the management of challenges and risks is possible with using an advanced technologies of secure networks but these technologies are not enough for information security over communication between sender and receiver. Therefore, an additional mechanisms of security are needed to secure information. [1], an origin of steganography word is Greek, steganography means "covered writing" or "concealed writing"[2]. The main difference between steganography and cryptography is keeping the existence of a message secret. The shared goal of steganography and cryptography is information protecting against malicious or unwanted persons or parties [3]. Steganography is one of the promising technologies helping to achieve the overall goal of secure delivery of information from its source to the authorized end-users. Steganography is the art or practice of concealing a file, image, or message within another a file, image, or message. The word steganography means "covered writing" or "concealed writing"[4]. Steganography is changing the digital media in a way that only the sender and the intended recipient is able to detect the message sent through it. On the other side steganalysis is the science of detecting hidden message [5].

2. STEGANOGHRAPHY. Steganography is changing the digital media in a way that only the sender and the intended recipient is able to detect the message sent through it. The following formula provides a very generic description of the pieces of the steganographic process: cover_medium + hidden data + stego_key = stego_medium[6]. An embedding algorithm embeds a secret information in a host video, the hiding process is performed with selected private or secret key to increase the complexity of hiding process. The general model of steganography is shown in figure (1). After embedding process, transmitting a stego- video to the receiver via transmission medium or communication channel is performed. The receiver extracts a hidden information which embedded using embedding technique by the sender from received stego- video with using same or another key according to type of steganography that selected initially. The receiver will apply an extraction technique on stego-video for that purpose. Via transmitting a stego- video from the sender to the receiver, there are many unauthorized persons or parties that notice a stego- video but without extracting the hidden contents of a stego- video [7]. The embedding techniques are selected according to type of domain, the types of embedding domains are spatial and frequency domains. The types of host or cover are text, audio, image and video[8]. The frequency domain is used in this work. The frequency domain is obtained via applying many transforms such as DCT, DWT and CvT on video. The embedding algorithm is different for each one of them according to nature of its frequency domain. Video Steganography is a technique to hide any kind of files in any extension or information into digital video format. Video which is the combination of pictures is used as carrier for hidden information. Video steganography uses video formats such as H.264, Mp4, MPEG, AVI, etc.[9]

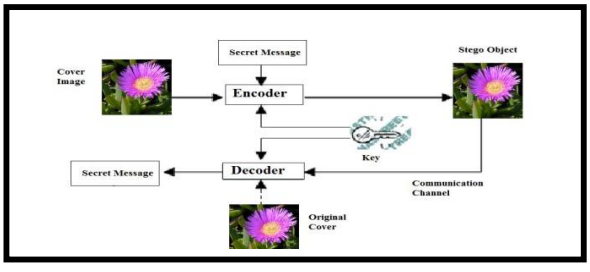

Figure 1. Basic steganography model.

3**. RELATED WORK.**Ramadhan J. [10] proposes a secure and robust video steganographic algorithm in discrete wavelet transform (DWT) and discrete cosine transform (DCT) domains based on the multiple object tracking

(MOT) algorithm and error correcting codes. By applying both Hamming and Bose, the secret message is preprocessed Chaudhuri, and Hocquenghem codes for encoding the secret data. First, motion-based MOT algorithm is implemented on host videos to distinguish the regions of interest in the moving objects. Then, the data hiding process is performed by concealing the secret message into the DWT and DCT coefficients of all motion regions in the video depending on foreground masks. Chang et al. [11] presented a data concealing algorithm using a High Efficiency Video Coding (HEVC) utilizing both DCT and Discrete Sine Transform (DST) methods. In this scheme, HEVC intra frames are used to conceal the hidden message without propagating the error of the distortion drift to the adjacent blocks. Blocks of quantized DCT (QDCT) and DST coefficients are selected for embedding the secret data by using a specific intra prediction mode. Ma et al. [12] presented a video data hiding for H.264 coding without having an error accumulation in the intra video frames. In the intra frame coding, the current block predicts its data from the encoded adjacent blocks, specifically from the boundary pixels of upper and left blocks. Thus, any embedding process that occurs in these blocks will propagate the distortion, negatively, to the current block, To select 4 × 4 QDCT coefficients of the luminance component for data embedding. Shahid et al. [13] This method embeds the secret message into the LSB of QDCT coefficients. Only nonzero QDCT coefficients are chosen for data hiding process, utilizing the predefined threshold, which directly depends on the size of secret information. What related to information hiding in digital video by using curvelet transform CvT, there is no researches related to this work.

4. The TECHNIQUE MODEL. The general structure of the proposed video hiding technique is shown in figure 2. It consists of many basic stages for all techniques of transformation (DCT , DWT and CvT) that are initialization stage, framing stage, preprocessing stage, transformation stage, embedding stage, inverse transformation stage and compression stage. All these stages are placed on sender side, after that the embedded video will be sent via communication channel and it exposes to four types of noise during the transmission in that channel of communication in simulation environment. But the stages that are placed on receiver side are decompression stage, post-framing stage, post-transformation stage, extraction stage and result evaluation stage. All those stages are shared and used for each type of transformation techniques (DCT , DWT and CvT). Some stages are same between DCT and DWT.

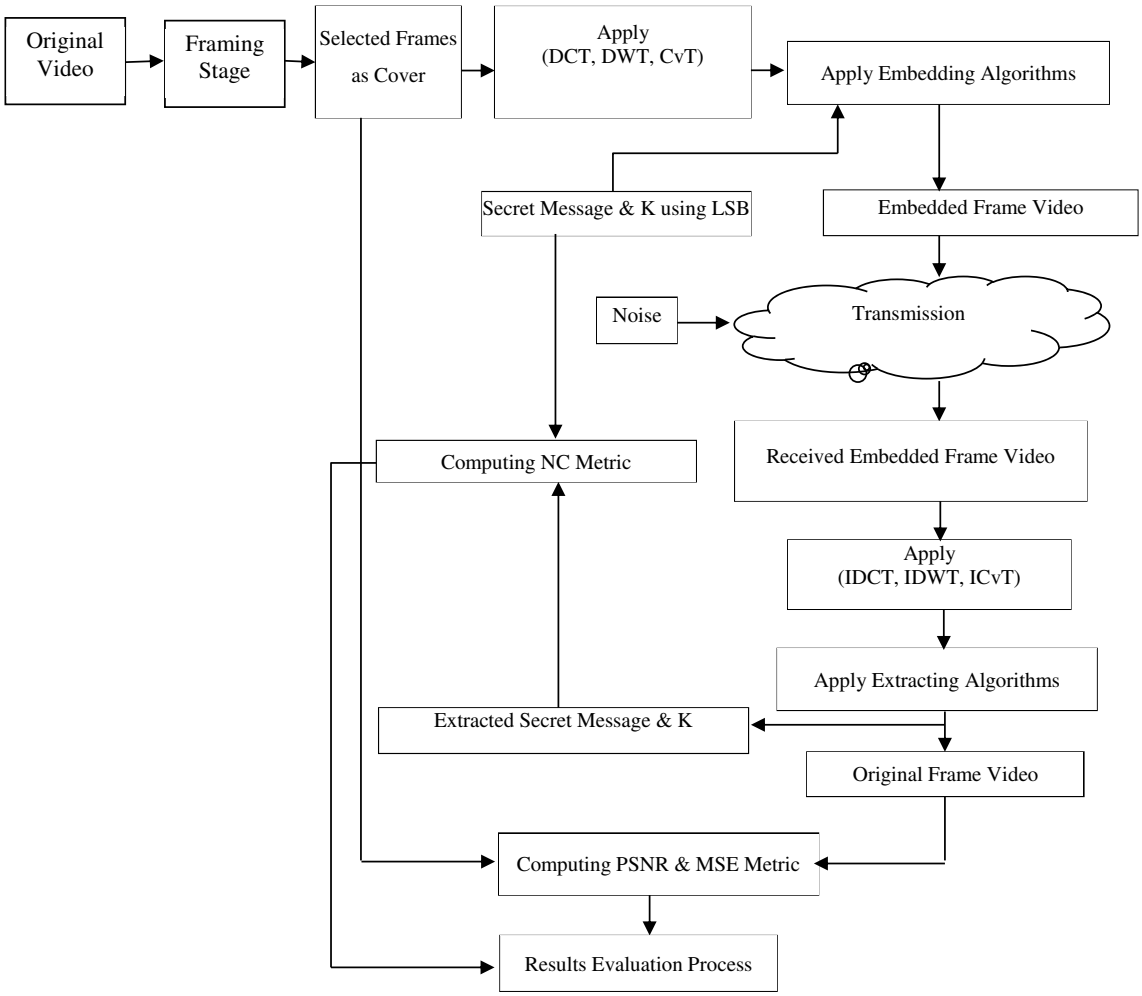

Figure 2: The general block diagram of the proposed technique.

4.1 HIDING PROCESS BY DCT & DWT

The embedding process in the DWT and DCT is the same, but there is just one difference between them. That difference is size of block in dividing phase of embedding stage; the size of block after dividing the frame into blocks is 4x4 in the DWT, while the size of block in the DCT is 8x8. The embedding stage of the DWT and DCT contains three phases, they are converting phase, dividing phase and hiding phase.

A. Converting Phase

In this phase, the sub secret information that is a string is converted into binary, and the total number of bits at each sub secret information is calculated. For example, if the required number for the secret information is equal to 1000 character, then each character of them can be represented in 7 bits because the text was written in english language.

B. Dividing Phase

This phase acts the difference point between the DWT and the DCT. In DWT case, the size of frame is 256x256 because of the resizing phase that is explained in framing stage previously, therefore, the transformed frame by DWT is divided into four sub bands, each block has size 4x4 to produce the enough area as cover for embedding the secret

information because the number of levels used is one. While in DCT case, the transformed frame is divided into sub blocks, each block has size of 8x8, since the resized frame has size of 256x256.

C. Hiding Phase

The hiding phase is the same for DCT and DWT, in the embedding phase, hides the bits of secret information in a chosen area in the frequency domain media of both, and then applies uniform quantization. The embedded process of secret information is in color video frames, where embedding the watermark is considered. The frame (F) is partitioned into blocks of 8x8 in DCT case and into 4x4 in DWT case where the secret information is embedded in the coefficients for DCT and DWT to get on embedded frame. The embedded binary secret information must be invisible to human eyes. Each binary secret information pixel value (0 or 1) is embedded in one block of the host frame of DCT and DWT. The secret information bits are to be hidden in the middle and high frequencies region of DCT, while in the DWT, the secret information bits are to be hidden in the high frequencies region. Since resizing phase each frame will be resized into 256x256, when the DWT is used, then each sub band of DWT has size 128x128. Therefore, the DWT domain will divide into blocks, each one of them has size 4x4. While the DCT is used, the size of the DCT domain is 256x256; therefore, the DCT domain will divide into blocks, each one of them has size 8x8. Each 4x4 and 8x8 blocks for DWT and DCT of a frame (F) is used to hide a single bit of secret information (S). The hiding of "1" or "0" is by using quantization function or directly without quantization to get on extracted secret information well in the coefficients; the inputs of the embedding algorithm are video frame (F) and the secret information (S), while the output of this algorithm is embedded frame. Algorithm 1 shows the embedding process of secret information in the DCT coefficients and Algorithm 2 shows the embedding process of secret information in the DWT coefficients.

Algorithm 1: Secret Information Embedding with DCT

Input: X is video frame, S is secret information
Output: embedded frame
Repeat
Read X.
Read S.
Convert S into binary.
Reshape S into vector.
c=1
Repeat
Compute DCT of X.
Compute quantization (Q) of the DCT coefficient.
if s(c)=1 then
DCT (u_7, v_7) = Q (u_7, v_7) + M;
else DCT (u_7, v_7) = Q(u_7, v_7) - M;
c=c+1;
Until all blocks of frame
Compute IDCT to reconstruct X.
Until all frames of video

Algorithm 2: Secret Information Embedding with DWT

Input: X is video frame, S is secret information.
Output: embedded frame.
Repeat
Read X.
Read S.
Convert S into binary.
Reshape S into vector.
c=1
Repeat
Compute DWT of X.
Compute quantization (Q) of the DWT coefficient.
if s(c)=1 then
DWT (u_3, v_3) = Q (u_3, v_3) + M;
else DWT (u_3, v_3) = Q (u_3, v_3) - M;
c=c+1
Until all blocks of frame.
Compute IDWT to reconstruct X.
Until all frames of video

4.2 HIDING PROCESS BY CVT

The embedding stage of the CvT consists of four phases that are:
A. Specification Phase
This phase includes three major steps that are shown in the following:
Step1: specify the first sub cell or array {1x1} from the fifth master cell {1x5} as the cover that carries the secret information.
Step2: specify the prepared secret information via the preprocessing stage.
Step3: specify the value of alpha that helps in hiding phase to give accepted results.
B. Converting Phase
The nature of values for the first sub cell or array {1x1} from the fifth master cell {1x5} as the cover is real numbers, while the prepared secret information is as text. Therefore, the prepared secret information is split into an individual character and each one of them will be converted into its related value in ASCII code domain. This process produces the compatibility between the cover and the secret information to supply the flowing for the procedures of embedding process correctly.
C. Hiding Phase
In this phase, the selected prepared secret information will be embedded in the first sub cell or array {1x1} which has size of 131x44from the fifth master cell {1x5} of the transformed frames of loaded video via applying the equation of secret information embedding, algorithm 3 shows secret information embedding operation in detail. The embedding equation that is used in this phase is as described follows:
Cover-emb(i,j)=[1+α*W(i,j)]*cover(i,j)] where: α is the embedding factor whose value is 0.0001, S is secret information, Cover is an original coefficient and Cover-emb is an embedded coefficient.

Algorithm 3: Secret Information Embedding with CvT
Input: X is video frame, S is secret information.
Output: embedded frame (X').
Repeat
Select the prepared secret information.
Convert the prepared secret information into vector.
Dividing the prepared secret information into set of sub secret information equally
Determine the value of the embedding factor (alpha).
c=1 // number of selected frames of video
Apply CvT to X
Select the cell {1x5}{1x1} that has size of 131x44 as cover.
Convert the cell {1x5}{1x1} into vector.
For j=1 to number of sub secret information
For k=1 to length of sub secret information
Apply the equation:
cover-emb(j,k)=[1+α* S(j,k)]*cover(j,k)
End for k
c=c+1;
End for j
Apply ICvT to reconstruct X
Until all frames of video.

The purpose of quantization step is to embed and extract the secret information without original (No reference) video which may be the hiding of "1" or "0" is directly made without quantization to get a good extracted secret information in the coefficients, but in extract quantization should be found for comparison between the result of quantization for DWT or DCT coefficients with DWT or DCT coefficients before quantization process. The quantization equations are as shown below.

$$Q(m_3, n_3) = \text{round}\left(\frac{WT(m_3,n_3)}{3M}\right). (3M) \quad \ldots(1)$$

$$Q(u_7, v_7) = \text{round}\left(\frac{DCT(u_7,v_7)}{3M}\right). (3M) \quad \ldots (2)$$

where 3M represents quality step, Q (m_3, n_3) is the quantized DWT coefficients, DWT (m_3, n_3) is DWT coefficient values and Q (u_7, v_7) is the quantized DCT coefficients, DCT (u_7, v_7) is DCT coefficient values, M is the embedding secret information strength=1,2,3,4.
If quantization equation is used in embedding, then each secret information pixel W(j) equals 0 or 1is embedded in the block in order as follows:

DWT (m_3, n_3)=Q(m_3, n_3) +M if S(j)=1. … (3)
DWT (m_3, n_3)=Q(m_3, n_3) - M if S(j)=0. … (4)
DCT (u_7, v_7)=Q(u_7, v_7) +M if S(j)=1. … (5)
DCT(u_7, v_7)=Q(u_7, v_7)-M if S(j)=0. … (6)
for j = 1…..length of the secret information.

If the quantization is not used in the embedding process, then each secret information pixel S(j) that equals (0 or 1) is embedded in the block (m_3, n_3) when the DWT is used and in the block (u_7, v_7) when the DCT used in order as follows:

DWT(m_3, n_3)= DWT (m_3, n_3)+M if S(j) =1. … (7)
DWT (m_3, n_3) = DWT (m_3, n_3)- M if S(j)=0. … (8)
DCT (u_7, v_7) =DCT (u_7, v_7)+M if S(j) =1. … (9)
DCT (u_7, v_7) =DCT (u_7, v_7)-M if S(j)=0. … (10)

The inputs to the quantization algorithm are the original frame with N×N dimension, quantization step (QS) and quality factor (QF). The output of the quantization algorithm is quantized frame. Algorithm 4 shows the main steps of the quantization process that are used in the embedding stage for DWT and DCT as follows:

Algorithm 4: Scalar Quantization
Input: Original frame, Quantization Step (QS) and Quality Factor (QF).
Output: Quantized Image.
Repeat
Read Original frame.
Read QS and QF values.
for K1 = 1 to M
for K2 = 1 to M
for V = 1 to N
for U = 1 to N
Set Quantize[V, U] = (QS + (1 + V + U) × QF)
Original [K1+V, K2+U] =Round Original [K1+V, K2+U]/Quantize [V, U])
end loop U
end loop V
Increment loop K2 by N
Increment loop K1 by N
end loop K2
end loop K1
Until all frames of video.

4.3 Extraction Process of DWT and DCT

To extract the secret information from the embedded frame (F), apply the quantization step to DWT and DCT coefficients which is very necessary to compare to the result of quantization with DWT and DCT coefficients before quantization process, algorithm 5 shows the steps of secret information extraction process when the DCT is used and algorithm 6 shows the steps of secret information extraction process when the DWT is used.

Algorithm 5: Secret Information Extracting with DCT
Inputs: X' is embedded frame
Outputs: X' is degraded video frame, S' is degraded secret information.
Repeat
c=1
Repeat
Compute DCT of X'
Compute quantization(Q) of the DCT coefficient
Comparison the DCT coefficient with quantization result
if DCT (u_7, v_7) < Q(u_7, v_7) then
S'(c)=0;
else S'(c)=1;
c=c+1 continue…
Until all blocks of frame
Store S', the recovered secret information;

where Q (u_7, v_7) is the result of quantization, DCT (u_7, v_7) refers to the DCT coefficient values.

Algorithm 6: Secret Information Extracting with DWT
Inputs: X' is embedded frame.
Outputs: X' is degraded video frame, S' is degraded secret information.
Repeat
c=1
Repeat
Compute DWT of X'.
Compute quantization(Q) of the DWT coefficient.
Comparison the DWT coefficient with quantization result.
If DWT (u_3, v_3) < Q(u_3, v_3) then
S'(c)=0;
else S'(c)=1;
c=c+1
Until all blocks of frame.
Store S', the recovered secret information;

where Q (m_3, n_3) the result of quantization, DWT (m_3, n_3) refers to the DWT coefficient values, m is the embedding secret information strength=4 only. The embedding secret information strength takes the value (4) only, when secret information is extracted without distortion, if gives m the values 1, 2 and 3, then extract the secret information will be with distortion.

4.4 Extraction Process of CvT

In this process, to extract the secret information from embedded frame, algorithm 7 shows the steps of secret information extraction process when the CvT is used.

Algorithm 7: Secret Information Extracting with CvT
Inputs: X' is embedded frame
Outputs: X' is degraded video frame, S' is degraded secret information
Repeat
Determine the value of the embedding factor (alpha).
c=1 // number of embedded frames of received video
Apply CvT to embedded frame
Select the cell {1x5}{1x1}
reshape the cell {1x5}{1x1} into vector.
For j=1 to length of vector
Apply the equation:

$$W_{ext\,(j)}=\frac{1}{\alpha}\left[1-\frac{\mathbf{Cover-emb(j)}}{\mathbf{Cover(j)}}\right]$$

End for j
c=c+1;
Until all frames of received video

4.5 Evaluation Process

This process presents the last process of the work, the evaluation of the video steganography by using the DCT, DWT & CvT. Comparison of degraded secret information (S') with the original secret information (S) inserted, the metrics used to test the proposed technique are Normalized cross Correlation (NC) and Peak Signal to Noise Ratio (PSNR), After extracting the secret information, the NC is calculated to evaluate the effectiveness of the proposed technique. The NC is calculated between the original secret information S, and the extracted secret information S'. The hiding quality rating of the received media is estimated directly from the secret information

degradation. By depending on the value of NC that is calculated for all embedded frames of host videos, Algorithm 8 shows the calculation process.

Algorithm 8: Evaluation Process
Inputs:
- An original secret information S.
- Extracted secret information S'.

Outputs: metric results of video steganography.
Repeat
  Read an original secret information S.
  Read Extracted secret information S'.
    c=1
      Repeat
      Compute MSE for an original frame and degraded frame.
      Compute PSNR
      Compute NC for an original secret information S and degraded secret information S'.
      c=c+1
  Until all degraded frames
Store the values of NC, MSE and PSNR.
Analyzing obtained results.
Until all test videos.

4.6 Implementation Results

When the proposed technique for hiding a secret information in digital video is implemented, the digital video that used in this work has an extension .AVI. The distortion is introduced for degrading the frame because of the noise and compression process of video that are added. The evaluation process is performed via computing the following metrics NC, MSE and PSNR. The values of these metrics are calculated then evaluating the embedding process for each frame of host video. The degradation of the recovered secret information can be used as a measure of the robustness of proposed embedding algorithms in this work. The calculating of NC, MSE, and PSNR after extraction of the secret information from embedded frames of host video that are compressed and noised is shown in tables 1, 2 and 3 when the DCT, DWT and CvT are performed respectively without noise. the average values of extracted secret information with the original secret information with using compression are between (0.82 to 0.90) when the CvT is used, The NC value of frames depends on the nature of the frame that has colors. the average values of extracted secret information with the original secret information it is noted with using compression are between (0.83 to 0.75) when the DWT is used, and the average values of extracted secret information with the original secret information with using compression are between (0.77 to 0.69) when the DCT is used. All images before and after hiding with and without noise are illustrated in appendix A.

Table 1. The Metric values without noise with DCT.

Host Frames	NC	MSE	PSNR
F0	0.7167	93.3156	28.4312
F1	0.7456	88.2836	28.6720
F2	0.7057	94.8649	28.3597
F3	0.7345	91.1333	28.5340
F4	0.7156	94.3464	28.3835

Table 2. The Metric values without noise with DWT.

Host Frames	NC	MSE	PSNR
F0	0.7778	72.3266	29.5378
F1	0.8023	67.2746	29.8522
F2	0.7679	73.8499	29.4473
F3	0.7955	70.1213	29.6723
F4	0.7734	73.2456	29.4829

Table 3. The Metric values without noise with CvT.

Host Frames	NC	MSE	PSNR
F0	0.8478	58.2177	30.4802
F1	0.8700	53.1647	30.8745
F2	0.8368	59.7389	30.3682
F3	0.8644	56.0104	30.6481
F4	0.8423	59.1337	30.4124

4.6.1 Secret Information Extraction Time

The time consumption of the secret information extraction for each frame as cover of video is discussed here. Figure 3 shows the time of extraction for each frame in host video when the DCT, DWT and CvT, are used respectively, when DCT and DWT are used, the average time for each one of them is 0.86 second and 0.79 second respectively. The average time of extracted secret information without noise for set frames of host video when the CvT used is 0.66 second. The extraction time of secret information when the CvT used is less than extraction time of secret information when the DCT and DWT used. therefore, hiding a secret information by using CvT is more speed and efficient than other transforms such as DCT and DWT.

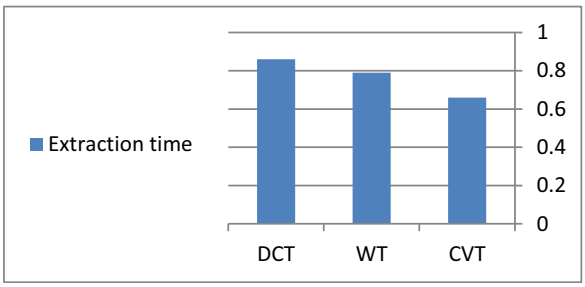

Figure 3. The Extraction Time for DCT, DWT and CvT

4.6.2 Performance with Noise

The secret information is embedded in the video before being compressed and/or transmitted via communication channel. In order to evaluate the performance of the proposed information hiding technique, a simulation of some of the impairments caused by a communication system is made, in this work, such as some types of noise that can be considered as an impairments caused by transmission mechanism used. There are four types of noise which will be chosen in this work with different values for each type of them as described below: Gaussian noise with rates: (0.001 as good, 0.01 as low and 0.04 as bad), Poisson noise (as low), Salt and pepper noise with rates: (0.02 as good, 0.05 as low and 0.07 as bad) and Speckle noise with rates: (0.01 as good, 0.03 as low, and 0.06 as bad). The calculating of NC, MSE, and PSNR after extraction of the secret information from compressed embedded frames when the DCT, DWT and CvT performed is shown in tables 4, 5 and 6 with Gaussian noise respectively.

Table 4.The Metric values with Gaussian noise by DCT.

Host Frames	NC	MSE	PSNR
F0	0.6560	117.4150	27.4335
F1	0.6857	112.3726	27.6241
F2	0.6467	118.9731	27.3763
F3	0.6746	115.2112	27.5158
F4	0.6546	118.3366	27.3996

Table 5. The Metric values with Gaussian noise by DWT.

Host Frames	NC	MSE	PSNR
F0	0.7467	78.2177	29.1977
F1	0.7707	73.1647	29.4877
F2	0.7368	79.7389	29.1141
F3	0.7639	76.0104	29.3220

F4	0.7421	79.1337	29.1471

Table 6. The Metric values with Gaussian noise by CvT.

Host Frames	NC	MSE	PSNR
F0	0.7692	73.4376	29.4716
F1	0.7901	68.2747	29.7882
F2	0.7524	74.8345	29.3897
F3	0.7845	72.1423	29.5489
F4	0.7612	74.2445	29.4241

When the CvT is used, the error rate is 8% approximately, while when the DWT used, the error rate is 11% approximately and the error rate is 14% approximately when the DCT is used. Figure 4 illustrates the relationship between the correct and error ratios of DCT, DWT and CvT, in the proposed hiding of secret information technique.

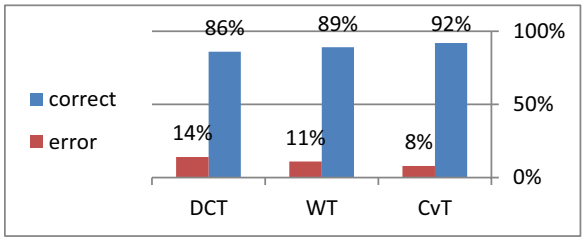

Figure 4. The error and correct ratios of DCT, DWT and CvT

5. Conclusions

The frame format consists of three color components (RGB) for individual pixel, the secret information could be embedded in one or more selected color channels. Some hiding schemes use the blue channel only because human eye is least sensitive to the blue component. In this work the secret information is hidden in red (R) color channel to ensure the best recovery of embedded information. The Poisson noise gives better result than other types of noise, while the Speckle noise gives the worst results. The secret information extraction time of the CvT is less than the secret information extraction time of the DWT and DCT; therefore, the CvT is the best one of them. The missing percentage of secret information in the extraction process is 10% approximately when different types of noise are used. Therefore, the proposed secret information technique is robust against some processes such as adding noise and compression so on. Finally, hiding a secret information in digital video by using CvT gives better results than DWT and DCT.

REFERENCES

[1] P. Kumar and V. K. Sharma, "Information security based on steganographyand cryptography techniques: A review" *International Journal of Advanced Research in Computer Science and Software Engineering- volume 4, Issue 10,October2014.*
[2] R. Gupta, S. Gupta, and A. Singhal, *"Importance and techniques of Information Hiding," International Journal of Computer Trend and Technolog(IJCTT)- volume 9 number 5- Mar 2014*
[3] T. Morkel, J.H.P Eloff and M. S. Olivier *, "An Overview of Image Steganoghraphy"* Information and Computer Security Architecture (ICSA), Research Group, Department of Computer Science, University of Pretoria, 0002, Pretoria, South Africa.
[4] Jayeeta Majumder, Sweta Mangal "An Overview of Image Steganography using LSB Technique "IJCA, 2012
[5] Vladimír BÁNOCI, Gabriel BUGÁR, Dušan LEVICKÝ "A Novel Method of Image Steganography in DWT Domain" IEEE, 2011.
[6] [4new] Arvind kumar, km. Pooja "Steganography – A Data Hiding Technique" IJCA volume 9, issue 7, 2010.

[7] M.junej, P.S.sandhu "*Improved information security using Steganography and Image Segmentation during transmission",* Computer Science and Engineering Department, Rayat and Bahra Institute of Engineering and Technology (RBIEBT), Sahauran (Punjab), India.
[8] D. Bhowmik,"Robust Watermarking Techniques For Scalable Coded Image And Video", PhD thesis, Department of Electronic and Electrical Engineering, The University of Sheffield, p.13-34, 2010.
[9] Swetha V, Prajith V and Kshema V, " Data Hiding Using Video Steganography -A Survey", IJCSET, Vol 5, Issue 6, 2015
[10] Ramadan J. Mstafa , Khaled M. Elleithy , and Eman Abdelfattah," A Robust and Secure Video Steganography Method in DWT-DCT Domains Based on Multiple Object Tracking and ECC", 2017.
[11] P.-C. Chang, K.-L. Chung, J.-J. Chen, C.-H. Lin, and T.-J. Lin, ''A DCT/DST-based error propagation-free data hiding algorithm for HEVC intra-coded frames,'' J. Vis. Commun. Image Represent., vol. 25, no. 2, pp. 239–253, Feb. 2014.
[12] X. Ma, Z. Li, H. Tu, and B. Zhang, ''A data hiding algorithm for H.264/AVC video streams without intra-frame distortion drift,'' IEEE Trans. Circuits Syst. Video Technol., vol. 20, no. 10, pp. 1320–1330, Oct. 2010.
[13] Z. Shahid, M. Chaumont, and W. Puech, ''Considering the reconstruction loop for data hiding of intra- and inter-frames of H.264/AVC,'' Signal, Image Video Process., vol. 7, no. 1, pp. 75–93, Jan. 2013.

.

APPENDIX A

(a)

(b)

Figure 1. (a) Original Frame (b) embedded Frame after compression.

(a)

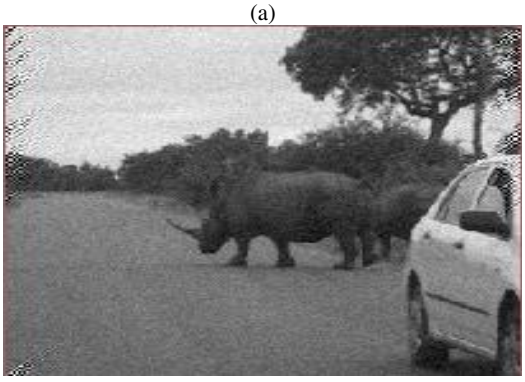

(b)

(c)

(d)

Figure 2: (a) Original Frame, (b) Embedded Frame with Gaussian noise rate (0.001), (c) Embedded Frame with Gaussian noise rate (0.01) (d) Embedded Frame with Gaussian noise rate (0.04).

(a)

(b)

Figure 3: (a) Original Frame, (b) Embedded Frame with Poisson noise

(a)

(b)

(c)

(d)

Figure 4. (a) Original Frame, (b) Embedded Frame with Salt & Pepper noise rate (0.02), (c) Embedded Frame with Salt & Pepper noise rate (0.05), (d) Embedded Frame with Salt & Pepper noise rate (0.07).

(a)

(b)

(c)

(d)

Figure 5. (a) Original Frame, (b) Embedded Frame with Speckle noise rate (0.01), (c) Embedded Frame with Speckle noise rate (0.03), (d) Embedded Frame with Speckle noise rate (0.06).

Medical image security using modified chaos-based cryptography approach

Medical image security using modified chaos-based cryptography approach

Methaq Talib Gatta and Shahad Thamear Abd Al-latief

Computer Science Department, University of Mustansiriya, Baghdad, Iraq

Abstract. The progressive development in telecommunication and networking technologies have led to the increased popularity of telemedicine usage which involve storage and transfer of medical images and related information so security concern is emerged. This paper presents a method to provide the security to the medical images since its play a major role in people healthcare organizations. The main idea in this work based on the chaotic sequence in order to provide efficient encryption method that allows reconstructing the original image from the encrypted image with high quality and minimum distortion in its content and doesn't effect in human treatment and diagnosing. Experimental results prove the efficiency of the proposed method using some of statistical measures and robust correlation between original image and decrypted image.

1. Introduction

Recently; hospitals and medicinal appliances produce images in digital forms with the ability of storing and transfer these images electronically which improves the efficiency of the health care services institution [1]. These images plays a prime role in evaluate the oddity in the human body and have its importance to provide accurate diagnosing with only a still image "A Picture worth Thousand Words"[2].With the remarkable development in communication technologies and the need of fast and secure treatments from remote location lead to phenomenal growth in the number of medical images that are transmitted daily [3] in to the open network, this result in many threat to these images by malicious attacks so the security of these medical image is essential and require reliable, fast and powerful security system [4]. There is no single encryption algorithm that is suitable for all image types, many popular encryption standard have been proposed such as Advanced Encryption Standard (AES) and Data Encryption Standard (DES), these standards are designed to the textual data encryption and the message can be decrypted by using the same key used for encryption so it is poorly suitable to the image encryption because it doesn't meet the image requirements such as redundancy, high data capacity, strong correlation between pixels [5]. There are many researchers noticed the strong relationship between the chaos theory and the cryptography systems which can be used to achieve the desired level of image security because of the chaotic system strong properties such as high sensitivity to the initial conditions and parameters ,aperiodicity, etc. any successful cryptosystem must have the diffusion and confusion effects, in order to be robust against several attacks[6],the chaos-based cryptography can achieve these two effects[7]. In this work the one dimensional standard chaotic logistic map 1D(SLM) is used for medical images cryptography by acting as a random numbers generator that input to the chaos-based cryptography modified algorithm steps depending on some determined number of iterations and specific algorithm for each step to have the desired level of security. Many researchers try to design image cryptography systems by using chaos, in [8] Zhang et al. proposed medical image protection scheme based on Arnold cat map to shuffle the image pixels and use the logistic map to change

the pixels values by a chosen number of the rounds for encryption and have proven its efficiency and security. In [9] Zhang et al. proposed a way to compress and encrypt the medical images which the plain image is compressed and encrypted by chaos-based Bernoulli measurement matrix, which is generated by the control of the Chebyshev map and perform a second level of protection by encrypt the result by permutation-diffusion type chaotic cipher, in [10] Rakesh S et al. present image encryption based on block scrambling using the chaotic Arnold cat map and also scramble the whole image again using the same map then the image is encrypted using a chaotic sequence generated using symmetric keys. In [11] Goce et al. present a block encryption algorithm based on two well-known chaotic maps exponential and logistic and have proven its efficiency against most of attacks rather than brute force attack.

2. Modified Method

This paper introduces the modified chaos-based cryptography algorithm by the use of the traditional architecture by Fridrich [12] in order to protect the security of medical images. The modification is presented through used the chaotic map rather than the two dimensional baker map as used in Fridrich's work; it is a symmetric block encryption. This architecture mainly consist of two main stages: confusion and diffusion for medical image pixels where confusion applied to changing pixels locations in the original medical image and diffusion step applied to perform a transformation on pixels to change their values to remove correlation between pixels [13], 1D chaotic map is used as a key generator that known as standard logistic map (SLM) and its control parameter and initial value as a secret key for the cryptography process. Block diagram of the medical image encryption process shows in 'figure 1'.

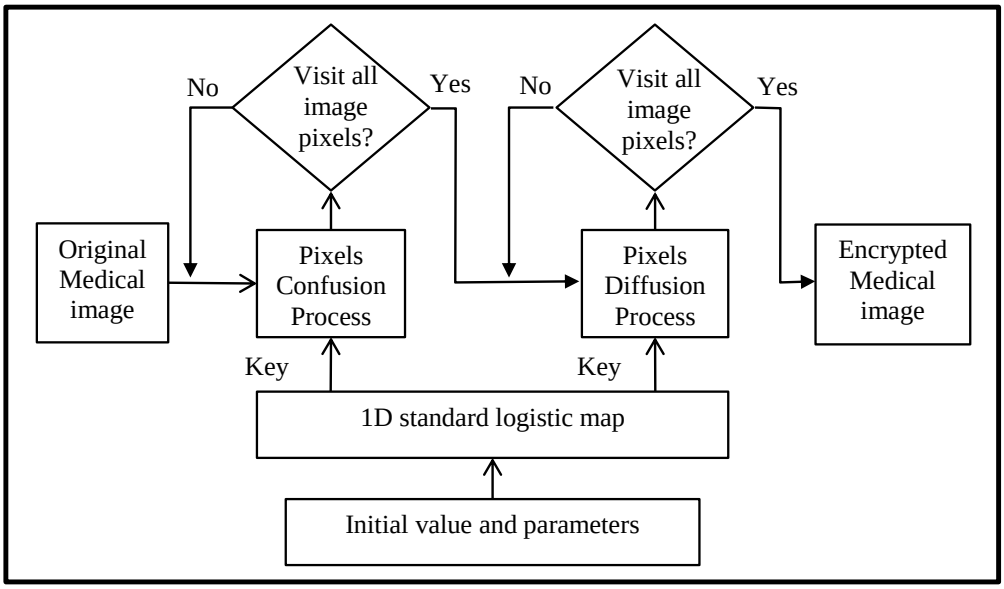

Figure 1. Block diagram of medical image encryption process.

The input for the proposed encryption process is a gray-scale image that is get of image database [14]. The medical image in this work can take different size of rows and columns. The main steps of image encryption process shows in algorithm 1:

Algorithm 1. Medical image encryption process

Input: Encrypted medical image, initial value, parameters.

Output: Encrypted medical image.

Begin:

Step 1: Read the desired gray-scale medical image and save its pixels in to 2D array that suits the cryptography process.

Step 2: Use the1D standard logistic map as random key generator and its initial condition and its control parameter as image encryption secret key which given in equation (1).

$$x_{n+1} = \mu x_n(1 - x_n) \quad (1)$$

Where μ is the system control parameter and the system is chaotic when $0< \mu \leq 4$ and $x_0 \in [0, 1]$, this work use x_0=0.4 and μ =3.87 as the secret key value.

Step 3: Confuse the pixels position in the array by using the random values generated from 1D standard logistic map and change the pixels positions depending on modified confusion equation.

Step 4: Diffuse the pixels of the image depending on the random values generated from the 1D Standard logistic map by performing some transformation on the image pixels using modified equation to give them new values that produce ciphered image with uniform histogram shape.

Step 5: Iterate step (3) and step (4) until all image pixels are visited.

End

After complete the image encryption process, the encrypted image can be send through communication network or store in database with secure mode. At the other side, the decryption process is applied on encrypted image by invers order of the encryption process. The main steps of image decryption process shows in algorithm (2):

Algorithm 2. Medical image decryption process

Input: Encrypted medical image, initial value, parameters.

Output: Original medical image.

Begin:

Step 1: Read the gray-scale ciphered image and store it into 2D array of pixels.

Step 2: Enter the same key used in encryption into the key generator which it is the initial value and the control parameter of the 1D standard logistic map, same values that is used in the encryption process.

Step 3: The pixels of the image are diffused by perform inverse transformation and return the value of each pixel to its original value.

Step 4: Confuse the pixels in inverse order and return pixels into their original positions in the original image.

Step 5: Iterate step (3) and step (4) for all image pixels.

End

3. Experimental Results

In this section some results are described to show the performance and security of the proposed algorithm. The experiments are performed on three MRI medical images with the use of MATLAB 2016b programing language.

3.1. Histogram Analysis

In the following experiments the original, ciphered and recovered images and their histograms are described in figure 2. It's obvious that the histogram of the ciphered image is completely different from the histogram of the original one and almost has a uniform distribution this makes

statistical attacks difficult because the ciphered image doesn't provide any chance to employ any kind of it.

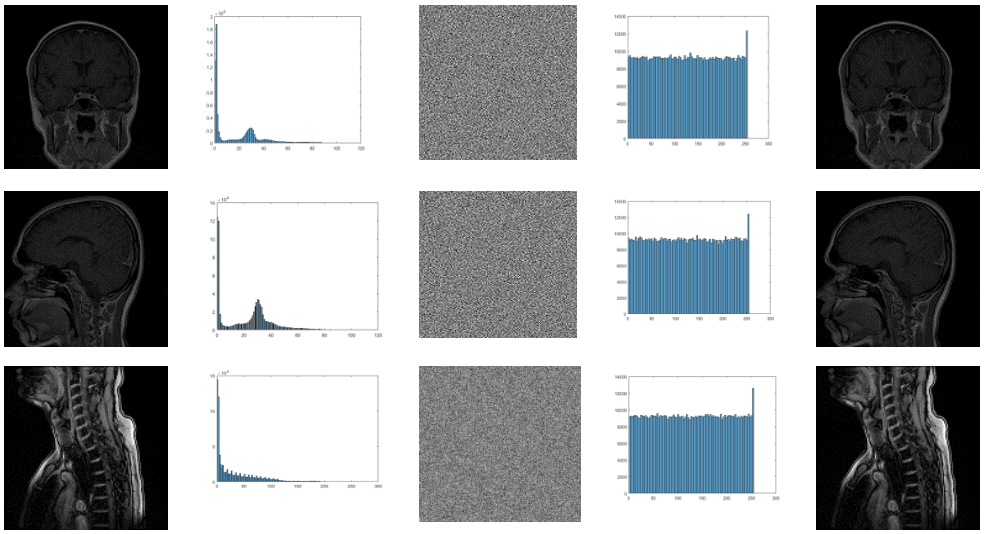

Figure 2. Experimental results of the modified encryption method: from the first to the fifth column are: original image, histogram of the original image, ciphered image, histogram of the ciphered image, and the recovered images, respectively.

3.2. Entropy Analysis

It is important property founded in information theory by Shannon [6] to give idea about them, the randomness and the unpredictability of an information source. Equation (2) used to calculate the entropy value [15].

$$H(m) = -\sum_{I=0}^{2^N-1} P(m_i)\, log_2\, P(m_i) \tag{2}$$

Where $P(m_i)$ is the probability of existence of the gray level value of pixel m_i in the m image and the log is taken to represent them in term of bits; since the gray-scale image pixel values is 256 gray levels then its contain 8 bits so the ideal entropy value to the secure cryptosystem must be 8 [16]. The entropies of the introduced medical images and their ciphered version are presented in table 1. It is evident that the entropies of the ciphered images are extremely close to the theoretical value of 8 which make the system able to resist the entropy attacks.

Table 1. Entropies of the original images and ciphered images.

Tested image	Original image	Ciphered image
MRI-brain	4.7571	7.9993
MRI -sinuses	5.1074	7.9993
MRI- neck	6.1344	7.9994

3.3. Time Analysis

The required time in image encryption process is very important aspect and depends on the used encryption method complexity. This work uses Java v8 in medical image cryptography algorithm implementation. Table 2, illustrate time analysis result of the previous three medical images.

Table 2. Time Analysis Results

Tested image	Encryption process	Decryption process
MRI-brain	0.282 sec	0.422 sec
MRI -sinuses	0.421 sec	0.337 sec
MRI- neck	0.671 sec	0.419 sec

4. Conclusions

In this paper medical image cryptography method is presented that based on chaos theory by using one of the most simple and popular one dimensional chaotic map which named standard logistic map. The results that have been shown proved that this method has an acceptable level of security rather than it is robust against statistical attacks and entropy attack.

References

[1] Zhang R and Liu L 2010 Security models and requirements for healthcare application clouds *IEEE 3rd Inter. Con. on Cloud Com.* USA 268-75.
[2] Vimala S and Nath B 2015 A survey on medical images *Inter. J. Research in Science Eng. Tech.* IJRSET **02** 673-79
[3] Puech W and Rodrigues J M 2004 A new crypto-watermarking method for medical images safe transfer 12th Eur. Con. Signal Proc. Australia 1481-84.
[4] Mohan A K Saranya M R and Anusudha K 2014 Separable reversible data hiding using chaotic encryption and histogram shifting *Inter. J. Simulation Sys. Tech.* IJSSST **15**.
[5] Pareek N K, Patidar V and Sud K 2006 Image encryption using chaotic logistic map Image Vis. Computing **24** 926-34
[6] Shannon C 1949 Communication theory of secrecy systems *Bell Labs Tech. J.* **28** 656-715.
[7] Kocarev L 2001 Chaos-based cryptography: a brief overview *IEEE Circuits Sys. Mag.* **21** 6-21.
[8] Zhang L B, Zhu Z L, Yang B Q, Liu W Y, Zhu H F and Zou M Y 2015 Cryptanalysis and improvement of an efficient and secure medical image protection scheme *Mathematical Pro. Eng*.
[9] Zhang L B, Zhu Z L, Yang B Q, Liu W Y, Zhu H F, Zou M Y 2015 Medical image encryption and compression scheme using compressive sensing and pixel swapping based permutation approach *Mathematical Pro. Eng.*
[10] Rakesh S., Kaller A, Shadakshari B C and Annappa B 2012 Image encryption using block based uniform scrambling and chaotic logistic mapping *Inter. J. Cryptography and Information Security* IJCIS **02** 49-57.
[11] Jakimoski G and Kocarev L 2001 Chaos and cryptography: block encryption ciphers based on chaotic *maps IEEE Trans. Circuites and Systems I: Foun. Theo. App.* **48** 163-9.
[12] Fridrich J 1998 Symmetric ciphers based on two-dimensional chaotic maps *Inter. J. Bifurcation and chaos* **08** 1259-84.
[13] Misra A, Gupta A and Rai D 2011 Analyzing the parameters of chaos based image encryption schemes *World Appl. Programming* **01** 294-99.
[14] Gaata M and Hantoosh F 2016 An Efficient Image Encryption Technique using Chaotic Logistic Map and RC4 Stream Cipher *Inter. J. Modern Trends Eng. Research* (IJMTER) **03**.
[15] Ponnain D and Chandranbabu K 2016 Security analysis of an image encryption algorithm based on paired interpermuting planes and a modified scheme *Optic-Inter. J. Light and Electron Opt.* **127** 8111-23.
[16] Ahmad J and Fawad A 2012 Efficiency analysis and security evaluation of image encryption schemes *Inter. J. Video and Image Processing N.W. Sec.* **12** 25.

Implementation of 4-way Superscalar Hash MIPS Processor Using FPGA

Implementation of 4-way Superscalar Hash MIPS Processor Using FPGA

Safaa Sahib Omran[1], Laith Fouad Jumma[2]

[1] College of Electrical and Electronic Techniques, Computer Engineering Techniques

[2] College of Electrical and Electronic Techniques, Computer Engineering Techniques

[1] Omran_safaa@ymail.com , [2]Laith1993@gmail.com

Abstract. Due to the quick advancements in the personal communications systems and wireless communications, giving data security has turned into a more essential subject. This security idea turns into a more confounded subject when next-generation system requirements and constant calculation speed are considered in real-time. Hash functions are among the most essential cryptographic primitives and utilized as a part of the many fields of signature authentication and communication integrity. These functions are utilized to acquire a settled size unique fingerprint or hash value of an arbitrary length of message. In this paper, Secure Hash Algorithms (SHA) of types SHA-1, SHA-2 (SHA-224, SHA-256) and SHA-3 (BLAKE) are implemented on Field-Programmable Gate Array (FPGA) in a processor structure. The design is described and implemented using a hardware description language, namely VHSIC "Very High Speed Integrated Circuit" Hardware Description Language (VHDL). Since the logical operation of the hash types of (SHA-1, SHA-224, SHA-256 and SHA-3) are 32-bits, so a Superscalar Hash Microprocessor without Interlocked Pipelines (MIPS) processor are designed with only few instructions that were required in invoking the desired Hash algorithms, when the four types of hash algorithms executed sequentially using the designed processor, the total time required equal to approximately 342 us, with a throughput of 4.8 Mbps while the required to execute the same four hash algorithms using the designed four-way superscalar is reduced to 237 us with improved the throughput to 5.1 Mbps.

Keywords: MIPS, FPGA, SHA-1, SHA-2, BLAKE.

1.Introduction

Cryptography is an important science of building protocols or plans that qualify users to transmit data over a risky path without victimizing the transmission confidentiality or the authenticity.

Contemporary cryptography is used in many fields of applications to ensure the safety of not only data, but also for commercial applications such as electronic payment schemes and voting. The basic building blocks are classified into block ciphers, stream cipher and hash function. They occupy a substantial role in a vast applications. The modern technologies such as online banking, online trading, email, ATMs and mobile applications claim efficient and secure schemes. The most important matter in crypto algorithm design is the harmonization and trade-off between efficiency and security, also the required property from integrity, authentication and confidentiality determine the field of security used. One of the most important concepts of cryptography is protecting the confidentiality and authenticity of data [1]. The hash functions deal with two important codes which are very useful with hash applications, these codes are: Hash Message Authentication Code (HMAC) and Message Integrity Check (MIC). These codes are providing an important property to the hash functions which is the collision resistance.

2.Related Work

In 2003, N. Sklavos et. al. designed a high speed Architecture for SHA-1 and RIPEMD-160. Pipelined technique is applied to achieve operation mode for RIPEMD-160 and SHA-1 [3].
In 2013, Fatma et. al. they implement an efficient hardware of secure hash algorithms (SHA-3) BLAKE-256 and they report the result implantation of BLAKE-256 on FPGA Xilinx Virtex 7, Virtex 6 and Virtex 5. They report the performance of its design [4].

In 2015, Mestiri et. al. suggested a new plan for the SHA-256 and SHA-512 hash algorithms. The proposed scheme has been performed by Xilinx Vertex- 5 FPGA [5].

In 2016, Mohamoud et. al. studied the computation bottlenecks of SHA-3 on a 32-bit MIPS processor and introduced two of ASIP architecture to increase performance of SHA-3 which designed on FPGA Xilinx Virtex 6 [6].

In this paper, SHA-1, SHA-224, SHA-256 and SHA-3 (BLAKE) are implemented in 4-way superscalar Hash MIPS processor using FPGA.

3.Four-way Superscalar Hash MIPS Processor Design

Firstly a MIPS processor was implemented for executing the hash algorithms sequentially. The design consist of two interacting parts:32-bits datapath and control unit. The datapath consist of an ALU, a register file, a message computation block and constant port. Then superscalar processor is an advanced technique that enables the processor to execute more than one instruction per clock cycle [7]. This approach is achieved by replicating the internal components of the processor, so that it can launch multiple instructions in each clock cycle. The general name of this technique is multiple issues. Hence, in this section a four-way unit's 32-bit superscalar MIPS processor is designed. This processor is capable for executing the algorithms for SHA-1, SHA-224, SHA-256 and BLAKE[8][9][10], since the variables for these hash algorithms are 32-bits. Figure 1 shows a general block diagram for this 4-way superscalar processor. As shown in the figure, four units were duplicated to enable the processor for executing 4 instructions per each clock.

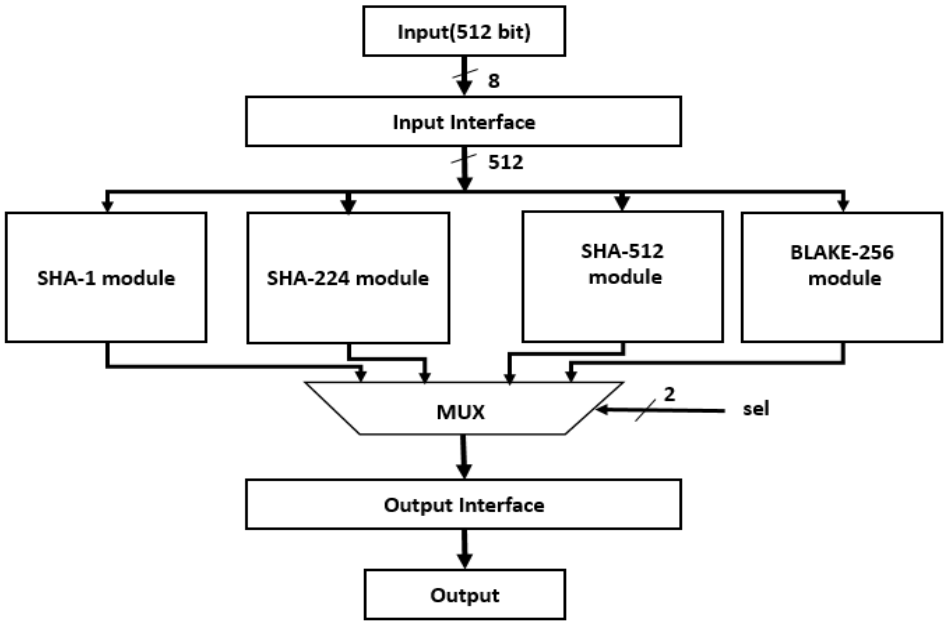

Figure 1: Block diagram for 4-way superscalar processor

The complete design of a 32-bit 4-way superscalar Hash MIPS processor consists of two interacting parts:

1. Four datapath.
2. Four Control unit.

The design has the ability to execute fourth instructions in clock cycle with some limitation. 'Figure 2' shows the complete design of the single-cycle Hash MIPS processor with its datapath and control unit.

3.1 Four Datapath

A four-way Superscalar has four copies of hardware to execute four instructions simultaneously. All elements in datapath are duplicated except program counter and memories, to allow four instructions pass through it at the same time. Register file's ports and memories' ports are duplicated in turns to be capable to execute four instructions simultaneously. The following sections present the differential units that required in this 4-way superscalar MIPS processor.

3.2 Four Control Units

Four datapaths were needed four control units to guarantee execute four instructions correctly. Each control unit consists of main control as single-cycle MIPS processor. It has the same signal with same meaning.

3.3 Register File

It consists of 32 registers each of 32-bit in size. The register file's ports are duplicated. It has eight read ports (RD1, RD2, RD3,,,,, RD8) and four write port (WD, WD1, WD2, WD3). Register file used ports (RD1, RD2, WD, A1, A2, and A3) to communicate with 32-bit datapath 1, and signal WE1 is provided from control unit 1 to register file, this considers entire execution path 0. Also it is used ports (RD3, RD4, WD1, A4, A5, and A6) to communicate with 32-bit datapath 2, and signal WE2 is provided from control unit 2 to register file, this considers execution path 1.and so on in path 2 and path 3.

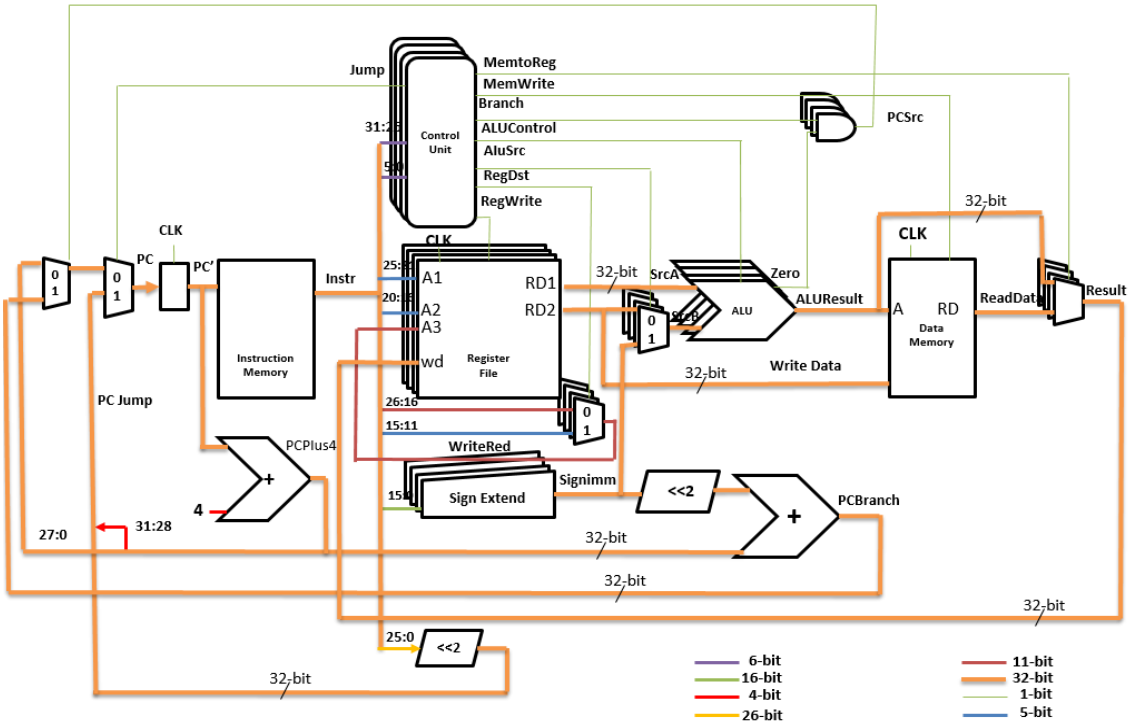

Figure 2: Block Diagram of 32-bit Superscalar Hash MIPS Processor

The SHA-1, SHA-224, SHA-256 and BLAKE each use varies instructions, table 1 shows all the designed instructions and the requirement from these instruction for each hash algorithm.

Table 1: Instruction need for SHA-1, SHA-224, SHA-256 and BLAKE.

Instruction	SHA-1	SHA-224	SHA-256	BLAKE
XOR	Y	Y	Y	Y
JMP	Y	Y	Y	Y
BEQ	Y	Y	Y	Y
ADDI	Y	Y	Y	Y
LOAD	Y	Y	Y	Y
STORE	Y	Y	Y	Y
AND	Y	Y	Y	Y
NOT	Y	Y	Y	Y
OR	Y	N	N	Y
ADD	Y	Y	Y	Y

<<< 1	Y	N	N	N
<<< 5	Y	N	N	N
<<< 10	Y	N	N	N
<<< 30	Y	N	N	N
>>> 2	N	Y	Y	N
>>> 6	N	Y	Y	N
>>> 7	N	Y	Y	Y
>>> 8	N	N	N	Y
>>> 11	N	Y	Y	N
>>> 12	N	N	N	Y
>>> 13	N	Y	Y	N
>>> 16	N	N	N	Y
>>> 17	N	Y	Y	N
>>> 18	N	Y	Y	N
>>> 19	N	Y	Y	N
>>> 22	N	Y	Y	N
>>> 25	N	Y	Y	N
>> 3	N	Y	Y	N
>> 10	N	Y	Y	N

Simulation results and Discussions

Superscalar MIPS processor of 32-bit is tested with a plaintext “abc” to produce fixed 160,256,224 and 256 bit for SHA-1, SHA-256, SHA-224 and BLAKE-256. This 4-wat superscalar processor is simulated using the Virtex 7 because the required component for this processor is greater than the available component exists in Spartan-3an. The testing figures of hash function are shown in 'figure 3'.

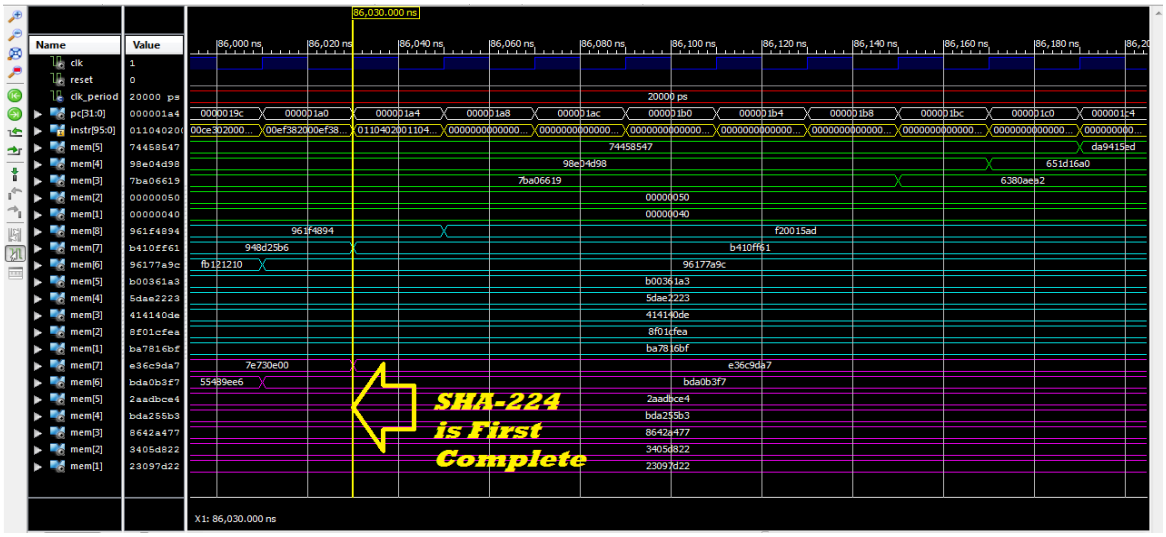

SHA-224 is first complete at t=86030 ns

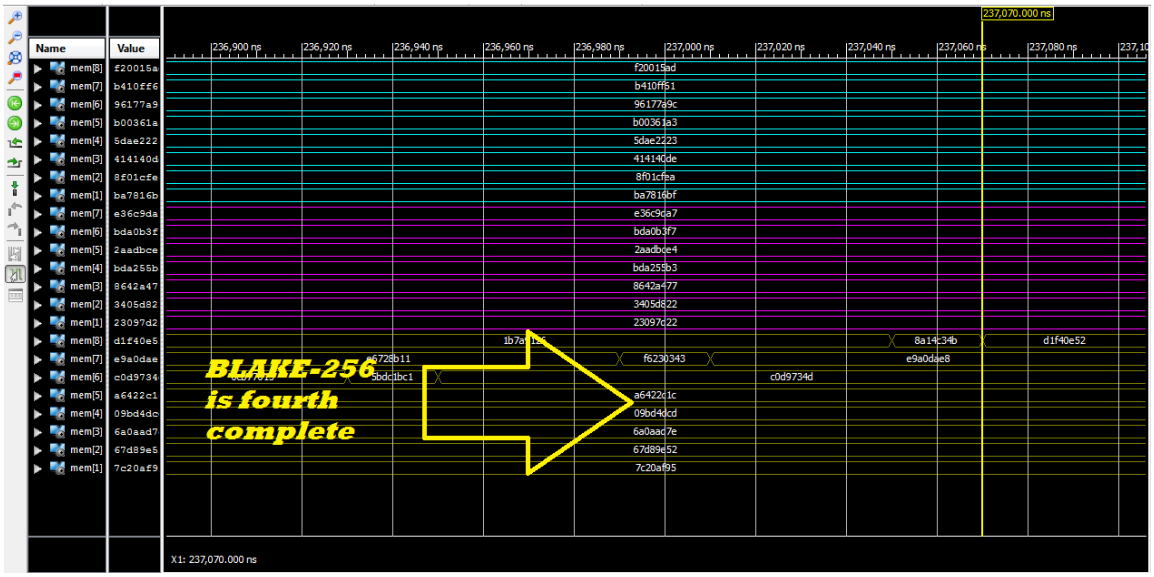

BLAKE-256 is fourth complete at t=237070 ns

Table 2 shows the throughput, power and time required to complete a 64-bit Hash MIPS processor.

Table 2: 4-way Superscalar Hash MIPS processor with its throughput, power and time to completed

Hash	Time	Throughput	Power
SHA-1	*136870 ns*	3.7 *Mbps*	0.039(Watt)
SHA-224	*86030 ns*	*5.6 Mbps*	
SHA-256	*86050 ns*	*5.6 Mbps*	
BLAKE-256	*237070 ns*	*5.1 Mbps*	

The execution time for our design can be enhanced by using a pipeline processor in which will increase the value of throughput. The designed processor in single cycle MIPS processor which easy to design but the drawback of this processor tht all instructions must be executed in fixed time (same no.of clk cycle) which is limited by the slowest instruction, from this table SHA-224 is first completed with t=86030 ns and with only one clock SHA-256 is second completed, third SHA-1 is complete with t=136870 ns and last BLAKE is completed with t= 237070 ns. Table 3 summarizes the FPGA resources used in a 32-bit Hash MIPS processor.

Table 3: FPGA resource utilization.

Device Utilization Summary	
Logic Utilization	4-way Superscalar
Number of Slice Flip Flops	32777
Number of 4 input LUTs	118691
Number of occupied Slices	32777
Number of bonded IOBs	262

4.Conclusions

A hash SHA-1, SHA-224, SHA-256, and BLAKE-256 was implemented using FPGA Virtex-7. A superscalar MIPS processor was designed using VHDL Xilinx ISE software language with only instructions that Hash need. The time required is executing each algorithm along in sequential orders takes about 342 usec with throughput of 4.8 Mbps, while the required time is executing the four algorithms simultaneously by using the 4-way superscalar processor is reduced to 237 us with throughput of 5.1 Mbps. This study is a starting point for future studies and can be extended to invoke the algorithm for SHA-1, SHA-224, SHA-256, and BLAKE-256 by using a Multicore MIPS processor.

Reference

[1] Ö. KÜÇÜK, "Design and Analysis of Cryptographic Hash Functions", Heverlee (Belgium): © Katholieke Universiteit Leuven – Faculty of Engineering, 2012.

[2] L. C. Washington, "Introduction to Cryptography, Wade Trappe": Wireless Information Network Laboratory, 2006.

[3] N. Sklavos, G. Dimitroulakos and O. Koufopavlou, “An Ultra High Speed Architecture for VLSI Implementation of Hash Functions”, Proceedings of the 10th IEEE International Conference on Electronics, Circuits and Systems (ICECS 2003) pp. 990-993 Vol.3, 2003.

[4] F. Kahri, B. Bouallegue, M. Machhout and R. Tourki, "An FPGA implementation of the SHA-3: The BLAKE Hash Function," 10th International Multi-Conference on Systems, Signals & Devices (SSD), Tunisia, 18-21, March, 2013.

[5] H. Mestiri, F. Kahri, B. Bouallegue and M. Machhout, "Efficient FPGA Hardware Implementation of Secure Hash Function SHA-2," I.J. Computer Network and Information Security, pp. 9-15, 2015.

[6] In 2015, Yi wang et. al. proposed a novel SHA-3 implemented using set execution based on a 32-bit LEON3 processor with reducing execution cycles and code size.

[7] M. A. Elmohr, M. A. Saleh, A. S. Eissa, K. E. Ahmed, M. M. Farag, "Hardware Implementation of A SHA-3 Application-Specific Instruction Set Processor,"28th International Conference on Microelectronics (ICM), 17 20,December,2016.

[8] In 2017, S. S. Omran at. al. designed a hash processor for SHA-1 and SHA-2 algorithms by using Multithreading MIPS processor using the Xilinx Spartan-3AN

[9] J. L. Hennessy, D. A. Patterson, “Computer Organization and Design: The Hardware/Software Interface”, 4th ed., Waltham, USA: Morgan Kaufmann, 2012.

[10] J.P Aumasson, L. Henzen, W. Meier, R. C.W. Phan, "SHA-3 proposal BLAKE", version 1.3, December, 16, 2010.

Using SAFRAN Software to Assess Radiological Hazards from Dismantling of Tammuz-2 Reactor Core at Al-tuwaitha Nuclear Site

IOP Conf. Series: Journal of Physics: Conf. Series **1003** (2018) 012038 doi:10.1088/1742-6596/1003/1/012038

Using SAFRAN Software to Assess Radiological Hazards from Dismantling of Tammuz-2 Reactor Core at Al-tuwaitha Nuclear Site

Mezher Abed Gatea[1,1], Anwar A Ahmed, Saad jundee kadhum, Hasan Mohammed Ali and Abbas Hussein Muheisn

[1]Iraqi Decommissioning Directorate, Ministry of Science and Technology, Iraq

[1]Corresponding Author, Chief Engineer, e-mail: mizher.abed@gmail.com

Abstract. The Safety Assessment Framework (SAFRAN) software has implemented here for radiological safety analysis; to verify that the dose acceptance criteria and safety goals are met with a high degree of confidence for dismantling of Tammuz-2 reactor core at Al-tuwaitha nuclear site. The activities characterizing, dismantling and packaging were practiced to manage the generated radioactive waste. Dose to the worker was considered an endpoint-scenario while dose to the public has neglected due to that Tammuz-2 facility is located in a restricted zone and 30m berm surrounded Al-tuwaitha site. Safety assessment for dismantling worker endpoint-scenario based on maximum external dose at component position level in the reactor pool and internal dose via airborne activity while, for characterizing and packaging worker endpoints scenarios have been done via external dose only because no evidence for airborne radioactivity hazards outside the reactor pool. The in-situ measurements approved that reactor core components are radiologically activated by Co-60 radioisotope. SAFRAN results showed that the maximum received dose for workers are (1.85, 0.64 and 1.3mSv/y) for activities dismantling, characterizing and packaging of reactor core components respectively. Hence, the radiological hazards remain below the low level hazard and within the acceptable annual dose for workers in radiation field
.

1. Introduction

For facilities, decommissioning is the final phase in the life cycle after siting, design, construction and operation. It is a complex process involving operations such as detailed surveys, decontamination and dismantling of equipment and facilities, demolition of buildings and structures, and the management of the resulting radioactive and other hazardous waste and materials, while taking into account the need to provide for the health and safety of workers and the general public, and protection of the environment. A general requirement in decommissioning is the development of a decommissioning plan which includes, or has associated with it, an evaluation of the potential radiological consequences to the public and workers during planned decommissioning activities and as a result of any credible accidents that might occur during these activities [1]. Safety assessment can contribute directly to safety by identifying potential hazards and appropriate mitigatory measures that can be put in place to protect workers, the public and the environment. Safety assessments are used to show that facilities will comply or continue to comply with established safety principles, standards and licensing conditions [2]. Hence, it is a process which is required to evaluate the safety of radioactive waste management facilities and activities [3,4,5,6].

There are many sites in Iraq have some degree of radiological contamination and require decommissioning and remediation in order to ensure radiological safety. Many of these sites are located at the nuclear research center at Al-tuwaitha which suffered substantial physical damage during the first Gulf War and several have been subject to looting of materials and equipment as a consequence of the challenging security situation in the country [7]. Tammuz-2 reactor 'figure 1' core 'figure 2' is one of nuclear facilities located within Al-tuwaitha nuclear site which need decommissioning. It is swimming pool type reactor operates in a maximum thermal power of 500kW, used for training, neutron radiography and for research purposes. The reactor was totally destroyed in the 1991 Gulf War and has been de-fuelled [8]. The reactor pool is approximately at the center of the building, between levels (0 and – 7 m). It is parallelepiped in form, with (4m×4m) cross-section area, corresponding to a volume of (112 m^3), made of a stainless steel liner, (6mm) thick. This liner is embedded in a reinforced concrete wall, providing the mechanical strength of structure and a biological shield. The pool block is fully separate from the floors at level (0) and (– 4m), to avoid transmission of a shock wave resulting from a borax type explosion in the pool block to the external walls.

Figure 1. Tamuz-2 reactor facility

Figure 2. Core of Tamuz-2 reactor

A probabilistic safety assessment approach is provided in the (Safety Assessment Plan and report for the Decommissioning of Tammuz-2 Reactor).

On the other hand, a key parameter in any decision making process for selecting the appropriate measures is the distribution of individual doses to the population affected by the radioactive materials in the area. The inhalation of contaminated dust is often a major exposure pathway, and sometimes the associated doses cannot be measured, even though the contamination levels may be rather high. In such cases the doses should be estimated on the basis of model calculations, with input from the radiological monitoring programme and with realistic scenarios [9].

The Safety Assessment Framework (SAFRAN) software tool was implemented here for safety analysis [10]. It developed to apply the methodology developed within the Safety Assessment Driving Radioactive Waste Management Solutions (SADRWMS) project. The International Atomic Energy Agency (IAEA) organized the International Project on SADRWMS to examine international approaches to safety assessment for predisposal management of all types of radioactive waste, including disused sources, small volumes of waste, legacy and decommissioning waste, operational waste, and large volume naturally occurring radioactive material residues. The initial outcome of the SADRWMS Project was achieved through the development of a series of flowcharts which were intended to improve the mechanisms for application of safety assessment methodologies for predisposal management of radioactive materials [11].

The deterministic safety analysis is used here to verify that the dose acceptance criteria and safety goals are met with a high degree of confidence for all works. A deterministic approach to safety assessment and the identification of safety control measures are recommended as being effective in providing adequate protection for workers and the public during decommissioning activities. However, probabilistic approaches can also be applied in a complementary manner.

It is important to ensure appropriate consideration of radioactive waste management in the development of safety assessment for decommissioning. For this purpose, it is essential to establish clear boundaries and interfaces between waste management and decommissioning activities and the scope of the associated safety assessments.

2. Materials and Methods

- MIP10 digital meter (Canberra Company) with STTC Geiger Muller probe for measuring high dose of Gamma radiation with range (0.3µSv/h-10Sv/h) 'figure (3-a)'.
- Radeye meter with two probes, the first is Scintillation detector probe (NaI crystal) (41S/MHV) model for measuring Gamma dose rate (unit µSv/h), and the second is ZnS Scintillation detector (DP6BD) model with 100cm2 active area for measuring Alpha, Beta and Gamma contamination (unit Bq/cm2) 'figure (3-b)'.
- Interceptor (Thermo Company) consists of (2) CZT finder and identification detectors and (1) 3He neutron detector 'figure (3-c)'.
- Ludlum (type 3030) Alpha Beta radiation sample counter. It has radiation detector ZnS(Ag) adhered to plastic scintillation material with 0.4mg/cm2 aluminized window 'figure (3-d)'.
- The particulates monitor LB9140 is used for measuring airborne Alpha/Beta particles in the presence of naturally occurring (Radon) activity and fluctuating Gamma backgrounds. Si-CAM detector unit 600mm2 for simultaneous separated Alpha/Beta measurement on a flat dust collection area of 25x25mm2. Air flow rate of approximately 3.3m3/h is possible 'figure (3-e)'.
- Scale of 1000kg maximum load used for weighing the radioactive dismantled segmented and forklift machine 'figure (3-f)' for lifting and transferring the segments into specified accumulation zone.

For portable radiological detection devices, a daily response check for each instrument is done by using standard radiation sources. Then it compares with the calibration certificates which supplied by the manufactured company for each instrument.

Figure 3-a. MIP10

Figure 3-b. Radeye

Figure 3-c. Interceptor

Figure 3-d. Ludlum

Figure 3-e. LB9140

Figure 3-f. Scale and Forklift

Figure 3. The used instruments

Safety assessment calculations have done by using SAFRAN (Safety Assessment Framework) tool version 2.3.2.7 software that incorporates the methodologies developed in SADRWMS (Safety Assessment Driven Radioactive Waste Management Solutions) project. SAFRAN calculations are based on the maximum external dose to the worker that comes from practicing to fulfill work activity. For dismantling activity, the maximum external dose is determined with accordance to worker position

for dismantling each component which mentioned in the components description and the maximum doses mentioned in (table 1). For characterization activity, the maximum external dose for characterizing reactor core in step by step manner was the maximum dose at the top of reactor core while, the maximum external dose that taken from characterization of each component after removing outside the reactor core is the same dose that worker of packaging activity undergo (table 2).

SAFRAN calculations for internal doses which came from the inhalation pathway are based on the maximum Co-60 concentration in air during work. The results of particulates monitor LB9140 device showed that the maximum Co-60 concentrations in air at reactor core are (0.001Bq/m^3) but, there is no evidence to present concentrations outside the reactor core. Assessment for affecting of internal doses have been used for worker who charged in dismantling activity while, workers of characterizing and packaging activities are assess due to effect of external dose only with the judgment results of Co-60 concentrations inside and outside the reactor pool.

The assessments covered work took place over 91 day period which spent to fulfill dismantling and removal of Tammuz-2 reactor core. One type of endpoints was considered in exposure assessment scenarios. It refers to worker who contributed in dismantling and removal of reactor core. In this assessment the worker endpoint is defined as a cumulative endpoint in SAFRAN. The worst case is a generic worker who charged with different activities. The annual dose for this worker is then calculated as the sum of all exposures for all the mentioned activities. Dose to the public was neglected and is not numerically assessed in the SAFRAN file due to that Tamuz2 facility is located in a restricted zone far away from the public, relatively low level radioactivity for the affected area, no evidence for airborne radioactivity hazards outside the reactor core and 30m berm surrounded Al-tuwiatha site. Assessment for accident conditions, were also neglected because no accident occurs in all work activities. The main components in Tamuz-2 reactor core which was dismantled and removed are:-

- Dummy are four experimental cells, made of net alloy AG-3, its form simulate the actual fuel cell, each one has cross-section area (8.4x8.4cm), length 80cm, thickness 5mm, contains four iron resistance rods.
- Upper chimney is nonradioactive item, made of stainless steel, 4.25m length, 5mm thickness, bolted with movable upper grid with 22 screws; it is positioned at level -4.25m measured from the top of reactor pool.
- Movable upper grid is nonradioactive material, made of net alloy AG-3, fixed at the top with upper chimney by 22 screws and fixed with AG-3 Aluminum chimney at the bottom by 22 screws. It is position at level -5m and -6m measured from the top of reactor pool.
- AG-3 Aluminum chimney was aligned with and extends the core grid (15cm) above the top surface of the pool water. The chimney assembly consists of two parts; a lower section made of AG-3 net alloy (thickness 2.5cm, height 80cm) and bolted to the core grid. An upper section made of stainless steel (thickness 5mm, height 4.2m). It was at -6m from the top of reactor pool.
- Zircoloy sheets are four plates compose of solid AG-3 net alloy. Two of them have (120×62×3.35cm) dimensions and another have (120×71×3.35cm). Zircoloy plates are positioned in core grid holes to provide shielding. It was at -6m from the top of reactor pool.
- Control rods are connected to their drive mechanisms by shafts located inside the control rod guide thimbles. The guide thimbles can be inserted into any core channel. Each drive mechanism was bolted to the control rod drive stand, which was perforated with a large number of holes to accommodate these bolts. The drive mechanisms can be placed in the position on the control rod drive stand required to insert the control rod in the core. Control rods are 6rods, 0.5cm thickness, (3.5″x3.5″) section area, 1.65m length and 6kg weight for each one. It was at -6m from the top of reactor pool.

- Internal core grid is made of AG-3 net alloy, has (56) square channels measuring (3.5″) on a side and the channels height was (1.1m).Thickness of the external wall measured at core level was (3.5mm).Channels were separated by (3mm) thick walls.
- External core grids are made of 150mm thicknesses net alloy AG-3 are designed to support the experiment rigs installed around the outside of the core. Two of them have dimensions (1.4x0.65m) and weighing 274kg while, another two have dimensions (2x0.65m), (0.7x0.6m) and weighing 378.4kg, 151kg respectively. It was at -6m from the top of reactor pool.
- Water box composes of a vertically-positioned, truncated cone made of AG-3 net alloy and weighing 700kg. This cone is formed by mechanically-welded elements and bolted to eight anchor studs adjustable by screws and located on the pool liner, for leveling vertical positioning. The lower part of the cone was closed by a plate, made of AG-3 net alloy (80mm) thick and perforated with (56) recessed holes, used to anchor support shafts for fuel elements or control rod guide thimbles. This plate positions the core assembly on the bottom of the pool and supports the weight of the core. It was at level -7m from the top of reactor pool.

The activities radiological characterization, dismantling and packaging were practiced to manage radioactive waste according to work time for each activity 28h/y, 225h/y and 18h/y respectively. Work time was 3h/day, 5day/week, 4week/month and 12month/year. The activities are:-

- Characterization is an initial step in the safety assessment process to provide a reliable database of information on quantity and type of radionuclides. It requires a logical approach in order to obtain the data necessary for planning a decommissioning program. The characterization program provides radiological information, which enables decisions on dismantling and removal of components and equipment. The characterization procedure has been done according to Multi-agency Radiation Survey and Site Investigation Manual (MARSSIM) [12]; standard approach for implementing the necessary radiological survey which derived by Nuclear Regulatory Commission, the U.S. Department of Energy, the U.S. Environmental Protection Agency and the U.S. Department of Defense and this guidance document used in the most of nuclear facilities under the decommissioning. The characterization program comprises review of historical information, in situ measurements, review and evaluation of the obtained data. The in situ measurement represents the flagship of the characterization program which involves dose rate measuring of reactor core and each segment, radionuclide identifying and taking swipe test for each segment to assure no loose contamination. The radiological characterization worker is positioned at the ground level 'figure 4' to measure the dose rate each 1m along the depth from the bottom to the top of reactor pool (before and after dismantling of each segment). The characterization was done by using Geiger Muller probe with cable detector 40m length. The average readings for each level were taken by measuring one and eight readings at the center and the surrounded area respectively. Then, each dismantled segment was obeyed characterization after removal 'figure 5' from the reactor core; to be adequate for packaging and transferring into specified accumulation zone.

Figure 4. Reactor core characterization

Figure 5. Component characterization

- Dismantling manners have been selected on the basis of previous experience on international decommissioning projects, taking into account availability of the dismantling technique and the low doses that existed inside the reactor core. Working area has been laid out and equipped in accordance with the applicable health and safety, fire protection and radiation protection requirements. Workers have provided with the industrial safety requirements like safety shoes, head covers, helmets, thick gloves and working suits. They also provided with radiation protection requirements like full face mask and personal radiation detection devices 'Figure 6'. The priority was given to dismantle and remove the Dummy from reactor core due to its relatively high dose (63mSv/h) which forms harmful to workers. Dummy removal is so important step and need to remove debris and dust from the reactor pool and core which generated from the destroyed of the reactor building during the second Gulf War in 1991. A simple hand tools were made to remove the rubbles while, compressed air system used to agitate the settled soil in reactor core and suck it up by a vacuum cleaner system to pack it exactly in the connected barrel and minimize the aerosols. The touched dose rate of the Dummy outer face is (63mSv/h) which need to attenuate into no more than (2mSv/h) [13], to be agreed with the waste acceptance criteria for the final waste receptor. Hence, a special container was designated to containerize the Dummy after removal. The manufactured Dummy container 'figure 7' is Carbon steel embedded by a pure lead layer of (12mm) thickness which cast in special ovens in the General Company for Batteries/Ministry of Industry to avoid formation of vocabularies during casting and assure that the touched dose rate of the container within the acceptable dose. Dismantling and containerize the four Dummy in the manufactured container has done by manufacturing a steel basket to hold the Dummy (through annular ring) during lifting it from its place into the container which placed away from the work area, to avoid the unjustifiable dose. Three times experimental lifting had made to train the worker man of crane to avoid accidents might be occurring. After Dummy removal, an encased steel structure by plastic glass was constructed above the reactor pool 'figure 8', to permit the light entering and protect the workers and the reactor pool from the weather variations. The structure also contains (2ton) overhead traveling crane to left and transfers the dismantled segments outside the reactor pool. Workers under control of radiation protection limitations and industrial safety requirements are dismantled components from top to the bottom of reactor pool. The dismantled worker was provided with the required hand tool and positioned at level facing the required segment in reactor core to unbolt the screws that fixed the segment 'figure 9' then, transferring it by the overhead crane outside the reactor pool.

Figure 6. Worker status

Figure 7. Dummy container

Figure 8. Structuring of reactor core

Figure 9. Dismantling of Upper chimney

- Packaging of reactor core segments have done according to Waste Acceptance Criteria (WAC) forms that established by Radioactive Waste Treatment Directorate (RWTD)/Ministry of Science and Technology (MoST) which is responsible for the final waste status. It is important to note that WAC guidelines are agreed with IAEA-TECDOC-1515 [14]. Hence, each dismantled piece of reactor core was warped in a thick nylon stratum and was stored in freight container by using suitable equipment like forklift machine to assure a safety distance for packaging worker and transferring each segment safely due to its relatively heavy weights 'figures 10, 11and 12'.



Figure 10. Packaging **Figure 11.** Transferring **Figure 12**. Store

Regulatory limitations which implemented here are (20mSv/y) maximum dose to the workers from all pathways; (0.4Bq/cm^2) clearance levels for surface contamination of radioisotopes have β and γ emitters, (0.1Bq/g) clearance levels for Co-60 radioisotopes in bulk materials [15,16,17].

To assure that the received doses within the principal As Low As Reasonably Achievable, the main safety principles for protection from the ionization radiation have been implemented here like calculation and limitation of work time according to in process safety assessment, increasing the distance (as possible) between the worker and the radiation source, using suitable containers to containerize the dismantling components and only the number of the necessary required workers have been permitted to fulfill the target activity.

3. Results and Discussion

With accordance to laboratory analysis of swipes tests which were taken from each component, sides of reactor pool, ground of reactor pool and the scattered materials; there is no evidence for loose contamination. The in situ measurements (by portable detectors) approved that all components are radiologically activated by Co-60 radioisotope. The manner in process survey was followed by measuring dose rate in reactor pool after dismantling and removal of any component as indicated in (table 1). The dose rate for each component after dismantling and removal away from reactor core also measured and tabulated in (table 2) below.

Table 1. The step by step in situ measuring of maximum dose rate by (μSv/h) units.

Height from the top of reactor pool (m)	**-7**	**-6.5**	**-6**	**-5**	**-4**	**-3**	**-2**	**-1**	**0**
Dose before Dummy removal	9900	63000	1900	79	60.3	47.8	21.6	17.9	13.6
Dose after Dummy removal	39	40	40	37	4.5	3.3	2.6	0.7	0.5
Dose after ampules removal	37	38	38	36	4.5	3.3	2.6	0.6	0.5
Dose after AG-3 chimney removal	37	38	38	35	4.0	3.0	2.4	0.5	0.5
Dose after Zircoloy sheets removal	75	80	78	65	2.6	0.85	0.7	0.6	0.3
Dose after Control rods removal	66	72	68	45	1.7	0.73	0.5	0.5	0.3
Dose after Internal core grid removal	3.4	4	2.88	0.65	0.15	B.G[a]	B.G	B.G	B.G
Dose after External grids removal	3.1	0.4	0.1	B.G	B.G	B.G	B.G	B.G	B.G
Dose after water box removal	B.G	B.G	B.G	B.G	B.G	B.G	B.G	B.G	B.G

[a]B.G = radiological Background = 0.09 μSv/h

Table 2. Dose rate for each component away from reactor pool.

Pool component	Contact Dose (µSv/h)
Dummy	63000
Ampules	550
Upper chimney and Movable upper grid	nonradioactive
AG-3 Aluminum chimney	1.21
Zircoloy sheets	79.8
Control rods	8.04
Internal core grid	63.5
External core grids	3.88
Water box	3.15

Results of SAFRAN calculations are printed in 'figures 13, 14 and 15' for worker endpoint who charged at dismantling, characterizing and packaging activities respectively.

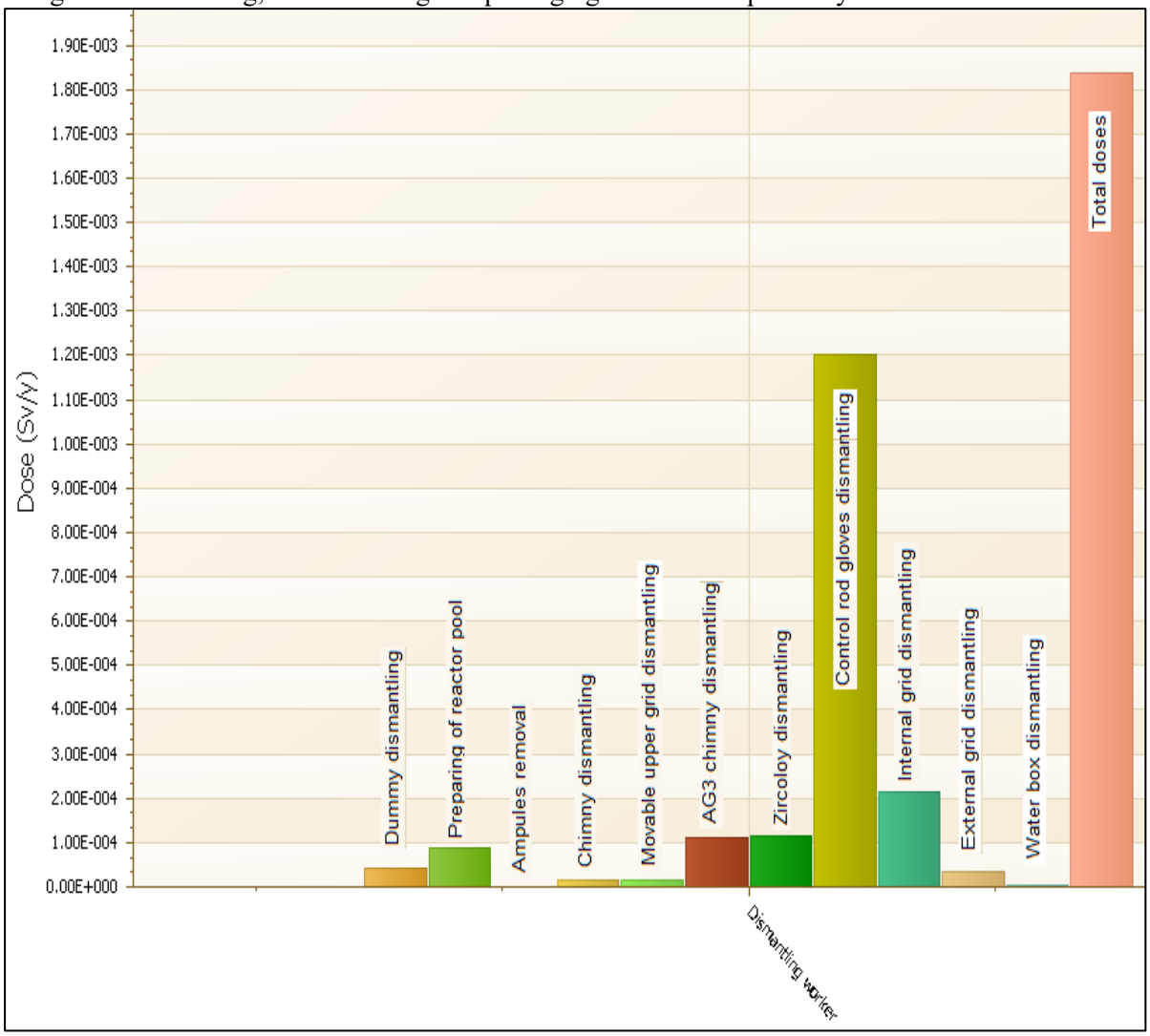

Figure 13. Dismantling scenario

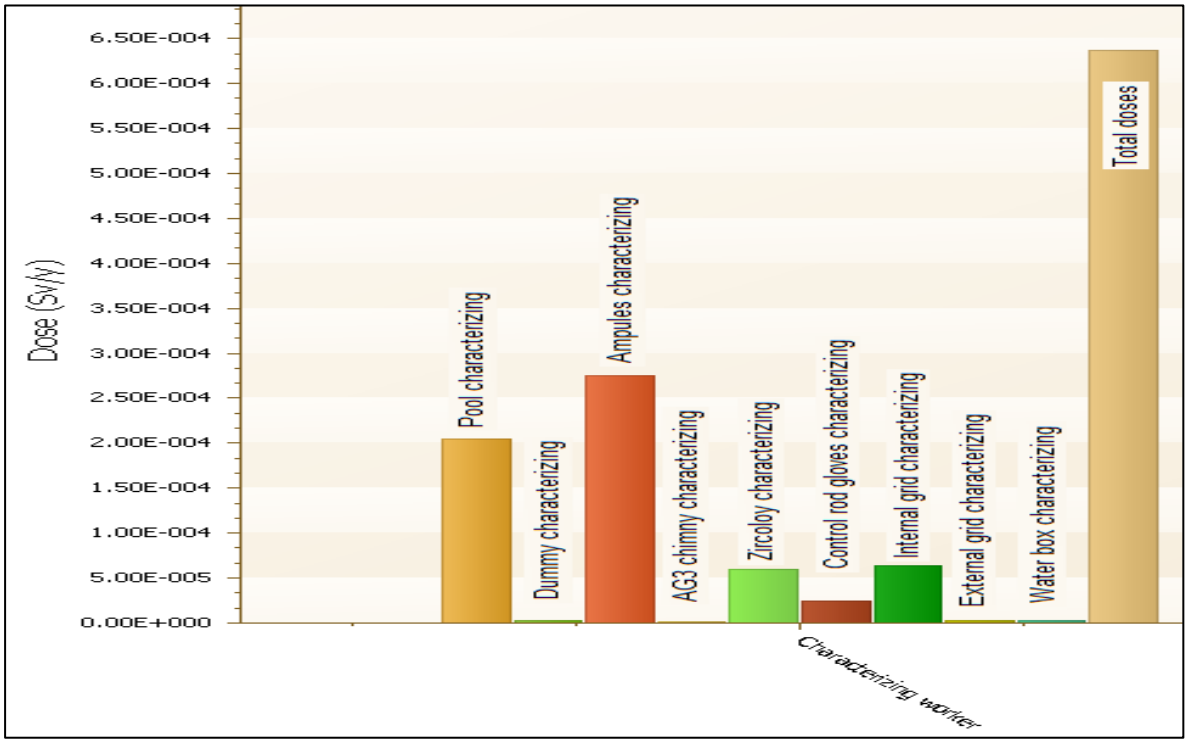

Figure 14. Characterization scenario

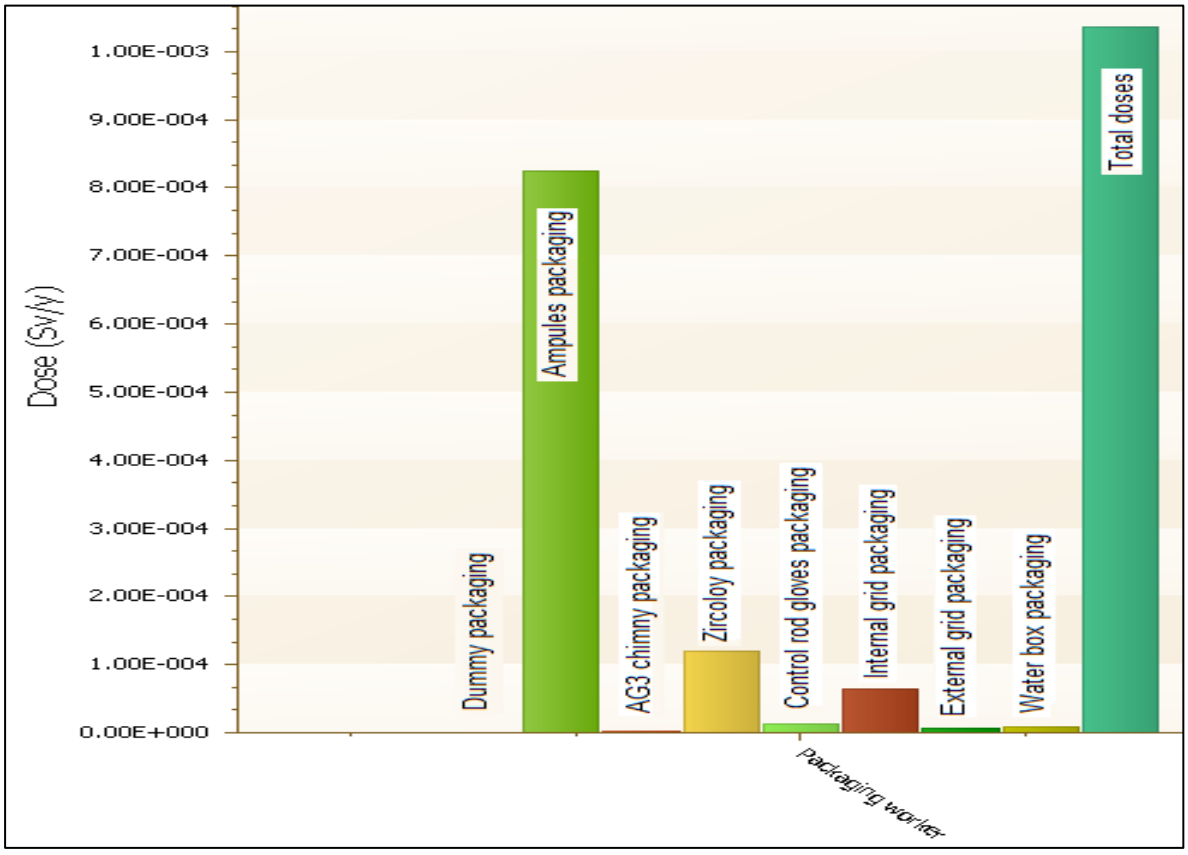

Figure 15. Packaging scenario

Table 1 shows the in situ measurement for dose rate by held detectors which has done with step by step manner. The dose rate was taken each 1m from the bottom to the top of reactor core depth after removing of every component. We can also see that the dose rate decreases after every removing process of components but the dose increases in case of Zircoloy removal and this actual matter because Zircoloy sheets work as a biological shield for reactor core.

Table 2 represents the maximum touched dose for each component which measured after dismantling and removal of a component outside the reactor core.

'Figure 13' indicates the dose rate that effected to the dismantling group of reactor core equipment. The worst case does at dismantling and removal of control rods gloves stage. The received dose rate in this stage (1.2mSv/y) formed 65% from the total dose rate (1.85mSv/y) which was received from the overall dismantling process but, in this context the total received dose rate (1.85mSv/y) remained below the allowable dose rate (20mSv/y) and formed about (9.25%).

'Figure 14' represents the received dose rate to the field measurement worker during characterizing of reactor core and ultimately characterizing of the each segment after dismantling. In this stage, the total received dose rate (0.64mSv/y) formed (3.2%) of the permissible dose rate (20mSv/y).

'Figure 15' shows the received dose rate to the field pretreatment group. This stage comprises packaging and relocating of the dismantling reactor core segments. The total received dose rate was (1.3mSv/y) which formed (6.5%) from the permissible dose rate (20mSv/y).

From 'figures 13 and 14', the worst case is at characterizing and packaging of ampules which scattered at reactor pool ground. The dose is 0.28mSv/y for characterizing worker and 0.83mSv/y for packaging worker which formed 44% and 64% from the total received doses for each case.

4. Conclusion

A hazard identification and radiological risk assessment study was conducted for the implemented activities to fulfill dismantling and removal works of Tammuz-2 reactor pool and core. Safety assessment results proved that the radiological hazard for all endpoint-scenarios remain below the low level hazard and within the acceptable annul dose for the worker in radiation field. Assessment taking into account specific aspects like contact dose rates, concentration of contaminants in air. The measures which were identified in the safety assessment are elicited through detail characterization and formally laid down in operational procedures and work instructions.

The International Commission on Radiological Protection (ICRP) derives the limit of an average of (20mSv/y) over five years for the occupational dose limit and (1mSv/y) for the public dose limit. The maximum worker dose is (1.85, 0.64 and 1.3mSv/y) for activities dismantling, characterizing and packaging of reactor core components respectively which formed (9.25%, 3.2% and 6.5%) from annul permissible dose (20mSv/y). Dose to the public was neglected and no accident was mentioned during works. Thus, the implemented manners to complete decommissioning of Tammuz-2 reactor core are considered to be adequate for the associated radiological risks As Low As Reasonably Achievable (ALARA).

References

[1] IAEA 2005 standard format and content for safety related decommissioning documents IAEA safety reports series No. 45 Vienna
[2] IAEA 2013 Safety Assessment for Decommissioning IAEA safety reports series No. 77 Vienna
[3] IAEA 2013 Radiation Protection and Safety of Radiation Sources IAEA Safety Standards Series GSR Part 3 Vienna
[4] IAEA 2007 Fundamental Principles of Security IAEA Safety Fundamentals No SF – 1 Vienna
[5] IAEA 2010 Pre-disposal Management of Radioactive Waste IAEA Safety Standards GSR-5 Vienna
[6] IAEA 2010.Assessment of the safety of facilities and activities IAEA General Safety Requirements GSR-4 Vienna

[7] Mousa M A, Al-Atia A B, Tuama H, Al-Mubarak M, Danneels J, John R C, Ken S and Roger C 2007 Decommissioning of The Iraq Former Nuclear Complex Proceedings of the 11th International Conference on Environmental Remediation and Radioactive Waste Management ICEM 2007 Belgium
[8] Ahmed A A, Jarjies A S, Al-Bakhat Y M, Abbas K, Nouri S, Nabeel H A, Ahmed S, Abdul Sahib k, Abdulhadi Q A, Walaa S W and Shamasldin E S 2013 Decommissioning of Tammuz-2 Research Reactor Iraqi Decommissioning Directorate (IDD) Iraq
[9] IAEA 2007 Remediation Process for Areas Affected by Past Activities and Accidents IAEA Safety Standards Series No. WS-G-3.1 Vienna
[10] SAFRAN tool and SAFRAN User Guide (http://goto.iaea.org/safran).
[11] IAEA 2011 Safety Guide for Safety Case and Safety Assessment for Predisposal Facilities and Activities IAEA Safety Series DS 284 Vienna
[12] Nuclear Regulatory Commission, the U.S. Department of Energy, the U.S. Environmental Protection Agency and the U.S. Department of Defense 2000 Multi-agency Radiation Survey and Site Investigation Manual (MARSSIM) NUREG-1575 Rev.1; EPA 402-R-97-016 Rev.1; DOE/EH-0624 Rev.1 Nuclear Regulatory Commission USA
[13] Radioactive Waste Treatment Directorate 2009 Waste Acceptance Criteria Form Ministry of Science and Technology (Form no. 1) Iraq
[14] IAEA 2006 Development of Specifications for Radioactive Waste Packages IAEA TECDOC1515 ISSN 1011-4289 Vienna
[15] Radiation Protection Center (RPC) 2012 Concentration Values for Clearance Levels of Radionuclides in Solid and Liquid Waste Ministry of Environment Iraq
[16] IAEA 2004 Application of the concepts of Exclusion, Exemption and Clearance IAEA Safety Guide No.RS-G-1.7 Vienna
[17] IAEA 2005 Derivation of Activity Concentration Values for Exclusion, Exemption and Clearance IAEA Safety Series No.44 Vienna

Achieving Real-Time Tracking Mobile Wireless Sensors Using SE-KFA

IOP Conf. Series: Journal of Physics: Conf. Series **1003** (2018) 012039 doi:10.1088/1742-6596/1003/1/012039

Achieving Real-Time Tracking Mobile Wireless Sensors Using SE-KFA

Dr. Haider Kadhim Hoomod[1], Sadeem Marouf M. Al-Chalabi[2]

[1] Computer Science Dept., Al-Mustansiriyah University, Baghdad, Iraq
[2]Informatics Institute for Postgraduate Studies, Iraqi Commission for Computer & Informatics, Baghdad, Iraq

Corresponding address drhjnew@gmail.com**,** sadeemalchalabi@gmail.com

Abstract. Nowadays, Real-Time Achievement is very important in different fields, like: Auto transport control, some medical applications, celestial body tracking, controlling agent movements, detections and monitoring, etc. This can be tested by different kinds of detection devices, which named "sensors" as such as: infrared sensors, ultrasonic sensor, radars in general, laser light sensor, and so like. Ultrasonic Sensor is the most fundamental one and it has great impact and challenges comparing with others especially when navigating (as an agent). In this paper, concerning to the ultrasonic sensor, sensor(s) detecting and delimitation by themselves then navigate inside a limited area to estimating Real-Time using Speed Equation with Kalman Filter Algorithm as an intelligent estimation algorithm. Then trying to calculate the error comparing to the factual rate of tracking. This paper used Ultrasonic Sensor HC-SR04 with Arduino-UNO as Microcontroller.

1. INTRODUCTION

Arising to the progresses in mobile wireless devices and technologies, Real-Time (RT) be important with a development of necessities, e.g., system of movable agents in RT navigation systems. Various kinds of new applications needs to intend about the RT, which are putted in use to record the distances and tracking with some conditions of the entities in the surroundings. Each RT detections may be deals with a sensitive deadline on its termination time and it is necessary to meet these deadline conditions for safety or cost (as an examples). Demands may be certified as lasting queries and govern in the system up to their deadlines have been expired. As an examples, a RT of a mobile agent may convince a navigation demand for the better way from its current location to its others destinations, surely the better trail will have to be permanency traced over RT until the agent get its destination[1, 2]. So, RT defined as an idiom used to distinguish system of computer that get the reaction at the same range as they trigged the order[3].

Choosing the mobile wireless sensor depending on the innate of the required projects. Some complexities appear when using mobile sensors because more of them are affected with material such as cotton, sponge, unshaped object[4]. Moreover, It could be impressed as well with humidity, wind, heat, interference waves, etc. [5].

In a pursuit of agent applications, the mobile sensors which can detect itself by itself as a target at a firmed time that kept in a lively mode while the others nodes in deactivate mode, so as to save power (energy) until the agent be near (or reach) the distinct desired points. To continuously observing mobile agent, multi sensors must be in active mode just before agent be close with them (the distinct desired points).

This tracking over RT calculations can be applied through various algorithms such: Kalman filter Algorithm (KFA), which is a well-known mathematical technique, KF is an predicator that estimate and correct the circumstance of wide range for linear processes as a future location of a mobile object, it

could configured for single or multiple objects for tracking, unfortunately, with KF the object should move in static velocity or with constant acceleration. It is important to mention that KF algorithm consists two steps: prediction and correction (the update phase) by calculating the previous states for estimate the current state. The correction phase is uses the current state such as object location, speed to correct the status[6].

As a related works for this achievement, Multiple or single models which used tracking methods with estimation are provoke many researchers and institutions for estimate RT. Here are some synopsis of several studies and researches:

-Saptarshi Bandyopadhyay, et al. in 2016 IEEE conference, the Consensus Filter of Bayesian (BCF) used for monitoring and tracking the movements of a targets in RT according to a collective networks of multi-sensing agents. and by consensus achieved for the best predicate of the expected of the target's distributions states comparing with (LogOP), (BCF) algorithms and conditions on the communications networks topologies has been resolved[7].

-Philipp Kohler, et al, produced in 2013 an experimental for examined the use of cost-effectiveness, ultrasonic sensors widely used for the tracking vehicles especially with high velocities, However, the result take concerning about blind-spot-surveillance and lane-change decision systems is analyzed. the detection rate approach is delivered with RT calculations[8].

-Georges S. Aoude, et al in (2011), the researchers introduced an algorithm called RR-GP as a dilation of the closed-loop rapidly exploring random trees (CL-RRT) algorithm to calculate reachable blocks of movements for agent in RT. Furthermore, the concept showed a necessary achievements in a cost and accuracy[9].

-Boris Babenko, et al. wrote in 2009 that Multiple Instance Learning (MIL) tracers which unbind the confusion of agent appearance using multiple proposals of the agent and then improvably tracks the mobile agent with the online sundry instance learning algorithm. [10].

-H. He, et al. In 2008 (IEEE) had designed a range measurements tools using (S3C2410). The finesse improved using temperature indemnity module in RT[11].

-Y. Jang, et al. In 2007 (IEEE) had adopted a mobile walking distances measurements system which having 90% of perfection in RT[12].

-C. C. Chang, et al. In 2004 (IEEE) had searched the ultrasonic measurements systems for underwater operation. It uses ultrasonic kit, laser system beside a camera upon a system for 3-D location controls, it found the error rate equal to (±1) for each 35cm, but when added GIC filter working in RT, the error reduced to 0.6[13].

The remains of this paper, 2^{ed} section mentioned around a criteria for selection an agent, 3th and 4th Parts are the specific details around the equipment and tools (Hardware / Software) which were used in a proposal system, 5rd section contain the proposed system, 6th part is the proposed system navigation, then 7th is the experimental results and discussion, the Penultimate part is for the conclusion and future works.

2. CRITERIA SELECTING A SUITABLE AGENT FOR REAL-TIME ACHIEVMENT

Many kinds of sensors can be found in the markets, it's an important to choose the suitable one, that mean the selection should impact some fundamentals criteria such: accuracy, range, distance, usability, cost and others[14].

like this proposal, a robotic model build to do a real test by placing sensor(s) up of movable robot, then make some processing to find the agent by itself and its locations (exact position) that can deal with a static known environment[15].

The concept's work for most of sensors is depending on the reflection of waves as in figure (1), the time duration that leaves the trigger pin until reflecting to the echo pin dividing by 2 should obtain the distance of that object (agent)[16, 17].

Meanwhile, with developments, different types of sensing technologies have been developed and examined to avert conflict among critical area of construction equipment[18]. However, in different

environments, the performance of sensing technologies disparate, such as movable agents or with static objects. This variance appears many testing standards protocols to appraise the overall system performance and the pattern of objective which is looking for estimations to the next positions and RT.

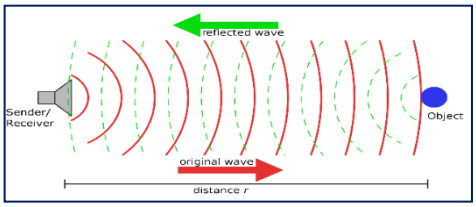

Figure 1. Concept Work of Sensor

Nevertheless, concerning to the exemplary caution when these kinds of sensors are used, RT could be impacted and achieved[19].

With scientific fields, normally sensor waves has different frequencies, the frequency range varies depending on the type for that subject. Figure (2) explain the concept of the interplaying between sensor and its environment[20].

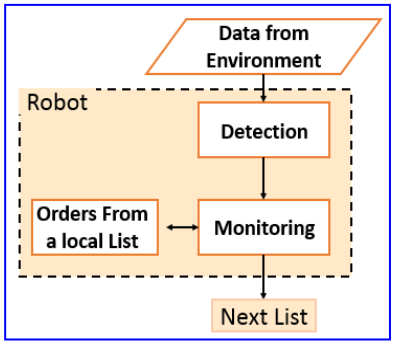

Figure 2. Concept Attractive Between Environment and Sensor

3. HARDWARE REQUIREMENTS

A. Ultrasonic Sensor (UsS): In this excrement, two HC-SR04 ultrasonic sensor has been chosen.

B. Arduino Microcontroller: Two (Microcontrollers) arduino UNO Board is used.

C. Transceiver Bluetooth: Two TB has been used, One of them connected with the automotive agent and the other connected to the computers, the data transmitted wirelessly between these two MC by two TcBT.

D. Steeper Motor (H-Bridge): Dual H Bridge- DC Drive L298N usually used for controlling motors speed and direction.

E. 4*4 Robotic Car: Four programmable DC-Motors, as a chase for picking up the whole kits for navigations.

4. SOFTWARE REQUIREMENTS

A. ARDUINO 1.5.6-r2: Using open-source arduino language for writing and uploading the arduino code, which named IDE Processing Language[21]. Additionally, the parameters can be monitored by the serial port online or offline by saving the result into a list (database).

B. VB.NET: Using VB.net environment for programing the algorithms for collecting all the results those needing for estimation RT.

5. THE PROPOSED SYSTEM

Generally, monitoring and tracing some mobile wireless sensors (MWS) provoke the researchers and developers to concentrate on the mechanisms that tracking reliance to the RT. The proposed system

looking for improvement and increasing the facilities on the agent navigation that traveling through static environment.

As related with these systems, surely the agent need a microcontroller(s) for controlling and guiding the robotic agent to do some coordination with the leader sensors. Then, Speed Equation - Kalman Filter Algorithms (SE-KFA) will used for achieving RT. and improved the efficiency as will appear in dissections section.

At the beginning, lets understand the whole algorithm which drown as a scheme in figure (3).

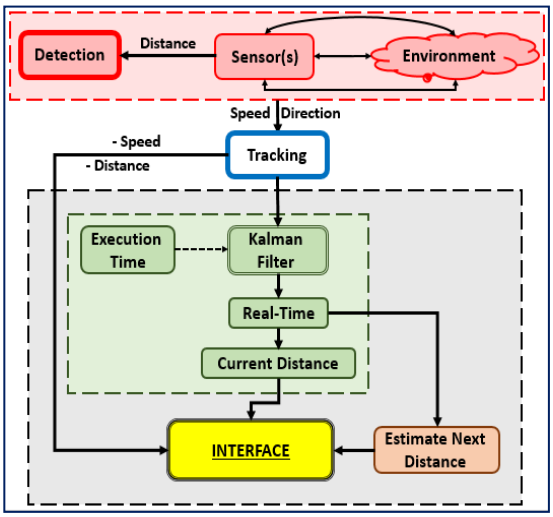

Figure 3. Scheme for Estimation Concept Work

This scheme consist two main stages:

1. The vision environment represented by the surrounded regions of the sensor(s) that could achieved the detection step. After detection step, the identifier step realized and the conditions for tracking has been achieved.

2. Second stage, represented by algorithms, the processed that accruing in the computer.

This proposal select a static / partially observed environment. When sensor turn on, the trigger sent its bullet and waiting for reflections while received by receiver pin (echo), certainly, this is controlled and calculated through microcontroller. By estimation, the total time travel dividing by two, distance can be obtained positively, these parameters achieved by mathematical speed in equation (1).

$$\boldsymbol{D = (T * V)/2} \quad (1)$$

Where: **D** = Distance, **T** = Time, **V** = Velocity

According to this tracking, distance (d) and time (T) has been collected. It is a good idea to mention that time (t) referring to the event at that distance, and distance (d) referring to the farness from the obstacle at this distinct point of time. Moreover, the distinct time that Microcontroller execution time for processing is (t_{mc}). Therefore, the input could be as in figure (4) below:

t	t_{mc}	d

Figure 4. Monitoring Controller Scheme

According to the equations of KFA, parameters (t, t_{mc}, d) treated in algorithm (1) below. Which explain the interactive between parameters obtained and SE-KFA until RT achieved:

ALGORITHM (1)

1. **Input:** i, dis , disTime, tmc, mct
2. exe[i] = tmc + mct

```
3.      t[i] = disTime
4.      d[i] = dis
5.      if ( i > 0 ) then
6.              Δt[i] = t[i] – t[i-1]
7.              Δd[i] = d[i-1] – d[i]
8.              if ( i = 1 ) then
9.                      Tt[1] = 1
10.                     Rte[1] = 0
11.                     St[1] = Δt[i]
12.                     NTE[1] = t[i] + St[1]
13.             else
14.                     Tt[i] = 1 – (Δt[i-1] - Δt[i] )/( Δt[i] )
15.                     Rte[i] = ( NET[i-1] – t[i] ) / t[i]
16.                     St[i] = Δt[i] × ( Tt[i] – Rte[i] )
17.                     NTE[i] = t[i] + St[i]
18.             End if
19.             S[i] = Δd[i] / St[i]
20.             array = SORT (s)
21.             If (count (array) mod 2 = 0 ) then
22.             x̃ = ( array( count(array) / 2 ) + array(( count( array ) / 2 ) + 1 )) / 2
23.             else
24.                     x̃ = array( count(array) / 2)
25.             End if
26.             ES[i] = 2 × si[i] - x̃
27.             ENAL[i] = d[i] – ( ES[i] × St[i] )
28.             ETt[i] = exe[i] × ( Tt[i] – Rte[i] )
29.             EAL[i] = d[i] – ( S[i] * ETt[i] )
30.             Output: ENAL[i], EAL[i]
31.     End if
```

The algorithm above cleared that the time (t_i) and next distance (d_{i+1}) appear the predicates for the mobile agent reliance on the amounts of its previous experience by taking the amount of change over time (Δt_i) which resulting from subtracting the present time devoid of previous time (t_{i-1}), As well as, taking the change in distance (Δd_i) by subtracting the current distance from the previous distance (d_{i-1}).

To calculates the amount of new time variation (Δt_{i+1}), the variation amount of the next time disparity is require for calculations, for take in consecrations the challenges (side effectiveness) that affected sensor(s) while processes. The percentage of time taken (T_t)[1] is calculated by changing the current time variation (Δt_i) relative to the previous time variation (Δt_{i-1}), and this ratio is subtracted from 1 to obtain the percentage of time taken (T_t).

This procedure (the calculation of the amount of time variety) also depends on the amount of error ratio (RTe)[2], which also depends on the ratio of variety in the amount of next time estimation (NTE_{i-1}) relatively to the current time (t_i).

For calculating the supposed time (St_i) for that period which collecting from the multiplication of the amount of (Tt_i) with (RTE_i) insofar of current variety of time (Δt_i) which is used to calculate the current

[1] The initial value of (T_t) = 1

[2] The initial error (RT_e) = 0.0

speed and also if it associated with the variety in distance (Δd_i) and even to calculate the value of (NTE_i) if combined with the current time (t_i).

In order to estimate the next location of the agent ($ENAL_i$), speed estimation (ES_{i+1}) should calculate, which resulting from double value of current speed (S_i) subtracting from the arithmetic mean of the preciouses velocities ($\hat{Y}_i$). When speed estimation achieved, ($ENAL_{i+1}$) can be reached successfully by subtracting the current distance (D_i) from the result of multiplied speed estimation (ES_{i+1}) multiplexing by time estimation (St_i). The algorithm processing can be represented as flow diagram in figure (5) below.

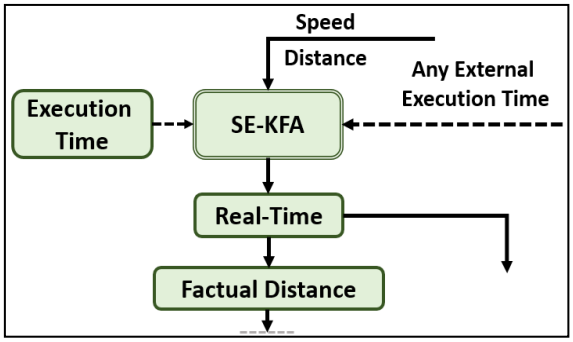

Figure 5. SE-KFA Processes

6. PROPOSED ESTIMATION ALGORITHM

Numerous kinds of experimental proposals has designed as a physical testing model, in this experimental, there are movable agent in the static environment. The navigation concepts are illustrated in figure (6):

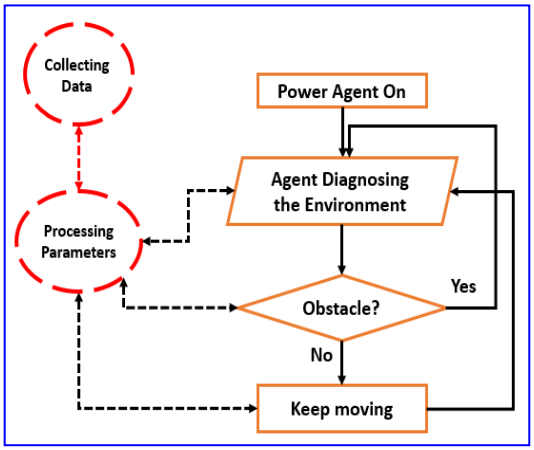

Figure 6. Flow Diagram for Navigation Concept

This navigation done by arduino, UsS and others tools (as above-mentioned in the requirement section) which controlling the whole operation. car robot (the agent) which can move forward, backward, left and right with different speeds and avoiding obstacles, this is depending on the algorithms that used for tracking. Figure (7) as a flowchart clarifying this roving algorithm. According to these general-purpose data, RT can be estimated. And calculate error deviation through Mean- Root Square deviation Equation (MRSD)[3]. And do mean testing by Standard Deviation (SD)[4]. For more information it is a good idea to see ref.[22].

[3] RMSD: used for measure differences between population values which predicted for an estimator and the values successfully observed.

[4] SD: is a criterion that used to determine the magnitude of variation or dispersal of a set of data values.

$$MRSD = \sqrt{\frac{\sum_{i=1}^{n}(\hat{y}_i - y_i)^2}{n}} \quad (2)$$

Where: **yi** = depended variable, **ŷi** = predicted values for observation **i**, **n** = different predictions.

$$SD = \sqrt{\frac{1}{N-1}\sum_{i=1}^{N}(x_i - \bar{x})^2} \quad (3)$$

Where: $x_1, x_2, x_3, \ldots x_n$ = observed values, $\bar{x}$ = mean value, **N** = the size of the sample

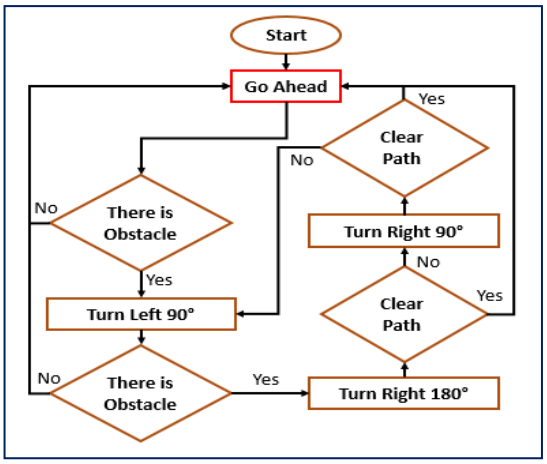

Figure 7. Flowchart for the Roving

7. RESULTS AND DISCUTION

The proposed technique has applied using VB.NET 2008 for test and calculate the RT estimation according to algorithm 1. IDE Processing Language V.1.8.4 for uploading the demanded code into the arduino MC for collecting parameters and controlling the agent that has been used. The computer specification was Corei5 with Ram 4G.

The experiments done three times for readings (25, 50 and 100) iterations in sequences, which implemented in static environment with (300*300cm). The initial distance started with 283.7cm and decreasing by (Δd) as an average according to the iterations that shown in table I.

Table I shown the excremental result for the time and distance error between the readings values and the estimations values, that measured using RMSD to calculate the differences between them, and SD to measure the quantify of the amount of variation for the set of mean square error between them.

The measured of RMSD with different iterations for the distance shown in figure (8, 9 and 10) and for the time shown in figure (11, 12 and 13).

Table 1. The Average Parameters for Delta-Distance by three deference sequences reading.

Readings	Average Δd	RMSD t	SD t	RMSD d	SD d
25	2.7876	0.139174	0.0922492	5.674394	4.28679
50	2.39586	0.103399	0.0730302	4.294559	3.26957
100	2.28603	0.080976	0.0559782	3.360349	2.56172

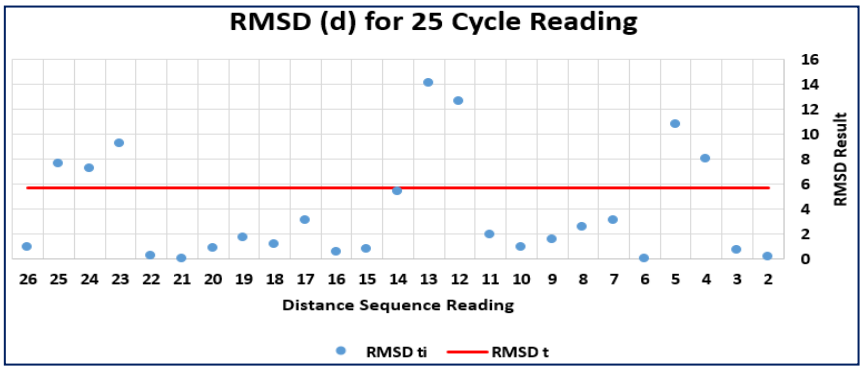

Figure 8. Error Rate for Mean over $RMSD_d$ for 25 Cyclic Readings

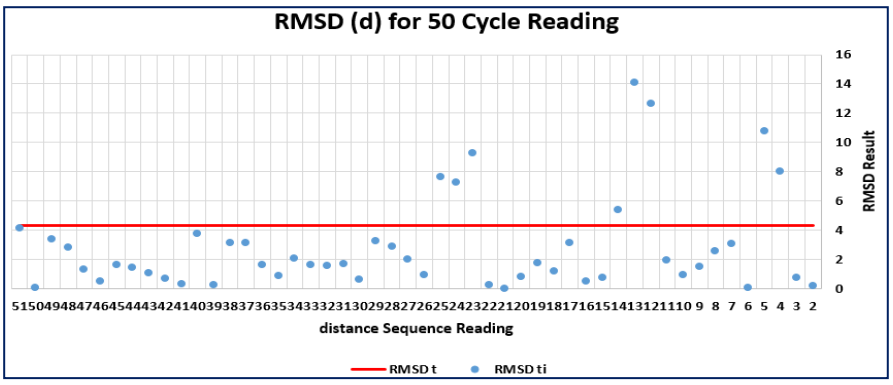

Figure 10. Error Rate for Mean over $RMSD_d$ for 50 Cyclic Reading

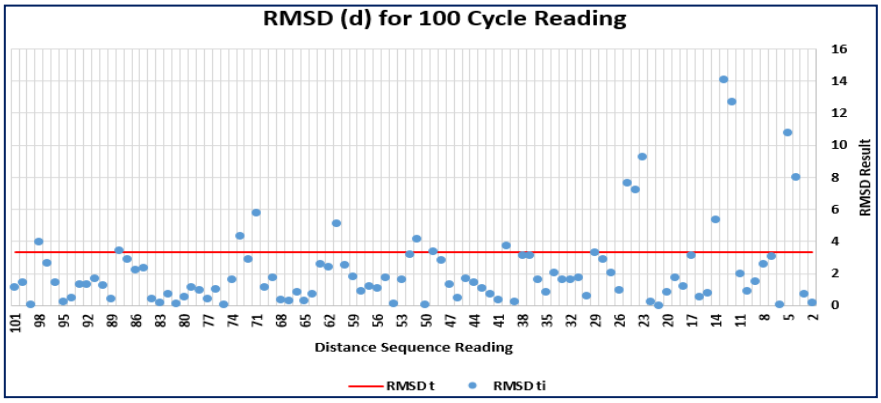

Figure 9. Error Rate for Mean over $RMSD_d$ for 100 Cyclic Reading

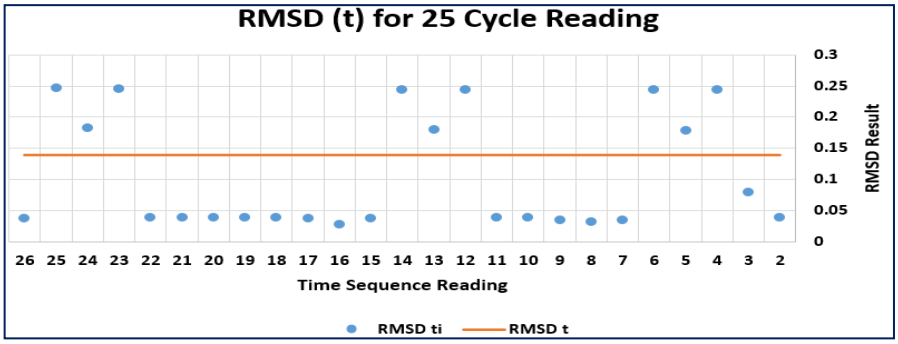

Figure 11. Error Rate for Mean over $RMSD_t$ for 25 Cyclic Reading

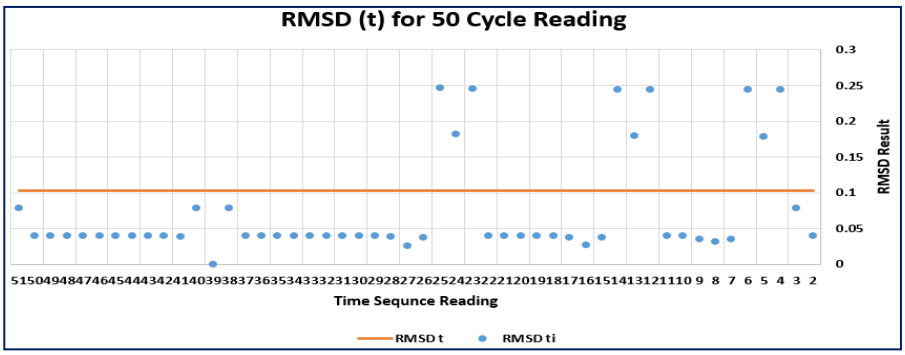

Figure 12. Error Rate for Mean over $RMSD_t$ for 50 Cyclic Reading

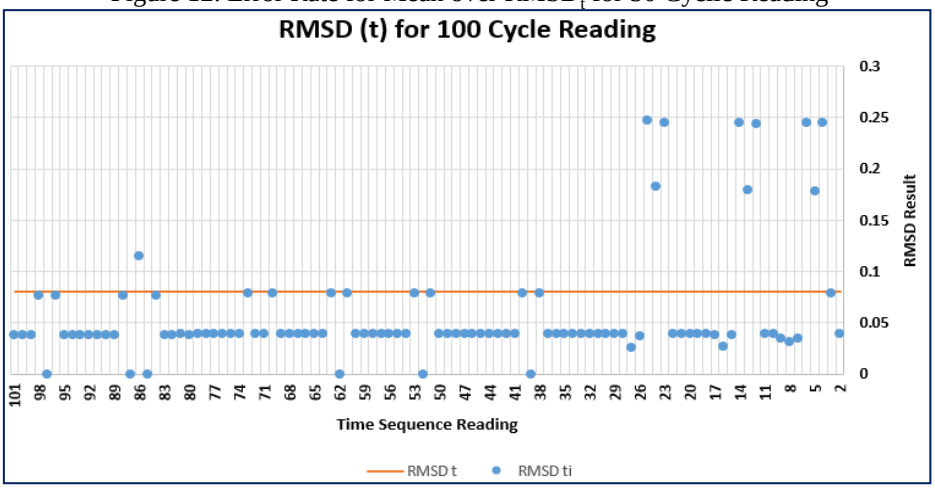

Figure 13. Error Rate for Mean over $RMSD_t$ for 100 Cyclic Reading

8. CONCILIATION AND FUTURE WORKS

In this paper, authors present an extensive study for tracking mobile wireless sensor to estimate Real-Time using SE-KFA. The errors between readings and estimations values for the time and distance measured using RMSD and SD with different iterations (25, 50 and 100). The experimental result shows that the RMSD value going to be closer to the stable state (sense to zero area) whenever collecting more readings as figure (14) which clarified these changeability. It is clear that when sensor did 25 readings (for both time and distance) the RMSD was 43%, 32% when 50 readings used, and finally 25% with 100 readings.

As future works, it could possible to use others types of sensors such laser sensor or any other perfect sensor for distance measurements to achieve RT and also could possible to test the impact of a curve movements with SE-KFA .

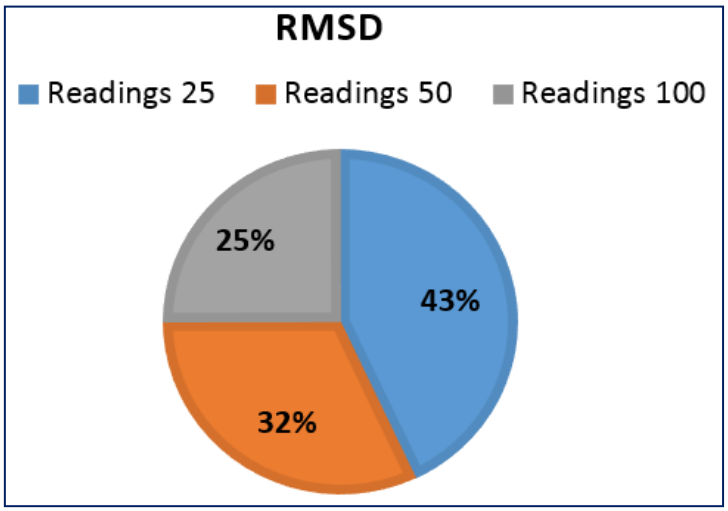

Figure 14. The Ratios for RMSD

9. REFERENCES

[1] K.-Y. Lam, A. Kwan, and K. Ramamritham, "RTMonitor: Real-time data monitoring using mobile agent technologies," in *Proceedings of the 28th international conference on Very Large Data Bases*, 2002, pp. 1063-1066.

[2] G. S. Aoude, B. D. Luders, J. M. Joseph, N. Roy, and J. P. How, "Probabilistically safe motion planning to avoid dynamic obstacles with uncertain motion patterns," *Autonomous Robots*, vol. **35**, pp. 51-76, 2013.

[3] T. E. R. F. real-time. (n.d.). The American Heritage® New Dictionary of Cultural Literacy, 2017 from Dictionary.com, "*NDCL," T. AH, Ed.*, ed: USA Heritage, 2017.

[4] D. Marioli, C. Narduzzi, C. Offelli, D. Petri, E. Sardini, and A. Taroni, "Digital time-of-flight measurement for ultrasonic sensors," *IEEE Transactions on Instrumentation and Measurement*, vol. **41**, pp. 93-97, 1992.

[5] K. Ohtani and M. Baba, *Shape Recognition and Position Measurement of an Object Using an Ultrasonic Sensor Array*: INTECH Open Access Publisher, 2012.

[6] S. S. Pathan, A. Al-Hamadi, and B. Michaelis, "Intelligent feature-guided multi-object tracking using Kalman filter," in *Computer, Control and Communication, 2009. IC4 2009. 2nd International Conference on*, 2009, pp. 1-6.

[7] S. C. Bandyopadhyay, Soon-Jo, "Distributed estimation using bayesian consensus filtering," in *American Control Conference (ACC), 2016*, 2016, pp. 634-641.

[8] P. C. Kohler, Christian Verl, Alexander, "Vehicle tracking using ultrasonic sensors & joined particle weighting," in *Robotics and Automation (ICRA), 2013 IEEE International Conference on*, 2013, pp. 2900-2905.

[9] G. Aoude, J. Joseph, N. Roy, and J. How, "Mobile agent trajectory prediction using Bayesian nonparametric reachability trees," in *Infotech@ Aerospace 2011*, ed, 2011, p. 1512.

[10] B. Babenko, M.-H. Yang, and S. Belongie, "Visual tracking with online multiple instance learning," in *Computer Vision and Pattern Recognition, 2009. CVPR 2009. IEEE Conference on*, 2009, pp. 983-990.

[11] H. He and J. Liu, "The design of ultrasonic distance measurement system based on S3C2410," in *Intelligent Computation Technology and Automation (ICICTA), 2008 International Conference on*, Proceedings of the IEEE International Conference on Intelligent Computation Technology and Automation,Oct. 2008, pp. 44-47. , 2008, pp. 44-47.

[12] Y. Jang, S. Shin, J. W. Lee, and S. Kim, "A preliminary study for portable walking distance measurement system using ultrasonic sensors," in *2007 29th Annual International Conference of the IEEE Engineering in Medicine and Biology Society*, Proceedings of the 29th Annual IEEE International Conference of the EMBS, France, Aug. 2007, pp. 5290-5293, 2007, pp. 5290-5293.

[13] C. C. Chang, C. Y. Chang, and Y. T. Cheng, "Distance measurement technology development at remotely teleoperated robotic manipulator system for underwater constructions," in *Underwater Technology, 2004. UT'04. 2004 International Symposium on*, 2004, pp. 333-338.

[14] M. Kelman, "Distance Measurement via Using of Ultrasonic Sensor," *Journal of Automation and Control*, vol. **3**, pp. 71-74, 2015 2015.

[15] Y. Golhar and U. Shrawankar, "Human Gesture Detection & Recognition: A Need of an Era," 2016.

[16] Y. Qi, C. B. Soh, E. Gunawan, K.-S. Low, and R. Thomas, "Assessment of foot trajectory for human gait phase detection using wireless ultrasonic sensor network," *IEEE Transactions on Neural Systems and Rehabilitation Engineering*, vol. **24**, pp. 88-97, 2016.

[17] H. K. Hoomod and S. M. M. Al-Chalabi, "Objects Detection and Angles Effectiveness by Ultrasonic Sensors HC-SR04.", IJSR, Vol. **6** P. 6, 2017

[18] T. Guenther and A. Kroll, "Automated detection of compressed air leaks using a scanning ultrasonic sensor system," in *Sensors Applications Symposium (SAS), 2016 IEEE*, pp. 1-6.

[19] S. Choe, F. Leite, D. Seedah, and C. Caldas, "Evaluation of sensing technology for the prevention of backover accidents in construction work zones," *Journal of information technology in construction*, vol. **19**, pp. 1-19, January 2014 2014.

[20] D. S. Vidhya, M. D. P. Rebelo, M. C. J. DSilva, M. L. W. Fernandes, and M. C. J. Costa, "Obstacle Detection using Ultrasonic Sensors," vol. **2**, p. 316, APR 2016.

[21] A. DAusilio, "Arduino: A low-cost multipurpose lab equipment," *Behavior research methods*, vol. **44**, pp. 305-313, 2011.

[22] S. J. Finney, C. DiStefano, and J. P. Kopp, "Overview of estimation methods and preconditions for their application with structural equation modeling," in *Principles and Methods of Test Construction: Standards and Recent Advances* vol. **3**, ed, 2017.

Acknowledgment
Special thanks for MSc. Atheer M. Al-Chalabi for all his advises and supporting.

Applying self-organizing map and modified radial based neural network for clustering and routing optimal path in wireless network

IOP Conf. Series: Journal of Physics: Conf. Series **1003** (2018) 012040 doi:10.1088/1742-6596/1003/1/012040

Applying self-organizing map and modified radial based neural network for clustering and routing optimal path in wireless network

Haider K Hoomod and Tuka Kareem Jebur
Al-Mustansariyhi University-Education College-Computer Science Dept. Iraq .Baghdad
Drhjnew@gmail.com , tukakareem9@gmail.com

Abstract: Mobile ad hoc networks (MANETs) play a critical role in today's wireless ad hoc network research and consist of active nodes that can be in motion freely. Because it consider very important problem in this network, we suggested proposed method based on modified radial basis function networks RBFN and Self-Organizing Map SOM. These networks can be improved by the use of clusters because of huge congestion in the whole network. In such a system, the performance of MANET is improved by splitting the whole network into various clusters using SOM. The performance of clustering is improved by the cluster head selection and number of clusters. Modified Radial Based Neural Network is very simple, adaptable and efficient method to increase the life time of nodes, packet delivery ratio and the throughput of the network will increase and connection become more useful because the optimal path has the best parameters from other paths including the best bitrate and best life link with minimum delays. Proposed routing algorithm depends on the group of factors and parameters to select the path between two points in the wireless network. The SOM clustering average time (1-10 msec for stall nodes) and (8-75 msec for mobile nodes). While the routing time range (92-510 msec).The proposed system is faster than the Dijkstra by 150-300%, and faster from the RBFNN (without modify) by 145-180%.

Keyword: ad hoc wireless network, MANET, Clustering, routing , wireless network clustering, modified Radial based neural network, SOM .

1. Introduction

An ad-hoc networks are collections of wireless mobile-nodes dynamical forming as temporary networks without using of any exists networks infrastructure or centralizes-administration.

The router is a free to moving random and organizing them-selves arbitrarily; thus, the topology of wireless network maybe changes rapidly/unpredictably Multi-hop, mobilities, large networks size combine with devices heterogeneity, band-width, and battery-power constraint making the designs of appropriate routing-protocols are major challenges [1].

Mobiles Ad-Hoc Networks (MANETs) are self-organized networks, thus, ad hoc considered Self configuring infrastructures-less networks of mobile devices connects by together. MANETs devices are free in moving in-dependently in any directions, and will therefore changes their links to another devices frequently. This move will be produced changing of its links to other devices considerably. Each must forward traffic unrelated to its own use, and therefore be a router hence, the major challenge of constructing MANET's is to continue keep the information collected for routing traffics [1]. MANETs can possessing characteristics likes(Bandwidth constrained, variables capacity-links, Energy-constrained Operations, Limited-Physical Security, Dynamics networks topologies, Frequent-routing update , an infrastructure-less, self-organized and multi hop networks with frequently changes the topologies causing the wireless links broken and re-establish on the fly [2].

The Routing in network can define as the process of choosing the paths in a network to convey network traffic. For this, the need to design routing protocol which seamlessly acclimatized with changing network topology that was unavoidable. As a consequence to the routing in this network

became one of the most important challenging missions [3]. Hence routing in MANETs became one of the most challenging tasks. Routing in networking is the process of selecting paths in a network to send network traffic. Therefore, the need to design a novel routing protocol which seamlessly adapt to changing network topology was inevitable [4].

The Clustering, is a method to gathering nodes into groups. These groups are contained by the network and they are known as clusters. A cluster is basically a subset of nodes of the network that satisfies a certain property [5,6]. Hence, the clustering can be define as a way to rearrange all nodes into small groups are defined as Cluster Head (CH) and cluster members that are determined with the same rule. Every clustering algorithm consists of two mechanisms: cluster formation and cluster maintenance.

Many researches in wireless network routing explored and suggested algorithm to find the optimal shortest path for nodes. In order to supply an overview of former work and to supply a basic theoretical understanding of the considered topic, some recent researches presented by different authors are reviewed and quote in this section. Some of these researches about the applying neural networks to find optimal path in wireless network.

2. Related Works

Many researches deal with the optimal shortest path in the wireless network like:

Kourosh Dadashtabar Ahmadi, et al in 2015[7] they present a new centralized adaptive Energy Based Clustering protocol through the application of Self organizing map neural networks (called EBC-S) which can cluster sensor nodes, based on their energy level and coordinates. they applying some maximum energy nodes as weights of SOM map units; so that the nodes with higher energy attract the nearest nodes with lower energy levels. So a cluster may not necessarily contain adjacent nodes. The new algorithm enables us to form energy balanced clusters and equally distribute energy consumption on whole network space. Simulation results show the considerable profit of our proposed protocol over LEACH and LEA2C (another SOM based protocol); by increasing the network lifetime and insuring more network coverage.

Siddesh.G.K, et al. in 2011[8] proposed a routing protocol in ad-hoc wireless network using software computing's technique like neutral's network, fuzzy logics and genetic algorithm. Performed simulation uses various existing protocols like power aware routing protocol, proactive, reactive and hybrid routing protocols. Authors use software computing's share to improving the protocol performance in very dramatic terms, establishing the link between the nodes in minimum time and find the optimal route to a large network.

S. Gangwar, K. Kumar & M. Mittal in 2015 [9] They have implemented ART1 neural network over the cluster head selection as a part of the routing technique which selects the cluster head depending on residual energy of the mobile node after the completion of every data transmission. After simulating the results showed that ART1 algorithm or simply ART1 has optimized the problem of cluster head selection and consequently optimized residual energy. And the network lifetime is increased up to 58% as compared to traditional routing techniques.

X. S. Asha Shiny and R. Jagadeesh Kannan in 2015[10], they proposed an Energy-Efficient-Clustering Protocols based on Self-Organizing Maps (EECPSOMs) in MANETs. The proposal program can be clustering sensors-nodes depends on additions parameters such as energy-levels and weights of sensor-nodes. Self Organized Mapping (SOM) helping in formatting cluster, so that nodes with higher-energy attracts the nearest-nodes with low-energy levels. Also, the method enabling to forms energy-balanced cluster and distributes the energy consumptions in an equivalently manner. And the EECPSOM results proving the minimizing the energy using and make energy efficient to lifetime of the networks.

3. **Radial Basis Function Networks:**

This type is distinctive kind in neural network and the radial basis function is activation function of this network [11]. It is very popular network and can be used for control and classification problems function approximation, time series prediction [12]. It has several distinctive features compared with other type of neural network: is faster learning speed, more compact topology, and universal approximation, therefore, it is different from other neural networks. This network has been widely applied in many engineering fields and science [12]. Radial Basis Function Networks (RBFNs) are comprised of three layers: input layer, hidden layer and output layer (as shown in figure 1)[13]. The input layer passes the input vector x = (x1, x2, . . . , xn) to the RBF layer. That later - which is a hidden layer of H RBF units - using transforms the input to new vector y = (y1, y2, . . . , yh) that is subsequently passed to the output layer using the linear transformation. Then the final result f = (f1, f2, . . . , fn) can be expressed as:

$$k(x) = \sum_{j=1}^{h} wjkyj = \sum_{j=1}^{h} wjk\Phi\left(\frac{||x-cj||}{bj}\right) \qquad (1)$$

where fk is the output of the kth unit of the output layer [14], c_j is the center vector for neuron j, b_j are weights to be determined.

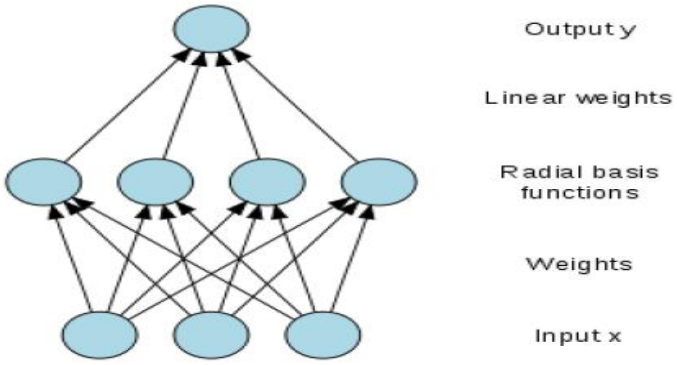

Figure 1. RBF network Example [13].

4. Self-Organizing Map Neural Network (SOM)

A SOM or Self-Organizing Features Maps (SOFMs) are an un-supervising neural network consisting of neurons organize on a regular low-dimensional grids. Each neuron is presented by an n-dimensional weight vector where n is equal to the dimensions of input vectors. Weight vectors (or synapses) connect the input layer to output layer which is called map or competitive layer .[7]

SOMs operate in two-modes: Trainings and Mappings modes. The training-mode built the maps use inputs examples. Training is competitive-processing called vector-quantization. SOMs consist of many nodes (or neuron). Each node is associated with a light-vector of the similar dimensions as the input-data vectors and positions in the map-space. The normal nodes arrangements are a regular-spacing in a hexagonal (or rectangular) grids. SOMs describe a mapping from a higher-dimensional of input-spaces to a lower-dimensional map spaces. The practices to place vectors from data-space onto the maps are for finding the nodes with the closest light-vector to the vector-data taken from data-spaces and to assigning the map-coordinates of these nodes to these vectors.[6,7]

5. The Proposed System

The main proposed system goal is to enhancing the performance of the Ad hoc and MANET wireless network operations and services that effected by their characteristics such as no preexisted infrastructure and high dynamic topology caused unpredictable change of their nodes location and

status (nodes may enter and leave the network duo to broken routing links and packed lose, drop packed so it needed recalculate their broken routing links information). These problems cause consumes processing time, memory, device power that introduces overhead traffic on the network and reduces network life time, limited transmission range, limited coverage area.

Hence, this proposed system was designed and implemented to avoiding some of these problems for these networks types by using methods (clustering and adaptive routing neural network based) to get new adaptive routing algorithm for ad hoc and MANET wireless network (depending on the important role performance (routing delay, bandwidth, distance, no. of hops to reach the destination)).

Using neural network to controlling messages passing in network by finding the optimal path from source to distention. In this proposed system, the RBFN modified to work as router to getting the optimal path for the wireless network (like MANETs). The proposed system stages are:

1. **Clustering:** apply self-organizing map neural network to determine best cluster head and optimal number of clusters with their nodes.
2. **Finding optimal path:** applying the new proposed MRBFN network to find the optimal rout from source to destination. Figure 2 shows the flow chart of the proposed system.

At first step, reading the N nodes in wireless network, then clustering operation will setup to find the clusters number in the network using SOM neural network with n nodes (mobile and stall nodes). SOM will selects cluster heads for every cluster using path weights of nodes, and configure the clusters according to nearest to center of cluster, assigning roles to (CH node) and determined the member node and getaway node for each cluster.

5.1 Modified Radial Based Function Neural Network (MRBFNN)

RBF network is feed forward neural network and using cluster, it is simpler and has three layer the training process, it is generally faster, and the output result determined by hidden layer only so it considers fast and give approximation value to desirable result, it is trained by hybrid learning algorithms by using unsupervised learning supervised learning to reduce the error.

MRBFNN considers efficient method to increase network lifetime and find the optimal path in wireless network from source to destination. In this stage, the proposed modified RBFN is used to find the optimal shortest path. Algorithm (1) shows the proposed modified RBFNN operation to find optimal path. In this algorithm, the proposed method depends on the information from the above stages like (number of CH, the path terminal points p1-p2, number of nodes, all paths information, network parameters and features).

In this modification, the hidden layers' weights to the outputs layer are adjusted and measured depending on the parallel "Moore-Penrose generalized pseudo-inverse". The parallel Moore-Penrose pseudo inverse algorithm gaining some matter over general gradients algorithm such as stop criterions, learning rates, and epochs number and local's minima's, has been useful for real time application because it is low trainings times and generalization abilities due to applying to all weights in parallel.

The modification of the Gaussian kernel is, by adding some K-mean operations feature. The main factor of the K-Means clustering is the Euclidean distances computing among points to center of cluster. The average Euclidean distance for all nodes to the cluster center also computed and used in the adjusting the basis functions for paths selecting. The new basis's functions are taken to be modified Gaussian's:

$$\varphi(||x\text{-}cj||) = \exp\{\frac{||x-cj||2+2Emj}{2Emj62i}\} \qquad (2)$$

The variable sigma, σ, defines the width or radius of the bell-shape and is something that has to be determined empirically, the outputs from the hidden units are φ, the set centres of hidden units are cj, the inputs are x, and Em is the average Euclidean distance points closest to the cluster center for the (jth) hidden unit in the hidden layer.

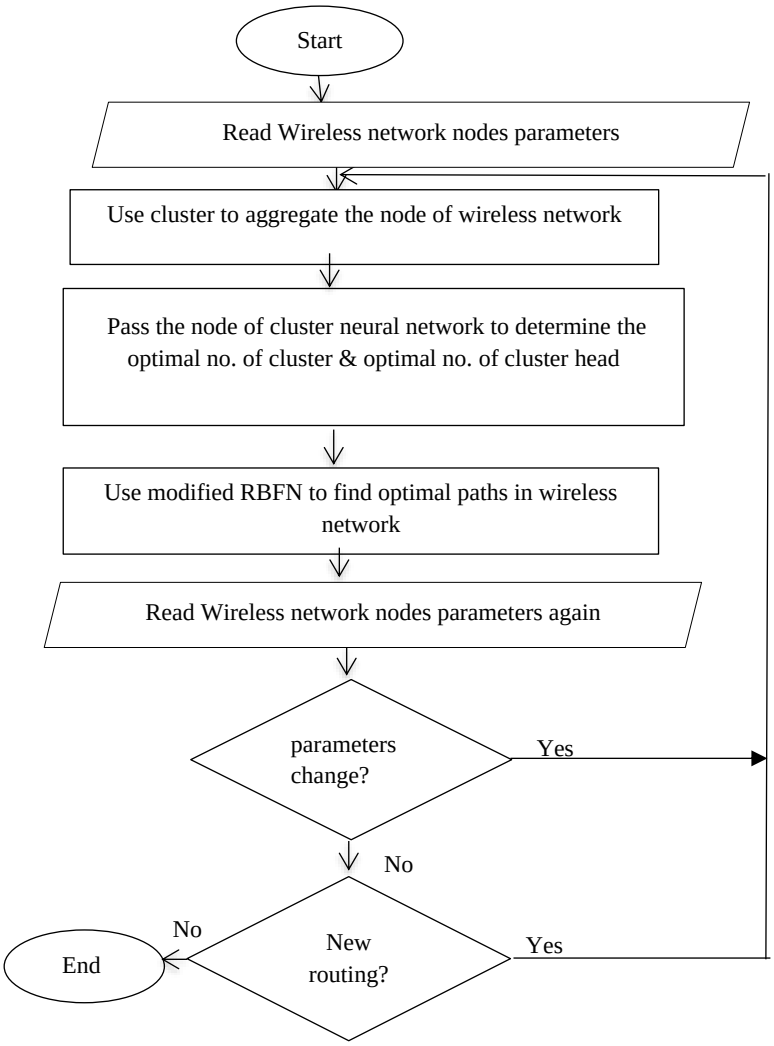

Figure 2. Flow Chart of the Proposed System

Mostly, the activation function center and distribution must have same data characteristics. Here, the center and width of Gaussians are selected using K-means clustering features (like Euclidean distance). The proposed modified RBFN neural network will initialize using the parameters like number of the layers nodes. In this proposed system, the modified RBFN input layer has size equal to all input information, hidden layer dynamic change depends on the errors of results until get the optimal paths, but it designed to initialized by 10 nodes (as defaults), and the output layer has also dynamic size starts with 30 nodes represent the number of nodes of the optimal path and change depends on the optimal path nodes.

The modified RBFN learning by using the smallest Euclidean distances for the clusters, and learning operation will be optimizing by other wireless nodes parameters (clusters size regions, packed

size, (dynamic or non-dynamic), link costs). The optimization will guide to get the optimal paths between two nodes in wireless network; not only on the distance between them.

A**lgorithm 1: Modified RBFN to find optimal path**

Start:
Input: patterns nodes connection and paths, k: no. of clusters, number of intra path p1, inter path p2, number of CH all from SOM algorithm
Output: find the optimal path

Note: Hidden layer: weight $W_{i\ j}$ =1,2, ... The neurons activated in this layer to find the shortest path that have smallest values E_{ij}.
Step1. Initialize Modified RBFNN and initialized the parameter k = {k1, k2, ..., kn} of nodes.
Step2. Select the best Q that has the short path from all paths with minima E_{ij} using:
Q = min E_{ij} // in Hidden layer
And has best other wireless nodes parameters (clusters size regions, packed size, Dynamic or non-dynamic, link costs).
Step3. Initialize the weights vector Wight kept as fixed while the hidden to output weights are learned with minimum distance and apply eqn. (2).

$$\varphi(||x-cj||) = \exp\{\frac{||x-cj||2+2Emj}{2Emj62i}\}$$

Step4. Select the minimum Euclidian's distances of B_{ij}

$$Bij = Q \sum\sum_{j,i=1,2..m} \|p1-p2\|$$

And optimized by other wireless nodes parameters (clusters size regions, packed size, (Dynamic or non-dynamic), link costs).
Step5. Update the value of weights vector using Moore-Penrose pseudo-inverse as follows:
$(W)_{ij} = w_{ij}$, $(\Phi)_{pj} = \varphi(x_p)$, and $(T)_{pi} = \{t_{ip}\}$.
D= dimensional input vector xp = $\{x_p: i = 1, ..., D\}$
K1= dimensional target output tp = $\{t_p: i = 1, ..., K1\}$.
Widths $\{\sigma_j\}$ Wights w_{ij}
Step6. iteratively Repeats Step (2-5).
Step7. Neurons have smallest's values of E_{ij} is output. //Outputs Layers
End

6. Results and Discussion

There are many results can be achieved from applying the proposed system based on the network cases and parameters distributions. The configuration of wireless network effects the results of clustering and routing because these proposed algorithms depend on their parameters. So, the results of the proposed system will take effect changing the network parameters like (bitrate, link costs (hops no.), distances, dynamic and fixed topologies(mobility), network size, number of nodes, packed size, shape and size regions).

Many evaluation criteria were used to test the results of routing protocol, but in our proposed system the time will take as the main evaluation due to the virtually of the wireless network used in our tests .

Figures (3-4) show an example of the SOM clustering and MRBFN routing results. While the tables (1-4) show the results of optimal path for MRBFN routing and Dijkstra algorithm. Table (5) shows the network parameters. The SOM clustering average time (1-10 msec for stall nodes) and (8-75 msec for mobile nodes). The proposed system is faster than the Dijkstra by 150-300%, and faster from the RBFNN (without modify) by 145-180%.

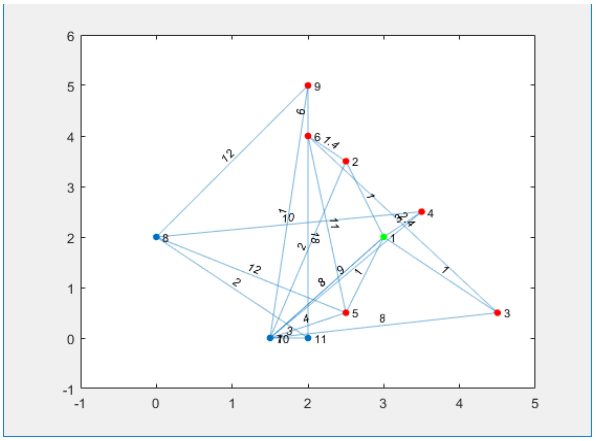

a) Optimal number of cluster head when Using SOM with (10 nodes)

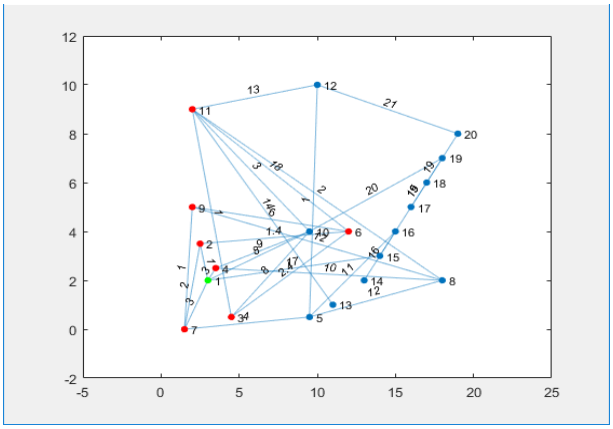

b) optimal number of cluster head when using SOM with (20 nodes)

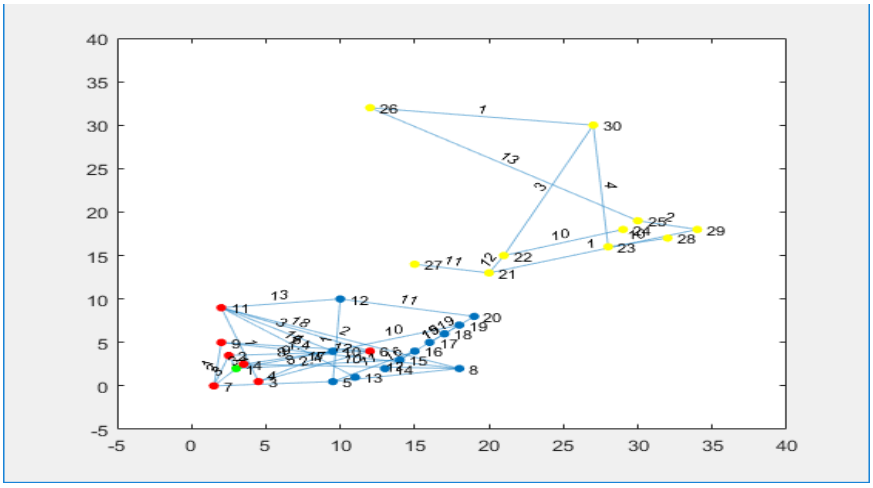

c) Optimal number of cluster head when using SOM with (30 nodes 2 cluster)

Figure 3. Optimal number of cluster head when using SOM with (10, 20 and 30 nodes).

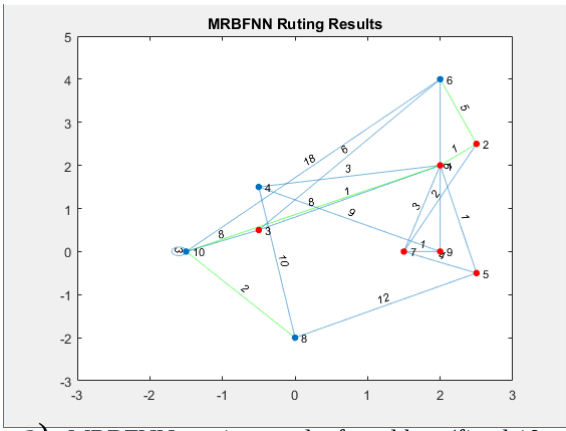

a) MRBFNN routing results for ad hoc (fixed 10 nodes 2 clusters). The optimal path between node 6 and node 8 is: 6 2 1 10 8

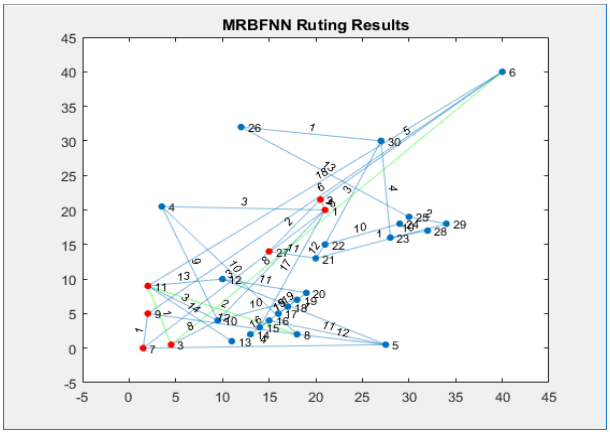

b) MRBFNN routing results for ad hoc (fixed 30 nodes 2 clusters). The optimal path between (6 and 8) nodes is: 6 3 11 8

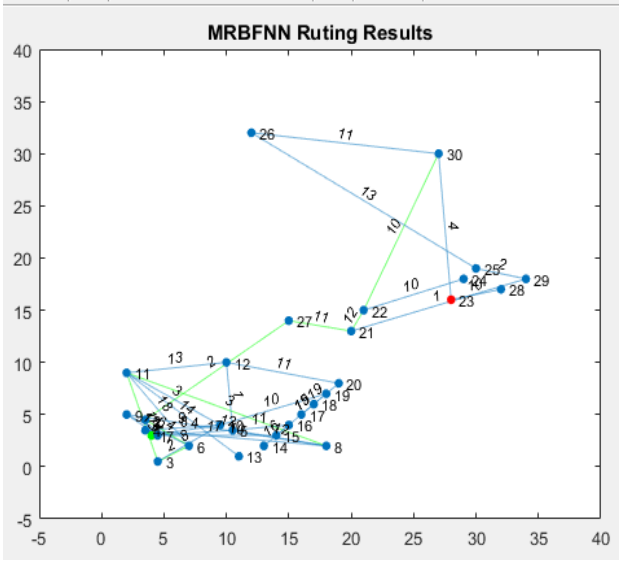

Start state

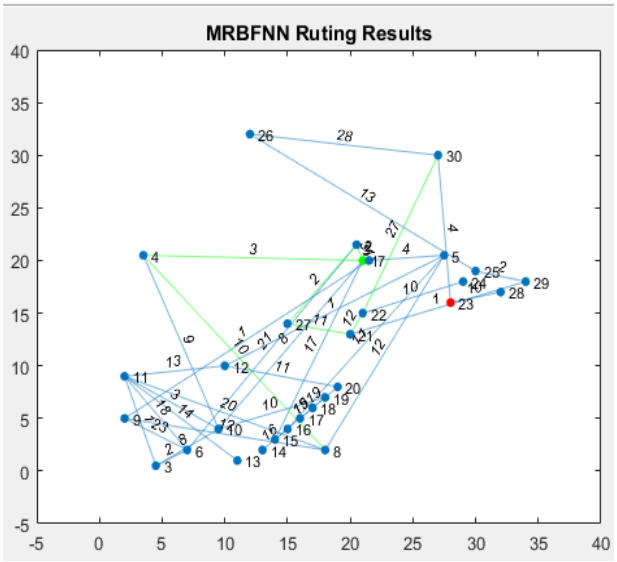

Final state

b) MRBFNN routing results for ad hoc (dynamic 30 nodes 2 clusters). Optimal path between (8 and 30) nodes change from 30 22 21 27 2 6 3 11 8 to 30 22 21 27 21 4 8 due the changing of network status and links costs distances, and bitrates (move some nodes)

Figure 4. The Proposed MRBFNN Routing Results Examples.

Table 1 The proposed system routing results for 10 nodes (fixed topology) first approach.

samples	Dijkstra Time(avg.)	MRBFNN time(avg.)	RBFNN time(avg.)	Avg. bitrate(kbs)	Avg. links costs	Avg. Distance	Cover nodes
Net1	0.41328	0.09211	0.14563	1-100	1-10	1-10	all
Net2	0.41677	0.09321	0. 14666	1-800	1-10	1-10	all
Net3	0.41638	0.09406	0. 14721	1-1000	1-10	1-10	all
Net4	0.41767	0.09425	0. 14655	1-1000	1-10	1-10	all

Table 2 The proposed system routing results for 10 nodes (one-two nodes mobile).

Samples	Dijkstra Time(avg.)	MRBFNN time(avg.)	RBFNN time(avg.)	Avg. bitrate(kbs)	Avg. links costs	Avg. Distance	Cover nodes
Net1	0.60893	0.11089	0.23410	1-100	1-14	1-12	all
Net2	0.61071	0.11107	0.24089	1-800	1-14	1-12	all
Net3	0.61189	0.11110	0.24066	1-1000	1-14	1-12	all
Net4	0.62839	0.11119	0.24100	1-1000	1-14	1-12	all

Table 3 the proposed system routing results for 10 nodes (three nodes mobile).

Samples	Dijkstra Time(avg.)	MRBFNN time(avg.)	RBFNN time(avg.)	Avg. bitrate(kbs)	Avg. links costs	Avg. Distance	Cover nodes
Net1	0.92111	0.32319	0.42310	1-100	1-16	1-15	all
Net2	0.92201	0.32440	0.43423	1-800	1-16	1-15	all
Net3	0.92288	0.32474	0.43111	1-1000	1-16	1-15	all
Net4	0.92376	0.32489	0.42980	1-1000	1-16	1-15	all

Table 4 The proposed system routing results for 10 nodes (five nodes mobile).

Samples	Dijkstra Time(avg.)	MRBFNN time(avg.)	RBFNN time(avg.)	Avg. bitrate(kbs)	Avg. links costs	Avg. Distance	Cover nodes
Net1	1.52985	0.50897	0.72410	1-100	1-19	1-17	all
Net2	1.54453	0.50991	0.72657	1-800	1-19	1-17	all
Net3	1.55190	0.51072	0.73780	1-1000	1-19	1-17	all
Net4	1.57340	0.51098	0.73067	1-1000	1-19	1-17	all

Table 5 the network parameters.

Parameter	Description
Routing Protocols	(CBRP +neural net.) or neural net.
Size of Region	2 km
Shape of Region	Random
Number of Nodes	10,50 and 100
Packet Size	20-64kb (random and fixed)
Cluster Head	2,3 and 5
Simulation Environment	Dynamic, fixed
Channel Type	Wireless Channel
Network Type	Ad hoc and mobile ad hoc
Connection protocol	UDP (User Datagram Protocol)
Node Distance	Different
Node Link Cost	Different
Node Link Bitrate	Random

7. Conclusions

MANETs one type of wireless networks and uses in many fields but this wireless network has many disadvantages such as Bandwidth-constrained, limited translation range, energy- constrained operation, limited physical security, dynamic network topology and packet lose and linked breakage hence finding optimal path in this network is a problem and need to solving with intelligent technique to overtake these challenges.

As shown from the results and ratios, the proposed routing algorithm is more speed and efficient than Dijkstra due to the intelligence technique in selecting the optimal path, and the different parameters used in selecting the optimal path between nodes. The SOM is also very fast in the node clustering and increase the performance of the optimal paths selecting by our proposed system. High speed routing will increase the throughput of the network, the life time of nodes, and connection links become more useful. The packet delivered ratio is also increase because the optimal path has the best parameters from other paths including the best bitrate and best life link with minimum delays.

References

[1] Navpreet Kaur, Sangeeta Monga, 2014," Comparisons of Wired and Wireless Networks: AReview", *International Journal of Advanced Engineering Technology.*

[2] Anuj K. Gupta, Harsh Sadawarti, and Anil K. Verma, November 2011," Review of Various Routing Protocols for MANETs", *International Journal of Information and Electronics Engineering*, Vol. **1**, No. 3

[3] Naveen Garg1, Kiran Aswal2 and Dinesh C Dobhal, 2012, " A Review of Routing Protocols in Mobile Ad Hoc Networks", *International Journal of Information Technology and Knowledge Management* January-June, Vo**l** 5, No. 1, pp. 177-180.

[4] Vanita Rani PG Student, Dr. Renu Dhir, 2013." A Study of Ad-Hoc Network: A Review", *International Journal of Advanced Research in Computer Science and Software Engineering*, Volume **3**, Issue 3, March.

[5] M. Anupama and Bachala Sathyanarayana, 2011" Survey of Cluster Based Routing Protocols in Mobile Ad hoc Networks ", *International Journal of Computer Theory and Engineering*, Vol. **3**, No. 6, December.

[6] Heni Kaaniche and Farouk Kamoun ,2010 "Mobility Prediction in Wireless Ad Hoc Networks Using Neural Networks", *Journal of Telecommunications*, Vol.**2**, Issue 1, April.

[7] Kourosh Dadashtabar Ahmadi , Morteza Barari and Neda Enami, 2015"Energy Based Clustering Self Organizing Map Protocol for Wireless Sensor Networks ", international journal of information & communication technology research , vol.**7** no. 1.

[8] Siddesh.G.K, K.N.Muralidhara, Manjula.N.Harihar, 2011 " Routing in Ad Hoc Wireless Networks using Soft Computing Techniques and Performance Evaluation using Hyper Net Simulator", *International Journal of Soft Computing and Engineering* (IJSCE)ISSN: 2231-2307,Vol. **1**, Issue 3, July.

[9] S. Gangwar, K. Kumar and M. Mittal, 2015 "Cluster Head Selection in Mobile Ad-hoc Network (MANET) Using ART1 Neural Network", *African Journal of Computing & ICT*, Vol. **8**. No. 1, March.

[10] X. S. Asha Shiny and R. Jagadeesh Kannan, 2015 " Energy Efficient Clustering Protocol using Self Organizing Map in MANET", *Indian Journal of Science and Technology*, Vol. **8**(28), October.

[11] Parvinder Kaur, Dr. Dalveer Kaur & Dr. Rajiv Mahajan, 2015" The Literature Survey on Manet, Routing Protocols and Metrics", *Global Journal of Computer Science and Technology: E Network, Web & Security*, Vol. **15** Issue 1 Version 1.0.

[12] Tuba Kurban and Erkan Beşdok, "A Comparison of RBF Neural Network Training Algorithms for Inertial Sensor Based Terrain Classification, 2009", *Geomatics Engineering, Engineering Faculty, Erciyes University, Turkey*, 9, 6312-6329; doi:10.3390/s90806312.

[13] Navpreet Kaur, Kuldeep Singh, Hardeep Kaur, 2014 "Radial Basis Function (RBF) Based Routing Optimization for Wireless Sensor Network", *international Journal of Advanced Research in Computer and Communication Engineering* Vol. 3, Issue 6, June.

[14] Larysa Aharkava, 2010" Artificial neural networks and self-organization for knowledge extraction", Master thesis, department of Theoretical Computer Science and Mathematical Logic.

Bayesian Estimation of Reliability Burr Type XII Under Al-Bayyatis' Suggest Loss Function with Numerical Solution

IOP Conf. Series: Journal of Physics: Conf. Series **1003** (2018) 012041 doi:10.1088/1742-6596/1003/1/012041

Bayesian Estimation of Reliability Burr Type XII Under Al-Bayyatis' Suggest Loss Function with Numerical Solution

Amal A. Mohammed [1,2], Sudad K. Abraheem[3,4] and Nadia J. Fezaa Al-Obedy [5,6]

Department of ways & Transportation, College of Engineering, Mustansiriyah University, Baghdad, Iraq.
Department of Mathematics, College of Science, Mustansiriyah University, Baghdad, Iraq.
Department of Mathematics, College of Science, Mustansiriyah University, Baghdad, Iraq.

dr.amal70@uomustansiriyah.edu.iq and orcid.org/0000-0003-4832-4197.
sudad1968@uomustansiriyah.edu.iq and orcid.org/0000-0002-2629-9093.
abualhassan76@uomustansiriyah.edu.iq and orcid.org/0000-0003-1134-4979.

Abstract. In this paper is considered with Burr type XII distribution. The maximum likelihood, Bayes methods of estimation are used for estimating the unknown scale parameter (α). Al-Bayyatis' loss function and suggest loss function are used to find the reliability with the least loss. So the reliability function is expanded in terms of a set of power function. For this performance, the Matlab (ver.9) is used in computations and some examples are **given**.

Keywords: Bayes methods, reliability function, Bayyatis', expanded, power function.

1. Introduction

The Burr type XII distribution is one of the most important distributions that belong in the Burr family of distributions was introduced by Burr(1942) [1], and make this distribution (Burr XII) a real importance in the last decades for importance it use in practical situations, this distribution applied in the reliability study, theory of probability, statistics, view time of the failure and economic measurement. It has been introduced by many authors some of whom are Makhdoom, I. [2], Erika, H. [3], Feroze, N. [4], Yarmohammadi, M. [5], Kleiber [6]. Research aims to estimate the reliability function for α when the shape parameter λ is

known by using maximum likelihood and Bayes methods with prior distribution depends on Fisher information's and loss functions.

In this work, Al- Bayyatis' [7], suggested Al- Bayyatis' and numerical method(expansion method) are used to comparison between the estimators that to see, first the best method, secondly the suitability approved loss functions in research. Expansion method is a simple way to find approximate solution based on expanding function [8, 9] or interpolation function [10].

The Burr type XII distribution is continuous probability distribution on (0,∞) for non-negative random variable, the probability density and cumulative distribution function of Burr type XII distribution random variable are given by [1,11]:

$$f(t;\,\alpha,\lambda) = \alpha\lambda t^{\lambda-1}\left(1+t^{\lambda}\right)^{-(\alpha+1)} \;\; ; \;\; 0 < t < \infty \tag{1}$$

$$F(t;\,\alpha,\lambda) = 1-\left(1+t^{\lambda}\right)^{-\alpha} \;\; ; \;\; 0 < t < \infty \tag{2}$$

where $\alpha > 0$ and $\lambda > 0$ are the scale and shape parameters respectively.

The corresponding reliability function $R(t)$ and failure rate function $h(t)$, at mission time t are given as [1, 11].

$$R(t) = 1-F(t;\,\alpha,\lambda) = \left(1+t^{\lambda}\right)^{-\alpha} \;\; ; \;\; 0 < t < \infty \quad \alpha,\lambda > 0 \tag{3}$$

$$h(t) = \frac{f(t)}{R(t)} = \alpha\lambda\, t^{\lambda-1}\left(1+t^{\lambda}\right)^{-1} \;\; ; \;\; 0 < t < \infty \quad \alpha,\lambda > 0 \tag{4}$$

2. Maximum Likelihood Estimation:[12]

Let $t = (t_1, t_2, \ldots, t_n)$ be the life time of a random sample of size n drawn independently from Burr type XII distribution defined by equation(1). The likelihood function for the given sample observations is defined as:

$$L\left(\alpha,\lambda|\underline{t}\right) = \prod_{i=1}^{n} f(t_i|\alpha,\lambda) = \alpha^n\lambda^n \prod_{i=1}^{n} t_i^{\lambda-1}\, e^{-(\alpha+1)\sum_{i=1}^{n} ln\left(1+t_i^{\lambda}\right)} \tag{5}$$

$$ln(L) = n\,ln(\alpha) + n\,ln(\lambda) + (\lambda-1)\sum_{i=1}^{n} ln(t_i) - (\alpha+1)\sum_{i=1}^{n} ln(1+t_i^{\lambda})$$

The MLE of unknown scale parameter α, denoted by $\hat{\alpha}_{ML}$, assuming that the other shape parameter λ is known yields by taking the derivative of natural log- likelihood function with respect to α and setting it equal to zero as:

$$\hat{\alpha}_{ML} = \frac{n}{w_2} \quad where \quad w_2 = \sum_{i=1}^{n} ln(1+t_i^{\lambda}) \tag{6}$$

The MLE's of $R(t)$ and $h(t)$, based on the invariant property of the MLE are defined as:

$$R(t) = \left(1+t^{\lambda}\right)^{-\hat{\alpha}_{ML}} \tag{7}$$

$$h(t) = \hat{\alpha}_{ML}\lambda\, t^{\lambda-1}\left(1+t^{\lambda}\right)^{-1} \tag{8}$$

where $\hat{\alpha}_{ML}$ as in equation(6).

3. Bayes Estimator:[4, 13, 14]

Consider the estimation of value of random parameter α, given a related observation $t = (t_1, t_2, \ldots, t_n)$, from Bayes' rule the posterior probability density function of parameter α given t can be expressed as:

$$\pi(\alpha|t) = L(\alpha|t)g(\alpha)\left(\int_{\alpha} L(\alpha|t)g(\alpha)d\alpha\right)^{-1} \quad (9)$$

Therefor two variables terms in equation(9) one term is likelihood function $L(\alpha \mid t)$ and the second is prior probability of the parameter $g(\alpha)$.
Now to find the prior density function $g(\alpha) \propto \sqrt{I(\alpha)}$,[15].
Where

$$I(\alpha) = -n\,E\left[\frac{\partial^2 \ln f(t)}{\partial \alpha^2}\right]$$

And

$$\ln f(t|\alpha,\lambda) = \ln\alpha + \ln\lambda + (\lambda-1)\ln t - (\alpha+1)\ln(1+t^{\lambda})$$

Then

$$I(\alpha) = n\,\alpha^{-2}$$

And

$$g(\alpha) = k\sqrt{n}\,\alpha^{-1} \;;\quad \alpha > 0 \quad (10)$$

To posterior distribution of the unknown parameter α of Burr type XII distribution have been obtained by combining equation(9) with equation(10) as:

$$\pi(\alpha|\underline{t}) = \alpha^n\lambda^n e^{w_1-(\alpha+1)\,w_2}\,k\,\sqrt{n}\,\alpha^{-1}\left(\int_0^{\infty}\alpha^n\lambda^n e^{w_1-(\alpha+1)\,w_2}\,k\,\sqrt{n}\,\alpha^{-1}\,d\alpha\right)^{-1}$$

Where $w_1 = (\lambda-1)\sum_{i=1}^{n}\ln(t_i)$ *and* $w_2 = \sum_{i=1}^{n}\ln(1+t_i^{\lambda})$

Then

$$\pi(\alpha|\underline{t}) = \alpha^{n-1}e^{-\alpha\,w_2}\left(\int_0^{\infty}\alpha^{n-1}e^{-\alpha\,w_2}\,d\alpha\right)^{-1}$$

Now, using the transformation $y = \alpha\,w_2$ or $\alpha = y / w_2$ then $d\alpha = dy / w_2$, we can get the final formula as:

$$\pi(\alpha|\underline{t}) = w_2^n\alpha^{n-1}e^{-\alpha\,w_2}\,(\Gamma(n)\,)^{-1} \quad (11)$$

4. Loss Functions
Bayes estimation depending on the posterior distribution is based in minimization of a Bayessian loss (risk) function which defined as an average cost – of – error function [16]. There are two type of loss function. Al - Bayyatis' loss function [7, 15] and Al - Bayyatis' suggest loss function.
This two types of loss functions can be expressed respectively as:

$$L_1(\hat{R}(t), R(t)) = R^c(t)(\hat{R}(t) - R(t))^2 \quad (12)$$

So, Bayes estimator of R(t) based on Al - Bayyatis' loss function denoted by $\hat{R}(t)_{BB}$ can be obtained as:

$$\hat{R}(t)_{BB} = E_{\pi}[L\left(\hat{R}(t), R(t)\right)] = E_{\pi}[\,R^c(t)\left(\hat{R}(t) - R(t)\right)^2\,]$$

$$= \int_{\alpha} R^{c}(t)\left(\hat{R}^{2}(t) - 2\hat{R}(t)R(t) + R^{2}(t)\right)\pi(\alpha|t)d\alpha$$

$$= \hat{R}^{2}(t)\int_{\alpha} R^{c}(t)\pi(\alpha|t)d\alpha - 2\hat{R}(t)\int_{\alpha} R^{c+1}(t)\pi(\alpha|t)d\alpha + \int_{\alpha} R^{c+2}(t)\pi(\alpha|t)d\alpha$$

$$= \hat{R}^{2}(t)E(R^{c}(t)|\underline{t}) - 2\hat{R}(t)E(R^{c+1}(t)|\underline{t}) + E(R^{c+2}(t)|\underline{t})$$

Now if $\frac{\partial f(\hat{R}(t),R(t))}{\partial \hat{R}} = 0$ *we have,*

$$2\hat{R}(t)E(R^{c}(t)|\underline{t}) - 2E(R^{c+1}(t)|\underline{t}) = 0$$

Then

$$\hat{R}(t)_{BB} = \frac{E(R^{c+1}(t)|\underline{t})}{E(R^{c}(t)|\underline{t})} \quad (13)$$

Where

$$E(R^{c}(t)|\underline{t}) = \int_{0}^{\infty} R^{c}(t)\pi\left(\alpha\middle|\underline{t}\right)d\alpha$$

From equation(11) we conclude that,

$$E(R^{c}(t)|\underline{t}) = w_{2}^{n}\left[w_{2} + c\,ln\left(1 + t^{\lambda}\right)\right]^{-n} \quad (14)$$

By the same procedure we find,

$$E(R^{c+1}(t)|\underline{t}) = \int_{0}^{\infty} R^{c+1}(t)\pi\left(\alpha\middle|\underline{t}\right)d\alpha$$

And

$$E(R^{c+1}(t)|\underline{t}) = w_{2}^{n}\left[w_{2} + (c+1)\,ln\left(1 + t^{\lambda}\right)\right]^{-n} \quad (15)$$

Put equation(14) and equation(15) in equation(13) we obtain,

$$\hat{R}(t)_{BB} = \left[w_{2} + c\,ln\left(1 + t^{\lambda}\right)\right]^{n}\left[w_{2} + (c+1)\,ln\left(1 + t^{\lambda}\right)\right]^{-n} \quad (16)$$

Bayes estimators of R(t) based on Al-Bayyaties' suggest loss function denoted by $\hat{R}(t)_{BBs}$ *can be obtained as:*

$$L_{2}\left(\hat{R}(t), R(t)\right) = R^{1.5}(t)R^{c}(t)(\hat{R}(t) - R(t))^{2} \quad (17)$$

$$\hat{R}(t)_{BBs} = E_{\pi}[L\left(\hat{R}(t), R(t)\right)] = E_{\pi}[\,R^{c+1.5}(t)\left(\hat{R}(t) - R(t)\right)^{2}\,]$$

$$= \int_{\alpha} R^{c+1.5}(t)\left(\hat{R}^{2}(t) - 2\hat{R}(t)R(t) + R^{2}(t)\right)\pi(\alpha|t)d\alpha$$

$$= \hat{R}^{2}(t)\int_{\alpha} R^{c+1.5}(t)\pi(\alpha|t)d\alpha - 2\hat{R}(t)\int_{\alpha} R^{c+2.5}(t)\pi(\alpha|t)d\alpha + \int_{\alpha} R^{c+3.5}(t)\pi(\alpha|t)d\alpha$$

$$= \hat{R}^{2}(t)E(R^{c+1.5}(t)|\underline{t}) - 2\hat{R}(t)E(R^{c+2.5}(t)|\underline{t}) + E(R^{c+3.5}(t)|\underline{t})$$

Now if $\frac{\partial f(\hat{R}(t),R(t))}{\partial \hat{R}} = 0$ *we have,*

$$2\hat{R}(t)E(R^{c+1.5}(t)|\underline{t}) - 2E(R^{c+2.5}(t)|\underline{t}) = 0$$

Then

$$\hat{R}(t)_{BBs} = \frac{E(R^{c+2.5}(t)|\underline{t})}{E(R^{c+1.5}(t)|\underline{t})} \tag{18}$$

Where

$$E(R^{c+2.5}(t)|\underline{t}) = \int_{\alpha} R^{c+2.5}(t)\pi(\alpha|\underline{t})d\alpha$$

$$= \int_0^{\infty} [e^{-\alpha\, ln(1+t^{\lambda})}]^{c+2.5}\, w_2^n \alpha^{n-1} e^{-\alpha\, w_2}\, (\Gamma(n))^{-1} d\alpha$$

Simplify the above equation we find:

$$E(R^{c+2.5}(t)|\underline{t}) = w_2^n\left[w_2 + (c+2.5)\, ln(1+t^{\lambda})\right]^{-n} \tag{19}$$

By the same procedure we obtain,

$$E(R^{c+1.5}(t)|\underline{t}) = \int_{\alpha} R^{c+1.5}(t)\pi(\alpha|\underline{t})d\alpha$$

And

$$E(R^{c+1.5}(t)|\underline{t}) = w_2^n\left[w_2 + (c+1.5)\, ln(1+t^{\lambda})\right]^{-n} \tag{20}$$

Put equation(19) and equation(20) in equation(18) we get,

$$\hat{R}(t)_{BBs} = \left[w_2 + (c+1.5)\, ln(1+t^{\lambda})\right]^n \left[w_2 + (c + 2.5)\, ln(1+t^{\lambda})\right]^{-n} \tag{21}$$

5. Estimate Reliability Function Using Expansion Method

In this section, we will discuss how to find the reliability function numerically using expansion method, in which $R(t)$ is expanded of a set of known function $Q_i(t)$ as [8, 10]:

$$R_n(t) = \sum_{i=1}^{n} c_i Q_i(t) \qquad 0 < t < \infty \tag{22}$$

Where c_i are expansion coefficients to be determined and $Q_i(t)$ are the expansion functions to be chosen, in this work we take $Q_i(t) = t^{i-1}$.
Now, we choose arbitrary points $\{t_1, t_2, \ldots, t_n\}$ in the subinterval $[t_1, t_n]$, this leads to:

$$R_n(t_j) = \sum_{i=1}^{n} c_i Q_i(t_j) \qquad j = 1, 2, \ldots, n \tag{23}$$

Using equation(7) to substitute $R(t)$ into equation(23) yields:

$$\sum_{i=1}^{n} c_i Q_i(t_j) = (1 + t_j^{\lambda})^{-\hat{\alpha}_{ML}} \qquad j = 1, 2, \ldots, n \tag{24}$$

Hence equation(24) is a system of (n) equations in (n) unknowns c_i , $i = 1, 2, \ldots, n$.
Rewrite this system in matrix form as:

$$AC = B \tag{25}$$

Where

$$A=\begin{bmatrix}1 & t_1 & \dots & t_1^{n-1}\\ 1 & t_2 & \dots & t_2^{n-1}\\ \vdots & & & \\ 1 & t_n & \dots & t_n^{n-1}\end{bmatrix},\qquad C=\begin{bmatrix}c_1\\ c_2\\ \vdots\\ c_n\end{bmatrix}\qquad and\qquad B=\begin{bmatrix}\left(1+t_1^{\lambda}\right)^{-\widehat{\alpha}_{ML}}\\ \left(1+t_2^{\lambda}\right)^{-\widehat{\alpha}_{ML}}\\ \vdots\\ \left(1+t_n^{\lambda}\right)^{-\widehat{\alpha}_{ML}}\end{bmatrix}$$

Obviously, the matrix A contains (n) independent columns.

Finally, solve the system in equation(25) for coefficients c_i's using Gauss- elimination which satisfy equation(22) the approximate solution of reliability function $R(t)$.

6. Test Examples

In this section, we present some test examples for different values (n) and (λ) show in tables (2-10) to show the effectiveness of the methods using in this work to estimate reliability function. As well as, in table (1) we take different values for c to find best estimate value of reliability function using Al-Bayyati's and Al-Bayyati's suggest loss function.

Table 1: Examples(1-9) with different values c to find $R_{BB}(t)$ and $R_{BBs}(t)$

Examples / c	$err_1=\sum(R(t)-R_{BB}(t))^2$			$err_2=\sum(R(t)-R_{BBs}(t))^2$		
	0	- 0.5	-2	0	- 0.5	-2
Example 1 n=10 , λ=1	0.0033	1.8447e-006	0.0361	0.0474	0.0278	1.8447e-006
Example 2 n=25 , λ=1	0.0014	1.0842e-007	0.0134	0.0210	0.0120	1.0842e-007
Example 3 n=50 , λ=1	6.6864e-004	8.8325e-009	0.0063	0.0104	0.0059	8.8325e-009
Example 4 n=10 , λ=1.5	0.0032	2.2925e-006	0.0342	0.0477	0.0279	2.2925e-006
Example 5 n=25 , λ=1.5	0.0014	1.3818e-007	0.0133	0.0212	0.0121	1.3818e-007
Example 6 n=50 , λ=1.5	6.7079e-004	9.2995e-009	0.0063	0.0105	0.0060	9.2995e-009
Example 7 n=10 , λ=2	0.0032	2.6267e-006	0.0321	0.0475	0.0276	2.6267e-006
Example 8 n=25 , λ=2	0.0013	1.6210e-007	0.0129	0.0211	0.0120	1.6210e-007
Example 9 n=50 , λ=2	6.7228e-004	9.5432e-009	0.0063	0.0105	0.0060	9.5432e-009

Table 2: Example 1 with $n=10$ and $\lambda=1$.

t	R(t)	$R_{BB}(t)$ c= -0.5	$R_{BBs}(t)$ c= -2	$R_n(t)$	$err_1=(R(t)-R_{BB}(t))^2$	$err_2=(R(t)-R_{BBs}(t))^2$	$err_3=(R(t)-R_n(t))^2$
0.1	0.8933	0.8933	0.8933	0.8933	1.1418e-012	1.1418e-012	0
0.4	0.6715	0.6715	0.6715	0.6715	1.2494e-009	1.2494e-009	0
0.8	0.4987	0.4986	0.4986	0.4987	1.9602e-008	1.9602e-008	7.7037e-032
1	0.4403	0.4401	0.4401	0.4403	4.1095e-008	4.1095e-008	4.9304e-032

1.2	0.3933	0.3930	0.3930	0.3933	7.1070e-008	7.1070e-008	7.7037e-032
1.4	0.3548	0.3545	0.3545	0.3548	1.0843e-007	1.0843e-007	6.0397e-031
2	0.2725	0.2720	0.2720	0.2725	2.4993e-007	2.4993e-007	1.2326e-032
2.5	0.2270	0.2264	0.2264	0.2270	3.8174e-007	3.8174e-007	6.2400e-030
2.8	0.2060	0.2053	0.2053	0.2060	4.6031e-007	4.6031e-007	2.3304e-030
3	0.1938	0.1931	0.1931	0.1938	5.1126e-007	5.1126e-007	2.6652e-029
				∑(err)	1.8447e-006	1.8447e-006	3.6042e-029

Table 3: Example 2 with $n=25$ and $\lambda=1$.

t	R(t)	$R_{BB}(t)$ c= -0.5	$R_{BBs}(t)$ c= -2	$R_n(t)$	$err_1=(R(t)-R_{BB}(t))^2$	$err_2=(R(t)-R_{BBs}(t))^2$	$err_3=(R(t)-R_n(t))^2$
0.1	0.8693	0.8693	0.8693	0.8693	1.0152e-013	1.0152e-013	1.2326e-032
0.18	0.7841	0.7841	0.7841	0.7841	2.2652e-012	2.2652e-012	1.2326e-032
0.26	0.7120	0.7120	0.7120	0.7120	1.3845e-011	1.3845e-011	1.2326e-032
0.34	0.6504	0.6504	0.6504	0.6504	4.7649e-011	4.7649e-011	4.9304e-032
0.42	0.5973	0.5973	0.5973	0.5973	1.1887e-010	1.1887e-010	4.9304e-032
0.5	0.55100.	0.5510	0.5510	0.5510	2.4185e-010	2.4185e-010	1.1093e-031
0.58	5105	0.5105	0.5105	0.5105	4.2798e-010	4.2798e-010	4.9304e-032
0.66	0.4748	0.4748	0.4748	0.4748	6.8481e-010	6.8481e-010	7.7037e-032
0.74	0.4430	0.4430	0.4430	0.4430	1.0160e-009	1.0160e-009	3.0815e-033
0.82	0.4147	0.4147	0.4147	0.4147	1.4219e-009	1.4219e-009	2.7733e-032
0.9	0.3893	0.3893	0.3893	0.3893	1.8999e-009	1.8999e-009	3.0815e-031
0.98	0.3664	0.3664	0.3664	0.3664	2.4455e-009	2.4455e-009	4.9304e-032
1.06	0.3457	0.3456	0.3456	0.3457	3.0528e-009	3.0528e-009	4.4373e-031
1.14	0.3269	0.3268	0.3268	0.3269	3.7149e-009	3.7149e-009	8.9856e-030
1.22	0.3097	0.3096	0.3096	0.3097	4.4245e-009	4.4245e-009	4.9304e-032
1.3	0.2940	0.2939	0.2939	0.2940	5.1744e-009	5.1744e-009	1.1093e-031
1.38	0.2796	0.2795	0.2795	0.2796	5.9574e-009	5.9574e-009	2.0831e-030
1.46	0.2663	0.2662	0.2662	0.2663	6.7665e-009	6.7665e-009	1.0690e-027
1.54	0.2541	0.2540	0.2540	0.2541	7.5955e-009	7.5955e-009	1.5023e-026
1.62	0.2428	0.2427	0.2427	0.2428	8.4382e-009	8.4382e-009	7.1012e-026
1.7	0.2323	0.2322	0.2322	0.2323	9.2895e-009	9.2895e-009	2.3067e-025
1.78	0.2225	0.2224	0.2224	0.2225	1.0144e-008	1.0144e-008	1.2752e-025
1.86	0.2134	0.2133	0.2133	0.2134	1.0998e-008	1.0998e-008	1.5667e-024
1.94	0.2049	0.2048	0.2048	0.2049	1.1848e-008	1.1848e-008	7.2929e-024
2.02	0.1970	0.1969	0.1969	0.1970	1.2690e-008	1.2690e-008	1.3806e-023
				∑(err)	1.0842e-007	1.0842e-007	2.3111e-023

Table 4: Example 3 with $n=50$ and $\lambda=1$.

t	$R(t)$	$R_{BB}(t)$ $c= -0.5$	$R_{BBs}(t)$ $c= -2$	$R_n(t)$	$err_1=$ $(R(t)- R_{BB}(t))^2$	$err_2=$ $(R(t)- R_{BBs}(t))^2$	$err_3=$ $(R(t)- R_n(t))^2$
2	0.5581	0.5581	0.5581	0.5581	1.3621e-011	1.3621e-011	4.9304e-032
2.32	0.5289	0.5289	0.5289	0.5289	2.0770e-011	2.0770e-011	1.2326e-032
2.42	0.5206	0.5206	0.5206	0.5206	2.3303e-011	2.3303e-011	8.1715e-023
2.52	0.5127	0.5127	0.5127	0.5127	2.5971e-011	2.5971e-011	2.4573e-023
2.74	0.4964	0.4964	0.4964	0.4964	3.2295e-011	3.2295e-011	1.2717e-024
2.84	0.4895	0.4895	0.4895	0.4895	3.5365e-011	3.5365e-011	5.1877e-025
3.06	0.4753	0.4753	0.4753	0.4753	4.2522e-011	4.2522e-011	4.6773e-026
3.16	0.4692	0.4692	0.4692	0.4692	4.5947e-011	4.5947e-011	2.3542e-026
3.38	0.4565	0.4565	0.4565	0.4565	5.3831e-011	5.3831e-011	3.3522e-027
3.48	0.4511	0.4511	0.4511	0.4511	5.7563e-011	5.7563e-011	2.2159e-027
3.70	0.4397	0.4397	0.4397	0.4397	6.6075e-011	6.6075e-011	3.8616e-028
3.80	0.4349	0.4349	0.4349	0.4349	7.0071e-011	7.0071e-011	1.4244e-028
4.02	0.4246	0.4246	0.4246	0.4246	7.9119e-011	7.9119e-011	1.5886e-027
4.12	0.4202	0.4202	0.4202	0.4202	8.3339e-011	8.3339e-011	1.4671e-029
4.34	0.4109	0.4109	0.4109	0.4109	9.2838e-011	9.2838e-011	9.6635e-030
4.44	0.4069	0.4069	0.4069	0.4069	9.7246e-011	9.7246e-011	3.3152e-028
4.66	0.3984	0.3984	0.3984	0.3984	1.0712e-010	1.0712e-010	5.1518e-027
4.76	0.3947	0.3947	0.3947	0.3947	1.1169e-010	1.1169e-010	6.3013e-027
4.98	0.3870	0.3870	0.3870	0.3870	1.2187e-010	1.2187e-010	5.6712e-028
5.08	0.3836	0.3836	0.3836	0.3836	1.2657e-010	1.2657e-010	2.4960e-029
5.30	0.3764	0.3764	0.3764	0.3764	1.3701e-010	1.3701e-010	3.4644e-026
5.40	0.3733	0.3733	0.3733	0.3733	1.4180e-010	1.4180e-010	9.3081e-027
5.62	0.3666	0.3666	0.3666	0.3666	1.5245e-010	1.5245e-010	4.9156e-026
5.72	0.3637	0.3637	0.3637	0.3637	1.5732e-010	1.5732e-010	2.2547e-026
5.94	0.3576	0.3576	0.3576	0.3576	1.6812e-010	1.6812e-010	9.9397e-027
6.04	0.3548	0.3548	0.3548	0.3548	1.7306e-010	1.7306e-010	2.3211e-025
6.26	0.3491	0.3491	0.3491	0.3491	1.8398e-010	1.8398e-010	3.9010e-026
6.36	0.3466	0.3466	0.3466	0.3466	1.8897e-010	1.8897e-010	1.2474e-026
6.58	0.3412	0.3412	0.3412	0.3412	1.9998e-010	1.9998e-010	3.2198e-025
6.68	0.3388	0.3388	0.3388	0.3388	2.0500e-010	2.0500e-010	8.1076e-024
6.90	0.3338	0.3338	0.3338	0.3338	2.1606e-010	2.1606e-010	2.3789e-023
7	0.3316	0.3316	0.3316	0.3316	2.2110e-010	2.2110e-010	8.0821e-023
7.22	0.3268	0.3268	0.3268	0.3268	2.3220e-010	2.3220e-010	7.6091e-023
7.32	0.3247	0.3247	0.3247	0.3247	2.3724e-010	2.3724e-010	6.1830e-024
7.54	0.3203	0.3203	0.3203	0.3203	2.4835e-010	2.4835e-010	4.9469e-023
7.64	0.3183	0.3183	0.3183	0.3183	2.5340e-010	2.5340e-010	3.9522e-022
7.86	0.3141	0.3141	0.3141	0.3141	2.6449e-010	2.6449e-010	1.2097e-021
7.96	0.3122	0.3122	0.3122	0.3122	2.6953e-010	2.6953e-010	1.1574e-021
8.18	0.3082	0.3082	0.3082	0.3082	2.8061e-010	2.8061e-010	7.7454e-022
8.28	0.3064	0.3064	0.3064	0.3064	2.8563e-010	2.8563e-010	6.3895e-023
8.50	0.3027	0.3027	0.3027	0.3027	2.9666e-010	2.9666e-010	8.8217e-021
8.60	0.3010	0.3010	0.3010	0.3010	3.0167e-010	3.0167e-010	6.1066e-021
8.82	0.2974	0.2974	0.2974	0.2974	3.1265e-010	3.1265e-010	1.7008e-020
8.92	0.2958	0.2958	0.2958	0.2958	3.1762e-010	3.1762e-010	3.9456e-020
9.14	0.2924	0.2924	0.2924	0.2924	3.2854e-010	3.2854e-010	1.0227e-019
9.24	0.2908	0.2908	0.2908	0.2908	3.3349e-010	3.3349e-010	4.3066e-019
9.46	0.2876	0.2876	0.2876	0.2876	3.4434e-010	3.4434e-010	1.2504e-018
9.56	0.2861	0.2861	0.2861	0.2861	3.4925e-010	3.4925e-010	1.1715e-017
9.78	0.2830	0.2830	0.2830	0.2830	3.6002e-010	3.6002e-010	4.1687e-016
9.88	0.2816	0.2816	0.2816	0.2816	3.6489e-010	3.6489e-010	9.4904e-015
				$\sum(err)$	8.8325e-009	8.8325e-009	9.9209e-015

Table 5: Example 4 with $n=10$ and $\lambda=1.5$.

t	R(t)	$R_{BB}(t)$ c= -0.5	$R_{BBs}(t)$ c= -2	$R_n(t)$	$err_1=(R(t)-R_{BB}(t))^2$	$err_2=(R(t)-R_{BBs}(t))^2$	$err_3=(R(t)-R_n(t))^2$
0.1	0.9688	0.9688	0.9688	0.9688	6.6588e-016	6.6588e-016	1.2326e-032
0.4	0.7946	0.7946	0.7946	0.7946	6.4743e-011	6.4743e-011	4.9304e-032
0.8	0.5768	0.5768	0.5768	0.5768	6.4141e-009	6.4141e-009	1.2326e-032
1	0.4933	0.4932	0.4932	0.4933	2.1056e-008	2.1056e-008	4.9304e-032
1.2	0.4251	0.4249	0.4249	0.4251	4.9264e-008	4.9264e-008	2.7733e-032
1.4	0.3694	0.3691	0.3691	0.3694	9.2662e-008	9.2662e-008	1.1124e-030
2	0.2545	0.2540	0.2540	0.2545	2.9642e-007	2.9642e-007	9.9840e-031
2.5	0.1957	0.1950	0.1950	0.1957	5.0299e-007	5.0299e-007	4.5490e-029
2.8	0.1701	0.1693	0.1693	0.1701	6.2386e-007	6.2386e-007	2.5016e-027
3	0.1558	0.1550	0.1550	0.1558	6.9972e-007	6.9972e-007	9.7634e-029
				∑(err)	2.2925e-006	2.2925e-006	2.6469e-027

Table 6: Example 5 with $n=25$ and $\lambda=1.5$.

t	R(t)	$R_{BB}(t)$ c= -0.5	$R_{BBs}(t)$ c= -2	$R_n(t)$	$err_1=(R(t)-R_{BB}(t))^2$	$err_2=(R(t)-R_{BBs}(t))^2$	$err_3=(R(t)-R_n(t))^2$
0.1	0.9574	0.9574	0.9574	0.9574	1.1136e-016	1.1136e-016	1.2326e-032
0.18	0.9022	0.9022	0.9022	0.9022	1.7250e-014	1.7250e-014	1.2326e-032
0.26	0.8401	0.8401	0.8401	0.8401	3.5061e-013	3.5061e-013	1.2326e-032
0.34	0.7764	0.7764	0.7764	0.7764	2.8155e-012	2.8155e-012	1.9722e-031
0.42	0.7140	0.7140	0.7140	0.7140	1.3243e-011	1.3243e-011	0
0.5	0.6547	0.6547	0.6547	0.6547	4.4026e-011	4.4026e-011	9.9840e-031
0.58	0.5994	0.5993	0.5993	0.5994	1.1491e-010	1.1491e-010	6.0397e-031
0.66	0.5484	0.5484	0.5484	0.5484	2.5127e-010	2.5127e-010	6.9819e-028
0.74	0.5019	0.5019	0.5019	0.5019	4.8042e-010	4.8042e-010	6.5146e-027
0.82	0.4598	0.4597	0.4597	0.4598	8.2751e-010	8.2751e-010	2.3755e-027
0.9	0.4216	0.4216	0.4216	0.4216	1.3120e-009	1.3120e-009	1.3301e-027
0.98	0.3872	0.3871	0.3871	0.3872	1.9455e-009	1.9455e-009	9.7917e-026
1.06	0.3562	0.3561	0.3561	0.3562	2.7312e-009	2.7312e-009	5.5398e-028
1.14	0.3282	0.3281	0.3281	0.3282	3.6641e-009	3.6641e-009	1.4572e-024
1.22	0.3030	0.3029	0.3029	0.3030	4.7326e-009	4.7326e-009	1.2125e-023
1.3	0.2802	0.2802	0.2802	0.2802	5.9202e-009	5.9202e-009	1.6546e-022
1.38	0.2597	0.2596	0.2596	0.2597	7.2068e-009	7.2068e-009	1.9974e-020
1.46	0.2411	0.2410	0.2410	0.2411	8.5709e-009	8.5709e-009	1.7236e-020
1.54	0.2242	0.2241	0.2241	0.2242	9.9903e-009	9.9903e-009	2.4527e-019
1.62	0.2089	0.2088	0.2088	0.2089	1.1444e-008	1.1444e-008	4.4877e-018
1.7	0.1950	0.1949	0.1949	0.1950	1.2911e-008	1.2911e-008	3.2471e-017
1.78	0.1823	0.1822	0.1822	0.1823	1.4374e-008	1.4374e-008	5.6542e-018
1.86	0.1708	0.1706	0.1706	0.1708	1.5818e-008	1.5818e-008	2.2854e-017
1.94	0.1602	0.1600	0.1600	0.1602	1.7228e-008	1.7228e-008	4.9706e-020
2.02	0.1505	0.1503	0.1503	0.1505	1.8593e-008	1.8593e-008	5.1313e-016

				∑(err)	1.3818e-007	1.3818e-007	5.7893e-016

Table 7: Example 6 with $n=50$ and $\lambda=1.5$.

t	R(t)	$R_{BB}(t)$ c= -0.5	$R_{BBs}(t)$ c= -2	$R_n(t)$	$err_1=(R(t)-R_{BB}(t))^2$	$err_2=(R(t)-R_{BBs}(t))^2$	$err_3=(R(t)-R_n(t))^2$
2	0.6021	0.6021	0.6021	0.6021	6.8681e-012	6.8681e-012	0
2.32	0.5648	0.5648	0.5648	0.5648	1.2316e-011	1.2316e-011	4.4373e-031
2.42	0.5543	0.5543	0.5543	0.5543	1.4402e-011	1.4402e-011	2.6704e-021
2.52	0.5443	0.5443	0.5443	0.5443	1.6670e-011	1.6670e-011	8.0094e-022
2.74	0.5238	0.5238	0.5238	0.5238	2.2294e-011	2.2294e-011	4.1185e-023
2.84	0.5151	0.5151	0.5151	0.5151	2.5131e-011	2.5131e-011	1.6646e-023
3.06	0.4972	0.4972	0.4972	0.4972	3.1966e-011	3.1966e-011	1.4931e-024
3.16	0.4896	0.4896	0.4896	0.4896	3.5332e-011	3.5332e-011	7.4905e-025
3.38	0.4739	0.4739	0.4739	0.4739	4.3275e-011	4.3275e-011	1.1410e-025
3.48	0.4672	0.4672	0.4672	0.4672	4.7119e-011	4.7119e-011	6.7839e-026
3.70	0.4532	0.4532	0.4532	0.4532	5.6052e-011	5.6052e-011	1.7558e-026
3.80	0.4473	0.4473	0.4473	0.4473	6.0317e-011	6.0317e-011	9.0845e-027
4.02	0.4348	0.4348	0.4348	0.4348	7.0116e-011	7.0116e-011	1.1277e-026
4.12	0.4294	0.4294	0.4294	0.4294	7.4747e-011	7.4747e-011	5.4018e-027
4.34	0.4182	0.4182	0.4182	0.4182	8.5291e-011	8.5291e-011	9.9767e-028
4.44	0.4134	0.4134	0.4134	0.4134	9.0234e-011	9.0234e-011	8.0150e-028
4.66	0.4032	0.4032	0.4032	0.4032	1.0141e-010	1.0141e-010	7.2933e-026
4.76	0.3988	0.3988	0.3988	0.3988	1.0662e-010	1.0662e-010	2.2764e-025
4.98	0.3896	0.3896	0.3896	0.3896	1.1832e-010	1.1832e-010	4.1595e-026
5.08	0.3856	0.3856	0.3856	0.3856	1.2375e-010	1.2375e-010	4.0873e-026
5.30	0.3771	0.3771	0.3771	0.3771	1.3589e-010	1.3589e-010	6.2530e-025
5.40	0.3735	0.3735	0.3735	0.3735	1.4149e-010	1.4149e-010	6.3075e-025
5.62	0.3657	0.3657	0.3657	0.3657	1.5399e-010	1.5399e-010	3.5168e-025
5.72	0.3623	0.3623	0.3623	0.3623	1.5974e-010	1.5974e-010	9.8892e-026
5.94	0.3551	0.3551	0.3551	0.3551	1.7252e-010	1.7252e-010	3.7232e-026
6.04	0.3520	0.3520	0.3520	0.3520	1.7838e-010	1.7838e-010	2.5872e-025
6.26	0.3454	0.3454	0.3454	0.3454	1.9137e-010	1.9137e-010	1.0480e-024
6.36	0.3425	0.3425	0.3425	0.3425	1.9732e-010	1.9732e-010	2.4162e-025
6.58	0.3363	0.3363	0.3363	0.3363	2.1048e-010	2.1048e-010	1.6116e-023
6.68	0.3336	0.3336	0.3336	0.3336	2.1649e-010	2.1649e-010	1.0042e-022
6.90	0.3278	0.3278	0.3278	0.3278	2.2976e-010	2.2976e-010	1.7003e-022
7	0.3253	0.3253	0.3253	0.3253	2.3581e-010	2.3581e-010	1.9976e-022
7.22	0.3199	0.3199	0.3199	0.3199	2.4916e-010	2.4916e-010	1.4473e-021
7.32	0.3176	0.3176	0.3176	0.3176	2.5524e-010	2.5524e-010	6.9660e-022
7.54	0.3125	0.3125	0.3125	0.3125	2.6862e-010	2.6862e-010	6.8745e-023
7.64	0.3103	0.3103	0.3103	0.3103	2.7471e-010	2.7471e-010	6.9777e-021
7.86	0.3056	0.3056	0.3056	0.3056	2.8810e-010	2.8810e-010	5.8813e-021
7.96	0.3035	0.3035	0.3035	0.3035	2.9418e-010	2.9418e-010	6.3011e-021
8.18	0.2990	0.2990	0.2990	0.2990	3.0755e-010	3.0755e-010	1.2746e-021
8.28	0.2971	0.2971	0.2971	0.2971	3.1361e-010	3.1361e-010	2.2608e-021
8.50	0.2929	0.2929	0.2929	0.2929	3.2694e-010	3.2694e-010	9.4352e-020
8.60	0.2910	0.2910	0.2910	0.2910	3.3298e-010	3.3298e-010	4.1293e-020
8.82	0.2870	0.2870	0.2870	0.2870	3.4625e-010	3.4625e-010	9.5578e-022
8.92	0.2852	0.2852	0.2852	0.2852	3.5226e-010	3.5226e-010	8.1584e-019
9.14	0.2815	0.2815	0.2815	0.2815	3.6544e-010	3.6544e-010	3.1544e-018
9.24	0.2798	0.2798	0.2798	0.2798	3.7141e-010	3.7141e-010	9.4712e-018
9.46	0.2762	0.2762	0.2762	0.2762	3.8450e-010	3.8450e-010	2.4142e-017
9.56	0.2746	0.2746	0.2746	0.2746	3.9042e-010	3.9042e-010	1.4663e-016
9.78	0.2712	0.2712	0.2712	0.2712	4.0341e-010	4.0341e-010	8.0046e-015
9.88	0.2697	0.2697	0.2697	0.2697	4.0928e-010	4.0928e-010	1.7202e-013
				∑(err)	9.2995e-009	9.2995e-009	1.8021e-013

Table 8: Example 7 with $n=10$ and $\lambda=2$.

t	R(t)	$R_{BB}(t)$ c= -0.5	$R_{BBs}(t)$ c= -2	$R_n(t)$	$err_1=(R(t)-R_{BB}(t))^2$	$err_2=(R(t)-R_{BBs}(t))^2$	$err_3=(R(t)-R_n(t))^2$
0.1	0.9913	0.9913	0.9913	0.9913	3.0243e-019	3.0243e-019	4.9304e-032
0.4	0.8779	0.8779	0.8779	0.8779	2.6124e-012	2.6124e-012	4.9304e-032
0.8	0.6478	0.6478	0.6478	0.6478	1.9515e-009	1.9515e-009	1.1093e-031
1	0.5443	0.5442	0.5442	0.5443	1.0428e-008	1.0428e-008	0
1.2	0.4571	0.4570	0.4570	0.4571	3.3428e-008	3.3428e-008	3.0815e-031
1.4	0.3859	0.3856	0.3856	0.3859	7.7260e-008	7.7260e-008	1.9722e-031
2	0.2436	0.2430	0.2430	0.2436	3.2816e-007	3.2816e-007	1.3833e-029
2.5	0.1758	0.1750	0.1750	0.1758	5.9512e-007	5.9512e-007	6.9333e-031
2.8	0.1477	0.1469	0.1469	0.1477	7.4516e-007	7.4516e-007	4.7190e-027
3	0.1326	0.1317	0.1317	0.1326	8.3517e-007	8.3517e-007	8.0871e-029
				$\sum$(err)	2.6267e-006	2.6267e-006	4.8151e-027

Table 9: Example 8 with $n=25$ and $\lambda=2$.

t	R(t)	$R_{BB}(t)$ c= -0.5	$R_{BBs}(t)$ c= -2	$R_n(t)$	$err_1=(R(t)-R_{BB}(t))^2$	$err_2=(R(t)-R_{BBs}(t))^2$	$err_3=(R(t)-R_n(t))^2$
0.1	0.9871	0.9871	0.9871	0.9871	8.3572e-020	8.3572e-020	0
0.18	0.9592	0.9592	0.9592	0.9592	8.5462e-017	8.5462e-017	1.2326e-032
0.26	0.9181	0.9181	0.9181	0.9181	5.8359e-015	5.8359e-015	1.2326e-032
0.34	0.8668	0.8668	0.8668	0.8668	1.1380e-013	1.1380e-013	0
0.42	0.8088	0.8088	0.8088	0.8088	1.0628e-012	1.0628e-012	1.2326e-032
0.5	0.7471	0.7471	0.7471	0.7471	6.0905e-012	6.0905e-012	1.2326e-032
0.58	0.6847	0.6847	0.6847	0.6847	2.4633e-011	2.4633e-011	4.9304e-032
0.66	0.6235	0.6235	0.6235	0.6235	7.6794e-011	7.6794e-011	1.2326e-032
0.74	0.5652	0.5652	0.5652	0.5652	1.9588e-010	1.9588e-010	4.4373e-031
0.82	0.5108	0.5108	0.5108	0.5108	4.2655e-010	4.2655e-010	4.9304e-032
0.9	0.4606	0.4606	0.4606	0.4606	8.1835e-010	8.1835e-010	4.4373e-031
0.98	0.4150	0.4150	0.4150	0.4150	1.4167e-009	1.4167e-009	2.0831e-030
1.06	0.3739	0.3738	0.3738	0.3739	2.2546e-009	2.2546e-009	2.4159e-030
1.14	0.3369	0.3369	0.3369	0.3369	3.3468e-009	3.3468e-009	3.8834e-028
1.22	0.3039	0.3039	0.3039	0.3039	4.6883e-009	4.6883e-009	6.0829e-027
1.3	0.2745	0.2744	0.2744	0.2745	6.2562e-009	6.2562e-009	3.8311e-026
1.38	0.2483	0.2483	0.2483	0.2483	8.0133e-009	8.0133e-009	2.5954e-025
1.46	0.2251	0.2250	0.2250	0.2251	9.9135e-009	9.9135e-009	4.0537e-026
1.54	0.2044	0.2043	0.2043	0.2044	1.1907e-008	1.1907e-008	1.3145e-023
1.62	0.1860	0.1858	0.1858	0.1860	1.3943e-008	1.3943e-008	9.7434e-023
1.7	0.1695	0.1694	0.1694	0.1695	1.5975e-008	1.5975e-008	4.2834e-022
1.78	0.1549	0.1548	0.1548	0.1549	1.7962e-008	1.7962e-008	8.7317e-022
1.86	0.1418	0.1417	0.1417	0.1418	1.9869e-008	1.9869e-008	5.9782e-023
1.94	0.1301	0.1300	0.1300	0.1301	2.1668e-008	2.1668e-008	1.5725e-020
2.02	0.1196	0.1195	0.1195	0.1196	2.3340e-008	2.3340e-008	5.8485e-020
				∑(err)	1.6210e-007	1.6210e-007	7.5682e-020

Table 10: Example 9 with $n=50$ and $\lambda=2$.

t	R(t)	$R_{BB}(t)$ c= -0.5	$R_{BBs}(t)$ c= -2	$R_n(t)$	$err_1=(R(t)-R_{BB}(t))^2$	$err_2=(R(t)-R_{BBs}(t))^2$	$err_3=(R(t)-R_n(t))^2$
2	0.6275	0.6275	0.6275	0.6275	4.4773e-012	4.4773e-012	3.0815e-031
2.32	0.5847	0.5847	0.5847	0.5847	9.0701e-012	9.0701e-012	2.4159e-030
2.42	0.5727	0.5727	0.5727	0.5727	1.0925e-011	1.0925e-011	1.0306e-020
2.52	0.5613	0.5613	0.5613	0.5613	1.2984e-011	1.2984e-011	3.1970e-021
2.74	0.5380	0.5380	0.5380	0.5380	1.8238e-011	1.8238e-011	1.7493e-022
2.84	0.5282	0.5282	0.5282	0.5282	2.0951e-011	2.0951e-011	7.2753e-023
3.06	0.5082	0.5082	0.5082	0.5082	2.7612e-011	2.7612e-011	6.8854e-024
3.16	0.4997	0.4997	0.4997	0.4997	3.0946e-011	3.0946e-011	3.5561e-024
3.38	0.4822	0.4822	0.4822	0.4822	3.8918e-011	3.8918e-011	5.6870e-025
3.48	0.4747	0.4747	0.4747	0.4747	4.2819e-011	4.2819e-011	3.6009e-025
3.70	0.4594	0.4593	0.4593	0.4594	5.1970e-011	5.1970e-011	8.9092e-026
3.80	0.4528	0.4528	0.4528	0.4528	5.6374e-011	5.6374e-011	5.1371e-026
4.02	0.4391	0.4391	0.4391	0.4391	6.6558e-011	6.6558e-011	4.5842e-026
4.12	0.4333	0.4333	0.4333	0.4333	7.1398e-011	7.1398e-011	1.6700e-026
4.34	0.4211	0.4211	0.4211	0.4211	8.2471e-011	8.2471e-011	2.3017e-026
4.44	0.4159	0.4158	0.4158	0.4159	8.7684e-011	8.7684e-011	1.4337e-025
4.66	0.4049	0.4049	0.4049	0.4049	9.9508e-011	9.9508e-011	7.6285e-025
4.76	0.4002	0.4001	0.4001	0.4002	1.0503e-010	1.0503e-010	1.7016e-024
4.98	0.3902	0.3902	0.3902	0.3902	1.1748e-010	1.1748e-010	8.0193e-025
5.08	0.3859	0.3859	0.3859	0.3859	1.2327e-010	1.2327e-010	2.8399e-027
5.30	0.3769	0.3769	0.3769	0.3769	1.3623e-010	1.3623e-010	4.2923e-024
5.40	0.3730	0.3730	0.3730	0.3730	1.4222e-010	1.4222e-010	8.8365e-024
5.62	0.3647	0.3647	0.3647	0.3647	1.5560e-010	1.5560e-010	3.4926e-024
5.72	0.3611	0.3611	0.3611	0.3611	1.6176e-010	1.6176e-010	4.5978e-025
5.94	0.3536	0.3535	0.3535	0.3536	1.7546e-010	1.7546e-010	1.5701e-024
6.04	0.3502	0.3502	0.3502	0.3502	1.8175e-010	1.8175e-010	3.4836e-023
6.26	0.3433	0.3432	0.3432	0.3433	1.9571e-010	1.9571e-010	5.7274e-024
6.36	0.3402	0.3402	0.3402	0.3402	2.0209e-010	2.0209e-010	2.5957e-025
6.58	0.3337	0.3337	0.3337	0.3337	2.1623e-010	2.1623e-010	1.3075e-022
6.68	0.3309	0.3309	0.3309	0.3309	2.2269e-010	2.2269e-010	2.7277e-022
6.90	0.3249	0.3248	0.3248	0.3249	2.3695e-010	2.3695e-010	1.1490e-021
7	0.3222	0.3222	0.3222	0.3222	2.4345e-010	2.4345e-010	5.0502e-021
7.22	0.3166	0.3166	0.3166	0.3166	2.5779e-010	2.5779e-010	5.7815e-021
7.32	0.3141	0.3141	0.3141	0.3141	2.6432e-010	2.6432e-010	5.5759e-021
7.54	0.3089	0.3089	0.3089	0.3089	2.7869e-010	2.7869e-010	3.0832e-020
7.64	0.3066	0.3066	0.3066	0.3066	2.8523e-010	2.8523e-010	8.1902e-020
7.86	0.3017	0.3016	0.3016	0.3017	2.9960e-010	2.9960e-010	2.7340e-021
7.96	0.2995	0.2995	0.2995	0.2995	3.0613e-010	3.0613e-010	4.1711e-020
8.18	0.2949	0.2949	0.2949	0.2949	3.2047e-010	3.2047e-010	2.5769e-019
8.28	0.2928	0.2928	0.2928	0.2928	3.2698e-010	3.2698e-010	3.3919e-020
8.50	0.2885	0.2885	0.2885	0.2885	3.4126e-010	3.4126e-010	5.7492e-019
8.60	0.2866	0.2866	0.2866	0.2866	3.4774e-010	3.4774e-010	2.5936e-020
8.82	0.2825	0.2824	0.2824	0.2825	3.6194e-010	3.6194e-010	3.0940e-018
8.92	0.2806	0.2806	0.2806	0.2806	3.6838e-010	3.6838e-010	1.7247e-018
9.14	0.2768	0.2767	0.2767	0.2768	3.8249e-010	3.8249e-010	1.9214e-017
9.24	0.2750	0.2750	0.2750	0.2750	3.8887e-010	3.8887e-010	6.4654e-017
9.46	0.2714	0.2713	0.2713	0.2714	4.0286e-010	4.0286e-010	1.5953e-016
9.56	0.2697	0.2697	0.2697	0.2697	4.0920e-010	4.0920e-010	1.9396e-015
9.78	0.2662	0.2662	0.2662	0.2662	4.2306e-010	4.2306e-010	7.3408e-014
9.88	0.2647	0.2647	0.2647	0.2647	4.2933e-010	4.2933e-010	1.5866e-012

				∑(err)	9.5432e-009	9.5432e-009	1.6622e-012

7. Conclusions

1-From table (1) for all examples the best estimation of reliability Al-Bayyati's loss function (R_{BB}) at ($c = -1/2$) and the best estimation of reliability Al-Bayyati's suggest loss function (R_{BBs}) at ($c = -2$).

2-From examples, the tables(2-10) with ($n= 10, 25, 50$, $\lambda = 1, 1.5, 2$) it appears that:

- The numerical method gives best estimate values than reliability Al-Bayyati's loss function (R_{BB}) with best c ($c = -1/2$) and the reliability Al-Bayyati's suggest loss function (R_{BBs}) with ($c = -2$).
- Where the sample sizes under study are increases, the estimation methods and numerical method are approaches to the maximum likelihood estimation.

References

[1] Burr W I 1942 Cumulative Frequency Distribution (Annals of Mathematical Statistics) **13** pp 215-232.
[2] Makhodoom I and Jafair A 2011 *Bayesian Estimations on the Burr Type XII* Distribution Using Grouped and Un-Grouped Data (Australian Journal of Basic and Applied Sciences) **5** No. 6 pp 1525-1531.
[3] Erika H 2000 Estimation of the Scale Parameter in Burr distribution (Department of Applied Mathematics and Statistics Comenius University) Bratistave.
[4] Feroze N and Aslam M 2012 Bayesian Analysis of Burr Type X Distribution Order Complete and Censored Samples
[5] Yarmohammadi M and Pazira H 2010 Minimax Estimations of the Parameter of the Burr Type XII Distributio*n* (Australian Journal of Basic and Applied Sciences) **4** No. **12** pp 6611-6622.
[6] Kleiber and Kotz 2003 The Burr Distribution Table 2-4 pp 51.
[7] Al-Bayyatis H N 2002 Comparing Methods of estimating Webull Failure Models Using Simulation (Ph.D. Thesis College of Administration and Economic, Baghdad Univ., Iraq).
[8] Mohammed A A and Ibraheem S K 2010 Approximated Solution of Higher-Order Linear Fredholm Integro-Differential Equations by Computing of Singular Value Decomposition(SVD) (*Engineering&Technology Journal*) **28** No.14 pp 4722-4729.
[9] Shihab S N and Mohammed A A 2012 An Efficient Algorithm for nth Order Integro-Differential Equations Using New Haar Wavelets Matrix Designation (*International Journal of Emerging Technologies in Computational and Applied Sciences(IJETCAS))* **2**(1) Aug. Nov. pp 32-35.
[10] Atkinson K E 1997 The Numerical Solution of Integral Equations of the Second Kind (Cambridge University Press).
[11] Solimon A A 2002 Reliability Estimation Inneralized Life Model with Application to the Burr-XII (IEEE Tran-On Reliability) **51** pp 337-343.
[12] Shao Q 2004 Notes on Maximum Likelihood Estimation for the Three-Parameter Burr-XII Distribution (Computational Statistics and Datd Analysis) **45** pp 675-687.
[13] Reshi J A, Ahmed A and Ahmed S P 2014 Bayesion Analysis of Scale Parameter of the Generalized Inverse Rayleigh Model Using Different Loss Functions (*International Journal of Modern Mathematical Sciences*) **10**(2) pp 151-162.

[14] Tahir M and Saleem M 2011 On Relation Ship Between Some Bayesian and Clasical Estimators (*Pakistan Journal of life and Social Science*) **8** No. 2 pp 159-161.
[15] Zheng G and Gastwirh J L 2000 Where is the Fisher Information in an Ordered Sample (Statistica Sinica) **10** pp 1267-1280.
[16] Wenbo Y and Jinyun X 2016 Bayesian Estimation of Reliability of Geometric

Strong Convergence of Iteration Processes for Infinite Family of General Extended Mappings

Strong Convergence of Iteration Processes for Infinite Family of General Extended Mappings

Zena Hussein Maibed

Department of Mathematic, College of Education for Pure Science/ Ibn Al-Haitham, University of Baghdad

mrs_ zena.hussein @yahoo.com

Abstract. The aim of this paper, we introduce a concept of general extended mapping which is independent of nonexpansive mapping and give an iteration process of families of quasi nonexpansive and of general extended mappings. Also, the existence of common fixed point are studied for these process in the Hilbert spaces.

1. Introduction

Let $\mathcal{H}$ be a real Hilbert space $\emptyset \neq C \subseteq \mathcal{H}$, we say that, $f: C \longrightarrow C$ is $non-expansive$ if $\|z-w\| \geq \|f(z)-f(w)\|$ for each $z, w \in C$. On the other hand, any multivalued mapping B is called monotone if:

$< z_1 - z_2, w_1 - w_1 > \geq 0 \quad \forall z_i \in D(B)$, for all $w_i \in B(z_i)$. And it is called maximal monotone if for all $(z,h) \in \mathcal{H} \times \mathcal{H}, \langle z-w, h-k \rangle \geq 0$ and for all $(w,k) \in gph(B)$ then we get, $h \in B(z)$.The Monotone mappings play important role in optimization Theory, see the books($[1]-[5]$).The convergence of the iteration processes are studied by many researchers see($[6]-[15]$).

Now, we recall the following

Lemma(1.1) ***[16]***

Let $< \alpha_n >$ and $< \beta_n >$ are sequences of nonnegative number such that $\alpha_{n+1} \leq \alpha_n + \beta_n$, *for each* $n \geq 1$. *If* $\sum_{n=o}^{\infty} \alpha_n$ *converge then* $\lim_{n\to\infty} \alpha_n$ *exists.*

Lemma(1.2) ***[7]***

If $\langle \alpha_n \rangle$ *is a sequence of positive real number satisfy:* $(1-\gamma_n)\alpha_n + \delta_n \geq \alpha_{n+1}$, $n \geq 0$

Such that $\langle \gamma_n \rangle$ sequence lies in (0,1) and $\langle \delta_n \rangle$ real sequence if the following conditions holds

$\sum_{n=0}^{\infty} \gamma_n = \infty$ *and* $\lim_{n\to\infty} sup \frac{\delta_n}{\gamma_n} \leq 0$ *or* $\sum_{n=1}^{\infty} |\delta_n| < \infty$. *Then* $\alpha_n \to 0$

$as\ n \to \infty$.

2. Main Results

Now, we define an iteration processes for sequence of general extended mapping and then study the convergence for these processes.

2.1.Definition

A mapping f is called general extended mapping if for each sequence $\langle z_n \rangle$ in [0,1] converges to 0 there exists a non – negative real number z such that

$$(1 - z_n)||x - w||^2 + z_n\|x - f_x - (w - f_w)\|^2 + z\langle x - f_x, w - f_w\rangle$$

$\geq ||fx - fw||^2$,*for all* $x, w \in C$

The concept of general extended mapping is independent of concepts nonexpansive mapping. As shown by the examples:

2.2.Example

Let $\mathcal{H}$ be a normed space $f: (0,\infty) \longrightarrow (0,\infty)$ such that $f(x) = 2x$..

the mapping f is not nonexpansive and it is general extended mapping .Then for any sequence $\langle z_n \rangle$ in [0,1] converges to 0 there exists $z > 0$ such that, $z = \frac{2}{\langle x - f_x, y - f_y \rangle}||x - y||^2$ and satisfy

$$(1 - z_n)||x - w||^2 + z_n[||x - f_x - w - f_w||]^2 + z\langle x - f_x, w - f_w\rangle \geq ||fx - fw||^2$$

2.3.Example

Let $\mathcal{H}$ be a normed space , $f: \mathcal{H} \longrightarrow \mathcal{H}$ such that $f(x) = x$.

It is clear that the mapping f is not general extended mapping but it is nonexpansive .

2.4..Theorem

If $\{A_j, j = 1, \ldots, m\}$ are maximal monotone operators and C is nonempty convex closed in $\mathcal{H}$, $\langle T_n \rangle$ is bounded sequence of general extended mappings and $\langle f_n \rangle$ is a sequence of quasi − nonexpansive. Let $\langle w_n \rangle$ define as

$z_n = (1 - \beta_n) f_n w_n + \beta_n w_n$

$$w_{n+1} = (1 - \alpha_n)T_n z_n + \alpha_n(\sum_{j=1}^{m} \gamma_{n,j} \; J^j_{r_{n,j}} \; z_n + (1 - \sum_{j=1}^{m} \gamma_{n,j}) f_n w_n$$

where $\langle \alpha_n \rangle, \langle \beta_n \rangle$ *are two sequences in [0,1] converges to 0,* $\langle \gamma_{n,i} \rangle$ *sequence in* R^+, *and* $\alpha_n + \beta_n = 1$

1-$\sum_{j=1}^{m} \gamma_{n,j}$ *is bounded*

$\sum \beta_n = \infty$ *and* $\sum \|T_n z_n\| < \infty$

If $\cap_{j=1}^{m} A_i^{-1}(0) \cap (\cap F(T_n)) \cap (\cap F(f_n)) \neq \emptyset$. *Then* $\langle w_n \rangle \longrightarrow \check{x}$, *where* $\check{x}$ *lies in of* $(\cap F(f_n)) \cap (\cap_{i=1}^{m} F(J^j_{r_{n,j}}))$.

Proof

Let $q \in \cap_{n \in N} F(T_n) \cap (\cap_{j=1}^{m} A_j^{-1}(0))$

$$\|z_n - q\|^2 \leq (1 - \beta_n)\|f_n w_n - q\|^2 + \beta_n \|w_n - q\|^2$$

$$\|w_{n+1} - q\|^2 \leq (1 - \beta_n)\|w_n - q\|^2 + \beta_n \|w_n - q\|^2 = \|w_n - q\|^2$$

$$\|w_{n+1} - q\|^2 \leq (1 - \alpha_n)\|T_n z_n - q\|^2 + \alpha_n(\sum_{j=1}^{m} \gamma_{n,j} \; \left\| J^j_{r_{n,j}} \; z_n - q \right\|^2 + (1 - \sum_{j=1}^{m} \gamma_{n,j}) \|f_n w_n - q\|^2$$

By definition of general extended mapping, we have, for any sequence $s_{nk} \in [0,1]$ *then there exist* $s_n > 0$ (*shortly we write them* s_n *and* s *respectively*) *such that*

$$\|w_{n+1} - q\|^2 \leq (1 - \alpha_n)[(1 - s_n)\|z_n - q\|^2 + s_n[\|q - T_n q\|.\|z_n - T_n z_n - (q - T_n q\|]^2 + z\langle w_n - T_n w_n, (q - T_n q)\rangle] + \alpha_n(\sum_{j=1}^{m} \gamma_{n,j} \; \|z_n - q\|^2 + (1 - \sum_{j=1}^{m} \gamma_{n,j}) \|w_n - q\|^2$$

$$\leq (1 - \alpha_n)[(1 - s_n)\|z_n - q\|^2] + \alpha_n(\sum_{j=1}^{m} \gamma_{n,j} \; \|z_n - q\|^2 + (1 - \sum_{j=1}^{m} \gamma_{n,j}) \|w_n - q\|^2$$

$$\|w_{n+1} - q\|^2 \leq (1 - \alpha_n)\|w_n - q\|^2 + \alpha_n(\sum_{j=1}^{m} \gamma_{n,j} \; \|w_n - q\|^2 + (1 - \sum_{j=1}^{m} \gamma_{n,j}) \|w_n - q\|^2 = \|w_n - q\|^2$$

Hence $\langle w_n \rangle$ *is bounded sequence* $\Rightarrow \exists \langle w_{nk} \rangle$ *subsequence of* $\langle w_n \rangle$ *and* $w_{nk} \rightharpoonup \check{x}$

$$||z_n - z_{n-1}|| = ||(1-\beta_n)f_n w_n - (1-\beta_{n-1})f_{n-1}w_{n-1} + \beta_n w_n - \beta_{n-1} w_{n-1}||$$
$$\leq ||\alpha_n f_n w_n - \alpha_{n-1} f_{n-1} w_{n-1} + \beta_n w_n - \beta_{n-1} w_{n-1}||$$
$$\leq \alpha_{n-1}\big|f_n w_n - f_{n-1} w_{n-1}\big| + \beta_{n-1}\big|w_n - w_{n-1}\big| + |\alpha_n - \alpha_{n-1}|\|f_n w_n\| + |\beta_n - \beta_{n-1}|\|w_n\|$$

$$\|w_n - w_{n+1}\| \leq \Big\|(1-\alpha_{n-1})T_{n-1}z_{n-1} + \alpha_{n-1}\Big(\sum_{j=1}^{m}\gamma_{n-1,j}\, J^j_{r_{n-1,j}}\, z_{n-1} + \Big(1 - \sum_{j=1}^{m}\gamma_{n-1,j}\Big) f_{n-1}w_{n-1} - (1-\alpha_n)T_n z_n - \alpha_n\Big(\sum_{j=1}^{m}\gamma_{n,j}\, J^j_{r_{n,j}}\, z_n + \Big(1 - \sum_{j=1}^{m}\gamma_{n,j}\Big) f_n w_n\Big\|$$
$$\leq \Big\|\beta_{n-1}T_{n-1}z_{n-1} - \beta_n T_n z_n + \alpha_{n-1}\sum_{j=1}^{m}\gamma_{n-1,j}\, J^j_{r_{n-1,j}}\, z_{n-1} - \alpha_n \sum_{j=1}^{m}\gamma_{n,j}\, J^j_{r_{n,j}}\, z_n + \alpha_{n-1}\Big(1 - \sum_{j=1}^{m}\gamma_{n-1,j}\Big) f_{n-1}w_{n-1} + \alpha_n\Big(1 - \sum_{j=1}^{m}\gamma_{n,j}\Big) f_n w_n\Big\|$$
$$+|\alpha_{n-1} - \alpha_{n-1}|\Big\|\Big(1 - \textstyle\sum_{i=1}^{m}\gamma_{n,j}\Big) f_n w_n\Big\|$$

But $\langle J^j_{r_{n,j}}\, z_n\rangle$, $\langle f_n\rangle$ $\langle T_n\rangle$ *are bounded sequences.*

$||w_n - w_{n-1}|| \longrightarrow 0$ *as* $n \longrightarrow \infty$

And hence $||z_n - z_{n-1}|| \longrightarrow 0$ *as* $n \longrightarrow \infty$

To prove that $||w_n - f_n w_n|| \longrightarrow 0$ *as* $n \longrightarrow \infty$

Since $\|w_n - q\| + \|f_n w_n - w_n\| \geq \|w_{n+1} - q\|$

and $\lim_{n\to\infty}\|w_n - q\|$ *exists, Therefore*

$$-\|f_n w_n - w_n\| \leq \|w_n - q\| - \|w_{n+1} - q\| \longrightarrow 0 \text{ as } n \longrightarrow \infty$$

So, $\|f_n w_n - w_n\| \to 0$ *as* $n \to \infty$

Also, as the same way we get,

$||w_n - J^j_{r_{n,j}} w_n|| \longrightarrow 0$ *as* $n \longrightarrow \infty$, *for each* $j = 1,2,3,\ldots$

But $w_{nk} \rightharpoonup \breve{x}$*.So,* $\breve{x} \in \cap_{n\in N} F(f_n)$ *and* $\breve{x} \in \cap_{j=1}^{m} F(J^j_{r_{n,j}})$

$$||z_n - \breve{x}|| \leq (1-\beta_n)\,||f_n w_n - \breve{x}|| + \beta_n||w_n - \breve{x}||$$
$$\leq (1-\beta_n)\,||w_n - \breve{x}|| + \beta_n||w_n - \breve{x}|| = ||w_n - \breve{x}||$$

$|| w_{n+1} - \check{x}||^2 \leq (1-\alpha_n) || T_n z_n - \check{x}||^2 +$

$\alpha_n[\sum_{j=1}^{m} \gamma_{n,j} || J^j_{r_{n,j}} z_n - \check{x}||^2 + (1 - \sum_{j=1}^{m} \gamma_{n,j}) \|f_n w_n - \check{x}\|^2]$
$\leq (1-\alpha_n) || T_n z_n - \check{x}||^2 + \alpha_n[\sum_{j=1}^{m} \gamma_{n,j} || z_n - \check{x}||^2 + (1 - \sum_{j=1}^{m} \gamma_{n,j}) \|w_n - \check{x}\|^2]$

$|| w_{n+1} - \check{x}||^2 \leq (1-\alpha_n) || T_n z_n - \check{x}||^2 + \alpha_n[\sum_{j=1}^{m} \gamma_{n,j} || w_n - \check{x}||^2 + (1 - \sum_{i=1}^{m} \gamma_{n,i}) \|w_n - \check{x}\|^2] \leq (1-\beta_n) || w_n - \check{x}||^2 + \beta_n || T_n z_n - \check{x}||^2$

By lemma (1.2) $\Longrightarrow || w_n - \check{x} ||^2 \longrightarrow 0$ *as* $n \longrightarrow \infty$. ■

2.5.Theorem
Let A_j, {j =1, . . ., m} are maximal operators ,$\langle T_n \rangle$ is bounded sequence of general extended mappings and $\langle f_n \rangle$ is sequence of quasi − nonexpansive mappings. If $\langle w_n \rangle$ define as:

$z_n = (1 - \beta_n) w_n + \beta_n f_n (w_n)$

$w_{n+1} = (1 - \alpha_n) T_n z_n + \sum_{j=1}^{m} \alpha_{n,j} J^j_{r_{n,j}} z_n$

where $\langle \alpha_n \rangle , \langle \beta_n \rangle$ are sequences in [0,1] and satisfied the following conditions

i. $\alpha_n + \beta_n = 1$
ii. $\sum \beta_n = \infty, \sum \|T_n z_n\| < \infty$ and $\sum_{j=1}^{m} \alpha_{n,j} = \alpha_n$.
iii. If $\cap_{j=1}^{m} A_j^{-1}(0) \cap \big(\cap F(T_n) \big) \cap \big(\cap F(f_n) \big) \neq \emptyset$.

Then $\langle w_n \rangle \longrightarrow \check{x}$, where $\check{x}$ be a common fixed point of T_n, for all $n \in N$.

Proof

Let $q \in \cap_{j=1}^{m} A_i^{-1}(0) \cap \big(\cap F(T_n) \big) \cap \big(\cap F(f_n) \big)$

$|| z_n - q|| \leq (1 - \beta_n)||w_n - q|| + \beta_n ||f_n (w_n) - q||$
$\leq (1 - \beta_n)||w_n - q|| + \beta_n ||w_n - q|| = || w_n - q||$

$||w_{n+1} - q||^2 \leq (1 - \alpha_n)||T_n z_n - q||^2 + \sum_{j=1}^{m} \alpha_{n,j} || J^j_{r_{n,j}} z_n - q||^2$

By definition of general extended mapping we have, for any sequence $s_{nk} \in [0,1]$ then there exist $s_n > 0$ (shortly we write them s_n and s respectively) such that

$$\begin{aligned} \big||w_{n+1} - q|\big|^2 \leq & \\ & \leq (1-\alpha_n)[(1 - s_n)||z_n - q||^2 + s_n[\, ||q - T_n q||.||z_n - T_n z_n - (q - T_n q||]^2 \\ & + z\,\langle w_n - T_n w_n, (q - T_n q)\rangle] + \sum_{j=1}^{m} \alpha_{n,j} \|z_n - q\|^2 \\ & = (1 - \alpha_n)\big||z_n - q|\big|^2 + \alpha_n \big||z_n - q|\big|^2 \leq ||z_n - q||^2 \leq ||w_n - q||^2 \end{aligned}$$

Hence $\langle w_n \rangle$ *is bounded sequence* $\Rightarrow \exists\, \langle w_{nk} \rangle$ *subsequence of* $\langle\ w_n\ \rangle$ *and* $w_{nk} \rightharpoonup \check{x}$

$|| z_n - z_{n-1}|| = ||(1 - \beta_n) w_n + \beta_n f_n (w_n) - (1 - \beta_{n-1}) w_{n-1} - \beta_{n-1} f_n (w_{n-1}) ||$

$$\leq (1-\beta_{n-1})|| w_n - w_{n-1}|| + \beta_{n-1}\|f_n(w_n) - f_{n-1}(w_{n-1})\|$$
$$+ |(1-\beta_{n-1}) - (1-\beta_{n-1})|\,||w_{n+1} - w_n|| + |\beta_{n-1} - \beta_{n-1}|\|f_n(w_n)\|$$

$||w_n - w_{n-1}|| \leq ||(1-\alpha_n)T_n z_n + \sum_{j=1}^{m}\alpha_{n,j} J^j_{r_{n,j}} z_n - (1-\alpha_{n-1})T_{n-1}z_{n-1} - \sum_{j=1}^{m}\alpha_{n-1,j} z_{n-1}||$

$\leq (1-\alpha_{n-1})||T_n z_n - T_{n-1}z_{n-1}|| + |(1-\alpha_{n-1}) - (1-\alpha_n)|\|T_n z_n\|$
$$+ \left|\sum_{j=1}^{m}\alpha_{n-1,j} - \sum_{j=1}^{m}\alpha_{n,j}\right| \left\|J^j_{r_{n,j}} z_n\right\|$$
$$+ \sum_{j=1}^{m}\alpha_{n-1,j} \left\|J^j_{r_{n,j}} z_n - J^j_{r_{n-1,j}} z_{n-1}\right\|$$

$||w_{n+1} - w_n|| = \beta_{n-1}||T_n z_n - T_{n-1}z_{n-1}|| + |\beta_{n-1} - \beta_{n-1}|\|T_n z_n\| + |\alpha_{n-1} - \alpha_n| \left\|J^j_{r_{n,j}} z_n\right\| +$
$\alpha_{n-1}\left\|J^j_{r_{n,j}} z_n - J^j_{r_{n-1,j}} z_{n-1}\right\|$.

But $\langle J^i_{r_{n,i}} z_n\rangle$, $\langle f_n\rangle$ *and* $\langle T_n\rangle$ *are bounded sequences then we get,*

$||w_n - w_{n-1}|| \longrightarrow 0$ *as* $n \longrightarrow \infty$.

And hence $||z_n - z_{n-1}|| \longrightarrow 0$ *as* $n \longrightarrow \infty$.

To prove that $||x_n - f_n x_n|| \longrightarrow 0$ *as* $n \longrightarrow \infty$

Since $\|w_{n+1} - q\| \leq \|w_n - q\| + \|f_n w_n - w_n\|$

and $\lim_{n\to\infty}\|w_n - q\|$ *exists, Therefore*

$-\|f_n w_n - w_n\| \leq \|w_n - q\| - \|w_{n+1} - q\| \longrightarrow 0$ *as* $n \longrightarrow \infty$

So, $\|f_n w_n - w_n\| \to 0$ *as* $n \to \infty$

Also, as the same way we get,

$||w_n - J^i_{r_{n,i}} w_n|| \longrightarrow 0$ *as* $n \longrightarrow \infty$, *for each* $i = 1,2,3,\ldots$

But $w_{nk} \rightharpoonup \breve{x}$. *Therefore,* $\breve{x} \in \cap_{n\in N} F(f_n)$ *and* $\breve{x} \in \bigcap_{i=1}^{m} F(J^i_{r_{n,i}})$

$||w_n - \breve{x}|| \leq (1-\beta_n)||w_n - \breve{x}|| + \beta_n||f_n(w_n) - \breve{x}||$
$$\leq (1-\beta_n)||w_n - \breve{x}|| + \beta_n||w_n - \breve{x}|| = ||w_n - \breve{x}||$$

$$||w_{n+1} - \breve{x}||^2 \leq (1-\alpha_n)||T_n z_n - \breve{x}||^2 + \sum_{j=1}^{m}\alpha_{n,j} ||J^j_{r_{n,j}} z_n - \breve{x}||^2$$
$$\leq (1-\alpha_n)||T_n z_n - \breve{x}||^2 + \sum_{j=1}^{m}\alpha_{n,j} ||z_n - \breve{x}||^2$$
$$\leq (1-\alpha_n)||T_n z_n - \breve{x}||^2 + \alpha_n ||w_n - \breve{x}||^2$$
$$\leq (1-\beta_n)||w_n - \breve{x}||^2 + \beta_n ||T_n z_n - \breve{x}||^2$$

By lemma (1.2) we get, $||w_n - \breve{x}||^2 \longrightarrow 0$ *as* $n \longrightarrow \infty$.

References

[1] Bauschke H. H. and Combettes P. L. 2011 Convex Analysis and Monotone Operator Theory in Hilbert Spaces, *Springer-Verlag*.
[2] Borwein J. M. and Vanderwerff J. D. 2010 Convex Functions, *Cambridge University Press*.
[3] Burachik R. S. and Iusem A. N. 2008 Set-Valued Mappings and Enlargements of Monotone Operators, *Springer-Verlag*, Vol.24.
[4] Simons S. 2008 From Hahn-Banach to Monotonicity, *Springer-Verlag*.
[5] Alinescu C. Z ˇ 2002 Convex Analysis in General Vector Spaces, *world Scientific Publishing*.
[6] Xu H. K. 2002 A nother Control Condition In an Iterative Method For Non-expansive Mappings, *Bull austral. Math .soc* , Vol.65, pp.109-113.
[7] Xu H. K. 2002 Iterative Algorithm For Nonlinear Operators ,*J. London. Math. Soc.*, pp..240-256.
[8] Moudafi A. 2000 Viscosity Approximation Method For Fixed Point Problems, *Journal of Mathematical Analysis and Applications*, Vol.241, pp.46-55.
[9] Xu H. K. 2004 Viscosity Approximation Methods For Nonexpansive Mapping, *J. Math Anal .Appl.* ,Vol.298, pp.279-291.
[10] Kamimura S., Takahashi W. 2000 Approximating Solutions of Maximal Monotone Operators in Hilbert Spaces, *J. Approx. Theory*, Vol.106, pp.226-240.
[11] Mabeed Z. H. 2011 Strongly Convergence Theorems of Ishikawa Iteration Process With Errors in Banach Space, *Journal of Qadisiyah Computer Science and Mathematics*, Vol. 3, pp.1-8.
[12] Abed S. S. ,Maibed Z . H. 2016 Convergence Theorems of Iterative Schemes For Non-expansive Mappings, *journal of advances in mathematics* ,Vol. 12, pp.6845-6851.
[13] Abed S. S .,Maibed Z. H. 2017 Convergence Theorems For Maximal Montone Operators By Family of Non_spreading Mappings, *(IJSR)* , pp.2319-7064.
[14] Lemoto S . and Takahashi W. 2009 Approximating Common Fixed Points of Non-expansive Mapping and Non-spreading Mappings In Hilbert Space, *Nonlinear Analysis*, Vol.71, pp.2082_2089.
[15] Aoyama K . and kohsaka F. and Takahashi W. 2011 Proximal Point Methods for Monotone operator in Banach space , *Taiwanese Journal of Math* ,Vol.15,No.1, pp. 259-281.
[16] Tan K. K. and XU H. K . 1993 Approximating Fixed Points of Non-expansive Mappings By The Ishikawa Iteration process, *J .Math .Anal.Appl*., Vol.178, pp.301-308.

COPRIME MODULES AND OTHER RELATED TOPICS

COPRIME MODULES AND OTHER RELATED TOPICS

A.M.Inaam and K.I. Rasha
Department of mathematics,college of education
Ibn-Al-Haitham , university of Baghdad.

Abstract. Let R be a commutative ring with unity and let M be a unitary R-module. In this paper we study the relationships between coprime modules and other kinds of modules.

1.Introduction

Let R be a commutative ring with unity and let M be an R-module. M is called coprime module (dual notion of prime modules) if $\underset{R}{\text{ann}}\, M = \underset{R}{\text{ann}} \frac{M}{N}$ for every proper submodule N of M [7].

Note that $\underset{R}{\text{ann}} \frac{M}{N} = [N :_R M]$.Equivalently M is coprime R-module if and only if M is second,see [17] (where M second if for every $r \in R$, the homothety r^* on M is either zero or surjective where a homothety r^* on M means $r^* \in \underset{R}{\text{End}}(M)$ and $r^*(x) = r\,x$ for each x in M [24].

The main purpose of this this paper is to study the relationships between coprime R-modules and other kinds of modules such as prime modules, Noetherian, Artinian, cohopfian, hopfian, anti-hopfian,fully stable and M-coprime modules and give the necessary and(or) sufficient condition under which these concepts with coprime R-modules are equivalent.

Recall that an R-module M is called a prime module if $\underset{R}{\text{ann}}\, N = \underset{R}{\text{ann}}\, M$ for all non-zero submodule N of M [12],[9]. Equivalently M is prime if for every $r \in R$, the homothety r^* on M is either zero or injective [21, Proposition (1.1.15)].

Proposition (2.1) Let M be an R-module such that $r\,M \cap N = r\,N$ for each proper submodule N of M; $r \in R$.If M is prime, then M is coprime.

Proof: Let $r \in [N :_R M]$, then $r\,M \subseteq N$. Since $r\,M \cap N = r\,N$, then $r\,M = r\,N$, hence for every $m \in M$, there exists $n \in N$ such that $r\,m = r\,n$, so $r\,(m - n) = 0$, that is $r \in \underset{R}{\text{ann}}\,(m - n)$. But M is prime, so $\underset{R}{\text{ann}}\,(m - n) = \underset{R}{\text{ann}}\, M$ by [21, proposition (1.1.15)]. Thus $r \in \underset{R}{\text{ann}}\, M$ and M is coprime. ■

We notice that the condition $r\,M \cap N = r\,N$ for all proper submodule N of M can not be dropped from proposition (2.1), for example Z as Z-module is prime, but not coprime ,where if N = 2Z, then $4Z \cap N \neq 4N = 8Z$

Recall that an R-module M is said to be ***F-regular*** if every submodule of M is pure, see [14], where a submodule N of M is called ***pure*** if I M $\cap$ N = I N for every ideal I of R, and hence r M $\cap$ N = r N for every $r \in$ R, see [14].A ring R is regular (in sense of von Neumann) if I $\cap$ J=IJ. Equivalently R is a regular ring if for any $a \in$R there exists x$\in$R such that $a= a^2x$.

Hence, we have the following result.

Corollary (2.2): Let M be a F-regular R-module. If M is prime , then M is coprime.

The following result shows that the concepts of coprime and prime are equivalent in the class of regular rings (in sense of von Neumann) .

Corollary (2.3): Let R be a regular ring, then M is a prime R-module if and only if M is a coprime R-module.

Proof: Let M be a prime module, since R is regular, then every R-module is F-regular. Hence the result follows by corollary (2.2).

To prove the converse, let M be a coprime R-module, then $\overline{R} = R / \operatorname{ann}_R M$ is an integral domain,see [17,note (8)]. But R is a regular ring, so $\overline{R}$ is a regular domain. Thus $\overline{R}$ is a field, and hence by [3, Rem. and Ex. 1.1.3 (6)] M is a prime $\overline{R}$-module, which implies that M is a prime R-module. ■

Recall that an R-module M is called ***divisible*** if for each non-zero divisor r of R, r M = M, see [22, p.32].

As another consequence of prop. (2.1), we have the following result.

Corollary (2.4): Let M be a prime module over an integral domain and every proper submodule of M is divisible, then M is coprime.

Proof: Let N be a proper submodule of M. Then r N =N for each $r \in$ R, $r \neq 0$. Hence r M $\cap$ N = r M $\cap$ r N = r N. Thus we have the result by proposition (2.1).■

We notice that the condition every submodule of M is divisible can not be dropped for example:

Z as Z-module is prime, but not coprime and every submodule of Z is not divisible.

Recall that an R-module M is called ***semisimple*** if every submodule N of M is a direct summand, see [19, p.107], where a suubmodule N of an R-module M is said to be ***direct summand*** of M if and only if there exists a submodule K of M such that M = N$\oplus$K, see [19,p.31], [6,p.61].

Note (2.5): A semisimple R-module need not be coprime, for example:

Z_6 as Z-module is semisimple and not coprime.

Also, in the class of semisimple modules the concepts coprime and prime modules are equivalent.

Proposition (2.6): Let M be a semisimple R-module, then M is a prime R-module if and only if M is a coprime R-module.

Proof: Let M be a prime module, to prove M is a coprime module, let N be a proper submodule of M; that is there exists a submodule W of M such that $N \oplus W = M$. Since M is prime, then $\underset{R}{\text{ann}}\, M = \underset{R}{\text{ann}}\, W$. But $W \cong \frac{M}{N}$, so it is easy to check that $\underset{R}{\text{ann}}\, W = \underset{R}{\text{ann}}\, \frac{M}{N}$, and so $\underset{R}{\text{ann}}\, M = \underset{R}{\text{ann}}\, \frac{M}{N}$. Thus M is coprime.

To prove the converse, let N be a submodule of M, then there exists a submodule W of M such that $N \oplus W = M$; that is $N \cong \frac{M}{W}$ and $\underset{R}{\text{ann}}\, N = \underset{R}{\text{ann}}\, \frac{M}{W}$. Since M is a coprime R-module, then $\underset{R}{\text{ann}}\, \frac{M}{W} = \underset{R}{\text{ann}}\, M$, which implies that $\underset{R}{\text{ann}}\, M = \underset{R}{\text{ann}}\, N$. Thus M is a prime R-module. ■

Note that the condition of semisimple in proposition (2.6) is necessary for example:

Z_{P^∞} is coprime, but it is not semisimple and not prime.

Compare the following result with proposition (1.1.16) in [21] (Let M be a prime R-module, let N be a proper submodule of M, if N is second, then N is prime).

Proposition (2.7): Let M be a coprime R-module and N be a proper submodule of M, if N is a prime R-submodule, then N is a coprime R-module.

Proof: Let $r \in R$ and let r^* be a homothety on N, to prove either $r \in \underset{R}{\text{ann}}\, N$ or r^* is surjective. Assume that $r \notin \underset{R}{\text{ann}}\, N$, hence $r \notin \underset{R}{\text{ann}}\, M$. But M is a coprime R-module, then by [17, corollary (9)] $r\,M = M$.

Let $y \in N$, then $y \in M = r\,M$, that is there exists $m \in M$ such that $y = r\,m$. But $r\,m \in N$ and N is a prime submodule, implies that $m \in N$ or $r \in [N :_R M]$. If $r \in [N :_R M]$, then $r\,M \subseteq N$, so M = N which is a contradiction. Thus $m \in N$ and so $r^*(m) = r\,m = y$. Therefore r^* is surjective. ■

S.Yassemi introduced the following theorem without proof, we give its proof for completeness.

Theorem (2.8):[24] If M is a non-zero finitely generated coprime R-module, then M is prime.

Proof: To prove M is prime, we shall prove $\operatorname{ann}_R(x) = \operatorname{ann}_R M$ for every $x \in M$, $x \neq 0$. It is clear that $\operatorname{ann}_R M \subseteq \operatorname{ann}_R(x)$. Assume that $\operatorname{ann}_R(x) \not\subseteq \operatorname{ann}_R M$ for some $x \in M$, $x \neq 0$, then there exists $r \in R$ such that $r \in \operatorname{ann}_R(x)$ and $r \notin \operatorname{ann}_R M$. Since M is coprime and $r \notin \operatorname{ann}_R M$, then by[13 ,corollary (9)] r M = M. But M is a finitely generated R-module, so by [18, p.50] there exists $r' \in R$ such that $(1 - r r')M = 0$. Thus $x = r' r x = 0$ which is a contradiction, so $r \in \operatorname{ann}_R M$ and $\operatorname{ann}_R(x) = \operatorname{ann}_R M$. ■

The condition M is finitely generated can not be dropped from theorem (2.8). Consider the Z-module Z_{p^∞}, This module is coprime and it is not finitely generated. However it is not prime because if N = $< \frac{1}{p^2} + Z >$, then $p^2 Z$ = ann N ≠ ann M = (0).

Recall that an R-module M is said to be ***Noetherian*** if every submodule of M is finitely generated, see [8, Proposition. 6.2, p.75].

The following result follows directly from (*2*.8).

Corollary (2.9): Let M be a Noetherian R-module if M is coprime, then M is prime.

Proof: Since M is Noetherian, then M is finitely generated. Hence the result obtained by theorem (2.8). ■

Recall that a proper submodule N of an R-module M is called ***fully invariant*** if for each $f \in \operatorname{End}_R(M)$, $f(N) \subseteq N$. M is called ***duo*** if every submodule of M is fully invariant, see [25].

Let M be an R-module, it is well known that we can consider M as E-module, where E = $\operatorname{End}_R(M)$ as follows for any $f \in E$, $m \in M$, $f(m) \in M$

To give the next result first we need the following lemmas.

Lemma (2.10): If M is a ***duo*** R-module, then every R-submodule is E-submodule.

Proof: The proof is obvious. ■

Lemma (2.11): Let M be a ***duo*** R-module, if M is a prime E-module, then M is a prime R-module.

Proof: Let N be an R-submodule. To prove $\operatorname{ann}_R M = \operatorname{ann}_R N$, let $r \in \operatorname{ann}_R N$, then $r N = 0$. Define $f : M \longrightarrow M$ by $f(m) = r m$. Hence $f(N) = r N = 0$. But by lemma (2.10), N is an E-submodule, thus $f \in \operatorname{ann}_E N = \operatorname{ann}_E M$ because M is a prime E-module. Then $f(M) = r M = 0$. Thus $r \in \operatorname{ann}_R M$. ■

Recall that an R-module is called ***finendo*** if M is finitely generated over endomorphism ring $\operatorname{End}_R(M)$, see [15].

Corollary (2.12): Let M be a finendo ***duo*** coprime E-module, then M is a prime R-module.

Proof: Since M is finendo coprime E-module, then M is a finitely generated coprime E-module, hence by Theorem (2.8), M is a prime E-module, so that by lemma (2.11) M is a prime R-module. ■

Recall that an R-module M is called ***hopfian*** if for every $f \in \operatorname{End}_R(M)$ f is surjective, then f is injective, see [16].

Proposition (2.13): If M is a hopfian coprime R-module, then M is prime.

Proof: Since M is a coprime R-module, then every non-zero homothety r^* is surjective. But M is a hopfian R-module, hence r^* is injective. Thus M is a prime R-module, see [21,proposition (1.1.15)]. ■

Recall that an R-module M is said to be ***cohopfian*** if for every $f \in \operatorname{End}_R(M)$, f is injective, then f is surjective, see [10].

The following theorem shows that cohopfian R-module is a sufficient condition for prime module to be coprime.

Proposition (2.14): Let M be a cohopfian R-module, if M is prime, then M is coprime.

Proof: Let $r \in R$, let r^* be a non-zero homothety on M. Since M is prime,then by[21, proposition (1.1.15)] r^* is injective. But M is cohopfian, hence r^* is surjective. Thus M is a coprime R-module. ■

From proposition (2.14) and Theorem (2.8) we have.

Corollary (2.15): If M is a finitely generated cohopfian R-module, then M is prime if and only if M is coprime.

Recall that an R-module M is called ***Artinian*** if M satisfies a decreasing chain conditions (dcc) on submodules of M.

S.Yassemi in [24] introduced the following result.

proposition (2.16): Let M be an Artinian R-module, if M is prime, then M is coprime.

Since every Artinian is cohopfian, then we get the following directly by (2.15).

Corollary (2.17): If M is a finitely generated Artinian R-module, then M is prime if and only if M is coprime.

Now, we can give the following result.

Proposition (2.18): If M is a coprime E –module, then M is cohopfian, where $E = \underset{R}{End}(M)$.

Proof: Since M is a coprime E-module, then by [17, corollary (9)] either $f(M) = 0$ or $f(M) = M$ for all $f \in E$, that is either $f = 0$ or surjective. Thus every injective mapping is surjective; that is M is cohopfian. ■

Similarly, we have the following result.

Proposition (2.19): Let M be a prime E-module, then M is hopfian, where $E = \underset{R}{End}(M)$.

Proof: Let $f \in \underset{R}{End}(M)$ such that f is surjective to prove f is injective, let $m \in \ker f$, hence $f(m) = 0$. But M is a prime E-module, then by [21, proposition (1.1.15)] (0) is a prime E-submodule. It follows that either $m = 0$ or $f \in \underset{E}{ann} M = 0$. But $f \neq 0$, so $m = 0$. Therefore f is injective. ■

Recall that a non-simple R-module M is called ***antihopfian*** if $M \cong M / N$ for all proper submodule N of M, see [16].

Remark (2.20):

1. It is clear that every anti-hopfian R-module M is a coprime R-module, but the converse may not be true, since the Z-module Q is coprime, and it is not anti-hopfian because $Q \ncong Q / Z$.
2. Every anti-hopfian R-module M is coprime E-module, where $E = \underset{R}{End}(M)$.

Proof: By [4, prop.1.3.1] every $f \in E$, $f = 0$ or f is surjective. Thus $f(M) = 0$ or $f(M) = M$; that is M is a coprime E-module, by [17, corollary (9)]. ■

Recall that if an R-module E is extension of an R-module M, then E is an essential extension of M, if for every non-zero submodule E′ of E, $E' \cap M \neq 0$ [22,p.40].

We recall that an R-module is an ***injective hull (envelope)*** of an R-module M if and only if E is a minimal injective extension of M, where E is a minimal injective extension of M if:

1. E is injective.
2. Whenever E′ is a proper submodule of E contains M, then E′ is not injective, see [22,p.43].

We used the symbol $\hat{M}$ to denote an injective hull of M.

To give the next result, we need the following remark.

Remark (2.21): Let M be a module over an integral domain, then $\hat{M}$ is a coprime R-module.

Proof: Since $\hat{M}$ is an injective and R is an integral domain, then by [17, corollary (33)] we have $\hat{M}$ is a coprime R-module. ■

The following result shows that the injective hull of any coprime R-module is coprime.

Corollary (2.22): If M is a coprime R-module, then $\hat{M}$ is a coprime R-module.

Proof: Since M is a coprime R-module, then $\overline{R} = R / \operatorname{ann}_R M$ is an integral domain. Hence M is a module over an integral domain $\overline{R}$. Then by remark (2.21), $\hat{M}$ is coprime $\overline{R}$-module, and by [17,corollary (11)] we have $\hat{M}$ is a coprime R-module. ■

We notice that the converse of this corollary is not true in general as it is shown by the following example:

For the Z-module Z, $\hat{Z} = Q$ is a coprime Z-module, but Z is not coprime.

The following proposition shows that the converse of corollary (22) is true under certain condition.

Proposition (2.23): Let M be an R-module such that $[U :_R M] = [U :_R \hat{M}]$ for every proper submodule U of M, if $\hat{M}$ is a coprime R-module, then M is coprime R-module.

Proof: $\operatorname{ann}_R M \subseteq [U :_R M]$ for every proper submodule U of M. Since $\hat{M}$ is coprime, then $[U :_R \hat{M}] = \operatorname{ann}_R \hat{M}$. But by assumption $[U :_R M] = [U :_R \hat{M}]$, that is $\operatorname{ann}_R M \subseteq \operatorname{ann}_R \hat{M}$. Thus $\operatorname{ann}_R M = \operatorname{ann}_R \hat{M} = [U :_R \hat{M}] = [U :_R M]$. Therefore M is coprime. ■

Also, the converse of proposition (2.22) holds under the class of modules over regular ring.

Proposition (2.24): Let R be a regular ring. If $\hat{M}$ is a coprime R-modul , then M is a coprime R-module.

Proof: Follows by [17, proposition (16)]. ■

Recall that an R-module M is called ***fully-stable*** if each submodule N of M is stable, where a submodule N of M is called ***stable*** if $f(N) \subseteq N$ for each R-homomorphism f from N into M, see [1].

A module M is called ***fully pseudo-stable*** (abbreviated p-stable) if each submodule of M is pseudo-stable, where a submodule N of M is said to be pseudo-stable if $f(N) \subseteq N$ for each R-monomorphism $f: N \longrightarrow M$, see [1, Definition 2.1, ch.2].

It is clear that every fully stable is fully p-stable, see [1].

Remarks (2.25):

1. fully-stable module may not be coprime module, for example: for all $n \in Z_+$, Z_n is a fully-stable Z-module by [1] but Z_n is a coprime Z-module if and only if n is prime.

2. A coprime module may not be fully stable as the following example shows:

Q / Z as Z-module is coprime by [21,corollary (2.1.13)]. But by [1, Ex. 1.2 (c), ch.1] it is not fully stable.

Recall that a module M over an integral domain R is **non-torsion** if there exists $m \in M$ such that $\operatorname{ann}_R(m) = 0$. Thus a torsion free R-module is non-torsion.

However, we have the following result.

Proposition (2.26): Let M be a non-torsion fully p-stable (stable) over an integral domain R, then M is faithful coprime.

Proof: By [1, Theorem 1.5, ch.3] and [1, Corollary 1.6, ch.3] we have M is divisible and so by [17, remark (29)], we have the result. ■

Corollary (2.27): Let M be torsion free over an integral domain R. If M is fully stable (p-stable), then M is faithful coprime.

Recall that an R-module M is called ***quasi-injective*** if for every submodule N of M, every R-homomorphism of N into M can be extended to an R-endomorphism of M, see [15].

Next, we have the following.

Proposition (2.28): Let M be multiplication non-torsion over a Dedekind domain R, then the following statements are equivalent:

1. M is a quasi-injective R-module.

2. M is a fully-stable R-module.

3. M is an injective R-module.

4. M is a divisible R-module.

5. M is a faithful coprime R-module.

Proof: (1) $\Leftrightarrow$ (2) follows by [1, Corollary 2.3, ch.3].

(2) $\Leftrightarrow$ (3) follows by [1, Corollary 1.8, ch.3].

(3) $\Leftrightarrow$ (4) $\Leftrightarrow$ (5). see [17, Proposition (35)].

(3) $\Leftrightarrow$ (1). It is obvious. ■

Notice that a fully stable module need not be prime module for example:
Z_6 as Z-module is fully stable and not prime.

Now, we have the following.

Theorem (2.29): Let M be a prime fully stable (P-stable) R-module. Then M is a coprime R-module.

Proof: Since M is a prime R-module, then $\overline{R} = R / \operatorname{ann}_R M$ is an integral domain and by [20], [11] M is a torsion free $\overline{R}$-module. But M is a fully stable (p-stable) R-module, so M is a fully stable (p-stable) $\overline{R}$-module, by [1,Prop.2.12,ch.3]. Then by corollary (2.27) M is coprime $\overline{R}$-module. Thus by [17,corollary (11)] M is a coprime R-module. ■

To give our next result, we need the following lemma.

Lemma (2.30): If M is a fully stable prime R-module, then M is cyclic.

Proof: Since M is fully stable, then by [1, Prop. 2.5,ch.3], $[\operatorname{ann}_R M : \operatorname{ann}_R x] \subseteq [x :_R M]$ for each x in M. But M is prime, so $\operatorname{ann}_R M = \operatorname{ann}_R x$ for every $x \in M$, $x \neq 0$. Hence $[\operatorname{ann}_R M : \operatorname{ann}_R M] = [x :_R M]$; that is $R = [x :_R M]$, which implies that $M = (x)$. ■

Corollary (2.31): Let M be a fully stable R-module. Then the following statements are equivalent.

1. M is a prime R-module.

2. M is a cyclic coprime R-module.

3. M is a simple R-module.

Proof: (1) → (2) follows by Theorem (2.29) and lemma (2.30).

(2) → (3) follows by [17, Rem. and Ex. 3 (6)].

(3) → (1). It is clear. ■

Recall that a submodule N of an R-module M is called ***annihilator submodule*** if $N = \operatorname{ann}_M I$ for some ideal I of R, see [2].

Equivalently, $N = \operatorname{ann}_M \operatorname{ann}_R N$.

Next, we can give the following proposition.

Proposition (2.32): If every submodule of an R-module M is an annihilator submodule and $\operatorname{ann}_R M$ is a prime ideal, then M is a coprime module.

Proof: Let N be a proper submodule of M. Then $N = \operatorname{ann}_M I$ for some ideal I of R. To prove $[N :_R M] = \operatorname{ann}_R M$, let $r \in [N :_R M]$, then $r M \subseteq N = \operatorname{ann}_M I$. Hence $r I M = 0$. Thus $r I \subseteq \operatorname{ann}_R M$, which implies that $r \in \operatorname{ann}_R M$ or $I \subseteq \operatorname{ann}_R M$. If $I \subseteq \operatorname{ann}_R M$, then $I M = 0$, and so $M \subseteq \operatorname{ann}_M I = N$, so $M = N$ which is a contradiction. Thus $r \in \operatorname{ann}_R M$, so $[N :_R M] = \operatorname{ann}_R M$ and M is coprime. ■

Hence, we have the following result.

Corollary (2.33): Let M be a fully stable finitely generated module over a dedekind domain with $\operatorname{ann}_R M$ is prime, then M is coprime.

Proof: By [1, Corollary 1.22, ch.3] every submodule N of M is an annihilator submodule. Hence by proposition (2.32), M is coprime. ■

As another consequence of (2.32), we have the following result:

Corollary (2.34): If M is a finitely generated multiplication R-module over a Dedekind domain and $\operatorname{ann}_R M$ is a prime ideal, then the following statements are equivalent.

1. M is a fully-stable R-module.

2. For every submodule N of M, N is an annihilator.

3. M is a coprime R-module.

4. M is a q-injective R-module.

Proof:

(1) $\Leftrightarrow$ (2) follows by [1, Corollary 1.22,ch.3].

(2) $\rightarrow$ (3) follows by corollary (2.32).

(3) $\rightarrow$ (4). M is a coprime multiplication R-module, implies M is simple. Hence M is q-injective.

(4) $\rightarrow$ (1) follows by [1, Proposition 2.1,ch.3]. ■

Corollary (2.35): Let M be a finitely generated prime module over Dedekind domain, then the following statements are equivalent.

1. M is a fully stable.

2. For any submodule N of M, N is an annihilator submodule.

3. M is simple, (and hence it is coprime).

4. M is a multiplication q-injective R-module.

Proof:

(1) $\Leftrightarrow$ (2). See [1, Proposition 1.22,ch.3].

(2) $\rightarrow$ (3). Since M is a prime R-module, then for every non-zero submodule N of M $\operatorname{ann}_R M = \operatorname{ann}_R N$. Hence $M = \operatorname{ann}_M \operatorname{ann}_R M = \operatorname{ann}_M \operatorname{ann}_R N = N$. Thus M is a simple R-module, and so it is coprime.

(3) $\rightarrow$ (4) is clear.

(4) $\rightarrow$ (1) follows by [1, Corollary 2.3,ch.3]. ■

R.Ameri, Y.Talebi and M.Maghsoomi in [12] introduced the notion of M-coprime module by the following definition.

Definition (2.36): A module X is said to be ***M-coprime*** if $\underset{R}{\mathrm{Hom}}(X,M) \neq 0$ and T*r* M (X) = T*r* M (X/Y) for every submodule Y of X such that $\underset{R}{\mathrm{Hom}}(X/Y,M) \neq 0$, where T*r* M (X) = $\sum$ {Im *f*; *f* $\in$ $\underset{R}{\mathrm{Hom}}(X,M)$}.

Recall that if M is an R-module and U is a non-empty set of R-modules, M is said to be generated by U if M is a summution of submodules which are homomorphic images of modules in U, see [19, Definition 3.3.1,p.52].

Examples (2.37):

1. Let M be the Z-module Z_6. If U = {Z_6 / ($\bar{2}$), Z_6 / ($\bar{3}$)}, then it is clear that M is generated by U.

   However, M is not generated by U = {Z_6 / ($\bar{2}$)}.
2. Let M = Z_{P^∞} as Z-module. Let U = { Z_{P^∞} /G}, where G is a submodule of Z_{P^∞}. $Z_{P^\infty} \cong Z_{P^\infty}$ /G. Thus Z_{P^∞} is a generated by U.
3. Let U ={Z_5/(0)}. Z_5 is a generated by U.
4. Let M = $Z_2 \oplus Z_2$ and N = $Z_2 \oplus (\bar{0})$. M / N $\cong$ Z_2. M is generated by M / N.

R. Ameri, Y.Talebi and Maghsoomi in [5] gave the following:

Theorem (2.38): [5] Let M be an R-module. The following statements are equivalent.

1. M is M-coprime.
2. M is generated by every non-zero factor module of M.

Note that the second statement is given as a definition of "coprime module", see [23, Exc. (16), p.103].

However, we have the following.

Proposition (2.39): If M is M-coprime, then M is coprime R-module.

In order to prove this proposition, we state and prove the following lemma.

Lemma (2.40): If $f : X \longrightarrow Y$ is an epimorphism, where X and Y are two R-modules, then $\underset{R}{\mathrm{ann}}(X) \subseteq \underset{R}{\mathrm{ann}}(Y)$.

Proof: Clear. ■

Now, we are ready to prove proposition (2.39).

Proof: If M is M-coprime. Let N be a proper submodule of an R-module M, then M is generated by M / N. Thus M = $\sum_{i\in\wedge} w_i$; $\wedge$ is some index set, where w_i is a homomorphic image of M / N. By lemma (2.40) we have for any $i \in \wedge$ $\underset{R}{ann}(M/N) \subseteq \underset{R}{ann} w_i$. Thus $\underset{R}{ann}(M/N) \subseteq \bigcap_{i\in\wedge} \underset{R}{ann}\, w_i = \underset{R}{ann}(\sum_{i\in\wedge} w_i) = \underset{R}{ann} M$.

Thus $\underset{R}{ann}(M/N) \subseteq \underset{R}{ann} M$, that is $\underset{R}{ann}(M/N) = \underset{R}{ann} M$ and M is coprime.■

We notice that the converse of proposition (2.39) is not true in general as the following example shows:

Consider the Z-module M = Q $\oplus$ Z_{P^∞} and N = Q $\oplus$ (0) be a submodule of M. M is coprime Z-module and M / N $\cong$ Z_{P^∞} . Thus M is not generated by M / N = { Z_{P^∞} }.

Recall that an R-module X is said to be ***comonoform*** if every non-zero homomorphism *f* : X $\longrightarrow$ X / Y is epimorphism, where Y is any submodule of X, see [5].

According to the above definition we have.

Remark (2.41): Every comonoform R-module is coprime.

Proof: Since M is comonoform, then by [5, Corollary 2.9], M is M-coprime and by proposition (2.39) we have M is coprime. ■

We notice that the converse of remark (2.41) may be false as the following example shows:

Let M be the Z-module Q $\oplus$ Q, M is a coprime Z-module. If N = Z $\oplus$ (0), then M / N = $\frac{Q \oplus Q}{Z \oplus (0)} \cong Q / Z \oplus Q$.

Define *f* : M $\longrightarrow$ M / N by *f* (*a*,*b*) = (*a* + Z,0), *f* is Z-homomorphism, but not epimorphism, so M is not comonoform.

REFERENCES

[1] M.S.Abass., (1990), **"On Fully Stable Modules"**, Ph.D. Thesis, Univ.of Baghdad.

[2] Z. Abdul-Baste and P. F. Smith, (1988), **"Multiplication Modules"**, Comm.in Algebra, Vol.16, pp. (755-779).
[3] H.M.Abdul-Razak, (1999), **"Quasi-Prime Modules and Quasi-Prime Submodule"**, M.D. Thesis, Univ. of Baghdad.
[4] H.KH.Al-Awadi, (2000), **"Anti-Hopfian Module and Restricted Anti-Hopfian"**, M.Sc. Thesis, Univ.of Baghdad.

[5] R.Ameri, Y.Talebi and M.Maghsoomi, (2008), **"M^X-Condition and Co-Prime Modules"**, International Journal of Algebra, Vol. 2, No.11, pp.(525-532).
[6] F.W.Anderson and K.R.Fuller,(1973),**"Rings and Categories of Modules"**, Univ. of Oregon

[7] S.Annin, (2002), **"Associated and Attached Primes Over Non Commutative Rings"**, Ph.D. Thesis, Univ.of Berkeley.

[8] M.F.Atiyah and I.G.Macdonald, (1969), **"Introduction to Commutative Algebra"**, Univ.of Oxford

[9] J.A.Beachy, (1976), **"Some Aspects of Non-Commutative Localization"**, Lecture Notes in Mathematics, Vo.545, Springer Verlage, Heildelberg, New York.

[10] G.F.Birkenmeier**, (1976),** "On The Cancellation of Quasi-Injetive Modules"**, Comm. In Algebra, Vol.49, No. 2, pp.(101-109).**

[11] J.Dauns, (1980), **"Prime Modules and One-Sided Ideals in 'Ring Theory and Algebra III""**, (Proccedings of the third Oklahoma Conference), B.R.MCDonald (editor) (Dekker, New Yourk), pp.(301-344).

[12]G.Desale, W.K.Nicholson, (1981), **"Endoprimitive Rings"**, J.Algebra, Vol.70, pp.(548-560).
[13] C.Faith, (1972), **"Modules Finite Over Endomorphism Ring"**, Lecture Notes in Mathematics, Springer-Verlag, Heidelberg, New Yourk, Vol. 246.

[14] D.J.Fieldhouse, (1969), **"PureTheories"**, Math. Ann.,Vol.184, pp.(1-18).
[15] M.Harda, (1965), **"Note on Quasi-Injective Modules "**, Osakaj, Math, Vol.2, pp.(531-356).
[16] Y.Hirano and I.Mogani, (1986), **"On Restricted Anti-Hopfian Modules"**, Math. J. Okayama Univ., Vol.28, pp.(119-131).
[17] A.M.Inaam and K.I.Rasha, (2010)**,"Dual Notion of Prime modules"**,Ibn Al-Haitham journal for pure and applied science,Vol.23, No.3,pp.(226-236).
[18] I.Kaplanskj, (1974), **"Commutative Rings"**, The Univ. of Chicago Press, Chicago & London
[19] F.Kasch, (1982), **"Modules and Rings"**, Acadimic Press, London.

[20] C.P.Lu, (1984), **"Prime Submodule of Modules"**, Comment, Math.Univ.St.Paul, Vol.23, No.1, pp. (61-69).

[21] K.I.Rasha, (2009), **Dual Notions Of Prime Submodules And Prime Modules, *(2009)***, M.Sc.. Thesis, Univ. of Baghdad.

[22] D.W.Sharp and P.Vamous, (1972), **"Injective Modules"**, Cambridge Univ. Press, London

[23] R.Wisbauer, (1996), **"Modules and Algebras: Bimodule Structure and Group Actiona and Algebra "**, Heinnch-Hein University Dusseldorf.

[24] S.M.Yassemi, (2001), **"The Dual Notion of Prime Submodule"**, Arch.Math. (Bron), Vol.37, pp. (273-278).

[25] A.C. Özcan,A.Harmaci,(2006), "**Duo Modules**",Glasgow Math.j.48 (2006)533-545.

When *m-lindelof* sets are mx-semi closed

IOP Conf. Series: Journal of Physics: Conf. Series **1003** (2018) 012044 doi:10.1088/1742-6596/1003/1/012044

When m-*lindelof* sets are mx-semi closed

Haider Jebur Ali, Marwa Makki Dahham

Department of Mathematics, College of Science, Mustansiriyah University, Baghdad, Iraqi

haiderali89@yahoo.com, marwamakki111@gmail.com

Abstract. This paper is devoted to introduce new concepts so called m-L(sc)-spaces. Several theorems related to these concepts are proved, further properties are studied as well as the relationships between these concepts with another types of m-L(sc)-spaces are investigated.

Key words. mx-open set, m-compact, m-lindelof , m-Lc-spaces, m-lindelof and mx -semi closed.

1. Introduction

It is known that there is no relation between m-Lindelof space and mx-closed sets, so this point stimulated some researchers to introduce a new concept namely m-Lc-spaces [1], these are the spaces (m-Lc-spaces) in which every m-Lindelof subset is mx-closed.

In 2015 the author [2] introduced a new concept, namely, m-K_2 (=A non-empty set X with an m-space is said to be m -K_2 if mx-cl (A) is m-compact in X for a subset A of a m-space X, whenever X is m-compact). The basic definitions that are needed in this work are recalled. A space(X,mx) means a m-space where a sub family mx of the power set $P(X)$, such that ϕ and X belong to mx [3]. Each member of mx is said to be mx-open set and the complement of an mx-open set is said to be mx-closed set. We denote the (X,mx) by m-space. For a subset A of a m-space X, the mx-interior of A and the mx-closure of A are defined as follows :

mx-$cl(A)$ $=\cap\{F: A \subseteq F, X\text{-}F$ is mx-open$\}$

mx-$int(A) = \cup\{U: U \subseteq A, U \in m_X\}$

Note that mx$-cl(A)$(mx$-int(A)$) is not necessarily mx-closed (mx-open). The m-space need not to be a topological space and the union and the intersection of any two mx-open sets are not necessarily to be mx-open [3], as we show in the following example:

Example: Let $X = \{a, b, c\}$, mx$= \{\phi, X\{b, c\}, \{a, b\}, \{a\}, \{c\}\}$.

Then (X, mx) is m-space but it is not topological space, since

$\{b, c\} \cap \{a, b\} = \{b\} \notin$ mx and $\{a\} \cup \{c\} = \{a, c\} \notin$mx. [2]. The authors [3] introduce the following definitions:

An m-space m_x on a non-empty set X is said to have the property (γ) if the intersection of finite number of m_x-open sets is m_x-open. An m -space m_x on a non-empty set X is said to have the property (β) if the union of any family of subsets of m_x belong to m_x. A nonempty set X with m -space is said to be m -compact if every cover of X with m_x-open sets has a finite sub cover [4]. An empty set X with m-space m_x is said to be m-lindelof if every cover of X with m_x-open sets has countable sub cover [5]. Every m -compact set is m-lindelof but the convers is not true [2]. For example:

The m-discrete space (X, τ_D), where X is infinite countable set, and $\tau_D = discrete$ m-Space, then (X, τ_D) is m-lindelof, which is not m-compact [2]. An m-space X which has (β) property is m_x-T_1-

space if and only if every singleton set is m_x-closed [2]. A set A is an m-space X is called m-regular if for each m_x-closed set F in X and $x \in X$ with$x \notin F$, there exist disjoint m_x-open sets U, V in X with $x \in U$ and $F \subseteq V$ by [6]. Every m-compact subset of m_x-T_2-space has the properties (β) & (γ) is m_x-closed [7].

On m-lindelof sets are m_X −semi closed

Definition (1): A space X is called m-L(sc)-space if every m -lindelof subset of X is m_x-semi closed.

Example (1): In the space (X, τ_D), such that X is a non-empty set, then every lindelof subset of X is closed means that X is L c-space.

Remark (1): Every m-L c-space is m-L(sc)-space, but the convers may not be true.

Example (2): Let R be the real line, N be a subset of R (where N is natural numbers) and $\tau = \{U \subseteq R | U = R \text{ or } U \cap N = \phi\}$. It is clear (X, τ) is an m-space. Then (R, τ) is m- L(sc)-space but it is not m -LC-space, since R consists of rational numbers and irrational numbers, then if we take a m-lindelof subset K of irrational numbers so it is finite set (since the m -lindelof set in irrational numbers is just a finite set), K is not m_x-closed set since it is not intersects N , but it is an m_x-semi closed, since there exists an m_x-closed subset $K \cup N$ of irrational number Q^c such that $K = m_x\text{-int}(K \cup N) \subseteq K \subseteq K \cup N$. Now if we take the rational number set Q, it is a countable then it is an m-lindelof set , the set Q-N is an m-lindelof and m_x-semi closed but not m_x-closed, there exists an m_x-closed subset $(Q\text{-}N) \cup N \text{ of } Q\text{-}N$ such that $Q\text{-}N = m_x\text{-int}((Q\text{-}N) \cup N) \subseteq Q\text{-}N \subseteq (Q\text{-}N) \cup N$.

Remark (2): Every m-L(sc)-space is m -k(sc)-space, but the convers may not be true.

Example (3): The m-space (R, τ_u) is a m-T_2 −space , so it is a m -k(sc)-space, but it is not m - L(sc)-space since if we take the natural N it is countable, then it is
m -lindelof, but not m_x-semi closed because the only m_x-closed set which contain N is just R but $R = m_x\text{-int}(R) \nsubseteq N \subseteq R$, so (N, τ_u) is not m -L(sc)-space.
Proposition (1): Every m -L(sc)-space is m -sT_1-space, whenever X has the property $(s\beta)$.

Proof: If X is an m -L(sc)-space, then it is clear that the set$\{x\}$ is an m -lindelof subset of X which is m -L(sc)-space, then $\{x\}$ is m_x-semi closed subset of X for all $x \in X$, hence, X is m -T_1.

Definition (2): A subset F in an m-space X is called m_x- F_σ –closed if it is the union of countably many m_x-closed sets. A set G is called m_x -G_δ-open if it is the intersection of countably many m_x-open sets.

Remark (3): Every m_x-closed set is m_x- F_σ –closed and m_x-open set is m_x-G_δ-open, but the convers is not true for example (2).

Definition (3): A space X is called m-p-space if every m_x-G_δ-open set in X is m_x-open.

Theorem (1): Every m- T_2-space and m-p-space is m- L(sc)-space, whenever X has the property (β).

Proof: Let L be an m-lindelof subset of X and $x \notin L$, so for each $l \in L$, such that $l \neq x$, but X is m-T_2-space means that there exists $U, V \in m_X$, such that $l \in U$, $x \in V$ *and*
$U \cap V = \phi$. Now, let $\{U_\propto\}_{\propto \in \Lambda}$ be an m open cover to L which is m-lindelof, that is $L = \bigcup_{i=1}^{n} U_{\propto i}$, thus, $\bigcup_{i=1}^{n} U_{\propto i}$ is a cover to L , put $V^{\setminus} = \bigcap_{i=1}^{\infty} V_{\propto i}$, then $V^{\setminus}$ is m_x-G_δ −open set but X is m-p-space, so $V^{\setminus}$ is m_x-open in X, then $x \in V^{/} \subseteq L^c$, that is x is an m_x-interior point to L^c this implies L^c is m_x-open set in X, hence, L is m_x-closed in X, but every m_x-closed is m_x-semi closed. Then X is m-L(sc)-space.
Definition (4): An m-space X is said to be m-L(θc)-space if every m-lindelof subset of X is m_x-θ-closed.

Example (4): (X, τ_D), where X is countable set, satisfy definition (4).

Definition (5): A space X is called θ-p-space if every θ-G_δ-open set in X is θ-open.
Definition (6): An m-space X is called m-θ-p-space if every m_x-θ-open set in X is m_x-θ-open.
Corollary (1): Every m-θ-T_2 and m-θ-p-space are m-L(θc)-space.
Proof: Let M be an m-lindelof subset and $x \notin M$, so for each $m \in M$ such that $m \neq x$, but X is m-θT_2 (means that) there exists $U, V \in \tau_\theta$ such that $m \in U, x \in V$ and $U \cap V = \emptyset$. Now, let$\{ U_\propto\}_{\propto\in\Omega}$, be an m_x-θ-open cover to M, which is a lindelof; that is $M = \bigcap_{i=1}^{\infty} U_{\propto i}$, so $\bigcup_{i=1}^{\infty} U_{\propto i}$ is a cover to M. Put $V^{\setminus}$=$\bigcap_{i=1}^{\infty} V_{\propto i}$, then V$^{\setminus}$ is m_x-$\theta - open$, but X is m-θ-p-space, so V$^{\setminus}$ is m_x-open in X. Then x$\in V^{\setminus} \subseteq M^c$ that is x is an m_x-θ −interior points to M^c. This implies, M^c is m_x-θ-open set in X, so M is m_x-θ-closed in X. Then X is m-L(θc)-space■

Definition (7): Let X be an m-space and Y be a subspace of it, a subset U_Y is said to be m_X-open in Y if there exists an m_x-open setU_x in X such that $U_Y = U_X \cap Y$.

Definition (8): let X be an m-space and Y be a subspace of it, a subset U_Y is said to be m_Y-closed in Y if there exists an m_X-closed set U_X in X such that $U_Y = U_X \cap Y$.

Example (5): $X = \{a, b, c, d\}, Y = \{a, c\}, \tau_X = \{\phi, X\}, \tau_Y = \{\phi, Y\}$ satisfies definition (8).

Definition (9): Let (X, τ_X) be an m-space and Y$\subseteq X$, then the subspace topology of Y in X is $\tau_Y = \{Y \cap U / U \in \tau_X\}$.

Proposition (2): Let X be an m-space, a subset U of X is m_X-open if and only if, $\forall x \in U, x \in m_X - int(U)$, wherever X has the property(β).
Proof: Let U is m_x-open in X, and $x \in U$ by taking $U = G$, then $x \in U = G \subseteq U$
X is an m_x-interior point of U but x is an arbitrary, hence, $\forall x \in U, x$ is an m_x-interior point to U. Conversely, since $\forall x \in U$, there exists an m_x-open set G containing x and contained in U, so $U = \bigcup_{\propto\in\nearrow} G_\propto$, but X has a property(β), thus, $\bigcup_{\propto\in\nearrow} G_\propto$ is m_x-open, that is U is m_x-open sets. ■
Proposition (3): Let X and Y be two m-spaces, a function $f: X \longrightarrow Y$ is m-continuous iff the inverse image under f of every m_x-open (m_x-closed) set in Y is m_x-open (m_x-closed) in X with property(β).

Proof: Let f be an m-continuous function and let H be an m_x-open in Y (to prove that $f^{-1}(H)$ be am m_x-open in X). If f^{-1}(H)=$\emptyset$, then there is nothing to prove. Thus, let f^{-1}(H)$\neq \emptyset$ and let $x \in f^{-1}(H)$ $that$ is $f(x) \in H$. Since f is m-continuous there exists an m_x-open set G in X such that $x \in G$ and $f(G) \subseteq H$ (means that) $x \in G \subseteq f^{-1}(H), so$ x is an interior point, $f^{-1}(H)$ is m_x-open in X
Conversely, assume that $f^{-1}(H)$ be an m_x-open in X,$\forall m_X$-open set H in Y (to prove that f is m-continuous at $x \in X$). Let H be any m_x-open set in Y such that f($(x) \in H \rightarrow x \in f^{-1}(H)$, by hypothesis $f^{-1}(H)$is m_x-open in X. If $f^{-1}(H) = G$, then G is an m_x-open set in X containing x such that $f(G) = f\left(f^{-1}(H)\right) \subseteq H$, hence, f is an m-continuous function ■
The proof of closeness is the same.

Theorem (2): let (X, m_X) and (Y, m_Y) be m-spaces and B be a base for m_Y on Y, a function $f: (X, m_X) \longrightarrow (Y, m_Y)$ is m-continuous if and only if
$\forall B \in B, f^{-1}(B) is$ m_X-open in X, whenever X and Y have the property (β).
Proof: Let f be an m-continuous and $B \in B$ since B be an m_x-open in Y, then $f^{-1}(B)$is m_x-open in X (by proposition (3))
Conversely, (Given $f^{-1}(B)$ is m_x-open in$X$) $\forall B \in$B and let H be an m_x-open in Y, then H is a union pf member of B (means that)
$H = \cup \{\mathcal{B}_\propto : \mathcal{B}_\alpha \epsilon B$ for some $\alpha \epsilon \lambda\}$. Therefore, $f^{-1}(H) = f^{-1}(\cup\{$B_$\propto$:B for some $\alpha\in\wedge\}) = \cup \{f^{-1}(\{\mathcal{B}_\propto : \mathcal{B}_\alpha \epsilon B$ for $some$ $\alpha \epsilon \lambda\}$, which is an m_x-open in X. Since each $f^{-1}(\mathcal{B}_\propto)$ is $m_X -$ $open$ in X and X has the property (β), hence f is m-continuous. ■

Theorem (3): Let X and Y be an m-spaces a function f from a space X to a space Y is m-continuous if $f(mx-cl(A)) \subset mx-cl(f(A))$, for every A$\subset X$,whenever X and Y have the property (β).

Proof: Let f be an m-continuous, since m_x-cl(f(A)) is m_x-closed in Y , then
$f^{-1}(m_X\text{-}cl(f(A))$ is m_x-closed in X and therefore
m_X-cl$(f^{-1}(m_X$-cl(f(A))$= f^{-1}(m_X\text{-}cl(f(A))\ldots(1)$, now
f(A)$\subset m_X\text{-}cl(U)$
A$\subseteq f^{-1}(f(A)) \subset f^{-1}(m_X\text{-}cl(f(A)) \Longrightarrow A \subset f^{-1}(m_x$-cl(f(A))
$\Longrightarrow m_X\text{-}cl(A) \subseteq m_X\text{-}cl(f^{-1}(m_X\text{-}cl(f(A))) = f^{-1}(m_X\text{-}cl(f(A))$by (1)
$\Longrightarrow f(m_X\text{-}cl(A)) \subset m_X\text{-}cl(f(A))$

Lemma (1): Let f:X$\rightarrow Y$ be an injective and m-continuous function from an m-space X in to a space Y if F is a m_x-semi closed set in X. then $f(F)$ is also m_x-semi closed in Y with property (β).

Proof: let $f(F) \subseteq Y$, for some m_x-semi closed F in X, since f is (one to one), so F=$f^{-1}(f(F))$, so F^c is m_x-semi open in X, that is there is U is m_x-open subset of X such that U$\subseteq F^c \subseteq m_X - cl(U)$,f(U)$\subseteq f(F^c) \subseteq f(m_X$-cl(U)), and since f is
$m-continuous,,then\ f(m_X$-cl(U))$\subseteq m_X\text{-}cl(f(U))$. This yields,
f(U) $\subseteq f(F^c)) \subseteq m_X\text{-}cl(f(U))$, then $f(F^c)$ is m_X-semi open set in Y, Hence, $f(F)$ is m_X-semi closed in Y.

Lemma (2): Let (X, m_X) and (Y, m_Y) be two m-spaces and let f:X$\rightarrow Y$ be an m-homeomorphism function from a space X to a space Y. If F is m_x-semi closed in Y, then $f^{-1}(F)$ is also m_x-semi closed in X with property (β).
Proof: let $f^{-1}(F) \subseteq X$, for some m_x-semi closed F in Y and $f(f^{-1}(F))$ (fis onto), then there exists G be an m_X-closed set in Y, such that
$m_x\text{-}int(G) \subseteq F \subseteq G, f^{-1}(m_X$-int(G))$\subseteq f^{-1}(F) \subseteq f^{-1}(G)$, and since
f is m-homeomorphism, then $m_x\text{-}int(f^{-1}(G)) \subseteq f^{-1}(m_X\text{-}int(G))$. Thus, $m_X\text{-}int(f^{-1}(G)) \subseteq f^{-1}(F)\subseteq f^{-1}(G)$, therefore, $f^{-1}(F)$ is m_x-semi closed in X.

Lemma (3): If F is m_x-semi closed in X, and Y is a subspace of X, then $F \cap Y$ is m_x-semi closed in Y.

Proof:
Since F is m_x-semi closed in X, then there exists m_X-closed set $G\ of\ X$ such that $m_X - int(G)_{in\,X} \subseteq F \subseteq G_{in\,X}$, so $m_X - int(G)_{inY}$
$= m_X - int(G)_{in\,X} \cap Y \subseteq F \cap Y \subseteq G_{inX} \cap Y = G_{inY}$
$m_X - int(G)_{inY} \subseteq F \cap Y \subseteq G_{inY}$, therefore, F$\cap Y$ is m_x-semi closed in Y.

Proposition (4): The property of space being m-L(sc)-space is a topological property, whenever X has the property (β).

Proof: let f:X$\rightarrow$Y be an m-homeomorphism function from an m-L(s c)-space X into a space Y, we aim to show that Y is also m-L(sc)-space. Let M be a m-lindelof subset of Y, but f^{-1} is m-continuos m_x-semi closed in X. Since f is onto, then M=f(f^{-1}(M)) and by lemma (2), then M is m_x-semi closed of Y, therefore, Y is an m-L(sc)-space ■

Definition (10): An m-space X is called m-sLc-space if every m_x-semi lindelof is m_x-closed. For example, (R, τ_{cof}), where τ_{cof} be a co-finite m- space.

Definition (11): An m-space X is called m-sL(sc)-space if every m_x-semi lindelof is m_x-semi closed.

Lemma (4): If a set A is m_x-semi closed in X and F is a m_x-closed set in a space X, then A$\cup F$ is m_x-semi closed in F and also in X.

Proposition (5): Suppose that $X=X_1 \cup X_2$, Then, X_1 is m_x- closed L(sc)-subspace of X and X_2 is m_x-closed Lc-subspace of X , then X is m- L(sc)-space .

Proof: Let M be an m-lindelof subset of X, then $M \cap X_1$ is an m_x-closed in M, which is m-lindelof in X and so $M \cap X_1$ *is* $m-$lindelof of X , but $M \cap X_1 \subseteq X_1$, which is m-L(sc)-space, then $M \cap X_1$ is m_X-semi closed in X_1, and $M \bigcap X_2$ is m_X-closed in M which is m$-$lindelof. Then, $M \bigcap X_2$ is m-lindelof of X, but $M \bigcap X_2 \subseteq X_2$, which is m-Lc-space, then $M \cap X_2$ is m_X-closed in X_2, but $M = (M \cap X_1) \cup (M, X_2)$, and so M is m_X-semi closed in X (by lemma(4)) ■

Proposition (6): Let (Y, τ_Y) be an m- subspace of (X, τ_X), then for every A$\subset Y$ we have $m_X - cl(A)_{in\,Y} = m_X - cl(A)_{in\,X} \cap Y$.

Proof: $m_X - cl(A)_{in\,Y} = \cap \{k: k\ is\ m_X-$closed in $Y\ and\ A \subset k\} = \cap \{F \cap Y: F\ is\ m_X - closed\ in\ X\ and\ A \subset F \cap Y\} = \cap \{F: F\ is\ m_X$-closed in X and $A \subset F\} \cap Y = m_X - cl(A)_{in\,X} \cap Y$ ■

Lemma (5): If W is m_x-semi closed in X and Y$\subseteq X$, then $M \cap Y\ is\ m_X-$semi closed in Y.

Proof: Since W is m_x-semi closed in X, then there exists m_X -closed set $F\ of\ X$ such that $m_X - int(F)_{in\,X} \subseteq W \subseteq F_{in\,X}$, so $m_X - int(F)_{inY} = m_X - int(F)_{in\,X} \cap Y \subseteq W \cap Y \subseteq F_{inX} \cap Y = F_{inY}$ $m_X - int(F)_{inY} \subseteq W \cap Y \subseteq F_{inY}$, therefore, W$\bigcap Y\ is\ m_X-$semi closed in Y ■

Proposition (7): Every m-locally compact L(sc)-space is an m-sT_2-space.

Proof: let X be an m-locally compact L (sc)-space, then it is m-locally compact K(sc)-space, hence X is an sT_2-space. Let X be m-locally compact and m-K(sc)-space, then X is an m-T_2-space.

Proposition (8): The property of space being m-L(sc)-space is a hereditary property.

Proof: let (X, τ) be am m-L(sc)-space and let $(Y, \tau^{\backslash})$ be a subspace of (X, τ) (to prove that $Y\ is\ m-L$(sc)$-$space). Let M be an m-lindelof in Y

Since M$\subseteq$Y$\subseteq$X

Then $M\ is\ m-lindelof\ in\ X$, and since X is m-L(sc)-space

then we get that $M_{inX}\ is\ m_X-$semi closed $in\ X$. since $M_{inY} = M_{inX} \cap Y$ is m_X-semi closed in Y by (lemma(5))

$\therefore (Y, \tau^{\backslash})$ is m-L(sc)-space■

Definition (12): Let X be an m-space, and let $A \subseteq X$. A subset A is said to be m-semi lindelof if A is m-semi lindelof subspace of X.

Remark (4): Every m-semi lindelof space is m-lindelof space, but the converse may be not true.

Example (6): Let (X, τ) be an m-space such that, X=R (the real line), and $\tau = \{r_a: a \in R\} \cup \{R\}$ be an m-space defined on X such that $r_a = \{x: x \in R\ and\ x \geq a\}$. Then, (X, τ) is an m-lindelof but not m_x-semi lindelof space, since if we take a family B=$\{\{r_1\}\} \cup \{a\}$:a$< 1\}$ m_x-semi open cover to X, $\{r_1\} \cup \{a\}$ is m_x-semi open set for each a$\in R$, and since $\{r_1\} \subseteq \{r_1\} \cup \{a\} \subseteq m_X - cl(\{r_1\}) = R$, such that this family of m_x-semi open sets cannot be reducible to a countable subcover since R-r_a uncountable set.

Definition (13): An m-space X is called hereditary m_x-semi lindelof if every subspace of X is m_x-semi lindelof.

Proposition (9): For a hereditary m_x-semi lindelof space X, the following statements are equivalent:

X is an m-sLc-space.

X is a countable discrete space.

Proof: To prove X is discrete space, let A be any subset of X, then it is an m_x-semi lindelof ,which is an m-sLc-space, then A is m_x-closed. Also, $X - A$ is m_x-semi lindelod subset of X, then it is an m_x-closed in X, hence, A is m_x-open, which implies X is discrete and X is countable , since every m_x-semi lindelof is m-lindelof and as follows the fact m-lindelof is discrete space if it is countable)
Conversely, let G is m_x-semi lindelof so it is an m-lindelof in X, which is a discrete space, so G is an m_x-closed subset of X. Therefore, X is an m-sLc-space.

Lemma (6): Every m_x-semi closed subset of m_x-semi lindelof space is m_x-semi lindelof.

Proof: let W be an m_x-semi closed subset of X, where X is m_x-semi lindelof space and suppose $\{\{G_\propto\}_{\propto\in\Omega}$ be an m_x-semi open cover of W (means that)$W = \bigcup_{\propto\in\Omega} G_\alpha$, so $X = \bigcup_{\alpha\in\Omega} G_\alpha \cup W^c$, but X is m_x-semi lindelof space, then X=$\bigcup_{i=1}^{\infty} G_\propto \cup W^c$, W$\subseteq \bigcup_{i=1}^{\infty} G_{\propto i}$, therefore W is m_x-semi lindelof.

Proposition (10): Suppose that X=$X_1 \cup X_2$, where X_1 and X_2 are m_x-closed sLc-subspaces in X, then X is also m-sLc-space.

proof : let W be m-semi lindelof of X , then it is m-lindelof, so $W \cap X_1$ and $W \cap X_2$ are m_x-semi closed in W, then it is m_x-semi closed in W, which is m-semi lindelof. Thus, $W \cap X_1$and $W \cap X_2$ are m-semi lindelof subsets of X (by lemma(6)). Since $W \cap X_1$ is subset $of\ X_i, i = 1,2$
which is m-sLc-space, thus W$\cap X_i$ is m_x-closed in X_i. Since X_i is m_x-closed in X, then $W \cap X_i$ is m_x-closed in X, but $W = (W \cap X_1) \cup (W \cap X_2)$, and so W is m_x-closed in X, therefore, X is m-sLc-space ■

Definition (14): An m-space (X, m_X) is said to be an m-locally L(sc)-space if each point has m_x-open neighborhood, which is an m-L(sc)-subspace. Clearly, every m-L(sc)-space is m-locally L(sc)-space, but the converse may be not true.

Example (7): let (R,τ_D) be a discrete m-space, then R be an m-locally L(sc)-space, where it is an m-Lc-space.

Lemma (7): let $A \subseteq Y \subseteq X$,and A is m_x-semi open set in Y. A set A be an m_x-semi open set in X if Y is an m_x-open subspace of X.

Proof: Since A is m_x-semi open in Y, then there exists an m_x-open set G of Y such that G$\subseteq A \subseteq m_X - cl(G)_{in\,Y}$, but m_X-$cl(G)_{in\,Y} = m_X - cl(G)_{in\,X} \cap Y$, then $G \subseteq A \subseteq m_X - cl(G)_{inY} \subseteq m_X - cl(G)_{in\,X}$. Then, A is m_X-semi open in X ■

Theorem (4): An m-space X is an m-L(sc)-space if and only if each point has m_x-cl open neighborhood that is m-L(SC)-space.

Proof: If X is an m-L(sc)-space, then for each $x \in X$, X itself is m_x-cl open neighborhood , which is an m-L(sc)-space. Conversely, let $L \subseteq X$ be an m-lindelof subset X and let $x \notin L$, choose an m_x-cl open neighborhood W_x of x in X such that W_x is an m-L(sc)-subspace $W_x \cap L$ is m-lindelof in the sub space W_x, which is an m-L(sc)-space. Therefore, it is m_x-semi closed in W_x but $W_x - (W_x \cap L) = W_x - L$ is m_x-semi open in W_x which is m_x-open in X. Thus, $W_x - L$ is m_x-semi open in X (by lemma (7)), that is L is m_x-semi closed in X, then X is an m-L(sc)-space ■
Proposition (11): Every m-locally L(sc)-space is a m-sT_1-space with property (β).
Proof: If X is not sT_1-space (means that) there exist $x, y \in X, x \neq y$ such that for all m_X-semi open set contains y, also contains x . Since $X\ is$ m-locally L(sc)-space, let U be an m_x-open neighborhood of x such that (U,τ_Y) is m-L(sc)-space, so $(U, \tau_Y)$is $m - sT_1$ −space, thus $\{x\}$is m_X-semi open in U ,then U-$\{x\}$is m_X-semi open in U and since U is m_X-open in X , then U-$\{x\}is\ m_X$-open in X (by lemma (7)), but $y \in U - \{x\}$ and $U - \{x\}$ does not contain x , but this is a contradiction, then X is m-sT_1-space ■

Proposition (12): The property of a m-space being m-locally L(sc)-space is H-property.
Proof: let (X, m_X) be an m-locally L(sc)-space, and let A$\subseteq X$. By assumption for $x \in A$,there exists $U \in m_X$ such that U is an $m-$L(sc)-subspace $of\ X$ not that $V = U \cap A$ is an m_x-open neighborhood of x in A and V is an m-L(sc)-subspace of A (since m-L(sc)-space is hereditary property), then (A, m_{X_A}) is an m-locally L(sc)-space.

Proposition (13): The property of a m-space being locally L(sc)-space is a topological property.

Proof: Let f : $(X, m_X) \to (Y, m_Y)$ be an m-homeomorphism function and let (X, m_X) be an m-locally L(sc)-space. Let y$\in Y$, choose $x \in X$ such that $f(x) = y$. Since $(X, m_X)$is m-locally L(sc)-space, then there exists $U \in m_X$ such that $x \in U$and U is an m-L(sc)-space . Since f is m_X-open , then $f(U)$is an m_X-open neighborhood of y in (Y, m_Y), and since f is m-homeomorphism function, then $f(U)$ is an m-L(sc)-subspace of (Y,m_Y), therefore, (Y,m_Y) is an m-locally L(sc)-space ■

References

[1] Al-mohamadawi.H J 2005 Certain types of Lc-spaces Thesis submitted to the college of education Al-mustansiriyah University
[2] Abu-Ragheef H A 2015 On some types of kc-spaces and Lc-spaces Thesis submitted to the college of education Al-mustansiriyah University
[3] Maki H 1996 On generalizing semi open sets and preopen sets Report for meeting on Topological spaces Theory and it is Applications Yastsushiro collge of Technology pp13-18
[4] Saleh M 2004 On θ-closed sets and some forms of continuity Archirum mathematicum (Brno) **40** pp 383-393
[5] Ali H J 2010 Strong and weak forms of m-lindelof spaces Editorial board of Zenco J for pure and Appl. Sciences Salahaddin university Hawler-Iraqi Kurdistan Region,special issue **22** pp 60-64
[6] Noiri T and popa V A 2009 Generalization of some forms of g-irresolute function. *European Journal of Pure and Applied Mathematics* **2** 4 pp 473-493
[7] Muthana H A and Ali H J 2014 Some types of m-compact functions *Journal of Sci. AL-mustansiriyah university* **25** 4

Mathematical analysis on the cosets of subgroup in the group of E-convex sets

Mathematical analysis on the cosets of subgroup in the group of E-convex sets

Nada Mohammed Abbas[1] and Ruma Kareem K. Ajeena[2]

[1,2]Mathematics Department, Education College for Pure Sciences, University of Babylon, Iraq

nadaalsafar333@gmail.com and ruma.usm@gmail.com

Abstract. In this work, analyzing the cosets of the subgroup in the group of L – convex sets is presented as a new and powerful tool in the topics of the convex analysis and abstract algebra. On L – convex sets, the properties of these cosets are proved mathematically. Most important theorem on a finite group of L – convex sets theory which is the Lagrange's Theorem has been proved. As well as, the mathematical proof of the quotient group of L – convex sets is presented.

Keywords: L – convex sets, Group of L – convex sets, Subgroup of L – convex sets, Cosets of L – convex sets, Quotient group of L – convex sets.

1. Introduction

The convex sets and convex functions are studied by many researchers. These concepts have been extended into L – convex sets and L – convex functions respectively by Youness [1]. In addition to, Suneja, Lalitha and Govil [2] follow the Youness study through characterizing the L – convex sets and proving some certain inequalities. On these sets, some properties are discussed and proved [2]. On the set of the L – convex sets, the axioms of the group are proved under the addition operation [3]. With addition operation, the set of the L – convex sets also formed a subgroup. One can observe that the intersection on the subgroups of the L – convex sets is also a subgroup of the L – convex sets. On the other hand, the union of two subgroups of the L – convex sets is also a subgroup of the L – convex sets with some conditions [3]. Our work in this paper will focus on using these sets,namely the L – convex sets [1], to build new algebraic structures. In this work, first the L – convex sets and their operations, the group law on the set of L – convex sets and subgroup of this group have been studied. On the subgroup of the group on the L – convex sets, the left (right) cosets have been analyzed mathematically as the main points in this paper. The Lagrange's Theorem on a finite group of L – convex sets is also proved. Finally, the concept of the quotient group has been displayed as well in this work. The outline of this paper shows: Section 2 gives a summary of the mathematical background to clarify the L – convex sets, the algebraic properties and the operations on L – convex sets, the group law on the L – convex sets and the subgroup of the L – convex sets. Section 3 explains the proposed idea of the cosets of a subgroup of the L – convex sets. New proposed definition and theorems related to these cosets of a subgroup on the L – convex sets are presented and proved. Section 4 reviews the concept of the nomral subgroup of the L – convex sets and proves a new important theorem related to this concept. Section 5 displays the

defintion of quotient group on the $L-$ convex sets and how to prove this group on the $L-$ convex sets. Finally, Section 6 draws the conclusions.

2. Mathematical Background

This section presents some important basic facts which are starting with the $L-$convex sets and their operations, the group law on the $L-$convex sets and the subgroup of the $L-$convex sets. The explanations of these concepts have been presented as follows.

Definition 2.1. Let $\mathrm{a} = (a_1, \mathrm{a}_2,..., \mathrm{a}_n)$ and $\mathrm{b} = (b_1, \mathrm{b}_2,..., \mathrm{b}_n)$ be two elements in R^n. The inner product [4,5,6] between a and b can be defined by $<\mathrm{a},b> = \mathrm{a}_1\,\mathrm{b}_1 + \mathrm{a}_2 b_2 + ... + \mathrm{a}_n\,\mathrm{b}_n$.

Definition 2.2. Let L be a map from R^n into R^n. A set $\mathrm{W} \subseteq \mathrm{R}^n$ is called $L-$convex set if $(1-\kappa)L(\mathrm{a}) + \kappa\,\mathrm{L}(\mathrm{b}) \in \mathrm{W}$ for $a,b \in \mathrm{W}$ with $0 \le \kappa \le 1$ [8].

Remark 2.1. Based on the study of Youness [1], one can prove:

- Every convex set is $L-$convex set with L is an identity map.
- If W is $L-$convex then $L(W) \subseteq \mathrm{W}$.
- If W is convex and $L(\mathrm{W}) \subseteq \mathrm{W}$ for a map L then W is $L-$ convex.
- The intersection of the $L-$convex sets is also $L-$convex.
- The union of $L-$convex sets is not is not necessarily $L-$convex; see the following example.

Example 2.3. consider $L: R^2 \to R^2$ be defined as $L(a,b) = (2b/3 - a/3, b/3 + 4a/3)$ and consider the two sets

$$W_1 = \{(a,b) \in R^2 : (a,b) = \kappa_1(0,0) + \kappa_2(2,1) + \kappa_3(0,3)\},$$
$$W_2 = \{(a,b) \in R^2 : (a,b) = \kappa_1(0,0) + \kappa_2(0,3) + \kappa_3(-2,-1)\}$$

With $\kappa_1, \kappa_2, \kappa_3 \ge 0, \sum_{i=1}^{3} \kappa_i = 1.$ the two sets W_1 and W_2 are $L-$convex ,but $W_1 \cup W_2$ is not $L-$convex.

Theorem 2.4. The union of two $L-$convex sets is also $L-$convex set if and only if one is contained in another one.

On the $L-$convex sets , the mathematical operations have been studied through the following propositions [2].

Theorem 2.5. Let W_1 and W_2 be $L-$convex sets. Let $L: \mathrm{R}^n \to \mathrm{R}^n$ be linear. Then $\eta W_1 + \eta W_2$ is an $L-$convex set convex for all η which is a real number [2].

A special case of Theorem (2.5) can be obtained through the following corollary.
Corollary 2.6. If $\eta = 0$ and W is $L-$convex. Then $0W$ is $L-$convex set.
Remark 2.7. In Corollary (2.5), the $L-$convex set, namely $0W$, will be considered as an identity element in the additive group G of the $L-$convex sets.

On the other hand, some definitions on the group of the set of $L-$convex sets are presented. Further theorems which have been proved to show that the axioms of the additive group are verified on the set $L-$convex sets is displayed [3]. These definitions and theorems are discussed as follows.

Definition 2.*8*. Let G be a collection of all $L-$ convex sets W_i with a linear map $L:\mathrm{R}^n \to \mathrm{R}^n$ and $i = 1,2,...,n$. The binary operation $+$ on G is a function $+ : G\times G \to G$. That is a rule that assigns to each order pair $(W_i , W_i) \in G\times G$ into an element $W_i + W_i \in G$ [3].

Definition 2.*9*. Let G be a nonempty $L-$convex sets with a linear map $L:\mathrm{R}^n \to \mathrm{R}^n$. Let $+$ be a binary operation on G. Then the mathematical system $(G,+)$ is called a group if the following axioms are holds [3]:

- If $W_1, W_2 \in G$, where W_1, W_2 are $L-$convex sets then $W_1 + W_2$ is an $L-$convex sets and $W_1 + W_2 \in G$
- If W is an element in G then there exists an element $0W = e$ in G such that $W + 0W = W$. The element $0W$ is called identity element of G.
- For each $W \in G$, there exists $-W \in G$ such that $W + (-W) = -W + W = e = 0W$. An element $-W$ is called an inverse element of M and it is denoted by $-W = (W)^{-1}$.
- For all $W_1, W_2, W_3 \in G$ then $(W_1 + W_2) + W_3 = W_1 + (W_2 + W_3)$.

Definition 2.10. The group G is called abelian if $W_1 + W_2 = W_2 + W_1$, for all W_1, W_2.

Theorem 2.11. For all $W_1 + W_2 \in G$, where W_1 and W_2 are $E-$convex sets, then $W_1 + W_2 = W_2 + W_1$.

Theorem 2.12. For all W_1, W_2 and W_3 in a group G, where W_1, W_2 and W_3 are $L-$convex sets, then $(W_1 + W_2) + W_3 = W_1 + (W_2 + W_3)$ (that is an associative law of the addition operation) [3].

Theorem 2.12. In a group of the $L-$convex sets, an additive identity $0W$ is an unique element.

Theorem 2.13. Suppose W_1, W_2 and W_3 are elements (that is, $L-$convex sets) in a group G. If $W_1 + W_2 = W_3 + W_2$. Then $W_1 = W_3$. And if $W_2 + W_1 = W_2 + W_3$. Then $W_1 = W_3$ [3].

Theorem 2.14. For each element W in a group G of the $L-$ convex sets, there is a unique inverse element $-W$ in G such that $W + (-W) = (-W) + W = 0\,W$.

Theorem 2.15. If W_1 and W_2 are two elements in a group G of the $L-$convex sets then $-(W_1 + W_2) = -W_1 - W_2$.

Theorem 2.16. If G is a group of the $L-$convex sets then $-(-W) = W$.

The mathematical proofs of the above theorems can be seen in [3].

On a set of all $L-$convex sets with addition operation, new mathematical structure can be created. This structure is called subgroup (see [9,10,11]) of the set of all $L-$convex sets. New definitions and theorems are presented as follows.

Definition 2.17. Let G be a group of the $L-$convex sets. A subset H of a group G is a subgroup [3] if

- $0W = e \in H$
- If $W_1, W_2 \in H$, then $W_1 + W_2 \in H$;
- If $W \in H$, then $-W \in H$.

Example 2.18. The set $\{0W\}$ and G are always subgroups of a group G [3].

Definition 2.19. A subgroup H of a group G is called a proper subgroup if $H \neq G$. Whereas, a subgroup H of a group G is called a nontrivial if $H \neq \{0W\}$ [3].

Theorem 2.20. A subset H of a group G is a subgroup if and only if H is a nonempty set and if $W_1, W_2 \in H$, then $W_1 + (-W_2) \in H$ [3].

Theorem 2.21. Let H_1 and H_2 be two subgroups of a group G. Then $H_1 \cap H_2$ is a subgroup of G [3].

Theorem 2.22. Let H_1 and H_2 be two subgroups of the $L-$ convex sets of a group G of the $L-$ convex sets. Then $H_1 \cup H_2$ is a subgroup of $L-$convex sets of G if and only if $H_1 \subseteq H_2$ or $H_2 \subseteq H_1$. The Cosets of a subgroup H of the $L-$convex sets [3].
The full proofs of the previous theorems, namely Theorems 2.10, 2.11 and 2.12 have been presented in [3].

3. The cosets of a subgroup of the $L-$convex sets

In this section, the mathematical concepts on the cosets of a subgroup of the $L-$convex sets are proposed as a new contribution in this work. These concepts are discussed as follows.

Definition 3.1. Let H be a subgroup of the group G of the $L-$ convex sets. For any $W \in G$. The set $W + H = \{W + h : h \in H\}$ is called the left coset of H in G which contains W and $H + W = \{h + W : h \in H\}$ is called the right Coset of H in G containing W The element W is called the Coset representative of $W + H$.

Theorem 3.2. Suppose G is a group of the $L-$ convex sets W. Let H is a subgroup of G Let $L : R^n \to R^n$ is a linear map with $L(W) = W$ for some $W \in R^n$. Then the left Coset $W + H$ is a $L-$ convex set.

Proof. Let $W + h_1, W + h_2 \in W + H$, where h_1, h_2 are the $L-$ convex sets in subgroup H and $0 \leq \kappa \leq 1$. Then

$$\begin{aligned}\kappa[L(W + h_1)] + (1-\kappa)L(W + h_2) &= \kappa[L(W) + L(h_1)] + (1-\kappa)[L(W) + L(h_2)] \\ &= \kappa L(W) + \kappa L(h_1) + (1-\kappa)L(W) + (1-\kappa)L(h_2) \\ &= \kappa L(W) + (1-\kappa)L(W) + \kappa L(h_1) + (1-\kappa)L(h_2) \\ &= \kappa L(W) + (1-\kappa)W + [\kappa L(h_1) + (1-\kappa)L(h_2)] \in W + H\end{aligned}$$

So, the left coset $W + H$ is an $L-$ convex set. ■

Theorem 3.3. Let G be a group of the $L-$ convex sets. Suppose H is a subgroup of G. Let $W_1 \in G$ then $W_1 \in W_1 + H$.

Proof. The element $W_e \in W_1 + H$ and $W_1 + W_e \in W_1 + H$. Since $W_1 + W_e = W_1 \in W_1 + H$. So $W_1 \in W_1 + H$. ■

Theorem 3.4. Suppose G is a group of the $L-$ convex sets. Let H be a subgroup of G and $W_1 \in G$. Then $W_1 + H = H$ if and only if $W_1 \in H$.

Proof. Assume that $W_1 + H = H$. From Theorem (2), $W_1 \in W_1 + H$. Since $W_1 + H = H$, then $W_1 \in H$. Conversely, assume that $W_1 \in H$. Again, from Theorem (2) $W_1 \in W_1 + H$. Then

$$W_1 + H \subseteq H. \tag{1}$$

On the other hand, $W_1 \in H$ then $-W_1 \in H$. Let $W \in H$, then $-W_1 + W \in H$. So, $-W_1 + W = h$, for some $h \in H$. Hence $W = W_1 + h \in W_1 + H$. Therefore,

$$H \subseteq W_1 + H. \tag{2}$$

From (1) and (2), one can obtain $W_1 + H = H$.

Theorem 3.5. Suppose G is a group of the $L-$convex sets. Let H be a subgroup of G. For any $W_1, W_2 \in G$, then $W_1 + H = W_2 + H$ if and only if $W_1 \in W_2 + H$. ■

Proof. Assume $W_1 + H = W_2 + H$. Based on Theorem (3.2), one can get $W_1 \in W_2 + H$. Conversely, assume $W_1 \in W_2 + H$. Then $W_1 = W_2 + h$, for some $h \in H$.
So $W_1 + H = (W_2 + h) + H$. Hence $W_1 + H = W_2 + (h + H)$. Therefore $W_1 + H = W_2 + H$. ■

Theorem 3.6. Suppose G is a group of the $L-$ convex sets. Let H be a subgroup of G and let $W_1, W_2 \in G$. Then either $W_1 + H = W_2 + H$ or $W_1 + H \bigcap W_2 + H = \phi$.

Proof. Assume that $W_1 + H \bigcap W_2 + H \neq \phi$. Let $W \in (W_1 + H \bigcap W_2 + H)$.
Then $W \in W_1 + H$ and $W \in W_2 + H$. So $W = W_1 + h_1$ and $W = W_2 + h_2$. Therefore,
$W_1 + h_1 = W_2 + h_2$. Hence $(W_1 + h_1) + H = (W_2 + h_2) + H$. A This leads to
$W_1 + (h_1 + H) = W_2 + (h_2 + H)$. So $W_1 + H = W_2 + H$. ■

Theorem 3.7. Suppose G is a group of the $L-$ convex sets. A subgroup H of G and let $W_1, W_2 \in G$. Then $W_1 + H = W_2 + H$ if and only if $-W_1 + W_2 \in H$.

Proof. Assume that $W_1 + H = W_2 + H$ if and only if $-W_1 + (W_1 + H) = -W_1 + (W_2 + H)$ if and only if $(-W_1 + W_1) + H = (-W_1 + W_2) + H$ if and only if $H = (-W_1 + W_2) + H$ if and only if $-W_1 + W_2 \in H$ based on Theorem (3.3). ■

Theorem 3.8. Let H be a subgroup of a group G which has elements are the $L-$ convex sets. Suppose $W_1, W_2 \in G$. Then $|W_1 + H| = |W_2 + H|$.

Proof. Let $\varphi : W_1 + H \to W_2 + H$ which is defined by $\varphi(W_1 + h) = W_2 + h$, for all $E-$ convex set $h \in H$. Suppose h_1, h_2 are two $E-$ convex set in H. we need first To prove that φ is one to one function . Assume that $\varphi(W_1 + h_1) = \varphi(W_1 + h_2)$. Then $W_2 + h_1 = W_2 + h_2$. So $h_1 = h_2$. Thus, $W_1 + h_1 = W_1 + h_2$. So φ is a one to one function. Now, it is clear that the function φ is onto. Let $W \in W_2 + H$. Then $W = W_2 + h$ for some $h \in H$. So $W = \varphi(W_1 + h)$. Hence φ is one to one and onto function. Therefore, $|W_1 + H| = |W_2 + H|$.
■

Theorem 3.9. Let H be a subgroup of a group G which has elements are the $L-$ convex sets. Suppose $W_1 \in G$. Then $W_1 + H = H + W_1$ if and only if $H = W_1 + H + (-W_1)$.

Proof. $W_1 + H = H + W_1$ if and only if $(W_1 + H) + (-W_1) = (H + W_1) + (-W_1)$ if and only if $W_1 + H + (-W_1) = H + (W_1 + (-W_1))$ if and only if $W_1 + H + (-W_1) = H + W_e$ if and only if $W_1 + H + (-W_1) = H$. ■

Theorem 3.10. Let H be a subgroup of a group G which has elements are the $L-$ convex sets. Suppose $W_1 \in G$. Then $W_1 + H$ is a subgroup of G if and only if $W_1 \in H$.

Proof. Assume that $W_1 + H$ is a subgroup of G Then $W_e \in W_1 + H$ and $W_e \in H = W_e + H$. So $W_e \in W_1 + H$ and $W_e + H$. Then $W_1 + H \bigcap W_e + H \neq \phi$. By Theorem (3.5) we have $W_1 + H = W_e + H$. So $W_1 + H = H$. By Theorem (3.3) $W_1 \in H$. Conversely, assume that $W_1 \in H$. So $W_1 + H = H$. Since H is a subgroup of a group G So $W_1 + H$ is a subgroup of a group G. ■

Theorem 3.11. (Lagrange's Theorem). If G is a finite group of $L-$ convex sets and H be a subgroup of a group G. Then $|G|$ is divisible by $|H|$ and the number of the distinct cosets of H in G is $|G|/|H|$.

Proof. Let $W_1 + H, W_2 + H, ..., W_r + H$ be the distinct left cosets of H in G. Then, for each $W \in G$, then $W + H = W_i + H$ for some i. Also, $W \in W + H$. Thus, $\forall$ element in G, so this element is in one of the cosets $W_i + H$.

In other words,

$$G = W_1 + H \bigcup W_2 + H \bigcup ... \bigcup W_r + H.$$

But $W_i + H \neq W_j + H$ for $i \neq j$. So this union is disjoint, so that

$$|G| = |W_1 + H| + |W_2 + H| + ... + |W_r + H|.$$

Since $|W_i + H| = |H|$ $\forall\ i$, this leads to

$$|G| = |H| + |H| + ... + |H|.$$

In other words, $|G| = r \cdot |H|$. Then $|H|$ divides $|G|$. Thus, $\exists\ r$ of distinct cosets of H in G, namely

$$r = \frac{|G|}{|H|}.$$ ■

4. A normal subgroup of $L-$ convex sets

In the following section, a normal subgroup of $L-$ convex sets will be discussed as follows.

Definition 4.1. A subgroup H of a group G of the $L-$ convex sets is called a normal subgroup of G if $W + H = H + W$, for all $W \in G$. A normal subgroup H of G can be denoted by $H \lhd G$.

The notation of the $W + H = H + W$ means that $W + h_1 = h_2 + W$.

Theorem 4.2. A subgroup H of a group G of the $L-$ convex sets is normal in G if and only if $W+H+(-W)\subseteq H$, for all $W\in G$.

Proof. Assume that $H\lhd G$ then $W+H=H+W$, for all $W\in G$ Since $W+H+(-W)=H$. Then $W+H+(-W)\subseteq H$.

Conversely, $W+H+(-W)\subseteq H$, for all $W\in G$. So $-W\in G$ and $-W+H+(-(-W))\subseteq H$. Then

$$-W+H+W\subseteq H. \tag{3}$$

So $W+(-W)+H+W\subseteq W+H$. We have $H+W\subseteq W+H$. Hence

$$H\subseteq W+H+(-W). \tag{4}$$

From (3) and (4), we have $W+H+(-W)=H$. Hence $W+H=H+W$. Consequently, $H\lhd G$. ■

Remark 4.3. The above theorem can be written as $H\lhd G$ if and only if $W+\mathrm{h}+(-W)\in \mathrm{H}$, for all $W\in \mathrm{G}$.

5 . A quotient group of the $L-$ convex sets

On the set of $L-$ convex sets, a quotient group has been created. The important concepts of this group are discussed as follows.

Definition 5.1. If $H\lhd G$ then the set of left (or right) cosets of H in a group G of the $L-$ convex sets is given by the set

$$G\setminus H=\{W+H:W\in G\}, \tag{5}$$

which is called the quotient group of G by H (or the factor group of G by H).

Theorem 5.2. (Quotient group). Let G be a group of the $L-$ convex sets and let $H\lhd G$. Then the set $G\setminus H=\{W+H:W\in G\}$ is a group under the operation

$$(W_1+H)+(W_2+H)=W_1+W_2+H.$$

Proof. Firstly, we want to show the given operation is well defined. For some elements $W_1,W_1',W_2,W_2'\in \mathrm{G}$, assume $W_1+\mathrm{H}=W_1'+\mathrm{H}$ and $W_2+\mathrm{H}=W_2'+\mathrm{H}$.

Since $W_1'\in W_1'+\mathrm{H}$ and $W_1'\mathrm{H}=W_1+\mathrm{H}$, then $W_1'\in W_1+\mathrm{H}$ and $W_1'=W_1+\mathrm{h}_1$, for some $\mathrm{h}_1\in \mathrm{H}$. Similarly, $W_2'\in W_2'+\mathrm{H}$ and $W_2'+\mathrm{H}=W_2+\mathrm{H}$, then $W_2'\in W_2+\mathrm{H}$ and $W_2'=W_1+\mathrm{h}_2$, for some $\mathrm{h}_2\in \mathrm{H}$.

$$\begin{aligned} W_1'+W_2'+\mathrm{H}&=(W_1+\mathrm{h}_1)+(W_2+\mathrm{h}_2)+\mathrm{H}\\ &=(W_1+\mathrm{h}_1)+(W_2+\mathrm{H})\\ &=W_1+\mathrm{h}_1+\mathrm{H}+W_2 \end{aligned}$$

$$= W_1 + H + W_2$$
$$= W_1 + W_2 + H .$$

Now, let $W_1 + H$, $W_2 + H$,$W_3 + H \in G\backslash H$. Then

$$\left[(W_1 + H) + (W_2 + H)\right] + (W_3 + H) = (W_1 + W_2 + H) + (W_3 + H) = W_1 + (W_2 + W_3) + H$$
$$= (W_1 + H) + (W_2 + W_3) + H$$
$$= (W_1 + H) + \left[(W_2 + H) + (W_3 + H)\right].$$

The element $W_e + H = H$ is the identity element because

$$(W_e + H) + (W + H) = (W_e + W) + H$$
$$= W + H,$$

for all $W \in G$. Similarly,

$$(W + H) + (W_e + H) = W + H ,$$

for all $W \in G$. The inverse of $W + H$ is $-(W + H) = (-W) + H,$ because

$$(-W) + H + (W + H) = (-W + W) + H = W_e + H = H .$$

Similarly, $(W + H) + (-W) + H = W + (-W) + H = H$.

Thus $G \backslash H$ is a group under the operation $(W_1 + H) + (W_2 + H) = W_1 + W_2 + H.$ ■

6.Conclusions

A new contribution on the set of the $L-$convex sets with addition operation is proposed. This contribution focuses on analysing the cosets of the subgroup of $L-$convex sets. This analysis considers as a new and powerful tool which connects the convex analysis with abstract algebra. On the cosets of the subgroup of $L-$convex sets, the fundamental properties have been proved mathematically. The Lagrange's Theorem on a finite group of $L-$convex sets is proved. A normal subgroup of $L-$convex sets and a quotient group of $L-$convex sets are discussed as well to give new bright spots in the topics of the convex analysis and abstract algebra.

References

[1] E. A. Youness, E-convex sets, E-convex functions and E-convex programming, J.Optim. Theory Appl., 102(3), pp. 439-450, 1999
[2] J. Sheiba Grace and P. Thangavelu , Properties of E-convex Sets, Tamsui Oxford Journal of Mathematical Sciences 25(1), pp. 1-7, 2009.
[3] M. A. Nada and K. K. A. Ruma, The group law on the E- convex sets, International Journal of Pure and Applied Mathematics, July 7, 2017. (Submitted).
[4] R.T. Rockafellar, “Convex Analysis”, Princeton University Press, 1969.
[5] J. B Hiriart-Urruty, C. Lemarechal, "Fundamentals of Convex Analysis ", Springer,2001.
[6] Goffman, C. and Pedrick, G. “First Course in Functional Analysis”, Chelsea Publishing Co., New York,1983.
[7] Klee, V. L., Jr. “Convex sets in linear spaces, II. Duke Math. J. 18, pp. 875-883, 1951.

[8] Tukey, J. W. "Some notes on the separation of convex sets". Portugaliae Math. 3, pp. 95-102, 1942.
[9] J. Thomas. "*Abstract algebra: theory and applications*". Stephen F. Austin State University, 2014.
[10] P. Charles C., "*A book of abstract algebra*". Courier Corporation, 2010.
[11] J. Nathan. , "Basic algebra I". Courier Corporation, 2012.

Generalized Differential Operator on Bistarlike and Biconvex Functions Associated By Quasi-Subordination

Generalized Differential Operator on Bistarlike and Biconvex Functions Associated By Quasi-Subordination

Abdul Rahman S. Juma[1] , Mohammed H. Saloomi [2]

[1]Department of Mathematics,University of Anbar,Ramadi,Iraq.
[2]Department of Mathematics,University of Baghdad,Baghdad,Iraq.

dr_juma@hotmail.com[1], mohammed_h1963@yahoo.com[2]

Abstract. In this paper, the generalized differential operator is applied to derive some subclasses of function class σ of bi-univalent functions defined in unit disk 𝔘. We estimate the bounds of the coefficients a_2 and a_3 for all functions which belong to the derived subclasses of σ.

Keywords: Holomorphic function, Quasi-subordination, Bistarlike function, Biconvex function, Bi-univalent function.

1. Introduction

Let $\mathcal{A}$ be the class of all functions f of the following form

$$f(z) = z + \sum_{n=2}^{\infty} a_n z^n \ , \qquad (1.1)$$

which are holomorphic in unit disk 𝔘

𝔘 ={z:|z|<1}

and normalized by the conditions f (0)=0 and f'(0)=1. Let S denote the class of all univalent and holomorphic functions.

Let φ(z) be holomorphic function in 𝔘 and|φ(z)| ≤ 1, such that

$$\varphi(z) = A_0 + A_1 z + A_2 z^2 + A_3 z^3 + \cdots , \qquad (1.2)$$

Where $A_0, A_1, A_2, A_3, \ldots$ are real. Let ϕ (z) be a holomorphic and univalent function with positive real part in𝔘, ϕ(0)=1, ϕ′(0)>0 and ϕ(𝔘) is a region starlike with the respect to 1and symmetric with the respect to the real axis. Further, let

$$\phi(z) = 1 + B_1 z + B_2 z^2 + B_3 z^3 + \cdots , \qquad (1.3)$$

where $B_1, B_2, B_3, \ldots$ are real and $B_1>0$.

Here, we suppose that the functions φ and ϕ are hold the above conditions one or otherwise stated.

The Koebe one–quarter Theorem [1] states that the image of 𝔘 under every function f in S contains a disk of radius $\frac{1}{4}$. So each univalent function has an inverse $g = f^{-1}$ satisfying

$$f^{-1}(f(z)) = z, \ (z \in \mathfrak{U}),$$

$$f\,(f^{-1}(\omega)) = \omega,\ (|\omega| < r_{\circ}(f)\ ,\ r_{\circ}(f) \geq \frac{1}{4}\ ), \qquad (1.4)$$

A holomorphic function is called bi-univalent in $\mathfrak{U}$ if both f and f^{-1} are univalent in $\mathfrak{U}$. By σ, we denote the class of all bi-univalent functions defined in (1.1). Since f in σ has the form (1.1), the computation proves that the invers $g = f^{-1}$ has the following expansion

$$g\,(\omega) = f^{-1}(\omega) = \omega - a_2\,\omega^2 + (2a_2^2 - a_3)\omega^3 - \cdots . \qquad (1.5)$$

A holomorphic function f is *subordinate* to holomorphic function g, written by

$$f \prec g \ \text{ or } f(z) \prec g(z)\ (z \in \mathfrak{U}), \qquad (1.6)$$

provided there is holomorphic function $\hbar$ defined on $\mathfrak{U}$,with $\hbar\,(0)=0$ and$|\hbar(z)| <1$ such that $f(z) = g(\hbar(z))$. Moreover if g is univalent in$\mathfrak{U}$, then $f(z) \prec g(z)$ is equivalent to $f(0) = g(0)$ and $f(\mathfrak{U}) \subset g(\mathfrak{U})$. For more details on the notion of subordination.(see [1]).

In [2], the concept of quasi-subordinate introduced by Robertson. For holomorphic functions f and g in $\mathfrak{U}$, the function f is *quasi-subordination* to , written as follows:

$$f(z) \prec_q g(z)\ (z \in \mathfrak{U}) \qquad (1.7)$$

if there exist holomorphic functions φ and $\hbar$ with $|\varphi(z)| \leq 1$, $\hbar\,(0) = 0$ and $|\hbar\,(z)|<1$ such that $f(z) = \varphi(z)g(\hbar(z))$. $(z \in \mathfrak{U})$.

Note that when $\varphi(z) = 1$, then $f(z) = g(\hbar(z))$ so that $f(z) \prec g(z)$ in $\mathfrak{U}$. Also notice that, if $\hbar\,(z)= z$, then $f(z) = \varphi(z)\,g(z)$ and it is said that f is *majorized* by g , in $\mathfrak{U}$. From previous statement it is clear that quasi-subordination is generalization of subordination as well as majorization. (For more details related to quasi-subordination see [2].)

Ma and Minda in [3] indicated to the unified classes by $S^*(\phi)$ and $K(\phi)$ and defined as following

$$S^*(\phi) := \{ f \in \mathcal{A} : \frac{zf'(z)}{f(z)} \prec \phi(z);\ z \in \mathfrak{U}\ \}, \qquad (1.8)$$

$$K(\phi) := \{ f \in \mathcal{A} : 1 + \frac{zf''(z)}{f'(z)} \prec \phi(z);\ z \in \mathfrak{U}\ \}.$$

The classes $S^*(\phi)$ and $K(\phi)$ are amplification of a classical set of starlike and convex functions. (See [3]).

El-Ashwah and Kanas in [4] studied the classes

$$S_q^*(\gamma,\phi) := \{ f \in \mathcal{A} : \frac{1}{\gamma}\,(\frac{zf'(z)}{f(z)} - 1) \prec_q \phi(z)-1; z \in \mathfrak{U}, 0 \neq \gamma \in \mathbb{C}\},$$

$$K_q(\gamma,\phi) := \{ f \in \mathcal{A} : \frac{1}{\gamma}\,(\frac{zf''(z)}{f(z)}) \prec_q \phi(z)-1; z \in \mathfrak{U}, 0 \neq \gamma \in \mathbb{C}\}.$$

If $\varphi(z) \equiv 1$, the classes $S_q^*(\gamma,\phi)$ and $K_q(\gamma,\phi)$ convert respectively, to $S^*(\gamma,\phi)$ and $K^*(\gamma,\phi)$ of Ma.Minda starlike and convex functions of order γ ($\gamma \in \mathbb{C} \setminus \{0\}$), in unit disk $\mathfrak{U}$ ([5]). The classes $S_q^*(\gamma,\phi)$ and $K_q(\gamma,\phi)$ minimize, to $S^*(\phi)$ and $K(\phi)$, respectively. When γ=1, that are similar to Ma.Minda starlike and convex functions, determined by Mohd and Darus [6].

Let $\phi(b,d; z)$ be function defined by

$$\phi(b, d; z) = \sum_{n=0}^{\infty} \frac{(b)_n}{(d)_n} z^{n+1},\ (d \neq 0, -1, -2, \ldots..\ z \in \mathfrak{U}),$$

where $(\alpha)_n$ denote the Pochhammer symbol defined by

$$(\alpha)_k = \begin{cases} 1 & \text{for } k = 0,\ \alpha \in \mathbb{C} \setminus \{0\}, \\ \alpha(\alpha+1)(\alpha+2) \ldots\ldots\ldots (\alpha + k - 1) & \text{for } k \in \mathbb{N} = \{1,2,3 \ldots.\},\ \alpha \in \mathbb{C}. \end{cases}$$

In [7] corresponding to the function $\phi(b, d; z)$,the generalized deferential operator defined as

$$D_{\lambda}^{m}(b, d) f : \mathfrak{U} \longrightarrow \mathfrak{U},$$

$$D_{\lambda}^{0}(b, d) f(z) = f(z) * \phi(b,d; z)$$

$$D_{\lambda}^{1}(b, d) f(z) = (1 - \lambda)(f(z) * \phi(b,d; z)) + \lambda z(f(z) * \phi(b,d;z))'$$

$$D_{\lambda}^{m}(b, d) f(z) = D_{\lambda}^{1}\left(D_{\lambda}^{m-1}(b, d) f(z)\right)$$

Let $f \in \mathcal{A}$, then from last two relations, we may deduce that

$$D_{\lambda}^{m}(b, d) f(z) = z + \sum_{n=2}^{\infty} [1 + (n-1)\lambda]^m \frac{(b)_{n-1}}{(d)_{n-1}} a_n z^n,$$

where $m \in N_{\circ} = \{0,1,2 \ldots\ldots\}$, and $\lambda \geq 0$.

From the last relation, we have

$$z(D_{\lambda}^{m}(b, d) f(z))' = bD_{\lambda}^{m}(b+1, d) f(z) - (b-1)\, D_{\lambda}^{m}(b, d) f(z),$$

and
$\lambda z(D_{\lambda}^{m}(b,d)f(z))' = D_{\lambda}^{m+1}(b,d)f(z) - (1-\lambda) D_{\lambda}^{m}(b,d)f(z)$.
Lately, Srivastava et al. [8] found estimates for coefficients of the first two factors $|a_2|$ and $|a_3|$. For the functions of these classes, we use this motivation in this research to define a unified subclass of bi- univalent function class σ as follows.
A function $f \in \sigma$ defined in (1.1) is said to be in the class $\mathcal{M}_{q,\sigma}^{\alpha,\lambda}\mathcal{D}^{m}(b,d,\gamma,\phi)$ if the quasi-subordination conditions are satisfied:
$\frac{1}{\gamma}[(1-\alpha)\frac{z(\mathcal{D}_{\lambda}^{m+1}(b,d)f(z))'}{\mathcal{D}_{\lambda}^{m+1}(b,d)f(z)} + \alpha\{1+\frac{z(\mathcal{D}_{\lambda}^{m+1}(b,d)f(z))''}{(\mathcal{D}_{\lambda}^{m+1}(b,d)f(z))'}\}-1] \prec_q \phi(z) - 1,$
$\frac{1}{\gamma}[(1-\alpha)\frac{w(\mathcal{G}_{\lambda}^{m+1}(b,d)g(w))'}{\mathcal{G}_{\lambda}^{m+1}(b,d)g(w)} + \alpha\{1+\frac{w(\mathcal{G}_{\lambda}^{m+1}(b,d)g(w))''}{(\mathcal{G}_{\lambda}^{m+1}(b,d)g(w))'}\}-1] \prec_q \phi(w) - 1,$
where $g(w) = f^{-1}(w)$ given by (1.5), and
$\mathcal{D}_{\lambda}^{m+1}(b,d)f(z) = (1-\lambda)\mathcal{D}_{\lambda}^{m}(b,d)f(z) + \lambda z(\mathcal{D}_{\lambda}^{m}(b,d)f(z))'$
$\mathcal{G}_{\lambda}^{m+1}(b,d)g(w) = (1-\lambda)\mathcal{G}_{\lambda}^{m}(b,d)g(w) + \lambda w(\mathcal{G}_{\lambda}^{m}(b,d)g(w))'$, $0 \le \lambda \le 1$. (see [7])
For special values of α,λ,γ,b, d, m,ϕ and φ(z), the class $\mathcal{M}_{q,\sigma}^{\alpha,\lambda}\mathcal{D}^{m}(b,d,\gamma,\phi)$ unify known and new classes.

Remark (1.1): *Putting λ=0 in the class $\mathcal{M}_{q,\sigma}^{\alpha,\lambda}\mathcal{D}^{m}(b,d,\gamma,\phi)$, we get*

$$\mathcal{M}_{q,\sigma}^{\alpha,0}\mathcal{D}^{m}(b,d,\gamma,\phi) := \mathcal{M}_{q,\sigma}^{\alpha,}\mathcal{D}^{m}(b,d,\gamma,\phi).$$

For b=d and m =0, we have the class $\mathcal{M}_{q,\sigma}^{\alpha,\lambda}(\gamma,\phi)$ was introduced and studied by N.Magesh,V.K.Balaji and J.Yamini [9].

In particular for b=d, m =0, and γ=1, we have the class

$$\mathcal{M}_{q,\sigma}^{\alpha,}\mathcal{D}^{0}(b,b,1,\phi) := \mathcal{M}_{q,\sigma}^{\alpha,}(\phi),$$

which introduced by Goyal and Kumar [10]. In this case for $\varphi(z) \equiv 1$, we get

$$\mathcal{M}_{q,\sigma}^{\alpha,}(\phi) := \mathcal{M}_{\sigma}^{\alpha,}(\phi),$$

this class was studied by Ali et al. [11,12].

Remark(1.2): *Putting λ=α=0 in the class $\mathcal{M}_{q,\sigma}^{\alpha,\lambda}\mathcal{D}^{m}(b,d,\gamma,\phi)$,we get*

$$\mathcal{M}_{q,\sigma}^{0,0}\mathcal{D}^{m}(b,d,\gamma,\phi) := \mathcal{M}_{q,\sigma}\mathcal{D}^{m}(b,d,\gamma,\phi).$$

In special case for γ=1,b=d and m =0, we have the class $\mathcal{M}_{q,\sigma}\mathcal{D}^{0}(b,b,1,\phi) = S_{q,\sigma}^{*}(\phi)$, was introduced by Goyal and Kumar [10].We observe that, for $\varphi(z) \equiv 1$, we get the class

$$S_{q,\sigma}^{*}(\gamma,\phi) := S_{\sigma}^{*}(\gamma,\phi),$$

was studied by Deniz [12].

Remark(1.3): *For λ=0 and α=1 in this class $\mathcal{M}_{q,\sigma}^{\alpha,\lambda}\mathcal{D}^{m}(b,d,\gamma,\phi)$, we obtain*

$$\mathcal{M}_{q,\sigma}^{1,0}\mathcal{D}^{m}(b,d,\gamma,\phi) := \mathcal{M}_{q,\sigma}^{1}\mathcal{D}^{m}(b,d,\gamma,\phi).$$

In particular, put b=d, m =0,and γ=1,we obtain $\mathcal{M}_{q,\sigma}^{1}\mathcal{D}^{0}(b,b,1,\phi) := K_{q\sigma,}(\phi)$ this is special case of the class $\mathcal{M}_{q,\sigma}^{\alpha,}(\phi)$ when α=1,this class was studied by Goyal and Kumar [10].

Remark (1.4): *Put α=0, we get the class $\mathcal{M}_{q,\sigma}^{0,\lambda}\mathcal{D}^{m}(b,d,\gamma,\phi) \equiv \mathcal{M}_{q,\sigma}\mathcal{D}^{m}(b,d,\lambda,\gamma,\phi)$ which defined as follow.*

A function $f\in\sigma$ is in the class$\mathcal{M}_{q,\sigma}\mathcal{D}^m(b,d,\lambda,\gamma,\phi)$, $\gamma\in\mathbb{C}\setminus\{0\}$, $0\leq\lambda\leq1$ if the quasi-subordination conditions are satisfied:

$$\frac{1}{\gamma}\left[\frac{z(\mathcal{D}_\lambda^m(b,d)f(z))'+\lambda z^2(\mathcal{D}_\lambda^m(b,d)f(z))''}{(1-\lambda)\mathcal{D}_\lambda^m(b,d)f(z)+\lambda z(\mathcal{D}_\lambda^m(b,d)f(z))'}-1\right]\prec_q\phi(z)-1,$$

and

$$\frac{1}{\gamma}\left[\frac{w(\mathcal{G}_\lambda^m(b,d)g(w))'+\lambda w^2(\mathcal{G}_\lambda^m(b,d)g(w))''}{(1-\lambda)\mathcal{G}_\lambda^m(b,d)g(w)+\lambda w(\mathcal{G}_\lambda^m(b,d)g(w))'}-1\right]\prec_q\phi(w)-1.$$

In particular for b=d and m =0 in above class, we obtain the class

$$\mathcal{M}_{q,\sigma}\mathcal{D}^0(b,d,\lambda,\gamma,\phi):=\mathcal{P}_{q,\sigma}(\gamma,\lambda,\phi).$$

The functions of the class $\mathcal{P}_{q,\sigma}(\gamma,\lambda,\phi)$ are called bi-convex and bi-starlike functions of complex order γ of Ma-Minda type. This class was studied by Nanjundan, Vitalrao and Jagadesan [9].

Remark(1.5): *Putting α=1, we get the class $\mathcal{M}_{q,\sigma}^{1,\lambda}\mathcal{D}^m(b,d,\gamma,\phi)\equiv\mathcal{M}_{q,\sigma,\lambda}\mathcal{D}^m(b,d,\gamma,\phi)$ which is defined as follow.*

A function $f\in\sigma$ is said to be in the class $\mathcal{M}_{q,\sigma,\lambda}\mathcal{D}^m(b,d,\gamma,\phi)$, $\gamma\in\mathbb{C}\setminus\{0\}$, $0\leq\lambda\leq1$, if the following conditions are satisfied

$$\frac{1}{\gamma}\left[\frac{z(\mathcal{D}_\lambda^{\mathrm{m}}(\mathrm{b,d})f(z))'+(1+2\lambda)z^2(\mathcal{D}_\lambda^{\mathrm{m}}(\mathrm{b,d})f(z))''+\lambda z^3(\mathcal{D}_\lambda^{\mathrm{m}}(\mathrm{b,d})f(z))'''}{z(\mathcal{D}_\lambda^{\mathrm{m}}(\mathrm{b,d})f(z))'+\lambda z^2(\mathcal{D}_\lambda^{\mathrm{m}}(\mathrm{b,d})f(z))''}\right]-1\prec_q\phi(z)-1,$$

and

$$\frac{1}{\gamma}\left[\frac{w(\mathcal{G}_\lambda^{\mathrm{m}}(\mathrm{b,d})g(w))'+(1+2\lambda)w^2(\mathcal{G}_\lambda^{\mathrm{m}}(\mathrm{b,d})g(w))''+\lambda w^3(\mathcal{G}_\lambda^{\mathrm{m}}(\mathrm{b,d})g(w))'''}{w(\mathcal{G}_\lambda^{\mathrm{m}}(\mathrm{b,d})g(w))'+\lambda w^2(\mathcal{G}_\lambda^{\mathrm{m}}(\mathrm{b,d})g(w))''}\right]-1\prec_q\phi(w)-1.$$

In particular for b=d and m =0 in above class, we obtain the class

$$\mathcal{M}_{q,\sigma}^{\lambda}\mathcal{D}^0(b,b,\gamma,\phi)\equiv\mathcal{K}_{q,\sigma}(\gamma,\lambda,\phi)$$

was studied by Nanjundan, Vitalrao and Jagadesan [9].

To find out our results, we needed to talk about the following lemma.

Lemma (1.6)*[13]. If $p\in\mathcal{P}$, then $|c_j|\leq2$ for each j, where $\mathcal{P}$ is the family of all functions p, holomorphic in $\mathfrak{U}$, for which*

$$\mathrm{Re}\{p(z)\}>0,\ (z\in\mathfrak{U}),$$

where

$$p(z)=1+c_1z+c_2z^2+c_3z^3+\cdots,\ (z\in\mathfrak{U}).$$

2. Coefficients Bounds

In this section, we find the initial Taylor coefficients $|a_2|$ and $|a_3|$ for functions in class $\mathcal{M}_{q,\sigma}^{\alpha,\lambda}\mathcal{D}^m(b,d,\gamma,\phi)$.

Theorem(2.1): *If f belonging to the class $\mathcal{M}_{q,\sigma}^{\alpha,\lambda}\mathcal{D}^m(b,d,\gamma,\phi)$, then*

$$|a_2|\leq \frac{|\gamma||A_\circ|B_1\sqrt{B_1}}{\sqrt{\left|\gamma[2(1+2\alpha)(1+2\lambda)^{m+1}\frac{(b)_2}{(d)_2}-(1+3\alpha)(1+\lambda)^{2(m+1)}\{\frac{(b)_1}{(d)_1}\}^2]A_\circ {B_1}^2-(1+\alpha)^2(1+\lambda)^{2(m+1)}\{\frac{(b)_1}{(d)_1}\}^2(B_2-B_1)\right|}} \quad (2.1)$$

$$|a_3|\leq \frac{|\gamma|^2|A_\circ|^2{B_1}^3}{\left|\gamma[2(1+2\alpha)(1+2\lambda)^{m+1}\frac{(b)_1}{(d)_1}-(1+3\alpha)(1+\lambda)^{2(m+1)}\{\frac{(b)_1}{(d)_1}\}^2]A_\circ {B_1}^2-(1+\alpha)^2(1+\lambda)^{2(m+1)}\{\frac{(b)_1}{(d)_1}\}^2(B_2-B_1)\right|} + \frac{|\gamma||A_1|B_1}{2(1+2\alpha)(1+2\lambda)^{m+1}\frac{(b)_2}{(d)_2}}+\frac{|\gamma||A_\circ|B_1}{2(1+2\alpha)(1+2\lambda)^{m+1}\frac{(b)_2}{(d)_2}} \quad (2.2)$$

Proof: Let $f \in \mathcal{M}_{q,\sigma}^{\alpha,\lambda}\mathcal{D}^m(b,d,\gamma,\phi)$ and $g=f^{-1}$. Then there exist holomorphic functions u, v: $\mathfrak{U}\to\mathfrak{U}$, with u(0)=v(0)=0, such that

$$\frac{1}{\gamma}[(1-\alpha)\frac{z(\mathcal{D}_\lambda^{m+1}(b,d)f(z))'}{\mathcal{D}_\lambda^{m+1}(b,d)f(z)}+\alpha\{1+\frac{z(\mathcal{D}_\lambda^{m+1}(b,d)f(z))''}{(\mathcal{D}_\lambda^{m+1}(b,d)f(z))'}\}-1]=\varphi(z)(\phi(z)-1), \quad (2.3)$$

$$\frac{1}{\gamma}[(1-\alpha)\frac{w(\mathcal{G}_\lambda^{m+1}(b,d)g(w))'}{\mathcal{G}_\lambda^{m+1}(b,d)g(w)}+\alpha\{1+\frac{w(\mathcal{G}_\lambda^{m+1}(b,d)g(w))''}{(\mathcal{G}_\lambda^{m+1}(b,d)g(w))'}\}-1]=\varphi(w)(\phi(w)-1). \quad (2.4)$$

Now, we define the functions p and q by

$$p(z)=\frac{1+u(z)}{1-u(z)}=1+c_1z+c_2z^2+c_3z^3+\cdots$$

and

$$q(z)=\frac{1+v(z)}{1-v(z)}=1+b_1z+b_2z^2+b_3z^3+\cdots,$$

It is obvious, Re p(z) >0 and Re q(z) >0 . From last two relations, we derive

$$u(z)=\frac{p(z)-1}{p(z)+1}=\frac{1}{2}[c_1z+(c_2-\frac{c_1^2}{2})z^2+\cdots \quad (2.5)$$

$$v(z)=\frac{qz-1}{q(z)+1}=\frac{1}{2}[b_1z+(b_2-\frac{b_1^2}{2})z^2+\cdots. \quad (2.6)$$

It is obvious that p and q are holomorphic functions in $\mathfrak{U}$ with $p(0)=q(0)=1$.

Using (2.5), (2.6) in (2.3) and (2.4), respectively, we obtain

$$\frac{1}{\gamma}[(1-\alpha)\frac{z(\mathcal{D}_\lambda^{m+1}(b,d)f(z))'}{\mathcal{D}_\lambda^{m+1}(b,d)f(z)}+\alpha\{1+\frac{z(\mathcal{D}_\lambda^{m+1}(b,d)f(z))''}{(\mathcal{D}_\lambda^{m+1}(b,d)f(z))'}\}-1]=\varphi(z)(\phi\left(\frac{p(z)-1}{p(z)+1}\right)-1), \quad (2.7)$$

$$\frac{1}{\gamma}[(1-\alpha)\frac{w(\mathcal{G}_\lambda^{m+1}(b,d)g(w))'}{\mathcal{G}_\lambda^{m+1}(b,d)g(w)}+\alpha\{1+\frac{w(\mathcal{G}_\lambda^{m+1}(b,d)g(w))''}{(\mathcal{G}_\lambda^{m+1}(b,d)g(w))'}\}-1]=\varphi(w)(\phi\left(\frac{q(z)-1}{q(z)+1}\right)-1). \quad (2.8)$$

Utilize (2.5), (2.6) together with (1.3) it is evident that

$$\varphi(z)(\phi\left(\frac{p(z)-1}{p(z)+1}\right)-1)=\frac{1}{2}A_\circ B_1C_1z+\{\frac{1}{2}A_1B_1C_1+\frac{1}{2}A_\circ B_1(C_2-\frac{c_1^2}{2})+\frac{1}{4}A_\circ B_2c_1^2\}z^2+\ldots \quad (2.9)$$

$$\varphi(w)(\phi\left(\frac{q(z)-1}{q(z)+1}\right)-1)=\frac{1}{2}A_\circ B_1b_1w+\{\frac{1}{2}A_1B_1b_1+\frac{1}{2}A_\circ B_1(b_2-\frac{b_1^2}{2})+\frac{1}{4}A_\circ B_2b_1^2\}w^2+\ldots.. \quad (2.10)$$

It follows from (2.7),(2,8),(2.9) and (2.10) that

$$\frac{1}{\gamma}(1+\alpha)(1+\lambda)^{m+1}\frac{(b)_1}{(d)_1}a_2=\frac{1}{2}A_\circ B_1C_1 \quad (2.11)$$

$$\frac{1}{\gamma}[2(1+2\alpha)(1+2\lambda)^{m+1}\frac{(b)_2}{(d)_2}a_3-(1+3\alpha)(1+\lambda)^{2(m+1)}(\frac{(b)_1}{(d)_1})^2a_2^2]=\frac{1}{2}A_1B_1C_1+$$
$$\frac{1}{2}A_\circ B_1(C_2-\frac{c_1^2}{2})+\frac{1}{4}A_\circ B_2c_1^2\} \quad (2.12)$$

$$\frac{-1}{\gamma}(1+\alpha)(1+\lambda)^{m+1}\frac{(b)_1}{(d)_1}a_2=\frac{1}{2}A_\circ B_1b_1 \quad (2.13)$$

$$\frac{1}{\gamma}[(4(1+2\alpha)(1+2\lambda)^{m+1}\frac{(b)_2}{(d)_2}-(1+3\alpha)(1+\lambda)^{2(m+1)}(\frac{(b)_1}{(d)_1})^2)a_2^2-2(1+2\alpha)$$
$$(1+2\lambda)^{m+1}\frac{(b)_2}{(d)_2}a_3]=\frac{1}{2}A_1B_1b_1+\frac{1}{2}A_\circ B_1(b_2-\frac{b_1^2}{2})+\frac{1}{4}A_\circ B_2b_1^2\}. \quad (2.14)$$

From (2.11) and (2.13), we obtain

$$c_1=-b_1 \quad (2.15)$$

and

$$a_2=\frac{\gamma A_\circ B_1C_1}{2(1+\alpha)(1+\lambda)^{m+1}\frac{(b)_1}{(d)_1}}=\frac{-\gamma A_\circ B_1b_1}{2(1+\alpha)(1+\lambda)^{m+1}\frac{(b)_1}{(d)_1}} \quad (2.16)$$

$$8(1+\alpha)^2(1+\lambda)^{2(m+1)}a_2^2=\gamma^2{A_\circ}^2{B_1}^2(\frac{(b)_1}{(d)_1})^2({b_1}^2+{C_1}^2), \quad (2.17)$$

adding (2.12) and (2.14) it follows that

$$\frac{a_2^2}{\gamma}[(4(1+2\alpha)(1+2\lambda)^{m+1}\frac{(b)_2}{(d)_2}-(1+3\alpha)(1+\lambda)^{2(m+1)}(\frac{(b)_1}{(d)_1})^2)]=\frac{1}{2}A_\circ B_1(c_2+b_2)$$
$$+\frac{A_\circ(B_2-B_1)}{4}(c_1^2+b_1^2). \quad (2.18)$$

Substituting (2.15) and (2.16) into (2.18), we have

$$a_2^2=\frac{\gamma^2{A_\circ}^2{B_1}^3(c_2+b_2)}{4\gamma[(1+2\alpha)(1+2\lambda)^{m+1}\frac{(b)_2}{(d)_2}-(1+3\alpha)(1+\lambda)^{2(m+1)}(\frac{(b)_1}{(d)_1})^2]{A_\circ B_1}^2-4(B_2-B_1)(1+\alpha)^2(1+\lambda)^{2(m+1)}(\frac{(b)_1}{(d)_1})^2}. \quad (2.19)$$

Applying Lemma (1.6), we get the desired inequality (2.1).

Subtracting (2.12) from (2.14) and computation using (2.15), we obtain

$$a_3=a_2^2+\frac{\gamma A_1B_1C_1}{4(1+2\alpha)(1+2\lambda)^{m+1}\frac{(b)_2}{(d)_2}}+\frac{\gamma A_\circ B_1(c_2-b_2)}{8(1+2\alpha)(1+2\lambda)^{m+1}\frac{(b)_2}{(d)_2}}.$$

By applying for Lemma (1.6) again, we had the estimate (2.2).

Taking special values for α and λ in previous theorem, we obtain the following results

Corollary (2.2): *Let* $\gamma\in\mathbb{C}\setminus\{0\}$ *and* $\alpha\geq 0$. *If* $f\in\mathcal{M}_{q,\sigma}^{\alpha,}\mathcal{D}^m(b,d,\gamma,\phi)$, *then*

$$|a_2|\leq\frac{|\gamma||A_\circ|B_1\sqrt{B_1}}{\sqrt{\left|\gamma[2(1+2\alpha)\frac{(b)_2}{(d)_2}-(1+3\alpha)\{\frac{(b)_1}{(d)_1}\}^2]{A_\circ B_1}^2-(1+\alpha)^2\{\frac{(b)_1}{(d)_1}\}^2(B_2-B_1)\right|}}$$

and

$$|a_3| \leq \frac{|\gamma|^2|A_\circ|^2{B_1}^3}{\left|\gamma[2(1+2\alpha)\frac{(b)_1}{(d)_1}-(1+3\alpha)\{\frac{(b)_1}{(d)_1}\}^2]{A_\circ}{B_1}^2-(1+\alpha)^2\{\frac{(b)_1}{(d)_1}\}^2(\mathrm{B_2}-\mathrm{B_1})\right|}+\frac{|\gamma||A_1|B_1}{2(1+2\alpha)\frac{(b)_2}{(d)_2}}+\frac{|\gamma||A_\circ|B_1}{2(1+2\alpha)\frac{(b)_2}{(d)_2}}$$

Remark (2.3): *For b=d and m =0, the above corollary reduces [9, Corollary 12, p.5].*

Corollary (2.4): *Let f be in the class $\mathcal{M}_{q,\sigma}\mathcal{D}^m(b,d,\gamma,\phi)$, and $\gamma\in\mathbb{C}-\{0\}$,$\alpha\geq 0$. Then*

$$|a_2|\leq\frac{|\gamma||A_\circ|B_1\sqrt{B_1}}{\sqrt{\left|\gamma[2\frac{(b)_2}{(d)_2}-\{\frac{(b)_1}{(d)_1}\}^2]{A_\circ}{B_1}^2-\{\frac{(b)_1}{(d)_1}\}^2(\mathrm{B_2}-\mathrm{B_1})\right|}}$$

and

$$|a_3| \leq \frac{|\gamma|^2|A_\circ|^2{B_1}^3}{\left|\gamma[2\frac{(b)_1}{(d)_1}-\{\frac{(b)_1}{(d)_1}\}^2]{A_\circ}{B_1}^2-\{\frac{(b)_1}{(d)_1}\}^2(\mathrm{B_2}-\mathrm{B_1})\right|}+\frac{|\gamma||A_1|B_1}{2\frac{(b)_2}{(d)_2}}+\frac{|\gamma||A_\circ|B_1}{2\frac{(b)_2}{(d)_2}}$$

Remark (2.5): *For $b=d$ and $m=0$, the Corollary (2.4) reduces to [9, Corollary 9, p.5].*

Corollary (2.6): *Let f be in the class $\mathcal{M}^1_{q,\sigma}\mathcal{D}^m(b,d,\gamma,\phi)$, and $\gamma\in\mathbb{C}-\{0\}$,.Then*

$$|a_2|\leq\frac{|\gamma||A_\circ|B_1\sqrt{B_1}}{\sqrt{\left|\gamma[6\frac{(b)_2}{(c)_2}-4\{\frac{(b)_1}{(c)_1}\}^2]{A_\circ}{B_1}^2-4\{\frac{(b)_1}{(c)_1}\}^2(\mathrm{B_2}-\mathrm{B_1})\right|}}$$

and

$$|a_3| \leq \frac{|\gamma|^2|A_\circ|^2{B_1}^3}{\left|\gamma[6\frac{(b)_1}{(c)_1}-4\{\frac{(b)_1}{(c)_1}\}^2]{A_\circ}{B_1}^2-4\{\frac{(b)_1}{(c)_1}\}^2(\mathrm{B_2}-\mathrm{B_1})\right|}+\frac{|\gamma||A_1|B_1}{6\frac{(b)_2}{(c)_2}}+\frac{|\gamma||A_\circ|B_1}{6\frac{(b)_2}{(c)_2}}$$

Remark (2.7): *For b=d and m =0, the Corollary (2.6) reduces to[9, Corollary 11,p.5].*

Corollary (2.8): *Let f be in the class $\mathcal{M}_{q,\sigma}\mathcal{D}^m(b,d,\lambda,\gamma,\phi)$, and $\gamma\in\mathbb{C}-\{0\}$ and $0\leq\lambda\leq 1$. Then*

$$|a_2|\leq\frac{|\gamma||A_\circ|B_1\sqrt{B_1}}{\sqrt{\left|\gamma[2(1+2\lambda)^{m+1}\frac{(b)_2}{(c)_2}-(1+\lambda)^{2(m+1)}\{\frac{(b)_1}{(c)_1}\}^2]{A_\circ}{B_1}^2-(1+\lambda)^{2(m+1)}\{\frac{(b)_1}{(c)_1}\}^2(\mathrm{B_2}-\mathrm{B_1})\right|}}$$

and

$$|a_3| \leq \frac{|\gamma|^2|A_\circ|^2{B_1}^3}{\left|\gamma[2(1+2\lambda)^{m+1}\frac{(b)_1}{(c)_1}-(1+\lambda)^{2(m+1)}\{\frac{(b)_1}{(c)_1}\}^2]{A_\circ}{B_1}^2-(1+\lambda)^{2(m+1)}\{\frac{(b)_1}{(c)_1}\}^2(\mathrm{B_2}-\mathrm{B_1})\right|}+\frac{|\gamma||A_1|B_1}{2(1+2\lambda)^{m+1}\frac{(b)_2}{(c)_2}}+\frac{|\gamma||A_\circ|B_1}{2(1+2\lambda)^{m+1}\frac{(b)_2}{(c)_2}}$$

Remark (2.9):*By taking b=d and m =0,the above corollary gives to the result obtained in Corollary (13) in [9].*

Corollary (2.10): *If f be in the class $\mathcal{M}^\lambda_{q,\sigma}\mathcal{D}^m(b,d,\lambda,\gamma,\phi)$, $\gamma\in\mathbb{C}-\{0\}$ and $0\leq\lambda\leq 1$, then*

$$|a_2|\leq\frac{|\gamma||A_\circ|B_1\sqrt{B_1}}{\sqrt{\left|\gamma[6(1+2\lambda)^{m+1}\frac{(b)_2}{(c)_2}-4(1+\lambda)^{2(m+1)}\{\frac{(b)_1}{(c)_1}\}^2]{A_\circ}{B_1}^2-4(1+\lambda)^{2(m+1)}\{\frac{(b)_1}{(c)_1}\}^2(\mathrm{B_2}-\mathrm{B_1})\right|}}$$

and

$$|a_3| \leq \frac{|\gamma|^2|A_\circ|^2{B_1}^3}{\left|\gamma[6(1+2\lambda)^{m+1}\frac{(b)_1}{(c)_1}-4(1+\lambda)^{2(m+1)}\{\frac{(b)_1}{(c)_1}\}^2]{A_\circ}{B_1}^2-4(1+\lambda)^{2(m+1)}\{\frac{(b)_1}{(c)_1}\}^2(\mathrm{B_2}-\mathrm{B_1})\right|}+\frac{|\gamma||A_1|B_1}{6(1+2\lambda)^{m+1}\frac{(b)_2}{(c)_2}}+\frac{|\gamma||A_\circ|B_1}{6(1+2\lambda)^{m+1}\frac{(b)_2}{(c)_2}}$$

Remark (2.11): *If we set b=d and m =0, the above corollary leads to get coefficient estimates $|a_2|$ and $|a_3|$ in the class $K_{q\sigma,}(\gamma, \lambda, \phi)$.[9, Corollary 14, p.5].*

References

[1] P. Duren, 1977, Subordination in complex analysis, Lecture Note in Mathematics, Springer, Berlin. Germany, 599, 22-29.
[2] M. S. Robertson, 1970, Quasisubordination and coefficient conjectures, Bulletin of American Mathematical Society, 76. 1-9.
[3] W. C. Ma and D. Minda, 1994, A unified treatment of some special classes of univalent functions, in Proceedings of the Conference on Complex Analysis, Tianjin,1992,vol. I of Lecture Notes for Analysis, International Press, Cambridge, Mass, USA, 157–169,
[4] R. El-Ashwah and S. Kanas, 2015, Fekete-Szego inequalities for quasi-subordination functions classes of complex order, *Kyungpook Mathematical Journal*, **55**(3), 679–688.
[5] V. Ravichandran, Y. Polatoglu, M. Bolcal, and A. Sen, 2005, Certain subclasses of starlike and convex functions of complex order, *Hacettepe Journal of Mathematics and Statistics*, **34**, 9–15.
[6] M. H. Mohd and M. Darus, 2012, Fekete-Szego problems for quasi-subordination classes, Abstract and Applied Analysis. Art. ID 192956, 1-14.
[7] C. Selvaraj and K. R. Karthikeyan, 2009, Differential subordination and superordination for analytic functions defined using a family of generalized differential operators, Tomis Vniversitas Ovidiana. **17**(1),201-210.
[8] H. M. Srivastava, A. K. Mishra, and P. Gochhayat, 2010, Certain subclasses of analytic and bi-univalent functions, Applied Mathematics Letters, **23**(10), 1188–1192.
[9] N. Magesh, V. K. Balaji and J. Yamini, 2016, Certain subclasses of bi-starlike and bi-convex functions based on quasi-subordination," Abstract and Applied Analysis, Article ID 3102960,1- 6.
[10] S. P. Goyal and R. Kumar, 2015, Coefficient estimates and quasi- subordination properties associated with certain subclasses of analytic and bi-univalent functions, Mathematica Slovaca, 65(**3**), 533-544.
[11] R. M. Ali, S. K. Lee, V. Ravichandran, and S. Supramaniam, 2012, Coefficient estimates for bi-univalent Ma-MINda starlike and convex functions, Applied Mathematics Letters, 25(**3**), 344–351.
[12] E. Deniz, 2013, Certain subclasses of bi-univalent functions satisfying subordinate conditions, *Journal of Classical Analysis*, **2**(1), 49-60.
[13] C. Pommerenke, 1975, Univalent Functions, Vandenhoeck & Ruprecht, Gottingen, Germany.

Essentially semismall Quasi-Dedekind module relative to a module

Essentially semismall Quasi-Dedekind module relative to a module

Mukdad Q Hussain

Department of Computer Sciences, College of Education for pure science, Diyala University, Diyala, Iraq.

Abstract. Let R be associative ring with identity and M be a unitary R-module. In this paper study the direct summand of essentially semismall quasi-Dedekind module and prove that the direct sum of essentially semismall quasi-Dedekind modules need not be essentially semismall quasi-Dedekind and give the definition of essentially semismall quasi-Dedekind relative to a module with some examples, also give some of their basic properties and some examples that illustrate these properties.

Keywords. Semismall modules, Quasi-Dedekind module.

1. Introduction

In this paper study the direct summand of essentially semismall quasi-Dedekind module and prove that the direct sum of essentially semismall quasi-Dedekind modules need not be essentially semismall quasi-Dedekind. Also, give the definition of essentially semismall Quasi-Dedekind relative to a module.

A submodule A of an R-module M is called small in M ($A \ll M$) if whenever a submodule B of M with $M = A + B$ implies $B = M$ [1].

An R-submodule N of an R-module M is called essentially small ($N \ll_e M$), if for every nonzero small submodule K of M, $K \cap N \neq \{0\}$. Equivalently, for each $0 \neq x \in M$, there exists $0 \neq r \in R$ such that $0 \neq rx \in N$.

A proper submodule A of an R-module M is called semismall in M ($A \ll_S M$) if $A = 0$ or $A/K \ll M/K$ for all nonzero submodules K of A [1].

A submodule N of an R-module M is called semismall invertible if $N^{-1}N = M$, where $N^{-1} = \{x \in R_T: xN \ll_s M\}$ and R_T is the localization of R at T in the usual sence, $T = \{s \in S: sm = 0$ for some $m \in M$, then $m = 0\}$, where S is the set of all nonzero divisors of R.

An R-module M is called semismall quasi-Dedekind, if every nonzero R submodule N of M is semismall quasi-invertible; that is $Hom(M/N, M) = \{0\}$, for all $\{0\} \neq N \ll_s M$.

A ring R is semismall quasi-Dedekind if R is a semismall quasi-Dedekind R-module.

An R-module M is called essentially semismall quasi-Dedekind if $Hom(M/N, M) = \{0\}$ for all $N \ll_{se} M$.

A ring R is essentially semismall quasi-Dedekind if R is an essentially semismall quasi-Dedekind R-module. The property of essentially semismall quasi-Dedekind module is inherited by direct summand.

Proposition1 A direct summand of an essentially semismall Quasi-Dedekind module is an essentially semismall Quasi-Dedekind module.

Proof: Let J is an essentially semismall Quasi-Dedekind R-module and let $E \leq^{\oplus} J$, then $J = E \oplus V$ for some submodule $V \leq J$. Let $f \in End_R(E)$, $f \neq 0$, to prove that Kerf $\ll_{se}$ E. Consider the following: $J \xrightarrow{\rho} E \xrightarrow{f} E \xrightarrow{i} J$, where ρ is the natural projection, and i is the inclusion mapping. Hence $h = i \circ f \circ \rho \in End_R(J)$ and $h \neq 0$, so Kerh $\ll_{se}$ J and since kerf ⊆ kerh then Kerf $\ll_{se}$ J. Now assume that Kerf $\ll_{se}$ E, this implies Kerh $\ll_{se}$ J and so get a contradiction.
Let x + y be any nonzero element of J, where $x \in E$, $y \in V$. If $x \neq 0$ and ($y = 0$ or $y \neq 0$), then since Kerf $\ll_{se}$ E, there exists $0 \neq r \in R$ such that $0 \neq rx \in$ kerf. Hence rx + ry ≠ 0, because if rx+ry = 0, then rx = - ry ∈ E∩V = {0} which is a contradiction. Also h (rx + ry) = 0; that is $0 \neq r(x+y) \in$ kerh. If $x = 0$ and $y \neq 0$, then x + y = y ≠ 0 and 1.y = y, h (y) = iofoρ(0 + y) = iof(0) = f(0) = 0; that is $0 \neq 1(x+y) = y \in$ kerh. Therefore Kerh $\ll_{se}$ J which is a contradiction. Thus the assumption is false and hence Kerf $\ll_{se}$ E; that is E is an essentially semismall Quasi-Dedekind R-module.
The next example show the direct sum of essentially semismall Quasi-Dedekind modules is not necessarily essentially semismall Quasi-Dedekind module.

Example2 It is known that Z and Z_2 are essentially semismall Quasi-Dedekind as Z-modules. But N = Z⊕ Z_2 is not essentially semismall Quasi-Dedekind Z-module. since if $f : N \longrightarrow N$ define by $f(x, \bar{y}) = (0, \bar{x})$, $x \in Z$, $\bar{y} \in Z_2$, then $f \neq 0$ and $Kerf = \{(x, \bar{y}) \in N : f(x, \bar{y}) = (0, \bar{0})\} = \{(x, \bar{y}) \in N : \bar{x} = \bar{0}\} = 2Z \oplus Z_2$ .Hence kerf $\ll_{se} N$. Thus $N = Z \oplus Z_2$ is not essentially semismall quasi-Dedekind as a Z-module .

Let M and N be R-modules. M is an essentially semismall quasi-Dedekind (K-nonsingular) relative to N if, for all $f \in Hom(M, N)$, $f \neq 0$, implies Kerf $\ll_{se}$ M.

Remarks and Examples 3

1) Let J be an R-module. Then J is essentially semismall Quasi-Dedekind if and only if J is essentially semismall Quasi-Dedekind relative to J.
2) Let J be an essentially semismall Quasi-Dedekind R-module. Then J is an essentially semismall Quasi-Dedekind relative to E, for all E ≤ J.

Proof: Let E ≤ J. If E = J, then J is an essentially semismall Quasi-Dedekind relative to E. If E ⊊ J, assume that $f \in Hom(J, E)$, $f \neq 0$. Hence $i \circ f \in End_R(J)$, $(i \circ f) \neq 0$, where i is the inclusion mapping. Since J is an essentially semismall Quasi-Dedekind R-module, then Ker (iof) $\ll_{se}$ J. But Kerf = Ker (iof), thus Kerf $\ll_{se}$ J and so J is an essentially semismall quasi-Dedekind relative to E.

3) Every uniform R-module J is an essentially semismall Quasi-Dedekind relative to N, where N is any R-module.
4) Any semisimple R-module M is an essentially semismall Quasi-Dedekind relative to E, where E is any R-module.
5) Z12 is not essentially semismall quasi-Dedekind relative to Z6, since there exists h: Z12 → Z6 defined by $h(\bar{x}) = 3\bar{x}$ for all $\bar{x} \in$ Z12, hence kerh = $(\bar{2})$ ≪se Z12.

Theorem4 Let $\{O_i\}_{i\in\Lambda}$ be a family of modules. Then $M = \oplus_{i\in\Lambda} O_i$ is essentially semismall quasi-Dedekind *if and only if* O_i is an essentially semismall Quasi-Dedekind relative to O_j, for all $i, j \in \Lambda$.

Proof: give the details of proof of this theorem for $i \in \Lambda = \{1, 2\}$, and the proof for any Λ is similarly.

$\Rightarrow$) Since $M = M_1 \oplus M_2$ is an essentially semismall quasi-Dedekind R-module, then by Prop1, M_1 and M_2 are essentially semismall quasi-Dedekind R-modules. So M_1 is an essentially semismall quasi-Dedekind relative to M_1 and M_2 is an essentially semismall quasi-Dedekind relative to M_2. Now, to prove that M_1 is an essentially semismall quasi-Dedekind relative to M_2. Let $f: M_1 \to M_2$, $f \neq 0$. Consider the following: $M \xrightarrow{\rho} M_1 \xrightarrow{f} M_2 \xrightarrow{i} M$, where ρ is the natural projection, and i is the inclusion mapping. Then $h = iof \circ \rho \in End_R(M)$ and $h \neq 0$, thus $Ker\, h \ll_{se} M$, but $kerf \subseteq kerh$ which implies $Ker\, f \ll_{se} M$. Now, to prove that $Kerf \ll_{se} M_1$. Suppose that $Kerf \ll_{se} M_1$, then $ker\, f \oplus M_2 \ll_{se} M_1 \oplus M_2 = M$, to show that $ker\, h = ker\, f \oplus M_2$: Let $x \in ker\, f$, $y \in M_2$, $h(x + y) = iofo\rho(x + y) = iof(x) = f(x) = 0$, thus $ker\, f \oplus M_2 \subseteq ker\, h$, and let $x + y \in ker\, h \subseteq M_1 \oplus M_2$, so $x \in M_1$, $y \in M_2$, since $h(x+y) = 0$ implies $(iofo\rho)(x + y) = 0$, so $iof(x) = 0$ then $f(x) = 0$; that is $x \in Ker\, f$, thus $ker\, h \subseteq ker\, f \oplus M_1$. Hence $kerh = kerf \oplus M_2 \ll_{se} M_1 \oplus M_2 = M$, which is a contradiction. Therefore $Kerf \ll_{se} M_1$ and hence M1 is an essentially semismall quasi-Dedekind relative to M_2.
Similarly, M_2 is an essentially semismall quasi–Dedekind relative to M_1.

$\Leftarrow$) Assume $\psi: M \to M$ such that $ker\,\psi \ll_{se} M$, so $ker\,\psi \cap M_1 \ll_{se} M_1$. Let $\psi|_{M_1} : M_1 \longrightarrow M$ such that $\psi|_{M_1}(x) = \psi(x+0)$, $\forall\ x \in M_1$, then $Ker(\psi|_{M_1}) = Ker\,\psi \cap M_1$, to see this: let $x \in Ker(\psi|_{M_1})$ implies $0 = \psi|_{M_1}(x) = \psi(x+0) = \psi(x)$. It follows that $x \in ker\,\psi \cap M_1$. Also, let $x \in ker\,\psi \cap M_1$, so $x \in M_1$ and $0 = \psi(x) = \psi(x+0) = \psi|_{M_1}(x)$, so $x \in Ker(\psi|_{M_1})$. Consider the following: $M_1 \xrightarrow{\psi|_{M_1}} M \xrightarrow{\rho_1} M_1$ and $M_1 \xrightarrow{\psi|_{M_1}} M \xrightarrow{\rho_2} M_2$, where ρ_1, ρ_2 are the natural projections. Claim that $Ker(\rho_1 o \psi|_{M_1}) \cap Ker(\rho_2 o \psi|_{M_1}) \supseteq Ker\,\psi|_{M_1}$. To prove our assertion: Let $x \in Ker(\psi|_{M_1})$ then $\psi|_{M_1}(x) = 0$, hence $\rho_1 o \psi|_{M_1}(x) = \rho_1(\psi|_{M_1}(x)) = \rho_1(0) = 0$ $\rho_2 o \psi|_{M_1}(x) = \rho_2(\psi|_{M_1}(x)) = \rho_2(0) = 0$.,Thus $x \in Ker(\rho_1 o \psi|_{M_1}) \cap Ker(\rho_2 o \psi|_{M_1})$; that is $Ker(\rho_1 o \psi|_{M_1}) \cap Ker(\rho_2 o \psi|_{M_1}) \supseteq Ker\,\psi|_{M_1}$. But $Ker(\psi|_{M_1}) = Ker\,\psi \cap M_1 \ll_{se} M_1$, so $Ker(\rho_1 o \psi|_{M_1}) \cap Ker(\rho_2 o \psi|_{M_1}) \ll_{se} M_1$ and hence $Ker(\rho_1 o \psi|_{M_1}) \ll_{se} M_1$ and $Ker(\rho_2 o \psi|_{M_1}) \ll_{se} M_1$. But M_1 is an essentially semismall quasi-Dedekind relative to M_1 and M_1

is essentially semismall quasi-Dedekind relative to M_2, through hypothesis. So that $\rho_1 o \psi \big|_{M_1} = 0$, $\rho_2 o \psi \big|_{M_1} = 0$ …(1), by a similar way, obtain $\rho_1 o \psi \big|_{M_2} = 0$, $\rho_2 o \psi \big|_{M_2} = 0$ …(2). Hence by (1) and (2), have $\psi = 0$.

Proposition5 Let J be an essentially semismall Quasi-Dedekind (K-nonsingular) module , and let $N \leq j$ Whether $E \ll_{se} E_i \leq^{\oplus} M$, for all I = 1,2, then $E_1 = E_2$.

Proof Consider the endomorphism $(I - \rho_1)\rho_2$, ρ_1 is the natural projections of J onto N_i , i = 1 , 2 ; that is $\rho_1 : J \to E_1$, $\rho_2 : J \to E_2$. Since $E \subseteq E_1$ and $E \subseteq E_2$, so $d_1(e) = e$, $d_2(e) = e$, for all $e \in E$. Hence for each $e \in E$ $([I - d_1]\, d_2)(e) = I - d_1(d_2(e)) = I - d_1(e) = I(e) - d_1(e) = 0$, so $E \subseteq \ker([I - d_1]\, d_2)$ ….(1). Since $E_2 \leq^{\oplus} J$, so there exists $k_2 \leq J$ such that $E_2 \oplus k_2 = J$, and since for each $k \in K_2$, $([I-d_1]\, d_2)(k) = (I-d_1)(d_2)(k) = (I-d_1)(0) = 0$ implies $k_2 \subseteq \ker([I-\rho_1]\, \rho_2)$…(2). Now, from (1) and (2) $E \oplus K_2 \subseteq \ker([I-\rho_1]\, \rho_2)$, but $E \ll_{se} E_2$, $K_2 \ll_{se} K_2$, so $E \oplus K_2 \ll_{se} E_2 \oplus K_2 = J$. Hence ker $([I-\rho_1]\, \rho_2) \ll_{se} J$, so $(I-\rho_1)\rho_2 = 0$ (since J is an Essentially semismall Quasi-Dedekind module). It follows that $\rho_2 = \rho_1 o \rho_2$. Now, to prove that $E_2 \subseteq E_1$. Let $u \in E_2$, then $\rho_2(u) = u$. Hence $d_1(d_2(u)) = d_1(u)$, then $d_1(u) = d_2(u) = u$. Hence $x \in E_1$, thus $E2 \subseteq E_1$. Similarly by taking $(I - \rho_2)\rho_1$ and showing it is zero, then obtain $E_1 \subseteq E_2$. Thus $E1 = E_2$.

References

[1] F.Kasch. Modules and rings. Academic Press. London, 1982.

The Approximate Solution of Fractional Damped Burger's Equation and its Statistical Properties

The Approximate Solution of Fractional Damped Burger's Equation and its Statistical Properties

Wurood R. Abd AL- Hussein[1], Mahmood A, Shamran[2] Suaad N. Kadhim[3] and Saad N. AL-Azzawi[2]

1Al-Isra'a University College – Baghdad - IRAQ
2Dept. of Math., College of Science for Women, Univ. of Baghdad
3Dept. of Math., College of Science, Univ. of Baghdad

wowomath91@yahoo.com , Mahmood_areiby@yahoo.com ,
Saad_naji2007@yahoo.com

Abstract. The aim of this paper is to extend the variational iteration method(VIM) to find the approximate solution of fractional damped Burger's equation and finding its statistical concepts.

Keywords Fractional calculus, Fractional damped Burger's equation, Caputo derivative, variational iteration method (VIM), statistical concepts.

1. Introduction

Nonlinear fractional partial differential equations are widely used to describe many important phenomena and dynamic processes such as engineering, acoustic, viscoelasticity, electromagnetics [4, 13]. In general, there is no method that yields an exact solution for nonlinear fractional differential equations.

Burger's equation is a fundamental partial differential equation in fluid mechanics. It is also a very important model encountered in several areas of applied mathematics such as heat conduction, acoustic waves, gas dynamics and traffic flow[9].The one dimensional nonlinear Burger's equation was first introduced in 1915 by Bateman H., [1], who found its steady solutions descriptive of certain viscous flows. It was later proposed by Burger J. M.(1948) [3] as one of a class of equation describing mathematical models of turbulence. Later the Burger's equation was studied by Cole J. D., (1951) [5] who gave a theoretical solution, based on Fourier series analysis, using the appropriate initial and boundary conditions. Gorguis A., (2005) [6] gives comparison between Cole - Hopf transformation and Decomposition method for solving Burger ′s equation. Momani S., (2006) [10] has presented nonperturbative analytical solutions of the space-and time-fractional Burger's equations by Adomian decomposition method. Inc (2008) [7] used variational iteration method for solving space-time fractional Burger's equations. Wang Qi. (2008) [14] extend the application of the homotopy perturbation and Adomian decomposition methods to construct approximate solutions for the nonlinear fractional KdV-Burger's equation. Biazar J. and Aminikhah H., (2009) [2] solve Burger's equation by using variational iteration method (VIM) by which Approximate solution can be found and which is better than ADM. In (2011) Pandey

K. and Verma L., [11] gave a note on Crank Nicolson scheme for Burger's equation without Hopf-Cole transformation solutions are obtained by ignoring nonlinear term.

2. Preliminaries

In this section, we present the basic definitions and properties of the fractional calculus theory, which are used further in this paper.

2.1. Definition [8]

A real valued function $f(x)$, $x > 0$, is said to be in the space C_μ, $\mu \in \mathbb{R}$, if there exists a real number p, $p > \mu$, such that $f(x) = x^p f_1(x)$, where $f_1(x) \in C[0,\infty)$, and it is said to be in the space C_μ^n if $f^{(n)}(x) \in C_\mu$, $n \in \mathbb{N}_0 = \mathbb{N} \cup \{0\}$.

2.2. Definition [8]

The Riemann-Liouville fractional integral operator of order $\alpha \geq 0$, of a function $f(x) \in C_\mu$, $\mu \geq -1$is defined as:

$$J^\alpha f(x) = \frac{1}{\Gamma(\alpha)} \int_0^x (x-t)^{\alpha-1} f(t)dt, \; x > 0 \qquad (1)$$

$$J^0 f(x) = f(x)$$

Properties of the operator J^αcan be found for $f \in C_\mu$, $\mu \geq -1$, $\alpha, \beta \geq 0$ and $\gamma > -1$as follows:

1. $J^\alpha J^\beta f(x) = J^{\alpha+\beta} f(x) = J^\beta J^\alpha f(x)$;
2. $J^\alpha C = \frac{C}{\Gamma(\alpha+1)} x^\alpha$, C is constant ;
3. $J^\alpha x^\gamma = \frac{\Gamma(\gamma+1)}{\Gamma(\alpha+\gamma+1)} x^{\alpha+\gamma}$.

2.3. Definition [7,8]

The fractional derivative of $f(x)$ in the Caputo sense is defined as:

$$D^\alpha f(x) = J^{n-\alpha} D^n f(x) = \frac{1}{\Gamma(n-\alpha)} \int_0^x (x-t)^{n-\alpha-1} f^{(n)}(t)dt \text{ , } \alpha > 0 \qquad (2)$$

For $n-1 < \alpha \leq n$, $n \in \mathbb{N}$, $x > 0$and $\Gamma(.)$ is the gamma function.

2.4. Definition [7,8]

For n be the smallest integer that exceeds α, the Caputo time- fractional derivative of a function $u\,(x,t)$ of order $\alpha > 0$ is defined as:

$$D_t^\alpha u(x,t) = \frac{\partial^\alpha u(x,t)}{\partial t^\alpha} = \begin{cases} \frac{1}{\Gamma(n-\alpha)} \int_0^t (t-\tau)^{n-\alpha-1} \frac{\partial^n u(x,\tau)}{\partial \tau^n} d\tau, n-1 < \alpha < n \\ \frac{\partial^n u(x,t)}{\partial t^n}, \qquad \alpha = n \in \mathbb{N} \end{cases}$$

and the space-fractional derivative operator of order $\beta > 0$ is defined as:

$$D_x^\beta u(x,t) = \frac{\partial^\beta u(x,t)}{\partial x^\beta} = \begin{cases} \frac{1}{\Gamma(n-\beta)} \int_0^x (x-\theta)^{n-\beta-1} \frac{\partial^n u(\theta,t)}{\partial \theta^n} d\theta, n-1 < \beta < n \\ \frac{\partial^n u(x,t)}{\partial x^n}, \qquad \beta = n \in \mathbb{N} \end{cases}$$

Satisfies the following properties:

1. $D^\alpha C = 0$, C constant;
2. $D^\alpha x^\gamma = \frac{\Gamma(\gamma+1)}{\Gamma(\gamma-\alpha+1)} x^{\gamma-\alpha}$, $x > 0$, $\gamma > -1$;

3. $D^{\alpha}\left(\sum_{i=0}^{m} c_i f_i(x,t)\right) = \sum_{i=0}^{m} c_i D^{\alpha} f_i(x,t)$, where $c_0, c_1, \ldots, c_m$ are constant.

2.5. Lemma [7]

If $n-1 < \alpha \leq n$, $f \in C_{\mu}^{n}$, $n \in \mathbb{N}$ and ≥ -1, then;

$D_a^{\alpha} J_a^{\alpha} f(x) = f(x)$,

$J_a^{\alpha} D_a^{\alpha} f(x) = f(x) - \sum_{k=0}^{n-1} f^{k}(0^{+}) \frac{(x-a)^k}{k!}$, where $x > 0$

3.Finding Approximate Solution and Using Statistical Tests for Reliability of the Solution

The fractional damped Burger's equation is:

$$u_t^{(\alpha)} + uu_x - u_{xx} + \lambda u = 0 \quad , 0 < \alpha \leq 1, \quad x \in \mathbb{R}, \quad t \geq 0, \lambda > 0 \tag{3}$$

We can reduce equation (3), by take the transformation;

$$\xi(x,t) = kx + \frac{ct^{\alpha}}{\Gamma(\alpha+1)} + \xi_0 \tag{4}$$

Where k, c, ξ_0 are constants, by using this transformation to get:

$$u_t^{(\alpha)} = u_t^{(\alpha)}(\xi) = u'(\xi) D_t^{\alpha} \xi = u'(\xi) \frac{c}{\Gamma(\alpha+1)} \frac{\Gamma(\alpha+1)}{\Gamma(\alpha-\alpha+1)} = cu'(\xi)$$

And

$$uu_x = u(\xi)\big(u(\xi)\big)_x = ku(\xi)u'(\xi)$$

Also

$$u_{xx} = (u(\xi))_{xx} = (ku'(\xi))_x = k(ku''(\xi)) = k^2 u''(\xi)$$

So by this transformation for ξ, equation (3) can be turned into the following nonlinear ordinary differential equation of second order with respect to the variable ξ;

$$cu'(\xi) + ku(\xi)u'(\xi) - k^2 u''(\xi) + u(\xi) = 0, \quad u'(\xi) = \frac{du}{d\xi} \tag{5}$$

Integrating (5) from 0 to ξ to get:

$$cu(\xi) - cu(0) + \frac{k}{2}u^2(\xi) - \frac{k}{2}u^2(0) - k^2 u'(\xi) + k^2 u'(0) + \lambda \int_0^{\xi} u(t)dt = 0$$

Let $L = k^2 u'(0) - cu(0) - \frac{k}{2}u^2(0)$

So to obtain;

$$cu(\xi) + \frac{k}{2}u^2(\xi) - k^2 u'(\xi) + \lambda \int_0^{\xi} u(t)dt + L = 0 \tag{6}$$

Now, integrating (6) from 0 to ξ to get:

$$\int_0^{\xi} cu(t)dt + \frac{k}{2}\int_0^{\xi} u^2(t)dt - k^2 u(\xi) + k^2 u(0) + \lambda \int_0^{\xi} (\xi - t)u(t)dt + L\xi = 0$$

So

$$u(\xi) = u(0) + \frac{L\xi}{k^2} + \frac{1}{k^2}\int_0^{\xi}[cu(t) + \frac{k}{2}u^2(t) + \lambda(\xi - t)u(t)]dt \quad (7)$$

Equation (7) can be solved by variational iteration method (VIM) and because of the uniform convergence, few terms are enough for good accuracy [12], to obtain;

$$u_0(\xi) = u(0) + \frac{L\xi}{k^2}$$

$$u_1(\xi) = \left(\frac{cu(0)}{k^2} + \frac{u^2(0)}{2k}\right)\xi + \left(\frac{cL}{k^4} + \frac{\lambda u(0)}{2k^2}\right)\xi^2 + \left(\frac{L^2}{2k^5} + \frac{\lambda L}{2k^2}\right)\xi^3$$

$$u_2(\xi) = \left(\frac{cu(0)}{2k^4} + \frac{u^2(0)}{4k^3}\right)\xi^2 + \left(\frac{cL}{3k^6} + \frac{\lambda u(0)}{6k^4}\right)\xi^3 + \left(\frac{L^2}{8k^7} + \frac{\lambda L}{8k^6}\right)\xi^4$$

$$u_3(\xi) = \left(\frac{cu(0)}{6k^6} + \frac{u^2(0)}{12k^5}\right)\xi^3 + \left(\frac{cL}{12k^8} + \frac{\lambda u(0)}{24k^6}\right)\xi^4 + \left(\frac{L^2}{40k^9} + \frac{\lambda L}{40k^8}\right)\xi^5$$

⋮

And so on.
Substituting these quantities into (4) we have:

$$u_0(x,t) = u(0) + (\frac{L}{k^2})(kx + \frac{ct^\alpha}{\Gamma(\alpha+1)} + \xi_0)$$

$$u_1(x,t) = \left(\frac{cu(0)}{k^2} + \frac{u^2(0)}{2k}\right)\left(kx + \frac{ct^\alpha}{\Gamma(\alpha+1)} + \xi_0\right) + \left(\frac{cL}{k^4} + \frac{\lambda u(0)}{2k^2}\right)\left(kx + \frac{ct^\alpha}{\Gamma(\alpha+1)} + \xi_0\right)^2 + \left(\frac{L^2}{2k^5} + \frac{\lambda L}{2k^2}\right)(kx + \frac{ct^\alpha}{\Gamma(\alpha+1)} + \xi_0)^3$$

$$u_2(x,t) = \left(\frac{cu(0)}{2k^4} + \frac{u^2(0)}{4k^3}\right)\left(kx + \frac{ct^\alpha}{\Gamma(\alpha+1)} + \xi_0\right)^2 + \left(\frac{cL}{3k^6} + \frac{\lambda u(0)}{6k^4}\right)\left(kx + \frac{ct^\alpha}{\Gamma(\alpha+1)} + \xi_0\right)^3 + \left(\frac{L^2}{8k^7} + \frac{\lambda L}{8k^6}\right)(kx + \frac{ct^\alpha}{\Gamma(\alpha+1)} + \xi_0)^4$$

$$u_3(x,t) = \left(\frac{cu(0)}{6k^6} + \frac{u^2(0)}{12k^5}\right)\left(kx + \frac{ct^\alpha}{\Gamma(\alpha+1)} + \xi_0\right)^3 + \left(\frac{cL}{12k^8} + \frac{\lambda u(0)}{24k^6}\right)\left(kx + \frac{ct^\alpha}{\Gamma(\alpha+1)} + \xi_0\right)^4 + \left(\frac{L^2}{40k^9} + \frac{\lambda L}{40k^8}\right)(kx + \frac{ct^\alpha}{\Gamma(\alpha+1)} + \xi_0)^5$$

⋮

And so on.
The solution of fractional damped Burger's equation is:

$$\begin{aligned} u(x,t) &= \sum_{i=0}^{\infty} u_i(x,t) = u_0(x,t) + u_1(x,t) + u_2(x,t) + u_3(x,t) + \cdots \\ &= u(0) + (\frac{L}{k^2})\left(kx + \frac{ct^\alpha}{\Gamma(\alpha+1)} + \xi_0\right) + \left(\frac{cu(0)}{k^2} + \frac{u^2(0)}{2k}\right)\left(kx + \frac{ct^\alpha}{\Gamma(\alpha+1)} + \xi_0\right) \\ &+ \left(\frac{cL}{k^4} + \frac{\lambda u(0)}{2k^2}\right)\left(kx + \frac{ct^\alpha}{\Gamma(\alpha+1)} + \xi_0\right)^2 + \left(\frac{L^2}{2k^5} + \frac{\lambda L}{2k^4}\right)(kx + \frac{ct^\alpha}{\Gamma(\alpha+1)} + \xi_0)^3 \\ &+ \left(\frac{cu(0)}{2k^4} + \frac{u^2(0)}{4k^3}\right)\left(kx + \frac{ct^\alpha}{\Gamma(\alpha+1)} + \xi_0\right)^2 + \left(\frac{cL}{3k^6} + \frac{\lambda u(0)}{6k^4}\right)\left(kx + \frac{ct^\alpha}{\Gamma(\alpha+1)} + \xi_0\right)^3 \end{aligned} \quad (8)$$

$$+\left(\frac{L^2}{8k^7}+\frac{\lambda L}{8k^6}\right)\left(kx+\frac{ct^\alpha}{\Gamma(\alpha+1)}+\xi_0\right)^4+\left(\frac{cu(0)}{6k^6}+\frac{u^2(0)}{12k^5}\right)\left(kx+\frac{ct^\alpha}{\Gamma(\alpha+1)}+\xi_0\right)^3$$
$$+\left(\frac{cL}{12k^8}+\frac{\lambda u(0)}{24k^6}\right)\left(kx+\frac{ct^\alpha}{\Gamma(\alpha+1)}+\xi_0\right)^4+\left(\frac{L^2}{40k^9}+\frac{\lambda L}{40k^8}\right)\left(kx+\frac{ct^\alpha}{\Gamma(\alpha+1)}+\xi_0\right)^5+\cdots$$

As a special case let $L=\lambda=u(0)=1$ and $\xi_0=0$. Then

$$u(x,t)=1+\left(\frac{1}{k^2}\right)\left(kx+\frac{ct^\alpha}{\Gamma(\alpha+1)}\right)+\left(\frac{c}{k^2}+\frac{1}{2k}\right)\left(kx+\frac{ct^\alpha}{\Gamma(\alpha+1)}\right)$$
$$+\left(\frac{c}{k^4}+\frac{1}{2k^2}\right)\left(kx+\frac{ct^\alpha}{\Gamma(\alpha+1)}\right)^2+\left(\frac{1}{2k^5}+\frac{1}{2k^4}\right)\left(kx+\frac{ct^\alpha}{\Gamma(\alpha+1)}\right)^3 \quad (9)$$
$$+\left(\frac{c}{2k^4}+\frac{1}{4k^3}\right)\left(kx+\frac{ct^\alpha}{\Gamma(\alpha+1)}\right)^2+\left(\frac{c}{3k^6}+\frac{1}{6k^4}\right)\left(kx+\frac{ct^\alpha}{\Gamma(\alpha+1)}\right)^3$$
$$+\left(\frac{1}{8k^7}+\frac{1}{8k^6}\right)\left(kx+\frac{ct^\alpha}{\Gamma(\alpha+1)}\right)^4+\left(\frac{c}{6k^6}+\frac{1}{12k^5}\right)\left(kx+\frac{ct^\alpha}{\Gamma(\alpha+1)}\right)^3$$
$$+\left(\frac{c}{12k^8}+\frac{1}{24k^6}\right)\left(kx+\frac{ct^\alpha}{\Gamma(\alpha+1)}\right)^4+\left(\frac{1}{40k^9}+\frac{1}{40k^8}\right)\left(kx+\frac{ct^\alpha}{\Gamma(\alpha+1)}\right)^5+\cdots$$

It is known that any interval $[a\,,b]$ is homeomorphic to $[0\,,1]$ by the transformation $t=(x-a)/(b-a)$.

Let the traveling wave solution (9) be a probability density function if:

$$\int_0^1\int_0^1 u(x\,,t)dxdt=1$$

$$1+\left(\frac{1+c}{k^2}+\frac{1}{2k}\right)\left(k+\frac{c}{\Gamma(\alpha+2)}\right)+\left(\frac{1}{2k^2}+\frac{1}{4k^3}+\frac{3c}{2k^4}\right)\left(\frac{k^2}{3}+\frac{ck}{\Gamma(\alpha+2)}+\frac{c^2}{(2\alpha+1)(\Gamma(\alpha+1))^2}\right)+\left(\frac{c}{6k^2}+\frac{2}{3k^4}+\frac{7}{12k^5}+\frac{c}{3k^6}\right)\left(\frac{k^3}{4}+\frac{ck^2}{\Gamma(\alpha+2)}+\frac{3kc^2}{2(2\alpha+1)(\Gamma(\alpha+1))^2}+\frac{c^3}{(3\alpha+1)(\Gamma(\alpha+1))^3}\right)$$
$$+\left(\frac{1}{6k^6}+\frac{1}{8k^7}+\frac{c}{12k^8}\right)\left(\frac{k^4}{5}+\frac{ck^3}{\Gamma(\alpha+2)}+\frac{2k^2c^2}{(2\alpha+1)(\Gamma(\alpha+1))^2}+\frac{2kc^3}{(3\alpha+1)(\Gamma(\alpha+1))^3}\right) \quad (10)$$
$$+\frac{c^4}{(4\alpha+1)(\Gamma(\alpha+1))^4}\Big)+\left(\frac{1}{40k^9}+\frac{1}{40k^8}\right)\left(\frac{k^5}{6}+\frac{ck^4}{\Gamma(\alpha+2)}+\frac{5k^3c^2}{2(2\alpha+1)(\Gamma(\alpha+1))^2}+\frac{10k^2c^3}{3(3\alpha+1)(\Gamma(\alpha+1))^3}\right.$$
$$\left.+\frac{5kc^4}{2(4\alpha+1)(\Gamma(\alpha+1))^4}+\frac{c^5}{(5\alpha+1)(\Gamma(\alpha+1))^5}\right)+\cdots=1$$

Now, let k = –1, $\alpha=\frac{9}{10}$ then by using numerical analysis (Newton-Raphson method) we find the value of c from equation (10) which has one solution

$$f(c)=-0.4292-0.4486c+0.0967c^2+0.5142c^3+0.0934c^4+0.0073c^5$$

c =1.0873

Substituting these values into (9) then the probability density function is:

$$u(x\,,t)=1-x+1.1302t^{\frac{9}{10}}-0.5873x+0.6638t^{\frac{9}{10}}+1.5873x^2-3.5881xt^{\frac{9}{10}}$$
$$+2.0278t^{\frac{9}{5}}+0.2937x^2-0.6639xt^{\frac{9}{10}}+0.2299t^{\frac{9}{5}}-0.5291x^3+0.7639t^{\frac{27}{10}}$$

$$+1.7940x^2t^{\frac{9}{10}} - 2.0278xt^{\frac{9}{5}} - 0.0979x^3 + 0.1413t^{\frac{27}{10}} + 0.3319x^2t^{\frac{9}{10}}$$
$$-0.3752xt^{\frac{9}{5}} + 0.1323x^4 + 0.2159t^{\frac{18}{5}} - 0.5981x^3t^{\frac{9}{10}} + 1.0141x^2t^{\frac{9}{5}}$$
$$-0.7641xt^{\frac{27}{10}}$$

Remark

We will choose the probability density functions $u_1^*(x)$ and $u_1^{**}(t)$ which satisfy the conditions $E(x) > 0$, $E(x^2) > 0$ and $E(x) > E(x^2)$, Also $E(t) > 0$, $E(t^2) > 0$ and $E(t) > E(t^2)$, $var(x) > 0$, $var(t) > 0$. The correlation coefficient lies in$[-1, 1]$.

$$u_1(x,t) = 1 - x + 1.1302t^{\frac{9}{10}} - 0.5873x + 0.6638t^{\frac{9}{10}} + 1.5873x^2 - 3.5881xt^{\frac{9}{10}}$$
$$+0.2937x^2 - 0.6639xt^{\frac{9}{10}} + 0.2299t^{\frac{9}{5}} - 0.5291x^3 + 0.7639t^{\frac{27}{10}}$$
$$+1.7940x^2t^{\frac{9}{10}} - 2.0278xt^{\frac{9}{5}} - 0.0979x^3 + 0.1413t^{\frac{27}{10}} + 0.3319x^2t^{\frac{9}{10}}$$
$$-0.3752xt^{\frac{9}{5}} + 0.1323x^4 + 0.2159t^{\frac{18}{5}} - 0.5981x^3t^{\frac{9}{10}} + 1.0141x^2t^{\frac{9}{5}}$$
$$-0.7641xt^{\frac{27}{10}}$$

(I) The moments

To evaluate the expected values $E(x)$, $E(t)$, $E(xt)$ and the second moments $E(x^2)$, $E(t^2)$ we need $u_1^*(x)$ and $u_1^{**}(t)$ .we find them as follows:

$$u_1^*(x) = \int_0^1 u_1(x,t)dt$$
$$= 1 - x + 0.5948 - 0.5873x + 0.3494 + 1.5873x^2 - 1.8885x + 0.2937x^2$$
$$-0.3494x + 0.0821 - 0.5291x^3 + 0.2065 + 0.9442x^2 - 0.7242x$$
$$-0.0979x^3 + 0.0382 + 0.1747x^2 - 0.1340x + 0.1323x^4 + 0.0469$$
$$-0.3148x^3 + 0.3622x^2 - 0.2065x$$

$$u_1^{**}(t) = \int_0^1 u_1(x,t)dx$$
$$= 1 - 0.5000 + 1.1302t^{\frac{9}{10}} - 0.2937 + 0.6638t^{\frac{9}{10}} + 0.5291 - 1.7941t^{\frac{9}{10}}$$
$$+0.0979 - 0.3319t^{\frac{9}{10}} + 0.2299t^{\frac{9}{5}} - 0.1323 + 0.7639t^{\frac{27}{10}} - 0.5980t^{\frac{9}{10}}$$
$$-1.0139t^{\frac{9}{5}} - 0.0245 + 0.1413t^{\frac{27}{10}} + 0.1106t^{\frac{9}{10}} - 0.1876t^{\frac{9}{5}} + 0.0265$$
$$+0.2159t^{\frac{18}{5}} - 0.1495t^{\frac{9}{10}} + 0.3380t^{\frac{9}{5}} - 0.3821t^{\frac{27}{10}}$$

(1) Expected Value of x

$$\mathrm{E}(x) = \int_0^1 x u_1^*(x)dx$$
$$= 0.2035$$

(2) Expected Value of t

$$\mathrm{E}(t) = \int_0^1 t u_1^{**}(\mathrm{t})d\mathrm{t}$$
$$= 0.4127$$

It means that the first expected length of the wave is concentrated at value 0.2035, which is the middle of the wave which agrees with nature.

Also the first expected time of wave is concentrated at 0.4127, which means that the wave takes a long time which agrees with nature.

(3) The Second Moment of x

$$\mathbf{E}(x^2)=\int_0^1 x^2 u_1^*(x)dx$$
$$= 0.0843$$

(4) The Second Moment of t

$$\mathbf{E}(t^2) = \int_0^1 t^2 u_1^{**}(t)dt$$
$$= 0.2850$$

$\mathrm{E}(x) > \mathrm{E}(x^2)$ shows that the first wave is stronger than the second.

The second expected length of the wave is concentrated at 0.0843, which means that the length begins to disperse (scatter) which agrees with nature.

The second expected time of the wave is concentrated at 0.2850, which means that the wave stay for a short time which agrees with nature.

(5) The Expected Value of xt

$$\mathbf{E}(xt) = \int_0^1 \int_0^1 xt\, u_1(x,t)dxdt$$
$$= 0.0791$$

This joint expected value for length and time of the wave is 0.0791, which means short wave and which agrees with nature.

(II) The Variance

(1) Variance of x

$$\sigma_x^2 = E(x^2) - [\mathrm{E}(x)]^2$$
$$= 0.0429$$

(2) Variance of t

$$\sigma_t^2 = E(t^2) - [\mathrm{E}(t)]^2$$
$$= 0.1147$$

The variation for length of wave is 0.0429, so that the separation is very small. This means that the power of the wave is focused in the middle of the wave and separation begins from the first wave which agrees with nature.

The variation for time of wave is 0.1147, so that the separation is small. This means that the time of a separated wave begins from the first wave and so on which agrees with nature.

(III) The Covariance

$$Cov(x,t) = \mathrm{E}(xt) - \mathrm{E}(x)\mathrm{E}(t)$$
$$= -0.0048$$

The range of deviation of the length and time of the wave from its expected values is very small which agrees with nature.

(IV) The Correlation Coefficient

$$\rho = \frac{cov(x,t)}{\sqrt{var(x)}\sqrt{var(t)}}$$
$$= -0.0685$$

This means that the relation between the amplitude of the wave and time is strong (high amplitude corresponding to the beginning of the wave in terms of length and time) and vice versa which agrees with nature.

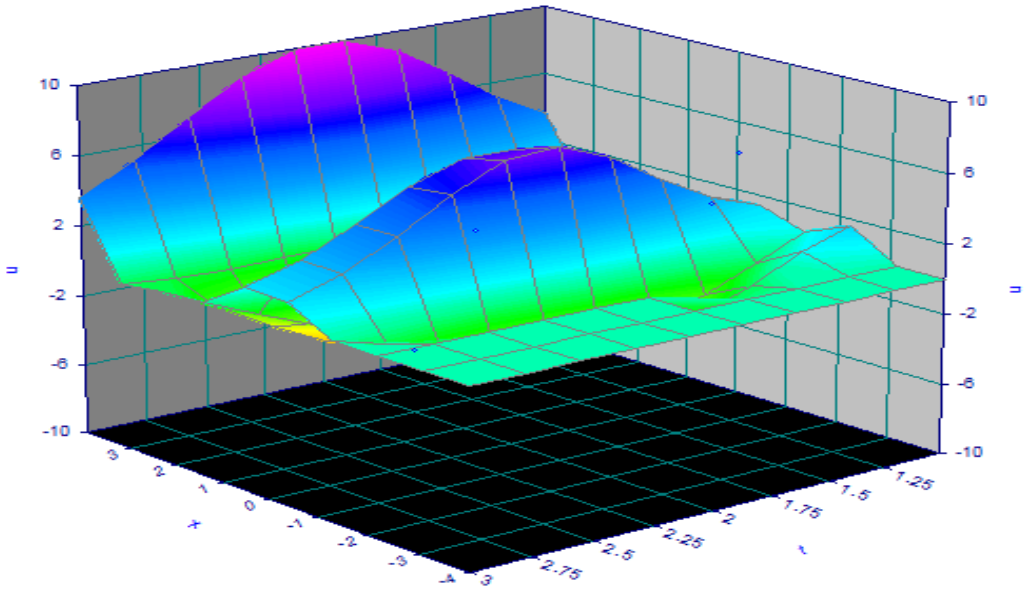

Figure 1 represents the traveling wave solution when –4< x < 4, 1 < t <3 and –10< u <10.

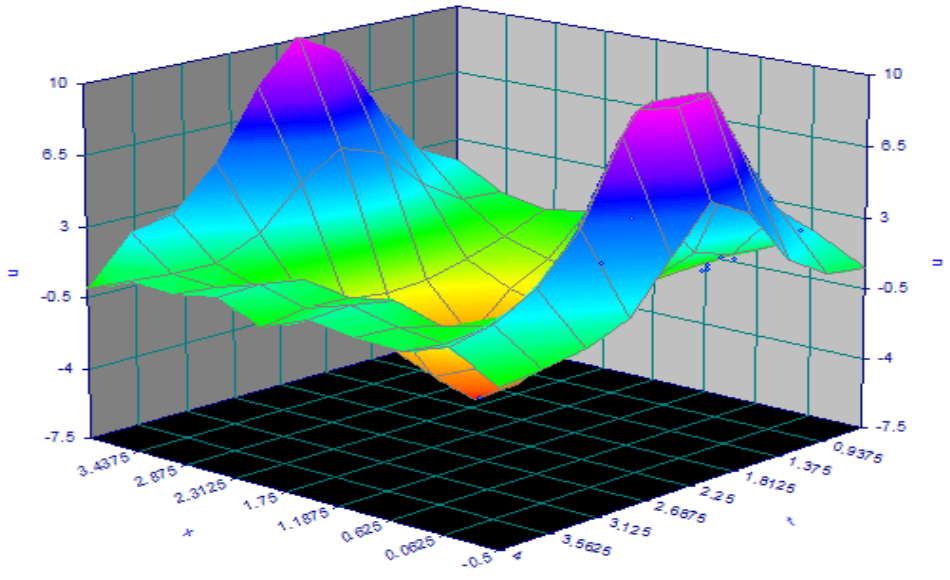

Figure 2 represents the traveling wave solution when –0.5< $\boldsymbol{x}$ < 4, 0.5 < $\boldsymbol{t}$ < 4 and –7.5< $\boldsymbol{u}$< 10.

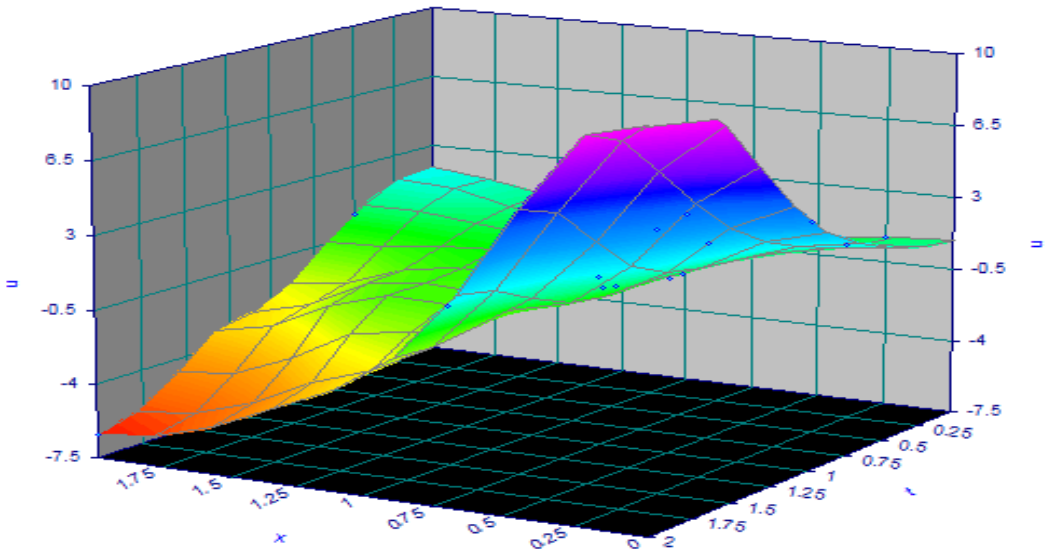

Figure 3 represents the traveling wave solution when $0< \boldsymbol{x} < 2$, $0 < \boldsymbol{t} < 2$ and $-7.5< \boldsymbol{u}< 10$.

References

[1] Bateman H., Some Recent Researches on the Motion of Fluids, Mon. Weather Rev., (1915), Vol. **43**, Issue 4, pp. 163-170.

[2] Blazer J. and Aminikhah H., Exact and Numerical Solutions for Nonlinear Burgers Equation by VIM, Mathematical and Computing Modeling, (2009),Vol. **49**, Issue 7-8, pp. 1394-1400.

[3] Burger J. M., A Mathematical Model Illustrating the Theory of Turbulence, Adv. Appl. Mech., (1948), Vol. **1**, pp. 171-199.

[4] Caputo M., ,Linear Models of Dissipation Whose Q is Almost Frequency Independent, Part II, *J. Roy. Austral. Soc*.**13**. (1967), PP. 529-539.

[5] Cole J. D ,On a Quasi Linear Parabolic Equations Occurring in Aerodynamics, *Quart. Appl. Math*., (1951), Vol. **9**, No. 3, pp. 225-236.

[6] Gorguis A., A Comparison between Cole-Hopf Transformation and Decomposition Method for Solving Burgers Equations, Applied Mathematics and Computation, (2006), Vol. **173**, No. 1, pp. 126-136.

[7] Inc M., The Approximate and Exact Solutions of the Space-and Time-Fractional Burgers equations with Initial Conditions by Variational Iteration Method , *J. Math. Anal. Appl,* (2008), Vol. **345**, No. 1, PP. 476-484.

[8] Kurulay M., The Approximate and Exact Solutions of the Space- and Time-Fractional Burgers Equations, (2010), Ijrras, Vol. **3**, No. 3, pp. 257-263.

[9] Maleknejad K., Babolian E., Shaerlar A.J. and Jahnagir M., Operational Matrices for Solving Burgers Equation by Using Block-Pulse Functions with Error Analysis,*Australian journal of Basic and Applied Sciences.* (2011), Vol. **5**, PP. 602-609.

[10] Momani S., Non-Perturbative Analytical Solutions of the Space-and Time-Fractional Burgers Equations, Chaos, Solutions and Fractals, (2006), Vol. **28**, No. 4, pp. 930-937.

[11] Pandey K. and Verma L., A Note on Crank Nicolson Scheme for Burgers Equation, Applied Mathematics, (2011), Vol. **11**, pp. 883-889.
[12] Rahman M., Integral Equations and their Applications, WIT press, Southampton, Boston(2007).
[13] Samko SG. , Kilbas AA.and Marichev OI., Fractional Integrals and Derivatives: Theory and Applications, Yverdon: Gordon and Breach(1993).
[14] Wang Qi. ,Homotopy Perturbation Method for Fractional KdV-Burger's Equation, Chaos, Solutions and Fractals. (2008), Vol. **35**, No. 5, PP. 843-850.

Using the Ridge Regression Procedures to Estimate the Multiple Linear Regression Coefficients

Using the Ridge Regression Procedures to Estimate the Multiple Linear Regression Coefficients

HazimMansoorGorgees[1] ,FatimahAssim Mahdi[2]

[1]Baghdad University, College of Pure Science, Ibn Al-Haithem
[2]Baghdad University, College of Pure Science, Ibn Al-Haithem

fatima_assim92@yahoo.com, hazim5656@yahoo.com

Abstract. This article concerns with comparing the performance of different types of ordinary ridge regression estimators that have been already proposed to estimate the regression parameters when the near exact linear relationships among the explanatory variables is presented. For this situations we employ the data obtained from tagi gas filling company during the period (2008-2010). The main result we reached is that the method based on the condition number performs better than other methods since it has smaller mean square error (MSE) than the other stated methods.

Keywords : Ordinary ridge regression, Ridge Parameter, Multicollinearity, Condition number, mean square error (MSE).

1.Introduction

Let us consider the classical linear regression model $y = X\beta + \varepsilon$ (1)

Where y is (n×1) vector of response variable X is (n×p) matrix of explanatory variables , β is (p×1) vector if unknown parameters and ε is (n×1) vector of unobservable random errors where $E(\varepsilon) = 0$, $var(\varepsilon) = \sigma^2 I$

The problem of multicollinearity occurs when there exist a linear relationship or an approximate linear relationship among two or more explanatory variables. It can be thought of as a situation where two or more explanatory variables in the data set move together, as a consequence it is impossible to use this data set to decide which of the explanatory variables produced the observed variation in the response variable. Indicators of multicollinearity include a very high correlation among two or more explanatory variables, a very small (near zero) eigen values of the correlation matrix of explanatory variables, a too large condition numbers. and the Farrer- Gloubar test based on the χ^2 statistic.

2.Ordinary Ridge Regression Estimator

The most popular method that been proposed to deal with the multicollinearty problem is the ordinary ridge regression estimation method which is a modification of ordinary least squares method to allow biased estimators of regression coefficients. The ridge estimator depend completely upon an exogenous parameter (k say) known as ridge parameter.

For any $k \geq 0$, the corresponding ordinary ridge regression estimator denoted by b_{ORR} is defined as

$$b_{ORR} = (X'X + k)^{-1} X'y \quad (2)$$

Where the ridge parameter k ≥ 0 is a constant selected by the researcher a ccording to some intuitively plausible criteria put forward by Hoerl and Kennard [1].

3.The choice of Ridge Parameter

The ordinary ridge regression estimator does not provide a unique solution to the multicollinearity problem, instead, it provides a class of solutions which depend upon the ridge parameter k. No explicit optimum value can be found for k. Yet, several stochastic choices have been proposed for this parameter. Some of these choices may be summarized as follows

Hoerl and Kennard (1970) suggested a graphical method called ridge trace to select the value of the ridge parameter [1]. When viewing the ridge trace the analyst picks the value of k for which the regression coefficients have stabilized. Often, the regression coefficients will vary widely for small values of k and then stabilize. One have to choose the smallest value of k (which introduces the smallest bias) after which the regression coefficients have seem to be constant.

Hoerl, kennard and Baldwin (1975) proposed a new approach to select the value of the ridge parameter as follows [1].

$$\hat{k}_{HKB} = \frac{\rho s^2}{b'_{OLS}\, b_{OLS}} \quad (3)$$

Where P is the number of explanatory variables, s^2 is the OLS estimator of σ^2 and b_{OLS} is the ordinary least squares estimator of the vector β.

Lawless and wang (1976) suggested choosing the value of k by employing the formula [2].

$$\hat{k}_{LW} = \frac{\rho s^2}{b'_{OLS}\, X'X\, b_{OLS}} \quad (4)$$

Assuming that the regression coefficients vector β has a certain prior distributions srivastava (2002) followed Bayesian approach to estimate the ridge parameter [2]. He concluded that is

$$\hat{k}_{Bayes} = Max[0, \frac{tr(X'X)}{[\frac{n-p-3}{n-p-1}(\frac{b'_{OLS}\, X'X\, b_{OLS}}{s^2} - P]}] \quad (5)$$

Where tr(X'X) denote the trace of the matrix X'X [4].

Gorgees, H. M. and Mahdi, F.A.(2017) utilized the concept of condition number to select the ridge parameter [5].

The condition number is defined to be the ratio of the largest to the smallest singular value of the matrix X of explanatory variables [5].

The proposed estimator denoted as $\hat{k}_{CN}$ is defined to be

$$\hat{k}_{CN} = Max[0, \frac{\rho s^2}{b'_{OLS}\, b_{OLS}} - \frac{1}{CN}] \quad (6)$$

Where CN refferd to the condition number.

Numerical Example

In this section we apply the procedures already discussed making use of the data obtained from Tagi gas filling company through the time period 2008-2016 .

We want to assess the effects of four explanatory variable x_1, x_2, x_3, x_4 on the response variable y , where y represents the annual output of liquid gas cylinders and the explanatory variables x_1, x_2, x_3, x_4 refer to craftsmen, adminstrators, technicians and engineers respectively. The following linear regression model is assumed to specify the relationship between the response variable and the explanatory variables

$$y_i = \beta_0 + \beta_1 x_{i1} + \beta_2 x_{i2} + \beta_3 x_{i3} + \beta_4 x_{i4} + \varepsilon_i \qquad (7)$$

Table (1). Values of the explanatory variables x_1, x_2, x_3, x_4 and the response variable y

Y	X_1	X_2	X_3	X_4
29024876	2186	490	1673	312
29024876	2184	464	1673	325
28259383	2397	510	1836	357
31691496	2552	544	1955	380
32655027	2575	549	1973	383
33691061	2828	604	2166	421
35441678	2787	593	2135	415
36872615	2929	624	2244	436
39256145	3297	702	2524	490

Table (2). Descriptive Statistics

variable	N	Minimum	Maximum	Mean	Standard .Deviation
Y	9	28259383	39256145	32879684.11	3813683.112
X_1	9	2184	3297	2637.222	363.51127
X_2	9	464	702	564.4444	74.2460
X_3	9	1673	2524	2019.889	278.35249
X_4	9	312	490	391	56.16939

Table (3). Matrix of Correlation coefficients

	Y	X_1	X_2	X_3	X_4
Y	1.0000	0.9578	0.9596	0.9578	0.9498
X_1	0.9578	1.0000	0.9951	1.0000	0.9974

X_2	0.9596	0.9951	1.0000	0.9949	0.9855
X_3	0.9578	1.0000	0.9949	1.0000	0.9976
X_4	0.9498	0.9974	0.9855	0.9976	1.0000

Table (4). Analyses of eigenvalues for correlation and matrix condition numbers

Eigen value	Condition numbers
31.882165	1
0.117604	271.0976
0.000219	145580.7
0.000009	3542462.8

Table (5). Eigenvectors of correlation matrix

X_1	X_2	X_3	X_4
-0.5670	0.0527	1.08514	0.5009
0.4087	-0.7635	-1.11670	0.4988
-0.4183	0.0697	1.10856	0.5009
0.5800	0.6398	-1.11163	0.4994

Table (6). ANOVA in case of OLS

Source	d.f	Sum of squares	Mean square	F test
Regression	4	7.793412	1.948353	37.724434
Residual	4	0.206587	0.051646	

Total	8	8		

Table (7). ANOVA in case of $b_{k_{HKB}}$

Source	d.f	Sum of squares	Mean square	F test
Regression	4	7.714816	1.928704	27.052126
Residual	4	0.285183	0.071295	
Total	8	8		

Table (8). ANOVA in case of $b_{k_{LW}}$

Source	d.f	Sum of squares	Mean square	F test
Regression	4	7.370573	1.842643	11.709980
Residual	4	0.629426	0.157356	
Total	8	8		

Table (9). ANOVA in case of $b_{k_{Bayes}}$

Source	d.f	Sum of squares	Mean square	F test
Regression	4	7.304121	1.826030	10.496257
Residual	4	0.695878	0.173969	
Total	8	8		

Table (10). ANOVA in the case of $b_{k_{CN}}$

Source	d.f	Sum of squares	Mean square	F test

Regression	4	7.603587	1.900896	19.180991
Residual	4	0.396412	0.099103	
Total	8	8		

4.Conclusions and Discussion

Many indicators ensure the presence of malticollinearity problem such as the large values of the correlation coefficients as it is shown in table (3) moreover the very small eigenvalues (near zero) which imply a very large condition number as it is displayed in table (4) .

The ANOVA tables displayed that the ordinary ridge regression estimator based on $\hat{k}_{HKB}$ is the best followed by the estimator based on the condition number $\hat{k}_{CN}$ in the sense of residual mean square as it is shown (6),(7),(10),(8),(9).

For the purpose of future works we can use other methods to overcome to the multicollinearity problem such as the generalized inverse estimator, Liu estimator, the restricted ridge regression estimator and Jackknife ridge regression estimator.

References

[1] Hoerl, A.E. and Kennard, R.W. (1970); " Ridge Regression Biased Estimation for Non orthogonal problems " ,Techno metrics, Vol.12,pp 55-67.

[2] Srivastava, M.S.(2002); "Methods of Multivariate Statistics", Wiley, New York.

[3] Pasha, G.R., Shah, M.A. and Ghosia (2004);"Estimation and Analysis of Regression Coefficients When Explanatory Variables are Correlated", *Journal of Research (Science)* ,Vol.15,No.1,pp 97-100.

[4] Lindley, D.V. and Smith, A. F. M.(1972); "Bayes Estimators for Linear Models (with Discussions)", *J. Roy. Statist. Soc.* B 34, pp 1-41.

[5] Gorgees, H. M. and Mahdi, F.A. (2017); "An Alternative Approach for Selecting Ridge Parameter for Ordinary Ridge Regression Estimator*", International Journal of Science and Research (IJSR).*ISSN 2319-7064.

Fibrewise soft ideal topological space

Fibrewise soft ideal topological space

Yousif Y Yousif *, Mohammed A H Ghafel**

Department of Mathematics, College of Education for Pure Science (Ibn Al-haitham), Baghdad University, Baghdad-Iraq.

*yoyayousif@yahoo.com, **h0142164@gmail.com

Abstract. In this work we explain and discuss new notion of fibrewise topological spaces, calledfibrewise soft ideal topological spaces, Also, we show the notions of fibrewise closed soft ideal topological spaces, fibrewise open soft ideal topological spaces and fibrewise soft near ideal topological spaces.

Keywords. Soft set, soft continuous, soft ideal, fibrewise soft ideal topological spaces, fibrewise closed soft ideal topological spaces, fibrewise open soft ideal topological spaces, fibrewise soft near ideal topological spaces.

1. Introduction and Preliminaries.

To begin with our work in the type of fibrewise sets over a given set, called the base set. If the base set is denoted by$B$, then a fibrewise set over B consists of a set H together with a function$P : H \to B$, called the projection. For all point b of B the fibre over b is the subset $H_b = P^{-1}(b)$ of H; fibres may be empty because we do not require P to be surjective, in addition for all subset B^* of B we consider $H_{B^*} = P^{-1}(B^*)$ as a fibrewise set over B^* with the projection determined by P.Molodtsov [23] generalized with the introduction of soft sets the traditional concept of a set in the classical researches. With the introduction of the applications of soft sets [22], the soft set theory has been the research topic and has received attention gradually [5, 19, 24, 26]. The applications of the soft sets are redetected so as to develop and consolidate this theory, utilizing these new applications; auni-int decision-making method was established [7]. Numerous notions of general topology were involved in soft sets and then authors developed theories about soft topological spaces. Shabir and Naz [28] mentioned this term to define soft topological space. After that definition, I. Zorlutuna et al. [34], Aygunoglu et al. [6] and Hussain et al. [15] continued to search the properties of soft topological space.This topic has an excellent potential for applications in many branches of mathematics. In 1990, Jankovic and Hamlett [17] using a specific topological τ introduced another topological$\tau^*(I)$, which satisfies$\tau \subset \tau^*(I)$. In 1952, Hashimoto [12, 13] introducing the concept of ideal continuity. Then Jankovic and Hamlett [11] introduced I-open set in ideal topological spaces. Future, Abd El-Monsef [1] defined I-continuity for functions**.** The notion of soft ideal was first given by R. Sahin and A. Kucuk [27]. Kale and Guler [18] introduced the concept of soft ideal and discuss the properties thesoft ideal topological space. The purpose of this paper is introduced a new class of fibrewise topology called fibrewise soft ideal topological space are introduced and few of their properties are investigated, we built on some of the result in [2, 20, 29, 30, 31, 32, 33].

Definition 1.1. [16]Let$H$ and K be afibrewise sets over B, with projections $P_H : H \to B$ and$P_K : K \to B$, respectively, a function $\phi : H \to K$ issaid to befibrewise if $P_K \circ \phi = P_H$, in other words if $\phi(H_b) \subset K_b$for all point b of B.
Note that a fibrewise function $\phi : H \to K$ over Blimitedsby restriction, a fibrewise function $\phi_{B^*} : H_{B^*} \to K_{B^*}$ over B^* for all subset B^* of B .

Definition 1.2.[23] Let$H$ be an initial universe and E be a set of parameters. Assume that$P(H)$denote the power set of H and E be a non-empty subset of A. A pair (F, E) is called a soft set over H, where F is a function given by $F : E \to P(H)$. In other words, a soft set over H is a parameterized familyof subset of the universe H.For $\varepsilon \epsilon E$, $F(\varepsilon)$may be considered like the set of ε_approximate elements of the soft set (F, E). observe that the set of all soft sets over H will be denoted by $S(H)$.

Example 1.3. [23] Assume that we have six houses in the universe $H = \{h_1, h_2, h_3, h_4, h_5, h_6\}$ under consideration, and that $A = \{e_1, e_2, e_3, e_4, e_5\}$ is a set of decision parameters. The $e_i (i = 1, 2, 3, 4, 5)$ stand for the parameters ''expensive'', ''beautiful'', ''wooden'', ''cheap'', and ''in green surroundings'', respectively. Consider the functionF_A given by ''houses (.)''; (.) is to be filled in by one of the parameters $e_i \in A$. For instance,$F_E(e_1)$ means''houses (expensive)'', and its functional value is the set $\{h \in H : h$ is an expensive house$\}$. Assume that $E = \{e_1, e_3, e_4\} \subset A$ and $F_E(e_1) = \{h_1, h_4\}$, $F_E(e_3) = H$,and $F_E(e_4) = \{h_1, h_3, h_5\}$. Then, we can view the soft set F_E like consisting of the next collection of approximations:$F_E = \{(e_1, \{h_2, h_4\}), (e_3, H), (e_4, \{h_1, h_3, h_5\})\}$.

Definition 1.4.[22] A soft set (F, E) over H is said to be a null soft if $F(e) = \Phi$ for all $e \in E$ and this denoted by $\widetilde{\Phi}$. Also, (F, E) is said to be an absolute soft set if $F(e) = H$, for all $e \in E$ and this denoted by $\widetilde{H}$.

Definition 1.5.[22]

(a) The union of two soft sets of $(F, A)$and (G, B)over the common universe $H$is the soft set (L, C), where$C = A \cup B$and for all $e \in C$,

$$L(e) = \begin{cases} F(e) & if\ e \in A - B \\ G(e) & if\ e \in B - A \\ F(e) \cup G(e) & if\ e \in A \cap B \end{cases}$$

We write $(F, A) \ \widetilde{\cup}\ (G, B) = (L, C)$.

(b) The intersection (L, C) of two soft sets (F, A), (G, B) over a common universe H, denoted by $(F, A) \ \widetilde{\cap}\ (G, B)$, is defined as $C = A \cap B$, and $H(e) = F(e) \cap G(e)$for all $e \in C$.

Definition 1.6. [28] Let τ be the collection of soft sets over H, then τ is said to be a soft topology on H if
(a) $\widetilde{\Phi}, \widetilde{H} \ \widetilde{\in}\ \tau$
(b) the union of any number of soft sets in τ belongs to τ
(c) the intersection of any two soft sets in τ belongs to τ.

The triplet $(H, \tau, E)$is called a soft topological space over H.The members of τ are called soft open sets in H. Also, a soft set (F, A) is called a soft closed if the complement $(F, A)^c$ belongs to τ.

Example 1.7.[28]Let $H = \{h_1, h_2, h_3\}$, $E = \{e_1, e_2\}$ and $\tau = \{\widetilde{\Phi}, \widetilde{H}, (F_1, E), (F_2, E), (F_3, E), (F_4, E)\}$ where $(F_1, E), (F_2, E), (F_3, E), (F_4, E)$ are soft sets over H,defined asthe following
$F_1(e_1) = \{h_1\}$, $F_2(e_2) = \{h_1\}$,
$F_2(e_1) = \{h_2, h_3\}$, $F_2(e_2) = \{h_1, h_2\}$,
$F_3(e_1) = \{h_1, h_2\}$, $F_3(e_2) = H$,
$F_4(e_1) = \{h_1, h_2\}$, $F_4(e_2) = \{h_1, h_3\}$.

Then τ defines a soft topology on $H$and hence $(H,\tau,E)$is a soft topological space over.

Definition 1.8. [25]

(a) A soft set (F,E) over $H$is said to be a soft element if $\exists e \in E$such that $F(e)$ is a singleton, say,$\{h\}$and $(e') = \Phi$, $\forall e'(\neq e) \in E$. Such a soft element is denoted by F_e^h. For simplicity of notation we denote such soft element as $\tilde{h}$. Let $SE(H,E)$ be the set of all soft elements of the universal set H.

(b) A soft set (F,E) is said to be a soft neighbourhood (briefly soft nbd) of the soft set (L,E) if there exists a soft set $(G,E) \,\widetilde{\in}\, \tilde{\tau}$such that $(L,E) \,\widetilde{\subseteq}\, (G,A) \,\widetilde{\subseteq}\, (F,E)$. If $(L,E) = \tilde{h}$, then (F,E) is said to be a soft nbdof the soft element $\tilde{h}$. The soft neighbourhood system of soft element $\tilde{h}$, denoted by$N(\tilde{h})$, is the family of all its soft neighbourhood. The soft open neighbourhood system of soft element $\tilde{h}$, denoted by $V(\tilde{h})$, is the family of all its soft open neighbourhood.

Definition 1.9.[28]

Let $(H,\tilde{\tau},E)$ be a soft topological space and (F,E) be a soft set over H. Then, the soft closure of (F,E), denoted $\overline{(F,E)}$, is defined as the soft intersection of all soft closed super sets of (F,E).

Note that $\overline{(F,E)}$ is the smallest soft closed set that containing(F,E).

Definition 1.10.[8]

(a) Let $(H,\tilde{\tau},E)$ be a soft topological space over H and Kbe a non-empty subset of H, then the collection $\tau_K = \{\widetilde{K} \,\widetilde{\cap}\, (F,E)\colon (F,E) \,\widetilde{\in}\, \tilde{\tau}\}$ is called a soft subspace topology on K. Hence, (K,τ_K,E) is called a soft topological subspace of (H,τ,E).

(b) A soft basis of a soft topological space (H,τ,E) is a subcollection $\widetilde{\mathcal{B}}$ of τ such that every element of τ can be expressed as the union of elements of $\widetilde{\mathcal{B}}$.

Definition 1.8. [10] A soft ideal I is a nonempty collection of soft sets over H if

(a) If $(F,E) \,\widetilde{\in}\, I$, $(G,E) \,\widetilde{\subset}\, (F,E)$, then$(G,E) \,\widetilde{\in}\, I$

(b) If$(F,E) \,\widetilde{\in}\, I$, $(G,E) \,\widetilde{\in}\, I$,then $(F,E) \,\widetilde{\cup}\, (G,E) \,\widetilde{\in}\, I$.

A soft topological space (H,τ,E) with a soft ideal $I$is said to be soft ideal topological space and denoted by (H,τ,E,I).

Definition 1.9. [10]Let(F,E)be a soft set in a soft ideal topological space (H,τ,E,I) and $(\cdot)^*$ be a soft operator from $S(H)$ to $S(H)$. Then the soft local function of (F,E) defined by $(F,E)^*(I,\tau)$ = $\{\tilde{h}\colon (U,E) \,\widetilde{\cap}\, (F,E) \,\widetilde{\notin}\, I$ for every $(U,E) \,\widetilde{\in}\, \tilde{V}(\tilde{h})$ denoted by $(F,E)^*$ simply. Moreover, the soft set operator Cl^* is said to be a soft * −closure and is defined as $Cl^*(F,E) = (F,E) \,\widetilde{\cup}\, (F,E)^*$ for a soft subset(F,E).

Definition 1.10. [21] Let H and K be two non-empty sets and E be the parameter set. Let$\{f_e : H \to K, e \in E\}$ be a collection of functions. Then a function $\tilde{f} : \mathrm{SE}(H,E) \to \mathrm{SE}(K,E)$ defined by $\tilde{f}(e_h) = e_{f_e(h)}$ is called a soft function, where $\mathrm{SE}(H,E)$ and $\mathrm{SE}(K,E)$ are sets of all soft elements of the soft sets $\widetilde{H}$ and $\widetilde{K}$ respectively.

Definition 1.11. [3]

(a) A soft subset (F,E) of an soft ideal topological space $(H,\tilde{\tau},E,I)$ is a soft I-open (briefly S.I-open) if $(F,E) \,\widetilde{\subseteq}\, int(F,E)^*$.

(b) A soft subset (F,E) of a soft ideal topological space $(H,\tilde{\tau},E,I)$ is a soft I-closed (briefly S.I-closed) if it is complement is a soft I-open.

(c) A soft function $\phi : (H, \tilde{\tau}, E, I) \to (K, \tilde{\sigma}, L)$ is said to be an soft ideal continuous (briefly S.I-continuous) if the inverse image of every soft open set of K is a soft I-open set in H.
(d) An soft ideal topological space $(H, \tilde{\tau}, E, I)$ is said to be a soft near I-compact (briefly S.j.I-compact) if for every soft near ideal open caver (briefly S.j.I-open cover) $\{(W_i, E_i): i \in \Delta\}$ of H, there exists a finite subset Δ_o of Δ such that $\tilde{H} - \{(W_i, E_i): i \in \Delta_o\} \in I$, where $j \in \{\alpha, S, P, b, \beta\}$.[4]

Lemma 1.12.[3]For any S.I-open set (F, E) of a space (H, τ, E, I), we have $(F, E)^* = (int(F, E)^*)^*$.

Definition 1.13.A subset $A$of an ideal topological space H is said to be
(a) α-I-open set [14] if $A \subset int\,(Cl^*(int(A)))$.
(b) pre-I-open set [1]if $A \subset int(Cl^*(A))$.
(c) sime-I-open set [14]if$A \subset Cl^*(int(A))$.
(d) b-open set [9] if$A \subset Cl^*(int(S)) \cup int(Cl^*(A))$.
(e) β-I-open set [14] if$A \subset Cl^*(int(Cl^*(A)))$.

Lemma 1.14. [3]For every soft function$\phi : (H, \tau, E, I) \to (K, \sigma, L)$, $\phi(I)$is an soft ideal continuous over$K$.

2- FIBERWISE SOFT IDEAL TOPOLOGICAL SPACES

During this section, we introduced a definition of fibrewise soft ideal topological space and its related properties.

Definition 2.1. Assume that (B, Ω, G) is a soft topology space the fibrewise soft ideal topology space (briefly, F.W.S.I-topological space) on a fibrewise set H over Bmeany any soft ideal topology space on H for which the projection function is S.I-continuous.

F.W.S. topological space and F.W.S.I-topological space this two concepts areThe following examples explain that.

Example 2.2. Let (H, τ, E, I) be a F.W.S.I-topological space over (B, Ω, G) given as follows : $H = \{h_1, h_2, h_3, h_4\}$, $E = \{e\}$, $\tau = \{\tilde{\Phi}, \tilde{H}, \{(e, \{h_3\})\}, \{(e, \{h_1, h_2\})\}, \{(e, \{h_1, h_2, h_3\})\}\}$, $I = \{\tilde{\Phi}, \{(e, \{h_1\})\}\}$, $B = \{a, b, c, d\}$, $G = \{g\}$, $\Omega = \{\tilde{\Phi}, \tilde{B}, \{(g, \{b, c, d\})\}\}$. Furthermore, assume that$f : H \to B$, $f(h_1) = a$, $f(h_2) = b$,$f(h_3) = c$, $f(h_4) = d$,$u : E \to G$, $u(e) = g$. Then the soft function $P_{fu} : (H, \tau, E, I) \to (B, \Omega, G)$ is soft I – continuous but is not soft continuous. Thus, (H, τ, E, I) is F.W.S.I-topological space but not F.W.S.topological space.

Example 2.3. Let(H, τ, E, I)be a F.W.S.I-topological space over (B, Ω, G) given asfollows: $H = \{h_1, h_2, h_3, h_4\}$, $E = \{e\}$, $\tau = \{\tilde{\Phi}, \tilde{H}, \{(e, \{h_4\})\}, \{(e, \{h_1, h_3\})\}, \{(e, \{h_1, h_3, h_4\})\}$,$I = \{\tilde{\Phi}, \{(e, \{h_3\})\}, \{(e, \{h_4\})\}, \{(e, \{h_3, h_4\})\}\}$, $B = \{a, b, c, d\}$, $G = \{g\}$, $\Omega = \{\tilde{\Phi}, \tilde{B}, \{(g, \{a, c, d\})\}\}$. Furthermore, assume that$f : H \to B$, $f(h_1) = a$, $f(h_2) = b$,$f(h_3) = c$, $f(h_4) = d$,$u : E \to G$, $u(e) = g$. Then the soft function $P_{fu} : (H, \tau, E, I) \to (B, \Omega, G)$ is soft continuous but is not S.I-continuous. Thus, (H, τ, E, I) is F.W.S. topological space but not F.W.S.I-topological space.

Proposition 2.4. The following statements are equivalent.
(a) $(H, \tau, E, I)$is F.W.S.I-topological space over (B, Ω, G),
(b) For each soft element in (H, τ, E) and each soft open in (B, Ω, G)containing the image of soft element, there exist S.I-open of(H, τ, E, I) containing soft element such that the image of S.I-open containing in soft open,
(c) For each soft element in (H, τ, E) and each soft open in (B, Ω, G) containing the image of soft element, $(H_{(M,G)})^*$is nbd of soft element.

Proof.(a)⇔(b)Suppose that (H, τ, E, I) is F.W.S.I-topological space over (B, Ω, G), then there exist the projection function$P_{fu}: (H, \tau, E, I) \to (B, \Omega, G)$is S.I-continuous. To proof For each soft element in (H, τ, E) and each soft open in (B, Ω, G) containing the image of soft element, there exist S.I-open of

(H,τ,E,I) containing soft element such that the image of S.I-open containing in soft open, since $(M,G)\ \tilde{\in}\ \Omega$ containing $P_{fu}(\tilde{h})$, then by (a) $H_{(M,G)}$ is S.I-open in H. By taking $(F,E)=H_{(M,G)}$ which containing $P_{fu}(\tilde{h})$, thus $P_{fu}(F,E)\ \tilde{\subseteq}\ (M,G)$.
(b)⇒(c) Sincesoft open in (B,Ω,G) containing the image of soft element, then by (b) there exists (F,E) is S.I-open of (H,τ,E,I)containing $P_{fu}(\tilde{h})$, such that $P_{fu}(F,E)\ \tilde{\subseteq}\ (M,G)$. So$\tilde{h}\ \tilde{\in}\ (F,E)\ \tilde{\subseteq}\ int((F,E)^*)\ \tilde{\subseteq}\ int(H_{(M,G)})^*\ \tilde{\subseteq}\ (H_{(M,G)})^*$. Hence $(H_{(M,G)})^*$is anbd of $\tilde{h}$.
(c)⇒(a) Since soft open in (B,Ω,G) containing the image of soft element, then by (c) $(H_{(M,G)})^*$is a softnbd of$\tilde{h}$, then there exist a soft set $(F,E)\ \tilde{\in}\ \tau$ such that $\tilde{h}\ \tilde{\in}\ (\mathrm{F,E})\ \tilde{\subseteq}\ (\mathrm{H_{(M,G)}})^*$, then $H_{(M,G)}$ is S.I-open, then P_{fu} is S.I-continuous, thus $(H,\tau,E,I)$is F.W.S.I-topological spaces.

Proposition 2.5.$(H,\tau,E,I)$is F.W.S.I-topological space over (B,Ω,G) if and only if the graph soft function $g:(H,\tau,E)\to(H,\tau,E)\times(B,\Omega,G)$, defined by $g(\tilde{h})=(\tilde{h},f(\tilde{h}))$, for each $\tilde{h}\ \tilde{\in}\ H$, is S.I-continuous.
Proof .(⇒) Suppose that (H,τ,E,I) is F.W.S.I-topological space over (B,Ω,G), then there exist the projection function $P_{fu}:(H,\tau,E,\ I)\to(B,\Omega,G)$ is S.I-continuous. For proof g is S.I-continuous, let $\tilde{h}\ \tilde{\in}\ H$ and $(W,E\times G)$ be any soft open of $H\times B$containing $g(\tilde{h})=(\tilde{h},f(\tilde{h}))$. Thus we have a basic soft open set $(F,E)\times(M,G)$ such that $g(\tilde{h})=\left(\tilde{h},f(\tilde{h})\right)\ \tilde{\in}\ (F,E)\times(M,G)\ \tilde{\subseteq}\ (W,E\times G)$. Since (H,τ,E,I) is F.W.S.I-topological space, then $P_{fu}$is S.I-continuous, we have a S.I-open set (L,E) of (H,τ,E) containing $(\tilde{h})$such that$P_{fu}(L,E)\ \tilde{\subseteq}\ (M,G)$. Because $(L,E)\ \tilde{\cap}\ (F,E)$is soft ideal open of$(H,\tau,E,I)$ and $(L,E)\ \tilde{\cap}\ (F,E)\ \tilde{\subseteq}\ (F,E)$ then $g\big((F,E)\ \tilde{\cap}\ (L,E)\big)\ \tilde{\subseteq}\ (F,E)\times(M,G)\ \tilde{\subseteq}\ (W,E\times G)$.This explains that g is S.I-continuous.
(⇐)assume that g is S.I-continuous. For proof (H,τ,E,I) is F.W.S.I-topological spaces i.e., the projection function$P_{fu}:(H,\tau,E,\ I)\to(B,\Omega,G)$ is S.I-continuous, let $\tilde{h}\ \tilde{\in}\ H$and (M,G) be any soft open set of (B,Ω,G)containing $P_{fu}(\tilde{h})$. Then $H\times(M,G)$ is soft open in $(H,\tau,E)\times(B,\Omega,G)$. Because g is S.I-continuous, we have(F,E) is S.I-open in (H,τ,E,I) containing $\tilde{h}$such that $g(F,E)\ \tilde{\subseteq}\ H\times(M,G)$. Hence, we get$P_{fu}(F,E)\ \tilde{\subseteq}\ (M,G)$.This explains that P_{fu} is S.I-continuous. Thus (H,τ,E,I) is F.W.S.I-topological space.
Proposition 2.6. Let(H,τ,E,I) be a F.W.S.I-topological space over (B,Ω,G). Then $(H_{B^*},\tau_{B^*},E_{B^*},I_{B^*})$ is F.W.S. I-topological space over (B^*,Ω^*,G^*) for each open subspace $(B^*,\Omega^*,G^*)$of (B,Ω,G).
Proof. Suppose that (H,τ,E,I) is F.W.S.I-topological space over (B,Ω,G),then there exist the projection function $P_{fu}:(H,\tau,E,I)\to(B,\Omega,G)$ is S.I-continuous. To show that $(H_{B^*},\tau_{B^*},E_{B^*},I_{B^*})$ is F.W.S.I-topological over (B^*,Ω^*,G^*)i.e.,the projection function$P_{B^*(fu)}:(H_{B^*},\tau_{B^*},E_{B^*},I_{B^*})\to(B^*,\Omega^*,G^*)$ is S.I-continuous. Assume(M,G) isa soft open subset of (B,Ω,G), then $(M,G)\ \tilde{\cap}\ (B^*,G^*)$is soft open in subspace (B^*,Ω^*,G^*) andso $H_{(M,G)}\ \tilde{\subseteq}\ int(H_{(M,G)})^*$, then $H_{(M,G)}\ \tilde{\cap}\ (H_{B^*},E_{B^*})\ \tilde{\subseteq}\ int\big(H_{(M,G)}\big)^*\ \tilde{\cap}\ (H_{B^*},E_{B^*})$. This $(H_{B^*},E_{B^*})_{(M,G)}=H_{(M,G)}\ \tilde{\cap}\ (H_{B^*},E_{B^*})\ \tilde{\subseteq}\ (H_{B^*},E_{B^*})_{(M,G)}\ \tilde{\subseteq}\ int((H_{B^*},E_{B^*})\ \tilde{\cap}\ (H_{(M,G)}))^*=\ int((H_{B^*},E_{B^*})_{(M,G)})^*$. This we have that $(H_{B^*},E_{B^*})_{(M,G)}$ is S.I-open of$(H_{B^*},E_{B^*},I_{B^*})$. This shows that $P_{B^*(fu)}$ is S.I-continuous, then$(H_{B^*},\tau_{B^*},E_{B^*},I_{B^*})$is F.W.S.I-topological space.

Proposition 2.7. Assume that (H,τ,E,I) is F.W.S. I-topological space over $(B,\Omega,G)$and for all member (H_i,E_i) of a soft open covering of (H,τ,E). Then $(H_{iB^*},E_{iB^*},I_{iB^*})$ is F.W.S.I-topological spaces over(B^*,Ω^*,G^*) for each open subspace $(B^*,\Omega^*,G^*)$of (B,Ω,G).

Proof. The proof is like to previous proposition.

Definition 2.8. Let $\phi:(H,\tau,E,I)\to(K,\sigma,L,J)$ be a function ϕ is called soft near irresolute(briefly, S. j-I-irresolute) if the inverse image of soft j-I-open set in K is soft j-I-open in H, where $j\in\{\alpha,S,P,b,\beta\}$.

Definition 2.9.A F.W.S.I-topological space (H,τ,E,I) over (B,Ω,G,J) is called fibrewise soft near ideal irresolute (briefly, F.W.S. I-irresolute) if the projection $P_{fu}$is soft j-I-irresolute where $j\in\{\alpha,S,P,b,\beta\}$.

Proposition 2.10. Let (H,τ,E,I) be a F.W.S.I-topological space over (B,Ω,G) and $(H_{(M,G)^*})\cong(H_{(M,G)})^*$ for each soft subset $(M,G)$of (B,Ω,G). Then (H,τ,E,I) is F.W.S.I-irresolute.

Proof. Suppose that (H,τ,E,I) is F.W.S.I-topological space over (B,Ω,G), then there exist the projection function $P_{fu}:(H,\tau,E,I)\to(B,\Omega,G)$is S.I-continuous. For proof (H,τ,E,I) is F.W.S.I-irresolute, then there exist the projection function $P_{fu}:(H,\tau,E,I)\to(B,\Omega,G,J)$is soft I-irresolute. Let (M,G) be any S.I-open set of (B,Ω,G,J). By lemma (1.13), we have $(M,G)^*=(int(M,G)^*)^*$. Therefore, we have $H_{(M,G)^*}$=$H_{(int(M,G)^*)^*}$,such $(H_{(M,G)})^*\cong(H_{int(M,G)^*})^*$, $H_{(M,G)}\cong H_{int(M,G)^*}$.so$H_{(M,G)}$ is S.I-open in (H,τ,E,I),then P_{fu} is soft I-irresolute, thus (H,τ,E,I) is F.W.S.I-irresolute.

Remark 2.11. Assume that $\phi:(H,\tau,E,I)\to(K,\sigma,L)$ is afibrewise soft ideal function and $\psi:(K,\sigma,L,M)\to(Z,\vartheta,C)$ is fibrewise soft ideal function, where $(H,\tau,E,I),(K,\sigma,L,M),(Z,\vartheta,C,N)$ are F.W.S. I-topological space over (B,Ω,G) thenthe composition $\phi o\psi:(H,\tau,E,I)\to(Z,\vartheta,C)$ is need not fibrewise soft ideal function, in general, like shown by the next example.

Example 2.12. Let $H=Z=\{h_1,h_2,h_3\}$, $K=\{h_1,h_2,h_3,h_4\}$, $B=\{a,b,c\}$, $E=L=C=\{e\}$, $G=\{g\}$, with soft topologies, $\tau=\{\widetilde{\Phi},\widetilde{H},\{(e,\{h_1\})\}\}$,$\sigma=\{\widetilde{\Phi},\widetilde{K},\{(e,\{h_1,h_3\})\}\}$, $\vartheta=\{\widetilde{\Phi},\widetilde{Z},\{(e,\{h_3\})\},\{(e,\{h_2,h_3\})\}\}$,$\Omega=\{\widetilde{\Phi},\widetilde{B}\}$,$I=\{\widetilde{\Phi},\{(e,\{h_3\})\}\}$, $M=\{\widetilde{\Phi},\{(e,\{h_1\})\}\}$. Let$(H,\tau,E,I)$and (K,σ,L,M), (Z,ϑ,C,N) is F.W.S.I-topological spaces over (B,Ω,G). Define the identity function$f$from H, Z to B,let$U$ be a identify function from E, $C$to$G$ and define $q:K\to B$, $d:L\to G$ as: $q(h_1)=a$, $q(h_2)=q(h_4)=b$, $q(h_3)=c$, $d(e)=g$. Then the soft function $P_{H(fu)}:(H,\tau,E,I)\to(B,\Omega,G)$, $P_{K(qd)}:(K,\sigma,L,M)\to(B,\Omega,G)$ and $P_{z(tv)}:(Z,\vartheta,C,N)\to(B,\Omega,G)$are S.I-continuous. And define identity function $\phi:(H,\tau,E,I)\to(K,\sigma,L)$,$\psi:(K,\sigma,L,M)\to(Z,\vartheta,C)$ define as: $\psi(\tilde{h}_{1\tilde{b}})=\tilde{h}_{1\tilde{b}}$, $\psi(\tilde{h}_{2\tilde{b}})=\psi(\tilde{h}_{4\tilde{b}})=\tilde{h}_{2\tilde{b}}$, $\psi(\tilde{h}_{3\tilde{b}})=\tilde{h}_{3\tilde{b}}$ where$\tilde{b}\cong B$. It clear that both ϕ and $\psi$are S.I-continuous function. However, the composition function $\phi o\psi$ is not S.I-continuous function because $\{(e,\{h_3\})\}$ is S. open in (Z,ϑ,C), but $(\phi o\psi)^{-1}\{(e,\{h_3\})\}=\{(e,\{h_3\})\}$ is not S.I-open in (H,τ,E,I).

Proposition 2.13. Let $\phi:(H,\tau,E,I)\to(K,\sigma,L)$be a fibrewise soft function, where(K,σ,L,M)aF.W.S.I-topological space over $(B,\Omega,G)$and (H,τ,E,I) has the induced F.W.S. I-topology,the follow are hold:

(a) If ϕ is soft continuous and for each F.W.S. I-topological space (Z,γ,C,N), a fibrewise soft function $\psi:(Z,\gamma,M,C)\to(H,\tau,E)$ is S.I-continuousthenthe composition $\phi\circ\psi:(Z,\gamma,C,N)\to(K,\sigma,L)$ is S.I-continuous.

(b) If ϕ is S.I-continuous and for each F.W.S. I-topological space (Z,γ,C,N), a fibrewise soft function $\psi:(Z,\gamma,M,C)\to(H,\tau,E,I)$ is soft I-irresolute then the composition $\phi\circ\psi:(Z,\gamma,C,N)\to(K,\sigma,L)$ is S.I-continuous.

Proof.(a)Assume that ψ is S.I-continuous. Let$\tilde{z}\cong Z_{\tilde{b}}$, where $\tilde{b}\cong B$ and (N,L) soft open set of $(\phi\circ\psi)(\tilde{z})=\tilde{k}\cong K_{\tilde{b}}$ in (K,σ,L). becauseϕ is soft continuous, $\phi^{-1}(N,L)$is a soft open set containing $\psi(\tilde{z})=\tilde{h}\cong H_{\tilde{b}}$in (H,τ,E). Becauseψ is S.I-continuous, then$\psi^{-1}(\phi^{-1}(N,L))$ is a S.I-open set containing $\tilde{z}\in Z_{\tilde{b}}$ in (Z,γ,C) and $\psi^{-1}(\phi^{-1}(N,L)$=$(\phi\circ\psi)^{-1}(N,L)$ is a S.I-open set containing $\tilde{z}\in Z_{\tilde{b}}$in (Z,γ,C,N).

(b)The proof is similar to the proof of (a).

3.Fibrewise Soft Ideal Closed and Soft Ideal Open Topological Spaces.

During this part, we explain the ideas of fibrewise soft ideal closed, soft ideal open topological spaces. Several topological properties on the obtained concepts are studied.

Definition 3.1.A function$\phi:(H,\tau,E,I)\to(K,\sigma,L)$ is called:

(a) Soft ideal open (briefly, S.I-open) function if the image of all S.I-open set in H is soft open set in K.

(b) Soft ideal closed (briefly, S. I-closed) function if the image of all S.I-closed set in H is soft closed set in K.

Definition 3.2. A F.W.S.I-topological space (H,τ,E,I) over (B,Ω,G) is called fibrewise soft ideal closed (briefly, F.W.S. I-closed) if the projection function is S. I-closed.
Definition 3.3. A F.W.S.I-topological space (H,τ,E,I) over (B,Ω,G) is called fibrewise soft ideal open (briefly, F.W.S. I-open) if the projection function is S.I-open.

F.W.S.I-open and F.W.S. open arethis two concepts are independent.

Example 3.4. Let (H,τ,E,I) bea F.W.S. I-topological space over (B,Ω,G) given likethe following:$H=\{h_1,h_2\}, E=\{e_1,e_2\},\tau=\{\widetilde{\Phi},\widetilde{H},\{(e_1,\{h_2\})\}, \quad I=\{\widetilde{\Phi},\{(e_1,\{h_1\})\},\{(e_2,\{h_2\})\},\{(e_1,\{h_1\}),(e_2,\{h_2\})\}\}$, $B=\{a,b\}$, $G=\{g_1,g_2\}$, $\Omega=\{\widetilde{\Phi},\widetilde{B},\{(g_1,\{a\})\},\{(g_2,\{b\})\},\{(g_1,\{a\}),(g_2,\{b\})\}\}$. Also, let $f:H\to B$, $f(h_1)=a$, $f(h_2)=b$, $u:E\to G$, $u(e_1)=g_1$, $u(e_2)=g_2$. Then soft function $P_{fu}:(H,\tau,E,I)\to(B,\Omega,G)$ is S. I-pen but is not S. open. Thus, (H,τ,E,I) is F.W.S. I-open but not F.W.S.open.

Example 3.5. Let (H,τ,E,I)be a F.W.S. I-topological space over(B,Ω,G) given likethe following: $H=\{h_1,h_2\}, E=\{e_1,e_2\}, \quad \tau=\{\widetilde{\Phi},\widetilde{H},\{(e_1,\{h_1\}),(e_2,\{h_2\})\}\}, \quad I=\{\widetilde{\Phi},\widetilde{H},\{(e_1,\{h_1\})\},\{(e_2,\{h_2\})\},\{(e_1,\{h_1\}),(e_2,\{h_2\})\}\}, \quad B=\{a,b\}, \quad G=\{g_1,g_2\}, \quad \Omega=\{\widetilde{\Phi},\widetilde{B},\{(g_1,\{a\})\},\{g_2,\{b\}\}\},\{(g_1,\{a\}),(g_2,\{b\})\}\}$. Also, let $f:H\to B$, $f(h_1)=a$, $f(h_2)=b$, $u:E\to G$, $u(e_1)=g_1$, $u(e_2)=g_2$. Then soft function $P_{fu}:(H,\tau,E,I)\to(B,\Omega,G)$ is S. open but is not S.I-open. Thus, (H,τ,E,I) is F.W.S. I-open but not F.W.S. open.

Proposition 3.6. Assume that (H,τ,E,I) is a F.W.S.I-open over (B,Ω,G)then for each soft element in (H,τ,E) and each soft nbd$(F,E)^*$ of the soft element, there exists soft open of (B,Ω,G) containing the image of soft element such that soft open containing in image of soft nbd
Proof. Suppose that (H,τ,E,I) is F.W.S.I-open, then there exist the projectionfunction$P_{fu}:(H,\tau,E,I)\to(B,\Omega,G)$is a S.I-open function. To proof for each soft element and each soft nbd(F,E) of the soft element, there exists soft open of (B,Ω,G) containing the image of soft element such that soft open containing in image of soft nbd, since for each soft element $\tilde{h}\,\widetilde{\in}\,H$ and each soft nbd$(F,E)^*$of$\tilde{h}$, then there existsS.I-open(U,E)in (H,τ,E) such that $\tilde{h}\,\widetilde{\in}\,(U,E)\,\widetilde{\subseteq}\,(F,E)^*$. Since $P_{fu}$is S.I-open, $(M,G)=P_{fu}(U,E)$ is soft open of (B,Ω,G) and $P_{fu}(\tilde{h})\,\widetilde{\in}\,(M,G)\,\widetilde{\subseteq}\,P_{fu}(F,E)^*$.

Proposition 3.7. Let (H,τ,E,I) be a F.W.S. I-topological space over (B,Ω,G). then(H,τ,E,I) is F.W.S. I-open (res. F.W.S.I-closed) if and for all fibre soft $(H_{\tilde{b}},E_{\tilde{b}})$of (H,τ,E) and all S.I-open (res. S.I-open)subset (F,E) of $(H_{\tilde{b}},E_{\tilde{b}})$ in (H,τ,E), there is a softopen (soft closed) subset (F,G) of $\tilde{b}$where $(H_{(F,G)},E_{(F,G)})\,\widetilde{\subseteq}\,(F,E)$.
Proof.(⇒)Suppose that (H,τ,E,I) is F.W.S.I-open (res. F.W.S.I-closed) then there existthe projection function$P_{fu}:(H,\tau,E,I)\to(B,\Omega,G)$ isS.I-open(res. soft I-closed). Now, let $\tilde{b}\,\widetilde{\in}\,B$ and (F,E)S.I-open(res. soft I-closed)subset of $(H_{\tilde{b}},E_{\tilde{b}})$ in (H,τ,E), then $(H,E)\_(F,E)$ is soft I-closed (res. S.I-open) in (H,τ,E), this implies $P_{fu}((H,E)-(F,E))$ issoft open (res. soft closed) in (B,Ω,E), let $(F,G)=(B,G)-P_{fu}((H,E)-(F,E))$, then (F,G)a soft open (res. soft closed) subset of $\tilde{b}$ in $(B,\Omega,G)$and$\big(H_{(F,E)},E_{(F,E)}\big)=H_{(F,G)}=(H,E)-H_{(P_{fu}((H,E)-(F,E))}\,\widetilde{\subseteq}\,(F,E)$.
(⇐)Suppose that the assumption hold and there exist the projection function$P_{fu}:(H,\tau,E,I)\to(B,\Omega,G)$ is soft I-closed. Now, let (F,C) be a S. I-closed subset of (H,τ,E,I) and $\tilde{b}\,\widetilde{\in}\,(B,G)-P_{fu}(F,C)$ and each S.I-open set (F,E) of fibre soft $(H_{\tilde{b}},E_{\tilde{b}})$ in (H,τ,E,I). By assumption we have a soft open (F,G) of $\tilde{b}$ such that $(H_{(F,G)},E_{(F,G)})\,\widetilde{\subseteq}\,(F,E)$. It is easy to show that $(F,G)\,\widetilde{\subseteq}\,(B,G)-P_{fu}(F,C)$,hence $(B,G)-P_{fu}(F,C)$ is soft open in (B,Ω,G) and this implies $P_{fu}(F,C)$ is softclosed in (B,Ω,G) and P_{fu} is soft I-closed.Thus, $(H,\tau,E,I)$is F.W.S. I-closed. For a S.I-open function, we can prove similarly.

Proposition 3.8. Assume that$\phi : (H, \tau, E, I) \to (K, \sigma, L)$is a fibrewise S.I-open function, where (K, σ, L, M)a F.W.S.I-topological space over $(B, \Omega, G))$ and (H, τ, E, I) has the induced F.W.S. I-topologyand for each F.W.S. I-topological space (Z, γ, C, N), a fibrewise soft function $\psi: (Z, \gamma, C, N) \to (H, \tau, E)$ is S.I-open then the composition $\phi \circ \psi: (Z, \gamma, C, N) \to (K, \sigma, L)$ is S.I-open.
Proof. Assume that ψ is S.I-open. Let $\tilde{z} \tilde{\in} Z_{\tilde{b}}$, where $\tilde{b} \tilde{\in} B$ and (N, L)S.I-open set in (Z, γ, C, N). Since Ψ is S.I-open, $\psi(N, L)$ is a soft open set containing $\psi(\tilde{z}) = \tilde{h} \tilde{\in} H_{\tilde{b}}$ in (H, τ, E). Becauseϕ is S.I-open, then$\psi(\phi(N, L))$ is a soft open set containing $(\phi o \psi)(\tilde{z}) = \tilde{k} \tilde{\in} K_{\tilde{b}}$ in (K, σ, L) and $\psi(\phi(N, L)=(\phi o \psi)(N, L)$ is a soft open set containing $\tilde{k} \in K_{\tilde{b}}$in (K, σ, L).

4. Fibrewise soft near ideal topological spaces

Definition 4.1. The F.W.S.I-topological space (H, τ, E, I) over (B, Ω, G) is named fibrewise soft near I-compact (briefly, F.W.S. j-I-compact) if the soft ideal topological space (H, τ, E, I) is soft j-I-compact, where $\in \{\alpha, S, P, b, \beta\}$.

Remark 4.2. In F.W.S.I-topological space we work over at soft topological base space B, say. When B is a point-space the theory reduces to that of ordinary soft topology. A F.W.S.I-topological (resp., S.j-I-topological) space over B is just a soft ideal topological (resp., S. j-I-topological) space H together with a soft ideal continuous (resp., S.j-I-continuous) the projectionfunction$P_{fu} : (H, \tau, E, I) \to (B, \Omega, G)$. So the implication between F.W.S.I-topological spaces and the families of F.W.S.j-I-topological spaces are given in the following diagram where $j \in \{\alpha, S, P, b, \beta\}$.

F.W.S.I-topological space
⇓
F.W.S.α-I-topological space ⇒ F.W.S. S-I-topological space
⇓⇓
F.W.S. P-I-topological space ⇒F.W.S.b-I-topological space ⇒ F.W.S. β-I-topological space.

Example 4.3. Let (H, τ, E, I) be a F.W.S. I-topological space over (B, Ω, G) given like the following : $H = \{h_1, h_2, h_3, h_4\}$, $E = \{e\}$, $\tau = \{\tilde{\Phi}, \tilde{H}, \{(e, \{h_1\})\}, \{(e, \{h_2\})\}, \{(e, \{h_1, h_2\})\}, \{(e, \{h_1, h_2, h_4\})\}\}$, $I = \{\tilde{\Phi}, \{(e, \{h_1\})\}, \{(e, \{h_3\})\}, \{(e, \{h_1, h_3\})\}\}$, $B = \{a, b, c, d\}$, $G = \{g\}$, $\Omega = \{\tilde{\Phi}, \tilde{B}, \{(g, \{a, b\})\}\}$. Also, let $f: H \to B$, $f(h_1) = a$, $f(h_2) = b, f(h_3) = c, f(h_4) = d, u : E \to G$, $u(e) = g$. Then the soft function $P_{fu}: (H, \tau, E, I) \to (B, \Omega, G)$ is S.α-I-continuous but is not S.I-continuous. Thus, (H, τ, E, I) is F.W.S.α-I-topological space but not F.W.S.I-topological space.

Example 4.4. Let (H, τ, E, I) be a F.W.S. I-topological space over (B, Ω, G) given like the following : $H = \{h_1, h_2, h_3, h_4\}$, $E = \{e\}$, $\tau = \{\tilde{\Phi}, \tilde{H}, \{(e, \{h_1\})\}, \{(e, \{h_2\})\}, \{(e, \{h_1, h_2\})\}, \{(e, \{h_1, h_2, h_4\})\}\}$, $I = \{\tilde{\Phi}, \{(e, \{h_1\})\}, \{(e, \{h_3\})\}, \{(e, \{h_1, h_3\})\}\}$, $B = \{a, b, c, d\}$, $G = \{g\}$, $\Omega = \{\tilde{\Phi}, \tilde{B}, \{(g, \{a, b\})\}\}$. Also, let $f: H \to B$, $f(h_1) = a$, $f(h_2) = b$, $f(h_3) = c, f(h_4) = d, u : E \to G$, $u(e) = g$. Then the soft function $P_{fu}: (H, \tau, E, I) \to (B, \Omega, G)$ is S.α-I-continuous but is not S.I-continuous. Thus, (H, τ, E, I) is F.W.S.α-I-topological space but not F.W.S.I-topological space.

Example 4.5. Let (H, τ, E, I) be a F.W.S. I-topological space over (B, Ω, G) given like the following : $H = \{h_1, h_2, h_3, h_4\}$, $E = \{e\}$, $\tau = \{\tilde{\Phi}, \tilde{H}, \{(e, \{h_1\})\}, \{(e, \{h_2, h_3\})\}, \{(e, \{h_1, h_2, h_3\})\}\}$, $I = \{\tilde{\Phi}, \{(e, \{h_1\})\}, \{(e, \{h_4\})\}, \{(e, \{h_1, h_4\})\}\}$, $B = \{a, b, c, d\}$, $G = \{g\}$, $\Omega = \{\tilde{\Phi}, \tilde{B}, \{(g, \{a, b, d\})\}\}$. Also, let $f: H \to B$, $f(h_1) = a$, $f(h_2) = b$, $f(h_3) = c, f(h_4) = d$, $u : E \to G$, $u(e) = g$. Then the soft function $P_{fu}: (H, \tau, E, I) \to (B, \Omega, G)$ is S.P-I-continuous but is not S.α-I-continuous. Thus, (H, τ, E, I) is F.W.S.P-I-topological space but not F.W.S.α-I-topological space.

Example 4.6. Let (H,τ,E,I) be a F.W.S. I-topological space over (B,Ω,G) given like the following : $H=\{h_1,h_2,h_3,h_4\}$, $E=\{e\}$, $\tau=\{\widetilde{\Phi},\widetilde{H},\{(e,\{h_2\})\},\{(e,\{h_1,h_3\})\},\{(e,\{h_1,h_2,h_3\})\}\}$, $I=\{\widetilde{\Phi},\{(e,\{h_1\})\},\{(e,\{h_4\})\},\{(e,\{h_1,h_4\})\}\}$, $B=\{a,b,c,d\}$, $G=\{g\}$, $\Omega=\{\widetilde{\Phi},\tilde{B},\{(g,\{a,b,d\})\}\}$. Also, let $f:H\to B$, $f(h_1)=a$, $f(h_2)=b$, $f(h_3)=c,f(h_4)=d$,$u:E\to G$, $u(e)=g$. Then the soft function $P_{fu}:(H,\tau,E,I)\to(B,\Omega,G)$ is S. S-I-continuous but is not S.α-I-continuous. Thus, (H,τ,E,I) is F.W.S.S-I-topological space but not F.W.S.α-I-topological space.

Example 4.7. Let (H,τ,E,I) be a F.W.S. I-topological space over (B,Ω,G) given like the following : $H=\{h_1,h_2,h_3,h_4\}$, $E=\{e\}$, $\tau=\{\widetilde{\Phi},\widetilde{H},\{(e,\{h_1\})\},\{(e,\{h_4\})\},\{(e,\{h_1,h_4\})\}\}$, $I=\{\widetilde{\Phi},\{(e,\{h_3\})\}\}$,$B=\{a,b,c,d\}$, $G=\{g\}$, $\Omega=\{\widetilde{\Phi},\tilde{B},\{(g,\{a,d\})\},\{(g,\{a\})\},\{(g,\{d\})\}\}$. Also, let $f:H\to B$, $f(h_1)=d$, $f(h_2)=b$, $f(h_3)=d,f(h_4)=b$,$u:E\to G$, $u(e)=g$. Then the soft function $P_{fu}:(H,\tau,E,I)\to(B,\Omega,G)$ is S.b-I-continuous but is not S. P-I-continuous. Thus, (H,τ,E,I) is F.W.S.b-I-topological space but not F.W.S.P-I-topological space.

Example 4.8. Let (H,τ,E,I) be a F.W.S.I-topological space over (B,Ω,G) given like the following : $H=\{h_1,h_2,h_3\}$, $E=\{e\}$, $\tau=\{\widetilde{\Phi},\widetilde{H},\{(e,\{h_1,h_2\})\}\}$, $I=\{\widetilde{\Phi},\{(e,\{h_3\})\}\}$, $B=\{a,b,c\}$, $G=\{g\}$, $\Omega=\{\widetilde{\Phi},\tilde{B},\{(g,\{a,b\})\}\}$. Also, let $f:H\to B$, $f(h_1)=a$, $f(h_2)=c$, $f(h_3)=b$,$u:E\to G$, $u(e)=g$. Then the soft function $P_{fu}:(H,\tau,E,I)\to(B,\Omega,G)$ is soft b-I-continuous but is not soft S-I-continuous. Thus, (H,τ,E,I) is F.W.S.b-I-topological space but not F.W.S.S-I-topological space.

Proposition 4.9. Let $\phi:(H,\tau,E,I)\to(K,\sigma,L)$be a fibrewise soft ideal function, where(K,σ,L,M)a F.W.S.j-I-topological space over(B,Ω,G) and(H,τ,E,I) has the induced F.W.S.j-I-topology. If ϕ is soft continuous and for each F.W.S. j-I-topological space (Z,γ,C,N), a fibrewise soft function $\psi:(Z,\gamma,M,C)\to(H,\tau,E)$ is soft j-I-continuous then the composition $\phi\circ\psi:(Z,\gamma,C,N)\to(K,\sigma,L)$ is soft j-I-continuous, where $j\in\{\alpha,S,P,b,\beta\}$.
Proof . The proof is similar to that of Theorem 2.12.(a).

Proposition 4.10. Let(H,τ,E,I) be a F.W.S.j-I-topological space over (B,Ω,G). Then $(H_{B^*},\tau_{B^*},E_{B^*},I_{B^*})$ is F.W.S. j-I-topological space over (B^*,Ω^*,G^*) for each open subspace $(B^*,\Omega^*,G^*)$of (B,Ω,G), where $j\in\{\alpha,S,P,b,\beta\}$.
Proof. The proof is similar to that of Theorem 2.6.

Proposition 4.11. Assume that (H,τ,E,I) is F.W.S.j-I-topological space over (B,Ω,G) if and only if the graph soft function $g:(H,\tau,E)\to(H,\tau,E)\times(B,\Omega,G)$, defined by $g(\tilde{h})=(\tilde{h},f(\tilde{h}))$, for every$\tilde{h}\cong H$, is S. j-I-continuous, where $j\in\{\alpha,S,P,b,\beta\}$.
Proof. The proof is similar to that of Theorem 2.5.

Proposition 4.12. Let $\phi:(H,\tau,E,I)\to(K,\sigma,L,M)$be aS.j-I-irresolute fibrewisesurjective, where (H,τ,E,I) and (K,σ,L,M) are F.W.S.I-topological spaces over (B,Ω,G).If (H,τ,E,I) is F.W.S.j-I-compact then (K,σ,L,M) is so, where $j\in\{\alpha,S,P,b,\beta\}$.
Proof. Let $\phi:(H,\tau,E,I)\to(K,\sigma,L,M)$ be a S. j-I-irresoluteand (H,τ,E,I) is F.W.S.j-I-compact,then there exist the projection function$P_{H(fu)}:(H,\tau,E,I)\to(B,\Omega,G)$ is S. j-I-compact. For proof (K,σ,L,M) is F.W.S.j-I-compacti.e., the projection function$P_{K(qd)}:(K,\sigma,L,)\to(B,\Omega,G)$ is S.j-I-compact, since let $\{(W_i,E_i):i\in\Delta\}$ an S.I-open cover of K_b, where $b\in B$. Then $\phi^{-1}\{(W_i,E_i):i\in\Delta\}$ is S.I-open cover of $H_{\tilde{b}}$, where$\tilde{b}\in B$. There exists from the hypothesis a finite subset Δ_o of Δsuch that $\widetilde{H}-\widetilde{\cup}\{\phi^{-1}(W_i,E_i):i\in\Delta_o\}\in I$. Thus, $\phi\{\widetilde{H}-\widetilde{\cup}\{\phi^{-1}(W_i,E_i):i\in\Delta_o\}\in J$which explains that is $P_{K(qd)}$ soft j-I-compact. Thus (K,σ,L,M)F.W.S.j-I-compact, where $j\in\{\alpha,S,P,b,\beta\}$.

Definition 4.13 The F.W.S. topological space (H,τ,E,I) over(B,Ω,G) is called fibrewise soft near ideal connected (briefly F.W.S. j-I-connected) if $H_{\tilde{b}}$where$\tilde{b}\ \tilde{\in}\ B$is not the union of two disjoint non-empty S.j-I-open sets of (H,τ,E,I),where$j \in \{\alpha,S,P,b,\beta\}$.

Proposition 4.14. Assume that $\phi:(H,\tau,E,I)\to(K,\sigma,L,M)$ isaS.j-I-irresolute fibrewise surjection function, when (H,τ,E,I) also (K,σ,L,M) are F.W.S. topological spaces over (B,Ω,G). If (H,τ,E,I) is F.W.S. j-I-connected then so is (K,σ,L,M), where $j \in \{\alpha,S,P,b,\beta\}$.

Proof. Let (K,σ,L,M) be a F.W.S.I-topological space over (B,Ω,G), then there existthe projection function $P_{K(qd)}:(K,\sigma,L,M)\to(B,\Omega,G)$ is S.I-continuous. To proof (K,σ,L,M) is F.W.S.j-I-connected, Suppose that (K,σ,L,M) is not F.W.S.j-I-connected, then there exist non-empty disjoint S.j-I-open subset (F,L), (G,L) of (K,σ,L,M) such that $(F,L)\ \tilde{\cup}\ (G,L)=K_{\tilde{b}}$, where $\tilde{b}\ \tilde{\in}\ B$. Since ϕ is soft j-I-irresolute, we have $\phi^{-1}(F,L)$, $\phi^{-1}(G,L)$ are non-empty disjoint in (H,τ,E,I). Moreover,$\phi^{-1}(F,L)\ \tilde{\cup}\ \phi^{-1}(G,L)=H_{\tilde{b}}$. This shows that (H,τ,E,I) is not F.W.S.j-I-connected. This is a contradiction and hence (K,σ,L,M) is F.W.S.j-I-connected, where $j \in \{\alpha,S,P,b,\beta\}$.

References

[1] M.E. Abd El-Monsef, E.F. Lashien, A.A.Nasef. On I-open sets and I-continuous functions. *Kyungpook Math. J.,* 1992, 32 (1): 21-30.
[2] A. A. Abo Khadra, S. S. Mahmoud and Y. Y. Yousif. fibrewise near topological spaces. *Journal of Computing, USA,* 2012, 4 (5): 223-230.
[3] M. Akdağ, F. rol. Soft I-Sets and Soft I-Continuity of Functions. *Gazi Univ. Journal of Science*, 2014, 27(3):923-932.
[4] M.Akdağ, F.Erol, Y.Bingö. Soft Sime-I-Continuity Functions. *Gazi Univ. Journal of Science*, 2015, 28(1):37- 44.
[5] M. I. Ali, F. Feng, X. Liu, W. K. Min, M. Shabir. On some new operations in soft set theory, *Computer and Mathematics with Applications*, 2009, 57: 1547-1553.
[6] A. Aygunoglu. H. Aygun, Some notes on soft topological spaces. *Neural Comput and Applic, Neural Comput. andApplic*, 2012, 21(1):113-119.
[7] N. Cagman, S. Enginoglu. Soft set theory and uniint decision making. *European Journal of Operational Research*, 2010, 207: 848-855.
[8] N. Çağman, S. Karataş Enginoğlu. Soft topology. *Computers and Mathematics with Applicatons,* 2011, 62:351-358.
[9] A. CaksuGuler, G. Aslim. B-I-open sets and decomposition of continuity via idealization, Proceedings of Institute of Mathematics and Mechanics. *National Academy of Sciences of Azerbaijan*, 2005, 22: 27–32.
[10] F. Feng, Y.B. Zhao. Soft semirings. *Computer and Mathematics with Applications*, 2008, 56: 2621-2628.
[11] T.R. Hamlett, D. Jankovic. Ideals in topological spaces and the set operator Ψ. *Bollettino U.M.I.*, 1990, 7: 863-874.
[12] H. Hashimoto. On the topology and its applications. *Fund. Math.*, 1976, 91, 5-10.
[13] H. Hashimoto. On some local properties on spaces. *Math. Japonica*, II, 1952: 127-134.
[14] E. Hatir, T. Noiri, On decompositions of continuity via idealization. *ActaMathematicaHungarica*, 2002, 96 (4): 341–349.
[15] S. Hussain, B. Ahmedi. Some properties of soft topological spaces. *Neural Comput and Appl.*, Inf. Sci., 2011, 62: 4058-4067.
[16] I. M. James. Fibrewise Topology. *Cambridge University Paress,* 1989.
[17] D. Jankovic, T.R. Hamlett. New topologies from old via ideals. *Amer. Math. Monthly, 1990,* 97 (4): 295-310.
[18] G. Kale, A.C. Guler. On Soft Ideal Topological Spaces.

[19] D. V. Kovkov, V. M. Kolbanov, D. A. Molodtsov. Soft sets theory-based optimization. *Journal of Computer and Systems Sciences International*, 2007, 46: 872-880.
[20] S. S. Mahmoud, Y. Y. Yousif. Fibrewise near separation axioms, *International Mathematical Forum, Hikari Ltd, Bulgaria*, 2012, 7 (35): 1725-1736.
[21] S. Mon., M. Chiney, S. K. Samanta, Urysohn's lemma, Tietze's. Extension theorem in soft topology. *Annals of Fuzzy Mathematics and Informatics*, 2011, 2 (1): 1—130 .
[22] P. K. Maji, R. Biswas, A. R. Roy. Soft set theory. *Computer and Math. with Appl.,* 2003:555-562..
[23] D, Moldtsov, Soft set theory-First results, *Comput. Math. Appl.* 37(4–5), 19–31, (1999).
[24] D. Molodtsov, V.Y. Leonov, D.V. Kovkov. Soft sets technique and its application. *NechetkieSistemy i MyagkieVychisleniya,* 2006, 1 (1): 8–39.
[25] S.K. Nazmul, S.K. Samanta. Neighbourhood properties of soft topological spaces. *Annals of Fuzzy Mathematics and Informatics*, 2013, 6(1): 1-15.
[26] D. Pei, D. Miao., X. Hu, Q. Liu, A. Skowron, T. Y. Lin, R. R.Yager, B. Zhang. From soft sets to information systems in (Eds.). *Proceedings of Granular Computing*, *IEEE*, 2005, 2: 617-621.
[27] R. Sahin and A. Kucuk, Soft filters and their convergence properties, *Ann. Fuzzy Math. Inform*. 2013, 6(3): 529–543.
[28] M. Shabir, M. Naz. On soft topological spaces. *Comput. Math. Appl.*, 2011, 61: 1786-1799.
[29] Y. Y. Yousif. Some result on fibrewise Lindelöf and locally Lindelöf Topological space. *Ibn Al-haitham Journal science,* 2009, 22 (3):191-198.
[30] Y. Y. Yousif. Some result on fibrewise Topological space. *Ibn Al-haitham Journal for pure and Applied science. University of Baghdad – Collage of Education - Ibn Al-haitham,* 2008, 21 (2): 118-132.
[31] Y. Y. Yousif, L. A. Hussain. Fibrewise bitopolgical Spaces. *International Journal of Science and Research (IJSR*), 2017*,* 6 (2): 978-982.
[32] Y. Y. Yousif, M. A. Hussain. Fibrewise Soft Topolgical Spaces. *International Journal of Science and Research (IJSR),* 2017*,* 6 (2):1010-1019.
[33] Y. Y. Yousif, M. A. Hussain. Fibrewise soft near separation Axiom. *The 23thScientific conference of collage of Education. AL. Mustansiriyah Universtity, 2017: 26-27.*
[34] I. Zorlutuna, M. Akdag, W. K. Min, S. Atmaca. Remarks on soft topological spaces. *Annals of Fuzzy Mathematics and Informatics,* 2012, 3(2): 171-185.

Application of Weyl Module In The Case Of Two Rows

Application of Weyl Module In The Case Of Two Rows

Haytham R. Hassan 1, Niran Sabah Jasim 2

1 Department of Mathematic, College of Science, Al-Mustansiriyah University
2 Department of Mathematic, College of Education for Pure Science/ Ibn Al-Haitham, University of Baghdad

1 haythamhassaan@yahoo.com , 2 sabahniran @gmail.com

Abstract. The target of this work is to study the two rows resolution of Weyl module, and locate the terms and the exactness of the Weyl Resolution in the Case of Partition (8,7).

1. Introduction

Let R be a commutative ring with identity (1) and $\hat{o}$ be a free R-module. The divided power algebra $D\hat{o} = \sum_{i\geq 0} D_i\hat{o}$ can be defined as the graded commutative algebra generated by x^i where $x \in \hat{o}$ and i is a non-negative integer, and $D_i\hat{o}$ is the divided power algebra of degree i.

A partition of length $\ell(\lambda) = n$ is a sequence $\lambda = (\lambda_1, \lambda_2, ..., \lambda_n)$ of non-negative integers in non-increasing order $\lambda_1 \geq \lambda_2 \geq ... \geq \lambda_n > 0$. The weight of a partition λ is $|\lambda| = \lambda_1 + \lambda_2 + ... + \lambda_n$.

A relative sequence is a pair $((\lambda, \mu)$ of sequence such that $\mu \leq \lambda$ and denoted by λ / μ.

If both λ and μ are partitions then the relative sequence λ / μ is called skew partition.

The authors in [1] remodel the resolution for the two rowed Weyl module $K_{\lambda/\mu}\hat{o}$ as:

$\lambda / \mu =$ 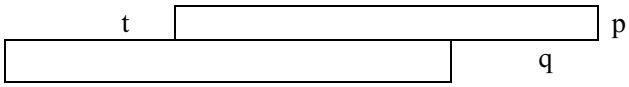

For $K_{\lambda/\mu}\hat{o} = \mathrm{Im}(d'_{\lambda/\mu})$ where $d'_{\lambda/\mu} : D\hat{o} \longrightarrow \wedge\hat{o}$ (Weyl map), so we have

$$\Sigma D_{p+\kappa} \otimes D_{q-\kappa} \xrightarrow{\square} D_p \otimes D_q \xrightarrow{d'_{\lambda/\mu}} K_{\lambda/\mu \to 0}$$

And by using letter place the maps will be

$$\begin{pmatrix} w & 1^{(p+\kappa)} \\ w' & 2^{(q-\kappa)} \end{pmatrix} \xrightarrow{\partial_{21}^{(\kappa)}} \begin{pmatrix} w & 1^{(p)} \quad 2^{(\kappa)} \\ w' & 2^{(q-\kappa)} \end{pmatrix} \longrightarrow \sum_{w} \begin{pmatrix} w_{(1)} & (t+1)'(t+2)'...(p+t)' \\ w'w_{(2)} & 1'2'3'...q' \end{pmatrix},$$

where $w \otimes w' \in D_{p+\kappa} \otimes D_{q-\kappa}$, $\square = \sum_{\kappa=t+1}^{q} \partial_{21}^{(\kappa)}$ is the box map and $d'_{\lambda/\mu} = \partial_{q'2}...\partial_{1'2}\partial_{(p+t)'1}...\partial_{(t+1)'1}$ is the composition of place polarizations from position place {1,2} to negative place {1', 2',…,(p + t)'}.

In [2] the authors illustrate that □ transmit an element $x \otimes y$ of $D_{p+\kappa} \otimes D_{q-\kappa}$ to $\sum x_p \otimes x'_\kappa y$ where $\sum x_p \otimes x'_\kappa$ is the component of the diagonal of x in $D_p \otimes D_\kappa$.

The author in [3] introduces these notions as follows:

Let Z_{21} be the free generator of divided power algebra $D(Z_{21})$ in one generator. The divided power element $Z_{21}^{(\kappa)}$ of degree κ of the free generator Z_{21} acts on $D_{p+\kappa} \otimes D_{q-\kappa}$ by place polarization of degree κ from place 1 to place 2.

The (graded) algebra. $A = D(Z_{21})$ act on the graded module $M = D_{p+\kappa} \otimes D_{q-\kappa} = \Sigma M_{q-\kappa}$ (the degree of the second factor determines the grading).

M is a (graded) left A-module, where for $w = Z_{21}^{(\kappa)} \in A$ and $v \in D_{\beta_1} \otimes D_{\beta_2}$, so we have:

$$w(v) = Z_{21}^{(\kappa)}(v) = \partial_{21}^{(\kappa)}(v)$$

If we take (t^+) graded strand of degree q

$$M_\bullet : 0 \longrightarrow M_{q-t} \xrightarrow{\partial_s} ... \longrightarrow M_\ell \xrightarrow{\partial_s} ... M_1 \xrightarrow{\partial_s} M_0$$

Of the bar complex Bar (M , A; S, •) where $S = \{x\}$.

As in [4] we define the maps $\{S_i\}$ as follows:

$$S_0 : D_p \otimes D_q \longrightarrow \sum_{\kappa>0} Z_{21}^{(t+\kappa)} x D_{p+t+\kappa} \otimes D_{q-t-\kappa}$$

$$\begin{pmatrix} w & 1^{(p)} \quad 2^{(\kappa)} \\ w' & 2^{(q-\kappa)} \end{pmatrix} \longrightarrow \begin{cases} 0 & \text{if } \kappa \le t \\ Z_{21}^{(\kappa)} x \begin{pmatrix} w & 1^{(p+\kappa)} \\ w' & 2^{(q-\kappa)} \end{pmatrix} & \text{if } \kappa > t \end{cases}$$

And for the higher dimensions as

$$S_{\ell-1} : \sum_{\kappa_i>0} Z_{21}^{(t+\kappa_1)} x Z_{21}^{(\kappa_2)} x \ ... \ Z_{21}^{(\kappa_{\ell-1})} x D_{p+t+|\kappa|} \otimes D_{q-t-|\kappa|} \longrightarrow$$

$$Z_{21}^{(t+\kappa_1)} x Z_{21}^{(\kappa_2)} x \ ... \ Z_{21}^{(\kappa_{\ell-1})} x Z_{21}^{(\kappa_\ell)} x D_{p+t+|\kappa|} \otimes D_{q-t-|\kappa|}$$

$$Z_{21}^{(t+\kappa_1)} x\, Z_{21}^{(\kappa_2)} x \ \ldots\ Z_{21}^{(\kappa_{t-1})} x \begin{pmatrix} w & 1^{(p+t+|\kappa|)} \quad 2^{(m)} \\ w' & 2^{(q-t-|\kappa|-m)} \end{pmatrix} \longrightarrow$$

$$\begin{cases} 0 & \text{if } m=0 \\ Z_{21}^{(t+\kappa_1)} x\, Z_{21}^{(\kappa_2)} x \ \ldots\ Z_{21}^{(\kappa_{t-1})} x\, Z_{21}^{(m)} x \begin{pmatrix} w & 1^{(p+t+|\kappa|+m)} \\ w' & 2^{(q-t-|\kappa|-m)} \end{pmatrix} & \text{if } m>0 \end{cases}$$

The authors in [1], [2] and [5] described the written of the modules of the resolution as:

M_i for i = 0,1,…, q – t, with

$M_0 = D_p \otimes D_q$

and

$$M_i = Z_{21}^{(t+\kappa_1)} x\, Z_{21}^{(\kappa_2)} x \ \ldots\ Z_{21}^{(\kappa_i)} x\, D_{p+t+|\kappa|} \otimes D_{q-t-|\kappa|} \quad \text{for } i \geq 1$$

2. Terms of the Weyl Resolution in the Case of Partition (8,7)

In this section we submit the terms of characteristic free resolution in the case of partition (8,7).

$$M_0 = D_8 \otimes D_7$$

$$M_1 = Z_{21}^{(1)} x\ D_9 \otimes D_6 \oplus Z_{21}^{(2)} x\, D_{10} \otimes D_5 \oplus Z_{21}^{(3)} x\, D_{11} \otimes D_4 \oplus Z_{21}^{(4)} x\, D_{12} \otimes D_3 \oplus Z_{21}^{(5)} x\, D_{13} \otimes D_2 \oplus$$
$$Z_{21}^{(6)} x\, D_{14} \otimes D_1 \oplus Z_{21}^{(7)} x\, D_{15} \otimes D_0$$

$$M_2 = Z_{21}^{(1)} x\, Z_{21}^{(1)} x\, D_{10} \otimes D_5 \oplus Z_{21}^{(2)} x\, Z_{21}^{(1)} x\, D_{11} \otimes D_4 \oplus Z_{21}^{(1)} x\, Z_{21}^{(2)} x\, D_{11} \otimes D_4 \oplus Z_{21}^{(2)} x\, Z_{21}^{(2)} x\, D_{12} \otimes D_3 \oplus$$
$$Z_{21}^{(3)} x\, Z_{21}^{(1)} x\, D_{12} \otimes D_3 \oplus Z_{21}^{(1)} x\, Z_{21}^{(3)} x\, D_{12} \otimes D_3 \oplus Z_{21}^{(4)} x\, Z_{21}^{(1)} x\, D_{13} \otimes D_2 \oplus Z_{21}^{(1)} x\, Z_{21}^{(4)} x\, D_{13} \otimes D_2 \oplus$$
$$Z_{21}^{(3)} x\, Z_{21}^{(2)} x\, D_{13} \otimes D_2 \oplus Z_{21}^{(2)} x\, Z_{21}^{(3)} x\, D_{13} \otimes D_2 \oplus Z_{21}^{(5)} x\, Z_{21}^{(1)} x\, D_{14} \otimes D_1 \oplus Z_{21}^{(1)} x\, Z_{21}^{(5)} x\, D_{14} \otimes D_1 \oplus$$
$$Z_{21}^{(3)} x\, Z_{21}^{(3)} x\, D_{14} \otimes D_1 \oplus Z_{21}^{(2)} x\, Z_{21}^{(4)} x\, D_{14} \otimes D_1 \oplus Z_{21}^{(4)} x\, Z_{21}^{(2)} x\, D_{14} \otimes D_1 \oplus Z_{21}^{(6)} x\, Z_{21}^{(1)} x\, D_{15} \otimes D_0 \oplus$$
$$Z_{21}^{(1)} x\, Z_{21}^{(6)} x\, D_{15} \otimes D_0 \oplus Z_{21}^{(2)} x\, Z_{21}^{(5)} x\, D_{15} \otimes D_0 \oplus Z_{21}^{(5)} x\, Z_{21}^{(2)} x\, D_{15} \otimes D_0 \oplus Z_{21}^{(3)} x\, Z_{21}^{(4)} x\, D_{15} \otimes D_0 \oplus$$
$$Z_{21}^{(4)} x\, Z_{21}^{(3)} x\, D_{15} \otimes D_0$$

$$M_3 = Z_{21}^{(1)} x\, Z_{21}^{(1)} x\, Z_{21}^{(1)} x\, D_{11} \otimes D_4 \oplus Z_{21}^{(2)} x\, Z_{21}^{(1)} x\, Z_{21}^{(1)} x\, D_{12} \otimes D_3 \oplus Z_{21}^{(1)} x\, Z_{21}^{(2)} x\, Z_{21}^{(1)} x\, D_{12} \otimes D_3 \oplus$$
$$Z_{21}^{(1)} x\, Z_{21}^{(1)} x\, Z_{21}^{(2)} x\, D_{12} \otimes D_3 \oplus Z_{21}^{(3)} x\, Z_{21}^{(1)} x\, Z_{21}^{(1)} x\, D_{13} \otimes D_2 \oplus Z_{21}^{(1)} x\, Z_{21}^{(3)} x\, Z_{21}^{(1)} x\, D_{13} \otimes D_2 \oplus$$
$$Z_{21}^{(1)} x\, Z_{21}^{(1)} x\, Z_{21}^{(3)} x\, D_{13} \otimes D_2 \oplus Z_{21}^{(2)} x\, Z_{21}^{(2)} x\, Z_{21}^{(1)} x\, D_{13} \otimes D_2 \oplus Z_{21}^{(2)} x\, Z_{21}^{(1)} x\, Z_{21}^{(2)} x\, D_{13} \otimes D_2 \oplus$$

$$Z_{21}^{(1)} x Z_{21}^{(2)} x Z_{21}^{(2)} x D_{13} \otimes D_2 \oplus Z_{21}^{(4)} x Z_{21}^{(1)} x Z_{21}^{(1)} x D_{14} \otimes D_1 \oplus Z_{21}^{(1)} x Z_{21}^{(4)} x Z_{21}^{(1)} x D_{14} \otimes D_1 \oplus$$
$$Z_{21}^{(1)} x Z_{21}^{(1)} x Z_{21}^{(4)} x D_{14} \otimes D_1 \oplus Z_{21}^{(3)} x Z_{21}^{(2)} x Z_{21}^{(1)} x D_{14} \otimes D_1 \oplus Z_{21}^{(3)} x Z_{21}^{(1)} x Z_{21}^{(2)} x D_{14} \otimes D_1 \oplus$$
$$Z_{21}^{(2)} x Z_{21}^{(3)} x Z_{21}^{(1)} x D_{14} \otimes D_1 \oplus Z_{21}^{(2)} x Z_{21}^{(1)} x Z_{21}^{(3)} x D_{14} \otimes D_1 \oplus Z_{21}^{(1)} x Z_{21}^{(2)} x Z_{21}^{(3)} x D_{14} \otimes D_1 \oplus$$
$$Z_{21}^{(1)} x Z_{21}^{(3)} x Z_{21}^{(2)} x D_{14} \otimes D_1 \oplus Z_{21}^{(2)} x Z_{21}^{(2)} x Z_{21}^{(2)} x D_{14} \otimes D_1 \oplus Z_{21}^{(5)} x Z_{21}^{(1)} x Z_{21}^{(1)} x D_{15} \otimes D_0 \oplus$$
$$Z_{21}^{(1)} x Z_{21}^{(5)} x Z_{21}^{(1)} x D_{15} \otimes D_0 \oplus Z_{21}^{(1)} x Z_{21}^{(1)} x Z_{21}^{(5)} x D_{15} \otimes D_0 \oplus Z_{21}^{(2)} x Z_{21}^{(2)} x Z_{21}^{(3)} x D_{15} \otimes D_0 \oplus$$
$$Z_{21}^{(2)} x Z_{21}^{(3)} x Z_{21}^{(2)} x D_{15} \otimes D_0 \oplus Z_{21}^{(3)} x Z_{21}^{(2)} x Z_{21}^{(2)} x D_{15} \otimes D_0 \oplus Z_{21}^{(3)} x Z_{21}^{(3)} x Z_{21}^{(1)} x D_{15} \otimes D_0 \oplus$$
$$Z_{21}^{(3)} x Z_{21}^{(1)} x Z_{21}^{(3)} x D_{15} \otimes D_0 \oplus Z_{21}^{(1)} x Z_{21}^{(3)} x Z_{21}^{(3)} x D_{15} \otimes D_0 \oplus Z_{21}^{(2)} x Z_{21}^{(4)} x Z_{21}^{(1)} x D_{15} \otimes D_0 \oplus$$
$$Z_{21}^{(2)} x Z_{21}^{(1)} x Z_{21}^{(4)} x D_{15} \otimes D_0 \oplus Z_{21}^{(4)} x Z_{21}^{(2)} x Z_{21}^{(1)} x D_{15} \otimes D_0 \oplus Z_{21}^{(4)} x Z_{21}^{(1)} x Z_{21}^{(2)} x D_{15} \otimes D_0 \oplus$$
$$Z_{21}^{(1)} x Z_{21}^{(4)} x Z_{21}^{(2)} x D_{15} \otimes D_0 \oplus Z_{21}^{(1)} x Z_{21}^{(2)} x Z_{21}^{(4)} x D_{15} \otimes D_0$$

$$M_4 = Z_{21}^{(1)} x Z_{21}^{(1)} x Z_{21}^{(1)} x Z_{21}^{(1)} x D_{12} \otimes D_3 \oplus Z_{21}^{(2)} x Z_{21}^{(1)} x Z_{21}^{(1)} x Z_{21}^{(1)} x D_{13} \otimes D_2 \oplus$$
$$Z_{21}^{(1)} x Z_{21}^{(2)} x Z_{21}^{(1)} x Z_{21}^{(1)} x D_{13} \otimes D_2 \oplus Z_{21}^{(1)} x Z_{21}^{(1)} x Z_{21}^{(2)} x Z_{21}^{(1)} x D_{13} \otimes D_2 \oplus$$
$$Z_{21}^{(1)} x Z_{21}^{(1)} x Z_{21}^{(1)} x Z_{21}^{(2)} x D_{13} \otimes D_2 \oplus Z_{21}^{(3)} x Z_{21}^{(1)} x Z_{21}^{(1)} x Z_{21}^{(1)} x D_{14} \otimes D_1 \oplus$$
$$Z_{21}^{(1)} x Z_{21}^{(3)} x Z_{21}^{(1)} x Z_{21}^{(1)} x D_{14} \otimes D_1 \oplus Z_{21}^{(1)} x Z_{21}^{(1)} x Z_{21}^{(3)} x Z_{21}^{(1)} x D_{14} \otimes D_1 \oplus$$
$$Z_{21}^{(1)} x Z_{21}^{(1)} x Z_{21}^{(1)} x Z_{21}^{(3)} x D_{14} \otimes D_1 \oplus Z_{21}^{(2)} x Z_{21}^{(2)} x Z_{21}^{(1)} x Z_{21}^{(1)} x D_{14} \otimes D_1 \oplus$$
$$Z_{21}^{(2)} x Z_{21}^{(1)} x Z_{21}^{(2)} x Z_{21}^{(1)} x D_{14} \otimes D_1 \oplus Z_{21}^{(2)} x Z_{21}^{(1)} x Z_{21}^{(1)} x Z_{21}^{(2)} x D_{14} \otimes D_1 \oplus$$
$$Z_{21}^{(1)} x Z_{21}^{(2)} x Z_{21}^{(2)} x Z_{21}^{(1)} x D_{14} \otimes D_1 \oplus Z_{21}^{(1)} x Z_{21}^{(1)} x Z_{21}^{(2)} x Z_{21}^{(2)} x D_{14} \otimes D_1 \oplus$$
$$Z_{21}^{(1)} x Z_{21}^{(2)} x Z_{21}^{(1)} x Z_{21}^{(2)} x D_{14} \otimes D_1 \oplus Z_{21}^{(4)} x Z_{21}^{(1)} x Z_{21}^{(1)} x Z_{21}^{(1)} x D_{15} \otimes D_0 \oplus$$
$$Z_{21}^{(1)} x Z_{21}^{(4)} x Z_{21}^{(1)} x Z_{21}^{(1)} x D_{15} \otimes D_0 \oplus Z_{21}^{(1)} x Z_{21}^{(1)} x Z_{21}^{(4)} x Z_{21}^{(1)} x D_{15} \otimes D_0 \oplus$$
$$Z_{21}^{(1)} x Z_{21}^{(1)} x Z_{21}^{(1)} x Z_{21}^{(4)} x D_{15} \otimes D_0 \oplus Z_{21}^{(2)} x Z_{21}^{(3)} x Z_{21}^{(1)} x Z_{21}^{(1)} x D_{15} \otimes D_0 \oplus$$
$$Z_{21}^{(2)} x Z_{21}^{(1)} x Z_{21}^{(3)} x Z_{21}^{(1)} x D_{15} \otimes D_0 \oplus Z_{21}^{(2)} x Z_{21}^{(1)} x Z_{21}^{(1)} x Z_{21}^{(3)} x D_{15} \otimes D_0 \oplus$$
$$Z_{21}^{(3)} x Z_{21}^{(2)} x Z_{21}^{(1)} x Z_{21}^{(1)} x D_{15} \otimes D_0 \oplus Z_{21}^{(3)} x Z_{21}^{(1)} x Z_{21}^{(2)} x Z_{21}^{(1)} x D_{15} \otimes D_0 \oplus$$
$$Z_{21}^{(3)} x Z_{21}^{(1)} x Z_{21}^{(1)} x Z_{21}^{(2)} x D_{15} \otimes D_0 \oplus Z_{21}^{(1)} x Z_{21}^{(1)} x Z_{21}^{(2)} x Z_{21}^{(3)} x D_{15} \otimes D_0 \oplus$$
$$Z_{21}^{(1)} x Z_{21}^{(1)} x Z_{21}^{(3)} x Z_{21}^{(2)} x D_{15} \otimes D_0 \oplus Z_{21}^{(1)} x Z_{21}^{(2)} x Z_{21}^{(1)} x Z_{21}^{(3)} x D_{15} \otimes D_0 \oplus$$
$$Z_{21}^{(1)} x Z_{21}^{(3)} x Z_{21}^{(1)} x Z_{21}^{(2)} x D_{15} \otimes D_0 \oplus Z_{21}^{(1)} x Z_{21}^{(3)} x Z_{21}^{(2)} x Z_{21}^{(1)} x D_{15} \otimes D_0 \oplus$$
$$Z_{21}^{(1)} x Z_{21}^{(2)} x Z_{21}^{(3)} x Z_{21}^{(1)} x D_{15} \otimes D_0 \oplus Z_{21}^{(2)} x Z_{21}^{(2)} x Z_{21}^{(2)} x Z_{21}^{(1)} x D_{15} \otimes D_0 \oplus$$

$$Z_{21}^{(2)} x Z_{21}^{(2)} x Z_{21}^{(1)} x Z_{21}^{(2)} x D_{15} \otimes D_0 \oplus Z_{21}^{(2)} x Z_{21}^{(1)} x Z_{21}^{(2)} x Z_{21}^{(2)} x D_{15} \otimes D_0 \oplus$$
$$Z_{21}^{(1)} x Z_{21}^{(2)} x Z_{21}^{(2)} x Z_{21}^{(2)} x D_{15} \otimes D_0$$

$$M_5 = Z_{21}^{(1)} x Z_{21}^{(1)} x Z_{21}^{(1)} x Z_{21}^{(1)} x Z_{21}^{(1)} x D_{13} \otimes D_2 \oplus Z_{21}^{(2)} x Z_{21}^{(1)} x Z_{21}^{(1)} x Z_{21}^{(1)} x Z_{21}^{(1)} x D_{14} \otimes D_1 \oplus$$
$$Z_{21}^{(1)} x Z_{21}^{(2)} x Z_{21}^{(1)} x Z_{21}^{(1)} x Z_{21}^{(1)} x D_{14} \otimes D_1 \oplus Z_{21}^{(1)} x Z_{21}^{(1)} x Z_{21}^{(2)} x Z_{21}^{(1)} x Z_{21}^{(1)} x D_{14} \otimes D_1 \oplus$$
$$Z_{21}^{(1)} x Z_{21}^{(1)} x Z_{21}^{(1)} x Z_{21}^{(2)} x Z_{21}^{(1)} x D_{14} \otimes D_1 \oplus Z_{21}^{(1)} x Z_{21}^{(1)} x Z_{21}^{(1)} x Z_{21}^{(1)} x Z_{21}^{(2)} x D_{14} \otimes D_1 \oplus$$
$$Z_{21}^{(3)} x Z_{21}^{(1)} x Z_{21}^{(1)} x Z_{21}^{(1)} x Z_{21}^{(1)} x D_{15} \otimes D_0 \oplus Z_{21}^{(1)} x Z_{21}^{(3)} x Z_{21}^{(1)} x Z_{21}^{(1)} x Z_{21}^{(2)} x D_{15} \otimes D_0 \oplus$$
$$Z_{21}^{(1)} x Z_{21}^{(1)} x Z_{21}^{(3)} x Z_{21}^{(1)} x Z_{21}^{(1)} x D_{15} \otimes D_0 \oplus Z_{21}^{(1)} x Z_{21}^{(1)} x Z_{21}^{(1)} x Z_{21}^{(3)} x Z_{21}^{(1)} x D_{15} \otimes D_0 \oplus$$
$$Z_{21}^{(1)} x Z_{21}^{(1)} x Z_{21}^{(1)} x Z_{21}^{(1)} x Z_{21}^{(3)} x D_{15} \otimes D_0 \oplus Z_{21}^{(2)} x Z_{21}^{(2)} x Z_{21}^{(1)} x Z_{21}^{(1)} x Z_{21}^{(1)} x D_{15} \otimes D_0 \oplus$$
$$Z_{21}^{(2)} x Z_{21}^{(1)} x Z_{21}^{(2)} x Z_{21}^{(1)} x Z_{21}^{(1)} x D_{15} \otimes D_0 \oplus Z_{21}^{(2)} x Z_{21}^{(1)} x Z_{21}^{(1)} x Z_{21}^{(1)} x Z_{21}^{(2)} x D_{15} \otimes D_0 \oplus$$
$$Z_{21}^{(2)} x Z_{21}^{(1)} x Z_{21}^{(1)} x Z_{21}^{(2)} x Z_{21}^{(1)} x D_{15} \otimes D_0 \oplus Z_{21}^{(1)} x Z_{21}^{(2)} x Z_{21}^{(2)} x Z_{21}^{(1)} x Z_{21}^{(1)} x D_{15} \otimes D_0 \oplus$$
$$Z_{21}^{(1)} x Z_{21}^{(2)} x Z_{21}^{(1)} x Z_{21}^{(2)} x Z_{21}^{(1)} x D_{15} \otimes D_0 \oplus Z_{21}^{(1)} x Z_{21}^{(2)} x Z_{21}^{(1)} x Z_{21}^{(1)} x Z_{21}^{(2)} x D_{15} \otimes D_0 \oplus$$
$$Z_{21}^{(1)} x Z_{21}^{(1)} x Z_{21}^{(2)} x Z_{21}^{(2)} x Z_{21}^{(1)} x D_{15} \otimes D_0 \oplus Z_{21}^{(1)} x Z_{21}^{(1)} x Z_{21}^{(1)} x Z_{21}^{(2)} x Z_{21}^{(2)} x D_{15} \otimes D_0 \oplus$$
$$Z_{21}^{(1)} x Z_{21}^{(1)} x Z_{21}^{(2)} x Z_{21}^{(1)} x Z_{21}^{(2)} x D_{15} \otimes D_0$$

$$M_6 = Z_{21}^{(1)} x Z_{21}^{(1)} x Z_{21}^{(1)} x Z_{21}^{(1)} x Z_{21}^{(1)} x Z_{21}^{(1)} x D_{14} \otimes D_1 \oplus Z_{21}^{(2)} x Z_{21}^{(1)} x Z_{21}^{(1)} x Z_{21}^{(1)} x Z_{21}^{(1)} x Z_{21}^{(1)} x D_{15} \otimes D_0 \oplus$$
$$Z_{21}^{(1)} x Z_{21}^{(2)} x Z_{21}^{(1)} x Z_{21}^{(1)} x Z_{21}^{(1)} x Z_{21}^{(1)} x D_{15} \otimes D_0 \oplus Z_{21}^{(1)} x Z_{21}^{(1)} x Z_{21}^{(2)} x Z_{21}^{(1)} x Z_{21}^{(1)} x Z_{21}^{(1)} x D_{15} \otimes D_0 \oplus$$
$$Z_{21}^{(1)} x Z_{21}^{(1)} x Z_{21}^{(1)} x Z_{21}^{(2)} x Z_{21}^{(1)} x Z_{21}^{(1)} x D_{15} \otimes D_0 \oplus Z_{21}^{(1)} x Z_{21}^{(1)} x Z_{21}^{(1)} x Z_{21}^{(1)} x Z_{21}^{(2)} x Z_{21}^{(1)} x D_{15} \otimes D_0 \oplus$$
$$Z_{21}^{(1)} x Z_{21}^{(1)} x Z_{21}^{(1)} x Z_{21}^{(1)} x Z_{21}^{(1)} x Z_{21}^{(2)} x D_{15} \otimes D_0$$

$$M_7 = Z_{21}^{(1)} x Z_{21}^{(1)} x Z_{21}^{(1)} x Z_{21}^{(1)} x Z_{21}^{(1)} x Z_{21}^{(1)} x Z_{21}^{(1)} x D_{15} \otimes D_0$$

3. The Exactness of the Weyl Resolution in the Case of Partition (8,7)

This section clarify the construction of a contracting homotopies $\{ S_i \}$ in the case of partition (8,7) where i = 1,2, …, 6 as follows:

$S_0 : D_8 \otimes D_7 \longrightarrow \sum_{\kappa > 0} Z_{21}^{(\kappa)} x D_{8+\kappa} \otimes D_{7-\kappa}$ such that

$$S_0\left(\left(\begin{array}{c|cc} w & 1^{(8)} & 2^{(\kappa)} \\ w' & 2^{(7-\kappa)} & \end{array}\right)\right)=\begin{cases} 0 & \text{if } \kappa \le 0 \\ Z_{21}^{(\kappa)} x \left(\begin{array}{c|c} w & 1^{(8+\kappa)} \\ w' & 2^{(7-\kappa)} \end{array}\right) & \text{if } \kappa = 1,2,...,7 \end{cases}$$

$$S_1 : \sum_{\kappa>0} Z_{21}^{(\kappa)} x\, D_{8+\kappa} \otimes D_{7-\kappa} \longrightarrow Z_{21}^{(\kappa_1)} x\, Z_{21}^{(\kappa_2)} x\, D_{8+\kappa} \otimes D_{7-\kappa}$$

such that

$$S_1\left(Z_{21}^{(\kappa)} x \left(\begin{array}{c|cc} w & 1^{(8+\kappa)} & 2^{(m)} \\ w' & 2^{(7-\kappa-m)} & \end{array}\right)\right)=\begin{cases} 0 & \text{if } m=0 \\ Z_{21}^{(\kappa)} x\, Z_{21}^{(m)} x \left(\begin{array}{c|c} w & 1^{(8+\kappa+m)} \\ w' & 2^{(7-\kappa-m)} \end{array}\right) & \text{if } m=1,2,...,6 \end{cases}$$

$$S_2 : \sum_{\kappa_i>0} Z_{21}^{(\kappa_1)} x\, Z_{21}^{(\kappa_2)} x\, D_{8+|\kappa|} \otimes D_{7-|\kappa|} \longrightarrow Z_{21}^{(\kappa_1)} x\, Z_{21}^{(\kappa_2)} x\, Z_{21}^{(\kappa_3)} x\, D_{8+|\kappa|} \otimes D_{7-|\kappa|}$$

such that

$$S_2\left(Z_{21}^{(\kappa_1)} x\, Z_{21}^{(\kappa_2)} x \left(\begin{array}{c|cc} w & 1^{(8+|\kappa|)} & 2^{(\wp)} \\ w' & 2^{(7-|\kappa|-m)} & \end{array}\right)\right)=\begin{cases} 0 & \text{if } m=0 \\ Z_{21}^{(\kappa_1)} x\, Z_{21}^{(\kappa_2)} x\, Z_{21}^{(m)} x \left(\begin{array}{c|c} w & 1^{(8+|\kappa|+m)} \\ w' & 2^{(7-|\kappa|-m)} \end{array}\right) & \text{if } m=1,2,...,5 \end{cases},$$

where $|\kappa| = \kappa_1 + \kappa_2$.

$$S_3 : \sum_{\kappa_i>0} Z_{21}^{(\kappa_1)} x\, Z_{21}^{(\kappa_2)} x\, Z_{21}^{(\kappa_3)} x\, D_{8+|\kappa|} \otimes D_{7-|\kappa|} \longrightarrow Z_{21}^{(\kappa_1)} x\, Z_{21}^{(\kappa_2)} x\, Z_{21}^{(\kappa_3)} x\, Z_{21}^{(\kappa_4)} x\, D_{8+|\kappa|} \otimes D_{7-|\kappa|}$$

such that

$$S_3\left(Z_{21}^{(\kappa_1)} x\, Z_{21}^{(\kappa_2)} x\, Z_{21}^{(\kappa_3)} x \left(\begin{array}{c|cc} w & 1^{(8+|\kappa|)} & 2^{(m)} \\ w' & 2^{(7-|\kappa|-m)} & \end{array}\right)\right)=\begin{cases} 0 & \text{if } m=0 \\ Z_{21}^{(\kappa_1)} x\, Z_{21}^{(\kappa_2)} x\, Z_{21}^{(\kappa_3)} x\, Z_{21}^{(m)} x \left(\begin{array}{c|c} w & 1^{(8+|\kappa|+m)} \\ w' & 2^{(7-|\kappa|-m)} \end{array}\right) & \text{if } m=1,2,3,4 \end{cases},$$

where $|\kappa| = \kappa 1 + \kappa 2 + \kappa 3$.

$$S_4 : \sum_{\kappa_i>0} Z_{21}^{(\kappa_1)} x\, Z_{21}^{(\kappa_2)} x\, Z_{21}^{(\kappa_3)} x\, Z_{21}^{(\kappa_4)} x\, D_{8+|\kappa|} \otimes D_{7-|\kappa|} \longrightarrow Z_{21}^{(\kappa_1)} x\, Z_{21}^{(\kappa_2)} x\, Z_{21}^{(\kappa_3)} x\, Z_{21}^{(\kappa_4)} x\, Z_{21}^{(\kappa_5)} x\, D_{8+|\kappa|} \otimes D_{7-|\kappa|}$$

such that

$$S_4\left(Z_{21}^{(\kappa_1)} x\, Z_{21}^{(\kappa_2)} x\, Z_{21}^{(\kappa_3)} x\, Z_{21}^{(\kappa_4)} x \left(\begin{array}{c|cc} w & 1^{(8+|\kappa|)} & 2^{(m)} \\ w' & 2^{(7-|\kappa|-m)} & \end{array}\right)\right)$$

$$=\begin{cases} 0 & \text{if } m=0 \\ Z_{21}^{(\kappa_1)} x\, Z_{21}^{(\kappa_2)} x\, Z_{21}^{(\kappa_3)} x\, Z_{21}^{(\kappa_4)} x\, Z_{21}^{(m)} x \left(\begin{array}{c|c} w & 1^{(8+|\kappa|+m)} \\ w' & 2^{(7-|\kappa|-m)} \end{array}\right) & \text{if } m=1,2,3 \end{cases},$$

where $|\kappa| = \kappa_1 + \kappa_2 + \kappa_3 + \kappa_4$.

$$S_5 : \sum_{\kappa_i > 0} Z_{21}^{(\kappa_1)} x Z_{21}^{(\kappa_2)} x Z_{21}^{(\kappa_3)} x Z_{21}^{(\kappa_4)} x Z_{21}^{(\kappa_5)} x D_{8+|\kappa|} \otimes D_{7-|\kappa|} \to Z_{21}^{(\kappa_1)} x Z_{21}^{(\kappa_2)} x Z_{21}^{(\kappa_3)} x Z_{21}^{(\kappa_4)} x Z_{21}^{(\kappa_5)} x Z_{21}^{(\kappa_6)} x D_{8+|\kappa|} \otimes D_{7-|\kappa|}$$ such that

$$S_5\left(Z_{21}^{(\kappa_1)} x Z_{21}^{(\kappa_2)} x Z_{21}^{(\kappa_3)} x Z_{21}^{(\kappa_4)} x Z_{21}^{(\kappa_5)} x \begin{pmatrix} w & 1^{(8+|\kappa|)} & 2^{(m)} \\ w' & 2^{(7-|\kappa|-m)} & \end{pmatrix} \right)$$

$$= \begin{cases} 0 & \text{if} \quad m = 0 \\ Z_{21}^{(\kappa_1)} x Z_{21}^{(\kappa_2)} x Z_{21}^{(\kappa_3)} x Z_{21}^{(\kappa_4)} x Z_{21}^{(\kappa_5)} x Z_{21}^{(m)} x \begin{pmatrix} w & 1^{(8+|\kappa|+m)} \\ w' & 2^{(7-|\kappa|-m)} \end{pmatrix} & \text{if} \quad m = 1,2 \end{cases},$$

where $|\kappa| = \kappa_1 + \kappa_2 + \kappa_3 + \kappa_4 + \kappa_5$.

$$S_6 : \sum_{\kappa_i > 0} Z_{21}^{(\kappa_1)} x Z_{21}^{(\kappa_2)} x Z_{21}^{(\kappa_3)} x Z_{21}^{(\kappa_4)} x Z_{21}^{(\kappa_5)} x Z_{21}^{(\kappa_6)} x D_{8+|\kappa|} \otimes D_{7-|\kappa|} \longrightarrow$$
$$Z_{21}^{(\kappa_1)} x Z_{21}^{(\kappa_2)} x Z_{21}^{(\kappa_3)} x Z_{21}^{(\kappa_4)} x Z_{21}^{(\kappa_5)} x Z_{21}^{(\kappa_6)} x Z_{21}^{(\kappa_7)} x D_{8+|\kappa|} \otimes D_{7-|\kappa|}$$

such that

$$S_6\left(Z_{21}^{(\kappa_1)} x Z_{21}^{(\kappa_2)} x Z_{21}^{(\kappa_3)} x Z_{21}^{(\kappa_4)} x Z_{21}^{(\kappa_5)} x Z_{21}^{(\kappa_6)} x \begin{pmatrix} w & 1^{(8+|\kappa|)} & 2^{(m)} \\ w' & 2^{(7-|\kappa|-m)} & \end{pmatrix} \right)$$

$$= \begin{cases} 0 & \text{if} \quad m = 0 \\ Z_{21}^{(\kappa_1)} x Z_{21}^{(\kappa_2)} x Z_{21}^{(\kappa_3)} x Z_{21}^{(\kappa_4)} x Z_{21}^{(\kappa_5)} x Z_{21}^{(\kappa_6)} x Z_{21}^{(m)} x \begin{pmatrix} w & 1^{(8+|\kappa|+m)} \\ w' & 2^{(7-|\kappa|-m)} \end{pmatrix} & \text{if} \quad m = 1 \end{cases},$$

where $|\kappa| = \kappa_1 + \kappa_2 + \kappa_3 + \kappa_4 + \kappa_5 + \kappa_6$.

So we possess the posterior scheme:-

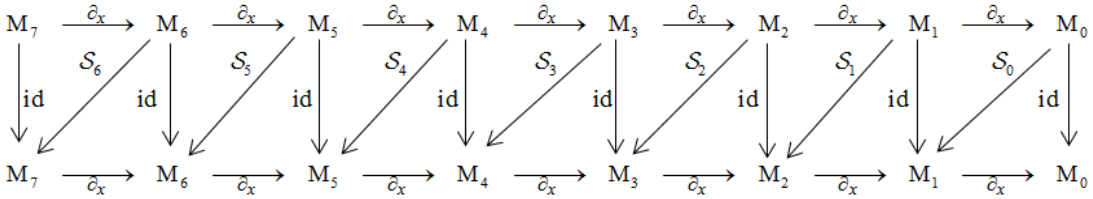

Now we possess

$$S_0 \partial_x \left(Z_{21}^{(\kappa)} x \begin{pmatrix} w & 1^{(8+\kappa)} & 2^{(m)} \\ w' & 2^{(7-\kappa-m)} & \end{pmatrix} \right) = S_0 \partial_{21}^{(\kappa)} \begin{pmatrix} w & 1^{(8+\kappa)} & 2^{(m)} \\ w' & 2^{(7-\kappa-m)} & \end{pmatrix} = \begin{pmatrix} \kappa + m \\ m \end{pmatrix} Z_{21}^{(\kappa+m)} x \begin{pmatrix} w & 1^{(8+\kappa+m)} \\ w' & 2^{(7-\kappa-m)} \end{pmatrix},$$

and

$$\partial_x \mathrm{S}_1\left(\mathrm{Z}_{21}^{(\kappa)} x \begin{pmatrix} \mathrm{w} & 1^{(8+\kappa)} & 2^{(m)} \\ \mathrm{w}' & 2^{(7-\kappa-m)} & \end{pmatrix}\right) = \partial_x\left(\mathrm{Z}_{21}^{(\kappa)} x \mathrm{Z}_{21}^{(m)} x \begin{pmatrix} \mathrm{w} & 1^{(8+\kappa+m)} \\ \mathrm{w}' & 2^{(7-\kappa-m)} \end{pmatrix}\right)$$
$$= -\binom{\kappa+m}{m} \mathrm{Z}_{21}^{(\kappa+m)} \begin{pmatrix} \mathrm{w} & 1^{(8+\kappa+m)} \\ \mathrm{w}' & 2^{(7-\kappa-m)} \end{pmatrix} + \mathrm{Z}_{21}^{(\kappa)} x \begin{pmatrix} \mathrm{w} & 1^{(8+\kappa)} & 2^{(m)} \\ \mathrm{w}' & 2^{(7-\kappa-m)} & \end{pmatrix}$$

It is lucid that $\mathrm{S}_0\partial_x + \partial_x \mathrm{S}_1 = \mathrm{id}$.

$$\mathrm{S}_1\partial_x\left(\mathrm{Z}_{21}^{(\kappa_1)} x \mathrm{Z}_{21}^{(\kappa_2)} x \begin{pmatrix} \mathrm{w} & 1^{(8+|\kappa|)} & 2^{(m)} \\ \mathrm{w}' & 2^{(7-|\kappa|-m)} & \end{pmatrix}\right)$$
$$= \mathrm{S}_1\left[-\binom{|\kappa|}{\kappa_2} \mathrm{Z}_{21}^{(|\kappa|)} x \begin{pmatrix} \mathrm{w} & 1^{(8+|\kappa|)} & 2^{(m)} \\ \mathrm{w}' & 2^{(7-|\kappa|-m)} & \end{pmatrix} + \mathrm{Z}_{21}^{(\kappa_1)} x\, \partial_{21}^{(\kappa_2)} \begin{pmatrix} \mathrm{w} & 1^{(8+|\kappa|)} & 2^{(m)} \\ \mathrm{w}' & 2^{(7-|\kappa|-m)} & \end{pmatrix}\right]$$
$$= -\binom{|\kappa|}{\kappa_2} \mathrm{Z}_{21}^{(|\kappa|)} x \mathrm{Z}_{21}^{(m)} x \begin{pmatrix} \mathrm{w} & 1^{(8+|\kappa|+m)} \\ \mathrm{w}' & 2^{(7-|\kappa|-m)} \end{pmatrix} + \binom{\kappa_2+m}{m} \mathrm{Z}_{21}^{(\kappa_1)} x \mathrm{Z}_{21}^{(\kappa_2+m)} x \begin{pmatrix} \mathrm{w} & 1^{(8+|\kappa|+m)} \\ \mathrm{w}' & 2^{(7-|\kappa|-m)} \end{pmatrix},$$

and

$$\partial_x \mathrm{S}_2\left(\mathrm{Z}_{21}^{(\kappa_1)} x \mathrm{Z}_{21}^{(\kappa_2)} x \begin{pmatrix} \mathrm{w} & 1^{(8+|\kappa|)} & 2^{(m)} \\ \mathrm{w}' & 2^{(7-|\kappa|-m)} & \end{pmatrix}\right) = \partial_x\left(\mathrm{Z}_{21}^{(\kappa_1)} x \mathrm{Z}_{21}^{(\kappa_2)} x \mathrm{Z}_{21}^{(m)} x \begin{pmatrix} \mathrm{w} & 1^{(8+|\kappa|+m)} \\ \mathrm{w}' & 2^{(7-|\kappa|-m)} \end{pmatrix}\right)$$
$$= \binom{|\kappa|}{\kappa_2} \mathrm{Z}_{21}^{(|\kappa|)} x \mathrm{Z}_{21}^{(m)} x \begin{pmatrix} \mathrm{w} & 1^{(8+|\kappa|+m)} \\ \mathrm{w}' & 2^{(7-|\kappa|-m)} \end{pmatrix} - \binom{\kappa_2+m}{m} \mathrm{Z}_{21}^{(\kappa_1)} x \mathrm{Z}_{21}^{(\kappa_2+m)} x \begin{pmatrix} \mathrm{w} & 1^{(8+|\kappa|+m)} \\ \mathrm{w}' & 2^{(7-|\kappa|-m)} \end{pmatrix} + \mathrm{Z}_{21}^{(\kappa_1)} x \mathrm{Z}_{21}^{(\kappa_2)} x$$
$$\begin{pmatrix} \mathrm{w} & 1^{(8+|\kappa|)} & 2^{(m)} \\ \mathrm{w}' & 2^{(7-|\kappa|-m)} & \end{pmatrix},$$

where $|\kappa| = \kappa_1 + \kappa_2$.

It is lucid that $\mathrm{S}_1\partial_x + \partial_x \mathrm{S}_2 = \mathrm{id}$.

$$S_2\partial_x\left(Z_{21}^{(\kappa_1)}xZ_{21}^{(\kappa_2)}xZ_{21}^{(\kappa_3)}x\begin{pmatrix} w & 1^{(8+|\kappa|)} & 2^{(m)} \\ w' & 2^{(7-|\kappa|-m)} & \end{pmatrix}\right)$$

$$= S_2\left[\binom{\kappa_1+\kappa_2}{\kappa_2}Z_{21}^{(\kappa_1+\kappa_2)}xZ_{21}^{(\kappa_3)}x\begin{pmatrix} w & 1^{(8+|\kappa|)} & 2^{(m)} \\ w' & 2^{(7-|\kappa|-m)} & \end{pmatrix}-\binom{\kappa_2+\kappa_3}{\kappa_3}Z_{21}^{(\kappa_1)}xZ_{21}^{(\kappa_2+\kappa_3)}x\begin{pmatrix} w & 1^{(8+|\kappa|)} & 2^{(m)} \\ w' & 2^{(7-|\kappa|-m)} & \end{pmatrix}+\right.$$

$$\left.Z_{21}^{(\kappa_1)}xZ_{21}^{(\kappa_2)}x\ \partial_{21}^{(\kappa_3)}\begin{pmatrix} w & 1^{(8+|\kappa|)} & 2^{(m)} \\ w' & 2^{(7-|\kappa|-m)} & \end{pmatrix}\right]$$

$$=\binom{\kappa_1+\kappa_2}{\kappa_2}Z_{21}^{(\kappa_1+\kappa_2)}xZ_{21}^{(\kappa_3)}xZ_{21}^{(m)}x\begin{pmatrix} w & 1^{(8+|\kappa|+m)} \\ w' & 2^{(7-|\kappa|-m)} \end{pmatrix}-\binom{\kappa_2+\kappa_3}{\kappa_3}Z_{21}^{(\kappa_1)}xZ_{21}^{(\kappa_2+\kappa_3)}xZ_{21}^{(m)}x\begin{pmatrix} w & 1^{(8+|\kappa|+m)} \\ w' & 2^{(7-|\kappa|-m)} \end{pmatrix}+$$

$$\binom{\kappa_3+m}{m}Z_{21}^{(\kappa_1)}xZ_{21}^{(\kappa_2)}xZ_{21}^{(\kappa_3+m)}x\begin{pmatrix} w & 1^{(8+|\kappa|+m)} \\ w' & 2^{(7-|\kappa|-m)} \end{pmatrix},$$

and

$$\partial_x S_3\left(Z_{21}^{(\kappa_1)}xZ_{21}^{(\kappa_2)}xZ_{21}^{(\kappa_3)}x\begin{pmatrix} w & 1^{(8+|\kappa|)} & 2^{(m)} \\ w' & 2^{(7-|\kappa|-m)} & \end{pmatrix}\right)=\partial_x\left(Z_{21}^{(\kappa_1)}xZ_{21}^{(\kappa_2)}xZ_{21}^{(\kappa_3)}xZ_{21}^{(m)}x\begin{pmatrix} w & 1^{(8+|\kappa|+m)} \\ w' & 2^{(7-|\kappa|-m)} \end{pmatrix}\right)$$

$$=-\binom{\kappa_1+\kappa_2}{\kappa_2}Z_{21}^{(\kappa_1+\kappa_2)}xZ_{21}^{(\kappa_3)}xZ_{21}^{(m)}x\begin{pmatrix} w & 1^{(8+|\kappa|+m)} \\ w' & 2^{(7-|\kappa|-m)} \end{pmatrix}+\binom{\kappa_2+\kappa_3}{\kappa_3}Z_{21}^{(\kappa_1)}xZ_{21}^{(\kappa_2+\kappa_3)}xZ_{21}^{(m)}x\begin{pmatrix} w & 1^{(8+|\kappa|+m)} \\ w' & 2^{(7-|\kappa|-m)} \end{pmatrix}-$$

$$\binom{\kappa_3+m}{m}Z_{21}^{(\kappa_1)}xZ_{21}^{(\kappa_2)}xZ_{21}^{(\kappa_3+m)}x\begin{pmatrix} w & 1^{(8+|\kappa|+m)} \\ w' & 2^{(7-|\kappa|-m)} \end{pmatrix}+Z_{21}^{(\kappa_1)}xZ_{21}^{(\kappa_2)}xZ_{21}^{(\kappa_3)}x\ \partial_{21}^{(m)}\begin{pmatrix} w & 1^{(8+|\kappa|+m)} \\ w' & 2^{(7-|\kappa|-m)} \end{pmatrix}$$

$$=-\binom{\kappa_1+\kappa_2}{\kappa_2}Z_{21}^{(\kappa_1+\kappa_2)}xZ_{21}^{(\kappa_3)}xZ_{21}^{(m)}x\begin{pmatrix} w & 1^{(8+|\kappa|+m)} \\ w' & 2^{(7-|\kappa|-m)} \end{pmatrix}+\binom{\kappa_2+\kappa_3}{\kappa_3}Z_{21}^{(\kappa_1)}xZ_{21}^{(\kappa_2+\kappa_3)}xZ_{21}^{(m)}x\begin{pmatrix} w & 1^{(8+|\kappa|+m)} \\ w' & 2^{(7-|\kappa|-m)} \end{pmatrix}-$$

$$\binom{\kappa_3+m}{m}Z_{21}^{(\kappa_1)}xZ_{21}^{(\kappa_2)}xZ_{21}^{(\kappa_3+m)}x\begin{pmatrix} w & 1^{(8+|\kappa|+m)} \\ w' & 2^{(7-|\kappa|-m)} \end{pmatrix}+Z_{21}^{(\kappa_1)}xZ_{21}^{(\kappa_2)}xZ_{21}^{(\kappa_3)}x\begin{pmatrix} w & 1^{(8+|\kappa|)} & 2^{(m)} \\ w' & 2^{(7-|\kappa|-m)} & \end{pmatrix},$$

where $|\kappa| = \kappa_1 + \kappa_2 + \kappa_3$.

It is lucid that $S_2\partial_x + \partial_x S_3 = \mathrm{id}$.

$$S_3\partial_x\left(Z_{21}^{(\kappa_1)}xZ_{21}^{(\kappa_2)}xZ_{21}^{(\kappa_3)}xZ_{21}^{(\kappa_4)}x\begin{pmatrix} w & 1^{(8+|\kappa|)} & 2^{(m)} \\ w' & 2^{(7-|\kappa|-m)} & \end{pmatrix}\right)$$

$$= S_3\left[-\binom{\kappa_1+\kappa_2}{\kappa_2} Z_{21}^{(\kappa_1+\kappa_2)} x\, Z_{21}^{(\kappa_3)} x\, Z_{21}^{(\kappa_4)} x \begin{pmatrix} w & 1^{(8+|\kappa|)} & 2^{(m)} \\ w' & 2^{(7-|\kappa|-m)} & \end{pmatrix} + \binom{\kappa_2+\kappa_3}{\kappa_3} Z_{21}^{(\kappa_1)} x\, Z_{21}^{(\kappa_2+\kappa_3)} x \right.$$

$$Z_{21}^{(\kappa_4)} x \begin{pmatrix} w & 1^{(8+|\kappa|)} & 2^{(m)} \\ w' & 2^{(7-|\kappa|-m)} & \end{pmatrix} - \binom{\kappa_3+\kappa_4}{\kappa_4} Z_{21}^{(\kappa_1)} x\, Z_{21}^{(\kappa_2)} x\, Z_{21}^{(\kappa_3+\kappa_4)} x \begin{pmatrix} w & 1^{(8+|\kappa|)} & 2^{(m)} \\ w' & 2^{(7-|\kappa|-m)} & \end{pmatrix} +$$

$$\left. Z_{21}^{(\kappa_1)} x\, Z_{21}^{(\kappa_2)} x Z_{21}^{(\kappa_3)} x\, \partial_{21}^{(\kappa_4)} \begin{pmatrix} w & 1^{(8+|\kappa|)} & 2^{(m)} \\ w' & 2^{(7-|\kappa|-m)} & \end{pmatrix} \right]$$

$$= -\binom{\kappa_1+\kappa_2}{\kappa_2} Z_{21}^{(\kappa_1+\kappa_2)} x\, Z_{21}^{(\kappa_3)} x\, Z_{21}^{(\kappa_4)} x\, Z_{21}^{(m)} x \begin{pmatrix} w & 1^{(8+|\kappa|+m)} \\ w' & 2^{(7-|\kappa|-m)} \end{pmatrix} + \binom{\kappa_2+\kappa_3}{\kappa_3} Z_{21}^{(\kappa_1)} x\, Z_{21}^{(\kappa_2+\kappa_3)} x$$

$$Z_{21}^{(\kappa_4)} x\, Z_{21}^{(m)} x \begin{pmatrix} w & 1^{(8+|\kappa|+m)} \\ w' & 2^{(7-|\kappa|-m)} \end{pmatrix} - \binom{\kappa_3+\kappa_4}{\kappa_4} Z_{21}^{(\kappa_1)} x\, Z_{21}^{(\kappa_2)} x\, Z_{21}^{(\kappa_3+\kappa_4)} x\, Z_{21}^{(m)} x \begin{pmatrix} w & 1^{(8+|\kappa|+m)} \\ w' & 2^{(7-|\kappa|-m)} \end{pmatrix} +$$

$$\binom{\kappa_4+m}{m} Z_{21}^{(\kappa_1)} x\, Z_{21}^{(\kappa_2)} x Z_{21}^{(\kappa_3)} x\, Z_{21}^{(\kappa_4+m)} x \begin{pmatrix} w & 1^{(8+|\kappa|+m)} \\ w' & 2^{(7-|\kappa|-m)} \end{pmatrix},$$

and

$$\partial_x S_4 \left(Z_{21}^{(\kappa_1)} x\, Z_{21}^{(\kappa_2)} x\, Z_{21}^{(\kappa_3)} x\, Z_{21}^{(\kappa_4)} x \begin{pmatrix} w & 1^{(8+|\kappa|)} & 2^{(m)} \\ w' & 2^{(7-|\kappa|-m)} & \end{pmatrix} \right)$$

$$= \partial_x \left(Z_{21}^{(\kappa_1)} x\, Z_{21}^{(\kappa_2)} x\, Z_{21}^{(\kappa_3)} x\, Z_{21}^{(\kappa_4)} x\, Z_{21}^{(m)} x \begin{pmatrix} w & 1^{(8+|\kappa|+m)} \\ w' & 2^{(7-|\kappa|-m)} \end{pmatrix} \right)$$

$$= \binom{\kappa_1+\kappa_2}{\kappa_2} Z_{21}^{(\kappa_1+\kappa_2)} x\, Z_{21}^{(\kappa_3)} x\, Z_{21}^{(\kappa_4)} x\, Z_{21}^{(m)} x \begin{pmatrix} w & 1^{(8+|\kappa|+m)} \\ w' & 2^{(7-|\kappa|-m)} \end{pmatrix} - \binom{\kappa_2+\kappa_3}{\kappa_3} Z_{21}^{(\kappa_1)} x\, Z_{21}^{(\kappa_2+\kappa_3)} x\, Z_{21}^{(\kappa_4)} x$$

$$Z_{21}^{(m)} x \begin{pmatrix} w & 1^{(8+|\kappa|+m)} \\ w' & 2^{(7-|\kappa|-m)} \end{pmatrix} + \binom{\kappa_3+\kappa_4}{\kappa_4} Z_{21}^{(\kappa_1)} x\, Z_{21}^{(\kappa_2)} x\, Z_{21}^{(\kappa_3+\kappa_4)} x\, Z_{21}^{(m)} x \begin{pmatrix} w & 1^{(8+|\kappa|+m)} \\ w' & 2^{(7-|\kappa|-m)} \end{pmatrix} - \binom{\kappa_4+m}{m}$$

$$Z_{21}^{(\kappa_1)} x\, Z_{21}^{(\kappa_2)} x\, Z_{21}^{(\kappa_3)} x\, Z_{21}^{(\kappa_4+m)} x \begin{pmatrix} w & 1^{(8+|\kappa|+m)} \\ w' & 2^{(7-|\kappa|-m)} \end{pmatrix} + Z_{21}^{(\kappa_1)} x\, Z_{21}^{(\kappa_2)} x\, Z_{21}^{(\kappa_3)} x\, Z_{21}^{(\kappa_4)} x\, \partial_{21}^{(m)} \begin{pmatrix} w & 1^{(8+|\kappa|+m)} \\ w' & 2^{(7-|\kappa|-m)} \end{pmatrix}$$

$$= \binom{\kappa_1+\kappa_2}{\kappa_2} Z_{21}^{(\kappa_1+\kappa_2)} x Z_{21}^{(\kappa_3)} x Z_{21}^{(\kappa_4)} x Z_{21}^{(m)} x \begin{pmatrix} w \\ w' \end{pmatrix} \begin{matrix} 1^{(8+|\kappa|+m)} \\ 2^{(7-|\kappa|-m)} \end{matrix} - \binom{\kappa_2+\kappa_3}{\kappa_3} Z_{21}^{(\kappa_1)} x Z_{21}^{(\kappa_2+\kappa_3)} x Z_{21}^{(\kappa_4)} x Z_{21}^{(m)} x$$

$$\begin{pmatrix} w \\ w' \end{pmatrix} \begin{matrix} 1^{(8+|\kappa|+m)} \\ 2^{(7-|\kappa|-m)} \end{matrix} + \binom{\kappa_3+\kappa_4}{\kappa_4} Z_{21}^{(\kappa_1)} x Z_{21}^{(\kappa_2)} x Z_{21}^{(\kappa_3+\kappa_4)} x Z_{21}^{(m)} x \begin{pmatrix} w \\ w' \end{pmatrix} \begin{matrix} 1^{(8+|\kappa|+m)} \\ 2^{(7-|\kappa|-m)} \end{matrix} - \binom{\kappa_4+m}{m} Z_{21}^{(\kappa_1)} x Z_{21}^{(\kappa_2)} x$$

$$Z_{21}^{(\kappa_3)} x Z_{21}^{(\kappa_4+m)} x \begin{pmatrix} w \\ w' \end{pmatrix} \begin{matrix} 1^{(8+|\kappa|+m)} \\ 2^{(7-|\kappa|-m)} \end{matrix} + Z_{21}^{(\kappa_1)} x Z_{21}^{(\kappa_2)} x Z_{21}^{(\kappa_3)} x Z_{21}^{(\kappa_4)} x \begin{pmatrix} w \\ w' \end{pmatrix} \begin{matrix} 1^{(8+|\kappa|)} & 2^{(m)} \\ 2^{(7-|\kappa|-m)} & \end{matrix} ,$$

where $|\kappa| = \kappa_1 + \kappa_2 + \kappa_3 + \kappa_4$.

It is lucid that $S_3\partial_x + \partial_x S_4 = \mathrm{id}$.

$$S_4\partial_x \left(Z_{21}^{(\kappa_1)} x Z_{21}^{(\kappa_2)} x Z_{21}^{(\kappa_3)} x Z_{21}^{(\kappa_4)} x Z_{21}^{(\kappa_5)} x \begin{pmatrix} w \\ w' \end{pmatrix} \begin{matrix} 1^{(8+|\kappa|)} & 2^{(m)} \\ 2^{(7-|\kappa|-m)} & \end{matrix} \right)$$

$$= S_4 \left[\binom{\kappa_1+\kappa_2}{\kappa_2} Z_{21}^{(\kappa_1+\kappa_2)} x Z_{21}^{(\kappa_3)} x Z_{21}^{(\kappa_4)} x Z_{21}^{(\kappa_5)} x \begin{pmatrix} w \\ w' \end{pmatrix} \begin{matrix} 1^{(8+|\kappa|)} & 2^{(m)} \\ 2^{(7-|\kappa|-m)} & \end{matrix} - \binom{\kappa_2+\kappa_3}{\kappa_3} Z_{21}^{(\kappa_1)} x Z_{21}^{(\kappa_2+\kappa_3)} x Z_{21}^{(\kappa_4)} x Z_{21}^{(\kappa_5)} x \right.$$

$$\begin{pmatrix} w \\ w' \end{pmatrix} \begin{matrix} 1^{(8+|\kappa|)} & 2^{(m)} \\ 2^{(7-|\kappa|-m)} & \end{matrix} + \binom{\kappa_3+\kappa_4}{\kappa_4} Z_{21}^{(\kappa_1)} x Z_{21}^{(\kappa_2)} x Z_{21}^{(\kappa_3+\kappa_4)} x Z_{21}^{(\kappa_5)} x \begin{pmatrix} w \\ w' \end{pmatrix} \begin{matrix} 1^{(8+|\kappa|)} & 2^{(m)} \\ 2^{(7-|\kappa|-m)} & \end{matrix} - \binom{\kappa_4+\kappa_5}{\kappa_5} Z_{21}^{(\kappa_1)} x$$

$$\left. Z_{21}^{(\kappa_2)} x Z_{21}^{(\kappa_3)} x Z_{21}^{(\kappa_4+\kappa_5)} x \begin{pmatrix} w \\ w' \end{pmatrix} \begin{matrix} 1^{(8+|\kappa|)} & 2^{(m)} \\ 2^{(7-|\kappa|-m)} & \end{matrix} + Z_{21}^{(\kappa_1)} x Z_{21}^{(\kappa_2)} x Z_{21}^{(\kappa_3)} x Z_{21}^{(\kappa_4)} x \partial_{21}^{(\kappa_5)} \begin{pmatrix} w \\ w' \end{pmatrix} \begin{matrix} 1^{(8+|\kappa|)} & 2^{(m)} \\ 2^{(7-|\kappa|-m)} & \end{matrix} \right]$$

$$= \binom{\kappa_1+\kappa_2}{\kappa_2} Z_{21}^{(\kappa_1+\kappa_2)} x Z_{21}^{(\kappa_3)} x Z_{21}^{(\kappa_4)} x Z_{21}^{(\kappa_5)} x Z_{21}^{(m)} x \begin{pmatrix} w \\ w' \end{pmatrix} \begin{matrix} 1^{(8+|\kappa|+m)} \\ 2^{(7-|\kappa|-m)} \end{matrix} - \binom{\kappa_2+\kappa_3}{\kappa_3} Z_{21}^{(\kappa_1)} x Z_{21}^{(\kappa_2+\kappa_3)} x Z_{21}^{(\kappa_4)} x$$

$$Z_{21}^{(\kappa_5)} x Z_{21}^{(m)} x \begin{pmatrix} w \\ w' \end{pmatrix} \begin{matrix} 1^{(8+|\kappa|+m)} \\ 2^{(7-|\kappa|-m)} \end{matrix} + \binom{\kappa_3+\kappa_4}{\kappa_4} Z_{21}^{(\kappa_1)} x Z_{21}^{(\kappa_2)} x Z_{21}^{(\kappa_3+\kappa_4)} x Z_{21}^{(\kappa_5)} x Z_{21}^{(m)} x \begin{pmatrix} w \\ w' \end{pmatrix} \begin{matrix} 1^{(8+|\kappa|+m)} \\ 2^{(7-|\kappa|-m)} \end{matrix} -$$

$$\binom{\kappa_4+\kappa_5}{\kappa_5} Z_{21}^{(\kappa_1)} x Z_{21}^{(\kappa_2)} x Z_{21}^{(\kappa_3)} x Z_{21}^{(\kappa_4+\kappa_5)} x Z_{21}^{(m)} x \begin{pmatrix} w \\ w' \end{pmatrix} \begin{matrix} 1^{(8+|\kappa|+m)} \\ 2^{(7-|\kappa|-m)} \end{matrix} + \binom{\kappa_5+m}{m} Z_{21}^{(\kappa_1)} x Z_{21}^{(\kappa_2)} x Z_{21}^{(\kappa_3)} x$$

$$Z_{21}^{(\kappa_4)} x Z_{21}^{(\kappa_5+m)} x \begin{pmatrix} w \\ w' \end{pmatrix} \begin{matrix} 1^{(8+|\kappa|+m)} \\ 2^{(7-|\kappa|-m)} \end{matrix} ,$$

and

$$\partial_x S_5 \left(Z_{21}^{(\kappa_1)} x Z_{21}^{(\kappa_2)} x Z_{21}^{(\kappa_3)} x Z_{21}^{(\kappa_4)} x Z_{21}^{(\kappa_5)} x \begin{pmatrix} w \\ w' \end{pmatrix} \begin{matrix} 1^{(8+|\kappa|)} & 2^{(m)} \\ 2^{(7-|\kappa|-m)} & \end{matrix} \right)$$

$$= \partial_x \left(Z_{21}^{(\kappa_1)} x Z_{21}^{(\kappa_2)} x Z_{21}^{(\kappa_3)} x Z_{21}^{(\kappa_4)} x Z_{21}^{(\kappa_5)} x Z_{21}^{(m)} x \begin{pmatrix} w \\ w' \end{pmatrix} \begin{matrix} 1^{(8+|\kappa|+m)} \\ 2^{(7-|\kappa|-m)} \end{matrix} \right)$$

$$= -\binom{\kappa_1+\kappa_2}{\kappa_2} Z_{21}^{(\kappa_1+\kappa_2)} x\, Z_{21}^{(\kappa_3)} x\, Z_{21}^{(\kappa_4)} x\, Z_{21}^{(\kappa_5)} x\, Z_{21}^{(m)} x \begin{pmatrix} w \\ w' \end{pmatrix} \begin{matrix} 1^{(8+|\kappa|+m)} \\ 2^{(7-|\kappa|-m)} \end{matrix} + \binom{\kappa_2+\kappa_3}{\kappa_3} Z_{21}^{(\kappa_1)} x\, Z_{21}^{(\kappa_2+\kappa_3)} x\, Z_{21}^{(\kappa_4)} x$$

$$Z_{21}^{(\kappa_5)} x\, Z_{21}^{(m)} x \begin{pmatrix} w \\ w' \end{pmatrix} \begin{matrix} 1^{(8+|\kappa|+m)} \\ 2^{(7-|\kappa|-m)} \end{matrix} - \binom{\kappa_3+\kappa_4}{\kappa_4} Z_{21}^{(\kappa_1)} x\, Z_{21}^{(\kappa_2)} x\, Z_{21}^{(\kappa_3+\kappa_4)} x\, Z_{21}^{(\kappa_5)} x\, Z_{21}^{(m)} x \begin{pmatrix} w \\ w' \end{pmatrix} \begin{matrix} 1^{(8+|\kappa|+m)} \\ 2^{(7-|\kappa|-m)} \end{matrix} +$$

$$\binom{\kappa_4+\kappa_5}{\kappa_4} Z_{21}^{(\kappa_1)} x\, Z_{21}^{(\kappa_2)} x\, Z_{21}^{(\kappa_3)} x\, Z_{21}^{(\kappa_4+\kappa_5)} x\, Z_{21}^{(m)} x \begin{pmatrix} w \\ w' \end{pmatrix} \begin{matrix} 1^{(8+|\kappa|+m)} \\ 2^{(7-|\kappa|-m)} \end{matrix} - \binom{\kappa_5+m}{m} Z_{21}^{(\kappa_1)} x\, Z_{21}^{(\kappa_2)} x\, Z_{21}^{(\kappa_3)} x\, Z_{21}^{(\kappa_4)} x$$

$$Z_{21}^{(\kappa_5+m)} x \begin{pmatrix} w \\ w' \end{pmatrix} \begin{matrix} 1^{(8+|\kappa|+m)} \\ 2^{(7-|\kappa|-m)} \end{matrix} + Z_{21}^{(\kappa_1)} x\, Z_{21}^{(\kappa_2)} x\, Z_{21}^{(\kappa_3)} x\, Z_{21}^{(\kappa_4)} x\, Z_{21}^{(\kappa_5)} x\, \partial_{21}^{(m)} \begin{pmatrix} w \\ w' \end{pmatrix} \begin{matrix} 1^{(8+|\kappa|+m)} \\ 2^{(7-|\kappa|-m)} \end{matrix}$$

$$= -\binom{\kappa_1+\kappa_2}{\kappa_2} Z_{21}^{(\kappa_1+\kappa_2)} x\, Z_{21}^{(\kappa_3)} x\, Z_{21}^{(\kappa_4)} x\, Z_{21}^{(\kappa_5)} x\; Z_{21}^{(m)} x \begin{pmatrix} w \\ w' \end{pmatrix} \begin{matrix} 1^{(8+|\kappa|+m)} \\ 2^{(7-|\kappa|-m)} \end{matrix} + \binom{\kappa_2+\kappa_3}{\kappa_3} Z_{21}^{(\kappa_1)} x\, Z_{21}^{(\kappa_2+\kappa_3)} x\, Z_{21}^{(\kappa_4)} x$$

$$Z_{21}^{(\kappa_5)} x\, Z_{21}^{(m)} x \begin{pmatrix} w \\ w' \end{pmatrix} \begin{matrix} 1^{(8+|\kappa|+m)} \\ 2^{(7-|\kappa|-m)} \end{matrix} - \binom{\kappa_3+\kappa_4}{\kappa_4} Z_{21}^{(\kappa_1)} x\, Z_{21}^{(\kappa_2)} x\, Z_{21}^{(\kappa_3+\kappa_4)} x\, Z_{21}^{(\kappa_5)} x\, Z_{21}^{(m)} x \begin{pmatrix} w \\ w' \end{pmatrix} \begin{matrix} 1^{(8+|\kappa|+m)} \\ 2^{(7-|\kappa|-m)} \end{matrix} +$$

$$\binom{\kappa_4+\kappa_5}{\kappa_4} Z_{21}^{(\kappa_1)} x\, Z_{21}^{(\kappa_2)} x\, Z_{21}^{(\kappa_3)} x\, Z_{21}^{(\kappa_4+\kappa_5)} x\, Z_{21}^{(m)} x \begin{pmatrix} w \\ w' \end{pmatrix} \begin{matrix} 1^{(8+|\kappa|+m)} \\ 2^{(7-|\kappa|-m)} \end{matrix} - \binom{\kappa_5+m}{m} Z_{21}^{(\kappa_1)} x\, Z_{21}^{(\kappa_2)} x\, Z_{21}^{(\kappa_3)} x$$

$$Z_{21}^{(\kappa_4)} x\, Z_{21}^{(\kappa_5+m)} x \begin{pmatrix} w \\ w' \end{pmatrix} \begin{matrix} 1^{(8+|\kappa|+m)} \\ 2^{(7-|\kappa|-m)} \end{matrix} + Z_{21}^{(\kappa_1)} x\, Z_{21}^{(\kappa_2)} x\, Z_{21}^{(\kappa_3)} x\, Z_{21}^{(\kappa_4)} x\, Z_{21}^{(\kappa_5)} x \begin{pmatrix} w \\ w' \end{pmatrix} \begin{matrix} 1^{(8+|\kappa|)} & 2^{(m)} \\ 2^{(7-|\kappa|-m)} & \end{matrix} ,$$

where $|\kappa| = \kappa_1 + \kappa_2 + \kappa_3 + \kappa_4 + \kappa_5$.

It is lucid that $S_4\partial_x + \partial_x S_5 = \mathrm{id}$.

$$S_5\partial_x \left(Z_{21}^{(\kappa_1)} x\, Z_{21}^{(\kappa_2)} x\, Z_{21}^{(\kappa_3)} x\, Z_{21}^{(\kappa_4)} x\, Z_{21}^{(\kappa_5)} x\, Z_{21}^{(\kappa_6)} x \begin{pmatrix} w \\ w' \end{pmatrix} \begin{matrix} 1^{(8+|\kappa|)} & 2^{(m)} \\ 2^{(7-|\kappa|-m)} & \end{matrix} \right)$$

$$= S_5\left[-\binom{\kappa_1+\kappa_2}{\kappa_2} Z_{21}^{(\kappa_1+\kappa_2)} x\, Z_{21}^{(\kappa_3)} x\, Z_{21}^{(\kappa_4)} x\, Z_{21}^{(\kappa_5)} x\, Z_{21}^{(\kappa_6)} x \begin{pmatrix} w \\ w' \end{vmatrix} \begin{matrix} 1^{(8+|\kappa|)} & 2^{(m)} \\ 2^{(7-|\kappa|-m)} & \end{matrix} \right) + \binom{\kappa_2+\kappa_3}{\kappa_3} Z_{21}^{(\kappa_1)} x$$

$$Z_{21}^{(\kappa_2+\kappa_3)} x\, Z_{21}^{(\kappa_4)} x\, Z_{21}^{(\kappa_5)} x\, Z_{21}^{(\kappa_6)} x \begin{pmatrix} w \\ w' \end{vmatrix} \begin{matrix} 1^{(8+|\kappa|)} & 2^{(m)} \\ 2^{(7-|\kappa|-m)} & \end{matrix} \right) - \binom{\kappa_3+\kappa_4}{\kappa_4} Z_{21}^{(\kappa_1)} x\, Z_{21}^{(\kappa_2)} x\, Z_{21}^{(\kappa_3+\kappa_4)} x\, Z_{21}^{(\kappa_5)} x\, Z_{21}^{(\kappa_6)} x$$

$$\begin{pmatrix} w \\ w' \end{vmatrix} \begin{matrix} 1^{(8+|\kappa|)} & 2^{(m)} \\ 2^{(7-|\kappa|-m)} & \end{matrix} \right) + \binom{\kappa_4+\kappa_5}{\kappa_5} Z_{21}^{(\kappa_1)} x\, Z_{21}^{(\kappa_2)} x\, Z_{21}^{(\kappa_3)} x\, Z_{21}^{(\kappa_4+\kappa_5)} x\, Z_{21}^{(\kappa_6)} x \begin{pmatrix} w \\ w' \end{vmatrix} \begin{matrix} 1^{(8+|\kappa|)} & 2^{(m)} \\ 2^{(7-|\kappa|-m)} & \end{matrix} \right) - \binom{\kappa_5+\kappa_6}{\kappa_6} Z_{21}^{(\kappa_1)} x$$

$$Z_{21}^{(\kappa_2)} x\, Z_{21}^{(\kappa_3)} x\, Z_{21}^{(\kappa_4)} x\, Z_{21}^{(\kappa_5+\kappa_6)} x \begin{pmatrix} w \\ w' \end{vmatrix} \begin{matrix} 1^{(8+|\kappa|)} & 2^{(m)} \\ 2^{(7-|\kappa|-\wp)} & \end{matrix} \right) + Z_{21}^{(\kappa_1)} x\, Z_{21}^{(\kappa_2)} x\, Z_{21}^{(\kappa_3)} x\, Z_{21}^{(\kappa_4)} x\; Z_{21}^{(\kappa_5)} x\, \partial_{21}^{(\kappa_6)} \begin{pmatrix} w \\ w' \end{vmatrix} \begin{matrix} 1^{(8+|\kappa|)} & 2^{(m)} \\ 2^{(7-|\kappa|-m)} & \end{matrix} \right) \Bigg]$$

$$= -\binom{\kappa_1+\kappa_2}{\kappa_2} Z_{21}^{(\kappa_1+\kappa_2)} x\, Z_{21}^{(\kappa_3)} x\, Z_{21}^{(\kappa_4)} x\, Z_{21}^{(\kappa_5)} x\, Z_{21}^{(\kappa_6)} x\, Z_{21}^{(m)} x \begin{pmatrix} w \\ w' \end{vmatrix} \begin{matrix} 1^{(8+|\kappa|+m)} \\ 2^{(7-|\kappa|-m)} \end{matrix} \right) + \binom{\kappa_2+\kappa_3}{\kappa_3} Z_{21}^{(\kappa_1)} x\, Z_{21}^{(\kappa_2+\kappa_3)} x$$

$$Z_{21}^{(\kappa_4)} x\, Z_{21}^{(\kappa_5)} x\, Z_{21}^{(\kappa_6)} x\, Z_{21}^{(m)} x \begin{pmatrix} w \\ w' \end{vmatrix} \begin{matrix} 1^{(8+|\kappa|+m)} \\ 2^{(7-|\kappa|-m)} \end{matrix} \right) - \binom{\kappa_3+\kappa_4}{\kappa_4} Z_{21}^{(\kappa_1)} x\, Z_{21}^{(\kappa_2)} x\, Z_{21}^{(\kappa_3+\kappa_4)} x\, Z_{21}^{(\kappa_5)} x\, Z_{21}^{(\kappa_6)} x\, Z_{21}^{(m)} x$$

$$\begin{pmatrix} w \\ w' \end{vmatrix} \begin{matrix} 1^{(8+|\kappa|+m)} \\ 2^{(7-|\kappa|-m)} \end{matrix} \right) + \binom{\kappa_4+\kappa_5}{\kappa_5} Z_{21}^{(\kappa_1)} x\, Z_{21}^{(\kappa_2)} x\, Z_{21}^{(\kappa_3)} x\, Z_{21}^{(\kappa_4+\kappa_5)} x\, Z_{21}^{(\kappa_6)} x\, Z_{21}^{(m)} x \begin{pmatrix} w \\ w' \end{vmatrix} \begin{matrix} 1^{(8+|\kappa|+m)} \\ 2^{(7-|\kappa|-m)} \end{matrix} \right) - \binom{\kappa_5+\kappa_6}{\kappa_6}$$

$$Z_{21}^{(\kappa_1)} x\, Z_{21}^{(\kappa_2)} x\, Z_{21}^{(\kappa_3)} x\, Z_{21}^{(\kappa_4)} x\, Z_{21}^{(\kappa_5+\kappa_6)} x\, Z_{21}^{(m)} x \begin{pmatrix} w \\ w' \end{vmatrix} \begin{matrix} 1^{(8+|\kappa|+m)} \\ 2^{(7-|\kappa|-m)} \end{matrix} \right) + \binom{\kappa_6+m}{m} Z_{21}^{(\kappa_1)} x\, Z_{21}^{(\kappa_2)} x\, Z_{21}^{(\kappa_3)} x\, Z_{21}^{(\kappa_4)} x$$

$$Z_{21}^{(\kappa_5)} x\, Z_{21}^{(\kappa_6+m)} x \begin{pmatrix} w \\ w' \end{vmatrix} \begin{matrix} 1^{(8+|\kappa|+m)} \\ 2^{(7-|\kappa|-m)} \end{matrix} \right) ,$$

and

$$\partial_x S_6 \left(Z_{21}^{(\kappa_1)} x\, Z_{21}^{(\kappa_2)} x\, Z_{21}^{(\kappa_3)} x\, Z_{21}^{(\kappa_4)} x\, Z_{21}^{(\kappa_5)} x\, Z_{21}^{(\kappa_6)} x \begin{pmatrix} w \\ w' \end{vmatrix} \begin{matrix} 1^{(8+|\kappa|)} & 2^{(m)} \\ 2^{(7-|\kappa|-m)} & \end{matrix} \right) \right)$$

$$= \partial_x \left(Z_{21}^{(\kappa_1)} x\, Z_{21}^{(\kappa_2)} x\, Z_{21}^{(\kappa_3)} x\, Z_{21}^{(\kappa_4)} x\, Z_{21}^{(\kappa_5)} x\, Z_{21}^{(\kappa_6)} x\, Z_{21}^{(m)} x \begin{pmatrix} w \\ w' \end{vmatrix} \begin{matrix} 1^{(8+|\kappa|+m)} \\ 2^{(7-|\kappa|-m)} \end{matrix} \right) \right)$$

$$= \binom{\kappa_1+\kappa_2}{\kappa_2} Z_{21}^{(\kappa_1+\kappa_2)} x Z_{21}^{(\kappa_3)} x Z_{21}^{(\kappa_4)} x Z_{21}^{(\kappa_5)} x Z_{21}^{(\kappa_6)} x Z_{21}^{(m)} x \begin{pmatrix} w & 1^{(8+|\kappa|+m)} \\ w' & 2^{(7-|\kappa|-m)} \end{pmatrix} - \binom{\kappa_2+\kappa_3}{\kappa_3} Z_{21}^{(\kappa_1)} x Z_{21}^{(\kappa_2+\kappa_3)} x$$

$$Z_{21}^{(\kappa_4)} x Z_{21}^{(\kappa_5)} x Z_{21}^{(\kappa_6)} x Z_{21}^{(m)} x \begin{pmatrix} w & 1^{(8+|\kappa|+m)} \\ w' & 2^{(7-|\kappa|-m)} \end{pmatrix} + \binom{\kappa_3+\kappa_4}{\kappa_4} Z_{21}^{(\kappa_1)} x Z_{21}^{(\kappa_2)} x Z_{21}^{(\kappa_3+\kappa_4)} x Z_{21}^{(\kappa_5)} x Z_{21}^{(\kappa_6)} x Z_{21}^{(m)} x$$

$$\begin{pmatrix} w & 1^{(8+|\kappa|+m)} \\ w' & 2^{(7-|\kappa|-m)} \end{pmatrix} - \binom{\kappa_4+\kappa_5}{\kappa_4} Z_{21}^{(\kappa_1)} x Z_{21}^{(\kappa_2)} x Z_{21}^{(\kappa_3)} x Z_{21}^{(\kappa_4+\kappa_5)} x Z_{21}^{(\kappa_6)} x Z_{21}^{(m)} x \begin{pmatrix} w & 1^{(8+|\kappa|+m)} \\ w' & 2^{(7-|\kappa|-m)} \end{pmatrix} + \binom{\kappa_5+\kappa_6}{\kappa_6}$$

$$Z_{21}^{(\kappa_1)} x Z_{21}^{(\kappa_2)} x Z_{21}^{(\kappa_3)} x Z_{21}^{(\kappa_4)} x Z_{21}^{(\kappa_5+\kappa_6)} x Z_{21}^{(m)} x \begin{pmatrix} w & 1^{(8+|\kappa|+m)} \\ w' & 2^{(7-|\kappa|-m)} \end{pmatrix} - \binom{\kappa_6+m}{m} Z_{21}^{(\kappa_1)} x Z_{21}^{(\kappa_2)} x Z_{21}^{(\kappa_3)} x Z_{21}^{(\kappa_4)} x$$

$$Z_{21}^{(\kappa_5)} x Z_{21}^{(\kappa_6+m)} x \begin{pmatrix} w & 1^{(8+|\kappa|+m)} \\ w' & 2^{(7-|\kappa|-m)} \end{pmatrix} + Z_{21}^{(\kappa_1)} x Z_{21}^{(\kappa_2)} x Z_{21}^{(\kappa_3)} x Z_{21}^{(\kappa_4)} x Z_{21}^{(\kappa_5)} x Z_{21}^{(\kappa_6)} x \partial_{21}^{(m)} \begin{pmatrix} w & 1^{(8+|\kappa|+m)} \\ w' & 2^{(7-|\kappa|-m)} \end{pmatrix}$$

$$= \binom{\kappa_1+\kappa_2}{\kappa_2} Z_{21}^{(\kappa_1+\kappa_2)} x Z_{21}^{(\kappa_3)} x Z_{21}^{(\kappa_4)} x Z_{21}^{(\kappa_5)} x Z_{21}^{(\kappa_6)} x Z_{21}^{(m)} x \begin{pmatrix} w & 1^{(8+|\kappa|+m)} \\ w' & 2^{(7-|\kappa|-m)} \end{pmatrix} - \binom{\kappa_2+\kappa_3}{\kappa_3} Z_{21}^{(\kappa_1)} x Z_{21}^{(\kappa_2+\kappa_3)} x$$

$$Z_{21}^{(\kappa_4)} x Z_{21}^{(\kappa_5)} x Z_{21}^{(\kappa_6)} x Z_{21}^{(m)} x \begin{pmatrix} w & 1^{(8+|\kappa|+m)} \\ w' & 2^{(7-|\kappa|-m)} \end{pmatrix} + \binom{\kappa_3+\kappa_4}{\kappa_4} Z_{21}^{(\kappa_1)} x Z_{21}^{(\kappa_2)} x Z_{21}^{(\kappa_3+\kappa_4)} x Z_{21}^{(\kappa_5)} x Z_{21}^{(\kappa_6)} x Z_{21}^{(m)} x$$

$$\begin{pmatrix} w & 1^{(8+|\kappa|+m)} \\ w' & 2^{(7-|\kappa|-m)} \end{pmatrix} - \binom{\kappa_4+\kappa_5}{\kappa_4} Z_{21}^{(\kappa_1)} x Z_{21}^{(\kappa_2)} x Z_{21}^{(\kappa_3)} x Z_{21}^{(\kappa_4+\kappa_5)} x Z_{21}^{(\kappa_6)} x Z_{21}^{(m)} x \begin{pmatrix} w & 1^{(8+|\kappa|+m)} \\ w' & 2^{(7-|\kappa|-m)} \end{pmatrix} + \binom{\kappa_5+\kappa_6}{\kappa_6}$$

$$Z_{21}^{(\kappa_1)} x Z_{21}^{(\kappa_2)} x Z_{21}^{(\kappa_3)} x Z_{21}^{(\kappa_4)} x Z_{21}^{(\kappa_5+\kappa_6)} x Z_{21}^{(m)} x \begin{pmatrix} w & 1^{(8+|\kappa|+m)} \\ w' & 2^{(7-|\kappa|-m)} \end{pmatrix} - \binom{\kappa_6+m}{m} Z_{21}^{(\kappa_1)} x Z_{21}^{(\kappa_2)} x Z_{21}^{(\kappa_3)} x Z_{21}^{(\kappa_4)} x$$

$$Z_{21}^{(\kappa_5)} x Z_{21}^{(\kappa_6+m)} x \begin{pmatrix} w & 1^{(8+|\kappa|+m)} \\ w' & 2^{(7-|\kappa|-m)} \end{pmatrix} + Z_{21}^{(\kappa_1)} x Z_{21}^{(\kappa_2)} x Z_{21}^{(\kappa_3)} x Z_{21}^{(\kappa_4)} x Z_{21}^{(\kappa_5)} x Z_{21}^{(\kappa_6)} x \begin{pmatrix} w & 1^{(8+|\kappa|)} & 2^{(m)} \\ w' & 2^{(7-|\kappa|-m)} & \end{pmatrix},$$

where $|\kappa| = \kappa_1 + \kappa_2 + \kappa_3 + \kappa_4 + \kappa_5 + \kappa_6$.

It is lucid that $S_5\partial_x + \partial_x S_6 = \mathrm{id}$.

From above we get $\{S_0, S_1, S_2, S_3, S_4, S_5, S_6\}$ is a contracting homotopy [6] which mean our complex is exact.

References

[1] David A.Buchsbaum and Gian C.Rota 1993 Projective Resolution of Weyl Modules, *Natl.Acad.Sci.USA* Vol. 90 pp.2448-2450.
[2] David A.Buchsbaum and Brian D.Taylor 2003 Homotopies for Resolution of Skew-Hook Shapes, *Adv. In Applied Math*. Vol.30 pp.26-43.
[3] David A.Buchsbaum 2004 A Characteristic Free Example of Lascoux Resolution, and Letter Place Mathods for Intertwining Numbers, *European Journal of Gombinatorics* Vol.25, (), pp.1169-1179.
[4] David A.Buchsbaum 2001 Resolution of Weyl Modules: The Rota Touch, *Algebraic Combinatorics and Computer Science* pp.97-109.

[5] David A.Buchsbaum and Gian C.Rota 1994, A new Construction in Homological Algebra, *Natl.Acad.Sci., USA* Vol.91 pp.4115-4119.
[6] Vermani L.R. 2003 An Elementary Approach to Homological Algebra, Chapman and Hall/CRC, *Monographs and Surveys in Pure and Applied Mathematics*, 130.

Solution Of nth-Order Ordinary Differential Equations Using Lie Group

IOP Conf. Series: Journal of Physics: Conf. Series **1003** (2018) 012052 doi:10.1088/1742-6596/1003/1/012052

Solution Of nth-Order Ordinary Differential Equations Using Lie Group

1Eman Ali Hussain and 2 Zainab Mohammed Alwan

1Asst. Prof, Dr., Department of Mathematics, College of Science, University ofAL-Mustansiriyah, Iraq
2Asst. Lecturer .,Department of Mathematics, College of Science, University of AL-Mustansiriyah, Iraq

dreman@uomustansiriyah.edu.iq, lionwight_2009@uomustansiriyah.edu.iq

Abstract. In the recent work, methods of solution nth-order linear and nonlinear ODE′s of Lie group was introduced and the calculations of Lie point symmetries with higher order for ODEs were also achieved .

1. Introduction

symmetry of DE mapped any solution to another one of DE. Symmetry based on methods to attack (in particular, non-linear) deterministic differential equations were introduced long ago. Generally the symmetries of a mathematical object are to be its invertible morphisms to itself . Symmetries of DEs are examined by [1],[2].Lie symmetries of DEs may be used to construct exact solutions for the equations ,the author in [4] realize a group and abelian group of symmetry, while authors in [3] define group of transformation (1-parameter Lie group of point transformation (1-P.L.G.O.P.T)), invariant of (function, Lie group of transformation , family of surface) also he established canonical coordinate and specified example group of scaling. Furthermore ,he established the first fundamental theorem of Lie and construct an example of this theorem. Where the authors in [9] realize an invariant surface . Now in this work we insert the employment symmetry method to solve higher order of ODE. Moreover we employed this method to solve two cases of linear and nonlinear ODE's and give applications for that.

2. Preliminaries

In this section, some fundamental and necessary concepts were inserted in theory of symmetries which are needed later in studying Lie point of DE's and driving appropriate applications for the method .

Definition (2.1),[3],[5],[6]: Lie group transformations of (ϵ)

$$x^* = W(x;\epsilon) \qquad \ldots(2.1)$$

By employing Taylor expansion about neighborhood of $\epsilon=0$ and law of composition

$$x^{*}=x+\left[\frac{\partial W}{\partial \in}(x;\in)\big|_{\in=0}\right]\in+\left[\frac{\partial^{2}W}{\partial \in^{2}}(x;\in)\big|_{\in=0}\right]\frac{\in^{2}}{2!}+.....$$

$$x^{*}=x+\left[\frac{\partial W}{\partial \in}(x;\in)\big|_{\in=0}\right]\in+O(\in^{2}) \qquad \ldots(2.2)$$

$$x^{*}=x+\in \xi(x) \qquad \ldots(2.3)$$

Where

$$\xi(x)=\frac{\partial W}{\partial \in}(x;\in)\big|_{\in=0} \qquad \ldots(2.4)$$

The transformation (T) of equation (2.3) is said to be the infinitesimal transformation (I.T) of (2.1),where component $\xi(x)=(\xi_1(x),\xi_2(x),\ldots,\xi_n(x))$ are said to be the infinitesimal vector field of group(2.1).

Definition (2.2),[7],[4]: The infinitesimal operator may be sometimes called infinitesimal generator, group operator, Lie operator, group generator, admitted operator, group admitted, symmetry operator, infinitesimal symmetry, invariant group or Lie symmetry (2.1):

$$X=X(x)=\xi(x).\nabla=\sum_{i=1}^{M}\xi_1(x)\frac{\partial}{\partial x_i} \qquad \ldots(2.5)$$

$$\nabla=\left(\frac{\partial}{\partial x_1},\frac{\partial}{\partial x_2},\ldots,\frac{\partial}{\partial x_\iota}\right) \qquad \ldots(2.6)$$

Where, ∇ is the gradient operator .

Theorem (2.1),[3],[2]:
The (1-P.L.G.O.P.T) of (2.1) equal to:

$$\mathbf{x}^{*}=e^{\in X}\mathbf{x}=\sum_{k=0}^{\infty}\frac{\in^{k}}{k!}X^{k}\mathbf{x} \qquad \ldots(2.7)$$

Where $X^{k}=X\,X^{k-1},K=1,2,....and\ X^{0}=I$

2.1. Invariance of a Lie Group
In this section, an introducing and studying the invariance principle because since Lie group analysis based on it.

Definition(2.3),[8]: A mark $x\in R^{N}$ is called invariant mark if it stay same by every (L.G.O.P.T), i.e. x*= x ,for all ∈.
Theorem (2.2)[8]: A point x∈ RN is said to be invariant point of a (L.G.O.P.T) (2.1) with (2. 5) iff

$$\xi_r(x)=0;\forall r=1,2,...,M \qquad \ldots(2.8)$$

Remark (2.1),[10]:

1-Any (1-P.L.G.O.P.T) of plane has exactly one independent invariant.

2-Each (1-P.L.G.O.P.T) of M(x) has exactly N-1 functionally independent invariants for M .Then the characteristic equation is follow

$$XM(x)=\sum_{i=1}^{N}\xi^i(x)\frac{\partial M}{\partial x^i}=0$$

$$\ldots(2.9)\quad \frac{dx^1}{\zeta^1(x)}=\frac{dx^2}{\zeta^2(x)}=.....=\frac{dx^N}{\zeta^N(x)},\ dM=0 \qquad \ldots(2.10)$$

We get J1(x), J2(x),..., JN-1(x) where

J1(x) =c1, J2(x) =c2,…,JN-1(x) =cN-1, c1,c2,..,cN-1 are constants

3-Any set of N-1 functionally independent invariants is called a basis of invariants for M, and M(x) = ϕ(J1(x), J2(x),..., JN-1(x)) ,is an invariant function.

Theorem (2.3) [9], [3] : M(x) is called Invariance Criterion under (2.1) iff

$$X\ M(x)\equiv 0 \qquad \ldots(2.11)$$

$$M(x)=0 \qquad \ldots(2.12)$$

2.2. Prolongation Formula,[10]:

The derivatives y′, y″ ,… under performance of point transformations:

$x^*=M(x,y;\epsilon)$ …(2.13)

$y^*=N(x,y;\epsilon)$ …(2.14)

We write by employing the total differentiation of these transformation as:

$$D=\frac{\partial}{\partial x}+y'\frac{\partial}{\partial y}+y''\frac{\partial}{\partial y'}+..... \qquad \ldots(2.15)$$

Whereas the determination the 1,2-derivatives can be put as:

$$y^{*'}\equiv\frac{dy^*}{dx^*}=\frac{DN}{DM}=\frac{N_x+y'N_y}{M_x+y'M_y}\equiv P(x,y,y';\in) \qquad \ldots(2.16)$$

$$y^{*\prime\prime} \equiv \frac{dy^{*\prime}}{dx^{*}} = \frac{D\,P}{DN} = \frac{P_x + y'\,P_y + y''P_{y'}}{N_x + y'\,N_y} \qquad \ldots(2.17)$$

Now,group P of point transformations (2.13),(2.14) and besides the transformation (2.15) one can get the first prolongation denoted by $P^{(1)}$, and the space of three variables (x,y,y′).Moreover by the transformation (2.17) we find the group $P^{(2)}$ in the space (x,y,y′,y″),also the higher prolongations , $P^{(1)}$, $P^{(2)}$ were recognized in:

$$P^{(1)} = \zeta\frac{\partial}{\partial x} + \eta\frac{\partial}{\partial y} \zeta_1 \frac{\partial}{\partial y'}, \zeta_1 = D(\eta) - y'D(\zeta) \qquad \ldots(2.18)$$

$$P^{(2)} = P^{(1)} + \zeta_2, \zeta_2 \frac{\partial}{\partial y''} = D(\zeta_1) - y''D(\zeta) \qquad \ldots(2.19)$$

We said of (2.18) and (2.19) are first and 1, 2- prolongation

$$\frac{dx^{*}}{d\in} = \zeta(x^{*}, y^{*}) \;,\; x^{*}\big|_{\in=0} = x$$

$$\frac{dy^{*}}{d\in} = \eta(x^{*}, y^{*}) \;,\; y^{*}\big|_{\in=0} = y \qquad \ldots(2.20)$$

Where

$$\zeta_1 = D(\eta) - y'D(\zeta) = \eta_x + (\eta_y - \zeta_x)\,y' - y'\zeta_y$$

$$\begin{aligned}\zeta_2 &= D(\zeta_1) - y''D(\zeta) = \eta_{xx} + (2\eta_{xy} - \zeta_{xx})\,y' \\ &+ (\eta_{yy} - 2\zeta_{xy})\,y'^2 - y'^3\zeta_{yy} + (\eta_y - 2\zeta_x - 3y'\zeta_y)\,y'' \\ \zeta_3 &= \eta_{xxx} + (3\eta_{xxy} - \zeta_{xxx})\,y' + 3(\eta_{xyy} - \zeta_{xxy})\,y'^2 + (\eta_{yyy} - 3\zeta_{xyy})\,y'^3 \\ &- \zeta_{yyy}\,y'^4 + 3\{\eta_{xy} - \zeta_{xx} + (\eta_{yy} - 3\zeta_{xy})\,y' - 2\zeta_{yy}\,y'^2\}y'' \\ &- 3\zeta_y\,y''^2 + \{\eta_y - 3\zeta_x - 4\zeta_y\,y'\}y'''\end{aligned} \qquad \ldots(2.21)$$

2.3. Prolongation Formulas in Multidimension,[11]:

This following with to multidimensional situation (with independent x^i , i=1,..,n, and dependent variables u^α , α=1,…,m

Now, the reformulating the prolongation of (2.18),(2.19) reduce to :

$$X = \zeta^i \frac{\partial}{\partial x^i} + \eta^\alpha \frac{\partial}{\partial u^\alpha} \qquad \ldots(2.22)$$

With consideration of the the form

$$X^{(1)} = X + \zeta_i^{\alpha} \frac{\partial}{u_i^{\alpha}}$$

$$X^{(2)} = X^{(1)} + \zeta_{ij}^{\alpha} \frac{\partial}{\partial u_{ij}^{\alpha}} \qquad \ldots(2.23)$$

Where

$$\zeta_i^{\alpha} = D_i(\eta^{\alpha}) - u_j^{\alpha} D_i(\zeta^j)$$

$$\zeta_{ij}^{\alpha} = D_j(\zeta_i^{\alpha}) - u_{ik}^{\alpha} D_j(\zeta^k) \qquad \ldots(2.24)$$

And

$$D_i = \frac{\partial}{\partial x^i} + u_i^{\alpha} \frac{\partial}{\partial u^{\alpha}} + u_{ij}^{\alpha} \frac{\partial}{\partial u_{ij}^{\alpha}} + ... \qquad \ldots(2.25)$$

2.4. Extended Prolongation of Lie Group and Infinitesimals:
the study of convenient extended prolongation for (1-P.L.G.O.P.T) and admitted by a kth-order with one dependent variable y and one independent variable x .

Theorem (2.4),[3]:
The (L.G.O.T) (2.13),(2.14) extends to its kth extension , k≥2 , in a form (1- P.L.G.O.P.T). It cuts on $(x,y,y_1,\ldots,y_k)$-space:

$$X^{*} = M(x, y; \in)$$
$$y^{*} = N(x, y; \in) \qquad \ldots.(2.26)$$
$$y^{*'} = N_1(x, y, y'; \in)$$
.....
$$y^{*k} = N_k(x, y, y', ..., y^k) = \frac{\frac{\partial N_{k-1}}{\partial x} + y' \frac{\partial N_{k-1}}{\partial y} + ... + y^k \frac{\partial N_{k-1}}{\partial y^{k-1}}}{\frac{\partial M_{k-1}}{\partial x}(x; \in) + y' \frac{\partial M_{k-1}}{\partial y}(x; \in)}$$

Where $N_1 = N_1(x, y, y', \ldots, y^k; \in)$ is defined by (2.26), $N_{k-1} = N_{k-1}(x, y, y', \ldots, y^{k-1}; \in)$

2.5. Extended Infinitesimals transformations of Lie group of 1-Dependent Variable and 1- Independent Variable,[3]:
Consider the (1-P.L.G.O.T)

$x^* = M(x,y;\epsilon) = x + \epsilon\, \xi(x,y) + O(\epsilon^2)$ …(2.27)

$y^* = N(x,y;\epsilon) = y + \epsilon\, \eta(x,y) + O(\epsilon^2)$ …(2.28)

has $\xi(x) = (\xi(x,y), \eta(x,y))$
with vector field

$$X = \zeta(x,y)\frac{\partial}{\partial x} + \eta(x,y)\frac{\partial}{\partial y} \qquad \ldots(2.29)$$

Now, kth extending (2.27),(2.28) leads:

$x^*=M(x,y;\epsilon)= x+ \epsilon\, \xi(x,y)+ O(\epsilon^2)$

$y^*=N(x,y;\epsilon)= y+ \epsilon\, \eta(x,y)+ O(\epsilon^2)$ …(2.30)

$y^{*\prime}= N_1(x,y,y';\epsilon)= y'+\epsilon\, \eta^{(1)}(x,y,y')+ O(\epsilon^2)$

……..

$y^{*k}= N_k(x,y,y',\ldots,y_k;\epsilon)= y_k+\epsilon\, \eta^{(k)}(x,y,y',\ldots,y_k)+O(\epsilon^2)$

The above expression has infinitesimal of the form

$(\xi(x,y), \eta(x,y), \eta^{(1)}(x,y,y'),\ldots, \eta^{(k)}(x,y,y',..,y_k))$, …(2.31)

Then the vector field of (2.29) The above expression:

$$X^{k} = \zeta(x,y)\frac{\partial}{\partial x} + \eta(x,y)\frac{\partial}{\partial y} + \eta^{(1)}(x,y,y')\frac{\partial}{\partial y'} + \ldots + \eta^{(1)}(x,y,y',\ldots,y^{k})\frac{\partial}{\partial y^{k}} \qquad \ldots(2.32)$$

Where k=1,2,.. ,Explicit formula for the expanded infinitesimals η^k is held.

Theorem (2.5),[3]: Consider

$$\eta^{(k)}(x,y,y',\ldots,y^{k}) = \frac{D\,\eta^{(k-1)}}{Dx} - y^{k}\,\frac{D\zeta(x,y)}{Dx},\ k = 1,2,\ldots \qquad \ldots(2.33)$$

where $\eta^{(0)} = \eta(x,y)$

3. Lie group of higher order for ODE's:

Consider nth-order ODE given as:

$V(x,y,y',y'',\ldots,y^{(n)}) = 0$ …(3.1)

Which can takes the following cases

1- **Case I:** equation (3.1) is non -linear.

2-**Case II:** The following equation (linear).

$$m_n(x)\,y^{(n)} + m_{n-1}(x)\,y^{(n-1)} + \ldots + m_1(x)\,y' + m_0(x)\,y = Q(x) \qquad \ldots(3.2)$$

Where $m_0, m_1, \ldots, m_n$ are constant with $m_n \neq 0$, we solved (3.1), (3.2) in 2-casese:

Algorithm (1): we will insert this procedure involved by following steps to calculate the Lie point symmetry of higher order ODEs for case I :

Step 1: Write all terms of equation (3.1) on the left hand side.

Step 2: Write the generator of symmetry with unknown ξ and η of the form:

$$X = \zeta(x, y)\frac{\partial}{\partial x^{i}} + \eta(x, y)\frac{\partial}{\partial y^{\alpha}}$$

Step 3: Write n-prolongation of the symmetry generator X in style:

$$X^{[n]} = X + \zeta^{(1)}\frac{\partial}{\partial y'} + \zeta^{(2)}\frac{\partial}{\partial y''} + ... + \zeta^{(n)}\frac{\partial}{\partial y^{n}}$$

Step 4: Apply the prolonged generator X[n] on V of (3.1) we locate the following:

$$X^{[n]}\left(V(x, y, y', y'', ..., y^{(n)})\right)\Big|_{V=0} = 0$$

Step 5: By using expansion of $\zeta^{(1)}, \zeta^{(2)}, \zeta^{(3)}$ from (2.21) and $\zeta^{(4)}, \zeta^{(5)}, ..., \zeta^{(n)}$ found by using maple package.

Step 6: Separate the expanded expression with respect to the derivatives of the dependent variables and their powers resulting in determined system of linear homogenous ODE's in the terms of ξ and η.

Step 7: Find the general solution.

Algorithm (2): We , calculate the Lie point symmetry of higher order ODEs for case II are give in the following steps:

Step 1: write all terms of equation (3.2) on the left hand side.

Step 2: Write the vector filed of the form:

$$X = \zeta(x, y)\frac{\partial}{\partial x} + \eta(x, y)\frac{\partial}{\partial y}$$

Step 3: We need find n-prolongation in style:

$$X^{[n]} = X + \zeta^{(1)}\frac{\partial}{\partial y'} + \zeta^{(2)}\frac{\partial}{\partial y''} + ... + \zeta^{(n)}\frac{\partial}{\partial y^{n}}$$

Step 4: Write $X^{[n]}\left(y^{(n)} - \frac{1}{m_n}(Q(x) - m_{n-1}y^{(n-1)} - .... - m_1 y' - m_0 y)\right)\Big|_{y^{(n)} = \frac{1}{m_n}(Q(x) - m_{n-1}y^{(n-1)} - .... - m_1 y' - m_0 y)} = 0$

Step 5: By using expansion of $\zeta^{(1)}, \zeta^{(2)}, \zeta^{(3)}$ from (2.21) and $\zeta^{(4)}, \zeta^{(5)}, ..., \zeta^{(n)}$ found by using maple package.

Step 6: Now replacing $y^{(n)}$ by $\frac{1}{m_n}(Q(x) - m_{n-1}y^{(n-1)} - .... - m_1 y' - m_0 y)$

Step 7: Find the general solution.

4. Applications

The followings are some examples of higher order of ODEs solved by using above algorithm (1).

Example (1): Consider the 10th- order of ODE in:

$$y^{(10)} = \frac{1}{x^{3}}y' y^{2} \qquad \ldots(4.1)$$

Now , calculate the Lie point symmetry of (4.1) with respect vector filed:

$$X = \zeta(x, y)\frac{\partial}{\partial x} + \eta(x, y)\frac{\partial}{\partial y} \quad \ldots(4.2)$$

considering 10th- prolongation in a style:

$$X^{[10]} = X + \zeta^{(1)}\frac{\partial}{\partial y'} + \zeta^{(2)}\frac{\partial}{\partial y''} + \ldots. + \zeta^{(10)}\frac{\partial}{\partial y^{10}} \quad \ldots(4.3)$$

$$\frac{3}{x^4} y' y^2 \zeta - \frac{2}{x^3} y' y \eta - \frac{1}{x^3} y^2 \zeta^{(1)} + \zeta^{(10)} = 0 \quad \ldots(4.4)$$

Now, by using expansion $\zeta^{(1)}, \zeta^{(2)}$ *and* $\zeta^{(3)}$ of (2.21) ,*where* $\zeta^{(4)}, \ldots, \zeta^{(10)}$ found by maple package ,and replacing $y^{(10)}$ by $\frac{1}{x^3}\ y'\ y^2$

we a result the general solution

$$\zeta = c_1 x \quad \ldots(4.5)$$

$$\eta = -3c_1\ y \quad \ldots(4.6)$$

Then (4.1) has Lie point symmetry

$$X_1 = x\frac{\partial}{\partial x} - 3\ y\frac{\partial}{\partial y} \quad \ldots(4.7)$$

Example(2): The 5th–order of ODE for (case II) is :

$$y^{(5)} = y^{-(F+1)}$$,F is constant …(4.8)

The vector field

$$X = \zeta(x, y)\frac{\partial}{\partial x} + \eta(x, y)\frac{\partial}{\partial y} \quad \ldots(4.9)$$

we must calculate:

$$X^{[5]}\left(y^{(5)} - y^{-(k+1)}\right)\Big|_{y^{(5)} = y^{-(k+1)}} = 0 \quad \ldots(4.10)$$

The five extension compute In a manner:

$$X^{[5]} = X + \zeta^{(1)}\partial y' + \zeta^{(2)}\partial y'' + \zeta^{(3)}\partial y''' + \zeta^{(4)}\partial y'''' + \zeta^{(I5)}\partial y'''' \quad \ldots(4.11)$$

Where

$$\eta^{(i)}(x, y, y', \ldots, y^{(i)}) = \frac{d\,\zeta^{(i-1)}}{d\,x} - y^{(i)}\frac{d\,\zeta}{d\,x}, i = 1,2,3,4,5 \quad \ldots(4.12)$$

With $\eta^{(i)}=\frac{d^i y}{dx^i}$, $\eta^{(0)}=\zeta^{(0)}=\eta(x,y)$

and $\frac{d}{dx}$ is the total differentiation realize:

$$\frac{d}{dx}=\frac{\partial}{\partial x}+y'\frac{\partial}{\partial y}+y''\frac{\partial}{\partial y'}+y'''\frac{\partial}{\partial y''}+... \quad \ldots(4.13)$$

The determining equation of (4.10) is given as follows:

$$(\zeta^{(5)}+(F+1)\eta y^{-(F+2)})\Big|_{y^{(5)}=y^{-(F+1)}}=0 \quad \ldots(4.14)$$

by using maple package we get the following result

$$\eta=5c_1 y \quad \ldots(4.15)$$

$$\zeta=(F+2)c_1 x+c_2 \quad \ldots(4.16)$$

Where c_1 and c_2 are constants , then equation (4.8) has 2-generators are:

$$X_1=\partial x$$
$$X_2=(F+2)x\,\partial x+5y\,\partial y \quad \ldots(4.17)$$

Example(3): Consider the 15th- order of ODE for (case II) is the form

$$y^{(15)}=\frac{y'^2}{y^3} \quad \ldots(4.18)$$

the Lie point symmetry of (4.18) with respect vector filed:

$$X=\zeta(x,y)\frac{\partial}{\partial x}+\eta(x,y)\frac{\partial}{\partial y} \quad \ldots(4.19)$$

we needed 15th- prolongation of (4.19) :

$$X^{[15]}=X+\zeta^{(1)}\frac{\partial}{\partial y'}+\zeta^{(2)}\frac{\partial}{\partial y''}+\zeta^{(3)}\frac{\partial}{\partial y'''}+...+\zeta^{(15)}\frac{\partial}{\partial y^{(15)}} \quad \ldots(4.20)$$

Equation (4.19) generates a point symmetry of (4.18)if the determining equation

$$\xi^{(15)}-2\xi^{(1)}\frac{y'}{y^3}+3\eta\frac{y'^2}{y^4}=0 \quad \ldots(4.21)$$

Where $\zeta^{(1)}$, $\zeta^{(2)}$, $\zeta^{(3)}$ are given by (2.21) respectively *and* $\zeta^{(4)},...,\zeta^{(15)}$ found

by maple package ,we get the general solution :

$$\zeta = c_1 x + c_2 \quad \ldots(4.22)$$

$$\eta = \frac{13}{2} c_1 y \quad \ldots(4.23)$$

5. Conclusion

The Lie group method is an efficient technique to solve higher order of ODEs and can be applied for solved linear and nonlinear for nth-order of ODE's

Reference

[1] Stephani H 1989 *Differential Equations: Their Solutions Using Symmetry* (Cambridge University Press,NewYork).

[2] Olver P J 1987 *Group Invariant Solutions of Differential Equations* Siam J. Appl. Math. **Vol.(47)** No.2 .PP. 263-277.

[3] Bluman G W and Kumei S 1989 *Symmetry and Differential Equations* (Springer-Verlag, New York, NY, USA).

[4] Cantwell B J 2002 *Introduction to Symmetry Analysis* (Cambridge University Press: Cambridge, UK).

[5] Dresner L 1999 *Application of Lie's Theory of Ordinary and Partial Differential Equations* (USA, British Library) .

[6] Stephani H 1989 *Differential Equations: Their Solution using Symmetries* (Cambridge University Press, Cambridge,UK).

[7] Bluman G W , Anco S C and Cheviakov A F 2009 *Applications of Symmetry Methods to Partial Differential Equations* (Springer, New York, NY, USA).

[8] Bluman G W and Anco S C 2002 *Symmetry and Integration Methods for Differential Equations* (Springer, New York, NY, USA).

[9] Bluman G W and Cole J D 1974 *Similarity Methods Differential Equations* (Springer-Verlag, New York, NY, USA).

[10] Ibragimov N H 1994 *CRC Handbook of Lie Group Analysis of Differential Equation* (Vol. I,

CRC Press, USA) .

[11] Grigoriev Y N et al 2010 *symmetries of Integro-Differential Equations: With Application in Mechaincs and Plasma Physics* (Lect . Notes Phys.806,Springer,Dordrecht, DOI:10.1007/978-90-481-3797-8) .

Effect of radial magnetic field on peristaltic transport of Jeffrey fluid in curved channel with heat / mass transfer

IOP Conf. Series: Journal of Physics: Conf. Series **1003** (2018) 012053 doi:10.1088/1742-6596/1003/1/012053

Effect of radial magnetic field on peristaltic transport of Jeffrey fluid in curved channel with heat /mass transfer

Ahmed M.Abdulhadi[1], Tamara S. Ahmed[2]

College of science[1], university of Baghdad,

Collage of education for pure science (ibn al Haitham)[2],university of Baghdad,

ahm6161@yahoo.com,

Tamaraalshareef@yahoo.com

Abstract.in this paper, we deals with the impact of radialiy magnetic field on the peristaltic transport of Jeffrey fluid through a curved channel with two dimensional. The effect of slip condition on velocity, the non-slip condition on temperature and conversation is performed. The heat and mass transfer are considered under the influence of various parameters. The flow is investigated under the assumption of long wave length and low Reynolds number approximations. The distribution of temperature and concentration are discussed for various parameters governing the flow with the simultaneous effects of Brinkman number, Soret number and Schmidt number.

1- Introduction

Peristaltic transport of fluid is quite popular topic of research amongst the mathematicians, physiologists and engineers. Such popularity of this topic is due to occurrence of peristalsis in the physiological and engineering processes. The peristaltic pumping is a mechanism for fluid transport induced by progressive wave of contraction and relaxation along the distensible tube. Fluid transport in view of peristalsis is an important biological mechanism responsible for various physiological functions of the organs in the human body. Particularly such mechanism is in urine passage from kidney to bladder through ureter, chyme movement in the gastrointestinal tract, ovum movement in the female fallopian tube, transport of spermatozoa in ducts efferent of male reproductive tract, transport of lymph in lymphatic vessels such as arterioles, capillaries, venules and in esophagus during food swallowing process. Practically the peristaltic pumps are desighned by engineers for pumping corrosive fluids without contact with the walls of the pumping machinery. In nuclear industry the peristaltic pumping has been found in corrosive fluid or sensitive fluids, sanitary fluids, transport of slurries and noxious fluids. Latham [1], Jaffrin and Shapiro [2], Shapiro et al. [3] and Fung [4] were the first who made a detailed analysis on peristaltic pumping. It is also noted that initial attempts for

peristalsis have been made for viscous liquids. This is not adequate since most of the materials in the physiological and engineering processes are non-Newtonian. There are three types of non-Newtonian fluids (i.e.), 1. Differential type. 2. Rate type. 3. Integral type. The non-Newtonian fluids which exhibit the characteristic of relaxation or retardation times are belong to rate type fluids. Maxwell fluid is one of the subclass of rate type fluids which contains only relaxation time behavior. The only draw back of this fluid model is that it does not explain the retardation time behavior. Therefore to fill this gap, Jeffrey fluid model is considered this model shows the behavior of linearly viscoelastic polymer industries. Moreover the Jeffrey fluid model is comparatively simple linear model using time derivatives instead of convective derivatives for example the oldroyd-B fluid model does, it represents a different rheological behavior from that of the Newtonian fluid. In view of diverse characteristics of non-Newtonian materials, various constitutive equations have been suggested. Among such constitutive equations there is one for Jeffrey fluid which has been already utilized for peristaltic transport in both symmetric and asymmetric channel (see [5 ,6,7,8,9].

Influence of applied magnetic field on peristaltic activity is important in connection with certain problems of the movement of the conductive physiological fluids, e.g. , blood and the blood pump machines, magnetic drug targeting and relevant process of human digestive system. Such consideration is also useful in treating gastro paresis, chronic constipation and morbid obesity, for more details can one see [10 ,11]. The convective heat transfer is of excessive significance in procedures in which high temperatures are involved for instance, gas turbines, nuclear plants, storage of thermal energy etc. Referring to numerous industrial and engineering processes. The convective boundary conditions are also more practical in material drying, transpiration cooling process etc. Also impact of heat transfer in peristaltic transport of fluid is quite significant in food processing, oxygenation, hemodialysis, tissues conduction, heat convection for blood flow from the pores of tissues and radiation between environment and its surface. Mass transfer is useful in the a fore mentioned processes. Especially mass transfer cannot be under estimated when nutrients diffuse out from the blood to neighboring tissues. Further mass transfer involvement is quite prevalent in distillation, chemical impurities diffusion, membrane separation and combustion process. It should be noted that relationships between fluxes and driving potentials occur when both heat and mass transfer act simultaneously. Here temperature gradient generates energy flux. However mass flux and composition gradients are due to temperature gradient (which is called soret effect). It is noted that all the a fore mentioned studies on peristaltic transport have been conducted for peristalsis in straight channels which is not realistic always since most of the pipes, arteries and glandular ducts are curved. Thus some advancements have been made for peristalsis using curvilinear coordinates. Abbasi et al.[12] initiated such analysis for peristaltic transport of viscous fluids. Sato et al. [13] extend the work of sato et al. in wave frame of reference. Later some attempts [14 , 15,16 ,17] have been presented to address. The curvature effects on peristalsis of fluids in a channel. In these attempts mostly the constant magnetic field are considered. Recently, Hayat et al. [18] is given in their work to explore the characteristics of radial magnetic field on peristaltic transport of Jeffrey fluid in a curved channel. Heat transfer is characterized there by utilizing convective condition. Hayat et al. [19] investigated the effect of radial magnetic field on the peristaltic flow of Jeffrey liquid in curved channel with complaint walls.

Influence of applied magnetic field on peristaltic activity is important in connection with certain problems of the movement of the conductive physiological fluids, e.g. , blood and the blood pump machines, magnetic drug targeting and relevant process of human digestive system. Such consideration is also useful in treating gastro paresis, chronic constipation and morbid obesity, for more details can one see [10 ,11]. The convective heat transfer is of excessive significance in procedures in which high temperatures are involved for instance, gas turbines, nuclear plants, storage of thermal energy etc. Referring to numerous industrial and engineering processes. The convective boundary conditions are also more practical in material drying, transpiration cooling process etc. Also impact of heat transfer in peristaltic transport of fluid is quite significant in food processing, oxygenation, hemodialysis, tissues conduction, heat convection for blood flow from the pores of

tissues and radiation between environment and its surface. Mass transfer is useful in the a fore mentioned processes. Especially mass transfer cannot be under estimated when nutrients diffuse out from the blood to neighboring tissues. Further mass transfer involvement is quite prevalent in distillation, chemical impurities diffusion, membrane separation and combustion process. It should be noted that relationships between fluxes and driving potentials occur when both heat and mass transfer act simultaneously. Here temperature gradient generates energy flux. However mass flux and composition gradients are due to temperature gradient (which is called soret effect). It is noted that all the a fore mentioned studies on peristaltic transport have been conducted for peristalsis in straight channels which is not realistic always since most of the pipes, arteries and glandular ducts are curved. Thus some advancements have been made for peristalsis using curvilinear coordinates. Abbasi et al.[12] initiated such analysis for peristaltic transport of viscous fluids. Sato et al. [13] extend the work of sato et al. in wave frame of reference. Later some attempts [14 , 15,16 ,17] have been presented to address. The curvature effects on peristalsis of fluids in a channel. In these attempts mostly the constant magnetic field are considered. Recently, Hayat et al. [18] is given in their work to explore the characteristics of radial magnetic field on peristaltic transport of Jeffrey fluid in a curved channel. Heat transfer is characterized there by utilizing convective condition. Hayat et al. [19] investigated the effect of radial magnetic field on the peristaltic flow of Jeffrey liquid in curved channel with complaint walls.

Now, in our work, we investigated the effect of radial magnetic field on the peristaltic flow of Jeffrey fluid in curved channel by using the effect of heat and mass transfer. The effects of viscous dissipation and thermophoresis are considered in the transport equations such as the effect of Brinkman number (Br), Schmidt number (Sc) and soret number (Sr). the slip boundary conditions on velocity, and non-slip boundary conditions on temperature and conservation are considered. The equations are simplified by using long wave length and low Reynolds number approximations. The graphical results are obtained to explain the effects of parameters entering in the problem.

2- Mathematical formulation

Consider two- dimensional motion of an viscous incompressible Jeffrey fluid in a curved channel of width $(2a)$, centre at 0° and radius at R as shown in figure (1). The flow is generated due to the transverse deflections of sinusoidal waves of small amplitudes (b) that are imposed on the flexible walls of the channel. The inertial effects are assumed to be small. The lower and upper walls of the channel are maintained at the same temperature T_0 and concentration C_0. The equations of the walls of channel are described as follows:

$$\bar{r} = \mp H(\overline{X}, \bar{t}) = \mp a \mp b \cos\left(\frac{2\pi}{\lambda}(\overline{X} - C\bar{t})\right) \quad \text{.....(1)}$$

Where $\overline{X}$ is the axial distance, $\bar{r}$ is the radial distance, a is the radius of the stationary curved channel, b is the wave amplitude, λ is the wave length, $\bar{t}$ is the time and the wave length is large compared with the channel width (a) that is $(\frac{a}{\lambda} << 1)$.

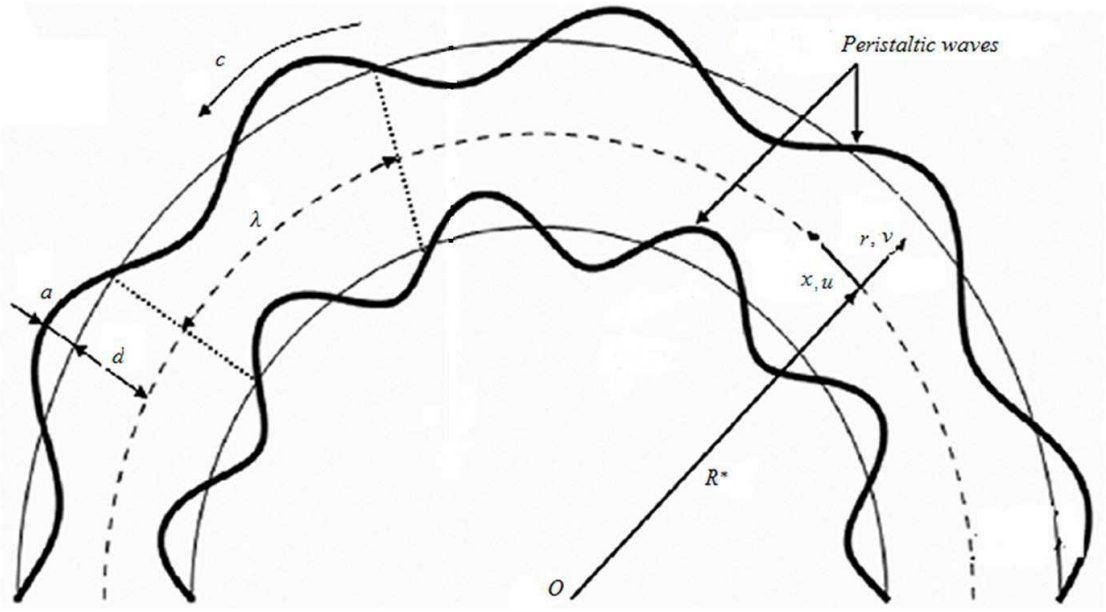

Figure 1 .geometry of the problem

3- Constitutive equations

The constitutive equations for a Jeffrey fluid given by : [20]

$$\bar{t} = -\bar{P}\bar{I} + \bar{S}, \qquad \text{.....(2)}$$

$$\bar{S} = \frac{\mu}{1+\lambda_1}(\dot{\bar{\gamma}} + \lambda_2 \ddot{\bar{\gamma}}) \qquad \text{.....(3)}$$

Where $\bar{t}$ and $\bar{S}$ Cauchy stress tensor and extra stress tensor, respectively, $\bar{P}$ is the pressure, $\bar{I}$ is the identity tensor, μ is dynamic viscosity, λ_1 is the ratio of relaxation to retardation times, λ_2 is the retardation time, $\dot{\bar{\gamma}}$ is the shear rate and dots over the quantities indicate differentiation with respect to time.

Let $\bar{V} = [\bar{U}(\bar{r}, \bar{X}, \bar{t}), \bar{V}(\bar{r}, \bar{X}, \bar{t}), 0]$ be the velocity vector in the curvilinear coordinates $(\bar{r}, \bar{X})$.

$$(grad\bar{V}) = (\nabla\bar{V}) = \begin{pmatrix} \frac{\partial\bar{V}}{\partial\bar{r}} & \frac{R}{\bar{r}+R}\frac{\partial\bar{V}}{\partial\bar{X}} - \frac{\bar{U}}{\bar{r}+R} \\ \frac{\partial\bar{U}}{\partial\bar{r}} & \frac{R}{\bar{r}+R}\frac{\partial\bar{U}}{\partial\bar{X}} + \frac{\bar{V}}{\bar{r}+R} \end{pmatrix} \qquad \text{.....(4)}$$

The strain E is defined by :

$$e = \tfrac{1}{2}[(\nabla\bar{V}) + (\nabla\bar{V})^{T}] \qquad \text{.....(5)}$$

The shear strain or shear rate $\dot{\bar{\gamma}}$ is defined by :

$$\dot{\bar{\gamma}} = 2e = \begin{pmatrix} 2\frac{\partial \bar{V}}{\partial \bar{r}} & \frac{\partial \bar{U}}{\partial \bar{r}} + \frac{R}{\bar{r}+R}\frac{\partial \bar{V}}{\partial \bar{X}} - \frac{\bar{U}}{\bar{r}+R} \\ \frac{\partial \bar{U}}{\partial \bar{r}} + \frac{R}{\bar{r}+R}\frac{\partial \bar{V}}{\partial \bar{X}} - \frac{\bar{U}}{\bar{r}+R} & 2(\frac{R}{\bar{r}+R}\frac{\partial \bar{U}}{\partial \bar{X}} + \frac{\bar{V}}{\bar{r}+R}) \end{pmatrix} \quad \text{.....(6)}$$

So, we have:

$$\dot{\bar{\gamma}}_{\bar{r}\bar{r}} = 2\frac{\partial \bar{V}}{\partial \bar{r}},\ \dot{\bar{\gamma}}_{\bar{r}\bar{X}} = \dot{\bar{\gamma}}_{\bar{X}\bar{r}} = \frac{\partial \bar{U}}{\partial \bar{r}} + \frac{R}{\bar{r}+R}\frac{\partial \bar{V}}{\partial \bar{X}} - \frac{\bar{U}}{\bar{r}+R},\ \dot{\bar{\gamma}}_{\bar{X}\bar{X}} = 2(\frac{R}{\bar{r}+R}\frac{\partial \bar{U}}{\partial \bar{X}} + \frac{\bar{V}}{\bar{r}+R}) \quad \text{....(7)}$$

Now, define $\ddot{\bar{\gamma}}$ as follows:

$$\ddot{\bar{\gamma}} = \frac{D}{Dt}\dot{\bar{\gamma}} = (\frac{\partial}{\partial \bar{t}} + \bar{V}.\nabla).\dot{\bar{\gamma}} = \frac{\partial}{\partial \bar{t}}\dot{\bar{\gamma}} + (\bar{V}.\nabla)\dot{\bar{\gamma}}, \quad \text{.....(8)}$$

in which

$$\bar{V}.\nabla = \frac{R}{\bar{r}+R}\bar{U}\frac{\partial}{\partial \bar{X}} + \bar{V}\frac{\partial}{\partial \bar{r}}, \quad \text{.....(9)}$$

Thus we have :

$$\ddot{\bar{\gamma}}_{\bar{r}\bar{r}} = \frac{\partial}{\partial \bar{t}}\dot{\bar{\gamma}}_{\bar{r}\bar{r}} + (\frac{R}{\bar{r}+R}\bar{U}\frac{\partial}{\partial \bar{X}} + \bar{V}\frac{\partial}{\partial \bar{r}})\dot{\bar{\gamma}}_{\bar{r}\bar{r}}$$
$$= 2[\frac{\partial}{\partial \bar{t}} + (\frac{R}{\bar{r}+R}\bar{U}\frac{\partial}{\partial \bar{X}} + \bar{V}\frac{\partial}{\partial \bar{r}})]\frac{\partial \bar{V}}{\partial \bar{r}}, \quad \text{.....(10)}$$

$$\ddot{\bar{\gamma}}_{\bar{r}\bar{X}} = \frac{\partial}{\partial \bar{t}}\dot{\bar{\gamma}}_{\bar{r}\bar{X}} + (\frac{R}{\bar{r}+R}\bar{U}\frac{\partial}{\partial \bar{X}} + \bar{V}\frac{\partial}{\partial \bar{r}})\dot{\bar{\gamma}}_{\bar{r}\bar{X}}$$
$$= [\frac{\partial}{\partial \bar{t}} + (\frac{R}{\bar{r}+R}\bar{U}\frac{\partial}{\partial \bar{X}} + \bar{V}\frac{\partial}{\partial \bar{r}})](\frac{\partial \bar{U}}{\partial \bar{r}} + \frac{R}{\bar{r}+R}\frac{\partial \bar{V}}{\partial \bar{X}} - \frac{\bar{U}}{\bar{r}+R}), \quad \text{.....(11)}$$

$$\ddot{\bar{\gamma}}_{\bar{X}\bar{X}} = \frac{\partial}{\partial \bar{t}}\dot{\bar{\gamma}}_{\bar{X}\bar{X}} + (\frac{R}{\bar{r}+R}\bar{U}\frac{\partial}{\partial \bar{X}} + \bar{V}\frac{\partial}{\partial \bar{r}})\dot{\bar{\gamma}}_{\bar{X}\bar{X}}$$
$$= 2[\frac{\partial}{\partial \bar{t}} + (\frac{R}{\bar{r}+R}\bar{U}\frac{\partial}{\partial \bar{X}} + \bar{V}\frac{\partial}{\partial \bar{r}})](\frac{R}{\bar{r}+R}\frac{\partial \bar{U}}{\partial \bar{X}} + \frac{\bar{V}}{\bar{r}+R}), \quad \text{.....(12)}$$

The components of shear tensor (S) are :

$$S=\begin{pmatrix} S_{\bar{r}\bar{r}} & S_{\bar{r}\bar{X}} \\ S_{\bar{X}\bar{r}} & S_{\bar{X}\bar{X}} \end{pmatrix}$$

$$S_{\bar{r}\bar{r}}=\frac{\mu}{1+\lambda_1}(\dot{\gamma}_{\bar{r}\bar{r}}+\lambda_2\ddot{\gamma}_{\bar{r}\bar{r}})$$

$$=\frac{\mu}{1+\lambda_1}(2\frac{\partial\bar{V}}{\partial\bar{r}}+2\lambda_2[\frac{\partial}{\partial\bar{t}}+(\frac{R}{\bar{r}+R}\bar{U}\frac{\partial}{\partial\bar{X}}+\bar{V}\frac{\partial}{\partial\bar{r}})]\frac{\partial\bar{V}}{\partial\bar{r}})$$

$$=\frac{2\mu}{1+\lambda_1}(1+\lambda_2[\frac{\partial}{\partial\bar{t}}+(\frac{R}{\bar{r}+R}\bar{U}\frac{\partial}{\partial\bar{X}}+\bar{V}\frac{\partial}{\partial\bar{r}})]\frac{\partial\bar{V}}{\partial\bar{r}} \qquad \text{.....(13)}$$

$$S_{\bar{r}\bar{X}}=\frac{\mu}{1+\lambda_1}(\dot{\gamma}_{\bar{r}\bar{X}}+\lambda_2\ddot{\gamma}_{\bar{r}\bar{X}})$$

$$=\frac{\mu}{1+\lambda_1}((\frac{\partial\bar{U}}{\partial\bar{r}}+\frac{R}{\bar{r}+R}\frac{\partial\bar{V}}{\partial\bar{X}}-\frac{\bar{U}}{\bar{r}+R})+\lambda_2[\frac{\partial}{\partial\bar{t}}+(\frac{R}{\bar{r}+R}\bar{U}\frac{\partial}{\partial\bar{X}}+\bar{V}\frac{\partial}{\partial\bar{r}}]$$

$$=\frac{\mu}{1+\lambda_1}(1+\lambda_2[\frac{\partial}{\partial\bar{t}}+\frac{R}{\bar{r}+R}\bar{U}\frac{\partial}{\partial\bar{X}}+\bar{V}\frac{\partial}{\partial\bar{r}}])(\frac{\partial\bar{U}}{\partial\bar{r}}+\frac{R}{\bar{r}+R}\frac{\partial\bar{V}}{\partial\bar{X}}-\frac{\bar{U}}{\bar{r}+R}) \qquad \text{.....(14)}$$

$$=\frac{\mu}{1+\lambda_1}(2(\frac{R}{\bar{r}+R}\frac{\partial\bar{U}}{\partial\bar{X}}+\frac{\bar{V}}{\bar{r}+R})+\lambda_2[\frac{\partial}{\partial\bar{t}}+\frac{R}{\bar{r}+R}\bar{U}\frac{\partial}{\partial\bar{X}}+\bar{V}\frac{\partial}{\partial\bar{r}}](2(\frac{R}{\bar{r}+R}\frac{\partial\bar{U}}{\partial\bar{X}}+\frac{\bar{V}}{\bar{r}+R})))$$

$$=\frac{2\mu}{1+\lambda_1}(1+\lambda_2[\frac{\partial}{\partial\bar{t}}+\frac{R}{\bar{r}+R}\bar{U}\frac{\partial}{\partial\bar{X}}+\bar{V}\frac{\partial}{\partial\bar{r}}])(\frac{R}{\bar{r}+R}\frac{\partial\bar{U}}{\partial\bar{X}}+\frac{\bar{V}}{\bar{r}+R}), \qquad \text{.....(15)}$$

4- Calculation of Lorentz force

Fluid in this problem is flowing under the influence of radially varying magnetic field of the form [19]:

$$\bar{B}=\frac{RB_0}{\bar{R}+\bar{r}}e_{\bar{r}} \qquad \text{.....(1)}$$

The type of magnetic field given through eq.(1) satisfies the Maxwell equations. Velocity field for present flow configuration is taken of the form :

$\bar{V}=[\bar{U}(\bar{r},\bar{X},\bar{t}),\bar{V}(\bar{r},\bar{X},\bar{t}),0]$ where $\bar{U}$ and $\bar{V}$ are the axial and radial components of the velocity respectively.

The Lorentz force $\bar{F}$ in view of the magnetic and velocity fields mentioned above takes the following form:

$$\bar{J} = \bar{V} \times \bar{B} = \begin{vmatrix} e_{\bar{X}} & e_{\bar{r}} & e_{\bar{Z}} \\ \bar{U} & \bar{V} & 0 \\ 0 & \frac{R}{R+\bar{r}} B_0 & 0 \end{vmatrix} = \frac{R}{R+\bar{r}} \bar{U} B_0 e_{\bar{Z}} \quad \text{.....(2)}$$

$$\sigma \times \bar{J} = \frac{R}{R+\bar{r}} \sigma \bar{U} B_0 e_{\bar{Z}} \quad \text{.....(3)}$$

Utilization of ohms law gives the following expression :

$$\bar{F} = \bar{J} \times \bar{B} = \begin{vmatrix} e_{\bar{X}} & e_{\bar{r}} & e_{\bar{Z}} \\ 0 & 0 & \frac{R}{R+\bar{r}} \sigma \bar{U} B_0 \\ 0 & \frac{R}{R+\bar{r}} B_0 & 0 \end{vmatrix} = -(\frac{R}{R+\bar{r}})^2 \sigma \bar{U} B_0{}^2 e_{\bar{X}} \quad \text{.....(4)}$$

That is

$$\bar{F} = [-\sigma(\frac{R}{R+\bar{r}})^2 \bar{U} B_0{}^2, 0, 0] \quad \text{.....(5)}$$

where B_0 is the strength of applied magnetic field, $e_{\bar{r}}$ is the unit vector in the radial direction, $\bar{J}$ is the current density and σ is the electric conductivity of fluid, $\bar{B}$ is the magnetic field. It is observed that the effect of magnetic field appear in the flow of axial direction.

5- Basic equations

The basic equations governing the non-Newtonian in compressible viscous Jeffrey fluid are given by:

The continuity equation is given by:

$$\frac{R}{\bar{r}+R} \frac{\partial \bar{U}}{\partial \bar{X}} + \frac{\partial \bar{V}}{\partial \bar{r}} + \frac{\bar{V}}{\bar{r}+R} = 0 \quad \text{.....(16)}$$

The momentum equations are given by:

$$\rho(\frac{\partial \bar{U}}{\partial \bar{t}} + \bar{V} \frac{\partial \bar{U}}{\partial \bar{r}} + \frac{R}{\bar{r}+R} \bar{U} \frac{\partial \bar{U}}{\partial \bar{X}} + \frac{\bar{U}.\bar{V}}{\bar{r}+R}) = -\frac{R}{\bar{r}+R} \frac{\partial \bar{P}}{\partial \bar{X}} + \frac{R}{\bar{r}+R} \frac{\partial}{\partial \bar{X}} S_{\bar{X}\bar{X}} + \frac{1}{(\bar{r}+R)^2}$$

$$\frac{\partial}{\partial \bar{r}} \left\{ (\bar{r}+R)^2 S_{\bar{X}\bar{r}} \right\} - \sigma(\frac{R}{\bar{r}+R})^2 \mathrm{B}_0{}^2 \bar{U} \quad \text{.....(17)}$$

$$\rho(\frac{\partial \bar{V}}{\partial \bar{t}} + \bar{V} \frac{\partial \bar{V}}{\partial \bar{r}} + \frac{R}{\bar{r}+R} \bar{U} \frac{\partial \bar{V}}{\partial \bar{X}} - \frac{\bar{U}^2}{\bar{r}+R}) = -\frac{\partial \bar{P}}{\partial \bar{r}} + \frac{1}{\bar{r}+R} \frac{\partial}{\partial \bar{r}} \left\{ (\bar{r}+R) S_{\bar{r}\bar{r}} \right\} + \frac{R}{\bar{r}+R} \frac{\partial}{\partial \bar{X}} S_{\bar{X}\bar{r}}$$

$$\frac{1}{\bar{r}+R} S_{\bar{X}\bar{X}} \quad \text{.....(18)}$$

The temperature equation is given by :

$$\rho C_p(\frac{\partial}{\partial \bar{t}}+\bar{V}\frac{\partial}{\partial \bar{r}}+\frac{R\bar{U}}{\bar{r}+R}\frac{\partial}{\partial \bar{X}})T = k_1[\frac{\partial^2 T}{\partial \bar{r}^2}+\frac{1}{\bar{r}+R}\frac{\partial T}{\partial \bar{r}}+(\frac{R}{\bar{r}+R})^2\frac{\partial^2 T}{\partial \bar{X}^2}]+$$
$$(S_{\bar{r}\bar{r}}-S_{\bar{X}\bar{X}})\frac{\partial \bar{V}}{\partial \bar{r}}+S_{\bar{X}\bar{r}}(\frac{\partial \bar{U}}{\partial \bar{r}}+\frac{R}{\bar{r}+R}\frac{\partial \bar{V}}{\partial \bar{X}}-\frac{\bar{U}}{\bar{r}+R}) \quad .....(19)$$

The concentration equation is given by :

$$[\frac{\partial}{\partial \bar{t}}+\bar{V}\frac{\partial}{\partial \bar{r}}+\frac{R}{\bar{r}+R}\bar{U}\frac{\partial}{\partial \bar{X}}]\bar{C} = D[\frac{\partial^2}{\partial \bar{r}^2}+\frac{1}{\bar{r}+R}\frac{\partial}{\partial \bar{r}}+(\frac{R}{\bar{r}+R})^2\frac{\partial^2}{\partial \bar{X}^2}]\bar{C}+$$
$$\frac{DK_T}{T_m}[\frac{\partial^2}{\partial \bar{r}^2}+\frac{1}{\bar{r}+R}\frac{\partial}{\partial \bar{r}}+(\frac{R}{\bar{r}+R})^2\frac{\partial^2}{\partial \bar{X}^2}]T \quad .....(20)$$

Where P is the pressure, ρ is the density, C_p is the specific heat, K_1 is the thermal conductivity, D is the diffusion coefficient of the diffusing species, T_m the mean fluid temperature, K_T is the thermal diffusion ratio, T and $\bar{C}$ denote the fluid temperature and concentration respectively.

6- Method of solution :

In order to simplify the governing equations of motion, temperature and concentration we may introduce the following dimensionless transformations as follows:

$$x=\frac{\bar{X}}{\lambda},\ r=\frac{\bar{r}}{a},\ u=\frac{\bar{U}}{c},\ v=\frac{\bar{V}}{\delta c},\ t=\frac{c\bar{t}}{\lambda},\quad h=\frac{\bar{H}}{a},\ \varphi=\frac{b}{a},\ \delta=\frac{a}{\lambda},\ K=\frac{R}{a},\ p=\frac{a^2\bar{P}}{\mu c\lambda},$$
$$\mathrm{Re}=\frac{\rho c a}{\mu},\ M^2=\frac{\sigma B_0^2 a^2}{\mu},\ \mathrm{S}=\frac{a\bar{S}}{\mu C},\ \mathrm{F}=\frac{Q}{aC},\ \theta=\frac{T-T_0}{T_0},\ \phi=\frac{\bar{C}-\bar{C_0}}{\bar{C_0}},\ \alpha_3=\mathrm{SC}=\frac{\mu}{\rho D},$$
$$\alpha_2=\mathrm{Sr}=\frac{\rho D K_T T_0}{\mu T_m \bar{C_0}},\ P\mathrm{r}=\frac{\mu C_p}{k_1},\quad \mathrm{Ec}=\frac{C^2}{C_p T_0},\ \alpha_1=\mathrm{Pr}.Ec=Br,\ \mathrm{u}=\frac{\partial \psi}{\partial r},\ \mathrm{v}=\frac{-K}{r+K}\frac{\partial \psi}{\partial x} \quad .....(21)$$

In which (Re) is the Reynolds number, F is the volume flow rate, δ is the wave number, ϕ is the amplitude ratio or the occlusion parameter, K is the curvature parameter, Pr is the prandtl number, Ec is the Eckert number, Sc is the Schmidt number, Sr is the soret number, ψ is the stream function, Br is brinkman number, θ is the temperature distribution and σ is the concentration of species.

Now substituting (21) into equations (13)-(15) and into equations (16)-(20) we have:

$$\frac{k}{(r+k)}.\frac{C}{\lambda}\frac{\partial u}{\partial x}+\frac{C}{\lambda}\frac{\partial v}{\partial r}+\frac{C}{\lambda}\frac{v}{(r+k)}=0 \quad .....(22)$$

Multiplying both sides of (22) by $(\frac{\lambda}{C})$ we get :

$$\frac{k}{(r+k)}\frac{\partial u}{\partial x}+\frac{\partial v}{\partial r}+\frac{v}{(r+k)}=0 \quad .....(23)$$

From eq.(17) we have:

$$\rho\frac{C^2}{\lambda}(\frac{\partial u}{\partial t}+v\frac{\partial u}{\partial r}+\frac{k}{(r+k)}u\frac{\partial u}{\partial x}+\frac{uv}{(r+k)})=-\frac{k}{(r+k)}\frac{C\mu}{a^2}\frac{\partial P}{\partial x}+\frac{k}{(r+k)}$$
$$\frac{1}{\lambda}\frac{\mu C}{a}\frac{\partial}{\partial x}S_{xx}+\frac{\mu C}{a^2(r+k)^2}.\frac{\partial}{\partial r}\{(r+k)^2S_{xr}\}-\sigma(\frac{k}{(r+k)})^2B_0{}^2Cu. \quad .....(24)$$

Now, multiplying sides of (24) by $(\frac{a^2}{C\mu})$ we get:

Now, in the laboratory frame $(\bar{r},\overline{X})$ the flow is unsteady, however if treated it as steady flow in the wave frame (r, x), thus we have:

$$\mathrm{Re}\,\delta(v\frac{\partial u}{\partial r}+\frac{k}{(r+k)}u\frac{\partial u}{\partial x}+\frac{uv}{(r+k)})=-\frac{k}{(r+k)}\frac{\partial P}{\partial x}+\frac{k}{(r+k)}\delta\frac{\partial}{\partial x}S_{xx}+\frac{1}{(r+k)^2}.$$
$$\frac{\partial}{\partial r}\{(r+k)^2S_{xr}\}-(\frac{k}{(r+k)})^2M^2u. \quad .....(25)$$

From eq.(18) we have:

$$\rho\frac{C^2}{a}(\delta^2\frac{\partial v}{\partial t}+\delta^2v\frac{\partial v}{\partial r}+\frac{k}{(r+k)}\delta^2u\frac{\partial v}{\partial x}-\frac{u^2}{(r+k)})=-\frac{C\lambda\mu}{a^3}\frac{\partial P}{\partial r}+\frac{\mu C}{a^2(r+k)}$$
$$\frac{\partial}{\partial r}\{(r+k)S_{rr}\}+\frac{k}{(r+k)}\frac{\mu C}{\lambda a}\frac{\partial}{\partial x}S_{xr}-\frac{\mu C}{a^2(r+k)}S_{xx} \quad .....(26)$$

Now, multiplying both sides of (26) by $(\frac{a^3}{C\lambda\mu})$ we get:

$$\mathrm{Re}\,\delta(\delta^2v\frac{\partial v}{\partial r}+\frac{k}{(r+k)}\delta^2u\frac{\partial v}{\partial x}-\frac{u^2}{(r+k)})=-\frac{\partial P}{\partial r}+\delta\frac{\partial}{\partial r}\{(r+k)S_{rr}\}+\frac{k}{(r+k)}\delta^2$$
$$\frac{\partial}{\partial x}S_{xr}-\frac{\delta}{(r+k)}S_{xx} \quad .....(27)$$

From eq. (19) we have:

$$\rho C_p\frac{C}{\lambda}[\frac{\partial T}{\partial t}+v\frac{\partial T}{\partial r}+\frac{k}{(r+k)}u\frac{\partial T}{\partial x})=\frac{k_1}{a^2}[\frac{\partial^2T}{\partial r^2}+\frac{1}{(r+k)}\frac{\partial T}{\partial r}+(\frac{k}{(r+k)})^2\delta^2\frac{\partial^2T}{\partial x^2}]+\frac{\mu C}{a}\frac{C}{\lambda}$$
$$(S_{rr}-S_{xx})\frac{\partial v}{\partial r}+\frac{\mu C}{a}\frac{C}{a}S_{rx}(\frac{\partial u}{\partial r}+\delta^2\frac{k}{(r+k)}\frac{\partial v}{\partial x}-\frac{u}{(r+k)}) \quad .....(28)$$

Now, multiplying both sides of (28) by $(\frac{a^2}{k_1})$ we get :

$$\rho C_p \frac{C}{\lambda}\frac{a^2}{k_1}\frac{\mu}{\mu}[\frac{\partial T}{\partial t}+v\frac{\partial T}{\partial r}+\frac{k}{(r+k)}u\frac{\partial T}{\partial x})=[\frac{\partial^2 T}{\partial r^2}+\frac{1}{(r+k)}\frac{\partial T}{\partial r}+(\frac{k}{(r+k)})^2\delta^2\frac{\partial^2 T}{\partial x^2}]+$$

$$\frac{\mu C^2}{\lambda}\frac{a}{k_1}(S_{rr}-S_{xx})\frac{\partial v}{\partial r}+\frac{\mu C^2}{k_1}S_{rx}(\frac{\partial u}{\partial r}+\delta^2\frac{k}{(r+k)}\frac{\partial v}{\partial x}-\frac{u}{(r+k)}) \quad .....(29)$$

$$Now,\ since\quad \theta=\frac{T-T_0}{T_0}\Rightarrow T-T_0=\theta T_0\Rightarrow T=\theta T_0+T_0\Rightarrow \partial T=T_0\partial\theta \quad .....(30)$$

Thus, we can write eq.(29) by the following form:

$$\rho C_p \frac{C}{\lambda}\frac{a^2}{k_1}\frac{\mu}{\mu}T_0[\frac{\partial \theta}{\partial t}+v\frac{\partial \theta}{\partial r}+\frac{k}{(r+k)}u\frac{\partial \theta}{\partial x})=T_0[\frac{\partial^2 \theta}{\partial r^2}+\frac{1}{(r+k)}\frac{\partial \theta}{\partial r}+(\frac{k}{r+k})^2\delta^2\frac{\partial^2 \theta}{\partial x^2}]+$$

$$\frac{\mu C^2}{k_1}\delta(S_{rr}-S_{xx})\frac{\partial v}{\partial r}+\frac{\mu C^2}{k_1}S_{rx}(\frac{\partial u}{\partial r}+\delta^2\frac{k}{(r+k)}\frac{\partial v}{\partial x}-\frac{u}{(r+k)}) \quad .....(31)$$

Multiplying both sides of eq.(31) by $(\frac{1}{T_0})$ we have:

$$\mathrm{Re}\,\mathrm{Pr}\,\delta[v\frac{\partial \theta}{\partial r}+\frac{k}{(r+k)}u\frac{\partial \theta}{\partial x})=[\frac{\partial^2 \theta}{\partial r^2}+\frac{1}{(r+k)}\frac{\partial \theta}{\partial r}+(\frac{k}{r+k})^2\delta^2\frac{\partial^2 \theta}{\partial x^2}]+$$

$$\frac{C^2}{C_pT_0}\frac{\mu C_p}{k_1}\delta(S_{rr}-S_{xx})\frac{\partial v}{\partial r}+\frac{C^2}{C_pT_0}\frac{\mu C_p}{k_1}S_{rx}(\frac{\partial u}{\partial r}+\delta^2\frac{k}{(r+k)}\frac{\partial v}{\partial x}-\frac{u}{(r+k)}). \quad .....(32)$$

Eq.(32) can be written as the following form:

$$\mathrm{Re}\,\mathrm{Pr}\,\delta[v\frac{\partial \theta}{\partial r}+\frac{k}{(r+k)}u\frac{\partial \theta}{\partial x})=[\frac{\partial^2 \theta}{\partial r^2}+\frac{1}{(r+k)}\frac{\partial \theta}{\partial r}+(\frac{k}{r+k})^2\delta^2\frac{\partial^2 \theta}{\partial x^2}]+Ec\,\mathrm{Pr}\,\delta(S_{rr}-S_{xx})$$

$$\frac{\partial v}{\partial r}+Ec\,\mathrm{Pr}\,S_{rx}(\frac{\partial u}{\partial r}+\delta^2\frac{k}{(r+k)}\frac{\partial v}{\partial x}-\frac{u}{(r+k)}). \quad .....(33)$$

From eq.(20) we have:

$$\frac{\overline{C}}{\lambda}[\frac{\partial \overline{C}}{\partial t}+v\frac{\partial \overline{C}}{\partial r}+\frac{k}{(r+k)}u\frac{\partial \overline{C}}{\partial x}]=\frac{D}{a^2}[\frac{\partial^2 \overline{C}}{\partial r^2}+\frac{1}{(r+k)}\frac{\partial \overline{C}}{\partial r}+(\frac{k}{(r+k)})^2\delta^2\frac{\partial^2 \overline{C}}{\partial x^2}]+\frac{DK_T}{T_m}\frac{1}{a^2}$$

$$[\frac{\partial^2 T}{\partial r^2}+\frac{1}{(r+k)}\frac{\partial T}{\partial r}+(\frac{k}{(r+k)})^2\delta^2\frac{\partial^2 T}{\partial x^2}]. \quad .....(34)$$

Multiplying both sides of (34) by $(\frac{a^2}{D})$ we get:

$$\frac{\overline{C}}{\lambda}\frac{a^2}{D}[\frac{\partial \overline{C}}{\partial t}+v\frac{\partial \overline{C}}{\partial r}+\frac{k}{(r+k)}u\frac{\partial \overline{C}}{\partial x}]=[\frac{\partial^2 \overline{C}}{\partial r^2}+\frac{1}{(r+k)}\frac{\partial \overline{C}}{\partial r}+(\frac{k}{(r+k)})^2\delta^2\frac{\partial^2 \overline{C}}{\partial x^2}]+\frac{DK_T}{T_m}\frac{1}{a^2}$$

$$\frac{a^2}{D}[\frac{\partial^2 T}{\partial r^2}+\frac{1}{(r+k)}\frac{\partial T}{\partial r}+(\frac{k}{(r+k)})^2\delta^2\frac{\partial^2 T}{\partial x^2}]. \quad .....(35)$$

But we have $\theta = \frac{T - T_0}{T_0}$ and $\phi = \frac{\overline{C} - \overline{C_0}}{\overline{C_0}}$ thus $\partial T = T_0 \partial\theta$ and $\partial\overline{C} = \overline{C_0}\partial\phi$

So, we can write (35) by the following form:

$$\frac{\overline{C}}{\lambda}\frac{a^2}{D}\overline{C_0}\frac{\rho}{\rho}[\frac{\partial\phi}{\partial t} + v\frac{\partial\phi}{\partial r} + \frac{k}{(r+k)}u\frac{\partial\phi}{\partial x}] = \overline{C_0}[\frac{\partial^2\phi}{\partial r^2} + \frac{1}{(r+k)}\frac{\partial\phi}{\partial r} + (\frac{k}{(r+k)})^2\delta^2\frac{\partial^2\phi}{\partial x^2}]$$

$$+\frac{DK_T}{T_m}\frac{1}{D}T_0[\frac{\partial^2\theta}{\partial r^2} + \frac{1}{(r+k)}\frac{\partial\theta}{\partial r} + (\frac{k}{(r+k)})^2\delta^2\frac{\partial^2\theta}{\partial x^2}]. \quad .....(36)$$

Multiplying both sides of (36) by $(\frac{1}{\overline{C_0}})$ we get :

$$\mathrm{Re}\,\delta Sc[v\frac{\partial\phi}{\partial r} + \frac{k}{(r+k)}u\frac{\partial\phi}{\partial x}] = [\frac{\partial^2\phi}{\partial r^2} + \frac{1}{(r+k)}\frac{\partial\phi}{\partial r} + \delta^2(\frac{k}{(r+k)})^2\frac{\partial^2\phi}{\partial x^2}] + Sr.Sc[\frac{\partial^2\theta}{\partial r^2} +$$

$$\frac{1}{(r+k)}\frac{\partial\theta}{\partial r} + \delta^2(\frac{k}{(r+k)})^2\frac{\partial^2\theta}{\partial x^2}]. \quad .....(37)$$

From eq.(13) we have:

$$\frac{\mu C}{a}S_{rr} = \frac{2\mu}{1+\lambda_1}(1+\lambda_2\frac{C}{\lambda}[\frac{\partial}{\partial t} + (\frac{k}{(r+k)})u\frac{\partial}{\partial x} + v\frac{\partial}{\partial r})]\frac{\partial v}{\partial r} \quad .....(38)$$

Multiplying both sides of (38) by $\frac{a}{C\mu}$ we get:

$$S_{rr} = \frac{2\cancel{\mu}}{1+\lambda_1}\frac{\cancel{C}}{\lambda}\frac{a}{\cancel{C\mu}}(1+\lambda_2\frac{C}{\lambda}\frac{a}{a}[\frac{\partial}{\partial t} + (\frac{k}{(r+k)})u\frac{\partial}{\partial x} + v\frac{\partial}{\partial r})]\frac{\partial v}{\partial r}$$

$$S_{rr} = \frac{2\delta}{1+\lambda_1}(1+\frac{\lambda_2 C\delta}{a}[(\frac{k}{(r+k)})u\frac{\partial}{\partial x} + v\frac{\partial}{\partial r})]\frac{\partial v}{\partial r} \quad .....(39)$$

From eq.(14) we have

$$\frac{\mu C}{a}S_{rx} = \frac{\mu}{1+\lambda_1}\frac{C}{a}(1+\lambda_2\frac{C}{\lambda}\frac{a}{a}[\frac{\partial}{\partial t} + \frac{k}{(r+k)}u\frac{\partial}{\partial x} + v\frac{\partial}{\partial r}])(\frac{\partial u}{\partial r} + \frac{k}{(r+k)}\delta^2\frac{\partial v}{\partial x} - \frac{u}{(r+k)})...(40)$$

Multiplying both sides of (40) by $(\frac{a}{\mu C})$ we have:

$$S_{rx} = \frac{1}{1+\lambda_1}(1+\frac{\lambda_2 C\delta}{a}[\frac{\partial}{\partial t} + \frac{k}{(r+k)}u\frac{\partial}{\partial x} + v\frac{\partial}{\partial r}])(\frac{\partial u}{\partial r} + \frac{k}{(r+k)}\delta^2\frac{\partial v}{\partial x} - \frac{u}{(r+k)}) \quad .....(41)$$

From eq.(15) we have:

$$\frac{\mu C}{a}S_{xx} = \frac{2\mu}{1+\lambda_1}(1+\lambda_2\frac{C}{\lambda}[\frac{\partial}{\partial t}+\frac{k}{(r+k)}u\frac{\partial}{\partial x}+v\frac{\partial}{\partial r}])\frac{C}{\lambda}(\frac{k}{(r+k)}\frac{\partial u}{\partial x}+\frac{v}{(r+k)}), \quad \text{.....(42)}$$

Multiplying both sides of (42) by $(\frac{a}{\mu C})$ we get:

$$S_{xx} = \frac{2\delta}{1+\lambda_1}(1+\frac{\lambda_2 C\delta}{a}[\frac{k}{(r+k)}u\frac{\partial}{\partial x}+v\frac{\partial}{\partial r}])(\frac{k}{(r+k)}\frac{\partial u}{\partial x}+\frac{v}{(r+k)}), \quad \text{.....(43)}$$

The general solution of the governing equations (25)-(43) in the general case seems to be impossible, therefore we shall can fine the analysis under the assumption of small wave length $(\delta << 1)$ and low Reynolds number approximation, thus we can write the above equations in the form of stream function:

$$\frac{\partial P}{\partial r} = 0 \quad \text{....(44)}$$

$$\frac{\partial P}{\partial x} = \frac{1}{k(r+k)}.\frac{\partial}{\partial r}\{(r+k)^2 S_{xr}\} - \frac{k}{r+k}.M^2\frac{\partial \psi}{\partial r} \quad \text{....(45)}$$

$$S_{rr} = 0,\ S_{xx} = 0, S_{rx} = \frac{1}{1+\lambda_1}(\frac{\partial^2\psi}{\partial r^2} - \frac{1}{(r+k)}\frac{\partial\psi}{\partial r}) \quad \text{.....(46)}$$

$$0 = \frac{\partial^2\theta}{\partial r^2}+\frac{1}{(r+k)}\frac{\partial\theta}{\partial r}+BrS_{rx}(\frac{\partial^2\psi}{\partial r^2} - \frac{1}{(r+k)}\frac{\partial\psi}{\partial r}) \quad \text{.....(47)}$$

$$0 = \frac{\partial^2\phi}{\partial r^2}+\frac{1}{(r+k)}\frac{\partial\phi}{\partial r}+SrSc(\frac{\partial^2\theta}{\partial r^2} - \frac{1}{(r+k)}\frac{\partial\theta}{\partial r}) \quad \text{.....(48)}$$

The corresponding dimensionless boundary conditions are given by:

$$\psi = \mp\frac{F}{2},\ \frac{\partial^2\psi}{\partial r^2}\mp\alpha\frac{\partial\psi}{\partial r} = 0,\ \theta = 0,\ \phi = 0 \quad \text{at } r = \mp h = \mp(1+\varphi\cos 2\pi(x-t)) \quad \text{.....(49)}$$

The relation between volume flow rate and time average flow rate is []:

$$F(x,t) = Q + 2(h(x,t)-1) \quad \text{.....(50)}$$

The non-dimensional expression for the average rise in pressure ΔP is given as follows:

$$\Delta P = (\int_0^1 \frac{\partial P}{\partial x}dx)_{r=0,\ t=0.5} \quad \text{.....(51)}$$

Solution of the problem

Equation (40) shows that P depends on x only. Thus if we diff. equation (41) with respect to r, we have the closed form solution as follows:

$$\psi = a_4 + a_3 K_r + a_3 \frac{r^2}{2} - a_2 \frac{(K+r)^{1-n_1}}{-1+n_1} + a_1 \frac{(K+r)^{1+n_1}}{1+n_1};$$

$$where \ \ n_1 = \sqrt{1+k^2 M^2 (1+\lambda_1)}; \qquad \text{. ....(52)}$$

$$\theta = -\frac{-a_2^2 (1+n_1)^2 (K+r)^{-2n_1} \alpha_1}{4n_1^2 (1+\lambda_1)} - \frac{a_1^2 (-1+n_1)^2 (K+r)^{2n_1} \alpha_1}{4n_1^2 (1+\lambda_1)} + c_2 + c_1 Log(k+r) +$$

$$\frac{a_1 a_2 (-1+n_1)^2 \alpha_1 Log(k+r)^2}{1+\lambda_1} \qquad \text{.....(53)}$$

$$\phi = \frac{a_2^2 (1+n_1)^2 (K+r)^{-2n_1} \alpha_1 \alpha_2 \alpha_3}{4n_1^2 (1+\lambda_1)} + \frac{a_1^2 (-1+n_1)^2 (K+r)^{2n_1} \alpha_1 \alpha_2 \alpha_3}{4n_1^2 (1+\lambda_1)} + c_4 + c_3 Log(k+r) -$$

$$\frac{a_1 a_2 (-1+n_1)^2 \alpha_1 \alpha_2 \alpha_3 Log(k+r)^2}{1+\lambda_1} \qquad \text{.....(54)}$$

In which $c_i, i = 1,2,3,4$ in eq.(6-53) and (6-54) can be found by using boundary conditions(49).

7- Results and Discussion

In this section, the numerical and computation results are discussed for the problem of an incompressible viscous non-Newtonian Jeffrey fluid in the curved channel with heat and mass transfer through the graphical illustrations of some important results. (MATHEMATICA) program is used to find out numerical and illustrations.

7-1 Pumping characteristics

We plot the expression for ΔP in eq.(51) against Q for various values of parameters of interest in figures (2)-(6). The effect of these parameters on ΔP have been evaluated numerically using (MATHEMATICA) program and the results are presented graphically. Impact of Hartmann number (M). The amplitudes ratio (φ), Jeffrey parameter (λ_1), culvature parameter (k) and slip parameter (α) have been pointed out. Pumping regions can be divided into three regions which are (retrograde pumping which is described by ($\Delta P > 0,\ Q < 0$), Co-pumping which is described by ($\Delta P < 0,\ Q > 0$) and free pumping which is described by($\Delta P = 0$)). In figure (2) the effect of parameter M on ΔP against Q are seen, observed that an increase in M causes increase on the regions of ($\Delta P > 0,\ Q \in (-1,0)$),($\Delta P < 0,\ Q \in (0,0.3)$), ($\Delta P = 0$) and decrease in the region of ($\Delta P < 0,\ Q \in (0.5,1)$), also we observed that the curves of pumping are intersected in the point (0.288, -1.504) in the fourth quadrant. Influence of parameter (φ) on ΔP is plotted in figure (3) which is showed that an increase in (φ) causes rise in all regions of pumping that is in the regions of ($\Delta P > 0,\ Q \in (-1,0)$),($\Delta P < 0,\ Q \in (0,0.5)$), ($\Delta P = 0$) and the curves of pumping are intersected in the point (0.7674,-2.863) in the fourth quadrant. The effects of parameters λ_1 and α are plotted in 'figure 4', 'figure 5' respectively, which is noted that an increase in these parameters lead to

increase in all pumping of regions. Opposite behavior is shown for the effect of (k) on pressure rise against Q, which is illustrated in 'figure.6'.

7-2 pressure gradient distribution

Effects of various parameters on the pressure gradient versus x have been illustrated in figures (7)-(12). These figures are scratched at the fixed values of (r=0.2,t=0.5). from figure (7) displays the effect of parameter (M) on pressure gradient, it is noticed that an increase in M leads to reduce in pressure gradient. Figure (8) illustrates the effect of the parameter φ on pressure gradient, it is observed that pressure gradient decrease on (-0.2, 0.2) and increase on the regions (-0.4,-0.2) and (0.2, 0.4). the impact of parameters λ_1 and α are plotted in figures (9) and (10) respectively which is observed that an increase in these parameters lead to rise in pressure gradient. Figure (11) displays the effect of (k) on pressure gradient, it is noticed that there is slightly increase in pressure gradient with an increase of (k). opposite behavior is observed for the effect of Q on pressure gradient and it is displayed in the figure (12).

7-3 velocity distribution

Influence of different parameters on the velocity distribution have been illustrated in figures (13)-(18). These figures are scratched at the fixed value of (x=0.2, t=0.05). from figure (13) displays the effect of Hartmann number parameter (M) on velocity u, it is noticed that the velocity increase at upper wall on region of $r \in [0.5,1]$ and decrease at lower wall on region of $r \in [0.5,1]$ and decrease at lower wall on the region of $r \in [-1,0]$. Figure (14), illustrates the effect of the parameter φ on velocity, we see that velocity u increase on upper and lower walls of channel with an increase of φ. From figure (15), it observed that there is similar behavior of Jeffrey parameter λ_1 of parameter M on velocity u. it is noticed from figures (13), (14) and (15) of effects of parameters M, φ and λ_1 that is the velocity u is not symmetric in curved channel (for small values of culvature parameter k) and it is symmetric in straight channel (for large values of k). figure (16) show that velocity distribution increase at upper part of channel and decrease at lower part of channel with an increase of culvature parameter k, and it is noticed that for large values of k (straight channel) the velocity profiles are symmetric figure (17) show that velocity distribution u decrease at the central line and increase at the walls of channel with an increase values of slip parameter (α). The effect of parameter Q on velocity is display in figure (18), it is observed that an increase in Q leads to increase in velocity at the central line and walls. In all graphs of figures of velocity distribution are parabolic graph.

7-4 trapping phenomenon

The effects of various parameter like $M, \varphi, \lambda_1, k, \alpha$ and Q on trapping can be seen through figures (19)-(24). 'Figure 19' show that the size of trapped bolus increase with an increase of

value of M in the upper and lower part of channel. 'Figure 20'is plotted for the effect of φ on trapping. It can be seen that there is a change in shape of trapping bolus and these bolus taken protraction in shape and increasing in the both sides of channel with an increase of φ. 'Figure 21' show that the size of bolus decrease with an increase of λ_1 on trapping. It means that λ_1 plays the resistive role for stream lines flow. It is further observed that for viscous fluid ($\lambda_1 = 0$) this size of trapping bolus is larger than Jeffrey fluid ($\lambda_1 \neq 0$). The effect of culveture parameter k on trapping is displayed in 'figure 22' which is noted that there is same behavior of effect λ_1 on trapping. The influence of slip parameter α on trapping is analyzed in figure (23), it showed that there is clear decreasing in size of bolus with an increase of α. The effect of parameter Q on trapping is shown in figure (24), it is noticed that there is clear increasing in size of bolus with an increase of Q.

7-5 Temperature characteristics

the expressions for temperature are given by eq.(53). The effects of various parameters on temperature for fixed values of (x=0.2, t=0.05) are shown, the results are presented in fig (25)-(31). From 'figure 25' it can found that temperature profile decrease at the central line with an increase of parameter (M). the effect of parameter φ on temperature profile is plotted in figure26), it is noticed that temperature increase at the central line and the walls of channel with an increase of φ. 'Figure 27' showed the influence of parameter λ_1, it is observed that an increase in λ_1 leads to decrease in temperature profile at the central line of channel, that is temperature profile θ is smaller for non-Newtonian fluid ($\lambda_1 \neq 0$) when compared with viscous fluid ($\lambda_1 = 0$). The effect of parameter k is noticed in 'figure 28', it is observed that an increase in k leads to decrease in temperature profile at the central line of channel with an increase of k. figure (29), illustrate the influence of parameter α which is behaved similar to effect of M on temperature. The effect of Brinkman number (Br) on temperature is displayed in figure (30), which is showed that an increase in (Br) lead to rising up on temperature, it is only due to the fact that (Br) incorporates viscous dissipation effects which expands the fluid temperature. 'Figure 31' illustrated the influence of parameter (Q) on temperature, which is noticed that the temperature increasing with an increase of Q at the central line of channel. In all graphs of temperature distribution of effects of all parameters mentioned above that the profiles of velocity are not symmetric in curved channel and it is symmetric in straight channel.

7-6 Mass transfer distribution

The expression for concentration are given by eq.(54). The effects of various parameters on concentration for fixed values of (x=0.2, t=0.05) are shown, the results are presented in fig (32)-(40). The profile of concentration is reverse of profile of temperature and the parameters behaved opposite manner on concentration than a temperature distribution. The effects of parameters $M, \lambda_1, k, \varphi, \alpha, Br, Sr, Sc$ and Q on concentration are plotted in figures (32)-(40). The effect of

M, λ_1, k and α are plotted in figures(32), (33), (34) and (35)respectively. It is noticed that an increase in these last parameters lead to an increase on concentration opposite behavior is obtained for the parameters φ, Br, Sr, Sc and Q which is illustrated into figures(36), (37), (38), (39), (40). In fact the reason behind the reducing of concentration when we increase the values of (Sc) is due that the mass diffusion decrease which show decrease in concentration. We observed that all graphs of concentration distribution are not symmetric in curved channel and it has symmetry characteristic in straight channel.

8- concluding Remarks

The present study deals with the combined effects of radial magnetic and heat/mass transfer on the peristaltic transport of viscous incompressible Jeffrey fluid in curved channel. We obtained the exact solution of the problem under long wave length and low Reynolds number assumptions. The results are analyzed for different values of parameters namely Hartmann number (M), amplitude ratio φ, Jeffrey parameter λ_1, culvature parameter (k), slip parameter α, time flow rate (Q), Brinkman number(Br). Thus through our work we observe the following notations:

1. At the upper part of curved channel, the axial velocity increase with an increase of M, φ, λ_1, k and α.
2. At the lower part of channel, the axial velocity increase with an increase of φ and α and decreasing with an increase of M, λ_1, k.
3. At the central line, the axial velocity increase with an increase of Q and decrease with an increase of α.
4. The profiles of velocity are parabolic and they are symmetric for large values of culvature parameter (k) (straight channel) and non-symmetric for curved channel.
5. The size of trapping bolus increase at both parts of channel with an increase of $M, \varphi,$ Q and decrease with an increase of λ_1, k and α.
6. The pressure gradient of fluid increase with an increase of λ_1, k, α and decrease with an increase of M, Q.
7. The pressure gradient increase into regions of $0.2 < x < 0.4, -0.4 < x < -0.2$ with an increase of φ and decrease into region $-0.2 < x < 0.2$.
8. The temperature profile increase with an increase of φ, Br and Q and decrease with an increase of M, λ_1, k and α.
9. The concentration distribution decrease with an increase of Sr and Sc. Opposite behavior for concentration profile is noted when compared with temperature.
10. The profiles of temperature and concentration are symmetric for large values of culvature parameter k (straight channel) and non-symmetric for curved channel for small values of k.
11. Pressure rise of fluid increase with an increase of $\varphi, \lambda_1, \alpha$ and decrease with an increase of k.
12. The impact of Hartmann number on pressure rise against mean flow rate Qis wobbling.
13. The curves of pressure rise are intersected at different regions.

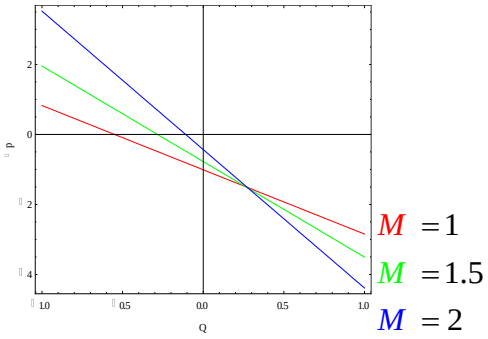

Figure 2: Effect of M on Δp

$\varphi = 0.2, t = 0.5, \lambda_1 = 1, k = 2, \alpha = 0.1$

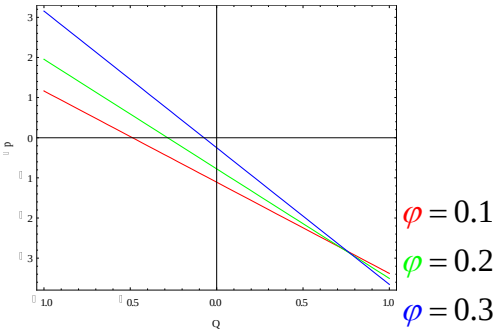

Figure 3: Effect of φ on Δp

$M = 1.5, t = 0.5, \lambda_1 = 1, k = 2, \alpha = 0.1$

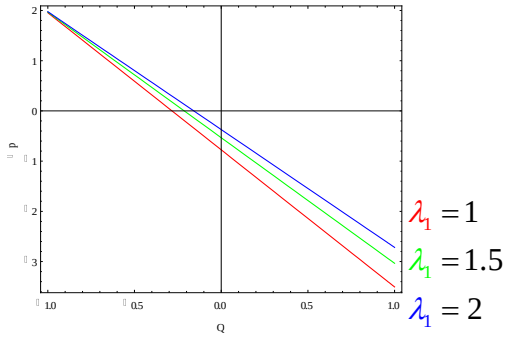

Figure 4: Effect of (λ_1) on Δp

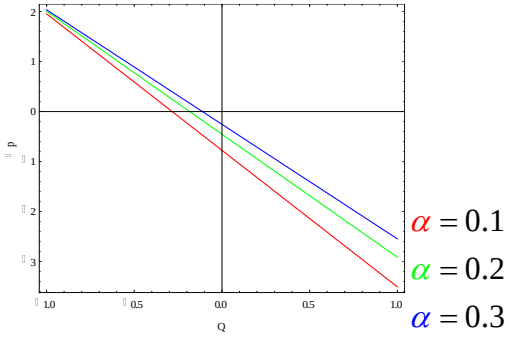

Figure 5: Effect of (α) on Δp

$M = 1.5, t = 0.5, \varphi = 0.2, k = 2, \alpha = 0.1$

$M = 1.5, t = 0.5, \varphi = 0.2, k = 2, \lambda_1 = 1$

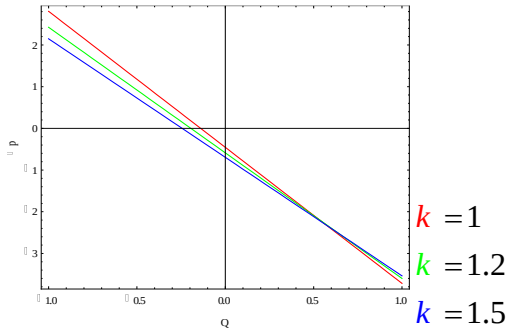

Figure 6: Effect of (k) on Δp

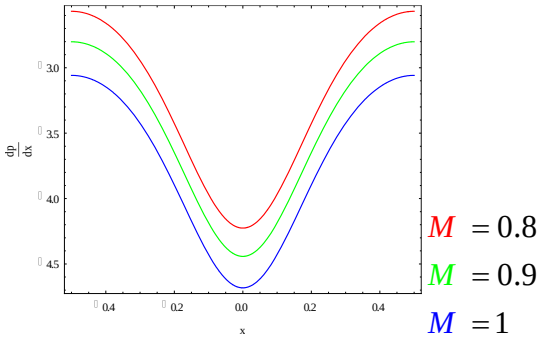

Figure 7: Effect of M on gradient

$M = 1.5, t = 0.5, \varphi = 0.2, \lambda_1 = 1, \alpha = 0.1$

$\varphi = 0.2, t = 0.5, \lambda_1 = 1, k = 2, \alpha = 0.1,$

$Q = 2, r = 0.2$

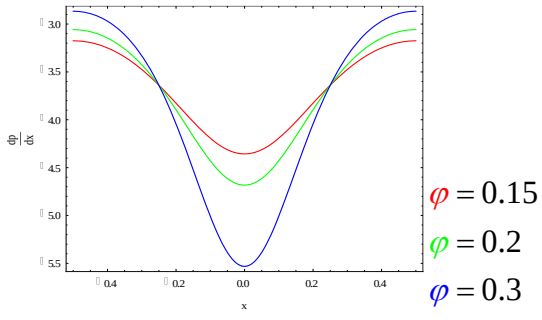

Figure 8: Effect of φ on gradient

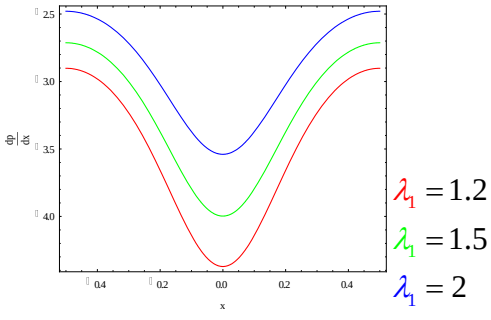

Figure 9: Effect of (λ_1) on gradient

$M = 1, t = 0.5, \lambda_1 = 1, k = 2, \alpha = 0.1,$
$Q = 2, r = 0.2$

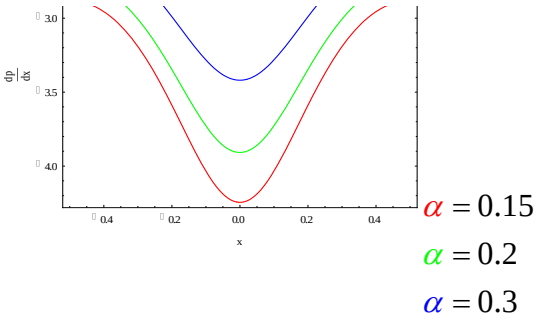

Figure 10. Effect of (α) on gradient

$\varphi = 0.2, M = 1, t = 0.5, k = 2, \lambda_1 = 1$
$Q = 2, r = 0.2$

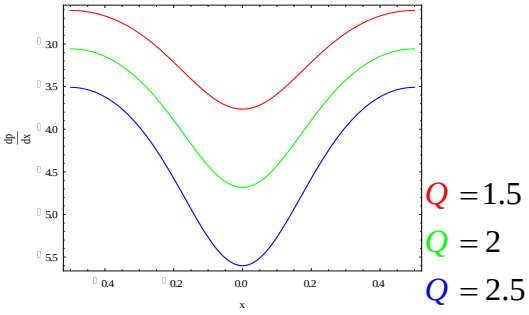

Figure 12. Effect of (Q)on gradient

$\varphi = 0.2, M = 1, t = 0.5, \lambda_1 = 1, \alpha = 0.1$
$k = 2, r = 0.2$

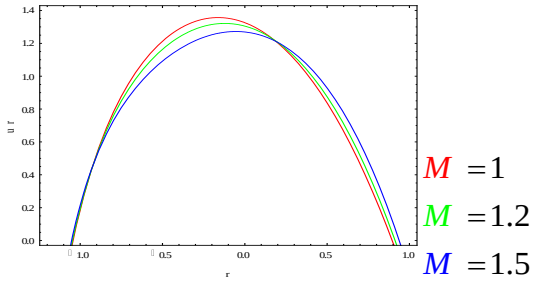

Figure13-a. Effect of (M) on velocity u

$\varphi = 0.2, t = 0.05, \lambda_1 = 1, \alpha = 0.1, Q = 1.5$
$x = 0.2$ when (k = 2), (curved channel)

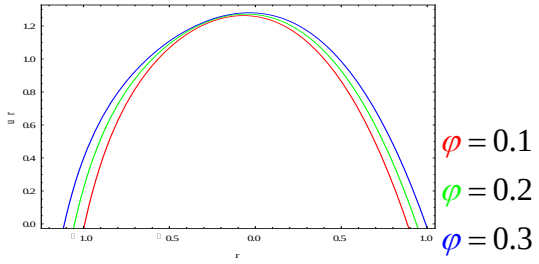

Figure14-a. Effect of (φ) on velocity u

$\varphi = 0.2, M = 1, t = 0.5, k = 2, \alpha = 0.1,$
$Q = 2, r = 0.2$

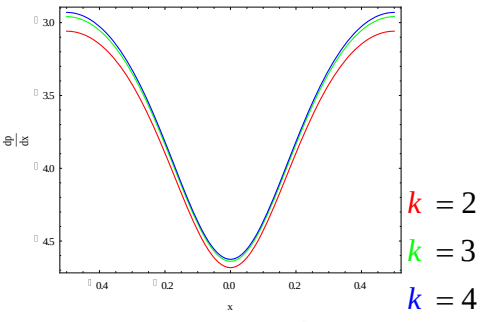

Figure 11. Effect of (k)on gradient

$\varphi = 0.2, M = 1, t = 0.5, \lambda_1 = 1, \alpha = 0.1$
$Q = 2, r = 0.2$

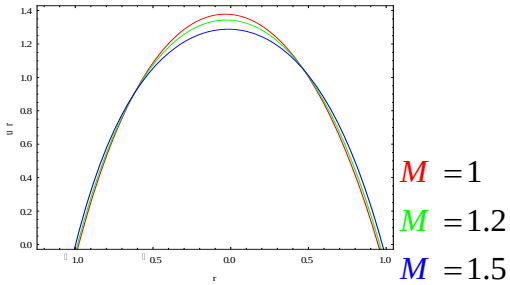

Figure13-b .Effect of (M) on velocity u

$\varphi = 0.2, t = 0.05, \lambda_1 = 1, \alpha = 0.1, Q = 1.5$
$x = 0.2$ when (k = 10), (straight channel)

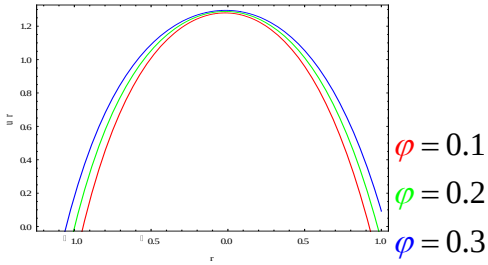

Figure14-b. Effect of (φ) on velocity u

$M = 1.5, t = 0.05, \lambda_1 = 1, \alpha = 0.1, Q = 1.5$

$x = 0.2$ when (k = 2), (curved channel)

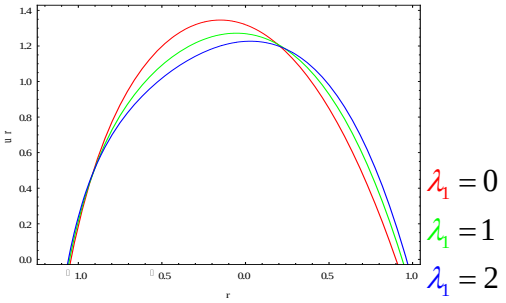

Figure15-a. Effect of (λ_1) on velocity u

$M = 1.5, t = 0.05, \lambda_1 = 1, \alpha = 0.1, Q = 1.5$

$x = 0.2$ when (k = 10), (straight channel)

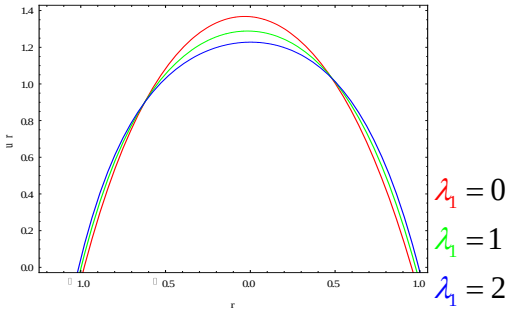

Figure15-b. Effect of (λ_1) on velocity u

$M = 1.5, t = 0.05, \varphi = 0.2, \alpha = 0.1, Q = 1.5$

$x = 0.2$ when (k = 2), (curved channel)

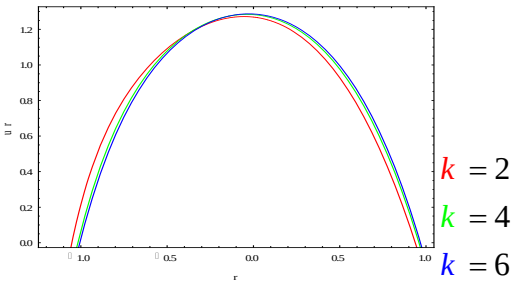

Figure 16-a. Effect of (k) on velocity u

$M = 1.5, t = 0.05, \varphi = 0.2, \alpha = 0.1, Q = 1.5$

$x = 0.2$, (curved channel)

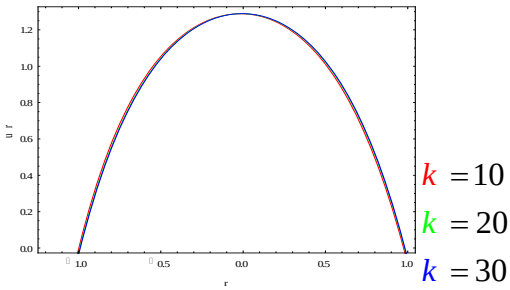

Figure 16-b. Effect of (k) on velocity u

$M = 1.5, t = 0.05, \varphi = 0.2, \alpha = 0.1, Q = 1.5$

$x = 0.2$, (straight channel)

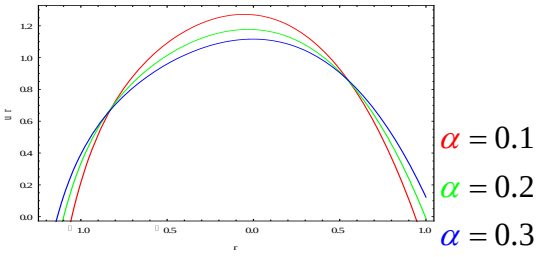

Figure17-a. Effect of (α) on velocity u

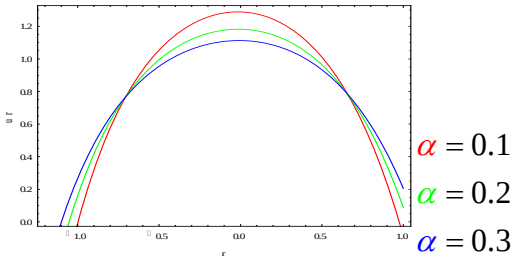

Figure17-b. Effect of (α) on velocity u

$M = 1.5, t = 0.05, \varphi = 0.2, \lambda_1 = 1, Q = 1.5$

$x = 0.2$ when (k = 2), (curved channel)

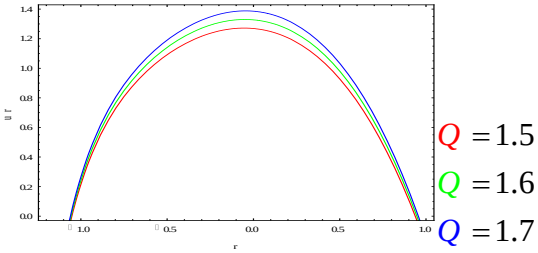

Figure18-a. Effect of (Q) on velocity u

$M = 1.5, t = 0.05, \varphi = 0.2, \lambda_1 = 1, Q = 1.5$

$x = 0.2$ when (k = 10), (straight channel)

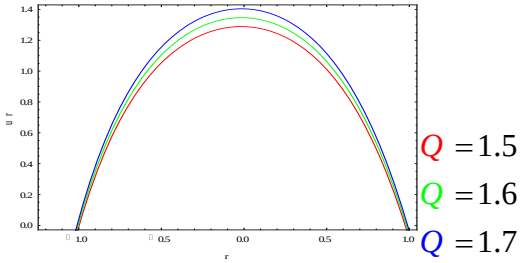

Figure18-b. Effect of (Q) on velocity u

$M = 1.5, t = 0.05, \varphi = 0.2, \lambda_1 = 1, \alpha = 0.1$

$x = 0.2$ when (k = 2), (curved channel)

$M = 1.5, t = 0.05, \varphi = 0.2, \lambda_1 = 1, \alpha = 0.1$

$x = 0.2$ when (k = 10), (straight channel)

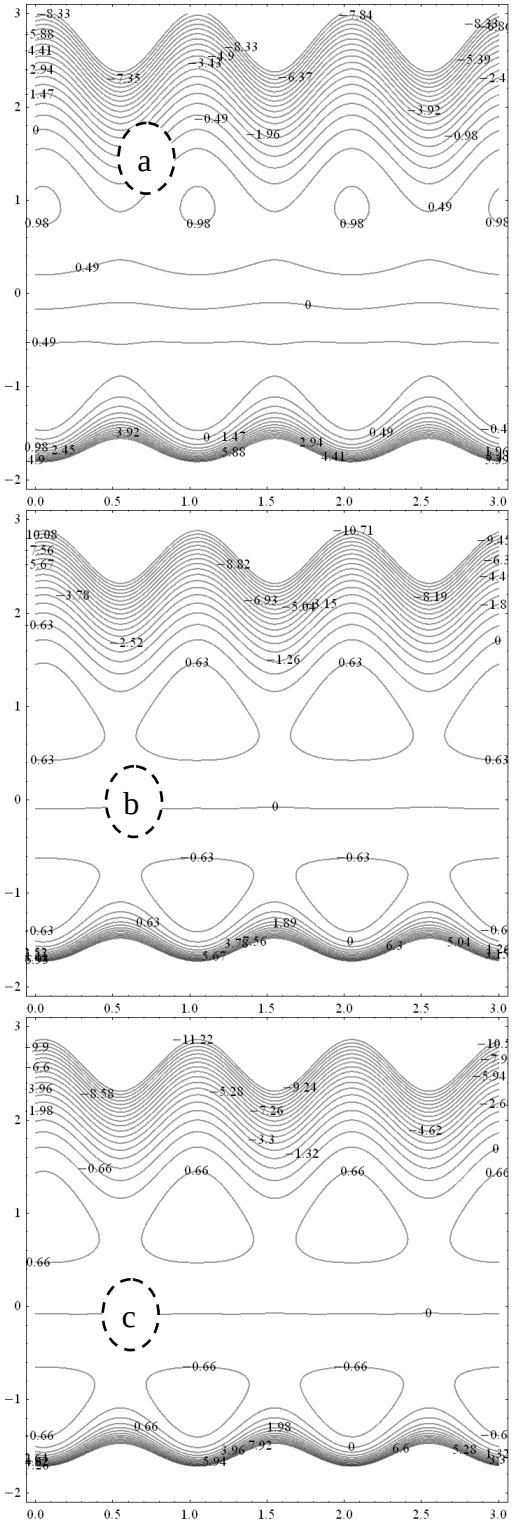

Figure 19 . Stream lines for $t = 0.05, \varphi = 0.2, \lambda_1 = 1, k = 2,$ $\alpha = 0.1, Q = 1.5$ (a)M = 0.9, (b) M = 1.5, (c) M = 1.6

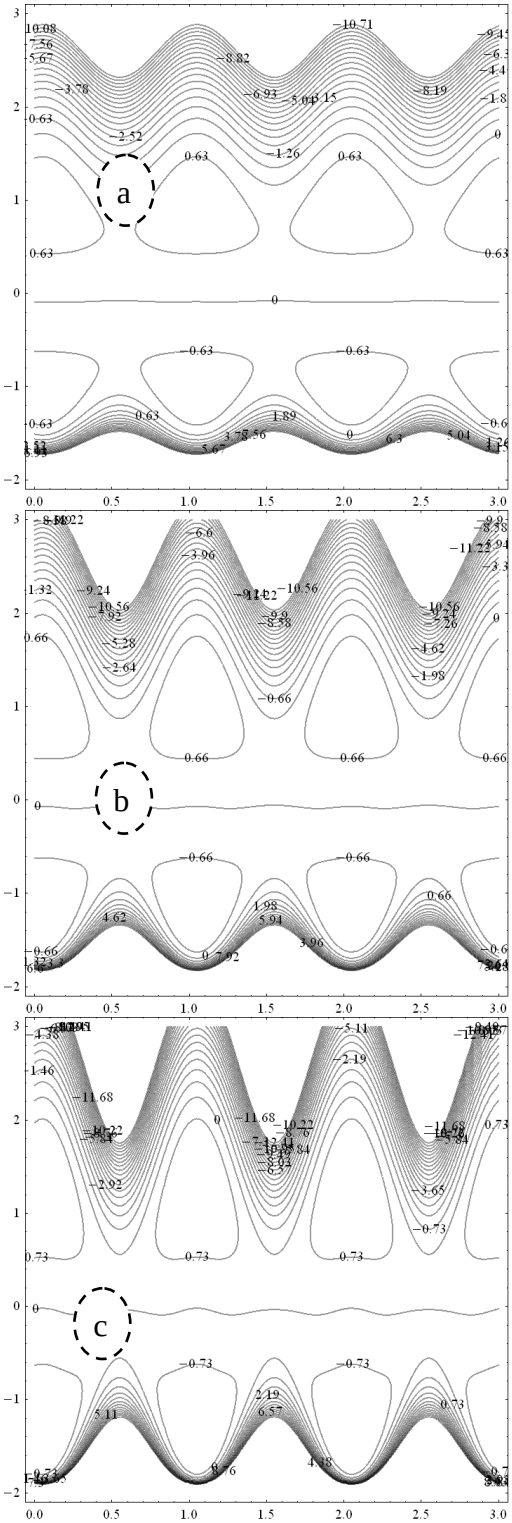

Figure 20. Stream lines for $M = 1.5, t = 0.05, \lambda_1 = 1, k = 2,$ $\alpha = 0.1, Q = 1.5$ (a)$\varphi = 0.2$, (b) $\varphi = 0.4$, (c) $\varphi = 0.6$

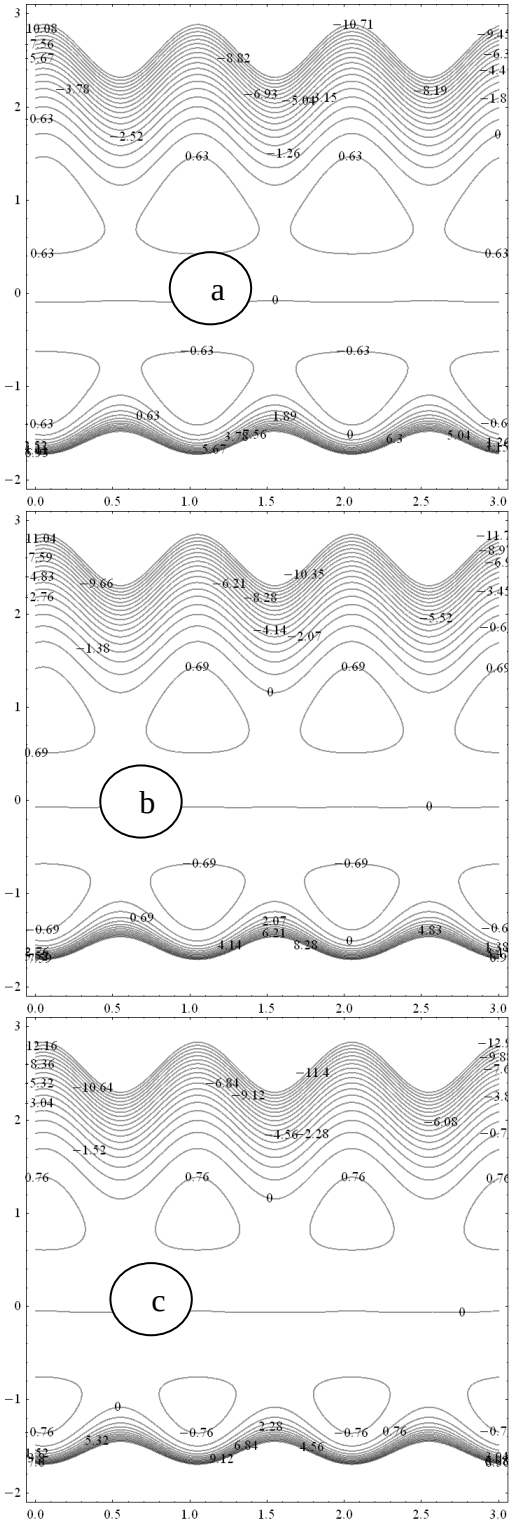

Figure 21. Stream lines for $M = 1.5, t = 0.05, \varphi = 0.2, k = 2,$ $\alpha = 0.1, Q = 1.5$ (a) $\lambda_1 = 1$, (b) $\lambda_1 = 1.5$, (c) $\lambda_1 = 2$

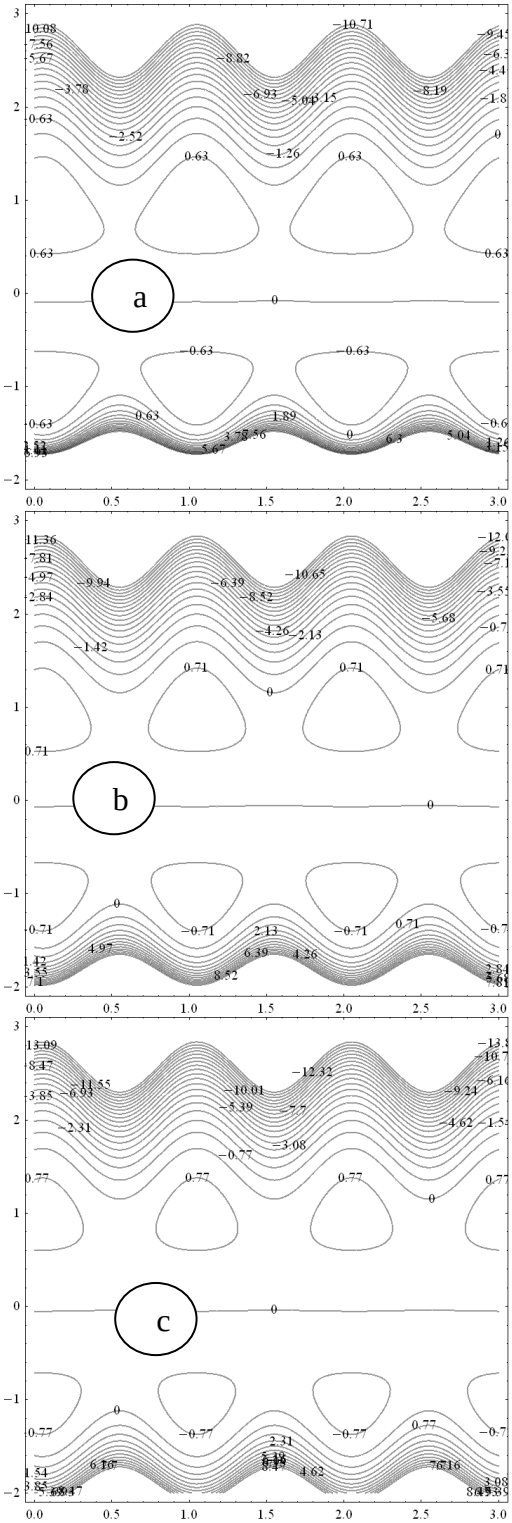

Figure 22. Stream lines for $M = 1.5, t = 0.05, \varphi = 0.2, \lambda_1 = 1,$ $\alpha = 0.1, Q = 1.5$ (a) $k = 2$, (b) $k = 3$, (c) $k = 4$

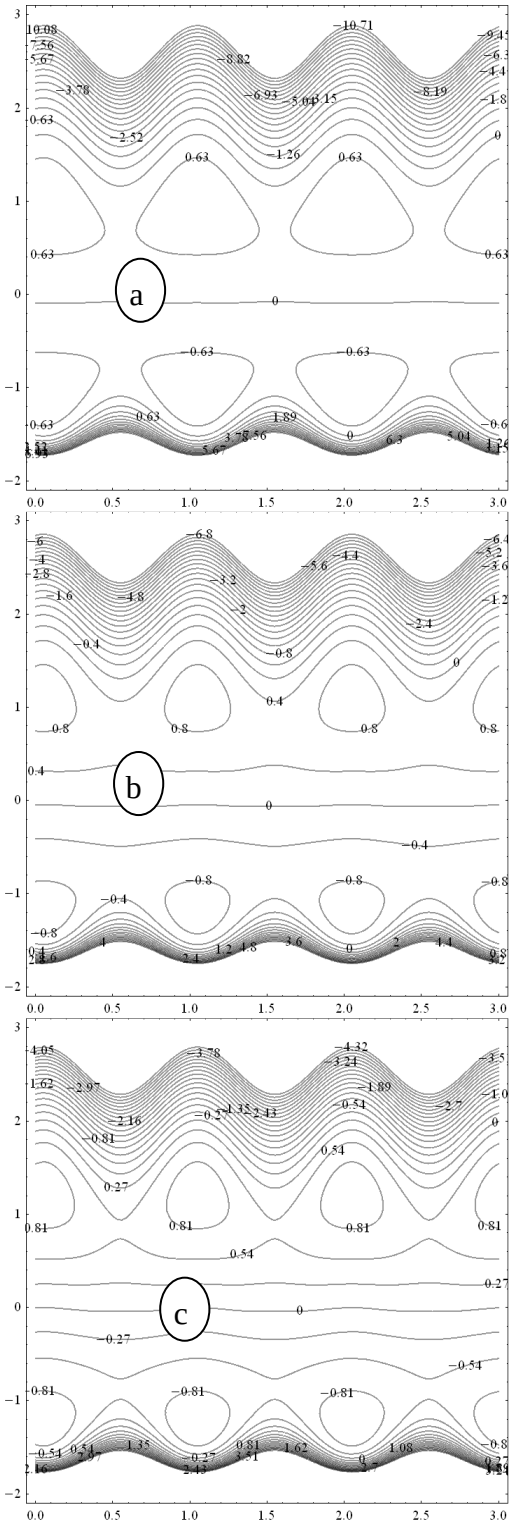

Figure 23. Stream lines for $M = 1.5, t = 0.05, \varphi = 0.2, \lambda_1 = 1,$ $k = 2, Q = 1.5$ (a)$\alpha = 0.1$, (b)$\alpha = 0.3$, (c) $\alpha = 0.5$

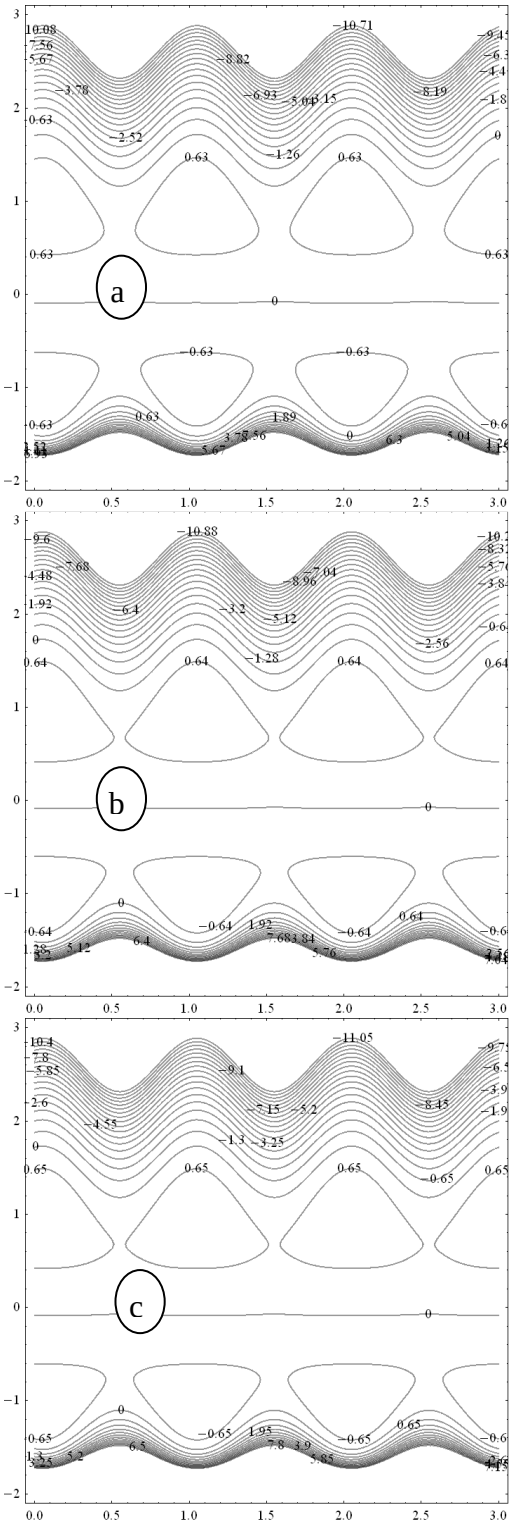

Figure 24. Stream lines for $M = 1.5, t = 0.05, \varphi = 0.2, \lambda_1 = 1,$ $\alpha = 0.1, k = 2,$ (a)$Q = 1.5$, (b)$Q = 1.6$, (c) $Q = 1.62$

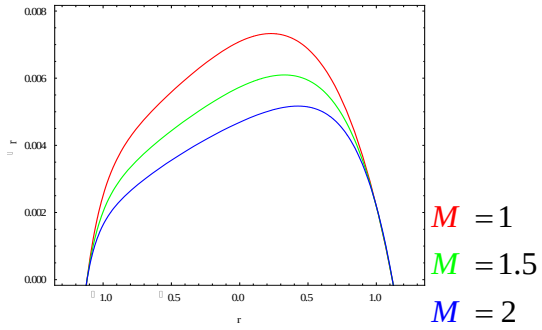

Figure 25-a. Effect of (M)on Temperature
$\varphi = 0.2, t = 0.05, \lambda_1 = 1, \alpha = 0.1, \alpha_1 = 0.01,$
$Q = 1.5 x = 0.2$ when (k = 2), (curved channel)

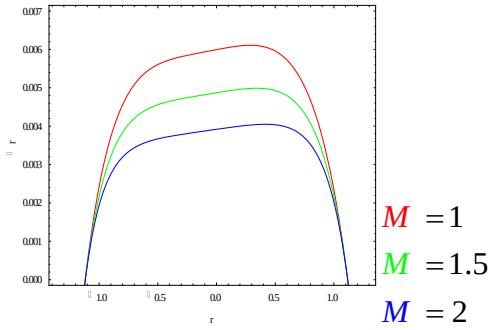

Figure 25-b. Effect of M on Temperature
$\varphi = 0.2, t = 0.05, \lambda_1 = 1, \alpha = 0.1, \alpha_1 = 0.01,$
$Q = 1.5 x = 0.2$ when (k = 10), (straight channel)

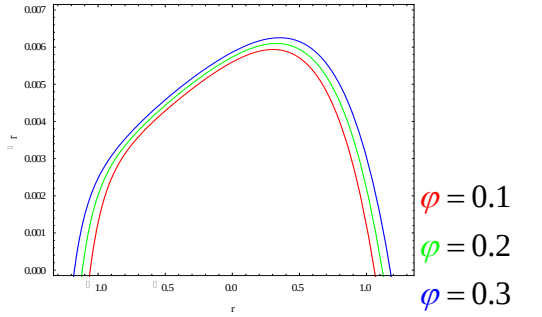

Figure 26a. Effect of φ on Temperature
$t = 0.05, M = 1.5, \lambda_1 = 1, \alpha = 0.1, \alpha_1 = 0.01,$
$Q = 1.5, x = 0.2$ when (k = 2), (curved channel)

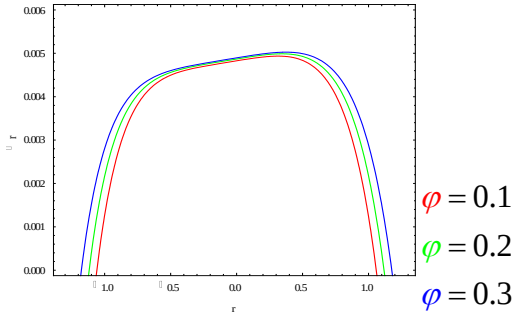

Figure 26b. Effect of φ on Temperature
$t = 0.05, M = 1.5, \lambda_1 = 1, \alpha = 0.1, \alpha_1 = 0.01,$
$Q = 1.5, x = 0.2$ when (k = 10), (straight channel)

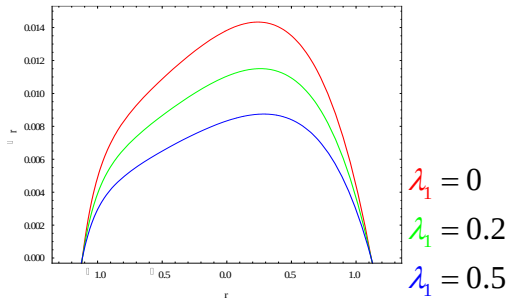

Figure 27-a. Effect of λ_1 on Temperature
$\varphi = 0.2, t = 0.05, M = 1.5, \alpha = 0.1, \alpha_1 = 0.01,$
$Q = 1.5, x = 0.2$ when (k = 2), (curved channel)

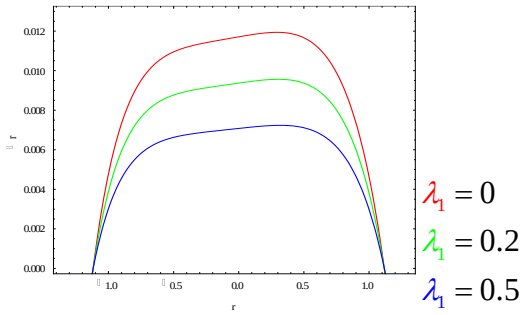

Figure 27-b. Effect of λ_1 on Temperature
$\varphi = 0.2, t = 0.05, M = 1.5, \alpha = 0.1, \alpha_1 = 0.01,$
$Q = 1.5, x = 0.2$ when (k = 10), (straight channel)

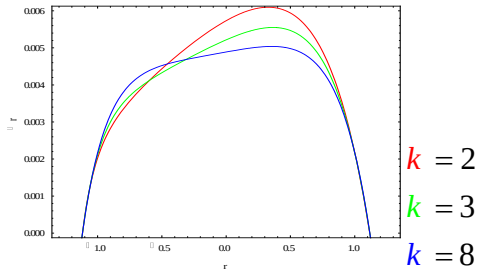

Figure 28. Effect of k on Temperature
$\varphi = 0.2, t = 0.05, M = 1.5, \lambda_1 = 1, \alpha = 0.1,$
$\alpha_1 = 0.01, Q = 1.5, x = 0.2$

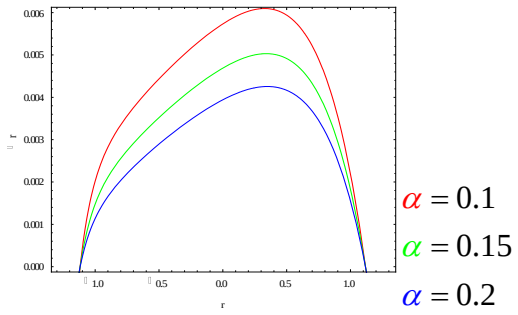

Figure 29-a. Effect of α on Temperature

$\varphi = 0.2, t = 0.05, M = 1.5, \lambda_1 = 1, \alpha_1 = 0.01,$

$Q = 1.5, x = 0.2$ when (k = 2), (curved channel)

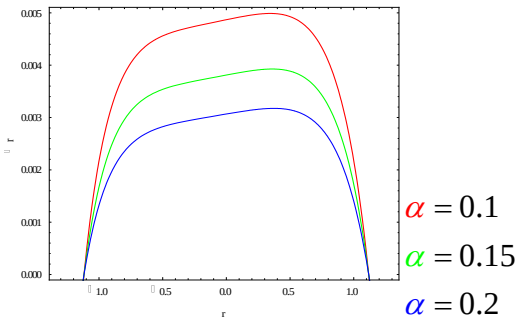

Figure 29-b. Effect of α on Temperature

$\varphi = 0.2, t = 0.05, M = 1.5, \lambda_1 = 1, \alpha_1 = 0.01,$

$Q = 1.5, x = 0.2$ when (k = 10), (straight channel)

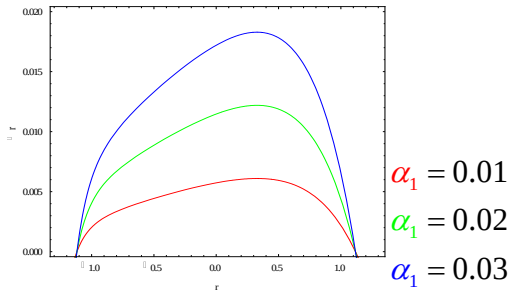

Figure 30-a. Effect of α_1 on Temperature

$\varphi = 0.2, t = 0.05, M = 1.5, \lambda_1 = 1, \alpha = 0.1$

$Q = 1.5, x = 0.2$ when (k = 2), (curved channel)

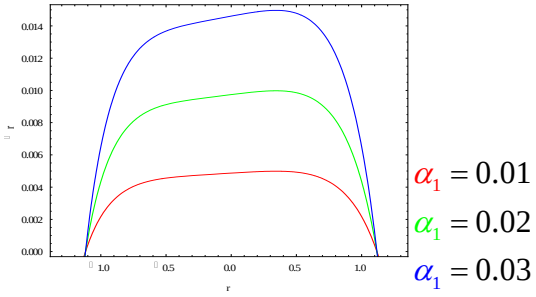

Figure 30-b. Effect of α_1 on Temperature

$\varphi = 0.2, t = 0.05, M = 1.5, \lambda_1 = 1, \alpha = 0.1$

$Q = 1.5, x = 0.2$ when (k = 10), (straight channel)

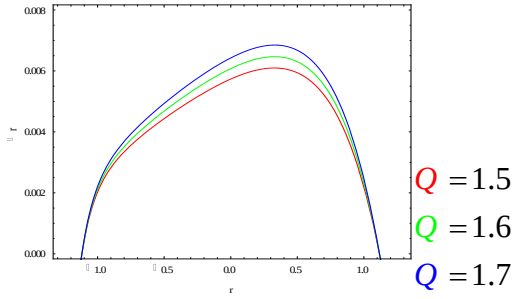

Figure 31-a. Effect of Q on Temperature

$\varphi = 0.2, t = 0.05, M = 1.5, \lambda_1 = 1, \alpha = 0.1,$

$\alpha_1 = 0.01, x = 0.2$ when (k = 2)(curved channel)

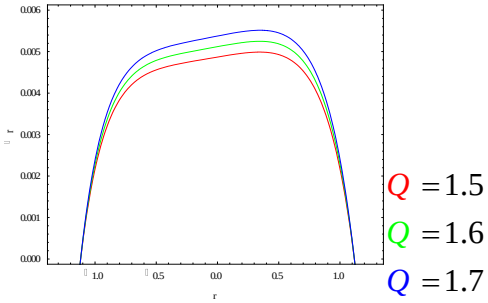

Figure 31-b.Effect of Q on Temperature

$\varphi = 0.2, t = 0.05, M = 1.5, \lambda_1 = 1, \alpha = 0.1,$

$\alpha_1 = 0.01, x = 0.2$ when (k = 10)(straight channel)

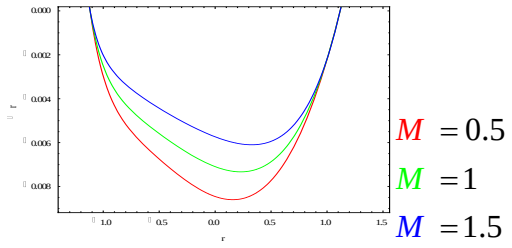

Figure 32-a. Effect of M on mass transfer

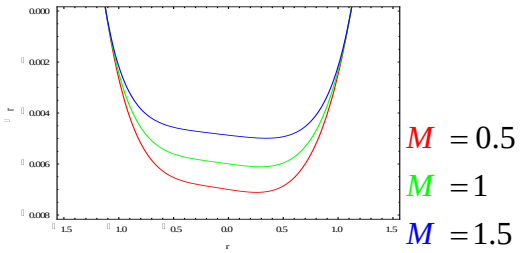

Figure 32-b. Effect of M on mass transfer

$\varphi = 0.2, t = 0.05, \lambda_1 = 1, \alpha = 0.1, \alpha_1 = 0.01,$
$\alpha_2 = 1, \alpha_3 = 1, Q = 1.5, x = 0.2$ when (k = 2),
(curved channel)

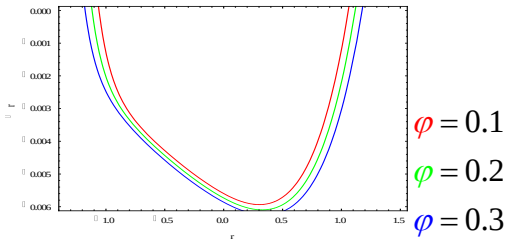

Figure 33-a. Effect of φ on mass transfer

$\varphi = 0.2, t = 0.05, \lambda_1 = 1, \alpha = 0.1, \alpha_1 = 0.01,$
$\alpha_2 = 1, \alpha_3 = 1, Q = 1.5, x = 0.2$ when (k = 10),
(straight channel)

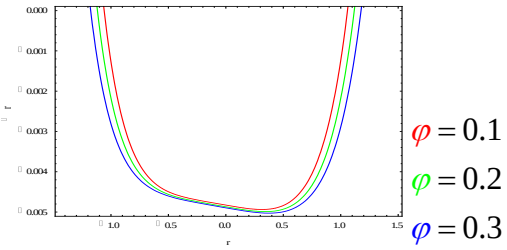

Figure 33-b. Effect of φ on mass transfer

$M = 1.5, t = 0.05, \lambda_1 = 1, \alpha = 0.1, \alpha_1 = 0.01,$
$\alpha_2 = 1, \alpha_3 = 1, Q = 1.5, x = 0.2$ when (k = 2),
(curved channel)

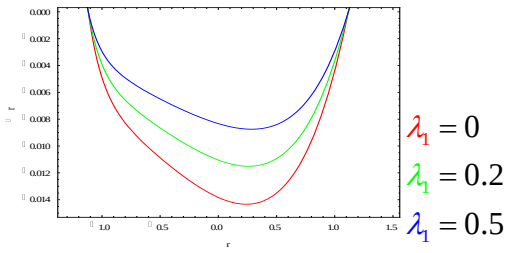

Figure 34-a. Effect of λ_1 on mass transfer

$M = 1.5, t = 0.05, \lambda_1 = 1, \alpha = 0.1, \alpha_1 = 0.01,$
$\alpha_2 = 1, \alpha_3 = 1, Q = 1.5, x = 0.2$ when (k = 10),
(straight channel)

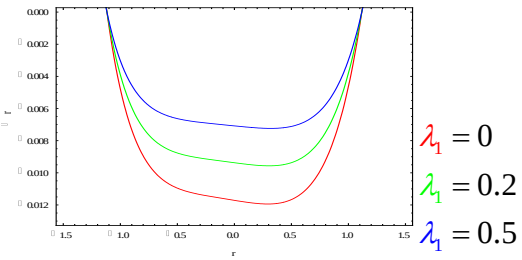

Figure 34-b. Effect of λ_1 on mass transfer

$\varphi = 0.2, M = 1.5, t = 0.05, \alpha = 0.1, \alpha_1 = 0.01,$
$\alpha_2 = 1, \alpha_3 = 1, Q = 1.5, x = 0.2$ when (k = 2),
(curved channel)

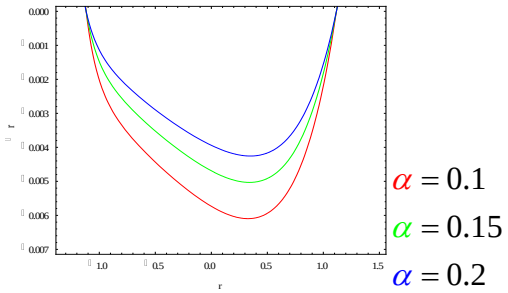

Figure 35-a.Effect of α on mass transfer

$\varphi = 0.2, t = 0.05, M = 1.5, \lambda_1 = 1, \alpha_1 = 0.01,$
$\alpha_2 = 1, \alpha_3 = 1, Q = 1.5, x = 0.2$ when (k = 2),
(curved channel)

$\varphi = 0.2, M = 1.5, t = 0.05, \alpha = 0.1, \alpha_1 = 0.01,$
$\alpha_2 = 1, \alpha_3 = 1, Q = 1.5, x = 0.2$ when (k = 10),
(straight channel)

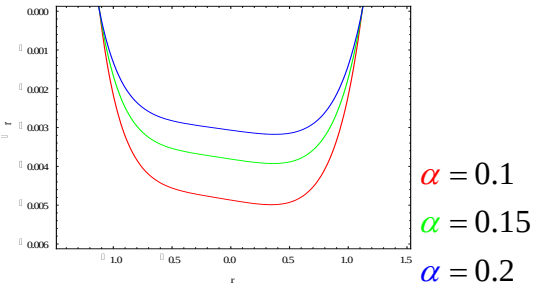

Figure 35-b. Effect of α on mass transfer

$\varphi = 0.2, t = 0.05, M = 1.5, \lambda_1 = 1, \alpha_1 = 0.01,$
$\alpha_2 = 1, \alpha_3 = 1, Q = 1.5, x = 0.2$ when (k = 10),
(straight channel)

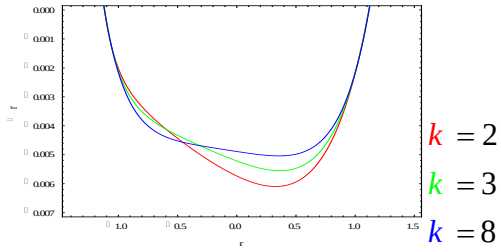

Figure 36. Effect of k on mass transfer

$\varphi = 0.2, t = 0.05, M = 1.5, \lambda_1 = 1, \alpha_1 = 0.01,$

$\alpha = 0.1, \alpha_2 = 1, \alpha_3 = 1, Q = 1.5, x = 0.2$

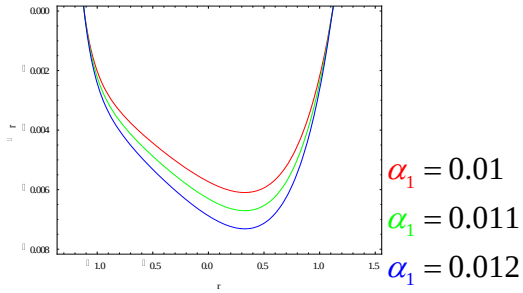

Figure 37-a. Effect of α_1 on mass transfer

$\varphi = 0.2, t = 0.05, M = 1.5, \lambda_1 = 1, \alpha = 0.1,$

$\alpha_2 = 1, \alpha_3 = 1, Q = 1.5, x = 0.2$ when (k = 2),

(curved channel)

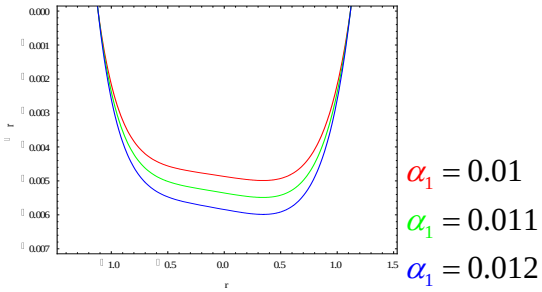

Figure 37-b. Effect of α_1 on mass transfer

$\varphi = 0.2, t = 0.05, M = 1.5, \lambda_1 = 1, \alpha = 0.1,$

$\alpha_2 = 1, \alpha_3 = 1, Q = 1.5, x = 0.2$ when (k = 10),

(straight channel)

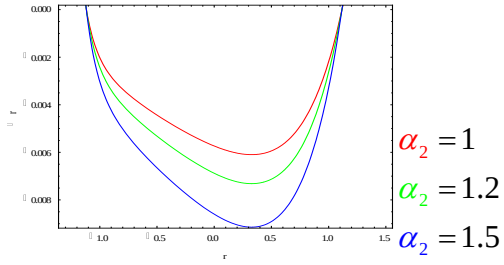

Figure 38-a. Effect of α_2 on mass transfer

$\varphi = 0.2, t = 0.05, M = 1.5, \lambda_1 = 1, \alpha = 0.1,$

$\alpha_1 = 0.01, \alpha_3 = 1, Q = 1.5, x = 0.2$ when (k = 2),

(curved channel)

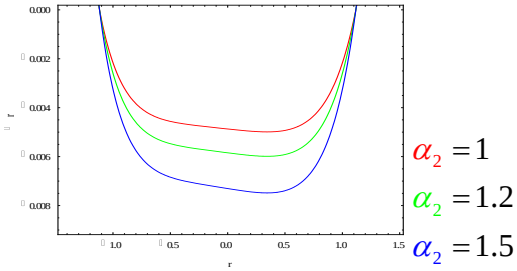

Figure 38-b. Effect of α_2 on mass transfer

$\varphi = 0.2, t = 0.05, M = 1.5, \lambda_1 = 1, \alpha = 0.1,$

$\alpha_1 = 0.01, \alpha_3 = 1, Q = 1.5, x = 0.2$ when (k = 10),

(straight channel)

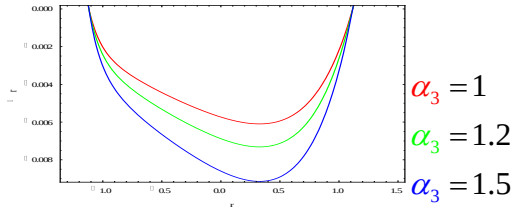

Figure 39-a. Effect of α_3 on mass transfer

$\varphi = 0.2, t = 0.05, M = 1.5, \lambda_1 = 1, \alpha = 0.1,$

$\alpha_1 = 0.01, \alpha_2 = 1, Q = 1.5, x = 0.2$ when (k = 2),

(curved channel)

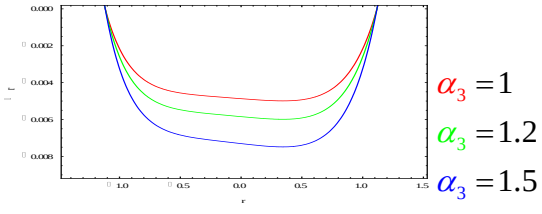

Figure 39-b.Effect of α_3 on mass transfer

$\varphi = 0.2, t = 0.05, M = 1.5, \lambda_1 = 1, \alpha = 0.1,$

$\alpha_1 = 0.01, \alpha_2 = 1, Q = 1.5, x = 0.2$ when (k = 10),

(straight channel)

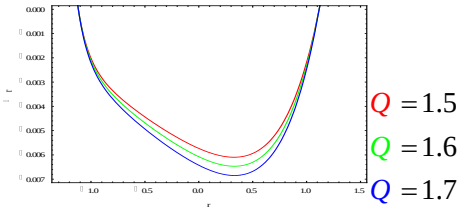

Figure 40-a. Effect of Q on mass transfer

$\varphi = 0.2, t = 0.05, M = 1.5, \lambda_1 = 1, \alpha = 0.1,$

$\alpha_1 = 0.01, \alpha_2 = 1, \alpha_3 = 1, x = 0.2$ when (k = 2),

(curved channel)

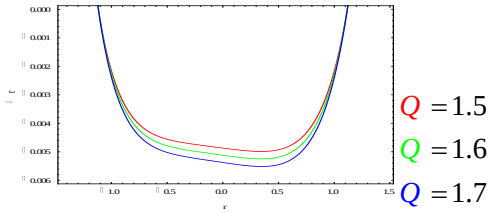

Figure 40-b. Effect of Q on mass transfer

$\varphi = 0.2, t = 0.05, M = 1.5, \lambda_1 = 1, \alpha = 0.1,$

$\alpha_1 = 0.01, \alpha_2 = 1, \alpha_3 = 1, x = 0.2$ when (k = 10),

(straight channel)

REFERENCES

[1] Latham, T.W., "Fluid motion in peristaltic pump, "M. S Thesis, Massachusetts Institute of Technology, Cambridge Massachusetts, U.S.A (1966).

[2] Shapiro, A. H., Jaffrin M. Y. and Weinberg S. L., "Peristaltic pumping with long wave length at low Reynolds number," *Journal of Fluid Mechanics*, **37**,pp. 799-825 (1969).

[3] Shapiro, A. H., "Pumping and retrograde diffusion in peristaltic waves," *Proceedings of the Workshop Ureteral Reftm Children,* National Academy of Science, Washington, D.C., U.S. (1967).

[4] Fung, Y. C., "Peristaltic pumping: a bio engineering model," *Proceedings of the Workshop Ureteral Reftm Children,* National Academy of Science, Washington, D.C., U.S. (1971).

[5] Hayat, T., Ali, N. and Asghar, S., "An analysis of peristaltic transport for flow of a Jeffrey fluid," *Acta Mechanic*a, **193**, pp. 101-112 (2007).

[6] Hayat, T., Yasmin, H., Alhuthali, M. S. and Kutbi, M.A., "Peristaltic flow of a non-Newtonian fluid in an asymmetric channel with convective boundary conditions, "J*ournal of Mechanics*, **29**, pp. 599-607

[7] . Ebaid, A., "Remarks on the homotopy perturbation method for the peristaltic flow of Jeffrey fluid with nano-particles in an asymmetric channel," *Computers& Mathematics with Applications*, **68**, pp. 77-85(2014).

[8] . Nadeem, S. and Akram, S., "Peristaltic flow of a Jeffrey fluid in a rectangular duct," *Nonlinear Analysis: Real World Applications*, **11**, pp. 4238-4247(2010).

[9] Kothandapani, M. and Srinivas, S., "Peristaltic transport of a Jeffrey fluid under the effect of magnetic field in an asymmetric channel," *International Journal of Non-Linear Mechanics*, **43**, pp. 915-924(2008).

[10] Tripathi, D. and Beg, O. A., "A study of unsteady physiological magneto-fluid flow and heat transfer through a finite length channel by peristaltic pumping ,"*Proceedings of the institution of mechanical Engineers, Part H: Journal of Engineering in Medicine*, DOI: 10.1177/0954411912449946 (2012).

[11] Jalilian, E., Onen, D., Neshev, E. and Mintchev, M.P., "Implantable neural electrical stimulator for external control of gastrointestinal motility," *Medical Engineering & Physics*, **29**, pp. 238-252 (2007).

[12] Abbasi, F. M., Hayat, T. and Ahmad, B., "Peristaltic flow in an asymmetric channel with convective boundary conditions and Joule heating," *Journal of Central South University*, **21**, pp. 1411-1416 (2014).

[13] Sato, H., Kawai, T., Fujita, T. and Okabe, M., "Two dimensional peristaltic flow in curved channels, "*The Japan Society of Mechanical Engineers B*, **66**,pp. 679-685 (2000).

[14] Ali, N., Sajid, M. and Hayat, T., "Long wave length flow analysis in a curved channel," *Zeitschrift fürNaturforschung A*, **65**, pp. 191-196 (2010).

[15] Ali, N., Sajid, M., Javed, T. and Abbas, Z., "Non-Newtonian fluid flow induced by peristaltic waves in a curved channel," *European Journal of Mechanics - B/Fluids*, **29**, pp. 387-394 (2010).
[16] Hayat, T., Quratulain., Rafiq, M., Alsaadi, F. and Ayub, M., "Soret and Dufour effects on peristaltic transport in curved channel with radial magnetic field and convective conditions," *Journal of Magnetism and Magnetic Materials*, **405**, pp. 358-369(2016).
[17] Hayat, T., Abbasi, F. M., Ahmed, B. and Alsaedi, A., "Peristaltic transport of Carreau-Yasuda fluid in a curved channel with slip effects," *PLOS ONE*, **9**,e95070 (2014).
[18] T. Hayat. , S. Farooq. , A. Alsaedi. , "MHD Peristaltic flow in a curved channel with convective condition" *Nonlinear Analysis and Applied Mathematics Research Group Department of Mathematics King Abdulaziz University Jeddah, Saudi Arabia*
[19] Tasawar Hayat[1]. , Hina Zahir[2]. , Anum Tanveer.[2] , Ahmad Alsaedi[2]. , " Soret and Dufour effects on MHD peristaltic transport of Jeffrey fluid in a curved channel with convective boundary conditions" Department of Mathematics, Quaid-I-Azam University 45320, Islamabad 44000, Pakistan, **2** Department of Electrical and Computer Engineering, Faculty of Engineering, King Abdulaziz University, Jeddah 21589,Saudi Arabia.
[20] V. K. Narla. , K. M. Prasad. , J. V. Ramanamurthy. , "Peristaltic transport of Jeffrey Nano fluid in curved channels" Gitam university, Department of mathematics , Hayderabad, India, National institute of technology, Department of mathematics, waragal-506004,,India.

On direct theorems for best polynomial approximation

On direct theorems for best polynomial approximation

A A Auad[1] ,R S AbdulJabbar[1]

[1] Department of mathematicsCollege of Education for Pure Science – AlAnbar University

Abstract This paper is to obtain similarity for the best approximation degree of functions which are unbounded in $L_{p,\alpha}(A=[0,1])$which called weighted space by algebraic polynomials $E_n^H(f)_{p,\alpha}$ and the best approximation degree in the same space on the interval $[0,2\pi]$ by trigonometric polynomials $E_n^T(f)_{p,\alpha}$ of direct wellknown theorems in forms the average modules

1 Introduction

Recently several papers have been devoted to study polynomial approximation with constraints In particular [16] polynomial approximation was considered Although several problems concerning algebraic approximation or trigonometric approximation have been studied the theory as well as developed as the one classical polynomial approximation In this paper we present some algebraic polynomial and trigonometric polynomials to approximate unbounded functions in terms average modules in weighted space $L_{p,\alpha}([0,1])$ and $L_{p,\alpha}([0,2\pi],(1\le p<\infty)$ respectivly Approximation of functions have integrable bounded derivative $f^{(k)}$ on closed intervals well be considered in other papers Let $A=[0,1]$ in algebraic polynomials $A=[0,2\pi]$ in trigonometric polynomials approximation W be the suitable set of all weight functions on $A\ni|f(x)|\le M\alpha(x)\ \forall x\in A\ M$ positive real number $\alpha: A\to\mathbb{R}^+$weight function and denoted by $L_{p,\alpha}(A)$ the space of unbounded functions $f: A\to\mathbb{R}$, $(1\le p<\infty)$ with the norm defined by:

$$\|f\|_{p,\alpha}=\left(\int_A\left|\frac{f(x)}{\alpha(x)}\right|^p dx\right)^{1/p} \tag{1}$$

The kth average module is used in this paper

$$\tau_k(f,\delta)_{p,\alpha}=\|\omega_k(f\ ,\cdot,\delta)\|_{p,\alpha} \tag{2}$$

Where

$$\omega_k(f\ ,\cdot\ ,\delta)=\sup\{\left|\Delta_h^k f(x)\right|; t,t+h\in[\,x-\tfrac{\delta}{2}\,,x+\tfrac{\delta}{2},]\} \tag{3}$$

$$\Delta_h^k f(x)=\begin{cases}\sum_{i=0}^k(-1)^{k+i}\binom{k}{i}f(x+ih) & if\ \ x,x+h\in X\\ 0 & otherwise\end{cases} \tag{4}$$

And

$$\omega_k(f,\delta)_{p,\alpha}=\left\|\Delta_h^k f(\cdot)\right\|_{p,\alpha} \tag{5}$$

As far as we know average modules of this type were first used by Sendov and Popov (1998) use this modules for $p = 1$ for Housdorff approximation by pointwise monotonic functions and established several of its basic properties

Combine all algebraic polynomials on $A = [0,1]$ of degree equals n or less in a set say H_n The best approximation degree of f in the space $L_{p,\alpha}(A)$ is defined as:

$$E_n^H(f)_{p,\alpha} = \inf\{\|f - P_n\|_{p,\alpha};\ P_n \in H_n\} \tag{6}$$

Also define the set T_n which contains every trigonometric polynomials of order n or less Then the best approximation degree of $f \in L_{p,\alpha}(A)$ is defined by

$$E_n^T(f)_{p,\alpha} = \inf\{\|f - t_n\|_{p,\alpha};\ t_n \in T_n\} \tag{7}$$

2 Auxiliary Results

We shall use the following supplementary results:

2.1 Lemma [4]

Let f be an element in $L_{p,\alpha}(A), (1 \le p < \infty)$ Then

$$\tau(f, \lambda\delta)_{p,\alpha} \le (\lambda + 1)\tau(f, \delta)_{p,\alpha}$$

2.2 Lemma

Let f be an element in $L_{p,\alpha}(A), (1 \le p < \infty)$ Then

$$\tau_k(f, \lambda\delta)_{p,\alpha} \le (\lambda + 1)^k\ \tau_k(f, \delta)_{p,\alpha} \qquad \lambda > 0$$

Proof

We have $\omega_k(f, \lambda\delta) \le (\lambda + 1)^k\ \omega_k(f, \delta)$ see [4]

So from (2) $\tau_k(f, \lambda\delta)_{p,\alpha} = \|\omega_k(f, \cdot, \lambda\delta)\|_{p,\alpha}$

$$\le \left\|(1 + \lambda)^k \omega_k(f, \cdot, \lambda\delta)\right\|_{p,\alpha}$$

$$= \left|(1 + \lambda)^k\right| \|\omega_k(f, \cdot, \lambda\delta)\|_{p,\alpha}$$

$$= (1 + \lambda)^k \tau_k(f, \lambda)_{p,\alpha}$$

2.3 Lemma

Let f be an element in $L_{p,\alpha}(A), (1 \le p < \infty)$

Then $\tau_k(f, \delta)_{p,\alpha} \le \delta\|f'\|_{p,\alpha}$

Proof

From (3) we have:

$$\omega(f, x, \delta) = \sup\{|f(x_1) - f(x_2)|, where\ x_1, x_2 \in [x - \tfrac{\delta}{2}, x + \tfrac{\delta}{2}]\}$$

$$= \sup\left\{\left|\int_{x_1}^{x_2} f'(u)du\right|, where\ x_1, x_2 \in [x - \tfrac{\delta}{2}, x + \tfrac{\delta}{2}]\right\}$$

$$\le \int_{x-\frac{\delta}{2}}^{x+\frac{\delta}{2}} f(t)dt = \int_0^{\delta} f'(x - t)dt$$

Also equation (2) yields:

$$\tau_k(f, \delta)_{p,\alpha} = \|\omega_k(f, \cdot, \delta)\|_{p,\alpha}$$

$$\leq \left\| \int_0^{\delta} f'(x-t)dt \right\|_{p,\alpha}$$
$$\leq \int_0^{\delta} \|f'(x-t)\|_{p,\alpha} dt$$
$$= \delta \|f'\|_{p,\alpha}$$

More generally the kth average modules can be estimated by means of norm in weighted space of the kth derivative of the function *f*

$\tau_k(f,\delta)_{p,\alpha} \leq c(k)\delta^k \left\| f^{(k)} \right\|_{p,\alpha}$

Where c is absolute constant depended on k

24 Lemma

Let $A = [0,1]$, f be an element in , $L_{p,\alpha}(A), (1 \leq p < \infty)$ Then for any natural number n the following is true:

$$E_n^H(f)_{p,\alpha} \leq (n+1)E_{n-1}^n(f')_{p,\alpha}$$

Proof

Let $P_n \in H_n$, $f(0) = 0$, and from (6) we have

$$E_{n-1}(f')_{p,\alpha} = \inf\{\|f' - P_n\|_{p,\alpha},\ P_n \in H_n\}$$

For $x \in A$ we consider the polynomial where c is absolute constant

$$q_n(x) = \{\int_0^x p_n(u)du + \sum_{i=0}^{k-n-1} h_i \int_0^x g_i(u)du\} \geq 0$$

Set $p_n(x) = 0$ for $x < 0$ Then

$$\left(E_n(f)_{p,\alpha}(u)\right)^p \leq \|f - q_n\|_{p,\alpha}^p = \int_A \left|\frac{f(x)-q_n(x)}{\alpha(x)}\right|^p dx$$

$$= \int_A \left|\frac{\int_0^x (f'(u)-p_n(u))du - \sum_{i=0}^{x-n-1} h_i \int_0^x g(u)du}{\alpha(x)}\right|^p dx$$

$$\leq \int_A \left|\frac{\int_{x-n-1}^x (f'(u)-p_n(u))du}{\alpha(x)}\right|^p dx$$

$$= \int_0^{n+1} \left(\int_A \left|\frac{(f'(x-(n+1)+u)-p_n(x-(n+1)+u)}{\alpha(x)}\right|^p dx\right) du$$

$$\leq \int_0^{n+1} \left(E_{n-1}^H(f')_{p,\alpha}\right)^p du = (n+1)E_{n-1}^n(f')_{p,\alpha}$$

3 Main results

We consider the approximation of unbounded function $f(x)$ defined on $[0,1]$ by algebraic polynomials

3.1Theorem

If *f* unbounded function defined on $A = [0,1]$ then

$$E_n^H(f)_{p,\alpha} \leq C(p)\tau(f,\delta)_{p,\alpha};\ (1 \leq p < \infty)$$

Where *C* is constant depends on *p*

Proof

Assume

$$g(x) = \sup_{u \in A} f(u) \tag{8}$$

It's clear that $g_n \in H_n$
From (3) we get

$$\omega(f, x, \delta) = \sup_{x \in A}\{|f(x) - g_n(x)|\}$$

So by using (1)(2)(3) and (6)

$$E_n^H(f)_{p,\alpha} = \inf\{\|f - g_n\|_{p,\alpha} \ , g_n \in H_n\}$$

$$\leq \left[\int_A \left|\frac{f(t) - g_n(t)}{\alpha(t)}\right|^p dt\right]^{1/p}$$

$$\leq \left[\int_A \sup\{\left|\frac{f(t)-g_n(t)}{\alpha(t)}\right|^p\}dt\right]^{1/p}$$

$$= \left[\int_A \{\left|\frac{\sup\{f(t)-g_n(t)\}}{\alpha(t)}\right|^p\}dt\right]^{1/p}$$

$$= \left[\int_A \{\left|\frac{\omega(f,t,\delta)}{\alpha(t)}\right|^p\}dt\right]^{1/p}$$

$$= \|\omega(f, t, \delta)\|_{p,\alpha}$$

$$\leq C(p)\tau(f, \delta)_{p,\alpha}$$

3.2 Theorem

Let f be an element in $L_{p,\alpha}(A), A = [0,1]$, $(1 \leq p < \infty)$ with nth derivative $f^{(n)}$ Then

$$E_n^H(f)_{p,\alpha} \leq C(n+1)\tau(f^{(n)}, \delta)_{p,\alpha}$$

Where *C* is absolute constant depended on *p*

Proof

By (23) Lemma and 31 Theorem we obtain

$$E_n^H(f)_{p,\alpha} \leq (n+1)E_{n-1}^H(f')_{p,\alpha} \leq (n+1)\cdot nE_{n-2}^H(f'')_{p,\alpha} \leq \cdots \leq (n+1)!\, E_0^H\left(f^{(n)}\right)_{p,\alpha}$$

$$\leq C(p)(n+1)!\,\tau\left(f^{(n)}, \delta\right)_{p,\alpha} \leq C(p)\tau(f(u))_{p,\alpha}$$

Where

$$C = \max\{C(p)(n+1)!, C(p)\}. \quad \blacksquare$$

Now we can state the following theorems by trigonometric polynomials on $[0,2\pi]$

3.3 Theorem

Let f be an element in $L_{p,\alpha}(A), A = [0,2\pi],\ (1 \le p < \infty)$ then:

$$E_n^T(f)_{p,\alpha} \le K\tau\left(f, {}^1/_n\right)_{p,\alpha}$$

Where K is constant

Proof

Put $$\boldsymbol{a_i = \frac{i\pi}{n},\quad i = 0,1,2,\dots,2n.}$$

$$b_i = \frac{a_i + a_{in}}{2},\quad i = 0,1,2,\dots,2n$$

$$b_{2n+1} = b_1$$

We define the trigonometric polynomial t_n as following:

$$t_n(x) = \begin{cases} \sup\limits_{\mathrm{u}\in[a_{i-1},a_i]} \{f(x)\}\ for\ a_i = b_i, i = 0,1,2,\dots,2n \\ \max\{t_n(b_i), t_n(b_{i+1}) for\ x = a_i\ , i = 0,1,2,\dots,2n\} \\ t_n(0) = t_n(2\pi) \\ linear\ and\ continuous\ for\ x\epsilon[a_{i-1}, b_i\ ], i = 0,1,2,\dots,2n \end{cases}$$

It is clear that $t_n(x) \ge f(x)$ for $x\epsilon[0,2\pi] = X$ and $t_n \in T_n$
The derivative $t_n'(x)$ exist at every point in A
If $x \in [a_{i-1}, b_i\ ]$ then t_n is linear and continuous from definition of t_n

$$\text{So}\quad |f(x) - t_n(x)| \le \frac{2n}{\pi}\ \omega(f(x), \tfrac{4\pi}{n})$$

From (7) (21) Lemma

$$E_n^T(f)_{p,\alpha} \le \|f - t_n\|_{p,\alpha}$$

$$\le \sup\left(\int_{\mathrm{A}} \left|\frac{\{f(t)-t_n(t)\}}{\alpha(t)}\right|^p dt\right)^{1/\mathrm{p}}$$

$$\le \left(\int_{\mathrm{A}} \left|\frac{\sup\{f(t)-t_n(t)\}}{\alpha(t)}\right|^p dt\right)^{1/\mathrm{p}}$$

$$\le \left(\int_{\mathrm{A}} \left|\frac{\omega(f,t,\frac{4\pi}{n}\}}{\alpha(t)}\right|^p dt\right)^{1/\mathrm{p}}$$

$$\le \left\|\omega(f,\cdot,\tfrac{4\pi}{n}\right\|_{p,\alpha}$$

$$\le (4\pi + 1)\tau\left(f, {}^1/_n\right)_{p,\alpha}$$

$$\le C\tau\left(f, {}^1/_n\right)_{p,\alpha}\ \blacksquare$$

*3.4Theorem***:**

Let f be an element in $L_{p,\alpha}(A), A = [0,2\pi],\ (1 \le p < \infty)$ then:

$$E_n^T(f)_{p,\alpha} \le (\tfrac{c}{n})^k \tau\big(f^{(k)},\delta\big)_{p,\alpha} where\ \delta = \tfrac{1}{n}$$

C is absolute constant

Proof:
From (33) Theorem (21) Lemmas and (22) we get

$$E_n^T(f)_{p,\alpha} \le (\tfrac{c}{n})^k\, \tau\left(f,\tfrac{1}{n}\right)_{p,\alpha}$$

$$\le (\tfrac{c}{n})^k \left\|f^{(k)}\right\|_{p,\alpha}$$

$$\le (\tfrac{c}{n})^k \underbrace{\sup}_{0<h<\delta} (\int_A \{\left|\tfrac{f^{(k)}(t)-f^{(k)}(t+h)}{\alpha(t)}\right|^p\}dt)^{1/p}$$

$$\le (\tfrac{c}{n})^k (\int_A \{\left|\tfrac{\sup\{f^{(k)}(t)-f^{(k)}(t+h)\}}{\alpha(t)}\right|^p\}dt)^{1/p}$$

$$\le (\tfrac{c}{n})^k (\int_A \{\left|\tfrac{\omega(f^{(k)},t,\delta)}{\alpha(t)}\right|^p\}dt)^{1/p}$$

$$\le \left(\tfrac{c}{n}\right)^k \tau\big(f^{(k)},\delta\big)_{p,\alpha} \quad \blacksquare$$

References:

[1] Bastmant J and Morales L 2009 Positive linear operator and continuous function on unbounded intervals Jean *Journal Approximation* **1** 2 145173
[2] Corcamo J 2003 On uniform approximation by some classical Bernsteintype operator *Journal Math analysis and applications* **279** 625638
[3] Dai F Ditzian Z and Tikinov S2008 Sharp Jackson inequalities *Journal approximation theory* **151** 86112
[4] Devore R and Lorentz G 1993 Constrictive approximation Springer Verlag Berlin
[5] Dragonov B 2002 A new modulus of smoothing for trigonometric polynomial approximation **8** 4 465499
[6] Dragonov B and Parvanov P 2011 On estimating the rate of best trigonometric approximation by Modulus of smoothing Acta Mathematics Hungar 360379
[7] Sendov B and Popov V1998 The Average moduli of smoothness Wileg New York

Persons Camp Using Interpolation Method

Persons Camp Using Interpolation Method

Luma Naji Mohammed Tawfiq1 , Israa Najm Abood2

[1]College of Education for Pure Science Ibn Al-Haitham, Baghdad University,Iraq
[2]College of Science, Diyala University, Iraq
Author to whom correspondence should be addressed;

luma.n.m@ihcoedu.uobaghdad.edu.iq1 , snamath1982@gmail.com2

Abstract.The aim of this paper is to estimate the rate of contaminated soils by using suitable interpolation method as an alternative accurate tool to evaluate the concentration of heavy metals in soil then compared with standard universal value to determine the rate of contamination in the soil. In particular, interpolation methods are extensively applied in the models of the different phenomena where experimental data must be used in computer studies where expressions of those data are required.

In this paper the extended divided difference method in two dimensions is used to solve suggested problem. Then, the modification method is applied to estimate the rate of contaminated soils of displaced persons camp in Diyala Governorate, in Iraq.

Keywords: Interpolation method, divided difference method, Soil contamination, Heavy metals.

1.Introduction

The paper emphasizes the importance of the numerical analysis in applications, being provided a systematic presentation of the methods and techniques of numerical analysis and interpolation of the functions. Basically, there are many types of approximating functions. Thus, any analytical expression may be expressed as an approximating function, the most common types being*:* polynomials, trigonometric and exponential functions. Special attention is dedicated to polynomials which are the oldest and simplest methods of approximation.

A particular and important aspect in the numerical methods subject is the approximation of the different values, operation designated as interpolation, which is employed in most of the branches of the science, such as: engineering (Oanta, 2001, [1]), economics (Oanta, 2007, [2]), etc.

The problems of interpolation and approximate the functions of several independent variables are important but the methods are less well developed than in the case of functions of a single variable. An

immediate indication of the difficulties inherent in the higher dimensional case can be seen in the lack of uniqueness in the general interpolation problem. In many problems in engineering and science, the data consist of sets of discrete points, being required approximating functions which must have the following properties:

- The approximating function should be easy to determine;
- It should be easy to evaluate;
- It should be easy to differentiate;
- It should be easy implemented.

It can be noticed that polynomials satisfy all four these properties, moreover it have many important properties say: continuity and orthogonally.

The study of interpolation method and its applications in contamination of soil by heavy metals are firstly beginning with Tawfiq, et al., in 2015 [3-7]. In this paper the extending of divided difference method in two dimension are proposed then applied to estimate the concentration of heavy metals for displaced persons camp in Diyala Governorate in Iraq, then estimate the rate of contamination in that soil.

2.Polynomial Interpolation

We must find a real interpolation function F, which has to satisfy the following conditions*:*

$F(x_i) = y_i$, $i = 0,\ldots,n$.

The theoretical base of polynomial approximation is the Weierstrass theorem [8]. This theorem shows that any continuous function can be approximated with accuracy on an interval, using a polynomial function. The interpolation polynomial function is unique for a function on any given interval. The most know methods for polynomial interpolation are: Lagrange, Newton, divided difference, Hermite, spline, Birkhoff polynomial interpolation, trigonometric and rational interpolation (for details see [8-9]). In this paper we suggest divided difference method and its extended in two variable to solve suggested problem.

3.Divided Difference Method

Let *f(x)* be a continuous function given at the distinct point x_i, $i= 0,1,2,\ldots,n$, define the zeros divided difference of the function f with respect to x_i denoted $f[x_i]$ by

$$f[x_i] = f(x_i),$$

The first divided difference of the function f with respect to x_i and x_{i+1} denoted $f[x_0, x_1]$ and is defined as [8]:

$$f[x_0, x_1] = \frac{f[x_1] - f[x_0]}{x_1 - x_0}$$

The second divided difference denoted $f[x_i, x_{i+1}, x_{i+2}]$ and is defined as:

$$f[x_0, x_1, x_2] = \frac{f[x_1, x_2] - f[x_0, x_1]}{x_2 - x_0}$$

Similarly the nth divided difference relative to $x_0, x_1, \ldots, x_{n-1}, x_n$, is given by

$$f[x_0, x_1, \ldots\ldots, x_{n-1}, x_n] = \frac{f[x_1, x_2, \ldots\ldots, x_n] - f[x_0, x_1, \ldots\ldots, x_{n-1}]}{x_n - x_0}$$

The value of $f[x_0, x_1, \ldots\ldots, x_n]$ is independent of the order number $x_0, \ldots\ldots, x_n$.
i.e., if i= 0, 1, 2, then $f[x_o, x_1, x_2] = f[x_1, x_0, x_2] = f[x_2, x_1, x_0]$

Then a polynomial of degree n in x can be construct to interpolate through x_i, $i = 0, 1, \ldots, n$, as

$$P_n(x) = \sum_{i=0}^{n} f[x_0, x_1, \ldots, x_i](x - x_o)\ldots(x - x_{i-1}) \quad , \qquad (1)$$

Let $w_{i-1}(x) = \prod_{k=0}^{i-1}(x - x_k)$, so rewrite equation (1) as follow:

$$P_n(x) = \sum_{i=0}^{n} f[x_0, x_1, \dots, x_i]\, w_{i-1}(x) \quad , \tag{2}$$

4.Interpolation in Two Dimensions

In this section we define the interpolation in two dimensions and generalized divided difference formula in two dimensions. Given distinct point (x_0, y_0), (x_1, y_1),…, (x_m, y_n) in the (x, y)- plane, we have to find polynomial passing through these points by divided difference formula.

Consider the distinct point (x_i, y_j) are given as rectangular grid such: x_i , i= 0, 1, 2,…, m and y_j , j= 0, 1, 2,…, n, then a polynomial of degree m in x and n in y can be construct to interpolate through (x_i, y_j), by extend one dimension formula equation (2), this is, given by:

$$P_{m,n}(x,y) = \sum_{i=0}^{m} \sum_{j=0}^{n} w_{i-1}(x) w_{j-1}(y) f[x_0, x_1, \dots, x_i, y_0, y_1, \dots, y_j] \tag{3}$$

where; $w_{i-1}(x) = \prod_{k=0}^{i-1}(x - x_k)$, $w_{j-1}(y) = \prod_{k=0}^{j-1}(y - y_k)$, $w_{-1}(x) = 1$ and $w_{-1}(y) = 1$.

5.suggested Modification

There is an alternative method for generating approximations that has as it basis the divided difference at $x_0, x_1, \dots, x_n$, this alternative method uses the connection between the nth divided difference and the nth derivative of f and given in the following theorem

Theorem 1 [10]

If $f^{(n)}(x)$ is continuous in $[a, b]$ and $x_0, x_1, \dots, x_n$ are in [a, b] than

$$f[x_0, x_1, \dots, x_n] = \frac{f^{(n)}(\xi)}{n!}$$

where; min $(x_0, x_1, \dots, x_n) \le \xi \le \max(x_0, x_1, \dots x_n)$

A particular case of Theorem 1, is the following corollary.

Corollary 1

If $f^{(n)}(x)$ is continuous in a neighborhood of x than

$$f\left[\underbrace{x, x, .., x}_{n+1 terms}\right] = \frac{f^{(n)}(x)}{n!}$$

Since $z_{2i} = z_{2i+1} = x_i$ for each i we cannot define $f[z_{2i}, z_{2i+1}]$ by divided difference formula, however, if we assume based on theorem (1) that the reasonable substitution in this situation is $f[z_{2i}, z_{2i+1}] = f'(z_{2i}) = f'(x_i)$, we can use the entries: $f'(x_0), f'(x_1), \dots, f'(x_n)$, in place of undefined first divided differences: $f[z_0, z_1], f[z_2, z_3], \dots, f[z_{2n}, z_{2n+1}]$ respectively.

The remaining entries are generated in the same manner as in the Table (1). The modify polynomial is then given by

$$P_{2n+1}(x) = f[z_0] + \sum_{i=1}^{2n+1} f[z_0, z_1, \dots, z_i](x - z_0)(x - z_1) \dots (x - z_{i-1}). \tag{4}$$

Then equation (4) can be generalized in two variables formula as follows

(5)

$$P_{2m+1,2n+1}(x,y) = f[z_0,v_0] + \sum_{i=1}^{2m+1}\sum_{j=1}^{2n+1} f[z_0,z_1,\dots,z_i;\ v_0,v_1,\dots,v_j](x-z_0)\dots(x-z_{i-1})(y-v_0)\dots(y-v_{j-1})$$

For simplification,

$$P_{2m+1,2n+1}(x,y) = \sum_{i=0}^{2m+1}\sum_{j=0}^{2n+1} f[z_0,\dots,z_i,v_0,\dots,v_j]w_{i-1}(z)w_{j-1}(v) \quad (6)$$

where; $z_{2i} = z_{2i+1} = x_i \ \ and \ \ \ v_{2j} = v_{2j+1} = y_j$, for all $i = 1,2,\dots,m \ \ and \ \ j = 1,2,\dots,n$

Table 1: divided difference with suggested modification

F(z) z	First divided difference	Second divided difference
$f[z_0] = f(x_0)$ Z_0		
	$f[z_0,z_1] = f'(x_0)$	
$f[z_1] = f(x_0)$ Z_1		$f[z_0,z_1,z_2] = \frac{f[z_1,z_2]-f[z_0,z_1]}{z_2-z_0}$
	$f[z_1,z_2] = \frac{f[z_2]-f[z_1]}{z_2-z_1}$	
$f[z_2] = f(x_1)$ Z_2		$f[z_1,z_2,z_3] = \frac{f[z_2,z_3]-f[z_1,z_2]}{z_3-z_1}$
	$f[z_2,z_3] = f'(x_1)$	
$f[z_3] = f(x_1)$ Z_3		$f[z_2,z_3,z_4] = \frac{f[z_3,z_4]-f[z_2,z_3]}{z_4-z_1}$
	$f[z_3,z_4] = \frac{f[z_4]-f[z_3]}{z_4-z_3}$	
$f[z_4] = f(x_2)$ Z_4		$f[z_3,z_4,z_5] = \frac{f[z_4,z_5]-f[z_3,z_4]}{z_5-z_3}$
	$f[z_4,z_5] = f'(x_2)$	
$f[z_5] = f(x_2)$ Z_5		

Thus, theorem 1, can be generalize in more than one variable by the following corollary

Corollary 2
If $f(x)$ has a continuous derivative of order
$m \ in \ [a,b];\ x_0,\dots,x_p,\ y_0,\dots,y_q,z_0,\dots,z_r \ \ are \ in \ [a,b];$

$x_i \neq y_i, x_i \neq z_k \ , y_i \neq z_k, \ \forall \ i,j,k, 0 \leq p,q,r \leq m; then$

$$f[x_0,\dots,x_p,y_o,\dots,y_q,z_0,\dots,z_r] = \frac{1}{p!q!r!}\frac{\partial^p}{\partial x^p}\frac{\partial^q}{\partial y^q}\frac{\partial^r}{\partial z^r} f[x,y,z]|(\xi,\eta,\zeta)$$

where ; $\min(x_0,\dots,x_p) \leq \xi \leq \max(x_0,\dots,x_p)$, $\min(y_0,\dots,y_q) \leq \eta \leq \max(y_0,\dots,y_q)$,
$\min(z_0,\dots,z_r) \leq \zeta \leq \max(z_0,\dots,z_r)$,

Now, we can generalize the suggested modification in two variables and construct table (2) as the same manner of table (1) but in two variables.

Table 2: divided difference with suggested modification in two variables

(x_i, y_j)	$f[x_i, y_j]$	First divided difference	Second divided difference
(x_0, y_0)	$f[x_0, y_0]$		
		$\frac{\partial}{\partial x}\frac{\partial}{\partial y} f[x_0, y_0]$	
(x_o, y_0)	$f[x_0, y_0]$		$\frac{f[x_1, y_0] - f[x_0, y_0]}{(x_1 - x_0)}$
		$\frac{f[x_1, y_0] - f[x_0, y_0]}{(x_1 - x_0)}$	
(x_1, y_0)	$f[x_1, y_0]$		$\frac{f[x_1, y_0] - f[x_0, y_0]}{(x_1 - x_0)}$
		$\frac{\partial}{\partial x}\frac{\partial}{\partial y} f[x_1, y_0]$	
(x_1, y_0)	$f[x_1, y_0]$		$\frac{f[x_1, y_0, y_1] - f[x_0, x_1, y_0]}{(y_1 - x_0)}$
		$\frac{f[x_1, y_0, y_1] - f[x_0, x_1, y_0]}{(y_1 - x_0)}$	
(x_0, y_1)	$f[x_0, y_1]$		$\frac{f[x_1, y_0, y_1] - f[x_0, x_1, y_0]}{(y_1 - x_0)}$
		$\frac{\partial}{\partial x}\frac{\partial}{\partial y} f[x_0, y_1]$	
(x_0, y_1)	$f[x_0, y_1]$		$\frac{f[x_1, y_1] - f[x_0, y_1]}{(x_1 - x_0)}$
		$\frac{f[x_1, y_1] - f[x_0, y_1]}{(x_1 - x_0)}$	
(x_1, y_1)	$f[x_1, y_1]$		$\frac{f[x_1, y_1] - f[x_0, y_1]}{(x_1 - x_0)}$
		$\frac{\partial}{\partial x}\frac{\partial}{\partial y} f[x_1, y_1]$	
(x_1, y_1)	$f[x_1, y_1]$		

Now, to illustrate the importance of suggested method, we applied it to determine the concentration of heavy metals in soil, for estimate the rate of contamination in its soil.

6. Sampling

The area of study is muasker Saad displaced persons camp in Diyala Governorate, Iraq. The 8 soil samples were collected with depth (0- 10 cm) using iron shovel (the quantity of each sample was 1 kg), isolation of foreign materials such as plant leaves, debris etc. were removed from the collected soil samples then all the samples were put in plastic bags to measure the concentration of heavy metals (Cd, Cu, Cr, Fe, Ni, Pb and Zn). The samples are carefully collected from each source area in different land using types with a stainless steel spatula. They were air–dried in the laboratory, homogenized and sieved through a 2mm polyethylene sieve to remove large debris, stones and pebbles, after they were disaggregated with a porcelain pestle and mortar. Then these samples were stored in clean self–sealing plastic bags for further analysis. Metal determinations were done by X– ray fluorescence analysis (XRF). pH for all samples was measured in a study soil. Table 3 gave the laboratory results, which represent the initial data which used to interpolate and get approximate function depending on suggested method.

Table 3. Concentration of heavy metals calculated in laboratory.

Samples	measures of heavy metals												
	PH	Pb (S.M.C.=50)		Ni (S.M.C.=50)		Zn (S.M.C.=70)		Fe (S.M.C.=38000)		Cr (SMC.=100)		Cu (S.M.C=20)		**Cd (SMC =1)**
		conc.	Poll. Am.	conc.	Poll. Am.	conc.	Poll. Am.	conc.	Poll. Am.	Conc.	Poll. Am.	conc.	Poll. Am.	**conc.**
Sample 1	6	20	-30	64	14	124	54	12500	-25500	59.3	-40.7	14.6	-5.4	**ND**
Sample2	6.2	20.6	-29.4	64.2	14.2	126.5	56.5	13320	-24680	64.6	-35.4	16.6	-3.4	**ND**
Sample3	6.2	20.6	-29.4	64.2	14.2	126.5	56.5	13320	-24680	64.6	-35.4	16.6	-3.4	**ND**
Sample4	6.4	26.9	-23.1	96.6	46.6	113.2	43.2	24975	-13025	38.2	-61.8	23.6	3.6	**ND**
Sample5	6.4	26.9	-23.1	96.6	46.6	113.2	43.2	24975	-13025	38.2	-61.8	23.6	3.6	**ND**
Sample6	6.6	28.6	-21.4	104.9	54.9	126.5	56.5	21978	-16022	40.9	-59.1	26.9	6.9	**ND**
Sample7	6.6	28.6	-21.4	104.9	54.9	126.5	56.5	21978	-16022	40.9	-59.1	26.9	6.9	**ND**
Sample8	6.6	30.5	-19.5	128	78	128	58	25650	-12350	45	55	30.3	10.3	**ND**

7.Results and Discussion

The data obtained from laboratory dissecting represent the concentration of heavy metals for selected soils are interpolated by suggested method and get the concentration of those heavy metals but in any desire time and any neighboring area, then compared with standard universal for concentration of heavy metals in soil depending on [11] to determine the rate of contamination in soil in that time. We applied suggested method and the results illustrated in figure (1) for each heavy metals. Also, figure (2) illustrate PH of study area

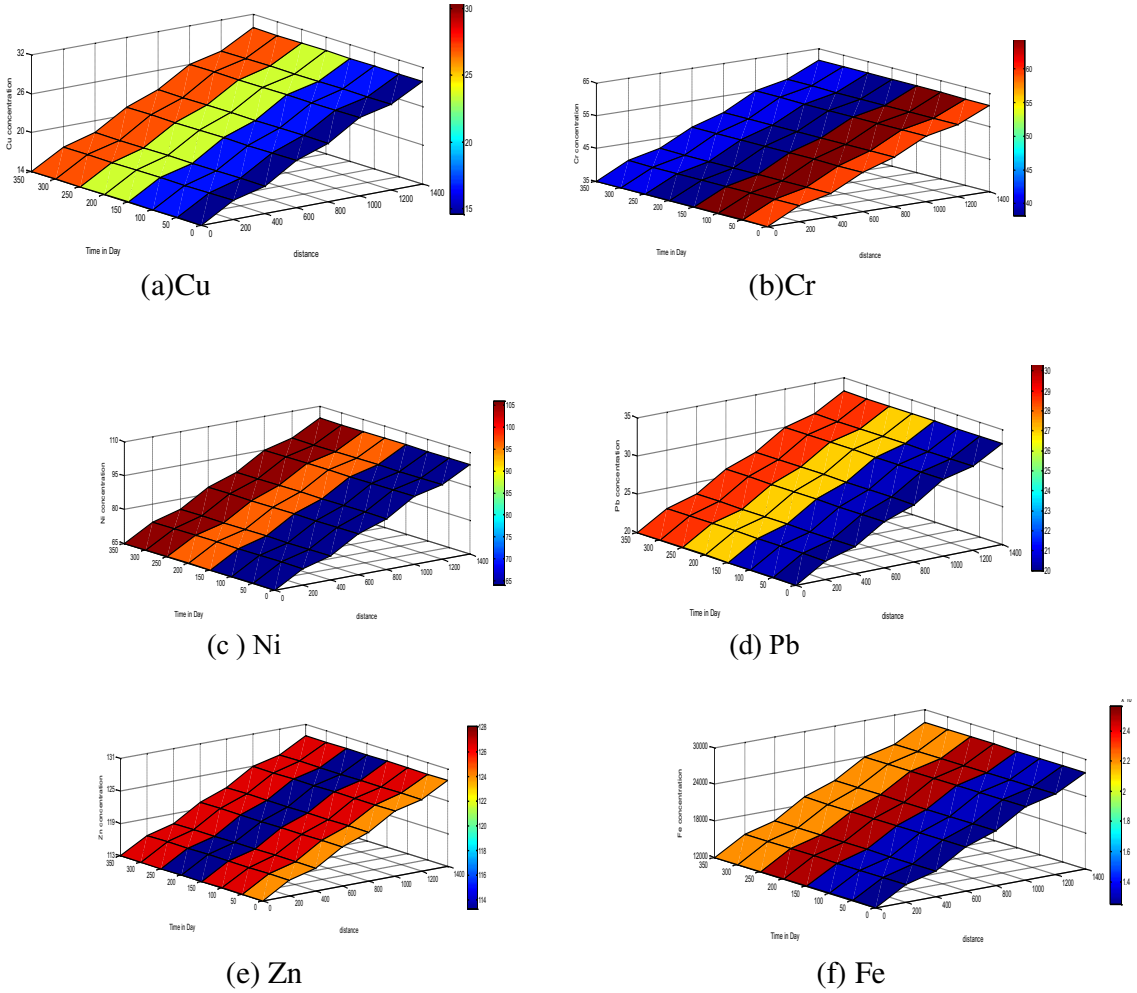

(a)Cu (b)Cr

(c) Ni (d) Pb

(e) Zn (f) Fe

Figure 1: concentration of heavy metals by suggested method

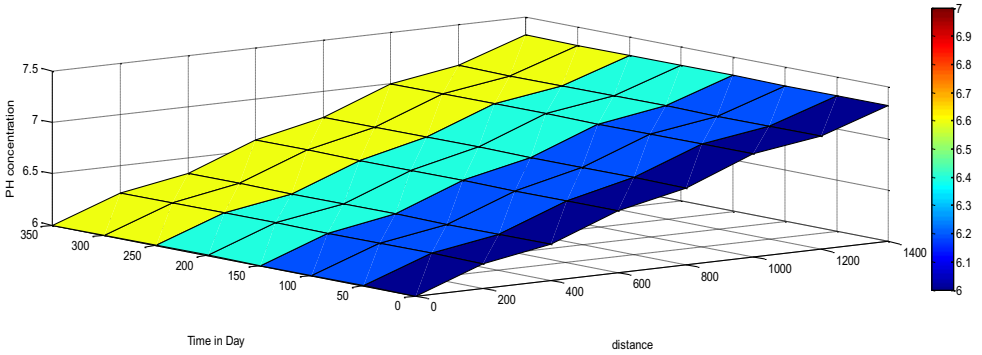

Figure 2: PH of study area by suggested method

'figure(3)', illustrate the accuracy of suggested method by using a comparison between the results of suggested method and laboratory dissecting. 'figure(4)', illustrate the concentration of heavy metals by suggested method for different years.

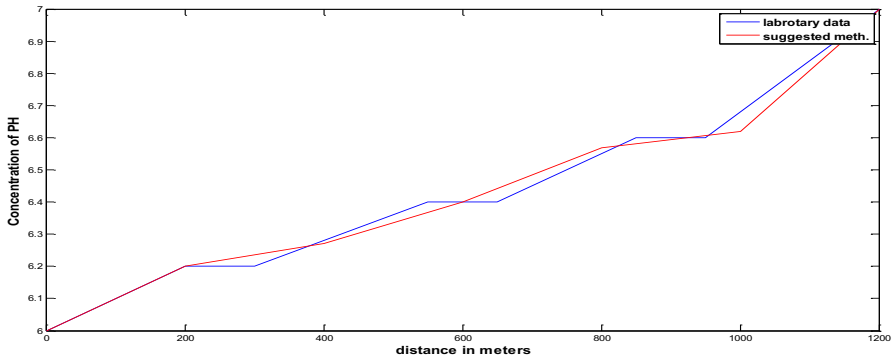

Figure 3: Comparison between suggested method and laboratory dissecting

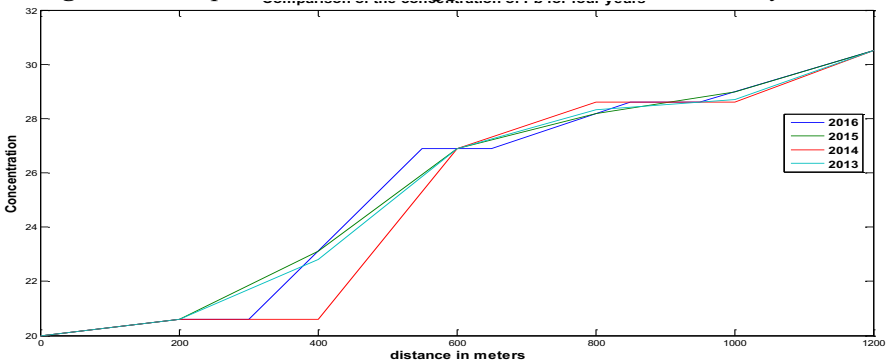

Figure 4: concentration of heavy metals by suggested method for different years

8.Conclusions

New approaches to interpolation of two variables is proposed by generalized one variable divided difference method then developed to increase the accuracy of results based on increase the data. Application in contamination soil is establish to illustrate the importance and efficiency of suggested method.

The results which obtained from the present work show that soil of muasker Saad displaced persons camp in Diyala Governorate, in Iraq were found to be significantly contaminated with metals like Cr, Ni, Pb and Zn at levels above the background concentration in the international soils, which may give rise to various health hazards, while the concentrations of Cd, Co and Fe were under the background concentration in soil. We noted that the comparison between concentrations of four years is introduced to determine the effect of displaced persons for increasing the contamination and figure (5) illustrate the rate of concentration for each heavy metals and sample. In addition the practical results showed the suggested method is easy implemented, high accuracy, efficient and rapid compared to other method.

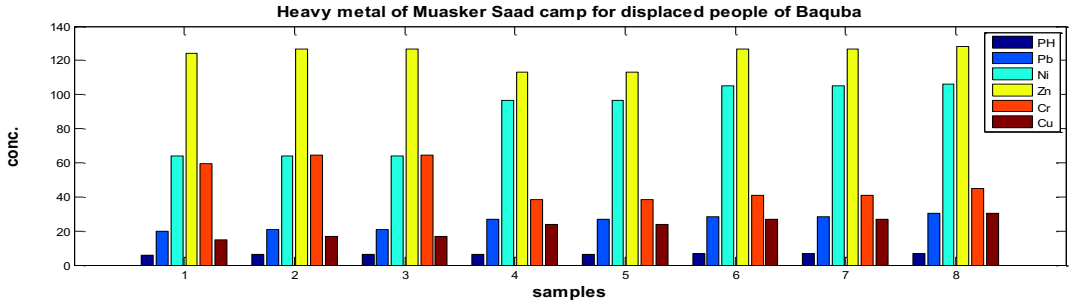

Figure 5: Rate of concentration for heavy metals in each sample

References

[1] Oanta, E. (2001), Study of The Strains and Stresses in The Block of Cylinders of The Naval Internal Combustion Engines, PhD Thesis, 'Cum laude', Mechanical Engineering, Politechnica University of Bucharest.

[2] Oanta, E. (2007), Numerical Methods and Models Applied in Economy, PhD Thesis, Informatics, Academy of Economical Studies of Bucharest, scientific guidance.

[3] Tawfiq, L.N.M; Jasim, K.A; and Abdulhmeed, E. O., 2015, Pollution of Soils by Heavy Metals in East Baghdad in Iraq, *International Journal of Innovative Science, Engineering & Technology*, Vol. **2**, Issue 6, pp: 181-187.

[4] Tawfiq, L.N.M; Jasim, K.A; and Abdulhmeed, E. O., 2015, Mathematical Model for Estimation the Concentration of Heavy Metals in Soil for Any Depth and Time and its Application in Iraq, *International Journal of Advanced Scientific and Technical Research*, Vol. **4**, Issue 5, pp: 718-726.

[5] Tawfiq, L.N.M; Jasim, K.A; and Abdulhmeed, E. O., 2016, Numerical Model for Estimation the Concentration of Heavy Metals in Soil and its Application In Iraq, *Global Journal Of Engineering Science And Researches*, Vol. **3**, No. 3, pp: 75-81.

[6] Tawfiq, L.N.M and Abood, I. N., 2017, Estimate the Heavy Metal Contamination in Soils Using Numerical Method and Its Application in Iraq, *International Journal of Basic & Applied Sciences IJBAS-IJENS*, Vol.**17**, No. 02, p:29-35.

[7] Tawfiq, L.N.M and Al- Khafaji, R.M., Mathematical Modeling and Soil Pollution, LAP Lambert Academic Publishing- 2016.

[8] Burden, L. R., and Faires, J. D., 2001, *Numerical Analysis*, Seventh Edition.

[9] Endre Süli and David F. Mayers, 2003, An *Introduction to Numerical Analysis*, Cambridge University Press, First published.

[10] Randall J. LeVeque, 2006, *Finite Difference Methods for Differential Equations*, University of Washington Press.

[11] Aziz, F. S., (1989), Ampient Air Quqlity in Selected Commercial Area in Baghdad City, M. Sc. Thesis, College of Engineering, University of Baghdad, pp: 72.

Steady State Radial Flow in Anisotropic and Homogenous in Confined Aquifers

IOP Conf. Series: Journal of Physics: Conf. Series **1003** (2018) 012056 doi:10.1088/1742-6596/1003/1/012056

Steady State Radial Flow in Anisotropic and Homogenous in Confined Aquifers

Luma Naji Mohammed Tawfiq[1] and Alaa K Jabber[3]

[1]Department of Mathematics, College of Education for Pure Science Ibn Al-Haitham, Baghdad University, Baghdad, Iraq.
[3]Department of Mathematics, College of Education, University of Al-Qadisiyah, Al Diwaniyah, Iraq.

luma.n.m@ihcoedu.uobaghdad.edu.iq, alaa_almosawi@qu.edu.iq.

Abstract. The purpose of this paper is to introduce the analysis of steady-state radial flow in an anisotropic and homogenous hydraulic property and discuss who we can estimate aquifer parameters from field pumping tests.

Keywords: Partial differential equation; Radial Flow; Anisotropic and Homogenous; Pumping tests.

1. Introduction

Pumping tests are one of the most important techniques used to obtain the properties and parameter of flow and transport problems underground (Kruseman and de Ridder, [1]; Batu, [2]). These properties are important because it is used to develop future work to extract groundwater from the ground. Water flow problems towards test wells with steady and unsteady conditions have been studied early. Thiem [3] and Theis [4] studied the groundwater flow in confined aquifers in the steady state.

Hantush in [5] illustrates the anisotropic aquifers are more apparent in nature, and the anisotropy has caused researchers and hydrologist to be worry because of its effect on the flow of water. To study the anisotropy of aquifers and get accurate solution Cihan et al, in [6] described the properties by the tensor property. The upper limit for the ratio of conductivity in anisotropic aquifers presented by Peijun and others [7]. Hantush [8] used the transformation of coordinate with unknown parameter Ki to convert the anisotropic domain to the isotropic domain to get the solutions of the problems.

We will study the following assumptions:

- Confined aquifer (i.e. confined top and bottom).
- A constant rate of flow Q.
- Reached the steady state (do not change in the head).
- Anisotropic and Homogenous hydraulic conductivity.

2. Steady-State Conditions

After very long time of pumping from the well, the water may reach state with no change in level, this state is called the steady state, at this time since the rate of recharge equal to the discharge rate then there is no growth in the cone of depression, in this case, we have $\frac{\partial h}{\partial t} = 0$.

3. Flow with Homogenous and Isotropic Hydraulic Conductivities

The isotropic and homogeneous property means hydraulic conductivity Kx = Ky = Kz = K where K is constant in space, there are many studies that have discussed this type of flow such that [10- 12].

4. Flow with Homogenous and Anisotropic Hydraulic Conductivities

In this paper, the radial flow will be studied in an anisotropic and homogenous property, i.e., hydraulic conductivity Kx ≠ Ky ≠ Kz but all k's are constant in space, and the equation presented here can be reduced from three dimensions to two by neglecting the vertical flow i.e. ∂h/∂z=0, in this case assume the following:

To radial flow in 2D, as in figure 1,

The standard equations that govern groundwater flow are derived using the principle of continuity and Darcy's law is as follow [9]:

$$T_x\left(\frac{\partial^2 h}{\partial x^2}\right) + T_y\left(\frac{\partial^2 h}{\partial y^2}\right) + T_z\left(\frac{\partial^2 h}{\partial z^2}\right) = S\frac{\partial h}{\partial t} \qquad (1)$$

Suppose that:

$$r = \sqrt{x^2 + y^2} \qquad (2)$$

And let

$$r' = \sqrt{\frac{T_y\, x^2 + T_x\, y^2}{T}}\,, \qquad T = \sqrt{T_x\, T_y} \qquad (3)$$

Assume that $x' = \sqrt{\frac{T_y}{T_x}}\, x \;\; and \;\; y' = \sqrt{\frac{T_x}{T_y}}\, y.$

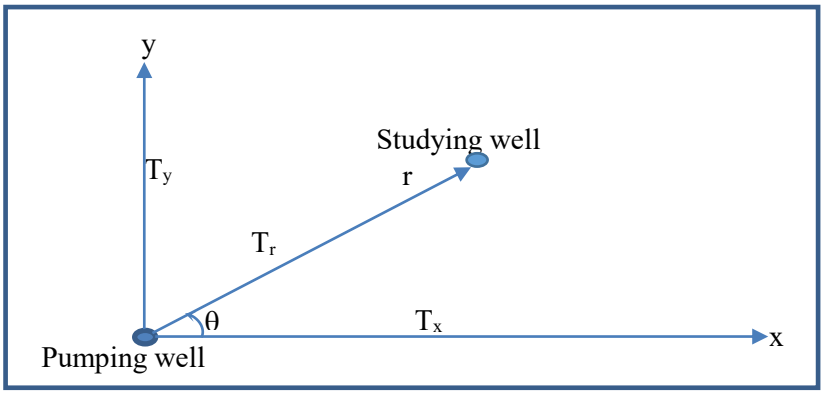

Figure 1: Illustrate the polar coordinates to the wells

Then

$$\frac{\partial r'}{\partial x}=\frac{T_y\ x}{T\ r'}\ ,\qquad \frac{\partial r'}{\partial y}=\frac{T_x\ y}{T\ r'}\ ,\qquad \frac{\partial^2 r'}{\partial x^2}=\frac{T\,T_y r'^2-{T_y}^2\,x^2}{T^2\,r'^3}\ ,\qquad \frac{\partial^2 r'}{\partial y^2}=\frac{T\,T_x r'^2-{T_x}^2\,y^2}{T^2\,r'^3}\quad (4)$$

We have

$$T_x\frac{\partial^2 h}{\partial x^2}=\ T_x\left[\frac{\partial h}{\partial r'}\frac{\partial^2 r'}{\partial x^2}+\frac{\partial^2 h}{\partial r'^2}\left(\frac{\partial r'}{\partial x}\right)^2\right]=\ T_x\left[\frac{\partial h}{\partial r'}\frac{T\,T_y r'^2-{T_y}^2\,x^2}{T^2\,r'^3}+\frac{\partial^2 h}{\partial r'^2}\left(\frac{T_y\ x}{T\ r'}\right)^2\right]$$
$$=\frac{T}{r'}\frac{\partial h}{\partial r'}-\frac{T_y\,x^2}{r'^3}\frac{\partial h}{\partial r'}+\frac{T_y\,x^2}{r'^2}\frac{\partial^2 h}{\partial r'^2}$$

So,

$$T_x\frac{\partial^2 h}{\partial x^2}=\frac{T}{r'}\frac{\partial h}{\partial r'}-\frac{T_y\,x^2}{r'^3}\frac{\partial h}{\partial r'}+\frac{T_y\,x^2}{r'^2}\frac{\partial^2 h}{\partial r'^2}\quad and\quad T_y\frac{\partial^2 h}{\partial y^2}=\frac{T}{r'}\frac{\partial h}{\partial r'}-\frac{T_x\,y^2}{r'^3}\frac{\partial h}{\partial r'}+\frac{T_x\,y^2}{r'^2}\frac{\partial^2 h}{\partial r'^2}$$

Hence, we get:

$$T_x\frac{\partial^2 h}{\partial x^2}+T_y\frac{\partial^2 h}{\partial y^2}=\frac{T}{r'}\frac{\partial h}{\partial r}-\frac{T_y\,x^2}{r'^3}\frac{\partial h}{\partial r}+\frac{T_y\,x^2}{r'^2}\frac{\partial^2 h}{\partial r^2}+\frac{T}{r'}\frac{\partial h}{\partial r}-\frac{T_x\,y^2}{r'^3}\frac{\partial h}{\partial r}+\frac{T_x\,y^2}{r'^2}\frac{\partial^2 h}{\partial r'^2}$$
$$=\frac{2T}{r'}\frac{\partial h}{\partial r'}-\frac{T_y\,x^2+T_x\,y^2}{r'^3}\frac{\partial h}{\partial r'}+\frac{T_y\,x^2+T_x\,y^2}{r'^2}\frac{\partial^2 h}{\partial r'^2}\ =\frac{T}{r'}\frac{\partial h}{\partial r'}+T\frac{\partial^2 h}{\partial r'^2}$$

i.e.,

$$T_x\frac{\partial^2 h}{\partial x^2}+T_y\frac{\partial^2 h}{\partial y^2}=T\left[\frac{1}{r'}\frac{\partial h}{\partial r'}+\frac{\partial^2 h}{\partial r'^2}\right]\qquad (5)$$

Now substitution equation (5) in equation (1):

$$T\left[\frac{1}{r'}\frac{\partial h}{\partial r'}+\frac{\partial^2 h}{\partial r'^2}\right]=S\frac{\partial h}{\partial t}\qquad (6)$$

Or

$$\frac{1}{r'}\frac{\partial h}{\partial r'}+\frac{\partial^2 h}{\partial r'^2}=\frac{S}{T}\frac{\partial h}{\partial t}\qquad (7)$$

From the polar coordinates $x=r\cos(\theta)$ and $y=r\sin(\theta)$, where θ is the angle between the point (studying well) and the positive x-axis, then from equation (3) we have:

$$r'=\sqrt{\frac{T_y\,x^2+T_x\,y^2}{T}}=\sqrt{\frac{T_y\,r^2cos^2(\theta)+T_x\,r^2sin^2(\theta)}{T}}$$

$$\therefore\quad r'\ =r\sqrt{\frac{T_y\,cos^2(\theta)+T_x\,sin^2(\theta)}{T}}\qquad (8)$$

Let $T_\theta = \sqrt{\frac{T_y \cos^2(\theta) + T_x \sin^2(\theta)}{T}}$

$$\therefore \quad r' = r\,T_\theta \tag{9}$$

5. Steady Flow in Confined Aquifer Case

In this case $\frac{\partial h}{\partial t} = 0$, then equation (7) becomes:

$$\frac{1}{r'}\frac{\partial h}{\partial r'} + \frac{\partial^2 h}{\partial r'^2} = 0 \tag{10}$$

Which can we write as:

$$\frac{1}{r'}\frac{\partial}{\partial r'}\left(r'\frac{\partial h}{\partial r'}\right) = 0 \tag{11}$$

Or

$$\frac{\partial}{\partial r'}\left(r'\frac{\partial h}{\partial r'}\right) = 0 \tag{12}$$

By integrated the two sides we get:

$$r'\frac{\partial h}{\partial r'} = C_1 \tag{13}$$

From Darcy's law:

$$\frac{Q}{2\pi T_r} = r\frac{\partial h}{\partial r} \tag{14}$$

Where T_r is the transmissivities in the r direction which is defined as Hantush, [8]

$$\mathrm{T_r} = \frac{\mathrm{T_y\,T_x}}{\mathrm{T_y}\cos^2(\theta) + \mathrm{T_x}\sin^2(\theta)} \tag{15}$$

From equation (9) $\frac{\partial r'}{\partial r} = T_\theta$ and r $= \frac{r'}{T_\theta}$, so:

$$\frac{Q}{2\pi T_r} = r\frac{\partial h}{\partial r} = \frac{r'}{T_\theta}\frac{\partial h}{\partial r'}\frac{\partial r'}{\partial r} = \frac{r'}{T_\theta}\frac{\partial h}{\partial r'}T_\theta = r'\frac{\partial h}{\partial r'}$$

$$\therefore \frac{Q}{2\pi T_r} = r'\frac{\partial h}{\partial r'} = C_1 \tag{16}$$

Now rewrite equation (16) as follows:

$$\partial h = \frac{Q}{2\pi T_r}\frac{\partial r'}{r'} \tag{17}$$

By integrated the two sides we get:

$$h = \frac{Q}{2\pi T_r} ln(r') + C_2 \qquad (18)$$

Alternatively, from equation (9) we can get:

$$h = \frac{Q}{2\pi T_r} \ln(r\, T_\theta) + C_2 \quad , \quad r > 0 \qquad (19)$$

If the radius of the well is r_v, see figure 2, the hydraulic head at a distance of r_v from the center of the well and in all directions is equal to h_v, then $h_v = \frac{Q}{2\pi T_{r_v}} ln(r_v\, T_{\theta_v}) + C_2$. Since the hydraulic head in all directions is equal to h_v, then we will choose the same direction to the r and this implies that $T_r = T_{rv}$ and $T_\theta = T_{\theta v}$, now from (19) we have:

$$h - h_v = \frac{Q}{2\pi T_r} [ln(r\, T_\theta\ ) - ln(r_v\, T_\theta\ )] = \frac{Q}{2\pi T_r} ln\left(\frac{r}{r_v}\right)$$

$$\therefore\ h = h_v + \frac{Q}{2\pi T_r} ln\left(\frac{r}{r_v}\right) \qquad (20)$$

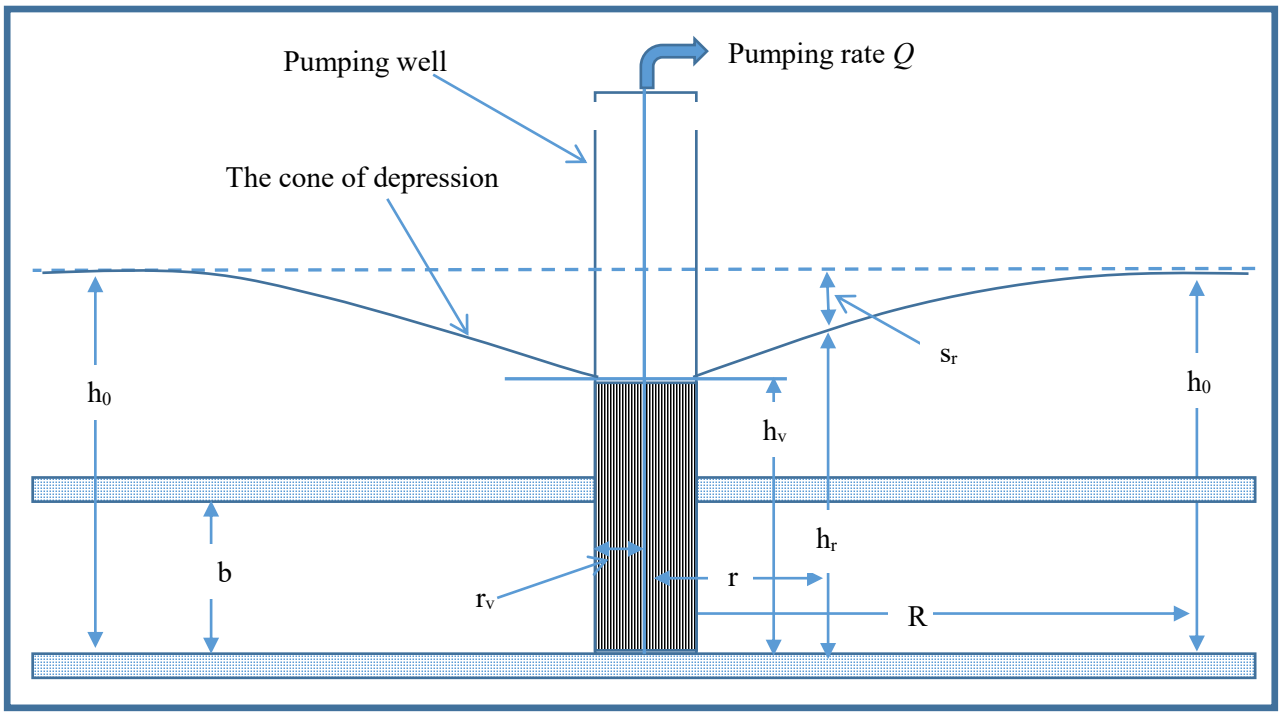

Figure 2: Illustrate the system of pumping

Another estimate to the constant C_2 can get by using boundary condition which specifies $h = h_o$ at $r = R$, Where R represents the largest radius of effect, see 'Figure (2)', then

$$h_0 = \frac{Q}{2\pi T_r} ln\left(R \sqrt{\frac{T_y\, cos^2(\theta_0) + T_x\, sin^2(\theta_0)}{T}}\right) + C_2$$

This implies too, after we choose the same direction:

$$C_2 = h_0 - \frac{Q}{2\pi T_r} ln\left(R \sqrt{\frac{T_y cos^2(\theta) + T_x sin^2(\theta)}{T}} \right)$$

Then equation (19) becomes:

$$h = \frac{Q}{2\pi T_r} ln\left(r \sqrt{\frac{T_y cos^2(\theta) + T_x sin^2(\theta)}{T}} \right) + h_0 - \frac{Q}{2\pi T_r} ln\left(R \sqrt{\frac{T_y cos^2(\theta) + T_x sin^2(\theta)}{T}} \right)$$

i.e.

$$h_0 - h = \frac{Q}{2\pi T_r} \left[ln\left(R \sqrt{\frac{T_y cos^2(\theta) + T_x sin^2(\theta)}{T}} \right) - ln\left(r \sqrt{\frac{T_y cos^2(\theta) + T_x sin^2(\theta)}{T}} \right) \right]$$
$$= \frac{Q}{2\pi T_r} \left[ln\left(\frac{R}{r}\right) \right] \qquad (21)$$

Where $h_0 - h$, is the drawdown s_r, for illustration see figure 2, at a radial distance r from the well.

For Example, if we have the pumping test system with pumping rate Q=1000 $\frac{\pi\, m^3}{s}$, h_v=10 m, r_v=1 m, the distance 100 m on all direction and the transmissivity studying in three case as following:

a) T_x=150 $\frac{m^2}{s}$, T_y=90 $\frac{m^2}{s}$. b) T_x=90 $\frac{m^2}{s}$, T_y=150 $\frac{m^2}{s}$. c) T_x=150 $\frac{m^2}{s}$, T_y=150 $\frac{m^2}{s}$.

By equation (19) we get the following results:

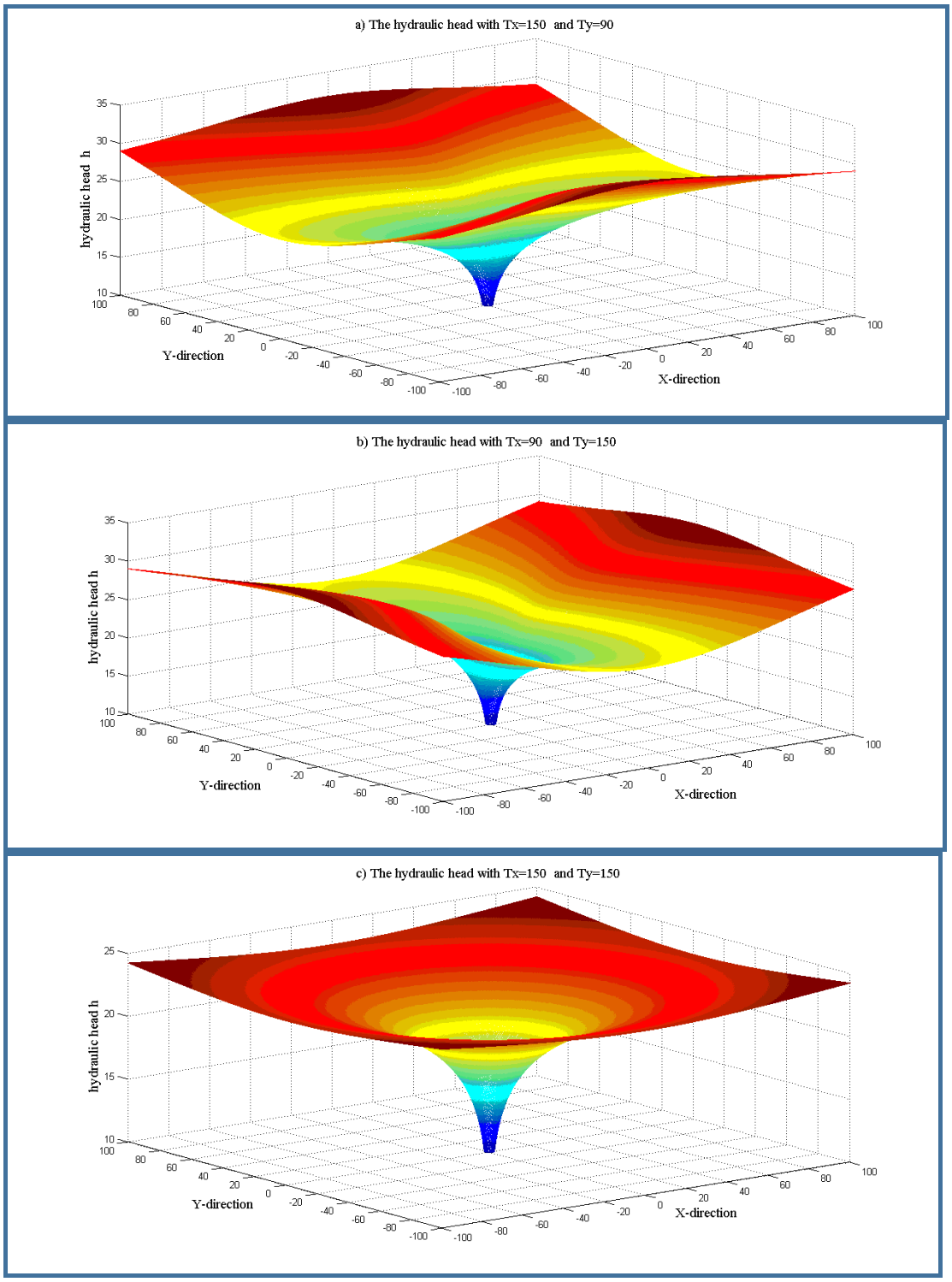

Figure 3 . (a,b,c): Illustrate the transmissivity effect on the hydraulic head

From the previous figures, we observe the transmissivity effect on the hydraulic head by the effect on the cone. In Figure (3.a) since $T_x > T_y$, this main axes of the ellipses are parallel to the x-axis, while in (3.b) since $T_x < T_y$, then this main axes of the ellipses are parallel to the y-axis, but in (3.c) the Conics are circles because of $T_x = T_y$.

6. Effect Radius

When the flow reaches a steady state, the curve of the hydraulic head is constant, i.e., there is a distance where the hydraulic head is not affected by the pumping process and the head equals to the initial value. This distance is called the effect radius and is used to locate other wells in the same region. We can calculate the effect radius from equation (20) as follows:

Suppose that the initial value of the hydraulic head is h_0 and h_v is the hydraulic head of the pumping well, for illustration, see figure 2, then equation (20) becomes:

$$h_0 - h_v = \frac{Q}{2\pi T_r} \ln\left(\frac{r}{r_v}\right) \rightarrow \frac{2\pi T_r (h_0 - h_v)}{Q} = \ln\left(\frac{r}{r_v}\right)$$

$$\rightarrow e^{\frac{2\pi T (h_0 - h_v)}{Q}} = \frac{r}{r_v}$$

$$\therefore \quad r = r_v e^{\frac{2\pi T_r (h_0 - h_v)}{Q}} \qquad (22)$$

Then by equation (22), we can calculate the radius in any direction θ.

For example, if we have the pumping test system with pumping rate Q=1000 $\frac{\pi\, m^3}{s}$, h_v=10 m, rv=1 m, initial head h_0 = 30 m and the transmissivity studying in three case as following:

a) T_x= 150 $\frac{m^2}{s}$, T_y= 90 $\frac{m^2}{s}$; b) Tx=90 $\frac{m^2}{s}$, Ty=150 $\frac{m^2}{s}$; c) T_x=150 $\frac{m^2}{s}$, T_y=150 $\frac{m^2}{s}$;

By equation (22) we get the following results:

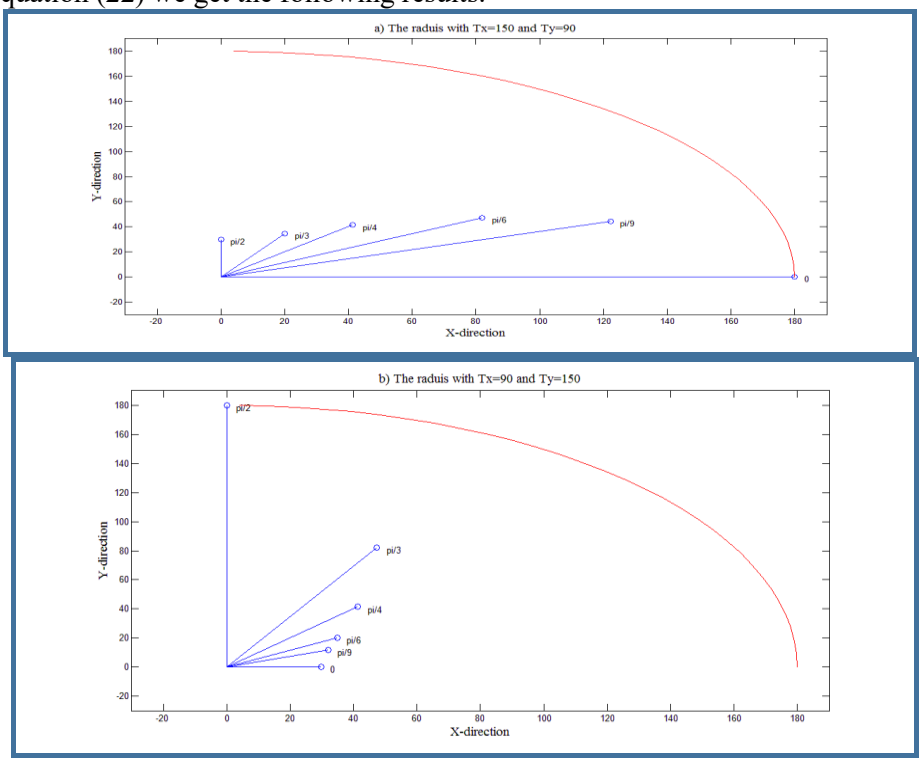

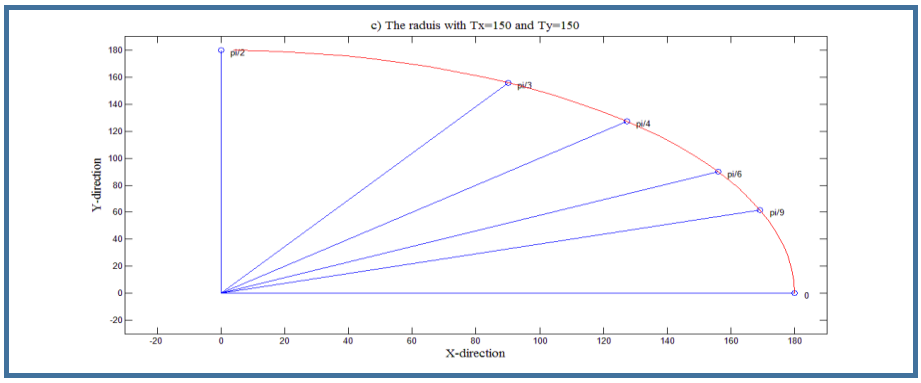

Figure 4. (a,b,c): Illustrate the radius of effect on the hydraulic head

Now to show the effect of the transmissivity on the radius for Example, if we have the pumping test system with pumping rate Q= 1000 $\frac{\pi\ m^3}{s}$, h_v=10 m, r_v=1, initial head h_0=30 m, T_y=90 $\frac{m^2}{s}$ and studying in three case as following: a) T_x=110 $\frac{m^2}{s}$; b) T_x=130 $\frac{m^2}{s}$; c) T_x=150 m^2/s. By equation (22) we get the following results:

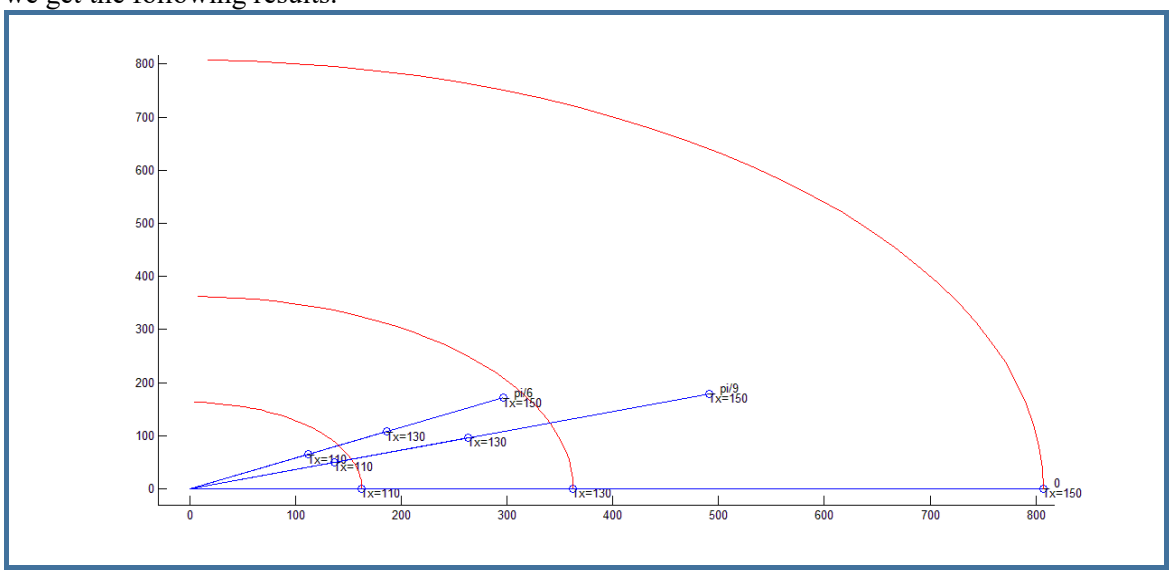

Figure 5: Illustrate the effect of the transmissivity on the radius

Which means that when increasing the transmissivity, the radius is increased. Similarly, we can study the effect of the transmissivity on y-direction.

7. Estimate the Transmissivity

We can estimate the transmissivity by using equation (20) as the following:

Suppose that the hydraulic head at another well, at rx distance in x-direction, is hx and hv is the hydraulic head of the pumping well, in this case θ= 0 and hence by (15) Tr = Tx, for more illustration, see figure 6 and 7, then by equation (20) we have:

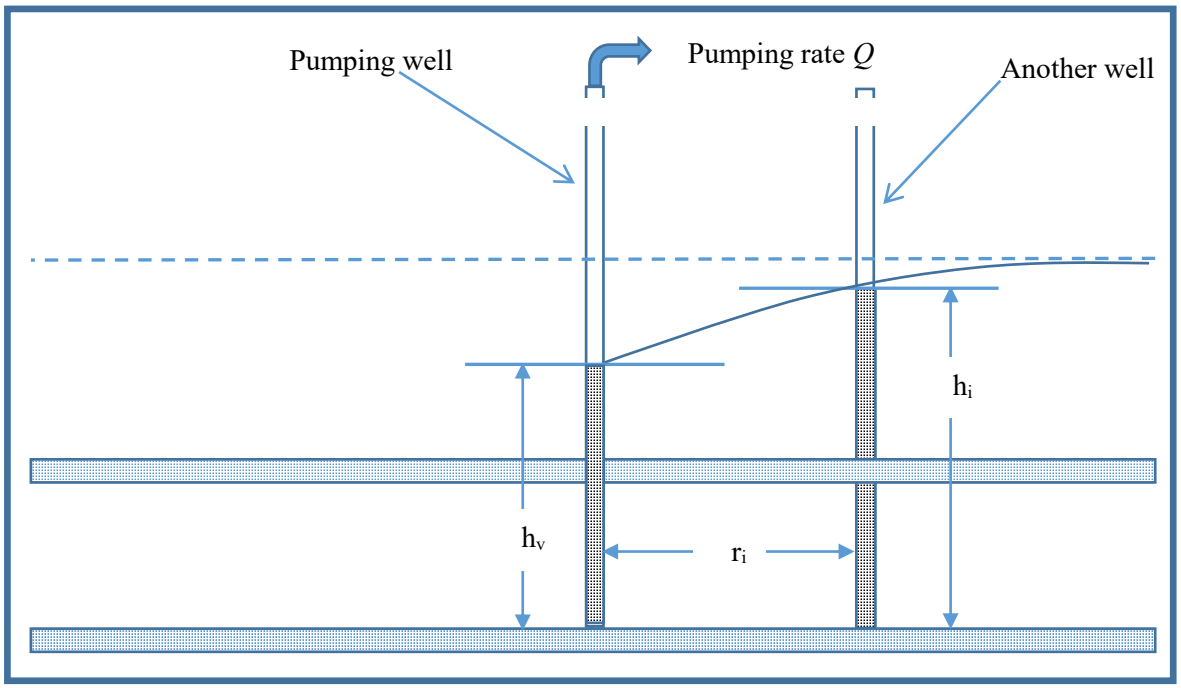

Figure 6: Illustrate the new well

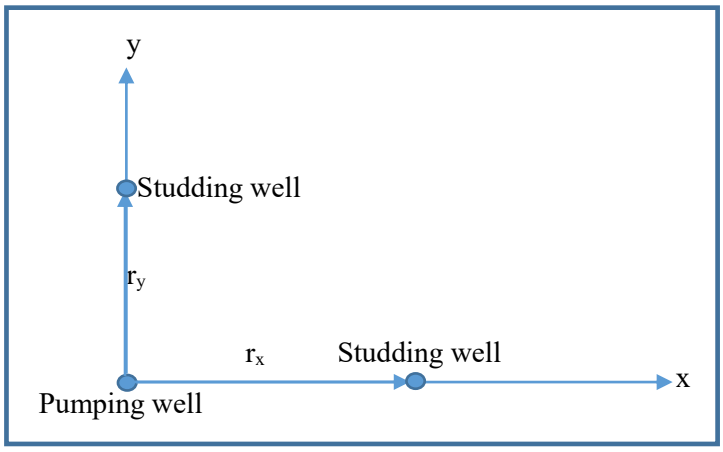

Figure 7: Illustrate the new well in direction

$$h_x - h_v = \frac{Q}{2\pi T_x} ln\left(\frac{r_x}{r_v}\right)$$

$$\therefore T_x = \frac{Q\ ln\left(\frac{r_x}{r_v}\right)}{2\pi\ (h_x - h_v)} \qquad (23)$$

From another hand in y-direction we have

$$T_y = \frac{Q\ ln\left(\frac{r_y}{r_v}\right)}{2\pi\ (h_y - h_v)} \qquad (24)$$

For example, if we have the same information of the example in section 4 and choose the following data illustrated in table 1, we get:

Table 1: Illustrated the data and results to compute T_x

$r_x = x$	h_x	T_x
6	13.66204096	150
11	15.68249364	150
16	16.93147181	150
21	17.83791752	150
26	18.54983119	150

The column T_x is calculated by (23), we can see that the transmissivity T_x is equal to that in the example in section 4 for all different distance r_x.

References

[1] Kruseman G P, de Ridder N.A. and Verweij J M 2000 *Analysis and evaluation of pumping test data* (Netherlands: International Institute for Land Reclamation and Improvement) 2nd edition.
[2] Batu V 1998 *Aquifer hydraulics: a comprehensive guide to hydrogeological data analysis* (Wiley : Interscience).
[3] Theis C V 1935 The Relation Between the Lowering of the Piezometric Surface and the Rate and Duration of Discharge of a Well Using Groundwater Storage *Transactions American Geophysical Union* **16** pp 519-24.
[4] Thiem G 1906 Hydrologische Methoden Thesis (German- Stuttgart: Leipzig – Gebhardt).
[5] Hantush Mahdi S 1966 Wells in Homogeneous Anisotropic Aquifers *Water Resources Research* **2** No. 2 pp 273-9.
[6] Cihan A, Zhou Q, Birkholzer J T and Kraemer S R 2014 Flow in horizontally anisotropic multilayered aquifer systems with leaky wells and aquitards *Water Resources Research* **50** pp741-7.
[7] Guo P, Liu Y and Stolle D 2015 Limit of Anisotropic Hydraulic Conductivity Ratio of Homogeneous Granular Materials *Vadose Zone Journal* **14** (11).
[8] Hantush Mahdi S 1966 Analysis of Data from Pumping Tests in Anisotropic Aquifers *Journal Of Geophysical Reserch* **71** (2) pp 421-6.
[9] Tawfiq L N M and Jabber A K 2016 Mathematical Modeling of Groundwater Flow *Global Journal of Engineering Science and Researches* **3** (10).
[10] Rushton K R 2003 *Groundwater Hydrology: Conceptual and Computational Models* (England: John Wiley & Sons Ltd).
[11] Waghmare R V 2016 Mathematical Modeling of Flow in Confined Aquifer *International Journal of Novel Research in Physics Chemistry & Mathematics* **3** (2) pp 1-16.
[12] Wang Xu-Sheng and Zhan H 2009 A New Solution of Transient Confined–Unconfined Flow Driven by a Pumping Well *Advances in Water Resources* **32** pp 1213–22.

Estimate the Effect of Rainwaters in Contaminated Soil by Using Simulink Technique

IOP Conf. Series: Journal of Physics: Conf. Series **1003** (2018) 012057 doi:10.1088/1742-6596/1003/1/012057

Estimate the Effect of Rainwaters in Contaminated Soil by Using Simulink Technique

Luma N M Tawfiq*, Mohammed A Hassan**

Department of Mathematics, Collage of Education for pure sciences- Ibn Al-Haitham, University Baghdad, Baghdad, Iraq.

*dr.lumanaji@yahoo.com, **alamery85@yahoo.com

Abstrac. The aim of this paper is to design a Simulink model which can estimate the effect of rainwaters in the contaminated soil by heavy metal. The paper suggests design of Simulink model to estimate concentration of heavy metals in soil depending on the given data. Then compared the results with laboratory inspecting to estimate the accuracy of suggested technique. Where the sample data selected from different zone in Baghdad before and after the rain to determine its effect. The practical results show the efficiency of suggested technique.

1. Introduction

Mathematical Models are simplified representations of some real world entity can be in equations or computer code are intended to mimic essential features while leaving out inessentials, that is, models describe our beliefs about how the world functions. Mathematical modeling aims to describe the different aspects of the real world, their interaction, and their dynamics through mathematics [1]. Simulink, associate degree add-on product to MATLAB, provides associate degree interactive, graphical environment for modeling, simulating. It enables rapid construction of virtual prototypes to explore style ideas at any level of detail with stripped effort. For modeling, Simulink provides a graphical programmer (GUI) for building models as block diagrams. It includes a comprehensive library of pre-defined blocks to be accustomed construct graphical models of systems exploitation drag-and-drop mouse operations. The user is in a position to supply associate degree "up-and-running" model that will otherwise need hours to create within the laboratory surroundings. It supports linear and nonlinear systems, sculptural in continuous-time, sampled time, or hybrid of the 2. Since students learn expeditiously with frequent feedback, the interactive nature of Simulink encourages you to do things out, you'll be able to modification parameters "on the fly" and immediately see what happens, for "what if" exploration. Lastly, and not the smallest amount, Simulink is integrated with MATLAB and knowledge are often simply shared between the programs.

2. Building a Simulink Model

Building a Simulink model of a problem hold by choosing the suitable blocks and connecting them depending on a means that represents the models. The Simulink model contains six distinct blocks, namely, sine wave, scope, gain, mux, clock, and to workspace. The wave could be a supply block from that a curving input signal originates. The signal is transferred through a line within the direction indicated by the arrow to the gain block. The gain block modifies its input (scales it by 5) and outputs a replacement signal through a line. The output of the gain block and also the output of the sine wave are combined within the electronic device (mux) to create a symptom vector. The signal vector is transferred through a line to the scope block accustomed show a symptom very like a cathode-ray

oscilloscope. Then the model must be creation, where creating is an operating model with Simulink, involves four basic steps as follow: Select desired blocks, Configure block parameters, Connect block inputs outputs, and Configure simulation parameters.

3. Suggested Simulink Design

The suggested model descriptions of the contamination of soils by heavy metals which are distributed throughout the soil system remain in the soil solution as iron, organic and inorganic complexes. Some of these heavy metals are mobile for uptake by plants. This mobility and availability depends on several factors including soil texture and PH [13]. Also, in the industrial regions, where some types of factories are active, several chemical and petrochemical processes would be also active. As a result, industrial water becomes contaminated with various substances which are harmful; these are sources of environmental contamination, which added in the description of the model equation. Then, the model equation, can be written as the relation between the change of concentration C ($\frac{\mathbf{mg}}{\mathbf{L}}$) of heavy metals proportionally with the change of time t (day-1) and the change of concentration of heavy metals proportionally with the change of space x (cm) multiplicand with the average pore-water velocity V ($\frac{\mathbf{cm}}{\mathbf{hr}}$). Then adding the fluid velocity in the reactor multiplicand with Dispersion parameter D ($\frac{\mathbf{cm^2}}{\mathbf{hr}}$). So, the model 'equation (1)' can be written as:

$$\frac{\partial C}{\partial t} = D\ \frac{\partial^2 C}{\partial^2 x} -\ V\ \frac{\partial C}{\partial x} \qquad (1)$$

Which is a second order linear PDE.

Where;

$C_\circ$: Initial concentration ($\frac{\mathbf{mg}}{\mathbf{L}}$).

The amount of each element retained by each soil ($\frac{\mathbf{mg}}{\mathbf{kg}}$) was calculated from the initial concentration in solution ($\frac{\mathbf{mg}}{\mathbf{L}}$) and the final concentration C in solution ($\frac{\mathbf{mg}}{\mathbf{L}}$).'Equation (1)', which can be represented as a mathematical model for spread of contamination through soil which can be used to determine the rate of contamination. we design Simulink model illustrated in 'figure 1'.

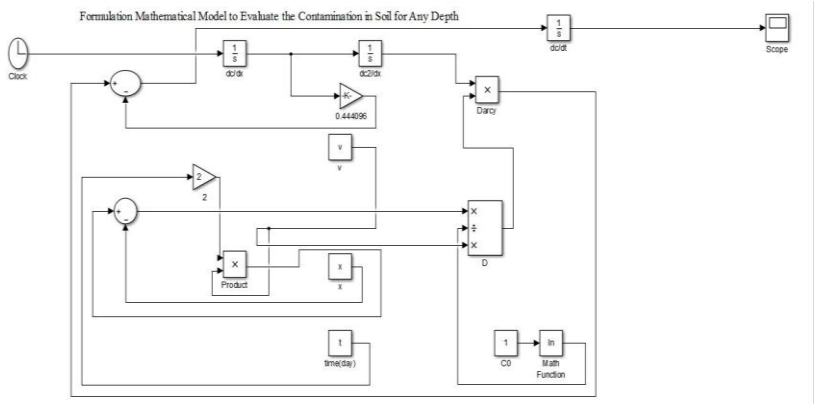

Figure 1. Design Simulink model for suggested problem.

4. Application of Suggested Design

The study area is a different zone in Baghdad city where the samples testing are selected from: residential, commercial and industrial land. Soil samples were collected different times before and after the rain for each zone, it's carefully collected with a stainless steel spatula. They were air-dried in the laboratory, homogenized and sieved through a 2-mm polyethylene sieve to remove large debris, stones and pebbles. Then these samples were stored in clean self- sealing plastic bags for further analysis. Concentration of metals such Pb, Zn, and Cd, are determinant by using XRF device and its mean are given in (table 1). This data are used as initial vale (initial concentrations (C_0) of heavy metals) which feeding suggested Simulink model.

Then the results of Simulink design (1) which represent the concentrations of these heavy metals are obtained. The results of laboratory and Simulink before rain given in Table 2, but after the rain are given in (table 3) and each the results are illustrated in 'figure 2' and 'figure 4'.

Table 1. Concentrations (C0) of heavy metals for different zone in Baghdad city.

Samples	Pb	Zn	Cd
State (1) before rain	70	190	3
State (1) after rain	28	85.5	2
State (2) before rain	192	370	2
State (2) after rain	65	63.2	1.5
State (3) before rain	340	140	10
State (3) after rain	72	98.2	8
State (4) before rain	125	120	3
State (4) after rain	81	78	2
State (5) before rain	150	120	5
State (5) after rain	51.1	59.1	2.6
State (6) before rain	54	170	2
State (6) after rain	39.5	89.5	1.7
State (7) before rain	410	100	5
State (7) after rain	80.3	71.5	2.4
State (8) before rain	300	165	2
State (8) after rain	101.2	90.5	1.1
State (9) before rain	90	50	2
State (9) after rain	50	47	1.5

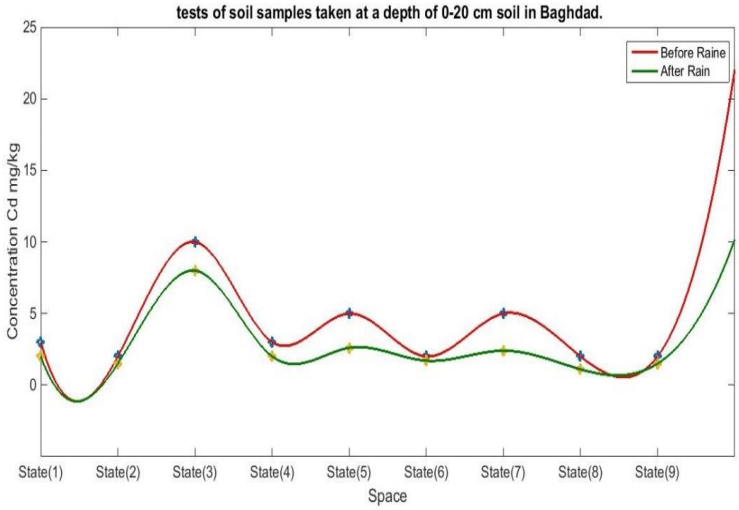

Figure 2. Concentrations of Cd before and after rain in Baghdad city.

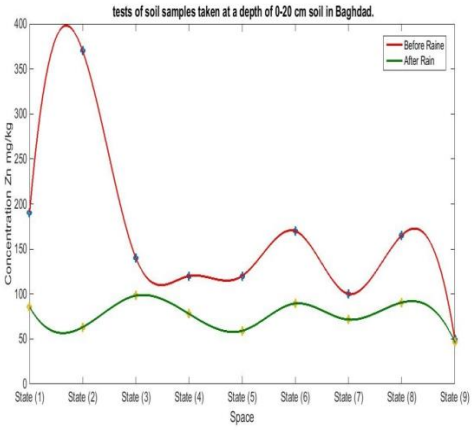

Figure 4. Concentrations of Zn before and after rain in Baghdad city

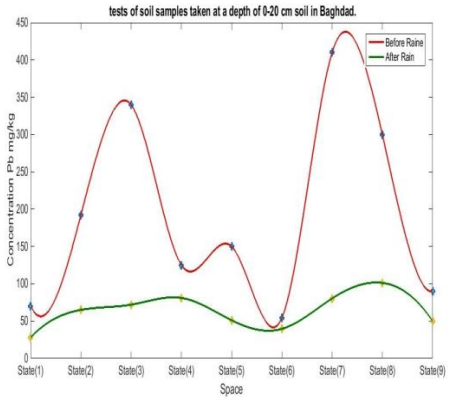

Figure 3. Concentrations of Pb before and after rain in Baghdad city.

Table 2. Concentration of Pb, Zn, and Cd before Rain.

No	Laboratory results Pb	Simulink results Pb	Laboratory results Zn	Simulink results Zn	laboratory results Cd ppm	Simulink results Cd
1	70	69	190	195	3	2
2	192	190	370	372	2	1
3	340	345	140	138	10	10.5
4	125	123	120	120	3	2.4
5	150	151	120	120	5	5.3

6	54	50	170	178	2	1.6
7	410	405	100	110	5	5.4
8	300	300	165	170	2	2
9	90	89	50	61	2	2

Table 3. Concentration of Pb, Zn, and Cd after Rain.

No	Laboratory results Pb	Simulink results Pb	Laboratory results Zn	Simulink results Zn	Laboratory results Cd	Simulink results Cd
1	28	30	85.5	80.9	2	1.6
2	65	70	63.2	60	1.5	0.8
3	72	72	98.2	99.3	8	8.6
4	81	85	78	78	2	1.8
5	51.1	50	59.1	58	2.6	2.8
6	39.5	38	89.5	90.1	1.7	1.6
7	80.3	80.5	71.5	70.1	2.4	2.6
8	101.2	103.4	90.5	92	1.1	0.9
9	50	51.2	47	49	1.5	1.1

5. Conclusions

The analysis of the result shows that there is a very good level of agreement between the experimental and simulated results obtained. This can also be confirmed by the numerical analysis of the result by using error / defect weights, Richardson extrapolation and higher order formula.
In conclusion, the suggested design can be considered to be a good representation of the estimating the concentrations of heavy metals in the soil.

The practical results show the effect of the rain for decreasing the rate of contamination in soil. The results of the analysis were showed that concentrations of zinc in the soil did not exceed the permissible limits, indicating the presence of contamination of this element in the soil of Baghdad city. Also, observed by measuring the concentration of Cd it had exceeded the permissible limits, which indicates the existence of this element in the soil of the city of Baghdad, and the reason for the increase in the concentration of this element is due to several reasons including the impact of industrial activities, but by less than in previous years due to suspension of many of these actors to work due to war conditions experienced by the country as well as the impact of adsorption by clay minerals and the presence of organic matter in the soil that play an important role in increasing concentrations of these elements as well as the weathering and irrigation and drainage.

References

[1] Bokil V A 2009 *Introduction to Mathematical Modeling* Spring
[2] Ajmalkhan M U and Showalter A M 1999 Effect of salinity on growth, ion contact, and osmotic relation. Stapf. *Journal of Plant Nutration* **22** 1 pp 191-204
[3] Kabata A and Pendias H 2016 *Trace Elements in Soils and Plants* 3rd Edition, CRC press, Washington D C p 550
[4] Tawfiq L N M and Al- Khafaji R M 2011 *Mathematical Modeling and Soil Pollution* (Lap Lambert Academic Publishing)
[5] Tawfiq L N M, Jasim K A and Abdulhmeed,E O 2015 Mathematical Model for Estimation the Concentration of Heavy Metals in Soil for Any Depth and Time and its Application in Iraq. *International Journal of Advanced Scientific and Technical Research*, **4** pp 718-726
[6] Luma N M Tawfiq and Farah F Ghazi 2015 Using Artificial Neural Network Technique for the Estimation of Cd Concentration in Contaminated Soils *International Journal of Innovations in Scientific Engineering* (*IJISE*) **1** 1 pp 1-7

[7] Luma N M Tawfiq and Farah F Ghazi 2016 Mathematical model for estimation the concentration of heavy metals in soil *MJ Journal on Applied Mathematics* **1** 1 pp 16-19
[8] Hamad M Salih, Luma. N M Tawfiq and Zainor R Yahya 2016 Estimate The Concentration of Heavy Metals in Soil by Using Trigonometric Cubic B-Spline Method and its Application in Baghdad, Iraq *Global Journal of Engineering Science and Researches* **3** 9 pp 13-20
[9] Tawfiq L N M and Jasim K A Abdulhmeed E O 2016 Numerical Model for Estimation the Concentration of Heavy Metals in Soil and its Application in Iraq *Global Journal of Engineering Science and Researches* **3** 3 pp 75-81
[10] Janette Worm and Tim v Hattum 2006 *Rainwater harvesting for domestic use, Agromisa Foundation and CTA Wageningen,* First edition

Estimation of Heavy Metals Contamination in the Soil of Zaafaraniya City Using the Neural Network

Estimation of Heavy Metals Contamination in the Soil of Zaafaraniya City Using the Neural Network

Farah F Ghazi

Department of Mathematics, College of Education for Pure Science Ibn Al-Haitham, Baghdad University.

mary_19862004@yahoo.com

Abstract. The aim of this paper is to estimate the heavy metals Contamination in soils which can be used to determine the rate of environmental contamination by using new technique depend on design feedback neural network as an alternative accurate technique. The network simulates to estimate the concentration of Cadmium (Cd), Nickel (Ni), Lead (Pb), Zinc (Zn) and Copper (Cu). Then to show the accuracy and efficiency of suggested design we applied the technique in Al- Zafaraniyah in Baghdad city. The results of this paper show that the suggested networks can be successfully applied to the rapid and accuracy estimation of concentration of heavy metals.

Keywords. Artificial Neural Network, Feedback Neural Network, Heavy metals.

1. Introduction

Mathematical modeling is important to describe the different problems in the real world and the solution of this modeling represents the solution for the problems in life, Quarteroni A. (2009) [1]. This paper studies and modifies a model equation to represent a suitable form which describes the environment contamination. Especially, soil contamination by heavy metals. We suggest the artificial neural network (ANN) as a technique to solve the model.

There are many studies for solving the soil contamination using ANN. For instance, Buszewski and Kowalkowski, 2006 [2] present the results of chemo metric treatment of data from experiment of column leaching to find dependencies between physicochemical parameters of soil and heavy metals concentration by using ANN model. Yetilmezsoy and Demirel, 2008 [3] used ANN model to predict the removal efficiency of Pb from aqueous solution. Kardam et al., 2010 [4] presented ANN model to describe the removal efficiency of Cadmium from aqueous solution using Shelled Moringa Oleifera Seed (SMOS) powder. Yin Li et al., 2011 [5] employed BP-NN model and Geographic Information System (GIS) for heavy metals descripted the spatial dynamics of distribution in Huizhou city. El-Badaoui et al., 2013 [6] predict the concentration of HMs in Moroccan river sediments relying on a number of physico-chemical parameters using ANNs. Pandhuripande et al., 2013 [7] estimated the concentration of Ni and Cr in aqueous solution with its physical properties using ANN. Krishna and Sree, 2014 [8] suggested the ANN for remove efficiency of Cr from aqueous solution used a Borasus flabellifer coir powder as adsorbent. Zongshu Wu et al., 2015 [9] explained the optimization way for

soil sampling to spatial distribution of heavy metals concentrations using ANN with genetic algorithm. Madhloom 2015[10] suggested using ANN to describe the removal efficiency of Cu from wastewater by fungal biomass.
This paper suggested an effective, low cost and easily accessible design of Artificial Neural Network to estimate soil contamination problems and compared the results with the traditional laboratory devices such X– ray fluorescence analysis (XRF) to illustrate the accuracy and the efficiency of the suggested technique. Note that all algorithms in this work implemented using MATLAB version 7.12.

2. Mathematical Model

The paper aims at developing equation of mathematical model given in [11, 12] that estimate the rate of concentration of HMs in soil. This aim can be achieved through the realization of the following objectives:

- Collection of data illustrating the concentration of some of HMs at different percentage of the soil with respect to depth.
- Developed the mathematical model equations for the concentration of HMs in the soil.
- Simulation of the model equation using software program Mat lab 2014 professional.
- Compare the result with the experimental data.

Models that include retention and release reactions of solutes with the soil matrix are needed. Retention and release reactions in soils include precipitation / dissolution, ion exchange, and adsorption / desorption reactions (Amacher et al. 1986) [13]. Retention and release are influenced by number of soil properties including texture, bulk density, power of hydrogen (PH), Electric Conductivity (EC), organic matter, and type and amount of clay minerals. Then the model equation which describes this problem has the form [14, 15]:

$$\rho \frac{\partial C}{\partial t} = D_L \frac{\partial^2 C}{\partial x^2} - V_x \frac{\partial C}{\partial x}, \quad 0 < x < \infty, \quad t > 0 \tag{1}$$

Which is a second order linear PDE, with initial - boundary conditions:

$$C(0,t) = C_0 \ \ and \ \ \frac{\partial C}{\partial x}(\infty, t) = 0.$$

$$C(x,0) = Cx$$

Where; C_0: Initial concentration.
C_x: Concentration for depth x ($\frac{\text{mg}}{\text{L}}$)
V_x: The average pore – water velocity, ($\frac{\text{cm}}{\text{hr}}$)
x: Soil depth (distance) (cm).
t : Time (day^{-1}).
ρ: Retardation factor. ($\frac{g}{cm^3}$)

The amount of each element retained by each soil ($\frac{\text{mg}}{\text{kg}}$) was calculated from the initial concentration in solution ($\frac{\text{mg}}{\text{L}}$) and the final concentration C in solution ($\frac{\text{mg}}{\text{L}}$). 'As in equation (1)', which can be represented as a mathematical model for spread of contamination through soils which can be used to determine the rate of contamination. The solution of model equation gives the concentration of the HMs in soil.

3. Solution & Design of the Model Equation

To solve that model we suggest artificial neural network (ANN) of type Feedback Neural Network (FBNN) used to estimate the concentration of HMs in Zafaraniyah soil.

We suggest a multilayer FBNN which consist three layers: input layer consist five input nodes, one hidden layer consist eleven hidden nodes with tansig. Transfer function and one node for output layer with purelin. Transfer function. The output of the suggest FBNN which represent the solution of trial can be written as:

$$C = N\,(x, t, c_0, s, p) \tag{2}$$

Where; x, t, c_0 are defined 'as in equation (2)', and s is the soil parameters defined; 'as in equation (1)', represent the weights.

4. Sampling

Baghdad City it was the capital of Iraq (33°14'-33°25'N, 44°31'-44°17'E), the climate with cold winters and dry hot in summers; the mean rainfall is about 151.8 mm. For the purpose of collection of soil samples, the study zone is Zafaraniyah was included in to 5 main types of land use viz. residential, agricultural, commercial, industrial and main roads [16]; and two main source zones, within each land use type viz. open zones and roadside. The sample zones are illustrated by geographic information system (GIS) give in 'figure 1'.

Soil samples were collected during winter season of 2016 with depth (0 – 40 cm) were carefully collected from different Zafaraniyah land using types with a stainless steel spatula and dried it in the laboratory and sieved through a 2mm polyethylene sieve to remove large debris, pebbles and stones, after they were disaggregated with a porcelain pestle and mortar. Then these samples were stored in clean self–sealing plastic bags for further analysis. Metal determinations were done by X– ray fluorescence analysis (XRF). The laboratory results for many states in Baghdad (Zafaraniyah) are given in (table 1).

Figure 1. Illustrate the study areas in Baghdad city- Zafaraniyah by GIS

Table 1. The laboratory results for Al- Zafaraniyah zone in Baghdad

Samples	Depth	Cu	Zn	Pb	Ni	1
State 1	0 – 20 cm	9.5	25	34.5	52	0.25
	20 – 40 cm	6	10	6.1	55	0.15
State 2	0 – 20 cm	11	18.8	9.7	66	0.7
	20 – 40 cm	12	25	8.8	80	0.2

State 3	0 – 20 cm	4.0	18	7.65	9.5	0.65
	20 – 40 cm	1.00	7	2.75	2.5	0.1
Average	0 – 20 cm	8.167	20.6	17.283	45.833	0.533
	20 – 40 cm	6.333	14	5.8833	42.5	0.15

'Figure 2' illustrates the training, testing and validation results when we used modified LM algorithm. Figure 3 illustrates the training, testing and validation results with regularization. 'Figure 4' illustrates the architecture of the FBNN.

We simulate suggested FBNN for Cd, Ni, Pb, Zn and Cu with the measured data. The comparison between the predicted concentrations and the measured data resulted in the performance function. (Table 2) gives the target values for training, testing and validation samples and regularization parameter γ of HMs. (Table 3) gives the accuracy of the train for time and epoch. 'Figure 5', 'figure 6', 'figure 7', 'figure 8' and 'figure 9' illustrates the performance of suggested design for concentration of Cd, Ni, Pb, Zn and Cu.

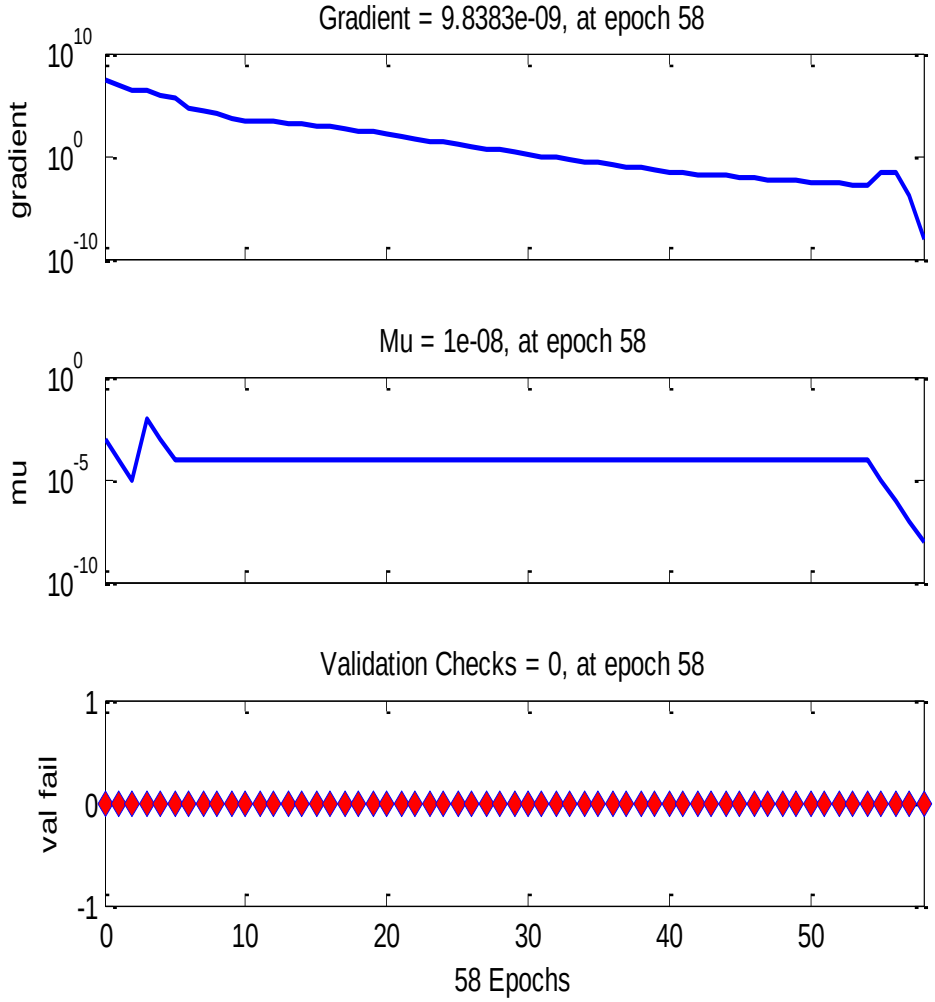

Figure 2. Training, testing and validation first FBNN by modify LM.

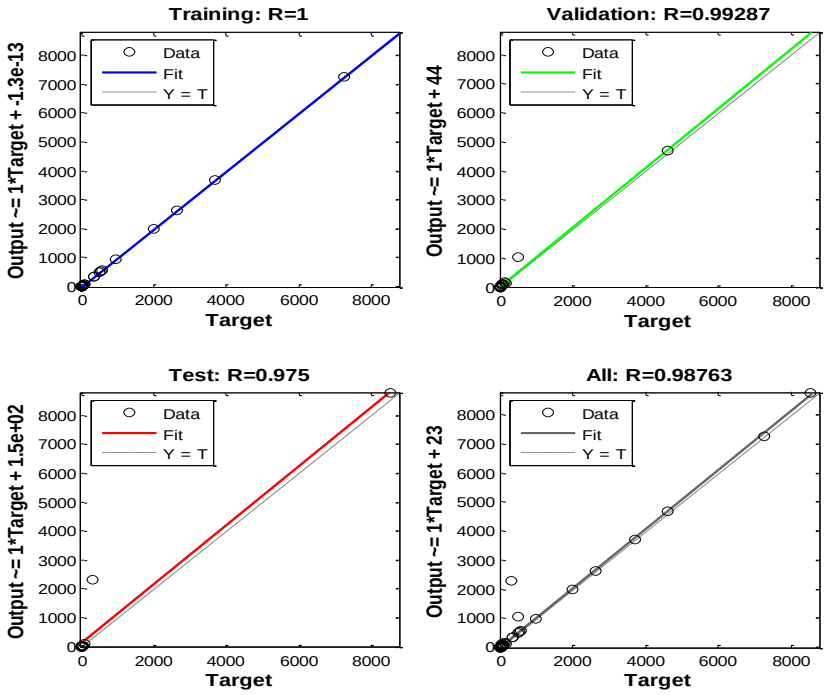

Figure 3. Training, testing and validation first FBNN with regularization.

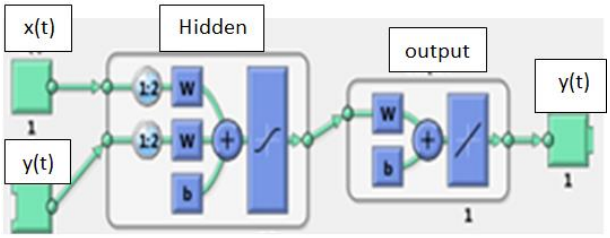

Figure 4. Architecture of the FBNN.

Table 2. Target values for concentration of HM.

Type	Target values	MSE	γ
Training	68	2.31128e -11	9.9999999 e-1
Validation	16	2.52614e -12	9.9999999 e-1
Testing	16	6.69947e -12	9.9999999 e-1

Table 3. The accuracy of the train for time and epoch.

Train Function	Performance of train	Epoch	Time	μ
Modify Trainlm	2.31e-11	252	00:00:06	1.00e-08

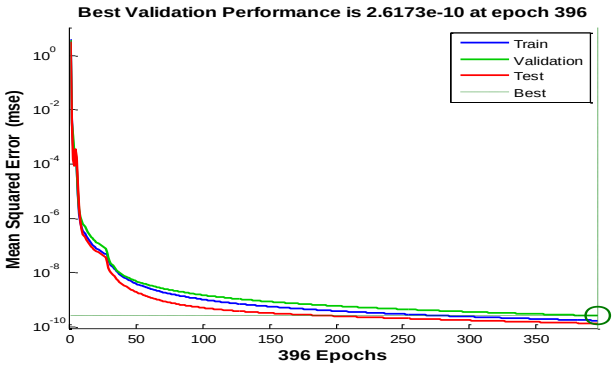

Figure 5. Performance of suggested FBNN for concentration of Cd

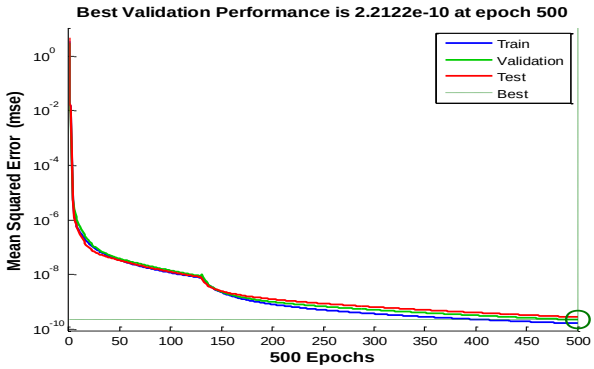

Figure 6. Performance of suggested FBNN for concentration of Ni.

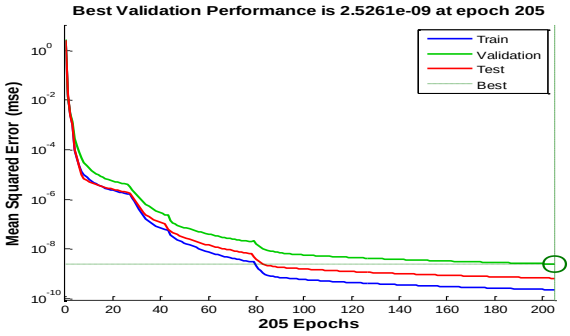

Figure 7. Performance of suggested FBNN for concentration of Pb

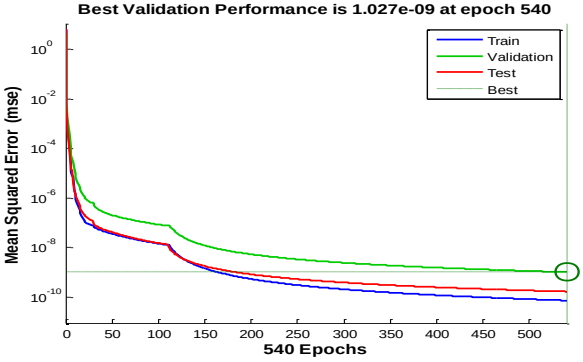

Figure 8. Performance of suggested FBNN for concentration of Zn

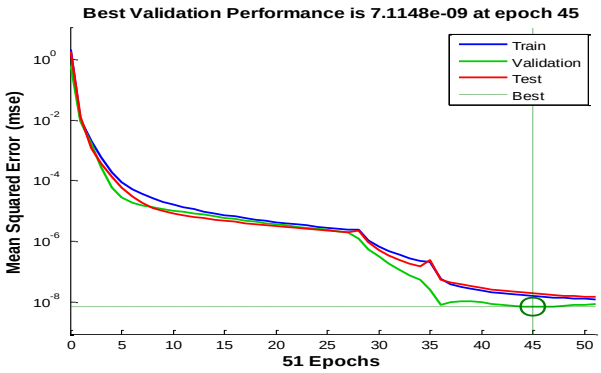

Figure 9. Performance of suggested FBNN for concentration of Cu

We applied the suggested design in Al- Zafaraniyah zone in Baghdad. Then comparing these results with that obtained by XRF which are illustrated in 'figure 10'.

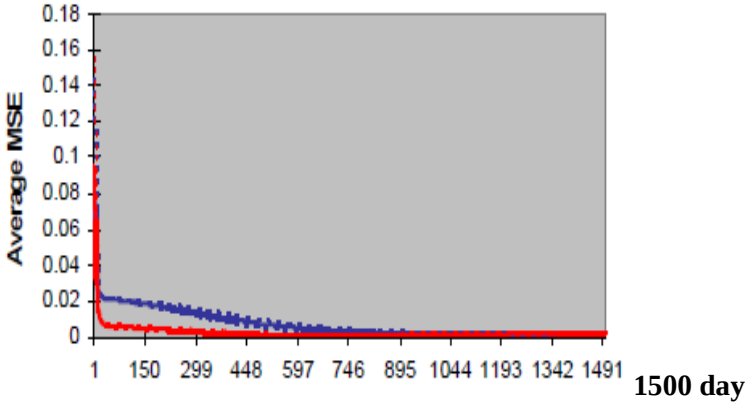

Figure 10. A Comparing of the concentration calculated by FBNN (blue curve) and by XRF (read curve).

5. Heavy metals and their effect on health

In nature there are 35 elements classified as metals, which of only 23 are HMs. This label appeared in the 1960s and was used to denote elements and compounds containing high atomic mass or high density metals and have adverse effects on healthy and the environment. It was initially named heavy metals, most of which had a higher density or an atomic mass than the carbon element, while the other metals were added to the list because they were similar in their properties to these minerals. Some HMs are found in nature, such as iron and copper, some of which are found at a lower rate such as gold, silver, chromium and lead. Heavy metals have been found to be of varying degrees of toxicity. The damage caused by them varies. Some of them affect the senses, including what affects the nerves, and internal members. Heavy metal compounds are used in a large number of applications for their excellent physical and chemical properties. They are good conductors of heat and electric current and their compounds are colored and have high stability. They are not affected by rapid weather conditions. They are highly susceptible to roads, clouds and formation. However, the most important result is the toxins that affect plants, humans and animals. Compounding the complexity of the problem is that it builds accumulative concentrations within the body, whether in the liver, muscle or fat, which increases the likelihood of human exposure to damage without knowing the direct cause [6].

6. Conclusion

The Scientific results showing the following:

- For comparing upon the depth of soil, we see the effect of depth on the concentration of HMs that are when the depth increase the concentrations of HMs are decrease, i.e., the concentration of HMs in depth 0 – 20 cm are larger than the concentration in depth 20 – 40 cm for the same soil.

- The developed of this model can be considered to be a good representation of that estimate the concentrations of HMs in the soil for any depth.
- The prediction errors of this technique are less than 10% compared with those of XRF. This technique is fast, convenient, sensitive, and can eliminate the interference among various species.

References

[1] Quarteroni A 2009 Mathematical Models in Science and Engineering Notices of the AMS **56** 1
[2] Buszewski B and Kowalkowski T 2006 A new model of heavy metal transport in the soil using non-linear artificial neural networks Journal of environmental engineering science **23** 4 pp 589-595
[3] Yetilmezsoy K and Demirel S 2008 Artificial Neural Network approach for modeling of Pb adsorption from aqueous solution by Antep pistachio (pistacia vera L.) shells Journal of Hazardous Materials **153** 3 pp.1288-1300
[4] Kardam A Raj K R Arora J K Srivastava M M and Srivastava S 2010 Artificial Neural Network Modeling for Sorption of Cadmium from Aqueous system by Shelled Moringa Oleifera Seed (SMOS) powder as an Agricultural waste Journal of Water Resource and Protection **2** 4 pp 339-344.
[5] Yin Li Chao-kui Li Jian-junTao and Li-dong Wang 2011 Study on Spatial Distribution of Soil Heavy metals in Huizhou city Based on BP- Artificial Neural Network Modeling and GIS Procedia Environmental Sciences Journal **10** part c pp1953-1960
[6] El Badaoui H Abdallaoui A Manssouri I and Lancelot L 2013Application of Artificial Neural Networks of MLP type for the prediction of the levels of Heavy Metals in Moroccan Aquatic Sediments International Journal of Computational Engineering Research **3** 6 pp 75-81.
[7] Pandharipande S L Deshmukh A R and Kalnake R 2013 Artificial Neural Network Modeling for Estimation of concentration of Ni (ll) and Cr (Vl) present in Aqueous Solution International Journal of Advances in Engineering & Technology **5** 2 pp 122-131 2231-1963
[8] Krishnaa D and Sree R P 2014 Artificial Neural Network (ANN) Approach for Modeling Chromium (VI) Adsorption From Aqueous Solution Using a Borasus Flabellifer Coir Powder International Journal of Applied Science and Engineering **12** 3 pp177-192
[9] Zongshu Wu Jiaoyan Ai Chaobing Deng Yajuan Cai and Zongming Wei 2015 Method for Optimal Arrangement of Soil Sampling Based on Neural Networks and Genetic Algorithms International Conference on Automation, Mechanical Control and Computational Engineering (AMCCE) 124 1951-6851
[10] Madhloom H M 2015 Modeling of Copper removal from simulated wastewater by adsorption on to fungal biomass using artificial neural network Global Journal on Advances in Pure & Applied Sciences **5** pp 35-44
[11] Tawfiq L N M Jasim K A and Abdulhmeed E O 2015 Mathematical Model for Estimation the Concentration of Heavy Metals in Soil for Any Depth and Time and its Application in Iraq International Journal of Advanced Scientific and Technical Research **4** 5 pp 718-726
[12] Luma N M T and Farah F G 2016 Mathematical model for estimation the concentration of heavy metals in soil MJ Journal on Applied Mathematics **1** 1 pp 16-19
[13] Amacher M C Kotuby-Amacher J Selim H M and Iskandar I K 1986 Retention and release of metals by soils--evaluation of several models Geoderma Science Direct **38** 1-4 pp 131-154.
[14] Selim H M Amacher M C and Iskandar L K 1990 Modeling the Transport of Heavy Metals in Soils, Monograph 90-2 U S army corps of engineering.
[15] Luma N M T and Farah F G 2016 New Technique to Estimate the Concentration of Heavy Metals in Soil Lap Lambert Academic Publishing Isbn-1: 978-3-659-87155-9.
[16] Luma N M T and Farah F G 2017 Heavy Metals Pollution in Soil and Its Influence in South of Iraq, International Journal of Discrete Mathematics **2** 3 pp 59-63

Action of Groups on the Projective Plane over the Field *GF*(41)

IOP Conf. Series: Journal of Physics: Conf. Series **1003** (2018) 012059 doi:10.1088/1742-6596/1003/1/012059

Action of Groups on the Projective Plane over the Field $GF(41)$

Emad Bakr Al-Zangana, Saja Abd Joudah

Department of Mathematic, College of Science–Mustansiriyah University, Iraq.

e.b.abdulkareem@uomustansiriyah.edu.iq, saja94.abd@gmail.com

Abstract. An k-arc is a set of k points of a projective plane such that some 2, but no 3 of them, are collinear. In this paper, an 5- arc of stabilizer group of type dihedral group of degree five, D_5 with five collinear points has been found in $PG(2,41)$. From this 5-arc, a unique 6-arc of stabilizer group of type alternating group of degree five, A_5 with ten B-points is found. Finally, the effects of D_5 and A_5 on the points of $PG(2,41)$ are discussed.

1. Introduction

Let $GF(q)$ denote the Galois field of q elements and $V(3,q) = \{(a_1, a_2, a_3) | a_i \in GF(q)\}$ be the respective vector space of row vectors of length three with entries in $GF(q)$. Let $PG(2,q)$ be the projective plane over the field $GF(q)$. The subspace of $PG(2,q)$ of dimension one is the zero set of the form of degree one

$$V(aX_0 + bX_1 + cX_2)$$

Which is called lines and the zero set of the form F of degree two:

$$V(F) = V(aX_0^2 + bX_1^2 + cX_2^2 + dX_0X_1 + eX_0X_2 + fX_1X_2)$$

It is called *plane quadric*. The number of points dually; the number of lines in $PG(2,q)$ is $q^2 + q + 1$. There are $q + 1$ points on each line dually; there are $q + 1$ lines passes through a point. For an introduction to coverings of vector spaces over finite fields and to the concept of projective plane, see [1, 2].

There are 1723 points and lines in $PG(2,41)$, 42 points on every line and 42 lines passing through each point.

Let α be the primitive element in $GF(41)$. The following matrix:

$$T = \begin{bmatrix} 0 & 1 & 0 \\ 0 & 0 & 1 \\ \alpha^{39} & 1 & 1 \end{bmatrix}$$

has been used to construct the points and lines of $PG(2,41)$ by the following way:

The points are $P(i) = [1,0,0]T^{i-1}$ and the lines are $\ell_i = \ell_1 T^{i-1}$, $i = 1, \dots, q^2 + q + 1$

Where $\ell_1 = V(X_2)$ be the line passing through points $P(X_0, X_1, X_2)$ with $X_2 = 0$. For detailed description of the representation of points and lines representations see [1, Chap. 4].

Definition 1.1[1]: A k-arc K or arc of degree 2 in $PG(2,q)$ with $k \geq 3$ is a set of k points such that every lines meets K in at most two points and there is some lines meeting K in exactly two points.

Definition 1.2 [1]: A line ℓ of $PG(2,\ q)$ is an i-secant of an k-arc K if $|\ell \cap K| = i$. A 2-secant is called a *bisecant*, a 1-secant a *unisecant* and a 0-secant is an *external line*. The number of bisecants through a point Q out of K is called the index of Q with respect to K.

Let c_i be the number of points of $PG(2,q)\backslash K$ with index exactly i. A point of index three is called a *Brianchon point* or B*-point* for short. The arc is called *complete* if $c_0 = 0$.

During this research, write $ij \cdot kl \cdot mn = P_iP_j \cap P_kP_l \cap P_mP_n$ for B-point. Some finite groups that appear in this research are listed below.
I = Trivial group.
C_n= Cyclic group of order n.
S_n= Symmetric group of degree n.
A_n= Alternating group of degree n.
D_n= Dihedral group of order $2n = \langle r, s | r^n = s^2 = (rs)^2 = 1 \rangle$.
For details and full descriptions about above groups of order less than 32, see [3].

In [1], a full classification and details of arcs in $PG(2,9)$ shows that there is a unique 5-arc with stabilizer group isomorphic to the dihedral group of degree five and a unique 6-arc with stabilizer group isomorphic to the alternating group of degree 5 with ten B-points. In [4], the same results have been obtained. In [5], theoretically existence of this 5-arc and 6-arc are proved. Also, there are many mathematicians study the effects of group on the projective plane as in [6]. In [7][8], the action of the groups D_5 and A_5 on the points of the projective plane over $GF(q), q = 19,29,31$ are studied.

The first aim of this paper is to compute the inequivalent 5-arcs and then show that there is a unique 5-arc in $PG(2,41)$ with stabilizer group isomorphic to D_5 with five collinear points. The second goal is to find the 6-arcs and to show that there is a unique 6-arc stabilized by group isomorphic to A_5 with ten B-points. The third aim is to examine the action of the groups D_5 and A_5 on the points of $PG(2,41)$.

2. Pentastigm with Collinearities of its Diagonal Points

Definition 2.1[1]: An k-stigm K in $PG(2,q)$ is a set of k points, no three of which are collinear, together with the $\frac{1}{2}k(k-1)$ lines that are join of pairs of the points. The points and lines are called vertices and sides of K, respectively. The intersection points of two sides of K which do not pass through the same vertex is called diagonal points.

During this research, the terminology pentastigm are used instead of a 5-stigm and write $ij \cdot kl$ instead of $P_iP_j \cap P_kP_l$.

Since the vertices of K form an n-arc, so, to construct a 5-stigm, started with unique projectively 4-arc, $\Gamma_{41} = \{U_0, U_1, U_2, U\}$ (*standard frame*) in $PG(2,q)$ which has stabilizers group isomorphic to S_4, where

$$U_0 = [1,0,0],\ U_1 = [0,1,0],\ U_2 = [0,0,1], U = [1,1,1].$$

By adding one point of index zero with respect to Γ_{41}, the 5-arcs have been constructed and the inequivalent ones have been found using mathematical programming language GAP.

Theorem 2.2: In $PG(2,41)$, there exist eighteen inequivalent 5-arcs through the frame Γ_{41} with parameters $[c_0, c_1, c_2] = [1333,370,15]$ as summarized in (table 1).

Table 1. Inequivalent 5-arc and their stabilizer group

No.	5-Arc	Stabilizer group types with its generators
1	$\mathcal{A}_1 = \Gamma_{41} \cup \{P(\alpha^{13}, \alpha^{12}, 1)\}$	I
2	$\mathcal{A}_2 = \Gamma_{41} \cup \{P(\alpha^{17}, \alpha^{22}, 1)\}$	$C_2 = \langle[[1,1,1],[0, \alpha^{12}, 0],[\alpha, \alpha^{37}, \alpha^2, \alpha^{20}]]\rangle$
3	$\mathcal{A}_3 = \Gamma_{41} \cup \{P(\alpha^{38}, \alpha^4, 1)\}$	I
4	$\mathcal{A}_4 = \Gamma_{41} \cup \{P(\alpha^{22}, \alpha^{13}, 1)\}$	$C_2 = \langle[[1,1,1],[0, \alpha^{36}, 0],[\alpha^2, \alpha^{33}, \alpha^{20}]]\rangle$
5	$\mathcal{A}_5 = \Gamma_{41} \cup \{P(\alpha^{35}, \alpha^{37}, 1)\}$	I
6	$\mathcal{A}_6 = \Gamma_{41} \cup \{P(\alpha^{38}, \alpha^{11}, 1)\}$	I
7	$\mathcal{A}_7 = \Gamma_{41} \cup \{P(\alpha^{32}, \alpha^{23}, 1)\}$	I
8	$\mathcal{A}_8 = \Gamma_{41} \cup \{P(\alpha^{11}, \alpha^{7}, 1)\}$	$C_2 = \langle[[0,0,1],[\alpha^{20}, \alpha^{20}, \alpha^{20}],[1,0,0]]\rangle$
9	$\mathcal{A}_9 = \Gamma_{41} \cup \{P(\alpha^6, \alpha^{16}, 1)\}$	I
10	$\mathcal{A}_{10} = \Gamma_{41} \cup \{P(\alpha^{26}, \alpha^{13}, 1)\}$	$C_2 = \langle[[0,0,\alpha^{20}],[0,\alpha,^{33}\ 0],[\alpha^6,0,0]]\rangle$
11	$\mathcal{A}_{11} = \Gamma_{41} \cup \{P(\alpha^{35}, \alpha^{11}, 1)\}$	$C_2 = \langle[[\alpha^8,0,0],[\alpha,^{15}\alpha^{31}, \alpha^{20}],[\alpha,^{11}\ \alpha^{11}, \alpha^{11}]]\rangle$
12	$\mathcal{A}_{12} = \Gamma_{41} \cup \{P(\alpha^{32}, \alpha^{39}, 1)\}$	$C_2 = \langle[[\alpha^{39}, \alpha^{39}, \alpha^{39}],[\alpha^{12}, \alpha^{19}, \alpha^{20}],[0,0,\alpha^{21}]]\rangle$
13	$\mathcal{A}_{13} = \Gamma_{41} \cup \{P(\alpha^{25}, \alpha^{14}, 1)\}$	$C_2 = \langle[[\alpha^5, \alpha^{34}, \alpha^{20}],[0,0,\alpha^{11}],[0,\alpha^{39},0]]\rangle$
14	$\mathcal{A}_{14} = \Gamma_{41} \cup \{P(\alpha^{36}, \alpha^{15}, 1)\}$	I
15	$\mathcal{A}_{15} = \Gamma_{41} \cup \{P(\alpha^{14}, \alpha^{32}, 1)\}$	$C_4 = \langle[[0,0,1],[0,\alpha^{32},0],[\alpha^{34}, \alpha^{12}, \alpha^{20}]]\rangle$
16	$\mathcal{A}_{16} = \Gamma_{41} \cup \{P(\alpha^{16}, \alpha^{22}, 1)\}$	I
17	$\mathcal{A}_{17} = \Gamma_{41} \cup \{P(\alpha^{39}, \alpha, 1)\}$	$D_5 = \langle r = [[\alpha,0,0],[1,1,1],[\alpha^{19}, \alpha^{21}, \alpha^{20}]]$ $s = [[0,\alpha^{22},0],[\alpha^{19}, \alpha^{21}, \alpha^{20}],[1,1,1]]\rangle$
18	$\mathcal{A}_{18} = \Gamma_{41} \cup \{P(\alpha^{34}, \alpha^{22}, 1)\}$	$C_2 = \langle[[\alpha^{37},0,0],[\alpha^{14}, \alpha^2, \alpha^{20}],[\alpha^{22}, \alpha^{22}, \alpha^{22}]]\rangle$

The condition to existence a pentastigm with five diagonal points are collinear in $PG(2,q)$ is that $x^2 - x - 1 = 0$ has solution in F_q [6]. Therefore, the following corollary holds.

Corollary 2.3: If $q = 41$, the equation $x^2 - x - 1 = 0$ has two solutions α^{21}, α^{39}, that is; $PG(2,41)$ has a pentastigm with five collinear diagonal points.

Theorem 2.4: In $PG(2,41)$, the pentastigm which has the 5-arc $\mathcal{A}_{17}$ as vertices has five diagonal points which are collinear on the line $\ell_{1562} = V(\alpha^{21}X_0 - X_1 + X_2)$ as shown below:

The diagonal points exactly are the points of index 2. Therefore, any 5-stigm has fifteen 15 diagonal.

(1) $01 \cdot 23 = P(1,1,0)$, (6) $02 \cdot 34 = P(0,\alpha,1)$, (11) $04 \cdot 13 = P(\alpha^{38},1,1)$,

(2) $01 \cdot 24 = P(1,0,1)$, (7) $03 \cdot 12 = P(\alpha^{19},1,0)$, (12) $04 \cdot 23 = P(\alpha,\alpha,1)$,

(3) $01 \cdot 34 = P(0,1,1)$, (8) $03 \cdot 14 = P(\alpha^{39},1,1)$, (13) $12 \cdot 34 = P(0,\alpha^{39},1)$,

(4) $02 \cdot 13 = P(\alpha^{38},1,0)$, (9) $03 \cdot 24 = P(1,\alpha,1)$, (14) $13 \cdot 24 = P(1,\alpha^{2},1)$,

(5) $02 \cdot 14 = P(\alpha^{39},0,1)$, (10) $04 \cdot 12 = P(\alpha^{38},0,1)$, (15) $14 \cdot 23 = P(\alpha^{39},\alpha^{39},1)$.

The only line which passes through the five diagonal points is

$$\ell_{1562} = \mathrm{V}(\alpha^{21}\mathrm{X}_0 - \mathrm{X}_1 + \mathrm{X}_2)$$

And the points are given below.

$$01 \cdot 34 = P(0,1,1) = 1562,$$
$$02 \cdot 14 = P(\alpha^{39},0,1) = 782,$$
$$03 \cdot 12 = P(\alpha^{19},1,0), = 1240,$$
$$04 \cdot 23 = P(\alpha,\alpha,1) = 322,$$
$$13 \cdot 24 = P(1,\alpha^{2},1) = 279.$$

3. Action of D_5 on $PG(2,41)$

Definition 3.1[1]: A non-singular plane quadric is called a *Conic*

In $PG(2,q)$, with $q \geq 4$, and there is a unique conic through a 5-arc [2]. Therefore, in $PG(2,41)$, from the 5-arc $\mathcal{A}_{17}$there is a unique conic through it as given bellow.

$$\begin{aligned} C_{\mathcal{A}_{17}} = & \quad V(X_0X_1 + \alpha^{20}X_0X_2 - \alpha^{20}X_1X_2) \\ = & \quad \{\alpha^{21}(t^2 - \alpha^{13}t), \alpha^{8}(1 - \alpha^{27}t), \alpha^{13}t | t \in F_{41} \cup \{\infty\}\}. \end{aligned}$$

From (Table 1), the Dihedral group D_5 generated by

$$r = \begin{bmatrix} \alpha & 0 & 0 \\ 1 & 1 & 1 \\ \alpha^{19} & \alpha^{12} & \alpha^{20} \end{bmatrix}, s = \begin{bmatrix} 0 & \alpha^{22} & 0 \\ \alpha^{19} & \alpha^{21} & \alpha^{20} \\ 1 & 1 & 1 \end{bmatrix}$$

Which stabilized the 5-arc $\mathcal{A}_{17}$ has the following effects on the points of $PG(2,41)$.

1- Fixes the conic $C_{\mathcal{A}_{17}}$.

2- Acts transitively on $\mathcal{A}_{17}$ since

$$(U_0, rs) \mapsto U_1,$$
$$(U_0, rs^3) \mapsto U_2,$$
$$(U_0, rs^4) \mapsto U,$$
$$(U_0, rs^2) \mapsto P(\alpha^{39}, \alpha, 1) = 112.$$

3- The elements of D_5 divided into two classes according to fixing points of $PG(2,41)$ by sending each point to itself as illustrated bellow.

Class 1: The five elements r, rs, rs^2, rs^3, rs^4 of order two fixes 43 points if acts on $PG(2,41)$ which is exactly line plus the diagonal point of $\mathcal{A}_{17}$

	$\ell_i \cup P_j$
r	$\ell_{320} \cup P(1,\alpha^2,1)$
rs	$\ell_3 \cup P(\alpha^{19},1,0)$
rs^2	$\ell_{375} \cup P(\alpha,\alpha,1)$
rs^3	$\ell_{807} \cup P(\alpha^{39},0,1)$
rs^4	$\ell_{292} \cup P(0,1,1)$

and 37 points if acts on the points of index zero which is precisely line with five points excluded.

	$\ell_i \setminus \{P_1, P_2, P_3, P_4, P_5\}$
r	$\ell_{320} \setminus \{P(1,0,0), P(1,\alpha^{39},1), P(\alpha^{37},\alpha^{39},1), P(0,\alpha^{39},1), P(\alpha^{39},\alpha^{39},1)\}$
rs	$\ell_3 \setminus \{P(0,0,1), P(\alpha^{39},1,1), P(1,\alpha,1), P(\alpha^{39},1,0), P(\alpha^{12},\alpha^{13},1)\}$
rs^2	$\ell_{375} \setminus \{P(0,1,0), P(\alpha^{38},1,1), P(\alpha^{38},\alpha^{38},1), P(\alpha^{38},0,1), P(\alpha^{38},\alpha,1)\}$
rs^3	$\ell_{807} \setminus \{P(\alpha^{39},\alpha^{27},1), P(1,1,1), P(0,\alpha,1), P(\alpha^{19},0,1), P(\alpha^{38},1,0)\}$
rs^4	$\ell_{292} \setminus \{P(\alpha^{39},\alpha,1), P(0,\alpha^{20},1), P(\alpha^{26},1,1), P(1,1,0), P(1,0,1)\}$

4- The lines ℓ_i, $i = 3,292,320,375,807$ have the property that unisecant to $\mathcal{A}_{17}$ and bisecant to $C_{\mathcal{A}_{17}}$.
Class 2: Each of the four element s, s^2, s^3, s^4 of order five fixes three points one of the points is $P(\alpha^{38}, \alpha^{39}, 1)$ which is the intersection point of the five lines ℓ_i, $i = 3,292,320,375,807$.

4. An 6-Arc with Stabilizer Group of Type A_5

The 6-arcs are computed after the action of the stabilizer groups on the points of index zeros. Then the in equivalent are founded as illustrated with details in the following theorem.
Theorem 4.1: In $PG(2,41)$, there are 2948 in equivalent 6-arcs through Γ_{41}. The stabilizers of the 6-arcs are partitions as given below.

2606: I
191: C_2
100: C_3
8:V_4; 9:C_4
1: C_5
22:S_3
8:A_4; 1:D_6
1:S_4
1:A_5

The unique 6-arc K with stabilizer group A_5 is just $\mathcal{A}_{17}$ union the intersection point of the lines ℓ_i, $i = 3, 292, 320, 375, 807$. The arc K in numeral form is

$$K = \{1,2,3,323,112,443\},$$

And its stabilizer group A_5 is given below.

$$A_5 = \langle a, b | a^2 = b^3 = (ab)^5 = 1 \rangle, \text{ where}$$

$$a = \begin{bmatrix} \alpha^{20} & 0 & 0 \\ 0 & 0 & \alpha^{20} \\ 0 & \alpha^{20} & 0 \end{bmatrix}, b = \begin{bmatrix} 0 & \alpha & 0 \\ \alpha^{20} & \alpha^{20} & \alpha^{20} \\ \alpha^{39} & \alpha & 1 \end{bmatrix}.$$

There are fifteen ways to choose three bisecants no two of which intersect on K as shown below.

$$(1)\ 12 \cdot 34 \cdot 56$$
$$(2)\ 12 \cdot 35 \cdot 46$$
$$(3)\ 12 \cdot 36 \cdot 45$$
$$(4)\ 13 \cdot 24 \cdot 56$$
$$(5)\ 13 \cdot 25 \cdot 46$$
$$(6)\ 13 \cdot 26 \cdot 45$$
$$(7)\ 14 \cdot 23 \cdot 56$$
$$(8)\ 14 \cdot 25 \cdot 36$$
$$(9)\ 14 \cdot 26 \cdot 35$$
$$(10)\ 15 \cdot 23 \cdot 46$$
$$(11)\ 15 \cdot 24 \cdot 36$$
$$(12)\ 15 \cdot 26 \cdot 34$$
$$(13)\ 16 \cdot 23 \cdot 45$$
$$(14)\ 16 \cdot 24 \cdot 35$$
$$(15) 16 \cdot 25 \cdot 34$$

These possibilities divided into two parts:

Part 1: Ten possibilities forms B-points as shown below.

(1) $12 \cdot 34 \cdot 56 = P(1,1,0) = 1561$

(2) $12 \cdot 35 \cdot 46 = P(\alpha^{38}, 1,0) = 1481$

(3) $13 \cdot 24 \cdot 56 = P(1, 0,1) = 1693$.

(4) $13 \cdot 26 \cdot 45 = P(\alpha^{38}, 0,1) = 1049$.

(5) $14 \cdot 25 \cdot 36 = P(\alpha^{39}, 1,1) = 4$.

(6) $14 \cdot 26 \cdot 35 = P(\alpha^{38}, 1,1) = 498$.

(7) $15 \cdot 23 \cdot 46 = P(0, \alpha, 1) = 485$.

(8) $15 \cdot 24 \cdot 36 = P(1, \alpha, 1) = 486$.

(9) $16 \cdot 23 \cdot 45 = P(0, \alpha^{39}, 1) = 947$.

(10) $16 \cdot 25 \cdot 34 = P(\alpha^{39}, \alpha^{39}, 1) = 1265$.

Let $K_{10} = \{4,485,486,498,947,1049,1265,1481,1561,1693\}$, set of B-points.

Theorem 4.1:

(i) The set K_{10} form incomplete 10-arc.

(ii) The set K_{10} partitions the 1723 lines of $PG(2,41)$ into 1348 external lines, 330 tangent lines and 45 bisecants lines.

(iii) K_{10} has parameters $[c_0, c_1, c_2, c_3, c_4, c_5] = [372, 1020, 210, 90, 15, 6]$.

Part 2: The remaining five possibilities constitute triangles, as shown below.

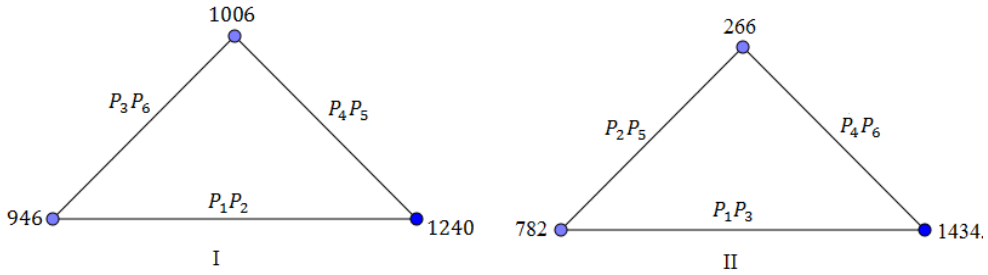

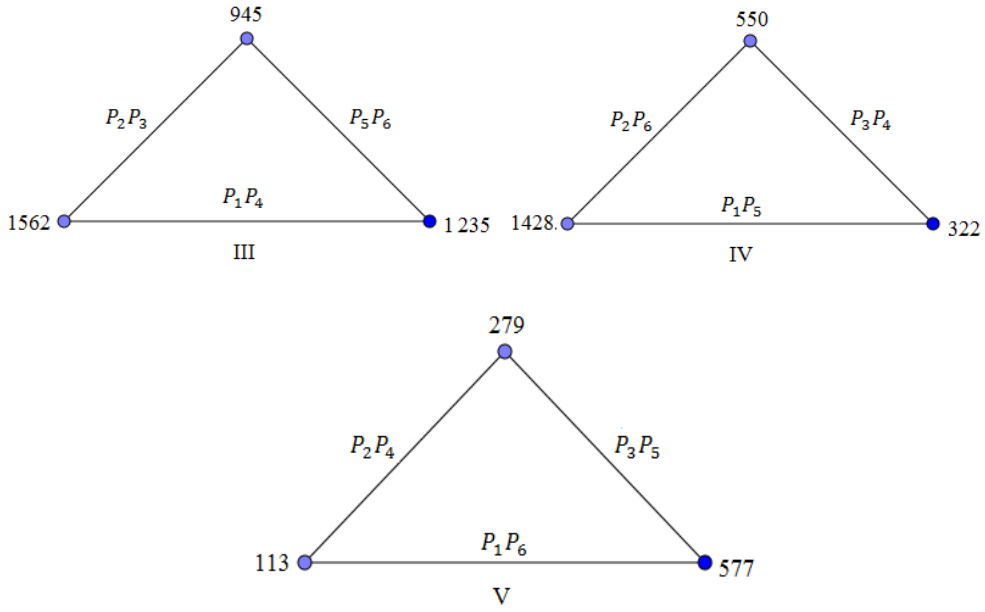

Where

$P_1P_2 = V(X_2)$ $P_3P_6 = V(\alpha^{19}X_0 - \alpha^{38}X_1)$ $P_4P_5 = V(\alpha^2X_0 - \alpha^{21}X_1 + \alpha^{20}X_2)$

$P_1P_3 = V(X_1)$ $P_2P_5 = V(X_0 + \alpha^{39}X_2)$ $P_4P_6 = V(\alpha^{21}X_0 - \alpha^{19}X_1 + \alpha^{20}X_2)$

$P_1P_4 = V(X_2 - X_1)$ $P_2P_3 = V(X_0)$ $P_5P_6 = V(\alpha^{20}X_0 - \alpha^{20}X_1 + X_2)$

$P_1P_5 = V(\alpha X_2 - X_1)$ $P_2P_6 = V(X_0 + \alpha^{38}X_2)$ $P_3P_4 = V(X_0 - X_1)$

$P_1P_6 = V(X_2 - \alpha^{39}X_1)$ $P_2P_4 = V(X_0 + X_2)$ $P_3P_5 = V(\alpha^{39}X_1 - \alpha X_0)$

And vertices of each triangle are given in numeral form.

Let the set of five triangles denote by $M = \{\mathrm{I}, \mathrm{II}, \mathrm{III}, \mathrm{IV}, \mathrm{V}\}$. The stabilizer group A_5 of K_{10} also fixes the set M of five triangles.

Example 4.2: The action of A_5 on I partition A_5 into five disjoint classes with twelve elements in each class as given below.

Class $1 = \{g \epsilon A_5 \mid g\mathrm{I} = \mathrm{I}\}$
I
$b \cdot bab$
$(abab^2)^4 \cdot (abab^2)^4$
$a \cdot (abab^2)^3$
$a \cdot (ab)^4$
$b \cdot abab^2$
$a \cdot (ab^2)^4$
$a \cdot (bab)^2$
$b \cdot (ab^2)^2$
$ab \cdot (abab^2)^3$
$(ab)^2 \cdot (ab^2)^2$
$(ab)^4 \cdot (abab^2)^4$

Class 2 = $\{g \epsilon A_5 \mid g\mathrm{I} = \mathrm{II}\}$
$b \cdot (ab)^4$
$b^2 \cdot (bab)^2$
$b \cdot (ab^2)^4$
$b \cdot (bab)^2$
$(ab)^3 \cdot (ab^2)^3$
$(bab)^3 \cdot (ab)^2$
$b \cdot a$
$(ab)^2 \cdot (abab^2)^2$
$(ab^2)^2 \cdot abab^2$
$b^2 \cdot (abab^2)^3$
$ab \cdot (ab^2)^2$
$b \cdot (abab^2)^3$
Class 3 = $\{g \epsilon A_5 \mid g\mathrm{I} = \mathrm{III}\}$
$(ab^2)^4 \cdot (abab^2)^3$
$(ab^2)^2 \cdot (abab^2)^2$
$(ab)^2 \cdot (abab^2)^3$
$ab^2 \cdot (ab^2)^2$
$(ab)^3 \cdot bab$
$a \cdot (ab^2)^3$
$a \cdot b$
$a \cdot ab$
$a \cdot (bab)^3$
$a \cdot (abab^2)^4$
$b^2 \cdot (ab)^3$
$b^2 \cdot abab^2$
Class 4 = $\{g \epsilon A_5 \mid g\mathrm{I} = \mathrm{IV}\}$
$ab \cdot (ab^2)^3$
$b \cdot (abab^2)^2$
$(ab)^3 \cdot (bab)^2$
$(ab)^3 \cdot (ab^2)^4$
$a \cdot bab$
$a \cdot b^2$
$b^2 \cdot (abab^2)^2$
$bab \cdot (ab^2)^3$
$a \cdot (ab^2)^2$
$b^2 \cdot (ab)^2$
$a \cdot (ab)^3$
$a \cdot abab^2$
Class 5 = $\{g \epsilon A_5 \mid g\mathrm{I} = \mathrm{V}\}$
$b \cdot (ab^2)^3$
$ab \cdot (abab^2)^2$
$a \cdot (ab)^2$
$a \cdot ab^2$
$a \cdot (abab^2)^2$

$(ab^2)^3 \cdot (ab)^4$
$(ab)^4 \cdot (abab^2)^3$
$(ab)^2 \cdot (ab^2)^3$
$b \cdot (abab^2)^4$
$b \cdot (bab)^3$
$a \cdot (bab)^4$
$(ab)^2 \cdot (abab^2)^4$

Theorem 4.3[5]: When $q = \pm 1 \pmod{10}$, then the set
$K^* = \{(1,0,1-2t), (1,0,2t-1), (1,2t,0), (1,-2t,0), (0,1,2t), (0,1,-2t)\}$,
when $4t^2 - 2t - 1 = 0$, constitute a 6-arc fixed by A_5.

Corollary 4.4:
1- In $GF(41)$, the equation $4t^2 - 2t - 1 = 0$ has two solutions, α^{13} and α^{35}.
2- For $t = \alpha^{13}$, the 6-arc
$K^* = \{(1, 0, \alpha^{21}), (1, 0, \alpha), (1, \alpha^{39}, 0), (1, \alpha^{19}, 0), (0,1, \alpha^{39}), (0,1, \alpha^{19})\}$
is equivalent to the 6-arc K by the matrix transformation:

$$T^* = \begin{bmatrix} \alpha^{28} & \alpha^{9} & 0 \\ \alpha^{26} & \alpha^{27} & \alpha^{14} \\ \alpha^{7} & \alpha^{8} & 0 \end{bmatrix}.$$

5. Conclusion

The effect of the stabilizer group D_5 of the unique 5-arc $\mathcal{A}_{17}$ on the points of $PG(2,41)$ depends on the order of its elements as follows.

(i) Let G^2 be the set of the five elements of D_5 of order two and G^5 be the set of four elements of D_5 of order five.

(ii) Each element of G^2 fixes a subset of the plane $PG(2,41)$ of length 43 by sending it to itself. These sets are exactly lines ℓ_i^* with extra points $P_i^*, i = 1, \ldots, 5$. The five extra points P_i^* are just the diagonal points of $\mathcal{A}_{17}$ and the lines ℓ_i^* are bisecants of the conic $C_{\mathcal{A}_{17}}$ and unisecants of $\mathcal{A}_{17}$.

(iii) Each element of G^5 fix three points, one of the points, P^*, is just the intersection point of the five lines ℓ_i^*.

6. Open Problem

Prove that, in $PG(2,q)$, $q \equiv \pm 1 \pmod{10}$, there is a unique 5-arc, $\mathfrak{D}$, fixed by group of type D_5 and a unique 6-arc, $\mathfrak{R}$, with the following properties.
Let G^2 be a set of the five elements of D_5 of order two and G^5 be a set of four elements of D_5 of order five.

(i) Each element of G^2 fix $q+2$ points of $PG(2,q)$ by sending each point to itself which is line, ℓ_i^*, union diagonal point of $\mathfrak{D}$, P_i^*.

(ii) Each element of G^2 fix $q-4$ points of index zero with respect to $\mathfrak{D}$ which is the line ℓ_i^* excluded five points.

(iii) Each element of G^5 fix
(a) if $q \equiv 1 \pmod{10}$ three points by sending each point to itself one of them is the common point of the five lines ℓ_i^*.
(b) if $q \equiv -1 \pmod{10}$ one points by sending it to itself which is the common point of the five lines ℓ_i^*.

(iv) The five lines ℓ_i^* are unisecant of $\mathfrak{D}$ and bisecant of the unique conic through $\mathfrak{D}$.

(v) The 6-arc $\mathfrak{R}$ is just $\mathfrak{D}$ union common point of the five lines ℓ_i^*.
A special cases of this problem proved for $q = 19,29,31,41$.

References

[1] Hirschfeld J W P 1998 *Projective geometries over finite fields* 2nd Edition Oxford Mathematical Monographs the Clarendon Press Oxford University Press New York
[2] Gallier J 2013 *Geometric methods and applications for computer science and engineering*. 2nd Edition Springer New York Dordrecht Heidelberg London
[3] Thomas A D and Wood G V 1980 Group tables Shiva Mathematics Series. Ser. 2 Devon Print Group Exeter Devon UK
[4] Sadeh A R 1984 Cubics surfaces with twenty seven lines over the eleven elements. Ph.D. Thesis, University of Sussex United Kingdom
[5] Storme L and Maldeghem V 1995 Primitive arcs in $PG(2,q)$. *J. Combin. Theory, Ser*. A **69** pp 200-216.
[6] Lorimer P 1993 The groups A_7, A_8 and a projective plane of order 16 *Australasian Journal of combinatorics* **8** pp 45-51
[7] Al-Zangana E B 2011 The geometry of the plane of order nineteen and its application to error-correcting codes Ph.D Thesis University of Sussex United Kingdom
[8] Al-Zangana E B 2013 Groups effect of types D_5 and A_5 on the points of projective plane over F_q, $q = 29,31$ *Ibn Al-Haitham Jour. for Pure & Appl. Sci.* **26** 3 pp 410-423.

Connecting on the Lattice Based Reductions for Computing the Generators in the ISD Method

Connecting on the Lattice Based Reductions for Computing the Generators in the ISD Method

Ruma K K Ajeena*, Sanaa K Kamal

Mathematics Department, Education College for Pure Sciences, University of Babylon, Iraq.

ruma.usm@gmail.com

Abstract. In this paper, the generalized Lagrange-Gauss reduction method to generate the generators in ISD method has been proposed. The comparison results on using the generalized Lagrange-Gauss reduction method and generalized extended Euclidean algorithm have been determined. As well as, the connection between the generalized Lagrange-Gauss Reduction and generalized extended Euclidean Algorithm to compute reduced bases to form the ISD generators in ISD elliptic scalar algorithm is presented.

Keywords: Elliptic curve cryptography, scalar multiplication, efficiently computable endomorphisms, ISD method, lattice basis reductions methods

1.Introduction

On the lattice basis reduction methods, the transformations of the given lattice bases into good lattice bases have been presented. These good bases consist of linearly independent vectors that reduced into the shortest and closest to orthogonal vectors. Some efficient algorithms have been proposed to achieve this task and getting good bases which are depending on the lattices rank.

The lattice bases of rank 2 in R^2 are reduced by the proposition of Lagrange and Gauss [1,2,3]. The Lagrange and Gauss algorithm (LGA) is implemented with the vectors v1 and v2 as inputs and returns the shortest vectors of v1 and v2. The LGA is closed to extended Euclidean algorithm (EEA) [4,5]. The EEA considered as another efficient way for reducing the lattice bases of rank 2. On the EEA, the reduction can be done with inputs $(n,\lambda),$ for positive integers n and λ with $n \geq \lambda,$ to get a sequence of integers f_i, g_i and h_i such that $nf_i + \lambda g_i = h_i$ for $i = 0,1,2,...,l,l+1,l+2,...,w-1$ with $w > l$ These integers can be used to form the shortest vectors v1 and v2 which considered as the elements in good lattice basis { v1, v2}.

Whereas, the lattice bases of rank 3 can be reduced using the Lenstra, Lenstra and Lov´asz algorithm, which is known by the LLL or L3 algorithm [4,5]. In this paper, our work focuses on the lattice bases of rank 2. The main idea of this research work is to generalize the Lagrange – Gauss algorithm (GLGA) for reducing 2-tuple of lattice bases that is employed to compute the generators in the ISD computation method [7,8,9,10,11,12]. The generalized extended Euclidean algorithm (GEEA) is presented as another efficient generalized algorithm to generate the ISD generators. Comparison results on using these generalized methods are explained by simple example. Based on these results, the connection between generalized methods, GLGA and GEEA can be done easily.

The rest of this paper is organized as follows: Section 2 reviews the mathematical background related to elliptic curves over finite fields and some important facts of lattices. Section 3 gives an explanation of the procedures of reducing the lattice basis in two dimensions. Section 4 discusses the generalized methods of two dimensional lattice bases reduction. Section 5 discusses the generators on the ISD computation method. Section 6 presents the comparison results on using these generalized methods, Lagrange-Gauss reduction method and extended Euclidean algorithm. Section 7 discusses the connection of the generalized Lagrange-Gauss reduction and generalized extended Euclidean algorithm. Finally, the conclusions are given in Section 8.

2.Mathematical background

This section discusses briefly some important mathematical concepts related to our research work in this paper. These concepts include the elliptic curve defined over prime fields and elementary fundamental definitions on lattices.

Definition 2.1.1. Suppose $p > 2, 3$. An elliptic curve E defined over F_p which is defined by

$$E : y^2 \equiv x^3 + cx + d \pmod{p} \tag{1}$$

where $c, d \in F_p$. The $\Delta=4c^3+27d^2 \not\equiv 0 \pmod{p}$ is defined to be a discriminant of E. All points (x,y) that satisfy elliptic curve equation (1) defined over F_p form a set that is given by

$$E(F_p) = \left\{(x, y) : x, y \in F_p, y^2 \equiv x^3 + cx + d \pmod{p}\right\} \cup \{\infty\}, \tag{2}$$

where ∞ is a point at infinity [2,3,4].

Definition 2.1.2. Let $P = (x_1, y_1) \in E(F_p)$ and $Q = (x_2, y_2) \in E(F_p)$, where $P \neq \pm Q$. Then the sum of two points P and Q is $P+Q = (x_3, y_3)$ [4], where

$$\begin{cases} x_3 \equiv \left(\dfrac{y_2 - y_1}{x_2 - x_1}\right)^2 - x_1 - x_2 \pmod{p}, \\ y_3 \equiv \left(\dfrac{y_2 - y_1}{x_2 - x_1}\right)(x_1 - x_3) - y_1 \pmod{p}. \end{cases} \tag{3}$$

Whereas, doubling the point P which lies on E can be computed by $2P = P+P=(x_3, y_3)$, where

$$\begin{cases} x_3 \equiv \left(\dfrac{3x_1^2 + a}{2y_1}\right)^2 - 2x_1 \pmod{p}, \\ y_3 \equiv \left(\dfrac{3x_1^2 + a}{2y_1}\right)(x_1 - x_3) - y_1 \pmod{p}. \end{cases} \tag{4}$$

Definition 2.1.3. Suppose k is a positive integer such that $k \in [1, n-1]$. The scalar multiplication kP on elliptic curve E can be defined by

$$kP = \underbrace{P + P + \cdots + P}_{k\text{-times}}, \tag{5}$$

where P is a point lies on E, which has a prime order n, defined over a prime field F_p [2,3,4].

Definition 2.1.4. Let $\{v_1,...,v_n\}$ be a set of linearly independent vectors in Z^m, with $m \geq n$. The set $\{v_1,...,v_n\}$ generates a lattice

$$L = \left\{ \sum_{i=1}^{n} l_i v_i : l_i \in Z \right\} \tag{6}$$

of linear combinations which are integers v_i. The vectors $v_1,...,v_n$ are called a lattice basis. The parameters n and m are the lattice rank and dimension respectively. A lattice has a full rank if $n = m$ [1,3].

Definition 2.1.5. Let $L \subset Z^m$ be a lattice. A sub-lattice is a subset $L' \subset L$ that is a lattice [1].

Definition 2.1.6. On a lattice L, a basis matrix V is an $n \times m$ matrix. It forms from the rows of the basis vectors v_i. On the row v_i, the $V_{i,j}$ is the $j-$ th entry. So, L can be expressed by

$$L = \{xV : x \in Z^n\}. \tag{7}$$

Lemma 2.1.1. Two $n \times m$ matrices V and V' generate the same lattice L if and only if V and V' are related by a unimodular matrix. In other words, $V' = UV$ where U is an $n \times n$ matrix with integer entries and determinant ± 1 [1].

Definition 2.1.2. Let $L \subset Z^2$ be a lattice. The parameters $\lambda_1, \lambda_2 \in Z$ are successive minima of L if λ_i, for i=1,2, is minimal such that there exist i vectors of linearly independent $v_i \in L, \| v_j \| \leq \lambda_i$ for $1 \leq j \leq i$. So, $0 < \lambda_1 \leq \lambda_2$ [1].

3.Two dimensional lattice basis reduction methods

Suppose $v_1, v_2 \in Z^2$ are two linearly independent vectors, which are a basis for the lattice *L*. The basic idea of the reduction methods on the lattice bases of rank 2 is to reduce the lengths of the basis vectors to be the shortest in compare with the original vectors. One of these reduction methods is Lagrange - Gauss method that will discuss as follows:

3.1The Lagrange-Gauss lattice basis reduction method

With the vectors v_1, v_2 in Z^2, the Lagrange – Gauss reduction idea [1,3] has been explained through the following mathematical concepts.

Definition 3.1.1. An ordered basis $v_1, v_2 \in Z^2$ is Lagrange-Gauss reduced if

$$\|v_1\| \leq \|v_2\| \leq \|v_2 + q v_1\| \text{ for all } q \in Z. \tag{8}$$

Theorem 3.1.1. Let λ_1, λ_2 be the successive minima of L. If L has an ordered basis $\{v_1, v_2\}$ that is Lagrange- Gauss reduced, then $\| v_i \| = \lambda_i$ for i = 1,2. [1].

Definition 3.1.2. Let $v_1, \ldots, v_n$ be the vectors in Z^n. We write $V_i = \| v_i \|^2 = \langle v_i, v_i \rangle$.

On the Lagrange-Gauss algorithm, a crucial ingredient defines by

$$\| v_2 - \mu v_1 \|^2 = V_2 - 2\mu < v_1, v_2 > + \mu^2 V_1 \tag{9}$$

Which is minimised at $\mu = < v_1, v_2 > / V_1$. Replacing v_2 by $v_2 - \lfloor \mu \rfloor v_1$, where $\lfloor \mu \rfloor$ is the nearest integer to μ. On Algorithm (3.1.1), the size of v_2 can be reduced based on v_1. the reduction formula $v_2 - \lfloor \mu \rfloor v_1$ is the familiar operation $h_{i+1} = h_{i-1} - \lfloor h_{i-1} / h_i \rfloor h_i$ that is computed from extended Euclidean algorithm [1].

Lemma 3.1.1. An ordered basis $\{v_1, v_2\}$ is Lagrange-Gauss reduced if and only if

$$\|v_1\| \leq \|v_2\| \leq \|v_2 + v_1\|. \tag{10}$$

Algorithm 3.1.1. Lagrange-Gauss lattice basis reduction method
Input: Basis $v_1, v_2 \in Z^2$ for a lattice L.
Output: Reduced basis (v_1, v_2) for L such that $\| v_i \| = \lambda_i$.

1: Compute $V_1 = \| v_1 \|^2$ and $\mu = < v_1, v_2 > / V_1$.
2: Calculate $v_2 = v_2 - \lfloor \mu \rfloor v_1$ and $V_2 = \| v_2 \|^2$.
3: While $V_2 < V_1$ do
4: Swap v_1 and v_2
5: If $V_2 = V_1$
6: Compute $\mu = < v_1, v_2 > / V_1$.
7: Calculate $v_2 = v_2 - \lfloor \mu \rfloor v_1$ and $V_2 = \| v_2 \|^2$.
8: Else
9: Stop and go to choose other vectors v_1 and v_2.
10: End if
11: End while
12: Return (v_1, v_2).

3.2 The extended Euclidean algorithm for reduction lattices

The Euclidean algorithm can be extended. Theorem (3.2.1) in [4, 5] is used to compute the tuples of variables g_i, f_i and h_i for $i = 0,1,2,...,l,l+1,l+2,...,w-1$ with $w > l$. On these tuples, some variables have been employed to form a two-dimensional reduced basis which is used to generate a lattice [5].

Theorem 3.2.1. (Extended Euclidean Algorithm (EEA)). If n and λ are two integers, not both zero, then there exist integers s and t such that:

$$gcd(n, \lambda) = g_i n + f_i \lambda = h_i. \tag{11}$$

for $i = 0,1,2,...,l,l+1,l+2,...,w-1$ with $w > l$. That is, $gcd(n, \lambda)$ can be expressed as a linear combination of n and λ [4,5].

Lemma 3.2.1 (Properties of the extended Euclidean algorithm [1,5]). Suppose tuples of variables s_i, t_i and r_i are defined by

$$g_i n + f_i \lambda = h_i \text{ for } i = 0,1,2,...,l,l+1,l+2,...,w-1 \text{ with } w > l, \tag{12}$$

Where $g_0 = 1, f_0 = 0, h_0 = n, g_1 = 0, f_1 = 1, h_1 = \lambda,$ are initial values. The values $h_i \geq 0$ for all i resulting from applying the EEA for given positive integers n and λ .Then

i. $h_i > h_{i+1} \geq 0$ for all $i \geq 0$.
ii. $| g_i | < | g_{i+1} |$ for all $i \geq 1$.
iii. $| f_i | < | f_{i+1} |$ for all $i \geq 0$.
iv. $h_{i-1} | f_i | + h_i | f_{i-1} | = n$ for all $i \geq 1$.
v. If i_j is odd then $(i-1)_j$ is even, so $f_{i_j} < 0$ and $f_{(i-1)_j} > 0$.

Assume l is a greatest index for $h_l \geq \sqrt{n}$. On Lemma (3.2.1) then the property (iv) becomes

$$h_l | f_{l+1} | + h_{l+1} | f_l | = n \text{ and } | f_{l+1} | < \sqrt{n} \text{ with } i = l+1.$$

Choose $v_1 = (h_{l+1}, -f_{l+1})$. The homomorphism $T : Z \times Z \to Z_n$ defined by $(a,b) \to a + b\lambda (mod\ n)$ then $T(v_1) = 0$. Further, $| f_{l+1} | < \sqrt{n}$ and $| h_{l+1} | < \sqrt{n}$, it is possible to compute $\| v_1 \| \leq \sqrt{2n}$. A vector v_2 is also chosen as the shortest vector $(h_l, -f_l)$ or $(h_{l+2}, -f_{l+2})$. Once again, from Equation (10) and

the homomorphism T, we have $T(v_2) = 0$. Experimentally, v_2 is also considered as a short vector. The v_1 and v_2 are linearly independent vectors. Otherwise, if $v_2 = (h_l, -f_l)$, then

$$\frac{h_{l+1}}{h_l} = \frac{-f_{l+1}}{-f_l} = \frac{f_{l+1}}{f_l}.$$

However, from Lemma (3.2.1)(i), $h_{l+1} = h_l < 1$, and from (iii), on the same Lemma, $|f_{l+1} = f_l| > 1$. This is contradictory. Hence, v_1 and v_2 are linearly independent [1].

4. The generalized lattice basis reduction methods in two dimensions

The generalization on the lattice reduction methods is discussed as follows.

4.1 The generalized computation of the extended Euclidean algorithm

The EEA has been used to form the generator in the GLV method. The generalized idea of the EEA can be used to form the ISD generators $\{v_3, v_4\}$ and $\{v_5, v_6\}$. The generalization of the EEA outputs $2-$tuples of variables for $j = 1,2$ as shown in the next lemma.

Lemma 4.1.1. (The generalized extended Euclidean algorithm (GEEA)). Let n be a positive integer and $\lambda = \langle \lambda_j \rangle$ be two tuple of integers, where $j = 1,2$ with $n \neq O$ or $\lambda \neq O$. For all j and $O = \langle 0 \rangle$ is a zero $2-$tuple. Then, an $2-$tuple of positive integers $D = \langle d_j \rangle = \langle \gcd(n, \lambda_j) \rangle$ is a $2-$tuple of the *gcds*. Furthermore, there exist two $2-$tuples of the integers $G = \langle g_i \rangle$ and $F = \langle f_i \rangle$ such that

$$\gcd(n, \lambda_j) = g_{i_j} n + f_{i_j} \lambda_j \text{ for } j = 1,2 \text{ and } i = 1,2,\ldots,l,l+1,\ldots,w, \text{ w} > l. \tag{13}$$

In other words, the expression of the $2-$tuple D is written by the linear combinations of the $2-$tuple λ and n [7].

4.2 The generalized Lagrange - Gauss lattice basis reduction method

The generalization on the method of Lagrange-Gauss lattice basis reduction is illustrated as follows.

Definition 4.2.1. An ordered bases v_1, v_2 and v_3, v_4 in Z^2 is a generalized Lagrange-Gauss reduced if

$$\|v_1\| \le \|v_2\| \le \|v_2 + q_1 v_1\| \text{ and } \|v_3\| \le \|v_4\| \le \|v_4 + q_2 v_3\|, \ \forall\, q_1, q_2 \in Z. \tag{14}$$

The reduced bases on the generalized Lagrange-Gauss (GLG) reduction method can be explained by following theorem.

Theorem 4.2.1. Let $\lambda_1, \lambda_2, \lambda_3, \lambda_4$ be the successive minima of L. If L has the ordered bases $\{v_1, v_2\}\{v_3, v_4\}$ which are the generalized Lagrange- Gauss reduced, then $\|v_i\| = \lambda_i$ for $i = 1,2,3,4$.

Definition 4.2.2. Let v_1, v_2, v_3, v_4 be the vectors in Z^2. We write $V_i = \|v_i\|^2 = \langle v_i, v_i \rangle$, for $i = 1,2,3,4$. On the generalized Lagrange-Gauss algorithm, the crucial points are

$$\|v_2 - \mu_1 v_1\|^2 = V_2 - 2\mu_1 \langle v_1, v_2 \rangle + \mu_1^2 V_1 \text{ and } \|v_4 - \mu_2 v_3\|^2 = V_4 - 2\mu_2 \langle v_3, v_4 \rangle + \mu_2^2 V_3 \tag{15}$$

Are minimised at $\mu_1 = \langle v_1, v_2 \rangle / V_1$ and $\mu_2 = \langle v_3, v_4 \rangle / V_3$ respectively. The vectors v_2 and v_4 are replaced by $v_2 - \lfloor \mu_1 \rfloor v_1$ and $v_4 - \lfloor \mu_2 \rfloor v_3$ respectively, where $\lfloor \mu_1 \rfloor$ and $\lfloor \mu_2 \rfloor$ are the smallest integers to μ_1 and μ_2. the size of v_2 and v_4 are reduced based on the vectors v_1 and v_3. The reduced

formulas $v_2 - \lfloor \mu_1 \rfloor v_1$ and $v_4 - \lfloor \mu_2 \rfloor v_3$ are familiar the operations to $r_{(i+1)_j} = r_{(i-1)_j} - \left\lfloor r_{(i-1)_j} / r_{i_j} \right\rfloor$ r_{i_j} which are computed from the generalized Euclidean algorithm for $j = 1,2.$

Lemma 4.2.1. The ordered bases $\{v_1, v_2\}$ and $\{v_3, v_4\}$ are Lagrange-Gauss reduced if and only if

$$\|v_1\| \le \|v_2\| \le \|v_2 + v_1\| \text{ and } \|v_3\| \le \|v_4\| \le \|v_4 + v_3\|. \tag{16}$$

Algorithm 4.2.1. The generalized Lagrange-Gauss Algorithm (GLGA)

Input: The bases $\{v_1, v_2\}, \{v_3, v_4\} \in Z^2$ for a lattice L.

Output: The shortest basis $\{v_1, v_2\}$ and $\{v_3, v_4\}$ for L such that $\|v_i\| = \lambda_i$ for $i = 1,2,3,4$.

1: Compute $V_1 = \|v_1\|^2$ and $V_3 = \|v_3\|^2$
2: Calculate $\mu_1 = \langle v_1, v_2 \rangle / V_1$ and $\mu_2 = \langle v_3, v_4 \rangle / V_3$.
3: Reduce $v_2 = v_2 - \lfloor \mu_1 \rfloor v_1$ and $v_4 = v_4 - \lfloor \mu_2 \rfloor v_3$.
4: Check $V_2 = \|v_2\|^2$ and $V_4 = \|v_4\|^2$.
5: While $V_2 < V_1$ do
6: Swap v_1 and v_2
7: If $V_2 = V_1$ then
8: Compute $\mu_1 = \langle v_1, v_2 \rangle / V_1$.
9: Reduce $v_2 = v_2 - \lfloor \mu_1 \rfloor v_1$
10: Check $V_2 = \|v_2\|^2$
11: Else
12: Stop and go to choose other vectors v_1 and v_2.
13: End if
14: End while
15: Return $\{v_1, v_2\}$.
16: While $V_4 < V_3$ do
17: Swap v_3 and v_4
18: If $V_4 = V_3$ then
19: Compute $\mu_2 = \langle v_3, v_4 \rangle / V_3$.
20: Reduce $v_4 = v_4 - \lfloor \mu_2 \rfloor v_3$
21: Check $V_4 = \|v_4\|^2$
22: Else
23: Stop and go to choose other vectors v_3 and v_4.
24: End if
25: End while
26: Return $\{v_3, v_4\}$.

5.Generating the generators on the ISD computation method

The generators of the ISD computation method for computing a scalar multiplication *kP*, which are called ISD generators, can be formed based on the following definition.

Definition 5.1. Suppose v_3, v_4 and v_5, v_6 are linearly independent vectors in the kernel of the homomorphism T that is defined by the formula:

$$T : Z \times Z \to Z = n$$
$$(x; y) \to x + y \lambda j \ (mod\ n). \tag{17}$$

The bases of a lattice *L*, $\{v_1,v_2\}$ and $\{v_3,v_4\}$, are called ISD generators if each components of each vector is relatively prime to other and the components on these vectors are bounded by the range [- $\sqrt{n}$, $\sqrt{n}$].

The existence of v_1,v_2 and v_3,v_4 in a sub-lattice L_s as the linear independent vectors as well as the shortness of them considers as *kerT* of a lattice $L = Z \times Z$. These vectors are computed by the GLGA (4.2.1) as the integer lattice points in two dimensions.

Algorithm 5.1. The ISD generators algorithm

Input: The bases $\{v_1,v_2\}, \{v_3,v_4\} \in Z^2$ for a lattice L.

Output: The shortest bases $\{v_1,v_2\}$ and $\{v_3,v_4\}$ for L such that $\| v_i \| = \lambda_i$ for $i = 1,2,3,4$.

1: Run the GLGA (4.2.1).

2: Return reduced based $\{v_1,v_2\}$ and $\{v_3,v_4\}$.

6.Comparison studies on the GLG reduction and GEEA

The ISD generators are the fundamental points in the ISD computation method that uses to compute an elliptic scalar multiplication. So, the computation for these generators requires applying one of two generalized algorithms, the GLGA or GEEA. Our discussion will be beginning with using the GLGA.

With the vectors $v_1 = (1,39)$, $v_2 = (0,67)$ and $v_3 = (1,28)$, $v_4 = (0,67)$, the GLGA can be applied by the following computations.

$$\lfloor \mu_1 \rfloor = \frac{\langle v_1,v_2 \rangle}{\langle v_1,v_1 \rangle} = \frac{2613}{1522} = 1 \text{ and } \lfloor \mu_2 \rfloor = \frac{\langle v_3,v_4 \rangle}{\langle v_3,v_3 \rangle} = \frac{1876}{785} = 2.$$

So, the first reduced vectors v_2 and v_4 are computed by

$$v_2 = v_2 - \lfloor \mu_1 \rfloor v_1 = (-1,28) \text{ and } v_4 = v_4 - \lfloor \mu_2 \rfloor v_3 = (-2,11).$$

Swapping v_2,v_4 with v_1,v_3 respectively. In other words, $v_1 = (-1,28)$ and $v_2 = (1,39)$. Whereas, $v_3 = (-2,11)$ and $v_4 = (1,28)$. Now, the next values of $\lfloor \mu_1 \rfloor$ and $\lfloor \mu_2 \rfloor$ are

$$\lfloor \mu_1 \rfloor = \frac{\langle v_1,v_2 \rangle}{\langle v_1,v_1 \rangle} = \frac{1091}{785} = 1 \text{ and } \lfloor \mu_2 \rfloor = \frac{\langle v_3,v_4 \rangle}{\langle v_3,v_3 \rangle} = \frac{306}{125} = 2.$$

So the new short vectors are

$$v_2 = v_2 - \lfloor \mu_1 \rfloor v_1 = (2,11) \text{ and } v_4 = v_4 - \lfloor \mu_2 \rfloor v_3 = (5,6).$$

Second swapping of the vectors v_2,v_4 with v_1,v_3 respectively produces

$$v_1 = (2,11),\ v_2 = (-1,28) \quad \text{and} \quad v_3 = (5,6),\ v_4 = (-2,11).$$

New values of $\lfloor \mu_1 \rfloor$ and $\lfloor \mu_2 \rfloor$ are

$$\lfloor \mu_1 \rfloor = \frac{\langle v_1,v_2 \rangle}{\langle v_1,v_1 \rangle} = \frac{306}{125} = 2 \text{ and } \lfloor \mu_2 \rfloor = \frac{\langle v_3,v_4 \rangle}{\langle v_3,v_3 \rangle} = \frac{60}{61} = 1.$$

New short vectors are

$$v_2 = v_2 - \lfloor \mu_1 \rfloor v_1 = (-5,6) \text{ and } v_4 = v_4 - \lfloor \mu_2 \rfloor v_3 = (-7,5).$$

Now, the vectors $v_3=(5,6)$ and $v_4=(-7,5)$. Swapping operation is stopped at this point, since $\|v_3\|<\|v_4\|$, therefore the shortest vectors are $v_3=(5,6)$ and $v_4=(-7,5)$.
Third swapping of the vectors v_2 with v_1 produces

$$v_1=(-5,6),\ v_2=(2,11)$$

New value of $\lfloor \mu_1 \rfloor$ is

$$\lfloor \mu_1 \rfloor = \frac{\langle v_1, v_2 \rangle}{\langle v_1, v_1 \rangle} = 1$$

New short vector is

$$v_2 = v_2 - \lfloor \mu_1 \rfloor v_1 = (7,-5)\ .$$

Now, the vectors $v_1=(-5,6)$ and $v_2=(7,-5)$. Swapping operation is stopped at this point, since $\|v_1\|<\|v_2\|$, therefore the shortest vectors are $v_1=(-5,6)$ and $v_2=(7,-5)$. Thus, the ISD generators can be formed by

$$\{v_1,v_2\}=\{(h_{(i+1)_1},-f_{(i+1)_1}),(h_{(i+2)_1},-f_{(i+2)_1})\}\{(6,-5),(-5,7)\}$$

and

$$\{v_3,v_4\}=\{(h_{(i+1)_2},-f_{(i+1)_2}),(h_{(i+2)_2},-f_{(i+2)_2})\}=\{(6,5),(5,-7)\}.$$

On the other hand, the application of the GEEA for the same values $(n,\lambda_1,\lambda_2)=(67,39,28)$ is achieved as follows.

With λ_1=39, n=67 and $f_{1_1}\leftarrow 1$, $g_{1_1}\leftarrow 0$, $f_{0_1}\leftarrow 0$, $g_{0_1}\leftarrow 1$.
$q\leftarrow\lfloor 67/39\rfloor=1$, $h\leftarrow 67-1(39)=28$, $f\leftarrow 0-1(1)=-1$, $g\leftarrow 1-1(0)=1$.

$n\leftarrow 39$, $\lambda_1\leftarrow 28$, $f_0\leftarrow 1$, $f_1\leftarrow -1$, $g_0\leftarrow 0$, $g_1\leftarrow 1$.
$q\leftarrow\lfloor 39/28\rfloor=1$, $h\leftarrow 39-1(28)=11$, $f\leftarrow 1-1(-1)=2$, $g\leftarrow 0-1=-1$.

$n\leftarrow 28$, $\lambda_1\leftarrow 11$, $f_0\leftarrow -1$, $f_1\leftarrow 2$, $g_0\leftarrow 1$, $g_1\leftarrow -1$.
$q\leftarrow\lfloor 28/11\rfloor=2$, $h\leftarrow 28-2(11)=6$, $f\leftarrow -1-2(2)=-5$, $g\leftarrow 1-2(-1)=3$.

$n\leftarrow 11$, $\lambda_1\leftarrow 6$, $f_0\leftarrow 2$, $f_1\leftarrow -5$, $g_0\leftarrow -1$, $g_1\leftarrow 3$.
$q\leftarrow\lfloor 11/6\rfloor=1$, $h\leftarrow 11-1(6)=5$, $f\leftarrow 2-1(-5)=7$, $g\leftarrow -1-1(3)=-4$.

$n\leftarrow 6$, $\lambda_1\leftarrow 5$, $f_0\leftarrow -5$, $f_1\leftarrow 7$, $g_0\leftarrow 3$, $g_1\leftarrow -4$.
$q\leftarrow\lfloor 6/5\rfloor=1$, $h\leftarrow 6-1(5)=1$, $f\leftarrow -5-1(7)=-12$, $g\leftarrow 3-1(-4)=7$.

$n\leftarrow 5$, $\lambda_1\leftarrow 1$, $f_0\leftarrow 7$, $f_1\leftarrow -12$, $g_0\leftarrow -4$, $g_1\leftarrow 7$.
$q\leftarrow\lfloor 5/1\rfloor=5$, $h\leftarrow 5-5(1)=0$, $f\leftarrow 7-5(-12)=67$, $g\leftarrow -4-5(7)=-39$.

$n\leftarrow 5$, $\lambda_1\leftarrow 1$, $f_0\leftarrow 7$, $f_1\leftarrow -12$, $g_0\leftarrow -4$, $g_1\leftarrow 7$.
So, $h=\{28,11,6,5,1,0\}$, $f=\{-1,2,-5,7,-12,67\}$ and g={1,-1,3,-4,7,-39}.

Whereas, with λ_2=28, n=67 and $f_{1_2}\leftarrow 1$, $g_{1_2}\leftarrow 0$, $f_{0_2}\leftarrow 0$, $g_{0_2}\leftarrow 1$.
$q\leftarrow\lfloor 67/28\rfloor=2$, $h\leftarrow 67-2(28)=56$, $f\leftarrow 0-2(1)=-2$, $g\leftarrow 1-2(0)=1$.

$n \leftarrow 28,\ \lambda_2 \leftarrow 11,\ \mathrm{f}_0 \leftarrow 1,\ \mathrm{f}_1 \leftarrow -2,\ \mathrm{g}_0 \leftarrow 0,\ \mathrm{g}_1 \leftarrow 1.$
$q \leftarrow \lfloor 28/11 \rfloor = 2,\ \mathrm{h} \leftarrow 28 - 2(11) = 6,\ f \leftarrow 1 - 2(-2) = 5,\ g \leftarrow 0 - 2(1) = -2.$

$n \leftarrow 11,\ \lambda_2 \leftarrow 6,\ \mathrm{f}_0 \leftarrow -2,\ \mathrm{f}_1 \leftarrow 5,\ \mathrm{g}_0 \leftarrow 1,\ \mathrm{g}_1 \leftarrow -2.$
$q \leftarrow \lfloor 11/6 \rfloor = 1,\ \mathrm{h} \leftarrow 11 - 1(6) = 5,\ f \leftarrow -2 - 1(5) = -7,\ \mathrm{g} \leftarrow 1 - 1(-2) = 3.$

$n \leftarrow 6,\ \lambda_2 \leftarrow 5,\ \mathrm{f}_0 \leftarrow 5,\ \mathrm{f}_1 \leftarrow -7,\ \mathrm{g}_0 \leftarrow -2,\ \mathrm{g}_1 \leftarrow 3.$
$q \leftarrow \lfloor 6/5 \rfloor = 1,\ \mathrm{h} \leftarrow 6 - 1(5) = 1,\ \mathrm{f} \leftarrow 5 - 1(-7) = 12,\ \mathrm{g} \leftarrow -2 - 1(3) = -5.$

$n \leftarrow 5,\ \lambda_2 \leftarrow 1,\ \mathrm{f}_0 \leftarrow -7,\ \mathrm{f}_1 \leftarrow 12,\ \mathrm{g}_0 \leftarrow 3,\ \mathrm{g}_1 \leftarrow -5.$
$q \leftarrow \lfloor 5/1 \rfloor = 5,\ \mathrm{h} \leftarrow 5 - 5(1) = 0,\ \mathrm{f} \leftarrow -7 - 5(12) = -67,\ \mathrm{g} \leftarrow 3 - 5(5) = 28.$

So, $h = \{11,6,5,1,0\}, f = \{-2,5,-7,12,-67\}$ and $g = \{1,-2,3,-5,28\}$.

Since the shortest vectors v_1 and v_2 on the GEEA are defined by

$$v_1 = (h_{(i+1)_1}, -f_{(i+1)_1}) = (6,-5),\ v_2 = (h_{(i+2)_1}, -f_{(i+2)_1}) = (-5,7) \text{ and } v_3 = (h_{(i+1)_2}, -f_{(i+1)_2}) = (6,5),$$
$$v_4 = (h_{(i+2)_2}, -f_{(i+2)_2}) = (5,-7).$$

Based on the comparison results on the GLGA and GEEA, one can conclude that the outputs on these algorithms are same. So, it is easy to connect between these generalized algorithms. Next section will discuss this connection.

7. Connecting between the GLGA and GEEA

In this section, some similarities and differences on the generalization of the Lagrange-Gauss algorithm and extended Euclid algorithm have been discussed. If $n, \lambda_j \in Z$ for $j = 1,2,$ then the generalized extended Euclidean algorithm produces a sequence of integers h_{i_j}, g_{i_j} and f_{i_j} such that

$$ng_{i_j} + \lambda_j f_{i_j} = \mathrm{h}_{i_j} \tag{18}$$

Where $|h_{i_j} f_{i_j}| < |n_j|$ and $|h_{i_j} g_{i_j}| < |\lambda_j|$. The precise formulae are $h_{(i+1)_j} = \mathrm{h}_{(i-1)_j} - q_j h_{i_j}$ and $f_{(i+1)_j} = \mathrm{f}_{(i-1)_j} - q_j f_{i_j}$ where $q_j = \lfloor f_{(i-1)_j} / f_{i_j} \rfloor$. The sequence $|h_{i_j}|$ is strictly decreasing. The initial values are $h_{0_j} = n,\ \mathrm{h}_{1_j} = \lambda_j,\ \mathrm{g}_{0_j} = 1_j,\ \mathrm{g}_{1_j} = 0_j,\ \mathrm{f}_{0_j} = 0_j,\ \mathrm{f}_{1_j} = 1_j.$ In other words the lattice with basis matrix

$$V_j = \begin{bmatrix} 0_j & \lambda_j \\ 1_j & n \end{bmatrix} = \begin{bmatrix} f_{1_j} & h_{1_j} \\ f_{0_j} & h_{0_j} \end{bmatrix} \tag{19}$$

contains the vectors

$$(f_{i_j}, h_{i_j}) = (g_{i_j}, f_{i_j}) V_j.$$

These vectors are shorter than the original vectors of the lattice. Now, If we suppose that the value of f_{i_j} is sufficiently small compared with h_{i_j} then one step of the generalized Lagrange- Gauss algorithm on V_j corresponds to one step of the generalized extended Euclidean algorithm. To see this, let $v_1 = (f_{(i+1)_1}, \mathrm{h}_{(i+1)_1}), v_3 = (f_{(i+1)_2}, \mathrm{h}_{(i+1)_2})$ and consider the GLGA with $v_2 = (f_{i_1}, \mathrm{h}_{i_1}), v_4 = (f_{i_2}, \mathrm{h}_{i_2})$ respectively. First compute the value

$$\mu_1 = \frac{\langle v_1, v_2 \rangle}{\langle v_1, v_1 \rangle} = \frac{\mathrm{f}_{(\mathrm{i}+1)_1}\mathrm{f}_{\mathrm{i}_1} + \mathrm{h}_{(\mathrm{i}+1)_1}\mathrm{h}_{\mathrm{i}_1}}{\mathrm{f}^2_{(\mathrm{i}+1)_1} + \mathrm{h}^2_{(\mathrm{i}+1)_1}} \tag{20}$$

and

$$\mu_2 = \frac{\langle v_3, v_4 \rangle}{\langle v_3, v_3 \rangle} = \frac{f_{(\mathrm{i}+1)_2} f_{\mathrm{i}_2} + \mathrm{h}_{(\mathrm{i}+1)_2}\mathrm{h}_{\mathrm{i}_2}}{f^2_{(\mathrm{i}+1)_2} + \mathrm{h}^2_{(\mathrm{i}+1)_2}}. \tag{21}$$

If f_{i_j} is a small value relative to h_{i_j}, for instance, in the first step, when $f_{1_j} = 1$) then

$$\lfloor \mu_j \rfloor = \lfloor h_{(i+1)_j} h_{i_j} / h^2_{(i+1)_j} \rfloor = \lfloor h_{i_j} / h_{(i+1)_j} \rfloor = q_j, \text{ for } j = 1, 2.$$

The reduced operations $v_2 = v_2 - \lfloor \mu_1 \rfloor v_1$ is $v_2 = \left(f_{i_1} - q_1 f_{(i+1)_1}, \mathrm{h}_{i_1} - q_1 h_{(i+1)_1}\right)$ and $v_4 = v_4 - \lfloor \mu_2 \rfloor v_3$, is $v_4 = \left(f_{i_2} - q_2 f_{(i+1)_2}, \mathrm{h}_{i_2} - q_2 h_{(i+1)_2}\right)$ which agree with the GEEA. Finally, the GALA compares the lengths of the vectors v_2, v_4 with v_1, v_3 respectively to check if these vectors should be swapped. When $f_{(i+1)_j}$ is small compared with $h_{(i+1)_j}$ then $\|v_2\|$ and $\|v_4\|$ are smaller than $\|v_1\|$ and $\|v_3\|$. So, the vectors are swapped and the matrix becomes

$$\begin{bmatrix} f_{i_j} - q_j f_{(i+1)_j} & h_{i_j} - q_j h_{(i+1)_j} \\ f_{(i+1)_j} & h_{(i+1)_j} \end{bmatrix},$$

as shown in the GEEA. The generalized algorithms start to deviate once f_{i_j}. Further, the GEEA runs until $h_{i_j} = 0$, in this case $f_{i_j} \approx n$, whereas the GLGA stops $h_{i_j} \approx f_{i_j}$.

8. Conclusions

For applying some efficient algorithms to compute a scalar multiplication *kP* on elliptic curves E defined over a prime fields F_p, the generators should be found. One of these generators are the ISD generators which consist of the linearly independent vectors v_1, v_2 and v_3, v_4. These vectors are the shortest vectors that form the bases on lattice *L* of rank 2. In this work, the generalization on the Lagrange-Gauss reduction method of basis lattice of rank 2 is proposed. On this generalization, the reduction of 2-tuple of integer vectors has been computed to give the good shortest bases lattice which are used to form the ISD generators $\{v_1, v_2\}$ and $\{v_3, v_4\}$.

The numerical results by simple example on the GLGA to generate ISD generators are compared with the numerical results that resulting from applying the GEEA. Based on the comparison results, the GLGA and GEEA can be connected to give the same numerical results of the ISD generators.

References

[1] Galbraith Steven D 2012 *Mathematics of public key cryptography* Cambridge University Press
[2] L C Washington 2006 *Elliptic curves: number theory and cryptography* CRC press
[3] J Hoffstein, J Pipher and J H Silverman 2008 *An introduction to mathematical cryptography* Springer
[4] G Robert P, L Robert J and V Scott A 2001 Faster point multiplication on elliptic curves with efficient endomorphisms Advances in Cryptology-CRYPTO pp 190-200
[6] K Dongryeol and L Seongan 2003 Integer decomposition for fast scalar multiplication on elliptic curves *Selected Areas in Crypto* pp 13-20

[7] R K K Ajeena 2015 Integer sub-decomposition (ISD) method for elliptic curve scalar multiplication *Diss. Universiti Sains Malaysia* pp 1-453
[8] R K K Ajeena and H Kamarulhaili 2013 Analysis on the elliptic scalar multiplication using integer sub decomposition method *Int. J. of Pu. and App. Math.* **87** 1 pp 95-114
[9] R K K Ajeena and H. Kamarulhaili 2014 Point Multiplication using Integer Sub- Decomposition for Elliptic Curve Cryptography *Appl. Math. & Inf. Sci.* **8** 2 pp 517-525
[10] R K K Ajeena and H Kamarulhaili 2014 Comparison Studies on Integer Decomposition Method for Elliptic Scalar Multiplication *Adva. Sci. Lett.* **20** 2 pp 526-530
[11] R K K Ajeena 2015 Upper Bound of Scalars in the Integer Sub-decomposition Method: The Theoretical Aspects *J. of Cont. Sci. and Eng.* **2** pp 91-101
[12] R K K Ajeena and H Kamarulhaili Two dimensional Sub-decomposition method for point multiplication on elliptic curves *J. of Math. Sci. : Adva. and Appl.* **25** pp 43-56

Weakly Coretractable Modules

Weakly Coretractable Modules

Inaam M A Hadi[1], Shukur N Al-aeashi[2]

[1]Department of Mathematics, College of Education for Pure Sciences (Ibn-Al-Haitham), University Of Baghdad, Iraq.
[2]Department of Urban Planning, College of Physical Planning, University of Kufa, Iraq.

[2]shukur. mobred@uokufa. edu. iq

Abstract: If R is a ring with identity and M is a unitary right R-module. Here we introduce the class of weakly coretractable module. Some basic properties are investigated and some relationships between these modules and other related one are introduced.

1. Introduction

Throughout this paper, R is a ring with unity and all modules are unitary right R-modules. The notion of coretractable module appeared in [3]. However, Amini [2], studied this concept as a dual of retrectable modules, "M is said to be coretractable if ∀N of M, there exists a nonzero mapping f∈Hom_R(M/N, M)"[3]. In [6], we introduced the concept of strongly coretractable modules, where " an R-module M is called strongly coretractable module if for all a submodule N of M, there exists a nonzero R-homomorphism f:M/N→M such that Imf+N=M"[6]. Equivalently, "M is strongly coretractable if for each a proper submodule N of M, there exists a nonzero mapping f∈End_R(M) such that Imf+N=M" [6], [7]. "It is clear that every strongly coretractable module is coretrectable, but not conversely for example the Z-module Z_4 is coretractable but not strongly coretractable module" and then some generalizations are introduced see [8], [9], [10] and [11]. We introduce the notion of weakly coretractable module, where an R-module M is called weakly coretractable if ∀K of M, there exists a nonzero mapping f∈End_R(M) such that f^2(K)=0. Clear that every coretractable is weakly coretrectable, but not conversely. Section one of this work is devoted to recall some basic properties of coretractable modules. Also we added some new results (up to our knowledge). In section two we introduced and studied weakly coretractable modules. Also many connections between it and other classes of modules were given.

2. On Coretractable Modules

First recall the following definition:

"Definition(1.1) [3]**:** An R-module M is called coretractable if for each a proper submodule S of M, there exists a nonzero R-homomorphism f:M/S→M".

Examples and Remarks (1.2):

(1) A module M is coretractable iff ∀S<M, ∃ 0≠f∈EndR(M) such that f(S)=0; S⊆kerf.

Proof: ($\Longrightarrow$) Suppose that S<M, $\exists$ f:M$\rightarrow$M, f$\neq$0 and f(S)=0. Define g:M/S$\rightarrow$M by g(m+S)=f(m), it is clear that g is well-defined R-homomorphism. Now, since f$\neq$0 and f(S)=0, then $\exists$ m$\in$M, m$\notin$S such that f(m) $\neq$0. Thus g(m+S)=f(m) $\neq$0. Thus HomR(M/S, M)$\neq$0 $\forall$S<M.

($\Longleftarrow$)Let S<M, since $\exists$ f:M/S$\rightarrow$M, f$\neq$0. It follows that f$\circ\pi$ $\in$EndR(M) and f$\circ\pi$(S)= f(π(S))=f(0)=0, where π is the natural epimorphism from M into M/S. Thus M is coretrectable.

(2) "Clearly every semisimple module is coretractable, and hence every R-module over a semisimple ring is coretractable [2].

But it may be that coretractable module not semisimple as the Z-module Z4.

(3) " Zp∞ is coretractable Z-module, since Zp∞/S$\cong$Zp∞ ($\forall$S< Zp∞)" [2].

(4) " Zn is coretractable Z-module ($\forall$n$\in$Z+)" [2].

(5) See the Z-module Q. Suppose Q is a coretractable module. Since Z<Q, $\exists$f $\in$EndR(Q), f$\neq$0 with f(Z)=0. Now, for any s/t$\in$Q, f(s/t)= f(1/t) s. But 0=f(1)= f(1/t) s, so f(1/t)=0 and hence f(s/t)=0. t=0; f=0, which is a contradiction. Thus Q is not coretractable module.

(6) See M=Z$\oplus$Z2 as Z-module. Let N=3Z $\oplus$Z2, M/N$\cong$Z3. But there is no nonzero mapping f:Z3$\rightarrow$ Z$\oplus$Z2, since if we assume there exists $\bar{x}$ $\in$Z3 and f($\bar{x}$)$\neq$(0, $\bar{0}$). So if f($\bar{x}$)=(n, $\bar{m}$), n$\neq$0, then f($\bar{x}$.3)=f($\bar{0}$)=(0, $\bar{0}$). On the other hand, f($\bar{x}$. 3)= f($\bar{x}$). 3= (n, $\bar{m}$). 3= (n. 3, $\bar{m}$. 3) $\neq$(0, $\bar{0}$) which is a contradiction. Similarly if f($\bar{x}$)=(0, $\bar{1}$), then f($\bar{x}$. 3)=f($\bar{0}$)=(0, $\bar{0}$), but f($\bar{x}$). 3=(0, $\bar{1}$). 3 $\neq$(0, $\bar{0}$) which is a contradiction. Thus Z$\oplus$Z2 is not coretrectable.

(7) See M=Z$\oplus$Z as Z-module. Let N=Z$\oplus$2Z suppose $\exists$ g$\in$EndZ(M), g$\neq$0, g(N)=0 then g(a, b)=0 $\forall$ a$\in$Z, b$\in$2Z. Now, for all odd integers x and y, x=2m+1 and y= 2n +1 for some n, m$\in$Z, g(x, y)= g(2m+1, 2n+1)= g(2m+1,2n)+g(0,1)= 0+ g(0,1)= g(0,1), but g(0, 2)= g(0, 1)2, then g(0, 1)=0, hence g(x,y)=0. Now for all even integer 2m and odd integer 2n+1; g(2m,2n+1)=g(2m,2n)+g(0,1)=0. Thus g(M)=0 that is g is a zero mapping which is a contradiction. Thus M is not coretractable module.

(8) Coretractability is preserved by an isomorphism.

Recall that "a submodule B of M is relative complement of A in M if B is maximal with respect to the property B$\cap$A=0 "[4]. "A submodule E of M is essential if $\forall$ W$\leq$M if E$\cap$W=0, then W=0(denoted E$\leq_e$M)" [4]. The following Proposition appears in[2] without proof.

Proposition(1.3): An R-module M is coretractable iff Hom_R(M/E, M)$\neq$0 $\forall$E$\leq_e$M.

Proof: It is clear.

Proposition(1.4): An R-module M is coretractable iff M is coretractable $\bar{R}$-module (where $\bar{R}$=R/annM).

Proof: Since every R-submodule of M is $\bar{R}$-submodule of M and conversely, also every R-homomorphism is an $\bar{R}$-homomorphism and conversely. Hence the result follows directly.

" A module M is cogenerator if every nonzero homomorphism f:$M_1\rightarrow M_2$ where M_1 and M_2 are modules, there is g:$M_2\rightarrow$M such that g$\circ$f $\neq$ 0 [5, P. 507] and [6, P. 53]. Equivalently an R-module M is called a cogenerator if for any R-module N and 0$\neq$x$\in$N, there exists g: N$\rightarrow$M such that g(x)$\neq$0" [5, P. 507].

Proposition(1.5): Every cogenerator R-module is coretractable module.

Proof: Let M be a cogenerator module and let S<M, then M/S$\neq$(0). Let x=m+S$\neq$0, $\exists$g:M/S $\rightarrow$M such that g(x) $\neq$0, that is g$\neq$0 and hence M is coretractable module.

The converse of Proposition(1.5) may be not true. Consider Z_2 is coretractable (by part (4)), but it is not cogenerator module. Since the only nonzero mapping from Z into Z_2 is given by:

$$g(x) = \begin{cases} \bar{0} & \text{if x is even integer} \\ \bar{1} & \text{if x is odd integer} \end{cases},$$

Thus for each nonzero even integer x, there is no g: Z$\rightarrow Z_2$ such that g(x)$\neq$0.

Corollary(1.6): For an R-module M, if $\prod_{i\in\Lambda}$M is a cogenerator module, then M is coretractable module.

Proof: By [5, Corollary19.7, P. 508], M is cogenerator and hence by Proposition(1.5), M is coretrectable.

Corollary(1.7): If R is cogenerator. Then any faithful R-module is coretrectable.

Proof: Take M is faithful R-module. Then by [5, Proposition(19. 19), P. 512], M is cogenerator and hence by Proposition(1. 5), M is a coretractable module.

Note that "for any module M and a cogenerator C, C⊕M is a cogenerator and so is a coretractable module, but M need not be coretractable module. So that Coretractability is not preserved by taking submodules, factor modules and direct summands "[2]. "However there are some special cases, but first recall that: a submodule S of an R-module M is called fully invariant if f(S) is contained in S for every R-endomorphism f of M" [4].

Proposition(1.8): [2] "Let M=F⊕L be a coretractable R-module. If F is a fully invariant submodule of M or F cogenerates M, then F is also coretrectable. In particular, if $\oplus_I$ F or $\prod_I$ F is coretractable for some index set I, then so is F".

Consider M=Z⊕Q, $End_Z(M) \cong \begin{pmatrix} EndZ & Hom(Q,Z) \\ Hom(Z,Q) & EndQ \end{pmatrix} = \begin{pmatrix} Z & 0 \\ Z & Q \end{pmatrix}$, so for any $\phi \in End_Z(M)$. $\phi = \begin{pmatrix} n & 0 \\ m & x \end{pmatrix}$, for some n, m∈Z and x∈Q. Then $\phi(Q) = \{ \begin{pmatrix} n & 0 \\ m & x \end{pmatrix} \begin{pmatrix} 0 \\ y \end{pmatrix}, y \in Q\} = \{ \begin{pmatrix} 0 \\ xy \end{pmatrix}, x, y \in Q\} \cong Q$. So $\phi(Q) \subseteq Q$. Thus Q is fully invariant in M, but Q isn't coretrectable. Thus M is not coretractable by Proposition(1.8).

Proposition(1.9): [2] " Let $M_1, M_2, \ldots, M_n$ be coretractable modules, then so is $\oplus_{i=1}^{n} M_i$" .

As application of Proposition(1.9), each of the Z-module $Z_4 \oplus Z_6 \oplus Z_8$, $Z_2 \oplus Z_8$, $Z_{p^\infty} \oplus Z_n$ (p is any prime number, $n \in Z_+$) is coretrectable.

Proposition(1.10): If M is module over commutative ring R such that $[N:_R M] = annM \neq annN \ \forall N$ of M. Then every factor module of M is a coretractable module, where $[N:_R M] = \{r \in R: Mr \subseteq N\}$ and $annN = \{r \in R: Nr = 0\}$.

Proof: Suppose L/N<M/N, so N<L<M. By 3rd fundamental isomorphism theorem (M/N)/(L/N)≅M/L. Hence there exists an isomorphism g:(M/N)/(L/N)→M/L. Since annL≠annM, then there exists t∈annL and t∉annM. Define f:M/L→M by f(m+L)=mt. Clear f is well-defined and R-homomorphism.

Consider the sequence $(M/N)/(L/N) \xrightarrow{g} M/L \xrightarrow{f} M \xrightarrow{\pi} M/N$; that is $\pi \circ f \circ g: (M/N)/(L/N) \rightarrow M/N$ and $\pi \circ f \circ g[(M/N)/(L/N)] = \pi \circ f(M/L) = \pi(Mt) = (Mt+N)/N \neq 0_{M/N}$ (since if Mt⊆N, then t∈[N:M]=annM which is a contradiction).

Proposition(1.11): If M is a module such that ∀S<M, $\exists D \leq^{\oplus} M$ such that S⊆D⊂M. Then M is coretrectable.

Proof: Let S<M. By hypothesis S ⊆ D ⊂M for some direct summand D of M, there is f:M/D⟶M, f≠0. Define h: M/S⟶ M/D by h(x+S)= x+D ∀x∈ M, then h is well-defined. Since f ≠ 0, there exists x +D∈M/D, x+D≠D and f(x+D)≠0; x∉D and hence x∉S. Thus x+S≠0 and $h(x+S)=x+D \neq 0_{M/D} = D$. Now, f∘h: M/S⟶M and f∘h ≠0 since f∘h(x+S)=f(h(x+S))= f(x+D)≠ 0. Therefore M is a coretractable module.

Recall that (Schur's Lemma) stated " If M is simple module, then S=End(M) is division ring " [4].

Proposition(1.12): An R-module M is simple iff M is coretractable and $End_R(M)$ is a division ring.

Proof: **(⇒)** Since M is simple, clearly M is coretractable and so $End_R(M)$ is division ring by Schur's Lemma.

(⇐) Let S< M and S≠0. As M is coretrectable, $\exists g \in End_R(M)$, g≠0 such that g(S)=0, hence g is not one-one and that contradiction with $End_R(M)$ is a division ring. Thus M is a simple module.

§2: Weakly coretractable Modules

In this section, we introduce the concept of weakly coretractable modules which is a generalization of coretractable modules. Several examples and many properties related with this concept are given.

Definition(2.1): An R-module M is called weakly coretractable module if ∀N of M, there exists $f\in End_R(M)$, $f\neq 0$ and $f^2(N)=0$; ($N \subseteq kerf^2$). A ring R is called weakly coretractable if R is a weakly coretractable R-module.

One can easy see that a module M is weakly coretractable if any proper submodule S of M, there is a nonzero homomorphism $f\in End_R(M)$ and there is $n\in Z_+$ with $f^n(S)=0$.

Examples and Remarks(2. 2):

(1) Every coretractable module is weakly coretrectable. But conversely;

Example(1): Consider $M=Z\oplus Z_2$ is not coretractable by Examples and Remarks(1.2(6)). $End_Z(M) \cong \begin{pmatrix} End(Z) & Hom(Z_2,Z) \\ Hom(Z,Z_2) & End(Z_2) \end{pmatrix}$, where $End(Z)\cong Z$, $Hom(Z_2,Z)=0$ and $Hom(Z, Z_2) \cong \{f_1, \text{zero map}\} \cong Z_2$ where $f_1(x)=\begin{cases} 0 & \text{if x is even} \\ 1 & \text{if x is odd} \end{cases}$ and $End(Z_2) \cong Z_2$. Any $f\in End_R(M)$ has one of the following form:

$\{\begin{pmatrix} n & 0 \\ \bar{1} & \bar{1} \end{pmatrix}, \begin{pmatrix} n & 0 \\ \bar{1} & \bar{0} \end{pmatrix}, \begin{pmatrix} n & 0 \\ \bar{0} & \bar{1} \end{pmatrix}, \begin{pmatrix} 0 & 0 \\ \bar{1} & \bar{1} \end{pmatrix}, \begin{pmatrix} 0 & 0 \\ \bar{1} & \bar{0} \end{pmatrix}, \begin{pmatrix} 0 & 0 \\ \bar{0} & \bar{1} \end{pmatrix}, \begin{pmatrix} 0 & 0 \\ \bar{0} & \bar{0} \end{pmatrix}, \begin{pmatrix} n & 0 \\ \bar{0} & \bar{0} \end{pmatrix}$: with $n\neq 0\}$.

Let N < M. If N contains (x, y) with $x\neq 0$, then there exists $f=\begin{pmatrix} 0 & 0 \\ \bar{1} & \bar{0} \end{pmatrix}$ and $f\neq 0$, since $f\begin{pmatrix} 3 \\ \bar{1} \end{pmatrix}=\begin{pmatrix} 0 \\ \bar{1} \end{pmatrix} \neq \begin{pmatrix} 0 \\ \bar{0} \end{pmatrix}$. But $f^2(M)=\begin{pmatrix} 0 \\ \bar{0} \end{pmatrix}$ since for each $\begin{pmatrix} x \\ \bar{y} \end{pmatrix} \in M$, $f^2\begin{pmatrix} x \\ \bar{y} \end{pmatrix} = f(f\begin{pmatrix} x \\ \bar{y} \end{pmatrix}) = f(\begin{pmatrix} 0 \\ \bar{1}.x \end{pmatrix}) = \begin{pmatrix} 0 \\ \bar{0} \end{pmatrix}$. Hence $f^2(N)=\begin{pmatrix} 0 \\ \bar{0} \end{pmatrix}$.
Otherwise, f(N) =0 (and hence $f^2(N)=0$), so M is weakly coretrectable.

Example(2): Consider $M=Z\oplus Z$ isn't coretractable module see Examples and Remarks(1. 2(7)). $End_Z(M) \cong \begin{pmatrix} Z & Z \\ Z & Z \end{pmatrix}$.

Let N < M. If N has an element (x, y) such that $x\neq y$, so there is $f=\begin{pmatrix} 1 & -1 \\ 1 & -1 \end{pmatrix} \in End_Z(M)$ and $f\begin{pmatrix} x \\ y \end{pmatrix}=\begin{pmatrix} x-y \\ x-y \end{pmatrix}\neq\begin{pmatrix} 0 \\ 0 \end{pmatrix}$. So $f(N)\neq 0$ but it is easy to check that $f^2(M)=0$, so $f^2(N)=0$. If all elements of N has the form (x, x), $x\in Z$. Then there exists also $f=\begin{pmatrix} 1 & 1 \\ -1 & -1 \end{pmatrix} \in End_Z(M)$, $f\begin{pmatrix} x \\ x \end{pmatrix}=\begin{pmatrix} 1 & 1 \\ -1 & -1 \end{pmatrix}\begin{pmatrix} x \\ x \end{pmatrix}=\begin{pmatrix} 2x \\ -2x \end{pmatrix}$. Thus $f\neq 0$, but $f^2\begin{pmatrix} x \\ x \end{pmatrix}=f\begin{pmatrix} 2x \\ -2x \end{pmatrix}=\begin{pmatrix} 1 & 1 \\ -1 & -1 \end{pmatrix}\begin{pmatrix} 2x \\ -2x \end{pmatrix}=\begin{pmatrix} 0 \\ 0 \end{pmatrix}$. Hence $f^2(N)=0$. Therefore M is weakly coretractable .

(2) A direct summand of weakly coretractable module may be not weakly coretrectable.

Consider $M=Z\oplus Z$ is weakly coretractable Z-module and Z is direct summand of M and it isn't weakly coretractable because for any proper submodule N of Z, N=<n> for some positive integer n and for any $f\in End_Z(Z)$, $f\neq 0$, $f(x)=xm$ for some $m\in Z$, $m\neq 0$, then $f\neq 0$ and so $f^2(N)\neq 0$.

(3) The epimorphism image of weakly coretractable module may be not necessary weakly coretrectable.

Consider $f:Z\oplus Z\to Z$ be a natural projection and $Z\oplus Z$ weakly coretrectable, but Z is not weakly coretractable .

(4) Every strongly coretractable R-module is coretractable and so it is weakly coretrectable.

(5) If M is an R-module with EndR(M) is semiprime. M is weakly coretractable iff M is coretrectable.

Proof: **(⟹)** Let S< M. As M is weakly coretrectable, so $\exists\ g\in End_R(M)$, $g\neq 0$ and $g^2(S)=0$. Since $End_R(M)$ is semiprime, $g^2\neq 0$ implies M is coretrectable.

(⟸) It is clear.

" A module M is strongly Rickart iff $kerf=r_M(f)$ is a fully invariant direct summand in M for all $f\in End_R(M)$" [1]. "If M is strongly Rickart module then for all $f\in End_R(M)$, $r_M(f)=r_M(f^2)$ (That is $kerf = kerf^2$)" [1, corollary(1.9)].

Proposition(2.3): If M is strongly Rickart module. M is weakly coretractable iff M is coretrectable.

Proof:**(⟹)** Let S<M. As M is weakly coretrectable, ∃g ∈End_R(M), g≠0 and S⊆kerg^2. As M is strongly Rickart, hence kerg = ker g^2 and hence S⊆ker g. Thus M is coretrectable.
(⟸) It is clear.
As application of this corollary, the following examples are introduced.
Examples(2.4):
(1) Q and Z as Z-module are strongly Rickart module. But each of Z and Q is not coretractable module, so they are not weakly coretractable modules.
(2)$Q⊕Z_2$ is strongly Rickart, but it's not coretractable and hence it's not weakly coretrectable.
(3)M=Z⊕Z is weakly coretractable Z-module but not coretractable (see Ex. and Rem. 2. 2(1)). However M is not strongly Rickart since there exists f ∈End_R(M) defined by f(a, b)=(a, 0), kerf=0⊕Z, but kerf is not fully invariant submodule since there exists g ∈ End_Z(M), g(a, b)=(b, 0), so g(kerf)=g(0⊕Z)=Z⊕0⊈kerf.

"A submodule N of M is stable if each f ∈Hom(N, M), f(N)⊆N and M is fully stable if every submodule of M is stable. Every stable submodule is fully invariant but not conversely ".
Proposition(2.5): Let M be an R-module. If M is a fully stable weakly coretractable R-module, then every submodule N of M is weakly coretrectable.
Proof: Let W<N. As M is weakly coretrectable, so ∃f∈EndR(M), f≠0 and f2(N)=0, let g=f lN: N→M. As M is fully stable g(N) ⊆ N, thus g ∈ EndR(N), then g2(W) =g (g(W)). But g2(W) ⊆g2(N) since W⊆N. But g2(N) = f2(N)=0. Thus g2(W)=0 and hence N is weakly coretrectable.
Proposition(2.6): Let M=M1⊕M2 where M1 and M2 are weakly coretractable modules. If M is duo module (or $annM_1$+$annM_2$=R or distributive module), then M is a weakly coretractable module.
Proof: Let N be a proper submodule of M. Since M is duo module(or $annM_1$+$annM_2$=R or distributive module), then N=(N∩M_1)⊕(N∩M_2)= N_1⊕N_2, where N_1= N∩M_1 and N_2= N∩M_2.
Case(1): N_1 = M_1 and N_2 < M_2.
There exists g ∈End_R(M_2), g≠0, g^2(N_2)=0 . Define h ∈End_R(M) by h(a,b) = (0, g(b)) ≠0 ∀ (a, b) ∈M. But h^2(a, b) = (0, g^2(b)) ∀ (a, b) ∈M, and so h^2(N_2)= 0.
Case(2): N_1 < M_1 and N_2 = M_2.
The proof is similar to case (1).
Case(3): N_1 < M_1 and N_2 < M_2.
Since M_1 and M_2 are weakly coretractable modules, there exist f ∈End_R(M_1), f≠ 0 and f^2(N_1)=0 and g ∈End_R(M_2), g≠ 0 and g^2 (N_2)= 0. Define h∈ End_R(M) by h(x,y)= (f(x), g(y)), h≠0 and h^2(N)= 0. Therefore M is weakly coretractable.
Proposition(2.7): Let M=M_1⊕M_2, where M_1 and M_2 are fully invariant in M and M is weakly coretrectable, then either M_1 or M_2 is weakly coretrectable.
Proof: Let N_1 and N_2 be proper submodule of M_1 and M_2 respectively. Then N=N_1⊕N_2 is a proper submodule of M. As M is weakly coretrectable, ∃f∈ End_R(M), f≠0, N⊆kerf^2.
As $End_Z(M) \cong \begin{pmatrix} End(M_1) & Hom(M_2, M_1) \\ Hom(M_1, M_2) & End(M_2) \end{pmatrix}$. But $Hom(M_2, M_1)=0$, $Hom(M_1, M_2)=0$, (since M_1 and M_2 are fully invariant in M). Thus $End_Z(M) \cong \begin{pmatrix} End(M_1) & 0 \\ 0 & End(M_2) \end{pmatrix}$ and so $f=\begin{pmatrix} f_1 & 0 \\ 0 & f_2 \end{pmatrix}$ for some $f_1 \in End(M_1), f_2 \in End(M_2)$. As f≠0, either f_1≠0 or f_2≠0. On other hand 0=f^2(N)=$f_1^2(N_1) \oplus f_2^2(N_2)$, that is $f_1^2(N_1)$= 0 and $f_2^2(N_2)$= 0. Thus either M_1 or M_2 is weakly coretractable.
"A submodule N of M is coquasi-invertible of M if Hom_R(M, N)= 0 [12, P. 8] and a nonzero R-module M is coquasi-Dedekind if every proper submodule of M is coquasi-invertible " [12, P. 32].
Also, M is coquasi-Dedekind if for each f∈EndR(M), f≠0, f is an epimomorphism [12, Theorem(2.1.4)].
Proposition(2.8): Let M be a weakly coretractable and coquasi-Dedekind module. If N is a proper fully invariant submodule of M, then M/N is weakly coretrectable.

Proof: Let U/N < M/N. Then U < M, but M is weakly coretrectable, so ∃f∈ EndR(M), f≠0 and f2(U)=0. Define g:M/N→M/N by g(m+N)=f(m)+N ∀m∈M. Then g is well-defined since N is fully invariant, also g is an R-homomorphism. Beside this g≠0 because if g=0, f(M)⊆N and so f ∈Hom(M, N) which is contradiction since M is coquasi-Dedekind. Now $g^2(U/N)=g(g(U/N)= g(f(U)+N)= f^2(U)+N= N=0_{M/N}$. Thus M/N is a weakly coretractable module.

The following gave a characterization for weakly coretractable ring R, when R is a commutative semiprime.

Proposition(2.9): If R is commutative semiprime. R is weakly coretractable iff for each proper ideal I of R, there exists $f:R/I^2 \rightarrow R$, f≠0.

Proof:**(⇒)** Let I < R. Hence I^2 < R and so ∃f∈End(R), f≠0 such that $f^2(I)=0$, f≠0. As f∈End(R) there exists r≠0, r∈R, f(x)=rx for all x∈R, hence $f^2(x)=r^2x$. Define $g:R/I^2\rightarrow R$, by $g(x+I^2)=f^2(x)$ for each x∈R. It easy to check that g is well-defined. As $g(1+I^2)=f^2(1)=r^2 \neq 0$, then g≠0.

(⇐) Let I < R. Then I^2 < R, and hence ∃$f:R/I^2\rightarrow R$, f≠0. Let g=f∘π, so that g∈End(R) and g ≠0, $g(I^2)=0$. Set g(1)=r. $g^2(I) = g(g(I)) = g(Ir)=Ir^2$. But $g(I^2)=I^2 r =0$, then $I^2 r^2= 0=(I r)^2$, and so Ir=0 since R is semiprime. Thus $g^2(I)=0$. Therefore R is weakly coretractable.

In the class of finitely generated faithful multiplication R-modules, weakly coretractability transferred from a module M to a ring R and conversely.

Theorem(2.10): If M is finitely generated faithful multiplication module. M is weakly coretractable iff R is weakly coretrectable, where R is commutative ring.

Proof: **(⇒)** Let I < R. Then N =MI < M, hence ∃f∈ $End_R(M)$, f≠0 and $f^2(N)=0$. But $f^2(N)=f^2(M)I=0$. As M is f. g. multiplication, M is scalar module, so ∃r ∈R, r ≠0 and f(m)=mr ∀m ∈M, hence f(M)=Mr. Thus $f^2(M)I=Mr^2I$. Now, define g:R→R by g(a)=ra, hence g≠0 and g(I)=rI. It follows that $g^2(I) = g(g(I)) =g(rI)= r^2I$. But $Mr^2I=0$ implies $r^2I\subseteq annM=0$; that is $r^2I=0$. Therefore $g^2(I)=0$ and R is weakly coretrectable.

(⇐) Let N=MI be a proper submodule of M. Then I is a proper ideal in R, so there exists f∈ $End_R(R)$ such that $f^2(I)=0$ and f≠0. Assume f(1)=r, then f(I)=Ir. Define h:M→M by h(x)=xr for each x ∈M, h is well-defined and $h^2(m)=h^2(\sum_{i=1}^{n} x_i a_i)$, x_i ∈M and a_i ∈ I, i= 1, 2, 3, …, n and m∈N. Hence $h^2(m)=\sum_{i=1}^{n} x_i r^2 a_i) = 0$ for each m ∈N and so $h^2(N)=0$. M is weakly coretrectable.

Proposition(2.11): Let M be an R-module, then the following statements are equivalent:

M is simple;

M is coretractable and $End_R(M)$ is a division ring;

M is weakly coretractable and $End_R(M)$ is a division ring.

Proof:**(1)⇔ (2)** It follows by Proposition(1.12).

(2)⇒(3) It is clear.

(3)⇒(1) suppose M is not simple; N < M and N≠0. As M is weakly coretrectable, so ∃g ∈$End_R(M)$, g≠0 and $g^2(N)=0$. Thus g^2 is not monomorphism. Hence $g^2\neq 0$ (since $End_R(M)$ is a division ring). But g ≠ 0, so g^{-1} exists and hence $g^{-1}g^2=g=0$ which is a contradiction. Thus M is simple.

References

[1] Al-Saadi S A and Ibrahiem T A 2014 Strongly Rickart Rings *Mathematical Theory and Modeling* **4** 8 pp 95-105

[2] Amini B, Ershad M and Sharif H 2009 Coretractable Modules *J. Aust. Math. Soc* **86** 3 pp 289-304.

[3] Clark J, Lomp C, Vanaja N and Wisbauer R 2006 Lifting Modules Frontiers In Mathematics (Basel-Boston-Berlin:Birkhäuser Basel)

[4] Goodearl K R 1973 *Ring Theory Nonsingular Rings And Modules*

[5] Lam T Y 1999 *Lectures on Modules and Rings* (Springer, New York)

[6] Hadi I M A and Al-aeashi S N 2017 *Strongly Coretractable Modules* Iraqi Journal of Science **58** 2C pp 1069-1075

[7] Hadi I M and Al-aeashi S N 2016 Strongly Coretractable Modules and Some Related Concepts *Journal of advances in Mathematics* **12** 12 pp 6881-88
[8] Hadi I M and Al-aeashi S N 2017 Y-coretractable and Strongly Y-Coretractable Modules *Asian Journal of Applied Sciences* **5** 2 pp 427-33
[9] Hadi I M and Al-aeashi S N 2017 P-coretractable and Strongly P-Coretractable Modules *Asian Journal of Applied Sciences* **5** 2 pp 477-82
[10] Hadi I M and Al-aeashi S N 2017 Studying Some Results about Completely Coretractable Ring (CC-ring) *Global Journal of Mathematics* **10** 1 644-47
[11] Hadi I M and Al-aeashi S N 2017 Some Results About Coretractable Modules *Journal of AL-Qadisiyah for computer science and mathematics* **9** 2 pp 40-48
[12] Yaseen S M 2003 *Coquasi-Dedekind Modules* Ph. D. Thesis University Of Baghdad Baghdad Iraq

Solving Modified Regularized Long Wave Equation Using Collocation Method

Solving Modified Regularized Long Wave Equation Using Collocation Method

Hamad Salih1,2, Luma Naji Mohammed Tawfiq3, Zainor Ridzuan Yahya1, Shazalina Mat Zin1

[1]Institute of Engineering Mathematics, Universiti Malaysia Perlis, 02600 Pauh, Perlis, Malaysia,
[2]Department of Mathematics, University of Anbar, Al-anbar, Iraq,
[3]Department of Mathematics, University of Bagdad, Bagdad, Iraq

Abstract. In this paper, we suggest collocation method depending on Cubic trigonometric B-spline (CuTBS) approach based on finite difference scheme to solve the modified regularized long wave equation. The single solitary wave motion was studied using the proposed method; thus the accuracy and efficiency of the suggested method were computed from the L_2 , L_∞ norms. Also, the von-Neumann method was used to study the linear stability analysis. The obtained results through the tested two problems exhibited that, the method is an effective numerical scheme to solve Modified Regularized Long Wave equation (MRLW).

Key word: Cubic Trigonometric B-spline method, Finite Difference, Regularized Long Wave Equation ,Von-Neumann method.

1. Introduction

Nonlinear partial differential equations can be effectively employed to express an assortment of physical and applied mathematical concerns. A non-linear partial differential equation is defined as a partial differential equation that comes with nonlinear terms. The numerical solutions derived from nonlinear partial differential equations are particularly useful for deciphering solitary waves of pulses or wave packets [1]. A model of the MRLW eq. can be utilized to symbolize the nonlinear PDEs

$$z_t + z_x + \varepsilon z^2 z_x - \mu z_{xxt} = 0 \tag{1}$$

with boundary conditions (BC)

$$z(a,t) = 0 \quad , z(b,t) = 0 \tag{2}$$

and the initial condition(IC)

$$z(a,0) = f(\mathrm{x}) \quad a \le x \le b \tag{3}$$

in which ε and μ represent positive parameters. Recognized as one of the foremost equations for nonlinear dispersive waves, the MRLW equation is applicable for a wide variety of issues. This includes phonon packets in nonlinear crystals, ion-acoustic waves in plasma and magneto hydrodynamic, ion-acoustic waves in plasma, pressure waves in liquid-gas bubble mixtures and down a tube, and transverse

waves in shallow water. The lumped galerkin technique based on cubic B-spline was employed to realize a solution to the MRLW equation. Karakoc et al. employed a numerical approach derived from a Petrow-Galerkin procedure to scrutinize the movement of a solitary wave. Their investigation, which delivered precise results, involved the use of quadratic weight functions and cubic B-spline finite elements [2-4]. The arrival to a numerical solution of the MRLW equation can be realized by way of the extended cubic B-spline procedure [5]. When it comes to ascertaining the value of parameter k, the approximation derived through the extended cubic B-spline algorithm has proven to be more exact than that of the cubic B-spline. Several methods have been introduced for realizing a numerical solution to the RLW equation for a solitary wave movement. Dag et al. [6-10] employed the collection method based on quartic B-spline. Other methods include interpolation functions, the quintic B-spline Galerkin finite element method, cubic B-spline functions, the least squares quadratic B-spline finite element method, and the least squares finite element method based on cubic B-spline. The results obtained through these methods were found to be more precise than those previously recorded in related literature.

B-splines are frequently employed for solutions to linear or nonlinear partial differential equations in the domains of engineering and science. The trigonometric B-spline based function is an option to the famous polynomial B-spline based function [11]. While the structure of the former is based on trigonometric functions, the structure of the latter is based on polynomial functions [12]. This study focuses on the arrival at a solution to the MRLW equation through trigonometric B-spline collocation procedures. The cubic trigonometric B-spline (TCuBS) was employed to realize a numerical solution to the non-linear Benjamin-Bona-Mahony-Burger equation, the coupled viscous Burgers' equation [13-14], as well as the generalized nonlinear Klein-Gordon wave equation [15-16].

2. Numerical Solution of MRLW equation.

The standard finite difference formula is applied for estimating the time derivative.

$$\frac{\partial z^n}{\partial t} = \frac{z^{n+1} - z^n}{\Delta t} \tag{4}$$

The use of (4) transforms equation (1) into

$$\frac{z^{n+1} - z^n}{\Delta t} - \mu \frac{(z_{xx})^{n+1} - (z_{xx})^n}{\Delta t} + z_x^n + \varepsilon (z^2 z_x)^n = 0 \tag{5}$$

And the use of the θ weighted technique facilitates the expression of the space derivatives of the MRLW equation (1) as

$$\frac{z^{n+1} - z^n}{\Delta t} - \mu \frac{(z_{xx})^{n+1} - (z_{xx})^n}{\Delta t} + \theta (z_x^{n+1} + \varepsilon (z^2 z_x)^{n+1}) + (1-\theta)(z_x^n + \varepsilon (z^2 z_x)^n) = 0 \tag{6}$$

The use of the rule [20]

$$(z^2)^{n+1} z_x{}^{n+1} = (z^n)^2 z_x{}^{n+1} + 2 z^n z_x^n z^{n+1} - 2 (z^n)^2 z_x^n$$

Allows for equation (6) to be generated as

$$\begin{aligned} & z^{n+1} - \mu z_{xx}^{n+1} + \Delta t \theta z_x^{n+1} + \Delta t \theta (z^n)^2 z_x{}^{n+1} + \Delta t \theta 2 z^n z_x^n z^{n+1} \\ & = z^n - \mu z_{xx}^n - \Delta t (1-\theta) z_x^n + \Delta t (1-\theta)(z^n)^2 z_x^n \end{aligned} \tag{7}$$

The system is regarded an explicit scheme if $\theta = 0$, a completely implicit scheme if $\theta = 1$ and a Crank-Nicolson scheme if $\theta = \frac{1}{2}$. As this study opted for the Crank-Nicolson procedure, equation (7) is converted into

$$z^{n+1}-\mu z_{xx}^{n+1}+\frac{\Delta t}{2}z_x^{n+1}+\frac{\Delta t}{2}(z^n)^2 z_x{}^{n+1}+\Delta t z^n z_x z^{n+1}$$
$$=z^n-\mu z_{xx}^n-\frac{\Delta t}{2}z_x^n+\frac{\Delta t}{2}(z^n)^2 z_x^n \tag{8}$$

3.1. CuTBS for Solving MRLW Equation

The basis function of the CuTBS is expressed as:

$$TB_{4,\mathrm{j}}(x)=\frac{1}{z}\begin{cases}a^3(x_j), & x\in[x_j,x_{j+1})\\ \mathrm{a}(x_j)\Big(\mathrm{a}(x_j)\,\mathrm{b}(x_{j+2})+b(x_{j+3})\,\mathrm{a}(x_{j+1})\Big)+b(x_{j+4})\,\mathrm{a}^2(x_{j+1}), & x\in[x_{j+1},x_{j+2})\\ \mathrm{b}(x_{j+4})\Big(\mathrm{a}(x_{j+1})\,\mathrm{b}(x_{j+3})+b(x_{j+4})\,\mathrm{a}(x_{j+2})\Big)+a(x_j)\,\mathrm{b}^2(x_{j+3}), & x\in[x_{j+2},x_{j+3})\\ b^3(x_{j+4}), & x\in[x_{j+3},x_{j+4}]\end{cases} \tag{9}$$

The values of $TB_{4,\mathrm{j}}(\mathrm{x}), TB'_{4,\mathrm{j}}(\mathrm{x})$ and $TB''_{4,\mathrm{j}}(\mathrm{x})$ at the knots x_j were calculated through equation (9) and registered in (Table 1).

Table 1: $TB_{4,i}(x)$ values and their derivatives.

x	x_j	x_{j+1}	x_{j+2}	x_{j+3}	x_{j+4}
$TB_{4,\mathrm{j}}$	0	p_1	p_2	p_1	0
$TB'_{4,\mathrm{j}}$	0	p_3	0	p_4	0
$TB''_{4,\mathrm{j}}$	0	p_5	p_6	p_5	0

where

$$p_1=\frac{\sin^2\left(\frac{h}{2}\right)}{\sin(h)\sin\left(\frac{3h}{2}\right)},\ p_2=\frac{2}{1+2\cos(h)},\ p_3=-\frac{3}{4\sin\left(\frac{3h}{2}\right)},\ p_4=\frac{3}{4\sin\left(\frac{3h}{2}\right)},$$
$$p_5=\frac{3\left(1+3\cos(h)\right)}{16\sin^2\left(\frac{h}{2}\right)\left(2\cos\left(\frac{h}{2}\right)+\cos\left(\frac{3h}{2}\right)\right)},\ p_6=-\frac{3\cos^2\left(\frac{h}{2}\right)}{\sin^2\left(\frac{h}{2}\right)\left(2+4\cos(h)\right)}$$

In keeping with the proposed procedure, the approximation algorithm for solving equation (1) is

$$z_j(x,t)=\sum_{j=-3}^{N-1}C_j(t)TB_{4,j}(x) \tag{10}$$

in which $C_j(\mathrm{t})$ are unidentified time dependents that need to be ascertained, $TB_{4,j}(x)$ is a CuTBS. The assessment process at each x_j involves only three non-zero basis functions. This circumstance is attributed to the local support properties of basis function. As such, the approximate solution calls for the values of

$TB_{4,j}(x)$ and its derivatives at nodal points to be identified. Approximate functions (9) and (10) were utilized for tabulating these derivatives. Here, the values at the knots Z_j^n of and their derivatives until the second order are:

$$\begin{cases} (z)_j^n = p_1 C_{j-3}^n + p_2 C_{j-2}^n + p_1 C_{j-1}^n, \\ \left(\dfrac{\partial z}{\partial x}\right)_j^n = p_3 C_{j-3}^n + p_4 C_{j-1}^n \\ \left(\dfrac{\partial^2 z}{\partial x^2}\right)_j^n = p_5 C_{j-3}^n + p_6 C_{j-2}^n + p_5 C_{j-1}^n \end{cases} \tag{11}$$

Equation (8) with the nodal values of w and its derivatives uses (11) to realize the difference equation below with the variables C_j, $\mathrm{j} = -3,...,\mathrm{N}-1$.

$$a_1 C_{j-3}^{n+1} + a_2 C_{j-2}^{n+1} + a_3 C_{j-1}^{n+1} = b_1 C_{j-3}^n + b_2 C_{j-2}^n + b_3 C_{j-1}^n \tag{12}$$

Here

$$a_1 = (1 + \varepsilon \Delta t z^n z_x^n) p_1 + (\frac{\Delta t}{2} + \frac{\Delta t \varepsilon}{2} (\mathrm{z}^n)^2) p_3 - \mu p_5 \quad , b_1 = (p_1 + (\frac{\Delta t \varepsilon}{2} (\mathrm{z}^n)^2 - \frac{\Delta t}{2}) p_3 - \mu p_5$$
$$a_2 = (1 + \varepsilon \Delta t z^n z_x^n) p_2 - \mu p_6 \qquad\qquad ,b_2 = p_2 - \mu p_6$$
$$a_3 = (1 + \varepsilon \Delta t z^n z_x^n) p_1 + (\frac{\Delta t}{2} + \frac{\Delta t \varepsilon}{2} (\mathrm{z}^n)^2) p_4 - \mu p_5 \quad ,b_3 = p_1 + (\frac{\Delta t \varepsilon}{2} (\mathrm{z}^n)^2 - \frac{\Delta t}{2}) p_4 - \mu p_5$$

the simplification of (12) gives rise to a system comprising the $(N+1)$ linear equation in the $(N+3)$ unknown $C^n = [\mathrm{C}_{j-3}^n, ..., \mathrm{C}_{N-1}^n]$ at the time level $t = t_{n+1}$, Equation (10), which is applied for acquiring the solution to the boundary conditions (2) is expressed as:

$$\begin{aligned} p_1 C_{-3}^{n+1} + p_2 C_{-2}^{n+1} + p_1 C_{-1}^{n+1} &= 0, \qquad j = 0, \\ p_1 C_{j-3}^{n+1} + p_2 C_{j-2}^{n+1} + p_1 C_{j-1}^{n+1} &= 0, \qquad j = N \end{aligned} \tag{13}$$

For equations (12) and (13), the system comprising $(N+3)\times(N+3)$ is expressed as:

$$M_{(N+3)\times(N+3)} C_{(N+3)\times 1}^{n+1} = Z_{(N+3)\times(N+3)} C_{(N+3)\times 1}^n$$

Initial state

Based on the initial conditions will calculate the initial vector C^0. The values of C^0 were obtained using the initial conditions and boundary values of the derivatives for the initial condition as below

$$\begin{cases} (z_j^0)_x = g'(\mathrm{x}_j) & j = 0 \\ z_j^0 = g(\mathrm{x}_j) & j = 0,1,...,N \\ (z_j^0)_x = g'(\mathrm{x}_j) & j = N \end{cases} \tag{14}$$

This generates the following $(N+3)\times(N+3)$ tridiagonal matrix system as follows.

$$A_{(N+3)\times(N+3)}K^{0}_{(N+3)\times 1}=d_{(N+3)\times 1}$$

where

$$K^{0}=[\mathrm{C}^{0}_{-3},\mathrm{C}^{0}_{-2},...,\mathrm{C}^{0}_{N-1}]^{T}\ ,\ d=[g^{'}(\mathrm{x}_0),g(\mathrm{x}_0),g(\mathrm{x}_1),...,g(\mathrm{x}_{N-1}),g(\mathrm{x}_N),g^{'}(\mathrm{x}_N)]^{T}$$

4. Stability Analysis

The Fourier method is introduced for an evaluation on the stability of the trigonometric cube B-spline method. For this purpose, Equation (1) is linearized by the assumption that quantity z^2 in the nonlinear term is unvarying β . The linearized configuration of the recommended procedure is expressed as

$$w_1C^{k+1}_{j-3}+w_2C^{k+1}_{j-2}+w_3C^{k+1}_{j-1}=u_1C^{k}_{j-3}+u_2C^{k}_{j-2}+u_3C^{k}_{j-1} \tag{15}$$

in which

$$\begin{aligned} w_1&=2\mathrm{p}_1+\Delta t(1+\varepsilon\beta)\mathrm{p}_3-2\mu\mathrm{p}_5 \quad ,\ u_1=2\mathrm{p}_1-\Delta t(1+\varepsilon\beta)\mathrm{p}_3-2\mu\mathrm{p}_5\\ w_2&=2\mathrm{p}_2+0-2\mu\mathrm{p}_6 \qquad\qquad\quad ,u_2=2\mathrm{p}_2-0-2\mu\mathrm{p}_6\\ w_3&=2\mathrm{p}_1+\Delta t(1+\varepsilon\beta)\mathrm{p}_4-2\mu\mathrm{p}_5 \quad ,u_3=2\mathrm{p}_1-\Delta t(1+\varepsilon\beta)\mathrm{p}_4-2\mu\mathrm{p}_5 \end{aligned}$$

the replaced Fourier mode $C^{k}_{j}=\varsigma^{k}e^{(\mathrm{i}m\eta h)}$, $i=\sqrt{-1}$ in Equation(15) gives rise to

$$\varsigma=\frac{X-iY}{X+iY} \tag{16}$$

Here,

$$\begin{aligned} \mathrm{X}&=(4\mathrm{p}_1-4\mu\mathrm{p}_5)\cos(\eta h)+(2\mathrm{p}_2-2\mu\mathrm{p}_6)\\ Y&=(2(1+\varepsilon\beta)\mathrm{p}_4)\sin(\eta\,\mathrm{h}) \end{aligned}$$

Thus, the stability condition $|\varsigma|\leq 1$, the modulus of Eq. (16) yields $|\varsigma|=1$, and as result the scheme will be unconditionally stable.

5. Numerical Experiments

This segment focuses on the computation for the L_2 and L_∞ error norms by way of the formula below:

$$L_\infty=\max|z^{exact}_i-z^{num}_i|,$$

$$L_2=\sqrt{h(\sum_{i}^{n}|z^{exact}_i-z^{num}_i|^2}$$

Also computed are the conservation laws through the formula [19]. In this formula C_1 represents the mass, C_2 the momentum and C_3 the energy.

$$C_1 = \int_a^b z(x,t)\,\mathrm{d}\,x,$$

$$C_2 = \int_a^b z(x,t)^2\,\mathrm{d}\,x,$$

$$C_3 = \int_a^b [z(x,t)^2 + \frac{1}{3}z(x,t)^3]\,\mathrm{d}\,x,$$

Example 1

The MRLW equation has an precise solution $\mathrm{z}(x,t) = 3c\sec h^2\left(\frac{1}{2}\sqrt{\frac{c}{1+c}}(x-(1+c)t-x_0)\right)$, initial conditions $\mathrm{z}(x,0) = 3c\sec h^2\left(\frac{1}{2}\sqrt{\frac{c}{1+c}}(x-x_0)\right)$ and boundary conditions $\mathrm{z}(0,t) = 0, \mathrm{z}(100,t) = 0$. $v = 1+c$ represents wave velocity and $x_0 = 40$ [1]. The calculation for numerical answers to this problem was derived through the cubic trigonometric B-spline procedure. The norms errors as well as the conservation laws at distinct time levels with the parameters $\varepsilon = \mu = 1$, c=0.3.0.09, $\Delta t = 0.025$ and $\Delta x = 0.2$ were computed and registered Tables 2 and 3 respectively .The computations of L_∞ and L_2 errors at various times revealed that the margin of error escalated in tandem with the increase in time. This gave rise to minor disparities in the C_1 , C_2 and C_3 values which amounted to below 10^{-3} ,10^{-6} and 10^{-7} respectively . The space–time graph for the approximation and exact solutions at t=5 and t=10 and c=0.3 is displayed in Figure 1.The table and figure show that the of L_∞ and L_2 errors are increasing as time increases

Table 2: c=0.3 , $\Delta t = 0.025$, $\Delta x = 0.2$, $0 \le x \le 100$ cubic trigonometric b-spline

T	L_2	L_∞	C_3	C_2	C_1
5	0.007226	0.001888	0.008865	0.127301	2.107066
10	0.014416	0.003845	0.008863	0.127302	2.106733
15	0.021575	0.005848	0.008858	0.127303	2.106135
20	0.028686	0.007867	0.008851	0.127304	2.104627

Table 3: $h = 0.2, \Delta t = 0.1, x_0 = 40, c = 0.09, 0 \le x \le 100$ cubic trigonometric b-spline

T	L_2	L_∞	C_3	C_2	C_1
5	0.072146	0.024671	0.142305	0.688049	3.759237
10	0.142238	0.049605	0.141782	0.688360	3.759894
15	0.208868	0.072388	0.140899	0.688638	3.760450
20	0.271397	0.092359	0.139735	0.688889	3.760882

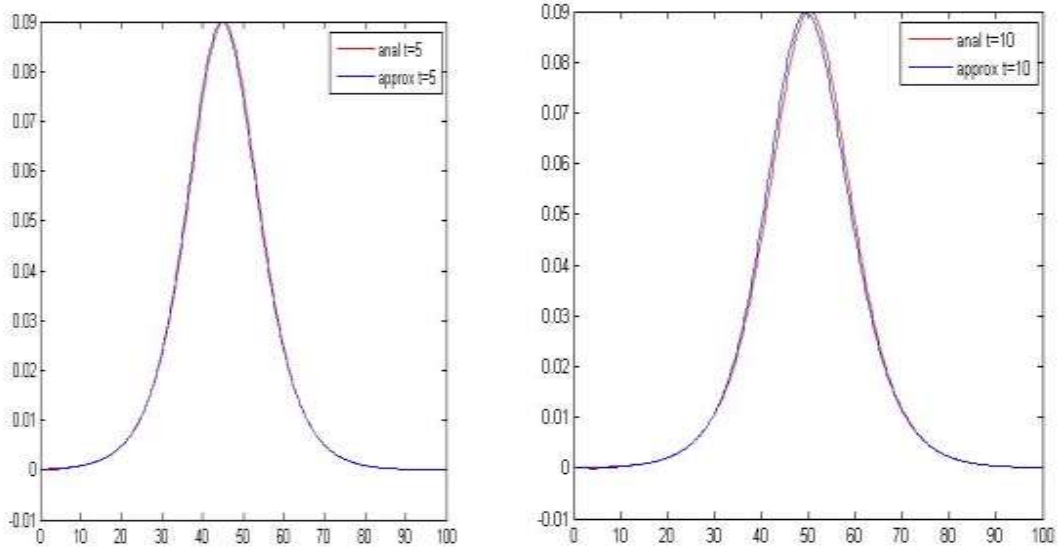

Figure 1: Approximation and exact solution by CuTBS at c=0.3 at different time levels

Example 2

We consider the motion of single wave equation (1) has exact solution in the form [21-23] $z(x,t) = b + 3c\sec h^2\left(k(x - x_0 - (b+c)t)\right)$ where b,c are constant and $k = \frac{1}{2}\sqrt{\frac{c}{\mu(\mathrm{b}+\mathrm{c})}}$ with initial condition $z(x,t) = b + 3c\sec h^2\left(\mathrm{k}(x - x_0)\right)$.We choose $\varepsilon = \mu = 1, x_0 = 40, c = 0.3, b = 1$ and $0 \le x \le 80$ the interval divided element of equal length $\Delta x = 0.2$ at time T =1 and $\Delta t = 0.01$. In Tables 4 lists the calculations of L_2 error at different time as observed the error increased when the time increased. This led to trivial differences in the C_1, C_2 and C_3 values. These differences did not exceed 10^{-2}.

Table 4: $c = 0.3, \varepsilon = \mu = 1, x_0 = 40, h = 0.2, \Delta t = 0.01, 0 \le x \le 80, T = 1$

T	L_2	C_3	C_2	C_1
0.1	1.099427	115.094176	97.940786	85.500228
0.2	1.102576	115.093482	97.952850	85.496447
0.3	1.107873	115.087847	97.971810	85.489544
0.4	1.115286	115.077166	97.998092	85.479538
0.5	1.124764	115.061282	98.032325	85.466455
0.6	1.136247	115.039984	98.075382	85.450329
0.7	1.149666	115.012988	98.128423	85.431207
0.8	1.164942	114.979925	98.192978	85.409143
0.9	1.181990	114.940312	98.271044	85.384209
1.0	1.200722	114.893519	98.365247	85.356491

6-Conclusion

The primary objective of this study is to confirm the effectiveness of the CuTBS procedure. This is in the context of realizing a solution to the unique kind of PDE by way of a one-dimensional nonlinear adapted regularized long wave equation. Two cases in point were investigated. Tables 2, 3 and 4 portray the errors acquired through the application of the proposed procedure on the MRLW equation. It was discovered that the errors increased in tandem with the rise in time. The applicability of this procedure is further enhanced by its elevated level of stability. This was verified through the Von Neumann stability analysis.

Reference

[1] Mohammadi, R. (2015). Exponential B-spline collocation method for numerical solution of the generalized regularized long wave equation. *Chinese Physics B*,*24*(5), 050206.

[2] Karakoc, S. B. G., Geyikli, T., & Bashan, A. (2013). A numerical solution of the modified regularized long wave (MRLW) equation using quartic B-splines.*TWMS Journal of Applied and Engineering Mathematics*, *3*(2), 231.

[3] Karakoc, S. B. G., Ucar, Y., & YAĞMURLU, N. (2015). Numerical solutions of the MRLW equation by cubic B-spline Galerkin finite element method. *Kuwait Journal of Science*, *42*(2).

[4] Karakoc, S. B. G., &Geyikli, T. (2013). Petrov-Galerkin finite element method for solving the MRLW equation. *Mathematical Sciences*, *7*(1), 1-10.

[5] Dağ, İ., Irk, D., & Sarı, M. (2013). The extended cubic B-spline algorithm for a modified regularized long wave equation. *Chinese Physics B*, *22*(4), 040207.

[6] Saka, B., &Dağ, İ. (2007). Quartic B-spline collocation algorithms for numerical solution of the RLW equation. *Numerical Methods for Partial Differential Equations*, *23*(3), 731-751.

[7] Dağ, İ., Saka, B., & Irk, D. (2006). Galerkin method for the numerical solution of the RLW equation using quintic B-splines. *Journal of Computational and Applied Mathematics*, *190*(1), 532-547.

[8] Dağ, İ., Saka, B., & Irk, D. (2004). Application of cubic B-splines for numerical solution of the RLW equation. *Applied Mathematics and Computation*, *159*(2), 373-389.

[9] Dağ, İ. (2000). Least-squares quadratic B-spline finite element method for the regularised long wave equation. *Computer Methods in Applied Mechanics and Engineering*, *182*(1), 205-215.

[10] Dağ, İ., &Özer, M. N. (2001). Approximation of the RLW equation by the least square cubic B-spline finite element method. *Applied Mathematical Modelling*, *25*(3), 221-231.

[11] Ersoy, O., & Dag, I. (2016). A Trigonometric Cubic B-spline Finite Element Method for Solving the Nonlinear Coupled Burger Equation. *arXiv preprint arXiv:1604.04419*

[12] Hamid, N. N., Majid, A. A., & Ismail, A. I. M. (2010). Cubic trigonometric B-spline applied to linear two-point boundary value problems of order two. *World Academic of Science, Engineering and Technology*, *47*, 478-803.

[13] Salih, H. M., Tawfiq, L. N. M., &Yahya, Z. R. (2016). Using Cubic Trigonometric B-Spline Method to Solve BBM-Burger Equation. IWNEST Conference Proceedings, 2, 1-9.

[14] Salih, H. M., Tawfiq, L. N. M., &Yahya, Z. R. (2016). Numerical Solution of the Coupled Viscous Burgers' Equation via Cubic Trigonometric B-spline Approach.*Math Stat*, *2*(011).

[15] Zin, S. M., Abbas, M., Majid, A. A., & Ismail, A. I. M. (2014). A new trigonometric spline approach to numerical solution of generalized nonlinear klien-gordon equation. *PloS one*, *9*(5), e95774.

[16] Zin, S. M., Majid, A. A., Ismail, A. I. M., & Abbas, M. (2014). Cubic Trigonometric B-spline Approach to Numerical Solution of Wave Equation. *World Academy of Science, Engineering and Technology, International Journal of Mathematical, Computational, Physical, Electrical and Computer Engineering*, *8*(10), 1302-1306.

[17] Zin, S. M. (2016).B-spline Collocation Approach for Solution Partial Differential Equation. Thesis
[18] Walz, G. (1997). Identities for trigonometric B-splines with an application to curve design. *BIT Numerical Mathematics*, *37*(1), 189-201.
[19] Olver, P. J. (1979). Euler operators and conservation laws of the BBM equation. In *Mathematical Proceedings of the Cambridge Philosophical Society*(Vol. 85, No. 01, pp. 143-160). Cambridge University Press.

[20] Islam, S. U., Haq, F. I., &Tirmizi, I. A. (2010). Collocation Method Using Quartic B-spline for Numerical Solution of the Modified Equal Width Wave Equation. *Journal of applied mathematics & informatics*, *28*(3_4), 611-624.
[21] Soliman, A. A., & Hussien, M. H. (2005). Collocation solution for RLW equation with septic spline. *Applied Mathematics and Computation*, *161*(2), 623-636.
[22] Soliman, A. A., & Raslan, K. R. (2001). Collocation method using quadratic B-spline for the RLW equation. *International journal of computer mathematics*, *78*(3), 399-412.
[23] Gardner, L. R. T., & Gardner, G. A. (1990). Solitary waves of the regularised long-wave equation. *Journal of Computational Physics*, *91*(2), 441-459.

FIBREWISE IJ-PERFECT BITOPOLOGICAL SPACES

FIBREWISE IJ-PERFECT BITOPOLOGICAL SPACES

Y.Y.Yousif, L.A.Hussain

Department of Mathematics, College of Education for Pure Science (Ibn Al-haitham), Baghdad University, Baghdad
yoyayousif@yahoo.com1, Liwaaalhashemy@gmail.com2

Abstract : The main purpose of this paper is to introduce a some concepts in fibrewise bitopological spaces which are called fibrewise ij , fibrewise ij -closed, fibrewise ij −compact, fibrewise ij-perfect, fibrewise weakly ij-closed, fibrewise almost ij-perfect, fibrewise ij^*-bitopological space respectively. In addition the concepts as ij-contact point, ij-adherent point, filter, filter base, ij-converges to a subset, ij-directed toward a set, ij-continuous, ij-closed functions, ij-rigid set, ij-continuous functions, weakly ij-closed, ij-H-set, almost ij-perfect, ij^*-continuous, pairwise Urysohn space, locally ij-QHC bitopological space are introduced and the main concept in this paper is fibrewise ij-perfect bitopological spaces. Several theorems and characterizations concerning with these concepts are studied.

Keywords : bitopological spaces, closed bitopological space, filter base, Fibrewise IJ-Perfect Bitopological Spaces

1. Introduction and Preliminaries.

In order to begin the category in the classification of fibrewise (briefly, F.W.) sets over a given set, named the base set, which say B. A F.W. set over B consists of a set M with a function $p: M \to B$, that is named the projection. The fibre over b for every point b in B is the subset $M_b = p^{-1}(b)$ of M. Perhaps, fibre will be empty since we do not require p is surjectve, also, for every subset B^* of B, we consider $M_{B^*} = p^{-1}(B^*)$ as a F.W. set over B^* with the projection determined by p. The alternative notation of M_{B^*} is sometime referred to as $M \mid B^*$. We consider the Cartesian product $B \times T$, for every set T, as a F.W. set over B by the first projection.

The bitopological spaces were first created by Kelly [١] in 1963 and after that a large number of researches have been completed to generalize the topological ideas to bitopological setting. A set M with two topologies τ_1 and τ_2 is called bitopological space [7] and is denoted by (M, τ_1, τ_2). By τ_i-open (resp., τ_i-closed), we shall mean the open (resp., closed) set with respect to τ_i in M, where $i = 1,2$. A is open (resp., closed) if it is both τ_1-open (resp., τ_1-closed) and τ_2-open (resp., τ_2-closed) in M. As well as, we built on some of the results in [1, 8, 13, 14, 15, 16,17, 18]. For other notations or notions which are not mentioned here we go behind closely I. M. James [5], R. Engelking [٤] and N. Bourbaki [3].

Definition:1.1. [5] If M and N with projections p_M and p_N, respectively, are F.W. sets over B, a function $\varphi: M \to N$ is named F.W. function if $p_N \, o \, \varphi = p_M$, or $\varphi(M_b) \subset N_b$ for every $b \in B$.

Definition: 1.2. [5] Let (B, Λ) be a topological space. The F.W. topology on a F.W. set M over B mean any topology on M makes the projection p is continuous.

Definition: 1.3. [5] The F.W. function $\varphi: M \to N$, where M and N are F.W. topological spaces over B is named:

Continuous if for every $x \in M_B$; $b \in B$, the inverse image of every open set of $\varphi(x)$ is an open set of x.

Open if for every $x \in M_B$; $b \in B$, the direct image of every open set of x is an open set of $\varphi(x)$.

Definition:1.4. [5] The F.W. topological space (M, τ) over (B, Λ) is named F.W. closed, (resp. F.W. open) if the projection p is closed (resp. open).

Definition: 1.5. [7] The triple (M, τ_1, τ_2) where M is a non-empty set and τ_1 and τ_2 are topologies on M is named bitopological spaces.

Definition:1.6. [7] A function $\varphi: (M, \tau_1, \tau_2) \to (N, \sigma_1, \sigma_2)$ is said to be τ_i-continuous (resp. τ_i-open and τ_i-closed), if the functions $\varphi: (M, \tau_i) \to (N, \sigma_i)$ are continuous (resp. open and closed), φ is named continuous (resp. open and closed) if it is τ_i-continuous (resp. τ_i-open and τ_i-closed) for every $i = 1,2$.

Definition:1.7. [13] Let $(B, \Lambda_1, \Lambda_2)$ be a bitopological space. The F.W. bitopology on a F.W. set M over B mean any bitopology on M makes the projection p is continuous.

Definition 1.8. [6] A point x in (M, τ_1, τ_2) is called an ij-contact point of a subset $A \subseteq M$ if and only if for every τ_i-open nbd U of x, $(\tau_{j-}cl(U)) \cap A \neq \emptyset$. The set of all ij-contact points of A is called the ij-closure of A and is denoted by $ij - cl(A)$. $A \subset M$ is called ij-closed if and only if $A = ij - cl(A)$, where $i, j = 1, 2, (i \neq j)$.

Definition 1.9 [3] A filter $\mathcal{F}$ on a set M is a nonempty collection of nonempty subsets of M with the properties:

(a) If $F_1, F_2 \in \mathcal{F}$, then $F_1 \cap F_2 \in \mathcal{F}$.

(b) If $F \in \mathcal{F}$ and F $\subseteq F^* \subseteq$ M, then $F^* \in \mathcal{F}$.

Definition 1.10. [3] A filter base $\mathcal{F}$ on a set M is a nonempty collection of nonempty subsets of M such that if $F_1, F_2 \in \mathcal{F}$ then $F_3 \subset F_1 \cap F_2$ for some $F_3 \in \mathcal{F}$.

Definition 1.11. [3] If $\mathcal{F}$ and $\mathcal{G}$ are filter bases on M, we say that $\mathcal{G}$ is finer than $\mathcal{F}$ (written as $\mathcal{F} < \mathcal{G}$) if for each $F \in \mathcal{F}$, there is $G \in \mathcal{G}$ such that $G \subseteq F$ and that $\mathcal{F}$ meets $\mathcal{G}$ if $F \cap G \neq \varphi$ for every $F \in \mathcal{F}$ and $G \in \mathcal{G}$.

Definition 1.12. [10] A filter base $\mathcal{F}$ on M i s said to be ij-converges to a subset A of M (written as $\mathcal{F} \xrightarrow{ij-con}$ A) if and only if for every τ_i-open cover $\mathcal{U}$ of A, there is a finite subfamily $\mathcal{U}_0$ of $\mathcal{U}$ and a number F of $\mathcal{F}$ such that $F \subset \cup \{\tau_j - cl(U): U \in \mathcal{U}_0\}$. If $x \in M$, we say $\mathcal{F} \xrightarrow{ij-con} x$ if and only if $\mathcal{F} \xrightarrow{ij-con} \{x\}$ or equivalently, τ_j-closure of every τ_i-open nbd of x contains some members of $\mathcal{F}$.

Definition 1.13. [2] A function $f: (M, \tau_1, \tau_2) \to (N, \sigma_1, \sigma_2)$ is called ij-continuous if and only if for any σ_i-open nbd V of $f(x)$, there exists a τ_i-open nbd U of x such that $f(\tau_j\text{-}cl(U)) \subset \sigma_j\text{-}cl(V)$, where $i, j = 1, 2$.

Definition 1.14. [2] A point x in a bitopological space (M, τ_1, τ_2) is called an ij-adherent point of a filter base $\mathcal{F}$ on M if and only if it is an ij-contact point of every number of $\mathcal{F}$. The set of all ij-adherent points of $\mathcal{F}$ is called the ij-adherence of $\mathcal{F}$ and is denoted by ij-ad $\mathcal{F}$, where $i, j = 1, 2$.

2. Fibrewise IJ-Perfect Bitopological Spaces.
In this section, we introduce the notion of ij-perfect bitopological, ij-rigidity spaces and investigate some of their basic properties.

Definition 2.1. Let $(B, \Lambda_1, \Lambda_2)$ be a bitopological space. The F.W. ij-bitopology on a F.W. set M over B mean any bitopology on M for which the projection p is ij-continuous, where $i, j = 1, 2$.

Definition 2.2. A function $f: (M, \tau_1, \tau_2) \to (N, \sigma_1, \sigma_2)$ is called ij-closed if the image of each ij-closed set in M is ij-closed set in N, where $i, j = 1, 2$.

Theorem 2.3. A function $f: (M, \tau_1, \tau_2) \to (N, \sigma_1, \sigma_2)$ is ij-closed if and only if $ij - cl(f(A)) \subset f(ij - cl(A))$ for each $A \subset M$, where $i, j = 1, 2$.
Proof. ($\Rightarrow$) Suppose that f is ij-closed. Let $A \subset M$, since f is ij-closed then $f(\text{ij} - \text{cl(A)})$ is ij-closed set in N, since ij $-$ cl(A) is closed in M. so, ij $-$ cl(f(A)) $\subset f(\text{ij} - \text{cl(A)})$.

($\Leftarrow$) Suppose that A is ij-closed set in M, so $A = \text{ij} - \text{cl(A)}$, but we have ij $-$ cl(f(A)) $\subset f(\text{ij} -$ cl(A)), thus $ij - cl(f(A)) \subset f(A)$, so $f(A)$ is ij-closed in M, therefore f is ij-closed.

Definition 2.4. A filter base $\mathcal{F}$ on bitopological space (M, τ_1, τ_2) is said to be ij $-$converges to a point $x \in M$ (written as $\mathcal{F} \xrightarrow{ij-con}$ x) if and only if every τ_i-open nbd U of x contains some elements of $\mathcal{F}$, where $i, j = 1, 2$.

Definition 2.5. A filter base $\mathcal{F}$ on bitopological space (M, τ_1, τ_2) is said to be ij-directed toward a set $A \subseteq M$, written as $\mathcal{F} \xrightarrow{ij-d} A$, if and only if every filter base $\mathcal{G}$ finer than $\mathcal{F}$ has an ij $-$adherent point in A, i.e. $(ij - ad\ \mathcal{G}) \cap A \neq \varphi$. We write $\mathcal{F} \xrightarrow{ij-d} x$ to mean $\mathcal{F} \xrightarrow{ij-d}$ {x}, where $x \in M$, where $i, j = 1, 2$.

Theorem 2.6. A point x in bitopological space (M, τ_1, τ_2) is an ij-adherent point of a filter base $\mathcal{F}$ on M if and only if there exists a filter base $\mathcal{F}^*$ finer than $\mathcal{F}$ such that $\mathcal{F}^* \xrightarrow{ij-con} x$, where $i, j = 1, 2$.

Proof. ($\Rightarrow$) Let x be an ij −adherent point of a filter base $\mathcal{F}$ on M, so it is an ij −contact point of every number of $\mathcal{F}$, then for every τ_i-open nbd U of x, we have $\tau_j - cl(U) \cap F \neq \varphi$ for every number F in $\mathcal{F}$. And thus $\tau_j - cl(U)$ contains a some member of any filter base $\mathcal{F}^*$ finer than $\mathcal{F}$, so that $\mathcal{F}^* \xrightarrow{ij-con} x$.

($\Leftarrow$) Suppose that x is not an ij −adherent point of a filter base $\mathcal{F}$ on M, so there exist $F \in \mathcal{F}$ such that x is not an ij −contact of F. Then there exists an τ_i-open nbd U of x such that $\tau_j - cl(U) \cap F = \varphi$. Denote by $\mathcal{F}^*$ the family of sets $F^* = F \cap (M - \tau_j\text{-}cl(U))$ for $F \in \mathcal{F}$, then the sets F^* are nonempty. Also $\mathcal{F}^*$ is a filter base and indeed it is finer than $\mathcal{F}$, because given $F_1^* = F_1 \cap (M\text{-}\tau_j\text{-}cl(U))$ and $F_2^* = F_2 \cap (M\text{-}\tau_j\text{-}cl(U))$, there is an $F_3 \subseteq F_1 \cap F_2$ and this gives $F_3^* = F_3 \cap (M\text{-}\tau_j\text{-}cl(U)) \subseteq F_1 \cap F_2 \cap (M\text{-}\tau_j\text{-}cl(U)) = F_1 \cap (M\text{-}\tau_j\text{-}cl(U)) \cap F_2 \cap (M\text{-}\tau_j\text{-}cl(U))$, by construction $\mathcal{F}^*$ not ij-convergent to x. This is a contradiction, and thus x is an ij-adherent point of a filter base $\mathcal{F}$ on M.

Theorem 2.7. Let $\mathcal{F}$ be a filter base on bitopological space (M, τ_1, τ_2), and a point $x \in M$, then $\mathcal{F} \xrightarrow{ij-con} x$ if and only if $\mathcal{F} \xrightarrow{ij-d} x$, where $i, j = 1, 2$.

Proof. ($\Leftarrow$) If $\mathcal{F}$ does not ij-converge to x, then there exists a τ_i-open nbd U of x such that $F \not\subset \tau_j\text{-}cl(U)$, for all $F \in \mathcal{F}$. Then $\mathcal{G} = \{(M\text{-}\tau_j\text{-}cl(U) \cap F : F \in \mathcal{F}\}$ is a filter base on M finer than $\mathcal{F}$, and clearly $x \notin ij$-adherence of $\mathcal{G}$. Thus $\mathcal{F}$ cannot be ij-directed towards x which is contradiction. So $\mathcal{F}$ is ij-converge to x.

($\Rightarrow$) Clear.

Definition 2.8. A function $f : (M, \tau_1, \tau_2) \to (N, \sigma_1, \sigma_2)$ is said to be ij-perfect if and only if for each filter base $\mathcal{F}$ on $f(M)$, ij-directed towards some subset A of $f(M)$, the filter base $f^{-1}(\mathcal{F})$ is ij-directed towards f^{-1}(A) in M. f is called pairwise ij-perfect if and only if f is 12 and 21-perfect, where $i, j = 1, 2$.

Definition 2.9. The F.W. bitopological space (M, τ_1, τ_2) over bitopological space $(B, \Lambda_1, \Lambda_2)$ is called F.W. ij-perfect if and only if the projection p is ij-perfect, where $i, j = 1, 2$.

In the following theorem we show that only points of N could be sufficient for the Subset A in definition [2.8] and hence ij-direction can be replaced in view of theorem [2.6] by ij-convergence.

Theorem 2.10. Let (M, τ_1, τ_2) be a F.W. bitopological space over bitopological space $(B, \Lambda_1, \Lambda_2)$. Then the following are equivalent:

(a) (M, τ_1, τ_2) is F.W. ij-perfect bitopological space.

(b) For each filter base $\mathcal{F}$ on $p(M)$, which is ij-convergent to a point b in B, $M_{\mathcal{F}} \xrightarrow{ij-d} M_b$.

(c) For any filter base $\mathcal{F}$ on M, ij-ad $p(\mathcal{F}) \subset p$ (ij-ad $\mathcal{F}$).

Proof. (a) ⇒ (b) Follows from theorem (2.7).

(b) ⇒ (c) Let $b \in$ ij-ad p $(\mathcal{F})$. Then by theorem (2.6), there is a filter base $\mathcal{G}$ on $p(M)$ finer than p $(\mathcal{F})$ such that $\xrightarrow{ij-con} b$. Let $\mathcal{U} = \{M_{\mathcal{G}} \cap F : G \in \mathcal{G}$ and $F \in \mathcal{F}\}$. Then $\mathcal{U}$ is a filter base on M finer than $M_{\mathcal{G}}$. Since $\mathcal{G} \xrightarrow{ij-d} b$, by theorem (2.7) and p is ij-perfect, $M_{\mathcal{G}} \xrightarrow{ij-d} M_b$. $\mathcal{U}$ being finer than $M_{\mathcal{G}}$, we have $M_b \cap$ (ij-ad $\mathcal{U}) \neq \varphi$. It is then clear that $M_b \cap$ (ij-ad $\mathcal{F}) \neq \varphi$. Thus $b \in p\ (ij - ad\ F)$.

(c) ⇒ (a) Let $\mathcal{F}$ be a filter base on $p(M)$ such that it is ij-directed towards some subset A of $p(M)$. Let $\mathcal{G}$ be a filter base on M finer than $M_{\mathcal{F}}$. Then $p(\mathcal{G})$ is a filter base on $p(M)$ finer than $\mathcal{F}$ and hence $A \cap (ij-ad\ p(\mathcal{G})) \neq \varphi$. Thus by (c) A ∩ p (ij − ad $\mathcal{G}$) ≠ φ so that $M_A \cap (ij-ad\ \mathcal{G}) \neq \varphi$. This shows that $M_{\mathcal{F}}$ is ij-directed towards M_A. Hence p is ij-perfect.

Definition 2.11. The function $f:(M,\tau_1,\tau_2) \to (N,\sigma_1,\sigma_2)$ is called ij-compact function if it is ij −continuous, ij −closed and for each filter base $\mathcal{F}$ in N then $f^{-1}(\mathcal{F})$ is filter base in M, where $i,j = 1,2$.

Definition 2.12 The F.W. ij −bitopological space (M,τ_1,τ_2) over bitopological space (B,Λ_1,Λ_2) is called F.W. ij −compact if and only if the projection p is ij −compact, where $i,j = 1,2$.

For example the bitopological product $B \times_B T$ is F.W. ij-compact over B, for all ij −compact space T, where $i,j = 1,2$.

Definition 2.13. The F.W. ij-bitopological space (M,τ_1,τ_2) over bitopological space (B,Λ_1,Λ_2) is called F.W. ij-closed if and only if the projection p is ij-closed, where $i,j = 1,2$.

Theorem 2.14. If the F.W. bitopological space (M,τ_1,τ_2) over a bitopological space (B,Λ_1,Λ_2) is ij-perfect, then it is ij-closed, where $i,j = 1,2$.

Proof. Assume that M is a F.W. ij perfect bitopological space over B, then the projection $p_M : M \to B$ is ij-perfect, to prove that it is ij-closed, by (2. 10 (a)⇒(c)) for any filter base $\mathcal{F}$ on M ij-ad p($\mathcal{F}$) ⊂ p(ij-ad ($\mathcal{F}$)), by theorem (2. 12) f is ij-closed if ij − cl f(A) ⊂ f(ij − cl(A) for all $A \subset M$, therefore p is ij-closed where $\mathcal{F} = \{A\}$.

Definition 2.15. A subset A of bitopological space (M,τ_1,τ_2) is said to be ij-rigid in M if and only if for each filter base $\mathcal{F}$ on M with $(ij-ad\ \mathcal{F}) \cap A = \varphi$, there is τ_i-open set U and $F \in \mathcal{F}$ such that $A \subset U$ and τ_j-$cl(U) \cap F = \varphi$, or equivalently, if and only if for each filter base $\mathcal{F}$ on M whenever $A \cap (ij-ad\ \mathcal{F}) = \varphi$, then for some $F \in \mathcal{F}$, $A \cap (ij-cl(F)) = \varphi$, where $i,j = 1,2$.

Theorem 2.16. If (M,τ_1,τ_2) is F.W. ij-closed bitopological space over bitopological space (B,Λ_1,Λ_2) such that each $M_b$where $b \in B$ is ij-rigid in M, then (M,τ_1,τ_2) is F.W. ij-perfect, where $i,j = 1,2$.

Proof. Assume that M is a F.W. ij-closed bitopological space over B, then the projection $p_M : M \to B$ exist, to prove that it is ij-perfect. Let $\mathcal{F}$ be a filter base on $p(M)$ such that $\mathcal{F} \xrightarrow{ij-con} b$ in B, for some $b \in B$. If $\mathcal{G}$ is a filter base on M finer than the filter base $M_{\mathcal{F}}$, then $p(\mathcal{G})$ is a filter base on B, finer than $\mathcal{F}$. Since $\mathcal{F} \xrightarrow{ij-d} b$ by theorem (2.6), $b \in$ ij-ad p($\mathcal{G}$), i.e., $b \in \cap\{ij-ad\ p(G) : G \in \mathcal{G}\}$ and hence $\{b \in \cap\{p(ij-ad\ (G) : G \in \mathcal{G}\}$ by theorem (2.12), since p is ij-closed. Then $M_b \cap$ ij-ad (G) ≠ φ, for all $G \in \mathcal{G}$. Hence for all $U \in \tau_i$ with $M_b \subset$ U, τ_j-cl(U) ∩ $G \neq \varphi$, for all $G \in \mathcal{G}$. Since M_b is ij-rigid, it then follows that $M_b \cap$ (ij-ad $\mathcal{G}$)≠ φ. Thus $M_{\mathcal{F}} \xrightarrow{ij-d} M_b$. Hence by theorem 2.10 (b)⇒(a), p is ij-perfect.

Theorem 2.17. If F.W. ij-bitopological space (M,τ_1,τ_2) over bitopological space (B,Λ_1,Λ_2) is ij-perfect, then it is ij-closed and for each $b \in B$, M_b is ij-rigid in M, where $i,j = 1,2$.

Proof. Assume that M is a F.W. ij-bitopological space over B, then the projection $p_M : M \to B$ exist and it is ij-continuous. Since p is an ij-perfect so it is ij-closed. To prove the other part, let $b \in B$, and suppose $\mathcal{F}$ is a filter base on M such that (ij-ad $\mathcal{F}$) ∩ M_b= φ. Then $b \notin p$ (ij-ad $\mathcal{F}$).

Since p is ij-perfect, by theorem (2.10 (a)⇒(c)) b $\notin$ ij $-$ ad p($\mathcal{F}$). Thus there exists an $F \in \mathcal{F}$ such that $b \notin$ ij-ad $p(F)$. There exists an Λ_i-open nbd V of b such that $\Lambda_j - cl(V) \cap p(F) = \varphi$. Since p is ij-continuous, for each $x \in M_b$ we shall get a τ_i-open nbd U_x of x such that $p(\tau_j - cl(U_x) \subset \Lambda_j - cl(V) \subset B - p(F)$. Then $p(\tau_j - cl(U_x) \cap p(F) = \varphi$, so that τ_j-cl-(U_x) $\cap F = \varphi$. Then $x \notin$ ij-cl(F), for all $x \in M_b$, so that $M_b \cap$ (ij-cl(F)) = φ, Hence M_b is ij-rigid in M.

Corollary 2.18. A F.W. ij-bitopological space (M, τ_1, τ_2) over bitopological space $(B, \Lambda_1, \Lambda_2)$ is ij-perfect if and only if it is ij-closed and each M_b, where $b \in B$ is ij-rigid in M, where $i, j = 1, 2$.

Next we show that the above theorem remains valid if F.W. ij-closedness bitopological space replaced by a strictly weak condition which we shall called F.W. weak ij-closedness bitopological space. Thus we define as follows.

Definition 2.19. A function $f : (M, \tau_1, \tau_2) \to (N, \sigma_1, \sigma_2)$ is said to be weakly ij-closed if for every $y \in f(M)$ and every τ_i-open set U containing $f^{-1}(y)$ in M, there exists a σ_i open nbd V of y such that f^{-1} (σ_j-cl(V)) $\subset \tau_j$-$cl(U)$, where $i, j = 1, 2$.

Definition 2.20. The F.W. ij-bitopological space (M, τ_1, τ_2) over bitopological space $(B, \Lambda_1, \Lambda_2)$ is called F.W. weakly ij-closed if and only if the projection p is weakly ij-closed, where $i, j = 1, 2$.

Lemma 2.21. [6] In space (M, τ_1, τ_2) if $U \in \tau_j$, then $ij - cl(U) = \tau_j - cl(U)$, where $i, j = 1, 2$.

Theorem 2.22. The F.W. ij-closed bitopological space (M, τ_1, τ_2) over bitopological space $(B, \Lambda_1, \Lambda_2)$ is weakly ij-closed, where $i, j = 1, 2$.

Proof. Assume that M is a F.W. weak ij-closed bitopological space over B, then the projection $p_M : M \to B$ exist and its weakly ij-closed. Let $b \in p(M)$ and let U be a τ_i-open set containing M_b in M. Now, by lemma (2.21) $\tau_j - cl\left(M - \tau_j - cl(U)\right) = ij - cl\left(M - \tau_j - cl(U)\right)$ and hence by theorem [2.1 ٢] and since p is ij-closed, we have ij-cl $p(M - \tau_j - cl(U)) \subset p[ij - cl(M - \tau_j - cl(U)]$. Now since $b \notin p[ij - cl(M - \tau_j - cl(U)]$, $b \notin ij - cl\, p(M - \tau_j$-$cl(U))$ and thus there exists an σ_i-open nbd V of b in B such that σ_j-$cl(V) \cap p(M - \tau_j - cl(U)) = \varphi$ which implies that $M_{(\sigma_j - \text{cl(V)})} \cap (M - \tau_j - cl(U)) = \varphi$ i.e., $M_{(\sigma_j - \text{cl(V)})} \subset \tau_j$-cl(U), and thus p is weakly ij-closed.

A F.W. weakly ij-closed is not necessarily to be F.W. ij-closed and the following example show This.

Example 2.23. Let τ_1, τ_2, Λ_1 and Λ_2 be any topologies and p : $(M, \tau_1, \tau_2) \to (B, \Lambda_1, \Lambda_2)$ be a constant function, then p is weakly ij-closed for $i, j = 1, 2$ and $(i \neq j)$. Now, let $M = B = IR$. If Λ_1 or Λ_2 is the discrete topology on B, then $p : (M, \tau_1, \tau_2) \to (B, \Lambda_1, \Lambda_2)$ given by $p(x) = 0$, for all $x \in M$, is neither 12-closed nor 21-closed, irrespectively of the topologies τ_1, τ_2 and Λ_2 (or Λ_1).

Theorem 2.24. Let (M, τ_1, τ_2) be F.W. ij-bitopological space over bitopological space $(B, \Lambda_1, \Lambda_2)$. Then (M, τ_1, τ_2) is F.W. ij-perfect if:

(a) (M, τ_1, τ_2) is F.W. weakly ij-closed bitopological space, and

(b) M_b is ij-rigid, for each $b \in B$.

Proof. Assume that M is a F.W. ij-bitopological space over B satisfying the conditions (a) and (b), then the projection $p_M : M \to B$ exist. To prove that p is ij-perfect we have to show in view of

theorem [2.1 ٦] that p is ij-closed. Let $b \in ij-cl\,p(A)$, for some non-null subset A of M, but $b \notin p\,(ij-cl(A))$. Then $\mathcal{H}=\{A\}$ is a filter base on M and (ij-ad $\mathcal{H}$) $\cap$ M_b = φ. By ij-rigidity of M_b, there is a τ_i-open set U containing M_b such that $\tau_j-cl(U)\cap A=\varphi$. By weak ij-closedness of p, there exists an Λ_i –open nbd V of b such that $M_{(\Lambda_j-\mathrm{cl(V)})}\subset\tau_j$ -cl(U), which implies that $M_{(\Lambda_j-\mathrm{cl(V)})}\cap A=\varphi$, i.e., $(\Lambda_j-cl(V))\cap p(A)=\varphi$, which is impossible since $b\in ij-cl\,p(A)$. Hence $b\in p(ij-cl(A))$. So f is ij-closed.

Definition 2.25.[11] A subset A in bitopological space (M,τ_1,τ_2) is called ij-H-set in M if and only if for each τ_i-open cover $\mathcal{A}$ of A, there is a finite sub collection $\mathcal{B}$ of $\mathcal{A}$ such that $A\subset\cup\{\tau_j-cl(U):U\in\mathcal{B}\}, i,j=1,2$. A is called a pairwise-H-set if and only if it is a 12- and 21-H-set. If A is an ij-H-set (pairwise-H-set) and $A=M$, then the space is called an ij-QHC (resp. pairwise QHC) space, where $i,j=1,2$.

Lemma 2.26.[10] A subset A of a bitopological space (M,τ_1,τ_2) is an ij-H-set if and only if for each filter base $\mathcal{F}$ on A, $(ij-ad\,\mathcal{F})\cap A\neq\varphi$, where $i,j=1,2$.
Proof. (⇒) Clear.
(⇐) Let $\mathcal{A}$ be a τ_i -open cover of A such that the union of τ_j -closure of any finite Sub collection of $\mathcal{A}$ is not cover A. Then $\mathcal{F}$ $\{A\setminus\cup_{\mathcal{B}}\tau_j$-cl(B) : $\mathcal{B}$ is finite sub collection of $\mathcal{A}\}$ is a filter base on A and (ij-ad $\mathcal{F}$) $\cap A=\varphi$. This contradiction so that A is ij-set.

Theorem 2.27. If (M,τ_1,τ_2) is F.W. ij-perfect bitopological space over bitopological space (B,Λ_1,Λ_2) and $B^*\subset B$ is an ij-H-set in B, then M_{B^*} is an ij-H-set in M, where $i,j=1,2$.
Proof. Assume that M is a F.W. ij-perfect bitopological space over B, then the projection $p_M: M\to B$ exist. Let $\mathcal{F}$ be a filter base on M_{B^*}, then $p(\mathcal{F})$ is a filter base on B^*. Since B^* is an ij-H-set in B, $B^*\cap ij-ad\,p(\mathcal{F})\neq\varphi$ by lemma (2.26). By theorem (2.10 (a)⇒(c)), $B^*\cap p(ij-ad\,(F))\neq\varphi$, so that M_{B^*} ∩ ij-ad $(\mathcal{F})\neq\varphi$. Hence by lemma (2.26), M_{B^*} is an ij-H-set in M. The converse of the above theorem is not true, is shown in the next example.

Example 2.28. Let $M=B=IR,\tau_1$ and τ_2 be the cofinite and discrete topologies on M and Λ_1, Λ_2 respectively denote the indiscrete and usual topologies on B. Suppose $p:(M,\tau_1,\tau_2)\to(B,\Lambda_1,\Lambda_2)$ is the identity function. Each subset of either of (M,τ_1,τ_2) and (B,Λ_1,Λ_2) is a 12-set. Now, any non-void finite set $A\subset M$ is 12-closed in M, but $p(A)$ (i.e., A) is not 12-closed in B (in fact, the only 12-closed subsets of B are B and φ).

Definition 2.29. A function $f:(M,\tau_1,\tau_2)\to(N,\sigma_1,\sigma_2)$ is said to be almost ij-perfect if for each ij-H-set K in N, $f^{-1}(K)$ is an ij-H-set in M, where $i,j=1,2$.

Definition 2.30. The F.W. ij-bitopological space (M,τ_1,τ_2) over bitopological space (B,Λ_1,Λ_2) is called F.W. almost ij-perfect if and only if the projection p is almost ij-perfect, where $i,j=1,2$. *By analogy to theorem (2.16), a sufficient condition for a function to be almost ij-perfect, is proved as follows.*

Theorem 2.31. Let (M,τ_1,τ_2) be F.W. ij- bitopological space over bitopological space (B,Λ_1,Λ_2) such that:
(a) $M_b$is ij-rigid, for each $b\in B$, and
(b) (M,τ_1,τ_2) is F.W. weakly ij-closed bitopological space.
Then (M,τ_1,τ_2) is F.W. almost ij-perfect bitopological space.

Proof. Assume that M is a F.W. ij-bitopological space over B, then the projection $p_M : M \to B$ exist and it is ij-continuous. Let B^* be an ij-H-set in B and let $\mathcal{F}$ be a filter base on M_{B^*}. Now $p(\mathcal{F})$ is a filter base on B^* and so by theorem (2.26), $(ij - ad\, p(\mathcal{F})) \cap B^* \neq \varphi$. Let $b \in [ij - ad\, p(\mathcal{F})] \cap B^*$. Suppose that $\mathcal{F}$ has no ij-ad point in M_{B^*} so that (ij-ad $(\mathcal{F})) \cap M_b = \varphi$. Since M_b is ij-rigid, there exists an $F \in \mathcal{F}$ and a τ_i-open set U containing M_b such that $F \cap \tau_j - cl(U) = \varphi$. By weak ij-closedness of p, there is a Λ_i-open nbd V of b such that $M_{(\Lambda_j - \mathrm{cl(V)})} \subset \tau_j - cl(U)$ which implies that $M_{(\Lambda_j - \mathrm{cl(V)})} \cap F = \varphi$, i.e., Λ_j-$cl(V) \cap p(F) = \varphi$, which is a contradiction. Thus by theorem (2.26), M_{B^*} is an ij-H-set in M and hence p is almost ij-perfect.

We now give some applications of ij-perfect functions. The following characterization theorem for an ij-continuous function is recalled to this end.

Theorem 2.32. A bitopological space (M, τ_1, τ_2) is F.W. ij-bitopological space over bitopological space $(B, \Lambda_1, \Lambda_2)$. if and only if $p(ij - cl(A)) \subset ij - cl(p(A))$, for each $A \subset M$, where $i, j = 1, 2$.

Proof. ($\Rightarrow$) Assume that M is a F.W. ij-bitopological space over B, then the projection $p_M : M \to B$ exist and it is ij-continuous. Suppose that $x \in ij - cl(A)$ and V is Λ_i-open nbd of $f(x)$. Since p is ij-continuous, there exists an τ_i-open nbd U of x such that $p(\tau_j - cl(U)) \subset \Lambda_j - cl(V)$. Since τ_j - $cl\,(U) \cap A \neq \varphi$, then Λ_j - $cl(V) \cap p(A) \neq \varphi$. So, $p(x) \in ij - cl(p(A))$. This shows $that\ p(ij - cl(A)) \subset ij - cl(p(A))$.

($\Leftarrow$) Clear.

Theorem 2.33. Let (M, τ_1, τ_2) be a F.W. ij-perfect bitopological space over bitopological space $(B, \Lambda_1, \Lambda_2)$. Then M_A preserves ij-rigidity, where $i, j = 1, 2$.

Proof. Assume that M is a F.W. ij-bitopological space over B, then the projection $p_M : M \to B$ exist and it is ij-continuous. Let A be an ij-rigid set in B and let $\mathcal{F}$ be a filter base on M such that $M_A \cap$ (ij- ad$(\mathcal{F})) = \varphi$. Since p is ij-perfect and $A \cap p(ij - ad(\mathcal{F})) = \varphi$ by theorem (2.10 (a) $\Rightarrow$ (c)) we get $A \cap (ij - ad\, p(\mathcal{F})) = \varphi$. Now A being an ij-rigid set in B, there exists an $F \in \mathcal{F}$ such that $A \cap ij - clp(F) = \varphi$. Since p is ij-continuous, by theorem (2.32) it follows that $A \cap p(ij - cl(F)) = \varphi$. Thus $M_A \cap (ij - cl(F)) = \varphi$. This proves that M_A is ij-rigid.

In order to investigate for the conditions under which a F.W. almost ij-perfect bitopological space may be F.W. ij-perfect bitopological space, we introduce the following definition.

Definition 2.34. A function $f: (M, \tau_1, \tau_2) \to (N, \sigma_1, \sigma_2)$ is said to be ij^*-continuous if and only if for any σ_j-open nbd V of $f(x)$, there exists a τ_i-open nbd U of x such that $f(\tau_j$-$cl(U)) \subset \sigma_i$-$cl(V)$, where $i, j = 1, 2$.

Definition 2.35. The F.W. ij-bitopological space (M, τ_1, τ_2) over bitopological space $(B, \Lambda_1, \Lambda_2)$ is called F.W. ij^*-bitopological space if and only if the projection p is ij^*-continuous, where $i, j = 1, 2$.

The relevance of the above definition to the characterization of F.W. ij-perfect bitopological space is quite apparent from the following result.

Definition 2.36. A bitopological space (M, τ_1, τ_2) is said to be pairwise Urysohn space if for $x, y \in M$ with $x \neq y$, there are τ_i-open nbd U of x and τ_j-open nbd V of y such that $\tau_j - cl(U) \cap \tau_i - cl(V) = \varphi$, where $i, j = 1, 2$.

Theorem 2.37. If (M,τ_1,τ_2) is F.W. ij^*-bitopological space on a pairwise Urysohn space (B,Λ_1,Λ_2), then it is F.W. ij-perfect bitopological space if and only if for every filter base $\mathcal{F}$ on M, if $p(\mathcal{F}) \xrightarrow{ij-con} b$ wher $b \in B$, then $ij-ad\,\mathcal{F} \neq \varphi$, where $i,j = 1,2$.

Proof. (⇒) Let $(\mathrm{M},\tau_1,\tau_2)$ be a F.W. $i\,j^*$-bitopological space on a pairwise Urysohn space $(\mathrm{B},\Lambda_1,\Lambda_2)$, then there is a ij^*-continuous projection function $p:(\mathrm{M},\tau_1,\tau_2) \to (\mathrm{B},\Lambda_1,\Lambda_2)$ and $p(\mathcal{F}) \xrightarrow{ij-con.} b$ where $b \in B$, for a filter base $\mathcal{F}$ on M. Then $M_{p(\mathcal{F})} \xrightarrow{ij-dir.} M_b$. Since $\mathcal{F}$ is finer than $M_{p(\mathcal{F})}$, $M_b \cap ij-ad\,\mathcal{F} \neq \varphi$, so that $ij-ad\,\mathcal{F} \neq \varphi$.

(⇐): Suppose that for every filter base $\mathcal{F}$ on M, $p(\mathcal{F}) \xrightarrow{ij-con.} b$ where $b \in B$ implies $ij-ad\,\mathcal{F} \neq \varphi$. Let $\mathcal{G}$ be a filter base on B such that $\mathcal{G} \xrightarrow{ij-con.} b$, and suppose that $\mathcal{G}^*$ is a filter base on M such that $\mathcal{G}^*$ is finer than $M_{\mathcal{G}}$. Then $p(\mathcal{G}^*)$ is finer than $\mathcal{G}$. So $p(\mathcal{G}^*) \xrightarrow{ij-con.} b$. Hence $ij-ad\,\mathcal{G}^* \neq \varphi$. Let $z \in B$ such that $z \neq b$. Then since B is pairwise Urysohn, there exist a Λ_i-open nbd U of b and Λ_j-open nbd V of z such that $\left(\Lambda_j - cl\,(U)\right) \cap \left(\Lambda_i - cl(V)\right) = \varphi$. Since $p(\mathcal{G}^*) \xrightarrow{ij-con.} b$, there exist a $G \in \mathcal{G}^*$ such that $p(G) \subset \Lambda_j - cl(U)$. Now, since p is ij^*-continuous, corresponding to each $x \in M_z$ there is a τ_i-open nbd W of x such that $p\left(\tau_j - cl(W)\right) \subset \Lambda_i - cl(V)$. Thus $\Lambda_j - cl(W) \cap G = \varphi$. It follows that $M_z \cap ij-\mathcal{G}^* = \varphi$, for each $z \in B - \{b\}$. Consequently $M_b \cap ij-ad\,\mathcal{G}^* \neq \varphi$, and p is ij- perfect and hence $(\mathrm{M},\tau_1,\tau_2)$ is F.W. ij^*-bitopology.

Definition 2.38. [9] A bitopological space (M,τ_1,τ_2) is said to be locally ij-QHC bitopological space if and only if for every $x \in M$, there is a τ_i-open nbd of x, which is an ij-H-set, where $i,j = 1,2$.

Lemma 2.39. [10] In a pairwise Urysohn bitopological space (M,τ_1,τ_2) an ij-H-set is ij-closed, where $i,j = 1,2$.

Corollary 2.40. Let (M,τ_1,τ_2) be a F.W. ij^*-bitopological space and ij-QHC on a pairwise Urysohn bitopological space (B,Λ_1,Λ_2), then (M,τ_1,τ_2) is F.W. ij-perfect bitopological space, where $i,j = 1,2$.

Theorem 2.41. Let (M,τ_1,τ_2) be a F.W. ij^*-bitopological space and locally ij-QHC on a Urysohn space (B,Λ_1,Λ_2), then (M,τ_1,τ_2) is F.W. ij^*-bitopological space if and only if it is F.W. almost ij-perfect, where $i,j = 1,2$.

Proof. (⇒) If $(\mathrm{M},\tau_1,\tau_2)$ is F.W. ij^*-bitopological space, then by corollary (2.40.), it is F.W. almost ij-perfect.

(⇐) Let $(\mathrm{M},\tau_1,\tau_2)$ is F.W. almost ij-perfect, then there exist almost ij-perfect projection function $p:(\mathrm{M},\tau_1,\tau_2) \to (\mathrm{B},\Lambda_1,\Lambda_2)$, and let $\mathcal{F}$ be any filter base on M and let $p(\mathcal{F}) \xrightarrow{ij-con.} b$ where $b \in B$. There are an ij-H-set B^* in B and Λ_i-open nbd V of b such that $b \in V \subseteq B^*$. Let $\mathcal{H} = \{\Lambda_j - cl(U) \cap p(F) \cap B^*; F \in \mathcal{F}$ and U is a Λ_i-open nbd of $b\}$. By lemma (2.39), B^* is ij-closed and hence no member of $\mathcal{H}$ is void. In fact, if not, let for some Λ_i-open nbd U of b and some $F \in \mathcal{F}$, $\Lambda_j - cl(U) \cap p(F) \cap B^* = \varphi$. Then $W = U \cap V$ since $y \in U \cap V \in \Lambda_i$ and $\Lambda_j - cl(W) = ij - cl(W) \subset ij - cl(B^*) = B^*$ by lemma (2.21). Now $\varphi = \Lambda_j - cl(W) \cap p(F) \cap B^* = \Lambda_j - cl(W) \cap p(F)$, which is not possible, since $p(\mathcal{F}) \xrightarrow{ij-con.} b$. Thus $\mathcal{H}$ is filter base on B, and is clearly finer than $p(\mathcal{F})$, so that $\mathcal{H} \xrightarrow{ij-con.} b$. Also $\mathcal{G} = \{M_H \cap F: H \in \mathcal{H}$ and $F \in \mathcal{F}\}$ is clearly a filter on M_{B^*}. Since p is almost ij-perfect, M_{B^*} is an ij-H-set and hence $ij-ad\,\mathcal{G} \cap M_{B^*} \neq \varphi$. Thus $ij-ad\,\mathcal{F} \neq \varphi$. Thus p is ij-perfect and by theorem (2.37) $(\mathrm{M},\tau_1,\tau_2)$ is F.W. ij^*-bitopological space.

We now give some application of F.W. ij-perfect bitopological space. The following characterization theorem for a F.W. ij-bitopological space is recalled to this end.

Theorem 2.42. A F.W. set M over B is F.W. ij-bitopological space if and only if $p(ij\text{-}cl(A)) \subset ij\text{-}clp(A)$ for each $A \subset M$, where $i, j = 1, 2$.
Proof: ($\Leftrightarrow$) Since M is a F.W. set over B, then there is projection p where $p: M \to B$. Now we have to prove that p is ij-continuous. But it directly by theorem (2.32).

Lemma 2.43. It was proved in (Sen and Nandi 1993) [12] that a bitopological space (M, τ_1, τ_2) is pairwise Hausdorff if and only if $\{m\} = ij - cl\{m\}$, for each $m \in M$. It then follows immediately in view of theorem (2.14).

Theorem 2.44. If (M, τ_1, τ_2) is a F.W. ij-perfect surjection bitopological space with M is a pairwise Hausdorff space on a bitopological space $(B, \Lambda_1, \Lambda_2)$, Then B is also pairwise Hausdorff.
Proof: Let $b_1, b_2 \in B$ such that $b_1 \neq b_2$. Since p is onto, then $M_{b1}, M_{b2} \in M$ and since p is one to one, then $M_{b1} \neq M_{b2}$. Since p is ij-perfect, so by theorem (2.14) it is ij-closed. By lemma (2.43) we have $\{M_{b1}\} = ij - cl\{M_{b1}\}$ and $\{M_{b2}\} = ij - cl\{M_{b2}\}$. Since p is pairwise Hausdorff. Now $p(ij - cl\{M_{b1}\}) = ij - cl\{b_1\}$ and $p(ij - cl\{M_{b2}\}) = ij - cl\{b_2\}$ since p is ij-closed. This mean $b_1 = ij - cl\{b_1\}$ and $b_2 = ij - cl\{b_2\}$. Hence B is pairwise Hausdorff.

Our next theorem give a characterization of an important class of F.W. bitopological space viz. the ij-QHC spaces in terms of F.W. ij-perfect bitopological space.

Theorem 2.45. For a bitopological space (M, τ_1, τ_2), the following statement are equivalent:

a) M is ij-QHC
b) The F.W. (M, τ_1, τ_2) is ij-perfect bitopological space with constant projection over B^* where B^* is a singleton with two equal bitopologies viz. the unique bitopology on B^*.
c) The F.W. $(B \times M, Q_1, Q_2)$ is ij-perfect bitopological space over $(B, \Lambda_1, \Lambda_2)$, where $Q_i = \Lambda_i \times \tau_j$. $i, j = 1, 2$ and $i \neq j$.

Proof: (a)⇒(b) Let p: $(M, \tau_1, \tau_2) \to (B^*, \Lambda_1, \Lambda_2)$ is a constant projection over B^* where B^* is a singleton with two equal bitopologies viz the unique bitopology on B^*. P is clearly ij-closed. Also, M_{B^*}, i.e. M is obviously ij-rigid since B^* is ij-QHC. Then by theorem (2.16) p is ij-perfect.
(b)⇒(a) Follows from theorem (2.33).

(a)⇒(C) Suppose that $(B \times M, Q_1, Q_2)$ is F.W. bitopological space over $(B, \Lambda_1, \Lambda_2)$ where $Q_i = \Lambda_i \times \tau_j$, $i, j = 1, 2$ and $i \neq j$, then there is a projection $p = \pi_i$: $(B \times M, Q_1, Q_2) \to (B, \Lambda_1, \Lambda_2)$. We show that π_i is ij- closed and for each $b \in B, M_B$ is ij-rigid in $B \times M$. Then the result will follow from theorem (2.16). Let $A \subset B \times M$ and $a \notin \pi_i(ij - cl(A))$. For each $m \in M, (a, m) \notin ij - cl(A)$, so that there exist a Λ_j-open nbd G_m of a and a τ_i-open nbd H_m of m such that $[Q_i - cl(G_m \times H_m)] \cap A = \varphi$. Since M is ij-QHC, $\{a\} \times M$ is a ij –H-set in $B \times M$. Thus there exist finitely many elements $m_1, m_2, m_3, \dots, m_n$ with $\{a\} \times M \subset \bigcup_{k=1}^{n} Q_i - cl(G_{m_k} \times H_{m_k})$. Now, $a \in \bigcap_{k=1}^{n} G_{m_k} = G$ which is a Λ_i-open nbd of a such that $(\Lambda_i - cl(G) \cap \pi_i(A) = \varphi$. Hence $a \notin ij - cl\pi_i(A)$ and thus $ij - cl\pi_i(A) \subset \pi(ij - cl(A))$. So π is ij-closed, by theorem (2.12). Next, let $b \in B$. To show that $(B \times M)_b = {\pi_i}^{-1}$(b) to be ij-rigid in $B \times M$. Let $\mathcal{F}$ be a filter base on $B \times M$ such that ${\pi_i}^{-1}$(b)$\cap ij - ad\,\mathcal{F} = \varphi$. For each $m \in M, (b, m) \notin ij - ad\,\mathcal{F}$. Thus there exist Λ_j-open nbd U_m of b in B, a τ_i −open nbd V_m of m in M and an $F_m \in \mathcal{F}$ such that $Q_i - cl(U_m \times V_m) \cap F_m = \varphi$. As show above, there exist finitely many elements $m_1, m_2, m_3, \dots, m_n$ of M such that $\{b\} \times M \subset \bigcup_{k=1}^{n} Q_i - cl(U_{m_k} \times V_{m_K})$. Putting $U = \bigcap_{k=1}^{n} U_{m_k}$ and choosing $F \in \mathcal{F}$ with $F \subset$

$\bigcap_{k=1}^{n} F_{m_k}$, we get $\{b\} \times M \subset U \times M \subset Q_j$ such that $Q_i - cl(U \times M) \cap F = \varphi$. Thus $\big(ij - cl(F)\big) \cap [{\pi_i}^{-1}(\text{b})] = \varphi$. Hence ${\pi_i}^{-1}$(b) is ij-rigid in $B \times M$.
(c)⇒(a) Taking $B^* = B$, we have that $p = \pi_i : B^* \times B \times \rightarrow B^*$ is ij-perfect . Therefore by theorem. (2.27) $B^* \times M$ is an ij-H-set and Hence M is ij-QHC.

References

[1] A. A. Abo Khadra, S. S. Mahmoud and Y. Y. Yousif, Fibrewise near topological spaces, *Journal of Computing*, USA, Vol4, Issue 5, May (2012), pp. 223-230.
[2] S. Bose and D. Sinha (1981): Almost open, almost closed, θ-continuous and almost quasi-compact mappings in bitopological spaces, Bull. Cal.Math. Soc. 73, 345.
[3] Bourbaki N., 1975, General Topology, Part I, Addison-Wesly, Reding, mass.
[4] nglking R., (1989), Outline of General Topology, Amsterdam.
[5] I. M. James, Fibrewise Topology, Cambridge University Press, London 1989.
[6] Kariofillis, C.G.(1986): On Pairwise Almost Compactness, Ann. Soc. Sci. Bruxelles 100, 129.
[7] J. C. Kelly, Bitopological spaces, Proc. London Math. Soc., Vol.13, 1963, pp.71-89.
[8] S. S. Mahmoud and Y. Y. Yousif, Fibrewise near separation axioms, International Mathematical Forum, Hikari Ltd, Bulgaria, Vol.7, No.35,(2012), pp.1725-1736.
[9] Mukherjee M. N., Nandi. J.N. and Sen S. K., Concerning Bitopological QHC Extenstion, Indian Jour. Pure. Appl. Math 27, (3), March (1996), pp.257-246
[10] Mukherjee M. N., Nandi. J.N. and Sen S. K., On Bitopological QHC spaces, Indian Jour. Pure. Appl. Math 27, (3), March (1996), pp.245-255
[11] Mukherjee, M. N. (1982): On pairwise almost compactness and pairwise-H-closedness in bitopological space Ann. Soc. Sci. Bruxelles 96. 98.
[12] Sen, S.K. and Nandi, J.N. (1993): Characterizations of some bitopological spaces, Ann, Soc. Sci. Bruxelles 48, 207.
[13] Y. Y. Yousif, L. A. Hussain, Fibrewise Bitopological Spaces, *Journal of International Journal of Science and Research (IJSR),* Vol. 6, (2017), pp 978-982.
[14] Y. Y. Yousif, L. A. Hussain, Fibrewise pairwise bi-Separation Axioms, *International Journal of Pure and Applied Mathematics IJPAM*, submitted.
[15] Y. Y. Yousif , M. A. Hussain, Fibrewise Soft Near Separation Axioms, preprint.
[16] Y. Y. Yousif , M. A. Hussain, Fibrewise Soft Topological Spaces, *International Journal of Science and Research (IJSR)* Volume 6 Issue 2, (2017), pp.1010-1019, February.
[17] Y. Y. Yousif, Some result on fibrewise Lindelöf and locally Lindelöf Topological space, *Ibn Al-haitham Journal science*, 191-198, Vol. 22, No. 3, (2009), pp. 191-198.
[18] Y. Y. Yousif, Some result on fibrewise Topological space, *Ibn Al-haitham Journal for pure and Applied science*. University of Baghdad – Collage of Education – Ibn Al-haitham Vol. 21, No. **2** , (2008), pp. 118-132.

Intuitionistic fuzzy n-fold KU-ideal of KU-algebra

IOP Conf. Series: Journal of Physics: Conf. Series **1003** (2018) 012064 doi:10.1088/1742-6596/1003/1/012064

Intuitionistic fuzzy n-fold KU-ideal of KU-algebra

Samy M Mostafa[1], Fatema F Kareem[2]

[1]Department of Mathematics, Faculty of Education, Ain Shams University, Roxy, Cairo, Egypt
[2]Department of Mathematics, Collage of Education for pure sciences- Ibn Al-Haitham, University Baghdad, Baghdad, Iraq.

fa_sa20072000@yahoo.com

Abstract. In this paper , we apply the notion of intuitionistic fuzzy n-fold KU-ideal of KU-algebra. Some types of ideals such as intuitionistic fuzzy KU-ideal, intuitionistic fuzzy closed ideal and intuitionistic fuzzy n-fold KU-ideal are studied. Also, the relations between intuitionistic fuzzy n-fold KU-ideal and intuitionistic fuzzy KU-ideal are discussed. Furthermore, a few results of intuitionistic fuzzy n- fold KU-ideals of a KU-algebra under homomorphism are discussed.

1. Introduction

In 1956, Zadeh introduced the concept of a fuzzy set [11]. After that, many papers studied the fuzzy set of different branches of mathematic such as topological space, vector space, groups, rings and modules. In fact the notion of intuitionistic fuzzy set is a generalization of fuzzy set. This concept is introduced by Atanassov [1]. Jun [2] studied an intuitionistic fuzzy ideal in BCK-algebra. He established the intuitionistic fuzzy subalgebra and ideal in BCK-algebra. In [3, 4, and 5] some authors introduced intuitionistic fuzzy set on different structures. The concept of fuzzy KU-ideal of KU-algebra is introduced0by Mostafa et al, in [6]. In this work, we introduce the notion of intuitionistic fuzzy set theory to n-fold KU-ideal of a KU-algebra as a natural generalization of n-fold fuzzy KU-ideal of KU-algebra. Moreover, we discuss some interesting properties between intuitionistic fuzzy n-fold KU- ideal and intuitionistic fuzzy KU- ideal.

2. Preliminaries

In this part, we present some definitions and background about KU-algebra.

Definition*2.1. [9, 10] Algebra* $(\chi,*,0)$ *is called a KU-algebra if it satisfies the following axioms:* $\forall \nu,\kappa,\omega \in \chi$.

(ku_1) $(\nu * \kappa) * [(\kappa * \omega)) * (\nu * \omega)] = 0$,

(ku_2) $\nu * 0 = 0$,

(ku_3) $0 * \nu = \nu$,

(ku_4) $\nu * \kappa = 0$ ***and*** $\kappa * \nu = 0$ ***implies*** $\nu = \kappa$,

(ku_5) $\nu * \nu = 0$.

The binary relation $\leq$ on χ is defining by the following:

$\nu \leq \kappa \Leftrightarrow \kappa * \nu = 0$. Thus $(\chi,*,0)$ satisfies the following conditions: For all $\nu,\kappa,\omega \in \chi$.

$(ku_{1\backslash})$: $[(\kappa * \omega) * (\nu * \omega)] \leq (\nu * \kappa)$

$(ku_{2\backslash})$: $0 \leq \nu$

$(ku_{3\backslash})$: $\nu \leq \kappa$ ***and*** $\kappa \leq \nu$ ***implies*** $\nu = \kappa$,

$(ku_{4\backslash})$: $\kappa * \nu \leq \nu$.

Theorem2.2 [6]: *In a KU-algebra* χ, *the following axioms are satisfied:* $\forall \nu,\kappa,\omega \in \chi$.

(1): $\nu \leq \kappa$ ***imply*** $\kappa * \omega \leq \nu * \omega$,

(2): $\nu * (\kappa * \omega) = \kappa * (\nu * \omega)$,

(3): $(\kappa * \nu) * \nu) \leq \kappa$.

Definition2.3 [9]: *A non-empty subset* S *of a KU- algebra* χ *is called KU- subalgebra of* χ *if* $\nu * \kappa \in S$ *whenever* $\nu,\kappa \in S$.

Definition2.4 **[6]:** A non - empty subset I of a KU- algebra χ is called an ideal of χ if for any $\nu,\kappa \in S$, then

(i) $\mathbf{0} \in I$,

(ii) $\nu * \kappa \in I$, $\nu \in I$ imply $\kappa \in I$.

Definition2.5 [6]: *A subset* I *of a KU-algebra* χ *is said to be an KU- ideal of* χ, *if*

(I_1) $0 \in I$

(I_2) For all $\nu,\kappa,\omega \in \chi$. If $\nu * (\kappa * \omega) \in I$ and $k \in I$ imply $\nu * \omega \in I$.

For any elements $\nu,\kappa \in \chi$, then $\nu^n * \kappa$ denotes $(\nu * (\nu * ...(\nu * \kappa))$, where ν occurs n times.

Definition2.6 [7,8]: *A non- empty subset* I *of a KU- algebra* χ *is called n- fold KU- ideal of* χ *if*
(1) $0 \in I$

(2) For all $\nu, \kappa, \omega \in \chi$, there exists a natural number n such that $\nu^n * \omega \in I$ whenever $\nu^n * (\kappa * \omega) \in I$ and $\kappa \in I$.

Obviously, **{0}** and χ itself are n-fold KU- ideal of χ for every positive integer n.

Definition2.7. **[10]:** Let $(\chi, *, 0)$ and $(\chi', *', 0')$ be KU- algebras, a homomorphism is a map $f : \chi \to \chi'$ satisfying $f(\nu * \kappa) = f(\nu) *' f(\kappa)$ for all $\nu, \kappa \in \chi$.

3. Intuitionistic Fuzzy set of a KU-algebra

An intuitionistic fuzzy set I in a non-empty set χ is an object having the form $I = \{(\nu, \mu_I, \beta_I) : \nu \in \chi\}$, where $\mu_I : \chi \to [0,1]$ is the degree membership and $\beta_I : \chi \to [0,1]$ is the degree non-membership of the element $\nu \in \chi$, and $0 \le \mu_I + \beta_I \le 1$ for all $\nu \in \chi$.

By brevity we use the form $I = (\chi, \mu_I, \beta_I)$.

Definition3.1. An intuitionistic fuzzy set $I = (\chi, \mu_I, \beta_I)$ of χ is called an intuitionistic fuzzy subalgebra of χ if, $\forall \nu, \kappa \in \chi$

(i) $\mu_I(\nu * \kappa) \ge \min\{\mu_I(\nu), \mu_I(\kappa)\}$

(ii) $\beta_I(\nu * \kappa) \ge \max\{\beta_I(\nu), \beta_I(\kappa)\}$

Lemma3.2. *If* $I = (\chi, \mu_I, \beta_I)$ *is intuitionistic fuzzy subalgebra of* χ, *then* $\beta_I(0) \le \beta_I(\nu)$ *and* $\mu_I(0) \ge \mu_I(\nu)$, $\forall \nu \in \chi$.
Proof. By definition3.1, the proof is complete.

Example3.3. *Let* $\chi = \{0, a, b, c, d\}$ *with the operation* $*$ *defined by the following table*

$*$	0	η	τ	γ	λ
0	0	η	τ	γ	λ
η	0	0	0	γ	λ
τ	0	η	0	γ	λ
γ	0	0	0	0	λ
λ	0	0	0	0	0

Then $(\chi,*,0)$ is a KU-algebra. Define an intuitionistic fuzzy set $I=(\chi,\mu_I,\beta_I)$ by $I=\{(0,1,0),(\eta,0.6,0.4),(\tau,0.4,0.6),(\gamma,0.3,0.7),(\lambda,0,1)\}$. Then $I=(\chi,\mu_I,\beta_I)$ is an intuitionistic fuzzy subalgebra of χ.

Definition3.4 **.**An intuitionistic fuzzy set $I=(\chi,\mu_I,\beta_I)$ of χ is called an intuitionistic fuzzy ideal, if: $\forall \nu,\kappa,o\in\chi$

(I1) $\mu_I(0)\geq\mu_I(\nu)$ and $\beta_I(0)\leq\beta_I(\nu)$

(I2) $\mu_I(\kappa)\geq\min\{\mu_I(\nu*\kappa),\mu_I(\nu)\}$ and $\beta_I(\kappa)\leq\max\{\beta_I(\nu*\kappa),\beta_I(\nu)\}$.

Definition3.5. An intuitionistic fuzzy set $I=(\chi,\mu_I,\beta_I)$ of χ is called an intuitionistic fuzzy closed ideal, if it satisfies (I2) and the following: $\mu_I(\nu*0)\geq\mu_I(\nu)$ and $\beta_I(\nu*0)\leq\beta_I(\nu)$, $\forall\nu\in\chi$.

Definition3.6. An intuitionistic fuzzy set $I=(\chi,\mu_I,\beta_I)$ of χ is called an intuitionistic fuzzy KU-ideal, if: For all $\nu,\kappa,\omega\in\chi$

(F1) $\mu_I(0)\geq\mu_I(\nu)$ and $\beta_I(0)\leq\beta_I(\nu)$

(F2) $\mu_I(\nu*\omega)\geq\min\{\mu_I(\nu*(\kappa*\omega)),\mu_I(\kappa)\}$ and $\beta_I(\nu*\omega)\leq\max\{\beta_I(\nu*(\kappa*\omega)),\beta_I(\kappa)\}$.

Definition3.7. Intuitionist fuzzy closed KU-ideal it satisfies (F2) and the following: For all $\nu\in\chi$ $\mu_I(\nu*0)\geq\mu_I(\nu)$ and $\beta_I(\nu*0)\leq\beta_I(\nu)$.

Proposition3.8. *Any intuitionistic fuzzy KU-ideal of* χ *isan intuitionistic fuzzy ideal.*

Proof. *Clear.*

Proposition3.9.*Every intuitionistic fuzzy closed KU-ideal of a KU-algebra* χ *is intuitionistic fuzzy KU-ideal.*
Proof. Clear.

Lemma3.10.*If* $I=(\chi,\mu_I,\beta_I)$ *is intuitionistic fuzzy KU-ideal of* χ *, then we have thefollowing* $\nu\leq\kappa\Rightarrow\mu_I(\nu)\geq\mu_I(\kappa)$ *and* $\beta_I(\nu)\leq\beta_I(\kappa)$*, for all* $\nu,\kappa\in\chi$.
Proof. Let $\nu,\kappa\in\chi$ such that $\nu\leq\kappa\Rightarrow\kappa*\nu=0$. Consider

$\mu_I(\nu)=\mu_I(0*\nu)\geq\min\{\mu_I(0*(\kappa*\nu)),\mu_I(\kappa)\}=\min\{\mu_I(\kappa*\nu),\mu_I(\kappa)\}=\mu_I(\kappa)$ and

$\beta_I(\nu)=\beta_I(0*\nu)\leq\max\{\beta_I(0*(\kappa*\nu)),\beta_I(\kappa)\}=\max\{\beta_I(\kappa*\nu),\beta_I(\kappa)\}=\beta_I(\kappa)$.

Definition 3.11. *Let* $I=(\chi,\mu_I,\beta_I)$ *be an intuitionistic fuzzy set of* χ *. The set* $V(\mu_I,\alpha)=\{\nu\in\chi:\mu_I(\nu)\geq\alpha\}$ *is called upper* α *-level of* μ_I *and the set* $W(\beta_I,\theta)=\{\nu\in\chi:\beta_I(\nu)\leq\theta\}$ *is called lower* θ *-level of* β_I *.*

4. Intuitionistic fuzzy n-fold KU-ideal

Definition4.1. An intuitionistic fuzzy set $I=(\chi,\mu_I,\beta_I)$ of χ is called an intuitionistic fuzzy n-fold KU-ideal of χ if, for all $\nu,\kappa,\omega\in\chi$

(N$_1$) $\mu_I(0)\geq\mu_I(\nu)$ and $\beta_I(0)\leq\beta_I(\nu)$,

(N$_2$) For $n\in N$, $\mu_I(\nu^n*\omega)\geq\min\{\mu_I(\nu^n*(\kappa*\omega)),\mu_I(\kappa)\}$ and

$\beta_I(\nu^n*\omega)\leq\max\{\beta_I(\nu^n*(\kappa*\omega)),\beta_I(\kappa)\}$.

Proposition4.2. *Every intuitionistic fuzzy n- fold KU-ideal of* χ *is an intuitionistic fuzzy ideal.*

Proof*. Clear.*

Lemma4.3. If $I=(\chi,\mu_I,\beta_I)$ is intuitionistic fuzzy n-fold KU-ideal of χ, then the sets $L=\{\nu\in\chi:\mu_I(\nu)=\mu_I(0)\}$ and $M=\{\nu\in\chi:\beta_I(\nu)=\beta_I(0)\}$ are n-fold KU-ideals of χ.

Proof. Since $0\in\chi$, $\mu_I(0)=\mu_I(0)$ and $\beta_I(0)=\beta_I(0)$, then $0\in L$, $0\in M$. So $L\neq\phi$

$M\neq\phi$. Let $(\nu^n*(\kappa*\omega))\in L$, $\kappa\in L$ implies $\mu_I(\nu^n*(\kappa*\omega))=\mu_I(0)$ and $\mu_I(\kappa)=\mu_I(0)$.

Since $\mu_I(\nu^n*\omega)\geq\min\{\mu_I(\nu^n*(\kappa*\omega)),\mu_I(\kappa)\}=\mu_I(0)$, then $(\nu^n*\omega))\in L$.

The proof is completed.

Theorem4.4. $I=(\chi,\mu_I,\beta_I)$ is intuitionistic fuzzy n-fold KU-ideal of a KU-algebra χ if and only if the upper α -level cut $V(\mu_I,\alpha)=\{\nu\in\chi:\mu_I(\nu)\geq\alpha\}$ and the nonempty lower θ -level cut $W(\beta_I,\theta)=\{\nu\in\chi:\beta_I(\nu)\leq\theta\}$ are n-fold KU-ideals of χ, for any $\alpha,\theta\in[0,1]$.

Proof. For any $\alpha,\theta\in[0,1]$, since $V(\mu_I,\alpha)\neq\phi$. Then

$\nu\in V(\mu_I,\alpha)\Rightarrow\mu_I(\nu)\geq\alpha\Rightarrow\mu_I(0)\geq\alpha\Rightarrow 0\in V(\mu_I,\alpha)$. Let $(\nu^n*(\kappa*\omega))\in V(\mu_I,\alpha)$ and $\kappa\in V(\mu_I,\alpha)$ implies $\mu_I(\nu^n*(\kappa*\omega))\geq\alpha$ and $\mu_I(\kappa)\geq\alpha$. So for all $\nu,\kappa,\omega\in\chi$,

$\mu_I(\nu^n*\omega))\geq\min\{\mu_I(\nu^n*(\kappa*\omega)),\mu_I(\kappa)\}\geq\min\{\alpha,\alpha\}=\alpha$. Therefore $(\nu^n*\omega)\in V(\mu_I,\alpha)$.

Hence $V(\mu_I,\alpha)$ is n-fold KU-ideal of χ. Also, we can prove $W(\beta_I,\theta)$ is n-fold KU-ideal of χ by Similar methods

Conversely, suppose that $V(\mu_I,\alpha)$ and $W(\beta_I,\theta)$ are n-fold KU-ideals of χ, for any $\alpha,\theta\in[0,1]$. Assume that $\nu,\kappa,\omega\in\chi$ such that $\mu_I(0)<\mu_I(\nu)$ and $\beta_I(0)>\beta_I(\nu)$. Let

$\alpha_0=\frac{1}{2}[\mu_I(0)+\mu_I(\nu)]$ *then* $\alpha_0<\mu_I(\nu),\ 0\le\mu_I(0)<\alpha_0<1\Rightarrow\nu\in V(\mu_I,\alpha)$. And since $V(\mu_I,t)$ is n-fold KU-ideal of χ, then $0\in V(\mu_I,\alpha)\Rightarrow\mu_I(0)\ge\alpha_0$, which is contradiction. Therefore $\mu_I(0)\ge\mu_I(\nu)$, for all $\nu\in\chi$. Similarly by taking $\theta_0=\frac{1}{2}[\beta_I(0)+\beta_I(x)]$, we can show that $\beta_I(0)\le\beta_I(\kappa)$, for any $\kappa\in\chi$. If Assume $\nu,\kappa,\omega\in\chi$ such that $\mu_I(\nu^n*\omega)<\min\{\mu_I(\nu^n*(\kappa*\omega)),\mu_I(\kappa)\}$. Put

$$\alpha_0=\frac{1}{2}[\mu_I(\nu^n*\omega)+\min\{\mu_I(\nu^n*(\kappa*\omega)),\mu_I(\kappa)\}]$$

$$\Rightarrow\alpha_0>\mu_I(\nu^n*\omega)\text{ and }\alpha_0<\min\{\mu_I(\nu^n*(\kappa*\omega)),\mu_I(\kappa)\}$$

$$\Rightarrow\alpha_0>\mu_I(\nu^n*\omega),\ \alpha_0<\mu_I(\nu^n*(\kappa*\omega))\text{ and }\alpha_0<\mu_I(\kappa)$$

$$\Rightarrow(\nu^n*\omega)\notin V(\mu_I,\alpha_0),(\nu^n*(\kappa*\omega))\in V(\mu_I,\alpha_0)\text{ and }\kappa\in V(\mu_I,\alpha_0)$$

This is contradiction. Therefore $\mu_I(\nu^n*\omega)\ge\min\{\mu_I(\nu^n*(\kappa*\omega)),\mu_I(\kappa)\}$ for any $\nu,\kappa,\omega\in\chi$. Similarly, we can prove $\beta_I(\nu^n*\omega)\le\max\{\beta_I(\nu^n*(\kappa*\omega)),\beta_I(\kappa)\}$ for any $\nu,\kappa,\omega\in\chi$. The proof is completed.

Theorem4.5. *$I=(\chi,\mu_I,\beta_I)$ isan intuitionistic fuzzy n-fold closed KU-ideal of χ $\Leftrightarrow$ the nonempty upper α -level cut $V(\mu_I,\alpha)$ and the nonempty lower θ -level cut $W(\beta_I,\theta)$ are n-fold closed KU-ideals of χ, for any $\alpha,\theta\in[0,1]$.*

Proof. The same method for Theorem4.4.

Definition4.6. *Let $f:\chi\to\chi'$ be a homomorphism of KU-algebra χ. For any intuitionistic fuzzy set $I=(\chi',\mu_I,\beta_I)$ in χ', we define a new intuitionistic fuzzy set $I^f=(\chi',\mu_I^f,\beta_I^f)$ in χ' by the following $\mu_I^f(\nu)=\mu_I(f(\nu))$, $\beta_I^f(\nu)=\beta_I(f(\nu)),\nu\in\chi$.*

Theorem4.7. *Let χ and χ' be two KU-algebras and f be a homomorphism from χ to χ'.*

(1) If $I=(\chi',\mu_I,\beta_I)$ is an intuitionistic fuzzy n-fold KU-ideal of χ', then $I^f=(\chi,\mu_I^f,\beta_I^f)$ is an intuitionistic fuzzy n-fold KU-ideal of χ.

(2) If $I^f=(\chi,\mu_I^f,\beta_I^f)$ is an intuitionistic fuzzy n-fold KU-ideal of χ, then $I=(\chi',\mu_I,\beta_I)$ is an intuitionistic fuzzy n-fold KU-ideal of χ'.

Proof. (1) For $\nu'\in\chi'$ there exists $\nu\in\chi$ such that $f(x)=x'$, we have

$\mu_I^f(0)=\mu_I(f(0))=\mu_I(0')\geq\mu_I(\nu')=\mu_I(f(\nu))=\mu_I^f(\nu)$ and

$\beta_I^f(0)=\beta_I(f(0))=\beta_I(0')\leq\beta_I(\nu')=\beta_I(f(\nu))=\beta_I^f(\nu)$. Let $\nu,\omega\in\chi$, $\kappa'\in\chi'$, then there exists $\kappa\in\chi$ such that $f(\kappa)=\kappa'$. It follows that

$$\mu_I^f(\nu^n*\omega)=\mu_I(f(\nu^n*\omega))=\mu_I(f(\nu^n)*f(\omega))\geq\min\{\mu_I(f(\nu^n)*(\kappa'*f(\omega)),\mu_I(\kappa')\}$$
$$=\min\{\mu_I(f(\nu^n)*(f(\kappa)*f(\omega)),\mu_I(f(\kappa))\}=\min\{\mu_I^f(\nu^n*(\kappa*\omega)),\mu_I^f(\kappa)\}$$

And

$$\beta_I^f(\nu^n*\omega)=\beta_I(f(\nu^n*\omega))=\beta_I(f(\nu^n)*f(\omega))\leq\max\{\beta_I(f(\nu^n)*(\kappa'*f(\omega)),\beta_I(\kappa')\}$$
$$=\max\{\beta_I(f(\nu^n)*(f(\kappa)*f(\omega)),\beta_I(f(\kappa))\}=\max\{\beta_I^f(\nu^n*(\kappa*\omega)),\beta_I^f(\kappa)\}$$

Hence $I^f=(\chi,\mu_I^f,\beta_I^f)$ is an intuitionistic fuzzy n-fold KU-ideal of χ.

(2) Since $f:\chi\to\chi'$ is onto mapping, then $\forall\nu,\kappa,\omega\in\chi'$ $\exists a,b,c\in\chi$ such that $f(a)=\nu$, $f(b)=\kappa$ and $f(c)=\omega$. So

$$\mu_I(\nu^n*\omega)=\mu_I(f(a^n)*f(c))=\mu_I(f(a^n*c))=\mu_I^f(a^n*c)\geq\min\{\mu_I^f(a^n*(b*c)),\mu_I^f(b)\}$$
$$=\min\{\mu_I(f(a^n)*(f(b)*f(c))),\mu_I(f(b))\}=\min\{\mu_I(\nu*(\kappa*\omega)),\mu_I(\kappa)\}$$

And

$$\beta_I(\nu^n*z)=\beta_I(f(a^n)*f(c))=\beta_I(f(a^n*c))=\beta_I^f(a^n*c)\leq\max\{\beta_I^f(a^n*(b*c)),\beta_I^f(b)\}$$
$$=\max\{\beta_I(f(a^n)*(f(b)*f(c))),\beta_I(f(b))\}=\max\{\beta_I(\nu*(\kappa*\omega)),\beta_I(\kappa)\}.$$

References

[1] Atanassov K. T.Intuitionistic fuzzy sets and Systems. 1986, 20: 87-96.
[2] Jun Y.B. Intuitionistic fuzzy ideal of BCK-algebras. *Int. J. Math. Sc.*, 2000, 24(**12**): 839-849.
[3] Lee K.M. Comparison of interval-valued fuzzy sets, intuitionistic fuzzy sets, and bipolar-valued fuzzy sets. *J. Fuzzy Logic intelligent Systems*, 2004, 14: 125-129.

[4] Satyanarayana B., Madhavi U. B., Prasad R.D. On foldness of intuitionistic fuzzy H-ideals in BCK-algebras. *International mathematical Forum*, 2010, 5(*45*): 2205-2211.
[5] Senapati T., Bhowmik M, Pal M. intuitionistic fuzzifications of ideals in BG-algebras, *Math.Aeterna*, 2012, 2 (**9**): 761-778.
[6] Mostafa S. M., Abd-Elnaby M.A, Yousef M.M.M. Fuzzy ideals of KU-Algebras. *International Mathematical Forum*, 2011, 6(**63**): 3139-3149.
[7] Mostafa S. M., Kareem F. F. N- fold commutative KU-algebras. *International Journal of Algebra*, 2014, 8 (**6**): 267-275.
[8] Mostafa S. M., Kareem F. F. fuzzy N-fold KU-ideals of KU-algebras. ***A****nnals of* ***F****uzzy* ***M****ath.* ***I****nform*, 2014, 6 (**8**): 987-1000.
[9] Prabpayak C., Leerawat U. On ideals and congruence in KU-algebras. scientia Magna Journal, 2009, 5(1): 54-57.
[10] Prabpayak C., Leerawat U. On isomorphisms of KU-algebras. *scientiamagna journal*, 2009, 5(**3**): 25-31.
[11] Zadeh L.A. Fuzzy Sets. Inform and Control, 1965, 8.

Classical Artinian Module and Related Topics

Classical Artinian Module and Related Topics

Majid M Abed, Faisal G AL-Sharqi

Department of Mathematics, Faculty of Education for Pure Scinces, University of Anbar, Iraq.

mnh_nn60@yahoo.com

Abstract. An R-module M is Artinian iff every non-empty set of submodules admits a minimal element. The aim of this paper, is studied three cases. The first case is to provide general properties about Artinian module. The second case is explaining the relationship between semisimple module and Artinian module and the third case is the study of Artinian module over division ring. In a short way, Artinian modules are characterized by the existence of minimal elements. This suggests a close analogy between Artinian module and other concepts. We proved that if M is projective, then it is Artinian. Also every Division module over Division ring is Artinian module. Any non-zero Sub-mod N of sem-simple R-module. If N is a non-zero Sub-mod of M, then N is Artinian as a module.

Keywords. Supplemented module, Radical supplemented, weakly supplemented, Artinian module, Division ring**.**

1. Introduction

Artinian modules have been studied by many researchers, but here we discus new relationships between Artinian module and other concepts. In [6], Wispaur ”showed a self projective M is a locally Artinian iff every cyclic module M=$\oplus$M-injective and f.cogenerated module”. In [2], Vanuynh and Wispaur, proved that, every f.g continuous right R-module is injective iff all simple right R-modules are injective. In [3], Matlis, developed a structure theory for Artinian modules over a comm Noetherian, 1-dimensional Cohen-Macaulay ring R. In [5], Abed proved that if every sub-module of M is a supplement in M, then M is a Artinian module. In Section 2, some properties of Artinian module are introduced. Also we studied some relations with others concepts in general. In Section 3, we choose two modules namely simple and sem-simple modules in order to explain the strong relation between Artinian module and these concepts. In Theorem 3.2, we proved that if M is projective, then it is Artinian. Finally, in Section 4, we look in general at the Artinian module over division ring Also, we proved that any module M over a ring Z_n is Artinian module if n = 5 and not Artinian module if n = 6 where n belong to Z and greater than zero.

In this paper, we studied the relationships between Artinian module and two concepts namely semi-simple module and Division ring. Our main results of this paper are Theorem 3.3 and Theorem 4.5.

2. Properties of Artinian Module

In this section, we give some properties of Artinian module and related it with others concepts in general. In order to focus on Art-module we need to define the following basic concepts.

Definition 2.1. (see [6]). Let R be a ring. A left R module is an abelian group M and an external law of composition" $\mu: R\times M \to M$, subject to the conditions that for all r; s∈R and m; n∈M we have:
(1) (r; m + n) = (r; m) + (r; n);
(2) (r + s; m) = (r; m) + (s; m);
(3) (rs; m) = (r; (s; m));
(4) if 1 ∈ R, then (1; m) = m.

Definition 2.2. (see [1]). A module M has (dcc) if it satisfy $M_1 \supseteq M_2 \supseteq M_n$ …there exists m^+ such that $M_m = M_n, \forall\ n \geq m$.

Definition 2.3. (see [1]). A module M is called Artinian, if it satisfy all the conditions in Definition 2.2.

From (Definition 2.2 and Definition 2.3), there is a relationship between these definitions and another concept is called minimal element. Therefore we need to introduce some information about this concept. If any sub-modules of a module have minimum condition, then any non empty collection of these sub-modules has minimal element (i.e. any subset A of some partially ordered set that is not greater than any other).

Example 2.4. ([4]). Let $M = (a/2^n) : a \text{ in } Z, n \geq 0$ and consider M as a Z-module. Not here that $Z \subseteq M \subseteq Q$. Also let T=M/N . Then T is Artinian module.

Lemma 2.5. (see [6]). IF every non-empty set of sub-modules of M has a minimal element; then every factor module of M is f.co-generated.

Theorem 2.6. Every non-zero Artinian R-module M has a minimal sub-modules.

Proof. Let M be an Artinian R-module such that $M \neq 0$. Let us take A equal to the collection of Sub-mods of M such that these Sub-mods are proper. Thus the Sub-mod (0) belong to A. Therefore $A \neq \phi$. So has minimal element, say K. Hence K is a minimal sub-module in M.

Theorem 2.7. If $\phi \neq N_i$ sub-modules of M has a minimal-element, then M is Artinian module.
Proof. From Lemma 2.5, every factor mod of M is finitely co-generated. Let we have (dcc) of M_i of submodule $N=(\cap N_i)/M$. So M/N is finitely co-generated. Now we must obtain $N=M_k$ for each k, i.e. $M_{k+1}=M_K$ for all i in N.

Remark 2.8. A module M with only finitely many sub-modules is Artinian module and from [5], we found the following three examples.

Example 2.9. All finite abelian groups over integer numbers are Artinian module. On the other hand, Z_Z is not Artinian module because $Z \supseteq <2> \supseteq <4> \supseteq <8> \ldots$ is not (dcc).

Example 2.10. As every sub-module is subspace with dimension ≤ dim(V) such that V is vector space, we can say finite-dimensional of V are Artinian module.
The dual of (Example 2.10) is not true. (see Example.2.11).

Example 2.11. All the finite dimensional vector spaces are not Artinian module.

Theorem 2.12. Let N_i be a Sub-modules of an Artinian module M. Let be a quotient-module. Then N_i and the quotient M/N are Artinian modules.
Proof. We take M is an Artinian module and N sub-module of M. We have any Sub-mod of N is also a sub-module of M. Hence any (dcc) of N is chain Sub-mods in M. So the result follows. Now any Sub-module of M/N as L/M such that L is a Sub-mod of M and contain N. Let us say Let us say $(L_1/N) \supseteq (L2/N) \supseteq \ldots$ be (dcc) of sub-modules in M/N . Thus $L_1 \supseteq L_2 \supseteq \ldots$ is a chain in M. Thus $L_m=L_n$ $n \geq m$ for some m.

The next theorem explain that the sum of any Artinian modules is also Artinian module.

Theorem 2.13. Let $A=\sum A_i$; i=1,. . . ,n. If A_1, A_2,. . . ,A_n are Artinian modules, then A is also Artinian module.
Proof. Let $A=\sum A_i$; i=1,. . . ,n. Assume that A is Artinian module. By induction on n; if n=1, there is nothing to prove. We claim that the case is true if m<n. Now $A=\sum A_i+A_n$; i=1,. . . ,n-1. Let $N=\sum A_i$; i=1, . . . , n^{-1}. Hence by induction hypothesis N is Artinian. We have

$$(A/N)=(N+(A_n/N)$$
$$= A_n/(N \cap A_n)$$

is alsoArtinian. Since (A/N) and N are Artinian, then A is Artinian module.

3. Artinian Module and Semi-simple Property

In order to describe the relationship between Artinian module and semi-simple property, we need to introduce some information about sem-simple-mod. Any module M is called semisimple module if every submodule of M is simple. One of the most important idea say any sem-simple module is Artinian module.
Lemma 3.1. Any semi-simple module M is Artinian module.
Proof. The proof is very easy, because for any sequence $M_1 \supseteq M_2 \supseteq \ldots M_n \supseteq \ldots$ of sub-module have decreasing property. This imply to the length is also decreasing (i.e M is Artinian module).

In the next theorem, we explain the relationship between projective module and Artinian module.

Theorem 3.2. Let M be an R-module. If M is projective module, then it is Artinian module.
Proof. Let M be an arbitrary sub-module of R. Then we have the following sequence

$$0 \rightarrow M \rightarrow R \rightarrow \xrightarrow{R} 0 \ldots (*).$$

But all the modules over R are projective. Then N/M Then N/M is projective. Hence (*) is splits. such that $N \leq R$ and $N \approx (R/M)$. Thus R is sem-simple. So, every module M of R is sem-simple. Then M is Artinian module (see Lemma 3.1).
The following theorem shows a Sub-module of semi-simple module is Artinian module.

Theorem 3.3. (see [1]). Let M be a sem-simple R-module. If N is a non-zero sub-modules of M, then N is Artinian as a module.

In order to understand Theorem 3.3, we must prove the next theorem.

Theorem 3.4. Let M be an R-module. If $N \leq M$ and N= M, then is the sum of a collection of simple sub-modules.

Proof. First we must show $N=\oplus M$. Let $N\leq M$ and $K\leq N$. We have $M=K\oplus L$ for sub-module L of M. Hence $N=(K\oplus L)\cap N=(K\cap N)\oplus (L\cap N)=K\oplus (L\cap N)$. Thus $N=\oplus N$. We claim that every sub-module $N\neq 0$ contains a simple module. Let $0\neq x\in N$. Let $\xi=L$ is a sub-module of N such that x not in L. Now Rx is a sub-modules of N and hence $N=Rx+U$ for some U. Thus x not in U. So ξ is non-empty. In order to benefit from zorn's Lemma, we obtain a max-element k in J. Then $N=K\oplus S$ for some sub-moduls S of N. We need to show S is simple module. Suppose S_0 is a proper sub-modules of S. Then $S=S0\oplus T$, $T\neq(0)$. Hence $N=K\oplus S_0\oplus T$. Now $K\oplus S_0$ and $K\oplus T$ both do not belong to I. Thus $x\in(K\oplus S_0)\cap(K\oplus T)$. Therefore $x=k_1+s=k_2+t$ for some $k_1, k_2\in K$, $s\in S$; $t\in T$. So $k_1-k_2+s-t=0$ and $k_1=k_2$, $s=t=0$. Thus $x=k_1=k_2\in K$ a contradiction. Hence S is simple.Let $M0=\sum\{S:S$ is simple of $M\}$there exists a sub-module U of M such that $M=M\oplus U$. If $U=(0)$, we are done. If $U\neq 0$), then U contains a simple Sub-mod. Thus $M=M_0$ is a sum of collection of simple sub-modules and so M is simple (see [1]). Hence N sem-simple and so is Artinian sub-module.

Corollary 3.5. Sum of the sem-simple modules are Artinian module.
Proof. Let $S=S_1+S_2+\ldots+S_n$ such that $S_1, S_2,\ldots,S_n$ are sem-simple mods. We have every sub-module of each S_n is simple. Hence each S_n are sem-simple and so S is a sem-simple Thus S Artinian module. (see Lemma 3.1).

Remark 3.6. We can rewrite a proof of (Theorem 2.12) by using sem-simple property in order to obtain M/N is Artinian module. See the following.

To prove quotient modules are Art-mod , we need to say if M is a semi-simple module and N subset of M so N Sub-mod of M/N. Then N has complement of $N\in M$. i.e. $M=N\oplus N\overline{N}$. Then Q equal to complement of N and so Q is equivalent to a Sub-module N of M. Thus Q is sem-simple and hence is Artinian module.

4. Artinian Module Over Division Ring

In this section, we study Artinian module over important ring namely Division ring. Some new results has been obtained in this section.

Definition 4.1. (See [4]). Let R be a ring. Then R is called Division ring if every $0\neq a$ is an element of R is a unit.

Remark 4.2. We know that Q, R, and C are Division rings. But Z and $M_n(R)$ are not Division rings. We say R is commutative field if R is a commutative Division ring. Also Q, R and C are fields but Z is not a field (not a Division ring).

Lemma 4.3. Every Division ring has no zero divisors.
Proof. Suppose that R is a Division ring. We must prove that R is integral domain. By contradiction, if $a.b = 0$, so $a\neq 0$ and $b\neq 0$. But $0\neq a$ in R. So the inverse of a in R. Thus $a^{-1}(ab) =a^{-1}(0)=0=(a^{-1}a)b=1.b=b=0$. Contradiction.

Theorem 4.4. Let D be a Division ring. Then every Division module is Artinian module.
Proof. Let V be a left Division module, and let W be a sub-module of V. Let Bbe a basis for W. Then there exists a basis, B_1, of V which contains B. Let $B_2=B_1\cap B$; and let W_1 be the span of B_2. Then $W_1\oplus W = V$. Thus V is sem-simple module and so is Artinian module. Any module M over integral domain is not Artinian module, because the converse of (Lemma 4.3) is not true in general.(i.e. there are integral domains which are not Division rings.

Remark 4.5. Let $(Z_n,+,.)$ be the ring of integers (where $n^+\in Z$). This is a commutative ring.

Theorem 4.6. Let D be a Division ring and let n^+ be an integer number. If $End_{D_i}(D_n)$ is a simple ring that is sem-simple as a left $End_{D_i}(D_n)$-module, then it is Artinian module.
Proof. If R is semi-simple, then by Wedderburn's Theorem (Let R be a sem-simple ring, then there is a finitely collection of integers $n_1,\ldots, n_k$, and Division rings $D_1,\ldots ,D_k$ such that $R \oplus End_{D_i}(D_{ni})$, i=1 to k). Then when k=1 is true. Thus $End_{D_i}(D_n)$ is Artinian module.

Example 4.7. If M is an R-module over the ring $(Z_n,+, .)$, then M is Artinian module. Let us take r any element in Z_n. We must prove r has unit element (i.e. r^{-1} exists). It is clear that the elements of Z_n are 1,…, n-1, for example, if n=5, then the elements are 1, 2, 3, 4 and so $1^{-1} = 1$, $2^{-1} = 3$, $3^{-1} = 2$ and $4^{-1} =4$. So Z_n is a division ring. Thus M is Artinian module.

Example 4.8. Any R-module M over $(Z_n,+, .)$ is not Art-mod such that n=6. We have $1^{-1} = 1$, but 2^{-1}, 3^{-1}, 4^{-1} have no inverse and $5^{-1} = 5$. So unit of $(Z_n) = 1, 5 = < 5 >$. Thus Z_n is not a division ring such that n=6, and hence M is not Artinian module.

Example 4.9. The Quaternions: Let D be the set of all symbols $a_0 + a_{1i} + a_{2j} + a_{3k}$ where $a_i \in R$. by term using the relations $i^2 = j^2 = k^2 = -1$ and ij = -jk = k; jk = -kj = i; ki = -ik = j. Then D is a non-commutative ring with zero and identity. Let $a_0 + a_{ji} + a_{2j} + a_{3k}$ be a non-zero element of D. Then not all the ai are zero. We have $(a_0 + a_{1i} + a_{2j} + a_{3k})(a_0 + a_{1i} + a_{2j} + a_{3k}) = (a_0)^2 + (a_1)^2 + (a_2)^2 + (a_3)^2$ f = 0. So letting $n = (a_0)^2 + (a_1)^2 + (a_2)^2 + (a_3)^2$, the element $(a_0/n)+(a_1/n)i+(a_2/n)j+(a_3/n)k$ is the inverse of $a_0 + a_{1i} + a_{2j} + a_{3k}$. Thus D is a D-ring. So p any module over D is Artinian.

Theorem 4.10. Let M be an R-module. If R has identity element, then not necessary R is comm, R and (0) are only left ideals. Then any module over R is Artinian module.
Proof. We have R not equal to {0} as 1 in R. Assume $a \in R$ not equal zero. Let $aR=\{ar: r \in R\}$. So aR is a right-ideal in R. Also {0} and R are right ideals in R. Hence aR equal to {0} or aR equal to R. But aR not equal to {0} in case 1 in R, so $ar = a \in ar$. Therefore aR= R. We have 1 in R, so a in R, a=1. So a^{-1} in R. Since a is an element such that only stipulation that a not equal to zero, so any $0 \neq x \in R$, the x^{-1} in R. Thus R is a Division ring and hence M is Artinian module

Corollary 4.11. Let R be a ring with p4 elements. If R have only (0) and R satisfy the conditions of ideals, then R has not Artinian module.
Proof. Let M be an R-module. Since $p \neq 2$, then Q_p is a non-commutative f.ring. But Wedderburn`s Theorem gives a finite Division ring is comm. So Q_p not be a Division ring, Thus M is not Art-mod.
Corollary 4.12. Let M be an R-module such that R have only two right ideals (0) and R. Then R is a Division ring and then has Artinian module or R is a ring has many prime number such that ab=0; a and b in R.

5. Conclusion

The relationship between Artinian module and other concepts was discussed in this paper. The main results are appeared clearly to achieve all objectives of this research, for example the first aim result is the sum of sem-simple-mod are Artinian module. The other result is, if M satisfy all conditions of projective module, then it is Artinian. Also, any module M over Division ring $(Z_n, +, .)$ is Artinian module.

Acknowledgments
The authors would like to thank the referee, whose careful reading and thoughtful comments have helped improve the paper.

References

[1] Eisenbud D 1970 Subring of Artinian and Noetherian Rings *Math Ann.* **185** 247
[2] D Vanhuynh and R Wisbaur 1990 Characterization of Locally Artinian Modules *Journal of Algebra* **132** 287
[3] E Maltis 1973 *Springer Lecture Notes* Springer-Verlag Berlin **198** 327
[4] J Hein 1979 Almost Artinian Module Math Scand **45**
[5] M M Abed 2015 Some Generalizations of Supplemented Module Related to Length Property Thesis Ph.D UKM-Malaysia.
[6] R.Wisbauer 1991 Foundation of Module and Ring Theory Gordon and Breach Reading University of Dusseldorf

Journal of Physics: Conference Series

ʎNαc – Continuous And ContraʎNαc-Continuous Mappings In Topological

ʎNαc - Continuous And ContraʎNαc-Continuous Mappings In Topological

NADIA MOHAMMED ALI ABBAS

Ministry of Education, Iraq
E-mail: mali.nadia@yahoo.com

Abstract: The aim of this paper is to introduce a class of ʎNαc - continuous mappings by using the concept ofʎNαc - open sets in topological spaces like: ʎNαc, ʎNαc*andʎNαc** - continuous mapping with some of their properties. Moreoverwe studied a new kind ofʎNαc- continuous mappings which we called contraʎNαc-continuous mappings with some of their applications.

Keywords:N_{α}–open;ʎ$N_{\alpha c}$- open;ʎ$N_{\alpha c}$- continuous mapping.

I.Introduction

Theconcept of mappings is very important.A new kind of mappings is given in this study which is named ʎNαc – continuous and contra ʎNαc– continuous mappings.An α – open set was first studied in 1965 byO. Njasted see [1]. Nα–open set was first studied in 2015 by N.A. Dawood and N.M.Ali see [2]. The ideaof an operationmappingʎon a spaceX was introduced by Ogatafor more details see [3]. The concepts of Nα-operation mapping and ʎNαC - open sets were first studied in 2015 by N.M.Ali, see [4].The idea of contra continuity in topological spaces was presented by Dontcher see [5]. Here, in this paperattempt has been made to employ the concept of ʎNαC- open sets to study some types of ʎNαc- continuous mappings like ʎNαc*, ʎNαc**continuous mappings, and contra- ʎNαc -continuous mappings. We shall mean in this study the space X is a topological space or a space. On the other handthe interior and closure of a subsetA of X we shall note by int (A) ,cl(A)respectively.

II.Preliminary Concepts And Results

In this section we shall recall some definitions,propositions, and properties of Nα- open; ʎNα - open and ʎNαc- open sets which we need to study the concept of ʎNαc - continuity.

Definition (2.1): [1]

A set A is an α-open if A⊆int (cl (int (A))), it's family isdenoted by αO (X), it'scomplement is called α - closed and denoted byαC (X).

Definition (2.2): [2]
A set A is N_α- open if ∃nonempty α- open set H s.t cl(H)⊆A ,it'scomplementis namedN_α− closed set,the family of N_α− open (N_α- closed)is denoted by$N_\alpha O(X)$, ($N_\alpha C(X)$) respectively.

Definition (2.3): [2]
A set A is N_α- clopen if A is N_α- open and N_α - closed set.

Proposition (2.4): [2]
Every clopen set is N_α- open set.
The set X is N_α- open in every topological space.

Definition (2.5): [4]
A mapping ʎ: NαO(X) →P(X) is called N_α- operation on $N_\alpha O(X)$ ifA⊆ʎ(A) for all nonempty N_α - open set A.

Remarks (2.6): [4]
(i) ʎ in above definition is called an identity Nα - operation if ʎ(A)=A for all A ϵ NαO(X)
(ii) (ii) If ʎ: NαO (X)→P(X) is any Nα - operation, then it is clear that ʎ(X) =X,ʎ(Ø)=Ø .
(iii) ʎ is named Nα- regular operation if ∀ Nα- open sets A ,B containingx∃Qϵ NαO(X) contains xsuch that ʎ(Q)⊆ʎ(A) ∩ ʎ(B).

Definition (2.7): [4]
Suppose that X is a topological space andʎ:NαO(X) → P(X)be Nα -operationdefined onNαO(X), thenA is ʎNα-open set if ∀xϵA∃nonempty Q ∈NαO(X) such that contains xand ʎ(Q)⊆A,it's complement is ʎNα-closed set ,the family of ʎNα-open(ʎNα-closed)is denoted by ʎNαO (X)ʎNαC (X) respectively.

Definition (2.8) [4]
A $ʎN_\alpha$- open set A is $ʎN_{\alpha c}$- open set if ∀ xϵ A ∃ closed set F such that xϵF⊆A and it's complement is called $ʎN_{\alpha o}$-closed, the family of all$ʎN_{\alpha c}$-open ($ʎN_{\alpha o}$-closed resp.) is denoted by ʎNαcO(X),(ʎNαOC(X)) respectively.

Remarks (2.9) [4]
(i) For any topological space X with Nα- operation ʎ, the set X and Ø are ʎNαc- open sets.
(ii) For any topological space X, we have ʎNαcO(X)⊆ʎNαO(X)⊆NαO(X)

Theorem (2.10) [4]
(i) Let {Aα}αϵ ɪ be any collection of ʎNαc - open sets ,then ∪Aα is ʎNαc - open set ∀ αϵ I.
(ii) Suppose A,Bϵ ʎNαcO(X) ,then A∩Bϵ ʎNαcO(X) such that ʎ is Nα - regular operation .

Theorem (2.11) [2]
Suppose that Y is a subspace of X such that A ⊆Y⊆X.Therefore:
(i) If A ϵ Nα O(X) (NαC(X)) respectively. Then Aϵ NαO(Y),(NαC(Y)) respectively.
(ii) If Aϵ Nα O(Y) (NαC(Y)) respectively. Then Aϵ NαO(X) (NαC(X)) respectively. , where Y is clopen set.

Theorem (2.12) [2]
Suppose thatX_1 , $X_2$are topological spaces. Then A_1, A_2areN_α - open sets inX_1 , X_2respectively if and only if $A_1 \times A_2$isN_α- open set in$X_1 \times X_2$.

Theorem (2.13) [4]
Suppose thatX_1 , $X_2$are topological spaces. ThenA_1,A_2 are $\Lambda N_{\alpha c}$ - open sets in X_1, , X_2respectively if and only if$A_1 \times A_2$ is $\Lambda N_{\alpha c}$ - open set in $X_1 \times X_2$.

Theorem (2.14)[4]
Suppose thatY is a subspace of Xsuch that $A \subseteq Y \subseteq X$. Then:
(i) If $A \in \Lambda N\alpha cO(X)$ ($\Lambda N\alpha oC(X)$) respectively, then$A \in \Lambda N\alpha cO(Y)$($\Lambda N\alpha oC(Y)$) respectively.
(ii)If$A \in \Lambda N\alpha cO(Y)$ ($\Lambda N\alpha oC(Y)$) respectively, then $A \in \Lambda N\alpha cO(X)$ ($\Lambda N\alpha oC(X)$) respectively, where Y is clopen set in X.

III . Some Kinds of $\Lambda N_{\alpha c}$ – Continuity

In this section, the concept of $\Lambda N_{\alpha c}$ -open set will be used to define some kinds of $\Lambda N_{\alpha c}$ -continuity like: $\Lambda N_{\alpha c}$ –continuous, $\Lambda N_{\alpha c}$*-continuous and $\Lambda N_{\alpha c}$** - continuous mappings and the relations between these kinds of mappings with proofs or counter examples

Definition (3.1)
Suppose that X_1,$X_2$are topological spaces such that $f : X_1 \to X_2$ isany mapping. Then f is named $\Lambda N_{\alpha c}$($\Lambda N_{\alpha c}$*($\Lambda N_{\alpha c}$**-continuous) mapping if$\forall A \in N_\alpha O(\Lambda N_{\alpha c} O(\Lambda N_{\alpha c} O(X_2))$ respectively, then $f^{-1}(A) \in \Lambda N_{\alpha c} o(\Lambda N_{\alpha c} O(N_\alpha O(X_1)$ respectively.

Now, we shall discuss the relations betweenabove kinds of mappings see the following Remarks:

Remarks (3.2)
(i) Every ΛNαc - continuous is ΛNαc* - continuous mapping .
(ii) Every ΛNαc* - continuous is ΛNαc** - continuous mapping .
Proof: It follows from (Rem.(2.9(ii))). The converse of (Rem.(3.2))is not true in general see(3.3) :

Example(3.3)
Consider X=Y={a,b,c},supposef:X→Ys.tf(a)=f(c)=c,f(b)=b,τ_x={X,{a},{b},{a,b}} ,NαO(X)={X,{b,c},{a,c},∅}.Let Λ:$N_\alpha O(X) \to P(X)$ be N_α- operation defined by:-

$$\Lambda(A) = \begin{cases} A & if \quad b \in A \\ X & if \quad b \notin A \end{cases}$$

ΛNαO(X)=ΛNαcO(X) = {X,{b,c},∅}.

tY= $\{Y, \{a, b\}, \{c\}, \emptyset\}$, NαO(Y)={Y,{a,c},{b,c},{c},{a,b}∅}.

ΛNαO (Y)={Y,{a,c},{b,c},{c},∅}.

ΛNαcO(Y)={Y,{a,c},{b,c},{c},∅}, Λ: NαO (Y)→P(Y) be Nα-opertion defined by

$$\Lambda(A) = \begin{cases} A & , if \ \ c \in A \\ Y, & if \ \ c \notin A \end{cases}$$

Thus f is $\Lambda N_{\alpha c}$** - continuous. But it is neither$\Lambda N_{\alpha c}$ - continuous nor$\Lambda N_{\alpha c}$* - continuous sincef^{-1}{a,c}∉Λ $N_{\alpha c}$O(X) , alsof^{-1}{c}={a,c}∉Λ$N_{\alpha c}$O(X).
We have the following diagram

$$\boxed{\Lambda N\alpha c- \text{ continuous}} \rightarrow \boxed{\Lambda N\alpha c * - \text{continuous}} \rightarrow \boxed{\Lambda N\alpha c ** - \text{continuous}}$$

Theorem (3.4)
Suppose thatf: X→Y is a mapping such thatX has N_α- regular operation.Therefore. The restriction mapping $f|_F$ of $\Lambda N_{\alpha c}$($\Lambda N_{\alpha c}$*($\Lambda N_{\alpha c}$**- continuous) mapping f to any subspace F $\subseteq$X where F ϵ $\Lambda N_{\alpha c}O(\Lambda N_{\alpha c}O(N_\alpha O(X))$respectively is also $\Lambda N_{\alpha c}$ ($\Lambda N_{\alpha c}$*($\Lambda N_{\alpha c}$** -continuous)) respectively.
Proof: We shall prove only the case for ($\Lambda N_{\alpha c}$)and the other cases by the same way. Assume that $f|_F$:F→Yis restriction mapping, assume thatB $\in N_\alpha O(Y)$, thus $f^{-1}(B)\in\Lambda N_{\alpha c}O(X)$ also F $\in\Lambda N_{\alpha c}O(X)$ sinceΛ is N_α- regular operation(by hypothesis)then by(Th. (2.10(ii))) $f^{-1}(B)$ $\cap$F$\in\Lambda N_{\alpha c}O(X)$ so$f^{-1}(B)$ $\cap$F$\in\Lambda N_{\alpha c}O(F)$ see(Th. (2.14). Therefore $(f|_F(B))^{-1}\in\Lambda N_{\alpha c}O(F)$,thus the proof is complete.

Theorem (3.5)
Suppose that f:X→Yis a mapping. Assume X=H∪W whenever H,W are disjoint clopen subsets of X. Therefore f is $\Lambda N_{\alpha c}$($\Lambda N_{\alpha c}$*($\Lambda N_{\alpha c}$** - continuous mapping) whenever the restriction mappings $f|_H$, $f|_W$is$\Lambda N_{\alpha c}$($\Lambda N_{\alpha c}$*($\Lambda N_{\alpha c}$**- continuous mappings)respectively.
Proof: We shall prove only the case of ($\Lambda N_{\alpha c}$),the other cases by the same way.Assume that$M\in N_\alpha O(Y)$,we have $f^{-1}(M)=(f|_H)^{-1}{}_{(M)}\cup(f|_W)^{-1}{}_{(M)}$,where $(f|_H)^{-1}$,$(f|_W)^{-1}\in\Lambda N_{\alpha c}O(H)$, $\Lambda N_{\alpha c}O(W)$ respectively. Thus$(f|_H)^{-1}$,$(f/_W)^{-1}\in\Lambda N_{\alpha c}O(X)$see (Th. (2.14)) →$f^{-1}(M)\in\Lambda N_{\alpha c}O(X)$see Th. (2.10(i))) .

Theorem (3.6)
Suppose that f:X→Y is a mapping , f_H:$f^{-1}{}_{(H)}$→Hdefined by$f_H(x) = f(x)$, where H is clopen set inY. Therefore f_H is $\Lambda N_{\alpha c}$($\Lambda N_{\alpha c}$*($\Lambda N_{\alpha c}$** - continuous)mapping whenever f is $\Lambda N_{\alpha c}$($\Lambda N_{\alpha c}$*($\Lambda N_{\alpha c}$** - continuous) mapping respectively.

Proof: We shall prove only the case of($\Lambda N_{\alpha c}$),the other cases by the same way. Assume that B $\in N_\alpha O(H)$ since H∈CO(Y), then B $\in$ $N_\alpha O(Y)$see(Th. (2.11)) hence $f^{-1}{}_{(B)}\in\Lambda N_{\alpha c}O(X)$ this implies $f^{-1}{}_{(B)}\in\Lambda N_{\alpha c}O(f^{-1}{}_{(H)})$ see(Th.(2.14) .

Theorem (3.7)
Assume that f:X_1 →$X_2$is any mapping , $X_2\subseteq X_3$.Therefore f : X_1 →X_3 is $\Lambda N_{\alpha c}$($\Lambda N_{\alpha c}$*($\Lambda N_{\alpha c}$** - continuous)mapping whenever f : X_1 →X_2 is $\Lambda N_{\alpha c}$($\Lambda N_{\alpha c}$* ($\Lambda N_{\alpha c}$** - continuous) mapping respectively.

Proof:We shall prove only the case for $\Lambda N_{\alpha c}$ and the other cases by the same way.
Assume that $M\in N_\alpha O(X_3)$ then $M\in N_\alpha O(X_2)$(see Th. (2.11)) hence,$f^{-1}{}_{(M)}\in\Lambda N_{\alpha c}O(X_1)$

Theorem (3.8)
Suppose that g: X→$X_\times$Yis a graph mapping of f:X→Y suchthat g(x)=(x, f(x)) ∀x∈X. Therefore f is $\Lambda N_{\alpha c}$($\Lambda N_{\alpha c}$*($\Lambda N_{\alpha c}$**- continuous) whenever g is $\Lambda N_{\alpha c}$($\Lambda N_{\alpha c}$*($\Lambda N_{\alpha c}$**- continuous) mapping respectively.

Proof: We shall prove only the first case .The other cases by the same way. Assume that$H\in$ $N_\alpha O(Y)$ because X $\in N_\alpha O(X)$ in every topological space see(propo.(2.4), this implies $X_\times H\in N_\alpha O(X_\times Y)$ see (Th. (2.12)) , thus $g^{-1}(X_\times H)$ $\in\Lambda N_{\alpha c}O(X)$ but $g^{-1}(X_\times H)=f^{-1}(H)$,thus$f^{-1}(H)$ $\in\Lambda N_{\alpha c}O(X)$.Therefore f is $\Lambda N_{\alpha c}$-continuous mapping.

Proposition (3.9)
Assume that f :X→Y ,g : Y→Ƶ are mappings. Therefore:

(i) The composition of tow ΛNαc(ΛNαc*- continuous mappings) is also ΛNαc(ΛNαc*- continuous mapping.

(ii) If f is ʎNαc**-continuous and g isʎNαc*-continuous, hence their composition isʎNαc**-continuous mapping.

Proof:By using Definition (3.1).

ıv.Contra $ʎN_{αc}$- Continuity

In this section the concept of $ʎN_{αc}$- open set will be used to define a new class of $ʎN_{αc}$- continuity which is called contra $ʎN_{αc}$- continuous mapping. Some theorems will be proved.

Definition (4.1)
Assume that f : X→Y is a mapping, then f is named contra $ʎN_{αc}$- continuousif for all H $∈N_αO(Y)$, then$f^{-1}(H)$ $ʎN_{αo}C(X)$.
Now we shall give equivalent theorems of Definition (4.1)

Theorem (4.2)
Assume that f : X→Yis a mapping. Therefore f is contra $ʎN_{αc}$- continuous if and only if for all F $∈N_αC(Y)$ then$f^{-1}(F)∈ʎN_{αc}O(X)$.
Proof: By using Definition (4.1).

Theorem (4.3)
Assume that f : X→Y is a mapping. Therefore f is contra $ʎN_{αc}$- continuous if and only if for all x∈X and for all F∈ $N_αC(Y)$ containing f(x) ∃G∈$ʎN_{αc}O(X)$ such that x∈ G , f(G)⊆ F.

Proof: Assume that f is contra $ʎN_{αc}$- continuous, supposex ∈ X , F∈ $N_αC(Y)$, then F'∈$N_αO(Y)$ thus$f^{-1}(F')$ ∈$ʎN_{αo}C(X)$where$f^{-1}(F')$ = $(f^{-1}(F))'$hence$f^{-1}(F)$ ∈$ʎN_{αc}O(X)$containing x. Put G=$f^{-1}(F)$, thenx ∈ G, f(G)⊆F. Conversely obvious.

Remark (4.3)
The concepts of $ʎN_{αc}$- continuous and contra $ʎN_{αc}$- continuous are independent see the following Examples:-

Example (1)
Suppose X={a, b, c}with τ ={X,{a},{b},{c}, φ},ʎ is identity $N_α$– operation. Assume f:X→X s.tf(a)=c , f(b)=a, f(c)=b $N_αO(X)$=ʎ $N_αO(X)$=ʎ $N_αcO(X)$={X,{b, c} , {a ,c} , {a, b},φ} . It is clear that f is$ʎN_{αc}$- continuous which is not contra $ʎN_{αc}$– continuous.

Example (2)
AssumeX ={a, b, c, d} with τ ={X,{b},{d},{b,d}, φ} , ʎ(A) is $N_α$- operation defined by $ʎ(A) = \begin{cases} cl(A) & if \quad d∈A \\ X & otherwise \end{cases}$
Conceder f:X→X by f(a)=f(c)=f(d)=d,f(b)=a, $N_α$ O(X)={X,{a, c, d},{a, b, c}φ}
$ʎN_αO(X)$={X,{a, c, d},φ}=$ʎN_{αc}O(X)$, $ʎN_{αo}C$ (X)={X,{b},φ}
It is easy tocheck that f is contra $ʎN_{αc}$-continuous which is not $ʎN_{αc}$- continuous since f^{-1}{a,b,c}={b}∉ʎ $N_{αc}O(X)$.

Theorem (4.4)
The restriction $f|_D$ of contra $ʎN_{αc}$- continuous mapping f:X→Y to any subspaceD⊆X where D∈ $ʎN_{αo}C(X)$ is also contra $ʎN_{αc}$- continuous .

Proof:Assume that M∈ $N_αO(Y)$, thus $f^{-1}(M)$ ∈ $ʎN_{αo}C(X)$,also D ∈$ʎN_{αo}C(X)$, hence$f^{-1}(M)$ ∩D ∈ $ʎN_{αo}C$ (X) ,so it is in D (see Th. (2.14)) ,but $(f|_D)^{-1}{}_{(M)}=f^{-1}{}_{(M)}$ ∩D. Thus the proof is complete.

Theorem (4.5)
Assume that f:X→Y is contra $\Lambda N_{\alpha c}$- continuous , then f_S:$f^{-1}(S)$→Sis also , where S is clopen subset of Y.
Proof : SupposeW$\epsilon N_\alpha O(S)$this implies Wϵ $N_\alpha O(Y)$ see (Th. (2.11)) , thus $f^{-1}(W) \epsilon \Lambda N_{\alpha o}C(X)$ where$f^{-1}(W) \subseteq f^{-1}(S) \subseteq X$ hence$f^{-1}(W) \epsilon \Lambda N_{\alpha o}C(f^{-1}(S))$.

Theorem (4.6)
Assume that f:X→Yis a mapping whereX =H∪F such that H,F are disjoint $\Lambda N_{\alpha o}$- closed sets of$X$.Therefore the restriction mappings $f|_H$, $f|_F$ of contra $\Lambda N_{\alpha c}$- continuous mapping f is also contra $\Lambda N_{\alpha c}$- continuous mappings .
Proof: Suppose G$\epsilon N_\alpha O(Y)$, thus$f^{-1}(G) \epsilon \Lambda N_{\alpha o}C(X)$ also H $\epsilon \Lambda N_{\alpha o}C(X)$, hence$H \cap f^{-1}(G) \epsilon \Lambda N_{\alpha o}C(X)$,so$H \cap f^{-1}(G) \epsilon \Lambda N_{\alpha o}C(H)$ but $(f|_H(G))^{-1}=f^{-1}(G) \cap H$. Thus $f|_H$ is contra $\Lambda N_{\alpha c}$- continuous mapping.
The proof of $f|_F$by the same way.

Remark (4.7)
The composition of two contra$\Lambda N_{\alpha c}$- continuous mappings is not true in general see the next:

Example(3)
Assumethat X={a ,b, c} ,τ={X,{a},{b},{c},φ} with anidentity Nα-operation Λ whereNαO(X)={X,{b, c},{a, c},{a ,b},φ} =ΛNαO(X) =ΛNαcO(X).
Assume thatY={a, b, c, d}=Z , τ= {Y,{b},{d},{b, d},φ}.
NαO(Y)={Y,{a,c,d},{a,b,c},φ},NαC(Y) ={Y,{b},{d},φ}. .
SupposeNα–operationΛ by$\Lambda(A) = \begin{cases} cl(A) & if \quad d \epsilon A \\ X & if \quad d \notin A \end{cases}$
ΛNαO(Y) =ΛNαcO(Y)= {Y,{a,c,d},φ }, suppose f:X→Y by f(a)=a , f(b)= f(c)= b.
Assume thatg:Y→Ƶby g(a)= g(c)= g(d)= a , g(b)=d ,τƵ={Ƶ,{a},{b},{a, b},φ},
NαO(Ƶ)={Ƶ,{b,c,d}, {a,c,d} ,φ}, NαC(Ƶ)={Ƶ,{a},{b} ,φ}, suppose Λ by $\Lambda(A) = \begin{cases} cl(int(A) & if d \epsilon A \\ Ƶ, & if d \notin A \end{cases}$
ΛNαO(Ƶ)= $\begin{cases} Ƶ, \{a,b,c\},\{a,b,d\},\{b,c,d\},\{a,c,d\},\{a,b\} \\ \{a,c\},\{a,d\},\{b,c\},\{b,d\},\{c,d\},\varphi \end{cases}$
ΛNαcO(Ƶ)={Ƶ,{c,d},{b,c,d},{a,c,d},φ}. It is easy to check that f and g are contra ΛNα c-continuous , but gof is not contra ΛNαc- continuous , since{a}ϵNαC(Ƶ) but(gof)-1 {a}={a}$\notin \Lambda$Nαc O(X).
Now we shall give some applications of contra $\Lambda N_{\alpha c}$- continuous mapping. First we shall give some definitions which we need in our work.

Definitions (4.8)
A space X is named:
(i) Nα (Nα-ultra (ΛNαc (ΛNαc –ultra)))- T2space if for all x ≠ y of X∃ two disjoint Nα-open(Nα- closed (ΛNαc- open (ΛNαo –closed)))sets C,D respectively such that xϵC , yϵD
(ii) Nα-ultra(ΛNαc-)normal space if for all pair nonempty disjoint Nα-clopen(Nα-closed) sets C,D can be separated by disjoint Nα-closed(ΛNαc- open) sets respectively.
(iii)Nα-strongly closed(ΛNαc- compact)space if for all Nα- closed(ΛNαc- open) cover of X respectively has finite subcover.

Theorem (4.9)
The inverse image of N_α- T_2 space under injective contra $\Lambda N_{\alpha c}$- continuous mapping f is $\Lambda N_{\alpha c}$- ultra T_2space.
Proof : Supposex≠y in X, becausef:X→Yis injective this impliesf(x)≠f(y) in Y, this implies∃ disjoint sets G,W∈$N_\alpha O(Y)$s.t f(x) ϵG, f(y) ϵW because f is contra $\Lambda N_{\alpha c}$- continuous then f

^{1}(G),f^{1}(W)∈ʎN$_{\alpha o}$C(X) s.t containing x, y and f^{1}(G) ∩f^{1}(W)=φ=f^{1}(G ∩W).Thus X is ʎN$_{\alpha c}$ - ultra T$_2$ space.

Theorem (4.10)
The inverse image of N$_\alpha$- ultraT$_2$ space under injective contra ʎN$_{\alpha c}$- continuous mapping f is ʎN$_{\alpha c}$-T$_2$space.
Proof : Assume x≠y in X, this impliesf(x)≠f(y)in Y, because Y isN$_\alpha$ ultra T$_2$ space, then ∃disjoint sets A, B∈N$_\alpha$C(Y) sets s.t f(x)∈A, f(y)∈B because f is contra ʎN$_{\alpha c}$- continuous, thus by (Th. (4.3)) ∃C,D∈ʎN$_{\alpha c}$O(X)s.t x ∈ C , y ∈ D and f(C)⊆A ,f(D)⊆B,this implies f(C)∩f(D)=f(C∩D)=φ⇨C∩D=φ⇨X is ʎN$_{\alpha c}$ - T$_2$ space.
We shall give the followingdefinition which we need in the following theorem

Definition (4.11)
Assume that f:X→Y is a mapping then f is named N$^*_\alpha$- closed mapping if for all G∈N$_\alpha$C(X),then f(G)∈ N$_\alpha$C(Y).

Theorem (4.12)
The inverse image of N$_\alpha$- ultra normal space under injective N$^*_\alpha$- closed contra ʎN$_{\alpha c}$-continuous mapping f is ʎN$_{\alpha c}$- normal space.
Proof:Suppose disjoint setsF$_1$, F$_2$∈N$_\alpha$C(X), becausef isN$^*_\alpha$- closedmapping , this implies f(F$_1$) , f(F$_2$)∈N$_\alpha$C(Y), becauseY isN$_\alpha$-ultra normal space then we have two disjoint N$_\alpha$- clopen sets B$_1$, B$_2$ofY s.t f(F$_1$)⊆B$_1$, f(F$_2$)⊆B$_2$ hence F$_1$⊆f^{1}(B$_1$) andF$_2$⊆f^{1}(B$_2$) becausef is injective contra ʎN$_{\alpha c}$-continuous mapping, this implies f^{1}(B$_1$) ,f^{1}(B$_2$) are disjoint ʎN$_{\alpha c}$- open sets. Thusthe proof is complete.

Theorem (4.13)
Let f:X→Y be a surjective contra ʎN$_{\alpha c}$- continuous mapping. Then if X is ʎN$_{\alpha c}$- compact space, then Y is N$_\alpha$- strongly closed space.
Proof : Let {V$_i$: i∈ I} be N$_\alpha$- closed cover of Y since f is contra ʎN$_{\alpha c}$- continuous mapping , thus{f^{1}(V$_i$) : i ∈ I } is ʎN$_{\alpha c}$- open cover of X , but X is ʎN$_{\alpha c}$- compact space, thus X has a finite subcover.
X=U{f^{1}(V$_i$) : i ∈ I$_o$ }, thus f (X) =U{ff^{1}(V$_i$) : i ∈ I$_o$ } since f is surjective. Thus Y =U {V$_i$: i ∈ I$_o$}⇨ Y is N$_\alpha$– strongly closed space.

V. Future Work

(i) We can use the concept of ʎNαc- open sets to study new kind of ʎNα c- compact spaces.
(ii) We can use the concept of ʎNαc- *open sets* to *study some types* of separation axioms.

References

[1] O. Njastad , On some classes of Nearly open sets , Pacific *J. Math.* , **15** (3) , 1965 , pp. 961 – 970 .
[2] N. A. Dawood , N. M. A. Al-Tabatabai , Nα- open sets and Nα- Regularity In Topological Spaces International *J. of Advanced Scientific and Technical Research* **5**,(3), (2015) , pp. 87 – 96 .
[3] H. Ogata,, *Operation on Topological Spaces and Associated Topology*,,Math. Japonica 3, **6**, (1999), pp. 175 – 184.
[4] N. M. Al- Tabatabai "ʎNαc- Open sets And ʎNαc – Separation Axioms In Topological Spaces" *International J. of Advanced ScientificandTechnical Research* **5** (6) September (2015) pp. 83 – 92 .
[5] J. Dontcher , Contra continuous and Strongly S- closed Spaces . *International J. Math. Math.Sci.* **19** (1996) pp. 303 – 310.

On Some Results of Topological Groupoid

On Some Results of Topological Groupoid

Taghreed Hur Majeed

Department of Mathematics- College of Education – Al-Mustansiriyah University

taghreedmajeed@yahoo.com

Abstract. Our main interest in this study is to look for groupoid space and topological groupoid. In this paper, we give some results of groupoid space and topological groupoid, which are properties of source proper topological groupoid (SP-groupoid). In the end we introduced remarks, propositions and theorems.

1.Introduction

The notion of groupoid as a generalization of that of group was found by Brandt [4]as a result of his work on the arithmetic of quaternary quadratic forms, generalizing the work of Gauss [3] for case of binary quadratic forms. This concept of groupoid now can be seen as a significant extension of the range of discourse, allowing for a more flexible and powerful approach to symmetry [2].The notion of groupoid action was introduce by Ehresmann (1959) [6] generalizing the group action in his work on the space of all isomorphisms between the fibers of a fiber bundle. On the other hand, Jean louis Tu [4] call the continuous action of topological groupoid G on a topological space E proper.

The present paper consists of two sections. In section one we introduce some definitions and propositions which we need in our work to give the definitions and theorems about categories, functor, fiber product, proper mapping, groupoid space and topological groupoid. In section two, we introduce the basic the construction of source proper topological groupoid SP-groupoid, propositions and theorems. These results are novel in the present time (to the best of our knowledge).

2.Groupoid Space and Topological Groupoid

Definition(1-1) [1]:

A groupoid is a pair of set (G,B) on which are given:

1. Two surjections $\alpha, \beta: G \to B$ called the source and the target map respectively.
2. An injection $w: B \to G$ called the unit map with $= I_B$, $\beta o w = I_B$ where $I_B: B \to B$ is the identity map.
3. A law of partial composition γ in G defined as a law of composition on the set $G \times G = \{(g, \acute{g}) \in G \times G , \alpha(g) = \beta(g')\}$ "fiber product of α and β over B" such that:

(a) $\gamma(g, \gamma(g_1, g_2) = \gamma(\gamma(g, g_1), g_2), \forall(g, g_1), (g_1, g_2) \in G * G$.

(b) $\alpha\big(\gamma(g_1, g_2)\big) = \alpha(g_2),\ \beta\big(\gamma(g_1, g_2)\big) = \beta(g_1)$ for each $(g, g_1) \in G * G$.

(c) $\gamma\left(g, w\big(\alpha(g)\big)\right) = g$ and $\gamma\big(w\big(\beta(g)\big), g\big) = g,$ for all $g \in G$.

4. A bijection $\sigma: G \to G$ called the inversion of G satisfying:
(a) $\alpha(\sigma(g)) = \beta(g),\ \beta(\sigma(g)) = \alpha(g),$ for all $g \in G$.
(b) $\gamma(\sigma(g), g) = w(\alpha(g)),\ \gamma(g, \sigma(g)) = w(\beta, g),$ for all $g \in G$.

We write $(g) = g^{-1}$, called the inverse element of $g \in G$ and $w(x) = \hat{x}$ called the unit element in G associated to the element $x \in B$. Also , we write $\gamma(g, \acute{g}) = g\acute{g}\,.G$ is called the groupoid and B is called the base. Also we say that G is a groupoid on B.

Example (1-2):
(1) Each non empty set B is a groupoid of base B where $= w = I_B$. This groupoid is called null groupoid.
(2) $GL(n, R)$ of base R is groupoid.

Definition(1-3) [5]:
Let f be a mapping of a topological space x into topological space Y. Then f is said to be proper map if f is continuous and the mapping $f \times I_Z: X \times Z \to Y \times Z$ is closed for every topological spac .

Proposition (1-4) [6]:
Let f and g be continuous maps then:
(i) If f and g are proper then gof is proper.
(ii) If gof is proper and f is surjective then g is proper.
(iii) If gof is proper and g is injective then f is proper.
(iv) If gof is proper and y is a Housdorff space then f is proper map.

Definition (1-5) [3]:
A topological groupoid is a groupoid (G,B) together with topologies on G and B such that the maps α, β, w, γ and σ are continuous where $G * G$. Has the subspace topology from $G \times G$. A topological subgroupoid is subgroupoid (H,A) with the subspace topology from (G,B).

Definition (1-6) [2]:
A morphism of topological groupoid is morphism of groupoids $(f, f_0): (G, B) \to (\acute{G}, \acute{B})$ such that f and f_0 are continuous. An isomorphism of topological groupoid is a morphism of topological groupoids such that $f: G \to \acute{G}$ is a homeomorphism.

Remark (1-7) [1]:
We denote by TG the category whose objects are topological groupoids and whose morphisms are continuous groupoid morphisms.

Example (1-8):
Any trivial groupoid $E \times \Gamma \times E$ is a topological groupoid where Γ is a topological group and E is a topological space.

Definition (1-9) [7]:
Let (G, B) be topological groupoid space, $\pi: E \to B$ be a continuous map and let $G * E$ denote the fiber product of α and π over B. A left action of G on (E, π, B) is a continuous map
$\varphi^*: G * E \to E$ such that:
(i) $\pi(\varphi^*(g, z)) = \beta(g)$ for each $(g, z) \in G * E$.
(ii) $\varphi^*(w(\pi(z)), z) = z$ for each $Z \in E$.
(iii) $\varphi^*(g, \varphi^*(\acute{g}, z)) = \varphi^*(\gamma(g, \acute{g})), z)$ for each $(g, \acute{g}) \in G * E$.
The bundle (E, π, B) together with action φ^* is called groupoid space and is denote by $G-$space, in similar way, we can define right action of G on (E, π, B).

3.Source Proper Topological groupoid (SP- groupoid):

Definition (2-1) [3]:

A topological groupoid (G,B) is called source proper groupoid "sp- groupoid" if:

(1) The source map $\alpha: G \to G$ is a proper.
(2) The base space B is a Housdorff.

Example (2-2):

Every compact topological groupoid G on a Housdorff space B is a Sp- groupoid , since the source map $\alpha: G \to B$ is proper map.

Proposition (2-3) [3]:

Let (G,B) be an sp- groupoid then:

(3) The inversion map $\sigma: G \to G$ is proper.
(4) The target map $\beta: G \to B$ is proper.
(5) The unit map $w: B \to G$ is proper .

Proposition (2-4):

Let $(f, f_0): (\mathrm{G}, \mathrm{B}) \to (G', B')$ and $(g, g_0): (G', B') \to (G'', B'')$ be morphism of Sp- groupoid such that gof is a proper map then the base map $g_0 o f_0: B \to B''$ is a proper map.

Proof :

Consider the following commutative diagram in topological groupoid.

$$\begin{array}{ccc} B & \xrightarrow{g_0 o f_0} & B'' \\ \mathrm{w} \downarrow & & \downarrow w'' \\ \mathrm{w(B)} & \xrightarrow{(gof)^*} & w''(B'') \end{array}$$

which w and w'' are both proper Proposition (2-3) and $(gof)^*$ is proper map since $w(B)$ is known subspace in G and $\acute{w}o(g_0, f_0)$ is proper map since $\acute{w}o(g_0, f_0) = (gof)^*$ and $(gof)^* ow$ is proper map proposition(1-4). Hence (g_0, f_0) is proper map, since w'' is injective continuous proposition (1-4).

Definition (2-5) [2]:

Let $(f_1, f_1'): (G_1, B_1) \to (G_1', B_1')$ and $(f_2, f_2'): (G_2, B_2) \to (G_2', B_2')$ each are proper maps, then the direct sum $(f_1 \oplus f_2, f_1' \oplus f_2'): (G_1 \oplus G_2, B_1 \oplus B_2) \to (G_1' \oplus G_2', B_1 \oplus B_2')$ is proper map.

Proposition (2-6):

Let $(f, f_0): (\mathrm{G}, \mathrm{B}) \to (G', B')$ and $(g, g_0): (\acute{G}, \acute{B}) \to (G'', B'')$ be morphisms of topological groupoid , if $(g0f)$ is an injective proper map and (G'', B'') is Sp-groupoid then (G, B) is Sp- groupoid.

Proof:

Consider the following commutative diagram in topological groupoid.

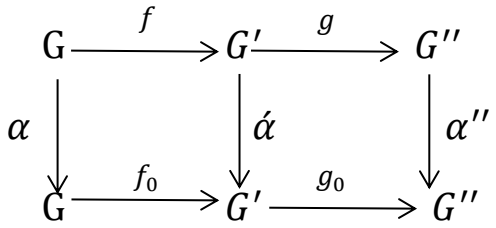

i.e $\acute{\alpha} o f = f_0 o \alpha$
$\bar{\bar{\alpha}} o g = g_0 o \acute{\alpha}$
$\bar{\bar{\alpha}} o (gof) = (g_0, f_0) o \alpha$
(gof) and $\bar{\bar{\alpha}}$ are proper map (G'', B'') is Sp- groupoid and then
$\alpha'' o (gof)$ is proper map ,proposition (1-4) and then $(g_0, f_0) o \alpha$ is proper.
Hence α is proper map since (g_0, f_0) is injective continuous proposition (1-4).

Proposition (2-7):
Let (f, f_0): (G, B) → (G', B') and (g, g_0): (G', B') → (G'', B'') be morphisms of topological groupoid , if (gof): $G \to \bar{\bar{G}}$ is surjective proper map and (G, B) is Sp-groupoid then (G'', B'') is Sp- groupoid.
Proof:
Consider the following commutative diagram in topological groupoid.

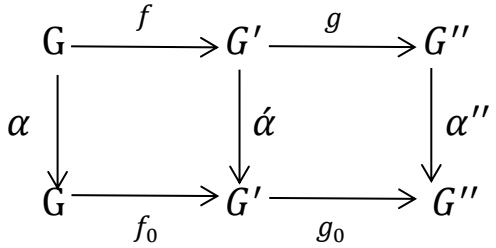

i.e $\alpha' o f = f_0 o \alpha$
$\alpha'' o g = g_0 o \alpha'$
$\alpha'' o (gof) = (g_0, f_0) o \alpha$
(gof) and α are proper map (G, B) is Sp-groupoid and then g_0, f_0 is proper map proposition (2-3)
Hence α is proper map then α'' is proper since (gof) is surjective continuous proposition(1-4).

Theorem (2-8):
Let (f_1, f_1'): (G, B) → (G_1, B_1)
(f_2, f_2'): (G_1, B_1) → (G_2, B_2)
⋮
and (f_n, f_n'): (G_n, B_n) → (G_n, B_n)
be morphisms of topological groupoid , if $(f_n o \dots o f_2 o f_1)$ is an injective proper map and (G_n, B_n) is Sp-groupoid then (G, B) is Sp-groupoid.

Proof:
Consider the following commutative diagram in topological groupoid

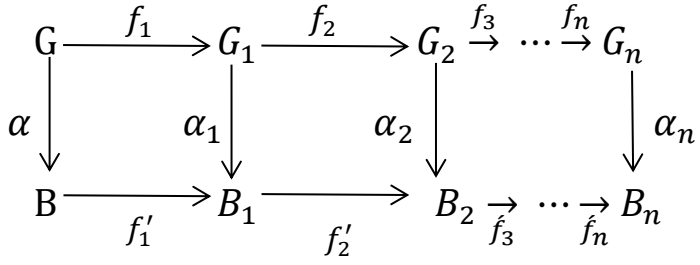

i.e $\alpha_n o(f_n o, \dots o f_2 o f_1) = (f_n' o \dots o f_2' o f_1') o \alpha$

$(f_n, \dots o f_2 o f_1)$ and α_n are proper map, (G_n, B_n) is Sp- groupoid and then $\alpha_n o(f_n o \dots o f_2 o f_1)$ is proper map proposition(1-4). And then $(f_n' o \dots o f_2' o f_1') o \alpha$ is proper .since α is proper map (proposition(2-5)).

Theorem (2-9):
Let (f_1, f_1'): $(\mathrm{G}, \mathrm{B}) \to (G_1, B_1)$
(f_2, f_2'): $(G_1, B_1) \to (G_2, B_2)$
$\vdots$
and (f_n, f_n'): $(G_{n-1}, B_{n-1}) \to (G_n, B_n)$
be morphisms of topological groupoid ,then $f_n o \dots o f_2 o f_1 : G \to G_n$ is surjective proper map and (G, B) is Sp-groupoid.
Proof:

Consider the following commutative diagram in topological groupoid

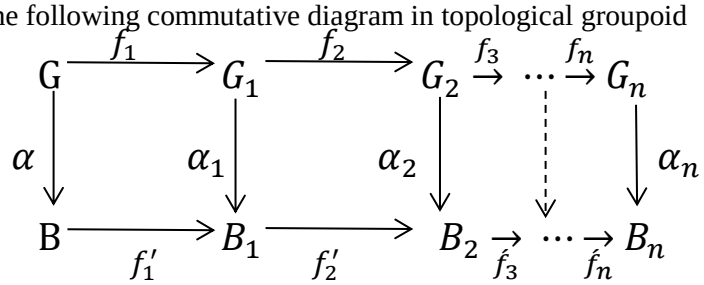

i.e $\alpha_n o(f_n o, \dots o f_2 o f_1) = (f_n' o \dots o f_2' o f_1') o \alpha$

$(f_n' o \dots o f_2' o f_1') \; and \; \alpha$ are proper map. Since (G, B) is Sp-groupoid $(f_n' o \dots o f_2' o f_1')$ is proper proposition (1-4). Hence α_{n-1} is proper map then α_n is proper since $(f_n o, \dots o f_2 o f_1)$ is surjective continuous proposition (2-6).

Theorem (2-10):
Let (f_1, f_1'): $(\mathrm{G}^1, \mathrm{B}^1) \to (\mathrm{G}^2, \mathrm{B}^2)$
(f_2, f_2'): $(\mathrm{G}^2, \mathrm{B}^2) \to (\mathrm{G}^3, \mathrm{B}^3)$
$\vdots$
and (f_n, f_n'): $(\mathrm{G}^{n-1}, \mathrm{B}^{n-1}) \to (\mathrm{G}^n, \mathrm{B}^n)$
be morphisms of topological groupoid , if $(f_n o, \dots o f_2 o f_1)$ is an injective proper map and $(\mathrm{G}^n, \mathrm{B}^n)$ is Sp- groupoid then (G, B) is Sp-groupoid.

Proof:

Consider the following commutative diagram in topological groupoid

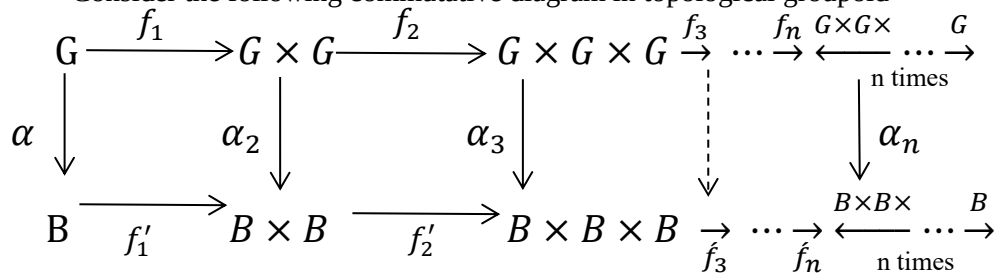

i.e $(f_n o, \dots o f_2 o f_1)$ and α_n are proper map , $(\mathrm{G}^n, \mathrm{B}^n)$ is Sp- groupoid and then $\alpha_n o(f_n o, \dots o f_2 o f_1)$ is proper map (proposition (1-4)) , and then $(f_n' o \dots o f_2' o f_1')$ is proper. Hence α is proper map.

Theorem (2-11):
Let (f_1, f_1'): $(\mathrm{G}, \mathrm{B}) \to (\mathrm{G}^2, \mathrm{B}^2)$
(f_2, f_2'): $(\mathrm{G}^2, \mathrm{B}^2) \to (\mathrm{G}^3, \mathrm{B}^3)$
$\vdots$
and (f_n, f_n'): $(\mathrm{G}^{n-1}, \mathrm{B}^{n-1}) \to (\mathrm{G}^n, \mathrm{B}^n)$
be morphisms of topological groupoid , then $(f_n o \dots o f_2 0 f_1)$: $G \to G^n$ is surjective proper map and $(\mathrm{G}^n, \mathrm{B}^n)$ is Sp-groupoid.
Proof:
Consider the following commutative diagram in topological groupoid

$$\begin{array}{ccccccccccc}
\mathrm{G} & \xrightarrow{f_1} & G \times G & \xrightarrow{f_2} & G \times G \times G & \xrightarrow{f_3} & \cdots \to & \underset{\text{n times}}{\overset{f_n \; G\times G\times}{\longleftarrow}} & \cdots \to & G \\
\alpha \downarrow & & \alpha_2 \downarrow & & \alpha_3 \downarrow & & \alpha_3 \downarrow & & \alpha_n \downarrow & \\
\mathrm{B} & \xrightarrow[f_1']{} & B \times B & \xrightarrow[f_2']{} & B \times B \times B & \xrightarrow[\acute{f}_3]{} & \cdots \to & \underset{\text{n times}}{\overset{\acute{f}_n \; B\times B\times}{\longleftarrow}} & \cdots \to & B
\end{array}$$

i.e $\alpha_n o(f_n o, \dots o f_2 o f_1) = (f_n' o \dots o f_2' o f_1')\, o\alpha$
$(f_n' o \dots o f_2' o f_1')$ and α are proper map since (G, B) is Sp- groupoid and $(f_n' o \dots o f_2' o f_1')$ is proper proposition (1-4). Hence α_{n-1} is proper map then α_n is proper since $(f_n o \dots o f_2 o f_1)$ is surjective continuous (Theorem (2-8)).

Proposition (2-12):
Let (f_1, f_1'): $(G_1, B_1) \to (G_1', B_1')$ and (f_2, f_2'): $(G_2, B_2) \to (G_2', B_2')$ be morphisms of Sp- groupoid such that $f_1 \oplus g_1$ is a proper map then the$f_1' \oplus f_2'$: $B_1 \oplus B_2 \to B_1' \oplus B_2'$ is proper map.

Proof:
Consider the following commutative diagram in topological groupoid[TG].

$$\begin{array}{ccc}
B_1 \oplus B_2 & \xrightarrow{f_1 \oplus f_2} & B_1' \oplus B_2' \\
w \downarrow & & \downarrow \acute{w} \\
w(B_1 \oplus B_2) & \xrightarrow{(f_1 \oplus f_2)^*} & w'(B_1' \oplus B_2')
\end{array}$$

In which w and $\acute{w}$ are both proper proposition (2-3) and $(f_1 + f_2)^*$ is proper map since $w(B_1 \oplus B_2)$ is closed subspace in $(G_1 \oplus G_2)$ and $(f_1 \oplus f_2)$ is proper map since

$w'o(f_1 \oplus f_2) = (f_1 \oplus f_2)^* ow$ and $(f_1 \oplus f_2)^* ow$ is proper map since $\acute{w}$ is injective continuous.

Theorem (2-11):
Let $(f_1 \oplus f_2 , f_1' \oplus f_2') = (\mathrm{G}, \mathrm{B}) \to (G', B')$, (G, B) are Sp-groupoid then $f_1 \oplus f_2 : G_1 \oplus G_2 = G \to B_1 \oplus B_2 = B$ and
$f_1' \oplus f_2' : G_1' \oplus G_2' = G \to B_1' \oplus B_2' = \acute{B}$ are proper maps.
Proof:
The map $f_1 \oplus f_2$ is bijective continuous map and its inverse is $(f_1 \oplus f_2)^{-1}(g) = (f_1 \oplus f_2)(g)^{-1}$, $\forall g \in G$ which is continuous so $f_1 \oplus f_2$ is homomorphism and then $f_1 \oplus f_2$ is proper map, and $f_1' \oplus f_2'$ is proper map.

References

[1] Brown, R. 1989 Symmetry, Groupoids and Higher dimensional analogons, computer Math. Application, Vol.17, No(1-3), pp.49-57.
[2] Chiriac. L. 2009 On topological groupoid and multiple Indentities, (BADS), number 1(59), pp.67-78.
[3] Gursuy, M., H. 2005 Topological group- groupoids and their Covering, Indian Pure and appl. Math., Vol.36(a), pp.493-502.
[4] Hamza, S., H. 2007 Certain types of groupoids spaces, A thesis AL-Mustansiriyah University, Collage of Sciences, Department of Mathemeatics.
[5] Mackenzie, K. 1987 Lie groupoids and Lie algebroids in differential Geometry, London Math. Soc. Lecture note series Cambridge University press.
[6] Meyer .R. 2012 On the Category of groupoids, GAP Anogia.
[7] Moerdijk, I. 2002 Orbifolds as Groupoids an Introdution, Madison W., pp. 205-222.
[8] Tu, J.L. 2004 Non-Hansdorff Groupoid , proper actions and K-theory, Document a math-a, pp.565-597.

Using Simulation Technique to overcome the multi-collinearity problem for estimating fuzzy linear regression parameters.

Using Simulation Technique to overcome the multi-collinearity problem for estimating fuzzy linear regression parameters.

Hazim Mansoor Gorgees[1] and Mariam Mohammed Hilal[2]

[1] Department of Mathematics, College of Education for Pure Science, Ibn-Al-Haitham, University of Baghdad, Iraq hazim5656@yahoo.com
[2] Department of Mathematics, College of Education for Pure Science, Ibn-Al-Haitham, University of Baghdad, Iraq marmoon80@yahoo.com

Abstract: Fatigue cracking is one of the common types of pavement distresses and is an indicator of structural failure; cracks allow moisture infiltration, roughness, may further deteriorate to a pothole. Some causes of pavement deterioration are: traffic loading; environment influences; drainage deficiencies; materials quality problems; construction deficiencies and external contributors. Many researchers have made models that contain many variables like asphalt content, asphalt viscosity, fatigue life, stiffness of asphalt mixture, temperature and other parameters that affect the fatigue life. For this situation, a fuzzy linear regression model was employed and analyzed by using the traditional methods and our proposed method in order to overcome the multi-collinearity problem. The total spread error was used as a criterion to compare the performance of the studied methods. Simulation program was used to obtain the required results.

Keywords: triangular Fuzzy numbers; Fuzzy linear regression; Least Square method; principle component method and linear programming problem.

1. Introduction:

Regression analysis is a powerful and comprehensive method for analyzing relationships between a response variable (depended variable) and one or more explanatory variables (independent variables). Inferential problems associated with regression model involve the estimation of the model parameters and prediction of response variable from knowledge of explanatory variables, based on a set of crisp data. Moreover, it is usually assumed that the parameters of underlying model are exact numbers (i.e. the relationship between variables is crisp). But in the complex systems, such as the systems existing in biology, agriculture, engineering and economy, we frequently cannot get the exact numerical data for the information of systems because of the complexity of systems themselves, the vagueness in people's thinking and judgment and the influence of various uncertain factors existing in boundary fuzzy environment around the systems. For this situation, the traditional least squares regression may not be applicable. We need therefore to investigate some soft methods for dealing with these situations. Fuzzy set theory provides suitable tools for regression analysis when the relationship between variables is vaguely defined and the observations are reported as imprecise quantities.

After introducing fuzzy set theory, several approaches to fuzzy regression have been developed by many researchers.

Studies related to fuzzy linear regression may be roughly divided into two approaches, namely, linear programming based methods (possibilistic approach) and fuzzy least squares methods (least squares approach) [2].

The main contribution of this work is to investigate the fuzzy regression model with the existence of multi-collinearity, and suggesting a method to deal with this problem.

2. Fuzzy regression methods:
Several studies related with the fuzzy linear regression started after introducing fuzzy set theory by Zadi (1961) [6].

At the first time Tanaka et, al. (1982) proposed a linear regression model with fuzzy parameters and crisp observed data, Their method has been developed in different directions by some researchers.

Tanaka's approach is essentially based on transforming the problem of fitting a fuzzy model on a data set to a linear programming problem.

Tanaka et, al regarded a fuzzy data as a possibility distribution. They supposed that the deviations between the observed values and the estimated values are due to the fuzziness of the system structure being investigated. This structure was represented as a fuzzy linear function whose parameters were given by fuzzy sets with membership functions regarded as possibility functions, instead of as probability functions [4].

Fuzzy linear regression models may be classified into three main categories according to the fuzziness of input and output data. Specifically [5]:

i. Each of input and output data are fuzzy.
ii. Input data are crisp but output data are fuzzy.
iii. Each of input and output data are crisp.

The basic model assumes a fuzzy linear function as:

$$\tilde{y}_i = \tilde{\beta}_0 + \tilde{\beta}_1 X_{i1} + \tilde{\beta}_2 X_{i2} + \cdots + + \tilde{\beta}_p X_{ip} \quad , \quad for\ i = 1,2,\dots,n \tag{1}$$

Which can be written as:

$$(y_i, e_i) = (\alpha_0, c_0) + (\alpha_1, c_1) X_{i1} + (\alpha_2, c_2) X_{i2} + \cdots + + (\alpha_p, c_p) X_{ip} \tag{2}$$

Where $\tilde{y}_i = (y_i, e_i)$ the fuzzy output with symmetric triangular numbers, y_i are the central values and e_i the spread values.

$\tilde{\beta}_j = (\alpha_j, c_j)$ are fuzzy coefficients presented in the form of symmetric triangular fuzzy numbers where α_j denote the central value of the parameter and c_j are its spread (assuming to be equal from the left and the right), $c_j \geq 0,\ j = 1, 2, \dots, p$.

$x_i = \left(x_{i1}, x_{i2}, \dots, x_{ip}\right)^T$ are the vectors of crisp explanatory variables.

In order to analyze the fuzzy linear regression, different approaches were followed. In the following sections, some of these approaches are considered.

3. Tanaka's model:
In (FLR) analysis, some assumptions concerned traditional regression analyses are relaxed and the uncertainty is represented by a fuzzy relationship between the input and output.
The present paper considers first the model of Tanaka which is a pioneer for such models.

The linear programming formula of the fuzzy regression problem can be written as follows [1]:

$$Minimize\ S = \sum_{i=1}^{n} \sum_{j=0}^{p} c_j |x_{ij}| \tag{3}$$

Subject to:

$$\sum_{j=0}^{p} \alpha_j x_{ij} + (1-h) \sum_{j=0}^{p} c_j |x_{ij}| \geq y_i + (1-h) e_i \tag{4}$$

$$\sum_{j=0}^{p} \alpha_j x_{ij} - (1-h)\sum_{j=0}^{p} c_j |x_{ij}| \le y_i - (1-h)e_i \quad (5)$$

$$c_j \ge 0, \alpha_j \in R, \quad x_{i0} = 1, \quad i = 1,2,\dots,n, \quad 0 \le h \le 1 \quad (6)$$

The h value (degree of confidence) is selected by the decision maker, where h is belongs to [0, 1].

4. Savic & Pedrycz approach

Savic and Pedrycz formulated the fuzzy regression by combining the ordinary least squares with minimum fuzziness criterion. The method is constructed in two successive steps. The first step employs ordinary least square regression to obtain fuzzy regression parameters. The minimum fuzziness criterion is used in the second step to find the spread of fuzzy regression parameters.

In the first step, the available information about the value of the center of the fuzzy observations is used to fit a regression line to the data.

In fact, the fuzzy data are regressed as simplified crisp data and the regression analysis is conducted as it is an ordinary least squares regression. The results of this step are employed as center values of the fuzzy regression parameters.

In the next step, the minimum fuzziness criterion is used to determine fuzzy parameters. Spreads of the fuzzy parameters are obtained by equation (4), (5) as the minimum fuzziness method with the distinction of employing the fuzzy centers of regression parameters resulting from the first step [3].

5. Proposed method:

Our proposed method is to deal with case of multi-collinearity among the crisp explanatory variables and it is a modification of Savic-Pedrycz method.

This method summarized as follows:

The principal component is used instead of ordinary least squares regression to determine fuzzy center values of fuzzy regression coefficients in the first step.

The minimum fuzziness criterion is used in the second step to find the spread of fuzzy regression coefficients.

6. Experimental study:

By using MATLAB program we generate a response variable and a set of four explanatory variables each with 54 observations including the two cases represented by absence and existence of the multi-collinearity problem among the explanatory variables.

In table 1 the upper and lower bound for each variable in the model is represented.

Table 1. Upper and lower bound for each variables**.**

Y	[0.026670837, 0.888949719]
X1	[-8.517193191,-7.35597863]
X2	[8.160232492, 8.803874764]
X3	[-0.798507696, -0.198450939]
X4	[2.114, 7.87]

Where:

x_{1j}: Initial tensile strain at 5th repetition of bending beam, (the first independent variable).

x_{2j}: Initial flexural stiffness modulus, (the second independent variable).

x_{3j}: stress level, (the third independent variable).

$\boldsymbol{x_{4j}}$: Percent air void, (the fourth independent variable).

Case 1: With absence of multi-collinearity:

By using MATLAB programs a simulation model was constructed to determine which of ordinary least square method and principal component method performed well by using MSE as a measure of performance on the data generated with the absence of multi-collinearity problem.

The MSE for the estimated regression coefficients vector is calculated for the two methods of estimation, namely: ordinary least square and principal component methods, the results are presented in table 2.

Table 2. MSE for each of ordinary least square and principal component methods in case 1

Method	Least Square	Principal Component
MSE	0.072587730448981	0.073574164021569

It is clear that the MSE obtained by using ordinary least square method is less than the MSE obtained by the principal component method and hence we use it in the first step in the Savic & Pedrycz method. The results are given in table 3.

Table 3. Results of Savic & Pedrycz method with the absence of multi-collinearity**.**

	Crisp Data		fuzzy data before using Lp		Outputs fuzzy data for Savic & Pedrycz method	
	Y	$\hat{y}$ from Least square	y_i=centers	e_i= spread	$\hat{y}_i$=center	$\hat{e}_i$=spread
1	0.320934739	0.530105004	0.425519872	0.003191399	0.425519872	-0.017816269
2	0.320934739	0.420191835	0.370563287	0.002779225	0.370563287	-0.014443484
3	0.320934739	0.490701692	0.405818216	0.003043637	0.405818216	-0.018787358
4	0.280926490	0.427526520	0.354226505	0.002656699	0.354226505	-0.014348966
5	0.260305654	0.632918337	0.446611996	0.003349590	0.446611996	-0.017298886
6	0.239250631	0.428689555	0.333970093	0.002504776	0.333970093	-0.015259780
7	0.217742741	0.442487666	0.330115204	0.002475864	0.330115204	-0.015420197
8	0.195762075	0.383626278	0.289694177	0.002172706	0.289694177	-0.015275427
9	0.150295937	0.491335795	0.320815866	0.002406119	0.320815866	-0.014428609
10	0.150295937	0.391775792	0.271035865	0.002032769	0.271035865	-0.015398435
11	0.126763423	0.415877221	0.271320322	0.002034902	0.271320322	-0.013921750
12	0.807977244	0.369585481	0.588781362	0.004415860	0.588781362	-0.014050905
13	0.795855349	0.663047842	0.729451595	0.005470887	0.729451595	-0.018441464
14	0.795855349	0.657698408	0.726776879	0.005450827	0.726776879	-0.018500297
15	0.783584708	0.566444445	0.675014577	0.005062609	0.675014577	-0.017380940
16	0.771161626	0.597104955	0.684133290	0.005131000	0.68413329	-0.017595542
17	0.758582267	0.553902497	0.656242382	0.004921818	0.656242382	-0.017662343
18	0.888949719	0.446272860	0.667611290	0.005007085	0.66761129	-0.013837324
19	0.877775964	0.609846373	0.743811169	0.005578584	0.743811169	-0.016330189
20	0.866475944	0.610947816	0.738711880	0.005540339	0.73871188	-0.014749717

21	0.855046772	0.577084493	0.716065633	0.005370492	0.716065633	-0.017882873
22	0.843485463	0.503996112	0.673740787	0.005053056	0.673740787	-0.017169953
23	0.831788925	0.460026590	0.645907757	0.004844308	0.645907757	-0.016952461
24	0.831788925	0.642020554	0.736904739	0.005526786	0.736904739	-0.017336998
25	0.819953958	0.545927039	0.682940498	0.005122054	0.682940498	-0.016511235
26	0.102663757	0.596615555	0.349639656	0.002622297	0.349639656	-0.017699486
27	0.102663757	0.379508573	0.241086165	0.001808146	0.241086165	-0.014317014
28	0.077968924	0.453416925	0.265692925	0.001992697	0.265692925	-0.013519796
29	0.026670837	0.550280277	0.288475557	0.002163567	0.288475557	-0.018507507
30	0.026670837	0.449680429	0.238175633	0.001786317	0.238175633	-0.012999200
31	0.026670837	0.397810488	0.212240662	0.001591805	0.212240662	-0.014364646
32	0.466656233	0.428370061	0.447513147	0.003356349	0.447513147	-0.013863897
33	0.432167891	0.476967772	0.454567832	0.003409259	0.454567832	-0.015471171
34	0.378097120	0.460531222	0.419314171	0.003144856	0.419314171	-0.015262542
35	0.359403715	0.603911906	0.481657811	0.003612434	0.481657811	-0.016957828
36	0.340354198	0.430101599	0.385227899	0.002889209	0.385227899	-0.015189745
37	0.745842651	0.550479202	0.648160926	0.004861207	0.648160926	-0.013959254
38	0.732938639	0.456923848	0.594931244	0.004461984	0.594931244	-0.013588835
39	0.706620070	0.455797047	0.581208559	0.004359064	0.581208559	-0.014140663
40	0.706620070	0.574450752	0.640535411	0.004804016	0.640535411	-0.016887809
41	0.693196393	0.313627301	0.503411847	0.003775589	0.503411847	-0.014553533
42	0.679590067	0.414537292	0.547063679	0.004102978	0.547063679	-0.013465081
43	0.665796052	0.478687971	0.572242011	0.004291815	0.572242011	-0.014191015
44	0.217742741	0.552805753	0.385274247	0.002889557	0.385274247	-0.014551307
45	0.195762075	0.392199941	0.293981008	0.002204858	0.293981008	-0.013172825
46	0.150295937	0.558361824	0.354328880	0.002657467	0.35432888	-0.015348713
47	0.150295937	0.404027765	0.277161851	0.002078714	0.277161851	-0.013190680
48	0.651809098	0.453559022	0.552684060	0.004145130	0.55268406	-0.015763193
49	0.637623730	0.532883518	0.585253624	0.004389402	0.585253624	-0.014941584
50	0.623234239	0.310807838	0.467021039	0.003502658	0.467021039	-0.013188539
51	0.608634663	0.495090923	0.551862793	0.004138971	0.551862793	-0.014880833
52	0.578780077	0.430174518	0.504477297	0.003783580	0.504477297	-0.013665970
53	0.563511756	0.430329059	0.496920407	0.003726903	0.496920407	-0.014290175
54	0.532257434	0.401889512	0.467073473	0.003503051	0.467073473	-0.014217675

The regression equation is:

$$\hat{y}_i = (-1.490128592, 0.010058366) + (-0.070576875, 0.00476394)x_{1j} + (0.18802968, 0.0012692)x_{2j} + (-0.030835988, 0.000208143)x_{3j} + (-0.037044369, 0.00025005)x_{4j}$$

We found that the total spread is equal to 3.219421578.

Case 2: With existence of multi-collinearity:

As in case 1, we construct a simulation model by using MATLB program in order to determine which of the estimation methods mentioned earlier is the best with the existence of multi-collinearity problem among the explanatory variables. The MSE is employed as an indicator of the performance for each method.

Table 4. MSE for each of ordinary least square and principal component methods in case 2**.**

Method	Least Square	Principal Component
MSE	8.265371434 e-07	4.656612873e-10

It is obvious that the value of MSE obtained by using principal component method is less than the value of MSE obtained by the least square method. Hence we use it in the first step of Savic & Pedrycz method instead of ordinary least square used in case 1 and this is our proposed method.

The results are shown in table 5.

Table 5. Results of the proposed method for h=0.5**.**

	Crisp Data		fuzzy data before using Lp		Outputs fuzzy data for Savic & Pedrycz method	
	Y	$\hat{y}$ from Least square	y_i=centers	e_i= spread	$\hat{y}_i$=center	$\hat{e}_i$=spread
1	0.795855349	0.533955501	0.664905425	0.004986791	0.664905425	-0.000313579
2	0.831788925	0.539194706	0.685491816	0.005141189	0.685491816	-0.000320426
3	0.706620070	0.696688391	0.701654231	0.005262407	0.701654231	-0.000535658
4	0.866475944	0.534984229	0.700730087	0.005255476	0.700730087	-0.000312889
5	0.843485463	0.539053396	0.691269429	0.005184521	0.691269429	-0.000318504
6	0.102663757	0.492721863	0.297692810	0.002232696	0.297692810	-0.000298454
7	0.280926490	0.482235488	0.381580989	0.002861857	0.381580989	-0.000286444
8	0.432167891	0.481470893	0.456819392	0.003426145	0.456819392	-0.000286136
9	0.563511756	0.358990964	0.461251360	0.003459385	0.461251360	-0.000091028
10	0.706620070	0.481310401	0.593965236	0.004454739	0.593965236	-0.000285413
11	0.359403715	0.363570315	0.361487015	0.002711153	0.361487015	-0.000095316
12	0.320934739	0.354302892	0.337618816	0.002532141	0.337618816	-0.000085584
13	0.260305654	0.703472427	0.481889041	0.003614168	0.481889041	-0.000544755
14	0.795855349	0.704991027	0.750423188	0.005628174	0.750423188	-0.000546512
15	0.217742741	0.626542831	0.422142786	0.003166071	0.422142786	-0.000501723
16	0.499994677	0.624612005	0.562303341	0.004217275	0.562303341	-0.000497840
17	0.637623730	0.692686196	0.665154963	0.004988662	0.665154963	-0.000530677
18	0.758582267	0.695628501	0.727105384	0.005453290	0.727105384	-0.000538158
19	0.888949719	0.695770302	0.792360010	0.005942700	0.792360010	-0.000534973
20	0.483464380	0.542200716	0.512832548	0.003846244	0.512832548	-0.000322047
21	0.623234239	0.704501694	0.663867967	0.004979010	0.663867967	-0.000546002
22	0.745842651	0.632608619	0.689225635	0.005169192	0.689225635	-0.000510209
23	0.877775964	0.703805551	0.790790757	0.005930931	0.790790757	-0.000547298
24	0.679590067	0.541732542	0.610661304	0.004579960	0.610661304	-0.000321121
25	0.665796052	0.490908859	0.578352455	0.004337643	0.578352455	-0.000297864
26	0.516256160	0.632774123	0.574515142	0.004308864	0.574515142	-0.000508422
27	0.608634663	0.632489688	0.620562175	0.004654216	0.620562175	-0.000511252
28	0.819953958	0.704466146	0.762210052	0.005716575	0.762210052	-0.000546353
29	0.771161626	0.632619566	0.701890596	0.005264179	0.701890596	-0.000509946
30	0.578780077	0.703900330	0.641340204	0.004810052	0.641340204	-0.000546493

31	0.732938639	0.632557031	0.682747835	0.005120609	0.682747835	-0.000510588
32	0.466656233	0.703778885	0.585217559	0.004389132	0.585217559	-0.000547690
33	0.340354198	0.490855363	0.415604780	0.003117036	0.415604780	-0.000298418
34	0.466656233	0.490973951	0.478815092	0.003591113	0.478815092	-0.000297404
35	0.855046772	0.531341454	0.693194113	0.005198956	0.693194113	-0.000308819
36	0.651809098	0.481730148	0.566769623	0.004250772	0.566769623	-0.000283916
37	0.783584708	0.321595839	0.552590274	0.004144427	0.552590274	-0.000063644
38	0.320934739	0.354412909	0.337673824	0.002532554	0.337673824	-0.000082272
39	0.807977244	0.319792813	0.563885029	0.004229138	0.563885029	-0.000065364
40	0.693196393	0.533288437	0.613242415	0.004599318	0.613242415	-0.000310859
41	0.532257434	0.479042290	0.505649862	0.003792374	0.505649862	-0.000284260
42	0.831788925	0.322478210	0.577133567	0.004328502	0.577133567	-0.000069188
43	0.150295937	0.354861788	0.252578863	0.001894341	0.252578863	-0.000082508
44	0.320934739	0.352647895	0.336791317	0.002525935	0.336791317	-0.000079474
45	0.026670837	0.320134898	0.173402868	0.001300522	0.173402868	-0.000065099
46	0.126763423	0.392077689	0.259420556	0.001945654	0.259420556	-0.000101878
47	0.026670837	0.321870219	0.174270528	0.001307029	0.174270528	-0.000064823
48	0.239250631	0.533300277	0.386275454	0.002897066	0.386275454	-0.000313073
49	0.378097120	0.361530531	0.369813826	0.002773604	0.369813826	-0.000093156
50	0.102663757	0.320140324	0.211402040	0.001585515	0.211402040	-0.000066470
51	0.150295937	0.391939729	0.271117833	0.002033384	0.271117833	-0.000101943
52	0.077968924	0.320696887	0.199332906	0.001494997	0.199332906	-0.000065515
53	0.195762075	0.354711495	0.275236785	0.002064276	0.275236785	-0.000084119
54	0.026670837	0.352632175	0.189651506	0.001422386	0.189651506	-0.000083099

The regression equation is:

$$\hat{y}_i = (-1.03, 0.0006585036534) + (-0.1752, 0.0000954758854)x_{1j} + (0.001, 0.0000098591951)x_{2j} + (-0.3, 0.0006085055554)x_{3j} + (-0.00231, 0.0000031222914)x_{4j}$$

The value of total spread for this method is 0.098339323.

7. Conclusions

From our experimental study the following Conclusions are pointed out

1. With absence of multi-collinearity problem, it was found that the least squares method is better than principal component method in the sense of MSE as it is shown in table 2.
   Consequently, the least squares estimators were used as centered values in the first step of Savic & Pedrycz method, whose results were agree with the engineering theory beyond the nature of asphalt, the results yield from applying Savic & Pedrycz method include that the initial tensile strain, stress level and percent air void have a negative influence on fatigue life while initial flexural stiffness modulus has positive influence on fatigue life.
2. With existence of multi-collinearity problem, it was found that the principal component method is better than least squares method in the sense of MSE as it is shown in table 4.
   Hence, the principal component estimators were used as center values in the first step of Savic & Pedrycz method. Again the results of Savic & Pedrycz method were coincide with the engineering theory beyond the nature of asphalt since each of initial tensile strain, stress level and percent air void have a negative effect on fatigue life, while initial flexural stiffness modulus has positive effect on fatigue life.

Reference:

[1] Akdemir, Hande and Tiryaki, F., 2013, "Using fuzzy linear regression to estimate relationship between forest fires and meteorological conditions", *Applications and Applied Mathematics, ISSN*: 1932-8366, Vol. 8, Issue 2 PP: 673-683.
[2] Alsoltany, S. N. and Alnaqash, I. A., (2015), "Estimating Fuzzy Linear Regression Model for Air Pollution Predictions in Baghdad City", *Journal of Al-Nahrain University*, Vol. 18 (2), PP. 157-166.
[3] savic, A., Dragan and Pedrycz, Witold, 1991, "Evaluation of fuzzy linear regression models", *Fuzzy Sets and Systems*, Vol. 39, PP. 51-63.
[4] Tanaka, H., Uejima, S. and Asai, K., 1982, "Linear Regression Analysis with Fuzzy Model", *IEEE Transactions on Systems, Man, and Cybernetics*, VOL. SMC-12, NO. 6.
[5] Yang, M. S. and Lin, T. S., (2002), "Fuzzy least-squares linear regression analysis for fuzzy input-output data", *Fuzzy Sets and Systems* 126 (2002), PP. 389-399.
[6] Zadeh, L. A., 1965, "Fuzzy Sets ", *Academic Press Inc*, 8(3), PP. 338-353.

Study the effect of flow rate on some physical properties of different polymeric solutions

IOP Conf. Series: Journal of Physics: Conf. Series **1003** (2018) 012069 doi:10.1088/1742-6596/1003/1/012069

Study the effect of flow rate on some physical properties of different polymeric solutions

A R Jabur [1,*], M A Najim [1] and Sh A Abd Al- Rahman[1]

[1]Department of Materials Engineering, University of Technology, Baghdad/ Iraq

[*]130020@uotechnology.edu.iq

Abstract: In this study, three different polymers were used to produce electrospun scaffolds, polyvinyl alcohol (PVA) in a concentration of 8% w/v, nylon 6 in a concentration of 25% w/v, and poly (vinylpyrrolidone) (PVP) in a concentration of 4% w/v. These three polymer solutions were electrospun at different flow rates, to compare the effect of flow rate on the porosity, fiber diameter, and pore size of the scaffolds prepared from these polymer solutions. The flow rate range for PVA electrospinning started with (o.5, 1, 1.2, 1.5, and 2) ml/hr. While for nylon 6, the flow rate range started with (0.1, 0.5, 1, 1.5, and 2) ml/hr.; and for PVP, it started with (0.5, 0.7, 1, 1.2, and 1.5) ml/hr. It was observed that increasing the flow rate resulted in decreasing the porosity % and pore size due to increasing fiber diameter.

Keywords: Electrospinning,PVA, scaffold, flow rate, porosity, nanofiber, pore size.

1. Introduction

Porosity and pore size has been shown to be a key determinant of the success of tissue engineered scaffolds. A high degree of open porosity and an appropriate pore size are necessary for cell spreading and penetration inside the scaffold as well as to offer proper exchange of nutrients and waste between the scaffold and the surrounding tissues. Electrospinning technique offers an attractive method for mimicking the natural extracellular matrix (ECM) for tissue engineering applications. However, a major problem in electrospinning is the accumulation of fibers, resulting in poor porosity and small pore size. The porosity and pore sizes in the electrospun scaffolds are highly dependent on the fiber diameter which is mainly affected by the flow rate during electrospinning process [1]. The basic mechanism of electrospinning involves ejection of a solution containing a dissolved polymer in the proper solvent through a metallic nozzle by electrostatic attraction to generate ultrafine fibers, which are deposited onto a grounded metal collector. The resultant structure is a randomly oriented micro- or nanofiber network mesh with a highly open porous structure [2]. Figure 1 illustrates the basic schematic of electrospinning technique [3]. In order to get uniform nanofiber, many investigations on the effective parameters such as surface tension, viscosity, capillary-collector distance, flow rate, applied voltage, and solution temperature have been studied [3]. Flow rate is considered one of the process parameters affecting electrospinning technique. Increasing the flow rate tends to increase fiber diameter and bead diameter [4]. The high flow rate also results in residual solvent in the deposited fibers because it doesn't take the necessary time to evaporate which may cause the fibers to fuse together [5].

Controlling the fiber diameter in electrospinning is possible by adjusting the electrospinning parameters like solution concentration, applied voltage, flow rate, capillary- collector distance and all the other solution and process parameters. Unlike fiber diameter, controlling the pore size and porosity% is more difficult and is

highly related with the fiber diameter [6]. Choosing the scaffold material is related to the application. PVA is one of the semi-crystalline hydrophilic polymers, dissolve in water and it's the largest volume synthetic resin produced in the world. The excellent physical properties, chemical resistance, biocompatibility and biodegradability of PVA have led to the development of various commercial products based on this polymer. PVA is characterized by being a biodegradable polymer and the degradation products are water and carbon dioxide. Therefore, it is used in many biomedical and pharmaceutical applications, due to its characteristics such as: nontoxic, noncarcinogenic, and bioadhesive properties with the ease of processing [7].

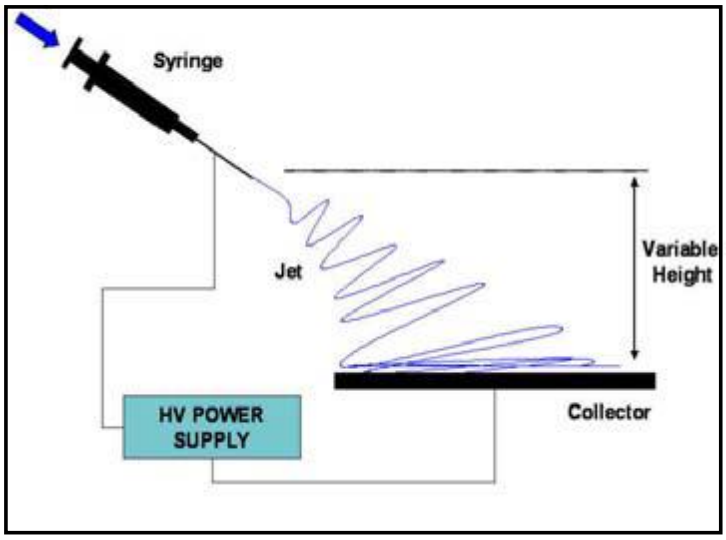

Figure 1. Schematic illustration of electrospinning technique [3].

Electrospunnanofibers from nylon 6 already found a number of applications. Nylon 6 has a superior fiber forming ability. It is a biodegradable and biocompatible synthetic polymer with good mechanical properties, which are further enhanced by hydrogen bonds. Unlike other polymers, such as polyethylene oxide and PVA, nylon 6 is resistant to both humidity and water [8]. Poly (vinyl pyrrolidone) (PVP) is known as an important amorphous polymer, with excellent biocompatiblity, low chemical toxicity, high solubility in most organic solvents, good spinnability, and ability to interact with a wide range of hydrophilic materials [9]. The aim of this study is to compare the effect of increasing flow rate on some important physical properties of electrospun scaffold which are porosity %, pore size and fiber diameter; using three different polymers which are PVA, nylon 6, and PVP which are used widely in tissue engineering due to their biocompatibility and biodegradability.

2. Materials and Methods

2.1. Preparation of solutions

(PVA, molecular weight 124000) was purchased from (Gerhard Buchmann KG Tuttlingen / Germany). Distilled water was used as a solvent to prepare the solution with a concentration of 8% w/v. using magnetic stirrer at 70°C.

Nylon 6 was purchased from SIGMA-ALDRICH CHEMINE Gmbh, USA; the molecular weight for the repeated unit is equal to 113.16 g/mol., the relative density for Nylon 6 at 25°C is equal to 1084 g/ml, and the melting point is equal to 220°C. Nylon 6 solution was prepared in a concentration of 25% w/v, with formic acid as a solvent by using magnetic stirrer at room temperature.

The used Poly (vinylpyrrolidone) (PVP), with molecular weight equal to 1,300,000 g/mol., was dissolved using ethanol in a concentration of 4% w/v with magnetic stirring at room temperature.

2.2. Fabrication of nanofiber scaffold

Electrospinning process is performed by (NaBondElectrospinning from NaBondTecchnologies Co.). The polymer solution has been kept in a plastic syringe with 10 ml capacity. A metal capillary needle with inside diameter equal to 0.6 mm has been attached to the plastic syringe; this metallic needle is connected to positive side of high voltage. The syringe is then fixed on a syringe pump obtained from (NaBond Technologies Co). An aluminum square plate (14.5*14.5 cm) has been used as a collector for nanofibers. The end of the capillary has been always positioned in such a way aligned with the center of the plate collector. The set-up is illustrated in Figure 2 and Table 1 shows the electrospinning conditions used in this research.

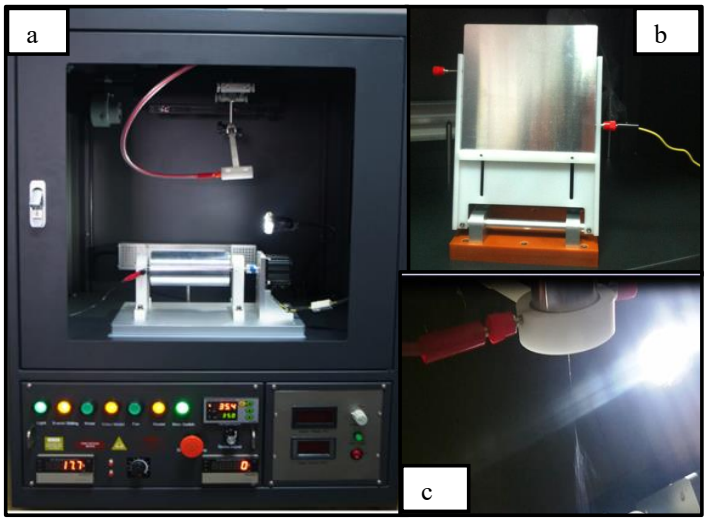

Figure 2. Electrospinning apparatus, (a) Chamber of electrospinning; (b) plate collector; (c) metallic needle.

Table 1. Electrospinning parameters used in preparing scaffolds.

Electrospinning parameters	PVA	Nylon 6	PVP
High voltage applied	20 KV	20 KV	15 KV
Capillary- collector distance	15 cm	15 cm	10 cm
Concentration%	8%	25%	4%

2.3. Porosity% test

The porosity% of the prepared specimens was determined by using Archimedes principle. Ethanol was selected as the displacement liquid since it penetrates inside the specimen without swelling or shrinking the matrix [10]. The specimens were individually immersed in a cylinder containing a determined volume of ethanol (V1). Each sample was immersed for 5 min. with inducing pore filling by physically press air from the scaffold. The total volume of ethanol and ethanol filled scaffold became (V2). Finally, the scaffold filled with ethanol was removed from the cylinder, and the residual ethanol volume was recorded as (V3) [11]. The Porosity percentage of each scaffold was calculated by the equation (1) [11].

$$P\% = ((V1 - V3)/(V2 - V3)) \times 100\% \quad (1)$$

2.4. Statistical analysis

The statistical analysis for fiber diameter and pore size was accomplished using scanning electron microscope (SEM) images and AutoCAD 2010 software, as shown in Figure 3. The number of the selected data of fibers and pores in each image was 100. The average fiber diameter and average pore size with the standard deviation were calculated using Excel.

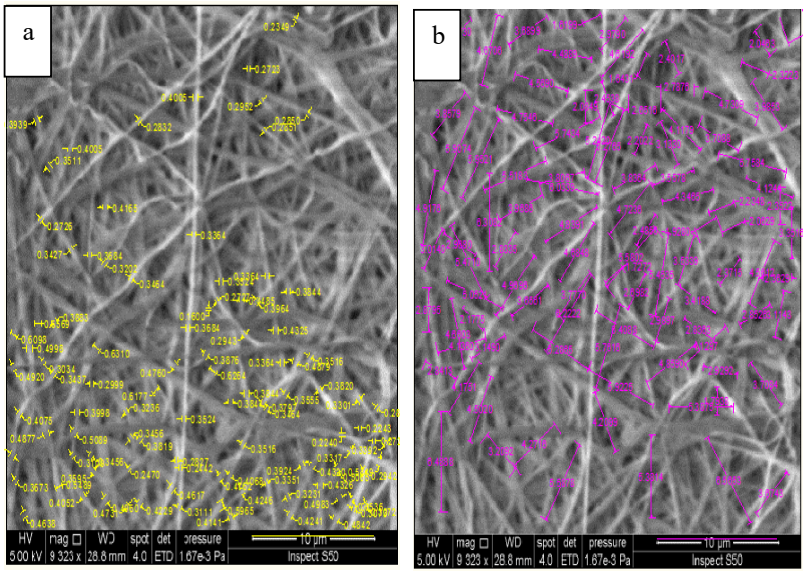

Figure 3. SEM images in AutoCAD 2010 software for measuring the dimensions of 100 fibers and pores, (a) Fibers; (b) pores.

3. Results and Discussion

The average fiber diameter and average pore size for the prepared scaffolds were determined depending on one flow rate (0.5 ml/hr.), using the scanning electron microscope (SEM) images shown in Figure 4. The results showed that using the same flow rate for different prepared polymer solutions resulted in different average fiber diameter and pore size. The highest fiber diameter resulted in the scaffold prepared from 8% w/v PVA, while the smallest average fiber diameter resulted in the scaffold prepared from 25% w/v nylon6. Although increasing the polymer concentration resulted in increasing fiber diameter [12], but with different polymers and different molecular weight this may not become true, because decreasing the molecular weight resulted in decreasing the fiber diameter. The largest average pore size resulted in 4% PVP scaffold, while the smallest average pore size resulted in the scaffold prepared from 25% w/v nylon6. The small fiber diameter resulted also in small pore size and this may be attributed to the high entanglement between the fibers which reduced the pore size or may be resulted from the beads formation. The beads formation was obvious in the scaffold prepared from 25% w/v nylon6 as shown in Fig. 4b. For scaffold application the high pore size is necessary for cell penetration and spread inside the scaffold to mimic the scaffold structure and form a three dimensional tissue after scaffold degradation [13]. Table 2 shows the results of the average fiber diameter and average pore size for the prepared scaffolds with flow rate equal to 0.5 ml/hr. with the calculated standard deviation in fiber diameter and pore size.

Table 2. The results of the average fiber diameter and average pore size with the calculated standard deviation using Excel.

Scaffold type	Average fiber diameter (nm)	Standard Deviation ± nm in fiber diameter	Average pore size (nm)	Standard Deviation ± nm in pore size
8% PVA, flow rate 0.5 ml/hr.	504.24	133.38	2031.8	755.61
25% nylon6, flow rate 0.5 ml/hr.	123.07	30.214	1381.15	835.8

4% PVP, flow rate 0.5 ml/hr.	383.38	94.78	3900.75	1318.25

The porosity % test results based on Archimedes principle showed a decrease in the porosity% with increasing the flow rate as shown in Figure 5 (a,b and c). This may be attributed to the increase in the fiber diameter with increasing the flow rate due to the increase in the amount of the delivered polymer through the metallic needle [14, 15]. The increase in flow rate leads sometimes to beads formation especially when the polymer concentration or the molecular weight of the polymer were low leading to lower viscosity levels, high solvent to polymer ratio and beads formation [16,17]. This occurred in nylon6 scaffold as shown from the SEM image Figure 4.b, the lower molecular weight levels leads to beads formation and this in turn caused low average pore size and decreased porosity %. For the tissue engineering applications; where the porosity% and big pore size are important, the lower flow rate is predominant, because lower polymer amount will be delivered leading to lower fiber diameter and lower porosity%. From the three used polymers in this research both PVA and PVP started with approximately the same porosity %, and a decrease was noticed with increasing the flow rate. For nylon6 scaffold the porosity% at 0.1 ml/hr. was much lower than that for PVA and PVP scaffolds at 0.5 ml/hr. flow rate, and also decreased with increasing the flow rate. Therefore lower flow rate is required for nylon 6 to achieve good porosity levels for tissue engineering applications; or increasing the molecular weight of the used polymer in order to increase the viscosity and reduce the beads formation that decrease the porosity%.

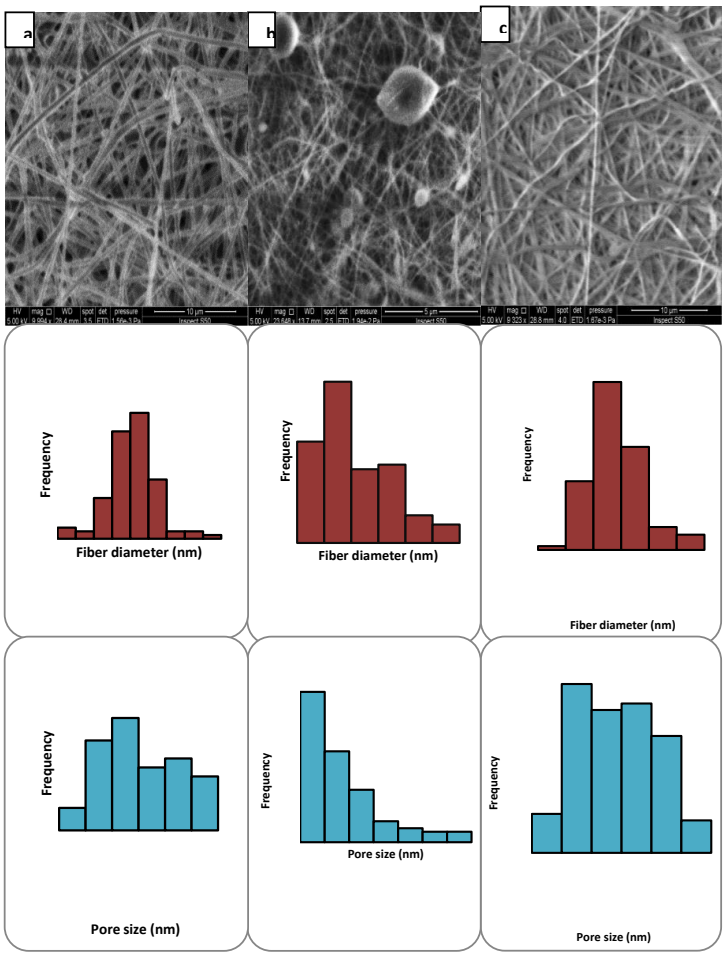

Figure 4. (a) SEM image and statistical analysis of 8% PVA with 0.5 ml/hr. flow rate, the magnification is equal to 9994 X; (b) SEM image and statistical analysis of 25% nylon 6 with 0.5 ml/hr. flow rate, the magnification is equal to 23648 X; (c) SEM image and statistical analysis of 4% PVP with 0.5 ml/hr. flow rate, the magnification is equal to 9323X.

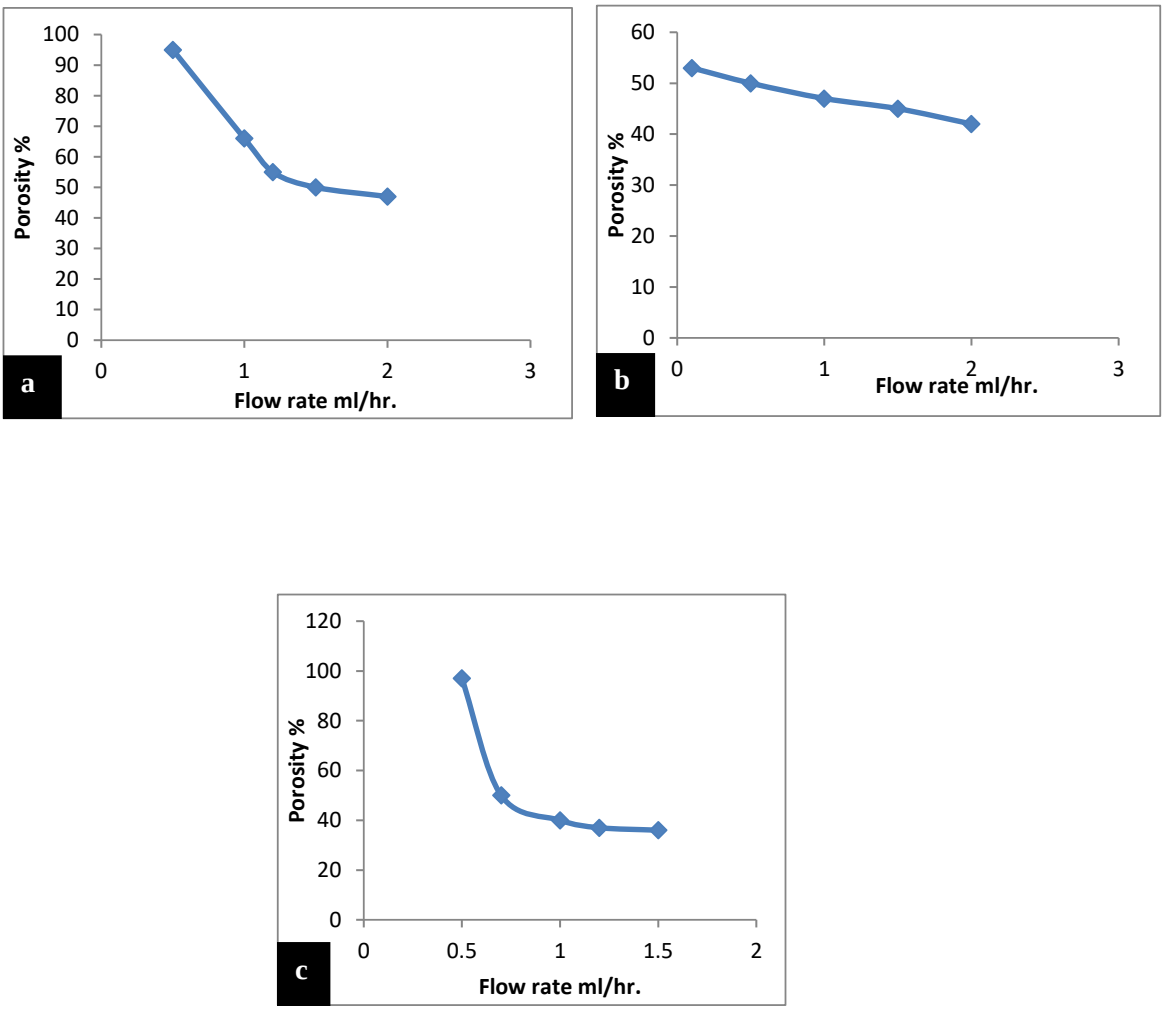

Figure 5. The effect of increasing flow rate on the porosity %. (a) PVA scaffold, (b) Nylon6 scaffold, and (c) PVP scaffold.

4.Conclusion

Increasing the flow rate, the porosity% will be decreased due to increasing the fiber diameter. Besides, using polymers with lower molecular weight resulted in beads formation which may leads to decreasing the pore size and porosity%.

References

[1] Soliman S, Sant S, Nichol JW, Khabiry M, Traversa E and Khademhosseini A. 2011. Controlling the porosity of fibrous scaffolds by modulating the fiber diameter and packing density. *Journal of Biomedical Materials Research Part A*. **96(3)**:566-74.

[2] Gunavathi P, Ramachandran T and Chellamani KP. 2012.Characterization of nanomembrane using nylon-6 and nylon-6/poly (e-caprolactine) blend. *Indian journal of fibre & textile research,* **37.** 211-16.

[3] Zargham S, Bazgir S, Tavakoli A, Rashidi A S and Damerchely R. 2012. The effect of flow rate on morphology and deposition area of electrospun nylon 6 nanofiber. *Journal of Engineered Fabrics & Fibers (JEFF)*, *7***(4)**.42-49.

[4] Thompson CJ, Chase GG, Yarin AL and Reneker DH. 2007. Effects of parameters on nanofiber diameter determined from electrospinning model. *Polymer*. Nov 2;**48(23)**:6913-22.
[5] Jabur AR, Al-Hassani ES, Al-Shammari AM, Najim MA, Hassan AA and Ahmed AA.2017. Evaluation of stem cells' growth on electrospun polycaprolactone (PCL) scaffolds used for soft tissue applications. *Energy Procedia*. **119**:61-71.
[6] Stepanyan R, Subbotin A, Cuperus L, Boonen P, Dorschu M, Oosterlinck F and Bulters M. 2014 Oct 27. Fiber diameter control in electrospinning. *Applied Physics Letters*.**105(17)** 173105.
[7] Subramanian UM, Kumar SV, Nagiah N and Sivagnanam UT. 2014 Feb 19. Fabrication of polyvinyl alcohol-polyvinylpyrrolidone blend scaffolds via electrospinning for tissue engineering applications. *International Journal of Polymeric Materials and Polymeric Biomaterials*.**63(9)**. 476-85.
[8] Matulevicius J, Kliucininkas L, Martuzevicius D, Krugly E, Tichonovas M and Baltrusaitis J. 2014 Jan 1. Design and characterization of electrospun polyamide nanofiber media for air filtration applications. *Journal of nanomaterials.* 2014. **14**.
[9] Huang S, Zhou L, Li MC, Wu Q, Kojima Y and Zhou D. 2016 Jun 28. Preparation and properties of electrospun poly (vinyl pyrrolidone)/cellulose nanocrystal/silver nanoparticle composite fibers. *Materials*. **9(7)**:523.
[10] Wattanutchariya W and Changkowchai W. 2014. Characterization of porous scaffold from chitosan-gelatin/hydroxyapatite for bone grafting. *InProceedings of the International MultiConference of Engineers and Computer Scientists* .**Vol. 2**, pp. 12-14.
[11] Guan J, Stankus JJ and Wagner WR. 2006 Mar 1. Development of composite porous scaffolds based on collagen and biodegradable poly (ester urethane) urea. *Cell transplantation*.**15(1) :**17-27.
[12] Thompson CJ, Chase GG, Yarin AL and Reneker DH. 2007 Nov 2. Effects of parameters on nanofiber diameter determined from electrospinning model. *Polymer*.**48(23)**:6913-22.
[13] Zafar M, Najeeb S, Khurshid Z, Vazirzadeh M, Zohaib S, Najeeb B and Sefat F. 2016 Jan 26. Potential of electrospun nanofibers for biomedical and dental applications. *Materials*.**9(2):**73.
[14] Pillay V, Dott C, Choonara YE, Tyagi C, Tomar L, Kumar P, du Toit LC and Ndesendo VM. 2013 Feb 13. A review of the effect of processing variables on the fabrication of electrospun nanofibers for drug delivery applications. *Journal of Nanomaterials*.**2013**.
[15] Jabur AR, Abbas LK and Aldain SM. 2015. The effects of operating parameters on the morphology of electrospun polyvinyl alcohol nanofibres. *InThe International 3rd. Scientific Conference of the College of Science, Journal of University of Kerbala 2015* (pp. 35-46).
[16] Shahreen L and Chase GG. 2015 Sep 1. Effects of electrospinning solution properties on formation of beads in Tio2 fibers with PdO particles. *Journal of Engineered Fabrics & Fibers (JEFF)*.**10(3).**
[17] Chayad FA, Jabur AR and Jalal NM. 2015 Dec 31. Effect of MWCNT addition on improving the electrical conductivity and activation energy of electrospun nylon films. *Karbala International Journal of Modern Science*.**1(4):**187-93.

The Enhancement Of UV Sensor Response By Zinc Oxide Nanorods / Reduced Graphene Oxide Bilayer Nanocomposites Film

The Enhancement Of UV Sensor Response By Zinc Oxide Nanorods /Reduced Graphene Oxide Bilayer Nanocomposites Film

Ali A A Mohammed[1,2,a], AB Suriani[1,2,b] and Akram R Jabur[3] .

[1]Nanotechnology Research Centre, Faculty of Science and Mathematics,
Universiti Pendidikan Sultan Idris, 35900 Tanjung Malim, Perak, Malaysia
[2]Departement of Physics, Faculty of Science and Mathematics,
Universiti Pendidikan Sultan Idris, 35900 Tanjung Malim, Perak, Malaysia
[3]Department of Materials Engineering, University of Technology, Baghdad, Iraq

ashanwer9@gmail.com[a] ,absuriani@yahoo.com[b] ,bakram.jabut@gmail.com[b]

Abstract. Zinc oxide nanorods (ZnO NRs) /reduced graphene oxide (rGO) nanocomposites assisted by sodium dodecyl sulfate surfactant (ZnO NRs/rGO-SDS) showed a good response for UV sensor application that has sensitivity of around ~32.54. Whereas, the UV sensor response on pristine ZnO NRs showed almost 15 times lower response than the ZnO NRs/rGO-SDS nanocomposites. The pristine ZnO NRs were prepared by sol-gel immersion method before rGO solution was sprayed on the ZnO films using spraying method. The GO solution was produced via electrochemical exfoliation method at 0.1 M SDS electrolyte then the solution was reduced using hydrazine hydrate under 24 hours magnetic stirring at a temperature of around ~100 °C. The samples were characterized using energy dispersive X-ray, field emission scanning electron microscope, micro-Raman, ultraviolet visible, , X-ray diffraction, UV lamp and four-point probe measurement. The aim of this study was to improve the UV sensor response based on ZnO/rGO-SDS nanocomposites. In conclusion, the fabricated ZnO NRs/rGO-SDS nanocomposites assisted with SDS is a good candidate for the use in UV sensor applications as compared to pristine ZnO NRs films.

.

1. Introduction

The Ultraviolet sensor (UV) becomes interesting research field due to it has many applications such as flame detection, space research, missile launching detection, optical communication, environmental monitoring and so on [1]. The UV sensor was fabricated based on due to its properties [2], ZnO has direct energy gap 3.37eV and it has also binding exciton energy ~60 meV [3]. In the recent years, a lot of effort has been devoted to improve different nanostructure of ZnO such as nanowire (NWs) [4], Nanorods (NRs) [5] nanotubes [6] nanoplate [7] and nanobelts [6] . There are a lot of literature reports on preparation of ZnO nanostructure by many methods such as; vapour liquid solid (VLS) [8], vapour–solid

(VS) [9], magnetron sputtering [10], pulse laser deposition (PLD) [11], metal organic chemical vapour deposition (MOCVD) [12], chemical vapour deposition (CVD) [13], hydrothermal [14] and arc discharge [15] used to obtained one dimensional semiconductor nanostructure technique, But all these methods were complex to controlled parameters [16]. There are another simple way to syntheses ZnO based on one dimensional nanostructure namely sol-gel immersion methods [17], this method has many advantages such as; low cost process, low temperature deposition process, environment friendly and, simple set up [18]. Pristine ZnO has been showed weak responsivity and small operating sensitivity UV detector. Jiang et al. [19] they reported the responsivity of pristine ZnO thin film is so poor to applied in practical applications. Coung et al.[20] they hybrid ZnO nanorods with nanostructure from GO/CNT, They found the ZnO NRs increase absorption ultraviolet after hybrid by spray coated on top of ZnO NRs. The ZnO also composite with rGO for many application and shows a big improvement such as hybrid ZnO/rGO for photocatalyst application [21], and also showed improvement in the supercapacitor applications where synthesis by sol-gel method [22]. The graphene shows good improving in tensile strength and electrical conductivity by compositing with aluminum based on pyrolysis method [23]. The rGO shows also enhancement in photovoltaic performance [24]. Thus, it seems the structure of rGO has an advantageous to improve the UV sensitivity and responsivity and it's the main objective to this study.

2. Experimental procedures:

2.1 Preparation of MgZnO seed layer

In this study MgZnO used as a seed layer for both pristine and hybrid samples; the MgZnO was deposit on the glass substrate (2×2) cm^2. The quartz substrate was cleaned with DI water one time and with acetone two times in ultra–sonicated by water bath (Hwashin Technology Power sonic 410, 50 Hz) at room temperature for 5 minute for each time. The MgZnO solution was produced from [0.88 g zinc acetate dehydrate ($Zn(CH_3COO)_2.2H_2O$), 0.44 g magnesium nitrate hexahydrate ($Mg(NO_3)_2.6H_2O$), 0.25 ml of stabilizer mono-ethanolamine (C_2H_7NO), and 10 ml of 2-methoxyethanol ($C_3H_8O_2$) as a solvent]. The solution was sonicated at 50 °C for 30 minutes, the finally step was stirred the solution for 2 hours at room temperature to get a clean and homogeneous solution. The solution prepared was deposit on the glass substrate by spin-coating method at 3000 rpm for 60 second, 10 drops for each layer than preheated in the oven model (memmert 30-1060, type UF 55) for 10 minutes at 150°C by using spin-coater model (WS-400 BZ-6NPP/A1/AR1), this process were repeated for 5 times. The final annealing for the samples at 500 °C for 1 hour in the furnace two-zone tube, model (2ZTF-1100-20-35).

2.2 Preparation of pristine ZnO nanorods and ZnO nanorods hybrid with rGO-SDS

The ZnO NRs were grown on the MgZnO seed layer that was deposit on the glass substrate. The solution was prepared by mixing (1.409 g) hexamethylenetetramine ($C_6H_{12}N_4$), HMT with (2.79 g) from zinc nitrate hexahydrate $Zn(NO_3)_3.6H_2O$ in (200ml) deionised (DI) water. The solvent sonicated at room temperature for 30 minutes and then stirred at room temperature for 2 hours to get a clean and homogeneous solution. The samples placed down facing top position in the bottle, where the bottle immersion in the water bath at 95 °C for 4 hours. After immersion process the samples were taken out of the bottle and cleaned by rinsing in DI water, and then the samples dried in oven at 130 °C for 10 minutes. The samples were post annealed in two-zone furnace at 500 °C for 1 hour. To hybrid the pristine ZnO NRs with rGO-SDS, where spray 0.1M concentration of rGO-SDS on the top of the ZnO samples by spray coating method, and annealed the samples at 400 °C for 1hour in furnace tow-zone tube. The prepared samples were coated with Aurum (Au), where (Au) as an electrode by using sputters coater model (EMITECH K550X) for current–voltage (I–V) measurements.

The morphology surface of images and cross –section of the samples examined by field emission scanning electron microscopy (FESEM) model (HITACHI SU8020). The Energy Dispersive X-ray (EDX)

model (E-MAX) where used to know the chemical compounds of the pristine ZnO NRs and hybrid ZnO NRs/rGO-SDS. Raman spectroscopy was used to investigate the crystal phase by using wavelength 633 nm, model (Renishaw inVia Reflex). The properties of ZnO NRs crystallinity were studied via X-ray diffraction model (Bruker D8 Advance). The optical properties of ZnO were investigated by using ultraviolent-visible spectrophotometer model (Cary 60 UV-Vis). The UV lamp model (UVGL-55 Handheld) was used to investigate sensor performance supported by measurement sensor system model (Keithley 2400). The four-point probes were used to investigate the electrical properties of ZnO and ZnO/rGO-SDS by using device model (SR-4-6) supported by system model (Keithley 2400).

3. Result and discussion

FESEM image shown in 'Figure (1)' for pristine ZnO NRs and hybrid with rGO-SDS where grown by sol-gel method as shown below.

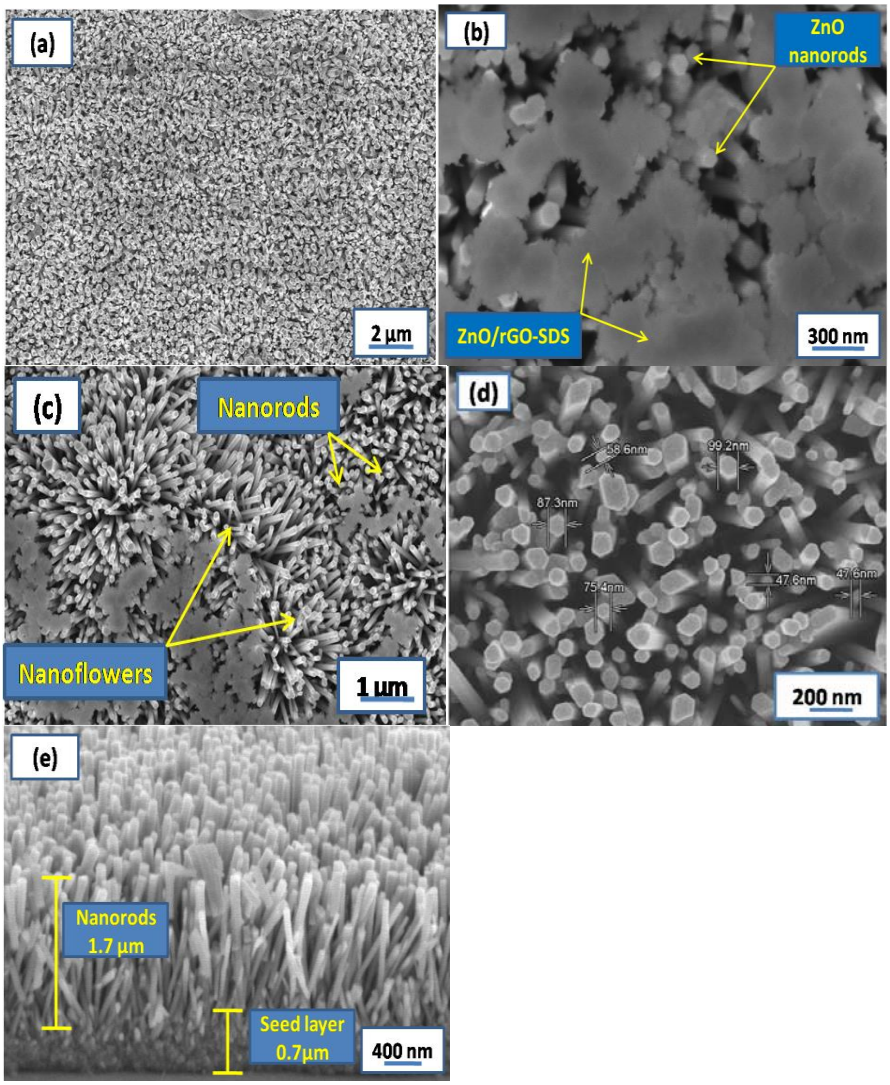

Figure 1. (a) Top surface morphology of ZnO. (b) Top surface of ZnO/rGO-SDS nanorods. (d) Top surface of ZnO with diameter of ZnO/GO-SDS nanorods. (c) Top surface of ZnO nanorods and nanoflower. (e) Cross-section of ZnO nanorods.

'Figure (1)' shows the morphologies surface for ZnO NRs pristine where the magnification was very low, the low magnification shows the ZnO NRs grown on top of MgZnO as seed layer have very high dense and uniform sample. However, Fig 2 (b) shows that rGO-SDS deposit on top of NRs by spray coating method. According to Fig 1 (c) the image shown that the grown a small amount of nanoflowers on top of ZnO NRs. Fig 1 (d) shows that the diameter of ZnO NRs around 47.6 nm up to 99.2 nm according to FESEM image and shows also very clearly that the ZnO NRs have hexagonal shape. However, the cross-section image of ZnO NRs Fig 1(e) shows that the ZnO NRs aligned shape with length around 1.7 µm and thickness of MgZnO was around 0.7 µm.

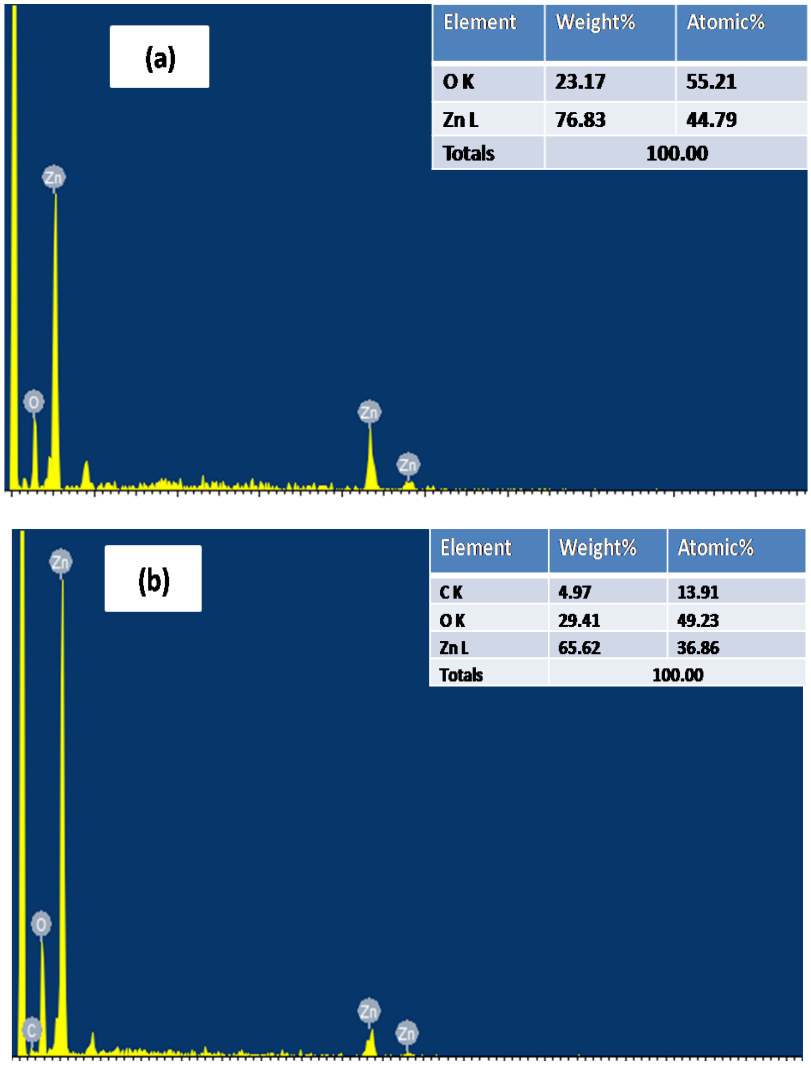

Figure 2. Energy dispersive X-ray spectroscopy (EDX) of (a) ZnO nanorods and (b) ZnO/rGO-SDS nanocomposites.

The ZnO NRs and ZnO NRs/rGO-SDS samples where syntheses by sol-gel immersion method for 4 hours at 95^0C tested by Energy dispersive X-ray spectroscopy (EDX) model (E-MAX). to know the chemical composition for hours we examined the sample by EDX. Fig. 2 (a) shows (EDX) spectrum for ZnO NRs, where can observe very clearly have four peaks contain three of these peaks are zinc and one peak is oxygen. Fig 2 (b) shows there are five peaks three peaks are ZnO, one peak is carbon and one peak is oxygen, Fig 2 (b) shows carbon according to rGO where deposit on top of the ZnO NRs by spray coating

method. However, the samples prepared have very small amount of impurities according to theoretical stoichiometric proved by (Bari et al. 2009 & Tarwal et al. 2011) the O =19.7% and Zn=80.3%.

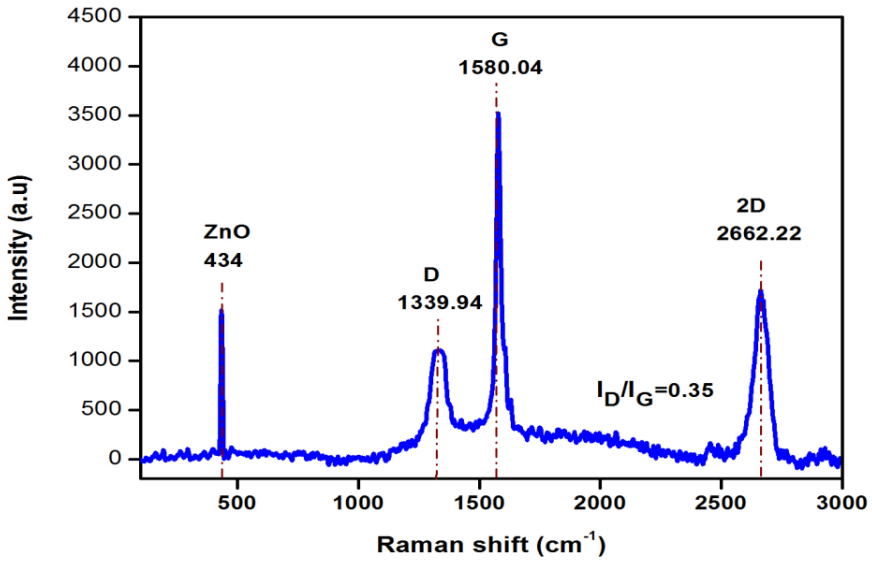

Figure 3. Raman shift for ZnO/rGO-SDS nanocomposites

The suitable technique to test and shown the crystal structure for GO synthesis via electrochemical exfoliation method is Raman spectroscopy Fig 3 show the sharp peak of ZnO NRs was around 434 cm^{-1} E_2 (high) mode corresponds to non-polar optical phonon. However, the peak 434 cm^{-1} related to the oxygen atoms motion and the active branch of a typical Raman for wurtzite hexagonal ZnO NRs and higher wavenumber is a red-shifted. The presence of E_2(h) vibrational mode in Fig 3 indicates clearly ZnO NRs structure is a hexagonal wurtzite [25]. Fig 3 shows appear D band at 1339.94 cm^{-1} due to surface modification process for graphite rod. However, the G band appears at 1580.04 cm^{-1} corresponding to carbon orbital sp^2-hybridized. The intensity of D band in Fig 3 is not very high comparing to G band that prove the sample has a good structure and the diffraction not so big. Fig 3 also shows 2D band at 2662.22 cm^{-1} which it's appear due to there are multilayer of GO also it shows high intensity which is indicate the sample has a few layer of GO only. The I_D/I_G ratio calculated corresponding to 'Figure (2)' and shows smallest ratio 0.35, the smallest ratio indicate that the rGO has defects and least sp^3 bond due to decrease the oxygen contain groups [26].

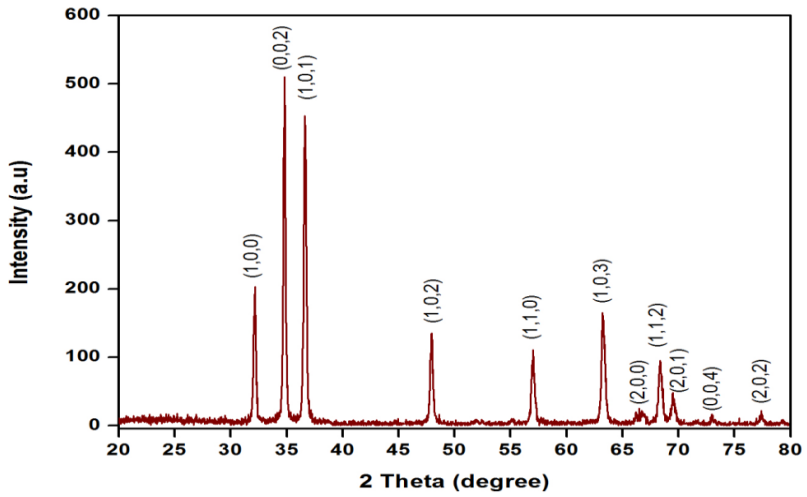

Figure 4. XRD pattern for ZnO nanorods

'Figure (4)' shows the ZnO NRs XRD pattern synthesis by sol-gel method where grown top on MgZnO. Fig 4 shows a highest peak it was at 33.4º (0,0,2) and (1,0,1) at 36.6º and shows that the ZnO NRs sample has a very high purity and degree of crystallinity. The pattern of XRD in Fig 4 shows the diffraction of peaks placed between 20º and 80º that prove the sample has hexagonal wurtzite phase. However these peaks all shows that the sample has no diffraction and it has also very clear hexagonal wurtzite phase according to reported file number (JCPDS#36-1451). That means this sample doesn't have impurity structure effect or shows another peaks.

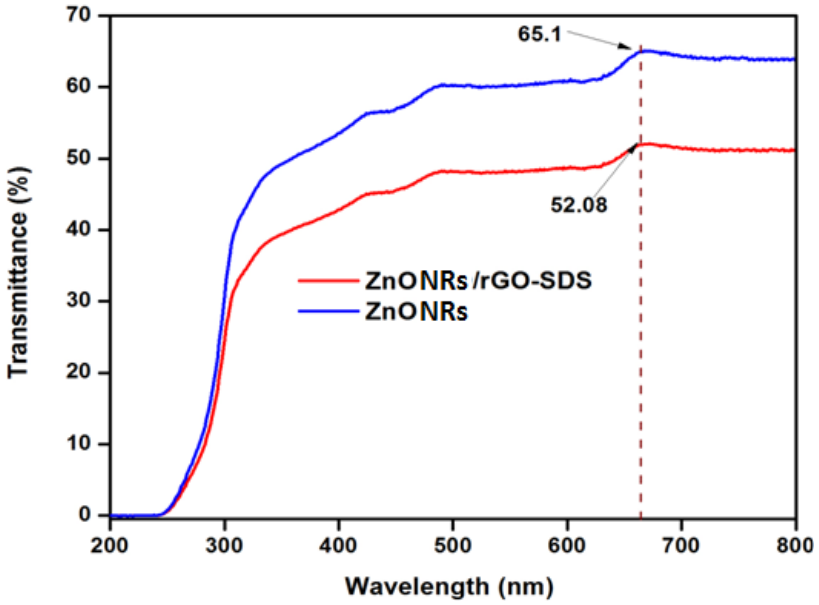

Figure 5. Transmittance spectra of ZnO nanorods and ZnO/rGO-SDS nanocomposites.

'Figure(5)' shows optical transmittance spectrum of ZnO NRs/rGO-SDS nanocomposites, and pristine ZnO NRs with wavelength rated between (200 up to 800) nm. The transmittance of pristine ZnO NRs

was~65% as shown in Fig 5 and the transmittance of ZnO NRs / rGO-SDS nanocomposites was~52% as shown in Fig 5 at wavelength 672 nm. According to 'Figure(5)' it's very clearly that pristine ZnO NRs has higher transmittance comparing to pristine ZnO NRs/rGO-SDS. The ZnO NRs/rGO-SDS show lower transmittance because of extra layer of rGO assisted by SDS spray on top of ZnO NRs as shown in 'Figure(1)' (b). However, the pristine ZnO NRs and ZnO NRs/rGO-SDS nanocomposites have a good transparent in visible in the range of electromagnetic spectrum but show very low and at approximately been around zero at 380 nm in the range of ultraviolet spectrum.

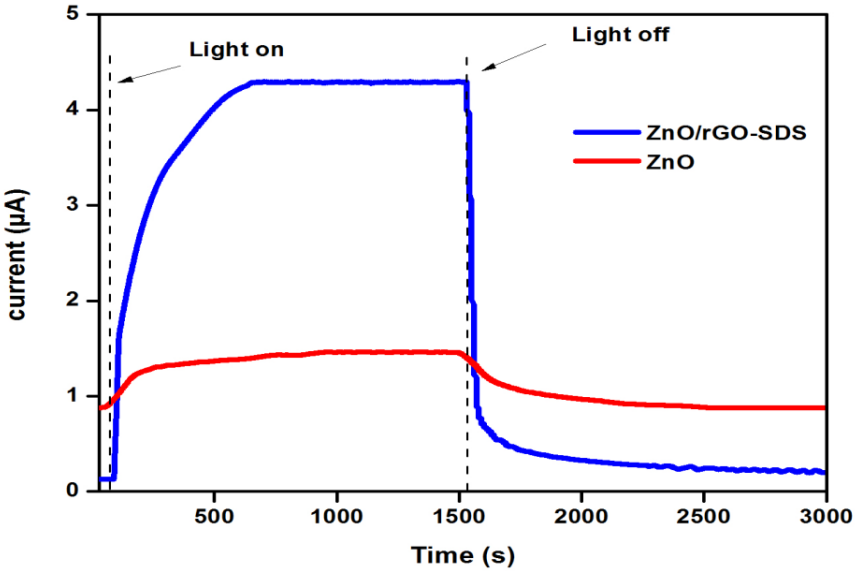

Figure 6. Photocurrent of pristine ZnO and ZnO/rGO-SDS, illumination by UV light (365 nm).

This research focus on UV sensing for pristine ZnO NRs and ZnO NRs/rGO-SDS, where the samples tested by UV lamp model (UVGL-55 Handheld) with illuminations 365 nm supported by system model (Keithley 2400). According to Fig 6 shows the effective of UV sensor for pristine ZnO NRs and ZnO NRs/rGO-SDS where deposit by spray coating method on top of ZnO NRs. The ZnO NRs/rGO-SDS nanocomposite shows a very high sensitivity comparing to ZnO NRs (32.54 and 2.4) respectively according to equation no.1 as shown below. However, ZnO NRs/rGO-SDS and ZnO NRs responsivity were around (180 and 30) mA/W respectively according to equation no.2 [27] as shown below. The good result of ZnO NRs/rGO-SDS due to high surface area of rGO-SDS because of it has one tail to open the GO sheet. The one tail of SDS its help the photon movements easily because of that the sensitivity and responsivity improved. The Aurum (Au) was as an electrode where deposit by using sputters coater model (EMITECH K550X) for current–voltage (I–V) measurements on top of the pristine ZnO NRs and ZnO NRs/rGO-SDS nanocomposites. The response of photocurrent for the samples prepared under UV illuminations with 5V bias can explained according to ZnO NRs and ZnO NRs/rGO-SDS band gap is smaller than photon energy of UV light. However, the illuminated ZnO NRs and ZnO NRs/rGO-SDS by UV light leading to generated mobile carrier in form of electron jumped from valance band to conduction band.

$$S=I_{ph}/I_d \quad (1)$$

$$R= [I_{ph}-I_d /P_{op}] \quad (2)$$

Where: $I_{ph:}$ is the photocurrent.

I_d is dark current.

P_{op} is the optical power of UV lamp

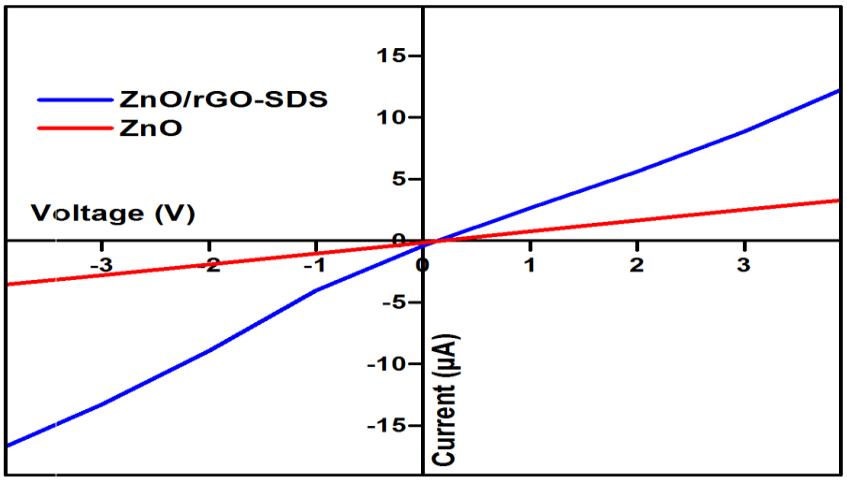

Figure 7. I-V measurement of ZnO and ZnO/rGO-SDS.

'Figure (7)'. shows the I-V curve characterization of pristine ZnO NRs and ZnO NRs/rGO-SDS better where done by using four-point probes model (SR-4-6) supported with system model (Keithley 2400) in room temperature. The ZnO NRs when coated by rGO-SDS shows a good result and it was best than pristine ZnO NRs. The ZnO NRs/rGO-SDS nanocomposites show a better result than the ZnO NRs due to the higher surface area because of rGO assisted by SDS has one tail to open the GO sheet. However, high surface area leads to increasing in the opportunity of photon movement. 'Figure (7)' shows the resistivity decreases when ZnO NRs spray by rGO-SDS due to high surface area.

4. Conclusion:

ZnO NRs grown on top of MgZnO as seed layer have very high dense and uniform sample**,** rGO-SDS deposit on top of NRs by spray coating method grown a small amount of nanoflowers on top of ZnO NRs**,** ZnO NRs have hexagonal shape,crystal structure for GO synthesis via electrochemical exfoliation method is Raman spectroscopy show the sharp peak of ZnO NRs was E_2 (high) mode corresponds to non-polar optical phonon**.** The presence of E_2(h) vibrational mode indicates clearly ZnO NRs structure is a hexagonal wurtzite. The pristine ZnO NRs and ZnO/rGO-SDS nanocomposites have good transparent in visible in the range of electromagnetic spectrum but show very low and at range of ultraviolet spectrum. The ZnO NRs/rGO-SDS nanocomposite shows a very high sensitivity to UV comparing to ZnO NRs. The illuminated ZnO NRs and ZnO NRs/rGO-SDS by UV light leading to generated mobile carrier in form of electron jumped from valance band to conduction band. ZnO NRs when coated by rGO-SDS shows a good result and it was best than pristine ZnO NRs. The ZnO NRs/rGO-SDS nanocomposites show a better result than the ZnO NRs due to the higher surface area because of rGO assisted by SDS has one tail to open the GO sheet. However, high surface area leads to increasing in the opportunity of photon movement.

Acknowledgment:

The authors would like to express their appreciation to the National Nanotechnology Directorate Division (2014-0015-102-03) and Fundamental Research Grant Scheme (Grant Code: 2015-0154-102-02) for their financial support.

Reference:

[1] E. Monroy, F. Omn s, and F. Calle, "Wide-bandgap semiconductor ultraviolet photodetectors," *Semicond. Sci. Technol.*, **vol. 18,** no. 4, pp. R33–R51, 2003.
[2] B. Gong *et al.*, "UV irradiation assisted growth of ZnO nanowires on optical fiber surface," *Appl. Surf. Sci.*, **vol. 406,** pp. 294–300, 2017.
[3] T. Author, J. Society, and P. Physiologists, "1, 2 ," **vol. 14,** no. 1, pp. 1–36, 2009.
[4] Y. Li, F. Della Valle, M. Simonnet, I. Yamada, and J.-J. Delaunay, "High-performance UV detector made of ultra-long ZnO bridging nanowires.," *Nanotechnology*, **vol. 20,** no. 4, p. 45501, 2009.
[5] C. Nanoscale, "Nanoscale PAPER A highly sensitive ultraviolet sensor based on a facile in situ solution-grown," pp. 258–264, 2011.
[6] Y. Lv, Z. Zhang, J. Yan, W. Zhao, C. Zhai, and J. Liu, "Growth mechanism and photoluminescence property of hydrothermal oriented ZnO nanostructures evolving from nanorods to nanoplates," *J. Alloys Compd.*, **vol. 718,** pp. 161–169, 2017.
[7] S. T. Tan, A. Ali Umar, and M. M. Salleh, "(001)-Faceted hexagonal ZnO nanoplate thin film synthesis and the heterogeneous catalytic reduction of 4-nitrophenol characterization," *J. Alloys Compd.*, **vol. 650,** pp. 299–304, 2015.
[8] P. Electronics, "Growth of ZnO nanostructures by vapor – liquid – solid method," **vol. 30,** pp. 27–30, 2007.
[9] A. Umar, S. H. Kim, Y. Lee, K. S. Nahm, and Y. B. Ã. Hahn, "Catalyst-free large-quantity synthesis of ZnO nanorods by a vapor – solid growth mechanism : Structural and optical properties," **vol. 282**, pp. 131–136, 2005.
[10] R. Hong, H. Qi, J. Huang, H. He, Z. Fan, and J. Shao, "Influence of oxygen partial pressure on the structure and photoluminescence of direct current reactive magnetron sputtering ZnO thin films," **vol. 473,** pp. 58–62, 2005.
[11] Y. Sun, G. M. Fuge, and M. N. R. Ashfold, "Growth of aligned ZnO nanorod arrays by catalyst-free pulsed laser deposition methods," **vol. 396,** pp. 21–26, 2004.
[12] W. Lee, M. Jeong, and J. Myoung, "Catalyst-free growth of ZnO nanowires by metal-organic chemical vapour deposition (MOCVD) and thermal evaporation," **vol. 52,** pp. 3949–3957, 2004.
[13] J. Wu and S. Liu, "Low-Temperature Growth of Well-Aligned ZnO Nanorods by Chemical Vapor Deposition," **vol. 21,** no. 5, 2012.
[14] M. Guo, P. Diao, and S. Cai, "Hydrothermal growth of well-aligned ZnO nanorod arrays : Dependence of morphology and alignment ordering upon preparing conditions," **vol. 178,** pp. 1864–1873, 2005.
[15] F. Fang, J. Kennedy, D. A. Carder, J. Futter, P. Murmu, and A. Markwitz, "Modulation of Field Emission Properties of ZnO Nanorods During Arc Discharge," **vol. 10,** no. 12, pp. 8239–8243, 2010.
[16] W. Lee and J.-Y. Leem, "Ultraviolet Photoresponse Properties of Li-Doped ZnO Thin Films Prepared by Sol–Gel Spin-Coating Method," *J. Nanosci. Nanotechnol.*, **vol. 17,** no. 8, pp. 5697–5700, 2017.
[17] A. Chelouche, T. Touam, D. Djouadi, and A. Aksas, "Synthesis and characterizations of new morphological ZnO and Ce-doped ZnO powders by sol-gel process," *Optik (Stuttg).*, **vol. 125**, no. 19, pp. 5626–5629, 2014.
[18] L. Armelao, M. Fabrizio, S. Gialanella, and F. Zordan, "Sol – gel synthesis and characterisation of ZnO-based nanosystems," pp. 90–96, 2001.
[19] D. Jiang *et al.*, "Ultraviolet Schottky detector based on epitaxial ZnO thin film," *Solid. State. Electron.*, **vol. 52,** no. 5, pp. 679–682, 2008.

[20] T. V. Cuong *et al.*, "Solution-processed semitransparent p-n graphene oxide: CNT/ZnO heterojunction diodes for visible-blind UV sensors," *Phys. Status Solidi Appl. Mater. Sci.*, **vol. 208**, no. 4, pp. 943–946, 2011.
[21] P. Thangaraj, M. Ramalinga, S. Sepulveda-guzman, and M. A. Gracia-pinilla, "Ultrasound assisted synthesis of morphology tunable rGO : ZnO hybrid nanostructures and their optical and UV-A light driven photocatalysis," *J. Lumin.*, **vol. 186,** pp. 53–61, 2017.
[22] A. B. Suriani *et al.*, "Electrical enhancement of radiation-vulcanized natural rubber latex added with reduced graphene oxide additives for supercapacitor electrodes," *J. Mater. Sci.*, **vol. 52,** no. 11, pp. 6611–6622, 2017.
[23] F. A. Chyada, A. R. Jabur, and H. A. Alwan, "Effect addition of graphene on electrical conductivity and tensile strength for Recycled electric power transmission wires," *Energy Procedia*, **vol. 119,** pp. 121–130, 2017.
[24] A. B. Suriani *et al.*, "Enhanced photovoltaic performance using reduced graphene oxide assisted by triple-tail surfactant as an efficient and low-cost counter electrode for dye-sensitized solar cells," *Optik (Stuttg).*, **vol. 139,** 2017.
[25] E. Manikandan, V. Murugan, G. Kavitha, P. Babu, and M. Maaza, "Nanoflower rod wire-like structures of dual metal (Al and Cr) doped ZnO thin films: Structural, optical and electronic properties," *Mater. Lett.*, **vol. 131**, pp. 225–228, 2014.
[26] F. Tu, S. Liu, T. Wu, G. Jin, and C. Pan, "Porous graphene as cathode material for lithium ion capacitor with high electrochemical performance," *Powder Technol.*, **vol. 253**, pp. 580–583, 2014.
[27] M. H. Mamat *et al.*, "Effects of Annealing Environments on the Solution-Grown , Aligned Aluminium-Doped Zinc Oxide Nanorod-Array-Based Ultraviolet Photoconductive Sensor," **vol. 2012**, no. Cvd, 2012.

The partial substitution of copper with nickel oxide on the Structural and electrical properties of $HgBa_2 Ca_2 Cu_{3x}Ni_x O_{8+\delta}$ superconducting compound

The partial substitution of copper with nickel oxide on the Structural and electrical properties of $HgBa_2Ca_2Cu_{3x}Ni_xO_{8+\delta}$ superconducting compound

K A Jasim L A Mohammed

Physics Department / College of Education for Pure Science Ibn AlHaitham / University of Baghdad / Baghdad / Iraq

Abstract: The present study the partial substitution of copper with nickel on of $HgBa_2Ca_2Cu_{3x}Ni_xO_{8+\delta}$ superconducting compound where x=002040608 Samples were prepared by solid state reaction method with sintering temperature 850C0 for 24h. By using Xray powder diffraction structural of the samples were studied. The XRD analysis's showed the structures a polycrystalline with tetragonal diagram with majority 1223 phase and the change of the nickel concentrations produce a change in lattice parameters of the lattice a b and c axis c/a density of mass ρm and volume fraction Vphase**.** Four probe apparatus was using to test the electrical resistivity to defined the critical temperature at zero resistivity Tc offset Optimum Tc offset was found from $HgBa_2Ca_2Cu_{24}Ni_{06}O_{8+\delta}$ sample with transition temperature its equal to 137K

Keywords $HgBa_2Ca_2Cu_3O_{8+\delta}$, superconductivity, critical temperature, XRD

1. Introduction

The superconductivity of the material when cooled at very low temperatures is characterized by loss of electrical resistance to zero and expel the magnetic field outside the material [1] The Phenomenon of superconductivity was first noted in mercury in 1911 when electrical resistance of pure mercury went to zero about 4K Understanding of this behavior was not clearly known until 1957 when three physicists suggested BCS theory which governs the emergence of superconductivity[2]
$HgBa_2Ca_nCu_nO_{2n+2+\delta}$ system has a high critical temperature at n=3 The first member of the family n=1 has a critical temperature of 94K The second one n=2 has Tc =127K The third member of this family n=3 has a sharp superconducting transition at 133 K [34] It is well known that the $HgBa_2Ca_2Cu_xO_{8+\delta}$ synthesis of single phase has been found very complicated due to high volatility of Hg at elevated the temperatures when these phase formation occurs

The properties and stability of the $HgBa_2Ca_nCu_nO_{2n+2+\delta}$ family of phases can be substantially improved by partial substitution of same element in the rock salt layer 3–5 they bring in more oxygen in the oxygen deficient HgO δ layer leading to phase stability The higher oxidation state cations also

lead to hole optimization in the hole deficient as grown Hg1223 phase thus producing optimum critical transition temperature Tc [5] In this paper was focused on the study the effect the partial substitution of copper with nickel oxide on the structural and optical properties of the superconducting

2. Experimental

The $HgBa_2Ca_2Cu_{3x}Ni_xO_{8+\delta}$ with x=0020406 and 08 high critical temperature superconducting HTS was synthesized by solid state reaction process Using the required amounts of pure powders materials high purity oxides 9999% of HgONiO BaOCaO and CuO and in Commensurate with the molecular weights accordingly for these chemical formulas

$$\mathbf{HgO + 2\ BaO + 2CaO + 3xCuO + x\ NiO \rightarrow Hg}\boldsymbol{Ba_2Ca_2Cu_{3-x}Ni_xO_{8+\delta}}$$

The reactants were measured by using a sensitive balance whose sensitivity order 10^4 g The reactants were mixed jointly by a gate mortar a sufficient quantity of methanol was to homogenize the mixture dry slurry during grinding process for nearly from 40 to 60 minute Mixture was putted in alumina crucible and dehydrated for in the oven at 120°C The mixture was compressed into the discshape as pellets with diameter 15 cm and 03 cm thick by hydraulic compress under a 7 ton/cm^2 pressure Disks putted in a furnace and sintered at 850°C for 24 hours with the rate of 5 °C/min and then cooled to the room temperature by same rate Structure of crystal such as phase of crystalline the polycrystalline amorphous grain size and parameter of lattice of all samples prepared were examined by XRD technique system SHIMADZU Japan XRD 600 by records the intensity in the range of Bragg's angle θ from 2080 Cu Kα radiation source of wavelength λ=15405 Å was employed with generator setting of current 20 mA and voltage 40 kV The surface morphology of these specimens observed from the AFM technique through using SPM model AA3000 contact mode spectrometer supplied by Angstrom Advanced Inc[6]

3. Results and Discussions

3.1. Structural Properties

The Xray diffraction pattern of $\mathbf{Hg}\boldsymbol{Ba_2Ca_2Cu_{3-x}Ni_xO_{8+\delta}}$ samples with x=0020406and 08 are shown in Fig1 We can show from this figure that all the samples have polycrystalline nature with tetragonal phase formation The peaks are observed due to diffraction from different planes shows mixed phases

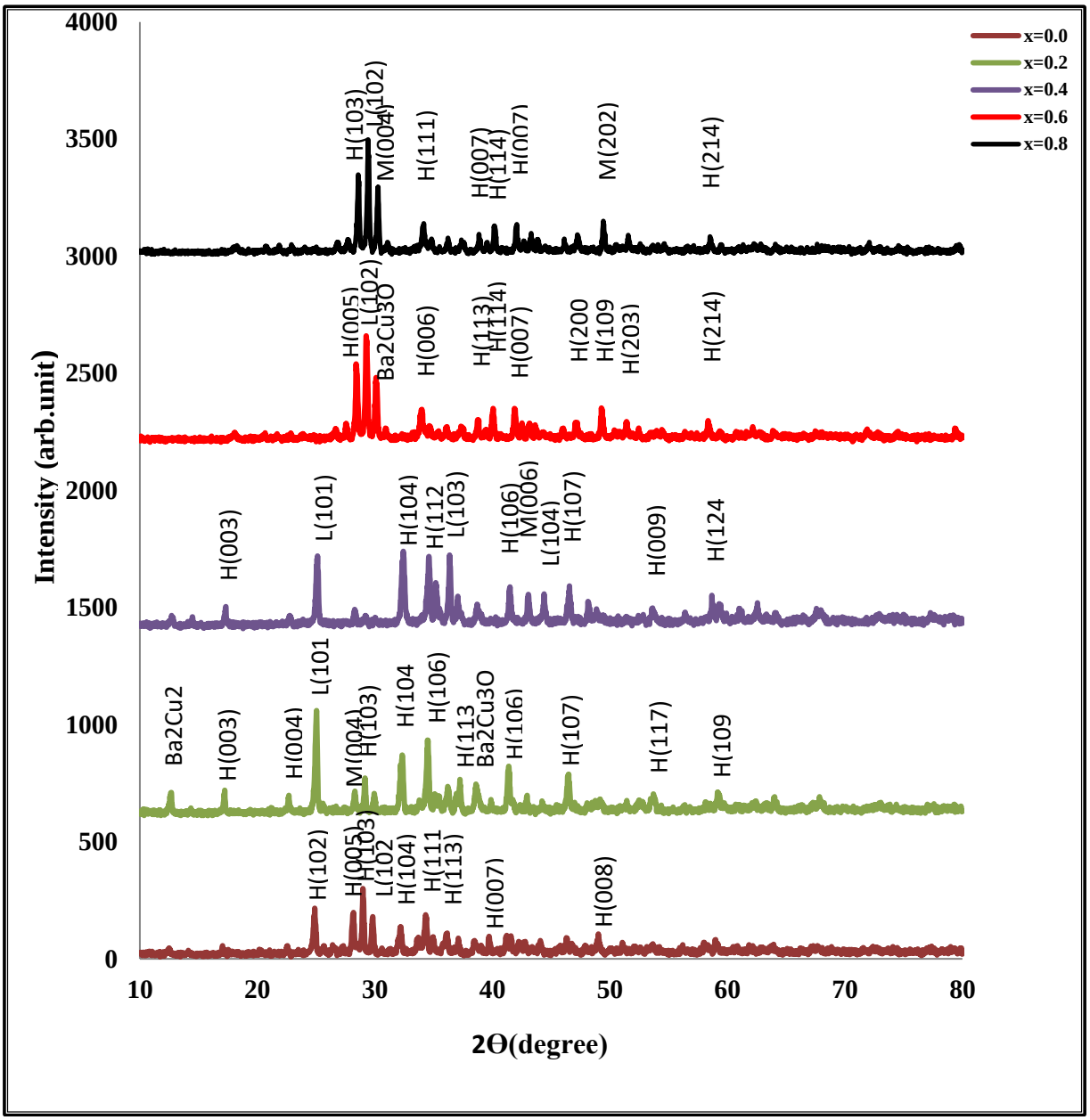

Figure 1. X-ray diffraction pattern of Hg$Ba_2Ca_2Cu_{3-x}Ni_xO_{8+\delta}$ x=0, 0.2, 0.4, 0.6 and 0.8

For the stoichiometric nominal composition of the Hg$Ba_2Ca_2Cu_{3-x}Ni_xO_{8+\delta}$ samples it was found that content a high phase Hg1223 and low phase Hg1212 and some impurity phases of Ba_2Cu_3O $Ba_2Cu_2O$and $Ba_2Cu_3O_5$ with vanishingly small concentrations of unknown phases In order to calculate the volume fraction of the phase the following formula will be used [78]

$$Vph = \frac{\sum I^{o}}{\sum I^{o}+\sum I1+\sum I2} *100\% \qquad (1)$$

It was found that the increase Ni concentration from 006 produce increasing from 757370% t0 829590 and decrease to 788173 when Ni=08
the mass densities d_m were calculated by using following equation

$$\rho x\text{-}ray\ d_m = Mwt/N_A V \qquad (2)$$

Where
ρ xray d_m is density calculated from XRD in units mg/cm ^{3}
N_A is Avogadro number 6022*10^{23} mol^1
Mwt is molecular weight V is volume of unit cell which equal a^2*c for tetragnal system molecular weight It was found that the increase Ni concentration from
The resistivity measurement is given as a function of temperature by using the four point probe technique at temperature range 300K The value of ρ is found by using the relation[910]

$$\rho = \frac{V}{I}\frac{wt}{L} \qquad (3)$$

Where V is the voltage I is the current w is the width *t* is the thickness and L is the length

$$G_s = \frac{0.9\,\lambda}{\beta\cos(\theta)} \qquad (4)$$

Where the wavelength λ of Xray θ is angle of the diffraction and β is FWHM[11]
These data of transition temperatures a b c/a and volume fraction of high phase V1223ph phase V1212ph phase V1201ph as shown in Table 1 it observed increases high phase by increasing the concentration of Ni oxide
It was found that substituting with NiO show that a tetragonal structure with lattice parameter value c creased006 with increasing of the critical temperature T_C this corresponds to the results [12]

Table1 the value of parameters a,b,c with different substitution and the critical transition temperature Tc

X	a=b (A˚)	c(A˚)	c/a ratio	v(A˚)³	dm(gm/cm³)	V ph(1223)%	V p*h*(1212)%	V ph(1201)%	Vp impurities%	T_c(K)
0	3.8038	15.7117	4.0982	230.9309	6.2848	74.7270	16.100	1.2180	7.9540	119
0.2	3.8813	15.8075	4.2478	218.9034	6.6227	75.7370	4.5570	13.9410	5.7640	123
0.4	3.9732	15.8753	3.9955	250.6125	5.7783	78.4210	7.6310	8.4210	5.5260	130
0.6	4.0798	16.2484	3.9826	270.4508	5.3485	82.9590	8.2470	7.7010	1.0910	137
0.8	3.9064	16.0123	4.0989	244.3471	5.9133	78.8173	6.5868	14.5958	3.5179	129

Fig2 shows the electrical resistivity versus temperature for $HgBa_2Ca_2Cu_{3-x}Ni_xO_{8+\delta}$ compound where the critical temperature is determined from this figure[13] we observed that substitution of NiO leads to increase T_C to T_C=137K because of increasing of c axis leads to increase in the CuO layer These results were almost identical to those reported in reference [14] The optimum $T_{c0ffset}$ was found from $HgBa_2Ca_2Cu_{24}Ni_{06}O_{8+\delta}$ sample with transition temperature 137K x=0.6

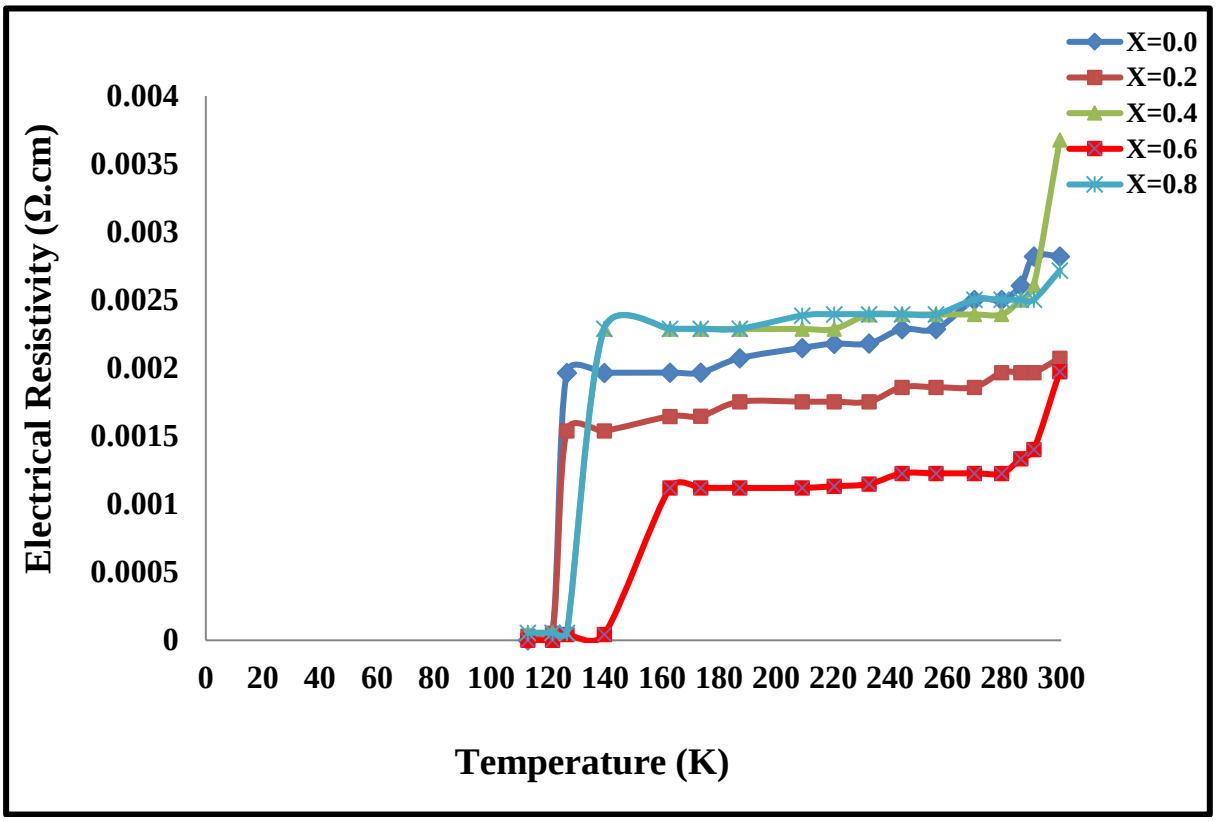

Figure 2. Shows the electrical resistivity versus temperature

The surface morphology of $HgBa_2Ca_2Cu_{3-x}Ni_xO_{8+\delta}$ where x=0, 0.2, 0.4, 0.6 and 0.8 was observed using AFM Figure 3 shows the AFM images of these plats with sintering 858^{0}C for 24 h substrate the values of average size range were found to be dependent on the Ni content shown in Table 2 and Grain size nm

We denote decreasing in value Grain size and Avg Diameter by increasing the concentration of Ni oxide from 004 and then increasing

Table 2 The value of Grain size Roughness Root mean square

x	Grain size(nm)	Roughness (nm)	Root mean square(nm)	Avg. Diameter (nm)	D_m (gm/cm³)	$T_{c(oFF)}$ K	$T_{c(oN)}$K
0	545.2484	0.278	0.365	225.99	6.2848	116	121
0.2	380.2717	0.159	0.219	84.26	6.6227	121	124
0.4	254.2405	1.18	1.36	79.99	5.7783	128.9	131.9
0.6	401.7333	1.76	2.03	105.44	5.3485	131	143
0.8	448.865	0.372	0.54	124.10	5.9133	129	130

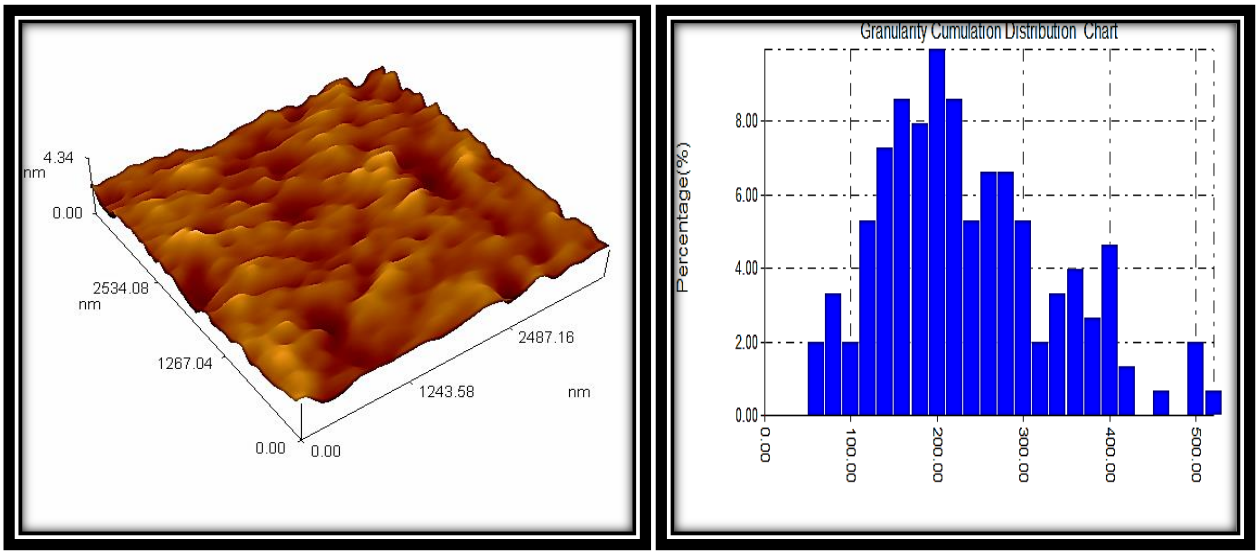
4.34
nm
0.00
2534.08
nm
1267.04
0.00
0.00
1243.58
2487.16
nm
Granularity Cumulation Distribution Chart
Percentage(%)
8.00
6.00
4.00
2.00
0.00
0.00
100.00
200.00
300.00
400.00
500.00

1

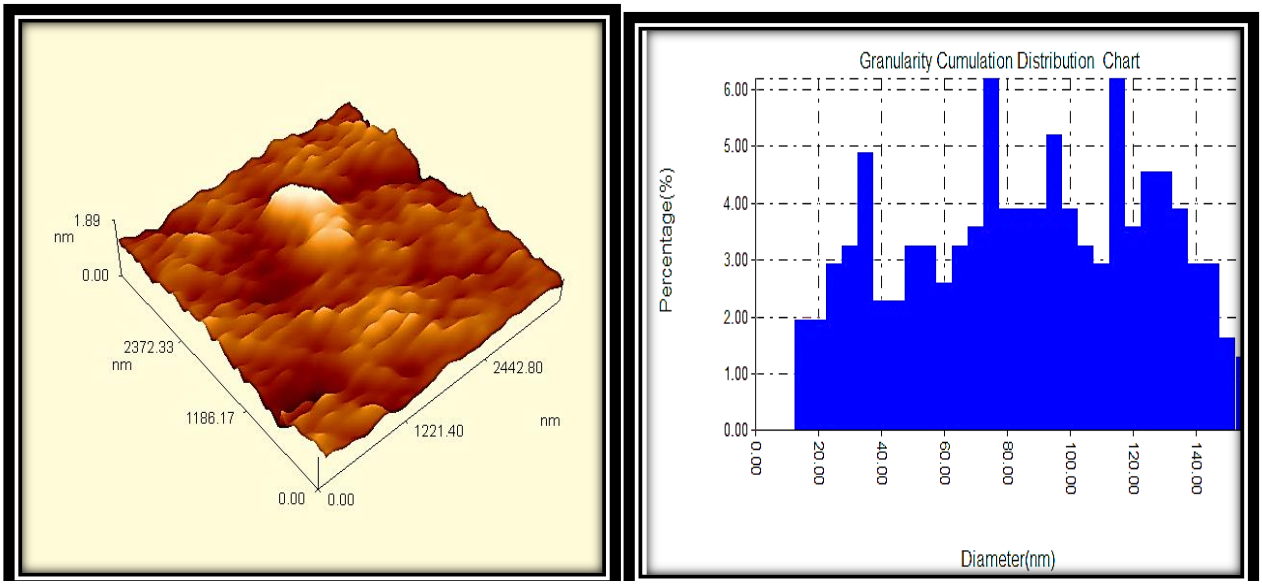
1.89
nm
0.00
2372.33
nm
1186.17
0.00
0.00
1221.40
2442.80
nm
Granularity Cumulation Distribution Chart
Percentage(%)
6.00
5.00
4.00
3.00
2.00
1.00
0.00
0.00
20.00
40.00
60.00
80.00
100.00
120.00
140.00
Diameter(nm)

2

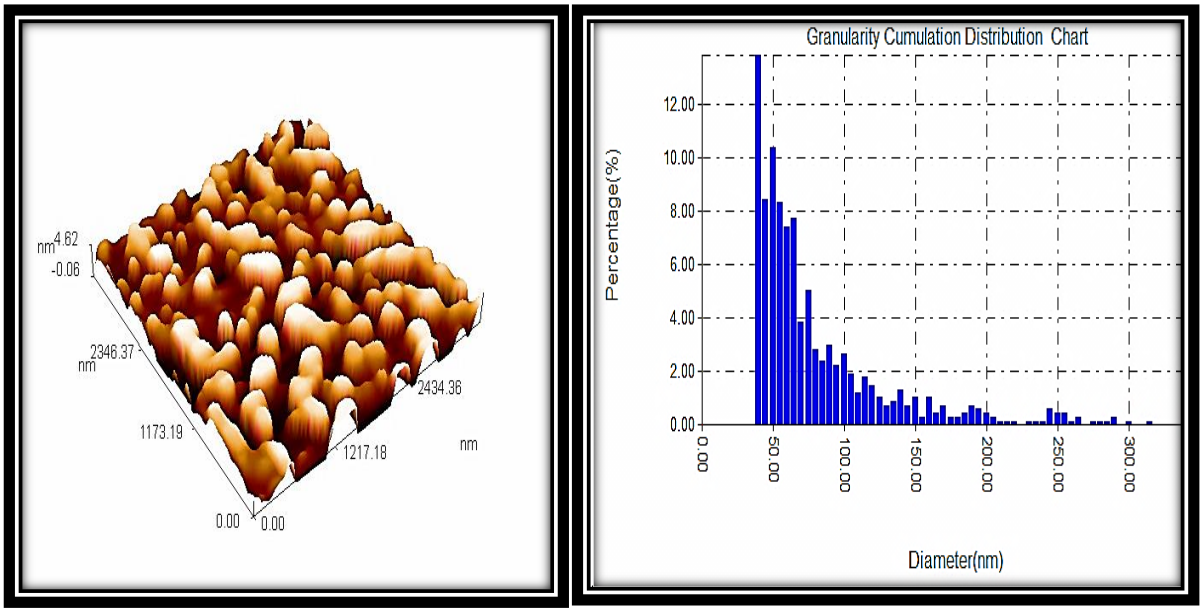
nm 4.82
-0.06
2346.37
nm
1173.19
0.00
0.00
1217.18
2434.36
nm
Granularity Cumulation Distribution Chart
Percentage(%)
12.00
10.00
8.00
6.00
4.00
2.00
0.00
0.00
50.00
100.00
150.00
200.00
250.00
300.00
Diameter(nm)

3

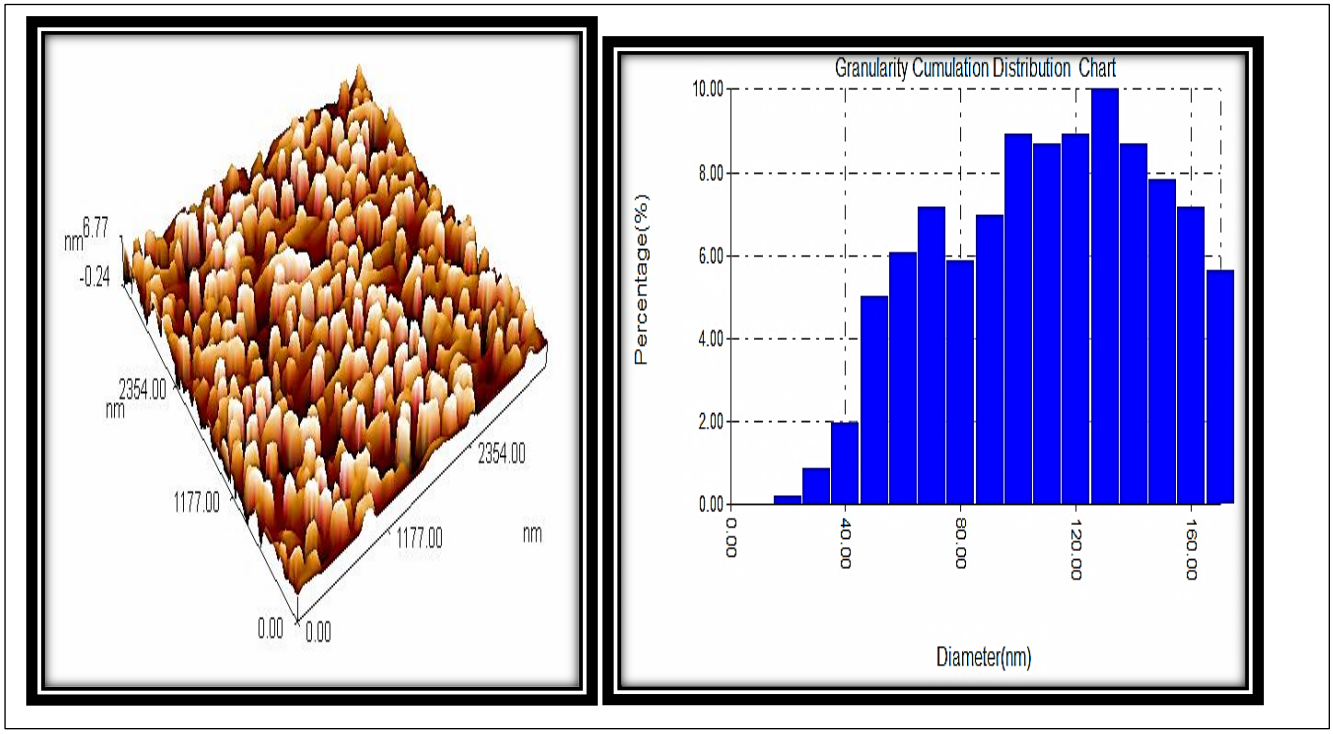
nm 6.77
-0.24
2354.00
nm
1177.00
0.00
0.00
1177.00
2354.00
nm
Granularity Cumulation Distribution Chart
Percentage(%)
10.00
8.00
6.00
4.00
2.00
0.00
0.00
40.00
80.00
120.00
160.00
Diameter(nm)

4

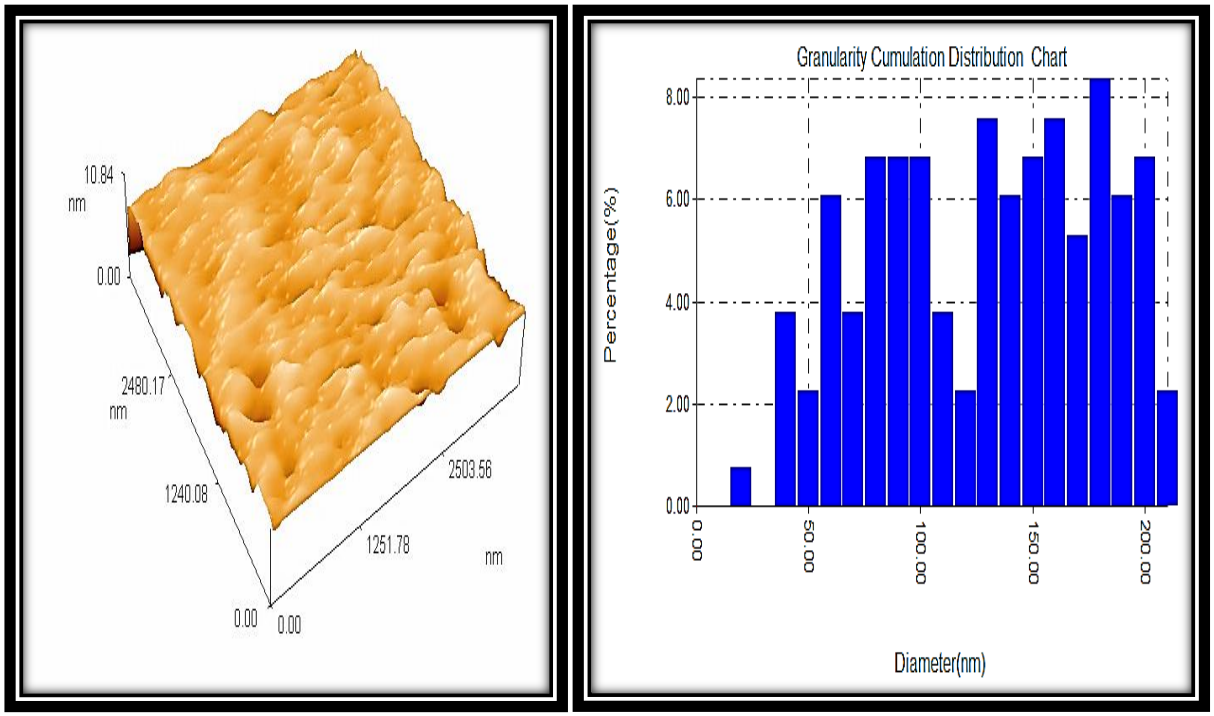

5

Figure 3. Reveals the 3D AFM images and the chart distribution of Hg$Ba_2Ca_2Cu_{3-x}Ni_xO_{8+\delta}$

4. Conclusions

In the present work we have successfully synthesized Hg$Ba_2Ca_2Cu_{3-x}Ni_xO_{8+\delta}$ high Tc superconducting compounds x= 0, 0.2, 0.4, 0.6and 0.8 specimen have been synthesized through the three step SSR doing

The XRD data collected from various samples show that all the samples are polycrystalline and correspond to Hg1223 phase The critical transition temperature Tc of the partial substitution of copper by nickel oxide on the of Hg$Ba_2Ca_2Cu_{3-x}Ni_xO_{8+\delta}$ with x = 0, 0.2, 0.4, 0.6and 0.8 range between119-137K The partial substitution of copper by nickel oxide on the of Hg$Ba_2Ca_2Cu_{3-x}Ni_xO_{8+\delta}$ with x = 0, 0.2, 0.4, 0.6and 0.8 has found a the best Tc value obtained for the compound is x = 0.6

Xray analyses have shown a tetragonal phase and there is an increasing in c axis lattice constant with the increasing of concentration of NiO then a decreasing

References

[1] Z M Galaiewicz 1970superconductivity Quantum Fluids V 29 Pergamon press Warszawa 3
[2] Taoreed O Owolabi Kabiru O Akande and Sunday O Olatunji 2016 Computational Intelligence Approach for Estimating Superconducting Transition Temperature of Disordered MgB2 Superconductors Using Room Temperature Resistivity Applied Computational Intelligence and Soft Computing 1709827 7
[3] G Y Hermiz2008 Effect of Pressure on the Properties of $HgBa_2Ca_2Cu_3O_{8+\delta}$ HTSC System *Iraqi Journal of Physics* **5** 175
[4] Md Atikur Rahman1 Md Zahidur Rahaman2 Md Nurush Samsuddoha2015 A Review on Cuprate Based Superconducting Materials Including Characteristics and Applications American *Journal of Physics and Applications* 39
[5] A Schilling M Gantoni H V Niessen and H R1993 Otl phys C V**215** 1 2 11
[6] Bushra K H Al Maiyaly Shatha H Mahdi et al 2015 Synthesis and Characterization of $Hg_{1-x}Cd_xBa_2Ca_2Cu_3O$ thin film Superconductors prepared by DC Sputtering *Journal of Chemical Biological and Physical Sciences* **5** 3 2630 2941
[7] ASimon PSMukherjee MSSarma and ADDamodaram1994JMater Sci **29** 50 59
[8] BIJU A2007 structure and transport properties of pure earth modified Bi Pbsuperconductors thesis university of kerala 52
[9] Ebtisam Khalil Alwan Albeyaty 2007Effect of n variation on Tc of $Hg_{0.8}Tl_{0.2}Ba_2Can-1Cu_nO_{2n+2+\delta}$ compounds MS Thesis Baghdad university college of science 38 39
[10] VZ Kresin and S A Wolf1990 Fundamentals of Superconductivity Ch 1 Plenum Press New York
[11] CD Lokhande Mater1991 Chemical Physics 27
[12] M F Alias G Y Hermiz A F AbdulAmeer L K Abbas 2009 Effect of In Substitution on TC and superconducting properties of the $Hg_{1-x}In_xBa_{2y}Sr_yCa_2Cu_3O_{8+\delta}$ Proceeding of 3rd scientific conference of the College of Science University of Baghdad 22 59
[13] M Al Beayaty 2014 Thermal properties of $Bi_{1.7}Pb_{0.3}Sr_2Ca_{2-x}MnxCu_3$ $O_{10+\delta}$ superconducting system University of Baghdad 59 61
[14] Noor S Abed Sabah J Fathi Kareem A Jassim 2017 Effect of Partial substitution of Ag on the Structural and Electrical Properties of High Temperature $HgBa_2Ca_2Cu_3O_{8+\delta}$ Superconductor *International Journal of Recent Research and Applied* **4** 76

Repeatability and Reversibility of the Humidity Sensor Based on Photonic Crystal Fiber Interferometer

Repeatability and Reversibility of the Humidity Sensor Based on Photonic Crystal Fiber Interferometer

S S Hindal1, H J Taher2

[1] Materials Research Directorate, Ministry of Science & Technology, Iraq.
[2] Institute of Laser for Postgraduate Studies, University of Baghdad, Iraq.

Abstract. The RH sensor operation based on water vapor adsorption and desorption at the silica-air interface within the PCF. Sensor fabrication is simple; it includes splicing and cleaving the PCF with SMF only. PCF (LMA-10) with a certain length spliced to SMF (Corning-28). The PCFI spectrum exhibits good sensitivity to the variations of humidity. The PCFI response is observed for range of relative humidity values from (27% RH to 85% RH), the interference peaks position is found to be shifted to longer wavelength as the humidity increases. In this work, a 6cm length of PCFs is used, and it shows a sensitivity of (2.41pm / %RH), good repeatability, and reversible in nature. This humidity sensor has distinguished features as that the sensor does not require the use of a hygroscopic material, robust, compact size, immunity to electromagnetic interference, and it has potential applications for high humidity environments.

Keywords: Humidity sensors, Optical fiber sensor, Photonic crystal fiber, Interferometers, Repeatability.

1. Introduction

The Photonic Crystal Fiber (PCF), which is also called holey fiber or Microstructured Optical Fiber (MOF) appeared in the mid-1990s. PCF has a periodic layout of micro holes that run along the entire length of the fiber. There are two types of PCF cross sections: a solid silica core surrounded by air–silica cladding, where the mechanism of light-guiding is provided by means of the Modified Total Internal Reflection (M-TIR), or a hollow core surrounded by air–silica cladding, where the light-guiding mechanism is based on the effect that called Photonic Band Gap (PBG) effect [1].

The presence of air holes in PCF provides a possibility of light propagation in air, or instead of that gives the ability to inject gases/liquids into the air holes. This provides a well-controlled interaction between light and matter leading to novel sensing applications that cannot get it with conventional optical fibers [2, 3]. The applications of PCF in sensing domains dividing it into two sub-branches, depending on the parameter that is measured. These two subbranches are physical (curvature sensor, temperature sensor, vibration sensor, electric and magnetic sensor, and pressure sensor) and biochemical sensors (gas sensor, humidity sensor, pH sensor, and molecular sensor) [4].

Humidity is an important factor in different fields such as agriculture, food process and storage, chemical, biomedical, weather conditions monitoring, civil engineering, and electronic, etc.[5]. Humidity indicates to the water vapor content in the air. It is one of the most measured physical quantities. The measurements of humidity can be stated in a variety of units and terms. The ratio of the water vapor partial pressure to the equilibrium vapor pressure of water at the same temperature is called Relative Humidity (RH). It is expressed as a percentage, using the following expression [6]:

$$RH = \frac{P_w}{P_{ws}} 100\% \quad (1)$$

Where Pw is the water vapor partial pressure and Pws is the saturation pressure of water vapor. RH is the relative measurement because it is a function of temperature [6]. Conventional electronic relative humidity sensors are based on monitoring the electrical capacitance or conductivity changes, and because of electrical leakage (especially in a high humidity environment), this types of sensors have the disadvantage of inaccuracy. So, the optical RH sensors (compared with electronic RH sensors) offer any features, such as low weight, small size, immunity to electromagnetic interference, and remote monitoring. There are wide ranges of relative humidity sensing techniques based on optical fibers, including plastic

optical fibers, long period gratings, Fiber Bragg Gratings, Surface Plasmon Resonance, and tapered optical fibers [7].

Relative Humidity (RH) sensor based on a PCFI has been submitted in this paper, which has a unique feature such as the sensor doesn't need any hygroscopic material to measure humidity and its tip is made of (silica) single material. For an interferometric type fiber optic RH sensor, the sensing mechanism relies on the perturbation of the light signal phase properties that traveling in the optical fiber introduced by the humidity change. The phase change detection is realized by mixing the interest signal with a signal of the reference , then converting the phase difference into wavelength shift or change of the optical intensity [6]. In this paper, the element sensing is just stub of PCF spliced to SMF, this forms the reflection-type PCFI, and the sensor spectrum exhibits good sensitivity to the variations of humidity.

2.Experimental:-

"Humidity sensor based on reflection type of the PCFI has been proposed. First, the coating of the PCF (LMA-10) stub and conventional optical fiber (Corning, SMF-28) are removed by using a mechanical stripping. Then, the second step is cleaving the PCF and SMF, which is done by fiber cleaver, and the third step is cleaning the fibers. Then, the PCF (LMA-10) stub is spliced to single mode optical fiber (SMF-28, Corning) by a splicing machine. The photonic crystal fiber (LMA-10) designed for an endless single-mode operation is used, it has four layers of air holes arranged in a hexagonal pattern around a solid silica core, the fiber has a core size diameter of (10μm), voids with a diameter of (3.1μm), pitch of (6.6μm) and outer diameter of (125μm). These PCF dimensions (LMA-10) alignment and splicing with the SMF with a splicing machine, and due to mode-field diameter (MFD) mismatch compared to other PCFs, the loss was minimize. During the splicing process and due to surface tension, the PCF voids collapse within a microscopic region (~300μm) near the splice point, as shown in the 'figure 1'.

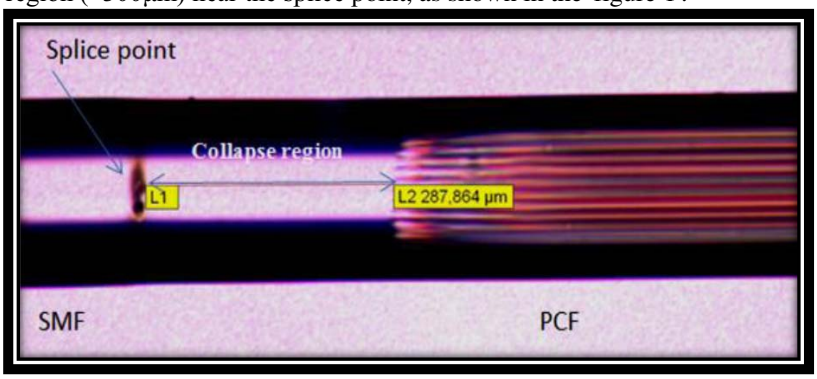

Figure1. The microscope image of splice zone between PCF (LMA-10) and the SMF

The PCF is cleaved with a cleaving machine after the splicing, so that the PCF end acts as a reflecting surface (Mirror). PCF holes are left open to the ambient atmosphere. The mechanism of light guidance in PCF is by (M-TIR).

"The PCFI working principle relies on the modes excitation and recombination occurring in the PCF zone in which the PCF voids are collapsed. The fundamental SMF mode diffract when it enters the collapsed region of the PCF. So, excitation of two core modes in the PCF occurs, due to the diffraction, the mode broadens. Then modes transfer until they reach the PCF cleaved end from where they are reflected. Then, reflected modes are recombined as single core mode, when they re-enter the collapsed region [8, 9]. 'Figure 2' show the setup of the humidity sensor based on PCFI, light source (1550nm) is launched to the interferometer through the Fiber Optic Circulator (FOC), and light that reflected from the cleaved end is fed to the Optical Spectrum Analyzer (OSA)".

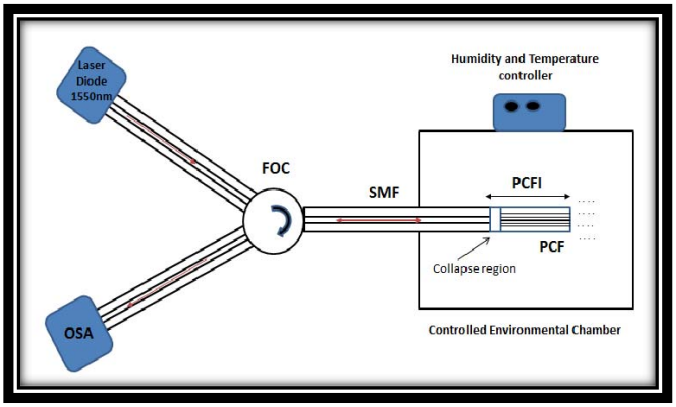

Figure2. Experimental setup of RH sensor based on PCFI

In this setup, the interference peaks shift is tracking with high resolution. Different lengths of the PCF section used to show the sensitivity dependence on PCF length.

The fabricated sensor response to humidity variations is studied (at room temperature and normal atmospheric pressure) by putting the sensor in an environmental chamber (which is a cuboid-shape sealed chamber), fabricated from Polyvinyl chloride (PVC) plastic. It consists of dry/wet air flow system that can vary the internal humidity in the chamber" (27%RH - 85%RH), there are three fans (the first fan is pumped a dry air from container containing a silica gel, the second fan pumps a wet air from container containing distilled water and heater (70watt), and the last fan is on the surface of chamber to expel the air). A calibrated electronic humidity (XMT9007-8 temperature & humidity control instrument) is used for monitoring humidity and temperature inside the environmental chamber.

3.Result and Discussion:-

The response of the PCFI is observed for a range of humidity values (27%, 30%, 40%, 50%, 60%, 70%, 80%, and 85%) RH. The position of the interference peak is found shifted within the humidity variations to the longer wavelength (red shift).The sensitivity of the sensor is calculated by dividing the experimentally measured PCFI response to the relative humidity. The Relative Humidity (RH) response of the PCFI device is studied with 6cm PCF lengths and different ambient relative humidity values (at room temperature and normal atmospheric pressure).'Figures (3)' shows the shifting of the interference peak of the reflected light from PCFI for the submitted sensors for 6cm lengths of PCF.

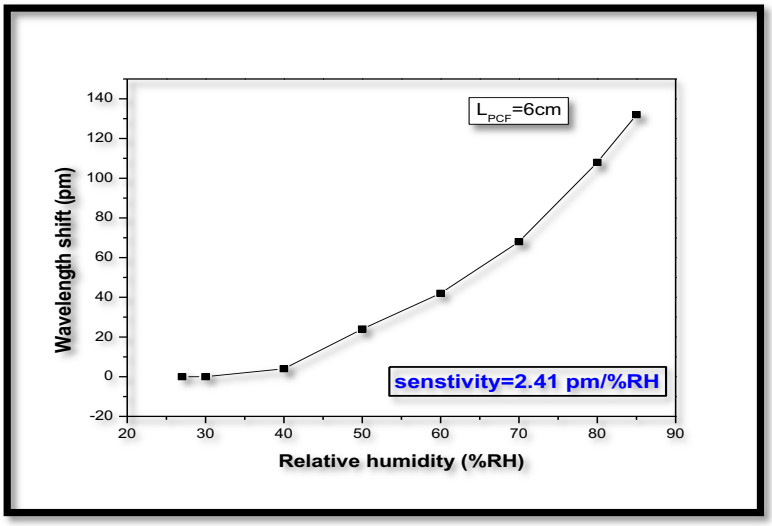

Figure3. Interference peaks shift of the sensor with respect to relative humidity,

and for 6cm lengths of PCF

From the previous figure, it is observed that there is no shifting in interference peak between (27%-40%) RH region, the shift is to appear for relative humidity value 40% RH. This is because water has hydrogen-bonded network (ice-like), which increase as relative humidity increases from 0% to 30%."The structure of liquid water starts appearing in RH range of 30-60%, while the ice-like structure continues growing to saturation [10].

The sensitivity in pm/%RH calculated from the linear fitting of relative humidity versus wavelength curve. It is observed that PCFI with length (6cm) shows sensitivity (2.41pm/%RH).

The variation of the RH sensor response at a wavelength (λ=1550 nm) to the cycle of RH-increasing and RH-decreasing, is shown in 'figure 4', RH is changed from 27% to 85%, and the PCF length is (6cm). From this figure, it can be observed that PCFI has reversibility at room temperature, its shift in reflection spectrum (after one humidity increasing/decreasing cycle) returns to the same value. Minor hysteresis is observed during the cycle.

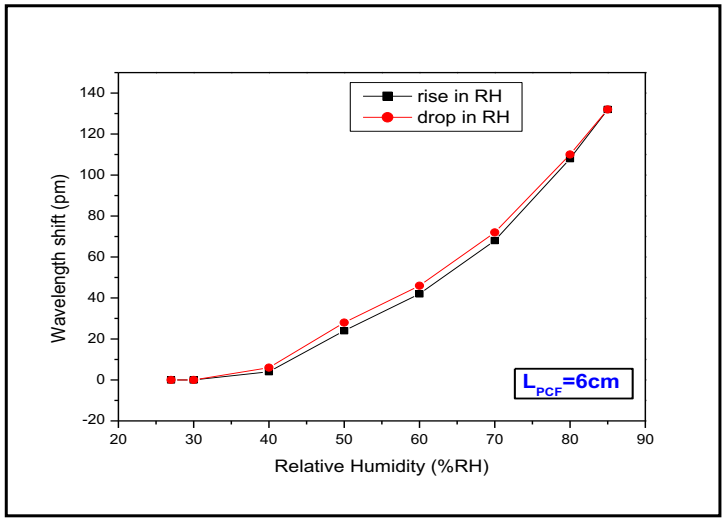

Figure4. The hysteresis loop of RH sensor with PCF length (6cm)

The reversibility is due to the fact that the adsorption is a reversible process, so the effective refractive index modulation of cladding (neff) occurs according to the values of ambient humidity which lead to change position of the interference pattern. The cladding mode effective index increases as increase in humidity, so the PCFI interference pattern shift toward longer wavelengths and vice versa. Also, the RH sensor repeatability over a large RH range (27%-85%) RH is demonstrated with the time gap of one week, and with (6cm) PCFI length, the sensor shows a good repeatability, shown in 'figure 5'.

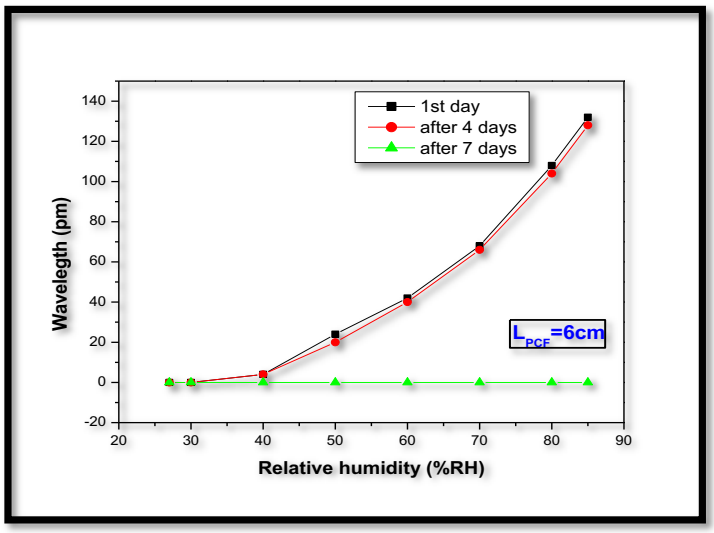

Figure5. The repeatability of the RH sensor with PCF length (6cm)

In this figure, the two curves (first day, and after 4 days) represent the measurements taken for the RH sensor with a time gap of (4 days), and they show a good repeatability for the humidity changes. This is because when the PCF is exposed to air for the first time, chemisorption happens only one time, which causes the formation of a single layer of a (Si-OH) group on the PCF surface (requires heating to desorb).

The physisorption takes place in this group, and form multiple layers of water molecules on the surface of the PCF and also it is a reversible process at room temperature in equilibrium with the ambient RH. So, under laboratory conditions the RH sensor is reusable.

Since the chamber locally made and environment nature in Iraq always contaminated generally and because this sensor depends on narrow silica microholes, so it has implications for contamination (dust particles) and degradation in varying degrees relying on the environment nature, as it clear in the behavior of the sensor after a week, as shown in the previous figure . To overcome this limitation can use different methods: recalibration sensor head after a specific period of time and then reuse of the head of the sensor during another time period, or protect the head of the sensor by attaching filters to it. The other way to remove the contaminants without damaging the sensor head and make the sensor reusable is the ultrasonic cleaning with heating.

4.Conclusion:-

Mach-Zehnder interferometer (MZI) for humidity detection based on PCF is demonstrated; this PCFI is simple and operates in reflection mode. Its fabrication involves splicing short pieces of one end of PCF (LMA-10) with SMF (Corning-28), and cleave the free end of PCF to act as a mirror, and the RH sensor does not require to using of any hygroscopic material.

The sensor sensitivity of the RH depends on the PCF length, and the sensor with 6cm PCF length has a sensitivity of the sensor is 2.41pm/%RH in the RH ranges of 40-85%. The RH sensor has reversibility at room temperature, and shows a good repeatability for humidity changes.

References:-

[1] Massaro A 2012 Photonic Crystals–Introduction, Applications and Theory InTech. (2012) 356 p.
[2] Frazao O, Santos J, Araujo F, and Ferreira L 2008 Optical sensing with photonic crystal fibers *Laser & Photonics Reviews* **2**(6): 449-459.
[3] Chen J 2010 Nanochemistry and Sensing in Photonic Crystal Fibers *Max-Planck Institute for the Science of Light* University of Erlangen-Nuremberg (2010).
[4] Pinto A M and Lopez-Amo 2012 Photonic crystal fibers for sensing applications *Journal of Sensors* 1-21.
[5] Alwis L, Sun T, and Grattan K 2013 Optical fibre-based sensor technology for humidity and moisture measurement: Review of recent progress *Measurement* **46**(10): 4052-4074.
[6] Mathew J 2013 Development of Novel Fiber Optic Humidity, Sensors and Their Derived Applications Dublin Institute of Technology.
[7] Wu Q, Semenova Y, Mathew J, Wang P, and Farrell G 2011 Humidity sensor based on a single-mode hetero-core fiber structure *Optics Letters* **36** (10), 1752-1754.
[8] Villatoro J, Minkovich V, Pruneri V, and Badenes G 2007 Simple all-microstructured-optical-fiber interferometer built via fusion splicing *Optics Express* **15**(4): 1491-1496.
[9] Villatoro J, Kreuzer M, Jha R, Minkovich V, Finazzi V, Badenes G, and Pruneri V 2009 Photonic crystal fiber interferometer for chemical vapor detection with high sensitivity *Optics Express* **17**(3): 1447-1453.
[10] David B, and Seong H J 2005 Evolution of the adsorbed water layer structure on silicon oxide at room temperature *The Journal of Physical Chemistry* B **109**(35): 16760-16763.

Enhanced photo-response of porous silicon photo-detectors by embeddingTitanium-dioxide nano-particles

Enhanced photo-response of porous silicon photo-detectors by embeddingTitanium-dioxide nano-particles

Hiba M Ali[1,2], Sameer A Makki[1], Ahmed N Abd[3]

[1]Department of Physics, College of Education for Pure Sciences/ Ibn- Al-Haithem, University of Baghdad, Baghdad ,Iraq
[3]Department of Physics, Collage of Science, Al- Mustansiriyah University/ Baghdad/ Iraq.

[1,2] hibamumtazali@yahoo.com

Abstract: Porous silicon (n-PS) films can be prepared by photoelectochemical etching (PECE) Silicon chips n - types with 15 (mA /cm2), in15 minutes etching time on the fabrication nano-sized pore arrangement. By using X-ray diffraction measurement and atomic power microscopy characteristics (AFM), PS was investigated. It was also evaluated the crystallites size from (XRD) for the PS nanoscale. The atomic force microscopy confirmed the nano-metric size chemical fictionalization through the electrochemical etching that was shown on the PS surface chemical composition. The atomic power microscopy checks showed the roughness of the silicon surface. It is also notified (TiO2) preparation nano-particles that were prepared by pulse laser eradication in ethanol (PLAL) technique through irradiation with a Nd:YAG laser pulses TiO2 target that is sunk in methanol using 400 mJ of laser energy. It has been studied the structural, optical and morphological of TiO2NPs.It has been detected that through XRD measurement , (TiO2) NPs have been Tetragonal crystal structure. While with AFM measurements, it has been realized that the synthesized TiO2 particles are spherical with an average particle size in the (82 nm) range. It has been determined that the energy band gap of TiO2 NPs from optical properties and set to be in (5eV) range .The transmittance and reflectance spectra have determined the TiO2 NPs optical constants. It was reported the effectiveness of TiO2 NPs expansion on the PS Photodetector properties which exposes the benefits in (Al/PS/Si/Al). The built-in tension values depend on the etching time current density and laser flounce. Al/TiO2/PS/Si/Al photo-detector heterojunction have two response peaks that are situated at 350 nm and (700 -800nm) with max sensitivity ≈ 0.7 A/W. The maximum given detectivity is 9.38at ≈ 780 nm wavelength.

Keyword: Titanium oxide ,XRD,AFM,thin film,photodetector, porous silicon.

1.Introduction

Titanium dioxide is a non-toxic, so metal oxide like TiO2 thin film have been a generallesson for different applications such as solar cells,photodetecter, protective coating and gas sensors [1, 2]. Pulsed laser ablation in ethanol (PLAL) has been employed to output large size of nanomaterials, which have shown a

variety of chemical, optical, magnetic, and electronic properties[3]. For fellow ship, student have centralize on the synthesis of variety materials using this technique in gas phases and liquid with solid [4-5]. Differential number for the every of nanostructures using PLAL, which depend on the precursor materials, the laser parameters and the surrounding conditions, TiO2 is a very suitable oxide material for solar cell and photodetector applications, because of its extraordinary depress ability of photogenerated holes. Thin films are prepared by different preparing methods, TiO2 is considered as one of the most important semiconductors having high photo-catalytic activity, non-toxicity and premium chemical immutability at different stipulation [6], Thin films can be deposited using several techniques such as, pulse laser ablation ,chemical vapor deposition (CVD) [7] ,spray pyrolysis [8], magnetron sputtering [9] & sol-gel [10] technique. In these methods, sol-gel methods have been notable beneficial, including thin film microstructure uniformity and low at every temperature and cost. Homogeneous layers on different substrates at low cost and it depend on the choice of refractive index and thickness of the layer by changing verbosity stipulation. Thin film crystalline size supposes for were allowed by, X-ray Diffraction (XRD) and using atomic force microscopy(AFM).

2. Experimental

The thin film silicon wafer n-type (100) with resistivity of (2-20) Ω . cm range. The silicon wafer was chemically cleaned . The substrates divided into oblong with (1.5×1.5 cm) areas and 0.1 μm thickness. All layers were precipitated through an evaporation system on the wafer. Photolectrochemical etching PECE (executes in a mixture of (1:1) / (40%) HF – Ethanol at room temperature using (Au) electrode as 15 mA/cm2 Current densities that was applied for 15 minutes etching time and the etched sample area was(0.785 cm2) as in 'figure 1'.

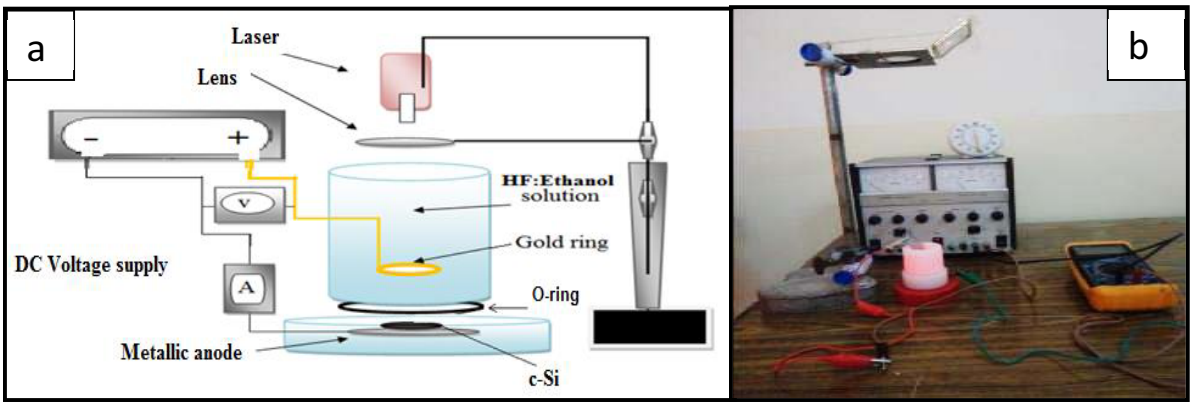

Figure 1. a) The schematic diagram of PEC system and b) The photographic image of PEC system.

'Figure 1' shows 1 and 3D AFM images of n-PS c synthesized with 15mA/cm2 current density and 15 minutes etching time. It has columnar grains and their average grain size is in the range of 82 nm. The average roughness is (2.43 nm), the AFM image of the irradiated surface exhibits coarser grind and rough surface. The RMS 2.86 nm. The 3D AFM image shows nearly uniform porous surface with valleys and hills and few grains have size larger than the others.

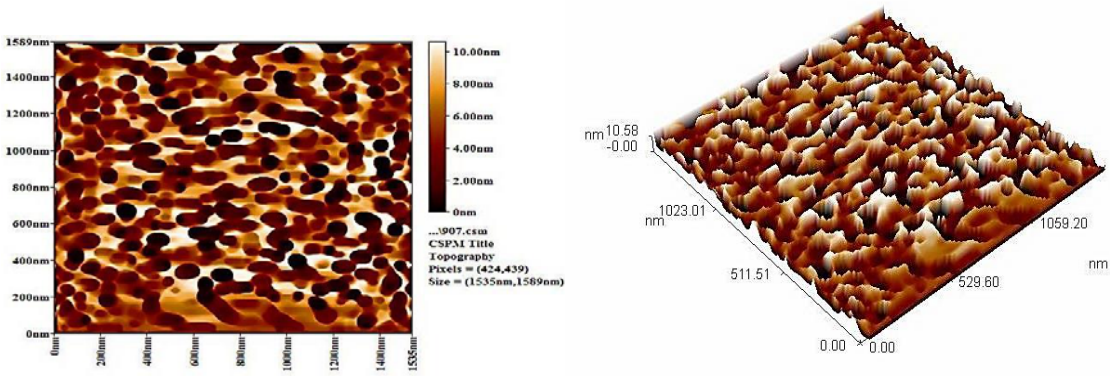

Figure 2. 2 and 3D AFM images of n-PS surface synthesized at 15 mA/cm2and 15min etching times.

Titanium dioxide nano-particles were created using TiO2 laser ablation under the bullet of (1 cm^2) diameter in methanol at room heat. The colloidal sol. Were influenced by the TiO2 pellet brilliance with Nd:YAG laser pulses that were run at λ = 1064 nm . The target was TiO2 which was set up in the filled quartz bottom (5 ml) of solution. Above the target,it was synthesized colloidal solutions by using irradiated pellet of (TiO2) with Nd:YAG laser puleses at λ= 1064 nm (HUAFEI type), It was fixed the laser fluence usage for ablation at 1.32 J/cm2 and at five minutes as in 'figure 3'.

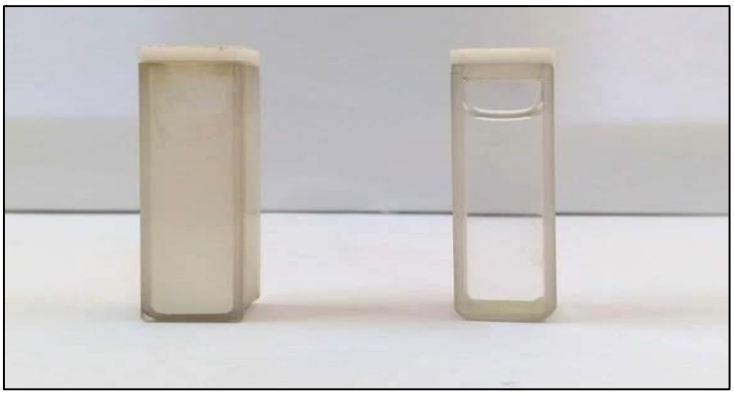

Figure 3. Methanol and Colloidal suspensions of TiO_2 at 1.32 J/cm^2 pulse laser fluence from left to right.

TiO_2 thin films were deposited on glass and n-Si substrates by by drop (5 drops) casting method, then the samples were annealed at 100°C for 1 hour . XRD-6000 was used to study the deposited films crystalline and structure. Transmission electron microscope (TEM) and (AFM) scanning probe microscope was used to study the film morphology and by utilizing UV–VIS double beam spectrophotometer, thin films absorption was measured.

3. Results and Discussion

3. 1 Structure and optical investigation of TiO2 nanoparticles morphology:

XRD analysis is managed to determine the phases and the grain size. XRD types for the investigated TiO2 sample prepared by laser ablation in ethanol and deposited on a glass substrate by the drop casting method .The XRD patterns for samples , show only nine peaks at 25.34, 37.91, 48.16, 54, 55.18, 62,79,70.39 and

75.15 corresponding to (101), (004), (200), (105), (211), (213), (216), (120) and (215) planes respectively . These results in agreement with the standard TiO_2 XRD [X-ray diffraction data file [00-021-1272]. It was accounted the crystallite size (D) by using the Scherrer's formulation. $D = 0.94\ \lambda / \beta\ Cos\theta$ [10], where λ (1.54056 Å) is the X-ray wavelength, θ is the Bragg's angle and β is the full width at half maximum (FWHM) of the diffraction peak in radians. The calculated value of D is presented in (table 1). It can be seen from the values of D that the as-grown TiO_2 layer presents a monocrystalline structure. The macrostrain $(\varepsilon)= \beta\cos(\theta)/4$ and dislocation density $(\delta)=1/D^2$ have been calculated [11] and their results are demonstrated in (table 1) : micro-strain and dislocation density where w = the FWHM and D = the crystallite size.

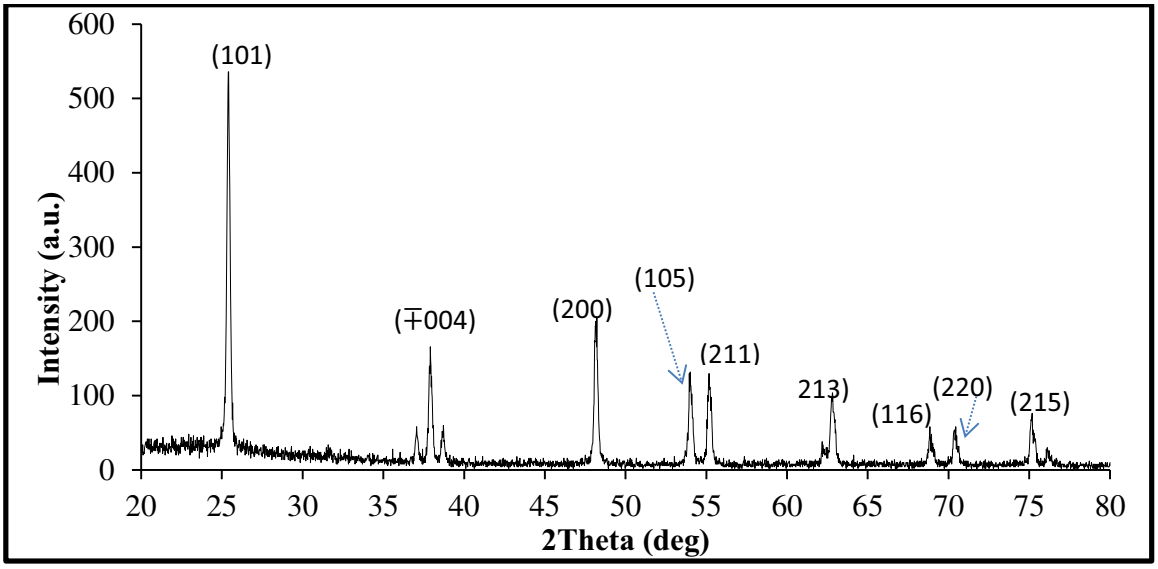

Figure 4. XRD pattern of Tio_2 films nanoparticles

Table 1. X-ray Diffraction appointment TiO2

2 Theta (deg)	β (deg)	(hkl) planes	D (nm)	$\eta\times10^{-5}$ $lines^{-2}.m^{-4}$	$\delta x10^{14}$ $(lines.m^{-2})$
25.4377	0.2308	(101)	35.09983	9.871841	8.116894
37.9183	0.212	(004)	39.42599	8.78862	6.433316
48.1607	0.2232	(200)	38.80699	8.928804	6.640184
54.0053	0.2068	(105)	42.92989	8.0713	5.426009
55.1802	0.2252	(211)	39.63381	8.742536	6.366026
62.7984	0.230	(213)	40.31191	8.595474	6.153655
68.8576	0.208	(116)	46.14684	7.50864	4.69587
70.3934	0.2087	(220)	46.42786	7.463191	4.639195
75.1598	0.2114	(215)	47.27955	7.32875	4.473561

'Figure 5' demonstrates the spectrum transition on TiO_2NPS, this transmittance reaches the maximum value 50% at the UV wavelength (280 nm) then reduces at (380 nm) and increase slowly over that, this is the feature of high nanoparticles transmittance at these wavelengths thus, the transmission increased as wavelength increased [12].

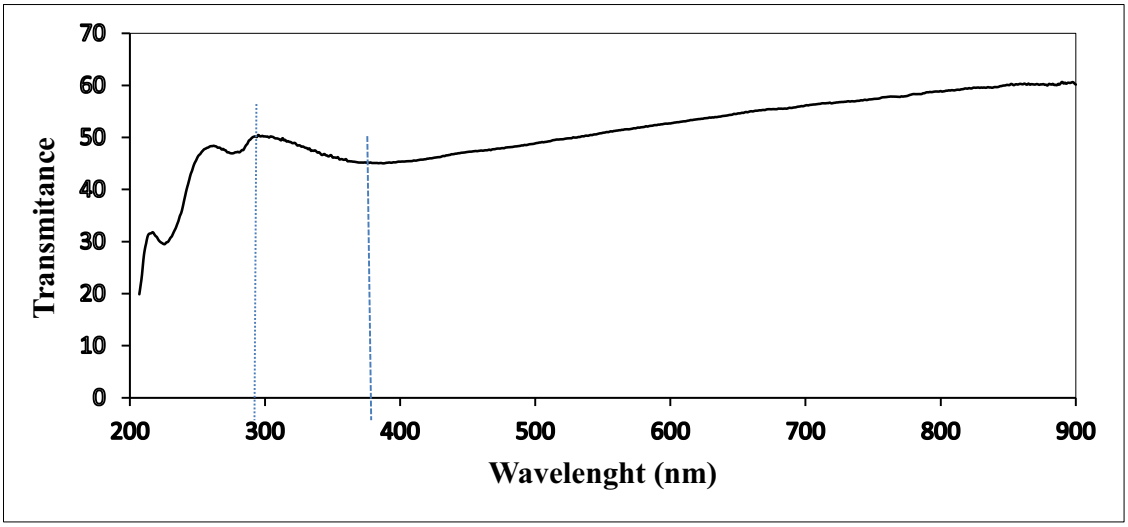

Figure 5. Optical Spectrum transmittance of TiO_2

The TiO_2 energy gaps of nanoparticles were evaluated by using Tauc relation:

$$\alpha h\nu = (h\nu - Eg\ )^{\frac{1}{2}} \quad (1)$$

Where Eg is the band gap energy, α is the absorption coefficient, A is constant $h\nu$ is the photon energy. 'Figure 6' displays TiO_2 band gap that was measured from the square plot of $(\alpha h\nu)^2$ against photon energy hν (where α = the absorption coefficient) by extrapolating the curve linear part toward the photon energy axis can be found to become (5eV and 5.7 eV). The two energy gap may refer to the absorption edge flux which is because of the energy band structure and the difference of state density with the energy level, this variation can also be assign to the low film thickness.

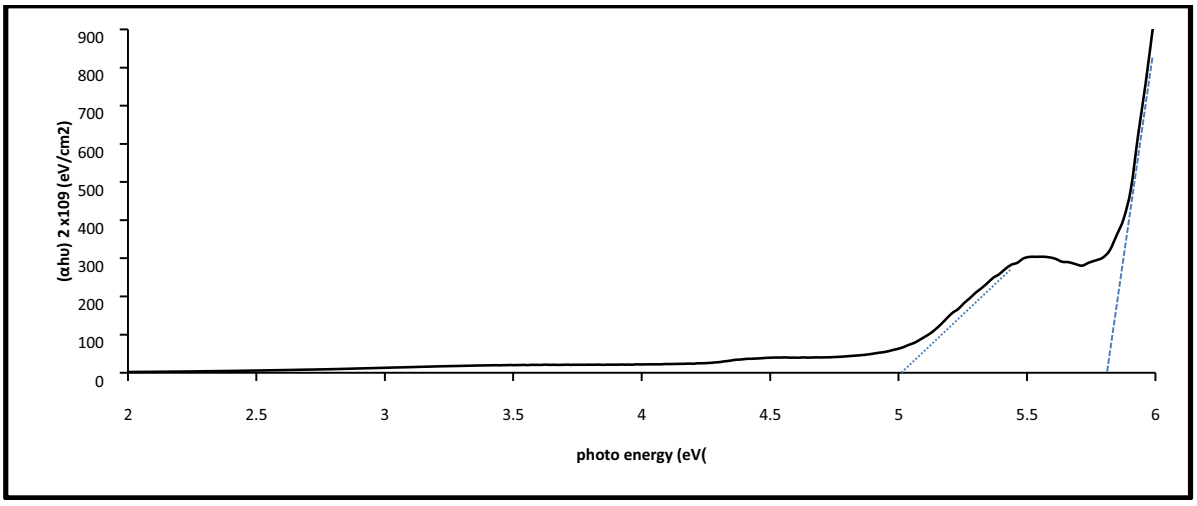

Figure 6. $(\alpha h\nu)^2$ versus optical energy gap of TiO_2 nanoparticles

'Figure 7' shows I–V features of Al / TiO_2 nano-particles layer contact prepared with 1.32J/cm^2 without any post heat at the dark room temperature. It obviously displays an ohmic contact over the whole utilized voltage range. Hall effect measurements which were carried out for TiO_2 at room temperature, these measurements assured the n-type conductivity of the collected TiO_2 nanoparticles, This is attributed to the

decreasing of titanium to the oxygen rate due to the increasing of Hall mobility. This result is in agreement with AFM and XRD results and because of the structural deficiency reducing.

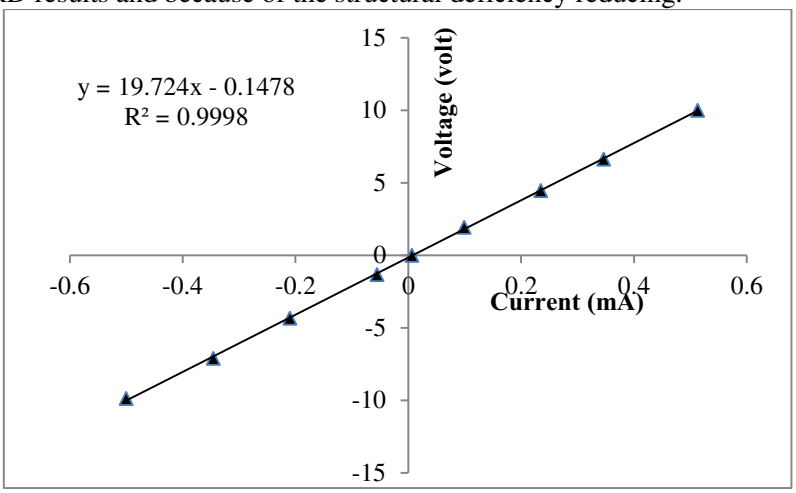

Figure. 7. Room temperature I–V characteristics of Al /TiO_2 nano-particles contact

The TEM image and particle size distributions of TiO2 NPS prepared by laser fluency are shown in 'figure 8' The TEM images show that theTiO2 NPs are well crystallized and are mostly separated. The images confirm that the particles have a spherical shape and the particle size was in the range of (44-68 nm).The production of different sizes particles at fixed laser fluency can be explained on the basis that the newly formed nanoparticles, which lie in the direction of laser radiation will have smaller sizes due to their successive interaction with laser pulses by the interpulse absorption process [13].

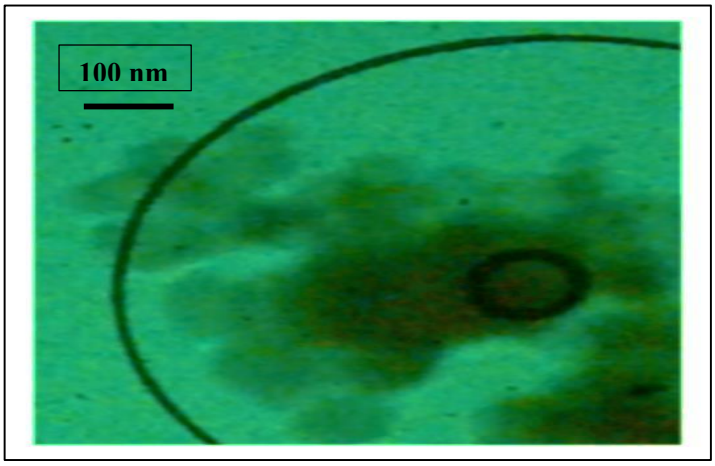

Figure 8. TEM images of TiO_2 nanoparticles

Al/TiO_2/n-Si/Al heterojunction photodetector was fabricated by using Al metal as an ohmic contacts. The capacity measuring is considered as a function of inverse voltage (C-V) to Al/TiO_2/n-Si/Al structure that were done by using (LCZ) meter at (10 kHz). Width of the depletion layer and charge-carrier density (N_d) for the two devices are studied by using the 'as in equation (2)'[14].

$$W = \sqrt{\left(\frac{2\varepsilon_{PSi}}{qN_d}\right)V_{bi}} \quad (2)$$

$$N_d = \frac{2}{q\,\varepsilon_{PSi}\,\varepsilon^2}.\frac{dV}{dc^{-2}} \quad (3)$$

(ε_{PSi}) is the dielectric constant, dV/dc^{-2} is the tendency revers. For current–voltage measurements, a (UNI-T-UT33C digital electrometer, Tektronics CDM 250 multimeters and double Farnel LT30/2, from (0 - 10V) were utilized. Spectral responsivity measurement was performed using a monochromator (Joban-Yvon monochromator) running at (200-900) nm wavelength range, while the current measurement was achieved by using a 8010 DMM Fluke digital millimeter. Capacitance-voltage characteristics of Al/TiO_2/PS/n-Si/Al is shown in Figure 9 under different reverse ranging (0-6)V. This figure shows that the capacitance decrease with increasing the supplied reverse voltage, it is noticed that the capacity decreases (non-linear) with increasing the reverse alignment voltage 'as in equation (2)'.This attitude refers to the depletion region width increasing, this in turn leads to decrease the capacity at the junction sides.

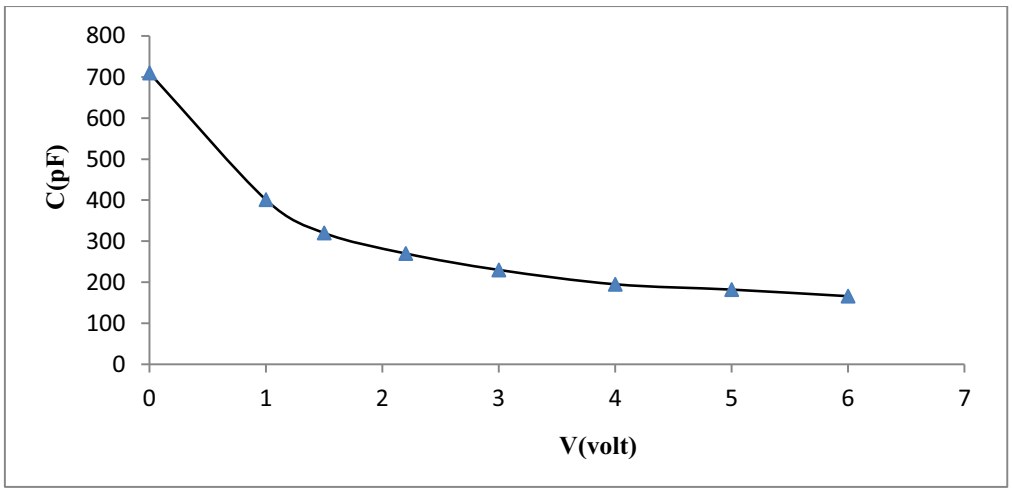

Figure 9. (C-V) Characteristics plot for Al/TiO_2/PS/n-Si/Al Hetrojunction

Capacitance- Voltage properties can be employed to estimate and calculate, heterojunction most important Parameters, such as built-in – voltage (V_{bi}) , depletion region, Carrier concentration , which clear idea concerning . The charge distribution, though out the lager C-V characteristics.

Shown in 'Figure 10 'which represents a linear relation the inverse of the square of capacitance ($1/C^2$) versus the reverse bias voltage for Al/TiO_2/PS/n-Si/Al a linear relation is observed in both cases. Also, it can be noticed from the figure Al/TiO_2/PS/n-Si/Al Will be affected by the application of reverse bias , that the depletion region seems to be extended , inversely it will be getting smaller thickness when forward bias will be applied . The depletion can be treated as a capacitor, with capacitance, C.

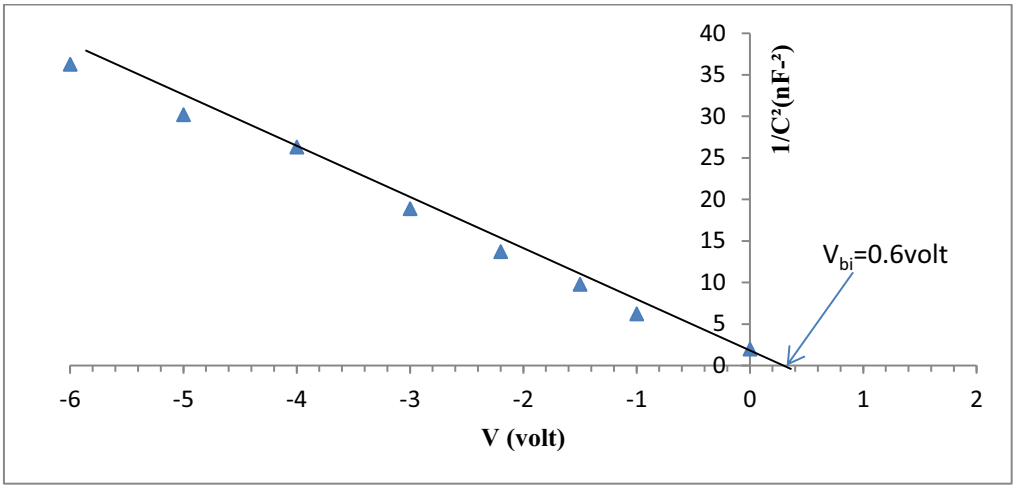

Figure 10. $1/C^2$ versus reverse voltage of Al/TiO_2/PS/n-Si/Al Heterojunction

'Figure 11' shows the I-V dark features in both directions (forward and reverse) of Al /TiO_2/PS/n-Si/Al photo-detector that is designed with 15 mA /cm2 current density and constant etching time of 12 minutes. The forward current of all photo-detector is very poor at voltages less than 0.6 V. This current known as reassembly current that takes place at low voltages only. It is created when each electron is excited form valence band in order to obtain the balance back. The second zone at high voltage demonstrates the spreading or bending area, which depends on crowded resistance. In this zone, the chafe voltage is able to deliver electrons with sufficient energy for penetrating the barrier between the two cross sides.

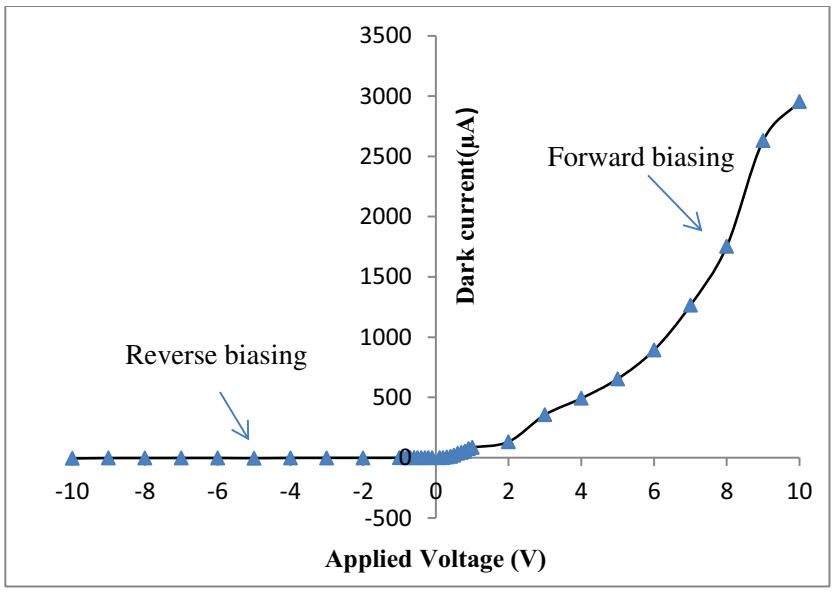

Figure 11. I-V characteristic under forward reverse bais of the Al/TiO2/PS/n-Si/Al

The best features for photodetector heterojunction are the optoelectronic ones, as the incident light power converts to photocurrent can be determined by these features. It can see in figure 12 the invert current-voltage features of the device Al/TiO2/PS/Si/Al that are measured in dark and under diverse light intensity glow, the photo-current under (40 W/m^2)Tungsten lamp lighting. It can be noticed that the inverse current

value at a given voltage for Al/TiO2/PS/Si/Al heterojunction under illumination can be higher comparing with in the dark.

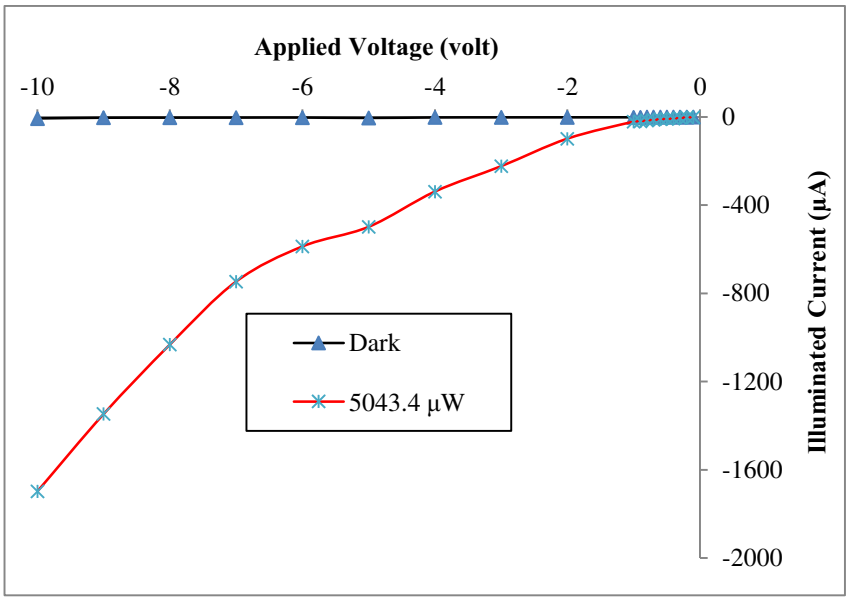

Figure 12. Dark and illuminated (I-V) characteristic of Al/TiO2// PS/n-Si/AL Photodetector.

It is inspected the spectral structures responsive through the wavelength range of (200–900) nm with 4V bias , as in equation (4)' [15]:

$$R_\lambda = \frac{I_{ph}}{P_{in}}(\text{A/W}) \quad (4)$$

As (I_{ph}) = the photo-current and (P_{in}) = the input power.

The structure of TiO_2/PS/n-Si consists of two heterojunction, the first heterojunction is between the TiO_2 layer and porous siliconTiO_2/PS and the second heterojunction is made between the porous silicon layer and crystalline Silicon (PS/Si) . Thus TiO_2 /PS/n-Si have two depletion regions.

Figures 13 display the spectral responsive plots as a wavelength function TiO_2/ PS / n-Si structure prepared at etching time 15 min and 15 mA/cm^2 current density. In figure 11 it can see the spectral response curve of TiO_2 / PS / n-Si containing two response peaks ; the first one is situated at (252 nm) because of the absorption edge of TiO_2 nanoparticles , where's the second one is placed at (780nm) because of the silicon absorption edge.

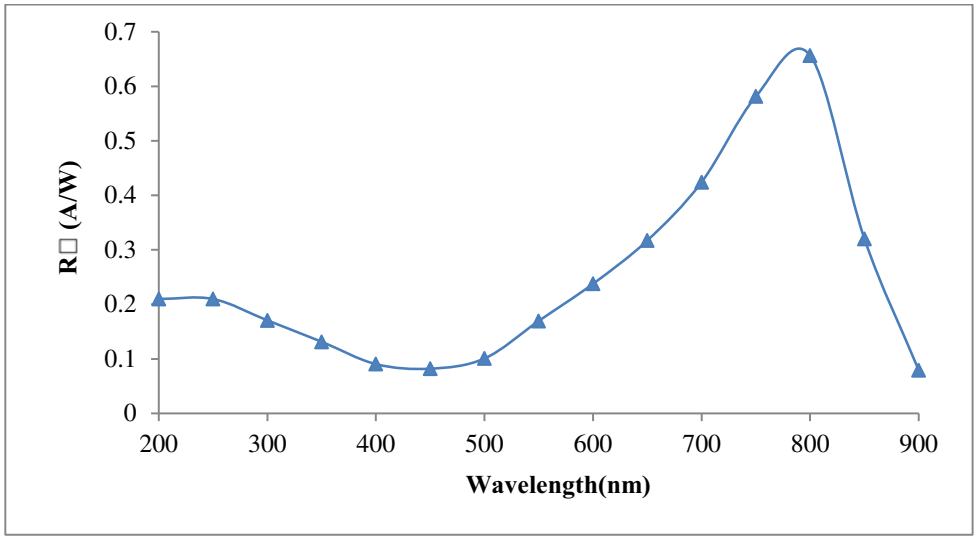

Figure.13. Responsivity as a function of TiO_2/PS /n-Si photo-detectors wavelength.

Deteectivity is reciprocal noise equivalent power of detectors since it depends on the detector area. In order to supply a" Figure of Merit" factor that depends on the actual detector properties, not on how large it occurs .It a term called detectivity that takes the formation [16]:

$$D_\lambda = \frac{1}{NEP} = \frac{R_\lambda}{I_n} \quad (5)$$

(I_n) = noise current and it can occaionaly be expressed as:

$$D_\lambda = \frac{S/N}{P_{in}} \quad (6)$$

S = the signal, N = the noise and P_{in} = the input power .

The symbol D_λ represents detectivity and can be stated as D-star that is known (NEP square value)

$$D_\lambda = R_\lambda \frac{A^{1/2}.\Delta f^{1/2}}{I_n} \quad (7)$$

$$I_n = \sqrt{2qI_d}\sqrt{\Delta f} \quad (8)$$

Δf = the noise bandwidth. D_λ is independent of the detector area. Therefore the directivity can measure the radical quality of the detector material itself. When a D_λ value for an optical detector is measured, this is generally measured through a system where the incident light is modified or divided at a frequency (f) in order to make an AC signal, which is later enlarged with an extention band-width Δf. These quantities should be specific. The subordenation of $D_\lambda$on the wavelength (λ) and the marking D_λ(λ, f, ΔF) can express the frequency where the measurement and the bandwidth are made. So the reference band-width is often (1Hz). The D_λ (λ, f, ΔF) units refer to the detector that is proper to detect weak signals in the noise existence [17]. The importance parameters for photodetector are the certain detectivity which perform a low detectable power. Therefore; the detector display is similar with this parameter. In figure (14) it can see the specific detectivity as a function of wavelength for TiO_2 /PS /n-Si Photo-detectors at 15 minutes of etching time and 15 mA /cm^2 current density.

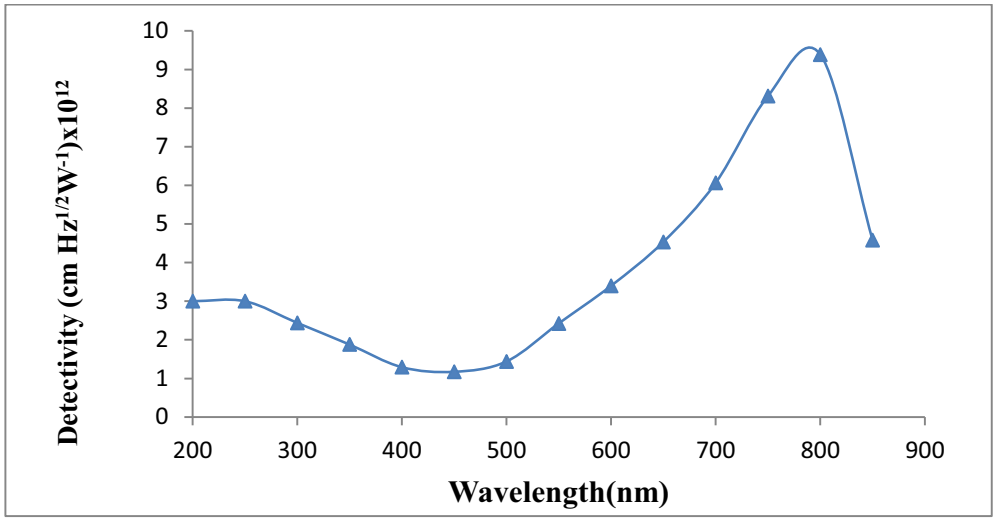

Figure 14. Spectral detectivity plots for TiO_2 PS/n-Si photodetector.

4.Conclusions

By using laser eradication in methanol at 400 mJ laser flunes,TiO2 NPS were in nanosized. The optical characteristic detected that theTiO2 NPS band gap was specified by the quantum size effectiveness. (XRD) measure exposed that the TiO2 NPS was polycrystalline and had only the tetragonal crystal structure.

TiO2NPS deposition onto PS developed the properties, porous photodetectors. The Al/TiO2/PS/Si/Al photo-detector spectral responsivity was found to be (0.7 A/W) at Dλ 780 nm wavelength because of the silicon absorption edge and porous silicon, was about (0.2A/W) at λ= 200 nm wavelength due to the TiO2 NPS absorption edge. The highest value of the specific detectivity (Dλ) was pointed to be 9.38 X 1012 W-1 .cm.Hz-1 and situated at (780 nm) wavelength for Al/TiO2/PS/Si/Al photodetector.

References

[1] Chen X and Mao S S 2007 Titanium dioxide nanomaterials: synthesis, properties, modifications, and applications Chemical Reviews **107** pp 2891-2959
[2] Fujishima A, Rao T N and Tryk D A 2000 Titanium dioxide photocatalysis. *Journal of Photochemistry and Photobiology C*: Photochemistry Reviews **1** pp 1-21
[3] Kumar M and Kumar D 2010 The Deposition of Nanocrys-talline TiO2 Thin Film on Silicon Using Sol-Gel Tech-nique and its Characterization Microelectronic Engi-neering **87** 3 pp 447-450
[4] Tian J, Chen, L, Dai J, Wang X, Yin Y and Wu P 2009 Preparation and Characterization of TiO2, ZnO, and TiO2/ZnO Nanofilms via Sol–Gel Process Ceramics International **35** pp 2261-2270
[5] Morteza S G and Alireza R B 2008 High Transparent Sol- Gel Derived Nanostructured TiO2 Thin Film *Materials Letters* **62** pp 361-364
[6] Dong J K, Sung H H, Sung H O and Eui J K 2002 Influence of Calcination Temperature on Structural and Optical Properties of TiO2 Thin Films Prepared by Sol-Gel Dip Coating. *Materials Letters* **57** pp 355-360
[7] Jiaguo Y, Xiujian Z and Qingnan Z 2001 Photocatalytic Activity of Nanometer TiO2 Thin Films Prepared by The Sol–Gel Method Materials Chemistry and Physic **69** pp 25–29
[8] Gong W, Zheng Z, Zheng J, Hu X, and Gao W 2007 Water soluble CdS nanoparticles with controllable size prepared via femtosecond laser ablation *J. App. Phys*. **102** 6

[9] Tian J, Chen L, Yin Y, Wang X, Dai J, Zhu Z, Liu X and Wu P 2009 Photocatalyst of TiO2/ZnO Nano Composite Film: Preparation, Characterization, and Photodegradation Activity of Methy Orange. Surface & Coatings Technology **204** pp 205-214
[10] K Girija, S Thirumalairajan, S M Mohan and J Chandrasekaran 2009 Structral, Morphological and Optical Studies Of CdSe Thin Films From Ammonia Bath *Chalocogenide Letters* **68** pp 351-357
[11] D. A. Sheikh, S. J. Connell and R. S. Dummer 2008 Durable silver coating for Kepler Space Telescope primary mirror Proc. Of SPIE 7010
[12] J D Wolfe, N L Thomas, 2000 Durable silver coating for mirrors US Patent 6 078 **6** p 25.
[13] C T Chu, P D Fuqua and J D Barrie 2006 Corrosion characterization of durable silver coatings by electrochemical impedance spectroscopy and accelerated environmental testing *Appl. Opt*. **45** 7 pp 1583-1593
[14] S F Pellicori 1980 Scattering defects in silver mirror coatings *Applied Optics* **19** 18 pp 3096-3098
[15] Kocareva T, Grozdanov I, Pejova Ag and AgO 2001 Thin Film Formation in Ag+ -Trieth-anolamine Solutions*, Materials Letters* **47** pp 319-323
[16] K Girija, S Thirumalairajan, S M Mohan and J Chandrasekaran 2009 Structral, Morphological And Optical Studies Of CdSe Thin Films From Ammonia Bath *Chalocogenide Letters* **6** 8 pp 351-357

Design of Light Trapping Solar Cell System by Using Zemax Program

IOP Conf. Series: Journal of Physics: Conf. Series **1003** (2018) 012074 doi:10.1088/1742-6596/1003/1/012074

Design of Light Trapping Solar Cell System by Using Zemax Program

A B Hasan[1] , S A Husain[1]

[1]physics department, College of education for pure sciences-Ibn Alhaitham, University of Baghdad, Iraq

Abstract : square micro lenses array have been designed (by using Zemax optical design program) to concentrate solar radiation into variable slits that reaching light to solar cell . This technique to increase the efficiency of solar system by trapping light due to internal reflection of light by mirrors that placed between upper and lower side of solar cell, therefore increasing optical path through the solar cell, and then increasing chance of photon absorption.
The results show priority of solar system that have slit of (0.2 mm) , and acceptance angle of (20°) that give acceptable efficiency of solar system .

1. Introduction

solar concentrators are most important solar system that deal with solar radiation and incident angle to increase efficiency. There are many configurations of solar concentrator designs, all of them reduce the effective area of receiving surface, one of those configurations is trapping light system [1]. Trapping light system uses holes or slits as a radiation windows to the system, also uses mirrors to increasing internal reflection of radiation into the system and don't escape to outside of it.

In this work; trapping light concentrator system (figure 1) has been designed, including square micro lenses array (20X20 lenses) has area (20 cm^2) with packing factor (100%) concentrate light at focal plane where a diaphragm (with slits) is placed to allow light passing through it and reaching the solar cell. The internal side of diaphragm has mirror to achieving internal reflections, and increasing optical path, consequently increasing photons absorption [2].

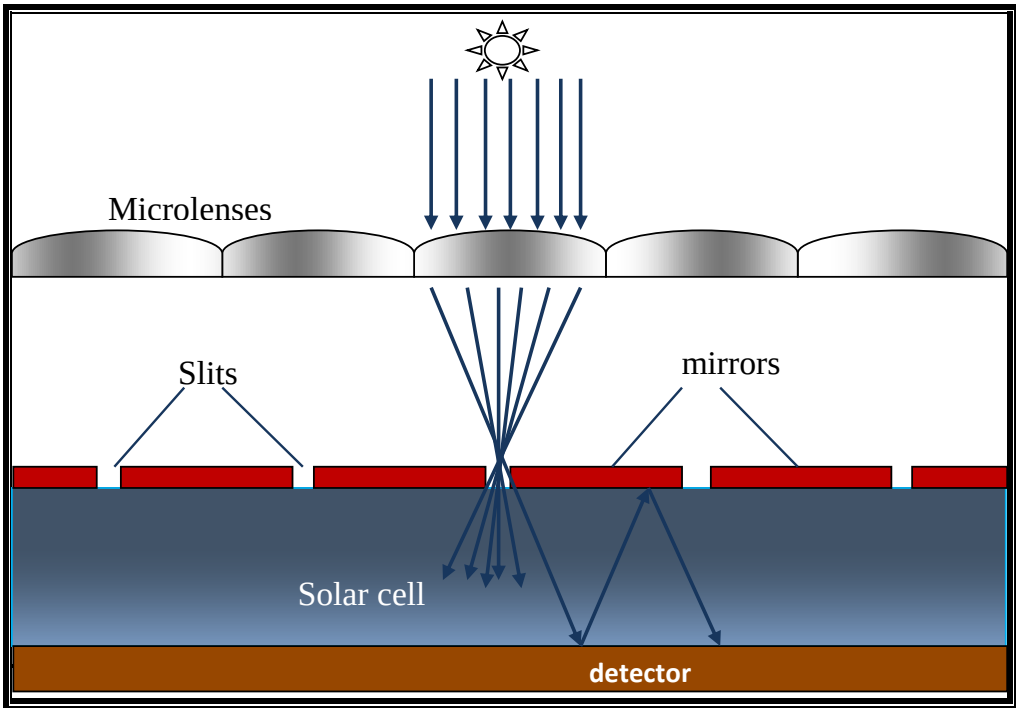

Figure 1: trapping light concentrator system

Trapping light system has been interested by researchers and designers, because of its importance to improve solar systems. J. Gjessing investigates the potential for light-trapping in thin silicon solar cells by the use of various photonic crystal back-side structures [3]. Jason H. Karp and Joseph E. Ford used a conventional concentrator photovoltaic (CPV) systems focus sunlight directly onto a PV cell micro-optic waveguide concentrators sunlight is coupled directly into the waveguide without absorption or wavelength conversion [4]. K. Tvingsted et al, demonstrate a novel light trapping configuration based on an array of micro lenses in conjunction with a self aligned array of micro apertures located in a highly reflecting mirror[5].

2. Optical design

zemax optical design program has been used to design the trapping light concentrator system, by using non sequential ray tracing mode of (1000) analyses rays and power of (1 watt). The total ray that strike the bottom of the cell and the optical power was detected by detector that fixed beneath the cell, also it has the same dimensions of the cell.

The type of borosilicate crown glass (BK7) has been used to designing lenses array, because of it has broad spectral transmission and highly environmental resistance. Despite of square lenses not favorable for imaging system because it has more aberrations than circular lenses, but it has perfect packing factor (100%) that is important in non-imaging system (solar concentrator), which the aberration is not considerable in system like that.

Crystalline Silicon has been used to designing solar cell, which has band gap matching photon energy of solar radiation that reaching the earth.

3. Results

there are many tools in zemax to evaluate design efficiency . The most important tools is the detector viewer that used in non-sequential ray tracing mode. It measures total incident rays hit the detector, and irradiance distribution that illustrate the optical power in unit area. Also detector give a picture about homogeneity of ray distribution.

Figure (2) illustrate detector measurements (T.H) of trapping system have different width of slits for variable incident angle. This procedure to evaluate effect of slits width of the system, and evaluate effect of incident angle and acceptance angle that is very considerable for solar concentrator systems, because sun position is vary during the day and must used maximum angle that give a good efficiency (acceptance angle).

Figure (2) shows different slit width (0.1 – 1 mm) with different incident angle (0^o – 70^o). It shows maximum values of detector measurements at normal incident angle (0^o) of all used samples and acceptance angle of (25^o), and shows curves degradation at increasing incident angle, this is normal effect because of design configuration that has narrow slits allow a certain ray direction to pass through into the system.

Figure (2) illustrates priority of slit (0.1 mm) and then (0.2 mm) and so on. Because the narrower slit make maximum trapping so decreasing ray escaping chance out the system.

Figure (3) illustrates detector measurements for trapping solar system has different thickness (1 – 5 mm) of solar cell at different incident angle. the difference of cell thickness may be used in multi layers cell that has broad spectral absorption. The figure shows priority for cell sample of thickness (1 mm) and decreasing the detector measurements by increasing incident angle.

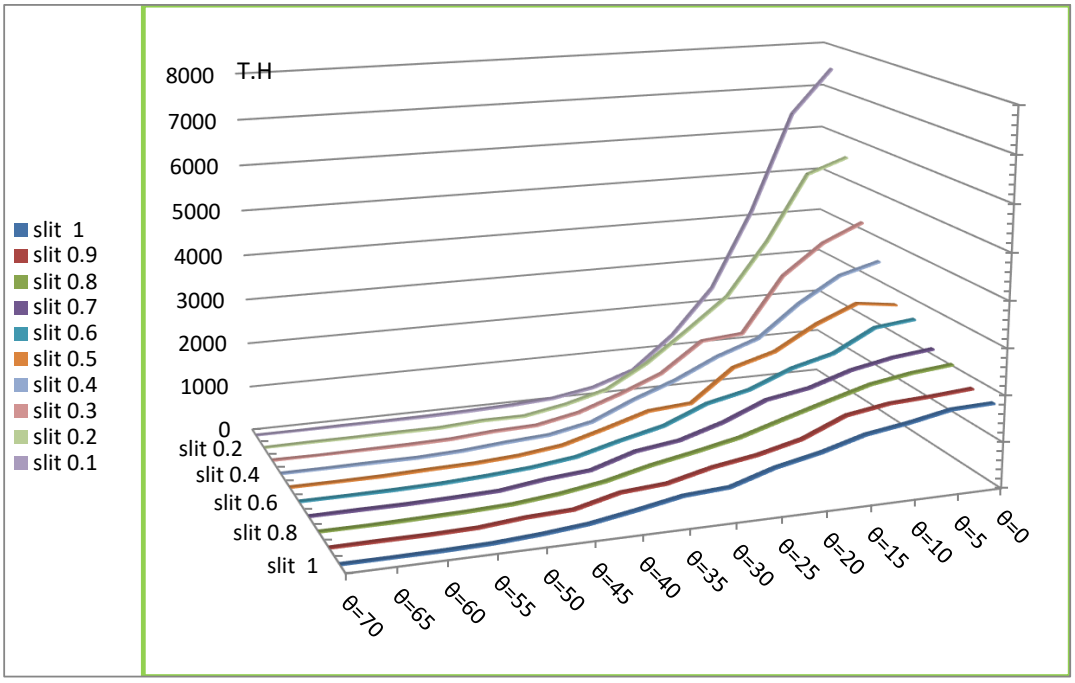

Figure (2): detector measurements of trapping solar system has different slit width for different incident angle.

Figure (4) illustrates the relation between slit width and cell thickness. It shows detector measurements in all samples gradually decreases when increasing values of slit width and cell thickness.

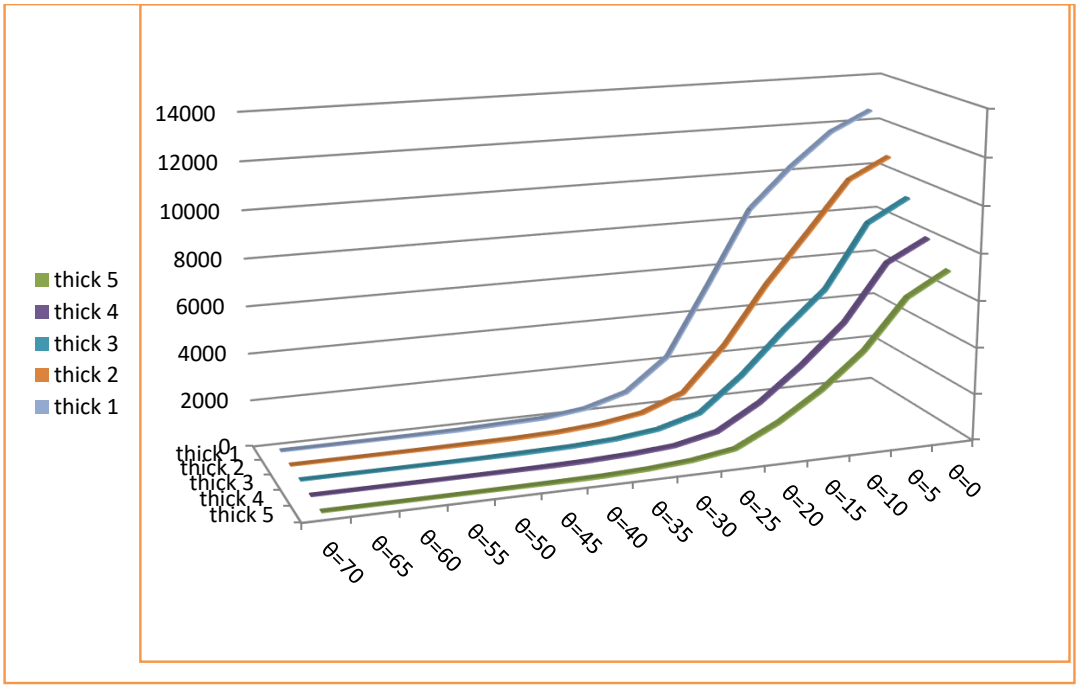

Figure (3): detector measurements of trapping solar system has different cell thickness for different incident angle.

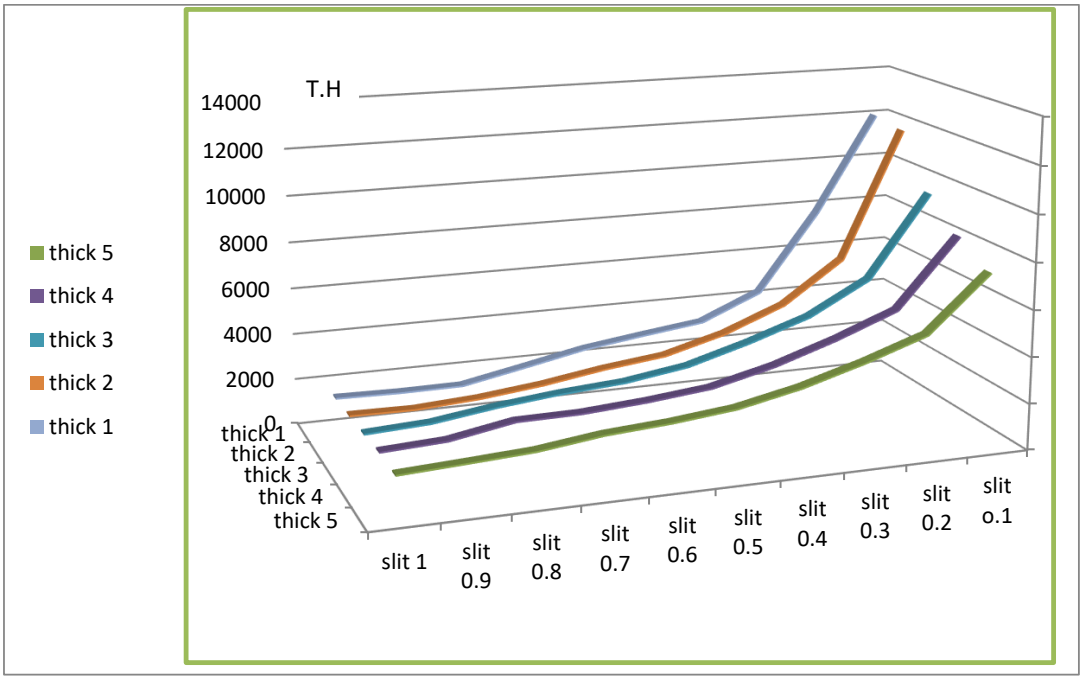

Figure (4): the relation between slit width and cell thickness

Figure (5) illustrates total optical power the reach the detector of trapping solar system have different slits width at different incident angle. It shows maximizing the power in all samples, but gradually decreases when increasing values of slit width and incident angle.

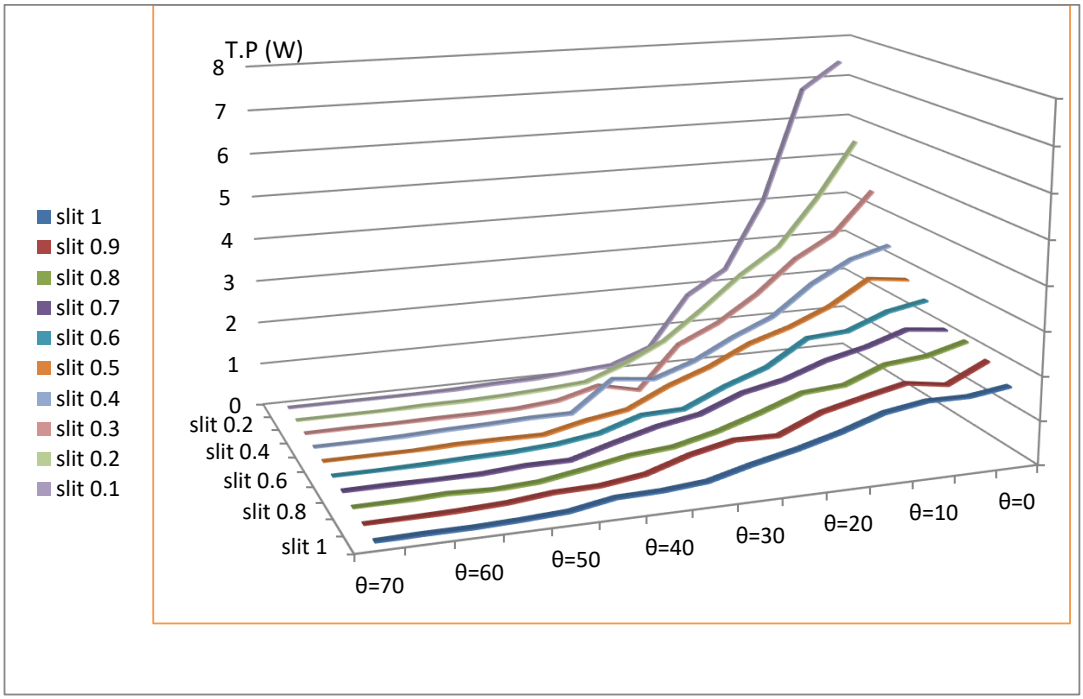

Figure (5): optical power of trapping solar system has different slit width for different incident angle.

Figure (6) shows the irradiance distribution (E_e) on the detector of samples that has different slit width at different incident angle. It shows slightly variations of irradiance distribution for all samples, because of design configuration nature that give internal reflections at all different samples.

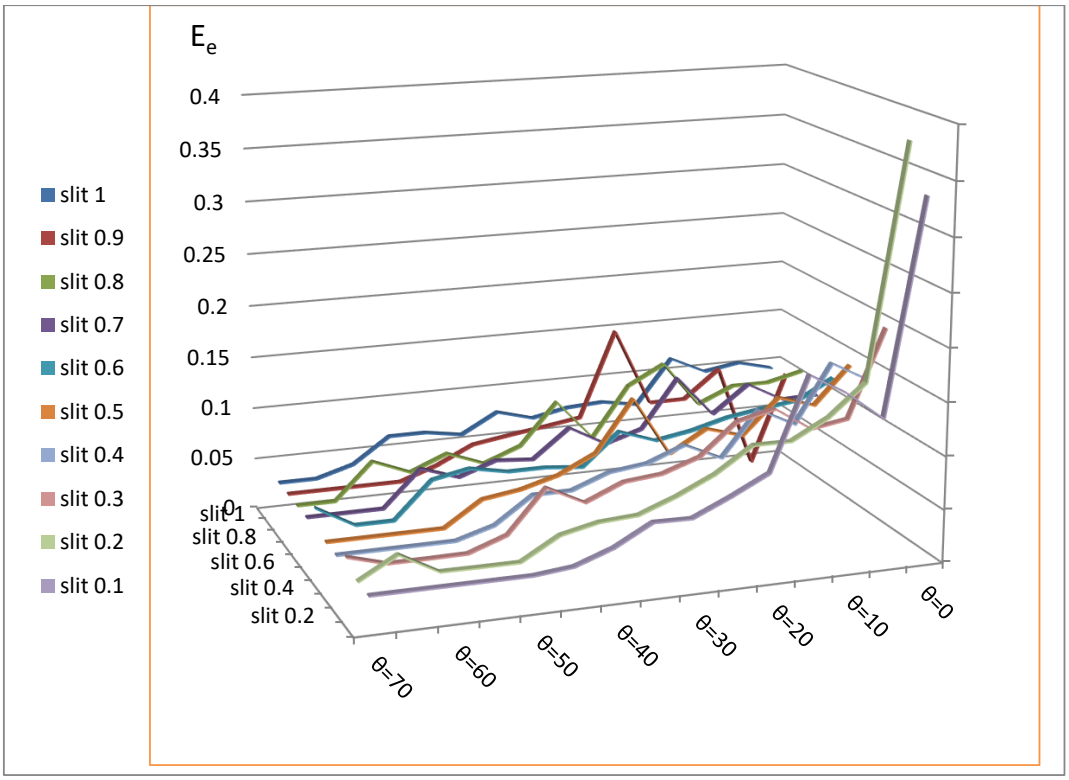

Figure (6): irradiance distribution of trapping solar system has different slit width for different incident angle.

References

1. P. M. Stella, D. G. Nieraeth, (Validation of the SCARLET Advanced Array on DSl). California Institute of Technology, Pasadena 1998.
2. Likai Li , Allen Y. Yi, (Design and fabrication of a freeform microlenses array for uniform beam shaping), Microsyst Technol vol. 17, pp. 1713–1720, 2011.
3. J. Gjessing, (Photonic crystals for light trapping in solar cells). Thesis submitted for University of Oslo, October, 2011.
4. Jason H. Karp and Joseph E. Ford, (Planar micro-optic solar concentration using multiple imaging lenses into a common slab waveguide), Proc. of SPIE Vol. 7407, 2009.
5. K. Tvingstedt, S. Dal Zilio, O. Inganäs1 and M. Tormen (Trapping light with micro lenses in thin film organic photovoltaic cells) Optical Society of America Vol. 16, No. 26, 2008

Practical Study for the Properties of Hueckel Edge Detection Operator

Practical Study for the Properties of Hueckel Edge Detection Operator

Hameed M Abdul Jabbar, Amal J Hatem, Inbethaq M A Abdul Ameer

Physics Department, College of Education for Pure Science (Ibn Al-Haitham), University of Baghdad, Iraq.

Abstract. The first practical study for the Hueckel edge detection operator was presented in this research, where it is tested on standard step edge set images. A number of criteria were adopted to evaluate its practical performance, which is the accuracy in detecting the edges direction, the error in the edges location (dislocation), edges width, the calculated edge goodness criterion and the consumed execution time. These criteria were studied with the edge direction and the used disk radius of the Hueckel edge detection operator. Important notes were recorded for the performance of this operator depending on the direction of the edge and/or with the radius of the used disk. There is a variation in the performance of the operator in terms of precision in detecting of the edges direction and position. A discussion was presented for the all criteria adopted in the research.

1. Introduction

Edge detection is an important field in the image processing science as a pre- or post-processing step since the edges play a major part in the recognizing the objects in the human vision. Many edge detectors are proposed in the literature that vary in its concept or complexity, but in general, they are classified into two groups [1]. The gradient edge detectors and the fitting edge detector, the first group is widely used in the image processing analysis, since it is easy to implement and they don't consume a lot of the computer resources. But they suffer from major fault, which is their sensitivity to the presence of noise, where their ability to detect the edge degrades dramatically [2]. The other group (fitting edge detection), they are designed to override the sensitivity to the presence of the noise, but their algorithms are complex and consume a lot of the computer resources comparing to the gradient edge detector group, therefore, they are used rarely in the image processing fields [3].

Hueckel edge detector is one of the famous detectors in the fitting edge detector group, its algorithm published by Hueckel, but he didn't reveal its full derivation [4 and 5]. Few researchers mentioned Hueckel edge detector in their literature and very fewer how tries to analysis it, therefore, Hueckel edge detector suffers from the lake in analysis especially in the practical studies in spite of some researchers try to analyze it theoretically [6 and 7], but it still needs more analysis.

This study tries to put some insight on the Hueckel edge detector performance in the practical approach that didn't study by other researchers.

2. Research Methodology

The restrictions and conditions that adopted by Hueckel in his papers [3 and 4] are adopted in this research besides other restriction, which are:

- In 'figure 1', eight standard step edge images set created that represent the edges in the directions 0^o, 30^o, 45^o, 60^o, 90^o, 120^o, 135^o and 150^o to be used in this study.

Figure 1. Standard step edge of the images set for the edge directions 0º, 30º, 45º, 60º, 90º, 120º, 135º and 150º respectively

- The value 0.9 for the edge goodness is considered as a threshold value for detecting edges.
- To nullify the rounding error of the periphery of the disk, the area of the sliding window outside the disk is considered to be equal to the void area inside the disk, where the following empirically equation is used (disk radius = 0.53305 × slide window size).
- All possible edge directions are considered in the Hueckel algorithm (the one-degree angular difference is used).
- The range (2-9) pixel is used for the sliding window size in the Hueckel edge detection algorithm with a single pixel difference between two successive sliding windows, which represent the range.

The perfect edge for these images is calculated using a logical condition to locate it since the test set images are binary. 'Figure 2' shows the perfect calculated edges.

Figure 2. Standard images edges calculated using logical condition for the edge directions 0º, 30º, 45º, 60º, 90º, 120º, 135º and 150º respectively

These edges are used as a reference to qualify the edges that founded by using Hueckel edge detection algorithm.

3. Results and Discussion

The set the standard step edge images are used in the Hueckel edge detection and the following edge parameters are calculated:

3.1. Edge Detectability

Applying Hueckel edge detection algorithm on the standard set images of the step edge image for different disk size can be summarized using figure 3, where the number of the detected points that classified by the Hueckel algorithm as edge points, from it we can notice the following:

i) Hueckel edge detection can be used to detect edges starting from the disk radius R=1.5992, and its efficiency increases with disk radius.

ii) The number of the detected edge point has a forward relationship with the disk size and the number keep increasing with the disk radius tell it to give the edges an exaggerated shape.

iii) The length of the detected edge is shortening with the disk radius by comparing with the edge length that detected using logical conditions. This is expected since no extended in the image dimension are applied in this research, therefore, a number of the image rows and columns will neglect in order to operate Hueckel algorithm.

To overtake the exaggerated shape of the detected edge, a customized simple (2×2) element erosion morphological thinning operator is applied to remove the excessive points. The customization in the erosion thinning operator is made to maintain the straightness of the thinned edge (without branching in the edge ends), 'figure 4' illustrates the edges before and after the thinning process, which will have adopted in the rest of this research.

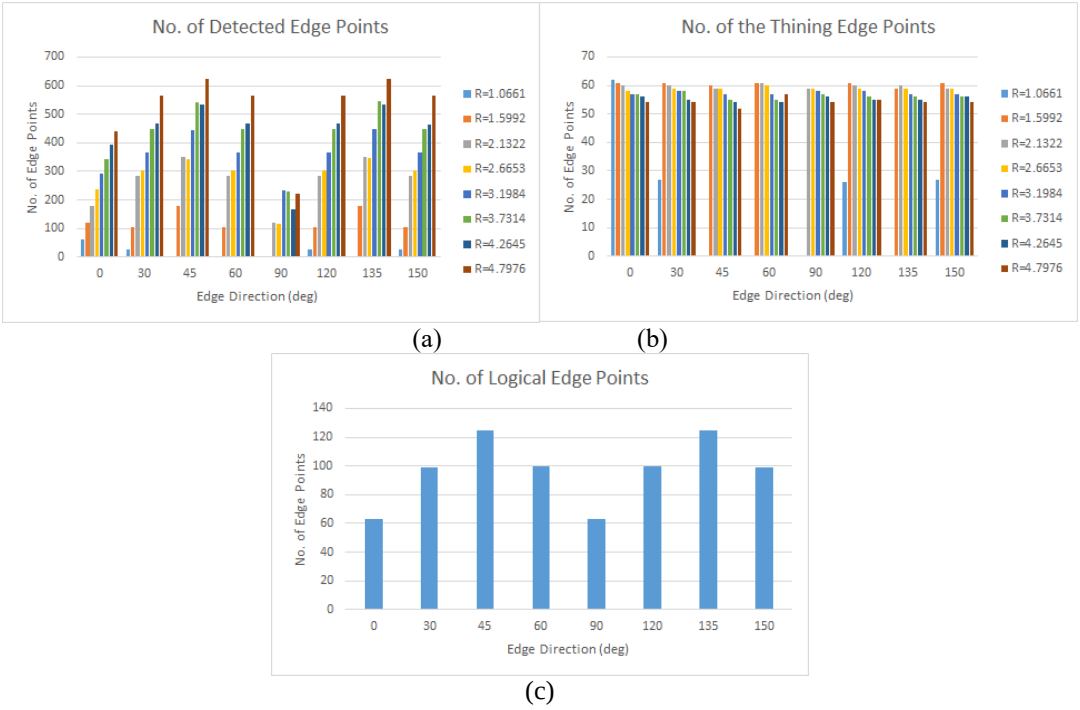

Figure 3. Number of the edge points: (a) the direct results after applying Hueckel algorithm, (b) after erosion edge thinning, (c) the real number of edge points detected using logical conditions.

Figure 4. Hueckel edge detection algorithm results: a) for angle 0, slide window size 6, b) its standard simple element erosion thinning, c) the customized simple element erosion thinning, d) for angle 150, slide window size 8, e) its standard simple element erosion thinning, c) the customized simple element erosion thinning.

After thinning process, the number of the edge points stabilized regarding the number of the detected edge points or the disk radius, except for the reduction in the detected edge length that mentioned in mentioned in (iii).

3.2. Edge Direction Accuracy

The edge direction for the edges images set was calculated for different disk size. Hueckel algorithm for some edge direction gives a range of number that related to that edge direction instead of giving a unique edge direction, therefore, the mean and the standard deviation (STD) of edge direction for points that belong to the founded edge are calculated, see ‘figure 5’.

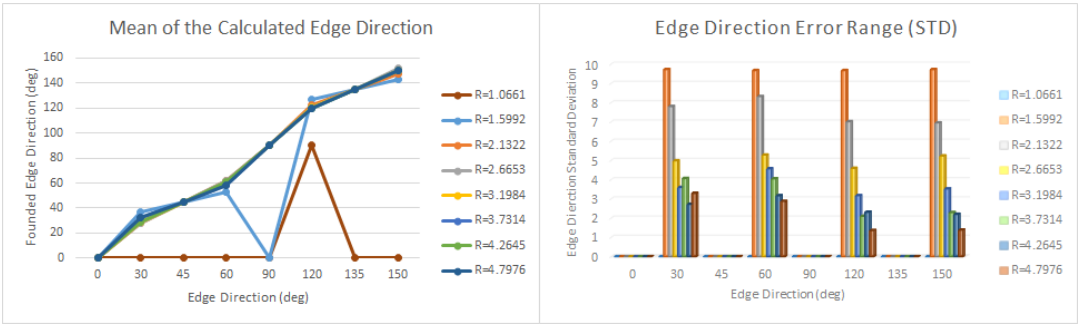

(a) (b)

Figure 5. Edge direction for the calculated edges: (a) the edge direction mean (b) edge direction error range (STD)

In 'figure 5', the following notices can be devised:

i) For the angles 0º, 45º, 90º, and 135º, Hueckel algorithm success to determine the edge direction without error (zero STD) while for the other their edge directions there is a small deviation from the correct value and that due to rounding error.

ii) For the angle 90º, it was more difficult for the Hueckel algorithm to detect it, it needed 2.1322 as disk radius to be able to detect the edge in that direction.

iii) The calculated edge direction accuracy increase with the disk radius.

3.3. Edge Dislocation

The Dislocation (the distance from the real edge location) for the detected edge is calculated from the exact edge (the logical edge), as is illustrated in 'figure 6'.

In 'figure 6' we can notice the following:

i) For the edge direction of 135º the calculated edge location coincides with the exact edge location (no dislocation).

ii) The dislocation value for the edge direction other than 135º was ranging from 1-3 pixels, most of the error came from the thinning process.

iii) There is no variation (SD) in the edge dislocation values for the direction 0º, 45º, 90º, and 135º in the most cases, while for other edge direction it was very small value comparing to the dislocation mean.

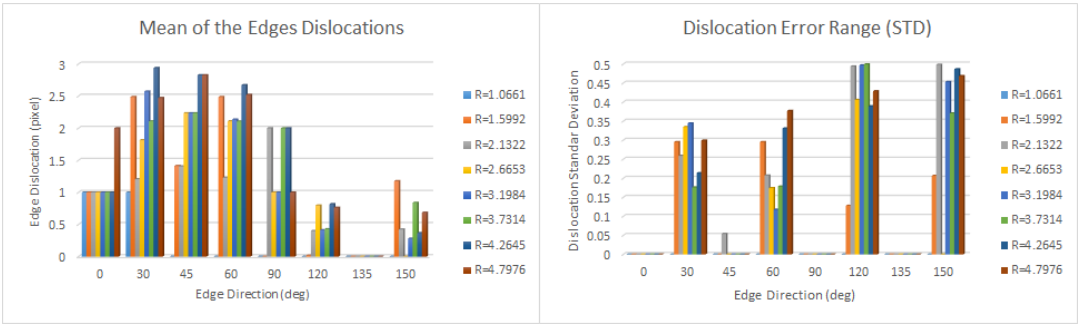

(a) (b)

Figure 6. Dislocation vale of the calculated edges: (a) mean dislocation value (b) dislocation variation (STD).

3.4. Edge Goodness Value

To evaluate the Hueckel edge detection algorithm, the maximum, minimum, mean and variation in the value of the edge goodness criterion are calculated to analyze it.

'Figure 7', give a representation of the edge goodness behaviour with edge direction and disk radius, and the following points can be noticed:

i) The edge goodness criterion is inefficient with the small disk radius (i.e. less than 2.1322) because the maximum value for the edge goodness criterion is less than 0.9.

ii) Starting from disk radius 2.1322 the edge goodness criterion record high values even when its mean value becomes low (for the radii 2.6653, 3.1984 and 4.7976), but it has high variation values (STD) for the other radius.

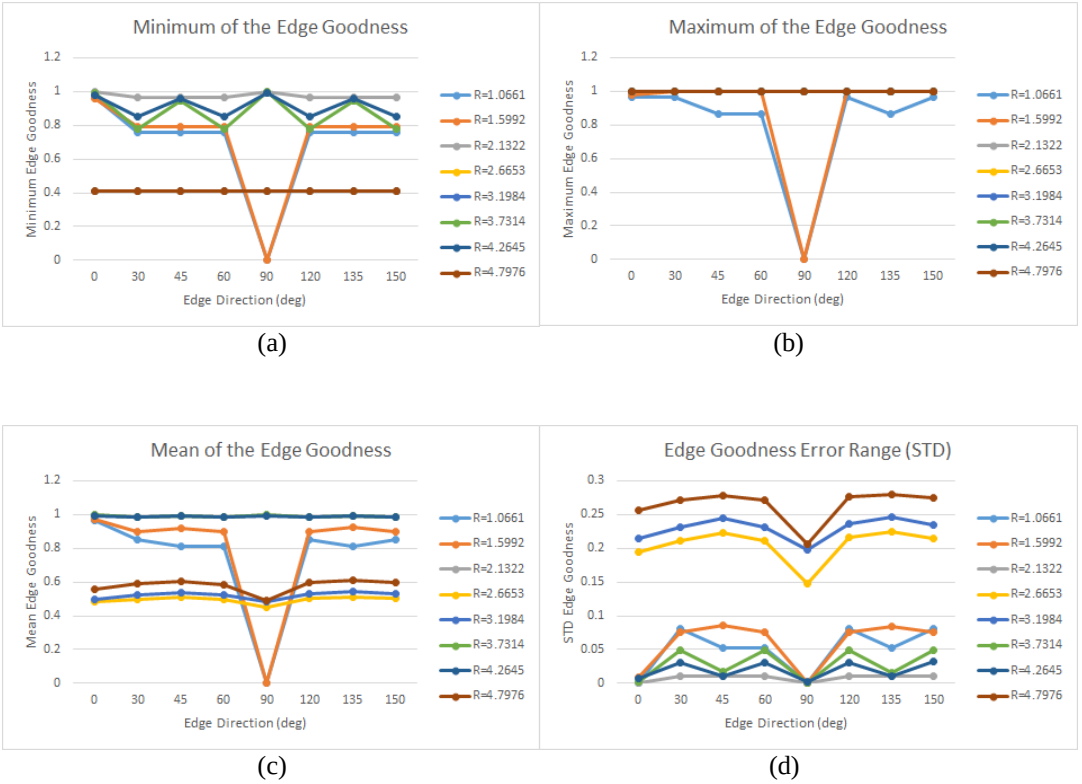

(a) (b)

(c) (d)

Figure 7. The edge goodness recorded values with edge radius and edge direction: (a) minimum value, (b) maximum value, mean vale, variation (STD).

3.5. Execution Time

The execution time of applying Hueckel edge detection algorithm with different disk radius and different edge directions are calculated, see figure 8.

'Figure 8', give a representation of the execution time behaviour with edge direction and disk radius, and the following notices can be devised:

i) The execution time differs depending on the edge direction, in which, the edge direction for 0°, 30° and 135° recorded the lowest execution time. On the contrary with the edge direction 45° and 60°, which it recorded the highest execution time due to the interpolation process that Hueckel edge detection algorithm performs in order to detect it.

ii) In general, the execution time increases with the disk radius, which is not obvious in the execution time results due to the small dimensions of the sample set images, as it recorded by Abduljabar [3].

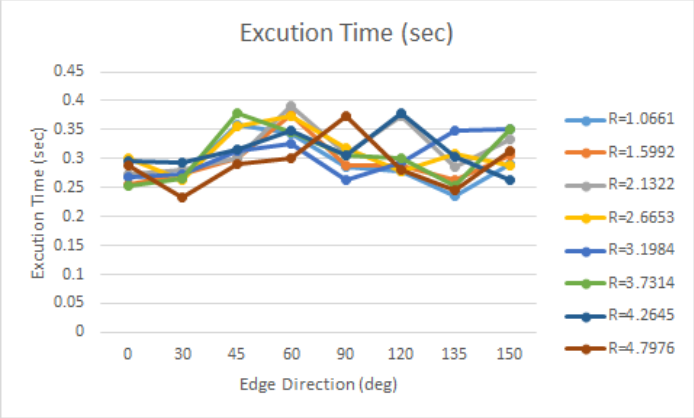

Figure 8. Recorded execution time for the Hueckel edge detection algorithm

4. Conclusions

Hueckel edge detection algorithm gives strongly connected edge with high immunity to noise, from the obtained results, the following conclusions can be derived:

1. The minimum valid disk radius that can be used in the Hueckel edge detection algorithm which makes it fully operate is starting from 2.3122 pixels.
2. The detected edge of the high disk radius suffers from exaggerating edge width that can be eliminated by using a customized simple (2×2) element erosion thinning process.
3. The detected edge direction accuracy increases with the disk radius.
4. The best value that can be used good edge direction with acceptable edge occurred when the disk radius is 1.5992 and 2.1322 (i.e. slid window size is 3 and 4 pixels) which represent the half radius values that recommended by Hueckel.
5. The recorded dislocation in the detected edge location is mainly due to the thinning process.

References

[1] Pratt W K 2007 Digital image processing. 4th ed. (John Wiley & Sons, Inc.) p 468
[2] Marques O 2011 *Practical image and video processing using MATLAB* IEEE Press p 337.
[3] Abdul-Jabbar H M, Taghreed A H Naji, Amal J Hatem and Inbethaq M A Abdul Ameer 2017 Studying Hueckel edge detector using binary step edge image *Ibn Al-Haitham Journal for Pure and Applied Science* **30** 1 pp 20-28
[4] Hueckel, M 1971 An operator which locates edges in digitized pictures *Journal of the Association for Computing Machinery* **18** 1 pp 113-125
[5] Hueckel M 1973 A local visual operator which recognizes edges and lines *Journal of the Association for Computing Machinery* **20** 4 pp 634-647
[6] Nevatia R 1982 *Machine perception* (Prentice. Hall, Inc., Englewood Cliffs) New Jersey 112
[7] Nevatia R Note 1977 Evaluation of a simplified Hueckel edge-line detector *Computer Graphics and Image Processing* **6 pp** 582-588

Reaching to a featured formula to deduce the energy of the heaviest particles producing from the controlled thermonuclear fusion reactions

Reaching to a featured formula to deduce the energy of the heaviest particles producing from the controlled thermonuclear fusion reactions

Raad H Majeed[1], Osamah N Oudah[2]

[1]Department of physics/ college of education for pure science (ibn-al-haitham)/ University of Baghdad, Iraq
[2]Department of physics/ college of education, University of Al-Qadisiyah, Iraq.

[1]raad.h.m@ihcoedu.uobaghdad.edu.iq

[2]osamah.oudah@qu.edu.iq

Abstract. Thermonuclear fusion reaction plays an important role in developing and construction any power plant system. Studying the physical behavior for the possible mechanism governed energies released by the fusion products to precise understanding the related kinematics. In this work a theoretical formula controlled the general applied thermonuclear fusion reactions is achieved to calculating the fusion products energy depending upon the reactants physical properties and therefore, one can calculate other parameters governed a given reaction. By using this formula, the energy spectrum of ^{4}He produced from T-^{3}He fusion reaction has been sketched with respect to reaction angle and incident energy ranged from (0.08-0.6) MeV.

1. Introduction

A fusion reaction is a subatomic process where two light nuclei are obliged together, so they will fuse producing energy. Energy yield because of the mass of the sum of masses of the individual nuclei greater than the mass of the combination of fusion reaction. If the combined nuclear mass is less than that of iron at the binding energy curve, then the nuclear particles will be more tightly bound than they were in the lighter nuclei and that decrease in energy released from mass based on the Einstein's equation [1].

Fusion has the ability to offer basic steady source of energy for the future, Fusion energy represented a clean source of energy with a basic fuel that is plentiful, inexpensive, and available to all human beings. It is presently being produced in the universe in stellar systems and on earth as a thermonuclear or hydrogen weapons.

To use fusion in producing energy, the fuel must be in the plasma state. In a usual state of matter, it is complicated to get fusion reactions. The reason is most of the kinetic energies of reactant are rapidly lost by means stopping power (processes like excitation and ionization of the constitutive atoms and

dissociation of the molecules)[2], so with the evolution of fusion researches, in particular the "ion-driven inertial confinement fusion" and "fast ignition" , the stopping power in plasmas has interest subject. The stopping data of different ion beams through the plasmas containing various materials is needed to the fusion research. Besides fusion fuels, some other materials such as C and Be are usually utilize in the design of fusion targets or fusion devices of fast ignition driven by ions. During the implosion process, these materials will mix with fusion fuels inevitably, which will affect the heating of fused ions. Fast charged particles passing through matter are lose their energy gradually in many small steps. Stopping power is defined as, the average energy loss of the particle per unit path length. Stopping power is very important for many parts of basic science, especially for all technological applicat [3, 4].

The cross section for atomic and molecular processes are larger by many times of magnitude than those for fusion reactions. These unwanted events can be obviated if the fuel is in the plasma state by the high-temperature plasma ions, which have energies high enough to transcend the Coulomb barrier [2].

It follows from the above discussion, in order to fuse nuclei, the electromagnetic repulsive force between protons must be transcend, oncoming nuclei come close enough with each other making the strong force to be active, On other hand the Coulomb barrier is effects and have minimum value for hydrogen. [5].

2. Tritium fuel and 3He

Tritium and ^{3}He are extremely vital to nuclear science side by side to Deuterium, as they are some of the major isotopes used in most nuclear fusion reactions mentioned in the table (1). The two main types of reactions by Tritium and ^{3}He is T-^{3}He fusion reaction, Broken down, the T-^{3}He fusion reaction looks like:

$$T + {}^3He \rightarrow D + {}^4He$$

$$T + {}^3He \rightarrow D + {}^4He$$

$$T + {}^3He \rightarrow p + {}^5He$$

As you can see from above, Appearance of more than one product formation, each of them release a different amount of energy. However, the reaction that releases the protons, which also released about the same amount of energy that the other have, rarely occurs. It is much less probable than the other reactions.

In a nuclear reaction, it is noted that the reaction rate is very important, in addition, it is the main part responsible for determining the factor of the releasing energy. This reaction rate is consists of three parts: The Maxwell-Boltzmann velocity, the cross-section and the Gamow factor.

Distribution of particle speeds described by the Maxwell Boltzmann velocity distribution, the velocities in this distribution given by [6]:

$$f(v) = A\, v^2\, e^{\frac{-mv^2}{2\,kT}} \tag{1}$$

A is constant given by

$$A = 2\pi(mkT)^3 \tag{2}$$

$f(v)$ is the relative probability that you can find a particle with speed between $v\ and\ v + dv$ in a collection of particles that are all in a thermally equal state at a constant temperature T.

Since E= 1/2 mv^2, the Maxwell-Boltzmann probability distribution can also be written as a function of the kinetic energy as [6]:

$$f(E) = [m\pi\ (mkT)^3]\ E\frac{1}{2}\ e^{\frac{-E}{kT}} \tag{3}$$

The first step toward determined the energy generated by T-^{3}He fusion reaction is to explore the microscopic physics of nuclear collisions. This perception is to relative moving to the macroscopic scale for determine the power releasing in magnetic fusion reactor. The microscopic concepts include the cross section etc. the probabilities of fusion reactions are quantitatively fixing as the cross sections, one of the essential physical quantities is the fusion cross section, it benefits parameter in the fusion engineering and design, the cross-section describes in quantitative frame the probability that a pair of T and ^{3}He nuclei will comes to a nuclear fusion reaction. For more specifically, suppose the ^{3}He nucleus is stationary and the T nucleus is come toward it with a velocity v, considering that the ^{3}He is the target particle while the T is the incident particle. The interactions like this called a hard-sphere collision. With a view to hard-sphere collision to occur, conservation of energy is needed with respect to the center of mass frame, the sum of initial kinetic energies of the T and ^{3}He when they are far from each other must overcome the Coulomb energy calculated at the surface of the particle when they come close to each other. If this is not happen, the T and ^{3}He are repelled away from each other before they collide. In mathematical treat, a collision occurs when: [7]

$$\frac{M_T}{2}\left(\frac{4_{He}}{M_T+4_{He}}\,V\right)^2+\frac{4_{He}}{2}\left(\frac{M_T}{M_T+4_{He}}\,V\right)^2 \geq \frac{e^2}{4\pi\varepsilon_0 d} \tag{4}$$

By observing Figure. 1 The T-^{3}He cross-section has a peak of about 0.1 barns at $T_T \approx 1000$ KeV. [7, 8]

Particle accelerators provide a good study of the fusion. Accelerated H, D, T, ^{3}He, ^{4}He particles are used to bombard targets of these nuclides [9]. Well known plots of these cross sections have been given by approximate sketch illustrated here.

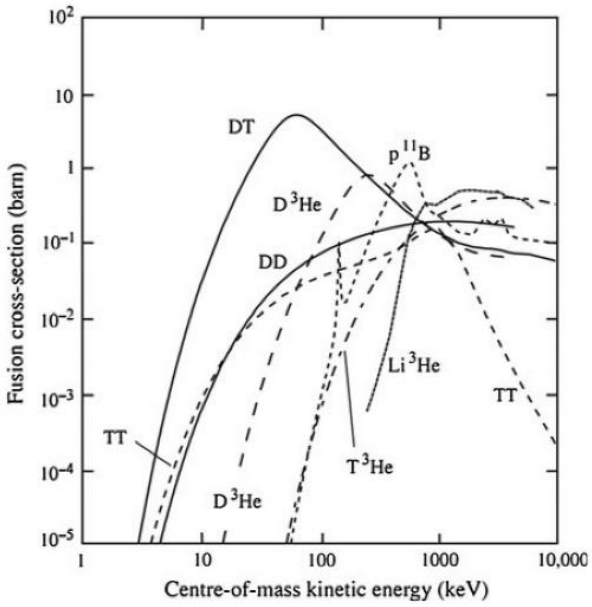

Figure 1. Fusion reaction cross-sections as a function of the incident particle energy, for the nuclear fusion reactions. [2]

The energy released from nuclear fusion reactions is the sacrifice of the mass. Thus, the energy of fusion Q can considered as part of the reaction equation, so the equation of T-^{3}He fusion is:

$$\text{T} + {}^3\text{He} \longrightarrow \text{D} + {}^4\text{He} + 14.320\ \text{MeV}$$

The release of (Q) 14.320 MeV per ^{4}He nuclide formed is interesting because that both the reactants and products are at very high temperature, a considerable amount of fusion energy is released as short-wave X- or γ-ray radiation.

Taking all the reactions into account, fusion doesn't produce radioactive ash or waste. For this reason, fusion is considered clean and environmental friendly for energy generation [2].

3. Calculations and results

An important notation related to the products energy from any nuclear reaction are essentially depend upon the so called Q-value equation given below which can be written based on conservation of mass-energy and linear momentum laws

$$Q = \varepsilon_{product}\left(1 + \frac{M_3}{M_4}\right) - \varepsilon_{incident}\left(1 - \frac{M_1}{M_4}\right) - \frac{2\sqrt[2]{M_1 M_3\, \varepsilon_{incident}\, \varepsilon_{product}}}{M_4}\ \mathrm{COS}\,\theta \qquad (5)$$

Q-value equation has independence concerning the reaction mechanisms (as compound nucleus, scattering, etc.), And here masses can be replaced without any intense mistakes by the corresponding integer-valued mass numbers A, For more accurate work, the neutral atomic masses are used.

The general fundamentals physicals equations for calculating the energies related with the released particles from any nuclear reaction based on the laws of energy and momentum conservations given by [10,11].

$$\sqrt[2]{\varepsilon_{product}} = v \pm \sqrt[2]{v^2 + w} \qquad (6)$$

$$\text{Where}\quad v = \frac{\sqrt[2]{M_1 M_3\ \varepsilon_{incident}}}{(M_3+M_4)}\cos\varphi \ \text{, and}\ w = \frac{M_4\, Q + \varepsilon_{incident}\,(M_4 - M_1)}{(M_3+M_4)}$$

The energy parameter $\varepsilon_{product}$ can be treated as the neutron, proton, and alpha particles energies etc. corresponding to the specific or given fusion reaction under study, Also The symbols M_1, M_2, M_3, M_4, present the masses for the reactant and product particles respectively.

In our work, we concentrated on the T-^{3}He thermonuclear fusion reaction, in which can present an important reaction in applied systems or devices, and all materials appear in any reaction play as a fuels for operating such small or mini scale devices or large scale devices, i.e.; (Dense Plasma Focus and Tokamak systems).

By substituting the values of the masses for the corresponding chosen fusion reactions, and taken into account some mathematical treatment, we simply bring to a general standard formula for calculating the energy of the heaviest emitted particles (Alpha) $\boldsymbol{\varepsilon_\alpha}$ and other particles, given:

$$\varepsilon_\alpha = \frac{L_1\, Q + L_2\ \varepsilon_{incident}}{L_3}\left[\sqrt{1 + S_1\, G\ - S_2\, G \sin^2\varphi} + \sqrt{S_3\, G}\ \cos\varphi\right]^2 \qquad (7)$$

$$\text{Where}\ G = \frac{P\ \varepsilon_{incident}}{L_1\, Q + L_2\ \varepsilon_{incident}}$$

Referring that L_1, L_2, L_3, P, S_1, S_2, and S_3 are constants see (table 1), Q mean the Q- value for the specific fusion reaction and $\varepsilon_{incident}$, is the bombarding projectile energy in which have a wide range of energies corresponding to a specific or given experimental or theoretical studies. G represents a variable depending upon the bombarding projectile energies, While φ is the reaction angles for heaviest products particles measured in lab coordinates with respect to a direction of the incident particle. Their corresponding values are completely described in the following table for common fusion reactions.

Table 1. The useful constants for common fusion reactions.

Thermonuclear fusion reaction	probability	L_1	L_2	L_3	P	S_1	S_2	S_3	Q MeV
${}_1^2D+{}_1^2D \rightarrow {}^3$He + neutron	50%	2	*2/3*	8	1	*5/3*	3	3	3.269
${}_1^2D+{}_1^2D \rightarrow {}_1^3T$+ proton	50%	2	*2/3*	8	1	*5/3*	3	3	4.033
${}_1^2D + {}_1^3T \rightarrow {}^4$He + neutron	100%	5	-10	25	1	13	8	8	17.589
${}_1^2D + {}^3$He $\rightarrow {}^4$He + proton	100%	5	-10	25	1	13	8	8	18.353
${}_1^3T + {}_1^3T \rightarrow {}^4$He +2 neutron	100%	2	-3	6	2	2	1	1	11.332
${}_1^3T + {}^3He \rightarrow {}_1^2D + {}^4He$	43%	2	-3	6	2	2	1	1	14.320
${}_1^3T + {}^3He \rightarrow p + {}^5He$	6%	6	-24	36	1	27	15	15	14.320

'Figure 2', 'figure 3' and 'figure 4' described the variation for the fusion energies of ${}^4He$ for versus bombarding projectiles energies of the T-^{3}He thermonuclear fusion reaction.

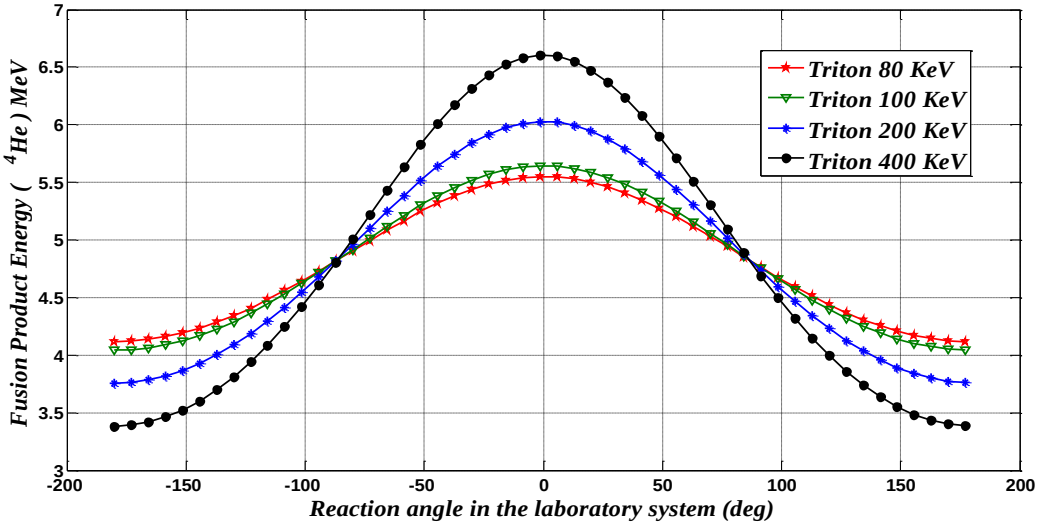

Figure 2. ^{4}He fusion products energy spectrum for T-^{3}He fusion reaction

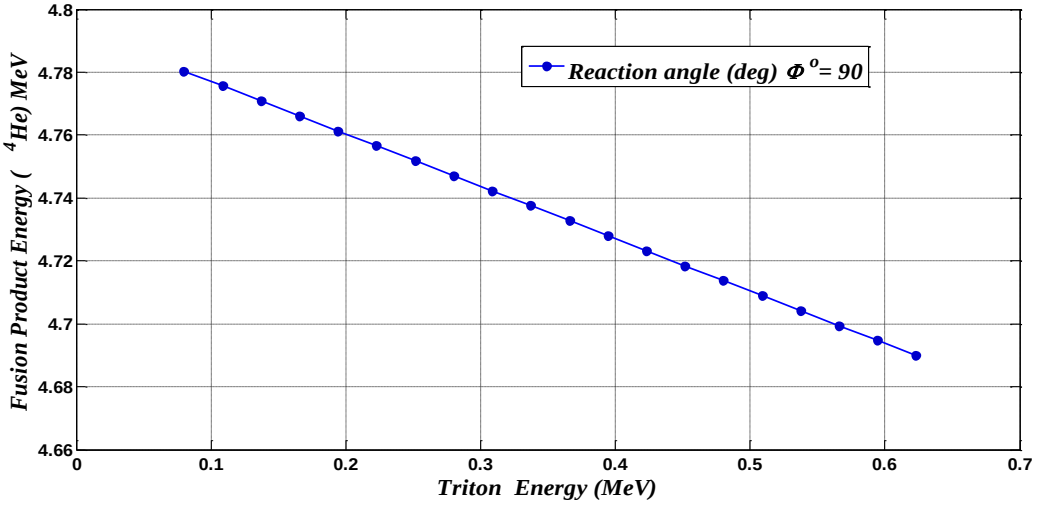

Figure 3. Variation of ^{4}He fusion energies with the incident Triton energies for T-^{3}He fusion reaction.

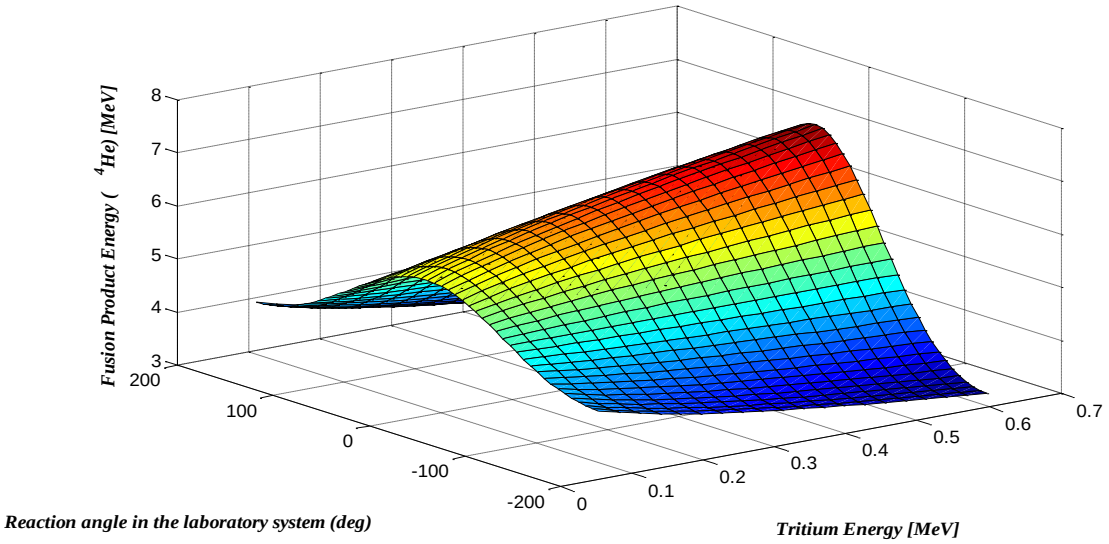

Figure 4. Fusion product energy distribution as a function of both a) Reaction angle b) Incident Triton energy.

Table 2. Variation of reaction angles for heavies and lightest fusion product controlling the thermonuclear fusion reaction $^{3}_{1}T$+ 3He → $^{2}_{1}D$+ 4He + 14.320 MeV.

Reaction angles in the laboratory system (deg)		Incident Triton Energy														
		0.08 [MeV]			0.1 [MeV]			0.2 [MeV]			0.4 [MeV]			0.6 [MeV]		
		Products energy MeV		Q value MeV	Products energy MeV		Q value MeV	Products energy MeV		Q value MeV	Products energy MeV		Q value MeV	Products energy MeV		Q value MeV
θ_D	φ_{4He}	D	4_{He}		D	4_{He}		D	4_{He}		D	4_{He}		D	4_{He}	
0	180	10.2825	4.1175	14.4000	10.3773	4.0427	14.4200	10.7610	3.7590	14.5200	11.3366	3.3834	14.7200	11.8052	3.1148	14.9200
30	150	10.1797	4.2006	14.3803	10.2614	4.1340	14.3954	10.5918	3.8794	14.4712	11.0860	3.5373	14.6233	11.4874	3.2887	14.7761
60	120	9.9040	4.4364	14.3404	9.9513	4.3943	14.3456	10.1425	4.2293	14.3718	10.4285	3.9969	14.4254	10.6607	3.8196	14.4803
90	90	9.5394	4.7804	14.3198	9.5427	4.7771	14.3198	9.5591	4.7604	14.3195	9.5918	4.7271	14.3189	9.6246	4.6938	14.3184
120	60	9.1882	5.1511	14.3393	9.1508	5.1932	14.3440	9.0092	5.3582	14.3674	8.8223	5.5907	14.4130	8.6892	5.7681	14.4573
150	30	8.9393	5.4403	14.3796	8.8742	5.5202	14.3944	8.6270	5.8416	14.4686	8.2990	6.3171	14.6161	8.0639	6.6992	14.7631
180	0	8.8500	5.5500	14.4000	8.7752	5.6448	14.4200	8.4913	6.0287	14.5200	8.1156	6.6044	14.7200	7.8469	7.0731	14.9200

4. Conclusion and discussion

The higher effective fusion cross section, the higher the probability of fusion. In general, the probability of fusion increases with the kinetic energy of the nuclei. Kinetic energies of nuclei are proportional to their temperatures in T, so the T-^{3}He fusion has the highest cross section nearly 1000 KeV temperature.

The energy of a reaction product depends on the masses of the particles involved in the reaction (it is fortunate that substantial reductions occur in fusion collisions between the light nuclei) and on the velocities of reactants, the reactants have Maxwellian velocity distributions.

The maximum fusion energies for the heaviest product obtained at zero reaction angle φ, the minimum than at 180^{o}. The most common collisions are those that lead to the deviation of the fusion product by angle 90^{o}.

It is necessary to see that we arrive or bring excellent facts which reflect the rule or the basic phenomena of resulting the fusion triton with energies corresponding to the reaction angles and this results completely described in (table 2)

Our conclusion concerned that we arrive a suitable agreement between the calculated results and the corresponding experimental results and in terms one can be used our theoretical model simply to calculate the interested fusion parameters and other related parameters and this fact can be related by observing the Alpha particles, neutrons, and proton fusion products energy spectrums for the different types of the interested thermonuclear fusion reactions.

References

[1] Zohuri B 2016 Plasma physics and controlled thermonuclear reaction driven fusion energy Springer
[2] Tanabe T 2016 Tritium: Fuel of Fusion Reactors Springer
[3] He B Meng X and Wang J 2016 Energy loss of an energetic Ga ion in hot Au plasmas Matter and Radiation at Extremes 1 5 257-63
[4] Sarsam M N 2017 Stopping Power for Proton Interacting with Aluminum, Beryllium, and Carbon Using Different Formulas. Al-Qadisiyah Journal Of Pure Science 18 1 135-44
[5] Bobin J L 2014 Controlled thermonuclear fusion, world scientific publishing co. pte. Ltd.
[6] Robert E 2017 *Nuclear Engineering Fundamentals: A Practical Perspective* (Masterson CRC Press) 1 edition
[7] Friedberg 2007 J Plasma physics and fusion energy, Cambridge University Press. https://doi.org/10.1017/CBO9780511755705
[8] Bosch H S and Hale G M 1992 Improved formulas for fusion cross-sections and thermal reactivities Nuclear Fusion 32 4 611-31
[9] McCracken G and Stott P 2012 Fusion: The Energy of the Universe Academic Press.
[10] Bielajew A F 2014 Introduction to Special Relativity Quantum Mechanics and Nuclear Physics for Nuclear Engineers The University of Michigan
[11] Evans R D 1955 The atomic nucleus (Mcgraw-Hill book company inc.)

Effect of particle size of TiO2 and additive materials to improve dye sensitized solar cells efficiency

Effect of particle size of TiO_2 and additive materials to improve dye sensitized solar cells efficiency

Falah H Ali[1, 3] , Dheyaa B Alwan[2]

[1] Phsics Department, College of Science, University of Baghdad, Iraq.
[2] Ministry of Education, Karkh / 1, secondary distinguished Harthiya of Baghdad, Iraq.
[3] Falah_h75@yahoo.com

Abstract. It became a great interest Dye-sensitized solar cells (DSSC) as a successful alternative to silicon solar cells in terms of cost and simplicity. These cells rely on a semi-conductive material of electricity TiO_2 nanocrystalline which encapsulates glass electrodes from the connected side at a temperature 450°C. In this work, the effect of nanoparticle size shows the size of atoms. The smaller the size of the atoms, the greater the surface area and thus the sufficient absorption of the dye and the stimulation of electrons, where increasing surface area increases efficiency. Then a limited amount was added and at a certain concentration, which led to a reasonable improvement in efficiency. According to this procedure commercially available TiO_2 (10 nm,25 nm,33 nm, 50 nm) standard. A TiO_2 paste was prepared by mixing commercial TiO_2, ethanol, distilled water, F:SnO_2 (FTO film thickness 14 μm) conductive glasses. By using Dr. Blade method we got films with appropriate thicknesses, then by using several particle sizes (10 nm,25 nm ,33 nm, 50 nm) ,many efficiencies were founded (2.39 %, 2.1 %,1.85 %,1.65%) respectively. Improved solar cell efficiency after addition of several chemical materials and the best that got is Cu $(NO_3)_2$. Efficiency became for (10 nm) (2.61 %, 2.34 %,2.1%,1.85%) respectively under 40 mW/cm^2 .

Keywords: DSSC, TiO_2, Efficiency, particle size, film thickness, additive.

1. Introduction

Titanium dioxide semi-conductive material future expected due to its high photochemical stability, low production and cost. Titanium nanoparticles are small and very accurate to increase surface area. This material is promising in many applications such as dyes, adsorbents and catalytic support [1-3]. In all cases, when the particle size of the surface is very small in nanometer so that the ratio of surface to size is large, Some new optical properties can be expected [4]. Dye solar cells convert visible light into electricity. Their work is based on wide band gap semiconductors. a solar cell (DSSC) is composed of two electrical poles connected to one side ،the first pole is covered with a layer of TiO_2 called anode electrode. The second pole is covered with platinum or carbon called this cathode pole. In addition to An electrolyte solution consisting of (redox couple like iodide/tri-iodide). When Solar radiation falls on DSSC many electrons present in the layer of the earth are excited. They are injected into the conduction band of TiO_2 porous film ، Then transfer them to glass through layer TiO_2 [5]. The TiO_2 films prepared

on Fluorine doped tin oxide glass annealing temperature 723 K (450^{o}C), the immersion time may be the uniquely influential factor to be analyzed at this stage since it is related to the dye concentration Ru (N719) 5x10^{-4}M. Films that were immersed for 5.5 h yielded the highest efficiency, this gets in the first electrode [6]. The electrolyte solution has an important role in obtaining high efficiency of adding suitable chemicals, its usefulness to enhance open circuit. As a result, increase efficiency (η) in DSSC [7]. Found highest value efficiency of ruthenium with a base TiO_2 film reached 11%–12%, but became undesirable because of its high cost[8]. Electrical additives are very important when adding a specific amount of electrolyte solution to improve and enhance performance solar cell. Increase or decrease specified amount leads to deterioration solar cell and low efficiency solar cell [9]. In this work, different sizes atoms TiO_2 nanopowder were used to demonstrate the effect of particle size on cell efficiency. The smaller TiO_2 volume, greater the surface area, and more efficient the result. The spectrometry of the Ruthenium dye on spectral range from 300 to 800 nm, the morphology of TiO_2 paste films, The photovoltaic parameters of the fabricated cells were determined. Enhances solar cell efficiency with electrical additives.

2. Materials

The following materials were used Iodine (I_2) and Potassium Iodide (KI) were purchased from (Erftstadt, Germany). ethanol, acetonitrile and Ethylene glycol from Aldrich, acetic acid solution-from SCR-China, FTO (7 Ohm/sq) transmission(80%) and ruthenium dye (N719) both supplied by a company [Solaronix] from Switzerland.TiO_2 nanocrystalline (anatase 10,25 nm) purity (99.9%) supplied [MK nano. Canada]. TiO_2 nanocrystalline (anatase 33, 50 nm) purity (97%) was supplied by [China]. Cu $(NO_3)_2$ and $AlCl_3$ supplied from (G.P.R- England). Solar power Meter (TES-1333 Digital Radiation Detector-China). Digital device for measuring voltages and current - China.and distilled water.

2.1. Preparation of the TiO_2-water paste

The composition of TiO_2 paste could affect the homogeneity and aggregates concentration of the TiO_2 electrode as well. Contents of acetic acid and water in TiO_2 pastes significantly decreased aggregation of nanoparticles of DSSC [10]. Prepare a paste TiO_2 in the following way, so that mixing solution becomes acidic powder and a hydrogen number (pH = 3).We add several drops of nitric acid to (6ml) from the deionized water, then add above to (6g) of nanoparticles TiO_2 nanoparticles. According to Dr. Blade's method [11].

2.2. Doctor blade Technique

used a special adhesive tape from three sides thick 10 μm.We place drops of dough prepared on side glass connector. Pull rod glass and move it slowly and with regular movement to film thickness as regular as the tape separator. The limitation of this technique is difficult to find an appropriate spacing material with a thickness of 1- 7μm [12].

2.3. Collecting the Cell

We collect the first face of film TiO_2 with the second face covered with carbon coated surface face to face in the form of a sandwich (Cathode and anode). We put at least two drops of electrolyte solution to be spread in all parts film TiO_2. sealed by using a Surlyn thermoplastic frame (to prevent leakage of the electrolyte solution).The complete cell was then taken to sunlight for harvesting energy.

2.4. Cell efficiency

Dye-sensitized solar cell efficiency it is the ratio of electrical output at power point and the power of incident radiation (Pin). The solar energy-to-electricity conversion efficiency (η) was determined by the

equation (1), after calculating the following parameters open-circuit voltage V_{oc}, short-circuit current density J_{sc} and fill factor FF.[13] .

$$FF = \frac{I_{max} \times V_{max}}{I_{sc} \times V_{oc}} \quad (1)$$

$$\eta = \frac{FF \times J_{sc} \times V_{oc}}{P_{in}} \quad (2)$$

3. Results and discussion

3.1. Absorption dye

In figure (1), three absorption regions (330,360 and 380) nm were observed in the ultraviolet region of the solar spectrum.

Ruthenium dye concentration ($5x10^{-4}$M).Highest peak absorption found in the visible region of the solar spectrum (510 nm) ,so solar cell efficiency was limited.

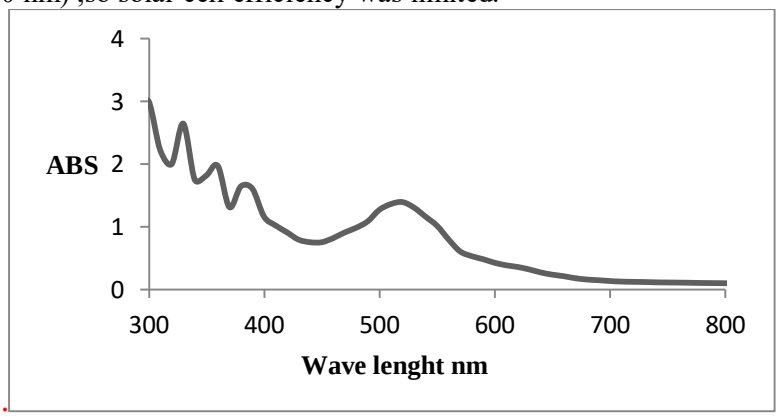

Figure (1) Absorption spectrum N719 dye

3.2. Effect of thickness on efficiency

Thickness and homogenization film is an important factor in solar cell performance. Film thickness at certain values is important for increasing efficiency. Electrons are close to the surface, interaction is rapid. The temperature used for depositing film 450 ºC under lighting 40 mW/cm^2 illumination, because it is compatible with the highest light response and no scratches and cracks. The best efficiency obtained in this work is 2.39% cell with a TiO_2 film thickness of 14µm. As in figure(2).

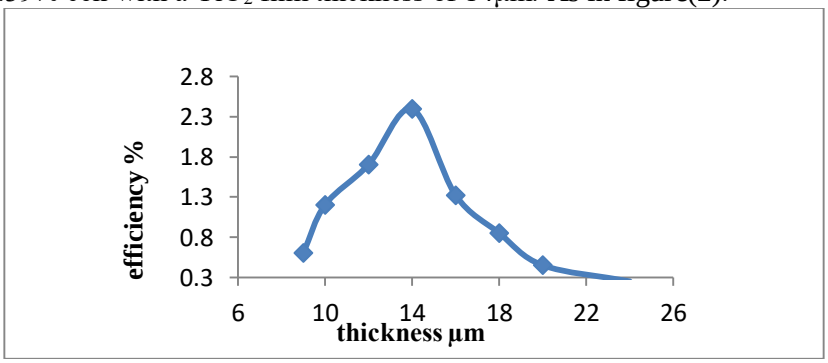

Figure (2) effect of thickness on efficiency

3.3. Effect Particle Size on efficiency

The volume of an atom is a very important factor in solar cell efficiency ,where reducing of particle size to a certain extent that process of recombination more and near to surface, the process is faster. For this reason, the catalytic activity of nanomaterial has increased with reduced particle size, increasing efficiency because reactions occur on the surface so the surface energy becomes more dominant in the process and the distance is short to surface for the desired reaction. Figure (3) shows the effect of particle size on efficiency.

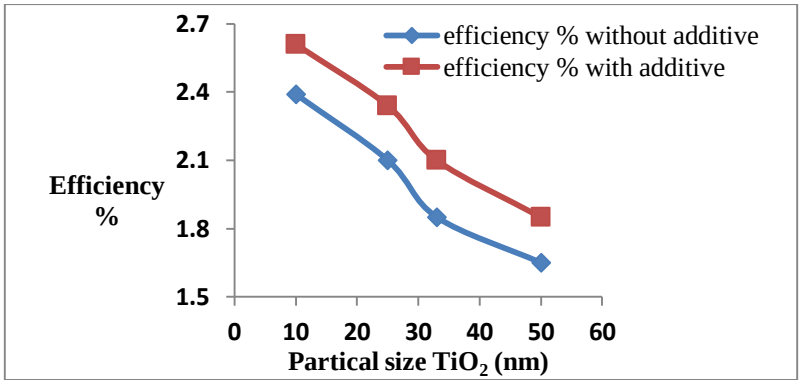

Figure (3) Effect Particle Size on efficiency

3.4. Influence Current density with and without additive on efficiency

Addition some materials to electrolyte solution led to improve efficiency, including copper nitrate 0.002 (g/10ml) figure (4) ,This addition increase the electron transfer speed and thus improving of the electrical conductivity. As in table (1) that shows short circuit current is increase after additive (1.98 mA/cm^2) .

Table (1) Influence of additive on efficiency

grain size TiO_2 µm	Without additive				With additive $Cu(NO_3)_2$			
	I_{sc}	V_{oc}	%FF	%η	I_{sc}	V_{oc}	%FF	% η
10	1.95	0.55	89	2.39	1.98	0.62	85	2.61
25	1.83	0.55	83	2.1	2	0.57	82	2.34
33	1.8	0.54	76	1.85	1.83	0.55	83	2.1
50	1.6	0.55	75	1.65	1.8	0.54	76	1.85

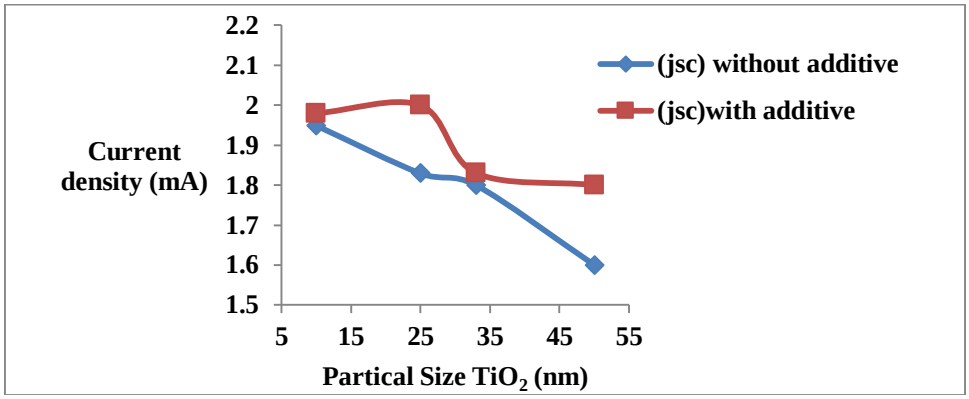

Figure (4) Influence Current density with particle size

*3.5. **Effect adding concentration on efficiency***

To get a good efficiency at best concentration, it is necessary to choose an appropriate concentration of the chemical additive $Cu(NO_3)_2$. After the work of several samples with different concentrations, concentration (0.002g/10ml) was selected. as shown table (2). Where efficiency solar cell before adding (2.39 %) became after adding $Cu(NO_3)_2$ (2.61 %), It is the best efficiency for best concentration. It mean more concentration than (0.002 g/10ml) led to less efficiency as illustrated in figure(5).

Table (2) additive concentration with efficiency

Concentration Type additive. g/10ml	GLASS CELLS			
	Isc	Voc	%FF	% η
0.00025	1.1	0.4	49	0.5
0.0005	1.3	0.65	60	1.3
0.001	1.9	0.55	83	2.17
0.002	1.98	0.62	85	2.61
0.003	1.7	0.51	85	1.72
0.005	1	0.5	63	0.79
0.01	0.49	0.52	60	0.38

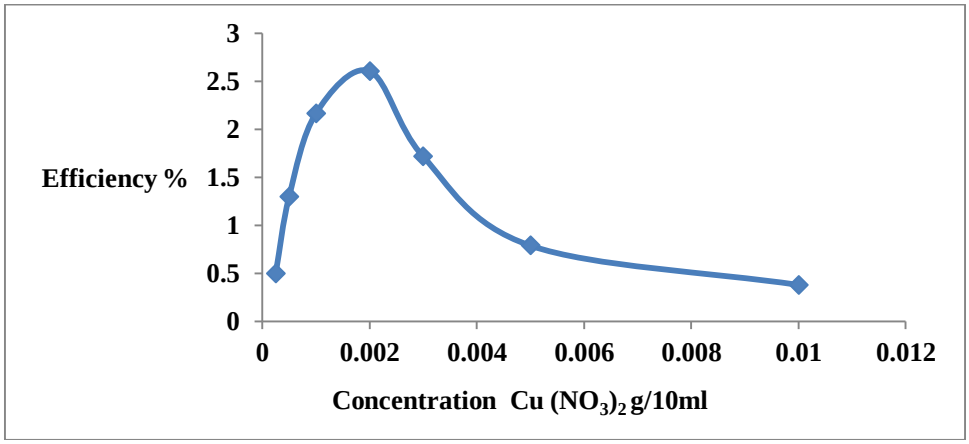

Figure (5) concentration with efficiency

4. AFM investigation

optical properties of the layer were identified TiO_2 size (10 nm) deposited on surface glass and most important root mean square (Rms) and histogram, after treatment thermally degree (450^0C) as shown in figure (6) which refers to lack of small microorganisms combined with the rate of diameter (44.35 nm), where roughness surface is equal (12.5 nm) ,So efficiency has increased.

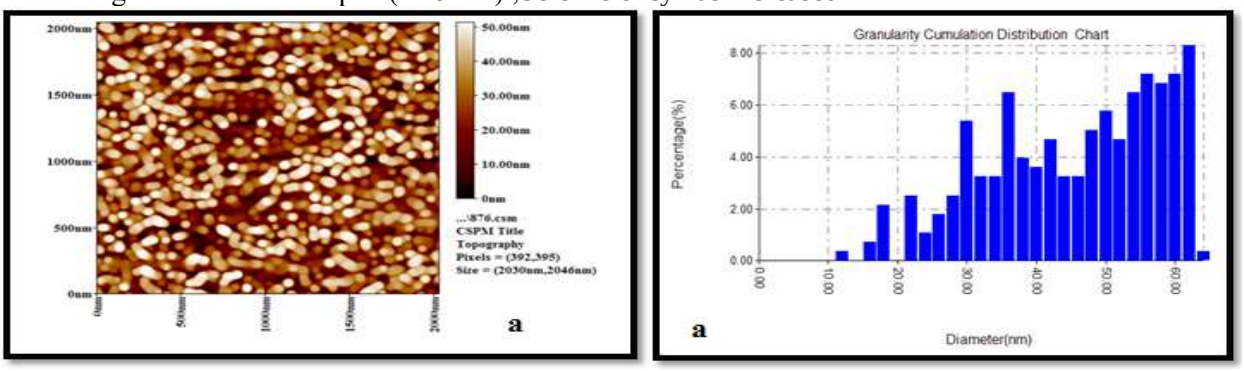

Figure (6) roughness surface and histogram TiO_2 (10 nm)

Shapes (7,8,9) shows pictures (2D) and sample chart respectively. Table (3) shows three films have a lower surface roughness first model (7), surface roughness (1.82nm) is very low and R.m.s (2.07nm) addition to accumulation of particles will lead to bad light activity, As well as other models (8,9), lower value (R.m.s) Caused a decrease roughness surface ,result is less that relationship between surface area and roughness surface due to a decrease in the size of the grain , this enhance in dye absorption by layer TiO_2 then increased the efficiency.

Table (3) optical properties layers of TiO_2 (AFM)

Particle size TiO_2	Avr.Diameter Nm	R.m.s nm	Surface .Avr Ratio	Roughness Avr(nm)
10	44.35	12.5	34.7	10.5
25	107.31	2.07	0.378	1.82
33	65.66	9.761	0. 932	7.544
50	103.6	1.15	0.125	0.826

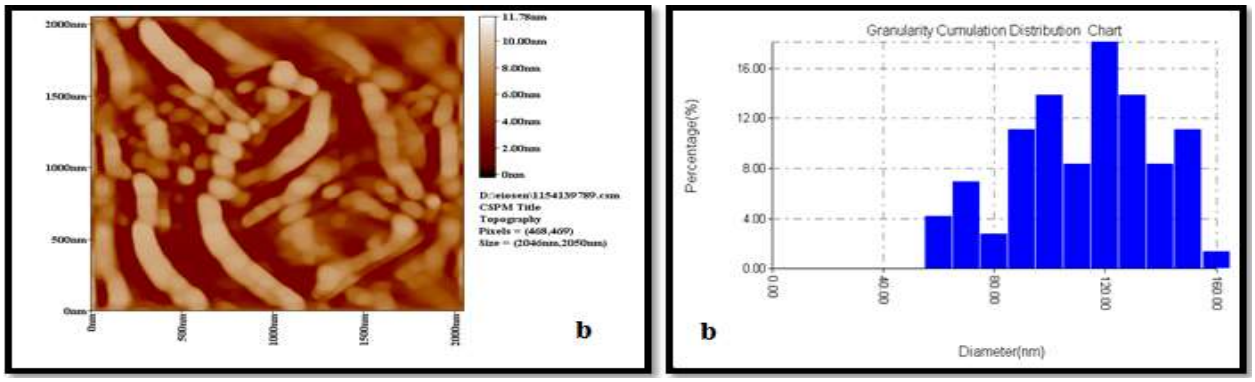

Figure (7) roughness surface and histogram TiO_2 (25 nm)

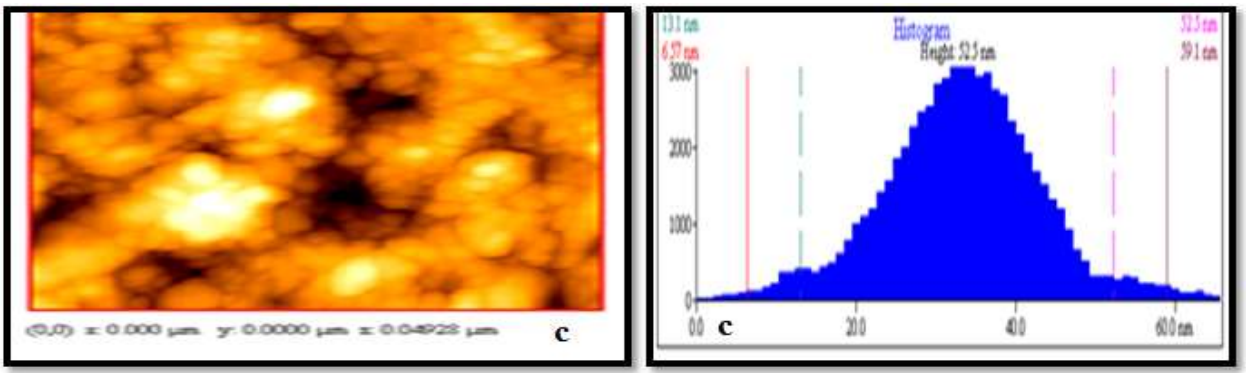

Figure (8) roughness surface and histogram TiO_2 (33 nm)

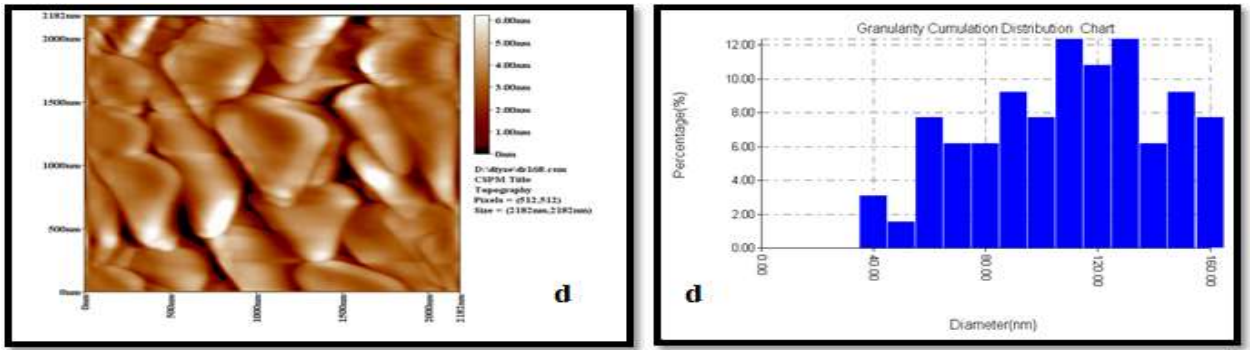

Figure (9) film roughness and histogram TiO_2 (50 nm)

5. Conclusions

There are many parameters affect on the performance of the solar cell. These factors include grain size, film thickness, and chemical additives. We have obtained efficiency greater at volume TiO_2 (10 nm) (2.39 %),where increasing of surface area is relative to the size of the small particle, thus increasing surface roughness, because of increasing of electron transfer speed and increasing current density . In case of sizes (25 nm,33 nm and 50 nm) surface area decreased due to large particle size and low surface roughness resulting reduced efficiency.

References

[1] G Ramakrishna and H N Ghosh 2003 Effect of particle size on the reactivity of quantum size ZnO nanoparticles and charge-transfer dynamics with adsorbed catechols, *Langmuir* ,**19** ,505.

[2] M M Rahman, K M Krishna, T Soga, T Jimbo and M Umeno 1999 Optical properties and X-ray photoelectron spectroscopic study of pure and Pb-doped TiO_2 thin films, *J. Phys. Chem. Solids,* **60** ,201.

[3] E Pelizzetti and C Minero 1993 Mechanism of the photo-oxidative degradation of organic pollutants over TiO_2 particles, *Electrochem. Acta* ,**38**, 47.

[4] Falah H Ali , Wesam A A Twej and AbdulKareem Al-Khafaji 2015 Structural and Optical Properties of Al-doped TiO2 Thin Films Prepared by Dip-Coating Method, *J. Spectro. Mol. Phys.*, vol. **10** (2015) 10, 91-96.

[5] Arman Sedghi and Hoda Nourmohammadi Miankushki 2012 Influence of TiO_2 Electrode Properties on Performance of Dye-Sensitized Solar Cells *Int. J. Electrochem. Sci.,* **7** (2012) 12078 – 12089.

[6] Wesam A A Twej, Mohanad M Azzawi, A S Hasaani and Dheyaa B Alwan 2014 Natural and chemically synthesized DSSC efficiency upgrading using silver nitrate additive, *Electrochemistry,* **5**(5), (2014) 142-148.

[7] Maeng Eun Lee, Moon Sung Kang, and Kwang Hwi Cho. 2013 , A Density Functional Theory Study of Additives in Electrolytes of a Dye Sensitized Solar Cell, *Bull Korean Chem. Soc*,**34**,(2013) 8.

[8] Dheyaa B Alwan 2016 Effect of Solvent type and Annealing Temperature on Efficiency for Eosin -y Dye Sensitized Solar Cells , *Iraqi Journal of Science*, Vol. **57**, No.4A, (2016) pp: 2429-2435.

[9] Jihuai Wu, Zhang Lan, Sanchun Hao, Pingjiang Li, Jianming Lin, Miaoliang Huang, Leqing Fang and Yunfang Huang 2008 Progress on the electrolytes for dye-sensitized solar cells. *Pure Appl. Chem.*,**80** (11), (2008) pp. 2241–2258.

[10] Pavol Gemeiner, and Milan Mikula 2013 The efficiency of dye sensitized solar cells with various compositions of TiO_2 based screen printed photoactive electrodes. *Acta Chimica Slovaca,* Vol. **6** (1), (2013) pp. 29-34.

[11] AbdulKareem, A Al-Khafaji, Dheyaa B Alwan, Falah H Ali, and Wesam A A Twej 2016 Influence of Grain Size, Electrode Type and Additives on Dye Sensitized Solar Cells Efficiency *ESAIJ*, **12**(6), (2016) 217-223.

[12] Sabarinath, S Subaganesh Rajni, K S and Ramachandran 2014 Fabrication and optimization of parameters for dye sensitized solar cell *IJRET*, **3**(1), (2014) 2319- 2321.

[13] B Pradhan, S K Batabyal and A J Pal 2007 "Vertically Aligned ZnO Nanowire Arrays in Rose Bengal-Based Dye-Sensitized Solar Cells," *Solar Energy Materials and Solar Cells*, Vol. **91**, No. 9, (2007) 769-773.

Evaluation of the Epoxy/Antimony Trioxide Nanocomposites as Flame Retardant

Evaluation of the Epoxy/Antimony Trioxide Nanocomposites as Flame Retardant

Balqees M Dheyaa[1],Widad H Jassim[2] and Noor A Hameed[2]

[1]Department of Applied Sciences, University of Technology
[2]Department of Physics, College of Education for Pure Science Ibn-Al-Haithm, University of Baghdad

Abstract. Antimony trioxide nanopowder was added for epoxy resin in various amount weight percentages (0, 2, 4, 6, 8, and 10) wt% to increase the combustion resistance and decrease the flammability for it. The study included three standard tests used to measure: limiting oxygen index (LOI), rate of burning (R.B), burning extent (E.B), burning time (T.B), maximum flame height (H) and residue percentage after burning in order to determine the effectiveness of the used additives to decrease the flammability of epoxy resin and increase the combustion resistance. Thermal test was done by using Lee's disk to measure the thermal conductivity coefficient. The thermal stability and degradation kinetics of epoxy resin without reinforcement and with reinforcement by (10 wt%) were studied by using thermogravimetric analysis (TGA). The recorded results indicated that epoxy reinforced by (10 wt%) has a good effect as flame retardants for epoxy resin and active to inhibit burning and reduce the flammability.

Keywords: Flame Retardant, Antimony Trioxide Nanopowder, Composite Material, Epoxy Resin and Inorganic Retardants.

1.Introduction

Flame retardants are defined as chemical materials that have the ability to withstand direct flame where it works to increase ignition resistance and reduce rate of flame spread and it is added to the material that doesn't have the ability to resist flame to improve its properties [1-3].

These materials are either additives called external flame retardants, which are an ineffective chemical additives added and mixed with polymeric materials without any chemical reaction with them, or as part of the polymer structure called the internal flame retardants[4].

Two methods are known to inhibit the flame, the first method is preventing the oxygen from reaching to flame zone by generating non-combustible gases which cause poisoning the flame by free radicals and extinction it, the second method depends on the thermal flame theory which states that the flame retardants need to thermal energy to disintegrate which leads to the reduction of the heat surface material to temperature less than the temperature of ignition and thus the burning will stop [5-7].

There are four primary materials which work to retard flame in various ways. These materials include nitrogen, phosphorus, halogenated and inorganic flame retardants [8,9].

Antimony trioxide is an inorganic compound with the formula Sb2O3, which has stability in high temperatures so it is used as a flame retardant in engineering materials.

Antimony trioxide has chemical formula (Sb2O3) or (Sb4O6) depending on its internal structure, where the cubic structure is colorless, while the orthorhombic structure is white. The cubic antimony trioxide is stable under temperature 570ºC and the orthorhombic is stable above temperature 570ºC [10].

The aim from this study is manufacture flame retardant composite material by adding nano antimony trioxide which was used as flame retardants to epoxy resin to increase the combustion resistance and decrease the flammability for it

2.Experimental Part

2.1. Materials

2.1.1.Polymer

Epoxy resin and hardener type (amine), imported from Sikadur-52 company, USA. Epoxy and hardener were used in this study in ratio of (2:1) for curing.

2.1.2.Flame retardant

Antimony trioxide nanopowder is supplied from Hongwu International Group Ltd, China with purity 99.5%, particles size (20-30) nm and orthorhombic phase (Valetinite) which have white color.

2.2 Synthesis

The samples of flame retardancy are formed by hand lay-up molding. Molded samples are a sheets shape in the dimensions of (13x13x0.3) cm. These sheets of epoxy resin were prepared for each percentage weight (0, 2, 4, 6, 8 and 10%) of flame retardant materials (antimony trioxide nanopowder), then the samples are cut by laser and have smooth edges according to the tests method. For limiting oxygen index (L.O.I), rate of burning (R.B) and maximum height of flame (H) testing, the specimens were chosen and each one has a length of ((130 ± 5), (130 ± 5) and (125± 5)) mm, width of ((6.5 ± 0.5), (12.5 ± 0.5) and (10 ± 0.1)) mm, respectively and thickness of (3.0 ± 0.1) mm. The specimens for thermal conductivity testing were a tablet shape and chosen each one that has a width of (40 ± 0.2) mm and thickness of (4.0 ± 0.1) mm. The weight of samples for thermogravimetric analysis (TGA) testing was 17gm.

2.3. Characterization

The flammability of polymers was determined by limiting oxygen index (L.O.I) (ASTM: D-2863)**.** The rate of burning (R.B), average extent of burning (A.E.B) and average time of burning (A.T.B) are measured according to (ASTM: D-635). The maximum height of flame (H) and the amount of loss in weight of polymer are measured according to (ASTM: D-3014). The thermal conductivity coefficient was estimated by Lee's disk test. The thermal degradation was studied using thermogravimetric analysis which carried out by (differential scanning calorimetry), model STA PT-1000 linseis, Germany.

3.Result and Discussion

3.1 Limiting oxygen index (L.O.I) test

L.O.I is the most widely used test to determine the flammability of polymer. It was measured by (ASTM: D-2863) method and calculated from the following equation[11]:

$$n\% = O_2 (O_2+N_2)^{-1}{}_x \, 100 \qquad (1)$$

Where:
n% : limited oxygen index.
O_2 : volumetric speed flow of oxygen (ml / sec).

N_2 : volumetric speed flow of nitrogen (ml / sec).

The results obtained are represent in table 1, and show the L.O.I increased with the increase of the reinforcement ratios (directly proportional).

Table 1. L.O.I for EP. with reinforcement ratios

Type of additive	Additives%					
	Non	2	4	6	8	10
Sb_2O_3	19.59	21.18	22.17	22.7	23.07	23.8

The limiting oxygen index (L.O.I) increased with the increase of the reinforcement ratios is due to the release of the oxygen root, which works to remove the active free radicals in the flame chain and inhibit the process of thermal fragmentation that occurs at the outset of the flame because of its effect in reducing the amount of heat generated by the flame.

3.2. Rate of burning (R.B) test

A.T.B in minutes and A.E.B were measured by (ASTM: D-635) method and calculated from the equations (2) and (3), respectively [12]:

$$ATB = (\sum(t-30)) \text{ (No. of samples)}^{-1} \quad (2)$$

$$ABE = (100-X) \text{ (No. of samples)}^{-1} \quad (3)$$

Where

t **:** time of burning (min).

X: length of the unburned part of the model when self-extinguishing occurs (cm).

Others variables were calculated from (ASTM: D-635) method in addition to A.E.B are:

R.B: rate of burning (cm / min).

S.E: self extinguishing .

N.B: the ignition non continuity of the specimen after the removal of heat source.

The result obtained from these tests showed that, the rate of burning of the epoxy resin with the additives has a continuous reduction with the increase of the percentage weight of additives, as in table 2, which showed the flame speed curves of flame retardation for resin.

Table 2. (A.T.B), (A.E.B), (R.B), (S.E) and (N.B) for EP. with reinforcement ratios

Test	Additives %					
	Non	2	4	6	8	10
A.T.B	5.35	6.71	7.3	3.22	2.52	2.25
A.E.B	10.3	10.3	10.3	4.1	1.8	1.4
R.B	1.92	1.73	1.69	1.2	0.57	0.49
S.E	-	-	-	Yes	Yes	Yes
N.B	-	-	-	-	-	-

The rate of burning (R.B) decreased with the increase of the reinforcement ratios due to the formation of non-flammable gases such as (CO) reduces flammable volatile substances and provides an inert atmosphere that forms a cover between oxygen and the burned area where it prevents or reduces oxygen from reaching the flame. Char, which is former of thermal decomposition, forms a barrier that protects the polymer from heat.

3.3. Maximum height of flame (H) test

The weight percentage for the residual of the burning material was measured by (ASTM: D-3014) method and calculated by the following relationship [13]*:*

$$PWR = ((W_1-W_2)(W_1)^{-1})_x100 \quad (4)$$

Where

W_1: weight of the sample before combustion (gm).

W_2: weight of residual material after combustion (gm).

PWR: percentage weight of the residual of burning material.

H: maximum height of flame reached (cm).

Table (3), show the results of the measurement of flame height for EP. with various amount weight percentages of Sb_2O_3.

Table 3. H for EP. with reinforcement ratios

Test	Additives%					
	Non	2	4	6	8	10
W_1(gm)	4.56	4.95	5.03	5.14	5.22	5.31
W_2(gm)	1.37	1.16	1.24	1.32	1.36	1.47
PWR%	69.95	76.56	75.34	74.31	73.94	72.31
H(cm)	12.3	9.9	7.6	6	4.8	3.7

Table (3), revealed the most effective additive at 10% where the flame height (H) is decreased from 12.3cm to 3.7cm and shows that the flame height (H) decrease with the increase of the reinforcement ratio (inversely proportional) because of the formation of carbonaceous char, which leads to the detention of oxygen from the polymer material and thus contribute to the cessation of ignition or reduce the flame.

3.4. Thermal conductivity test

Thermal conductivity coefficient (K) was calculated by thermal conductivity test. Thermal conductivity is a measure of the ability of a materials to allow the transport of heat from warmer regions to colder regions through the material. Coefficient of thermal conductivity (K) is the amount of heat conducted per second normally across unit area perpendicular to the direction of heat conduction at unit temperature gradient. It is measured in watts per Kelvin-meter ($W.k^{-1}.m^{-1}$) or in IP units ($Btu.hr^{-1}.ft^{-1}.F^{-1}$) [14]. Lee's disk test is one method used to determine the thermal conductivity coefficient of additives.

A value of thermal conductivity coefficient of the specimens (K) of thickness (d) and radius (r) is calculated by using the following equation [15]:

$$K\ (T_B-T_A/d_S) = e\ [T_A+2/r\ (d_A+d_S/4)\ T_A+d_ST_B/2r] \quad (5)$$

Where:

d_S, d_A, d_B and d_C : are the thickness of the sample and the disks respectively (mm).

T_A, T_B and T_C : are the temperature of the disks A, B and C (ºC).

e : quantity of thermal energy would be emitted from exposed area of the surface ($W/m^2.ºC$) calculated by using following equation [16]:

$$IV= \pi\ r^2\ e\ (T_A+T_B) + 2\pi\ r\ e\ [d_AT_A+d_S/2(T_A+T_B) + d_BT_B + d_CT_C] \quad (6)$$

Where:

V: is the difference potential across the heater.

I : is the current which flows through it.

Table (4), shows the obtained results of measurements of thermal conductivity coefficient (W/m.ºC) for EP. with different reinforcement ratios which increasing with the increase of the percentages of reinforcement added (directly proportional).

Table 4. K for EP. with reinforcement ratios

Type of additive	Additives%					
	Non	2	4	6	8	10
Sb_2O_3	0.37957	0.45171	0.49234	0.48312	0.44425	0.25773

This test was runned to determine the effectiveness of antimony trioxide nanopowder on thermal insulation or thermal conductivity at low temperatures where the thermal conductivity of composite material begins to rise with the increase of the reinforcement ratios, the reason for this is that the addition nano particle to polymer works to reduce the degree of cross linking between the molecular chains that give them larger freedom of movement and increase the ability to vibration movement so the heat passing through the composite material collides with the Sb_2O_3 grains that begin to absorb the heat. This absorption leads to a reduction in the passage of heat through the material, which reduces the thermal conductivity, but after a period of time and at high temperature, these grains begin to vibrate (thermal excitation) due to high temperature, and this vibration causes the heat rush through the composite material, leading to increase thermal conductivity.

The absorption of Sb_2O_3 of the heat is increased by increasing its proportion within the composite material thus it becomes a good conductor of heat.

3.5. Thermogravimetric Analysis (TGA)

Thermogravimetry (TG) is one of the thermal analysis which is used to characterize a wide variety of materials and provide supplementary characterization information to the thermal technique (DSC). It measures the amount and rate (velocity) of change in the mass of a sample as a function of temperature or time in a controlled atmosphere [17]. In this work, TGA is used to know the thermal stability of polymers and the effect of additives on thermal stability for these polymers. 'Figure 1', illustrate the TGA results of EP. without additive and with (10 wt%) additive.

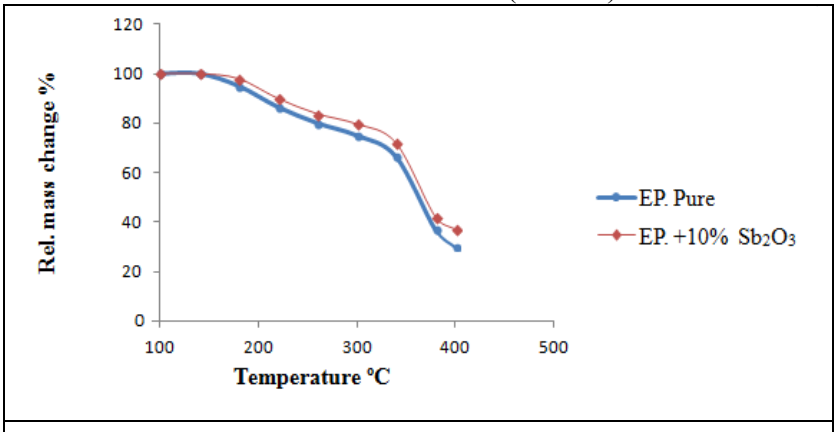

Figure 1. TGA curves of neat epoxy and epoxy/ 10% Sb2O3 nanocomposite

In two samples a change in peak was observed due to different melting behaviors of composite materials. There is no change in the starting of melting thermogram and there was a marginal increase

in the ending of it. The glass transition temperature for the pure sample is 111.5 ºC and for the reinforced sample is 115.5 ºC this difference is due to the nanoparticle penetrates inside the base material and works to fill and reduce the gaps that formed during the molding process, which gave better thermal properties. The weight loss at rel. mass change (98%) is due to the epoxy resin loses humidity by evaporation process and at 95% occurs because the epoxy begins to decompose.

4.Conclusions

The used additive was effective in reducing the flame and preventing the combustion of epoxy resin. The limiting oxygen index (L.O.I), thermal conductivity and thermal stability increases, rate of burning (R.B) and maximum flame height (H) decreases with the increase of the reinforcement ratios. Self extinguishing (S.E) occurred at the weight percentages (6, 8 and 10%).

References

[1] Moslem A 2003 Study using of antimony trioxide material as a flame retardant material Babylon University - Iraq
[2] Al-Jeebory A, Al-Mosawi A and Al-Bdiry M 2008 Experimental study of the effect of zinc borate on flame retardancy of carbon- kevlar hybrid fibers reinforced composite materials Al-Qadisiya *Journal For Engineering Sciences* Vol. **1** No. 1
[3] Ugal J and Jimaa R 2012 Study the synergetic activity of aluminium tri hydroxide with zinc oxide as flame retardants for unsaturated polyester resin The First Scientific Conference the Collage of Education for Pure Sciences
[4] Faris A, Abbas H and Al-Thuwaini M 2012 Study of the effect of synergistic action of additives in increasing the resistance of burning of epoxy resin College of Science City University *Journal* Vol. **4** No. 2
[5] Salaman A 2013 Improving thermal resistance for polymeric material reinforced by fibers by using of flame retardants from antimony trioxide The Iraqi *Journal For Mechanical And Material Engineering* Vol.**13** No. 1
[6] Al-Jeebory A, Al-Mosawi A and Jaseem K 2009 Improving thermal resistance for polymeric material reinforced by fibers by using of flame retardants material layer Al-*Qadisiya Journal For Engineering Sciences* Vol. **2** No. 2
[7] Mohammad A 1993 Plastic Chemistry Books House Publishing – Mosul
[8] Al-Mosawi A, Rijab M, Alwash N and Salaman A 2013 Fire retardancy characteristics of polymeric composite materials *J. Baghdad for Sci*. Vol. **10** No. 3
[9] Ibrahim A, Humza M, Abdullah Z and Salama A 2010 Using of hybrid flame retardants to increase thermal erosion resistance for advanced composite materials First Engineering Scientific Conference College of Engineering –University of Diyala p 148-156
[10] Abbas S 2011 Effect of flame retardant material addition on thermal conductivity of polymeric composite material reinforced by fibers *Journal of Technical* Vol. **24** No. 6
[11] Jaffer H and Mokhilif M 2011 Effect of triammonium orthophosphate on fire retardation of epoxy resin reinforced with wood flour, *Baghdad Science Journal* Vol. **8** No. 2
[12] Jima'a R 2012 Flame retardancy of unsaturated polyester resin by using some metal oxides and salt University of Baghdad - Iraq
[13] Mahmoode Z 2015 Using of some inorganic additives as flame retardants for low density polyethylene and unsaturated polyester University of Baghdad - Iraq
[14] Kakani S and Kakani A 2004 Material Science New Age International (P) Ltd., Publishers
[15] Alrubaiy S 2008 Preparation and study of some physical and mechanical properties of hybrid epoxy particulate composites doctoral dissertation, Baghdad
[16] Mocutkevic J and Banys J 2013 Epoxy resin/carbon black composites below the percolation threshold, *Journal of Nanoscience and Nanotechnology* Vol. **13** No.8
[17] Hatakeyama T and Quinn F 1999 Thermal analysis: fundamentals and applications to polymer science John Wiley & Sons Ltd.

Measure of Backscatter for small particles of atmosphere by lasers

Measure of Backscatter for small particles of atmosphere by lasers

Mariam M Abud

Department of Physics, College of Education for Pure Sciences/ Ibn- Al-Haithem, University of Baghdad, Baghdad ,Iraq

Abstract. It developed a program for the atmosphere to study the backscattering for contents gas &Molecules, Aerosol, Fog, clouds and rain droplets. By using Rayleigh, Mie and geometric scattering.The aim of research Using different types of lasers from various optical region to calculate differential cross scatter section and backscatter of atmosphere component in one layer from height 10-2000m. 180o is backscattering angle using ISA standard sea level condition P=1013.25 (kpa) at t0 =15 ◦ C.and then calculated the density of molecules and water vapor molecules represented D in kg/m3 .Results reflected index consist of the large value of the real part and imaginary m=1.463-0.028i.this research diff. scatter cross section of different component of atmosphere layer decreased vs. wavelengths . The purpose of lider research to find backscatter from UV to IR laser within the optical range in the atmosphere and measurement of excitation and analysis of backscatter signals. Recently, the atmosphere of Iraq has become full of dust and pollution, so by knowing the differential cross scatter section and backscatter of atmosphere. Relation between total Rayleigh scatter coefficient & type of particles include fog and clouds, Aerosols and Water Droplet (-0.01, 0.025,- 0.005) m-1/sr-1.

1. Introduction

Light strikes a medium, it is scattered or absorbed. Scattering is the spread of light in several directions are far away from original direction after collision with a specific particle and include several physical meanings are, Reflection, refraction, diffraction etc. All just forms of scattering.

The atmosphere interaction of importance in determine the received lidar signal elastic process Mie scattering when $d>>\lambda$ (aerosols) and Rayleigh scattering ($d<<\lambda$) when interact with some gas molecules.

Rayleigh [1] is the elastic scattering of light by particles much smaller than the wavelength of the radiation. Rayleigh scattering does not change the state of material; hence it is parametric process [2]. Whose size is similar to the wavelength such as water droplets in the atmosphere is necessary [3].

Mie scattering, make it is useful formalism when using scattered light to measure particle size Kear et., al[4] Mie theory is used in commutations applied in laser diffraction analysis. It is widely used since the 1990s and officially recommended for particles below 50 μm [5].

The various of sky colour at sunset, from red to the blue is caused by Rayleigh scattering by atmospheric gas particles which are much smaller than the wavelengths of visible light, also the ratio of grey/white colour of the clouds is caused by Mie scattering by water droplets when are of compare that size of the wavelengths of visible light [5].LIDAR is brief of light detection and ranging use light matter interaction. The LIDAR system based on the fundamental second and third harmonic emission lines of Nd: YAG laser collected the backscatter Raman return from nitrogen at visible and ultraviolet

wavelengths. In Addition, the water vapor Raman –shifted backscatter return from UV laser line is used to retrieve the water vapor as a function of relative humidity [6]. During previous researches Eldlen [7],Owens[8] presented an depth treatment of indices of refraction at CO_2 in free air ,pure CO_2 and water vapor , they opinion were provided for dependence on temp. , pressure and compositions.Dr. fouad Ismail is studied some of the atmospheric effects(aerosols and Rain) on a three specified laser beams (785, 850, and 1550) nm, like absorption and scattered of (Mie and Rayleigh) for the atmospheric, with horizontal propagation range between (0.01– 4) km at a stander condition in a middle summer season[9]. That study of some atmosphere effect in Baghdad city to calculate the average transmittance.

2. Theory

Light interaction with matter was three kinds of scattering [10] include:Elastic scattering – the wavelength (frequency) of the scattered light is the same as the incident light (Rayleigh and Mie scattering),Inelastic scattering – the emitted radiation has a wavelength different from that of the incident radiation (Raman scattering, fluorescence) and Quasi-elastic scattering – the wavelength (frequency) of the scattered light shifts (e.g., in moving matter due to Doppler effects).Size of the diffuser is that Rayleigh(d<<1) and Mie d~1 and geometric d>>1, where d is the dimensionless size parameter is given by:

$$d=\frac{2\pi r}{\lambda} \tag{1}$$

Where r is the particle radius of diffuser, and λ is the wavelength of incident radiation. The refractive index of the scattering particle, is commonly represented by the complex nature as:

$$m= n - ik \tag{2}$$

Complex refractive Index, where the real part (n) no absorbing part and imaging part (k) represent absorbing part.The scattering parameters can express for the Rayleigh and Mie solutions by using coordinate system can be seen in 'Figure 1'.

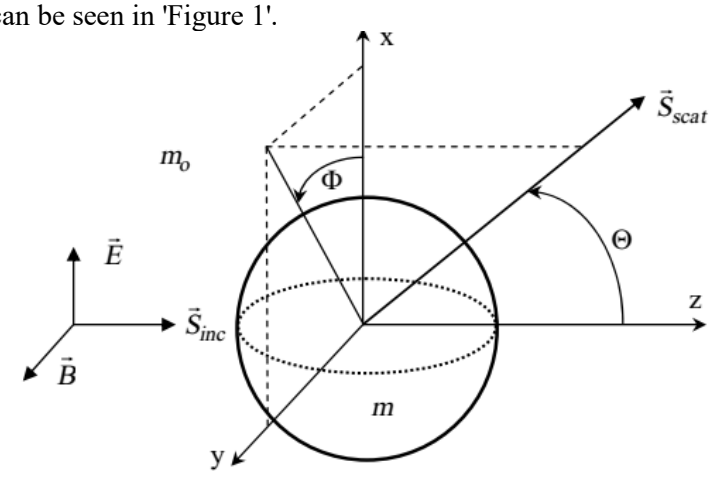

Figure 1. Coordinate geometry for the Rayleigh and Mie scattering [10].

The Rayleigh differential scattering cross section for polarized, monochromatic light is given by [11]:

$$\frac{d\sigma_R}{d\Omega} = [\,\pi^2(n^2\text{-}1)^2\,/N^2\lambda^4]\,[cos^2\Phi\, cos^2\Theta + sin^2\Phi] \tag{3}$$

where *n* is the index of refraction of the atmosphere, *N* is the density of molecules, λ is the wavelength of the optical radiation, and ϕ and θ are the spherical coordinate angles of the scattered polarized light referenced to the direction of the incident light. Equation (3), shorter-wavelength light (i.e., blue) is

more strongly scattered out from a propagating beam than the longer wavelengths (i.e., red), which is consistent with the preceding comments regarding the color of the sky or the sunset.
The total Rayleigh scattering cross section can be determined from Eq. (3) by integrating over 4π steradians is obtained [12]:

$$\sigma_{R(total)=}\left[\frac{8}{3}\right][\pi^2\,(n^2-1)^2\,/N^2\,\lambda^4] \quad (4)$$

The total Rayleigh scattering extinction coefficient as:

$$N\sigma_{R\,(total)} = 1.18\,x\,10^{-8}[\,\frac{550(nm)}{\lambda}]^4\,cm^{-1} \quad (5)$$

The molecular Rayleigh backscatter cross section for the atmosphere (θ =180 °) has been given by Collins and Russell for polarized incident light (and received scattered light of the same polarization [12] :

$$\sigma_R = 5.45x\,10^{-28}\,[\frac{550(nm)}{\lambda(nm)}]^4\,cm^2\,sr^{-1} \quad (6)$$

$$\sigma_r\,(\lambda)= 5.45.10^{-32}\,[\frac{550}{\lambda}]^{4.09} \quad m^2\,sr^{-1} \quad (7)$$

The efficiency to scatter light is found analytically to be in the case of spherical molecules:

$$Q_{scat} = Q_{ext}=\frac{8}{3}\,(\frac{\pi\,d}{\lambda})^4\,[\frac{m^2-1}{m^2+1}]^2 \quad (8)$$

Where Qsca is the scattering efficiency. The ratio πd/λ is called the size parameter, m is index of refraction, d the diameter of the molecule and λ the wavelength. The scattering coefficient due to nm spherical molecules will be:

$$\sigma_m = n_m\,\pi r^2\,Q_{ext}=\frac{32\,\pi^3\,(m-1)^2}{3\,\lambda^4}\,k\,T\,\frac{6+3\delta}{6-3\delta} \quad (9)$$

Where K is the Boltzmann's constant, T is the temperature and P is the pressure; δ is a correction factor (depolarization factor) which accounts for the anisotropy of the molecules.

The efficiencies of the particles are calculated for scattering (Qsca), backscattering (Qback), and extinction (Qext). The relationships for extinction, scattering, backscattering and absorption efficiencies (which are functions of r, λ and m) respectively [13].

3. Material and Method

A model put to measure the matter vertical distribution use differential backscatter laser technique requires the simulated emission of two laser beams.$\lambda_1 = 551.3784\ \mu m\ and\ \lambda_2 = 991.4376\ \mu m$.The light detected and ranging system includes several laser sources, optical devices to reduce the divergence, telescope to collects light scattered back. Optical analyzer system with detectors such as: interference filters or spectrometers.Input the program atmosphere some parameters such as depolarization factor 0.035, pollutant concentration ratio 0.05 and gas constant (R) in 8.314 (J/mol.K)

Use one layer of atmosphere is height from 10-20000 (m) and scattering angle degree (0 °) [10] 180° is backscattering. Using different type lasers rang resolved measurements can be obtained using (pulsed lasers).A model put to measure the matter vertical distribution use differential backscatter laser technique requires the simulated emission of two laser beams.$\lambda_1 = 551.3784\ \mu m\ and\ \lambda_2 = 991.4376\ \mu m$.This research base of program atmosphere in one layer to be calculated .using ISA standard sea level condition P=1013.25 (kpa) at t_0 =15 ° C. and then calculated the density of molecules and water vapor molecules represented D in kg/m^3 , can calculated by pressure of dry air $P_{d,}$ pressure of water vapor P_v, to get total air pressure P= $P_{d,}$+ P_v.Where gas constant for dry air R_d(kg*K)=287.05=R/M_d .formula to determine the saturation vapor pressure [12] and vapor pressure

from relative humidity. Scattering (Rayleigh, Mie and geometric .the section of lider system as shown as in 'Figure 2'.

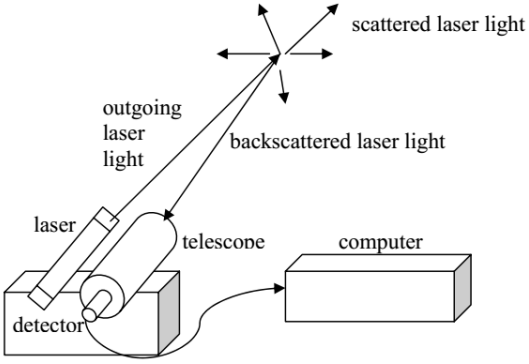

Figure 2. Represent the diagram of some parts of a lidar system [13]

4. Results

Using different types of lasers from various optical region such as Ruby (λ=694 nm), Nd:YAG (NIR λ=1064 nm) with optical parameter oscillation(OPO Oscill) and second harmonic oscillator (SHO)by using nonlinear tech. to get lasers output with a suitable wavelength for optical communication such as(266,355,532)nm and NaCl Excimer laser (213 nm) ,Dye laser, Alexander, Ruby, diode lasers, CO and CO_2 and then calculated the density of molecules and water vapor molecules represented D in kg/m^3 .Results reflected index consist of the large value of the real part and imaginary m=1.463-0.028i is a value contain real and imaginary parts wave number ($k=2\pi$) , are function of wavelength (λ) since d=kr. For all values of the total differential scattering cross section due to of laser wavelengths. When wavelengths increased vs. decreased of diff. scatter cross section of different component of atmosphere layer. Data are presented in table 1, forward and backscatter for different particle component of atmosphere by satisfy of equation (7).

Table1. Explained relation between total diff. scatter cross section and various laser wavelengths

Wavelengths (nm)	total diff. scatter cross section (m^2/molecules .sr)
213	0.9999683
266	-9.082651E-3
355	7.8736169E-5
532	-6.1117958E-7
694	4.3884187E-9
1064	-2.9883885E-11
1550	2.1874425E-13
1600	-1.7892321E-15
10600	1.111201E-17

The results in the table 2 showed that the components of atmosphere in one layer, the program atmosphere have given total Rayleigh scatter coefficient (m^{-1}/sr^{-1}) the backscatter by using equation (9) for the scattering coefficient due to nm spherical molecules as shown in table 2.

Table 2. Relation between total Rayleigh scatter coefficient & type of particles

total Rayleigh scatter coefficient(m^{-1}/sr^{-1})	Types of Particles
6.5	Molecules & Gas
-0.01	Aerosols
0.025	Fog & Clouds
-0.005	Water Droplet

5. Conclusion

In this program, all types of laser have been given Rayleigh backscattering unless Nacl Excimer (λ=213 nm), studied forward and backscatter with use Nd:YAG (opooscill) with different cross section (6.1E-7 – 4.38E-9)m^2/molecules.sr

It is observed from values of total diff. scatter cross section that decrease by increasing the wavelengths. These values fluctuated due to the diffusion of light between the various components in the size of atmospheric component produced the complex interactions of scattered rays that results to different paths with the same scattering angle 180 degree .Note the wavelength for 213 nm and 10600nm , hence these cross-sections vary by forward and backscatter during 9 values between value and other of total Rayleigh backscatter cross section and total Rayleigh scatter coefficient is great value in gas and molecules.

References

[1] David W. Hahn July. Light Scattering Theory. Department of Mechanical and Aerospace Engineering, University of Florida, 2009.

[2] Bohren, C. F., Huffmann, D. R. Absorption and scattering of light by small particles. New York: Wiley-Interscience. 2010, ISBN 3: 527-40664.

[3] Armin G.1, Andreas B.1, Volker W.1, Jens Strohbach1, Jochen F., Roland Potthast, Ina Mattis. A Backscatter Lidar Forward Operator for Particle-Representing Atmospheric Chemistry Models. Atmos. Chem. Phys. Discuss., Manuscript under review for journal Atmos. Chem. Phys.Published, 2016.

[4] Kear-Padilla He, L, Lieberman L.L, , Andrews S.H, J.M. Rapid in situ determination of total oil concentration in water using ultraviolet fluorescence and light scattering coupled with artificial neural networks. Analytica Chimica Acta, 2003, 478 (2): 245, doi:10.1016/S0003-2670(02)01471-X.

[5] Lindner, H, Fritz, Gerhard, Glatter, Otto. Measurements on Concentrated Oil in Water Emulsions Using Static Light Scattering. *Journal of Colloid and Interface Science*, 2001, 242: 239 doi:10.1006/jcis.2001.7754.

[6] Otero. L.A, Ristori .P.R, Quel. E.J. Multiwavelength aerosol and water vapor Raman lidar system at CEILAP, Buenos Aires, *Argentina. Opt pura Ap*, 2006, 41(**2**): 171-175.
[7] Eldlen, B. the refractive index of air, Metrologia, 1966, 2: 71-80.
[8] Owens, J. C. Optical refractive index of air dependence on pressure, temperature and composition. Appl. Opt., 1967, 6: 51-59.
[9] Fouad Abdul Kareem Ismail. Study the attenuation of the atmospheric effects on laser beam (785, 850, 1550) nm in free space propagation. A Thesis of Ph.D degree of of Doctor of Philosophy in Physics, College of Education Al-Mustansiriyah University, 2008.
[10] David W. Hahn. Light Scattering Theory. Department of Mechanical and Aerospace Engineering University of Florida, 2009.
[11] Measures. R. Laser Remote Sensing. Wiley-Interscience, John Wiley & Sons, 1984.
[12] Dennis K. Killinger, James H. Churnside , Laurence S. Rothman ,Center for Laser Atmospheric Sensin Department of Physics Uniyersity of South Florida,Tampa , Florida,National Oceanic and Atmospheric Administrati Enyironmental Technology Laboratory ,Boulder , Colorad,Air Force Geophysics Directorate/Phillips Lab,Optical Enyironment Diyision,Hanscom AFB , Massachusett, ATMOSPHERIC OPTICS,ch44, 1997: 14-15.
[13] Mariana A. Development of Lider Techniques to Estimate atmosphere optical Propertes. A dissertation submitted to the Johns Hopkins University in conformity with the requirements for the degree of Doctor of Philosophy, 2005.

Radiological Risk Assessments for Occupational Exposure at Fuel Fabrication Facility in AlTuwaitha Site Baghdad – Iraq by using RESRAD Computer Code

Radiological Risk Assessments for Occupational Exposure at Fuel Fabrication Facility in AlTuwaitha Site Baghdad – Iraq by using RESRAD Computer Code

Ziadoon H Ibrahim[1], S A Ibrahim[2], M K Mohammed[1] ,A H Shaban[2]

[1]Central Laboratories Directorate Ministry of Science and Technology

[2]Department of Physics College of Education Ibn AlHaitham University of Baghdad

Abstract . The purpose of this study is to evaluate the radiological risks for workers for one year of their activities at Fuel Fabrication Facility (FFF) so as to make the necessary protection to prevent or minimize risks resulted from these activities this site now is under the Iraqi decommissioning program (40) Soil samples surface and subsurface were collected from different positions of this facility and analyzed by gamma rays spectroscopy technique High Purity Germanium detector (HPGe) was used It was found out admixture of radioactive isotopes (^{232}Th ^{40}K ^{238}U ^{235}U^{137}Cs) according to the laboratory results the highest values were (975758) for ^{238}U (21203) for ^{235}U (218) for ^{232}Th (4046) for ^{40}K and (129) for ^{137}Cs in (Bqkg^{1}) unit The annual total radiation dose and risks were estimated by using RESRAD (onsite) 70 computer code The highest total radiation dose was (5617μSv/year) in area that represented by soil sample (S7) and the radiological risks morbidity and mortality (118E02 8661E03) respectively in the same area

1 Introduction

Italian fuel fabrication facility (FFF) is located in AlTwaitha site at Iraq / Baghdad at 33o 1257 North and 44o 31822 East It was previously belong to the Iraqi Atomic Energy Commission (IAEC) The total area of this site was about (13 km2) the concern facility FFF area around (37400 m2) Each soil sample represent (100 m2) from this facility were as in 'figure 6' During the second Gulf war (1991) it was completely destroyed and now is subjected to the Iraqi decommissioning project(IDP) The facility was contaminated by Uranium radionuclides (238U235U) in soil concrete equipments and scrap materials

Dose and risk estimation managements were carried out according to single or numerous radionuclides and the radiation types (alpha beta gamma) to demonstrate compliance with regulations[12] Radiological dose and risk assessment done at the beginning of project during decommissioning or decontamination and after cleanup of a site[3] It was used pathway analysis and exposure scenarios

A radiological dose is afforded by a likely exposed individual because of a specific exposure[45]

- External doses happen when the body is exposed to radioactive material outside the body
- Internal doses take place from radioactive exposure to material entered into the body by inhalation or ingestion
- skinny absorption doses happen from skin absorption of radionuclides (Tritium or open wound)

The dose can be centralized to particular organs or spread across the whole body due to the radionuclide intake or organ exposed by the nature of work The total dose is the sum of all pathways such as external exposure inhalation and ingestion[67] The radiation dose and risk was evaluated by using ResRad (onsite) 70 computer code The results of soil samples were regarded after analyzing in laboratory so as to characterize the radionuclides concentrations which represent the chosen zones A radiological risk evaluation is a probability assessment of deadly cancer over the existence of an exposed It can express the radiation cancer health risks through terms of death and incidence a risk of 1×10^4 means the possible for an exposed individual having a deadly cancer is one in 10000 persons The concept of risk constrain provide a basic level of protection for the individuals from a source and serves as an upper bound on the individual risk in optimization of protection for that source According to International Atomic Energy Agency (IAEA) safety standards the relation between dose and cancer risk development is well described for high doses of most radiation kinds the exposure scenarios pathways and environmental parameters values should be identified to the workers

The suitable radiological risk factor is (1×10^6 to 1×10^4) [89]The radiological dose and risk evaluation can be helpful through

- To support a lot of kinds of decisions like operational controls to make certain that the radiation exposures are safe and reasonable time limitations arrival controls personal protective equipment and storage requirements
- Decisions to remediation and decontamination objectives (getting the site clean enough the effectiveness different in assessments actions in terms of limiting future radiation exposures and the possible future uses of the site)
- Storage treatment disposal facility operation and design The necessity in design and operation features for a facility workers protection public protection during operations and facility closure

The information that needed to manage these assessments are the source material features physical regulations location and exposure scenarios (Workers' activities environmental pathways onsite direct exposure surface water or groundwater contamination and soil contamination)[10]

2 ResRad computer code

In order to assess contaminated sites it can use a suite of software tools developed by the US Department of Energy to assessing radiation dose and risks from residual radioactive material under different scenarios using suitable parameters [810] Four kinds of scenarios are being used Resident Farmer (RFS) Suburban Resident (SRS) Industrial Worker (IWS) and Recreationist (RS) RESRAD code Version 70 was used in the research and IW scenario was carried out for being benefited with decommissioning work table 1 shows the parameters that applied in this scenario

Table 1 Factors values of the Industrial Workers scenario Dose Library

Parameter	(Unit)	Quantity
Area	square meters	100
Exposure time	Hour/year	1250
Inhalation rate	m^3/year	11400
Indoor time fraction (occupancy factor)	[]	005
outdoor time fraction (occupancy factor)	[]	014
Contaminated fraction of food (plant meet and aquatic food)	kg/year	0
The amount of the annual soil ingestion	g/year	365
Soil and dust density	g/cm^3	15
Wind speed	m/s	2
Contaminated zone erosion rate	m/year	0001
Contaminated zone total porosity	[]	04
Saturated zone effective porosity	[]	02

Contaminated zone hydraulic conductivity	m/year	10
Length parallel to aquifer flow	m	100
Thickness of contaminated soil	m	020
Cover Depth	m	000
Time for calculation	year	0130100
Drinking water	Liter/year	0
Milk	Liter/year	0

3 Materials and methods

The equipment that used are sampling tools core sample milling machine sieve of 750 μm mesh size drying oven weighting scale sample container global position system (GPS) as shown in 'figures 12' portable device for radiological survey(LUDLUM 2241 2RK) type 4410 sodium iodide scintillation detector and Gamma Spectroscopy system (Canberra) as shown in 'figures 45' Gamma spectroscopy system consists of a detector preamplifier pulseheight analyzer(DSA1000) lead shield multichannel analyzer (MCA) with 8192 channel and vertical high purity germanium (HPGe) detector with relative efficiency 40% and resolution (<18keV) based on measurements of 1332 MeV gamma ray at photo peak of ^{60}Co source Both high voltage supply and amplifier device are compact in one unit (DSA1000) detector shield with a cavity adequate to 10 cm Lead absorbed grid from Cadmium 16mm and Copper 04mm to reduce radiological background as shown in 'figure 5'

3.1. Samples Collecting

The samples was collected (40) (surface and subsurface) from the Fuel Fabrication Facility at depth of 15cm and 6 samples at 40 cm depth each sample represent the studied area (100m^2) from facility three samples were collected from outside AlTuwaitha site to determine the background levels Samples were labeled and coded in all locations by using (GPS) where the samples taken from the mass of the sample was one kilogram[5]

3.2. Preparing samples method

By putting each soil sample in a drying oven at 100°C for one hour to make sure of removing any remaining of moisture samples preparation was managed then the dried samples was milled till to be a fine powder using grinder for pulverizing the soil sample A 750 μm mesh is used to sieve the soil samples to obtain uniform particle sizes The volume was (500ml) that was kept in sealed Marinelli Beaker with plastic strip to avoid the escaping of (^{222}Rn) and (^{220}Rn) from the samples as shown in 'figure 3' after that it was stored for one month so that the Uranium238 and Thorium 232 chains could reach to the radiological equilibrium [79]

3.3. Samples analysis

Gamma Spectroscopy system (Canberra) was used to analyze soil samples A library of radionuclide's which contained the energy of the characteristic gamma emissions of each radionuclide and their corresponding emissions probabilities were built from the date supplied in the software (Genie 2000)^{238}U radioactivity concentration was determined by gamma energy (1001keV) that is belong to the Protactinium isotope (^{234m}Pa) for high radionuclide concentration samples and by (60932 keV) that is belong to the Bismuth (^{214}Bi) to low concentration^{235}U was determined at gamma energy (1438 keV 1633 keV 1857 keV and 2053 keV)which are belong to the same isotope the corrected activity in Genie 2000 software was depended whereas the thorium (^{232}Th) was determined at (9117keV) gamma energy by energy is belong to ^{228}Ac ^{40}K and ^{137}Cs isotopes which can be determined at 14608 and 662keV peak energy respectively it should be noticed that all concentrations were determined in (Bq /kg) unit[11]

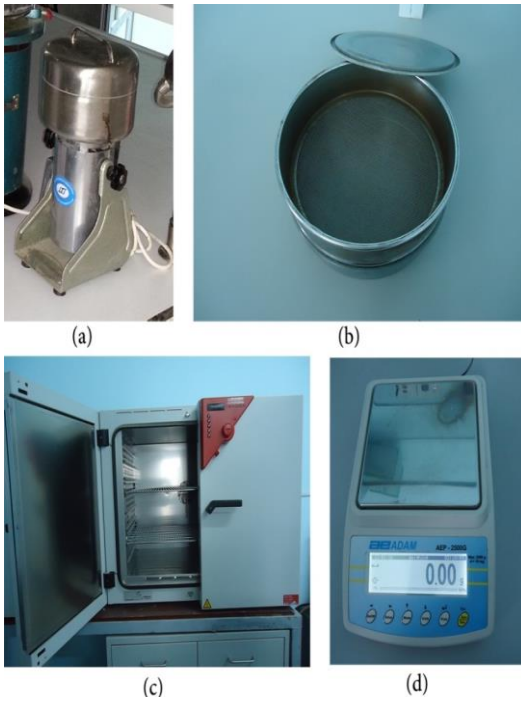

Figure 1. a milling machine for soil sample (b) sieve (c) oven (d) weighing scale.

Figure 2. trowel tool used to collect sample, handheld GPS unit.

Figure 3. A prepared soil samples filling in 500 ml Marinelli beaker.

Figure 4. Gamma spectrometry system.

Figure 5. Ludlum dose rate meter.

3.4. Samples analysis results

Three samples were analyzed using gamma spectrometry system with consider that samples are as the radiation background in order to compare results with the selected areas The (40) mentioned samples were analyzed the radiological activity concentration can be seen in table 2 and 'figures 67' Table 3 shows the higher and lower radiological activity concentration in samples

Table 2 Activity concentration in soil samples

Sample code	Coordenate North	East	Radionuclide concentration Bq/kg ^{238}U	^{235}U	^{232}Th	^{40}K ^{137}Cs
S1	33° 12014	44° 30757	128±09	BDL**	129±11	4755±12 BDL
S2	33° 11970	44° 30789	13±085	BDL	149±112	2997±171 25±032
S3 Sub*	33° 12013	44° 30755	148±095	BDL	7±16	392±145 BDL
S4 Sub	33° 11984	44° 30770	184±114	BDL	161±1	3345±20 BDL
S5 Sub	33° 11946	44° 30774	125±13	BDL	84±12	453±15 BDL
S6	33° 11962	44° 30776	62116	149±89	86±13	258±113 73±085
S7	33° 11958	44° 30778	975758	21203	BDL	3796±444 BDL
S8	33° 11949	44° 30780	18952	4044	138±28	281±105 BDL
S9	33° 11972	44° 30770	166±13	BDL	153±17	3127 BDL
S10	33° 11996	44° 30754	91±1	BDL	135±18	346±11 32±05
S11	33° 12003	44° 30744	141±13	BDL	99±15	2594±21 24±05
S12	33° 11985	44° 30745	115±12	BDL	11±15	2683±209 39±05
S13	33 ° 11952	44° 30776	11942	2904	123±16	2702 43±066
S14	33° 11954	44° 30768	94525	21535	BDL	335±11 BDL
S15	33° 11964	44° 30719	749005	15592	BDL	3636 BDL
S16	33° 11971	44° 30962	153174	3656	BDL	2534 BDL

Sample code	Coordenate North	East	Radionuclide concentration Bq/kg ^{238}U	^{235}U	^{232}Th	^{40}K ^{137}Cs
S17	33° 11967	44° 30964	224630	4161	BDL	BDL BDL

S18	33° 11956	44° 30735	377785	6744	BDL	BDL	BDL
S19	33° 11968	44° 30721	539612	13083	BDL	332	BDL
S20	33° 11981	44° 30741	342493	8179	BDL	2836	BDL
S21Sub	33° 11924	44° 30672	11±085	BDL	149±112	316±121	BDL
S22Sub	33° 11996	44° 30647	14±084	BDL	159±112	2737±171	BDL
S23	33° 12010	44° 30732	108206	BDL	15	2902	57
S24	33° 11990	44° 30711	86086	878	157	3566	44
S25	33° 11973	44° 30726	121765	2269	171	3312	22
S26Sub	33° 11938	44° 30752	163	BDL	142	3285	BDL
S27	33° 11939	44° 30736	193956	4367	BDL	2759	BDL
S28	33° 11961	44° 30702	42731	936	163	2873	5
S29	33° 11933	44° 30721	66290	14822	158	3336	BDL
S30	33° 11980	44° 30686	5215	929	182	2872	34
S31	33° 11960	44° 30691	201993	40615	BDL	2417	BDL
S32	33° 11962	44° 30689	2865425	5466	BDL	4046	BDL
S33	33° 11913	44° 30723	178346	35246	212	3952	15
S34	33° 11980	44° 30670	31428	559	218	3393	71
S35	33° 11932	44° 30703	55974	1236	144	3436	BDL
S36	33° 11960	44° 30667	26063	557	106	2956	32
S37	33° 11930	44° 30690	1021	2125	118	3172	79
S38	33° 11914	44° 30692	69084	1419	119	2038	129
S39	33° 11963	44° 30668	169014	299	877	2188	BDL
S40	33° 11897	44° 30670	169±089	BDL	118±075	2374±145	17±025

S3 Sub soil sample sub surface BDL below detection limit

Table 3 Summary of the activity concentration of soil sample

	Sample code	*^{238}U Bq/kg*	*^{235}U Bq/kg*	*^{232}Th Bq/kg*	*^{40}K Bq/kg*	*^{137}Cs Bq/kg*
Highest sample	S7	975758	21203	BDL	3796±444	BDL
Lowest sample	S10	91±1	BDL	135±18	346±11	32±05
Average background	BG	878	BDL	1326	28398	BDL

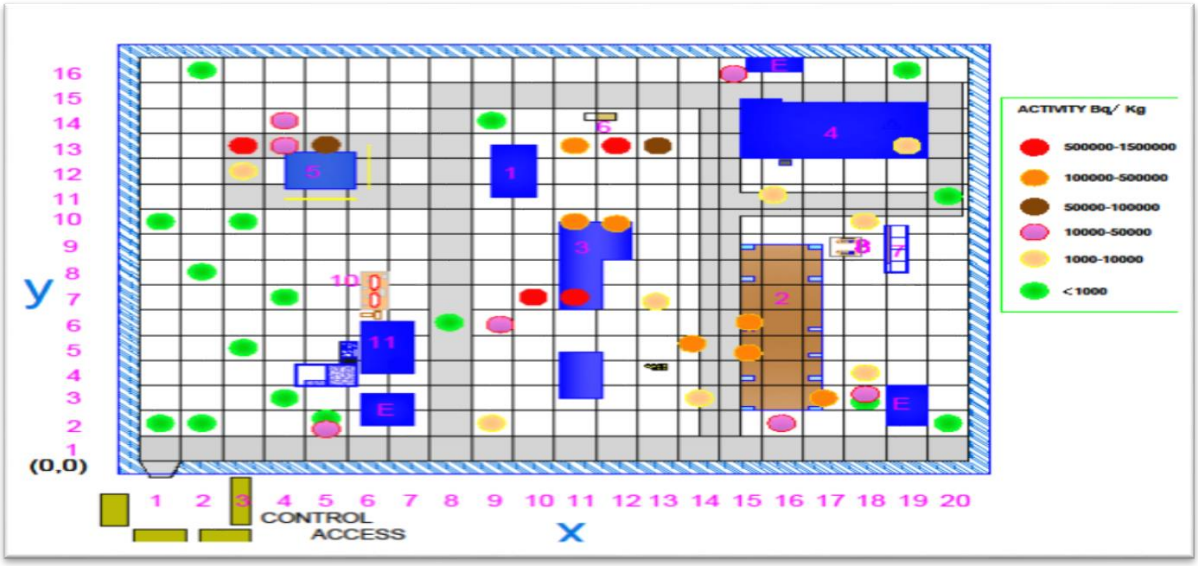

Figure 6 location of sampling in FFF and ^{238}U concentration activity levels(Bqkg^{1})

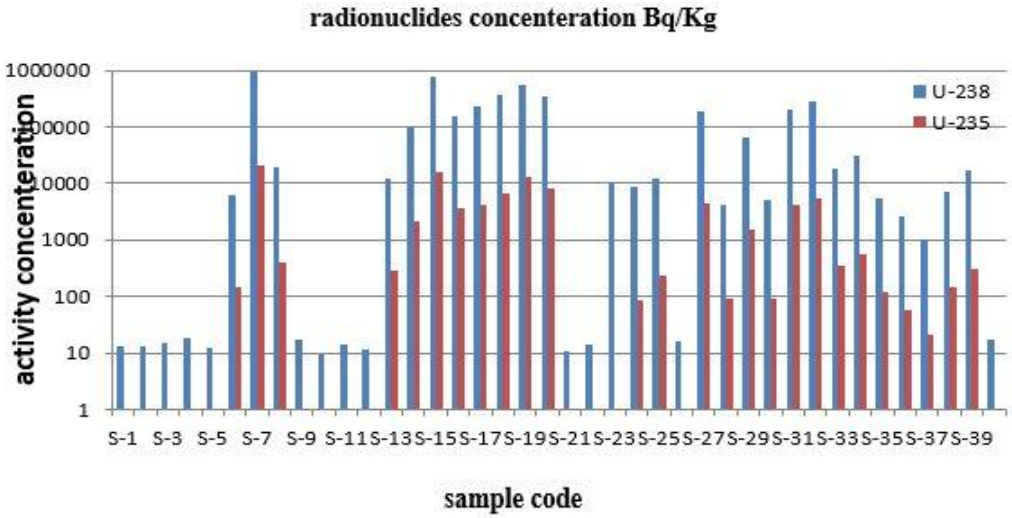

Figure 7 Radioactivity concentration in soil samples

4 The radiological dose and risks results

The radiation dose and risks was analyzed to workers by using RESRAD onsite computer codethe industrial scenario (IS) in RESRAD was applied with the limited exposure pathways because it is suitable with the workers in FFF to their activities in decommissioning project The RESRAD code used a pathway analysis method in which the relation between radionuclides concentrations in soil with dose and risks to a member of workers that expressed as a pathways sum which is the sum of products of pathway factors correspond to pathways involving radionuclides that can be transported or from radiation that can be emitted[11] Table 1 shows the input values for RESRAD software parameters Table 4 and 'figures 89' show the annual radiological dose and risk (morbidity and fatal mortality)

Table 4 Total radiological dose and risk in FFF

Sample code	Total annual dose µSv/yr	Radiological risk Morbidity	Mortality	Sample code	Total annual dose µSv/yr	Radiological risk Morbidity	Mortality
S6	4383	9324E05	6421E05	S27	1102E+03	2311E03	1595E03
S7	5617E+03	118E02	8124E03	S28	3309E+01	7078E05	4870E05
S8	1160E+02	2444E04	1686E04	S29	3899E+02	8184E04	5647E04
S13	7723E+01	1632E04	1125E04	S30	3776E+01	8051E05	5543E05
S14	5527E+02	1160E03	8002E04	S31	1143E+03	2396E03	1654E03
S15	4283E+03	8973E03	6194E03	S32	1647E+03	3451E03	2382E03
S16	8766E+02	1838E03	1268E03	S33	1139E+02	2407E04	1659E04
S17	1272E+03	2665E03	1840E03	S34	1883E+02	3965E04	2735E04
S18	2139E+03	4480E03	3093E03	S35	4175E+01	8909E05	6132E05
S19	3139E+03	6579E03	4540E03	S36	2329E+01	5032E05	3458E05
S20	1753E+03	3668E03	2535E03	S37	1249E+01	2727E05	1870E05
S23	6394E+01	1353E04	9332E05	S38	4653E+01	9865E05	6797E05
S24	5670E+01	1205E04	8305E05	S39	1008E+02	2122E04	1464E04
S25	7804E+01	1651E04	1138E04				

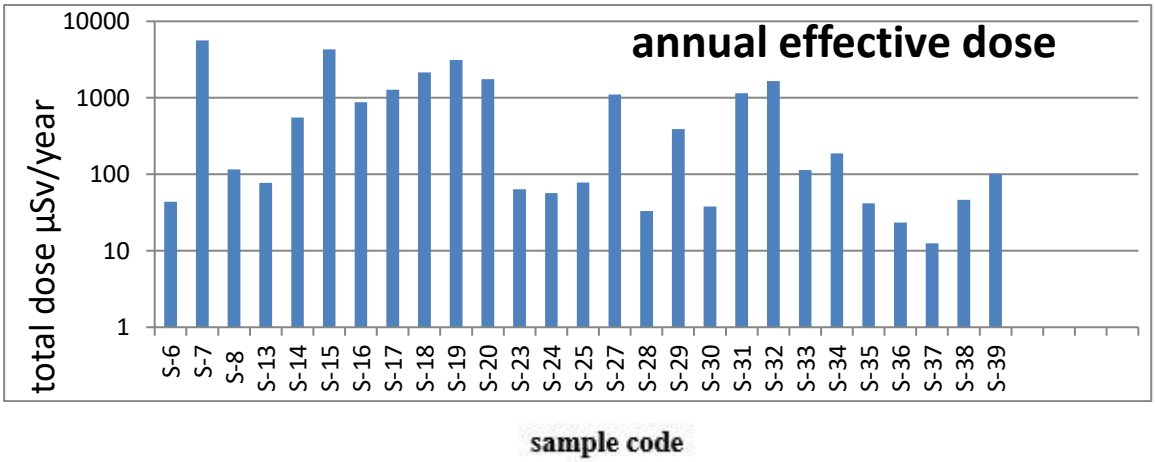

Figure 8 The annual effective dose for selected area

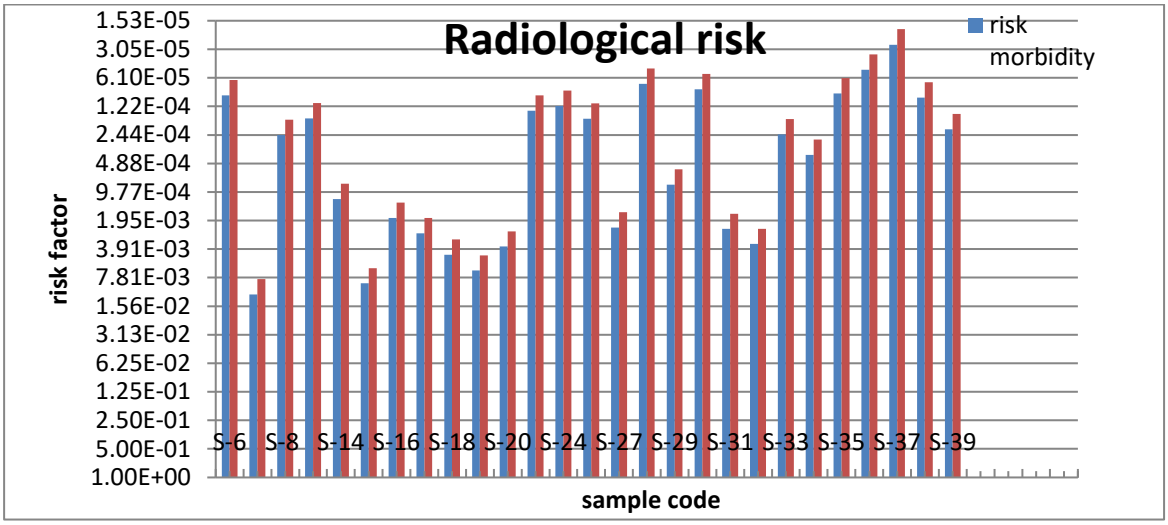

Figure 9 The annual radiological risk factor for selected area

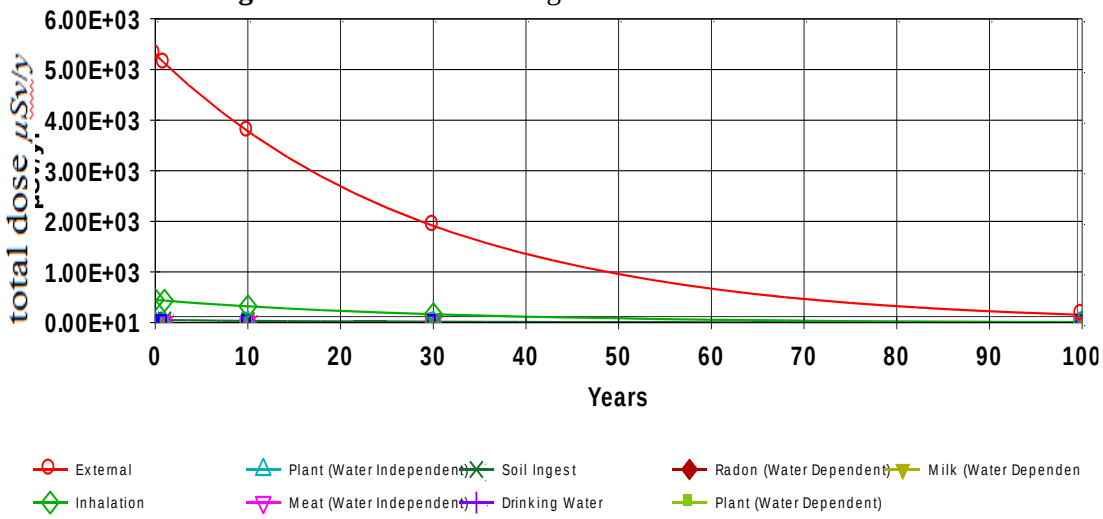

Figure 10 The total radiological dose to highest area(S7) by pathways components

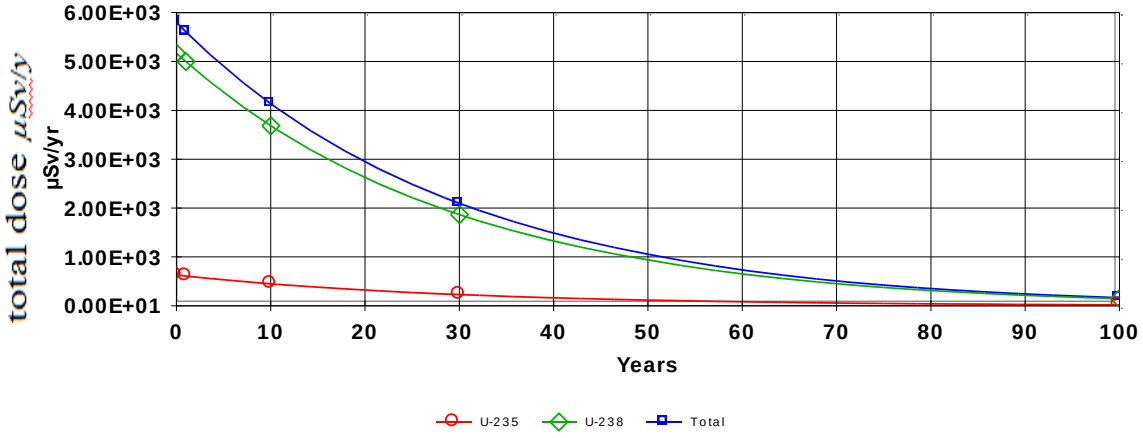

Figure 11 The total radiological dose to highest area(S7) by the radionuclides

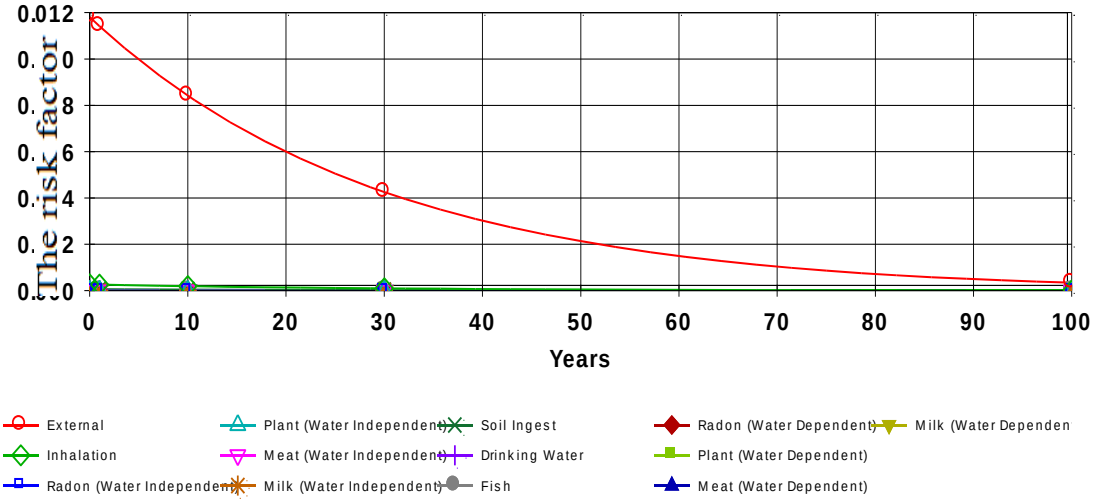

Figure 12 The radiological risk factor for highest area (S7)by pathways components

5. Discussion

(40) soil samples were collected from the fuel fabrication facility according to the results obtained from laboratory analysis as in table 2 there were a presence of high concentrations of (^{238}U ^{235}U) radionuclides in(27) soil sample above background level the highest radiation dose for the chosen area of (S7) was (5617µSv/year) and risk (118x10^{2} 8124x10^{3}person/year) morbidity and mortality respectively The total radiation dose and risk factor were conducted to (27) areas because of these areas have residual radioactive material depending on soil samples analysis results In 'figure 10' it can see the contribution and participation of each by path ways components in the total radiation dose and risks such as external ingestion and inhalation As shown in 'figure 11' the total radiological dose to highest area (S7) area along 100 years by contribution of the radionuclides ^{238}U is the highest radionuclide that contribute in radiation dose and risk In 'figures 1011 and 12' there are decreasing in radiation dose and risks over the time integration from RESRAD program report(19) areas were determined over to the risk limit that illustrated in table 4 and 'figures 89' these areas are (S781314 15161718192023 2527 29 31323334 39)

6. Conclusions and Recommendations

The radiological risk depend on total dose from the results of this research there are a rising in nineteen areas in FFF each area in this study represent 100 m^{2} that mean 1900 m^{2} from 37400 m^{2} (5%) from total FFF area over the risk limit2700 m^{2} from 37400m^{2} are contaminated (72%) under this study Radiation protection program must conduct for workers in these areas by decreasing the working hours wearing protective clothing and suitable equipment's From one area that represented by soil sample the external exposure of all radionuclides that dominant on the exposure pathways (inhalation and ingestion) therefore must focus on the precaution and protection workers from external dose by taking in to account the working time is the major factor from radiation exposure Time factor can solve by reduce the daily number of working hours or use the alternative system for workers ^{238}U is the highest radionuclide that contributes in radiation dose and risk because of the obviously high difference in concentration activity between ^{238}U and another radionuclides by analyzed soil samples Because of the long life ^{238}U (about 45x10^{9} year)the radiological dose and risk reduce over the time but slightly by radioactive decay of all radionuclide but the second basis is environmental condition that play main role to reduce dose and risk from transport the contaminants by wind and leaching them underground that fine in 'figures 101112'

The highest areas (S7 S15 S17 S18 S19 S20 S27 S31 S32) must controlled by surrounding with warning label to prevent anyone reach them and putting a plan to decontamination as well as other contaminated areas

Acknowledgments
I would like to thank the assistance that given from physicists team in/ Decommissioning Directorate and to acknowledge the Radiation Measurements Department/ Central Laboratories Directorate at Ministry of Science and Technology

References

[1] Council of the European Union 1996 laying down basic safety standards for the protection of the health of workers and the general public against the dangers arising from ionizing radiation
[2] United Nations Scientific Committee on the effect of Atomic Radiation UNSCEAR 2000 Sources effect and risks of ionizing radiation
[3] International Atomic Energy Agency IAEA 2008 safety standards series No WsG52 decommissioning of facilities using radioactive material safety guide Vienna 2008
[4] International Atomic Energy Agency IAEA 1996 Safety Series Reports No 115 International basic safety standards for protection against ionizing radiation and for the safety of radiation sources Vienna
[5] Till JE and and Helen A G 2008 radiological risk assessment and environmental analysis Oxford University Press 2008
[6] Agbalagba E Avwiri G and ChadUmoreh Y 2012 Gamma spectroscopy measurement of natural radioactivity and assessment of radiation hazard indices in soil samples from oil fields environment of Delta State Nigeria *Journal of environmental radioactivity* **109** page 6470
[7] Michael G Stabin 2007 Radiation protection and dosimetry an introduction to health physics Springer Science and Business Media
[8] International Commission On Radiation Units And Measurements 1993 Quantities and units in radiation protection dosimetry report No 51 Icru Bethesda
[9] Department of energy and the US Nuclear regulatory commission The US nuclear regulatory commission 2014 RESRAD onsite version 70 computer code the Environmental science Division of Argonne National Laboratory
[10] C Yu Cheng and S Kamboj 2015 RESRAD for radiological risk assessment comparison with EPA cercla ToolsPRG and DCC calculators argonne national laboratory
[11] Ibrahim NK 2016 radioactive contamination and radiological risk assessment of the destroyed nuclear facilities at AlTuwaitha nuclear site PhD Thesis University of AlMustansiriyah College of Science

Multispectral and Panchromatic used Enhancement Resolution and Study Effective Enhancement on Supervised and Unsupervised Classification Land – Cover

Multispectral and Panchromatic used Enhancement Resolution and Study Effective Enhancement on Supervised and Unsupervised Classification Land – Cover

S S Salman, W A Abbas

Department of Clinical Laboratory Science, College of Pharmacy, University of Baghdad, Baghdad, Iraq.

Abstract. The goal of the study is to support analysis Enhancement of Resolution and study effect on classification methods on bands spectral information of specific and quantitative approaches. In this study introduce a method to enhancement resolution Landsat 8 of combining the bands spectral of 30 meters resolution with panchromatic band 8 of 15 meters resolution, because of importance multispectral imagery to extracting land - cover. Classification methods used in this study to classify several lands -covers recorded from OLI- 8 imagery. Two methods of Data mining can be classified as either supervised or unsupervised. In supervised methods, there is a particular predefined target, that means the algorithm learn which values of the target are associated with which values of the predictor sample. K-nearest neighbors and maximum likelihood algorithms examine in this work as supervised methods. In other hand, no sample identified as target in unsupervised methods, the algorithm of data extraction searches for structure and patterns between all the variables, represented by Fuzzy C-mean clustering method as one of the unsupervised methods, NDVI vegetation index used to compare the results of classification method, the percent of dense vegetation in maximum likelihood method give a best results.

Keywords. Panchromatic Band, NDVI, Maximum likelihood and supervised Classification, Enhancement resolution**.**

1. Introduction

In Research of environment the applications of R.S meaningful tool. where R.S successful to extract land - cover map and classification of the spectral image [1, 2], monitoring and detection real time of deforestation [3, 4], guess production and vegetation area [5] and pollution monitoring [6].
Ehlers fusion method used to enhancement resolution to obtain land cover data by remote sensing and interpretation of imagery through merge high-resolution panchromatic band (15 meters) with bands - spectral imagery of 30 meters.

Image classification is usually applied in an optical pattern, object recognize, in medical applications and industrial processes [7]. Methods of classification (unsupervised, supervised) develop to give the solution of scientific problems [8], Fuzzy C-mean clustering method as one of unsupervised methods [9], where K-NN and MLC techniques an example of supervised classification [10, 11], which can be

divided into two-stage first: calibration depends on spectral signature of various bands obtain from training to known class labels, second: estimation class which applied to other un-known location.

2. Methodology

The study area was located in the northwest provinces of Iraq between Tikrit and Kirkuk, at 43.30°→ 43.45°E longitude, and 34.40°→34. 50°N latitude, datum WGS 84 and UTM projection, zone 38. The image is high quality and does not contain clouds, the study area is surrounded by wheat plantations 'Figure 1'.

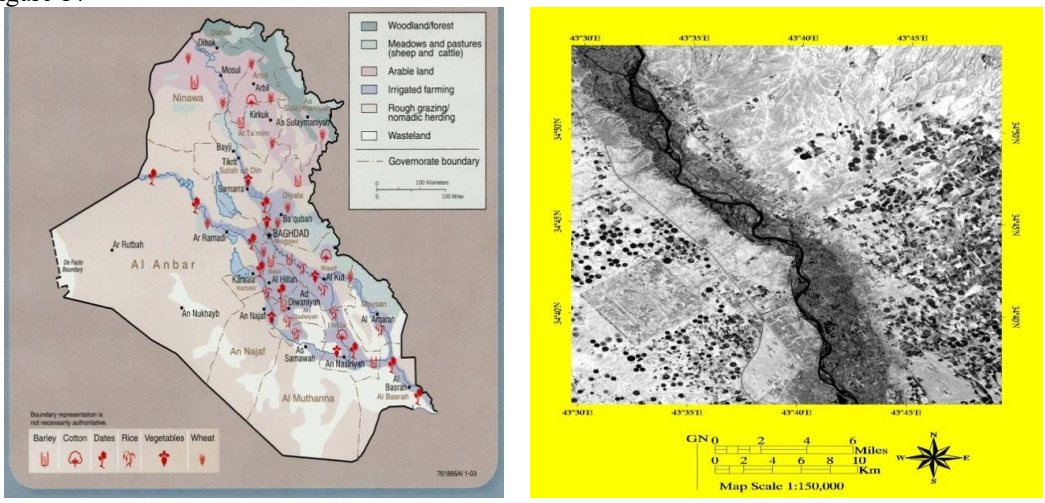

a **b**

Figure 1. (a) Land use map of Iraq country lies between the geographic coordinates lat. 37.38°→ 28.5°N, and Long. 38.70°→48.75°E. (b) photomap of the study area.

The data of study area acquire from the free website (http://landsat.usgs.gov/landsat8.php) of OLI satellite for February (2014, 2015). OLI -8 consist of 11 bands, 1-7, 9 bands with spatial resolution 30 meters, band 8 (panchromatic) is 15 meters resolution while bands 10, 11 with 100-meter spatial resolution. OLI - 8 presented on February 11, 2013, include two senses (Thermal Infrared, Operational Land Imager), the image produce from OLI- 8 of 16 bit (65536 gray level), and coverage study area every 16 days.

Ehlers fusion, image classification methods, true color composite image and panchromatic image of the study area (2014, 2015) was applied using Matlab 2013 and Erdas software 2014. 'Figure 2' show the true color image and panchromatic.

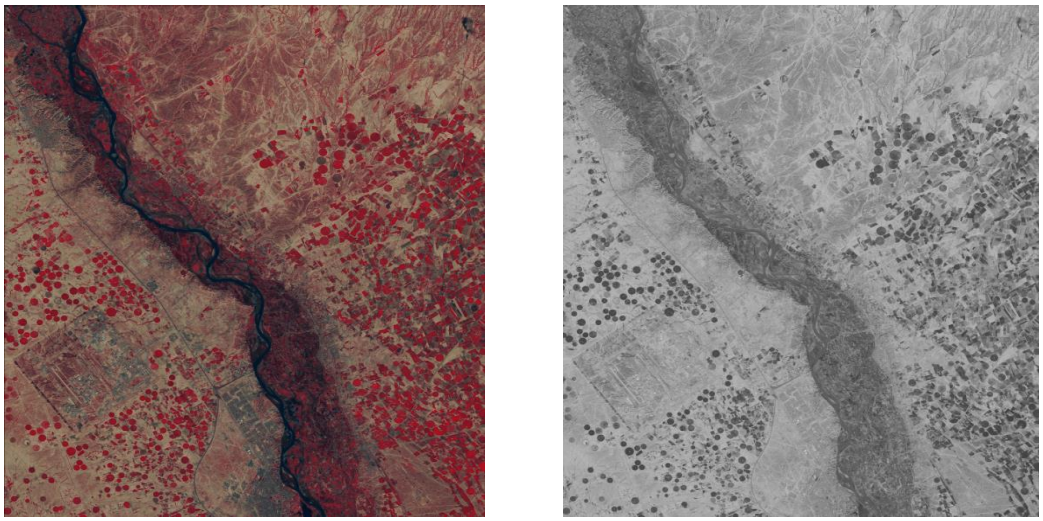

a b

Figure 2. (a) True color composite image (size 1002×1202) pixels, spatial resolution 30 m resolution 30 m of the study area, **(b)** panchromatic image b8(size 2004×2404) resolution 15 m of the study area.

3. Ehlers fusion

The algorithm of Ehlers Fusion is merging of two images different in spatial resolution to create a new image with new properties.Fusion differentiated into three ways: scale of pixel, Acknowledge and feature [12] .pixel scale fusion algorithm is often used in image pansharpening [13]. These methods depend on a group of arithmetic processing (PCA, Fourier Transform, HIS, wavelet transform,) [14].The algorithm of Ehlers Fusion implemented by steps:

1. Multispectral image transformation in intensity hue saturation.
2. Apply Fast Fourier Transform (FFT) and low-pass filter in the result of step 1.
3. Apply (FFT) and high pass filter in the panchromatic image.
4. Apply inverse FFT and the results are combining.
5. Inverse intensity hue saturation transformation apply to output a fused color (RGB) image

The algorithm implements for three bands till all bands are fused with the panchromatic band. The result of fusion is presented in 'Figure 3'.

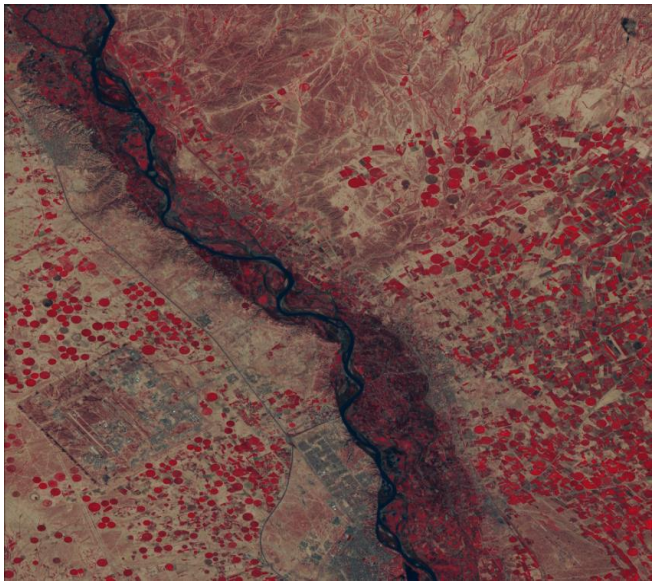

Figure3. Pansharpened image True Color Composite(size 2004×2404) resolution 15 m of the study area (Feb.2015)

4. Green Vegetation Index

One vegetation indicator for dense vegetation assessment is called *Normalized Difference Vegetation Index (NDVI)*, the range of NDVI (0.2 – 0.8) for healthy plants. NDVI is calculated on a per-pixel basis as the difference between the reflectance of red band and reflectance of near infrared band from an image:

$$NDVI = \frac{\rho_{NIR} - \rho_R}{\rho_{NIR} + \rho_R} \quad (1)$$

Where ρ represent the reflectance, the result show in figure (4) and percentage of dense vegetation from land cover show in table (1).

Table 1. Percentage of dense vegetation from NDVI method.

Year	Percentage area%
2014	14.53
2015	14.28

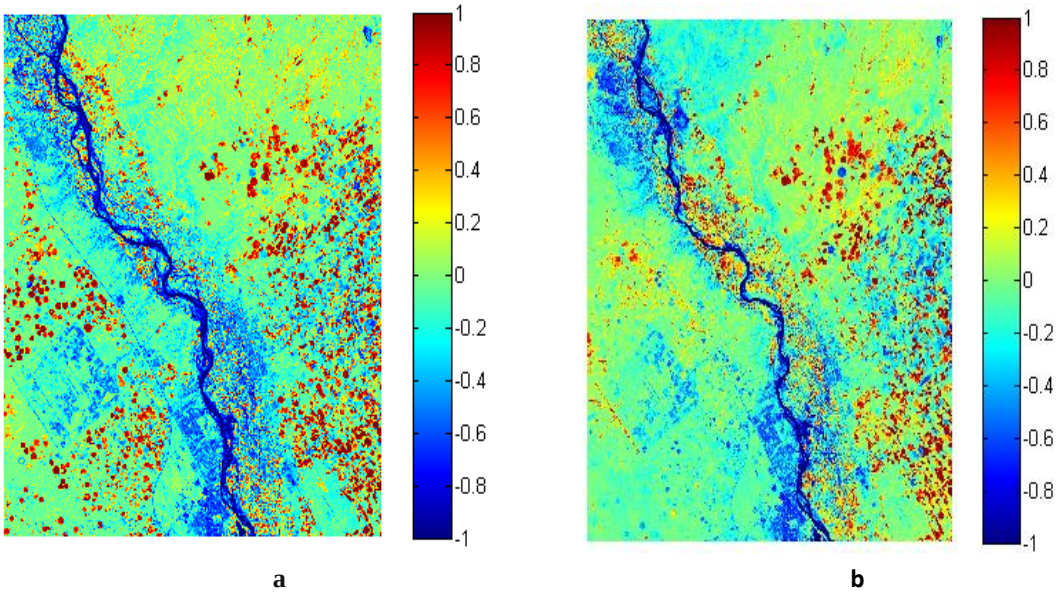

Figure 4. Normalized Difference Vegetation Index (NDVI), (a) 2014, (b) 2015.

5. Unsupervised classification

Fuzzy c-mean clustering FCM method is widely applied to dividing data into homogeneous classes with respect to some given criterion. , this algorithm presented by [9].Which based on minimizing an object function (J_q) as follow:

$$J_q = \sum_{i=1}^{n}\sum_{j=1}^{m} U_{ij}^{q}\, d(x_i, \theta_j) \quad (2)$$

Where *d* is the distance between the center of clusters θj and data x_i, *u* is fuzzy membership of data x_i to cluster with center θ_j *and u* calculated from the equation 3:

$$\boldsymbol{u_{ij}} \in [\,\mathbf{0},\mathbf{1}], \sum_{j=1}^{n} \boldsymbol{u_{ij}} = \mathbf{1} \quad \& \quad 0 < \sum_{j=1}^{n} \boldsymbol{u_{ij}} < n \quad (3)$$

The $\boldsymbol{u_{ij}}$ function and center $\boldsymbol{\theta_j}$ of each cluster are calculated from:

$$\boldsymbol{u_{ij}} = \left(\sum_{k=1}^{m} (\boldsymbol{d}(\boldsymbol{x_i}, \boldsymbol{\theta_j}) / \boldsymbol{d}(\boldsymbol{x_i}, \boldsymbol{\theta_k}))^{\left(\frac{2}{q}-1\right)}\right)^{-1} \quad (4)$$

$$\boldsymbol{\theta_j} = \frac{\sum_{i=1}^{N} \boldsymbol{u_{ij}^{q}} \boldsymbol{x_i}}{\sum_{i=1}^{N} \boldsymbol{u_{ij}^{q}}} \quad (5)$$

The object function of FCM optimize by frequent update of the $\boldsymbol{u_{ij}}$ function and centers($\boldsymbol{\theta_j}$) of clusters till the different between two iteration is smaller than a threshold, the results of method show in Figure 5 and percentage of each class of land cover show in Table 2, where the accuracy calculated depend on dense vegetation percent from NDVI method.

Table 2. Percentage classes of Enhanced Resolution and original band using FCM method.

Year	Name class	Percentage classes of original Resolution		Percentage classes of Enhanced Resolution	
		Percentage area%	Accuracy	Percentage area%	Accuracy
2014	**Water**	3.1%		3.3%	
	Wet Soil	22.7%		24.9%	
	Dry Soil	16.3%		16.5%	
	Dense Vegetation	15.3%	94.7%	15.4%	94.01%
	Wet Vegetation	16.6%		16.0%	
	Dry Vegetation	26.1%		23.9%	
2015	**Water**	1.6%		1.8%	
	Wet Soil	24.6%		25.2%	
	Dry Soil	18.6%		17.8%	
	Dense Vegetation	12.2%	85.43%	11.9%	83.33%
	Wet Vegetation	17.2%		18.2%	
	Dry Vegetation	25.8%		25.1%	

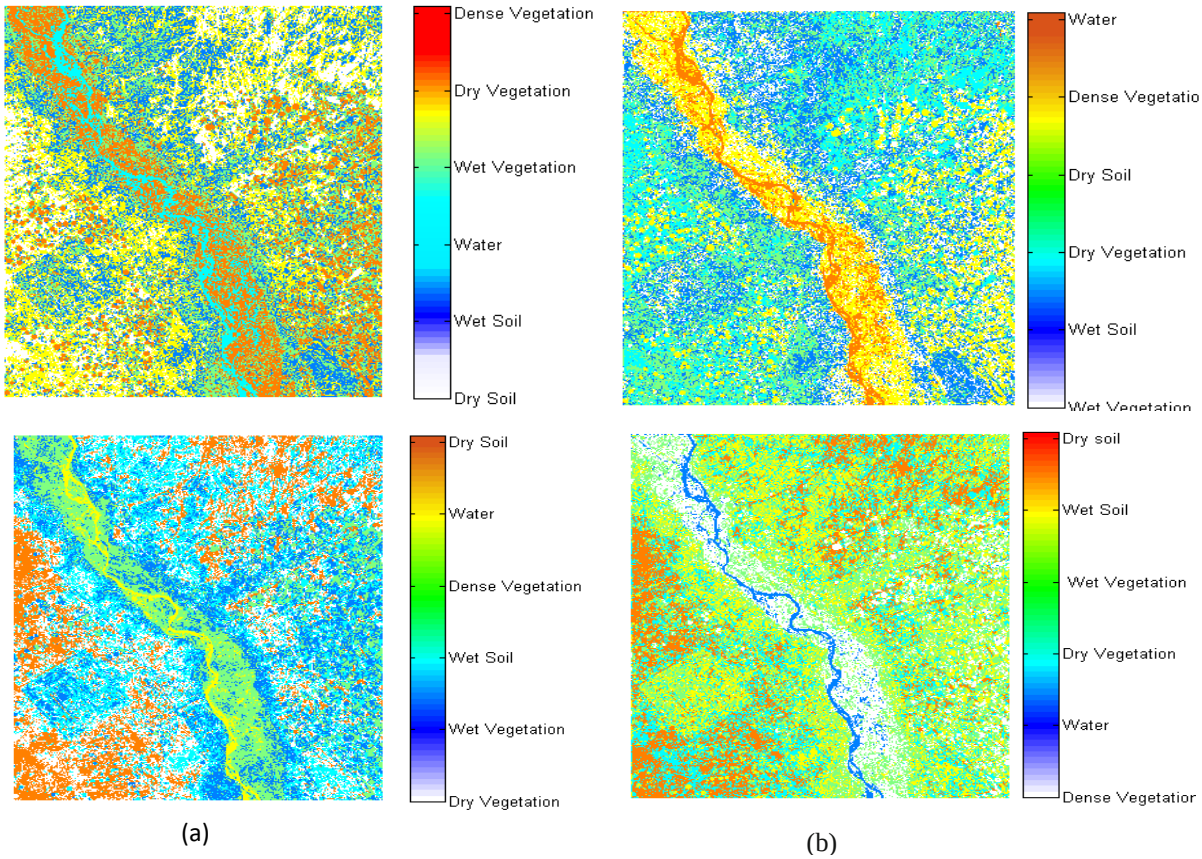

Figure 5. (a) FCM Classification of Original OLI Bands Composite(size 1002×1202), (b) Pansharpened image True Color Composite(size 2004×2404) ,first row (2014),Second row(2015).

6. Supervised classification

6.1. K-Nearest Neighbor Algorithm

The K-nearest neighbor method program is one of the most celebrated classification algorithms used for expecting the class of a sample with unspecified class based on its neighbor records class [15], it's an exemplify of instance-based *learning*, in which the set of data is stored as training data, so that a classification for unclassified sample may be found merely by comparing it to the closest records in the training set [16].The steps of the algorithm as follows:

1. The distance between of input sample and training samples are calculated.
2. Depending on distance select the K-nearest neighbor to arrange the training samples.
3. The class which has the majority of the k-nearest neighbors is used.

The important parameter in K-nearest neighbor method is K value, its proper value depends on the data apportionment [16], the results of method shown in Figure 6 and percentage of each class of land cover shown in the Table 3.

Table 3. Percentage classes of Enhanced Resolution and original band using K-nearest neighbor method.

Year	Name class	Percentage classes of original Resolution		Percentage classes of Enhanced Resolution	
		Percentage area%	Accuracy	Percentage area%	Accuracy
2014	**Water**	2.9%		3.0%	
	Wet Soil	19.1%		19.4%	
	Dry Soil	22.2%		20.7%	
	Dense Vegetation	16.4%	87.13%	17.8%	77.49%
	Wet Vegetation	14.5%		14.0%	
	Dry Vegetation	24.8%		25.2%	
2015	**Water**	1.7%		2.0%	
	Wet Soil	14.9%		2.0%	
	Dry Soil	25.3%		23.2%	
	Dense Vegetation	15.2%	93.55%	16.7%	83.05%
	Wet Vegetation	21.4%		21.7%	
	Dry Vegetation	21.0%		19.4%	

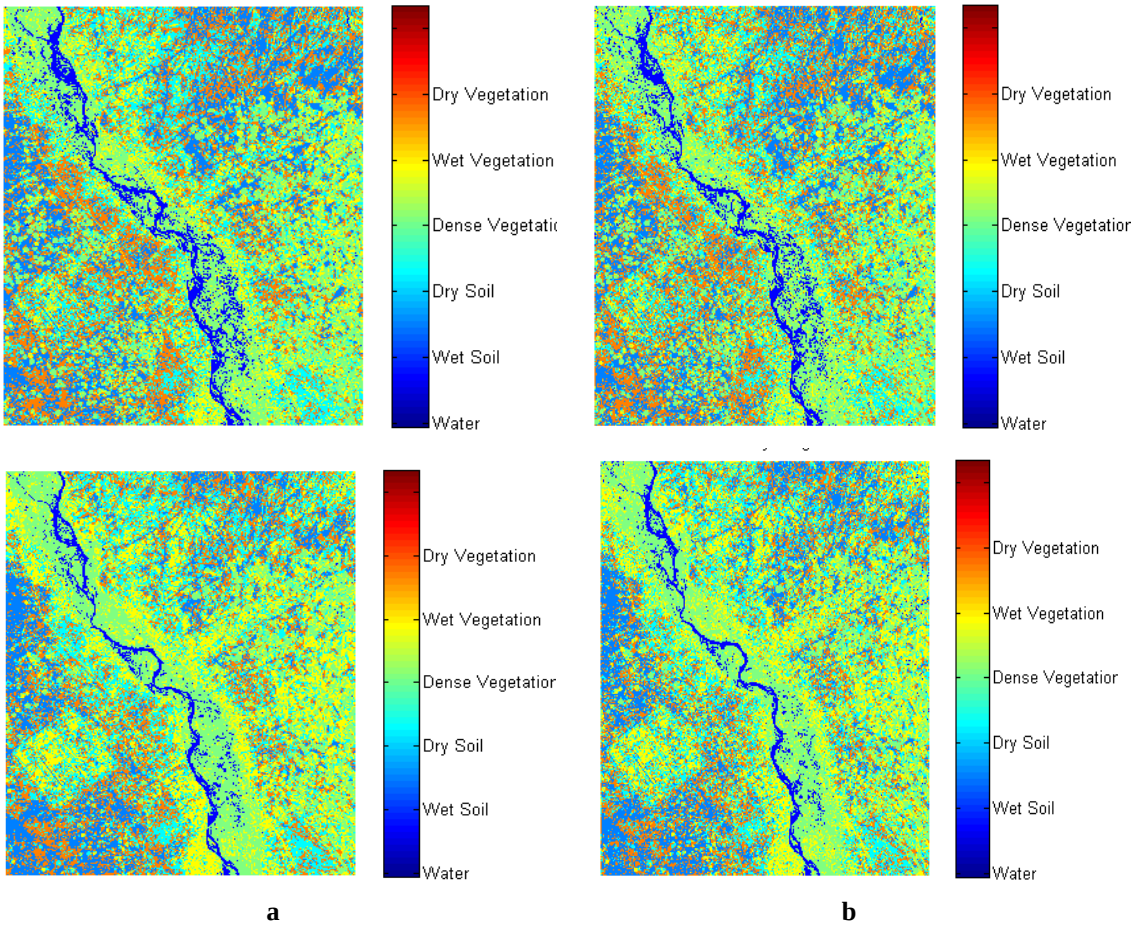

Figure 6. (a) The K-nearest neighbor Classification of Original OLI Bands Composite(size 1002×1202), (b) Pansharpened image True Color Composite(size 2004×2404) ,first row (2014),Second row(2015).

6. 2 Supervised Maximum Likelihood Classification image

The popular method used to classification Landsat imageries is Maximum Likelihood Classification (MLC) which applied in this study as one of the supervised methods.The algorithm depends on predefined 6 classes as training (Dense Vegetation, Wet Vegetation, Dry Vegetation, Water, Wet Soil, and Dry Soil), the steps of implementing the method as follow:

1. Six types of land cover specified in the study area as training classes set.
2. The pixels are selected from each training classes using the information of land cover for the study area.
3. Mean vector and covariance matrix are evaluated for each class.
4. Jeffries-Matusita (JM) distance used to measure the class separability of normal distribution for two training classes by the following [17] :

$$J_{ij} = \sqrt{2(1 - e^{-\alpha})} \quad (6)$$

Where α is the Bhattacharyya distance is defined as:

$$\alpha = \frac{1}{8}(\mu_i - \mu_j)^t \left[\frac{C_i+C_j)}{2}\right]^{-1} (\mu_i - \mu_j) + \frac{1}{2} ln[\frac{\left|\frac{C_i+C_j}{2}\right|}{\sqrt{|C_i||C_j|}} \quad (7)$$

μ is the means of vector and c is covariance matrices, Jij ranges from 0 to 2.0, where J ij> 1.9 indicates good separability of classes.

Moderate separability for 1.0 ≤ J ij ≤1.9 and poor separability for J ij < 1.0,

5. The last step, classified each pixel in the image into one of the six land cover types.

The results of method classification (MLC) show in figure (7) and percentage of each class of land cover shown in the Table 4.

Table 4. Percentage classes of Enhanced Resolution and original band using Maximum Likelihood Classification method.

Year	Name class	Percentage classes of original Resolution		Percentage classes of Enhanced Resolution	
		Percentage area%	Accuracy	Percentage area%	Accuracy
2014	**Water**	0.7%		0.8%	
	Wet Soil	29.2%		23.7%	
	Dry Soil	7%		4.2%	
	Dense Vegetation	15.7%	91.94%	15.1%	96.07%
	Wet Vegetation	18.2%		9.1%	
	Dry Vegetation	29.0%		46.9%	
2015	**Water**	0.7%		0.9%	
	Wet Soil	23.5%		19.6%	
	Dry Soil	1.6%		4.0%	
	Dense Vegetation	14.6%	97.7%	14.8%	96.35%
	Wet Vegetation	20.8%		18.0%	
	Dry Vegetation	38.1%		42.8%	

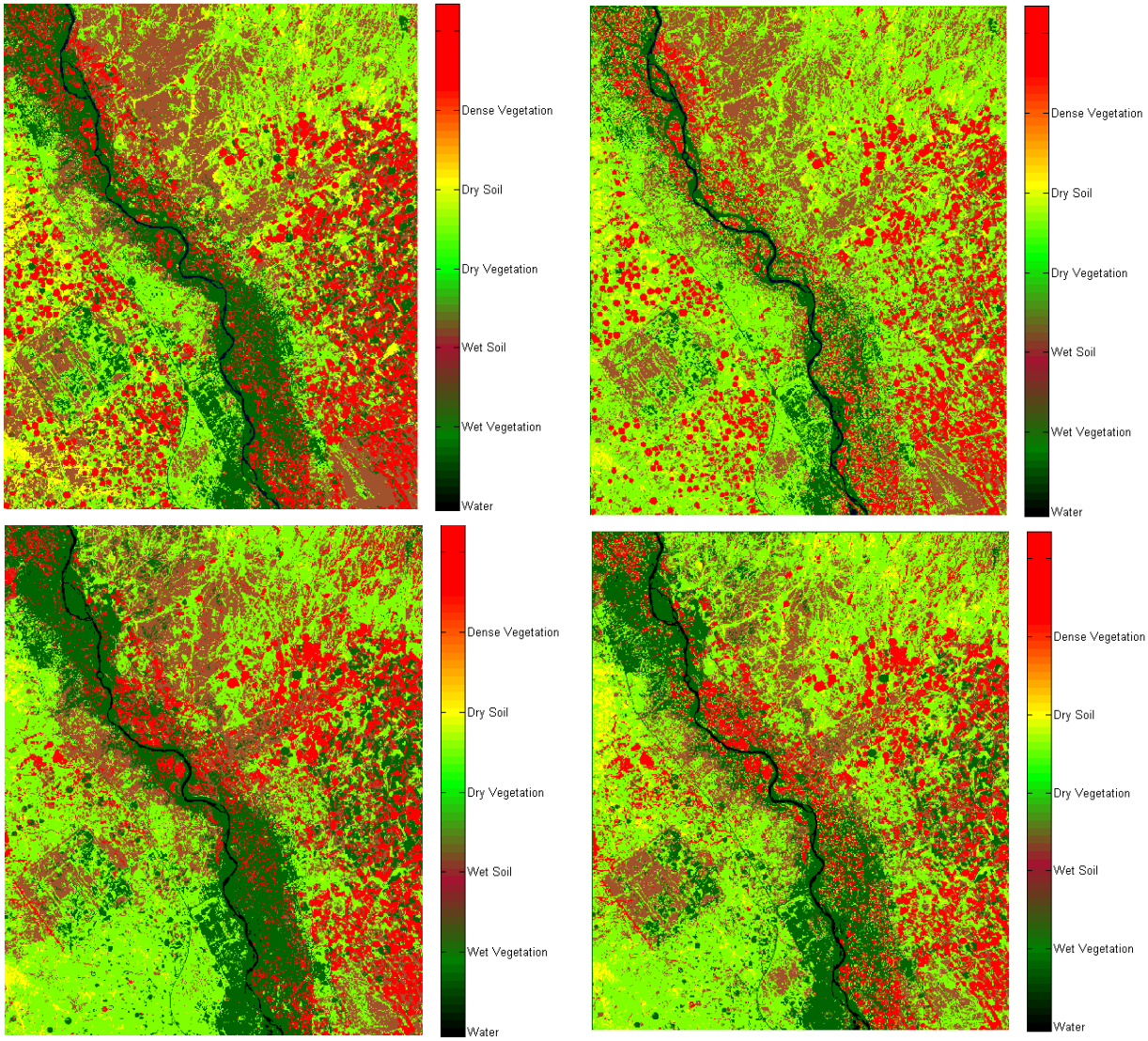

Figure 7. (a) The Maximum Likelihood Classification of Original OLI Bands Composite(size 1002×1202), (b) Pansharpened image True Color Composite(size 2004×2404), First row (2014), Second row(2015).

7. Conclusion

The possibility of merging multi - spectral bands with a panchromatic band made OLI - 8 it has been a good spatial resolution to detect and classification Land - cover. Properties of Land – cover can be extracted effectively with image classification, the first problem we have encountered was the lack of accurate records issued by the Iraqi Ministry of Agriculture for the true percent of the study area (Because of the occupation ISIS parts of the study area). For this purpose, the research team has

compared the result of Normalized difference vegetation index (NDVI) with methods classification to install the percentage of land cover and make sure the data was correct.

The results showed that supervised classification (MLC) is the most powerful methods when accurate training data is provided where the percentage of dense vegetative areas give a very good accuracy, that means the MLC method is useful in the classification of homogeneous areas .while the result of KNN method smaller than MLC with lower accuracy, It is due to the fact that the study area has an overlap between different species.

FCM method takes a long time to classify image depend on the number of iterations to minimizing an object function, we conclude that FCM method being useful in the classification of overlapping areas when getting a suitable number of iteration.

Ehlers fusion was applied as Enhancement method in this study is good for monitoring changes in land cover and is considered an important way to improve the accuracy of land sat 8 images.

References

[1] Powell S L, Cohen W B ,Yang Z,Pierce J D, Alberti M. Quantification of impervious surface in the Snohomish water resources inventory area of Western Washington from 1972-2006. *Remote Sens. Environ.* 2008, 112: 1895–1908.

[2] Joshi P K K, Roy P S, Singh S, Agrawal S, Yadav D. Vegetation cover mapping in India using multi-temporal IRS Wide Field Sensor (WiFS) data. *Remote Sens. Environ.,* 2006, 103: 190–202.

[3] Potapov P, Hansen M C, Stehman S V, Loveland T R, Pittman K. Combining MODIS and Landsat imagery to estimate and map boreal forest cover loss. *Remote Sens. Environ.,* 2008, 112: 3708–3719.

[4] Dennison P E, Roberts D A. Daytime fire detection using airborne hyperspectral data. *Remote Sens. Environ.*, 2009, 113: 1646–1657.

[5] Liu JY, Liu ML, Tian HQ, Zhuang DF, Zhang ZX, Zhang W, Tang XM, Deng XZ. Spatial and temporal patterns of China's cropland during 1990-2000: an analysis based on Landsat TM data. *Remote Sens. Environ.*, 2005, 98: 442–456.

[6] Zhu HW, Basir O. An adaptive fuzzy evidential nearest neighbor formulation for classifying remote sensing images. *IEEE Trans. Geosci. Remote Sens*., 2005, 43: 1874–1889.

[7] Muller KR , Mika S, Ratsch, G, Tsuda K, Scholkopf B. An introduction to kernel-based learning algorithms. *IEEE Trans. Neural Networks*, 2005, 12: 181–201.

[8] Richards JA, Jia X. Remote Sensing Digital Image Analysis, *an Introduction, 4th ed.; Springer-Verlag*, Secaucus, NJ, USA, 2006.

[9] Balafar MA, Ramli A R, Mashohor S. Edge-preserving clustering algorithms and their application for MRI image segmentation. *Proceedings of the international multiconference of engineers and computer scientists,1, IMECS*, March 17-19, Hong Kong, 2010.

[10] Cleveland W, Devlin S. Locally weighted regression: an approach to regression analysis by local fitting. *J. Amer. Statist. Assoc.,* 1988, 83: 596–610.

[11] Franco-Lopez H, Ek A, Bauer M. Estimation and mapping of forest stand density, volume, and cover type using the k-nearest neighbor's method. *Remote Sens. Environ*., 2001, 77: 251–274.

[12] Ehlers M, Klonus S, strand PJ, Rosso P. Multi- sensor image fusion for pansharpening in remote sensing. *International Journal of Image and Data Fusion*., 2010, 1(1): 25-45.

[13] Zhang Y. Understanding Image Fusion. *Photogrammetric Engineering and Remote Sensing*, 2004, 70 (6): 657-661.

[14] Lasaponara R, Masini N. Satellite Remote Sensing, A New Tool for Archaeology. *Remote Sensing and Digital Image Processing*, Chapter 4, Springer, 2012, 16: 87-109.

[15] Maryam K A. Method to Improve the Accuracy of K-Nearest Neighbor Algorithm International *Journal of Computer Engineering and Information Technology,* 2016, 8 (6); 90–95, Available online at: www.ijceit.org .

[16] Sayali D, Jadhav, Channe H P. Comparative Study of K-NN, Naive Bayes and Decision Tree Classification Techniques. *International Journal of Science and Research* (*IJSR*) ISSN (Online): 2319-7064, 2013.
[17] Richards JA. Remote sensing digital image analysis: *An introduction. Springer-Verlag*, Berlin, Germany, 1999.

The Effects of micro Aluminum fillers In Epoxy resin on the thermal conductivity

The Effects of micro Aluminum fillers In Epoxy resin on the thermal conductivity

Kareem A Jasim* , **Rihab N Fadhil****

Department of Physics, College of Education for pure science, University of Baghdad, Baghdad, Iraq.

*kareem.a.j@ihcoedu.uobaghdad.edu.iq, **rahb_naser@yahoo.com

Abstract. A hand lay-up molding method was used to prepare Epoxy/ Aluminum composites. As a matrix used Epoxy resin (EP) with reinforced by Aluminum particles. The preparation technique includes preparing carousel mold with different weight percentage of fillers (0, 0.05, 0.15, 0.25, 0.35, and 0.45). Standard specimens (in 30 mm diameter) were prepared to the thermal conductivity tests. The result of experimental thermal conductivity (k), for EP/ Aluminum composites show that , k increase with increasing Aluminums percentage and it have maximum values of (1.4595 W/m .K).

Keywords: Epoxy/ Aluminum composites, thermal conductivity, Epoxy resin, Aluminum.

1. Introduction

The defined of composite material as: “A substance consisting of two or more of two materials, insoluble in one another, which are joint to form a useful engineering material possessing certain properties not possessed by the constituents” [1].

Such materials offer advantages over conventional isotropic structural materials such as aluminum, and other sorts of metal .These advantages involve high strength, low weight, and good fatigue strength and corrosion resistance [2].

Polymer composite materials, based on a polymer matrix and inorganic micro particle fillers, have dragged great attention among researchers, due to improvements in different properties including thermal, electrical, optical and mechanical properties [3]. The polymer composite collects the advantages of polymer (e.g., ductility, dielectric, flexibility, and process ability) and the advantages of the filler materials (e.g., hardness and the stability thermal). Epoxy resins are used to generate structural adhesives helpful to large portions requisitions. Epoxy built adhesives will security an extensive variety about substrates includes composites, metals, pottery and elastic. They might be figured should confer heat and compound safety What's more will show hole filling Furthermore different obliged properties. Adhesives in light of Epoxy resins would skilled about accomplishing precise highshear qualities and would utilize extensively clinched alongside structural holding provisions in the air ship industry [4].

2. Thermal conductivity

Thermal conductivity is the capacity of a material to heat conducting. This quantity represents the rate of heat flow per unit time in a homogenous material under steady conditions, per unit area, per unit temperature gradient in a direction perpendicular to area [5].Polymers are often utilized as thermal insulators because of their low thermal conductivities. For these materials, the transfer of energy is accomplished by the rotation and vibration of the molecules chain [6].

Imply that free bath and the temperature gradient in (equ.1) are because of the random nature of the thermal conductivity procedures into the expression for the thermal flux [7]. The heat transfer method depends upon several factors, consisting of sort of material, temperature and case of the thermal material. Specifically there are two mechanisms for heat transfer through a solid substance [8].

- Free electrons and lattice vibration in solid conductors are the dominant mechanism of temperature transfer.
- The phonons in solid insulator substances are the unique mechanism.

Consistent with the first clear assertion proposed via Fourier, heat flow through a substance is proportional to the temperature gradient, as the following Equation:

$$q = -k\frac{\mathrm{d}T}{\mathrm{d}x} \tag{1}$$

Where q: the thermal energy flux transmitted across a unit area per unit time. k is the coefficient of thermal conductivity, and (dT/dx) is the gradient of temperature. The unit of q is W/m^2 and the unit of k is W/m. k [9]. Most conveniently in describe term for Thermal conduction is the scattering of phonons, via other phonons, or by using electrons [10].

Through the 'figure 1', the substance S was contained between two copper discs B and C, and the heater between B and a third copper disc A. The temperatures of all the copper discs were measured with a thermometer. When the discs had were assembled they were varnished to give them the same emissivity, and the whole apparatus was suspended in an enclosure of constant temperature. In the theory given below, the following symbols are used [11]:

IV: rate of supply of energy to the heater, after the steady state has been reached.

e: heat loss per second per sq.cm for each 1˚ increase of discs temperature, over that of enclosure.

T: excess of temperature over that of the enclosure.

d: thickness of disc, r: radius of disc.

The heat received per second by disc A and given up to air is:

$$(\pi r^2 + 2\pi\, r\, dA)\, e\, TA \tag{2}$$

The heat received per second by S and given up to air from its exposed surface or passed on to A is

$$e\, TA(\pi\, r2 + 2\pi\, r\, dA) + 2\pi\, r\, ds\, (1/2)(\, TA+TB) \tag{3}$$

In terms of IV can be obtained, since the total heat supplied must be equal to that given up by the various surfaces:

$$H=I.V = \pi\, r^2 e\, (TA+TB) + 2\pi re\, [(1/2)\, dS\, (TA+TB) + dATA+dBTB +dCTC] \tag{4}$$

So, thermal conductivity becomes:

$$KT\, ((TB - TA)/dS) = e\, [TA+ (2/r)\, (dA+ (1/4)\, dS)\, TA+ (1/2r)dSTB] \tag{5}$$

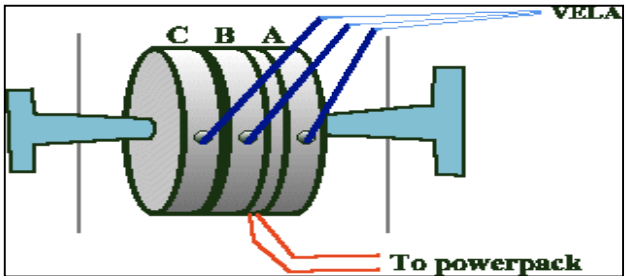

Figure 1: Schematic diagram of Lee's disc.

3. Thermal Conductivity in Composites

So as to attain material with desired thermal, electric, physical, and mechanical residences, polymers combined with deffrent types of fillers are used as matrix materials .The thermal conductivity of compsite materials, which can be represented as multiphase substance, depends upon thermal conductivity, proportion, and the distribution of the phase [12]. The distribution of the phase consists of its shape, size, volume reaction, orientation, weight percent, and conductivity relative to the heat flow direction path [8, 10, and12]. Agari et al. (1990), studied thermal conductivity of a polymer (PS and PS composite), filled with particles (quartz or Al2O3) for extensive variety from volume concentration. The results showed that thermal conductivity increased from low to super-high of filler con in order will get materials with wanted thermal, mechanical, electrical and physical properties, polymers mixed with different kinds of fillers (particles or fibers) are used as matrix material. The thermal conductivity of composite materials depends up on proportion, and the distribution of the phase [12]. In 1995 studied Torquto and Rintoul the impact of interface on the characteristic of composite media for metallic particles in epoxy matrices for different volume friction they developed rigorous bounds on the thermal conductivity effective of dispersion. [6]. Tavaman (2002) studied the thermal conductivity effective of composites filled with particles .His results were compared with experimental data of micro sized Al2O3 particles filled with HDPE composites [13].

Asmaa, Harith and Ekram (2010), studied The Effect of metals as Additives on Thermal conductivity of Epoxy Resin. They obtained results show increase thermal conductivity with increasing weight per cent age for Epoxy/Aluminum and Epoxy/Copper composites. While thermal conductivity for Ep/Fe composite show slight increase [14] Those primary destinations of the research will be with get ready and test tests about particulate composite, which comprises for epoxy resin as a matrix, with metal powder (Aluminum) about different weight percentage (0, 0.05, 0.15, 0.25, 0.35, and 0.45) as fillers. Those Examine expects with examine the impact for filler weight percentage and its sort on the thermal conductivity of the composite.

4. Experimental

For thermal tests, the procedures of preparing EP/Al composites with different additive weight percentage (0, 0.05, 0.15, 0.25, 0.35, and 0.45) percentage) were almost similar. The materials used to prepare the test samples ware epoxy resin (EP Euxit 50) production of Swisschem with the hardener (Euxit 50 KII) as a matrix and metal particle Al has average diameter of (7.1228 µm) of purity (99.0) as fillers. (Table 1) summarizes the materials and some of their properties. The chemical structure of epoxy resin is shown in ‘figure 2’.

Table1. Some of properties of the used material

Material	*Sample*	*Density (g/cm^3)*	*Thermal conductivity (W/m. K)*
Epoxy	*EP*	*1.05*	-------
Aluminum	*Al*	*2.7*	*247(9)*

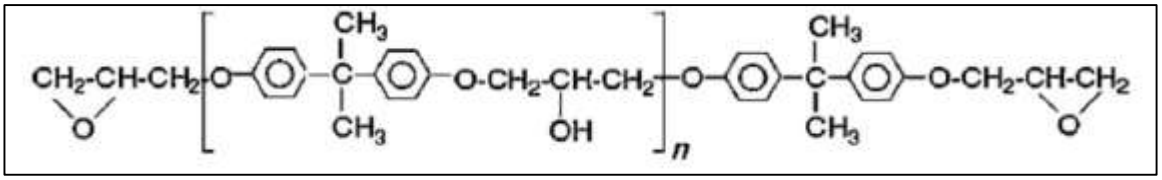

Figure 2: Epoxy structure [15].

A hand lay-up method was used to prepare all the specimens in this work .Samples composed of epoxy resin with Aluminum powder at different weight percentage (0%, 5%, 15%, 25%, 35%, and 45%), and the ratio of Epoxy to hardener is (5:2).To get good homogeneity between epoxy resin and Aluminum powder, homogenizer device at 700 rpm with 10 minutes to have good distribution for particles in epoxy resin. Vacuum system was used to remove the bubble before cast the composites in earlier prepared mold, blend was then poured into the mould, allowed to cure for 24 hours at room temperature (26 ± 2) ^{o}C.

Lee's disc was used to calculate the thermal conductivity. the prepared samples have a diameter 30 mm as shown in 'Figure 3' and 'Figure 4', the temperatures were measured by thermometers to calculate Heat current (H) and thermal conductivity (K) were calculated by using 'equation (4) and ' equation (5)' [16]. The experimental values for epoxy (0.671688 W/m. K)

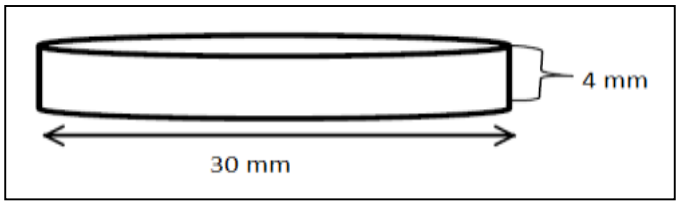

Figure 3. Dimension of thermal conductivity Test Specimens.

Figure 4: Photograph of Thermal conductivity Test Specimens for Epoxy and Epoxy/ Aluminum composites.

5. Results and Discussion

A Scanning Electron Microscope (SEM) with a magnifying force 5µm was used to calculate the average diameter partical for Al (7.1228µm) as shown in 'figure 5'.

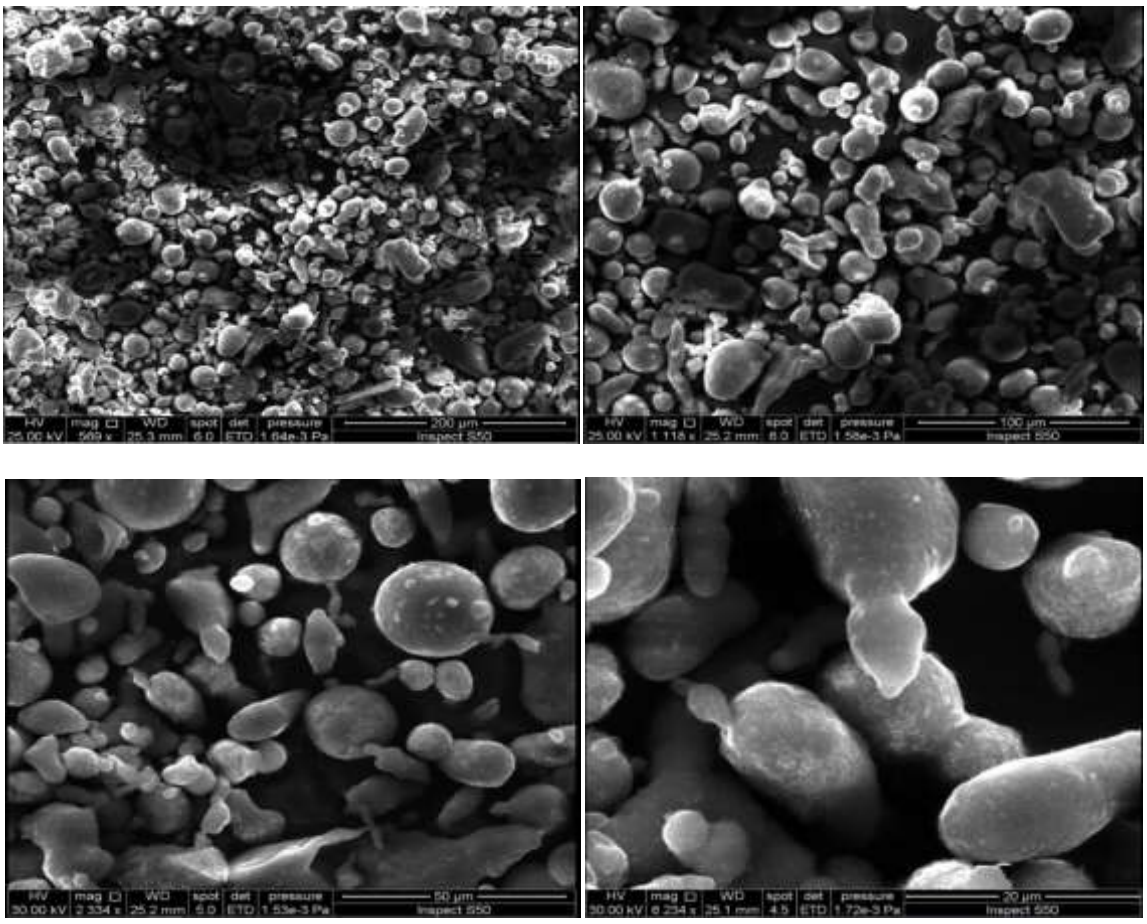

Figure 5. SEM image for Al

The results appear that k values for increase with increasing weight percentage from reinforcement, the maximum value 1.459549 W/m. K at 45% filler weight percentage for EP/Al composite as shown in (table 2). This table includes the type and weight percentage affect thermal conductivity of the composite.

Table 2. Thermal conductivity k for EP/Al composite

Wt%	V%	K (W/m. K)
0%	0	0.671688
5%	2.005731	0.732399
15%	6.422018	0.857353
25%	11.47541	0.976934
35%	17.31449	1.104591
45%	24.13793	1.459549

'Figure 6' shows the obtained results of thermal conductivity for EP/Al composites under study state. It is clear that k for Epoxy/Aluminum composites increase with increasing wt% of filler, this can be due to the well separation of the particles, that there is no interaction between them.

A phonon is a collective excitation in a periodic, elastic arrangement of atoms or molecules in condensed matter, such as solids and some liquids [17].

Aluminum has thermal conductivity and its value (247 W/m. K) [9]. When you add (5%) percentage of Aluminum to epoxy found that there was an increase in thermal conductivity by (0.060711) on thermal conductivity for epoxy.

The reason for this that when you mix epoxy with Al, Aluminum granules will spread in the matrix material at random according to manufacturing process, The presence of these particles plays an important role in the transition process.

When the sample surface bearing its thermal shed will move this energy from the higher temperature zone to the region least heat the heat transfer mechanism in the composite that depend on heat transfer phenomena by phonons and electrons. Upon arrival of a quantity of heat to the polymer chains and molecules made up a bunch of phonons which in turn will travel or absorb by Aluminum granules, transporting energy by electrons to the surrounding area leading to heat transfer from the higher temperature zone to the region least heat. Thermal conductivity for composites increase with increasing wt% of filler, The consequences show that the thermal conductivity increase for all composites .additionally it's affected by the type and weight percentage of additive, this end result is in a good agreement with general theory of the thermal conductivity of composites, which has been predicted that the addition of a second phase with thermal conductivity different than that of the matrix can be effect on the thermal conductivity of the resulting composite [18].

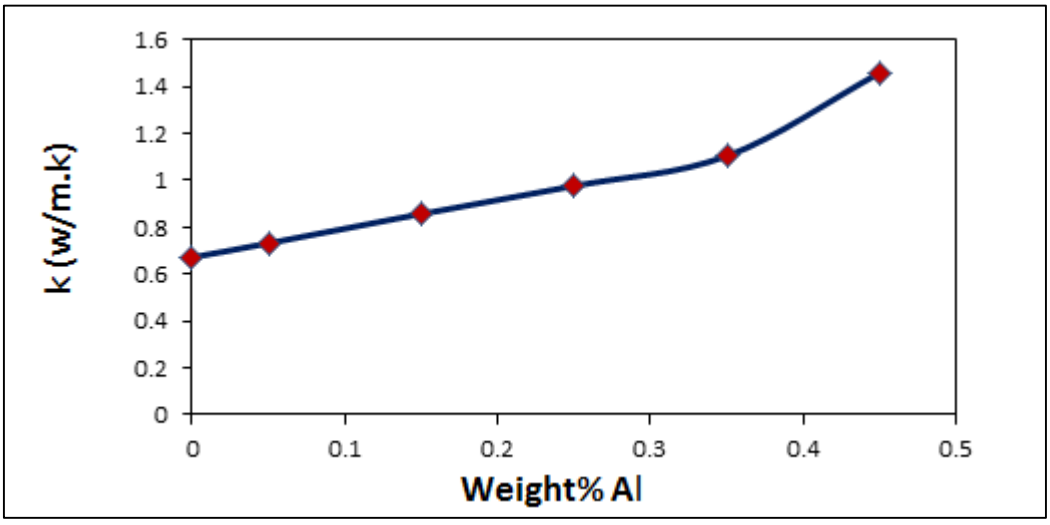

Figure 6. K vs. wt% of EP/ Al composite.

6. Conclusions

Composites were preparation using Epoxy resin as a matrix with metal particles Al which have average diameter (7.1228µm) as fillers with different weight percentage of fillers (0, 0.05, 0.15, 0.25, 0.35, and 0.45). Increase thermal conductivity for (EP/Al) composites with increasing addition rates of fillers, where maximum value (1.459549 (W/m. K)) at (45%Al), which increased by (117.3%) compared with epoxy.

References

[1] William Callister D 2006 Jr *Materials Science and Engineering An Introduction* 7th Edition PP 520-528
[2] Kullör L P and Spriner 2003 *Mechanics of Composite Structures* (Cambridge University Press Stanford)
[3] Koo J H 2006 *Polymer Nano composite Processing Characterization and Application* Mc. GrawHill companies USA
[4] Lubin and George 2013 *Handbook of composites* Springer Science & Business Media
[5] Harper Charles A 1975 *Handbook of plastics and elastomers*
[6] Callister W D and David G Rethwisch 2007 *Materials science and engineering an introduction* **7** (New York: Wiley)
[7] P F Intropera and V Dewit 1981 *Fundamental to Heat Transfer* (John Willey and Sons Inc. USA)
[8] Jaffer H I and Al-Shamri Z R 2002 *Iraqi J. Sci* **43c** 2
[9] Callister D 2000 *Fundamentals of materials Science and Engineering* Jr August Ch 17 S-254
[10] Wang W Ga Q and Yan Yang S 2001 *Acta polymerica Sinic a* **1** 1-4
[11] Kadhim B B 2005 Mechanical and thermal properties and ablation simulation of resole resin composites Ph D Thesis College of Science University of Baghdad.
[12] Kamoto J O and Ishida H 1999 *J Appl Poly Sci* **72** 1689
[13] Rondeaus F, Bedy P H and Rey J M 2001 Cryogenic Engineering Conference (John Willy and Sons USA)
[14] Shawky A H Jafeer and AL Ajaj Ekram 2010 The Effect of metals as Additives on Thermal conductivity of Epoxy Resin *Iraqi Journal of Physics* **8** 12 pp 74 -79
[15] Jean-Pierre Pascault and Roberto J J Williams 2010 *Epoxy Polymers* (WILEY-VCH Verl GmbH & Co. KGaA, Weinheim)
[16] Keblinski P and Phillpot S R 2002 *J Heat and Mass Transfer* **45** 4 pp 855-863
[17] Schwabl Franz 2008 *Advanced Quantum Mechanics* 4th Ed Springer PP 253 ISBN 978 3 540 85062 5.
[18] Russel L M Johnson L T and Hasselman D P 1987 *J Phys D Appl Phys* **20** 261

Study of vegetation cover distribution using DVI, PVI, WDVI indices with 2D-space plot

Study of vegetation cover distribution using DVI, PVI, WDVI indices with 2D-space plot

Taghreed A H Naji

Department of Physics, College of Education for Pure Sciences/ Ibn- Al-Haithem, University of Baghdad, Baghdad ,Iraq

Taghreednaji1972@gmail.com

Abstract. The present work aims to study the effect of using vegetation indices technique on image segmentation for subdividing an image into the homogeneous regions. Three of these vegetation indices technique has been adopted (i.e. Difference Vegetation-Index (DVI), Perpendicular Vegetation Index (PVI) and Weighted Difference Vegetation Index (WDVI)) for detecting and monitoring vegetation distribution and healthiness. Image binarization method being followed the implementation of the indices to isolating the vegetation areas from the image background. The separated agriculture regions from other land use regions and their percentages are presented for two years (2001 and 2002) of the (ETM+) scenes. The counted areas resulted from 2D-space plot technique and the separated vegetated areas resulted from the using of the vegetation indices are also presented. The separated agriculture regions from the implementation of the DVI-index have proved better than other used indices. Because it showed better coincident approximately with 2D-space plot segmentation.

Keyword. Image segmentation, vegetation indices, image binarization technique.

1. Introduction

Multispectral scanning measurements are used for predicting and assessing vegetative characteristics. Such as; plant leaf area, total biomass, chlorophyll content, plant height and plant stress by vegetation indices [1]. It is a number value that is generated by some algebraic combination of remotely sensed spectral bands to estimate the vegetation amount for image pixel. It is a measurement of vegetation greenness or health on remote sensing images, it has been developed to use for environmental monitoring. Vegetation absorption for energy spectral bands is very high in visible and invisible bands from 0.4 µm to 0.7 µm and 1.3 µm to 2.5 µm, due to the presence of chlorophyll pigment and water in the vegetation leaves, so the vegetation appear very dark. While in (0.7-1.3) µm bands, Vegetation appear very brighter and scattering for light, due to the internal structure of vegetation leaves cells. Vegetation indices will yield high values for this bands [2].

In this research, three vegetation indices are adopted to be implemented, as Difference Vegetation Index (DVI), Perpendicular Vegetation Index (PVI) and Weighted Difference Vegetation Index (WDVI) indices. The 2D-space segmentation has been utilized for the purpose of comparison with vegetation

indices results. This method based on dividing the Near Infrared "NIR" and Red "R" diagram into two regions (vegetation and non-vegetation areas) corresponding to their reflectance values.

2. Materials and methods

2.1 The available data

The region of interest (ROI) has been chosen and used in this work is Al Fit'ha situated north Salah al-Den province, cover (130 km2), upper left point lat. 35° 17' 14.70" N, long. 43° 22' 51.22" E, lower right point lat. 35° 09' 49.16" N, long. 43° 29' 40.19" E. As it is obvious, the area involves the junction region between the Tigris and the Lower Al-Zab Rivers which contains different types of Landcover classes. Images in 'figure 1' show this ROI; the available images were two temporally ETM+ exposure at 2001, and 2002. They have been acquired by Landsat-7, with spatial resolution of (28.5m).

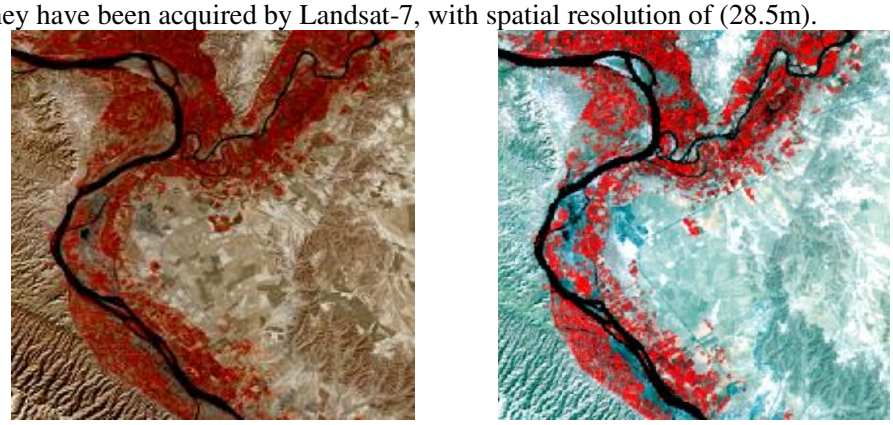

a b

Figure 1. a-First Time (2001) the original scene, b- Second Time (2002), at the same size, with resolution of (28.5m).

2.2 Detection and separation of vegetation areas

The vegetation indices are developed by the world food monitoring organizations to assist future drought warning system [3]. There are many functionally information of vegetation indices, while some provide biophysical content. They have been grouped into four types including slope based, distance based, orthogonal transformation and plant water sensitive vegetation indices depend on spectral bands combination [4].

Vegetation indices have been computed via arrays arithmetic the details of these indices, as their equations mentioned for DVI, PVI and WDVI indices.

The DVI- index is a slope based group, and was obtained by subtracting the red reflectance from the near-infrared reflectance. It is simpler than NDVI-index but it is prone to measurement errors in the Near Infrared (NIR) and Red (R) bands because it is not normalized by their sum. This index as computationally easier than PVI-index. The range of this index is infinite and the index is given 'as in equation (1)' [5]:

$$DVI = NIR - R \tag{1}$$

The PVI-index is a distance based group, and was designed to assume that the perpendicular space of the pixel from the soil line is linearly depended on the vegetation area; it attempts to eliminate difference in soil background, applicable for arid and semiarid regions. The higher PVI -index values indicate to the effect of brighter soil background, at the expense of incomplete vegetation. This allows creating different slopes for soil lines. PVI-index is affected by atmospheric fluctuations and it given different data, so

atmospheric correction should been performed on the data before implemented this index. The range of this index is -1 → +1, given 'as in equation (2)' [2]:

$$PVI = (\sin(a) \times NIR) - (\cos(a) \times R) \quad (2)$$

Where: (a) is the angle between the soil line and the NIR axis.

WDVI-index has been used to overcome high PVI values, which due to the brighter soil background. This index is based on distance too, and it assumes that the ratio between NIR and Red reflectance of bare soil is constant. WDVI- index has mathematically simpler from PVI-index, but it has an infinite range. Like PVI-index, it is very affected by atmospheric fluctuations. This index is given 'as in equation (3)' [6 and 2]:

$$WDVI = NIR - (g \times R) \quad (3)$$

Where: (g) is the slope of the soil line.

The 2D- space plot technique for image segmentation has been adopted to surmount the mutation in segmented areas, by identify the threshold values locally which depended on image features reflectance. This method is separated the vegetation and non-vegetation regions on the space diagram between the Near-Infrared (NIR) and Red (R) spectral bands.

In order to identify pixels most likely contain significant vegetation, a simple threshold values may be implemented to the vegetation indices. Selection of threshold values depended on the pixel values in the vegetation indices images. The vegetated areas appear green when viewed as logically binary images. To monitor the vegetation covers, the following percentage and area's counting relationships are implemented:

$$\rho_v = (N_v/N_t) \times 100 \quad (4)$$

$$A_t = N_t \times R^2 \quad (5)$$

$$A_v = A_t \times \rho_v \quad (6)$$

Where:

P_v = is the percentage of vegetation class.

N_v = is the number of pixels within the vegetation class.

N_t = is the total number of pixels within the processed image.

A_t = is the total area of image, measured by square kilometer.

A_v = is the area of vegetation class, measured by square kilometer.

R^2 = is resolution of the satellite image data; i.e. (28.5 × 28.5 m2) for the Landsat (ETM+) data.

There are many of change detection algorithms; one of the most common algorithms which used in this research is "Image Differencing". This algorithm involves subtracting each digital number (DN) value of first time image from that of the second time image and adding a specific positive constant to avoid negative values. The subtraction results produced three levels of information: positive and negative values in area of feature changes, and zero values in area of no changes; mathematically:

$$CD\ (i,j) = DN_2\ (i,j) - DN_1\ (i,j) + C \quad (7)$$

Where:

CD (i, j): is the produced image of changes.

DN1 (i, j): the first time image.

DN2 (i, j): the second time image.

C: is a positive constant ranging from (0 to 255) for 8- bit image.

(i, j): row's and column's number, respectively.

3. Results and discussion

Many vegetation indices have been developed and used for exploring vegetated areas. Three of them have been adopted in this research to detect the vegetation covers for the ROI satellite images. These images are used to illustrate the effect of performing these indices, are shown in 'figure 1', false color scenes (Band2, Band3, and Band4) are combined, by smaller size extracted temporal.

Three indices formula have been used to exploring the vegetated regions on these images, shown in 'figure 2'. The vegetation cover of the ROI using DVI- index was 25.64 km2 at 2001 and 26.91 km2 at 2002 (i.e. 19.72 and 20.70%, respectively). The ROI is decreased in the surface of vegetation from 24.70 to 26.94 km^2 between 2001 and 2002 (i.e. 19 and 20.72%, respectively) using PVI- index. The WDVI-index has been found to be more sensitive than the PVI-index. This index was used to minimize the effect of soil reflectance variation. The change of vegetated area showed decreases in the surface of vegetation from 24.87 to 27.56 km^2 at the periods 2001 and 2002, (i.e. 19.13 and 21.20%, respectively). The differences between the percentage areas of vegetated areas using different vegetation indices due to the utilized threshold assigned for each differences.

To split the vegetation regions from other land cover classes, different suitable threshold have been used (i.e. all pixels < threshold have been assigned to represent background (non-vegetation cover), while those ≥ threshold have been regarded as to represent the vegetation cover), the splitting or slicing results are demonstrated in 'figure 3'.

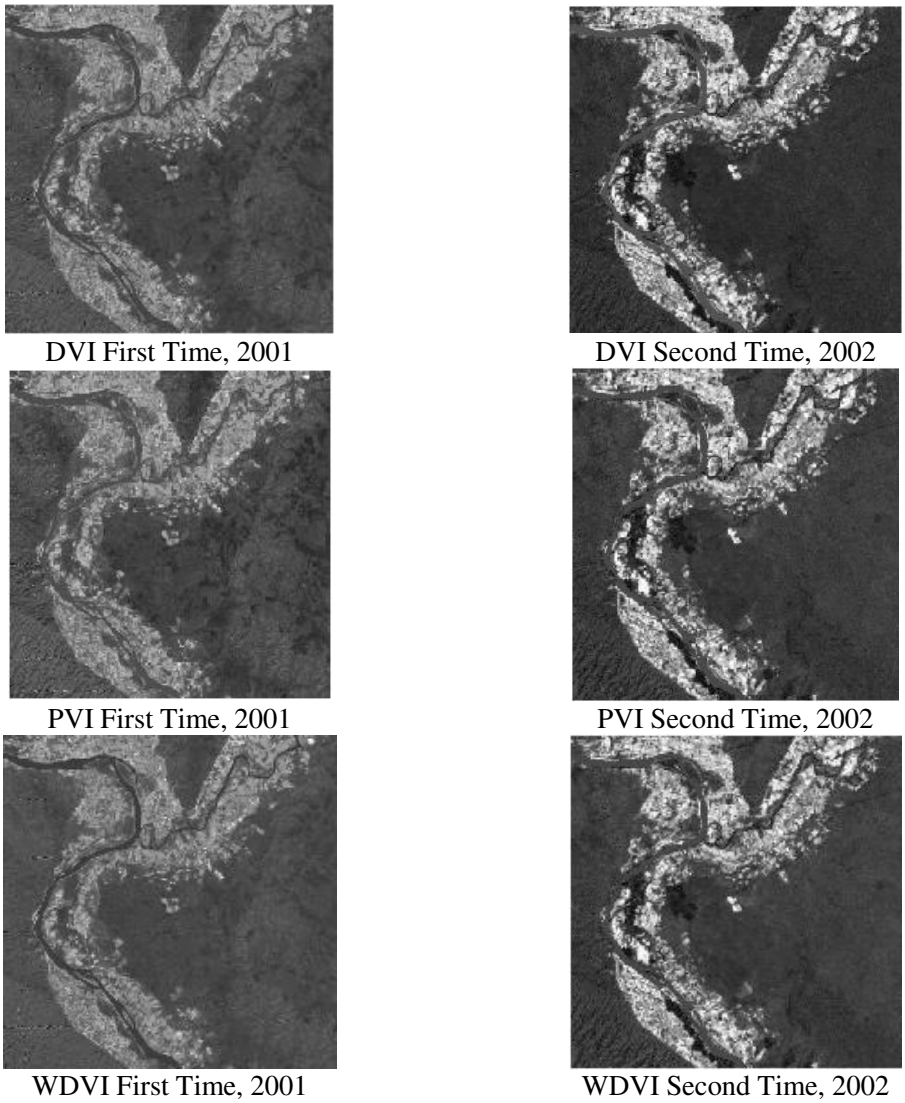

Figure 2. The vegetation indices effects on the multi-temporal images (2001 and 2002)

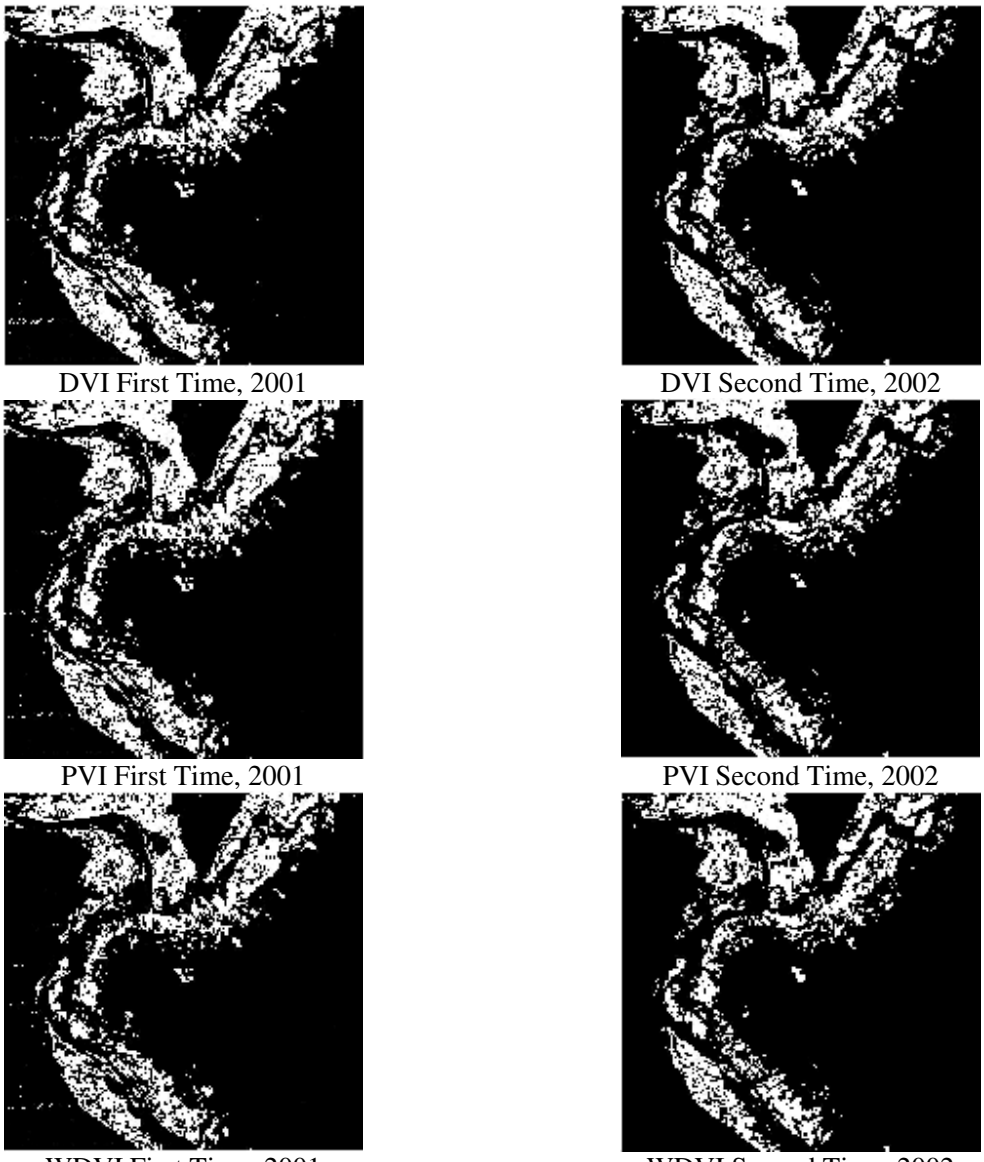

Figure 3. Vegetation layers, binaries by decided threshold (given in table 1)

To compare the implementation of the vegetation indices with 2D-space plot segmenting results, 'figure 4' shows the studied areas as to consist either vegetated and non-vegetated regions, coloring them into green (for vegetated areas), and blue (non-vegetated areas). (Table 1) presents the percentage area of the vegetated covers within the processed images, show right column of 'figure 4'. Two dimension space diagram is plotted by projecting the thresholded colored images on them, shown in the left column of 'figure 4'.

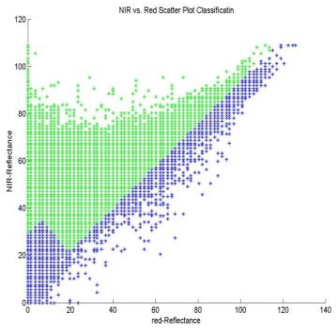

2D-space plot method for First -Time image (2001)

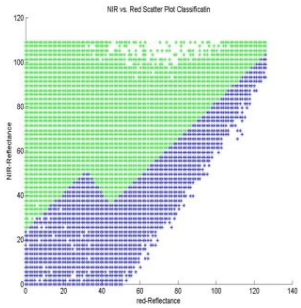

2D-space plot method for Second - Time image (2002)

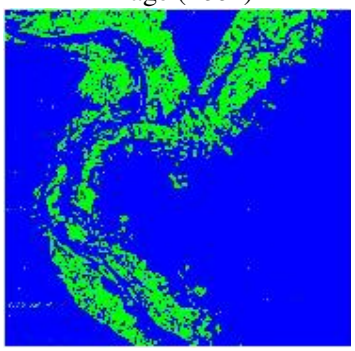

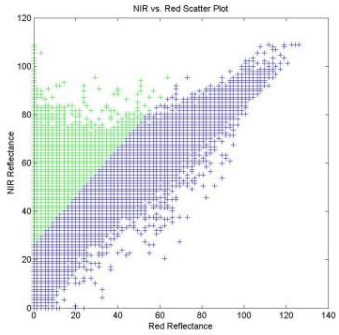

DVI First Time, 2001

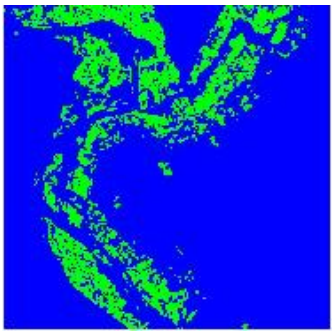

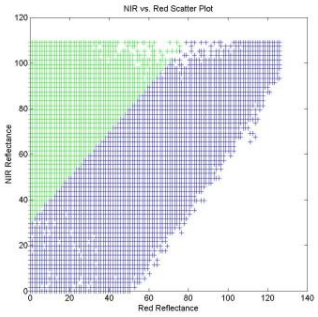

DVI Second Time, 2002

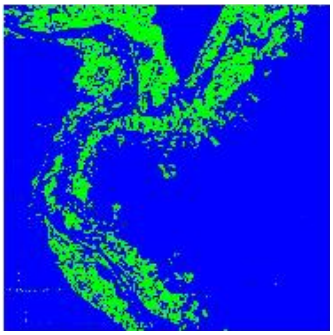

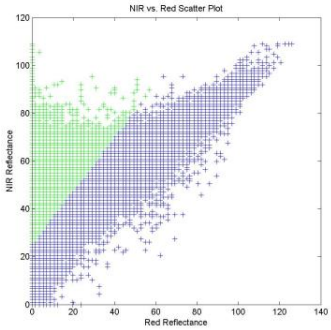

PVI First Time, 2001

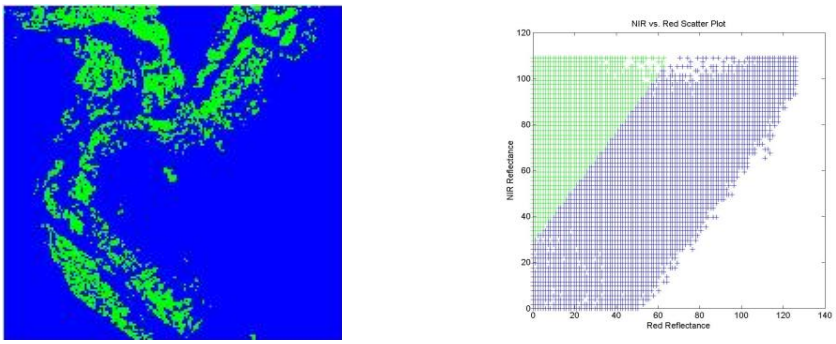

PVI Second Time, 2002

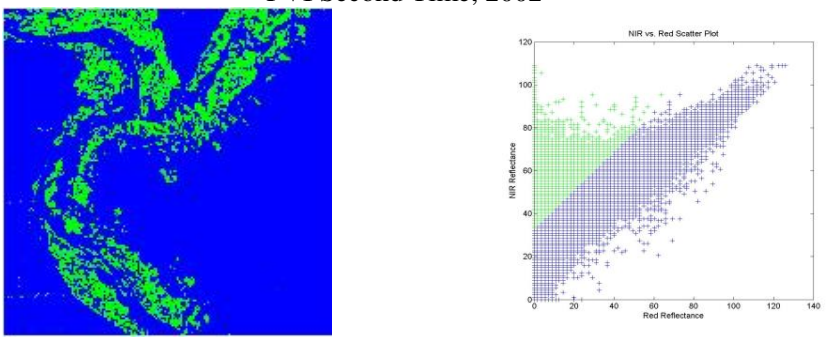

WDVI First Time, 2001

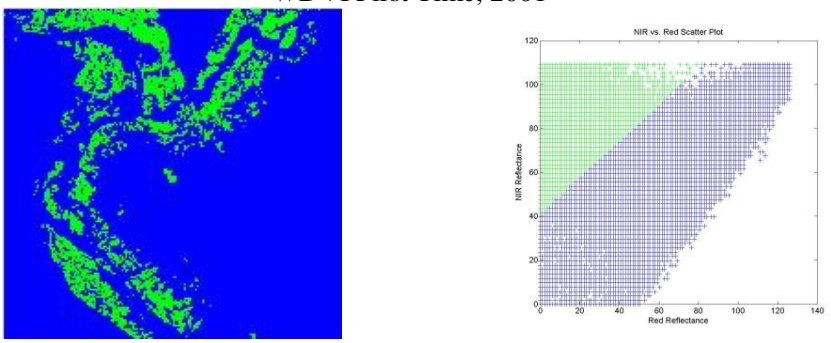

WDVI Second Time, 2002

Figure 4. Thresholded images and their 2D-space plots, produced by projecting the values of thresholded images on the original 2D-space plots

Table 1. List of threshold values, and percentage vegetation coverage for vegetation indices images (First, and Second Time)

Index	**First Time (2001)**			**Second Time (2002)**		
	Threshold	**%Percentage**	**Area km2**	**Threshold**	**%Percentage**	**Area km2**
DVI	115	19.72	25.64	110	21.72	27.94
PVI	120	19	24.70	110	21.70	27.91
WDVI	115	19.13	24.87	110	20.20	26.56

In this research, 'as in equation (7)' has been utilized to discriminate the changes in vegetated areas for the period 2001 to 2002, as illustrated in 'figure 5'. Image differencing algorithm has been applied on previous images before and after utilizing the vegetation indices to detect the changes in vegetation areas.

The changes in the vegetation areas with the percentage variations, with and without implementing vegetation indices, are listed in (table 2).

This study has been performed and built using ArcGIS10.3, ENVI 4.5 software's and MATLAB R2013a language.

Table 2. Vegetation changes during period 2001 to 2002, utilizing vegetation indices

The vegetation cover in the entire study area without implementing vegetation indices was 201.67 km^2 representing 155.13%.		
Implementing Vegetation Indices	**%Percentage**	**Area km^2**
DVI	13.92	17.80
PVI	13.62	17.41
WDVI	12.26	16.24

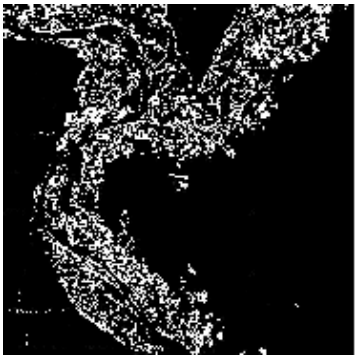

DVI layer

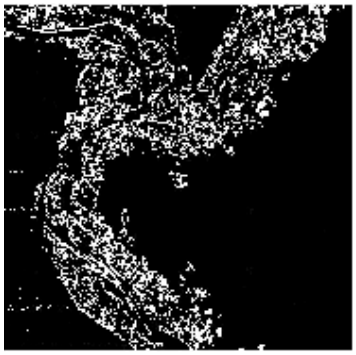

PVI layer

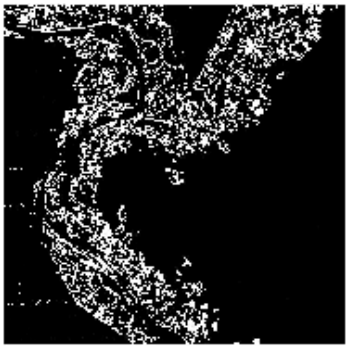

WDVI layer

Figure 5: Vegetation layers changes, using differencing images method

4. Conclusion

Vegetation index must be applicable as good indicator of vegetated cover, and have overcome the undesirable influence of soil background and other effects. Because the vegetation exhibits higher reflectance in NIR band and strong absorption (low reflectance) in R band. In this work, different indices for vegetation have been implemented to differentiate vegetated areas using multispectral temporal scenes to study of vegetation cover density and distribution; these were (DVI, PVI and WDVI). For detecting vegetation changes the vegetation index and 2D-space plot technique can be compared. The differences between vegetated areas, using different vegetation indices, have been interpreted due to the utilized

threshold assigned for each of them. Generally, the implementation of indices yield brighter grey levels for the healthy vegetated areas, and darker grays for other parts of land cover. However, any deficient result may be referred to spectrally and reflectively affected scenes. As listed in tabulated results, the vegetated areas are mostly less in the first time (2001); this may be caused by the effect of climatic; annual rainfall, evaporation and irrigation, or agriculture policy. As it has been noticed in 'figure 4', the (DVI) index showed better performance than others, because it showed better coincident approximately with 2D-space plot segmentation technique. The research results can be more conformable to fact, when they were depended on field measurements of the study area for detecting vegetation areas and assessing its case.

References

[1] Paul J Pinter Jr, Jerry L Hatfield, James S Schepers, Edward M Barnes and M Susan Moran 2003 Remote Sensing for Crop Management *Photogrammetric Engineering and Remote Sensing* American Society for Photogrammetry and Remote Sensing Inc. **69** 6 pp 647-664

[2] Terrill W Ray 1994 A FAQ on Vegetation in Remote Sensing Division of Geological and Planetary Sciences California Institute of Technology

[3] Paul Jude Gibson and Clare H. Power 2000 *Introductory Remote Sensing: Digital Image Processing and Applications* (Routledge 11 New Fetter Lane).

[4] Reza Jafari 2007 Arid Land Condition Assessment and Monitoring using Multispectral and Hyperspectral Imagery PhD. Thesis the University of Adelaide Australia

[5] Charles R Perry Jr and Lyle F. Lautenschlager 1983 Functional Equivalence of Spectral Vegetation Indices U.S D. A. jSB.S. Johnson Space Center SC2 Houston Texas

[6] Peng Gong, Ruiliang Pu, G S Biging and M R Larrieu 2003 Estimation of Forest Leaf Area Index Using Vegetation Indices Derived From Hyperion Hyperspectral Data *IEEE Transactions on geosciences and remote sensing* **41** 6

Fabrication and characterization study of ZnTe/n-Si heterojunction solar cell application

Fabrication and characterization study of ZnTe/n-Si heterojunction solar cell application

BushraK H AlMaiyaly[1], Bushra H Hussein Auday H Shaban

Department of physics College of Education For Pure Science (Ibn AlHaitham) University of Baghdad Baghdad Iraq

drbushra2009 @yahoocom

Abstract. Different thicknesses (150 250 and 350) ±20 nm has been deposited on the glass substrate and nSi wafer to fabricate ZnTe/n-Si heterojunction solar cell by vacuum evaporation technique Structural optical electrical and photovoltaic properties are investigated for the samples. The structural characteristics studied via X ray analyses indicated that the films are polycrystalline besides having a cubic (zinc blende) structure also average diameter and surface roughness calculated from AFM images The optical measurements of the deposited films were performed in different thicknesses to determine the transmission spectrum as a function of incident wavelength in the range of wavelength (4001000) nm and the optical energy gap calculated from the optical absorption spectra was found to reduse with thickness The IV characteristic at (dark and illuminated) and CV measurement for ZnTe/n-Si heterojunction shows the good rectifying behaviour under dark condition. The measurements of opencircuit voltage (V_{OC}) short-circuit current density (J_{SC}) fill factor (FF) and quantum fficiencies of the ZnTe/n-Si heterojunction are calculated for all samples The results of these studies are presented and discussed in this paper

Keywords ZnTe/ n-Si heterojunction optical band gap structural properties solar cell

1 Introduction

Assembly IIIV compound semiconductors including cadmium selenide (CdSe) zinc selenide (ZnSe) zinc telluride (ZnTe) and cadmium telluride (CdTe) have established significant attention owing to their low cost however high absorption coefficients in their applications to a variety of solid state devices [1] Zinc telluride as a significant II–VI group semiconductor has a moderate and direct band gap of (17 to 24) eV at room temperature also has broadly used in modern technologies of optoelectronic [23] ZnTe thin films are broadly used in manufacturing different solid state optoelectronic devices (photo detectors solar cells light emitting diodes laser diodes microwave devices etc) due to its specific optical and electrical properties (high transparency in visible and infrared regions and low electrical resistivity etc) [45] ZnTeis an broadly investigated compound because of good optoelectronic properties mainly in the area of heterojunction solar cells The electrical and optical properties of ZnTe thin films can be optimized besides resistivity can be changed with dopant sort and concentration [67] Zinc telluride has a zincblende lattice and expansion of 83×10^{6}K Most heterostructures including ZnTe are characterized by very low lattice mis match For example it is 07% for InAsZnTe structure 009% for GaSbZnTe and 026% for GaAsZnTe [8] ZnTe thin films have been prepared by different techniques including magnetron sputtering [9] pulsed laser

deposition (PLD) thermal evaporation molecular beam epitaxy (MBE) [10] electron beam [11] closed space sublimation (CSS) [12] electrodeposition [13] etcThe aim of this study was focused on the construction and characterization of ZnTe nSi heterojunction for solar cells with different thin film thickness utilizing thermal evaporation technique

2 Experimental

In this study n type Si wafer substrates with crystal orientation (111) indirect energy gap of 11eV diameter 762mm and thickness (508±15)µm which used to study the ZnTe/ n-Si heterojunction these substrates were put in diluted 1% HF solution to eradicate the nativeoxide washed by deionized water several times then dry using soft paper Secondly prepared glass slides were usedas asubstrate were used to study the structural electrical and optical properties of ZnTe films these glass slides were cleaned with chromic acid ultrasonic cleaner detergent water distilled water and then with acetone High purity (99999)% ZnTe was used as a source material for the evaporation with thicknesses [150 250 and 350] nm were deposited by thermal vacuum evaporation using (Edwards – Unit 306) system All thicknesses were determined with an optical interferometer method a suitable shape design for molybdenum boats were used for films evaporation also used spiral cord from Tungsten for deposition aluminum poles Xray diffraction (SHIMADZU Japan XRD 6000) diffractometer system with CuKα radiation (λ = 15418 Å) was used to identify the structural of the deposited films while topography surfaces investigations were carried out using atomic force microscopy (AFM) Optical transmission measurements and the band gap (Eg) were performed with (UVVisible 1800 spectrophotometer) Hall effect and the capacitance–voltage measurement of is determined by using HMS3000 Hall measurement setting and by using (LRC meter Winsted 8105G) at a fixed frequency of (10 kHz)The IV characteristics of the ZnTe/ n-Si heterojunction were measured using a DC power supply (F302 Farnell Instrument) and (keithley digital electrometer 616) The measurements were performed in dark and under light

3 Results and discussion

'Figure 1' displays the XRD spectrum of different thickness (150 250 and 350) ±20 nm of ZnTe thin films It is observed from XRD pattern of films that the all thickness films have polycrystalline and have cubic structure four noticeable peaks (111) (200) (220) and (311) and the prominent peak was (111) this is agreement with other studies [1415] The FWHM of the prominent peak decreases with increasing thickness due to a drop in the defects as a result of shrinking of the grain boundaries large crystallite size has been observed for film of thickness 350nm because of fast growth of crystallite and by reason of the reduction in grain boundaries this process results removal of the defects in the films a similar behavior was observed in other studies for different thickness [16]

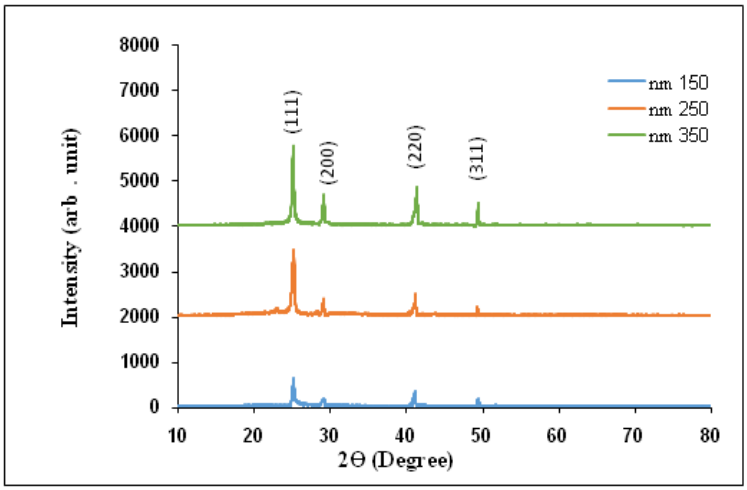

Figure 1 XRD designs of ZnTe thin films at different thickness (150 250 and 350) nm

From the Scherer's relation [17] the average crystallite size ($\boldsymbol{CS}$) of ZnTe thin films was calculated

$$(\boldsymbol{CS}) = \frac{\mathbf{094}\boldsymbol{\lambda}}{\beta \boldsymbol{cos\theta}} \ldots\ldots\ldots\ldots\ldots\ldots\ldots\ldots\ldots\ldots\ldots\ldots (1)$$

Where λ is wavelength of radiation β is full width half maxima of the main peak and θ the diffraction angle Table 1 shows the values of 2θ d_{hkl} full width half maxima and the average crystallite sizeofthe main peak

Table 1 The X ray diffraction parameters of ZnTe thin films of different thickness

film thicknesses (nm)	2 θ(deg)	d_{hkl} (Å)	β(deg)	$\boldsymbol{CS}$ (nm)
150	252991	35175	04093	2078
250	252747	35209	04240	2492
350	252325	35266	02439	3487

'Figure 2' shows the three dimensional (3D) AFM images of ZnTe thin films with different thickness we can be observed that the films are found to be uniform and densely packed without any cracks or pinholes and the average grain size was increased as the film thickness increase and the surface roughness values equal to (9393 11057 and 1374 nm) for the different thickness (150 250 and 350) nm respectively due to growth of some crystal planes the results agreement with X ray diffraction data Table 2 shows the values of grain sizesand surface roughness for different thickness

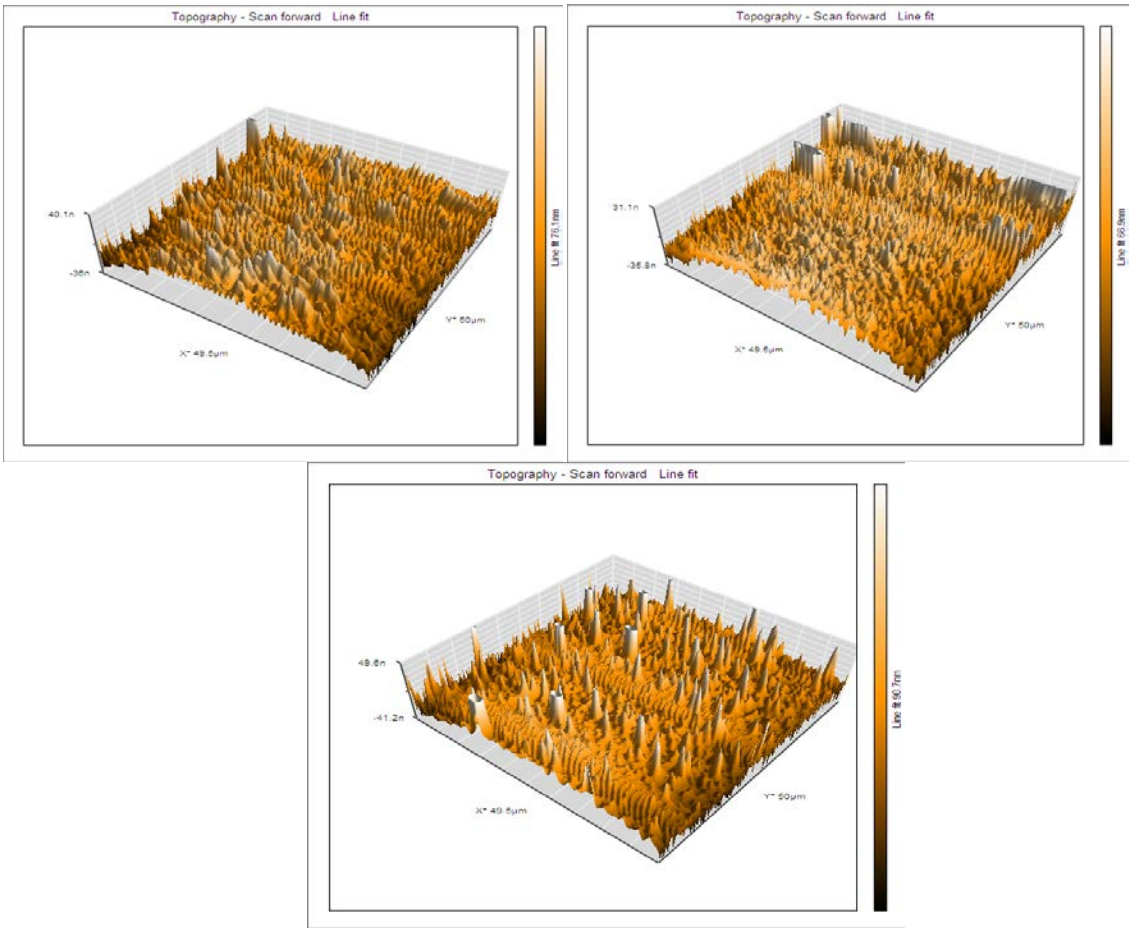

Figure 2 3D images of ZnTe thin films different thickness (150 250 and 350) nm

Table 2 The average grain size and roughness of ZnTe thin films of 3 different thickness

Film thicknesses (nm)	Grain Size (nm)	Roughness average (nm)
150	688	9393
250	8165	11057
350	1294	1374

'Figure 3(ab)' demonstrates that the characteristic measured spectral transmittance and reflectance spectra of ZnTe films of three different thicknesses It is shown that the maximum value of 6862% being reached for ZnTe thin films with lower thicknesses (150 nm) and the transmission decreasingly increasing the thicknesses(from 150 to 350) nm as a result of increase in the density of the film and due to highly transparent similar behavior has reported by other studies [18] Figure 3(b) shows the reflectance spectra of films increased rapidly in visible region and then decreases with the increase of wave length from the range of (830 to 1000) nm with the increase in thicknesses

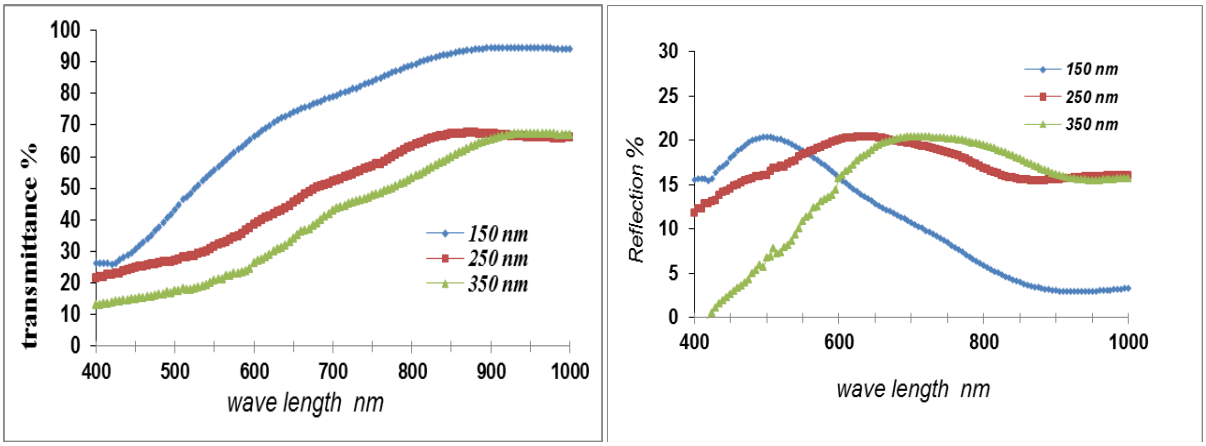

(a) **(b)**

Figure 3 The spectral transmittance and reflectance spectra of ZnTe thin films different thickness (150 250 and 350) nm

The optical band gap of the ZnTe thin films is calculated using the expression [19]

$$\alpha h\upsilon = B(h\upsilon - Eg)^{r} \ldots\ldots\ldots\ldots\ldots\ldots\ldots\ldots\ldots\ldots\ldots\ldots (2)$$

Where B is constant α is the absorptioncoefficient **hυ**is the photon energy Eg is the optical band gap and **r** is constant may take values 2 3 12 32 depending on the material and the type of the optical transition The optical band gap energy E_g was obtained from the intercept on the photon energy axis after extrapolating of the straight line section of the curve of $(\alpha h\nu)^2$ versus (hν) plot Figure 4 expressions $(\alpha h\upsilon)^2$ against the photon energy (hυ) for different thicknesses (from 150 to 350)nm the energy band gap decrease from [202 eV to 182eV] by means of high film thicknesses there are several energy levels resulted in several overlapping energy bands in the band gap of these films The overlapping energy bands tend to decrease the energy band gap resulting in lower band gaps for increase on film thicknesses [20]

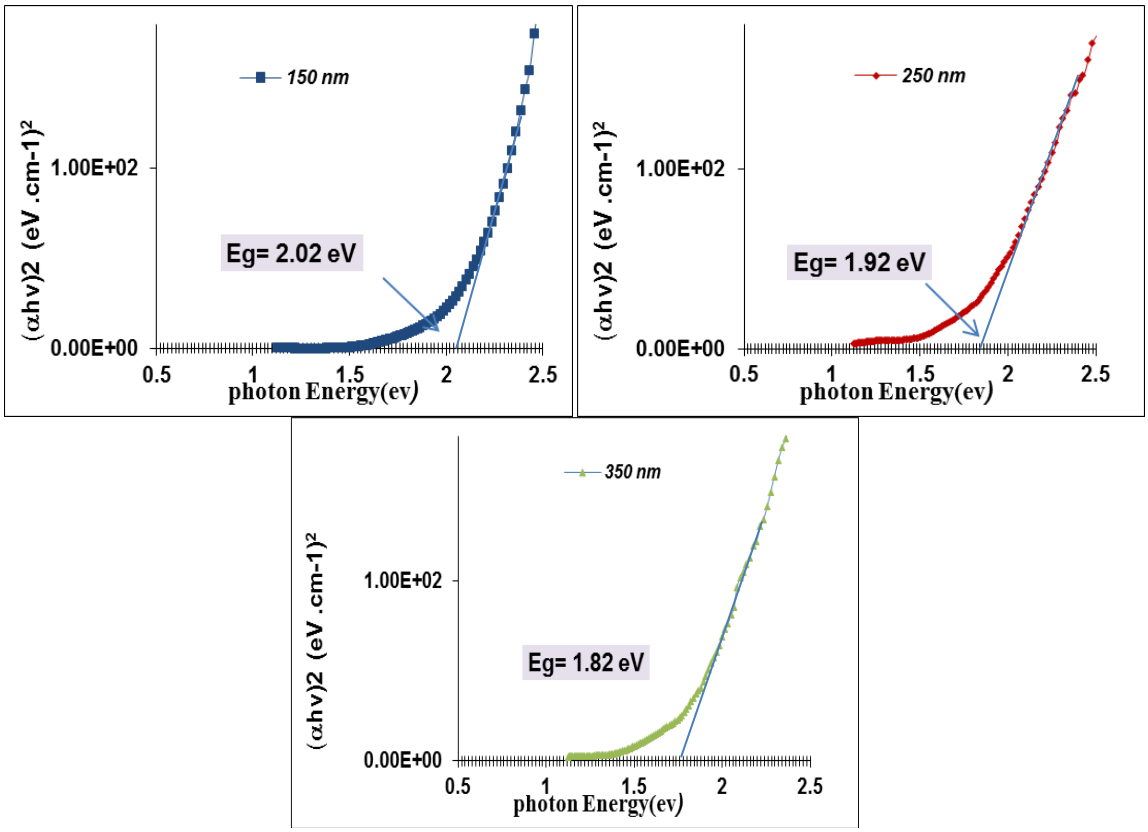

Figure 4 Variation of $(\alpha h\upsilon)^2$ verse photon energy ZnTe thin films different thickness

From Hall measurements can be estimated the type of charge carriers concentration and Hall mobility the positive sign of the hall coefficient indicates the conductive nature of the film is ptype Figure 5(ab) shows the variations of carriers concentration and Hall mobility with thickness respectively we can notice from the figure that the carrier concentration increased with increasing thickness due to drop in the resistivity the ultimate change in resistivity is due to the corresponding grain size Also we see increases in the Hall mobility with increasing thickness where there is a direct proportion between the carrier's concentration and the conductivity [21]

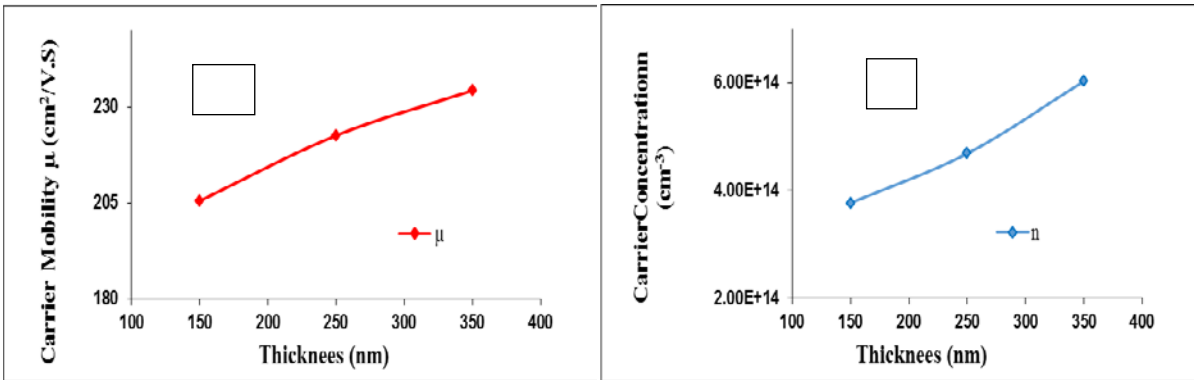

Figure 5 The variations of **a** carriers concentration **b** Hall mobility with different thickness

Figure 6 shows change heterojunction capacity of unit area with reverse bias voltage at frequency (10 KHz) for different thickness the junction capacitance per unit area can be calculated using the expression [22]

$$C = \left[\frac{q\ \varepsilon_n\ \varepsilon_p\ N_n\ N_p}{2\left(\varepsilon_n\ N_n + \varepsilon_p\ N_p\right)} \right]^{1/2} \left(V_{bi} - V\right)^{-1/2} \quad \text{.....(3)}$$

Where Nn and Np are the donor and acceptor concentrations $\varepsilon_n$and ε_p are the dielectric constants of n and p type semiconductors respectively V_{bi} is the builtinjunction potential and V_d is the applied voltage and the width of the depletion region can be calculated via [23]

$$W = \frac{\varepsilon_S}{C_0} \quad \text{.....(4)}$$

$$\varepsilon_S = \frac{\varepsilon_n \varepsilon_p}{\varepsilon_n + \varepsilon_p} \quad \text{.....(5)}$$

Where Co is the capacitance on zero biasing voltage also ε_s is dielectric constant of heterojunction for different thickness The scheme of $1C^2$ vs V is a straight line which means that the junction was of an abrupt type the intercept with the voltage axis gives the value of the builtin potential Table 3 shows the capacitance (Co) at (zero bias voltage) decreases with the increasing of ZnTe thickness due to the increasing of the depletion region where the increasing in the carrier concentration leads to a decrease of the capacitance The results have a good agreement with other studies [24]

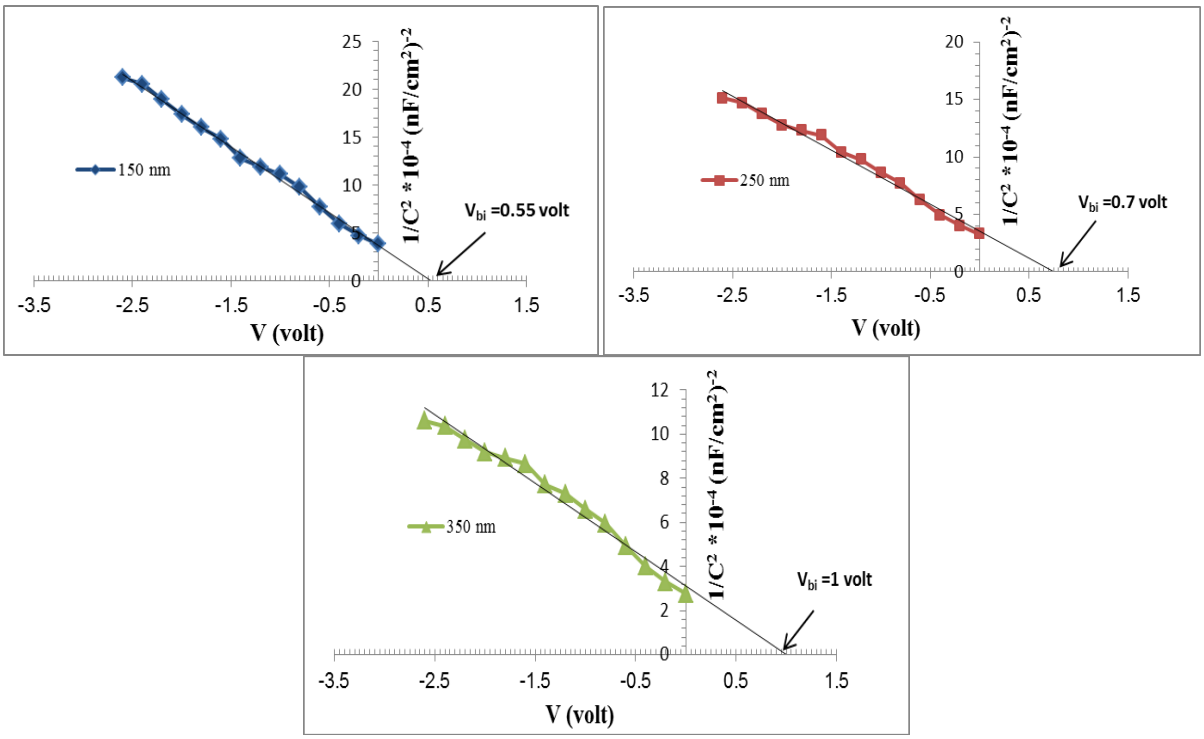

Figure 6 Variation of $1C^2$ with reverse bias voltage for ZnTe /n-Si hetero junction with different thickness

Table 3 Values of *Co* W NA and V_{bi} for ZnTe nSi heterojunction for different thickness

Thickness(nm)	C_o(nfcm^2)	W(nm)	V_{bi}(Volt)	N_A (cm^3)
150	5668	86	055	144E+13
250	5308	9182	07	283E+13
350	522	9322	1	356E+13

The (I–V) characterizes of ZnTe/ n-Si heterojunction solar cell with different thickness (150 250 and 350)nm can be calculated by the two expressions [25]

$$I = I_S\left(\exp\left(\frac{qV}{\beta K_B T}\right)-1\right)-I_L \quad \text{.....(6)}$$

$$\beta = \frac{q}{K_B T}\frac{dV}{d(\ln I)} \quad \text{.....(7)}$$

Where $\mathbf{I_s}$ Saturation current $\mathbf{I_L}$ Illumination current **I** The total Solar cell current **V** applied voltage **β** is the ideality factor **T** Temperature in Kelvin $\mathbf{K_B}$ Boltzmann constant and **q** electron charge Figure 7 and Table 4 shows the barrier height (Φ_{ba}) and the reverse saturation current density it is clear that the ideality factor barrier height decrease and saturation current upsurge with increasing of thickness where this behavior attributed to improvement of crystal structure this result agrees with [26]. Also Figure 8 shows the (I–V) curve in dark and under illumination where the photocurrent produced by the (100 mWcm^2) white lamp the current values rise exponentially by way of increasing in the forward bias voltage besides the device has high forward current Moreover the photovoltaic conversion efficiency (η %)and fill factor (*FF*) can be calculated from two expressions [25]

$$\eta = \frac{P_m}{P_{in}} x100\% = \frac{I_m V_m}{P_{in}} x100\% \quad \text{.....(8)}$$

$$F.F = \frac{J_m V_m}{J_{sc} V_{oc}} \quad \text{.....(9)}$$

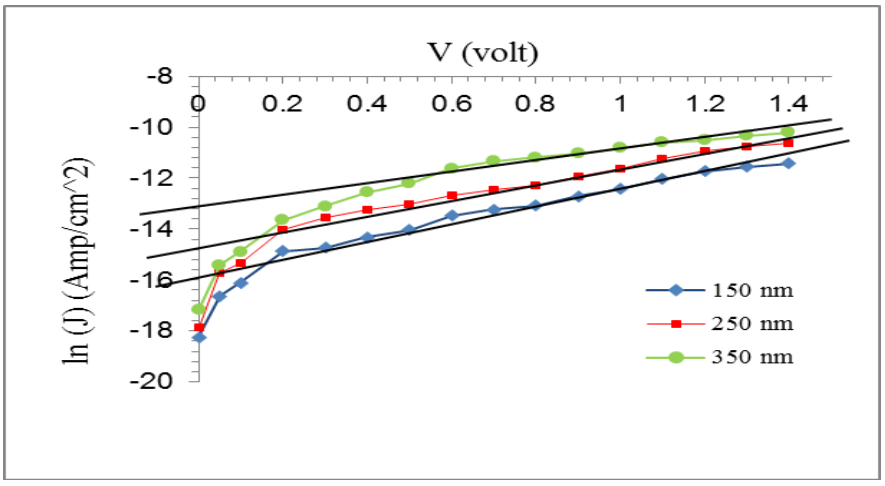

Figure 7 ln(J_s) with V for dark forward bias at different thicknesses

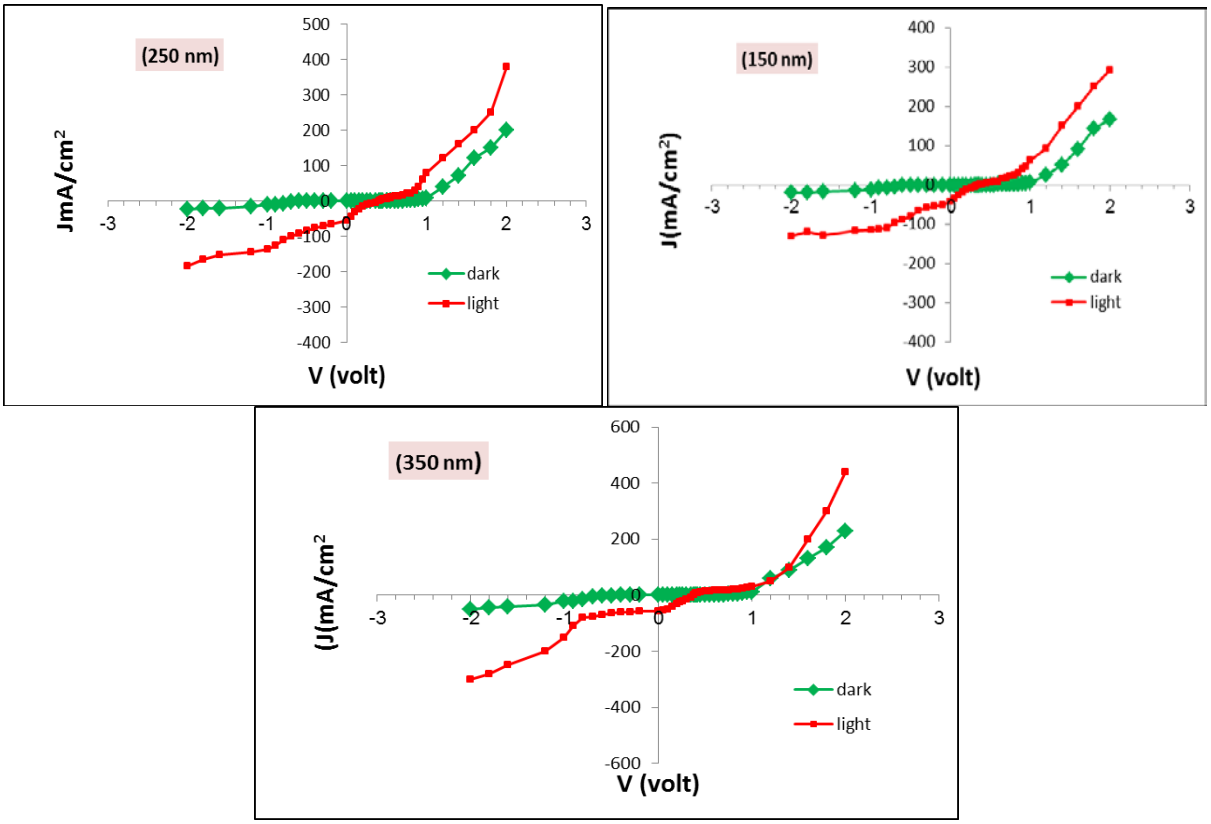

Figure 8 IV characteristics of ZnTe nSi heterojunction solar cell dark and under illumination

Table 4 Ideality factor Barrier height and Saturation current density values at different thickness

Thickness(nm)	Ideality Factor	Saturation Current Density(J_S) (μAcm^2)	Barrier Height (Φb) (eV)
150	1821	0112	0833
250	1698	031	0807
350	1532	137	0769

The open circuit voltage (V_{oc}) short circuit current (I_{sc}) fill factor (FF) and conversion efficiency (η_s%) results are shown in Table 5 we can find with increasing thickness the photovoltaic effect increasing that is clear in thickness (350 nm) where the conversion efficiency for ZnTe nSi heterojunction solar cell with (350nm) is much higher than (150) nm ZnTeSi heterojunction this behavior attributed to increase in photo generated current (I_{ph}) our results nearly agreement with other studies [27]

Table 5 The measurement with different thickness for ZnTe nSi heterojunction solar cell

Thickness (nm)	V_{oc} (Volt)	J_{sc} ($mAcm^2$)	V_{max} (Volt)	J_{max} ($mAcm^2$)	FF	η %
150	04	18	02	123	0341667	246
250	022	40	015	25	0426136	375
350	02	55	013	40	0472727	52

4 Conclusions

ZnTe thin films were prepared using thermal evaporation technique for different thickness (150 250 and 350)nm all films deposited on glass and silicon substrates at room temperature From XRD analysis it was found that the film is polycrystalline having the zinc blende structure with prominent peak was observed along (111) plane the ZnTe thin film for (350 nm) show large crystallite size with optimum surface roughness and low transmittance spectrum with appropriate band gap also the high Hall mobility value carriers concentration and low capacitance for (350 nm) thickness A photovoltaic device consisting of a ZnTe nSi heterojunction solar cell for (350 nm) have ideal behavior in ideality factor saturation current density and higher efficiency measurements this maximum was found to be 52% at ZnTe optimum thickness (350 nm)

References

[1] Dong Hun Shin Jung Su Moon Park 2003 Electrochemical Preparation of Zinc Telluride Films on Gold Electrodes *Journal of the Electrochemical Society***150** 5 342346
[2] Lin Bao Shun Zhang Rui Lu Wei Sun Qun Ling Fang 2015 ptype ZnTeGa nanowires controlled doping and optoelectronic device application *RSCAdv***5** 13324
[3] MS Hossain R Islam K A Khan 2010 Structural Elemental compositions and Optical properties of ZnTeV *thin films Chalcogenide Letters***7** 1 21 29
[4] N Amin K Sopian M Konagai 2007 *Sol Energ Mat Sol C***91** 1202
[5] H YChao J HCheng J Y Lu YHChang C L Cheng YFChen 2010ChenGrowth and characterization of typeII ZnOZnTe coreshell nanowire arrays for solar cell applications *Super lattice Microst***47** 160
[6] A KSAqili A Maqsood and Z Ali2001Optical and Xray studies of low resistive films by immersion in Cu solution *Appl SurfSci***180** 73 80
[7] NB Chaure J PNair R Jayakrishan V Ganesan and R K Pandey1998Effect of CuDoping on the morphology of ZnTe films electrodeposited from nonaqueousbath*Thin Solid Films***324** 78
[8] K Z Yahiya ET Salem M SMuhammad 2008 Optical Constants of Zinc Telluride Thin Films in the Visible and NearInfrared Regions*Eng&Tech***26**5
[9] D Zeng W Jie H Zhou YYang 2011Effect of sputtering power on the properties of $Cd_{1-x}Zn_xTe$ films deposited by radio frequency magnetron sputteringOriginal*Thin Solid Films***519** 4158
[10] O Toma SAntohe 2014 Optical and morphological investigations of thermal vacuum evaporated ZnTe thin films*Letters***11** 3 11 611 618
[11] A M Salem T M Dahy Y A Elgendy 2008Thickness dependence of optical parameters for ZnTe thin films deposited by electron beam gun evaporation technique. *Physica B***403** 3027
[12] O de Melo E M Larramendi JMDuart MH Velez J Stangl HSitter Structure and growth rate of ZnTe films grown by isothermal closed space sublimation*JCryst Growth*2007 **307** 253
[13] V S John T Mahalingam J P Chu 2005Synthesis and characterization of copper doped zinc telluride thin films *Solid State Electron***49** 3
[14] Gowrish K Rao Kasturi V Bangera G K Shivakumar 2010 Studies on the Photoconductivity of vacuum deposited ZnTe thin films *Materials Research Bulletin***45** 10 13571360
[15] JW Orton BJ Goldsmith JA Chapman MA Powell 1982 The mechanism of photoconductivity in polycrystalline cadmium sulphide layers *Journal of Applied Physics* 531602
[16] G K R Å 2010 Studies on the photoconductivity of vacuum deposited ZnTe thin films *Materials Research Bulletin***45** 10 1357 1360
[17] M J Yousef 1987 *Solid state physics*

[18] W S Wang I Bhat 1997The properties of ZnTe layers heteroepitaxially grown on Si using atmospheric metalorganic chemical vapor deposition*Materials Chemistry and Physics***5** 80
[19] Zimmermann Horst2010 Integrated Silicon Optoelectronics *Engineering Electronics & Electrical Engineering* Springer Series in Optical Sciences
[20] N A Okereke I A EzenwaandA J Ekpunobi 2011 Effect of thickness on the optical properties Of Zinc Selenide thin films *Journal of NonOxide Glasses***3** 3 105 111
[21] A K S Aqili A Maqsood Z Ali 2001 *Applied Surface Science***180** 1
[22] H Lewerenz 2004Development of copper indium disulfide into a solar materia*Solar Energy Materials and Solar Cells* 83 4 395407
[23] N K Kwok 2002 *Complete guide to Semiconductor Devices* 2nd Edition Wiley IEEE Press USA
[24] H M Zeyada MM ElNahass 2010 Characterization of 223 dihydro1 5dimethyl3oxo2phenyl1Hpyrazol4ylimino 2 4 nitrophenyl acetonitrile and ZnO nanocrystallite structure thin films for application in solar cells. *JApplPhys* **49** 10 301
[25] D A Neamen 2003 *semiconductors physics and Devices Basic Principles* Third edition copyright© McGraw Hill Companies
[26] Hussein Kh Rasheed Ramiz Ah AlAnssar ImanKaJebur NisreenKh Abdalameer 2016 Surface Morphology and Photolumincense Properties of aGaAsZn Solar Celles International *Journal of Scientific & Engineering Research***7** 5
[27] Bernabe Mari and HanifUllah 2016 Numerical study of the influence of ZnTe thickness on CdS ZnTe solar cell performance *EurPhys J Appl Phys***74** 2

Wind Turbine Bearing Diagnostics Based on Vibration Monitoring

Wind Turbine Bearing Diagnostics Based on Vibration Monitoring

H T Kadhim[1], F H Mahmood [2], and A K Resen[3]

[1]Ministry of Higher Education and Scientific Research, Baghdad, Iraq
[2] Remote Sensing Unit, College of Science, Baghdad University, Baghdad, Iraq
[3] Ministry of Science and Technology, Renewable Energy Directorate, Baghdad, Iraq

Abstract. Reliability maintenance can be considered as an accurate condition monitoring system which increasing beneficial and decreasing the cost production of wind energy. Supporting low friction of wind turbine rotating shaft is the main task of rolling element bearing and it is the main part that suffers from failure. The rolling failures elements have an economic impact and may lead to malfunctions and catastrophic failures. This paper concentrates on the vibration monitoring as a Non-Destructive Technique for assessing and demonstrates the feasibility of vibration monitoring for small wind turbine bearing defects based on LabVIEW software. Many bearings defects were created, such as inner race defect, outer race defect, and ball spin defect. The spectra data were recorded and compared with the theoretical results. The accelerometer with 4331 NI USB DAQ was utilized to acquiring, analyzed, and recorded. The experimental results were showed the vibration technique is suitable for diagnostic the defects that will be occurred in the small wind turbine bearings and developing a fault in the bearing which leads to increasing the vibration amplitude or peaks in the spectrum.

1. Introduction

In the last few years, there has been a growing interest in the vibration monitoring has been gaining importance in recent years [1]. The current paper focused on the wind turbine (WT) bearing diagnostics based on the vibration monitoring. Vibration is one of the most established procedures utilized as a part of the field of wind turbine condition monitoring (WTCM) and it is typically used to recognize wind turbine faults like bearings faults, mechanical imbalance etc.as mentioned in [2,3]. This technique applicable on the wind turbine bearings, moving parts to decide mechanical and electrical issues as for damages, bearing issues, mechanical detachment, unbalanced, twisted shafts, tower vibrations, blades vibrations, electrical issues, reverberation issues. Bearing condition has been famously and dependably measured by means of machine vibration [4], also, it is problem is broadly gotten as the main issue for wind turbine prepare condition checking among all subsystems as studied in [5,6]. This is true as stressed Brian McNiff in his study [7], bearing failure is the main problem of turbine gearbox. Specifically, it was called attention to that it has been a tendency to destroy in various rates. It can be pointed that among the moving parts in a planetary gearbox, both the middle and high-speed shaft-supporting bearings have a tendency to fail at the quickest rate [8]. Also, the vibration measurement and spectrum analysis can be considered as a typical choice for bearing monitoring and diagnostics and rolling element bearing fault diagnosis [9, 10] targets at identifying the underlying anomalies based on the corresponding condition monitoring information. for summed up faults of

bearing, the bearing deficiency attributes have been seen observed in the WT vibration; for summed up faults of bearing, a critical broadband changes caused by the faults have been seen in the WT vibration spectrum [11]. It is possible to measure the vibration by utilizing vibration sensors, such as accelerometer what's more, vibration speed transducers [12]. Estimations ought to be gone up against the bearing, bearing reinforcement housing, or other structural parts that altogether react to the dynamic force and describe the general vibration of the machine. It has been perceived that WT vibration is a dependable warning to identify bearing issues. In this way, vibration observing is attractive proceeding, and well-acknowledged specification is accessible, for example, ISO 10816 [13]. Accelerometers are utilized as vibration sensors and it can be situated on rotor bearing [14]. Vibration signals from accelerometers have the upside of giving a wide unique range and wide frequency range. 'Figure 1' shows a bearing made out of the external race, inward race, moving component, fixing [15].

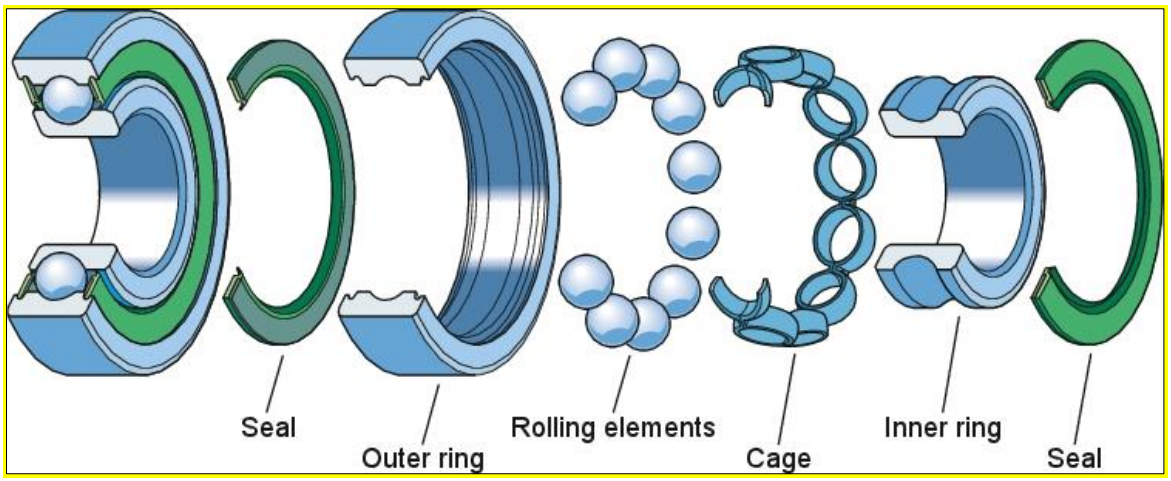

Figure1. The rolling bearing component.

Faults in bearing may be occurred due to crack in outer race, hole in the outer race, corrosion, deformation of the protective shield, etc. 'Figure 2' shows the types of bearing faults that can be detected by monitoring the increased vibration in high-frequency spectra.

Figure 2. The bearing faults. (a) Crack in the outer race (b) Deformation of the protective shield (c) Corrosion (d) Hole in the outer race.

The causes of bearing vibration are the outside time changing qualities between the portions and the transmission instrument of the WT amid the bearing operation however different signal processing procedures have been created to examine and interpret waveform and multidimensional information to extricate valuable data for promoting analytic and prognostic reason [14]. It can be outlined four kinds of deficiencies are recognized on the moving bearing relying upon where the fault happens. The

alleged bearing defect frequency ascertained on the premise of bearing parameters and rotational frequency relates to each of these faults and the following formulas are used to determine bearing defect frequencies:

Ball Pass Frequency Inner (BPFI)

$$\text{BPFI (Hz)} = \frac{N_b}{2}\left(1 + \frac{B_d}{P_d}\cos\theta\right) \times RPM \quad (1)$$

Ball Pass Frequency Outer (BPFO)

$$\text{BPFO(Hz)} = \frac{N_b}{2}\left(1 - \frac{B_d}{P_d}\cos\theta\right) \times RPM \quad (2)$$

Fundamental Train Frequency (FTF) (Cage)

$$\text{FTF(Hz)} = \frac{1}{2}\left(1 - \frac{B_d}{P_d}\cos\theta\right) \times RPM \quad (3)$$

Ball Spin Frequency (rolling element)

$$\text{BSF(Hz)} = \frac{P_d}{2B_d}\left(1 - \left(\frac{B_d}{P_d}\right)^2 (\cos\theta)^2\right) \times RPM \quad (4)$$

Where: N_b: No. of balls or rollers, B_d: Ball diameter (mm), P_d: Bearing pitch diameter (mm), θ: contact of angle, RPM: Rotational speed (Hz).

2. Test Procedure

For diagnostic the most popular defects in wind turbine bearing many experiments were carried out in the Renewable Energy LAB at Ministry of Science and Technology. In order to verify the validity of the diagnostic method as shown in Figure 3, an experimental rig was designed and fabricated.

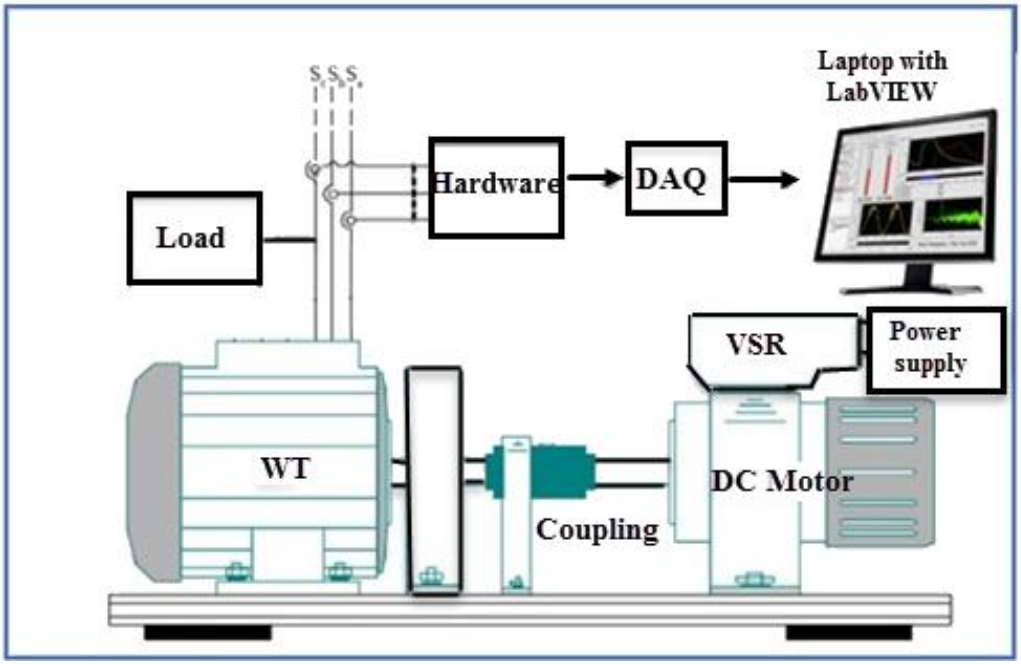

Figure 3. Test Rig.

The bearing type of SWG wind turbine 300 watts was used in this study which is 6205RZ deep groove ball bearing. The structure of the bearing is given in 'figure 4' and its main geometric parameters can be found in (table 1).

Table 1. Summarizes the geometric parameters of wind turbine bearing.

Pitch diameter (Pd)	Roller no.	Roller diameter (Bd)	Contact angle (ß)
52 mm	9	10 mm	0

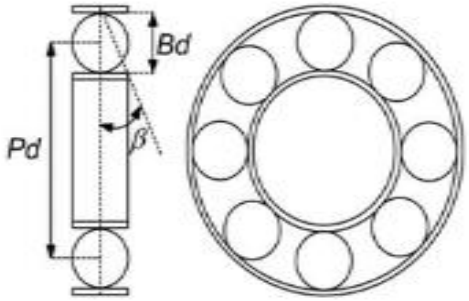

Figure 4. Deep groove bearing.

To provide the WT with regular speed, a speed control was used through a mechanical coupling which is connected to the DC motor and WT. The bearing vibration signals were acquired by using the piezoelectric accelerometer. According to the fact that accelerometers are climb on the bearing by the magnetic method. So, signal translated to NI USB DAQ-4431 device which is used for vibration readings. Input and output channels are integrated for stimulus-response tests. The sample rate is set to be 25000 Sample/second. As can be seen from 'figure 5', the signal was processed by Zoom Fast Fourier Transform (ZFFT) to relatively small bandwidth within the spectrum.

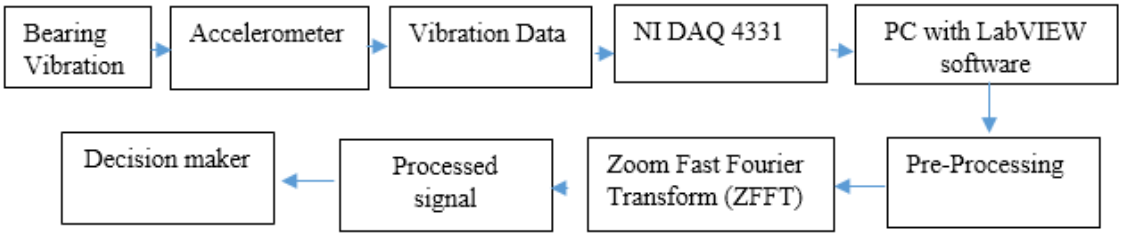

Figure 5. Flowchart of the vibration signal processing

According to the (table 1) geometric parameters must be determined to calculate the characteristic frequencies or orders of rolling-element bearings. The vibration which produced by the bearing changes causes a fault starts to build up when a rolling part experiences a discontinuity of line tracking, a signal is watched and RMS indicator in the front panel of the program will be glow when the vibration value exceeds the threshold value which is determined by the observer as shown in 'figure 6'.

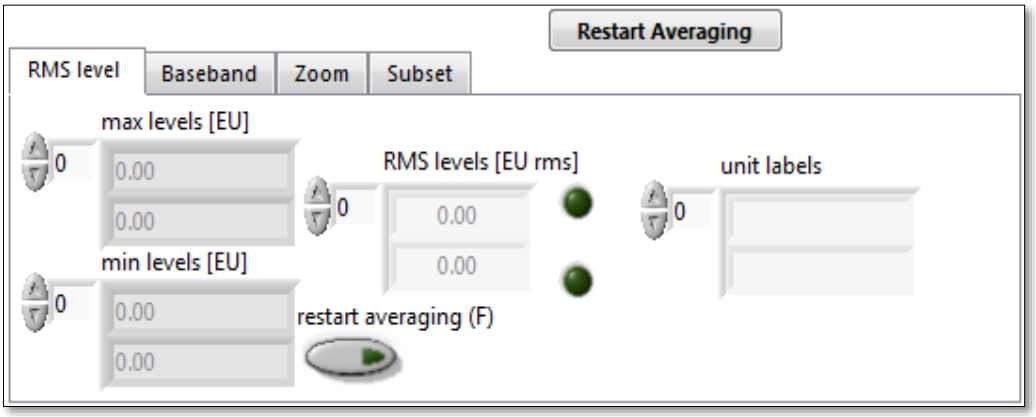

Figure 6. RMS indicator

The subsequent signals of vibration repeated continuously at a specific rate according to the position of the discontinuity and also the bearing structural. From (table 1), the bearing is after nine tests, are called BPFI, BPFO, and BSF individually. These measured the vibration signals of bearing at different shaft speed (2.5, 5, and 7.5 Hz) as shown in (table 2).

Table 2. Fault frequencies and adjacent harmonic frequencies for 2.5, and 7.5 Hz shaft speed

No load condition =7.5 Hz			
Notation	Fault frequency multiplier	Fault frequency (Hz)	Harmonic frequency
BPFI	5.1	38.5	39
BPFO	3.6	27.3	28
BSF	2.5	19	19
Half load condition =5 Hz			
BPFI	5.1	26.7	28
BPFO	3.6	18.2	18
BSF	2.5	12.6	13
Full load condition =2.5 Hz			
BPFI	5.1	13.3	13
BPFO	3.6	9.1	9
BSF	2.5	6.3	6

3. Test results

Depending on the tabulated results, some analysis spectra are clearly discussed. ‘Figure 7’, ‘figure 8’ and ‘figure 9’, showing BPFI, BPFO, and BSF fault frequencies respectively. The velocity waveforms as will reveal bearing damage, looseness, rubs, unbalance, misalignment and other conditions that have a high frequency and occur frequently.

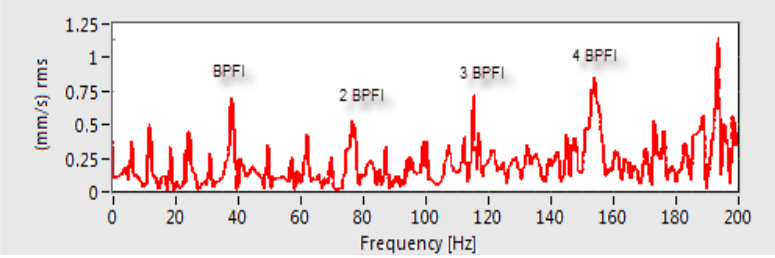

Figure 7. BPFI at shaft speed = 7.5 Hz

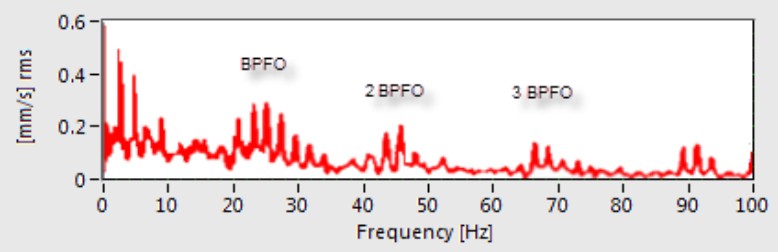

Figure 8. BPFO at shaft speed = 7.5 Hz

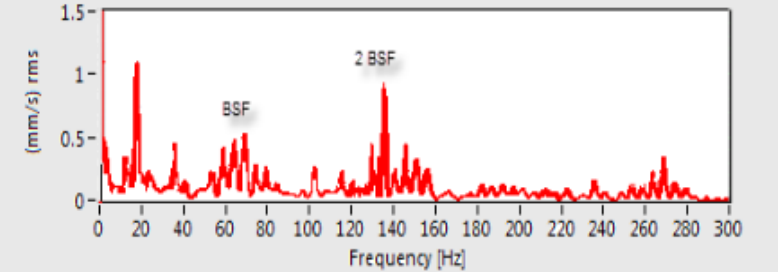

Figure 9. BSF at shaft speed = 7.5 Hz

'Figure 10' illustrates the BPFI, BPFO, and BSF spectrum at 7.5 Hz shaft speed. The method for determining displacement from velocity is the same as determining velocity from acceleration– therefore to go from acceleration to displacement needs two stages of processing, as shown in Figure 11. 'Figure 11' show criterion displacement movement for BSF fault of a wind turbine at 7.5 Hz shaft speeds. This type of waveforms can provide indications to wind turbine status that is not always evident in the frequency spectrum.

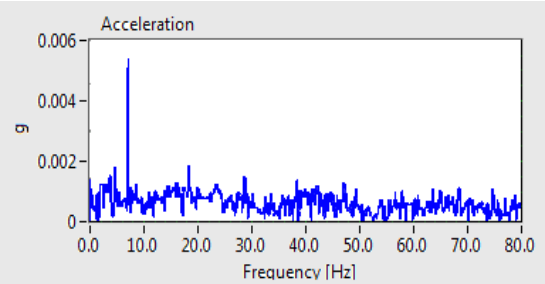

Figure 10: illustrate BPFO, BPFI, and BSF at 7.5 Hz shaft speed

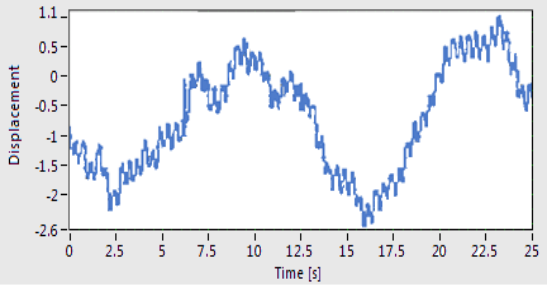

Figure 11. The criterion displacement movement at 7.5 Hz shaft speed

4. Conclusions

The results showed that developing a fault in bearing lead to appearing vibration amplitude or peaks in the spectrum. Spectrum monitoring and analysis are very useful because it is recording exactly what happened in the wind turbine from one moment to the next because the spectrum will have a "spike" when some fault or defect occurred and will record or capture the event. In addition, the spectrum may have harmonics, sidebands will reveal what happened. The fast Fourier transforms (FFT) have a high scope in vibration analysis. An FFT can be considered as especially benefit method. When a problem wind turbine occurs, FFT can tell us the position of the fault, the cause of the fault. BY knowing a certain wind turbine problem that occurs at definite pulsation it can determine the FFT spectrum. From study conditions, it can be concluded that the vibration technique suitable for diagnostic the defects occurred in the small wind turbine bearing.

References

[1] Abbasion S Rafsanjani A Farshidianfar A and Irani N 2007 Rolling element bearings multi-fault classification based on the wavelet denoising and support vector machine *Mech. Syst. Signal Process.* **21** pp 2933–45
[2] Choudhury A and Paliwal D 2016 Application of Frequency B-Spline Wavelets for Detection of Defects in Rolling Bearings *Procedia Eng.* **144** pp 289–96
[3] Jardine A Lin D and Banjevic D 2006 A review on machinery diagnostics and prognostics implementing condition-based maintenance *Mech. Syst. Signal Process.* **20** pp 1483–510
[4] Jayaswal P Wadhwani A and Mulchandani K 2008 Machine fault signature analysis *Int. J. Rotating Mach.*
[5] Korkua S Lee W and Kwan C 2011 Design and Implementation of ZigBee based Vibration Monitoring and Analysis for Electrical Machines *Int. Conf. Wirel. Networks - ICWN.*
[6] Lan Y et al. 2016 A two-step fault diagnosis framework for rolling element bearings with imbalanced data 2016 *13th Int. Conf. Ubiquitous Robot* Ambient Intell. 620–25
[7] Mcgowan J G et al. 2006 Condition monitoring and prognosis of utility-scale wind turbines Condition monitoring and prognosis of utility-scale wind turbines
[8] B. Mcniff and M L Industry The Gearbox Reliability Collaborative
[9] Önel I Y and Benbouzid M E 2008 Induction motor bearing failure detection and diagnosis: Park and Concordia transform approaches comparative study *IEEE/ASME Trans. Mechatronics* **13** pp 257–62
[10] Randall R B and Antoni J 2011 Rolling element bearing diagnostics-A tutorial *Mech. Syst. Signal Process.* **25** pp 485–520
[11] Bellini A Filippetti F Franceschini G Tassoni C and Kliman G B 2001 Quantitative Evaluation of Induction Motor Broken Bars by Means of Electrical Signature Analysis *IEEE Transactions on Industry Applications* **37** 5
[12] Safizadeh M S and Latifi S K 2014 Using multi-sensor data fusion for vibration fault diagnosis of rolling element bearings by accelerometer and load cell *Inf. Fusion* **18** pp 1–8
[13] Si L Wang Z Liu X Tan C, Xu J and Zheng K 2015 Multi-sensor data fusion identification for shearer cutting conditions based on parallel quasi-newton neural networks and the Dempster-Shafer theory *Sensors (Switzerland)* **15** 28772–95
[14] Wang W Q Ismail F and Farid M 2001 Assessment of Gear Damage Monitoring Techniques Using Vibration Measurements *Mech. Syst. Signal Process* **15** 905–22
[15] Wilkinson M Spianto F and Knowles M 2006 Towards the zero maintenance wind turbine *41st Int. Univ. Power Eng. Conf. UPEC Conf. Proceedings* **1** 74–8

Synthesis and characterization of porous silicon gas sensors

Synthesis and characterization of porous silicon gas sensors

Roaa A abbas[1], Alwan M Alwan[2], Zainab T Abdulhamied[1]

[1]Ministry of science and technology (directorate of material researches)

[2]University of Technology (Applied Sciences Department)

noor_ok_2@yahoo.com

Abstract. In this work, photo-electrochemical etching process of n-type Silicon of resistivity(10 Ω.cm) and (100) orientation , using two illumination sources IR and violet wavelength in HF acid have been used to produce PSi gas detection device. The fabrication process was carried out at a fixed etching current density of 25mA/cm2and at different etching time (5, 10, 15 and 20) min and (8, 16, 24, and 30) min. Two configurations of gas sensor configuration planer and sandwich have been made and investigated. The morphological properties have been studied using SEM ,the FTIR measurement show that the (Si-Hx) and (Si-O-Si) absorption peak were increases with increasing etching time ,and Photoluminescence properties of PSi layer show decrease in the peak of PL peak toward the violet shift. The gas detection process is made on the CO2 gas at different operating temperature and fixed gas concentration. In the planner structure, the gas sensing was measured through, the change in the resistance readout as a function to the exposure time, while for sandwich structure J-V characteristic have been made to determine the sensitivity.

1. Introduction

PSi is one of the most important substance because of its perfect morphological, electrical, and mechanical characteristic [']. The high surface area to volume ratio is about (500-1000m2/cm3) of PSi, the ease of manufacturing, several morphology can be obtain for different preparation condition result in the formation very promising material for developing a smart systems-on-chip sensors. Several modern gas sensing systems are has been developed as a means for comparing both the performance and the physical sensing gas sensor is defined as any device that assesses one or more characteristics of a sample of gas [2]. The Photo _electrochemical Etching (PECE) is a combined between the electrochemical etching process and photochemical etching where light or laser illuminating on the silicon electrode during the anodization process can be utilized to modify the micro porous and macro porous properties. Where At the top layer due to light absorption, which leads to further reduction in size the number of nano-crystallites and PSi layer thickness were affected by illumination wavelength [3]. The following equation shows the overall reactions for the pore formation. The following equation shows the overall reactions for the pore formation [4]:

$$Si + 6HF \rightarrow H_2SiF_6 + H_2 + 2H^+ + 2e^- \quad (1)$$

There are two specific configuration of sensing mechanism Planar and Sandwich structure. In the first one the electrical current will pass in the porous layer only while in the second mechanism the current will flow cross the porous layer and formed silicon hetrojunction between PSi and Si the sensing process will vary based on the current flow in the porous layer and the PSi/Si junction. It is important to use porous silicon instead of silicon in the gas sensor application this is due to the increasing in responsively, ease of manufacturing by etching process which is simple and cheap, also it can be produced with different morphology, and can use several techniques to obtain the readout[5].

2. Basic Gas Sensing Characteristics

The main parameter of the gas sensor including the gas responsivity(R), gas concentration, sensing limit of gas detection, response(τ_{res}) and recovery time(τ_{rec}),and the detection temperature [6] . These parameters are varied based on the porous silicon parameter especially the pore size, porosity, and surface to the volume ratio.

2.1Response time and recovery time

One of the most important parameter of the gas sensor device is the response time (τ res) which can be defined as the exploited time for the gas sensor device to make dramatic change in the physical parameter from the beginning of the reaction until getting to a stable readout when it reached spatial percentage scale (generally take as 95%) of the last value, in response to the changing in the input [7]. The reduction in the response time is a good properties for gas detection device. With high gas concentration, the response time is short. So in the case of operation with low concentration of the toxic gases must be careful because long response time would be dangerous. The response time for typical gas sensor is in the order of a few minute or lower than that [8].

2.2 Selectivity

Generally the selectivity of the gas sensor device is defined as the capacity of sensor to characterize a given gas concentration with the presence of other gases at the same sensing condition [9]. For example the O_2 sensing device dose not response to another gases like CO, NO and NH_3, so this device considered as a selective device. The selectivity of nano material based gas sensor device is given by the following equation [10].

$$\mathbf{Si + 6HF \rightarrow H_2SiF_6 + H_2 + 2H^+ + 2e} \qquad (2)$$

2.3 Detection Limit

The detection limit is defined as the minimum magnitude of the calculated that can be determine by the sensor, on the other word is the lower value of gas concentration that can be sensed by gas detection device. The sensing device performance enhanced with decreasing the detection limt [11].

2.4 Gas response (sensitivity)

The gas responsivity for gas detection device can be define as the dramatically change in the resistance or other physical quantities of the sensor surface before and after exposure to gas. The researchers have used different mathematical terms to define the gas response as shown in the following equations [12].

$$R = \frac{R_a - R_g}{R_a} \times 100 = \frac{\Delta R}{R_a} \times 100\% \qquad (3)$$

$$R = \frac{I_a - I_g}{I_g} \times 100 = \frac{\Delta I}{I_g} \times 100\% \quad (4)$$

Where Ra is the resistance of the sensor in the presence of atmospheric air, while Rg the device resistance after exposure to the gas, Ia the essential current of PSi sensor in the presence of atmospheric air, and Ig is the current after exposure to gas. The sensitivity is the capability to sense a lower concentrations of using gas [13]. Sensitivity characterizes the magnitude of a response to a particular analyse [14]. The sensitivity can be recorded as a ratio between some measure of the response and the concentration of analyse being delivered.

3. Experimental part

A commercially available Si wafer (100) n-type of resistivity (10Ω.cm) and thickness (625µm) were used. The experimental setup consisted of power supply, ammeter and aqueous (HF) acid in Teflon cell with ethanol to prevent the aggregation of H_2 bubbles , and laser .The PSi formation condition including for IR (810nm) and intensity (2W/cm^2) the etching times 5,10,15, and 20min, the HF concentration of about 24% . While for violet (405nm) and intensity (20mw/cm^2) the HF concentration of about 16%and fixed current density 25mA/cm^{2}Also there were two electrodes, the Si wafer connected to the anode and platinum used as the cathode .The PSi silicon sample were prepared by PECE process with constant current density (25mA/cm^2) for both lasers ,and at different etching time of about 5to 20 min for IR illuminated PSi samples and 8 to 30 min for violet illuminated samples and the etching solution consisted of HF :ethanol :H_2O(1:1:1),and the HF concentration was(16%). Experimental setup is shown in 'Figure 1'.

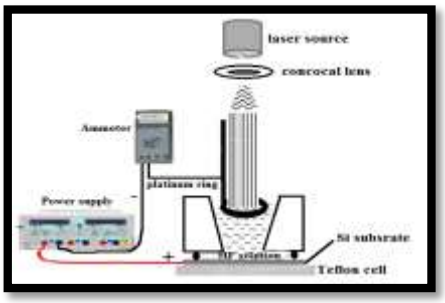

Figure 1. The schematic of PECE.

After the formation process the gas sensor application required deposition of AL electrode. Two configuration of electrode have been done for planer structure of gas sensor grid mask with thickness 250nm on the PSi surface have been formed and for sandwich structure the electrode made on the upper PSi surface with thickness (5-20nm) and lower PSi surface with AL electrode, as shown in the following Figure 2.This deposition was done by using the vacuum thermal evaporation.

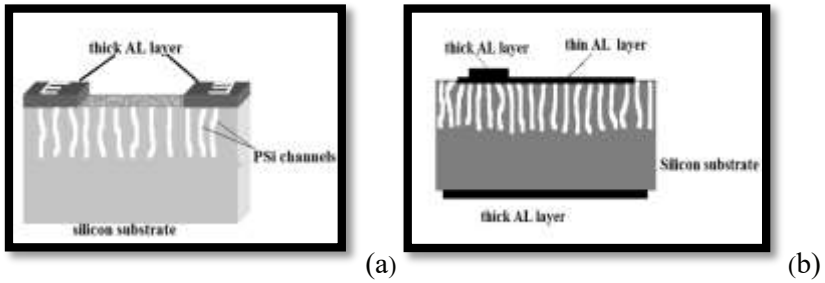

(a) (b)

Figure 2. PSi sample (a)planer (b) sandwich

4. Result and discussion

4.1Characteristic of porous silicon layer

One of the most important structural properties of PSi material is the formation pores (or porosity %), the PSi preparation parameter including (HF) concentration, laser properties such as (wavelength, illumination intensity), and the percentage of the doping in the Si wafer. All these parameters monitoring the nanosize of the pore, how the channel distributed, the channel connectivity. The most common structure of the PSi preparation are circular pores with 'branching' through the surface. Also it can be noted that the nanosize of the high thickness porous silicon reduced with the depth of layer. The porosity% (P %) and layer thickness of PSi (d) can be calculated gravitationally by the following equations[15].

$$P = (M_1 - M_2) / (M_1 - M_3) \quad (5)$$

$$d = (M_1 - M_3) / (\rho \times A_{PSi}) \quad (6)$$

Where M_1,the PSi sample mass before anodization process, M_2, the PSi sample mass after anodization process ,and M_3, the sample mass after removing the PSi layer using NaOH electrolyte, ρ, the Si bulk density and its unit is (g/cm^3) ,and APSi, the PSi area in (cm^2).

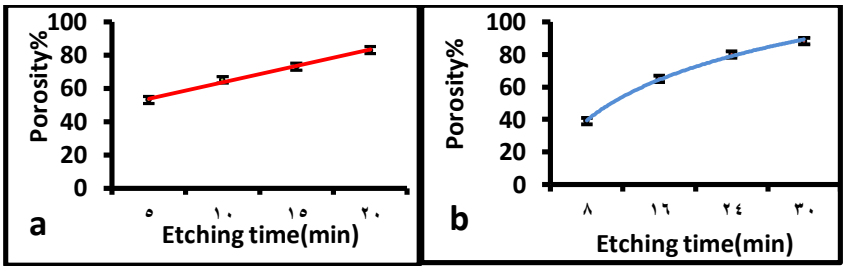

Figure 3. The porosity of the porous silicon as a function to the etching time for two illumination wave length (a) IR (810nm), (b) and violet (405nm).

'Figure 3a' shows the case of IR, after certain time the porosity increased linearly and reaching to high value of about 83% .The increasing of etching time to higher value of 20min ,the PSi layer became Fragile with low mechanical properties. For case of violet illumination of 'figure b', the porosity increased with increasing the etching time in an exponentially relationship , and the maximum value was about 88% at 30min etching time .The higher etching time allowed deeper penetration through silicon region and produced more pore, and this results was comparable with the results obtain by other researchers[16]. The relationship between the layer thickness and the etching time shown in the Figure 4. In this Figure the value of the PSi thickness layer increased with increasing etching time. The higher value of the layer thickness was about (38.43μm) and (23.8μm) for IR and violet illumination respectively.

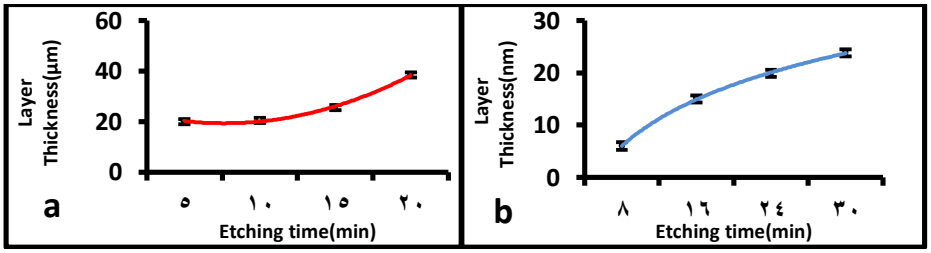

Figure 4. The layer thickness of the porous silicon as a function to the etching time for two illumination wave length (a) IR (810nm), (b) and violet (405nm).

The layer thickness of IR was much greater than that of violet illumination. This was due to the increasing of the absorption depth for (810nm), where the absorption depth was about (12.9μm) while for violet (405nm) it was about (100nm). Long laser wavelength increases the penetration depth of incident photons and the etching would occur at region away from the porous layer and inside the deep silicon regions so much greater e-h pairs would be generated and this would increasing the silicon dissolution process. The morphological properties of porous layer like ,pore shape ,pore width ,and the wall thickness between the adjacent pores are strongly depended on the etching parameters especially the etching time ,current density ,and the laser illumination conditions (intensity and wavelength) [17, 18].These properties of (PSi) have been investigated by direct imaging for the structure by using Scanning Electron Microscope (SEM) .

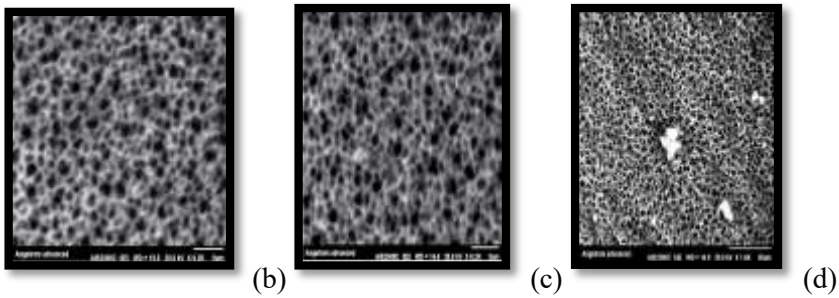

Figure (5). SEM image (top- view) of IR illuminated porous layer ,2W/cm2illumination intensity (a)5,(b)10,(c)15,and(d)20min) with6200 magnification for (a, b and c) and with1600 magnification for d.

The increasing of the etching time would improve the silicon dissolution mechanism due to increases the amount of the photo generated e-h pairs and hence the pore size and the pores overlapping process leading to synthesis the rectangular form (pores). From this images, some basic observations may be taken into account based on the ;(i) Pore size of the porous layer seems as a macro pores with different pore shapes nearly spherical and rectangular forms ;(ii) The pores was randomly distributed on the silicon surface, the large value of the pore sizes may be attributed to the increase of e-h pairs within the porous layer, which enhanced the silicon dissolution process between the nearest-neighbor pores. The non-uniformity of Gaussian distribution of the laser beam intensity led to make the etching rate having different values and hence resulting a porous layer with different pore size. While for the PSi sample prepared with violet laser the formation of this rare morphology was studied by ***Cláudia*** [19], according to the analysis of removing the silicon atoms remains enhancing the surface in homogeneity due to the local changes in the electric field distribution. This type of morphology occurred at high value of applied voltage where (30V) DC was supplied across the silicon and pt electrodes compared with (1.5-2V) in the case of IR illumination. By comparing the SEM images, we can observe that the increasing of the etching time would lead to increase the density of the cross -like pore structure. The growth rate of the pore across the PSi layer was not constant along the depth. This referred to the fact that etching occurs only in the pore tip but also in the pore walls. The high electric filed at the pore corner maybe responsible for this behaviour, where high bias voltage led to so -called pore wall break down [19].

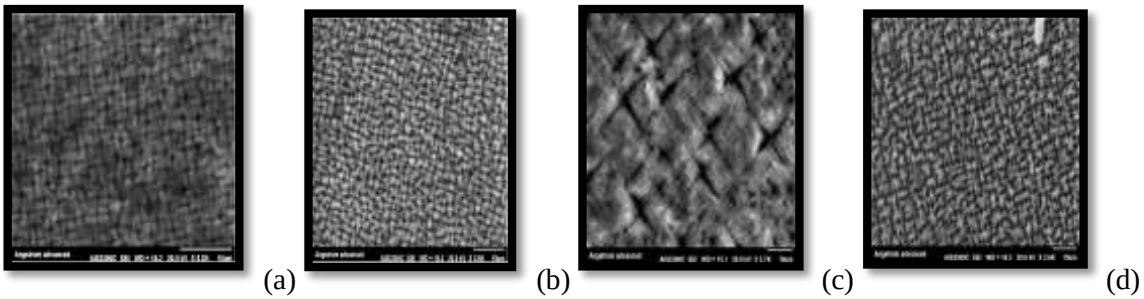

Figure 6. SEM image(top view)of violet illumination PSi layer prepared and (20mW/cm2) illumination intensity(a)8,(b)16,(c)24,(d)30min with 3600 magnification for(a,b,and d)and2700 magnification for c .

4.2Photoluminescence studies

Photoluminescence spectroscopy has emerged as an important tool for studying the optical properties of PSi materials suited for gas detection process. PL studies was carried out using He-Cd laser system operating at 325nm wavelength. The PL spectra of PSi prepared with different etching times under two illumination wavelength IR and violet as showing in the following figure respectively. The PL spectra of PSi were dominded by strong and broad emission peak spanning over a large part visible region. i.e PSi sample showed strong emission wavelength in the range (500-750nm). The emission was attributed to the radiation carrier recombination process in the silicon nano region .The PL intensity increased with increases the etching time with blue shift in the peak position.

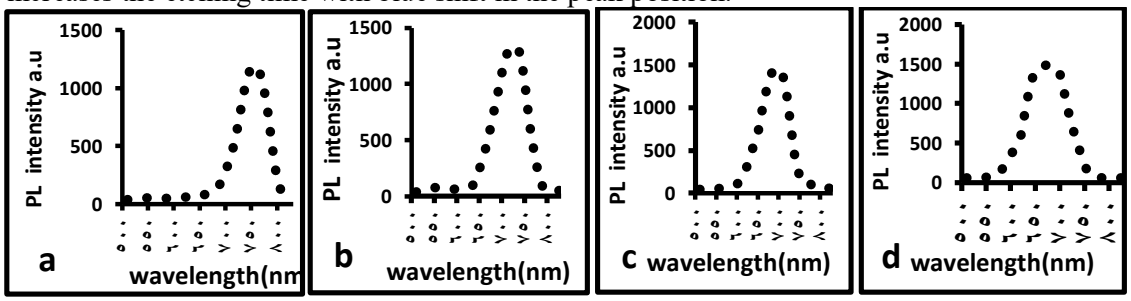

Figure (7). Illustrates the PL spectra of IR PSi sample at different etching times, (a) 5min (b) 10min, (c) 15 min, and (d) 20 min.

While 'Figure 8', displays the PL spectra of sample prepared with violet laser the increasing of the etching time showed a strong emission at different wavelengths 655, 605, 573, and535nm respectively, with a blue shift in the peak position.

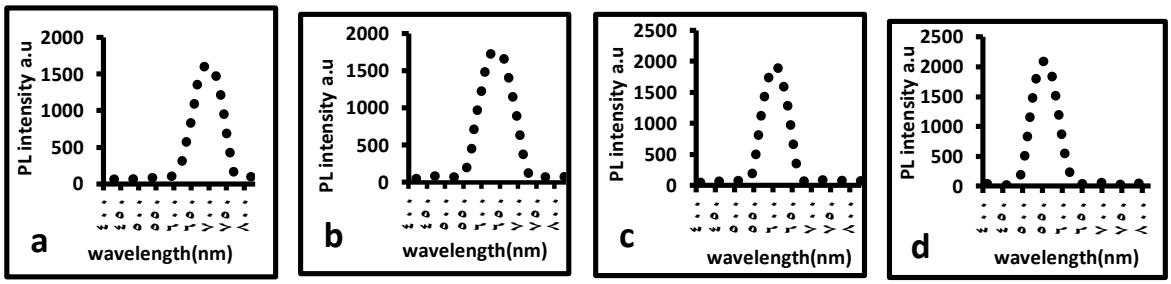

Figure 8. Illustrates the PL spectra of violet PSi sample at different etching times, (a) 8min, (b) 16min, (c) 24 min, and (d)30 min.

By comparing the PL spectra of Figure 7 and 8, it can be recognized that the PL spectra of violet illumination, the PL intensity with short emission wavelength has high value. While for the samples prepared by an 810 nm, there was low PL intensity and this would be as a result of bigger nanocrystile size due to its small photon energy (1.53eV), which was not sufficient enough to initiate the absorption and reduce the silicon nano size. To PL contribution limit so the increasing of the illumination wavelength (decreasing the photon energy) led to synthesis larger silicon nano size. When the silicon sample illuminated with short wavelength (405nm), the photon energy was (3.062eV). The average of the silicon nano crystallite, energy gap of the porous layer, the peak of PL intensity and emission which determine from the above figures and according to the following equation [20] are showed in Table 1.

$$E_{g\,(PSi)}=h\,c/\lambda_{max} \quad (7)$$

$$E_{g(PSi)}=Eg_{(S)}+88.34/L^{1.37} \quad (8)$$

Where h is blank constant, c is the light speed ,and λ max is obtain from the PL curve and then can determine the nano size L.

Table 1. Illustrates, PL emission wavelength, PL intensity, energy band gap, and silicon nano size as a function to the etching time for two illumination wavelength IR and violet

Illumination Source	Etching time(min)	PL peak Wavelength(nm)	PL intensity (a.u)	Eg PSi eV	Nano silicon size(nm)
IR	5	752	1200	1.7	3.9
	10	720	1335	1.72	3.8
	15	688	1466	1.8	3.4
	20	675	1500	1.84	3.3
Violet	8	680	1705	1.82	3.4
	16	630	1780	1.97	2.9
	24	600	1950	2.06	2.75
	30	560	2100	2.21	2.72

4.3Gas sensor properties

The gas sensing performance of two types of porous silicon configuration (planer and sandwich structure) were studied at different operation temperatures.

4.3.1Sandwich structure mode

Sensing mechanism of this mode of operation was based on the response of the current density -voltage characteristic across the porous silicon /crystalline silicon junction.

4.3.1.1Current density –voltage characteristic of sensor without gas

'Figure 9a' , 'Figure 9b' , 'Figure 9c' and 'Figure 9d' and 'Figure 10a' , 'Figure 10b' , 'Figure 10c' and 'Figure 10d' present the J-V characteristics of IR illuminated and violet illuminated sandwich (Al/n PSi/n-Si/Al) structure at different temperatures from (25-150C°). All measurements were taken in the range from (0 – 5V).

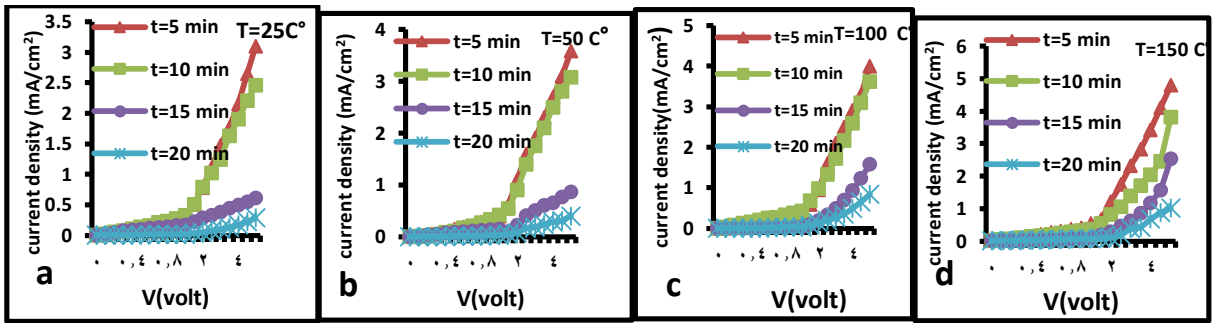

Figure 9. J-V characteristic for IR illuminated porous samples at the different temperatures (a)25 C°, ,(b)50C° ,(c)100 C°, (d) and 150C°for different etching times(5,10,15,and20 min).

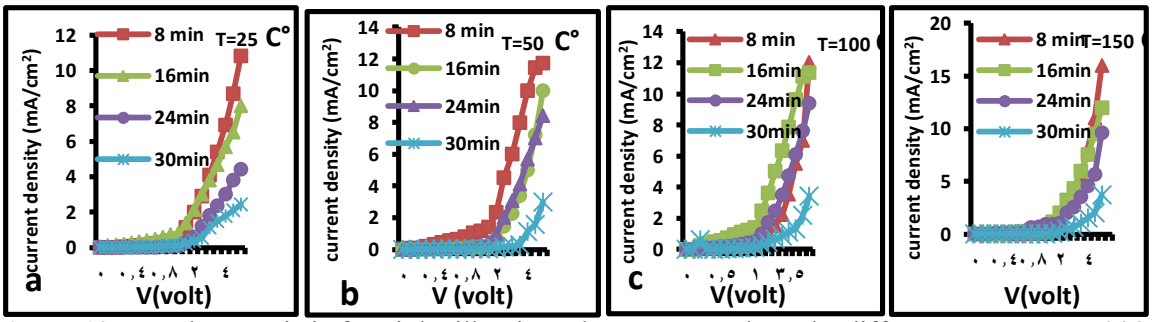

Figure 10. J-V characteristic for violet illuminated porous sample at the different temperature (a)25 C°, (b)50C°, (c)100 C°,, (d)and 150C°for different etching times(8,16,24,and 30min).

From these curves, we can observe that the current passing in the absence of gas molecule was varied according to the porosity and the layer thickness of the porous layer. The following facts can be conclude.

1-At fixed temperature the forward current passing through the fabricated sandwich structures deceased with increasing the etching times for both types of illuminated porous silicon samples. This behavior was due to the increasing the porosity and layer thickness with increasing the etching time ,where the increasing of the porosity led to decrease both of the dielectric constant of the porous silicon layer and the mobility of the charge carrier.

2- At fixed etching time the value of the forward current increased slightly with increasing the operation temperatures from 25C° to 150C° due to the increase of the thermal generated charge carrier with temperature.

In prepared device, the forward current density –voltage (J-V) behavior followed a power law relationship ($J \alpha V^2$) which indicated the space charge current attributed to the carriers drifting through the high resistivity luminescence Psi. According to the suggested model by ***Pang. C etal*** [21] for the carrier transport in PSi photoluminescence device was rectifying. In forward bias, the (J-V) characteristics exhibits a power-law relationship ($J=kv^m$) where k was proportionality factor depended on the characteristics of the porous layer and m=2 which implied that the total current of the device was dominated by carrier transport in the high resistivity luminescence. The device can be modeled as an intrinsic semiconductor luminescence sandwich between two conduction material Aluminum electrode and the n-type silicon substrate. The intrinsic semiconductor (PSi layer) contained a limited amount of thermally generated free carrier. In forward bias, electron and hole were injected into PSi layer .When the injected carrier concentration became comparable to the thermally generated concentration, the J-V characteristics of the device deviated from ohmic behavior according to the equation.

$$I_{PSi} = \epsilon_{rPSi}\, \epsilon 0\, \mu_{eff}\, V^2/d^3 \qquad (9)$$

Under the pressure of about (5%) ppm CO_2 the current density –voltage characteristic with gas. For both curves, exposure to CO_2 gas did not change the shape of J-V characteristic (still rectifying)but the values of the current at presence of CO_2 gas were higher than that of the case without gas ,the variation in the current indicating that the sensor was very sensitive to CO_2 gas. The variation of the current at maximum applied voltage +5V at fixed operation temperature before and after exposure to CO_2 gas increased with increasing the etching time. The structure of (Al/nPSi/n-Si/Al) with violet illuminated samples has higher variation in current compared with structure of (Al/nPSi/n-Si/Al) with IR illuminated samples. The increasing of the current density for all samples related to the role of the CO_2 molecules where desorption of the molecule on the PSi layer was due to the Vander **Waals** interaction which would lead to modify the dielectric constant of the porous layer, whereas we see in the presence of theCO_2 gas would enhance the current flow in the fabricated sensor. According to theCO_2 molecules that acted as acceptor, this would lead to an increasing the free carrier concentration [14].

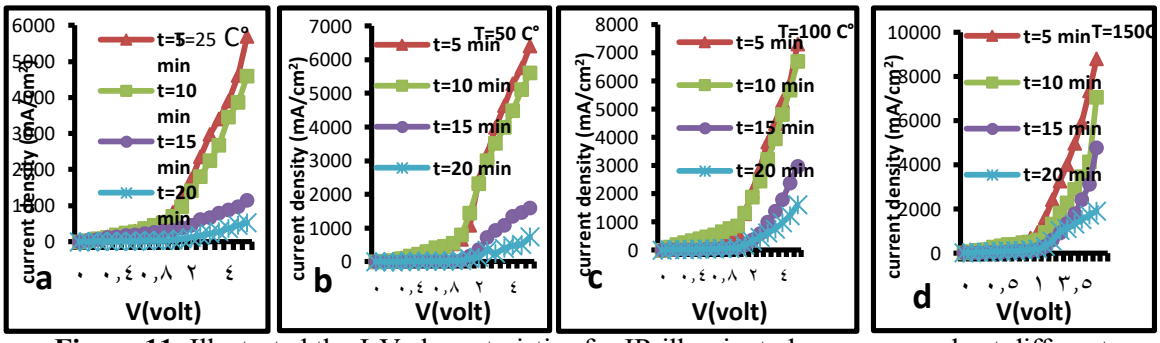

Figure 11. Illustrated the J-V characteristics for IR illuminated porous sample at different temperatures (a)25 C°, ,(b)50C°, (c)100 C°, (d) and150C° under CO2 gas at pressure of about (5%)ppm.

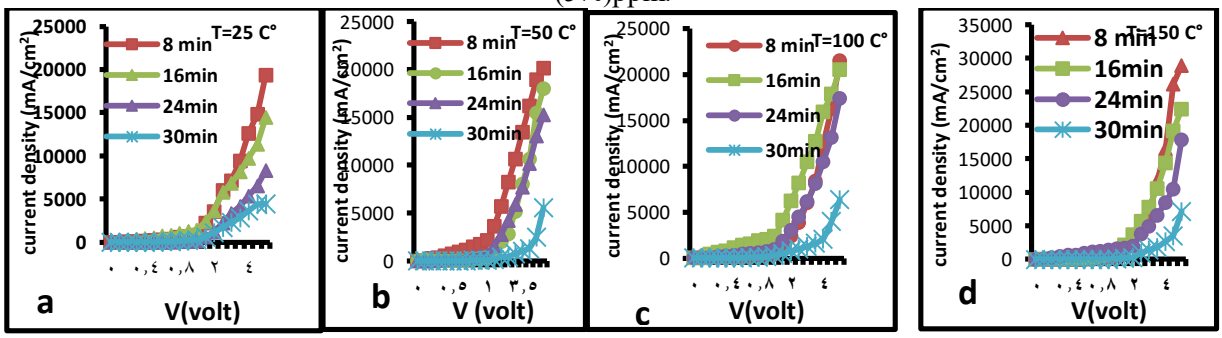

Figure 12. Illustrated the J-V characteristics for violet illuminated porous sample at different temperatures (a)25 ,(b)50C°, (c)100, (d)150C° under CO2 gas at pressure of about (5%)ppm.

The variation of the maximum detection sensitivity at fixed opreating voltage 5V with operating temperature in the range from room temperature to 150C° of the porous layer shown in the figure (13). The sensing test was performed using (5%ppm) CO_2. Temperature variations revaled the current passing through the sensor ,so the sensitivity of the device increased with raising in the operating temperature from(50 to 150) C° and reached a maximum at 150 C°. Also by comparing figure (a) and(b) it clear to us that the violet illuminated sample have higher sensitivity than the IR illuminated sample. This is due to to the fact that the increasing of the effective dielectric constantof the porous layer under CO_2 exposure. This may be attributed to the rate of the adsorption of the CO_2gas molecules on active porous layer increased with riasing in the operating temperature. This causes a rapid increasing in the passing charge carriers and hence an increasing in the sensitivity as shown in Figure 13.

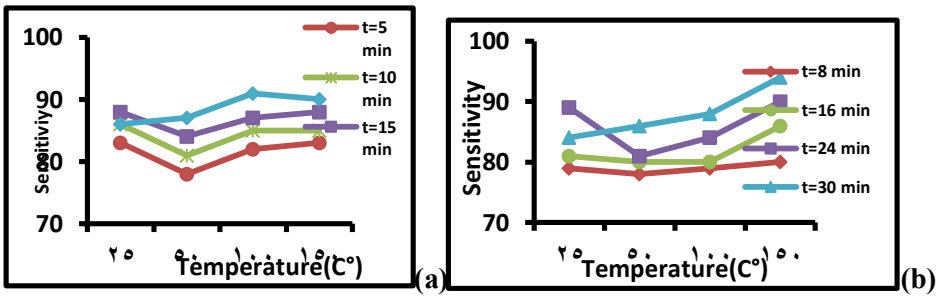

Figure 13. The variation of the sensitivity at 5V applied voltage for porous sample with operating temperatures (a) IR illuminated PSi (b) violet illuminated PSi.

4.3.2 Planer structure mode

The sensing mechanism of this type of sensors operation was based on the recording the variation of the resistance of the porous layer. Parallel strip electrodes with two opposite E latter were used for measuring the electrical resistance of PSi device. The resistance was measured at different temperature and fixed operating voltage of about 3volt.

4.3.2.1 Dynamic response

Dynamic response of the planer structure gas sensor at fixed concentration of using gases for two type of porous silicon substrates IR and violet illuminated PSi samples.

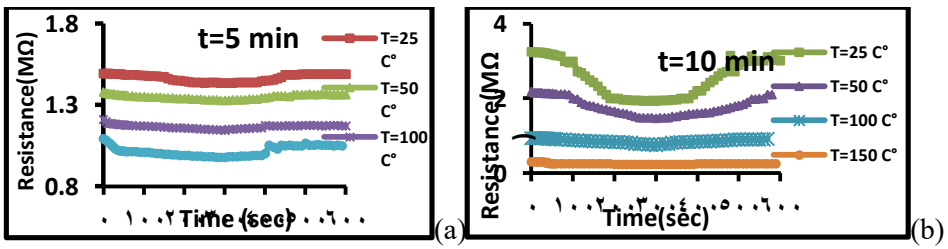

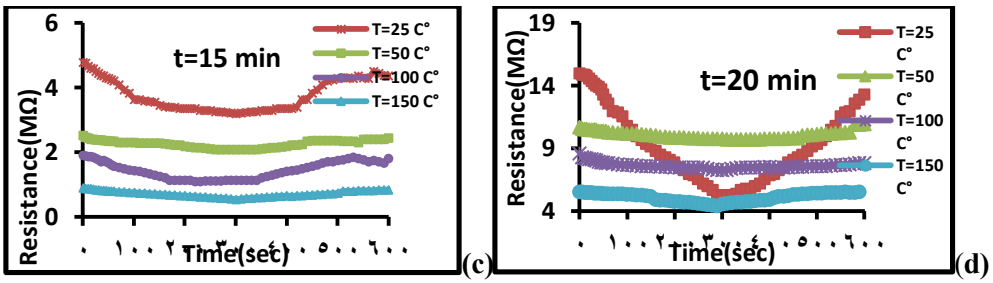

Figure 14. Dynamic response of IR illuminated PSi sample planer structure sensor at different temperatures under CO2 concentration (5%)ppm at specific etching times ,(a)5 min ,(b)10min, (c) 15min and,(d)20min,at current density (25mA/cm2),and fixed i intensity of about(2W/cm2).

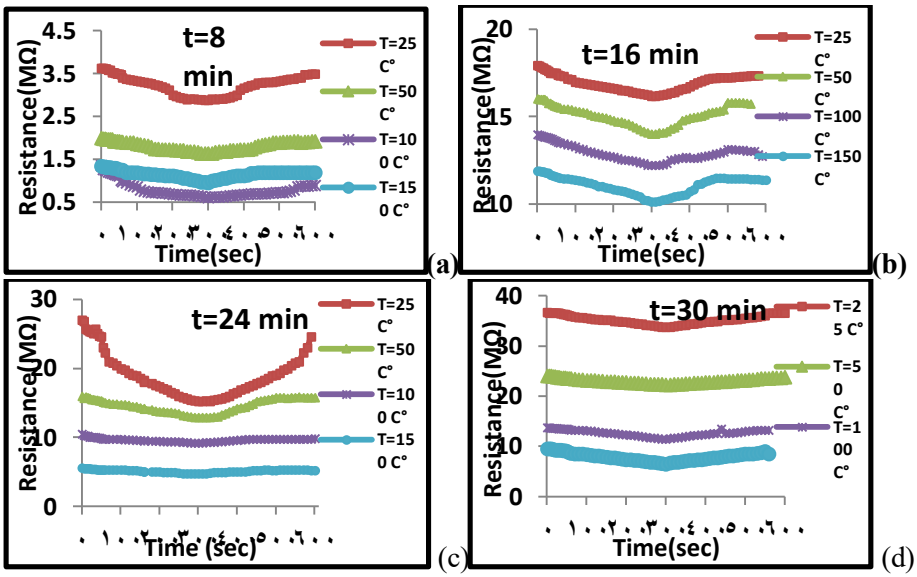

Figure 15. Dynamic response of violet illuminated sample planer structure sensor at different temperatures under CO_2 concentration (5%)ppm at specific etching times ,(a) 8 min,(b)16min,(c)24min and,(d)30min ,at current density (25mA/cm^2),and fixed illumination intensity of about(20mW/cm^2)

From the dynamic response curves, it's easily to observe that a large resistance variation is recorded. The resistance of porous layer recovers slowly and tend to retain to the initial value for IR and violet illuminated samples at different temperature and specific etching time. The resistance of porous layer shows a decrease from higher value to lower value and the numerical value of the resistance is varied according to the etching time and the temperature. The resistance value, before and after exposure to CO_2 gas of PSi layer has been tabulated in the following table also the response and recovery time for all planer structure PSi sample sensor.

Table 2. Dynamic response for planer configuration porous with IR illuminated PSi layer.

tching time (min)	Temperature (C°)	Maximum resistance(MΩ)	Minimum resistance(MΩ)	Response time(sec)	Recover time(sec)	Maximum sensitivity
IR 5min	25	1.493	1.435	130	120	3.884796
	50	1.377	1.327	100	160	3.631082
	100	1.21	1.143	110	80	5.53719
	150	1.092	0.977	60	80	10.53114
10 min	25	3.244	1.93	140	100	40.50555
	50	2.194	1.472	120	200	14
	100	0.938	0.751	150	180	17.91045
	150	0.303	0.236	90	100	21.05611
15min	25	4.78	3.2	125	170	33.05439
	50	2.52	2.1	150	140	16.66667
	100	1.92	1.113	160	200	42.03125
	150	0.915	0.561	165	210	38.68852
20 min	25	15	5.2	50	75	65.33333
	50	10.96	9.74	155	180	16.56704
	100	8.62	7.29	140	200	15.42923
	150	5.56	4.44	170	150	19.2446

Table 3. Shows dynamic response for planer configuration porous sensor with violet illuminated PSi layer.

Etching time (min)	Temperature (C°)	Maximum resistance (MΩ)	Minimum resistance (MΩ)	Response time(sec)	Recover time(sec)	Maximum Sensitivity
violet 8min	25	3.622	2.88	130	110	20.04
	50	1.99	1.63	140	115	18.0402
	100	1.352	0.611	50	90	54.80769
	150	1.33	0.955	75	100	37.36842
16 min	25	17.9	16.17	240	170	9.66
	50	15.99	14	200	200	12.44528
	100	13.94	12.19	190	200	11.47776
	150	11.85	10.1	195	110	13.75527
24min	25	27	15.2	140	80	43.7
	50	16	12.88	140	90	19.5
	100	10.5	9.23	160	120	12.09524
	150	5.59	4.77	150	140	14.66905
30 min	25	36.78	35.09	220	200	4.46
	50	23.36	21.97	160	180	5.89
	100	13.28	12.55	140	120	5.639098
	150	9.52	8.63	150	140	9.822362

1. Resistance –time characteristic of sensor without gas.

The resistance of the PSi layer between the deposited metallic electrodes in the case of absence of CO_2 gas molecule varied according to the etching time, illumination wavelength, and the operating temperature. From the Tables 2 and 3 we can list the following facts:

1-For fixed type of PSi sample, the resistance of the PSi was increases with increasing the etching time. This behavior is due to the quantum confinement effect for the charge carrier in the depletion process. This will lead to decreases the effective charge carriers which contribute to conductance process in PSi layer. The increasing of these bonds and the effects of depletional charge carriers would lead to the increase the charge depleted region (w) according to the passion's equation. So the central silicon channel would be dropped to large extent.

2-The resistance of IR illuminated PSi gas sensor samples in general was less than that of violet illuminated samples due to the fact that the density of the dangling bonds Si-H_x and Si-O-Si.

Resistance –time characteristic of sensor with presence of gas.

The resistance of PSi layer in the presence of gas CO_2 molecule as a function to the time was varied according to the type of PSi layer. Also the sensitivity, the response time, and recovery time depended on the PSi layer. The following facts can be deduced.

1-The sensitivity of IR illuminated PSi samples was higher than that o of the violet illumination PSi gas sensor samples.

2-At fixed etching time the response time PSi gas sensor was slightly varied with increasing the operating temperature from (25-150C°).

3-For fixed etching time the recovery time was often higher than the response time for both PSi substrate, including a fast rate for adsorption than for desorption of CO_2 gas from the porous matrix. For the performance of the fabricated porous silicon planer structure, we have realized a sensor which the resistance decreased down to (one or two order) of magnitude in the presence of carbon dioxide. To interpret quantitatively this behaviour, we discussed the performance of the sensor according to the activity of the dangling bonds (Si-H) associated with porous silicon. Based on the ***D. stievenard and Deresmes*** model [22]. The conductivity and hence the resistivity was governed by width of the channel resulting from the partial depletion of silicon located between pores. This partial depletion region was resulting from the charges trapped on the surface states associated with the partially oxidation of porous silicon (Si-SiO_2) where SiO_2 was the native silicon oxide. In order to explain the electrical behaviour of the sensor, we proposed the following schematic representation (4.28). Due to the partially oxidation of PSi which occurred spontaneously during aging process ,there were a thin layer of SiO_2 and associated interface states having density (δ) cm^{-2}, there was a depleted region in the silicon material over the region(w).So the effective silicon channel has a width (d-2w)in which the carriers can move when the applied voltage was applied on the planer .junction[23].

$$w=\delta/N_D \qquad (10)$$

Where N_D is the doping level in the silicon. So the conductivity of the sensor was govern by (δ). The effect of the gas was to passivate the active dangling bonds through screening mechanism, so that (w) decreases and the width of the channels increases. In our samples, d is the order (0.7μm). The density of the dangling bonds was about 10^{12}_10^{13} cm^{-2}. As the initial doping of Si was in the order of ($4.1*10^{14}cm^{-3}$), there were enough DB to passivate the free carriers. We found that (w) was in the order of ($0.02*10^{-14}$nm) so the central channel can be easily pinched.

5. Conclusions

PSi based gas sensor substrate were fabricated by photo-electrochemical etching process the sensitivity will modify according to the porous silicon morphology. Higher sensitivity was obtained. The maximum porosity with lower porous layer thickness was obtained with violet illuminated PSi sample rather than the IR illuminated PSi sample. The IR illuminated PSi layer has surface morphology of pore- like structure at etching time ranging from(5-20min),while violet illuminated PSi layer has surface morphology of cross- like structure with different sizes. The gas sensor performance was chanced according to the gas sensor configurations and characteristics of the porous layer. The porous silicon gas sensitivity was increase with increase the pore size within the porous layer. Efficient porous silicon gas sensor can be fabricated in sandwich configuration mode from a thin porous layer rather than thick porous layer.

Reference

[1] Hirschman K, Tsybeskov L, Duttagupta SP, Fauchet PM, Nature, 1996, 384: 338-341.
[2] K H C, Li, Tsai, Sarathy, J, Shih, S, Campbell, JC, Hance, BK, White, JM. Thermal treatment studies of the photoluminescence intensity of porous silicon. *Appl Phys Lett*, 1991, 59 (**22**): 2814-2816.
[3] Bisi O, Stefano Ossicini, Pavesi L. Porous silicon: a quantum sponge structure for silicon based optoelectronics Surface Science Reports. 2000, 38: 1-126.
[4] Barillaro G, Bruschi P, Diligenti A, Nannini A. Fabrication of regular silicon microstructures by photo-electrochemical etching of silicon. phys. stat. sol. (c), WILEY-VCH Verlag GmbH & Co. KGaA, Weinheim, 2005, 2 (9): 3198–3202/ DOI 10.1002/pssc.200461110.
[5] Korotcenkov G, Beongki K Cho. Porous Semiconductors: Advanced Material for Gas Sensor Applications. CRITICAL REVIEWS IN SOLID STATE AND MATERIAL SCIENCES · FEBRUARY, DOI: 10.1080/2010 10408430903245369.
[6] Shi L, Naik AJT, Goodall JBM, Tighe C, Gruar R, Binions R, Parkin I, Darr J. Highly sensitive ZnO nanorod- and nanoprism-based NO2 gas sensors: size and shape control using a continuous hydrothermal pilot plant. Langmuir, 2013, 29 (33):10603–10609.
[7] ztu¨rk S, Kılınc N¸ ztu¨rk Z.Z O, Fabrication of ZnO nanorods or NO2 sensor applications: effect of dimensions and electrode position. *J. Alloys Compd*, 2013, 581: 196–201.
[8] Oh E, H,Choi Y, Jung,H, Cho S, Kim JC, Lee KH.,. Kang S, W, Kim J, Yun JY, SH. Jeong. High-performance NO_2 gas sensor based on ZnO nanorod grown by ultrasonic irradiation. Sens. Actuators B: Chem., 2009, 141(1): 239–243.
[9] Chougule M A, Sen S, Patil VB. Fabrication of nanostructured ZnO thin film sensor for NO_2 monitoring. Ceram. 2012, 38 (4): 2685–2692.
[10] Rajesh Kumar O, Al-Dossary, Girish Kumar, Ahmad Umar. Zinc Oxide Nanostructures for NO_2 Gas–Sensor Applications. Nano-Micro Lett., DOI 10.1007/s40820-014-0023-3.
[11] Rajesh Kumar, Al-Dossary, Girish Kumar Ahmad Umar. Zinc Oxide Nanostructures for NO_2 Gas–Sensor Applications. Nano-Micro Lett., DOI 10.1007/s40820-014-0023-3.
[12] Shi L, Naik A.JT, Goodall J.BM., Tighe C, Gruar R, Binions R, Parkin I, Darr J. Highly sensitive ZnO nanorod-and nanoprism-based NO_2 gas sensors. size and shape control using a continuous hydrothermal pilot plant. Langmuir, 2013, 29 (33): 10603–10609.
[13] Tamaki J, Miura N, Yamazoe N. Sensors and Actuators B3, 1991, 147.
[14] Watanabe, Okada T, Choe I, Sens. Actuators B Chem., 1996, 33: 194 -197.
[15] Ulhir A. Electrolytic shaping of germanium and silicon. *Bell System Technology Journal*, 1956, 35: 333-47.
[16] Matthias S, Muller F, Gosele U. Controlled nouniformity in macroporous silicon pore growth. *Appl. Phys. Lett.*, 2005, 87 (**22**).
[17] Yorikawa H, Muramatsu S. Silicon nano-structure. *Appl. Phys. Lett*., 1998, 197 (**644**).
[18] Koker L., Kolasinki K.W, *J. Phys Chem*., 2000, 2: 277.
[19] Cláudia R, Miranda B, Maurício R. Baldan, Antonio F. Beloto. Morphological and Optical Characteristics of Porous Silicon Produced by Anodization Process in HF-Acetonitrile and HF-Ethanol Solutions. *J. Braz. Chem. Soc*., 2008, 19 (**4**): 769-774.
[20] Lehmann V, Jobst B, Muschik T, Kux A, Petrova V -Koch, Jpn. *J. Appl. Phys*., 1993, 32: **2095**.
[21] Peng C. Hirschmanand K.D, Fauchet P M. *J. Appl. Phys*, 1996, 80: **295**.
[22] Stievenard, D, Deresmes, D. Are electrical properties of an aluminium-orous silicon junction governed by dangling bonds? *Appl. Phys. Lett*., 1995, 67: **1570**.
[23] J. Gardner, H. Shin, E. Hines. An electronic nose system to diagnose disease. Sensors and Actuators B., 2000, 70: 19-24.

Recycling the construction and demolition waste to produce polymer concrete

Recycling the construction and demolition waste to produce polymer concrete

Mohammad T. Hamza [1] and Dr. Awham M. Hameed [1]

[1] Applied Sciences Department, University of Technology, Iraq, Baghdad.

mohammad_tahir_84@yahoo.com

Abstract. The sustainable management for solid wastes of the construction and demolition waste stimulates searching for safety applications for these wastes. The aim of this research is recycling of construction and demolition waste with some different types of polymeric resins to be used in manufacturing process of polymer mortar or polymer concrete, and studying their mechanical and physical properties, and also Specify how the values of compressive strength and the density are affected via the different parameters. In this research two types of construction and demolition waste were used as aggregates replacement (i.e. waste cement/concrete debris, and the waste blocks) while the two types of polymer resins (i.e. Unsaturated polyester and Epoxy) as cement replacements. The used weight percentages of the resins were changed within (10, 20, 25 and 30) % to manufacture this polymer concrete.

Keyword: polymer concrete, demolition waste, Unsaturated polyester, Epoxy.

1-Introduction

Concrete is a synthetic stone that is a mixture of water, admixture, binding material and additives. The world concrete commonly means Portland cement concrete (PCC), in that binder is Portland cement If the binder is synthetic resin of polymer, then we talk about synthetic resin polymer concrete (PC) (Now on the currently accepted term 'polymer concrete' is to be used) [1].

Polymer concrete (PC) is a comparatively young building material. It is primarily used for repairs, and for formation of sidewalks and wear-resistant stratum [2]. Research works in the literature [2] mostly test the properties of concrete purposed for given purposes. For enable the publishing of a new material, its mechanical and physical characteristics should be tested methodically. Many researches of several years aim to discover the characteristics of polymer concrete (PC) in detail, inclusive compressive strengths, flexural strengths, slow plasticity, fire resistance, and the relationship between concrete and concrete, and between polymer concrete and reinforcement rods.

The strengths and physical properties of polymer concrete mostly depend on the kinds of binder and admixture. In case of Portland cement concretes, standard strength is determined at 28 days [1]. It is also known that in case of cement concretes, strength is increasing continuously, and subsequent solidification can be observed even after 28 days of age. One of the most favorable properties of polymer concrete is extremely rapid strengthening, showing values approaching final strength as early at several days of age [4] [5]. However, there is no reference in the literature to long-term time-dependent rise in strength.

In situation of Portland cement concrete (PCC), the strength and physical characteristics of concrete are basically fixed by the state of affairs of production [1]. Decisive circumstances of production include temperature, and the duration of mixing and compaction. Previous study [3] to its the first objective is to get to know how the strength properties (compressive strength) of polymer concrete of a given composition change in function of time (from mixing to 90 days of age) while the second objective of it is to study how the strength properties (compressive strengths) of UP polymer concrete are influenced by the quality and duration of mixing and compaction. The current study aims to recycle the construction and demolition waste for using again to produce the polymer concrete after the mixing process with different polymeric resins in various weight ratios.

2-Materials

2.1. Epoxy

Sikadur-52 is a 2 parts, solvent free, low viscosity injection-liquids, based on high strength epoxy resins produced by (Sika yapi Kimyasallari A.S. Turkiye). Table (1) illustrates some mechanical and physical properties of epoxy resin

This epoxy resin has kindly adhesion to the concrete, mortar, stone, steel and wood. Sikadur-52 is applied to fill and seal voids and cracks in structures, for example bridges and another civil engineering building, industrial and indoor buildings, e.g. columns, beams, ground, walls, floors and water keep structures. It not only forms an influential barrier against water sweating and corrosion strengthen media, but it also Structural aspect bonds the concrete Parts together.

Table 1. Show the properties of epoxy

Mechanical & Physical prop. of epoxy		
Density	1.0850 g/cm^3	at 20 ^{o}C
Compressive strength	52 MPa	after 7 days at 23^{o}C
Flexural strength	61 MPa	After 7 days at 23^{o}C
Tensile strength	37 MPa	After 7 days at 23^{o}C
E-Modules	Flexural strength 1800 MPa	after 7 days at 23^{o}C
Thermal expansion coefficient	8.9×10^{-5} ^{o}C^{-1}	from -20 ^{O}C to 40^{o}C

2.2. Polyester

Unsaturated polyester **(UPE)** resins are the most usually used for the composites industry. Polyester resins have a good equilibrium of mechanical, electrical and chemical characteristics. Unsaturated polyester resin it was used in this research is produced by K.S.A. Typical the properties of the unsaturated polyester resin are described in Table (2) and (3).

Table 2. Show physical Properties of unsaturated polyester resin

physical properties of unsaturated polyester		
Density	1.9-2.0 kg/dm^3	At +25 ^{O}C
Percentage of Styrene	22 %	At +25 ^{O}C
Viscosity	1000 mPa . s	At +25 ^{O}C
Color	Purple	At +25 ^{O}C
Specific weight	1.15	At +25 ^{O}C
Hardener time	6 minutes	At +25 ^{O}C

Table 3. Show mechanical properties of unsaturated polyester

Mechanical properties of unsaturated polyester			
	Dry value	Weigh value	Units
Tensile strength	91.5	88.3	N/mm^2
Tensile modulus	9.30	7.71	KN/mm^2
Flexural strength	176	164	N/mm^2
Flexural modulus	7.38	6.59	KN/mm^2
Glass contain	27.4	------	%

The polyester resin has good chemical resistance characteristics. The chemical environment has to be well-known before polyester or vinylester resin can be selected. Polyester resins are suitable in weak alkalis and excellent in weak acid environments.

2.3. Sand

AL-Ukhaider natural sand was used throughout this work. The physical properties of aggregate according to Limits of the Iraqi Specification No.45/1984 illustrated in Table 4.

Table 4. Show Physical properties of sand.

density	2.65 g/cm^3
Sulfate content %	0.2
Absorption%	0.6
Thermal conductivity	0.7766 (W/m.K)

2.4. Construction and Demolition waste

- Waste cement/concrete debris
- Waste blocks. Show in figure (1).

(A) **(B)**

Figure 1. Show Construction and Demolition waste **(A)** waste cement/concrete debris **(B)** waste blocks

Some processes were made on this aggregate such as crushing, grinding, sieving, before mixing with polymeric resin as binder. Table (5) shows some properties of these two types of aggregates.

Table 5. Physical properties for aggregates.

Samples	**Loose bulk density g/cm^3**	**Specific gravity**	**Percentage of voids %**
Waste Blocks	0.995	1.255	0.207
Waste Cement	1.209	1.522	0.205

3-Experimental Work

3.1. Mixing of Concrete

For preparing the polymer concrete (PC), a dry mixing had been done for both two types of aggregate for 3 minutes and then the unsaturated polyester resin (UP) or epoxy (EP) were added to the mixture after mixing with the hardener with weight ratio 0.01% for (UP) and (2:1) for (EP).

3.2. Casting and Curing of the Specimens

Before casting, the molds were carefully oiled to be ready for casting the fresh concrete. The polymer concrete was cast in 3 layers for all samples, respectively layer was compacted by a rod then all samples were wet-cured at room temperature and removed the molds after one day.

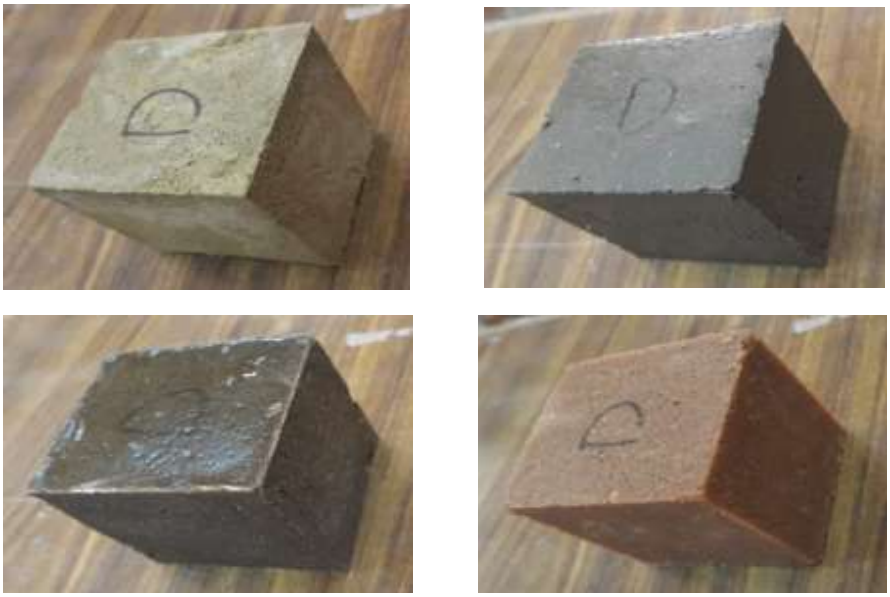

Figure 2. Show the samples

Table 6. Show the prepared samples (1)

Aggregates with Percentage of Epoxy resin			
Samples	Aggregates	Polymer resin	Percentage of resin
SCEP	N. sand + concrete Debris	Epoxy	20 %
SWEP	N. sand + waste Blocks	Epoxy	15 %

Table 7. Show the prepared samples (2)

Aggregates with Percentage of Unsaturated polyester resin			
Samples	Aggregates	Polymer resin	Percentage of resin
SCUP	N. sand + concrete Debris N: natural	Unsaturated polyester	30 %
SWUP	N. sand + waste Blocks	Unsaturated polyester	25 %

4-Test Procedures

4.1. Compressive strength

The compressive strengths test was calculated consistent with B.S.1881, part 116 [6]. This test was made on 50 mm^3 cubes using an electrical testing machine with measurements of 2000 kN. The compressive strengths of the samples were calculated by applying the equation 1.

$$\text{Compressive strength} = F\ (\text{force})/A\ (\text{area}) \quad (1)$$

C = Compressive strengths in (MPa).
F = The maximum load up to failure in (N).
A = Initial cross sectional area of specimens in (mm^2).

4.2. Bulk Density

This test was calculated consistent with the ASTM C138 [7]. Where the density was calculated by dividing the total mass of all materials. The bulk density was calculated by applying equation (2)

$$\text{Bulk density} = M\ (\text{mass}) / V\ (\text{volume}) \quad (2)$$

ρ = Bulk density in (g/cm^3), **M=** Mass in (g) and **V=** Volume in (cm^3).

5-Results and Discussions

5.1. Bulk Density

The density of case-hardened concrete is a responsibility of the densities of the initial components, mix quantities, initial and final water contented, air contented, degree of consolidation, degree of hydration, volume variations, and consequent gain or loss of water, amongst additional factors.

Dependence on these operators creates density an effective indicator of the homogeneousness of raw materials, mixing, batching, placing, sampling, and testing. Table (8) shows the bulk density values of various types of concrete before curing.

Table 8. Show Results of the density

Samples	Percentage of resin	Density	Unit
SCUP	30 %	1.748	g/cm^3
SWUP	25 %	1.854	g/cm^3
SCEP	20 %	1.934	g/cm^3
SWEP	15 %	1.642	g/cm^3

5.2. Compressive strength

Compressive strengths test the most important characteristic of concrete subsequently the first consideration in structural design, is that the structural components must be capable of transport the imposed loads. Table (9) shows the Compressive strength values of various types of concrete before curing.

Table 9. Show Results of the Compressive strength

Sample	Percentage of resin	Compressive strength	Unit
SCUP	30 %	80.48	MPa
SWUP	25 %	132.55	MPa
SCEP	20 %	121.93	MPa
SWEP	15 %	56.65	MPa

References

[1] Balázs, Gy.: "Építőanyagok és kémia", Tankönyv kiadó, Budapest, 1984
[2] ACI Committe 548.: Polymer Concrete – Structural Applications State-of-the Art Report, 1996
[3] Farkas, Gy., Nemeth, O.I.: "Experimental study of polymer concrete's mechanical properties" Proceeding of 15th International Conference on Civil Engineering and Architecture, Csíksomlyó, pp.117-123., 2011
[4] ACI 548.1R-09: "Guide For The Use Of Polymer In Concrete, Chapter 4 – Polymer Concrete", reported by ACI Committee, PP.11-16., 2009
[5] Fowler, D. W. , Polymers in Concrete, ACI SP-214, PP. 111-117, 2003.
[6] B.S.1881, Part 116, "Method for Determination of Compressive Strength of Concrete Cubes", British Standard Institution, 1989.
[7] ASTM C138 "Standard Test Method for Density (Unit Weight), Yield, and Air Content (Gravimetric) of Concrete" Annual Book of ASTM Standards Vol. 04-02/2004.

Theoretical Calculation of the Electron Transport Parameters and Energy Distribution Function for CF3I with noble gases mixtures using Monte Carlo simulation program

IOP Conf. Series: Journal of Physics: Conf. Series **1003** (2018) 012089 doi:10.1088/1742-6596/1003/1/012089

Theoretical Calculation of the Electron Transport Parameters and Energy Distribution Function for CF3I with noble gases mixtures using Monte Carlo simulation program

Enas A Jawad

physics department, College of education for pure sciences-Ibn Alhaitham, University of Baghdad, Iraq

Abstract. In this paper, The Monte Carlo simulation program has been used to calculation the electron energy distribution function (EEDF) and electric transport parameters for the gas mixtures of The trif leoroiodo methane (CF3I) 'environment friendly' with a noble gases (Argon, Helium , kryptos, Neon and Xenon).

The electron transport parameters are assessed in the range of E/N (E is the electric field and N is the gas number density of background gas molecules) between 100 to 2000Td (1 Townsend =10-17 V cm2) at room temperature. These parameters, namely are electron mean energy (ε) , the density –normalized longitudinal diffusion coefficient (NDL) and the density –normalized mobility (μN) .

In contrast, the impact of CF3I in the noble gases mixture is strongly apparent in the values for the electron mean energy, the density –normalized longitudinal diffusion coefficient and the density –normalized mobility. Note in the results of the calculation agreed well with the experimental results.

1.Introduction

The electron transport parameters have been studied for a wide range of applied electric field. These parameters, such as ,the drift velocity, mobility, diffusion coefficient, ionization coefficient, and electron mean energy are knowledge in collision cross section and EEDF personification the backbone of the electron swarm behavior of gas in discharge of plasma [1].

The numerical solution of the Boltzmann **EQUATION** yields the electron energy distribution with the electric field E and gas number density N as parameters.

trifluoroiodomethane (CF3I) has been found to be a potential high voltage insulator[2,3]. Generally, CF3I is colorless and nonflammable [4,5]. From an environmental point of view, CF3I presents a weak global warming potential (GWP) of 1–5 against approximately 23900 for SF6[6,7]. CF3I is considered as a low environmental impact gas and is attracting widespread attention for comprehensive study. However, CF3I has a high boiling point -22.5 C0, as reported in Ref. [8,9].

The electron transport in a gas under the effect of an electric field E can be simulated with the help of a Monte Carlo method [10-15].

In this work the Monte Carlo simulation technique for ion transport that accounts for limited gas temperature is used to calculate electron transport parameters of CF3I with noble gas mixture at temperature T=300 K. transport parameters are determined as a function of E/N for various rates of increase of the electric field [16].

In this paper is calculation the electron energy distribution function and electron transport parameters for trifluoroiodomethane mixtures with a noble gases (Argon, Helium , kryptos, Neon and Xenon) by using Monte Carlo simulation program.

2.Theory

The Boltzmann equation describes the time evolution of the electron energy distribution function *f* (*r*, *v*, t).

The Boltzmann equation for electrons in an ionized gas is [17] .

$$\frac{\partial f}{\partial t} + V.\nabla_r f - \alpha.\nabla_r f = \beta(f) \quad \text{.....(1)}$$

Where $\alpha = -eE/m$ represents the acceleration of the electrons due to the external electric field *E*, and β is the collision operator.

The Boltzmann equation maybe written as[18,19] .

$$\left(\frac{\partial}{\partial t} + v.\nabla_r + \frac{eE}{m}.\nabla_v\right) f(r,v,t) = \left(\frac{\delta}{\delta t}\right) \quad \text{.....(2)}$$

where , $f(r,v,t)$ is the electrons distribution at time t and spatial location r, *v* is the velocity of charge particles and ∇_V is the gradient in V-space .

And $\left(\frac{\delta}{\delta t}\right)$ is an integral collision which accounts for electron energy transferred in elastic and inelastic collision [20,21]

The electron mean energy $(\varepsilon)$is, [22,23]:

$$\varepsilon = \int_0^\infty \epsilon^{3/2} f_0 \, d\epsilon \quad \text{.....(3)}$$

Values of f_0 are calculated from Boltzmann's equation using all collision cross-sections.

The relation between drift velocity *w* and distribution function of electron energy is given by [24,25]:

$$w = -\frac{1}{3}\left(\frac{2}{m}\right)^{1/2} \frac{eE}{N} \int_0^\infty \frac{\epsilon}{q_m(\epsilon)} \frac{df_0}{d\epsilon} d\epsilon \quad \text{.....(4)}$$

Where ϵ is the electron energy in (eV) , *m* is the electron mass, *e* is the elementary charge and $q_m$is the momentum transfer cross section (in cm2).

The mobility is defined as the proportionally coefficient between the drift velocity of a charged particle and electric field. The mobility of electrons is (in cm^2/V)[26,27]:

$$\mu_e = \frac{e}{m\nu_m} = \frac{w}{E} \quad \text{.....(5)}$$

Where $v_m$represent the electron momentum- transfer collision frequency.

The density-normalized mobility (μN) is defined as:

$$(\mu N) = -\frac{\vartheta}{3}\int_0^{\infty}\frac{\epsilon}{q_m}\frac{\partial f_0}{\partial \epsilon}d\epsilon \quad \text{.....(6)}$$

And the density-normalized longitudinal diffusion coefficient is defined as:

$$ND_L = \frac{V_1}{3N}\left[E\int_0^{\infty}\frac{\epsilon}{qT}\frac{\partial}{\partial\epsilon}\left(f_1\epsilon^{-1/2}\right)d\epsilon + \int_0^{\infty}\frac{\epsilon^{1/2}}{qT}f_0 d\epsilon\right] - (\bar{w}_0 A_2 - \bar{w}_1 A_1 - \bar{w}_{02}) \quad \text{.....(7)}$$

Where V_1 is the speed of electron, q_T is the total cross section, *fn* and *n* ϖ (n = 0, 1, 2) are respectively the electron energy distributions of various orders and their eigen values. V_1, *n* ϖ , 0*n* ϖ , and An are given by[28-30]

$$V_1 = \left(\frac{2\epsilon}{m}\right)^{1/2} \quad \text{.....(8)}$$

$$\bar{w}_0 = V_1 N\int_0^{\infty}\epsilon^{1/2}q_i f_0 d\epsilon \quad \text{.....(9)}$$

$$\bar{w}_1 = -\frac{V_1 E}{3N}\int_0^{\infty}\frac{\epsilon}{qT}\frac{\partial}{\partial\epsilon}\left(f_0\epsilon^{-1/2}\right)d\epsilon + (\bar{w}_0 A_1 - \bar{w}_{01}) \quad \text{.....(10)}$$

$$\bar{w}_{01} = V_1 N\int_0^{\infty}\epsilon^{1/2}q_1 f_n d\epsilon \quad \text{.....(11)}$$

$$A_n = \int_0^{\infty} f_n\, d\epsilon \quad \text{.....(12)}$$

Where q_i is the ionization cross section.

3.Result

To calculate the electron mean energy and the others transport parameters using the Monte Carlo simulation program, find out about the accreditation of the momentum transfer cross section on the electron energy is basis,We present the results of The electron mean energy , the density –normalized longitudinal diffusion coefficient and the density –normalized mobility as functions of E/N for mixtures CF3Igas with noble gases (Ar,Kr, Xe, He and Ne) have been calculated in the E/N range 100 < E/N < 2000 Td are recorded in Table (1-6).

Tables (1-3) note the computed results for the electron mean energy , the density –normalized longitudinal diffusion coefficient and the density –normalized mobility as a function of E/N , respectively in pure CF_3I and pure noble gases.

Tables (4) clarify the calculated results for the electron mean energy, in various ratios of CF_3I mixtures with (Argon, Helium , kryptos, Neon and Xenon) gases.

Tables (5) clarify the computed results for the density –normalized longitudinal diffusion coefficient, in different ratios of CF_3I mixtures with (Argon, Helium , kryptos, Neon and Xenon) gases .

Tables (6) explain the calculated results for the density –normalized mobility,in various proportions of CF_3I mixtures with (Argon, Helium , kryptos, Neon and Xenon) gases .

'Figure (1)' exhibit the behavior of the electrons energy dependence distribution function for different cases of the factor (E/N) and , figure (2) show the variety in the mean energy of electrons as a function of E/N , which increases with increase of E/N and they appear clearly effect of adding noble gases(Argon, Helium , kryptos, Neon and Xenon) to the trifleoroiodo methane (CF_3I) gas in increasing due to the change in the various types of collision processes.

Figure (3) show the density –normalized mobility for different ratios of mixtures CF_3I with noble gases, we notice that it decreases by increasing E/N.

The gas density normalized longitudinal diffusion coefficient ND_L, the product of the gas number density N and the longitudinal diffusion coefficient D_L for CF_3I mixtures with noble gases, is plotted in Figure (4)as a function of E/N.

in figure (5) for pure CF_3I. The results demonstrate a good agreement with the experimental values [31].

4.Conclusion

In this study, we have examined the behavior of electrons in uniform electric fields using a Monte Carlo simulation. Electron transport parameters were calculated as a function of reduced electric fields E/N.

calculation the electron energy distribution function and the transport parameters for The trifleoroiodo methane (CF_3I) 'environment friendly' with a noble gases (Argon, Helium , kryptos, Neon and Xenon) in the E/N range of 100 - 2000 Td.

In this work, the simulation results give values for electron mean energy, the density –normalized longitudinal diffusion coefficient (ND_L) the density –normalized mobility (μN) and electron energy distribution as functions of reduced electric field.

Table 1. The calculate electron Mean Energy(ε)(eV) in pure of CF3I and Noble gases (Ar, He, Kr,Ne and Xe).

E/N(Td)	Xe	Ne	Kr	He	Ar	CF_3I
100	4.486	12.87	5.607	12.82	6.666	2.938
200	4.642	13.93	5.827	14.87	6.978	3.215
300	4.819	15.25	6.078	18.12	7.275	3.52
400	5.025	16.85	6.361	23.64	7.61	3.846
500	5.272	18.81	6.698	32.44	8.012	4.191
600	5.578	21.23	7.106	44.96	8.507	4.557
700	5.969	24.3	7.614	61.71	9.134	4.946
800	6.484	27.88	8.262	83.97	9.955	5.366
900	7.18	32.45	9.106	113.9	11.006	5.829
1000	8.138	38.12	10.21	155.3	12.62	6.352
1200	9.472	45.21	11.67	215.1	14.94	6.963
1400	11.32	54.2	13.58	305.3	18.52	7.706
1600	13.83	65.89	16.03	449.9	24.18	8.901
1800	17.17	81.69	19.16	688.13	33	9.901
2000	21.52	104.1	23.08	1153	46.64	11.62

Table 2: The calculate density –normalized mobility (μN) $\times 10^{23}$ (m Vs)$^{-1}$,for electron in pure of CF_3I and Noble gases (Ar, He, Kr,Ne and Xe).

E/N(Td)	Xe	Ne	Kr	He	Ar	CF_3I
100	5.444	24.16	7.356	2.83	8.195	6.84
200	5.431	22.91	7.196	3.14	7.847	6.365
300	5.441	21.66	7.052	3.638	7.651	5.986
400	5.476	20.43	6.924	4.39	7.494	5.675
500	5.537	19.23	6.814	5.267	7.359	5.41
600	5.631	18.07	6.719	6.019	7.247	5.178
700	5.764	16.92	6.642	6.514	7.167	4.969
800	5.945	15.89	6.58	6.772	7.138	4.779
900	6.175	14.87	6.535	6.83	7.169	4.604
1000	6.44	13.88	6.6486	6.777	7.286	4.443
1200	6.727	12.93	6.413	6.674	7.496	4.295
1400	6.97	12.03	6.298	6.582	7.791	4.167
1600	7.123	11.2	6.115	6.559	8.152	4.066
1800	7.127	10.48	5.856	6.559	8.524	3.997
2000	6.988	9.914	5.528	6.896	8.82	3.95

Table 3.The calculate density –normalized longitudinal diffusion coefficient $(ND_L)\times 10^{24}$(m s)^{1},for electron in pure of CF_3I and Noble gases (Ar, He, Kr,Ne and Xe).

E/N(Td)	Xe	Ne	Kr	He	Ar	CF_3I
100	4.034	25.15	7.346	24.27	6.761	1.985
200	3.963	25.66	7.026	32.94	6.594	1.993
300	3.881	26.27	6.65	52.11	6.457	2.009
400	3.791	27.03	6.237	94.28	6.332	2.031
500	3.7	27.97	5.849	164.6	6.23	2.06
600	3.613	29.17	5.517	255.1	6.167	2.093
700	3.553	30.62	5.275	359.3	6.17	2.133
800	3.576	32.47	5.147	479.4	6.289	2.179
900	3.726	34.74	5.159	622.5	6.597	2.233
1000	4.079	37.52	5.329	806.3	7.255	2.296
1200	4.702	40.9	5.671	1061	8.546	2.375
1400	5.641	45.11	6.194	1444	10.9	2.482
1600	6.911	50.6	6.881	2076	15.14	2.642
1800	8.499	58.42	7.705	3223	21.93	2.895
2000	10.36	70.56	8.64	5527	32.41	3.293

Table 4.The calculate electron Mean Energy(ε)(eV) in various mixture of CF_3I with Noble gases (Ar, He, Kr,Ne and Xe).

	20% ε (eV)					40% ε (eV)				
E/N(Td)	Xe	Ne	Kr	He	Ar	Xe	Ne	Kr	He	Ar
100	3.067	3.21	3.148	3.172	3.176	3.244	3.596	3.425	3.496	3.5
200	3.355	3.515	3.444	3.475	3.477	3.541	3.928	3.739	3.825	3.822
300	3.666	3.842	3.763	3.801	3.8	3.851	4.278	4.069	4.173	4.161
400	3.992	4.187	4.099	4.145	4.14	4.172	4.648	4.412	4.541	4.516
500	4.335	4.552	4.453	4.509	4.494	4.507	5.044	4.773	4.934	4.89
600	4.627	4.941	4.826	4.897	4.87	4.862	5.473	5.155	5.36	5.278

700	5.084	5.36	5.226	5.315	5.282	5.246	5.946	5.567	5.831	5.712
800	5.507	5.822	5.661	5.776	5.726	5.673	6.483	6.023	6.366	6.301
900	5.981	6.343	6.146	6.296	6.221	6.165	7.112	6.542	6.994	6.827
1000	6.53	6.949	6.706	6.902	6.79	6.754	7.876	7.156	7.763	7.445
1200	7.191	7.683	7.375	7.638	7.971	7.488	8.842	7.913	8.749	8.204
1400	8.018	8.61	8.211	8.571	8.322	8.439	10.11	8.884	10.07	9.181
1600	9.1	9.827	9.298	9.807	9.435	9.716	11.81	10.17	11.89	10.49
1800	10.56	11.48	10.76	11.5	10.95	11.47	14.13	11.91	14.42	12.47
2000	12.58	13.75	12.75	13.85	13.05	13.87	17.26	14.25	17.88	15.15

	60% ε (eV)					80% ε (eV)				
E/N(Td)	Xe	Ne	Kr	He	Ar	Xe	Ne	Kr	He	Ar
100	3.5	4.179	3.812	3.973	3.962	3.889	5.26	4.411	4.825	4.712
200	3.793	4.544	4.137	4.333	4.303	4.147	5.706	4.73	5.258	5.068
300	4.091	4.932	4.472	4.717	4.658	4.408	6.2	5.057	5.739	5.438
400	4.397	5.35	4.82	5.129	5.029	4.678	6.762	5.399	6.288	5.793
500	4.716	5.809	5.186	5.581	5.398	4.969	7.416	5.764	6.939	6.231
600	5.058	6.322	5.577	6.089	5.834	5.293	8.202	6.164	7.744	6.696
700	5.437	6.915	6.006	6.678	6.301	5.67	9.172	6.621	8.788	7.22
800	5.874	7.622	6.493	7.388	6.827	6.13	10.4	7.162	10.21	7.84
900	6.398	8.494	7.066	8.284	7.445	6.711	11.97	7.829	12.2	8.607
1000	7.051	9.607	7.768	9.461	8.204	7.475	14.03	8.681	15.05	9.599
1200	7.899	11.07	8.662	11.09	9.181	8.506	16.72	9.793	19.03	10.94
1400	9.035	13.02	9.833	13.37	10.49	9.921	20.23	11.27	24.45	12.83
1600	10.59	15.64	11.4	16.52	12.32	11.87	24.81	13.21	31.69	15.56
1800	12.72	19.12	13.49	20.81	14.91	14.52	30.75	15.76	41.35	19.56
2000	15.62	23.71	16.25	26.5	18.57	18.05	38.48	19.05	54.4	25.22

Table 5. The calculate density –normalized mobility (μN) (m Vs)$^{-1}$for electron in various mixture of CF_3I with Noble gases (Ar, He, Kr,Ne and Xe).

	20% μN×10^{23}(m Vs)$^{-1}$					40% μN×10^{23}(m Vs)$^{-1}$				
E/N(Td)	Xe	Ne	Kr	He	Ar	Xe	Ne	Kr	He	Ar
100	6.517	7.779	7.134	7.478	7.402	6.152	9.254	7.499	8.423	8.037
200	6.086	7.314	6.64	7.041	6.904	5.795	8.878	7.025	8.021	7.496
300	5.755	6.932	6.243	6.683	6.493	5.535	8.37	6.64	7.68	7.037
400	5.494	6.605	5.914	6.379	6.145	5.338	8.006	6.322	7.381	6.639
500	5.28	6.318	5.634	6.113	5.841	5.185	7.677	6.058	7.115	6.29
600	5.098	6.06	5.391	5.876	5.585	5.063	7.375	5.839	6.875	5.996
700	4.941	5.82	5.176	5.661	5.334	4964	7.093	5.656	6.656	5.714
800	4.809	5.607	4.985	5.463	5.115	4.883	6.813	5.505	6.456	5.471
900	4.678	5.405	4.814	5.282	4.918	48.16	6.584	5.382	6.278	5.261
1000	4.566	5.218	4.661	5.117	4.743	4.763	6.361	5.283	6.131	5.085
1200	4.469	5.052	4.528	4.974	4.592	4.729	6.171	5.2	6.029	4.949
1400	4.393	4.915	4.42	4.865	4.473	4.719	6.015	5.151	5.979	4.858
1600	4.346	4.811	4.34	4.794	4.392	4.733	5.89	5.099	5.974	4.816
1800	4.324	4.738	4.286	4.76	4.349	4.759	5.771	5.026	5.974	4.811
2000	4.313	4.674	4.243	4.736	4.329	4.766	5624	4.907	5.925	4.813

60% $\mu N\times10^{23}(m\ Vs)^{-1}$						80% $\mu N\times10^{23}(m\ Vs)^{-1}$				
E/N(Td)	Xe	Ne	Kr	He	Ar	Xe	Ne	Kr	He	Ar
100	5.763	11.81	7.375	9.916	8.659	5.434	17.05	7.418	1.263	8.95
200	5.52	11.27	6.874	9.551	8.062	5.332	16.29	7.044	1.236	8.336
300	5.35	10.79	6.469	9.231	7.547	5.272	15.57	6.741	1.212	7.816
400	5.236	10.34	6134	8.947	7.1	5.242	14.88	6.496	1.192	7.456
500	5.154	9.925	5.85	8.693	6.757	5.238	14.211	6.294	1.174	7.036
600	5.1	9.531	5.607	8.465	6.388	5.256	13.56	6.14	1.173	6.724
700	5.066	9.157	5.398	8.265	6.074	5.298	12.94	6.01	1.179	6.482
800	5.051	8.806	5.218	8.101	5.585	5.5661	12.35	5.912	1.199	6.299
900	5.053	8.482	5.063	7.99	5.654	5.458	11.79	5.836	1.235	6.176
1000	5.076	8.192	4.93	7.959	5.5	5.585	11.26	5.779	1.277	6.119
1200	5.124	7.937	4.822	8	5.418	5.74	10.72	5.731	1.31	6.13
1400	5.195	7.703	4.739	8.08	5.38	5.903	10.17	5.678	1.322	6.205
1600	5.277	7.462	4.681	8.141	5.4	6.043	9.588	5.593	1.307	6.322
1800	5.339	7.184	4.63	8.09	5.452	6.109	8.976	5.454	1.269	6.44
2000	5.34	6.851	4.564	7.9	5.477	6.066	8.348	5.48	1.218	6.512

Table 6. The calculate density –normalized longitudinal diffusion coefficient (ND_L) $(m\ s)^{-1}$for electron in various mixture of CF_3I with Noble gases (Ar, He, Kr,Ne and Xe).

20% $ND_L\times10^{24}(m\ s)^{-1}$						40% $ND_L\times10^{24}(m\ s)^{-1}$				
E/N(Td)	Xe	Ne	Kr	He	Ar	Xe	Ne	Kr	He	Ar
100	2.079	2.418	2.283	2.242	2.339	2.199	3.112	2.669	2.624	2.831
200	2.077	2.433	2.284	2.268	2.346	2.188	3.153	2.656	2.68	2.831
300	2.085	2.453	2.292	2.303	2.36	2.189	3.203	2.651	2.744	2.836
400	2.102	2.502	2.307	2.344	2.338	2.201	3.26	2.654	2.815	2.847
500	2.126	2.544	2.328	2.392	2.405	2.222	3.325	2.665	2.896	2.864
600	2.159	2.593	2.356	2.446	2.435	2.255	3.4	2.685	2.986	2.885
700	2.2	2.649	2.391	2.509	2.472	2.3	3.486	2.73	3.09	2.916
800	2.252	2.714	2.435	2.58	2.517	2.361	3.585	2.757	3.212	2.957
900	2.315	2.79	2.489	2.66	2.57	2.44	3.708	2.815	3.363	3.012
1000	2.396	2.88	2.559	2.767	2639	2.549	3.868	2,898	3.565	3.091
1200	2.504	3.008	2.653	2.904	2.732	2.705	4.099	3.02	3.863	3.217
1400	2.659	3.188	2.791	3.106	2.872	2.94	4.446	3.209	4.323	3.424
1600	2.899	3.466	3.005	3.419	3.097	3.3	5971	3.5	5.034	3.775
1800	3.27	3.899	3.339	3.911	3.465	3.844	5.728	3.944	6.065	4.344
2000	3.827	4.355	3.838	4.632	4.035	4.61	6.735	4.558	7.419	5.197

60% $\mu N\times10^{23}(m\ Vs)^{-1}$						80% $\mu N\times10^{23}(m\ Vs)^{-1}$				
E/N(Td)	Xe	Ne	Kr	He	Ar	Xe	Ne	Kr	He	Ar
100	5.763	11.81	7.375	9.916	8.659	5.434	17.05	7.418	1.263	8.95
200	5.52	11.27	6.874	9.551	8.062	5.332	16.29	7.044	1.236	8.336
300	5.35	10.79	6.469	9.231	7.547	5.272	15.57	6.741	1.212	7.816
400	5.236	10.34	6134	8.947	7.1	5.242	14.88	6.496	1.192	7.456
500	5.154	9.925	5.85	8.693	6.757	5.238	14.211	6.294	1.174	7.036
600	5.1	9.531	5.607	8.465	6.388	5.256	13.56	6.14	1.173	6.724

700	5.066	9.157	5.398	8.265	6.074	5.298	12.94	6.01	1.179	6.482
800	5.051	8.806	5.218	8.101	5.585	5.5661	12.35	5.912	1.199	6.299
900	5.053	8.482	5.063	7.99	5.654	5.458	11.79	5.836	1.235	6.176
1000	5.076	8.192	4.93	7.959	5.5	5.585	11.26	5.779	1.277	6.119
1200	5.124	7.937	4.822	8	5.418	5.74	10.72	5.731	1.31	6.13
1400	5.195	7.703	4.739	8.08	5.38	5.903	10.17	5.678	1.322	6.205
1600	5.277	7.462	4.681	8.141	5.4	6.043	9.588	5.593	1.307	6.322
1800	5.339	7.184	4.63	8.09	5.452	6.109	8.976	5.454	1.269	6.44
2000	5.34	6.851	4.564	7.9	5.477	6.066	8.348	5.48	1.218	6.512

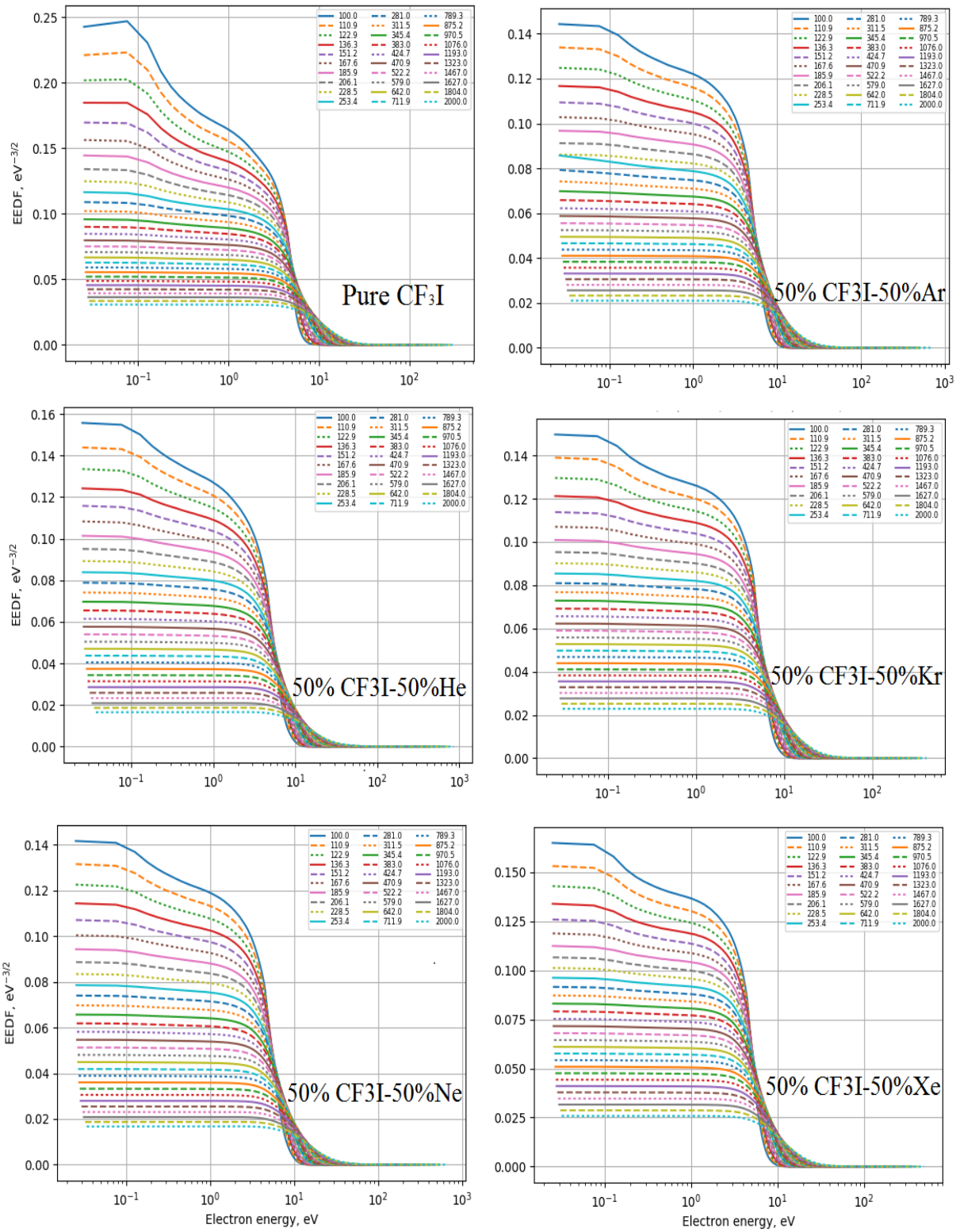

Figure(1). The electron energy distribution function versus the electron energy for pure CF3I and mixture with noble gaseous (50/50%) .

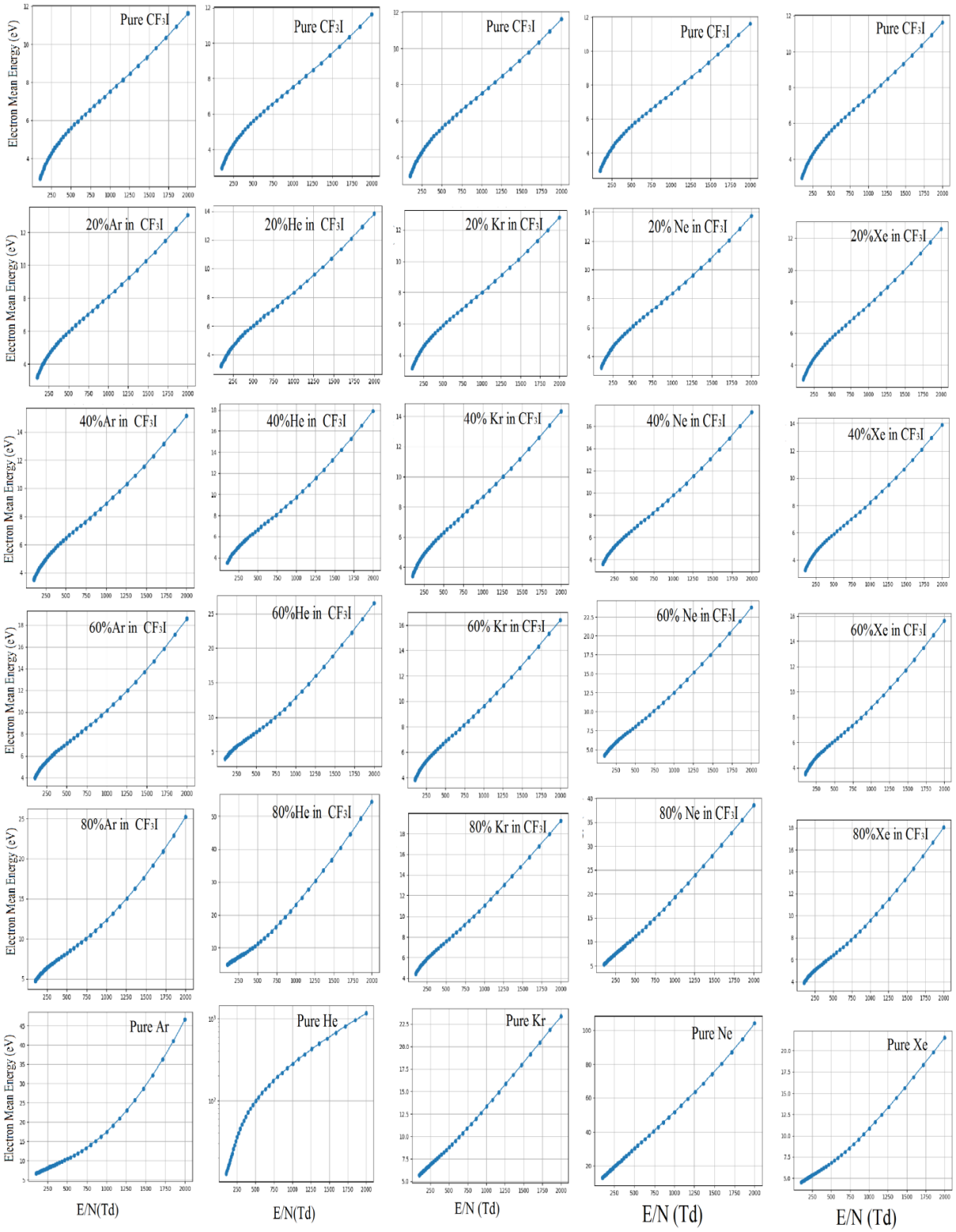

Figure(2). The electron mean energy as a function of E/N in various mixture of CF_3I with Noble gases (Ar, He, Kr,Ne and Xe).

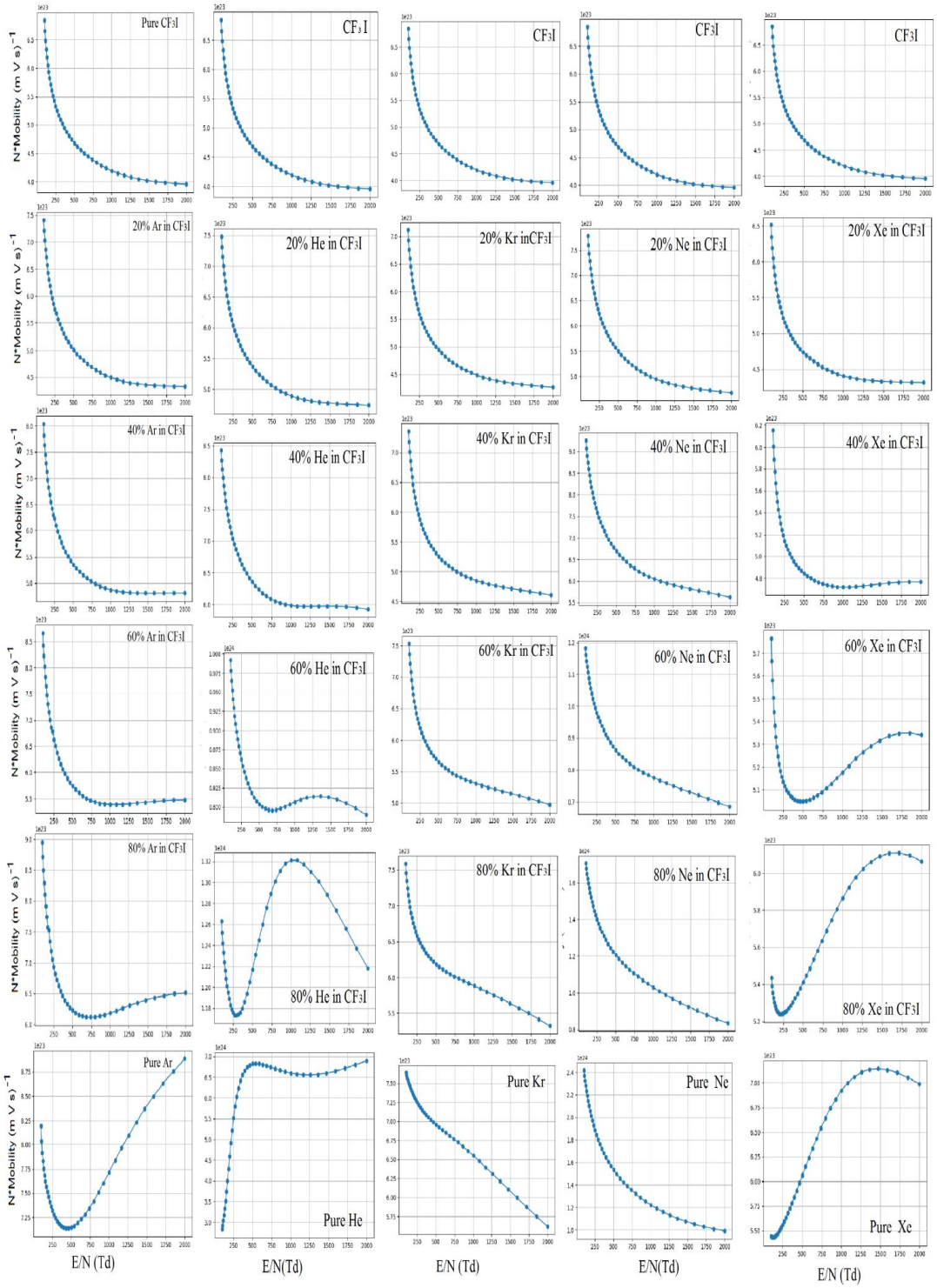

Figure(3). The density –normalized mobility as a function of E/N in various mixture of CF_3I with Noble gases (Ar, He, Kr,Ne and Xe).

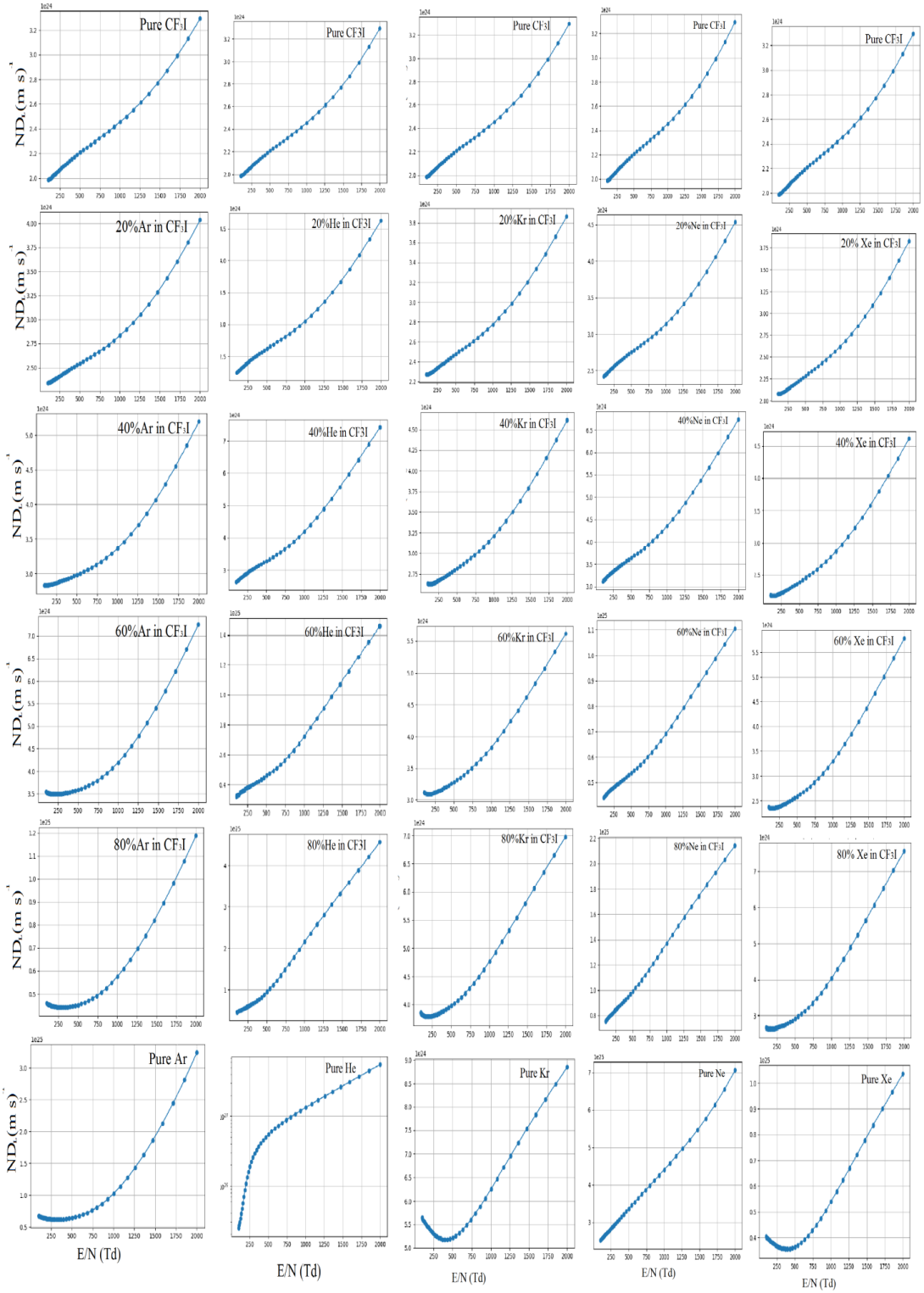

Figure(4). density –normalized longitudinal diffusion coefficient as a function of E/N in various mixture of CF_3I with Noble gases (Ar, He, Kr,Ne and Xe).

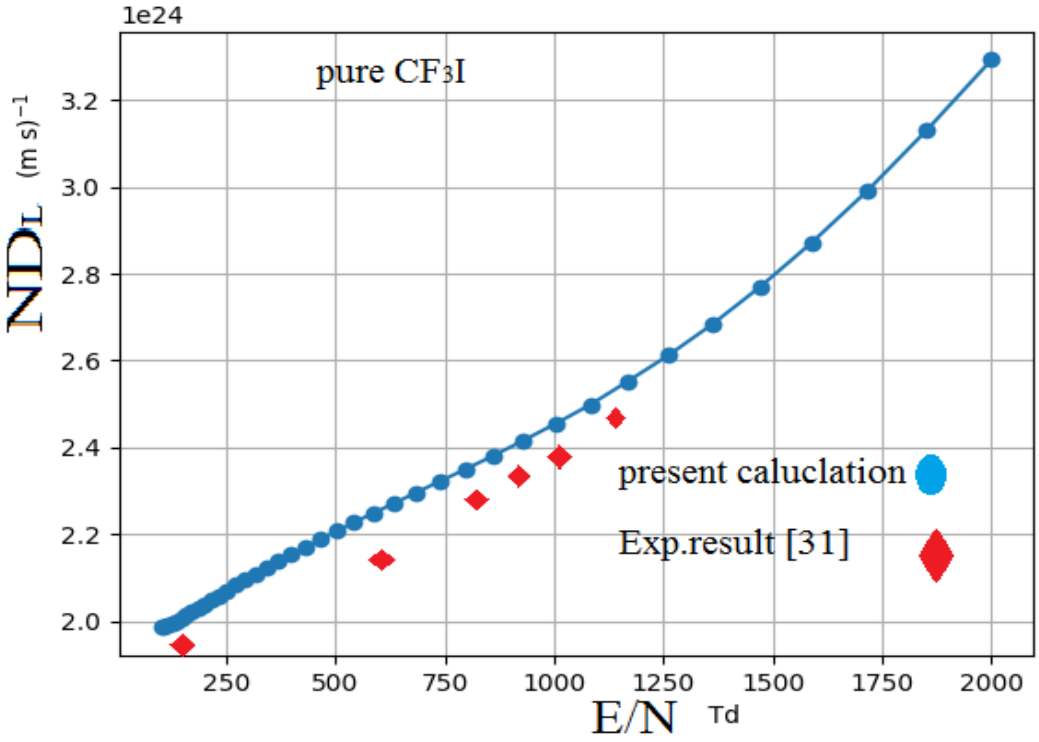

Figure(5). density –normalized longitudinal diffusion coefficient as a function of E/N of pure CF_3I.

Reference:

[1] Dahl Dominik A ., Teich Timm H . and Christian Franck M .,(2012), "Obtaining precise electron swarm parameters from a pulsed Townsend setup", *J.Phys*. D*: Appl. Phys*. **45**,485201 (pp9).

[2] S. Nakauchi, D. Tosu, S. Matsuoka, Kumada A, Hidaka K, 2006, Proc. XVI Int. Conf. on Gas Discharges and their Applications. 1, pp 365-369, Xi'an, China.

[3] Taki M, Hiromi O, Maekawa . Mizoguchi D, Mizoguchi H, Yanabu S, 2006, Proc. XVI Int. Conf. on Gas Discharges and their Applications. 2, pp 793-796, Xi'an, China.

[4] Christophorou L G and Olthoff J K 2000 *J. Phys. Chem. Ref. Data* **29553**.

[5] Solomon S, Burkholder J.B, Ravishankra A.R, and. García R.R, 1994 *J. Geophys. Res. D* **99**, 20929.

[6] Cressault Y, Connord V, Hingana H, Teulet P and Gleizes A 2011 *J. Phys. D: Appl. Phys*. **44** 495202

[7] Solomon S, Burkholder J, Ravishankara .A and Garcia R 1994 *J. Geophys. Res. 99 20929*

[8] Duan Y Y, Zhu M S and Han L Z 1996 Fluid Phase Equilib. 121 227

[9] I. Rozum, P. Limão-Vieira, S. Eden, J. Tennyson, and N.*J. Mason, 2006 J. Phys. Chem. Ref. Data* **35**, 267.

[10] Grapperhaus M. J. and Kushner M. J. (1997). A Semi-analytic Radio Frequency Sheath Model Integrated into a two dimensional Hybrid Model for Plasma Processing Reactors, *J Appl. Phys*. **81**(2): 569-577.

[11] Tessarotto M., WhiteR. B. and Zheng L-J. (1994). Monte Carlo approach to Collisional Transport, *Phys. Plasmas* **1**(8): 2603-2613.

[12] Ardehali M. (1994). Monte Carlo Simulation of Ion Transport through Radio Frequency Collisional Sheaths, *J Vac. Sci. Techno!. A*. **12**(6): 3242-3244.

[13] Helin W., Zuli L. and Darning L. (1996). Monte Carlo Simulation for Electron NeutralCollision Processes in Normal and Abnormal Discharge Cathode Sheath Region, Vacuum **47**(9): 1065-1072.
[14] Stache J. (1994). Hybrid Modeling ofDeposition Profiles in Magnetron Sputtering Systems, *J Vac. Sci. Techno!. A.* **12**(5); 2867-2873.
[15] Nathan S. S., Rao G. M. and Mohan S. (1998). Transport of Sputtered Atoms in Facing Targets Sputtering Geometry: A Numerical Simulation Study, *J. Appl. Phys*. **84**(1): 564-571.
[16] Rabie M, Haefliger P, Chachereau A and Franck C M, (2015), "Obtaining electron attachment cross sections by means of linear inversion of swarm parameters", *J. Phys. D: Appl. Phys.* **48** ,075201 (7pp).
[17] Morgan W.L., Penetrane B.M., Computer physics communication CPC, Vol.**58**, PP. 127-152, 1990.
[18] Edward A. and Eral Mc Daniel W., 1988, "Transport properties of ions in gases", John Wiely and Sons, Inc.
[19] Morgan W.L. and Penetrane B.M., 1990, Computer physics communication CPC, Vol.**58**, PP. 127-152.
[20] 20.Willett C. S.: Introduction to gas lasers: population inversion mechanisms; with emphasis on selective excitation processes, 1st Ed, Pergamon Press, New York(1974).
[21] Christophorou L.G. and Olthoff JK, 2000 *J. Phys. Chem. Ref. Data*, **29** 553.
[22] Wang Y. & Olthoff J.K, (1999) : Ion energy distributions in inductively coupled radio-frequency discharges in argon, nitrogen, oxygen, chlorine, and their mixtures, *Journal of Applied Physics*, vol.**85**, 6358-6365.
[23] Houghton J.T., Meira Filho L.G., Callander B.A., N. Harris, Kattenberg A., Maskell K., Climate Change 1995: The Science of Climate Change (Cambridge University Press, Cambridge, 1996).
[24] 24 Nighan W. L., Electron energy distribution and collision rats in electrically excited N2, CO and CO2, Phys. Rev., 1970, 2, 1989-2000.
[25] Morgan W.L.:Electron collision cross sections for tetraethoxysilane, *Journal of Applied Physics*, vol. **92**, pp. 1663-1667 (2002).
[26] Truesdell C., *J. Chem. Phys*, Vol. **37**, P. 2336, (1962).
[27] Hernández-Ávila J.L., Basurto E., and de Urquijo J., 2002 *J. Phys. D* **35**, 2264,
[28] Tuan D. A., 2012 “Determination of Electron Collision Cross Sections for F2, Cl2 Molecules, and Electron Transport Coefficients in Mixture Gases as Pro-spective Substitutes for the SF6 Gas in Industrial Applications”,PhD Dissertation, Dongguk Univ., Korea.
[29] Kimura M and Nakamura Y 2010 *J. Phys. D: Appl. Phys*. **43** 145202
[30] Phelps A and Pitchford L 1985 Phys. Rev. A 31 2932.
[31] de Urquijo J, Jua´rez A M, Basurto E and Herna´ndez-A´ vila J L ,2007 *J. Phys. D: Appl. Phys.* **40** 2205.

Structural and optical properties of colloidal InZnO NPs prepared by laser ablation in liquid

IOP Conf. Series: Journal of Physics: Conf. Series **1003** (2018) 012090 doi:10.1088/1742-6596/1003/1/012090

Structural and optical properties of colloidal InZnO NPs prepared by laser ablation in liquid

Maryam M khlewee, Khawla S Khashan

Department of Applied Science, University of Technology, Baghdad, Iraq.

Abstract. In the current work, colloidal of InZnO NPs were produced by pulsed laser ablation in liquid (PLAL) method. The effect of indium content on the structural, morphological and optical of the InZnO NPs was confirmed by Fourier transform infrared spectroscopy, Scanning electron microscopy, and UV-visible spectroscopy. The FTIR spectra showed the presence of the metal-oxide bond. The SEM exhibit different morphological aspects according to the (In/Zn) ratio. The optical transmittance of InZnO NPs has high value around 70 % in the visible region and the band gap value was varied between 3.29 to 3.25 eV.

1. Introduction

Transparent conducting oxides (TCO) like In_2O_3, SnO_2, and ZnO, have been most studied [1, 2]. Indium is an expensive and rare element, pure and doped ZnO films are investigated as an alternate candidate. Furthermore, these compounds are inexpensive, abundant, nontoxic and offer noticeably high chemical and thermal stabilities [3]. Because of that reason, ZnO is a promising material for various technological applications like electro-luminescent displays [4], heated mirrors [5], Schottky diodes [6], solar cells [7], and chemical sensors [8]. N-type ZnO with wide bandgap semiconductor (E_g=3.2 eV), its electrical conductivity is fundamentally via to intrinsic defects (interstitial zinc atoms, oxygen vacancies) and could be enhanced by adding group VII (F) or group III doping (B, Ga, In, Al) [9]. Doping type has been chosen to take into account the fact that the impurity size of the ionic radius mast is similar to that of the substituted ion, in order to avoid lattice distortions. The efficiency of the doping element is related to its electro-negativity and its ionic radius. Different approaches were utilized to generate indium doped zinc oxide IZO nanostructures like chemical vapor deposition [10], chemical method [11, 12], thermal evaporation [13, 14], sol-gel [15], pulsed laser deposition [16] and spray pyrolysis [17]. Among them, pulsed laser ablation in liquids (PLAL) is a simple and clean technique, and it does not need any pressure and temperature, also can utilize to produce a new compound of nanomaterials with the new phase [18, 19]. The size and shape of these nanoparticles depend on the ablation features such as energy, wavelength, number of pulse and pulse duration. [20]. In general, there is no data of In-doped ZnO via PLAL process. Therefore, here prepared colloidal of IZO utilized laser ablation in liquid and the influence indium doped on structural and optical properties were investigated.

2. Experimental details

The indium zinc oxide nanoparticles (IZO-NPs) were prepared via PLAL methods. A 1064 nm Q-switched Nd:YAG laser (9ns) was used to produce the nanoparticles. These techniques have two processes; the first step for ZnO-NPs production was accomplished via PLA of a Zn target (99.99% purity) immersed in a 3ml DIW. The second step is the doping process achieved by replacing the zinc target by Indium plate (99.99%) for the same surrounding liquid that contains the zinc nanoparticles previously. The pulse laser energy was constant in the range (80mJ) for a different ablation time that ranged (2, 3, 4 and 5) min.

To study the chemical assignment and bonds of undoped ZnO-NPs and doped with different in concentration used Fourier Infrared Spectroscopy (FTIR) from (BRUKER-7613). The scan of the FTIR probes in ranging from (500 to 3000 cm-1) for synthesized sample. The optical transmittance can be found via OPTIMA (SP-3000 Plus) double beam, These were achieved at ambient conditions utilizing quartz cell with (1 cm) optical path. Finally, the morphology was assessed using Scanning Electron Microscope (SEM) (type Tescan VEGA3, Czech).

3. Results and discussion

'Figure 1' the FTIR-spectrum of IZONPs are shown. The broad peaks around the region from 3000 to 4000 cm^{-1} show the presence of - OH is stretching vibrations. The peaks at 1635 cm^{-1} and 1636 cm^{-1} related to stretching vibrations of C-C. Also, several distinguishing bands got among a range of 500 - 800 $cm^{-1}$are owing to the existence of a bond (for In−O and Zn−O) [21]. While bands at 613cm^{-1}, 615cm^{-1}, 616cm^{-1}, 627 $cm^{-1}$and 630 cm^{-1} for InZnO-NPs. These results agree with the reference [13, 14, 16].

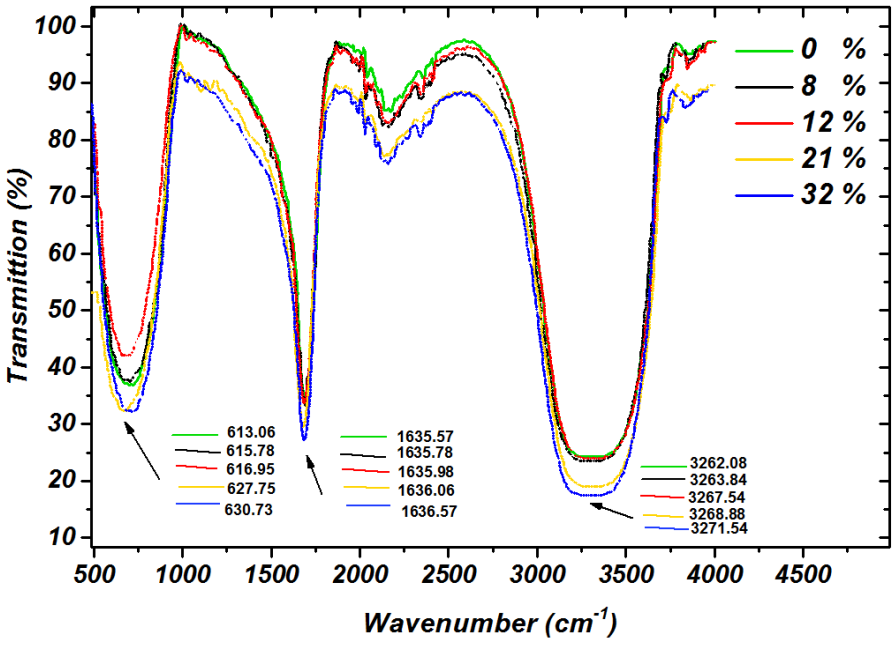

Figure 1. FTIR spectrums of ZnO suspensions doping with different In concentration.

'Figure 2' shows views of zinc oxide with different in concentration. The images show alter in morphology from hierarchical nanostructures, including the flower structure in (0%) ZnO with diameter ~ (3.9 µm) to nano-structures consist of flakes, droplets and slight nano-rods like structure with mean width ~ (100 nm) and mean length ~ (6 µm) for ZnO doped with 32%. In general, at ($[In^{3+}] = 8\%$), there are three major morphologies: (1) one of them is the one that shows clusters of

tiny particles with loose appearance, (2) the shard-like flake with flower, (3) the rods-shaped particles were observed (mean width ~187 nm, mean length ~12µm), and these continued to grow as the ablation time was increased. On indium doping the hierarchical ZnO nano-structures lack their morphology ($[In^{3+}] = 12\%$) and cauliflower-like structure has appeared. For ($[In^{3+}] = 21\%$), the rod's surface disappears and the conglomerates are composed of agglomerated tiny particles, and to structures with different morphology like flakes, droplets and small nano-rods ($[In^{3+}] = 32\%$). These results are good agreement with data in reference [11].

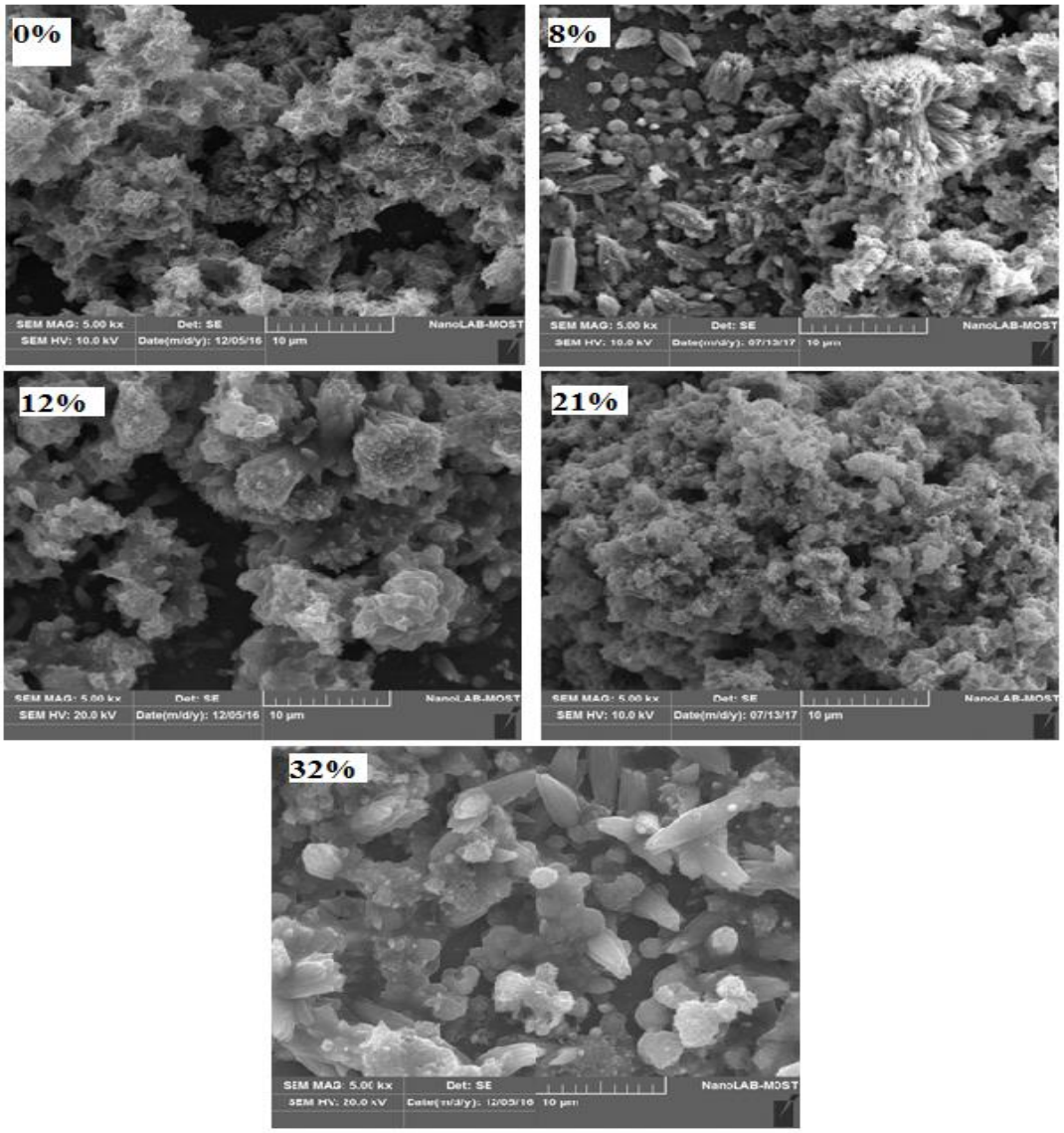

Figure 2. SEM images of in doped ZnO structure with various concentrations.

'Figure 3' shows the transmittance spectra for undoped ZnO nanoparticles observed suspensions and doped with different indium concentration, which seen the broad peak around 300 nm for ZnONPs. With doping absorption, broad shifted a bit near lower wavelengths, which mean a red-shift in the transmission spectra [10, 22]. Also can notice, increased transmission intensity because light

scattering is high on an irregular surface of the in doped nano-structures, that increased as in concentration increased, that result is in good agreement with [12]. The high transmission in the UV wavelength was attached to the essential transmission and includes the transition of electrons among the band, this was used to locate the energy gap (E_g) in a semiconductor [12]. Doping with 21% and 32% show superior transparency over 70% in the entire visible-light in the NIR wavelength region, indicating that In content has negligible effects on the transmittance and the enhanced of visible-NIR range due to the improvement of crystallinity of IZO [13,15]. The higher transmittance at 32%, which indicates good homogeneity [23].

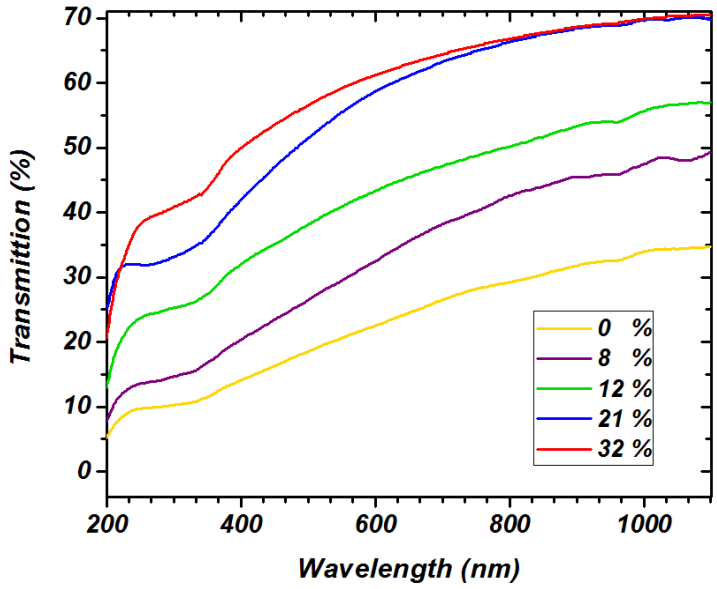

Figure 3. UV- Vis. Transmittance spectra of ZnO-NPs suspensions (0%) with different In doping concentration.

'Figure 4' shows the direct band gap values were obtained by an extrapolation of the linear portion in a plot of $(\alpha h\nu)^2$ against hν, notes that the energy gap of ZnO-NPs suspensions before doping equal (E_g = 3.29 eV). While, after doping ZnO-NPs with different in concentrations, the value of the energy gap was decreased from (Eg=3.28, 3.27, 3.26 to 3.25), which shown in 'figure 3', these results were good agreement with reference [10, 12, 15]. This shift was associated with the majority carrier concentration [12]. The band shifts noted among doping are owing to vagaries in nano crystal structure. Also, corresponding for the theory of "semiconductor – metal" transition, a E_g reduction as the impurity is additional than the "Mott-critical" density [24] therefore, doping indicates to recognizable reducing of the gap. When In doped insert to the ZnO lattices, the specified edge states establish at the sites of doped, with a decrease of gap Refs [25, 26].

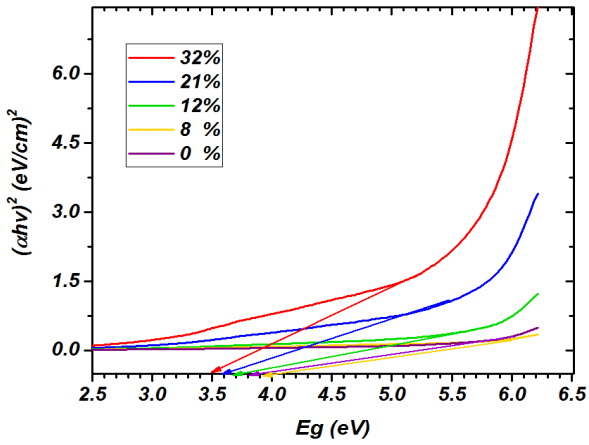

Figure 4. Optical band gap of ZnO-NPs suspensions (0%) with different in doping concentration.

4. Conclusions

Good quality InZnO NPs were prepared using the pulse laser ablation in liquid method. The existence of metal-oxide (In-O and Zn-O) bond was identified from FTIR spectra. SEM studies have revealed that the surface morphology of the films with changed from hierarchical nanostructures with flower-like morphology in pure *ZnO* to rods after doping in (32%). The IZO nanoparticles showed an average optical transmittance around 70 % in the visible region; meanwhile, the band gap value was decrease varied between 3.29 and 3.25 eV.

References

[1] Nouneh K, Oyama M, Diaz R, Abd-Lefdil M, Kityk I V and Bousmina M 2011 *J. Alloys and Compounds* **509** 5 2631-38
[2] Abd-Lefdil M, Douayar A, Belayachi A, Reshak A H, Fedorchuk A O, Pramodini S, Poornesh P Nagaraja K K and Nagaraja H S 2014 *J. Alloys and Compounds* **584** pp 7-12
[3] Hsu H C, Tseng Y K, Cheng H M, Kuo J H and Hsieh W F 2014 *J. Crystal. Growth* **261** 520-5
[4] Yi L, Hou Y, Zhao H , He D, Xu Z, Wang Y and Xu X 2000 *Displays* **21** 4 147-9
[5] Wang Z, Chen Q and Cai X 2005 *J. Appli. Surf. Sci* **239** 3 262-7
[6] Park W I, Yi G C, Kim J W and Park S M 2003 *J. Appli Phys* **82** 24 4358-60
[7] Contreras M A, Egaas B, Ramanathan K, Hiltner J, Swartzlander A, Hasoon F and Noufi R 1999 *Research and applications*, **7** 4 311-6
[8] Wan Q, Li Q H, Chen Y J, Wang T H, He X L, Li J P and Lin C L 2004 J. *Appli Phys* **84** 18 3654-6
[9] Klaus E, Andreas K and Bernd R 2008 *Transparent Conductive Zinc Oxide: Basics and Applications in Thin Film Solar Cells.*Springer
[10] Tang K, Gu S, Liu J, Ye J, Zhu S and Zheng Y 2015 J. *Alloys and Compounds* **653** 643-8
[11] Sharma M and Jeevanandam P 2014 *J. Chemistry* **53**A 561-5
[12] Chava R K and Kang M 2017 J. *Alloys and Compounds* **692** pp 67-76
[13] Sugumaran S, Ahmad M N B, Jamlos M F, Bellan C S, Pattiyappan S, Rajamani R and Sivaraman R K 2015 *Optical Materials* **49** 348-56
[14] Sugumaran S, Ahmad M N B, Jamlos M F, Bellan C S, Chandran S and Sivaraj M 2016 *Optical Materials* **54** pp 67-73
[15] Kim M S, Yim K G, Kim S, Nam G, Lee D Y, Kim J S,Kim J S and Leem J Y 2012 *Acta Physica Polonica-Series A General Physics* **121** 1 217
[16] Fang H W, Hsieh T E and Juang J Y 2014 *Solar Energy Materials and Solar Cells* **121** 176-81
[17] Shinde S S, Shinde P S, Bhosale C H and Rajpure K Y 2008 *J. Physics D: Applied Physics* **41** 10 105109
[18] Khashan K S and Mohsin M H 2015 *Surface Review and Letters* **22** 4 1550055
[19] Khashan K and Abbas S F 2016 *International Journal of Modern Physics B* **30** 14 1650080

[20] Hamad A H, Khashan K S and Hadi A A 2016 In *Applications of Laser Ablation-Thin Film Deposition Nanomaterial Synthesis and Surface Modification* InTech.
[21] Bheeman D, Sugumaran S, Mathan R, Sivanesan D and Bellan C S 2014 *Nanoscience and Nanotechnology* **6** 6 457-63
[22] Lee M Y, Song M K, Seo J H and Kim M H 2015 *J. Appli Phys* **54** 6 065201
[23] Thomas R and Dube D C 2000 *J. Appli Phys* **39** 4R 1771
[24] Wander A, Schedin F, Steadman P, Norris A, McGrath R, Turner T S, Thornton G and Harrison N M 2001 *Physical review* **86** 17 3811
[25] Morales A E, Zaldivar M H and Pal U 2006 *Optical Materials* **29** 1 100-4
[26] Mehra S, Bergerud A, Milliron D J, Chan E M and Salleo A 2016 *Chemistry of Materials* **28** 10 3454-34

Spatial and Temporal Temperature trends on Iraq during 1980-2015

Spatial and Temporal Temperature trends on Iraq during 1980-2015

Yassen K. Al-Timimi[1], Aws A. Al-Khudhairy[2]

[1] Atmosphere department, College of Science, Al-Mustansiriyah University , IRAQ

[2] Atmosphere department, College of Science, Al-Mustansiriyah University, IRAQ

awssss_ali@yahoo.com

Abstract. Monthly Mean surface air temperature at 23 stations in Iraq were analyzed for temporal trends and spatial variation during 1980-2015.Seasonal and annual temperature was analyzed using Mann-Kendall test to detect the significant trend .The results of temporal analysis showed that during winter ,spring , summer and Autumn have a positive trend in all the parts of Iraq. A tendency has also been observed towards warmer years, with significantly warmer summer and spring periods and slightly warmer autumn and winter, the highest increase is (3.5)°C in Basrah during the summer. The results of spatial analyze using the ArcGIS showed that the seasonal temperature can be divided into two or three distinct areas with high temperature in the south and decreasing towards north, where the trend of spatial temperature were decreasing from south to the north in all the four seasons.

Keywords: Trend, temperature, Mann-Kendall, ArcGIS, Iraq.

1.Introduction

Temperature is one of the most influential elements of Meteorological and Climatological Components, Cause its directly affected in our lives. The global average surface temperature has increased in the 20th century by about (0.6°C). Recent studies reveal a significant worldwide warming and a general increase in frequencies and persistence of high temperatures, one of the major concerns with that potential change in climate is the increase in extreme events will occur. Generally the global surface temperature has been increasing over the past 100 years by presumably due to the greenhouse effect, as a result of increasing concentrations of carbon dioxide and other greenhouse gases into the atmosphere. This warming trend has exhibited considerable temporal and spatial variability [1]. Global mean air surface temperature has risen in the Twentieth century, and it's expected to rise by (1.8-4.0)°C in the twenty first century [2]. Because global and regional effects of global warming become apparent that cause the studies on monitoring global and regional temperature change have sharply increased in the last few decades. Global average surface air temperature has increase by (0.13°C) to (0.03°C) per decade over the last 50 years according to (IPCC) Intergovernmental Panel on Climate Change Which is one of the most important association providing data on the global warming changes and it's established back in 1988 [3]. Many regional studies have also indicated a positive trend in temperature although the changes slightly vary from one region to another indicated, the annual mean temperature has

increased between (0.5°C) and (1.58°C) in the south parts of Canada over the 20th century. With an intense warming trend of (+0.08°C +0.03°C) per decade over Europe, Where Europe has the highest increase (0.43°C) over the last 30 Years [4]. The analysis of temperature all over the world has shown that the increase is not only in mean annual but also in seasonal, monthly, maximum and minimum temperature [5]. Worldwide analysis of air temperature changes And the studies shown that temperature has increased in both Hemispheres. But warming was more dominant in the northern hemisphere in the last 50 years [6]. Many regional studies have also indicates a positive trend in temperature although the changes slightly vary from one region to another [7]. Mediterranean is the most affected area in the world from global warming, these intensified increased in temperature may cause potential evaporation, water Deficit and forest fire risk [8]. This study aimed to examine the spatial and temporal temperature trends in annual and seasonal mean temperatures in Iraq for 35 years time period (1980-2015) by using Mann-Kendall non-parametric test and Sen's method.

2. Experimental

2.1 Study Area and Data

The study area is represented by Iraq, where geographically Iraq is located in the semi-tropical latitude in the Northern Hemisphere between latitudes (29.5°-37.5°N) north the equator, and between longitudes (38.45°-48.45°E) east of Greenwich line. Also, Iraq lies in the south west of Asian continent in the northern part of the Arab homeland, the north border is with turkey, Syria, Jordan from the west, Kuwait and Kingdom Saudi Arabia from south and Iran from the east. And this location determines the closeness or the distance of Iraq from water bodies which have clear impact in the climate and thermal properties of Iraq, where the Mediterranean Sea and the Arabian Gulf are the most influential water bodies in Iraq [9].

In this study a historical records of monthly mean temperature were acquired from the Iraqi Meteorological Organization and Seismology (IMOS) for thirty five years of the period (1980-2015). The long term data were collected from 23 ground weather stations located at different regions of the country. As shown in Table 1 and 'Figure 1'.

Table (1): Meteorological stations that used in the study

Station	Station Number	Longitude	Latitude	Elevation
Amara	680	47.17	31.83	9.5
Baghdad	650	44.4	33.3	31.7
Biji	631	43.53	34.9	115.5
Basrah	689	47.78	30.52	2
Diwaniya	672	44.95	31.95	20
Haditha	634	42.35	34.13	108
Hella	657	44.45	32.45	27
Kerbela	626	44.05	32.57	29
Khanqin	637	45.38	34.35	202
Kirkuk	621	44.35	35.47	331
Kut	665	45.75	32.49	17
Mosul	608	43.15	36.31	223
Najaf	670	44.32	31.95	53
Nasiriya	676	46.23	31.02	5
Rabiah	602	42.1	36.37	382
Ramadi	645	43.32	33.83	48
Rutba	642	40.28	33.03	630.1
Samawa	674	45.27	31.27	11.4
Sinjar	604	41.83	36.32	583

Sulaymaniya	623	45.45	35.53	843
Teleafer	603	42.48	36.37	373
Arbil	616	44	36.15	420
Salahaddin	611	44.2	36.38	1075

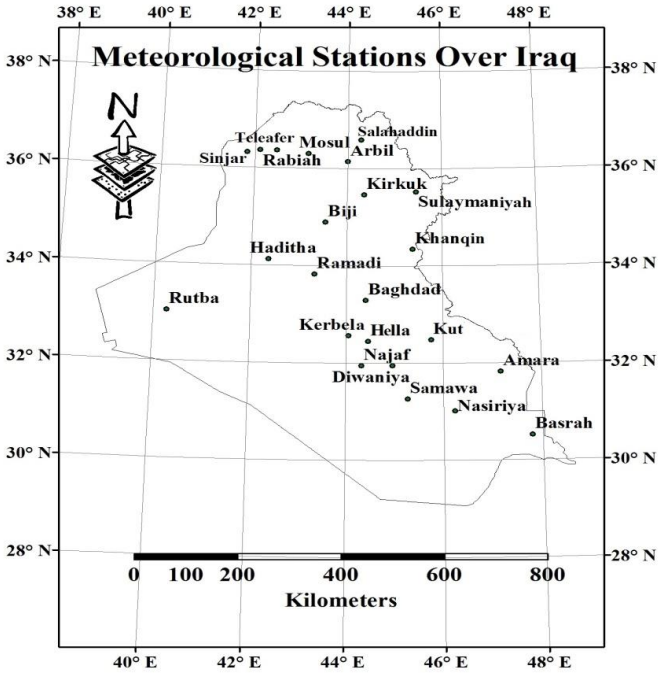

Figure 1. Meteorological stations in Iraq

2.2 Mann-Kendall Test (MK)

Simple linear regression analysis could give us a primary indication of existence of trend in times series data, whereas another method, such as the non-parametric Mann-Kendall (MK) test, which usually used in hydrologic data analysis, can used to detect trends that are monotonic but not necessarily linear. The MK test does need the assumption of normality, and only indicates the direction but not the magnitude of significant trends [10]. This test is usable in the situations where values xi of a time series may subjected to

$$x_i = f(t_i) + \varepsilon_i \qquad (1)$$

The $f(t_i)$ is continuous monotonic growing or diminishing function with time, while εi presumed to came from same division with zero mean. Thus we can assume that the difference in the division is constant with time.

For testing the null hypothesis when there is no trend for example the monitoring xi are randomly arrange with time, with the substitution hypothesis whereas a rising or declining monotonic trend. For computation of this statistical test MAKESENS which is a brief to Mann-Kendall test and Sen's method exploits both, so the S statistics and the normal approximation Z statistics in Gilbert are called [11]. For time series with less than 10 data points the S test is used, and for time series with 10 or more data points the normal approximation is used.

Trends were detected in the time series by means of Mann-Kendall test. The Mann-Kendall method has been suggested by the world meteorological organization to assess the trend in environment data time series.

The Mann-Kendall test statistic S is given by:

$$S = \sum_{k=1}^{n-1} \sum_{j=k+1}^{n} sgn(x_j - x_k), \tag{2}$$

x_j and x_k represents the annual values in years j and k, $j>k$, respectively, and

$$sgn\,(x_j - x_k) = \begin{cases} 1 & if\ x_j - x_k > 0 \\ 0 & if\ x_j - x_k = 0 \\ -1 & if\ x_j - x_k < 0 \end{cases} \tag{3}$$

When n is 9 or lower, the absolute value of S is match straight to the theoretical distribution of S obtained by Mann-Kendall [11].

The Z statistics used When the number of Values ten or further. When n is at minimum 10 thereafter normal approximation test is applied. Although whether there are various tied values for example a similar values in the time series, this may decrease veracity of the normal distribution when the number of values near ten. The contrast of S calculated by equation (4) with consideration that ties would be display as:

$$VAR(S) = \frac{1}{18}\left[n(n-1)(2n+5) - \sum_{p=1}^{q} t_p\,(t_p - 1)(2t_p + 5)\right] \tag{4}$$

Where
q the number of tied groups.
t_p the number of data values on the p^{th} group.
The values of S and $VAR(S)$ are applied for calculating the Z test as fallows

$$Z = \begin{cases} \dfrac{S-1}{\sqrt{VAR(S)}} & if\ S > 0 \\ 0 & if\ S = 0 \\ \dfrac{S+1}{\sqrt{VAR(S)}} & if\ S < 0 \end{cases} \tag{5}$$

The existence of a statistically significant trend is estimated by using the Z value. A positive (negative) value of Z indicates an upward (downward) trend [11].

3. Results & Discussion

3.1 Temporal Analysis

The statically significant levels, high (0.01), medium (0.05) and low (0.1) were used in this study. The estimate for magnitude of slope (Q) was computed for significant trends in (ºC/Year). Mann–Kendall test was used to identify the pattern for the analysis of seasonal and annual mean temperature. Figures (2-5) shows the trends of temperature in four standard stations .it can be seen that there is a slight increase during winter season. In spring season the results reveal an increase in all the trends. While in summer, the trends of mean temperature shows the most increasing trends between the seasons. Autumn season is characterized by increasing trends in mean temperature with a slight increase or almost the same as in spring season.

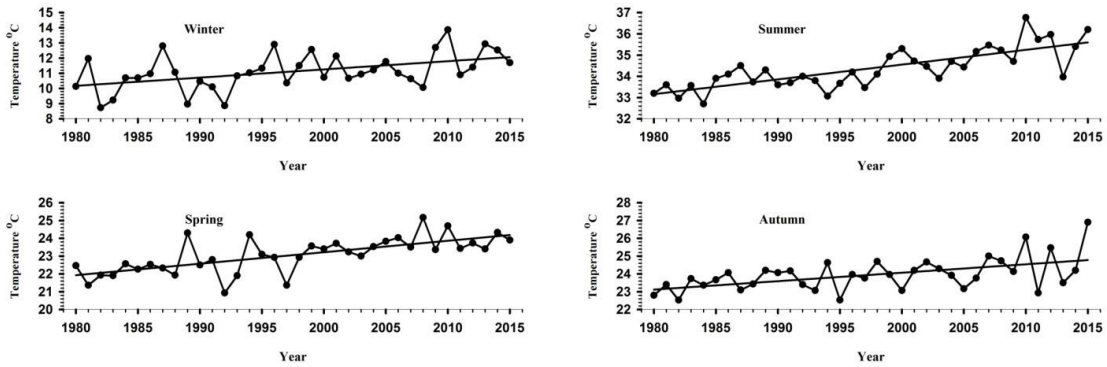

(a)

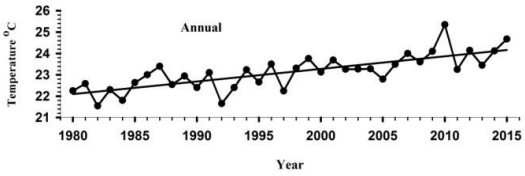

(b)

Figure (2): (a) Seasonally and (b) annually mean temperature at Baghdad Station

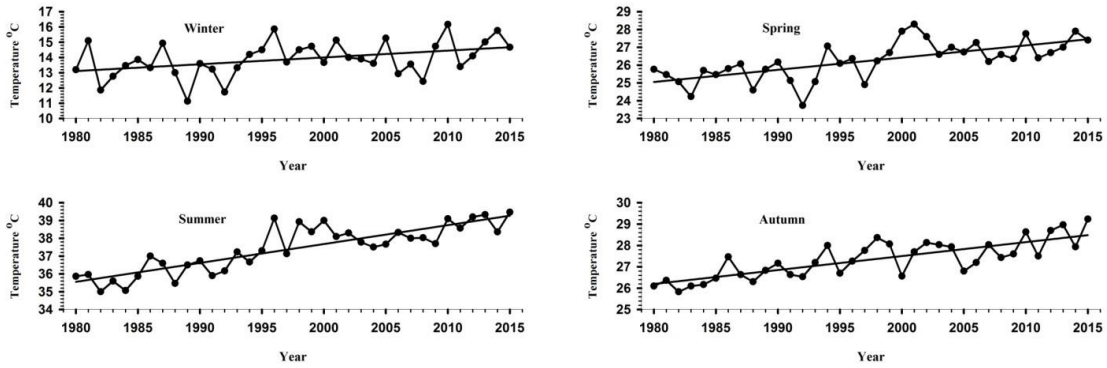

(a)

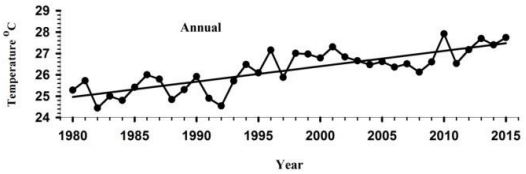

(b)

Figure (3): (a) Seasonally and (b) annually mean temperature at Basrah Station

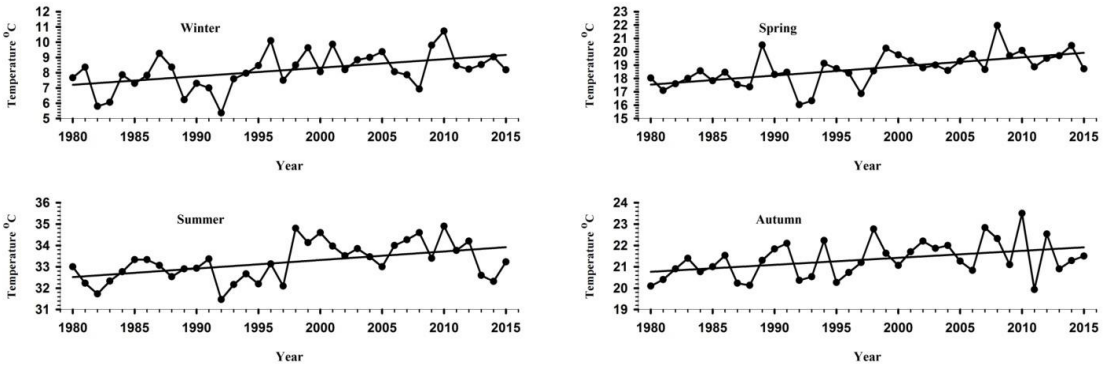

(a)

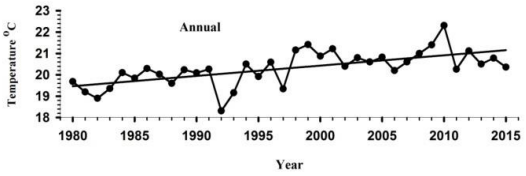

(b)

Figure (4): (a) Seasonally and (b) annually mean temperature at Mosul Station

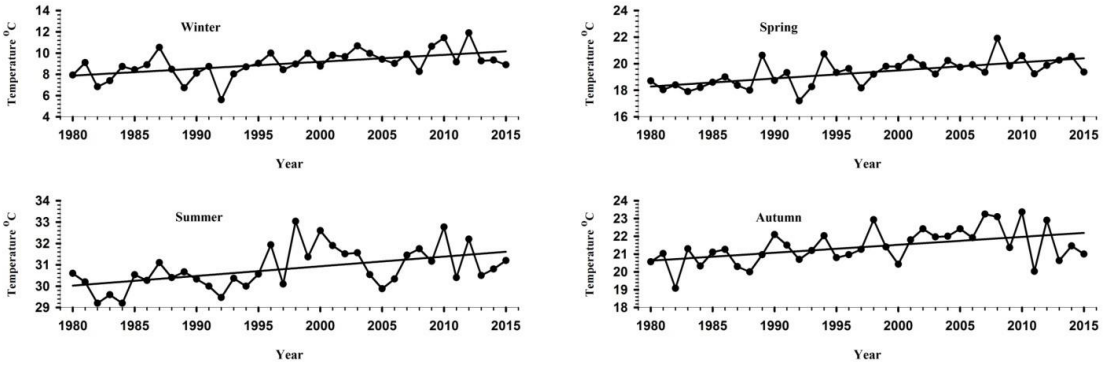

(a)

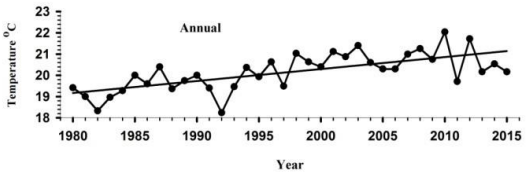

(b)

Figure (5): (a) Seasonally and (b) annually mean temperature at Rutba Station

From the table (2) The results of annual analysis shows the highest increase in Q(ºC/Year) was (0.07) noticed in Basrah station, And the lowest increase was (0.05) noticed in Mosul station. Seasonally the highest increase in Q(ºC/Year) (0.10) noticed In Summer season at Basrah station. And the lowest was (0.04) Noticed in Autumn Season at both Baghdad and Mosul stations and in Spring season at Mosul and Rutba.

Table 2: Seasonally & annually of Mann-Kendall Results For T_{mean}

Seasonally								
	Baghdad		Basrah		Mosul		Rutba	
	Z	Q(ºC/Year)	Z	Q(ºC/Year)	Z	Q(ºC/Year)	Z	Q(ºC/Year)
Winter	2.77	0.05	2.48	0.05	2.97	0.05	2.77	0.06
Spring	4.54	0.06	4.43	0.07	3.85	0.06	4.54	0.06
Summer	5.16	0.07	5.71	0.10	2.80	0.04	5.16	0.04
Autumn	3.09	0.04	5.13	0.07	2.95	0.04	3.09	0.05
Annually								
	5.59	0.06	4.91	0.07	4.24	0.05	5.59	0.06

3.2 Spatial Analysis

Seasonal mean temperature over Iraq during the period 1980-2015 is displayed in figure (6). The results reveal that the mean temperature in the south part of Iraq was higher than the other parts of the country. In winter season, the temperature distribution over Iraq is can be divided into two distinct areas, the north and the west regions are below 10ºC Which covers about 38% of the country, While the center and the southern parts that covers the other 62% of the studied area are 10-15ºC as shown in Figure (6a) and table (3). The lowest Mean temperature T_{Mean} in winter season was 5.6ºC and the highest value 13.9ºC. In summer, temperatures increased in the whole country, and the temperature distribution over Iraq can be divided into three distinct areas, The lowest temperature observed in the northern parts of the country was below 30ºC, the center up to the north and the western regions experiments temperature between 30-35ºC which is covers about 58% of the study area, and the southern regions was more than 35ºC Which covers about 40% as shown in (Figure 6b) and table (3). The lowest Mean temperature T_{Mean} in summer season was 29.2ºC and the highest value 37.4ºC.The study area during spring season divided into four regions, the highest mean temperature observed in the southern region of the country with temperature 25-30ºC, the central regions which covers about 57% of country is between 20-25ºC, and the north and west regions with temperatures between 15-20ºC, with a small region in the northeast of Iraq with temperature below 15ºC as shown in Figure (6c) and table (3). In autumn, the study area divided into three distinct areas, moderate temperature are observed all over the country with temperatures below 20ºC in a small region in the northeast part of the country, the other northern region and center of the country to the east and west regions which cover more than 63% of the study area are with temperatures 20-

25ºC, and the southern parts with temperatures more than 25ºC as shown in Figure (6d) and table (3). The lowest Mean temperature T_{Mean} in autumn season was 19.2ºC and the highest value 27.3ºC.

From the 'figure 7' and table 4 annual mean temperature distribution over Iraq can be divided into three distinct areas the lowest mean averaged temperature is noticed in the northern region of the country which cover about 8% of the study area with temperatures between 15-20ºC, the central region that occupy about 69% of the studied area are with temperatures between20-25ºC, and the highest mean temperature noticed in the south part of the country above 25ºC which cover about 23% of the country as shown in (Figure 7). The lowest Mean temperature T_{Mean} annually was 17.2ºC and the highest value 26.3ºC.

(a)Winter

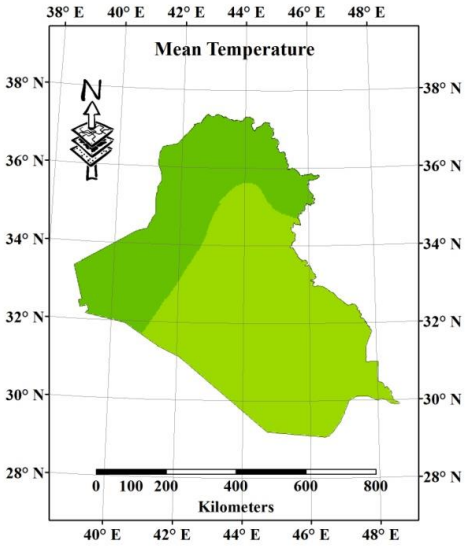

(b)Summer

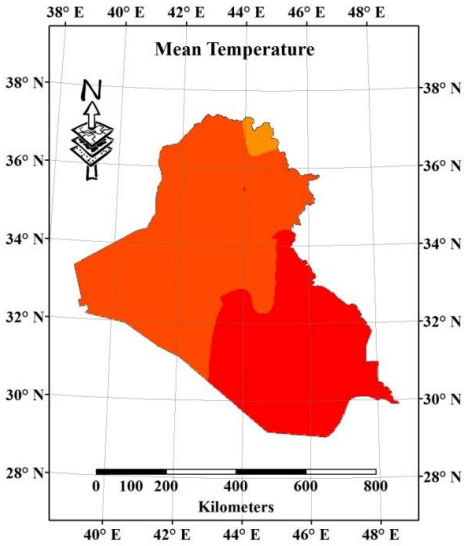

(c)Spring

(d)Autumn

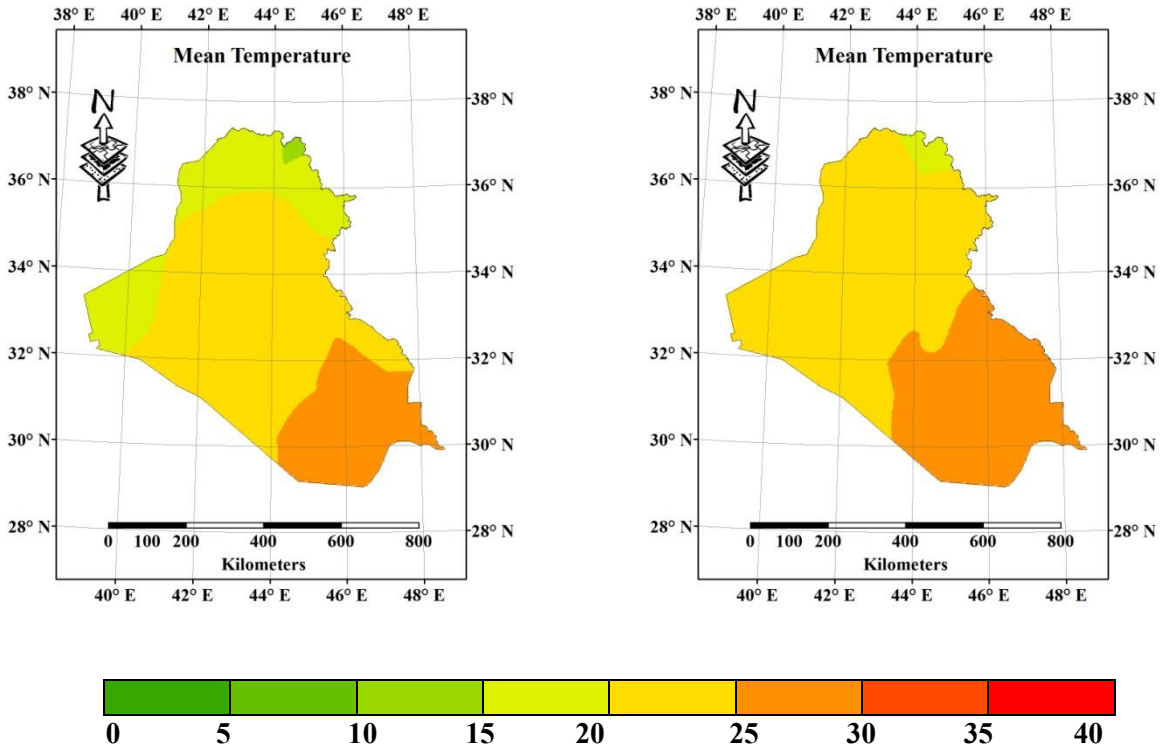

Figure 6. Spatial Distribution of Seasonal Mean Temperature (T_{Mean}) in (ºC) over Iraq for the period 1980-2015 By Kriging Technique in ArcGis

Table (3): Seasonal T_{mean} over Iraq for the period 1980-2015

Winter Mean Temperature (T_{Mean})			
Classes Color	Class Category	Count	Frequency Percent
	2	14464	37.94%
	3	23653	62.06%
		Sum = 38117	100%
Lowest T_{Mean} in Winter is 5.6 ºC			
Highest T_{Mean} in Winter is 13.9 ºC			

Summer Mean Temperature (T_{Mean})			
Classes Color	Class Category	Count	Frequency Percent
	6	669	1.76%
	7	22230	58.32%
	8	15218	39.92%
		Sum = 38117	100%
Lowest T_{Mean} in Summer is 29.2 ºC			
Highest T_{Mean} in Summer is 37.4 ºC			

Spring Mean Temperature (T_{Mean})			
Classes Color	Class Category	Count	Frequency Percent
	3	259	0.68%
	4	8453	22.18%
	5	21585	56.62%
	6	7820	20.52%
		Sum = 38117	100%
Lowest T_{Mean} in Spring is 14.7 ºC			
Highest T_{Mean} in Spring is 26.3 ºC			

Autumn Mean Temperature (T_{Mean})			
Classes Color	Class Category	Count	Frequency Percent
	4	830	2.18%
	5	24090	63.20%
	6	13197	34.62%
		Sum = 38117	100%
Lowest T_{Mean} in Autumn is 19.2 ºC			
Highest T_{Mean} in Autumn is 27.3 ºC			

Classes Color								
Class Category	1	2	3	4	5	6	7	8
Temperature in ºC	0-5	5-10	10-15	15-20	20-25	25-30	30-35	35-40

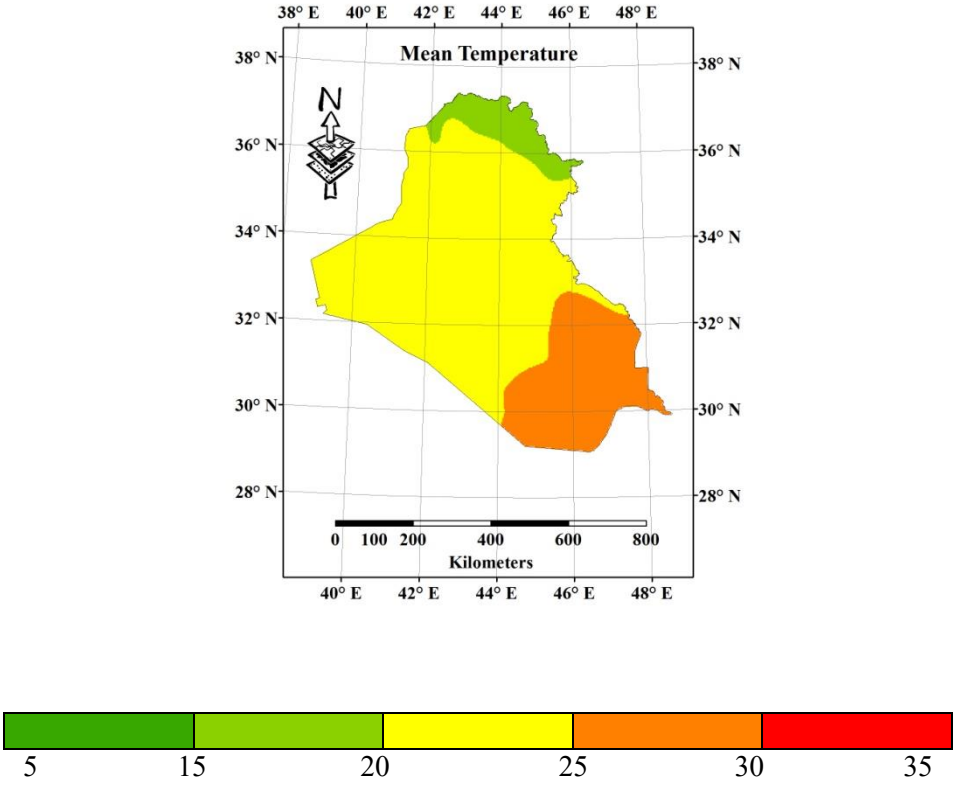

Figure 7. Spatial Distribution of Annual Mean temperature in (°C) over Iraq for the period 1980-2015 By Kriging Technique in ArcGis

Table (4): Annual (T_{mean}) over Iraq for the period 1980-2015

Annual Mean Temperature (T_{Mean})			
Classes Color	Class Category	Count	Frequency Percent
	2	2973	7.80%
	3	26410	69.29%
	4	8734	22.91%
		Sum = 38117	100%
Lowest T_{Mean} annually is 17.2 °C			
Highest T_{Mean} annually is 26.3 °C			

Classes Color					
Class Category	1	2	3	4	5
Temperature In °C	10-15	15-20	20-25	25-30	30-35

4. Conclusions

This study investigated the seasonal and annual variability on mean temperature in Iraq. The results show that trends of mean temperature for annual series, the trends in various regions are increased in northern and southern Iraq. The trend of increasing mean temperature was about (2.1ºC/year). In winter season, the increasing trend of mean temperature was (1.75ºC/year) in northern of Iraq and the same in the middle and southern region in Iraq. The increasing trend of autumn mean temperature was the same value in northern and middle parts of Iraq (1.4ºC/year) and increase in the south to (2.45ºC/year). In spring the rising trend of mean temperature was (2.1ºC/year) in the northern and the middle region of the country and reach (2.45ºC/year) in the south region. The highest value of increasing trend of mean temperature was in southern part of Iraq during the summer with value (3.5ºC/year).

The results of the spatial analysis of mean temperature show that the mean temperature gradient is found to be from the south to the north of Iraq. Seasonally the study area can be divided into two or three distinct areas with high temperature in the south and decreasing toward north.

References

[1] Jones, P.D., Raper, S.C.B., Bradley, R.S., Diaz, H.F., Kelly, P. M., Wigley, T.M. L., 1986, "A northern hemisphere surface air temperature variations: 1851-1984.," *American Meteorological Society,* vol. 25, pp. 161-179, February 1986.

[2] Brohan P, Kennedy JJ, Harris I, Tett SFB, Jones PD, "Uncertainty estimates in regional and global observed temperature change: A new data set from 1850," *journal of geophysical Research Atmospheres,* vol. 111, no. D12106, DOI: 10.1029/2005JD006548., 2006 june 24.

[3] Solomon, S., D. Qin, M. Tignor and H.L. Miller, "Climate Change : The physical Science Basis," Cambridge University Press, Cambridge, United Kingdom, 2007.

[4] Luterbacher. J., D. Diertrich, E. Xoplaki, M. Grosjean and H. Wanne, " European seasonal and annual temperature variability, trends and extremes since 1500," Science, vol. 303, pp. 1499-1503, 2004 March 5.

[5] Pielke, R.A., C.A. Davey, D. Niyogi, S. Fall, J. Steinweg-Woods, K. Gallo, R. hale, R. Mahmood, S. Foster, R.T. McNider and P. Blanken, "Unresolved issueswith assessment of multidecadal global and land surface temperature trends," Geophysical Research, vol. 112, no. D24S08, doi:10. 1029/2006JD008229, 2007.

[6] Rabetez, M. and M. Reinhard, "Monthly air temperature trends in Switzerland 1901-2000 and 1975-2004," *Theoretical and Applied Climatology,* vol. 91, pp. 27-34, 2007 june 27.

[7] Stafford, J.M., G. Wendler and J.Curtis, " Temperature and precipitation of Alaska:50 year trend analysis," *Theoretical and Applied Climatology,* vol. 67, pp. 33-44, 2000 March 21.

[8] Miro, J.J., M.J. Esrela and M. Milla'n, "Summer temperature trends in a Mediterranean area (Valancia Region)," *CONTRIBUTIONS to SCIENCE,* vol. 3, p. 331–342, 2007.

[9] Al Quraishi, Dhiyaa AlDeen Abd Al Hussien Ewaeed.(2008)."thermal properties of the middle and south part of Sedimentary plain in Iraq".Msc Thesis,College of education Ibn Rushed,Baghdad Unversity.

[10] Soman, M.R., Krishnakumar, K.,Singh, N., 1988.Decreassing trend in the rainfall of Kerala. Current science 57,7-12.

[11] Gilbert, R.O., 1987. "Statistical Methods for environmental pollution monitoring". Van Nostrand Reinhold, New York.

Measuring of nonlinear properties of spatial light modulator with different wavelengths

Measuring of nonlinear properties of spatial light modulator with different wavelengths

Farah G. Khalid[1]*, Samar Younis Al-Dabagh[2], Sudad S. Ahmed[3], Aseel I. Mahmood[4], Kais Al-Naimee[3]

1 Baghdad University / Collage of Agriculture / Basic of Science department/Baghdad/ Iraq

2 Baghdad University / Collage of Science for Women / Physics department /Baghdad/ Iraq

3 Baghdad University / Collage of Science / Physics department /Baghdad/ Iraq

4 Ministry of Science and Technology / material research directorate / Baghdad/ Iraq

* E-mail: farah_physicalaf70@yahoo.com

Abstract. The non-linear optical properties of Spatial Light Modulator(SLM) represented by Nonlinear Refractive Index (NLR) and nonlinear Absorption coefficient has been measured in this work using highly sensitive method known as Z-scan technique for different wavelengths (red and green). The capability to do instant measurements of different nonlinear optical parameters lead to consider these techniques as a one of the most desired and effective methods that could apply for different materials. The results showed that the NLR were in the same power for the different wavelengths while the nonlinear absorption is higher in case of green laser.

Keyword: SLM; Nematic Liquid Crystal, Z-scan technique

1-Introduction

Liquid Crystals (LC's) are materials that have one or more intermediate phase(s) between solid and liquid phases. In this intermediate phase, they retain the ability to flow like ordinary liquid, but also possess long-range orientational order. Some liquid crystals may also have positional order as well. Liquid crystalline phases, which classified according to their orientational and positional orders. The nematic phase has only orientational order, while the chiralnematic (cholesteric) phase has orientational order resembling the

nematic phase, but possess a helical layer structure as well. This spontaneous helical director configuration makes it more difficult to reorient a cholesteric than a nematic, liquid crystalline phases are illustrated in 'figure 1' [1, 2].Liquid crystals are widely employed in display applications (LCDs). They are used to construct Light valves and Spatial Light Modulators (SLMs) utilized in real-time image processing and optical computing applications. They are also used to fabricate optical limiting and optical switching devices, highly sensitive temperature sensors and thermo-graphical devices, among many other usages. Their sensitivity to polarization distribution makes them even more useful for future possible applications [3].

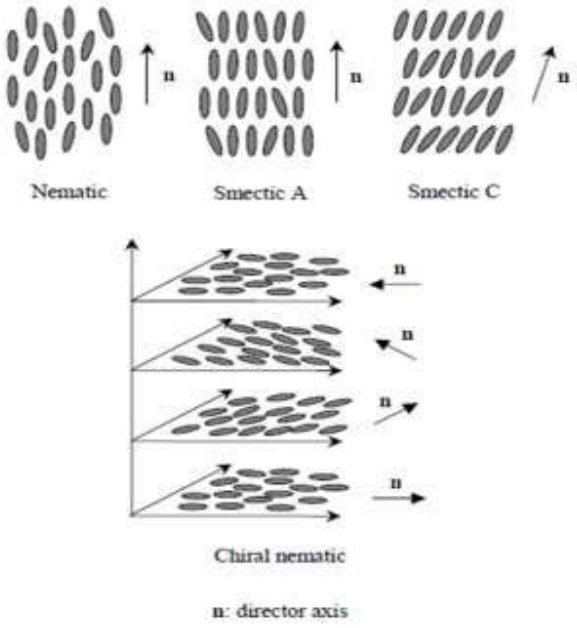

Figure 1. liquid crystalline phases [1].

Nonlinear isotropic materials exhibit nonlinear optical responses when their optical properties are field-dependent. Usually, in order to observe nonlinear responses, high field strength or high optical intensity from a high-power pulsed laser is required. The strong anisotropic and molecular rotation of the LC's lead to highly nonlinear optical response so, the refractive index of them change under applied stimulate (electric or magnetic field) or low optical intensity from CW laser [3].

S. Bahae et al. [4], were the first group whom introduce the z-scan technique, which could be defined as a highly simple sensitive method compared with interferometric method, from this technique the nonlinear parameters of liquids and sold could behind.

In Z-Scan technique, a sample is scanned along the optical axis in the focal region of a single Gaussian TEM00 beam. The transmission through the sample, with and without an aperture in the far field is then recorded. The transmission with an aperture (closed aperture) characterizes the sign and magnitude of the nonlinear index, while the transmission without an aperture (open aperture) characterizes the nonlinear absorption. This is a simple and sensitive technique for measuring the change in phase induced on a laser beam upon propagation through a nonlinear material. It gives both the sign and magnitude of this phase change, $\Delta\Phi_o$ which is simply related to the nonlinear refractive index, n_2 [5, 6].

2-Experimental work

In this work, z-scan technique is used to measure the nonlinear parameters of SLM cell which has an array of 90◦ nematic LC., Holoeye LC2002 SLM from Sony has been used. This type contains a Sony SVGA (800*600) LC micro display and driver electronics, the wavelength range of this SLM is (400-650) nm, LCD thickness is 20µm. the experiment was carried out at room temperature.

In this work we used two different lasers wavelengths to study the nonlinear properties of SLM the first one is He:Ne laser (λ=632.8nm) and the second one is green semiconductor laser (λ=532 nm). The beam is focused to a small spot by a positive lens with focal length 15 cm. The Z-scan technique, which is a simple experiment, used to measure intensity dependent nonlinear susceptibilities of materials. In this technique, the material sample (SLM)is passed through extensive Gaussian beam along the z-direction, and the far field intensity versus sample position Z-scan curve, predicated on a local response, gives the real and imaginary part of third order susceptibility. In the closed-aperture (window), Z-Scan measures the change in intensity of a beam, focused by lens as the sample passes through the focused area. Photo-detector (or power meter) collects the light that passes through an axially centered aperture in the far field. The change in on axis intensity is caused by self-focusing either self-defocusing by the sample (the SLM in our case) as it travels through the beam waist. A TEM_{00}Gaussianbeam has maximum intensity at the center and will create a change in index of refraction forming a lens in a SLM as shown in 'figure 2' [7].

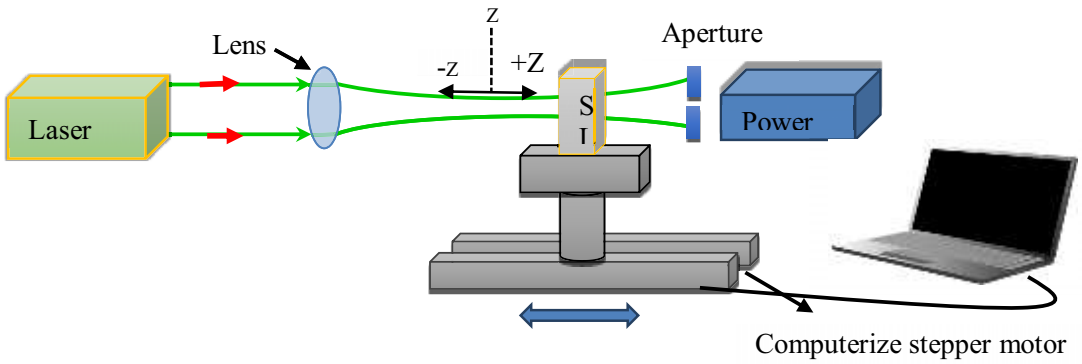

Figure 2. Closed aperture Z-Scan, the blue arrow indicate the direction of movement.

While when the aperture is moved we get an open aperture (window) method, here the Z-Scan measures the change in intensity of the focused beam, as it clear in 'figure 3', in the far-field at detector, which captures the entire beam. Multi-photon absorption in SLM caused changing in output intensity as the SLM travels through the focused beam waist. In the focused area, the intensity is in its maximum value, so we get largest nonlinear absorption. At the "tails" of the Z-scan curve, where | Z | >> Zo, the beam intensity is too weak to elicit nonlinear effects. The higher order of multi-photon absorption present in the measurement depends on the wavelength of the laser source and the energy levels of the SLM [7].

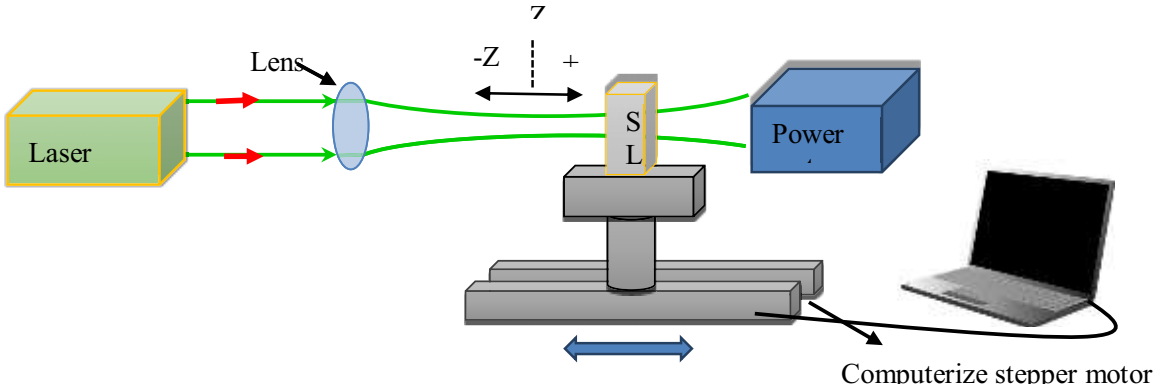

Figure 3. Open-aperture Z-Scan, the blue arrow indicate the direction of movement.

The relative on-axis transmittance of the SLM, which is obtained (at the small aperture of the far-field detector), is given by [8]:

$$T(Z,\Delta\phi_0) = 1 - \frac{4\Delta\phi_0 Z/Z_0}{[(Z^2/Z_0^2)+9][(Z^2/Z_0^2)+1]} \quad (1)$$

Where T is the transmission of laser light through the aperture, which is a function of the sample position Z, and Z_0 is Rayleigh wavelength and $\Delta\Phi_o$ is the on-axis phase shift at the focus zone, and it's measured through the following equation [8]:

$$\Delta T_{p-v} \approx 0.406(1-S)^{0.25}\,\Delta\phi_o \quad (2)$$

The ΔT_{p-v} is measured by get the difference between the normalized peak and valley transmittance and S is linear transmittance of the aperture, which is calculated from the following formula [8]:

$$S = 1 - \exp\,(-2r_a^2/w_a^2) \quad (3)$$

Where r^a represent aperture radius and w^a is the beam radius at the aperture, the nonlinear refractive index could be found through the following equation [9]:

$$n_2 = \Delta\phi_0 / I_0 L_{eff} k \quad (4)$$

where, k = 2π /λ , λ is the laser wavelength, I_o is the maximum intensity within the SLM at the focus and the Leff Effective thickness, which is given by [10]:

$$L_{eff} = [1 - \exp(-\alpha_0 L)]/\alpha_0 \quad (5)$$

Where α_0 is the linear absorption coefficient of the samples and it is obtained through the, Beer-Lambert law that defines based on $\alpha = -\left(\frac{1}{l}\right) \ln I/I_0$ in the linear regime of the experiment. While the nonlinear absorbance coefficient given by the following equation [10]:

$$\gamma = 2\sqrt{2}\Delta T / I_0 L_{eff} \quad (6)$$

3-Experimental results

The spectral absorbance of the SLM was measured by use of an UV-VIS spectrophotometer, which is shown 'figure 4'.

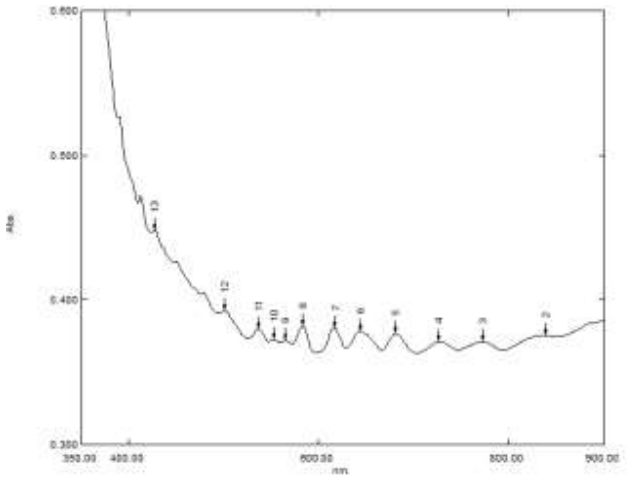

Figure 4. UV-VIS absorbance spectra of SLM

The Rayleigh wavelength (Z_0) is equal to 3.1 cm to green laser and 2.7cm to the red one and they both are greater than the SLM thickness, which is, allows considering the interaction between the laser pulse and the SLM to occur at just one location and not to distribute out over the entire interaction length.
The results of typical Z-scan normalized transmittance measurement for the SLM in case of used He:Ne Laser is shown in 'figures 5' and results illustrated in table 1.

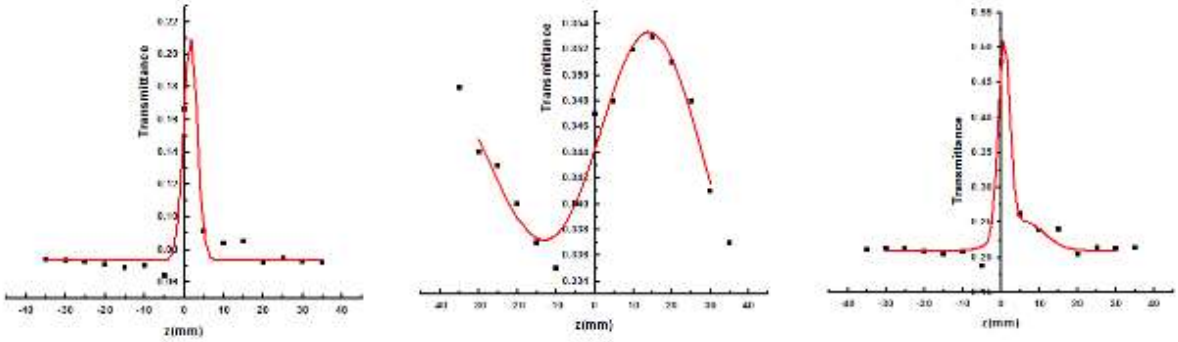

(a) Open aperture (b) Closed aperture (c) Closed aperture/open aperture

Figure 5. Normalized transmittance curve of SLM for He:Ne laser

Table 1. The linear And nonlinear optical properties of SLM for He:Ne laser

Case	$n_2(\frac{w}{cm^2})$	$\gamma(\frac{cm}{mw})$	$\alpha(\mu m^{-1})$
Closed. Aperture	12.965*10-8	0.0249	0.203
Closed. aperture/open,aperture	1.2554*10-7	-	-

While the results of typical z –scan normalized transmittance measurement for the SLM in case of used green semiconductor Laser are shown in figures 6 and results illustrated in Table 2.

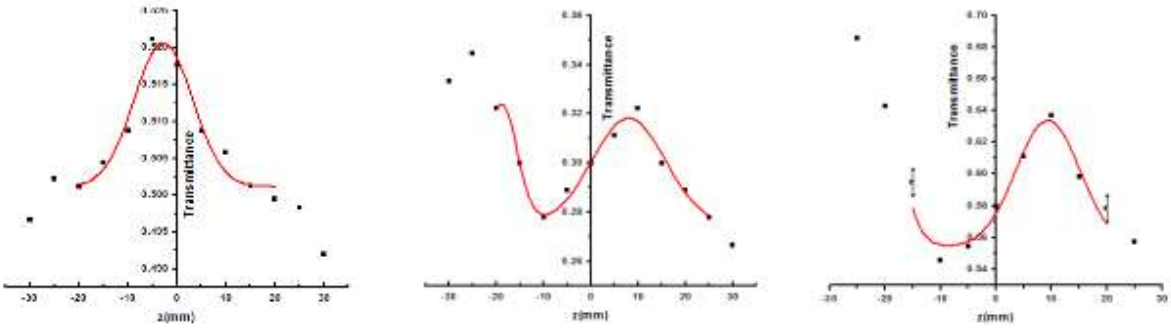

(a) Open aperture (b) Closed aperture (c) Closed aperture/open aperture

Figure 6. Normalized transmittance curve of SLM for Green semiconductor laser

Table 2. The linear and Nonlinear Optical properties of SLM for green semiconductor laser

Case	$n_2(\frac{w}{cm^2})$	$\gamma(\frac{cm}{mw})$	$\alpha(\mu m^{-1})$
Closed aperture	$9.927*10^{-8}$	0.286	0.162
Closed aperture/open aperture	$2.053*10^{-7}$	-	-

The resulted behavior of the SLM shows a positive z-scan profile starting linearly at (z<0) (far from focus) where the laser beam intensity is low and non linear refraction is negligible in this case the transmittance still constant, when the SLM began to move towards the focus the intensity began to increase, self-lensing will occur in the SLM and the laser beam will be collimated on the aperture which is located in front of the detector, so the higher transmission of the laser beam will be passed through the aperture until it reach to its maximum at the focus (z=0)then this maximum intensity began to drop after passing the focus zone and the behavior return to its linearity as the sample moved at (z>0). The non linear absorption of the SLM is calculated utilizing open aperture z-scan measurement, the behavior is changed from linear far from the beam waist (-z) then to nonlinear at (z=0) then return to its linear behavior at (+z) which change its intensity, this change is caused by two photon absorption in the sample travels through beam waist. S. Saadi et al [11], determine the real part of the third order nonlinear susceptibility of SLM utilizing Z-scan technique using He:Ne laser which is in a good agreement with our results related with He: Ne laser.

4-Conclusions

An investigation of the optical nonlinearity of SLM by using two different sources have been carried out in this work. The nonlinear refractive index, $n_2$of SLM cell which contains of an array of twisted nematic LC was measured using the single Beam z-scan technique for excitation wavelength, 632.8 nm, and 532 nm in the CW regime. The sign of the nonlinear refractive index was found to be positive so the experiment confirmed that the nonlinear phenomenon was caused byself-focusing process, the value of nonlinear refractive index for two wavelengths were in the same power.

The nonlinear absorption experiments were carried utilizing open aperture z-scan measurements, the value of this coefficient is lower when Red laser was used.

References

[1] de Gennes G 1974 The physics of liquid crystals, Clarendon Press, Oxford.
[2] Collings J and Hird M 1997 Introduction to liquid crystals: Chemistry and physics, Taylor & Francis, Bristol
[3] Moerner W and Silence S 1994 Polymeric photorefractive materials, *Chem. Rev*. 94, 127-155.
[4] Sheik-Bahae M, Said A., and Van Stryland E., 1989.High –sensitivity, single beam n_2 measurements, *Opt. Lett*. **14**, 17, 955 -975
[5] Masud P 2015 Experimental studies on the nonlinear optical properties of liNbO3 crystal, *Am. J. Sci. Ind. Res*., **6**,4, 69-73
[6] Zidan M and Allahham A2015 Z-Scan Measurements of the Third-Order Optical Nonlinearity of a C60 Doped Poly(dimethylacetylendicarboxylate), *ACTA PHYSICA POLONICA A*, **128** ,25-28.

[7] de Nalda R, del Coso R, Requejo-Isidro J, Olivares J, Suarez-Garcia A, Solis J, and Afonso C , 2002 Limits to the determination of the nonlinear refractive index by the Z-scan method, *Journal of the Optical Society of America B*, **19**, 2, 289-296.
[8] Sheik-Bahae M, Said A, and Wai T 1990 Sensitive measurement of optical nonlinearities using a single beam, *IEEE Journal of Quantum Electronic*, **26**, 4, 760-769.
[9] Wang Y, and Saffman M, 2004 Z-scan formula for two-level atoms, *Opt. communications*, **241**, 513-520.
[10] Sheik –Bahae M, Said A, Wai T, and Van Stryland E 2007 Sensitive Measurement of Optical Nonlinearities Using a single Beam, *IEEE LEOS NEWSLETTER*,**21**, 1,17-26.
[11] Saadi S , Al Naimee K and Ahmed S 2017 Third-order nonlinear optical properties of Spatial Light Modulator, *Australian Journal of Basic and Applied Sciences*, **11**,7, 42-48.

Enhance the performance of liquid crystal as an optical switch by doping CdS quantum dots

Enhance the performance of liquid crystal as an optical switch by doping CdS quantum dots

Sudad S Ahmed[1], Rawa K Ibrahim[2, 1], Kais Al- Naimee[1], Asama N Naje, Omar A Ibrahim[1], K A Majeed[1]

[1]Department of Physics, College of Science, University of Baghdad, Baghdad, Iraq
[2]Laser &Electro-Optic Centre, Advanced Materials Research Directorial, Ministry of Science and Technology, Baghdad, Iraq

[2,1]rawak2070@gmail.com

Abstract. The electrical and optical properties results were studied for Cadmium Sulphide (CdS) Nanoparticles/ Nematic liquid crystal (5CB) mixtures. Doping of CdS nanoparticles increases the spontaneous polarization and response time, the increase is due to large dipole-dipole interaction between the liquid crystal (LC) molecules and CdS nanoparticles, which increase the anchoring energy. The electro-optic measurements revealed a decrease (~40%) in threshold voltage, and faster response time in doped sample cells than Pure 4'-n-pentyl-4-cyanobiphenyl (5CB) nematic liquid crystal.

1. Introduction

Liquid crystal (LC) devices are great interest elements of modern life because of the pervasiveness of their application as a spatial light modulator (SLM), optical antennas, and flat panel display devices.Doping the nematic liquid crystals (NLC) type 4'-n-pentyl-4-cyanobiphenyl (5CB) with small amounts of nanoparticles can stupendously modify the electro-optic response of the NLC host material. Nanoparticles effects result from the influence of these nanoparticles in the liquid crystal/substrate interface, and nanoparticles in the bulk. In this paper, these effects were studied. The Fréedericksz transition happened due to the distribution in the orientational order of the nematic liquid crystal 5CB doped with CdS quantum dots is also studied, as these dispersions are known from earlier studies to affect the initial alignment layers[1].Low operation voltage is one of the most decisive operators for developing liquid crystal display devices. Nanoparticles doping is a facile method of achieving low threshold voltage [2]. A type of semiconductor material, CdS nanoparticles, have been doped into the nematic liquid crystal. The response time and frequency cut off of nanoparticles-doped liquid crystal were also studied in this work. In addition, there are some parameters as phase transition temperature, orientational order, and dielectric constants have interest effect cause the threshold voltage reduction, and make the doped materials have the same variation behavior with the threshold voltage as they are correlated with the nanoparticles size and doping concentration [3].Some of the semiconductor nanoparticles as TiO2 , ZnO , CdS have been studied for improved the physical properties in case if they doped in liquid crystal [4-8].

In the present paper, an attempt has been made to study the effect of CdS nanoparticles on the electro-optic properties of 5CB LC.

2. Experimental Work

The preparation of Cadmium Sulphide CdS quantum dots (CdS QDs) achieved using the Chemical method , Initially Cadmium chloride CdCl2, Paraffin, and Olic acid, were mixed in proper way and heated under argon gas with temperature at l60 0C then the Sulfur (S) dissolved in Paraffin Oil to get solution that heated to 2200C . When the solution achieved, the CdS QDs synthesis by mixing this two solution with mole ratio 2:l . The CdS QDs were purified by repeated dissolution in a mixture of toluene: methanol.The detailed synthesis of CdS nanoparticles is also reported in previously published methods [9]. The liquid crystal material was 5CB from Sigma Aldrich Company, has been used as the host material. The LC sample cells of thickness 2mm were fabricated using indium tin oxide (ITO) coated transparent glass substrates has sheet resistance 25Ω and aligning layers of polyimide (PVA) deposited on it. The polyamide layer act as the planar alignment of 5CB LC molecules. The polyimide layers were scribed by a fleecy material in order to provide a uniform planar alignment of LC. The cell was assembled so that the rubbing directions of the opposite aligning layers were antiparallel. The cell gap was done by the glass spacers of appropriate size, (20 μm). The pure and doped NLC samples were prepared using doping of CdS NPs with two concentration of 0.05wt%, 0.25 wt% into NLC. The homogenized mixture of CdS /NLC was then filled in the space of LC sample cells (middle of the cell layers) by capillary action and sealed using adhesive materials. The electrodes for the LC cell were connected at the ITO surface of the cells using the Aluminum material.

The electro-optical measurements were carried out using the experimental setup puts in ‘figure l’. The sample cell was set between two linear polarizers so that the angle between the polarizers plan is 90^0, while the angle between the polarizer plan and the rubbing direction of polyimide layer was 45°. The electro-optical variations were recorded on a digital storage oscilloscope (Tektronix TDS2024B).

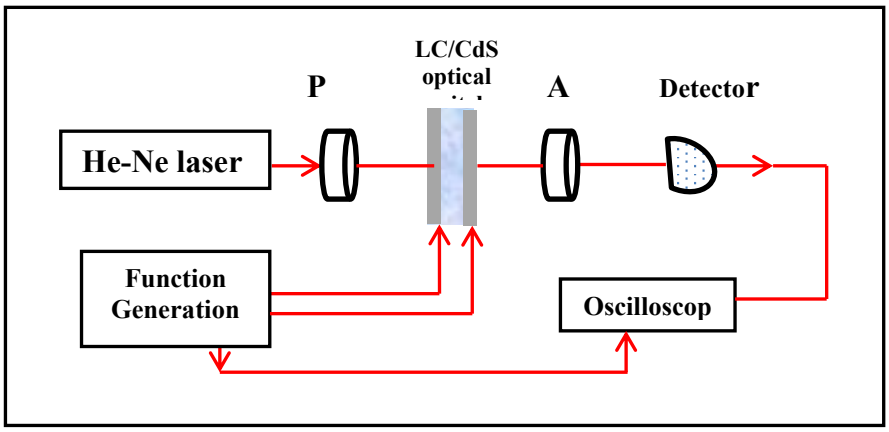

Figure l. Experimental setup for measuring the electro-optical properties of the LC samples.

3. Results and Discussions

3.1. The Structure, Morphology and the Shape of CdS QDs:

The XRD test has patterns of the prepared CdS QDs shows the presence of the diffraction peaks at the (l00), (002), (l0l), (220) planes. All peaks in the XRD pattern give indicate to the structure, which is hexagonal wurtzite structure. ‘Figure 2a’ shows the XRD patterns of CdS QDs, which have peak position illustrate in ‘figure 2 b’, which are agreed with the standard data get from PCPDFWIN. The average particle size of the CdS QDs calculated from the Scherrer formula is (6.62 nm).

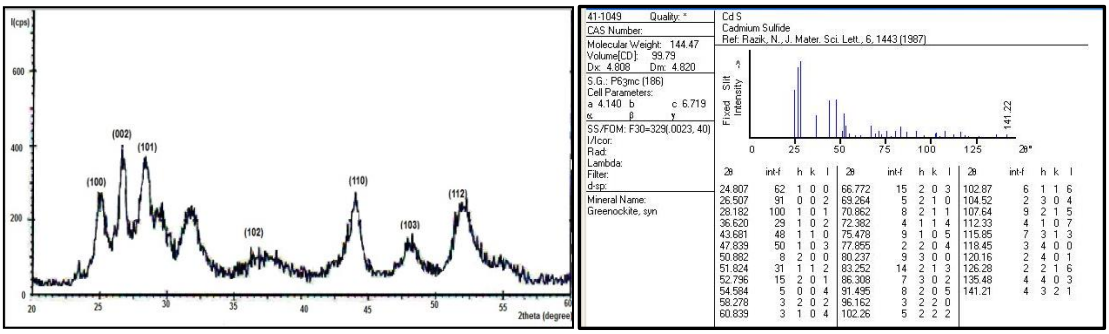

(a) (b)

Figure 2. The XRD patterns for (a) prepared CdS QDs and (b) Bulk CdS.

The SEM image of CdS QDs shows the spherical clusters of CdS QDs, while the grain size estimated was about 20nm as shown in figure 3.

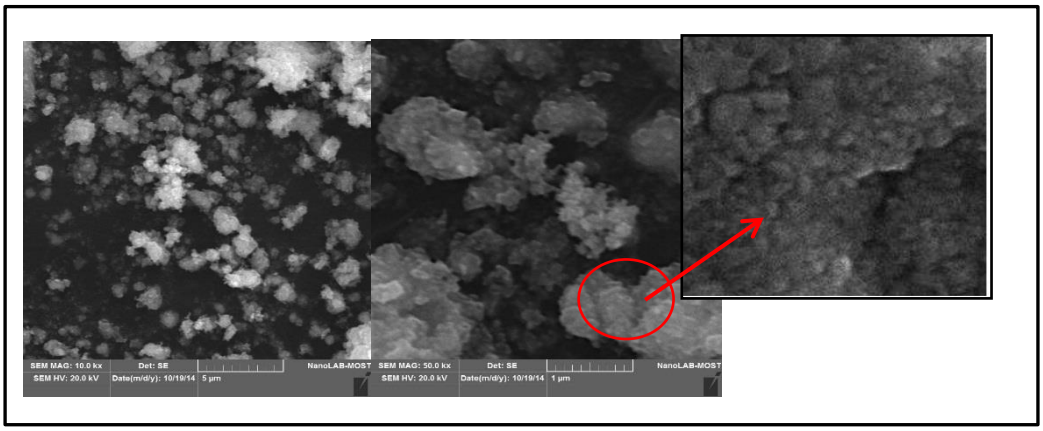

Figure 3. The SEM images of CdS QDs.

The EDX analysis of CdS QDs to get the purity and the concentration of each compounded inside the CdS film was the Cadmium 34 at% and the sulfur l4 at % as shown in ‘figure 4’.

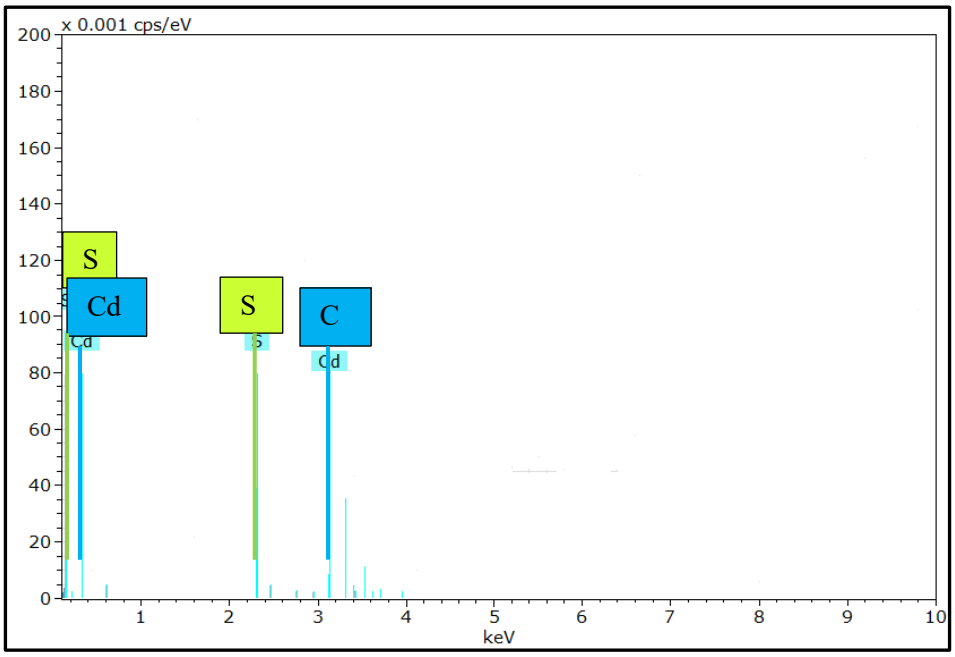

Figure 4. The EDX of CdS QDs

3.2. The Electro-optic Properties

3.2.1. Frequency Response

The frequency that the device of LC/CdS have maximum transmittance as an optical switch is 200 Hz for pure LC optical switch device, while for the tow devices that have the concentration of doping with 0.05 wt% and 0.25wt%, the frequency response for these was 250 Hz as in ‘figure 5’.

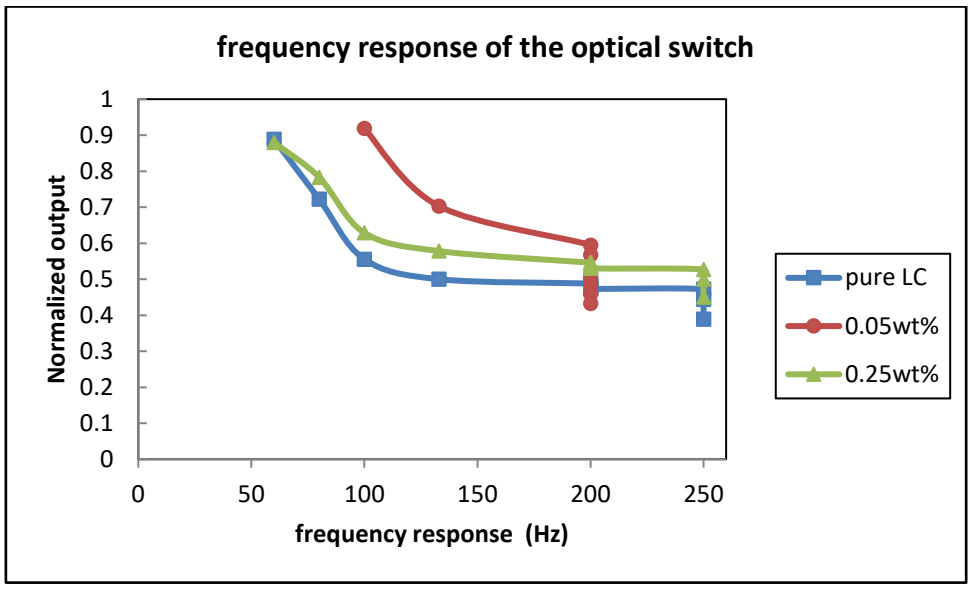

Figure 5. The Frequency Response of the Pure LC, LC/CdS with 0.05wt% and with 0.25wt% optical switch

3.2.2. Threshold Voltage

The threshold voltage of the LC device and LC/CdS optical switch is measured when it starts to respond. 'Figure 6' shows the relation between applied voltage and output voltage record from the detector as a function of the transmission of the pure LC and for LC/ CdS with tow concentration of doping. The threshold voltage was l.4 volt for pure LC optical switch while for LC/CdS optical switch was 1 V, for both doping concentration 0.05 wt% and 0.25 wt%.

The threshold voltage has reduced with the addition of nanoparticles in the pure nematic liquid crystal optical switch because of the increased charge density of the nano-nematic composite system which reduced an energy barrier. The doping of CdS NP (0.25% by weight) nano-particle in the LC layer generates free electron, CdS NP, these generated free electrons enter into the LC layer and therefore charge density increases near the interface. This results in the smaller electric field and thus a smaller threshold voltage is required.

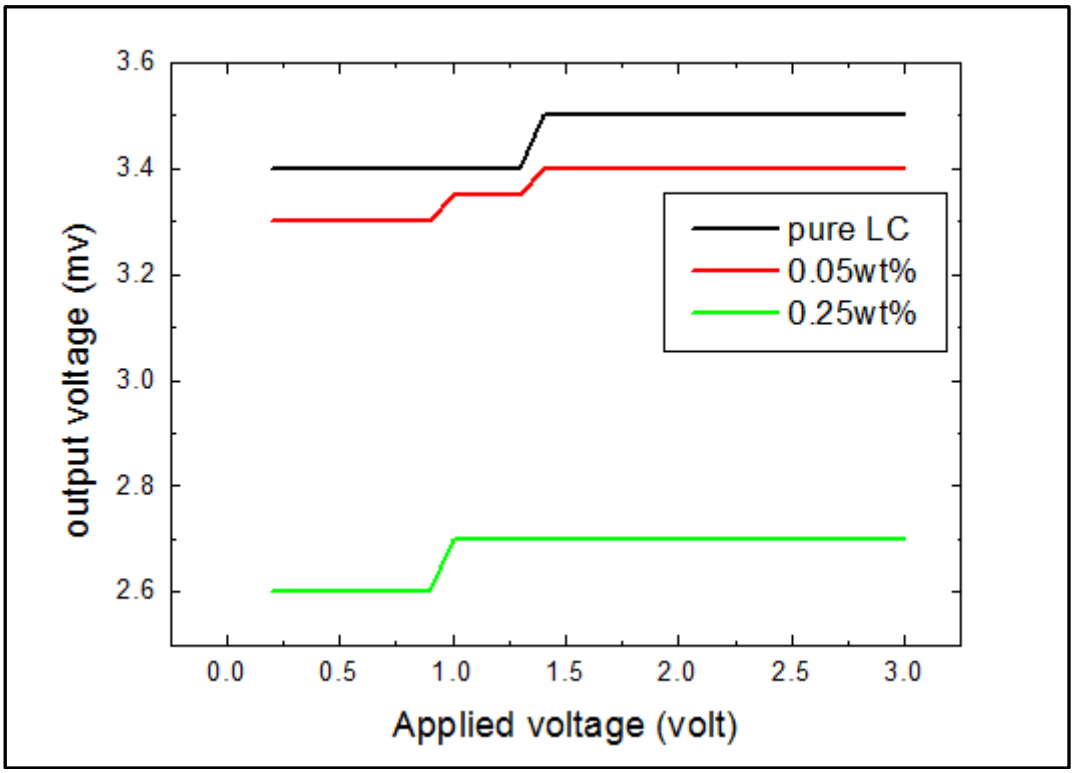

Figure 6. The Threshold Voltage of Pure LC, 0.05wt %, and 0.25wt% Optical Switch

3.2.3. Rise Time

The rise time have been calculated from l0% to 90% of the steady state of the signal of the response voltage of the pure LC optical switch device that shown in 'figure 7', which was 7.5ms.while the rise time for LC/CdS optical switch can be illustrated in table (l) which was 5 ms for the 0.05wt% and 4ms for the 0.25wt%. 'figure 8' shows the response signal of LC/CdS optical switch.

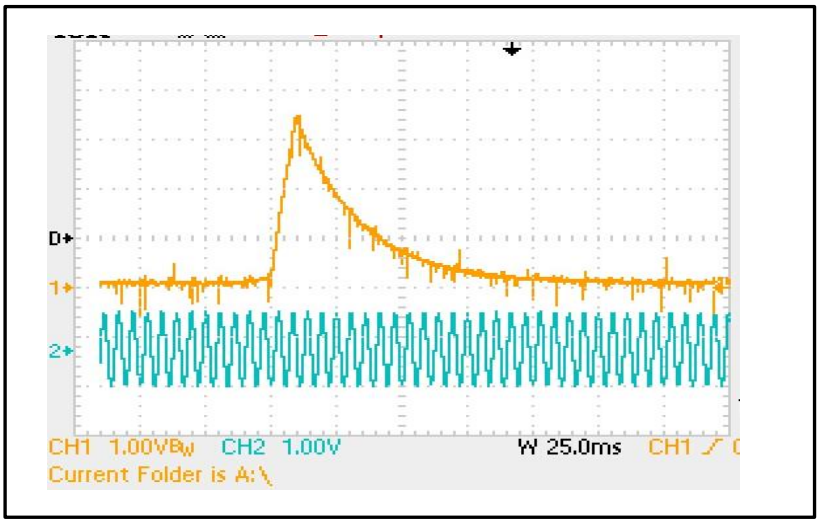

Figure 7. The Response Signal of Pure LC Optical Switch

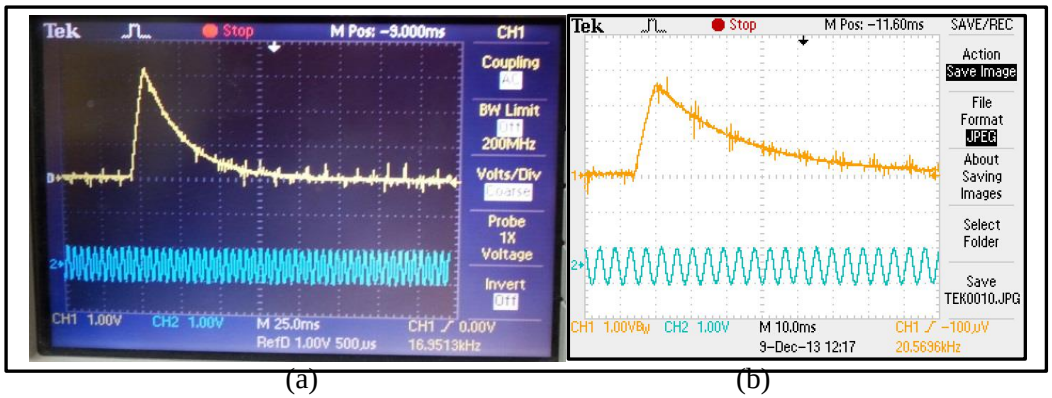

(a) (b)

Figure 8 . The signal response of LC/CdS QDs optical switch, (a) for 0.05 wt%,(b) 0.25wt%

The addition of nanoparticle provides enhancement interaction to the dipole moment of nematic liquid crystal molecules. Therefore, the higher concentration of nanoparticles causes to decrease the response time of NPs/NLC mixture. The mechanics of CdS nanoparticle in liquid crystals is based on the orientational vector distribution of the dipole moment of nanoparticle and that can be characterized by an orientational order parameter. This distribution catalyzes the coupling strength to increase the responding for liquid crystals and stabilizes the nematic phase of the liquid crystal.

3.2.4. Fall Time

The fall time calculated from90% to l0% of the steady state of the signal was 58.75 ms for the pure LCoptical switch, while the fall time was 55 ms for the 0.05wt% and 50ms for the 0.25wt%.

3.2.5. Response Time

The response time calculated from 0% to 62.5% of the steady state of the signal was l2.5 ms for pure LC optical switch. While the response time was 4.375 ms for the 0.05wt% and 3 ms for the 0.25wt%.

4. Conclusions

The effect of CdS QDs doping into nematic liquid crystal mixture has been studied electro-optic measurements. Doping of CdS QDs improves the response time and threshold voltage than pure NLC, due to the tremendous increase in dipole moment of NLC molecules.A decrease in the threshold voltage about 40% was also noticed in the doped sample than pure NLC sample, that showing an improved switching behavior. The cutoff frequency of CdS/NLC optical switch was250 Hz, which greater than Pure LC optical switch (200Hz). Fast response time from l2.5ms for pure LC to 4.3 ms for 0.05wt% sample and 3ms for 0.25 wt% sample.

References

[1] Urbanski M Mirzaei J Hegmann T and Kitzerow H 2014 Nanoparticle Doping in Nematic Liquid Crystals: Distinction between Surface and Bulk Effects by Numerical Simulations *Chem Phys Chem* **l5** l395–404

[2] Zhang T Zhong C and Xu J 2009 CdS-Nanoparticle-Doped Liquid Crystal Displays Showing Low Threshold Voltage *Jpn.J.Appl.Phys*. **48** pp l-6

[3] Kinkead B and Hegmann T 2010 Effects of size capping agent and concentration of CdSe and CdTe quantum dots doped into a nematic liquid crystal on the optical and electro-optic properties of the final colloidal liquid crystal mixture *Journal of Materials Chemistry* **20** 448–58

[4] Lee W Choi J Na H et al. 2009 Low-power operation of vertically aligned liquid-crysta system via anatase-TiO2 nanoparticle dispersion *Optics Letters* **34** 3653–5
[5] Joshi T Kumar A Prakash J and Biradar A 2010 Low power operation of ferroelectric liquid crystal system dispersed with zinc oxide nanoparticles *Applied Physics Letters* **96** 25
[6] Tripathi P Misra A Manohar S Gupta S and Manohar R 2012 Improved dielectric and electro-optical parameters of ZnO nano-particle (8% Cu2+) doped nematic liquid crystal, *Journal of Molecular Structure* **l035** 37l–7
[7] Tripathi P Misra A Pandey K Yadav S and Manohar R 2013 Abnormal switching behavior of nanoparticle composite systems *Journal Phase Transition* **86** 12

Dispersion Parameters of Polyvinyl Alcohol Films doped with Fe

Dispersion Parameters of Polyvinyl Alcohol Films doped with Fe

Nadir F Habubi[1], Khalid H Abass[2], Chiad S Sami[1], Duha M A Latif[3], Jandow N Nidhal[1], A Ismaeel Al Baidhany[1]

[1]Department of Physics, College of Education, Mustansiriyah University, Baghdad, Iraq
[2]Department of Physics, College of Education for Pure Sciences, University of Babylon, Babylon, Iraq
[3]Department of Physics, College of Education for Pure Sciences, University of Baghdad, Baghdad, Iraq.

nadirfadhil@uomustansiriyah.edu.iq, pure.khalid.haneen@uobabylon.edu.iq, dr.sami@uomustansiriyah.edu.iq, nidhaljandow@uomustansiriyah.edu.iq, ismaeel_2000@uomustansiriyah.edu.iq.

Abstract. Polyvinyl alcohol polymer was dissolved in water in order to prepare films with different concentration of Fe utilizing casting method. The optical properties were obtained by recording the transmittance spectrum in the wavelength range (300-900) nm. The dispersion parameters were calculated using the Wemple–DiDomenico method. Dispersion energy (E_d) and the single oscillator energy of electronic transition (E_o) were decreased with the increasing of Fe content in the PVA-Fe films. While Urbach energy was increased. The energy gap decreased from 4.08 eV to 3.52 eV for PVA: 4% Fe film.

1. Introduction

PVA has attained great importance due to, its high dielectric strength, high charge storage capacity. Electrical and optical properties of PVA can be tailored by doping. It was notified that the PVA based electrolyte contains water, which improves the conductivity and maintains the dimensional constancy of the electrolyte [1]. Polymers doped with metal particles helps in enhancing the kinetics of the ionic species through the compound by motivating better vicinity of the required ions within the polymer/metal composite [2], and its (Metal/polymer composites) have appealing great importance in recent years because of the unique properties of metals and polymers built into them. The doping transition metal halides into PVA are serious for limiting and monitoring the operational characteristic of the different PVA composites [3, 4].

Polymer blends were taken place in the vision of broad application concerning systems and devices. The addition of dopant to the polymer matrix will affect electrical, electrochemical and optical properties and can be tuned to obtain new properties for diverse applications [5, 6]. In this study, the prepare of PVA-Fe composite was done by casting solution method and the study of Urbach energy and dispersion parameters of this composite were obtained.

2. Materials and Methods

Matrix Polymer of polyvinyl alcohol with molecular weight 10000 g/mol (supplied from BDH Chemicals England) was employed to obtain a polymeric Solution. $FeCl_3$ (supplied from Metck Chemicals Germany) was used as a doping agent embedded in PVA matrix with (2% and 4%) volumetric concentration. This composite was deposited by casting method at ambient temperature to obtain films in order to study their optical properties. Transmittance and absorbance spectra were recorded by spectrophotometer Schimadzu (Japan) in the wavelength range (300-900 nm).

3. Results and discussion

Transmittance spectra of PVA-Fe with various content of Fe are registered by spectrophotometer in the range 300-900 nm. Transmittance against wavelength is presented in 'figure 1', which shows that the transmittance decreased with the increasing of Fe content in the PVA-Fe films, make these films less transparency.

'Figure 2' shows the variation of reflectance with a wavelength of PVA-Fe films. The reflectance increased sharply with the increase of wavelength until 500 nm and decreased with the increasing of Fe content in this region, while it's taken stable values with wavelength until 900 nm of wavelength and changed slightly with increasing Fe content.

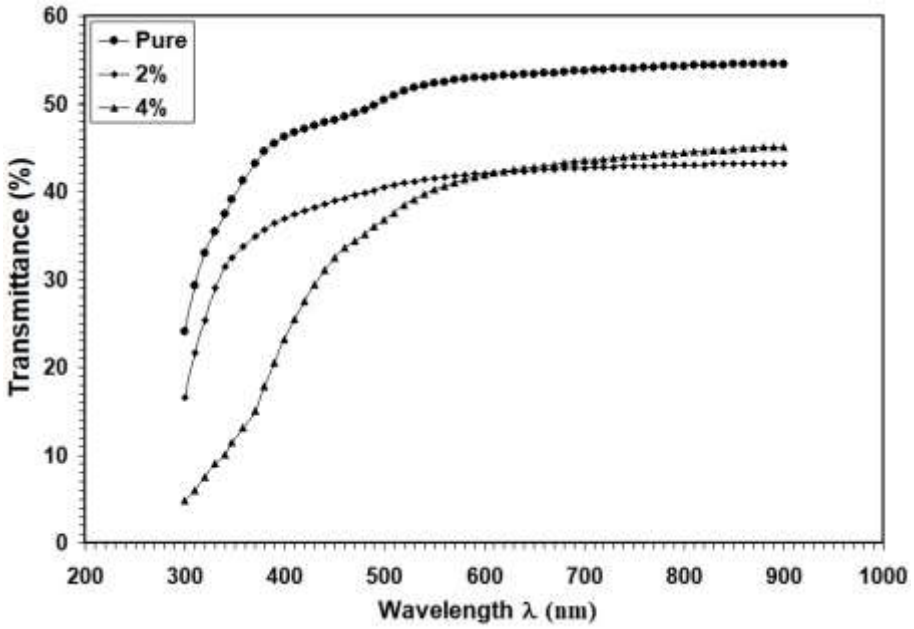

Figure 1. Transmittance via wavelength of PVA-Fe composite with various content of Fe.

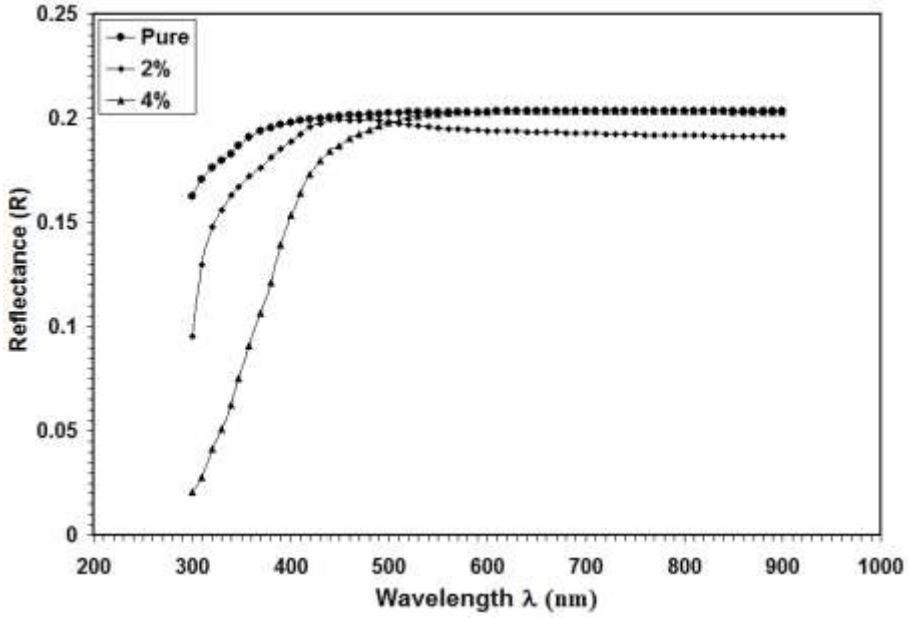

Figure 2. The refractive spectra of PVA-Fe composite with various content of Fe.

Real (ε_r) and imaginary (ε_i) parts of dielectric constant are calculated 'as in equation (1) and equation (2)' [7]:

$$\varepsilon_1 = n^2 - k^2 \quad (1)$$

$$\varepsilon_2 = 2nk \quad (2)$$

Where (n) is the index of refraction and (k) is the extinction coefficient. The variations of these parameters PVA-Fe wavelength are presented in 'figures 3' and 'figures 4'. From these figures, it can be seen that both parts are decreased with the increasing of Fe content.

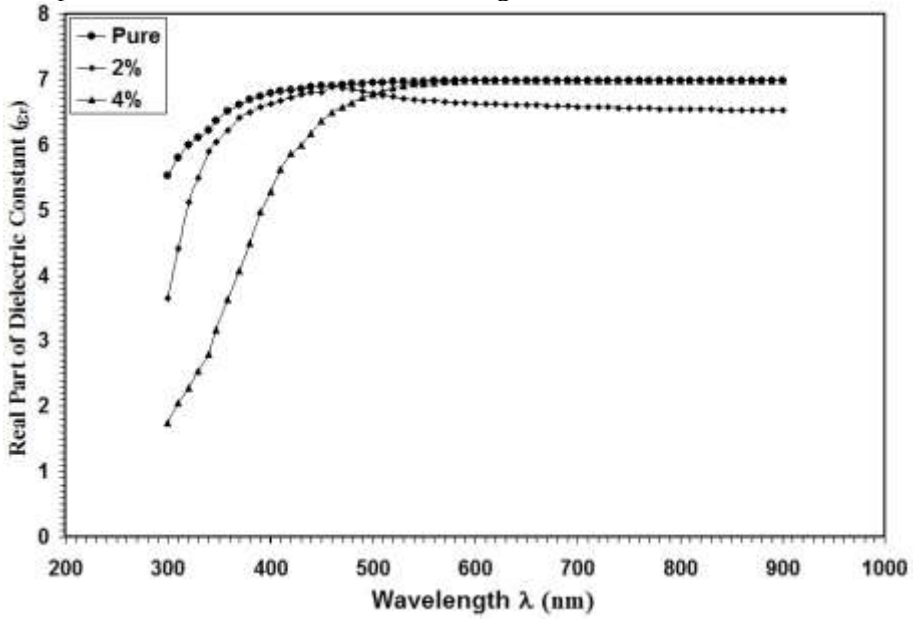

Figure 3. The real part of the dielectric constant of PVA-Fe composite with various content of Fe.

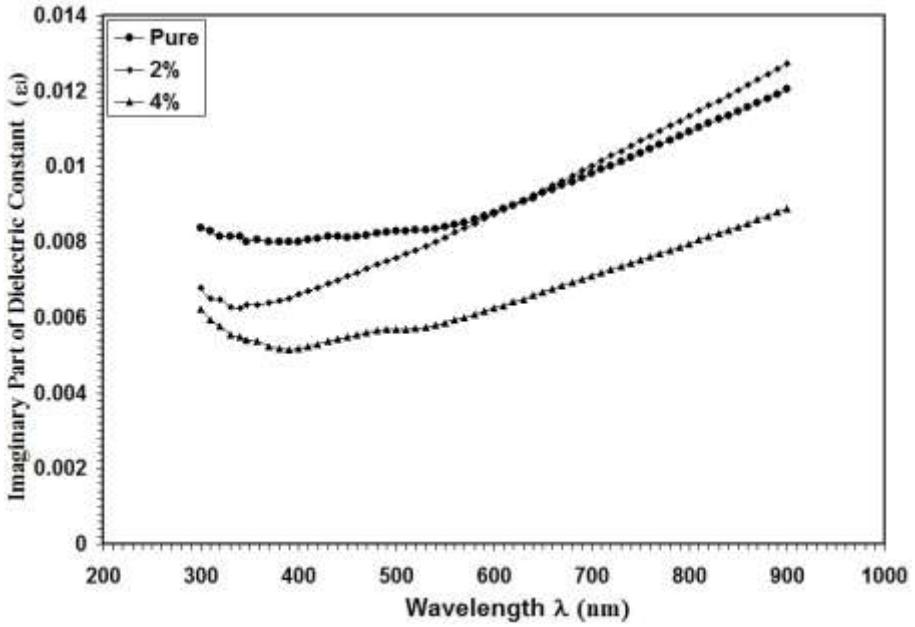

Figure 4. The imaginary part of the dielectric constant of PVA-Fe composite with various content of Fe.

The Urbach energy (E_U) was mentioned to the width of the exponential absorption edge, also called Urbach tails [8]. It can determine 'as in equation (3)' [9]:

$$\alpha = \alpha_o \exp\left(\frac{E}{E_U}\right) \quad (3)$$

Where (E) denoted photon energy and (α_o) is fixed. Variations of ln α with photon energy (hυ) for PVA-Fe films are presented in 'figure 5'. The values of Urbach energy for PVA-Fe films are listed in (table 1), which increased with the increasing of Fe content in the PVA-Fe films.

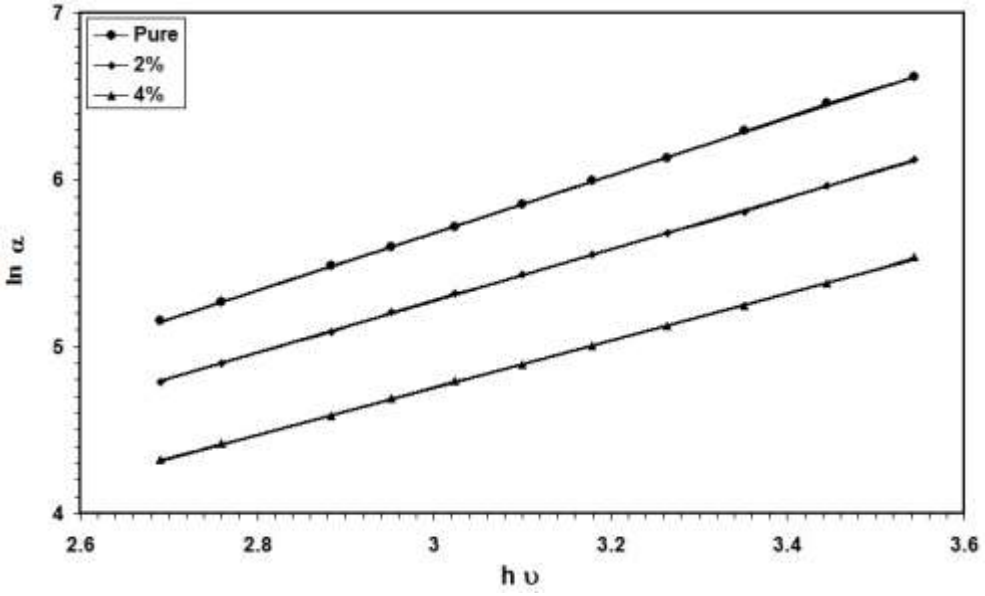

Figure 5. The Urbach energy of PVA-Fe composite with various content of Fe.

The dispersion parameters are very important in many applications such as optical communication and in the design of optical devices [10]. From Wemple–DiDomenico it can describe the dispersion parameters 'as in equation (4)' [11]:

$$n^2 = 1 + \frac{E_d E_o}{E_o^2 - (h\upsilon)^2} \quad (4)$$

Where E_d is the dispersion energy, E_o denotes single oscillator energy of the electronic transition, and n denotes refractive index. To estimate the values of E_d and E_o, it can plot $(n^2-1)^{-1}$ in the x-axis and $(h\upsilon)^2$ in the y-axis, as shown in Figure 6. E_d and E_o were obtained from slope $(E_d\ E_o)^{-1}$ and opposed (E_o/E_d) [12]. Energy gap (E_g) values were estimated from the energy of the single oscillator of the relation $E_o \approx E_g$ [12]. The values of E_d, E_o, and E_g are listed in (table 1). From the Table, the values of E_d, E_o, and E_g decrease with the increasing of Fe content in the PVA-Fe films. The index of refraction (n_∞) for the PVA-Fe films were gained by the interception of the perpendicular axis in Figure 6.

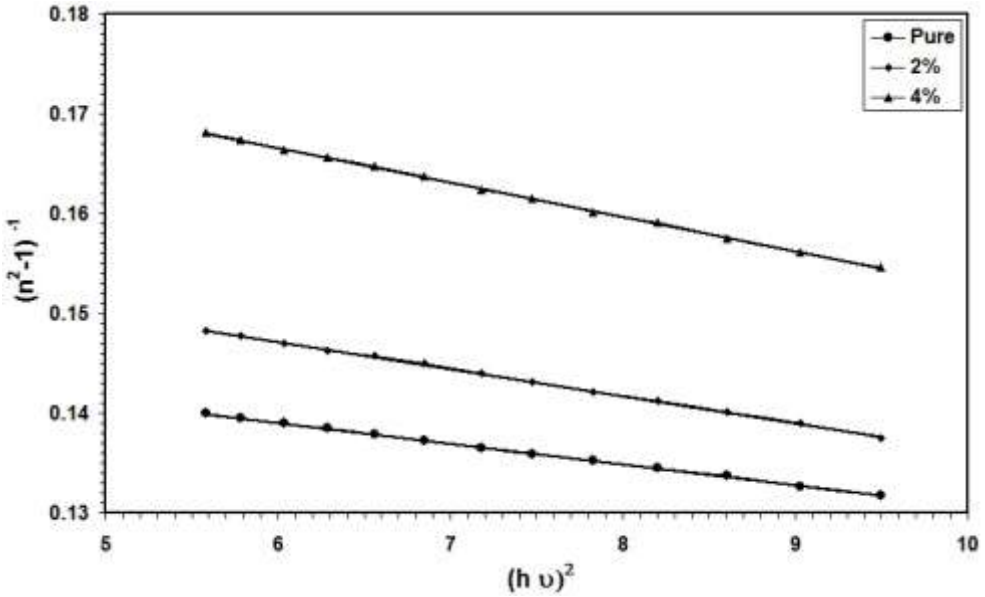

Figure 6. The $(n^2-1)^{-1}$ versus $(h\upsilon)^2$ of PVA-Fe composite with various content of Fe.

The Sellmier or Cauchy expressions for the refractive index depends on the wavelength $(n(\lambda))$ which are purely mathematical fitting 'as in equation (5)' [11]:

$$n^2(\lambda) - 1 = \frac{S_o \lambda_o^2}{1 - (\frac{\lambda_o}{\lambda})^2} \quad (5)$$

Where λ_o denote the average oscillator position and S_o denote the average oscillator strength. These parameters can be determined from the plot of $(n^2-1)^{-1}$ versus λ^2 as illustrated in 'figure 7'. The slope who produces straight line accord $1/S_o$, and the infinite-wavelength intercept accord $1/S_o\lambda_o^2$ [13]. The values of S_o and λ_o are recorded in (table 1). The value of S_o was increased with the increase of Fe content in the PVA-Fe films, while λ_o value was decreased.

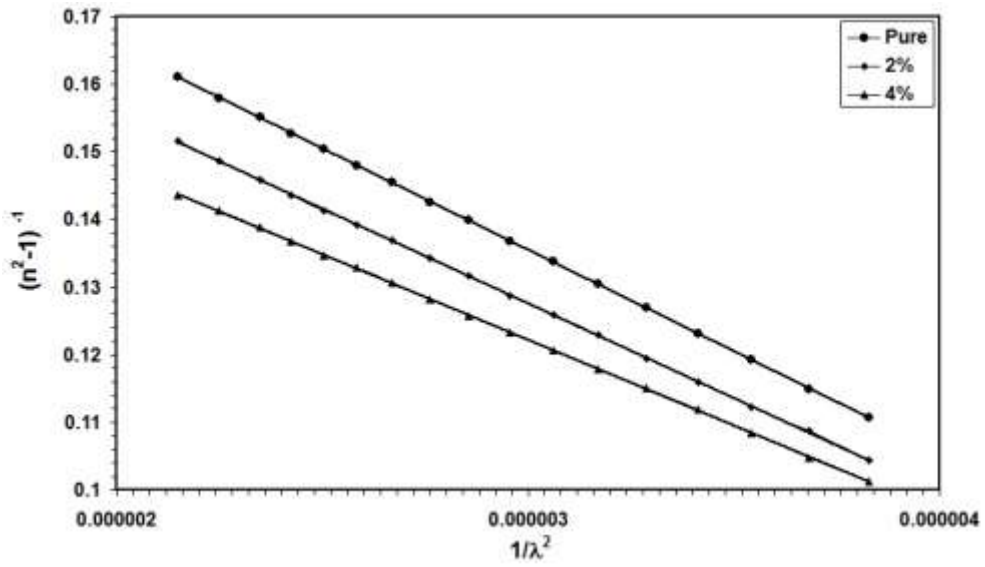

Figure 7. The $(n^2-1)^{-1}$ versus $1/\lambda^2$ of PVA-Fe composite with various content of Fe.

The moments of the imaginary part of the optical spectrum (M_{-1}, M_{-3}) of PVA-Fe films are estimated 'as in equation (6) and equation (7)' [14]:

$$E_o^2 = \frac{M_{-1}}{M_{-3}} \tag{6}$$

$$E_d^2 = \frac{M_{-1}^3}{M_{-3}} \tag{7}$$

Values of M_{-1} and M_{-3} are recorded by Table (1). From the Table, It could be noticed that optical moments M_{-1}, M_{-3} decrease by the increasing of Fe content in the PVA-Fe films.

Table. Optical parameters of PVA-Fe composite with various content of Fe.

PVA and doped PVA	E_d (eV)	E_o (eV)	E_g (eV)	ε_∞	n(o)	M_{-1}	M_{-3} eV^{-2}	S_o $x10^{13}$ m^{-2}	λ_o nm	E_U meV
Pure	58.32	8.16	4.08	8.14	2.85	7.14	0.127	3.33	426	588
2 %	49.69	7.45	3.72	7.66	2.77	6.67	0.120	3.57	410	649
4 %	41.47	7.05	3.52	6.88	2.62	5.88	0.118	4.00	387	709

4. Conclusion

Polyvinyl alcohol polymer was dissolved by water to prepare films with various content of Fe by solution casting method. The Urbach energy was increased with the increase of Fe content in the PVA-Fe films, while the energy gap decreased that calculate using Wemple–DiDomenico equation. Dispersion energy (E_d) and single oscillator energy of electronic transition (E_o) decrease with increasing of Fe content in the PVA-Fe films.

Acknowledgments

The authors would like to thank Mustansiriyah University (www.uomustansiriyah.edu.iq) Baghdad-Iraq, Baghdad University and Babylon University for their support in the present work.

References

[1] Vargas M A Vargas R A and Mellander B E 2000 *Electrochim Acta* **45** 1399-403
[2] Khan S D Ahmed B Raghuvanshi S K and Wahab M A 2014 *Indian Journal of Pure and Applied Physics* **52** 192-7
[3] Bhajantri R F Ravindrachary V Harisha A Crasta V Nayak S P and B Poojary 2006 *Polymer* **47** 3591-8
[4] Chiad S S Oboudi S F Abass K H and Habubi N F 2012 *Iraqi J. of Polymers* **16** 2 10-8
[5] Abdel-Fattah A A El-Kelany M. and Abdel Rehim F 1996 *Radiat. Phys. Chem.* **48** 4 pp 497–503
[6] Mustafa I S Azman N M Rahman A A Ramli R M and Kamari H M 2013 *Journal of Engineering Science* **9** 61–9
[7] Hodgson J N 1970 *Chapman and Hall Ltd.* 11 New Fetter Lane. London EC4.
[8] Abass K H 2015 Physical *Chemistry An Indian Journal* **10** 1 pp 19-24
[9] Urbach F 1953 *Phys. Rev*. **92** 1324
[10] Caglar M, Ilican S and Caglar Y 2009 *Thin Solid Films* **517** 5023-8
[11] WEMPLE S H and DIDOMENICO JR M 1969 *J. Appl. Phys*. **40** 2 720-34
[12] Mishjil K A Chiad S S Abass K H, and Habubi N F 2016 *Materials Focus* **5** 471–5
[13] Chiad S S Oboudi S F Toma Z A and Habubi N F 2013 *Atti Della Fondazionegiorgioronchi* **118** 5 689-98.
[14] Abass K H and Latif D M A 2016 *International Journal of Chem. Tech Research* **9** 9 332-8

Estimation of geometrical shapes of mass-formed nuclei (A=102-178) from the calculation of deformation parameters for two elements (*Sn* & *Yb*)

IOP Conf. Series: Journal of Physics: Conf. Series **1003** (2018) 012095 doi:10.1088/1742-6596/1003/1/012095

Estimation of geometrical shapes of mass-formed nuclei (A=102-178) from the calculation of deformation parameters for two elements (Sn & Yb)

Sameera A. Ebrahiem[1],Haider A. Zghaier[2]

[1]Department of PhysicsCollage of Education Ibn Al-HaithemUniversity of Baghdad

[1]Council of MinistersIraqi Radioactive Sources RegulatoryAuthority

Abstract. The present research focused on the studying of even- even nuclei forms for elements with mass numbers greater than 100 ($A > 100$) for ($^{102-134}_{50}Sn$&$^{152-178}_{70}Yb$) isotopes. Which included the study of deformation parameters (β_2) derived from the Reduced Electric Transition Probability $B(E2)\uparrow$ based on the energy of the first Excited State (2^+), and distortion parameter (δ) from Intrinsic Electric Quadrupole Moments (Q_0). Roots Mean Square Radii $< r^2 >^{1/2}$were also calculated and compared with theoretical values.The diversity of nuclei forms for selected isotopes and their differences was observed by plotting three-dimensional shapes (axially symmetric) in addition to drawing two-dimensional shapes of single element isotopes to distinguish between them by using semi-major (a) and semi minor (b) axes.

1.Introduction

The atomic nucleus mirrors condition is the protons and neutrons shell structure which are the formation of it with regard that the shells are totally filled, it has been discussed a "magic" ball-shaped nucleus. Most nucleuses may have an orientation for being deformed on the grounds that their shells are partially filled off. The most commonly experienced shapes are elongated (prolate) or prostrated (oblate) as shown in figure (1-1); shapes can change from nucleus to another respectively by aggregation or dislocating a proton or neutron. It is appropriate in some cases to rearrange protons or neutrons at the same nucleus so that the shape can be changed. Thus, nucleus selfsame can suppose several shapes alike different energy states. When the states approach in energy (one thousand of the nucleus's obligated energy), due to quantum mechanics laws, these various shapes can be mixed and nucleus may get along with different shapes.

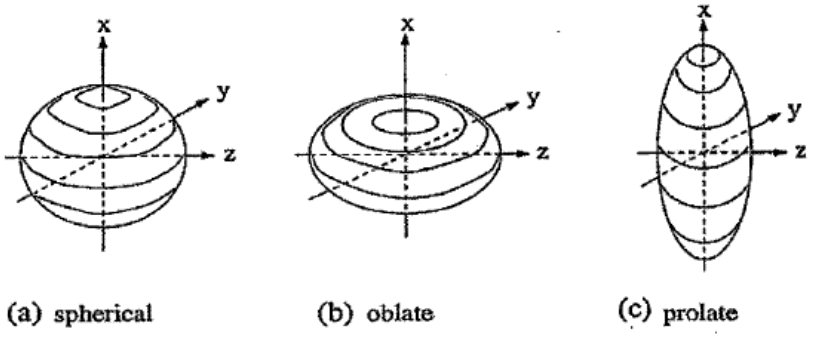

Figure (1.1). A diagrammatic representation of three of a nuclear shapes (a) Spherical, (b) Oblate, (c) Prolate. The x-axis donates to the symmetry axis of the oblate and prolate shapes.

2.Theoretical

2.1.Nuclear Shape

The nuclear shape is generally spherical when nuclei are stable. This attempt is to lower the surface energy. However, small parts from spheres are observed, such as, in the area $150 < A < 190$. These deformations can only be quantified by using the ratio[1]:

$$\boldsymbol{\delta = \frac{\Delta R}{R}} \qquad (\mathbf{1})$$

Where:
R = The nuclear radius average
ΔR = The difference between semi- minor and semi- major axes.

$$\boldsymbol{\Delta R = (b - a)} \qquad (\mathbf{2})$$

For a sphere $\Delta R = 0$.

2.2.Nuclear Surface Deformations:

The collective motion can be explained as nuclear surface vibrations and rotations in the geometrical collective model that was firstly suggested by Bohr and Mottelson [2], where a nucleus modeled like a charged liquid drop and the moving nuclear surface may be expressed quite generally by an extension in spherical consistent with time-dependent shape parameters that are considered as coefficients[3,4]:

$$\boldsymbol{R(\theta, \emptyset, t) = R_{av}[1 + \sum_{\lambda=0}^{\infty} \sum_{\mu=-\lambda}^{\lambda} \alpha_{\lambda\mu}(t) Y(\theta, \emptyset)]} \qquad (\mathbf{3})$$

Where:
$R(\theta, \phi, t)$: Indicates the nuclear radius in the direction $(\theta, \emptyset)$ at time t as shown in figure (1.2),
R_{av}: The average nucleus radius.
$\alpha_{\lambda\mu}$: Are the deformation variables.
λ: determines the multipole or mode of nuclear motion.
μ: is the projection of λ on the z-axis.
$Y(\theta, \emptyset)$: is the spherical harmonic.

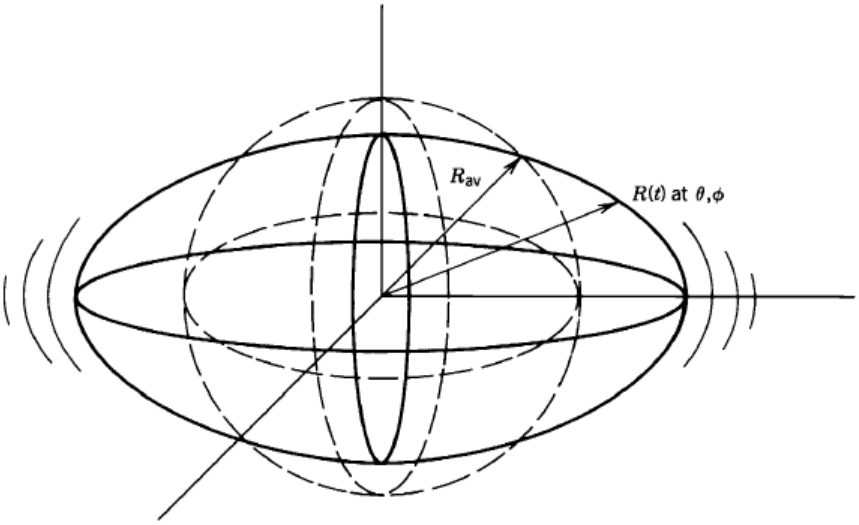

Figure (1.2). A vibrating nucleus with a spherical equilibrium shape. The time-dependent coordinate R(t) locates a point on the surface in the direction $(\theta, \emptyset)$[4].

The quadrupole deformation parameter β_2, is related to the spheroid axes [5]:

$$\boldsymbol{\beta_2 = \frac{4}{3}\sqrt{\frac{\pi}{5}}\frac{\Delta R}{R_{av}} = 1.06\frac{\Delta R}{R_{av}}} \quad (4)$$

Where:
The average radius $R_{av} = R_0 A^{1/3}$.
ΔR: The difference between both of the semi-major and minor axes. As long as the value of β_2 is larger, the nucleus becomes more disfigured.

2.3.The Root Mean Square Charge Radius (Isotopes Shift)
The root mean square (rms) nuclear charge radius $R = \langle r^2 \rangle^{1/2}$, with one another nuclear ground-state properties, is considered the key nuclear materials information which refer to stated nuclear structure effectiveness, for instance: shell closures and a deformation starting. [6].

The root mean square (rms) radius, $\langle r^2 \rangle^{1/2}$,is deduced directly from the distribution of scattered electrons; for a uniformly charged sphere, the squared charge distribution radius $\langle r^2 \rangle$ [8,4]:

$$\boldsymbol{\langle r^2 \rangle = \frac{3}{5}R^2 = \frac{3}{5}R_0^2 A^{2/3} > 100} \quad (5)$$

Where:
A: Mass number
R: is the radius of the sphere
A: Mass number
$R = R_0 A^{1/3}$.

2.4.Electric Quadrupole Moment
The charge allocation in a nucleus can be described in terms of electric multipole moments and pursued from the classical electrostatics thoughts [9]. Several nuclei have constant quadrupole

moments which may experimentally be measured. These nuclei are expected to have oval shape with a symmetrical axis. This proposition, has classically led to define the intrinsic quadrupole moment as the following equation [10]:

$$\boldsymbol{Q_0 = \int d^3\rho(r)\left(3z^2 - r^2\right)} \quad (6)$$

Where
$\rho(r)$: Radial charge density of the proton.
r: Charge radius.

If Q_0 is consider to be calculated for a homogeneously charged ellipsoid with charge Ze and semi-axes (a) and (b). With (b) pointing along the z axis, Q_0 will be[11]:

$$\boldsymbol{Q_0 = \frac{2}{5}Z\left(a^2 - b^2\right)} \quad (7)$$

If the deviation from sphericity is not very large, the average radius: $R = 1/2\ (a + b)$ and $\Delta R = (b - a)$from equation (2) can be presented and with $\delta = \Delta R/R$, from equation (1), the quadrupole moment is[11]:

$$\boldsymbol{Q_0 = \frac{4}{5}ZR^2\delta} \quad (8)$$

The nucleus quadrupole distortion parameter values δ calculated from the equation[12]:

$$\boldsymbol{\delta = 0.75\ Q_0/(Z\langle r^2\rangle)} \quad (9)$$

The semi-axes $(a)$and (b) are gained from the two following equations [13].

$$\boldsymbol{a = \sqrt{\langle r^2\rangle(1.66 - \frac{2\delta}{0.9})}} \quad (10)$$

$$\boldsymbol{b = \sqrt{5\langle r^2\rangle - 2a^2}} \quad (11)$$

2.5.Quadrupole Deformations
In general, nuclei with Z or N far from a magic number are deformed. The so-called quadrupole is the most ordinary deformations where the nucleus may have a prolate (rugby ball) or oblate (cushion) shape, as shown in 'figure 1'. A quadrupole deformation holds one symmetry axis (z axis) [14].

It is notorious that the axially symmetric deformed nucleus shape is explained by the deformation parameter (β_2) which is connected to the quadrupole moment (Q_0) and represents the homogeneous charge distribution [15,16]:

$$\boldsymbol{\beta_2 = \frac{\sqrt{5\pi}}{3}\frac{Q_0}{ZR_0^2}} \quad (12)$$

Where
(Z): The atomic number.
$R_0 = 1.2 \times A^{1/3}$ fm.
(β_2): The deformation parameter and $(\beta_2 < 1)$.

2.6.The reduced electric quadrupole transition probability $(\boldsymbol{E2})\uparrow$

Radioactive electromagnetic transformations between nuclear states are a perfect path to achieve nuclear structure and to experiment nuclear structure models [17]. $B(E2)$ Transmission play a definitive role to determine the lifetimes of nuclear states average, the nuclear deformation parameter β, the volume of essential electric quadrupole moments and the energy of low-lying nuclei levels. Great quadrupole moments and transmissions forces refer to the collective effects in which many nucleons can participate[18]. From here the reduced electric quadrupole transition likelihood, B(E2)↑, from the spin 0^+ ground state to the first excited spin 2^+ state is specified by[19]:

$$\boldsymbol{B(E2:0^+ \rightarrow 2^+) = \frac{5}{16\pi} e^2 Q_0^2} \quad (13)$$

Where

$B(E2)\uparrow$:reduced electric quadrupole transition probability in the unit of (e^2b^2)**.**

Q_0 : is intrinsic quadrupole momentin unit of barn (b)**.**

The $B(E2)\uparrow$ values are requisite experiential quantities that have no dependence on nuclear models. A quantity in which the model is thought to be depended on, is perfectly useful as it is the deformation parameter (β_2).. Presuming a uniform charge distribution out to the distance $R(\theta,\phi)$ and zero charge beyond, (β_2). is associated to $B(E2)\uparrow$ by the formulation [20]

$$\boldsymbol{\beta_2 = \left(4\pi / 3ZR_0^2\right)\left[B(E2)\uparrow / e^2\right]^{\frac{1}{2}}} \quad (14)$$

$$\boldsymbol{{R_0}^2 = \left(1.2 \times A^{\frac{1}{3}}\ fm\right)^2 = 0.0144A^{2/3}b} \quad (15)$$

In accordance with the global systematic, the energy acknowledgement E (KeV) of the 2^+ state is whole that is required of creating a prediction for the corresponding $B(E2)\uparrow(e^2b^2)$ value [18]:

$$\boldsymbol{B(E2)\uparrow = 2.6 \times E^{-1}Z^2A^{-\frac{2}{3}}} \quad (16)$$

3.Calculation and Results

3.1.Deformation Parameters$(\boldsymbol{\beta_2})$

Deformation Parameters(β_2) derived from Reduced Electric Transition Probability $B(E2)\uparrow$of even-even nucleus for the $(Sn\ \&\ Yb)$ isotopes were counted using the equation (14). this equation contains many Parameters must be obtained:

3.1.1.Reduced Electric Transition Probability $B(E2)\uparrow: 0^+ \rightarrow 2^+$ from the ground 0^+ to the first excited 2^+ states calculated by using equation (16). The energy $E(KeV)$ of the first excited state 2^+ was obtained from the reference (18).

3.1.2. Average Nuclear Radius R_0^2 *calculated using equation*(15).

3.2. The Deformation Parameters $(\boldsymbol{\delta})$

The other method for calculation of distortion parameter (δ) is by using the intrinsic quadrupole moments (Q_0) Equation (9). To evaluate this, the following variables must be available:

3.2.1.The Mean Square Charge Radius $\langle r^2 \rangle$ *which is obtained from equation (5) for* $A > 100$.

3.2.2Intrinsic Quadrupole Moments (Q_0)*of nuclei were calculated from the equation (13). These values were compared with the Predicted values of* Q_0 *for SSANM form reference[18].All these values were tabulated in tables* (1)*, and* (2).

3.3.The major axis (a) and minor axis (b) were counted by using Eq. (10) and (11) respectively. The deference ΔR *between (a) and (b) were counted also by using Eq. (1), (2), and (4) respectively. All these values are tabulated in the (3) and (4) tables.*

Table* 1.Isotopes Mass Number*$(\mathbf{A})$*, Neutron Number* $(\mathbf{N})$*, Gamma Energy of the First Excited State* $\mathbf{2_1^+(E_\gamma)}$*, Nuclear Average Radius (*$\mathbf{R_0^2}$*), Reduced Electric Transition Probability* $(\mathbf{B(E2)} \uparrow$ *in unit*

				Theoretical Value		***Present Work***				
(Z)	(A)	(N)	$E_\gamma(KeV)$	$B(E2)\uparrow$ (e^2b^2) *for* $(SSANM)$	β_2*for* $(SSANM)$ $(P.w.)$	R_0^2	$B(E2)\uparrow$ (e^2b^2)	$Q_\circ$ *(b)*	β_2	δ
	102	52	1472 *22*	0.051	0.0602	0.3144	0.2023	1.4260	0.1199	0.1080
	104	54	1260.1 *3*	0.116	0.0896	0.3185	0.2332	1.5313	0.1271	0.1145
	106	56	1207.7 *5*	0.195	0.1147	0.3225	0.2403	1.5543	0.1273	0.1147
	108	58	1206.07 *10*	0.281	0.1360	0.3266	0.2376	1.5457	0.1251	0.1127
	110	60	1211.89 *15*	0.361	0.1523	0.3306	0.2336	1.5325	0.1225	0.1104
	112	62	1256.85 *7*	0.407	0.1597	0.3346	0.2226	1.4959	0.1181	0.1064
	114	64	1299.92 *7*	0.406	0.1577	0.3386	0.2127	1.4622	0.1141	0.1028
	116	66	1293.560 *8*	0.394	0.1535	0.3425	0.2113	1.4573	0.1124	0.1013
50	118	68	1229.666 *16*	0.379	0.1489	0.3464	0.2197	1.4862	0.1134	0.1021
	120	70	1171.34 *19*	0.365	0.1445	0.3503	0.2281	1.5143	0.1142	0.1029
	122	72	1140.55 *3*	0.286	0.1265	0.3542	0.2317	1.5261	0.1138	0.1026
	124	74	1131.739 *17*	0.190	0.1020	0.3581	0.2310	1.5238	0.1124	0.1013
	126	76	1141.15 *4*	0.111	0.0771	0.3619	0.2266	1.5094	0.1102	0.0993
	128	78	1168.83 *4*	0.035	0.0527	0.3657	0.2190	1.4836	0.1072	0.0966
	130	80	1221.26 *5*	0.017	0.0296	0.3695	0.2074	1.4440	0.1032	0.0930
	132	82	4041.1 *4*	Sph	--------	0.3733	0.0620	0.7898	0.0559	0.0504
	134	84	725 *2*	0.060	0.0344	0.3771	0.3424	1.8553	0.1300	0.1171

Table 2. Isotopes Mass Number(A), Neutron Number (N), Gamma Energy of the First Excited State 2^+ (E_γ), Nuclear Average Radius (R_0^2), Reduced Electric Transition Probability $(B(E2)\uparrow$ in

				Theoretical Value		***Present Work***				
(Z)	(A)	(N)	$E_\gamma(KeV)$	$B(E2)\uparrow$ (e^2b^2) *for* $(SSANM)$	β_2*for* $(SSANM)$ $(P.w.)$	R_0^2	$B(E2)\uparrow$ (e^2b^2)	$Q_\circ$ *(b)*	β_2	δ
	152	82	1531.4 *5*	1.189	0.1591	0.4101	0.2921	1.7136	0.0789	0.0711
	154	84	821.3 *2*	1.972	0.2031	0.4137	0.5399	2.3298	0.1063	0.0958
70	156	86	536.4 *1*	2.566	0.2297	0.4173	0.8196	2.8704	0.1298	0.1170
	158	88	358.2 *1*	3.195	0.2542	0.4209	1.2169	3.7977	0.1569	0.1413
	160	90	243.1 *1*	3.609	0.2679	0.4244	1.7782	4.2280	0.1880	0.1694
	162	92	166.85 *4*	3.982	0.2790	0.4279	2.5694	5.0824	0.2241	0.2020

164	94	123.36 *4*	4.299	0.2876	0.4314	3.4469	5.8866	0.2575	0.2320
166	96	102.37 *3*	4.569	0.2941	0.4349	4.1203	6.4359	0.2793	0.2517
168	98	87.73 *1*	4.836	0.3001	0.4384	4.7696	6.9245	0.2981	0.2686
170	100	84.25474 *8*	5.097	0.3057	0.4419	4.9273	7.0381	0.3006	0.2709
172	102	78.7427 *5*	5.186	0.3060	0.4454	5.2313	7.2519	0.3073	0.2769
174	104	76.471 *1*	5.025	0.2989	0.4488	5.3453	7.3305	0.3083	0.2778
176	106	82.13 *2*	4.866	0.2919	0.4522	4.9392	7.0466	0.2941	0.2650
178	108	84 *3*	4.659	0.2835	0.4557	4.7930	6.9415	0.2875	0.2591

of e^2b^2, Quadrupole Moment (Q_o) in unit of barn, and Deformation Parameters (β_2, δ) for ($_{50}Sn$).

Table 3. Mass number (A), Neutron Number (N), Root Mean Square Radii $< r^2 >^{1/2}$, Major and minor axes(a,b) and the difference between them (Δ R) by two method for ($_{50}Sn$) Isotopes.

(Z)	(A)	(N)	***Theoretical Value***	***Present Work***				
			$\langle r^2\rangle^{1/2}$ *fm*	$\langle r^2\rangle^{1/2}$ *fm*	$a\ (fm)$	$b\ (fm)$	ΔR_1	ΔR_2	ΔR_3
	102	52		4.4503	2.5197	3.0908	0.5400	0.5711	0.6358
	104	54		4.4792	2.5151	3.1216	0.5761	0.6065	0.6784
	106	56		4.5077	2.5226	3.1323	0.5810	0.6097	0.6842
	108	58	4.5605	4.5359	2.5345	3.1355	0.5742	0.6010	0.6762
	110	60	4.5785	4.5637	2.5469	3.1377	0.5659	0.5907	0.6664
	112	62	4.5948	4.5912	2.5624	3.1343	0.5490	0.5719	0.6465
	114	64	4.6099	4.6183	2.5772	3.1318	0.5335	0.5546	0.6283
	116	66	4.6250	4.6452	2.5877	3.1358	0.5287	0.5481	0.6225
50	118	68	4.6393	4.6717	2.5934	3.1476	0.5361	0.5541	0.6313
	120	70	4.6519	4.6980	2.5991	3.1589	0.5431	0.5598	0.6396
	122	72	4.6634	4.7239	2.6070	3.1665	0.5444	0.5596	0.6411
	124	74	4.6735	4.7496	2.6166	3.1709	0.5406	0.5543	0.6366
	126	76	4.6833	4.7750	2.6277	3.1727	0.5327	0.5450	0.6273
	128	78	4.6921	4.8002	2.6401	3.1719	0.5208	0.5318	0.6133
	130	80	4.7019	4.8250	2.6541	3.1681	0.5043	0.5140	0.5938
	132	82	4.7093	4.8496	2.7459	3.0279	0.2744	0.2820	0.3231
	134	84		4.8740	2.6181	3.2651	0.6414	0.6470	0.7553

Table 4. Mass number (A), Neutron Number (N), Root Mean Square Radii $< r^2 >^{1/2}$, Major and minor axes(a,b) and the difference between them (Δ R) by two method for ($_{70}Yb$) Isotopes

(Z)	(A)	(N)	***Theoretical Value***	***Present Work***				
			$\langle r^2\rangle^{1/2}$ *fm*	$\langle r^2\rangle^{1/2}$ *fm*	$a\ (fm)$	$b\ (fm)$	ΔR_1	ΔR_2	ΔR_3
	152	82	5.0423	5.0831	2.7693	3.1745	0.4058	0.4051	0.4778
	154	84	5.0875	5.1053	2.7244	3.2683	0.5493	0.5439	0.6468
	156	86	5.1219	5.1274	2.6856	3.3483	0.6738	0.6627	0.7935
70	158	88	5.1498	5.1492	2.6391	3.4375	0.8176	0.7985	0.8628
	160	90	5.1781	5.1708	2.5829	3.5372	0.9842	0.9543	1.1589
	162	92	5.2054	5.1923	2.5146	3.6490	1.1782	1.1344	1.3874

164	94	5.2307	5.2135	2.4497	3.7505	1.3590	1.3008	1.6004
166	96	5.2525	5.2346	2.4077	3.8183	1.4799	1.4106	1.7426
168	98	5.2702	5.2556	2.3711	3.8773	1.5859	1.5062	1.8675
170	100	5.2853	5.2764	2.3702	3.8918	1.6055	1.5215	1.8906
172	102	5.2995	5.2970	2.3598	3.9176	1.6479	1.5578	1.9405
174	104	5.3108	5.3174	2.3622	3.9277	1.6593	1.5655	1.9540
176	106	5.3215	5.3377	2.3985	3.8965	1.5890	1.4980	1.8711
178	108		5.3579	2.4177	3.8858	1.5594	1.4681	1.8363

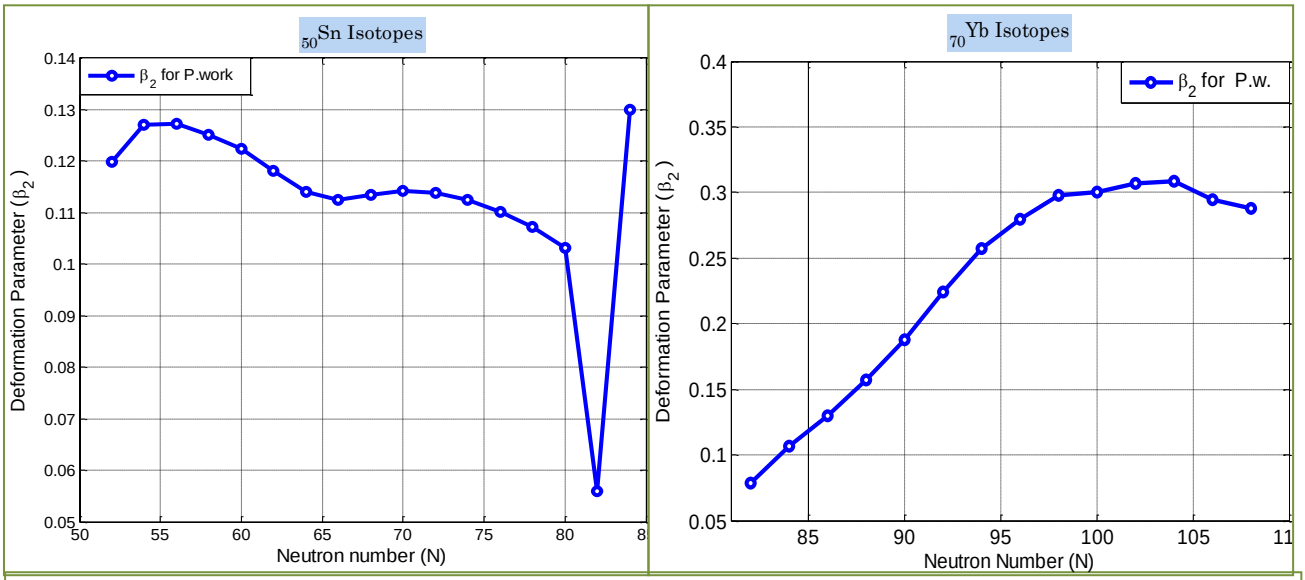

Figure 3. Deformation Parameter (β_2) values as a function of neutron Number (N)for the ($_{50}$Sn) and ($_{70}$Yb) Isotopes.

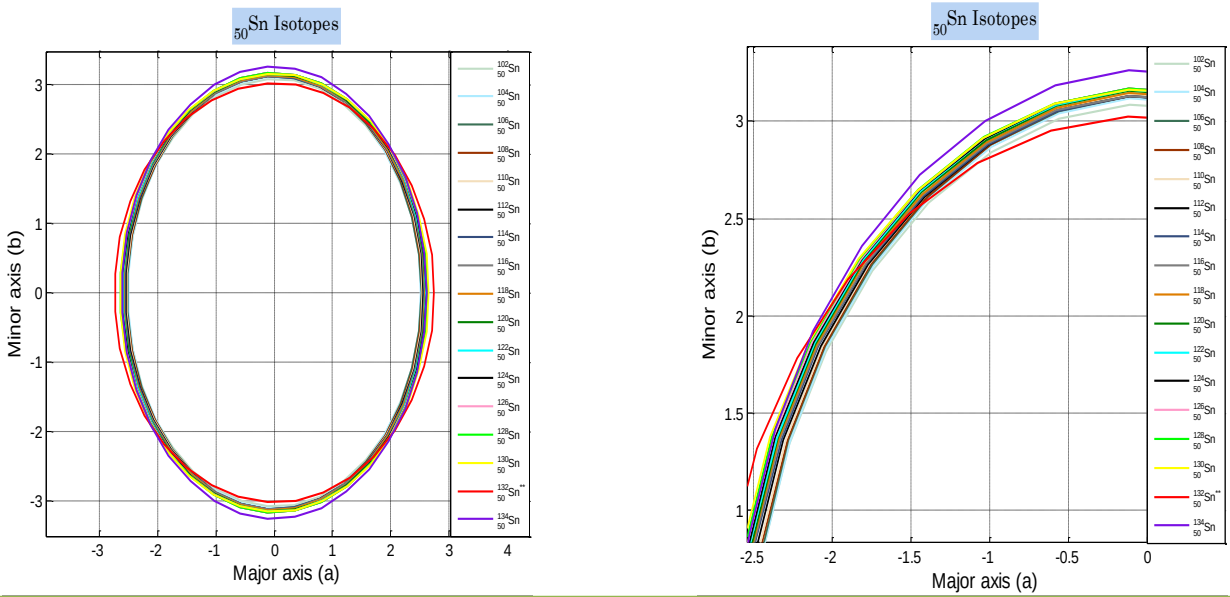

Figure 4. Shapes of axially symmetric quadrupole deformation for $_{50}Sn$isotope from major (a) and minor (b) axes.

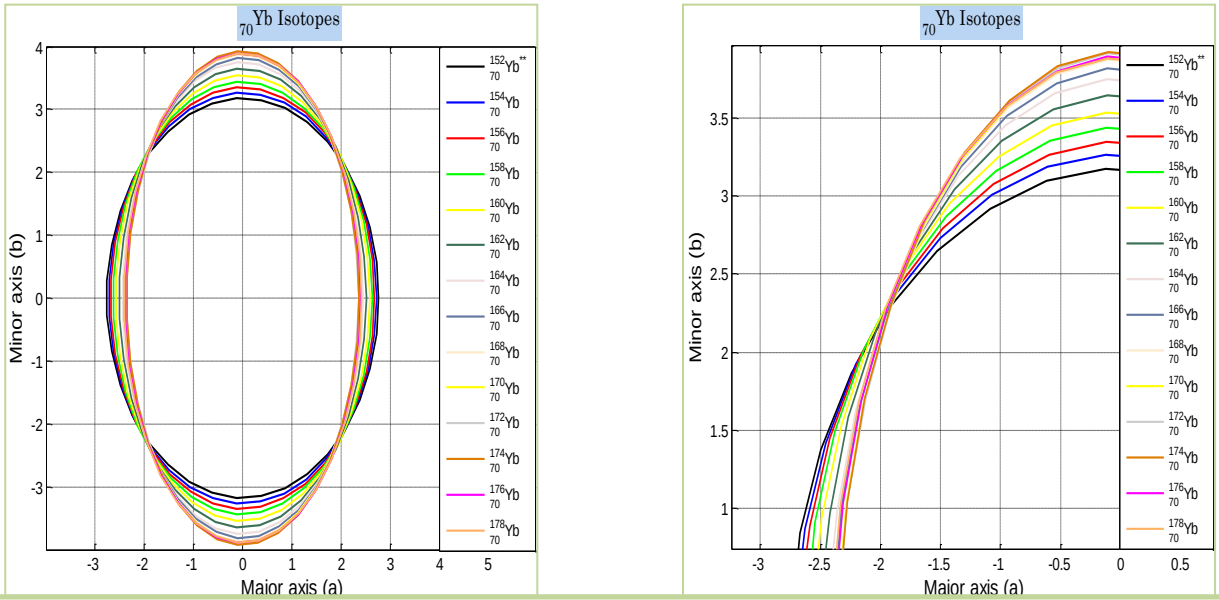

Figure 5. Shapes of axially symmetric quadrupole deformation for $_{70}Dy$isotope from major (a) and minor (b) axes.

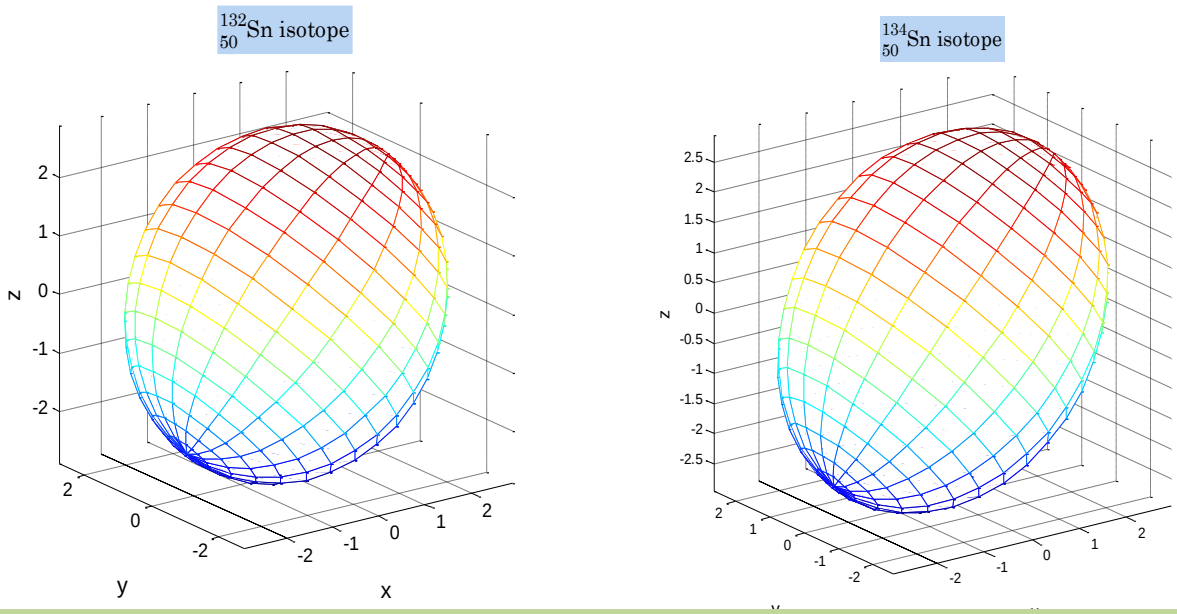

Figure 6.3-D Shapes of axially symmetric quadrupole deformation for $_{50}Sn$isotope from major (a) and minor (b) axes.

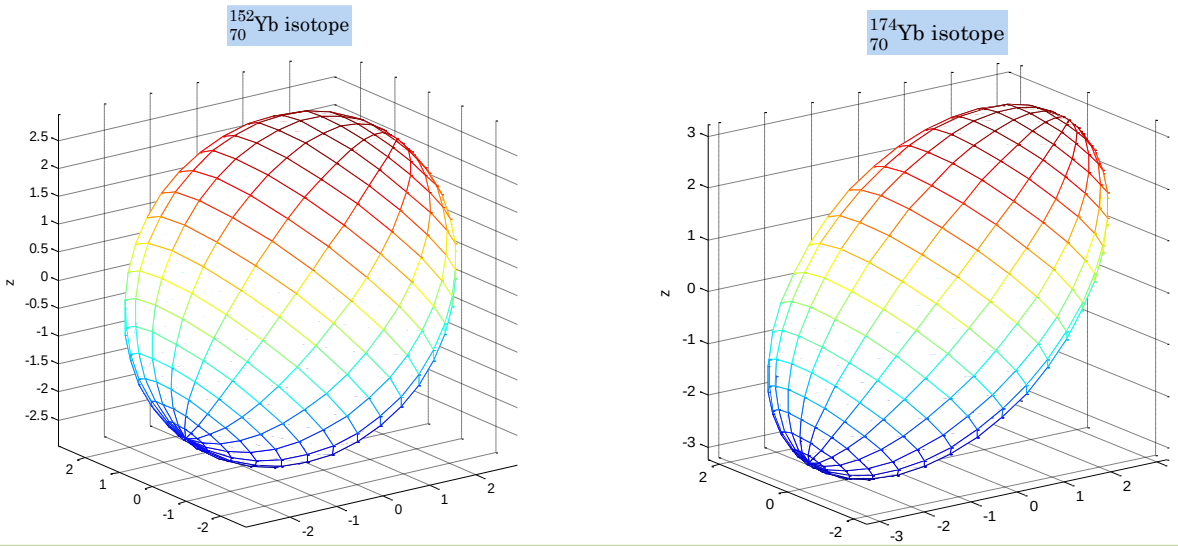

Figure 7.3-D Shapes of axially symmetric quadrupole deformation for $_{70}Yb$isotope from major (a) and minor (b) axes.

4.Discussion

From observation the values of the electric quadrupole moments $B(E2)\uparrow$ of selected elements, tables (1-1) &(1-2), we found that these values vary according to their mass numbers (number of protons and

neutrons), and when we approaching to the magic numbers of protons and/or neutrons, the values of $B(E2)\uparrow$ become less than those of the other isotopes of the same element, in other words the values of deformation (β_2) become as low as possible and, therefore, this isotope with magic numbers is more stable than others.

On the other hand, we also found when the mass numbers are less than 150 $(A < 150)$, the values of intrinsic quadrupole moments are seems to be less than those of with mass number between 150 and $180(150 < A < 180)$, this is belonged to collective behavior (vibrational and rotational) of nucleons.

Also in the even-even nuclei that appear collective behavior. The energy of the first excited state (2^+) appears to be decrease sort of smoothly as a function of A(except the regions near closed shells).

From observable values of the root mean square charge radii$\langle r^2\rangle^{1/2}$, table (1.3) to (1.4), we found that these values increased as the mass number A increasing. For comparison purposes, it was found that the calculated values of $\langle r^2\rangle^{1/2}$ (P.w.) correspond well to the experimental values of $\langle r^2\rangle^{1/2}$ from references [].

What has been mentioned above can be explained in detail in the following paragraphs.

4-1 Strontium Isotopes $^{102-134}_{50}\boldsymbol{Sn}$

Clearly from table $(1-1)$, that the lowest value of the deformation Parameter is for the ($^{132}_{50}$Sn) equal to $(\beta_2 = 0.0559)$and the largest value of deformation parameteris for ($^{134}_{50}$Sn) $(\beta_2 = 0.1300)$. The remaining values of β_2 are ranging between these two values. This is due to the fact that the nucleus of the ($^{182}_{50}$Sn) is one of the nucleus with double magic numbers$(Z = 50, N = 82)$, and therefore this nucleus is more stable than others. Furthermore, the energy level of the first excited state 2^+ is very high $(E_\gamma = 4041.1$ KeV), (the gap is large between the ground and the first excited states, thus the hardness of transfer nucleons between these two states), compared with the energy levels of the same states for others. This means that the nucleus of $^{132}_{50}$Sn isotope has closed shall, spherically Symmetric, and be especially stable.

More nucleons are added outside the closed shell in the($^{134}_{50}$Sn) isotope and the energy level of the first excited state 2^+ is$(E_\gamma = 725$ KeV). All these factors are encouraging the small deformation of this nuclide.

These results are confirmed in Figure (1-3), which shows the relationship between deformation parameters (β_2) as a function of neutrons numbers (N). It is clear that the distortion of nuclides decreases as neutron numbers close to the magic number of (82). Then the value of (β_2) begins to increase thereafter as the (N) increased, which mean increase of nucleons outside closed shell.

Generally speaking all nuclide of the isotopes of ($_{50}$Sn)show a small deviation from the spherical shape, with the exception of the isotope($^{132}_{50}$Sn) as shown in the 'figure 4'. Also 'figure 6' show the 3-D shapes of the smallest and highest values of deformation Parameter of $_{50}$Sn Isotopes

4-2 Ytterbium Isotopes $^{152-178}_{70}\boldsymbol{Yb}$

From observable table 2 , we find that it starts with $^{152}_{70}Yb$, where the number of neutrons represent a magic number $(N = 82)$ and the number of protons $(Z = 70)$, The energy of the first excited state 2^+ $(E_\gamma = 1531.4$ KeV) (the gap is large between the ground and the first excited states, thus the hardness of transfer nucleons between these two states), So that the reduced electric transmission probability $B(E2)\uparrow$ is low and therefore the β_2 will be at its minimum value$(\beta_2 = 0.0789)$, this will lead that the nuclide of this isotope is more stable, almost spherical and the most tightly bound shape.

From same table, values of (β_2)will increase with increase(N) until reach to the confined area between $(92 \le N \le 108)$, deformation values are approximately equal and ranging from $(\beta_2 = 0.2241)$ with $(E_\gamma = 166.85$ KeV) for $^{162}_{70}Yb$to $(\beta_2 = 0.2875)$ with $(E_\gamma = 84$ KeV)for $^{178}_{70}Yb$.

the maximum value of $(\beta_2 = 0.3083)$ for $(^{162}_{70}Yb)$, this is due to the low energy value of the first excited state $(E_\gamma = 76\ \text{KeV})$ which is in turn leads to maximum value of $B(E2)\uparrow$ and then the highest value of deformation. This seems to be clear in the 'figure 3' which shows the relationship between $\beta_2$as a function of the neutrons number (N). As a result, these nuclei will be less stable, non-spherical shape and will be more elongated.

On the other hand from observable table 2 we find the distortion values (δ) derived from Q_0, become as low as possible because it started with magic number $(N = 82)$ and the values of the intrinsic electric quadrupole moment become on its minimum value. When add more nucleons in the shell or sub-shell outside close shell this will lead to restrict the vibrations of wholly or partially to one direction (polarization the core), and the nucleus can get a permanent deformation.

'Figure 5' shows the differences between these values of deformation Parameters (β_2) based on the values of major and minor axes (a, b) respectively. Also 'figure 7' show the 3-D shapes of the smallest and highest values of deformation Parameter of $_{70}$Yb Isotopes.

References

[1]. SAMUEL S.M. WONG, "Introductory Nuclear Physics", Second Edition, ©2004 WILEY-VCH VerlagGmbII& Co. KGaA, Weinheim.

[2]. A. Bohr and B. R. Mottelson, "Nuclear structure, Vol.II, Nuclear Deformations", copyright ©1998 by World Scientific Publishing Co. Pte. Ltd.

[3]. A. Al-Sayed and A. Y. Abul-Magd," Level statistics of deformed even-even nuclei", DOI: 10.1103/*PhysRevC*.**74**.037301(2006).

[4]. Kenneth S. Krane, "Introductory Nuclear Physics", copyright © 1988, by Joun Willey &Sons, Inc.

[5]. R.R.Roy and B.P. Nigam, "Nuclear Physics Theory and Experiment", copyright©1967 By John Wiley & Sons, INC

[6]. W. Greiner· J. A. Maruhn,"Nuclear Models" © Springer- Verlag Berlin Heidelberg 1996.

[7]. Neugart R. and Neyens G." Nuclear Moments" Department of Physics, University of Mainz, Germany (2005).

[8]. Boboshin I., Ishkhanov B., Komarov S., Orlin V., Peskov N., and Varlamov V., "Investigation of Quadrupole Deformation of Nucleus and its Surface Dynamic Vibrations" International Conference on Nuclear Data for Science and Technology.DOI: 10.1051/ndata:07103 P.65-68 (2007).

[9]. Gerda Neyens,"Nuclear magnetic and quadrupole moments for nuclear structure research on exotic nuclei" Rep. Prog. Phys. 66 (2003) 633–689 © 2003 IOP Publishing *Ltd. Printed in the UK*.

[10]. S. Mohammadi,"Quadrupole Moment Calculation of Deformed Nuclei",Journal of Physics: Conference Series 381 (2012) 012129. doi:10.1088/1742-6596/381/1/012129.

[11].Ernest M Henley and Alejandro Garcia, "SUBATOMIC PHYSICS (3rd Edition)", Copyright © 2007 by World Scientific Publishing Co. *Pte. Ltd.*

[12].I.Boboshin, B. Ishkhanov, and S. Komarov, "Investigation of quadrupole deformation of nucleus and its surface dynamic vibrations", *International Conference on Nuclear Data for Science and Technology*,©2008 CEA, published by EDP Sciences.

[13]. Ali AbdulwahabRidha,"Deformation parameters and nuclear radius of Zirconium (Zr) isotopes using the Deformed Shell Model", *Wasit Journal for Science & Medicine* 2009 **2** (1) : (115 - 125).

[14].Jean-Louis Basdevant, James Rich & Michel Spiro, "Fundamentals in Nuclear Physics, from Nuclear Structure to Cosmology", ©2005 Springer Science+Business Media, Inc.

[15]. F. Ertugrala, E. Guliyev, and A.A. Kuliev," Quadrupole Moments and Deformation Parameters of the $^{166\text{-}180}$Hf, $^{180\text{-}186}$W and $^{152\text{-}168}$Sm Isotopes", DOI: 10.12693/APhysPolA.128.B-254, ACTA PHYSICA POLONICA A, (2015).

[16]. J. Margraf, R.D. Heil, U. Kneissl, and U. Maier, "Deformation dependence of low lying M1strengths in even isotopes", PHYSICAL REVIE%' C VOLUME 47, NUMBER 4 APRIL 1993.
[17] A. Bohr and B. R. Mottelson, "Nuclear Structure, Volume II: Nuclear Deformations", (World Scientific, Singapore, 1998).
[18].S. Raman, C. W. Nestor, and P. Tikkanen, At. Data Nucl. Data Tables 78, 1 (2001).
[19]. M. Haberichter,P. H. C. Lau, and N. S. Manton, "Electromagnetic Transition Strengths for Light Nuclei in the Skyrme model", Kent Academic Repository, (2015).
[20].Subramanian Raman, "A Tale of Two Compilations: Quadrupole Deformations and Internal Conversion Coefficients", *Journal of Nuclear Science and Technology*, **39**: sup2, (2002), 450-454, DOI: 10.1080/00223131. 2002.10875137.

The Effect of Oxygen Flow on the Transition Temperature of Hg0.75Pb0.25Sr2-yBayCa2Cu3O8+ δ Superconductors

The Effect of Oxygen Flow on the Transition Temperature of Hg0.75Pb0.25Sr2-yBayCa2Cu3O8+ δ Superconductors

Kareem A Jasim, Raghad S Al-Khafaji

Department of Physics, College of Education for Pure Sciences/ bn- Al-Haithem, University of Baghdad, Baghdad,Iraq

raghadsubhiabbas@yahoo.com

Abstract. In this paper, there are three different high temperature superconductors which are Hg0.75Pb0.25Sr2-y BayCa2Cu3O8+δ with deferent weight fractions y = 0.10, 0.20 and 0.25 that have been prepared successfully by solid state reaction and the samples have been equipped with/without O2 flow. The optimum calcinations is 1073 K and the sintering process that has been achieved within 1128-1133 K. Transition temperature Tc has been found by using four probe technique through electrical resistivity measurements. The greatest Tc that has been found for Hg0.75Pb0.25Sr1.75 Ba0.25Ca2Cu3O8.31 is 115 oK. Oxygen content (O2) flow exhibits high-phased superconductors that is similar to the samples prepared without O2. Investigation of X-ray diffraction (XRD) is revealed (tetragonal structure) by the c-axis lattice parameter increasing of the samples substituted with Ba. It has been established, from the calculated results, that the Ba variation concentrations of all samples products a modification in the density (ρm), (c/a) and volume fraction (VPh(2223)).

1. Introduction

Many magnificent attempts have been achieved recently to develop the constancy of the Hg-1223 phase. Much efforts have been practiced in the production of Hg-Base high Temperature Superconductor (HTSC) phases manner, because of their sensitivity excess towards polluting from humidity and carbon dioxide. HgBa2Ca (n-1)CunO2n+2+δ phases synthesize is not so stable as the other HTSC phases of cuprate oxide group [1-3]. The majority effective method to advance the stability of the Hg-1223 phase is doing appropriate cationic exchange for Hg, which has oxidation states upper than that of Hg+2. Various substituted cationic like, Tl+3, Sn+4, Bi+3, Pb+4, Mo+4, 5, Re+4, etc have made an effort [4-7]. The effect of this cationic replacements on the superconducting possessions are different. Furthermore, they lead to superior chemical stability [8, 9]. By (Ba) substituting to the (Sr) lesser cation in Hg0.8Tl0.2Ba2Ca2Cu3O8+ δ which supply reservoir clog conduct to reduce the reaching between the superconductivity CuO2 blocks, that may improve the interlayer pair strength and cause a modification to irreversible line to higher fields [10,11]. They gain extra oxygen in the oxygen lacking HgO δ layer

conducting to phase stability. In this paper, it has been substituted the Ba at the Sr site in the oxygen deficient Sr-O layer of Hg0,75Pb0.25Sr2Ca2Cu3O8+ δ superconductor, which is synthesized by solid state reaction technique.

2. Experimental Setup

The synthesis of $Hg_{0.75}Pb_{0.25}Sr_{2-y}Ba_yCa_2Cu_3O_{8+\delta}$ HTSC phases (y = 0.10, 0.20 and 0.25) have been composed in a solid state reaction technique by three steps, suitable weights of started material (99.998% from May & Baker LTD Dagenham England). Each reaction that has been weighted of, HgO, Pb_2O_3, $SrNO_3$, $BaCO_3$, $CaCO_3$ and CuO as powders by utilizing a sensitive balance. The powders of ($BaCO_3$, $SrNO_3$, $CaCO_3$ and CuO), in the first stage are mixed collectively by utilizing agate mortar, the procedure of crushing take about (30-50) minute to homogeneous. Then, product mixture that is dehydrated by an oven at 473 ^oK. The mixture is placed in (programmable tube furnace) and exposed to 1073 ^oK temperature for about three hours with a rate of 473 ^oK/hr, then exposed to room temperature (RT) ambient by the similar heating amount of calcinations. This process is achieved to eliminate NO_3 and CO_2 gas from the prepared mixture.

The Sr2-yBayCa2Cu3O7 precursor of the second step is mixed with HgO and Pb2O3 to get the insignificant compositions Hg0.75Pb0.25Sr2-yBayCa2Cu3O8+δ. After that, powders is pressed into disc-designed pellets of (1.3 cm) diameter, and (0.2-0.3 cm) thickness, employing hydraulic press of type (Specac) underneath a pressure of 8 ton/cm2. The acquired pellets are presintered in air ambience with a rate of 473 oK/hr for twenty hours at 1128-1133 oK, then cooled down to RT by similar heating proportion.

The final step, pellets are re-pulverized, re-pressed and re-sintered in air and oxygen (oxygen rate 0.6 L/min) at the equivalent range of temperature for (24 hours) and then cooled at 773 oK, after that is annealed under oxygen for (4 hours) and then exposed to cool at room temperature by similar rate of heating. The examination of the (resistivity corresponding temperature), the excess of oxygen δ (O2) Δ (O2), in addition to measured transition temp. Tc, lattice paramètres (a, b, c and c/a) and mass density ρM have been described eleswhere [12-14]. The prepared specimens structure is identified by utilizing (X-ray diffractometer (XRD) - Philips) which have the following specifications, the source of Cukα, current of (20 mA), voltage of (40 KV) and wave length (1.5405 A0).

3. Results and discussion

The quality diffusion coefficient of oxygen has been carefully determined which is critical grandness in optimizing the amply dense of polycrystalline samples [15-18]. 'Figure1' shows the resistivity as function of temperature for all $Hg_{0.75}Pb_{0.25}Sr_{2-y}Ba_yCa_2Cu_3O_{8+\delta}$ samples prepared with or without oxygen treatments. The samples with oxygen treatments demonstrated a good high temperature superconductor while the samples that are without oxygen given lower T_c, because T_c increases with the increasing of δ [19, 20]. The zero-resistivity critical temperature $T_{c(offset)}$ increases systematically with increasing in concentration of Sr**.** The results of transition temperature $T_{c(offset)}$ for gaining $Hg_{0.75}Pb_{0.25}Sr_{1.9}Ba_{0.1}Ca_2Cu_3O_{8.141}$, $Hg_{0.75}Pb_{0.25}Sr_{1.8}Ba_{0.2}Ca_2Cu_3O_{8.191}$, $Hg_{0.75}Pb_{0.25}Sr_{1.75}Ba_{0.25}Ca_2Cu_3O_{8..310}$, phases are 95, 98 and 117 ^oK, respectively. The data of T_{c1} without O_2 flow and T_{c2} with flow of O_2 are enumerated in the (table 1).

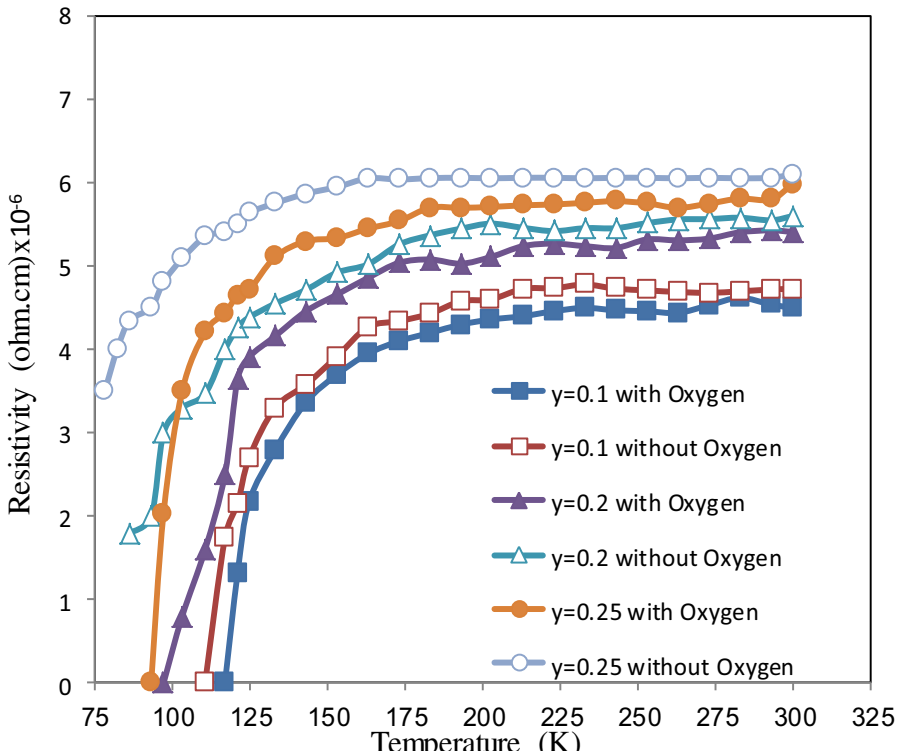

Figure 1. Dependence of temperature with resistivity for $Hg_{0.75}Pb_{0.25}Sr_{2-y}Ba_yCa_2Cu_3O_{8+\delta}$ at indicated values of y (y = 0.10, y = 0.20, y = 0.25).

Employing of flow rate with oxygen higher than 0.3 L/min produces deformed samples. Which is assigned the dropping of melting point, as indicated by Koyama et al. [18]. The oxygen stoichiometry Bi-based and Hg-based superconductors of δ=0 are unbalanced [19], but the structure can be stabilized by interpolating of extra oxygen, which will produce greater cavities in the CuO_2 layers. The increasing of the cavities concentrations in the high-T_c phase will conduct the development of the T_{c1} and T_{c2} [21, 22]. In this work all the synthesized samples are applied to whole structural identifications via X-ray diffraction. The resulted data of XRD for samples having various Ba concentrations are entirely polycrystalline and agree to Hg (Pb)-1223 phases. The results of XRD also show some impureness phases by tiny concentrations. The illustration XRD pattern is revealed in ‘figure 2’.

Table 1. Tc1 without oxygen flow, Tc2 with oxygen flow, oxygen content, δ(O2) with O2 flow, Δ(O2) without O2 flow, lattice parameters (a, b, and c) and mass density ρM for diffèrent composition of Hg0.75Pb0.25Sr2-yBayCa2Cu3O8+δ

y	Tc_1(°K)	Tc_2(°K)	$\delta(O_2)$	$\Delta(O_2)$	$a(A^0)$	$b(A^0)$	$c(A^0)$	c/a	ρ_M (g/cm^3)
0.10	-----	95	0.141	0.071	3.829	3.829	15.41	4.0245	5.7547
0.20	-----	98	0.191	0.086	3.830	3.831	15.43	4.0287	5.7617
0.25	103	117	0.310	0.207	3.833	3.834	15.44	4.0281	5.8041

Obviously, It can be noticed through the XRD spectra that there are two essential phases in all production specimens of high Tc phase (1223), low Tc phase (1212) and a little amount of impureness phases of (Ca, Sr)$_2$CuO$_3$, CaPbO$_4$ and CuO. The presence of other than two phases can be related to the (stacking faults) along the c-axis. In all samples of $Hg_{0.75}Pb_{0.25}Sr_{2-y}Ba_yCa_2Cu_3O_{8+\delta}$ systems, the high phases augmented by Ba increasing. It has been observed that many following reflections that are ordering the cations and/or displacing of an ion or oxygen defects (the oxygen deficiency increases when Ba is replaced by Sr which has lesser ionic radius compared to Ba). This is similar to the result of a heterogeneous structure which causes the deformation of the c-parameter rising. The distortion of the structure is always reflected as the cause of the great conduction in the perovskite multi-layer state which proposes rising to several type of polarization at sufficient high-Tc, this polarization will allow holes or electrons to move along distance without undergoing scattering progression.

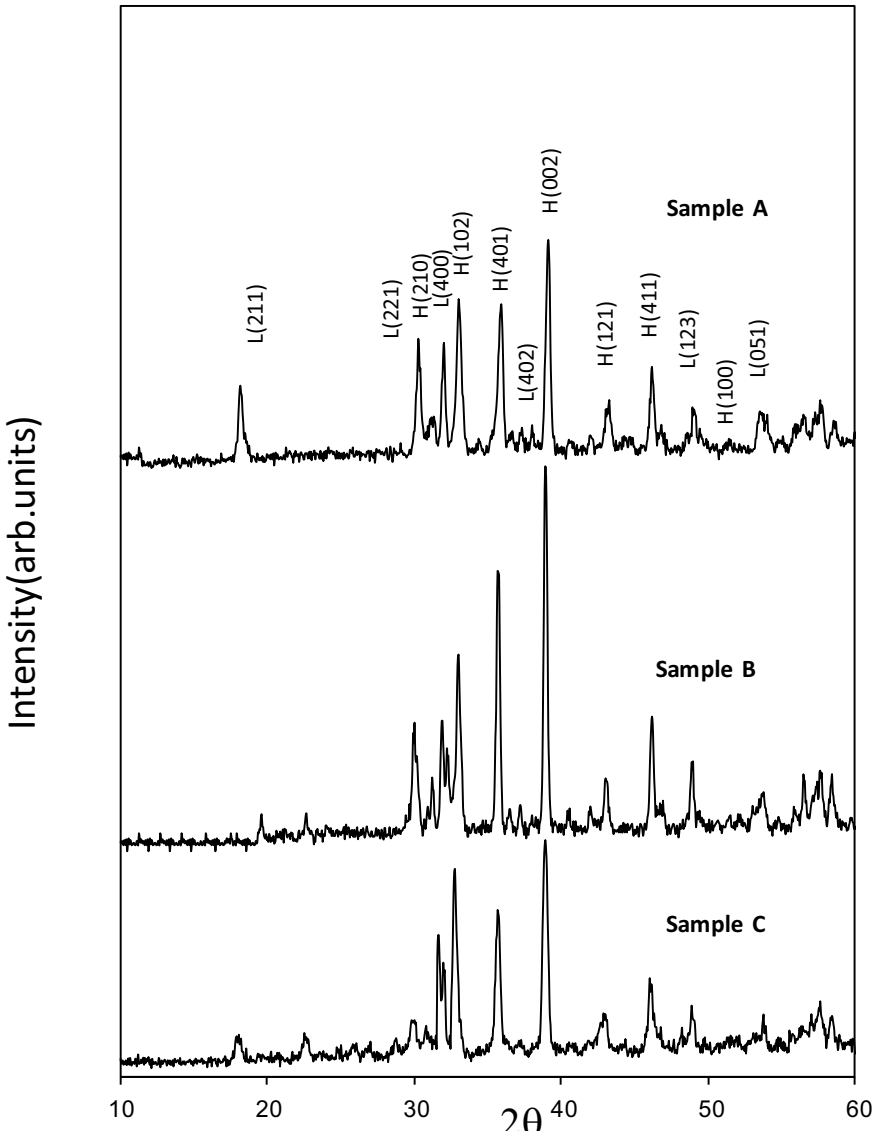

Figure 2. XRD data collected from various samples for Hg0.75Pb0.25Sr2-yBayCa2Cu3O8+ δ at indicated y (a: y = 0.10, b: y = 0.20, c: y = 0.25)

Utilization the software which is established on (Cohen,s least square procedure [13]), the parametric of lattice which has been computed through d-values and (hkl) reflections of the detected X-ray diffraction design, and the obtained values are arranged at the (table 1).

4. Conclusions

$Hg_{0.75}Pb_{0.25}Sr_{2-y}Ba_yCa_2Cu_3O_{8+\delta}$ high-Tc superconducting compounds (y = 0.10, 0.20 and 0.25) without/with oxygen treatment, have been synthesized by utilizing three-steps of solid state reaction technique successfully. Special significant of correlation between superconducting characterizations and the observed microstructural has been investigated by way of effect the coincident doping of Ba at Sr site for Sr-O_2 layer

in $Hg_{0.75}Pb_{0.25}Sr_2Ca_2Cu_3O_{8+\delta}$ .The results of XRD data conducted from various composed samples show that they are wholly polycrystalline and agree to Hg(Pb)-1223 phase. Critical transition temperature Tc (0ffset) of the Sr doped Hg (Pb)-1223 compounds range between 93- 115 ^oK. Obtained results are yelled T_c increasing with the increases of δ (oxygen content). Furthermore the change of Ba concentrations for all composed samples gives a modification in the density ρ_m, c/a and volume fraction $V_{Ph(2223)}$.

References

[1] Putilin S N, Antipov E V, Chmaissem O and Marezio M, 1993 *Nature* **362** p 226
[2] Runde M 1992 *Phys. Rev. B*. **45** p 7375
[3] Breitzke H, Eremin I, Manske D, Antipov EV and Leuders K 2004 *Physica* **C 406** pp 27–36
[4] Jin H, Zhao WC, Lou FM, Zhang K, Ruan KQ, Wang CY, Liu Q M, Cao L Z, Zhang YH, Chen Z J and Hu Z Q 1997 *Physica **C*** **843** pp 282–287
[5] Kareem A J and Raghad S Al-Khafaji 2017 *Journal of Applied and Physical Sciences* **3** pp 26-31
[6] Kreem A J 2012 *Turk J Phys* **36** pp 245 – 251
[7] Rajiv G, Verma G D, Tiwari R S and Srivastava O N 2001 *Bull. Mater. Sci* **24** pp 523–528
[8] Rajiv G, Verma G D, Tiwari R S and Srivastava O N 2003 *Cryst. Res. Technol* **38** pp 760 – 766
[9] Dinesh V, Singh R K and Sanjay S 1997 *Indian Journal of Engineering & Materials Sciences* **4** pp 225-231
[10] Pickett W E *Iranian Journal of Physics Research* **6** 11
[11] Yusuke S, Takato K, Satoshi H and Ken I 2015 *IEEE Transaction on Applied Superconductivity* **25** p 2323
[12] Kareem A J 2012 *Journal of superconductivity and novel magnetism* **25**
[13] Kreem A J and Alwan T J 2009 *Journal of Superconductivity and Novel Magnetism* **22** 8
[14] Kreem A J, Alwan T, H. K. Al-Lamy and Mansour H L 2011 *Journal of superconductivity and novel magnetism* **24**
[15] Kreem A J 2008 *Ibn Al-Haitham Journal pure and applied sciences* **21**
[16] Pandey A K, Verma G D and Srivastava O N 1998 *Physica* **C 306** pp 47-57
[17] Ferguson I F and Rogerson A H 1984 *Comput. Phys. Commun* **32** 95
[18] Koyoma S, Endo U, Kawai T 1989 *Advances in superconductivity* **833**
[19] Khaled J, Komatsu T and Sato R 1997 *J ceramic socity of Jap* **105** 279
[20] Matsumoto A and Kitaguchi H 2014 *Supercond. Sci. Technol* **27**
[21] Xing G, Wang M, Fan X and Tang X 1993 *Appl. Phys*. **A56** 99
[22] Yusuke S, Takato K, Satoshi H and Ken 2015 *IEEE Transaction on Applied Superconductivity* **253**

La+3 effectiveness replacement on the ferrite material ($Cu_{0,2}Zn_{0,45}La_xFe_{2-x}O_4$) On the structural and electrical and magnetic features

La+3 effectiveness replacement on the ferrite material $(Cu_{0,2}Zn_{0,45}La_xFe_{2-x}O_4)$ On the structural and electrical and magnetic features

Farouq I Hussain, Rusul Alaa Najem

Baghdad University-Physics Department ,College of Education for pure science – Ibn Al-Haitham

Abstract. Nano ferrite with chemical formula ($Ni_{0.35}Cu_{0.2}Zn_{0.45}La_xFe_{2-x}O_4$) , were chemically collected utilizing sol-gel auto – combustion procedure for the values of (X=0.0, 0.025, 0.05 and 0.075). The prepared samples were calcined at ($900°C$) for (2h), the formation of ferrite was assured using (XRD) and (SEM) techniques. X-ray diffractometer result shows that ferrite have spinal cubic phase with a particle size ranging from (22-29 nm),the Lattice constant and density (ρx-ray) increased with La+3content while the porosity was noticed to decrease. And have been studied dielectric properties It was also observed that the value of the dielectric constant and the dielectric loss factor decreased by increasing the frequency. The increase in alternating conductivity (σa.c) was also observed with increasing frequency.

1. Introduction

Rare-earth-materials have good dielectric characteristics with high electrical resistivity. Thus, these rare earth ions replacement into spinel ferrites may modify the magnetic and electrical features and also have big influential on the magnetic disparity system creating the spinel ferrite as favorable materials that can be replaced into the Hexa-ferrite or garnets [1,2]. Ferrites electrical properties depend on the micro-structure, chemical combination and assembly technique [3]. Lanthanum is considered the second lightest rare earth element in the lanthanide chain. It is silvery white color metal and can be found in monazite and bastnasite ores. This element has special quality comparing with other (REE), like being simple electronic spectrum which is beneficial for experiential analysis since it has the lowest vapor pressure and highest boiling point at its fusion point; and at atmospherically pressure lanthanum is considered the only superconducting among other (REE) [4]. Different procedures were used so as to synthesize the soft spinel ferrite materials (e.g. chemical co-precipitation [5], hydrothermal [6], mechano-chemical [7], micro emulsion [5], rheological phase reaction [8], and also sol-gel [9].

2. Experimental

2.1 Materials and Synthesis:

The Nano-ferrites of the composition ($Ni_{0.35}Cu_{0.2}Zn_{0.45}\ LaxFe_{2-x}O_4$) were (X equals 0.0, 0.025, 0.05 & 0.075) that prepared using sol-gel-auto-combustion technique by below mentioned raw materials. In order to prepare (Ni0.35 Cu0.2Zn0. 45)Lax Fe2−xO4 ferrite with x = 0.0, 0.025, 0.05 and 0.075 compositions, it was used analytical stage for: [Ni(NO3)2•6H2O], [Zn(NO3)2•6H2O],

[Cu(NO3)2•3H2O], [Fe(NO3)3•9H2O], [C6H8O7•H2O] and [La(NO3)3]. It was solved citric acid and metal nitrates in deionized water, all these are collected in glass beaker and mixed well at room temperatures by hot plate magnetic stirrers with high speed, Ammonia solution was added slowly the form of drops into the mixed solution to control its pH until reach threats from 7 with continuous rotation. Gradually increase in temperature to reaches of 80˚C in order to turn it into a gel then was burnt in a self-propagating ignition way to get a formation of a feathery movable powder the as-burnt predecessor powder was later calcined at (900 °C) for 4 hours after that it was pressed using a die with (1.5cm) diameter to make specimens in a pellet shapes. The pressing load used was (7ton/cm2) and the specimens held for 2min. under pressure using a hydraulic press of a maximum load (15) ton.

2.2 Characterization:

The structural characterization of the prepared nano ferrites was performed by X-ray diffraction analysis and Scanning Electron microscopic analysis and EDX technique. XRD analysis confirms the phase formation and SEM analysis reveals the structural morphology. Nano-ferrites dielectric features were deliberated by LCR meter range of 50 KHz to 1MHz. Dielectric parameters like constant (ε ′) and loss tangent (tan δ) were calculated using LCR meter

3. Results and discussion:

3.1 Structural analysis

XRD prototypes of (Ni0.35 Cu0.20Zn0. 45) LaxFe2−xO4 Nano crystals, for all the samples with (x = 0.00, 0.025, 0.050, & 0.075) as in Figure 1. (XRD) patterns disclose a single stage cubic spinel arrangement with few traces of minor stage. In addition, diffraction peaks that were noticed could be allocated to the reflection flat surface of [111, 220, 311, 400, 422, 511 and 440] which might be indexed to a single-stage Ni-Cu-Zn ferrite nano-crystal. in the interim, the peak matching to 2θ = 32.21 is due to minor stage at the grain limitations for (✦) La FeO3 (ICDD PDF #37±1493) excluding for the cubic spinel phase. LaFeO3 intensity peak has risen with the increasing in La+3 ion concentration [10].

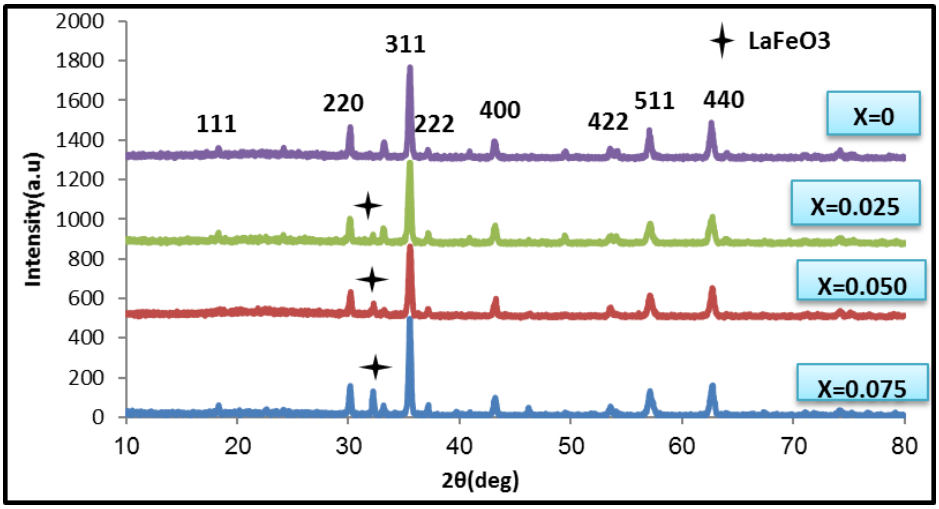

Figure 1. (XRD) patterns sample of $Ni_{0.35}Cu_{0.2}Zn_{0.45}La_xFe_{2-x}O_4$

The individual lattice parameter structure was detected as the relation below: [11].

$$d_{hkl} = \frac{a}{(h^2 + k^2 + l^2)^{-\frac{1}{2}}} \quad (1)$$

(α) = lattice constant, (d) = inter-planar distance and (h, k, l) are the Miller indicators

The sample's rate crystallite size is determined using the Scherer's equation [12] .

$$D = \left(\frac{K\lambda}{\beta_{hkl}\cos\theta}\right) \quad (2)$$

Where (D) = crystallite size, β = diffraction line full width at maximum half intensity that is counted in radians, is x-ray wavelength (Cu kα radiation, 1.5405Å) and θ is the Bragg angle, and Williamson-Hall formula

$$\beta_{hkl}\cos\theta = \frac{K\lambda}{D} + [4\varepsilon\sin\theta] \quad (3)$$

The actual (X-ray) density of the samples was calculated using the formula [13] ,

$$\rho_{x-ray} = \frac{ZM_{wt}}{N_a V} \quad (4)$$

Here; M = sample molecular weight per (Kg), N = number of Avogadro (per mol) and a = lattice parameter (Å). The samples bulk densities as the following formulation,

$$\rho_b = \frac{m}{\pi h r^2} \quad (5)$$

m = mass per (Kg), r = radius (m) and h = the pellet height per (m).

The following relation can calculate the porosity percentage [14]

$$P = 1 - \frac{\rho}{\rho_{X-ray}} \times 100\% \quad (6)$$

The observed increase in the lattice constant (a) that might be related with the La+3 increasing contentment where the La+3 ionic radius (1.6061) can be bigger in comparing with the one of Fe+3ion (0.645) that replacing iron ions on octahedral B-site which in turn can cause inequelity in the structure. For this reason, the lattice constant has to be enlarged with the La+3 increasing contentment through the exchange operation [15, 16]. The samples crystallite size can be observed with lanthanum concentration increasing. This is consistent with the results reported for La+ 3doped Ni–Cu–Zn ferrite [17]. The X-ray density increases linearly with lanthanum ion content and this can be correlated with the increase of atomic weight of La+3 substituted for Fe+3 of lower atomic mass. The magnitudes of bulk densities are smaller than that of the corresponding X-ray densities and this difference in magnitude may be attributed to the existence of pores in the bulk samples. The porosity is observed to decrease with La+3 content.

Table 1: Effectiveness of La+3 doping on the lattice parameter, crystallite size, actual (X-ray) density, Bulk density, porosity of (Ni0.3 5 Cu0.20Zn0.45) LaxFe2−xO4 system

Sample	X concentrations	Lattice Constant (a)	DSh (nm)	DW-H (nm)	ρx-ray (g/cm3)	ρ (g/cm3)	Porosity %
C0	**0**	8.353	28.35	29.50	5.43	3.56	34.39
C1	**0.025**	8.3771	26.11	28.29	5.43	3.67	32.31
C2	**0.050**	8.3732	27.00	27.73	5.47	3.72	32.04
C3	**0.075**	8.3745	32.20	33.81	5.51	3.80	31.02

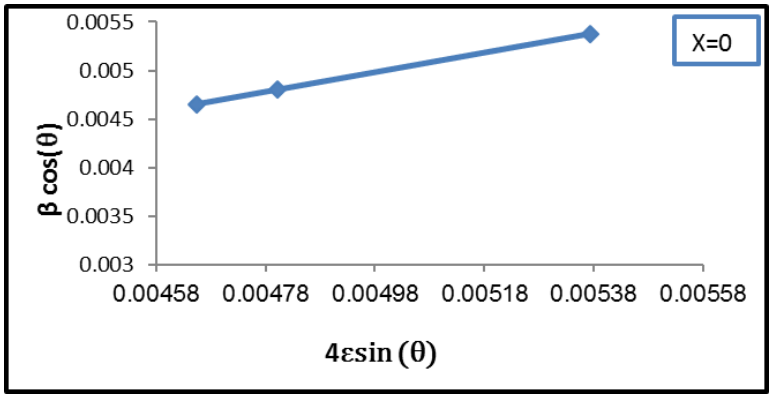

Figure 2. Hall – Williamson plots of (Ni0.3 5 Cu0.20Zn0.4 5) LaxFe2−xO4

3.2 SEM Analysis:

The SEM images of various compositions of NiCuZnLa ferrites were shown in the 'figure (3)'. The SEM images reveal that the particles are spherical in shape and are agglomared in nature. . 'Figure (4)' shows the EDX images of all (Ni0.35 Cu0.20Zn0.4 5) LaxFe2−xO4 ferrite nanoparticles calcined at 900 °C. The characteristic peaks of Ni, Cu, Zn, La, Fe and O elements were observed in EDX spectra.

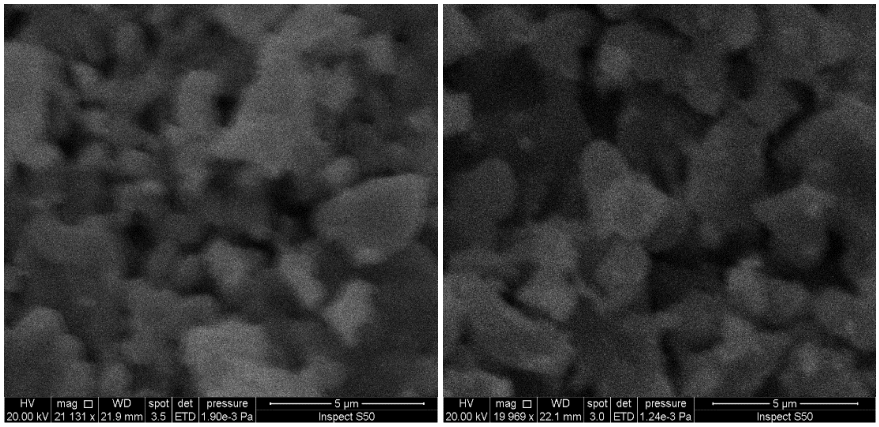

Figure 3. Hall – Williamson plots of (Ni0.3 5 Cu0.20Zn0.4 5) LaxFe2−xO4

.3. SEM photographs of (Ni0.35 Cu0.20Zn0. 45)LaxFe2−xO4 ferrites with (A) x = 0.00, (B) x = 0.075.

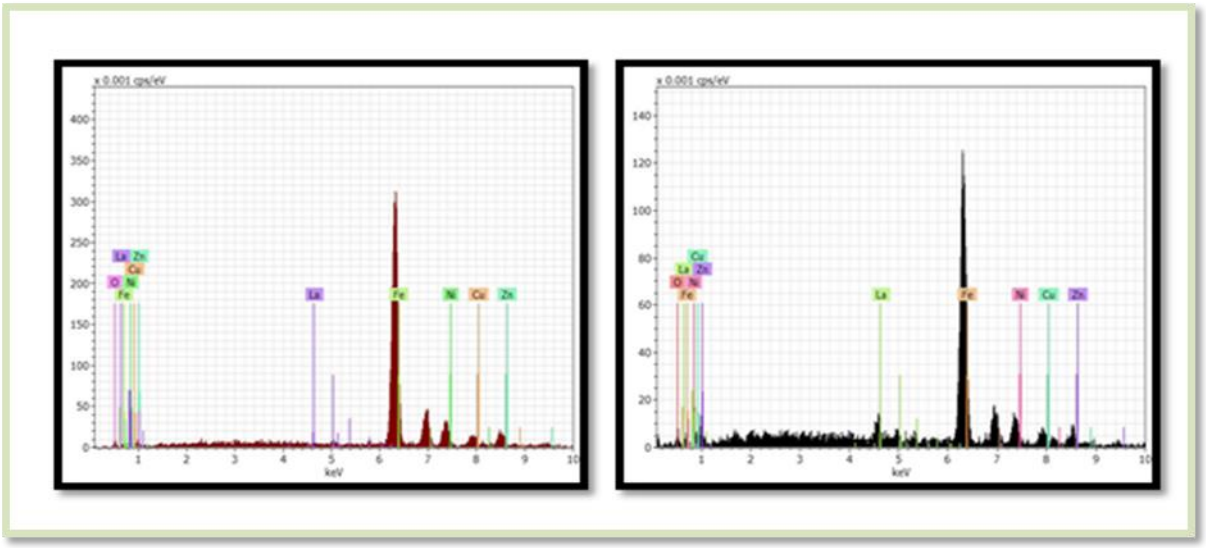

Figure 4. EDX pattern (Ni0.35 Cu0.20Zn0.45) LaxFe2−xO4 ferrite nanoparticles with (A) x = 0.00, (B) x = 0.075.

3.3 Electrical Properties:

The electrical properties of La doped NiCuZn ferrite ($Ni_{0.35}Cu_{0.2}Zn_{0.45}Fe_{2-x}O_4$), with (X=0.0, 0.025, 0.05 and 0.075) of Lanthanum additions include the A.c and D. c conductivity, dielectric properties.

3.4. Dielectric properties:

With the following equation, dielectric constant real part was detailed [18],

$$\varepsilon_r' = \frac{c\,t}{\varepsilon_o A} \tag{7}$$

C = the capacitance measured value, d = the thickness in centimeters, A = the surface area in cm^2 , ε_0 = air dielectric permittivity (8.854×10-14 F/cm). The dielectric imaginary part loss εr" can be shown as below [18],

$$\varepsilon_r'' = \tan\delta\ \varepsilon_r' \tag{8}$$

'Figures(5)' and (6) show the dependence of the real and imaginary part of dielectric constantε_r', εr", for bulk (Ni0.35 Cu0.20Zn0. 45) LaxFe2−xO4 on the frequency ω, for different lanthanum doping contents. The real and imaginary parts of dielectric constant for all samples decrease with increasing of frequency. This behavior agrees well with Debby's type relaxation process. The real and imaginary parts of dielectric constant reach a constant value for all the samples above certain greater frequency, this agrees with the result of references [19]. It can be observed from Figures 4 that the imaginary parts of dielectric constant εr", increases with frequency.

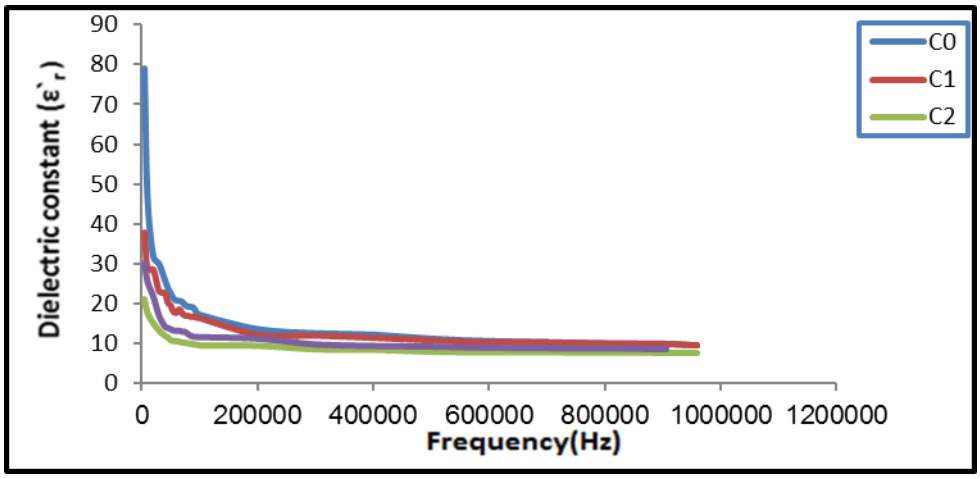

Figure 5. Real part variation of ($\varepsilon_r^{'}$) of dielectric constant with frequency for (Ni0.35 Cu0.20Zn0.4 5) LaxFe2−xO4 at different La contents.

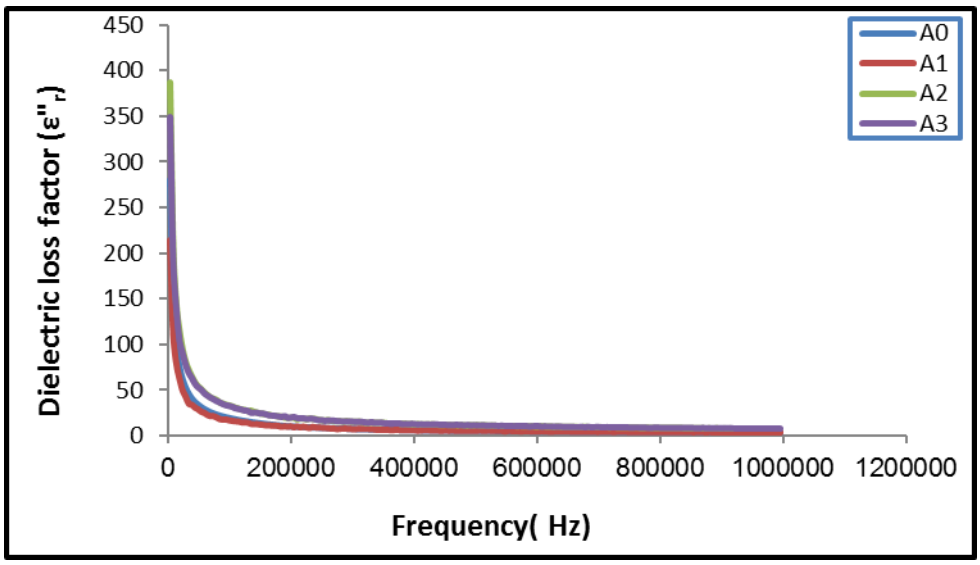

Figure .6. Variation of imaginary part (εr") of dielectric constant with frequency for at (Ni0.35 Cu0.20Zn0.4 5) LaxFe2−xO4 different La contents.

3.5. A.C. conductivity:

The A.C. conductivity was evaluated using the relation [18],

$$\sigma_{a.c} = 2\pi f\ \varepsilon_o \varepsilon_r^{'} \tan\delta \tag{9}$$

'Figure (7)' shows the ac conductivity differences with frequency (50Hz-1MHz). The ac conductivity increases with increasing frequency for all specimens, which is the normal behavior of ferrites this agrees with the result of references [20].

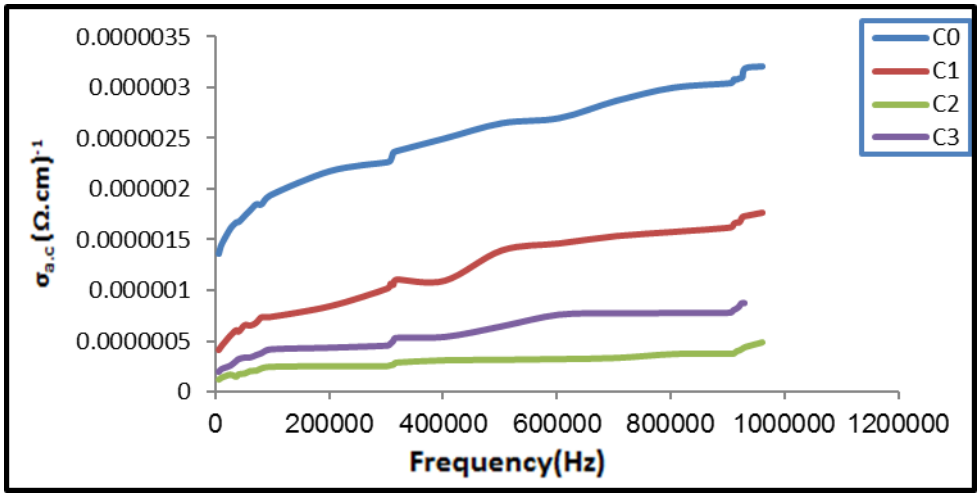

Figure7. A.C electrical conductivity as a function of frequency for with (Ni0.35 Cu0.20Zn0. 45) LaxFe2−xO4 different contents of La.

3.6. D.C conductivity:

In the following equation D.C conductivity can be calculated:

$$\sigma_{D.C} = \frac{d}{AR} \quad (10)$$

Where R is the resistance .A (m2) it represents the area of the pole, d (m) is the thickness of pellet. From table (2) obtained that dc conductivity decrease with increasing (La+3) content.

Table 2. The DC conductivity

Concentration (X)	$\sigma_{D.C}$ ***10^-19 (Ω.cm)**
0.00	2.51
0.025	2.32
0.050	2.41
0.075	2.43

3.7. Magnetic properties:

The magnetic examinations results displayed that the (X=0.05) rate with chemical formulation (Ni0.35Cu0.2Zn0.45 LaxFe2-XO4) own a considerable magnetic features in comparing with other samples due to its best hysteresis circuit in order that it can realize the conditions of utilizing it as a cores in transducers and electrical engines.

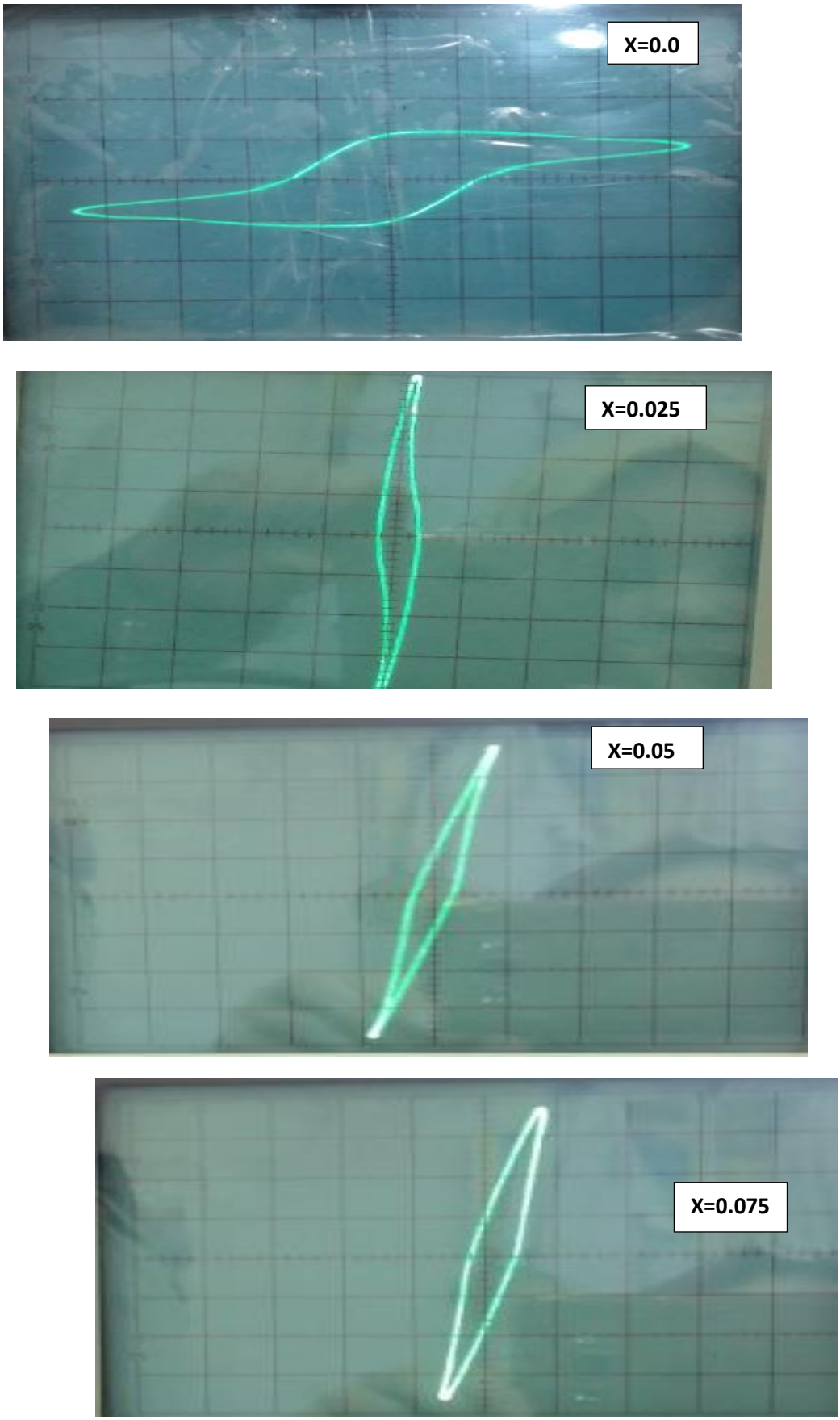

Figure 8. Room temperature hysteresis curves of (Ni0.35Cu0.2Zn0.45 LaxFe2-XO4) samples

4. Conclusions

The (Ni0.35 Cu0.20Zn0.4 5) LaxFe2−xO4 where (x= 0.0, 0.025, 0.050 and 0.075) Nano ferrites were all set by Sol-Gel technique. (XRD) studies clearly showed formations of the crystalline structure of (Ni0.35 Cu0.20Zn0. 45) LaxFe2−xO4 is cubic spinal stricture phase ferrite and The Average crystallite size (D) was calculated as (27-33nm) using Williamson's Hall and Debary -shere equation, the It was found out that lattice parameter increases with increasing lanthanum content. Whereas porosity decreases with increasing lanthanum content. The veritable and fictional part of dielectric constant decreases with increasing of frequency, whilst the A.C electrical conductivity can increase with frequency increasing .and D.C conductivity decreases with increasing lanthanum content. The magnetic examination results presented that the (X=0.05) rate has a considerable magnetic properties in comparing with other samples because of its best hysteresis loop so that it can realize the conditions of utilizing it, as the cores in transducers and electrical motors.

References

[1] Shinde TJ, Gadkari AB, Vasambekar PN. 2012 Influence of Nd+ 3substitution on structural, electrical and magnetic properties of nanocrystal line nickel ferrites. *Journal of Alloys and Compounds*. **513**:80.

[2] Pervaiz E, Gul I, editors. 2013Influence of rare earth (Gd+3) on structural, gigahertz dielectric and magnetic studies of cobalt ferrite. *Journal of Physics*: Conference Series,439012015 IOP Publishing.

[3] A. Verma, R. Chatterjee, 2006 “Effect of zinc concentration on the structural, electrical and magnetic properties of mixed Mn–Zn and Ni–Zn ferrites synthesized by the citrate precursor technique” *J. Magn. Magn. Mater*. Vol. **306**, PP. 313-320.

[4] Krishnamurthy N, Gupta CK. Extractive Metallurgy of Rare Earths: CRC Press; 2004. [5] . Dar MA, Shah J, Siddiqui W, Kotnala R. Study of structure and magnetic properties of Ni±Zn ferrite nano-particles synthesized via co-precipitation and reverse micro-emulsion technique. Applied Nano science.; 4(6):675.

[6] KoÈseoğlu Y, Bay M, Tan M, Baykal A, SoÈ zeri H, Top kaya R, et al. 2014 Magnetic and dielectric properties of Mn0.2Ni0.8Fe2O4 nanoparticles synthesized by PEG-assisted hydrothermal method. *Journal of Nanoparticle Research*.;**13**(5):2235.

[7] Yang H, Zhang X, Ao W, Qiu G. 2004 Formation of NiFe2O4 nanoparticles by mechanochemical reaction. Materials Research Bulletin.; 39(6):833.

[8] Jing J, Liangchao L, Feng X. 2007 Structural analysis and magnetic properties of Gd-doped Li-Ni ferrites prepared using rheological phase reaction method. *Journal of Rare Earths*.; **25**(1):79.

[9] Hussain A, Abbas T, Niazi SB. 2013 Preparation Of Ni1− xMnxFe2O4 Ferrites By Sol Gel Method And Study Of Their Cation Distribution.In Ceramics International.; **39**(2):1221-1225.

[10] BRK A R Bugad, T R Mane, D H Bobade Structural and micro structural properties La3+ substituted Mg-Zn ferrites prepared by Co-precipitation method,CTBC' s *Int. Res. J* **l** 2 (7 (Special)), 104 - 108

[11] Cullity BD. Elements of X-ray Diffraction. California: Addison – Wesley; 1978.

[12] Gao F, Qin G, Li Y, Jiang Q, Luo L, Zhao K, et al. 2016 One-pot synthesis of La-doped SnO2 layered nanoarrays with an enhanced gas-sensing performance toward acetone. RSC Advances.; 6(13):10298-310.

[13] K. Rama Krishna, Dachipalli Ravinder, K. Vijaya Kumar, Utpal S. Joshi, V. A. Rana, Abrham Lincon,. 2012.Dielectric Properties of Ni-Zn Ferrites Synthesized by Citrate Gel Method.World *Journal Of Condensed Matter Physics*.**2**.57-60

[14] Aghav PS, Dhage VN, Mane ML, Shengule DR, Dorik RG, Jadhav KM. 2011 Effect of aluminum substitution on the structural and magnetic properties of cobalt ferrite synthesized by sol–gel auto combustion process. *Phys B*; **406**: 4350 – 5

[15] Wang Y, Xu F, Li L, Liu H, Qiu H, Jiang J. 2008 Magnetic properties of La-substituted Ni-Zn-Cr ferrites via rheological phase synthesis.*Journal Of Materials Chemistry and Physics*.; **112**(3):769-73.

[16] Anupama MK, Rudraswamy B. 2016 Effect of Gd+3-Cr+3 ion substitution on the structural, electrical and magnetic properties of Ni-Zn ferrite nanoparticles. IOP Conference Series: *Materials Science and Engineering*.; **149**(1):012194.
[17] Roy, P. K., and J. Bera. 2007 "Enhancement of the magnetic properties of Ni–Cu–Zn ferrites with the substitution of a small fraction of lanthanum for iron. "Materials research bulletin 42.1: 77-83.
[18] Kambale R C, Adhate N R, Chougule B K and Kolekar Y D 2010 *J. Alloys Compd.* **491** 372
[19] R. S. Devan, Y .D. Kolekar and B. K. Coagula, 2006 "Effect Of Cobalt Substitution on The Properties of Nickel–Copper Ferrite",*J. Physics: Condensed Matter*, **18**, ,43.
[20] P.A. Noorkhan and S. Kalayne, 2012"Synthesis, Characterization Ac Conductivity of Nickel Ferrite", *Journal of Engineering Research and Applications*,**2**, , 681-685.

Journal of Physics: Conference Series

Partial substitution of Zn Effects on the Structural and Electrical Properties of High Temperature $Hg_{0.95}Ag_{0.05}Ba_2Ca_2Cu_3O_{8+\delta}$ Superconductors

Partial substitution of Zn Effects on the Structural and Electrical Properties of High Temperature $Hg_{0.95}Ag_{0.05}Ba_2Ca_2Cu_3O_{8+\delta}$ Superconductors

Noor S. Abed [1], Sabah J. Fathi [1], Kareem A. Jassim[2] & Shatha H. Mahdi[2]

[1]Department of Physics, College of Sciences, Kirkuk University, Kirkuk, Iraq.
[2]University of Baghdad, College of Education, for pure science, of pure science Ibn - Al-Haithem, Department of Physics, Iraq.
bilalahmed983339@yahoo.com, shatha246@yahoo.com

Abstract. The effect of the Ag partial substitution at Hg site in HgO_δ layer and Zn partial substitution at Ca site in CaO layer on the structure ,T_c ,electrical properties , and oxygen content for Hg-1223 have been studied . Bulk polycrystalline $Hg_{1-x}Ag_xBa_2Ca_{2-y}Zn_yCu_3O_{8+\delta}$ compound samples with x=0.05 and y =0.0, 0.05, 0.1, 0.15, 0.2, 0.25, and 0.3, are synthesized by a solid state reaction process. Structural properties are studied by using X-ray powder pattern, the high temperature phase superconductor (Hg-1223) of the tetragonal structure didn't change with the partial substitution of Zn and Ag ions , lattice parameters c ,c/a are established to vary with Ag and Zn- substitution. The surface morphology has been studied by using atomic force microscopes (AFM), showed that all specimens have good crystalline and homogeneous surface. Also give a best nano size value is 75.72 nm at x=0.05 and y=0.3. Four probe technique is used to measure T_c. The T_c were found to be increases from 129 K to 147 K and oxygen content were found to be increases with increasing Zn. In addition, dielectric properties (dielectric constant, dielectric loss factor, and the alternating electrical conductivity) are characterized directly by relating with Ag and Zn concentration.

Keywords: HgBa2Ca2Cu3O8+δ, Superconductor, Solid state reaction method, Structural Properties.

1. Introduction

Superconductivity is a phenomenon, which was observed by Kammerlingh Onnes in 1911. When temperature decreases to below a critical value, electric resistance of a superconductor disappeared and the magnetic field is expelled [1]. The first member of HgBa2Can-1CunO2n+2+δ series, was HgBa2CuO4+δ, fabricated by Putilin et. al. in 1993 [2]. In 1993 Schlling et. al. [3,4] concluded that the critical temperature was equal to 133 K for a compound Hg Ba Ca Cu O. This has achieved a significant jump in the critical temperature of superconducting compounds at high temperatures. The highest values of Tc which were calculated for HgBa2Can-1CunO2n+2+δ series were 97K [5] , 123K [6] 127K [7], and 133K [8], for Hg-1201, Hg-1234 phases, Hg-1212, and Hg-1223 respectively. The Tc value of Hg-1223 raise up to 164 K under high pressures of 30 GPa [9,10]. HBCCO superconductor phases most important series of all HTSC cuprates because of the high Tc and the extra oxygen existence appear by this series [11]. There are difficulties in preparation of Hg-based superconductors, because of the toxic mercury steam and the low decomposition temperatures of the compounds containing mercury and the relative instability of these materials. All cuprates are very sentient to carries doping and, it was found that the most efficient way to enhance the stabilization of the Hg-1223 phase is by partial substitution with cations having oxidation states higher than +2 i.e. higher than Hg+2 (e.g. Tl+3, Re+4 etc) [12,13,14]. All the superconducting phases of the HgBa2Can-1CunO2n+2+δ system crystallize with a tetragonal cell having the symmetry of space group P4/mmm. The a-parameter is ~ 3.5 Å and the c-parameters of the various phases follow the formula c ~ 9.5 +

3.2(n-1) Å, n being the number of Cu-O planes in the structure. The crystal structures are based on the layer sequence: (BaO)(HgOδ)(BaO)(CuO2)[(n-1)(Ca)(CuO2)](n-1)(BaO) The blocks (BaO)(HgOδ)(BaO) have the rock-salt structure with a thickness of about 5.5 Å and alternate with blocks (CuO2)[(Ca)(CuO2)](n-1) having a perovskite-like structure with an approximate thickness of [4.0 + 3.16(n-1)] Å . The crystal structures of Hg-based superconductors consist of two generic building blocks [15,16]: the vital, superconducting copper-oxide layers or planes, and the insulating block layers which can act as electronically active charge-reservoirs for hole or electron donation to the copper-oxygen layers. The copper-oxide layers can be thought of as being derived from the perovskite structure-type by deintercalation of oxygen from between the copper-oxide planes, while the insulating block is derived from the rock-salt structure. The aim of this paper was investigated the effect of partial substitution of Ag in Hg site and Zn nano scale in Ca site, on the oxygen content, structural, and electrical properties of HgBa2Ca2Cu3O8+δ HTSC compounds to make the characteristic more better .

2. Experimental

The $Hg_{1-x}Ag_xBa_2Ca_{2-y}Zn_yCu_3O_{8+\delta}$ samples with different Zn (y=0.0, 0.05, 0.1, 0.15, 0.2, 0.25, and 0.3) and Ag (x=0.05) were prepared by using a solid state reaction method using mixed oxides powder of HgO, AgO, ZnO, BaO, CaO and CuO with a purity of 99.99%. The starting materials were mixed and ground in a gate mortar. Isopropanol is added during the grinding process to avoid the loss of parts of the powder during the grinding process. Then it is placed inside an electric oven at a temperature of 100 C^0 to remove the isopropanol alcohol. The powder was pressed into disc shaped pellets (1.5 cm) in diameter and (0.3 cm) thickness, using hydraulic press under a pressure of (7 ton/cm^2) .The pellets were sintered in air at (850) C^0 for (24) hours with a rate of (5C°/min) then cooled to room temperature by same rate of heating. Four probe technique is applied for electric resistivity measurements of the prepared samples in a temperature from 300 down to 77 K, and to calculate the critical temperature (T_c) by using the relation:

$$\rho = \frac{(R*A)}{L} \dots\dots (1)$$

Where R is electric resistance, A is area and L is length of specimens. The structure properties of the 1223-phase was checked using X-ray diffraction technique using (Shimadzu XRD-6000) diffractometer with source Cu-Kα (1.5406 Å) radiation. The lattice parameters a, b and c were calculated by using d-values and (hkl) reflection of the observed XRD using standard card of Hg-1223 (ICDD-045-0615). The oxygen content determined using a chemical method called iodometric titration was described elsewhere [17]. The volume fraction for any phase determined by using the relation:

$$Vph = \frac{\sum I^{\circ}}{\sum I^{\circ}+\sum I1+\sum I2+\sum In} *100\,\% \dots\dots (2)$$

Where I° is the XRD peak intensity of the phase which was determined, I1, I2,…In are the peaks intensity of all XRD. The mass density(dm)determined by using the relation:

$$d_m\left(\frac{gm}{cm^3}\right) = \frac{M_{wt}}{N_A \times V} \dots\dots (3)$$

Where $N_A$is Avogadro number ($6.022*10^{23}$ mol^{-1}), $M_{wt}$is molecular weight, V is volume of unit cell which equal (a^2*c) for tetragonal system. LCR meter (Hewlett-Packard, USA)- HP-R2C unit 4274A in the range (100 kHz–10 MHz) and the Agilent 4275B LCR meter of (Agilent Technologies Japan, Ltd.) are employed for dielectric measurements at the room temperature with frequency range (50 Hz – 1 MHz). Silver electrode is applied to both surfaces of the specimen. The capacitance (C) was recorded, then dielectric constant (ε_r'), dielectric loss factor (ε_r''), and the alternating electrical conductivity ($\sigma_{a.c}$) have been calculated by using the following expressions [18]:

$$\varepsilon_r' = \frac{C.t}{A.\varepsilon_\circ} \dots\dots (4)$$

$$\varepsilon_r'' = \varepsilon_r'.D \dots\dots (5)$$

$$\sigma_{A.C} = 2\pi f \varepsilon_r'' \dots\dots (6)$$

Where t is the thickness of the pellet (0.3cm), $\varepsilon_\circ$ is the permittivity of space ($8.85*10^{-12}$ F/m), A is the effective cross area of the applied electrode, and D is dissipation factor.

3. Results and Discussion

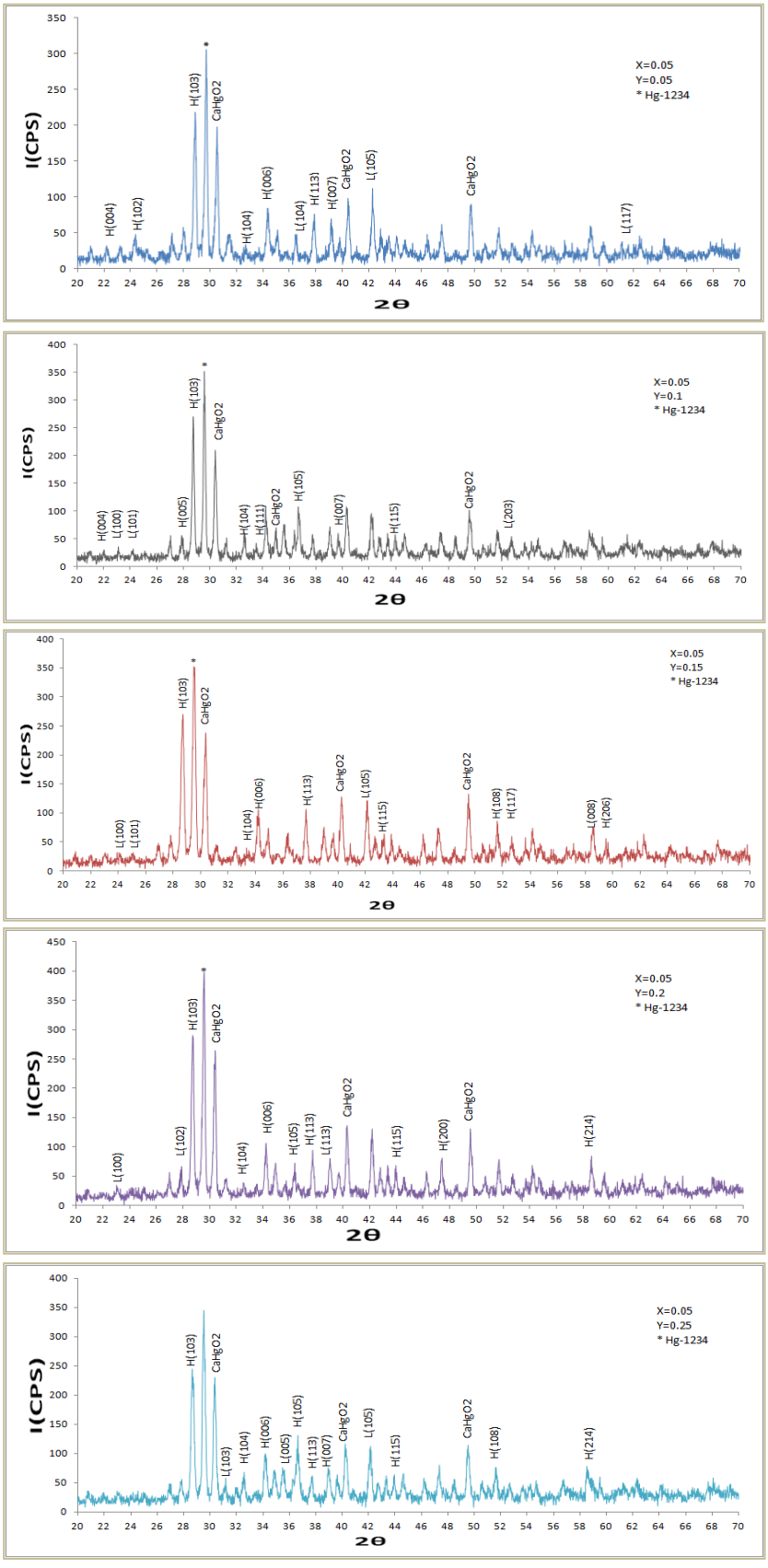

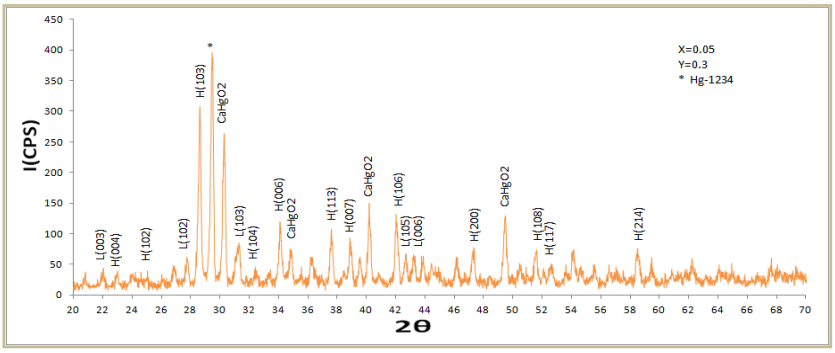

Figure 1. XRD pattern of Hg1-xAgxBa2Ca2-yZnyCu3O8+δ, superconductor compounds with x=(0.0, 0.05, 0.1, 0.15, 0.2, 0.25, 0.3)

'Figure(1)', shows series XRD patterns for $Hg_{1-x}Ag_xBa_2Ca_{2-y}Zn_yCu_3O_{8+\delta}$ compound with Ag=0.05 and different Zn (y=0.0, 0.05, 0.1, 0.15, 0.2, 0.25, and 0.3).

The figure observes high transition temperature phase (Hg-1223 phase) with a small amount of the second phase Hg-1212 (low phase) and Hg-1234 for all compounds that have been composed during synthesizes of samples which are agreement with reference [19] . Furthermore, it is significant to notice that a small amount of impurity such as ($CaHgO_2$) is present. The appearance of more than two phases could be related to the stacking faults along the c-axis. It can be clearly seen from table-1 that with increasing Zn content, the lattice parameters (a) for all samples are close to each other ($a \approx 3.83$ Å), while c parameter and ratio (c/a) is significantly increasing . This increases indicate to partial replacement of Ca atoms by Zn, and Hg atoms by Ag since the ionic radii of Ag^{+2} (1.26 A^0) is larger than that of Hg^{+2} (1.02 A^0) which render c-parameter to be longer or get deformed This will be a driving force to the pairing generation of superconductor holes forming bosons which are the current carriers in our superconductor, and the volume of lattice become bigger that explains the reason behind the decrease of T_c .

Table 1. Lattice parameters of $Hg_{1-x}Ag_xBa_2Ca_{2-y}Zn_yCu_3O_{8+\delta}$, superconductor compounds with x=0.05 and y=(0.0, 0.05, 0.1, 0.15, 0.2, 0.25,and 0.3) .

X=0.05						
y	**a=b(A°)**	**c(A°)**	**c/a ratio**	**v(A°)³**	**d_m (gm/cm³)**	**V-ph (1223)**
0.05	3.8393	15.7966	4.1144	232.845	6.2082	73.92
0.1	3.8364	15.7974	4.1177	232.505	6.2263	75.49
0.15	3.8353	15.8254	4.1262	232.784	6.2279	79.37
0.2	3.8348	15.8362	4.1296	232.882	6.2343	80.92
0.25	3.8341	15.8511	4.1342	233.016	6.2397	82.11
0.3	3.8338	15.8715	4.1398	233.279	6.2417	82.55

3.1. T_c and Oxygen Content Results :

The change of T_c is related with δ .Oxygen content increase with increase Zn concentration as presented in the Table-2. Since the substitution of Ag in Hg site leads to produce chemical pressure in HgO_δ layer. generally increase the pressure mean increases the hole which lead to disorders in structure, and this disorder is found reflected the T_c (δ) behavior. At x=0.3, the oxygen content (δ) and T_c gets a maximum value. These results were almost identical to those reported in references [20].

Table 2. Oxygen content and critical temperature (T_c) of $Hg_{1-x}Ag_xBa_2Ca_{2-y}Zn_yCu_3O_{8+\delta}$, superconductor compounds with x=0.05 and y=(0.0, 0.05, 0.1, 0.15, 0.2, 0.25,and 0.3).

X=0.05		
y	**T_c (K)**	**δ**
0.05	129	0.3419
0.1	136	0.3684
0.15	137	0.4050
0.2	140	0.5238
0.25	144	0.5376
0.3	147	0.5521

'Figure(2)' show the electrical resistivity as function of temperature for $Hg_{1-x}Ag_xBa_2Ca_{2-y}Zn_yCu_3O_{8+\delta}$, superconductor compounds with x=0.05 and y=(0.0, 0.05, 0.1, 0.15, 0.2, 0.25,and 0.3) HTSC. Samples shows a metallic behavior, followed by a superconductivity transition with T_c =129, 136, 137, 140, 144, and 147K respectively. This Due to firstly, the Ag and Zn partial substitution may lead to change in the carrier density of states indicating unlike magnetic moments, secondly, the positive contribution of the Ag element to the coupling process in the CuO layer which responsible for the superconductivity, leads to an increase in the c-lattice parameter ,which leads to raise in T_c values.

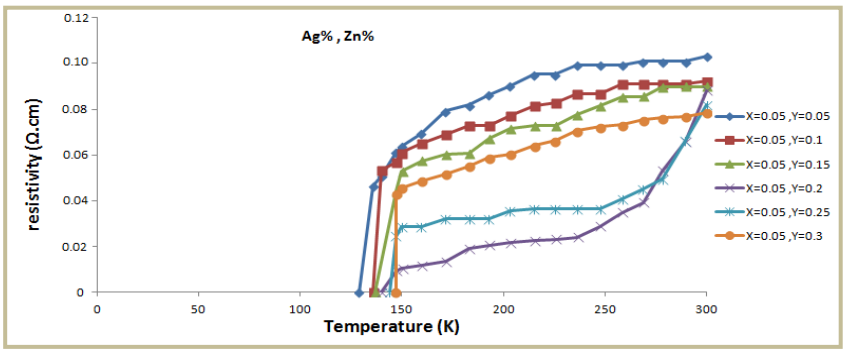

Figure 2. The electrical resistivity vs. temperature behavior of of $Hg_{1-x}Ag_xBa_2Ca_{2-y}Zn_yCu_3O_{8+\delta}$, superconductor compounds with x=0.05 and y=(0.0, 0.05, 0.1, 0.15, 0.2, 0.25,and 0.3) .

'Figure(3)' show T_c as a function of Ag content from 0.0 to 0.3. It is found that, with increasing of Ag contents, the T_c will increase.

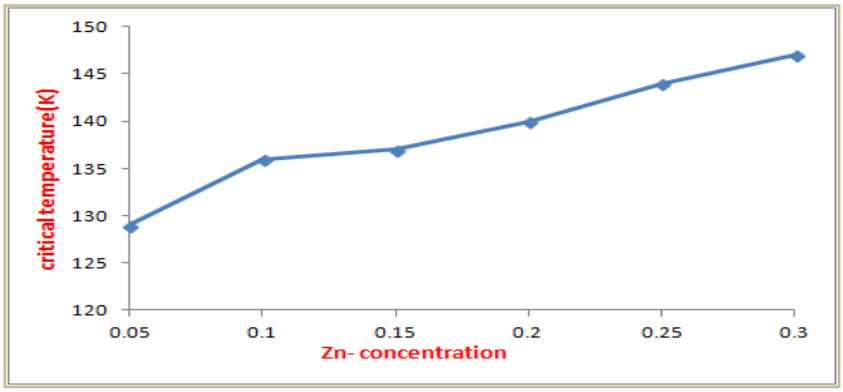

Figure 3. The critical temperature vs. Zn concentration of $Hg_{1-x}Ag_xBa_2Ca_{2-y}Zn_yCu_3O_{8+\delta}$, superconductor compounds with x=0.05 and y=(0.0, 0.05, 0.1, 0.15, 0.2, 0.25,and 0.3).

3.2. Dielectric Results :

The variations in the real part (ε_r'), the dielectric loss factor (ε_r''), and the alternating electrical conductivity ($\sigma_{a.c}$) of $Hg_{1-x}Ag_xBa_2Ca_{2-y}Zn_yCu_3O_{8+\delta}$, superconductor compounds with x=0.05 and y=(0.0, 0.05, 0.1, 0.15, 0.2, 0.25,and 0.3) at room temperature, as a function of frequency within the frequency (50Hz-1MHz) are shown in figure-4,figure-5, and figure-6. The dielectric constant (ε_r') and dielectric loss factor (ε_r'') decreasing with increasing frequency from (50Hz) to (1MHz) at room temperature with the effect of Zn doping. This is due to the ionic radii of Zn which is substituted with Ca smaller than it. The real part of the dielectric constant (ε_r') awards the magnitude of the part of energy which is stored within the material when the electrical field is applied to the material. Inter grains are the most likely places at which this energy can be stored, and the dielectric loss factor (ε_r'') express the absorption and the attenuation of energy. The value of the alternating electrical conductivity ($\sigma_{a.c}$) increases with the increase of frequency. At low frequencies, the number of electrons which transmit is few, because the amount of kinetic energy in which the electrons must have to cross the crystal is few, that means the alternating electrical conductivity ($\sigma_{a.c}$) is few and the dielectric loss factor increase. At high frequencies the amount of kinetic energy in which the electrons must have to cross the crystalline increases, so the number of electrons transmitted is more, so ($\sigma_{a.c}$) increasing and the dielectric loss factor decrease. These results were almost identical to those reported in references [21].

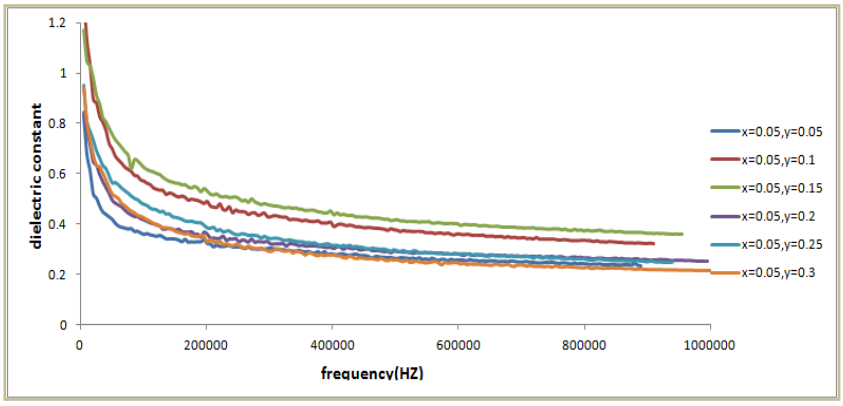

Figure 4. The dielectric constant(ε_r') as function of frequency of $Hg_{1-x}Ag_xBa_2Ca_{2-y}Zn_yCu_3O_{8+\delta}$, superconductor compounds with x=0.05 and y=(0.0, 0.05, 0.1, 0.15, 0.2, 0.25,and 0.3).

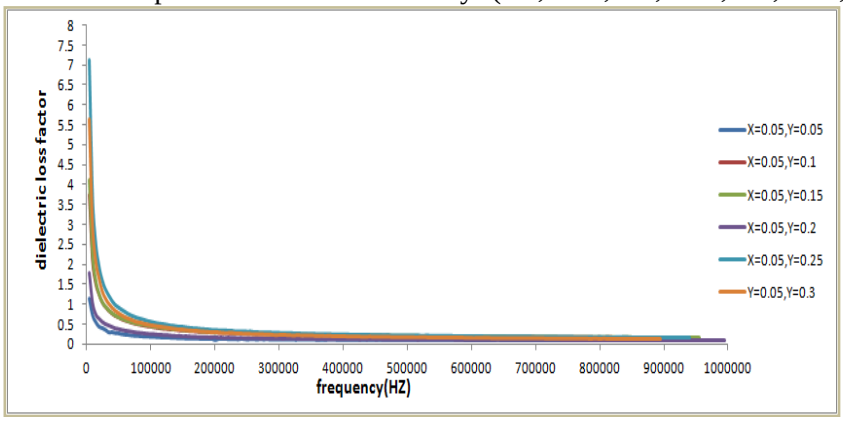

Figure 5. The dielectric loss factor (ε_r'') as function of frequency of $Hg_{1-x}Ag_xBa_2Ca_{2-y}Zn_yCu_3O_{8+\delta}$, superconductor compounds with x=0.05 and y=(0.0, 0.05, 0.1, 0.15, 0.2, 0.25,and 0.3).

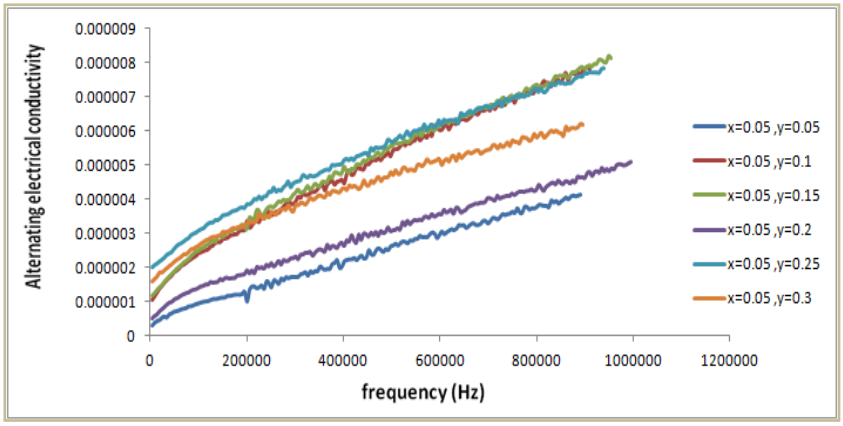

Figure 6. The alternating electrical conductivity ($\sigma_{a.c}$)as function of frequency for $Hg_{1-x}Ag_xBa_2Ca_{2-y}Zn_yCu_3O_{8+\delta}$, superconductor compounds with x=0.05 and y=(0.0, 0.05, 0.1, 0.15, 0.2, 0.25,and 0.3).

3.3. AFM Results :

After the preparation of the samples by solid state interaction method. Using a nanometer agate mortar, the elements were converted to small dimensions and imaged by an atomic force microscope. Figure-7 represent 3D AFM images of $Hg_{1-x}Ag_xBa_2Ca_{2-y}Zn_yCu_3O_{8+\delta}$, superconductor compounds with x=0.05 and y=(0.05, 0.1, 0.15, 0.2, 0.25,and 0.3). It was noted that there are tortuosity, areas of high and low density with nano scale dimensions different from one site to another location within the sample .The Surface roughness and average diameter of $Hg_{1-x}Ag_xBa_2Ca_{2-y}Zn_yCu_3O_{8+\delta}$, superconductor compounds with x=0.05 and y=(0.05, 0.1, 0.15, 0.2, 0.25,and 0.3) which presented in the Table-3 shows that all specimens have good crystalline and homogeneous surface give a best Nano size value is 75.72 nm at y=0.3 and x=0.05**.**

Table 3. Surface roughness and average diameter for $Hg_{1-x}Ag_xBa_2Ca_{2-y}Zn_yCu_3O_{8+\delta}$, compounds .

X=0.05		
x	**Surface roughness**	**average diameter**
0.05	0.433 nm	182.94 nm
0.1	0.205 nm	166.56 nm
0.15	0.717 nm	121.51 nm
0.2	0.769 nm	95.76 nm
0.25	0.387 nm	89.80 nm
0.3	0.136 nm	75.72 nm

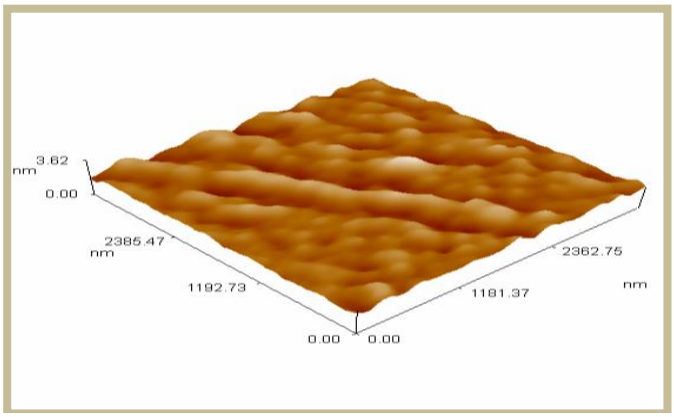

x=0.05 , y=0.05

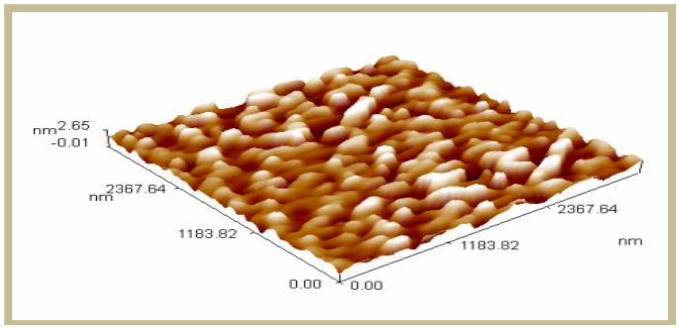

x=0.05 , y=0.1

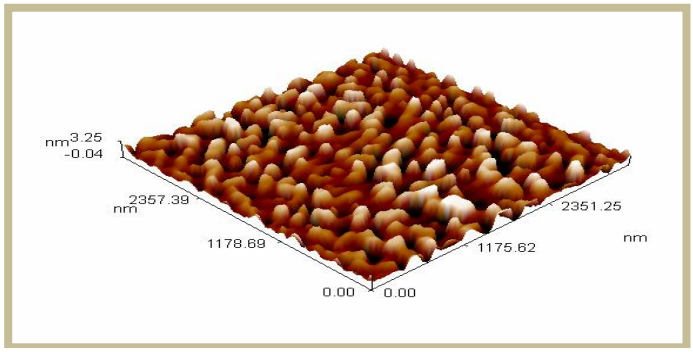

x=0.05 , y=0.15

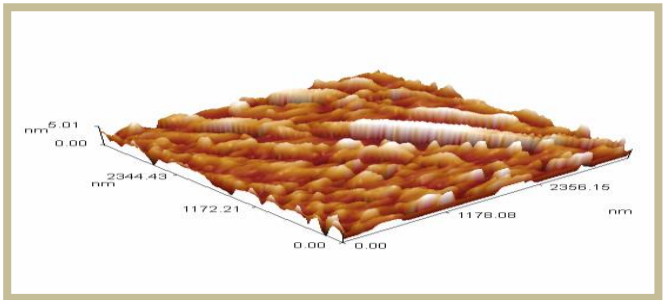

x=0.05 , y=0.2

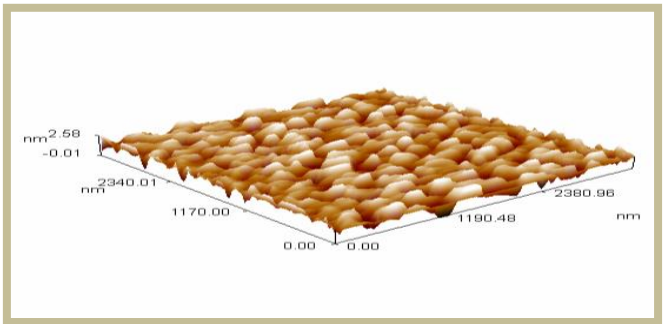

x=0.05 , y=0.25

Figure 7. AFM Images of $Hg_{1-x}Ag_xBa_2Ca_{2-y}Zn_yCu_3O_{8+\delta}$, with different y

4. Conclusions

In the present paper, it was investigated Hg1-xAgxBa2Ca2-yZnyCu3O8+δ,, superconductor compound with Ag x=0.05 and different Zn y=(0.0, 0.05, 0.1, 0.15, 0.2, 0.25, and 0.3) which prepared by using a solid state reaction method. XRD pattern analyses have showed tetragonal structure with high ratio of Hg-1223 superconductor phase, and , the c-axis lattice constant increase, as the zinc incorporation is increased, the content of high phase and the critical transition temperatures ,are increase . The best value for y is that the best substitution ratio for Zn in the compound Hg1-

xAgxBa2Ca2-yZnyCu3O8+δ, is at x = 0.05 and y=0.3 where a high percentage of phase Hg-1223 appears. The substitution of Zn in Ca for the compounds Hg0.95Ag0.05Ba2Ca2-yZnyCu3O8+δ,has exhibited a maximum value of oxygen content δ (0.5521) and Tc (147 K) at y=0.3, since the substitution produced of local pressure, hole carrier concentration, variation electronic state and its distribution. AFM results showed that the samples have good crystalline and homogeneous surface and gives the best nano size value is 75.72 nm at y=0.3. In addition, the dielectric properties are directly decreasing with increasing the frequency from (50Hz) to (1MHz) with Zn content.

References

[1] M. Monteverde, M. Nunez-Regueiro, C. Acha, D. A. Pavlov, K. A. Lokshin, S. N. Putilin, E. V. Antipov, Physica C: Superconductivity, 408-410 (2004) 23-24.
[2] N. Putilin, E. V. Antipov, O. Chmaissem and M. Marezio, Nature, **362** pp.226, (1993).
[3] Schilling A., Jeandupeux O., Guo J. D., et al. Magnetization and resistivity study on the 130 K superconductor in the Hg–Ba–Ca–Cu–O system. *Physica C*, **216**: pp. 6–11,(1993).
[4] Schilling, M. Cantoni, J. D. Guo, and H. R. Ott, "Superconductivity above 130 K in the Hg-Ba-Ca-Cu-O system," *Nature* **363**, 56 (1993).
[5] Fukuoka, A. Tokiwa – Yamamoto et. al., *Physics C*, Vol. **13**, No. 265, (1996).
[6] R. Usami, S. Adachi, M. Itoh, et. al. *Physica C*, **262** (1996) 21.
[7] Tokiwa - Yamamoto, S. Adachi, K. Isawa et.al., Advances in Superconductivity, VI /Proc.ISS' 93 (Oct 26 - 29, 1993 Hiroshima, Japan) eds. T. Fujita, Y. Shiohara ,Springer – Verlag Tokyo, P. 247, (1994).
[8] K. Isawa, A. Tokiwa - Yamamoto, M. *Itoh et. al. Physica C*, **222** (1994) 33.
[9] C. W. Chu, L. Gao, F. Chen, Z. J. Huang, R. L. Meng, and Y. Y. Xue, "Superconductivity above 150 K in HgBa2Ca2Cu3O8+δ δ at high pressures," *Nature* **365**, 323 (1993).
[10] H. Takahashi, A. Tokiwa-Yamamoto, N. Môri, S. Adachi, H. Yamauchi, and S. Tanaka, "Large enhancement of Tc in the 134 K superconductor HgBa2Ca2Cu3O under high pressure," *Physica C* **218**, 1 (1993).
[11] R. Giri, H. K. Singh, R. S. Tiwari and O. N. S. *rivastava Mater. Sci*., Vol. **24**, No. 5, pp. 523–528, (2001).
[12] N.H. Hur, N.H. Kim, K.W. Lee, K.H. Yoo, Y.K. Park and J.C. *Park "PhysicaC*" V**234**, p.19, 1994.
[13] Lin C. T., Yan Y., Peters K., et. al. "Flux growth Hg1-xRexBa2Can-1CunO2n+2+δ single crystals by self-atmosphere*". Physica C* ,pp. 300: 141–150 ,(1998).
[14] Sin A., Cunha A.G., Calleja A., et. al. "Formation and stability of HgCaO2, a competing phase in the synthesis of Hg1-xRexBa2Ca2Cu3O8+δ superconductor". *Physica C*, **306**, pp. 34–46, (1998).
[15] P.V.P.S.S. Sastry, Y. Li, J. Su, and J. Schwartz, "Attempts to fabricate thick HgPb1223superconducting films on silver," *Physica C* **335**, 112 (2000).
[16] P.V.P.S.S. Sastry, Y. Li, J. Su, K.W. Hamill, M. Chatard, and J. Schwartz, "Effect of silver interface on the formation and stability of HgPb1223 superconductors," Advances in Cryogenic Engineering *(Materials*) 46(B), **715** (2000).
[17] K. A. Jassim, PhD thesis, Physics Department, College of Science, University of Baghdad, Iraq (2005).
[18] I Abou-Aly, M. F. Mostafa, I. H. Ibrahim, R. Awad and M. A. Al-Hajji, "Electrical and magnetic properties of Hg0.3Tl0.7Ba2Ca3Cu4O10+δ doped with Ni and Ag," Superconductor Science and Technology, vol. 15, no. 6, (2002).
[19] Kareem A. Jasim , Raghad S. Al-Khafaji "The study of the properties of Hg0.6Tl0.4Ba2Ca2(Cu1-xAgx)3O8+δ compound" *Journal of Applied and Physical Sciences*, **3**(1): 26-31, (2017).
[20] M. M. Abbas "Influences of the Cu Substitution at Hg Site in Hg1-xCuxBa2Ca2Cu3O8+δ Superconductors" *Iraqi Journal of Physics*, Vol. **5**, No. 1, PP 1-6, (2008).
[21] Noor Q. Fadhel, Shatha Hashim Mahdi, Kareem Ali Jasim "study the effect of (Y2O3,SbO2) additives on the dielectrically properties of [Hg-1223] compound" *International Journal for Sciences and Technology* ,Vol.**11**, No.1,(2016).

Chaotic behaviour of the Rossler model and its analysis by using bifurcations of limit cycles and chaotic attractors

Chaotic behaviour of the Rossler model and its analysis by using bifurcations of limit cycles and chaotic attractors

K M Ibrahim[1], R K Jamal[2] and F H Ali[2]

1) Department of Physics, College of Education for Pure Science (Ibn Al-Haitham), University of Baghdad, Baghdad, Iraq.

2) Department of Physics, College of Science, University of Baghdad, Baghdad, Iraq.

E-mail: km11140@yahoo.com

Abstract.The behaviour of certain dynamical nonlinear systems are described in term as chaos, i.e., systems' variables change with the time, displaying very sensitivity to initial conditions of chaotic dynamics. In this paper, we study archetype systems of ordinary differential equations in two-dimensional phase spaces of the Rössler model. A system displays continuous time chaos and is explained by three coupled nonlinear differential equations. We study its characteristics and determine the control parameters that lead to different behavior of the system output, periodic, quasi-periodic and chaos. The time series, attractor, Fast Fourier Transformation and bifurcation diagram for different values have been described.

Keywords: Chaos, Rossler model, attractor, bifurcation diagram.

1. Introduction

Term "chaos" is used to describe the behavior of certain dynamical nonlinear systems, i.e., systems' variables change with the time exhibiting very sensitivity to initial conditions of chaotic dynamics. This sensitivity of chaotic systems' behavior manifest exhibits almost random, which shows as an exponential evolution of perturbations in the initial conditions. [1]. Nonlinear systems appear in all domains of engineering, chemistry, physics, economics, biology and sociology. Paradigms of nonlinear chaotic systems contain neural network models, planetary climate prediction models, turbulence, data compression, nonlinear dynamical economics, mixing liquid with low power exhaustion, processing information , circuits and devices which have high performance, and preventing the collapse of systems' power [2]. Within the chaos and dynamical systems field for low dimensional systems, the Lorenz and the Rössler models are two paradigmatic problems that have been frequently studied. Most of the results have been expressed in models of three-dimensional, where, due to the limited phase-space only low-dimensional chaos can be noticed [3]. Chaotic systems are described by one direction of exponential spreading [4]. The three-dimensional Rössler system was originally conceived as a simple model for studying chaos. With only one nonlinear term it can be thought of as a simplification of the well-known Lorenz system and as a minimal model for continuous-time chaos [5].

Continuous chaos has been first described by E.N. Lorenz in a model of turbulence, under the name of deterministic nonperiodic flow [6]. The same model has lately been obtained to apply to lasers also, demonstrating the phenomenon of chaos in lasers [7]. The chaotic of dynamical behavior possible in nonlinear systems (for example, electronic) depends only on the set of state variables concerned [8]. The electronic circuit that has the simple physical approach is designed to emulate the system for investigating of a chaotic system. This approach has some evident features. Firstly chaotic electronic oscillators are generated and it can be shown on the oscilloscope and noticed quickly. Secondly this approach avoids the uncertainties arise from statistical errors and systematic in numerical emulations, for example the discretization and round-off errors in the numeral procedures or finite time approximation of a quantity that is properly described by an unlimited time integral [9]. An excellent instrument for the study of chaotic behavior is nonlinear electronic circuits. Some of these electronic circuits treat time as a discrete variable, using analog multipliers and sample-and-hold sub circuits to model iterated maps such as the logistic map [10]. In spite of their easiness of designing and ubiquity, electronic systems have rarely been made utilize of so far in experimental dynamics [8]. In this work we use a simple electronic system agree to simple third order differential equations to describe Rössler model. It is include only simple electronic elements such as operational amplifiers, resistors, and capacitors. Moreover, with small variations, they hold the possibility for very exact comparisons between experiment and theory.

2. Rössler Model

The Rössler model [7] are given by these three equations:

$$\frac{dx}{dt} = -(y + z) \quad (1)$$

$$\frac{dy}{dt} = x + ay \quad (2)$$

$$\frac{dz}{dt} = b + xz - cz \quad (3)$$

where *a, b* and *c* are real parameters, The values firstly studied by Rössler were *a* & b =0.2 and *c*=5.7 and x, y and z are the three variables which evolves with the time. the first two equations have linear terms that create oscillations in the variable x and y. The last equation has only one nonlinear term (xz) so the expected chaotic behavior is appeared from that the system.

Continuous chaos is minimal of this system for three reasons at least: its nonlinearity is minimum because it has single quadratic term, a chaotic attractor is generated with a one lobe, in contrast to the Lorenz attractor that has two lobes, and its phase-space has the minimum dimension three [11]. The chaotic behavior in Rössler model can be described by the time series and the trajectories in the phase space as shown in Figure 1 when the control parameter c is varied. When the parameter c changed, and keeping a and b fixed at a = 0.2 and b = 0.2. We noticed that the time series is periodic and the attractor is a limit cycle at c=2.3 (Figure 1(a) and (b)) and it is period doubling and its attractor have two loops represented to two different amplitude in time series when c= 2.9 as shown in Figure 2(a) and (b). More increasing in value of c we obtained another period-doubling bifurcation creates the 4-loop shown at 4.1. We noticed the dynamics exhibit chaotic behavior at c= 5.7 when the time series shows different spikes with high and low amplitudes. The chaotic attractor is rather different from others attractors. It looks very strange (strange attractor). The FFT of this state demonstrates the signature of chaotic behavior, where the distribution is exponential decay (see Figure 4(a), (b), and (c)).

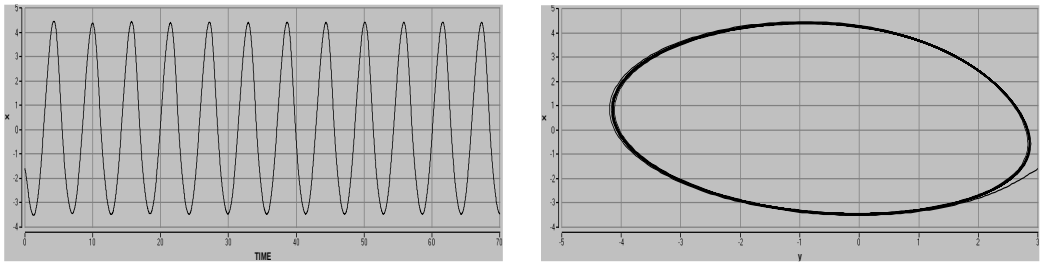

a) b)

Figure.1 Numerical simulation results (a) time series of a system at c= 2.3, (b) the corresponding attractor.

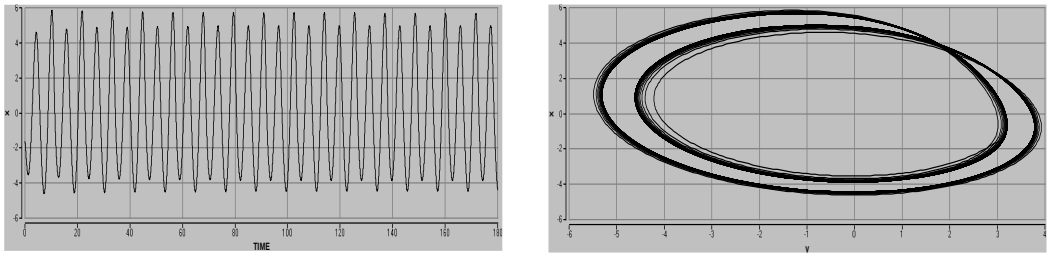

a) b)

Figure.2 Numerical simulation results (a) time series of a system at c= 2.9, (b) the corresponding attractor.

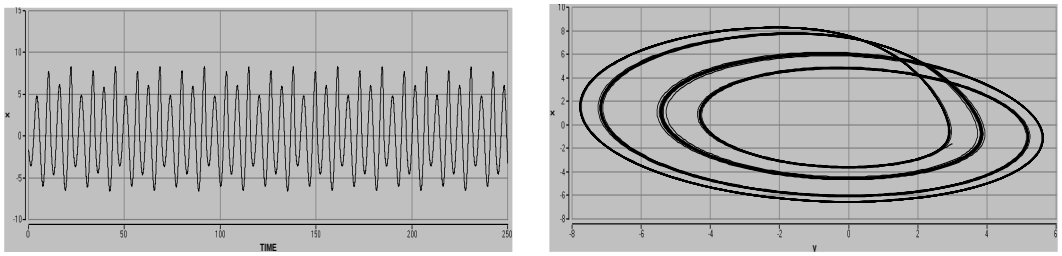

a) b)

Figure.3 Numerical simulation results (a) time series of a system at c= 4.1, (b) the corresponding attractor.

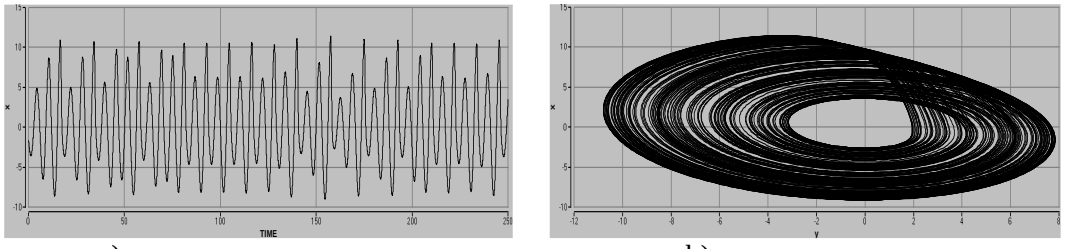

a) b)

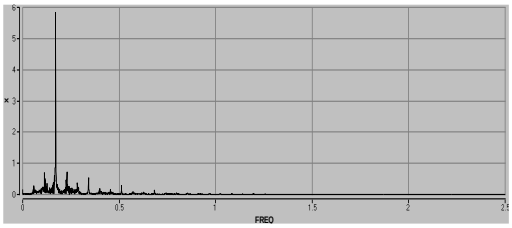

c)

Figure 4 Numerical simulation results (a) time series of a system at c=5.7, (b) the corresponding attractor. (c) The corresponding FFT.

Poincaré originally developed bifurcation theory. It is utilized to describe specific variation in system's behavior, in terms of the type and the number of solutions, under the change of one or more parameters on which the system depends [1]. The analysis was used to obtain the bifurcation diagram, which has a period-doubling route to chaos (Figure 5). When the value of c is changing from 0.7 to maximum value 8, the range of x scale in the time series is divided into various parts. In the range of $0.7 \leq c \leq 2.4$ the dynamic is periodic. For $2.5 \leq c \leq 3.6$, the period doubling behavior of the system is observed. At c value between 3.7 and 4.1 the system behaves as second period doubling behavior of the system, and finally, the chaos behavior region is starting from $c \geq 4.2$.

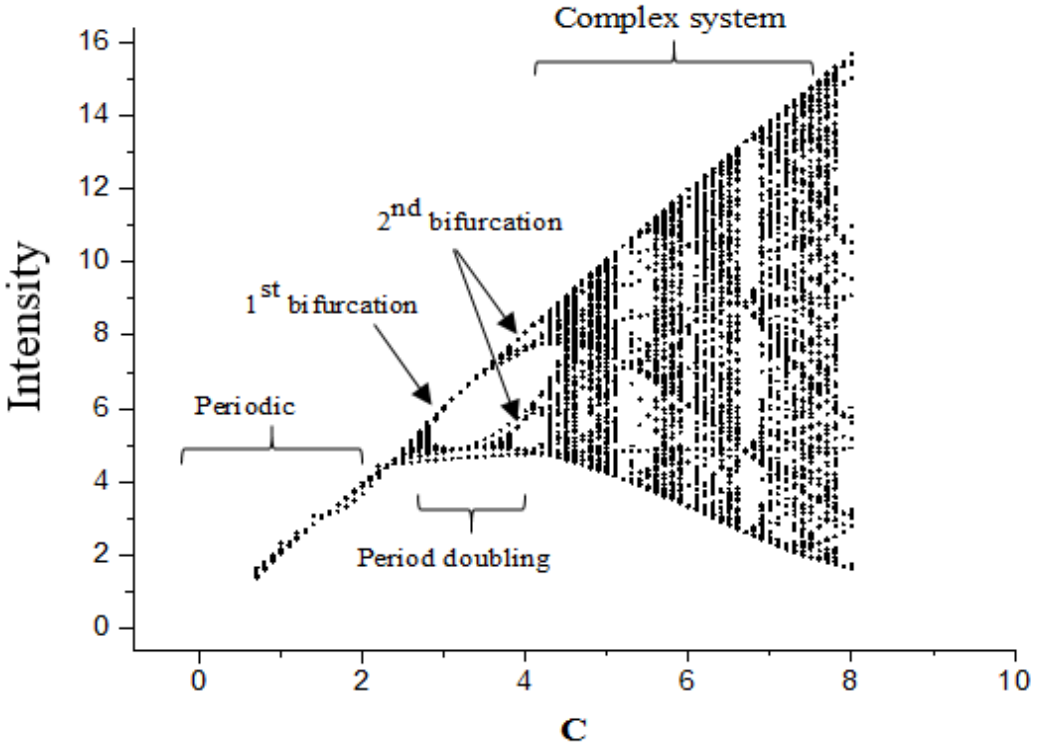

Figure 5.The Bifurcation diagram for the Rossler model. The intensity as a function of the control parameter c for the a and b values are constant and equal to 0.2

3. Experimental Setup

The electronic circuit solves the 3 coupled differential equations of the Rössler attractor shown in figure 6, by replacing the nonlinear element by an analog multiplier chip. The circuits consist of resistors, capacitors, operational amplifiers and potentiometers (variable resistors). The output voltages *X*, *Y* and *Z* are registered with an oscilloscope which represents of the Rössler system. All op-amps powered by a ±12 V power source.

The experimental time series and attractor are shown in Figures 7 and 8 when the control parameter varied (variable resistor). The dynamic displays period doubling when the value of R varied from (15-22.5) KΩ as shown in Figure 7. We notice the time series has two different amplitudes (see Figure 7(a)) and its attractor appears with two loops as represented in Figure 7(b), gradually increasing in control parameter the dynamics exhibit chaos and Rössler attractor obtained at 50 KΩ. Figure 8 a, b and c show respectively the time series of Rössler chaos, its attractor and corresponding FFT.

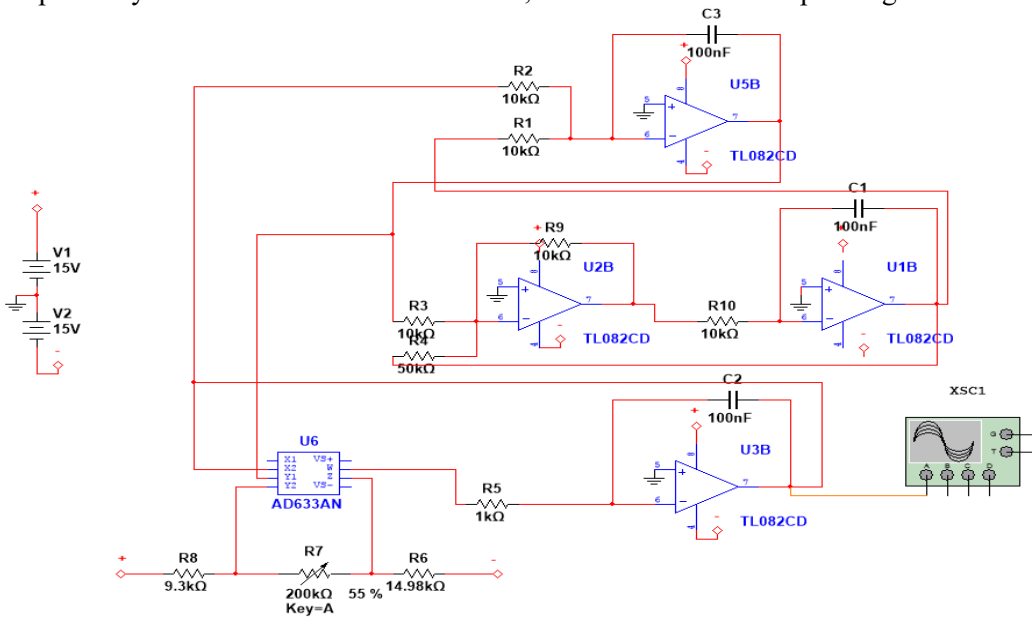

Figure 6. Schematic of Rossler drive circuit using MultiSIM 13.0.

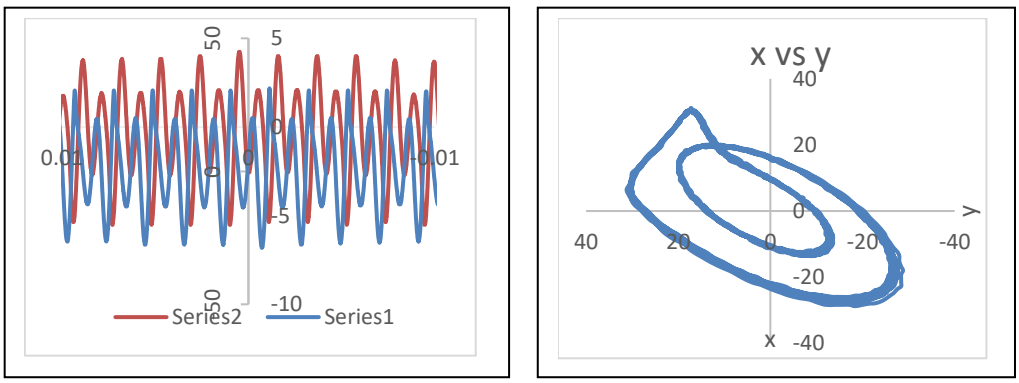

a) b)

Figure 7 a) experimental results (a) time series of a system at R= 15 KΩ, (b) the corresponding attractor.

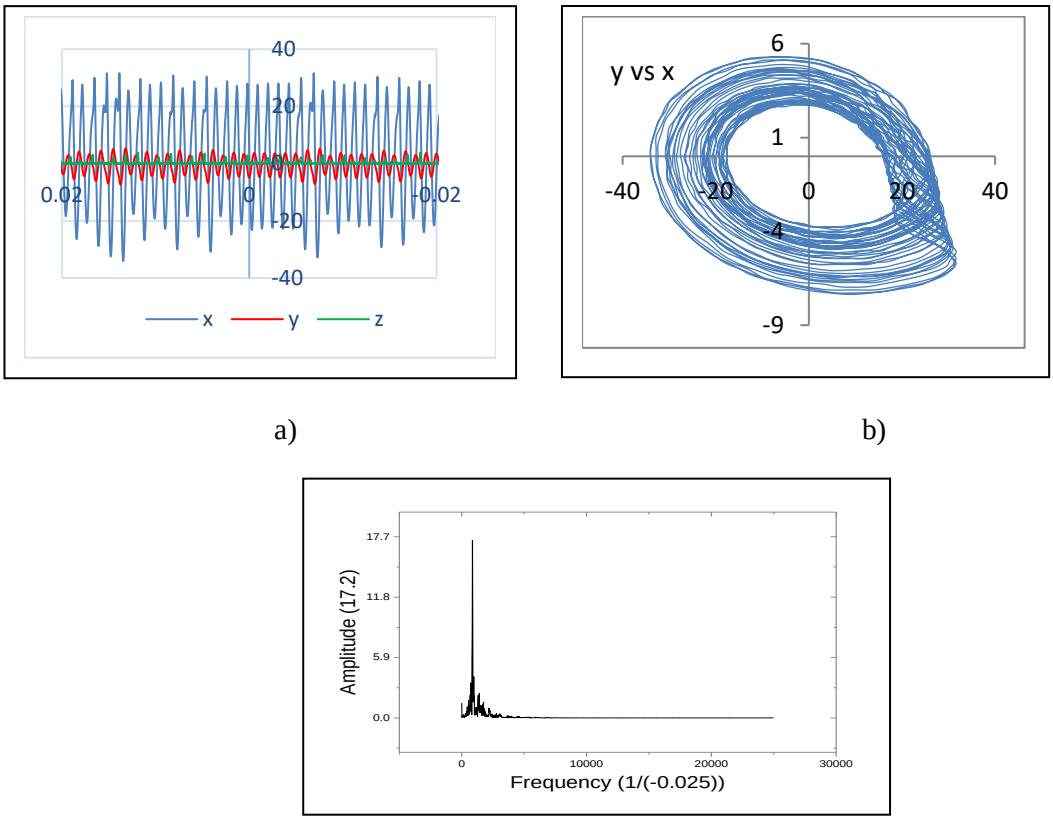

Figure 7 a) experimental results (a) time series of a system at R= 50 KΩ, (b) the corresponding attractor, (c) The corresponding FFT.

Conclusions

The Rössler model described continuous-time chaos, it exhibits a period-doubling route to chaos by increasing in the parameter c and keeping a and b fixed at 0.2. We obtained typical Rössler attractor at 5.7 of the value of c. in this paper we use bifurcation diagram to analyze the results, which it gives information about the behavior for all value of the parameter. Experimental design of the electronic circuit to study Rössler attractor is easier than Lorenz circuit because the third equation of the Rössler system has only a single nonlinear term.

References

[1] A. Sambas, M. Sanjaya W. S., and M. Mamat, 2013, Journal of Engineering Science and Technology Review **6** (4) 66-73.
[2] Qais H. Alsafasfeh, Mohammad S. Al-Arni, 2011, Circuits and Systems **2,** 101-105.
[3] R. Barrio, F. Blesa, S. Serrano, 2009, Physica D **238,** 1087_1100
[4] R. Barrio, M.A. Martinez, S. Serrano, D. Wilczak, 2015, Physics Letters A **379**(38), 2300-2305.
[5] A E Botha and W Dednam, 2015, Proceedings of the 59th Annual Conference of the SAIP **59**, 571.
[6] E N. Lorenz, 1963, J. Atmos. Sci. **20 (2),** 130.
[7] O,E. Rössler, 1976, PHYSICS LETTERS, A **57**,397.
[8] O,E. Rössler, 1983, Z. Naturforsch. **38**a, 788.
[9] A T Azar and V Sundarapandian, 2015, Studies in Computational Intelligence, Springer-Verlag, Germany **581**, ISBN 978-3-319-13131-3.
[10] K Kiers, D. Schmidt, J. C. Sprott, 2004, Am. J. Phys. **72**, 503-509**.**
[11] P Gaspard, 2005, Encyclopedia of Nonlinear Science, Routledge, New York, pp. 808-811.

Preparation and characterization of copper oxide nanoparticles decorated carbon nanoparticles using laser ablation in liquid

Preparation and characterization of copper oxide nanoparticles decorated carbon nanoparticles using laser ablation in liquid

K S Khashan[1], M S Jabir[2], F A Abdulameer [1, 2]

[1]Department of Applied Science, Division of Laser Physics, University of Technology, Baghdad, Iraq.
[2]Department of Applied Science, Division of Biotechnology, University of Technology, Baghdad, Iraq.

[1,2]eng.farahabdulkareem89@gmail.com

Abstract. Carbon nanoparticles CNPs decorated by copper oxide nano-sized particles would be successfully equipped using technique named pulsed laser ablation in liquid. The XRD pattern proved the presence of phases assigned to carbon and different phases of copper oxide. The chemical structure of the as-prepared nanoparticles samples was decided by Energy Dispersive Spectrum (EDS) measurement. EDS analysis results show the contents of Carbon, Oxygen and Copper in the final product. These nanoparticles were spherical shaped with a size distribution 10 to 80 nm or carbon nanoparticles and 5 to 50 nm for carbon decorated copper oxide nanoparticles, according to Transmission Electron Microscopy (TEM) images and particle-size distribution histogram. It was found that after doping with copper oxide, nanoparticles become smaller and more regular in shape. Optical absorption spectra of prepared nanoparticles were measured using UV–VIS spectroscopy. The absorption spectrum of carbon nanoparticles without doping indicates absorption peak at about 228 nm. After doping with copper oxide, absorption shows appearance of new absorption peak at about (254-264) nm, which is referred to the movement of the charge between 2p and 4s band of Cu^{2+} ions.

Keywords. Nanoparticles (NPs), pulsed laser ablation in liquid medium (PLAL), Transmission Electron Microscopy (TEM), Copper Oxide.

1. Introduction

Carbon is a standout amongst the most various components in nature. Carbon-based nanomaterial has pulled in more interest for late years. There are extensive variety of carbon nanostructures have been synthesized, for example, carbon nanotubes, fullerenes, Nano fibers, Nano diamond, carbon nanoparticles, and different carbonaceous nanomaterial [1]. Carbon nanoparticles (CNPs), which assign to the type of round carbon-related nanomaterial, display numerous superior optical characteristics, such as stabilized photoluminescence property (PL), wide excitation wavelengths (λex) and tunable radiation. Among luminescent semiconductor substrate such as quantum dots, CNPs

exhibit further advantages of biological compatibility, minimum cell toxicity, effortless functionalization, perfect solubility in water circumference. Therefore, CNPs have encountered developing respect in many promising fields, for example, imaging in biomedicine, delivery of drugs in body, optoelectronic [2].

Furthermore, it could be the host to therapeutic agents, attributable to their great surface functional groups such as amine, amide, carbonyl, alcoholic hydroxyl [3]. Nanoparticles of metal oxides are already greatly synthesized because of their unique applications. Nano-copper oxide (CuO) is p-type narrow band gap semiconductor (1.2 eV at room temperature) is basically utilized in a part of numerous applications, for example, catalysis, photo-catalysis, gas sensors, solar energy transformation, and electronics [4].

Other carbon compounds broadly examined are the carbon-containing nanoparticles, usually called carbon nanocomposites. These matters have gotten fabulous notice because of exceptional properties.

Like high surface area and regular pore dimension, thermal and mechanical steadiness [1]. Nanoparticles of metal or metal oxide, which were propped on small dimensional of carbon Nano-scale materials have created noteworthy enthusiasm for different applications. These nanoparticles are extremely stable since they are embedded in the carbon matrix [1].

The incorporation of different metal oxide nanostructures on surface of carbon Nano-dimensions substrate let them to be helpful for many applications not just due to particular physical and chemical properties of upheld particles, but furthermore to their big area of the surface, sprightly weight, high mechanical quality, and great electrical and thermal transfer features [5].

Different techniques have been utilized for the preparation of carbon nanomaterial decorated by semiconductor nano-scale particles [6, 7, 8, and 3]. Pulsed laser ablation in liquid environment (PLAL) is a one of these methods. It is well-known system to produce NPs, where solid positioned in a colloidal medium [9]. Thus, Laser Ablation in solution is a strategy to manufacture a wide range of nanostructure materials. In its procedure, laser beam, which is an intensive one, is illuminate surface of metal target resulting in the generation of plasma plume within the fluid–target binding forming micro-bubbles. These bubbles grow to achieve a specific basic mix of pressure and temperature and after that collapse [10]. The result is generation and expulsion of Nano-dimension clusters from the objective substrate into the restricting environment, ensuing the fashioning of solutions of nanoparticles. Morphology, size and chemistry of Nano-scale particles surface could be administered through varying parameters of used laser, type of the desired material and liquid circumference [11]. PLAL can use to prepare an extensive variety of novel substances and the final products are typically inside the shape of nanoparticles that stay suspended within the liquid medium, and can be separated by filtration and evaporation of the liquid [12]. In addition, this method is simple and does not require a vacuum system [13]. In this work, carbon nanoparticles decorated with different copper oxide nanoparticles ratio were prepared using PLAL and characterization of these nanoparticles were studied by several techniques.

2. The Used Matters and Techniques

2.1 NPs Solution Production

Carbon doped by copper oxide nanoparticles would be synthesized by irradiation of a pure graphite pellet (99.9% purity, diameter of 0.5 cm and thickness of 2 mm) with laser, which is positioned at a vessel base and immersed by 3 ml of de-ionized water. Q-switched Nd:YAG laser of following features was employed to produce the nanoparticles: wavelength of 1064 nm, frequency of 1 Hz, pulse width of 9 ns, and laser fluence of 10.6 J/cm^2 for 75 pulses. After production of carbon nanoparticles, copper target (96.53% purity, diameter of 1.5 cm and thickness of 3mm) was put in these carbon nanoparticles colloidal and was ablated by same laser at different doping ratio.

2.2 Characterization

Prepared carbon nanoparticles doped with copper oxide Nano-colloids were distinguished by both optical and structural methods. A double-beam UV–Vis spectrophotometer (Schimatzu) was utilized to register optical absorption of NPs colloids in the range 200-800 nm. Photoluminescence (PL) was measured to determine energy structure of nanoparticles by (Elico, S174, spectrofluorometeric

detector, Shimadzu RF-551). The measurement was carried out in Science collage /University of Baghdad. X-ray diffraction (XRD) measurements of NPs colloidal, which dropped and dried on glass slides, were achieved using Shimadzu XRD 6000 with Cu-Kα radiation source at 2θ angle = (10°–80°). Transmission electron microscope (TEM -type Philips) was used to discuss the morphological properties of the NPs. Samples were prepared for TEM analysis by dropping Nano-colloids onto a model copper grid coated with gold (contains about 200 meshes). EDS measurements were done by (Inspect S 50 /FEI Company/ Netherlands) at Al-Khofa University. Samples were prepared for EDS by dropping few drops of solutions on slides of glassy substrate and let it dry for ten minutes.

3. Result and discussion

'Figure 1' shows the optical absorption spectra of colloidal NPs. UV-visible spectrum of synthesized carbon nanoparticles without doping indicates absorption peak at about 228 nm. This may be contributed the $\pi \rightarrow \pi^*$ transition typically found in the carbon which is in a range of 180 - 280 nm [14]. It is of the aromatic sp^2 domains, and leads to very low fluorescence intensity [2]. While after doping with copper oxide, the optical absorption shows appearance of new absorption peak at about (254-264) nm, which indicates the charge transformation among what named 2*p* oxygen orbital's and 4*s* of Cu^{2+} ions [15]. Change in the UV-visible spectrum could be due to complex formation between copper and CNPs.

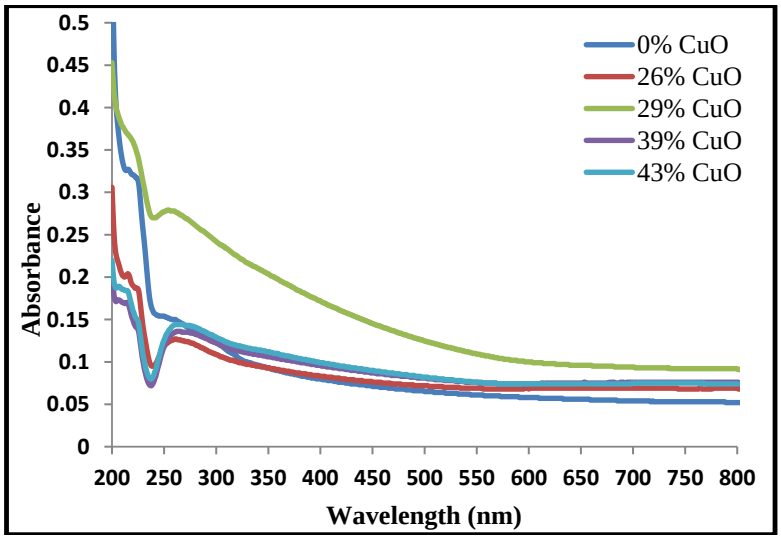

Figure 1. Absorbance spectra of carbon nanoparticles prepared at 10.6 J/cm^2 in de-ionized water (0%) and then doped with different ratio (26, 29, 39 and 43) % of CuO NPs.

The photo luminescent spectra of the synthesized carbon decorated copper oxide nanoparticles were studied using the same excitation wavelengths of 350 nm as shown in 'figure 2'. PL spectra for all suspensions are ranging from 390 to 550 nm. The maximum intensity of fluorescent emission was obtained between (452-460) nm, which is correlated with blue wavelength [14].

The photoluminescence intensity yield of the C-CuO NPs was observed to be highest for carbon NPs alone than that of the other samples. This could be due to the quenching of the luminescence of carbon NPs in the presence of CuO [16].

XRD measurements were studied through interval scan from 10º to 80º. In XRD spectrum of CNPs made by laser at fluence of 10.6 J/cm^2 for 75 pulses in 'figure 3', there are significant diffraction pattern that could be viewed at 2θ of 26.58° and 43.78º, which returning to the (002), and (101) reflection phases of carbon respectively (JCPDS No.41-1478 and 06-0675) [17]. While in XRD pattern of carbon NPs decorated with copper oxide NPs of different concentration (26%, 29%, 39%, 43%), new peaks of copper oxide will be appeared at 2θ (38.5° and 48.64° corresponded to (111), (202) crystal planes of CuO with monoclinic phase, respectively. The peaks have well consent with the standard pattern of monoclinic CuO (JCPDS Card No. 05-0661) [18].

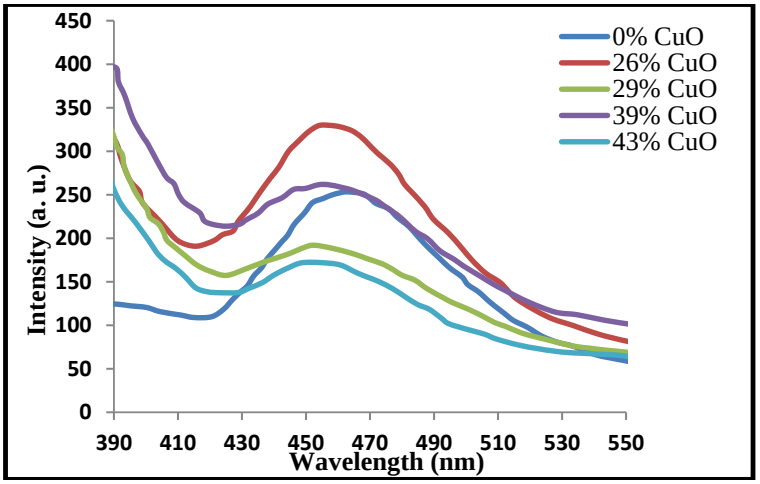

Figure 2. Photoluminescence spectra of carbon nanoparticles doped with different ratios (26, 29, 39 and 43) % of copper oxide nanoparticles.

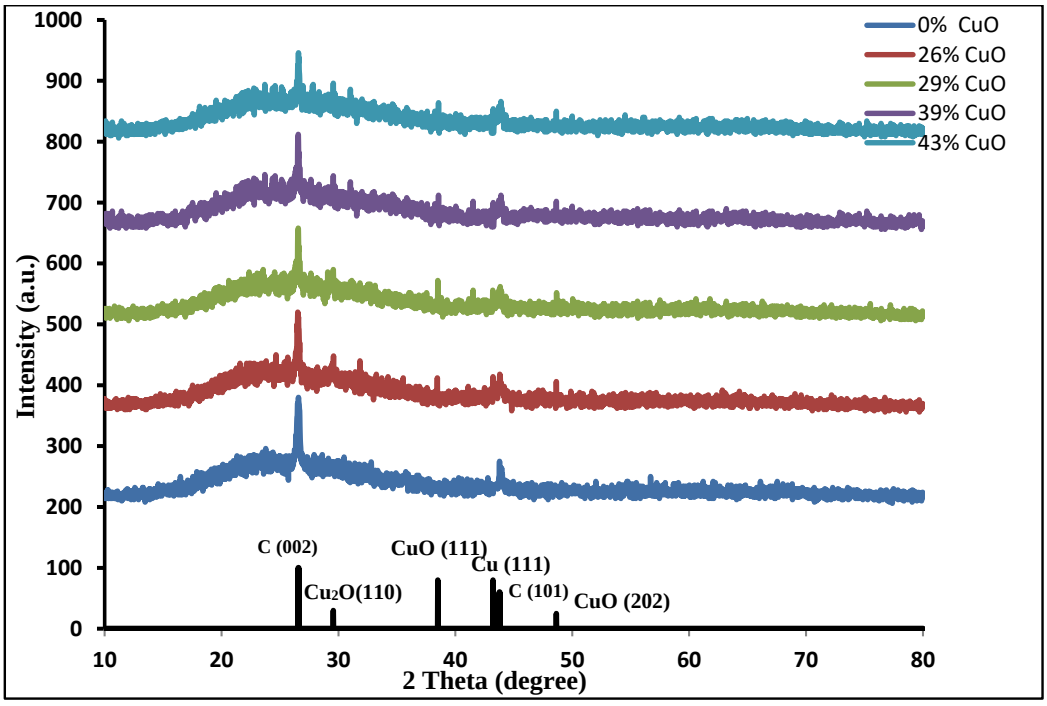

Figure 3. XRD pattern of carbon nanoparticles doped with different ratios (26, 29, 39 and 43) % of copper oxide nanoparticles.

In addition, typical diffraction peak of Cu_2O (110) and Cu (111) is observable in the XRD pattern for carbon doped by copper oxide nanoparticles at $2\theta = 43.2°$ and 29.56° respectively. It can be seen that intensity pattern of carbon nanoparticles still observable in the XRD pattern for carbon doped copper oxide nanoparticles. It can be ascribed to the fact that CNPs cannot be reduced under the Nano composite preparation conditions [19].

The morphology and particle size of prepared nanoparticles was determined by TEM images and the particle size distribution histogram. It was found to be in a range of 10–80 nm for carbon Nano-dimensional particles synthesized with laser ablation in de-ionized water at 10.6 J/cm^2 as shown in 'figure 4'.

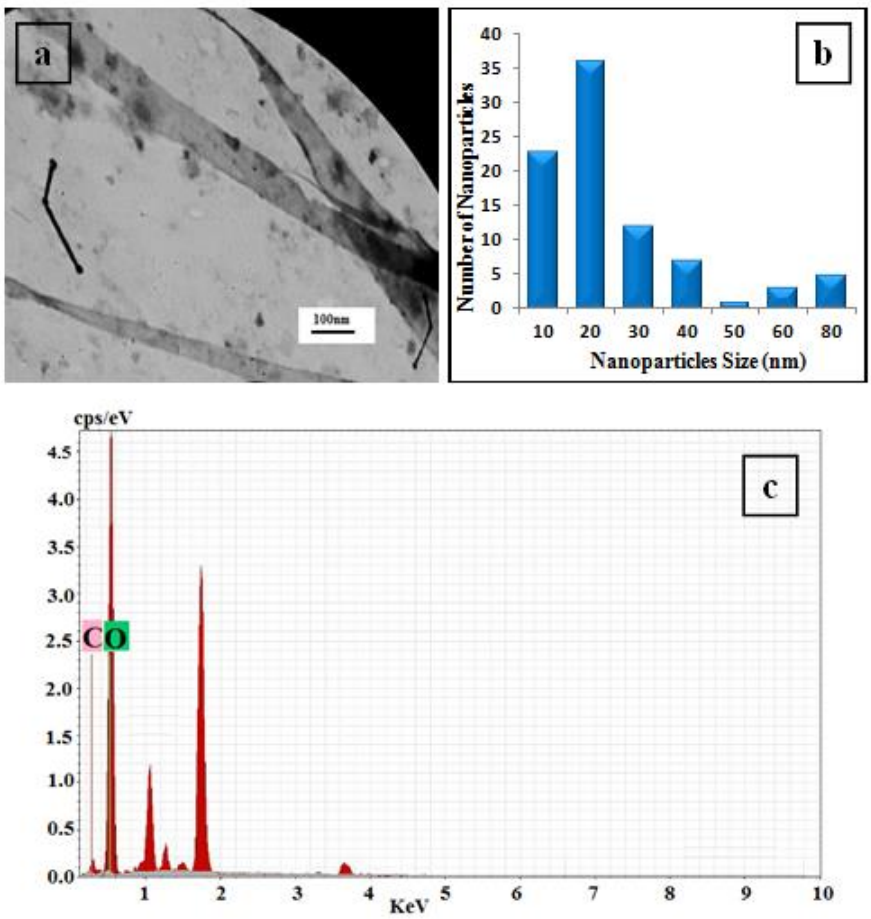

Figure 4. (a) TEM image of carbon nanoparticles prepared by laser ablation of carbon target in de-ionized water at 10.6 J/cm^2 laser fluence (0% CuO), (b) Size distribution of prepared carbon nanoparticles, and (c) EDS spectrum of nanoparticles.

TEM image shows little aggregation of nanoparticles due to a small electrostatic repulsive force between them produced by the electric double layer on the nanoparticles' surfaces [20]. The chemical composition of the as-synthesized carbon nanoparticles samples was determined by Energy Dispersive Spectrum (EDS) measurement. EDX spectra in 'figure 4c' indicated the presence of only C, and O in the collodial (O was from the TEM grid) [12].

While 'figure 5' show morphology, size distribution, and chemical composition for carbon nanoparticles decorated by copper oxide nanoparticles with ratio 43% CuO. It can be seen that the nanoparticles are mostly of spherical shape with a size distribution between 5 to 50 nm, as depicted in the size histogram in the figure inset. It was found that after doping with copper oxide, nanoparticles become smaller and more regular in shape and turn over shape that is more spherical. Carbon-metal oxide NPs are formed by binding metal to the peripheral carboxylic bonds of carbon by ion exchange. The result is carbon nanoparticles surrounded by metal oxide nanoparticles, so peripheral charges of carbon can help in stabilizing the metal particles in solution.

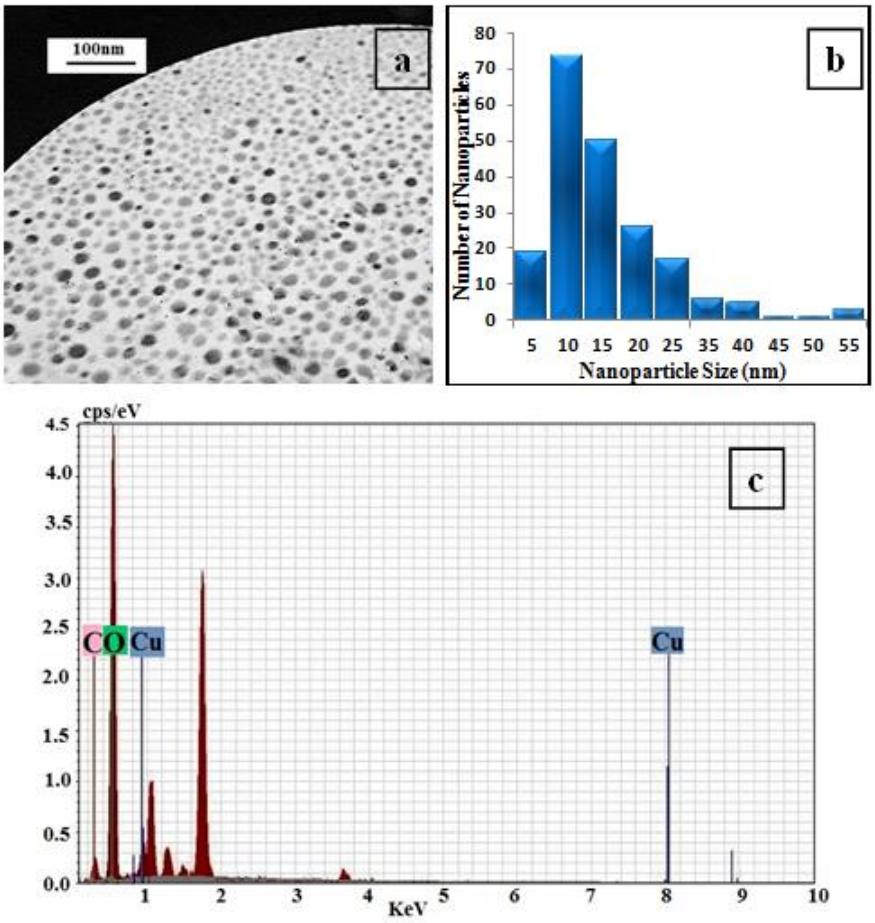

Figure 5. (a) TEM image of carbon nanoparticles doped with 43% of copper oxide nanoparticles prepared by laser ablation, (b) Size distribution of prepared nanoparticles, and (c) EDS spectrum of nanoparticles.

EDS analysis results show the contents of Carbon, Oxygen and Copper in the final product. The ratio of weight (%) of C, O, and Cu matters in the as-prepared final nanoparticles sample are 9.82, 12.25, and 4.11, respectively.

4. Conclusions

In conclusion, Carbon nanoparticles decorated by copper oxide Nano-colloidal had been effectively manufactured by ablation with pulsed laser technique in a liquid medium. It is found that doping of carbon nanoparticles with copper oxide nanoparticles will result in formation of decorated nanoparticles that are more uniform in shape and smaller. In addition, that doping will cause quenching of photoluminescence spectra of carbon nanoparticles.

Acknowledgements

We would be acknowledged to the Department of Applied Science, University of Technology, Baghdad, Iraq for offering assistance.

References

[1] Krolow M Z, Hartwig C A, Link G C, Raubach C W, Pereira J S F, Picoloto R S, Gonçalves M R F, N Carreño L V and Mesko M F 2013 Synthesis and characterisation of carbon nanocomposites *Carbon Nanostructures* 3 pp 33-47

[2] Hu Q, Meng X, Choi M M F, Gong X and Chan W 2016 Elucidating the structural of carbon nanoparticles by ultra-performance liquid chromatography coupled with electrospray ionisation quadrupole time of- flight tandem mass spectrometry *Analytica Chimica Acta* **911** pp 100-107
[3] Palashuddin M, Goswami U, Ghosh S S and Chattopadhyay A 2015 Cu2+- embedded carbon nanoparticle as an anticancer agent. *J. Mater. Chem.* **B** 3 pp 5673-5677
[4] Jeyakumari A P, Ramakrishnan M, Nithyanandhi Y and Renuka S 2017 Structural and antibacterial activity of copper oxide nano particles *IOSR JAP* pp 57-63
[5] LinY, Baggett D W, Kim J, Siochi E J, and Connell J W 2011 Instantaneous formation of metal and metal oxide nanoparticles on carbon nanotubes and graphene via solvent-free microwave Heating *ACS Appl. Mater* 3 pp 1652–1664
[6] Abbaspourrad A, Verissimo C, Gelamo R V, da Silva M M, Vaz A R, Rouxinol F P M, Alves O L and Moshkalev S A 2013 Gas Sensors Based on Multiwall Carbon Nanotubes Decorated with Different Metal Oxides Nanoparticles Smart *Nanocomposites* **1** pp 13-18
[7] Athanassiou E K, Grass R N and Stark W J 2006 Large-scale production of carbon-coated copper nanoparticles for sensor applications *Nanotechnology* **17** pp 1668–1673
[8] Johan M R, Suhaimy S H M and Yusof Y 2014 Physico-Chemical studies of cuprous oxide (cu2o) nanoparticles coated on amorphous carbon nanotubes (α-cnts) *Applied Surface Science* **289** pp 450– 454
[9] Khashan K S, Sulaiman G M and Mahdi R 2017 Preparation of iron oxide nanoparticles-decorated carbon nanotube using laser ablation in liquid and their antimicrobial activity *Artificial Cells Nanomedicine and Biotechnology* pp 1-11
[10] Al-Hamaoy A, Chikarakara E, Jawad H, Gupta K, Kumar D, Ramachandra Rao M S, Krishnamurthy S, Morshed M M, Fox E, Brougham D, He X, Vázquez M and Brabazon D 2014 Liquid phase pulsed laser ablation: a route to fabricate different carbon nanostructures *Applied Surface Science* **302** pp 141-144
[11] Bagga K, McCann R, Wang M, Stalcup A, Vázquez M and Brabazon D 2015 Laser assisted synthesis of carbon nanoparticles with controlled viscosities for printing applications *Journal of Colloid and Interface Science* **447** pp 263-268
[12] Yang L, May P W, Yin L, Smith J A and Rosser K N 2007 Growth of diamond nanocrystals by pulsed laser ablation of graphite in liquid.*Diamond & Related Materials* **16** pp 725–729
[13] Thongpool V, Phunpueok A Piriyawong V, Limsuwan S and Limsuwan P 2013 Pulsed laser ablation of graphite target in dimethyformamide *Energy Procedia* **34** pp 610-616
[14] Thongpool V, Asanithi P and Limsuwan P 2012 Synthesis of carbon particles using laser ablation in ethanol. *Procedia Engineering* **32** pp 1054-1060
[15] Nath A and Khare A 2011 Size induced structural modifications in copper oxide nanoparticles synthesized via laser ablation in liquids *Journal of Applied Physics* 110 043111-1-043111-6
[16] Raja S and Deepa M 2015 Synthesis and characterization of polyaniline-copper (ii) oxide nanocomposite by wet chemical route *Indian Journal of Advances in Chemical Science* **3** pp 198-203
[17] Thongpool V, Denchitcharoen S, Asanithi P and Limsuwan P 2011 Preparation of carbon nanoparticles by long pulsed laser ablation in water with different laser energies. *Advanced Materials Research* **214** pp 402-405
[18] Chen C, Yu C and Fu X W 2014 Wang Z B. Synthesis of graphite oxide-wrapped cuo nanocomposites for electrocatalytic oxidation of glucose synthesis and reactivity in inorganic *Metal-Organic and Nano-Metal Chemistry* **44** pp 1521-1525
[19] Mahmoodi N M, Rezaei P, Ghotbei C and Kazemeini M 2016 Copper oxide-carbon nanotube (cuo/cnt) nanocomposite: synthesis and photocatalytic dye degradation from colored textile wastewater *Fibers and Polymers* **17** pp 1842-1848
[20] Khashan K S and Mohsin M H 2013 Synthesis of polyynes by laser ablation of graphite in Ethanol *Iraqi Journal of Physics* **11** pp 37-47

Doping And Annealing Effect On Evaporation Of ZnO Thin Films

Doping And Annealing Effect On Evaporation Of ZnO Thin Films

Auday H Shaban*, Samir A. maki, Shahd A. hussain,

Department of physics/ College of Education For Pure Science (Ibn Al-Haitham), University of Baghdad, Baghdad, Iraq

auday.h.s@ihcoedu.uobaghdad.edu.iq*

Abstract. The present study carried out to show the structure and optical properties of doped ZnO:Sn thin films that have been deposition on a glass substrate by thermal evaporation (using Zn metal). The percentage of dopant is (3, 5, 7, & 9)%. The annealing temperature was 200 oC fixed for one hour annealing time. The result of XRD shows the presence of (100), (002) and (101) are the diffraction peaks of all thin films. The crystalline size was found to be increased with Sn doping. The FWHM values of the peaks were found to increase with doping. The direct optical band gap was calculated and found to be (3.24, 3.21, 3.2, 2.72, 2.88) e.V for pure and doped thin films respectively.

Keywords ZnO, optical properties, Sn doping, thermal evaporation.

1. Introduction

The transparent conducting oxides (TCO) has an interest wide range of application in solar cells, gas sensors, light emitted diode (LED), etc. Zinc Oxide can prepare by spray pyrolysis [1], sol-gel, chemical vapor deposition (CVD) and reactive evaporation. Among these methods, the thermal evaporation technique is a simple method and low-cost procedure [2]. Zinc Oxide is a semiconductor from II-VI group. it has a direct band gap 3.37 e.V and free excitation energy 60 Me.V [3]. Generally, it has polycrystalline with Wurtzite hexagonal structure [4]. In present study Tin (Sn+4) have a chosen as doping in ZnO matrix of ZnO as it will easily replace the (Zn+2) ions with (Sn+4) ions and create two more electron vacancies. In such condition, it will produce good conductivity and also alter some structural properties. It is known that the substitution of Sn does not produce large lattice distortion parent matrix (ZnO) because of its almost equal radius. Much of previous studies on pure ZnO and Sn-doped ZnO thin films with various concentration (3, 5, 7 & 9)% were deposited by thermal evaporation technique on the effect of the annealing process[5]. The properties of the deposited ZnO and ZnO:Sn films depend on the deposition parameters such as substrate temperature, the evaporation rate of Zinc metal and Tin concentration.

2. Experimental techniques

Thermal evaporation was used to deposit pure Zn at room temperature and under vacuum about 10^{-5} (mbar) using Edward coating unit. The thin films were coated on a glass substrate at thickness 200 nm. The distance between the substrate to the source was 8 cm and the metal was placed in a molybdenum boat in thermal evaporation system. After deposition of Zn metal on a glass slide, the films were followed by thermal oxidation in air using furnace at temperature 400 C^{o} with flow rates of oxygen 2.5 litters/ min for two hours to form ZnO thin films. After oxidation the samples were cooled at room temperature. The doping percentage of Tin varies (0 - 9) % were deposited on ZnO thin films then diffused by heating temperature 140 C^{o} for one hour. All the pure and doped thin films were annealed at 200 C^{o}. The structural properties were studied by X-ray diffraction using a (model (E306) with Cu Kα radiation (λ_{cu} = 0.154056 nm) as the source. The crystalline size was studied from Scherrer's formula. The influence of annealing time on the structure of thin films was investigated. The optical transmission and absorption of pure and doped ZnO were studied by UV-visible spectrophotometer with range (300-1100) nm.

3. Result and discussion:

1- The effect of doping:

A- Structural properties

'Figure (1)' shows the X-ray diffraction of pure ZnO and doped thin films at different doping percentage. The peaks of XRD show that thin films are polycrystalline with a hexagonal structure (ASTM-00-019-1365) with orientation peaks (100), (002) and (101). With increase Sn content. The changes of peaks intensity depend on the level of Sn Doping. The value of the preferred orientation for pure ZnO thin film is (100) which is agree with **[3],** the peaks intensity is the domain orientation with respect to (002) and (101).

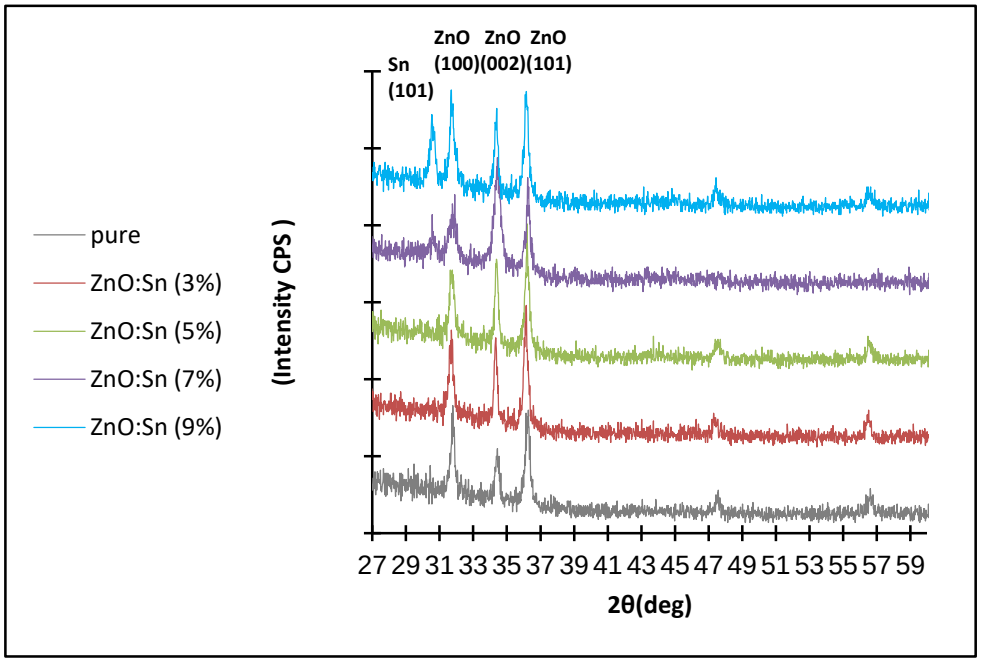

Figure 1. X-ray diffraction of ZnO:Sn thin films with different doping.

Table (1) shows the variation of intensity is dependent on the rate of the Sn impurities. The preferred orientation direction depends on Sn content. The value of pure ZnO films I(100) is a high intensity compared to both I(002) and I(101). At doping (3%) the value of I(100) is reducing until we reach (7%) compared to pure ZnO. the value of I(101) for doping (5%) continues to increase and the domain orientation becomes (101). At doping (7%) the value of I(002) is increased compared to (5%) and the value of I(101) decrease, therefore, the preferred orientation is (002). At doping (9%) the value of (002) decrease compared to (7%) while I(100) increased then the value of I(002), I(101), therefore again a preferred orientation along I(100) similar to pure ZnO. It is clearly noticed that was a peak appeared for Sn at (7%) and this peak increased at (9%). These results match the ASTM cards (00-019-1365) for Sn. The previous results refer to (impurities with limit percentages improves the crystalline structure) because it will reduce the crystal defects. The impurities atoms made their own atomic states except at 9% doping, where at this percentage, a reverse impact appears on the structural properties.

Table 1. shows the variation of intensity of XRD doping thin films.

Sn %	$I_{(100)}$	$I_{(002)}$	$I_{(101)}$	Preferred orientation	Sn $I_{(101)}$
o	166	110	156	100	
3%	164	154	194	101	
5%	140	150	202	101	
7%	140	188	162	002	114
9%	176	152	174	100	144

Table (2) indicates the diffraction angle (2θ), full width at half maximum (FWHM) and crystallite size (D) was calculated by using Scherrer's equation (1): **[6]**

$$C.S = \frac{0.9\,\lambda}{\beta cos\theta} \quad \text{.....(1)}$$

Where **λ**: is the wavelength (A)
β : is the full width at half maximum (FWHM) of diffraction peak.
θ : Bragg angle.
The number of dislocation was calculated by equation (2):

$$\delta = \frac{1}{(C.S)2} \quad \text{.....(2)}$$

Where **δ** : dislocation density (Dislocation line/nm^2).
C.S: crystalline size (nm^2).
That obtained by x-ray diffraction for all peaks. The crystal size was decreased with increasing impurities except for 9% and an increase of dislocation δ. The dislocation is an indication of the crystals quality and Crystallization Level. The relation between dislocations and square particale size is [$\delta \propto D^{-2}$] **[7]** through a table (2) appears an increasing of layers with increasing impurities.

Table 2. X-ray diffraction of the peaks of ZnO thin films.

Sample	β (deg)	D (nm)	δ * 10^{14} (line.m^{-2})
ZnO (pure)	0.27	29.91	11.3
ZnO:Sn (3%)	0.27	31.2	11.09
ZnO:Sn (5%)	0.27	30.4	11.5
ZnO:Sn(7%)	0.28	29.3	11.7
ZnO:Sn(9%)	0.44	19.1	30.1

b- Optical properties

'Figure 2' illustrated the optical transmittance spectra with respect to wavelength for ZnO: Sn thin films. The films show high transmission and low absorption and reflection. The transmittance of ZnO thin films decreases with increasing doping percentages. This behavior happened because of the creation of local states, gained from the impurities, at energy gap between valance and conduction bands, which increase absorption. It is also shown from the figure that the highest transmission was for pure Zinc Oxide thin films, reaching Its transmission is about (90)% of the wavelengths within the infrared region (800-900) nm **[4]** and this is the least absorption. The previous behavior makes the ability to use the properties of ZnO thin film as a transparent material for vehicles and airplanes windows, also as IR detector shields **[8].**

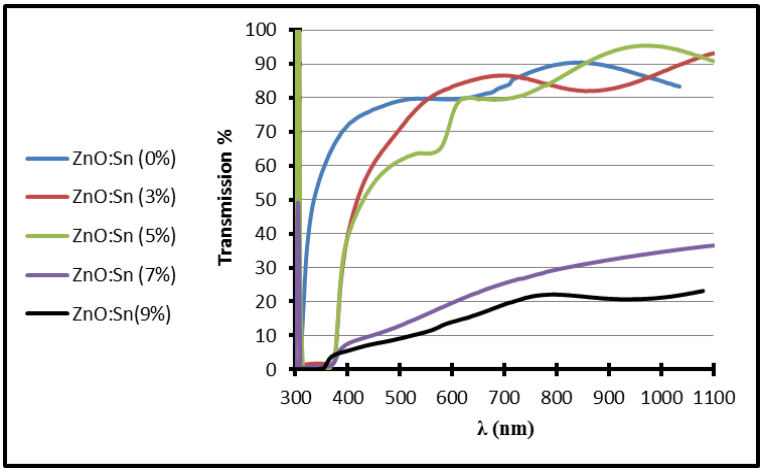

Figure 2. Transmittance spectra as a function of wavelength.

'Figure 3' , 'Figure 4' illustrated the increasing of absorption and reflection curve with increasing doping percentages. The reason for this behavior is the increasing of local states at energy gap **[8]**. Doping thin films were recorded with a precipitation rate of (9) % in the study that showed higher absorption compared to the absorption of the thin films prepared from pure and doping.

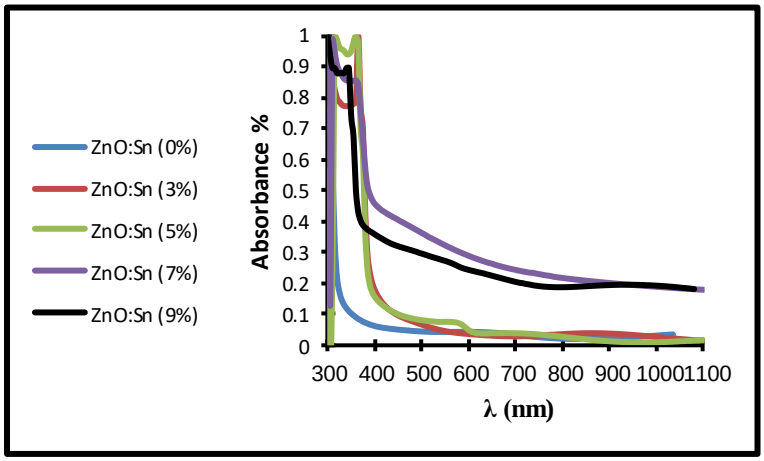

Figure 3. Absorbance spectrum as a function of wavelength.

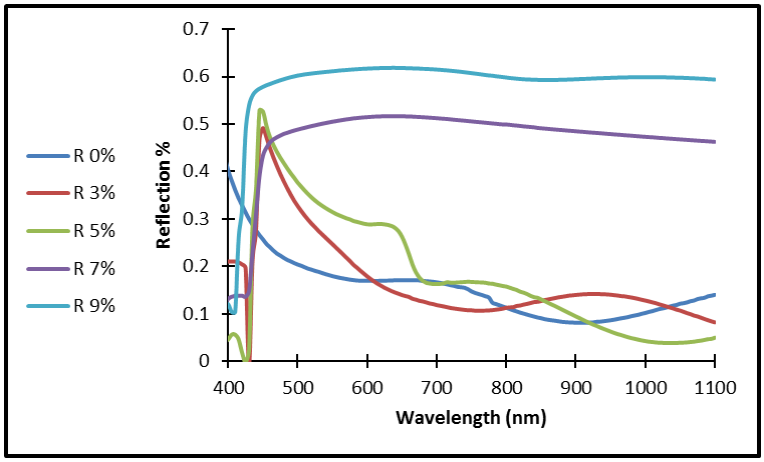

Figure 4. Reflection spectrum as a function of wavelength.

'Figure 5' illustrates the changes in the absorption coefficient as a function of the photon energy. The absorption coefficient generally begins a gradual increase as photon energy increases at ranges (2.2 - 2.9) eV for doping thin films. By increasing doping rate the absorption coefficient increases with low photonic energy. The higher value of absorption coefficient is greater than (10^4) cm^{-1}, indicate to direct electronic transitions between the valence and conduction bands at these energies. The absorption coefficient has a maximum value at ($9*10^4$) cm^{-1}. At the energy range (2.85 - 3.3) eV, the absorption coefficient remains almost constant.

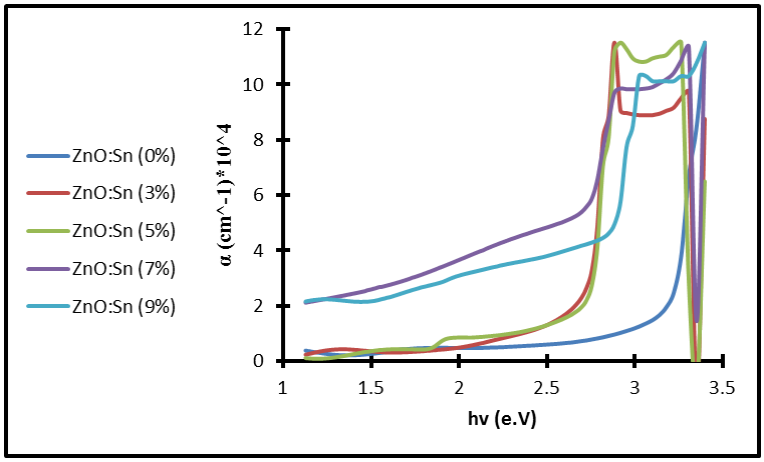

Figure 5. Absorption coefficient with different percentages.

The optical energy gap between the thin films material is the standard path to use these materials in industries. ZnO has a direct band gap dependence of the absorption coefficient can be calculated by Tauc's equation (3) [9]:

$$\alpha h\nu = B(h\nu - E_g)^n \quad \ldots\ldots\ldots\ldots (3)$$

where α: is absorption coefficient.
hv: the photo of energy.
B: constant.
Eg: the energy gap.
n: constant the type of electronic transition.

'Figure (6)' illustrated the relation between (hν) and $(\alpha h\nu)^2$ and the modification process to achieve the intercept with X-axis.
The band gap of the pure ZnO thin films is 3.24 eV **[10].** After doping the band gap is decrease to (2.72 eV) for (7 %) dopant this due to additional levels below the conduction band **[9]**. At level (9%) the energy gap is increases because of increase in the band tail width **[6].** Table (3) illustrates the variation value of energy gap with doping concentration.

Table 3. the change of energy gap with different doping.

sample	Energy gap (e.V)
pure	3.24
3%	3.21
5%	3.2
7%	2.72
9%	2.88

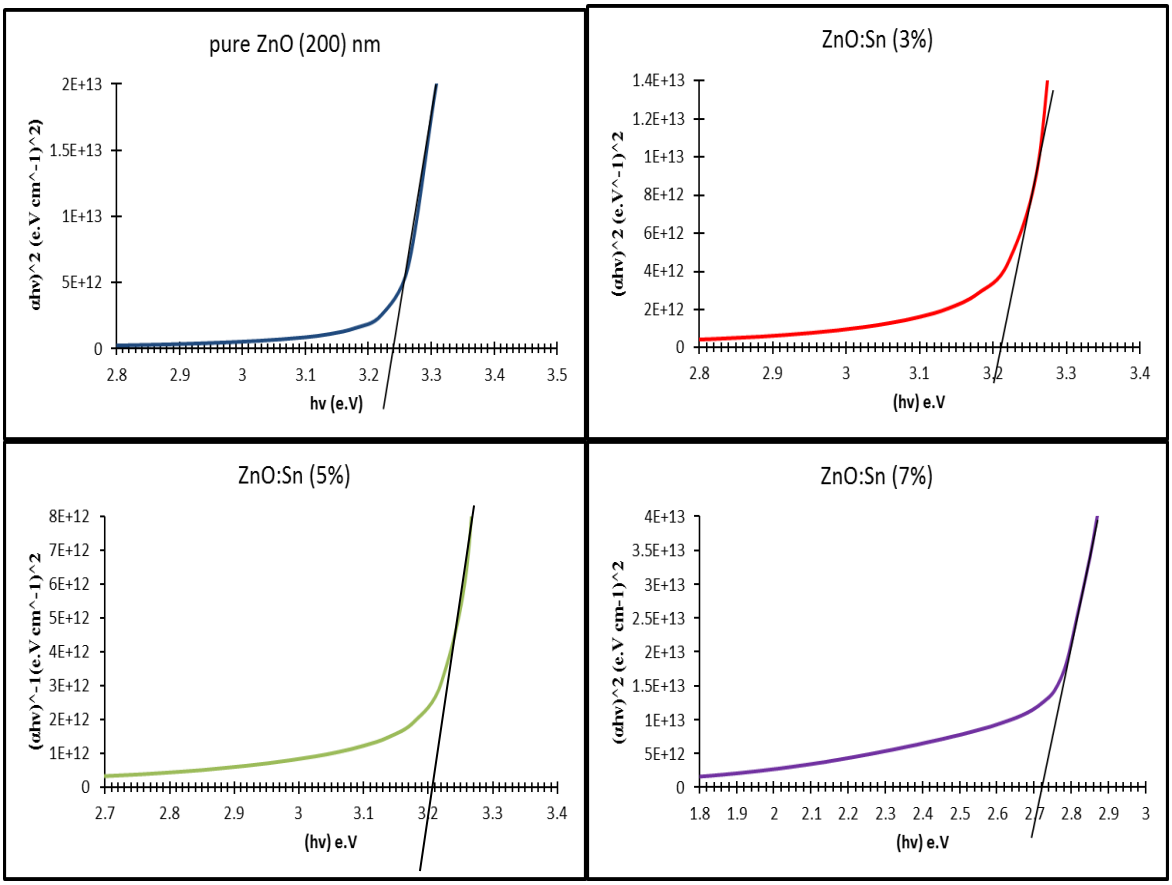

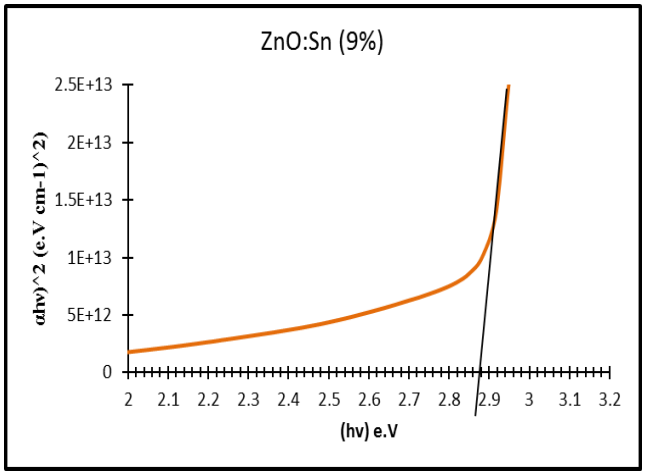

Figure 6. Energy gap for pure and doped ZnO thin films.

a- The effect of annealing
b- Structural properties

'Figures 7' illustrate X-ray diffraction of doping Zinc Oxide thin films after annealing. It show the effects on the domain peak which make it higher and more crystal order. Comparing the results between XRD and ASTM, which appear to be matched, before annealing. Table (4) shows the comparing values. This behavior gained from annealing process which makes the atoms with bigger energies and reorders the structure. The reason behind reduce the peaks, except the domain one, is the reorder process done with the domain direction.

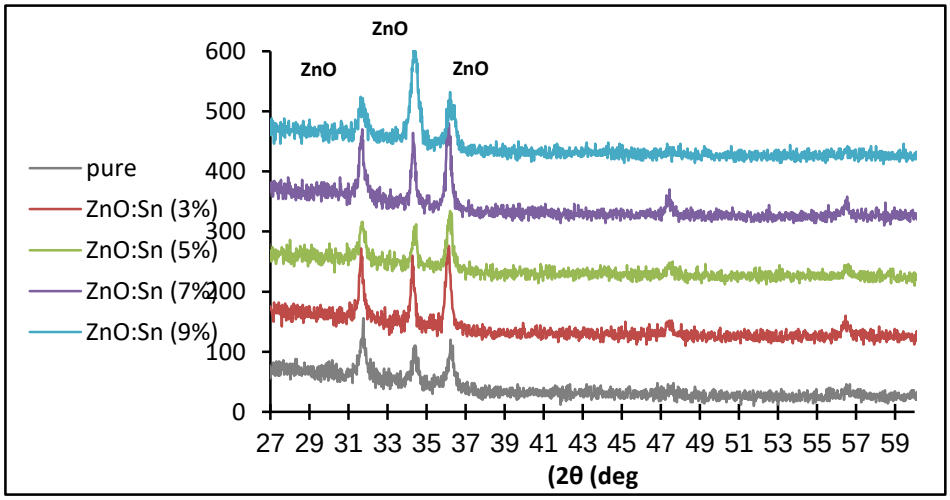

Figure 7. X-ray diffraction for ZnO thin films after annealing.

Table (4) shows the diffraction angle (2θ), full width at half maximum (FWHM) and crystalline size (D) was obtained by x-ray diffraction for all peaks. Table (4) illustrate Improved thin films the pure and doped with percentage 5 & 9%.

Table 4. X-ray diffraction for doped ZnO:Sn thin films after annealing.

Samples	FWHM (deg)	D (nm)	$\delta * 10^{14}$ (line.m^{-2})
ZnO (pure)	0.33	24.9	16.1
ZnO:Sn (3%)	0.27	30.6	10.8
ZnO:Sn (5%)	0.31	26.3	15

ZnO:Sn (7%)	0.27	30.7	10.8
ZnO:Sn (9%)	0.45	18.02	30.8

Table (6) illustrated the grain size for 9% was less size than after annealing. The FWHM curve is wider at the middle based on Scherer equation, which shows a nanocrystaline structure.

c- Optical properties

Optical measurements of doped thin films after annealing were performed. The transmission decrease of pure ZnO thin films after annealed at 200 C° was below 70%. Figure shows the transmittance increase with increasing wave length. The transmittance values decrease with increasing impurities. The annealing effects on the transmittance and makes them decrease than before annealing **[11].**

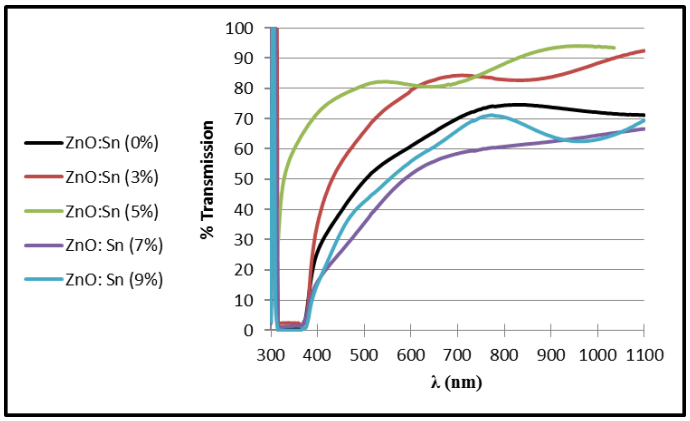

Figure 8. Transmission spectra forZnO:Sn films after annealing.

'Figure (9) & (10)' illustrated the absorption and reflection spectra for ZnO pure and doped thin films after annealing with respect to photon energy. This figure shows the increase of absorption and reflection with annealing and displacement of optical absorption edge to the region of higher wave length. The absorption spectra for ZnO thin films gradually decrease with increasing impurities, except for the pure sample which shows an increase in transmittance.

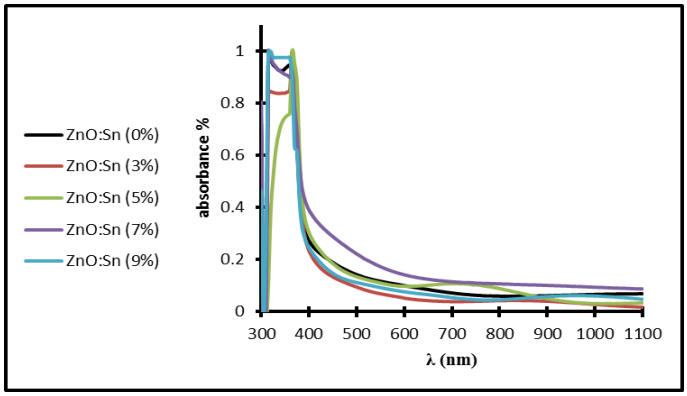

Figure 9. Absorbance spectra for pure and doped ZnO filmsafter annealing.

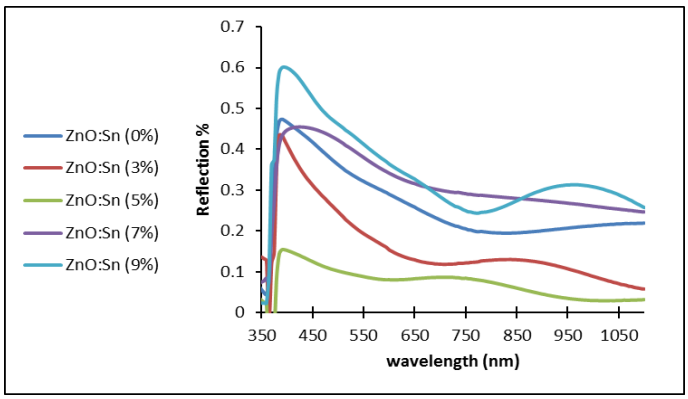

Figure 10. Reflection spectra for pure and doped ZnO films after annealing.

The absorption coefficients appear to be increase gradually with increasing photon energy. The absorption coefficients reduce with increasing impurities. The higher value appears at 9% after annealing. This figure shows that the absorbance coefficient values for pure and doped thin films after annealing is ($\alpha > 10^4$ cm^{-1}) indicate that the electronic transition is of the direct type.

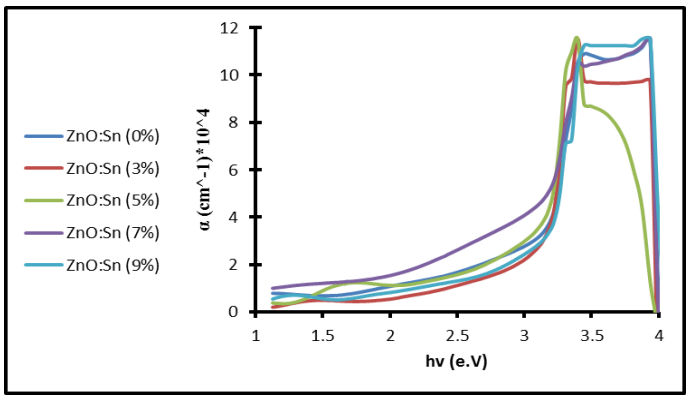

Figure 11. Absorption coefficient forZnO:Sn after annealing.

'Figure (12)' illustrate the changes of energy gap for pure and doped thin films after annealing. The figure shows the decrease of energy gap directly compare with energy gap before annealing because appearance of band tail resulting from defects associated with the presence of cavities and surface roughness **[3].** Table (5) illustrates the variation value of energy gap with doping concentration after annealing.

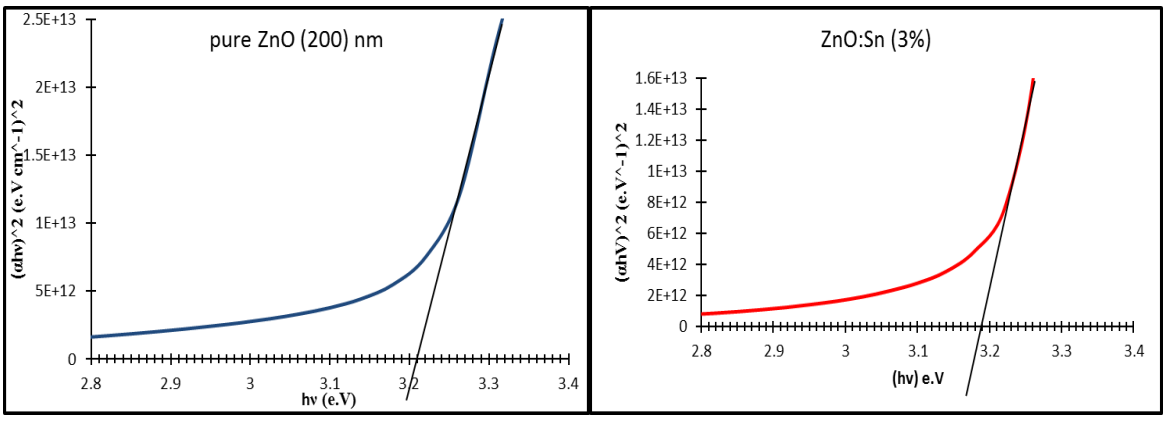

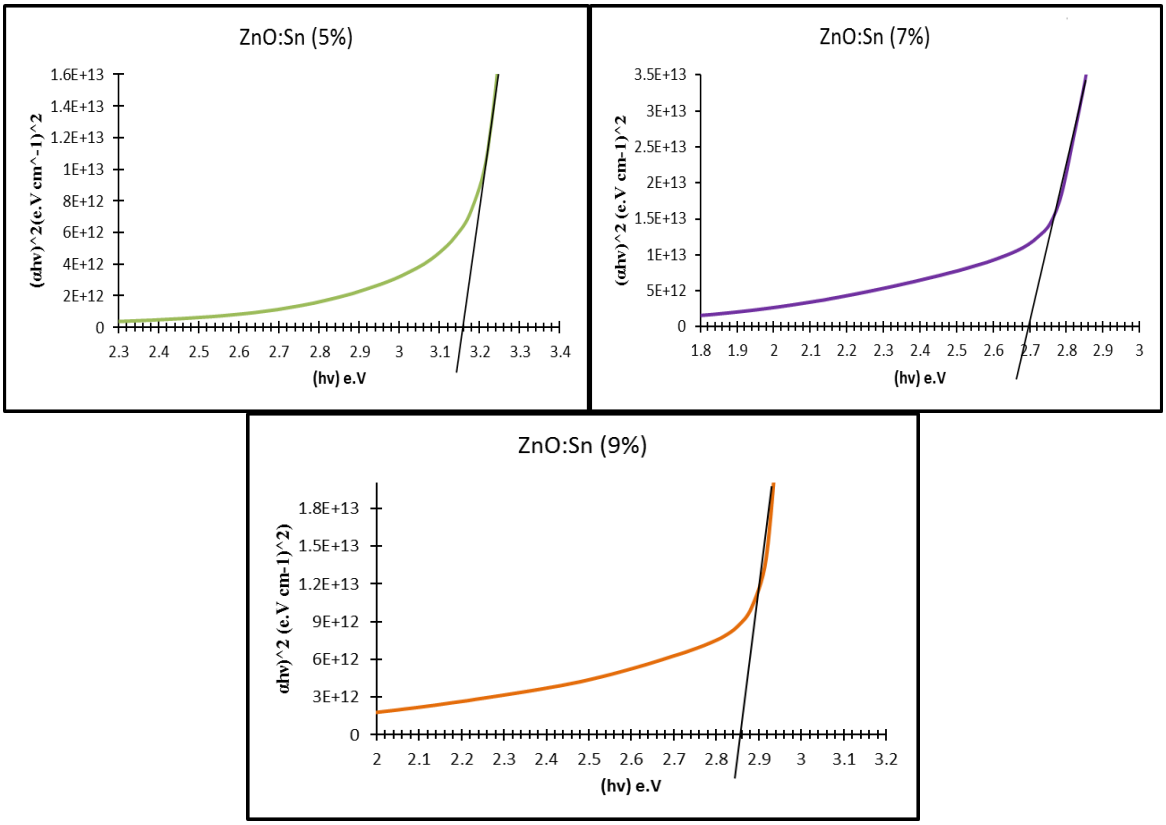

Figure 12. Energy gap for ZnO:Sn thin film after annealing.

Table 5. The change of energy gap after annealing.

sample	Energy gap (e.V)
pure	3.21
3%	3.19
5%	3.16
7%	2.7
9%	2.86

4. Conclusion

The films are apolycrystalline hexagonal structure wurtzite, and the preffered orientation for pure ZnO is (101) and varied with increase doping due to change of growth orentation. it is observed the value of crystaline size for (0, 3 and 5) % do not change, while at percantage (7 & 9) % shows increase the crystalline size. After annealng shows improvements for pure and doped at (5 & 9) % increase the crystalline size and decrease the FWHM. From optical properties show the best transmission for the effect of doping is about 95% for ZnO that due to complete oxidation of films, after anealing the transmission enhanced for thin films doping. The optical band gap decrease with doping reach to 5% then observe wideing due to Burstein –Moss effect. After annealing thin films show decrease the band gap effect of narrowing is attributed to film disorder.

References

[1] F.Z. Bedia, A. Bedia M. Aillerie, N. Maloufi, B. Benyoucef (2015), Structural, Optical and Electrical Properties of Sn-doped Zinc Oxide Transparent Films Interesting for Organic Solar Cells (OSCs), Energy Procedia, 74, 539-546.

[2] Sowmya Palimar. Kasturi V. Bangera, G. K. Shivakumar (2013), Study of the doping of thermally evaporated zinc oxide thin films with indium and indium oxide, applied nanoscience, **3**(6), pp:549–553.

[3] N. sadananda Kumar, Kasturi V. Bangera, G. K. Shivakumar (2014), Effect of annealing on the properties of zinc oxide nanofiber thin films grown by spray pyrolysis technique, applied nanosience, **4**(2), pp:209–216.

[4] N. chahmat, T. souier, A.Mokri, M.Bououdina, M.S.Aida, M.Ghers (2014), Structure, microstructure and optical properties of Sn-doped ZnO thin films, *journal of alloys and compounds*, **593**, pp:148-153.

[5] V .Ganesh, I.S. Yahia, S. AlFaify, Mohd. Shkir (2016), Sn-doped ZnO nanocrystalline thin films with enhanced linear and nonlinear optical properties for optoelectronic applications, *journal physics and chemistry of solids*, **100**, pp:115-125.

[6] Nadia chahmat et.al (2012), effect of Sn doping on the properties of ZnO thin films prepared by spray pyrolysis, *journal of modern physics*, **3**, pp:1781-1785.

[7] M. Ashraf, S. M. J. Akhtara, A.F. Khanb, Z. Ali, A. Qayyum (2011), Effect of annealing on structural and optoelectronic properties of nanostructured ZnSe thin films, *Journal of Alloys and Compounds*, **509**, pp:2414–2419.

[8] Sabri J. Mohammed, Khalaf. I. Khaleel, Qutaibah A. Abd-Aljabbar, (2013), Study the Doping Effect of Nickel on the Optical Properties of (ZnO) Thin Films, *Tikrit Journal of Pure Science*, **18**(4), pp:175-182.

[9] Sowmya Palimar, Kasturi V. Bangera, G. K. Shivakumar (2012), Highly conducting and transparent Ga2O3 doped ZnO thin films prepared by thermal evaporation method, Semiconductors, **46**(12), pp 1545–1548.

[10] Sowmya palimar, Kasturi V. Banger, G.K. Shivakumar (2012), study of the aluminum oxide doped zinc oxide thin films prepared by thermal evaporation technique, *journal of applied science*, **12**(16), pp:1775-1777.

[11] N. H. Sheeba, Sunil C. Vattappalam, Johns Naduvath, P. V. Sreenivasan, Sunny Mathew, Rachel Reena Philip (2014), effect of Sn doping on properties of transparent ZnO thin films prepared by thermal evaporation technique, chemical physical letters, **635**, pp: 290-294.

The Effect of Multi Wall Carbon Nanotubes on Some Physical Properties of Epoxy Matrix

The Effect of Multi Wall Carbon Nanotubes on Some Physical Properties of Epoxy Matrix

Tagreed M. Al-Saadi[1], Suad hammed Aleabi[1], Entisar E. Al-Obodi[2], Hadeel Abdul-Jabbar Abbas[1]

[1] Department of physics, College of Education for Pure Sciences – Ibn Al-Haitham, University of Baghdad ,Iraq
[2] Department of Chemistry, College of Education for Pure Sciences – Ibn Al-Haitham, University of Baghdad ,Iraq

E-mail: tagreedmm2000@gmail.com

Abstract. This research involves using epoxy resin as a matrix for making a composite material , while the multi wall carbon nanotubes (MWNCTs) is used as a reinforcing material with different fractions (0.0,0.02 , 0.04 , 0.06) of the matrix weight.

The mechanical (hardness), electrical (dielectric constant , dielectric loss factor , dielectric strength , electrical conductivity) , and thermal properties (thermal conductivity) were studied . The results showed the increase of hardness, thermal conductivity , electrical conductivity and break down strength with the increase of MWCNT concentration , but the behavior of dielectric loss factor and dielectric constant is opposite that.

Keywords : Epoxy resin , MWCNT , Electrical properties , Hardness , Thermal conductivity.

1. Introduction

Epoxy resin is one of the polymers has used as a matrix of fiber reinforced composites for advanced application [1] . Addition of MWCNTs results in significant improvement of epoxy resin [2,3].The researchers in recent years have reported to use of CNTs in metals [4],ceramic[5]and polymers[6],so they have paid much attention to the unique properties of CNTs [7-11]has led to their use in development of the next generation of new composites [12].

CNTs ,owe to their attractive electrical, mechanical, and thermal properties with chemical stability, have found a wide range of applications consist of nanomodifier of both thermoplastic and thermoset [13,14].That unique properties led to a variety of applications as sensors , energy conversation , energy storage devices ,radiation sources , field emission displays , interconnects ,coatings , hydrogen media[15-17] ,aerospace industry [18] and others.

The aim of this study was to investigate the structural , electrical, thermal and mechanical properties of epoxy / MWCNTs composite for different concentrations of MWCNTs.

2. Experimental

2.1.Matrix material

In this study(thortex) epoxy (EP) resin was used ,because it has an excellent adhesion , low shrinkage and good dimensional stability .

The epoxy resin is formed by a reaction of peroxides with a hardener Metaphynelendiamine (MPDA) used with epoxy by ratio (1 : 3) .

2.2.Carbon nanotubes

The nanolabas based manufacturer of carbon nanotubes, which can be exact to customer specifications . Our criteria carbon nanotubes products , including multi wall (MWCNTs) , nanotubes used in this work and single wall nanotube (SWNT) and double nanotubes (DWCNTs) . The MWCNTs were used in the research have purity about (95 %), the tube diameter ranges (30 - 50) nm and the tube length ranges from(3 to1) μm .

2.3.*Samples preparation*

The hand lay- up technique has been used to prepare sheets of composites .The carbon nanotube in different weight fractions (0, 2, 4 , 6) % by weight of the sample mixed with amount of epoxy . The dimension was made according to the shape and size of the samples are per ASTM involve the samples of tensile test , hardness , thermal conductivity and electrical conductivity .

2.4.Measurement

2.4.1. Hardness

The hardness was measured by instrument Shore (D) and the device used for this test kind (shore D hardness tester TH 210) , that is a tool by stitches in needle the surface of the sample and then record the number which comes out the screen of the device .

2.4.2.*Thermal conductivity*

Thermal conductivity coefficient was measured by using lee's disk (manufacture by Griffin and George ⁄England) , thermal conductivity coefficient can be calculated from the following equations [19] :

$$K\ \frac{(T_2 - T_1)}{d_s} = e\left[T_1 + \frac{2}{r}\left(d_1 + \frac{d_s}{2}\right)T_1 + \frac{d_s - T_2}{r}\right] \quad \ldots\ldots\ldots (1)$$

And the terms (e) can be evaluated from [10] .

$$I\,V = \pi r^2 e\,(T_1 + T_3) + 2\pi r e\left[d_1 T_1 d_s \frac{(T_1 + T_2)}{2} + d_2 T_2 + d_3 T_3\right] \ldots\ldots\ldots (2)$$

K : thermal conductivity coefficient (W / m .˚C) .
e : represents amount of thermal energy passing through unit area per second disk material .
d_1 , d_2 : represent thickness of the disk (mm) .
d_s : thickness of the sample (mm) .

2.4.3.*Electrical conductivity*

In the insulating materials the electrical resistance , three electrodes cell or (guard ring electrode method) was used to study the effect of the temperature and the filler addition on volume resistivity of polymer composite . Resistivity (ρ) value was calculated by using the relation [20] :

$$\rho = \frac{RA}{L} \quad \ldots\ldots\ldots (3)$$

L : the length (m) .
ρ : the resistivity of the material (Ω . m) .
A : the cross sectional area (m^2) .
R :the resistance of the object (Ω) .
Where conductivity was calculated by using the equation :

$$\sigma = \frac{1}{\rho} \quad \ldots\ldots\ldots (4)$$

2.4.4.*Dielectric strength*

In this test we used instrument (Rang HV - 50 Hz , 30 Kv) and the specimen used in ASTM standard in dimension length (10 mm) and the diameter (10 mm) .

The breakdown strength (dielectric strength) is calculated from the equation [21] :

$$E_{br} = \frac{V_{br}}{h} \quad (V/m \text{ or } Kv/m) \quad \ldots\ldots\ldots (5)$$

h : represents the thickness (mm) .

V_{br} : the maximum break down (Kv) .

2.4.5.*Dielectric constant and dielectric loss factor*

Complex permittivity (ε) is defined as the product of the relative permittivity multiplied by the vacuum permittivity constant (ε_o= 8.85 x 10^{-12})F /m. In equation (6) ,ε , D and E are the electric permitivity , electric flux density (q /m^2) and electric field intensity (V /m) respectively .

$$D = \varepsilon E \quad \ldots\ldots\ldots (6)$$

Complex relative permittivity (ε_r) consists of two real and imaginary parts . The real part ($\bar{\varepsilon}$) is known dielectric constant or charge storage and the imaginary part($\bar{\varepsilon}''$) is known as dielectric losses or loss factor ($\varepsilon_r = \bar{\varepsilon} - j\,\bar{\varepsilon}''$) . The imaginary part indicates the ability of material in absorption of ratio frequency waves .So , high value of this parameter (loss factor) indicates materials with high absorption properties [22]

The loss tangent known as dielectric loss or tan , is described by equation (7) . This parameter represents the ability of converting the stored energy in the material to heat energy . High loss factor ($\bar{\varepsilon}''$) and high loss tangent (tanδ) show high ability of the materials in absorbing the radio waves [23].

$$tan\delta = \frac{\bar{\varepsilon}''}{\bar{\varepsilon}} = \sigma\varepsilon_o\varepsilon_r \quad \ldots\ldots\ldots (7)$$

3. Results and Discussion

3.1.X-ray diffraction

The patterns of X-ray diffraction (XRD) are carried out using (Shimadzu XRD-6000) with Cu $K\alpha_1$ radiation powder diffractometer .X-ray diffraction patterns of pure and reinforcement epoxy with MWCNTs are shown in Figure (1). The crystalline phase of CNT is represented by a strong 26.36° (002) reflection. The intensity of the (002) peak associate with CNT is stronger than other x-ray diffraction peaks due to presence of the more tangled nanotubes in the pattern of 6% CNT.

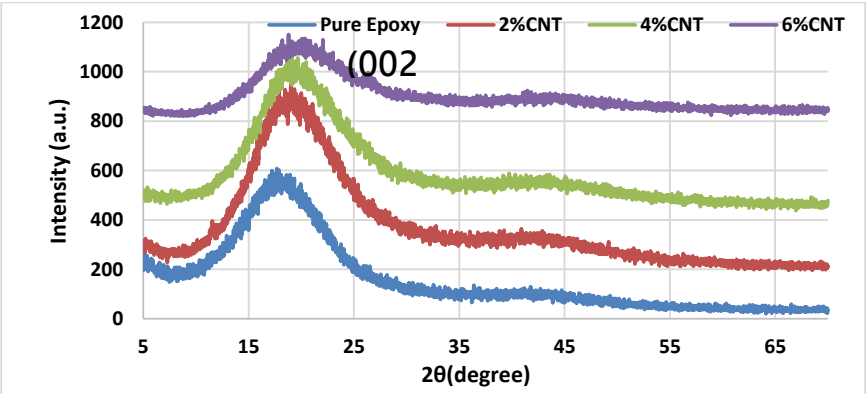

Figure 1. X-ray patterns of pure and reinforcement epoxy

3.2.Mechanical properties

- Hardness

In this study had found that the hardness increased with the increasing of the weight fraction of MWCNTs due to stacking and overlap , which decrease the movement of polymer molecules which caused to increase the resistance of material to scratch , cut and becoming high resistance to plastic deformation .The hardness of materials depends on the kind of the forces according to the atoms in the material because the strong interlink between the phases of MWCNTs and epoxy increases the cohering of mixture which results in increasing the hardness [24] the result is shown in 'Figure (2)'.

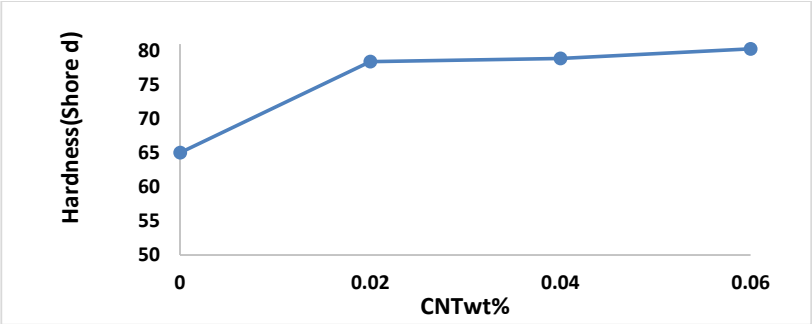

Figure 2. Variation of Hardness with CNT concentration

3.3.Thermal properties

- Thermal conductivity

The epoxies are insulators and very weak thermal conductors , fillers and fibers must be introduced within epoxy in order to provide thermal transfer . The thermal conductivity of an epoxy will be determined by the percentage of filler loading , and the choice of filler , the process of thermal energy transfer depends on the structure nature of the material and there are two ways for the transition of thermal energy which are lattice waves and free electrons . Transmitted thermal energy in insulating materials is by phonons and this process occurs as a result of oscillation molecules as the move to the frequency as a result of neighboring molecules are linked together the bonds [25] . Thermal conductivity coefficient of MWCNTs K_{CNT}= 3000 W ⁄m . ˚C [26] . 'Figure (3)' shows that the thermal conductivity coefficient increase with the increasing of weight fraction of MWCNTs.

The modification of epoxy matrix might cause decrease in the mean distance between neighboring chains, hence to increase elastic constant reason the intermolecular interaction ,the result , thermal resistant is decreased , and , hence thermal conductivity is increased .

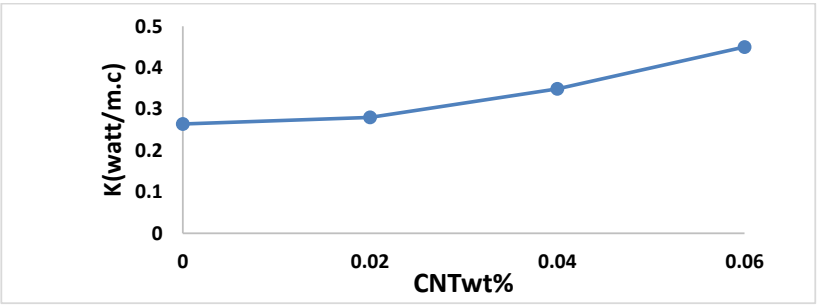

Figure 3. Variation of thermal conductivity coefficient with CNT concentration

3.4. Dielectrical properties

3.4.1 *Electrical conductivity*

Electrical conductivity was calculated from equation (4), the results are show in figure (4).In 'figure(4)' observed increasing of electrical conductivity with the increase of the frequency and we can observed in the same figure increased the electrical conductivity with increase the weight fraction of (CNT) , specially at the higher electrical conductivity in the weight fraction (0.06) of (CNT)% . This increased could be attributed to increase segmental mobility of polymer chains near the filler particles [27] .

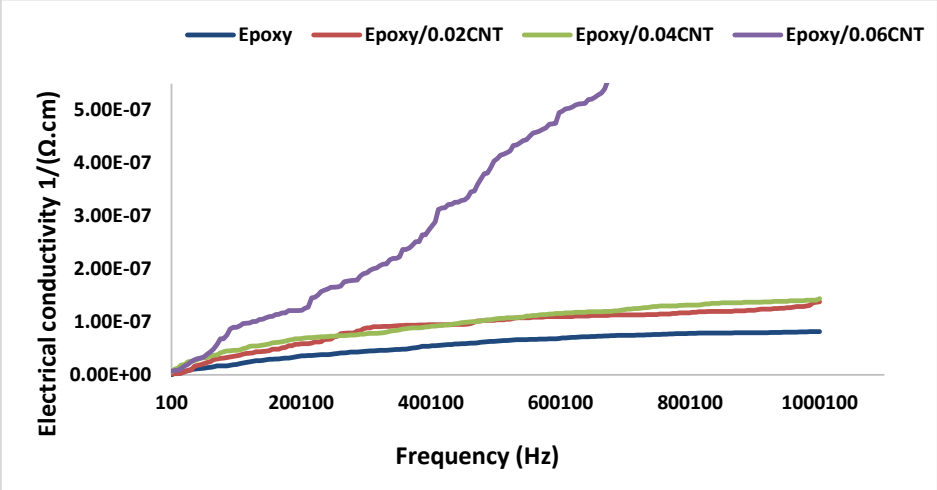

Figure 4. Variation of Electrical conductivity with Frequency for different concentration of MWCNT

Also the electrical conductivity increased with increasing weight fraction of MWCNTs, that could be describe to increase of ionic charge carriers which might be increased due to increasing filler content [28] ,this shown in this figure (4) .The electrical conductivity increases with the increase of frequency we can explain this relation according to the resistivity where the effect of the frequency on resistivity of carbon nanotubes/ epoxy . It is interesting that when the higher frequency the impedance of the sample decreases significantly indicating that the impedance of the sample is dominated by the capacitance of epoxy matrix [29] . Inasmuch, the conductivity equals reciprocal the resistivity , hence the conductivity increases with the increase of frequency .

3.4.2*. Dielectric constant , Dielectric loss factor and Dielectric strength*

'Figure (5)' , represents the relation between dielectric constant and frequency , figure (6) represents the dielectric loss factor with frequency , from both figures observed same behavior , when the frequency is increasing the dielectric constant and dielectric loss factor decrease in the other hand the dielectric constant is increasing with increase weight fraction of CNTs ,while the behavior of dielectric loss factor is opposite that. Several articles have studies the complex permittivity of different types of the carbon of nanotubes at low frequencies (1 MHz) , studied showed an extremely dependence of the real and imaginary of relative permittivity on frequency and weight fraction of the (CNTs) in the polymer matrix . From the result both parts of relative permittivity at megahertz frequency were very high but at gigahertz frequency they showed extremely low values [30] .

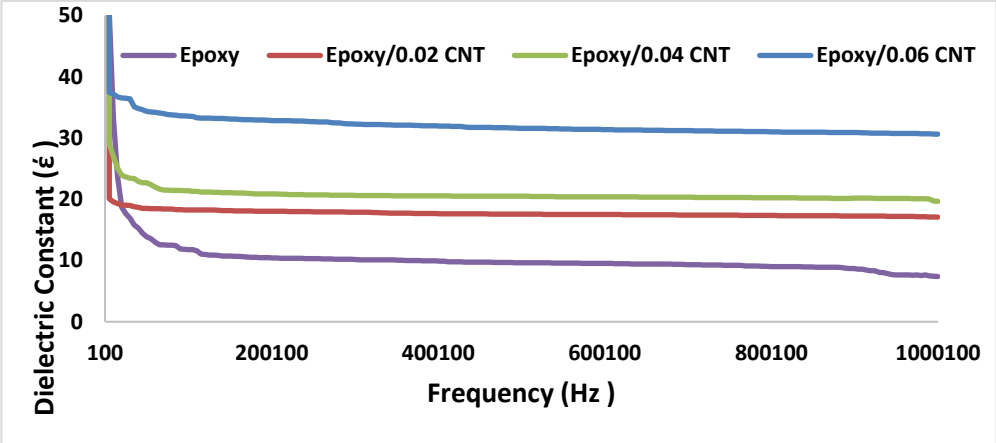

Figure 5. Variation of Dielectric Constant with Frequency for different concentration of MWCNT

In most of nanocomposite the imaginary part of permittivity is smaller than the real part[31] . Whereas , according to equation (7) the increase of the loss factor (imaginary part of permittivity ε) of nanocomposites leads to materials with high absorption properties are not suitable for use in electromagnetic waves reflector structures [32] .

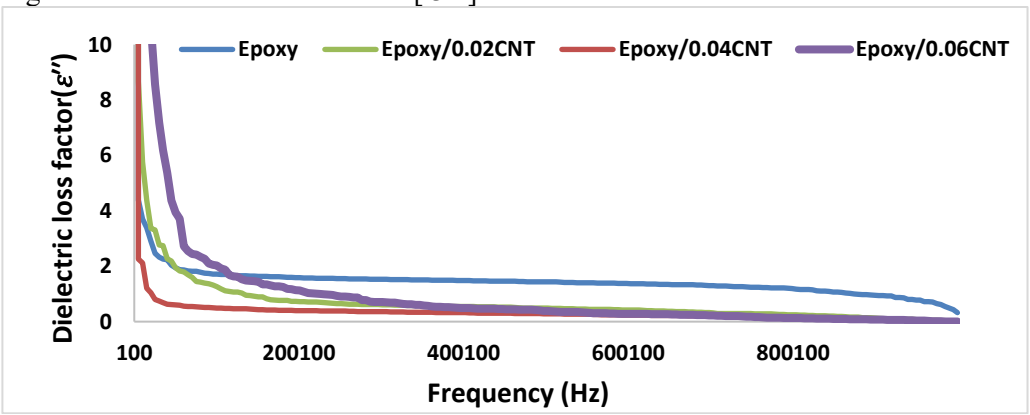

Figure 6. Variation of Dielectric loss factor with Frequency for different concentration of MWCNT

'Figure (7)' represented the relation between the break down and weight fraction of CNTs% . The results showed in this figure the increase of the break down strength with the increase of the weight fraction and we can explain this relation . In most the polymers⁄CNTs composite ,because the agglomeration of filler particles at vicinity of favorable the bundle structure is formed [33] . In this respect , it becomes apparent that filler EP⁄CNT composites contain few CNT weight content are dispersed as isolated agglomerates in the epoxy rather than network of linked particles .

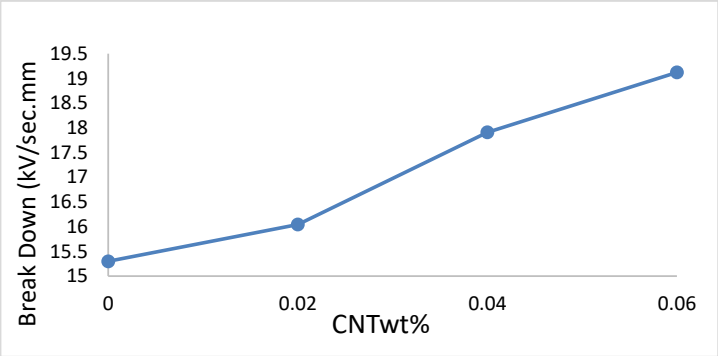

Figure 7. Variation of Break Down with CNT concentration

Conclusions

In this study , MWCNTs used as a filler in epoxy resin . Four samples with different weight fractions (0, 2 , 4 , 6)wt % of MWCNTs were made . The results showed the epoxy composites filled with a few weight fraction CNTs gives better mechanical properties than pure epoxy , also give better thermal and electrical properties, because the (CNTs) have a good mechanical , thermal and electrical properties .

References

[1] Marcio Rodrigo, Loosa, Luiz Antonio Ferreira Coelhoa, Sérgio Henrique Pezzina, Sandro Campos Amico 2008 Materials Research 11(3) 347
[2] Thostenson ET, Chou TW 2006 Carbon 44 3022
[3] Yang Y, Gupta MC, Zalameda JN, Winfree WP 2008 Micro Nano Lett. 3(2) 35
[4] Xu CL, Wei BQ, Ma RZ, Liang J, Ma XK, Wu H 1999 Carbon 37(5) 855
[5] Peigney A, Flahaut E, Laurent C, Chastel F, Rousset A. Aligned 2002 Chemical Physics Letters 352(1-2) 20
[6] Shen J, Huang W, Wu L, Hu Y, Ye M 2007 Comp. Sci. *Tech*. **67**(1516) 3041
[7] Ounaies, Z., Park, C., Wise, K.E., Siochi, E.J., Harrison, J.S 2003 Comp. Sci. Tech. 631637
[8] Gojny F.H., Malte H.G.W., Fiedler B., Ian A.K., Bauhofer W., Windle A., Schulte K. 2006 Polymer 47(6)2036
[9] Novak I., Krupa C 2003 Euro. *Poly. J*. **39** (3) 585
[10] Yang K.,Gu M., Guo Y., Pan X., Mu G.2009 Carbon 47,1723
[11] Meng-KaoYeh,Tsung-HanHsieh,Nyan-HwaTai 2008 Mat. Sci. Eng. A 483 289
[12] S. IIJIMA 1991 Nature 354 56
[13] Ray H. Baughman, Anvar A. Zakhidov, Walt A. de Heer 2002 Science 297 787
[14] Yang Y, Gupta MC, Zalameda JN, Winfree WP 2008 Micro Nano Lett. 3(2)35
[15] Erin Camponeschi, Bill Florkowski, Richard Vance, Glenn Garrett, Hamid Garmestani, and RinaTannenbaum 2006 Langmuir 22(4)1858
[16] Yu-HsuanLiao,OlivierMarietta-Tondin , ZhiyongLiang ,ChuckZhang ,BenWang 2004 Mater Sci. Eng. A 385(1-2)175
[17] Ami Eitan, Kuiyang Jiang, Doug Dukes, Rodney Andrews, and Linda S. Schadl 2003 Chem. Mater.15(16)198
[18] Jeena Jose Karippal, H. N. Narasimha Murthy, K. S. Rai, M. Krishna, And M. Sreejith 2010 Poly.-Plastics Tech. Eng. 49 1207
[19] Kleinholz R. and Molinier G. 1986 Vetrotex Fiber World 10(22)13
[20] Murthy BSR ,Dr.Krishna A . Rama and Krishna B.V Rama 2004 *IE (I) Journal - MC* **84**
[21] Younes K.J. Alesawy 2005 Master Thesis , College of Science , Al - Mustansiriya university
[22] Chin W ,LucL. , Hsu WK 2011 carbon 49 4648
[23] KuH 2003 *J. compos Mater* **37** 22

[24] Qi , H . J ,Toyce K and Boyce M . C 2006 *J .Rub , chem. Technol*. **76** (2) 419
[25] Incropera P .F , Dewitt D. D 1981 "Fundemental Of Heat Transfer John wi ; ey and Sons *Inc*
[26] Fisher F .T . , Bradshaw R .D . , Brinson L .C 2002 *Appl .phys .Lett* . **24** (80)4647
[27] Kawamoto Y . , NaguraN .andTsuchihashiS 2006 *J. of American Ceramic Socity* **57**(11)489.
[28] Sankara S . , Arayanan Potty N .and Abdul KhdarM . 2000 *Bull mater .Sci*, **23**(5)361
[29] GojnyF .H . , WichmannM .H . , Fielder B . , Banhover W. , Schulte K . , 2005 comp. part A ; Appl. Sci. manuf. 36 1525
[30] Wu J , Kong L (2004) *Appl .phys .Lett* .**84** 4956
[31] Liu Z , Bai G , Huang Y , May , DuF , Li F , Guo T , chen Y 2007 , Carbon 45 821
[32] Watts pcp , ponnampalam DR , Hsu WK , Barnes A, chambers B 2003 *Chem .phys .lett* . **378** 609
[33] Petra P , Tschke M , A , G Ingo , A Sergej D , Dirk L 2004) ., *J. of polymer* **45** 8863

Preparing and Study the effects of Composite Coatings in Protection of Oil Pipes from the Risk of Corrosion that resulting from Associated water with Petroleum Products

Preparing and Study the effects of Composite Coatings in Protection of Oil Pipes from the Risk of Corrosion that resulting from Associated water with Petroleum Products

A R Al – Sarraf[1] , M A Yaseen[1]

[1]University of Baghdad collage of Education For Pure Science-Ibn Al Haitham

Baghdad-Iraq

E-mail :MO_199345@yahoo.com

Abstract.In order to inhibit the metallic corrosion in the oil pipelines,the protection method with composite coating of Unsaturated polyester and reinforced by Caolin at weight percentage (20%) was studied .where, the work samples were classified into two groups according to internal composite coatings layers for all group of these samples.The first group is nitrocellulose coating reinforced by nano and Micro Powder of Mgo ,The Second group is sodium silicate coating reinforced by nano powder of Mgo ,The following weight percentages (0%,1%,3% and5%) were adopted as reinforcement ratios for nano powders,as well as the weight percentages (0%,3%,5% and7%) as reinforcement ratios for micro powders Tribology properties and Electrochemical Corrosion Resistance by Polarization method (Tafel) and Adhesion Strength were studied, The results showed an improvement in the corrosion resistance of protected steel by coatings compare with uncoated steel, As well as improvement in mechanical properties and adhesion strength of composite coatings.

1-Introduction.

The problem of corrosion has received great attention from many researchers in order to arrive at effective solutions to reduce this problem. This is evident to us through research completed and worked to find appropriate solutions to reduce the problem of corrosion and the effects of it through a number of modern engineering methods that ensure addressing the problem at the lowest cost and time of possible scenarios. The risk of corrosion lies in the diversity of its forms and the multiplicity of its causes. Therefore, there are many ways and means of protecting it [1].One of the most common ways of protecting the pipes from the risk of corrosion, which was adopted by many researchers is the protection method of coating as one of the effective methods of protection because of the distinct characteristics in the protection of steel pipes from corrosion. One of the most common ways of protecting the pipes from the risk of corrosion, which was adopted by many researchers is the protection method of coating as one of the effective methods of protection because of the distinct properties in the protection of steel pipes from corrosion.

2. Experimental part

2.1 the stage of the preparation of steel samples

Steel pipe was cut to two dimensions (15×15×3mm) and (30×30×3mm) After the cutting process, solid carbonization was done on the samples .where the samples immersed in (100g coke + 4g barium carbonate).the carbonization process was done at (1.5hr) and (950°C),and then the samples coated with iron oxide as a corrosion resistant layer,and added (0.25g) of Hydrazine hydrate per (100g) of iron oxide coating in order to remove the oxygen from it.see the 'figure1'and 'figure2'.

2.2 coating by reinforced Sodium silicate

Group of the samples coated with a layer of sodium silicate, reinforced by magnesium oxide Nano powder. It was reinforced by (0%,1%,3%and 5%).the mixture was mixed into a glass beaker by Hot Plate Stirrer,then the sodium Silicate poured on the samples and left to reach to the case of full dryness**.**see 'figure 3'.

Figure 1. A photograph of carbonated Samples

Figure 2. A photograph of the Samples after coating by iron oxide

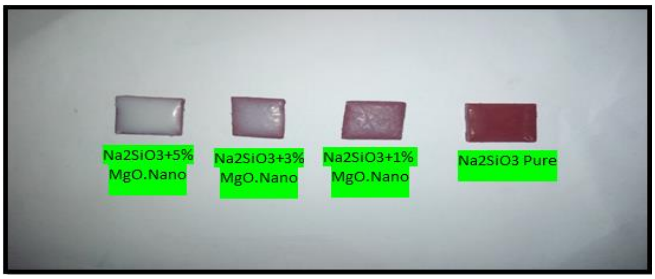

Figure 3. A photograph of Samples coated with Sodium silicate reinforced by (MgO.Nano).

2.2 Coating by reinforced Nitrocellulose

Another Group of samples coated with Nitrocellulose reinforced by magnesium oxide Nano powder with percentages (0%,1%,3%and 5%).and also reinforcement with magnesium oxide Micro powder with percentages (0%,3%,5%and 7%).and used (aluminum citrate powder) by percentage (0.75g) to disperse the reinforcement powders.the coatings was mixed by use an electrical mixer type (RW-20), the samples coated by use the hand brush and left to dry.notes 'figure 4'.

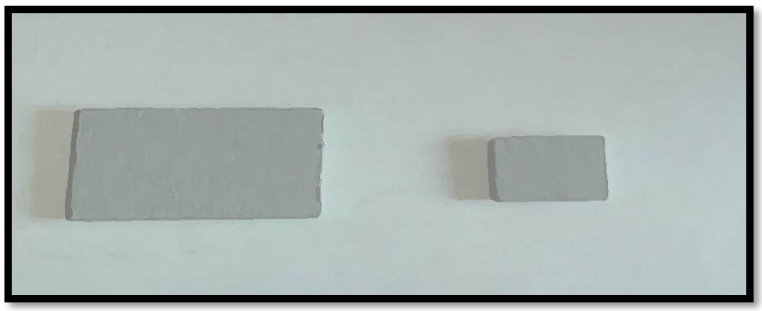

Figure 4.A photograph of Samples coated with Nitrocellulose reinforced by (MgO. Nano /Micro).

2.3 Coating with reinforced Unsaturated Polyester

The composite polyester prepared by mixing the polyester with kaolin powder at different weight percentages (5%,10%,15%,20% and 25%).and the samples coated by using the hand brush.notes 'figure 5'

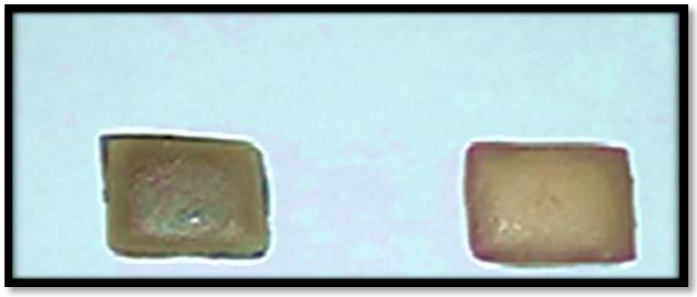

Figure 5. A photograph of Samples coated with reinforced unsaturated polyester and already coated with composite coatings (Nitrocellulose/Sodium silicate).

3.Results and discussion

3.1 Hardness Test

The results of the surface hardness test in Figure 6 and Table 1 for the composite coatings (Sodium silicate and Nitro cellulose) showed an improvement in the surface hardness values with increasing the ratio of (Nano/Micro) powder. When increasing the weight ratio of additives, this increase led to raising the hardness of sodium silicate from 68.NO in the case of non-reinforced silicates up to its highest value 71.NO,at weight percentage(5%).In the case of Nitro cellulose, we notice an increase in the hardness values in both of (nano /micro) powders, where the highest hardness value in the nano-reinforcement was recorded at 3% which is 87.1NO,and the value of hardness with the micro-reinforcement was recorded at 5% is 87.5NO,Compared with unreinforced case which recorded the value 84.6NO. The high surface hardness due to the reinforcement particles that improve mechanical properties of materials composite, This is consistent with Saeid and Rafiq [2].and the reinforcement particles are working on impeding dislocations movement,this confirmed by the researcher Higgins [3].

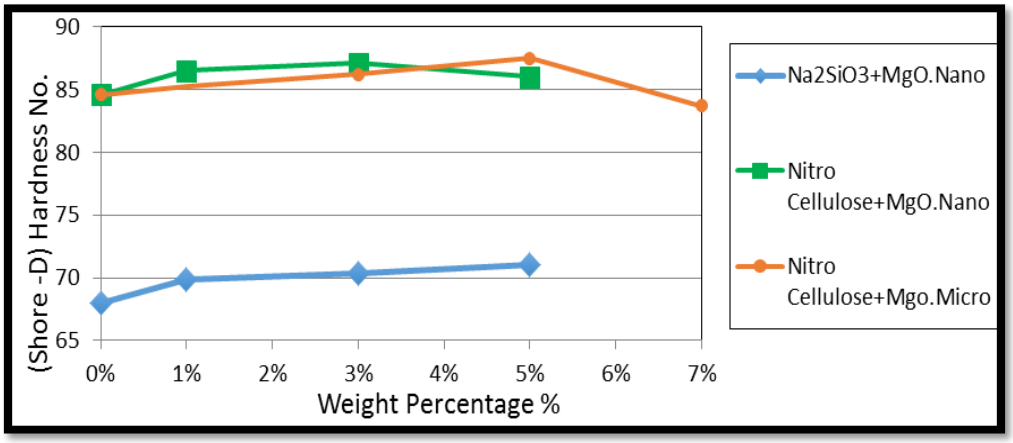

Figure 6..Effect of ratio of additives on surface Hardness for prepared composite coatings.

Table 1. Hardness values for composite coatings at the best weight percentages.

Types of composite coatings		Hardness NO.
Sodium Silicate	Non-reinforcement	68
	Reinforced with 5%MgO.Nano	71
Nitrocellulose	Non-reinforcement	84.6
	Reinforced with 3%MgO.Nano	87.1
	Reinforced with 5%MgO.Micro	87.5

3.2. Wear rate test

The results of the wear rate test, Figure 7 and Table 2 showed a decrease in the wear rate of the composite coatings. The wear rate of the sodium silicate is lower compared with non-reinforced.The wear rate decreased from $7.7282*10^{-6}$gm/cm in the case of the non-reinforced sodium silicate to $0.4246*10^{-6}$gm/cm when reinforced by 5% ,where the particles of magnesia which has high hardness acts to deform ofthe matrix material and improve the toughness of the composite body.This is consistent with Samal and Bal[4].The wear rate decreased with the increase of weight percentages reinforcement of (Nano/Micro)the magnesium for Nitrocellulose coating,where the wear rate was $5.0955*10^{-6}$gm/cm before reinforcement,and then started to decrease further to its optimum value $0.6794*10^{-6}$gm/cm at 3% the nano-reinforced and $1.1040*10^{-6}$gm/cm at 5% of the micro-reinforced.from Figure 8.shows the superiority of reinforcement by nano-particles on reinforcement by micro-particles in improve the tributological properties because of the grain size of the nano powders that allow to particles to enter inside the polymeric chains,that led to increase in compact and cohesion of the composite material. Consequently, the wear rate become lower This confirms the interpretation of the researcher Praveen et al [5].

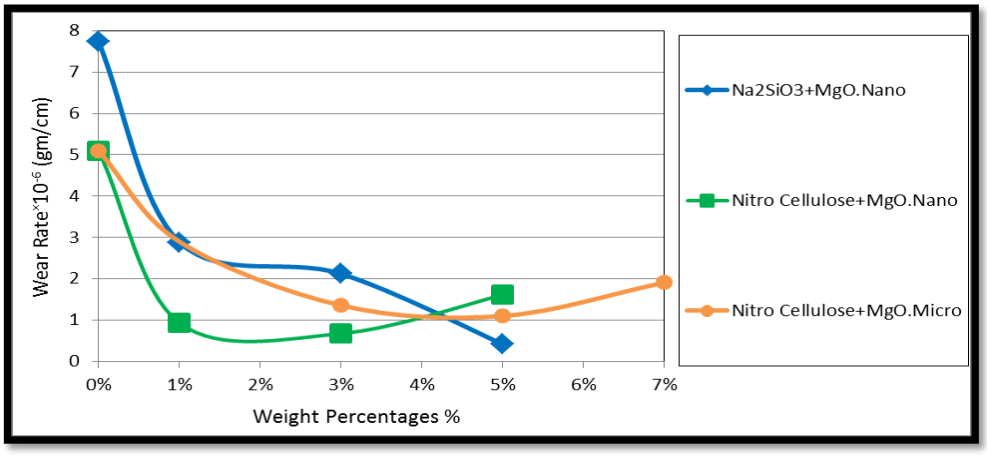

Figure 7. Effect of change in the ratio of additives on the wear rate of the composite coatings at fixed operating conditions.

Table 2. Wear rate for composite coatings at the best weight percentages.

Types of composite coatings		Wear rate×10^{-6}
Sodium silicate	Non-reinforcement	7.7282
	Reinforced with 5%MgO.Nano	0.4246
Nitrocellulose	Non-reinforcement	5.0955
	Reinforced with 3%MgO.Nano	0.6794
	Reinforced with 5%MgO.Micro	1.1040

3.3 The Surface hardness test of the reinforced polyester coating layer

From Figure 8 and Table 3 show the improvement in the surface hardness values of the Unsaturated polyester coating, and which reinforced by kaolin particles. Where The surface hardness increases with the increase of the reinforcement ratios to reach to the highest hardness value at 20%.which was 76.8NO.Compared with its value for unsaturated polyester which was 76.8NO.Here,showe the effect of additive in the participation of the matrix to bear the stresses placed on the surface of composite.this based on the interpretation of the researcher Higgins [3].

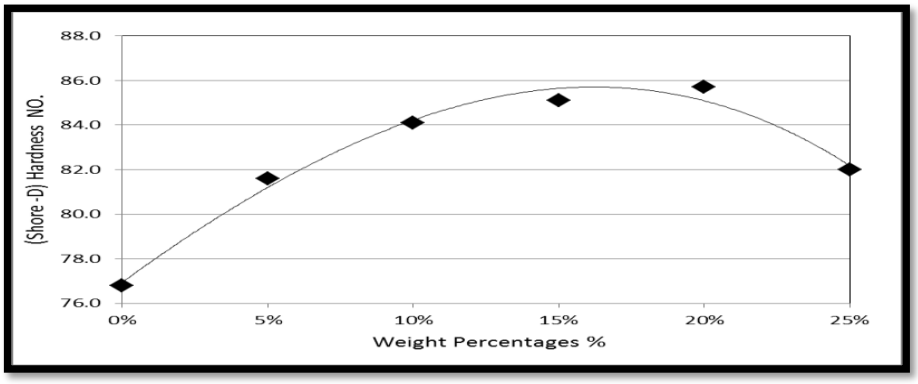

Figure 8. Effect of the percentages of additives (kaolin) on the surface hardness of the unsaturated polyester coating.

Weight percentages of kaolin	Surface hardness NO. (Shore-D)
0%	76.8
5%	81.6
10%	84.1
15%	85.1
20%	85.7

Table3. The values of Surface hardness for unsaturated polyester composite reinforced with different percentages of kaolin.

3.4 The Wear rate Test of reinforced Unsaturated Polyester layer

The results of the wear test for kaolin-reinforced polyester with different reinforcement ratios, showed a significant decrease in wear rate with increase the weight percentages of kaolin as shown in Figure 9 and Table 4.The wear rate was lowest at 20%Which is $0.545*10^{-7}$gm/cm and represents the lowest value compared with the value of wear at the unreinforced polyester, which is recorded at $3.639*10^{-7}$gm/cm.This is consistent with the researcher Oleiwi [6].This decrease in the value of wear is due to the role played by the particles of reinforcement in reducing the Sliding Contact between the surfaces of the objects,as described by d'Almeida et al [7].from Figure 9 We note an increase in wear rate at percentage (25%) of kaolin because of the weakness in toughness and cohesion of the composite due to the increase of the reinforcement percentages above the required limit,that's agrees with the researcher AL-Abbasi [8].

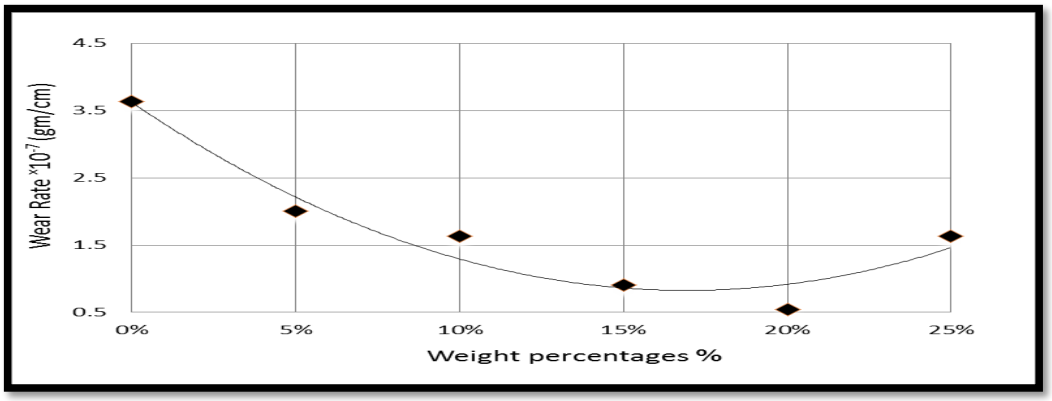

Figure 9. Effect of the change in the percentages of add itives on the wear rate of composite polyester.

Table 4.the wear rate of reinforced unsaturated polyester by different percentages of kaolin.

Weight percentages of kaolin	Wear rate$\times 10^{-7}$
0%	3.639
5%	2.001
10%	1.637
15%	0.909
20%	0.545
25%	1.637

3.5 Electrochemical Corrosion Test after coating with composite coatings layer

The results obtained from Figure 10 and Table 5 of the electrochemical corrosion test (Tafel) show a change in the density of the corrosion current and the corrosion potential of the steel samples protected by layers of composite coatings.Where,The values of the corrosion currents and the corrosion potentials of all the coated samples decreased to be more nobleness compare with their value of the uncoated steel sample.The practical results showed improvement in the values of protection against corrosion caused by the associated water with the oil product, and this reflects the important role played by those composite layers, specifically the final layer of unsaturated polyester As a stable protection layer with high resistance to degradation in the aqueous medium.this agrees with the researcher's opinion Thair et al [9].

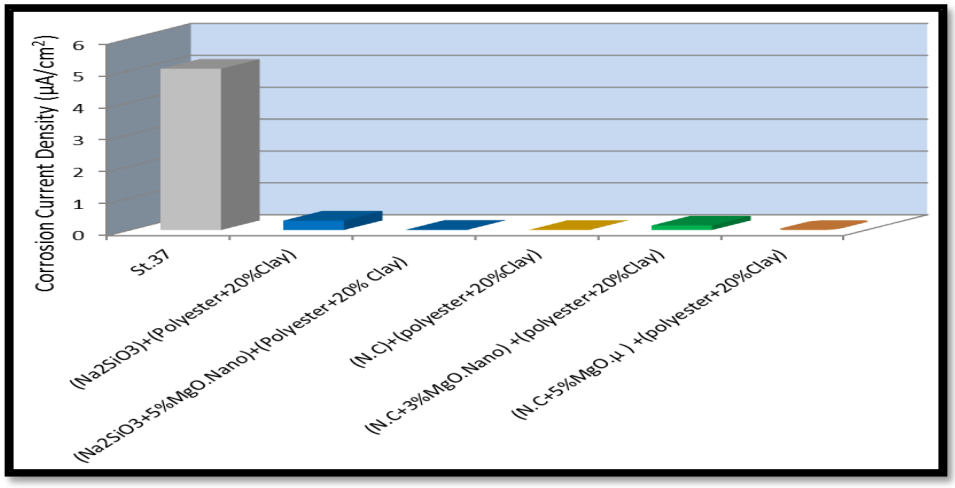

Figure 10. Change of the density of the corrosion currents for composite coatings.

Table 5. Corrosion currents density and corrosion voltages of composite coatings.

Types of composite coatings	I_{Corr} µA/cm^2	V_{Corr} (mv)
St.37	5.06	-569
(Na2SiO3) + (polyester+20%clay)	0.29576	155.8 -
(Na2SiO3+5%MgO.Nano) + (polyester+20%clay)	0.01075	-264.3
(polyester+20% clay)) +N.C(	0.00460	-20.5
3%MgO.Nano) +(polyester+20%clay)+N.C(	0.14345	-33.7
(N.C+ 5%MgO.Micro)+ (polyester+20%Clay)	0.00870	-218.2

3.6 Adhesion strength test

From the results that obtained from Figure11 and Table 6 of adhesion strength of the coatings, show the improvement in adhesion strength where recorded adhesion strength in the case of (pure sodium silicate + reinforced polyester) 83Pa, and reinforced sodium silicate with 5% of magnesium oxide nano particles, showed a high adhesion strength 117 pa. As for the other model of composite coatings (pure Nitrocellulose+ reinforced polyester),recorded the value of adhesion strength 626 P.and also when reinforcing Nitrocellulose with 3% of (MgO.nano+ Reinforced polyester or 5% of (MgO.micro +Reinforced polyester) where adhesion strength recorded the following values 523Pa and 482Pa respectively, but these values are low compared to their previous value (the case of the non-reinforced coating layers).The adhesion strength is Attribute to several reasons, including strength of the mechanical interlock between the different coating layers on one hand,and the

coating layers and the steel surface on the other hand, as well as the forces of the Vander Wals between the different coating layers, as described by Abbas [10].

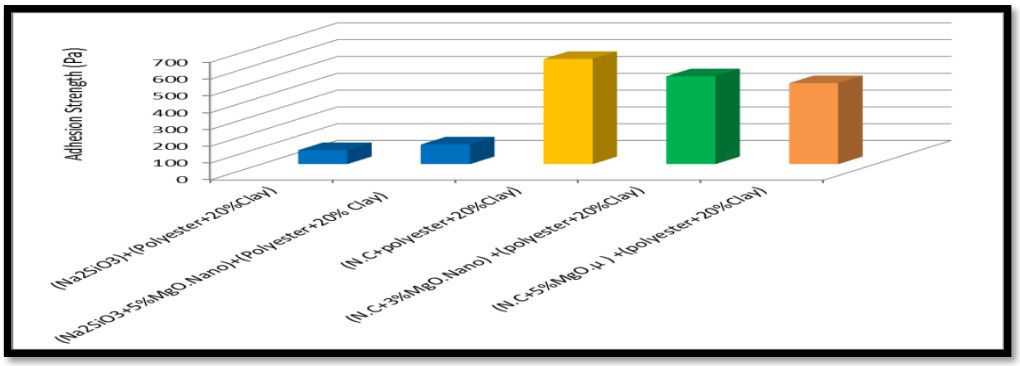

Figure 11.Adhesive strength values for composite coatings.

Table 6. Adhesive strength values for composite coatings.

Types of composite coatings	(Pa) Adhesive strength
(Na2SiO3)+ (Polyester+20%Clay)	83
(Na2SiO3+5%MgO.Nano)+(Polyester+20% Clay)	117
(N.C) + (polyester+20%Clay)	626
(N.C+3%MgO.Nano) + (polyester+20%Clay)	523
(N.C+5%MgO.μ) + (polyester+20%Clay)	482

4-Conclusions

The sliding wear resistance,as well as surface hardness are improving with the increase of additives for all composite coating.The adhesion strength of the composite coatings(reinforced Sodium silicate + reinforced Polyester)increases more than in the case of unreinforced coating layers.while,the adhesion strength of the composite coatings(reinforced nitrocellulose+reinforced polyester)decrease more than unreinforced coatings.The electrochemical corrosion test of the coated samples showed the effects of these coatings on the protection of steel from the corrosion risk of associated water with the oil products when compared these results with result of steel without protection.and from results obtained we note the excellence of protection with (reinforced nitrocellulose+reinforced polyester) more than (reinforced Sodium silicate+ reinforced Polyester).

Acknowledgments

Thanks to every one who helped me to complete this research.

References

[1] Al-Abdullatif M 2007 Design and optimization of cathodic protection systems used in prevention of pipelines corrosion PhD dissertation college of engineering chemical engineering department king saud university kingdom of saudi arabia p.p.21–3

[2] Saeid A and Rafiq S 2011 Stadying mechanical properties for polyethylene composites rein for by fish shell particles *Engineering and Technology Journal* **29** 620–607

[3] Higgins R A 1973 Engineering Metallurgy, London

[4] Samal S and Bal S 2008 Carbon nanotube ceramic matrix composites *Journal of Minerals & Materials Characterization &Engineering* **7** 367–366

[5] Praveen G, Girisha K and Yogeesha H 2014 Synthesis, characterization and mechanical properties of a356.1 aluminium alloy matrix composite reinforced with mgo nanoparticles *International Journal of Engineering Science Invention* 3 59–53

[6] Oleiwi J 2010 Astudy of wear rate behavior of polyester reinforced by silica (sio2) particles *The Iraqi Journal For Mechanical And Material Engineering* **10** 118–108

[7] d'Almeida J, Ribeiro F, and Alves I 2009 Wear behavior of a polymer- matrix composite reinforced with residues from ahydrometallurgical process *Polymer-Plastics Technology and Engineering* **48** 1309–1304

[8] AL-Abbasi S 2015 Preparation of composite materials reinforced by carbon for treatment of corrosion in oil distillation towers master thesis department of applied sciences university of technology

[9] Thair L,Jassim I,Al-Khuzaie S,Hammody J and Kalile M 2016 Corrosion protection of carbon steel oil pipelines by unsaturated polyester/clay composite coating *American Scientific Research Journal for Engineering,Technologyand Sciences ASRJETS* **18** 119–108

[10] Abbas R A 2007 Preparation adhesive material reinforced of graphite particles and study electrical and mechanical and thermal properties *Um Salama Journal* **4** 415–407

Study of the effect of electromagnetic fields on indoor and outdoor radon concentrations

Study of the effect of electromagnetic fields on indoor and outdoor radon concentrations

Lina M Haider[1], N R Shareef[1], H H Darwoysh[2] and H L Mansour[2]

[1]University of Baghdad, College of Education for pure sciences, Ibn AlHaitham, Baghdad, Iraq

[2] Physics Department, College of Education, University of Al- Mustansiriyah, Baghdad, Iraq

Corresponding author: Lina Majeed Haider: linamh_1978@yahoo.com

Abstract: In the present work, the effect of electromagnetic fields produced by high voltage power lines(132kV) and indoor equipments on the indoor and outdoor average radon concentrations in Al-Kazaliya and Hay Al-Adil regions in Baghdad city were studied using CR-39 track detectors and a gauss-meter.Results of measurements of the present study, have shown that the highest value for the indoor average radon concentration (76.56± 8.44 Bq/ m^3) was recorded for sample A_1(Hay Al-Adel) at a distance of (20 m) from the high voltage power lines , while the lowest value for the indoor average radon concentration (30.46 ± 8.44 Bq/ m^3) was recorded for sample A_3 (Hay Al-Adil) at a distance of (50 m) from the high voltage power lines. The indoor gaussmeter measurements were found to be ranged from (30.2 mG) to (38.5 mG). The higest value for outdoor average radon concentration and the highest gaussmeter measurements were found for sample (1), with values (92.63 ±11.2 Bq/ m^3) and (87.24 ± 2.85 mG), directly under the high voltage power lines respectively, while the lowest outdoor average radon concentration and the lowest gaussmeter measurements were found in sample (4),with values (34.19 ± 6.33 Bq/ m^3) and (1.16 ± 0.14 Bq/ m^3),), at a distance of (120 m) from the high voltage power lines respectively. The results of the present work have shown that there might be an influence of the electromagnetic field on radon concentrations in areas which were close to high voltage power lines and houses which have used many electric equipment for a long period of time.

Keywards : Power lines, Radon,Gaussmeter,CR-39. Electromagnetic.

1-Introduction;

A group at the International Agency for Research on Cancer worked and classified that exposure to low-frequency magnetic fields for long time will causes cancer[1].In(2005), a large-scale case-control study from Britain, showed an association between proximity of residence at birth near high voltage power lines and the risk of childhood leukemia[2].The association extended beyond distances where the power line-induced(ELF-MF) exceed background levels, which suggested that the association was not explained by the magnetic field, but perhaps by some other risk factor.Several studies have looked for potential confounders which could explain the observed association between (ELF-MF), and childhood leukemia [3,4]. Radon progeny like other airborne particles (tobacco smoke, chemical pollutants, spores, bacteria and viruses) might be affect our health, which can be inhalated [5,6]. Many researchers have found that the deposition of these particles increasing under the high voltage power lines [7].For that they have suggested that the electric field that result from these lines can breakdown the air electrically,that give positive and negative ions and charge particles when they pass through ions,which finally increased the affect on health by increasing exposure[8]. Radon (an alpha emitter)is an odorless, naturally occurring radioactive gas that comes from the soil. Radon and its radioactive decay products (porgeny) are found in easily measurable concentrations in all outdoors air and in higher

concentrations indoors. Studies of tens of thousands of miners exposed to high concentrations of radon and its decay products show that they cause lung cancer, however, these studies found no significant increase in other forms of cancer due to exposure to radon and its decay products[9].Contribution of radon and its progeny to the total effective dose has been reported to be more than (50%) [10]. The risk of lung cancer from exposure to radon and radon decay products depends on their concentrations in air and the length of time a person is exposed to the radon source[11].Radon as a cause of leukemia has also been discussed by Richardson et al [12]. It has been reported that indoor radon exposure is associated with the risk of leukemia and other cancers such as melanoma and cancers of the kidney and prostate [13]. Exposure to radon has become a global concern due to its health hazards inside dwellings[14-16]. CR-39 detector is considered one of the best detectors to record the tracks of alpha particles and nuclear fission fragments, because of the advantage of its high sensitivity and efficiency [17, 18].The aim of this work is to study

a probable behavior of radon in fields like electromagnetic produced by high voltage power lines(132kV),in addition to the effects of the electromagnetic fields from indoor electrical equipment.

2-Experimental Method:

The CR-39 track detectors, (128) pieces, with dimensions (1x1 cm^2) and thickness of (250 μm) have been distributed in (22) houses,(16 indoors and 6 outdoors) for the period of one month for the purpose of natural exposure**.** After the exposure time, (30day), the (CR-39) track detectors were etched in (6.25N) (NaOH) solution at temperature of (60 ^oC) for (5 h), and the tracks density were recorded using an optical microscope with magnification (400X). The density of the tracks (ρ) of the samples were calculated according to the following relation [' ٩].:

$$\rho = \frac{N_{ave}}{A} \quad (1)$$

Where:

N_{ave} **:** is the average number of total pits(track). A **:** is the area of field view.

An example of a photograph for the observed tracks of one of the studied samples is shown in Figure (1). Radon gas concentration in the samples were obtained by the comparison between track densities registered on the detectors of the sample and that of the standard samples which are shown in Figure(2), using the relation [3]:

$$C_X = C_s(\rho_x / \rho_s) \quad (2)$$

$$Cx = \rho_x / \text{slope} \quad (3)$$

Where:

C_x**:** is the radon gas concentration in the unknown sample. C_s**:** is the radon gas concentration in the standard sample. ρ_x**:**is the track density of the unknown sample (track/mm^2). ρ_s**:**is the track density of the standard sample (track/mm^2).

A calibration curve [20]for outdoor measurements ,see Fig(2), and calibration constant(0.161 track.m3/ Bq. day.mm2) for indoor measurements [21],have been employed in the present work for the determination of the radon concentrations. On the other hand,it have been measured the electromagnetic fields intensity under high voltage lines (132 kV), which were passed through the area of Al- Kazaliya region (K-symbol),and Hay Al-Adil (A- symbol) to Al-Maree station in Baghdad city using a milligauss meter which was designed by Shreef [22],and it is shown in the Figure (3) and Table(1) represent there results. For the studied houses,a computer program was designed (in Matlab language),to calculate the electromagnetic field intensity for every studied device, which contains the intensity, type of the device , distance at (30 cm),and the time for using the device ,(60% for more frequently used),(30% for moderate frequently used) and (10% for less frequently used), as shown in Table (2) and Table (3) for high voltage lines (132 kV). Table(1) illustrates the values of the induce electromagnetic field emissions which were previously obtained for the different electrical devices inside the houses near the high voltage power lines[22]. Table(2) displays the results of radon concentrations which were obtained for the same places for the years (2006) and (2008)[20], and also for the current study(2016). Also included in Table (2), the measured intensity values of the electromagnetic field emissions in the present study (2016).

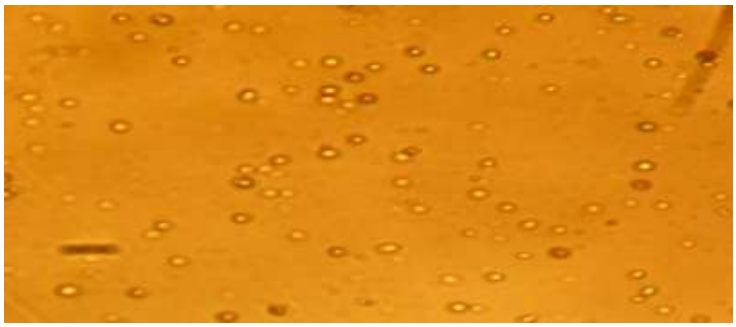

Figure (1): Photograph of the observed tracks for a sample obtained in present work.

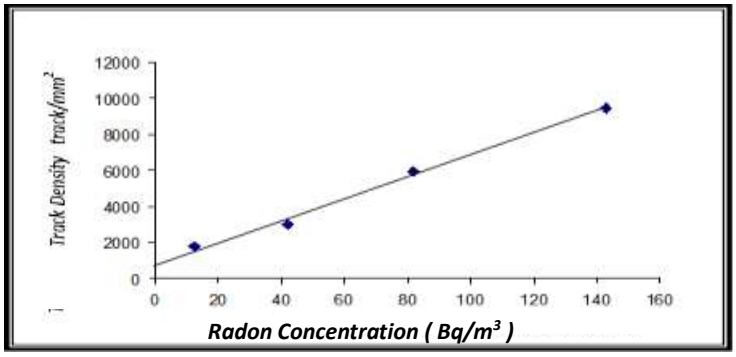

Figure (2): Calibration curve between track density and outdoor radon concentration employed in the present work[20].

Figure (3): Photograph of mlligauss-meter used in the present work[22].

Table (1): Electromagnetic emission (EME) values at different distances[22].

	EME (milli-gauss)			
Electric device name	15 cm	30 cm	60 cm	120 cm
Can opener	٦٥٠	١٦٠	٢٧	٥
Hair dryer	٣٥٠	٢	١	٠
Vacuum cleaner	٣٥٠	٧٠	١٠	٠
Electric saw	٢٥٠	٤٠	٤	٠
Food mixer	١٠٠	٢٥	٠	٠
Food processor	١٢٥	٢٠	٢	٠

Heater (fan)	١٥٠	٢٥	١٠	٠
Printer	١٠٠	٣٠	٥	١
Shaving machine	١٢٥٠	٢٥	٠	٠
Air conditioner	٣	٢	٠	٠
Battery charger	٣٥	١٠	٢	٠
Electronic clock	١٠	٠	٠	٠
Clothes dryer	٢	٢	٠	٠
Fluorescent lamp	٤٥	١٠	٥	٠
Dishwasher	٣٠	١٠	٢	٠
Fan (desktop)	٥	١	٠	٠
Clothes iron	١	٠	٠	٠
Refrigerator	٢	١	٠	٠
Television	١٥	١٠	٠	٠
Computer monitor	٢٠	٦	٣	٠
Computer(desktop)	٣	٢	٠	٠
Computer (laptop)	٥	٠	٠	٠
Electric oven	١٠	٥	٠	٠

Table (2): Indoor average radon concentrations and average electromagnetic field emission (intensity)(EME) for different distances from high voltage power lines

Indoor					
Sample no.	d (m)	Average radon concentration (Bq/m^3) * for different studied years			Gauss-meter measurements (mG) * 2016[p.w]
		2006[22]	2008[22]	2016[p.w]	
K_1	15	69.99±11.5	73.3±11.9	74.86±2.2	33.5
K_2	15		72.9±7.2	73.19±6.8	33.5
K_3	٣٥	67.34±3.4	69±15.34	73.46±2.7	36.2
K_4	٣٥	55.8±6.37	53.7±6.3	52.11±8.42	36.2
K_5	٥٠	41.76±11.08	56.26±16.1	58.49±12.10	38.5
K_6	١٢٠	35.37±7.21	39.63±9.73	40.87±6.1	30.5
A_1	20	-----	74.16±5.3	76.56±8.44	38.5
A_2	40	-----	65.6±4.9	62.88±8.33	38.5
A_3	50	-----	25.9±8.9	30.46±5.83	30.2
A_4	60	-----	43.47±4.9	46.96±7.12	34.8

*** The average of (10) measurements. [p.w]: Present work.**

Table (3): Outdoor average radon concentrations and average electromagnetic field emission (intensity) (EME) for different distances from high voltage power lines.

Outdoor					
Sample no.	d (m)	Averge radon concentration (Bq/m^3) * for different studied years			Gauasmeter measurments (mG)* 2016[p.w]
		2006[22]	2008[22]	2016[p.w]	
1	٠	80.12±15.9	84.39±13.7	92.63±11.2	87.24±2.85
2	٣٠	34.9±5.3	77.9±8.01	48.33±8.16	5.32±0.69
3	٥٠	33.67±10.8	46.5±17.9	37.66±6.24	2.45±0.32
4	١٢٠	31.96±11.5	30.68±5.54	34.19±6.33	1.16±0.14

*** The average of (10) measurements. [p.w]: Present work.**

3- Results and discussion:

From Table(2), it can be noticed that ,apart from (K_4), and (A_2) samples and for a fixed distance from the high voltage power lines, values of the indoor average radon concentrations were found to be increased with the time (measuring year). The higest value for the indoor average radon concentration (76.56 ± 8.44 Bq/ m^3), was recorded for sample (A_1),(Hay Al-Adil),at a distance of (20 m) from the high voltage power lines,(present study in 2016),while the lowest indoor average radon concentrations (25.9 ± 8.9 Bq/ m^3), was recorded for(A_3) sample, (Hay Al-Adil), at a distance of (50m) from the high voltage power lines in (2008) by Raheem [20]. However ,from the present study in (2016),the lowest indoor average radon concentration (30.46 ± 5.83Bq/ m^3), was also recorded for sample(A_3), (Hay Al-Adil), at a distance of (50 m)from the high power lines.For all samples studied in the present work, the gaussmeter measurements were found to be ranged from (30.2 mG)to (38.5 mG). From Table (3),and for the present study in 2016,it can be noticed that, the outdoor average radon concentrations and the gaussmeter measurements were found to be decreased as the sample distance from the high voltage power lines was increased .The highest outdoor average radon concentration and the highest gaussmeter measurements were found for sample (1),with values (92.63 ± 11.2Bq/ m^3) and (87.24 ± 2.85Bq/ m^3) respectively, directly under the high voltage power lines.While the lowest outdoor average radon concentrations and the lowest gaussmeter measurements were found for sample(4), whith values (34.19 ± 6.33Bq/ m^3) and (1.16 ± 0.14 mG) respectively at distance (120 m) from the high voltage power lines. From Tables (2&3), it can be noticed that a significant differences were found in radon gas concentrations outside the houses near to the high voltage power lines, also the increasing of the electrical power supplied now adays from the source might be accounted for these differences, which were in agreement with the other previous studies [20]. Also we have found that an increase in radon gas concentrations in some houses which might be due to the excessive use of electrical devices, although these houses have been selected on the basis of similarity of designs and building materials. These differences might have resulted due to the differences in the usage duration of these electrical devices, nature and the resulting field. Form the above present results it can be noticed that the presence of the residential houses near to high voltage power lines might led to an increase in radon gas concentration inside and outside these houses, In addition, the fields produced from high usage of electrical devices which might also produced high electromagnetic fields as it was shown in Tables(1,2,3). This could give a high risk and side effects to the human health.To reduced these effects, we suggest that and through this study to activate some proper precautions to avoid the radon gas concentrations by using a certain substances which have low diffusion factors to radon gas which can lead to a high gas absorption capability ,or, by increasing ventilation inside these houses, as well as residential building areas shoud be situated more than about (50) meter from the electrical high voltage power lines, if possible. Alternatively,we can use underground cables to the minimize the electromagnetic fileds,because in this case it will be grounded and the electromagnetic fileds will decrease more rapidly because the cables will have smaller distance between them. Because the underground lines are not frequently used and they are often situated at very short distances from high electrical uasge areas, which could cause high electromagnetic fields, however, it will have only little effects on,for example ,for the ground floor, basement apartments, shops, gardens, pavements etc. Since higher power consumption means the existing high voltagepower lines will emit greater electromagnetic fields, the radiation emitted by cables nowadays has more aggravating waveform,so that the extensive use of electronic non-linear load devices such as fluorescent lamps, AC adapters, dimmer electronic switches, inverter air conditioners, plasma TVs, photovoltaic systems etc.,will result in deformation of the plain sinusoidal signal of (50-60)Hz mains with high frequency harmonics. This phenomenon is called "Dirty Electricity" because it causes overheating of the neutral conductor and premature aging of equipment. Some scientists believe that the new waveform of the power grid is particularly burdensome for humans [23]. A previons Research at the University of Bristol [24], have shown that the presence of high levels of low-frequency electromagnetic fields near the high voltage cables, have increases up to 18 times the accumulation of radon particles. As it is well documented , elevated radon levels are also associated with lung cancer [25].

4-Conclusions :

From the present study,and in general for a fixed distance from the high voltage power lines ,values of the indoor average radon concentrations were found to be increased with time(measuring years). Also the average outdoor radon concentrations , and the gauasmeter measurements were found to be decreased as the sample distance from the high power lines was increased . Finally , it can be concluded from this study ,the presence of the residential houses near to high voltage power lines might led to an increase in radon gas concentraions inside and outside these houses.

Aeknowledgements: The authers would like to thank Dr.Raafat Al-H.M.for fruitful and valuable discussion.

References :

[1] IARC working group on the evaluation of carcinogenic risks to humans, (2002), Non-ionizing radiation, Part 1: Static and extremely low-frequency (ELF) electric and magnetic fields. In: IARC Monographs on the Evaluation of Carcinogenic Risks to Humans volume 80. Lyon: IARC Press.

[2] Draper G, Vincent T, Kroll ME, Swanson J. ,(2005),Childhood cancer in relation to distance from high voltage power lines in England and Wales: a case-control study. BMJ 330: pp.1290–1292.

[3] Rasheed , E.M., (2017),Determination the concentration of radon gas and exhalation rate in some phosphate fertilizer using CR-39 track *detector,Iraqi Journal of Physics*, **15**,No.32,pp.136-144.

[4] Kroll ME, Swanson J, Vincent TJ, Draper GJ, (2010),Childhood cancer and magnetic fields from high-voltage power lines in England and Wales: a case-control study. *Br J Cancer* **103**:pp. 1122–1127 doi:10.1038/sj.bjc.6605795.

[5]WHO, (2007), Extremely low frequency fields. Geneva: World Health Organization. (Environmental health criteria 238).

[6] AGNIR - Advisory Group on Non-Ionising Radiation, (2004), Particle deposition in the vicinity of power lines and possible effects on health. Chilton: National Radiological Protection Board, (Documents of the NRPB, Vol.15,No.1).

[7] Fews AP, Henshaw DL, Keitch PA, Close JJ, Wilding RJ, (1999), Increased exposure to pollutant aerosols under high voltage power lines. *Int J RadiatBiol* ,**75**:pp. 1505–1521.

[8] Fews AP, Henshaw DL, Wilding RJ, Keitch PA, (1999), Corona ions from powerlines and increased exposure to pollutant aerosols. *Int J RadiatBiol* ,**75**:pp. 1523–1531.

[9] National Research Council ,(1999), Health Effects of Exposure to Radon – BEIR VI.

[10] UNSCEAR,(2000),Report of the United Nations Scientific Committee onthe Effects of Atomic Radiation to the General Assembly. ANNEX B.,Exposures from natural radiation sources.

[11]Environmental Health Division – Radiochemistry Unit of Wisconsin State Laboratory of Hygiene (2008),www.slh.wisc.edu/radiochem/results.html.

[12] Richardson, R.B., Eatough, J.P., Hensshaw, D.L.,(1991),Dose to red bone marrow from natural radon and thoron exposure.*Br.J. Radiol*,**64**(763),pp. 608-624.

[13] Henshaw,D.L.,Etough, J.P., Richardson,R.B., (1990),Radon as a causative factor in induction of myeloid leukaemia and other cancers.Lancet, **335**,pp. 1008-1012.

[14] IAEA, (2003), Radiation Protection Against Radon in Workplaces Other than Mines. In: Safety Report Series,vol.33, pp.11-12.

[15] USEPA Environments Division, (2004),A Citizen's Guide to Radon: the Guide to Protecting Yourself and Your Family from Radon. Washington DC 20460 US EPA402-K-02-006.

[16] WHO,(2009), Handbook on Indoor Radon.A Public Health Perspective.

[17] FleischerR. L., Price P. B. and Walker R.M., (1975), Nuclear Tracks in Solids, Principles and Applications. (Berkeley, USA, University of California Press).

[18] Misdaq M.A. and OuabiH.,(2006), ^{238}U and ^{232}Th concentrations in various potable waters in Morocco, *J.of Rad.Analy. Nucl.Chem*., Vol.270(3), pp.543-553.

[19] Mahdi K. H., Ishnayyin H.G..and Haider L. M.,(2015), Radon Concentration and its Doses in Dwellings of Baghdad City and In Dora Refinery Using Nuclear Track Detector (CR-39*), J. Chem. Bio. Phy. Sci. Sec. C*, Vol.**5**(3), pp.3336-3350.

[20] Raheem Z. J., (2009),The Effect of High Voltage Power Lines on Radon Concertrations in Air Using Solid State Nuelear Track Detector CR-39 in Baghdad City,MSc.thesis,Baghdad University,College of Education for pure science Ibn Alhaithem.

[21] Al-Rakabi M.S.K., (2015), Study of Radioactivity and Radon gas Emanation in Some Iraqi Governorates, Ph.D. thesis, College of EducationAL-Mustansiriyah University.

[22] Shareef N. R. ,(2913),The Measurement of Electromagnetic wave Emitted from Home Appliance by Milligauss meter, *Ibn Al-Haitham Jour. for Pure & Appl. Sci*. Vol. **26** (2)pp.131-136 .

[23] Havas M, (2006), Electromagnetic hypersensitivity: biological effects of dirty electricity with emphasis on diabetes and multiple sclerosis.

[24] HenshawD.L., Ross A.N., Fews A.P. and Preece A.W., (1996), Enhanced deposition of radon daughter nuclei in the vicinity of power frequency electromagnetic fields., Physics Laboratory, University of Bristol, U.K.

[25] Tawfiq N.F.,and Jaleel J.,(2015),Radon concentrations in soil and, Radon Exhalation Rate at

AL-DORA Refinery and Surrounding Area in Baghdad, Detection, 3, pp.37-44.

Photoluminescence Spectra From The Direct Energy Gap of a-SiQDs

Photoluminescence Spectra From The Direct Energy Gap of a-SiQDs

Nidhal M. Abdul-Ameer[1], Moafak C. Abdulrida[2], Shatha M. Abdul-Hakeem[3]

[1]Department of Physics,College of Education for pure Science (Ibn Al-Haitham), University of Baghdad, adamiayh, Baghdad, Iraq.
[2]Department of Laser and Optoelectronics Engineering, Kut College University, Wasit, Iraq.
[3]Department of Physics,College of Science, University of Baghdad, Baghdad-Iraq.

[1]dr.nidhalmoosa@gmail.com, [2]moafak.c.1950@ieee.org

Abstract. A theoretical model for radiative recombination in amorphous silicon quantum dots (a-SiQDs) was developed. In this model, for the first time, the coexistence of both spatial and quantum confinements were considered. Also, it is found that the photoluminescence exhibits significant size dependence in the range (1-4) nm of the quantum dots. a-SiQDs show visible light emission peak energies and high radiative quantum efficiency at room temperature ,in contrast to bulk a-Si structures. The quantum efficiency is sensitive to any change in defect density (the volume nonradiative centers density and/or the surface nonradiative centers density) but, with small dots sizes, the quantum efficiency is insensitive to such defects. Our analysis shows that the photoluminescence intensity increases or decreases by the effect of radiative quantum efficiency. By controlling the size of a-SiQDs, we note that the energy of emission can be tuned. The blue shift is attributed to quantum confinement effect. Meanwhile, the spatial confinement effect is clearly observed in red shift in emission spectra. we found a good agreement with the experimental published data. Therefore, we assert that a-SiQDs material is a promising candidate for visible, tunable, and high performance devices of light emitting.

Keyword. photoluminescence, Amorphous silicon, Quantum Dots, Confinement.

1. Introduction

One of the key components needed to induce photoluminescence in silicon is the presence of materials of low dimensional (nanostructures) [1].Therefore; SiQDs is considered a promising material to open a number of technological relevant and scientifically challenging areas that deal with atomic scales [2]. The structures of quantum dot, in general, used quantum confinement to shift the luminescence of silicon into the visible region [3]. Thus, the effect of quantum confinement is considered to be one of the mechanisms of illumination; however, it differs from other mechanisms by controlling the size that can be tunable[4,5]. Therefore; the spectrum of SiQDs can be tuned continuously across the visible spectrum [6,7], where the wavelength of the emitted light, from green to infrared, is controlled by the size of dots [8,9]. However, in the process of searching for more efficient materials of less dimension, it has been shown that the amorphous silicon dots, a-SiQDs, may be a suitable material for this purpose [10,11]. In fact, there are two

important advantages of bulk amorphous silicon compared to crystalline silicon [4,10] : Firstly, the energy gap of a-Si (1.6 eV) is greater than of c-Si (1.1 eV). Second, the luminescence efficiency in a-Si is higher than c-Si, due to structural disturbance. Thus. This material , a-Si, will be a good candidate for emitters of short wavelength light [12,13].

The efficient visible light emission from a-SiQDs has attracted much interest from researchers both in terms of basic physics and applications to silicon-based devices. It is known that; the radiative recombination processes are involved in this phenomenon, but its mechanism is still a matter of debate. In fact, the mechanism of the photoluminescence is the main issue of the current research [14]. It is studied first by Dunstan and Boulitrop[15], for a bulk a-Si. In the case of a-Si nanostructures, Estes and Moddel[16,17]are developed this model, which is depending on the spatial confinement. Calculations were made using a simple model of radiative recombination in amorphous silicon nanostructure of 2-D , 1-D and 0-D. Their calculations showed a significant size dependence of the photoluminescence. They believed, the spatial confinement effects exist only and no quantum confinement. Also, in 1997 [18], they reported on the influence of doping, temperature, porosity, band gap, and oxidation on the photoluminescence properties ofporous a-Si. With the same manner of Estes and Moddel opinion, a complete analysis of the light emission properties of porous a-Si:H was produced by I. Solomon etal.[19]. The measurements of Light emission and optical absorption energy of a-SiQDswith different sizes revealed that tuning of the light emission is possible by controlling the size of the a-SiQDs. This important performance is achieved by Nae-Man Park etal.[13], who prove the possibility of existence of the quantum confinement in a-SiQDs. They also fabricated an orange light emitting diode (LED) by using a-SiQDs with a mean size of 2 nm [4]. F. Karbassian etal. [20] show that nanocrystals emit light around a wavelength of 550 nm. Multilayer structures have been fabricated to increase the PL intensity by separating luminescent nanocrystal layers with a 5 nm-thick layer of silicon oxynitride. By methods of optical spectroscopy and Raman spectroscopy, N.G. Galkin etal. show that embedded NC form intensive peaks in the reflectance spectra at energies up to 2.5 eV and Raman peaks and a photoluminescence andelectroluminescence at room temperature were firstly observed [21]. Theoretically, K. Nishioetal.[10,11] studied the light emission properties of a-SiQDs by using the continuous random network (CRN) model.Their tight-binding calculations, for direct band-to-band recombination, reproduce the peak energies of experimental photoluminescence results,obtained by [13].

In fact, many treatments are used to convert this material into an efficient photo-emitting material. One of these treatments is the concept of the confinement. In this paper, we are trying open new considerations on the mechanism of photoluminescence for a-SiQDs model. In fact, these considerations are consisting the dynamic of the confinements (the spatial and the quantum) ,which suggests the coexistence of both the spatial and the quantum confinement's effects in amorphous silicon nanostructure material [22].To clarify this proposal, we have used the experimental data of (Egvs.Rt) to obtain a theoretical relation via a fitting process [13]. Thus, the comparison between these two confinements is reflected in our results. We have analysis the results of this model by starting the concepts of both confinements with their characteristic lengths, where are considered special features of a-SiQDs model. We were also studying the most important parameters which have affected on the intensity of photoluminescence, for both types of the confinement. Finally, the tuning is one of an applications parameter of this study that is resulting from the controlling of the sphere's sizes, where the red and blue shifting is discussed.

2.The Model

In previous our paper [22], we had believed that *a-SiQDs* changes the nature of amorphous silicon optical band gap from indirect to direct transition material. In fact, these structures, it is note that : the first; zero- phonon optical transitions are allowed , second; oscillator strength of the zero- phonon transition is significantly enhanced [23]. Thus, it is expected, the properties of light emission will be improved [24].

Now, we describe our model with both concepts the spatial and the quantum confinements to produce the photoluminescence from a-SiQDs.

In the spatial confinement, the common model of recombination is used in the amorphous silicon which suggested by *Street* [25],where the defects provide the dominant recombination centers as illustrated in 'Figure

1a', which is represented the bulk case of a-Si. The distance from a defect at which the nonradiative and radiative recombination rates are equal, a nonradiative capture radius,$\boldsymbol{R_C}$, a round the defect is defined [19]. Thus; the size of capture can be considered as a sphere surrounding the defect [26] as shown in 'figure 1b'. When the electron-hole pair into the sphere, it recombines nonradiatively; otherwise, it recombines radiatively [19, 26]. In this case, the electron-hole pairs can recombine either radiatively or nonradiatively. Alternatively, the capture radius, $\boldsymbol{R_C}$, may be seen as the characteristic length explored by a photocreated electron-hole pair before its radiative recombination [19]. The spatial confined for ***a-Si*** is represented in 'figure 1b'.

In view of the fact that the values of *Rc* must not adopts as a randomly, that takes the form [16, 17]:

$$R_C = \left\{\frac{3}{4\pi N_{nr}} \ln\left[\left(\frac{1}{\eta_O} - 1\right) \exp\left(\frac{T}{T_O}\right) + 1\right]\right\}^{\frac{1}{3}} \quad (1)$$

where $N_{nr}$is the volume nonradiative recombination density (cm^{-3}), $T_o$is an experimentally determined constant and η_o is the low temperature maximum quantum efficiency limit. We used in this paper the values for bulk a-Si:H [27] $\eta_{o\sim}0.998$ and $T_{o\sim}23K$.

In *a-SiQDs* structure, we suppose the amorphous silicon nanocrystals are grown in a silicon nitride film by one of the deposition technique as shown in 'figure 1c'. The probability for a photocarrier of encountering a nonradiative center is no more given by the dark sphere volume but the volume of the intersection of the dark spheres with quantum dots nanostructures [19]. When the characteristic size of the quantum dot is smaller than R_C, hence the nonradiative recombination probability is decreased. Also, from 'figure 1' can notice that; the periodicity due to a superstructure is absent [14], which is called also superlattice. It is important, in this research, to mention that; the localization radius in this model has the same meaning ofthe effective Bohr radius, R_o, which is estimated to be 10Å [16,17].

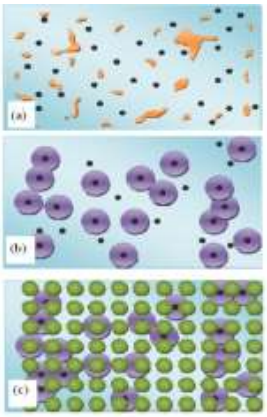

Figure 1. a- illustrates the case of bulk a-Si with defects. Dark spheres are represented the nonradiative capture regions.b- the same bulk film with the spatial confinement,the circles are the capture volume with radius, RC. c- In this case, the spatial confinement is still considered, where a-Si-QDs are etching in the film.

Since quantum dots usually consist of tens to thousands of atoms, geometric considerations promote a very high surface-to-volume ratio, compared to the bulk version of the same quantum dot material [28].The volume, $V = \frac{4}{3}\pi R^3$, and surface area,$A = 4\,\pi R^2$, of spherical dot are taken as the ordinary geometric expression for this shape. But, the concept of R is different from one magnitude to another. When the magnitude of R lies in the range of active quantum dots, Rrepresents the dot radius, R_t. In this case, the model is treated as the nanostructure material. But, if R has a magnitude more than this range, then it will be the nonradiative capture radius, R_C that is considered. It is clear that, the material should be treated as a bulk in this case. As a consequence, R_C can be used as a probe of $R_t$according to its magnitude in this work. Therefore, there are three different cases for the volume and the surface area of spherical dot; where R_t may be less than R_C, equal to R_C, or more than R_C, in both cases $R_t \leq R_C$ the characteristic length is considered as the radius of the quantum dot itself. According to this assumption, different cases for capture volume, $\boldsymbol{V_C}$, and surface capture area, $\boldsymbol{A_C}$, can be computed as shows in (table 1).

Table 1. The different cases of the capture volume, Vc, and the surface capture area.

	$\boldsymbol{R_t < R_C}$	$\boldsymbol{R_t = R_C}$	$\boldsymbol{R_t > R_C}$
$\boldsymbol{V_C}$	$\frac{4}{3} = \pi R_t^3$	$\frac{4}{3}\pi R_C^3$	$\frac{4}{3}\pi R_C^3$
$\boldsymbol{A_C}$	$4\pi R_t^2$	$4\pi R_t^2$	0

From table (1), it can be said that when$R_t \leq R_C$, the material behaves as quantum dots nanostructure. While when $R_t > R_C$, follows the bulk ***a-Si***. 'Figure 2' describes the different cases of capture volume V_C and surface capture area A_C according to the relation between $R_C$and R_t.

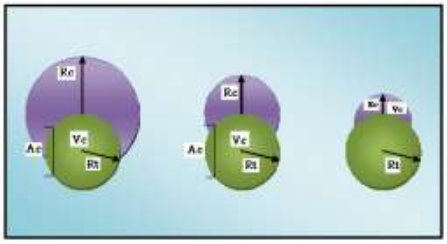

Figure 2. According to the relation between R_C and R_t, the different cases of the capture volume, V_C, and the surface capture area, A_C, as indicated in table 1. In front of the circle is the quantum dot with radius R_t, while behind the circle is the capture region with radius R_C. In each case, this region has different size because it has different nonradiative center density.

According to the **Anderson -Mott** picture of amorphous semiconductors [29], a rigid-band model is assumed [15,16]. The **Mott-Davis**model is suggested to satisfy this purpose**.** In this model, radiative recombination take place via tunneling between the deepest accessible energy conduction and valence states in the respective band tail [10,15,16,19], without Stokes Shift [16,17]. Radiative transition to /or from defect levels near midgap is not considered here [16,17] because this transition is not occurred at only one band. The surfaces do not additional radiative recombination paths are assumed [17], since, in general, the surface transitions is nonradiative process. On the other hand, nonradiative recombination occurs through a tunnel to a nonradiative defect center when this center is within the capture volume,***Vc***[16,19]. We have assumed that the surface is additional nonradiative states due to excess dangling bond. It is important to note that; in *a-SiQDs* structure, carriers will find deeper energy paths within the volumes of spheres. While in bulk, carriers may recombine through only a few low energy tail or defect [16].

The carriers at the spatial confinement have smaller volumes, this led to increasing the average luminescence energy and efficiency [16,17]. The quantum confinement is making to convert an indirect optical transition into a direct one [14]. Radiative recombination becomes more efficient since the electron and hole wavefunctions overlap, leading to a faster recombination for size decreasing of nanocrystal [1]. In fact, studying the effect of quantum confinement in ***a-Si*** as a function of dimension can yield important informations about the physical processes which are related to the carrier mobility [13]. Recombination at interface states or other defect states away from the quantum dots form competitive nonradiative recombination paths [1].

The net effect of the quantum confinement is a reduction of carrier mobility and a widening of mobility gap [16,30]. By using the best fitting for the experimental data that is achieved by *Park etal.*[13], this effect is done in the *a-SiQDs* model. According to the theory of effective mass, an infinite potential barrier is assumed, therefore, the energy gap, E_{QD}, for three-dimensionally confined ***a-SiQDs*** model is expressed as [4, 12, 13].

$$\mathrm{E_{QD}} = \mathrm{E_{g(bulk)}} + \frac{\mathrm{C}}{\mathrm{R_t^2}} \tag{2}$$

Where $E_{g(bulk)}$is the bulk of the *a-Si* band gap that takes the value (1.56 eV) obtained from the best fit for the experimental data which is mentioned above. This value is very close to the values reported in literature for bulk ***a-Si*** [31]. R_t is the radius of the dot and C is the confinement parameter. This parameter is about (2.4 eV nm^2).

Since the density of states function in amorphous silicon is changed as the energy depth increase [31], the density of states function for *a-SiQDs* model is still under debate and search [10]. Therefore; some assumptions must be taken in account for this model: the electronic states are assumed to be the same as those of bulk *a-Si* [16,17], where the estimation for *a-SiQDs* is often carried out in an analogous manner [11]. The exponential band tails are supposed to be independent of size [10,16,17]. This led to estimate the probability that no band tail states exist in volume comparable with *a-SiQDs* [10,11]. Also, for simplicity, Fermi energy level is considered constant throughout the structure and is located near midgap [16].

In this work, in contrast to *Dunstan* and *Boulitrop*, the entire density of states are considered, including both exponential band- tail and quadratic band states as potential luminescence sites [16,17]. The amorphous-silicon density-of states function ($cm^{-3}eV^{-1}$) for conduction band is given by[16]:

$$N_{CO}(E) = \begin{cases} N_{CO} exp\left(\frac{E}{E_{CO}}\right) for E \le E_C \equiv 0 \\ N_{CO}\left(\frac{2}{E_{CO}}\right)^{\frac{1}{2}} (E - E_C)^{\frac{1}{2}} for E > E_C \end{cases} \tag{3}$$

Where $E_C \equiv 0$ is the conduction -band energy at which the band and tail state densities are equal, $N_{CO}$is the effective density of states (cm^{-3}) at E_C, and E is the energy relative to E_C.

$E_{CO}$the slope of the band tail energy, which is defined as the characteristic energy which describes the width of the Urbach edge, thefore; E_{CO} is a measure of the width of the localized state distribution [32], which is given by [33]:

$$E_{CO} = kT \tag{4}$$

The valence –band has a similar form for $N_V(E)$**,** where E is valence band energy relative to the energy $E_V \equiv 0$ at which the band and tail state densities are in equal. As in conduction band , $\mathrm{E_{VO}}$ is obtained by [33]:

$$(E_{VO})^2 = (E_{VO})^2_{T=0} + (kT)^2 \tag{5}$$

Where the second term is represented the room temperature energy.

The process of thermalization is considered as a characteristic feature of amorphous semiconductors [25]. Accordingly, photoluminescence carriers are presumed quickly thermalize down or above (for conduction or valence band, respectively) through localized states in the band tails [16, 19, 32]. These carriers reach to the deepest energy states before recombination within some distance *R* [16, 19]. It must be mentioned, the deepest state for conduction band means the lowest state and the highest state for valence band [19].

The carriers' separation arises from the diffusion of carriers in the extended states during the thermalization process [19]. It could be considered as the initial distance of electron-hole pairs may have spatial distribution even immediately after photoexcitation [34].

When the density of states drops $(E_C V_C)^{-1}$at energy in the conduction band tail, this energy is equal to [26]:

$$\Delta E_C = E_C \ln(V_C N_{CO}) \quad (6)$$

which is defined as the thermalization energy for electrons that lie below the conduction band mobility edge. While the energy for holes that lies above the valence band mobility edge is named the thermalization energy. The valence band had the same expression.

Now, it is easy to calculate the total number of states which are contributed in these transitions for both conduction and valence bands.

For an electron injected at an energy ΔE_C above E_C, the total number of accessible conduction –band states below ΔE_C and within the capture volume, V_C, is given by[16]:

$$n_C = V_C \int_{-\infty}^{\Delta E_C} N_C(E) dE \quad (7)$$

The function of probability density for conduction band , $P_{C(lowesttstate)}\ (E)$, which is gives the probability that the lowest-energy conduction band state within the capture volume lies between E and $E + dE$. It is then the probability that $n_C - 1$ states lie above the energy E times the probability that n_C^{th} state is between $E$and $E + dE$, which is denoted by $P_{C(\,n-1states)}(E)$

Assuming that these ***n*** states are independent $P_C(E)$is thus:

$$P_C(E) = P_{C(lowesttstate)}(E) P_{C(n-1states)}(E) \quad (8)$$

$$P_C(E) = V_C N_C(E) \left(\frac{\int_E^{\Delta E_C} N_C(E) dE}{\int_{-\infty}^{\Delta E_C} N_C(E)} \right)^{n_C - 1} \quad (9)$$

A similar expression applied for the probability density function of highest-energy valence-band hole states, $P_V(E)$.

The normalized luminescence photon flux spectrum,$P(hv)$, is the convolution of probability density function of deepest energy conduction$P_C(E)$ and valence $P_V(E)$ band states within the capture volume [15,16,17,19].

$$P(hv) = P_C(E)^* P_V(E) \quad (10)$$

$$P(hv) = \int_{hv - \Delta E_V - E_g}^{\Delta E_C} P(E) P_V\big(hv - E_g - E\big) dE \quad (11)$$

It should be noted that the two E values are in different reference frames [16], E_g is the band gap energy of *a-Si* (1.6 eV) in the case of spatial confinement, but it's value is already different as the size of dots in the case of quantum confinement [35].

Since the luminescence spectrum is a function of the capture volume, it should be spatially averaged and multiplied by photon energy to obtain the net intensity spectra for *a-SiQDs*, which was computed numerically [16]:

$$I_{0D} = 3\, hv \eta_{OD} P(hv) \quad (12)$$

Where hv is the excitation energy ,with taking into account the intensity of photoluminescence is proportional to the recombination rate [34]. $\eta_{OD}$is the internal radiative quantum efficiency.

For bulk *a-Si*, the internal radiative quantum efficiency is determined by solving the nearest neighbor distribution function for randomly dispersed sea of electrons and holes or defects [25,19]. This distribution function is applied to nonradiative tunneling of an electron to a defect [36], then it can be given:-

$$\eta = e^{\left(\frac{4}{3}\pi R_C^3 N_{nr}\right)} \quad (13)$$

where $N_{nr}$is the volume nonradiative recombination center density(cm^{-3}).

But, for *a-SiQDs* model the equation (13) is taken for different situations depending on the size of the dot. Meanwhile, no change occurs in case $(R_t > R_C)$, but R_C is replace by $R_t$for the case $(R_t \leq R_C)$. Thus, equation (13) become:

$$\eta = e^{\left(\frac{4}{3}\pi R_t^3 N_{nr}\right)} \quad (14)$$

Besides the effect of volume nonradiative recombination center density, the effect of the surface nonradiative recombination center density, N_{snr} (cm^{-2})is also considered. Therefore, the equation (14) is replaced by:-

$$\eta_{OD} = e^{\left(\frac{4}{3}\pi R_t^3 N_{nr}\right)} e^{(4\,\pi R_t^2 N_{snr})} \quad (15)$$

where the number of surface atoms is a large proportion of the total number of atoms [28]. In fact, the above expression simply gives the probability of not finding a nonradiative recombination center within the capture volume but the surface capture area does not exist [16].

In this model, the quantum efficiency is defined as the ratio of the light-color volume, which is shown in Fig.(1c), to the whole volume [19]. The quantum efficiency is improved by breaking the bulk momentum space selection rule (quantum confinement effects) [3] and by reducing the efficiency of the nonradiative channels for the recombination because of the localization of the carriers (effects both spatial and quantum confinement) [3, 5].

3.The Results and Discussion

In this paper, we are dealing with the term of the characteristic length at more position. Generally, this term is separated between two cases, processes, values, etc. Therefore; we will be analysis as its positions in this section.

In the case of the spatial confinement for the bulk material, the characteristic length is the capture radius, R_C, where the tunneling process of the carriers is assumed. From 'equation (1)', there are two quantities which are essentially affected on the value of the capture radius, R_C. The first is the temperature energy, that is estimated by the room temperature **(***T=300K***)**. The other quantity is the volume nonradiative center density, N_{nr}. The capture radius versus nonradiative center density is illustrated in 'figure 3'.

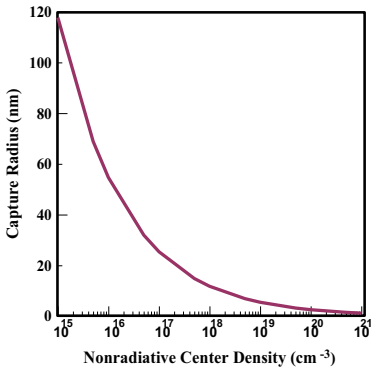

Figure 3. The capture radius is represented the characteristic length for bulk a-Si as a function of volume nonradiative center density.

It is clear from 'figure 3' that the value of capture radius, R_C is decreasing, (and so on the capture volume ,V_C), when the volume nonradiative center density is increasing. Since free carriers can move around and access a larger volume of amorphous silicon, they stand a greater chance of finding nonradiative recombination centers or very deep tail states [16]. With taking into account the carriers have enough thermal energy to diffuse a considerable distance before being trapped and recombined..

In the case of the spatial confinement for quantum dot nanostructures, the characteristic length is submitted to the relation between the quantum dot radius, R_t, and the capture radius, R_C. In fact, this relation may be explained, because of the tunneling rate is proportional to $(exp(-R/R_O))$ [26]; therefore, the tunneling is almost considered the shorter distance. As a consequence, the characteristic length is the quantum

dot radius, R_t when$R_t \leq R_C$. But; it is remained as the capture radius, R_C in case $R_t > R_C$which is represented the bulk material.

As an electron shows properties of a particle and a wave, if the size is small, the electron energy spectrum is quantized [1]. Therefore; the magnitude order of the electron and the hole de Broglie's wavelength is comparable with the confinement dimension [37]. Thus, the characteristic length in the case of the quantum confinement is the de Broglie wavelength, λ_B. We are computed λ_B for *a-SiQDs* from [38,39,40]:-

$$\lambda_B = \frac{h}{P} = \frac{h}{m^* v_{th}}$$

where v_{th} is the thermal velocity, and P is the momentum, which its magnitude is about **(*4.4* *nm*)**. In general, the characteristic length in this case is considered as a criterion for the confinement. When the wavelengths of the emitting energy are larger than the λ_B, the confinement is described as a weak. While it is considered a strong if the wavelengths are smaller than λ_B.

It is useful to mention this; the total number of states is included both radiative and nonradiative states. 'figure 4' illustrates the number of nonradiative states as a function of the quantum dot size. In fact, this figure is confirming that; *first*, the contribution of the valence band states in the tunneling processing are more than for the conduction band states. *Second*; the carriers are tunnelling nonradiatively in the valence band which is more than the case in conduction band. *Third*, the number of nonradiative states, in both bands, is decreasing when the size is decreasing. This means the transitions, in only one band, is decreased when the size is decreased. In a very small size, the number of nonradiative states is closing to zero. In this case, the small sizes almost have the radiative states. We can say the transitions between the two bands are occurred more in the small size.

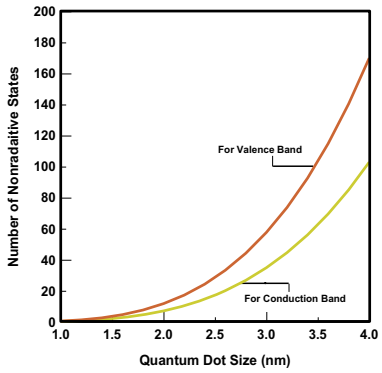

Figure 4. The number of nonradiative states versus the quantum dot size for conduction and valence bands.

.

As a consequence, the ratio of the carriers which are ready to tunnelling radiatively in the conduction band is higher than in the valence band. Therefore, the contribution of the radiative transitions for conduction band is more than the radiative transitions for valence band. This distinct in the 'figure 5', where the probability density function is plotted versus the quantum dot size. In fact, this result is in agreement with analysis the number of nonradiative states in both conduction and valence band.

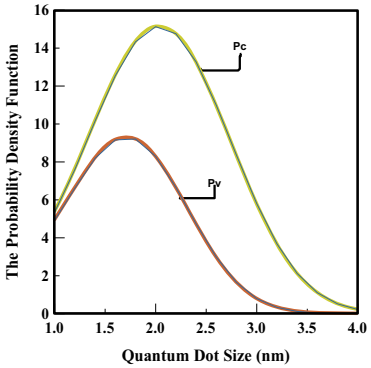

Figure 5. The probability density function versus the quantum dot size for conduction and valence bands.

In fact, these results represent the internal quantum efficiency only and do not reflect losses associated with light escaping the structure. Since, the effective index of refraction is considerably lower than that for bulk *a-Si*, hence a greater fraction of the luminescent light may escape as the angle for total internal reflection larger than for the bulk case [16, 17].

Both surface and volume nonradiative recombination center densities affect on the quantum efficiency value. Besides of that; the value of quantum efficiency is also affected by the quantum dot size. One of the methods for improving the quantum efficiency is to reduce nonradiative defect [5]. Therefore, the expression of 'equation (15)', as mentioned previously, simply gives the probability of not finding a nonradiative recombination center within the capture volume and on the surface capture density. From 'figure 6a', one can see the effect of structure size on the quantum efficiency for *a-SiQDs* structure with different values of the volume nonradiative center density. We found, the quantum efficiency is increased when the volume nonradiative center density is decreased at each fixing value of the surface nonradiative density. This dip in efficiency is due to combination of relatively large surface area and relatively large volume of the structure so that carriers are exposed to a maximal number of nonradiative sites [16,17]. Actually, this behavior is reasonable and logical because of the decreasing in the carriers which are recombined radiatively. In fact, at low densities of the volume nonradiative center $(10^{15} - 10^{17})\ cm^{-3}$ the quantum efficiency value is sensitive to the changing in magnitude of surface nonradiative density. Whereas the degree of the sensitivity is less at high densities $(10^{19} - 10^{21})\ cm^{-3}$; therefore, we can note that; the changing is not great. At small sizes, the near unity quantum efficiency of the quantum dots results simply from there being very few states, and hence a small probability of a nonradiative recombination center, within these sizes. When the dot size is increased, the states, generally, are increasing at each size. This leads to increase the probability of existence nonradiative states, which have the nonradiative recombination centers. As a consequence, in this case, the quantum efficiency value is comedown.

The surface nonradiative density is played a very important role in the magnitude of the quantum efficiency, as we noted in previous section. The reason of this relate to the atoms of surface atoms which have a large proportion in the quantum dot. In fact, It is considered to be a very effective in the value of quantum efficiency [41]. The surface nonradiative density versus the quantum dot size is indicated in 'figure 6b'. To consider the effect of surface nonradiative density, we have fixed the volume nonradiative density. Whenever the density of the volume nonradiative is increased, the sites of nonradiative centers is increased too because the combination of surface area with the volume of the structure. Therefore; the value of quantum efficiency is comedown by increasing the density of the volume nonradiative.

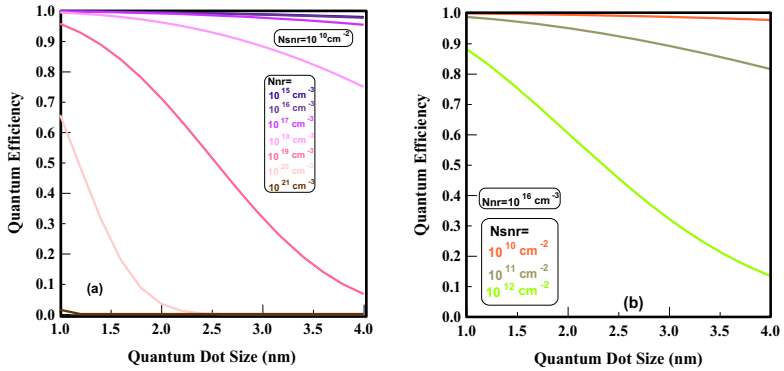

Figure 6. The quantum efficiency versus the quantum dot size with different values of a- the volume nonradiative recombination center density (10^{15} cm^{-3} - 10^{21} cm^{-3}) for the surface nonradiative recombination center density $10^{10}cm^{-2}$ value. b- the surface nonradiative recombination center density (10^{10} cm^{-2} – $10^{12}cm^{-2}$) for thevolume nonradiative recombination center density $10^{16}cm^{-3}$ value

'figure 7' shows the quantum efficiency versus the volume nonradiative center density for all the sizes of spheres in this work. In the 'figure 7a' , the surface nonradiative density is assumed to be $10^{10}cm^{-2}$. It is appeared from this figure, the quantum efficiency value for all sizes has not affected by the increasing the density until closing the value $10^{17}cm^{-3}$, where the quantum efficiency value at near unity. In other words, the quantum efficiency is independent on the density in this range. But, the quantum efficiency is starting of the decreasing after the density of value $10^{17}cm^{-3}$. Then, the dip is very clear appeared at high density, where the number of sites nonradiative is increased. On the other hand, the size of the quantum dot plays an important role in the value of quantum efficiency. As we see in this figure; its value increases with the reducing the size. The reason of this refers to increasing the number of the carriers which are recombined radiatively. Also, this means, the probability of not finding nonradiative center has been highly when the size is smaller. While 'figure 7b' shows the quantum efficiency as a function of the surface nonradiative density. We can see from this figure, the quantum efficiency is very sensitive to any changing in surface nonradiative density. At the same magnitude of the volume nonradiative density, the quantum efficiency is increasing with the reducing of the size; with taking in account this increasing is excessive. In fact, this increasing result from the dominantly of the radiative recombination because the decreasing of nonradiative center on the surface area of quantum dot.

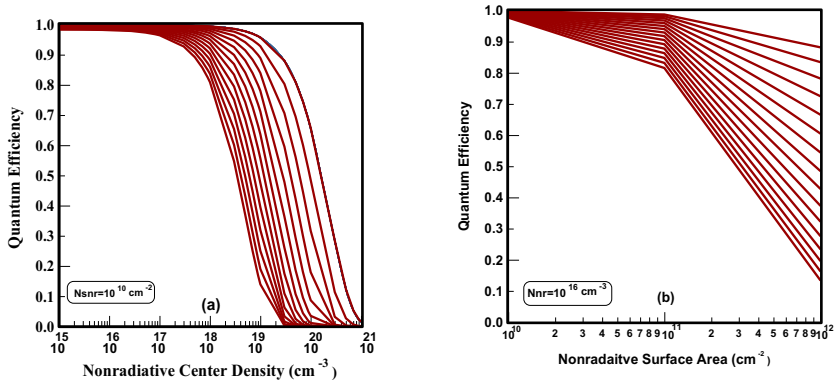

Figure 7. The effect of structure sizes (from 1 to 4 nm) on the quantum efficiency as a function of (a) the volume nonradiative recombination center density, the surface nonradiative recombination center density is

fixed at value 10^{10}. of (b) the surface nonradiative recombination center density,the volume nonradiative recombination center density is establish atvalue10^{16}cm^{-3}.

From equation (12), we can distinguish the parameters which are contributed on the photoluminescence intensity magnitude. These parameters are the quantum efficiency, the photon flux (more details of photon flux in pervious paper Ref. [35] , and the magnitude of the excited photon energy. According in pervious paper [35], they are four regions, each region has a practically behavior differs from another region.We are chosen from each region only one size for both cases of spatial and quantum confinements. These sizes are $(3.6)\ nm, (2.8)\ nm, (2)\ nm, (1.2)\ nm$ for the four regions respectively. In all figures in this section, the photoluminescence intensity is represented as a function of the photon energy.

Here, we indicate the role of every parameter, which affected on the photoluminescence intensity as mentioned above. The effect of quantum efficiency is shown clearly when the intensity magnitude is increasing or decreasing by changing the volume nonradiative density and/or the surface nonradiative area. We note from all figures that; as a general sequence, the intensity magnitude is decreasing with the increase of volume nonradiative density. But, this magnitude is more comedowns when the surface nonradiative area is increased. The reason for this behavior related by the increase of the number of nonradiative recombination centers.

The effect of photon flux shows the behavior of the intensity, where this behavior has only one style although the intensity magnitude is decreasing or increasing [35]. This leads us to think, the period of optical transitions in the various sizes of quantum dots has the same procedure, and thus the photoluminescence spectrum has the same shape.In amorphous semiconductors, Urbach edge (the exponential part of the absorption edge) is due to optical transitions involving localized states. In fact, the width of the Urbach edge is determined by the Urbach energy, therefore; this energy is a measure of the width of the localized states distribution [32]. Because of this energy is depended on the temperature energy, thus, In this work, the magnitude of Urbach energy, for both conduction and valence bands, is estimated at room temperature.

Since the photoluminescence dynamics of *a-SiQDs* is determined by the recombination of carriers localized in the band tail state, therefore; the broad photoluminescence spectra of *a-SiQDs* is due to various of the radiative transition energy in the band tail state within a quantum dot [24]. However, the full width at half maximum (*FWHM*) of this spectra can be estimated from the Urbach energy [19]. In the case of spatial confinement, the spectra exhibit a line width of approximately *0.22 eV* for all the dot sizes. While in the case of quantum confinement, the broadening of spectra is increasing from *0.22 eV* to *0.225eV* with decreasing the dot size, in which exhibits the *Gaussian-like* shape in both cases. We can explain the first case as; a significant shift of the mobility edge to higher energies being not or less affected [19], whereas the second case suggests; the dot structure affects the distribution of localized states in the band states [32]. In other words, the size effect is inducing a broadening of Urbach energy. It is useful to mention that; besides of the linewidths of spectra are varied by the quantum dot size, they are also varied by local environment [6].

In all figures of photoluminescence intensity, there are differences in the maximum magnitude of the photoluminescence intensity between the spatial and the quantum confinements, where the magnitude for the quantum confinement is higher than for the spatial confinement. The reason of that retain to enhancement of radiative recombination for the case of quantum confinement. Since the emission occurs from the lowest energy states in the conduction band to highest energy states in the valence band [6], the energy of the electron-hole pair, then the number of available states , is increased because the increasing of the excited photon energy [3], that is considered one of the consequences the quantum confinement effects.

Figur 8 a and b illustrates the photoluminescence intensity for the first region, a bulk-like region at the spatial and the quantum confinements respectively. At high densities$(10^{20}, 10^{21})\ cm^{-3}$,this behavior dose not affected by the change of surface nonradiative density. This improves, at this region, the behavior of the intensity to be close to the bulk mode when the radius becomes larger. In other words, the nanostructure mode is appeared partially upon the volume nonradiative density. Also, the intensity magnitude is decreasing with the increasing of surface nonradiative area because the nonradiative centers are increasing.

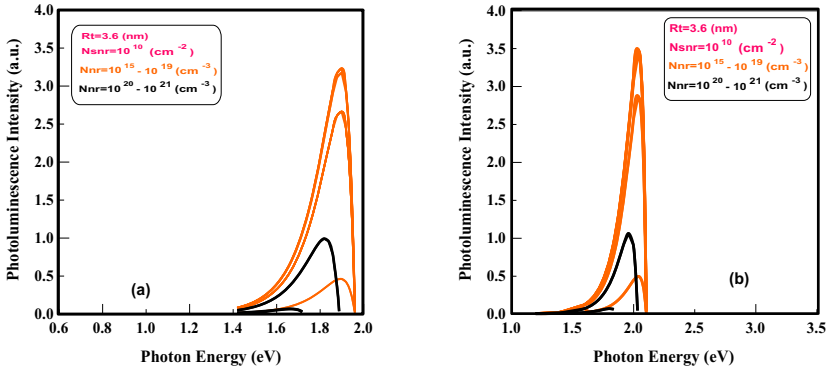

Figure 8. The photoluminescence intensity as a function of photon energy for the bulk- like region for 3.6 nm size, Nsnr=10^{10}cm^{-2} a- at the spatial confinement b- at the quantum confinement.

In 'figure 9' , the spectra of photoluminescence intesity at the large-dot region is indicated . While this spectra at the medium-dot region is shown in 'figure 10'. Finally, the spectra at the small-dot region is indicated in 'figure 11'.

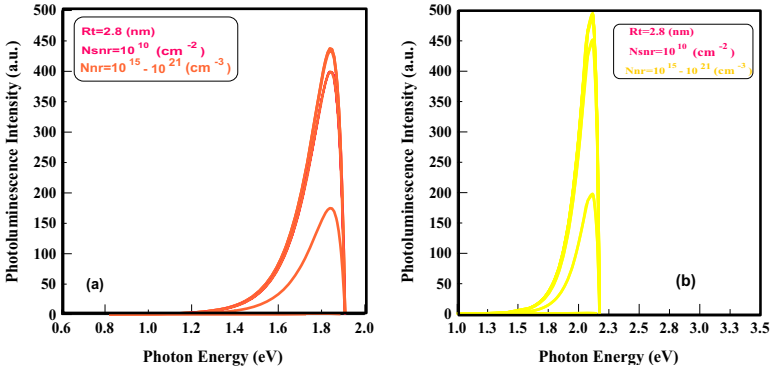

Figure 9. The photoluminescence intensity as a function of photon energy for the large-dot region, for 2.8 nm size, Nsnr=10^{10}cm^{-2} a- at the spatial confinement b- at the quantum confinement

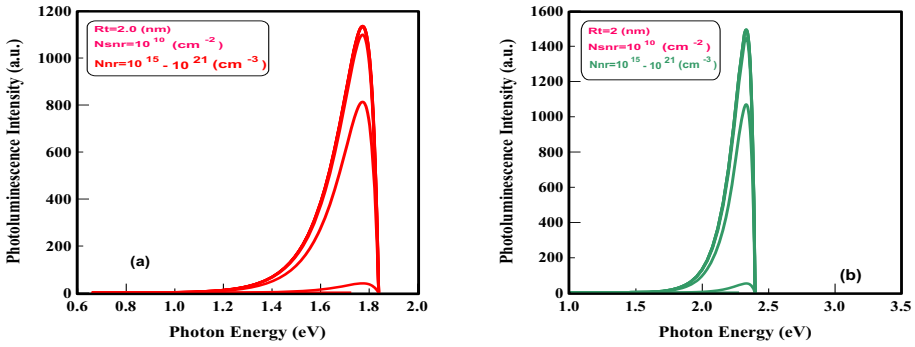

Figure 10: The photoluminescence intensity as a function of photon energy for the medium-dot region, for 2 nm size, Nsnr=10^{10}cm^{-2} a- at the spatial confinement b- at the quantum confinement

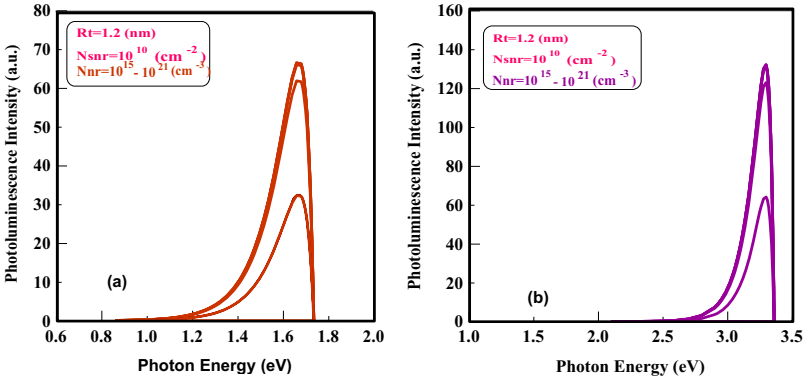

Figure 11. Thephotoluminescence intensity as a function of photon energy for the small-dot region, for 1.2 nm size, Nsnr=10^{10}cm^{-2} a- at the sparial confinementb- at the quantum confinement

One of the major outcomes of this study is the realization, the crystallivity is not necessary for visible light emission from nanostructures. Such these structures yield emission energy tunable from near-infrared to the visible range [42]. In fact, the wavelength of the emitted light is controlled by the size and the composition of the dots [9]. In this work, we illustrate the effect of both cases of confinement (the spatial and the quantum) on the emitted light from *a-SiQDs*.

'Figure 12a' illustrates the energy can be shifted toward a larger wavelengths (*red shifting*) of all sizes are used for the spatial confinement case. In this figure indicates nominally $(2.0-1.6)eV$ peak energies in the orange-red room temperature photoluminescence band with decreasing the dot size. In fact, the mechanism of the orange-red photoluminescence originating from the long-lined surface states [43]**.** This led us to suggest that; the optical transitions occur under the condition $(E \geq E_g)$,where E is the excitation energy, and the excitation states decrease when the dot size is decreasing. [41,44]**.** While It is clear in 'figure 12b' that; the energy can be shifted toward a smaller wavelengths (*blue shifting*), which indicates the peak energy as a function of dot size. Also, the peak energies have the range 2 eV to 4 eV in the (*red to blue*) room temperature photoluminescence band with reducing the size of dot. The mechanism of the red-blue photoluminescence relates to the quantum confinement effects. This mechanism can be explained as follow; since the energy levels are shifting to higher magnitude with the dot size decreasing, the energy gap is changed from size to another. Under the condition $(E \geq E_g)$, each size have a privacy feature in its transition energy, which takes a high magnitude whenever the dot size is deceased.The explaining of *red shifting* and *blue shifting* will present with more details in Ref [22].

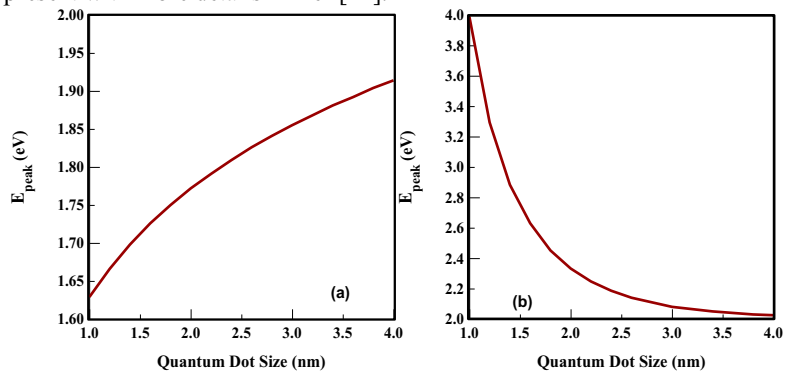

Figure 12. a- The peak energy as a function of the dot size at the spatial confinement. b-The peak energy as a function of the dot size at the quantum confinement.

'figure 13' shows the emission color that could be changed by controlling the dot size, where the tuning of the photoluminescence emission from $(0.7-0.3)\,\mu m$. For example, the dot size corresponding to red, green, and blue emission color were $(3.6, 2.2, \text{and } 1.2)nm$respectively. In fact, the tuning of emission color and efficient emission can be achieved by quantum confinement effects [4, 45, 46, 47], where quantum confinement effects make silicon a likely candidate for full-color displays [4].

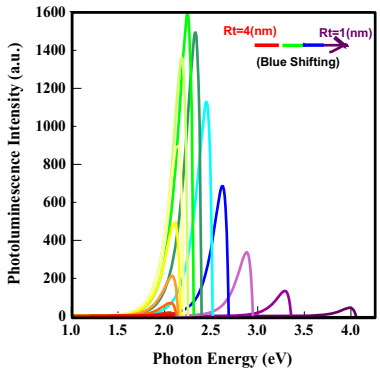

Figure 13. The photoluminescence as a function of photon energy for all used sizes at the quantum confinement.

the results of photoluminescence *a-SiQDs*model are reviewed with the parameters that affect the photoluminescence's value. In this section, progress the development of amorphous silicon photoluminescence is introduced by 'figure 14'. This is done , first, by considering the Dunstan and Boulitrop model (Fig.(14) , that has peak energy at about 1.4eV for *a-Si: H*. The second curve represents porous *a-Si*, this material attracted more attention after Canham's discovery in 1990, its peak energy is about 1.75eV. The model of *a-SiQDs* for Estes and Moddel, with a size 2.5nm, has its peak energy at 1.75eV. This model depends on the spatial confinement. But, the peak energy shifts to 2 eV when the model considers the quantum confinement rather than the spatial confinement for a2nm size as Nishio et al. model. For the same size and with the consideration of both confinements (the spatial and the quantum) in our work, the peak energy has the value 2.2eV.

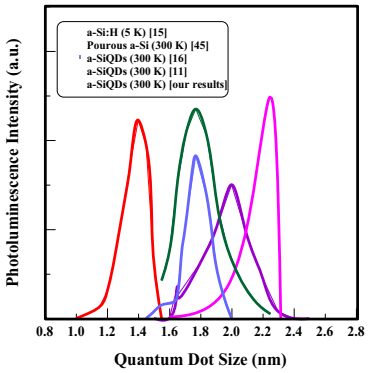

Figure 14: Progress the development of photoluminescence a-Si models.

It is clear from the development steps of ***a-Si*** models that the photoluminescence is shifting into the visible region. In fact, this improvement means that; the amorphous silicon material can be considered as a good candidate as a light-emitting material. 'figure 15' indicates the agreement between our results and the experimental data of *Park et al* [13] . This agreement leads to the assumption of the coexistence of the spatial and the quantum confinement in this model.

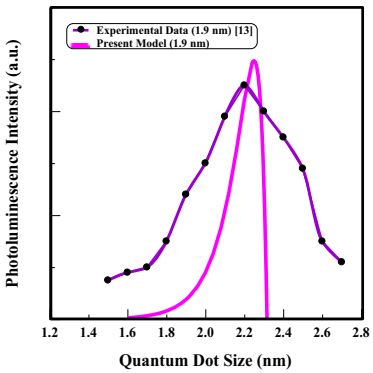

Figure 15. The comparison between our results withthe experimental data.

4. Conclusion

In this work, a simple theoretical model for photoluminescence in *a-SiQDs* is designed, which considers the coexistence of both confinements (the spatial and the quantum).At room temperature, the radiative quantum efficiency is very sensitive to the change in the volume nonradiative density or/and the surface nonradiative density, while it is insensitive at small dot size.The photoluminescence intensity increases or decreases due to the effect of the quantum efficiency, while its shape style reflects the behavior of photon flux. By controlling the sizes of *a-SiQDs* , the emission spectra can be tuned from red to blue (visible region). But, its noted that: blue shifting come from the effect of quantum confinement which is differ from the effect of spatial confinement that is result in the red shifting.

Aknowledgment

The authors would like to thank Dr. Ahlam H. Jaffar Al-Mousawi for her valuable discussion

Reference

[1] D Gutkowicz-Krusin, C R Wronski and T Tiedje 1981 *Appl. Phys. Lett*. **38** 2 pp 87-90
[2] C Bostedt 2002 Electronic Structure of Germanium Nano crystal Films Probed with Synchrotron Radiation Ph.D. Thesis Universtät Hamburg
[3] G Allan, C Delerue and M Lannoo 1997 *Appl. Phys. Lett.* **71** 9 pp 1189-1191
[4] N M Park, T S Kim and S J Park 2001 *Appl. Phys. Lett*.**78** 17 pp 2575-2577
[5] B H Kim, C H Cho, T W Kim, N M P ark, G Y Sung and S Park 2005 *Appl. Phys. Lett.*, **86** 7 pp 091908-1-091908-3
[6] C Kittle 2004 *Introduction to Solid State Physics* 8th edition (John Wile & Sons)
[7] T Toyama, Y Nakai, A Asano and H Okamoto 2002 *Journal of Non-Crystalline Solids* 299-302 pp 290-294.
[8] U Banin, J C Lee, A A Guzelian, A V Kadavanich and A P Alivisatos 1997 Superlattices and Microstructures **22** 4 pp 560-567
[9] J S Williams, RG Elliman, H H Tan, P Lever, J Wong Leung and C Jagadish 2002 Materials Forum **26** pp 74-80
[10] K Nishio, J Koga, T Yamaguchi and F Yonezawa 2002 *Journal of Non-Crystalline Solids* 312-314 pp 323-326
[11] K Nishio, J Koga, T Yamaguchi and F Yonezawa 2003 *Phys. Rev*. B67 195304-1- 195304-5

[12] H S Kwach, Y Sun, Y H Cho, N M Park and S J Park 2003 *Appl. Phys. Lett*. **83** 14 pp 2901-2903
[13] N M Park, C J Choi, T Y Seong and S J Park 2001 *Phys. Rev. Lett*. **86** 7 p 1355
[14] T Takagahara and K Takeda 1992 *Phys. Rev*., **B46** 23 pp 15578-15581
[15] D J Dunstan and F Boulitrop 1984 *Phys. Rev*.**B30** 10 pp 5945-5957
[16] M J Estes and G Moddel1996 *Phys. Rev.***B54** 20 pp 14633-14641
[17] M J Estes and G Moddel 1996 *Appl. Phys. Lett*. **68** 13 pp 1814- 1816
[18] M J Estes, L R Hirsch, S Wichart and G Moddel J 1997 *Appl. Phys*. **82** 4 pp 1832-1840
[19] R B Wehrspohn, J N Chazalviel, F Ozanam and I Solomon 1999 *Eur. Phys. J*. **B8** pp 179-193
[20] F Karbassian, S Rajabali, S Mohajerzadeh and R Talei 2013Scientia Iranica F**20** 3 pp 1063–1066
[21] N G Galkin, K N Galkin, S A Dotsenko, D L Goroshko, A V Shevlyagin, E A Chusovitin and I M Chernev 2017 *EPJ Web of Conferences* 13202006
[22] N M Abdul-Ameer and M C Abdulrida 2011 *Journal of Modern Physics* **2** pp 1530-1537
[23] A Irrera, D Pacifici, M Miritello, G Franzo and F Priolo 2008 *Appl.Phys. Lett.* **81** 10 pp 1866-1868
[24] Y kamemitus,Y Fukunishi and T Kushida 2000, *Appl. Phys. Lett.* **77** 2 pp 211-213
[25] J I Pankove 1984 *Semiconductors and Semimetal* Hydrogenated Amorphous Silicon Part B optical properties Academic Press INC. **21**
[26] T Tiedje, B Abeles and B G Brooks 1985 *Phys. Rev. Lett.* **54** 23 pp 2545-2547
[27] R W Collins, M A Paesler and W Paul 1980 Solid State Commun **34** p 833
[28] A Dumbrava, V Ciupina and G Prodan 2005 *Rom Journ Phys* **50** 7-8 pp 831-836
[29] N F Mott and E A Davis 1979 *Electronic Processes in Non-Crystalline Material* Printed in Great Britain by J. W. Arrow Smith LTD
[30] S Oğűt, R Chelikowsky and S G Louie 1997 *Phys. Rev. Lett.* 791-4
[31] K Tanaka, E Moruyama, T Shimada and H Okamoto 1999 *Amorphous Silicon* John Wiley & Sons Ltd.Translated by T Sato
[32] B Abeles and T Tiedje 1983 *Phys. Rev. Lett.* **51** 21 pp 2003-2005
[33] N Nedev, E Manolov, Tz Ivanov, B Pantchev, G Beshkov, R Durnya, K Gmucová and V Nadazdy2005 *Journal of Optoelectronics and Advanced Materials* **7** 1 pp 507 – 511
[34] K Soki, K Murayama and M Tachiya 2005 *Phys. Rev*. **B71** pp 235212-1- 235212-7
[35] M C Abdulrida, N M Abdul-Ameer and Sh M Abdul-Hakeem 2012 *Turk J Phys* 36197 – 205
[36] C Tsang and R A 1978 *Street, Philos. Mag*. **B37** p 601
[37] A Irrera 2003 Light Emitting Devices based on Silicon Nano structures Universita DegliStudi Di Catania Ph.D. Thesis
[38] S M Sze 2007 *Semiconductors Devices Physics and Technology* 3th edition (John Wiley &Sons, Inc.)
[39] E Bennici 2003 Amorphous Silicon based Photoni Crystals Scuola Di Dottorato Ph.D. Thesis
[40] J M Martinez-Duart, R J Martin-Palma and F Agullo-Rueda 2006 *Nanotechnology For Microelectronics and Optoelectronics* Elesvier B.V. AE Amsterdam
[41] N M Park, T Y Kim, G Y Sung, B H. Kim, S J Park, K S Cho, J H Shin, J K. Lee and M Nastasi 2004 Mat. Res. Soc. Symp. Proc 817 L1.4.1-L1.4.6 Material Research Society
[42] F Giorgis, C F Pirri, C Vinegoni and L Pavesi 1999 *Phys. Rev.* **B60** 16 pp 11572-11576
[43] Y Kanemitsu 1994 *Phys. Rev.***B49** 23 pp 16845 -16848
[44] N M Park, T Y Kim, K H Kim, G Y Sung, B H Kim, S J Park, K S Cho, J H Shin, J K Lee and M Nastasi 2005 *Journal of Electrochemical Society* **152** 6 pp G445-G447
[45] J M Perez, J Villalobs, P McNell, J Prasad, R Cheek and J Kelber 1992 *Appl. Phys. Lett*. **61** 5 pp 563-565
[46] T W Kim, C H Cho, B H Kim and S J Park 2006 *Appl. Phys. Lett.* **88** pp 123102-1-123102-3
[47] T Y Kim, N M Park, K H Kim, G Y Sung, Y W Ok, T Y Seong and C J Choi 2004 *Appl. Phys. Lett*. **85** 22 pp 5355-5357

Interaction of (O,Ar)ions with Prostate tissue

Interaction of (O,Ar)ions with Prostate tissue

Dr.Bashair Mohammed Saied[1] , SaadNafea Yaqoob[2]

[1]Department of Physics/College of Education Ibn Al-Haitham for Pure Scienes-University of Baghdad –Iraq[2]Ministry of Education.

Abstract. The use of Ion beam in cancer therapy allows an accurate irradiation of the tumor with minimum collateral damage in surrounding healthy tissue, for this purpose we calculate the energy loss for (O,Ar) ions beams with (prostate tissue) in energy rang(0.001-200) MeV using different theoretical and semi-empirical formulation.The stopping power values calculated using semi-empirical approaches SRIM ,CaSP and SRIM Dictionary compound.

Keywords: SRIM, Stopping power , Range, CaSP

1-Introduction

The interaction of charged particles with substances enters a number of medical fields and nuclear reactions; the interaction of heavy charged particles differs from the interactions of lighter particles such as protons and alpha particles. The therapeutic mode, which uses particles larger than the size of the protons or neutrons as carbon atoms compared to the proton particle, is more positive due to the ionic density of its last orbit. Thus, the damage associated with the synthesis of the RNA molecule in a single cell often occurs, the cancerous repair on the output damage. This increases the biological efficiency of the dose by a factor of (1.5-3) compared with the use of protons. A database in which the appropriate particle and energy can be selected to irradiate the infected tissue and prevent the passage of the particle into adjacent non-infected tissue, causing adverse medical effects on the patient, the aim of the present work is to study the interaction of heavy ions with biological materials, including tissues of the human body; therefore The range and stopping power of heavy ions interacting with the prostate tissue will be studied using several methods these are SRIM program (Stopping and Range of Ions in Matter) , SRIM Dictionary of compound and CaspConvolution approximation for Swift Particles.

2-Theory

Bethe –Bloch expression for the stopping power of a heavy charge particle derived using relativistic quantum mechanics is given by:

$$-\frac{dE}{dx}=\frac{4\pi nz^2K_0{}^2e^4}{m_0v^2}[\ln\frac{2m_0v^2}{I}-\ln(1-\frac{v^2}{c^2})-\frac{v^2}{c^2}] \qquad \text{- - (1)}$$

Where Z: charge of the incident particle n: number of electrons per unit volume. m_0: rest mass of electron.V: velocity of incident particle. e: electron charge. K_0: 1/4 ЛЄ $_0$ I: mean excitation or the ionization energy of the medium. This equation shows dependence of (dE / dx) on the velocity of interacted particle but (In $\frac{2m_0v^2}{I}$) gives almost no variation or negligible change on (v).Various stopping power table and relations have been reported by many researchers. The Stopping power of compound material was found the suspension following relationship [1]:

$$\frac{dE}{dx} = \sum_i w_i (\frac{dE}{dx})_i \quad (2)$$

The range of charged particle is computed by numerical integration of the stopping power .The range (R) is continuous Slowing down approximation (Csda) is given by:

$$R = \int_0^R dx = \int_{T_0}^{0} \frac{-dE}{-\frac{dE}{dx}} = \int_{T_1}^{T_0} \frac{dE}{S} = \int_{T_1}^{T_0} \frac{dE}{S} + R_1(T_1) \quad (3)$$

Where , dx: path length variable of integration .S: stopping power .T_0: the initial kinetic energy of the charge particles.T_1: some limit of energy below the calculation cannot be performed. In the present work we compared some famous and available theoretical (Casp 5.2)[2] and semi-empirical (SRIM 2008)[3] procedures of stopping power calculation has been checked using statistical analysis of deficits between computed and experimental data of (prostate tissue) for (O and Ar) ions in energy range of (0.001-200) MeV .The range formulas were obtained by directly integrating the reciprocal of stopping power for (O and Ar) ions and the values of the range for the (prostate tissue) are calculated and compared with (SRIM).

3- Results and discussion

In the Present work the measurements of the mass stopping power and range of Oxygen and Argon ions in the elements of human prostate tissue (C=8.9%,H=10.5%,K=0.2%,N=2.5%,Na=0.2%,O=77.4% ,P= 0.1%andS=0.2%) [4] with energy (0.001-200MeV) have been done using the (SRIM 2008), (Casp 5.2) and (SRIM Dictionary for compound) programs. Figures (1,2,3,5,6,7) show these measurements.

1-We obtained the following semi-empirical formula for mass stopping power for Oxygen and Argon ions by calculation of the weighted average for mass stopping power were calculated, compared with three methods:

$$y = \frac{a + bx}{1 + cx + dx^2} \quad (4)$$

For Oxygen ion:

a=1.034616681518439×10^3 c=5.032663585116284×10^{-1}

b=8.279294927675910×10^3 d=1.493493210978582×10^{-2}

For Argon ion:

a=7.89905925250 41×10^{-3} c=1.216823437206584×10^{-1}

b=5.227187249176428 d=8.528044147114153×10-4

2-The following semi-empirical equation were obtained

$$y = a(b^x)x^c \quad (5)$$

For Range of Oxygen and Argon ions in prostate.

For Oxygen ion:

$a=9.032281090756985\times10^{-5}$ b=1.003441574946905

c=1.058292747260118

For Argon ion:

$a=3.853934858221334\times10^{-1}$ b=1.004322123852577

$c=4.438398758353817\times10^{-1}$

3-We note that the maximum value of mass stopping powers found in Hydrogen element, because of Hydrogen was gas molecules in the traversing path of the heavy ions and hence the more probability of interaction and more energy loosed [5].

4-We found that the maximum value of energy the Oxygen and Argon ions can lose along its path in prostate tissue are (11245.28 MeV.cm^2/g) which correspond to the energy (8.001 MeV) .and (29.03 MeV.cm^2/g) which correspond to the energy (34.001 MeV) respectively. Figures (4),(8) illustrates this.

5-We note from figures(9and10) that the Range correspond to energy which can lose along its path of Oxygen ion in prostate tissue is (0.000838545g/cm^2) in energy (8.001 MeV) ,while the same relation for Argon ion is (2.134648313 g/cm^2) in energy (34.001 MeV).Figs (9),(10) illustrates this.

6-From figures (4),(8) note that the theoretical values are consistent with the practical values of the mass stopping power values for Oxygen and Argon ions in prostate tissue indicating the validity of the present results.

7-From figures (9),(10) note that the theoretical values correspond to the experimental values of the range for Oxygen and Argon ions in prostate tissue this indicate the validity of the present results .

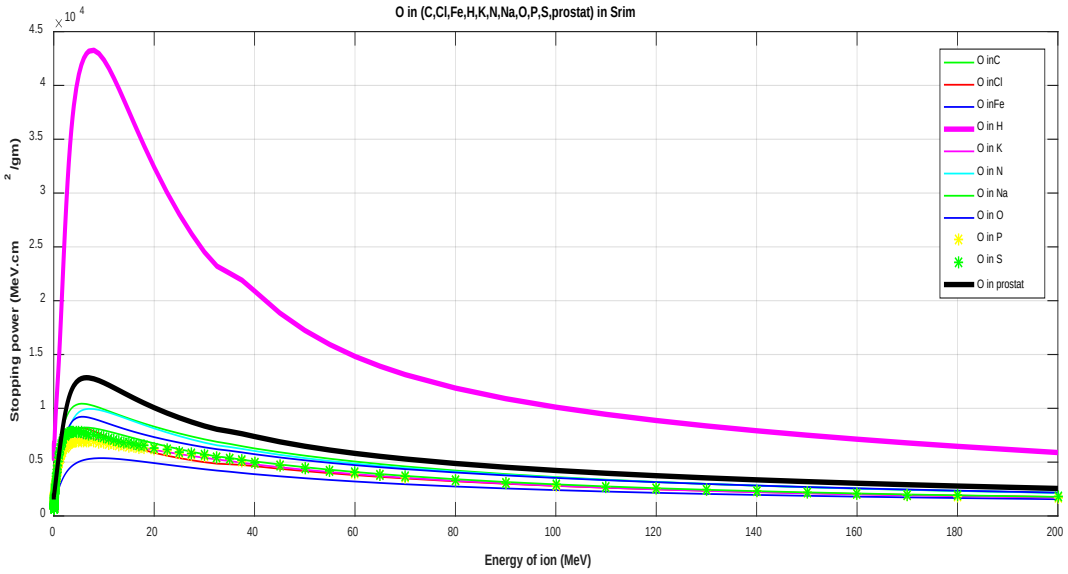

Figure1.ass stopping power for Oxygen in (C,Cl,Fe,H,K,N,Na,O,P,S,prostat) by using SRIM program

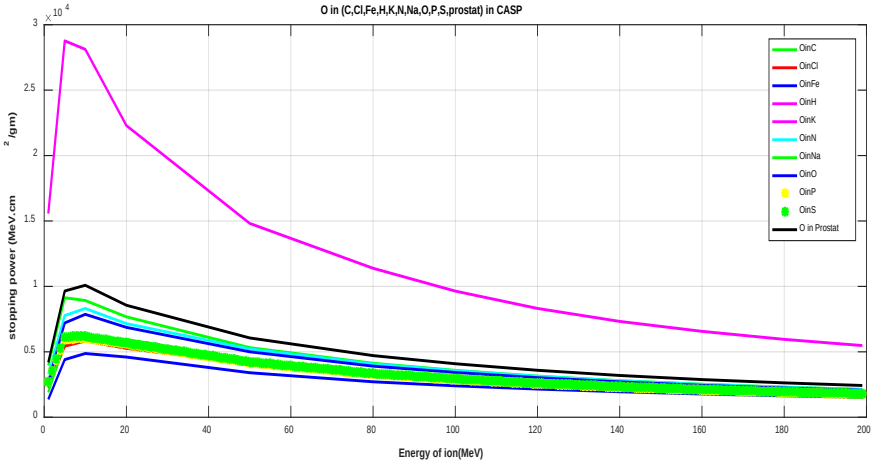

Figure 2. Mass stopping power for Oxygen in (C,Cl,Fe,H,K,N,Na,O,P,S,prostat) by using CaSP program

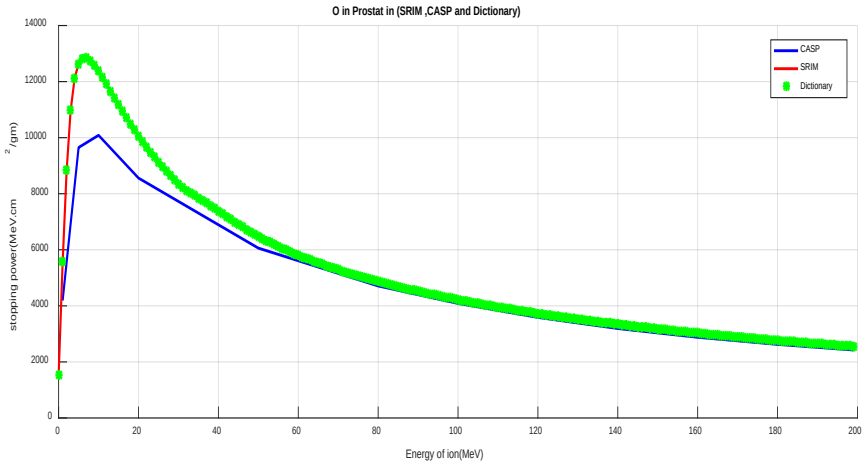

Figure 3.Mass stopping power for Oxygen in prostate tissue (by using SRIM,CASP,

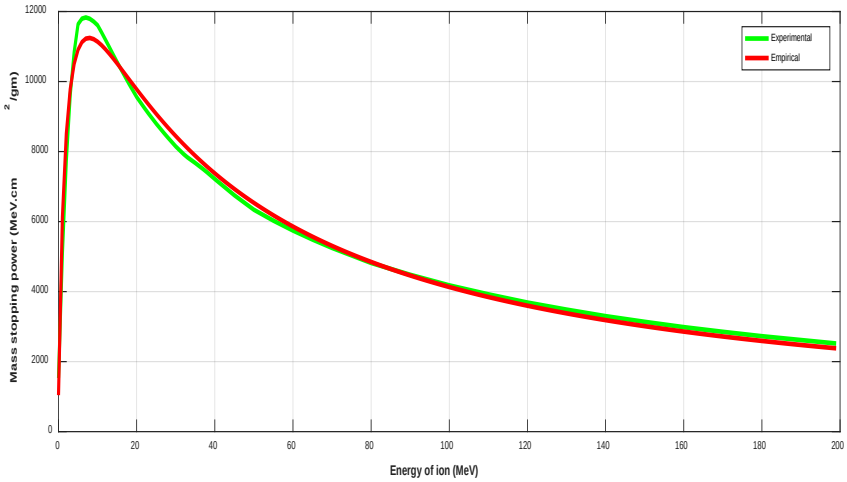

Figure 4. Experimental [3] and empirical mass stopping power of (O) ion in prostate tissue

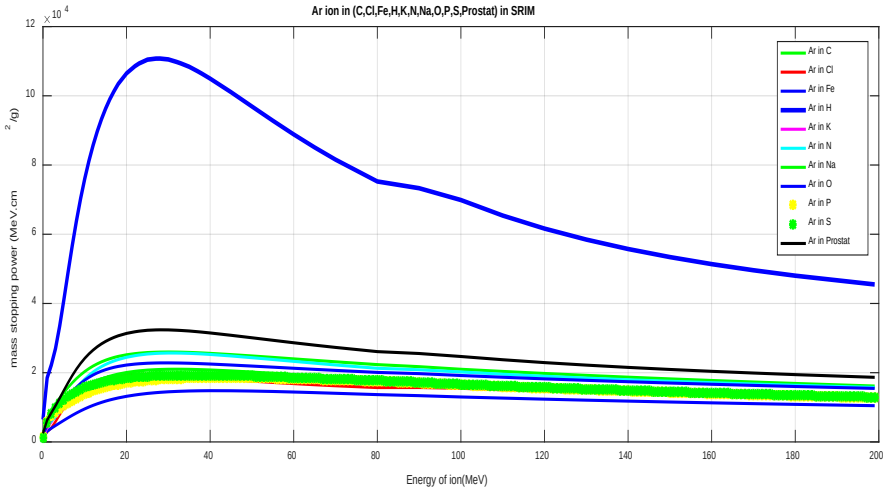

Figure 5. Mass stopping power for Argon in (C,Cl,Fe,H,K,N,Na,O,P,S,prostat) by using SRIM

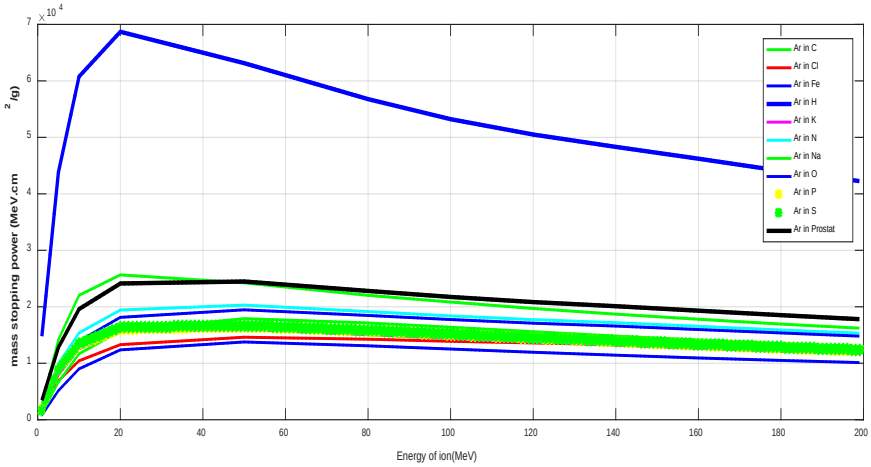

Figure 6. Mass stopping power for Argon in (C,Cl,Fe,H,K,N,Na,O,P,S,prostat) by using CASP program

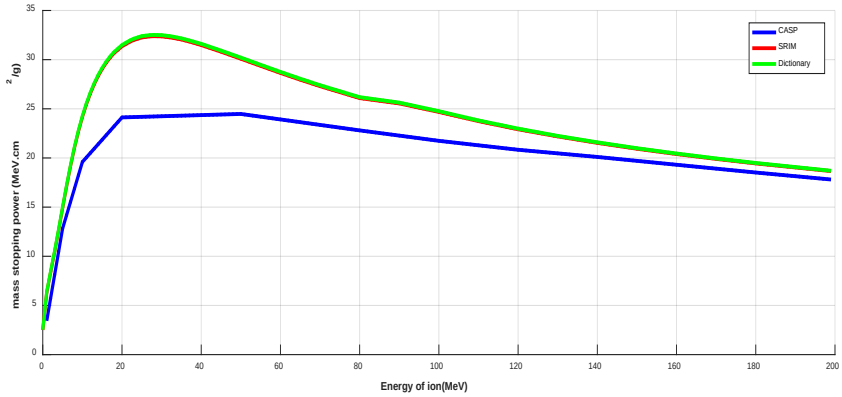

Figure7. Mass stopping power for Argon in prostate tissue by using (SRIM,CASP, SRIM Dictionary) programs

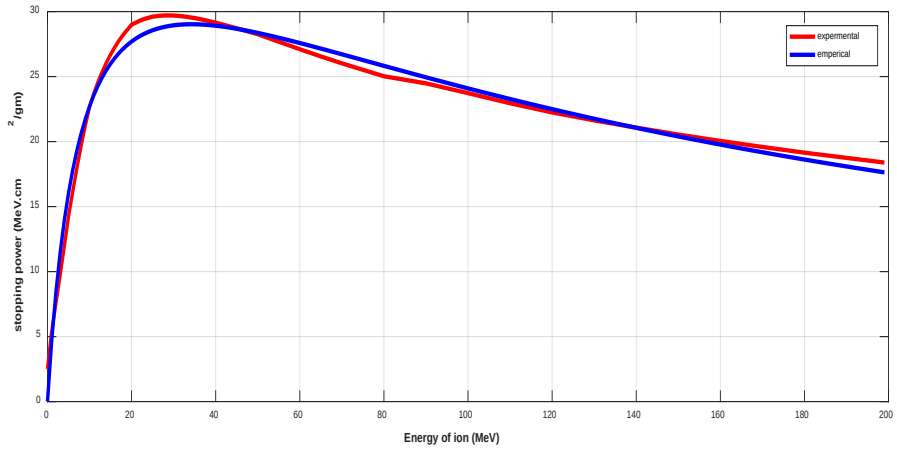

Figure 8. Experimental [3] and empirical mass stopping power of (Ar)in prostate tissue

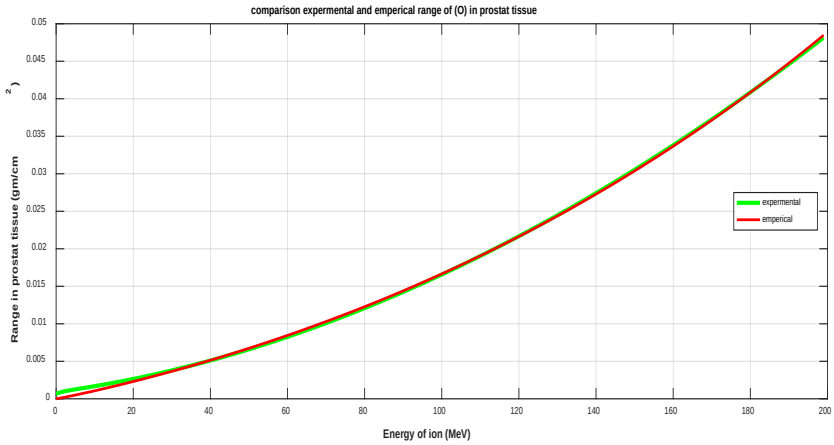

Figure 9. Experimental[2] and empirical Range of (O)ion in prostate tissue

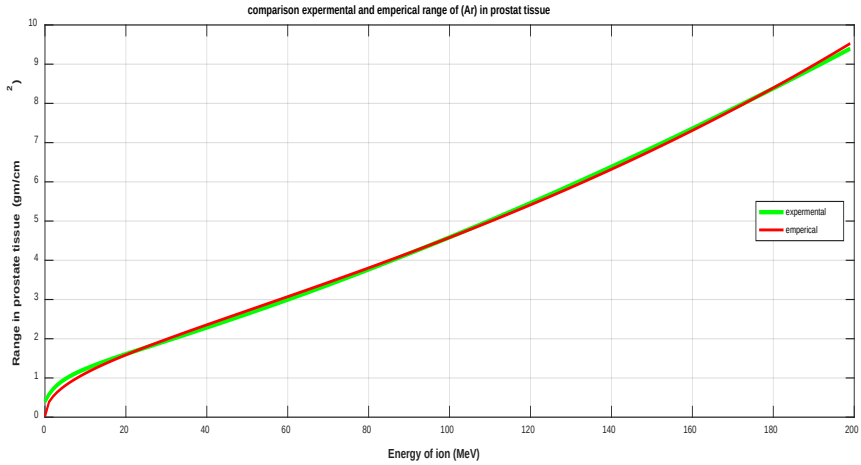

Figure 10. Experimental [2] and empirical Range of (Ar)ionin prostate tissue

Conclusions

1- A database of these ions can be provided to the treating physician from dealing with these ions for the treatment of cancerous tumors in the prostate.
2- We conclude that the Hydrogen atoms are most responsible to energy losing in the human prostate tissue.
3- The maximum value of energy the Oxygen and Argon ions can lose along its path in prostate tissue are (11245.28 MeV.cm^2/g) which correspond to the energy (8.001 MeV) .and (29.03 MeV.cm^2/g) which correspond to the energy (34.001 MeV) respectively.
4- The range correspond to energy which can lose along its path of Oxygen ion in prostate tissue is (0.000838545g/cm^2) in energy (8.001 MeV) ,while the same relation for Argon ion is (2.134648313 g/cm^2) in energy (34.001 MeV.

References

[1] Don Groom, Energy loss in matter by heavy particles, Particle data group notes, (8 December 1993), PDG-93-06.
[2] P.Lgrand,G.Schiwietz,R,Gabreva, Advances in Quantum Chemistry. Vo. l45, Elsevier,SanDiego, 2004,p:7(Casp)
[3] J.F.Ziegler,SRIM<http:www.srim.org/>.
[4] H.Q.Woodard and D.R.White,Department of Biophysics,Memorial Sloan-Kettering Cancer Center1986 London EC1A7BE.
[5] Mahalesh D. et al., International Journal of Science, Technology & Management 2015.

Novel Relationship among Spiral Arm Pitch Angles (p) and momentum parameter of the host spiral galaxies

Novel Relationship among Spiral Arm Pitch Angles (p) and momentum parameter of the host spiral galaxies

Ismaeel Al-Baidhany[1,2], Hayfa G Rashid[1,3] , Sami S Chiad[1,4], Nadir F Habubi[1,5], Nidhal N Jandow[1,6], Wasmaa A Jabbar[1,7], khalid H Abass[2,1]

[1]Department of Physics, College of Education, Mustansiriyah University, Baghdad, Iraq
[2]Department of Physics, College of Education for Pure Sciences, University of Babylon, Iraq,

[1,2]ismaeel_2000@uomustansiriyah.edu.iq, [1,3]dr.hayfa@uomustansiriyah.edu.iq, [1,4]dr.sami@uomustansiriyah.edu.iq, [1,5]nadirfadhil@uomustansiriyah.edu.iq, [1,6]nidhaljandow@uomustansiriyah.edu.iq, [1,7]wasmaajabbar@uomustansiriyah.edu.iq,pure, [2,1]khalid.haneen@uobabylon.edu.iq

Abstract. In this study, we have found a novel relationship among spiral arm pitch angles (p) and momentum parameter of the host spiral galaxies. In this study, we measured the momentum parameter for specimen of Spitzer/IRAC 3.6 μm images of 41 spiral galaxies evaluated employing a relation(Mbulge σ*/c)where Mbulge is mass of the bulge and σ* is the stellar velocity dispersion. We have taken velocity dispersions (σ*) from the literature. In order to determine the spiral arm pitch angles. The selection of specimen of nearly face-on spiral galaxies and employ IRAF ellipse to indicate the ellipticity and major-axis position angle so as to deproject the images to face-on, employing 2D Fast Fourier Transform decomposition mehtod. The specified bulge mass (Mbulge) using the virial theorem was include.

1. Introduction

Astronomers observed many types of black holes, which can be classified into three groups: stellar mass black holes, intermediate mass black holes (IMBHs) and supermassive black holes (SMBHs) [1]. The distinction between normal black holes and SMBHs is that normal black holes are believed to be the endpoint of stellar evolution for the most massive stars. The possible end products of stellar evolution are white dwarfs, neutron stars (usually observed as pulsars), and black holes. Stars that have masses greater than around 5 times the mass of the Sun may end up as a black hole [2]. A SMBH is the largest type of black hole [3].

It is becoming significantly clear that the energy output from SMBHs at the centers of galaxies play an important role to know the mechanism of nuclear energy and consistence and the estimation of SMBHs and their steward galaxies [4, 5]. In addition, the energy emitted by rising SMBHs plays a significant turn in the forming characteristic of galaxies shell and the properties of their host galaxy, possibly by being regulated by energy feedback from its center [6, 7, 8, 9].

Supermassive black hole in the center of almost all galaxies strongly correlates with the central stellar velocity dispersion (σ*) (MBH-σ*) [5,10,11] with the total stellar mass or brilliance of bulge (Mbulge), (Lbul) [12,13,14,15], for rotational velocity or dark matter halo [9], with the concentration of a galaxy's light [16], for bulge effective radius [13], the host bulge Sersic index [16,17], via

gravitational binding energy [19], for radio and inner core ,length and radius respectively [20], with the kinetic energy of random motions (Mbulσ2) [22,23,24,25].

Many of previous studies have found the MBH−Mbulσ relevance using sundry independent galaxy specimen, with good positive results, meaning the (MBH− Mbulσ) relevance could be utilized as an indirect measure of the SMBH mass in the center of galaxies [25].

Astronomers have found that spiral arm pitch angle does not rely measurably on image waveband [26, 27].

The aim of this paper is the study of the cited scaling relations that involve bulge properties (MBH–Md,sσ, MBH–Md,s, Md.sσ− P and Md,s− P) in images of selected galaxies.

The paper is structured as follows. In the next section we briefly describe our sample, in Sect. 3 the methods are presented to estimate the bulge (stellar and dynamical)masses and estimate the momentum parameter, Section 4 is an analysis and discussion of the results. The conclusions are given in Sect. 5.

2. Sample

The sample in this research consists of selected galaxies using the Spitzer Space Telescope at 3.6μm. The major request was the momentum estimation parameter of conformable host galaxies ($M_d\sigma$ & $M_s\sigma$) is an estimation of bulge mass and stellar velocity dispersion. The measure the bulge dynamical mass was verified by stratifying the isothermal model [28, 29] and measured bulge stellar mass using the calibration by [50]. The dispersion velocity of galaxy hosts was evaluated from old researchers as depicted in (table 1).

The speciman consists of Hubble types extended from Sa to Sc, so it is conceivable to measure pitch angle for every galaxy with slope (ranging from 25 to 65 degrees) using ELLIPSE in IRAF [27, 30].

Table 1. Galaxies parameters

Name (1)	**Leda Type (2)**	**SMBH (M_{BH}-σ) (3)**	**P (deg.) (4)**	**σ (km/sec) (3)**	**$M_{dyn}(M_\odot)$ (4)**	**$M_s(M_\odot)$ (5)**	**$M_{dyn}\sigma$ (6)**	**$M_s\sigma$ (7)**
Circinus	Sb	6.418±0.1	26.7	75	9.67±0.19	9.72±0.1	3.87±0.2	3.883±0.13
IC 2560	SBb	7.469±0.2	16.3	137	11±0.4	10.7±0.2	5.73±0.4	5.433±0.02
NGC 224	Sb	7.794±0.23	8.5±1.3	160±8	10.6±0.5	10.7±0.3	5.45±0.2	5.568±0.03
NGC 613	Sbc	7.309±0.2	23.68±1.77(1)	125.3±18.9	10.1±0.3	10.4±0.5	4.75±0.3	5.055±0.07
NGC 1022	SBa	6.902±0.3	19.83±3.6(1)	99	10.1±0.17	10.10.14	4.54±0.3	4.541±0.04
NGC 1068	Sb	7.63±0.05	17.3±2.2(2)	151±7	10.4±0.11	11.2±0.1	5.21±0.3	6.017±0.03
NGC 1097	SBb	7.627±0.18	16.7±2.62(3)	150	10.6±0.13	10.8±0.4	5.40±0.4	5.602±0.06
NGC 1300	Sbc	7.568±0.17	12.7±1.8	145±22	10.5±0.08	10.6±0.1	5.27±0.4	5.372±0.09
NGC 1350	Sab	7.251±0.04	20.57±5.38(1)	120.91±2.08*	10.3±0.13	10.4±0.1	4.92±0.4	5.024±0.05
NGC 1353	Sb	6.594±0.13	36.6±5.4(1)	83	9.11±0.73	9.43±0.3	3.39±0.3	3.728±0.08
NGC 1357	Sab	7.252±0.03	16.16±3.48(1)	121±14	10.1±0.02	10.3±0.2	4.72±0.3	4.925±0.05
NGC 1365	Sb	7.639±0.07	15.4±2.4(3)	151±20	10.3±0.25	10.4±0.2	5.1±0.17	5.217±0.02
NGC 1398	SBab	8.264±0.08	6.2±2(3)	216±20	10.8±0.23	10.9±0.1	5.92±0.3	6.02±0.35
NGC 1433	SBab	6.615±0.05	25.82±3.79(1)	84±9	9.5±0.034	10.2±0.4	3.79±0.4	4.508±0.07
NGC 1566	SAB	6.919±0.07	21.31±4.78(3)	100±10	9.6±0.032	9.77±0.3	4.05±0.4	4.22±0.083
NGC 1672	Sb	7.388±0.14	18.22±14.07(3)	130.8±2.09*	10.1±0.57	9.93±0.3	4.79±0.6	4.63±0.036
NGC 1808	Sa	7.601±0.11	23.65±7.77(1)	148	9.89±0.3	10.2±0.1	4.23±0.3	4.99±0.025
NGC 2442	Sbc	7.516±0.12	14.95±4.2(1)	140.74±2.18*	10.5±0. 32	10.4±0.4	5.25±0.4	5.15±0.015
NGC 3031	Sab	7.544±0.04	15.4±8.6	143±7	10.7±0.14	10.9±0.1	5.57±0.3	5.664±0.01
NGC 3227	SABa	7.35±0.16	12.9±9	128±13	10.9±0.06	10.7±0.4	5.57±0.3	5.37±0.15
NGC 3368	SABa	7.267±0.06	14±1.4	122±(28,24)	10.5±0.03	10.8±0.3	5.12±0.1	5.42±0.047
NGC 3511	SABc	6.803±0.07	28.21±2.27(1)	93.56±2.04*	9.51±0.13	9.58±0.1	3.90±0.4	3.97±0.096
NGC 3521	SABb	7.384±0.05	21.86±6.34(3)	130.5±7.1	10.3±0.07	10.4±0.4	4.98±0.9	5.08±0.073
NGC 3673	Sb	7.2±0.011	19.34±4.38(1)	117.45±2.07*	10.3±0.08	10.3±0.1	4.89±0.2	4.899±0.08

NGC 3783	SBab	6.83±0.021	22.73±2.58[(1)]	95±10	9.31±0.03	9.42±0.2	3.72±0.3	3.835±0.35
NGC 3887	Sbc	6.954±0.04	24.4±2.6[(2)]	102.01±2.05*	9.75±0.08	9.63±0.3	4.22±0.2	4.1±0.051
NGC 4030	Sbc	7.544±0.06	19.8±3.2[(2)]	122.43±2.1*	10.7±0.08	10.9±0.3	5.33±0.4	5.53±0.037
NGC 4151	SABa	7.696±0.07	11.8±1.8	156±8	10.3±0.07	10.5±0.3	5.14±0.4	5.346±0.07
NGC 4258	SABb	7.58±0.012	7.7±4.2	146±15	10.8±0.18	11.2±0.7	5.58±0.4	5.988±0.08
NGC 4462	SBab	7.579±0.02	17.2±5.42[(1)]	146±8	10.6±0.07	10.7±0.2	5.38±0.2	5.485±0.08
NGC 4594	Sa	8.448±0.01	6.1	240±12	11.4±0.09	11.3±0,4	6.61±0.4	6.510±0.32
NGC 4699	SABb	8.256±0.05	6.2±2.2[(1)]	215±10	10.7±0.06	10.8±0.2	5.82±0.5	5.92±0.35
NGC 5054	Sbc	6.996±0.06	25.57±3.73[(1)]	104.48±2.05*	9.9±0.13	10.2±0.3	4.39±0.2	4.69±0.071
NGC 5055	Sbc	6.937±0.08	14.9±6.9	101±5	9.84±0.37	9.95±0.5	4.30±0.3	4.41±0.043
NGC 6300	SBb	6.811±0.05	24.3±3.8[(1)]	94±5	9.82±0.04	10±0.053	4.2±0.07	4.406±0.06
NGC 6744	SABb	7.117±0.07	21.28±3.8	112±25	10.3±0.19	10.3±0.5	4.85±0.2	4.858±0.09
NGC 6902	SBab	7.578±0.04	13.71±2.3[(3)]	145.86±2.1*	10.6±0.84	10.6±0.5	5.38±0.3	5.45±0.35
NGC 7213	Sa	7.993±0.03	7.05±0.28[(1)]	185±20	11±0.048	10.9±0.4	5.99±0.4	5.894±0.06
NGC 7531	SABb	7.065±0.09	18.31±9.09[(1)]	108.7±5.6	10.2±0.08	10.2±0.5	4.72±0.6	4.75±0.021
NGC 7582	SBab	7.469±0.09	14.7±7.44[(3)]	137±20	10.7±0.08	10.9±0.5	5.43±0.5	5.61±0.082
NGC 7727	SABa	7.955±0.07	15.94±6.39[(1)]	181±10	10.9±0.06	11.1±0.4	5.87±0.3	6.07±0.079

3. Methods

*3.1 Measurement of SMBHs using MBH-σ**

There are a variety of techniques for measuring supermassive black hole masses. For this study we have selected galaxies which have SMBH mass estimates and applied two correlations. We applied the correlation between supermassive black hole mass (M_{BH}) and host-galaxy bulge velocity dispersion (σ_*) (M_{BH}-σ_*) [10, 11, 18].

The M_{BH}-σ_*relation supports the notion of regulated formation mechanisms and co-evolution for the galaxy's central black hole mass and the bulge velocity dispersion [9, 31, 32].

The M_{BH}– σ_* relation is one of the most common techniques used to estimate the mass of SMBH at the center of a spiral galaxy [13]. This is done by measuring the velocity dispersion of stars in the galactic bulge. This method was based on the observation that supermassive black hole masses correlate with the dispersion velocity of the surrounding stellar component (bulge) of spiral galaxies [10, 11, 17, 18]. Because BH masses found in late-type spirals and spheroidal galaxies have lower mass, we used the M_{BH}- σ_* relation since it has the least scatter [33, 34].

The velocity dispersion (σ_*) of classical bulges and pseudobulges in spiral galaxies were converted to SMBH masses using the following relation [5]:

$$M_{BH}(\sigma *) = 10^{8.13\pm0.06}\left(\frac{\sigma*}{200} km\ s^{-1}\right)^{4.02\pm0.32} \quad (1)$$

Using selected galaxies noticed with Spitzer at 3.6μm along with MBH-σ* relation, SMBH masses were determined. Stellar velocity dispersions were obtained in host galaxies from a literature search, and using the correlation between (Vc) and (σ*) (where Vc and σ* measured in (km s-1) [9].

$$logV_c = (0.84 \pm 0.09) log\sigma + (0.55 \pm 0.19) \quad (2)$$

This correlation is a good link between SMBHs and dark matter haloes [9].

3.2 Measuring SMBHs using spiral arm pitch angle

One of the more interesting methods to find SMBH masses in late-type galaxies use the relationship between SMBH mass in the nuclei of disk galaxies and spiral arm pitch angle (P) (a measure of the tightness of spiral structure) [30, 35]. Seigar et al. (2008) found that SMBHs are linked by a strong correlation with P. Additionally, a correlation between P and rotation curve shear (S) was discovered [26, 40, 42].

Previous studies described logarithmic spiral in polar coordinates [27, 36, 37, 38, 39, 40, 41, 61]. This is a special kind of spiral curve that describes the arm in disk galaxies:

$$r = r_o e^{\theta \tan(\varphi)} \quad (3)$$

Where r is radius, θ is central angle, r_0 is initial radius when θ = 0, and pitch angle is $-90 \leq \phi \leq 90$.

Because the spiral arm pitch angle has been shown to be independent of the wavelength at which it is measured, multi-band images were used to determine it for our sample of spiral galaxies [26].

Spiral arm pitch angles were measured using a two-dimensional fast Fourier transform (2DFFT) decomposition with logarithmic spirals of Spitzer/IRAC 3.6 μm images of 63 galaxies, with inclinations of $30^{\hat{}} \leq i \leq 60^{\hat{}}$. The 2DFFT program analyzes images of spiral galaxies and categorizes their pitch angles and number of arms. The two-dimensional fast Fourier transform decomposition program is fully described by [45].

The amplitude of each Fourier component is given by:

$$A(m,p) = \frac{\sum_{i=1}^{I}\sum_{j}^{J}\ln(r,\theta)exp[-i(m\theta+p*lnr)]}{\sum_{i=1}^{I}\sum_{j}^{J}ln(r,\theta)} \quad (4)$$

where r and θ are polar coordinates, I(lnr, θ) is the intensity at position (lnr, θ), m represents the number of arms or modes, and p is the variable associated with the pitch angle P defined by $P = -(m/p_{max})$.

IRAF was used to estimate ellipticity values and major-axis position angle in order to deproject 3.6 μm galaxy images to fully face-on by assuming circular outer isophotes. ELLIPSE in IRAF was used to derive inclination angle (α); [43, 44], which is defined by:

$\alpha = \cos^{-1}(b/a)$,

Where (a) is the semi-major axis and (b) is the semi-minor axis. Where the value 0^{o} describes a face-on galaxy and 90^{o} describes an edge-on galaxy.

Two-dimensional fast Fourier Transform [45] was then utilized the deprojected 3.6 μm images.

3.3 Measurement of the dynamical bulge mass

In this part the methods used to derive the dynamical bulge mass are described. Bulge's dynamical mass (M_{dyn}) were determined utilizing the virial theorem, i.e. the virial bulge mass given by

$$M_{dyn} = \frac{KR_e\sigma^2}{G} \quad (5)$$

Where k is a model dependent dimensionless constant [28] or is function of the Sérsic index n. [29, 46]. K is a constant throughout the galaxy in the isothermal model, and its value is determined numerically, K=3 [47], 8/3 [13], 3 [18] and 5 [29], we follow Sani (2011) to use k = 5 instead of 8/3 or 3.

Where k is function of the Sérsic index n [13,] as in [28, 29], σ_*, R_e and G are host-galaxy bulge velocity dispersion, bulge effective radius and gravitational constant respectively.

3.4 Estimation of stellar mass (M_*)

Many researchers [13, 29, 48] have extensively used the J, I, and K band luminosity to compute stellar mass by assuming a mass-to-light ratio M/L [48]. Bell & de Jong (2001, 2003) [48, 49] established a relation between optical colors (e.g., B−R, B−V).

These former studies of optical colors of disk galaxies do not supply γ values for the Spitzer/IRAC bands, thus they couldn't employed. A novel relevance was used to gain γ in 3.6-μm Spitzer/IRAC. Such relevance is amidst γ^{K} and γ in the 3.6-μm waveband was notified by Se-Heon Oh [50]:

$$\gamma^{3.6} = B^{3.6}x\gamma^{k}x\,A^{3.6} \quad (6)$$

Where $A^{3.6} = -0.05$ and $B^{3.6} = 0.92$

A relevance among the (γ^{K}) and optical colors is given by,

$$log_{10}(\gamma)^{k} = b^{k}x\ optical\ colors + a^{k} \quad (7)$$

Where a^{K} and b^{K} are coefficients.

3.5 Measurement of the bulge luminosity (L_{bulge})

The measurement of the bulge luminosity depend on a two-dimensional decomposition program to model Spitzer/IRAC 3.6 um images [51]. The bulge luminosity was determined for a sample of 41 spiral galaxies by applying the two-dimensional multicomponent decomposition technique. In this style, an exponential function was employed to depict disc:

$$I_d(r) = I_{od}exp[-(r/h_r)],$$

Where I_{od} is disc central surface density, h_r is disc radial scalength, and r is disc radius. Bulge is determined with Sersic function:

$$I_b(r_b) = I_{ob} exp\left[1(\frac{r_b}{h_b}\right] \quad (8)$$

Where I_{ob} is central surface density of bulge, h_b is the scale parameter of the bulge, and â=1/n with n=sérsic index. The effective radius, r_e, of bulge was estimated by converting h_b,
$r_e = (b_n)^n h_b$

Where value of b_n is a proportionality constant defined such that Ã(2n) = 2ã(2n,b_n). Ã and ã are the complete and incomplete gamma functions, respectively. Approximation $b_n \approx 2.17n_b - 0.355$ [51] was used, where n_b is the bulge Sersic index
The bars and ovals are evaluated using Ferrers or Sersic function:

$$I_{bar}(r_{bar}) = I_{bar}((1 - \frac{r_{bar}}{a_{bar}})^2)^{n_{bar}+0.5} \qquad r_{bar} < a_{bar}$$
$$= 0 \qquad r_{bar} > a_{bar} \quad (9)$$

Where I_{0bar} is the central surface brightness of the b_{ar}, a_{bar} is the bar major axis, and n_{bar} is the exponent of the bar model defining the shape of the bar radial profile.

First, foreground stars were removed and all point sources from the Spitzer 3.6 ìm images were masked out by using SExtractor [52]. In order to change surface brightness units to mag arcsec^{-2}, the next form was used:

$$\mu_{3.6\,\mu m} = -2.5\, log_{10}\left[\frac{S_{3.6\,\mu m} x 2.35 x 10^{-5}}{ZP_3}\, .6\mu m\right] \quad (10)$$

Where $S_{3.6im}$ is the flux value of the 3.6 ìm band in units of MJy sr^{-1}, $ZP_{3.6im}$ is the IRAC zero magnitude flux density in Jy and is 280.9 [53].

Apparent magnitude was converted to absolute magnitude was convert using luminosity distance and absorption in the galaxies according to the NED[1] database.

4. Results and discussions

(Table 1) lists the SMBH masses, spiral arm pitch angles, the central stellar velocity dispersion, bulge dynamical masses, bulge stellar masses, and the momentum parameter of the dynamical and stellar bulge, respectively.

This work, was studied scaling relations describe trends that are observed between important physical properties (SMBH masses, spiral arm pitch angles, bulge dynamical masses, bulge stellar masses, and the momentum parameter of the dynamical and stellar bulge) of spiral galaxies. in this work, we studied the scaling relations describe trends that are observed between important physical properties (SMBH masses, spiral arm pitch angles, bulge dynamical masses, bulge stellar masses, and the momentum parameter of the dynamical and stellar bulge) of spiral galaxies. The studied relations were:

$$log_{10}M_{BH} = b + mlog_{10}x$$
$$log_{10}M_{bul}\sigma = b + mlog_{10}x$$
$$log_{10}M_{bul} = b + mlog_{10}x$$

Where b and m are the intercept and the slope of the relation, x is a parameter of the bulge or spiral arm pitch angle. We used ‘equations (1, 4 and 5)’ to predict the values of M_{BH}, M_{bul}, $M_{bul}\sigma$ in other galaxies once we know the value of x.

In this study, the ordinary linear regression of MBH, M_{bul}, and M_{bul} σ on x were performed for the spiral galaxies.

‘Figures 1’ and ‘figure 2’ show the SMBH masses as a function of $M_{dyn}\sigma$ and $M_s\sigma$, for 41 galaxies respectively. Pearson’s linear correlation coefficient for a correlation between M_{BH}-$M_{dyn}\sigma$ and M_{BH}-$M_*\sigma$ relations are 0.77 and 0.79, respectively. The slopes of these relations are 0.675 and 0.686

respectively, meaning that no a considerable variation amidst M_{BH}-$M_{dyn}\sigma$ relation and M_{BH}-$M_s\sigma$ relation.

The fitting results of the M_{BH}-$M_{dyn}\sigma$ and M_{BH}-$M_s\sigma$ correlations are presented in (table 4) agrees with [25, 54, 55].

From the results of the Pearson's linear correlation coefficient and the significance level at which the null hypothesis of zero correlation is disproved is 3σ. This means that the masses of BHs in the nuclei of disk galaxies can be determined directly from a measurement of their momentum parameter.

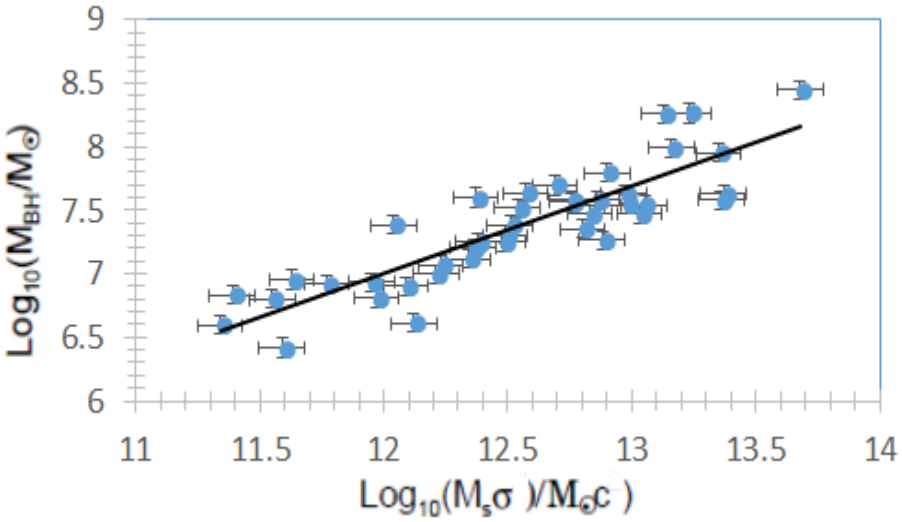

Figure 1. SMBH masses from M_{BH}-σ relation via the momentum parameter ($M_{dyn}\sigma$).

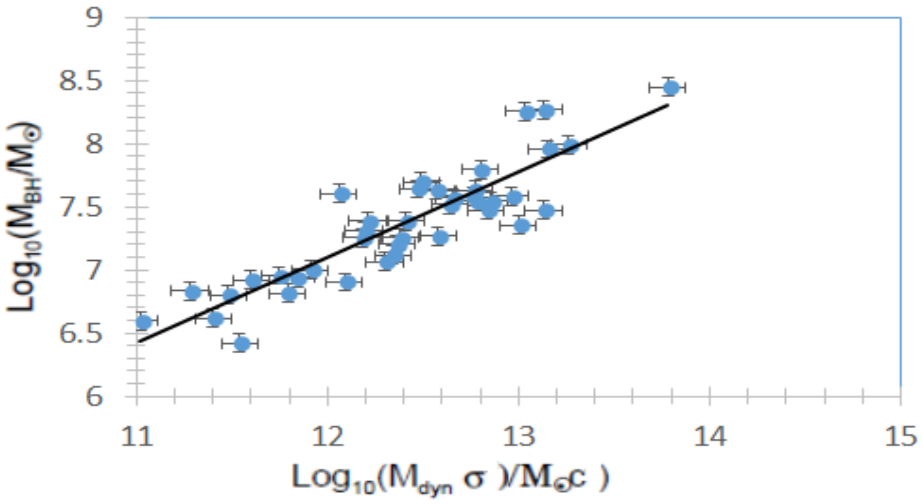

Figure 2. SMBH masses from MBH-σ relation via momentum parameter (Mσ).

As Seigar et al. (2008) have shown in [30], the slopes (0.07) and intercepts (8.44) of black hole-pitch angle correlation is very consistent with our results. This result agrees with [30, 35].

In 'figure 3' shows of the relation of spiral arm pitch angles and SMBH masses.

According to the results of this study, we can confident that for galaxies the of the spiral arms pitch angle should correlate well to the parts of galaxies coevolve with black hole, bulge luminosity, bulge mass,...etc.. The fitting result of M_{BH}-P correlation is shown in (table 4).

The relation of M_{BH}-P in this study agrees with that obtained in [30, 35]:

$Log_{10}\ M_{BH}=(8.44 \pm 0.1) - (0.07 \pm 0.005)\ P$ [30]

'Figures 4' and 'figure 5' depict SMBH masse versus M_{dyn} and M_s for spiral galaxy, where the masses were determined using 'equations (4)' and (5)'. Fitting results of M_{BH}-M_{dyn} and M_{BH}-M_s correlations are presented in (table 4).

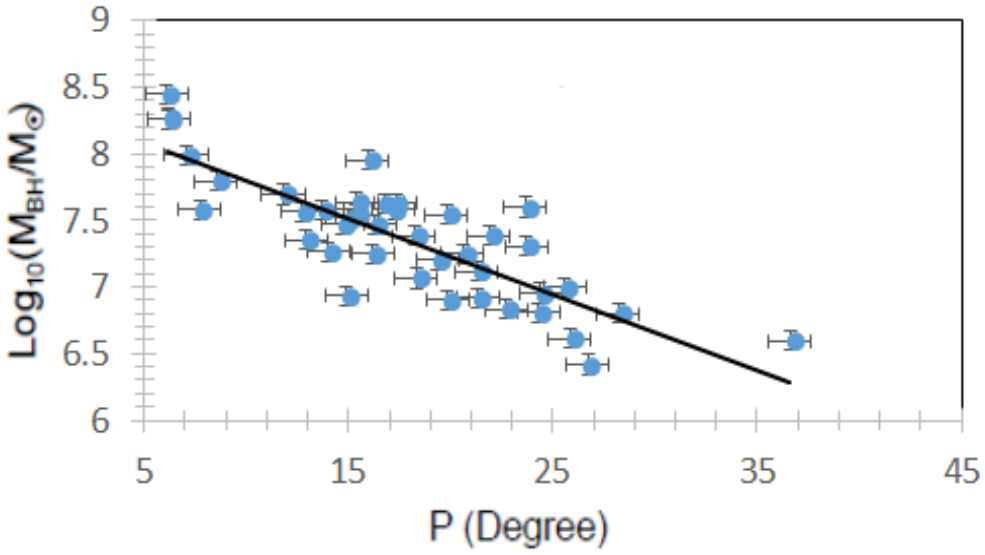

Figure 3. SMBH mass from M_{BH}-σ relation versus spiral arm pitch angle (P).

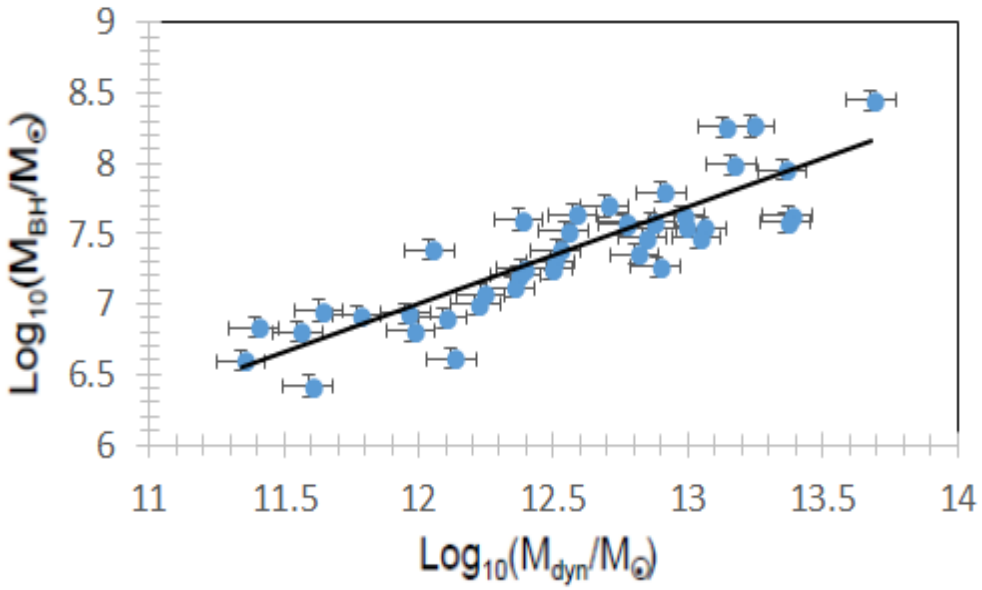

Figure 4. SMBH mass from M_{BH}-σ relation versus bulge dynamical mass (M_{dyn}).

The following conclusion can be estimated from these figures that the best fitting line for M_{BH} - M_s and M_{BH} - M_d relations are shown in (table 4). These results contain data on galaxies with two types of bulges (classical bulges and pseudo-bulges).

Pearson's linear correlation coefficient for a correlation between M_{BH}- M_{dyn}, and M_{BH} –M_s are 0.81 and 0.83, respectively, whereas the slope of the M_{BH} - M_d and M_{BH} − M_s relations are 0.68 and 0.67 respectively. Due to the Difference of M^*/M_d ratio, the establishment of little difference between

values from both relations can be seen, which might be concerned with mass contribution from dark matter [21]. Astronomers shown that dynamical mass of bulges is dominated by the stellar mass, with a negligible contribution of dark matter and gas [56, 57].

'Figure 4' and 'figure 5' indicate that M_{dyn} and M_s correlated well with (M_{BH}).These results confirmed the result that [25, 55, 58] found a good correspondence between the values from both relations M_{BH}-M_d and M_{BH}-M_s for Spiral galaxies, due spiral galaxies following the same M_{BH}–σ* relation [34].

The fitting results of the relationship between bulge mass (M_{dyn} and M_s) and spiral arm pitch angle by the linear regression method are summarized in (table 4).

The introduce of M_{dyn} - P and M_s - P relations for selected galaxies are illustrated in Figures 6 and 7.

Our data have shown the concerned SMBHs in the evolution, or co-evolution, of their host galaxies (bulge dynamical mass, bulge stellar mass, spiral arm pitch angle,.....ect.) [13, 59].

Recently discovered an important relation between the SMBHs mass and the spiral arm pitch angle of the galaxy (M_{BH}–P) relation by [30], whereas [24] found the relation between SMBH mass and M_{bul}σ. 'Figures 8' and 'figure 9' illustrated the momentum parameter of the host spiral galaxies versus spiral arm pitch angle for 41 spiral galaxies. In all the figures, the solid line is fir to spiral galaxies.

The momentum parameter of the host spiral galaxies (M_{dyn}σ* and M_sσ*) correlate with P. It is very clear that there is a correlation concerning M_{dyn}σand M_sσ with P. The fitting results of M_{dyn}σ–P, M_s-P correlations are shown in (table 4).

The comparison between our result and other in works were shown in (table 2).

Table 2. A comparison with previous studies

Relation	a	B	r	References
MBH-Md	-1.64±2.55 -9.01±1.96 -1.05±2.0	0.87±0.25 1.58±0.10 0.81±0.2	0.68	[60]
MBH-P	8.21±0.16 8.44±0.10	-0.062±0.009 -0.076±0.005	-0.81, 99.7% -0.91, 99.99%	[30, 35]
MBH-Mdσ2	4.55±0.8 2.36±0.62 4.88±0.56	0.75±0.22 1.37±0.17 0.66±0.16	0.68	[60]

Table 3. Regression result for the selected galaxies

Relation	b	m	r
M_{BH} - M_d	-1.22 ± 0.03	0.68 ±0.05	0.76
M_{BH} – M_s	-1.006 ± 0.06	0.675 ±0.07	0.79
M_{BH} - P	8.373 ± 0.5	-0.056 ± 0.002	-0.68
M_{BH} – M_dσ	1.006 ± 0.04	0.675 ± 0.03	0.79
M_{BH} – M_sσ	1.22 ± 0.05	0.68± 0.04	0.76
M_d - P	13.76 ± 0.17	-0.069 ± 0.006	-0.63
M_s - P	13.76 ± 0.22	-0.077 ± 0.003	0.71
M_dσ- P	13.76 ± 0.46	-0.069 ± 0.0049	-0.63
M_sσ-P	13.76 ± 0.044	-0.077 ± 0.0065	0.71

Table 4. Scaling relation for log M•= b + mlogx for the selected galaxies

Relation	The best fitting line for the relation
M_{BH} - M_d	$\log_{10} M_{BH} = (-1.22 \pm 0.03) + (0.68 \pm 0.05) \log_{10}(M_{dyn})$
M_{BH} – M_s	$\log_{10} M_{BH} = (-1.006 \pm 0.06) + (0.675 \pm 0.07) \log_{10}(M_s)$
M_{BH} - P	$\log_{10} M_{BH} = (8.373 \pm 0.5) + (0.056 \pm 0.02)P$
M_{BH} – M_dσ	$\log_{10} M_{BH} = (1.006 \pm 0.04) + (0.675 \pm 0.03) \log_{10}(M_{dyn}\sigma)$

$M_{BH} - M_s\sigma$	$\log_{10} \mathbf{M_{BH}} = (1.22 \pm 0.05) + (0.68 \pm 0.04)\log_{10}(\mathbf{M_s\sigma})$
M_d - P	$\log_{10} \mathbf{M_d} = (13.76 \pm 0.17) + (0.069 \pm 0.006)\mathbf{P}$
M_s – P	$\log_{10} \mathbf{M_s} = (13.76 \pm 0.22) + (0.077 \pm 0.003)\log_{10}(\mathbf{M_{dyn}})$
$M_d\sigma$- P	$\log_{10} \mathbf{M_{dyn}}\,\boldsymbol{\sigma} = (13.76 \pm 0.46) + (0.069 \pm 0.0049)\mathbf{P}$
$M_s\sigma$-P	$\log_{10} \mathbf{M_s\sigma} = (13.13 \pm 0.44) + (0.077 \pm 0.0065)\mathbf{P}$

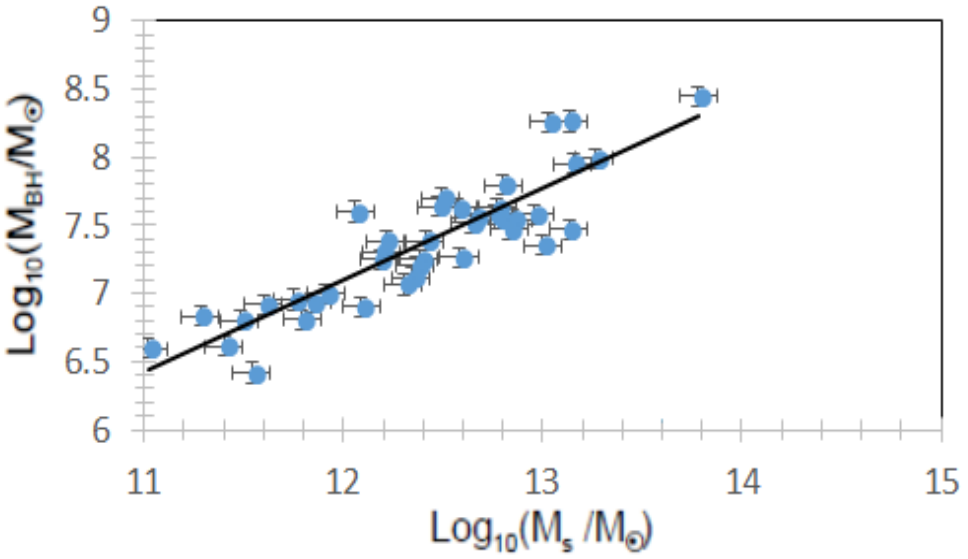

Figure 5. SMBH mass from MBH-σ relation versus bulge stellar mass (Ms).

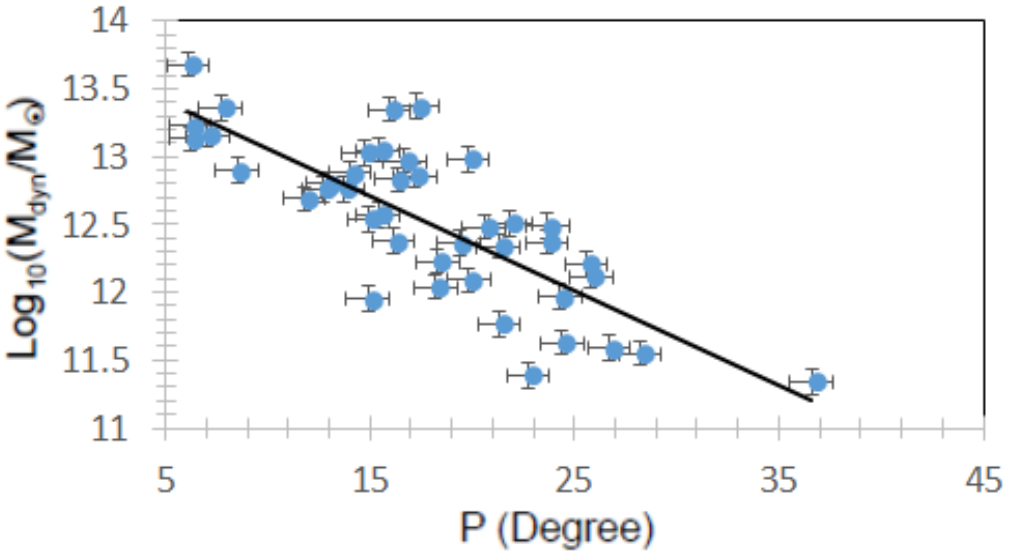

Figure 6. Bulge dynamical masses versus spiral arm pitch angle.

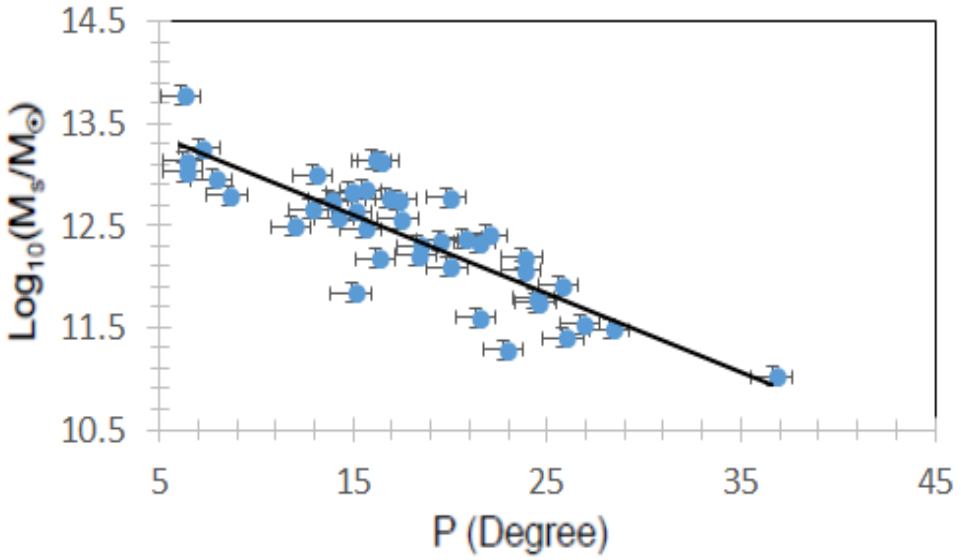

Figure 7. Bulge stellar masses versus spiral arm pitch angle.

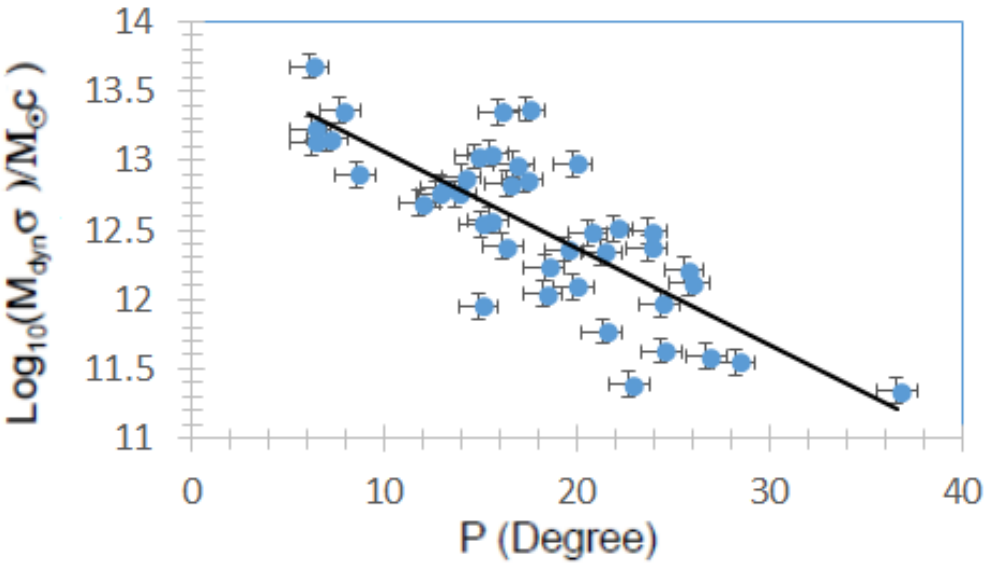

Figure 8. Momentum parameter for bulge dynamical masses versus spiral arm pitch angle.

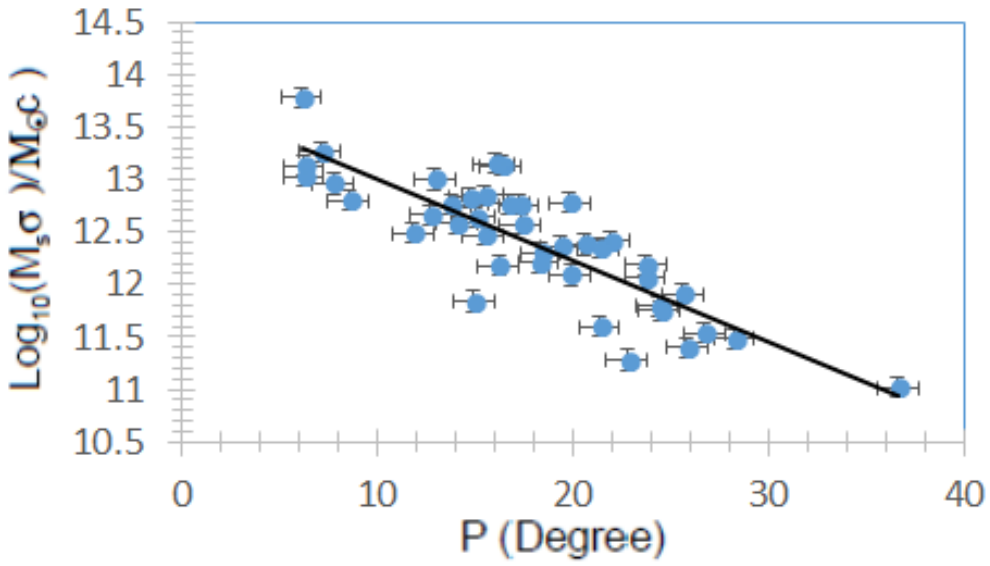

Figure 9. Momentum parameter for bulge stellar masses versus spiral arm pitch angle.

5. Conclusion

From isothermal model and the calibration by Se-Heon Oh [50], we calculated the bulge dynamical and stellar masses in 41 spiral galaxies. We used $M_{dyn}\sigma$ and $M_s\sigma$ to calculate the momentum parameter for the bulge stellar masses and the bulge dynamical mass.

We have gained preferable-fit lines of four relevance. Through them, we have establish M_{BH} - M_{dyn}, M_{BH}- M_s, M_{BH}– P, M_{BH} – $M_{dyn}\sigma$,, M_{BH} – $M_s\sigma$,, M_{dyn} – P, M_s – P, M_{dyn} – P, and $M_s\sigma$– P have a linear correlation coefficient 0.76, 0.79, 0.68, 0.79, 0.76, 0.63, 0.71, 0.63 and 0.71 respectively. Moreover, the momentum parameter in the bulge correlates well with pitch angle too. We conclude that pitch angle is perfect tool to specify indirect measurements of the dynamical bulge mass, stellar bulge mass, and momentum parameter in bulges. As well, these results underscore the importance of further understanding the role of the host galaxies in the growth of SMBHs.

Acknowledgement

The authors would like to thank Mustansiriyah University (www.uomustansiriyah.edu.iq) Baghdad-Iraq, Baghdad University and Babylon University for their support in the present work.

References

[1] Gebhardt K, Rich R and Ho L 2005 *ApJ* **634** 1093
[2] Valeri P, Frolov and Igor D 1998 *Black Hole Physics: Basic Concepts and New Developments*, (Kluwer academic).
[3] Heckman T and Kauffmann G 2011 *Science* **333** 182
[4] Rees M J 1984 *A Ann. Rev. Astr. Ap.*pp 22 471
[5] Tremaine S, Gebhardt K and Bender R 2002 *ApJ* pp 574-740
[6] Al-Baidhany I A, Seigar M, Treuthardt P, Sierra A, Davis B, Kennefick D, Kennefick J, Lacy C, Toma Z and Jabbar W 2014 *Journal of the Arkansas Academy of Science* **68** 25
[7] Kormendy J, Cornell M, Block D, Knapen J and Allard E 2006 *ApJ*, pp 642- 765
[8] Kormendy J and Fisher D 2008 ASP Conference Series 396
[9] Ferrarese L 2002 *ApJ* **578** 90
[10] Ferrarese L and Merritt D 2000 *ApJ* **9** 539
[11] Gebhardt K, Bender R and Bower 2000 ApJ, , **13**, 539.

[12] Magorrian J, Tremaine S and Richstone D 1998 *AJ* **115** 2285
[13] Marconi A and Hunt L, 2003 *ApJ* **589** 21
[14] Häring N and Rix H 2004 *ApJ* **604** 89
[15] Gültekin K, Richstone D O and Gebhardt K 2009 *ApJ* **695** 1577
[16] Graham A, Erwin P, Caon N and Trujillo I 2001 *ApJ* **11** 563
[17] Graham A and Driver S P 2007 *ApJ*, **655** 77
[18] Graham A W, Onken C A, Athanassoula E and Combes F 2011 **412** 2211
[19] Aller M C and Richstone D O 2007 *ApJ* **665** 120
[20] Lauer T, Faber S and Richstone D 2007 *ApJ* **662** 808
[21] Lauer T R, Tremaine S and Rich stone D 2007 Faber Selection S M *ApJ* **670** 249
[22] Feoli A and Mele D 2005 *Int. Jour. Mod. Phys*. **D14** 1861
[23] Feoli A and Mele D 2007 *Int. Jour. Mod. Phys.* **D16** 1261
[24] Feoli A and Mancini L 2009 *ApJ* **703** 1502
[25] Mancini L and Feoli A 2012 A&A **537** A48
[26] Seigar M S, Bullock J S, Barth A J and Ho L C 2006 *ApJ* **645** 1012
[27] Seigar M S, Ho L C and Barth A J 2006 Bulletin of the AAS **38** 1190
[28] Hu J 2009 ArXiv 0908.2028v1
[29] Sani E, Marconi A, Hunt L K and Risaliti G 2011 MNRAS **413** 1479
[30] Seigar M S, Kennefick D, Kennefick J and Lacy C H S 2008 *ApJ* **678** L93
[31] Ho L C and Kim M 2016 *ApJ* **821** 48
[32] Ferrarese L and et al 2006 *ApJS* **164** 334
[33] Barth A J, Greene J E and Ho L C 2005 *ApJL* **619** L151
[34] Greene J E and Ho L C 2006 *ApJ* **641** L21
[35] Berrier JOEL C and et al 2013 *ApJ* **769** 132
[36] Lin C C and Shu F H 1964 *ApJ* **140** 646
[37] Kennicutt R C 1981 *AJ* **86** 1847
[38] Elmegreen B G, Elmegreen D M and Hirst A C 2004 *ApJ* **612** 191
[39] Seigar M S and James P A 1998 MNRAS **299** 672
[40] Seigar M S and James P A 1998 MNRAS **299** 685
[41] Seigar M S and James P A 2002 **337** 1113
[42] Seigar M S, Block D L, Puerari I and Chorney N E 2005 MNRAS **59** 1065
[43] Hubble E P 1926 *ApJ* **64** 321
[44] Jedrzejewski R I 1987 MNRAS **226** 747
[45] Schröder M F, Pastoriza M G, Kepler S O and Puerari I 1994 A&AS **108** 41
[46] Cappellari M and et al 2006 MNRAS **366** 1126
[47] Gebhardt K and et al 2003 *ApJ* **583** 92
[48] Bell E F and de Jong R S 2001 *ApJ* **550** 212
[49] Bell E F, McIntosh D H, Katz N and Weinberg M D 2003 *ApJS* **149** 289
[50] Oh S H, de Blok W J G, Walter F, Brinks E and Kennicutt R C 2008 *AJ* **136** 2761
[51] Bertin E and Arnouts S 1996 A&AS **117** 393
[52] Reach W T, Morris P, Boulanger F and Okumura K 2003 **164** 384
[53] Soker N and Meiron Y 2011 MNRAS **411** 1803
[54] Mancini L, Feoli A, Marulli F and van den Bergh S 2011 *Gen. Rel. Grav.***43** 1007
[55] Drory N, Bender R and Hopp U 2004 *ApJ* **616** L103
[56] Tamm A, Tempel E, Tenjes P, Tihhonova O and Tuvikene T 2012 A&A **A4** 546
[57] Ho L C 2009 *ApJ* **699** 626
[58] Treuthardt P, Seigar M S, Sierra A D, Al-Baidhany I, Salo H, Kennefick D, Kennefick J and C H S Lacy 2012 **423** 3118
[59] Benedetto E, Fallarino M T and Feoli A 2013 A&A **558** A108
[60] Vallée J P 2002 *ApJ* **566** 261

Effects of FeCl3 additives on optical parameters of PVA

Effects of FeCl3 additives on optical parameters of PVA

Duha M A Latif[1], Sami S Chiad[2], Muhssen S Erhayief[2], Khalid H Abass[3], Nadir F Habubi[2], Hadi A Hussin[2]

[1]Department of Physics, Education for Pure Sciences, Baghdad University, Baghdad, Iraq,[2]Department of Physics, College of Education, Mustansiriyah University, Baghdad, Iraq ,[3]Department of Physics, College of Education for Pure Sciences, University Babylon, Babylon, Iraq

[2]dr.sami@uomustansiriyah.edu.iq, dr.muhssensalbookh@uomustansiriyah.edu.iq, [3]pure.khalid.haneen@uobabylon.edu.iq, nadirfadhil@uomustansiriyah.edu.iq, [2]hadi.ahmed@uomustansiriayh.edu.iq

Abstract. PVA doped FeCl3 have been deposited utilizing casting technique. Absorption spectrum was registered in the wavelengths (300-900 nm) utilizing UV-Visible spectrophotometer. Optical constants behavior such as, absorbance, absorption coefficient, and skin depth were studied. It was found these parameters were increased as Fe content increase. While the extinction coefficient and optical conductivity was decreased. The energy gap of PVA-Fe films were decreased from 4 eV for the PVA film to 3.5 eV for the PVA: 4 % Fe film.

Keywords: Poly (vinyl alcohol), Optical parameters, optical energy gap.

1. Introduction

Poly (vinyl alcohol) (PVA) has gained great importance , as it has a unique properties such as, crystalline polymer, solubility in water is high, its dissolution needs the breaking of the crystal structure and poverty to be carried out at high temperature [1-4]. Ionization of atoms and separation of molecules occur leading to the formation of charged species both ionic and free radicals [5].

Different composite materials latterly synthesized by starting from different polymers and a broad assortment of dopants like metals, oxides and inorganic salts [6]. Polymeric films have been widely used in industry especially in the measurement of electron beam dosimetry [7]. The motivated physical and chemical characteristics of polymer-metal composites showing the composites as conductive or semi-conductive materials, hence it gives the chance to use these materials in many applications, like, design the integrated circuits, optoelectronic devices, solid-state batteries [8,9]. In this study, the PVA-Fe composite by casting solution method is prepared in order to study the optical properties of this composite.

2. Materials and Methods

Polymeric solution of high purity Poly (vinyl alcohol) (molecular weight 10000 g/mol) was used as a matrix element in this work, which was Supplied from (BDH Chemicals). $FeCl_3$ supplied from (Merck chemicals Germany) with a volumetric percentage of (2% and 4%) was used to obtain Films of PVA:Fe utilizing casting method .Absorbance spectrum in the wavelength range (300-900 nm) was calculated to obtain the optical constants.

3. Results and discussion

Absorbance spectra of PVA with various content of Fe (0, 2, and 4% wt.) were depicted in Figure 1, which was recorded by spectrophotometer in the range of 300-900 nm, using casting method as a film with thickness 1.5 µm. The absorbance decreased with the increasing of wavelength, while it increased with the increasing of Fe content in the PVA-Fe films.

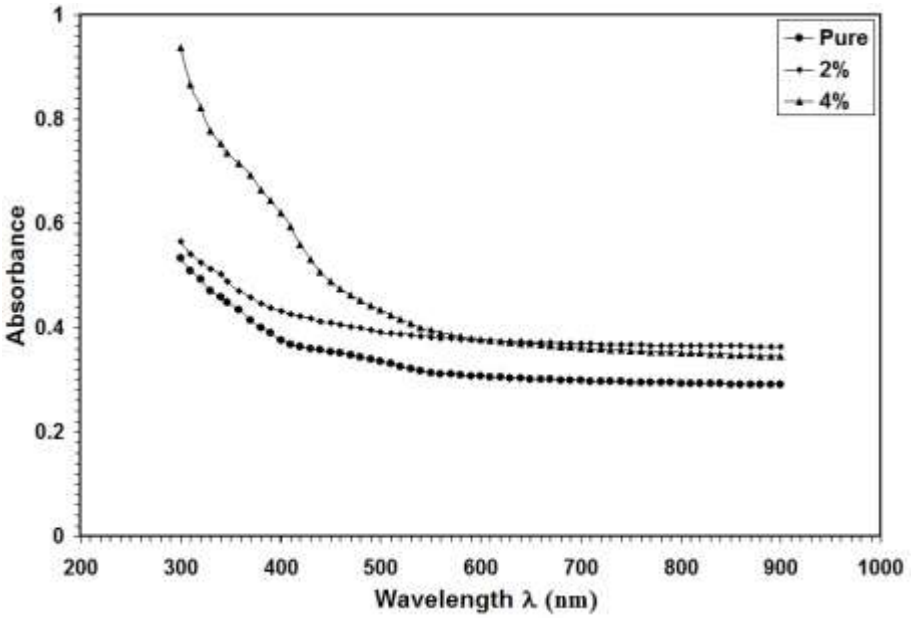

Figure 1. Absorbance versus wavelength of PVA-Fe composite with various content of Fe.

The absorption coefficient (α) of PVA-Fe was estimated by the following formula [10]:

$$\alpha = \frac{2.303A}{d} \qquad (1)$$

Where (A) is the absorbance and (d) is the film thickness. Absorption coefficients via wavelength was presented in Figure 2, from this figure, it can be seen that absorption coefficient were increased by increasing Fe content in the PVA-Fe films.

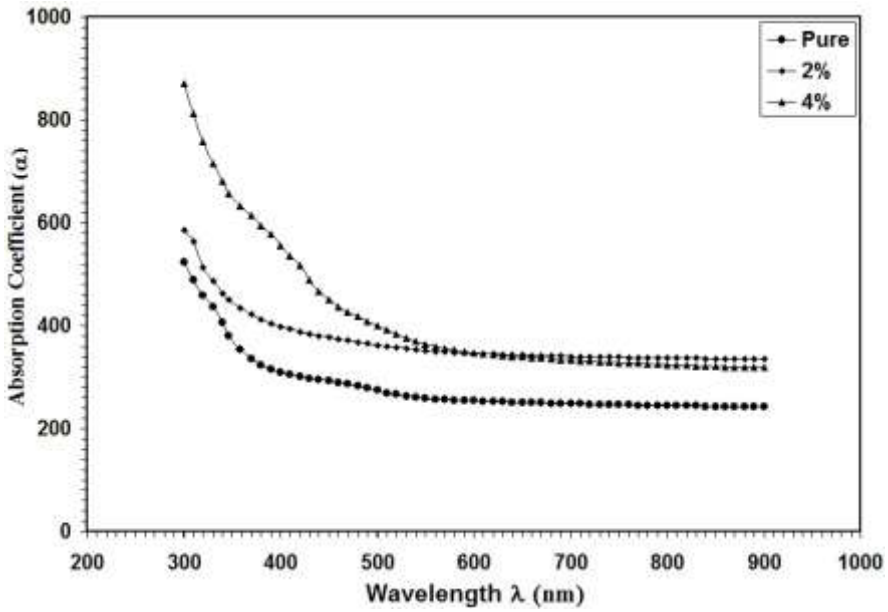

Figure 2. The absorption coefficient of PVA-Fe composite with various content of Fe.

The extinction coefficient (k) of PVA-Fe films were calculated from the following equation [11]:

$$k = \frac{\alpha\lambda}{4\pi} \qquad (2)$$

Where (α), (λ) are the absorption coefficient and incident photon wavelength respectively. Extinction coefficient versus wavelength was presented in the Figure 3 Same behavior of absorption coefficient was noticed in extinction coefficient with the increment of Fe content.
'Figure 4' depicts the relation between refractive index (n) and wavelength (λ) that obtained from the formula [12]:

$$n = \left[\left(\frac{4R}{(R-1)^2}\right) - K^2\right]^{1/2} + \frac{(R+1)}{(R-1)} \qquad (3)$$

Where (R) denoted reflectance, Refractive index of PVA-Fe films were decrease with the increase of Fe content up to 500 nm of wavelength, and then the changes in refractive index seem slightly increase up to 900 nm of wavelength.

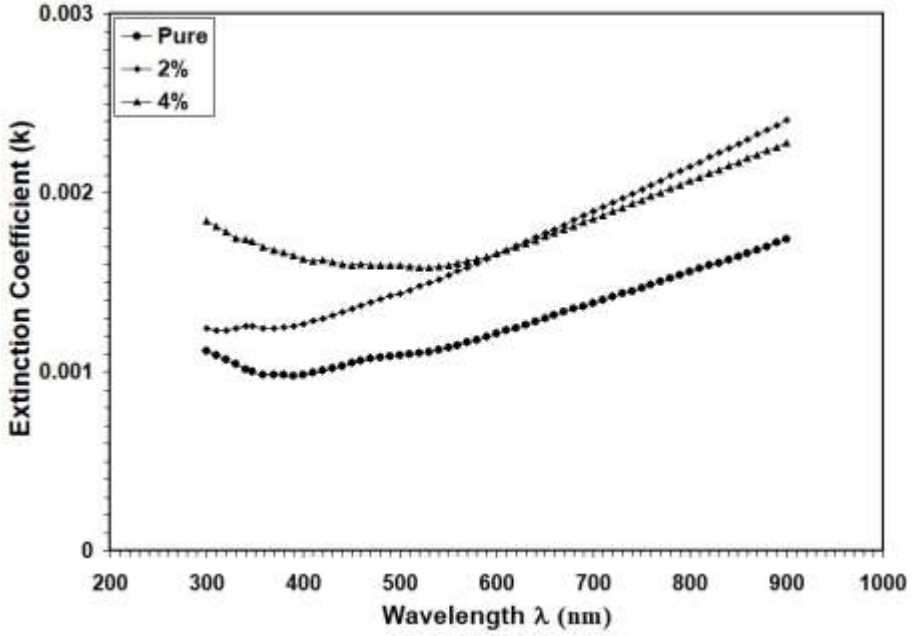

Figure 3. The extinction coefficient of PVA-Fe composite with various content of Fe.

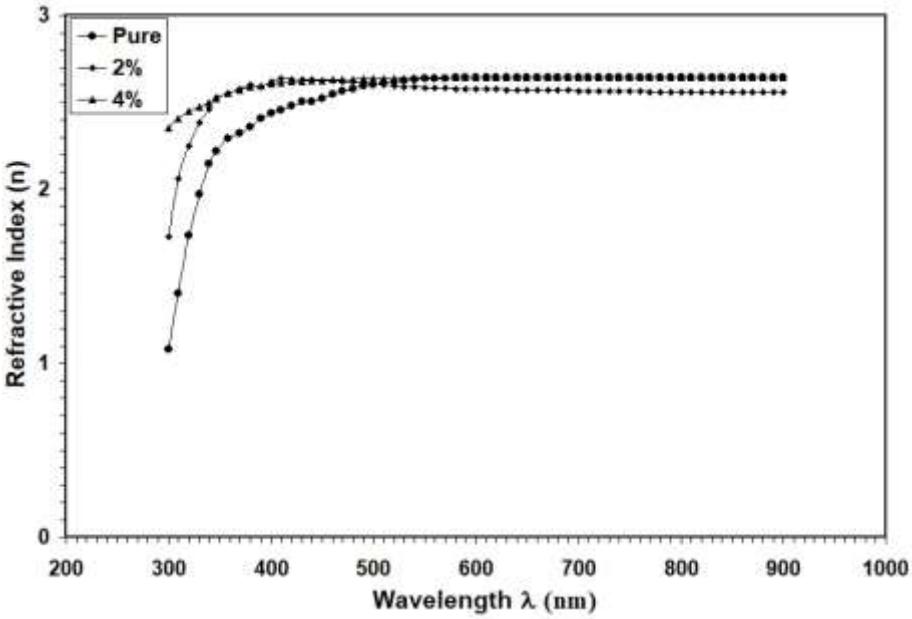

Figure 4. The absorbance spectra of PVA-Fe composite with various content of Fe**.**

The optical conductivity (σ) was calculated using the following formula [13]:

$$\sigma = \frac{\alpha n c}{4\pi} \qquad (4)$$

Where (c) is the velocity of light in the vacuum. The optical conductivity versus wavelength was presented in Figure5, which was increase with the increasing of Fe content in the PVA-Fe films.

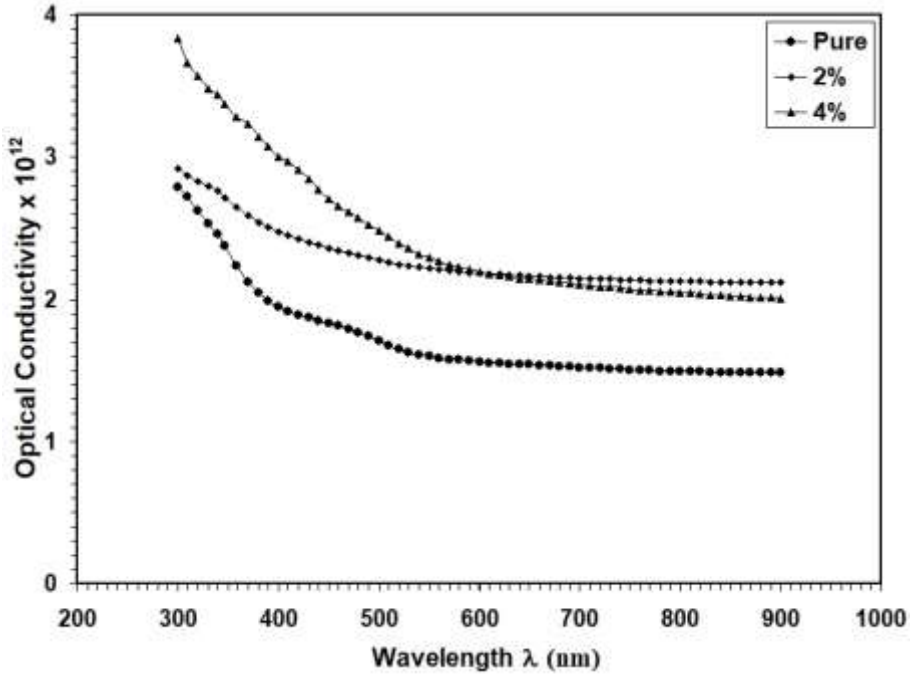

Figure 5. The optical conductivity of PVA-Fe composite with various content of Fe.

The skin depth increased with the increasing of Fe content in the PVA-Fe films as shown in the 'Figure 6'.

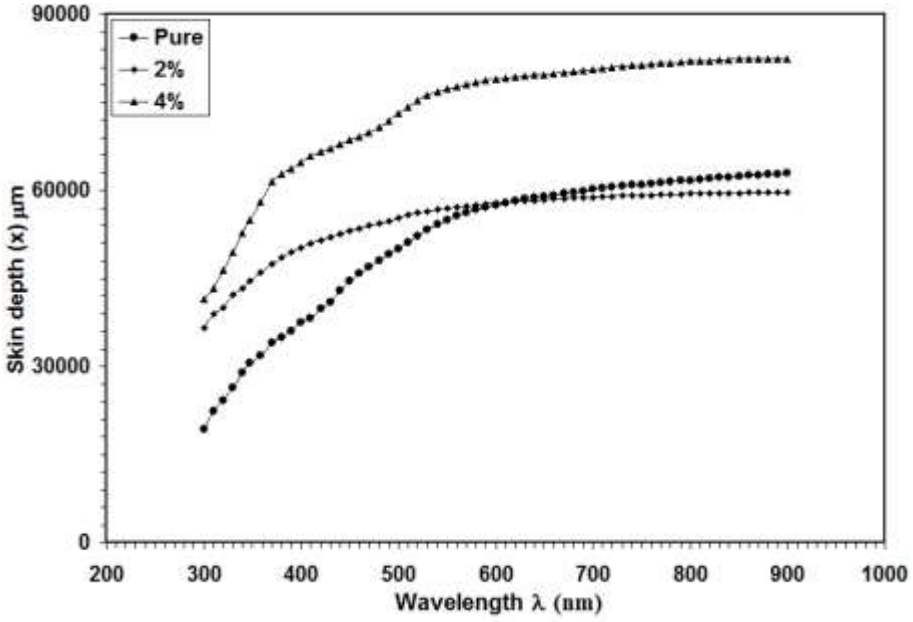

Figure 6. The skin depth of PVA-Fe composite with various content of Fe.

The optical band gap of PVA-Fe composites were estimated from absorption spectra .The energy gap it's found from Tauc relation [14]:

$$\alpha h\upsilon = B(h\upsilon - E_g)^m \quad (5)$$

Where (hυ) represent photon energy, (B) is a parameter depends on transition probability [15], and m = 1/2 or 2/3 [16]. By plotting $(\alpha h\upsilon)^2$ versus hυ, the band gap value can be obtained from Figures 7 - 9. From the figures, the energy gap decreased from 4 eV for the film PVA to 3.5 eV for the film PVA-4%Fe. The Fe content makes a network inside the PVA films leads to decrease the energy gap.

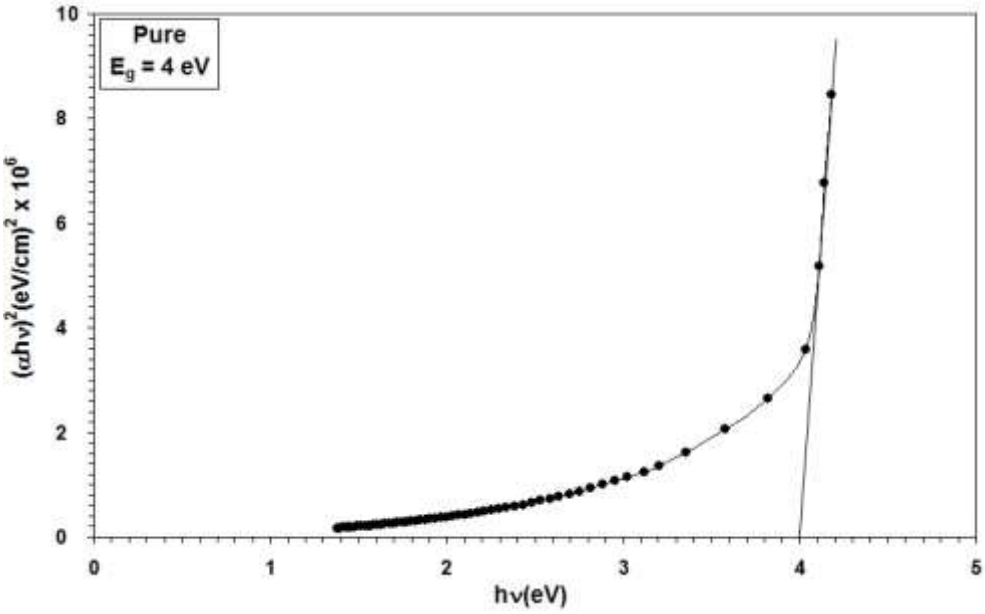

Figure7. Energy gap of PVA polymer.

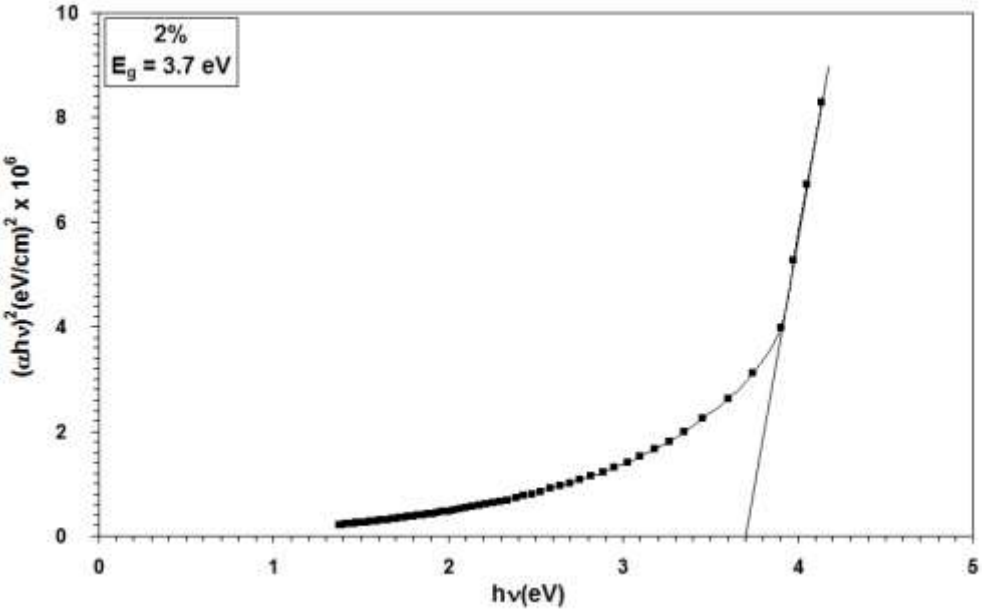

Figure 8. Energy gap of PVA-2 % Fe composite.

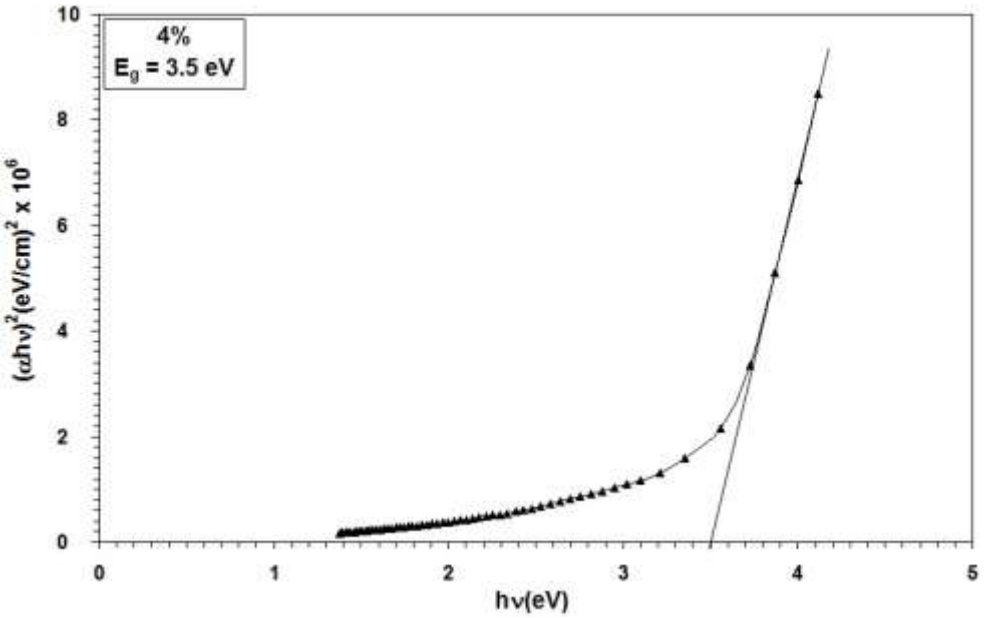

Figure 9. Energy gap of PVA-4 % Fe composite.

4. Conclusion

The films of PVA-Fe for various content of Fe are prepared by solution casting method. The absorbance spectra are recorded in the range of 300-900 nm. Absorbance, absorption coefficient, and skin depth increase with the increasing of Fe content in the PVA-Fe films, but extinction coefficient and optical conductivity are decreased. The energy gap of PVA-Fe films are decreased from 4 eV for the film PVA to 3.5 eV for the film PVA-4%Fe, make these films suitable in solar cell application.

Acknowledgments

The authors would like to thank Mustansiriyah University (www.uomustansiriyah.edu.iq) Baghdad-Iraq, Baghdad University and Babylon University for their support in the present work.

References

[1] Badr Y, Mahmoud M A, *J. Mater. Sci*., 2006, 41: 39-47.
[2] Florianczyk Z,Penczek S. Chemistry of Polymer (Oficyna Wydawnicaz Politechniiki. Warzawskiej, Warszawa), 1997.
[3] Habubi N F, Chiad S S, Mohammed R A. Atti Della Fondazionegiorgioronchi, 2011, 116 (3): 391-396.
[4] Vargas M.A, Vargas R A, Mellander B. E. Electrochim. Acta, 2000, 45: 1399–1403.
[5] Aleshin, AN, N B Mironkov, Suvarov A V, Conklin J A, Su J M., Kaner R B, Phys. Rev. B: Condens. Matter, 1996, 54: 11638-11643.
[6] Asogwa P, Ezugwu S, Ezema F, Superficies y, 2010, 23: 18–22.
[7] Adiyodi A K, Jyothy P V, Unnikrishnan N V, *J. Appl. Polym. Sci*., 2008, 113(2): 887–895.
[8] Reichmanis E, Donnel J O. ACS Symposium Series. (Washington, DC: American Chemical Society, 1993, 381 (527): 1–8.
[9] Omer M A A, Gar-elnabi M E M, Ahmed A H, Eidam G A, Khidir N A N, *International Journal of Science and Research* , 2013, 2 (9): 361-364.
[10] Abass K H, *International Letters of Chemistry*, Physics and Astronomy, 2015, 47: 178-184.

[11] Abass K H, Hadi Q M, Hamdan Sh L, Alagha M M, *physical Chemistry An Indian Journal,* 2015, 10 (2): 41-45.
[12] Aadim K A, Abass K H, Hadi Q M, *International Letters of Chemistry*, Physics and Astronomy, 2015, 56: 87-94.
[13] Oboudi S F, Chiad S S, Abass K H, Habubi N F, *Iraqi Journal of Physics,* 2014, 12 (24): 75-80.
[14] Tauc J, Menth A, Wood D, *Phys. Rev. Lett*., 1970, 25: 749-752.
[15] Dorranian D, Abedini Z, Hojabri A, Ghoranneviss M, *Journal of Non-Oxide Glasses,* 2009, 1(3): 217-229.
[16] Mishjil K A, Chiad S S, Abass K, Habubi N F, Materials Focus, 2016, 5: 471–475.

Experimental study of some shielding parameters for composite shields

Experimental study of some shielding parameters for composite shields

AHMED F MKHAIBER[1] ,ABDULRAHEEM DHEYAA[1]

[1] Department of Physics – College of Education for Pure sciences Ibn AlHaitham University of Baghdad Iraq

ahmfad2002@yahoocom

Abstract.In this study radiation protection shields have been prepared consist of composite materials have epoxy as a basis material and different reinforcing materials C Ni PbO and Bi with various reinforcing ratios 10 20 30 40 50 % and dimensions 1 ×10 ×10 cm For examination the suitability of using this shields to protect from gamma ray some shielding parameters were calculated like Linear attenuation coefficient μ Effective atomic numberZ_{effe} Heaviness and half value thickness $X_{1/2}$ for energy rang 1218 – 1480 KeV These parameters have been measured by using sodium iodide system NaITI with deferent radiation sources ^{152}Eu ^{60}Co and ^{137}CsThe results show that this parameters are effected by the reinforcing ratio and gamma ray energy it is found the linear attenuation coefficient and atomic effective number increases with reinforcing ratio increases and decreased with energy increasing especially with high concentrations 40 50 % and at low energies E_γ < 0662 MeV with certain energy while the values of $X_{1/2}$ is decrease with reinforcing ratio increases Heaviness was calculated too for all shields with respect to lead from its values we found that this shields lighter than lead which make it preferable to traditional material such as lead and concrete

Key words Attenuation coefficient Composite materials Gamma rays Shielding

1 Introduction

The continuation of development in nuclear technology led to make the radiation sources intervention in many relevant fields such as agriculture industry medicine nuclear power generation and scientific research[1] so the nuclear shields used to reduce the exposure to nuclear radiation and their secondary interactions with the material and to minimize the effects on human tissue[2] Most of these shields are made from different types of materials depending on the energy type of radiation availability of the shielding material [3] The polymerbased composites such as polyethylene polystyrene and epoxy have been selected in the field of radiation protection[4]In the recent years composite materials are employed in the gammaray shielding and showed good efficiency in this field Composite materials are multiphase materials that are obtained by artificial combination of different materials so as to attain properties that the individual components by themselves cannot attain[5] In our study we use composite material consist of epoxy as based material and C Ni PbO and Bi as reinforcing material with five reinforcing ratios 1020304050 %

2. Experimental part

2.1Counting system for gamma ray

The gamma rays counting system which is used in the search shown in figure 1

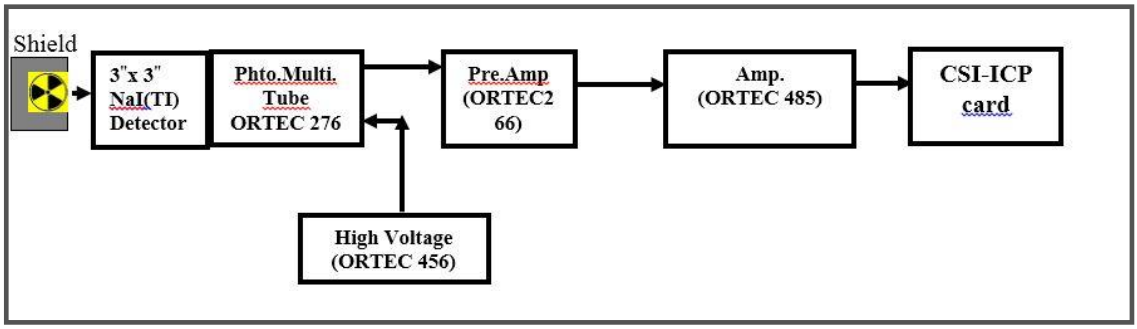

Figure 1 Diagram of counting system

2.2.Geometric arrangement of the system

For studying the attenuation coefficients we used a collimator to get a good geometry arrangement This collimator made of lead with dimensions 5x10x20 cm The detector was placed at 20 cm from the source Two collimators were used the first placed near the source and second placed near the detector and this arrangement was used to measure the total linear attenuation coefficient This arrangement was shown in figure 2

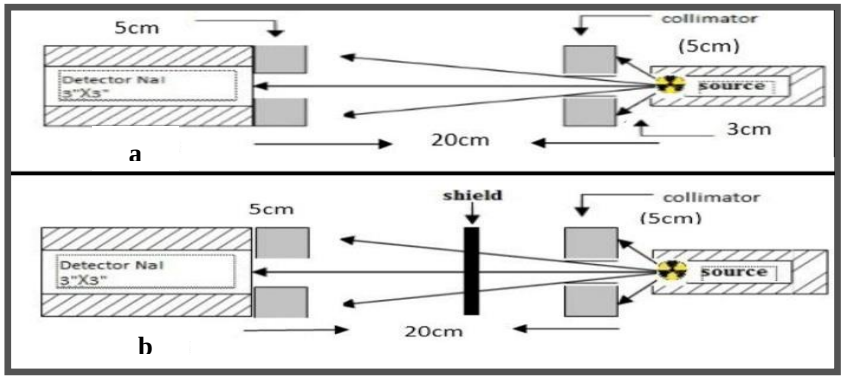

Figure 2 Good geometric arrangement for system

2.3.Materials

Epoxy resin was used as a matrix in the preparation of polymeric composite material which is one of the thermosetting polymers types The form of this resin will change from liquid to solid state by adding hardener which is transparent liquid added to the epoxy resin by 3 grams per 100 grams of resin at room temperature The reinforced materials are in powder form to get many types of composites as in table 1

Table 1 Reinforcement materials

Name of composite	Matrix	Reinforcement
Comp1	Epoxy	C
Comp2	Epoxy	Ni
Comp3	Epoxy	PbO_2
Comp4	Epoxy	Bi

3.Theoretical part

3.1.Linear attenuation coefficient

The linear attenuation coefficient μ is one of the most important parameters that describe the gamma rays penetrating process which depends on the energy of incident photons and atomic number or effective atomic number of the target and it is considered as the main factor for the derivation of other shielding parameters [6] When a package of gamma rays is passing through a substance each photon packet of photons either go out without interaction or displaced entirely from the package brokered by absorption or scattering If $I_\circ$ is the gamma rays original intensity which falling off on the slice thickness x the intensity of outgoing I_x is given by the following [7]

$$I_\times = I_\circ \, e^{\mu \times} \quad (1)$$

Where μ total linear attenuation coefficient

To apply the above equation there are two conditions must be provided the thickness of the absorbent material is to be small and the gamma rays beam is to be narrow and monoenergetic

3.2. Effective atomic number

The effective atomic number is one of the important parameters for the interaction of photons with the matter it is included in many of the technological and engineering fields [8] The atomic number of composite materials is not represented by integervalued as in the case of the elements but represents a numerical quantity called the effective atomic number which is calculated based on the percentage of the participation of each element in the composite material [9] The effective atomic number of composite materials calculated by the following equations [10]

$$Z_{matrix} = \frac{\sigma_a}{\sigma_e} \quad (2)$$

$$Z_{effe} = \sum_{i=1}^{2} w_i Z_i \quad (3)$$

Where σ_a atomic crosssection σ_e Electronic cross section Z_{matrix} Atomic number of the polymer Z_{effe} effective atomic number of composite material w_i the weight ratio of shielding materials Z_i atomic number of ith material in composite

3.3. Heaviness

The advantage of polymericbased composite materials is that its performance is best relative to its low density and the parameter which reflects this characteristic is called gravity where it calculated relatve to the lead by the following equation [12]

$$\text{Heaviness \%} = \frac{density\ of\ matrial}{lead\ density} \times 100\% \quad (4)$$

3.4.Halfvalue thickness $X_{1/2}$

The halfvalue thickness of an absorber is the thickness of the absorber material which makes the intensity of output gamma ray reduced to one half of its original intensity and can be calculated as [13]

$$X_{1/2} = \frac{0.693}{\mu} \quad (5)$$

4 Results and discussion

Linear attenuation coefficients were measured of all shields at different concentrations and energies 'Figures 36' show the relation between linear attenuation coefficient and concentration Of reinforced material It is clear from these figures that the values of the attenuation coefficient vary with concentration This can be returned to increase the absorption processes which due to the distribution of the additive material inside the matrix material and this is leading to increased density of the shields This meansthat the epoxy alone is not useful for use as a shield against gamma rays but when we add some reinforcement materials it is become possible to use as a shield against gamma rays and this result agrees with [14]

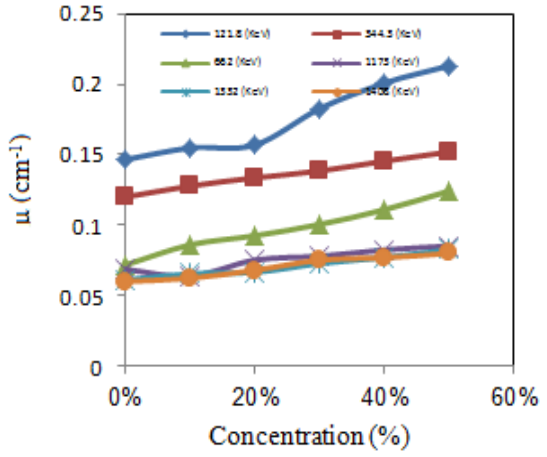

Figure 3. Attenuation Coefficient μ (cm^{-1}) as a function of concentration (%) for Comp1.

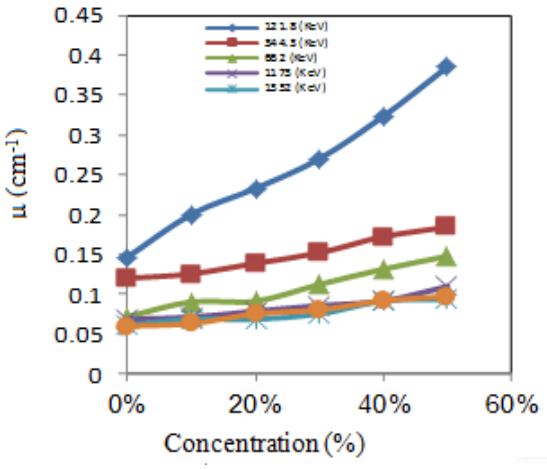

Figure 4. Attenuation Coefficient μ (cm^{-1}) as a function of concentration (%) for Comp2.

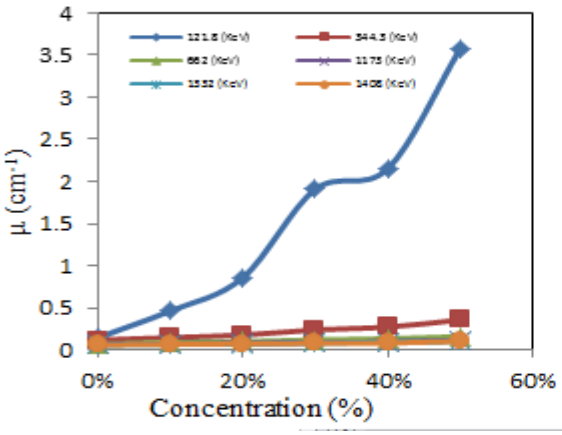

Figure 5. Attenuation Coefficient μ (cm^{-1}) as a function of concentration (%) for Comp3.

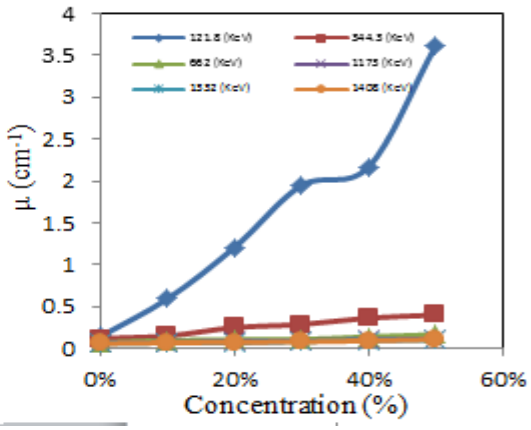

Figure 6). Attenuation Coefficient μ (cm^{-1}) as a function of concentration (%) for Comp4.

Attenuation coefficient as a function of gamma rays energy shown in figures 710 and it is clear from these figures that the attenuation coefficient decrease with energy increase and this is due to the interaction mechanism of gamma rays with a matter which depends on the energy values These figures show that the highest values of the attenuation coefficient are being within the low energy region for all types and concentrations of reinforcement materials and this can be interpreted to the dominance of the photoelectric effect which its crosssection is high in this region Then the attenuation coefficient decrease slowly down to the extent of highenergy which has the effect of the pair production is in control where there is no noticeable change in the values of the attenuation
Coefficient within this area and this is consistent with [15]

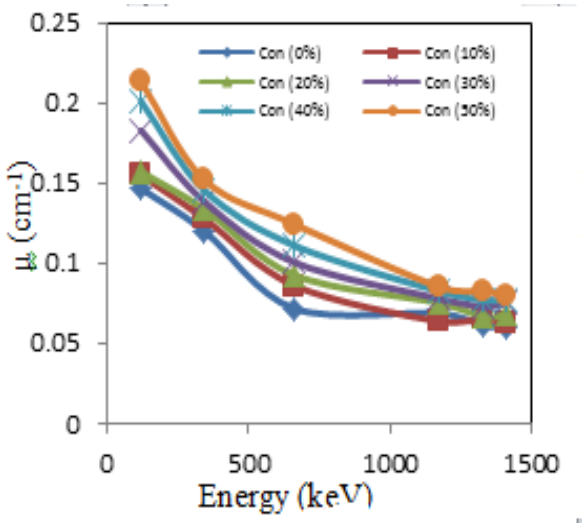

Figure 7. Attenuation Coefficient μ (cm-1) as a function of energy (keV) for Comp1

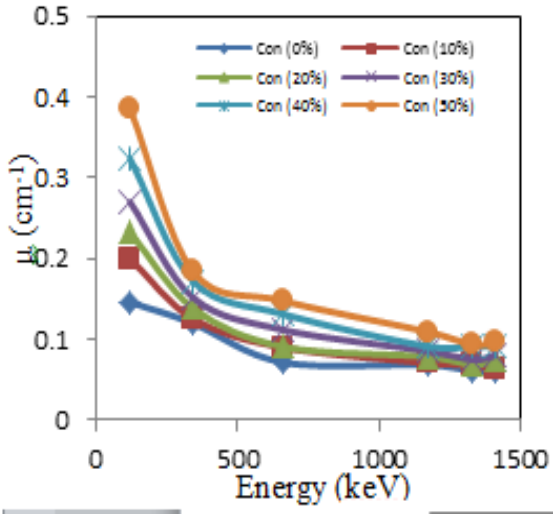

Figure 8. Attenuation Coefficient μ (cm^{-1}) as a function of energy (keV) for Comp2.

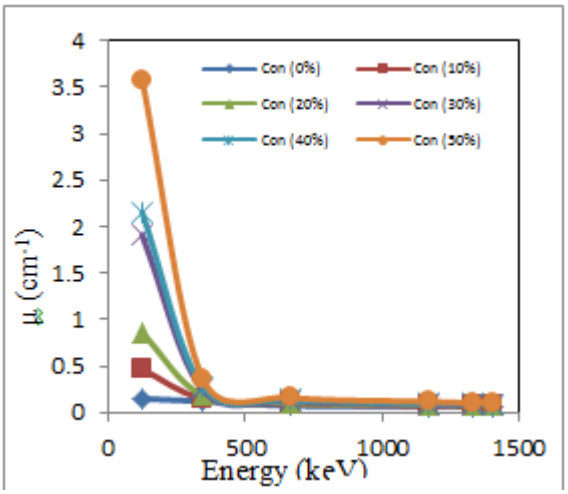

Figure 9. Attenuation Coefficient μ (cm^{-1}) as a function of energy (keV) for Comp3.

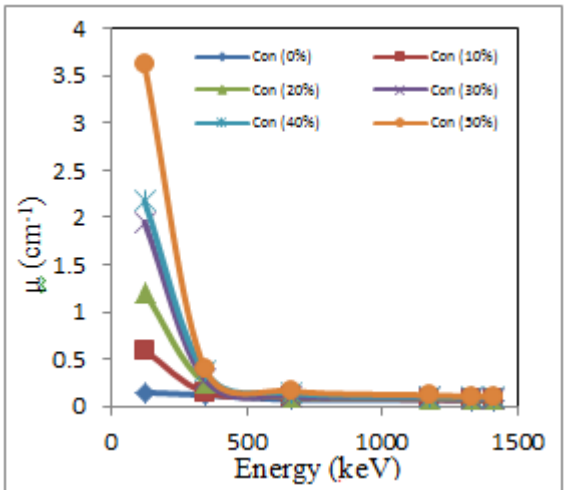

Figure 10. Attenuation Coefficient μ (cm^{-1}) as a function of energy (keV) for Comp4.

The effective atomic number was calculated for all shields at different concentrations and the result was plotted in figures 1114 From these figures we can note that the effective atomic number increases with increasing concentration of reinforcement material specially for Comp3 and Comp4 which have the highest value of Zeff and can be interpreted as an increase of the concentration of reinforcement material the attenuation coefficient will increase and thus increasing atomic number of shields This meaning that there is an improvement in the properties of the matrix material epoxy towards the properties of reinforcement material

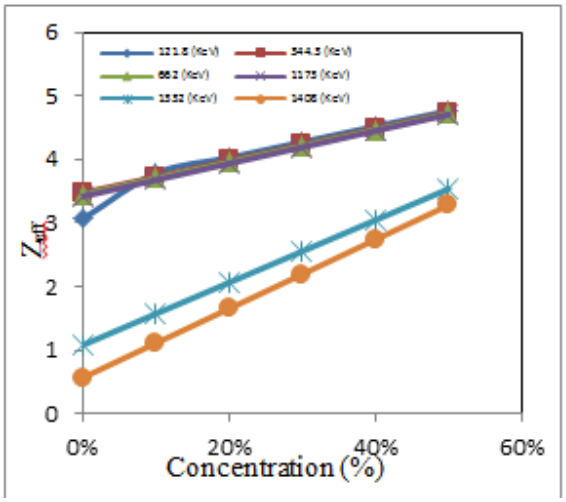

Figure 11. Effective atomic number Z_{eff} as a function of concentration (%) for Comp1.

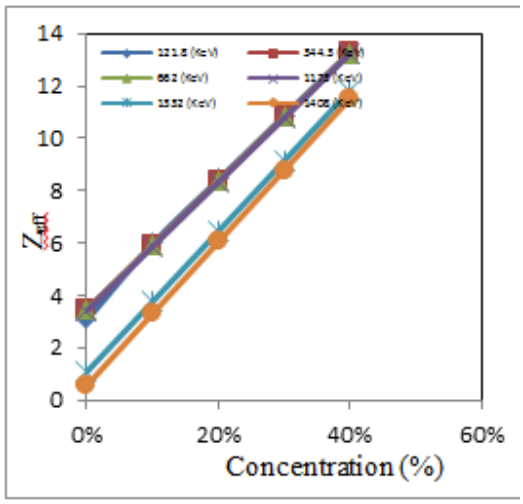

Figure 12. Effective atomic number Z_{eff} as a function of concentration (%) for Comp2.

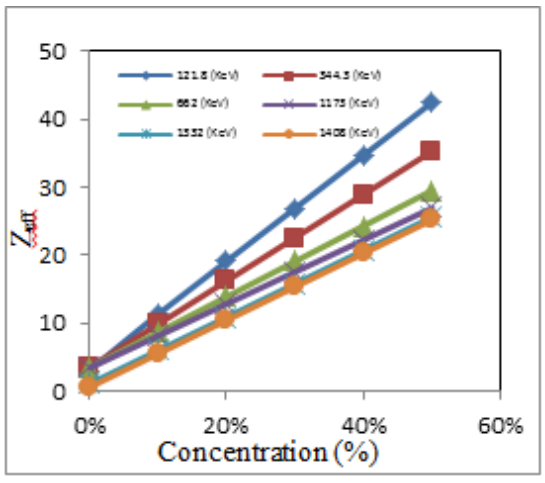

Figure 13. Effective atomic number Z_{eff} as a function of concentration (%) for Comp3.

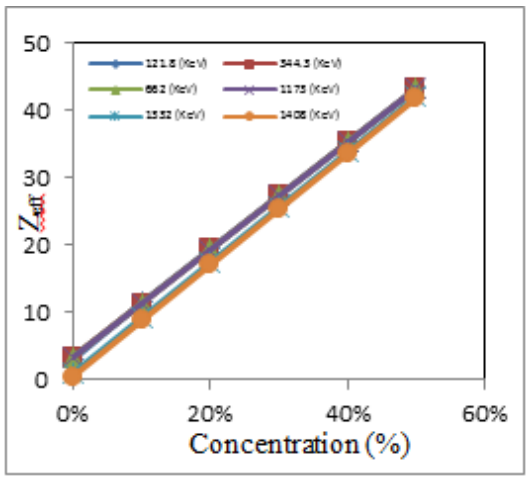

Figure 14. Effective atomic number Z_{eff} as a function of concentration (%) for Comp4.

.

The values of half value thickness $X_{1/2}$ for all shields were calculated at different concentrations The relationship between $X_{1/2}$ and concentration of reinforcement materials was plotted in the figures 1518

and it is noticeable from these figures that the half values thickness decreases with increasing concentration and that arise from the fact that the increase in the concentration of the additive material lead to improving the properties of the matrix material towards the attenuation of gamma radiation so this contribute in determining the appropriate thickness for this shields

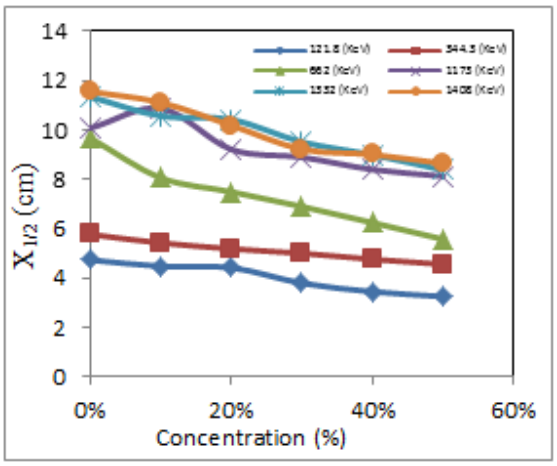

Figure 15. Half value thickness $X_{1/2}$ (cm) as a function of concentration (%) for Comp1.

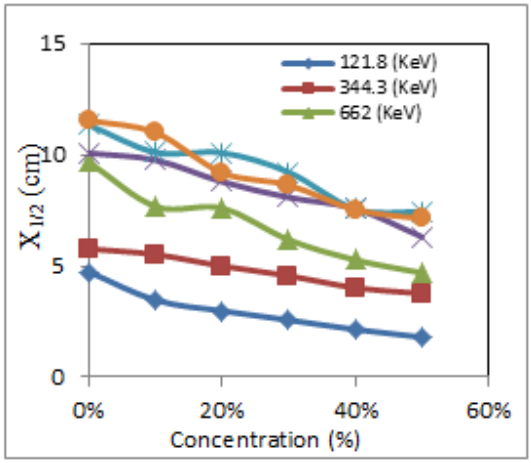

Figure 16. Half value thickness $X_{1/2}$ (cm) as a function of concentration (%) for Comp2.

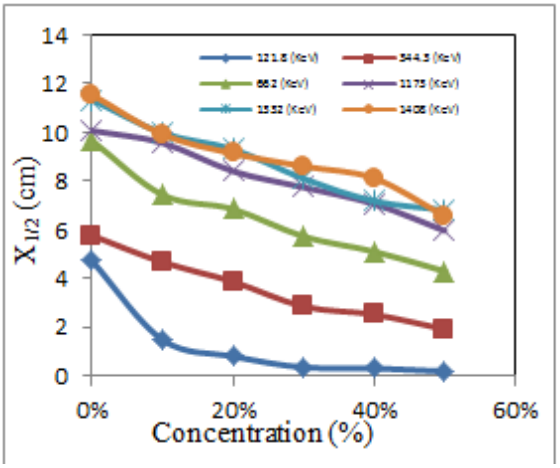

Figure 17. Half value thickness $X_{1/2}$ (cm) as a function of concentration (%) for Comp3..

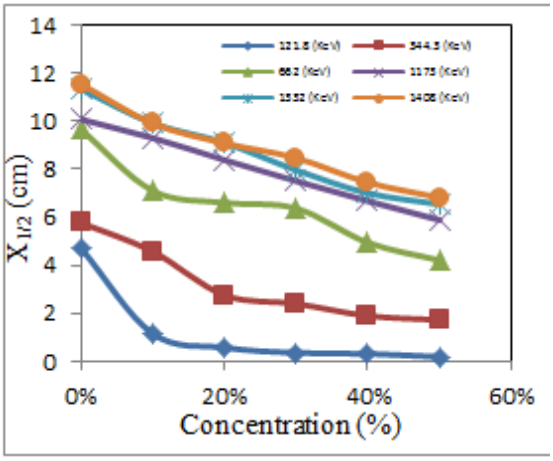

Figure 18. Half value thickness $X_{1/2}$ (cm) as a function of concentration (%) for Comp4.

The heaviness values were calculated and plotted as a function of the type of shield at a certain concentration 50%It is clear from figure 19 that manufactured shields from Polymeric Composite Material be light when it is compared with materials of conventional shielding such as lead and concrete as well as their performance as a radiation protection shields more receptive when adding high concentrations to it and when it is used with low energy and this agrees with the study [12]

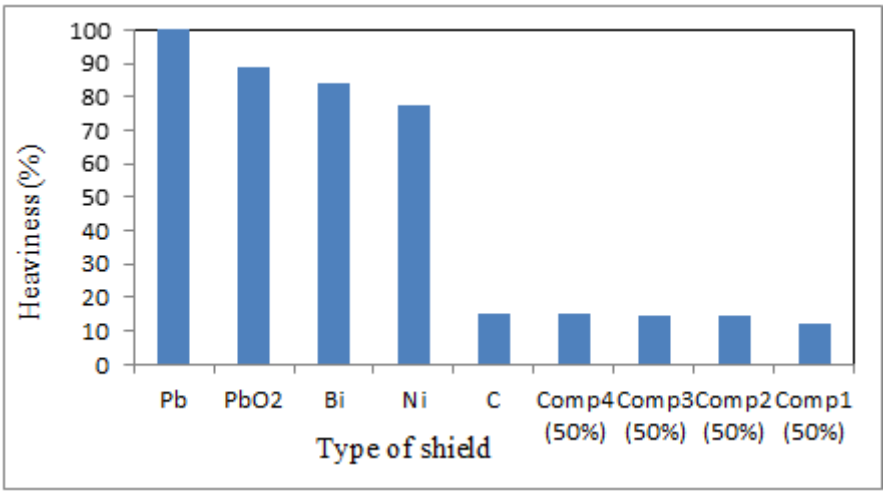

Figure 19 Heaviness % as a function of shield type

5 Conclusion

In this study we find that there is an improvement in the properties of the matrix material epoxy toward gamma rays shielding by adding some reinforcement materials where it is possible to use this shields in some nuclear applications such as radiation therapy rooms shielding as well as radioactive sources containers The results show that the shielding properties of these shields such as attenuation coefficient effective atomic number and others affected by increased reinforcement ratios it was found that the effectiveness of the shields was best in the case of increasing concentration of reinforcement materials ratio specially when using PbO as reinforcing materials due to its hiehg atomic number for lead

References

[1] Ripan B Hossain S and Abdus S 2015 Calculation of gammaray attenuation parameters for locally developed shielding material polyboron *journal of radiation research and applied sciences*
[2] Rahman I 2010 Calculation the number buildup factor of cylindrical samples for Brass Copper & lead **71** 146
[3] Hossain S Ripan B and Fazlul H 2016 Calculation Of GammaRay Attenuation parameters for locally developed ilmenitemagnetite concrete *J Bangladesh Acad Sci* **40** 11 21
[4] Garea S Sandu T and Constantin F 2010 Characterization of novel epoxy composites based on hybrid inorganic organic polyhedral oligomeric silsesquioxane *IntJPolymAnalCharact* **15** 119 128
[5] Deborah D and Chung L 2002 Composite material science and applications functional material for modern technologies *SpringerVerlag London Ltd*
[6] Singh V and Badiger N 2013 Study of mass attenuation coefficients effective atomic numbers and electron densities of carbon steel and stainless steels *JRadioprotect* **48** 431 443
[7] Wood J 1981 Computational methods in reactor shielding Pergamon Press UK
[8] Hine G 1952 The effective atomic numbers of materials for various gamma interactions *physics*

review **85** 725 737
[9] Pravina P Anita R and Govind K 2012 Effective atomic number and electron densities for L Arginine LR at several photon energies *journal of chemical and pharmaceutical research* **4** 2692 2696
[10] Olarinoyr I 2011 Variation of effective atomic numbers of some thermoluminescence and phantom materials with photon energies *research journal of chemical sciences* **1**
[11] Akkurt I Gunoglu K and Arda S 2014 Detection efficiency of NaITl detector in 5111332 Kev energy range *science and technology of nuclear installations* **article ID186798**
[12] Harish V Nagaiah Nand Harish H 2012 Lead oxides filled isophthalic resin polymer composite for gamma radiation shielding applications *Indian journal of pure and applied physics* **50**
[13] Mürsel S and Abdullah E 2014 Calculation of halfvalue thickness for aluminum absorbers by means of fractional calculus *Annals of Nuclear Energy* **63** 46 50
[14] Turguy K Osman G Erol K and Witold B 2013 Xray Gamma and neutron radiation tests on Epoxyferrochromium slag composites by experiments and monte carlo simulations *International journal of polymer analysis and characterization* **18** 224 231
[15] Mahdi K Ahmed Z and Mkhaiber A 2012 Calculation and study of gamma ray attenuation coefficients for different composites *Ibn AlHaitham Journal for Pure and Applied science* **25**

Fabrication & Characterization of AIAS/pSi Heterojunction Solar Cell

Fabrication & Characterization of AIAS/pSi Heterojunction Solar Cell

Hanan K Hassun[1], Auday H Shaban, Ebtisam M T Salman

Department of physics College of Education For Pure Science Ibn AlHaitham University of Baghdad Baghdad Iraq

hanan.kadhem@yahoo.com

Abstract: Silver Indium Aluminum Selenium AgIn1xAlxSe2 AIAS for x=01 thin films was deposited by thermal evaporation at RT and different 1thickness 100 150 and 200 nm on the glass Substrate and p2Si wafer to produce AIAS/p3Si heterojunctionsolarcell4 Structural optical electrical and photovoltaicproperties6 are investigated for the samples XRD analysis reveals that all the deposited AIAS films show polycrystalline structure without any change due to increase of thickness Average diameter and roughness calculated from AFM images shows an increase in its value with increasing thickness The optical absorbance and transmittance for samples are measured using a spectrometer type UV Visible 1800 spectra1photometer to study the energy6gap The electricalproperties7of heterojunction were obtained by IV8 dark and illuminated9 and C10Vmeasurement The ideality1 factor and the saturation2current density were calculated Under illuminated3the open circuit voltage Voc4 short circuit current density Jsc6 fill factor 6FF and quantum efficiencies were calculated The builtin potential 7Vbi carrier concentration and depletion width are measured with different9 thickness

Keywords: nAIAS/pSi heterojunction thin films solar cell

1. Introduction

The ternary chalcopyrite compounds of the group I–III[1]–VI_2 direct gap semiconductors have been studied in recent years for solar cell applications due to their material properties as an absorbed layer for tandem solar cell light emitting diodes optoelectronics and nonlinear optical devices [1]$AgInSe_2$ was first prepared from the original binary compounds by Hahnet et al [2]$AgInSe_2$thin films have been produced by several techniques such as coevaporation[34] ultrahigh vacuum pulsed laser deposition [5] horizontal Bridgman method [6] molecular beam epitaxial[7] and solid state microwave irradiation[8]The growing and properties of AIGS thin films and devices fabricated with various film compositions are presented[9]The aim of this study was focused on the fabrication and characterization of AIAS /pSi heterojunction for solar cells with different thin film thickness utilizing thermal evaporation technique

2. Experimental

Polycrystalline AIAS material alloy was prepared by fusing the mixture of the appropriate quantities of the elements Ag In Al and Se of high purity 99999% in evacuating fused quartz ampoules The compound of $AgIn_{1x}Al_xSe_2$were sealed in a quartz ampoule at a base pressure of 10^3TorrThe ampoule's temperature was raised from room temperature to 1200 K for five hour with a rate of 5 K/min in an electrical furnace The sample was left to cool slowly in the electrical furnace

The films of different thicknesses 100 150 and 200±20 nm were determined by using optical interferometer method and deposited by the thermal evaporation technique at room temperature using the Edward coating unit model E 306 of $3x10^6$Torr using with molybdenum boat were prepared onto a glass slide substrate and single crystal pSi 111 The area of heterojunction solar cell was 1 cm Xray diffraction XRD was used in order to identify the structural of the deposited $AgIn_{1x}Al_xSe_2$ films The average crystallite size C_S of AIAS thin films was calculated by using Scherer's formula [10]

$$C_S = \frac{0.94\lambda}{B\cos\theta_B} \quad \text{.....(1)}$$

λ = X ray wavelength β = full width at half maximum of the main peak and θ = reflection angle

The surface morphology and roughness were studied by atomic[6] force microscope AFM. The optical absorption spectrum of the prepared$AgIn_{1x}Al_xSe_2$ thin film will be considered through UV–VIS spectrophotometer at 25°C The energy gap E_g and the absorption coefficient were determined by equations [11 12]

$$\alpha h\upsilon = D\ h\upsilon - E_g^{\ r} \quad (2)$$

$$\alpha = 2303\ A/t \quad (3)$$

Where α is the absorption coefficient D is a constant dependent on the properties of the bands hν is the photon energy eV Eg is the optical energy gap eVr is constant and may take values 2 31/2 3/2 reliant on the material and the type of the optical transition A is the absorbance and t is the film thickness

Hall Effect measurements have been managed by Vander Pauw Ecopia HMS 3000 to determining majority carrier concentrations type of carrier and their mobility in thin films

IV characteristics of Al AIAS /pSi heterostructures in dark and under light were measured The Current – Voltage characteristics in illumination and dark is description by the equation respectively [13]

$$I = I_S\left(\exp\left(\frac{qV}{\beta K_B T}\right) - 1\right) - I_L \quad \text{.....(4)}$$

The ideality factor can calculated from equation

$$\beta = \frac{q}{K_B T}\frac{dV}{d(\ln I)} \quad \text{.....(5)}$$

Where I_s Saturation current I_L Illumination current I The total current Solar cell current V applied voltage positive forward bias and negative for reverse bias T Temperature in Kelvin K_B Boltzmann constant q electron charge β is the ideality factor related to the many physical properties of the heterojunction having a value between 1 and 2

The photovoltaic conversion efficiency and Fill Factor is given by [13]

$$\eta = \frac{P_m}{P_{in}} x100\% = \frac{I_m V_m}{P_{in}} x100\% \quad \text{.....(6)}$$

$$F.F = \frac{J_m V_m}{J_{sc} V_{oc}} \quad (7)$$

The capacitance–voltage C–V distinguishing for nAIAS/pSi heterojunction was obtained through LCZ meter at frequency = 10 MHz. The capacitance voltage measurements led to calculate different factors for example builtin potential junction capacitance charge carrier concentration and depletion region thickness from[14]

$$C = \left[\frac{q\,\varepsilon_n\,\varepsilon_p\,N_n\,N_p}{2\left(\varepsilon_n\,N_n + \varepsilon_p\,N_p\right)} \right]^{1/2} \left(V_{bi} - V\right)^{-1/2} \quad \text{.....(8)}$$

N_n and N_ρ are the donor concentrations in nAgInAlSe$_2$and the acceptor concentrations in pSiε_n and ε_p are the dielectric constants of nAgInAlSe$_2$ and pSi respectively V_{bi}^{i} is the built1 in potential and V is the applied voltage

$$W = \frac{\varepsilon_S}{C_0} \quad \text{.....(9)}$$

$$\varepsilon_S = \frac{\varepsilon_n \varepsilon_p}{\varepsilon_n + \varepsilon_p} \quad \text{.....(10)}$$

Where *W* is the width of the depletion region C_o is the capacitance at zero biasing voltage and ε_s is the dielectric constant of heterojunction

3. Results and discussion

'Figure 1'shows the XRD spectrum of different thickness 100 150 and 200 ±20 nm of AIAS thin films deposited on glass The patterns show that all the films have three main crystalline peaks the first peak located at 2θ ≈*2518*^{o}with the 112preferred orientation while the second peak appeared at 2θ ≈335^o with the 211 and the third peak appeared at 2θ ≈427^o with the 204 Table 1 show all the peaks observed in all films By increasing the film thickness the locations of the measured diffraction peaks do not change significantly but the intensities of the peaks increases This is due to the improvement of crystalline of the films being and crystallite size become larger from 1723 to 591 nm when increased the film thickness [15]

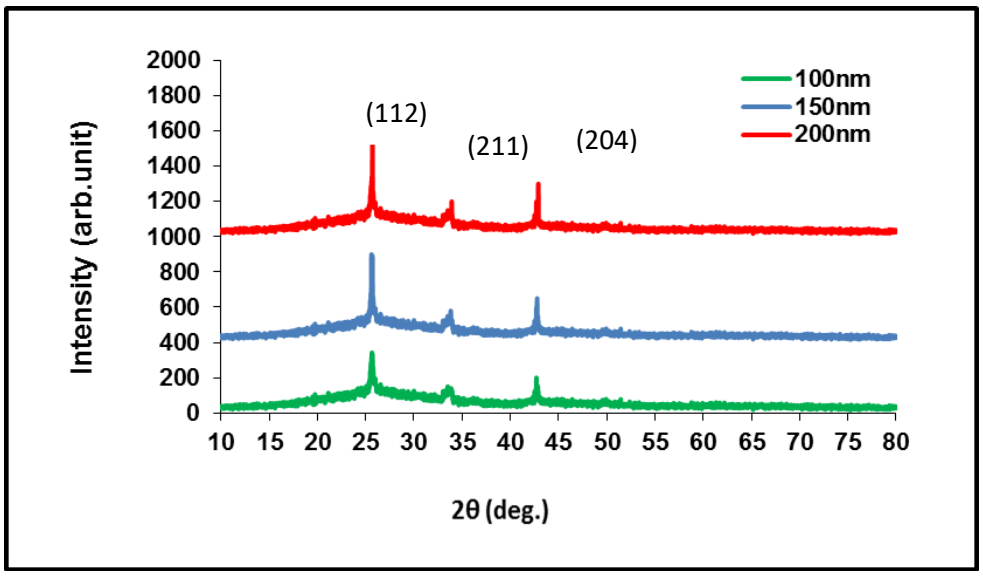

Figure 1. XRD patterns for AIAS thin films deposited on glass with different thicknesses 100,150 and 200 nm

Table 1. Structural parameters of AIAS thin films at different thicknesses

Thicknessnm	2θDeg	dhklExpÅ	hkl	βDeg	CSnm
100	2518	3532	112	04933	1723
	335	267	211		
	427	2115	204		
150	256	3475	112	0253	336
	3382	2647	211		
	4278	2111	204		
200	257	3462	112	0144	591
	3392	2639	211		
	429	2105	204		

'Figure 2' shows the AFM images of three dimensional 3D surface morphology of AIAS thin films with different thickness The surface roughness values and the grain size were measured and illustrated in table 2This is also supported by the Xray diffraction data The average diameter of AIAS thin films with respect to thickness seems to be larger in Figure 2 c than Figure 2 a 2b

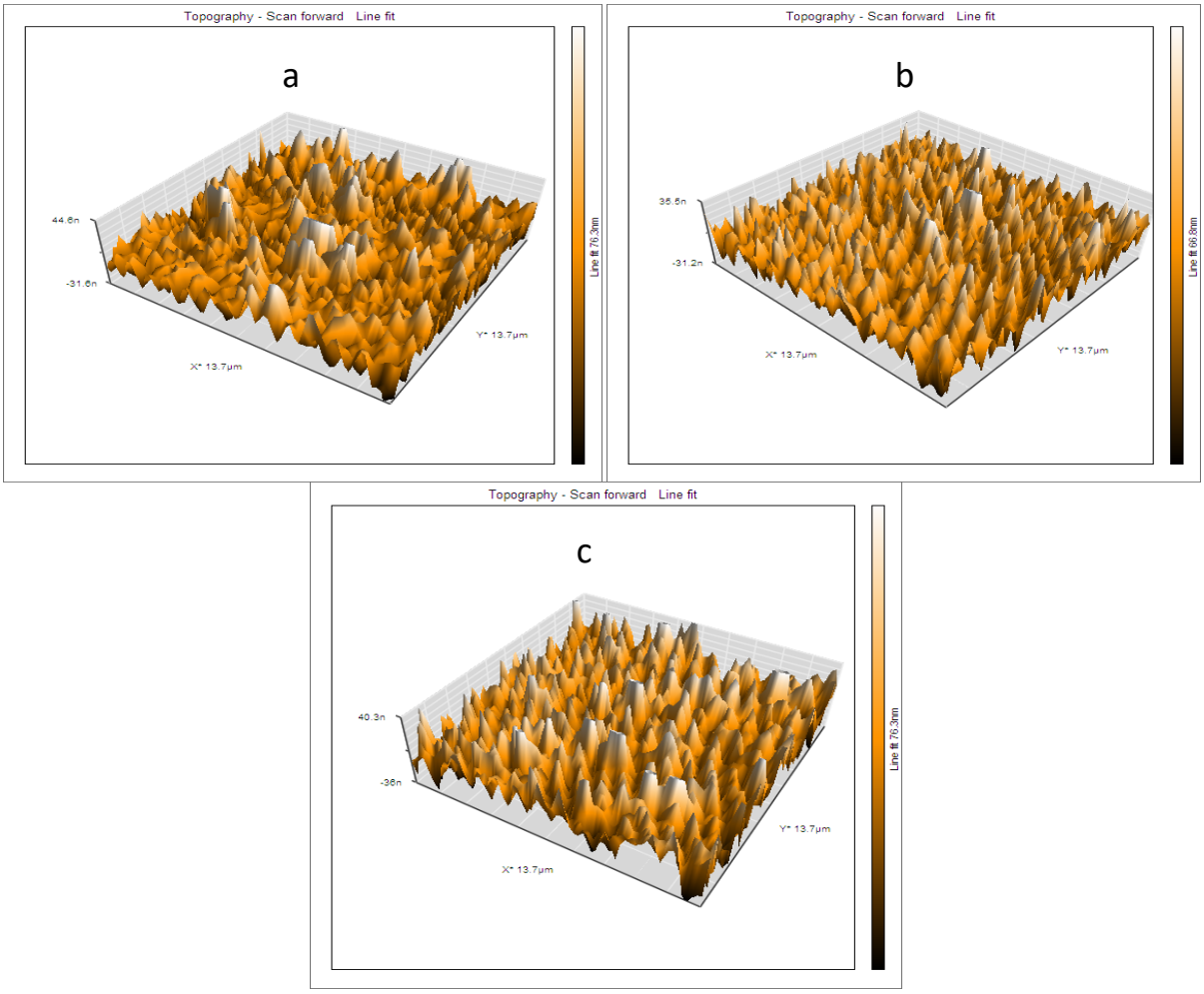

Figure 2. 3D AFM images of AIAS with thicknesses a 100 nm b 150 nm and c 200 nm

Table 2 The average grain size GS and roughness for AIAS thin films at different thickness

Thicknessnm	Grain size GSnm	Roughness average nm	rmsnm
100	992	1278	1695
150	128	1424	1943
200	152	3843	6590

In order to probe the energy transitions within AIAS films the optical properties measurements were studied The Absorbance and Transmittance spectrum of AIAS thin films was calculated as a function of wavelength at different thickness in figure 3The Absorbance spectrum for AIAS thin film increase with the increase of thickness The Absorbance values were between 40% and 85% These results agree with other researchers [15]

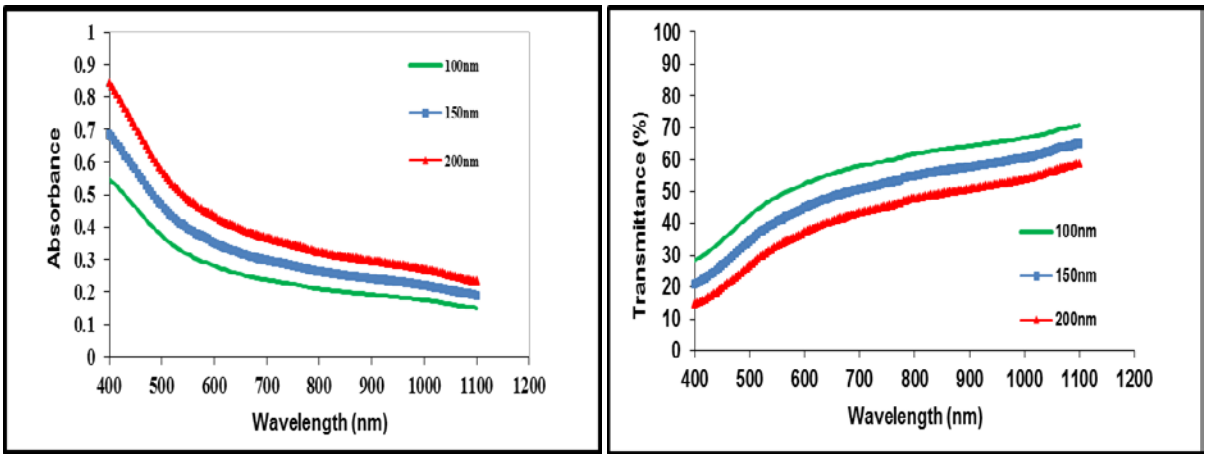

Figure 3. The Absorbance and Transmittance spectrum of AIAS with different thickness 100 nm 150 nm and 200 nm

The behavior of the transmittance spectra is opposite totally to that of the absorbance spectra From Figure 4 we can observe that the α values which has been calculated using equation 3 indeed own high amount reached above 10^5 cm^1 It was pointed that the α values in general increases as a function of different thickness which is attributed to an increase in absorbance of used films we found that the value of α increases from 0612 $\times 10^5 cm^{18}$with the increase of thickness The value of E_g^{opt} decreases from 198 to 172 to 155 eV with increase of thickness as shown in figure 4 The decrease in the band gap Eg^{opt} values may be describable of the increase in defect states near the bands this result is in agreement with reference [4]

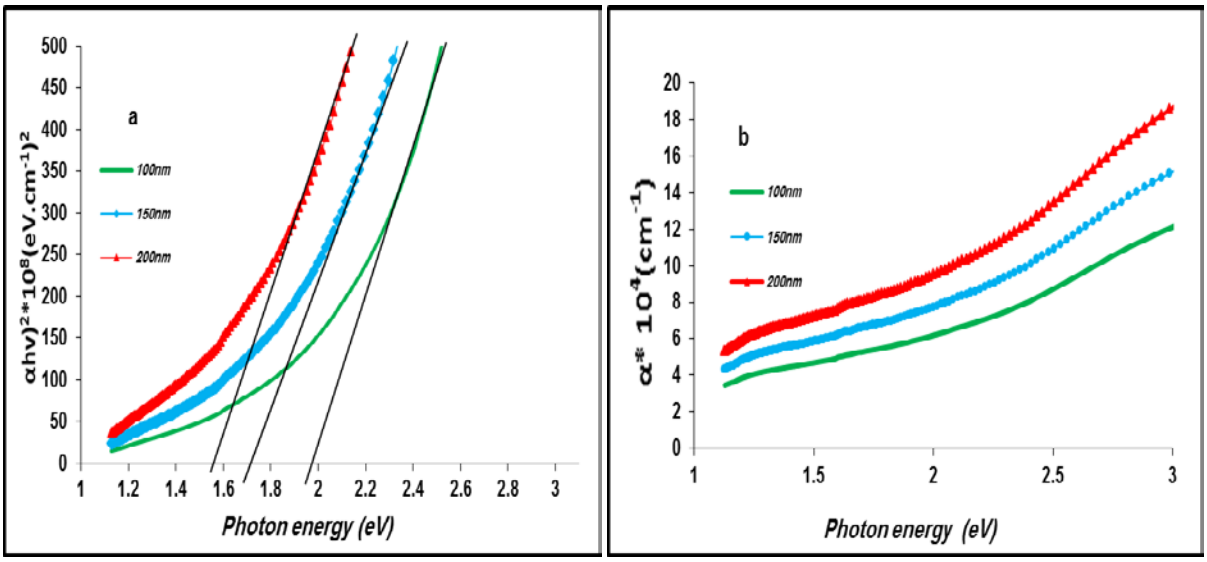

Figure 4. a Variation $\alpha h\upsilon^2$ verse photon energy **b** absorption coefficient verse photon energy of AIAS with different thickness 100 nm 150 nm and 200 nm

The type of charge carriers concentration n and Hall mobility μ_H has been estimated from Hall measurements These values are listed in table 3 The negative sign of the Hall coefficient indicates that the conductive nature of the film is ntypeie Electrons are the majority charge carriers ie Hall voltage decreasing with the increasing of the current The carrier concentration of the order $10^{16}cm^3$ is in a good agreement with reference [16] We can notice from table 3 that the carrier concentration and mobility increases with increasing of thickness

Table 3 Hall parameters for AIAS thin films at different thickness

Thicknessnm	R_H	$\mu_H cm^2/VS$	n cm^3	ρΩcm
100	8928571	7440476	7E+16	12
150	753012	125502	83E+16	6
200	6416838	1604209	974E+16	4

'Figure 5' illustrated IV curve of manufactured AIAS/Si heterojunction solar cells with different thickness100 150 and 200 ±20 nm at RTUsing equations 6 7 was the conversion efficiency and Fill Factor calculation as show in finger 5 and table 4the photo current produced by the 100 mW/cm^2 white lamp the results obtained where there is a clear increase in the value of the open circuit voltage V_{oc} and the value of short circuit current density J_{sc} maximum for both the current and the voltage value V_mJ_m and the value of efficiency solar cell in terms of efficiency increases in general with increasing thickness and this goes back as we have already improved the increase the surface roughness the absorption coefficient and charge carriers this result agrees with [17]

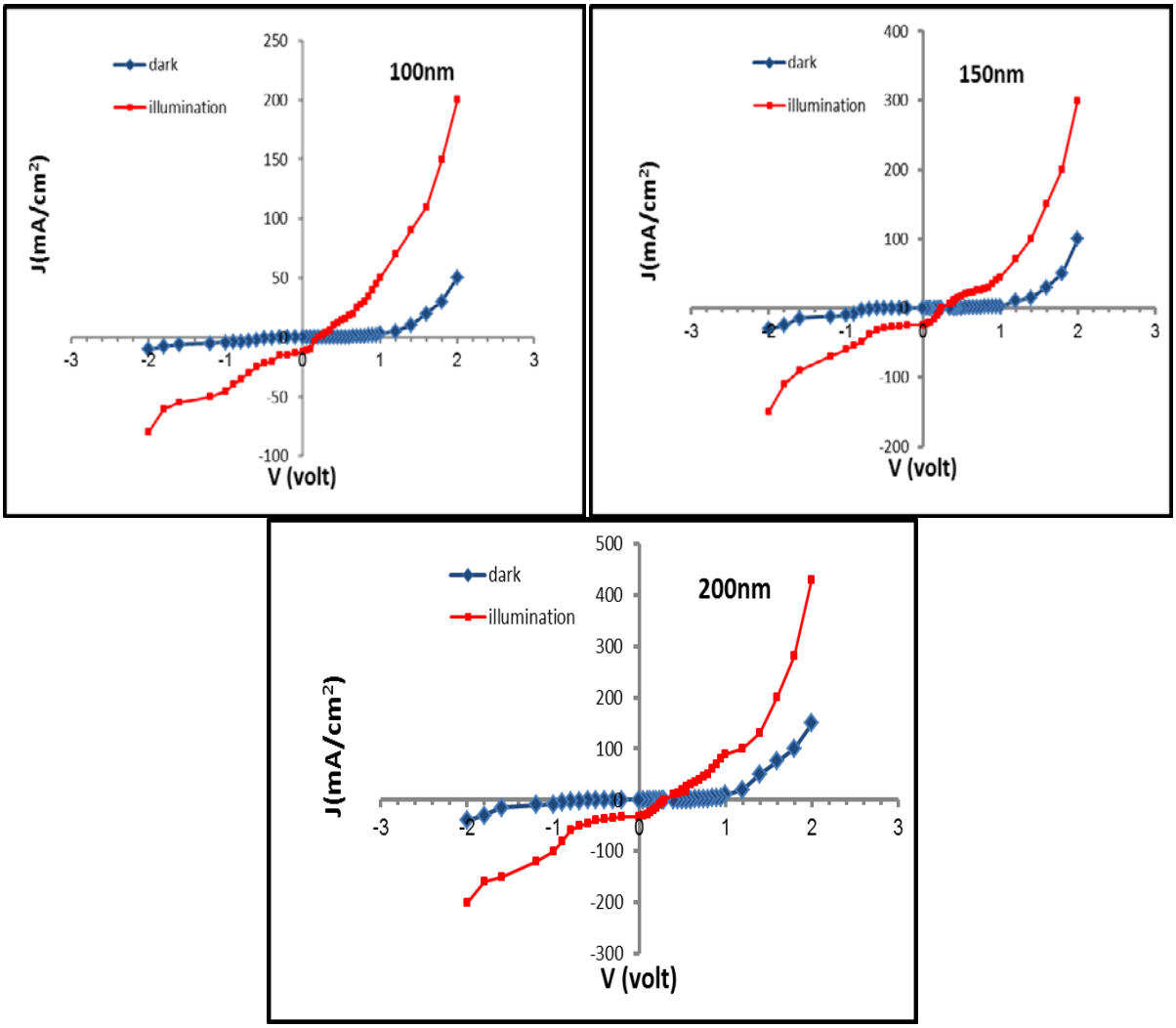

Figure 5. IV plots for AIAS/Si solar cell at thickness 100 150 200 nm in dark and under light

Table 4. The parameter for AIAS/Si heterojunction with respect to thicknesses

Thickness nm	V_{oc} Volt	J_{sc} mA/cm^2	V_{max} Volt	J_{max} mA/cm^2	FF	η %
100	02	12	01	10	0416667	1
150	024	25	015	17	0425	255
200	029	32	017	20	0366379	34

The ideality factor Φb and J_S of the $AgInAlSe_2$/Si heterojunction solar cell are gained from the grade of the straight line region forward bias in IV plots under dark by using equation 5 as show in figure 6 and Table 5the behavior of the current are change exponentially with voltage at V < 02 VThe decrease of ideality factor and Φb with the increasing of thickness while J_S increase This result agrees with [18]

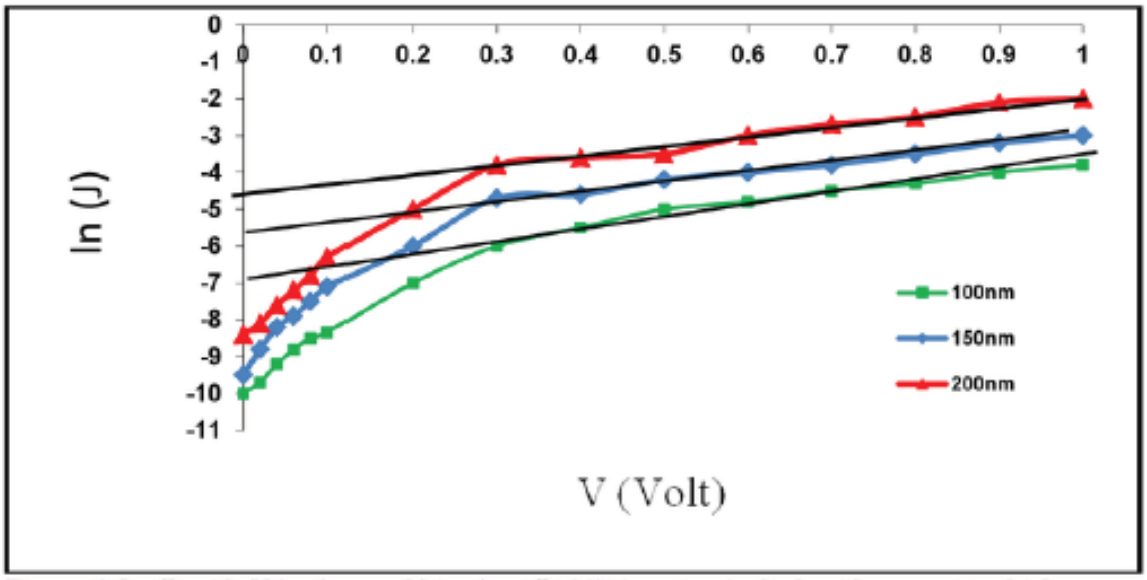

Figure 6 ln J with *V* for forward bias for AIAS/Si junction in dark with respect to thicknesses

Table 5. Ideality Factor and $J_S$for AIAS /Si junction at different thicknesses

Thickness*nm	Ideality Factor	Saturation Current DensityJ_SmA/cm^2	Barrier*HeightΦbeV
100	2193752	0000911882	060075
150	18263971	0003345965	056708
200	1668541	0008229747	054377

The capacitance voltage measurements led to calculate built in potential junction capacitance carrier concentration and depletion width Figure 7 illustrated 1/C^{2}V relation with respect to thickness amount For all samples it can be seen that junction capacitance is decrease with increasing bias voltage which can be explained by the expansion of depletion layer with the built in potential

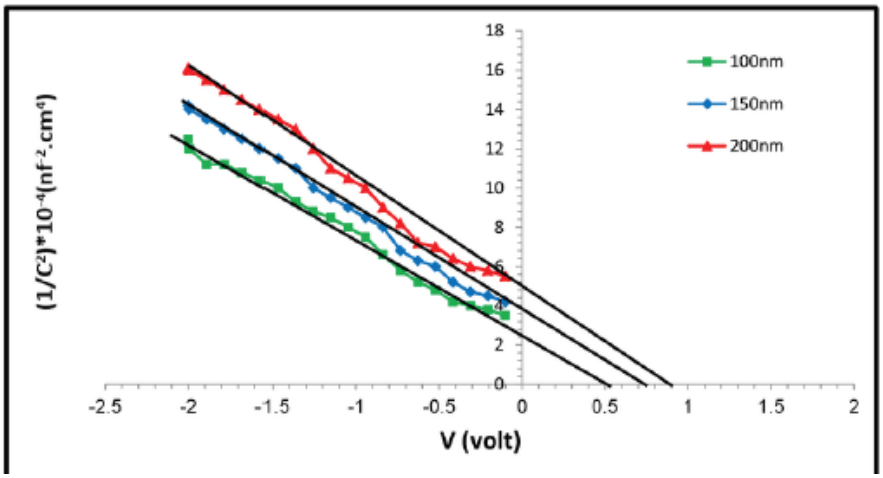

Figure 7. 1/C^2 as a function of reverse bias voltage for AIAS/Si heterojunction

'Figure7 'illustrated CV behavior of AIAS/Si solar cell Table 6 illustrated the relation between C_o and thickness which is reversely relative This behavior was attributed to the increase in W which tends to the improve V_{bii} The increasing of W due to increases in thickness because of the increasing in N_D which leads to a decrease of the capacitance The CV measurements show that the heterojunction of abrupt type because the relationship between inverted square amplitude $1/C^2$ with a voltage voltage of reverse bias is lined

Table 6. Variables of AIAS /Si heterojunction with different thickness

Thicknessnm	$C_o$nf/cm^2	W=ε_s/C_0 nm	V_{bi}Volt	N_D cm^3
100	6454972244	669	05	523001E+15
150	50	783	075	633278E+15
200	4472135955	876	09	77731E+15

4. Conclusions

After characterizing and analyzing the performance of the samples the conclusions are summarized as follows

The AIAS thin films were successfully deposited on glass and silicon substrates by thermal evaporation technique The XRD analysis shows that all the deposited films were polycrystalline and the crystallite size was highly oriented in 112 direction AIAS films exhibits a high value of absorption coefficient in the visible range of the electromagnetic spectrum the optical transitions in AIAS are direct and value of optical energy gap decreases with increasing of thickness *IV* measurements analyzed minutely for rectifying and photovoltaic behaviors For AIAS/Si heterojunction solar cell the ideality factor and J_S are obtained with respect to different thickness The diode exhibits an ideal behavior when the ideality factors become less than 2 The measurements were carried out under illuminate by incident power density equal to about 100 mW/cm^2 The forward relativity between quantum and thickness will get the maximum values of efficiency 34 when the thickness t = 200nm while CV curves showed that the abrupt type for prepared devices

References

[1] M Kaleli T Colakoglu M Parlak 2013 Production and characterization of layer by layer sputtered singlephase AgInSe2thin film by thermal selenization Applied Surface Science **286** 171 176

[2] H Hahn G Frank W Klingler AD Meyer G 1952 StöergerTernareChalkogenideZeitschrift fur AnorganischeChemie 271 153 170

[3] MC Santhosh Kumar and B Pradeep 2009 Effect of H^+ irradiation on the optical properties of vacuum evaporated $AgInSe_2$*thin films Appl Surf Sci***255** 8324 8327

[4] JJ Lee JD Lee BY Ahn HS Kim KH Kim 2007 Structural and Optical Properties of AgInSe2 Films Prepared on Indium Tin Oxide Substrates *J KorPhysSoc***50** 1099 1103

[5] H Mustafa D Hunter AK Pradhan UN Roy Y Cui A Burger Synthesis and characterization of $AgInSe_2$ for application in thin film solar cells *Thin Solid Films***515** 7001 7004

[6] IV Bodnar 2004 Properties of $AgGa_xIn_{1-x}Se_2$ Solid Solutions Inorg Mater 40 914918

[7] K Yamada N Hoshino T Nakada 2006 Crystallographic and electrical properties of wide gap Ag In_{1-x}Gax Se_2*thin films and solar cells SciTechnolAdv Mater***7** 4245

[8] JW Lekse AM Pischera JA Aitken 2007 Understanding solidstate microwave synthesis using the diamondlike semiconductor AgInSe2 as a case study Mater Res Bull **42** 395403

[9] Keiichirou Yamada Nobuyuki Hoshino TokioNakada 2006 Crystallographic and electrical properties of wide gap Ag $In_{1-x}Ga_x$ Se2 *thin films and solar cells Science and Technology of Advanced Materials***7** 42 45

[10] BD Cullity 1978 Elements of XRay diffraction 2nd edition copyright © by Addison Wesley

Publishing company *Inc*
[11] RutuparnaMohanty 2012 Electronic Properties of Ternary and Binary Compounds Thesis Submitted for the Award of the Degree of Master of Science Department of Physics National Institute of Technology
[12] MA Omer 1975 Elementary Solid State *Physics AddisoWe sly Publishing*
[13] D A Neamen 2003 Semiconductors physics and Devices Basic Principles Third edition copyright© McGraw Hill Companies *Inc*
[14] S M Sze 2007Physics of semiconductors Devices Third edition copyright© by John Wiley & Sons *Inc*
[15] S Murugana and KR Muralib 2014 Structural Optical and Electrical Studies on Pulse Plated $AgInSe_2$*Films ACTA PHYSICA POLONICA A***126** 3 727731
[16] Kenji Yoshino Aya Kinoshita Yasuhiro Shirahata Minoru Oshima Keita Nomoto Tsuyoshi YoshitakeShunji Ozaki Tetsuo Ikari 2008 Structural and electrical characterization of $AgInSe_2$ crystals grown by hotpress method *Journal of Physics Conference Series***14**
[17] Raviendra D JK1985 Sharma nCdS p$AgInSe_2$ solar cells by electro deposition physics status solidi a*Application and materials science***88** 1 365368
[18] S Mridha M Dutta Durga 2009Basak Photo response of nZnOpSiheterojunction towards ultraviolet visible lights thickness dependent behavior*J Mater Sci Mater Electron***20** 376

Design of Magnetic Charged Particle Lens Using Analytical Potential Formula

Design of Magnetic Charged Particle Lens Using Analytical Potential Formula

A H Al-Batat [1], M J Yaseen [1], S R Abbas [1], M S Al-Amshani [1] and **H S Hasan [2]**

[1]Department of Physics, College of Education, Mustansiriyah University, P.O.Box:46219, Baghdad, Iraq.

[2]Department of Physiology and Medical Physics, College of Medicine, Al-Nahrain University, P.O. Box: 70044, Kadhimiya, Baghdad, Iraq.

Abstract: In the current research was to benefit from the potential of the two cylindrical electric lenses to be used in the product a mathematical model from which, one can determine the magnetic field distribution of the charged particle objective lens. With aid of simulink in matlab environment, some simulink models have been building to determine the distribution of the target function and their related axial functions along the optical axis of the charged particle lens. The present study showed that the physical parameters (i.e., the maximum value, B_{max}, and the half width W of the field distribution) and the objective properties of the charged particle lens have been affected by varying the main geometrical parameter of the lens named the bore radius R.

Keywords: Electron Microscopy, Electron and Ion optics, Objective Magnetic Lenses, Aberration.

1. Introduction

The ultimate goal of high-performance electron microscopy is the acquisition of detailed information on the atomic structure, the chemical composition and the local electronic states of real objects [1]. Any axially symmetric magnetic field produced by current-carrying coils with or without ferromagnetic materials or by permanent magnets is known as a charged particle lens (magnetic lens) [2]. An axially symmetric electric or magnetic field can be used to focus a beam of electrons much as a light lens focuses visible rays. Electric or magnetic field that are axially symmetry, or a combination of the two, acts in a similar manner on the trajectories of electrons traveling through the field. Electrons that enter the field along paths close to the axis and nearly parallel to the axis experience a radial force which is proportional to the distance of electrons from the axis. The electron trajectories therefore, are deflected in proportional to their distance from axis, and the axially symmetric field acts as a lens. Figure1 illustrates an electric electron lens and a magnetic electron lens, respectively [3].

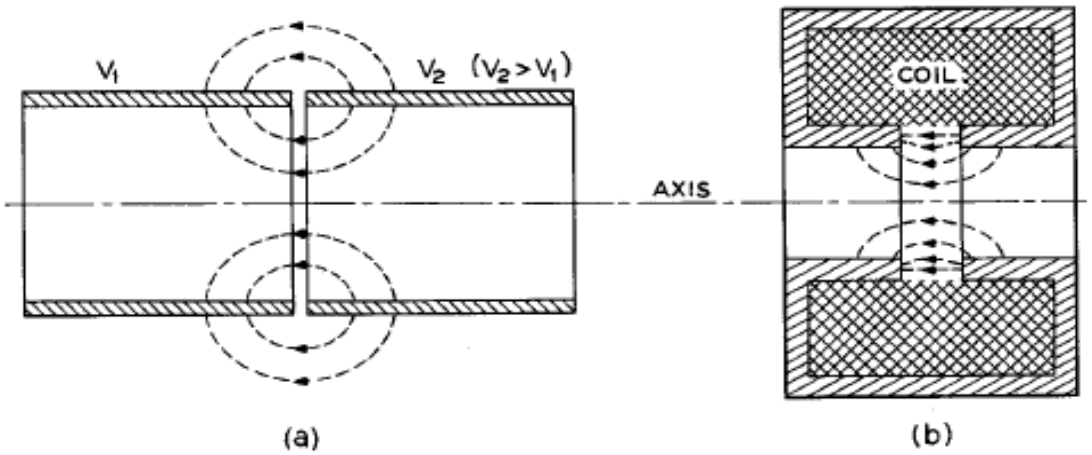

Figure 1. Type of lens: (a) an electric electron lens and, (b) a magnetic electron lens [3].

The vast majority of focusing elements used in electron and ion optics consists of axially symmetric electrostatic and/or magnetic fields that can represented by scalar potential functions [2]. Generally, electric and magnetic scalar potential distributions in electron optical devices are determined numerically with aid of some specific numerical methods such as the finite element method (FEM) or the finite difference method (FDM); see [4]. However, those may determine using some analytical target axial functions, see [5-6]. Hence, in the present article the latter procedure has been followed, where the axial magnetic scalar potential distribution of the magnetic lens has been evaluated using a convenience suggested target function in the domain of the optical axis of the lens under consideration.

2. Mathematical Remediation

The potential at distance r from the axis of an axially symmetric potential distribution is given in terms of the potential along the axis by [7],

$$V(r,z) = V(0,z) - \frac{r^2}{4}V''(0,z) + \frac{r^4}{64}V''''(0,z) - ..... \quad (1)$$

where V(0,z)=V(z) is the potential along the axis, and the primes indicate differentiation with respect to z [1]. By means of equation (1) the potential at all points in an axially symmetric potential region can be described in terms of the potential on the axis. For regions close to the axis we can neglect all higher order terms and take only the first two terms of this expression, so that the potential distribution in the meridional plane (r, z), can be determined as follows.

$$V(r,z) = V(0,z) - \frac{r^2}{4}V''(0,z) \quad (2)$$

However, in the present work the following target function has been used to determine the axial magnetic scalar potential distribution V(z) of the magnetic lens,

$$V(z) = \frac{1}{2}\left[(V_1 + V_2) + (V_2 - V_1)\tanh\left(\frac{1.32z}{R}\right)\right] \quad (3)$$

where V_1 and V_2 represents the potential values at terminals of the lens, i.e., $V_1=V_s$ and $V_2=V_f$, and R represents the pole piece radius. By using the equation [**B**=-μ_o**grad**V] the axial component of the magnetic field can be determined as follows,

$$B_z(z) = -\mu_o \frac{dV(z)}{dz} \tag{4}$$

where μ_o is the magnetic permeability in vacuum (4π x10^{-7} Hm^{-1}). Hence, by differentiating equation (3) by means of equation (4), one can get the axial magnetic field distribution component given by,

$$B_z(z) = \mu_o\left(\frac{V_2 - V_1}{2}\right)\left(\frac{1.32}{R}\right)sech^2\left(\frac{1.32z}{R}\right) \tag{5}$$

it is easy then to use equation (5) to assigning the imaging magnetic field distribution $B_z(z)$ along the optical axis $z_s \leq z \leq z_f$. Once the magnetic field is determined, the next step is to calculate the electron beam trajectory r(z) and its correspondence departure r'(z) along the axis of the lens. Typically, this task can be achieved by solving the paraxial ray equation given by the following ordinary second order differential equation [8],

$$r'' + \frac{\eta}{8V_r} B_z^2(z) r = 0 \tag{6}$$

where η is the mass m to the charge e ratio of the electron, and V_r is defined as the corrected relativistically accelerating voltage which is given by [9],

$$V_r = V_a\left(1 + \frac{eV_a}{2mc^2}\right) = V_a\left(1 + 0.978x10^{-6}V_a\right) \tag{7}$$

where V_a is the applied accelerating voltage. It is well known that the distinctive feature of magnetic lenses is that their optical properties are dependent on the charge to mass ratio of the particles [2]. To obtain the electron beam trajectory inside the electron optical device (the magnetic lens in the present work) the paraxial ray equation (6) can be solved analytically or numerically according to the constraints imposed in the study. However, the forth-order Runge-Kutta method has been used to solve the trajectory equation numerically in terms of the field distribution under zero magnification mode. A ''weak'' lens is one for which the focal length is long compared with the region of field. Suppose that an electron approaches such a lens along a path that is initially parallel to the axis but displaced a small distance from it. Equation (6) can be integration along the axis between points on either side of the lens where the field is zero, we obtain [3],

$$r'_f = -\frac{\eta}{8V_r}\int_{z_s}^{z_f} B_z^2(z) r dz \tag{8}$$

where z_s and z_f are points on the axis on opposite sides of the lens and beyond the region of field, and r'_f is the slope of the trajectory at $z=z_f$. If the focal length is long compared with the region of field, r will remain nearly constant in the region of field and can be taken outside the integral in equation (8). The focal length f_o for such a lens is then given by [3],

$$\frac{1}{f_o} = -\frac{r'_f}{r} = \frac{\eta}{8V_r}\int_{z_s}^{z_f} B_z^2(z) dz \tag{9}$$

The axial magnetic flux density would be proportional to the gradient of this is given by equation (5), then substituting this equation in equation (9), we obtain for the reciprocal of the focal length,

$$\frac{1}{f_o}=\frac{\eta\mu_o^2}{8V_r}\left(\frac{V_2-V_1}{2}\right)^2\left(\frac{1.32}{R}\right)^2\int_{z_s}^{z_f}sech^4\left(\frac{1.32z}{R}\right)dz \tag{10}$$

using the relations [$sech^2z=1-tanh^2z$] and [$sech^2zdz=d(\tanh z)$], we obtain,

$$\frac{1}{f_o}=\frac{\eta\mu_o^2}{8V_r}\left(\frac{V_2-V_1}{2}\right)^2\left(\frac{1.32}{R}\right)^2\left(\frac{R}{1.32}\right)\left[tanh\left(\frac{1.32z}{R}\right)-\frac{tanh^3}{3}\left(\frac{1.32z}{R}\right)\right]_{z_s}^{z_f} \tag{11}$$

$$\frac{1}{f_o}=\frac{\eta\mu_o^2}{8V_r}\left(\frac{V_2-V_1}{2}\right)^2\left(\frac{1.32}{R}\right)^2\left(\frac{R}{1.32}\right)\left(\frac{4}{3}\right)\approx\frac{\eta R\mu_o^2}{8V_r}\left(\frac{V_2-V_1}{2}\right)^2\left(\frac{1.32}{R}\right)^2 \tag{12}$$

where the points z_s and z_f have been taken to be effectively at ($-\infty$ and $+\infty$), respectively. The focal length f_o is therefore given by,

$$f_o=\frac{8V_r}{\eta R\mu_o^2\left(\frac{V_2-V_1}{2}\right)^2\left(\frac{1.32}{R}\right)^2} \tag{13}$$

If an electron trajectory after emerging on one side of a lens lies in a plane containing the axis, the trajectory after emerging from the lens will also lie in a plane containing the axis. However, the second plane is rotated about the axis from the first plane. The angle of rotation between the planes is given by [3],

$$\theta=\frac{\eta}{2}\int_{t_1}^{t_2}B_z\,dt=\frac{\eta}{2}\int_{z_s}^{z_f}B_z\frac{dz}{dz/dt}=\sqrt{\frac{\eta}{8V_r}}\int_{z_s}^{z_f}B_z(z)dz \tag{14}$$

where t_1 and t_2 are, respectively, the times at which the z coordinate of the electron is z_s and z_f, and where it is assumed that ż (dz/dt) is very nearly constant through the lens and is equal to $(2\eta V_r)^{1/2}$. If $B_z(z)$ is in the direction of travel of the electron, Θ is positive, then by substituting equation (5) in equation (14), we obtain the angle of rotation of electron along the terminals $z=z_s$ to $z=z_s$ as follows,

$$\theta=-\mu_o\sqrt{\frac{\eta}{8V_r}}\left(\frac{V_2-V_1}{2}\right)\left(\frac{1.32}{R}\right)\int_{z_s}^{z_f}\sec h^2\left(\frac{1.32z}{R}\right)dz$$

$$\theta=-\mu_o\sqrt{\frac{\eta}{8V_r}}\left(\frac{V_2-V_1}{2}\right)\left(\frac{1.32}{R}\right)\left(\frac{R}{1.32}\right)tanh\left(\frac{1.32z}{R}\right)$$

$$\theta=-\mu_o\left(\frac{V_2-V_1}{2}\right)\sqrt{\frac{\eta}{8V_r}}tanh\left(\frac{1.32z}{R}\right) \tag{15}$$

The final task of the synthesis approach is finding the profile of the electrode or pole piece of the electron optical device, however, equation (2) may be used to obtain the shape of the pole piece that produce the field distribution as follows [10-11],

$$R_P(z)=2\sqrt{\frac{V(z)-V_P}{V''(z)}} \tag{16}$$

where R_p is the radial height of the pole piece, V_P is the potential value at the pole piece surface, which is equivalent to half of the lens excitation NI in the case of symmetrical charged particle lens, and $V''(z)$ is the second derivative of the magnetic scalar potential V(z) which can be obtained from equation (3) as follows with aid of Simpson rule numerical method.

$$V''(z) = -(V_2 - V_1)\left(\frac{1.32}{R}\right)^2 \tanh\left(\frac{1.32z}{R}\right)\sec h^2\left(\frac{1.32z}{R}\right) \tag{17}$$

The spherical and chromatic aberration coefficients C_s and C_c of any axially symmetric magnetic lenses can be calculated using the following integral [8],

$$C_s = \frac{\eta}{128V_r}\int_{z_o}^{z_i}\left[\left(\frac{3e}{mV_r}\right) + B_z^4(z)r_\alpha^4(z) + 8B_z'^2(z)r_\alpha^4 - 8B_z^2(z)r_\alpha^2 r_\alpha'(z)\right]dz \tag{18}$$

$$C_c = \frac{\eta}{8V_r}\int_{z_o}^{z_i} B_z^2(z)\, r_\alpha^2(z)\, dz \tag{19}$$

where $r_\alpha(z)$ is the solution of the paraxial ray equation, and primes indicate differentiation with respect to the axial coordinate z.

3. Magnetic Lens Simulation

The Simulink is a companion application to Matlab, it deals with the engineering and scientific problems in terms of complete models. The Simulink can be considered as a powerful tool to solve different problems in terms of various blocks. Simulink in Matlab include comprehensive libraries. However, each library contains different specific blocks. Each block may be correspondent to a mathematical operation, such as: the addition, subtraction, multiplication, division, or matrices operations. Also, there are some blocks represents constants, signals, integrator, derivatives, gains, and waves. The input and output of each model can be obtained by specific blocks, such as: 'From workspace', 'To workspace', 'Scope' block, and 'XY Graph' block. The Simulink produces powerful complete models in the image processing, signal processing, communications, etc. Where, there are specific blocks determining the conversion, transformation, filtering, etc. All special mathematical functions, such as: trigonometric functions, inverse trigonometric functions, hyperbolic, inverse hyperbolic, exponential, logarithmic functions can be determined with aid of special blocks. Linear and nonlinear mathematical functions as well as polynomials also can be calculated with aid of Simulink. All logic and bit operations can be executed by special blocks, for more details see [12].

In this paper we used the direct Simulink method to simulate and determine the related axial functions of the magnetic lens under consideration in terms of different Simulink models. Figure 2 shows a Simulink model aiming to create the distributions of the axial potential and axial magnetic field which is buildup on the target axial magnetic potential function and the magnetic field distribution given in equations (3) and (5) respectively.

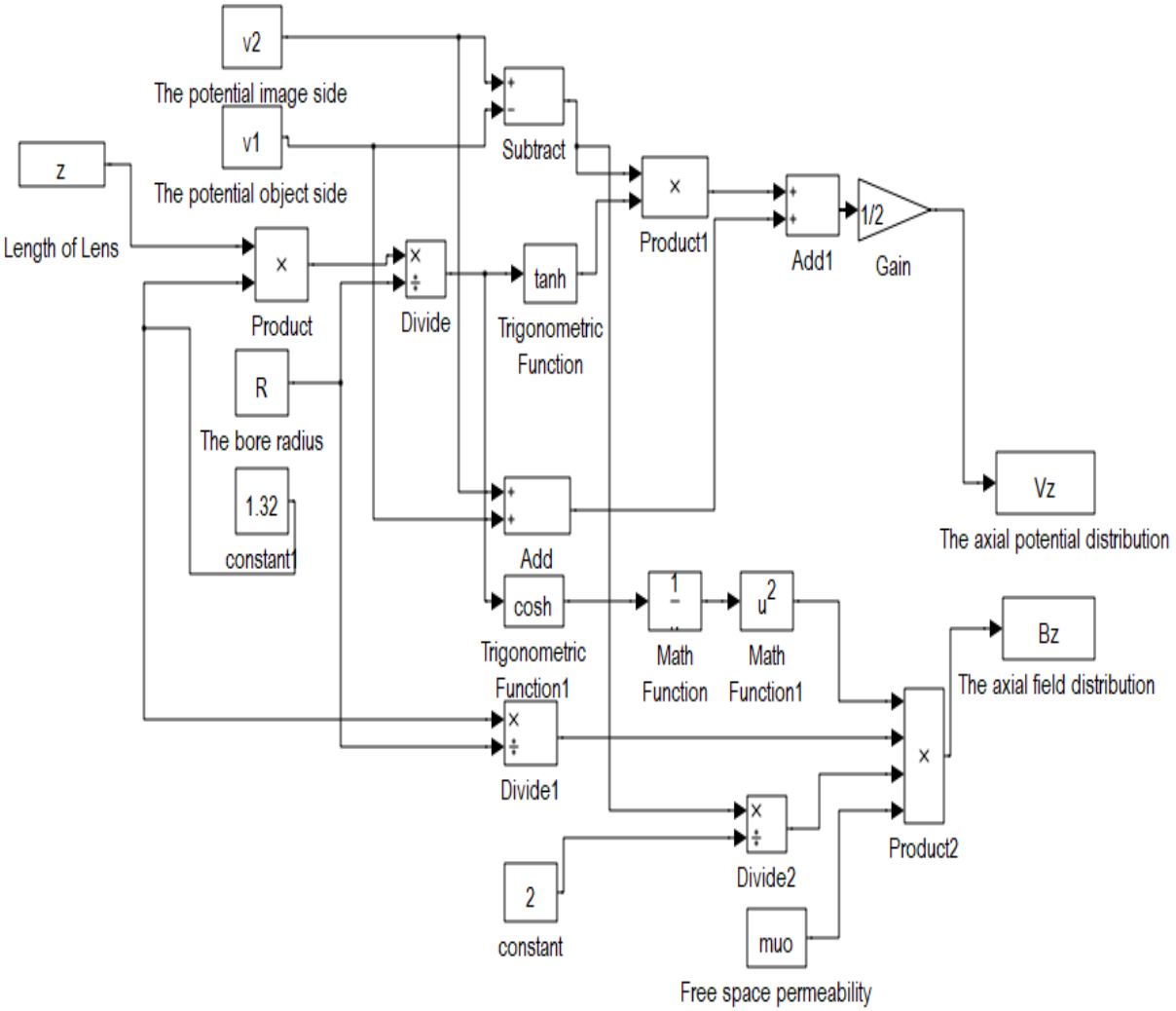

Figure 2. Simulink model for the axial magnetic scalar potential and axial field distributions.

With aid of equations (16) and (17), figure3 shows the Simulink model aiming in creation the shape of the pole piece and the distribution of the second derivative of the axial potential.

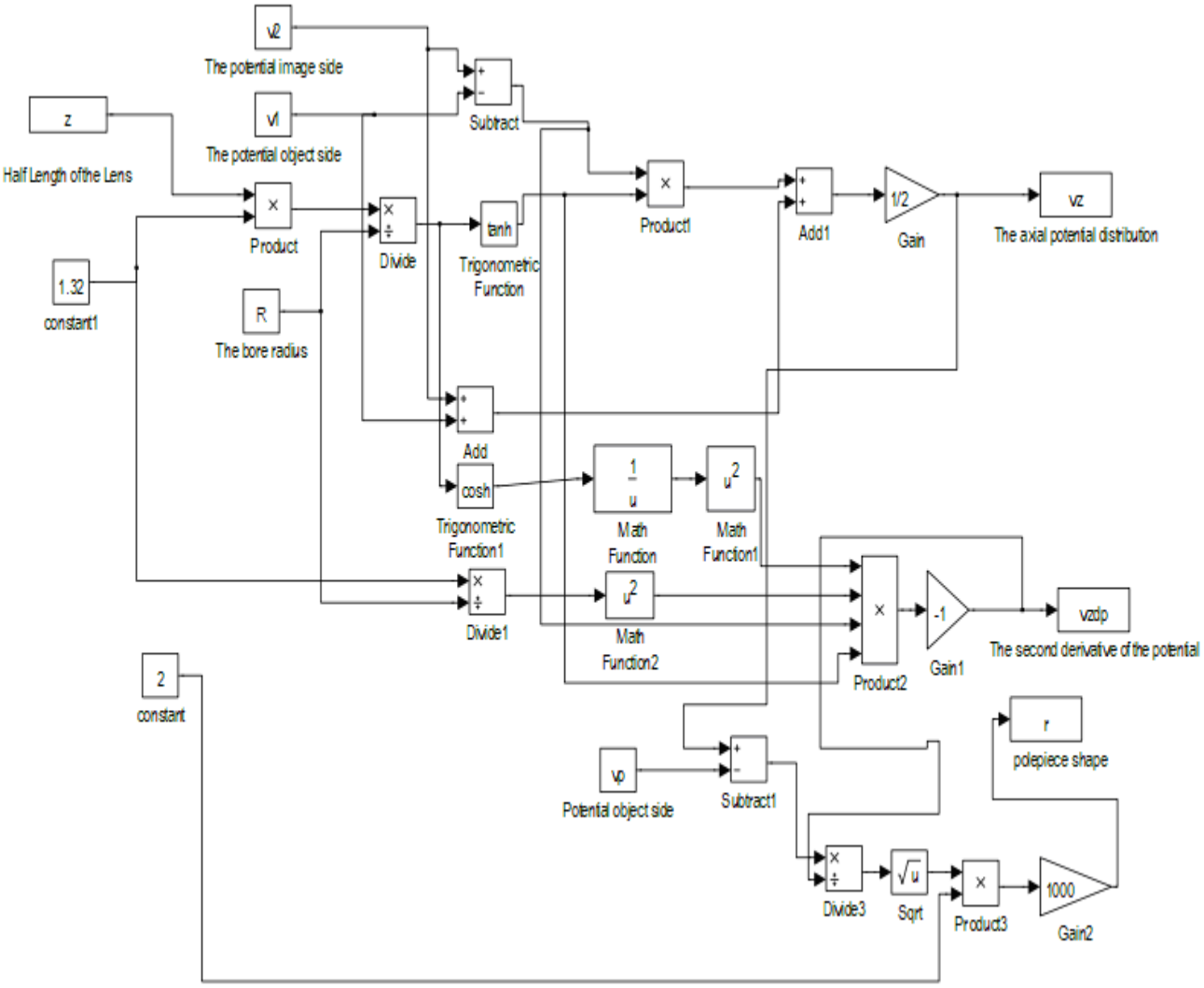

Figure 3. Simulink model for the axial magnetic scalar potential, V″(z) and pole shape.

The results of simulation in two mentioned models are the axial distributions of potential V(z), magnetic field B_z , and , V″(z) at specific input parameters as well as the shape of the pole piece plotted in 'figure 4' , 'figure 4' respectively.

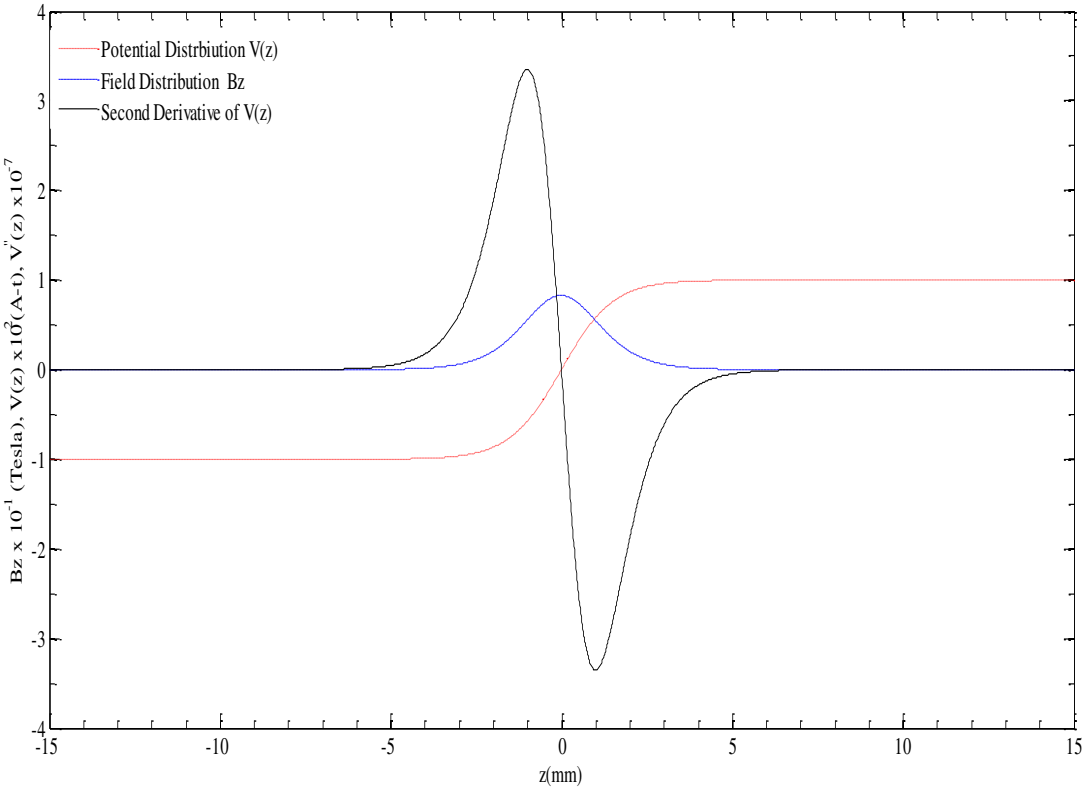

Figure 4. The axial distributions of V(z), $B_z(z)$ and V″(z) along the optical axis of the lens at $V_1=V_2=$-100A-t, R=2mm and L=30mm.

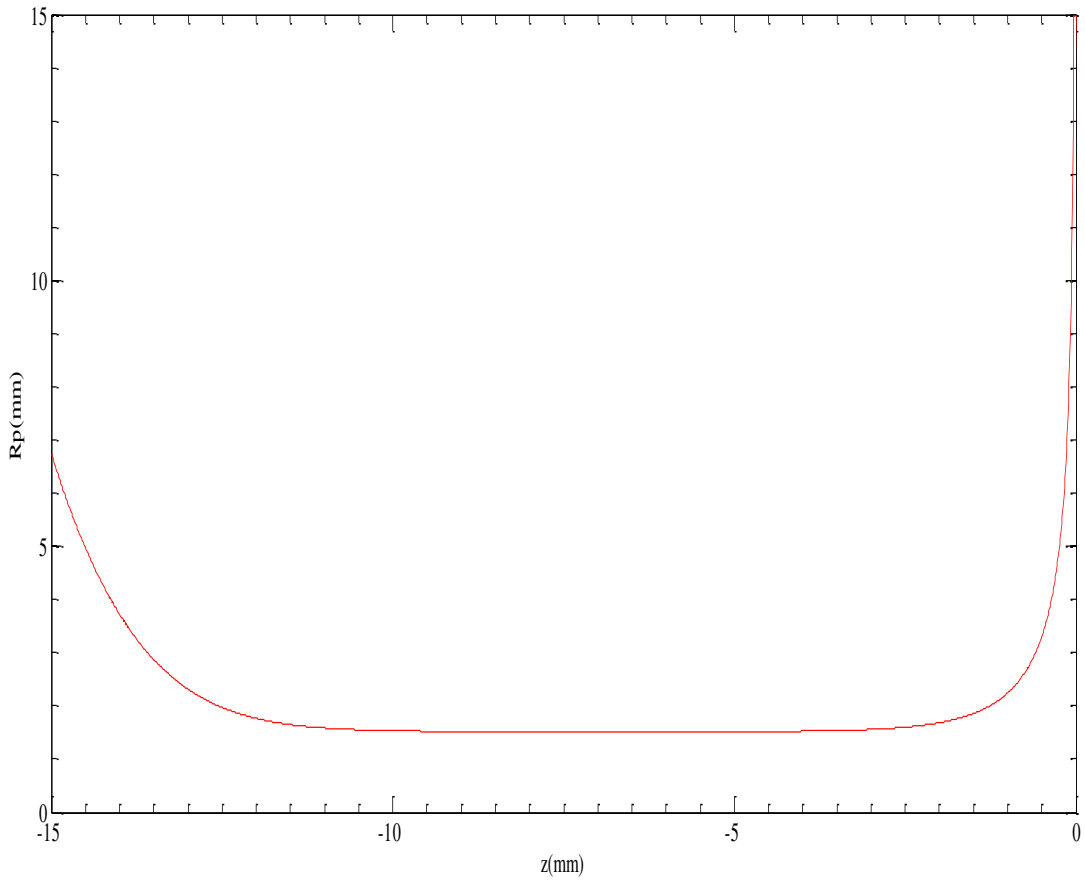

Figure 5. The profile of the magnetic pole piece at V_1=V_2=-100A-t, R=2mm and L=30mm.

4. Results and Discussion

To study the effect of the important optimization parameter in equation (3) that called pole piece radius of the lens (bore radius) R, the following five values of R are selected (1, 2, 3, 4, and 5 mm), the lens operates under the magnetic unsaturated mode, and other parameters are kept constant (the length of the lens is kept constant at 30 mm and the potentials at the terminals of the lens (i.e., at the object and image sides) are kept at V_1=-100A-t (Ampere-turn) and V_2=100A-t). Regarding the two equations (3) and (5), one can plot the magnetic scalar potential distribution and the magnetic field distribution, as shown in figures 6 and 7 where both figures are sketched for diverse values of the lens radius R. It is obvious that when the optimization parameter R is increased the peak field value B_{max} of the corresponding fields is affected and decreased. The lens excitation NI (Ampere-turn) is equal to the area under the curve of the magnetic field distribution which remains unchanged for all R values since the potential values V_1 and V_2 are kept constant. This means that the field distribution would be not more distributed along a large axial extension of the optical axis for large values of parameter R. It is noted that the magnetic scalar potential distribution curve plotted in figure 6 is affected by varying R values, so the potential gradient increases with increasing R. The magnetic pole pieces that produce the desired field distribution can be reconstructed with aid of equation (16), thus, figure 8 shows the half upper part of the double pole piece magnetic lens profile for various

values of the bore radius R. Figure 9, shows the angle of rotation of electron about the optical axis of the magnetic lens, at terminals z_s to z_f for diverse values of the bore radius R, this figure plotted according to equation (15). It will be mentioned that the angle of rotation decreasing with increasing the pole piece radius R.

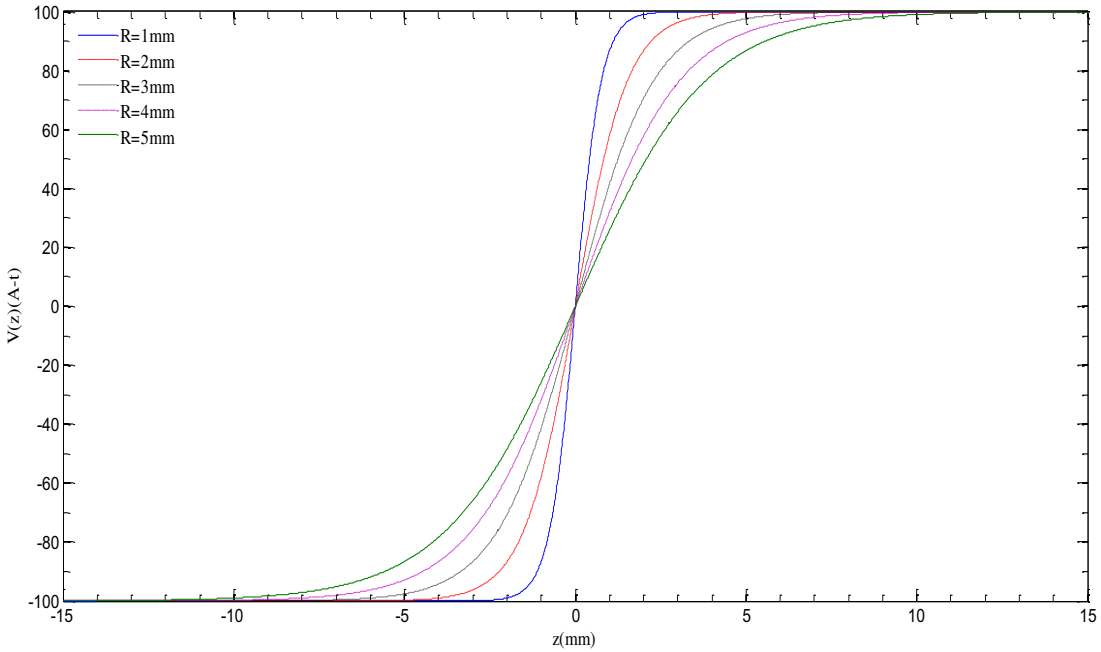

Figure 6. The axial magnetic scalar potential distribution for different values of the pole piece radius R.

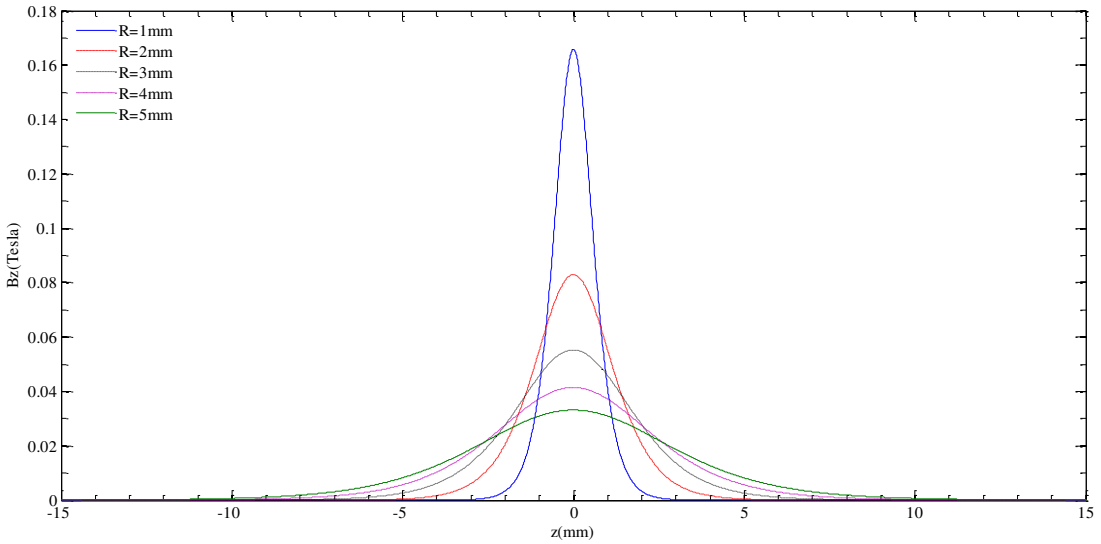

Figure 7. The axial magnetic field distribution for different values of the pole piece radius R.

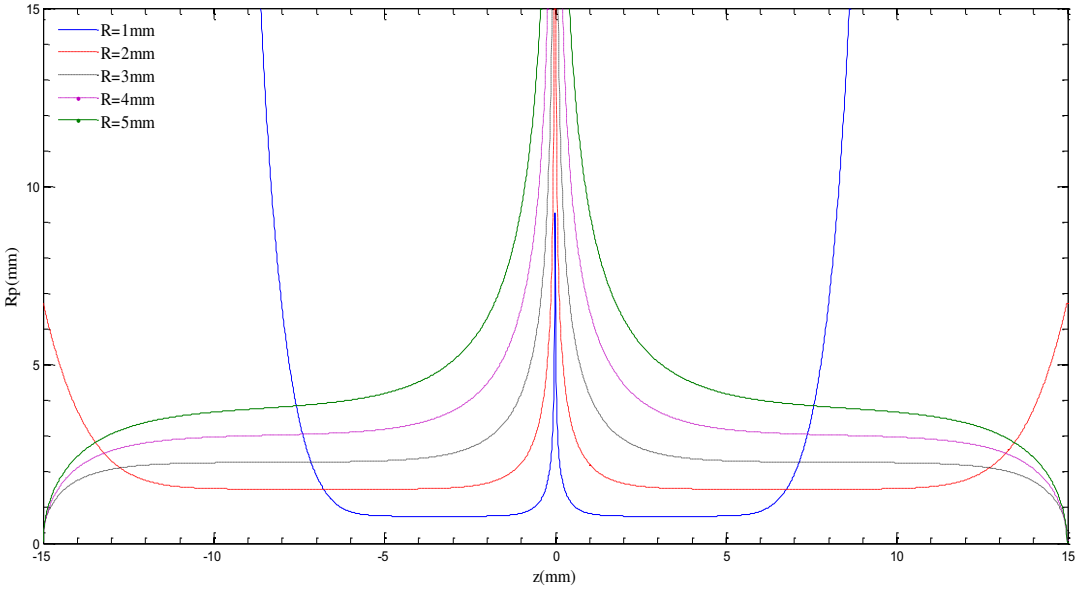

Figure 8. The half upper reconstructed magnetic pole piece shape for different values of the pole piece radius R

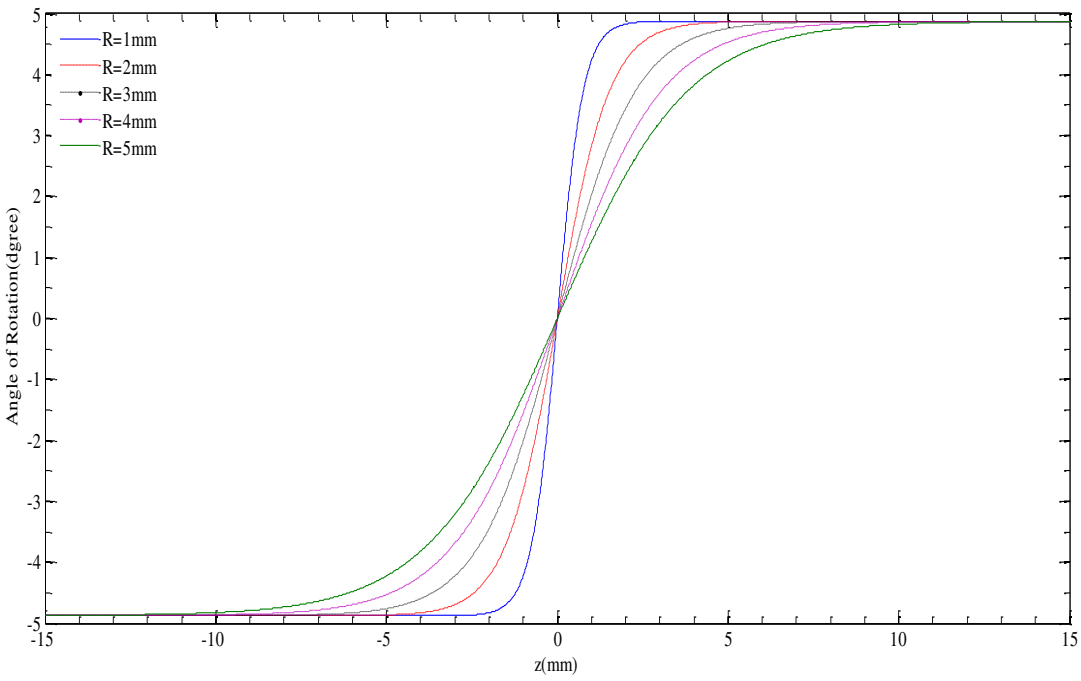

Figure 9. The angle of rotation of electron about the z-axis for different values of the pole piece radius R.

The important values of some design parameters are shown in Table (1). The columns in this table represent the setup values of the lens radius R, the maximum value of the magnetic field (peak values) B_{max}, the half width of the field W, and the area under the curve NI (excitation of the lens). The investigation shown that as the parameter R is increased, W also increasing, while B_{max} is decreasing, and NI remains almost constant.

Table 1. Lens design parameters for different values of pole piece radius R at V_2=-V_1=-100(A-t) and L=30mm.

R(mm)	B_{max}(T)	W(mm)	NI(A-t)
1	0.166	1.335	200
2	0.083	2.671	200
3	0.055	4.006	200
4	0.042	5.342	200
5	0.033	6.677	200

Table 2 shows the objective optical properties, the columns in this table represent the setup values of the lens radius R, the objective focal length f_o computed from the program and equation (13), the spherical aberration coefficient C_s and the chromatic aberration coefficient C_c. It will be noted from the Table 2 that all the optical properties are increasing with increasing R, with convergence in values between two focal lengths that are computed from the program and equation (13), which means that the objective optical properties of the objective magnetic lens affected and become worst by increasing the lens radius (bore radius) R.

Table 2. Optical objective properties for different values of pole piece radius R at V_2=V_1=-100(A-t) and L=30mm at NI/$Vr^{1/2}$=20.

R(mm)	f_o(mm) from the program	f_o(mm) from the equation (13)	C_s(mm)	C_c(mm)
1	0.514	0.408	0.248	0.356
2	1.027	0.816	0.498	0.712
3	1.540	1.224	0.748	1.068
4	2.054	1.632	0.998	1.423
5	2.566	2.040	1.247	1.778

5. Conclusions

In accordance with the aspects and results illustrated in the present work, several conclusions could be written down. However, the most important remarks can be summarized as follows;

1. The study showed that the optical properties have been worse when increasing the bore radius of the lens.
2. The study also showed that the area under the curve (excitation of the lens) and corrected relativistically, accelerating voltage remains nearly constant at different values of the radius of the lens.

References

[1] Rose H and Wan W 2005 Aberration correction in electron microscopy proceeding of particle Acce elerator conference, Knoxville,Tennessee, LBNI Berkeley, CA94720, USA, pp **44-48**

[2] Szilagyi M 1988 Electron and ion optics Plenum Press New York and London

[3] Klempere O 1953 Electron Optics,2nd Edition Cambridge University Press, Cambridge, England
[4] Munro M 1971 Computer- Aided Design Methods in Electron optics Ph.D. Thesis, University of Cambridge, UK.
[5] Al-Batat A H H '2013 Modeling and Design For Objective Charged *Particle Lens Journal of (IJAIE M),* vol **2,** Issue **10**, pp **25-32**
[6] A. H. H.Al-Batat A H H, Yaseen M J and Majeed M M 2011 Investigation of the projector Properties of the magnetic lenses using analy-tical function *Ibn Al-Haithom journal for pure and applied science*, vol **24**, No.**1** pp **63-71**
[7] Szilagyi M 1984 Reconstruction of Electrodes and Pole pieces from Optimized Axial Field Distributions of Electron and Ion Optical Systems *Appl. Phys. Lett.,* **45**, pp **499-501**
[8] El-Kareh A B and El-Kareh J C J 1970 Electron beams, lenses, and optics vol**2**, p**49,**(New York Academic)
[9] Klemprer O 1971Electron Optics **3**rd ed., (Cambridge)
[10] Szilagyi, M. 1985 Electron optical synthesis and optimization Proceeding of the IEEE, **73**, No. **3**
[11] Al. Batat A H H, Hasan H S, *Ibrahim Husin H M and Yaseen M J* 2016 Modulating Mathematical Function to be used in Electron Objective *Lens Journal of Advances in Physics Theories and Applications,* vol **57**, pp.**8-15**
[12] Karris T 2006 Introduction to Simulink with e

Effect of Electrical Current Stimulation on Pseudomonas Aeruginosa Growth

Effect of Electrical Current Stimulation on Pseudomonas Aeruginosa Growth

Auns Q Alneami[1], Eman G Khalil[2], Rana A. Mohsien[3] and Ali F. Albeldawi[4,5]

[1,2,4]Department of Biomedical Engineering, Al-Nahrain University, Baghdad, Iraq.
[3]College of biotechnology, Al Nahrain University, Baghdad, Iraq.
[5]Author to whom any correspondence.

E-Mail: uns_alneami@yahoo.com[1] , dr.emankhalil@yahoo.com[2] , rana1980@yahoo.com3 , ali_faisal79@yahoo.com 4

Abstract. The present study evaluates the effect of electrical current with different frequencies stimulation to kill pathogenic Pseudomonas aeruginosa (PA) bacteria in vitro using human safe level of electricity controlled by function generator. A wide range of frequencies has been used from 0.5 Hz-1.2 MHz to stimulate the bacteria at a voltage of 20 p-p volt for different periods of time (5 to 30) minutes. The culture of bacteria used Nickel, Nichrome, or Titanium electrode using agarose in phosphate buffer saline (PBS) and mixed with bacterial stock activated by trypticase soy broth (TSB). The results of frequencies between 0.5-1 KHz show the inhibition zone diameter of 20 mm in average at 30 minutes of stimulation. At frequencies between 3- 60 KHz the inhibition zone diameter was only 10mm for 30 minutes of stimulation. While the average of inhibition zone diameter increased to more than 30mm for 30 minutes of stimulation at frequencies between 80-120 KHz. From this study we conclude that at specific frequency (resonance frequency) (frequencies between 0.5-1 KHz) there was relatively large inhibition zone because the inductive reactance effect is equal to the value of capacitive reactance effect (XC = XL). At frequencies over than 60 KHz, maximum inhibition zone noticed because the capacitance impedance becomes negligible (only the small resistivity of the bacterial internal organs).

Keywords: bacteria, electrical stimulation, frequency effect, Pseudomonas aeruginosa.

1. Introduction

Recently scientists began to depend on developing a new techniques to treat infections caused by pathogenic bacteria or other microorganisms rather than antibiotics, that is belong to their harmful side effect or bacterial resistance to antibiotics [1] [2].

A lot of suggested techniques included and subjected to scientific research include using electrical stimulation (ES), laser, ultrasound, nano technology, electromagnetic radiations, etc. Electrical stimulation influence has a multiple variations that could change its ability to interact with living cells, these variables include voltage; current; frequency; polarization; and wave shape [3].

It is clear that high power electrical current more than 6 mA will be harm for human beings and could be fatal [4]. So the ability of electrical current lower than the effective value needs to be focused on to kill pathogenic bacteria. Pseudomonas aeruginosa is one of the most harmful bacteria which increase patients mortality rate in the hospitals because it is one of the antibiotic - resistant bacteria [5].

When alternating current (AC) pass through living body it will be resisted by extracellular matrix and intracellular matrix, where living cell such as bacteria act as capacitance (C) depending on the size

of the cell membrane[6][7]. Bacteria is a living cell that contain cell membrane which acts as capacitance too. The total impedance of the AC inside media containing living cells could be represented by the resistance (R) and reactance (XC) where the cell represented by R1 & C in the series and the extracellular matrix represents pure resistance (R2) parallel to the cell impedance as shown in 'figure (1)':

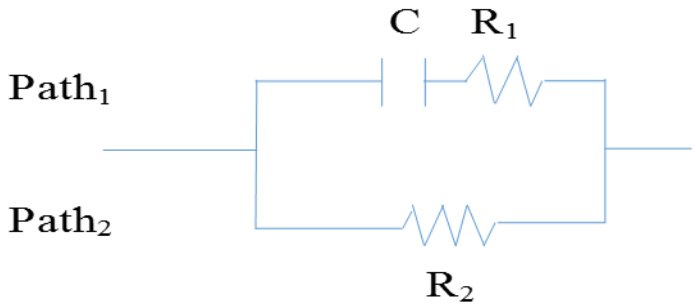

Figure 1. Pathway of intracellular ($path_1$) and extracellular ($path_2$) matrices

If the current frequency is zero, then the electrical current will pass totally through path2 because of higher impedance at path1 compare to path2 (i.e. reactance proportional inversely with frequency and equal to infinity, open circuit, at zero frequency according to equation 1), if the frequency increased then gradually part of AC will pass through path1 as the reactance effect decrease. At very high frequency total AC will pass through path1, according to the difference in the impedance between path1 and path2, there are three equations:

$$X_c = \frac{1}{2\pi f c} \quad (1)$$

$$Z_1 = \sqrt[2]{R_1^2 + X_c^2} \quad (2)$$

$$Z_2 = R_2^2 \quad (3)$$

Where:
Z_1: impedance of $path_1$,
Z_2: impedance of $path_2$, and
X_C: Reactance of path $_1$
f: is the frequency in hertz.
c: is the capacitance in micro farad

According to equations (2) and (3) if pathogenic PA treated by a suitable frequency of AC current that could kill bacteria avoiding human cell depending on the differences in reactance properties between the human cell membrane and bacterial cell membrane according to the differences in the composition and size of the cell membrane [6][7].

There are many differences between bacterial cells and live human cells, as illustrated in table 1 [8] [9] [10] [11]:

Table 1. Comparison between the human cell and the bacterial cell

Differences	Human cell	Bacterial cell
Cell	Human cells are in a group and not isolated. It is dependent on other cells for survival.	Cell is isolated and Independent. It survives as an individual on its own.
Cell wall	The wall is absent	Thick protective cell wall is present covering the whole cell.
Construction of cell membrane	Lipid bilayer with phosphate molecules. It is hydrophilic to external and hydrophobic in the inner wall.	Made of bilayer phospholipid. But the memebrance lacks sterols.
Cell wall has	Cytoplasmic bridges are present which help in inter-cellular	No cytoplasmic bridges as there is only one cell.

	transport in between neighbouring cells.	
Cell shape	Only spherical or oval	Cells can be of different shapes
Cell appendages (External parts)	Absent mostly. Except for example ciliated cells in respiratory tract & gut.	Present. Flagella for movement, pili for sexual reproduction.
Nucleus	Prominent nucleus with nuclear membrane. So called as eukaryote type.	Nucleus is Absent. Instead nuclear content like DNA are present in cytoplasm. No distinct nucleus, so called as prokaryote

Pseudomonas aeruginosa is an opportunistic human pathogen, gram negative, rod shaped, asporogenous, and monoflagellated bacterium that has an incredible nutritional versatility. It is a rod about 1-5 μm length and 0.5-1.0 μm wide. PA is an obligate respirer, using aerobic respiration as an optimal metabolism and can respire anaerobically on nitrate or other alternative electron acceptors [12]. PA can catabolize a ubiquitous range of organic molecules, including organic compounds like benzoate. This, makes PA is a very ubiquitous microorganism, for it has been found in wide environmental conditions such as soil, water, humans, animals, plants, sewage, and hospitals [13][14]. PA is the predominant inhabitant in all aquatic ecosystems, which contain high dissolved oxygen content, but its existence in low plant nutrients makes it clearly the most abundant organism [14][15][16].

2. Aim

The aim of the present study is to prove that in vitro the pathogenic bacteria can be inhibited by using low power alternative electrical current that is safe to human body.

3. Materials and Methods

3.1. Materials:

PA were isolated from human skin burns and preserved in the bacterial bank in Al Nahrain University/College of Biotechnology.

- A 60 mm plastic petri dish (100 piece) was obtained and two holes of 2.4mm in diameter were borne through the bottom of each, at distance 1cm apart from the centre. Two of 2 cm length, 2.5 mm-gauge Nickel electrodes (ESAB/VacPac electrodes) were fed through each hollow. A 1.1cm of the electrode inside the petri dish was perpendicular to the base of the petri dish, while the outside portion of the electrode was fixed in with epoxy cement parallel to the base of the dish, with a 0.9 cm overhang for the attachment of the function generator wires figure 2. Then petri dishes were sterilized by alcohol 70% and wiped with cotton, then alcohol 70% again and finally exposed to UV light of 9J/cm2 for 1 hour.

Figure 2. Petri dish with Nickel electrodes

- A movable wires (Nichrome inoculation loop gauge 24) were used as an electrodes to stimulate the cultured bacteria. A special setting as shown in figure 3 applied by hanging the sterilized

electrodes in the petri dish. Pouring the cultured media with PA, then it was left to solidify at room temperature (RT) and thus become ready to apply the electrical current.

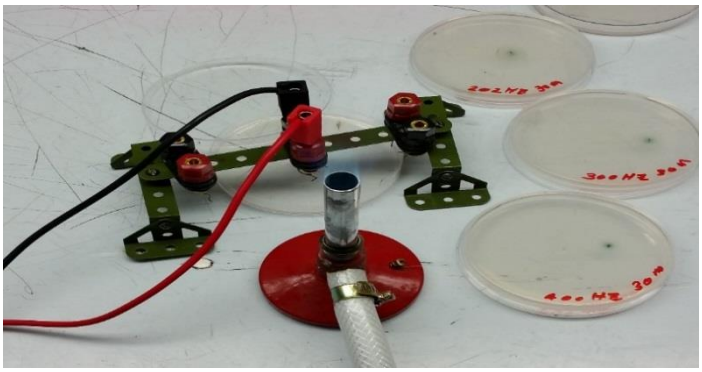

Figure 3. Petri dish and Nichrome wire electrodes

3.2. Instrumentation for electrical current application:

A function generator (FeelTech Model:FY3200S) as illustrated in figure 4.a was used in this study to stimulate bacteria by a customized range of frequency as follows (0.5, 1, 30, 70, 100, 300, 700, 1K, 3K, 7K, 10K, 30K, 120K, 1.1M, 1.2M) Hz at a constant value of continues sine wave 20 V_{p-p} AC current as shown in figure 4.b and for 10, 20, and 30 minutes. Two cables with alligator clips were used to deliver current to two petri dishes at the same time (two channels of the function generator were used simultaneously each in different frequency and each petri dish stimulated by only one of the mentioned frequency).

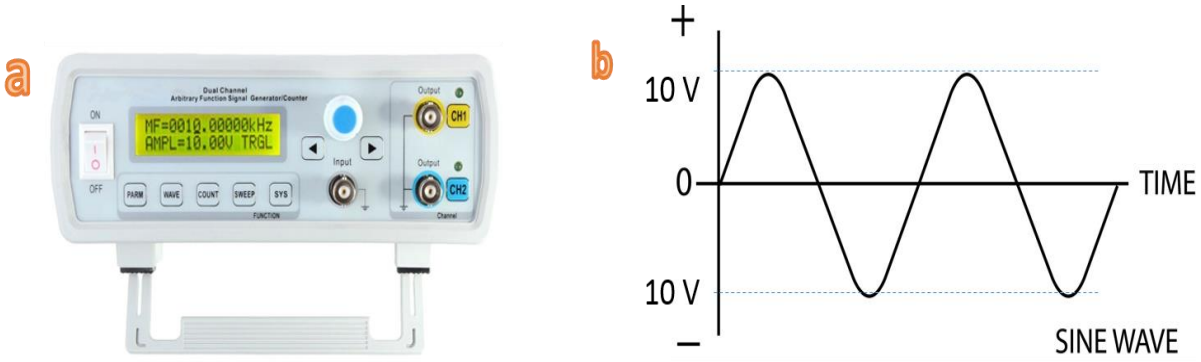

Figure 4. (a): Function Generator / FeelTech / Model: FY3200S and **(b)**: Sine wave 20 Vp-p AC current

4. Procedure:

The cultured PA were grown overnight to reach mid-exponential growth phase at 37°C in trypticase soy broth with a shaking incubator at speed of 200rpm.Next day 2gm agarose were added to 200ml of 0.1M phosphate-buffered saline, molded by using microwave for 140 sec., then was cooled to suitable temperature nearly (37°C) within (20 to 30) minutes. A 20 ml of TSB containing 10^6 colony-forming units (cfu) of PA / milliliter were added to the mixture and mixed well manually. Fifteen ml of the final mixture were added to each (13) sterile (60mm) petri dish using 20ml syringe [17]. Cultured petri dishes were used immediately after solidification at RT.

Two petri dishes cultured with PA were each stimulated with one of the customized electrical current stimulation mentioned previously, then another two petri dishes stimulated using two new different electrical current frequencies and the procedure was repeated to cover all the 12 values of the chosen frequencies. Each ES frequency was applied to a petri dish for 30 minute at room temperature (20-25 °C) inside sterile hood cabinet. Then each electrical stimulated petri dishes were incubated for another (20) hour at (37 ºC), the diameter of the inhibition zone (absence of bacterial growth) surrounding each

electrode was measured using ruler. Two measurements of each inhibition zone were taken perpendicular to each other, and both of them perpendicular to the electrode.
This procedure repeated four times for each frequency (i.e. totally four samples subjected to the same value of frequency).

These measurements were then averaged to obtain a value for the inhibition zone. Inter-tester reliability was determined using 1 × 3 repeated measures analysis of variance (ANOVA). No electrode corrosion, gas formation, and media discoloration were noticed except 2mm burning trace around positive and negative Nichrome electrodes. A set of 24 cultured petri dishes was incubated as mentioned previously, but without ES, considered as a control group.

All the procedure above was repeated again for 20minute and 10minute electrical stimulation for chosen samples at specific frequencies. Finally (96) samples were used including (24) control.

All samples passes through the following procedure to measure their growth inhibition zones:

- Step 1: This is mean that a quantity of TSB prepared and cultured by 10 percent of previously TSB cultured PA from refrigerator to activate bacteria then the sample incubated for 20-22 hours at 37°C shaking incubator at 200 rpm.
- Step 2: This mean that preparing agarose by adding 1gm of agarose to each 100 ml of 0.1 M PBS. Then solve the mixture totally by hand then microwave. After slight cooling to almost 37ºC a 10 percent of activated bacteria from step 1 is added to the mixture and mixed well manually then 15 ml of the mixture poured in 60 mm petri dish with built in electrodes. After solidification the sample stimulated by AC current of specific frequency for specific time and incubate the stimulated samples and the control (not stimulated) for 20-22 hours at 37ºC incubator.
- Step 3: checking the inhibition zone of the stimulated samples from step 2.

All samples pass through steps 1, 2, and 3 then finally the inhibition zone measured and recorded in a table.

5. Statistical Analysis

A 1 × 24 × 4 repeated measures analysis of variance ANOVA, $p < 0.05$, was performed to determine a possible main effect for (1) electrode polarity between two levels, (2) sixty types of ES based on (15 frequencies with 4 stimulation times), (3) number of samples stimulated for each type of stimulation (13×3 using Nichrome wire electrode, 8×3 by using built-in Nickel electrodes, and 3×3 using Titanium electrodes) while the fourth used as control.

6. Results

Tables 2, 3, 4, 5, 6, and 7 and related figures 5, 6, and 7 below show the practical result of the present study clarifying the inhibition zone at each examined frequency and time:

Table 2. Inhibition zone according to the frequency and time by using Nichrome electrodes

NO.	Freq. , Hz / Stimulation time (minute)	Inhibition zone, Anode, Cathode, (mm)
1.	0.562/30	15, 14
2.	5.04/30	16,15
3.	7.04/30	16,15
4.	30.44/30	16,15
5.	300/30	10,10
6.	500/30	10,8
7.	1K/30	10,10
8.	3K/10	10,8
9.	3K/12	6,4
10.	3K/30	11,10
11.	30.01K/30	15,9
12.	61.8K/12	4,4
13.	303K/15	12 , (24×16)

Table 3. Inhibition zone area related to AC stimulation frequency / Nichrome electrodes

Freq.	I.Z. area (mm²)
0.5	330
5	377
7	377
30	377
300	157
500	128
1000	155
3000	174
30000	240
300000	415

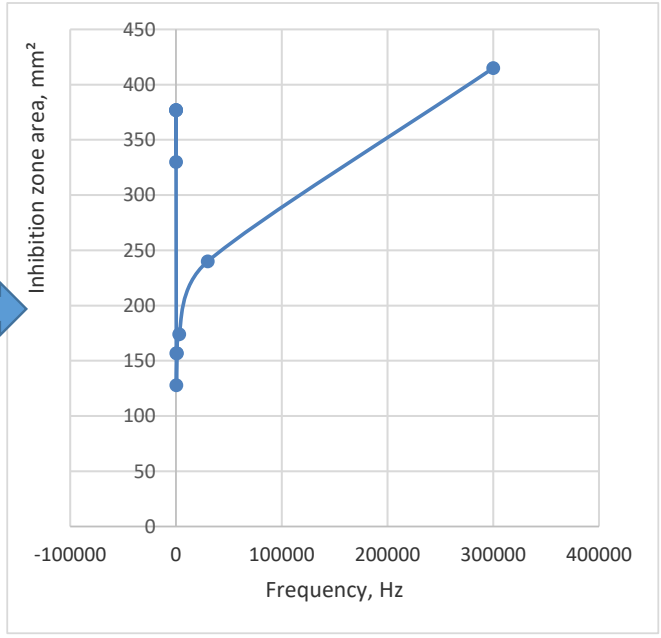

Figure 5. Shows the AC stimulation of PA by using Nichrome electrodes according to values as shown in table 3.

Table 4. Inhibition zone according to the frequency and time by using Titanium electrodes

NO.	Freq. , Hz / Stimulation time (minute)	Inhibition zone Anode (mm)
1.	700/30	0 but Lighter growth
2.	120K/30	(35, 30) mm ellipse at one side. Closely total killing.
3.	1.1M/20	(35, 30) mm ellipse at one side. Closely total killing.

Table 5. Inhibition zone area related to AC stimulation frequency/Titanium electrodes

Freq.	I.Z. area, (mm^2)
700	0
120000	825
1100000	825

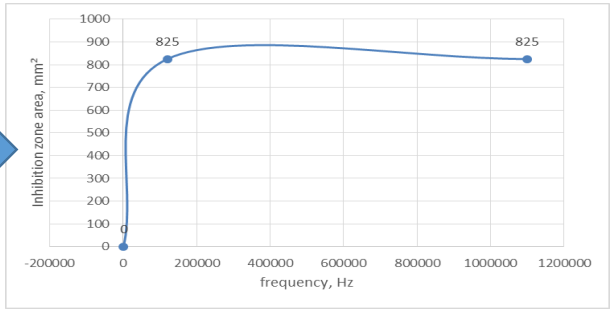

Figure 6. Shows the AC stimulation of PA by using Titanium electrodes according to values as shown in table 5.

Table 6. Inhibition zone according to the frequency and time by using Nickel electrodes

NO.	Freq. , Hz / Stimulation time (minute)	Inhibition zone Anode , Cathode, (mm)
1.	0.5/30	(20×30), 15.6
2.	30/30	20, 15
3.	300/30	28, 15
4.	80K/20	26, 15
5.	100K/20	34, 20
6.	120KHz/20	33, 24
7.	120KHz/30	Nearly total inhibition
8.	1.2M/30	100% inhibition

Table 7. Inhibition zone area related to AC stimulation frequency/Nickel electrodes

Freq.	I.Z. area (mm^2)
0.5	660
30	491
300	792
80000	707
100000	1222
120000	2827

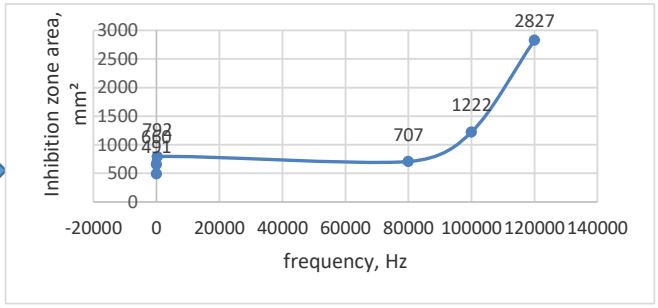

Figure 7. Shows the AC stimulation of PA by using Nickel electrodes according to values as shown in table 7.

* Da: diameter of inhibition zone at anode
* Dc: diameter of inhibition zone at cathode

The figures (8,9,10,11,12, 13) below show some photos´ results (as clear as possible photos have been chosen, taken into account that glue drops leave its trace around built in Nickel electrodes):

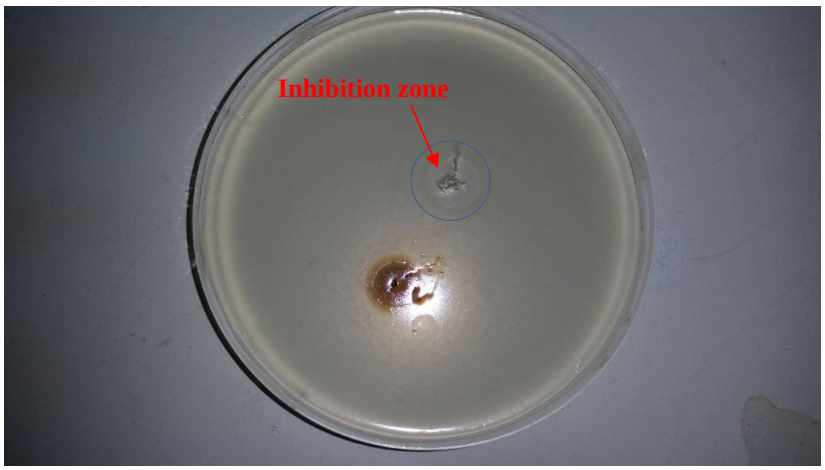

Figure 8. Inhibition zone of 5 mm burning trace at anode side using movable Nichrome electrodes at 3 KHz for 10 minutes.

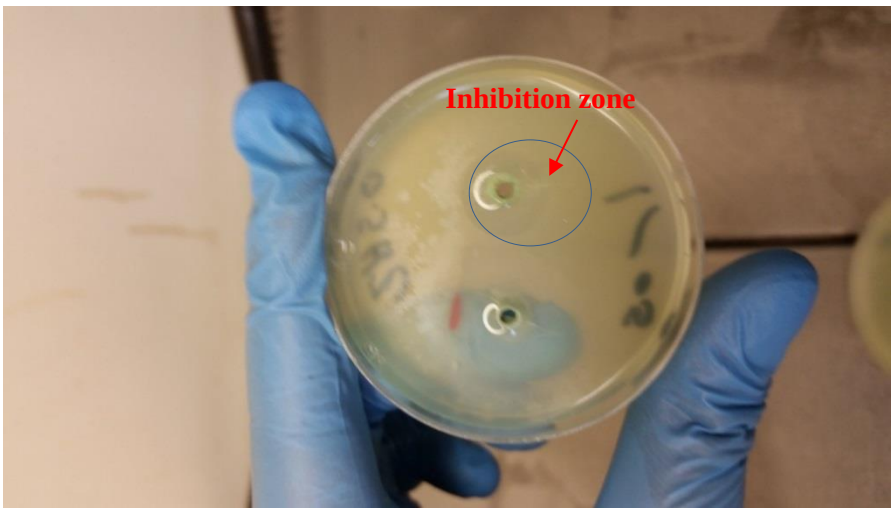

Figure 9. Inhibition zone of 25×15 mm using built-in Nickel electrodes at 0.5 Hz for 30 minutes.

Figure 10. Inhibition zone of 20×15 mm, using built-in Nickel electrodes at 30 Hz for 30 minutes.

Figure 11. Inhibition zone of 28×15 mm using built-in Nickel electrodes at 300 Hz for 30 minutes.

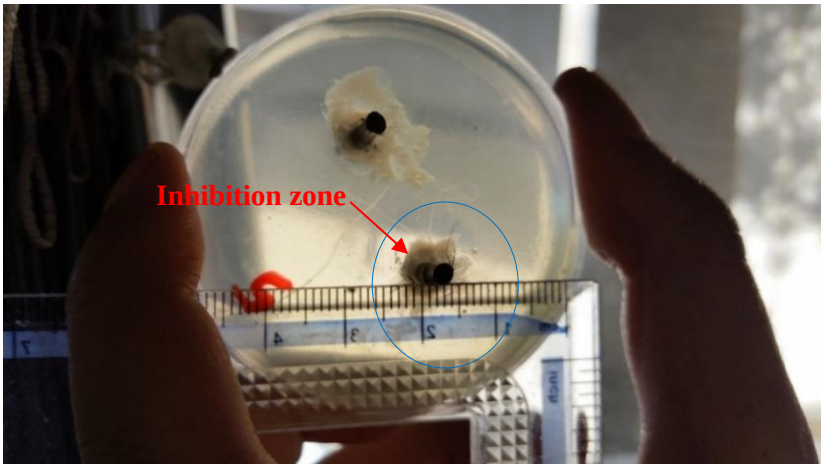

Figure 12. Inhibition zone of 33×24 mm using built-in Nickel electrodes at 100 KHz for 30 minutes.

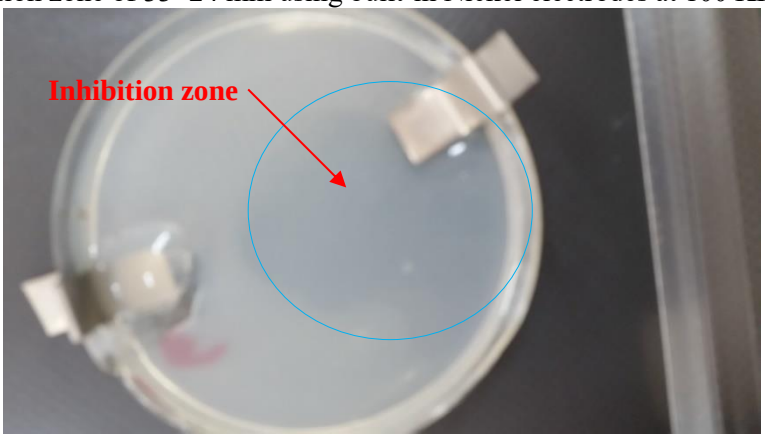

Figure 13. Inhibition zone of 35×30 mm, closely total bactericidal effect using built-in Titanium electrodes at 120 KHz for 30 minutes.

7. Discussion

The various values of AC current frequencies can inhibit PA growth in different inhibition levels. A significant inhibition zone diameter observed when low frequencies were applied (between 0.5 Hz and 1 KHz), in comparison with higher frequencies (between 3 Hz and 60 KHz), but there is no significant difference in their effect between each other (similar inhibition zone) which is agree with Fadel M. Ali et al. in [2013] whose results indicated that exposure to positive square pulsed electric fields can inhibit bacterial growth at particular resonance frequencies 0.7 Hz and 0.5 Hz and clearly act on cellular activity as well as cause changes in molecular structure that affect (inhibition) the cellular division or proliferation [18]. While increasing frequencies between 3 KHz and 60 KHz show smaller inhibition zone. The inhibition zone area increased significantly after stimulation by electrical current of frequencies between 80 KHz and 300 KHz .The inhibition zone increased at all frequencies levels by increasing stimulation power and time. This meant that bacterial membrane acts as capacitive resistance while increasing frequency the capacitance reactance decrease leading to decrease cell impedance and therefore more current (electrons) passes through bacterial cell and cause higher interaction leading to faster inhibition of cells and occurrence of larger inhibition zone.

We clearly notice that at frequencies less than 60 KHz the inhibition zone was less than 5 mm at short stimulation time (20 minutes) while it was 20 mm for samples stimulated by 120 KHz for the same time.

This study confirmed that low power of 20 V_{p-p} and less than 5μA was enough to inhibit PA pathogenic bacteria, these values of electrical current is theoretically safe to the human body.

It must be referred to the effect of burning in the cathode and anode sides of the stimulation electrodes which must be avoided in future study by using wider electrodes cross section area. There was no noticeable corrosion and coloration on the Nickel or Nichrome wire electrodes by examined

using naked eye while using stainless steel wire show some physical effects in previous study [19] but more tests needed to find the exact amount of corrosion if any.

It was also clear that Nickel electrodes cause either bacterial attraction towards the electrodes or toxic effect or both depending on frequency (i.e. in some frequencies the bacteria aggregate in areas around electrodes and the inhibition zone was observed in the remaining cultured area of the petri dish even in control sample because of either old PA isolate or may be due to the dual effect of Nickel; toxic and attraction), it is also important to mention that different bacterial isolates shows similar, but not identical, reactions to different electrical frequencies values stimulation.

It was only clear that wide area of Titanium electrodes cause no burning effect on the samples.

8. Conclusion

This study aimed to investigate the effect of changing the frequencies of low voltage and power alternative electrical current (values theoretically safe to humane body) on PA growth and it was found that low electrical current values can inhibit PA growth and the inhibition significantly increased at high frequencies more than 80 KHz and reach maximum at 120 KHz.

9. Recommendations for Future Work:

- This study recommends additional investigation about Nickel effect on PA growth.
- Using wide plates of inert material as an electrode to avoid burning effect.
- Developing a methodology work on to measure the suitable frequency that can effectively kill any species of bacteria and can be programmed to find out if it is safe to human tissues, and can be applied to use it as a therapy in addition to the other therapeutic strategies.
- Additional studies should be established to prove that in general high frequencies have no harmful side effects on human body and especially on organs their functions related to electrical stimulation such as the heart and nervous system.

References:

[1] J. a Feedar, L. C. Kloth, and G. D. Gentzkow, "Chronic dermal ulcer healing enhanced with monophasic pulsed electrical stimulation*," Phys. Ther.,* vol. **71**, no. 9, pp. 639–49, 1991.

[2] G. Rizzoni, T. T. Hartley, and T. O. S. U. Giorgio Rizzoni, Principles And Applications Of Electrical Engineering / Chapter 1 Introduction to Electrical Engineering, 4th ed. McGraw-Hill Higher Education, 2003.

[3] C.L. Wadhwa, Basic Electrical Engineering, 4th ed. 2007.

[4] S. T. T. Ards, IEEE Recommended Practice for Electrical Safety in Industrial and Commercial Power Systems. 2012.

[5] J. W. Peterson, "Medical Microbiology/Chapter 7 Bacterial Pathogenesis," Med. Microbiol. 4th Ed., no. 1, pp. 1–20, 2013.

[6] S. R. Iqbal, "Physics of Bio-electrical Impedance Analysis : Phase Angle and its Application," Adv. *Life Sci. Technol*., vol. **9**, no. 23, pp. 4–12, 2013.

[7] M. Bodenstein, M. David, and K. Markstaller, "Principles of electrical impedance tomography and its clinical application," Crit. Care Med., vol. **37**, no. 2, pp. 713–724, 2009.

[8] T. Vellai and G. Vida, "The origin of eukaryotes: the difference between prokaryotic and eukaryotic cells*," Proc. R. Soc. B Biol. Sci.*, vol. **266**, no. 1428, pp. 1571–1577, 1999.

[9] C. F. Riddel, Jennifer, "All about Cells Literacy Foundations Science : Biology." 2012.

[10] G. Orchard, B. Nation, and Institute of Biomedical Science (Great Britain), "Cell structure and function," p. 500, 2014.

[11] W. M. Gerald Karp, Janet Iwasa, "Karp's Cell and Molecular Biology: Concepts and Experiments, Chp.1/1. 2 | Basic Properties of Cells," pp. 3–23, 2016.

[12] P. Kenneth Todar, "Pseudomonas aeruginosa © 2004," pp. 1–10, 2004.

[13] K. N. Unni, P. Priji, V. A. Geoffroy, M. Doble, et al., "Pseudomonas aeruginosa BUP2 — A Novel Strain Isolated from Malabari Goat Produces Type 2 Pyoverdine," 2014.

[14] J. B. Lyczak, C. L. Cannon, and G. B. Pier, "Establishment of Pseudomonas Aeruginosa Infection: Lessons from a versatile opportunist," Microbes and Infection, vol. 2, no. 9. pp. 1051–1060, 2000.

[15] K. Poole, "Pseudomonas aeruginosa: resistance to the max," Front. *Microbiol*. vol. **2**, no. 65, pp. 1–13, 2011.
[16] H. Leclerc, J. Bartram, J. A. Cotruvo, et al., "Relationships between common water bacteria & pathogens in drinking-water\r," World Heal. Organ. (WHO)Heterotrophic Plate Counts Drink. *Saf*., pp. 84–85, 2003.
[17] N. J. Szuminsky, a C. Albers, and P. and Unger, "Effect of narrow, pulsed high voltages on bacterial viability." *Phys. Ther*., vol. **74**, no. 7, pp. 660–667, 1994.
[18] F. M. Ali, A. M. Elkhatib, W. M. Aboutalib, et al., "Control of the Activity of Pseudomonas Aeruginosa by Positive Electric Impulses at Resonance Frequency," *J. Am. Sci*., vol. **9**, 2013.
[19] H. L. Merriman, C. Hegyi, and A. Albright-Overton, "A comparison of four electrical stimulation types on Staphylococcus aureus growth in vitro," *J. Rehabil. Res. Dev.,* vol. **41**, no. 2, pp. 139–46, 2004.Allowing the last numbered section of the paper.

Mathematical Calculations Of Heat Transfer For The CNC Deposition Platform Based On Chemical Thermal Method

Mathematical Calculations Of Heat Transfer For The CNC Deposition Platform Based On Chemical Thermal Method

Mohammed Sh. Essa[1], Bahaa T. Chiad[2], Khalil A. Hussein[1]

1 Ministry of Science and Technology, Renewable Energy Directorate, Solar Energy Research Center, Iraq, Baghdad
2 University of Baghdad, College of Science, Dept. of physics, Iraq, Baghdad

mohalnasban@yahoo.com

Abstract. Chemical thermal deposition techniques are highly depending on deposition platform temperature as well as surface substrate temperatures, so in this research thermal distribution and heat transfer was calculated to optimize the deposition platform temperature distribution, determine the power required for the heating element, to improve thermal homogeneity. Furthermore, calculate the dissipated thermal power from the deposition platform. Moreover, the thermal imager (thermal camera) was used to estimate the thermal destitution in addition to, the temperature allocation over 400cm2 heated plate area. In order to reach a plate temperature at 500 oC, a plate supported with an electrical heater of power (2000 W). Stainless steel plate of 12mm thickness was used as a heated plate and deposition platform and subjected to lab tests using element analyzer X-ray fluorescence system (XRF) to check its elemental composition and found the grade of stainless steel and found to be 316 L. The total heat losses calculated at this temperature was 612 W. Homemade heating element was used to heat the plate and can reach 450 oC with less than 15 min as recorded from the system.as well as the temperatures recorded and monitored using Arduino/UNO microcontroller with cold-junction-compensated K-thermocouple-to-digital converter type MAX6675.

Keywords: Heat transfer, Deposition platform, CNC, Chemical Thermal Method.

1-Introduction

Heat Transfer is the study of the rates of thermal energy motion. There are three modes of Heat Transfer: Conduction, Convection, and Radiation [1]. Conduction is concerned with the transfer of thermal energy through a material without bulk motion of the material. Conduction is the diffusion of thermal energy, i.e., the movement of thermal energy from regions of higher temperature to regions of lower temperature. On a microscopic level, this occurs due to the passing energy through molecular vibrations [2]. Convection is the process of heat transfer by displacing the macroscopic elements of a medium (molar volumes) [3]. Radiation is the transfer of thermal energy between two objects through electromagnetic waves. Unlike conduction and convection, radiation does not require a medium. In general, gasses do not take part in radiation heat transfer [4].

One of the many chemical thermal deposition methods is the chemical thermal spray pyrolysis system which is contained the following parts, spray head, carrier gas, heating element, and temperature controller [5]. Thermal stability and uniformity of temperature distribution are very important in spray deposition process because of this method highly dependence on thermal decomposition.
So in this work try to estimate the needed thermal power to achieve the required temperature with maximum stability and uniformity, as well as, design the heating element and temperature monitoring and controlling system.

2.Experimental

The nature and the surface of the substrates are extremely important because they greatly influence the properties of the films deposited onto them. Glass, quartz, and ceramics substrates are commonly used for polycrystalline films [6] [7]. In this work, the microscopic glass slides of (25.4mm x 76.2mm x 1.2mm) dimensions used as the substrate. There are some factors that effect on the film homogeneity, which are Substrate Temperature, deposition rate, spray time, distance, and air pressure. The substrate temperature has great importance in the preparing the homogeneous film, so we must choose the possible temperature to get the homogeneous film. We can measure the temperature of the substrate due to the thermocouple, which is connected to an electrical heater, and a large number of experiments did to get the possible temperature to get the homogeneous film.

The substrate heater (deposition platform) was an electrically controlled and monitored every 200 msec using Arduino UNO and analog to digital converter type MAX6675 with a K-type thermocouple. The controlling was done by a specially written instruction program code in C++, the latter facilitate the accurate real-time monitoring and controlling the deposition temperature during the process. The electric heater as illustrated in figure (1) is designed to equip the translated (X-Y) movable deposition platform with a thermal energy, which is suitable for the overall entire area of 400 cm2. Furthermore, homemade gridded deposition platform plat was stainless steel type 306L according to the handheld X-ray fluorescence XRF type Skyray Instrument EDX-Pocket III report as shown in figure (2). It has also been used the thermal camera (Fluke thermography type Ti10) to evaluate the performance efficiency of the home-made electrical heater by thermal images of the heated plate and surface temperature of the substrate.

Figure 1. Home-made electrical heater using tungsten wire and quartz tube.

Sample	NewSpec04-20160114131204	Used Time	20 sec
Supplier		Voltage	38 KV
Operator		Current	16 μA
Test Date	1/14/2016	WorkCurve	
GPS	de:;Latitude:;Altitude:;	Specification	
Element	Content	Limit	Result
Ti	ND	0	ND
V	0.1233	0	0.1233
Cr	18.1566	0	18.1566
Mn	1.5485	0	1.5485
Fe	63.9841	0	63.9841
Ni	15.0341	0	15.0341
Cu	0.1517	0	0.1517
Mo	1.0018	0	1.0018
W	ND	0	ND

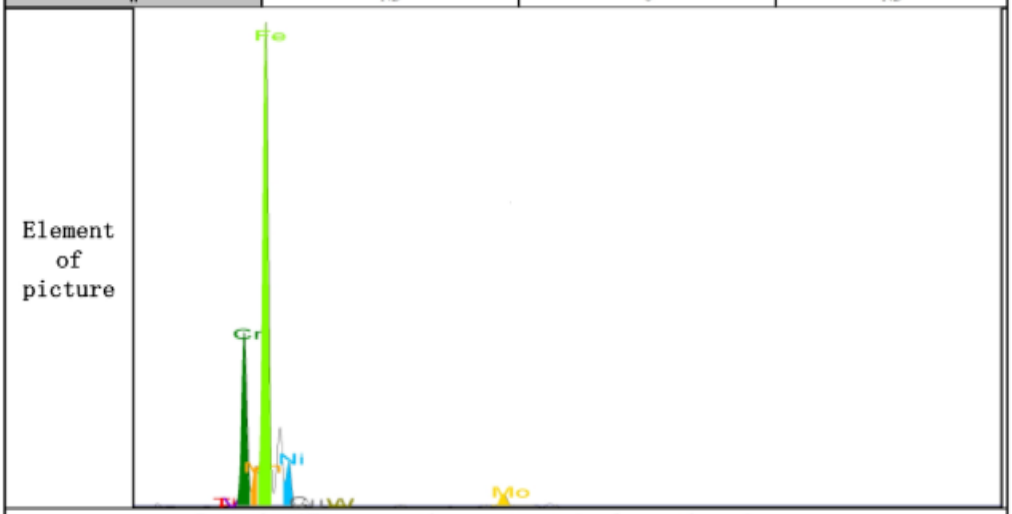

Remark: ND means the content is less than 2 ppm.

Figure 2. The XRF elements analyzer composition result for the home-made gridded hot plate

3.Calculation and Results

The basic heat transfer relationship for conduction is the Fourier equation:

$$Q = \frac{KA\Delta T}{L} \qquad (1)$$

Where **Q** is the rate of heat transfer, **K** the thermal conductivity of the material in this case **K** equal to (1.28) for the firebrick that used as a thermal insulator in the bottom and sidewall of the carriage. The Stainless Steel adopted in this work was (grade 306L) according to the XRF measurement and results, **L** is the thicknesses of the platform, **A** is the area of the heat transfer as shown in figure (3), and Δ**T** is the temperature difference of the heat transfer.

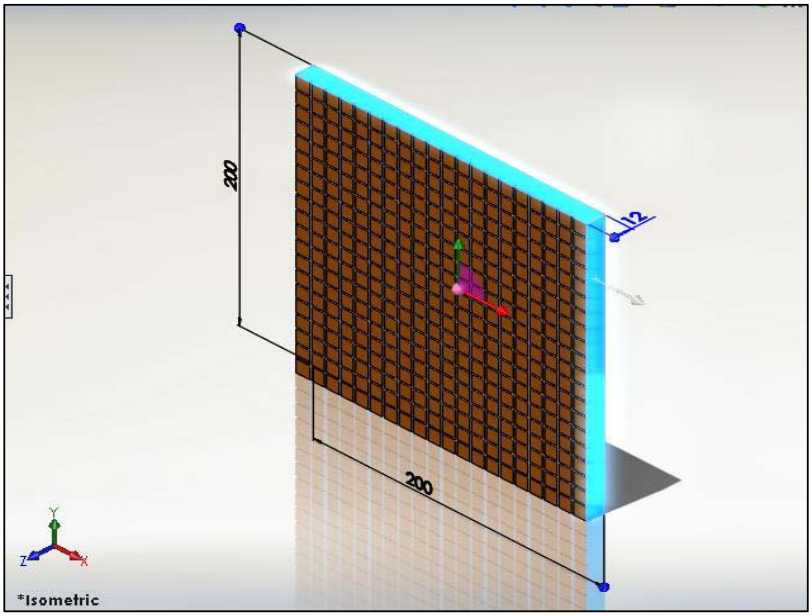

Figure 3. The gridded stainless steel heated plate designed and simulated using SolidWorks 2014, light side (light blue) refer to the area of thermal

Then:

The heat transfer from the side of the carriage as illustrated in figure (4) in red color, assume that the outside temperature of the fiber brick is 75 ℃. To calculate the thermal losses from the carriage wall.

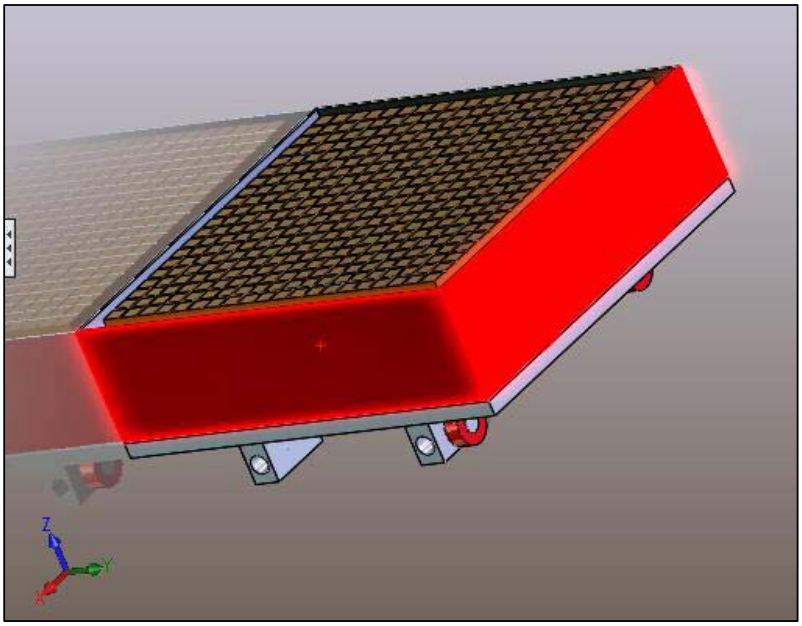

Figure 4. Sidewall of the carriage the red color refer to increasing the temperature of the sidewall

$$Q_{cond.} = \frac{KA\Delta T}{L} \qquad (2)$$

$$Q_{1.} = \frac{1.28 \times (0.012 \times 0.8)(500 - 75)}{0.006}$$

$$Q_{1.} = 870.4\ W$$

To evaluate the heat transfer by conduction from the lower surface of the plate.

$$Q_{2.} = \frac{1.28 \times (0.2 \times 0.2)(500 - 50)}{0.8}$$

$$Q_{2.} = 28.8\ W$$

To evaluate the heat transfer from the upper surface of the plate (by convection) as shown in 'figure (5)'.

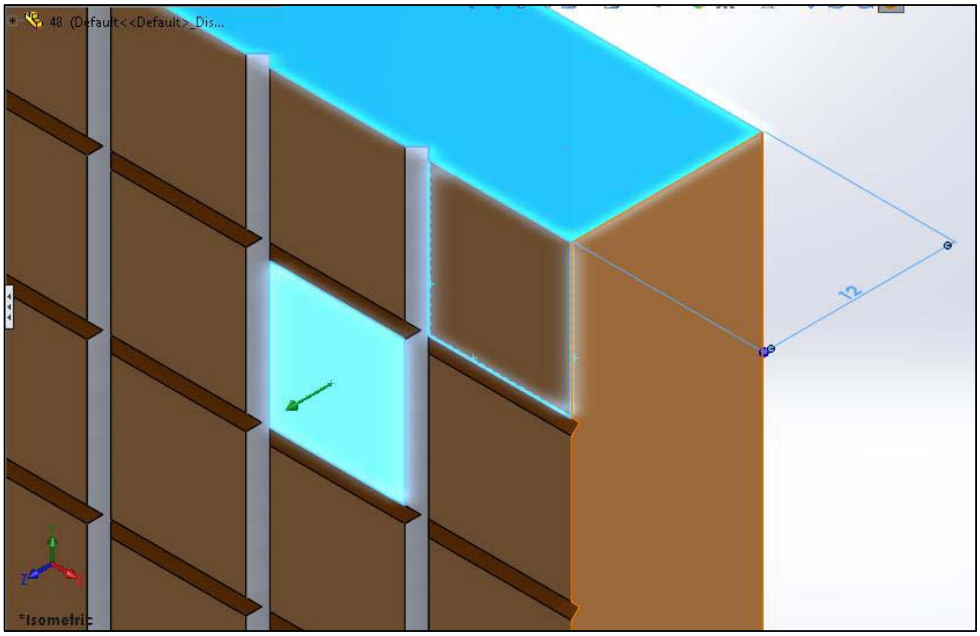

Figure 5. The upper-heated surface with projection of the X-Y movable deposition platform

Newton's Law of Cooling as expresses the heat Transfer rate in natural convection:

$$Q_{conv.} = hA(T_s - T_\infty) \quad (3)$$

Where: ***h*** is the heat transfer coefficient in (W/m.^{o}C).

The Nusselt number ***Nu*** in natural convection is in the following equation (4):

$$Nu = 0.54(Ra)^{\frac{1}{4}} \qquad 10^4 < Ra < 10^7 \quad (4)$$

Where $\boldsymbol{R_a}$ is the Rayleigh number, which is defined as the product of Grashof number and prandtl number, as:

$$R_a = G_r \,.\, \mathrm{P}_r = \frac{g.\beta(T_s - T_\infty)L^3}{\vartheta^2} \quad (5)$$

Where:
$\boldsymbol{g}$: gravitational acceleration m/s^2
$\boldsymbol{\beta}$: Coefficient of volume expansion, 1/k
$\boldsymbol{L}$: Characteristic of geometry, m
$\boldsymbol{\vartheta}$: Kinematics viscosity of fluid, m/s^2
Then, suppose the plate heated for 500℃ and exposed to atmospheric air at 20℃ we first determine the film temperature as:

$$T_f = \frac{T_s + T_\infty}{2} \quad (6)$$

$$T_f = \frac{500 + 20}{2} = 260\ ℃ = 533\ k$$

The Properties of air at $\boldsymbol{T_f}$:

$\beta = \frac{1}{533} = 1.87 * 10^{-3}\ K^{-1}$

$K = 4.39 * 10^2\ \frac{W}{m.k}$

$\vartheta = 2.88 * 10^{-5}\ N.\frac{s}{m^2}$

$P_r = 0.68$

$g = 9.81 \frac{m}{s^2}$

Then Rayleigh number can be found using equation (7):

$$R_a = G_r \,.\, P_r \quad (7)$$

$= 2.150606 * 10^5$

According to the equation (4) can calculate Nusselt number ***Nu*.**

$Nu = 0.54(2.150606)^{\frac{1}{4}}$

$Nu = 11.6$

$h = 16.5 \frac{W}{m^2 \ .℃}$

Then the heat transfer by convection is:

$Q_{conv.} = hA(T_s - T_\infty)$

$= 16.5\ (0.2 * 0.2)(500 - 50)$

$Q_{conv.} = 297\ W$

Now to evaluate the heat transfer from the upper surface of the plate by radiation as shown in figure (6) using equation (8)

$$Q_r = \sigma \epsilon f A (T_s^4 - T_\infty^4) \quad (8)$$

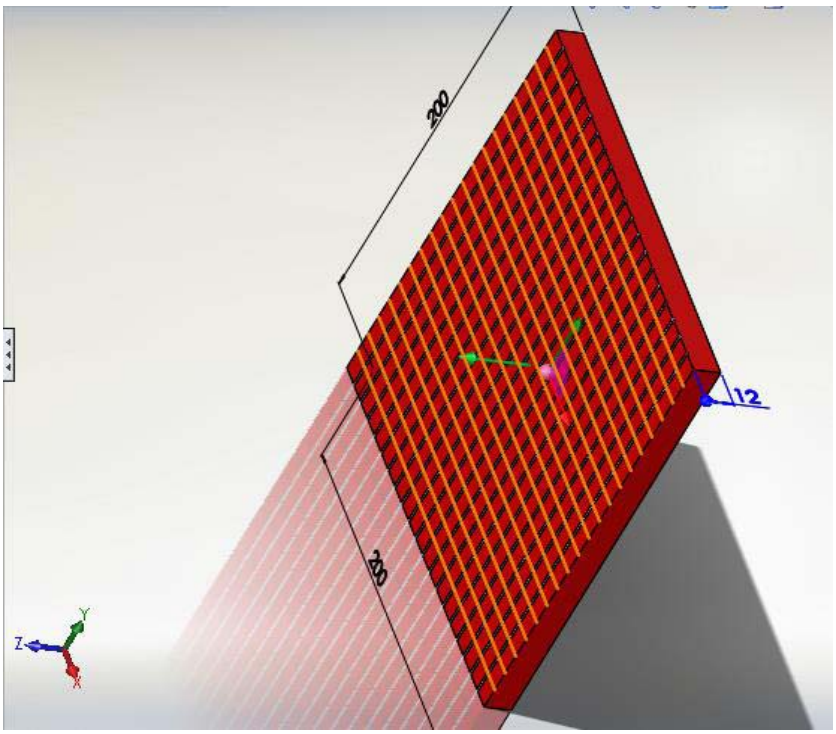

Figure 6. Upper surface heated plate with projection

$= 5.67 * 10^{-8} * 0.78 * 1 * (0.0 * 0.2)[(733)^4 - (298)^4]$

$Q_{conv} = 617\ W$

Then the total heat transfer calculated and needed to safely reach 500 ℃ is:

$$Q_T = Q_{conv} + Q_{cond} + Q_{rad} \quad (9)$$

$$Q_T = 1864.4\ W$$

While the electric heater designed to supply power according to the equation.

$$Q_{in} = 11_{Amp} * 220_{volt} = 2420\ W$$

Therefore, the inlet energy is quite enough to heat the plate more than 500 ℃ safely. The experimentally result results approved the uniform thermal distribution and temperature over all the examined area (400 cm2) as shown in figure (7), the latter explain the thermal energy detect and distributed as a function of temperature in histogram view, whereas the inset figure showed the uniformity of thermal energy and temperature distribution as well as the heat loss in the sidewall of the carriage.

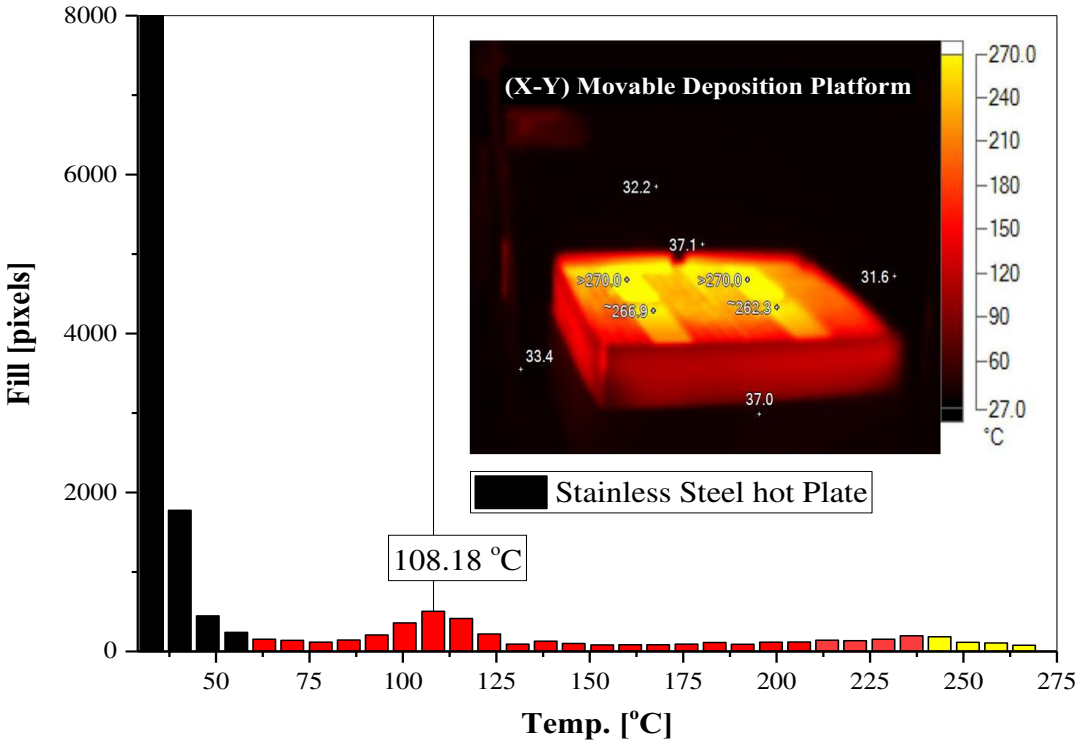

Figure 7. Histogram showed the thermal energy distributed overall the image, inset figure is the thermal image exhibited thermal and temperature distribution overall deposition area

4.Conclusion

The theoretical calculations of heat transfer showed that the total heat loss of all kinds is less than the designed capacity of the home-made electric heater that manufacturer, and therefore the heater has the ability to equip the deposition platform plate with uniform thermal energy and uniform temperature overall its area equally.

Acknowledgments

This work was supported by the laser and molecular lab. Physics Dept. college of science, Baghdad University. The author is indebted to Chief researcher Dr. Kamal Latief Hussien general manager of the Renewable Energy research & technology Directorate in the Ministry of Science and technology (M.O.S.T). The authors also like to thank Sabah Mohammed Hadi in the Solar Energy Research Center in (M.O.S.T).

References

[1] Theodore L 2011 Heat Transfer Applications for the Practicing Engineer (John Wiley & Sons, Inc.)
[2] Yunus A. Engel 2006 Heat and Mass Transfer
[3] Konstantin V. Frolov, Oleg N. Favorsky R A C and C F 2009 Mechanical Engineering, Energy Systems And Sustainable Development (EOLSS Publications)
[4] Seshan K 2002 Handbook Of Thin-Film Deposition Processes and Techniques (USA: William Andrew)
[5] Mooney J B and Radding S B 1982 Spray Pyrolysis Processing Annu. Rev. Mater. Sci. 12 81–101
[6] Mattox D M 2010 Handbook of physical vapor deposition (PVD) processing (William Andrew)
[7] Chopra K L 1969 Thin Film Phenomena (New York: McGraw-Hill,)

OLIFE: Tight Binding Code for Transmission Coefficient Calculation

IOP Conf. Series: Journal of Physics: Conf. Series **1003** (2018) 012114 doi:10.1088/1742-6596/1003/1/012114

OLIFE: Tight Binding Code for Transmission Coefficient Calculation

Zainelabideen Yousif Mijbil[1,2]

[1)] Chemistry and Physiology Department, Al-Qasim Green University, Al-Qasim Town Babylon, Iraq

[z)] Hillah, Babylon, Iraq, P. O. Box 385

z.ymijbil0@gmail.com , zymijbil@vet.uoqasim.edu.iq

Abstract A new and human-friendly transport calculation code has been developed. It requires a simple tight binding Hamiltonian as the only input file and uses a convenient graphical user interface to control calculations. The effect of magnetic field on the molecular junction has also been included. Furthermore the transmission coefficient can be calculated between any two points on the scatterer which ensures high flexibility to check the system. Therefore Olife can highly be recommended as an essential tool for pretesting, studying, and teaching electron transport in molecular devices that saves a lot of time and efforts.

1 Introduction

Molecular electronics field has enthused scientists worldwide for its spectacular features[1-3] such as high speed nanoscale junctions[4- 5] and the economical usage of power and resources[6]. Because of the nano-dimensions, quantum phenomena such as quantum tunneling [7-8] and quantum interference (QI)[9-11] are clearly revealed[12]. Therefore theoretical methods have continuously been developed to explain these phenomena [13 14] as well as the experimental techniques which eagerly seek to harness them [15]. However due to the complexity of the molecular structure[16, 17], junction design or both[18] the task has become far more intricate. Thus, theoreticians are working hard to analyse and investigate molecular behaviours[19, 20]. As a result, issues like the convenience[21] and efficiency of choosing a particular method for modelling and grasping signatures are the major difficulties theoreticians would definitely encounter[20-22]. Therefore these two problems will be closely examined in this paper.

The first problem we are aiming to discuss is the ability to easily simulate molecular structures and understanding electronic behaviours. Initially this issue stems basically from the intrinsic complexity of the molecule configuration [23-25]. For example porphyrin wheel is a single unit composed of an outer ring and inner spokes. The outer ring has six porphyrin molecules attached to each other by alkene chains on the circumference while the inner spokes consist of thirteen benzene molecules at the wheel

centre[26]. Therefore overcoming this problem requires theoretical methods capable of envisaging the main features of the molecule without considering their very elementary details. The approach that successfully ignores details but yet preserves the principle peculiarities is the first order tight binding (TB) approximation. Tight binding approach neglects all interactions except for those between the nearest neighbours[27,28]. Furthermore its validity has successfully approved through the impressive success[29] to capture the main features reflected in the transmission curve of the system[30] as it can be seen in the increased number of literature using this method[31-33]

The second obstacle is how convenient is to apply theoretical approaches. Results such as the transport coefficient calculation cannot be deduced entirely from TB alone. Therefore theories specialized in describing the ballistic transport through molecules should be combined with TB. Landauer-Büttiker theory is cornerstone approach in the field of molecular electronic transport[34]They have managed to describe the probability of transferring an electron from one side of the junction to the other side and have also taken into account the effect of the leads on the molecule transmission probability. Based on this theory commercial and academic packages namely Gollum[35] Sméagol[36] and ONETEP[37] have successfully described and calculated the conductance of a single molecule attached to external leads. However these softwares depend on other packages such as SIESTA[38] or Gaussian[39] to establish density functional Hamiltonian. As far as we know all transport codes including *Olife* need firstly the Hamiltonian of the system and secondly input instructions to derive the code. Although these packages may use simple tight binding Hamiltonian but they require sort of tedious inputs, a long preparation time, and finally their computing time itself can be very stressful especially for large systems in order just to be checked. On the other hand, efforts have been paid to make transmission calculations even simpler to be done and easy to be read. For instance Lambert and coworkers have suggested the Magic Ratio Rule (MRR) theory to compare between the conductance of different branches in hydrocarbon molecules such graphene and benzene[40]. The bottom line is that easy to use numerical methods are crucial to first check the system and then study it with inexpensive time limits

The main goal of this paper is to give a very easy and effective tool for transmission coefficient calculation. *Olife* code applies Landauer-Büttiker formalism based on a simple TB Hamiltonian of the system to depict the transmission features. It uses Matlab as programing language and offers a simple graphical user interface to facilitate the procedure of the calculations.

2 Methodology

In *Olife*, the transmission coefficient of the molecules is restricted to be calculated through two leads only The reason for this restriction is that the majority of experimental methods use two leads to measure the molecular conductance, for instance, the mechanical break junction (MBJ)[41] technique and scanning electron microscope (STM)[42]. However this temporary limitation is partially compensated by the merit that conductance can be calculated between any two points in the molecule which allows for high flexibility and practicality for testing the junction. A feature that, firstly, it is totally absent in experiments because they thoroughly depend on statistics for measurements[43 44] and secondly it is time and resources consuming in *ab-intio* calculations since the best scenario is to do the calculation via a linear scaling codes like SIESTA[45]. Therefore, *Olife* can be considered an indispensable tool for pre-testing the transmission behaviour of systems.

In this work and in order to calculate the transmission, the junction is divided into two parts as shown in 'Figure 1'. The first part is the external part which includes all leads and the second part namely the internal refers to the isolated molecule. These two parts can be combined together using Dyson's equation[46]:

$$\left(g(E)^{-1} - H\right)G(E) = I, \tag{1}$$

where E is the energy, $g(E)$ is the Green's functions of the separated parts of the junction, H is the connection Hamiltonian between the isolated molecule and leads, $G(E)$ is the total Green's function, and I is the identity matrix. The definitions of each part of Eq (1) are shown below

$$g(E)^{-1} = \begin{pmatrix} g_A^{-1} & 0 \\ 0 & g_B^{-1} \end{pmatrix} = \left(\begin{array}{cc:c} g_{A1}^{-1} & 0 & 0 \\ 0 & g_{A2}^{-1} & 0 \\ \hdashline 0 & 0 & g_B^{-1} \end{array}\right), \tag{2}$$

$$H = \left(\begin{array}{cc:c} 0 & 0 & h_{A1,B1} \\ 0 & 0 & h_{A2,B2} \\ \hdashline h_{A1,B1}^{\dagger} & h_{A2,B2}^{\dagger} & 0 \end{array}\right), \tag{3}$$

$$G(E) = \begin{pmatrix} G_{A1,A1} & G_{A1,A2} & G_{A1,B} \\ G_{A2,A1} & G_{A2,A2} & G_{A2,B} \\ G_{B,A1} & G_{B,A2} & G_{B,B} \end{pmatrix} \tag{4}$$

$$g_{Am}(E) = -\frac{e^{ik_m(E)}}{\gamma_m}, \quad m = 1, 2. \tag{5}$$

The leads are represented by their surface Green's function g_{AM}. The parameters γ_m and k_m are the coupling and wave number in the lead m respectively. The isolated molecule is represented by g_B which is given by

$$g_B = \left(E - H_B\right)^{-1}, \tag{6}$$

where H_B is the Hamiltonian of the isolated molecule and it is given by

$$H_B = \sum_{n=1}^{N} \varepsilon_n \left|n\right\rangle\left\langle n\right| + \sum_{n=1}^{N-1}\left[h_n \left|n\right\rangle\left\langle n+1\right| + h_n^{\dagger}\left|n+1\right\rangle\left\langle n\right|\right], \tag{7}$$

$$h_n = \gamma_n e^{-i\beta}, \tag{8}$$

where ε_n is the orbital onsite energy, n is the orbital index, N is the total number of sites, γ_n is the coupling energy, and β is the magnetic flux[47].

The retarded GF has two travelling waves; one moving to the left side of the scatterer and the other one moving to the right side. The left going waves are related to the reflection amplitudes while the right going waves are related to the transmission amplitude. These amplitudes can be deduced from the matrix elements of the total GF by using Fisher-Lee relation[48,49] which shows that

$$G_{a,a+1} = \frac{1}{i\hbar v} t\ e^{ik}, \tag{9}$$

$$G_{a,a} = \frac{1}{i\hbar v}(\ 1 + r\ ) \tag{10}$$

Therefore the transmission coefficient $T(E)$, the reflection coefficient $R(E)$, and finally the conductance $G(E)$ can be calculated from[49]

$$T(E) = \left|tt^*\right|^2, \quad R(E) = \left|rr^*\right|^2, \tag{11}$$

$$G(E) = \frac{2q^2}{h} \int dE\, T(E)\ (-\frac{\partial f}{\partial E}), \tag{12}$$

where r is the reflection amplitude and a and a+1 are the source point and post-scatterer point respectively. The group velocity is v, the electron charge is q, and $\hbar$ (=2π/h) where h is Planck's constant.

3 *Olife* Prerequisites

The only input file that *Olife* requires is the Hamiltonian of the system. This Hamiltonian can easily be built by hand for simple molecules or using some other softwares like Microsoft Excel or Matlab for big systems. In the supplementary information, a number of Hamiltonians has been included.

4. Tests and Results

4.1. Basic checks

The first example to test the results of the code is by assuming a perfectly crystalline one dimensional chain. The chain and the leads are all have the same onsite energies (= 0) and coupling elements (= 15) as the first case. The second example represents the same system but with weak coupling between the chain and the leads (equals to one third of the first case). The last scenario is when the coupling between the leads and the chain (molecule) is nullified. The results of the three cases are shown in Figure . These rudimentary examples are crucial to test the code because they clearly show the basic expected results of changing the transmission probability with the coupling between the molecule and the leads. In the first curve the transmission coefficient is equal to one because the system is purely periodic so that the de Broglie wave of the electron would have the same probability everywhere along the system. The third one shows zero $T(E)$ since the connection between the molecule and the leads is cut, i.e. the electron wave cannot move from one side to the other

4.2. Quantum interference

The moving de Broglie waves of the electrons in the molecule branches can interact with each other resulting in the so-called quantum interference[50]. To show that our code is able to illustrate quantum interferences, three types of connections of the leads to a single benzene ring have been separately considered. The first connection is the para connection where the two leads make 180 degrees with each other; the second one is the meta when the angle between the leads is 120 degrees; and finally an ortho configuration when the leads confine an angle of 60 degrees[51] as shown in Figure. All onsite energies are nullified. The coupling energies in the leads and benzene ring are equal to -1.5 whereas the coupling between the leads and the molecule was set to -0.5. The transmission curves at the centre of the band show that the para and ortho connections exhibit higher transmission values than meta configuration as shown in the inset of 'Figure'.

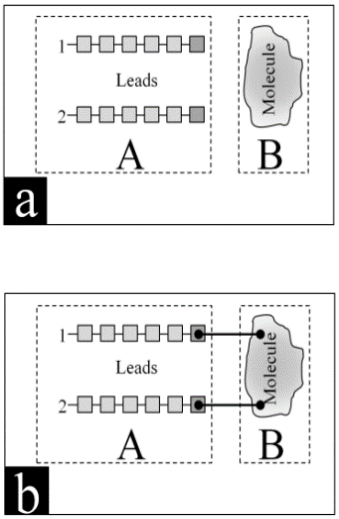

Figure 1 Junction configuration where it is divided into two parts: A shows the external part, namely the leads; B shows the internal part (molecule). Panels (a) and (b) illustrate a close and an open system respectively. One should notice that in both cases the leads do not interact directly with each other and only the surface part of the leads is connected to the molecule in the open system.

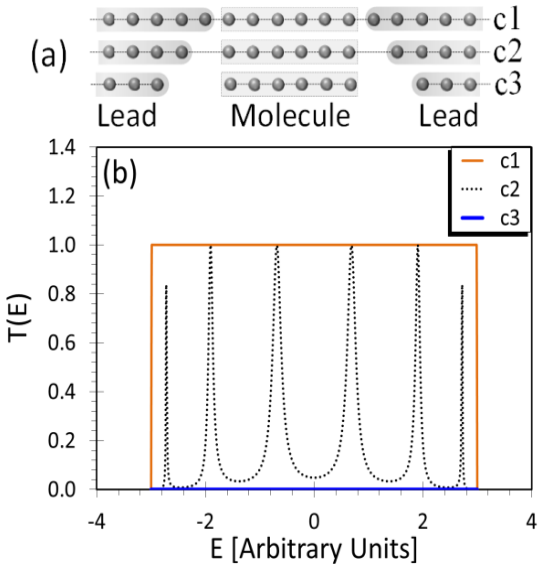

Figure 2 (a) Three schematic representations of a six-site system attached to two semi-infinite leads: c1 represents a perfectly crystalline system where all coupling and onsite energies are the same; c2 is the same system but with weak coupling to the leads; and c3 shows a detached molecule. (b) The transmission coefficient for each case. For more details see SI.1

4.3. Fano resonance

Fano resonance emerges in the transmission curve when a side group is attached to the main molecule, i.e. a localized state attached to the main continuum states. Fano resonance is very sensitive to any variations in the states of the extra connected molecule which results from changing the structure of the molecule or the surrounding environment[30-52]. Therefore to show that our code is capable of showing such a type of resonance, an extra site has been attached to six-site chain as shown in 'Figure a'. In this example all onsite energies are kept equal to zero and the coupling between the chain and leads is -0.5 which is the same for the coupling between the molecule and the attached unit. In addition, the coupling used for the chain was -1.5 and the values of the onsite of the pendant group are arbitrarily chosen to be -1 and 1.7 to produce distinctive states of Fano resonances. 'Figure b' illustrates the variation of the Fano resonance with change of the onsite energy of the pendant group.

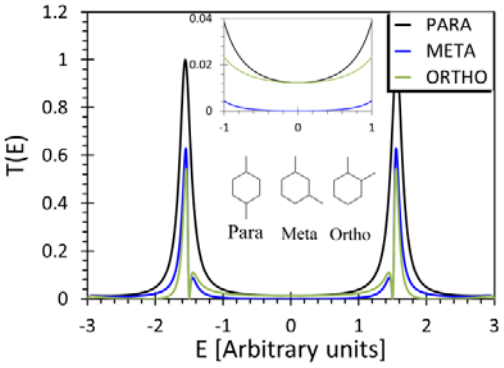

Figure 3 The transmission curve of a benzene ring connected in para, meta, and ortho configurations to two external leads. The above panel illustrates the transmission at the centre of the energy band and the lower panel shows the para, meta, and ortho configurations. More details can be found in the SI-2.

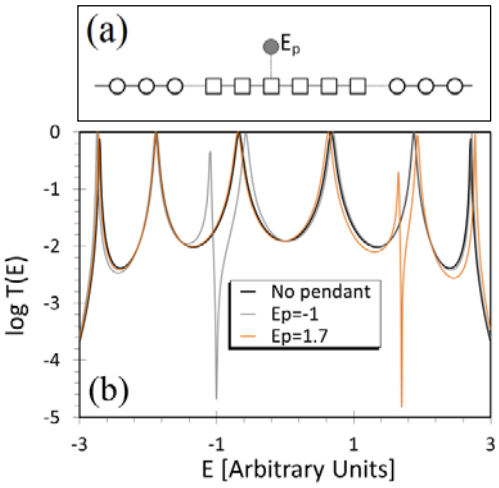

Figure 4 (a) A schematic represenation of a six-site chain attached at site number three to pendant goup with onsite energy E_p. (b) Transmssion coefficient of the chain when there is no pendant group and E_p is equal to -1 and 1.7. To keep clarity, more details can be found in the SI-3.

4.4. Magnetic field

Magnetic field is one of the main means to tune electron conductance in molecules[47-53] and understand phenomena like quantum Hall effect and de Haas–van Alphen effect[54]. For these reasons and to ensure a high applicability of *Olife*, we have included the effect of the magnetic field. The model system used to show the effect of the magnetic field is a benzene ring and the corresponding transmission curves are shown in Figure . The parameters used to produce the results in Figure are zero for all onsite energies and -1.5 for all coupling energies except for those between the leads and the benzene which set to -0.5.

4.5. Magic Ratio Rule

A beautiful and simple theory suggested by Lambert and his team is the Magic Ratio Rule (MRR) theory [40 55]. In this theory they have illustrated that constructive and destructive interferences can easily be deduced for graphene-like molecules without resorting to the expensive DFT calculations. The significance behind polycyclic aromatic hydrocarbons (PAHs) is that they represent perfect systems to understand the transport in molecular devices which use graphene as a building unit[40]. The calculations for some results of MRR are illustrated in Figure which shows the transmission coefficient of anthanthrene [40] and pyrene[55] molecules with different connection points. Figure a shows the effect of different connection points on the transmission coefficient of anthanthrene molecule which is schematically shown in Figure b and Figure c. The same procedure is repeated to obtain the results in Figure d which shows the transmission coefficient of pyrene molecule corresponding to the configurations shown in Figure e and Figure f. Our results are in good agreement with the related papers of the molecules. The parameters used in Figure a and Figure d are: all onsite energies are equal to zero, the coupling energies in the leads and molecules are -1.5, and the lead-molecule coupling was -0.5.

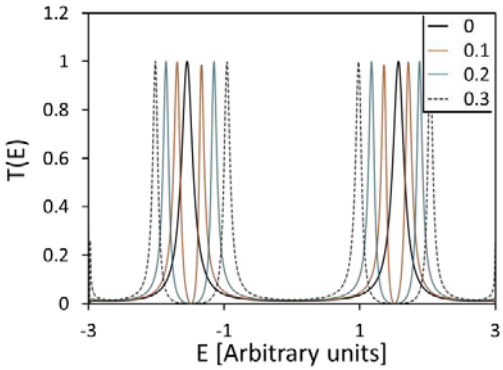

Figure 5 The effect of the magnetic field on the transmission resonances of benzene ring. For simplicity, the magnetic field is represented by arbitrary units.

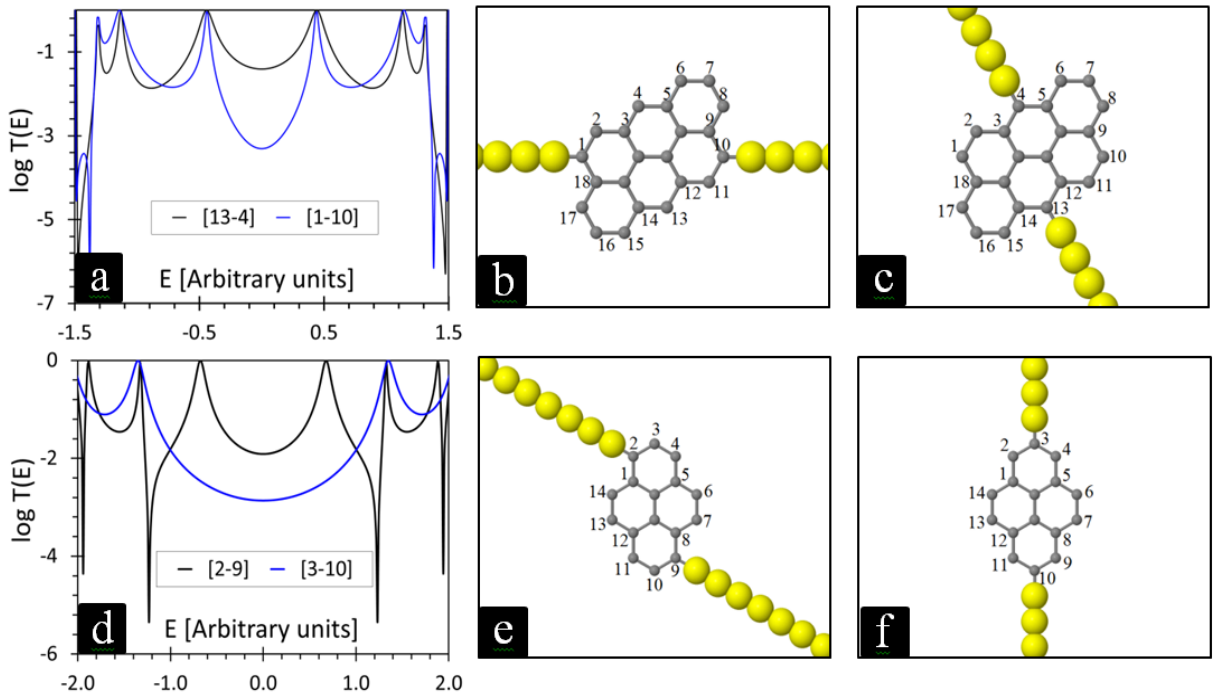

Figure 6 (a) and (d) show the transmission curves of anthanthrene and pyrene molecules respectively. The curves in (a) show the effect of different contact points of the leads to anthanthrene molecule which illustrated in (b) and (c). Similarly, (e) and (f) show the same effect on transmission coefficient (d) of pyrene molecule.

5 Conclusions

Olife is a very easy simple and efficient tool for transmission calculation because it uses very simple inputs. It is also very fast code owing to the fact that it uses simple tight binding Hamiltonians. Therefore this code is essential for studying pre-checking and teaching the transmission coefficient of molecules.

Acknowledgement

The author wants to thank Dr Ahmed Baqer Sharba for linguistic and scientific discussions.

References

[1] Livshits G I Stern A Rotem D Borovok N Eidelshtein G Migliore A Penzo E Wind S J Di Felice R Skourtis S S Cuevas J C Gurevich L Kotlyar A B and Porath D 2014 *Nat Nano* **9** 1040
[2] Han H Zhang Y Wang N Samani M K Ni Y Mijbil Z Y Edwards M Xiong S Sääskilahti K Murugesan M Fu Y Ye L Sadeghi H Bailey S Kosevich Y A Lambert C J Liu J and Volz S 2016 *Nat Comm* **7** 11281
[3] Mijbil Z Y 2012 *Chem Mat Res* **2** 8
[4] Reed M A 1999 *Proc IEEE* **87** 652
[5] Xiang D Wang X Jia C Lee T and Guo X 2015 From Concept to Function
[6] Liu R Ke SH Baranger H U and Yang W 2005 *J Chem Phys* **122** 044703
[7] Bogani L and Wernsdorfer W 2008 *Nat Mater* **7** 179
[8] Wernsdorfer W AliagaAlcalde N Hendrickson D N and Christou G 2002 *Nature* **416** 406
[9] Berritta M Manrique D Z and Lambert C J 2015 *Nanoscale* **7** 1096
[10] Lambert C J 2015 *Chem Soc Rev* **44** 875
[11] Sparks R E GarcíaSuárez V M Manrique D Z and Lambert C J 2011 *Phys Rev B* **83** 075437
[12] Xiang D Wang X Jia C Lee T and Guo X 2016 *Chem Rev* **116** 4318
[13] Breit G and Wigner E 1936 *Phys Rev* **49** 519
[14] Landauer R and Büttiker M 1985 *Phys Rev Lett* **54** 2049
[15] Parks J J Champagne A R Hutchison G R FloresTorres S Abruña H D and Ralph D C 2007 *Phys Rev Lett* **99** 026601
[16] Ozawa H Baghernejad M AlOwaedi O A Kaliginedi V Nagashima T Ferrer J Wandlowski T GarcíaSuárez V M Broekmann P Lambert C J and Haga M 2016 *Chem Euro J* **22** 12732
[17] Davidson R AlOwaedi O A Milan D C Zeng Q Tory J Hartl F Higgins S J Nichols R J Lambert C J and Low P J 2016 *Inorg Chem* **55** 2691
[18] Mol J A Lau C S Lewis W J M Sadeghi H Roche C Cnossen A Warner J H Lambert C J Anderson H L and Briggs G A D 2015 *Nanoscale* **7** 13181
[19] RinconGarcia L Ismael A K Evangeli C Grace I RubioBollinger G Porfyrakis K Agrait N and Lambert C J 2016 *Nat Mater* **15** 289
[20] Borges A and Solomon G C 2016 *J Chem Phys* **144** 194111
[21] Mijbil Z Y Abdulsattar M A and AbdulLettif A M 2011 *Nat Sci* **3** 11
[22] Péterfalvi C G and Lambert C J 2012 *Phys Rev B* **86** 085443
[23] Aggarwal A V Thiessen A Idelson A Kalle D Würsch D Stangl T Steiner F Jester SS Vogelsang J Höger S and Lupton J M 2013 *Nat Chem* **5** 964
[24] Langton M J Matichak J D Thompson A L and Anderson H L 2011 *Chem Sci* **2** 1897
[25] Davis N K S Thompson A L and Anderson H L 2011 *J Am Chem Soc* **133** 30
[26] Sprafke J K Kondratuk D V Wykes M Thompson A L Hoffmann M Drevinskas R Chen WH Yong C K Kärnbratt J Bullock J E Malfois M Wasielewski M R Albinsson B Herz L M Zigmantas D Beljonne D and Anderson H L 2011 *J Am Chem Soc* **133** 17262
[27] Hancock Y Uppstu A Saloriutta K Harju A and Puska M J 2010 *Phys Rev B* **81** 245402
[28] Nakada K Fujita M Dresselhaus G and Dresselhaus M S 1996 *Phys Rev B* **54** 17954
[29] Porezag D Frauenheim T Köhler T Seifert G and Kaschner R 1995 *Phys Rev B* **51** 12947
[30] Papadopoulos T A Grace I M and Lambert C J 2006 *Phys Rev B* **74** 193306
[31] White C T Li J Gunlycke D and Mintmire J W 2007 *Nano Lett* **7** 825
[32] Gunlycke D and White C T 2008 *Phys Rev B* **77** 115116
[33] Gunlycke D Areshkin D A and White C T 2007 *App Phys Lett* **90** 142104
[34] Büttiker M Imry Y Landauer R and Pinhas S 1985 *Phys Rev B* **31** 6207
[35] Ferrer J Lambert C J GarcíaSuárez V M Manrique D Z Visontai D Oroszlany L RodríguezFerradás R Grace I Bailey S W D Gillemot K Hatef S and Algharagholy L A 2014

New J Phys **16** 093029
[36] Rocha A R GarcíaSuárez V M Bailey S Lambert C Ferrer J and Sanvito S 2006 *Phys Rev B* **73** 085414
[37] Bell R A Dubois S M M Payne M C and Mostofi A A 2015 *Comp Phys Comm* **193** 78
[38] José M S Emilio A Julian D G Alberto G Javier J Pablo O and Daniel SP 2002 *J Phys: Cond Matt* **14** 2745
[39] Böhm M C 1984 *B Bunsengesell physik Chem* **88** 778
[40] Geng Y Sangtarash S Huang C Sadeghi H Fu Y Hong W Wandlowski T Decurtins S Lambert C J and Liu SX 2015 *J Am Chem Soc* **137** 4469
[41] Smit R H M Noat Y Untiedt C Lang N D van Hemert M C and van Ruitenbeek J M 2002 *Nature* **419** 906
[42] Scheer E Agrait N Cuevas J C Yeyati A L Ludoph B MartinRodero A Bollinger G R van Ruitenbeek J M and Urbina C 1998 *Nature* **394** 154
[43] Solomon G C 2016 *Nat Mater* **15** 254
[44] LINDSAY S M 2004 *Electrochem Soc interf* **13** 26
[45] Emilio A Anglada E Diéguez O Gale J D García A Junquera J Martin R M Ordejón P Pruneda J M SánchezPortal D and Soler J M 2008 *J Phys: Cond Matt* **20** 064208
[46] Sanvito S Lambert C J Jefferson J H and Bratkovsky A M 1999 *Phys Rev B* **59** 11936
[47] Rai D Hod O and Nitzan A 2011 *J Phys Chem Lett* **2** 2118
[48] Fisher D S and Lee P A 1981 *Phys Rev B* **23** 6851
[49] datta S *Electronic Transport in Mesoscopic Systems* 1995: Cambridge University Press
[50] Nozaki D Avdoshenko S M Sevinçli H and Cuniberti G 2014 *J App Phys* **116** 074308
[51] Solomon G C Andrews D Q Hansen T Goldsmith R H Wasielewski M R Van Duyne R P and Ratner M A 2008 *J Chem Phys* **129** 054701
[52] Ashwell G J Urasinska B Wang C Bryce M R Grace I and Lambert C J 2006 *Chem Comm* 4706
[53] Takami S Furumi S Shirai Y Sakka Y and Wakayama Y 2012 *J Mat Chem* **22** 8629
[54] Analytis J G Blundell S J and Ardavan A 2004 *Am J Phys* **72** 613
[55] Sangtarash S Huang C Sadeghi H Sorohhov G Hauser J Wandlowski T Hong W Decurtins S Liu SX and Lambert C J 2015 *J Am Chem Soc* **137** 11425

Effect of time variation on coating characteristic of Ti-6Al-4V alloy coated with TiO2 by dip coating method

Effect of time variation on coating characteristic of Ti-6Al-4V alloy coated with TiO2 by dip coating method

Shaymaa Hashim Aneed

Collage of Education / pure science, Physics Department, University of Baghdad/ Ibn Al-Haitham collage, Baghdad / Iraq.

shaimaahasheem1977@gmail.com

Abstract: In this reserch samples of Ti-6Al-4V alloy was coated with TiO2 layer by dip coating method in solution consist of 8 gm TiO2 nanoparticle dissolved in 100 ml. ethanol absolute (99%) and 1 gm P2O5, with various coating periods (1,2,3) minuts .The corrosion characteristics was investigated using (parstat 2273,USA made) ,the corrosion rate reach to7.047 × 10-4 mm/y for sample coated at 3 minutes compared with 8.266 × 10-3mm/y for uncoated sample . Then the samples immersed in simulated body fluid (SBF) synthesized in the laboratory for one month in order to investigate the osseointegration from hydroxyapatite biomimaticallyformed , the corrosion charactaristics also invistigated after immirsing in (SBF) and it was 1.479 × 10-4 mm/y . For each part of reaserch we test the optical microscopic images ,XRD and SEM in order to evaluate the results.

Keyword: dip coating ,TiO2 coting , biomimatic formation of hydroxyapatite

1. Introduction

Metallic biomaterials such as stainless steels, Co-Cr alloys, and titanium and its alloys are currently utilized as structural materials in artificial hip joints, bone plates and screws, and artificial dental roots; they are mainly used in implants that replace hard tissue[1,2] . Among biometals, titanium alloys have high biocompatibility, specific strength, and corrosion resistance, and exhibit the most suitable characteristics for biomedical applications. However, titanium and titanium alloys cannot meet all of the clinical requirements. One of the most popular titanium alloy, used today in medicine, is Ti-6Al-4V material [3, 4].In order to improve the titanium and its alloy corrosion resistance and oseointegration with bones ,many surface modification method was investigated by coating titanium and its alloy with biocompatible ceramics like TiO2, hydroxyapatite , alumina and zirconia [5], using many way for coating like electrophoretic deposition ,electrolytic deposition , plasma sputtering and dip coating [6-9]. Dip coating method considered the most easy and practical one, because it was not need a complex systems like plasma sputtering , very low coast ‘ with cheap equipment and different shapes coating for complex shapes .The dip coating very successful to do it in room temperature and don’t needed for vacuum system [10,11].In this research we coated Ti-6Al-4V with TiO2 by dip coating at different thickness and investigate the purity of TiO2 and phase structures by XRD and the resistance of corrosion characteristic by measuring polarization curve (Tafel) , ossiointegration also investigated by invetro biomimetic coating

achieved by immersing the coated samples in concentrated synthetic simulated body fluid for one months, testing the coated and biomimetic coated samples by optical microscope, XRD and SEM.

2. Materials and methods

Titanium samples with 20 mm diameter was grinded by 500 micron SiC grinding paper .Sonically cleaned by using ultrasonic bath for 15 min. twice in ethanol 96% (Sigma Aldrich, England) ,then was cleaned in ultrasonic bath by distilled water for 15 min. once time. Solution consist from 8 gm TiO2 nanoparticle (Skyspring nanoparticle, USA) dissolved in 100 ml. ethanol absolute 99% (Romell, England) and 1 gm P2O5 (Merick,England) was prepared. The samples immersed for different time (1, 2.3) min. in the prepared solution. Calcined in tubular furnace at 400 °C under air atmosphere for 1 hr. period and was let to cool overnight. The corrosion characteristics polarization curve (Tafel) for coated samples was measured by using (PARSTAT 2273, USA) .The coated samples tested by optical microscope, SEM, XRD. The coated samples was bimimatically tested by immersing in synthetic simulated body fluid (SBF) for one month in order to investigate the ossiointgration ,the prepared synthetic simulated body fluid chemical composition was tabled in table (1). The biomimatically coated samples was tested by optical microscope,SEM,XRD.

Table 1. Simulated body fluid (SBF) chemical composition [1].

Item	**Description**	**Concentration gm/l**
1	**Sodium Chloride**	**8.035**
2	**Sodium Bicarbonate**	**0.355**
3	**Potassium Chloride**	**0.225**
4	**Potassium Phosphate Dibasic Trihydrate**	**0.231**
5	**Magnesium Chloride Hexahydrate**	**0.311**
6	**Calcium Chloride**	**0.292**
7	**Sodium Sulfate**	**0.072**

3.Results and discussion

The polarization curve (Tafel) diagram for coated samples shows that the corrosion current decrease with increasing coating time compared with uncoated samples as shown in Figure 1 ,that was expected because the increasing in coating time lead to increase the thickness of coated layer as shown in Table 2.

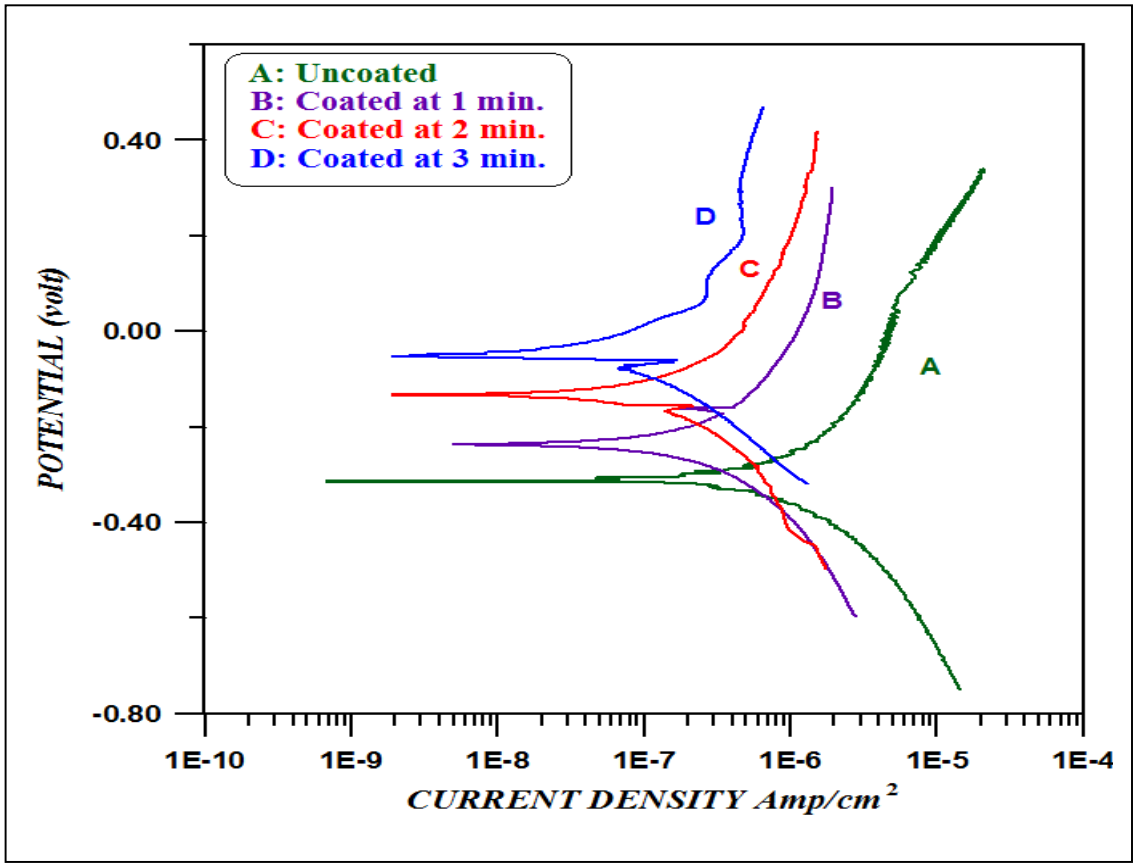

Figure 1. Polarization curves (Tafel) for Ti-6Al-4V coated samples with nanoparticle TiO2

Table 2.corrosion charecteristics and coated layer thickness for Ti-6Al-4V coated with nanoparticle TiO2

Coating time (min)	E corr. (volt)	I corr. (Amp)	Corr.rate (mm/y)	Layer thickness (μm)
uncoated	-0.315	9.5 × 10-7	8.266 × 10-3	0.0
1 min.	-0.236	1.8 × 10-7	1.566 × 10-3	40
2 min	-0.147	1.2 × 10-7	1.044 × 10-3	110
3min.	-0.561	8.1 × 10-7	7.047 × 10-4	150

The optical microscope images shows that the coating at 1 min was not uniform coating and there was uncoated area but with increasing coating time the coating was uniform and the morphology refer to the increasing with thickness as shown in 'Figure (2)'.

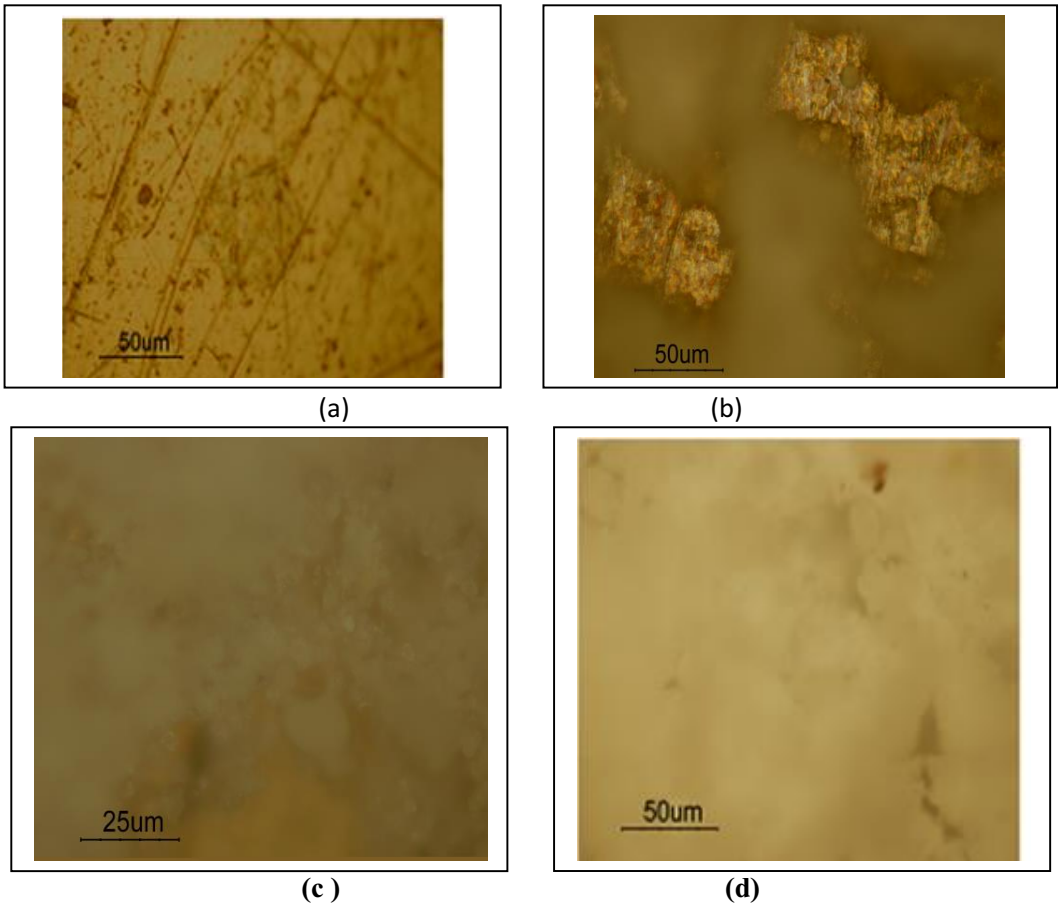

Figure 2. Optical microscope images for Ti-6Al-4V coated samples with nanoparticle TiO2 (a): uncoated, (b) 1min.coating, (c)2 min. coating (d)3 min. coating.

The SEM images for uncoated and coated samples at 3 min shows the morphology of the coated TiO2 as shown in 'Figure (4)'.

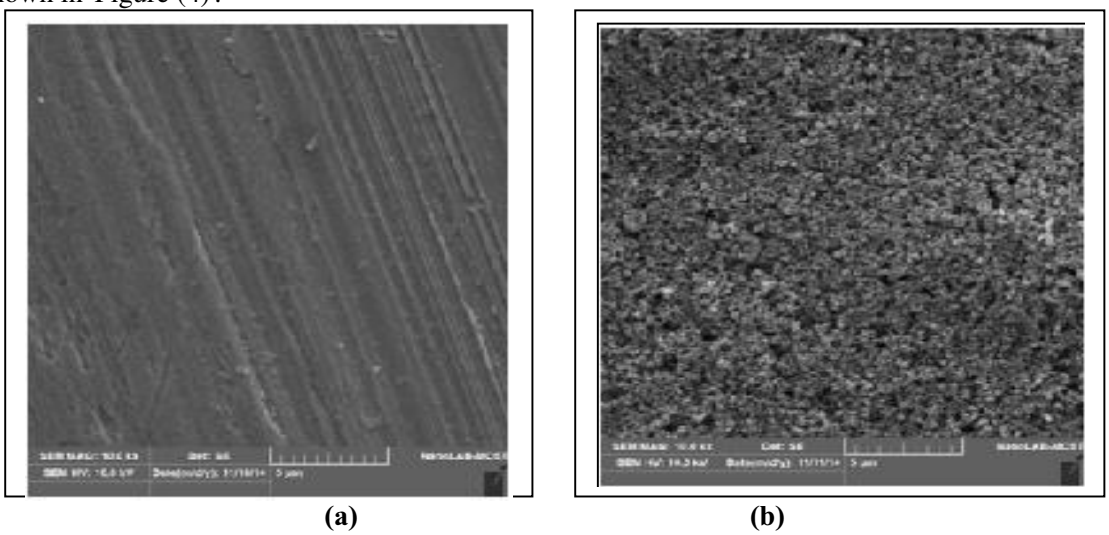

Figure 3. SEM images for Ti-6Al-4V coated samples with nanoparticle TiO2 (a): uncoated and (b): coated at 3 min.

The XRD pattern for the coated samples shows obviously the routile TiO2 coated on Ti-6Al-4V alloy as shown in Figure 5.

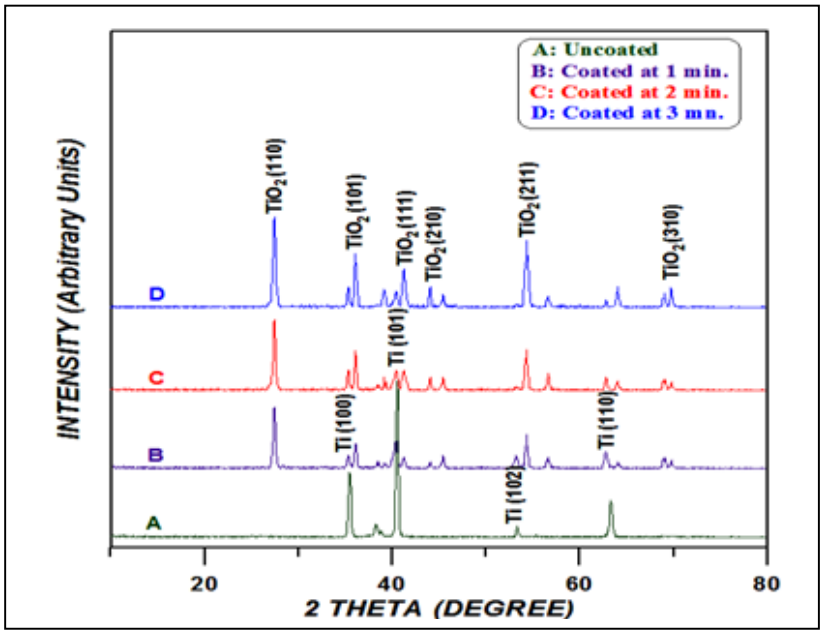

Figure 4. XRD pattern for Ti-6Al-4V coated samples with nanoparticleTiO2

The samples of Ti-6Al-4V coated with TiO2 immersion in SBF for one month to study resistance the alloy for corrosion. And this samples appear more nobility behavior in corrosion tests compared with un immersion sample because the hydroxyapatite formed from (SBF) and coated the samples fill all uncoated area and increase the coated layer thickness as shown in fig (6) and table (3)

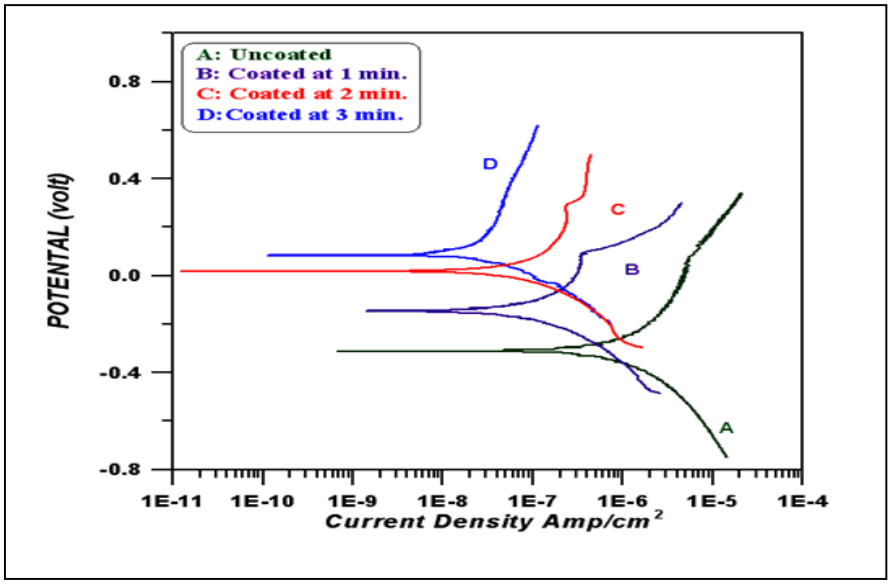

Figure 5. Figure Polarization curves (Tafel) for Ti-6Al-4V coated samples with nanoparticle TiO2 and immersed in (SBF) for one month.

Table (3) corrosion charecteristics and coated layer thickness for Ti-6Al- 4V coated with nanoparticle TiO2 and immersed in (SBF) for one month

Coating time (min)	E corr. (volt)	I corr. (Amp)	Corr.rate (mm/y)	Layer thickness (mm)
Uncoated	-0.315	9.5 × 10-7	8.266 × 10-3	0.0
1 min.	-0.157	0.9 × 10-8	8.613 × 10-4	75
2 min	0.028	5.4 × 10-7	4.698 × 10-3	170
3min.	0.869	1.71 × 10-7	1.479 × 10-4	230

The optical microscope images shows no uncoated area ,that means the hydroxyapatite that formed cover all the sample surface and casuseincrasing in thickness , the morphology also was different from the sampes that not immersed as shown in 'figure (7)'.

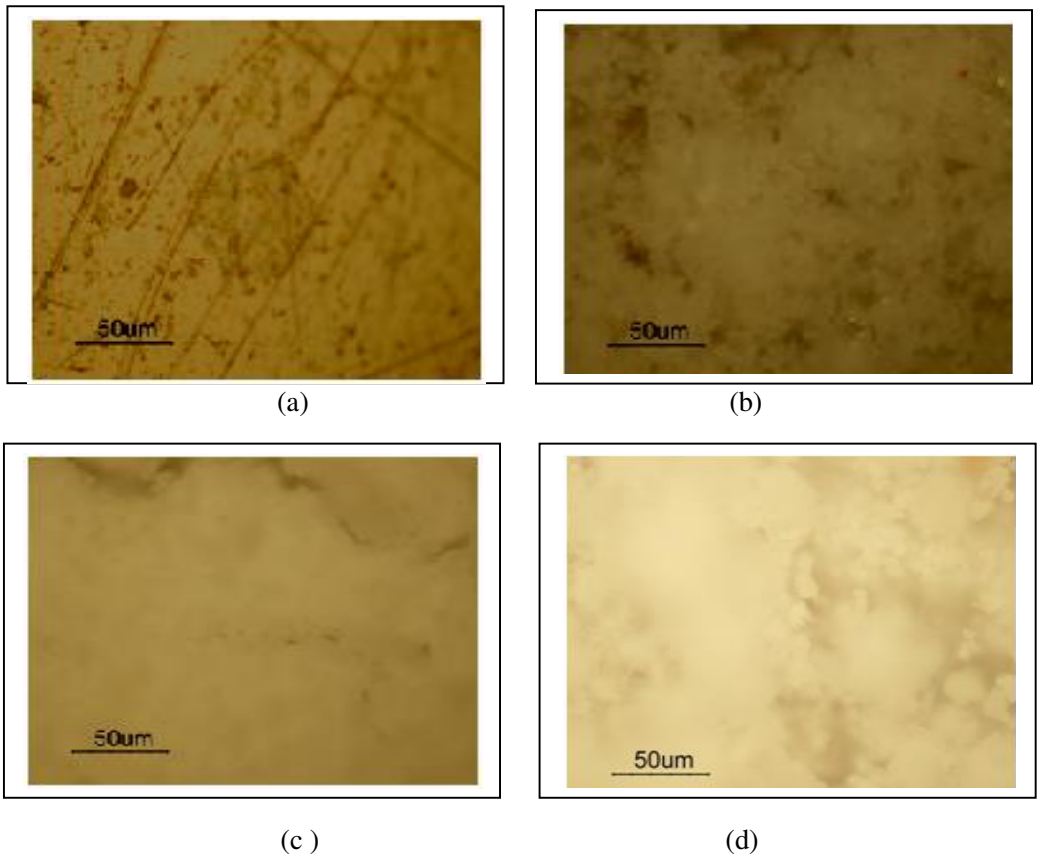

Figure 6 microscopic images for Ti-6Al-4V coated samples with nanoparticle TiO2 and immersed in (SBF) for one month(a): uncoated, (b) coated at 1min.,(c) coated at 2min.and(d): coated at 3min.

The SEM images shows a different morphology for the surface coated with TiO2 for 3 min. and immersed in (SBF) for one month as shown in fig (8) and the XRD pattern shows obviously appearance of hydroxyapatite with the rutile TiO2 as shown in fig (9) ,that is mean the coating has a good osseointegration if the Ti-6Al-4V alloy implants coated with TiO2 and will implanted in human body.

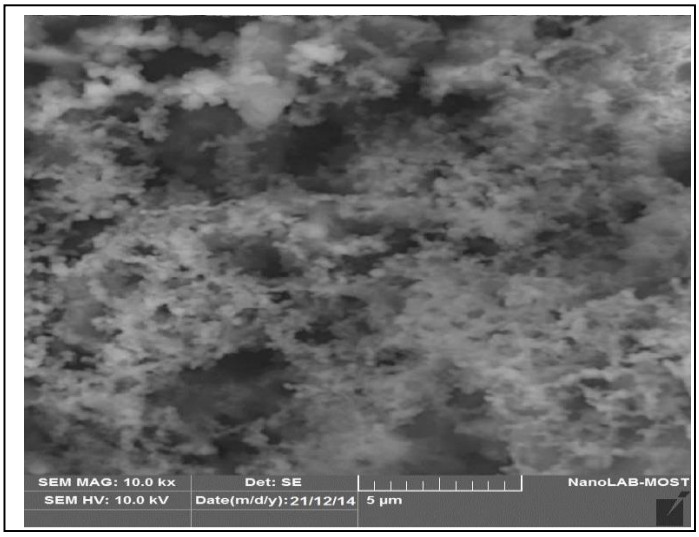

Figure 7 Ti-6Al-4V coated samples with nanoparticle TiO2 and immersed in (SBF) for one month.

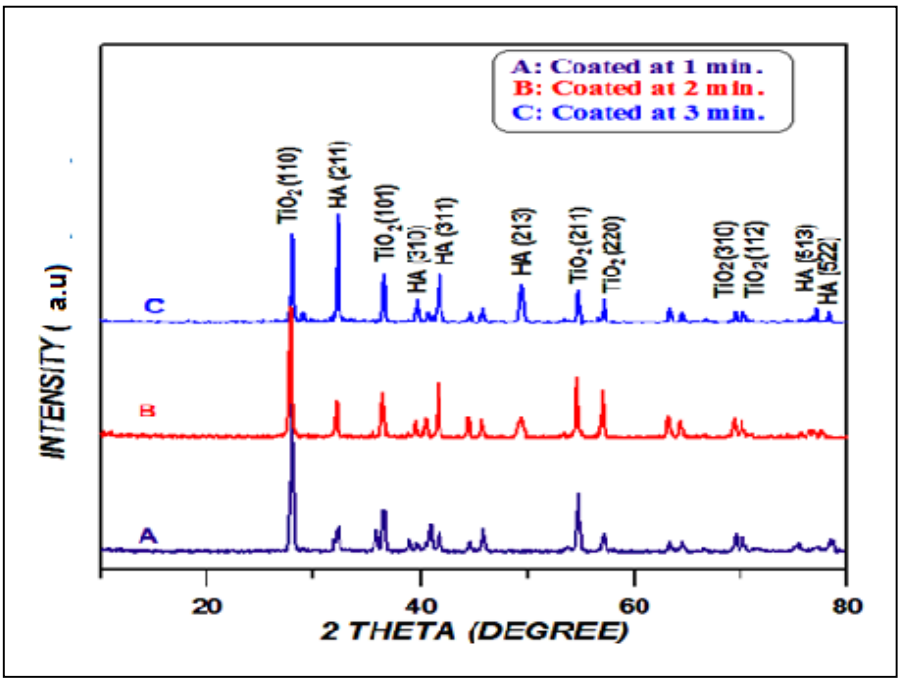

Figure 8 Ti-6Al-4V coated samples with nanoparticle TiO2 and immersed in (SBF) for one month.

4. Conclusion

The effect of increasing coating period of Ti-6Al-4V alloy with TiO_2 layer by dip coating improved the corrosion characteristics , the corrosion rate be 7.047×10^{-4} mm/y for 3 min period coated sample while the corrosion rate for uncoated samople was 8.266×10^{-3} mm/ y. The immersing in SBF for one month make more improve in corrosion characteristics ,where it reach to 1.479×10^{-4} mm/y for 3 min period coated sample , and also prove that there was biomimatically hydroxyapatite formed which refer to osseointegration with living bone if the samples implanted in human body.

References

[1] Yuhua Li, Chao Yang *, Haidong Zhao, Shengguan Qu, Xiaoqiang Li and Yuanyuan Li "New Developments of Ti-Based Alloys for Biomedical Applications", *Materials*, 2014, (7): 1709-1800.
[2] MitsuoNiinomi " Recent research and development in titanium alloys for biomedical applications and healthcare goods", *Science and Technology of Advanced Materials* ,2003(**4**): 445–454.
[3] Xuanyong Liu, Paul K. Chu and Chuanxian Ding "Surface modification of titanium, titanium alloys, and related materials for biomedical applications ", *Materials Science and Engineering* ,2004,R(**47**) :49–121.
[4] C. Veiga, J.P. Davim and A.J.R. Loureiro "properties and applications of titanium alloys: a brief review", *Rev.Adv. Mater. Sci*., 2012, (**32**):133-148.
[5] K.Niespodziana,K.Jurczyk and M.Jurczyk"The synthesis if titanium alloys for biomedical applications", *Rev.Adv.Mater.Sci.,*2008 ,(**18**): 236-240.
[6] A. R. Boccaccini , S. Keim1, R.Ma, Y. Li and I. Zhitomirsky " Electrophoretic deposition of biomaterials", *J. R. Soc. Interface* ,2010,(**7**): S581–S613.
[7] J. M. Zhang, C. J. Lin, Z. D. Feng And Z. W. Tian, 1998" Hydroxyapatite=metal composite coatings prepared by multi-step electrodeposition method", *journal of materials science letters,* , (17):1077- 1079.
[8] S.W.K. Kweh, K.A. Khor and P. Cheang "Plasma-sprayed hydroxyapatite (HA) coatings with flame-spheroidized feedstock: microstructure and mechanical properties", *Biomaterials*, 2000, (21):1223- 1234.
[9] Chun-Cheng Chen and Shinn-Jyh Ding"Effect of Heat Treatment on Characteristics of Plasma Sprayed Hydroxyapatite Coatings" *Materials Transactions*, 2006,47(**3**):935 – 940.
[10] Bora Mavis and A. CuneytTas " Dip Coating of Calcium Hydroxyapatite on Ti-6Al-4V Substrates",*J. Am. Ceram. Soc*., 2000, **83** (4):989–91.
[11] R.S. Sonawane , S.G. Hegde and M.K. Dongare " Preparation of titanium(IV) oxide thin film photocatalystby sol–gel dip coating " *Materials Chemistry and Physics* ,2002,(**77**): 744–750.

Study electron transport coefficients for Ar, O_2 and their mixtures by using EEDF program

Study electron transport coefficients for Ar, O_2 and their mixtures by using EEDF program

D S Abdul Majeed[1],B J Hussein[1], M K Jassim[1]

[1]Physics Department College of Education for Pure Science Ibn AL Haitham University of Baghdad

drbushrahussam@yahoocom

Abstract. We calculated the electron transport coefficient in Ar, O_2 and their mixtures for ratio of E/N where E denotes the electric field and N the density of gas atoms from $5 - 600$ Td $1\text{Td} = 10^{-17}\ \text{V.cm}^2$ The result and parameters mean energy mobility drift velocity and others are calculated by solving Boltzmann equation We study these gases because of its importance in thermal plasma such as shielding gas for arc welding of metals and alloys These results are useful to find best gas mixtures to reach appropriate transport parameter and to derive the same relevant cross section data

Keywords transport parameter coefficients Argon and oxygen uses and application Boltzmann equation

1. Introduction

The electron energy distribution functions EEDF play a fundamental role in plasma modeling The need of this function comes through the calculations of the reaction rates for electron collision reactions [1 – 3] The distribution functions such as Maxwellian Druyvesteyn and the solution of Boltzmann equation assume that elastic collisions are dominated and the effect of inelastic collisions on the distribution function is not important [4 – 5] However inelastic collisions of electrons with heavy particles play an essential role in the dropping of EEDF at higher electron energies On the other hand the electron transport properties can be derived from EEDF There are many resources help to figure out these properties The EEDF software package is one of those resources [6] This program gives results of the kinetic and transport coefficients of plasma in the pure and mixture of gases by numerically solving Boltzmann equation of EEDF in low – ionized plasma in an electric field In practical applications the inert gases can be mixed to specific gas in order to get special characteristic of the application In turn this needs to have accurate data about electron transport properties of gas mixtures The calculations data of a mixture of molecular Oxygen and Argon under a steady state electric field are presented in this paper There are several computational resources and numerical techniques used to find the transport properties One of them is presented in the EEDF software package This program gives results of the kinetic and transport coefficients of plasma in the mixture of gases by numerically solving Boltzmann equation of EEDF in low – ionized plasma in an electric field This program gives results of the kinetic and transport coefficients of plasma in the mixture of gases by numerically solving Boltzmann equation

of EEDF in low – ionized plasma in an electric field The gas mixtures of molecular Oxygen and Argon are very customary used for a lot of important plasma processes and plasma applications [6] The calculations of EEDF and transport coefficient of pure Argon and pure molecular oxygen and their mixtures are carried out under standard conditions $273\ ^0\text{K},\ 760\ \text{torr}$ by solving Boltzmann equation with two – term approximation using EEDF The range of reduced electric field is between 5 and 600 Td and the electron concentration is $1 \times 10^3\ \text{cm}^{-3}$ One of the goal of this paper is to compute electron drift velocity which is an important swarm parameter and may be useful to control electron energy [7]

2. Theory.

We use the program for numerical solution of Boltzmann equation for the electron energy distribution function EEDF in lowionized plasma in an electric field it is used for calculations of electron transport and kinetic coefficients in gas mixtures [8] In general the EEDF and the electron coefficients for the given discharge conditions can be calculated from the fundamental collision cross section data by solving Boltzmann equation The general form of Boltzmann equation [9]

$$(1)\left(\frac{\partial}{\partial t} + \upsilon.\nabla_r + \frac{eE}{m}.\nabla_\upsilon\right) f(r,\upsilon,t) = \left(\frac{\partial f}{\partial t}\right)_{\text{collisions}}$$

Where $f(r,\upsilon,t)$ is the distribution function for at time t and spatial location r with velocity υ The acceleration of charged particle is given by eE/m and $\partial f/\partial t$ states that $f(r,\upsilon,t)$ changes with time at fixed values of υ and r The term $\upsilon.\nabla_r$ describes that part of change due to an external force altering υ We calculate the time evolution of in mixture of atomic or molecular gases accelerated by electric field The program also computes the diffusion coefficient as [10]

$$D = \left(\frac{1}{3N}\right)\left(\frac{2e}{m}\right)\int_0^\infty f(\epsilon)\frac{\epsilon d\epsilon}{\sum \delta_s \sigma_s(\epsilon)} \qquad (2)$$

Where q_s is the concentration of the species N_s The term $\sigma_s(\epsilon_k)$ is the cross section for elastic scattering of species$s$ and f_k is the normalized distribution function
The drift velocity is given by [10]

$$(3)\quad \upsilon_d = -\frac{1}{3}\left(\frac{2e}{m}\right)^{\frac{1}{2}}\left(\frac{E}{N}\right)\int_0^\infty \frac{1}{\sum_s \delta_s \sigma_s(\epsilon)}\frac{df_0}{d\epsilon}\epsilon d\epsilon$$

Where ϵ is electron energy in eV N is the gas density in $\text{cm}^{-3}$and E/N is in Vcm^2 The electron density n_e is in cm^{-3} and $\delta_s = N_s/N$ The term σ_s is the momentum transfer cross section for species s
The electron mobility stated as the ability of charged particles such as electron to move through a medium in response to an electric field that is pulling them we can write as [11]

$$\mu = \frac{\upsilon_d}{E} \qquad (4)$$

And also can compute the electron mean energy by [12 13]

$$(5)\langle\epsilon\rangle = \int_0^\infty f_0\,(\epsilon)\epsilon^{\frac{3}{2}}d\epsilon$$

The Boltzmann equation describes an evolution of rarefied substance whose particles during a flow undergo binary interaction It describes the physical phenomena which are often of great importance for engineering and technological applications

3 Results and discussion

'Figure 1a', 'Figure 1b' exhibit the EEDF with Mean Electron Energy MEE for pure molecular Oxygen and pure Argon for different values of reduced electric field respectively

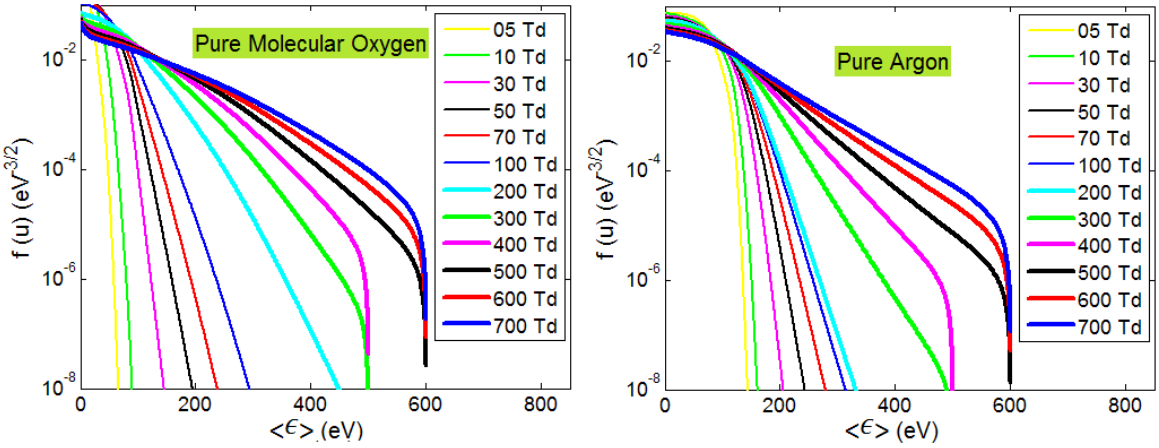

Figure1 a EEDF as a function of mean electron energy for various reduced electric fields E/N in pure molecular Oxygen and b pure Argon In both a and b the electron concentration is 1×10^3 cm^{-3} the gas temperature is 273 ^{0}K and the pressure is 760 torr

'Figure 2a',' Figure 2c' show the EEDF as a function of MEE for various reduced electric fields E/N in a described mixture It is manifesting that EEDF is strongly affected by the increasing of reduced electric field and thus the electron transport coefficients would remain affected The EEDFs for both pure molecular Oxygen and pure Argon hold different discrete curves for all electron energies due to the fact that electrons lose energy in inelastic collisions with atom In both figures applying a high E/N leads to a specific EEDF to evolve to a larger high energy tail Thus each curve is a specific depending on the value of E/N At the proximity of the origin ie at lower MEE the EEDF is low for higher E/N Near to the threshold of inelastic processes the EEDF which is strongly affected by E/N heats the electrons and thus increases the energy of cold electrons For constant value of MEE the EEDF increases as the E/N increased However as MEE increased the EEDF grows with increasing E/N

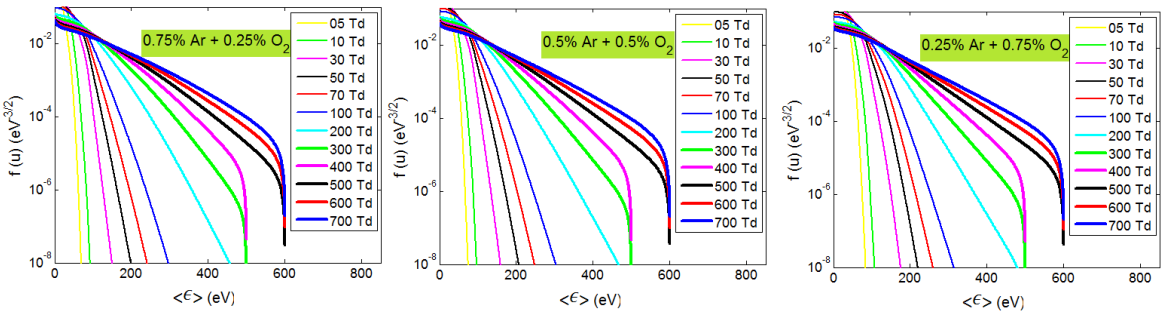

Figure 2 a The EEDF as a function of mean electron energy for various reduced electric fields E/N in a mixture of $0.75\%\ \mathrm{Ar} + 0.25\%\ \mathrm{O_2}$ 05e 2 The EEDF vslar Oxgy eld is between 3 b Mixture of $0.5\%\ \mathrm{Ar} + 0.5\%\ \mathrm{O_2}$ c Mixture of $0.25\%\ \mathrm{Ar} + 0.75\%\ \mathrm{O_2}$ In the entire calculations the electron concentration is 1×10^3 cm^{-3} the gas temperature is 273 ^{0}K and the pressure is 760 torr

'Figure 3a' shows that the MEE increases significantly as the E/N increased At $E/N \leq 350$ Td the pure Ar has upper curve and O_2 has lower curve while the curves of the mixtures are located between them Upper this value the curves are reflected the obverse The MEE of the mixtures are located between Ar and O_2 curves
The characteristic energy in pure Ar pure O_2 and their mixtures gases as a function of reduced electric field is shown in figures 3b It is clear that the characteristic energy for the pure Ar gas is higher than the pure O_2 gas and their used mixture gases For the three used mixtures of both gases the curves of the characteristic energy are located between that of pure Ar and O_2 gases The characteristic energy increases monotonously in exponentially manner with *E*/*N* until 500 Td then the increase becomes linear up from this value for all mixtures and its components

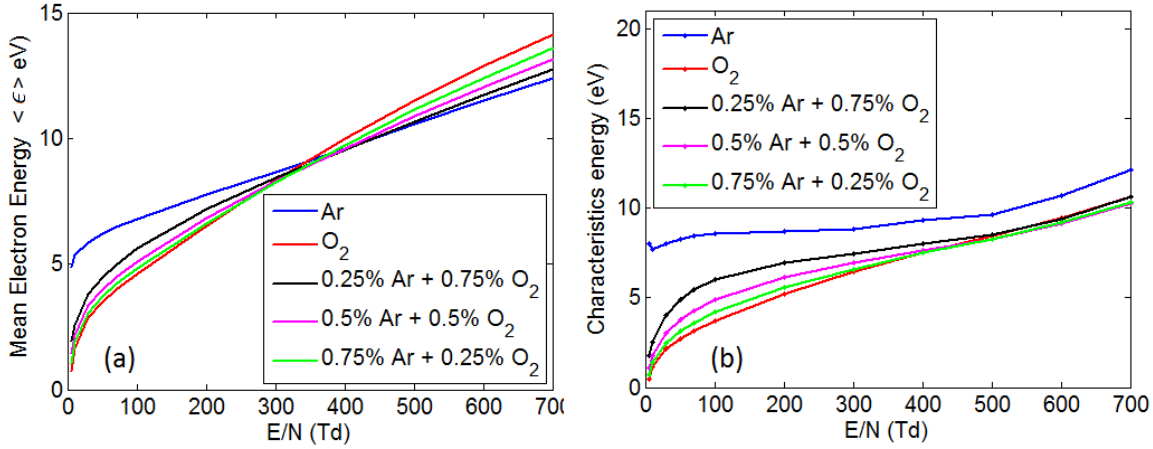

Figure 3 a Mean electron energy b Characteristic energy versus reduced field of a pure Ar O_2 and their mixtures the electron concentration is 1×10^3 cm^{-3} the gas temperature is 273 ^{0}K and the pressure is 760 torr

'Figure 4a' expresses the relation between Electron Diffusion Coefficient EDC and E/N for pure Ar O_2 and their mixtures At low E/N both pure Ar and O2 behave in a different way whilst the EDC decreases for Ar it is increasing for molecular oxygen Since EDC for O_2 is growing quickly from the start it is increasing in exponentially manner with E/N For Ar the curve of EDC against E/N looks like U shape However the curves are intersected at E/N =165 Td At lower of this value the entire values of EDC for O2 are less than for Ar Larger values of EDC than the intersection point the EDC for Ar are less than that for O2 Lower concentration used of Ar in the mixture gives similar behavior of pure Ar whilst lower concentration of O2 in the mixture yields similar behavior as pure O2 The 0.5% Ar $+$ 0.5% O_2 concentration of gas mixture gives a dual behavior of the both each pure gases This mixture obeys to the behavior of O2 at low E/N and to the behavior of Ar at large E/N Obviously at larger than E/N =165 Td the EDC of O2 is larger than all the mixtures and pure Ar
'Figure 4b' shows the electron mobility as a function E/N for a pure Ar and a pure O2 and their used mixtures The electron mobility of O2 is inversely exponential proportional with E/N This is due to the electron energy loss that results in through the collisions between the electrons and neutral molecules Clearly all the used gases mixtures have the same behavior The mobility of pure Ar is decreasing as the E/N increased at the $E/N \leq 100$ Td After this value the mobility of O2 has a plateau as E/N increased It is noted that both concentrations 50% Ar $+ 50\%$ O_2 and 75% Ar $+ 25\%$ O_2 give values of mobility are identical at low E/N but they separate at $E/N = 200$ Td The mixture 75% Ar $+$ 25% O_2 has higher values of mobility than the mixture 50% Ar $+ 50\%$ O_2 Also it is clear that the

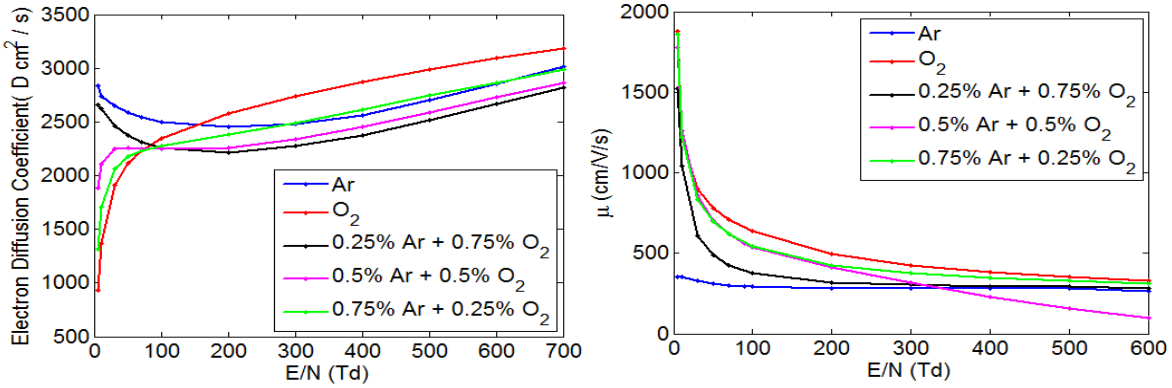

mobility of mixture $50\%\ \mathrm{Ar} + 50\%\ \mathrm{O_2}$ continues to decrease in a way such that it is lower than that for a pure Ar

Figure 4 a Electron diffusion coefficient b Mobility versus reduced field of a pure Ar O_2 and their mixtures the electron concentration is 1×10^3 cm^{-3} the gas temperature is 273 ^{0}K and the pressure is 760 torr

'Figure 5a' shows the electron drift velocity versus reduced electric field for pure molecular O_2 and pure Ar and their mentioned mixtures The conductivity of the gases/mixture is characterized by the electron drift velocity in electric field and is the rather important electron transport parameters [14] The drift velocities of Ar O_2 and their mixtures behave in similar manner They increase as the E/N increased The increase is linear but tends to be nonlinear at higher E/N Obviously the pure Ar has lower drift velocity whereas the O_2 has higher values for constant E/N Their mixtures drift velocities stand between them It increases as the concentration of O_2 increased Figure 5b shows the electron drift velocity versus reduced electric field for pure Ar and experimental data Although the experimental data are fairly in a good agreement with the value computed by the program at *E/N* lower than 300 Td but at higher value than 300 Td the experimental data are slightly lower than the resulted from the program The differences could be attributed to experimental results due to impurities in Ar However the two set of data show the same general shape and indicate that the program realistically describes the experimental data is 273 ^{0}K and the pressure is 760 torr

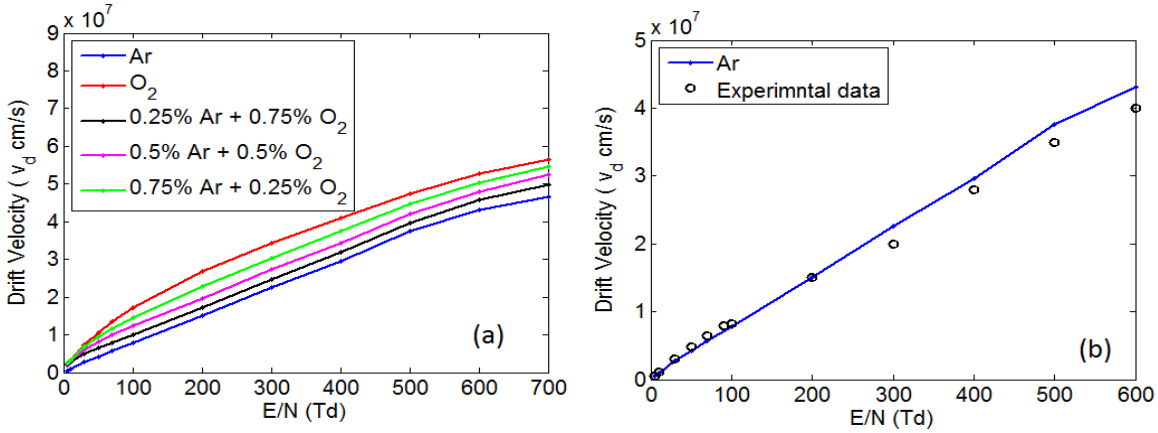

Figure 5 aThe drift velocity as a function of reduced field of a pure Ar O_2 and their mixtures b pure Ar with experimental data the electron concentration is 1×10^3 cm^{-3} the gas temperature

'Figure 6a' ,'Figure 6b' expresses the effect of electron temperature on electron diffusion coefficient and mobility for pure Ar gas at fixed pressure and plasma density The effect is to raise the curves of both parameters with *E*/*N* to a higher magnitude

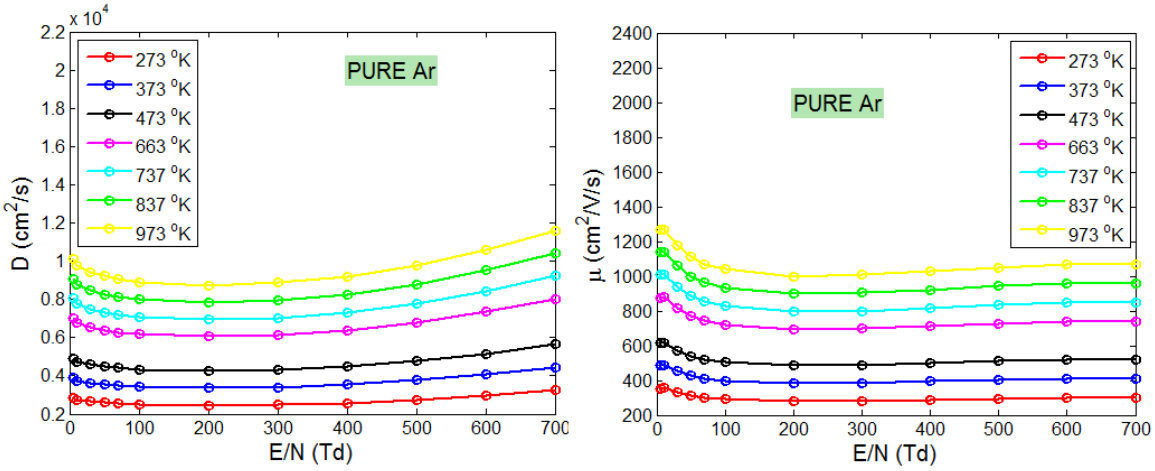

Figure 6 a Electron Diffusion Coefficient vs *E*/*N* of pure Ar for different electron temperatures b Electron Mobility vs *E*/*N* of pure Ar for different electron temperatures the electron concentration is 1×10^3 cm^{-3} and the pressure is 760 torr

'Figure 7a', 'Figure 7b' shows the effect of pressure on electron diffusion coefficient and mobility for pure for pure Ar gas at fixed electron temperature and plasma density As the pressures increased the curves of both parameters with *E*/*N* are going to be at lower magnitude

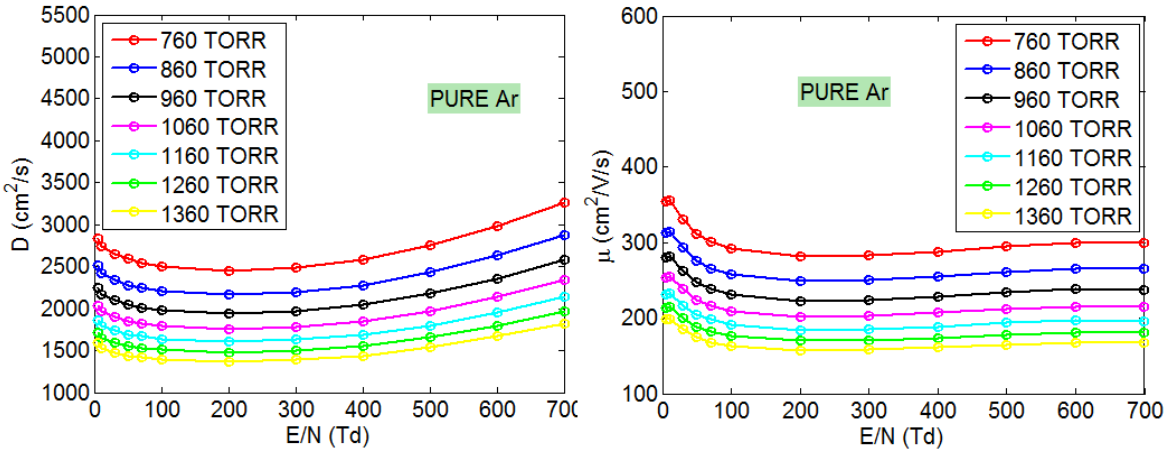

Figure 7 a Electron Diffusion Coefficient vs *E*/*N* of pure Ar for different pressures b Electron Mobility vs *E*/*N* of pure Ar for different pressures the electron concentration is 1×10^3 cm^{-3} and the temperature is 273 ^{0}K

4. Conclusion

We have introduced the transport coefficients of the electron in pure Ar and O_2 and their mixtures The coefficients result in can be adopted as model of plasma containing molecular Oxygen and Argon gases and their mixtures. We observed the effect of this mixture It was found that adding a small amount of Argon gas to molecular Oxygen gives better results in the values of transport coefficients The results of this mixture are satisfactory by comparing the drift velocity with the experimental results

Acknowledgments

The authors would like to thank physics Department College of Education for Pure Science Ibn AL Haitham University of Baghdad for their support in the present work

References

[1] Demidov V DeJoseph C Jr and Kudryavtsev A 2006 IEEE Transactions on plasma science **34** 3
[2] Meeks E and Ho P 2000 Handbook of Advanced Plasma Processing Techniques Springer Berlin Heidelberg
[3] Dahl D A Teich T H and Franck C M 2012 *Journal of Physics D Applied Physics* **45** 48 485201
[4] Boogaard A 2011 PhD thesis University of Twente Netherlands
[5] Behlman N 2009 MSc thesis Worcester Polytechnic Institute USA
[6] Dyatko N Kochetov I Napartovich A and Sukharev A 2005 EEDF the software package for calculations of the electron energy distribution function in gas mixtures
[7] Rabie M Haefliger P Chachereau A and Franck C M Journal of Physics D Applied Physics **48** 7 075201
[8] Jeon B 2003 *Journal of the Korean Physical Society* **43** 4 513 525
[9] Kuzmin D 2010 A Guide to Numerical Methods for Transport Equations Friedrich – Alexander university Germany
[10] Chen F F 1984 Introduction to plasma physics and controlled fusion Plenum Press New York and London
[11] Morgan W L and Penetrante B M 1990 Computer physics communication North Holland **58** 127 152
[12] Rockwood S D Greene A E 1980 Computer physics communication North Holland **19** 377 393
[13] Paul K Chu and XinPei Lu 2014 Low Temperature Plasma Technology Methods and Applications CRC Press USA
[14] Lisovskiy V Booth JP Landry K Douai D Cassagne V and Yegorenkov V 2006 *Journal of Physics D Applied Physics* **39** 660 665

Radon Concentration And Dose Assessment In Well Water Samples From Karbala Governorate Of Iraq

Radon Concentration And Dose Assessment In Well Water Samples From Karbala Governorate Of Iraq

I T Al-Alawy[1] and A A Hasan[2]

1,2Al-Mustansiriyah University, College of Science, Department of Physics

profimantarik@gmail.com[1]

Abstract. There are numerous studies around the world about radon concentrations and their risks to the health of human beings. One of the most important social characteristics is the use of water wells for irrigation, which is a major source of water pollution with radon gas. In the present study, six well water samples have been collected from different locations in Karbala governorate to investigate radon concentration level using CR-39 technique. The maximum value 4.112±2.0Bq/L was in Al-Hurr (Al-Qarih Al-Easariah) region, and the lowest concentration of radon was in Hay Ramadan region which is 2.156±1.4Bq/L, with an average value 2.84±1.65Bq/L. The highest result of annual effective dose (AED) was in Al-Hurr (Al-Qarih Al-Easariah) region which is equal to 15.00±3.9μSv/y, while the minimum was recorded in Hay Ramadan 7.86±2.8μSv/y, with an average value 10.35±3.1μSv/y. The current results have shown that the radon concentrations in well water samples are lower than the recommended limit 11.1Bq/L and the annual effective dose in these samples are lower than the permissible international limit 1mSv/y.

Keywords: Radon, well water, CR-39 detector, Karbala, Iraq.

1. Introduction

The radon is produced by radium decay and by recoil emanating of the material into the air or water. When underground well are opened, the radon is transported, by diffusion and convection, from the rocks to the environment through water or air circulation. The importance of each process depends on the geological nature of formation. Radon exhalation rate varies due to alterations in the differential air pressure, the uranium and radium levels, the working conditions, and the degree of ventilation. The underground well environment is complex and variable. Radon, after being exhaled, migrates along ventilation currents while it generates the solid decay products: ^{218}Po, ^{214}Pb, ^{214}Bi and ^{214}Po [1].

Radon is a radiant gas with a half-life 3.82days, odorless, tasteless, and colorless. Its density is 7.5 times that of air [2]. It dissolves in water easily and can spread through gases and water vapor [3]. It produced by naturally decay occurring Radium ^{226}Ra, which is a decay product of Uranium ^{238}U chain. Thoron ^{220}Rn with a half-life 56.6s is the result of the decay product of the ^{232}Th Thorium chain. Because of this short half-life, its emergence and emigration are limited to a few centimeters. Radon is inhaled in lung tissues. Its degradation by alpha emission causes ionization damage that causes lung cancer [4]. The second most important contributor to outdoor radon is emanation from well water sources. The radon in the water supply poses an inhalation and an ingestion risk. Radon can then be transported by well water to far large distances than by the diffusion process in a short time [5]. However, radon and its progeny can enter into human's body through ingestion and inhalation [6].

Therefore, human exposure to high concentrations of radon and its progeny for a long period of time leads to the growth of lung cancer [7]. Radon can dissolve and build up in water from underground sources. Radon in the water dissolves and escapes into the air throughout household water use, especially when it is heated. Radon levels in the air will increase for a short period of time when one uses his dishwasher, cooking, washing clothes, shower and bath. However, research has shown that the risk of lung cancer from respiration radon in the air is much greater than the risk of developing stomach cancer from drinking water containing radon [8, 9]. The objective of this study is to measure radon concentration and dose assessment in well water samples from selected areas in Karbala governorate using the CR-39 nuclear track detector, and assessment of the situation.

2. Materials and Methods

2.1. *Description* of the Studied Area

Karbala is a well-known Islamic city. It is famous by its holy and it's historical which gall in huge accidents, its dust witnessed on the most Nobel feature of martyrdom in the history. Karbala governorate situated about 108km in southwest of Baghdad, on the edge of desert in west of Euphrates River and on the east side of the Al- Husseiniya River. Its location at latitude (32°36′52″N), and longitude (44°1′27″E), and its elevation above sea level is (32m=104ft), with a total area of (52.856 km^2) and with population 1,378,000 at (2013). It is bordered by Anbar to the north and northwest, Al-Najaf to the south, and Al-Hillah and department of the Baghdad to the east [10], see Figure 1. This figure also explains the code and location of the underground areas in Karbala Governorate.

.

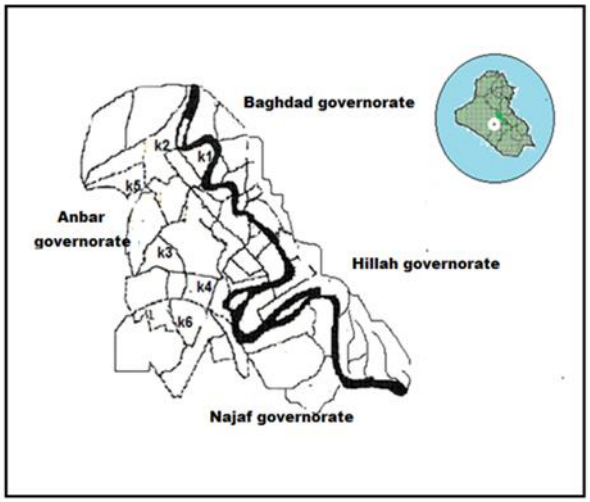

Figure 1. Well water locations at different regions

2.2. The Detector

CR-39 solid-state nuclear track detector (SSNTD) with thickness (500μm) is a $C_{12}H_{18}O_7$ polymer with density 1.36 gm/cm^3 and area of about ($1\times1cm^2$) has been used in the current work. It is sensitive to alpha particles of energy up to 40MeV. It was used as complement to detect alpha particles from ^{222}Rn and its daughter's nuclei. The concentrations of alpha particles which emitted from the radioactive element ^{222}Rn in selected samples were determined by using the nuclear track detector CR-39. The damage caused by alpha particles when penetrating the detector along its path can be observed by chemical etching and optical microscopy [11].

2.3. Collection and Preparation of Samples

Six samples have been collected from well water at different regions within the boundaries of the administrative Karbala governorate. They are Al-Wand, Alhurr (Alqarih Aleasariah), Hay Al-Hussein, Hay Ramadan, Ain Al-Tamur, and Hay-Al- Muathafin. Table 1 shows the symbol of these regions respectivily. The water samples were collected from the well water in the plastic containers after washing them with diluted hydrochloride. The acid works to reduce the absorption of radionuclides by the walls of the container and prevent algae growth. The water filtration using filter paper before the container is full to get rid of lingering in the water minutes.

2.4. The Exposure

A capacity of 0.250L of well water is kept in plastic container for 30days before measurements in order to achieve the secular equilibrium as shown in Figure 2.

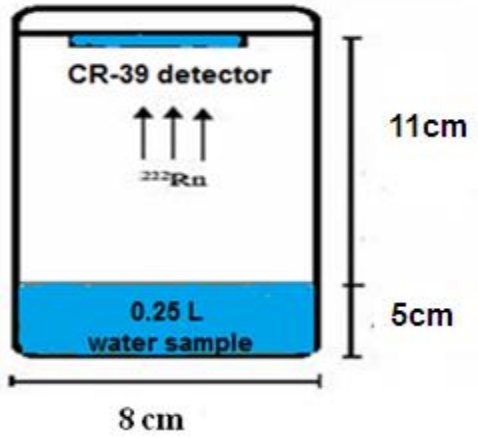

Figure 2. Plastic -can techniques used in this study.

Square piece of ($1\times1cm^2$) has been installed inside the upper lid of the can facing the water surface sample. The detector was exposed for a period of 60days during exposed period from 17-9-2016 to 15-11-2016, to be able to register alpha particles for 90 days after which samples were collected and chemically etching with 6.25 normality of sodium hydroxide (NaOH) at 60C° for 5h. It was then washed, dried, read the tracks and calculated their number in the unit area using an optical microscope with a magnification of 400X to identify and determine radon concentrations. These reagents were calibrated by exposing them to known concentrations of radon and its offspring in the designated chamber.

3. Theoretical Concentrations

3.1. Radon Concentration Measurements

The density of the tracks (ρ) in the samples was calculated according to the following Equation [12]:

$$Tracks\ density\ (\rho) = \frac{Average\ number\ of\ total\ pits\ (track)}{Area\ of\ the\ field\ view} \quad (1)$$

Radon concentrations in water samples were obtained by comparing the track densities recorded on the detectors of the samples and that of the standard water samples, which are shown in Figure 3, using the following relationship [13]:

$$C_x(sample)/\rho_x(sample) = C_x(standard)/\rho_x(standard) \quad (2)$$

$$C_x = \rho_x \cdot (C_s/\rho_s) \quad (3)$$

Where C_x and C_s are the radon concentration in the unknown and standard samples respectively. ρ_x and ρ_s are the density of the track of unknown and standard samples respectively. This relationship has been explained in Figure 3.

3.2. Annual Effective Dose in Water

This parameter was calculated for the individual popular due to intake consumption of radon according to the following Equation [14]:

$$AED\ (\mu Sv/y) = C_{R_n}\ C_{R_W}\ D_{C_W} \quad (4)$$

Where C_{R_n} is the radon-concentration for ingestion, C_{R_W} is the consumption-rate 730L/y and D_{C_W} is the dose-conversion factor (5×10^{-9}Sv/Bq) according to UNSCEAR [15].

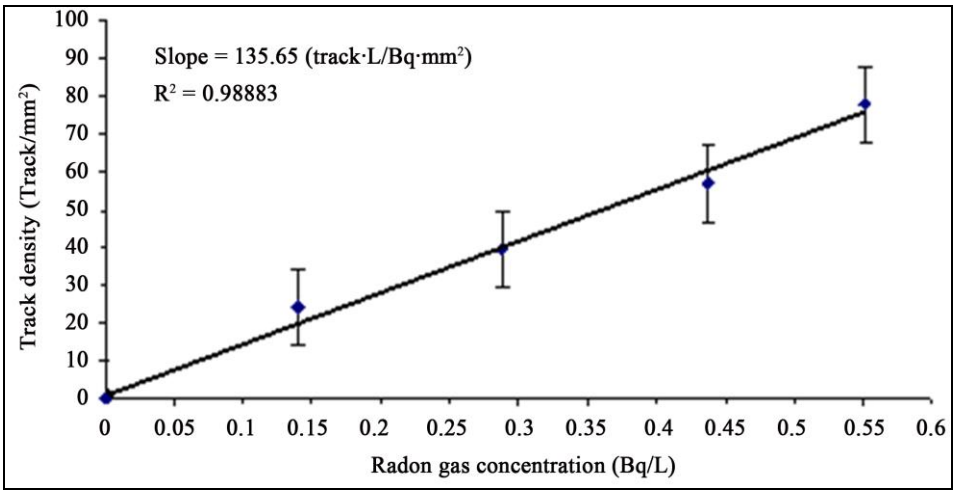

Figure 3. Relation between track density and

3.3. Determination of Some Radon Parameters

3.3.1. Radon Exhalation Rate. The radon exhalation rate (E_A) in any sample is defined as the flux of radon released from the surface of the material. The radon exhalation rate (surface exhalation rate) in units of ($Bq.m^{-2}.h^{-1}$) was calculated according to the following Equation [16]:

$$E_A = \frac{CV\lambda}{A[T+1/\lambda\,(e^{-\lambda T}-1)]} \quad (5)$$

Where C is the integrated-Radon exposure ($Bq.h.L^{-1}$); A is the surface area of the sample; V is the occupation of air volume in the can; λ is the decay constant of ^{222}Rn (0.1812 day^{-1}); and T is the exposure time (h).

3.3.2. Dissolved Radon Concentration. This parameter was calculated according to the following Equation [17]:

$$C_d\ (Bq/L) = C_{R_n}\ \lambda\ h\ T/L \quad (6)$$

Where C_{Rn} is the radon concentration for ingestion (Bq/L); λ is the decay constant of ^{222}Rn (0.1812 day^{-1}); h is the distance between the surface of the water sample and the detector; T is the exposure-time (h); and L is the depth of the sample (m).

4. Results and Discussion

Table(1) presented the results of radon concentrations in regions under study. Figure 4 shows the maximum concentration in Al-Hurr (Al-Qarih Al-Easariah) (K2) which was equal to 4.112±2.0Bq/L, while the minimum value of radon concentration was found in Hay-Ramadan (K4) which was equal to 2.156±1.4Bq/L. Al-Hurr (Al-Qarih Al-Easariah) (K2) was characterized by maximum annual effective dose 15.00±3.9μSv/y, and the minimum was found in Hay-Ramadan (K4) to be 7.86±2.8μSv/y, with an average value 10.35±3.1μSv/y, see 'Figure(5)'.

In addition, the average rate of radon exhalation (E_A) in well water samples was 3.778±0.6Bq/m^2.h. The maximum value 3.761±1.9Bq/m^2.h was in Al-Hurr (Al-Qarih Al-Easariah) (K2) and the minimum value was in Hay-Ramadan (K4) with a value 1.972±1.4Bq/m^2.h, as shown in 'Figure(6)'.

Figure 7 shows the variation of dissolved radon concentration (C_d) in well water samples. The highest value 122.941±11Bq/L was in Al-Hurr (Al-Qarih Al-Easariah) (K2), while the lowest concentration was in Hay-Ramadan (K4) which was equal to 64.46±8.0Bq/L, with mean value 84.8955±9.1Bq/L.

The current results for Karbala governorate showed that all concentrations was less than the recommended upper limit 300pCi/L which amount to 11.1Bq/L according to (USEPA, 2012)[18]. The annual effective dose in all studied samples was lower than the recommended limit 1mSv/y as recorded by (EPA, 2000) [19]. Therefore, all studied areas in Karbala are safe with respect to radon concentration.

Differences in the values of radon concentrations were observed among well water samples. These differences can arise because of the difference in the nature of the samples and the nuclei content of these samples. But the extremes values still found in the same regions that are Al-Hurr (Al-Qarih Al-Easariah) and Hay-Ramadan. The total annual effective dose of radon in well water of Karbala governorate were significantly lower than that of United Nations Scientific Committee on the Effects of Radiation (UNSCEAR, 2012) [20], World Health Organization (WHO, 2012) [21] which recommended limit for persons of 1mSv/y.

In 'Table (2)', a summary of the information gathered by other authors in different governorates of Iraq on the well water have been tabulated. The present dialogues showed that the radon concentration in some of the well water samples from the studied areas was either less or higher than the maximum value of the level of contaminant. The current results showed a close concentration of radon in the Sulaymaniyah governorate.

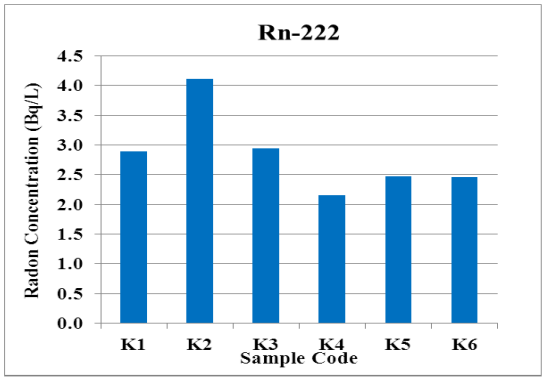

Figure 4. Radon concentration in well water

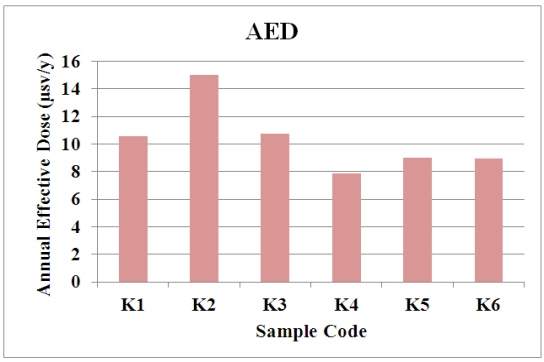

Figure 5. Annual effective dose in well water samples

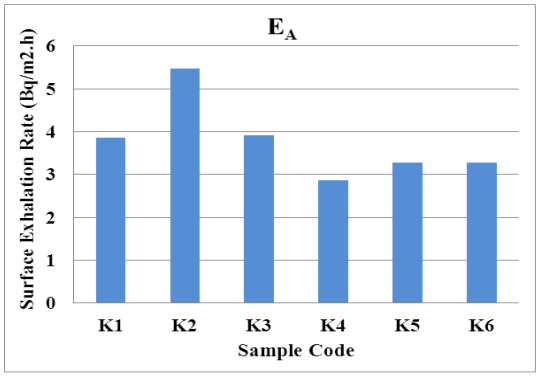

Figure 6. Surface exhalation rates in well water samples at different regions in Karbala

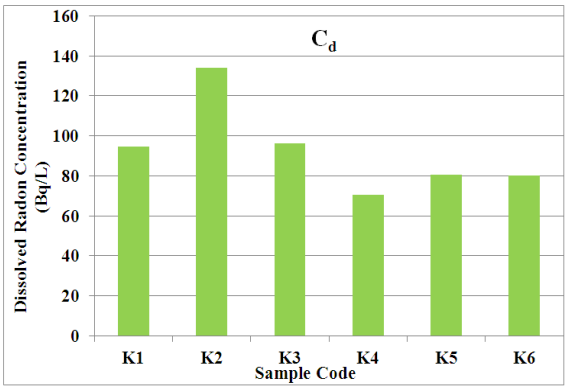

Figure 7. Dissolved radon concentration in well water

Table 1. Radon concentration (C_{R_n}), annual effective dose (AED), surface exhalation rate (E_A), and dissolved radon concentration in water (C_d), of well water samples for different regions in Karbala governorate.

Sample No.	Location Name / well depth(m)	Track density (track/mm²)	C_{R_n} (Bq/L)	AED ($\mu Sv/y$)	E_A ($Bq/m^2.h$)	C_d (Bq/L)
K1	Al-wand/7	392.9±2.9	2.896±1.7	10.57±3.2	2.649±1.6	86.585±9.3
K2	Al-Qarih Al-Esariah/240	557.8±4.5	4.112±2.0	15.00±3.9	3.761±1.9	122.941±11
K3	Hay Al-Hussein/12	399.7±2.8	2.946±1.7	10.75±3.3	2.695±1.7	88.08±9.4
K4	Hay Ramadan/12	292.5±2.6	2.156±1.4	7.86±2.8	1.972±1.4	64.46±8.0
K5	Ain Al-Tamur/100	335±3.5	2.47±1.5	9.01±3.0	2.259±1.5	73.848±8.6
K6	Hay Al-Muathafin/12	333.3±2.0	2.457±1.6	8.96±2.9	2.248±1.4	73.459±8.5
	Average	385.2±3.0	2.84±1.65	10.35±3.1	2.597±1.5	84.8955±9.1
	Maximum	557.8±4.5	4.112±2.0	15.00±3.9	3.761±1.9	122.941±11
	Minimum	292.5±2.6	2.156±1.4	7.86±2.8	1.972±1.4	64.46±8.0
	Global limit	…….	11.1 [18]	1mSv/y [19,20,21]	…….	……..

Table 2. Radon concentrations and annual effective dose in well water worldwide, using CR-39 technique, compared with the present work.

Location (Date of measurement)	C_{R_n} (Bq/L)	AED)($\mu Sv/y$	Ref.
Iraq/Akashat (2004)	0.11-0.158 well water	-------	Tawfiq et al. [22]
Iraq/ Sulaimany (2013)	2.756 well water	-------	Yousuf and Abullah [23]
Iraq/Karbala Al-Hindiyah city (2014)	0.549±0.041 well water	-------	Abdalsattar [24]
Iraq/Sulaymaniyah (2016)	0.979-1.320 well water	9.44 well water	Mohammed et al. [25]
Jordan/Irbid (1997)	3.1-5.7 with average 4.5±0.8 well water	-------	AL-Bataina et al. [26]
Scotland/Aberdeen Area (1993)	3-35 to 40-76 well water	20-400 well water	Al Doorie et al. [27]
Present work (2016)	2.84±3.06 well water	10.365±1.7 well water	Present work

5. Conclusions

The results of the present study provide well water level of radon concentration in province of Karbala. The highest value was found in well (K2) Al-Hurr (Al-Qarih Al-Easariah) region which was equal to 4.112±2.0Bq/L, while the lowest value was recorded in (K4) Hay-Ramadan to be

2.156±1.4Bq/L, with mean value of 2.84±1.65Bq/L. The results were less than the permissible limit 11.1 Bq/L given by USEPA, 2012. Therefore, all studied wells in Karbala governorate are safe as far as radon concentration is concerned. Even the annual effective dose values varied with respect to the increase in radon concentration and were significantly below the recommended limit given by UNSCEAR and WHO for members of the public of 1mSv/y. Therefore, the consumption of this well water does not cause any health risk to the population of Karbala governorate.

6. References

[1] ICRP, International Commission on Radiological Protection 1986, Radiation Protection of Workers in Mines, Annals of ICRP Publication, 47, 16, Canada, United States.
[2] Forkapić S, Bikit I, Čonkić Lj, Vesković M, Slivka J, Krmar M, Žikić-Todorović N, Varga E and Mrđa D 2006, Methods of Radon measurement, Facta Universitatis. Series: Physics, Chemistry and Technology, 1-10.
[3] Lee J K 1998, Radiological risk associated with naturally occurring radioactive nuclides in tap water and protection standards. Consumer Affairs Institute, Report on Debate on the Hazardousness of Radioactive Elements in Tap Water, 39-49.
[4] Lei Zhang C L A Q G 2008, Measurements of thoron and radon progeny concentrations in Beijing, China, Journal of Radiological Protection. 28 603–607.
[5] Singh M, Kumar M, Jain R K and Chatrath R P 1999, Radon in groundwater related to seismic events, Radiation Measurements, 30(4) 465-469.
[6] Ai N, Khan E U, Akhter P, Khan F and Waheed A 2010, Estimation of Mean annual Effective Dose through Radon Concentration in the Water and Indoor air of Islamabad and Murree, Radiation Protection Dosimetry, 141 183-191.
[7] Ramola R C, Choubey V M, Negi M S, Prasad Y and Prasad G 2008, Radon Occurrence in Soil Gas and Groundwater around an Active Landslide, Radiation Measurements, 43 98-101.
[8] CTDPH, Connecticut Department of Public Health 2017, Radon Program, List of Qualified Radon Mitigation Professionals.
[9] EPA, Environmental Protection Agency 1978, EPA/EERF-Manual-78-1 Radon in water sampling program.
[10] Wikipedia 2017, the free encyclopedia, List of cities and towns on the Euphrates River.
Eissa M F 2011, Optical Properties of CR-39 Track Etch Detectors Irradiated by Alpha Particles with Different Energies, Journal of Materials Science and Engineering, 52 6-31.
[11] Shahid M 2007, Improvement Calibration of Nuclear Track Detectors for Rare Particle Searches and Fragmentation Studies, Ph.D. Thesis, University of Bologna, Italy, Bologna: Italy.
[12] Durrani S A and Bull R K 1987, Solid State Nuclear Track Detection: Principles. Methods and Applications, Pergammon Press, U.K..
[13] Alam M N, Chowdhry M I, Kamal M, Ghose S, Islam M N and Awaruddin M 1999,
[14] Radiological assessment of drinking water of the Chittagong region of Bangladesh, Radiation Protection Dosimetry, 82 207-214.
[15] UNSCEAR, United Nations Scientific Committee on the Effects of Atomic Radiation 2000, Sources and Effects of Ionizing Radiation, Report to the General Assembly, New York: United Nations, 1 1-653.
[16] Ferreira A O, Pecequilo B R and Aquino R R 2011, Application of a Sealed Can Technique and CR-39 detectors for measuring radon emanation from undamaged granitic ornamental building materials, Radioprotection Journal, 46(6) 49-54.
[17] Kant K, Upadhyay S B and Chakarvarti S K 2005, Alpha activity in Indian thermal springs, Iranian Journal of Radiation Research, 2 197-204.
[18] USEPA, United States Environmental Protection Agency 2012, Edition of the Drinking Water Standards and Health Advisories. EPA 822-S-12-001 Office of Water U.S., Environmental Protection Agency Washington, DC..
[19] EPA, Environmental Protection Agency 2000, Technical Fact Sheet: Final Rule for (Non-

Radon) Radionuclides in Drinking Water, in EPA 815-F-00-013 November 2000.
[20] UNSCEAR, United Nations Scientific Committee on the Effects of Atomic Radiation 2012, Sources, Effects and Risks of Ionizing Radiation. Report to the General Assembly, with Scientific Annexes A and B Series, Annex A - Attributing health effects to ionizing radiation exposure and inferring risks. Annex B - Uncertainties in risk estimates for radiation-induced cancer. United Nations, New York.
[21] WHO, World Health Organization 2012, Progress on Drinking Water and Sanitation, World Health Organization, Geneva.
[22] Tawfiq N F, Al-Saji A W and Kadim K A 2004, Radon/Thorium Determination in Under Ground Water Using CR-39 Track Detector. Fourth Symposium on Use of Nuclear Techniques in Environmental Studies, 13-15 Sep. 2004, Yarmouk University, Irbid, Jordan.
[23] Yousuf R M and Abullah K O 2013, Measurement of Uranium and Radon Concentrations in Resources of Water from Sulaimany Governorate -Kurdistan Region-Iraq, Journal of Science and Technology, 3(6) 632-638.
[24] Abdalsattar K H 2014, Measurement of radon and radium concentrations in different types of water samples in Al-Hindiyah city of Karbala Governorate, Iraq, Journal of Kufa physics, 6(2) 69 -77.
[25] Mohammed FM, Najim R S and Mohammad Y K 2016, Estimation of radon and uranium concentrations in some selected wells water in Salahuddin province, Iraq, Journal European Academic Research, 3(10) 11511-11521.
[26] AL-Bataina B A, Ismail A M, Kullab M K, Abumurad K M and Mustafa H 1997, Radon Measurements in different types of natural waters in Jordan, Radiation Measurements,28(1-6)591-594.
[27] Al-Doorie F N, Heaton B and Martin C J 1993, A Study of Rn-222 in Well Water supplies in the area of Aberdeen, Scotland, Journal of Environmental Radioactivity, 18(2) 163-173.

Acknowledgement

We wish to express our deep thanks and gratitude to the Dean of the Faculty of Science and the Head of Physics Department at Al-Mustansiriyah University for their supporting this research. We would also like to extend our deep thanks to the Directorate of Water Resources in Karbala governorate for its assistance to collect samples.

Design and Simulation of Surface Plasmon Resonance Sensors for Environmental Monitoring

Design and Simulation of Surface Plasmon Resonance Sensors for Environmental Monitoring

Aseel I Mahmood[1,2], Rawa Kh Ibrahim[1], Aml I Mahmood[2], Zainab Kh Ibrahim[3]

[1]Material Research Directorate, Ministry of Science and Technology, Baghdad, Iraq
[2]Middle Technical University, Electrical Engineering Technical College, Baghdad, Iraq
3Mayoralty of Baghdad, Baghdad Water Authority Lab. And Q.C. Department, Baghdad, Iraq

[1,2]E-mail: aseelibrahim208@gmail.com

Abstract. In this work a Surface Plasmon Resonance (SPR) sensor based on Photonic Crystal Fiber (PCF) infiltrated with water samples has been proposed. To accurate detection of the sample properties, gold is used as plasmonic material. The air holes of PCF has been infiltrated with water samples, the optical properties of these samples has been taken from samples collected from Al-Qadisiya and Wathba lab. (east Tigris, Wathba, and Al-Rasheed) water projects at Baghdad- Iraq. Finite Element Method (FEM) has been used to study the sensor performance and fiber properties. From the numerical investigation we get maximum sensitivity circa 164.3 nm/RIU in the sensing range of 1.33 (of STD water) to 1.3431 (of river sample). The proposed sensor could be developed to detect f various high refractive index (RI) chemicals like the heavy metals in water.

Keyword. SPR; FEM; PCF; Optical sensing and sensors; environment monitoring

1. Introduction

Surface plasmon could be define as plasma oscillations supported by metal dielectric interface. The oscillations of charge density along this interface are define as surface plasma oscillations mode for the quantized oscillation of these modes; the quantized oscillations of the oscillated modes called surface plasmon mode. Theses modes are joined to longitudinal electric field; the field intensity suffering exponential decay in metal and dielectric materials. Due to this decay, the field intensity has maximum value at the metal- dielectric interface. Maxwell's equations for metal dielectric Refractive Index (RI) distribution are used to study the properties of the surface plasmon and decay of this decay, the origin of the phenomenon of Surface Plasmon Resonance (SPR) began theoretically studied in 1907 by Zenneck [1, 2].

Surface Plasmon Resonance sensors widely used in field of detection chemical and biological components which is very helpful in fields like environmental monitoring, food safety and medical diagnostics, with high sensitivity also no molecular labels are used [3]. Although, these sensors commercially available but they used only in laboratory due to their high cost and large size. So, to solve this problem a need for smaller and cheaper SPR sensor become a very important point, this is achieved by using optical fiber- based SPR sensors [4]. These sensors are based on different types of fibers, such as Single Mode Fiber (SMF), Multimode Fiber (MMF) and Photonic Crystal Fiber (PCF) [5].

In this work SPR-sensor based on PCF has been submitted, PCF's are special type of fibers, which have a periodic array of air holes with different shape, size, and distribution running along the entire length of the fiber. The existence of these holes allow controlling fiber properties like chromatic dispersion, high birefringence and non-linearity, which is not suitable in ordinary fibers [6, 7]. In addition, these holes could be infiltrated with different liquids and gases, which give them very good advantages in sensing applications [8], 'figure 1' shows different types of PCFs.

The SPR-PCF sensors working principle is based on the evanescent field that is generated due to the propagation of light through the region of core-cladding interface getting interaction between light and plasmonic surface. This lead to changing the RI of the infiltrated analyte and thus changing the RI of the guided light mode, so the resonant wavelength change and lead to detect the particles or molecules by measuring the shifting in resonant wavelength [9]. Gold and Silver are widely used as an active plasmonic materials, although Silver is easily oxidize but it commonly used than Gold due to its high conductivity and sharp resonant peak [10]. In this work Gold has been chosen as a plasmonic material to prevent the oxidation of Silver due to the infiltration of air holes with water samples.

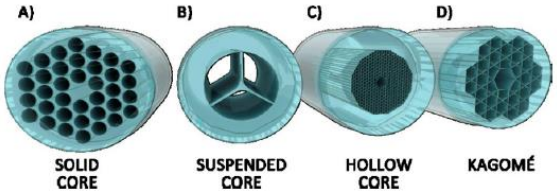

Figure 1. Some typical structures of MOFs (A) Solid Core-PCF, (B) Suspended core PCF; (C) Hollow Core-PCF, and (D) Kagom´e HC-PCF [7].

2. Simulation treatment

The submitted simulation has two air holes rings arranged in hexagonal shape as it shown in 'figure 2'. Light will be propagate in the air holes area, the SPR-PCF has hole to hole spacing (Λ) circa 1.2 µm, air hole diameter (d) 4 µm, normalized air hole size (d/Λ) is 3.3, and core diameter (r) 8 µm , the thickness of the gold layer (t) is about 2 µm. The refractive index of the fiber material is assumed 1.45.

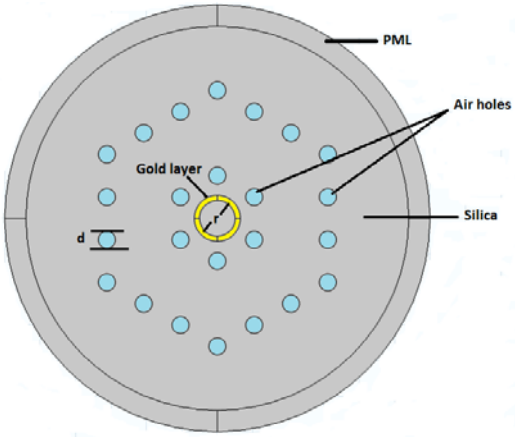

Figure 2. Schematic illustration of the proposed SPR-PCF sensor.

The analysis of this model has been done by Finite Element Method (FEM) with Perfectly Matched Layer (PML) boundary condition. The FEM has allowed the successful investigation of experiment the characters of mode and calculating the plasmonic mode complex propagation constant.

The complex formula of FEM is very helpful, to evaluate the fiber leakage or confinement losses, because of the holey region of fiber which is consists of finite number of air holes, the eigen value equation can be derived from the Maxwell equations 'as in equation (1)' [11]:

$$\nabla \times \left(\mu_r^{-1} \nabla \times \vec{E}\right) - k_0^2 \varepsilon_r \vec{E} = 0 \quad (1)$$

Where $(\vec{E})$ is the electric field, (k_0) is the wave number in vacuum, and (ε_r) and (μ_r) are the dielectric permittivity and magnetic permeability tensors, respectively. The eigen values are (β/k_0) the effective indices(n_{eff}), and the eigen vectors are the electric field components (E_x, E_y, E_z) [11].

The modal analyses have been applied on the cross section in the x-y plane of the SPR sensor when the wave is propagating in the z direction. The SPR-PCF cross-section in the transverse X – Y plane is divided into triangular elements with different shapes, sizes, and refractive indices by selecting suitable mesh.

PCF's considers as a single material fiber, they usually made of pure silica and they has the finite width of the cladding structures so they suffering from type of losses called the confinement losses or leakage losses L_c ; L_c in dB/m is given by [12]:

$$L_c = -20 \log_{10} e^{-k_0 Im[n_{eff}]} = 8.686 k_0 Im[n_{eff}] \quad (2)$$

Where, (k_0) free space propagation constant, and $\mathrm{Im}[n_{eff}]$ is the imaginary part of the complex effective refractive index (n_{eff}).

In this simulation, the Drude-Lorentz model will be used to study the dielectric constant of gold as it clear 'as in equation (3)' [13]:

$$\varepsilon_m = \varepsilon_\infty - \frac{\omega_D^2}{\omega(\omega + j\Gamma_D)} - \frac{\Delta\varepsilon\Omega_L^2}{(\omega^2 - \Omega_L^2) + j\Gamma_L\omega} \quad (3)$$

Where ε_m gold permittivity, ε_∞ gold permittivity in the high frequency, $\Delta\varepsilon$ is the weighting and equal to 1.09, ω is the guided light angular frequency, $\omega^D/2\pi = 2113.6$ THz is the plasma frequency, $\Gamma_D/2\pi$ =15.92 THz is the damping frequency, $\Omega_L/2\pi$=650.07 THz and $\Gamma_L/2\pi$=104.86 THz are the frequency and spectral width of the Lorentz oscillator.

3. Simulation results

To analyze the sensor characteristics, the air holes of the PCF is infiltrated with different samples of water, the optical characteristics of these samples are measured from real water samples collected from Al-Qadisiya and Wathba lab's water projects with wavelength range (0.6-1.6) μm.

FEM solver has been used to numerically simulate and investigate the designed model, the core-guided modes and plasmonic mode SPR-PCF. The single mode Gaussian distribution output of selected wavelength are illustrated in 'figure 3'.

The resonant curves for different water samples refractive indices (na1 = 1.33, na2 =1.3433, and na3 =1.3431) has been studied through investigate coupling properties of the sensor as it illustrated in 'figure 4'. The phase-matching wavelength condition occur when the real part of effective refractive index of the core-guided mode and that of the plasmonic mode intersect. From figure 4 the loss spectra of the core guided mode could be noticed which is mean that the largest energy transmission from the core guided mode to the plasmonic mode, Therefore, the intersections of the line of core mode and SPR mode represent the resonant wavelength. The resonant wavelengths for samples 1, 2, and 3 is 1.238, 1.399, and 1.41 µm respectively as it is shown in 'figure 5'.

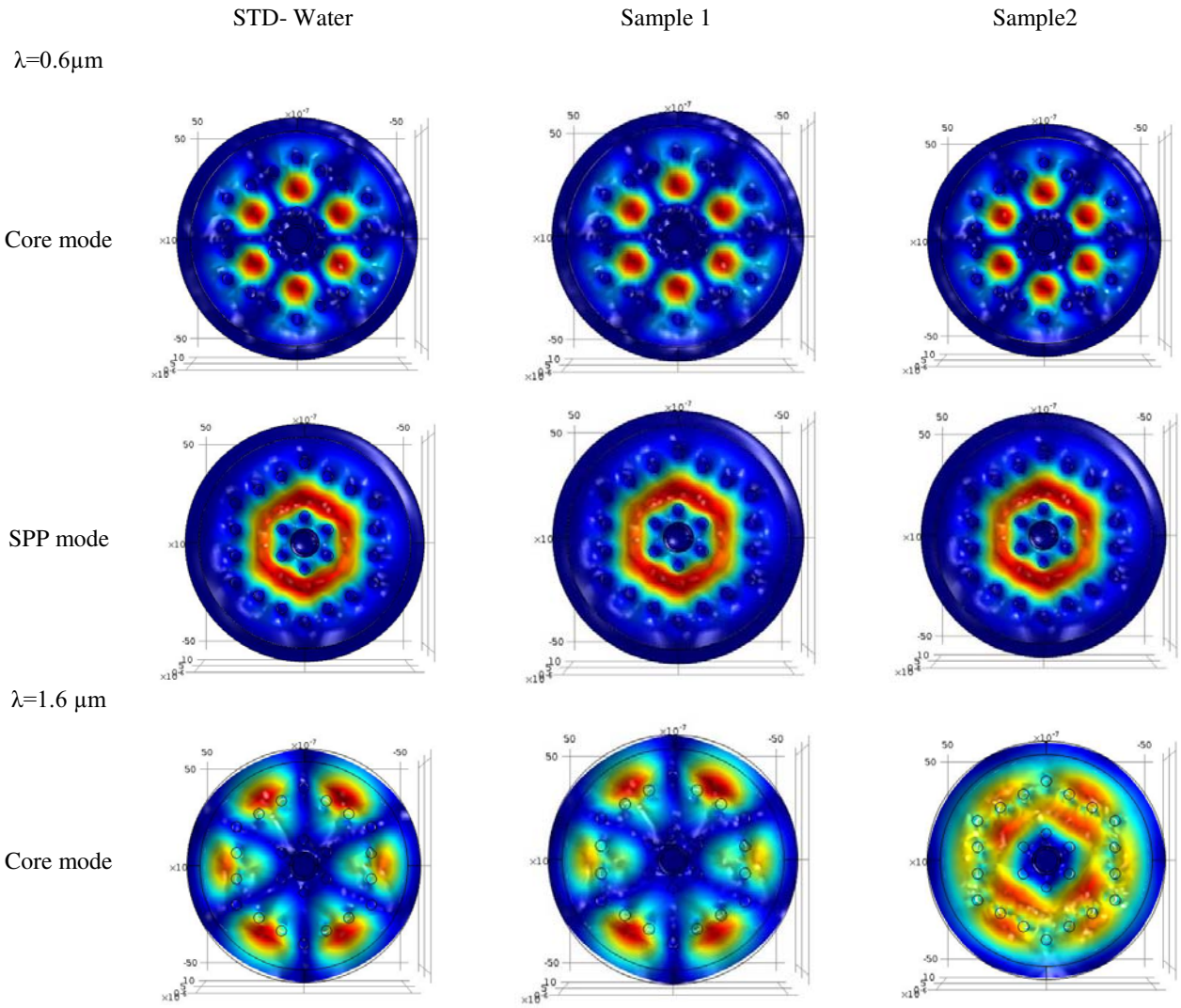

SPP mode

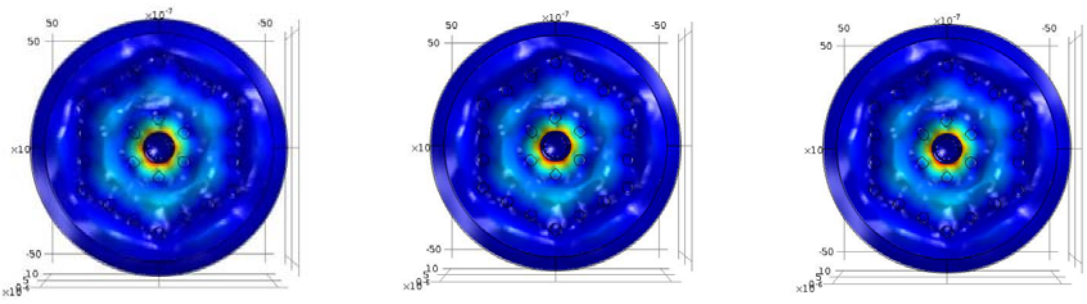

Figure 3. Single mode Gaussian distribution output of fundamental core and SPP mode for selective wavelength (o.6 and 1.6) µm.

The submitted sensor has resonant features through the depending of the resonant wavelength on the RI of the infiltrated liquid; the sensitivity is defined in the following equation [14]

$$S_\lambda = \frac{d\lambda_{peak}(n_a)}{dn_a} \quad (4)$$

The maximum sensitivity is 164.3 nm/RIU in range of RI 1.33 (STD water), 1.3431 (river sample) had been achieved.

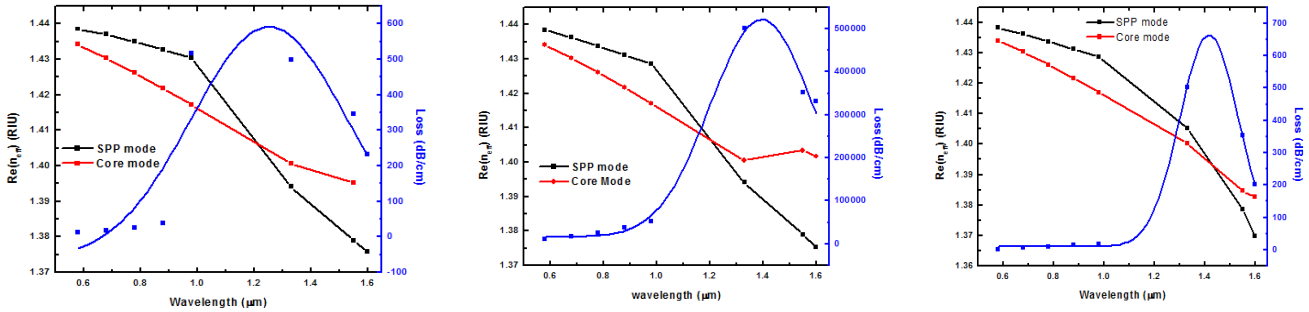

Figure 4. Calculated loss spectrum (blue line) core and SPP mode dispersion relation for water with RI's (a) (1.33), b (1.3433), and c (1.3431).

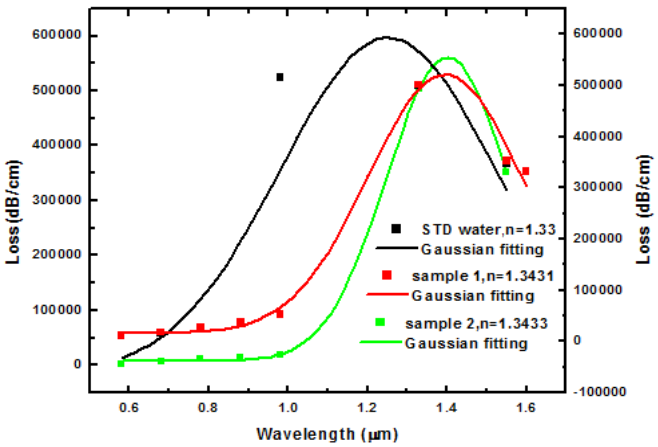

Figure 5. Resonant Wavelength for all samples.

4. Conclusion

Surface Plasmon Resonance sensor based on Photonic Crystal Fiber (SPR-PCF) coated with Gold layer and air holes filled with water samples has been submitted in this work. By finding the resonant wavelength or the peak of the transmission loss spectrum corresponding to the resonant wavelength of the SPR sensor we can detect identified the filled analyte . The sensor parameters of the fundamental mode had been studied by employing the FEM, The maximum sensitivity is 164.3 nm/RIU in the sensing range of 1.33 (STD water) –1.3431 (river sample) is obtained. Also it is possible to introduce the analytes refractive index range from 1.33 to 1.3431, which is infiltrated into the hole of the proposed sensor. Because of this high sensitivity this technique very recommended to be used for sensing applications in chemical and biological fields like detect the heavy metals in water in the field of environment monitoring.

References

[1] Sharma A, Jha R and Gupta B 2007 Fiber-Optic Sensors Based on Surface Plasmon Resonance: A Comprehensive Review IEEE *Sensor Journal* **7** 8 pp 1118-1129
[2] Zenneck J 1907 Uber die Fortpflanztmg ebener elektro-magnetischer Wellen langs einer ebenen Leiterflache und ihre Beziehung zur drahtlosen Telegraphie Annals der Physik. **23** pp 846–866
[3] Yang X C, Lu y, Liu B, and Yao J 2016 Temperature Sensor Based on Photonic Crystal Fiber Filled With Liquid and Silver Nanowires *IEEE Photonic Journal* **8** 3 6803309
[4] Akowuah E, Gorman T, Ademgil H, Haxha SH, Robinson G and Oliver J 2012 A Novel Compact Photonic Crystal Fibre Surface Plasmon Resonance Biosensor for an Aqueous Environment. Photonic Crystals - Innovative Systems Lasers and Waveguides In tech Publisher ISBN 978-953-51-0416-2
[5] Homola J 1999 Surface plasmon resonance sensors: review Sensors and Actuators B: Chemical **54** pp 3-15
[6] Birks T, Knight J, Cregan R and Ph Russell 1998 Single mode photonic crystal fiber with indefinitely large core IEEE publishing: Proceeding of the Conference on laser and electro-optics (CLEO) San Francisco USA
[7] Gorodetsky M, Savchenkov A, and Ilchenk V 1996 Ultimate Q of optical microsphere resonators. Optics Letters **21** 7 pp 453-455
[8] Joannopoulous J, Johnson S, Winn J and Meade R 2008 *Photonic crystals: modeling the flow light* 2nd edition Princeton University Press Princeton and Oxford
[9] Rifat A, Amouzad Mahdiraji G, Shee Y, Shawon M and Mahamd Adikan R 2016 A Novel Photonic Crystal Fiber Biosensor Using Surface Plasmon Resonance Procedia Engineering **140** pp 1 – 7
[10] Kravets V, Jalil R, Kim Y, Ansell D, Aznakayeva D, Thackray B, Britnell L, Belle B, Withers F, Radko I, Han Z, Bozhevolnyi S, Novoselov K , Geim A and Grigorenko A 2014 Graphene-protected copper and silver plasmonics Scientific reports 4 pp 1 -8
[11] Otupiri R, Akowuah E, Haxha S, Ademgil H, AbdelMalek F and Aggoun A 014 A Novel Birefrigent Photonic Crystal Fiber Surface Plasmon Resonance Biosensor *IEEE Photonic Journal* **6** 4 6801711
[12] Luan N, Wang R, Lv W, Lu Y and Yao J 2014 Surface Plasmon Resonance Temperature Sensor Based on Photonic Crystal Fibers Randomly Filled with Silver Nanowires Sensors **14** pp 16035-16045
[13] Wei Q, Shu-Guang L, Jian-Rong X , Xü-Jun X and Lei Z 2013. Numerical analysis of a photonic crystal fiber based on two polarized modes for biosensing applications, Chin. Phys. B. 22, 7, 074213-1-6.
[14] Rifat A Amouzad Mahdiraji G , Chow D, Shee Y, Ahmed R and Adikan F 2015 Photonic Crystal Fiber-Based Surface Plasmon Resonance Sensor with Selective Analyte Channels and Graphene-Silver Deposited Core Sensors **15** pp 11499-11510

Theoretical estimation of Photons flow rate Production in quark gluon interaction at high energies

IOP Conf. Series: Journal of Physics: Conf. Series **1003** (2018) 012119 doi:10.1088/1742-6596/1003/1/012119

Theoretical estimation of Photons flow rate Production in quark gluon interaction at high energies

Hadi J. M. Al-Agealy[1] ,Hyder Hamza Hussein [2] ,Saba Mustafa Hussein [3]

[1]Department of Physics, College of Education for pure Science, Baghdad University, Baghdad, Iraq.

[2]Department of Physics, College of Science, Kufa University, Iraq.

[3]Ministry of Education.

Abstract.photons emitted from higher energetic collisions in quark-gluon system have been theoretical studied depending on color quantum theory . A simple model for photons emission at quark-gluon system have been investigated . In this model, we use a quantum consideration which enhances to describing the quark system. The photons current rate are estimation for two system at different fugacity coefficient . We discussion the behavior of photons rate and quark gluon system properties in different photons energies with Boltzmann model. The photons rate depending on anisotropic coefficient : strong constant, photons energy, color number, fugacity parameter, thermal energy and critical energy of system are also discussed.

1-Introduction

High-energy physics had been established a basic theory for an elementary particles and interactions. Standard Model one of the most important model to establishment this. the physics of ultra-relativistic heavy-ion collision aimed to apply Standard Model theory on dynamically systems to study and understand the properties of nuclear matter [1]. Both Zweig and Gell-Mann independently had been introduced the quarks idea for building the matter in 1964 . Quarks in proton or neutron were helding together due to strong nuclear force. Beside the quarks ,the sciences introduce an idea that for any quarks corresponding antiquark have same properties except the charge was opposite for each other . Proton is composed of quarks and gluons. The spin values in proton is (1/2), it's coming from quarks the spin [2]. Quarks and gluons have a color quantum number that's makes quarks confined in hadron[3]. The particles protons and neutrons that contain quarks are called hadrons. Hadrons could be divided to baryons and mesons . Baryons are building of three quarks for protons and neutrons or antiquarks for anti neutrons and anti protons. On the other hand, mesons are bounding from pairs quark-antiquark confined by gluons[4]. The interacting

matter is found to exist in the form of a super fluid state called The quark-gluon plasma is the super fluid state that produce from quark gluon matter interaction and it was investigation in the Relativistic Heavy Ion Collision (RHIC) or/and Large Hadron Collider (LHC) [5–6]. Nuclear strong interaction could be establishing by Quantum Chromodynamics (QCD). QCD was theory dependent on the distance between quarks [7]. Moreover, the report from lattice QCD calculation proves the existence of such matter (QGP) at very high temperature [8]. In recent years ago, The photons production studies at relativistic heavy ion collisions has availabe from CERN experimental and RHIC experiments at BNL [9]. However, the theoretical studies of quark Gluon interaction Was utilize with resummation technique [[10] to estimation the photon self energy to evaluate the photonic rate.

2. Theory

To study and evaluation the photonic rate at quark gluon interaction is obtained the approximation rule from real time calculation of hard photonic production rate in order adopted at quantum field theory [11]. The photonic rate of the Gama emitted from quarks system per unit time per unit volume is given by self-energy retarded appropriate [12] .

$$\boldsymbol{E\frac{dN}{d^3Pd^4x}=-\frac{\alpha}{(2\pi)^3}\mathrm{Im}\prod_{\mu\vartheta}^{R}\frac{1}{e^{E_i/T}-1}} \quad (1)$$

The self-energy retarded propagators $\mathrm{Im}\prod_{\mu\vartheta}^{R}$ due to spectral representation can be given by [13].

$$\boldsymbol{Im\prod_{\mu}^{R,\mu}=-\frac{10\pi}{3}e^2\sum q_Q^2\left(e^{\frac{E_\gamma}{T}}-1\right)\times\int\frac{d^3k}{(2\pi)^3}\int_{-\infty}^{\infty}dw\int_{-\infty}^{\infty}dw^{\sim}\,\delta\left(E_\gamma-w-w^{\sim}\right)[f_{FD(q)}(w).f_{BE(g)}(w^{\sim})]Tr[\xi^{\mu}(k,\overline{k},-p)\rho^{*}(w,\overline{k})\rho(w-E_\gamma,\overline{k}-\overline{p})\xi^{\vartheta}(-\overline{k},-k,p)]} \quad (2)$$

Where $e^2$is the statical strength , q_Q^2 is quark charge , E_γ is the photonic energy ,T is the thermal energy of system , w frequency propagator of quark system, k is cut off parameter, $\xi^{\mu}(k,\overline{k},-p)$ is propagator of system , $\rho(w-E_\gamma,\overline{k}-\overline{p})$ is the density distribution of system ,$f_{FD(q)}$ and $f_{BE(g)}$ are the Jouttner distribution functions for quarks, anti-quarks and gluons and may be written as by[14].

$$\boldsymbol{f_{FD(q,\overline{q})}=\frac{\lambda_{(Q,\overline{Q})}\,e^{\pm\frac{\mu}{T}}}{e^{\frac{E_\gamma}{T}}+1}\ ,\ and\quad f_{BE(g)}=\frac{\lambda_G}{e^{\frac{E_\gamma}{T}}-1}} \quad (3)$$

where$\lambda_{(Q,\overline{Q})}$ is the fugacity of quark and anti quark,and λ_G is the fugacity of gluon

By substituting the Eqs.(2) and(3) in Eq.(1) and treatment mathematically ,the results is

$$\boldsymbol{\xi(\alpha_{esc},\lambda_Q\lambda_G,T,E)=\frac{10\alpha\alpha_{Str}}{9\pi^2}\,\lambda_Q\lambda_G\sum q_Q^2\ \ T^2e^{-\frac{E_\gamma}{T}}[Ln(\frac{2E_\gamma}{4\pi\alpha_{sc}T})+\frac{1}{2}-C_{Euler}]} \quad (4)$$

Where becomes. $C_{Euler}=0.577$is the Euler constant, α is electrodynamic strength approximated equally to $\alpha\approx\frac{1}{137}$, q_Q is the charge of quark and $\alpha_{Str}(P_m)$ is the strength quantum coupling that's may be written as[15].

$$\boldsymbol{\alpha_{Str}(P_m)=\frac{6\pi}{(33-2N_f)ln(\frac{P_m}{T_c})}} \quad (5)$$

Where$P_m$is the transfer momentum of media, N_f is the flavor quantum number and T_c is the transition critical energy.

3. Result

In this paper we evaluated the photonic rate at Compton processes for quark gluon interaction depending on extended the expression using the fugacity correlation .The evaluation are performed for quarks system have quntum flavor number N_f=2 and 4 for ug→dγ and Cg→dγ sytems respectivelly. Strength quantum coupling, photonic energy, color quantum number, thermal energy media , flavor number and fugacity correlation parameter are active parameters controlling on the photonic flow rate in quarks interactions at Compton processes. The photonic rate as fulfillment to estimation the strength quantum coupling for ug→dγ and Cg→dγ systems using Eq.(5) and the results is shown in table (1).

Table1. Strength quantum coupling estimation for ug→dγ and Cg→dγ systems at $T_c = 160\,, and\ 190$ MeV

		$\alpha_{Str}(P_m)$									
		P_m=1 Gev		P_m=2 Gev		P_m=3 Gev		P_m=4 Gev		P_m=5 Gev	
		Critical energy temperature T_c MeV									
system	N_F	190	160	190	160	190	160	190	160	190	160
$ug \rightarrow d\gamma$	2	0.335	0.367	0.247	0.264	0.214	0.227	0.195	0.206	0.183	0.192
$cg \rightarrow d\gamma$	4	0.389	0.426	0.286	0.306	0.248	0.263	0.226	0.239	0.212	0.223

The rate was evolution of two system using calculated date of the strength quantum coupling $\alpha_{Str}(P_m)$ that's shown in table (1) and matlab program with fugacity correlation parameter $\lambda_Q = 0.02$ and $\lambda_G = 0.09$ for quark and gluon [16]. Next parameter for the photonic rate is quark charge at both system .It is played more effective in photonic emission at system according to electromagnatic field effect. The quarks charge of system can be estimation using $\sum q_Q^2 = q_u^2 + q_d^2$ and$\sum q_Q^2 = q_c^2 + q_d^2$. However, the photonic rate is function of the fugacity parameter for quark and gluon that's was shown in Eq. (4). The photonic rate should be evaluation using Eq.(4) for both system by substituting the strength coupling α_{Str} ,photonic energy E_γ (GeV), thermal energy media T , fugacity parameter , quarks charge system $\sum q_Q^2$and Euler constant C_{Euler} . A MATLAB soft ware program has been using to evaluation the photonic rate for ug→dγ and and Cg→dγ systems using Eq.(4), the results are tabulated in tables (2),(3) ,(4) and(5) respectively.

Table 2. The evaluated result of photonic rate production$\xi(\alpha_{esc},\lambda_Q\lambda_G,T,E)$ in ug→dγ interaction at T_C=160 MeV.

	$\boldsymbol{\xi(\alpha_{esc},\lambda_Q\lambda_G,T,E)}$ $\boldsymbol{(GeV^2\,fm^4)^{-1}}$			
	Thermal energy of quarks system (T)MeV			
	150 MeV	200 MeV	250 MeV	300 Mev
$\boldsymbol{E_\gamma}$Gev	Strength quantum coupling$\boldsymbol{\alpha_{Str}(P_m)}$`			
	0. 25779	0.2764	0.30319	$\mathbf{0.34648}$
1	$8.4942x10^{-12}$	$2.682x10^{-10}$	$8.858x10^{-9}$	$\mathbf{1.972x10^{-9}}$
1.5	$4.208x10^{-13}$	$3.207x10^{-11}$	$1.84x10^{-10}$	$\mathbf{6.066x10^{-10}}$
2	$8.100x10^{-14}$	$3.218x10^{-12}$	$3.107x10^{-11}$	$\mathbf{1.460x10^{-10}}$
2.5	$3.261*10^{-15}$	$3.014x10^{-13}$	$4.853x10^{-12}$	$\mathbf{3.218x10^{-11}}$
3	$1.271x10^{-16}$	$2.724x10^{-14}$	$7.283x10^{-13}$	$\mathbf{6.789x10^{-12}}$

Table 3. The evaluated result of photonic rate production$\xi(\alpha_{esc},\lambda_Q\lambda_G,T,E)$ in ug→dγ interaction at T_C=190 MeV.

	$\boldsymbol{\xi(\alpha_{esc},\lambda_Q\lambda_G,T,E)}$ $\boldsymbol{(GeV^2\,fm^4)^{-1}}$			
	Thermal energy of quarks system (T)MeV			
	150 MeV	200 MeV	250 MeV	300 MeV
	Strength quantum coupling$\boldsymbol{\alpha_{Str}(P_m)}$`			
$\boldsymbol{E_\gamma}$Gev	0.378790	0.327648	0.296587	$\mathbf{0.2752668}$
1	$3.820x10^{-11}$	$2.645x10^{-10}$	$8.620x10^{-10}$	$\mathbf{1.891x10^{-9}}$
1.5	$1.943x10^{-12}$	$3.257x10^{-11}$	$1.854x10^{-10}$	$\mathbf{6.075x10^{-10}}$
2	$8.399x10^{-14}$	$3.307x10^{-12}$	$3.171x10^{-11}$	$\mathbf{1.460x10^{-10}}$
2.5	$3.402x10^{-15}$	$3.117x10^{-13}$	$4.987x10^{-12}$	$\mathbf{3.292x10^{-11}}$
3	$1.332x10^{-16}$	$2.829x10^{-14}$	$7.518x10^{-13}$	$\mathbf{6.976x10^{-12}}$

Table 4. The evaluated result of photonic rate production$\xi(\alpha_{esc},\lambda_Q\lambda_G,T,E)$ in Cg→dγ interaction at T_C=160 MeV.

	$\boldsymbol{\xi(\alpha_{esc},\lambda_Q\lambda_G,T,E)}$ $\boldsymbol{(GeV^2\,fm^4)^{-1}}$			
	Thermal energy of quarks system (T)MeV			
	150 MeV	200 MeV	250 MeV	300 MeV
$\boldsymbol{E_\gamma}$Gev	Strength quantum coupling$\boldsymbol{\alpha_{Str}(P_m)}$`			
	0.40674211	0.355924266	0.3244790019	**0.3026332043**
1	$3.796x10^{-11}$	$2.580x10^{-10}$	$8.189x10^{-10}$	$\mathbf{1.739x10^{-9}}$
1.5	$1.977x10^{-12}$	3.298x10^{-11}	$1.862x10^{-10}$	$\mathbf{6.036x10^{-10}}$
2	8.630x10^{-14}	$3.394x10^{-12}$	$3.244x10^{-11}$	$\mathbf{1.508x10^{-10}}$
2.5	$3.514x10^{-15}$	$3.224x10^{-13}$	$5.150x10^{-12}$	$\mathbf{3.390x10^{-11}}$
3	$1.417x10^{-16}$	$2.940x10^{-14}$	$7.810x10^{-13}$	$\mathbf{7.236x10^{-12}}$

Table 5. The evaluated result of photonic rate production$\xi(\alpha_{esc},\lambda_Q\lambda_G,T,E)$ in Cg→dγ interaction at T_C=190 MeV .

	$\boldsymbol{\xi(\alpha_{esc},\lambda_Q\lambda_G,T,E)}$ $\boldsymbol{(GeV^2\,fm^4)^{-1}}$			
	Thermal energy of quarks system (T)MeV			
	150 MeV	200 MeV	250 MeV	300 MeV
$\boldsymbol{E_\gamma}$Gev	Strength quantum coupling$\boldsymbol{\alpha_{Str}(P_m)}$`			
	0.44466763	0.38463064	0.3481683	**0.32313931**
1	$3.730x10^{-11}$	$6.075x10^{-12}$	$7.755x10^{-10}$	$\mathbf{1.605x10^{-9}}$
1.5	$2.012x10^{-12}$	7.378x10^{-12}	$1.858x10^{-10}$	$\mathbf{5.970x10^{-10}}$
2	8.893x10^{-14}	$3.468x10^{-12}$	$3.291x10^{-11}$	$\mathbf{1.521x10^{-10}}$
2.5	$3.652x10^{-15}$	$3.320x10^{-13}$	$5.269x10^{-12}$	$\mathbf{3.449x10^{-11}}$
3	$1.441x10^{-16}$	$3.042x10^{-14}$	$8.032x10^{-13}$	$\mathbf{7.407x10^{-12}}$

4. Discussion

The photonic rate in quark-gluon interaction at Compton proces have been studied and evaluation in term of a quantum chromodynamic theor . According to quantum chromodynamic postulate of field theory, the photons are emission by fluctuations of

propogation of both quarks and gluon system. In this research , we have calculation of photons produce from one-loop contributions.With a suitable quarks election in ug→dγ and Cg→dγ reaction systems the flow rate at Compton scattering are performed to the quantum flavor number 2 1nd 4 respectively. The electromagnetic coupling constant $\alpha \approx 1/137$ is much smaller than the strength coupling α_{Str} for strong interactions. In the results, the photonic producing during the quark gluon interaction at hadronic Phase as aresult the to large free path compare to lifetime of the system fireball. In tables(2to 5) , we can show the net photonic rate emission at different thermal energies T=.150 ,0.200,0.250 and 0.300GeV with the various photonic energy for Compton process. This indicate that results of flow rate of photons are highly effecte due to thermal energy for the system, and it seems to be large near the hot temperature . This leads to the fact of strength coupling is dependent on thermal energy and critical temperature dependent and when increasesd in thermal energy T lead to smaller Strength quantum coupling and the system approaching to the deconfined behavior that's means the quarks and gluons are weakly interaction in system. It means that increasing of thermal energy system increasing in photonic rate that's means in case of finite thermal energy , the increasing thermal energy lead to increase the size of droplet which refrers to good output photonic flow in respect of hadronic phase structure. In quark gluon interaction system the phase transition was opposite to thet hermal energy (temperature). This results at tables(2 to5) in all the system interaction , the simple model for this reactions is very advantage to study the photonic rate production at Compton processes.

It is founded to be very large rate in high temperature T=300 MeV for all system through the quarks interaction at Compton processes . Photon emission at Compton process is increased when the critical temperature is increased, and for both system the rate production in this process have been still a high at T_c=190 GeV. In tables (2-5) ,we can show the photonic rate at different critical temperature T =160 and 190 MeV through Compton process for quark quantum flavor numer n = 2 and 4,the photonic rates are showing to be increases with the thermal energy T of system . This increasing in photonic rate was effected due to themal energy temperature as well as the fugacity parameters of the system. So the photonic rate calculation of simple model with different quantum flavor number 2,and 4 has improvement the color quntum theory for the strong nuclear forces . Moreover, the results of photonic rate at tables (2-5) for two systems are suppressing by about a 1-5 factor , its hows that photonic rate results are approximated values at hadronic phase dependent on physical features of photons . Overall the data results in all tables indicate that Photonic rate production a function of decreases the strength quantum coupling and transverse momentum P_m for system incorporating with quantum flavor for quark . Finally, we conclusion that the effect of calculation strength quantum coupling factor on photonic rate by discussion of the behavior of strong nuclear forces and the rate was decrease due to decreases the strength quantum coupling and vice versa

5. Conclusion

In this research, we have been study and evaluation the photonic rate produce in Quark gluon interaction at hadronic phase. Its solving a set equation that preparing to evaluate the photonic rate based on the color quantum theory and using the Juttner function of distribution of the system,next we have obtained an expressions to evaluate the photonic production at Compton processes . . We could be concluded that photonic rate calculation of quark gluon interaction as a function of strength quantum coupling .However , we have evaluated the photonic rate in a hadronic phase at deferent photonic energies. We find that the increase of the thermal energy will change the photonic rate caused by the increase thermal energy system , making the net photonic rate strongly increasing of the photonic energy to emission .From results ,its shown that quark -gluon interaction at the Compton

scattering is the main feature of quantum chromodynamic theory and making to inderstanding the postulate of field theory,so the photonic yield is good sensor of quantum color hypothesis.

References

[1] Alessandro B, Antinori F, Belikov JA, Blume C, Dainese A, Foka P, Giubellino P, Hippolyte B, Kuhn C, Martinez G, Monteno M. 2006 *Journal of Physics G: Nuclear and Particle Physics*. **32(10)**, 1295.
[2] Kristin F H, 2005.PhD Thesis, Institute of Physics and Technology, University of Bergen, Bergen, Norway.
[3] Lee TD. Missing symmetries, 1992. *Nuclear Physics A*. **538**,3-13.
[4] Stephen A B, 2005, PhD Thesis, Particle Physics Group, School of Physics and Astronomy, University of Birmingham
[5] Adams J, Aggarwal MM, Ahammed Z, Amonett J, Anderson BD, Arkhipkin D, Averichev GS, Badyal SK, Bai Y, Balewski J, Barannikova O. 2005. *Nuclear Physics A.* **757(1-2)**,102-83.
[6] Adcox K, Adler SS, Afanasiev S, Aidala C, Ajitanand NN, Akiba Y, Al-Jamel A, Alexander J, Amirikas R, Aoki K, Aphecetche L.2005. *Nuclear Physics A*. **757(1-2)**,184-283.
[7] Grimbach A,.2008. Master Thesis in Computer Simulation in Science.
[8] Mastroserio A. 2007. *Acta Physica Polonica B*, **38(3).**
[9] Srivastava DK, Sinha BC. 2000. *Journal C-Particles and Fields.* **12(1)**,109-12.
[10] Frenkel, J. and Taylor, J.C., 1992. *Nuclear Physics B*, **374(1)**, 156-168.
[11] Le Bellac, M., 1996. Thermal Field Theory, *Cambridge Monographs on Mathematical Physics.*
[12] Gervais, H. and Jeon, S., 2012. *Physical Review C*, ***86*(3)**, 034904.
[13] Ilgenfriz E.M.,Muller P.M.,Sternbeck A.,Schiller A. and Bogolubsky I.L, *J of physics Brazillian* , **37**, 193-200.
[14] Long, J.L., He, Z.J., Ma, Y.G. and Liu, B., 2005. *Physical Review C*, *72*(6), 064907.
[15] Hadi J. M. Al-Agealy and Enass. J. Muhssen 2015.JCBPS; Section C; **5(4)**; 4389-96.
[16] Singh, S.S., 2014. In *Journal of Physics: Conference Series* , **535**, p. 012002). IOP Publishing.

Influence of Temperature on Nanosecond Pulse Amplification in Thulium Doped Fiber Lasers

Influence of Temperature on Nanosecond Pulse Amplification in Thulium Doped Fiber Lasers

Ali Abdulfattah[1,2*], Stefan Gausmann[1], Alex Sincore[1], Joshua Bradford[1], Nathan Bodnar[1,2], Justin Cook[1], Lawrence Shah[1,3] And Martin Richardson[1]

[1]Laser Plasma Laboratory, College of Optics & Photonics, University of Central Florida, 4304 Scorpius Street, Orlando, FL 32816, USA.
[2]Department of Electrical Engineering & Computer Science, University of Central Florida.
[3]Luminar Technologies, Inc., 12601 Research Parkway, Orlando, FL 32826, USA.

*Correspond Author email: aqa@creol.ucf.edu

Abstract. Thulium silica doped fiber (TDF) lasers are becoming important laser sources in both research and applications in industry. A key element of all high-power lasers is thermal management and its impact on laser performance. This is particularly important in TDF lasers, which utilize an unusual cross-relation pumping scheme, and are optically less efficient than other types of fiber lasers. The present work describes an experimental investigation of thermal management in a high power, high repetition-rate, pulsed Thulium (Tm) fiber laser. A tunable nanosecond TDF laser system across the 1838 nm – 1948 nm wavelength range, has been built to propagate 2μm signal seed pulses into a TDF amplifier, comprising a polarized large mode area (PLMA) thulium fiber (TDF) with a 793nm laser diode pump source. The PLMA TDF amplifier is thermally managed by a separately controlled cooling system with a temperature varied from 12ºC to 36ºC. The maximum output energy (~400 μJ), of the system is achieved at 12ºC at 1947 nm wavelength with ~32 W of absorbed pump power at 20 kHz with a pulse duration of ~ 74 ns.

1. Introduction

The broadband wavelength emission (1.7-2.1 μm) produced by the thulium-doped fiber (TDF) laser has attracted attention in many fields, from remote-sensing [1] to free space communication [2], medical therapy [3], mid-infrared generation via optical parametric oscillators [4], and material processing [5]. The particularly unique feature of TDF is the gain peak resulting from the $^3H_4$ – $^3F_6$ transition which can be optically pumped via the $^3H_4$ – $^3H_6$ absorption transition by commercial 793 nm laser diode pump sources. This contribution has promised high efficiencies greater than the standard quantum defect due to the 2-for-1 cross relaxation (CR) process between thulium ions [6-7]. The efficiency of CR is related to the ground state depletion [8]. In the ground state, the population of the Stark levels is related to the applied temperature. Thus, the lasing threshold will also relate to the applied temperature [9]. Likewise, the core/cladding area ratio of TDF, doping concentration, and fiber length significantly affect the CR process through the temperature dependent Boltzmann distribution [9].

Thulium-doped fibers are silica glass-based with 2-4 % thulium doping as the active laser material. Based on the quantum defect, the fiber core/cladding diameter, and nonradiative losses, the peak thermal load in TDF is approximately 8 times larger than in Ytterbium (Yb) for an equivalent fiber geometry. As a consequence, thermal management is crucial in TDF lasers to avoid thermal failure [10]. Frith et al. [9], found the TDF slope efficiency varies significantly based on the type of thermal management employed. For an uncooled TDF, a slope efficiency of 37% was reported, while for air cooling and conduction cooling, this figure jumps to 57% and 59% respectively. Johnson et al [11], used cryogenic thermal management within the -263 ^{o}C to 100 ^{o}C range of applied temperatures on the TDF. Temperature is an effective tool to increase the short wavelength lasing near 1850 nm. Cole et al [12], employed cryogenic temperatures from -196 ^{o}C to room temperature. When pumping with 1047 nm and 1410 nm, the resulting gain measured at -196 ^{o}C was 12 dB, compared with 7 dB measured at room temperature. The higher rate of nonradiative decay out of the $^{3}H_{4}$ level at room temperature is responsible for the lower gain observed. The current work examines the effect of temperature on the operation of a high power thulium fiber laser.

2. Experiment

The TDF laser system used in these studies consists of two stages, an oscillator and an amplifier, shown in Figure 1. The oscillator is a TDF-based tunable pulsed laser system, with 1838–1948 nm wavelength coverage. A 600 lines/mm gold-coated diffraction grating and an acousto-optic modulator (AOM) with an applied RF signal from a signal generator are used to select the desired wavelength and pulse duration, respectively. This TDF oscillator provides up to 2 W average power with a ~74 ns pulse duration at 20 kHz repetition rate.

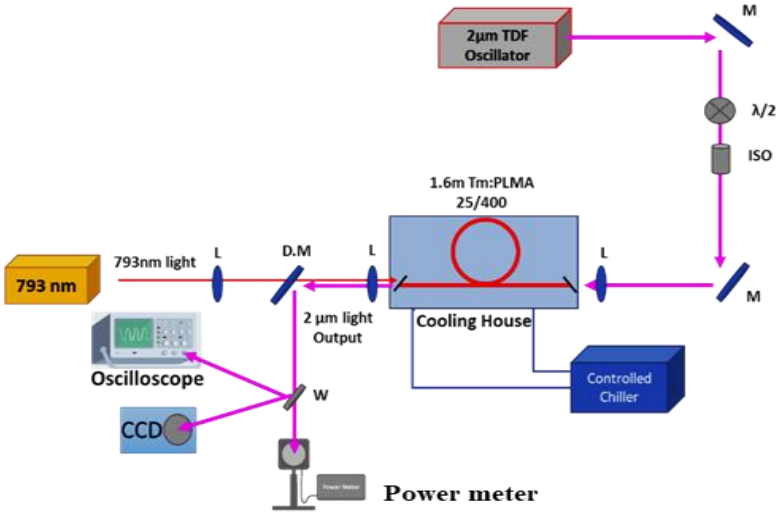

Figure 1. The optical layout of the experimental setup. L: Lens, M: Mirror, D.M: Dichroic Mirror, λ/2: Half-wave plate, ISO: Isolator, W: Wedge, CCD: CCD Camera.

A free space transition stage between the oscillator and amplifier serves to seed the oscillator signal into the TDF amplifier fiber and provides protection for both stages from feedback and crosstalk between them. This stage consists of two 45^{o} angle-of-incidence dichroic mirrors, coated for high-reflectivity (HR) operation at 2 µm and anti-reflective (AR) operation at 793 nm. A light valve, comprising a half-wave plate (λ/2) and isolator (ISO), is located between the mirrors to block any feedback. The seed signal suffers from an attenuation through the free space transition stage.

Because they are less efficient than Yb-doped fiber lasers, high power operation of TDF's are more dependent on the designs for thermal management. Designs using a water cooling basin [13] or a cryogenic cooling freezer [11-12] have been investigated. Here we have designed a homemade independently temperature controlled 1.3 m longitudinal aluminum cooling system comprising a V-shaped groove to hold the fiber. This is connected to a flowing water system to diagnostics flowing water cooling in a closed cycle with water chiller. A Termotek-AG P308 water chiller is used to verify the control temperature range from 10 to 36 °C. The fiber used in this amplifier is a 1.6 m PLMA TDF (TDF-25P/400) from Nufern. A 100 W, 793 nm DILAS diode laser with a 200 µm core delivery fiber was coupled into the PLMA-TDF through an in-house designed 1:1 aspheric telescope with a dichroic mirror (D.M) for HR operation at 2 µm to separate the amplified signal from the pump. A diagnostics stage consists of a beam profile camera (Pyrocam III from Spiricon), power meter (Coherent PM 10 model, 0.25-11 µm), an optical spectrum analyzer (AQ6375 from YOKOGAWA) and a digital oscilloscope (Tektronix DPO 3052) to measure the pulse width.

3. Results & Discussion

The focus of this study was to investigate the temperature effect on pre-lasing (ASE) and the lasing states. To ensure accuracy in the temperature, a 30 minute wait time was imposed after adjusting the temperature before commencing the experiments to assure the housing was stable at the desired temperature. In addition, care was taken to ensure that the TDF-PLMA test fiber facets were unburned and undamaged after the test.

The ASE experiments were performed by pumping the TDF-PLMA amplifier with a 793nm diode laser without the use of a seed signal, for applied temperatures of 15, 20, and 28 ºC. The ASE has different free lasing thresholds relative to each applied temperature, shown in Figure 2. The highest free-lasing threshold occurred at 15 ºC with 120 mW output power, showing a direct correlation between free lasing threshold and applied temperature. Lower fiber temperatures lead to higher free-lasing thresholds and lower lasing. However, still lower cooling temperatures, below 11 ºC, can lead to water condensation on the fiber. While the ASE spectrum has ~100 nm broadening width at 10dB, and slight differences in the optical signal to noise ratio (OSNR). The temperature dependent Boltzmann distribution of the electrons within the energy levels of thulium results in greater ground-state reabsorption of ASE at higher temperatures.

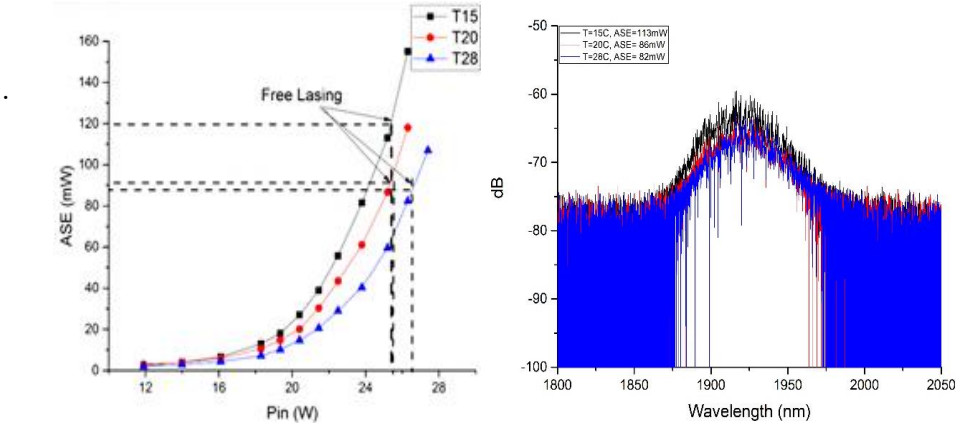

Figure 2. ASE power scale and spectrum related to the temperature

Four lasing wavelengths were selected to investigate the lasing behavior as a function of its spectrum: 1838 nm, 1877 nm, 1913 nm and 1947 nm. The 793 nm pump power launched into the TDF

amplifier was kept constant. Analogous to the ASE tests, a 30-minute wait time was employed for each of the applied temperatures were 15, 20, and 28 ºC.

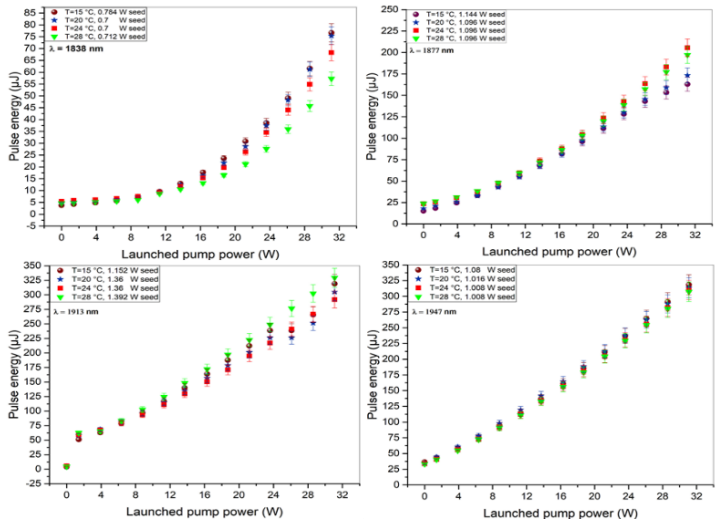

Figure 3. Amplified energy related to different applied temperatures (15, 20, 24, and 28 ºC), for four selective wavelengths 1838, 1877, 1913, and 1947 nm, at the same launched power scale, up to 32W.

'Figure (3)' shows the results for the case of the seeded TDF amplifier. The seed energy was 35 – 70 µJ depending on the wavelength selected, while the pulse amplification gain is 7.9-15.5 dB. This amplification factor depends on the wavelength selected relative to the ASE gain spectrum and the lasing spectrum. Shorter wavelengths display an exponential growth in the pulse energy with increasing launched pump power, while the pulse energy at longer wavelengths is seen to grow linearly. At shorter wavelengths, the effect of temperature on the pulse amplification is more pronounced than at longer wavelengths, especially near the free-lasing threshold. The absorbed pump is constant, so the inversion is fixed to provide a fixed amplification factor at a given wavelength. The sensitivity to temperature decreases from ~25% variance in output energy at 1838 nm to ~10% at 1947 nm. However, since longer wavelengths are generally preferred in TDF's, the temperature does not have a strong effect on the pulse amplification over the desired operating parameters.

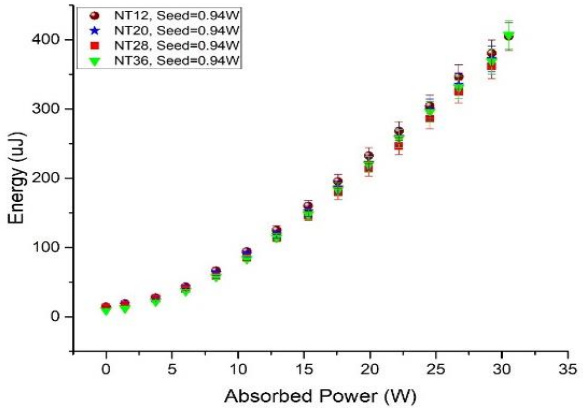

Figure 4. Amplified pulse energy for a fixed seed energy of 47 µJ with different applied temperatures 12 – 36 ºC at 1947 nm.

To investigate temperature effects further, the energy amplification at a wavelength of 1947 nm was investigated for a wider applied temperature range of 12-36 ºC, with a fixed seed energy of 47 µJ. The highest pulse energy obtained was ~ 400 µJ at both 12 and 36 ºC applied temperatures for 32 W absorbed power, shown in Figure 4. For temperatures lower than 12 ºC atmospheric condensation occurred on the fiber mounts. Overall, under a lab operation environment there is no recorded effect of the temperature on the TDF laser operation. However, the 12 - 20 ºC temperature is the likely range to avoid any damage our on the TDF facet.

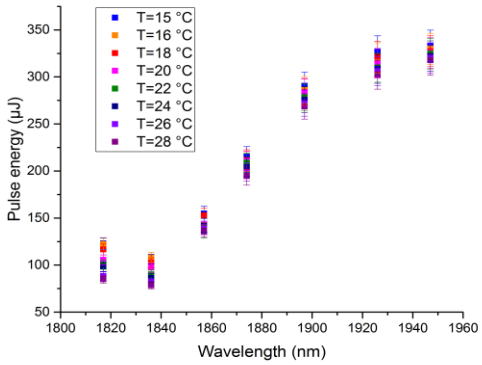

Figure 5. The relation between wavelength and pulse energy under different temperatures for TDF laser.

Finally, the relation between the wavelength and laser pulse amplification for different temperatures was investigated, Figure 5. The launched pump power was kept constant at 32 W. The highest output energies achieved were at longer wavelengths with an output of 350 µJ at 1947 nm. At increasing wavelengths, the extractable energy is more effective than at shorter wavelengths. No strong dependence on the temperature was observed. These results agree well with the higher gain observed at longer wavelengths in the TDF.

4. Conclusion

This work investigated experimentally the thermal management of TDF laser systems in the high repetition-rate nanosecond pulsed regime. The system consists of TDF oscillator and amplifier, providing a nanosecond pulsed tunable seed wavelength between 1810 – 1950 nm at 20 kHz rep. rate to produce up to 2 W average power. A free space transition stage between the oscillator and amplifier delivers the seed signal into the amplifier fiber as well as prevents optical feedback. A 1.6 m PLMA-TDF with up to 100 W available pump power at 793 nm provides the amplifier stage. The amplifier PLMA-TDF has thermal management control using an aluminum V-shaped cooling house with active temperature control from a water chiller. The applied temperature range examined in this study was 12-36 ºC. A negligible effect of the temperature on the PLMA-TDF laser gain was observed. Longer wavelength operation near 1947 nm is preferred to maximize the extracted energy from the amplifier, producing ~400 µJ pulse energies at 12 ºC

Acknowledgements

This work was supported by grants from the High Energy Laser – Joint Technology Office with Office of Naval Research (FA9451-15-D-0013), Air Force Office of Scientific Research (FA9550-15-1-0041), Army Research Office (W911NF-11-1-0297), and High Energy Laser – Joint Technology Office with Army Research Office (W911NF-12-1-0450), United State of America.

References

[1] Wang Q, Geng J and Jiang S 2013 *Optical Engineering* **53** 061609
[2] Li Z, Heidt A, Simakov N, Jung Y, Daniel J, Alam S and Richardson D 2013 *Optics Express* **21** 26450
[3] Herrmann T, Bach T, Imkamp F, Georgiou A, Burchardt M, Oelke M and Gross A 2010 *World Journal of Urology* **28** 45-51
[4] Gebhardt M, Gaida C, Kadwani P, Sincore A, Gehlich N, Jeon C, Shah L and Richardson M 2014 *Optics Letters* **39** 1212
[5] Mingareev I, Gehlich N, Bonhoff T, Abdulfattah A, Sincore A, Kadwani P, Shah L and Richardson M 2015 *The International Journal of Advanced Manufacturing Technology* **84** 2567-2578
[6] Dickinson, Ben, S. D. Jackson, and T. A. King, *Advanced Solid State Lasers*. Optical Society of America, 2000
[7] Tao M, Huang Q, Yu T, Yang P, Chen W and Ye X 2013 *2nd International Symposium on Laser Interaction with Matter (LIMIS 2012)*
[8] Frith G, Carter A, Samson B, Faroni J, Farley K, Tankala K and Town G 2010 *Fiber Lasers VII: Technology, Systems, and Applications*
[9] Gavin P. Frith, David G. Lancaster, Stuart D. Jackson 2004 *Proc. SPIE **5620**, Solid State Laser Technologies and Femtosecond Phenomena*
[10] Gregory D. Goodno, Lewis D. Book, Joshua E. Rothenberg, Mark E. Weber, Stanley B. Weiss 2011 *Optical Engineering* **50**(11), 111608
[11] Benjamin R. Johnson, Daniel J. Creeden, Scott D. Setzler 2017 *Proc. SPIE **10083**, Fiber Lasers XIV: Technology and Systems*, 100830J
[12] Cole B, Dennis M, *OFC 2001 Optical Fiber Communication Conference and Exhibit Technical Digest Post conference Edition* (IEEE Cat 01CH37171)
[13] Till Walbaum, Matthias Heinzig, Franz Beier, Andreas Liem, Thomas Schreiber, Ramona Eberhardt, Andreas Tünnermann 2016 *Proc. SPIE **9728**, Fiber Lasers XIII: Technology, Systems, and Applications*, 97280P

Antibacterial Activity Of ternary semiconductor compounds AgInSe2 Nanoparticles Synthesized by Simple Chemical Method

Antibacterial Activity Of ternary semiconductor compounds $AgInSe_2$ Nanoparticles Synthesized by Simple Chemical Method

A A Shehab[1], S A Fadaam[2] ,A N Abd[3], M H Mustafa[1]

[1]Department of physics/ College of Education For Pure Science Ibn AlHaitham University of Baghdad Baghdad Iraq

2Ministry of EducationDirectorate General for Education Baghdad ALRusafa /1 Baghdad Iraq

[3]Physics Department Collage of Science Al Mustansiriyah University/ Baghdad/ Iraq

Abstract: In this objectiveeAgInSe2Nanoparticles $AgInSe_2$ NP_s were prepared by a Simple chemical methoddSCM The optica structural l and morphological properties of the synthesized $AgInSe_2$ NPs swere investigated by using UVVI absorption atomic force microscopy AFMmfFourier TransformInfrared Spectroscopy and xray diffractionn The resistance of bacteria represents a trouble and the outlook for the use of antibiotics in the future until now uncertain It must be taken measures to decrease this problem antibacterial activity of the AgInSe2 nanoparticles were exposed against several pathogenic bacteriaa including Klebsiella pneumonia KPa Staphylococcus aureus Bacillus subtili Enterobacter Cloacae and *Esherichia Coli*by using a good spread method the results showed that $AgInSe_2$ NPs had inhibitory effect versus some pathogenic bacteria with suppression area 18 18 14 and 17 mm for S$AgInSe_2$ NPs had an inhibitory effect against S Bacillus Subtilis 11 mm K EnterobactercCloacae 12 mm

Keywords XRD AFM thin film Antibacterial AgInSe2

1. Introduction

Nanotechnology can be applied to various domains eg physical biological chemical and engineering sciences where sover new developing methods are being developed so as to study manipulate single atoms and molecules The metallic nanoparticles have different applications areas like cosmetics covering electronics packaging and biotechnology [1] The strong usage of chemotherapeutic antibacterial agents led to generate the eclestic pressure to promote the rising average in antibiotic resistance [2] Up growth of new strains bacteria that resist the present antibiotics has become a

significant public health problem which requires to develop novel bactericidal materials [3] In this consideration compounds composition or extraction for instance nanoparticles with antimicrobial features is significant and has applications of fighting against the evergrowing number of antibiotic resistant pathogenic bacteria that show a continual threat to human and animal health

2. Experimental

In the present work $AgInSe_2$ prepared of compound from alloy of ratio 112 Ag InSe lineage key –live equivalent to an atomic ratio of each compound The mixture in a furnace at a temperature reaches up to 1100 °C and left the sample inside furnace until it is cool gradually and then flushed sample and extract the broken substance than grinded substance by mill specials 15 g of $AgInSe_2$ NP_s was solution in 50 ml of ethanol was used throughout experiment after grinding as a powder The color of the mixture was black The sample was protected at 75 °C for 1 hour A considerable black deposit amount was made The particles were deposited on glass substrates at room temperature by using drop infusion technique 5 drops only to prepare the $AgInSe_2$ thin films at 80 °C thin films were dried

3. Results and Discussions

Figure 1 shows the Xray diffraction patterns for $AgInSe_2$ thin films on glass substrate As shown in Fig1 XRD patterns for $AgInSe_2$ It can be noticed that films are polycrystalline materials The figure 1 revels contain Many peaks at diffraction angle of 2570 2931 4188 4283 4974 5142 6068 6835and 7708 corresponding to 112 200 220204312116400316 and 424 and planes which have been compared with the standard XRD diffraction date file ASTM NO 000380952 Where it was found thin films are prepared with a tetrahedral structure

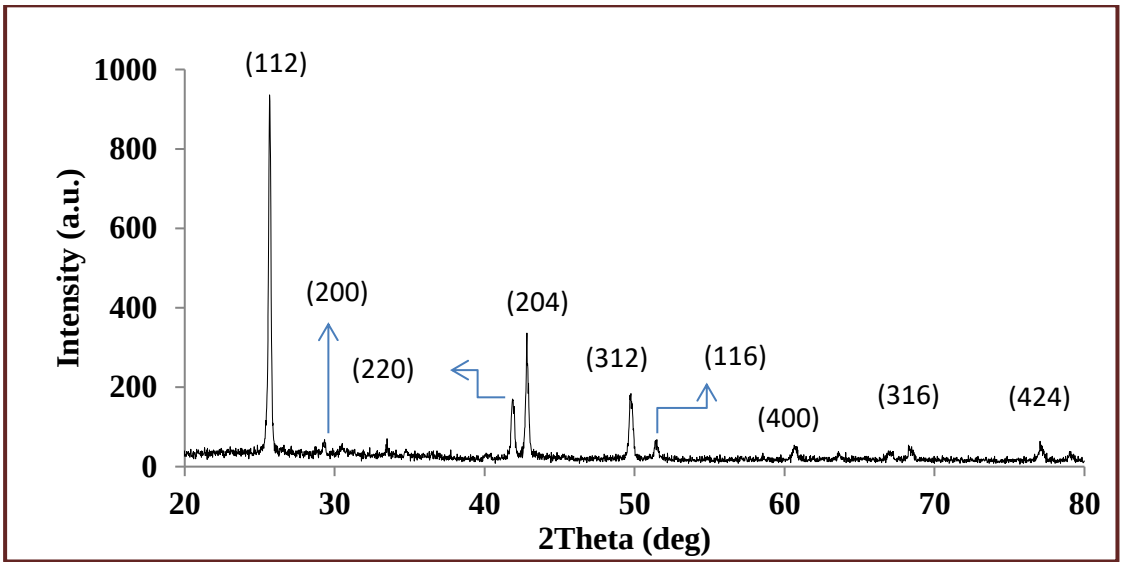

Figure 1. XRD spectra of $AgInSe_2$ films deposited on glass substrate

Through "DebyeScherrer's relation" it was calculated the crystallite size [5]

$$G_s = \frac{0.9\,\lambda}{\beta\cos(\theta)} \quad (1)$$

θ = the diffraction angle λ is the wavelength of xray and β is the FWHMIt can use the relations in equation 2 and 3 to evaluate the dis arrangement density δ and the strain η [6] as shown in Table 1

$$\eta = \frac{\beta \cos\theta}{4} \quad (2)$$

$$\delta = \frac{1}{G_s{}^2} \quad (3)$$

Table 1 2 theta crystallite size strain and dislocation density $AgInSe_2$ thin films

Sample	2 theta deg	hkl	G_s nm	η* 10^4lines^{2}m^4	δ10^{14}linesm^2
	257004	112	5468261	6899817	3344272
	29315	200	4640018	8131434	4644733
	418840	220	4676607	8067814	45723362
	4289399	204	6073208	6212532	2711214
$AgInSe_2$	497481	321	4400549	8573931	5164001
	514224	116	5360899	7037998	3479563
	606841	600	3939965	9576226	6441918
	68355	316	539066	6999142	3441249
	770873	424	4308368	8757376	538734

Figure 3 Methanol and Colloidal suspensions of TiO_2 at 132 J/cm^2 pulse laser fluence from left to right

'Figure 2' exposes the 3D AFM photos and the chart division of $AgInSe_2$ film on glass substrate It is fully wrapped with $AgInSe_2$ nanostructure spread regularely on the surface Table 2 clearly demostrates that the root mean square of surface roughness

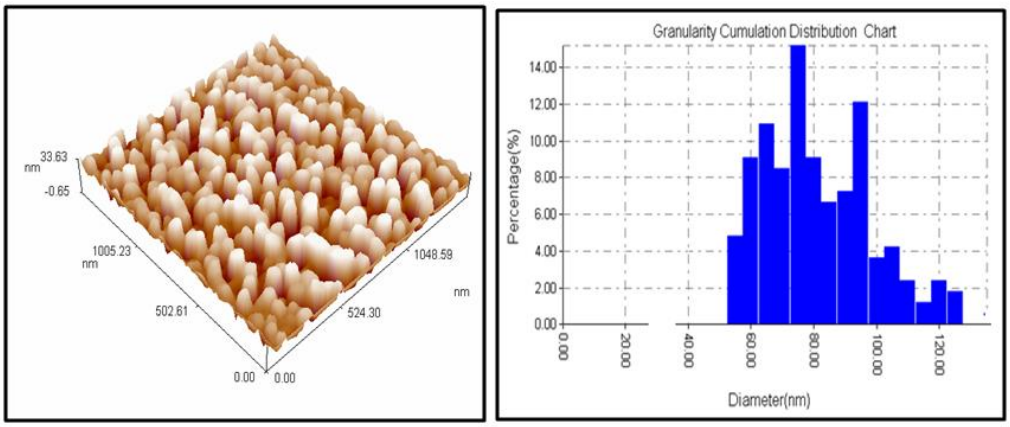

Figure 2 3D AFM images and Granularity accumulation distribution chart of $AgInSe_2$ thin film surface

Table 2 Rate grain roughness density and RMS of AgInSe2 thin films

Sample	Average grain nm	Roughness density nm	RMS nm
$AgInSe_2$	7926	723	838

' Figure 3' displays the FTIR spectrum of $AgInSe_2$ Sample that demonstrates many significant absorption peaks in zone of 400 3900 cm^1 broad absorption band is designated to $AgInSe_2$ expansion form $AgInSe_2$ spectra showed absorption bands as in table 3

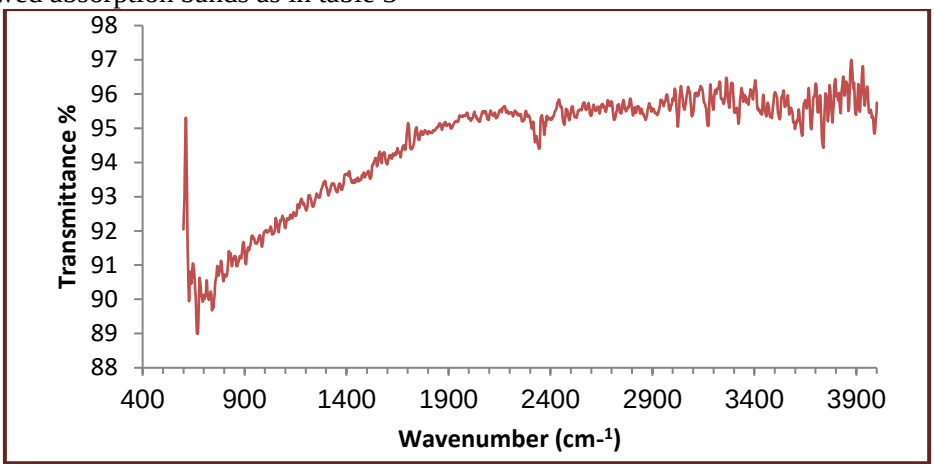

Figure 3 FTIR spectra of AgInSe2 thin film

Table 3 Chemical bonds and their IR resonance positions in $AgInSe_2$

Sample	Wavenumber cm^1
$AgInSe_2$	62689
	66932
	69440
	72526
	74069
	79763
	90657
	95672
	123448
	234359
	286632
	292418
	298591
	302448
	305727
	309392
	319808

'Figure 4' show optical micrographs of $AgInSe_2$ deposited on a glass substrate prepared by simple chemical method Furthermore the images exhibit a a good homogeneous and uniform thin film Also the surface is coarse and showed various colors there were noticed no crack and no void on layer surface

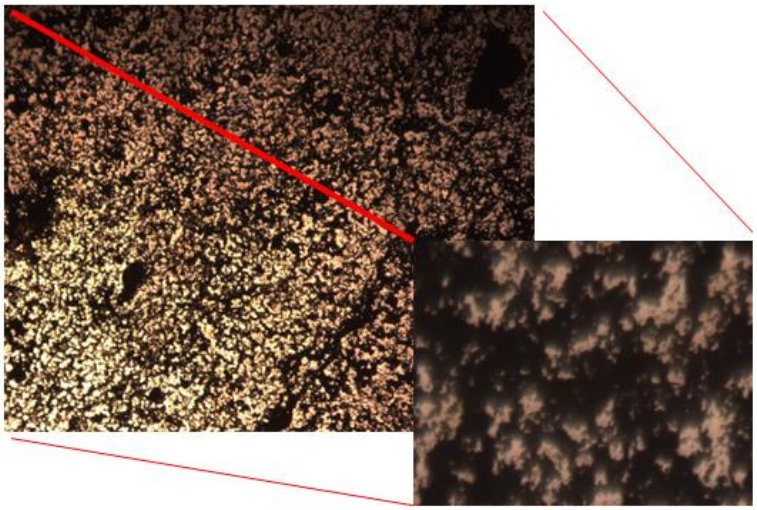

Figure 4. Optical micrographs of $AgInSe_2$ prepared by chemical method

By using chemical procedure PL emission spectra of AgInSe2 was measured with an excitation wavelength source 350254 nm and 70066 nm at 27 ºC temperature as shown in 'figure 5' Where excitation wavelength sourcenm agreeing 350254 with energy gap for optical properties

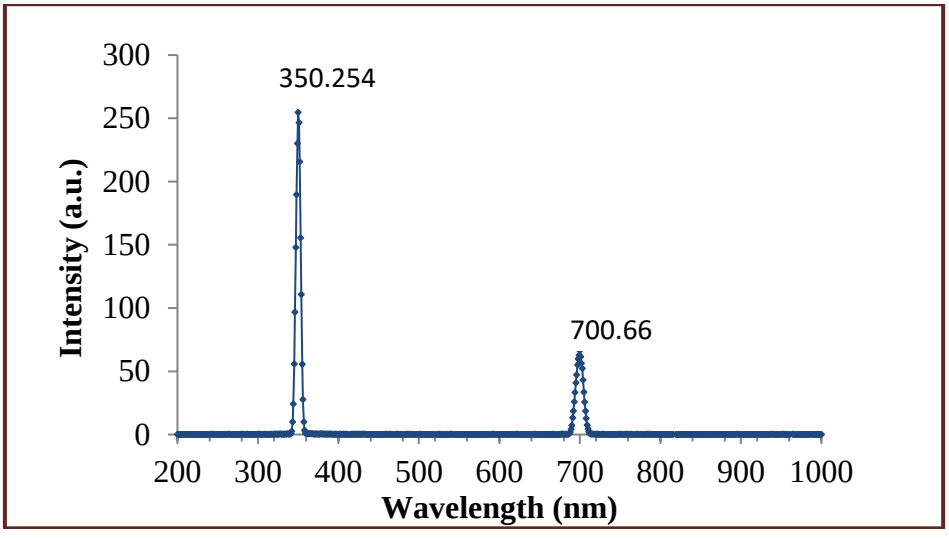

Figure 5. PL spectra of $AgInSe_2$

'Figure 6' shows displays the transmission as a function of wavelength of AgInSe2 thin films that are prepared using chemical procedure and deposited on a glass substrate It is noticed that the films give good translucence features at the spectral range 300 1100 nm The date is corrected for glass in UV regain the transmission is sharply increasing because of the width of the absorbed particle size Also the figure 5 the maximum value of transmittance 2058 nm

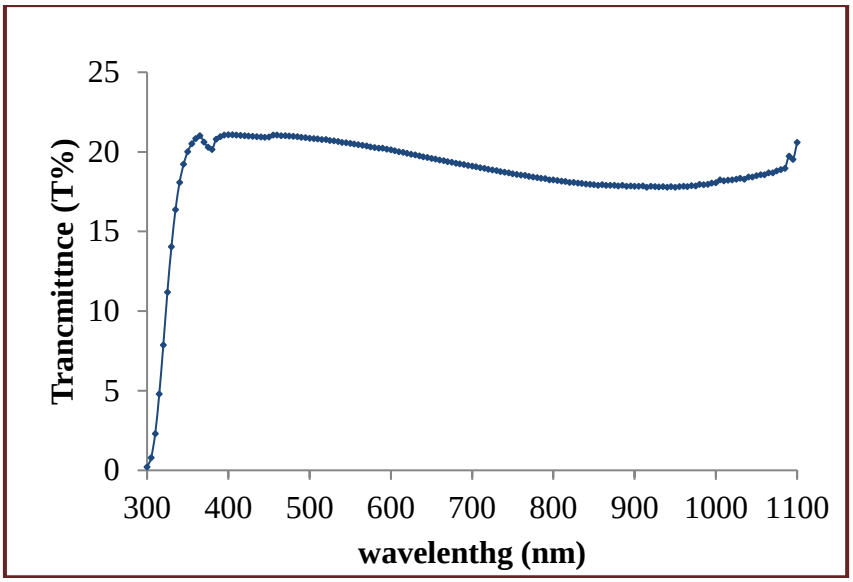

Figure 6. Optical transmittance of $AgInSe_2$ thin film

The optical energy gap of $AgInSe_2$ was calculated by the relation [7]

$$\alpha h\nu = A(h\nu - Eg)^n \quad (4)$$

Where A is a constant ν is the transition frequency is plank constant α is the absorption coefficient E_g is the energy gap and the exponent n characterizes the nature of band transition n= 05 corresponds to indirect band Fig7 shows that the band gap of $AgInSe_2$ thin films is which is chemically prepared and deposited on a glass substrate The measurement was from the square plot $\alpha h\nu^2$ toward photon energy hν considering α is the absorption coefficient by extrapolating the curve linear part toward the photon energy pivots The optical energy gap of AgInSe2 is found to be36 eV

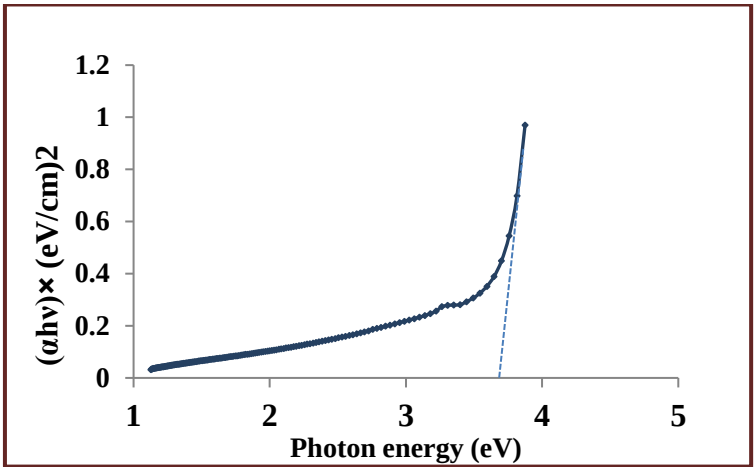

Figure 7. Plot of $\alpha h\nu^2$ versus hν curve of $AgInSe_2$

Staphylococciaureus Golden staphare gram positive bacteria described by individual cocci which have grapelike clusters also this bacteria are nonmotile nonspore forming [8] S aureus are volitional anaerobes that grow by aerobic respiration or by fermentation and can grow in a temperature range of 15 45 ℃ and at NaCl concentrations as high as 15 percent [9]S aureus antibiotic resistance is increased due to the firm protective coat Adhesions or MSCRAMMs microbial surface components recognizing adhesive matrix molecules expressed on the surface of the S Areas and promoted the adhesion of the bacteria to the host proteins such as fibronectin and fibrinogen S aureus is considered to be a main pathogen that colonizes and infects both hospitalized patients with deficiency immunity and healthy immunocompetent people inthe community In normal situation these bacterial types are found naturally in the nasopharynx and in skin and in nose but this minor infection are not life threatening however if S aureus violates the implict tissue because of wound of shock or surgery its characteristic local abscess lesion will be created but when reaches to the lymphatic channels or blood this might be the reason of septicaemia toxic shock Enterotoxin AE syndrome toxin1 TSST1 and exfoliative toxins A and B are toxins that occure outside the cells Enterotoxin ingestion is produced by S aureus that can be found in contaminated food may cause food poisoning.

Bacillus subtilis is agrampositive bacteria characterized byaerobic sporeforming rodshaped bacteria that are moving by peritrichous flagella The bacteria areextensively spread in the environment articularly in air oil and plant remains [8] Bsubtilis bacteria has anoptimal temperature 25 35ºC and the most optimal activit of Bsubtilis occurs at 37^0 Canda basic pH of 8 [4].

The distinction of these bacteria are their capability of producing endospores that are highly resistanttonot suitable environmental conditions and that also have ability to grow over a wide range of temperatures including that of the humanbody Bsubtilis amongthe studied bacterial strains in this study the following specific features were noticed

- They do not have virulence factor genes they may acquire such genes from other bacteria particularly from closely related bacteria within the genus
- Lecithinase an enzyme which rupture membranes of mammalian cells is one of B subtilis product however this enzyme has no correlation between it and human disease in B subtilis
- Subtilisin is an extracellular toxin that is produced by B subtilis this proteinaceous compound is able of causing allergic reactions in individuals who are over and over exposed to it [11]

Escherichia coli E coli It's one of the most popular gram negative bacteria E coli is considered as a facultative anaerobic bacteria that can grow with or without oxygen It can be distingwished by nonsporeforming motile rode shaped bacteria that ferments lactose [1] E coli is one of the mostcommon inhabitants of the human intestinal tractnormal flora its optimal growth occurs at 37°C [13] and the optimum pH growing in a culture at 37°C is 6070 also it has a minimum pH level of 44 and a maximum level of 90 required for growth [14]Figure 8 shows the effect Silver Indium Selenide AgInSe2 nanoparticles combined with different antibiotics was inspected against pathogenic bacteria by utilizing the disk spreading method The diameter of suppersion areas 10 mm around the diverse antibiotic discs included Staphylococcus aureus Bacillus subtilis Enterobacter cloacae and Esherichia Coli with and without Silver Indium Selenide nanoparticles against bacterial insulate were caculated Some antibiotics have antibacterial activities like Enterobacter cloacae that was increased in the existance of Silver Indium Selenide nanoparticles against K Pneumoniaisolates while others didn't affect Table 4 It is noticed a need of agents for killing bacteria because of the antibacterial agents resistance [15] Integrating the use of antibiotic nanoparticle unifies towards diminishing the resistance of antibiotic presently It is noticed that for given bacteria and traditional antibiotics [16] Roy et al[17] proposed the mechanisms which including the nanomaterials reaction with biological molecules and thought that bacteria can have a negative charge while metal oxides have a positive one this is the reason of the attraction between bacteria and treated surface that leads to themicrobe oxidizing and eventually dead Antibiotic molecules have considerable active groups like amino groups and hydroxyl which easily reacts with NPS by chelation causing a synergistic effectivness [18]

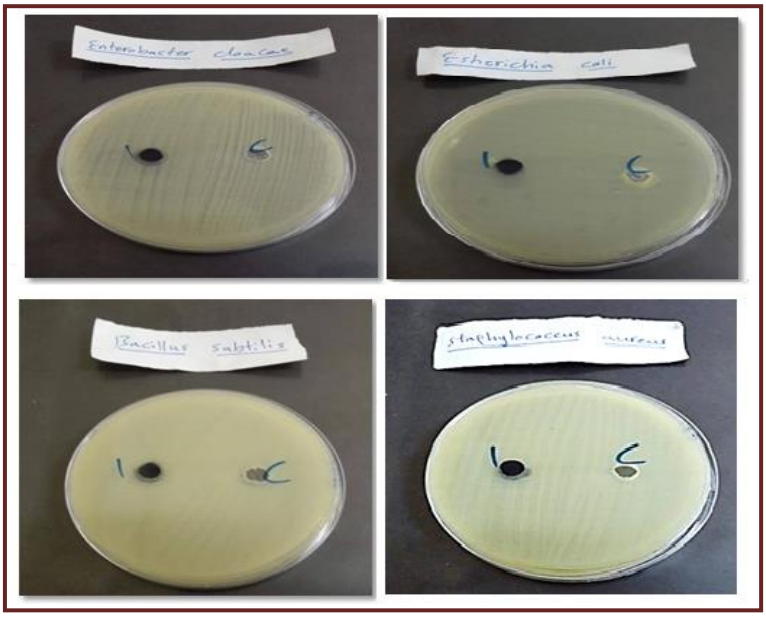

Figure 8. Zone of inhibition induced by $AgInSe_2NP_S$ suspended in ethanol solution prepared simple chemical method against pathogenic bacteria

Table 4 Combined effect between Antibiotics and Silver Indium Selenide nanoparticles against pathogenic bacteria

Compound	Staphylococcus aureus	Bacillus subtilis	Enterobacter cloacae	Esherichia Coli
Control	R	11mm	12mm	R

4. Conclusions

This work has been presented how AgInSe2NPS was prepared by chemical method simplicity value and rapid technique for the composition of AgInSe2 nanostructure The film action as is explained in the figures that display the film is a obvious transmition thin film with a fine crystallize Also the results show that cadmium and copper nanoparticles have an inhibitory effect against pathogenic bacterial isolates

References

[1] Rosarin FS and MirunaliniS 2011 Nobel Metallic Nanoparticles with Novel Biomedical Properties *J BioanalBiomed* **3** 4 8591
[2] Lee CR Cho IH Jeong BC Lee SH 2013 Strategies to Minimize Antibiotic Resistance *Int J Environ Res Public Health* **10** 9 4274 4305
[3] CLSI 2011 Performance standard for antimicrobial susceptibility testing TwentyFirst informational supplement M100S21 **31** 1
[4] RoyAS ParveenA Kuppakar ARand Prasad MNNA 2010 Effect of Nano Titanium Dioxide with Different Antibiotics against Methicillin Resistant Staphylococcus aureusJ Biomaterials and Nanobiotech **1** 37 41
[5] P Scherrer 1918Go¨tt Nachrichten Gesell **2** 98
[6] CD Lokhande 1991Mater ChemicalPhysics **27** 1
[7] CD Lokhande A Ennaoui PS Patil M Giersig M Muller K Diesner H Tributsch 1998 Thin Solid Films 330 70
[8] JOSEPH CM 1996 MENON CS Semicond Sci Techn **11** 1668
[9] SuchitraD Nageswara Rao A B N Ravindranath A Sakunthala Madhavendra S and Jayathirtha Rao V 2011 Silver Nanoparticle Synthesis From Lecanicillium Lecanii and Evalutionary Treatment on Cotton Fabrics by Measuring Their Improved Antibacterial Activity with Antibiotics against Staphylococcus aureus ATCC 29213 And E coli ATCC 25922 Strains" *International Journal of Pharmacy and Pharmaceutical Sciences* **3** 4 190 195
[10] SantosMM QueirozMJand BaptistaPV 2012 Enhancement of antibiotic effect via goldsilveralloy *nanoparticles J Nanopart* Res **14** 859
[11] Fayaz AM Balaji K Girilal M Yadav R Kalaichelvan PTandVenketesan R 2010 Biogenic synthesis of silver nanoparticles and their synergistic effect with antibiotics A study against grampositive and gramnegative bacteria NanomedNanotechnol Biol Med**6** 1 103 109
[12] Holt KB and Bard AJ Interaction of silver I ions with the respiratory chain of Escherichia coli 2005 An electrochemical and scanning electrochemical microscopy study of the antimicrobial mechanism of micromolar Ag Biochemistry 44
[13] HarrisLG Foster SJ and Richards RG 2002An introductionto Staphylococcus aureus and techniques for identifyingand quantifying Saureus adhesions in relation to adhesionto biomaterialsreview Europeancells andmaterials **4** 39 60
[14] HorstAK 2009 Antimicrobial effects of metaloxide nanoparticles The 2009NNINREU Research

Accomplishments 12 13
[15] Jalal RSaliani M and Goharshadi EK 2011 Effects of Phand concentration antibacterial activity of ZnO nanofluids against Staphylococcus aureus 1st NationalIranian New Chemistry Congress 885 890
[16] Jones N Ray B Ranjit KT and Manna AC 2008 Antibacterial activity of ZnO nanoparticles suspensions on a broad spectrum micro organisms Federation of European Microbiological Societies Microbial Letter **279** 71 76
[17] Karvani ZE andChehrazi P2011 Antibacterial activity of ZnO nanoparticles ongrampositive and gramnegative bacteria *African Journal of Microbiology Research***5** 12 1368 1373
[18] Todar K 2012Todar's online textbook bacteriology 2008 2012 p1 Availableat http text bookof bacteriologynet Saureushtml .

Theoretical Discussion of Electron Transport Rate Constant at TCNQ / Ge and TiO_2 System

IOP Conf. Series: Journal of Physics: Conf. Series **1003** (2018) 012122 doi:10.1088/1742-6596/1003/1/012122

Theoretical Discussion of Electron Transport Rate Constant at TCNQ / Ge and TiO_2 System

Hadi J M Al-agealy[1], B Alshafaay[2], Mohsin A Hassooni[1], Ahmed M Ashwiekh[1] Abbas K Sadoon[1], Raad H Majeed[1], Rawnaq Q Ghadhban[1], Shatha H Mahdi[1]

[1]Department of Physics, College of Education for pure science, Ibn Al-Haitham, Baghdad of University
[2]Department of Physics, College of Education, Kerbala of University.

Abstract. We have been studying and estimation the electronic transport constant at TCNQ / Ge and Tio2interface by means of tunneling potential (TP), transport energy reorientation (TER) , driving transition energy DTE and coupling coefficient constant. A simple quantum model for the transition processes was adapted to estimation and analysis depending on the quantum state for donor state$|\alpha_D>$ and acceptor state$|\alpha_A>$ and assuming continuum levels of the system. Evaluation results were performed for the surfaces of Ge and Tio2as best as for multilayer TCNQ. The results show an electronic transfer feature for electronic TCNQ density of states and a semiconductor behavior. The electronic rate constant result for both systems shows a good tool to election system in applied devices. All these results indicate the

1. Introduction

Charge transition reaction were fundamental steps processes in more biophysical and physical chemistry and study of condensing phase of electron transfer field in molecular electronics. Where its development of charge transfer theory by Marcus [1]. Electronics are such an elementary particles that mobile in molecular devices and movement at condensed phases due to fluctuations and/or external electromagnetic excitation [2]. Nonadiabatic charge transfer in molecular electronic via quantum mechanical tunneling was characteristic of processing limited from photosynthesis to conduction at molecular wires [3]. The special type of molecular have electronic properties was a multidisciplinary and active research area to study a fundamental process, such that charge transfer .The low-cost and molecular-sized make us to using, molecular electronic in much-applied research [4]. Marcus R was one famous scientist that provided to describe the transfer depending simple theory. Depending on the Marcus assumption of charge transfer reactions, there are a simple relation the rate reaction and the system fundamental quantities [5]. The exploitation of charge transfer reaction processes to construct more technological devices had already been proposing and needed to understand the transfer mechanism theoretically [6].The important challenging against the scientists today was developing the scale of molecular systems that could be controlling and signals processes, besides to producing more applied devices such as rectifiers, wires, transistors, memories and optoelectronic triggering switches [7]. On the other hand, the charge transfers at semiconductor surfaces include many important applications such that photoelectrolysis, photocatalysis, quantum confinement devices, waste processing, and solar cells [8].

The aims of this paper are to study and discuss the electronic transfer interaction at the molecule/semiconductor interface according to simple quantum model to gate result an expression enables us to evaluate the transfer rate flow of electrons through molecule/semiconductor systems. Wing the last numbered section of the paper.

2. Theory

The consideration of quantum theory assumes that the two wave function of system donor and acceptor are satisfied a linear function in the Hilbert space. The assume two wave function are $|\psi_D>$, and $|\psi_A>$ which refers to the electronic donor and accepter state function and given by [9].

$$|\boldsymbol{\psi_D(\epsilon)}>= \frac{e^{\left(-\frac{\epsilon^2}{2\theta^2}\right)}}{(2^i i!)^{\frac{1}{2}}(2\pi\theta^2)^{\frac{1}{4}}} \boldsymbol{H_i}(\frac{\epsilon}{\sqrt{2}\boldsymbol{\theta}})\boldsymbol{\theta} \tag{1}$$

$$|\boldsymbol{\psi_A(\epsilon)}>= \frac{1}{(2^i i!)^{\frac{1}{2}}(2\pi\theta^2)^{\frac{1}{4}}} \boldsymbol{H_i}(\frac{\epsilon}{\sqrt{2}\boldsymbol{\theta}}) \tag{2}$$

Here $\boldsymbol{\epsilon}$ is the effective transition energy, $\boldsymbol{\theta} = \sqrt{\boldsymbol{2\Delta k_B T}}$, H_i is Hermite polynomial.

According to Schrödinger assumption the distribution function $\boldsymbol{\rho(t)}$ for the electron transfer system. Maybe written due to Neuman 'as in equation (3)' [10].

$$\frac{\mathbf{d}}{\mathbf{dt}}\boldsymbol{\rho}(\boldsymbol{\epsilon},\mathbf{t}) = \hat{\mathbf{L}}\boldsymbol{\rho}(\boldsymbol{\epsilon},\mathbf{t}) \equiv \mathbf{H}\boldsymbol{\rho}(\boldsymbol{\epsilon},\mathbf{t}) \tag{3}$$

The Hamiltonian operators of the system can be written as [11].

$$\boldsymbol{\hat{H} = \hat{H}_{EL} + \hat{H}_{VIB} + \hat{H}_{INT}} \tag{4}$$

Where $\hat{H}_{EL}$ is the electronics Hamiltonian, $\hat{H}_{VIB}$ is the Hamiltonian for the classical dynamics oscillators and $\hat{H}_{INT}$ is the interaction between the electronic and the vibrational.According to the classical-quantum treatment [12], the density of electron transfer reduces to rate $\Pi(\epsilon, t)$ according to.

$$\boldsymbol{\Pi(\epsilon,t) = \frac{d}{dt}\rho(\epsilon,t) = H\rho(\epsilon,t)} = (\boldsymbol{\varrho + i\xi})\boldsymbol{\rho(\epsilon,t)} \tag{5}$$

Where ϱ, and ξ are the relaxation dynamics and for the electronic transition between two states and Eq. (6) lead to results.

$$\boldsymbol{\dot{\rho}_{aa}(\epsilon,t) = H_{aa}\rho_{aa} + i\bar{T}(\rho_{ab} - \rho_{ba})} \tag{6-A}$$

$$\boldsymbol{\dot{\rho}_{bb}(\epsilon,t) = H_{bb}\rho_{bb} - i\bar{T}(\rho_{ab} - \rho_{ba}} \tag{6-B}$$

$$\boldsymbol{\dot{\rho}_{ab}(\epsilon,t) = H_{ab}\rho_{ab} - i\omega_{ab}\rho_{ab} + i\frac{\bar{T}}{\hbar}(\rho_{aa} - \rho_{bb})} \tag{6-C}$$

$$\boldsymbol{\dot{\rho}_{ba}(\epsilon,t) = H_{ba}\rho_{ba} + i\omega_{ab}\rho_{ba} - i\frac{\bar{T}}{\hbar}(\rho_{aa} - \rho_{bb})} \tag{6-D}$$

Where $\bar{T}$is the coupling coefficient, w_{12} is the differences frequency between two free energies $U_1(E)$, and $U_2(E)$ given by[13].

$$\boldsymbol{\hbar\omega_{12} = U_1(E) - U_2(E) = \Delta + E_o} \tag{7}$$

For non-adiabatic limit of electron transfer Eq. (6-C) and (6-D) in time domain solution

$$\boldsymbol{\rho_{ab}(\epsilon,t) = \rho_{ba}(\epsilon,t) = i\bar{T}\int_0^t d\tau \int_{-\infty}^{\infty} d\epsilon_o G_{ab}(\epsilon,\tau|E_o)\,[\rho_{aa}(\epsilon_o,\mathbf{t}\mp\tau) - \rho_{bb}(\epsilon_o,\mathbf{t}\mp\tau)} \tag{8}$$

The operator of green functionG_{ab} is.

$$\boldsymbol{G_{ab}(\epsilon,\tau|\epsilon_o) = \langle\epsilon|e^{(H_{21}+i\omega_{12})t}|\epsilon_o\rangle} \tag{9}$$

Substitute 'equation (8)' in 'equation (6-A) and 'equation (6-B), to results.

$$\frac{d}{dt}\boldsymbol{\rho_{ii}(\epsilon,t)} = \boldsymbol{L_{ii}\rho_{ii}(\epsilon,t)} - \frac{2\pi}{\hbar}|\overline{T)}|^2 \boldsymbol{Re}\int_{-\infty}^{\infty} \boldsymbol{d\epsilon_o}\int_0^t \boldsymbol{d\tau\, G_{12}(E,\tau|E_o)[\rho_{ii}(E_o,\mathrm{t}-\tau) - \rho_{jj}(E_o,\mathrm{t}-\tau)} \quad (10)$$

for non adiabatic electron transfer is given by:

$$\boldsymbol{\Pi(\epsilon,t)} = \frac{2\pi}{\hbar}|\overline{T)}|^2 \boldsymbol{Re}\int_{-\infty}^{\infty} \boldsymbol{d\epsilon_o}\int_0^t \boldsymbol{d\tau\, G_{12}(\epsilon,\tau|E_o)[\rho_{aa}(\epsilon_o,\mathrm{t}-\tau) - \rho_{bb}(\epsilon_o,\mathrm{t}-\tau)} \quad (11)$$

Then result of evaluation Eq. (11) is:

$$\boldsymbol{\Pi(\epsilon,t)} = \frac{2\pi}{\hbar}(4\Delta \mathbf{k_B T})^{\frac{-1}{2}}|\overline{T)}|^2 \mathbf{exp} - \frac{\Delta}{4\mathbf{k_B T}}\left[\left[1 - \frac{1}{4\Delta \mathbf{k_B T}}\left(\frac{(\pi \mathbf{k_B T})^2}{4}\right) + \frac{1}{32\Delta^2 \mathbf{k_B}^2 T^2}\left(\frac{5(\pi \mathbf{k_B T})^4}{16}\right)\right]\right] \quad (12)$$

The reorientation transition energy Δ (eV) for electronic transition is [14]:

$$\Delta(\boldsymbol{n,\varepsilon}) = \frac{(\Delta e)^2}{8\pi\varepsilon_0}[\boldsymbol{f}(\mathbf{n},\boldsymbol{\varepsilon})\left(\frac{1}{R} - \frac{1}{2D}\right)] \quad (13)$$

Here$f_{(n,\varepsilon)}$is the polarity of system $f_{(n,\varepsilon)} = (\frac{1}{n^2} - \frac{1}{\varepsilon})$, n and ε are the optical and statistical dielectric constant, $\Delta e = e_D - e_A$ the difference in electron charge of donor and acceptor, *R is* molecule radius, and *D* is the distance between semiconductor and molecule. The radii of the molecule could be evaluation using [15].

$$\boldsymbol{R} = (\frac{3M}{4\pi N\rho})^{\frac{1}{3}} \quad (14)$$

Where M is the molecular weight, N is Avogadro's number, and ρ is the mass density.

3. Result and Discussion:

A theoretical discussion of electronic transport according to the quantum system that assumes depending on the experimental system to understanding the mechanism of charge transfer at the molecule /semiconductor interface. A two quantum state $|\psi_D(\epsilon)>$, and $|\psi_A(\epsilon)>$ for donor and acceptor system and the transfer of electrons via the interface of the system. The evaluation of the rate of electronic flow has been performed for TCNQ molecule with Ge and Tio2 semiconductor. It was evaluated using expression Eq. (12) due to the transition energy $\Delta(n,\varepsilon)(eV)$, the electronic coupling coefficient $\bar{T}$ for molecule and semiconductor state at room temperature. The rate expression indicates the behavior of electronic transfer through interface molecule/semiconductor. The mechanisms of electronic transfer at molecule/semiconductor system have been the discussion from evaluated flow rate and all transfer coefficient, one can be evaluated the transition energy $\Delta(n,\varepsilon)(eV)$ depending on the continuum model. To evaluated the transition energy, it could be estimated the radii of TCNQ molecule using expression Eq. (14) and substituting Avogadro's constant $N = 6.02\times10^{23}\frac{Molecule}{mol}$, molecular weight M=204.19[16], and density masses $\rho = 1.358$ [17], in Eq. (14), we can evaluate the values of radii for the molecule is 3.906109457.

Next, it can be calculating with inserting the transition energy radii and optical and dielectric constant from Table 1using Eq. (13) with a Mat lab program and substituting. Results are listed in tables (2,3)

Table 1. Properties of Ge and TiO_2 semiconductor.

Properties	**Ge[18]**	**TiO_2 [19]**
Atomic weight	72.60	79.866 [19]
Crystal structure	Diamond	Tetragonal rutile

Density (g/cm^3)	5.3267	4.23 [19]
Refractive index	4.0	2.609[19]
Dielectric Constant	16.0	15.10 [20]
Radius(Å)	1.7547	1.95612

Table 2. Data of transition energy $E_{met}^{liq}(eV)$ for electron transfer at TCNQ/ Ge system.

Solvent	$f(\mathbf{n},\varepsilon)$	Refractive Index [21]	Dielectric constant[21]	Transition energy
Acetunitnile	0.5289	1.3416	37.50	0.567
Propionitnile	0.5010	1.3636	27.20	0.564
Ethyleneolamine	0.3972	1.4513	12.90	0.456
Propanol-1	0.4731	1.3837	20.33	0.534
Dimethylsulfoxidl	0.4367	1.4773	46.68	0.487

Table 3. Data of transition energy $E_{met}^{liq}(eV)$ for electron transfer at TCNQ/ TiO_2 system

Solvent	$f(\mathbf{n},\varepsilon)$	**Refractive index[21]**	**Dielectric constant[21]**	**Transition energy**
Acetunitnile	0.5289	1.3416	37.50	0.643
Propionitnile	0.5010	1.3636	27.20	0.594
Ethyleneolamine	0.3972	1.4513	12.90	0.486
Propanol-1	0.4731	1.3837	20.33	0.578
Dimethylsulfoxidl	0.4367	1.4773	46.68	0.521

The coupling strength $\bar{T}$ between molecule level state and conduction band of semiconductor system is estimation using a typical result from experimental data 0.4, 0.45, 0.5, and 0.55)cm^{-1} depending on literature data in ref. [20] and exchange to $\bar{T} = 0.01115, 0.01177, 0.01239$,and 0.01363eV using transform parameter [20]. However, it has been evaluated the transition rate of electron transfer $\mathbb{R}_{e|t}$ for TCNQ/Ge, and TCNQ /TiO_2 systems using Eq.(12) with the result of transition energy $\Gamma(n, \varepsilon)$, and coupling strength $\bar{T}$. The electronic rate constant of electron transition from Eq. (12) using A MATLAB program .results are shown in tables (4,5).

Table 4. Theoretical data of electronic rate constant $\Pi(\epsilon, t)$(Sec^{-1}) at (TCNQ)/Ge system.

Rate of electron transfer $\Pi(\epsilon, t)\times10^{-29}$(sec^{-1})					
solvent	$\bar{T}$ (eV)				
	0.01115	0.01177	0.01239	0.01280	0.01363
Acetunitnile	1.22	1.36	1.51	1.82	1.99
Propionitnile	1.52	1.70	1.88	2.28	2.49
Ethyleneolamine	1.78	1.98	2.20	2.66	2.91
Propanol-1	5.07	5.66	6.27	7.59	8.29
Dimethylsulfoxidl	2.37	2.64	2.92	3.54	3.87

Table 5. Theoretical data of electronic rate constant $\Pi(\epsilon, t)$(Sec^{-1}) at (TCNQ)/ TiO_2 system.

Rate of electron transfer $\Pi(\epsilon, t) \times 10^{-25}(sec^{-1})$					
solvent	$\overline{T}$ (eV)				
	0.01115	0.0117	0.01239	0.01280	**0.01363**
		7			
Acetunitnile	1.43	1.56	1.75	1.98	**2.21**
Propionitnile	1.75	1.86	1.95	2.43	**2.74**
Ethyleneolamine	1.87	2.18	2.42	2.87	**3.41**
Propanol-1	5.86	5.96	6.47	7.89	**8.49**
Dimethylsulfoxidl	2.88	3.21	3.54	3.83	**4.17**

Analytical of results according to quantum theory indicates that a high potential barrier formed at the interface of molecule and semiconductor and the potential depending on nature of the material. A simple quantum model of donor acceptor are adapted to discussion transfer of electronic flow via interface according to the wave functions for the acceptor and donor electronic state levels at molecule and conduction band. The important factor that limited the transfer via potential is the coupling strength between donor and acceptor state. Data results in the table (4,5), show that the transfer increases when increases of coupling strength , this indicate the more of electron are cross interface and have energy large than potential and vice versa.

Another parameter effect on transfer rate is transition energy at molecule/semiconductor system. It is evaluated depending on continuum theory to approaches results of experimental data. Transfer energy is modeled depending on physical concepts such as optical and static dielectric constant for donor acceptor and solvent system. The fluctuation of polar media helped to reorientation system to transfer and find the system has large transfer flow when having large transition energy ,this means the system has large transition energy make more electron transfer cross interface because have large energy to drive cross potential at interface that showing from tables (2,3) and tables(4,5)and vice versa.

Tables (2,3) show that the transition energy increase with increasing the solvent dielectric constant and decreasing in rate compared with the system has small the solvent dielectric constant because the system has a small value of transition energy make orient system to transfer of electron. However, it is an increase the solvent refractive index refers to decrease in transition energies for systems.The flow charge proportional due to polarity function $f(\mathrm{n}, \varepsilon)$, and the system have small polarity results to decreasing transition energy and increases flow charge that showing in the table (4,5) for two system.

Apparently, it may be explained the transfer more electron in (TCNQ)/ TiO_2 system indicate this system have transition energy can drive more electronic to transfer potential and have rate larger than TCNQ)/Ge.

4. Conclusions

In this paper, it has been discussing the electronic rate at molecule / semiconductor interface system according on the simple quantum model. The transition energy has been estimated according to assume levels of all system are a continuum.

We concluded that electronic rate at interface system depends on transition energy, coupling strength, and polarity media.

The transition energy evaluation indicates that electronic rate flow is most probably in the system have large polarity.

Consequently, the system (TCNQ)/ TiO_2 have electronic rate transition large than TCNQ)/Ge, this indicates the physical properties of two semiconductors.

References

[1] Gray HB Winkler JR 2003 *Quarterly reviews of biophysics* **36** 3 341-72
[2] Chen H Ratner MA Schatz GC 2011 *The Journal of Physical Chemistry C* **115** 38 18810-21
[3] Nitzan A Jortner J Wilkie J Burin AL Ratner MA 2000 *The Journal of Physical Chemistry B.* **104** 24 5661-5
[4] Small DW Matyushov DV Voth GA 2003 *Journal of the American Chemical Society* **125** 24 7470-8
[5] Xiao T Song X 2013 *The Journal of chemical physics* **138** 11 114105
[6] Hennig D 2001 *Physical Review E* **64** 4 041908
[7] Albinsson B Eng MP Pettersson K Winters MU 2007 *Physical Chemistry Chemical Physics* **9** 44 5847-64
[8] Stier W Prezhdo OV 2002 *The Journal of Physical Chemistry B* **106** 33 8047-54
[9] Cao J 2000 *InAPS Meeting Abstracts*
[10] Cheche TO Hayashi M Lin SH 2000 *Journal of the Chinese Chemical Society* **47** 4 A729-39
[11] Hennig D Burbanks AD Osbaldestin 2011 Directed current in the Holstein system *Physical Review E* :031121
[12] Hadi J. M. Al-Ageal 2016 *Journal of Physical Science and Application* **1** 6 pp 1-11
[13] Al-Agealy H J M and AL-Obaidi R I N 2009 *Ibnal-Haitham J. For Pure& Appl. Sci*. **22** 2
[14] Creutz C Brunschwig BS Sutin N 2006 *The Journal of Physical Chemistry B.* **110** 50 25181-90
[15] Al-Aagealy HJ Hassooni MA 2014 *Journal of Chemical, Biological and Physical Sciences* **4** 3 2454
[16] Xue Y Ratner MA 2003 *Physical Review B* **68** 11 115406
[17] Nitzan A Ratner MA 2003 *Science* **300** 1384-9
[18] Hadi J M Al-Agealy 2014*Wasit Journal for Science & Medicine* **7** 4 278-297
[19] Cotton FA Wilkinson GM Murillo C. CA and Bochmann M 1999 Advances Inorganic Chemistry
[20] Zhu XY2004 *J. Phys. Chem. B* **108** 8778-93
[21] Kasap SO 2000 Principles of electrical engineering materials and devices. *McGraw-Hill Companies*

Hiding Information Using different lighting Color images

Hiding Information Using different lighting Color images

Ahlam Majead[1], Rash Awad[2], Salema S Salman[3]

[1]Dep. of Physics /College of Science / University of Al- Mustansiriyah.
[2]Dep. of Computer/College of Basic Education/ University of Al- Mustansiriyah.
[3]Dep. of Clinical Laboratory Science/College of Pharmacy/ University of Baghdad.

Abstract. The host medium for the secret message is one of the important principles for the designers of steganography method. In this study, the best color image was studied to carrying any secret image.The steganography approach based Lifting Wavelet Transform (LWT) and Least Significant Bits (LSBs) substitution. The proposed method offers lossless and unnoticeable changes in the contrast carrier color image and imperceptible by human visual system (HVS), especially the host images which was captured in dark lighting conditions.The aim of the study was to study the process of masking the data in colored images with different light intensities. The effect of the masking process was examined on the images that are classified by a minimum distance and the amount of noise and distortion in the image. The histogram and statistical characteristics of the cover image the results showed the efficient use of images taken with different light intensities in hiding data using the least important bit substitution method. This method succeeded in concealing textual data without distorting the original image (low light) Lire developments due to the concealment process.The digital image segmentation technique was used to distinguish small areas with masking. The result is that smooth homogeneous areas are less affected as a result of hiding comparing with high light areas. It is possible to use dark color images to send any secret message between two persons for the purpose of secret communication with good security.

1. Introduction

Steganography as the hiding of a note within another so that the attendance of the hidden note is undetectable. The key notion behind steganography is that the note to be dispatch is not detectable to the casual eye. In fact, people who they are not contemplating to be the recipients of the note should not even suspect that a hidden note occurs [1].

The conflict between steganography and cryptography is that in cryptography, one can tell that a note has been encrypted, but he cannot decode the note without knowing the conflict key. In steganography, the note itself may not be hard to decode, but the most public would not detect the appearance of the note. When combined, steganography and cryptography can supply two levels of security. Computer programs exist which encrypt a note using cryptography and hide the encryption within an image using steganography [2].

1.1. LSB encoding

LSB-based programs rely on image encoding in the least significant bits per bytes in image data. By doing this, the value of each pixel is changed slightly, but not enough to make noticeable changes in the image by HVS. The 24-bit color image is used 3 bytes per pixel, so each pixel can be the 3-bit encoding of a secret message. The modified image looks identical to the human eye, even compared to

the original. However, the 24-bit images are very large and are not the common way to send images around the Internet, so the fact that they are too large would be suspicious. There is a 256 image color image, where 1 bytes are used per pixel. A 640 x 480 image of this quality will be able to store 300 kilobytes of data. With a large enough image, one could even hide an image within another image [3, 4].

1.2. Wavelet Transform and Lifting Scheme

DWT is widely used for analyzing signals, steganography art, compression, and noise reducing. DWT implements multiresolution analysis of the signals that have an adjustable location in each of space (time) and frequency domains. Because of a large number of calculations required, there have been many research efforts to improve DWT and give new fast algorithms that are used for performance DWT. The lifting scheme has numerous benefits compared with classical DWT [5]. LWT usually requires less mathematical operations compared with traditional approach convolution. LWT achievement does not require additional memory because of the in-place calculation features of the lifting. This is particularly suitable for the devices implementation of with a limited memory.LWT scheme submitted integer to integer transformation appropriate for lossless processing signal [6].

1.3. Perception the Color Vision

To realize the color requirements must be met are- *:*

1. There should be a variation or differences in the length of light waves that you receive in the visible eye Ocean.
2. There should be a variation in optical reflections surfaces.
3. There should be two or more of the deliverables (Receptors) differ in their impact positive lengths that make up visible light.

Thus, the color does not create subjective and objective impressions but affect our assessment and our perception of time, size, weight, heat and noise, if you can achieve good vision and catching colors for what they are relying on day-lighting [7].

1.4. Phenomena Affecting the Color Vision

1.4.1. Port Kenji Phenomenon

Is the change in the maximum degree of luster in the light spectrum visible color, from yellow to green, brighter with long waves such as ,red .This color loses its brightness by reducing the spotlight on it more than it loses from the gloss of a short-wave color, blue for example. Because the retina loses its sensitivity to the color red first, when you reduce the lighting ,it loses its sensitivity to green and blue colors. The color red seems to be more of the blue ,brighter lighting ,while blue has more shine in the light and dark. This phenomenon is named after the discoverer of the world [7].

1.4.2. Post-image phenomenon After Image Phenomena

Defined as the sensory image in memory and mind after the removal of the external alarm. If the eye has adapted to a particular color through the stare for some time and then shifts toward considering the surface of white or gray on a particular color, the color CMOS will appear on this surface. White Light Fallon if I stared factor or catalyst with a red color and this phenomenon is called the post-image and understanding of this phenomenon is a result of the stress-optic 10 Green will appear.

When adapted to the retina on a specific color such as red ,it censors the red color found in suffering from a temporary stress, and when replacing the catalyst red white, these censors 'response becomes more powerful and not detect the rays reflected from the College of the surface .At the same time, they are insensitive towards green work at full efficiency.

1.5.Estimation Contrast

It's rare to see a solo and isolated color in the optic field as often noticed the existence of different colors happen simultaneously and instantaneously. This creates a visual effect and is strongly linked to the phenomenon posterior ,an eye generates color for visual color and drops a drive toward the adjacent color or is imposed by it. It may be noted that the phenomenon of simultaneous contrast between the two colors of complementary or integrated happens through a simple experiment by taking gray and surrounding it with a red background colored box .We note that the color gray has become a distortion of the green color (color CMOS red color). Contrast is the difference in the optical properties that make the picture elements to distinguish between the different elements by the difference in color and lighting [7].

2. Methodology

A number of images were taken with different lighting depending on the sunlight at different times of the day 'figure 1' showing the different lighting images.

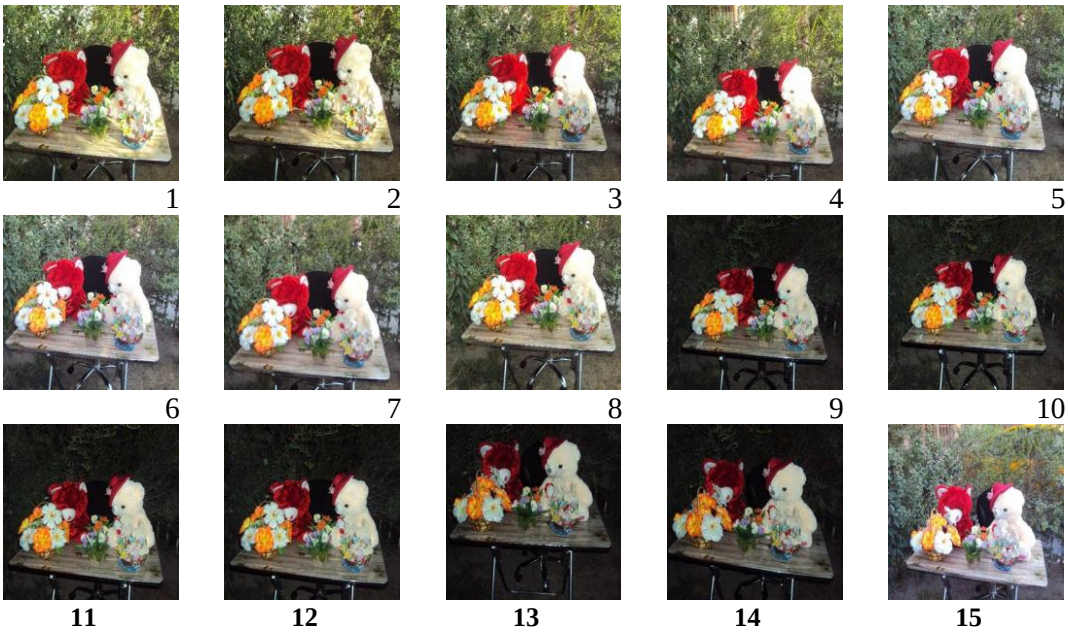

Figure 1. Different images with different contrast and lighting by using camera Sony

2.1. Hiding technique

A color image of size (110 * 100) pixels is hidden within host color image of different sizes (255 x 255) pixels and 400 x 400 pixels. The size of host image is increased with decreasing the number of LSB. The host image has been converted to the frequency domain using lifting wavelet transform technique (LWT). The process of replacing bits of host image bits with the secret image bits was done after converting both images to the binary system using Mat lab program techniques. (Tables 1), (table 2) and (table 3) show the runts of hiding secret image within different lighting host color images. 'Figures 2' 'Figures 3' showing the host images after performing hiding process and the secret message image.

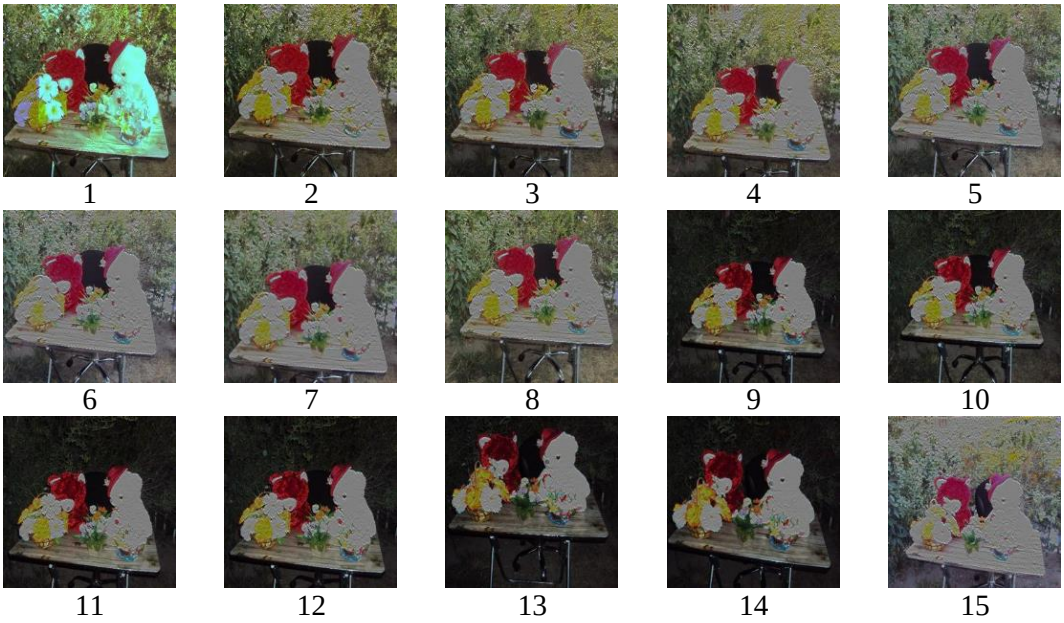

Figure 2. Host images after hiding using 1 LSB for each pixel

Figure 3. Secret message or secret color image

Table 1. The properties statistical of image before and after hiding using 2 bits (standard deviation, mean, contrast)

Image	Before hiding		
255x255	std	mean	contrast
1	0.0499	0.5337	0.0936
2	0.0556	0.4683	0.1187
3	0.0486	0.4758	0.1021
4	0.0459	0.5046	0.0910
5	0.0525	0.5105	0.1028
6	0.0505	0.5310	0.0952
7	0.0428	0.5178	0.0826
8	0.0580	0.4942	0.1174
9	0.1022	0.2445	0.4179
10	0.1014	0.2884	0.3515
11	0.1009	0.2660	0.3794

12	0.0988	0.2710	0.3647
13	0.0825	0.2333	0.3537
14	0.0823	0.2431	0.3387
15	0.0397	0.5384	0.0738

Table 2. The properties statistical of image before and after hiding using 2 bits (standard deviation, mean, contrast)

Image 255x255	After hiding using two bits size(110x110)			
	std	**mean**	**contrast**	**SNR**
1	0.0269	0.4040	0.0665	8.5e-5
2	0.0263	0.3688	0.0712	8.5e-5
3	0.0207	0.3838	0.0540	8.5e-5
4	0.0195	0.4040	0.0482	8.5e-5
5	0.0262	0.4110	0.0636	8.4e-5
6	0.0259	0.4225	0.0613	8.3e-5
7	0.0205	0.4164	0.0493	8.4e-5
8	0.0237	0.3973	0.0596	8.1e-5
9	0.0628	0.2102	0.2989	8.3e-5
10	0.0559	0.2437	0.2293	5.3e-5
11	0.0599	0.2238	0.2678	5.2e-5
12	0.0583	0.2270	0.2568	5.3e-5
13	0.0529	0.2047	0.2584	5.3e-5
14	0.0520	0.2105	0.2473	5.2e-5
15	0.0231	0.4319	0.0535	8.5e-5

Table 3. The properties statistical of image before and after hiding using 1 bits (standard deviation, mean, contrast)

Image 400×400	Before hiding			After hiding using one-bit size message(110x110)		
	std	mean	contrast	std	mean	contrast
1	0.0495	0.5301	0.0934	0.0408	0.4409	0.0926
2	0.0557	0.4666	0.1194	0.0359	0.3945	0.0910
3	0.0488	0.4742	0.1028	0.0407	0.4084	0.0997
4	0.0458	0.5030	0.0911	0.0411	0.4305	0.0955
5	0.0524	0.5086	0.1029	0.0419	0.4475	0.0936
6	0.0504	0.5297	0.0951	0.0458	0.4674	0.0980
7	0.0427	0.5162	0.0828	0.0455	0.4538	0.1003
8	0.058	0.4926	0.1176	0.0418	0.4284	0.0975
9	0.1017	0.2434	0.4177	0.0766	0.2202	0.3479
10	0.1009	0.2868	0.3518	0.0753	0.2579	0.2918
11	0.1007	0.2650	0.3798	0.0766	0.2373	0.3226
12	0.0987	0.2699	0.3657	0.0752	0.2412	0.3116
13	0.0823	0.2322	0.3543	0.0626	0.2123	0.2948
14	0.0820	0.2419	0.3391	0.0635	0.2202	0.2885
15	0.0397	0.5368	0.0739	0.0521	0.4791	0.1087

From the above tables, the results of the statistical measures indicated that the characteristics of the images that were hidden in them replaced with one bit of each pixel is the closest to the original image statistics before hiding. While the images hidden in the replacement of two bits of each pixel notes that they were more affected by the process of concealment. It is also noted that the images that were taken in low lighting condition and high light condition are the best as host images compared to those where taken at medium lighting condition.

2.2. Minimum Distance Classification

For each feature image, the distances towards class means are calculated, the steps of minimum distance are:

1. detection the shortest Euclidean distance to a mean class;
2. If the user-defined threshold is larger than shortest distance to a class mean, then this class name is assigned to the output pixel.
3. Else the undefined value is assigned.

To apply the classification algorithm, 20 blocks of different image regions were cut out, ‘figure 5’ shows the blocks taken from the images

The result of method classification showing in ‘Figures 6’ for images different lighting ‘figures 7’ and ‘figures 8’ showing the result classification method to host images after performing hiding process and the secret message image.

For the purpose of explain which regions are most affected by hiding using (1, 2) LSB, blocks of different image regions were cut out from homogeneous and heterogeneous regions as shown in ‘figure 9a’ and ‘figure 9b’. The properties histogram of homogeneous and heterogeneous regions was shown in ‘figure 10a’ and ‘figure 10b’.

Where we observe through the study of the histogram that the most affected regions of hiding are homogeneous regions, but heterogeneous regions less affected by the process of hiding.

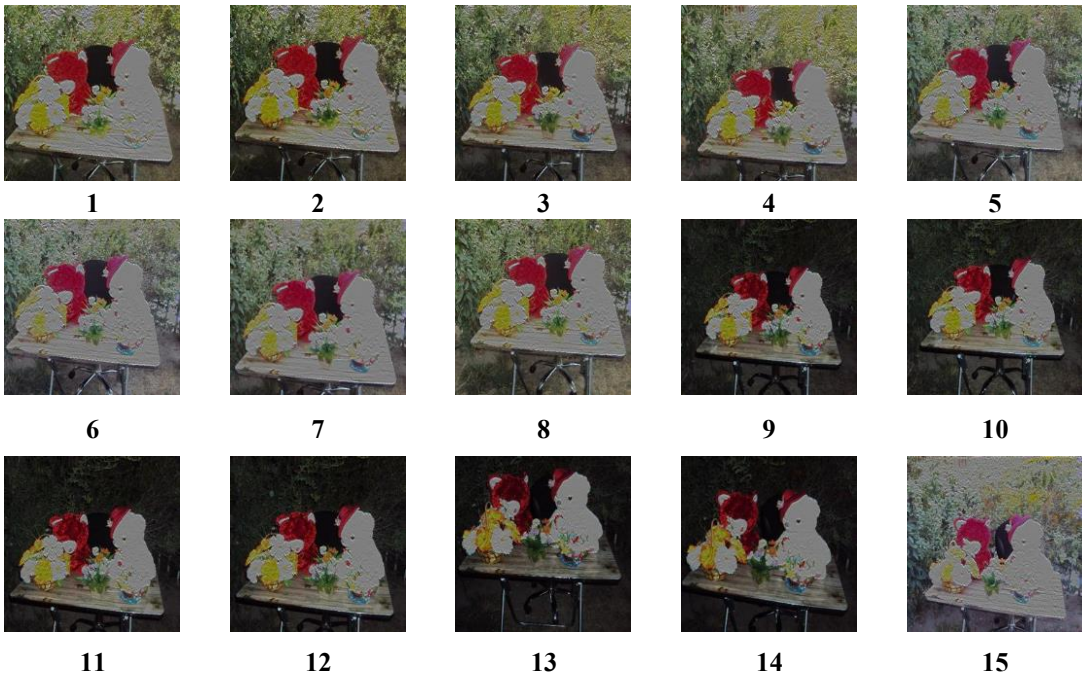

Figure 4. Host images after hiding using 2 LSB for each pixel

Figure 5. The blocks of regions from different lighting image

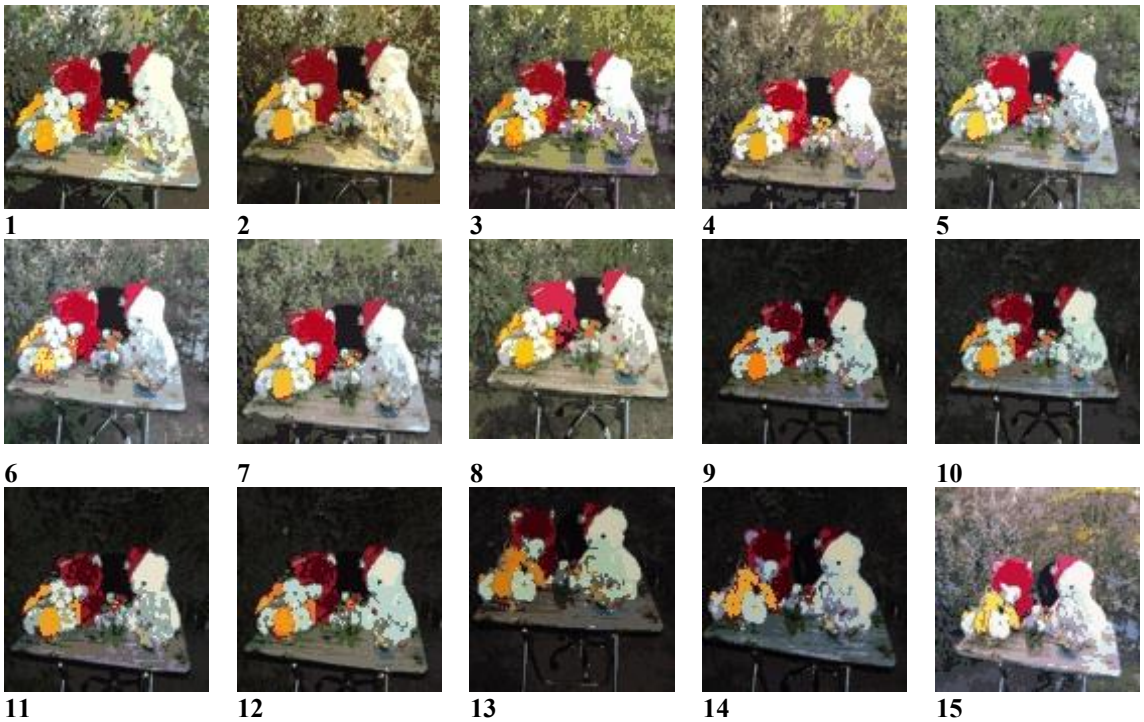

Figure 6. Original images applying classification method

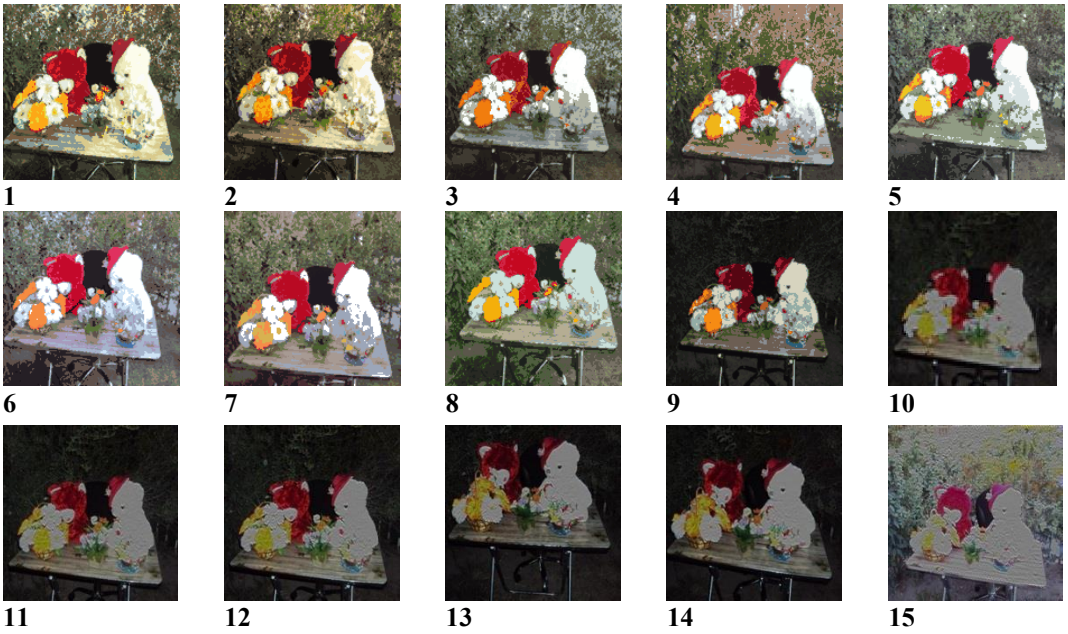

Figure 7. Host images after hiding using 1 LSB and applying classification method

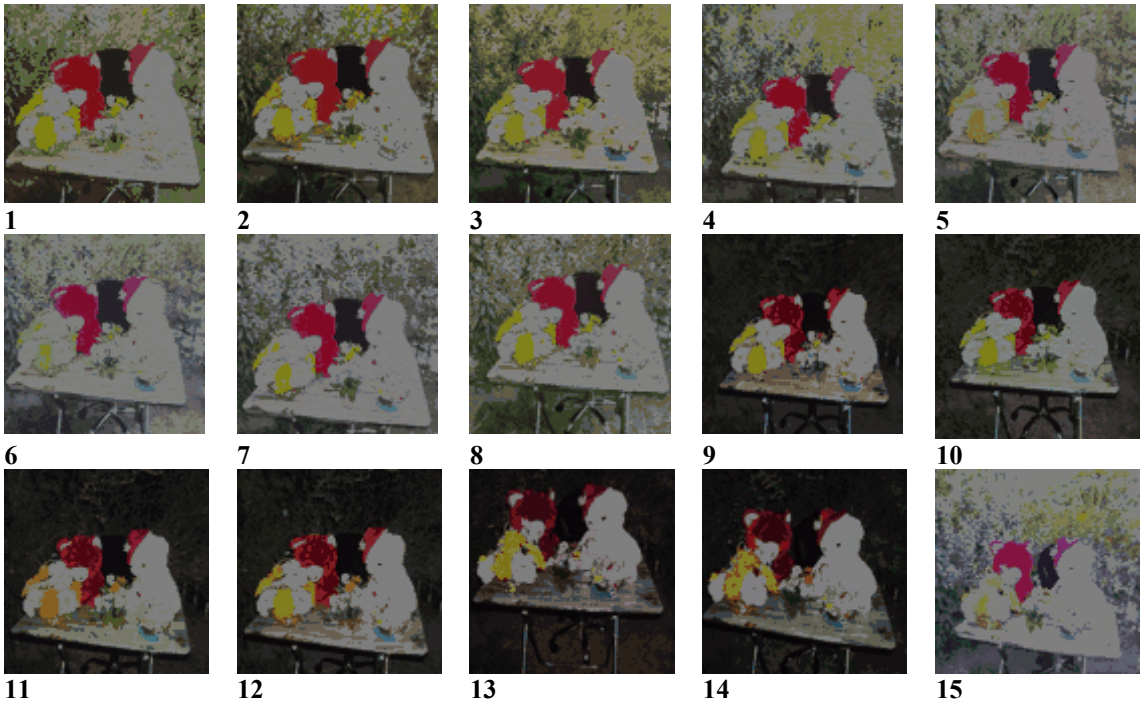

Figure 8. Host images after hiding using 2 LSB and applying classification method

Figure 9. Region (a) homogeneous ,(b) heterogeneous

Histogram for homogenous region for original image

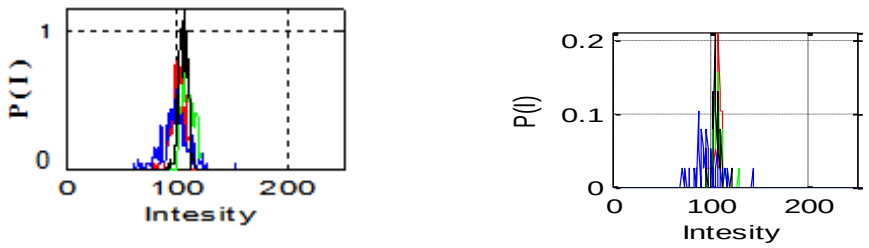

Histogram for homogenous region for images after apply hiding

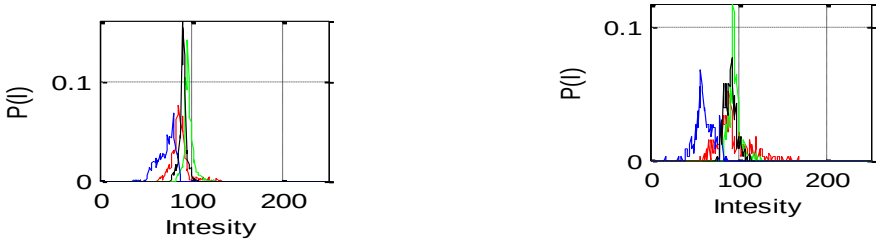

Figure 10 a. The histogram for homogenous region before and after apply hiding

Histogram for heterogeneous region for original image

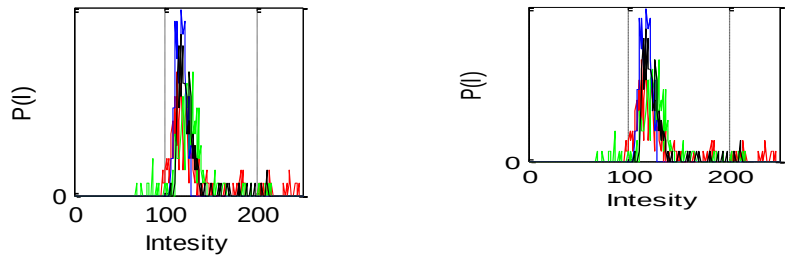

Histogram for heterogeneous region for image after apply hiding

Figure 10 b. The histogram for heterogeneous region before and after apply hiding

3. Conclusion

Steganography plays an important role in secret communication in digital worlds. The result of hiding show properties of images that were hidden in them replaced with one bit of each pixel is the closest to the original image statistics before hiding. While the images hidden in the replacement of two bits of each pixel notes that they were more affected by the process of hiding and to more secret using the images were lighting low. The result of classification method in this paper shows the smooth homogeneous areas are less affected as a result of hiding comparing with high light areas.

References

[1] Fridrich Goljan M Soukal D 2014 Searching for the Stego Key Proc SPIE Electronic Imaging Security Steganography and Watermarking of Multimedia Contents VI. **5306** pp 70–82
[2] Nivedhitha R 2012 Image Security using steganography and cryptographic techniques department of computers science & engineering Tamil Nadu India **3** 3
[3] Bouman C A 2013 Digital Image Processing
[4] Shalieder G 2012 Information hiding using Lest significant bit stegaoghy and cryptography department of electrical & electronics engineering YMCAUST Faridabad India V**6** pp 27-34
[5] Salehi S A Amirfattahi R 2011 VLSI Architectures of Lifting-Based Discrete Wavelet Transform Isfahan University of Technology
[6] Acharya T Chakraabati C 2006 A Survey on Lifting-based Discrete Wavelet Transform Architectures *Springer* **42** 3 321-39
[7] Frank M H and Rudolf M 1987 Color and Light in man –mad Environments New York 28-9

Enhance Video Film using Retnix method

Enhance Video Film using Retnix method

Rasha Awad[1], Ali A. Al-Zuky[2], Anwar H. Al-Saleh[3] and Haidar J. Mohamad[2]

[1] Computer Department, College of Basic Education, Mustansiriyah University, Baghdad, Iraq
[2] Physics Department, College of Science, Mustansiriyah University, Baghdad, Iraq
[3] Computer Department, College of Science, Mustansiriyah University, Baghdad, Iraq

1rashaheart_2005@yahoo.com ,prof.alialzuky@yahoo.com
anwar.alsaleh10@gmail.com,haidar_jawad2001@yahoo.com

Abstract. An enhancement technique used to improve the studied video quality. Algorithms like mean and standard deviation are used as a criterion within this paper, and it applied for each video clip that divided into 80 images. The studied filming environment has different light intensity (315, 566, and 644Lux). This different environment gives similar reality to the outdoor filming. The outputs of the suggested algorithm are compared with the results before applying it. This method is applied into two ways: first, it is applied for the full video clip to get the enhanced film; second, it is applied for every individual image to get the enhanced image then compiler them to get the enhanced film. This paper shows that the enhancement technique gives good quality video film depending on a statistical method, and it is recommended to use it in different application.

Keywords: enhancement, video frame enhancement, image quality, video processing.

1.Introduction

Image enhancement techniques (IET) used to enhance the quality of an image as seeming by a human. IET techniques are most useful because a lot of satellite images when studied on a color display, they provide insufficient information of image interpretation. Image enhancement used to correct geometric and radiometric deformities. Image enhancement ways are applied separately to each band of a multispectral image. Digital enhancing techniques considered one of the most satisfactory method compared with the photographic technique, because of the accuracy and wide different of digital processes [1, 2]. Methods of image enhancement mostly can be categorizing into two groups: Frequency Domain Methods, and Spatial Domain Methods. Some of contrast and lightness enhancement algorithms are used such as Histogram Equalization, Multi Scale Retinex algorithm and Contrast enhancement that depend on the physical contrast of simple images to enhance color images from any type of distortion such as noise, color shift, inverse transform for any operation and lightness change. Therefore, many efforts in image enhancement used sinusoidal screen, or a solitary patch of light on an unchanging background, which is well defined and approves with the recognized contrast [3]. Non-uniform lighting conditions and the night scenes have been studied depending on nonlinear transform [4]. While using Structural Similarity Index Metric (SSIM)

requires two images (optimal and original image) and evaluation of three different measures like luminance, contrast, and structure comparison which make this process difficult and slow [5]. Histogram modification technique used to enhance intensity contrast and brightness error [6]. A criterion called Quality Factor (QF) suggested to determine color image quality based on changing lightness and contrast with analyzing image by using methods depending on image quality assessments like, mean of locally (μ and σ) model, which suggest introduced two methods named Modified Retinex (MR) and Adaptive Histogram Equalization (AHE) to enhance color images based on changing lightness and contrasts [7]. Methods like Histogram Equalization, Retinex, and a combined between Retinex and wavelet are introduced to study the effect of the low lightness on the captured images using two types of camera [8].

In this study, we introduced famous method which called Multi Scale Retinex algorithm to be used as video enhancement.

2.Retinex Method

Image enhancement in general refining the explainable or observation of data within images for any watchers and giving improved input for other computerized image processing techniques. Image lighting consider interested parameter features in digital image processing. Lighting enhancement is commonly lead to focused problems in digital image processing [9].

Retinex method is bridging the gap between images and the human observation of scene. Retinex could achieve compensation for the blurring introduced by image development process, make efficient output as brightness change and functional range compression. Retinex Techniques divided into [9]:

1-Single Scale Retinex (SR)
2-Multi Scale Retinex (MR)
3-Multi Scale Retinex Color Restoration (MSRCR).

Multi Scale Retinex (MSR) is extended from Single Scale Retinex (SSR) where [10, 11]:

$$R_i(x, y, c) = \log[I_i(x, y)] - \log[F(x, y, c) \otimes I_i(x, y)] \tag{1}$$

meaning of $R_i(x, y, c)$ is the Gaussian shaped surrounding space constant of the production of channel i ($i \in$ R, G, B) at location x, y, c. $I_i(x, y)$ is the value of image pixel for channel I, and character $\otimes$ is convolution. Function $F(x, y, c)$ is Gaussian surrounds function which is written as [10, 11]:

$$F(x, y, c) = k \quad e^{-(\frac{x^2+y^2}{c^2})} \tag{2}$$

k is normalization constant [10]:

$$\iint F(x, y, c)dxdy = 1 \tag{3}$$

The output of MSR is then simply a weighted sum of all different SSR outputs [10, 11]:

$$R_{MSR}(x, y, w, c) = \sum_{n=1}^{N} W_n \, R_i(x, y, c_n) \tag{4}$$

where N is the number of scales, $R_i (x, y, c_n)$ the ith component of the nth scale, $R_{MSR} (x, y, w, c)$ the ith spectral element of the MSR output, and W_n is the weight related with the nth scale. It assumed that ($\sum W_n$=1). The above processing will deal with both negative and positive RGB values as a result, and the histogram will usually have big tails. Therefore, a final gain-offset is used as stated and discussed in additional details underneath. This method can lead that color within image becomes gray color, therefore an extra processing stage is anticipated [10, 11]:

$$R = I_{MSR}.L(x, y) \tag{5}$$

where L can be written as

$$L(x, y) = b\log[1 + a\frac{I_i(x, y)}{\sum_{i=1}^{3} I_i(x, y)}] \tag{6}$$

where the permission uses the form *log* (1+x) instead of *log* (x) to make sure to get a positive result. The values of a=125 and b=100 are suggested for a specific test images.

$$I_{Pi}(x, y) = g(L(x, y) + h) \tag{7}$$

In equation (7), The values of the gain offset g = 0.35 and h= 0.56 respectively [7]; I_{pi} is output image. In this paper, the value that used are w_1=w_2=w_3=1/3 and c_1=250, c_2=80, c_3=15 [10, 11].

3. Video frames enhancement

The recording process was recorded indoor using fixed camera, where the artificial light intensity controlled and measured by luxmeter with values (315, 644 and 566 Lux). The MR algorithm is used to enhance video frames that captured in different intensities. Moreover, σ and μ are computed for each image after and before the enhancement process. The algorithm that used is the same algorithm (1) except step (1) should be replaced to clip frames. The procedure analysis and enhancement steps as follow:

Algorithm (1) color frames lighting enhancement

Input:- color frame image I() OR clip frames.
Outputs:- color image enhanced
- computed (μ, σ) to each color frame images before and after the enhancement process.

Start Algorithm

1-Open color frame image frame Ii ( ), i= r, g, b OR clip frames.

2- Calculate Gaussian surrounds function $F(x, y, c_n) = (k)\exp(\frac{-(x^2 - y^2)}{c_n^2})$

k is constant normalization, c_n, n=3, {c_1=250, c_2=120, c_3=80} [7].

3-Compute SSR using: $R_i(x, y, c) = \log[I_i(x, y)] - \log[F(x, y, c_n) \otimes I_i(x, y)]$

4-Compute MSR using: $R_{MSR}(x, y, w, c) = \sum_{n=1}^{N} W_n R_i(x, y, c_n)$

Where N=3 {w_1=w_2=w_3=1/3}.

5-Calculate MSR with color repair by $I_i'(x, y) = b\log[1 + a\frac{I_i(x, y)}{\sum_{i=1}^{3} I_i(x, y)}]$, b =100 , a =125.

6- color image enhancement is gotten form gain offset using $IE_i(x,y)=0.35(I_i'(x, y)+0.56)$.

4.Results of lighting Enhancement of Color Video Clips Frame

4.1 Images of the colored target

These images are homogeneous in intensity and color, with size of (1080x1820) pixel. They are captured under different light conditions. Figure 1 shows these images with colored target

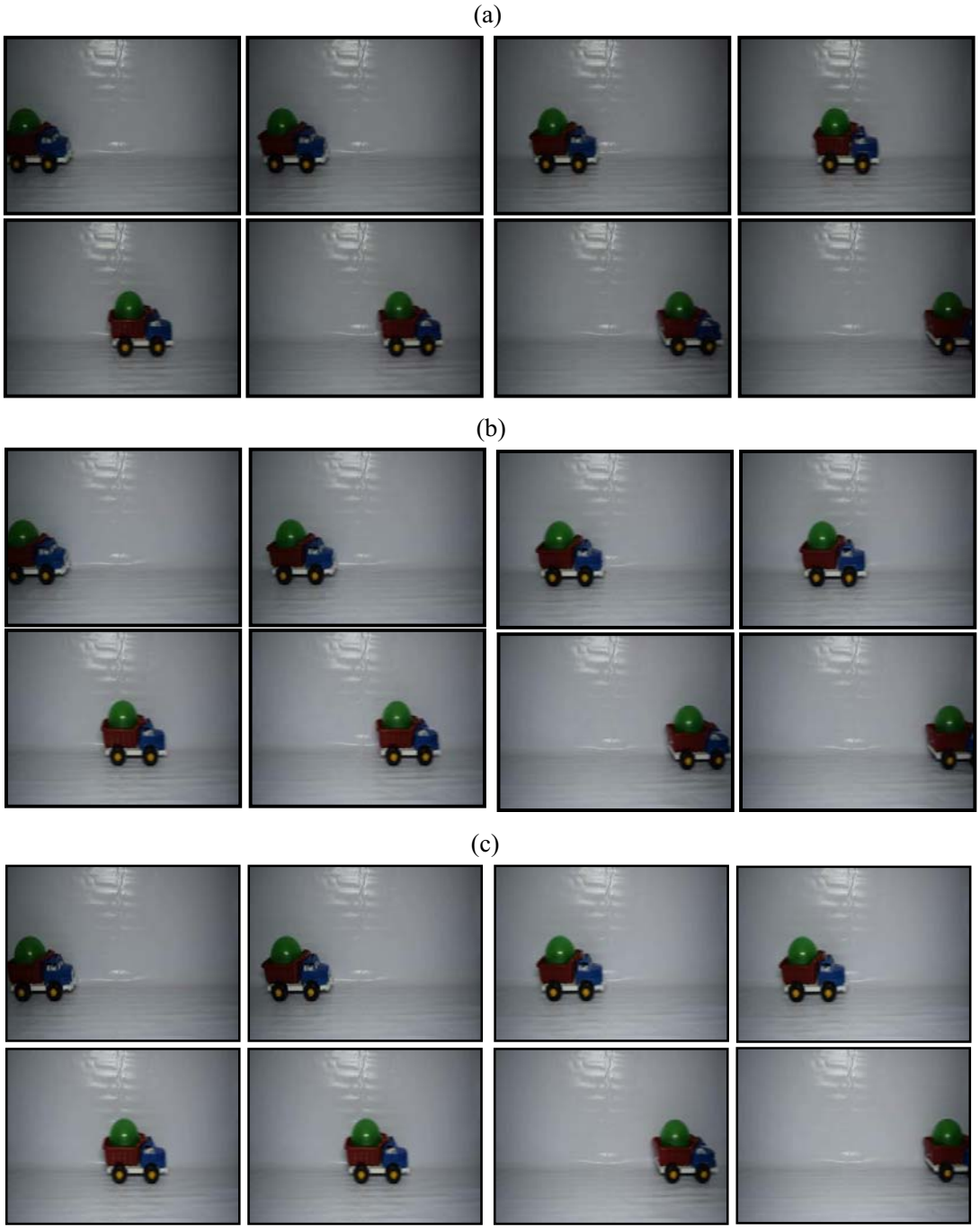

Figure 1. Images of the colored target light intensity (a) 64.4Lux, (b) 315Lux, and (c) 566 Lux.

4.2 Results of Enhancement using Retinex technique

The enhancement process is implanted by using algorithm (1). The results show that the enhanced regions are the high contrast regions (edges) which is a prove that this algorithm works properly. Moreover, enhanced the background and object color. The enhancement process is used for the recorded video with 80 frames, and it used for each frame individually as shown in figure 2.

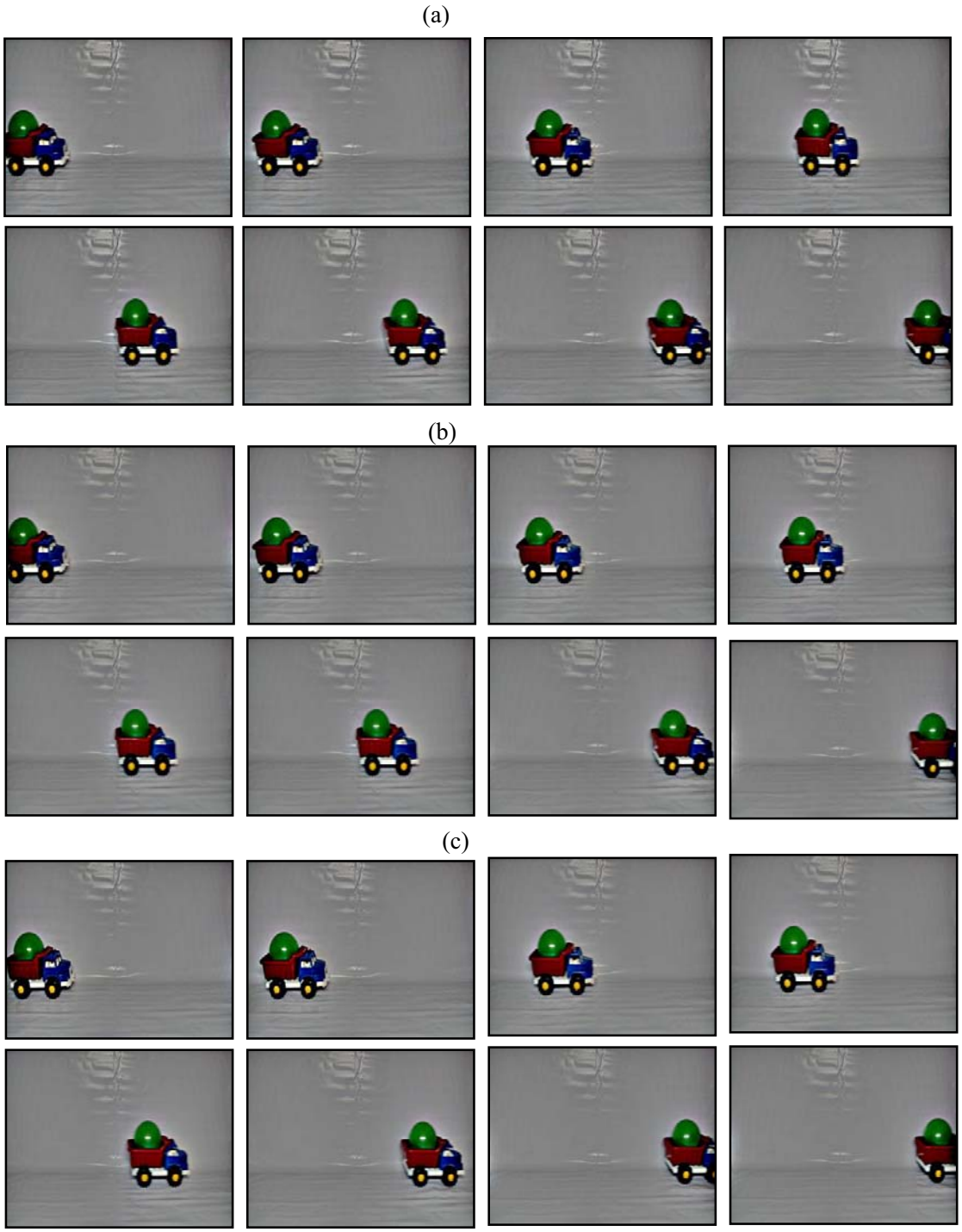

Figure 2. Images enhancement using Retinex technique for 80 frames individually

(a) Light Intensity = 64.4Lux (b) light Intensity = 315ux and (c) Light Intensity = 566 Lux.

Mean (μ) and standard deviation (σ) are computed individually as shown in figure 3. Mean curve has higher values at low light conditions and it is decay with frame image time at high light condition. While at mid light condition, μ have stabile behavior. Standard deviation (represent the small details within the image) behavior is increases for the three light conditions. The best increase is at low light conditions. In the legend, (-O) denoted to the original images while (–E) for the enhanced images.

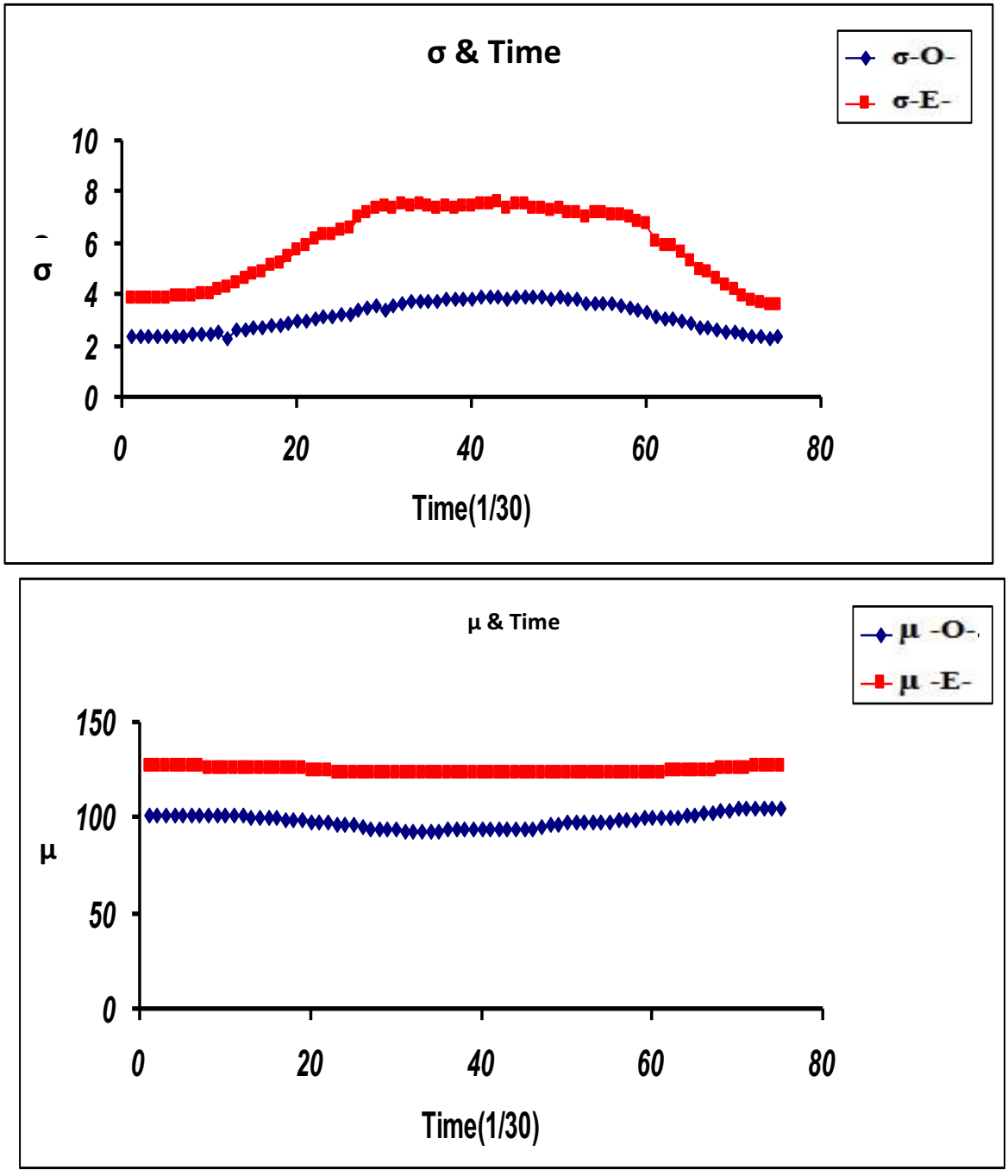

(a)

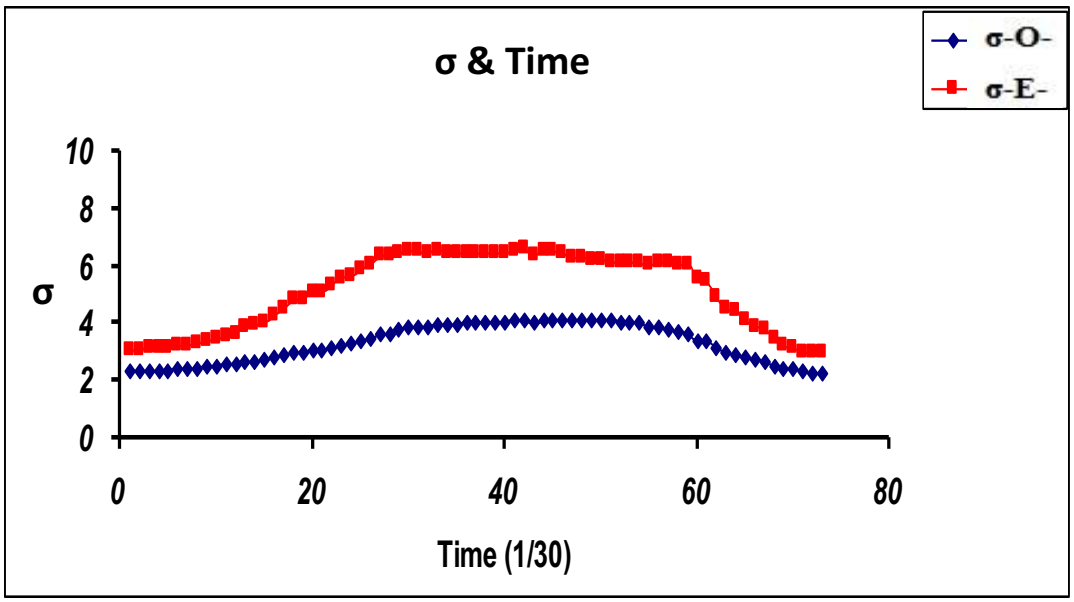
σ & Time
σ-O-
σ-E-
σ
10
8
6
4
2
0
0
20
40
60
80
Time (1/30)

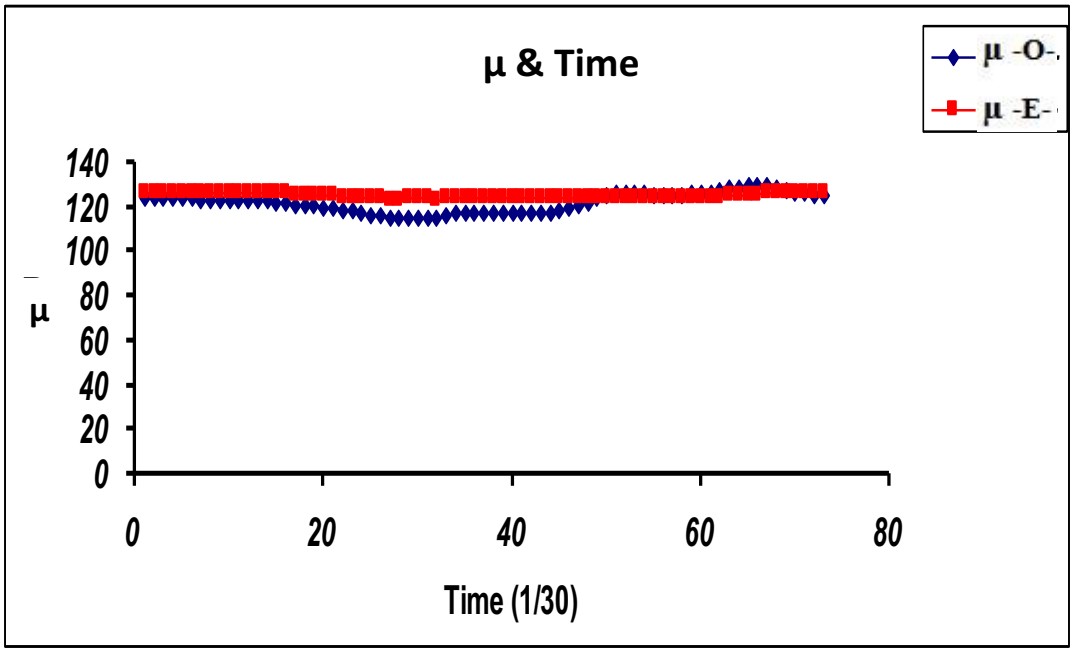
μ & Time
μ -O-
μ -E-
μ
140
120
100
80
60
40
20
0
0
20
40
60
80
Time (1/30)

(b)

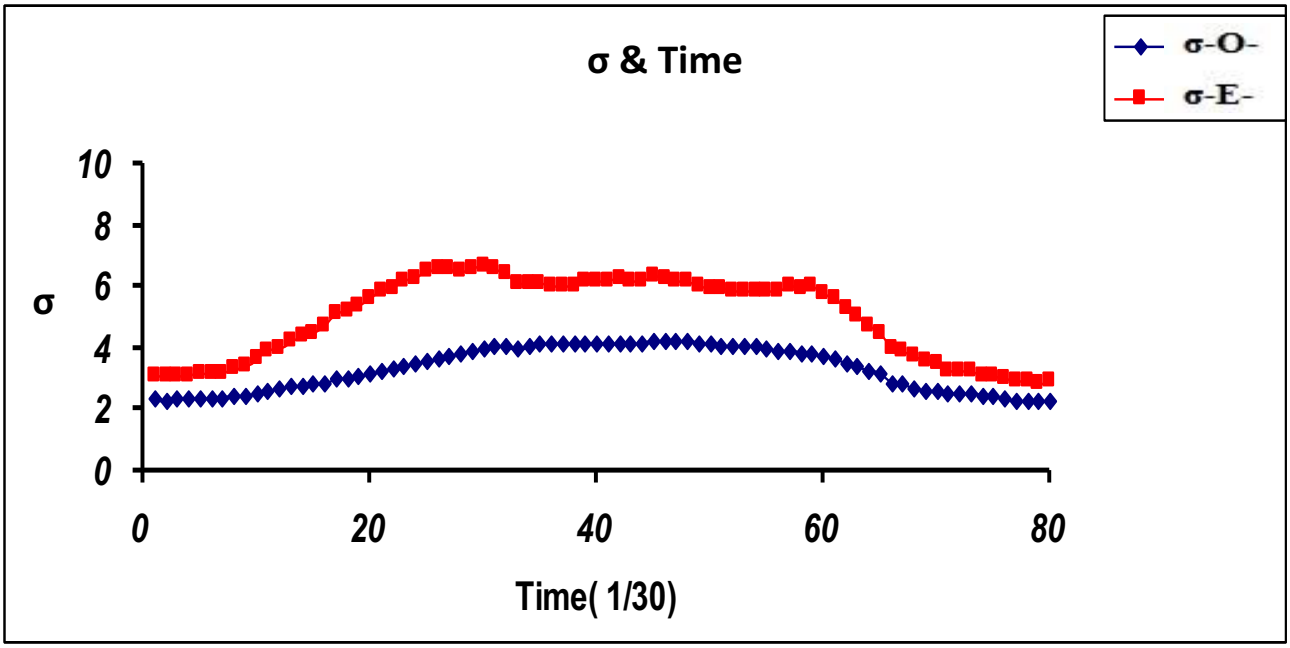

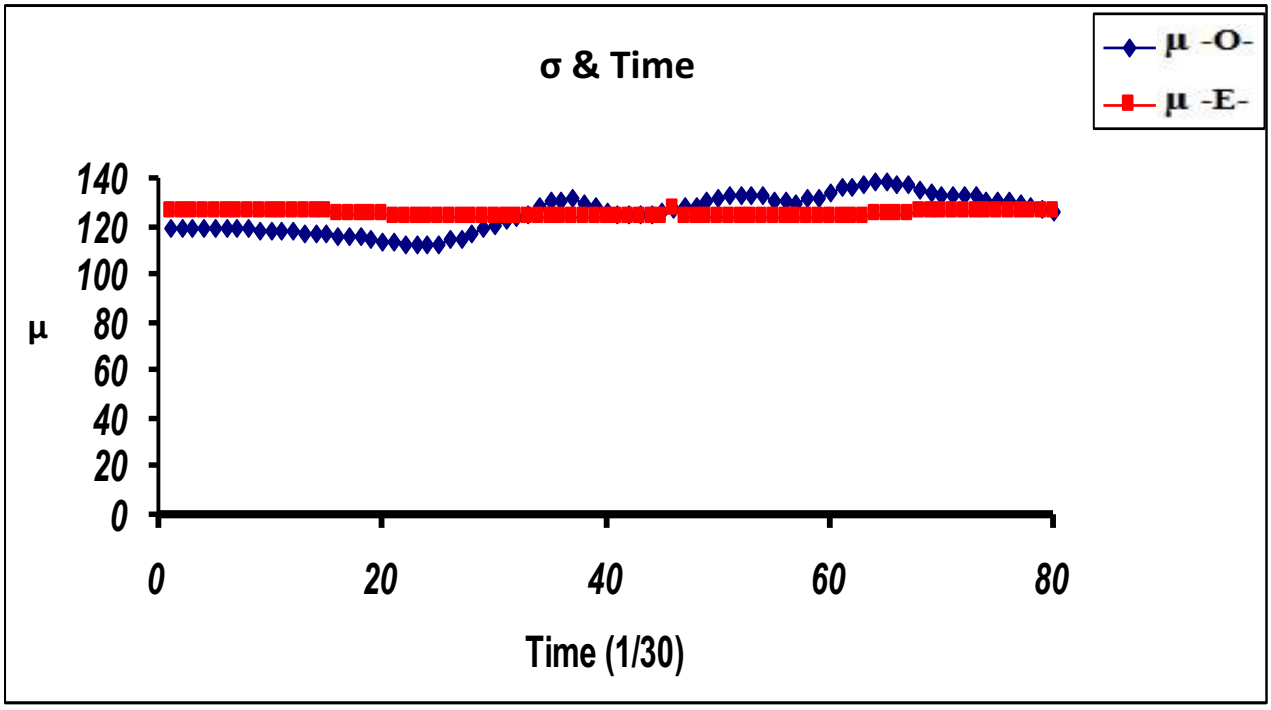

(c)

Figure 3. Values of σ & μ as a function to the number of frames of images enhancement individually where light intensity in (a) 64.4 Lux, (b) 316 Lux and (c) 566 Lux.

Figure 4 shows the results of using enhancement method to a recorded video with 80 frames as one process, which means that the loop in algorithm (1) takes the clip as one loop. It is the same behavior for the individual frame process where the mean curve has higher values at low light conditions and it is decay with frame image time at high light condition. While at mid light condition, μ have stabile behavior. Therefore, it is recommended to use this algorithm. In the legend, (-O) denoted to the original images while (–E) for the enhanced images.

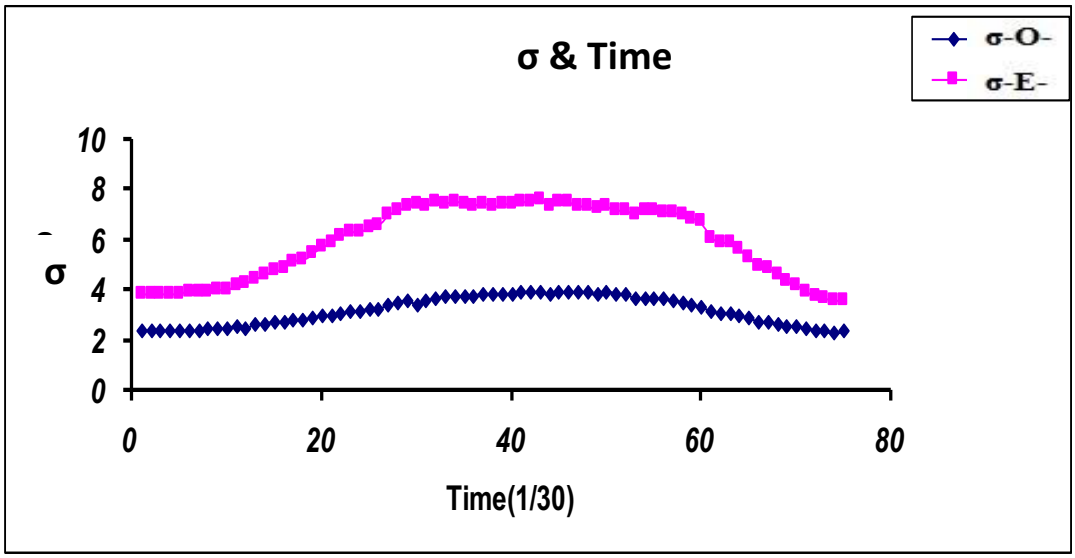

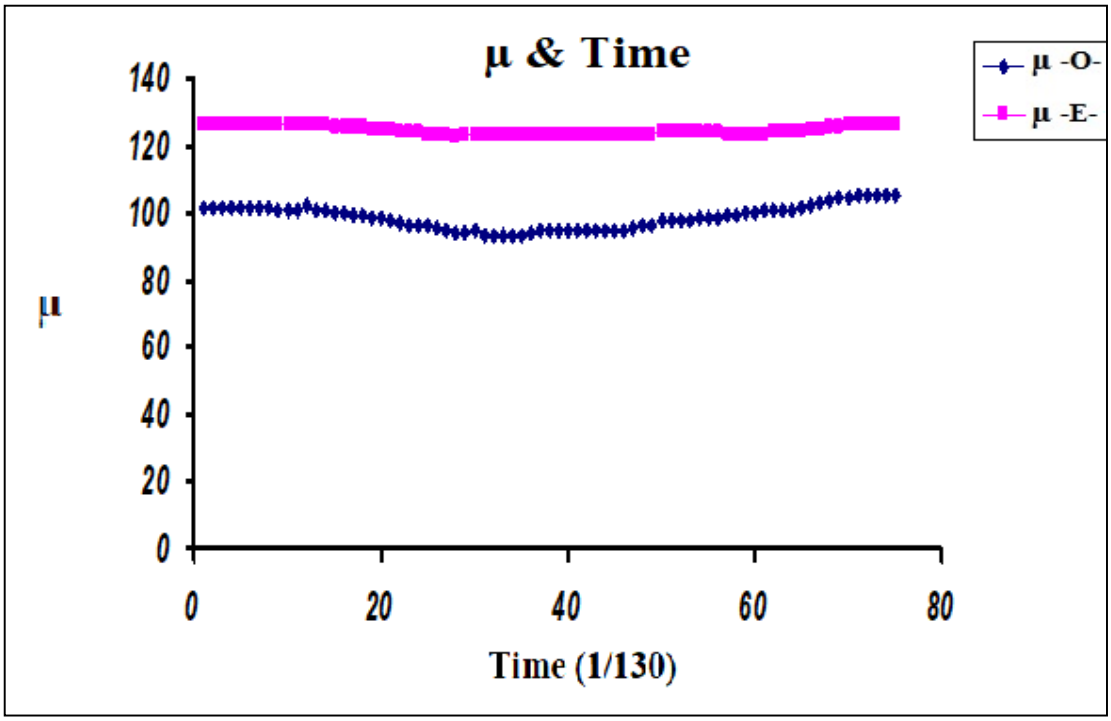

(a)

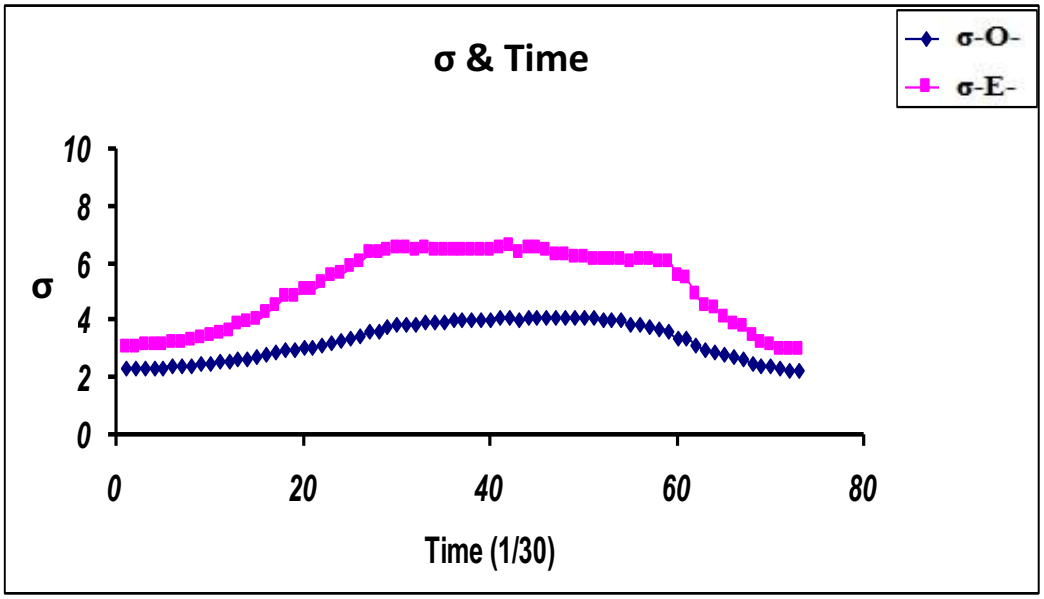
σ & Time
σ-O-
σ-E-
σ
10
8
6
4
2
0
0
20
40
60
80
Time (1/30)

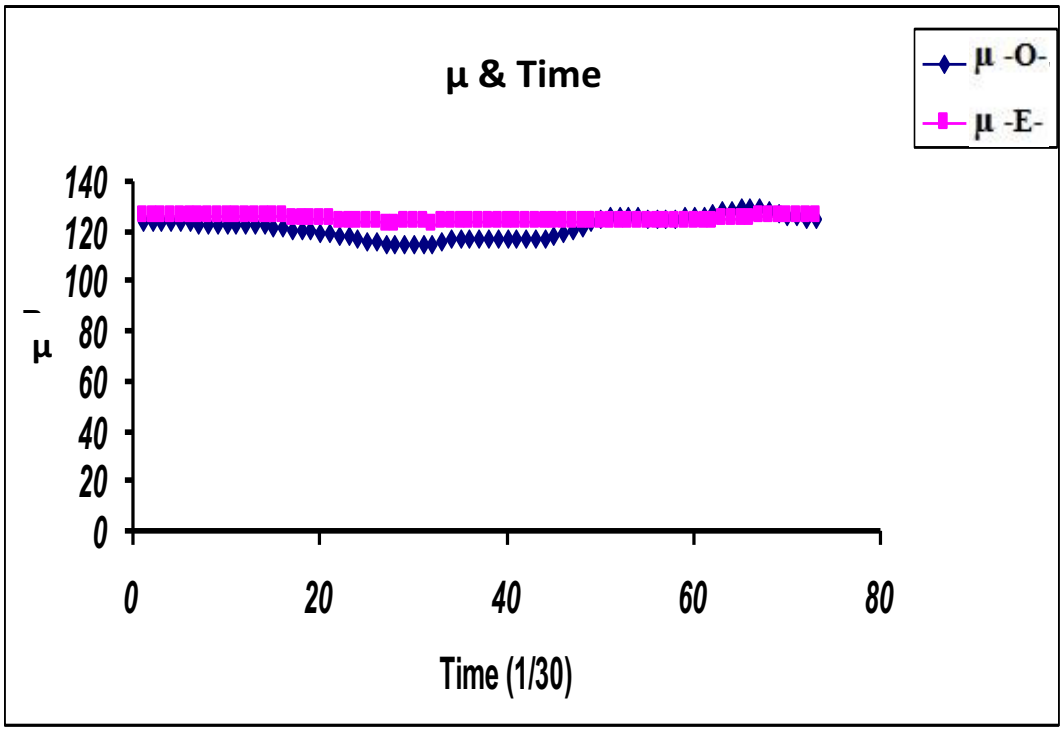
μ & Time
μ -O-
μ -E-
μ
140
120
100
80
60
40
20
0
0
20
40
60
80
Time (1/30)

(b)

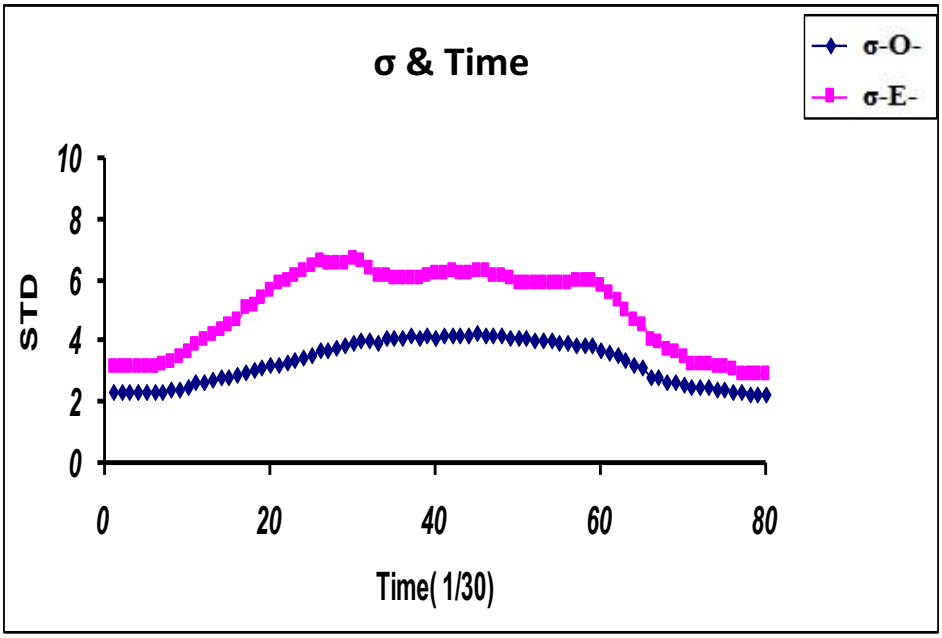

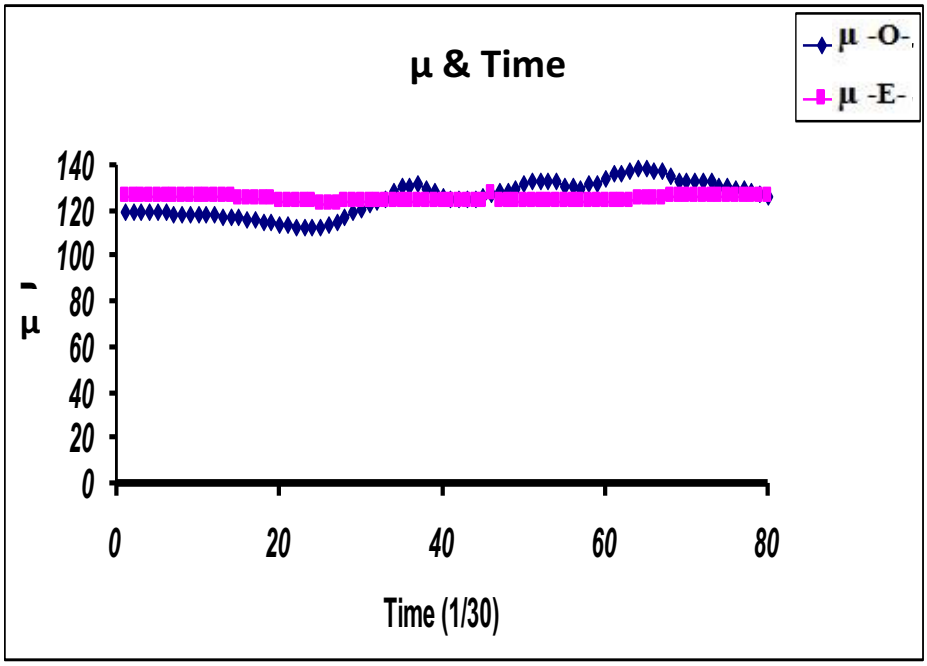

(c)

Figure 4. Values of σ & μ as a function to the number of frames for images enhancement of a recorded video with 80 frames where light intensity in (a) 64.4 Lux (b) 316 Lux and (c) 566 Lux

As a summary, the behaviour of σ and μ as a function of frame number, in both ways as taken as a package (clip frames) or individually (one frame), is the same because the area of the background in the image is bigger than the target. Which means that σ and μ for the target does not have an effect on the σ and μ for the image when Retinex apply on the frame. Therefore, the enhancement is matching in both cases.

5.Conclusions

The value of σ and μ for the video frames before and after enhancement are computed. The enhancement results are obvious depending on σ values because image contrast for the enhancement images is increased, and σ values are increased for all type of light conditions. While μ values didn't show any response at high light conditions.

The process of enhancement the video images of the two methods (continuous and separate) gave identical results, so we recommend using the continuous method of execution speed.

Retinex enhancement technique is adapted and applied on the video frames, where it showed good responds in enhancing the brightness and contrast of video images, especially at the moderate and middle light intensity.

References

[1] Palmer S E 1999 Vision Science: Photons to Phenomenology: MIT Press)
[2] Rakhi Chanana, Parneet Kaur Randhawa and Navneet Singh Randhawa 2011 Spatial Domain based Image Enhancement Techniques for Scanned Electron Microscope-SEM-images International *Journal of Computer Science Issues* **8** 580-6
[3] Peli E 1990 Contrast in complex images *Journal of the Optical Society of America A* **7** 2032-40
[4] Uçan O N and Öğüşlü E 2007 A non-linear technique for the enhancement of extremely non-uniform lighting images *Journal of Aeronautics and Space Technologies* **3** 37-47
[5] W.S. Malpica and Bovik A C 2009 SSIM based range image quality assessment. In: Fourth International workshop on Video Processing and Quality Metrics for Consumer Electronics Scottsdale Arizona, Arizona
[6] Gil D C, Farah R, Langlois J P, Bilodeau G-A and Savaria Y 2011 Comparative analysis of contrast enhancement algorithms in surveillance imaging. In: Circuits and Systems (ISCAS), 2011 IEEE International Symposium on: IEEE) pp 849-52
[7] Al-Khuzai H G D 2011 Enhancement of Color Images Captured at Different Lightening Conditions. In: Physics Department: Mustansiriyah University)
[8] Karam A J 2016 Analysis Study of the Captured Images Under Low Lightness. In: Physics deparetment: Mustansiriyah University)
[9] Bogdanova V 2010 Image Enhancement Using Retinex Algorithms and Epitomic Representation Cybernetics and Information Technologies 10
[10] Jobson D J, Rahman Z and Woodell G A 1997 A multiscale retinex for bridging the gap between color images and the human observation of scenes IEEE Transactions on Image Processing 6 965-76
[11] Jobson D J, Rahman Z and Woodell G A 1997 Properties and performance of a center/surround retinex IEEE Transactions on Image Processing 6 451-62

Structural properties different between two types of PE subjected to heat treatment

Structural properties different between two types of PE subjected to heat treatment

May Abdul Sattar Mohammed Najeeb, Kareem.A.Jasim and Dr. Nabil.N.Rammo

Collage of Education / pure science, Physics Department, University of Baghdad/ Ibn Al-Haitham collage, Baghdad / Iraq.

Abstract. In this study two modifications of polyethylene white (Pure one) and blue which is prepared with CaCo3 stabilized from polyethylene's tunnel have been studied by (XRD) subject to different temperatures at heat treatment. Both specimens show difference in the scattered X-ray intensity of the basal planes (110) and (200) with changing of the heat treatment.The degree of crystallinity of both modification of polyethylene (PE) has been studied. It has been looked that the white type is better than the blue type.

1. Introduction

Polymers have been selected for several reasons, including the use of common engineering materials for small, high performance parts and it offers many of the manufactures. Moreover, published research describing its structural characteristics appears to be under-represented because of its importance. Polymers are generally used in manufacturing and engineering [1, 2].

The analysis of X- ray powder diffraction patterns of samples of polyethylene (PE) revealed , in addition to traditional crystalline and amorphous components (amorphous phase) characterized by a diffuse scattering peak at the Kα diffraction angle of 80º(Cu – Kα radiation) [3, 4, 5].

In understanding of the degree of crystallinity for a polymer is important as crystallinity affects physical properties such as storage modules, permeability, density and melting temperature. While most of these manifestations of crystallinity can be determined a direct measure of degree of crystallinity provides a fundamental property from which these other physical properties can be predicted [6].

The aim of the present studies is to find the intensity of the crystalline, the intensity of amorphouse and the degree of crystallinity at a variable of heat treatment for samples white PE and blue PE.

2. Experimental

We used two sets (Twelve pieces) for samples from different sources of PE manufactured with different origins, the first set (six pieces) is a white PE and the second set (six pieces) is also manufactured blue PE. Two specimens of polymeric materials were prepared. These materials were prepared by casting. These specimens were cut with rectangular dimensions (2X3) cm. Both samples were treated at (25, 70, 90, 110, 120, melted) °C for each set separately in (Carbolite furnace) for 30 minutes. The crystallization of the material was determined by x-ray technique, where 2θ angle (10 – 80) degree. We're using to determine the starchier preparing.

3. Results and discussion

Some categories of materials shrink when they are exposed to thermal treatment if the area of the specimen weren't constrained during the treatment and free – area annealing allows more freedom for the molecular structure to be rearranged and may rise a shrinkage when the heat treatment rising ; In this work , these samples from this kind of materials. The maximum shrinkage when the sample melted (Liquid phase).

The alignment of the goniometer was periodically checked by recording the data for the standards (quartz and NaCl in the measurements in the reflection mode and a pentaerythritol single crystal in the measurements in the transmission mode). Three X – ray diffraction patterns measured for each sample were statistically processed with the use of the Microcal Origin 6.0 program to determine the average interplanar spacing's d_{hkl} and were then indexed with the use of the Powtool program.

To estimate the degree of crystallinity , we determined the integrated intensity of crystalline by add all numerical intensities in the range of peak , the total sum then will be the value of crystalline peak . Then we get integrated of amorphous region take back – ground intensities at start and end selected a above . The degree of crystallinity X_c of the samples was determined as :

$$X_c = [1+ (I_c / Ia)]^{-1} \times 100\% \quad (1)$$

Where I_c is the crystalline intensity, I_a is the amorphous intensity and X_c is the degree of crystalline [7], as shown in Table (1 and 2).

Table 1. The intensities of crystalline and amorphouse for white and blue PE.

T (°C)	Ic(White PE)(Count/Sec)	Ia(White PE)(Count/Sec)	Ic(Blue PE)(Count/Sec)	Ia(Blue PE)(Count/Sec)
25	138606	37593.6	31006	10731.6
70	250678	76430.2	34356	13887.5
90	119202	43718.4	51106	23501.3
110	213060	79171.4	30558	13112
120	220834	93913.6	25502	13684
melted	302516	133892	39694	27766.9

Table 2. The degree of crystalline in different temperatures to each.

T (°C)	Xc % White PE	Xc% Blue PE
25	78.66	74.29
70	76.60	71.21
90	73.16	68.50
110	72.91	67.08
120	70.16	66.50
melted	69.27	58.80

The accuracy of the determination was 5%.

The intergraded intensity of the reflection (110) at the 2θ angle of ~ 20.5º was taken as the crystalline component of PE , because peaks at large angles make an insignificant contribution to the scattering samples [8, 9, 10, 11, 12, 13] .

By using a above equation , the degree of crystallinity of the untreated sample and annealing samples at free area in the temperatures (25,70 , 90 , 110 , 120 , melted)°C did cause change in the degree of crystallinity . At 25 °C the maximum degree of crystallinity was obtained; it amounted to 78.66% and the minimum degree of crystallinity was obtained; it amounted to 69.27 %for White PE .While at 25 °C the maximum degree of the crystallinity was obtained; it amounted to 74.29 % and the minimum degree of the crystallinity was obtained; it amounted to 58.8 % for blue PE. The results of the degree of the crystallinity investigation in the two types are illustrated in Figures A (1, 2, 3, 4, 5, and 6) for white PE and Figures B (7, 8, 9, 10, 11, and 12) for blue PE.

We see that the angles of the intensity peaks are 21º.9/,23.º.5/,36º.3/ turn to a pure PE, but the angles 29º.8/, 36º.5/, 39º.5/, 43º.3/, 47º.8/ goes to the call site phase .
The reason of decreasing in the reflection peak (100) is the relaxation of the crystalline regions that found in the amorphous regions, this caused to increase the amorphous regions.

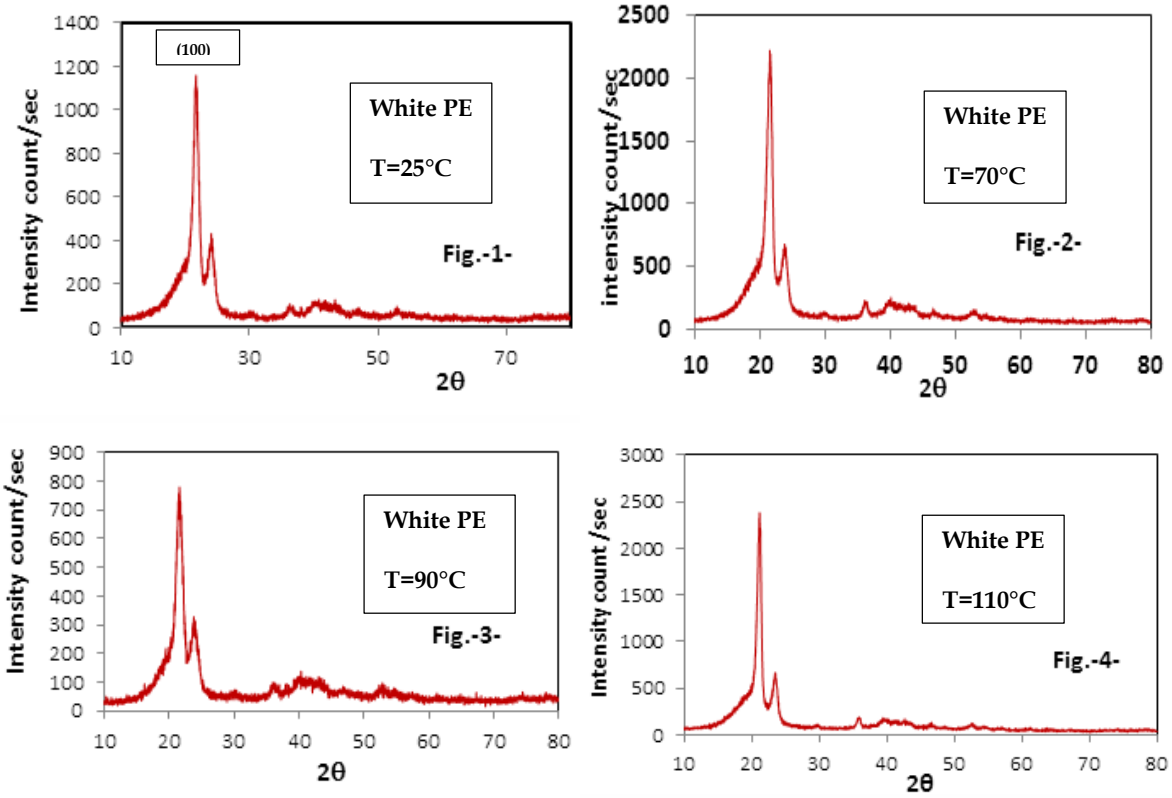

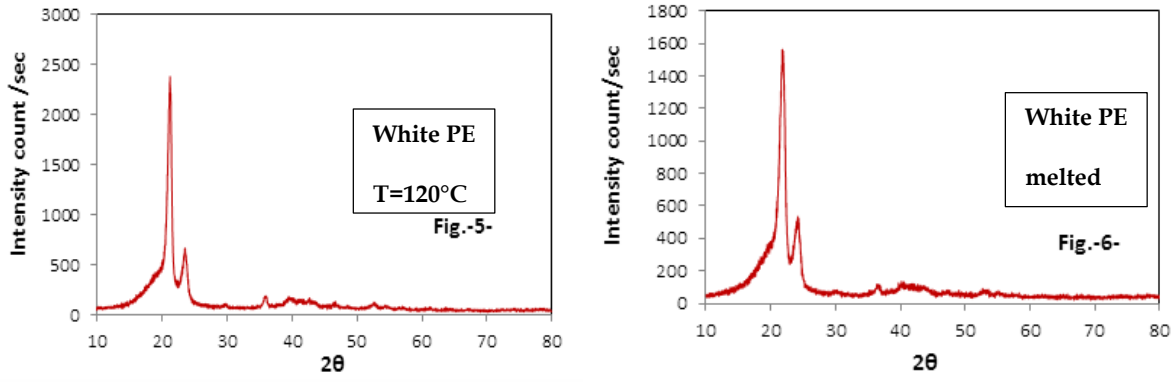

Figure A. The intensity vs Bragg's angle (2θ) of different temperatures for White PE.

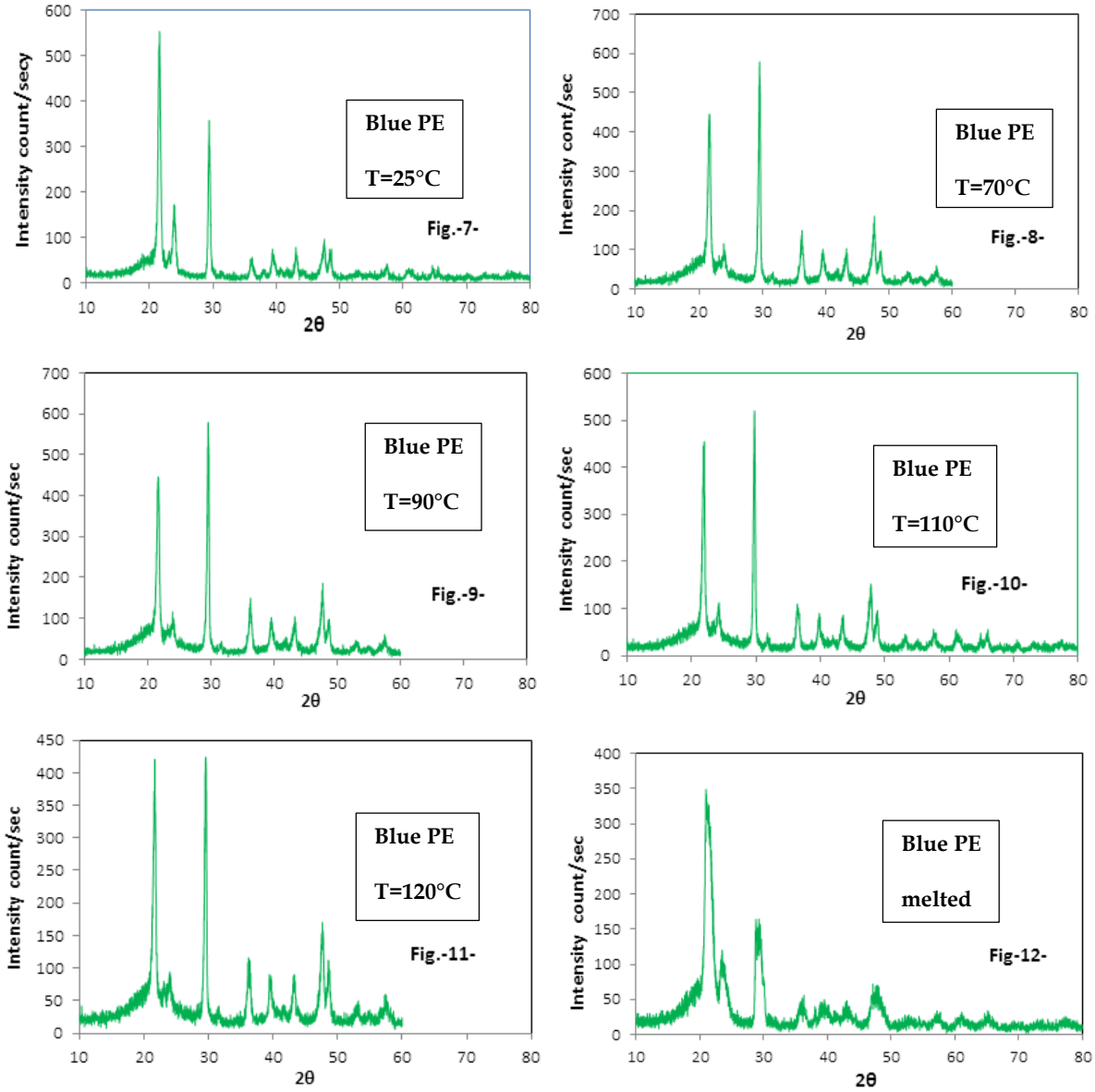

Figure B. The intensity vs. Bragg's angle (2θ) of different temperatures for Blue PE.

Generally in white PE, the degree of crystallinity decreased about 5% until the sample in melt temperature. This means that the polymer kept the semi crystalline property until above of melt temperature. But in blue PE, the degree of crystallinity decreased about 15% until the sample in melt temperature. This means that the callisite affected on the semi crystalline property until the above of melt temperature .'Figure (C)' shows the degree of the crystallites vs. temperature for white and blue PE.

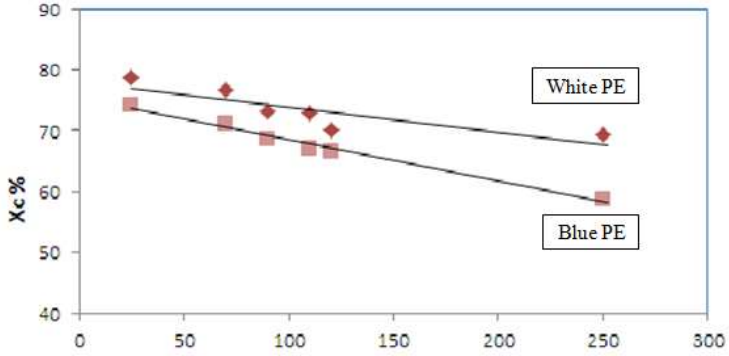

Figure C. degree of crystallinity vs different temperatures for (White & Blue) PE.

4. Conclusion

This method appeared more accuracy to find the degree of crystallinity with different heat treatment for white and blue PE which seen that the degree of crystallinity for a blue PE is lower than the degree of crystallinity for white PE because the callisite effected in the un arrangement for the crystalline regions. This caused to increase the amorphous regions with increasing the heat treatment in the heat cycle.

Note that the white and blue polymorphisms of A- B showed that the heat treatment has effect on the formation of the material as the material began to dissolve as the temperature increased in a different way to the material at 25°C .We also notice a change in the position of the integrated intensity of the reflection (110) indicated that the material began to respond to the heat treatment and received a change in the composition of the material.

References

[1] Polymer engineering and science, 1969, 9(5).
[2] Colloid. polymer Sci 265:209, 1987.
[3] Jian S., binsong at el. Determination of degree of crystallinity of nylon 1212 by WAXD. *Chinese journal of polymer science*, 2004, 22(5):491 -496.
[4] Fresenius J. Anal Chem, 1995, 353:778 – 784.
[5] Original Russion text , Ya-A. Lebedev …..etc, 2010, 55(4): 657-652.
[6] Polymer physics edition. *Journal of polymer science*, 1983, 21: 1133-1145.
[7] Polymer, 1978, 19.
[8] Handbook of Instrumental Techniques for Analytical Chimestry Ed. Frank settle Ch, 1997, 50.
[9] KAKUDO M. and RULLMAN. *Journal of polymer science*, 1960, xlv: 91-101.
[10] Kolodka E., Wang W. Szhu J. and Hamielec A. *J.Appl. polym. Sci*, 2004, 92, 307.
[11] Moly K.A. et al. *European polymer journal*, 2005, 41: 1410-1419 .
[12] Brandon Rawlings. *Crystallinity in polymers*, 2009, 12.
[13] Mulla S . M ., at el . Use of the X – Ray Diffraction Technique for polymer Characterization and studying the Effect of the Optical Accessories. *ARAI*, 2012, 6.

Investigation of Corrosion Protection in Oil Mineral Reservoirs by Nanocomposites Used as Coating Layers

Investigation of Corrosion Protection in Oil Mineral Reservoirs by Nanocomposites Used as Coating Layers

Abdulhameed R Al-Sarraf and Samer A Al-Saaidi

Physics Department, College of Education for Pure Science Ibn-Al-Haithm, University of Baghdad

Samerhawk@gmail.com

Abstract. In this study, a number of nanocomposites were prepared by adding magnesium oxide (MgO) with weight percentages (1, 2 & 3)% to cellulose nitrate and sodium silicate as an intermediate layer and other nanocomposites by adding MgO, coal coke and hybrid (MgO & coal coke with ratio 1:1) with weight percentages (1, 2 & 3)% to epoxy resin as final layer. The identity of the used metal is determined by spectrometer OE thermo. The nature and topography of the surface layers were examined by optical microscope and atomic force microscope (AFM). Mechanical properties are indicated by hardness, wear rate, impact strength and adhesion strength. The efficiency of the layers prepared to inhibit corrosion in the oil mineral reservoirs of the oil products distribution company was studied by electrochemical corrosion test in addition to the chemical corrosion test. The used metal is (St-37) according to (ASTM). It was found that the best intermediate layer (cellulose nitrate+3%MgO) and the final layer is the epoxy resin reinforced by 2% hybrid.

Keywords: Corrosion, Electrochemical Corrosion, Chemical Corrosion, Nanocomposoites, Cellulose Nitrate, Sodium Silicate, MgO, Hybrid Composite and Epoxy Resin.

1.Introduction

Corrosion is a natural and costly process of destruction like volcanic eruptions, floods, tornados and earthquakes. It's playing an important role in economics and safety, particularly for metals and alloys [1,2]. Corrosion is the destructive attack of a metal by electrochemical or chemical reaction with the environment. Steel has found wide application in a broad spectrum of industries and machinery; in spite of its tendency to corrosion. The corrosion of steel is a fundamental academic and industrial worry that has received a considerable amount of attention [3]. Inhibitors are one of the an important methods used for protecting materials against deterioration due to corrosion [4,5]. Several countries such as (the United Kingdom, China, Germany, the United States, Finland, Australia, India, Japan, Sweden and Kuwait) studied the cost of corrosion and found the annual corrosion costs from the Gross National Product (GNP) of each nation ranged from approximately 1 to 5 percent. The failures in oil and gas production ranged from 25 to 40% are due to corrosion. Consciousness to corrosion, acclimation of timely and appropriate control measures were in the reduction of corrosion failures [6,7].

The research aims to prepare nanocomposite coats in layers form (including sodium silicate and cellulose nitrate composites reinforced by 3 wt.% MgO as intermediate layer and epoxy resin reinforced by 2 wt.% hybrid (MgO & Coal coke) as final layer) in order to inhibit and protect the stainless steel alloy (St-37) from the chemical corrosion resulting from the oil product in the oil products distribution company (Opdc.)

2.Experimental Part

The metal used was analyzed by using spectrometer OE thermo ARL 3460 and has been found the classification of alloy is (St-37) a low Carbon (C = 0.16) and a moderate hardness (130HB = 13HRC) according to ASTM.

The metal piece exposed to corrosion as shown in 'Figure 1' and was taken from one of the reservoir in oil product distribution company (OPDC). The thickness was reduced from 6mm to 3mm and cut into two groups (1.5cmX1.5cm & 3cmX3cm) as shown in 'Figure 2'.

Figure 1. St-37 alloy exposed to corrosion

Figure 2. Samples after cutting

The carbonization process was performed at 950 ºC for 3 hours to eliminate the internal cracks and corrosion microwaves to make the surface of steel stronger and harder (hardness = 589 HB) due to the cohesion of the particles and the formation of surface to coating as shown in 'Figure 3'.

Figure 3. Samples after carbonization

Coating samples includes three stages:

2.1.First stage

After cleaning samples from impurities they were painted by red iron oxide as an initial layer as shown in 'Figure 4'.

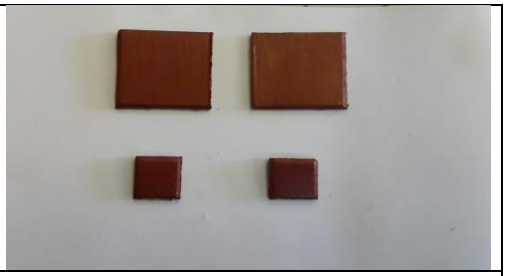

Figure 4. Samples coated by initial layer

2.2.Second stage

Samples were coated by pure cellulose nitrate, pure sodium silicate, cellulose nitrate reinforced by MgO with different percentages (1,2 & 3 wt.%) and sodium silicate reinforced for the same percentage as intermediate layer as shown in 'Figure 5', 'Figure 6', 'Figure 7' and 'Figure 8', respectively.

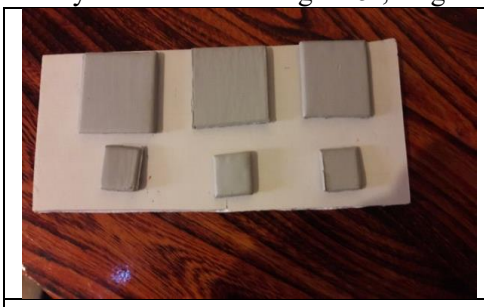

Figure 5. Samples coated by pure cellulose nitrate

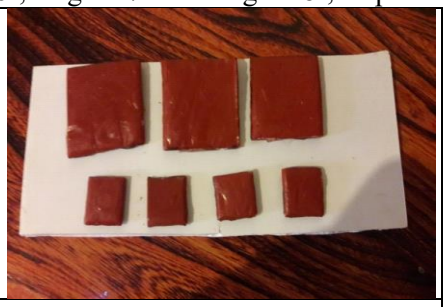

Figure 6. Samples coated by pure sodium silicate

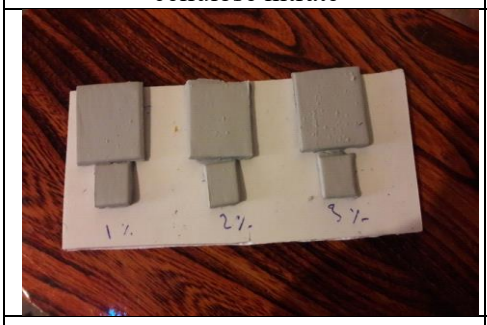

Figure 7. Samples coated by reinforced cellulose nitrate

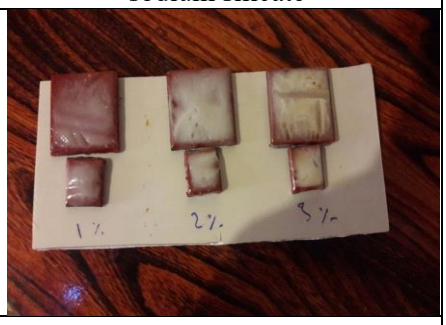

Figure 8. Samples coated by reinforced sodium silicate

The following tests were performed (adhesion force, electrochemical corrosion and chemical corrosion) by the samples coated with sodium silicate and cellulose nitrate reinforced by 3% MgO immersing in three types of oil products (gasoline, gasoil and kerosine) for 24, 48, 72 and 96 hours.

2.3.Third stage

Composite material was prepared from epoxy resin reinforced by nano magnesium oxide, coal coke and hybrid MgO & coal coke (1:1) all of them were with different percentages (1,2 & 3 wt.%) as final layer.

The following tests were performed (adhesion force, electrochemical corrosion and chemical corrosion) by the samples (hybrid composite with 2 wt.%) immersing in three types of oil products (gasoline, gasoil and kerosine) for 24, 48, 72 and 96 hours. Table 1, shows the specifications of used oil products.

3.Results and discussion

Based on the following tests: hardness and wear rate, the samples coated with sodium silicate and cellulose nitrate reinforced by 3% MgO were chosen as intermediate layer because they gave the best results compared to the other reinforcement ratios.

Based on the following tests: impact, hardness and wear rate, the hybrid composite with 2 wt.% was chosen as final layer because it gave best results compared with other composites.

Table 1. Specifications of oil products

Oil product	pH at 25ºC	Density gm/cm^3 at 15ºC	Sulfur content ppm
gasoline	6.78	0.710	10
gasoil	6.6	0.850	10
kerosine	7.16	0.801	10

The hardness and wear rate tests were carried out for the intermediate layer, their results were shown in table 2 and table 3.

Table 2. Values of surface hardness for prepared coatings with reinforcement ratios

Reinforcement ratio %	Surface Hardness	
	Sodium Silicate	Cellulose Nitrate
0	58.3	76.8
1	61.7	78.3
2	63.7	82.4
3	65.6	85.2

Table 3. Values of wear rate for prepared coatings with reinforcement ratios of intermediate layer

Reinforcement ratio %	Wear Rate (Intermediate layer)	
	Sodium Silicate*10 $^{-5}$	Cellulose Nitrate*10 $^{-5}$
0	9.031	7.0032
1	7.092	6.0018
2	5.38	2.0072
3	3.009	1.484

From table 2, we noticed that the increase in hardness with the increase of the reinforcement ratios is due to the nanoparticle penetrates inside the base material and works to fill and reduce the gaps that formed during the molding process, which gave better mechanical properties.

The increase in the reinforcement ratio leads to the decrease in the wear rate because of the increase in the rates of slippery communication between the touching surfaces as shown in table 3. From this, we conclude that the reinforcement ratio 3% gave the best results compared to the other reinforcement ratios.

The topography surface of the intermediate layer was studied by AFM microscope and its results are shown in ‘Figure 9’ and ‘Figure 10’. The nature and homogeneity of the surface of the coat were studied by the optical microscope and their results are shown in ‘Figure 11’ and ‘Figure 12’.

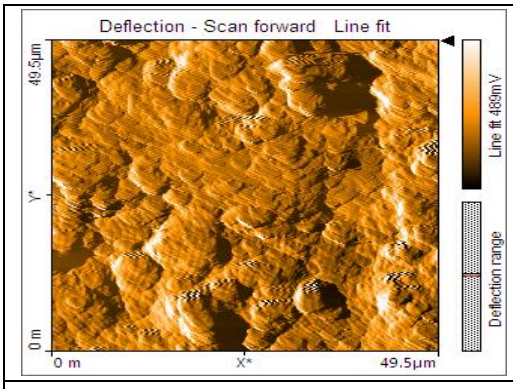

Figure 9. Topography intermediate layer (cellulose nitrate)

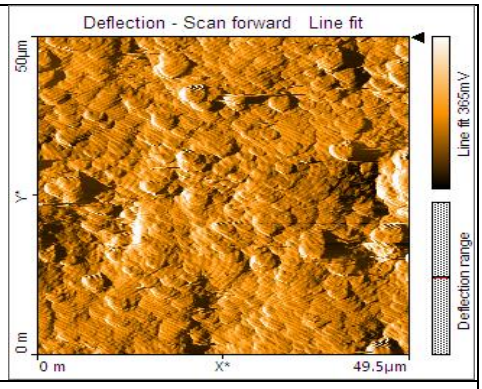

Figure 10. Topography intermediate layer (sodium silicate)

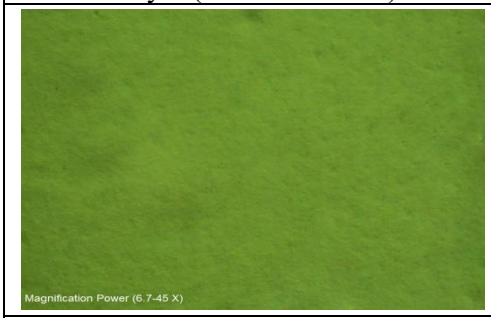

Figure 11. Nature surface of intermediate layer (cellulose nitrate)

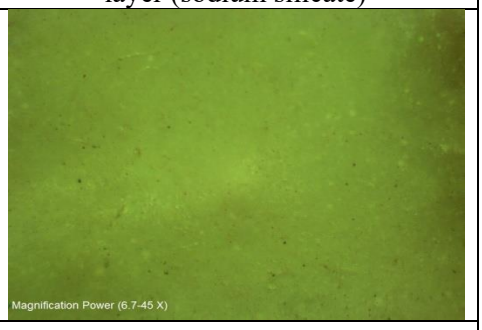

Figure 12. Nature surface of intermediate layer (sodium silicate)

Microscopic images showed that the reinforce by nano magnesium oxide increases the homogenization process thus obtaining better mechanical properties..

Table 4, shows the values of adhesion force of the intermediate layer. It was found adhesion force of the cellulose nitrate is better than of sodium silicate because the mechanical bonding of the cellulose nitrate with the steel surface is better than that of sodium silicate and the locations of sodium silicate at the surface are working as a store of adhesive material that used in the adhesive force measuring device.

Table 4. values of adhesion force of intermediate layer

Intermediate layer	Adhesion (Pa)
Sodium Silicate + 3% MgO	171
Cellulose Nitrate + 3% MgO	232

The lowest corrosion rate is the intermediate layer (Cellulose Nitrate + 3% MgO) works as a dielectric (inhibitory layer) oxidizes with the steel surface and union with oxygen prevents the corrosion metal, this reduces or stops the reaction. This is reported in table 5, 'Figure 13' and 'Figure 14'**.**

Table 5. Values of electrochemical corrosion of intermediate layer

Intermediate layer	Current density $\mu A/cm^2$	Weight lose gm/m^2	Penetration lose mm/a
Sodium Silicate + 3% MgO	117.22	29.3	1.36
Cellulose Nitrate + 3% MgO	2.75	0.687	0.0319

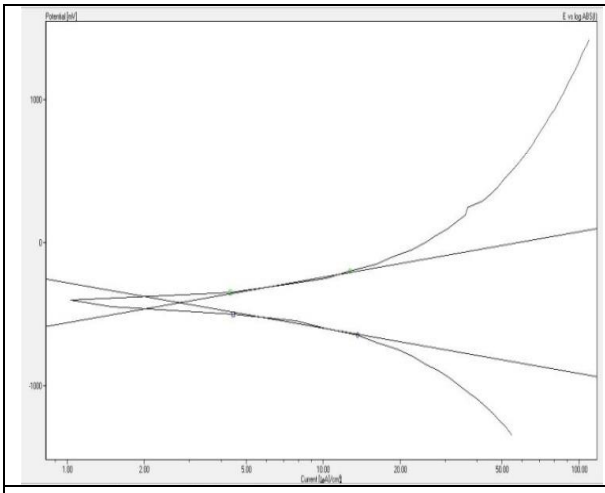

Figure 13. Electrochemical corrosion of intermediate layer (Cellulose Nitrate + 3% MgO)

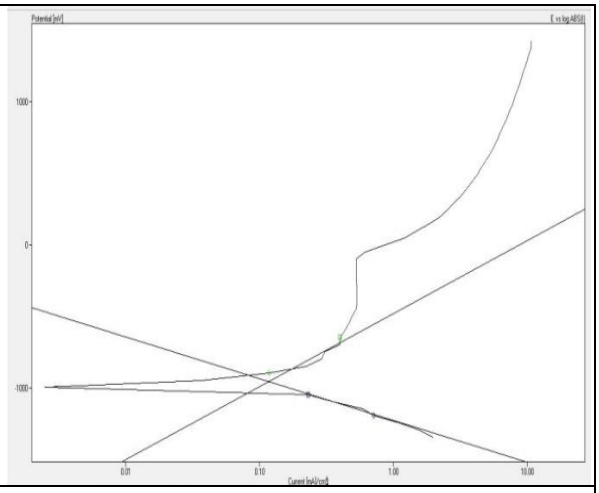

Figure 14. Electrochemical corrosion of intermediate layer (Sodium Silicate + 3% MgO)

'Figure 15' show the values of the chemical corrosion. The reason for the raise of the curve at (1&3) hours of immersion time for sodium silicate, this area is considered a polymer grout area which has an increase in weight and directly proportional to the density because the penetration of water is rapid through polymer chains which lead to increase the chemical bond between them. When the density of bonding increases the susceptibility to absorption of polymer decrease, the difference in concentration between the liquid and the area in which will penetrate during increase. The speed of diffusion is higher according to Fick's law of diffusion. The increased density leads to weight gain (bulge of the intermediate layer) and therefore the weight loss is greater, this means more corrosion and this is clear when samples immersion in gasoil product.

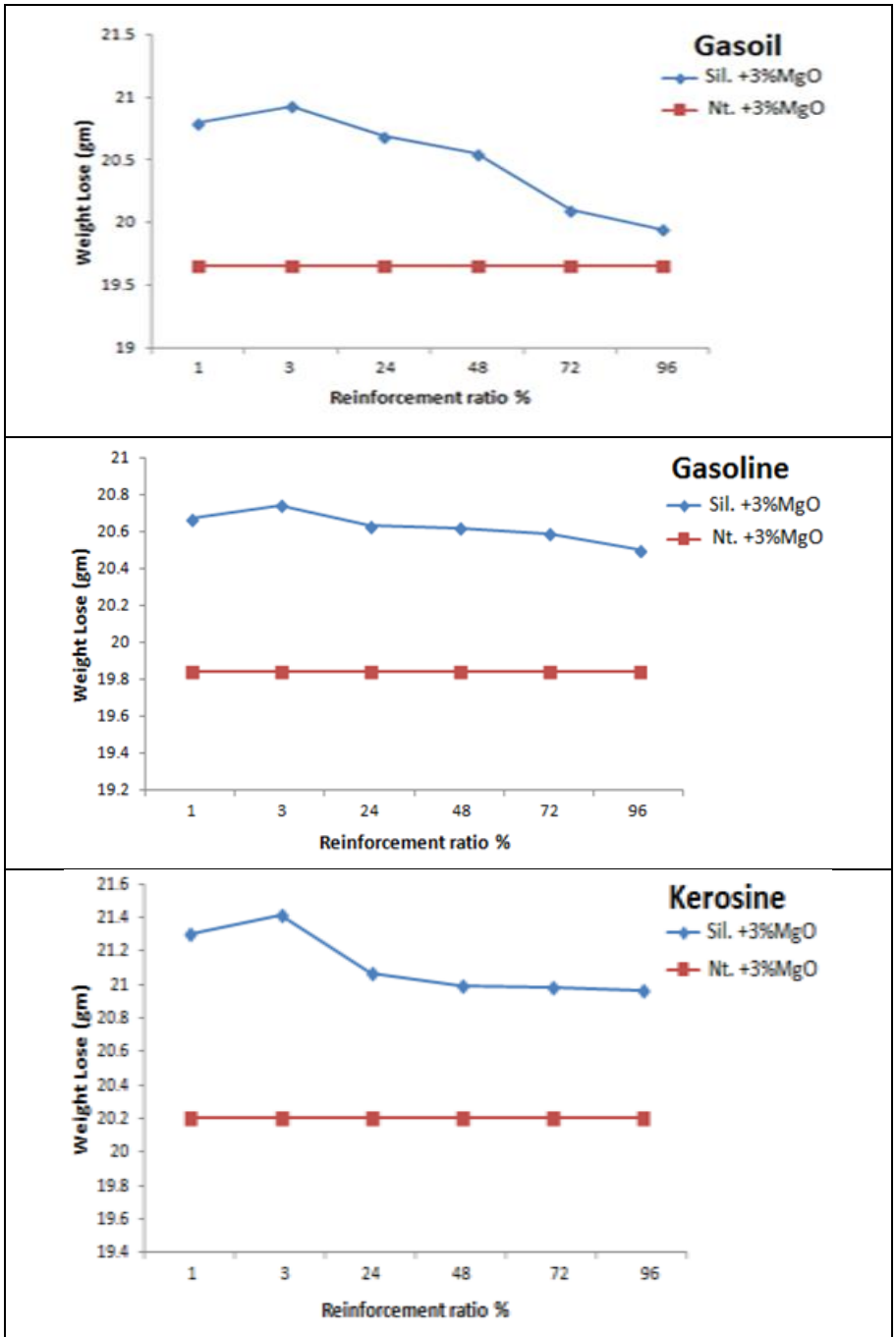

Figure 15. Relation between weight loss and rienforcement ratio of intermedidte layer

From the three tests above, the intermedidte layer (cellulose nitrate +3% MgO) gave the mechanical and chemical protection of the surface sample better than the intermedidte layer (sodium silicate +3% MgO) because the ratio of sand to soda 2:3 is called aquatic glass and it is considered a brittle material.

Impact strength, Hardness and wear rate tests were carried out for the final layer showing their results in table 6, table 7and table 8, respectively.

Table 6. Relation between reinforcement ratio and impact strength for final layer

Rienforcement ratio%	Pure	MgO	Coal coke	Mix
0	3.918	-	-	-
1	-	2.989	3.785	4.625
2	-	3.761	3.035	4.712
3	-	4.589	3.94	4.283

Table 7. Relation between reinforcement ratio and hardness for final layer

Rienforcement ratio %	Pure	MgO	Coal coke	Mix
0	67.5	-	-	-
1	-	70	79	80.2
2	-	77.6	79	84.1
3	-	79	76.4	79

Table 8. Relation between reinforcement ratio and weight loss for final layer

Rienforcement ratio %	Pure	MgO	Coal coke	Mix
0	1.009	-	-	-
1	-	3.009	5.027	3.0063
2	-	1.081	2.036	1.009
3	-	5.69	1.027	2.018

The hybrid material (2 wt.%) has the highest value of hardness due to the reinforcement particles that carry a large part from the loads applied on the composite material and works to prevent the spread of the cracks in order to increase the bond between the touching surfaces (matrix and reinforcement) as shown in 'Figure 16' and 'Figure 17', this leads to prevent the dislocation motion and the particles share the matrix phase in the carrying of forces and stresses, which leads to increase the impact strength. The hybrid composite with 2 wt.% was chosen because it gave best results according to the three tests above.

Table 9, shows the adhesion force of the final layer with the intermediate layer, from this we conclude that the adhesion of the final layer to the intermediate layer (cellulose nitrate +3% MgO) is better than the (sodium silicate +3% MgO).

Table 9. Values of adhesion force

Sample Intermediate layer) +(Final layer) (	Adhesion (Pa)
Sodium Silicate +3%MgO) +(2%hybride)(	137
(Cellulose Nitrate +3%MgO) +(2%hybride)	196

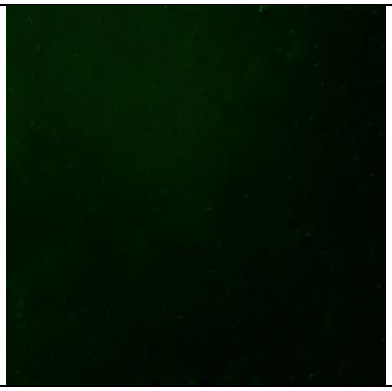

Figure 16. Nature surface of final layer

(a)

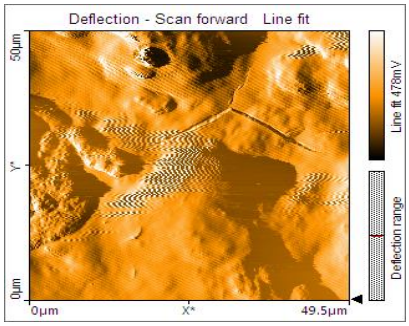

(b)

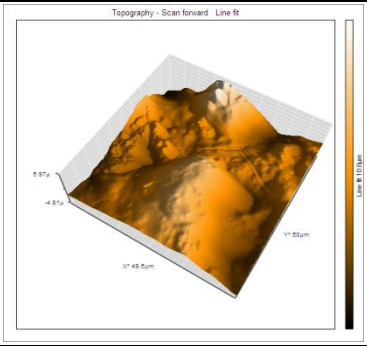

Figure 17. Topography surface of final layer (a) two direction (b) three direction

The relationship between the current density (current of the corrosion) and the potential shown in 'Figure 18' and 'Figure 19' is linear, this means that the increase of the current shall be with constant potential and any change in potential proof is that the corrosion occurred. The tangents represent the cathode and anodic behavior and the intersection point of these tangents represents the corrosion current.

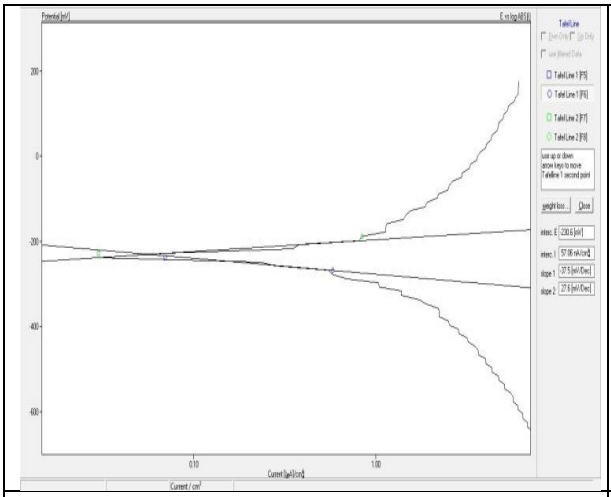

Figure 18. Electrochemical corrosion of (Cellulose Nitrate + 3% MgO) and final layer

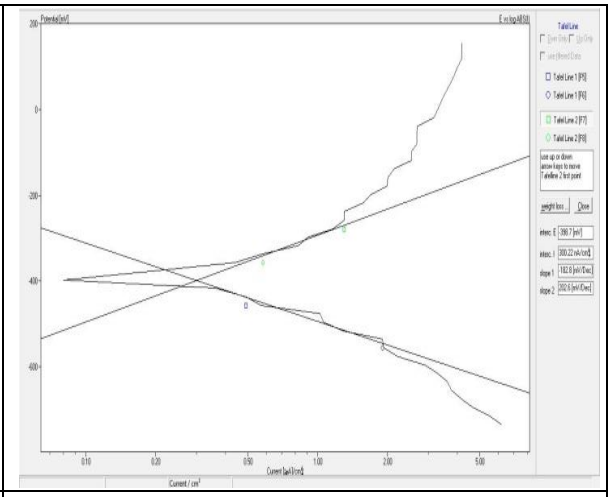

Figure 19. Electrochemical corrosion of (Sodium Silicate + 3% MgO) and final layer

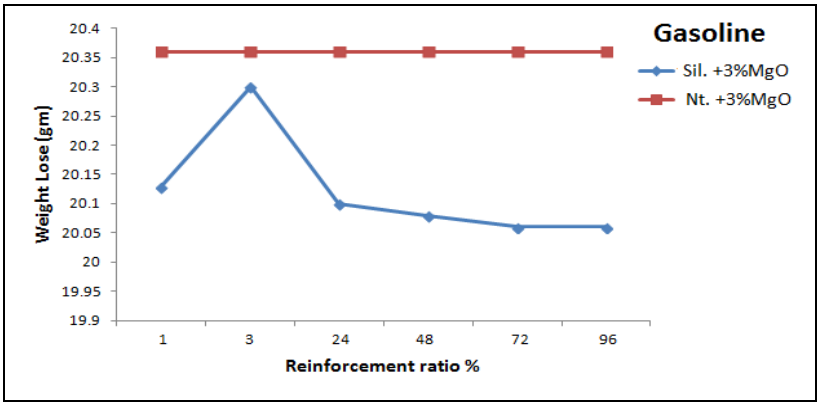

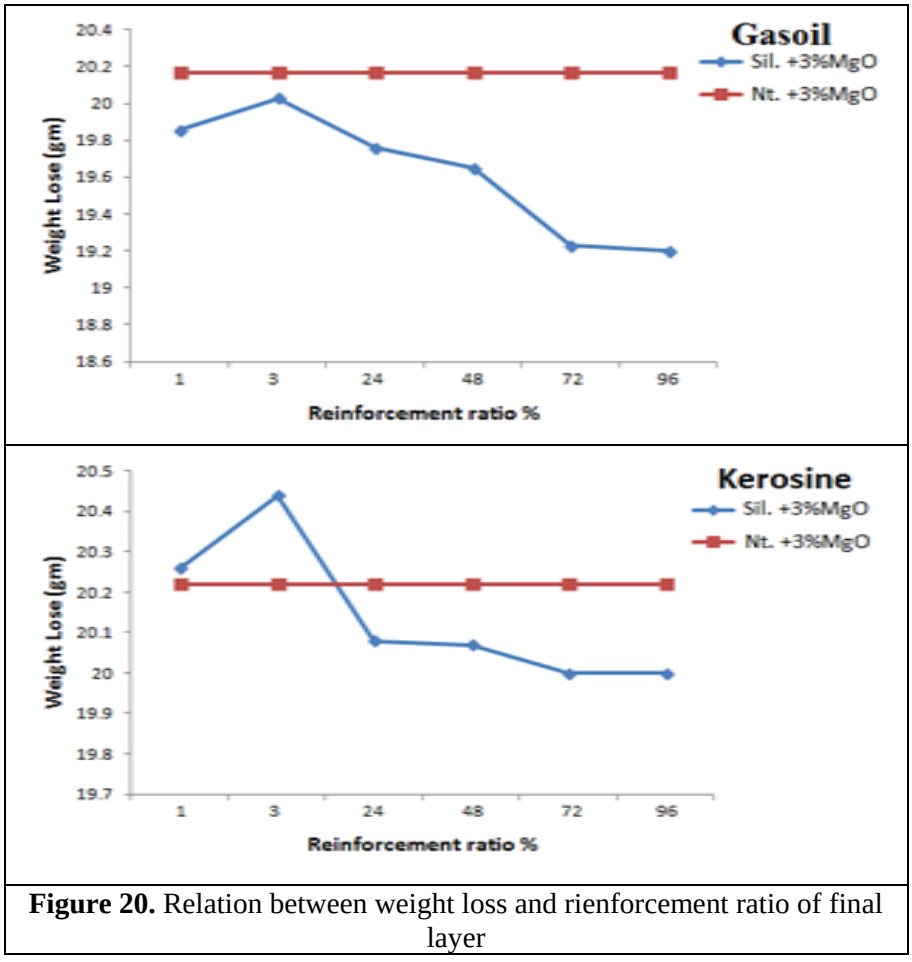

Figure 20. Relation between weight loss and rienforcement ratio of final layer

'Figure 20', the lowest corrosion rate is (final layer + cellulose nitrate + 3%MgO) because of the reduced potential of (cellulose nitrate +3%MgO) lies under the reduced potential of the steel in the chemical chain and works as a protective layer. Cellulose nitrate is a saturated and stable compound (inert) that does not dissolve in water so it gives chemical protection from corrosion by preventing moisture from reaching the steel surface and it is a good base for the cohesion of the final layer.

4.Conclusion

Mechanical properties increase with the increase of carbonation temperature and the reinforcement ratios of nanoparticles for sodium silicate and cellulose nitrates due to the elimination of internal cracks and the nanoparticles penetration within the polymer chain. The adhesion force of the (final layer + cellulose nitrates + 3%MgO) is greater than the (final layer + sodium silicate + 3%MgO) because of slippery communication between the two layers. Inhibitor coat reduce or stop corrosion metal in order to be united with oxygen and oxidizes with the steel surface.

The particles can be shared the matrix phase in the standing for of forces and stresses applied, which leads to increase the mechanical properties. The Resistance to chemical and electrochemical corrosion of the (final layer +cellulose nitrates + 3%MgO) is greater than the (final layer + sodium silicate + 3%MgO).The hybrid composite (2%) is better than the other hybrid composites according to the mechanical tests. The oil products (gasoline, gasoil and kerosion) are natural according to pH meter.

References

[1] Ahmad Z 2006 Principles of corrosion engineering and corrosion control *butterworth heinemann*
[2] Bentiss F, Traisnel M and Lagrenee M 2000 Substituted 1,3,4-oxadiazoles: a new class of corrosion inhibitors of mild steel in acidic media *Corros. Sci.* 42 p 127–146
[3] Khadom A 2010 Mathematical and quantum chemical studies for the corrosion inhibition of steel in HCl acid *Diyala journal of engineering sciences* Vol 03 No 01
[4] Trabanelli G 1991 Inhibitors an old remedy for a new challenge *Corrosion* 47 p 410– 419
[5] Khadom A, Yaro S, AlTaie S and Kadum A 2009 Electrochemical, activations and adsorption studies for the corrosion inhibition of low carbon steel in acidic media *Port. Electrochim. Acta* 27 p 699-712
[6] Hantoosh A 2010 Study of the effect of polymer inhibitors on the (Al-Cu) galvanic corrosion in hydrochloric acid *University of Technology*
[7] Sastri S, Hoey R and Revie W 1994 Corrosion in the mining industry *CIM Bulletin* Vol 87 No 976

The effect of replaced recycled glass on thermal conductivity and compression properties of cement

The effect of replaced recycled glass on thermal conductivity and compression properties of cement

A S khalil[1], M A Mahmoud[1], A AL-Hathal[1], M K Jawad[1], B M Mozahim[1]

Physics Department, College of Education for Pure Science (Ibn Al-Haitham), University of Baghdad, Iraq.

Asmaashawky67@yahoo.com

Abstract. This study deal with recycling of waste colorless glass bottles which are prepared as a powder and use them as an alternative for cement to save the environment from west and reduce some of cement(ceramic) damage and interactions with conserving physical properties of block concrete. Different weight percentage (0%, 2%, 4%, 5%, 6%, 8%, 10%, 15%, 20% and، 25%) of recycled glass bottle were use in this research to be replaced by a certain percentages of cement. Thermal conductivity was studied for prepared samples. Results show that the thermal conductivity decrease with the increase of weight percentage of glass powder comparing with the stander sample.

1. Introduction

Cement (Portland cement) is on kind of a ceramic material [1] The importance of ceramic materials in the possession of a high melting point, good mechanical chemical properties and they provide first-hand in most parts of the world [2,3].The most important hydraulic cement used extensively in various types of construction as mortars, grouting plasters, and concrete. The Portland cement mainly as calcium silicates and aluminates and even smaller quantities of potassium and sodium oxide may also be present [4]. Cement is one of the most cost and energy-intensive components of concrete. Across the world, significant environmental problems result from the manufacture of Portland cement. [5]. The heat produced by the hydration of cement may prevent freezing of the water in the capillaries of freshly placed concrete in cold weather, and a high evolution of heat is, therefore, advantageous [6]. Most of the world suffer from the problem of the accumulation of industrial waste and special waste resulting from the concentration of defective material or because of consumer use, such as broken glass and causing other environmental and health problems that require the development of practical solutions to get rid of them through the re-use or by taking advantage of them partial substitute for some construction materials (cement, sand,) involved in asphalt or concrete admixtures [7- 10]. The reuse of waste glass is one of the most important issues around the world due to the increase of solid wastes in the landfill and non-degradable nature at its disposal. The use of recycled waste glass in concrete has attracted much interest worldwide and numerous researchers have been carried out, showing the possibility of use of waste glass as building materials by partially replacing concrete mixtures (Shi and Zheng 2007)[11]. The glass powder pozzolanic of materials that can be added to concrete or mortar (pozzolanic material) or cement paste. pozzolanic materials are natural materials or industrial contain the active silica (amorphous) and which are the Association of properties when they

interact with calcium presence of water and varying unusual heat hydroxide, (Ca (OH)2) and calcium hydroxide is one of the outputs of the process of cement interaction with water Shown in the 'figure 1'. This research deal with replacing cement with recycling transparence bottle glass powder.

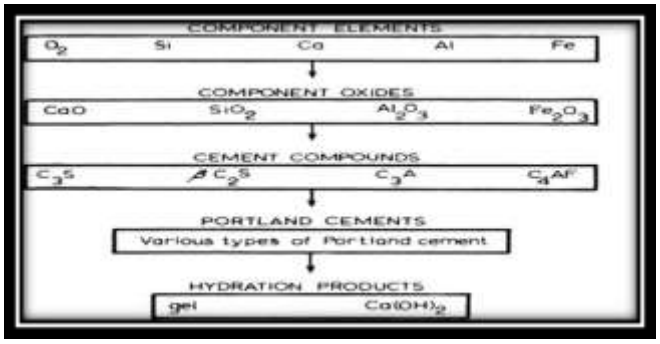

Figure 1. Schematic representation of the formation and hydration of Portland cement [12].

2. Experimental work

2.1. Cement

In this study, Portland cement was used, commercially known as (TASLUJA), which stored in dry place. Particle size was Examined by using Mastersizer 2000 laser diffraction particle size analyzer delivers rapid as shown in 'figure 2' and chemical analysis was used to study the cement Chemical composition and main compounds, the material analyzed according to ASTM C150- 02. The result agrees with the standard value as shown in (table 1) and (table 2) which show the calculation potential composition of Portland cement by Bogue's equation [13] as shown in 'figure 2'.

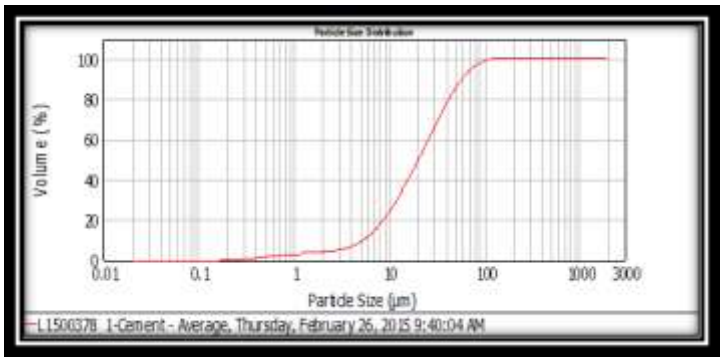

Figure 2. Particle size of cement. The diameter from (5.344 µm- 57.822 µm)

Table 1. Chemical composition and main compounds (Bogues) equation) of Portland cement

Element	Content %	Standard[14]
SO3	2.33%	3.0 max
Na2O	0.4366%	--
Fe2O3	2.611%	6.0 max
SiO2	24.24%	20 min
CaO	60.18%	--

K2O	0.698%	--
MgO	1.318%	6.0 max
AL2O3	2.53%	6.0 max
L.O.I	5.86%	--

Table 2. Potential composition result for Portland cement (Bogue's equations) [13]

C_3S	39.99
C_2S	39.33
C_3A	2.286
C_4AF	7.945

2.2. Fine aggregate (sand)

According to the ASTM C33-03, the proportion of salt in the sand used in this research studied and the results show a good agreement with standard values as shown in the (table 3). By sieving (1kg) of the used sand the particle size of sand was measured by using different size of sieves (9.5, 4.75, 2.36, 1.18, 0.60, 0.30, 0.15) mm respectively, and then weighing the outcome of sand for each sieve ,the result show a good agreement with standard values, as shown in (table 4)

Table 3. Chemical composition of sand

Element	Expe. Content %	Standard[15]
SO_3	0.6%	0.5%

Table 4.Grading of fine aggregate*

Sieve size(mm)	Weight % Passing by	Specification Limit[15]
9.5	100	100
4.75	93.2	90-100
2.36	84.2	75-100
1.18	68.0	55-90
0.60	37.8	35-59
0.30	19.6	8-30
0.15	8.8	0-10

2.3. Recycled Transparent Glass Bottles (RTGB)

The glass used in this study is from the waste, it is colorless glass bottles used as partial substitute for cement, at first all bottles washed carefully and then crushed in a mill specification. The particle size of the glass powder was examined by the Mastersizer 2000 laser diffraction particle size analyzer delivers rapid. The diameter is in between (3.733 μm- 51.938 μm) as shown in 'figure 3'

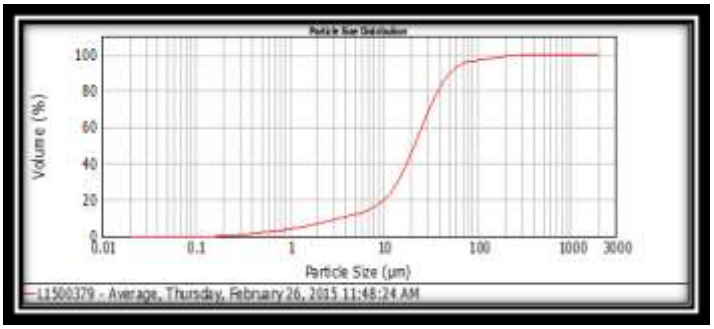

Figure3. The particle size of Glass powder.

3. Chemical analysis

The used Glass was analyzed according to ASTM C618 and the result showed a good agreement with standard values of element as shown in the (table 5).

Table 5. Chemical composition of glass powder

Element	Content %	stander %[14]
SO_3	0.7%	---
Na_2O	13.626%	12-15%
Fe_2O_3	1.321%	---
SiO_2	72.52%	73%
CaO	7.21%	10%
K_2O	0.227%	---
MgO	2.208%	---
AL_2O_3	1.75%	---
L.O.I	0.347%	---

4. Water

According to (IQS 1992/1703). Ordinary drinking water was used for all concrete admixtures.

5. Sample preparation

According to ASTM C133-97 standard, the molds were prepared by using wood. According to ASTM C109/C109M, the weight percentages of the used components of concrete, cement, sand, and water was (1:2.75:0.485) respectively. 'Figure 6' shows the Scheme Stages of sample preparation.

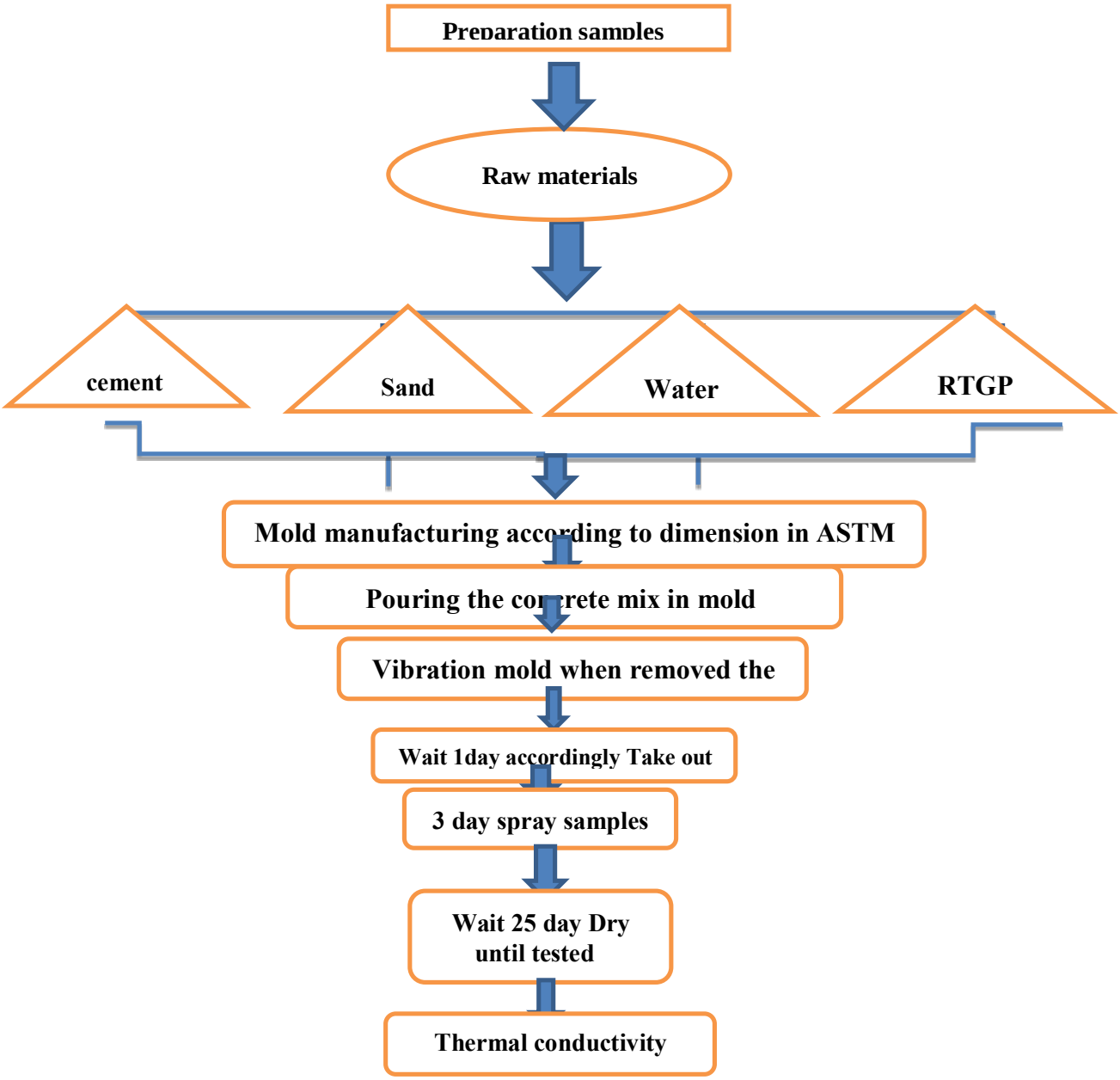

Figure 4. Scheme Stages of sample preparation.

6. Thermal Conductivity Measurement

Lee's disc method was used to measure thermal conductivity and Compressive test have been done According to ASTM C109/C109M-02 for prepared samples.

7. Results and discussion

The effect of waste glass addition on Thermal conductivity is shown in 'figure 7' and list in the (table 8). The result show that thermal conductivity coefficient gradually decreases with increasing of recycling glass content in specimen because of thermal conductivity of class is less than cement. Sand as a fine aggregate has a good thermal conductivity, replacing the cement with recycling glass powder

will reduce the ability of sand to heat transfer [16]. The recycled glass then will be function as sand in term aggregates are uniformly distributed in the mix but in same time reduce the ability of concrete to transfer heat. These results are a good agreement with by Krishnamoorthy [17].

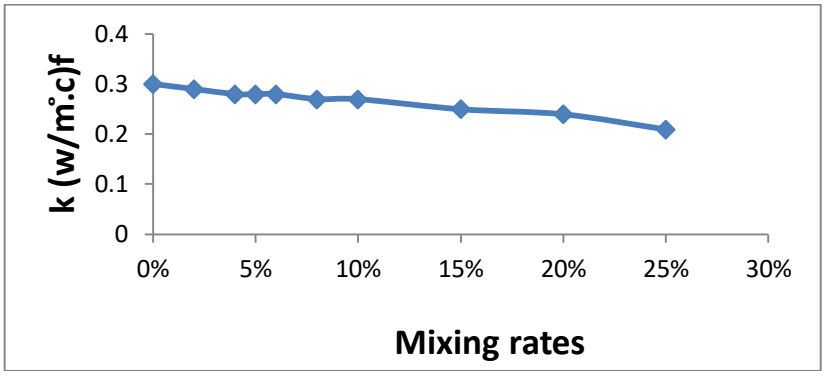

Figure 5. Thermal conductivity (K) vs Mixing rates for samples.

Table 6. Thermal conductivity results for concrete samples

Sample	K (W/m.℃)
1	0.30
2	0.29
3	0.28
4	0.28
5	0.27
6	0.27
7	0.27
8	0.25
9	0.22
10	0.21

Compressive strength results show that maximum value for compression strength was at 4% of additives and these results showed a decrease of maximum stress for concrete samples with increasing the weight percentage (wt. %) substituted cement which means decrease in adhesive material and the maximum stress increase in the low ratios as shown in the ‘figure 7’. increases of glass wt. % will lead to failure the samples 8, 9 and 10 which shows the vertical view spread of the cracks

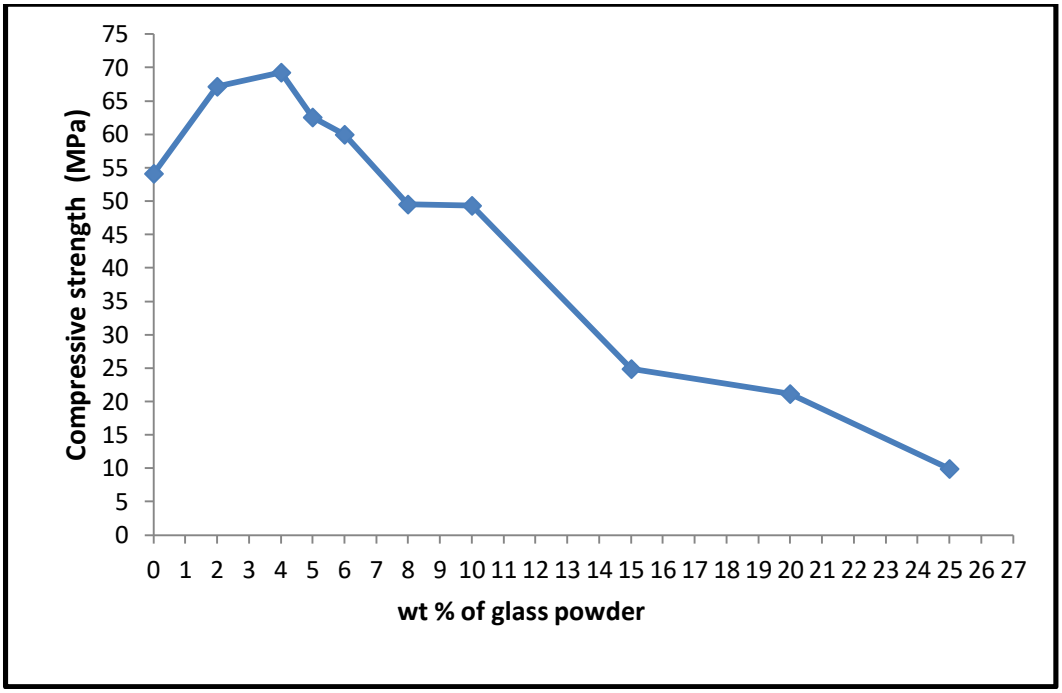

Figure 6. Compressive strength v.s to various percentages Replacement of Glass powder with cement.

8. Conclusion

Replacing cement with recycled glass bottles powder show that:

1. Possible to use west in a useful way to protect the environment and return to use with good production properties.
2. The obtained results show that thermal conductivity decrease with increasing wt% of replaced glass powder.
3. Compressive strength results show that maximum value for compression strength was at 4 %wt% replaced glass powder.

References

[1] Ryan W. and Fric C 1967 *Properties of Ceramic Raw Materials* John Wiley and Sons Inc. New York
[2] Zbigniew D and Jastrzebski 2014 *The Nature and properties of engineering materials* second edition
[3] ACI Committee 1977 Guide to Durable Concrete (ACI 74-53) *American Concrete Institute* Detroit Dec.
[4] Neville A M 1981 *Properties of Concrete* Fifth Edition pitman -1 publishing limited London UK
[5] Shi C Wu Y Riefler C and Wang H 2004 Characteristics and Pozzolanic Reactivity of Glass Powders *Cement and Concrete Research*
[6] Shayan A 2002 Value-added Utilisation of Waste Glass in Concrete *Iabse Symposium Melbourne*
[7] Eldin N N and Senouci A B 1993 Rubber-tire Particles as Concrete Aggregate *Journal of Materials in Civil Engineering* ASCE 478-96
[8] Chesner W Waste Glass and Sewage Sludge 1992 Ash Use in Asphalt Pavement Utilization of Waste Materials in Civil Engineering Construction *American Society of Civil Engineering*
[9] Shi C and Zheng K A 2007 review on the use of waste glasses in the production of cement and

concrete *Resources* Conservation and Recycling **52** 2 234–47
[10] BOGUE R H 1955 *Chemistry of Portland Cement* New York Reinhold
[11] Shehata MH Thomas MDA 2000 The effect of fly ash composition on the expansion of concrete due to alkali–silica reaction. *Cem Concr Res* **30** 1063–72
[12] Vandhiyan R Ramkumar K and Ramya R 2013 Experimental Study On Replacement Of Cement By Glass Powder *International Journal of Engineering Research and Technology (IJERT)* **2** 5
[13] ASTM C 150-02a Standard Specification for Coal Fly Ash and Raw or Calcined Natural Pozzolan for Use in Concrete.
[14] VERBECK G J and HASS W E 1951 Dilatometer method for determination of thermal coefficient of expansion of fine and coarse aggregate, *Proc. Highw. Res. Bd.* **30** 187–93
[15] Krishnamoorthy R R and Zujip J A 2013 Thermal Conductivity and Microstructure of Concrete Using Recycle Glass as a Fine Aggregate Replacement *Int. J. Emerg. Technol. Adv. Eng* **3** 8 463–71

Utilizing Laser-Induced Breakdown Spectroscopy Method to recognize chemical composition of low-carbon steel in $NH_3(NO)_4$ material

IOP Conf. Series: Journal of Physics: Conf. Series **1003** (2018) 012128 doi:10.1088/1742-6596/1003/1/012128

Utilizing Laser-Induced Breakdown Spectroscopy Method to recognize chemical composition of low-carbon steel in $NH_3(NO)_4$ material

Nissan Saud Oraibi

Physics Department, College of Science, Al-Nahrain Univ., Iraq.

nissansoud78@gmail.com

Abstract.A standoff laser Induced Break down Spectroscopy (L.I.B.S) technique has been used to characterization the organic materialsuch as $NH_3(NO)_4$, a Q-switched Nd:YAG laser (1064 nm wavelength, 9 ns pulse width and 1 Hz repetition rate, 300 mJ is focused to the targets to generate plasma. HR 4000 CG-UV-NIR spectrum analyzer was used to collect the generated plasmaemissions, specificsignature of each targets material can be obtained by analysis the plasma emission spectrum Peak ratio analysis technique is used for the identification of energetic materials.

Key words: Laser-Induced-Breakdown Spectroscopy, LIBS, plasma , low-carbon steel.

1.Introduction:

LIBS (Laser-Induced Breakdown Spectroscopy) is an atomic emission spectroscopic method, where a high energy pulsed laser concentrate onto a material that creats a passing high-density plasma as the laser ferocity overtakes the material breakdown threshold (~1-10 MW/cm2)[1]. Orienting the analytic breakdown to be ions and free electrons that make the plasma be recognized by atomic emission [2]. The Ultraviolet and apparent emission from the plasma is likely be spectrally determined for qualitative and quantitative analysis of the samples composition. This paper presents LIBS technique of the organic materials analysis through the analysis of their plasma spectrallines and measure their intensities and the conformityof that line with the basic components. This technique owns a lot of benefits as it is considered as an analytical technique which needs no sample planning, The analysis procedure is rapid and can be used for both samples (conducting and non-conducting) , disregarding to their physical status. LIBS can also be used to analyze hard materials that havethe difficulty of being digested or dissolved,. This technique is able to simulate multi-element determination and used in successful way even in difficult environmental conditions [3], [4]. So it is considered as a suitable technique for detecting and identifing the atmospheric environment performence [5]

2.Experiment

A graphic diagram of the experimental plan is displayed in Fig.1 in our experiments, energy source was a Q-switched Nd:YAG pulsed laser operative at the main wave-length (1064 nm), having pulse duration of 9 ns and 1Hz repetition rate. The energy per pulse at the target surface was fixed at a level of 300mJ. The laser beam was focused on the targets by a lens of focal length (10 cm). the targets were manure sample on a glass supstrate[6,7],

The laser spot was measured at the target surface using an optical microscope and gives a circle of area $5x10^{-3}cm^2$ and hence laser intensity of the order of 6.628 GW/cm^2 was calculated. Plasma emission spectroscopy was performed with an Ocean optics (HR 4000 CG-UV-NIR) spectrum

analyzer having resolution in(320-740 nm) wavelength interval. An optical fiber was positioned at (3 cm) distance from the targets surface(to captur as much as possible of emission spectrum) .

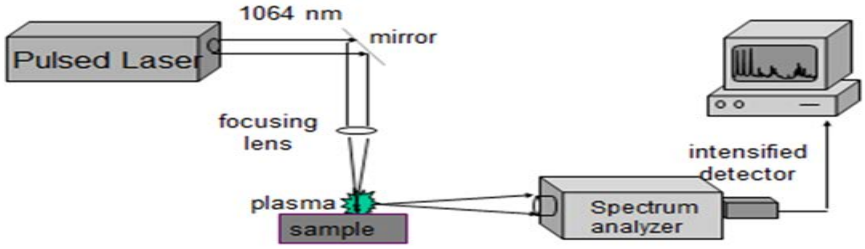

Figure 1.Experimental setup

3.Results and discussion

In depending on the elements spectral lines of dung sample that was analyzed in the LIBS, Figure 2demonstrates exemplary LIBS spectrum in various wavelength reach for the tested sample[8], in table1, elements that have been recognized in manure sample can be shown.In addition, other impurites were identified in small persentege, like (Al, Fe, S, H, N, and O)[9].

The absorved emission lines were situated on a beamy spectral background basicaly because of the technicality that invovles free electrons (inverse Bremsstrahlung, radiative recombination and photoionization) [10]. These peaks were assigned using(NIST) database [11].

Table 1. Analytical lines ofelements between the measurement and reference.

NIST element	NIST λ (nm)	[Intensity]	λ(wavelength) (nm)	Marker Number
H	373.4	0.005629	373.3673	1
Fe I	83.925	0.076838	383.9247	2
O	393.4	0.510173	393.2152	3
SII	397.02	0.282957	397.0158	4
Al II	22.787	0.179054	422.7759	5
Mn	45.582	0.100376	445.5798	6
FeII	18.638	0.027582	518.637	7
NII	558.859	0.122383	558.7551	8
N	589.9	0.580938	589.5827	9
SII	616.18	0.153727	616.1873	10
OII	657.11	0.119813	656.7277	11

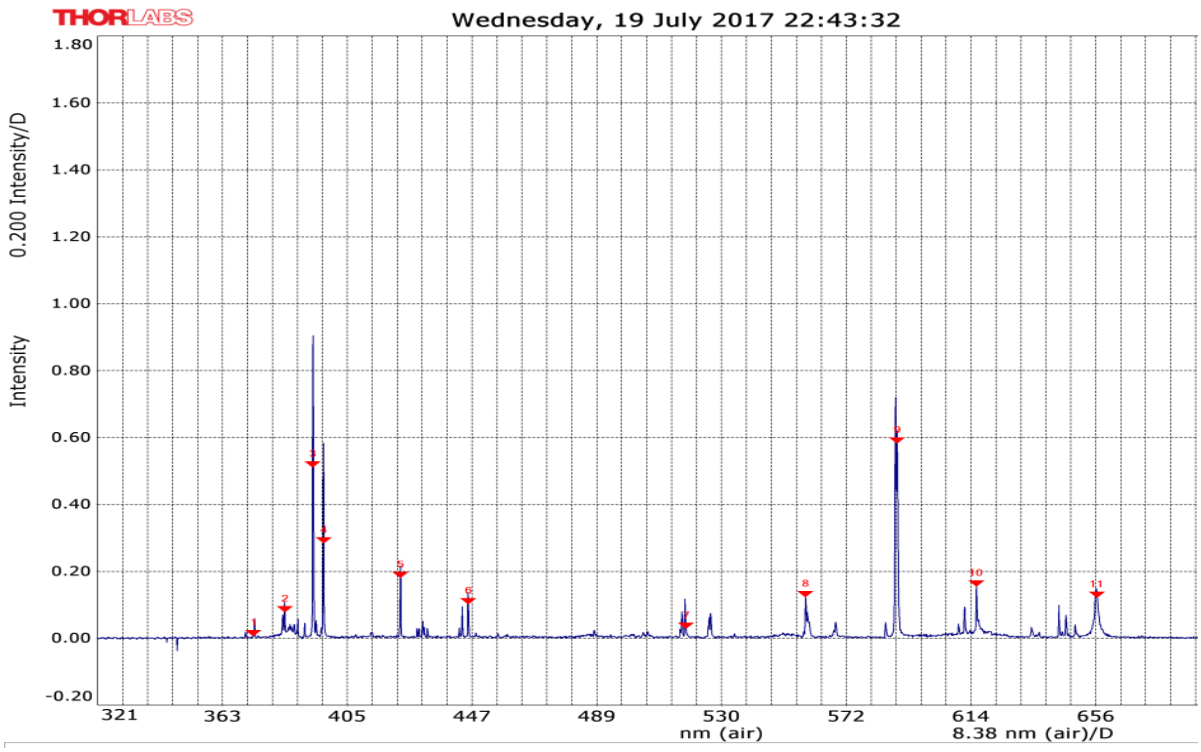

Figure 2. shown typical LIBS spectrum for the tested sample

4.Conclusions

evaluating the performance of LIBS for identification of the materials cmposition was done, LIBS spectra were recorded using a spectrum analyzer.An emission spectra tests were enough to identify between many materials.LIBS has low cost and high-quality system for analyzing in comparing with all other analysis technologies. LIBS displayed high sensitivity to identify some elements like: (H,N,Oand other elements). LIBS is a fast way to analyze the material, non-destructive and no sample preparation is required to gain beneficial results.

References

[1]Schade. W, Bohling.C,Hohmann. K., and Scheel. D, "Laser-induced plasma spectroscopy for mine detection and verification," Laser and Particle Beams **24(02),** (2006) 241–247.

[2]Radziemski .L.J, "Review of selected analytical applications of laser plasmas and laser ablation, 1987-1994," Microchem. J. 50(3), (1994) 218–234.

[3]Rusak .D.A, Castle.B. C,Smith B. W, and Winefordner .J. D, "Fundamentals and applications of laser-induced breakdown spectroscopy," Crit. Rev. Anal. Chem. **27,** (1997) 257–290.

[4]Samuels.A. C,DeLuciaJr. F. C, McNesby .K. L.andMiziolek .A, Appl. Opt., 42 (2003) 6205–6209.

[5]Morel .S,Leone. N, Adam .P and Amoroux .J, Appl. Opt., 42 (2003) 6184–6191.

[6]DeLuciaJr .F. C,Harmon. R. S,Mcnesby. K. L,WinkelJr. R. J. and MiziolekA, Appl. Opt. , 42, (2003) 6148–6152.

[7]Diwakar.P.K and Hahn. D.W,"Study of early laser-induced plasma dynamics: Transient electron density gradients via Thomson scattering and Stark Broadening, and the implications on laser-induced breakdown spectroscopy measurements", spectrochimicaacta. B,63 (2008) 1038-1046.

[8]Cremers.D.A and Radziemski.L.J, Handbook of Laser-Induced Breakdown Spectroscopy,1st ed., John Wiley & Sons Ltd., Chichester, (2006).

[9]Dadras .S, M.J.Torkamany and Sabbaghzadeh .J,"Characterization and comparison of iron and aluminium laser ablation with time-integrated emission spectroscopy of induced plasma",J.Phys. D: Appl. Phys. 41(2008) 225202.

[10]Rao. S. V,Sreedhar. S, Kumar .M. A, P. P.Kiran,Tewari S. P,Kumara. G. M,"Laser Induced Breakdown Spectroscopy of high energy materials using nanosecond, picosecond, and femtosecond pulses: Challenges and opportunities"Proc. of SPIE 3(2011)8173- 81731

[11]http://physics.nist.gov/PhysRefData/ASD

The role of Tin Oxide Concentration on The X-ray Diffraction, Morphology and Optical Properties of In2O3:SnO2 Thin Films

IOP Conf. Series: Journal of Physics: Conf. Series **1003** (2018) 012129 doi:10.1088/1742-6596/1003/1/012129

The role of Tin Oxide Concentration on The X-ray Diffraction, Morphology and Optical Properties of In2O3:SnO2 Thin Films

Bushra A.Hasan , Rusul M.Abdallah

University of Baghdad , College of Science ,Department of Physics

bushra_abhasan@yahoo.com

Abstract. Alloys were performed from In_2O_3 doped SnO_2 with different doping ratio by quenching from the melt technique. Pulsed Laser Deposition PLD was used to deposit thin films of different doping ratio In_2O_3 : SnO_2 (0, 1, 3, 5, 7 and 9 % wt.) on glass substrate at ambient temperature under vacuum of 10^{-3} bar thickness of ~100nm. The structural type ,grain size and morphology of the prepared alloys compounds and thin films were examined using X-ray diffraction and atomic force microscopy . The results showed that all alloys have polycrystalline structures and the peaks belonged to the preferred plane for crystal growth were identical with the ITO (Indium – Tin –Oxide) standard cards also another peaks were observed belonged to SnO_2 phase. The structures of thin films was also polycrystalline , and the predominate peaks are identical with standard cards ITO . On the other side the prepared thin films declared decrease a reduction of degree of crystallinity with the increase of doping ratio. Atomic Force Microscopy AFM measurements showed the average grain size and average surface roughness exhibit to change in systematic manner with the increase of doping ratio with tin oxide. The optical measurements show that the In_2O_3:SnO_2 thin films have a direct energy gap E_g^{opt} in the first stage decreases with the increase of doping ratio and then get to increase with further increase of doping ration, whereas reverse to that the optical constants such as refractive index (n), extinction coefficient (k) and dielectric constant (ε_r, ε_i) have a regular increase with the doping ratio by tin oxide and then decreases.

Keywords :thin films of In_2O_3:SnO_2, XRD, AFM, PLD, Optical Properties

1. Introduction

Indium tin oxide (ITO) is well-known as transparent conducting oxide (TCO) have a wide band gap~3.7eV . n-type semiconductor and it posses a low electrical resistivity [1-3]. Thin Films ITO is transparent but it have color when it is in bulk form bulk. The behavior of ITO similar to meats due to high conductivity, thin films exhibit to show high reflectivity in the near infrared region [4-5]. The lowest electrical resistivity and hence highest transparency transparency in the visible range suitable for many application can provided from ITO films. It is well known that the unique electrical and optical properties of ITO are depend upon the deposition method which can be modified by controlling the deposition parameters the unique properties. There are many deposition techniques to obtain high quality ITO films such as pulsed laser deposition[6], sol-gel [7] , RF and DC sputtering [8-9] . In the present work, ITO films were prepared by PLD on glass substrate and the, structural,morphology and optical properties of ITO films were examined.

2. Experimental Part

The alloy of In_2O_3:SnO_2 is were prepared by mixing the appropriate amount of high purity (99.99)indium oxide and tin oxide .An electronic balance with accuracy (10^{-4}gm)was used to weight the powder of the matrix material (Indium oxide) and the dopant material (tin oxide) . A quartz ampoule with length and internal diameter ~ 25 cm and ~ 8 mm respectively was used to heat the material to 1000°C and left at this temperature for 8 hours. In order to obtain homogeneous alloy the ampoules are constantly agitated. Cleaning glass slides substrates were used which were subjected to several steps to remove any contamination such as dust ,oily material ,grease and some oxides using soap solution , then the glass sildes were placed in a clean beaker containing distilled water and with ethanol solution then the glass slides were dried by blowing air. Thin films were deposited using pulsed lased deposition technique under vacuum of (10^{-3} Torr). Thin films were obtained by focusing Nd:YAG (Huafei Tongda Technology–Diamond-288 pattern EPLS) Q-switching operating type , wavelength1064 /532) nm, repetition frequency (1, 2, 3,4,5,6) , with applied voltage 220 volt . The incoming laser beam from a window will fall on a target make at angle 45° with it .X-ray diffraction (XRD) was used to check the structures of the prepared alloys and thin films . In the present work x-ray diffractrometer type (Miniflex II), with Cu-K_α x-ray tube (λ = 1.54056 Å) is used. The morphology is obtained using atomic force microscopy AFM.

UV/Visible spectrophotometer type SP-8001was used to study the optical properties of In_2O_3:SnO_2 films in the wavelength range 300-1100 nm. The optical parameters optical energy gap and the optical constants which imply the refractive index (n) , extinction coefficient (k) and real and imaginary parts of dielectric constants(ε_r,ε_i) were measured using the transmittance and absorbance as function of wavelength using the following equation respectively:

The refractive index value can be calculated from the formula :

$$n = \sqrt{\frac{4R}{(R-1)^2} - k^2} - \frac{(R+1)}{(R-1)} \quad \text{.....(1)}$$

Where R is the reflectance, and can be expressed by the relation [10]:

$$R = \frac{(n-1)^2 + k^2}{(n+1)^2 + k^2} \quad \text{.....(2)}$$

The extinction coefficient is given by the relation[11] :

$$k = \frac{\alpha\lambda}{4\pi} \quad \text{.....(3)}$$

Where λ is the wavelength of the incident radiation which is related to the absorption coefficient (α)which define as the reduction of light intensity per unit length , (α) is estimated from the equation :

$$\alpha = 2.303\frac{A}{t} \quad \text{.....(4)}$$

Where A is the absorbance and t is the sample thickness. The film thickness was measured by the Tolanasky interference method with an accuracy of ±10 nm[12]. The real and imaginary part of dielectric constant can be measured by using the following equations [13]:

$$(n - ik)^2 = \varepsilon_r - i\varepsilon_i \quad \text{..... (5)}$$

Where

$$\varepsilon_r = n^2 - k^2 \quad \text{.....(6)}$$

and $\varepsilon_i = 2nk$ .....(7)

3. Results and Discussion

'Figure 1' shows the X-ray diffraction patterns for In_2O_3 doped with different SnO_2 concentration powders. All the peaks of XRD patterns were analyzed and indexed using JCDD data base and compared with standards. All the ITO films are polycrystalline with body-centered cubic structure of In_2O_3. As can be seen from Fig. .1, the (222) peak is the most prominent, and the weak peaks are the (211), (400), (440),and (622) planes. The similar result was reported previously [14]. Intensity of (222),(321),(400),(440), and (622) planes which are the dominate planes of the ITO become more prominent as SnO_2 was introduced to the host material, i.e. with increase of wt.% of SnO_2 to 1% as shown in same figure which indicates the improvement of crystallinity of the compound [15]. The intensity of the same planes decreased with further increase of SnO_2 concentration up 5%, which indicates the crystallinity deformation of the compound . The crystallinity of the compound increases with the increase of doping ratio from 5 to 9 %. .The grain size of the predominant plane increased

from 22.9nm to 48.1 nm as SnO_2 was added to In_2O_3 , while the grain size was reduced with the continuous addition of SnO_2 up 5% . Then the grain size increases from with further increase of doping ratio and reach steady value at high doping ratio .Indeed the grain size increases 40.1 to 45.1 nm as when the doping ration increases from 5 to 9%.

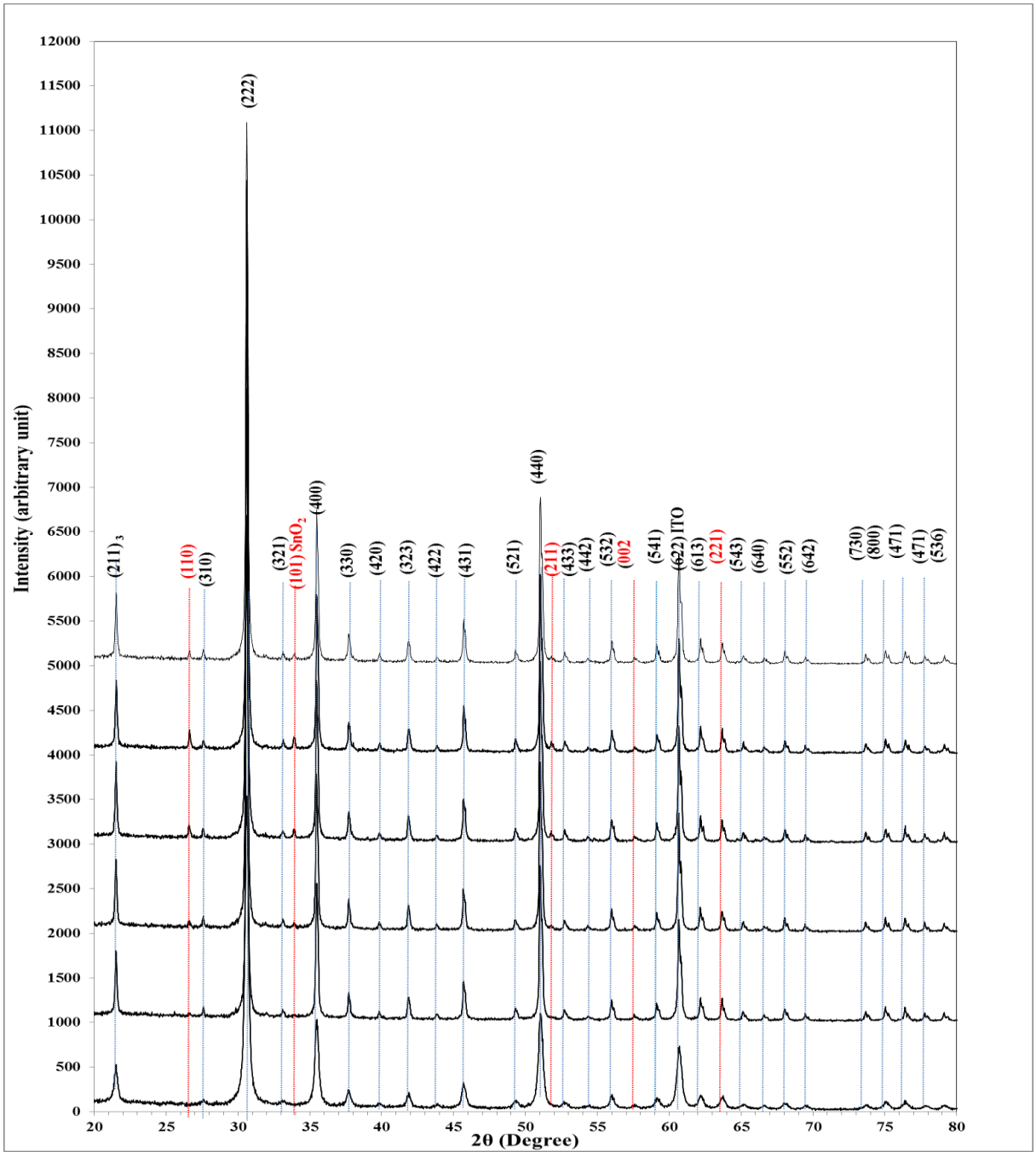

Figure 1: shows the XRD patterns of the pure In_2O_3 and doped with different concentrations of SnO_2 powder .

The X-ray diffraction patterns of pure In_2O_3 and In_2O_3:SnO_2 thin films deposited on glass substrates prepared by the PLD technique with different doping concentrations of SnO_2 (1, 3, 5, 7and 9) wt.% are shown in Fig.2.The XRD diffractograms revealed that In_2O_3:SnO_2 films become polycrystalline when deposited at room temperature substrate and crystallized in a cubic bixbyite structure (In_2O_3) [16-17]. The peaks observed for (2θ =30.4°) are associated to the plane (222) and other planes related to the ITO composite (400)(440)and (622) .The preferential growth of the In_2O_3:SnO_2 films is the (222) plane and this orientation is dependent on the deposition conditions [17]. In Table 1 it can be noticed the structural parameters: 2θ, d_{hkl}, (hkl), FWHM and G.S of deposited pure and In_2O_3 films at different SnO_2 doping ratio (1, 3, 5, 7and 9) %. In general, there was an increases in full width of half maximum FWHM with the increase of the doping ratio i.e. decrease of the crystalline size as the SnO_2 was introduced to the In_2O_3, but then the FWHM decreased(crystalline size increased)with the increase of doping ratio up 3% ,(increasing the doping ratio more caused a decrease of crystalline size).It can be noticed for the doping ratios(3%,5%,7%) the appearance of the peaks related to SnO_2 located at (2θ =26.4° , 33.78°) corresponds to the diffractions planes (110),(101).Theses peaks disappeared at high doping ratio , i.e. 9% SnO_2 indicates to the decrease of crystallization degree as indicated from the decrease of grain size at high doping ratio.

Table 1 :Illustrates the Structural parameters: 2θ, d_{hkl}, (hkl), FWHM and G.S of deposited In_2O_3 films at different SnO_2 doping ratio (1, 3, 5, 7and 9) %.

% SnO2	2θ (Deg.)	FWHM (Deg.)	d_{hkl} Exp.(Å)	G.S (nm)	d_{hkl} Std.(Å)	Phase	hkl
Pure	30.5088	0.2892	2.9277	28.5	2.9214	Cub. In_2O_3	(222)
1%	30.4767	0.3918	2.9307	21.0	2.9214	Cub. In_2O_3	(222)
3%	26.5238	0.1750	3.3579	46.6	3.3503	Tet.SnO_2	(110)
	30.5410	0.3049	2.9247	27.0	2.9214	Cub. In_2O_3	(222)

	33.8190	0.1264	2.6483	65.7	2.6441	Tet.SnO_2	(101)
	26.4596	0.2250	3.3659	36.3	3.3503	Tet.SnO_2	(110)
	30.4446	0.3649	2.9338	22.6	2.9214	Cub. In_2O_3	(222)
5%	33.7868	0.1928	2.6508	43.1	2.6441	Tet.SnO_2	(101)
	35.3294	0.1782	2.5385	46.8	2.5300	Cub. In_2O_3	(400)
	37.9004	0.1585	2.3720	53.0	2.3853	Cub. In_2O_3	(330)
	50.9480	0.1588	1.7910	55.4	1.7890	Cub. In_2O_3	(440)
	60.6856	0.1788	1.5248	51.5	1.5256	Cub. In_2O_3	(622)
	26.5560	0.2350	3.3539	34.7	3.3503	Tet.SnO_2	(110)
	30.5088	0.3744	2.9277	22.0	2.9214	Cub. In_2O_3	(222)
7%	33.8190	0.2571	2.6483	32.3	2.6441	Tet.SnO_2	(101)
	35.3937	0.1892	2.5340	44.1	2.5300	Cub. In_2O_3	(400)
	37.9646	0.1607	2.3681	52.3	2.3853	Cub. In_2O_3	(330)
	50.9480	0.1590	1.7910	55.3	1.7890	Cub. In_2O_3	(440)
	60.7177	0.1801	1.5241	51.1	1.5256	Cub. In_2O_3	(622)
	30.5731	0.3822	2.9217	21.5	2.9214	Cub. In_2O_3	(222)
9%	35.4580	0.1928	2.5296	43.3	2.5300	Cub. In_2O_3	(400)
	51.0123	0.1599	1.7889	55.0	1.7890	Cub. In_2O_3	(440)
	60.6213	0.1858	1.5263	49.5	1.5256	Cub. In_2O_3	(622)

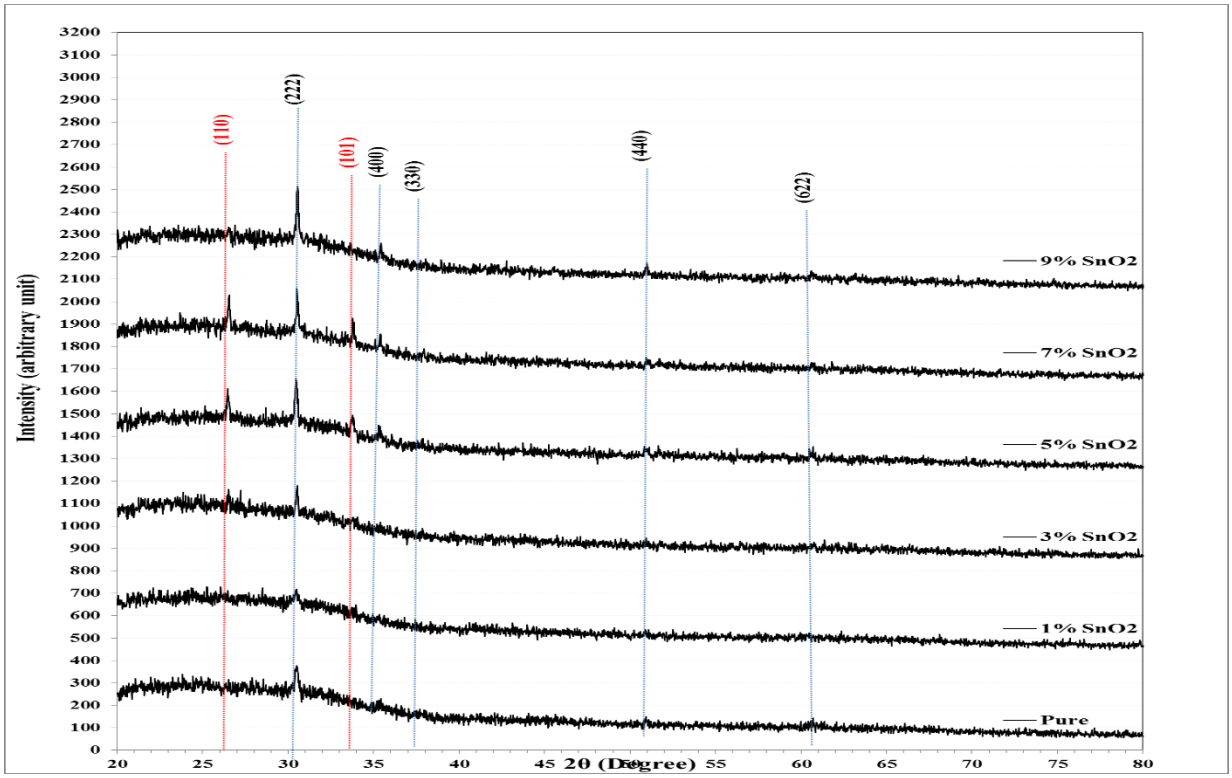

Figure 2: X-ray diffraction patterns of deposited pure In_2O_3 and doped with SnO_2films in different ratio (1, 3, 5, 7,and 9) %.

4. Atomic Force Microscopy Analysis (AFM)

The surface morphologies of In_2O_3:SnO_2 films are investigated using Atomic Force Microscopy (AFM). Fig.3 shows their surface morphologies pictures obtained from AFM. The obtained data are listed such as grain size and RMS roughness and peak –peak value are listed in Table 2 .This Table illustrates an increment in average diameter with doping ratio 1% then go down in 3% and increase at (5,7)%then go down . The roughness of the films shows increment by increasing doping but go down at 7% , while the doped film by 9% SnO_2 have maximum values of roughness and peak –peak value.

Table.2: AFM parameters for pure and doped In_2O_3 at different SnO_2 ratios deposited at room temperature.

% SnO_2	Average diameter (nm)	Average roughness (nm)	Peak-peak (nm)
0	52.48	0.458	2.21
1	100.22	14.6	62.9
3	79.12	22	102
5	87.57	24.3	109
7	105.59	11.5	103
9	90.95	26.8	112

Pure	1% SnO_2
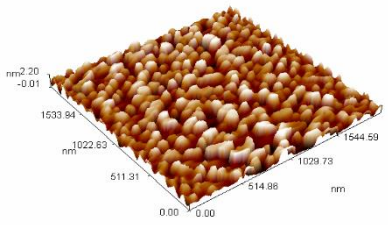	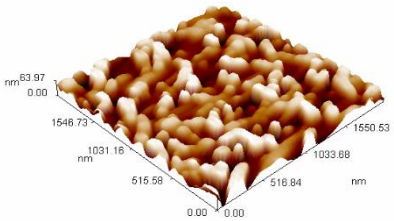

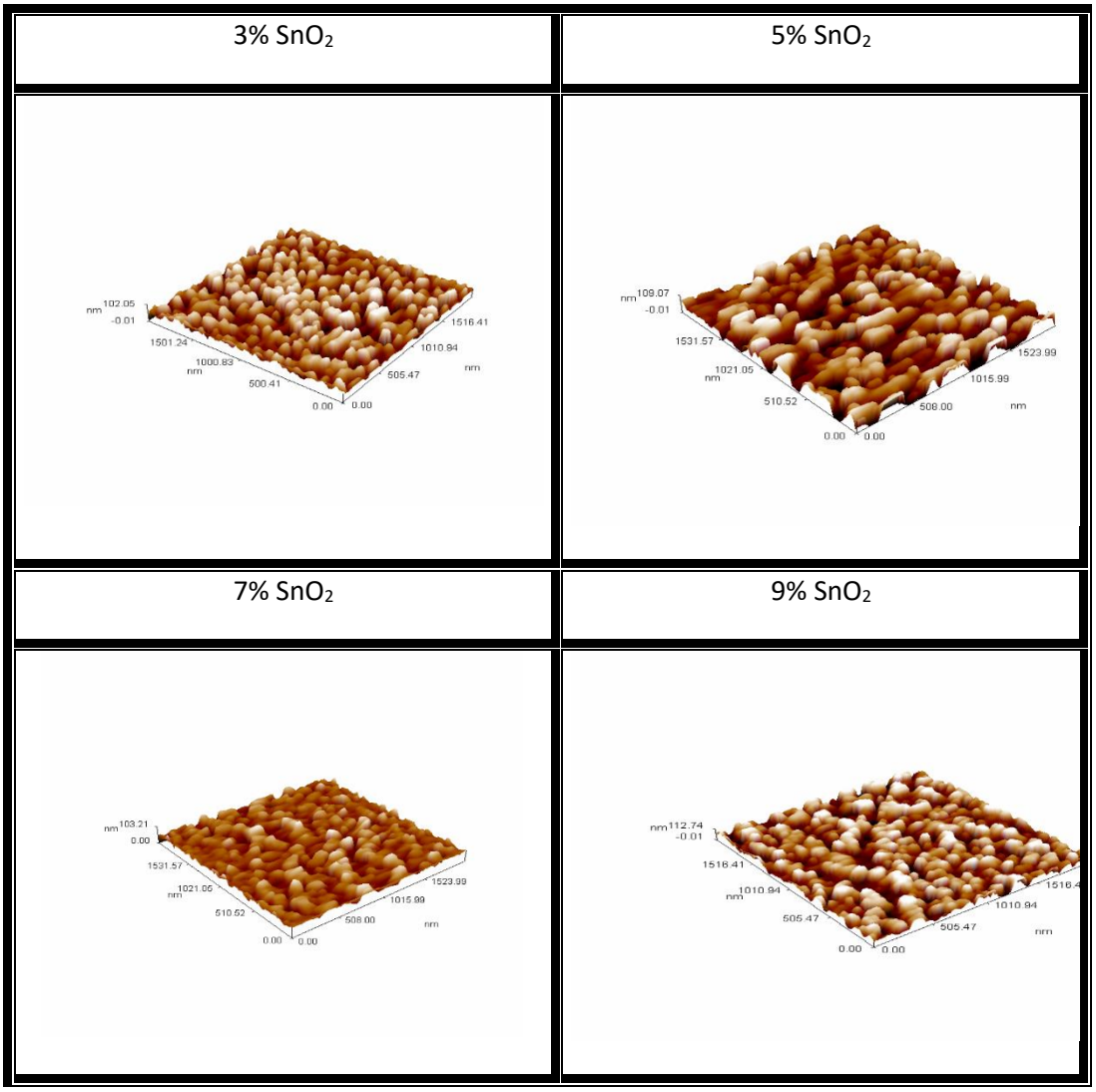

Figure .3 AFM images for of pure In_2O_3 thin film and In_2O_3 doped with SnO_2in different doping ratio.

5. The Optical Properties of In_2O_3:SnO_2 Films

The optical properties of pure In2O3 and doped with SnO2 at different ratio of (1, 3, 5, 7, and 9) wt. % films deposited on glass at room temperature have been determined using UV-visible near infrared region (300-1100)nm. The energy gap and optical constants have determined using the transmittance and the absorbance spectrum . Fig(4) transmittance spectra pure $In_2O_3$and doped with different concentrations of SnO_2.In general, we can observe from Fig.4 that transmittance is inversely proportional to concentration of tin oxide hence the transmission decreases with increasing SnO_2 concentration ratio until (7%)and then the transmission increases , which result from the increment of the reflection and absorption , this giving rise to shift the absorption edge to longer wavelength (red shift

) but the continues addition of tin oxide to the host material lead to shifts absorption edge toward shorter wavelength (higher energies) the behavior accompanied the increment of tin oxide concentration is related with reduction of grain size which in turn increases the lattice parameters and hence wide the energy gap as we seen in the next section.

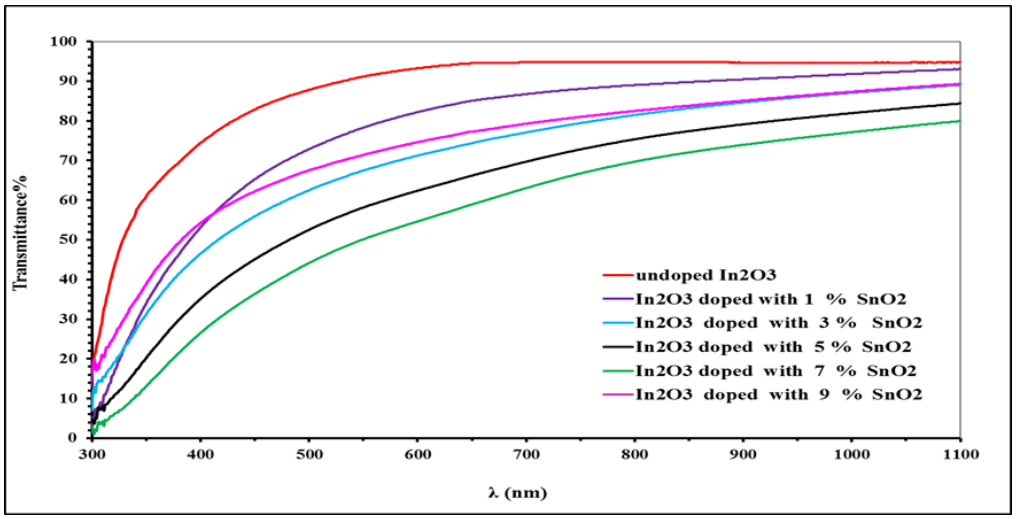

Figure 4 :The transmittance as a function of wavelength for pure $In_2O_3$and doped with different concentrations of SnO_2thin films deposited at R.T.

6. The Optical Energy Gap

The type of the optical transition as well as the optical energy gap values E_g^{opt} for thin films have been determined by applying the empirical Tauc equation. The plot diagram is shown in figure .5. between $(\alpha hv)^{1/r}$ and (hv) were r= 1/2 for allowed direct transition The extrapolation of the portion at $[(\alpha hv)^{1/r} = 0]$ gives the optical energy gap is shown in Fig.5 .It can be observe that direct band gap for pure In_2O_3 films is 3.6 eV . The energy gap was decreasing with increase of doping concentration, indeed the optical energy gap decreases from 3.35 to 3.08 eV as the doping ratio increases from 1% to 7% , this result it agreement with the energy gap of ITO .This reduction of energy gap values attributed to creation of new states of donor levels within the energy gap near the conduction band by the impurity addition to the host material , take place as a donor levels within the energy gap near the conduction band. Thus, causes the visual decrease of energy gap such that the material will absorb photon of lower energy. The optical energy gap decrease by increasing concentration of SnO_2 in the films ,can see it in the figures and Table.2. the optical energy gap return to increase with further increase of

doping ratio, indeed Eg increases to 3.23 eV at SnO_2 9% . This due to compensate the donor stated which were prohibited initially.

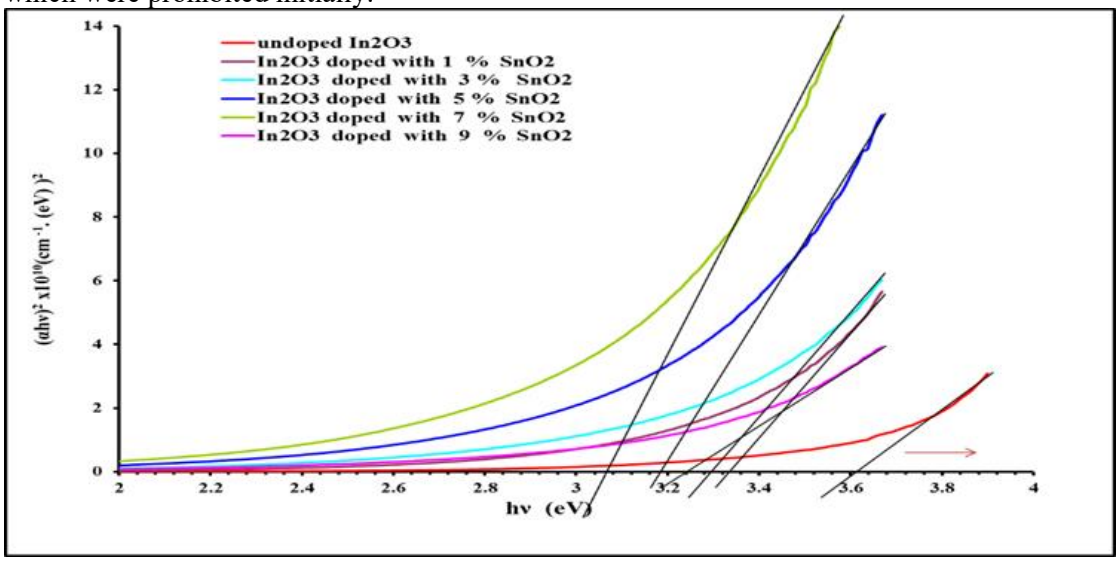

Figure 5 :The variation of $(\alpha h\upsilon)^2$ versus photon energy (hυ) for pure and doped In_2O_3 films with different concentrations of SnO_2 deposited at R.T.

The plot of the refractive index as a function of wavelength in the range (300-1100) nm for pure In_2O_3 and In_2O_3:SnO_2 thin films with different concentration of SnO_2 is shown in figure (6).The refractive index calculated according to the equation (3). It can be noticed from these figures that pure n at λ=500nm of In_2O_3 is 1.68 increases with increasing of the concentration of SnO_2. Indeed n increases to2.644 with the increase of doping ratio from 0 to 7% while n decrease to 2.292 at 9% doping ratio. The increase of n attributed to the reduction of transmittance giving rise to high opaque material while the reduction of n is related to the inverse manner. The values of refractive index are given in table (2)

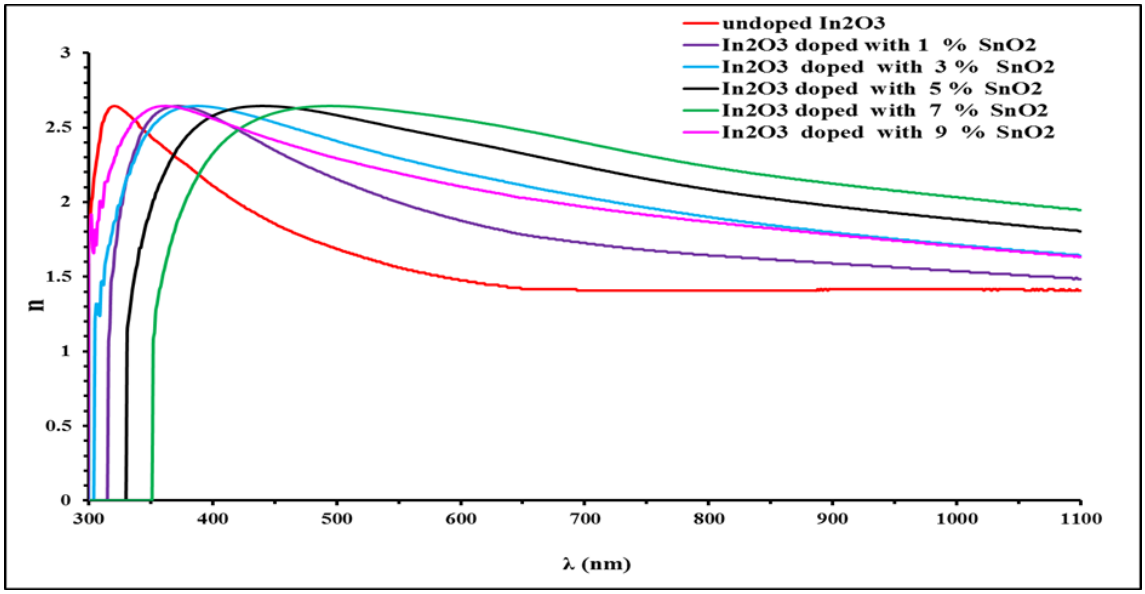

Figure 6: Refractive index as a function of wavelength for pure In_2O_3 and doped In_2O_3 films with different concentrations of SnO_2 deposited at R.T

Variation of the extinction coefficient as a function of wavelength for undoped and doped In_2O_3 films with different concentration are shown in Fig.(7). It is evident from this figure and Table(2) that the extinction coefficient exhibit to change in non regular manner with the increase of doping concentration .Indeed k at λ=500nm for pure In_2O_3 is 0.026 increases to 0.163 as the doping concentration increases from 0 to 7% but the k return to decreases to 0.078 at 9% doping ratio . The increase and the decrease of k is related with increase and decrease of absorption coefficient .

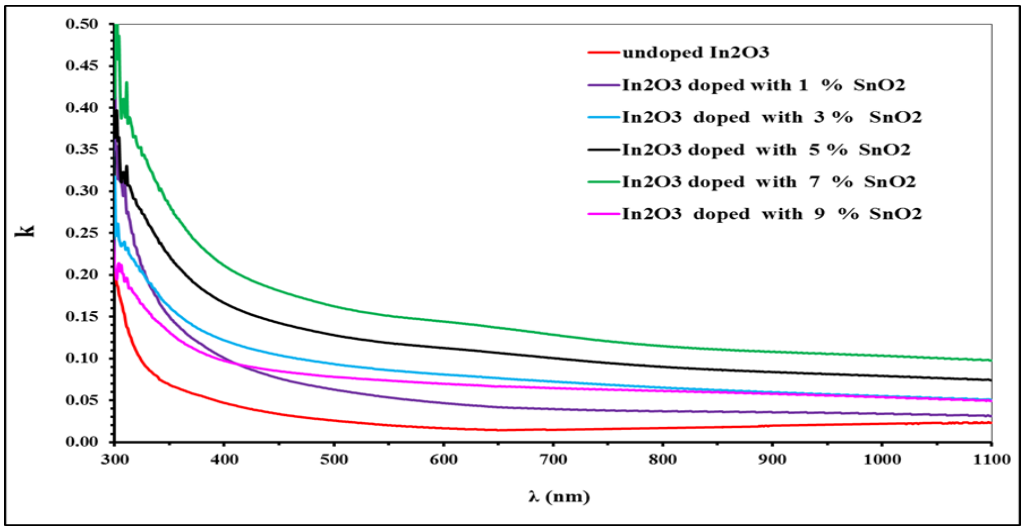

Figure 7: Extinction coefficient as a function of wavelength for pure and doped In_2O_3 thin films with different concentrations of SnO_2 deposited at R.T

The plot diagram of the real (ε_r) and imaginary (ε_i) parts of the dielectric constant values as a function of wavelength in the range (300–1100)μm for In_2O_3:SnO_2 films deposited at R.T with different concentration of SnO_2 , are shown in Figs (8and 9). Real part of dielectric constant ε_r exhibits to change in similar manner to that of the refractive index because of the smaller value of k^2 compared with n^2 , while imaginary part of dielectric constant ε_i has similar trend to that of extinction coefficient k. It can be observed that the real dielectric constant (ε_r) for pure equal to 2.83 increased to 4.68 when SnO_2 concentration changed from 0 to 7% and then return to decreased to2.644 with further increase of dopant material as shown in Table(3), and It is found that ε_i, increased with increasing of SnO_2 concentration and then return to fall with further increase of doping concentration. The behavior of ε_r and ε_i can be explained in similar ways to that of n and k .

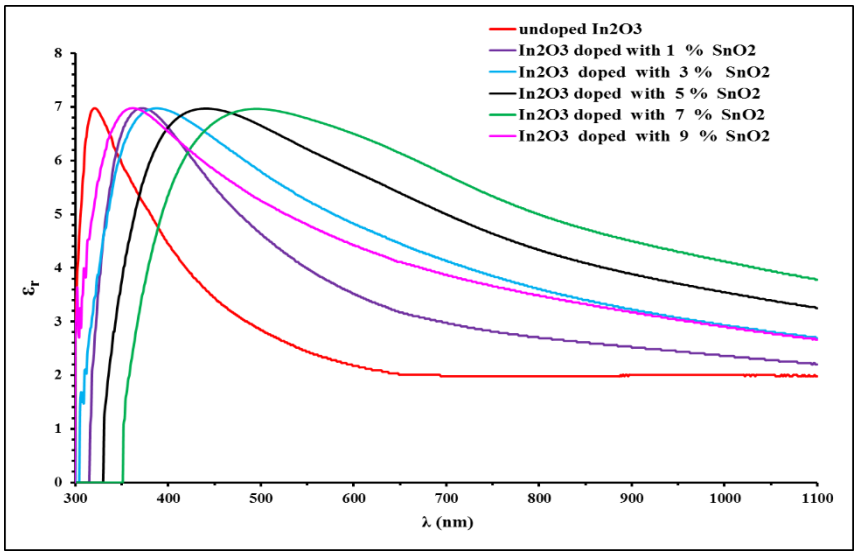

Figure.8:Variation of ε_r with wavelength of for pure and doped In_2O_3 thin films with different concentrations of SnO_2 deposited at R.T

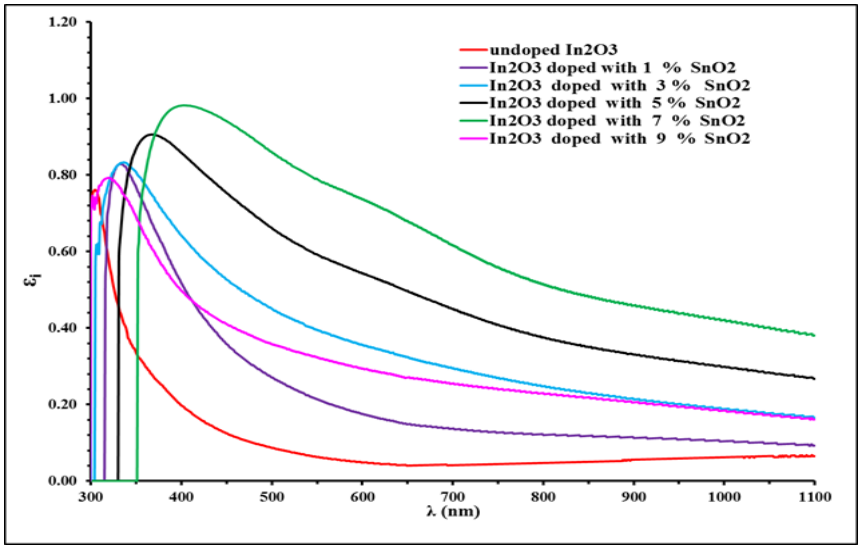

Figure .9 :Variation of ε_i with λ of pure In_2O_3 and In_2O_3: SnO_2thinfilms at different concentration of SnO_2 deposited at R.T

Table (3) Values of E_g and optical constants at λ=500 nm for pure and doped In_2O_3 with SnO_2 thin films with different doping concentrations(1, 3, 5 , 7and 9) %.

%SnO_2	T%	α (cm^{-1})	k	n	ε_r	ε_i	Eg (eV)
0	87.90	6448	0.026	1.684	2.836	0.086	3.60
1%	72.94	15776	0.063	2.152	4.627	0.270	3.35
3%	62.51	23491	0.094	2.409	5.796	0.451	3.25
5%	52.54	32184	0.128	2.583	6.654	0.662	3.15
7%	44.15	40878	0.163	2.644	6.963	0.860	3.08
9%	67.60	19576	0.078	2.292	5.245	0.357	3.23

7. Conclusions

1- The prepared In_2O_3:SnO_2 compounds and thin films are polycrystalline with a cubic structure with a preferential orientation along (222) direction.
2- The grain size, the average diameter and average roughness increases as tin oxide increases added to hast material but then reduced and the increases to reach steady state
3-Maximum diameter and average roughness obtained are 105.59 and 26.8 nm respectively.
3- The increasing of tin oxide concentration made all the prepared thin films more opaque throughout increasing the packing density and shifting the absorption edge to lower energies .
4- Increasing of tin oxide content in the prepared samples creates new states in the band gap which consequently giving rise to the visual decrease of the optical energy gap.

5-The transmittance and the optical energy increases ,while the optical constants decreases when compensation take place at high tin oxide concentration i.e .9%.

References

[1] N.G. Pramod, S.N. Pandey, and P.P. Sahay, Journal of Thermal Spray Technology, Volume 22(6) August (2013),1035.
[2]Kyung-Soo Park, Young-Jin Choi, Jin-Gu Kang,Yun-Mo Sung and Jae-Gwan Park, Nanotechnology, 22 (2011) 285712 (5pp)
[3] A. Ambrosini, A. Duarte, K.R. Poeppelmeier, M. Lane, C.R. Kannewurf, T.O. Mason, J. Solid State Chem. 153 (2000) 41.
[4]S.H. Brewer, S. Franzen, J. Phys. Chem. B 106 (2002) 12986
[5] O.N. Mryasov, A.J. Freeman, Phys. Rev. B (2001) 6423, Art. No.233111.
[6] J. B. Choi, J. H. Kim, K.A. Jeon, S. Y. Lee, Mat.science and Eng. B102 (2003) 376-379.
[7]T.F. Stoica, V.S. Teodorescu, M.G. Blanchin, M. Gortner, M.Losurdo, M. Zaharescu, Mater. Sci. Eng. B101 (2003)222.
[8]L. Kerkache, A. Layadi, A. Mosser, journal of Alloys and Compounds 485(2009) 46-50
[9]M. Nisha, M.K. Jayaraj, Appl.Surf.Sci 255(2008)1790-1795.
[10] J.L. PANKOV, *Optical Process in Semiconductors* (London 1971).
[11] W. KLOPFFER, *Introduction to Polymer Spectroscopy* (SpringerVerlag, 1984).
[12] 9-T.Matsushita, A.Suzuki, M.Okuda, H.Naitoh and T.Nakau,
Jap.J.App1.Phys., 22, 762 (1983).
[13] M. ALENSO, J. VENN, *Physics*, 2nd ed. (JohnWiley, 1971).
[14] J. George, C.S. Menon, Surf. Coat. Technol. 132, 45–48 (2000)
[15]. H.L. Ma, D.H. Zhang, P. Ma, S.Z. Win, S.Y. Li, Thin Solid Films ,263, 105–110 (1995)
[16] Dewei Chua, Yu-Ping Zeng, Dongliang Jianga, Yoshitake Masuda, Sensors and Actuators B 137 (2009) 630–636.
[17] N.G. Patel , P.D. Patel , V.S. Vaishnav , Sensors and Actuators B 96 (2003) 180–189.

Performance of Case-Based Reasoning Retrieval Using Classification Based on Associations versus Jcolibri and FreeCBR: A Further Validation Study

IOP Conf. Series: Journal of Physics: Conf. Series **1003** (2018) 012130 doi:10.1088/1742-6596/1003/1/012130

Performance of Case-Based Reasoning Retrieval Using Classification Based on Associations versus Jcolibri and FreeCBR: A Further Validation Study

Ahmed S. Aljuboori[1], Frans Coenen[2], Mohammed Nsaif[3], David J. Parsons[4]

[1] The School of Computing, Science and Engineering, University of Salford, Salford, M5 4WT, UK
College of Education for Pure Science Ibn-Al-Haitham, University of Baghdad, Iraq.
[2] The Department of Computer Science, The University of Liverpool, Liverpool L69 3BX, UK
[3] College of Education for Pure Science Ibn-Al-Haitham, University of Baghdad, Iraq.
[4] A visiting professor with the School of Computing, Science and Engineering, University of Salford, Salford, M5 4WT, UK

[1] a.s.aljuboori@edu.salford.ac.uk.
[2] coenen@liverpool.ac.uk
[3] mohammed.k.n@ihcoedu.uobaghdad.edu.iq
4 d.j.parsons@salford.ac.uk

Abstract. Case-Based Reasoning (CBR) plays a major role in expert system research. However, a critical problem can be met when a CBR system retrieves incorrect cases. Class Association Rules (CARs) have been utilized to offer a potential solution in a previous work. The aim of this paper was to perform further validation of Case-Based Reasoning using a Classification based on Association Rules (CBRAR) to enhance the performance of Similarity Based Retrieval (SBR). The CBRAR strategy uses a classed frequent pattern tree algorithm (FP-CAR) in order to disambiguate wrongly retrieved cases in CBR. The research reported in this paper makes contributions to both fields of CBR and Association Rules Mining (ARM) in that full target cases can be extracted from the FP-CAR algorithm without invoking P-trees and union operations. The dataset used in this paper provided more efficient results when the SBR retrieves unrelated answers. The accuracy of the proposed CBRAR system outperforms the results obtained by existing CBR tools such as Jcolibri and FreeCBR.

***Index Terms*— case-based reasoning, class association rules, partial trees, similarity-based reasoning.**

1 INTRODUCTION

This fundamental idea underpinning CBR is a technique which uses the experience of previous cases to help solving new problems [1]. [2] stated that A case is a group of experience that are collected, defined and stored in a case base. Principally, the cases are defined by a problem description and its own solution. Among the four main stages in Case Based Reasoning, retrieval is a key step, with success being heavily dependent on its performance. Its aim is to retrieve the most similar cases that can be positively utilised to assist solve a target problem.

Basically, retrieval is performed through a specific strategy referred to as 'Similarity of Based Retrieval' (SBR) [2]. In SBR technique, measures are subroutines can be utilised to identify cases importance by their similarity to the case problem. The solution is basically "associated" to the closest case to enable users to determine the rank of cases [3].

Class Association Rule (CAR) mining is one of the most significant and common data mining approaches. It can be efficiently utilised in any decision making as a classifier [4]. It produces classification rules based on ARs as an integration of both classification and association. The integrated framework of CARs suggested by [5] is achieved by discovering a special subset of Association Rules (ARs) where the right-hand side of the implication equation is confined to the classification class label. The concept of CARs was used in previous work to show that patterns of classed rules can be combined with a similar pattern in the context of CBR [6], [7]. ARs have also been used by [8] for deriving association information from a certain case base using different ARM approaches.

The originality of the work presented in this paper is the focus on the contribution when 'Data Mining' (DM) is integrated into CBR in a merged system. The retrieved cases will be more effective to one correct class rather than being just similar to multi classes. In addition, this paper is a further validation based on a former study which highlighted the use of ARs as one of the DM methods that can be used in order to enhance the outcome of the retrieval process. A key point of this paper, is that the P-trees and set union concept which have been developed in [7] are not invoked to let different rules to be joint to produce a more correct cases. Therefore, the proposed CBRAR can produce remove the ambiguity of the retrieved answers of existing CBR systems.

One of the shortcomings of our former approaches [6], [7] were the reliability of the outcomes. Therefore, a further objective of this paper is to provide more improved and validated outcomes using CBRAR. TABLE 1 shows that in our earlier research the CBRAR only resolved 3 out of 4 cases achieving 75% accuracy [6], and 4 out of 5 cases achieving 80% accuracy [7]. In this paper, without invoking the P-trees and union of two rules which gave rise to the FP-CAR algorithm, CBRAR resolved 12 cases of the dataset.

2 A BRIEF REVIEW OF RELATED WORK

CBR can be listed into four phases: retrieve – is to search and find the most similar cases, reuse – is to find what old cases can be reused, revise – is to apply the retrieved solution in a real world field and make sure it is correct, and retain – is to save the new solution and maintain it in CBR library as an experience [1]. Retrieval is a significant phase in the CBR cycle because if the system retrieves a wrong case, this could lead to a wrong decision. The main objective of this phase is to explore comparable cases that could be positively used to resolve a target problem. The process of retrieving a case starts with a (partial) matching of a new case, and finishes when the most similar cases are retrieved.

Some CBR methods retrieve a former case mainly based on the similarities among problem descriptors [9], [10]. Some approaches focus on deeper feature retrieval, [11], [12] and [13], while more recent methods attempt to utilise other knowledge to enhance SBR [14], [15]. The work presented in this paper further validates a new technique developed to improve the retrieval strategy. It also explores various methods by integrating other knowledge types into the CBR process. The cases build on similarities and the relative significance of features as a large part of the domain knowledge is required to explain the nature of why two cases are matched and how reliable the match is. In addition, the method of matching a case is described as hard or unachievable to obtain, because of the poor representation of the knowledge. By contrast, combined methods are capable of using the meaning of the problem. Therefore the description and its meaning make the similarity of matching cases obtainable [1].

CAR is one type of AR algorithms, which integrates association rule mining (finding all rules existing in the dataset that satisfy some constraints) and classification rule mining, (discovering a small set of rules in the database that forms an accurate classifier by focusing on mining a special subset of the existing ARs) [5]. It can be applied not only to linearly separable cases, but also to linearly inseparable cases, or where other linear classification approaches are not applicable [16]. One of CAR mining's advantages over conventional methods, for example support vector machine, is its interpretability. This is because classifiers are generated as a set of simple rules without much sacrifice of accuracy [17]. In addition, when applied to a medical dataset, for instance gene data, the CAR algorithm, which predicts a class label based on specific sets of differentially genes that are actually noticed in training samples, are expected to generate more biologically reasonable classifiers. This is because it is generally not single genes but groups of these genes that jointly define phenotypes i.e. drug responses [18]. In a CBR context, a CAR is represented as an AR in which a consequent holds the item built as a pair of a solution attribute and its value. This might be called a solution item. A CAR therefore has the form $X \Rightarrow y$, where $X \subseteq I$ is an itemset and $y \in I$ is a solution item. Considering this, it should

be noted that the form of a CAR X⇒ y allows the representation of correlation between an itemset X (i.e., a set of problem attributes) and a solution item y (i.e., the resultant solution) in an easy method. CAR mining is also considered to be an extension of the Apriori algorithm. In other words, the goal of CAR is to find all rules of the items of the form < cond_set, y > where cond_set is a set of items, and y ∈ Y where Y is the set of class labels. In addition, Association Rules can be employed in order to find significant relationships from case bases [8].

Accordingly, derived subsets of a set of CARs are the CARs whose resultant is limited to one label only. In the CBR scope, a CAR is a rule whose importance consists of the element is designed as a pair included a solution attribute and its real value [15]. In a specific case base storage, AK is programmed to describe the cause behind the specific problem's features and then associate with a solution. The proposed CBRAR strategy which presented in the earlier research [6] has been enhanced by containing the union set theory as well as the FP-CAR algorithm using a new dataset.

3 MATERIAL AND METHODS

This section gives a brief review of the characteristics of the newly validated dataset and its validated performance compared with the dataset used in [6], [7].

3.1 Balloon Dataset Characteristics

The Balloon dataset is utilised to test the FP-CAR algorithm. It has been used to determine the influence of prior knowledge e.g. experimental results, and experimental psychology, including learning and memory. Adult and stretch is one of the four dataset provided by Michael Pazzani within the UCI repository website. It is used for determining the status of inflating a balloon to acknowledge whether it is true or false according to its characteristics.

This dataset is used in the third series of experiments to support the theory behind our proposition. The attributes' values and characteristics that were used in the hash table and FP-CAR tree are as follows {A= act {Stretch, Dip}}, {B= age {Adult, Child}}, {C = colour {yellow, purple}}, {D=size {Small, Large}}. The values of attributes appear in the FP-CAR tree as a string. In addition, the class characteristic is {Class =c{True=c1, False=c2}}.

3.2 Performance of CBRAR using Balloon versus Acute Inflammation and Space Shuttle Datasets

The main objective of this paper is to present further validation results when integrating CARs into CBR to disambiguate the wrongly retrieved cases where a full case can be extracted from the CBRAR. A block diagram illustrating the proposed Strategy is given in Figure 1. It starts by combining existing data mining algorithms i.e. CAR and FPGrowth to obtain the FP-CAR algorithm. The diagram also shows that the FPCAR is prioritized to find a full pattern that can be compared with a target case, if a full match is recognized, a correct solution can be extracted from the frequent built tree and there is no need to use other knowledge i.e. P-trees and union to obtain an optimum tree. This Strategy was developed and explained in details by the author in [6], [7]. The FP-CAR algorithm consists of two stages. Firstly, it produces a FP-tree from a set of CARs [19]. Secondly, the P-tree concept [20] and table of implications are used to optimize the resultant FP-tree. The former two phases will then be processed to obtain an optimum tree. This tree can be likened to a new case referred as *Q* which is a super pattern to improve the performance of the Similarity-Based Reasoning.

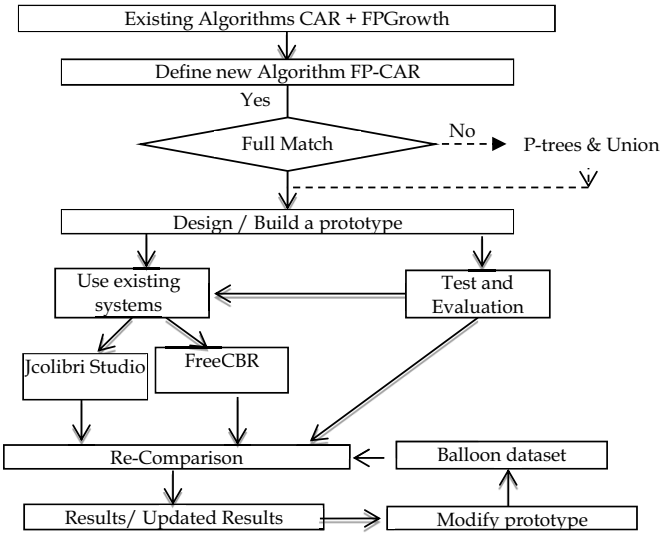

Figure 1. CBRAR Flow Diagram

In [6], a voting process was achieved by counting the value of longest length of edges that connect nodes of the updated FP-tree when a partial match is found. In addition, the P-trees technique was used so as to compensate any missing nodes in the tree if required to create an similar pattern to CBR queries. Therefore, 3 out 4 cases were resolved by the CBRAR when voting and P-trees are used. In [7], CBRAR was enhanced by the author when union is utilized at the top of P-trees. The shortcomings of [6] was the results accuracy. Thus, the purpose of Enhanced CBRAR was to suggest a better result utilising a new method based on union theory. Whilst, previous study only resolved two out of five cases, employing the joint of 2 rules has generated in the FP-CAR algorithms resolving four out of five cases. Therefore, the error is decreased and the accuracy rate is doubled with respect to the space shuttle dataset.

In this research, we remove one case from the CBR base storage till the system returns two different classes with the same percentage of similarity as shown in

TABLE 2. In the new conducted experiments an attempt to validate the FP-tree has been done and the rules allocated to one label as a root class have been obligated. Furthermore, this paper is implemented using Balloon dataset, where the CBRAR resolved more cases with less run time memory being used where no P-tree and union are required to resolve a target case. The mentioned datasets i.e. acute inflammations and space shuttle were previously tested to assess the former work of the researchers in [6], [7].

Ultimately, the outcomes gained utilizing the new validated dataset are likened with the outcomes of the Similarity Based Reasoning phase in order to choose the best answer. The chosen case is then likened with the outcome of the retrieved cases in order to ignore unassociated solutions.

4 EXPERIMENTAL RESULTS

In order to prove that the CBRAR has achieved better results, the accuracy of CBRAR is examined by conducting more experiments on a new dataset benchmarked from the UCI website, namely the Balloon dataset. Typically, one case is drawn from the CBR base to be counted as a new case for each experiment conducted by Jcolibri and FreeCBR. The Balloon dataset was utilised to calculate the accuracy rate of both CBRAR and CBR considering the same case base source as the input for both systems. Basically, when using Jcolibri the SBR returns the 5 most similar cases for a new target case. However, the preordained cases (1,2), 3, 4, 6, 8, 9, (11,12), 13, 14, (16,17), 18 and 19 all retrieved unrelated cases that misled the decision maker. This is because the whole returned cases had an identical ratio of similarity with two classes i.e. (*c1, c2*). Practically, the FreeCBR tool produces more cases than those returned by Jcolibri tool. In

TABLE 2, the outcomes are presented in the first column denotes the new arrived case *Q* and then the retrieved other cases using the Case-Based Reasoning tools i.e. NewCase(1,2). Then cases (3, 4, 6, 7 and 11 for Jcolibri) and one more case 12 for FreeCBR. The other column denotes to attributes which start with *A* then followed by 3 extra attributes *B,*

C and *D*. The class section associated with labels (c1, c2). Those "Accuracy" columns recap the assessment of Jcolibri, FreeCBR as welll as CBRAR. The terms TP and FP allude on true positive and false negative distinctly.

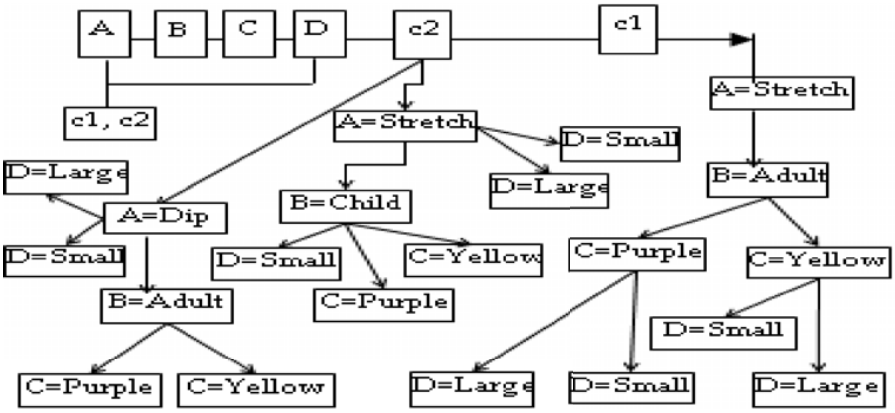

Figure. 2. FP-CAR Tree

TABLE 2 Indicates that to each new examined case utilizing CBR, five cases for those same similitude measure for 0. 866 would recouped by Jcolibri once those NewCases(1,2) is utilized. Jcolibri retrieved 2 TP also 3 FP cases with those same comparability proportion

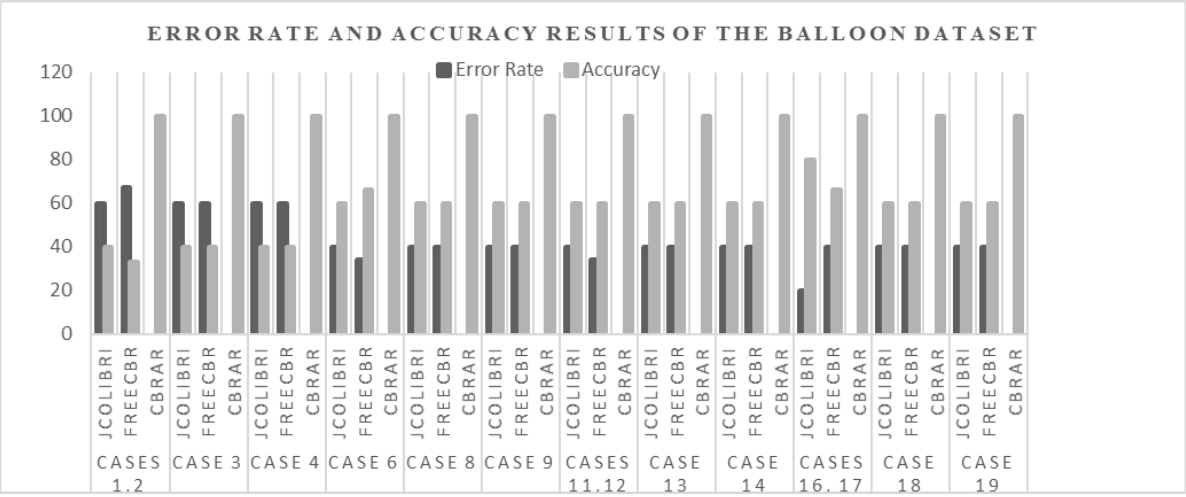

Figure. 3. Error Rate and Accuracy of Balloon Dataset

equal to 40%, whereas FreeCBR retrieved 6 cases, 2 TP Furthermore 4 FP for same similitude proportion of 50.0%, giving an accuracy rate of 33%. whilst CBRAR returned 1 TP case of evidence from the suggested model, giving a exactness about 100%.

In the second experiment, the NewCase3 has been applied to the CBR. Both Jcolibri and FreeCBR returned two TN and three TN with an accuracy of 40%. CBRAR returned 1 TN from the new system, achieving an accuracy of 100%. Third experiment, used NewCase4, Jcolibri and FreeCBR retrieved 2 TN and 3 FN cases for same similitude rate, equivalent to 40% accuracy and CBRAR returned 1 TN from the FP-CAR tree. inside the fourth test, Newcase6, Jcolibri retrieved 3 TP moreover 2 FP cases for the ones identical similitude ration, giving 60% accuracy, even as FreeCBR retrieved 6 instances, 4 TP what is extra 2 FP, undertaking an exactness charge from claiming 66%. CBRAR retrieved 1 TP case, giving an accuracy of 100%. In the 5th experiment, NewCase8 is applied, Jcolibri retrieved three TN and a couple of FN instances with the equal similarity ratio, giving 60% accuracy, and FreeCBR retrieved three

TN and a pair of FN, giving 60% accuracy. CBRAR retrieved 1 TN case from the new model which is the correct case hence achieving 100% accuracy and outperforming the performance of the CBR tools used. In the sixth experiments, NewCase9, Jcolibri retrieved 3 TN and 2 FN cases with the same similarity ratio, providing 60% accuracy, and FreeCBR retrieved 3 TN and 2 FN, providing 60% accuracy. CBRAR retrieved 1 TN case from the new strategy which is the correct case therefore giving 100% accuracy and outperforming the performance of the CBR tools used.

In the seventh experiment, using NewCases (11 ,12), Jcolibri returned three TP and two FP responses with similar percentages, presenting 60% accuracy, whilst FreeCBR returned four TP and two FP, registering 66% accuracy. CBRAR returned one TP case from the new version which is the correct case therefore giving 100% accuracy. In experiment 8, using NewCase13, Jcolibri and FreeCBR retrieved 3 TN and 2 FN cases with the same similarity percentage, and this achieved 60% accuracy. CBRAR retrieved 1 TN case from the new model which is the correct case hence achieving 100% accuracy. In experiment 9, which used NewCase14, Jcolibri and FreeCBR retrieved 3 TN and 2 FN cases with the same similarity, giving 60% accuracy. CBRAR retrieved 1 TN case from new model, and this equals to 100% and showing a better performance when compared with the CBR tools used. In the tenth experiment, using NewCases (16, 17), Jcolibri returned 4 TP and 1 FP instances registering same percentage of similarity, giving 80% accuracy, FreeCBR returned four TP and two FP, achieving 66% precision. CBRAR returned 1 TP instance which is the correct case hence achieving 100% accuracy. In the experiment 11, NewCase18 was used, Jcolibri retrieved 3 TN and 2 FN cases with the same similarity, and this achieved 60% accuracy, and FreeCBR retrieved 3 TN and 2 FN, giving 60% accuracy, whereas 1 TN case was retrieved by the CBRAR which is the correct case hence achieving 100% accuracy. In the twelfth experiment, NewCase19 applied to the CBR, Jcolibri and FreeCBR retrieved 3 TN and 2 FN cases with the same similarity ratio, giving 60% accuracy. From the new model CBRAR retrieved 1 TN case which is the correct case hence achieving 100% accuracy and outperforming the performance of the CBR tools used.

Table 2 also shows that, the NewCases((1,2), 6, (11,12) and (16,17)) have matched a full pattern within the FP-CAR algorithm without invoking the P-tree procedure to compensate the missing nodes as used in [6], [7]. The novel strategy (CBRAR) is a significant step in the machine learning field, where a target case can be drawn directly from FP-CAR for a further validation.

The consequences display that 34 out of the 60 Jcolibri retrieved instances are categorized as TP and TN giving fifty six% accuracy. via evaluation, 34 of the 64 instances retrieved through FreeCBR are categorized as TP and TN giving 53% accuracy. Nevertheless, both Jcolibri and FreeCBR provide confusing set of consequences. The proposed CBRAR system exhibits favorable element through both Jcolibri and FreeCBR through determining 12 out of 12 giving one hundred percent exactness as well as no ambiguity. Cases (1,2), 3, 4, 6, 8, 9, (11,12), 13, 14, (16,17), 18 and 19 in

TABLE 2 can be reworked in Figure. 2 to prove that CBRAR identifies a correct case using a frequent classed tree for a further validation study.

The most remarkable outcomes in this study is the significantly reduced error rates attained in [6],[7]. In Figure. 3 , the chart illustrates a comparison between Jcolibri and FreeCBR as traditional tools versus the suggested CBRAR explaining the error and accuracy rate. It can be seen that CBRAR offered many advantages and registered zero error percentage, which is considered the least amongst other rates. Thus, giving the highest accuracy and notably resolving 12 out of 12 cases accurately on the Balloon dataset as shown in Figure. 3.

TABLE 1. Validation of Balloon Dataset Vs Acute Inflammation and Space Shuttle Datasets

Dataset	Solved Cases			CBRAR Accuracy	CBRAR Error
	CBRAR	Jcolibri	FreeCBR		
Acute inflammation	3/4	14/20	29/35	75%	25%
Space Shuttle	4/5	10/18	13/21	80%	20%
Balloon	11/11	34/60	34/64	100%	0%

TABLE 2. Results of Wrong Retrieved Cases

Cases	Attributes					Accuracy		
	A	B	C	D	Class	Jcolibri	FreeCBR	CBRAR

NewCase1,2	**STRETCH**	**ADULT**	**YELLOW**	**SMALL**	**c1**	**0.866**	**50.0**	**100**
Case3	STRETCH	CHILD	YELLOW	SMALL	c2	TP	TP	TP
Case4	DIP	ADULT	YELLOW	SMALL	c2	TP	TP	
Case6	STRETCH	ADULT	YELLOW	LARGE	c1	FP	FP	
Case7	STRETCH	ADULT	YELLOW	LARGE	c1	FP	FP	
Case11	STRETCH	ADULT	PURPLE	SMALL	c1	FP	FP	
Case12	STRETCH	ADULT	PURPLE	SMALL	c1		FP	
NewCase3	**STRETCH**	**CHILD**	**YELLOW**	**SMALL**	**c2**	**0.866**	**50.0**	**100**
Case1	STRETCH	ADULT	YELLOW	SMALL	c1	TN	TN	
Case2	STRETCH	ADULT	YELLOW	SMALL	c1	TN	TN	TN
Case5	DIP	CHILD	YELLOW	SMALL	c2	FN	FN	
Case8	STRETCH	CHILD	YELLOW	LARGE	c2	FN	FN	
Case13	STRETCH	CHILD	PURPLE	SMALL	c2	FN	FN	
NewCase4	**DIP**	**ADULT**	**YELLOW**	**SMALL**	**c2**	**0.866**	**50.0**	**100**
Case1	STRETCH	ADULT	YELLOW	SMALL	c1	TN	TN	
Case2	STRETCH	ADULT	YELLOW	SMALL	c1	TN	TN	TN
Case5	DIP	CHILD	YELLOW	SMALL	c2	FN	FN	
Case9	DIP	ADULT	YELLOW	LARGE	c2	FN	FN	
Case14	DIP	ADULT	PURPLE	SMALL	c2	FN	FN	
NewCase6	**STRETCH**	**ADULT**	**YELLOW**	**LARGE**	**c1**	**0.866**	**50.0**	**100**
Case1	STRETCH	ADULT	YELLOW	SMALL	c1	TP	TP	
Case2	STRETCH	ADULT	YELLOW	SMALL	c1	TP	TP	
Case8	STRETCH	CHILD	YELLOW	LARGE	c2	FP	FP	TP
Case9	DIP	ADULT	YELLOW	LARGE	c2	FP	FP	
Case16	STRETCH	ADULT	PURPLE	LARGE	c1	TP	TP	
Case17	STRETCH	ADULT	PURPLE	LARGE	c1		TP	
NewCase8	**STRETCH**	**CHILD**	**YELLOW**	**LARGE**	**c2**	**0.866**	**50.0**	**100**
Case3	STRETCH	CHILD	YELLOW	SMALL	c2	TN	TN	
Case6	STRETCH	ADULT	YELLOW	LARGE	c1	FN	FN	TN
Case7	STRETCH	ADULT	YELLOW	LARGE	c1	FN	FN	
Case10	DIP	CHILD	YELLOW	LARGE	c2	TN	TN	
Case18	STRETCH	CHILD	PURPLE	LARGE	c2	TN	TN	
NewCase9	**DIP**	**ADULT**	**YELLOW**	**LARGE**	**c2**	**0.866**	**50.0**	**100**
Case4	DIP	ADULT	YELLOW	SMALL	c2	TN	TN	
Case6	STRETCH	ADULT	YELLOW	LARGE	c1	FN	FN	TN
Case7	STRETCH	ADULT	YELLOW	LARGE	c1	FN	FN	
Case10	DIP	CHILD	YELLOW	LARGE	c2	TN	TN	
Case19	DIP	ADULT	PURPLE	LARGE	c2	TN	TN	
NewCase11,12	**STRETCH**	**ADULT**	**PURPLE**	**SMALL**	**c1**	**0.866**	**50.0**	**100**
Case1	STRETCH	ADULT	YELLOW	SMALL	c1	TP	TP	
Case2	STRETCH	ADULT	YELLOW	SMALL	c1	TP	TP	
Case13	STRETCH	CHILD	PURPLE	SMALL	c2	FP	FP	TP
Case14	DIP	ADULT	PURPLE	SMALL	c2	FP	FP	
Case16	STRETCH	ADULT	PURPLE	LARGE	c1	TP	TP	
Case17	STRETCH	ADULT	PURPLE	LARGE	c1		TP	
NewCase13	**STRETCH**	**CHILD**	**PURPLE**	**SMALL**	**c2**	**0.866**	**50.0**	100
Case3	STRETCH	CHILD	YELLOW	SMALL	c2	TN	TN	TN
Case11	STRETCH	ADULT	PURPLE	SMALL	c1	FN	FN	
Case12	STRETCH	ADULT	PURPLE	SMALL	c1	FN	FN	
Case15	DIP	CHILD	PURPLE	SMALL	c2	TN	TN	
Case18	STRETCH	CHILD	PURPLE	LARGE	c2	TN	TN	
NewCase14	**DIP**	**ADULT**	**PURPLE**	**SMALL**	**c2**	**0.866**	**50.0**	**100**
Case4	DIP	ADULT	YELLOW	SMALL	c2	TN	TN	TN
Case11	STRETCH	ADULT	PURPLE	SMALL	c1	FN	FN	
Case12	STRETCH	ADULT	PURPLE	SMALL	c1	FN	FN	

Case15	DIP	CHILD	PURPLE	SMALL	c2	TN	TN	
Case19	DIP	ADULT	PURPLE	LARGE	c2	TN	TN	
NewCase16,17	**STRETCH**	**ADULT**	**PURPLE**	**LARGE**	**c1**	**0.866**	**50.0**	**100**
Case6	STRETCH	ADULT	YELLOW	LARGE	c1	TP	TP	TP
Case7	STRETCH	ADULT	YELLOW	LARGE	c1	TP	TP	
Case11	STRETCH	ADULT	PURPLE	SMALL	c1	TP	TP	
Case12	STRETCH	ADULT	PURPLE	SMALL	c1	TP	TP	
Case18	STRETCH	CHILD	PURPLE	LARGE	c2	FP	FP	
Case19	DIP	ADULT	PURPLE	LARGE	c2		FP	
NewCase18	**STRETCH**	**CHILD**	**PURPLE**	**LARGE**	**c2**	**0.866**	**50.0**	**100**
Case8	STRETCH	CHILD	YELLOW	LARGE	c2	TN	TN	TN
Case13	STRETCH	CHILD	PURPLE	SMALL	c2	TN	TN	
Case16	STRETCH	ADULT	PURPLE	LARGE	c1	FN	FN	
Case17	STRETCH	ADULT	PURPLE	LARGE	c1	FN	FN	
Case20	DIP	CHILD	PURPLE	LARGE	c2	TN	TN	
NewCase19	**DIP**	**ADULT**	**PURPLE**	**LARGE**	**c2**	**0.866**	**50.0**	**100**
Case9	DIP	ADULT	YELLOW	LARGE	c2	TN	TN	TN
Case14	DIP	ADULT	PURPLE	SMALL	c2	TN	TN	
Case16	STRETCH	ADULT	PURPLE	LARGE	c1	FN	FN	
Case17	STRETCH	ADULT	PURPLE	LARGE	c1	FN	FN	
Case20	DIP	CHILD	PURPLE	LARGE	c2	TN	TN	
Average						**56%**	**53%**	**100%**

5 CONCLUSION

To conclude, the P-trees and union of two rules was used in CBRAR [6], [7]. The assessment on the on the acute inflammation dataset recorded three out for four situations with seventy five percent of accuracy. On the space go back and forth dataset, it became possible to promote the previous system. The FP-CAR method resolved four out of five cases instead of two out of five cases via doubling the accuracy from forty to eighty percent, wherein it constructs far fewer common classed subsets than would be built from an actual FP-tree.The CBRAR approach has offered a better performance of Similarity Based Reasoning but needed more time and memory for resolving cases on the previous study. It makes use of a length voting technique likened to the TFPC set of rules wherein nodes preserve a value of object node at the same time as building the tree. moreover, the subsets of the common tree that meet the support and confidence, and longest length can be used to suit the pattern while indexed in a hash table. In this paper, a further validation achieved on the Balloon dataset showed that in NewCases ((1,2), 6, (11,12) and (16,17)) a superset was drawn directly from the FP-CAR in order for it to be matched with other CBR target cases. Furthermore, New Cases (3, 4, 8, 9, 13, 14, 18 and 19) were resolved using a P-tree has shown the ability of CBRAR to resolve more cases compared to our previous work. Jcolibri and FreeCBR as a CBR tools were contrasted to the CBRAR and an improved grade of accuracy was gained with the least error percentage up to this point. All unclear answers with similar percentage have been avoided by CBRAR as an advantage of using it over Jcolibri and FreeCBR. As a result of the outcomes offered on this research paper, extra datasets will be examined in order to generalise the proposed strategy.

References

[1] A. Aamodt and E. Plaza, “Case-based reasoning: Foundational issues, methodological variations, and system approaches,” *AI Commun.*, vol. 7, no. 1, pp. 39–59, 1994.
[2] R. Lopez De Mantaras *et al.*, “Retrieval, reuse, revision and retention in case-based reasoning,” *Knowl. Eng. Rev.*, vol. 20, no. 3, pp. 215–240, 2005.
[3] P. Perner, “Introduction to Case-Based Reasoning for Signals and Images. Case-Based Reasoning on Signals

and Images," in *Case-Based Reasoning on Images and Signals*, P. Perner, Ed. Springer Verlag, 2008, pp. 1–24.

[4] D. Nguyen, L. T. T. Nguyen, B. Vo, and T.-P. Hong, "A novel method for constrained class association rule mining," *Inf. Sci. (Ny).*, vol. 320, pp. 107–125, 2015.

[5] B. Ma, W. Liu, and Y. Hsu, "Integrating classification and association rule mining," in *Proceedings of the 4th Knowledge Discovery and Data Mining*, 1998.

[6] A. S. Aljuboori, F. Meziane, and D. J. Parsons, "A new strategy for case-based reasoning retrieval using classification based on association," in *12th MLDM International Conference*, 2016, p. pp 326-340.

[7] A. Aljuboori, "Enhancing case-based reasoning retrieval using classification based on associations," *2016 6th International Conference on Information Communication and Management (ICICM)*. pp. 52–56, 2016.

[8] Y.-B. Kang, S. Krishnaswamy, and A. Zaslavsky, "A Retrieval Strategy for Case-Based Reasoning Using Similarity and Association Knowledge," *IEEE Trans. Cybern.*, vol. 44, no. 4, pp. 473–487, 2014.

[9] P. Thagard, K. J. Holyoak, G. Nelson, and D. Gochfeld, "Analog retrieval by constraint satisfaction," *Artif. Intell.*, vol. 46, no. 3, pp. 259–310, 1990.

[10] Y. Orbach, M. E. Lamb, K. J. Sternberg, J. M. G. Williams, and S. Dawud-Noursi, "The effect of being a victim or witness of family violence on the retrieval of autobiographical memories," *Child Abuse Negl.*, vol. 25, no. 11, pp. 1427–1437, 2001.

[11] J. L. Arcos and E. Plaza, "A reflective architecture for integrated memory-based learning and reasoning," in *Topics in Case-Based Reasoning*, Springer, 1993, pp. 289–300.

[12] B. Li and H. Johan, "3D model retrieval using hybrid features and class information," *Multimed. Tools Appl.*, vol. 62, no. 3, pp. 821–846, 2013.

[13] J. Kendall-Morwick and D. Leake, "A Study of Two-Phase Retrieval for Process-Oriented Case-Based Reasoning," in *Successful Case-based Reasoning Applications-2*, Springer, 2014, pp. 7–27.

[14] M.-J. Huang, M.-Y. Chen, and S.-C. Lee, "Integrating data mining with case-based reasoning for chronic diseases prognosis and diagnosis," *Expert Syst. Appl.*, vol. 32, no. 3, pp. 856–867, 2007.

[15] V. / Aparna and M. Ingle, "Enriching Retrieval Process for Case Based Reasoning by using Vertical Association Knowledge with Correlation," *Int. J. Recent Innov. Trends Comput. Commun.*, vol. 2, no. 12, pp. 4114–4117, 2014.

[16] D. L. Sampson, T. J. Parker, Z. Upton, and C. P. Hurst, "A comparison of methods for classifying clinical samples based on proteomics data: a case study for statistical and machine learning approaches," *PLoS One*, vol. 6, no. 9, p. e24973, 2011.

[17] F. P. Pach, A. Gyenesei, and J. Abonyi, "Compact fuzzy association rule-based classifier," *Expert Syst. Appl.*, vol. 34, no. 4, pp. 2406–2416, 2008.

[18] A. R. Bateman, N. El-Hachem, A. H. Beck, H. J. W. L. Aerts, and B. Haibe-Kains, "Importance of collection in gene set enrichment analysis of drug response in cancer cell lines," *Sci. Rep.*, vol. 4, 2014.

[19] "TFPC Classification Association Rule Mining (CARM) Software." [Online]. Available: https://cgi.csc.liv.ac.uk/~frans/KDD/Software/Apriori-TFPC/Version2/aprioriTFPC.html. [Accessed: 15-Dec-2015].

[20] F. Coenen, P. Leng, and S. Ahmed, "Data structure for association rule mining: T-trees and P-trees," *IEEE Trans. Knowl. Data Eng.*, no. 6, pp. 774–778, 2004.